PHYSICAL REVIEW C

NUCLEAR PHYSICS

Editor
H. H. BARSCHALL

Associate Editors
G. J. DREISS M. S. WEISS

Editorial Board

Term ending 31 December 1980
DAVID B. FOSSAN
EVANS HAYWARD
DANIEL S. KOLTUN
CARL M. SHAKIN

Term ending 31 December 1981
GEORGE BERTSCH
FELIX BOEHM
JOHN W. MIHELICH
ROBERT VANDENBOSCH

Term ending 31 December 1982
PETER D. BARNES
J. C. HARDY
J. HÜFNER
JOHN W. NEGELE

Published by the
American Institute of Physics
for
The American Physical Society

Offices of the Society
and the Institute
135 East 45th Street
New York, N. Y 10017

Officers of the Society

President
HERMAN FESHBACH
Massachusetts Institute of Technology

Vice-President
ARTHUR L. SCHAWLOW
Stanford University

Vice-President Elect
MAURICE GOLDHABER
Brookhaven National Laboratory

Executive Secretary
W. W. HAVENS, JR.
Columbia University

Treasurer
OSEPH A. BURTON
Bell Laboratories
(retired)

Managing Editor of
The Physical Review
CHALMERS FRAZER
Brookhaven National Laboratory

Manuscripts for publication should be submitted in triplicate to the Editor, *Physical Review*, 1 Research Road, Ridge, N Y 11961 Submission is a representation that the manuscript has not been published previously nor is it currently under consideration for publication elsewhere. Th manuscript should be accompanied by a statement transferring copyright to APS. This writte transfer of copyright, which previously was assumed to be implicit in the act of submitting a man script, is needed under present U.S. copyright law. Requests for information or exceptions shoul be addressed to the Executive Secretary, The American Physical Society.

To support the cost of wide dissemination of research results through publication of journa pages, the authors' institutions are requested to pay a publication charge of $65 per page, whic if honored, entitles them to 100 free reprints. Nonpayment of the publication charge leads delays in publication. An additional $15 per article is requested for advance publication of th abstract in *Physical Review Abstracts*.

Subscription prices (tables below) for American Physical Society members only are for the fiscal year July 1, 1979-June 30, 1980. The prices in parentheses are nonmember subscription prices (January-December 1980)). Domestic subscription rates apply to U.S. & Possessions, Back-number price Single copies, $11.00.

	No. issues	Domestic	Foreign (incl. Can. & Mex.)	Optional air freight Europe	Optional air freight Asia
Physical Review C	12	$20.00 (85)	$29.00 (97)	$48.00(115)	$65.00(130)
Physical Review Index	1	3.50 (10)	7.50 (16)	10.50 (19)	11.50 (22
Physical Review A, B, C, D, & Index	73	120.00(530)	174.00(604)	266.00(710)	352.00(800

Microfilm subscriptions to *Physical Review A–D* (including indexes) are available on 16- and 35-mm film Send orders and inquiries to Dept. N/M, American Institute of Physics.

Subscriptions, renewals, address changes, and single-copy orders should be addressed to Subscription Fulfillment Division, American Institute of Physics. Allow at least six weeks advance notice. For address changes please send both old and new addresses, and, if possible, include an address stencil imprint from the mailing wrapper of a recent issue. A change-of-address form is included in every issue of *Physics Today*.

Copyright 1980, The American Physical Society

ermission is granted to quote from this journal with the customary acknowledgment of the source. To reprint a figure, table, or other cerpt requires, in addition, the consent of one of the original authors and notification of APS.

[illegible]ying fee is required when copies of articles are made for educational or research purposes by individuals or libraries (including those overnment and industrial institutions)

publication or reproduction for sale of articles or abstracts in this journal is permitted only under license from APS; in addition, APS may quire that permission also be obtained from one of the authors. Address inquiries to the Executive Secretary, The American Physical ciety)

Physical Review C is published once a month on the 1st of each month. Second-class postage rates paid at Woodbury, N. Y., and additional mailing offices.

SN 0556-2813

CODEN: PRVCAN

PHYSICAL REVIEW C

NUCLEAR PHYSICS

Accession Number
225390
Date 30-12-04

THIRD SERIES, VOLUME 21, NUMBER 5 *CONTENTS* MAY 1980

Nuclear Reactions

^{12}C(p,α^*)^{9}B reaction in the finite range microscopic distorted-wave Born-approximation formalism . . . . . S. K. Datta, W. R. Falk, S. P. Kwan, R. Abegg, and O. A. Abou-Zeid 1687
Photoneutron studies of $E1$, $M1$, and $E2$ excitations in ^{13}C . . . . . R. J. Holt, R. M. Laszewski, H. E. Jackson, J. E. Monahan, and J. R. Specht 1699
Quasi-free (α,2α) reaction induced by 140 MeV alpha particles on ^{9}Be, ^{12}C, ^{16}O, and ^{20}Ne . . . . . C. W. Wang, N. S. Chant, P. G. Roos, A. Nadasen, and T. A. Carey 1705
Separation of current and spin contributions to isovector $M1$ excitations by means of the (e,e') and (p,n) reactions . . . . . F. Petrovich, W. G. Love, and R. J. McCarthy 1718
Adiabatic limit of the Faddeev equations . . . . . L. R. Dodd and K. J. Nieukerke 1724
Scattering amplitudes and integral equations for the collision of two charged composite particles . . . . . E. O. Alt and W. Sandhas 1733
^{56}Fe(e,α) reaction and its relevance to the $E2$ isoscalar sum rule . . . . . D. M. Skopik, J. Asai, and J. J. Murphy II 1746
Nuclear excitation of ^{111}Cd by positron annihilation . . . . . Yoshihisa Watanabe, Takeshi Mukoyama, and Sakae Shimizu 1753
Statistical and pre-equilibrium (γ,α) cross sections of ^{90}Zr and their multipolarities via the ^{90}Zr (e,α) reaction . . . . . T. Tamae, T. Urano, M. Hirooka, and M. Sugawara 1758

Heavy Ions

Decay of deformed and superdeformed nuclei formed in heavy ion reactions . . . . . Marshall Blann 1770
Target residues from the reaction of 8 GeV ^{20}Ne with ^{181}Ta and ^{197}Au . . . . . D. J. Morrissey, W. Loveland, M. de Saint Simon, and G. T. Seaborg 1783
(^{7}Li,t) on $1f$-$2p$ shell nuclei . . . . . R. I. Cutler, K. W. Kemper, and A. Roy 1799
^{24}Mg(^{16}O, ^{12}C)^{28}Si and ^{24}Mg(^{16}O, ^{16}O) ^{24}Mg reactions at backward angles . . . . . M. Paul, S. J. Sanders, D. F. Geesaman, W. Henning, D. G. Kovar, C. Olmer, J. P. Schiffer, J. Barrette, and M. J. LeVine 1802
Resonant behavior of the ^{24}Mg(^{16}O, ^{12}C)^{28}Si reaction . . . . . S. J. Sanders, M. Paul, J. Cseh, D. F. Geesaman, W. Henning, D. G. Kovar, R. Kozub, C. Olmer, and J. P. Schiffer 1810
Complete fusion of ^{15}N + ^{27}Al . . . . . F. W. Prosser, Jr., R. A. Racca, K. Daneshvar, D. F. Geesaman, W. Henning, D. G. Kovar, K. E. Rehm, and S. L. Tabor 1819
Backward angle cross sections for ^{27}Al + ^{16}O reaction products . . . . . D. Shapira, J. L. C. Ford, Jr., J. Gomez del Campo, and P. H. Stelson 1824
Velocity dependence of the dynamic magnetic field acting on swift O and Sm ions . . . . . N. K. B. Shu, D. Melnik, J. M. Brennan, W. Semmler, and N. Benczer-Koller 1828
Spectroscopy of ^{213}At, ^{212}Po, and ^{210}Pb following ^{208}Pb + ^{7}Li . . . . . T. P. Sjoreen, U. Garg, and D. B. Fossan 1838
Exactly central heavy-ion collisions by nuclear hydrodynamics . . . . . Henry H. K. Tang and Cheuk-Yin Wong 1846

(Continued)

PHYSICAL REVIEW C THIRD SERIES, VOLUME 21, NUMBER 5 MAY 1980

Complete fusion of ^{12}C with ^{20}Ne ..... I. Tserruya, J. Barrette, S. Kubono, P. Braun-Munzinger, M. Gai, and C. D. Uhlhorn 1864

Closed-form description of heavy-ion transfer reactions based on distorted-waves theory .... W. E. Frahn 1870

Imaginary part of the ion-ion interaction potential .... B. Behera, K. C. Panda, and R. K. Satpathy 1883

Parametrization of exact-finite-range distorted-wave Born approximation overlap integral for reactions induced by heavy ions .... T. Udagawa, T. Tamura, and D. Price 1891

Intermediate Energy

Diffraction structure in back angle p-^{4}He elastic scattering .... L. G. Arnold, B. C. Clark, and R. L. Mercer 1899

Systematic features of the pion-nucleus interaction .... R. S. Bhalerao, L. C. Liu, and C. M. Shakin 1903

Probing inclusive production mechanisms with the $(p,2p)$ reaction .... David H. Boal 1913

Consistency between pion exchange currents and N-N potential in doubly radiative n-p capture .... A. Cambi, B. Mosconi, and P. Ricci 1921

Proton-^{4}He elastic scattering at intermediate energies .... G. A. Moss, L. G. Greeniaus, J. M. Cameron, D. A. Hutcheon, R. L. Liljestrand, C. A. Miller, G. Roy, B. K. S. Koene, W. T. H. van Oers, A. W. Stetz, A. Willis, and N. Willis 1932

Extraction of the πNN form factor from charged pion photoproduction .... C. A. Dominguez and Robert Beck Clark 1944

Relativistic calculation of radiative muon capture in hydrogen and ^{3}He .... Harold W. Fearing 1951

Relativistic description of πd elastic scattering in the (3,3) resonance region .... N. Giraud, C. Fayard, and G. H. Lamot 1959

Nuclear disintegration of some complex nuclei by 60-MeV muons .... C. J. Orth, J. D. Knight, K. Wolfsberg, and M. W. Johnson 1967

Interpretation of quasielastic pion scattering coincidence experiments .... Morton M. Sternheim and Richard R. Silbar 1974

Analysis of quasi-free scattering data in the impulse approximation .... Albert W. Stetz 1979

Proton-proton correlations, the fireball model, and inclusive pion spectrum .... E. Forest, S. Das Gupta, and C. S. Lam 1989

Local field corrections in π-nucleus scattering .... M. K. Banerjee and S. J. Wallace 1996

Photoproduction of pions from deuterons at medium energies .... J. D. Anand, V. S. Bhasin, and V. K. Gupta 2010

Radioactivity

Actinide muonic atom lifetimes deduced from muon-induced fission ..... W. W. Wilcke, M. W. Johnson, W. U. Schröder, D. Hilscher, J. R. Birkelund, J. R. Huizenga, J. C. Browne, and D. G. Perry 2019

$L_{2,3}$-subshell x-ray fluorescence and Coster-Kronig yields at $Z = 64$ and 67 ...... B. E. Gnade, R. Braga, and R. W. Fink 2025

Half-life of ^{241}Pu .... S. K. Aggarwal and H. C. Jain 2033

Levels of ^{230}Ac and ^{230}Th populated by decay of ^{230}Ra and ^{230}Ac .... J. Gilat, S. Katcoff, and L. K. Peker 2041

Nuclear Structure

Sturmian expansion method for bound state problems .... A. Deloff and J. Law 2048

Alternative methods for the solution of static Hartree-Fock and related problems .... M. Di Toro, G. Russo, and F. Duggan 2054

(Continued)

CONTENTS—*Continued*

HYSICAL REVIEW C **THIRD SERIES, VOLUME 21, NUMBER 5** **MAY 1980**

lass parameters in the adiabatic time-dependent Hartree-Fock approximation. I. Theoretical aspects; the case of a single collective variable . . . . M. J. Giannoni and P. Quentin 2060
lass parameters in the adiabatic time-dependent Hartree-Fock approximation. II. Results for the isoscalar quadrupole mode . . . . M. J. Giannoni and P. Quentin 2076

omments

Pion-nucleus optical potential including the nuclear Hamiltonian . . . . Humberto Garcilazo 2094

Communications

Glauber theory and N-N inelasticity . . . . William A. Friedman and Alvin M. Saperstein 2098
New isotope ^{199}Rn and evidence for an isomeric state ^{199}Rn^{m} . . . A. C. DiRienzo, H. A. Enge, S. B. Gazes, M. K. Salomaa, A. Sperduto, W. Schier, and H. E. Wegner 2101
Self-energy of the Δ resonance in finite nuclei and Fermi broadening . . . . R. S. Bhalerao, L. C. Liu, and C. M. Shakin 2103
Relative importance of neutron and proton components of nuclear transitions and comparative π^-/π^+ inelastic scattering . . . . B. A. Brown and B. H. Wildenthal 2107
^{12}C + ^{12}C intermediate structures correlated among elastic and reaction channels . . . . E. R. Cosman, R. Ledoux, and A. J. Lazzarini 2111
Interior probing capability in kaon-nucleus inelastic scattering . . . . Stephen R. Cotanch 2115
Pion electroproduction from the nucleon near threshold . . . . . . E. T. Dressler, N. Freed, and H. B. Miska 2119
Truncated pion-nucleon amplitudes and pion-nucleus interactions . . . . K. L. Kowalski 2122
Projection operator method for heavy ion reactions and application to ^{12}C + ^{12}C . . . . Thomas L. Larry and William P. Beres 2126
Existence of strongly bound states of pions in nuclei . . . . Javier Sesma 2130
Bremsstrahlung from ^{12}C + p near the 1.7-MeV resonance . . . . C. C. Trail, P. M. S. Lesser, A. H. Bond, Jr., M. K. Liou, and C. K. Liu 2131
Levels in ^{44}K via the ^{48}Ca(p,αn) reaction . . . . P. A. Mandò, G. Poggi, G. Lo Bianco, and N. Molho 2135

Errata

Erratum: Neutron capture cross sections on ^{138}Ba, ^{140,142}Ce, ^{175,176}Lu, and ^{181}Ta at 30 keV: Prerequisite for investigation of the ^{176}Lu cosmic clock [Phys. Rev. C 21, 534 (1980)] . . . . H. Beer and F. Käppeler 2139
Erratum: Intranuclear cascade calculation of high-energy heavy-ion interactions [Phys. Rev. C 20, 2227 (1979)] . . . . Y. Yariv and Z. Fraenkel 2139

Cumulative Author Index 2140

PHYSICAL REVIEW C

NUCLEAR PHYSICS

THIRD SERIES, VOLUME 21, NUMBER 6 *CONTENTS* **JUNE 1980**

A New Job in The American Physical Society i

Nuclear Reactions

Inelastic excitation of ^{12}C and ^{14}N by 122 MeV protons and implications for the effective nucleon-nucleon interaction . . . . J. R. Comfort, Sam M. Austin, P. T. Debevec, G. L. Moake, R. W. Finlay, and W. G. Love 2147
Scattering and reaction dynamics for the ^{12}C + p system . . . . J. R. Comfort and B. C. Karp 2162
Electroexcitation of odd-parity states in ^{27}Al . . . . R. S. Hicks, A. Hotta, J. B. Flanz, and H. deVries 2177
Neutron total cross section of sulfur: Single level to multilevel to optical model . . . . C. H. Johnson and R. R. Winters 2190
Wave-function formalisms in the channel coupling array theory of many-body scattering . . . . . F. S. Levin 2199
Proton-nucleus charge exchange measurements at 144 MeV as a test of one-pion exchange and the partially conserved axial vector current . . . . . G. L. Moake, L. J. Gutay, R. P. Scharenberg, P. T. Debevec, and P. A. Quin 2211
Reaction ^{27}Al(α,d)^{29}Si at 27.2 MeV . . . . L. C. Bland, H. T. Fortune, O. K. Gorpinich, Yu S. Stryuk, V. N. Shcherbin, and V. V. Tokarevski 2227
Finite range distorted-wave Born approximation analysis of (p,t) reactions with a realistic triton wave function . . . . M. F. Werby, M. R. Strayer, and M. A. Nagarajan 2235
^{210}Bi^{m}(d,t) reaction; ^{210}Bi(9^{-}) parentage of states in ^{209}Bi . . . . T. P. Cleary, W. D. Callender, and R. K. Sheline 2244
Global optical model potential for elastic deuteron scattering from 12 to 90 MeV . . . . . . W. W. Daehnick, J. D. Childs, and Z. Vrcelj 2253
W(p,t) reactions. I. Even targets . . . . M. H. Mortensen, R. R. Betts, and C. K. Bockelman 2275
W(p,t) reactions. II. Odd target . . . . M. H. Mortensen, R. R. Betts, and C. K. Bockelman 2288
Neutron rich ^{73}Ga and ^{79}As isotopes via the (α,p) reaction . . . G. Rotbard, M. Vergnes, G. Berrier-Ronsin, and J. Vernotte 2293
Interaction of 80-164 MeV protons with nickel isotopes . . . . M. E. Sadler, P. P. Singh, J. Jastrzebski, *L. L. Rutledge, Jr., and R. E. Segel* 2303
Gamma-ray lifetimes for parity doublets in ^{41}K, ^{41}Ca . . . . S. K. Saha, M. J. Maynard, B. C. Robertson, A. B. McDonald, and E. D. Earle 2322
Photon-absorption cross sections between 3 and 30 MeV . . . N. K. Sherman, C. K. Ross, and K. H. Lokan 2328

Heavy Ions

Factorization in high-energy nucleus-nucleus fragmentation cross sections . . . . . . J. Cugnon and R. Sartor 2342
^{12}C(^{6}Li,d)^{16}O $\rightarrow \alpha + {}^{12}$C reaction mechanism by means of angular correlation measurements . . . . A. Cunsolo, A. Foti, G. Immè, G. Pappalardo, G. Raciti, and N. Saunier 2345
Total fusion cross section for the ^{9}Be + ^{28}Si system . . . . J. S. Eck, J. R. Leigh, T. R. Ophel, and P. D. Clark 2352
Direct transfer reaction to discrete and continuum states . . . . M. C. Mermaz 2356

(Continued)

CONTENTS—*Continued*

PHYSICAL REVIEW C **THIRD SERIES, VOLUME 21, NUMBER 6** **JUNE 1980**

High-spin properties of ^{164}Er in the multiple band crossing region . . . . S. W. Yates, I. Y. Lee, N. R. Johnson, E. Eichler, L. L. Riedinger, M. W. Guidry, A. C. Kahler, D. Cline, R. S. Simon, P. A. Butler, P. Colombani, F. S. Stephens, R. M. Diamond, R. M. Ronningen, R. D. Hichwa, J. H. Hamilton, and E. L. Robinson 2366

Creation and observation of a pion condensate in high-energy heavy-ion collisions . . . . S. Krewald and J. W. Negele 2385

Dominance of strong absorption in ^{9}Be + ^{28}Si elastic scattering . . . . M. S. Zisman, J. G. Cramer, D. A. Goldberg, J. W. Watson, and R. M. DeVries 2398

Techniques for heavy-ion coupled-channels calculations. I. Long-range Coulomb coupling . . . . M. Rhoades-Brown, M. H. Macfarlane, and Steven C. Pieper 2417

Fusion of ^{16}O + ^{148,150,152,154}Sm at sub-barrier energies . . . . R. G. Stokstad, Y. Eisen, S. Kaplanis, D. Pelte, U. Smilansky, and I. Tserruya 2427

Techniques for heavy-ion coupled-channels calculations. II. Iterative solution of the coupled radial equations . . . . M. Rhoades-Brown, M. H. Macfarlane, and Steven C. Pieper 2436

Angular distributions and ranges of heavy products from quasi-elastic transfer reactions induced by heavy ions in ^{209}Bi . . . . D. Gardes, R. Bimbot, J. Maison, M. F. Rivet, A. Fleury, F. Hubert, and Y. Llabador 2447

Fission

Scission-point configuration of ^{252}Cf . . . . A. K. Sinha and G. K. Mehta 2467

Intermediate Energy

Neutron angular and energy distributions from 710-MeV alphas stopping in water, carbon, steel, and lead, and 640-MeV alphas stopping in lead . . . . R. A. Cecil, B. D. Anderson, A. R. Baldwin, R. Madey, A. Galonsky, P. Miller, L. Young, and F. M. Waterman 2471

800-MeV inelastic proton scattering from ^{40}Ca, ^{48}Ca, and ^{54}Fe . . . . G. S. Adams, Th. S. Bauer, G. Igo, G. Pauletta, C. A. Whitten, Jr., A. Wriekat, G. W. Hoffmann, G. R. Smith, and M. Gazzaly 2485

Electroexcitation of ^{6}Li with application to the reactions ${}^{6}\mathrm{Li}(\pi^-,\gamma)_{1s}{}^{6}\mathrm{He}(0^+,2^+)$ . . . . J. C. Bergstrom 2496

Phenomenological relativistic quantum mechanics of the $NN\pi$ system . . . . M. Betz and F. Coester 2505

Angular distributions of Sc fragments from the interaction of ^{238}U with 0.8–400 GeV protons . . . . D. R. Fortney and N. T. Porile 2511

Low-energy absorption of pions on nuclei and the real $\rho^2(r)$ potential . . . . Gerald A. Miller and J. V. Noble 2519

Products of stopped-pion interactions with Cu and Ta . . . . C. J. Orth, W. R. Daniels, B. J. Dropesky, R. A. Williams, G. C. Giesler, and J. N. Ginocchio 2524

Proton-deuteron elastic scattering at 800 MeV . . . . . E. Winkelmann, P. R. Bevington, M. W. McNaughton, H. B. Willard, F. H. Cverna, E. P. Chamberlin, and N. S. P. King 2535

Off-shell rescattering effects in the reaction $\pi^- + d \rightarrow 2n + \gamma$ . . . . G. F. de Téramond, J. Páez, and C. W. Soto Vargas 2542

Radioactivity

Decay of ^{180}Re: Search for octupole states in ^{180}W . . . . L. G. Mann, J. B. Carlson, R. G. Lanier, G. L. Struble, W. M. Buckley, R. K. Sheline, and Z. Singh 2547

Systematics of quasirotational states in $N = 88$ nuclei . . . . D. R. Zolnowski, M. B. Hughes, J. Hunt, and T. T. Sugihara 2556

g factors of the 80 and 1094 keV states of ^{168}Er . . . . Akira Furusawa, Masaaki Kanazawa, and Shogo Hayashibe 2575

Ground-state nuclear g factor of ^{97}Ru . . . . K. Leuthold, E. Hagn, H. Ernst, and E. Zech 2581

(Continued)

CONTENTS—*Continued*

PHYSICAL REVIEW C **THIRD SERIES, VOLUME 21, NUMBER 6** **JUNE 1980**

Level properties of $^{85}_{37}$Rb$_{48}$ from the decay of the ^{85}Kr and ^{85}Sr isomers and the cluster-vibration model . . . . . . R. A. Meyer, J. E. Fontanilla, N. L. Smith, C. F. Smith, R. C. Ragaini, and V. Paar 2590

Nuclear Structure

Inelastic scattering $E4$ transition probabilities in the $0d$, $1s$ shell . . . . B. A. Brown, W. Chung, and B. H. Wildenthal 2600
Single-particle states in nuclear matter and in finite nuclei . . . . R. Sartor and C. Mahaux 2613
Short-range correlations and the nuclear momentum density distribution for ^{16}O . . . . . . J. W. Van Orden, W. Truex, and M. K. Banerjee 2628
Use of the boson-expansion theory for the description of collective nuclei . . . . K. J. Weeks and T. Tamura 2632
Shape of eigenvalue distribution for bosons in scalar space . . . . V. K. B. Kota and V. Potbhare 2637
Nucleon-nucleon interaction as derived from the De Rújula, Georgi, Glashow phenomenological quark-quark potential . . . . C. S. Warke and R. Shanker 2643

Comments

Search for nuclear structure dependence of analyzing powers for the ($\vec{t},p$) reaction in medium mass nuclei . . . . Ronald E. Brown, J. A. Cizewski, J. W. Sunier, E. R. Flynn, P. Alford, E. Sugarbaker, and D. Ardouin 2663

Communications

Large absorption potential for the Ag + p reaction at sub-Coulomb energies . . . . A. Feigel, E. Finckh, K. Rüskamp, and U. Weise 2666
Importance of the breakup mechanism for composite particle scattering . . . . G. Baur, R. Shyam, F. Rösel, and D. Trautmann 2668
Evidence for statistical fluctuation in the fragmentation of ^{16}O at intermediate energies . . . . Che Ming Ko 2672
Projection operator method for finding energies and widths of shape resonances in heavy-ion collisions . . . . Thomas L. Larry and William P. Beres 2675
P-wave dispersive contribution to low-energy elastic π^{+2}H scattering . . . . R. M. Rockmore 2678
(π,p) absorption in ^{6,7}Li at 75 and 175 MeV . . . . Jan Källne, J. Davis, P. C. Gugelot, J. S. McCarthy, G. R. Smith, R. L. Boudrie, B. Höistad, and C. L. Morris 2681
Comparison of analyzing powers and polarizations for the charge symmetric reactions ^{2}H($\vec{d},p$)^{3}H and ^{2}H($\vec{d},n$)^{3}He . . . . J. J. Bevelacqua 2685
High energy scattering from a bound nucleon: Unitarity and closure approximation . . . . F. Cannata and S. A. Gurvitz 2687
Time-dependent quadrupole interactions in ^{129}I . . . . S. L. Gupta, Ashok Kumar, S. K. Soni, and S. C. Pancholi 2691
Composite particle emission from ^{65}Zn* . . . . H. Machner 2695

Cumulative Author Index 2699

HYSICAL REVIEW C VOLUME 21, NUMBER 5 MAY 1980

$^{12}C(p,\alpha^*)^9B$ reaction in the finite range microscopic distorted-wave Born-approximation formalism

S. K. Datta, W. R. Falk, S. P. Kwan, R. Abegg,* and O. A. Abou-Zeid

Cyclotron Laboratory, Department of Physics, University of Manitoba, Winnipeg, Manitoba, R3T 2N2, Canada

(Received 21 June 1979)

The differential cross sections for the $^{12}C(p,\alpha^*)^9B(g.s.)$ and $^{12}C(p,\alpha)^9B(g.s.)$ reactions were measured at forward angles at the proton energy of 45.2 MeV. The outgoing α^* particle (20.1 MeV, 0^+, $T=0$) was detected by measuring in coincidence the proton and triton breakup products. Finite range distorted-wave Born approximation and final state interaction calculations were employed in describing the reaction with the unbound emitted particle. The form factor for the distorted-wave Born-approximation analysis was calculated in a microscopic model employing Woods-Saxon wave functions for the three individual transferred nucleons. Microscopic wave functions for the α and α^* particles, due to Hackenbroich *et al.*, were used. Comparisons were also made with distorted-wave Born-approximation calculations using cluster transfer form factors. Relative normalizations between the (p,α^*) and the corresponding (p,α) angular distribution were found to be in good agreement with theoretical prediction from the microscopic model.

[NUCLEAR REACTIONS $^{12}C(p,\alpha^*)^9B$, $^{12}C(p,\alpha)^9B$, $E=45.2$ MeV; measured $\sigma(E_p, E_t, \theta)$, $E_{pt}=0.285$ MeV, $\sigma(E_\alpha, \theta)$; finite range DWBA analysis, microscopic and cluster form factors; final state interaction; relative normalization.]

I. INTRODUCTION

Study of nuclear reactions in which the outgoing particle is in a resonant state is a relatively new area. Its importance and usefulness in spectroscopic studies have been discussed by Robson.[1] There are two main advantages. First, this method is suitable for studying many resonant states for a fixed beam energy in contrast to the usual method involving many changes of bombarding energy. Second, advantage can be taken of the different quantum numbers (e.g., isospin) of the resonant state to populate selected states of the residual nucleus. This latter point was made in connection with $(p,\bar{d})$ reactions,[2] $\bar{d}$ being the singlet ($S=0$, $T=1$) unbound deuteron state. Typical examples of transfer reactions, involving unbound light particles, that have been studied include $(p,\bar{d})$ reactions,[2-4] $(^3He,\bar{d})$ reactions,[5,6] $(\alpha,{}^5He)$ and $(\alpha,{}^5Li)$ reactions,[7-11] and $(\alpha;{}^2He)$ reactions.[12,13] Recently (α,α^*) reactions[14,15] have also been investigated. To our knowledge, no work on (p,α^*) reactions has been reported to date.

The existence of α^*, the first excited state of the α particle (20.1 MeV, 0^+, $T=0$, unbound by 285 keV and decaying into proton and triton) was first indicated in the $^3H(d,pn)^3H$ experiment of Lefevre *et al.*,[16] which was analyzed by Werntz.[17] Subsequent corroborations came from analysis of proton-triton elastic scattering,[18,19] and more extensive study including $^3H(p,p)^3H$, $^3He(n,n)^3He$, $^3H(p,n)^3He$ channels by Meyerhof and collaborators.[20-22] A summary of the properties of this resonant state and references to other works are given by Fiarman and Meyerhof.[23]

Aside from adding to the general body of information involving transfer reactions with resonant particles, the present work was undertaken with a specific end in view. The microscopic finite range form factor approach of Falk *et al.*[24,25] for (p,α) reactions makes possible finite range distorted-wave Born approximation (DWBA) calculations where the details of the α and α^* wave functions can be incorporated. In a comparison between (p,α) and (p,α^*) reactions those aspects due to the different wave functions of α and α^* are emphasized and effects due to the other parameters which are kept the same in both reactions are minimized. Therefore, such a study provides an additional and more stringent test of the microscopic theory. The alternative finite range cluster form factor DWBA calculations,[26] which neglect internal structures of the transferred particle group, can also be compared to the data and its merits relative to the microscopic approach evaluated.

The absolute normalizations of the cross section angular distributions for the microscopic form factor calculations are difficult to determine[26] and only relative normalization between (p,α) and (p,α^*) angular distributions are, therefore, calculated. Janetzki *et al.*[6] have shown, in their study of the $(^3He,\bar{d})$ reaction, how to calculate the normalization factor for the reaction involving the unbound singlet deuteron. In their work the effect of the unbound emitted particle was taken

© 1980 The American Physical Society

into account using the final state formulation of Watson[27] and Migdal.[28] The enhancement in the energy differential cross section was calculated using a scattering length, effective range approximation of the Jost function for n-p scattering. Unlike the singlet deuteron, which is an antibound state (i.e., a pole on the negative imaginary k axis of the complex k plane), the α^* (singlet p-t) is a resonance. While the effective range approximation is valid on the positive real E axis (the pole being on the negative E axis) for $\tilde{d}$, for the α^* resonance a Breit-Wigner description must be used (the pole being in the positive energy region though not on the positive real E axis). Coulomb effects between the proton and triton from the α^* are also important. We followed, therefore, a slightly different method. The effect of the three body final state was still taken into account using the Watson-Migdal approach, but the unbound wave function of the α^* was expressed in terms of a Breit-Wigner energy dependent factor and a bound s-wave function. The development follows closely the method of Pong and Austern[8] but, unlike theirs, includes Coulomb interactions.

The experiment was carried out to measure ^{12}C(p, α^*)^{9}B and ^{12}C(p, α)^{9}B cross section angular distributions simultaneously. The target was chosen because of its known large cross section for the (p, α) reaction at our available energy.[29] The proton and triton products from α^* decay were detected in coincidence. The experimental details are given in Sec. II. Theoretical details for evaluating the (p, α^*) cross section—salient features of the Watson-Migdal final state formulation, our description of the unbound α^* wave function, and the relation of the measured cross section to the calculations—are set forth in Sec. III. The method of data analysis and the results are discussed in Secs. IV and V.

II. EXPERIMENT

The experiment was performed using a 45.2 MeV proton beam from the University of Manitoba variable energy cyclotron. The momentum analyzed beam impinged on a target at the center of a 56 cm diameter scattering chamber. The target was a self-supporting Mylar foil of thickness 0.25 mil, yielding a ^{12}C target of thickness 0.55 mg/cm^2. Mylar was used because of the availability of thick foils. Interference due to the presence of oxygen, the other major component in the target, was expected from the ^{16}O(p, α^*)^{13}N (3.51 MeV) peak. Subsequently, this reaction was found to have a negligible contribution and was ignored.

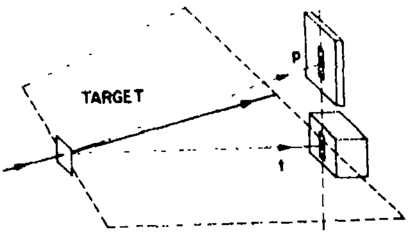

FIG. 1. Detection geometry for coincident detection of the breakup products from α^*.

The detector arrangement for detecting the proton and triton decay products from α^* is shown in Fig. 1. The triton was detected in a solid state ΔE-E-veto counter telescope of thicknesses 100 μm (ΔE) and 1000 μm (E), respectively. The collimating slit in front of the telescope detector was 0.315 by 0.956 cm. The proton was detected in a 1000 μm rectangular detector of 0.7 cm width and 2.4 cm height with a horizontal collimating slit of width 0.315 cm. The two detectors were mounted in a vertical plane; the triton detector slightly below the scattering plane and the proton detector above it. Both were at a distance of approximately 11 cm from the center of the target. The angular separation between midpoints of the two detectors subtended at the target was set at 20° on the basis of a kinematic calculation for the most efficient coincidence detection.

The protons and tritons from the α^* decay were detected using a slow-fast coincidence electronic arrangement. The slow logic signals from the timing single-channel analyzers in the proton and triton detection channels were fed into a coincidence unit and the output pulse after logic shaping was used as a common analog-to-digital converter (ADC) gate. The fast timing signals from the two channels were put into a time-to-amplitude converter (TAC) and the TAC output fed into an ADC. Particle identification in the telescope spectrum was performed by the data taking program on the basis of ΔE and E signals.

The energy resolution in the telescope spectrum was about 200 keV. No particle identification was made in the proton detector. Fortunately, competing reaction channels did not yield other particles within the region of interest of $E_p = 1$ to 8 MeV. The program displayed a two-dimensional spectrum of triton energy E_t vs proton energy E_p for coincident events in the two detection channels. A typical E_t-E_p plot corresponding to α^* scattering at angle $\theta_{\rm lab} = 20°$ is shown in Fig. 2. The fast timing coincidence constraint was imposed by software, selecting only events from this list that fell within the specified window of the TAC spectrum. The veto detector placed behind the triton telescope served to eliminate the large number of background events due to coincidence between elastic protons in the two detection chan-

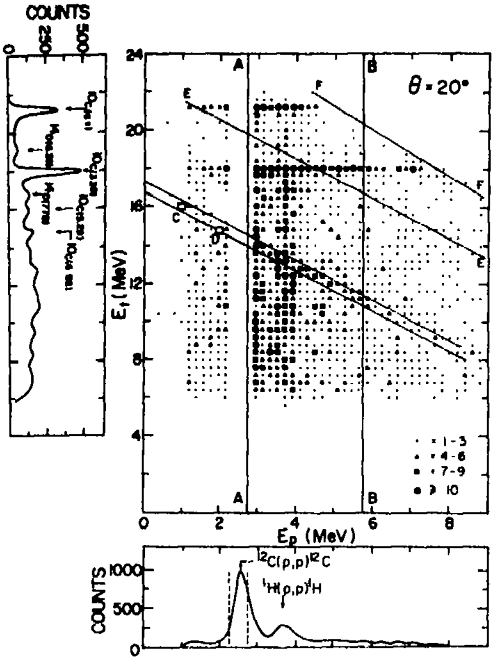

FIG. 2. Two-dimensional plot of proton-triton coincident events at laboratory scattering angle of α^*, $\theta = 20°$. The events projected along E_p and E_t axes are shown as spectra beside the axes. The events with a breakup energy of 285 keV are contained in the central band bounded by the two parallel oblique lines and the lines A and B. Boxes C and D denote locations of sequential decay events from $^{12}C(p,t)^{10}C^*$ (5·29) and $^{12}C(p,t)^{10}C^*$ (6·58), respectively. Loci E and F indicate locations of events from $^{16}O(p,t)^{14}O^* \rightarrow ^{13}N+p$ and $^{16}O(p,t)^{14}O^* \rightarrow ^{10}C+\alpha$, respectively. For clarity of presentation, events in the region $E_p = 2·3$ to $2·7$ MeV (dominated by the elastic proton peak) have been left out.

nels. Pileup rejection circuitry was also used to clean up the background.

The α-particle spectrum from the (p,α) reaction was collected simultaneously by feeding the summed $E+\Delta E$ signals from the telescope counter into a multichannel analyzer. No particle identification was necessary since all other competing channels produced peaks at the lower energy end of the spectrum due to either high negative Q values or loss of little energy in the combined ΔE-E counter.

The resolution achieved in the α spectrum was 200 keV. The proton beam was stopped and collected in a Faraday cup separated by a 2 cm airgap from the scattering chamber. Typical beam currents were 5 nA. Two NaI detectors were placed to the left and right of the beam at 15° from the chamber center to monitor target thickness. The necessary corrections due to evaporation of material from the target were made by normalizing the monitor peak counts to the charge collected in the Faraday cup.

The angular distributions for (p,α^*) and (p,α) were measured at laboratory angles 20° to 50°, at 10° intervals.

III. THEORY

A. Three body final state

Since the $^{12}C(p,\alpha^*)^9B$ reaction yields in the final state three particles, ^9B, proton, and triton, the usual two body direct reaction theories, e.g., the DWBA, cannot be applied straightforwardly in the description of the reaction process. Final state interaction between the emitted particles and the three particle kinematics must be taken into account over and above the primary reaction mechanism responsible for the production of the α^*.

It is assumed following Watson and Migdal[27,28] that the total Hamiltonian of the system can be written as $H = H_0 + V + U$ where H_0 is the Hamiltonian for three free particles, V is the potential which produces ^9B and α^* (emitted as a composite particle), and U is the final state potential between the proton and triton into which the α^* breaks up (final state interaction between other pairs are not considered). The Lippmann-Schwinger equation for this case can be written as[30,31]

$$\psi^{\pm} = \chi^{\pm} + (E - H_0 \pm i\epsilon)^{-1}(U+V)\psi^{\pm}, \tag{1}$$

where $\psi^{\pm}$ is the three particle scattering state, $\chi^{\pm}$ are the three free particle plane wave states, and E the total energy. The isolated scattering of the proton-triton through the potential U is given by

$$\phi^{\pm} = \chi^{\pm} + (E - H_0 \pm i\epsilon)^{-1}U\phi^{\pm}. \tag{2}$$

The transition matrix element T_{ba} between the entrance channel a ($^{12}C+p$) and the exit channel b ($^9B+p+t$) is given by

$$T_{ba} = \langle \chi_b^- | (U+V) | \psi_a^+ \rangle, \tag{3}$$

which after some algebra utilizing Eqs. (1) and (2), yields

$$T_{ba} = \langle \phi_b^- | V | \psi_a^+ \rangle + \langle \chi_b^- | U | \phi_a^+ \rangle. \tag{4}$$

Following Watson,[27] the two body interaction U is so chosen that the second term vanishes. A new wave function ψ_0 is defined for the case $U=0$, when from Eq. (1) for $U=0$,

$$\psi_0^{\pm} = \chi^{\pm} + (E - H_0 \pm i\epsilon)^{-1}V\psi_0^{\pm}. \tag{5}$$

Using this equation, after some further algebra, one gets

$$T_{ba} = \langle \phi_b^- | V | \psi_{0a}^+ \rangle + \langle \psi_b^- - \phi_b^- | U | \psi_{0a}^+ \rangle. \tag{6}$$

In the Watson approximation, the production potential V is assumed to be weak. (This is justified since the first Born approximation is often sufficient to describe the production process.) For such a case ψ_b tends to ϕ_b and the second term in Eq. (6) can be dropped. We have finally

$$T_{ba} = \langle \phi_b^- | V | \psi_{0a}^+ \rangle , \tag{7}$$

where ψ_{0a}^+ is the entrance channel (proton, ${}^{12}C = {}^9B + t$ bound state) wave function assuming no proton-triton final state interaction, V is an effective interaction, and ϕ_b is the exit channel (proton, triton, ${}^9B$) wave function where the proton and triton interact via a potential U and the residual nucleus does not interact with the p-t pair.

B. Unbound ejectile wave function

The exit channel wave function ϕ_b can be separated into three parts as

$$\phi_b = \phi_{pt}(\vec{k}, \vec{r})\, X(\vec{k}_b, \vec{R}_b) B(\vec{\xi}_B) , \tag{8}$$

where $\phi_{pt}(\vec{k}, \vec{r})$ is the wave function of the unbound p-t system, $X(\vec{k}_b, \vec{R}_b)$ is a relative wave function between the centers of mass of the p-t cluster and the residual nucleus, and $B(\vec{\xi}_B)$ is the intrinsic wave function of the residual nucleus. If we now make the usual DWBA approximation[26] for the transition amplitude we get

$$\begin{aligned} T_{ba} = \langle & \phi_{pt}^-(\vec{k}, \vec{r}), X^-(\vec{k}_b, \vec{R}_b) B(\vec{\xi}_B) | V_{pt}(\vec{r}) | \\ & \times X^+(\vec{k}_a, \vec{R}_a) A(\vec{\xi}_A) \rangle , \end{aligned} \tag{9}$$

where $X(\vec{k}_a, \vec{R}_a)$ is the relative wave function between the proton and ${}^{12}C$ in the entrance channel, $A(\vec{\xi}_A)$ is the intrinsic wave function of the target nucleus, and $V_{pt}(\vec{r})$ is the effective interaction. The intrinsic spin wave functions of proton and triton are implicit in this expression.

Depending upon whether the proton-triton unbound wave function ϕ_{pt} is dominated by a resonant structure or not, we use two different approaches to evaluate Eq. (9).

(i) *Breit-Wigner resonance.* According to Werntz,[19] the α^* appears as an $l = 0$, $S = 0$ (spin-singlet) resonance in p-t scattering at $E_{pt} = 285$ keV. For scattering states which are unbound by small energy we make the approximation following Pong and Austern[8]

$$V_{pt}(\vec{r}) \phi_{pt}^{(-)}(\vec{k}, \vec{r}) \approx A(k) V_{pt}(\vec{r}) W(\vec{k}, \vec{r}) , \tag{10}$$

where $A(k)$ carries the bulk of momentum dependence and $W(\vec{k}, \vec{r})$ is a relatively energy independent $l = 0$ bound state wave function localized and normalized to unity within some radius R_0. The bound state wave function W vanishes for large r, whereas ϕ_{pt} has an oscillatory tail. The approximation holds because V_{pt} is a short range nuclear potential. (Coulomb interactions between the proton and the nucleons in the triton are neglected in the microscopic form factor approach.)

Since $W(\vec{k}, \vec{r})$ is normalized to unity within some radius R_0, we can write

$$\begin{aligned} \int_{r=0}^{R_0} d^3r \, | \phi_{pt}^{(-)}(\vec{k}, \vec{r}) |^2 &= \int_0^{R_0} r^2 dr \, |A(k)|^2 |W(k, r)|^2 \\ &= |A(k)|^2 . \end{aligned} \tag{11}$$

Writing $\phi_{pt}^{(-)}(\vec{k}, \vec{r}) = [\chi(k, r)/r] Y_{00}(\hat{r})$ we get

$$|A(k)|^2 = \int_0^{R_0} dr \, |\chi(k, r)|^2 . \tag{12}$$

This is evaluated by standard techniques[8] (with modifications for charged particle) using at $r = R_0$,

$$\chi(k, r = R_0) = \sqrt{4\pi}\, e^{-i\sigma_0} \frac{e^{-i\delta_0}}{k} (F_0 \cos\delta_0 + G_0 \sin\delta_0) , \tag{13}$$

and neglecting Coulomb function derivatives dF_0/dk and dG_0/dk compared to $d\delta/dk$ over a sharp resonance. We get

$$|A(k)|^2 = 4\pi \frac{\hbar^2}{2mk} \frac{d\delta_0}{dE} . \tag{14}$$

For charged particle scattering, the resonant nuclear phase shift for a single level is given by[33]

$$\delta_0 = \tan^{-1} \frac{\frac{1}{2}\Gamma}{(E_0 - S_0\gamma^2 - E)} , \tag{15}$$

where Γ is $2P_0\gamma^2$, the penetrability P_0 is $ka_0/(F_0^2 + G_0^2)$, a_0 is the channel radius, γ^2 is the reduced width, E_0 is the resonance energy, and the shift function

$$S_0 = \tfrac{1}{2} k a_0 \left[\frac{d}{d(kr)} \ln(F_0^2 + G_0^2) \right]_{r=a_0} .$$

Using Eq. (15) in Eq. (14) we have the final expression

$$\begin{aligned} |A(k)|^2 &= 4\pi \frac{\hbar^2}{2mk} \frac{\frac{1}{2}\Gamma}{(E_0 - S_0\gamma^2 - E)^2 + \frac{1}{4}\Gamma^2} \\ &\quad + 4\pi \frac{\gamma^2 (E_0 - S_0\gamma^2 - E) \frac{1}{2k^2} \frac{dP_0}{dk} + P_0 \gamma^4 \frac{1}{2k^2} \frac{dS_0}{dk}}{(E_0 - S_0\gamma^2 - E)^2 + \frac{1}{4}\Gamma^2} \\ &= f_{s1} + f_{s2} . \end{aligned} \tag{16}$$

The first term f_{s1} is similar to that for neutral particles (in Ref. 8) except for the Coulomb shifted resonance energy in the denominator. But the second term f_{s2} is an entirely new one due to Coulomb effects. The relative importance of the two terms is shown in Fig. 3, where f_{s1} and $f_{s1} + f_{s2}$ are plotted as a function of the relative energy $E_{pt} = E = \hbar^2 k^2 / 2\mu$. The parameters for the calculation, $E_0 = 0.64$ MeV, $\gamma^2 = 3.35$ MeV, and $a_0 = 3.3$ fm are taken from Meyerhof and McElearney.[30]

The expression for the transition amplitude can

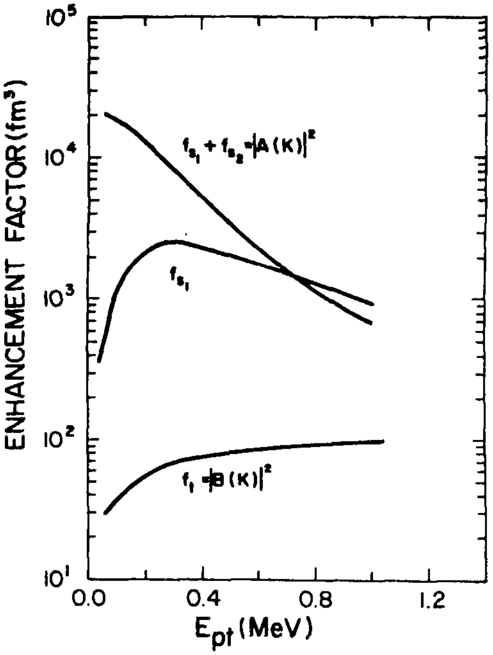

FIG. 3. Enhancement factors $|A(k)|^2=f_{s1}+f_{s2}$ for the singlet state and $|B(k)|^2=f_t$ for the triplet state, as functions of relative energy between the proton and triton. The quantities plotted are those given by expressions (16) and (23), with $N_0{}^2=1$.

now be written as follows, using Eq. (10),

$$T_{ba}=A(k)\langle W(\vec{k},\vec{r}),X^{(-)}(\vec{k}_b,\vec{R}_b)B(\vec{\xi}_B)|V_{pt}(\vec{r})|$$
$$\times X^{(+)}(\vec{k}_a,\vec{R}_a)A(\vec{\xi}_A)\rangle=A(k)T_{DW}^{(s)}, \qquad (17)$$

where T_{DW} is the usual DWBA amplitude in which α^* is treated as an $l=0$, p-t bound state. The superscript s denotes singlet state. The effect of the unbound nature of the ejectile is separated out in the factor $A(k)$, which is evaluated from Eq. (16). The quantity $|A(k)|^2$ is called the enhancement factor.

(ii) *Effective range approximation.* A nonresonant $l=0$, $S=1$ (spin-triplet) background underlying the α^* state, is also associated with the observed p-t spectrum. For this case, the momentum dependence of the wave function ϕ_{pt} is separated out in the following way.[31] The wave function for large r is

$$\phi_{pt}^{(-)}(\vec{k},\vec{r})=\sqrt{4\pi}\,e^{-i\sigma_0}\frac{e^{-i\delta_0}}{kr}(F_0\cos\delta_0+G_0\sin\delta_0)Y_{00}\,. \qquad (18)$$

For states of low relative momenta $kr\ll1$, $F_0(kr)=Ckr$, and $G_0(kr)=1/C$ (*Coulomb functions normalized to unit amplitude at infinity*), where $C^2=2\pi\eta/(e^{2\pi\eta}-1)$, $\eta=z_1z_2\mu e^2/\hbar^2k$. The effective range approximation for charged particles at small relative momentum is given by

$$C^2k\cot\delta_0=-\frac{1}{a}+\frac{r_e}{2}k^2-\frac{h(\eta)}{R}, \qquad (19)$$

where a = scattering length, r_e = effective range, $h(\eta)=\text{Re}\,[\Gamma'(1-i\eta)/\Gamma(1-i\eta)]-\ln\eta$, $R=\hbar^2/2\mu z_1z_2e^2$. Using this with the approximate expressions for F_0 and G_0 in Eq. (18) we get,

$$\phi_{pt}^{(-)}(\vec{k},\vec{r})=\sqrt{4\pi}\,e^{-i\sigma_0}\frac{e^{-i\delta_0}}{Ck}\sin\delta_0\left(\frac{1}{r}-\frac{1}{a}\right)Y_{00}(\hat{r})$$
$$=\sqrt{4\pi}\,e^{-i\sigma_0}\frac{e^{-i\delta_0}}{Ck}\sin\delta_0 f_{pt}(\vec{r})\,, \qquad (20)$$

where only the first term $C^2k\cot\delta_0=-1/a$ has been retained in the effective range expansion.

Introducing this in the expression for the transition amplitude, Eq. (9), we get

$$T_{ba}=\sqrt{4\pi}\,e^{-i\sigma_0}\frac{e^{-i\delta_0}\sin\delta_0}{Ck}$$
$$\times\langle f_{pt}(\vec{r}),X^{(-)}(\vec{k}_b,\vec{R}_b)B(\vec{\xi}_B)|V_{pt}(\vec{r})|$$
$$\times X^{(+)}(\vec{k}_a,\vec{R}_a)A(\vec{\xi}_A)\rangle\,. \qquad (21)$$

We can approximate $f_{pt}(r)=(1/r-1/a)$ by $N_0W_t(r)$ where $W_t(r)$ is a normalizable triplet bound state wave function and N_0 is a normalization constant of dimension $(\text{length})^{1/2}$ (Ref. 27). Putting this in Eq. (21) we have

$$T_{ba}=B(k)T_{DW}^{(t)}, \qquad (22)$$

where

$$B(k)=\sqrt{4\pi}\,e^{-i\sigma_0}\frac{e^{-i\delta_0}\sin\delta_0}{Ck}N_0$$

and

$$T_{DW}^{(t)}=\langle W_t(\vec{r}),X^{(-)}(\vec{k}_b,\vec{R}_b)B(\vec{\xi}_B)|V_{pt}(\vec{r})|$$
$$\times X^{(+)}(\vec{k}_a,\vec{R}_a)A(\vec{\xi}_A)\rangle$$

is the DWBA transition amplitude for the triplet state.

The enhancement factor, the quantity comparable to $|A(k)|^2$, is

$$|B(k)|^2=N_0{}^24\pi/(C^2k^2+C^4k^2\cot^2\delta_0)\,.$$

Using the effective range approximation (19) for $C^2k^2\cot^2\delta_0$ we get

$$|B(\vec{k})|^2$$
$$=N_0{}^2\frac{4\pi C^2}{\frac{2\mu}{\hbar^2}\left[C^4E_{pt}+\frac{\hbar^2}{2\mu}\left(-\frac{1}{a}-\frac{h(\eta)}{R}+\frac{\mu r_e}{\hbar^2}E_{pt}\right)\right]}=f_t\,. \qquad (23)$$

The variation of $|B(k)|^2 = f_t$, with energy E_{pt}, is shown in the lower part of Fig. 3. The parameters $a = 4.17$ fm and $r_e = 2.9$ fm are taken from Meyerhof and McElearney.[20]

Hence both for the Breit-Wigner resonance and the effective range approximation we are able to separate out the transition amplitude into two parts; a momentum dependent enhancement factor calculable from p-t scattering data and a DWBA transition amplitude.

C. Energy differential cross section

The energy differential cross section, in obvious notation, is related to the transition amplitude by

$$\sigma = \frac{d^3\sigma}{dE_{pt}\, d\Omega_{B\alpha^*}\, d\Omega_{pt}} = \frac{2\pi}{\hbar}\, \frac{1}{v}\, |T_{ba}|^2 \rho_{B\alpha^*} \rho_{pt}\,, \tag{24}$$

where $\rho_{B\alpha^*}$ and ρ_{pt} are the density of states in the residual nucleus -α^* system and proton-triton system, respectively, and v is the velocity of the incident proton. The density of states ρ_{pt} is given by[6]

$$\rho_{pt} = \frac{\mu_{pt} \hbar k_{pt}}{(2\pi\hbar)^3}\,. \tag{25}$$

Writing out the expression for T_{ba} from Eqs. (17) and (22) we have

$$\sigma^{(s)} = |A(k)|^2 \sigma_{\rm DW}^{(s)} \rho_{pt}$$

and (26)

$$\sigma^{(t)} = |B(k)|^2 \sigma_{\rm DW}^{(t)} \rho_{pt}\,,$$

where we have used

$$\frac{2\pi}{\hbar}\, \frac{1}{v}\, |T_{\rm DW}|^2 \rho_{B\alpha^*} = \sigma_{\rm DW}\,,$$

the cross section calculated from the DWBA formalism assuming α^* to be a bound state of the proton and triton. The observed cross section is an incoherent sum of the two with statistical weights $\frac{1}{4}$ for the singlet and $\frac{3}{4}$ for the triplet. Hence

$$\sigma^{(\rm c.m.)} = \frac{d^3\sigma^{(\rm c.m.)}}{dE_{pt}\, d\Omega_{B\alpha^*}\, d\Omega_{pt}}$$

$$= \tfrac{1}{4}\left[\, |A(k)|^2 \sigma_{\rm DW}^{(s)} + 3|B(k)|^2 \sigma_{\rm DW}^{(t)} \right] \rho_{pt}\,. \tag{27}$$

Now $T_{\rm DW}^{(t)}$ is different from $T_{\rm DW}^{(s)}$ for two reasons. First, it includes a radial bound state for the proton-triton system, $W_t(r) = (1/N_0)(1/r - 1/a)$ which is perhaps not realistic, and certainly cannot be used for very small values of r, unlike the radial bound state $W(k, r)$ for the singlet state. Secondly, the effective interaction V_{pt} is different for the triplet and singlet states.[2] Therefore, we write $\sigma_{\rm DW}^{(t)} = N_{ts} \sigma_{\rm DW}^{(s)}$, where N_{ts} is a constant to be determined from experimental data and the value of N_0^2 has been arbitrarily set to 1. N_{ts} is independent of angle because $W(r)$ is an $l = 0$ wave function and $V_{pt}(r)$ is a central interaction. Thus

$$\sigma^{(\rm c.m.)} = \sigma_{\rm DW}\left[\tfrac{1}{4}|A(k)|^2 + \frac{3N_{ts}}{4}|B(k)|^2\right]\rho_{pt}\,. \tag{28}$$

Now the experimental quantity measured is the laboratory energy differential cross section. This is expressed as

$$\frac{d^3\sigma^{(\rm lab)}}{dE_p\, d\Omega_p\, d\Omega_t} = J\sigma^{(\rm c.m.)}$$

$$= \tfrac{1}{4} J \sigma_{\rm DW} |A(k)|^2 \rho_{pt}$$

$$+ \frac{3N_{ts}}{4} J \sigma_{\rm DW} |B(k)|^2 \rho_{pt}$$

$$= \frac{\sigma_{\rm DW}}{4}(F_s + 3N_{ts}F_t)\,, \tag{29}$$

where F_s and F_t are defined by this equation. The Jacobian of transformation J is given by[6]

$$J = \frac{1}{\mu_{B\alpha^*} \mu_{pt} k_{B\alpha^*} k_{pt}}\; \frac{M_B m_p m_t k_p k_t}{M_B + m_t[1 + \mathbf{k}_t \cdot (\mathbf{k}_p - \mathbf{k}_i)/k_t^2]}\,, \tag{30}$$

where $\mu_{B\alpha^*}$ and μ_{pt} are reduced masses, $k_{B\alpha^*}$ and k_{pt} are relative momenta, M_B, m_p, m_t are particle masses, and k_i, k_p, k_t are incident and outgoing particle momenta.

IV. ANALYSIS

A. Data reduction

For the (p, α) reaction, the extraction of cross section data from the peak counts in the spectrum was done by standard techniques. Since the (p, α^*) reaction involves a three body final state, the data extraction is different and described below in detail.

For reactions with three particle final states, the energies of the two detected particles are related to each other through three body kinematic equations which have been described by Ohlsen.[23] The present work follows his prescription except for relativistic corrections in the entrance channel due to the high energy ($E = 45.2$ MeV) of the incident proton.

The coincident proton-triton events are shown in a two-dimensional plot in Fig. 2 with E_p, the proton energy as the x axis and E_t, the triton energy, as the y axis. The mean laboratory scattering angle θ, the angle at which the α^* would be detected if it did not break up, is 20°. The events of interest are inside the band shown, of a width of 400 keV. For a given detector geometry of small solid angles, e.g., polar angles θ_p, ϕ_p for the proton detector and θ_t, ϕ_t for the triton detector, the kinematic locus of events is approximately a straight line within the band and parallel to the edges. The large solid angles of the detectors were divided into smaller elements and kinematic loci calculated for each pair. All these loci were within the band shown.

The projected spectra along E_p and E_t axes obtained from the full two-dimensional plot are shown along the two axes. Positions of the various peaks obtained from the $^{12}C(p,t)^{10}C$ and $^{16}O(p,t)^{14}O$ reactions are indicated in the spectrum along the E_t axis. In the spectrum along the E_p axis two main peaks appear; the one centered at around 2.6 MeV is due to the energy deposited in the 1 mm thick proton detector by protons elastically scattered from ^{12}C and ^{16}O, while the other at 3.5 MeV is due to protons elastically scattered from hydrogen. Because of random coincidences between protons and tritons, large concentrations of events appear at the position of strong proton or triton peaks. For clarity of presentation, the portion of the two dimensional spectrum from $E_p = 2.3$ to 2.7 MeV has been omitted in Fig. 2.

The relative energy between proton-triton pairs is given by[15,33]

$$E_{pt}=\frac{1}{m_p+m_t}\times[m_tE_p+m_pE_t-2(m_pm_tE_pE_t)^{1/2}\cos\theta_{pt}], \quad (31)$$

where m_p, m_t are the masses of the two particles and θ_{pt} is the lab angle between the two detector elements. For α^* events, E_{pt} = breakup energy of $\alpha^* = 0.285$ MeV. There are two points on a kinematic locus which correspond to this value of E_{pt} for a given θ_{pt}. However, due to the large solid angles of detectors, we have to consider many pairs of detector elements. Consequently θ_{pt} varies over a wide range, and events of $E_{pt} = 0.285$ MeV occupy an extended segment within the band indicated by the region AB in Fig. 2. For our detector geometry, θ_{pt} varied from 11.5° to 25.8°.

To obtain the number of true α^* events in the region AB, background events due to other processes had to be subtracted. The background events were from random coincidences between tritons and protons and from sequential decays resulting in a triton and some other particle. Since the projected triton spectrum in the region of interest did not show pronounced discrete peaks, the random coincidences with elastic protons produced fairly uniform bands parallel to the E_t axis (the band centered at $E_p = 3.5$ MeV is distinctly visible in Fig. 2). Sequential decay processes $^{12}C(p,t)^{10}C^* \rightarrow {}^9B + p$ and $^{12}C(p,t)^{10}C^* \rightarrow {}^6Be + \alpha$ proceeding through particle unbound states (5.29 MeV, doublet and 6.58 MeV) in ^{10}C would generate events at the points C and D in Fig. 2. Three body final states from $^{16}O+p$ are indicated by loci E and F which are well outside the region of interest.

The number of events within the band and in the region AB was counted. Two parallel bands of equal width (400 keV) were drawn on both sides of the band of interest, at a distance of about 800 keV (measured along E_t axis) from the central band, and the number of events in these bands were taken as representative of the background due to random coincidences and subtracted from the counts obtained from the band of interest. The spectra of the total counts and the representative background projected onto the E_p axis are shown in the upper part of Fig. 4 for $\theta = 20°$ and 40°. The lower part of the figure shows the background subtracted spectra. The errors are due to counting statistics. No sequential events from $^{12}C(p,t)^{10}C^*$ (points C and D in Fig. 2) were observed.

The histograms represent number of counts $dN(\Omega_p, \Omega_t, E_p)\Delta E_p$ in an energy range ΔE_p. The region AB contains events of interest. However, because of the large solid angles of the detectors, the region AB contains not only the α^* events of $E_{pt} = 285$ keV but actually events in the energy range $E_{pt} = 100$ to 800 keV. The large range is necessary in view of the large width of the α^* resonance (~300 keV) and the experimental ener-

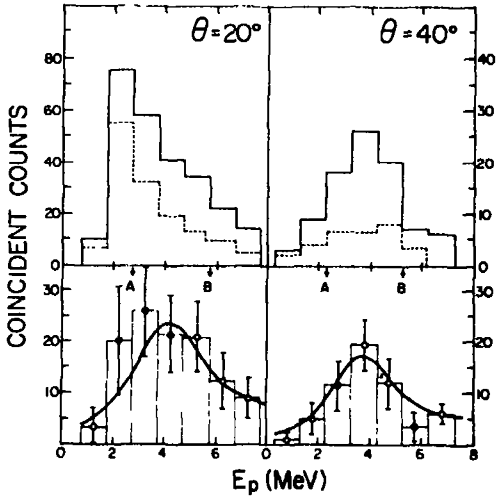

FIG. 4. Proton-triton coincident counts as functions of proton energy for laboratory scattering angles of α^*, $\theta = 20°$ and 40°. In the upper region are shown total counts (solid line) and background counts (dashed line). In the lower region, background subtracted counts are presented. The region AB (between the arrows) contain α^* events of breakup energy = 285 keV. The curves represent the functions $\sum_{ij}(g_{ij}^{(s)}+3N_{st}g_{ij}^{(t)})$ and the histograms the experimental data. See Sec. IV A for details.

gy resolution of 200 keV. The non α^* events are presumably due to the nonresonant triplet p-t component underlying the singlet α^* events. These are accounted for through the triplet terms in the cross section expression (29) as described below.

For a given pair of detector elements i-j with solid angles $\Delta\Omega_{pi}$ for the proton detector and $\Delta\Omega_{tj}$ for the triton detector, the number of coincident counts in an energy interval ΔE_p is given by

$$dN(\Delta\Omega_{pi},\Delta\Omega_{tj},\Delta E_p)\Delta E_p$$

$$=K\frac{d^3\sigma_{ij}^{(\mathrm{lab})}}{dE_p d\Omega_{pi} d\Omega_{tj}}\Delta\Omega_{pi}\Delta\Omega_{tj}\Delta E_p\,,\quad(32)$$

where $K=$ (target nuclei/cm^2) × (number of incident protons) and $d^3\sigma_{ij}^{(\mathrm{lab})}/dE_p d\Omega_{pi} d\Omega_{tj}$ is the laboratory energy differential cross section measured in the i-j pair. We use expression (29) and sum over all detector pairs i-j to get the total number of counts in an interval ΔE_p (corresponding to the histograms in Fig. 4),

$$dN(\Omega_p\Omega_t E_p)\Delta E_p$$

$$=K\sum_{ij}\tfrac{1}{4}\sigma_{\mathrm{DW}}(\theta_{ij})$$

$$\times[(F_s)_{ij}\Delta\Omega_{pi}\Delta\Omega_{tj}+3N_{ts}(F_t)_{ij}\Delta\Omega_{pi}\Delta\Omega_{tj}]\Delta E_p$$

$$=\tfrac{1}{4}K\sigma_{\mathrm{DW}}(\theta)\left[\sum_{ij}g_{ij}^{(s)}+3N_{ts}\sum_{ij}g_{ij}^{(t)}\right]\Delta E_p\,,\qquad(33)$$

where the variation of θ (the α^* polar scattering angle) among different i-j detector elements is neglected. For the worst case of $\theta=20°$, the minimum lab angle, the actual θ values for peripheral elements lie within ±0.5°. The detector element indices i run from 1 to 9 for the proton detector and j from 1 to 4 for the triton detector. Each element subtended an angle of 1.3° in the vertical plane at the target.

The expressions $\sum_{ij}g_{ij}^{(s)}$ and $\sum_{ij}g_{ij}^{(t)}$ were calculated by a computer program and are shown in Fig. 5. (The detailed expressions for the functions F_s and F_t as well as the parameters used in calculating them have been given in Sec. III.) It is noted that the shape and magnitude of the triplet term is considerably different from the singlet term.

Referring back to expression (33) we observe that $\frac{1}{4}K\sigma_{\mathrm{DW}}(\theta)\Delta E_p$ is a constant for a given θ. Therefore, the quantity in the square bracket $\sum_{ij}g_{ij}^{(s)}+3N_{ts}\sum_{ij}g_{ij}^{(t)}$ as a function of E_p must be similar in shape to the histogram spectrum in Fig. 4. These functions are represented by the curves in Fig. 4 and indeed the agreement between the curves and the histograms is reasonable within statistics. This agreement lends credence to our description of the process in terms of final state interactions in the Watson-Migdal picture. The curves in Fig. 4 were calculated using a value of $N_{ts}=10$. This was a representative value and any value from $N_{ts}=1$ to $N_{ts}=20$ could fit the spectra quite well. For values of N_{ts} much larger than 20, the flat triplet distribution (Fig. 3) dominates and the calculated curves do not resemble the experimental distributions of Fig. 4. Effectively, the triplet state makes, at most, a small contribution to the spectra which are dominated by the singlet. It is possible, in principle, though difficult in practice, to calculate N_{ts}, a factor proportional to radial integrals involving the effective interaction $V_{pt}(r)$ and the proton-triton bound state wave function $W(r)$ for the triplet and singlet states. No attempt was made in this analysis to evaluate this.

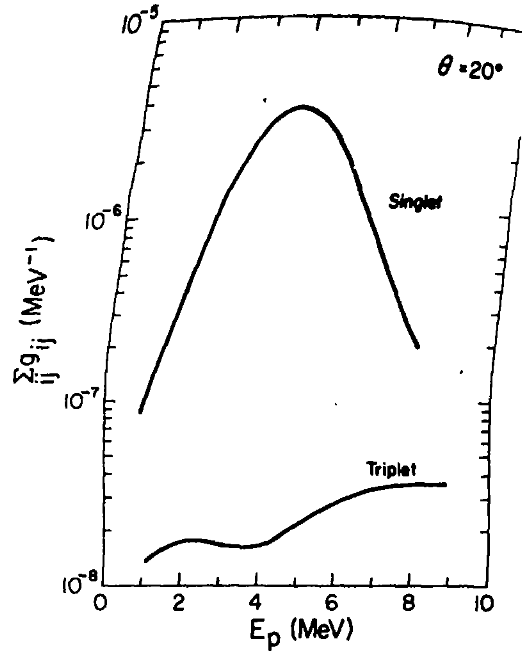

FIG. 5. The functions $\sum_{ij}g_{ij}$ for singlet and triplet states versus proton energy, at a laboratory scattering angle of α^*, $\theta=20°$.

Finally, we can define from Eq. (33),

$$\sigma_{\mathrm{DW}}(\theta)=\frac{\int_A^B dN\Delta E_p}{\frac{1}{4}K\int_A^B\sum_{ij}(g_{ij}^{(s)}+3N_{ts}g_{ij}^{(t)})\Delta E_p}$$

$$=\left[\frac{d\sigma(\theta)}{d\Omega}\right]_E\qquad(34)$$

and call $[d\sigma(\theta)/d\Omega]_E$ the "experimental differential ross section." This is the quantity we compare ith the DWBA cross section for the (p,α^*) reaction.

B. DWBA analysis

The transition amplitude for the (p,α) reaction in DWBA approximation is[25]

$$T_{DW}=\int d\vec{r}_{Ap}\int d\vec{r}_{B\alpha}\chi_\alpha^{*(-)}(\vec{k}_\alpha,\vec{r}_{B\alpha})\langle B\alpha|V_{pt}|Ap\rangle \times\chi_p^{(+)}(\vec{k}_p,\vec{r}_{Ap}). \quad (35)$$

The matrix element $\langle B\alpha|V_{pt}|Ap\rangle$ contains the radial form factor $F(\rho,R)$, where ρ is the separation between the incident proton and the center of mass of the transferred nucleon group and R is the separation between the residual nucleus and the same transferred nucleon group.

In the conventional cluster approach, the transferred nucleon group is treated as a triton cluster with no internal structure, the α particle being the bound state of the proton and triton and the target being the bound state of the triton and residual nucleus. The radial form factor is written as[26]

$$F(\rho,R)=U_{t_1}(R)V_{pt}(\rho)U_{t_2}(\rho), \quad (36)$$

where $U_{t_1}(R)$ is the radial bound state wave function of the triton-residual nuclear system, $V_{pt}(\rho)$ the effective interaction is an interaction potential between the proton and triton cluster, and $U_{t_2}(\rho)$ is the radial bound state wave function for the proton-triton system.

In the microscopic approach,[24,25] wave functions are calculated for each individual nucleon in the transferred group in a Woods-Saxon potential, and then combined to form the bound state wave function of the transferred cluster relative to the residual nucleus [corresponding to $U_{t_1}(R)$]. For the effective interaction, a Gaussian interaction of the form $V_0\exp(-\beta^2 r_{pi}^2)$ between the incident proton and each of the picked up ($i=1-3$) nucleons, is used. A microscopic wave function of the form $N_0\exp(-\eta^2\sum_{i<j=1}^4 r_{ij}^2)$ is used for the α particle [corresponding to $U_{t_2}(\rho)$]. Then[26]

$$F(\rho,R)=\sum_{nN}[e^{(-3\eta^2+\beta^2)\rho^2}\rho^n][a_{nN}R_{NL}(\nu_{c.m.},R)] \quad (37)$$

where R_{NL} is a radial harmonic oscillator wave function, $\nu_{c.m.}=[3(A-3)/A]\nu_{sm}$, $\nu_{sm}=0.392\ \text{fm}^{-2}$ being the nucleon shell model oscillator parameter, and a_{nN} are coefficients resulting from all the internal integrations in the construction of the form factor.

In the actual microscopic calculation, α and α^* wave functions of Hackenbroich *et al.*[34] were used. These are

$$\phi_\alpha=3.1854\times10^{-2}(e^{-0.0831r^2}+1.2656\times10^{-3}e^{-0.0311r^2}) \quad (38)$$

$$\phi_{\alpha^*}=2.2379\times10^{-2}(e^{-0.0831r^2}-8.1465\times10^{-4}e^{-0.0311r^2})$$

where $r^2=\sum_{i<j=1}^4 r_{ij}^2$, r_{ij} being the distance between i,j nucleons in the α particle. Since these wave functions are of the form $N_0(e^{-\eta_1^2r^2}+e^{-\eta_2^2r^2})$, rather than $N_0e^{-\eta^2r^2}$, the form factor becomes a sum of two terms of the type shown in Eq. (37). The range parameter for the Gaussian interaction was $1/\beta=1.47$ fm. The microscopic form factors $F(\rho,R)$ calculated for the (p,α) and (p,α^*) reactions are shown in Fig. 6.

The ρ dependence of the form factors is shown separately in Fig. 7 for a fixed value of $R=3.2$ fm. There is an extra node in the (p,α^*) form factor. The corresponding cluster quantity $V_{pt}(\rho)U_{t_2}(\rho)$ is also shown for comparison. All curves have been arbitrarily normalized at $\rho=0$ to the value of $F(\rho,R)$ for the microscopic calculation for (p,α).

In the form factor calculation for (p,α) and (p,α^*) reactions using the cluster transfer, the proton and triton were assumed to be bound in a $1s_{1/2}$ state with a separation energy of 19.82 MeV for the α particle and in a $2s_{1/2}$ state with an arbitrary small separation energy of 0.2 MeV for the α^* (actually unbound by 0.285 MeV). The geometrical parameters for the proton-triton bound state were taken from the optical model analysis of n-t scattering of Sherif and Podmore.[35] For the triton-^{9}B bound state, an $L=1$, $S=\frac{1}{2}$, $J=\frac{3}{2}$ configuration was assumed.

The DWBA cross sections $\sigma_{DW}(\theta)$ for the reactions were calculated with the computer code LOLA (Ref. 36). For the cluster calculation the

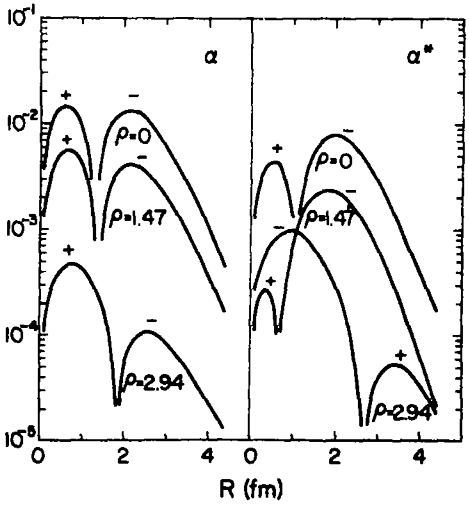

FIG. 6. Microscopic form factors $F(\rho,R)$ for $^{12}C(p,\alpha)^9B$ and $^{12}C(p,\alpha^*)^9B$ reactions.

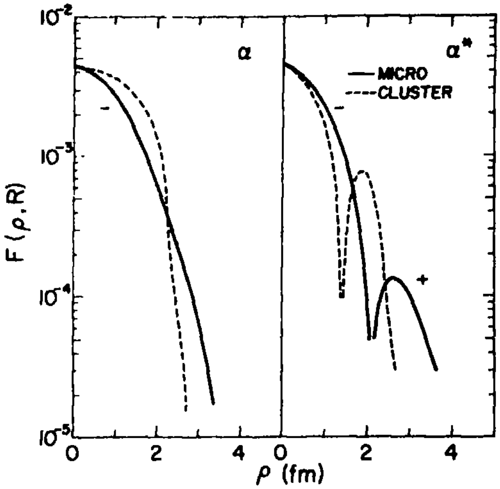

FIG. 7. The ρ dependence of $F(\rho, R)$ for $^{12}C(p, \alpha)^9B$ and $^{12}C(p, \alpha^*)^9B$ reactions. The solid and dashed curves are microscopic and cluster calculations respectively. The functions are plotted for a fixed value of $R = 3.2$ fm.

program was used as such and slight modifications were made to allow calculations with microscopic form factors. The optical model parameters for the distorted waves in the entrance and exit channel were taken from the $^{12}C(p, \alpha)^9B$ reaction study of Li and Hird.[29] In our experiment, the exit channel energies of the α and α^* were approximately 49 and 20 MeV. The Li-Hird parameters for the exit channel were obtained from fits to elastic scattering $^9Be(\alpha, \alpha)^9Be$ at $E_\alpha = 48$ MeV. So we also used an alternative set of parameters, due to Kuznetsov *et al.*,[37] in the exit channel obtained by fitting to $^9Be(\alpha, \alpha)^9Be$ at $E_\alpha = 26.6$ MeV. All parameters used in the calculations are summarized in Table I.

V. RESULTS AND DISCUSSIONS

The experimental cross sections and the DWBA calculations $[d\sigma(\theta)/d\Omega]_{DW}$ [formerly called $\sigma_{DW}(\theta)$] for the $^{12}C(p, \alpha)^9B(g.s.)$ and $^{12}C(p, \alpha^*)^9B(g.s.)$ reactions are shown in Fig. 8. For the (p, α^*) reaction, the experimental $[d\sigma(\theta)/d\Omega]_E$ is as defined in Eq. (34). The errors are due to counting statistics. The solid lines represent DWBA cross sections with microscopic form factors and the dashed lines are cluster calculations, both using Li-Hird parameters. The dashed-dotted line represents microscopic DWBA calculations for (p, α^*) with Kuznetsov[37] optical model parameters in the exit channel. The shape of angular distributions calculated from the two different form factors generally follow the trend of the data and both calculations perform comparably in the description of the shape of the angular distribution. The microscopic calculations with Li-Hird and Kuznetsov parameters yield comparable fits to the (p, α^*) distribution within the accuracy of our data. A calculation for (p, α) distributions using Kuznetsov parameters produced a rather worse fit and is not shown.

It was mentioned in the Introduction that the absolute normalization of the reaction is difficult to determine in the microscopic form factor approach. We therefore determined only the relative normalization between the (p, α^*) and (p, α) cross section distribution as a test of our theoretical description. We define,

$$\frac{\left\{\left[\frac{d\sigma(\theta)}{d\Omega}\right]_E \Big/ \left[\frac{d\sigma(\theta)}{d\Omega}\right]_{DW}\right\}^{(p,\alpha^*)}}{\left\{\left[\frac{d\sigma(\theta)}{d\Omega}\right]_E \Big/ \left[\frac{d\sigma(\theta)}{d\Omega}\right]_{DW}\right\}^{(p,\alpha)}} = N_{\alpha^*\alpha} \,. \tag{39}$$

TABLE I. Optical model and form factor parameters.

		Channel	V_0 (MeV)	R_0 (fm)	a_0 (fm)	W_V (MeV)	R_W (fm)	a_W (fm)	R_C (fm)
		$^{12}C + p$ Ref. 29	37.6	1.18	0.7	5.2	1.4	0.7	1.25
Optical parameters	Li-Hird	$^9B + \alpha$ Ref. 29	207.1	1.55	0.48	26.98	1.55	0.48	1.25
	Kuznetsov	$^9B + \alpha$ Ref. 37	175	1.37	0.57	15	1.5	0.6	1.25

	Channel	Separation energy (MeV)	R_0 (fm)	a_0 (fm)	V_{so} (MeV)	R_{so} (fm)	a_{so} (fm)
Cluster form factor	$^9B + t$	27.37	1.3	0.3			
	$p + t$	19.82	0.879	0.144			
Microscopic form factor	$^{11}C + n$ $^{11}B + p$	9.12	1.04	0.563	7.5	0.98	0.45

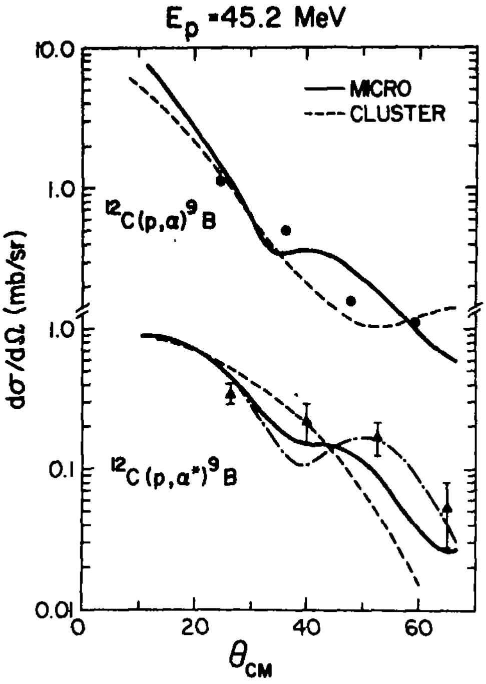

FIG. 8. Experimental differential cross section angular distributions for $^{12}C(p,\alpha)^9B$ and $^{12}C(p,\alpha^*)^9B$ reactions. The solid and dashed curves are DWBA calculations with microscopic and cluster form factors, respectively, both using Li-Hird parameters. The dashed-dotted curve is the microscopic DWBA calculation for (p,α^*) using Kuznetsov parameters. Each curve has been separately normalized to the data.

The value of $N_{\alpha^*\alpha}$ deduced from the current analysis for the calculations with Li-Hird parameters is 2.1 compared to the value of unity expected for a consistent theoretical description of the two reactions. This value corresponds to our choice of N_{ts}, the triplet to singlet cross section ratio [see Eq. (28)], to be equal to 10. As mentioned before, a range of values of N_{ts} fits the distribution shown in Fig. 4. This uncertainty in the value of N_{ts} affects the magnitude of $(d\sigma(\theta)/d\Omega)_F$ for (p,α^*) [in Eq. (34)], and therefore the normalization for the (p,α^*) cross section. However, the effect is not large; the uncertainty in the relative normalization factor $N_{\alpha^*\alpha}$ caused by a variation of N_{ts} from 1 to 20 is estimated at only 30%. Considering the widely different methods of description of the (p,α^*) and (p,α) reactions employed in our analysis and the approximate nature of the Watson model in evaluating three body final state effects, the value of $N_{\alpha^*\alpha} = 2.1 \pm 0.63$ represents good agreement between theory and experiment.

The normalization factor is also affected by the choice of optical parameters. If one chooses the Li-Hard calculation for (p,α) distribution and the Kuznetsov calculation for (p,α^*) distribution, the mean $N_{\alpha^*\alpha}$ has the rather gratifying value of 1.0. If Kuznetsov calculations are chosen for both (p,α) and (p,α^*) angular distributions, this factor comes out to be 1.5. This range of variation within factors of 2, for different optical model parameters, is acceptable. The more fundamental question of describing the α^* elastic scattering by α-particle optical model parameters is not answered by the above discussions.

The relative normalization factor $N_{\alpha^*\alpha}$ was similarly determined for the cluster calculations with Li-Hird parameters and was found to be 0.23. Since the proton-triton wave function was calculated as a single particle state, this number should be corrected by putting in the spectroscopic factors of α^* and α for $(p+t)$. In a simple model of $\alpha = p+t$, $S_\alpha = 2$. S_α^* was calculated from

$$S_\alpha^* = \frac{(\gamma_\lambda{}^2)_{\text{exp}}}{(\hbar^2/2ma^2)af_\lambda{}^2(a)}\,, \tag{40}$$

with $(\gamma_\lambda{}^2)_{\text{exp}} = 4.2$ MeV and channel radius $a = 3.0$ fm, obtained from Ref. 17. The radial part of the α^* wave function at $r = a$, $f_\lambda(a)/a$ was obtained from the LOLA cluster calculation. This yielded a value of $S_\alpha^* = 2.97$. Hence putting in $S_\alpha^*/S_\alpha \approx 1.5$, the corrected value of $N_{\alpha^*\alpha}$ for the cluster calculation, to be compared with the microscopic calculation was 0.15 ± 0.05. The error is due to the same reason as described for the microscopic calculation.

The microscopic form factor calculation would thus appear to give a much better description of the reaction than the cluster calculation. However, the latter calculation may not give the right result for two reasons. First, a bound state form factor was used for the α^* state which is actually unbound. A better method would be to perform the calculations for various binding energies and then extrapolate it to the unbound energy region. Second, the geometrical parameters for the Woods-Saxon well for the $p+t$ bound state (Table I) was chosen to be the same as those used for the α-particle $(p+t)$ bound state. This may introduce errors in the final result.

In conclusion, the microscopic description of the (p,α^*) reaction with three body final state effects yields good agreement with observations in the limited range of our experiment. Future investigation on other targets and over large angular and energy ranges should prove valuable in further testing of these models. Full three body reaction effects, inclusion of the Coulomb force in the two body potentials, and coupled-channels effects due to the neutron-^{3}He threshold near the α^* state are some aspects that should be investigated in more complete attempts at a description of the (p,α^*) reaction.

This work was supported in part by the Natural Sciences and Engineering Research Council of Canada.

---

*Present address: TRIUMF, University of British Columbia, Vancouver, B.C. V6T 1W5, Canada.

[1] D. Robson, Nucl. Phys. A204, 523 (1973).

[2] B. L. Cohen, E. C. May, and T. M. O'Keefe, Phys. Rev. 179, 962 (1969).

[3] B. L. Cohen, E. C. May, and T. M. O'Keefe, Phys. Rev. Lett. 18, 962 (1967).

[4] K. Nagatani, Phys. Lett. 27B, 187 (1968).

[5] W. Bohne, M. Hagen, H. Homeyer, H. Lettau, K. H. Maier, H. Morgenstern, and J. Schoer, Phys. Rev. Lett. 24, 1028 (1970).

[6] U. Janetzki, Q. K. K. Liu, D. Hahn, H. Homeyer, and J. Schoer, Nucl. Phys. A267, 285 (1976).

[7] G. Chenevert, N. S. Chant, I. Halpern, C. Glashausser, and D. L. Hendrie, Phys. Rev. Lett. 27, 434 (1971).

[8] W. S. Pong and N. Austern, Nucl. Phys. A221, 221 (1974).

[9] A. Saha, R. Kamermans, J. van Driel, and H. P. Morsch, Phys. Lett. 79B, 363 (1978).

[10] D. R. Brown, J. M. Moss, C. M. Rozsa, D. H. Youngblood, and J. D. Bronson, Nucl. Phys. A313, 157 (1979).

[11] N. E. Davison, Gh. Gregoire, Th. Delbar, K. Grotowski, and S. K. Datta (unpublished).

[12] R. Jahn, G. J. Wozniak, D. P. Stahel, and J. Cerny, Phys. Rev. Lett. 37, 812 (1976).

[13] R. Jahn, D. P. Stahel, G. J. Wozniak, R. J. de Meijer, and J. Cerny, Phys. Rev. C 18, 9 (1978).

[14] R. Jahn, D. P. Stahel, G. J. Wozniak, and J. Cerny, Phys. Lett 65B, 339 (1976).

[15] R. Kamermans, H. P. Morsch, R. J. de Meijer, and J. van Driel, Nucl. Phys. A314, 37 (1979).

[16] H. W. Lefevre, R. R. Borchers, and C. H. Poppe, Phys. Rev. 128, 1328 (1962).

[17] C. Werntz, Phys. Rev. 128, 1336 (1962).

[18] N. Jarmie, M. G. Silbert, D. B. Smith, and J. S. Loos, Phys. Rev. 130, 1987 (1963).

[19] C. Werntz, Phys. Rev. 133, B19 (1964).

[20] W. E. Meyerhof and J. N. McElearney, Nucl. Phys. 74, 533 (1965).

[21] W. E. Meyerhof, Rev. Mod. Phys. 37, 512 (1965).

[22] D. U. L. Yu and W. E. Meyerhof, Nucl. Phys. 80, 481 (1966).

[23] S. Fiarman and W. E. Meyerhof, Nucl. Phys. A206, 1 (1973).

[24] W. R. Falk, A. Djaloeis, and D. Ingham, Nucl. Phys. A252, 452 (1975).

[25] W. R. Falk, R. Abegg, and S. K. Datta, Nucl. Phys. A334, 445 (1980).

[26] N. Austern, R. M. Drisko, E. C. Halbert, and G. R. Satchler, Phys. Rev. 133, B3 (1964).

[27] K. M. Watson, Phys. Rev. 88, 1163 (1952).

[28] A. B. Migdal, Zh. Eksp. Teor. Fiz. 28, 3 (1955). [Sov. Phys.—JETP 1, 2 (1955)].

[29] T. Y. Li and B. Hird, Phys. Rev. 174, 1130 (1968).

[30] J. Gillespie, *Final State Interaction* (Holden-Day, San Francisco, 1964), p. 5.

[31] R. J. Slobodrian, Rep. Prog. Phys. 34, 175 (1971).

[32] A. M. Lane and R. G. Thomas, Rev. Mod. Phys. 30, 257 (1958).

[33] G. G. Ohlsen, Nucl. Instrum. Methods 37, 240 (1965).

[34] H. H. Hackenbroich, T. H. Seligman, and W. Zahn, Nucl. Phys. A259, 445 (1976). Note that the values of $\bar{\alpha}_1$ and $\bar{\alpha}_2$ given in this reference are in error by a factor of 4.

[35] H. S. Sherif and B. S. Podmore, in *Proceedings of the International Conference on Few Particle Problems*, edited by I. Slaus, S. A. Moszowski, R. P. Haddock, and W. T. H. van Oers (North-Holland, Amsterdam, 1972), p. 691.

[36] R. M. Devries, Computer Code LOLA, University of Rochester (unpublished).

[37] B. I. Kuznetsov and I. P. Chernov, Yad. Fiz. 20, 632 (1974) [Sov. J. Nucl. Phys. 20, 340 (1975)].

PHYSICAL REVIEW C VOLUME 21, NUMBER 5 MAY 1980

Photoneutron studies of $E1$, $M1$, and $E2$ excitations in ^{13}C

R. J. Holt, R. M. Laszewski,* H. E. Jackson, J. E. Monahan, and J. R. Specht
Argonne National Laboratory, Argonne, Illinois 60439

(Received 26 November 1979)

The angular distribution for the ^{13}C$(\gamma,n_0)^{12}$C reaction was observed in the energy region 6.5 to 9.3 MeV and at angles of 90° and 135°. The photoneutron measurements were analyzed in terms of a multilevel R-matrix formalism. The ^{12}C$(n,n)^{12}$C reaction channel was explicitly included in this analysis. The effects of potential capture were directly observed in the photoneutron spectra. The ground-state radiative widths for resonances in this energy region were deduced from the R-matrix interpretation of the results. The ground-state transition probabilities for $E1$ excitations at 7.69 and 8.19 MeV were found to be in good agreement with the predictions of the weak-coupling model.

[NUCLEAR REACTIONS ^{13}C$(\gamma,n_0)^{12}$C, $E_{\text{exc}} = 6.5-9.3$ MeV, measured $\sigma(\theta)$, $\theta = 90°, 135°$; deduced $\Gamma_{\gamma 0}$.]

I. INTRODUCTION

There have been numerous theoretical and experimental studies of low-lying levels in ^{13}C. The theoretical studies fall into two broad categories, the weak-coupling approach[1] and the more detailed shell-model calculations. The weak-coupling model[2-4] has been successful in describing the essential features of the ^{12}C$(n,n)^{12}$C reaction below a neutron energy of 5 MeV. The most notable of these calculations is the work of Lovas,[2] who used the Feshbach formalism and Reynolds *et al.*,[3] who used the coupled-channel approach of Tamura.[5] In fact, Reynolds *et al.* provided a detailed description of both the observed cross sections and polarizations in the ^{12}C$+n$ system. Unfortunately, the studies of electromagnetic transition rates in the mass 13 system have not been as successful. These transition matrix elements have been computed using bound-state shell-model wave functions. Barker[6] used a weak-coupling approach, while Jäger *et al.*[7] took into account all 1 $\hbar\omega$ configurations. Kissener *et al.*[8] improved upon the work of Jäger *et al.* by incorporating into the bound-state calculation an R-matrix theory to account for nuclear decay. Of course, the most detailed calculation in the 1-p shell nuclei is that of Cohen and Kurath.[9] These models differ rather markedly on predictions of the strengths of low-lying $E1$ excitations. For example, for the 8.19-MeV $E1$ excitation in ^{13}C, the weak-coupling model[6] predicts a value which is an order of magnitude greater than that of the full shell-model calculations.[7]

Although there have been numerous experimental studies[10-13] of the ^{13}C$(\gamma,n)^{12}$C reaction, the values of the ground-state radiative widths for the $E1$ excitations at 7.69 and 8.19 MeV remain uncertain. The difficulties in extracting $\Gamma_{\gamma 0}$, unambiguously, in ^{13}C arise from the effects of large direct photoneutron reaction processes and a strong level-level interference. Moreover, these strong interference effects have led to the questionable speculation that there is a new resonance[12] in ^{13}C at 7.88 MeV.

Consequently, we observed the ^{13}C$(\gamma,n_0)^{12}$C cross section with high resolution in the photon energy range 6.5 to 9.3 MeV and at angles of 90° and 135°. The results were interpreted in terms of a multilevel R-matrix analysis which was developed specifically for photoneutron studies. The (n,n) reaction channel was explicitly included in the analysis so that the ^{12}C$(n,n)^{12}$C reaction was simultaneously described. The ground-state radiative widths for the $E2$ excitation at 7.56 MeV, the $E1$ resonances at 7.69 and 8.19 MeV, and the $M1$ resonance at 8.89 MeV were deduced from the analysis. It was found that the $E1$ excitations are reproduced remarkably well by the weak-coupling model.

II. EXPERIMENTAL METHOD

The differential cross section for the ^{13}C$(\gamma,n_0)^{12}$C reaction was measured using the photoneutron facility at the Argonne high-current electron Linac. The operating mode of the Linac was selected to produce 10.0-MeV electron bursts of 35-ps duration, 200-A peak current, and at a rate of 800 Hz. The electron pulses were converted to bremsstrahlung in a 0.15-cm thick Ag foil. The ^{13}C sample (90.7% enrichment) was irradiated with bremsstrahlung. The sample was in the form of powder and encased in a rectangular, thin-walled (0.8 mm

© 1980 The American Physical Society

thick) Al holder of dimensions: 5.0-cm along the photon beam axis × 1.0-cm thick × 4.0-cm high. The photoneutrons traveled through two 11-m flight paths which were at angles of 90° and 135° with respect to the electron beam axis. The neutron energies were determined with high resolution (9.5 keV at $E_n = 1.5$ MeV and 34 keV at 4.0 MeV) using the time-of-flight method. The neutrons were detected in 2.5-cm thick NE110 plastic scintillation counters. The differential cross section was determined relative to the well-known cross section for the photodisintegration of the deuteron. The final cross sections are shown as the points in Fig. 1. The main features of the spectra are (1) a relatively large nonresonant cross section, (2) well-defined resonances at 7.56 and 8.89 MeV, and (3) a strong level-level interference pattern near 7.9 MeV. Except for the narrow resonance at 7.56 MeV, which was barely visible in the early photoneutron work,[10-13] the present observation at 90° is in excellent agreement with the previous measurements. Background effects were estimated by replacing the ^{13}C target with an identical ^{12}C sample. The background was found in this way to be < 10% of the foreground at all energies. Since the first excited state in ^{12}C occurs at 4.44 MeV, there is no ambiguity associated with nonground-state neutron transitions in this work.

III. PHOTONEUTRON PROCESSES IN ^{13}C

The photoexcitation processes of ^{13}C are summarized in Fig. 2. An $E1$ photon can excite $\frac{1}{2}^+$ or $\frac{3}{2}^+$ resonances in ^{13}C. These levels subsequently decay by emitting an $s_{1/2}$ or $d_{3/2}$ neutron, respectively. An $M1$ photon excites $\frac{1}{2}^-$ or $\frac{3}{2}^-$ resonances which decay to the ground state of ^{12}C by $p_{1/2}$ or $p_{3/2}$ neutrons. $E2$ photoexcitations are $\frac{3}{2}^-$ or $\frac{5}{2}^-$ and decay by $p_{3/2}$ or $f_{5/2}$ neutrons. All of these photoexcitation processes are explicitly included in the analysis. No multipolarities of order higher than $E2$ were considered. This restriction simplifies the analysis since the $d_{5/2}$ and $f_{7/2}$ neutron channels are ruled out. We note that the well-known $E_n = 2.08$-MeV, $\frac{5}{2}^+$ resonance is absent from the present data since it would require an $E3$ or $M2$ photoexcitation. In the energy region of the present work, there are no known $\frac{1}{2}^+$ or $\frac{3}{2}^-$ resonances. However, the nonresonant components of the $s_{1/2}$ and $p_{3/2}$ amplitudes were retained in the analysis. The expression for the photoneutron differential cross section was determined from the table of Carr and Baglin[14]:

$$\begin{aligned}\frac{d\sigma}{d\Omega} = \frac{\lambda_\gamma^2}{16}\Big(&[2|U_{s_{1/2}}|^2+2|U_{p_{1/2}}|^2+4|U_{p_{3/2}}(M1)|^2+4|U_{p_{3/2}}(E2)|^2+4|U_{d_{3/2}}|^2+6|U_{f_{5/2}}|^2]\\ &+\{U^*_{s_{1/2}}[4U_{p_{3/2}}(M1)-4U_{p_{1/2}}+6.928U_{p_{3/2}}(E2)]+U^*_{d_{3/2}}[4U_{p_{1/2}}-4U_{p_{3/2}}(M1)+1.386U_{p_{3/2}}(E2)+12.471U_{f_{5/2}}]\}\\ &\times P_1(\cos\theta)\\ &+\{-2|U_{d_{3/2}}|^2+U^*_{p_{3/2}}(M1)[-2U_{p_{3/2}}(M1)+6.928U_{p_{3/2}}(E2)-6.928U_{f_{5/2}}]\\ &\quad+U^*_{p_{1/2}}[-4U_{p_{3/2}}(M1)-6.928U_{p_{3/2}}(E2)+6.928U_{f_{5/2}}]+U^*_{p_{3/2}}(E2)[2U_{p_{3/2}}(E2)+1.714U_{f_{5/2}}]\\ &\quad+3.429|U_{f_{5/2}}|^2-4U^*_{s_{1/2}}U_{d_{3/2}}\}P_2(\cos\theta)\\ &+\{U^*_{d_{3/2}}[-5.543U_{f_{5/2}}-8.314U_{p_{3/2}}(E2)]-6.928U^*_{s_{1/2}}U_{f_{5/2}}\}P_3(\cos\theta)\\ &+[-3.429|U_{f_{5/2}}|^2-13.714U^*_{p_{3/2}}(E2)U_{f_{5/2}}]P_4(\cos\theta)\Big),\end{aligned} \tag{1}$$

where $U_{lJ}(\mathfrak{M}\mathcal{L})$ are the collision matrix elements for the (γ, n) channel. These matrix elements will be described in the following section.

IV. THE R-MATRIX ANALYSIS

The application of the R-matrix theory to photoneutron reactions was discussed in detail in Ref. 15. Only the elements essential to the present analysis will be discussed here. From Ref. 15, the collision matrix for the photoneutron reaction is given by

$$U_{\gamma n}^{(lJ\mathcal{L})} = -ie^{-i\phi_l}\sum_{\lambda\mu} A_{\lambda\mu}\Gamma_{\lambda lJ}^{1/2}\Gamma_{\mu\gamma_f lJ}^{1/2} + \left(\frac{8\pi(\mathcal{L}+1)}{\mathcal{L}\hbar v_n}\right)^{1/2}\frac{k_\gamma^{\mathcal{L}+1/2}}{(2\mathcal{L}+1)!!}(2J+1)^{-1/2}\langle\Psi_{f(J_f)}||H^{\mathcal{L}}||(I_l-e^{2i\phi_l}O_l)\varphi_{lJ}\rangle, \tag{2}$$

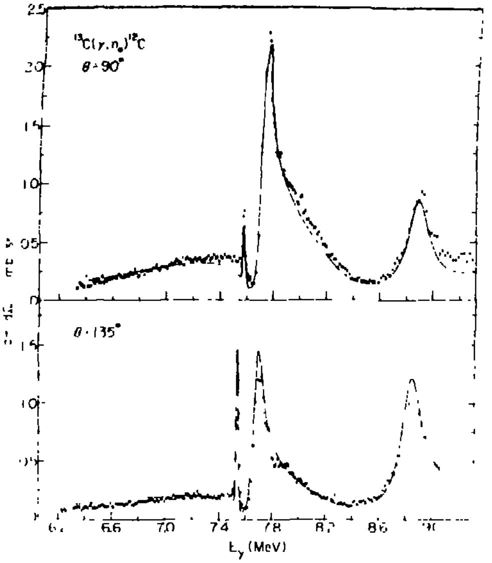

FIG. 1. High-resolution spectra for the $^{13}C(\gamma,n_0)^{12}C$ reaction at angles of 90° and 135°. The curves represent the results of an R-matrix analysis of the data.

where J is the spin of the excited state and J_f is the ground-state spin of ^{13}C in this case. The first term of Eq. (2) is due to internal capture or that component that arises from capture inside the channel radius. The second term is due to external capture. Outside the channel radius, the initial neutron-nucleus state is described by the scattering wave function. $H^{\mathfrak{L}}$ is the electromagnetic operator for either $E1$, $M1$, or $E2$ radiation in the present case. The contribution from the external capture term is due to the long-range nature of the electromagnetic interaction. The δ_{lJ} are the phase shifts which describe the neutron-nucleus scattering. Since only the photon and neutron channels are open in this energy range and since the neutron scattering cross section is $\gtrsim 10^3$ times greater than the photoneutron cross section, then Eq. (2) provides a complete representation of the photoneutron reaction.

The phase shifts were parametrized in terms of the R-function R_{lJ} in the following manner

$$\delta_{lJ}=-\phi_l+\tan^{-1}\{P_l R_{lJ}/[1-R_{lJ}(S_l-b_{lJ})]\},$$

where ϕ_l, S_l, P_l, and b_{lJ} are the hard-sphere phase shifts, shift factors, penetration factors, and boundary condition constants, respectively. The R function is given by

$$R_{lJ}=\sum_{\lambda}\frac{\gamma_{\lambda lJ}^2}{E_{\lambda lJ}-E}+R_{0lJ}+R_{1lJ}E\,,$$

where the last two terms describe the contributions from distant levels and $\gamma_{\lambda lJ}^2$ are the reduced widths. The most recent set of R-function parameters[16] were used in the present analysis.. The results of this R-function analysis of Ref. 16 are in excellent agreement with the total cross section, angular distributions, and neutron polarizations below a neutron energy of 4 MeV. These parameters are summarized in Table I. The final state wave function $\Psi_{f(J_f)}$ in Eq. (2) was taken to be a Whittaker function

$$\Psi_{f(J_f)}=\left(\frac{2}{R}\right)^{1/2}\theta_{fc_f}\frac{W_{c_f}(k_f r)}{W_{c_f}(k_f R)}\,\varphi_c(J_f,M_f)\,,$$

where θ_{fc_f} is the reduced width of Lane and Thomas[17]

$$\theta_{fc_f}=\gamma_{fc_f}/(\hbar^2/MR^2)^{1/2}$$

and k_f is the wave number corresponding to the binding energy of the neutron in ^{13}C. The $\theta_{1/2^-}$ was adjusted in order to fit the observed photoneutron cross section. This quantity is defined by the amount of nonresonant potential capture in the $^{13}C(\gamma,n_0)^{12}C$ reaction.

We now focus attention on the internal capture

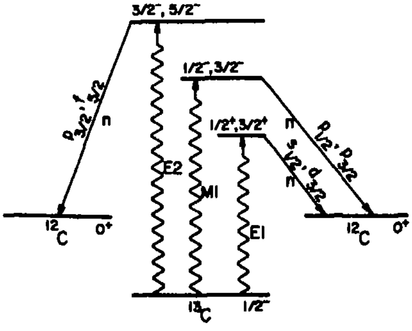

FIG. 2. Photoneutron processes in ^{13}C. The labels l_J on the neutron decay branch refer to the orbital angular momenta and total spins of the neutrons relative to the ^{12}C nucleus.

TABLE I. R-function parameters for the $^{12}C(n,n)^{12}C$ reaction and the present analysis. [Note that the $d_{5/2}$ and $f_{7/2}$ parameters are not necessary for the (γ,n) channel.] Channel radius, $R=4.61$ fm.

l_J	$E_{\lambda lJ}$ (MeV)	$\gamma_{\lambda lJ}^2$ (MeV)	R_{0lJ}	R_{1lJ} (MeV^{-1})	b_{lJ}
$s_{1/2}$	−1.887	0.666	0.0245	0.0	0.0
$p_{1/2}$	4.20	0.080	0.09	0.05	−0.2
$p_{3/2}$	−1.267	0.050	0.261	0.05	−0.18
	4.940	0.010			
$d_{3/2}$	2.930	0.165	0.250	0.0	−1.0
	3.510	0.968			
$f_{5/2}$	2.810	0.006	0.0	0.0	−1.3

component in Eq. (2). The $\Gamma_{\lambda l J}$ and $\Gamma_{\mu\gamma_f l J}$ are the neutron width and internal capture width, respectively. $A_{\lambda\mu}$ is the transformation which relates the internal wave function to the real wave function for a given resonance.

$$(A^{-1})_{\lambda\mu}=(E_{\gamma\lambda}-E)\delta_{\lambda\mu}-\xi_{\lambda\mu}\,,$$

where

$$\xi_{\lambda\mu}^{lJ}=\sum_{c}\left[(S_{l,c}-b_{lJ,c})+iP_{l,c}\right]\gamma_{\lambda lJ,c}\gamma_{\mu lJ,c}$$

and the sum is taken over all reaction channels. The internal capture widths were determined by a least-squares fit to the data. The R-matrix analysis is compared with the observed differential cross section in Fig. 1. The data are well described by the R-matrix interpretation. The deduced parameters are given in Table II. The width for the $\frac{5}{2}^-$ level was chosen to be approximately $\frac{1}{10}$ of the energy resolution of the time-of-flight spectrometer. The width of this level is known[18] to be small and without question smaller than 2 keV. However, for the present work we wish to extract the ground-state radiative width $\Gamma_{\gamma 0}$ and no error is introduced by this arbitrary choice as long as it is much smaller than the resolution function. In order to obtain the curves in Fig. 1, a triangular resolution function was folded in with the R-matrix calculation. This resolution function has a large effect upon the 7.56 MeV resonance. The effect of the resolution broadening is insignificant for the remaining spectrum.

The parameters that were allowed to vary in the present analysis were the $(\Gamma_{n\lambda})^{1/2}$, $(\Gamma_{\gamma_f\lambda})^{1/2}$, and $\theta_{1/2^-}$. Although, in principle, the magnitude of $(\Gamma_{n\lambda})^{1/2}$ can be determined from the reduced widths in Table I, a better fit was obtained by allowing them to vary. In Table III these widths are compared with those obtained from R-function analyses[16,19] of neutron elastic scattering. The neutron widths were deduced from the reduced widths with the following expression

$$\Gamma_{n\lambda}=2P_l(k_R R)\gamma_{\lambda n}^{2}\,,$$

where P_l is the penetration factor and k_R is the neutron wave number evaluated at the resonance energy. The widths for the $d_{3/2}$ resonances are in good agreement with the present work. However, the width of the $p_{1/2}$ level from Ref. 16 seems rather broad. Our result is in better agreement with the Yale R-function analysis[19] for that resonance. One possible explanation for this disagreement is that the R-function analysis of Ref. 16 was performed primarily for angular distribution data for the ^{12}C$(n,n)^{12}$C reaction below $E_n=4$ MeV, whereas that of Ref. 19 and the present work extended to approximately 5 MeV.

TABLE II. R-matrix parameters for ^{13}C$(\gamma,n_0)^{12}$C reaction: $R=4.61$ fm, $\theta_{1/2^-}=-0.524$.

$\mathfrak{ML}$	J^π	$E_{\gamma\lambda}$ (MeV)	$(\Gamma_{n\lambda})^{1/2}$ (MeV)$^{1/2}$	$(\Gamma_{\gamma f\lambda})^{1/2}$ (eV)$^{1/2}$
$E2$	$\frac{5}{2}^-$	7.534	0.045[a]	0.346
$E1$	$\frac{3}{2}^+$	7.636	0.412	2.068
$E1$	$\frac{3}{2}^+$	8.151	1.053	1.664
$M1$	$\frac{1}{2}^-$	8.861	0.412	−2.258
$E1$	$\frac{1}{2}^+$	11.000[b]	1.414	−2.966
$E1$	$\frac{3}{2}^+$	11.000[b]	1.414	−2.280

[a] This width was chosen to be 0.1 of the energy resolution spread at this energy.

[b] These resonances were arbitrarily placed here in order to account for the effects of distant levels.

TABLE III. Comparison of the values of Γ_n deduced from the present analysis with those from R-function analyses of elastic n-^{12}C scattering results.

E_γ (MeV)	J^π	Γ_n(MeV) Yale	ANL	Present work
7.69	$\frac{3}{2}^+$	0.15	0.15	0.17
8.19	$\frac{3}{2}^+$	1.11	1.15	1.11
8.89	$\frac{1}{2}^-$	0.20	0.24	0.17

V. RESULTS AND DISCUSSION

The collision matrix, Eq. (2), can be written in an equivalent manner in the level representation[15]

$$U_{\gamma n}^{(lJ\mathfrak{L})}=-ie^{-i\phi_l}\sum_{\gamma\mu}A_{\lambda\mu}\Gamma_{\lambda n}{}^{1/2}\left[\Gamma_{\mu\gamma}{}^{1/2}+(\delta\Gamma_{\mu\gamma})^{1/2}\right]$$

$$+U_{\gamma n}(\mathrm{HS})\,,$$

where $U_{\gamma n}$(HS) is the hard-sphere capture component. From the above expression it is clear that ground-state radiative widths depend upon both the internal capture width and the resonant component of external capture or the channel capture width $\delta\Gamma_{\gamma f}$. The amplitude for channel capture is given by the expression

$$(\delta\Gamma_{\gamma f})^{1/2}=\left[\frac{8\pi(\mathfrak{L}+1)}{\mathfrak{L}\hbar v_n}\right]^{1/2}\frac{k_\gamma^{\mathfrak{L}+1/2}}{(2\mathfrak{L}+1)!!}$$

$$\times\; e^{-i\phi_l}(2J+1)^{-1/2}$$

$$\times\;\Gamma_{\gamma n}{}^{1/2}\langle\Psi_{1/2^-}\|H^{(\mathfrak{L})}\|O_l\varphi_{l(J)}\rangle\,.$$

The way in which the integral in the above equation

TABLE IV. Deduced ground-state radiative widths for the $^{13}C(\gamma,n_0)^{12}C$ reaction.

E_γ (MeV)	$\mathfrak{M}\mathfrak{L}$	J^π	$\Gamma_{\gamma 0}$ (eV) Present work	Darmstadt
7.56	$E2$	$\frac{5}{2}^-$	0.11 ± 0.015	0.1150 ± 0.0062
7.69	$E1$	$\frac{3}{2}^+$	0.6 ± 0.1	
8.19	$E1$	$\frac{3}{2}^+$	7.0 ± 0.9	
8.89	$M1$	$\frac{1}{2}^-$	5.4 ± 0.5	3.36 ± 0.46

is computed was given in the Appendix of Ref. 15 and will not be discussed further. Then $\Gamma_{\gamma 0}$ is given by

$$\Gamma_{\gamma 0} \equiv \left| \Gamma_{\gamma f}^{1/2} + (\delta\Gamma_{\gamma f})^{1/2} \right|^2 .$$

This $\Gamma_{\gamma 0}$ is the quantity[20] that would be determined from a traditional area analysis of the data, i.e., this $\Gamma_{\gamma 0}$ governs the peak height of the resonance in the (γ,n) cross section. The final results are given in Table IV. For the 7.56-MeV, $E2$ excitation, we have extremely good agreement with the inelastic electron scattering results.[21] However, for the 8.89-MeV $M1$ excitation, the results of the present experiment disagree with the Darmstadt value[21] for the $M1$ component of the transition strength. The errors in our experimental values of $\Gamma_{\gamma 0}$ were estimated by taking extreme cases for the effects of distant levels in the (γ,n) channel. In addition, we fixed the Darmstadt value for $\Gamma_{\gamma 0}$ for the $M1$ excitation in our analysis and readjusted all the other parameters. We found no combination of the other parameters that would give a reasonable fit to the photoneutron cross sections. The origin of this discrepancy remains unknown. However, in the inelastic electron scattering process, the $\frac{1}{2}^-$ resonance can be excited by both $E0$ and $M1$ transitions. Unfortunately, in Ref. 21 there was no discussion of the method for unraveling the $M1$ radiative width from the $E0$ transition rate.

The deduced $\Gamma_{\gamma 0}$ are compared with theoretical predictions in Table V. The results for the $E1$ excitations are in remarkably good agreement with the early calculations of Barker[6] and in disagreement with the recent shell-model calculations of Jäger *et al.*[7] and Kissener *et al.*[8] Kurath[22] predicted the total strength for these two resonances and the results are in fair agreement with the present measurement. The Cohen-Kurath results overestimate the $M1$ transition rate for the 8.89-MeV resonance, but they are in fair agreement with the $E2$ transition.

It is surprising that the more detailed models underestimate the amount of $E1$ strength in the 7.69- and 8.19-MeV resonances. This present work provides additional evidence that the essential features of these resonances can be explained in terms of the weak-coupling model. This result was suggested in the work of Fukuda,[11] but the observed strength for the lower energy resonance was more than five times greater than the present observation. Of course, this is the magnitude of discrepancy one would expect from a traditional area analysis of these strongly interfering resonances.

It is noteworthy that the Lane reduced width for $^{12}C+n$, $\theta_{1/2^-} = -0.524$, is near the value obtained[18] for $^{16}O+n$, $\theta_{5/2^+} = -0.59$. This implies that ^{13}C is nearly as well represented as a ^{12}C core plus a neutron as ^{17}O can be described by a ^{16}O core and a neutron.

VI. CONCLUSIONS

The differential cross section for the $^{13}C(\gamma,n_0)^{12}C$ reaction was measured with high resolution throughout the photon energy range 6.5 to 9.3 MeV. These results were interpreted in terms of a multilevel, multichannel R-matrix analysis and the ground-state widths were extracted. The $\Gamma_{\gamma 0}$ of the $E2$ resonance at 7.56 MeV was found to agree well with the inelastic electron scattering results, while that of the $M1$ resonance at 8.89 MeV does not agree. The radiative widths for the two strongly interfering $E1$ excitations at 7.69 and 8.19 MeV were found to be in excellent agreement

TABLE V. Comparison of the deduced internal capture widths with theoretical predictions.

E_γ (MeV)	$\mathfrak{M}\mathfrak{L}$	$\Gamma_{\gamma 0}$ (eV) Present experiment	Barker	Jäger *et al.*	Kissener *et al.*	Kurath[a]
7.56	$E2$	0.11 ± 0.015				0.18
7.69	$E1$	0.6 ± 0.1	0.71	0.60	1.54	3.78[b]
8.19	$E1$	7.0 ± 0.9	5.49	0.53	0.89	
8.89	$M1$	5.4 ± 0.5			6.13	13.87–14.78

[a] References 9 and 22.

[b] Only the integrated strength from both $E1$ excitations is quoted.

with predictions of a weak-coupling model, while the strength of the 8.19-MeV resonance is in clear disagreement with the more sophisticated shell-model calculations. The direct component of the interaction was found to be large, indicating a need for calculations which include the single-particle nature of ^{13}C.

This research was performed under the auspices of the United States Department of Energy.

---

*Present address: Department of Physics, University of Illinois, Urbana-Champaign, Illinois 61801.

[1] A. M. Lane, Rev. Mod. Phys. 32, 519 (1960).

[2] I. Lovas, Nucl. Phys. 81, 353 (1966).

[3] J. T. Reynolds, C. T. Slavik, C. R. Lubitz, and N. C. Francis, Phys. Rev. 176, 1213 (1968).

[4] J. E. Purcell and M. R. Meder, Phys. Rev. C 16, 76 (1977).

[5] T. Tamura, Rev. Mod. Phys. 37, 679 (1965).

[6] F. C. Barker, Nucl. Phys. 28, 96 (1961).

[7] H. U. Jäger, H. R. Kissener, and R. A. Eramzhian, Nucl. Phys. A171, 16 (1971).

[8] H. R. Kissener, A. Asward, R. A. Eramzhian, and H. U. Jäger, Nucl. Phys. A219, 601 (1974).

[9] S. Cohen and D. Kurath, Nucl. Phys. 73, 1 (1965).

[10] W. Bertozzi, P. T. Demos, S. Kowalski, F. R. Paolini, C. P. Sargent, and W. Turchinetz, Nucl. Instrum. Methods 33, 199 (1965).

[11] K. Fukuda, Nucl. Phys. A156, 10 (1970).

[12] J. G. Woodworth, K. G. McNeill, J. W. Jury, P. D. Georgopulos, and R. G. Johnson, Can. J. Phys. 55, 1704 (1977).

[13] J. G. Woodworth, K. G. McNeil, J. W. Jury, R. A. Alvarez, B. L. Berman, D. D. Faul, and P. Meyer, Phys. Rev. C 19, 1667 (1979).

[14] R. W. Carr and J. E. Baglin, Nucl. Data Tables 10, 143 (1971).

[15] R. J. Holt, H. E. Jackson, R. M. Laszewski, J. E. Monahan, and J. R. Specht, Phys. Rev. C 18, 1962 (1978).

[16] A. Smith, R. Holt, and J. Whalen, Nucl. Sci. Eng. 70, 281 (1979).

[17] A. M. Lane and R. G. Thomas, Rev. Mod. Phys. 30, 257 (1958).

[18] S. Cierjacks, P. Forti, D. Kopsch, L. Kropp, J. Nebe, and H. Unfeld, Kernforschungszentrum Karlsruhe Report No. KFK-1000, 1968.

[19] R. J. Holt, F. W. K. Firk, R. Nath, and H. L. Schultz, Nucl. Phys. A213, 147 (1973).

[20] Note that this definition differs slightly from that of Ref. 15, since the expression for internal capture in Eq. (2) differs by a minus sign from that of Ref. 15.

[21] G. Wittwer, H.-G. Clerc, and G. A. Beer, Phys. Lett. 30B, 634 (1969).

[22] D. Kurath, private communication.

PHYSICAL REVIEW C VOLUME 21, NUMBER 5 MAY 1980

Quasi-free (α,2α) reaction induced by 140 MeV alpha particles on ^{9}Be, ^{12}C, ^{16}O, and ^{20}Ne

C. W. Wang,* N. S. Chant, P. G. Roos, A. Nadasen, and T. A. Carey
Department of Physics and Astronomy, University of Maryland, College Park, Maryland 20742

(Received 26 November 1979)

Measurements of the (α,2α) reaction on ^{9}Be, ^{12}C, ^{16}O, and ^{20}Ne targets at $E_\alpha = 140$ MeV were made at 20 angle pairs. The quasi-free knockout mechanism appears to dominate the reaction. The experimental data were analyzed with distorted-wave impulse approximation calculations. The factorization approximation employed in the calculations was tested explicitly and found to be valid. The shapes of the calculated energy sharing spectra are in satisfactory agreement with the data. The predicted absolute cross sections were found to be very sensitive to the cluster-core bound state radius parameter, and a bound state radius $R = 2.52A_c^{\,1/3}$ fm is necessary to obtain absolute spectroscopic factors consistent with existing theoretical values. Several possible explanations for this excessive value are suggested. Comparisons are made with other alpha knockout and transfer reactions.

[NUCLEAR REACTIONS ^{9}Be, ^{12}C, ^{16}O, ^{20}Ne (α, 2α), $E_\alpha = 140$ MeV; measured $\sigma(E_{\alpha 1}, E_{\alpha 2}, \theta_{\alpha 1}, \theta_{\alpha 2})$ DWIA analysis; deduced absolute spectroscopic factors.]

I. INTRODUCTION

Quasi-free knockout reactions have proved to be a powerful tool for the investigation of nuclear structure. Since the first experiment studying (p, 2p) reactions on light nuclei,[1] a considerable amount of experimental and theoretical work has been carried out on this subject. In situations where the quasi-free knockout reaction mechanism dominates, the (p, 2p) reaction can provide two types of information.[1-6] Firstly, the proton hole states in nuclei can be investigated, and secondly, one can study off-energy-shell p-p interactions. Similar information about nucleon clusters in nuclei can be obtained using quasi-free cluster knockout reactions.[4]

In this paper we present studies of alpha clustering using the (α, 2α) reaction at 140 MeV. In recent years alpha clustering in 1p and 2s1d shell nuclei has been studied using a variety of nuclear reactions. The (d, ^{6}Li), (^{3}He, ^{7}Be), (α, ^{8}Be), (^{6}Li, d), (^{7}Li, t), and (^{16}O, ^{12}C) alpha transfer reactions[7-13] has been studied and analyzed using distorted wave Born approximation (DWBA) and coupled channel Born approximation (CCBA) calculations.[14] However, most of these analyses are limited to extracting relative alpha spectroscopic factors. The (p, $p\alpha$) quasi-free knockout reaction has been investigated in several works.[15-18] Analyses of the experimental results at an incident energy of 100 MeV have shown that the plane wave impulse approximation (PWIA) reaction model is inadequate but that the data are well described by distorted wave impulse approximation (DWIA) calculations.[19-21] In these analyses the extracted *absolute* alpha cluster spectroscopic factors are found to be in good agreement with theoretical calculations.[22,23]

The (α, 2α) quasi-free knockout reaction on 1p and 2s1d shell nuclei has also been studied by other groups. Results for the ^{6,7}Li(α, 2α) reaction at $E_\alpha = 50$ to 80 MeV (Refs. 24 and 25) have been analyzed using the PWIA. Also a reaction mechanism study of ^{9}Be(α, 2α) at $E_\alpha = 40$ to 60 MeV has been reported.[26,27] In addition, data have been obtained for the ^{20}Ne(α, 2α) reaction at $E_\alpha = 78$ MeV (Ref. 28) and analyzed using the PWIA. Recently, Sherman *et al.*[29,30] have carried out extensive measurements of the (α, 2α) reaction on nine nuclei from ^{12}C to ^{66}Zn at $E_\alpha = 90$ MeV. Finally the ^{16}O, ^{28}Si(α, 2α) reactions have been studied at 0.65 and 0.85 GeV.[31]

The most complete (α, 2α) study is the work of Sherman *et al.*, at 90 MeV which poses some interesting problems. Using an approximate parametrized form for the distorted waves[32] quite good agreement was obtained with the shape of the energy sharing spectra and the results were insensitive to the type of bound state wave function used. The alpha spectroscopic factors obtained from this analysis are 2.9 ± 0.4 and 2.9 ± 0.5 for ^{12}C[α + ^{8}Be(g.s.)] and ^{16}O[α + ^{12}C(g.s.)], respectively, which should be compared to the theoretical values of 0.55 and 0.23 obtained by Kurath.[22] However, for the ^{16}O(α, 2α)^{12}C data of Sherman *et al.*, calculations by Chant and Roos,[19] using an exact partial wave expansion of the distorted waves and a Woods-Saxon bound state wave function with parameters chosen to reproduce the rms radius of ^{16}O, yield absolute spectroscopic factors roughly 100 times the theoretical prediction. In spite of this unexpected result, the ratio S_{0^+}/S_{2^+} of

© 1980 The American Physical Society

the spectroscopic factors for ^{12}C(g.s.) and the first excited state of ^{12}C(4.43 MeV, 2^+) was found to be $\frac{1}{4}$, fairly close to the value 1/5.7 of Kurath. At $E_\alpha = 850$ MeV, Chant and Roos obtained a value of 1.8 for S_α which is an upper limit since many levels contributed due to poor binding energy resolution of the experiment.[31]

Studies[33,34] of ^{16}O($\alpha, 2\alpha$)^{12}C(g.s.) at $E_\alpha = 25$ MeV and ^{16}O, ^{20}Ne($p, p\alpha$) at $E_p = 46.8$ MeV showed that the alpha removal reaction at these energies is dominated by sequential processes, while in the systematic study of Sherman *et al.*,[29,30] at $E_\alpha = 90$ MeV the quasi-free knockout mechanism appeared to dominate. Nevertheless, since the difficulties in Sherman's approximate DWIA analysis and in the exact DWIA treatment of Chant and Roos may arise from the presence of competing processes at this energy, we chose to study the ($\alpha, 2\alpha$) reaction at a higher energy, $E_\alpha = 140$ MeV, in the hope that the reaction mechanism might be more easily understood and hence more reliable nuclear structure information obtained. Results for ^{9}Be, ^{12}C, ^{16}O, and ^{20}Ne targets are presented. The experimental details and results are presented in Sec. II. A DWIA analysis of the data is presented in Sec. III. An important feature of this section is a series of explicit tests of the factorization approximation employed in the analysis which serve to establish the validity of the assumed reaction mechanism. As a prerequisite to a comparison of experimental and theoretical values for the alpha cluster spectroscopic factors it is important to be aware of the sensitivity of the results to the various parameters associated with the DWIA calculations. Thus, in Sec. III we also present studies of these sensitivities together with comparison of our results with theoretical predictions and the other experimental studies. Finally the implications of our results are discussed in Sec. IV.

II. EXPERIMENT

A. General description

A 140 MeV alpha beam from the University of Maryland sector-focused isochronous cyclotron was focused at the center of a 1.5 m diameter scattering chamber. The beam spot at the center of the target was 2 mm × 2 mm with an angular divergence of 5 mrad. Beam currents ranged from 15 to 100 nA depending on the detector angles.

The outgoing alpha particles were detected by two identical counter telescopes which were mounted coplanar with and on opposite sides of the beam. Each telescope consisted of a 300 μm silicon surface barrier ΔE detector followed by a 4 mm Si(Li) E detector mounted at 45° to provide an effective thickness of 5.65 mm which is sufficient to stop 140 MeV alpha particles. The solid angles subtended by the detectors were 1.35 and 1.39 msr, respectively.

For the ^{9}Be runs a self-supporting foil of 2.52 mg cm^{-2} thickness was used. For the other measurements, high purity ^{16}O, and ethane (C_2H_6) and isotopically enriched ^{20}Ne gases were used in a 12 cm diameter gas cell. The typical pressure was about 1 atmosphere. In order to define the gas target thickness and to prevent particles scattered by the gas cell windows from entering the detector telescopes, a double slit collimator system was used in front of each telescope. The overall angular resolution provided by the slit system was 1.9° and 2.8°, respectively.

Details of the experimental setup are discussed in Ref. 35. Briefly fast timing signals from the ΔE preamplifiers provided start and stop signals for a time-to-amplitude converter in order that real and accidental coincidences could be simultaneously stored. The timing resolution was approximately 3 ns. In addition a slow coincidence was required between the four detectors and the TAC signal. The analog signals from the four detectors and the TAC signal were gated by the slow coincidence and fed to analog-to-digital converters interfaced to an IBM 360/44 computer. Dead time losses were determined using a fourfold pulser unit triggered at a rate proportional to the beam current.

All ADC data were written, event by event, on magnetic tape for off-line reanalysis. In addition a very flexible data handling code permitted online calibration, particle identification, random coincidence subtraction, and one-and two-dimensional array accumulation.

On reanalysis two-dimensional spectra were constructed for the parameters F_3 vs T_1, where T_1 is the total energy deposited in one telescope and $F_3 = T_1 + T_2 + T_3$. Here T_2 is the energy deposited in the second telescope and T_3 the (computed) residual nucleus recoil energy. Clearly $F_3 = T_0 - B$, where T_0 is the incident kinetic energy and B the alpha binding energy in the target. Thus we refer to distributions of the parameter F_3 as "binding energy" spectra. Each F_3 vs T_1 spectrum was gated by the computer generated particle identification functions to correspond to alpha-alpha coincidences and random events were subtracted. The counts in each F_3 vs T_1 spectrum were summed along the kinematic line for each final state in the residual nucleus in bins of $\Delta T_1 = 2.4$ MeV. The resulting spectra were plotted as a function of T_1 yielding the energy sharing cross section $d^3\sigma/d\Omega_1 d\Omega_2 dT_1$.

The errors in the calculated cross sections are predominantly statistical. An error evaluation

TABLE I. Experimental angle pairs θ_1/θ_2 and minimum allowed recoil momenta q_{min}.

Target	θ_1/θ_2	q_{min} (MeV/c)
^{20}Ne	43.71°/−43.71°	0
	49.39°/−38.0°	0
	57.20°/−30.0°	0
	63.82°/−23.0°	0
^{16}O	43.16°/−43.16°	0
	55.97°/−30.0°	0
	63.82°/−23.0°	10
^{12}C	43.11°/−43.11°	0
	49.15°/−37.0°	0
	55.86°/−30.0°	0
	62.21°/−23.0°	0
^{9}Be	44.19°/−44.19°	0
	47.39°/−41.0°	0
	50.38°/−38.0°	0
	54.85°/−33.5°	0
	58.30°/−30.0°	0
	61.25°/−27.0°	0
	64.65°/−23.5°	0
	40.0°/−40.0°	69
	36.0°/−36.0°	125

showed the errors due to other sources such as random subtraction, solid angles, target thickness, gas pressure and temperature, current integrator, slit scattering, dead time correction, and bin size measurements could be neglected relative to the statistical errors.

B. Experimental results

The $(\alpha, 2\alpha)$ reaction yields were measured for ^{20}Ne, ^{16}O, ^{12}C, and ^{9}Be targets at 20 angle pairs with an incident energy $E_\alpha = 140$ MeV. Table I shows the data taken in the experiment, where q_{min} is the allowed minimum recoil momentum of the residual nucleus for the ground state transition. All but three of these angle pairs permit $q_{min} = 0$. At these so-called "quasi-free" angle pairs the reaction can proceed leaving the residual nucleus at rest.

The binding energy spectra for ^{20}Ne, ^{16}O, ^{12}C, and ^{9}Be$(\alpha, 2\alpha)$ reactions at symmetric quasi-free angles are shown in Fig. 1. Each binding energy spectrum shows a prominent isolated peak corresponding to the ground state of the residual nucleus. In the ^{20}Ne$(\alpha, 2\alpha)^{16}$O spectrum, a peak corresponding to the 6.05 and 6.13 MeV doublet of ^{16}O is also rather clear. Other states, due to poor counting statistics, could not be identified. In the ^{16}O$(\alpha, 2\alpha)^{12}$C spectrum, the 2^+(4.43 MeV) peak is comparable in magnitude to that of the ^{12}C(g.s.) transition. In addition, there is some evidence for a broad peak corresponding to the 4^+(14.0 MeV) state. The ground and first excited states of ^{8}Be in ^{12}C$(\alpha, 2\alpha)^8$Be are smeared somewhat in the binding energy spectrum. This is largely due to a slight gain shift of the detector telescopes and some nonlinearity of the F_3 functions in the F_3 vs T_1 spectra. However, the two-dimensional F_3 vs T_1 spectrum used to calculate the cross section had a much clearer separation of the two states. For ^{9}Be$(\alpha, 2\alpha)^5$He reaction, no ^{5}He state other than the ground state is seen in the binding energy spectrum.

The energy sharing spectrum for the transition leaving the residual nucleus in its ground state was extracted for each target and angular setting. Three additional spectra for ^{20}Ne$(\alpha, 2\alpha)^{16}$O(6 MeV), ^{16}O$(\alpha, 2\alpha)^{12}$C(4.43 MeV), and ^{12}C$(\alpha, 2\alpha)^8$Be(2.9 MeV) at the symmetric quasi-free angle pair were also obtained.

The ground state (g.s.) energy sharing spectra for the symmetric quasi-free angle pairs are presented in Fig. 2. There are several systematic

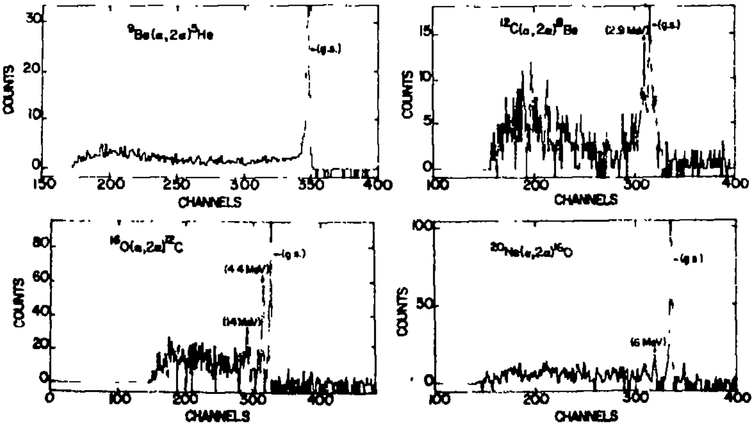

FIG. 1. Binding energy spectra for the $(\alpha, 2\alpha)$ reaction at 140 MeV on ^{9}Be, ^{12}C, ^{16}O, and ^{20}Ne.

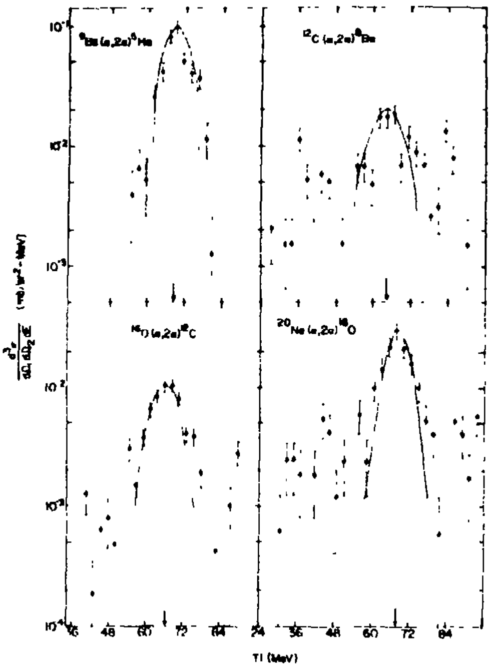

FIG. 2. Energy sharing spectra for the 140 MeV (α, 2α) reaction at symmetric quasi-free angle pairs on ^{9}Be, ^{12}C, ^{16}O, and ^{20}Ne leading to the ground states of the various residual nuclei. The arrows indicate the zero recoil momentum ($P_3 = 0$) points. The solid lines are DWIA predictions.

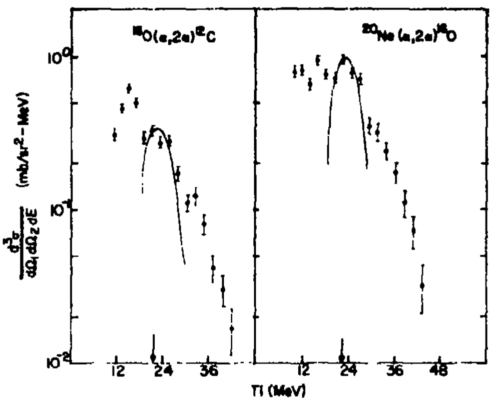

FIG. 3. Energy sharing spectra for ^{16}O$(\alpha,2\alpha)^{12}$C (g.s.) and ^{20}Ne$(\alpha,2\alpha)^{16}$O(g.s.) at $\theta_1/\theta_2 = 63.8°/-23°$. Arrows indicate minimum recoil momentum points and solid lines are DWIA predictions.

features which characterize these spectra. Firstly, the maximum in each quasi-free angle pair spectrum comes at the minimum recoil momentum of the residual nucleus. An arrow in each spectrum indicates this point. Secondly, the structure of the spectra is characterized by a broad, smooth bump which is characteristic of the quasi-free knockout mechanism for $L = 0$ transitions.[36] Spectra for nonsymmetric angle pairs, two of which are shown in Fig. 3, are very similar and the full width at the half maximum (FWHM) of the spectrum for each target is essentially independent of the particular angle pair when plotted against the momentum of the recoil nucleus rather than outgoing particle energy. The approximate widths are 70 MeV/c for ^{20}Ne$(\alpha,2\alpha)^{16}$O(g.s.), 90 MeV/c for ^{16}O$(\alpha,2\alpha)^{12}$C(g.s.), 90 MeV/c for ^{12}C$(\alpha,2\alpha)^8$Be(g.s.), and 70 MeV/c for ^{9}Be$(\alpha,2\alpha)^5$He(g.s.).

When one of the detector angles is less than 30° strong contributions from mechanisms other than knockout are evident. For example in Fig. 3 the data for ^{20}Ne$(\alpha,2\alpha)$ at $\theta_1/\theta_2 = 63.82°/-23°$ show a large yield on the lower energy side of the quasi-free distribution, although there is no well defined peak. In the same figure the data for ^{16}O show evidence of sequential alpha decay following inelastic scattering to levels in the target nucleus centered around 20 MeV excitation. In this excitation region many alpha decay channels are open and cannot be resolved in the experiment.

III. ANALYSIS

A. DWIA calculations

The theoretical analysis of the data was performed using the distorted wave impulse approximation code written by Chant and Roos.[19] The differential cross section for the reaction $A(\alpha,2\alpha)B$ for the knockout of an alpha particle with total angular momentum J and orbital angular momentum L is given by

$$\frac{d^3\sigma^{LJ}}{d\Omega_1\, d\Omega_2\, dT_1} = F_K S_{LJ} \frac{d\sigma}{d\Omega}\bigg|_{\alpha-\alpha} \sum_{\Lambda} |T_{BA}^{\alpha L\Lambda}|^2 , \tag{1}$$

where F_K is a kinematic factor, $d\sigma/d\Omega|_{\alpha-\alpha}$ is the two-body α-α cross section, and S_{LJ} is the cluster spectroscopic factor for specific L and J. The quantity

$$T_{BA}^{\alpha L\Lambda} = \frac{1}{(2L+1)^{1/2}} \int \chi_2^{(-)*}(\vec{r})\chi_1^{(-)*}(\vec{r})\chi_0^{(+)}(\gamma\vec{r}) \times \phi_{L\Lambda}^{\alpha}(\vec{r})\, d\vec{r} , \tag{2}$$

where the $\chi_i^{(\pm)}$ are distorted waves, $\gamma = B/A$, and $\phi_{L\Lambda}^{\alpha}(\vec{r})$ is the bound state wave function of the alpha cluster in the target nucleus. We refer to this quantity as the "distorted momentum distribution", since in the limit of no distortion $T_{BA}^{\alpha L\Lambda}$ reduces to $\phi_{L\Lambda}^{\alpha}$ in a momentum representation at the point $\vec{q}$

$= -\vec{p}_B$. In practice we shall see that distortion effects are quite severe for the present data.

It is important to note that Eq. (1) employs a factorized impulse approximation in which the two-body cross section enters as a multiplicative factor rather than as a t operator within the integrand of Eq. (2). Thus the integration over what is properly a fully off-energy-shell matrix element is replaced by the half off-shell value at the asymptotic kinematics. Furthermore, in practice we make the additional approximation of replacing $d\sigma/d\Omega\,|_{\alpha-\alpha}$ by the corresponding quantity determined from a measured (on-shell) two-body cross section. In analyzing $(p,p\alpha)$ data at 100 MeV, Roos *et al.*[17] found little error arose from the neglect of half off-shell effects, although there was some breakdown in the factorization approximation. This problem is investigated for the present data in Sec. III B.

B. Factorization test

In order to test our description of the assumed reaction mechanism we first divided the measured experimental cross sections at $p_B = 0$ by the kinematic factor F_K. According to Eq. (1) we have

$$\frac{d^3\sigma}{d\Omega_1\, d\Omega_2 dT_1}\Big/F_K = [S_\alpha |\phi(-\vec{p}_B)|^2]\, \frac{d\sigma}{d\Omega}\bigg|_{\alpha-\alpha}, \qquad (3)$$

where $|\phi(-\vec{p}_B)|^2 = \sum_\Lambda |T^{\alpha L\Lambda}_{BA}|^2$.

In principle S_α is constant. In addition, explicit DWIA calculations of the quantity $|\phi(-\vec{p}_B)|^2$ varied by less than ±10% at the $p_B = 0$ point over the entire angular range studied for all four targets. Thus, in the factorized DWIA, the ratio constructed in Eq. (3) should be proportional to the two-body cross section $d\sigma/d\Omega\,|_{\alpha-\alpha}$ to within this accuracy. Results are shown in Fig. 4 for all four targets studied plotted as a function of the two-body c.m. scattering angle. Also shown are measured free α-α cross sections at 120 and 140 MeV lab energy.[37,38] As indicated in Fig. 4, since the struck alpha particle is bound, the effective scattering energy (in the final state) is less than 140 MeV. It is found that, for all four targets, the ratios $(d^3\sigma/d\Omega_1 d\Omega_2 dT_1)/F_K$ can be normalized to lie between the free cross sections at 120 and 140 MeV and that the angular variation of the data points follows the free cross sections very closely over almost three orders of magnitude.

The result of the preceding series of factorization tests with the quasi-free angular distribution data is encouraging. However, there is no free α-α scattering data available at energies between 120 and 140 MeV and the uncertainties in the extracted half-shell cross sections are quite large. In order to choose a suitable energy for the free α-α cross section which is used to replace the half-shell cross section, three possible prescriptions were examined. On-shell α-α cross sections were obtained by interpolation at energies: (a) $E = T_f$, (b) $E = \frac{1}{2}(T_f + T_i)$, and (c) $E = T_i$. Using these cross sections the ratio of the experimental three-body cross section at $p_B = 0$ and the product $F_K\, d\sigma/d\Omega$ is compared with the calculated $|\phi(0)|^2$ at each angle for each of the $(\alpha, 2\alpha)$ reactions under investigation. Differences between the three prescriptions are not large. However, a careful comparison of the extracted $|\phi(0)|^2$ obtained from the on-shell cross section at the three different energies with the calculated $|\phi(0)|^2$ shows that the T_f prescription gives slightly better consistency between the experimental and calculated results. This result is in agreement with other investigations and with the result that the final energy prescription arises as the first term of a multiple scattering expansion based on the Faddeev equations.[39] It thus is used throughout the ensuing analyses.

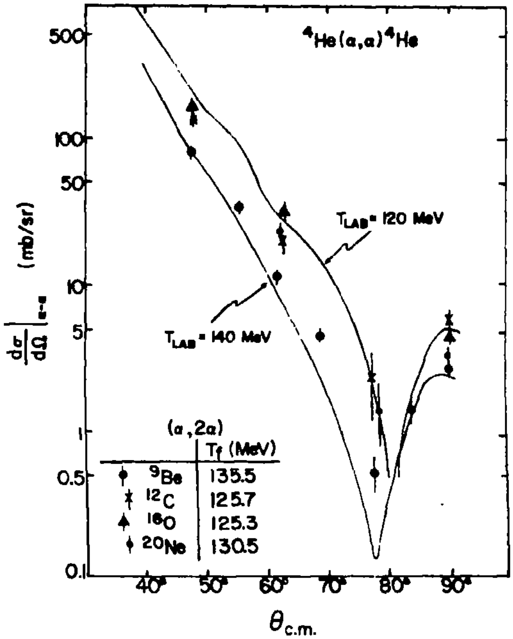

FIG. 4. Half-shell α-α cross sections extracted from 140 MeV (α,2α) reactions on ^{9}Be, ^{12}C, ^{16}O, and ^{20}Ne. The solid lines represent measured free α-α elastic scattering cross sections at 120 and 140 MeV.

These tests have been carried out with different sets of distorting and bound state parameters. The factorization characteristics are found to be insensitive to the choice of these parameters.

C. Comparison of DWIA calculations with experiment

In order to carry out the DWIA calculations it is necessary to evaluate both the distorted wave functions and the bound cluster "wave function" appearing in the integrand of Eq. (2). The latter quantity, $\phi^{\alpha}_{L\Lambda}(\vec{r})$, more properly represents the result of projecting the target nucleus wave function onto the product of the residual nucleus wave function and the internal wave function of an alpha particle in its ground state. Following common practice in both knockout and transfer reaction analyses we have replaced $\phi^{\alpha}_{L\Lambda}(r)$ in our calculations by an eigenfunction of a Woods-Saxon potential with an energy eigenvalue equal to the alpha particle separation energy. The principal quantum number N is chosen on the basis of conservation of oscillator shell model quanta. Thus

$$2(N-1)+L=\sum_{i=1}^{4} 2(n_i-1)+l_i\,, \tag{4}$$

where the n_i and l_i are individual nucleon principal quantum numbers and orbital angular momenta, respectively. Thus, assuming $(1s^4)(1p^n)$ configurations for $A \leq 16$, $L=0(2)$ transitions must have $N=3(2)$. For ^{20}Ne, if we assume an initial $(1s^4)(1p^{12})(2s1d)^4$ configuration, $L=0(2)$ transitions have $N=5(4)$.

Initially calculations were carried out using bound state potential parameters yielding a potential consistent with the known rms radii of the target nuclei. For the ^{16}O target the parameters used are listed in Table II. The values ($R=1.22\times 12^{1/3}$ fm, $a=0.76$ fm) are quite similar to the results of a folding procedure which was used successfully in an earlier analysis[17] of the $(p,p\alpha)$ reaction at 100 MeV. Also listed in Table II are potentials used for the incident and emitted alpha particles. Our notation is such that, for example, C139 is a potential obtained by fitting $\alpha+{}^{12}$C elastic scattering at a laboratory energy of 139 MeV. Notice that our use of $\alpha+{}^{12}$C potential parameters is consistent with the formal result[40] that the projectile-ejectile interaction is, in principle, included to all orders via the two-body t matrix.

Using the parameters C139/C139/C139 for the incident/emitted/emitted alpha particles for ^{16}O$(\alpha,2\alpha)^{12}$C(g.s.) at 140 MeV the shapes of the experimental distributions at three different angle pairs were reasonably well reproduced. Typical results are shown in Fig. 2. Somewhat surprisingly, however, the extracted spectroscopic factor S_α was approximately 25, more than 100 times the theoretical value of 0.23 predicted in the Kurath shell model calculations.[22] This result is similar to that obtained by Chant and Roos[19] in their DWIA analysis of the 90 MeV $(\alpha,2\alpha)$ data. Noting that, at $p_B=0$, the emitted alpha particle kinetic energies are each about 66 MeV the sets C139/C104/C104, C104/C104/C104, C139/C56/C56, C139/C56′/C56′ were tried. However, these calculations produced a variation in the spectroscopic factor of less than a factor of 3. Finally, to allow for the energy variation of the emitted alphas in the exit channel (between 40 and 90 MeV) calculations were carried out using the various combinations of potentials listed above with real potential strengths readjusted to yield volume integrals $J/4A$ corrected for an energy dependence of $-1.3\,E_{\text{c.m.}}$, where $E_{\text{c.m.}}$ is the c.m. energy. This is consistent with the observed variation of the real volume integral in the range $30<E<160$ MeV and $4<A<60$. In all cases the extracted spectroscopic factors were at least 30 times larger than the theoretical value.

A similar study[41] by Jain and Sarma of the sensitivity of the spectroscopic factor extracted from the 90 MeV ^{16}O$(\alpha,2\alpha)^{12}$C data[29,30] to the choice of optical parameters has been reported. These authors correctly point out that the optical parameters selected for the original calculations of Chant and Roos[19] are not in good agreement with appropriate elastic scattering data (being in fact obtained from fits to slightly heavier targets). By

TABLE II. Optical potential parameters[a] for ^{16}O$(\alpha,2\alpha)^{12}$C (g.s.) initial calculations.

Set series	V_0[b]	r_0	a	r_c	W_0	r_0'	a'	Ref.
B.S.[c]	72.5	1.22	0.76	1.24				
C139	108.1	1.22	0.76	1.26	16.9	1.85	0.47	52
C104	114.0	1.22	0.80	1.26	13.8	1.91	0.50	52
C56	151.9	1.24	0.665	1.4	28.05	1.24	0.64	53
C56′	216.8	1.3	0.58	1.4	38.05	1.5	0.32	53

[a] The optical potential is defined to be $V_{\text{opt}}=-V_0 f(r,r_0,a)-iW_0 f(r,r_0',a')+V_C$, where $f(r,r_0,a)=\{1+\exp[(r-r_0A^{1/3})/a]\}^{-1}$, A is the target mass, V_C is the Coulomb potential of a uniform charged sphere of radius $r_cA^{1/3}$.

[b] V_0 and W_0 in MeV: r_0, r_0', a, a', and r_c in fm.

[c] Bound state.

selecting optical parameters from the work of Pehl,[42] Jain and Sarma obtain improved fits to the relevant elastic scattering data and obtained a spectroscopic factor only about five times the theoretical value. We have carried out additional calculations which suggest that this reduction in S_α is a consequence not of the detailed improvements in the elastic scattering fits but rather of the fact that, in his early work, Pehl reported the shallowest potential from among the various discrete ambiguities. Specifically the potential of Ref. 42 has $V=33$ MeV and $J/4A$ roughly one fourth of the value derived from the energy dependence described above. In the light of more recent work[43] we argue that this choice is unphysical and does not satisfactorily remove the large discrepancy in S_α which we have noted.

Similar problems are encountered for the other targets. Initial calculations reproduced the shapes of the $(\alpha,2\alpha)$ distributions but gave spectroscopic factors of 9 for ^{9}Be, 11 for ^{12}C, and 27 for ^{20}Ne which are much larger than the theoretical values[21,22] of 0.57, 0.55, and 0.21, respectively. As found for ^{16}O reasonable variations in distorting parameters failed to remove the disagreement between theory and experiment.

Next a test of the sensitivity of the calculations to the bound state parameters was carried out. The results were found to be relatively insensitive to the diffuseness parameter "a" and to the Coulomb radius r_C. Variation of the bound state radius parameter r_0 produced no change in the shape of the energy sharing distribution, but resulted in significant changes in the predicted magnitude. To illustrate this effect we have plotted in Fig. 5 the distorted momentum distribution at $p_B=0$, $|\phi(0)|^2$, as a function of the bound state radius parameter r_0 for $^{16}\text{O}(\alpha,2\alpha)^{12}\text{C}(\text{g.s.})$ at $\theta_1=-\theta_2=43.16°$. In these calculations the distorting parameter set was C139/C139/C139. For the bound state, the parameters a and r_C were fixed at 0.76 and 1.3 fm, respectively, while the potential strength was readjusted at each value of r_0 to yield a solution with the empirical alpha separation energy. It is seen that the magnitude of $|\phi(0)|^2$ is increased by a factor of approximately 120 on changing r_0 from 1.2 to 2.52 fm which thus serves to reduce the extracted spectroscopic factor to approximately 0.23, the anticipated value.

It should be noted that the value $r_0=2.52$ fm for $^{16}\text{O}(\alpha,2\alpha)^{12}\text{C}(\text{g.s.})$ does not lead to noticeable deterioration in the fit to the shape of the energy sharing distribution. However, the associated 3S wave function has an rms radius of 4.37 fm while the rms radius of the potential is 3.56 fm. Both values are well in excess of the empirical rms radius of 2.65 fm for ^{16}O. Although the value $r_0=2.52$ fm is thus clearly excessive, it is important to note that comparable values have been used in analyses of alpha-transfer reactions in order to reproduce the experimental absolute cross sections (that is, to obtain absolute spectroscopic factors in agreement with shell model theories). For example, the authors of Refs. 11 and 12 used bound state well radii of $R=2.0A_c^{1/3}$ fm and $R=1.2\,(A_c^{1/3}+4^{1/3})$ fm, respectively, where A_c is the mass number of the core. These values are equivalent to $r_0=2.0$ and 2.05 fm for ^{16}O in our parametrization.

Our decision to characterize the enhanced $(\alpha,2\alpha)$ cross sections by an increased value of r_0 thus has the merit of consistency with transfer reaction analyses and is clearly preferable to the introduction of unphysical optical potentials in *both* knockout and transfer analyses. Nevertheless, it is a somewhat arbitrary device. We shall return to the question of the implications of this choice in Sec. III F. For the present we choose $r_0=2.52$ fm for all targets studied in order to investigate the resultant fits to the energy sharing distributions as well as the deduced spectroscopic factors.

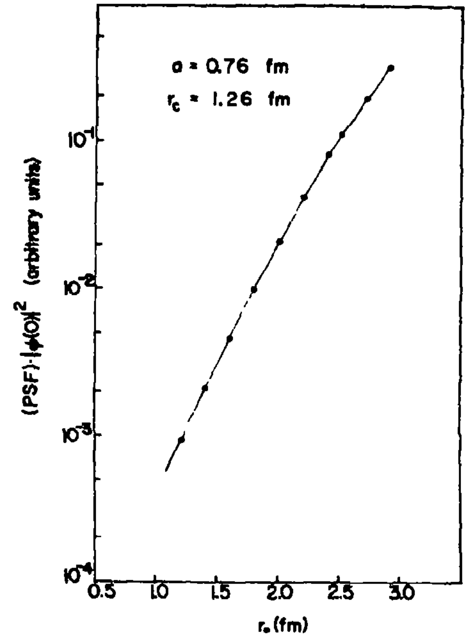

FIG. 5. Dependence of the quantity $|\phi(0)|^2$ on the bound state radius parameter r_0 for $^{16}\text{O}(\alpha,2\alpha)^{12}\text{C}(\text{g.s.})$ at $E_\alpha=140$ MeV. The diffuseness is held fixed at $a=0.76$ fm and the Coulomb radius parameter is $r_C=1.26$ fm.

Calculated energy sharing spectra for all four ground state transitions at the symmetric quasi-free angle pair are shown in Fig. 2. The optical parameters used are listed in Table III. It should be noted that, with the exception of ^{9}Be, these are pure $L = 0$ transitions. For ^{9}Be, as we have discussed previously,[17] roughly equal admixtures of $3S$ and $2D$ transitions are expected. These terms add incoherently and the curve shown in Fig. 2 is the summed result. As found for $(p, p\alpha)$ at 100 MeV the $2D$ admixture has little effect.

In general agreement between theory and experiment in Fig. 2 is good. Aside from the regions of sequential processes, comparable agreement is also apparent in Fig. 3 in which results are shown for the ground state transitions at asymmetric angle pairs.

D. Spectroscopic factors: ground state transitions

The ground state spectroscopic factors extracted from our 140 MeV data are shown in Table IV together with theoretical values obtained from structure calculations employing shell model[22] and SU$_3$ model[23] approaches. All data sets have been included with the exception of the ±36° angle pair for ^{9}Be which was poorly reproduced in the DWIA calculations. This difficulty can be attributed to the fact that this angle pair involves much higher momentum components in the alpha wave function than any other angle pair chosen. Specifically, the minimum value of p_B is 125 MeV/c which is to be compared with a distorted momentum distribution width of ±70 MeV/c for ^{9}Be. As a result the knockout cross section is suppressed, and accuracy in treating the bound state and distorted waves becomes more crucial. Also competing reaction mechanisms may play a more significant role.

From Table IV it is seen that the extracted spectroscopic factors for each target vary between ±20% and ±30% over the angular range studied. The uncertainties attached to the average spectroscopic factors quoted are merely standard deviations of the angular variations. Clearly many sources of relative and absolute errors have been ignored.

Agreement between theory and experiment is generally good. Clearly our choice of $r_0 = 2.52$ fm guarantees this result for ^{16}O. However, it is seen that this choice, made arbitrarily for the other targets, leads to an excellent description of the *relative* strengths for the four targets.

As a further test of our chosen bound state geometry, calculations were carried out for $(\alpha, 2\alpha)$ data obtained by other groups at lower energies. Results for the four targets under discussion are compared with our 140 MeV results in Table V. For ^{9}Be$(\alpha, 2\alpha)^5$He(g.s.) data at $E_\alpha = 55$, 49.2, and 42.8 MeV (Refs. 26 and 27) have been analyzed. It is surprising that at these low energies, where the quasi-free knockout reaction mechanism may be less dominant and the free α-α cross sections oscillate, we obtain an experimental spectroscopic factor consistent with that from 140 MeV data to within about 50%. The results of the same analysis of ^{12}C data at $E_\alpha = 90$ MeV (Ref. 29 and 30) and ^{16}O data at 90 MeV (Refs. 29 and 30), 52.5 and 46 MeV

TABLE III. Optical potential parameters[a] for final calculations.

Reaction	System	V_0[b]	r_0	a	r_c	W_0	r_0'	a'	r_{rms}	$J/4A$	Ref.
^{9}Be$(\alpha, 2\alpha)^5$He	$\alpha + ^9$Be	72.63	1.36	0.765	1.3	23.8	1.36	0.765		329	54
	$\alpha + ^5$He	72.63	1.36	0.765	1.3	23.8	1.36	0.765		396	54
	B.S.[c]	36.69	2.52	0.765	1.3				4.74	806	
^{12}C$(\alpha, 2\alpha)^8$Be	$\alpha + ^{12}$C	108.1	1.22	0.76	1.26	16.9	1.85	0.47		356	52
	$\alpha + ^8$Be	108.1	1.22	0.76	1.26	16.9	1.85	0.47		402	52
	B.S.	35.80 38.51[d]	2.52	0.655	1.26				4.03	700	
^{16}O$(\alpha, 2\alpha)^{12}$C	$\alpha + ^{16}$O	108.1	1.22	0.76	1.26	16.9	1.85	0.47		330	52
	$\alpha + ^{12}$C	108.1	1.22	0.76	1.26	16.9	1.85	0.47		356	52
	B.S.	30.50 35.13[d]	2.52	0.7825	1.26				4.37	604	
^{20}Ne$(\alpha, 2\alpha)^{16}$O	$\alpha + ^{20}$Ne	110.6	1.22	0.82	1.3	17.9	1.77	0.63		338	55
	$\alpha + ^{16}$O	110.6	1.22	0.82	1.3	17.9	1.77	0.63		358	55
	B.S.	46.34	2.52	0.78	1.3				5.44	892	

---

[a] The optical potential is defined to be $V_{opt} = -V_0 f(r, r_0, a) - iW_0 f(r, r_0', a') + V_C$, where $f(r, r_0, a) = [1 + \exp\{(r - r_0 A^{1/3})/a\}]^{-1}$; A is the target mass; V_C is the Coulomb potential of a uniform sphere of radius $r_c A^{1/3}$.

[b] V_0 and W_0 in MeV, r_0, r_0', a, a', r_C, and r_{rms} in fm, $J/4A$ in MeV fm^3.

[c] Bound state.

[d] When the core is left in its first excited state.

TABLE IV. Spectroscopic factors for angle pairs (θ_1/θ_2) extracted by means of the DWIA analysis. The average $\langle S_\alpha^{\rm exp}\rangle$ is a statistical average of all angle pairs.

Reaction	θ_1/θ_2	$S_\alpha^{\rm exp}$	$\langle S_\alpha^{\rm exp}\rangle$	$S_\alpha^{\rm theory}$	Ref.
^{9}Be(α, 2α)^{5}He(g.s.)	44.19°/−44.19°	0.656			
	47.39°/−41.0°	0.930			
	50.38°/−38.0°	0.574		0.57	22
	54.85°/−33.5°	0.635			
	58.39°/−30.0°	0.579	0.633 ± 0.120		
	61.25°/−27.0°	0.622			
	64.65°/−23.5°	0.540			
	40.0°/−40.0°	0.527			
^{12}C(α, 2α)^{8}Be(g.s.)	43.11°/−43.11°	0.641		0.674	47
	49.15°/−37.0°	0.682		0.55	22
	55.86°/−30.0°	0.421	0.558 ± 0.107	0.285	23
	62.21°/−23.0°	0.487		0.759	56
				0.675	56
^{16}O(α, 2α)^{12}C(g.s.)	43.16°/−43.16°	0.209		0.295	47
	55.97°/−30.0°	0.304		0.23	22
	63.82°/−23.0°	0.222	0.244 ± 0.046	0.296	23
				0.333	56
				0.296	56
^{20}Ne(α, 2α)^{16}O(g.s.)	43.71°/−43.71°	0.157			
	49.39°/−38.0°	0.235		0.21	23
	57.20°/−30.0°	0.220	0.202 ± 0.029	0.182	47
	63.82°/−23.0°	0.196			
^{12}C(α, 2α)^{8}Be(2.9 MeV)	43.16°/−43.16°	1.74	1.74	0.72	22
				0.592	23
^{16}O(α, 2α)^{12}C(4.43 MeV)	43.11°/−43.11	1.26	1.26	1.31	22
				1.48	23

Refs. 26 and 27) and ^{20}Ne data at 78 MeV (Ref. 28) re also shown in Table V. The results from the ^{2}C and ^{16}O data at 90 MeV are consistent with the esults from our own data to within a factor of 5. For the ^{16}O data at around 50 MeV the agreement is within a factor of 4. For ^{20}Ne at 78 MeV greement with our 140 MeV result is within the xperimental error. Considering the original isagreement of over a factor of 100, these dif- rences are not large.

The optical model parameters used for the lower ergy calculations are the same as those listed Table III. We have not investigated the sensitivity of the lower energy results to the choice of distorting potentials. Clearly there are large uncertainties and a more consistent description might be possible. An important ingredient of any improved analysis would be a more systematic treatment of the energy dependence of the alpha optical potential.

E. Transitions to the first excited states of ^{8}Be and ^{12}C

The overlaps of ^{12}C − α + ^{8}Be (2.9 MeV, 2$^+$) and ^{16}O − α + ^{12}C (4.43 MeV, 2$^+$) have also been investi*gated with the quasi-free knockout reactions* ^{12}C(α, 2α)^{8}Be (2.9 MeV) and ^{16}O(α, 2α)^{12}C(4.43 MeV) at angles 43.11°/−43.11° and 43.16°/−43.16°,

TABLE V. Spectroscopic factors $S_\alpha^{\rm exp}$ extracted by means of the DWIA analysis at symmetric quasi-free angle pairs.

Reactions	E_α (MeV)	$S_\alpha^{\rm exp}$	$\langle S^{\rm exp}\rangle E_\alpha$ − 140 MeV
^{9}Be(α, 2α)^{5}He(g.s.)	55	0.820 ± 0.082	
	49.2	0.655 ± 0.068	0.633
	42.8	0.936 ± 0.156	
^{12}C(α, 2α)^{8}Be(g.s.)	90	0.196 ± 0.014	0.558
^{16}O(α, 2α)^{12}C(g.s.)	90	0.0942 ± 0.011	
	52.5	0.982 ± 0.225	0.244
	46	0.687 ± 0.125	
^{20}Ne(α, 2α)^{16}O(g.s.)	76.6	0.149 ± 0.017	0.202

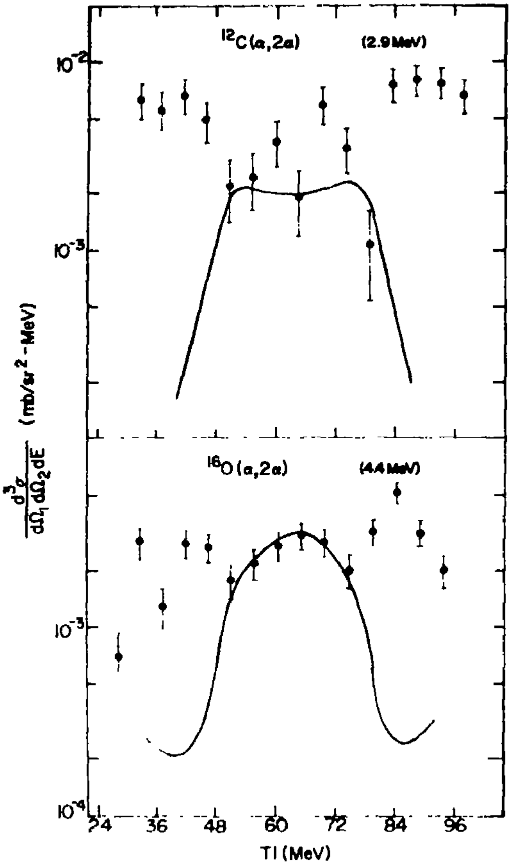

FIG. 6. Energy sharing spectra for ^{12}C(α,2α)^{8}Be (2.9 MeV) and ^{16}O(α,2α)^{12}C (4.43 MeV) at $\theta_1/\theta_2 \approx 43°/-43°$. The solid lines are DWIA predictions.

respectively. The measured energy sharing spectra are shown in Fig. 6. The distorting parameters and bound state radius and diffuseness parameters for the DWIA analysis are the same as those for the ground state transitions. Both states have spin and parity 2^+. The principal quantum number $N = 2$ and orbital angular momentum quantum number $L = 2$ are used for the analyses in both cases. The calculated energy sharing distributions can roughly reproduce the experimental data in the region where the two outgoing alpha particle energies are not very different. However, the overall fits are disappointing.

Alpha spectroscopic factors were extracted by comparing the data with the DWIA calculations near the minimum recoil momentum regions. The results are compared with theoretical estimates obtained using a $1p$ shell model[22] and by considering the nuclei as alpha chains,[23] in Table IV. The consistency between the experimental and theoretical values for the ^{16}O → α + ^{12}C(4.43 MeV) transition is remarkable while for the ^{12}C → α + ^{8}Be (2.9 MeV) transition agreement is within a factor of 3. A difficulty in this case is the possibility of $L = 0$ contributions to the transition which are permitted owing to the unbound nature of the final state and which may be present in $(p, p\alpha)$ data for the same transition.[17] Clearly data with improved statistics coupled with further reaction mechanism studies for the excited states are needed.

F. The alpha cluster bound state wave function

In the preceding sections we have seen that DWIA calculations for the $(\alpha, 2\alpha)$ reaction at 140 MeV are relatively insensitive to reasonable changes in the distorting potentials but are strongly dependent on the choice of bound state wave functions $\phi_{L\Lambda}^{\alpha}(\vec{r})$. Specifically, if we accept the theoretical absolute spectroscopic factors quoted as being correct to better than an order of magnitude, calculations using a bound state radius parameter $r_0 \sim 1.22$ fm seriously underestimate the observed absolute cross section. Such a choice for r_0 is "reasonable" in that the resultant wave function and potential have rms radii similar to the empirical target rms radii. However, in order to reproduce the observed cross sections the apparently excessive value of $r_0 = 2.52$ fm is needed. This choice leads to reasonable predicted absolute cross sections for all four targets at 140 MeV without deterioration in the fits to the shapes of the distributions. In addition, consistent absolute cross sections are obtained at lower energies (at least to within a factor of 2–3).

This behavior is in marked contrast to studies[1] of $(p, p\alpha)$ and (p, d^3He) reactions at 100 MeV on ^{9}Be and ^{12}C and in more recent studies[44,45] at the same energy on ^{16}O and ^{20}Ne. These authors used values of $r_0 \sim 1.1$–1.3 fm which is close to a foldi model geometry and thus quite different from our value of $r_0 = 2.52$ fm. However, as pointed out elsewhere[46] the predicted distorted momentum distributions for these $(p, p\alpha)$ transitions are not very sensitive to the radius parameter of the alpha-core bound state. Thus in Ref. 46 we noted that S_α for ^{16}O$(p, p\alpha)^{12}$C(g.s.) at 100 MeV changes by less than a factor of 2 when r_0 is changed from 1.09 to 2.3 fm.

Some of these features can be understood in terms of the radial localization of these reactions By integrating $T_{BA}^{\alpha L\Lambda}$ of Eq. (2), from r to infinity one obtains a calculated differential cross sectio $\sigma(r)$, which is a measure of the contribution to th reaction in the range from r to infinity. The difference $\Delta\sigma = \sigma(r) - \sigma(r + \Delta r)$ is thus a measure of the contribution to the reaction in the range from r to $r+\Delta r$. From a histogram of these differences against r one can investigate the reaction contribution from different values of r. Figure 7 shows the histogram for ^{16}O(α, 2α)^{12}C(g.s.) at $\theta_1/\theta_2 = 43.16°/-43.16°$, $p_B = 0$, and $E_\alpha = 140$ MeV. For the case of bound state radius parameter $r_0 = 1.22$ fm, one observes a dramatic interference near the region $r \sim r_0 A_c^{1/3}$. It is this calculation which seriously underestimates the experimental absolute cross section. Also shown in Fig. 7 is the corresponding histogram for $r_0 = 2.52$ fm, which leads to agreement with experiment. It is seen that the reaction is now localized to a region near 6.5 fm and that the interference region has been eliminated. At the lower end of Fig. 7 is the corresponding diagram for ^{16}O(p, $p\alpha$)^{12}C(g.s.) at 100 MeV using $r_0 = 1.3$ fm and $a = 0.65$ fm. These parameters lead to calculations in good agreement with experiment.[44] Here we see that the reaction is no longer localized in the extreme tail of the bound state wave function, and it is this feature which accounts for the more modest sensitivity to r_0.

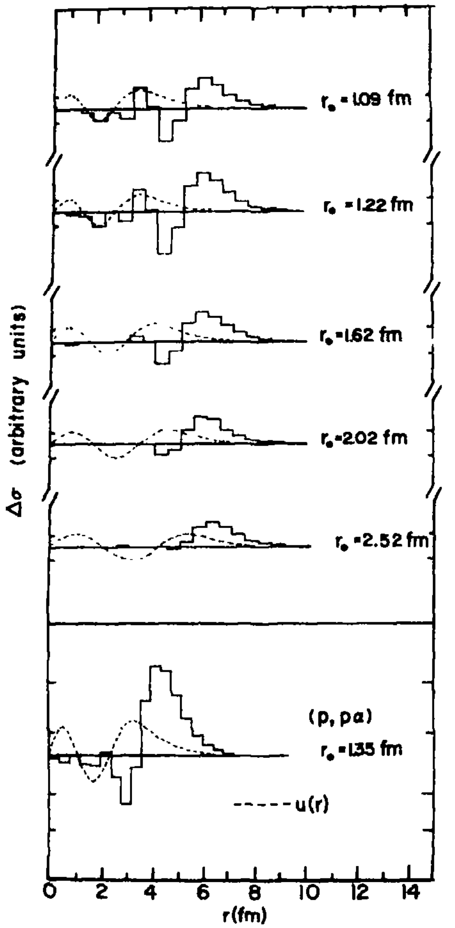

FIG. 7. Histograms of $\Delta\sigma$, the calculated contributions as a function of radius to the ^{16}O(α, 2α)^{12}C(g.s.) cross section at 140 MeV at $\theta_1/\theta_2 = 43.2°/-43.2°$. Shown are calculations for various values of r_0, the bound state radius parameters. Also shown is a histogram for ^{16}O(p, $p\alpha$)^{12}C(g.s.) at 100 MeV for $r_0 = 1.3$ fm. In each case the broken curve is the corresponding bound state radial wave function $u(r)$.

As mentioned briefly in Sec. IIIC our choice of $r_0 = 2.52$ fm is not inconsistent with the values used in alpha transfer reactions. Firstly the (α, ^{8}Be) reaction study of Ref. 11 obtained absolute alpha spectroscopic factors for eight 1p shell nuclei using an alpha core bound state radius parameter $r_0 = 2.0$ fm. Secondly, the analysis of the ^{12}C(^{16}O, ^{20}Ne)^{8}Be reaction data[12] used an α-^{16}O bound state radius $R = 1.2(16^{1/3} + 4^{1/3})$ fm, which corresponds to $r_0 = 1.96$ fm in our notation, to reproduce the experimental data. Thirdly, in analyzing the ^{16}O(d, ^{6}Li)^{12}C reaction Nagel and Koshel[44] were obliged to use a bound state radius $R = 1.27$ $(12^{1/3} + 4^{1/3})$ fm (which corresponds to $r_0 = 2.15$ fm in our notation) in order to reproduce the magnitude of the experimental cross section. These authors pointed out that the magnitude of the calculated cross section increased by a factor of 16 when the bound state radius changed from 1.25 $\times\, 12^{1/3}$ fm to the above value. This is to be compared with a factor of about 24 for a corresponding change in our ^{16}O(α, 2α)^{12}C(g.s.) analysis. Finally, two groups[47,48] have investigated the (^{3}He, ^{7}Be) reaction on 1p and 2s1d shell nuclei and extracted relative alpha spectroscopic factors. The authors of Ref. 47 used $r_0 = 1.2$ fm for ^{7}Be $\rightarrow {}^3$He + α while Audi *et al.*[48] used a bound state radius $R = 1.25$ $(A_c^{1/3} + 4^{1/3})$ fm. The results of Audi *et al.* are more consistent with the spectroscopic factors obtained in SU$_3$.

We have seen that while reasonable bound state geometry parameters work well for (p, $p\alpha$), most alpha transfer analyses and the (α, 2α) reaction at 140 MeV incident energy or less require bound state wave functions enhanced in the nuclear surface by up to an order of magnitude. The device we have selected to achieve this end, namely an increase in r_0, probably has no intrinsic significance. For example, as an alternative, we could have arbitrarily reduced the calculated cluster binding energy.

Yet another approach is that suggested by Jain,[49] who was able to reproduce both the shapes and absolute magnitudes of the 90 MeV data of Ref. 30 using a strong absorption model with a radius parameter $R = 1.15(A^{1/3} + 4^{1/3})$ fm where A is the target mass number. Unfortunately the success of the strong absorption model calculations does not greatly clarify the situation and more physical explanations for the apparent enhancement of $\phi^{*}_{LA}(r)$ are needed.

IV. DISCUSSION AND CONCLUSIONS

The present $(\alpha, 2\alpha)$ data suggest the dominance of the quasi-free knockout mechanism. The energy sharing data are well described by the DWIA calculations. Perhaps more importantly the angular dependence of the three-body cross section is in excellent agreement with that obtained in free $\alpha + \alpha$ scattering. However, in spite of consistency with alpha transfer analyses, the necessity of using bound state radii yielding rms radii significantly in excess of those expected is disturbing. Two possible explanations are suggested.

First one might conclude that surface clustering exists in excess of that predicted by the simple shell model calculations considered so far. To examine this question we have considered the treatment of the ^{16}O ground state by Brown and Green,[50] who include 2p-2h and 4p-4h admixtures. We expect an increased yield over our 0p-0h calculation, since these components lead to 4S and 5S bound state wave functions, respectively. Using the amplitudes of Brown and Green we obtain an enhancement in the DWIA cross section of only a factor of 3.5. In fact, any combination of the various components is insufficient to explain the present data using a bound state radius near $r_0 \simeq 1.2$ fm.

Thus more pronounced correlation effects than included in the calculations of Ref. 50 seem to be implied by the present data. However, this result is not at variance with the general success of structure calculations such as Ref. 50. Referring to Fig. 7 we see that nuclear radii of 6 to 7 fm appear to be responsible for the $(\alpha, 2\alpha)$ yield. In this region for the targets studied, nuclear densities are well below 1% of central density and it is only here that alpha clustering of order 100 times shell model estimates are implied by the data. In this regard it is of interest to compare the present results with charge distributions obtained in model independent analyses of electron scattering data. Using the bound alpha cluster wave function obtained with $r_0 = 2.52$ fm we can estimate the charge densities at $r = 6$–7 fm implied by the $(\alpha, 2\alpha)$ data. These are clearly crude estimates. However, it is interesting to note that the results are comparable to (or even exceed) values obtained from electron scattering. For example, for ^{12}C at $r = 7$ fm, Sick[51] obtained $\rho(r)/\rho(0) \sim 2.5 \times 10^{-4}$ from analysis of low momentum transfer electron scattering data whereas our ^{12}C$(\alpha, 2\alpha)^8$Be result is $\rho(r)/\rho(0) \sim 3.5 \times 10^{-4}$. Thus the $(\alpha, 2\alpha)$ data seem to imply that most of the nuclear matter at these very low densities has coalesced into alpha clusters.

As an alternative explanation of the present results we can consider alpha clustering in the surface region *induced* by the projectile. This would correspond to inelastic scattering to states with large alpha parentage followed by knockout. This is an appealing possibility since there exist (at least in ^{16}O) states near the alpha threshold[46] strongly excited in inelastic scattering. Thus, the second step would consist of knocking out an alpha particle weakly bound to the residual nucleus (and therefore having a large asymptotic tail). Unfortunately, no calculations for such processes exist at present. It is worth noting that not only is it necessary to fit the energy sharing distribution, both in shape and magnitude but also such calculations must reproduce the angular dependence of the $(\alpha, 2\alpha)$ cross section. As we have seen this is in excellent agreement with free $\alpha + \alpha$ scattering and thus seems to imply a one-step process. This feature of our data may well prove decisive since one might speculate that dominance of two-step processes would lead to some broadening of the angular distribution. Lastly, similar levels must exist in all four nuclei studied despite their rather different nuclear structure, since all show the same basic effect. Notice also that such calculations must reproduce the alpha transfer data, since similar bound state geometries are needed in those analyses.

ACKNOWLEDGMENTS

We are indebted to the operators and staff of the University of Maryland Cyclotron for their assistance in obtaining stable and reproducible beams. Calculations were carried out using the facilities of the University of Maryland Computer Science Center. Provision of time is gratefully acknowledged. This research was supported in part by the National Science Foundation.

*Present address: Tsing Hua University, Taiwan, R. O. C.

[1] O. Chamberlain and E. Segrè, Phys. Rev. 87, 81 (1952).

[2] J. M. Wilcox and B. J. Moyer, Phys. Rev. 99, 875 (1955).

[3] H. Tyrén, P. Hillman, and Th. A. J. Maris, Nuovo Cimento 6, 1507 (1957); Nucl. Phys. 7, 1 (1958) ; 7, 10 (1958); Phys. Rev. Lett. 5, 107 (1960).

[4] M. Riou, Rev. Mod. Phys. 37, 375 (1965).

[5] I. E. McCarthy, Rev. Mod. Phys. 37, 388 (1965).

[6] G. Jacob and Th. A. J. Maris, Rev. Mod. Phys. 38, 121 (1966); 45, 6 (1973).

[7] J. D. Cossairt *et al.*, Nucl. Phys. A261, 373 (1976).

[8] D J. Pisano and P. D. Parker, Phys. Rev. C 14, 475 (1976).

[9] M. E. Cobern, D. J. Pisano, and P. D. Parker, Phys. Rev. C 14, 491 (1976).

[10] N. Anantaraman *et al.*, Phys. Rev. Lett. 35, 1131 (1975).

[11] G. J. Wozniak, D. P. Stahel, J. Cerney, and N. A. Jelley, Phys. Rev. C 14, 815 (1976).

[12] H. Yoshida, Phys. Lett. 47B, 411 (1973).

[13] K. Bethge, Annu. Rev. Nucl. Sci. 20, 255 (1970).

[14] P. Nagel and R. D. Koshel, Phys. Rev. C 14, 1667 (1976).

[15] A. N. James and H. G. Pugh, Nucl. Phys. 42, 441 (1963).

[16] B. Gottschalk and S. L. Kannenberg, Phys. Rev. C 2, 24 (1970).

[17] P. G. Roos *et al.*, Phys. Rev. C 15, 69 (1977).

[18] A. A. Cowley *et al.*, Phys. Rev. C 15, 1650 (1977).

[19] N. S. Chant and P. G. Roos, Phys. Rev. C 15, 57 (1977).

[20] N. S. Chant and P. G. Roos, in *Proceedings of the Second International Conference on Clustering Phenomena in Nuclei, College Park, Maryland, 1975*, edited by D. A. Goldberg, J. B. Marion, and S. J. Wallace (ERDA Technical Information Center, Oak Ridge, Tennessee).

[21] P. G. Roos and N. S. Chant, in *Proceedings of the Second International Conference on Clustering Phenomena in Nuclei, College Park, Maryland, 1975*, edited by D. A. Goldberg, J. B. Marion, and S. J. Wallace (ERDA Technical Information Center, Oak Ridge, Tennessee).

[2] D. Kurath, Phys Rev. C 7, 1390 (1973).

[3] M. Ichimura, A. Arima, E. C. Halbert, and T. Terasawa, Nucl. Phys. A204, 225 (1973).

[4] J. W. Watson *et al.*, Nucl. Phys. A172, 513 (1971).

[5] M. Jain, P. G. Roos, H. G. Pugh, and H. D. Holmgren, Nucl. Phys. A153, 49 (1970); H. G. Pugh *et al.*, Phys. Rev. Lett 22, 408 (1969).

[6] A. Guichard *et al.*, Phys. Rev. C 4, 700 (1971).

[7] P. Gaillard *et al.*, Phys. Rev. Lett. 25, 593 (1970).

[8] M. B. Epstein, D. J. Margaziotis, N. S. P. King, and T. A. Cahill, Phys. Rev. C 9, 581 (1974).

[9] J. D. Sherman, Ph.D. thesis, University of California, Berkeley, 1973 (Report No. LBL-1690).

[30] J. D. Sherman, D. L. Hendrie, and M. S. Zisman, Phys. Rev C 13, 20 (1976).

[31] N. Chirapatpimol *et al.*, Nucl. Phys. A264, 379 (1976).

[32] I. E. McCarthy and D. L. Pursey, Phys. Rev. 122, 578 (1961).

[33] A. W. Parker, J. S. Allen, R. L. Yerke, and V. G. Scotland, Phys. Rev. 7, 1093 (1968).

[34] M. Epstein *et al.*, Phys. Rev. 178, 1698 (1969).

[35] C. W. Wang, Ph.D. thesis, University of Maryland, 1978 (unpublished).

[36] H. D. Holmgren, in *Proceedings of the International Conference on Clustering Phenomena in Nuclei, Bochum, Germany, 1969* (International Atomic Energy Agency, Vienna, Austria, 1969).

[37] A. Nadasen *et al.*, Phys. Rev. C 18, 2792 (1978); P. Frisbee, Ph.D. thesis, University of Maryland, 1972 (unpublished).

[38] P. Darriulat, G. Igo, H. G. Pugh, and H. D. Holmgren, Phys. Rev. 137, B315 (1965).

[39] E. F. Redish, G. J. Stephenson, Jr., and G. M. Lerner, Phys. Rev. C 2, 1665 (1970).

[40] D. F. Jackson and T. Berggren, Nucl. Phys. 62, 353 (1965).

[41] A. K. Jain and N. Sarma, *Clustering Aspects of Nuclear Structure and Nuclear Reactions*, edited by W. T. H. Van Oers, J. P. Svenne, J. S. C. McKee, and W. R. Falk (AIP, New York, 1978), p. 568.

[42] R. H. Pehl, Ph.D. thesis, Report No. UCRL 10993, 1963 (unpublished).

[43] See for example D. A. Goldberg and S. M. Smith, Phys. Rev. Lett. 33, 715 (1974); P. Gaillard *et al.*, Nucl. Phys. A131, 353 (1969).

[44] T. A. Carey, Ph.D. thesis, University of Maryland, 1979 (unpublished).

[45] N. S. Chant, *Clustering Aspects of Nuclear Structure and Nuclear Reactions*, edited by W. T H. Van Oers, J. P. Svenne, J. S. C. McKee, and W. R. Falk (AIP, New York, 1978), p. 415.

[46] N. S. Chant, P. G. Roos, and C. W. Wang, Phys. Rev. C 17, 8 (1978).

[47] C. Détraz, H. H. Duhm, and H. Hagner, Nucl. Phys. A147, 488 (1970).

[48] G. Audi, C. Détraz, M. Langevin, and F. Pougheon, Nucl. Phys. A237, 300 (1975).

[49] B. K. Jain, Nucl. Phys. A314, 51 (1979).

[50] G. E. Brown and A. M. Green, Nucl. Phys. 75, 401 (1966).

[51] I. Sick, Nucl. Phys. A218, 509 (1974).

[52] S. M. Smith *et al.*, Nucl. Phys. A207, 273 (1973).

[53] P. Gaillard *et al.*, Nucl. Phys. A131, 353 (1969).

[54] S. Matsuki *et al.*, J. Phys. Soc. Jpn. 26, 1344 (1969).

[55] H. Rebel *et al.*, Nucl. Phys. A182, 145 (1972).

[56] H. H. Gutbrod, H. Yoshida, and R. Bock, Nucl. Phys. A165, 240 (1971); P. Beregi, N. S. Zelenskaja, V. N. Neudatchin, and Yu. F. Smirnov, Nucl. Phys. 66, 513 (1965).

PHYSICAL REVIEW C VOLUME 21, NUMBER 5 MAY 1980

Separation of current and spin contributions to isovector $M1$ excitations by means of the (e,e') and (p,n) reactions

F. Petrovich
Department of Physics, Florida State University, Tallahassee, Florida 32306

W. G. Love
Department of Physics and Astronomy, University of Georgia, Athens, Georgia 30602

R. J. McCarthy
Department of Physics, Kent State University at Ashtabula, Ashtabula, Ohio 44004

(Received 10 October 1979)

The orbital current and spin contributions to isovector $M1$ excitations in light nuclei are studied microscopically by combining information from inelastic electron scattering at small momentum transfers with that obtained from recent measurements of (p,n) cross sections at forward angles. The (p,n) reaction is studied within the distorted-wave approximation using a G-matrix interaction and shell model wave functions and the (e,e') scattering is calculated in a plane wave approximation.

[NUCLEAR REACTIONS Charge exchange scattering, $E_p = 62$ MeV, cross sections; inelastic electron scattering; targets ^{12}C, ^{24}Mg, ^{28}Si.]

I. INTRODUCTION

Experimental studies of the (p,n) reaction at $E_p \gtrsim 60$ MeV, currently being carried out at the Indiana University Cyclotron Facility, will provide much new information on isovector modes of excitation in nuclei.[1-5] In one of the first (p,n) experiments, forward angle cross sections for the excitation of analogs of 1^+ $T=1$ levels in ^{12}C, ^{24}Mg, and ^{28}Si by 62 MeV protons were measured. We report here a study of the nature of the isovector dipole transitions in these nuclei based on the shell model wave functions of Cohen and Kurath (^{12}C) (Ref. 6) and Chung and Wildenthal (^{24}Mg, ^{28}Si).[7] It is shown that a *separate* measure of orbital current and spin transition matrix elements can be obtained by simultaneously considering information from the (p,n) reaction and corresponding information from low momentum transfer inelastic electron scattering.[8-11] The (p,n) reaction is interpreted within the distorted wave approximation and the G-matrix interaction of Bertsch *et al.*[12] is assumed for the effective interaction. The complete spin dependent isovector part of the interaction is compared with the one-pion exchange potential (OPEP) which is expected to be the leading term at small momentum transfer.

II. RELATION BETWEEN THE (e,e') AND (p,n) REACTIONS

For $0^+ \to J^\pi$ abnormal parity transitions it is common[8-11,13] to characterize the inelastic electron scattering cross sections by the reduced magnetic transition probability. The Born expression for this quantity, which is adequate for the discussion of electron scattering from light nuclei, is given by[13]

$$B(MJ\uparrow;q)=\left[\frac{(2J+1)!!}{q^{J-1}}\left(\frac{J}{J+1}\right)^{1/2}\frac{e\hbar}{2Mc}\right]^2 \times\left|\sum_{L,t}\left[C^s_{L}g^t_s\rho^{st}_{JL}(q)+C^l_{L}g^t_l\rho^{lt}_{JL}(q)\right]\right|^2, \quad (1)$$

where q is the momentum transfer, L is the orbital angular momentum transfer which is restricted to the values $J-1$ and $J+1$, t differentiates between isoscalar and isovector quantities, g^t_s and g^t_l are the spin and orbital g factors, $C^s_{J-1}=\frac{1}{2}(J+1)^{1/2}$, $C^l_{J-1}=2(J+1)^{-1/2}$, $C^s_{J+1}=-\frac{1}{2}J^{1/2}$, $C^l_{J+1}=2J^{-1/2}$, and $\rho^{st}_{JL}(q)$ and $\rho^{lt}_{JL}(q)$ are the momentum representations of the spin and orbital current transition densities defined by

$$\rho^{kt}_{JL}(q)=\left\langle J^\pi\left\|\sum_i j_L(qr_i)[Y_L(\hat r_i)\times O^k_i]^J\tau^t_i\right\|0\right\rangle, \quad (2)$$

where $\langle\|\ \|\rangle$ denotes a reduced matrix element,[14] $j_L(qr_i)$ is a spherical Bessel function, and O^k_i is $\vec\sigma_i$ or $\vec l_i$ as k is s or l. We are specifically interested in transitions with $J=t=1$ for which L can be 0 or 2. By expanding the Bessel functions in Eq. (2) about $q=0$ one easily obtains the two parameter formula[8-11] commonly used to describe the low q electron scattering data, i.e.,

$$B(MJ\uparrow;q)=B(MJ\uparrow;0)\left[1-\frac{J+3}{J+1}\frac{(qR_{tr})^2}{2(2J+3)}+\cdots\right]^2, \quad (3)$$

where $B(MJ\uparrow;0)$ is the reduced transition probability for γ decay and R_{tr} is the transition radius.

To see the connection between inelastic electron

© 1980 The American Physical Society

scattering and the (p,n) reaction for a $0^+ \to J^\pi$ abnormal parity transition, it is useful to examine the direct microscopic Born approximation expression for the (p,n) cross section. In the case of a local effective interaction with central, tensor, and spin-orbit parts this is[15-17]

$$\frac{d\sigma}{d\Omega} = \left(\frac{\mu}{2\pi\hbar^2}\right)^2 \frac{k_f}{k_i} (2J+1)8\pi$$
$$\times \left\{ \left| \sum_{L,t} v_t^{LS}(q) B_L^J \rho_{JL}^{st}(q) \right|^2 \right.$$
$$+ \sum_L \left| \sum_t \left[v_t^C(q) \rho_{JL}^{st}(q) + v_t^T(q) \sum_{L'} Z_{LL'}^J \rho_{JL'}^{st}(q) \right.\right.$$
$$\left.\left.\left. + v_t^{LS}(q) A_L^J \rho_J^{lt}(q) \right] \right|^2 \right\}, \qquad (4)$$

where the factors outside the curly brackets are the usual kinematical and statistical factors, $v^C(q)$, $v^T(q)$, and $v^{LS}(q)$ are the Bessel transforms of the spin-dependent central, tensor, and spin-orbit components of the effective interaction, L' is the orbital angular momentum transfer to the target when the tensor interaction is acting, A_L^J, B_L^J, and $Z_{LL'}^J$ are statistical coefficients which can be obtained elsewhere,[17-19] $\rho_{JL}^{st}(q)$ is the spin transition density, and $\rho_J^{lt}(q)$ is a linear combination of the orbital current densities. As in the discussion of Eqs. (1)–(3) we are specifically interested in the case $J = t = 1$ for which L and L' can each be either 0 or 2. A proper treatment of the (p,n) reaction requires, of course, the inclusion of distortion effects[20] and knockout exchange amplitudes.[21] These effects are not included explicitly in Eq. (4) ecause they complicate the relation without af- ecting its basic sense. Both distortion and knockout exchange are treated *exactly* in the final cal- lations of the (p,n) cross sections to be discuss- below. In the graphs of the effective interac- n to be shown, the knockout exchange ampli- ies for the central and spin-orbit interaction mponents are included in the interaction by ans of a well established approximation.[22,23] this point, it is clear from Eqs. (1) and (4) that connection between the (e,e') and (p,n) reac- ns for $0^+ \to J^\pi$ abnormal parity transitions is ually complicated.

III. RESULTS

Some of the essential results obtained from the ell model wave functions of Refs. 6 and 7 are mmarized in Table I and Fig. 1. The table lists e theoretical and experimental excitation energ- es, reduced transition probabilities $B(M1\uparrow)$, and ansition radii R_{tr} for the first $1^+T=1$ excitation in ^{12}C and the first four $1^+T=1$ levels in ^{24}Mg and ^{28}Si. The last two columns in the table contain the values of the theoretical $L=0$ spin and orbital current transition densities at $q=0$. The complete set ($L=0$ and $L=2$) of theoretical spin and orbital cur-

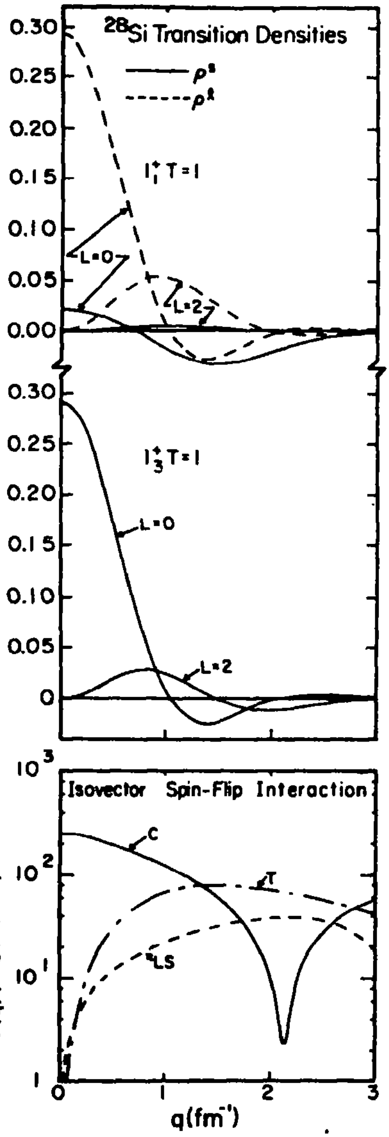

FIG. 1. The $L=0$ and $L=2$ spin and orbital current densities for the 1_1^+ and 1_3^+ $T=1$ excitations in ^{28}Si are compared with the isovector spin-flip parts of the G-matrix interaction of Ref. 12. For the 1_3^+ $T=1$ excitation the orbital current densities are too small to show in the graph. C, LS, and T refer to the central, spin-orbit, and tensor components of the interaction.

TABLE I. Comparison of shell model results with experiment for isovector $M1$ transitions in ^{12}C, ^{24}Mg, and ^{28}Si.

Nucleus	Final state	$E_x^{\text{exp}\,a}$ (MeV)	$E_x^{\text{th}\,b}$ (MeV)	$B(M1\uparrow)_{\text{exp}}{}^{a}$ ($e^2\,\text{fm}^2$)	$B(M1\uparrow)_{\text{th}}{}^{b}$ ($e^2\,\text{fm}^2$)	$R_{\text{tr}}^{\text{exp}\,a}$ (fm)	$R_{\text{tr}}^{\text{th}\,b}$ (fm)	$\rho_{10}^{s1}(0)$	$\rho_{10}^{l1}(0)$
^{12}C	1_1^+ $T=1$	15.11	15.08	$(3.22 \pm 0.33)\times 10^{-2}$	2.54×10^{-2}	2.70 ± 0.20	2.67	−0.221	0.026
^{24}Mg	1_1^+ $T=1$	9.97	10.22	$(1.30 \pm 0.21)\times 10^{-2}$	6.31×10^{-3}	3.05 ± 0.44	3.10	−0.035	−0.339
	1_2^+ $T=1$	10.72	11.14	$(4.10 \pm 0.77)\times 10^{-2}$	3.86×10^{-2}	2.94 ± 0.14	2.94	−0.221	−0.210
	1_3^+ $T=1$		13.30		3.41×10^{-2}		3.45	−0.156	0.361
	1_4^+ $T=1$		13.59		2.53×10^{-3}		2.75	0.090	−0.104
^{28}Si	1_1^+ $T=1$	10.48	12.05	$(5.99 \pm 2.75)\times 10^{-3}$	3.86×10^{-3}	3.90 ± 0.40	2.78	0.022	0.293
	1_2^+ $T=1$	10.86	12.29	$(1.28 \pm 0.27)\times 10^{-2}$	2.23×10^{-2}	2.98 ± 0.25	2.95	0.186	0.080
	1_3^+ $T=1$	11.41	13.28	$(4.01 \pm 0.77)\times 10^{-2}$	4.64×10^{-2}	2.58 ± 0.23	2.97	−0.292	0.001
	1_4^+ $T=1$	12.27	14.00	$(1.13 \pm 0.29)\times 10^{-2}$	5.26×10^{-3}	2.93 ± 0.36	2.87	−0.098	−0.001

[a] Reference 11.

[b] The ^{12}C results are from Ref. 6 while the ^{24}Mg and ^{28}Si results are from Ref. 7. Harmonic oscillator radial wave functions were used in the calculations with $b = 1.95$, 1.82, and 1.86 fm for ^{12}C, ^{24}Mg, and ^{28}Si, respectively.

rent transition densities for the 1_1^+ and 1_3^+ $T=1$ excitations in ^{28}Si are shown with the isovector spin-flip components of the G matrix interaction of Ref. 12 in Fig. 1.

From Table I it is clear that the theoretical wave functions give a good qualitative account of the experimental electromagnetic data. One can distinguish between two types of transitions. One type might be called current correlated, i.e., $\rho_{10}^{l1} \gg \rho_{10}^{s1}$. The 1_1^+ $T=1$ levels in both ^{24}Mg and ^{28}Si are of this type. These are weak in electron scattering because $g_l{}^1 \approx 0.1 g_s{}^1$. They are weaker still in the (p,n) reaction at low q because ρ_{10}^{l1} couples to the projectile through the spin-orbit interaction which is essentially zero at $q=0$. These levels were not seen in the 62 MeV experiment[1-5] being discussed here. The other type of transition might be called spin dominated, i.e., $g_s{}^1\rho_{10}^{s1} > g_l{}^1\rho_{10}^{l1}$. All of the other excitations in the table fall into this group. The current contributions to the spin dominated states in ^{24}Mg are considerably larger than those for the spin dominated states in ^{12}C and ^{28}Si. This occurs because of the open $j = 1d_{5/2}$ shell for ^{24}Mg. It is the $1d_{5/2} - 1d_{5/2}$ single particle transition which has the largest current matrix elements in the s-d shell.

Using the fact that the tensor interaction, the spin-orbit interaction, and the $L=2$ transition densities are small near $q=0$, Eqs. (1) and (4) reduce approximately to

$$B(M1\uparrow;q) \approx g\left(\frac{e\hbar}{2Mc}\right)^2 \left|\tfrac{1}{2}g_s{}^1\rho_{10}^{s1}(q) + g_l{}^1\rho_{10}^{l1}(q)\right|^2, \quad (5)$$

$$\frac{d\sigma}{d\Omega} \approx 8\pi\left(\frac{\mu}{2\pi\hbar^2}\right)^2 \frac{k_f}{k_i} 3\left|v_1^C(q)\rho_{10}^{s1}(q)\right|^2 \quad (6)$$

for the spin dominated transitions at low q. These relations clearly show that the scaling of the forward (p,n) cross sections for spin dominated transitions measures the scaling of the $L=0$ spin transition densities at low q and departures in the scaling of $M1$ rates and forward (p,n) cross sections are a direct consequence of the $L=0$ orbital current transition densities at low q.

Equations (5) and (6) do not allow for a model independent determination of $v_1^C(q)$ at low q since there are two experimental values, $B(M1\uparrow;q)$ and $d\sigma/d\Omega$, and two structure unknowns, ρ_{10}^{s1} and ρ_{10}^{l1}, for each transition. β decay is more useful in this regard because allowed Gamow-Teller decays provide a direct measure of $\rho_{10}^{s1}(0)$ (Refs. 24 and 25) which can be used in Eq. (6). The essential relation is

$$\langle\sigma\rangle^2 = 6\pi\left|\rho_{10}^{s1}(0)\right|^2, \quad (7)$$

where $\langle\sigma\rangle^2$ is the Gamow-Teller matrix element. There are no β-decay data available for transitions in ^{24}Mg and ^{28}Si. The ^{12}N$(1^+) \to {}^{12}$C(0^+) β^+ rate[10,20] implies that $\rho_{10}^{s1}(0) = 0.223$ for the $0^+ - 1_1^+$ $T=1$ transition in ^{12}C. This is quite close to the value of 0.221 obtained from the Cohen and Kurath wave functions so this transition serves to fix $v_1^C(q)$. In addition, it is concluded that the discrepancy between the experimental and theoretical $B(M1\uparrow)$ for this transition is associated with the orbital current transition density. Multiplication of $\rho_{10}^{l1}(0)$ in Table I by about −2 is sufficient to remove the discrepancy.

The results of theoretical distorted wave calculations are compared with the experimental (p,n) data in Fig. 2. The theoretical (p,n) cross sec-

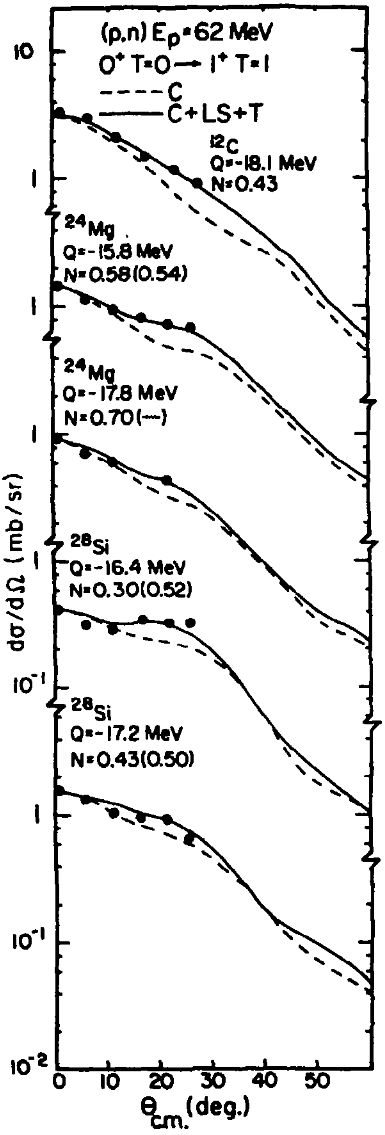

FIG. 2. The results of the distorted wave calculations ormalized to the data as described in the text. The ashed curves are the results obtained with the central omponents of the G-matrix interaction alone and the olid curves are the results obtained with the complete -matrix interaction. The levels observed in ^{24}Mg and Si correspond to the 1_1^+ and 1_2^+ $T=1$ excitations listed in able I.

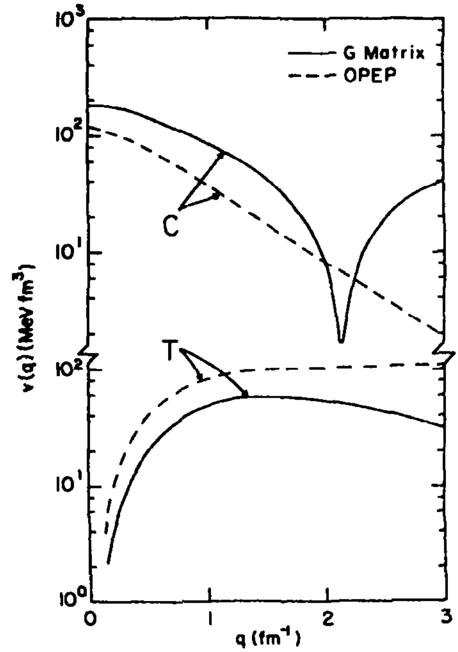

FIG. 3. A comparison of the central and tensor parts of the G-matrix interaction of Ref. 12 (reduced by the factor 1.4) with the corresponding parts of the OPEP.

ions have been calculated with the computer code WBA70 (Ref. 27) using the wave functions of Refs. and 7, the G matrix interaction of Ref. 12, and optical model parameters of Ref. 28. The theoretical results give a good reproduction of the shape of the experimental data, but have to be renormalized by factors $N = 0.3-0.7$ to reproduce the magnitude of the experimental cross sections. The noncentral components of the effective interaction make essentially no contributions to the (p,n) cross sections at 0°. They do enter and improve the shape of the (p,n) cross sections at larger angles. Much less scatter is obtained in the normalization factors if the theoretical wave functions are first normalized to the experimental $B(M1\uparrow)$. This is reflected in the normalization factors shown in parentheses in Fig. 2. This prescription was not applied to the ^{12}C transition because of the β-decay information discussed above. The calculation for the ^{24}Mg(p,n) transition to the analog of the 1_2^+ state was not renormalized either since the corresponding transition is not observed in (e,e'). The fact that this transition is seen in the (p,n) reaction but not in (e,e') experiments supports the large cancellation between spin and current terms predicted by the Chung-Wildenthal wave functions. This further emphasizes the complementary information which can be obtained from comparative studies of this type. Excluding the 1_2^+ state in ^{24}Mg, the final renormalization factors range from $N = 0.43$ to $N = 0.54$. One could attempt to reduce further the discrepancy between the normalization factor for ^{12}C compared to ^{24}Mg and ^{28}Si by making additional adjustments in the spin and orbital current densities for ^{24}Mg and ^{28}Si. Uncertainties in the effects of distortion for the scattering of 62 MeV protons from ^{12}C (Ref. 28) are, however, comparable to the existing discrepancy so this has not been done.

It is concluded from these results that the isovector spin-flip components of the G-matrix interaction of Ref. 12 are too strong by a factor of approximately 1.4 at low q. In keeping with current interest in describing the (p,n) reaction in terms of amplitudes which might be considered elementary,[29] the central and tensor components of the G-matrix interaction of Ref. 12 (reduced by 1.4) are compared with the corresponding components of the OPEP in Fig. 3. The corrected G matrix $v_1^C(0)$ is 180 MeV fm^3 which is to be compared with the OPEP value of 119 MeV fm^3, so that OPEP accounts for approximately 44% of the forward (p,n) cross sections at $E_p = 62$ MeV. The present calculations are currently being extended to the newer experimental (p,n) data for incident energies near 120 MeV.[1-5] Preliminary results[15,16,30] indicate that the t matrix interaction of Ref. 31 is adequate for describing the forward (p,n) cross sections for isovector $M1$ excitations near 120 MeV. OPEP accounts for about 60% of the forward (p,n) cross sections at this higher energy. These results are only in qualitative agreement with results based on partially conserved axial-vector current (PCAC) and the absorption model.[29]

IV. SUMMARY

In summary the manner in which experimental data from the (p,n) and (e,e') reactions at low momentum transfers can be used to separate the orbital current and spin contributions to isovector $M1$ transitions has been demonstrated. It was necessary to introduce the available β-decay rate for the single transition in ^{12}C to fix the strength of the effective interaction used in the description of the (p,n) reaction. Specific results are that the wave functions of Cohen and Kurath[8] give a good description of $\rho_{10}^{s1}(0)$, but not $\rho_{10}^{l1}(0)$, for the $0^+ \rightarrow 1_1^+$ $T = 1$ transition in ^{12}C while the Chung and Wildenthal wave functions[7] for ^{24}Mg and ^{28}Si give about the correct values for $\rho_{10}^{l1}(0)/\rho_{10}^{s1}(0)$, but miss somewhat on the overall magnitude of these quantities. The large orbital current contributions to the ^{24}Mg transitions is a striking feature of the latter wave functions that is consistent with the data. In addition it has been shown that the isovector spin-flip components of the G-matrix interaction of Ref. 12 are about 40% too strong and that the OPEP accounts for only about 44% of the forward angle (p,n) cross sections at $E_p = 62$ MeV.

ACKNOWLEDGMENTS

We would like to thank the authors of Refs. 1–5 for providing us with their data prior to publication and M. B. Greenfield for help with some of the calculations. Additional thanks go to D. Kurath and B. H. Wildenthal for helpful correspondence concerning their nuclear wave functions. This work was supported in part by the National Science Foundation.

---

[1] B. D. Anderson, D. E. Bainum, A Baldwin, C. C. Foster, C. D. Goodman, C. A. Goulding, M. B. Greenfield, J. N. Knudson, R. Madey, J. Rapaport, and T. R. Witten, IUCF Technical and Scientific Report 1977–1978 (unpublished), p. 117.

[2] C. D. Goodman, in *Proceedings of the LAMPF Workshop on Pion Single Charge Exchange, Los Alamos, 1979*, Report No. LA-7892C, p. 23.

[3] C. D. Goodman, in *The (p,n) Reaction and the Nucleon-Nucleon Force*, edited by C. D. Goodman *et al.* (Plenum, New York, 1980), p. 149.

[4] C. A. Goulding, M. B. Greenfield, C. C. Foster, T. E. Ward, J. Rapaport, D. E. Bainum, and C. D. Goodman, Nucl. Phys. A331, 29 (1979).

[5] B. Anderson, D. Bainum, A. Baldwin, C. C. Foster, A. I. Galonsky, C. D. Goodman, C. Goulding, D. Horen, J. Knudson, D. Lind, R. Madey, J. Rapaport, G. R. Satchler, S. D. Schery, G. Walker, J. Watson, T. Witten, and C. Zafiratos, IUCF Technical and Scientific Report 1978 (unpublished), p. 45.

[6] S. Cohen and D. Kurath, Nucl. Phys. 73, 1 (1965); A101, 1 (1976); D. Kurath, private communication.

[7] B. H. Wildenthal, in *The (p,n) Reaction and Nucleon-Nucleon Force*, edited by C. D. Goodman *et al.* (Plenum, New York, 1980), p. 89; W. Chung and B. H. Wildenthal (unpublished).

[8] L. W. Fagg, W. L. Bendel, R. A. Tobin, and H. T. Kaiser, Phys. Rev. 171, 1250 (1968).

[9] L. W. Fagg, W. L. Bendel, E. C. Jones, Jr., and S. Numrich, Phys. Rev. 187, 1378 (1969).

[10] B. T. Chertok, C. Sheffield, J. W. Lightbody, Jr., S. Penner, and D. Blum, Phys. Rev. C 8, 23 (1973).

[11] H. Theissen, *Springer Tracts in Modern Physics*, Vol. 65 (Springer, Berlin, 1972), p. 1.

[12] G. Bertsch, J. Borysowicz, H. McManus, and W. G. Love, Nucl. Phys. A284, 399 (1977).

[13] T. de Forest, Jr. and J. D. Walecka, Adv. Phys. 15, 1 (1966).

[14] D. M. Brink and G. R. Satchler, *Angular Momentum* (Oxford University Press, Oxford, 1962).

[15] F. Petrovich and W. G. Love, in *Proceedings of the LAMPF Workshop on Pion Single Charge Exchange, Los Alamos, 1979,* Report No. LA-7892C, addendum.

[16] F. Petrovich, in *The (p,n) Reaction and the Nucleon-Nucleon Force*, edited by C. D. Goodman *et al.* (Plenum, New York, 1980), p. 115.

[17] F. Petrovich and W. G. Love (unpublished).

[18] W. G. Love and L. J. Parish, Nucl. Phys. A157, 625 (1970).

[19] W. G. Love, Nucl. Phys. A192, 49 (1972).

[20] G. R. Satchler, Nucl. Phys. 55, 1 (1964).

[21] K. A. Amos, V. A. Madsen, and I. E. McCarthy, Nucl. Phys. A94, 103 (1967).

[22] F. Petrovich, H. McManus, V. A. Madsen, and J. Atkinson, Phys. Rev. Lett. 22, 895 (1969).

[23] W. G. Love, Nucl. Phys. A312, 160 (1978).

[24] J. D. Anderson, C. Wong, and V. A. Madsen, Phys. Rev. Lett. 24, 1074 (1970).

[25] A. Bohr and B. Mottelson, *Nuclear Structure* (Benjamin, New York, 1969), Vol. I, p. 345.

[26] F. Ajzenberg-Selove, Nucl. Phys. A248, 1 (1975).

[27] J. Raynal and R. Schaeffer, computer code DWBA70.

[28] C. B. Fulmer, J. B. Ball, A. Scott, and M. L. Whiten, Phys. Rev. 181, 1565 (1969).

[29] G. L. Moake, L. J. Gutay, R. P. Scharenberg, P. T. Debevec, and P. A. Quin, Phys. Rev. Lett. 43, 910 (1979); G. L. Moake, L. J. Gutay, R. P. Scharenberg, P. T. Debevec, and P. A. Quin (unpublished).

[30] W. G. Love, in *The (p,n) Reaction and the Nucleon-Nucleon Force*, edited by C. D. Goodman *et al.* (Plenum, New York, 1980), p. 23.

[31] W. G. Love, A. Scott, F. Todd Baker, W. P. Jones, and J. D. Wiggins, Jr., Phys. Lett. 73B, 277 (1978).

PHYSICAL REVIEW C VOLUME 21, NUMBER 5 MAY 1980

Adiabatic limit of the Faddeev equations

L. R. Dodd and K. J. Nieukerke
Department of Mathematical Physics, University of Adelaide, G.P.O. Box 498, Adelaide, South Australia, 5001

(Received 2 October 1979)

The adiabatic scattering of two heavy particles, interacting by the exchange of a third light particle, is considered from the Faddeev viewpoint. The Faddeev equations are reduced to an equivalent infinite set of coupled integral equations, which like the equations of the close-coupling scheme have two-body kinematics, and effective two-body interactions, but unlike the close-coupling equations, properly include the effects of breakup states. Complete sets of eigenstates of the kernels of the two-body Lippmann-Schwinger equations (Sturmian states) are used to effect the expansions. For the special case of separable interactions the equivalent set is shown to be finite. The effective interactions of the theory are examined in the adiabatic and static limits and compared with the potentials of the close-coupling scheme. In the limiting case the interactions are determined by a reduced form of the three-particle propagator and found to be local, leading to an alternative set of coupled differential equations for the three-body elastic amplitude. The effective potentials and their limiting forms are constructed for three specific examples, the Yamaguchi interaction, a nonrelativistic model of the nucleon-nucleon interaction, and a model of heavy-ion transfer scattering using δ-shell interactions

NUCLEAR REACTIONS Three-body scattering in molecular-mass limit. Sturmian reduction of Faddeev equations. Adiabatic and static limits of effective two-body interactions for Yamaguchi, δ-shell potentials, model nucleon-nucleon interaction.

I. INTRODUCTION

Although various forms of the Faddeev equations have been used extensively in recent years to explore the properties of three-body systems, much of this work has necessarily involved lengthy numerical calculations. Simple systems for which the equations can be solved exactly are few. Exact solutions in closed form for the one-dimensional model of three equal mass particles interacting with δ-function potentials have been displayed by Dodd[1] using the work of McGuire.[2] Other models which admit exact solutions have been discussed by Fuda,[3] McGuire and Hurst,[4] and Gaudin and Derrida.[5] The problem of two noninteracting particles scattering from a center of force has been analyzed from the Faddeev viewpoint by Amado.[6]

Despite the complexity of the three-body equations, the physical properties of some three-body systems are adequately described using only two-body dynamics. In these situations a derivation of approximate two-body equations from the three-body theory is of interest in providing a theoretical justification of the simplified two-body description. More importantly, consideration of such limiting cases should allow a useful check of the numerical solutions of the full three-body equations to be made. For example, the scattering of a weakly interacting particle on a tightly bound state of a pair of particles is essentially a two-body process. The solution of the Faddeev equations is given to a good approximation by a wave function that is the product of the bound state wave function and a wave function of the coordinate of the scattered particle relative to the c.m. of the pair. Corrections to the Lamb shift in deuterium, due to the finite size and polarizability of the deuteron,[7] and off-shell effects in pionic deuterium[8] have been calculated in a three-body perturbation theory based on this point of view.

Another class of three-body systems considered in this paper, for which the Faddeev equations have accessible limiting forms, are those where two heavy particles interact by the exchange of a light particle, which may bind to either of them. In this molecular-mass limit, exemplified by the H_2^+ ion, one expects that low energy processes will be well described by the adiabatic approximation[9] where the motion of the light particle is decoupled from the motion of the heavy particles.

Recently Fonseca and Shanley[10] have compared in the molecular-mass limit binding energies calculated from the Faddeev equations with separable potentials with values obtained using the adiabatic approximation. Agreement is very good, even when the mass ratio of the heavy to light particles is not particularly large ($M/m < 30$). Some years ago a similar comparison was made for a one-dimensional model with δ interactions.[11] Here the adiabatic approximation took a very simple form and the bound state spectrum calculated in this approximation was also in excellent agreement with the exact spectrum calculated from the Faddeev equations.

Our present interest in the adiabatic limit was stimulated by the work of one of us (K.N.) on a three-dimensional, three-body model of heavy-ion elastic transfer collisions using δ-shell poten-

© 1980 The American Physical Society

ials.[12] The δ shell was chosen because it is both ocal and separable, and its properties in momenum space simplify the angular momentum algebra. On the other hand, because of the analytic properies of the potential, the standard technique of contour rotation[13] cannot be used to solve the Faddeev equations, and rather complicated numerical methods are necessary.[14] One is faced with the problem of checking the results of a large numerical calculation. We have found that a conideration of the adiabatic limit provides an invaluable test of the validity of the numerical work. In this limit, independent solutions of the problem may be found by an entirely different method, namely by solving sets of coupled differenial equations, with effective local potentials as xplained in this paper.

Von Oertzen[15] has already discussed, on the basis of the exchange interaction, the effective potential acting between the heavy cores in the elastic transfer reaction. In the adiabatic limit he potential has a Yukawa form in coordinate space for large separations of the cores.[16] The range is fixed by the binding energy of the valence particle in the core. We obtain a similar result rom three-body theory.

Our purpose in this paper is to show how the adiabatic limit of a three-particle system with appropriate masses emerges from the Faddeev ormulation. In Sec. II our approach is to reduce he Faddeev equations to an infinite set of coupled Lippmann-Schwinger equations which formally have wo-body kinematics and which contain effective wo-body interactions. Although it is well known hat the Faddeev equations reduce to coupled twobody equations in the separable potential approximation, we wish to emphasize here that our method is more general. We make use of the complete set of eigenstates of the kernel of the two-body Lippmann-Schwinger equation to effect the expansions.[17,18] A rigorous set of coupled two-body equations, of the same form as the equations of he close-coupling approximation, is obtained. Unike the close-coupling equations, the effects of ntermediate continuum states have not been discarded in these equations.

In Sec. III the three-body system is taken to consist of two heavy identical particles and one light particle which may bind to either heavy. The efective two-body interactions of the theory are examined in the adiabatic limit. It is shown how hey may be reduced to the potentials which appear n the usual adiabatic approach. Corrections to the adiabatic solutions may be obtained by treating the differences between the exact effective potentials and their adiabatic limits as perturbations.

In Sec. IV specific examples are discussed. In IV A we deduce the form of the effective potential when the pair interaction is a Yamaguchi potential. In the adiabatic limit it is shown that the interaction between the heavy particles reduces to a local Yukawa interaction with space exchange (Majorana force). In IV B a nonrelativistic model[19] of the nucleon-nucleon interaction first proposed by Lovelace[20] and used by Thomas and Afnan[21] in their model of pion-deuteron scattering is discussed. In IV C the heavy-ion elastic transfer model with δ interactions is considered. Explicit forms for the exact effective potentials and their adiabatic limits are given. In the limiting case the potentials are local and the elastic amplitude may be obtained by solving a set of coupled differential equations. Some preliminary numerical calculations comparing the solutions of the differential equations, valid in the adiabatic limit, and the full Faddeev equations have been carried out. The results of these calculations will be presented in a subsequent paper.

II. EQUIVALENT TWO-BODY EQUATIONS

(A) Close-coupling scheme

Consider the scattering of particle 1 with momentum $\vec{p}$ relative to the c.m. of a bound state $\phi_\rho^{(1)}$ of particles 2 and 3. The Faddeev representation of the scattering state is

$$|\psi^+\rangle = |\psi^{(1)}\rangle + |\psi^{(2)}\rangle + |\psi^{(3)}\rangle\,, \tag{2.1}$$

with $\psi^{(i)}$ satisfying

$$|\psi^{(i)}\rangle = |\phi_\rho^{(i)}\rangle\delta_{i1} + \sum_{j\neq i} G_0 t_i |\psi^{(j)}\rangle\,, \tag{2.2}$$

where G_0 is the free Green's operator and t_i is the two-particle transition operator acting in the three-particle space.

In order to obtain a set of coupled equations to which the adiabatic approximation can be applied, we make a decomposition of the orbital $\psi^{(i)}$ in terms of a complete set of states $\phi_\alpha^{(i)}$ of the pair subsystem consisting of particles j and k,

$$|\psi^{(i)}\rangle = \sum_\alpha |\psi_\alpha^{(i)}\rangle|\phi_\alpha^{(i)}\rangle\,. \tag{2.3}$$

Among the states $\phi_\alpha^{(i)}$ are included the bound states of j and k. The state $\psi_\alpha^{(i)}$ depends only on the observables of particle i relative to the c.m. of j and k. Introducing (2.3) into (2.2), we obtain the coupled equations

$$\begin{aligned} |\psi_\alpha^{(i)}\rangle = {} & |\vec{p}\rangle\delta_{i1}\delta_{\alpha\rho} \\ & + \sum_{\substack{j\neq i\\ \beta}} \langle\phi_\alpha^{(i)}|G_0 t_i|\phi_\beta^{(j)}\rangle|\psi_\beta^{(j)}\rangle\,. \end{aligned} \tag{2.4}$$

For the bound states in the set $\phi_\alpha^{(i)}$, the kernel simplifies,

$$\begin{aligned} \langle\phi_\alpha^{(i)}|G_0 t_i|\phi_\beta^{(j)}\rangle &= \langle\phi_\alpha^{(i)}|(E-H_i)^{-1}v_i|\phi_\beta^{(j)}\rangle \\ &= g_0^{(i)}(E+\epsilon_\alpha^{(i)})V_{\alpha\beta}^{(ij)}\,. \end{aligned} \tag{2.5}$$

Here $g_0^{(i)}$ is the free two-body Green's operator depending only on the kinetic energy of particle i and the effective two-particle potentials $V_{\alpha\beta}^{(ij)}$ are defined by

$$V_{\alpha\beta}^{(ij)} = \langle\phi_\alpha^{(i)}|v_i|\phi_\beta^{(j)}\rangle . \tag{2.6}$$

Thus if the set (2.4) is truncated by retaining only bound states in the sum (2.3), a well-behaved set of coupled, two-body Lippman-Schwinger equations results, i.e.,

$$|\psi_\alpha^{(i)}\rangle = |\vec{p}\rangle\delta_{i1}\delta_{\rho\alpha} + \sum_{\substack{j\neq i\\ \beta}} g_0^{(i)}(E+\epsilon_\alpha^{(i)})V_{\alpha\beta}^{(ij)}|\psi_\beta^{(j)}\rangle . \tag{2.7}$$

It must be emphasized that the truncation which is necessary to obtain (2.7) excludes continuum eigenstates of the two-body subsystems, which should appear in the formal expansion (2.3). Consequently, the difficulties arising from states containing three separated particles, which the Faddeev equations (2.2) correctly take into account, are ignored.

(B) The Sturmian reduction

An alternative method of obtaining an infinite set of coupled two-body equations, having the advantages of the close-coupling set (2.7), but avoiding the difficulties of the continuum states, uses the eigenstates $\chi_\alpha^{(i)}$ of the kernel of the two-body Lippman-Schwinger equation

$$v_i g_0^{(i)}(\sigma_i)|\chi_\alpha^{(i)}(\sigma_i)\rangle = \lambda_\alpha^{(i)}(\sigma_i)|\chi_\alpha^{(i)}(\sigma_i)\rangle . \tag{2.8}$$

For a wide class of potentials, the kernel of (2.8) after symmetrization can be shown to be compact, ensuring the discreteness of the set $\chi_\alpha^{(i)}$ and leading to the orthonormality conditions

$$\langle\chi_\alpha^{(i)}|g_0^{(i)}(\sigma_i)|\chi_\beta^{(i)}\rangle = -\delta_{\alpha\beta}. \tag{2.9}$$

It is essential to note that the eigenvalues $\lambda_\alpha^{(i)}$ and the states $\chi_\alpha^{(i)}$ depend parametrically on the choice of the pair subenergy σ_i.

The orthonormality relations (2.9) hold strictly only for negative energies σ_i, but the defining equations (2.8) can usually be continued to energies above the two-body scattering threshold, with a suitable generalization of (2.9).[18]

From (2.8) and (2.9), it is easy to show that the transition operator has the form

$$t_i(\sigma_i) = -\sum_\alpha |\chi_\alpha^{(i)}(\sigma_i)\rangle\lambda_\alpha^{(i)}(\sigma_i) \times[1-\lambda_\alpha^{(i)}(\sigma_i)]^{-1}\langle\chi_\alpha^{(i)}(\sigma_i)| . \tag{2.10}$$

If there is a bound state $\phi_\rho^{(i)}$ of particles j and k with binding energy $\epsilon_\rho^{(i)}$, Eq. (2.8) implies that $\lambda_\rho^{(i)}(-\epsilon_\rho^{(i)})=1$. The relationship of the bound state $\phi_\rho^{(i)}$ and the eigenstate $\chi_\rho^{(i)}$ may be established by taking the residue of the transition operator (2.10) at the pole $\sigma_i = -\epsilon_\rho^{(i)}$ and comparing it with the usual spectral representation, with the result that

$$|\phi_\rho^{(i)}\rangle = -N_\rho^{(i)}g^0(-\epsilon_\rho^{(i)})|\chi_\rho^{(i)}(-\epsilon_\rho^{(i)})\rangle . \tag{2.11}$$

with normalization constant

$$N_\rho^{(i)} = \left[\frac{d\lambda_\rho^{(i)}}{d\sigma_i}\right]^{-1/2}_{\sigma_i=-\epsilon_\rho^{(i)}} . \tag{2.12}$$

If $\vec{p}_i$ is the momentum of particle i relative to the c.m. of particle j and k, then from (2.9) we see that the identity operator in the three-particle space has the representation

$$I = -\sum_\alpha\int g_0^{(i)}(\sigma_i)|\chi_\alpha^{(i)}\rangle|\vec{p}_i\rangle\langle\vec{p}_i|\langle\chi_\alpha^{(i)}|d^3p_i , \tag{2.13}$$

the states $\chi_\alpha^{(i)}$ are evaluated at the pair subenergies σ_i equal to the three-body energy E less the kinetic energy of particle i,

$$\sigma_i = E - p_i^2/2\mu^i . \tag{2.14}$$

In terms of the free Green's operator G_0 acting in the three-particle space, Eq. (2.13) may be written in the alternative form

$$I = -\sum_\alpha G_0(E)|\chi_\alpha^{(i)}(\sigma_i)\rangle\langle\chi_\alpha^{(i)}(\sigma_i)| . \tag{2.15}$$

This expression, together with (2.11), suggests that (2.3) be replaced by the expansion

$$|\psi^{(i)}\rangle = -\sum_\alpha G_0(E)|\chi_\alpha^{(i)}\rangle|\psi_\alpha^{(i)}\rangle N_\alpha^{(i)} , \tag{2.16}$$

with

$$|\psi_\alpha^{(i)}\rangle = \langle\chi_\alpha^{(i)}|\psi^{(i)}\rangle N_\alpha^{(i)} .$$

For eigenvectors associated with bound states, the normalization constant is fixed by Eq. (2.12); for other states $N_\alpha^{(i)}$ may be taken as unity.

With the help of (2.10) and (2.16), Eq. (2.2) yields the coupled equations

$$|\psi_\alpha^{(i)}\rangle = |\vec{p}\rangle\delta_{i1}\delta_{\alpha\rho} - \sum_{\substack{j\neq i\\ \beta}} \lambda_\alpha^{(i)}(1-\lambda_\alpha^{(i)})^{-1}(N_\alpha^{(i)})^{-2}V_{\alpha\beta}^{(ij)}|\psi_\beta^{(j)}\rangle ,$$

with

$$V_{\alpha\beta}^{(ij)} = N_\alpha^{(i)}\langle\chi_\alpha^{(i)}|G_0|\chi_\beta^{(j)}\rangle N_\beta^{(j)} . \tag{2.17}$$

At the bound state energy $\sigma_i = -\epsilon_\alpha^{(i)}$, the kernel of Eq. (2.17) has a pole since the eigenvalue $\lambda_\alpha^{(i)}(-\epsilon_\alpha^{(i)})$ is unity. To make this pole explicit we define $S_\alpha^{(i)}(\sigma_i)$ by

$$S_\alpha^{(i)}(\sigma_i)^2(\sigma_i+\epsilon_\alpha^{(i)})^{-1} = -\lambda_\alpha^{(i)}(\sigma_i)[1-\lambda_\alpha^{(i)}(\sigma_i)]^{-1}N_\alpha^{(i)-2} , \tag{2.18}$$

so that at the pole $S_\alpha^{(i)}(\sigma_i)=1$.

With the aid of factors $S_\alpha^{(i)}$, the kernel of Eqs. (2.17) may be symmetrized giving

$$|\tilde{\psi}_\alpha^{(i)}\rangle = |\vec{p}\rangle\delta_{i1}\delta_{\alpha\rho} + \sum_{\substack{j=1\\ \beta}} g_0(E+\epsilon_\alpha^{(i)})\tilde{V}_{\alpha\beta}^{(ij)}|\tilde{\psi}_\beta^{(j)}\rangle \tag{2.19}$$

with a symmetric potential

$$\tilde{V}_{\alpha\beta}^{(ij)} = N_\alpha^{(i)}S_\alpha^{(i)}(\sigma_i)\langle\chi_\alpha^{(i)}|G_0|\chi_\beta^{(j)}\rangle N_\beta^{(j)}S_\beta^{(j)}(\sigma_j)\,. \tag{2.20}$$

The coupled two-body equations (2.19), which result from the rigorous reduction of the Faddeev equations using the Sturmian states (2.8), will be called the Sturmian set and the approximate equations (2.7) will be referred to here as the close-coupling set. The two-body potentials (2.20) of the Sturmian set will be compared with the potentials (2.6) of the close-coupling set to examine the validity of the adiabatic approximation. First, however, we find suitable forms for the scattering amplitudes associated with the solutions of Eqs. (2.19).

(C) Scattering amplitudes

By definition, the amplitudes for elastic and inelastic scattering of particle 1 and the bound state ϕ_ρ of particles 2 and 3 are

$$\begin{aligned} A_{\tau\rho}^{(11)}(\vec{p}\,',\vec{p}) &= \langle\phi_\tau^{(1)}\vec{p}\,'|v_2+v_3|\psi^+\rangle \\ &= N_\tau^{(1)}\langle\chi_\tau^{(1)}\vec{p}\,'|G_0\sum_\alpha\{|\chi_\alpha^{(2)}\rangle\lambda_\alpha^{(2)}\langle\chi_\alpha^{(2)}| + |\chi_\alpha^{(3)}\rangle\lambda_\alpha^{(3)}\langle\chi_\alpha^{(3)}|\}|\psi^+\rangle\,, \end{aligned} \tag{2.21}$$

where the expansion of v_2 and v_3 in the eigenstates (2.8) and Eq. (2.11) have been used.

Now from (2.16)

$$\begin{aligned} \langle\chi_\rho^{(j)}|\psi^+\rangle &= \sum_i\langle\chi_\rho^{(j)}|\psi^{(i)}\rangle \\ &= N_\rho^{(j)}|\psi_\rho^{(j)}\rangle - \sum_{\substack{i\neq j\\ \alpha}} N_\rho^{(j)-1}V_{\rho\alpha}^{(ji)}|\psi_\alpha^{(i)}\rangle\,. \end{aligned} \tag{2.22}$$

On simplifying the result of substituting (2.22) in (2.21) with the integral equations (2.17), a convenient expression for the amplitudes (2.21) is obtained:

$$A_{\tau\rho}^{(11)}(\vec{p}\,',\vec{p}) = \sum_\alpha\{\langle\vec{p}\,'|V_{\tau\alpha}^{(12)}|\psi_\alpha^{(2)}\rangle + \langle\vec{p}\,'|V_{\tau\alpha}^{(13)}|\psi_\alpha^{(3)}\rangle\}\,. \tag{2.23}$$

In terms of the symmetrized potentials (2.20), we may define amplitudes

$$\tilde{A}_{\tau\rho}^{(11)}(\vec{p}\,',\vec{p}) = \sum_\alpha\{\langle\vec{p}\,'|\tilde{V}_{\tau\alpha}^{(12)}|\psi_\alpha^{(2)}\rangle + \langle\vec{p}\,'|\tilde{V}_{\tau\alpha}^{(13)}|\tilde{\psi}_\alpha^{(3)}\rangle\}\,. \tag{2.24}$$

It is straightforward using the on-shell condition (2.18) to show that the amplitudes (2.20) and (2.24) are equal on the energy shell, and thus yield the same cross sections.

Similar manipulations show that the rearrangement amplitudes with the same initial state as above but where particle 3 emerges with momentum $\vec{p}\,'$ leaving particles 1 and 2 in the bound state $\phi_\tau^{(3)}$ are

$$A_{\tau\rho}^{(31)}(\vec{p}\,',\vec{p}) = \sum_\alpha\{\langle\vec{p}\,'|\tilde{V}_{\tau\alpha}^{(32)}|\psi_\alpha^{(2)}\rangle + \langle\vec{p}\,'|\tilde{V}_{\tau\alpha}^{(31)}|\psi_\alpha^{(1)}\rangle\}\,. \tag{2.25}$$

The corresponding elastic and rearrangement amplitudes in the close-coupling scheme (2.7) have the same form as Eqs. (2.24) and (2.25) but with the potentials $\tilde{V}_{\tau\alpha}^{(ij)}$ of Eq. (2.20) replaced by the potentials $V_{\tau\alpha}^{(ij)}$ of Eq. (2.6), and the states $\tilde{\psi}_\alpha^{(i)}$ replaced by the states $\psi_\alpha^{(i)}$ calculated from Eq. (2.7) instead of (2.19).

We see that Eqs. (2.7) and (2.19) have the same two-body structure and in order to compare the close-coupling approximation, and hence the adiabatic approximation, with the Sturmian form of the Faddeev equations, we need only compare the approximate two-body potentials $V_{\tau\alpha}^{(ij)}$ with the exact two-body potentials $\tilde{V}_{\tau\alpha}^{(ij)}$. The additional complexity of three-body continuous spectra is contained in the symmetrization factors $S_\rho^{(i)}$ and the energy dependence of the eigenstates $\chi_\rho^{(i)}$ which appear in the exact potentials.

(D) Separable potentials

Finally, in this section we wish to remark that separable potential models are also included in our approach as special cases of the Sturmian reduction of Sec. II B.

Suppose that the potential v_i is separable, i.e.,

$$v_i = \sum_{\gamma=1}^{n}|\theta_\gamma^{(i)}\rangle\mu_\gamma^{(i)}\langle\theta_\gamma^{(i)}|\,, \tag{2.26}$$

where θ_γ are a set of n orthonormal vectors spanning a subspace R of the two-particle space. Let S be the set of integers $1,2,\ldots n$, and S' be the set $n+1,\ n+2,\ldots$. Substitution of (2.26) in Eq. (2.8) shows that n of the Sturmian states $\{|\chi_\alpha^{(i)}\rangle,\ \alpha\in S\}$

and their eigenvalues may be found by solving the finite set of linear equations

$$\sum_{\gamma \in S}\{\delta_{\rho\gamma}\lambda^{(1)} - \mu_\rho^{(1)}\langle\theta_\rho^{(1)}|g^{(1)}(\sigma_1)|\theta_\gamma^{(1)}\rangle\}C_\gamma = 0, \quad \rho \in S \tag{2.27}$$

for the *n* eigenvalues $\lambda^{(1)} = \lambda_\alpha^{(1)}$ and the associated components C_γ of $|\chi_\alpha^{(1)}\rangle$ in the subspace R, all other components of $|\chi_\alpha^{(1)}\rangle$ being zero. A complete set of Sturmian states may then be formed by adding to the states $\{|\chi_\alpha^{(1)}\rangle, \alpha \in S\}$ states $\{|\chi_\alpha^{(1)}\rangle, \alpha \in S'\}$ which are orthogonal to $g_0^{(1)}(\sigma_1)|\chi_\alpha^{(1)}\rangle$, $\alpha \in S$. Such states have eigenvalues $\lambda_\alpha^{(1)}$ of Eq. (2.8) which are identically zero and thus the states $\{|\chi_\alpha^{(1)}\rangle, \alpha \in S'\}$ make no contribution to the expansion (2.10), and hence do not appear in Eq. (2.19). Therefore for the case of separable potentials, the Faddeev equations may be reduced rigorously to the *finite* set of coupled two-body equations (2.19) with equivalent two-body potentials which are easily constructed from the solutions of the finite eigenvalue problem (2.27).

III. THE ADIABATIC LIMIT

In this section we examine the formal results of Sec. II in the particular kinematical situation of two identical heavy particles and one light particle, which may be described as the molecular-mass limit. We wish to simplify the equations of Sec. II under the adiabatic hypothesis, by which we mean that in a low energy collision the motion of the light particle may be uncoupled from the motion of the heavy particles.

Particles 1 and 3 are taken as the identical heavy particles of mass M and particle 2 as the light particle of mass m, which can form at least one bound state with either particle 1 or 3. Since we are interested in the effective forces generated by the exchange of the light particle, the interaction v_2 between the heavy particles is taken to vanish.

From the identity of particles 1 and 3, the amplitude $\bar{A}_{\tau\rho}^{11}$ is physically indistinguishable from the amplitude $\bar{A}_{\tau\rho}^{31}$ and the correctly symmetrized amplitude for elastic scattering is

$$\bar{A}_{\tau\rho}(\vec{p}\,',\vec{p}) = \sum_\alpha (\langle\vec{p}\,'|\bar{V}_{\tau\alpha}^{(13)}|\bar{\psi}_\alpha^{(3)}\rangle \pm \langle\vec{p}\,'|\bar{V}_{\tau\alpha}^{(31)}|\bar{\psi}_\alpha^{(1)}\rangle), \tag{3.1}$$

with the plus sign for identical bosons, and the minus for identical fermions. From Eq. (2.19), $|\bar{\psi}_\alpha^{(3)}\rangle$ and $|\bar{\psi}_\alpha^{(1)}\rangle$ are determined from

$$\begin{aligned} |\bar{\psi}_\alpha^{(1)}\rangle &= |\vec{p}\rangle\delta_{\alpha\rho} + \sum_\beta g_0(E+\epsilon_\alpha^{(1)})\bar{V}_{\alpha\beta}^{(13)}|\bar{\psi}_\beta^{(3)}\rangle, \\ |\bar{\psi}_\alpha^{(3)}\rangle &= \sum_\beta g_0(E+\epsilon_\alpha^{(3)})\bar{V}_{\alpha\beta}^{(31)}|\bar{\psi}_\beta^{(1)}\rangle. \end{aligned} \tag{3.2}$$

By symmetry $\chi_\alpha^{(1)}$ and $\chi_\alpha^{(3)}$ have the same functional form and since $\lambda_\alpha^{(1)} = \lambda_\alpha^{(3)}$, $\epsilon_\alpha^{(1)} = \epsilon_\alpha^{(3)} \equiv \epsilon_\alpha$ and $V_{\alpha\beta}^{(13)} = V_{\alpha\beta}^{(31)} = V_{\alpha\beta}$ are independent of the particle labels 1 and 3.

So defining

$$|\bar{\psi}_\alpha\rangle = |\bar{\psi}_\alpha^{(1)}\rangle \pm |\bar{\psi}_\alpha^{(3)}\rangle,$$

Eqs. (3.2) may be combined to give

$$|\bar{\psi}_\alpha\rangle = |\vec{p}\rangle\delta_{\alpha\rho} \pm \sum_\beta g_0(E+\epsilon_\alpha)\bar{V}_{\alpha\beta}|\bar{\psi}_\beta\rangle, \tag{3.3}$$

determining the elastic amplitude (3.1):

$$\bar{A}_{\tau\rho}(\vec{p}\,',\vec{p}) = \sum_\alpha \langle\vec{p}\,'|\bar{V}_{\tau\alpha}|\bar{\psi}_\alpha\rangle. \tag{3.4}$$

Similar considerations apply for the close-coupling approximation with the result that the elastic amplitude takes the same form as (3.4) with the scattering state calculated from Eq. (3.3), but using the potential $V_{\alpha\beta}$ of Eq. (2.6).

In its simplest form the adiabatic hypothesis implies that in a low energy collision the initial bound state is not disturbed by the scattering interaction so that the scattering state factorizes into a state describing the bound state of the light particle and a state describing the relative motion of the heavy particles $|\psi^+\rangle \sim |\psi_\rho^{(1)}\rangle|\phi_\rho^{(1)}\rangle$. But particles 1 and 3 are indistinguishable so the simplest acceptable form for the scattering state under the adiabatic hypothesis is

$$|\psi^+\rangle \sim |\psi_\rho^{(1)}\rangle|\phi_\rho^{(1)}\rangle \pm |\psi_\rho^{(3)}\rangle|\phi_\rho^{(3)}\rangle. \tag{3.5}$$

The same result can be obtained by retaining only the ground state $|\phi_\rho\rangle$ in the close-coupling decomposition. In this case $|\psi_\rho\rangle$ is determined by the equation

$$|\psi_\rho\rangle = |\vec{p}\rangle \pm g_0(E+\epsilon_\rho)V_{\rho\rho}|\psi_\rho\rangle. \tag{3.6}$$

The effective two-body potential is

$$V_{\rho\rho} = \langle\phi_\rho^{(1)}|v_1|\phi_\rho^{(3)}\rangle. \tag{3.7}$$

If the two-body interaction v_1 is local, the equivalent potential (3.7) in the position representation has the form

$$V_{\rho\rho}(\vec{R}) = \int \phi_\rho^{(1)}(\vec{r})v_1(\vec{r})\phi_\rho^{(3)}\left(\vec{R} + \frac{M}{M+m}\vec{r}\right)d^3r, \tag{3.8}$$

where $\vec{R}$ is the vector from particle 1 to the c.m. of particles 3 and 2. In the static mass limit $M/m \to \infty$, the equivalent potential is a function of the separation of the two heavy particles. The same exchange integral appears in the Born-Oppenheimer approximation, where the adiabatic hypothesis is applied to the Schrödinger equation, the energy of the three-body system being calculated for fixed values of the separation of the heavy particles.[9,18]

We now turn to the problem of applying the adiabatic hypothesis to the Faddeev equations. Proceeding as for the close-coupling scheme, we take as the simplest acceptable form for the scattering state [cf. Eq. (2.14)]

$$|\psi^+\rangle = -G_0|\chi_\rho^{(1)}\rangle|\phi_\rho^{(1)}\rangle N_\rho^{(1)} \pm G_0|\chi_\rho^{(3)}\rangle|\phi_\rho^{(3)}\rangle N_\rho^{(3)} ,$$

which leads to the equivalent two-body potential

$$\tilde{V}_{\rho\rho} = N_\rho^{(1)} S_\rho^{(1)}(\sigma_1)\langle\chi_\rho^{(1)}|G_0(E)|\chi_\rho^{(3)}\rangle S_\rho^{(3)}(\sigma_3) N_\rho^{(3)} . \qquad (3.9)$$

In contrast to (3.7), this potential is in general nonlocal, energy dependent, and non-Hermitian.

However, it is not difficult to establish that when taken on the energy shell the potential (3.9) reduces to (3.7) and hence, for low energies and in the static limit agrees with the Born-Oppenheimer form (3.8). To see this in detail consider the matrix element of the three-particle propagator in (3.9) between an initial momentum state $|\vec{p}\rangle$ and a final momentum state $|\vec{p}\,'\rangle$. With the help of Eq. (2.8) and the relation

$$G_0(E)|\chi_\rho^{(1)}\vec{p}\,'\rangle = g_0(\sigma')|\chi_\rho(\sigma')\rangle|\vec{p}\,'\rangle ,$$

where $\sigma' = E - p'^2/2\mu$ and $\mu = (M+m)M/(2M+m)$, we may write

$$\langle\vec{p}\,'\chi_\rho^{(1)}|G_0(E)|\chi_\rho^{(3)}\vec{p}\rangle = \lambda_\rho^{-1}(\sigma')\langle\vec{p}\,'\chi_\rho^{(1)}|G_0(E)v_1G_0(E)|\chi_\rho^{(3)}\vec{p}\rangle . \qquad (3.10)$$

Let $\delta' = \sigma' + \epsilon$ and $\delta = \sigma + \epsilon$, where $\sigma = E - p^2/2\mu$ and ϵ is the binding energy of the light particle with either of the heavies. The on-shell condition is then $\delta = \delta' = 0$. A simple perturbation calculation in powers of δ about $\delta = 0$, gives

$$\lambda_\rho(\sigma) = 1 + \delta\lambda_\rho^{(1)} - \delta^2\lambda_\rho^{(2)} + 0(\delta^3) , \qquad (3.11a)$$

with

$$\lambda_\rho^{(1)} = \langle\chi_\rho|g_0^2|\chi_\rho\rangle$$

and

$$\lambda_\rho^{(2)} = \langle\chi_\rho|g_0^3|\chi_\rho\rangle + \sum_{\beta\neq\rho}\frac{\lambda_\beta}{\lambda_\beta - 1}\langle\chi_\rho|g_0^2|\chi_\beta\rangle^2 .$$

Also

$$S_\rho^2(\sigma) = \frac{\lambda_\rho^{(1)}(1+\delta\lambda_\rho^{(1)})}{\lambda_\rho^{(1)} - \delta\lambda_\rho^{(2)}} + 0(\delta^2) \qquad (3.11b)$$

and

$$g_0(\sigma)|\chi(\sigma)\rangle = g_0|\chi_\rho\rangle(1 + \tfrac{1}{2}\delta\lambda_\rho^{(1)}) + \delta\sum_{\beta\neq\rho}\frac{g_0|\chi_\beta\rangle\langle\chi_\beta|g_0^2|\phi_\rho\rangle}{1-\lambda_\beta} + 0(\delta^2) . \qquad (3.11c)$$

Combining these results, the potential (3.9) may be expressed as

$$\langle\vec{p}\,'|\tilde{V}_{\rho\rho}|\vec{p}\rangle = \langle\vec{p}\,'|V_{\rho\rho}|\vec{p}\rangle + 0(\delta) + 0(\delta') . \qquad (3.12)$$

Thus, if the off-shell terms are neglected the potentials from the Sturmian expression and the close-coupling scheme agree. If in addition the static limit is taken, then both give rise to the same local potential.

The importance of the off-shell terms is, in general, difficult to estimate but their effect in particular models is discussed in the next section. We show there that the off-shell terms are multiplied by the mass ratio m/M and may therefore be expected to make only small corrections to the local potential of the Born-Oppenheimer approximation in the molecular-mass limit.

Since in the case of separable potentials the Sturmian expansion gives rise to a finite set of equivalent two-body equations, whereas those of the close-coupling scheme form an infinite set, it might be expected that calculations based upon the equivalent potentials (3.9) to be more accurate than those based on (3.8). This suggests that a useful method of treating situations where the adiabatic limit is expected to be valid would be to take the difference of potentials (3.9) and (3.7) as a perturbation acting on the solutions evaluated from the local effective potentials.

IV. EXAMPLES

(A) The Yamaguchi interaction

As our first example, we consider a specific two-body interaction between the light and heavy particles of the Yamaguchi form, used in numerous three-body calculations:

$$v = g|\theta\rangle\langle\theta| ,$$

with

$$\langle q|\theta\rangle = (q^2 + \alpha^2)^{-1} . \qquad (4.1)$$

The only nontrivial eigenvalue of Eq. (2.8) for this interaction is

$$\lambda = [(k_0 + \alpha)/(k + \alpha)]^2 . \qquad (4.2)$$

The momentum k is related to the energy σ of the subsystem by

$$k^2 = -2\mu\sigma , \qquad (4.3)$$

$\mu = Mm/(M+m)$ being the reduced mass, and k_0 is related to the binding energy ϵ by

$$k_0^2 = 2\mu\epsilon . \qquad (4.4)$$

The associated Sturmian vector with appropriate normalization is

$$|\chi\rangle = \frac{1}{\pi}\left(\frac{\alpha}{2\mu}\right)^{1/2}(\alpha + k)|\theta\rangle . \qquad (4.5)$$

In this case the factors S and N of Eq. (3.9) are

$$N^2 = \frac{k_0}{2\mu}(k_0+\alpha)\,, \tag{4.6}$$

$$S^2 = \frac{(k_0+\alpha)(k+k_0)}{k_0(k+k_0+2\alpha)}\,. \tag{4.7}$$

Since the interaction contains only one separable term, it follows from Sec. II D, that Eq. (3.3) reduces to just one equation which, it is important to note, gives the *exact* three-body scattering amplitude. The equivalent two-body potential, reproducing the *exact* elastic amplitude, may be determined explicitly using Eqs. (4.2), (4.5), (4.6), and (4.7) in Eq. (3.9) with the result that

$$\begin{aligned}\tilde{V}(\vec{p}\,',\vec{p}) = {} & \frac{1}{4\pi^2 m}(k_0+\alpha)^2\alpha(\alpha+k')(\alpha+k) \\ & \times\left[\frac{(k'+k_0)(k+k_0)}{(k'+k_0+2\alpha)(k+k_0+2\alpha)}\right]^{1/2} \\ & \times\frac{1}{\left(\vec{p}+\frac{M}{m+M}\vec{p}\,'\right)^2+\alpha^2}\,\frac{1}{\left(\vec{p}\,'+\frac{M}{m+M}\vec{p}\right)^2+\alpha^2} \\ & \times\frac{2m}{2mE-2\vec{p}\cdot\vec{p}\,'-\frac{m+M}{M}(p^2+p'^2)}\,,\end{aligned} \tag{4.8}$$

where the total energy of three-body system is

$$E = \frac{p_0^2}{2\mu}-\epsilon \tag{4.9}$$

and

$$\begin{aligned}k'^2 &= k_0^2+\eta(p'^2-p_0^2)\,,\\ k^2 &= k_0^2+\eta(p^2-p_0^2)\,,\end{aligned} \tag{4.10}$$

with

$$\eta = (m+2M)m/(M+m)^2\,.$$

We note that the off-shell terms associated with the symmetrization factors S are multiplied by the mass parameter η which tend to zero in the static limit $M\to\infty$.

The term in (4.8) involving the total energy, which comes from the three-body Green's operator may be written in a more suggestive form:

$$\begin{aligned}2\mu E-2\vec{p}\cdot\vec{p}\,'-\frac{m+M}{M}(p^2+p'^2) &= -2m\epsilon-(\vec{p}+\vec{p}\,')^2-\frac{m}{M}(p^2+p'^2-2p_0^2)\\ &\quad -\frac{m^2}{(M+m)M}p_0^2\,.\end{aligned} \tag{4.11}$$

The last term in (4.11) is second order in m/M and the penultimate term vanishes on the energy shell or in the static limit.

In seeking an approximate expression for the equivalent potential valid for small mass ratios, it seems reasonable to require that the approximate potential to first order reproduce the exact Born term, i.e., the equivalent potential and its approximation are equal on shell $p=p'=p_0$. With this constraint we are led to the potential

$$\tilde{V}(\vec{p}+\vec{p}\,') = -\frac{1}{2\pi^2 m}(k_0+\alpha)^2\alpha k_0 \times\frac{1}{[(\vec{p}+\vec{p}\,')^2+\alpha^2]^2}\,\frac{1}{[(\vec{p}+\vec{p}\,')^2+k_0^2]}\,. \tag{4.12}$$

This has the form of a local potential combined with a space exchange operation, as expected from the Born-Oppenheimer theory. It is easily checked that (4.12) agrees with the usual expression (3.7).

The potential (4.12) is further simplified if the zero-range limit $\alpha\to\infty$ of the two-body interaction is taken

$$\tilde{V}(\vec{p}+\vec{p}\,') = -\frac{k_0}{2\pi^2 m}\,\frac{1}{(\vec{p}+\vec{p}\,')^2+k_0^2}\,, \tag{4.13}$$

which is just the space exchange form of the Yukawa interaction, with an inverse range determined by the binding energy of the light and heavy particles. [The subtlety of these limiting processes should be emphasized. Zero-range forces may only be taken after the adiabatic constraints have been imposed. If the zero-range limit is taken prematurely, the kernel of the three-body equations is no longer compact due to the loss of the convergence factors in Eq. (4.8).] It is clear that for short-range two-body interactions, the tail of the equivalent potential in the three-body system always has a Yukawa form depending only on the binding energy of the two-particle subsystem and independent of the details of the two-particle interaction.

(B) Nonrelativistic model of the nucleon-nucleon potential

Consider the heavy particles of the preceding example as "nucleons" and the light particle as a "pion." In a simple bootstrap picture[20] of the nucleon, the binding energy of the pion with one of the nucleons is set equal to the rest mass of the pion, and the composite is regarded as being indistinguishable from the other nucleon. As in the three-body model of π-d scattering of Afnan and Thomas,[21] we introduce a further *ad hoc* antisymmetrization of the three-particle elastic amplitude to ensure that the pion is equally likely to bind to either nucleon in the final state. If P denotes the operation of exchanging the c.m. coordinate of the bound state of the light particle with one of the heavies with the coordinates of the other heavy, the elastic amplitude (3.4) becomes, with the additional antisymmetrization,

$$\tilde{A}_{\tau\rho}(\vec{p}\,',\vec{p}) = \frac{1}{\sqrt{2}}\sum_{\alpha}\{\langle\vec{p}\,'|\bar{V}_{\tau\alpha}|\tilde{\psi}_{\alpha}\rangle-\langle-\vec{p}|\bar{V}_{\tau\alpha}|\tilde{\psi}_{\alpha}\rangle\,,$$

with $|\vec{\psi}_\alpha\rangle$ now satisfying

$$|\vec{\psi}_\alpha\rangle = |\vec{\mathfrak{p}}\rangle\delta_{\alpha\rho} - \sum_\delta g_0(E+E_\alpha)P\tilde{V}_{\alpha\delta}|\vec{\psi}_\delta\rangle . \qquad (4.14)$$

The effective potential corresponding to (4.12) is now a local potential $P\tilde{V} = \tilde{V}(\vec{\mathfrak{p}} - \vec{\mathfrak{p}}')$ in the adiabatic limit. Furthermore, when the mass ratio $m/M \to 0$ this potential reduces to the familiar Yukawa potential.

This result has also been deduced more generally from minimal requirements of unitarity and analyticity in Ref. 19, and further discussion of the effective potential may be found there.

(C) The δ-shell potential

As a final example we take a local two-body potential confined to a thin shell of radius $r = r_0$,

$$v(r) = g\delta(r - r_0) . \qquad (4.15)$$

As mentioned in the Introduction, the numerical solution of the Faddeev equations with this interaction[12] initiated our interest in the adiabatic limit.

In momentum space the local potential (4.15) can be represented as an infinite sum of separable terms, $(2l+1)$ terms for each orbital angular momentum l,

$$v = g\sum_\alpha |\theta_\alpha\rangle\langle\theta_\alpha| , \qquad (4.16)$$

with

$$\langle\vec{\mathfrak{q}}|\theta_\alpha\rangle = \theta_{lm}(q) = \sqrt{2/\pi}\, r_0 j_l(qr_0)Y_l^m(\hat{q}) . \qquad (4.17)$$

Here the state label α stands for the orbital angular momentum quantum numbers l and m, j_l is a spherical Bessel function, and Y_l^m is the usual spherical harmonic. In this case the eigenvalues of Eq. (2.8) are

$$\lambda_l(\sigma) = -2i\mu kgr_0^2 j_l(kr_0)h_l^{(1)}(kr_0) , \qquad (4.18)$$

where $h_l^{(1)}$ is a spherical Hankel function and $k^2 = 2\mu\sigma$, μ being the reduced mass. The $(2l+1)$ fold degenerate Sturmian states associated with the eigenvalues (4.18) are related to the form factors (4.17) by

$$|\chi_{lm}(\sigma)\rangle = a_l(\sigma)|\theta_{lm}\rangle , \qquad (4.19)$$

with

$$a_l^{-2} = 2i\mu kr_0^2 j_l(kr_0)h_l(kr_0) .$$

The potentials (2.20) of the set of equations (2.19) which yield the exact three-body amplitudes for δ-shell scattering are readily constructed. An advantage of the form factor (4.17) is that the relation between the potential factors in the various two-body coordinate systems is easily obtained and consequently the angular momentum algebra in the partial wave equation for the effective potential (2.20) may be carried out.[13] The details of this and the numerical solution of the resulting equations will be presented elsewhere.

Here we confine our discussion to the molecular-mass limit discussed in Sec. III. We suppose that the potential is attractive ($g < 0$) and that there is a bound state of orbital angular momentum with binding energy $\epsilon_l = 2\mu k_l^2$ corresponding to the eigenvalue $\lambda_l(-\epsilon_l) = 1$ and the strength

$$g^{-1} = 2\mu k_l r_0 j_l(ik_l r_0)h_l(ik_l r_0) . \qquad (4.20)$$

From the definitions (2.12) and (2.18), the factors S_l and N_l needed for the construction of the effective potential (3.9) are

$$N_l^{-2} = -2\mu^2 gr_0 k_l^{-1} f_l'(ik_l) , \qquad (4.21)$$

with

$$f_l(k) = ikr_0 j_l(kr_0)h_l(kr_0)$$

and

$$S_l^2 = \frac{(k^2 + k_l^2)f_l'(ik_l)}{2k_l f_l(ik_l)[f_l(k) - f_l(ik_l)]} . \qquad (4.22)$$

In momentum space Eq. (3.3) becomes

$$\tilde{\psi}_\alpha(\vec{\mathfrak{p}}) = \delta(\vec{\mathfrak{p}} - \vec{\mathfrak{p}}'')\delta_{\alpha\rho} + \sum_{\alpha'}\int \frac{1}{\sigma + \epsilon_\alpha}\tilde{V}_{\alpha\alpha'}(\vec{\mathfrak{p}},\vec{\mathfrak{p}}')\tilde{\psi}_{\alpha'}(\vec{\mathfrak{p}}')d^3p' , \qquad (4.23)$$

with the effective potential

$$V_{\alpha\alpha'}(\vec{\mathfrak{p}},\vec{\mathfrak{p}}') = \frac{2mgN_lN_{l'}S_l(\sigma)S_{l'}(\sigma')\chi_{lm}\left(\frac{M}{m+M}\vec{\mathfrak{p}} + \vec{\mathfrak{p}}'\right)\chi_{l'm'}\left(-\vec{\mathfrak{p}} - \frac{M}{m+M}\vec{\mathfrak{p}}'\right)}{2mE - 2\vec{\mathfrak{p}}\cdot\vec{\mathfrak{p}}' - \frac{m+M}{M}(p^2 + p'^2)} \qquad (4.24)$$

with N_l, S_l, χ_{lm} defined by Eqs. (4.21), (4.22), (4.19), and (4.17).

As in Sec. III and the first example of this section, we take the adiabatic limit by setting the arguments σ and σ' of S_l, a_l and $S_{l'}$, $a_{l'}$ to their on-shell values. Again we note that in the static limit the effective potential is a function of $\vec{\mathfrak{p}} + \vec{\mathfrak{p}}'$, which suggests transforming Eq. (4.23) to configuration space. The Fourier transformation of Eq. (4.23) in the static limit yields

$$\psi_\alpha(\vec{r}) = \frac{e^{i\vec{p}''\cdot\vec{r}}}{(2\pi)^{3/2}}\delta_{\alpha\alpha'} + \sum_{\alpha'\neq\alpha}\int G_0(\vec{r} - \vec{r}')V_{\alpha\alpha'}(\vec{r}')\psi_{\alpha'}(-\vec{r}')d^3r' , \qquad (4.25)$$

with the potentials

$$V_{\alpha\alpha'}(\vec{r}') = -2mgN_lN_{l'}\int \frac{e^{-i\vec{q}\cdot\vec{r}'}\theta_{lm}(\vec{q})\theta_{l'm'}(-\vec{q})}{2m\epsilon_1+q^2}\,d^3q\,. \tag{4.26}$$

Equation (4.25) may be simplified by making a partial wave decomposition of the wave function ϕ_α:

$$\psi_\alpha(\vec{r}) = \psi_{lm}(\vec{r}) = \sum_{\substack{Lm\\ jn}}\left(\frac{2}{\pi}\right)^{1/2}(2j+1)i^L\begin{pmatrix} l & L & j\\ m & M & n\end{pmatrix}\begin{pmatrix} l & L & j\\ -n & 0 & n\end{pmatrix}Y_L^m(\vec{r})\psi^j_{Ll}(r)\,, \tag{4.27}$$

yielding the set of one-dimensional equations

$$\psi^j_{lL}(r) = j_L(rp'') + \sum_{l'L'}\int G_L(r,r')V^j_{LL'll'}(r')\psi^j_{l'L'}(r')r'^2dr'\,, \tag{4.28}$$

with the local potentials

$$V^j_{LL'll'} = \frac{[(2L+1)(2L'+1)(2l+1)(2l'+1)]^{1/2}}{4\pi}\sum_J(-1)^{J+j}\begin{Bmatrix} l & L & j\\ L' & l' & J\end{Bmatrix}\begin{pmatrix} L & L' & J\\ 0 & 0 & 0\end{pmatrix}\begin{pmatrix} l & l' & J\\ 0 & 0 & 0\end{pmatrix}W^J_{ll'}(r')\,, \tag{4.29}$$

with

$$W^J_{ll'}(r') = -16mgN_lN_{l'}r_0^2\int_0^\infty \frac{j_l(qr_0)j_{l'}(qr_0)j_J(qr')q^2dq}{(2m\epsilon_1+q^3)}\,. \tag{4.30}$$

Because of the local nature of the potentials it is simpler to solve the differential equations with appropriate boundary conditions corresponding to the integral equation (4.28). Thus, in the adiabatic and static limits we have obtained a set of coupled Schrödinger equations with local potentials, whose solutions form a very useful check of the solutions of the original Faddeev equations with the molecular-mass configuration. Finally, we note that if the zero-range limit of the δ-shell potential is also taken, the potential (4.30) vanishes for l and l' nonzero and, in fact, reduces to the Yukawa with exchange of our first example.

---

[1] L. R. Dodd, J. Math. Phys. (N. Y.) 11, 207 (1970); C. K. Majumdar, *ibid.* 13, 705 (1972).

[2] J. B. McGuire, J. Math. Phys. (N. Y.) 5, 622 (1964).

[3] M. G. Fuda, Phys. Rev. C 7, 1365 (1973).

[4] J. B. McGuire and C. A. Hurst, J. Math. Phys. (N. Y.) 13, 1595 (1972).

[5] M. Gaudin and B. Derrida, J. Phys. (Paris) 36, 1183 (1975).

[6] R. D. Amado, Phys. Rev. 158, 1414 (1967).

[7] L. R. Dodd and G. L. Strobel, Phys. Rev. 165, 1 (1968).

[8] L. R. Dodd and M. N. Sinha Roy, Phys. Lett. 84B, 389 (1979).

[9] T. Y. Wu and T. Ohmura, *Quantum Theory of Scattering* (Prentice-Hall, New Jersey, 1962), Sec. M4,5.

[10] A. C. Fonseca and P. E. Shanley, Ann. Phys (N. Y.) 117, 268 (1979).

[11] L. R. Dodd, Aust. J. Phys. 25, 507 (1972).

[12] K. J. Nieukerke, University of Adelaide Ph D. thesis, 1979.

[13] J. H. Hetherington and L. Schick, Phys. Rev. 137, B935 (1965); A. T. Stelbovics, Nucl. Phys. A288, 461 (1977).

[14] N. M. Larsen and J. H. Hetherington, Phys. Rev. C 9, 699 (1974); P. Doleschall, Nucl. Phys. A201, 264 (1972).

[15] W. von Oertzen, Nucl. Phys. A148, 529 (1970); W. von Oertzen and H. G. Bohlen, Phys. Rep. 19, 1 (1975).

[16] D. Brink, *Nuclear Forces* (Pergamon, New York, 1965).

[17] S. Weinberg, Phys. Rev. 131, 440 (1963).

[18] R. G. Newton, *Scattering Theory of Waves and Particles* (McGraw-Hill, New York, 1965).

[19] L. R. Dodd, Phys. Rev. C 18, 2796 (1978).

[20] C. Lovelace, Phys. Rev. 135, B1225 (1964).

[21] I. R. Afnan and A. W. Thomas, Phys. Rev. C 10, 109 (1974).

PHYSICAL REVIEW C VOLUME 21, NUMBER 5 MAY 1980

Scattering amplitudes and integral equations for the collision of two charged composite particles

E. O. Alt
Institut für Physik, Universität Mainz, Mainz, West Germany

W. Sandhas
Physikalisches Institut, Universität Bonn, Bonn, West Germany

(Received 8 March 1979)

Transition operators for the collision of two clusters composed of an arbitrary number of *charged* and neutral particles are represented as a sum of pure Coulomb and Coulomb-modified short-range operators. Sandwiching this relation between the corresponding channel states, correct two-fragment scattering amplitudes are obtained by adapting the conventional two-body screening and renormalization procedure. Furthermore, integral equations are derived for off-shell extensions of the full screened amplitudes and of the unscreened Coulomb-modified short-range amplitudes. For three particles, the final results coincide with those derived previously in a different approach. The proposed theory is valid for pure Coulomb scattering as well as for systems containing, in addition, two-body interactions of short range.

[NUCLEAR REACTIONS *N*-body scattering theory for charged particles. Scattering amplitudes for two-fragment collisions defined via screening and renormalization procedure. Derived effective two-body integral equations. Formalism also applicable to atomic problems.]

I. INTRODUCTION

In recent publications three-body scattering processes with two[1-3] or three[4] *charged* particles have been investigated by employing the quasiparticle method[5] which consists in replacing the original three-body integral equations by fully equivalent Lippmann-Schwinger (LS)-type matrix equations for effective two-body operators. By making use of the close analogy between this effective two-body formalism and the well-established genuine two-body Coulomb theory, scattering amplitudes for (in)elastic and rearrangement collisions of two fragments could be defined, and at the same time manageable integral equations for their calculation have been obtained.

In the present paper we develop an alternative approach which is based on the fundamental operator relations between the relevant quantities of the problem. Hereby, the previously derived expressions for the on-shell scattering amplitudes are reproduced in a direct and transparent manner. Consequently, their generalization to collisions of two fragments consisting of an arbitrary number of charged particles[6-14] becomes straightforward. We, moreover, show that these amplitudes may again be calculated from manageable integral equations.

The general idea of our procedure can be stated in the following way. As suggested by the results of Refs. 1–4, which are very much in accord with physical intuition, a *center-of-mass Coulomb potential*, acting between the total charges of the two fragments concentrated in their respective centers of mass, is introduced besides the original Coulomb interaction. We then derive a representation of the full transition amplitude as a pure center-of-mass two-body Coulomb amplitude, plus a Coulomb-modified short-range transition operator sandwiched between the bound state wave functions of the fragments and between the two-body Coulomb scattering states associated with their relative movement.

As in Refs. 1 to 4 the derivation of this representation is first performed for screened Coulomb potentials. Applying then the usual two-body renormalization and limiting procedure,[15-19] the occurring two-body Coulomb scattering amplitudes and states go over into the corresponding, explicitly known, unscreened quantities. However, no renormalization is needed when performing the zero-screening limit in the Coulomb-modified short-range transition operator sandwiched between bound states. For, in this expression there occurs, besides any short-ranged potentials, the difference between the original Coulomb interaction and the center-of-mass Coulomb potential. Expanding this difference into a multipole series with respect to the relative distance of the two fragments, the first nonvanishing term is the *dipole* term. Since it decreases sufficiently fast for large spatial separations, the transition to in-

© 1980 The American Physical Society

finite screening radius, indeed, poses no problems in this amplitude. Of course, the justification of the multipole expansion rests on the localization property of the cluster wave functions.

The screening technique used to *define* the relevant transition amplitudes represents also an appropriate *practical* method. For, it allows us to apply *any* method of short-range collision theory to calculate first the screened scattering amplitudes, and then to perform after renormalization the zero-screening limit, e.g., numerically.[20] One of these short-range methods is the quasiparticle approach of Ref. 5 which has the advantage of providing us with exact integral equations for off-shell extensions of the two-fragment amplitudes considered. Hence, we describe its application to the present problem, reproducing in this way the integral equations given for three particles in Refs. 1–4, and deriving their generalization to arbitrary particle numbers. In addition, the quasiparticle method leads to a second approach which is based on integral equations directly for the *unscreened* Coulomb-modified short-range transition amplitudes.

The paper is organized as follows. The simple example of the scattering of two particles interacting via short-ranged plus Coulomb potentials is recalled in Sec. II. Two-fragment collisions of three particles are dealt with in Sec. III, utilizing the close structural analogy of the three-body formalism of Ref. 5 with the two-body theory. The generalization to the scattering of two fragments built up of an arbitrary number of charged particles is contained in Sec. IV. Quasiparticle equations for the full screened amplitudes and for the unscreened Coulomb-modified short-range amplitudes are described in Sec. V for three, and in Sec. VI for N particles.

II. TWO-BODY COLLISIONS

We recapitulate in this section some aspects of the scattering theory of two charged particles[19] in a way which suggests straightforward generalization to two-fragment arrangement collisions with an arbitrary number of (charged) particles.

A. Operator relations

Let the Hamiltonian $H^{(R)}$ be composed of the kinetic energy part H_0, a short-ranged potential V^s, and a screened Coulomb potential V^R,

$$H^{(R)}=H_0+V^s+V^R\,, \tag{2.1}$$

with R denoting the screening radius. Then, the full resolvent, the free, and the "Coulomb-distorted free" resolvents, are given by

$$G^{(R)}(z)=(z-H_0-V^s-V^R)^{-1}=(z-H^{(R)})^{-1}\,, \tag{2.2}$$

$$G_0(z)=(z-H_0)^{-1}\,, \tag{2.3}$$

$$G^R(z)=(z-H_0-V^R)^{-1}\,. \tag{2.4}$$

Factoring out from $G^{(R)}$ the resolvents G_0 and G^R, respectively, and from G^R the resolvent G_0, by means of

$$G^{(R)}=G_0+G_0T^{(R)}G_0\,, \tag{2.5}$$

$$G^{(R)}=G^R+G^RT^{sR}G^R\,, \tag{2.6}$$

$$G^R=G_0+G_0T^RG_0\,, \tag{2.7}$$

the full transition operator $T^{(R)}$, the Coulomb-modified short-range operator T^{sR}, and the pure Coulomb transition operator T^R are introduced. These definitions emphasize the basic fact that appropriate *singularities of the Green's functions* have to be removed when going over to T operators. Moreover, the fundamental interrelationship

$$T^{(R)}=T^R+(1+T^RG_0)T^{sR}(1+G_0T^R) \tag{2.8}$$

is obtained in a particularly simple manner by equating the right-hand sides of (2.5) and (2.6), and by replacing the occurring resolvent G^R by the representation (2.7). Let us recall, however, that the definitions of the various T operators via Eqs. (2.5)–(2.7) are equivalent to the more conventional ones

$$T^{(R)}=V^s+V^R+(V^s+V^R)G^{(R)}(V^s+V^R)\,, \tag{2.9}$$

$$T^{sR}=V^s+V^sG^{(R)}V^s\,, \tag{2.10}$$

$$T^R=V^R+V^RG^RV^R\,. \tag{2.11}$$

B. Zero-screening limit

We are now going to perform the zero-screening limits of the transition amplitudes obtained by sandwiching the operators (2.9)–(2.11) between plane waves $|\vec{p}\rangle$. This is unproblematic for T^{sR} since in its definition (2.6) the singularities of G^R corresponding to the *Coulomb-distorted free movement* of the particles are separated off from $G^{(R)}$. In fact, the explicit representation (2.10) shows that the full resolvent $G^{(R)}$ appears in $\langle\vec{p}\,'|T^{sR}(E+i0)|\vec{p}\rangle$ between states $V^s|\vec{p}\rangle$ which are normalizable and smooth under appropriate conditions on V^s. Thus, the existence of the limit $R\to\infty$, which is denoted by $\langle\vec{p}\,'|T^{sC}(E+i0)|\vec{p}\rangle$, is guaranteed for all values of the initial and final momenta.

In contrast, the amplitudes $T^{(R)}$ and T^R are obtained by extracting from the respective Green's functions only those singularities which correspond to the *undistorted free relative motion*. Since such an unperturbed movement does not exist in the presence of unscreened Coulomb potentials, the performance of the limit $R\to\infty$ requires the well-known renormalization procedure.[15-18] In fact, the momentum representation of the relation (2.8) takes on the energy shell $[p' = p = (2\mu E)^{1/2}$, with μ being the reduced mass$]$ the form

$$\langle \vec{p}\,' | T^{(R)}(E+i0) | \vec{p} \rangle = \langle \vec{p}\,' | T^{R}(E+i0) | \vec{p} \rangle + \langle \vec{p}_R'^{(-)} | T^{sR}(E+i0) | \vec{p}_R^{(+)} \rangle \,, \tag{2.12}$$

with the screened Coulomb scattering states defined according to

$$|\vec{p}_R^{(\pm)}\rangle = [1 + G_0(E \pm i0) T^R(E \pm i0)] |\vec{p}\rangle \,. \tag{2.13}$$

When these wave functions are multiplied by the appropriate renormalization factors $Z_R^{\mp 1/2}(p)$, and the amplitude $\langle \vec{p}\,' | T^R(E+i0) | \vec{p} \rangle$ by $Z_R^{-1}(p)$, the unscreened Coulomb scattering states $|\vec{p}_C^{(\pm)}\rangle$ and the Coulomb amplitude $T^C(\vec{p}\,', \vec{p})$, respectively, are recovered in the zero screening limit. (For instance, in the case of exponential screening, $V^R(r) = e_1 e_2 \exp(-r/R)/r$, we have $Z_R(p) = \exp[-2ie_1 e_2(\mu/p)(\ln 2pR - C)]$. Here, e_i is the charge of particle i, and $C = 0.5772\ldots$ the Euler number.) Hence, the limit $R \to \infty$ exists in both terms on the right-hand side of Eq. (2.12) *after renormalization* by $Z_R^{-1}(p)$, thus providing the full transition amplitude for a short-ranged plus an unscreened Coulomb potential according to

$$T(\vec{p}\,', \vec{p}) = T^C(\vec{p}\,', \vec{p}) + \langle \vec{p}_C'^{(-)} | T^{sC}(E+i0) | \vec{p}_C^{(+)} \rangle \,. \tag{2.14}$$

C. Integral equations

These considerations immediately suggest two different approaches of how to proceed in practice. One of them consists in solving the partial-wave LS equations for $T^{(R)}$ and T^R for finite values of R, and subtracting the result of the latter from that of the former. Summing up these partial-wave contributions yields the Coulomb-modified short-range amplitude in the (screened) Coulomb representation, $\langle \vec{p}_R'^{(-)} | T^{sR}(E+i0) | \vec{p}_R^{(+)} \rangle$. Renormalizing then by $Z_R^{-1}(p)$ the corresponding on-shell elements, and repeating the calculation for successively increased values of R, the transition to large ("infinite") screening radii is performed numerically.[30]

Alternatively, we can calculate directly the unscreened Coulomb-modified short-range amplitude occurring in (2.14) by making use of the LS equation

$$T^{sC} = V^s + V^s G^C T^{sC} \tag{2.15}$$

and of the analytically known Coulomb wave functions. Equation (2.15) follows from (2.6) or (2.10) in the zero-screening limit which exists according to the above discussion.

In both methods we then have to add the explicitly known Coulomb amplitude $T^C(\vec{p}\,', \vec{p})$ in order to get the full amplitude via (2.14).

III. SCATTERING AMPLITUDES FOR TWO-FRAGMENT COLLISIONS OF THREE CHARGED PARTICLES

For short-ranged potentials the three-body theory was formulated in Ref. 5 in structural analogy to the two-body case. The same concept is now being used to extend the considerations of Sec. II to three particles interacting via potentials with Coulomb tails. We remark that the *pure* Coulomb scattering is contained as a special case in our treatment.

A. Operator relations

The interaction in the total Hamiltonian

$$H^{(R)} = H_0 + \sum_\gamma V_\gamma^S + \sum_\gamma V_\gamma^R = H_0 + V^S + V^R \tag{3.1}$$

is assumed to be a superposition of short-ranged pair potentials V_γ^S and screened Coulomb potentials V_γ^R acting between particles $\alpha, \beta \neq \gamma$ (here and in the following, the familiar cyclic notation is used).

Let us introduce, in addition, the screened Coulomb interaction v_α^R between particle α and the *center of mass* of particles β and γ. In coordinate space this potential reads

$$v_\alpha^R(\vec{\rho}_\alpha) = e_\alpha(e_\beta + e_\gamma) f_\alpha^R(\rho_\alpha)/\rho_\alpha \,, \tag{3.2}$$

with $\vec{\rho}_\alpha$ denoting the corresponding relative coordinate, and $e_\alpha, e_\beta, e_\gamma$ the charges of the three particles.[21-23] The screening function $f_\alpha^R(\rho_\alpha)$ has to be suitably chosen, e.g., exponentially decreasing. Now, the full resolvent, the channel, and the Coulomb-distorted channel resolvents, are introduced as

$$\begin{aligned} G^{(R)}(z) &= (z - H_0 - \sum_\gamma V_\gamma^S - \sum_\gamma V_\gamma^R)^{-1} \\ &= (z - H^{(R)})^{-1} \,, \end{aligned} \tag{3.3}$$

$$G_\alpha^{(R)}(z) = (z - H_0 - V_\alpha^S - V_\alpha^R)^{-1} \,, \tag{3.4}$$

$$g_\alpha^R(z) = (z - H_0 - V_\alpha^s - V_\alpha^R - v_\alpha^R)^{-1} \,. \tag{3.5}$$

We emphasize that in two-fragment reactions of the three particles the channel resolvents (3.4) and (3.5) play the same role as the resolvents (2.3) and (2.4) in the two-elementary particle case. This fact suggests defining the full transition operators $U_{\beta\alpha}^{(R)}$, the Coulomb-modified short-range operators $U_{\beta\alpha}^{sR}$, and the pure center-of-mass Coulomb operators t_α^R, in analogy to Eqs. (2.5)–(2.7), via

$$G^{(R)} = \delta_{\beta\alpha} G_\alpha^{(R)} + G_\beta^{(R)} U_{\beta\alpha}^{(R)} G_\alpha^{(R)} \,, \tag{3.6}$$

$$G^{(R)} = \delta_{\beta\alpha} g_\alpha^R + g_\beta^R U_{\beta\alpha}^{sR} g_\alpha^R \,, \tag{3.7}$$

$$g_\alpha^R = G_\alpha^{(R)} + G_\alpha^{(R)} t_\alpha^R G_\alpha^{(R)} \,. \tag{3.8}$$

Equating the right-hand sides of (3.6) and (3.7) and inserting the representation (3.8) of g_α^R we end up with the fundamental relation

$$U_{\beta\alpha}^{(R)} = \delta_{\beta\alpha} t_\alpha^R + (1 + t_\beta^R G_\beta^{(R)}) U_{\beta\alpha}^{SR} (1 + G_\alpha^{(R)} t_\alpha^R) \qquad (3.9)$$

which generalizes Eq. (2.8).

We mention that in writing the definitions (3.6) and (3.7) of $U_{\beta\alpha}^{(R)}$ and $U_{\beta\alpha}^{SR}$, respectively, we have followed the idea of Ref. 5, namely to introduce transition operators by extracting subsystem singularities from the full resolvent in a most symmetric way. Similarly to Eqs. (2.9)–(2.11), the various transition operators can also be represented in the explicit forms

$$U_{\beta\alpha}^{(R)} = \bar{\delta}_{\beta\alpha} G_\alpha^{(R)-1} + \bar{V}_\beta^{(R)} + \bar{V}_\beta^{(R)} G^{(R)} \bar{V}_\alpha^{(R)}, \qquad (3.10)$$

$$U_{\beta\alpha}^{SR} = \bar{\delta}_{\beta\alpha} (g_\alpha^R)^{-1} + (\bar{V}_\beta^{(R)} - v_\beta^R) + (\bar{V}_\beta^{(R)} - v_\beta^R) G^{(R)} (\bar{V}_\alpha^{(R)} - v_\alpha^R), \qquad (3.11)$$

$$t_\alpha^R = v_\alpha^R + v_\alpha^R g_\alpha^R v_\alpha^R. \qquad (3.12)$$

In (3.10) and (3.11) the channel potentials $\bar{V}_\alpha^{(R)}$ acting between the colliding fragments are

$$\bar{V}_\alpha^{(R)} = V^S + V^R - V_\alpha^S - V_\alpha^R = \sum_{\gamma \neq \alpha} V_\gamma^S + \sum_{\gamma \neq \alpha} V_\gamma^R. \qquad (3.13)$$

And, as usual, we have $\bar{\delta}_{\beta\alpha} = 1 - \delta_{\beta\alpha}$. Note, that the lack of symmetry of (3.10) under interchange of α and β is only apparent. For, we have $\bar{\delta}_{\beta\alpha} G_\alpha^{(R)-1} + \bar{V}_\beta^{(R)} = \bar{\delta}_{\beta\alpha} G_\beta^{(R)-1} + \bar{V}_\alpha^{(R)}$. A similar remark applies to (3.11). Of course, as in any short-range theory we could work also with unsymmetric post and prior transition operators[34] $U_{\beta\alpha}^{(R)\pm}$, which are related to $U_{\beta\alpha}^{(R)}$ via $U_{\beta\alpha}^{(R)} = \bar{\delta}_{\beta\alpha} G_\alpha^{(R)-1} + U_{\beta\alpha}^{(R)+} = \bar{\delta}_{\beta\alpha} G_\beta^{(R)-1} + U_{\beta\alpha}^{(R)-}$. Analogously, post and prior operators $U_{\beta\alpha}^{SR\pm}$ can be defined according to $U_{\beta\alpha}^{SR} = \bar{\delta}_{\beta\alpha} (g_\alpha^R)^{-1} + U_{\beta\alpha}^{SR+} = \bar{\delta}_{\beta\alpha} (g_\beta^R)^{-1} + U_{\beta\alpha}^{SR-}$. All these operators yield the same on-shell amplitudes when introduced in the respective expressions of relation (3.22) given below.

B. Zero-screening limit

The limit $R \to \infty$ is now investigated for the on-shell matrix elements of (3.9) between channel states[35]

$$|\Phi_{\alpha m}\rangle = |\psi_{\alpha m}\rangle |\vec{q}_\alpha\rangle \qquad (3.14)$$

belonging to the energy $E_{\alpha m} = q_\alpha^2/2M_\alpha + \hat{E}_{\alpha m}$. Here, $|\psi_{\alpha m}\rangle$ is the mth bound state wave function of the pair (β, γ) with binding energy $\hat{E}_{\alpha m}$, and the plane wave $|\vec{q}_\alpha\rangle$ describes the free motion of particle α relative to this bound state (M_α is the corresponding reduced mass). To simplify the notation the label R is suppressed on the states (3.14) and on the energies to which they belong.

Let us first consider the action of

$$[1 + G_\alpha^{(R)}(E_{\alpha m} \pm i0) t_\alpha^R (E_{\alpha m} \pm i0)] = [1 + g_\alpha^R (E_{\alpha m} \pm i0) v_\alpha^R] \qquad (3.15)$$

on $|\Phi_{\alpha m}\rangle$. For this purpose we associate with the operators v_α^R, $G_\alpha^{(R)}(z)$, and $g_\alpha^R(z)$, which act in the three-body space, potentials $\mathfrak{v}_\alpha^R$, "free Green's functions" $\mathfrak{g}_{0,\alpha}(z)$, and "Coulomb Green's functions" $\mathfrak{g}_\alpha^R(z)$, respectively, which are restricted to the relative momentum states $|\vec{q}_\alpha\rangle$. I.e., we define[36]

$$v_\alpha^R |\psi_{\alpha m}\rangle |\vec{q}_\alpha\rangle = |\psi_{\alpha m}\rangle \mathfrak{v}_\alpha^R |\vec{q}_\alpha\rangle, \qquad (3.16)$$

$$\mathfrak{g}_{0,\alpha}(z) = \left(z - \frac{Q_\alpha^2}{2M_\alpha}\right)^{-1}, \qquad (3.17)$$

$$\mathfrak{g}_\alpha^R(z) = \left(z - \frac{Q_\alpha^2}{2M_\alpha} - \mathfrak{v}_\alpha^R\right)^{-1}, \qquad (3.18)$$

where $\vec{Q}_\alpha$ are the relative momentum operators with eigenstates $|\vec{q}_\alpha\rangle$. Moreover, two-body Coulomb transition operators are defined by

$$\mathfrak{t}_\alpha^R(z) = \mathfrak{v}_\alpha^R + \mathfrak{v}_\alpha^R \mathfrak{g}_\alpha^R(z) \mathfrak{v}_\alpha^R. \qquad (3.19)$$

All these quantities satisfy, of course, the usual resolvent and transition operator LS equations as known from the two-body theory.

With these definitions we find

$$\begin{aligned}[1 + g_\alpha^R(E_{\alpha m} \pm i0) v_\alpha^R] |\psi_{\alpha m}\rangle |\vec{q}_\alpha\rangle &= |\psi_{\alpha m}\rangle \left[1 + \mathfrak{g}_\alpha^R\left(\frac{q_\alpha^2}{2M_\alpha} \pm i0\right) \mathfrak{v}_\alpha^R\right] |\vec{q}_\alpha\rangle \\ &= |\psi_{\alpha m}\rangle \left[1 + \mathfrak{g}_{0,\alpha}\left(\frac{q_\alpha^2}{2M_\alpha} \pm i0\right) \mathfrak{t}_\alpha^R\left(\frac{q_\alpha^2}{2M_\alpha} \pm i0\right)\right] |\vec{q}_\alpha\rangle \\ &= |\psi_{\alpha m}\rangle \omega_{\alpha,R}^{(\pm)} |\vec{q}_\alpha\rangle = |\psi_{\alpha m}\rangle |\vec{q}_{\alpha,R}^{(\pm)}\rangle. \end{aligned} \qquad (3.20)$$

That is, $[1 + G_\alpha^{(R)}(E_{\alpha m} \pm i0) t_\alpha^R (E_{\alpha m} \pm i0)]$ acts on $|\Phi_{\alpha m}\rangle$ as a Møller operator $\omega_{\alpha,R}^{(\pm)}$ with respect to $|\vec{q}_\alpha\rangle$, mapping the latter onto screened Coulomb scattering states $|\vec{q}_{\alpha,R}^{(\pm)}\rangle$ which characterize the Coulomb-distorted free movement of the two fragments. We furthermore see that

$$\begin{aligned}\langle \vec{q}_\alpha{}' | \langle \psi_{\alpha n} | t_\alpha^R (E_{\alpha m} + i0) | \psi_{\alpha m}\rangle |\vec{q}_\alpha\rangle &= \delta_{nm} \langle \vec{q}_\alpha{}' | \mathfrak{t}_\alpha^R (q_\alpha^2/2M_\alpha + i0) | \vec{q}_\alpha\rangle \\ &= \delta_{nm} \langle \vec{q}_\alpha{}' | \mathfrak{v}_\alpha^R | \vec{q}_{\alpha,R}^{(\pm)}\rangle \\ &= \delta_{nm} t_\alpha^R (\vec{q}_\alpha{}', \vec{q}_\alpha) \end{aligned} \qquad (3.21)$$

represents the screened two-body Coulomb scattering amplitude for particle α off the center of mass of particles β and γ. Sandwiched between channel states (3.14), our basic relation (3.9) consequently reads on the energy shell

$$\begin{aligned}\langle \vec{q}_\beta{}' | \langle \psi_{\beta n} | U_{\beta\alpha}^{(R)} (E_{\alpha m} + i0) | \psi_{\alpha m}\rangle |\vec{q}_\alpha\rangle &= \delta_{\beta\alpha} \delta_{nm} t_\alpha^R (\vec{q}_\alpha{}', \vec{q}_\alpha) \\ &\quad + \langle \vec{q}_{\beta,R}{}'^{(-)} | \langle \psi_{\beta n} | U_{\beta\alpha}^{SR} (E_{\alpha m} + i0) | \psi_{\alpha m}\rangle |\vec{q}_{\alpha,R}^{(+)}\rangle. \end{aligned} \qquad (3.22)$$

Proceeding as in Sec. II, we first demonstrate that the limit $R\to\infty$ can be performed without any problems in the *effective two-body operators* $\langle\psi_{\beta n}|U^{sR}_{\beta\alpha}|\psi_{\alpha m}\rangle$, the resulting unscreened quantities being denoted by $\langle\psi_{\beta n}|U^{sC}_{\beta\alpha}|\psi_{\alpha m}\rangle$. This is easily demonstrated with the help of the explicit representation (3.11) which yields

$$\begin{aligned}\langle\vec{q}\,'_\beta|\langle\psi_{\beta n}|U^{sR}_{\beta\alpha}|\psi_{\alpha m}\rangle|\vec{q}_\alpha\rangle &\doteq\langle\vec{q}\,'_\beta|\langle\psi_{\beta n}|[\bar{\delta}_{\beta\alpha}(g^R_\alpha)^{-1}+(\bar{V}^{(R)}_\beta-v^R_\beta)]|\psi_{\alpha m}\rangle|\vec{q}_\alpha\rangle\\&\quad+\langle\vec{q}\,'_\beta|\langle\psi_{\beta n}|(\bar{V}^{(R)}_\beta-v^R_\beta)G^{(R)}(\bar{V}^{(R)}_\alpha-v^R_\alpha)|\psi_{\alpha m}\rangle|\vec{q}_\alpha\rangle\,.\end{aligned}\tag{3.23}$$

As in the momentum representation of the corresponding two-body equation (2.10), the full Green's function $G^{(R)}$ occurs here between states $(\bar{V}^{(R)}_\alpha-v^R_\alpha)|\psi_{\alpha m}\rangle|\vec{q}_\alpha\rangle$ which are *normalizable*, a property which is shared even by their zero-screening limits $(\bar{V}_\alpha-v^C_\alpha)|\psi_{\alpha m}\rangle|\vec{q}_\alpha\rangle$. This is obvious for the short-ranged part $\bar{V}^s_\alpha$ of

$$\bar{V}_\alpha-v^C_\alpha=\sum_{\gamma\neq\alpha}V^s_\gamma+\sum_{\gamma\neq\alpha}V^C_\gamma-v^C_\alpha=\bar{V}^s_\alpha+\bar{V}^C_\alpha-v^C_\alpha\,,\tag{3.24}$$

but holds for the Coulomb terms, too. For, in position space the contribution of the latter is

$$\begin{aligned}\Big\langle\vec{\rho}_\alpha,\vec{r}_\alpha\Big|\Big(\sum_{\delta\neq\alpha}V^C_\delta-v^C_\alpha\Big)\Big|\psi_{\alpha m}\rangle|\vec{q}_\alpha\Big\rangle &=[e_\alpha e_\beta(r_\gamma{}^{-1}-\rho_\alpha{}^{-1})+e_\alpha e_\gamma(r_\beta{}^{-1}-\rho_\alpha{}^{-1})]\\&\quad\times\psi_{\alpha m}(\vec{r}_\alpha)\frac{e^{i\vec{q}_\alpha\cdot\vec{\rho}_\alpha}}{(2\pi)^{3/2}}\,,\end{aligned}\tag{3.25}$$

with the relative coordinate $\vec{r}_\gamma$ between particles α and β being expressed as a linear combination of $\vec{\rho}_\alpha$ and $\vec{r}_\alpha$,

$$\vec{r}_\gamma=\vec{\rho}_\alpha-\frac{m_\gamma}{m_\beta+m_\gamma}\vec{r}_\alpha\quad(\alpha,\beta,\gamma\ \text{cyclic})\tag{3.26}$$

and similarly for $\vec{r}_\beta$ (see Fig. 1). For sufficiently fast (e.g., exponentially) decreasing bound state wave functions $\psi_{\alpha m}(\vec{r}_\alpha)$, a multipole expansion of $r_\gamma{}^{-1}$ and $r_\beta{}^{-1}$ in powers of $\rho_\alpha{}^{-1}$ is justified. Thus, in fact, the first nonvanishing terms of $(r_\gamma{}^{-1}-\rho_\alpha{}^{-1})$ and $(r_\beta{}^{-1}-\rho_\alpha{}^{-1})$ are of the order $\rho_\alpha{}^{-2}$. Therewith the proof of our statement is completed.

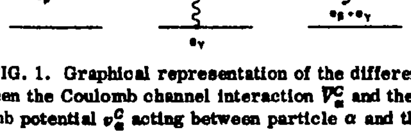
e_α
$e_\alpha e_\beta/r_\gamma$
e_β
+
e_α
$e_\alpha e_\gamma/r_\beta$
e_γ
−
e_α
$e_\alpha(e_\beta+e_\gamma)/\rho_\alpha$
$e_\beta+e_\gamma$

FIG. 1. Graphical representation of the difference between the Coulomb channel interaction $\bar{V}^C_\alpha$ and the Coulomb potential v^C_α acting between particle α and the center of mass of particles β and γ, in position space [cf. Eq. (3.25)].

Consequently, when the screening radius goes to infinity, divergencies can originate in (3.22) only from the *two-body* amplitudes $t^R_\alpha(\vec{q}\,'_\alpha,\vec{q}_\alpha)$ and scattering states $|\vec{q}^{(\pm)}_{\alpha,R}\rangle$. These divergencies, however, can be eliminated by the renormalization procedure of Sec. II. In fact, with the renormalization factor $Z_{\alpha,R}(q_\alpha)$ defined as in the two-body case,[27] we obtain the on-shell two-body Coulomb amplitude for scattering of particle α off the center of mass of particles β and γ via

$$t^R_\alpha(\vec{q}\,'_\alpha,\vec{q}_\alpha)Z_{\alpha,R}{}^{-1}(q_\alpha)\underset{R\to\infty}{\sim}t^C_\alpha(\vec{q}\,'_\alpha,\vec{q}_\alpha)\,,\tag{3.27}$$

and the corresponding Coulomb scattering states via

$$|\vec{q}^{(\pm)}_{\alpha,R}\rangle Z^{\mp1/2}_{\alpha,R}(q_\alpha)\underset{R\to\infty}{\sim}|\vec{q}^{(\pm)}_{\alpha,C}\rangle\,.\tag{3.28}$$

Thus, multiplying the whole equation (3.22) by $Z^{-1/2}_{\beta,R}(q'_\beta)Z^{-1/2}_{\alpha,R}(q_\alpha)$, we arrive in the limit $R\to\infty$ at the representation

$$\begin{aligned}\lim_{R\to\infty}Z^{-1/2}_{\beta,R}(q'_\beta)\langle\vec{q}\,'_\beta|\langle\psi_{\beta n}|U^{(R)}_{\beta\alpha}(E_{\alpha m}+i0)|\psi_{\alpha m}\rangle|\vec{q}_\alpha\rangle&\\ \times Z^{-1/2}_{\alpha,R}(q_\alpha)&\\ =\delta_{\beta\alpha}\delta_{nm}t^C_\alpha(\vec{q}\,'_\alpha,\vec{q}_\alpha)&\\ +\langle\vec{q}\,'^{(-)}_{\beta,C}|\langle\psi_{\beta n}|U^{sC}_{\beta\alpha}(E_{\alpha m}+i0)|\psi_{\alpha m}\rangle|\vec{q}^{(+)}_{\alpha,C}\rangle&\\ =T_{\beta n,\alpha m}(\vec{q}\,'_\beta,\vec{q}_\alpha)&\end{aligned}\tag{3.29}$$

for the transition amplitudes describing two-fragment processes of three charged particles.

Of course, our formalism remains valid if one of the bound particles in the incoming and outgoing states is neutral. This case has been discussed in detail in Ref. 3. Only the corresponding charge has to be set equal to zero in the above formulas. Furthermore, Eq. (3.29) simplifies considerably if the bound state or the elementary particle in the initial or in the final state is neutral. Then, the pure Coulomb amplitude is absent and the corresponding Coulomb scattering state has to be replaced by a plane wave. If, in particular, both in the initial and in the final state, one of the fragments is neutral, the limit $R\to\infty$ exists in the arrangement amplitudes without renormalization, i.e., no screening is necessary at all and conventional short-range scattering theory is applicable.[28]

Let us emphasize that the basic result (3.29) is valid also for pure Coulomb scattering, i.e., if $V^s_1=V^s_2=V^s_3=0$. For, our treatment yields also in this case a splitting of the interaction between the two fragments into a part which is of short range [cf. Eq. (3.25)] and the long-ranged Coulomb potential v^C_α. In other words, even *without* short-ranged pair potentials V^s_γ our formulation of two-fragment collisions of three particles is structurally equivalent to the genuine two-body problem with a Coulomb *plus* a short-ranged interaction, as discussed in Sec. II.

IV. GENERALIZATION TO N-PARTICLE SYSTEMS

For two-fragment collisions the formalism developed in Sec. III can be extended to arbitrary particle numbers in a straightforward manner.[6]

A. Operator relations

We denote by $a, b, \ldots$ two-fragment partitions of N distinguishable particles $1, 2, \ldots, N$. Then, the total Hamiltonian

$$H^{(R)} = H_0 + \sum_{i<j}^{N} V^S_{ij} + \sum_{i<j}^{N} V^R_{ij} = H_0 + V^S + V^R \tag{4.1}$$

with the short-ranged potentials $V^S_{ij} = V^S_{ji}$ and the screened Coulomb potentials V^R_{ij} is split, according to

$$H^{(R)} = H_a^{(R)} + \bar{V}_a^{(R)}, \tag{4.2}$$

into a channel Hamiltonian

$$H_a^{(R)} = H_0 + \sum_{\substack{i<j \\ (ij)\subset a}} (V^S_{ij} + V^R_{ij}) = H_0 + V^S_a + V^R_a \tag{4.3}$$

and the channel interaction

$$\bar{V}_a^{(R)} = \sum_{\substack{i<j \\ (ij)\not\subset a}} (V^S_{ij} + V^R_{ij}) = \bar{V}^S_a + \bar{V}^R_a . \tag{4.4}$$

Here, as usual, $(ij)\subset a$ means that both particles i and j are contained in the same fragment of the partition a.

Denoting by $\vec{\rho}_a$ the relative coordinate between the centers of mass of the two clusters of fragmentation a, we define as in (3.2) the Coulomb interaction v_a^R between them. In position space it reads explicitly

$$v_a^R(\vec{\rho}_a) = \sum_{\substack{i<j \\ (ij)\not\subset a}} \frac{e_i e_j}{\rho_a} f_a^R(\rho_a). \tag{4.5}$$

That is, it is obtained by replacing in all potentials V^R_{ij} which occur in the Coulomb part $\bar{V}^R_a$ of the channel interaction, the relative coordinates between particles i and j by the center-of-mass variable $\vec{\rho}_a$. This allows us to introduce, besides the resolvents $G^{(R)}$ of $H^{(R)}$, and $G_a^{(R)}$ of $H_a^{(R)}$, the generalization of the Coulomb-distorted channel resolvent (3.5),

$$g_a^R(z) = (z - H_a^{(R)} - v_a^R)^{-1}. \tag{4.6}$$

Then, analogously to (3.6)–(3.8), transition operators are defined as follows:

$$G^{(R)} = \delta_{ba} G_a^{(R)} + G_b^{(R)} U_{ba}^{(R)} G_a^{(R)}, \tag{4.7}$$

$$G^{(R)} = \delta_{ba} g_a^R + g_b^R U_{ba}^{SR} g_a^R, \tag{4.8}$$

$$g_a^R = G_a^{(R)} + G_a^{(R)} t_a^R G_a^{(R)}. \tag{4.9}$$

Their interrelationship is expressed by an equation similar to (3.9),

$$U_{ba}^{(R)} = \delta_{ba} t_a^R + (1 + t_b^R G_b^{(R)}) U_{ba}^{SR} (1 + G_a^{(R)} t_a^R). \tag{4.10}$$

For the various transition operators, explicit representations can again be derived which are of the form (3.10)–(3.12), with α, β replaced by a, b.

B. Zero-screening limit

Sandwiched between channel states belonging to the energy E_a, Eq. (4.10) becomes, by means of a generalization of the arguments leading to Eq. (3.22),

$$\begin{aligned}\langle \vec{q}_b' | \langle \psi_b | U_{ba}^{(R)}(E_a + i0) | \psi_a \rangle | \vec{q}_a \rangle &= \delta_{ba} t_a^R(\vec{q}_a', \vec{q}_a) \\ &\quad + \langle \vec{q}_{b,R}'^{(-)} | \langle \psi_b | U_{ba}^{SR}(E_a + i0) | \psi_a \rangle | \vec{q}_{a,R}^{(+)} \rangle . \end{aligned} \tag{4.11}$$

Here $|\psi_a\rangle = |\psi_a^{(1)}\rangle |\psi_a^{(2)}\rangle$ is a product of the bound state wave functions of the two asymptotically free fragments of partition a, and $\vec{q}_a$ their relative momentum. In order to simplify the notation the quantum numbers characterizing the bound states are suppressed. Furthermore, $t_a^R(\vec{q}_a', \vec{q}_a)$ denotes the *two-body* on-shell amplitudes for screened Coulomb scattering of the total charges of the two clusters situated in their respective centers of mass, and $|\vec{q}_{a,R}^{(\pm)}\rangle$ are the corresponding scattering states. Note that both quantities go over for infinite screening radius into their unscreened counterparts $t_a^C(\vec{q}_a', \vec{q}_a)$ and $|\vec{q}_{a,C}^{(\pm)}\rangle$, respectively, after having been subjected to the usual *two-body* renormalization procedure [compare Eqs. (3.27) and (3.28)].

Thus, it remains to be shown that the zero-screening limit exists for the matrix elements of the Coulomb-modified short-range transition operator between channel states,

$$\langle \vec{q}_b' | \langle \psi_b^{(2)} | \langle \psi_b^{(1)} | U_{ba}^{SR} | \psi_a^{(1)} \rangle | \psi_a^{(2)} \rangle | \vec{q}_a \rangle . \tag{4.12}$$

Making use of their explicit representation, Eq. (3.11) with a, b substituting α, β, we recognize that for $R \to \infty$ the full Green's function G occurs sandwiched between normalizable states which in position space read as

$$\begin{aligned}\langle \vec{\rho}_a | \langle \vec{x}_a^{(2)} | \langle \vec{x}_a^{(1)} | (\bar{V}_a - v_a^C) | \psi_a^{(1)} \rangle | \psi_a^{(2)} \rangle | \vec{q}_a \rangle &= \sum_{\substack{i<j \\ (ij)\not\subset a}} [V^S_{ij}(\vec{r}_{ij}) + e_i e_j (r_{ij}^{-1} - \rho_a^{-1})] \\ &\quad \times \psi_a^{(1)}(\vec{x}_a^{(1)}) \psi_a^{(2)}(\vec{x}_a^{(2)}) \frac{e^{i\vec{q}_a \cdot \vec{\rho}_a}}{(2\pi)^{3/2}} . \end{aligned} \tag{4.13}$$

Here, $\vec{x}_a^{(k)}$ collectively denotes the internal variables of cluster k of the partition a. Note that the relative coordinates $\vec{r}_{ij}$ between particles i and j

are given as a sum of $\vec{\rho}_a$ and a linear combination $l(\vec{x}_a^{(2)}, \vec{x}_a^{(1)})$ of the internal variables,

$$\vec{r}_{ij} = \pm\vec{\rho}_a + l(\vec{x}_a^{(2)}, \vec{x}_a^{(1)}) . \qquad (4.14)$$

In view of the strong decrease of the bound state wave functions $\psi_a^{(k)}(\vec{x}_a^{(k)})$, again a multipole expansion of r_{ij}^{-1} in powers of ρ_a^{-1} is justified, so that the first nonvanishing term of $(r_{ij}^{-1} - \rho_a^{-1})$ is of the order ρ_a^{-2}. This, however, implies that U_{ba}^{sC} *sandwiched between channel states exists without screening*. Consequently, after renormalization the zero-screening limit of both terms on the right-hand side of Eq. (4.11) exists, providing us with the two-fragment transition amplitude

$$\begin{aligned} T_{ba}(\vec{q}_b{}', \vec{q}_a) = {} & \delta_{ba} t_a^C(\vec{q}_a{}', \vec{q}_a) \\ & + \langle \vec{q}_{b,C}^{\,\prime(-)} | \langle \psi_b | U_{ba}^{sC}(E_a + i0) | \psi_a \rangle | \vec{q}_{a,C}^{\,(+)} \rangle , \end{aligned} \qquad (4.15)$$

represented as a superposition of a pure Coulomb two-body amplitude and a Coulomb-modified short-range amplitude in the Coulomb representation.

We finally mention that the discussion at the end of Sec. III concerning neutral fragments and the pure Coulomb problem carries over directly to the present general case.

V. INTEGRAL EQUATIONS FOR TWO-FRAGMENT SCATTERING AMPLITUDES: THREE-BODY CASE

The screening procedure used in Sec. III to *define* scattering amplitudes for two charged particles, one of which is composite, can also serve as a means to perform *practical calculations*. We may, indeed, evaluate for finite R the on-shell amplitudes (3.22)

$$T_{\beta n,\alpha m}^{(R)}(\vec{q}_\beta{}', \vec{q}_\alpha) = \langle \vec{q}_\beta{}' | \langle \psi_{\beta n} | U_{\beta\alpha}^{(R)}(E_{\alpha m} + i0) | \psi_{\alpha m} \rangle | \vec{q}_\alpha \rangle , \qquad (5.1)$$

with the help *of any* method known in short-range multichannel scattering theory. Subtracting from (5.1) the screened Coulomb amplitude (3.21) obtained by means of a two-body LS equation, and renormalizing this difference, the transition to infinite screening radius can be performed numerically (cf. the corresponding discussion at the end of Sec. II). In this way we arrive at the correct Coulomb-modified short-range transition amplitudes occurring in (3.29)

$$\begin{aligned} & T_{\beta n,\alpha m}^{sC}(\vec{q}_\beta{}', \vec{q}_\alpha) \\ & \quad = \langle \vec{q}_{\beta,C}^{\,\prime(-)} | \langle \psi_{\beta n} | U_{\beta\alpha}^{sC}(E_{\alpha m} + i0) | \psi_{\alpha m} \rangle | \vec{q}_{\alpha,C}^{\,(+)} \rangle . \end{aligned} \qquad (5.2)$$

Adding the explicitly known two-body center-of-mass Coulomb amplitude, the full transition amplitudes $T_{\beta n,\alpha m}(\vec{q}_\beta{}', \vec{q}_\alpha)$ are obtained according to (3.29).

One special method to calculate the two-fragment amplitudes (5.1) is provided by the *quasiparticle* approach[5,29] which is particularly well suited for the present problem. For, it yields *exact* integral equations directly for transition operators sandwiched between two-body bound states, i.e., for effective two-body amplitudes the on-shell elements of which coincide with the expressions (5.1). And just for such amplitudes our zero-screening procedure has been established.[28] We, therefore, describe in the following the application of the quasiparticle concept to $N = 3$.

A. Quasiparticle equations for the full amplitudes

The transition operators $U_{\beta\alpha}^{(R)}$ defined by (3.6) or (3.10) fulfill the Faddeev-type integral equations[5]

$$U_{\beta\alpha}^{(R)} = \bar{\delta}_{\beta\alpha} G_0^{-1} + \sum_\gamma \bar{\delta}_{\beta\gamma} T_\gamma^{(R)} G_0 U_{\gamma\alpha}^{(R)} . \qquad (5.3)$$

Here, $T_\gamma^{(R)}$ is the two-body T matrix (2.9) for subsystem γ read in the three-body space. Following the treatment of Ref. 5 (see also Ref. 29) we decompose $T_\gamma^{(R)}$ into a sum of N_γ separable terms and the rest $T_\gamma'^{(R)}$:

$$\begin{aligned} T_\gamma^{(R)}(z) = {} & \sum_{r,s=1}^{N_\gamma} | \varphi_{\gamma r}(z) \rangle\!\rangle \Delta_{\gamma,rs}(z) \langle\!\langle \varphi_{\gamma s}(z^*) | \\ & + T_\gamma'^{(R)}(z) . \end{aligned} \qquad (5.4)$$

Making use of this representation the three-body equations (5.3) are reduced *exactly* to *effective two two-body equations* of the Lippmann-Schwinger type which can be written in matrix notation as

$$\mathcal{T}^{(R)} = \mathcal{V}^{(R)} + \mathcal{V}^{(R)} \mathcal{G}_0 \mathcal{T}^{(R)} . \qquad (5.5)$$

Here, the elements of the amplitude, potential, and free Green's function matrices are defined by

$$\mathcal{T}_{\beta n,\alpha m}^{(R)}(z) = \langle\!\langle \varphi_{\beta n}(z^*) | G_0(z) U_{\beta\alpha}^{(R)}(z) G_0(z) | \varphi_{\alpha m}(z) \rangle\!\rangle , \qquad (5.6)$$

$$\mathcal{V}_{\beta n,\alpha m}^{(R)}(z) = \langle\!\langle \varphi_{\beta n}(z^*) | G_0(z) U_{\beta\alpha}'^{(R)}(z) G_0(z) | \varphi_{\alpha m}(z) \rangle\!\rangle , \qquad (5.7)$$

$$\mathcal{G}_{0;\beta n,\alpha m}(z) = \delta_{\beta\alpha} \Delta_{\alpha,nm}(z) . \qquad (5.8)$$

The operator $U_{\beta\alpha}'^{(R)}$ occurring in (5.7) satisfies Eq. (5.3) with $T_\gamma^{(R)}$ replaced by $T_\gamma'^{(R)}$:

$$U_{\beta\alpha}'^{(R)} = \bar{\delta}_{\beta\alpha} G_0^{-1} + \sum_\gamma \bar{\delta}_{\beta\gamma} T_\gamma'^{(R)} G_0 U_{\gamma\alpha}'^{(R)} . \qquad (5.9)$$

In praxis, the splitting (5.4) is usually based on a splitting of the potential

$$V_\gamma^{(R)} = V_\gamma^S + V_\gamma^R = \sum_{r=1}^{N_\gamma} | \chi_{\gamma r} \rangle \lambda_{\gamma r} \langle \chi_{\gamma r} | + V_\gamma'^{(R)} . \qquad (5.10)$$

Then, $| \varphi_{\gamma r}(z) \rangle\!\rangle$ is related to the form factor $| \chi_{\gamma r} \rangle$, which itself may be energy dependent, via

$$| \varphi_{\gamma r}(z) \rangle\!\rangle = [1 + T_\gamma'^{(R)}(z) G_0(z)] | \chi_{\gamma r} \rangle , \qquad (5.11)$$

with

$$T_\gamma^{\prime(R)} = V_\gamma^{\prime(R)} + V_\gamma^{\prime(R)} G_0 T_\gamma^{\prime(R)}. \tag{5.12}$$

And the inverse of the matrix Δ_γ is given by

$$[\Delta_\gamma^{-1}(z)]_{rs} = \delta_{rs}\lambda_{\gamma r}^{-1} - \langle \chi_{\gamma r}| G_0(z) |\psi_{\gamma s}(z)\rangle . \tag{5.13}$$

It is advantageous to choose the form factors $|\chi_{\gamma r}\rangle$ orthogonal to the bound states $|\psi_{\gamma m}\rangle$:

$$\lambda_{\gamma r}\langle \chi_{\gamma r}|\psi_{\gamma m}\rangle = \delta_{rm} \quad \text{for } r = 1, \ldots, N_\gamma \tag{5.14}$$

at the binding energies $\hat{E}_{\gamma m}$, $m = 1, \ldots, n_\gamma$ with $n_\gamma \leq N_\gamma$. Then the corresponding bound state poles show up only in the diagonal elements $\Delta_{\gamma,mm}$

$$\langle \vec{q}_\gamma{}'|\Delta_{\gamma,mm}(z)|\vec{q}_\gamma\rangle = \delta(\vec{q}_\gamma{}' - \vec{q}_\gamma)\, \frac{S_{\gamma,m}(z)}{z - q_\gamma{}^2/2M_\gamma - \hat{E}_{\gamma m}} \tag{5.15}$$

with $S_{\gamma,m}(z)$ being, in general, a complicated function of z which, however, as a consequence of (5.14), becomes unity for $z = q_\gamma{}^2/2M_\gamma + \hat{E}_{\gamma m}$. Consequently, the quantities

$$\mathcal{T}^{(R)}_{\beta n,\alpha m}(\vec{q}_\beta{}', \vec{q}_\alpha) = \langle \vec{q}_\beta{}'|\mathcal{T}^{(R)}_{\beta n,\alpha m}(E_{\alpha m} + i0)|\vec{q}_\alpha\rangle ,$$

with $n = 1, \ldots, n_\beta$ and $m = 1, \ldots, n_\alpha$ labeling two-body bound states, coincide on the energy shell with the transition amplitudes (5.1). In other words, solving Eq. (5.5) numerically and proceeding as described after (5.1), we end up with the desired arrangement scattering amplitudes for three charged particles. This procedure corresponds to the *first* practical approach described at the end of Sec. II.

B. Modified off-shell extension of the full amplitude

For the generalization of the *second* practical approach it proves convenient to introduce another off-shell continuation of the amplitude (5.1). It is defined by a LS equation of the form (5.5), but with $\mathcal{G}_0$ replaced by a more appropriate free matrix Green's function $\bar{\mathfrak{g}}_0$. Namely, for indices enumerating the two-body bound states, $\bar{\mathfrak{g}}_0$ is chosen to have only diagonal elements which are of the simple structure of a genuine two-body free Green's function, i.e., of the form (5.15) with $S_{\gamma,m}(z) = 1$ for *all* values of z. In other words, we define the elements of $\bar{\mathfrak{g}}_0$ via

$$\bar{\mathfrak{g}}_{0;\beta n,\alpha m}(z) = \begin{cases} \delta_{\beta\alpha}\delta_{nm}\mathfrak{g}_{0,\alpha}(z - \hat{E}_{\alpha m}), & \text{for } n = 1, \ldots, n_\beta \\ & \text{or } m = 1, \ldots, n_\alpha \\ \mathcal{G}_{0;\beta n,\alpha m}(z), & \text{otherwise}, \end{cases} \tag{5.16}$$

with $\mathfrak{g}_{0,\alpha}$ given by (3.17). Multiplying (5.5) from the right by $\mathcal{G}_0\bar{\mathfrak{g}}_0{}^{-1}$, we obtain again a matrix equation of the Lippmann-Schwinger structure

$$\bar{\mathcal{T}}^{(R)} = \bar{\mathfrak{V}}^{(R)} + \bar{\mathfrak{V}}^{(R)}\bar{\mathfrak{g}}_0\bar{\mathcal{T}}^{(R)} \tag{5.17}$$

for the matrix operator

$$\bar{\mathcal{T}}^{(R)} = \mathcal{T}^{(R)}\mathcal{G}_0\bar{\mathfrak{g}}_0{}^{-1}, \tag{5.18}$$

which contains the simpler free matrix Green's function $\bar{\mathfrak{g}}_0$ instead of $\mathcal{G}_0$.

From the above mentioned properties of $\mathcal{G}_0$ and $\bar{\mathfrak{g}}_0$ it follows that all elements $(\mathcal{G}_0\bar{\mathfrak{g}}_0{}^{-1})_{nm}$ with m denoting a two body bound state vanish, when applied onto $|\vec{q}_\alpha\rangle$ at the corresponding channel energy $E_{\alpha m}$, except the one with $n = m$ which, in fact, has the value one. Therefore, on the right-hand energy shell, $\bar{\mathcal{T}}^{(R)}$ coincides with $\mathcal{T}^{(R)}$,

$$\bar{\mathcal{T}}^{(R)}_{\beta n,\alpha m}(E_{\alpha m} + i0)\,|\vec{q}_\alpha\rangle = \mathcal{T}^{(R)}_{\beta n,\alpha m}(E_{\alpha m} + i0)|\vec{q}_\alpha\rangle \quad \text{for } m = 1, \ldots, n_\alpha . \tag{5.19}$$

In other words, $\bar{\mathcal{T}}^{(R)}$ and $\mathcal{T}^{(R)}$ represent different off-shell continuations of the amplitude (5.1). A relation similar to (5.19) holds true also between $\bar{\mathfrak{V}}^{(R)}$ and $\mathfrak{V}^{(R)}$. Henceforth, we will work with Eq. (5.17) instead of (5.5).

C. Quasiparticle equations for the unscreened Coulomb-modified short-range amplitudes

The two-body structure of the quasiparticle equations (5.5) and (5.17) suggests generalizing also the *second* practical approach described at the end of Sec. II. As mentioned above, the form (5.17) is particularly convenient for this purpose. In order to be able to perform all algebraic manipulations as in the genuine two-body case, an effective two-body Coulomb potential matrix $\bar{\mathfrak{v}}^R$ and an amplitude matrix $\bar{\mathfrak{t}}^R$ are associated with the operators (3.16) and (3.19) by means of

$$\bar{\mathfrak{v}}^R_{\beta n,\alpha m} = \begin{cases} \delta_{\beta\alpha}\delta_{nm}\mathfrak{v}^R_\alpha, & \text{for } n \text{ and } m \\ & \text{bound state indices} \\ 0, & \text{otherwise} \end{cases} \tag{5.20}$$

and

$$\bar{\mathfrak{t}}^R_{\beta n,\alpha m}(z) = \begin{cases} \delta_{\beta\alpha}\delta_{nm}\mathfrak{t}^R_\alpha(z - \hat{E}_{\alpha m}), & \text{for } n \text{ and } m \\ & \text{bound state indices} \\ 0, & \text{otherwise}. \end{cases} \tag{5.21}$$

To introduce nonvanishing elements in these matrices only for bound state indices is suggested by the desire to reproduce the on-shell relation (3.22 for the physical two-fragment amplitudes which are characterized by these indices [compare Eq. (5.27)]. The other $\mathcal{T}_{\beta n,\alpha m}$ in (5.6) for which n and m do *not* correspond to bound state indices, are purely auxiliary quantities, introduced in order to improve the accuracy. Hence, no renormalization procedure and consequently no splitting of the form (3.22), is needed for these terms. In this context it may be helpful to recall the argumenta-

22539 0
Date 30-12-04

tion employed in Refs. 3 and 4. There, by inspecting the kernels of the effective two-body integral equations, it was found that, due to the absence of physical-sheet poles in the effective propagators for nonbound state indices, no overlap with the singularity of $\mathfrak{v}_\alpha^R$ in the zero-screening limit can occur. Consequently, no renormalization procedure is necessary in these unphysical channels.

The Coulomb resolvent matrix corresponding to the definitions (5.16), (5.20), and (5.21) is then introduced by the conventional two-body relation

$$\tilde{\mathfrak{g}}^R=\tilde{\mathfrak{g}}_0+\tilde{\mathfrak{g}}_0\tilde{\mathfrak{t}}^R\tilde{\mathfrak{g}}_0\,, \tag{5.22}$$

or equivalently by

$$\tilde{\mathfrak{g}}^R=\tilde{\mathfrak{g}}_0+\tilde{\mathfrak{g}}_0\tilde{\mathfrak{v}}^R\tilde{\mathfrak{g}}^R\,. \tag{5.23}$$

Then, in complete analogy to (2.8), a Coulomb-distorted short-range amplitude $\mathcal{T}^{SR}$ is defined via

$$\tilde{\mathcal{T}}^{(R)}=\tilde{\mathfrak{t}}^R+(1+\tilde{\mathfrak{t}}^R\tilde{\mathfrak{g}}_0)\mathcal{T}^{SR}(1+\tilde{\mathfrak{g}}_0\tilde{\mathfrak{t}}^R)\,. \tag{5.24}$$

Introducing a potential matrix $\mathcal{V}^{SR}$ by means of

$$\tilde{\mathcal{V}}^{(R)}=\mathcal{V}^{SR}+\tilde{\mathfrak{v}}^R \tag{5.25}$$

we find that this amplitude satisfies the integral equation

$$\mathcal{T}^{SR}=\mathcal{V}^{SR}+\mathcal{V}^{SR}\tilde{\mathfrak{g}}^R\mathcal{T}^{SR}\,. \tag{5.26}$$

The definition (5.24) is closely related to (3.22), as becomes transparent by going over to the explicit notation. Indeed, for bound state indices $n=1,\ldots,n_\beta$ and $m=1,\ldots,n_\alpha$ it reads

$$\begin{aligned}\tilde{\mathcal{T}}^{(R)}_{\beta n,\alpha m}(z)&=\delta_{\beta\alpha}\delta_{nm}\mathfrak{t}_\alpha^R(z-\hat{E}_{\alpha m})\\&\quad+[(1+\mathfrak{t}_\beta^R(z-\hat{E}_{\beta n})\mathfrak{g}_{0,\beta}(z-\hat{E}_{\beta n})]\\&\quad\times\mathcal{T}^{SR}_{\beta n,\alpha m}(z)[1+\mathfrak{g}_{0,\alpha}(z-\hat{E}_{\alpha m})\mathfrak{t}_\alpha^R(z-\hat{E}_{\alpha m})]\,.\end{aligned} \tag{5.27}$$

Taking into account (3.20) and (3.21), we see that both the left-hand side and the first term on the right-hand side of (5.27), when sandwiched between plane waves $\langle\vec{q}\,'_\beta|$ and $|\vec{q}_\alpha\rangle$, coincide on the energy shell with the corresponding terms of (3.22). This implies on-shell the equality of the respective second terms, too, namely

$$\begin{aligned}\langle\vec{q}\,'^{(-)}_{\beta,R}|\langle\psi_{\beta n}|U^{SR}_{\beta\alpha}(E_{\alpha m}+i0)|\psi_{\alpha m}\rangle|\vec{q}^{\,(+)}_{\alpha,R}\rangle\\=\langle\vec{q}\,'^{(-)}_{\beta,R}|\mathcal{T}^{SR}_{\beta n,\alpha m}(E_{\alpha m}+i0)|\vec{q}^{\,(+)}_{\alpha,R}\rangle\,.\end{aligned} \tag{5.28}$$

From the investigation leading to Eq. (3.29) we know that the states $\langle\vec{q}\,'^{(-)}_{\beta,R}|$ and $|\vec{q}^{\,(+)}_{\alpha,R}\rangle$, multiplied by $Z^{-1/2}_{\beta,R}(q'_\beta)$ and $Z^{-1/2}_{\alpha,R}(q_\alpha)$, respectively, go over for $R\to\infty$ into the unscreened Coulomb scattering states. Furthermore, as has been shown in Sec. III, this limit can be performed immediately in $\langle\psi_{\beta n}|U^{SR}_{\beta\alpha}(E_{\alpha m}+i0)|\psi_{\alpha m}\rangle$, and consequently due to the equality (5.28) the same holds true for the quantity $\mathcal{T}^{SR}_{\beta n,\alpha m}(E_{\alpha m}+i0)$. Denoting the zero-screening limit of the latter by $\mathcal{T}^{SC}_{\beta n,\alpha m}(E_{\alpha m}+i0)$ we, therefore, end up with the representation

$$T^{SC}_{\beta n,\alpha m}(\vec{q}\,'_\beta,\vec{q}_\alpha)=\langle\vec{q}\,'^{(-)}_{\beta,C}|\mathcal{T}^{SC}_{\beta n,\alpha m}(E_{\alpha m}+i0)|\vec{q}^{\,(+)}_{\alpha,C}\rangle \tag{5.29}$$

for the *unscreened* Coulomb-modified short-range transition amplitude (5.2).

An integral equation for $\mathcal{T}^{SC}$ itself now follows directly by letting R go to infinity in Eq. (5.26). In this way, we arrive at the generalization of Eq. (2.15),

$$\mathcal{T}^{SC}=\mathcal{V}^{SC}+\mathcal{V}^{SC}\tilde{\mathfrak{g}}^C\mathcal{T}^{SC}\,. \tag{5.30}$$

Here, the Coulomb-modified short-ranged potential matrix

$$\mathcal{V}^{SC}=\tilde{\mathcal{V}}-\tilde{\mathfrak{v}}^C \tag{5.31}$$

and the Coulomb Green's function matrix $\tilde{\mathfrak{g}}^C$ are given by Eqs. (5.25) and (5.22), respectively, after having switched off the screening.

Let us briefly comment on the relation between the present approach and the one developed in Refs. 1–4. There, we demonstrated explicitly that $\mathcal{V}^{SC}$ does not contain contributions of infinite range. From this fact the validity of Eq. (5.30) and, as a consequence, the existence of $\mathcal{T}^{SC}$ could be inferred. Alternatively, in the present paper we started by directly proving the existence of $\mathcal{T}^{SC}$ from which then the validity of the integral equation (5.30) followed. However, whether Eq. (5.30) is also useful for practical calculations depends on properties of its kernel which go beyond those required for proving its validity. In fact, since $\mathcal{V}^{SC}$ is still of fairly long range it is even questionable whether the kernel $\mathcal{V}^{SC}\tilde{\mathfrak{g}}^C$ falls into that class for which standard integral equations theory is applicable. Certainly further investigations are needed to clarify this point.

For convenience we present our result (5.30) in explicit notation,

$$\begin{aligned}\mathcal{T}^{SC}_{\beta n,\alpha m}(z)=\mathcal{V}^{SC}_{\beta n,\alpha m}(z)+\sum_{\gamma\delta,rs}\mathcal{V}^{SC}_{\beta n,\gamma r}(z)\\\times\tilde{\mathfrak{g}}^C_{\gamma r,\delta s}(z)\mathcal{T}^{SC}_{\delta s,\alpha m}(z)\,,\end{aligned} \tag{5.32}$$

with

$$\mathcal{V}^{SC}_{\beta n,\alpha m}(z)=\begin{cases}\tilde{\mathcal{V}}_{\beta n,\alpha m}(z)-\delta_{\beta\alpha}\delta_{nm}\mathfrak{v}^C_\alpha\,, & \text{for } n \text{ or } m \text{ bound state indices}\\ \tilde{\mathcal{V}}_{\beta n,\alpha m}(z)\,, & \text{otherwise}\,,\end{cases} \tag{5.33}$$

and

$$\tilde{\mathfrak{g}}^C_{\beta n,\alpha m}(z)=\begin{cases}\delta_{\beta\alpha}\delta_{nm}\mathfrak{g}^C_\alpha(z-\hat{E}_{\alpha m})\,, & \text{for } n \text{ or } m \text{ bound state indices}\\ \mathfrak{g}_{0;\beta n,\alpha m}(z)\,, & \text{otherwise}\,.\end{cases} \tag{5.34}$$

We mention that from (5.21) and (5.27) it follows immediately that the full unscreened amplitude $\mathcal{T}_{\beta n,\alpha m}$ equals $\mathcal{T}^{SC}_{\beta n,\alpha m}$ if neither n nor m denote two-body bound states, i.e., if $n \neq 1,\ldots,n_\beta$ and $m \neq 1,\ldots,n_\alpha$. This is consistent with the fact that (5.32) goes over into (5.5) in this case. Solving Eq. (5.32) we therefore obtain, besides the full amplitudes for unphysical channels, the Coulomb-distorted amplitudes $\mathcal{T}^{SC}_{\beta n,\alpha m}$ for physical channels enumerated by $n(m) = 1,\ldots,n_\beta(n_\alpha)$. Sandwiching the latter ones between $\langle \vec{q}\,'^{(-)}_{\beta,C}|$ and $|\vec{q}^{(+)}_{\alpha,C}\rangle$, the full unscreened arrangement amplitudes are obtained via (5.29), (5.2), and (3.29).

This procedure is considerably simplified if the Coulomb interactions v^C_γ between the colliding clusters are repulsive. For, inserting the spectral decomposition of $g^C_\gamma(z-\hat{E}_{\gamma r})$ occurring via (5.34) in Eq. (5.32), we obtain relations which directly yield off-shell continuations of the amplitudes (5.2). In fact, we have for $m=1,\ldots,n_\alpha$ and $n=1,\ldots,n_\beta$

$$\begin{aligned}\langle \vec{q}\,'^{(-)}_{\beta,C}|\mathcal{T}^{SC}_{\beta n,\alpha m}(z)|\vec{q}^{(+)}_{\alpha,C}\rangle &= \langle \vec{q}\,'^{(-)}_{\beta,C}|\mathcal{V}^{SC}_{\beta n,\alpha m}(z)|\vec{q}^{(+)}_{\alpha,C}\rangle \\ &+\sum_\gamma\sum_{r=1}^{n_\gamma}\int d^3q''_\gamma \langle \vec{q}\,'^{(-)}_{\beta,C}|\mathcal{V}^{SC}_{\beta n,\gamma r}(z)|\vec{q}\,''^{(-)}_{\gamma,C}\rangle \frac{1}{z-\hat{E}_{\gamma r}-q''^2_\gamma/2M_\gamma}\langle \vec{q}\,''^{(-)}_{\gamma,C}|\mathcal{T}^{SC}_{\gamma r,\alpha m}(z)|\vec{q}^{(+)}_{\alpha,C}\rangle \\ &+\sum_\gamma\sum_{r,s=n_\gamma+1}^{N_\gamma}\int d^3q''_\gamma \langle \vec{q}\,'^{(-)}_{\beta,C}|\mathcal{V}_{\beta n,\gamma r}(z)|\vec{q}\,''_\gamma\rangle \mathcal{G}_{0;\gamma r,\gamma s}(z)\langle \vec{q}\,''_\gamma|\mathcal{T}^{SC}_{\gamma s,\alpha m}(z)|\vec{q}^{(+)}_{\alpha,C}\rangle\,, \end{aligned}\qquad(5.35)$$

and a similar relation with $\langle \vec{q}\,'^{(-)}_{\beta,C}|$ replaced by $\langle \vec{q}\,'_\beta|$ for the elements with $n = n_{\beta+1},\ldots,N_\beta$.

A final remark concerns the case of attractive Coulomb forces in one or more subsystems. Associating to each of the infinitely many two-body bound states a separable term in (5.4) would blow up the system of equations (5.5). In this case, it might be preferable to represent by separable terms in (5.4) only the dominant bound states, in particular those which are explicitly considered in the special physical situation, and to absorb the remaining ones via T'_γ into the definition of $U'_{\beta\alpha}$, cf. Eq. (5.9). Whether the quasi-Born series, which perturbatively determines the effective potential $\mathcal{V}$, and consequently also $\mathcal{V}^{SC}$, then still converges deserves further investigation.

D. Modified screening procedure

In the above definitions of three-body transition operators and effective two-body amplitudes *all* Coulomb potentials had been screened before applying the renormalization and limiting procedure. From the reasoning following Eq. (3.22) we know, on the other hand, that such a screening is actually required only for the center-of-mass Coulomb potential v^C_α when it is being used to define the two-body amplitudes t^C_α and the scattering states $|\vec{q}^{(\pm)}_{\alpha,C}\rangle$. In contrast, for the definition of the Coulomb-modified short-range amplitudes $\mathcal{T}^{SC}$ we could have worked from the very beginning with unscreened Coulomb potentials.

This fact has already been utilized in the *second* approach where, as shown in Sec. VC, the *unscreened* amplitude $\mathcal{T}^{SC}$ is obtained directly as solution of (5.30). But we expect that also the *first* practical approach, based on solving Eqs. (5.5) or (5.17), can be simplified in a corresponding manner. Indeed, according to the above considerations, the screening of the Coulomb interaction is expected to be unnecessary in most terms of the effective potential (5.7). To make this explicit we introduce the modified effective potential

$$\bar{\mathcal{V}}^{(R)} = \mathcal{V}^{SC} + \bar{v}^R \qquad (5.36)$$

which originates from (5.25) by replacing the Coulomb-modified short-ranged part $\mathcal{V}^{SR}$ by its zero-screening limit $\mathcal{V}^{SC}$. The representation (5.31) allows us to write (5.36) in the form

$$\bar{\mathcal{V}}^{(R)} = \bar{\mathcal{V}} - \bar{v}^C + \bar{v}^R \qquad (5.37)$$

which clearly shows that $\bar{\mathcal{V}}^{(R)}$ is obtained from the unscreened potential $\bar{\mathcal{V}}$ by screening only its long-ranged contribution $\bar{v}^C$.

Inserting $\bar{\mathcal{V}}^{(R)}$ instead of $\tilde{\mathcal{V}}^{(R)}$ in (5.17), a new screened amplitude $\bar{\mathcal{T}}^{(R)}$ is defined as

$$\bar{\mathcal{T}}^{(R)} = \bar{\mathcal{V}}^{(R)} + \bar{\mathcal{V}}^{(R)}\bar{g}_0\bar{\mathcal{T}}^{(R)}\,. \qquad (5.38)$$

Making use of the splitting (5.36) of $\bar{\mathcal{V}}^{(R)}$ we obtain the representation

$$\bar{\mathcal{T}}^{(R)} = \bar{t}^R + (1+\bar{t}^R\bar{g}_0)\bar{\mathcal{T}}^{SR}(1+\bar{g}_0\bar{t}^R)\,, \qquad (5.39)$$

where $\bar{\mathcal{T}}^{SR}$ is given as solution of

$$\bar{\mathcal{T}}^{SR} = \mathcal{V}^{SC} + \mathcal{V}^{SC}\bar{g}^R\bar{\mathcal{T}}^{SR}\,. \qquad (5.40)$$

Since this relation, which contains the screening only via $\bar{g}^R$, goes over into (5.30) for $R\to\infty$, its solution becomes identical with $\mathcal{T}^{SC}$ in this limit. Comparison of (5.39) and (5.24) then reveals that $\tilde{\mathcal{T}}^{(R)}$ and $\bar{\mathcal{T}}^{(R)}$ lead to the *same* unscreened amplitude (3.29) when subjected to the renormalization and limiting procedure. In other words, the *first* practical approach discussed in Sec. VA yields the ame on-shell arrangement amplitudes when being ased on the solutions of (5.38) instead of (5.5) or 5.17). However, the amount of work required for he numerical solution is drastically different for oth types of equations. For, when solving Eqs. 5.5) or (5.17) the full effective potential has to be ecalculated every time the value of R is increas- d. This, however, is a most time-consuming sk. In contrast, when Eq. (5.38) is used the bulk $\bar{\mathcal{V}}^{(R)}$ namely, $\mathcal{V}^{SC}$, has to be computed only once or a fixed energy) since the R dependence resides lely in the trivial term $\bar{v}^R$. Therefore, the pro- dure described in the present section represents considerable simplification of the first practical proach.

In addition, the present version is even more closely related to the corresponding method in the genuine two-body problem. Namely, as is the case *there, only that part of the potential* $\bar{\mathcal{V}}$ *has to be* screened which behaves like a pure Coulomb potential in the *relative* two-fragment coordinate, whereas $\mathcal{V}^{SC}$, which is of shorter range with respect to this variable although it contains two-body Coulomb potentials, remains unscreened.

Sections V D and V C, therefore, contain the most natural generalizations of the first and the second practical approach discussed for the two-body case in Sec. II.

VI. INTEGRAL EQUATIONS FOR TWO-FRAGMENT AMPLITUDES: N-BODY CASE

The method discussed at the beginning of Sec. V for $N=3$ can be extended immediately to arbitrary *particle numbers. First, the screened* amplitude (4.11),

$$T^{(R)}_{ba}(\vec{q}_b{}', \vec{q}_a) = \langle \vec{q}_b{}' | \langle \psi_b | U^{(R)}_{ba}(E_a + i0) | \psi_a \rangle | \vec{q}_a \rangle , \quad (6.1)$$

is calculated for finite R by means of *any* method applicable for purely short-ranged interactions. Subtracting from it the center-of-mass Coulomb amplitude $t^R_a(\vec{q}_a{}', \vec{q}_a)$ yields, on account of (4.11), the screened Coulomb-modified short-range amplitude. Renormalizing the latter, and repeating the calculation for increasing values of R, the zero-screening limit is approached numerically. By this procedure we end up with the unscreened Coulomb-modified short-range amplitude

$$T^{SC}_{ba}(\vec{q}_b{}', \vec{q}_a) = \langle \vec{q}_{b,C}{}'^{(-)} | \langle \psi_b | U^{SC}_{ba}(E_a + i0) | \psi_a \rangle | \vec{q}_{a,C}^{(+)} \rangle , \quad (6.2)$$

and according to (4.15) with the full unscreened scattering amplitude $T_{ba}(\vec{q}_b{}', \vec{q}_a)$.

Particularly appropriate for the calculation of the screened amplitude (6.1) is the generalization of the three-body quasiparticle method to N-body problems proposed in Ref. 30. For, it replaces in $(N-2)$ steps the original operator identities for $U^{(R)}_{ba}$ by exact equations for off-shell extensions $\mathcal{T}^{(R)}_{ba}$ of the *effective two-body* amplitudes $\langle \psi_b | U^{(R)}_{ba}(E_a + i0) | \psi_a \rangle$,

$$\mathcal{T}^{(R)}_{ba} = \mathcal{V}^{(R)}_{ba} + \sum_{c,d} \mathcal{V}^{(R)}_{bc} \mathcal{G}_{0;cd} \mathcal{T}^{(R)}_{da} . \quad (6.3)$$

For details of the definitions of the effective potential $\mathcal{V}^{(R)}$ and "free Green's function" $\mathcal{G}_0$ we refer to Ref. 30. There it is also shown that on the energy shell the physical reaction amplitude (6.1) can be obtained via

$$T^{(R)}_{ba}(\vec{q}_b{}', \vec{q}_a) = \langle \vec{q}_b{}' | \mathcal{T}^{(R)}_{ba}(E_a + i0) | \vec{q}_a \rangle . \quad (6.4)$$

Therefore, solving Eq. (6.3) and proceeding as discussed after Eq. (6.1), represents the N-body generalization of the *first* practical approach described in Sec. II. We remark that this method may again be simplified along the lines described in Sec. V D.

Of course, the *second* approach developed in Sec. V C can be extended to arbitrary particle numbers, too. For this purpose, it is again advantageous to work with, instead of (6.3), an equation containing the simpler free Green's function matrix $\bar{g}_0$, with elements

$$\bar{g}_{0;ba} = \begin{cases} \delta_{ba}\, g_{0,a}(z - \hat{E}_a) , & \text{for } b \text{ or } a \text{ denoting} \\ & \text{bound state channels} \\ \mathcal{G}_{0;ba} , & \text{otherwise} . \end{cases} \quad (6.5)$$

Here

$$g_{0,a}(z) = \left(z - \frac{Q_a{}^2}{2M_a} \right)^{-1} \quad (6.6)$$

is a genuine two-body free Green's function which acts on the relative momentum states $|\vec{q}_a\rangle$ only [cf. Eq. (3.17)]. Multiplication of (6.3) with $\mathcal{G}_0 \bar{g}_0{}^{-1}$ results in the N-body analog of (5.17):

$$\bar{\mathcal{T}}^{(R)}_{ba} = \bar{\mathcal{V}}^{(R)}_{ba} + \sum_{c,d} \bar{\mathcal{V}}^{(R)}_{bc} \bar{g}_{0;cd} \bar{\mathcal{T}}_{da} . \quad (6.7)$$

Since we assume $\mathcal{G}_0$ to be chosen such that it displays the same pole behavior as $\bar{g}_0$ (compare the discussion in Secs. V A and V B for the three-particle case), the solution $\bar{\mathcal{T}}^{(R)} = \mathcal{T}^{(R)} \mathcal{G}_0 \bar{g}_0{}^{-1}$ of (6.7) equals $\mathcal{T}^{(R)}$ on the right-hand energy shell.

Next we introduce a two-body Coulomb potential v^R_a describing the interaction between the charges of the two colliding fragments concentrated in their centers of mass, which is related to the N-body operator (4.5) according to

$$\langle \vec{q}_a{}' | v^R_a | \vec{q}_a \rangle = \langle \vec{q}_a{}' | \langle \psi_a | V^R_a | \psi_a \rangle | \vec{q}_a \rangle = v^R_a(\vec{q}_a{}' - \vec{q}_a) . \quad (6.8)$$

The corresponding two-body Coulomb resolvent g^R_a and Coulomb transition operator t^R_a are

$$\mathfrak{g}_a^R(z) = \left(z - \frac{Q_a^{\,2}}{2M_a} - \mathfrak{v}_a^R\right)^{-1} \tag{6.9}$$

and

$$t_a^R = \mathfrak{v}_a^R + \mathfrak{v}_a^R \mathfrak{g}_a^R \mathfrak{v}_a^R , \tag{6.10}$$

respectively. With the help of these quantities we define for bound state channels a and b an effective two-body amplitude $\mathcal{T}_{ba}^{SR}$, in analogy to (5.27), via

$$\begin{aligned}\bar{\mathcal{T}}_{ba}^{(R)}(z) = {} & \delta_{ba} t_a^R(z - \hat{E}_a) \\ & + [1 + t_b^R(z - \hat{E}_b) \mathfrak{g}_{0;b}(z - \hat{E}_b)] \\ & \times \mathcal{T}_{ba}^{SR}(z)[1 + \mathfrak{g}_{0;a}(z - \hat{E}_a) t_a^R(z - \hat{E}_a)] .\end{aligned} \tag{6.11}$$

For a or b *not* characterizing bound state channels, the first term on the right-hand side of (6.11) and either the right or the left bracket in the second term are missing. Sandwiching (6.11) between plane waves $\langle \vec{q}_b'|$ and $|\vec{q}_a\rangle$ and comparing with (4.11) we see that the left-hand sides and the first terms on the right-hand sides of both equations, respectively, coincide on the energy shell. Generalizing the argumentation following (5.28), we infer that the zero-screening limit of $\mathcal{T}^{SR}$, which we denote by $\mathcal{T}^{SC}$, is indeed related on the energy shell to the Coulomb-modified short-range amplitude (6.2) according to

$$T_{ba}^{SC}(\vec{q}_b', \vec{q}_a) = \langle \vec{q}_{b,C}'^{(-)} | \mathcal{T}_{ba}^{SC}(E_a + i0) | \vec{q}_{a,C}^{(+)} \rangle . \tag{6.12}$$

An integral equation directly for $\mathcal{T}^{SC}$ is now easily derived. For this purpose we introduce the zero-screening limits of the potentials $\bar{\mathfrak{V}}_{ba}^{(R)}$ and $\mathfrak{v}_a^R$, and of $\mathfrak{g}_a^R$, to be denoted by $\bar{\mathfrak{V}}_{ba}$, $\mathfrak{v}_a^C$, and $\mathfrak{g}_a^C$, respectively. As in (5.33), the short-ranged part $\mathfrak{V}^{SC}$ of $\bar{\mathfrak{V}}$ is obtained by subtracting from the latter the long-ranged Coulomb contribution,

$$\mathfrak{V}_{ba}^{SC} = \begin{cases} \bar{\mathfrak{V}}_{ba} - \delta_{ba}\mathfrak{v}_a^C , & \text{for } a \text{ or } b \text{ denoting} \\ & \text{bound state channels} \\ \bar{\mathfrak{V}}_{ba} , & \text{otherwise} . \end{cases} \tag{6.13}$$

Familiar algebra, then, leads immediately to the generalization of (5.32),

$$\mathcal{T}_{ba}^{SC} = \mathfrak{V}_{ba}^{SC} + \sum_{c,d} \mathfrak{V}_{bc}^{SC} \bar{\mathfrak{g}}_{cd}^{C} \mathcal{T}_{da}^{SC} . \tag{6.14}$$

Here the elements of the matrix Coulomb Green's function $\bar{\mathfrak{g}}^C(z)$ are defined by [cf. Eq. (5.34)]

$$\bar{\mathfrak{g}}_{ba}^C(z) = \begin{cases} \delta_{ba}\, \mathfrak{g}_a^C(z - \hat{E}_a) , & \text{for } b \text{ or } a \text{ denoting} \\ & \text{bound state channels} \\ \mathfrak{g}_{0;ba}(z) , & \text{otherwise} . \end{cases} \tag{6.15}$$

Solving (6.14) we, therefore, get without any screening procedure an amplitude $\mathcal{T}_{ba}^{SC}$. When sandwiched between the explicitly known two-body Coulomb states $\langle \vec{q}_{b,C}'^{(-)}|$ and $|\vec{q}_{a,C}^{(+)}\rangle$, it yields via (6.12) the Coulomb-modified short-range amplitude (6.2), and then by means of (4.15) the full transition amplitude $T_{ba}(\vec{q}_b', \vec{q}_a)$.

As emphasized in Sec. V C this method is simplified considerably if the Coulomb potential $\mathfrak{v}_a^C$ is repulsive. For, insertion of the spectral decomposition of the Coulomb Green's function $\mathfrak{g}_a^C$ occurring in (6.15) results in an integral equation directly for

$$\mathcal{T}_{ba}^{SC}(\vec{q}_b', \vec{q}_a) = \langle \vec{q}_{b,C}'^{(-)} | \mathcal{T}_{ba}^{SC} | \vec{q}_{a,C}^{(+)} \rangle , \tag{6.16}$$

which we need not write down explicitly since it generalizes the three-body equation (5.35) in an obvious way.

---

[1] E. O. Alt, in *Few Body Dynamics*, edited by A. N. Mitra *et al.* (North-Holland, Amsterdam, 1976).

[2] E. O. Alt, W. Sandhas, H. Zankel, and H. Ziegelmann, Phys. Rev. Lett. 37, 1537 (1976).

[3] E. O. Alt, W. Sandhas, and H. Ziegelmann, Phys. Rev. C 17, 1981 (1978).

[4] E. O. Alt, in *Few-Body Nuclear Physics*, edited by G. Pisent *et al.* (IAEA, Vienna, 1978); in *Few Body Systems and Nuclear Forces*, edited by H. F. K. Zingl *et al.* (Springer, Berlin, 1978).

[5] E. O. Alt, P. Grassberger, and W. Sandhas, Nucl. Phys. B2, 167 (1967).

[6] E. O. Alt and W. Sandhas, in *Few Body Systems and Nuclear Forces*, edited by H. F. K. Zingl *et al.* (Springer, Berlin, 1978).

[7] *For other attempts concerning the definition problem* see, e.g., Refs. 8–14.

[8] J. D. Dollard, J. Math. Phys. 5, 729 (1964); *ibid.* 9, 620 (1968).

[9] A. M. Veselova, Teor. Mat. Fiz. 13, 368 (1972).

[10] E. Prugovecki and J. Zorbas, Nucl. Phys. A213, 541 (1973).

[11] J. Zorbas, J. Phys. A7, 1557 (1974); Rep. Math. Phys. 9, 309 (1976).

[12] C. Chandler and A. G. Gibson, J. Math. Phys. 15, 291 (1974); *ibid.* 15, 1366 (1974).

[13] Gy. Bencze, Lett. Nuovo Cimento 17, 91 (1976).

[14] Gy. Bencze, G. Cattapan, and V. Vanzani, Lett. Nuovo Cimento 20, 248 (1977).

[15] R. H. Dalitz, Proc. R. Soc. London A206, 509 (1951).

[16] V. G. Gorshkov, Zh. Eksp. Teor. Fiz. 40, 1481 (1961) [Sov. Phys.—JETP 13, 1037 (1961)].

[17] J. R. Taylor, Nuovo Cimento B23, 313 (1974).

[18] M. D. Semon and J. R. Taylor, Nuovo Cimento A26, 4 (1975).

[19] Compare also Sec. II of Ref. 3.

[20] This approach has been used in Refs. 1 and 2 for calculations of proton–deuteron scattering observables.

[21] The intoduction of the center-of-mass Coulomb interaction v_α^R here and in Refs. 1–4 is the crucial ingredient which makes our formulation very different from, and more practical than, previous approaches (see Refs. 22, 23).

[22] J. V. Noble, Phys. Rev. 161, 945 (1967).

[23] Gy. Bencze, Nucl. Phys. A196, 135 (1972). See, however, P. U. Sauer in *Few-Body Nuclear Physics*, edited by G. Pisent *et al.* (IAEA, Vienna, 1978).

[24] C. Lovelace, Phys. Rev. 135, B1225 (1964).

[25] For our definitions of scattering amplitudes to be valid also beyond the breakup thresholds it is decisive that we always work with three-body operators sandwiched between two-body bound state wave functions. For an approach below threshold see A. M. Veselova, Teor. Mat. Fiz. 3, 326 (1970); See also L. D. Faddeev, in *Three Body Problem in Nuclear and Particle Physics*, edited by J. S. C. McKee and P. M. Rolph (North-Holland, Amsterdam, 1970).

[26] We mention that in Refs. 3 and 4 the operators v_α^R, $g_{0,\alpha}$, etc. have been denoted by $V_R^{0\alpha}$, $G_0^{0\alpha}$, etc.

[27] In the special case of exponentially screened Coulomb potentials

$$v_\alpha^R(\vec\rho_\alpha)=e_\alpha(e_\beta+e_\gamma)\exp(-\rho_\alpha/R)/\rho_\alpha,$$

the renormalization factor has the form

$$Z_{\alpha,R}(q_\alpha)=\exp[-2ie_\alpha(e_\beta+e_\gamma)M_\alpha/q_\alpha(\ln 2q_\alpha R-C)],$$

cf. the two-body analog in Sec. II.

[28] This has also been pointed out by L. D. Faddeev in *Three Body Problem in Nuclear and Particle Physics*, edited by J. S. C. McKee and P. M. Rolph (North-Holland, Amsterdam, 1970), referring to A. M. Veselova, Vestn. Leningr. Univ. 4, 148 (1968).

[29] E. O. Alt and W. Sandhas, Phys. Rev. C 18, 1088 (1978).

[30] P. Grassberger and W. Sandhas, Nucl. Phys. B2, 181 (1967).

PHYSICAL REVIEW C VOLUME 21, NUMBER 5 MAY 1980

^{56}Fe(e,α) reaction and its relevance to the $E2$ isoscalar sum rule

D. M. Skopik, J. Asai, and J. J. Murphy II
Saskatchewan Accelerator Laboratory, University of Saskatchewan, Saskatoon S7N 0W0, Canada

(Received 17 December 1979)

The cross section ^{56}Fe(e,α) has been measured as a function of α energy, lab angle, and incident electron energy. The analyses of these data using distorted-wave Born approximation virtual photon spectra have been performed in the framework of models suggested by the data. We find that the (e,α) channel exhausts a sizable percentage of the $E2$ isoscalar sum rule.

[NUCLEAR REACTIONS ^{56}Fe(e,α) measured $\sigma(E_0, E_\alpha, \theta_\alpha)$, obtained $\sigma(e,\alpha)$ and determined $\sigma^{E1}(\gamma,\alpha)$ and $\sigma^{E2}(\gamma,\alpha)$.]

I. INTRODUCTION

The work that we report here is an outgrowth of our earlier (e,α) experiments[1,2] in which the systematics of alpha emission from various nuclei after electron bombardment were studied. The primary motivation for this experiment, however, was the recent work by Wolynec *et al.*[3] in which it was concluded that the $E2$ isoscalar resonance for ^{58,60,62}Ni decays predominantly through the alpha channel. They reported that roughly 30–50% of the $E2$ sum rule was exhausted by the (γ,α) reaction, and while this percentage exhaustion has been lowered after reanalysis,[4] the conclusion is still that the (γ,α) channel is a dominant decay mode of the $E2$ isoscalar resonance for these nuclei.

We have measured the ^{56}Fe(e,α) cross section to see if a similar effect exists in this nucleus. As was the case in ^{60}Ni, the capture reaction ^{52}Cr(α,γ_0)^{56}Fe is small and the amount of $E2$ strength located near 16 MeV (60 $A^{-1/3}$) is less than 1%.[5] Hence the picture proposed by Wolynec *et al.* that the α's preferentially decay not to the ground state but rather to the first excited state in ^{52}Cr by s, d, or g waves may also be applicable in ^{56}Fe (see Fig. 1).

The technique that the National Bureau of Standards group used was to measure yields of the (e,α) cross section and then use a modified Lorentzian line shape to unfold the $E1$ and $E2$ cross sections. Subsequent analysis has shown that the $E1$ analysis is independent of an assumed line shape.[4] The indicator in their work that $E2$ transitions are an important factor is the rapid rise of the yield as the incident energy increases. This is due to the fact that the number of $E2$ virtual photons is greater than the number of $E1$ photons. If only $E1$ transitions were important, the slope of the isochromat would be much less, as is demonstrated by their (e,p) measurement which proceeds essentially by $E1$ processes. The point has been raised by the Glasgow group[6] that the increase in the isochromat as E_0 increases may be accounted for by a statistical model. We can fit our measured energy distributions with a statistical model that gives reasonable parameters (e.g., nuclear temperatures of ~0.3 MeV). Because of this we have looked as well at the angular dependence of the emitted α particles, since a statistical interpretation of data such as these would demand that the angular distribution be symmetric about 90°, whereas if direct or reso-

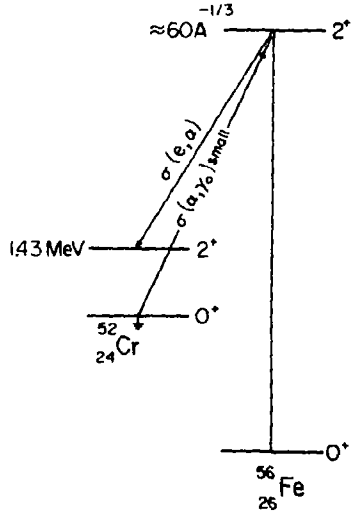

FIG. 1. $E2$ decay scheme for the ^{56}Fe(e,α) reaction, equivalent to the one proposed for ^{60}Ni by Wolynec *et al.* (Ref. 3). The ground state channel, as noted in the diagram is small (Ref. 5).

© 1980 The American Physical Society

nance effects are present the angular distributions may be asymmetric.[7]

II. EXPERIMENTAL PROCEDURE

The apparatus used in this experiment was similar to the one used in our earlier work.[1,3] The α particles were detected by a positive-ion spectrometer which consisted of five silicon surface barrier detectors positioned in the focal plane of a 127° double-focusing magnet. The beam current was measured by a nonintercepting ferrite monitor that was periodically calibrated with a Faraday cup.

The iron foils used in this experiment were 2.0 and 3.9 mg/cm^2. The thicknesses of the foils were determined by both direct micrometer measurement and by measuring the energy loss of 5.49 MeV α particles in passing through the foils.

The overall experimental uncertainty, reflecting errors in measuring the incident charge, target thickness, solid angle, and detector efficiencies, is ± 5%.

As well as electrodisintegration data, photodisintegration data were also taken by inserting a thin (22 mg/cm^2) Ta radiator in front of the target. Checks were made by varying the thickness of the radiator to ensure that a thin enough radiator was used, which allowed us to ignore thick target effects. The position of the radiator along the incident beam line was found not to affect the count rate of α particles in the spectrometer.

The radiator data were taken only to ascertain that we are justified in neglecting $E0$ continuum contributions to the (e,α) cross section. The $E0$ isoscalar resonance, located at $\sim 80A^{-1/3}$ MeV, is not expected to contribute at the excitation energies that we are predominantly measuring $E_x \lesssim 20$ MeV.

III. RESULTS

A. Energy spectra

The (e,α) cross section as a function of α energy was measured at a number of incident electron energies. The spectra at 35 and 100 MeV are shown in Fig. 2. The 100 MeV run was performed to add to the systematics that were studied in our earlier work. Since the virtual photon theories currently available do not include corrections for finite size effects the incident energy was kept at $E_0 \leq 50$ MeV for the main body of the experimental data. Above 60 MeV the point nucleus approximation made in deriving the virtual photon spectra is not valid.[8]

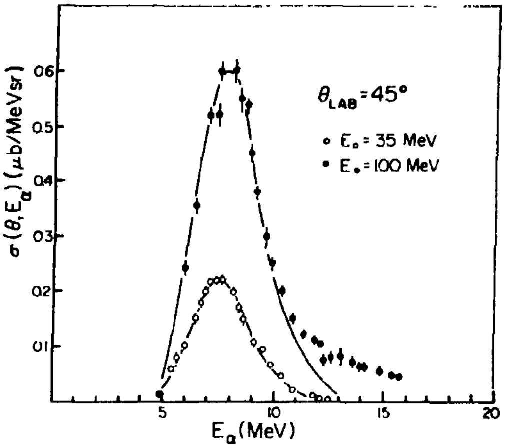

FIG. 2. Measured differential cross sections at $\theta_{LAB} = 45°$ for incident electron energies of 35 and 100 MeV. The solid lines are fits using the statistical model employed in our earlier studies of the (e,α) reaction from various nuclei. These fits result in a nuclear temperature of 0.3 MeV.

For cross sections as a function of α-particle energy we can use a statistical or evaporation interpretation of the (e,α) process to fit the data. These fits, shown in Fig. 2 by the solid lines, give nuclear temperatures of 0.3 MeV. However, the nuclear temperature is essentially determined by the Coulomb barrier and the penetrability, i.e., it is determined primarily by where the cross section peaks. These energy distributions are similar to those that we have measured for other nuclei. The value of 0.3 MeV for ^{56}Fe is not inconsistent with the systematics deduced from our other data.

B. Angular distribution

If a statistical model analysis of the data is adopted, then the angular distribution of α particles is expected to be symmetric about 90°. We have measured a six point angular distribution for $E_0 = 35$ MeV over a wide range of α-particle energies. Representative angular distribution data are shown in Fig. 3. The data have been analyzed by fitting to the form

$$\sigma(\theta, E) = a + b\sin^2\theta + c\sin^2\theta\cos\theta + d\sin^2\theta\cos^2\theta\,. \qquad (1)$$

In this form of fitting, the coefficient "c" arises from interference of opposite parity transitions. A finite value of c would not be explained by a statistical picture of the (e,α) process. The results of fitting the angular distribution data are shown in Fig. 4 and as can be seen, a finite value

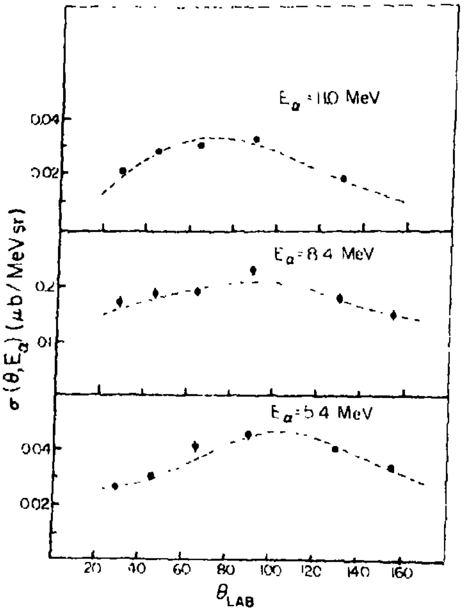

FIG. 3. Representative angular distributions that show the shift from backward to forward angles of α particles.

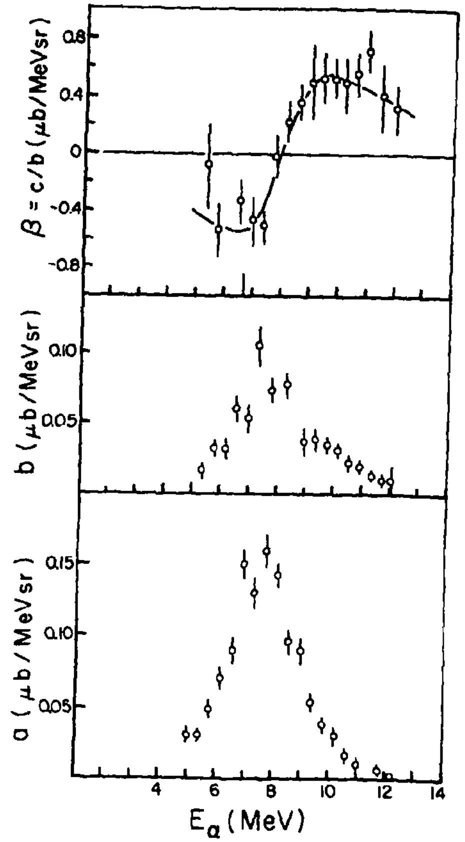

FIG. 4. Angular distribution coefficients (μb/MeV sr) that are found by fitting to Eq. (1). The asymmetry $\beta = c/b$ shows a change in sign that can be associated with resonance interference. The solid line is the result of fitting to an asymmetry defined in the text.

of the asymmetry, defined as $\beta = c/b$, is observed. A model-dependent explanation of the energy dependence of the asymmetry will be given in the next section.

The value of "d" was found to be consistent with zero over the range of α particles measured. This implies that d-wave emission of α particles is small. This result is consistent with the (α, γ_0) measurement since the decay to the ground state involves d-wave emission (recall that the capture results indicate a very small cross section) while decay to the 2^+ first excited state would involve primarily s-wave emission due to angular momentum arguments. As can be seen from the angular distribution data, a sizable isotropic term is measured, in marked contrast to the case when one restricts the α's to be emitted to the ground state, i.e., the capture results, where "a" is identically zero.

C. Isochromat data

At fixed α energies, the incident electron energy was varied from 26 to 50 MeV. Representative integrated over angle data are shown in Fig. 5, corresponding to an α energy near the peak in the energy distribution that is shown in Fig. 2. The analysis of these data will be explained in the next section.

IV. MODEL-DEPENDENT ANALYSES

A. Angular distribution data

To account for the energy dependence of the asymmetry in the angular distribution data, we assume that the transition matrix element can be written in the usual notation as being proportional to

$$\left\langle \phi_f \middle| r Y_{10} + \frac{f(r)}{E - E_R + \frac{1}{2} i \Gamma} Y_{20} \middle| \Phi_i \right\rangle ,$$

which leads to an asymmetry:

$$\beta = F_1 \left[\frac{(E - E_R)}{(E - E_R)^2 + \Gamma^2/4} \right] - F_2 \left[\frac{\Gamma}{(E - E_R)^2 + \Gamma^2/4} \right] .$$

The quantities F_1 and F_2 are determined by least squares fitting and are related to the $E1$ and $E2$

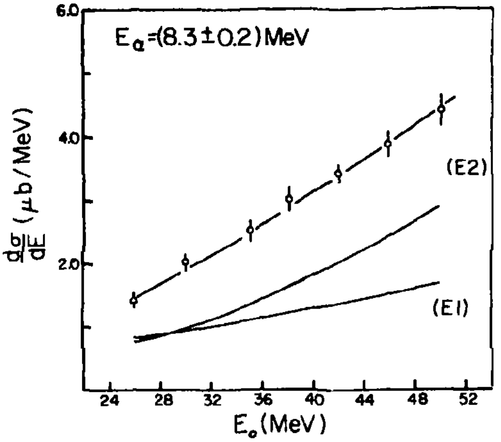

FIG. 5. The cross section $d\sigma/dE$ found by integrating over $d\Omega$ using the angular dependence shown in Fig. 4. These data are analyzed in terms of α particles making transitions to the 2^+ state in ^{52}Cr. The solid lines are the contributions to the cross section from $E1$ and $E2$ cross sections by least squares fitting Eq. (3).

matrix elements. All we are interested in here is to ascertain if the energy dependence of β can be explained by this simple model which contains resonance and direct interference terms.

The best fit to the data is shown by the solid line in Fig. 4. The resonance parameters determined are

$$\Gamma = 3.1 \pm 1.6 \text{ MeV},$$

$$E_R = 17.6 \pm 0.9 \text{ MeV } (8.0 \pm 0.4 \text{ MeV } \alpha \text{ energy}).$$

*Again, we point out that statistical processes in*volve symmetric distributions ($\beta = 0$) and direct processes alone cannot account for the change of sign in β.

B. Isochromat analysis

Since the angular distribution exhibits a definite asymmetry about 90°, we have analyzed our data assuming that the α particles are making transitions to the 2^+ first excited state in ^{52}Cr. In other words, we adopt the decay scheme that is shown in Fig. 1. We further assume that only $E1$ and $E2$ multipoles contribute to the cross section. The results of our real photon measurements that are discussed later rule out any significant contribution to the cross section from $E0$ transitions which are allowed in the electrodisintegration process but not in photodisintegration.

In general, the total electrodisintegration cross section can be expressed as

$$\sigma_{e,\alpha}(E_0) = \sum_l \int_{E_t}^{E_0} \sigma_{\gamma,\alpha}^{(l)} N^{(l)}(E_0, E_\gamma Z) \frac{dE_\gamma}{E_\gamma}, \tag{2}$$

where the sum over l encompasses all multipoles, and E_t is the threshold for the reaction.

The quantity $N^l(E_0, E_\gamma, Z)$ has been computed by Wright.[9] The distortion for the $E1$ and $E2$ spectrum defined as the distorted wave to plane wave ratio is shown in Figs. 6 and 7, respectively. *These distortions were used to calculate the pho*ton spectra in all the following analyses.

In charged particle experiments, a total cross section is seldom measured. The total cross section is defined as

$$\sigma_{e,\alpha}(E_0) = \int_0^{E_{\alpha\max}} \frac{d^2\sigma}{d\Omega\, dE}\, d\Omega\, dE,$$

where the experimentally determined quantity is $d^2\sigma/d\Omega\, dE$. Therefore, assuming that the α par*ticles are primarily emitted to the 2^+ excited* state in ^{52}Cr, the integral in Eq. (2) can be evaluated at fixed gamma ray energies, if the angular dependence is removed. The angular dependence was determined from the coefficients of the fit to the angular distribution data given by Eq. (1), evaluated at 45°, the angle at which the energy dependence was studied. These coefficients were assumed to be independent of the incident electron energy in this analysis. Thus we form the cross sections (isochromats)

$$\frac{d\sigma}{dE} = \sigma_{\gamma,\alpha}^{E1}(E_\gamma) \frac{N^{E1}(E_0, E_\gamma, Z)}{E_\gamma} + \sigma_{\gamma,\alpha}^{E2}(E_\gamma) \frac{N^{E2}(E_0, E_\gamma, Z)}{E_\gamma}. \tag{3}$$

These cross sections were then fitted by minimizing χ^2, which determined the quantities

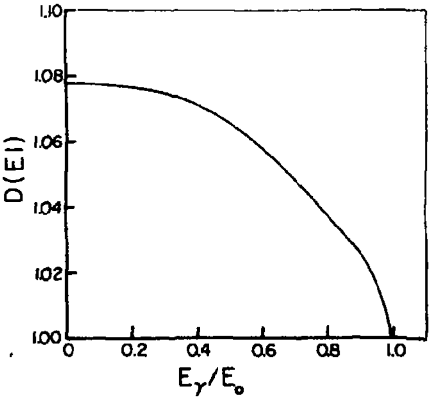

FIG. 6. $E1$ distortion factor defined as the ratio of distorted wave to plane wave virtual photon spectra.

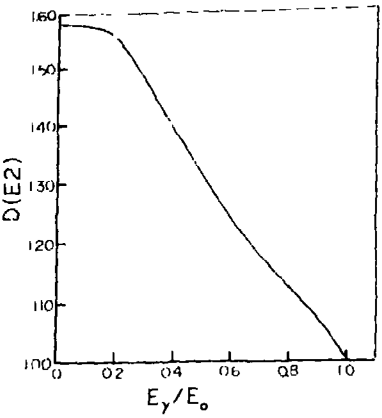

FIG. 7. *E*2 distortion factor.

$\sigma^{E1}_{\gamma,\alpha}(E_\gamma)$ and $\sigma^{E2}_{\gamma,\alpha}(E_\gamma)$. In Fig. 5, the fitted values of the E_1 and $E2$ contribution to $d\sigma/dE$ are shown for one of the isochromats. In Fig. 8 we show σ^{E1} and σ^{E2} for each of the seven isochromats that were measured. The areas were determined and the appropriate sum rules were found. By fitting these data to Lorentzian and Breit-Wigner line shapes the usual resonance parameters can be determined. These results are summarized in Table I. The width and position of the $E2$ resonance are consistent with those found using the angular distribution data. Note that the shape of the $E1$ cross sections in this analysis is primarily determined by the fact that $d^2\sigma/d\Omega dE$ rises, then falls, with the fit determining the relative amounts of $E1$ and $E2$ strength. The $E2$ strength, however, is determined essentially by the fact that the iso-

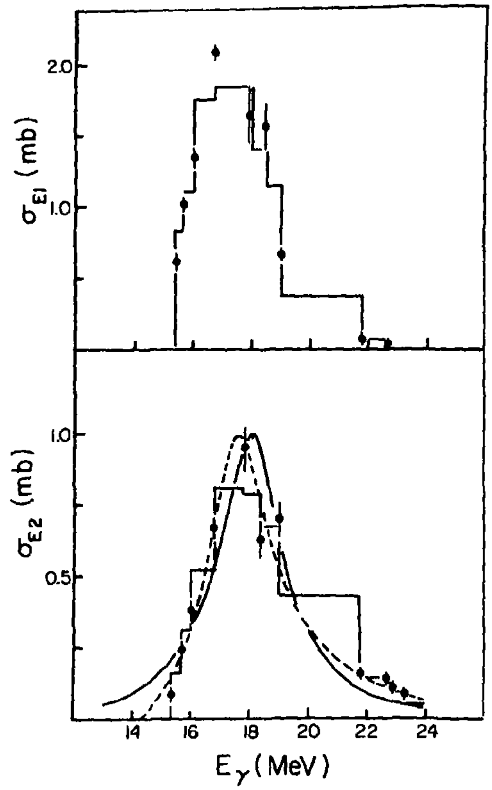

FIG. 8. Total *E*1 and *E*2 cross section determined from the isochromat analysis at seven α energies. The dashed line is the Lorentz line shape fit and the solid line is the Breit-Wigner line shape fit. The resonance parameters are summarized in Table I.

TABLE I. *E*2 integrated cross sections and resonance parameters determined by the isochromat analysis of Sec. IV B.

	Trapezoidal[a] integration	2nd order fit[a] integration	Lorentz line shape	Breit-Wigner line shape
$\int \sigma dE$ (mbMeV)	3.6 ± 0.3	3.8 ± 0.3	3.9 ± 0.1	3.9 ± 0.1
$\int \frac{\sigma dE}{E^2}$ (μb/MeV)	11.0 ± 1.0	11.3 ± 0.9	11.1 ± 1.6	11.1 ± 1.5
% of $E2$ sum rule[b]	28 ± 3	29 ± 2	29 ± 4	29 ± 4
E_R (MeV)			17.9 ± 0.2	18.1 ± 0.2
Γ (MeV)			2.8 ± 0.3	2.9 ± 0.3
σ_0 (mb)			1.00 ± 0.07	1.00 ± 0.06

[a] Reference 13.

[b] We have used the value $0.22Z^2/A^{1/3}$.

chromat rises more rapidly with E_0 near the peak in the measured cross section.

C. Total cross section analysis

The total cross section $\sigma_{e,\alpha}(E_0)$ was found by numerically integrating the cross sections $d^2\sigma/d\Omega dE$ over alpha energy and angle. The angular dependence at $E_0 = 35$ MeV was again assumed to be the same for all incident electron energies. [Taking 4π for the angular integration was found to produce a 4% difference in $\sigma_{e,\alpha}(E_0)$.]

The measured total cross section is shown in Fig. 9. If we analyze these data assuming specific line shapes for σ^{E1} and σ^{E2} in Eq. (2), the total $E1$ and $E2$ cross sections may be determined without an initial assumption with regard to the specific transition taking place, as was done in Sec. IV B. The total cross section was least squares fitted using

$$\sigma_{\text{B-W}} = \sigma_0 \frac{(\Gamma/2)^2}{(E_\gamma - E_R)^2 + (\Gamma/2)^2}$$

and

$$\sigma_L = \sigma_0 \frac{(E_\gamma \Gamma)^2}{(E_\gamma^2 - E_R^2)^2 + (E_\gamma \Gamma)^2} .$$

Since the fitting procedure used[10] can minimize χ^2 by varying parallel parameters, the χ^2 parabola is expected to be very shallow. In other words, the particular values of fitted parameters (Γ, E_R, and σ_0) in the above equations that are determined in the fit should not be taken as seriously as the amount of exhaustion that these parameters dictate for the appropriate sum rules.

We have used two methods for determining $\sigma^{(E1)}$ and $\sigma^{(E2)}$ this way. First, we have constrained the fit to give the values $E_R = 17.6$ MeV and $\Gamma = 3.1$ MeV for the $E2$ cross section. These were the parameters that were found from the angular distribution data. Second, we have allowed all the parameters to be fit (six in all) with no constraints. The results are summarized in Table II. As can be seen, the constrained and unconstrained fits give values with respect to the sum rules that are in good agreement.

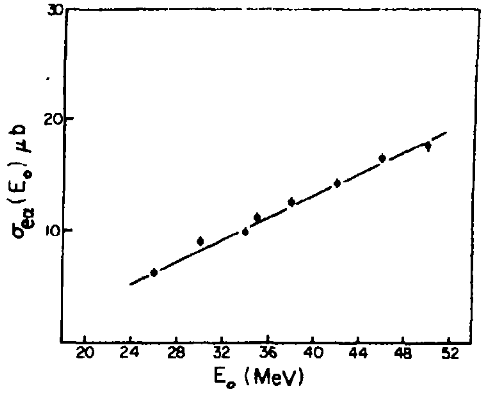

FIG. 9. The total electrodisintegration cross section for the (e,α) channel. The solid line is the result of least square fitting these data with Eq. (1). No appreciable difference was found for Lorentzian and Breit-Wigner line shapes.

Fits to the data assuming that the cross sections were either pure $E1$ or $E2$ resulted in an unsatisfactory χ^2 for either case. Both $E1$ and $E2$ components are required to obtain acceptable values of χ^2. It is also of some comfort that the unconstrained fits give values for E_R and Γ for the $E2$ line shapes that agree reasonably well with the values determined from the angular distribution data. Combining all of these results, we find that the (e,α) cross section exhausts 24 ± 8% of the isoscalar sum rule for ^{56}Fe which is 39 μb/MeV.[11] The $E1$ integrated cross sections determined by the various analysis procedures are summarized in Table III.

D. Real photon data

To ascertain that monopole transitions were not making a significant contribution to the electrodisintegration cross sections, data were also taken with a thin Ta foil inserted in the beam in front of

TABLE II. $E2$ integrated cross sections and resonance parameters determined by the total cross section analysis of Sec. IV C.

Line shape		σ_0 (mb)	Γ (MeV)	E_R (MeV)	$\int \sigma dE$ (mb MeV)	$\int \sigma dE/E^2$ (mb/MeV)	χ^2	% of $E2$ sum rule
Lorentz	a	0.72 ± 0.02	3.1	17.6	3.04 ± 1.55	8.74 ± 2.82	3.6	22 ± 7
	b	0.99 ± 0.03	2.2 ± 0.2	17.9 ± 0.4	3.14 ± 0.30	9.12 ± 0.42	3.4	23 ± 1
Breit-Wigner	a	0.75 ± 0.02	3.1	17.6	2.99 ± 1.40	8.92 ± 2.84	3.7	23 ± 7
	b	1.00 ± 0.02	2.3 ± 0.1	18.0 ± 0.6	3.13 ± 0.23	9.27 ± 0.15	3.4	24 ± 1

[a] Fit constrained to the $E2$ values of Γ and E_R found from the angular distribution analysis.
[b] Unconstrained fit.

TABLE III. Summary of the $E1$ integrated cross sections for the ^{56}Fe(e,α) reaction and the percentage exhaustion of the sum rule $60NZ/A$.

Analysis		$\int\sigma dE$ (mbMeV)	E_R (MeV)	Γ (MeV)	σ_0 (mb)	% of sum rule
Isochromats		6.41 ± 0.64				0.8 ± 0.1
Lorentz	a	10.51 ± 2.63	16.5 ± 3.1	4.04 ± 0.26	2.19 ± 0.02	1.3 ± 0.3
	b	10.44 ± 0.80	17.0 ± 2.5	4.14 ± 0.30	2.02 ± 0.02	1.2 ± 0.1
Breit-Wigner	a	9.87 ± 3.12	16.7 ± 3.5	4.09 ± 0.3	2.19 ± 0.03	1.2 ± 0.4
	b	9.98 ± 2.19	17.1 ± 2.8	4.25 ± 0.23	2.06 ± 0.02	1.2 ± 0.3

[a] Fit constrained to the $E2$ values of Γ and E_R found from the angular distribution analysis.

[b] Unconstrained fit.

the Fe foil.

The ratio of radiator in to radiator out measurements can be written as

$$\sigma(e+\gamma)/\sigma(e)=1+R$$

$$=1+\frac{\int_{E_t}^{E_0}\sum_{l}\sigma^{El}_{\gamma,\alpha}(E_\gamma)N_\gamma(E_0,E_\gamma)\frac{dE_\gamma}{E_\gamma}}{\int_{E_t}^{E_0}\sum_{l}\sigma^{El}_{\gamma,\alpha}(E_\gamma)N^{l}_{e}(E_0,E_\gamma,Z)\frac{dE_\gamma}{E_\gamma}}\,.$$

If monopole transitions dominate, then no difference between the radiator in and radiator out measurements would be observed since $R\to 0$ in this case. We find that R does not vanish. Furthermore, the quantity $1+R$ serves as a check on the integrated strength for the $E1$ and $E2$ cross sections found in the previous section. Using formula $3BS(e)$ in Koch and Motz[12] to calculate $N_\gamma(E_0,E_\gamma)$, we calculate the expected value of $\sigma(e+\gamma)/\sigma(e)$ and compare it with the experimental ratio.

These results, for three different incident electron energies 40, 45, and 49 MeV, give an average value of $(1+R)_{\text{theor}}/(1+R)_{\text{exp}}=1.00\pm0.02$. We only mean by $(1+R)_{\text{theor}}$ here the value expected using our extracted resonance parameters. We have not considered thick target bremsstrahlung due to the thinness of our radiator. Thus, our analyses would tend to agree more with the Schiff limit given by Hayward[4] for the ^{56}Fe percentage of the $E2$ sum, i.e., (18 ± 3)%.

V. CONCLUSION

We find that by considering various model-dependent analyses of the ^{56}Fe(e,α) cross section measurements that this channel exhausts a sizable percentage of the $E2$ sum rule (24 ± 8%). The angular distribution data which exhibit a definite asymmetry rule out a statistical interpretation as the sole explanation of the data and give reasonable consistency with the parameters determined from the energy-dependent analyses of the (e,α) cross section. Real photodisintegration data were taken that serve as a check on the extracted cross sections and analysis method. The measured ratios of real to virtual processes were consistent with the cross sections extracted from the electrodisintegration data.

ACKNOWLEDGMENTS

This work was partially supported by the National Sciences and Engineering Research Council of Canada. We wish to thank Dr. H. Weller and Dr. E. Hayward for useful discussions and communication of their work. We also thank Mr. L. Custead for assistance with some of the computer programming used in the analyses of the data and Dr. E. Tomusiak for many useful comments.

---

[1] J. J. Murphy *et al.*, Phys. Rev. C 18, 736 (1978).

[2] J. J. Murphy II, H. J. Gehrhardt, and D. M. Skopik, Nucl. Phys. A277, 69 (1977).

[3] E. Wolynec, W. R. Dodge, and E. Hayward, Phys. Rev. Lett. 42, 27 (1979).

[4] E. Hayward (private communication).

[5] H. R. Weller (private communication).

[6] J. C. McGeorge *et al.*, Nature (London) 280, 724 (1979).

[7] H. Feshbach, in *Nuclear Spectroscopy*, edited by F. Ajzenberg-Selove (Academic, New York, 1960), p. 625.

[8] D. S. Onley and L. E. Wright (private communication).

[9] L. E. Wright (private communication).

[10] K. Fielding, Commun. Assn. Comp. Mach. 13, 509 (1970).

[11] S. S. Hanna, in *Photonuclear Reactions*, edited by S. Costa and C. Schaerf (Springer, New York, 1977), p. 275.

[12] H. W. Koch and J. W. Motz, Rev. Mod. Phys. 31, 920 (1959).

[13] P. R. Bevington, in *Data Reduction and Error Analysis for the Physical Sciences* (McGraw-Hill, Toronto, 1969).

PHYSICAL REVIEW C VOLUME 21, NUMBER 5 MAY 1980

Nuclear excitation of ^{111}Cd by positron annihilation

Yoshihisa Watanabe,* Takeshi Mukoyama, and Sakae Shimizu
Institute for Chemical Research, Kyoto University, Kyoto, Japan

(Received 19 July 1979)

Nuclear excitation of ^{111}Cd by positron annihilation has been investigated. The experimental evidence for this process was searched by observing the 245-keV γ rays from ^{111}Cd^m after irradiation of natural cadmium foils by positrons from the β^+ decay of ^{64}Cu. For the excited level of 1330 keV in ^{111}Cd, the experimental cross section of the annihilation-excitation process has been estimated to be less than 8.6×10^{-25} cm^2. This upper limit is larger than the simple theoretical estimate. Further improvements of theoretical and experimental studies are discussed.

[NUCLEAR REACTIONS ^{111}Cd; evaluated excitation cross section for 1330-keV level by positron annihilation.]

I. INTRODUCTION

Among various modes of positron annihilation, there exists an annihilation process without emission of radiation. When the positron annihilates with the atomic electron strongly bound to the nucleus, the excess energy liberated in annihilation is given up to the nucleus, resulting in its excitation. This process was first predicted by Present and Chen in 1951.[1] According to their simple estimate, the total cross section for the annihilation process to excite ^{115}In to its principal activation level is in the order of 10^{-26} cm^2.

Neglecting the very small recoil energy of the nucleus, the energy liberated in annihilation and used to excite the nucleus is expressed by the simple relation

$$W = E_p + 2m_0c^2 - B_K\,, \tag{1}$$

where E_p is the kinetic energy of an incident positron, m_0 is the electron rest mass, and B_K is the binding energy of the K-shell electron in the target atom.

The first experimental evidence of this annihilation mode was established for ^{115}In by the present authors[2] in 1972. Recently more accurate experimental study was performed by us[3] and the cross sections of nuclear excitation by positron annihilation for 1078- and 1464-keV levels of ^{115}In were evaluated to be $(3.9\pm1.4)\times10^{-24}$ cm^2 and $(1.4\pm0.5)\times10^{-22}$ cm^2, respectively. Up to the present, no experimental study has been reported for other nuclides.

In the present paper, we report the nuclear excitation of ^{111}Cd by positron annihilation. The experiment has been made by observing the γ rays from the isomeric state ^{111}Cd^m after irradiation of cadmium foils by positrons emitted from a ^{64}Cu source. For ^{111}Cd, many excited levels have been observed, but only three of them, 740-, 1120-, and 1330-keV levels, are known to be excited by photons and have branches which decay to the ground state via the 396-keV isomeric state.[4] Of these three levels, the excitation probabilities to the 740- and 1120-keV levels by photon irradiation are more than three orders of magnitude smaller than that to the 1330-keV level.[4] In the present work, only the 1330-keV level is considered to be excited by positron annihilation.

The energy-level diagram of ^{111}Cd is shown in Fig. 1. The nuclear transitions relevant to the present experiment are indicated by the arrows. The isomeric state ^{111}Cd^m has a half-life of 48.7 min and decays to the ground state by emission of two γ rays, 151 and 245 keV, in cascade.[5] The nuclear excitation process to be studied has been observed by the use of 245-keV γ rays, since for the preceding transition of 151 keV the internal conversion coefficient ($\alpha_K = 1.53$[5]) is much larger than for the 245-keV transition ($\alpha_K = 0.0525$[5]).

II. EXPERIMENTAL

The experimental method is similar to that of our previous experiment for ^{115}In and has already been described in detail earlier.[3] Experimental conditions, however, are briefly presented here.

The positron source was produced by thermal neutron irradiation of a 20-mm diam × 241-mg/cm^2 thick copper disk in the Kyoto University Research Reactor (KUR). The intensity of this ^{64}Cu source is about 20 Ci.

Natural cadmium foils of 20-mm diam and 435-mg/cm^2 thickness were placed just above the positron source and irradiated by positrons for 3.5 h. This period was chosen so as to get maximum induced activity of ^{111}Cd. The target foil was covered with a thin rubber-hydrochloride film to protect

© 1980 The American Physical Society

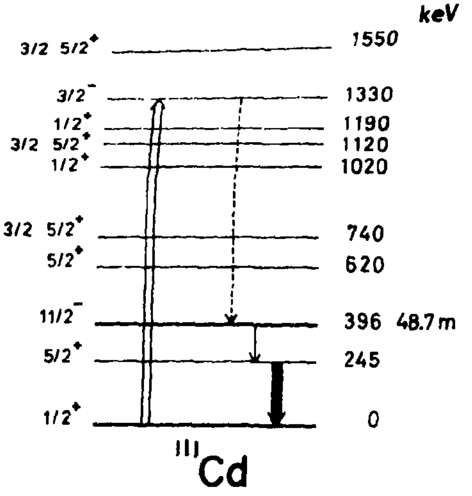

FIG. 1. A part of level diagram of ^{111}Cd. The transitions relevant to the present work are indicated by the arrows. The energies of three levels 740, 1120, and 1330 keV possible to be excited by photons are taken from Boivin, Cauchois, and Heno (Ref. 4). Other data are taken from Raman and Kim (Ref. 5).

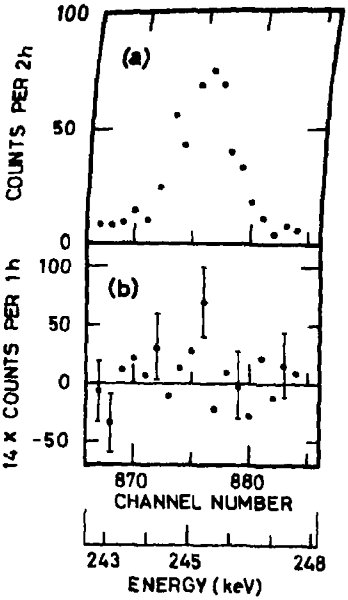

FIG. 2. Observed spectra of γ rays from natural cadmium foils. (a) After irradiation by γ rays in a 700-Ci ^{60}Co irradiation facility, by (γ, γ') reaction. (b) After irradiation by positrons from a 20-Ci ^{64}Cu source, by the positron annihilation process.

radioactive contamination by direct contact to the positron source. After positron irradiation, the 245-keV γ rays from ^{111}Cd^{m} were measured by a 75-cm^3 Ge(Li) detector for 1 h. The actual number of positrons incident on the target foil was determined in a similar manner to the previous work.[3]

Since this annihilation process has a resonance character, nuclear excitation can take place only for positrons with definite kinetic energy corresponding to Eq. (1). In order to estimate the cross section for this process, we need the number of positrons within the resonance width. For this purpose, the momentum spectrum of β^+ positrons was measured with a sector-type double-focusing β-ray spectrometer by the use of much weaker-intensity ^{64}Cu source of the same thickness as that of the 20-Ci source.

To estimate the reasonable profile of γ-ray spectrum from ^{111}Cd^{m}, a natural cadmium foil was irradiated in the 700-Ci ^{60}Co irradiation facility of our Institute[6] and photons from the isomeric level ^{111}Cd^{m} produced by (γ, γ') reaction were observed with the same measuring system as that used in the actual experiment. The result is shown in Fig. 2(a). From this observation the energy of γ rays and the half-life of the isomeric state have been determined to be 245.3 ± 0.4 keV and 49.7 ± 4.3 min, respectively.

III. RESULTS AND DISCUSSION

A. *Effective cross section*

The observed γ-ray spectrum from cadmium foils irradiated by positrons is shown in Fig. 2(b). This spectrum was obtained as a sum of the experimental results of typical 14 runs. The poor statistics make it difficult to discern distinctive features of a peak. Nevertheless, there is undoubtedly an excess of counts above the background around the peak position to be expected. Moreover, at the γ-ray energy of the isomeric transition in ^{111}Cd, there is a suggestion of a peak. However, considering the poor statistics of the present experiment, we cannot accept this as a definite observation of the isomeric transition. The counting rate under the peak was therefore used to set an upper limit of the process to be studied.

In order to deduce the upper limit of the cross section for nuclear excitation by positron annihilation, we must carefully examine the possibility of the competing processes which may excite the ^{111}Cd nucleus from the ground state to higher excited levels cascading down to the 396-keV isomeric state. As discussed in a previous paper,[3] the nuclear excitation by photons from the following four processes may contribute to the formation of this isomeric state, viz. (1) photons from the two-quantum annihilation in flight, (2) photons from the single-quantum annihilation, (3) 1346-keV photons of ^{64}Ni emitted from the ^{64}Cu positron source, and (4) bremsstrahlung of conversion electrons from the 1346-keV state of ^{64}Ni. For the 1330-keV excited level of ^{111}Cd, all of these possibilities were carefully estimated in a similar way to the previous cases of ^{115}In,[2,3] and concluded to be negligible.

Using the observed γ activity of ^{111}Cd^m induced by positron annihilation, the effective cross section for isomer production of ^{111}Cd by the annihilation-excitation process has been evaluated. This cross section is defined as the cross section for the total number of positrons impinging on the target. In the first approximation, we assume that the partial width of the excited level for transition to the isomeric state is equal to its total width. Then the effective cross section can be expressed as

$$\sigma_{eff}=\frac{C_\gamma(1+\alpha)(\lambda_2-\lambda_1)\exp(\lambda_2 t_s)}{N_0 n_p \epsilon[1-\exp(-\lambda_2 t_m)][\exp(-\lambda_1 t_r)-\exp(-\lambda_2 t_r)]}. \tag{2}$$

The symbols in the expression are as follows: C_γ = the observed counts of the 245-keV photons during the measuring period t_m, N_0 = the number of ^{111}Cd atoms in the natural cadmium foil per unit area (natural isotropic abundance of this nuclide[5] is 12.75%) [2.97×10^{20}], ϵ = the overall detection efficiency of the Ge(Li) detector for the 245-keV photons from the cadmium foil [$(4.8\pm0.1)\times10^{-3}$], n_p = the number of positrons impinging on the cadmium foil per unit time at the beginning of irradiation, α = the total internal conversion coefficient[7] of the 245-keV transition of ^{111}Cd (0.0619), t_r = the period of irradiation by positrons (3.5 h), t_s = the time elapsed between the end of positron irradiation and the start of measurement of the 245-keV photons (180 s), λ_1 = the decay constant of ^{64}Cu [$1.52\times10^{-5}s^{-1}$],[8] and λ_2 = the decay constant of ^{111}Cd^m [$(2.32\pm0.20)\times10^{-4}s^{-1}$, corresponding to $T_{1/2}=(49.7\pm4.3)$ min, the present work].

Inserting the experimental values of C_γ, n_p, and the numerical values of other factors into Eq. (2), the effective cross section was evaluated to be $\sigma_{eff}=(4.8\pm2.8)\times10^{-32}$ cm^2, as an average value of 16 experimental runs. The error contains the uncertainty due to the counting statistics and the errors of all the factors in Eq. (2). The large uncertainty is ascribed mainly to the poor statistics in measurements of the induced activity. Although the observed value is larger than the estimated uncertainty, this value was considered to be an upper limit of the effective cross section because we could not discern a definite peak, as described above.

B. Cross section

The relationship between the effective cross section and the cross section for annihilation-excitation is given by the expression

$$\sigma_{eff}=n\sigma\Gamma_{iso}/\Gamma, \tag{3}$$

where Γ_{iso} and Γ are the partial width for the transition to the isomeric state and the total width of the excited level, respectively, and n is the ratio of the number of positrons in the target foil within the interval of the resonance width Γ to the total number of positrons impinging on the target foil.

The ratio Γ_{iso}/Γ was determined by the relation between the integral cross section for the isomer production by photoexcitation $\int\sigma_{iso}(E)dE$ and the partial width for the direct transition to the ground state of the excited level Γ_0:

$$\int\sigma_{iso}(E)dE=\frac{\lambda^2}{4}g\Gamma_0\frac{\Gamma_{iso}}{\Gamma}. \tag{4}$$

Here λ is the wavelength of the photon with the resonance energy and the factor g is $(2J_1+1)/(2J_0+1)$, where J_1 and J_0 are the spins of the excited level and the ground state, respectively. Using the values of our previous experimental results,[9] $\int\sigma_{iso}(E)dE=(3.5\pm0.4)\times10^{-25}$ cm^2 eV, and $g\Gamma_0=(1.7\pm1.1)\times10^{-3}$ eV, obtained by Chertok and Booth,[10] the ratio Γ_{iso}/Γ was found to be 0.099 ± 0.065.

The total width of the 1330-keV level, Γ, was calculated from the values of $g\Gamma_0$ and Γ_0/Γ based on the following two assumptions: (1) The 1330-keV transition to the ground state is pure $E1$($J_1=\frac{3}{2}$), and (2) the total width of the excited level is equal to the sum of the partial width for the direct transition to the ground state Γ_0 and that for the transition to the isomeric state Γ_{iso}. Boivin *et al.*[4] concluded that the multipolarity for the upward transition to the 1330-keV level is neither $M1$ nor $E2$. Considering the large value of the photoexcitation cross section to this level, it is not reasonable to assume the multipolarity higher than $E2$. From the latter assumption, the branching ratio of the direct transition to the ground state Γ_0/Γ is expressed as $(1-\Gamma_{iso}/\Gamma)$, and the total level width is determined to be $\Gamma=(9.4\pm6.1)\times10^{-4}$ eV.

The factor n was evaluated by the same way as that discussed in the previous paper.[3] Because of difficulty in estimation of the positron distribution in the target, the positron spectrum at the arbitrary point in the target was approximated by the spectrum of positrons passing through the thin layer whose thickness corresponds to the distance from the target surface. In this approximation, the effect of backscattering of positrons in the target material is neglected. Using the measured spectrum, described in Sec. II, as the energy spectrum of the incident positrons, the factor n was calculated to be 4.9×10^{-8}.

Combining the effective cross section σ_{eff} determined above with the values of n and Γ_{iso}/Γ, the upper limit of the cross section for nuclear excitation of ^{111}Cd by positron annihilation has been evaluted to be 8.6×10^{-25} cm^2 by the use of Eq. (3).

According to the two-step model of Present and Chen,[1] the cross section of the annihilation-excitation process is given by

$$\sigma = \sigma_{aq}[\sigma_{ph}/(2l+1)\pi k^{-2}], \tag{5}$$

where σ_{aq} is the positron annihilation cross section with the K-shell electron with emission of a spherical wave of 2^l-pole radiation converging on the nucleus, σ_{ph} is the cross section of the nuclear photoexcitation by this photon, and k is the propagation number of the photon.

Provided that the multipolarity of the upward transition from the ground state to the excited level is $E1$, the cross section σ_{aq} is given by

$$\sigma_{aq} \doteq \pi\alpha^2 Z^3 \left(\frac{e^2}{m_0c^2}\right)^2 (\xi^2 + 2\xi + 3) \times (\xi+1)^{-9/2}(\xi-1)^{-1/2}, \tag{6}$$

where $\xi = (E_p + m_0c^2)/m_0c^2$. From this equation, σ_{aq} is calculated to be 2.0×10^{-25} cm^2 for the 1330-keV level in ^{111}Cd. On the other hand, the photoexcitation cross section σ_{ph} measured by us[9] is $(2.4 \pm 1.6) \times 10^{-22}$ cm^2.[11] Inserting these values into Eq. (5), the theoretical value of the cross section for annihilation-excitation was estimated to be 2.4×10^{-26} cm^2 in the case of pure $E1$ transition.

IV. CONCLUDING REMARKS

In the present work, nuclear excitation of ^{111}Cd by positron annihilation has been studied by observing γ rays from the isomeric state. The upper limit of the cross section for this annihilation process has been estimated to be in the order of 10^{-25} cm^2. This value is about 36 times larger than the two-step model proposed by Present and Chen.[1] However, their theory is based on rough assumptions, and we have already pointed out in our previous paper[3] that this annihilation mode should be treated theoretically in a one-step model. Recently Grechukhin and Soldatov[12] calculated the cross section for the nuclear excitation by positron annihilation by the use of Weisskopf single-particle nuclear transition matrix element. The cross section for ^{115}In is found to be $\sim 10^{-26}$ cm^2 for the case of $E1$ transition. It is hoped to perform similar calculations for ^{111}Cd.

Experimentally our counting statistics were poor. In order to estimate the experimental cross section and compare with the theoretical value, it is necessary to measure the induced activity in good statistics. For this purpose, the experiments with much stronger positron sources and enriched ^{111}Cd targets should be performed. Furthermore, there is a problem in estimating the positron spectrum in the target foil. Our method is based on a rough assumption, as has been discussed already in our earlier work.[3] The value of n estimated by our method may be smaller than more rigorous values and this fact leads to the larger value of σ.

Finally we have made many assumptions on the nuclear properties of the excited level of ^{111}Cd, such as energy, spin, multipolarity of the upward transition from the ground state, and branching ratio to the isomeric state. In order to compare the theory and experiment, more accurate data for these properties are needed.

ACKNOWLEDGMENTS

A part of this work was performed in the Research Reactor Institute of Kyoto University. The authors would like to thank Dr. M. Koyama and R. Matsushita for their kind help and valuable advice in preparation of the ^{64}Cu source. Thanks are also due to Dr. Y. Kawase for the use of the β-ray spectrometer and to R. Katano for cooperation in measurements.

---

*Present address: Department of Mathematics and Physics, National Defense Academy, Yokosuka, Japan.

[1] R. D. Present and S. C. Chen, Phys. Rev. 85, 447 (1952).

[2] T. Mukoyama and S. Shimizu, Phys. Rev. C 5, 95 (1972).

[3] Y. Watanabe, T. Mukoyama, and S. Shimizu, Phys. Rev C 19, 32 (1979).

[4] M. Boivin, Y. Cauchois, and Y. Heno, Nucl. Phys. A137, 520 (1969).

[5] S. Raman and H. J. Kim, Nucl. Data Sheets B6, 39 (1971).

[6] R. Katano, Bul. Inst. Chem. Res. Kyoto Univ. 48, 66 (1970).

[7] P. Sparrman, A. Marelius, T. Sundström, and H. Pettersson, Z. Phys. 192, 439 (1966).

[8] J. F. Emery, S. A. Reynolds, E. I. Wyatt, and G. I. Gleason, Nucl. Sci. Eng. 48, 319 (1972).

[9] Y. Watanabe and T. Mukoyama, Bul. Inst. Chem. Res. Kyoto Univ. 57, 72 (1979).

[10] B. T. Chertok and E. C. Booth, Nucl. Phys. 66, 230 (1965).

[11] In Ref. 9, we assumed the 1330-keV transition as $E2$ ($J_i = \frac{5}{2}$) and the photoexcitation cross section σ_{ph} was calculated to be $(3.5 \pm 2.3) \times 10^{-22}$ cm^2.

[12] D. P. Grechukhin and A. A. Soldatov, Zh. Eksp. Teor. Fiz. 74, 13 (1978) [Sov. Phys.—JETP 47, 6 (1978)].

PHYSICAL REVIEW C VOLUME 21, NUMBER 5 MAY 1980

Statistical and pre-equilibrium (γ,α) cross sections of ^{90}Zr and their multipolarities via the ^{90}Zr(e,α) reaction

T. Tamae,* T. Urano, M. Hirooka, and M. Sugawara
Laboratory of Nuclear Science, Tohoku University, Mikamine, Sendai, Japan

(Received 23 August 1979)

The (e,α) cross section in ^{90}Zr has been measured at incident electron energies from 13.5 MeV to 66.5 MeV for α particles between 6.9 and 16.8 MeV. The (γ,α) cross section was deduced from it assuming both $E1$ interaction and $E2$ interaction. The angular distribution of the (γ,α_0) cross section and an experiment using the bremsstrahlung plus electron beam make it clear that the $E1$ interaction is dominant over all the present energy range. The (γ,α) cross section extracted by using $E1$ virtual photon spectra has a large bump above the excitation energy of 30 MeV in addition to a bump in the giant dipole resonance region. The (γ,α_0) cross section also has a bump at the giant dipole resonance which exhausts most of the (γ,α) cross section in that region. The compound nucleus model was used successfully to explain the bump at the giant dipole resonance. The cross section above 30 MeV is discussed in terms of the pre-equilibrium α emission process combined with the quasi-deuteron model.

[NUCLEAR REACTIONS ^{90}Zr(e,α), $E_e = 13.5-66.5$ MeV; measured $d\sigma(e,\alpha)/d\Omega$, deduced $d\sigma(\gamma,\alpha)/d\Omega$ and $d\sigma(\gamma,\alpha_0)/d\Omega$. Angular distributions; (γ,α_0) at $E_e = 17.5$ MeV and (e,α) at $E_e = 40.0$ MeV, $\theta_\alpha = 45-135°$. Experiment using electron plus bremsstrahlung at $E_e = 60.0$ MeV. Calculations, compound nucleus model, and pre-equilibrium exciton model combined with quasi-deuteron model.]

I. INTRODUCTION

A number of studies have been made of alpha spectra in (γ,α) reactions on medium-weight nuclei.[1-9] Most cases have been explained quite well by statistical model calculations. In heavy nuclei such as In and Au, however, an excess of energetic α particles has been observed in comparison with those expected from the evaporation model.[5] Isotropic angular distributions were obtained for α particles with low energies in ^{63}Cu and Zn as expected by the statistical model.[9,10] On the other hand, α particles from heavier nuclei showed a strong forward peaking, which suggested a direct process.[9,11] Forward-peaked angular distributions were measured for the high energy component of α particles even in ^{60}Ni and ^{63}Cu (Refs. 11 and 12). The measurements of Flowers *et al.* showed that the high energy α particles exhibit a cross section in ^{60}Ni several orders of magnitude above the statistical model prediction,[12] and they suggested that the two-step process involving (γ,N) and (N,α) reactions might explain these experimental results [the symbol N means a nucleon (neutron or proton)].

In regard to the emission of an α particle from heavy nuclei, studies of the (n,α) and (p,α) reactions also have been carried out successfully in the framework of the pre-equilibrium exciton model, in which a performed α particle is emitted in the intranuclear cascade mechanism.[13-16]

The photonuclear reaction in the high energy region has been studied mainly on the basis of the quasi-deuteron model discussed by Levinger.[17] In the region above 150 MeV, the model has successfully predicted the production cross sections for high energy nucleons, energy and angular distributions of outgoing nucleons, as well as the presence of neutron-proton coincidences.[18-22] Also in the region under 150 MeV, several investigations have been made in the framework of this model,[23,24] and attempts have been made to take account of the scattering and reabsorption of the emerging nucleons by the target nucleus.[25-28] The intranuclear cascade model and the pre-equilibrium exciton model have been combined with the quasi-deuteron model to interpret photonuclear reactions above the giant resonance.[27,29,30]

The (γ,α) reaction on heavy nuclei is suitable for the study of the photonuclear reaction in the high energy region because α emission through the giant resonance is suppressed by the high Coulomb barrier. However, only a few such cross sections have been measured as a function of excitation energy, and there is little information on the reaction mechanism above the giant resonance region. In the giant resonance region, the (γ,α_0) and (α,γ_0) reactions have been studied on several nuclei lighter than the Ni isotopes.[31-36] The angular distributions of (γ,α_0) cross sections in such nuclei show that the $E2$ component is less than 10%

© 1980 The American Physical Society

of the $E1$ cross section. Recently Wolynec *et al.* have measured the (e,α) cross sections in the Ni isotopes up to 50 MeV and suggested a large $E2$ cross section should exist in the isoscalar giant quadrupole resonance (GQR) region.[37] They claimed that electroproduced α particles decay preferentially to the 2^+ first excited state. However, more work needs to be done in order to understand the reaction mechanism of the photoalpha reaction in this region. Moreover, the $E2$ contribution is uncertain in heavier nuclei and in the region above the giant resonance. It is important to understand correctly the contribution of the $E2$ interaction in these cases.

This paper presents measurements of the ^{90}Zr(γ,α) cross section up to 60 MeV, and gives the multipolarity for the cross section by means of an experiment using bremsstrahlung plus electrons. Angular distributions are given both for the (γ,α_0) and (e,α) reactions.

Also, the results of two kinds of calculation, the compound nucleus model and the pre-equilibrium exciton model combined with the quasi-deuteron model, are compared with the experimental cross sections.

II. EXPERIMENTAL PROCEDURES

The experiments were performed with electron beams from the Tohoku University electron Linac. An enriched ^{90}Zr target, of 97.80% purity and 5.08 mg/cm^2 thickness, was bombarded with elec-rons, whose energy resolution was fixed at 2.0%. Electron beam currents were monitored with a errite core monitor calibrated with an accuracy of 1%. Alpha particles were detected with a multiwire proportional counter (MWPC) placed in the ocal plane of a Browne-Buechener type broad range spectrometer.[38] The window of the MWPC s a 644 mm long and 30 mm wide aluminized Mylar sheet 12 μm thick, which is reinforced outside with 4 mm tungsten meshes of 200 μm diameter. A hundred sense wires made of 30 μm diameter gold-plated tungsten were stretched 3 mm apart providing energy and position resolu-ions of 0.6% and 3 mm respectively measured vertically to the direction of the particle orbits. The distance between the sense wire plane and cathode plane is 5 mm. High voltage of 1.2 kV was supplied to the sense wires and signals were aken out through capacitors. PR gas (90% Ar, 10% CH$_4$) at atmospheric pressure was used as he counter gas at a flow rate of 15–35 cm^3 per minute. Cards of charge-sensitive pre-amplifiers were attached directly to the chamber frame.

A set of signals on several successive wires is made by one incident particle as shown in Fig. 1 because its track is inclined to the MWPC at an acute angle (21.50°–37.52°). An electronics system identifies the signals as due to one particle. The entrance window plane of the MWPC is located in the focal plane, so that an incident particle intersects the focal plane at the point of the first wire of the successive wires which produce signals. The measurement of the sum of their pulse heights, which is proportional to the energy loss of the incident particle in the counter gas, allows particle identification.

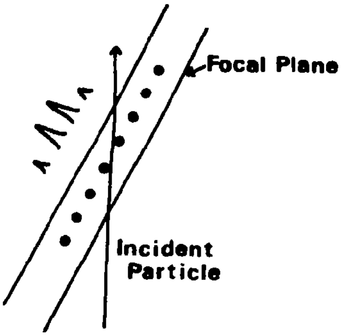

FIG. 1. An incident particle passes obliquely through the MWPC and makes signals on several successive wires.

Figure 2 shows the schematic diagram of the data acquisition system. It delivers the sum of pulse heights on the successive wires and the wire number of the first wire to the computer.

Figure 3 shows pulse height spectra from the MWPC. A discrimination level was set at an intermediate point of α particles and tritons. The pulse height of α particles is 10 times as large as that of protons, and can be discriminated from the proton background. Yields of deuterons, tritons, and ^{3}He particles are very small in medium-weight nuclei, and the background from them can be ignored.

An example of an α-particle energy spectrum is shown in Fig. 4. This was corrected for energy loss on the assumption that each α particle originated half-way through the target. The energy loss is about 0.7 MeV at α energy of 10 MeV. The experimental conditions are shown in Table I.

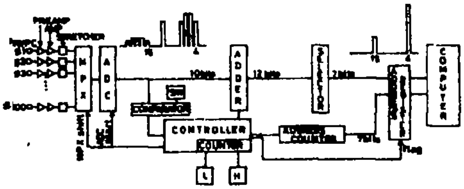

FIG. 2. Schematic diagram of the data acquisition system.

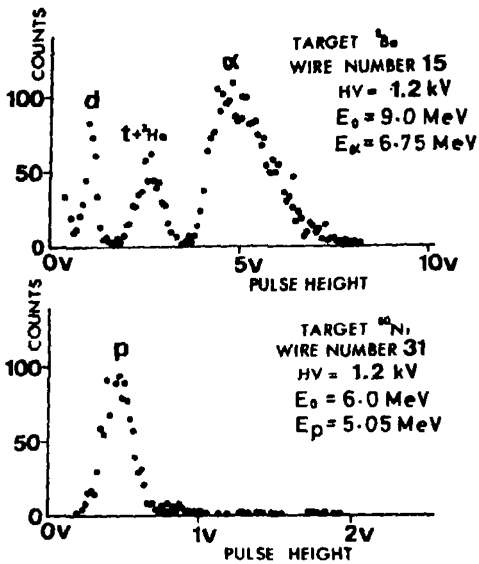

FIG. 3. Typical pulse height spectra from the MWPC.

III. EXPERIMENTS AND RESULTS

A (γ,α) and (γ,α_0) cross sections

The (e,α) differential cross section at 90° was measured at electron energies from 13.5 to 66.5 MeV at intervals of 0.5 MeV. Alpha particles between 6.9 and 16.8 MeV were summed after the correction for the solid angle of the detector. The result is shown in Fig. 5. The (e,α) cross section is related to the (γ,α) cross section, as follows:

$$\sigma^{(e,\alpha)}(E_e)=\sum_{\lambda L}\sigma_{\lambda L}^{(e,\alpha)}(E_e)\,, \tag{1}$$

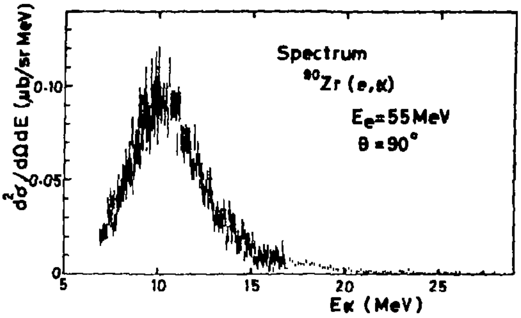

FIG. 4. (e,α) energy spectrum of ^{90}Zr at $\theta=90°$, for $E_e=55$ MeV. Alpha-particle energy was corrected for energy loss in half target thickness.

$$\sigma_{\lambda L}^{(e,\alpha)}(E_e)=\text{const}\times\int_0^{E_e}\sigma_{\lambda L}^{(\gamma,\alpha)}(E_\gamma)N_{\lambda L}^{VP}(E_e,E_\gamma)dE_\gamma\,, \tag{2}$$

where $N_{\lambda L}^{VP}(E_e,E_\gamma)$ is the virtual photon spectrum of energy E_γ and multipolarity λL for electron energy E_e. The extraction of the (γ,α) cross section from the (e,α) cross section was done first of all on the assumption that all of the α particles are attributed to the $E1$ interaction. The ^{90}Zr(γ,α) cross section was deduced by the variable-bin Penfold-Leiss method.[39-41] $E1$ virtual photon spectra used in the analysis were calculated from the analytical expression of Nascimento *et al.*,[42] which was obtained from a fit to the distorted-wave Born approximation (DWBA) calculations of Gargaro and Onley.[43] The analysis also took into account bremsstrahlung,[44] which came from the target and from the Ti vacuum window separating the scattering chamber from the accelerator at

TABLE I. Experimental conditions.

Experiment	Electron energy (MeV)	Spectrometer angle (degree)	α-particle energy (MeV)
(e,α) cross section	13.5–66.5 (interval 0.5)	90	6.9–16.8
(γ,α_0) cross section	14.0–23.5 (interval 0.5)	90	
Multipolarity	60.0	90	6.9–10.1 10.1–11.5 11.5–13.5 13.5–16.8
Angular distributions			
(γ,α_0)	17.5	45–135 (interval 15)	9.3–10.3
(e,α)	40.0	45–135 (interval 15)	10.1–11.5 11.5–13.5 13.5–16.8

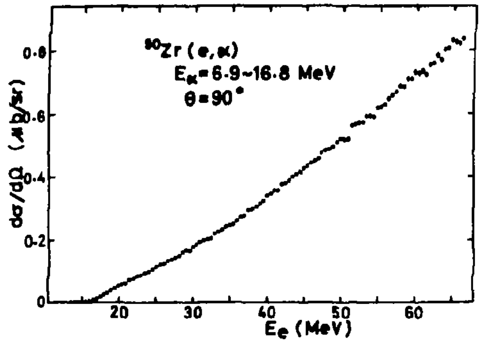

FIG. 5. Differential cross section of the (e,α) reaction at $\theta = 90°$.

the entrance of the scattering chamber.

The closed points in Fig. 6 give the (γ,α) cross section on ^{90}Zr. There is a broad bump above 30 MeV in addition to a peak at 18 MeV. The solid line in Fig. 6 is the (γ,n) cross section[45]; the position of the peak corresponds to the $T_<$ GDR, and the peak at 18 MeV in the (γ,α) cross section agrees with it.

The ^{90}Zr(γ,α_0) cross section, which is shown by the open circles in Fig. 6, was obtained from the higher energy part of the spectra measured with successive electron energies; the method is similar to that described in Ref. 46. It shows that the (γ,α_0) cross section dominates the (γ,α) cross section in the GDR region. It appears that the (γ,α_0) cross section surpasses the total (γ,α) cross section in the low energies because the missing part of α particles due to energy loss through the target was corrected for the (γ,α_0) cross section but not corrected for the (γ,α) cross section.

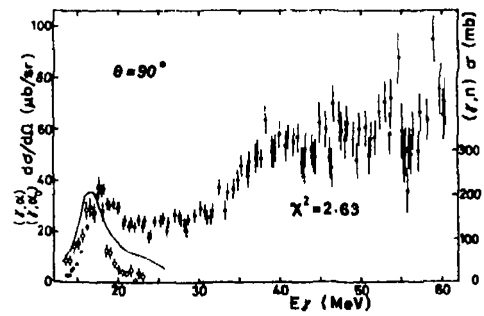

FIG. 6. Photoalpha differential cross section of ^{90}Zr (closed points) analyzed from the (e,α) cross section in Fig. 5 and ^{90}Zr(γ,α_0) differential cross section (open circles), at $\theta = 90°$. $E1$ interaction only was considered in these analyses. The value of χ^2 for the total (γ,α) cross section was calculated for the cross section smoothed by eye. Solid line shows ^{90}Zr(γ,n) cross section.

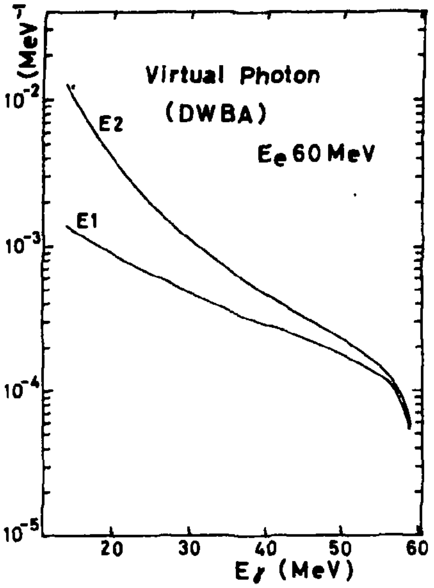

FIG. 7. Electric dipole and quadrupole virtual photon spectra for electrons of kinetic energy 60 MeV, scattered by a ^{90}Zr nucleus.

In the above analyses, only the $E1$ cross section was assumed to exist over the full energy region in which the experiments were made. However, a small $E2$ contribution to the cross section might have a considerable effect on the analyses because the $E2$ component of virtual photons is much larger than the $E1$ component, as shown in Fig. 7. Two additional analyses of the total (γ,α) cross section were made taking account of the $E2$ component:

(a) both $E1$ and $E2$ cross sections in the giant resonance region,

(b) $E1$ cross section in the giant resonance region and $E2$ cross section above 30 MeV.

The (e,α) cross section was fitted by $E1$ and $E2$ (γ,α) cross sections calculated from Eqs. (1) and (2) using Lorentz shapes for the cross sections. These were slightly corrected at low energies in order to make the (e,α) cross section vanish below a cutoff energy (the cutoff energy means the lowest electron energy that gives the lowest α energy considered):

TABLE II. Parameters of Lorentz shapes.

σ_1 (μb/sr)	Γ_1 (MeV)	E_1 (MeV)	σ_2 (μb/sr)	Γ_2 (MeV)	E_2 (MeV)	$E_{\rm cut}$ (MeV)	C (MeV)	χ^2
(a) $E1$ and $E2$ cross sections in the giant resonance region								
7.21	6.0	18.5	16.57	6.5	16.5	13.0	3.5	18.50
(b) $E1$ cross section in the giant resonance region and $E2$ cross section above 30 MeV								
24.75	7.5	18.5	24.02	21.0	38.0	13.0	3.5	3.08

$$\sigma_{\lambda L}^{(\gamma,\alpha)}(E_\gamma)=\sigma_{\lambda L}^{(\gamma,\alpha)}\frac{E_\gamma^2\Gamma_{\lambda L}^2}{(E_\gamma^2-E_{\lambda L}^2)^2+E_\gamma^2\Gamma_{\lambda L}^2}\quad\text{for } E_\gamma>E_{\rm cut}+C$$

$$=\frac{E_\gamma-E_{\rm cut}}{C}\,\sigma_{\lambda L}^{(\gamma,\alpha)}\frac{E_\gamma^2\Gamma_{\lambda L}^2}{(E_\gamma^2-E_{\lambda L}^2)^2+E_\gamma^2\Gamma_{\lambda L}^2}\quad\text{for } E_{\rm cut}<E_\gamma\leq E_{\rm cut}+C$$

$$=0\quad\text{for } E_\gamma\leq E_{\rm cut}\,. \tag{3}$$

An analytical formula by Nascimento *et al.*[42] was used for the $E1$ virtual photon spectrum, and the following formula for the $E2$ photon spectrum:

$$N_{E2}^{VP}(E_e,E_\gamma)=\frac{\alpha}{\pi E_\gamma}\left[\frac{E_0^2+E^2}{p^2}\ln\left(\frac{E_0E+pp'-m_e^2}{m_eE_\gamma}\right)+\frac{8}{3}\left(\frac{p'}{E_\gamma}\right)^2\right]+\frac{0.69}{E_0}\exp\left[-15\left(\frac{E_\gamma}{E_0}-0.65\right)^3-6.71\left(\frac{E_\gamma}{E_0}\right)\right], \tag{4}$$

where $E_0=E_e+m_e$, $E=E_0-E_\gamma$,

$p=(E_0^2-m_e^2)^{1/2}$, $p'=(E^2-m_e^2)^{1/2}$.

The first term of the right-hand side in Eq. (4) is the virtual photon spectrum given by Barber,[47] and the second term is a correction term. The values of the constants in the second term were determined so that the values calculated using the equation on ^{90}Zr agree with those given by DWBA calculations. The code presented by Onley[43] was used for the calculation.

The results using a least squares method are shown in Table II, and the (γ,α) cross sections obtained are given in Fig. 8. What we must do next is to assess the three cases. This problem will be discussed in the following sections.

B. Multipolarity of the ^{90}Zr(γ,α) cross section

In order to study the reaction process in detail, the (e,α) cross section was divided into four parts with particular α-particle energies: 6.9–10.1 MeV, 10.1–11.5 MeV, 11.5–13.5 MeV, and 13.5–16.8 MeV (Fig. 9), and the (γ,α) cross sections were deduced from them on the assumption that the (γ,α) cross sections consist of

(a) $E1$ cross section over the full energy range,

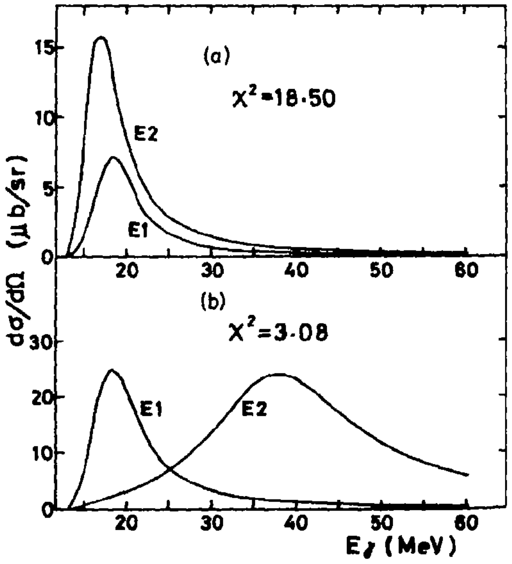

FIG. 8. Photoalpha differential cross sections reduced by taking account of the $E1$ and $E2$ components; (a) both $E1$ and $E2$ cross sections in the giant resonance region, (b) $E1$ cross section in the giant resonance region and $E2$ cross section above 30 MeV.

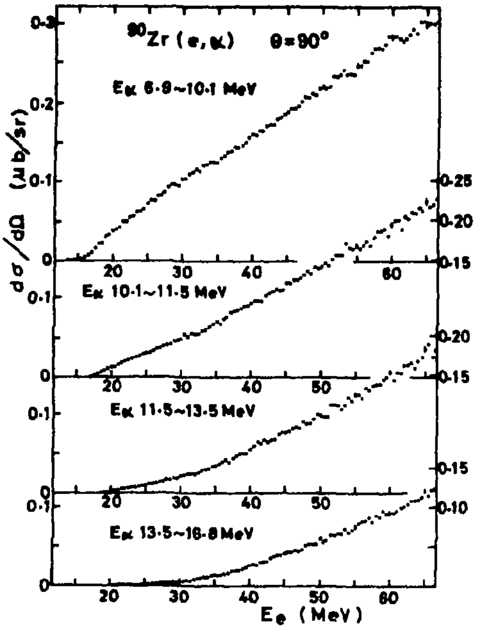

FIG. 9. ^{90}Zr(e, α) cross sections divided into four parts with particular α-particle energies.

(b) $E1$ and $E2$ cross sections in the giant resonance region,

(c) $E1$ cross section in the giant resonance region and $E2$ cross section above 30 MeV.

The method of fitting has been described in Sec. III A. The results are shown in Fig. 10 and in Table III. It was difficult to get a small χ^2 in case (b) although the parameters were changed over wide ranges. In this case, the sum of the four cross sections does not equal that shown in Fig. 8(a).

An experiment was performed to assess the three cases. Copper foils were placed in front of the ^{90}Zr target, so that the ^{90}Zr target was irradiated with bremsstrahlung from the copper foils plus electrons. The yield of α particles is given by

$$Y_{\lambda L}^{\mathrm{TOTAL}}(E_e,t)=Y_{\lambda L}^{\mathrm{BS}}(E_e,t)+Y_{\lambda L}^{\mathrm{VP}}(E_e)\,, \tag{5}$$

$$Y^{\mathrm{TOTAL}}(E_e,t)=\sum_{\lambda L} Y_{\lambda L}^{\mathrm{TOTAL}}(E_e,t)\,. \tag{6}$$

The first term of the right-hand side in Eq. (5) shows the yield associated with bremsstrahlung, and

$$Y_{\lambda L}^{\mathrm{BS}}(E_e,t)=\mathrm{const}\int_0^{E_e}\sigma_{\lambda L}^{(\gamma,\alpha)}(E_\gamma)N^{\mathrm{BS}}(E_e,t,E_\gamma)dE_\gamma\,, \tag{7}$$

where $N^{\mathrm{BS}}(E_e,t,E_\gamma)$ is the bremsstrahlung spectrum, t is the thickness of the copper foil, E_e is the electron energy, E_γ is the photon energy, and $\sigma_{\lambda L}^{(\gamma,\alpha)}(E_\gamma)$ is the (γ,α) cross section for multipolarity λL. The second term in Eq. (5) is the yield of α particles due to virtual photons of the multipolarity λL, and is given by

$$Y_{\lambda L}^{\mathrm{VP}}(E_e)=\mathrm{const}\times\int_0^{E_e}\sigma_{\lambda L}^{(\gamma,\alpha)}(E_\gamma)N_{\lambda L}^{\mathrm{VP}}(E_e,E_\gamma)dE_\gamma\,, \tag{8}$$

where $N_{\lambda L}^{\mathrm{VP}}(E_e,E_\gamma)$ is the number of virtual photons with multipolarity λL and photon energy E_γ due to an electron with energy E_e.

Now we consider $P(t)$:

$$P(t)=\frac{\sum_{\lambda L} Y_{\lambda L}^{\mathrm{TOTAL}}(E_e,t)}{\sum_{\lambda L} Y_{\lambda L}^{\mathrm{VP}}(E_e)}$$

$$=\frac{\sum_{\lambda L}\int_0^{E_e}\sigma_{\lambda L}^{(\gamma,\alpha)}(E_\gamma)N^{\mathrm{BS}}(E_e,t,E_\gamma)dE_\gamma}{\sum_{\lambda L}\int_0^{E_e}\sigma_{\lambda L}^{(\gamma,\alpha)}(E_\gamma)N_{\lambda L}^{\mathrm{VP}}(E_e,E_\gamma)dE_\gamma}+1\,. \tag{9}$$

The value obtained from the experiment is denoted $P_{\mathrm{exp}}(t)$:

$$P_{\mathrm{exp}}(t)=\frac{Y_{\mathrm{exp}}^{\mathrm{TOTAL}}(E_e,t)}{Y_{\mathrm{exp}}^{\mathrm{VP}}(E_e)}\,. \tag{10}$$

As shown in Fig. 7,

$$N_{E2}^{\mathrm{VP}}(E_e,E_\gamma)>N_{E1}^{\mathrm{VP}}(E_e,E_\gamma)\,, \tag{11}$$

and $N^{\mathrm{BS}}(E_e,t,E_\gamma)$ is the same for $E1$ and $E2$. Therefore the value of $P(t)$ for the $E1$ cross section will be greater than that for the $E2$ at the same t. The inclinations of $P(t)$ for higher multipolarities are gentler than the slope for the $E2$ because their virtual photons exceed $E2$ virtual photons. The slope for the $M1$ interaction will be close to that for the $E2$ because the $M1$ virtual photon spectrum is like the $E2$ (Refs. 43 and 47). In the case of the $E0$ interaction, the $E0$ transition with a real photon is forbidden, and the slope of $P(t)$ will be horizontal. One can decide whether the cross section is associated with the $E1$ interaction, the $E2$, or other interaction by comparing the measured and calculated $P(t)$ values.

The experiment was done with copper foils of four thicknesses: 139.3, 268.8, 399.2, and 536.6 mg/cm². The electron energy was 60 MeV, and emitted α particles were measured at 90° to the electron beam. Measurements were made for two values of magnetic field in the spectrometer, corresponding to α particles with $E_\alpha=6.0$–10.5 and $E_\alpha=9.4$–16.3 MeV. The experimental results for $P_{\mathrm{exp}}(t)$ are shown in Fig. 11 for four ranges of α-particle energy. These have been corrected for energy loss in the target, and correspond to the

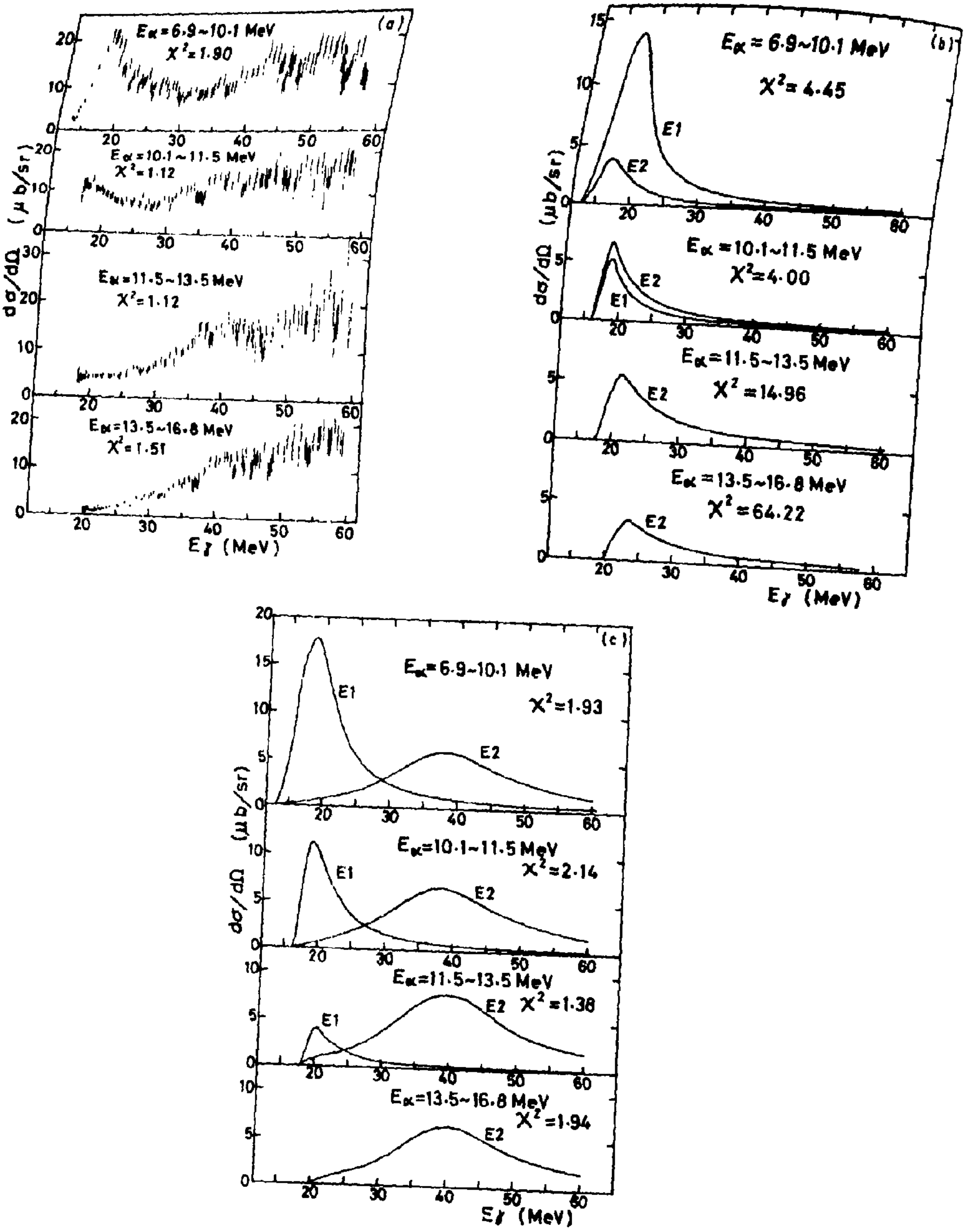

FIG. 10. ^{90}Zr(γ, α) cross sections analyzed from the (e, α) cross sections in Fig. 9. (a) An $E1$ cross section was assumed over the full energy range. The value of χ^2 was calculated for the cross sections smoothed by eye. (b) $E1$ and $E2$ cross sections were assumed in the giant resonance region. (c) An $E1$ cross section was assumed in the giant resonance region, and an $E2$ cross section above 30 MeV.

TABLE III. Parameters of Lorentz shapes.

E_α (MeV)	σ_1 (μb/sr)	Γ_1 (MeV)	E_1 (MeV)	σ_2 (μb/sr)	Γ_2 (MeV)	E_2 (MeV)	E_{cut} (MeV)	C (MeV)	χ^2
(b) $E1$ and $E2$ cross sections in the giant resonance region									
6.9–10.1	13.99	7.0	18.0	3.93	7.0	16.5	13.0	3.5	4.45
10.1–11.5	5.94	6.0	17.5	10.88	7.0	15.5	16.5	2.0	4.00
11.5–13.5	0.00	6.0	17.0	20.24	7.0	14.5	18.5	3.0	16.13
13.5–16.8	0.00	6.0	17.0	18.62	7.0	14.5	20.0	3.5	64.22
(c) $E1$ cross section in the giant resonance region and $E2$ cross section above 30 MeV									
6.9–10.1	17.61	7.5	18.5	6.07	20.0	38.0	13.0	3.0	1.93
10.1–11.5	11.65	7.5	18.5	6.60	20.0	38.0	16.5	2.0	2.14
11.5–13.5	4.85	7.5	18.5	7.79	20.0	39.0	18.5	2.0	1.38
13.5–16.8	0.00	7.5	18.5	6.41	20.0	40.0	20.0	2.0	1.94

ranges in Fig. 10. The calculated values are also shown in Fig. 11 for the $E1$ and $E2$ interactions.

In the calculation, bremsstrahlung spectra were calculated using a formula given by Schiff,[44] and virtual photon spectra by using a formula of Nascimento *et al.* and Eq. (4). In case (a), the (γ,α) cross sections in Fig. 10(a) were used for $\sigma_{E1}^{(\gamma,\alpha)}(E_\gamma)$ in Eq. (9) after smoothing by eye. The experimental results are very close to the values calculated on the assumption that all α particles are associated with the $E1$ interaction.

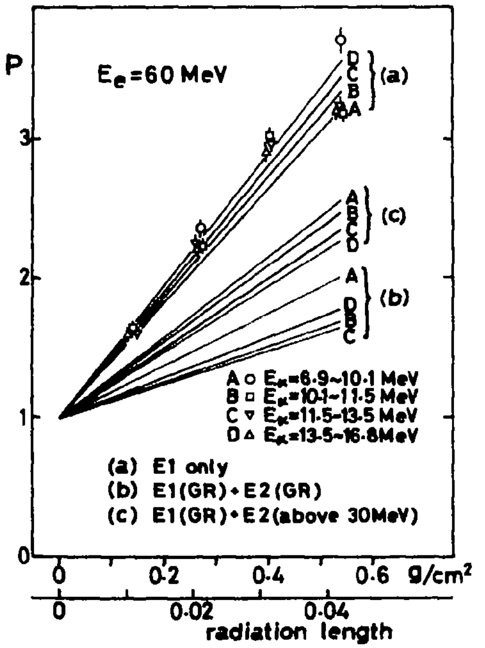

FIG. 11. Increase of α yields for thickness of bremsstrahlung target (Cu). Three sets of straight lines (a), (b), (c) correspond to (a), (b), (c) in Fig. 10.

C. Angular distributions

The angular distribution of the (γ,α_0) reaction was measured at an electron energy of 17.5 MeV. The $E1$ and $E2$ cross sections were determined using the expression[31]

$$W(\theta)=\frac{1}{4\pi}[\sigma_1(1-P_2)+\sigma_2(1+0.71P_2-1.71P_4) \\ -2.68(\sigma_1\sigma_2)^{1/2}\cos\theta_{12}(P_1-P_3)], \qquad (12)$$

where σ_1 and σ_2 are the $E1$ and $E2$ cross sections, and θ_{12} is the difference in phase between α-particle waves with $l=1$ and $l=2$. The result $\sigma_2/\sigma_1=0.009^{+0.040}_{-0.009}$ at $\langle E_\gamma\rangle=17.07\pm0.24$ MeV was obtained through the method of least squares (Fig. 12). The result shows that the $E2$ component for the ground state transition is very small and is consistent

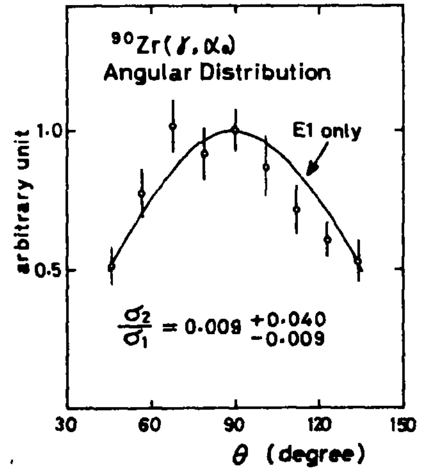

FIG. 12. Angular distribution of ^{90}Zr(γ,α_0) cross section at $E_\gamma=17.07\pm0.24$ MeV. A solid curve shows the calculation result for a pure $E1$ cross section.

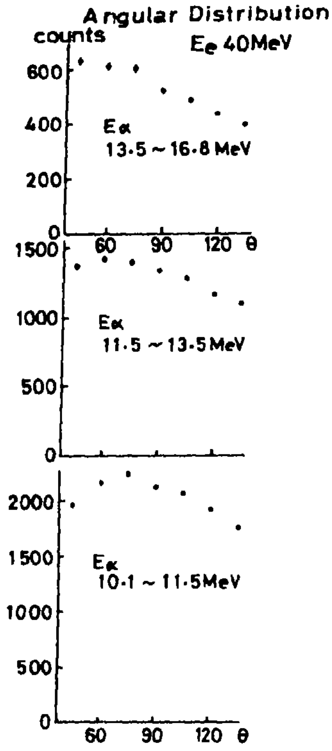

FIG. 13. Alpha-particle angular distributions at E_e = 40 MeV.

with the experiment of Sec. III B.

Angular distributions of α particles from ^{90}Zr were also measured for three ranges of α-particle energy with a 40 MeV electron beam. The result is shown in Fig. 13. The angular distribution is forward-peaked for the highest α-particle energy, and more symmetric about 90° for lower α-particle energies. As shown in Sec. III B, α particles above 13.5 MeV come from the $E1$ cross section above 30 MeV, and the forward-peaked angular distribution reflects the nature of the cross section above 30 MeV. These α particles cannot be explained by a compound nucleus process because the calculation based on a statistical theory gives a symmetric angular distribution at 90°. The forward peaking obtained experimentally suggests that these α particles are emitted relatively directly from earlier stages of the reaction. Interference with a small $E2$ component also may be necessary to explain the forward-peaked angular distribution. The more symmetric angular distribution for α particles with lower energies is due to a contribution from α particles emitted through the giant resonance [Fig. 10(a)]. As shown in Fig. 6, the (γ,α_0) cross section forms a large fraction of the (γ,α) cross section in the GDR region. The angular distribution tends to be nearly symmetric to 90° for lower α-particle energies because the angular distribution for the (γ,α_0) reaction is very similar to that of a pure $E1$ process (Fig. 12).

IV. DISCUSSION

In Secs. III B and III C, most α particles emitted through the (γ,α) reaction in ^{90}Zr are associated with the $E1$ interaction, and a broad bump exists above 30 MeV in addition to one in the GDR region. The reaction mechanism is discussed in this section.

A. Compound nucleus model

The (γ,α) cross section of ^{90}Zr has two bumps as shown in Fig. 6, one at 18 MeV corresponding to the GDR and the other above 30 MeV. In the giant resonance region, the (γ,α_0) cross section forms a major part of the (γ,α) cross section. This result is explained by the compound nucleus model. On the basis of the Hauser-Feshbach formula,[48] the (γ,α_0) cross section is expressed as

$$\sigma^{(\gamma,\alpha_0)}(E_\gamma)=\sigma^{\mathrm{CN}}(E_\gamma)\frac{T(\alpha_0)}{\sum\limits_{c} T_c}, \qquad (13)$$

where σ^{CN} is the compound nucleus formation cross section and $T(\alpha_0)$ is the transmission coefficient of the emitted α particle leading to the ground state of the residual nucleus. The denominator is the sum of the transmission coefficients for all possible decay channels.

Considering the angular distribution of the $E1$ interaction [see Eq. (12)], the differential cross section at 90° for the even-even nucleus is given by

$$\frac{d\sigma^{(\gamma,\alpha_0)}(E_\gamma)}{d\Omega}=\frac{3}{8\pi}\sigma^{\mathrm{CN}}(E_\gamma)\frac{T(\alpha_0)}{\sum\limits_{c} T_c}. \qquad (14)$$

Similarly, it is assumed that all neutrons are emitted through the compound nuclear process

$$\sigma^{(\gamma,n)}(E_\gamma)=\sigma^{\mathrm{CN}}(E_\gamma)\frac{\sum\limits_{c'} T_{c'}(n)}{\sum\limits_{c} T_c}. \qquad (15)$$

From Eqs. (14) and (15) it follows that

$$\frac{d\sigma^{(\gamma,\alpha_0)}(E_\gamma)}{d\Omega}=\frac{3}{8\pi}\frac{T(\alpha_0)}{\sum\limits_{c'} T_{c'}(n)}\sigma^{(\gamma,n)}(E_\gamma). \qquad (16)$$

The transmission coefficients were calculated using Woods-Saxon type optical potentials shown in Table IV, which had been obtained through the

TABLE IV. Optical potential parameters used for calculations of transmission coefficients.

	r_0 (fm)	a_0 (fm)	V_0 (MeV)	r_I (fm)	a_I (fm)	W_I (MeV)	V_{SO} (MeV)	r_C (fm)
(*n*)	1.25	0.65	$52.5-0.625E$	1.25	0.98	$5.4+0.4E$	$10.185-0.171E$	
(α)	1.553	0.631	34.63	1.553	0.631	17.35		1.4

experiments of α scattering[49] and neutron scattering.[50] On the assumption of an isotropic angular distribution for all α particles except those leading to the ground state, the (γ,α) cross section is written in the form

$$\frac{d\sigma^{(\gamma,\alpha)}(E_\gamma)}{d\Omega}=\frac{\sigma^{(\gamma,n)}(E_\gamma)}{\sum_{c'}T_{c'}(n)}\left[\frac{3}{8\pi}T(\alpha_0)+\frac{1}{4\pi}\sum_{i\neq 0}T(\alpha_i)\right]. \tag{17}$$

The solid lines in Fig. 14 are the cross sections calculated by Eqs. (16) and (17). Both (γ,α) and (γ,α_0) cross sections calculated by this model agree well with the experimental results in the giant resonance region. However, the (γ,α) cross section above 20 MeV is not explained by this model at all.

B. Pre-equilibrium exciton model combined with the quasi-deuteron model

The angular distribution of α particles emitted rom the region above 30 MeV shows a forward peaking as discussed in Sec. III C. This implies hat α particles from the excited state above 30 MeV are not always emitted through a compound nuclear process.

A calculation was made in the framework of the pre-equilibrium exciton model combined with the quasi-deuteron model. The photonuclear reaction above the giant resonance region has been successfully studied on the basis of the quasi-deuteron nodel, which was introduced by Levinger.[17] According to this model, a photon is absorbed through he photodisintegration of a correlated neutron-proton pair in the nucleus. Levinger showed that he absorption cross section could be written as

$$\sigma_\gamma(E_\gamma)=L\frac{NZ}{A}\sigma^D(E_\gamma), \tag{18}$$

where σ^D is the photodisintegration cross section or a free deuteron, and L is a constant which indicates the probability of this process compared with the disintegration of a free deuteron, whose value was obtained theoretically to be 6.4. Thereafter, different values of L have been obtained experimentally by many investigators, for example $L=2.8$ by Costa *et al.*[27] and $L=10.3$ by Garvey *et al.*[31]

In the case of the emission of α particles on medium-weight and heavy nuclei, the (*n*,α) and (*p*,α) reactions have been successfully studied in the pre-equilibrium exciton model,[13-16] An incoming particle, having entered the nucleus, hits a particle (proton, neutron, or preformed α particle) in the nucleus, and makes a particle-hole pair. A two-particle one-hole state (so-called three exciton state) formed in this way decays either by particle emission or by a transition to a five-exciton state through an exciton-particle scattering in the nucleus.

In the case of the pre-equilibrium exciton model combined with the quasi-deuteron model, the first stage of the reaction is characterized by a four exciton state (one-particle one-hole pairs which are made for both proton and neutron through the quasi-deuteron process). An alpha particle-hole pair can be formed for the first time in the six-exciton state.

The calculation of the (γ,α) reaction can be done with the same formalism as for the (*n*,α) or (*p*,α) reaction involving the pre-equilibrium exciton mo-

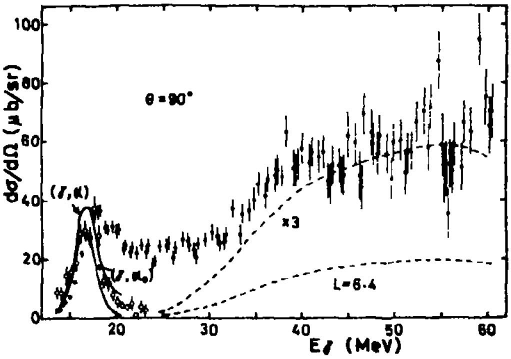

FIG. 14. Comparison of the compound nucleus model (solid lines) and the pre-equilibrium exciton model combined with the quasi-deuteron model (dashed lines) with the experimental ^{90}Zr(γ,α) cross section (closed points) and ^{90}Zr(γ,α_0) cross section (open circles).

del, with a slight modification:

$$\sigma^{(\gamma,\alpha)}(E)=\sigma_\gamma(E)\int\frac{m_\alpha\epsilon\sigma_{\mathrm{inv}}(\epsilon)g_R}{4\pi^3\hbar^2|M|^2g_C{}^5E^3}\,d\epsilon \times\sum_{\substack{n=6\\(\Delta n=2)}}^{\bar{n}}\left(\frac{g_RU}{g_CE}\right)^{(n-2)} \times(n^2-1)n\,\frac{\varphi K_{n-1}^{\alpha}}{\varphi K_n^{\alpha}+(1-\varphi)K_n^{\nu}}\,. \qquad (19)$$

Symbols in Eq. (19) are as follows:

$\sigma_\gamma(E)$ is the photon absorption cross section.

m_α and ϵ are the reduced mass of the α particle and its kinetic energy in the exit channel.

$\sigma_{\mathrm{inv}}(\epsilon)$ is the cross section for the inverse process: the absorption cross section for an α particle with the kinetic energy ϵ.

g_R and g_C are the single particle level density in the residual and target nucleus.

U and E are the excitation energy of the residual nucleus and that of the nucleus before decay.

n is the exciton number in each stage of the cascade, which varies only by two units.

$\bar{n}$ is the exciton number of the state at equilibrium.

M is the matrix element describing the transition from a state with n excitons to the subsequent state with $n+2$.

K_n^{α} and K_n^{ν} are factors for an α particle and a nucleon introducing the corrections due to charge conservation and assuming the α particle to have a level density equal to $g/4$.

φ is the probability for the nucleon in the intranuclear cascade to strike a preformed α particle.

The inverse cross section $\sigma_{\mathrm{inv}}(\epsilon)$ is represented by the formula

$$\sigma_{\mathrm{inv}}(\epsilon)=\pi\lambda^2\sum_l(2l+1)T_l(\epsilon) =\frac{\pi\hbar^2}{2m_\alpha\epsilon}\sum_l(2l+1)T_l(\epsilon)\,, \qquad (20)$$

where $T_l(\epsilon)$ is the transmission coefficient for an α particle with kinetic energy ϵ and angular momentum l.

The following relations were also used[15,51]:

$$|M|^2=8A^{-3}\ (\mathrm{MeV}^2)\,, \qquad (21)$$

$$g=\frac{6}{\pi^2}\frac{A}{7.5}\ (\mathrm{MeV}^{-1})\,, \qquad (22)$$

$$\bar{n}=(2Eg_C)^{1/2}\,. \qquad (23)$$

The photon-absorption cross section was calculated from Eq. (18) using the deuteron photodisintegration cross section σ^D presented by Partovi.[52] The parameter φ was assumed to be 0.2 (Ref. 15).

The differential cross section for the ^{90}Zr(γ,α) reaction was calculated using

$$\frac{d\sigma^{(\gamma,\alpha)}(E_\gamma)}{d\Omega}=\frac{1}{4\pi}\sigma^{(\gamma,\alpha)}(E_\gamma)\,. \qquad (24)$$

An isotropic angular distribution was assumed here. The calculated result is shown in Fig. 14 by a dashed line. It rises gradually with increasing excitation energy like the experimental result, although there is a slight difference in the absolute value. The value of L cannot be evaluated because the parameter φ in Eq. (19) is uncertain.

V. SUMMARY AND CONCLUSIONS

The total (e,α) cross section for ^{90}Zr and the four cross sections for particular alpha energy intervals can be described assuming a broad bump of $E1$ or $E2$ cross section above 30 MeV in addition to an $E1$ cross section in the GDR region. It is difficult to explain the (e,α) cross sections using $E1$ and $E2$ cross sections in the giant resonance region. The angular distribution of the (γ,α_0) cross section shows that the $E2$ component is not more than 1% of the $E1$ cross section at $E_\gamma=17$ MeV. The experiment using bremsstrahlung plus electrons indicates that almost all α particles are emitted through $E1$ excitation.

The angular distribution of α particles with high energies, which are associated with the cross section above 30 MeV, shows a forward peaking. This suggests that they should be emitted through earlier stages of the reaction than a compound nuclear process.

The calculation using the pre-equilibrium exciton model combined with the quasi-deuteron model gives a bump above 30 MeV like the experimental result. Some problems in the formula by Milazzo-Colli *et al.* used in this paper have been pointed out.[53] They have no serious influence on the calculation made in this paper. Very recently Flowers *et al.*[54] and members of our group[55] have successfully compared high energy parts of α-particle spectra from the (e,α) reaction in several heavy nuclei with ones calculated by the method of Wu and Chang.[30] Their results are consistent with the existence of the (γ,α) cross section above 30 MeV.

The cross sections in the giant resonance region, both (γ,α_0) and (γ,α), can be explained by the compound nucleus model.

ACKNOWLEDGMENTS

The authors are grateful to Professor K. Shoda and his colleagues for assistance with the experimental work and for valuable discussions. Dr. Y. Kawazoe helped them with discussions. The authors also wish to thank the accelerator group and the computer group for their assistance during the measurements.

*Present address: National Laboratory for High Energy Physics, Oho-Machi, Tsukuba-Gun, Ibaraki-Ken, 305 Japan.

[1] M. E. Toms and J. McElhinney, Phys. Rev. 111, 561 (1958).

[2] M. Kregar and B. Povh, Phys. Lett. 2, 103 (1962).

[3] M. Kregar and B. Povh, Nucl. Phys. 43, 170 (1963).

[4] J. A. Scheer, K. Schlüpmann, and F. Triantafyllidis, Nucl. Phys. 56, 113 (1964).

[5] L. Meneghetti and S.Vitale, Nucl. Phys. 61, 316 (1965).

[6] H. Hoffmann, B. Prowe, and H. Ullrich, Nucl. Phys. 85, 631 (1966).

[7] G. Kraft, R. Kosiek, R. Mundhenke, and J. Winter, Nucl. Phys. A118, 25 (1968).

[8] P. David, J. Debrus, F. Lübke, H. Mommsen, R. Schoenmackers, and G. Stein, Nucl. Phys. A221, 145 (1974).

[9] J. J. Murphy II, H. J. Gehrhardt, and D. M. Skopik, Nucl. Phys. A277, 69 (1977).

[10] N. A. Keller and D. B. McConnell, Can. J. Phys. 50, 1554 (1972).

[11] J. J. Murphy II, D. M. Skopik, J. Asai, and J. Uegaki, Phys. Rev. C 18, 736 (1978).

[12] A. G. Flowers, A. C. Shotter, D. Branford, J. C. McGeorge, and R. O. Owens, Phys. Rev. Lett. 40, 709 (1978).

[13] L. Colli-Milazzo and G. M. Marcazzan-Braga, Phys. Lett. 38B, 155 (1972).

[14] G. M. Braga-Marcazzan, L. Milazzo-Colli, and C. Signorini, Lett. Nuovo Cimento 6, 357 (1973).

[15] L. Milazzo-Colli and G. M. Braga-Marcazzan, Nucl. Phys. A210, 297 (1973).

[16] L. Milazzo-Colli, G. M. Braga-Marcazzan, M. Milazzo, and C. Signorini, Nucl. Phys. A218, 274 (1974).

[17] J. S. Levinger, Phys. Rev. 84, 43 (1951).

[18] A. C. Odian, P. C. Stein, A. Wattenberg, and B. T. Feld, Phys. Rev. 102, 837 (1956).

[19] M. Q. Barton and J. H. Smith, Phys. Rev. 110, 1143 (1958).

[20] P. C. Stein, A. C. Odian, A. Wattenberg, and R. Weinstein, Phys. Rev. 119, 348 (1960).

[21] J. Garvey, B. H. Patrick, J. G. Rutherglen, and I. L. Smith, Nucl. Phys. 70, 241 (1965).

[22] T. A. Gabriel, Phys. Rev. C 13, 240 (1976).

[23] S. Costa, L. Ferrero, and L. Pasqualini, Lett. Nuovo Cimento 1, 448 (1971).

[24] H. Schier and B. Schoch, Nucl. Phys. A229, 93 (1974).

[25] C. Whitehead, W. R. McMurray, M. J. Aitken, N. Middlemas, and C. H. Collie, Phys. Rev. 110, 941 (1958).

[26] N. N. Kaushal, E. J. Winhold, P. F. Yergin, H. A. Medicus, and R. H. Augustson, Phys. Rev. 175, 1330 (1968).

[27] T. A. Gabriel and R. G. Alsmiller Jr., Phys. Rev. 182, 1035 (1969).

[28] S. Costa, L. Ferrero, and L. Pasqualini, Lett. Nuovo Cimento 2, 665 (1971).

[29] V. S. Barashenkov, F. G. Gereghi, A. S. Iljinov, G. G. Jonsson, and V. D. Toneev, Nucl. Phys. A231, 462 (1974).

[30] J. R. Wu and C. C. Chang, Phys. Rev. C 16, 1812 (1977).

[31] L. Meyer-Schützmeister, Z. Vager, R. E. Segel, and P. P. Singh, Nucl. Phys. A108, 180 (1968).

[32] R. B. Watson, D. Branford, J. L. Black, and W. J. Caelli, Nucl. Phys. A203, 209 (1973).

[33] G. S. Foote, D. Branford, R. A. I. Bell, and R. B. Watson, Nucl. Phys. A220, 505 (1974).

[34] R. E. Peschel, J. M. Long, H. D. Shay, and D. A. Bromley, Nucl. Phys. A232, 269 (1974).

[35] G. S. Foote, D. Branford, D. C. Weisser, N. Shikazono, R. A. I. Bell, and F. C. P. Huang, Nucl. Phys. A263, 349 (1976).

[36] M. Sugawara, Proceedings of Kawatabi Conference of New Giant Resonance, Supplement to Research Report of Laboratory of Nuclear Science, Tohoku University, 8, 18 (1975).

[37] E. Wolynec, W. R. Dodge, and E. Hayward, Phys. Rev. Lett. 42, 27 (1979), and private communications.

[38] K. Shoda, M. Sugawara, T. Saito, and H. Miyase, Nucl. Phys. A221, 125 (1974).

[39] A. S. Penfold and J. E. Leiss, Phys. Rev. 114, 1332 (1959).

[40] H. H. Thies, Aust. J. Phys. 14, 174 (1961).

[41] E. Bramanis, T. K. Deague, R. S. Hicks, R. J. Hughes, E. G. Muirhead, R. H. Sambell, and R. J. J. Stewart, Nucl. Instrum. Methods 100, 59 (1972).

[42] I. C. Nascimento, E. Wolynec, and D. S. Onley, Nucl. Phys. A246, 210 (1975).

[43] W. W. Gargaro and D. S. Onley, Phys. Rev. C 4, 1032 (1971).

[44] L. I. Schiff, Phys. Rev. 83, 252 (1951).

[45] A. Lepretre, H. Beil, R. Bergere, P. Carlos, A. Veyssiere, and M. Sugawara, Nucl. Phys. A175, 609 (1971).

[46] M. Sugawara, T. Terasawa, T. Tamae, Y. Kawamura, H. Saito, and H. Tsubota, Nucl. Phys. A248, 477 (1975).

[47] W. C. Barber and T. Wiedling, Nucl. Phys. 18, 575 (1960).

[48] W. Hauser and H. Feshbach, Phys. Rev. 87, 366 (1952).

[49] F. Bjorklund and S. Fernback, Phys. Rev. 109, 1295 (1958).

[50] C. M. Perey and G. Perey, At. Data Nucl. Data Tables 17, 87 (1976).

[51] G. M. Braga-Marcazzan, E. Gadioli-Erba, L. Milazzo-Colli, and P. G. Sona, Phys. Rev. C 6, 1398 (1972).

[52] F. Partovi, Ann. Phys. (N.Y.) 27, 79 (1964).

[53] P. Obložinský, Phys. Lett. 74B, 6 (1978).

[54] A. G. Flowers, D. Branford, J. C. McGeorge, A. C. Shotter, P. Thorley, C. H. Zimmerman, R. O. Owens, and J. S. Pringle, Phys. Rev. Lett. 43, 323 (1979).

[55] T. Urano, M. Hirooka, and M. Sugawara, International Conference on Nuclear Physics with Electromagnetic Interactions, Abstracts of Contributed Papers, Mainz, 1979, 4.33.

PHYSICAL REVIEW C VOLUME 21, NUMBER 5 MAY 1980

Decay of deformed and superdeformed nuclei formed in heavy ion reactions

Marshall Blann
Lawrence Livermore Laboratory, Livermore, California 94550

(Received 13 September 1979)

The importance of considering the deformation of nuclei at high angular momenta in computing transmission coefficients for their decay is the major topic of this work. Deformations based on the rotating liquid drop model were used to generate transmission coefficients versus compound nucleus angular momentum. The results were then used in a Hauser-Feshbach code which included fission competition to assess the ultimate importance of deformation modified transmission coefficients. It was found that for a broad range of prolate nuclei (superdeformed) the course of deexcitation predicted changes totally from predominant fission to predominant α decay because of a new mechanism called α-decay amplification. The phase space relationships responsible for this new mechanism are presented. It is shown that this predicted new decay mode of superdeformed nuclei is consistent with a large body of existing experimental results, though more explicit experiments must be completed to confirm the new mechanism.

NUCLEAR REACTIONS Study effects on deexcitation from calculating transmission coefficients for superdeformed ^{56}Ni, ^{149}Tb nuclei formed by HI bombardment. Compare results with usual Hauser-Feshbach calculation assuming spherical nuclei.

I. INTRODUCTION

A large fraction of heavy ion reaction cross sections end up in evaporation residue (ER) and fissionlike products. Analysis of these reaction products often involves the statistical model in various degrees of sophistication (or lack thereof). The degree of agreement between theory and experiment is then interpreted as the reaction being, or not being, describable as decay of an equilibrated compound nucleus.

The flaw in this argument of course occurs if the model is used in an invalid form. Indeed the domain of application has been extended, almost without question, from a few tens of MeV of excitation and relatively low angular momenta, to excitations in excess of 100 MeV and angular momenta beyond the predicted limits of stability of the systems in question. Lack of agreement under these circumstances for experimental results versus model calculations may indicate more the inadequacy of the model input than difference in mechanism.

In an earlier work we examined changes in input to the Hauser-Feshbach (HF) statistical approach which might result from relaxation of the Pauli principle due to high excitation energy, and also due to particle emission during the coalescence and equilibration phases of heavy ion reactions.[1,2] In this work we investigate the importance of considering the high deformation of nuclei at high angular momenta in calculating the transmission coefficients (T_l) used as input into statistical codes.[3] The transmission coefficients determine the accessible phase space in the decay process, and can therefore have an exponential influence on final branching ratios.

The nuclear shapes used will be based on the rotating liquid drop model (RLD).[4] They will therefore be of a global nature, and will not reflect variations due to shell structure; the latter provides a vast area for discussion on its own merit. The very prolate nuclei at high angular momenta will be shown to be dominated by alpha decay, rather than fission, as the principal initial deexcitation mode when the ground state deformations are recognized in the T_l input. It will be shown that these results are consistent with many experimental observations, although definitive experiments remain to be done.

A brief description of the computer code used will be given in Sec. II. The calculation of transmission coefficients for spherical and deformed nuclei will be discussed in Sec. III. In Sec. IV results of various sets of calculations will be presented, such that the predictions of deexcitation of superdeformed nuclei will be more fully understood and, in particular, how these model predictions using T_l for deformed nuclei differ vastly from earlier predictions. Two systems will be calculated for illustrative purposes in order to show the mass dependence of deformation effects. These will be, respectively, the decay of ^{56}Ni at 172 MeV of excitation as formed by 214-MeV ^{16}O ions on ^{40}Ca, and ^{149}Tb nuclei at

© 1980 The American Physical Society

120 MeV of excitation as formed by 236-MeV ^{40}Ar on ^{109}Ag. Conclusions will be presented in Sec. V.

II. DESCRIPTION OF COMPUTER CODE

The code used for the calculations to be presented represents a minor modification of the Hauser-Feshbach (HF) MBII code[5]; the new code has been named ALERT. The logic of the code is represented pictorially in Fig. 1. The computer core is organized into files corresponding to a Chart-of-Nuclides-like region beginning with the compound nucleus at some excitation energy E, and with a partial reaction cross section distribution σ_I. The subroutines used to provide input to the HF calculation will be described shortly.

The ALERT code nuclides are each dimensioned 100 $\hbar \times 200$ MeV with a mesh size 1 MeV by 1 $\hbar$. Outgoing particles (n,p,α) may have energies to 60 MeV and angular momenta to 60 $\hbar$, also with 1 MeV and 1 $\hbar$ mesh size. The gamma-ray competition with particle emission has been limited arbitrarily to 15 MeV above the yrast energy at each value of the angular momentum and only dipole decay is considered. At present, an array 9 mass units wide by 7 Z units deep may be calculated (63 nuclides), although these dimensions could easily be extended.

As is illustrated in Fig. 1, n, p, α, fission, and sometimes γ-emission spectra are calculated, and the residual nuclide differential cross section elements are stored in the appropriate residual nuclide array. The particle emission spectra are also stored according to kinetic energy and angular momentum of the outgoing particles.

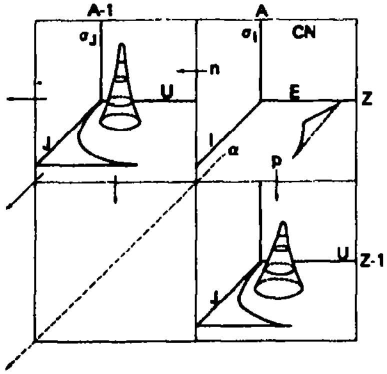

FIG. 1. Illustration of logic of the Hauser-Feshbach de ALERT which was used in calculations is presented rein. The control sequence and mesh sizes are dissed in Sec. II.

When no further particle emission or fission is possible from the compound nucleus, control transfers to the nucleus $A-1, Z$; this becomes the new compound nucleus, and the deexcitation calculation is continued for as many of the 20 000 E–J points as may be populated and capable of further deexcitation. The calculation continues to $A-2$, etc., then to $A-1$, $Z-1$, $A-2$, $Z-1$, etc., until all nuclides in the array specified by data input have had their population and deexcitation calculated.

The code has been written to read transmission coefficients from either an internally generated or separately generated files. Binding energies and Q values may be user supplied or internally generated using the Myers-Swiatecki–Lysekil mass formula.[6,7] Fission barriers and ground state rotational energies are generated using the RLD,[4] with subroutines from the Weisskopf-type[8] code ALICE[9]; entrance channel T_l are calculated from the parabolic model routine from code ALICE.[8,9] The angular momentum dependent level density was used in the form proposed by Lang,[10,11]

$$\rho(E,J) \propto (2J+1)E^{-2}\exp 2\{a[E-E_{\mathrm{rot}}(J)]\}^{1/2}. \tag{1}$$

Lang showed[10] that this expression, which gives no level density below the yrast line, is very much superior to the more commonly used exponential cutoff factor formulation. This level density, Eq. (1), was used in the code ALERT to evaluate the equation

$$P_\nu(\epsilon,I)\,d\epsilon = \frac{(2s_\nu+1)\sum_{l=0}^{\infty}T_l^\nu(\epsilon)\sum_{J=|I-l|}^{I+l}\rho(U,J)\,d\epsilon}{\int_{\epsilon=0}^{\infty}\sum_{\nu=1}^{3}(2s_\nu+1)\sum_{l=0}^{\infty}T_l^\nu(\epsilon)\sum_{J=|I-l|}^{I+l}\rho(U,J)\,d\epsilon}, \tag{2}$$

where symbols are defined in Table I.

III. CALCULATION OF TRANSMISSION COEFFICIENTS FOR SPHERICAL AND DEFORMED NUCLEI

A. Spherical nuclei

Standard global optical model parameter sets from the MBII code subroutines were used to generate T_l sets for nuclei beginning with the compound nucleus (A,Z) and for nuclides $(A-2, Z-1)$–$(A-10, Z-5)$.[5,12] This was done for n, p, and α particles at channel energies between 0.1 and 59.1 MeV in 1-MeV increments. Partial waves up to 60 $\hbar$ were permitted in the buffers chosen. Transmission coefficients were computed

TABLE I. Definition of symbols used.

T_l, $T_l(\epsilon)$, $T_l^{\nu}(\epsilon)$	Transmission coefficient; for channel energy ϵ; for particle type ν and orbital angular momentum $l\hbar$.
$P_\nu(\epsilon, I)d\epsilon$	Probability of emitting particle type ν with channel energy ϵ to $\epsilon + d\epsilon$ from compound nucleus of angular momentum I.
s_ν	Intrinsic spin of particle ν.
E	Compound nucleus excitation.
U	Residual nucleus excitation.
J	Residual nucleus angular momentum.
l	Orbital angular momentum of captured or emitted particle.
$\rho(U, J)$	Level density of nucleus at excitation energy U and angular momentum J.
a	Level density parameter; value used in this work is $A/10$ MeV^{-1}.
$E_{ROT}(J)$	Rotational energy of a nucleus with angular momentum J ($\hbar$).
μ	Reduced mass.
$\sigma_\nu(\epsilon)$	Inverse reaction cross section for particle ν with channel energy ϵ.
σ_{ER}	Evaporation residue cross section.
ER	Evaporation residue.

to values of 10^{-9}.

Classical sharp cutoff parameters (SCO) were also selected to reproduce, as nearly as possible, the optical model results. The sharp cutoff model T_l values were defined by

$$l_{max} = 0.187(2\mu\epsilon)^{1/2}(R + 3.4/\epsilon^{1/2}) \tag{3a}$$

for neutrons and

$$l_{max} = 0.187(2\mu\epsilon)^{1/2}(1 - V_{\nu,l}/\epsilon)^{1/2} R \tag{3b}$$

for protons and α particles, where

$$T_l(\epsilon) = 1 \text{ if } l < l_{max}, \tag{4a}$$

$$T_l(\epsilon) = 0 \text{ if } l > l_{max}. \tag{4b}$$

The radius R_ν is defined by

$$R_\nu = 1.21[(A - A_\nu)^{1/3} + A_\nu^{1/3}], \tag{5a}$$

and the potential by

$$V_\nu = \frac{(Z - Z_\nu)Z_\nu K_\nu}{R_\nu + 1.6}\ \text{MeV}, \tag{5b}$$

where $K_\nu = 1.32$ for α particles and 1.15 for protons. A comparison between the SCO result and the optical model result is shown in Fig. 2 for 30-MeV α particles incident on $^{52}_{26}$Fe. Results for neutrons and protons as calculated on the SCO are shown in Fig. 3. Symbols are defined in Table I.

B. Deformed nuclei

The rotating liquid drop model was used to estimate the maximum radius of the equilibrium deformed nucleus at various values of the angular momentum. Calculations were performed for each nucleus for $I = 5\hbar$ to $I = 95\hbar$ in $10\hbar$ increments. If the deformation exceeded the saddle point value, the saddle point result was taken. The latter procedure requires some discussion. First, calculation of input T_l for nuclei with angular momenta beyond the RLD stability limit does not require that this regime be considered in any particular deexcitation calculation. However, if the intrinsic excitation equilibration and particle emission decay rates are much greater than the rate of fission, such a calculation may

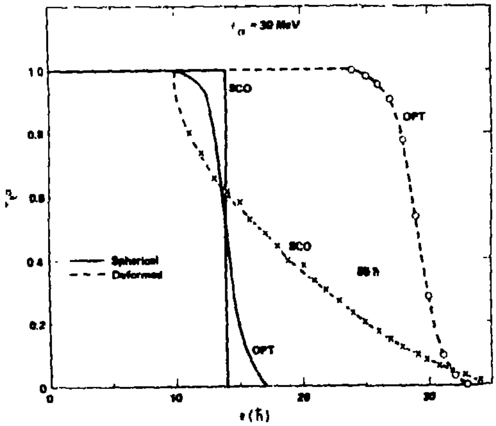

FIG. 2. Comparisons of several sets of transmission coefficients calculated for 30-MeV α particles incident on ^{52}Fe. Solid lines are for spherical systems, dashed lines for deformed systems. Results are shown for the SCO model and the optical model, plotted as T_l vs partial wave (abscissa). The deformed nucleus is at 55 $\hbar$.

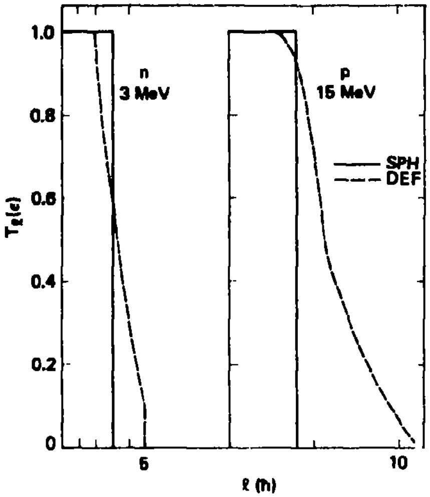

FIG. 3. Comparison of T_l (ordinate) for 3-MeV neutrons and 15-MeV protons from ^{58}Ni vs partial wave l. Results are from the SCO model for spherical and deformed (55 ħ) nuclei.

give valuable insights into the possible non-equilibrium decay modes.

Two procedures were followed for generating sets of transmission coefficients for deformed nuclei. One of these involved an averaging over the surface of the spheriod indicated by the RLD using the classical SCO approximation; the other was an extreme model in which the optical model radius was modified to generate T_l results appropriate for emission from the tips of the nuclei.[3]

In the classical SCO approximation the triaxial shapes were replaced by ellipsoids of revolution having a major axis to spherical axis ratio as given by RLD (Fig. 10 of Ref. 4) and a minor axis defined to be volume conserving. The ellipsoids of revolution were defined by

$$\frac{x^2}{c^2}+\frac{y^2}{a^2}=1\,, \tag{6}$$

where x is the symmetry axis and y is 90° to x.

The potential of such a spheroid at any point on the surface is given by[13]

$$V(x,y)=D-\tfrac{1}{2}Ax^2-\tfrac{1}{2}By^2\,, \tag{7}$$

where

$$D=\frac{3Z}{2c}K\,, \tag{8}$$

$$A=\frac{3Z}{\epsilon^3c^3}(K-1)\,, \tag{9}$$

$$B=\frac{3Z}{2\epsilon^3c^3}\left[\frac{1}{(1-\epsilon^2)}-K\right], \tag{10}$$

$$K=\frac{\ln[(1+\epsilon)/(1-\epsilon)]}{3\epsilon}\,, \tag{11}$$

and

$$\epsilon=(1-a^2/c^2)^{1/2}\,. \tag{12}$$

The eccentricity ϵ is real if a prolate spheroid and imaginary if an oblate spheroid.

The transmission coefficients were then defined as to the $l_{\max}$ at the surface of the spheroids at increments in radius where the maximum radii R_ν of Eq. (5) were replaced by

$$R'=\frac{R_{\max}}{R_0}R_\nu\,. \tag{13}$$

The symmetry axis was divided, between zero and R', into 50 increments. For each increment the surface area was approximated by

$$\Delta A_i\cong 2\pi y_i S_i\,, \tag{14}$$

where

$$S_i=[(y_i-y_{i-1})^2+(\Delta x)^2]^{1/2} \tag{15}$$

(and $\Delta x=0.02\ c$). The potential V_ν of Eq. (6) was replaced by $V_{\nu,i}$ calculated for (x_i, y_i) of each segment according to Eq. (7). The variation of $V(x,y)$ and R with x increment is shown in Fig. 4.

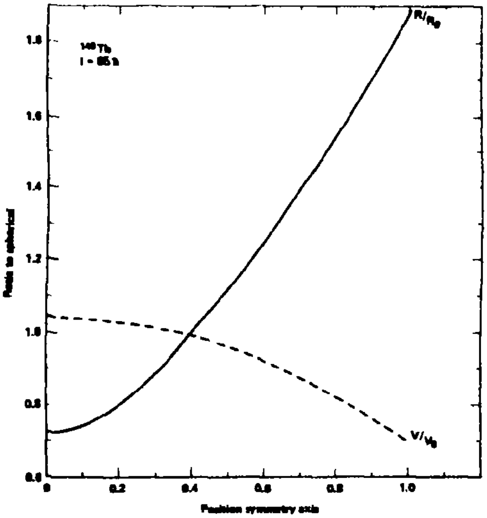

FIG. 4. Comparison of radius (R/R_0) and potential (V/V_0) ratios of a deformed nucleus to those of a spherical nucleus (ordinate) versus position along the symmetry axis (abscissa). The nucleus considered is ^{149}Tb at 85 ħ.

The T_l values were then averaged over the surface area by

$$T_l(\epsilon) = \sum_{A_i} \frac{\Delta A_i}{A_i} \delta_l \,, \tag{16}$$

where $\delta_l = 1$ if $l \le l_{max}$ and $\delta_l = 0$ if $l > l_{max}$.

A comparison between the T_l values calculated for α particles for a spherical and deformed nucleus via the SCO and optical models is shown in Fig. 2. A comparison of SCO model results for neutrons and protons for spherical and deformed nuclei is shown in Fig. 3.

In Fig. 2, the deformed optical potential result is shown for α particles. The optical model radii were modified by multiplying the radius parameter r_0 by R_{max}/R_0 for each value of l. The diffuseness parameter was left unchanged. The ratio of Coulomb barriers at the tip of the deformed nucleus to that at a point on the ground state spherical nucleus was computed via Eq. (7) and the charge of the optical model was altered to reproduce the calculated barrier height at the enlarged radius. This represents an extreme estimate of the effect to be expected from deformation. Comparisons between results using the SCO and optical model results might therefore give some indication as to whether results are very sensitive to the exact manner in which the T_l are calculated, or only to the fact that the deformation is included in some fashion in determining the T_l cutoff point. The point which needs to be accepted with caution is that we have computed the maximum T_l based on the deformation of the emitting nucleus. The question as to whether emission of the particle at large l can couple to a residual nucleus of considerably lower deformation has been begged. We feel that this question may best be answered by experiment.

The averaged SCO results may be seen to give T_l values which begin to cut off at lower l than the nondeformed SCO. This reflects the lower radii at the "waist" of the highly deformed nuclei. The averaged SCO results are generally lower than the extreme deformed optical results, as expected. Yet it will be shown that results are not terribly sensitive as to which T_l set is used. The relative shapes and Coulomb barriers, as a function of angular momenta, are summarized in Figs. 5 and 6 for the two sample systems (^{58}Ni and ^{149}Tb) considered in this work. It may be seen in these figures that the superdeformed region is entered quite rapidly once the transition to prolate shapes is made, and that a considerable reaction cross section exists for superdeformed nuclei with nonzero fission barriers.

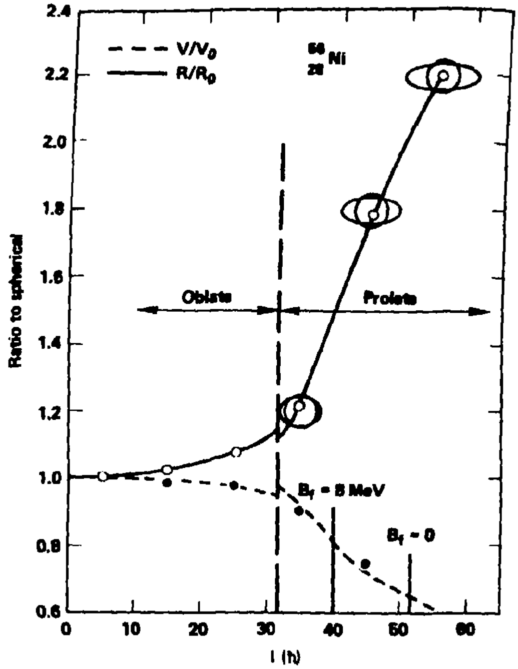

FIG. 5. Ratio to spherical of radii and potential for ^{58}Ni nuclei versus angular momenta (abscissa). Values of R and V were calculated as shown by the small open and closed points. The shapes of some of the nuclei are shown superimposed on a spherical projection of the same volume nucleus. The oblate and prolate/triaxial regions are indicated, as well as the values of the angular momentum for which the RLD predicts fission barriers of zero and 8 MeV.

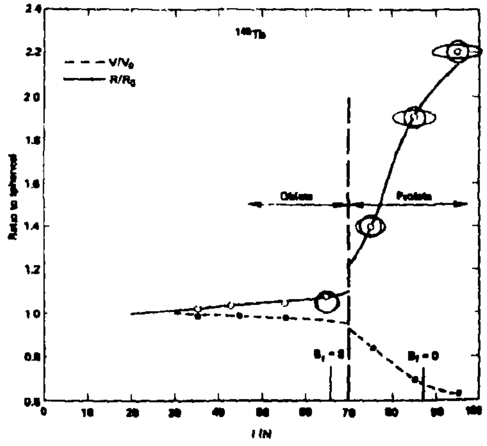

FIG. 6. As in Fig. 5 for the ^{149}Tb nucleus.

IV. RESULTS OF STATISTICAL DECAY CALCULATIONS FOR DEFORMED VERSUS SPHERICAL NUCLEI

A. E-J plane space comparisons

In order to appreciate results to be presented, it is worthwhile to examine the *E*–*J* space of the residual nuclei. This is shown in Figs. 7 and 8. The point of compound nucleus excitation is shown for each test system ($^{149}_{65}$Tb and $^{56}_{28}$Ni) for a single value of the entrance channel angular momentum, in each case for a superdeformed nucleus. Residual *U* and *J* are considered for α particle emission. There is an energy required for α binding energy and for the Coulomb barrier. For each value of the kinetic energy, there is a maximum *l* value which the outgoing particle can use to couple to lower (or higher) angular momenta. The loci of $l_{\max}$, coupled antiparallel with *I*, are shown in Figs. 7 and 8, for the α kinetic energy range from the Coulomb barrier to 39 MeV. The loci are shown for the SCO model for both spherical and for deformed nuclei. The results of this figure using optical model T_l values are essentially identical.

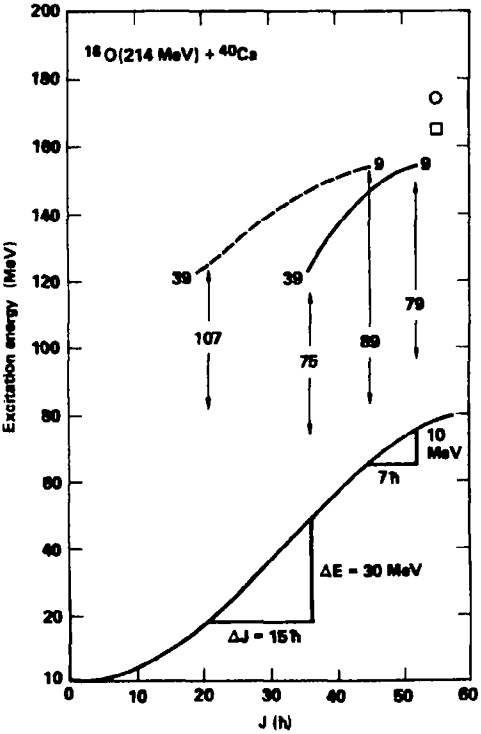

FIG. 7. The *E* vs *J* space for ^{56}Ni. The yrast line is from RLD. The circle represents the compound nucleus excitation (ordinate) for 214 MeV ^{16}O on ^{40}Ca, for a 55 ℏ partial wave in the entrance channel. The solid line represents the loci of minimum residual angular momenta and excitation when 9 to 39 MeV α particles are emitted, with T_l from the spherical SCO model. The dashed curve represents the same for the deformed SCO model. The effective excitation energies above the yrast line are indicated for several kinetic energies. Triangles below the yrast lines contrast the differences in minimum and maximum residual excitations for the two sets (spherical and deformed) of calculations.

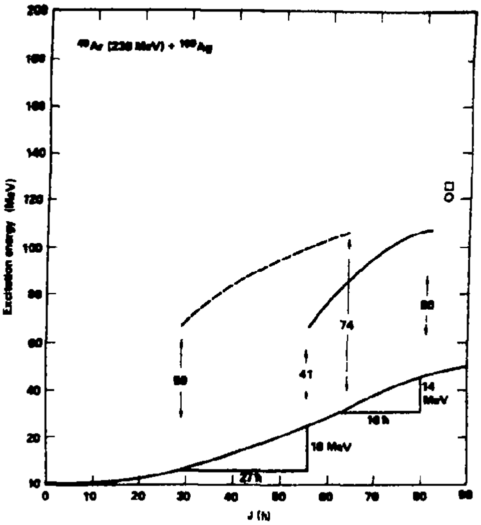

FIG. 8. As in Fig. 7, for the ^{149}Tb nucleus formed by 236-MeV ^{40}Ar + ^{109}Ag.

The consequences of using deformed versus spherical transmission coefficients may be understood qualitatively by comparing the loci of minimum residual angular momenta for the two cases. The *n* and *p* channels (cf. Fig. 3) do not show such a large change in T_l between spherical and deformed nuclei as do α particles, and deformation effects on fission rates are already explicitly considered via the RLD saddle point energy. The main change in deexcitation properties results from the enhanced α emission due to the much higher effective residual excitation accessible when deformation effects persist, as reflected in the nuclear level density [Eq. (1)].

For the ^{149}Tb case, the residual nucleus excitation range for emission of 9 to 39 MeV α particles is 60 to 41 MeV for spherical T_l, and 74 to 59 MeV when deformed T_l are considered. Since these energies enter the level densities (1) in an exponential way, a huge effect is to be expected. As a manyfold enhancement of α decay results, we refer to this as an α-decay amplification.

An even more dramatic, qualitatively different result obtains for the ^{56}Ni compound nucleus. Here the steepness of the yrast line permits the result that as the α-emission energy from the deformed nucleus goes from 8 to 39 MeV, the accessible residual excitation actually increases from 89 to 107 MeV. In contrast the excitation range decreases for the spherical case from 79 to 75 MeV over the same range. From these numbers one can see that α decay is enhanced over results at lower angular momenta using spherical T_l, but should be *very* strongly enhanced for deformed versus spherical T_l at high angular momenta. In this example an additional 30 MeV of residual excitation is available to the deformed system. The very large effect here might be called a superamplification from superdeformed nuclei. We turn next to quantitative results of these qualitative considerations.

B. Decay branching ratios and amplification factors

Branching ratios for first chance particle emission and for total fission deexcitation are summarized in Fig. 9 for ^{149}Tb and in Fig. 10 for ^{56}Ni. Results are compared for both spherical and deformed T_l.

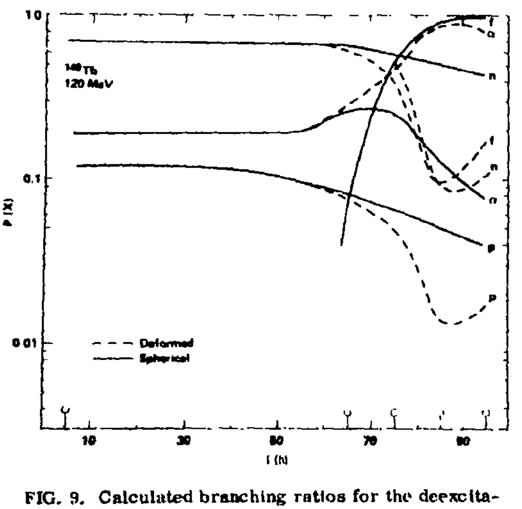

FIG. 9. Calculated branching ratios for the deexcitation of ^{149}Tb at 120 MeV of excitation versus initial angular momentum. The open circles near the abscissa represent the values of compound nucleus angular momenta for which results were calculated. Smooth curves were drawn through these points. Fission curves (f) represent total fission, whereas n, p, and α curves represent only first chance emission. Curves are for spherical (solid lines) and deformed nuclei (dashed lines).

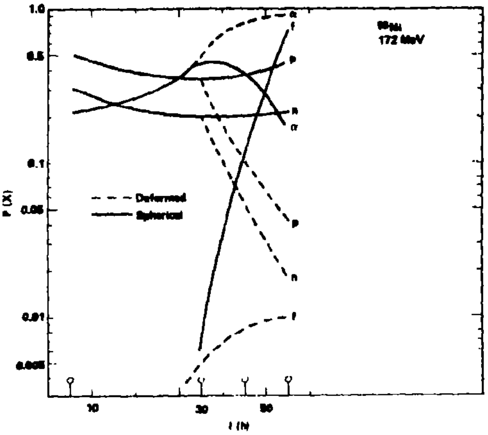

FIG. 10. As in Fig. 9 for decay of ^{56}Ni.

In each case, nucleon emission exceeds other decay modes at low angular momenta. Consider the "spherical" T_l emission as angular momentum increases. The α-emission probability initially increases with increasing I, as expected. Perhaps less anticipated is the subsequent decrease as angular momentum increases further. It may be seen that this is a consequence of the rapid increase in the fission width with increasing I. It illustrates as a side point the importance of including the fission channel in HI deexcitation calculations, e.g., to compute residual angular momentum distributions. At higher excitations, fission completely dominates the deexcitation. There should be no evaporation residues according to the spherical T_l calculation.

Next compare the branching ratios when T_l of deformed nuclei are used (the SCO model results were used in preparing Figs. 9 and 10). In both these cases the additional phase space available for α decay causes a huge increase in its emission rate such that this mode totally dominates the decay process; total fission drops to around 1% for ^{56}Ni at 55 $\hbar$, down from 74%, and to 10% for ^{149}Tb, down from 97%. The full liquid drop fission barriers were used in all the calculations, and $a_f/a_\nu = 1.0$ was assumed.

Numerical results of Figs. 9 and 10, with additional information, are summarized in Tables II and III. Results for ^{149}Tb deexcitation are summarized in Table IV for T_l computed with the optical model as described in Sec. IV.[3] In particular it is of interest to compute the α-decay amplification factor due to deformation. This amplification effect may be expressed in a quantitative fashion if it is assumed that the change in n and p decay rates due to using T_l charac-

TABLE II. Summary of $^{56}_{28}$Ni decay at 172-MeV excitation using sharp cutoff transmission coefficients for spherical and deformed nuclei.

	Spherical				Deformed			
$I(\hbar)$	5	35	45	55	5	35	45	55
$\sigma(I)$	4.1	26.7	34.2	41.7	4.1	26.7	34.2	41.7
f_n [a]	0.30	0.21	0.20	0.22		0.21	0.056	0.018
f_p	0.50	0.36	0.37	0.44		0.33	0.11	0.042
f_α	0.21	0.43	0.40	0.17		0.46	0.82	0.93
f_f [b]	0	0.0036	0.035	0.17		0.003	0.007	0.009
$f_{f\ \text{total}}$ [c]		0.006	0.094	0.74		0.005	0.008	0.010
Amplification for α decay						1.13	6.8	65
ϵ_α [d] (mp) (MeV)	13	18	20	13	13	19	28	36
$\langle J_\alpha \rangle$ $(\hbar)$ [e]		28.5	36.4	49.7		26.2	25.4	24.5
$\langle J_n \rangle$ $(\hbar)$ [f]	5.6	32.7	43.1	53.7	5.6	32.5	41.5	51.9

[a] Fraction decay by neutron channel.

[b] First chance fission fraction.

[c] Total fission fraction with multiple emission.

[d] Most probable kinetic energy.

[e] Average final angular momentum following emission of one α particle.

[f] Average final angular momentum following emission of one neutron.

teristic of deformed rather than spherical nuclei is negligible. One can then represent the fractional α decay from spherical or deformed nuclei as f^s_α and f^d_α, respectively; the rates of α decay as R^s_α and R^d_α, and the rate of n, p, and fission decay by R. The fraction of α decay from spherical and deformed nuclei can then be represented as

$$f^i_\alpha = \frac{R^i_\alpha}{R^i_\alpha + R}, \quad i = s \text{ or } d. \tag{17}$$

Then the amplification factor A, defined as the ratio of α-decay rates for the deformed versus spherical system is given by

TABLE III. Summary of $^{149}_{65}$Tb decay at 120-MeV excitation using transmission coefficients for spherical and deformed nuclei calculated in the sharp cutoff approximation. Liquid drop barriers were used.

	Spherical					Deformed			
$I(\hbar)$	5	65	75	85	95	65	75	85	95
$\sigma(I)$	1.43	17.0	19.6	22.2	24.8	17.0	19.6	22.2	24.8
f_n	0.70	0.65	0.59	0.50	0.44	0.62	0.43	0.090	0.11
f_p	0.12	0.079	0.064	0.06	0.040	0.075	0.051	0.0135	0.017
f_α	0.18	0.26	0.25	0.13	0.077	0.29	0.45	0.86	0.80
f_f	0	0.009	0.097	0.320	0.44	0.009	0.064	0.040	0.074
f^{total}_f	0	0.058	0.52	0.93	0.97	0.049	0.52	0.090	0.165
Amplification for α decay						1.16	2.4	41	48
ϵ_α(mp)	18	18	18	18	18	21	21	23	24
$\langle J_\alpha \rangle$ $(\hbar)$	7.0	58.8	68.0	79.7	97.4	58.4	64.2	56.9	65.6
$\langle J_n \rangle$ $(\hbar)$	5.7	63.4	73.4	84.3	93.8	63.2	73.0	83.1	92.8

TABLE IV. Summary of $^{149}_{65}$Tb decay at 120-MeV excitation using transmission coefficients for spherical and deformed nuclei calculated using the nuclear optical model.

	5 [a]	65	75	85	95	55	65	75	85	95
I (ħ)			Spherical nuclei					Deformed nuclei		
$\sigma(I)$ (mb)	1.43	17.0	19.6	22.2	24.8	14.4	17.0	19.6	22.2	24.8
f_n	0.63	0.49	0.33	0.23	0.19	0.53	0.45	0.21	0.037	0.052
f_p	0.11	0.065	0.040	0.025	0.020	0.084	0.065	0.033	0.009	0.015
f_α	0.25	0.31	0.23	0.10	0.058	0.35	0.37	0.62	0.92	0.88
f_f [b]	0.0014	0.139	0.40	0.64	0.73	0.038	0.12	0.14	0.032	0.056
$f_{f\ \mathrm{total}}$	0.0014	0.56	0.87	0.97	0.99	0.17	0.46	0.49	0.38	0.47
Amplification for α decay							1.3	7.4	104	120
ϵ_α(mp) (MeV)	21	21	21	20	19	21	21	21	23	24
J_α [c] (mp) (ħ)		59	68	80	92	49	58	63	63	67

[a] This column is characteristic of spherical nuclei at zero angular momentum; column 6 for 55 ħ should be approximately characteristic of spherical systems as well, since deformations are not large at 55 ħ.

[b] Liquid drop fission barriers reduced by 40% were used with $a_f/a_v = 1.03$.

[c] Most probable residual angular momentum following the emission of one α particle.

$$A = \frac{R_\alpha^d}{R_\alpha^s}\,\frac{f_\alpha^d(1-f_\alpha^s)}{f_\alpha^s(1-f_\alpha^d)}\,. \tag{18}$$

It may be seen in Table II (and III) that the α amplification for ^{56}Ni (^{149}Tb) starts to become significant above 35 ħ (65 ħ), exceeding a factor of 65 (40) by 55 ħ (85 ħ).

The phase space increase may be seen to cause such an amplification in α-emission rate that the predicted fission fate of the high I compound nuclei is highly suppressed. Furthermore, following the dominant α-decay mode in the first step of deexcitation, the residual nuclei are at very much lower J than would have been expected. This means that nuclei formed near (and perhaps beyond) the barrier disappearance point could α decay to a nuclide having a significant fission barrier. This nuclide might in turn undergo fission or deexcite to an ER by further particle emission.

Some comparisons might be made at this point to some relevant but probably inconclusive experimental results. Vigdor *et al.* have measured the ER excitation function for ^{16}O + ^{40}Ca at energies up to and including 214 MeV.[14] They report ER yields implying $l_{\mathrm{lim}} \approx 54$ ħ, with an estimate of $\leqslant 4\%$ fusion cross section being attributable to fission. This is consistent with the calculation using T_l for deformed nuclei, inconsistent with the result using spherical T_l values.

Additional comparisons are to be found in experimental results published by Britt *et al.*[15,16] One set involves the system ^{40}Ar + ^{109}Ag at incident ^{40}Ar energies of 169 to 337 MeV (lab).[15] Evaporation residue and fissionlike excitation functions were measured. The sum of fissionlike and ER cross sections imply fusion angular momenta beyond the liquid drop limit. This could have several interpretations. One of these is that the fissionlike yields measured (and reported to have some ambiguity of interpretation) are from a noncompound mechanism. Another is that the predicted initial α decay takes place, leaving a residual nucleus with finite fission barrier which then undergoes fission. This is very speculative on such weak evidence of course; more direct experiments are suggested.

Additional evidence—still not conclusive—is to be found in yet another result of Britt *et al.*[16] reproduced as Fig. 11 herein, with the kind permission of the authors. In Fig. 11 the $l_{\max}$ determined from γ-ray multiplicity measurements is shown as a function of excitation energy. The systems included are ^{40}Ar + ^{122}Sn, ^{86}Kr + ^{76}Ge. This curve seems to flatten at around 65 ħ. This could result from the fission limit, except that the σ_{ER} results imply yet higher l limits. (The latter also include points from ^{86}Kr and Cu and ^{40}Ar + ^{121}Sb.) This may also be seen in the $l_{\max}$ from ER measurements in Fig. 11. They clearly extend beyond the survival range expected for I, when deexcitation fission competition is included in the decay calculation. Both sets of results are consistent with deexcitation by α amplification at high angular momenta. The residual angular momenta are seen to limit around 65 ħ following

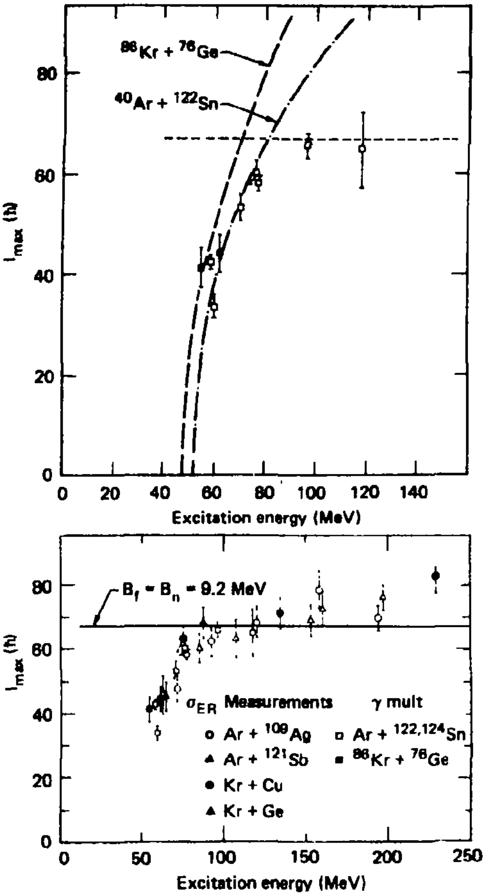

FIG. 11. Maximum angular momenta deduced from γ-ray multiplicity and evaporation residue excitation function measurements. These curves are reproduced from Ref. 15 with permission of the authors. This figure is discussed in Sec. IV.

emission of the first α particle (Tables III and IV) from the superdeformed region consistent with the γ-ray multiplicity results. This would also stabilize the residues against subsequent fission, consistent with the higher l_{max} deduced from the σ_{max} results (since the latter are inferred from the cross sections surviving fission deexcitation, whereas the γ-ray multiplicity is a measure of the actual angular momentum of the evaporation residues following particle emission).

Another result consistent with the change in deexcitation to be expected by consideration of deformation is found in product yield measurements. Plasil *et al.*[17] (and others as well) have found in measuring the nuclidic yields of evaporation residues, that more charged particles are apparently emitted than are predicted by ordinary evaporation theory. As Figs. 9 and 10 indicate, the superdeformation should enhance the charged particle emission substantially. This represents yet another observation consistent with the proposed new mechanism, yet still is inconclusive.

C. Kinetic energy spectra

The influence of superdeformation on the α kinetic energy spectra is shown in Tables II and IV and in Figs. 12 and 13. The most probable energies are summarized in the tables. For ^{149}Tb, spherical T_l calculations predict a reasonably invariant most probable kinetic energy with l, whereas deformed T_l values predict some increase at the higher l values. For the case of ^{56}Ni, the spherical T_l results predict most probable kinetic energies of 13–20 MeV for $l = 0$ to 45 ħ, then decreasing to 13 MeV. For the deformed case, the most probable energy continued to increase monotonically to 36 MeV at 55 ħ. This represents nearly a factor of 2 increase in peak kinetic energy over the spherical result. It may be seen in Fig. 13 that the superamplified α particles from ^{56}Ni are expected to extend with reasonable cross sections to energies up to 60 MeV from a purely evaporation, nonprecompound mechanism. This represents a rather surprising change from results of all earlier calculations for which spherical T_l values were used.

The high energy α particles are predicted to set in rather sharply in ^{56}Ni beyond 35 ħ as the superdeformed region is populated (see also Figs. 5 and 16). Vigdor *et al.*[14] measured ER angular distributions at a series of bombarding energies. They observe a bulge and extension to relatively high recoil angles at bombarding energies where the predicted superdeformed region is populated. Kinematic calculations show that the emission of one or two energetic α particles or a ^{8}Be emission could well explain this bulge. The deformed nucleus calculation would predict large ^{8}Be emission cross sections, whereas the spherical case would not. A coincidence experiment is presently being pursued by the Livermore heavy ion group to measure the spectrum of the light particles emitted in coincidence with the heavy fragment.

D. Multiple particle emission patterns

It is of some interest to see how the total deexcitation pattern varies for the various T_l inputs under discussion. Figures 14–17 indicate the particle emission cross sections for deexcitation by the n, p, α, and fission channels for a ^{56}Ni compound nucleus initially populated at 55ħ. The results are shown using SCO T_l values for

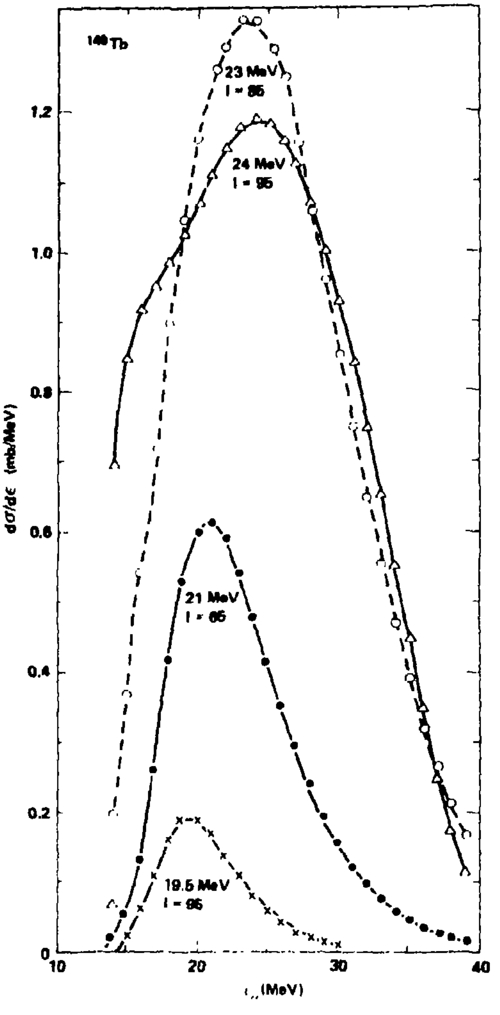

FIG. 12. First chance α spectra calculated for decay of ^{148}Tb for different entrance channel angular momenta. The most probable kinetic energies are shown by each spectrum. All spectra are computed using T_l for deformed nuclei using the SCO model, except for the lower curve for $l = 95\ \hbar$, for which spherical nucleus T_l (SCO) were used.

both spherical and deformed nuclei. Results are also shown using optical model T_l for spherical nuclei, and the optical model tip emission assumption for deformed nuclei. In Fig. 18 a result is shown at 45 $\hbar$ using the SCO for deformed nuclei.

For both sets of spherical T_l (SCO Fig. 14 and optical model Fig. 15) very similar deexcitation patterns are predicted. In each case, first chance fission is comparable to all other decay channels, as is α decay. In both cases fission accounts for 75% of the deexcitation when multiple particle emission is considered. Nucleon emission is in both cases the dominant overall nonfission mode of deexcitation.

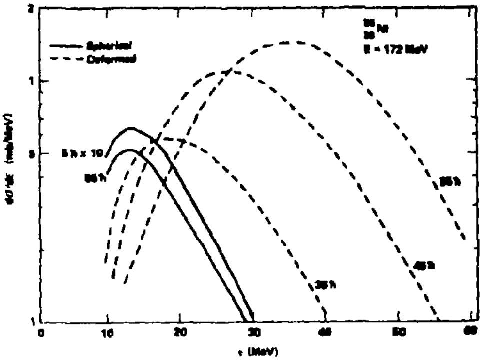

FIG. 13. First chance α spectra calculated for decay of ^{56}Ni at 172-MeV excitation using spherical and deformed SCO transmission coefficients. The compound nucleus angular momentum for which each spectrum was computed is shown by the spectrum.

Next consider the two sets of results (Figs. 16 and 17) using deformed T_l values. In each case total fission falls to below 0.5% for first chance fission, and below 1% over all channels, independent of the T_l set used. In each case, first chance α decay accounts for at least 95% of the decay. And in each case, second and third alpha particles are of the same order of magnitude as nucleon emission. The similarities of results from the two sets of calculations with deformed nuclei again emphasize that the α-decay amplification is not strongly dependent on how the T_l are calculated, but rather result from recognizing that the deformation and large radii do exist, and that this allows some high partial waves for the emitted α particles. Figure 18 shows that the α amplification and fission suppression persist strongly at 45 $\hbar$, as is shown by reference to Table II.

V. CONCLUSIONS

We have stressed that the RLD which seems to properly and semiquantitatively predict the disappearance of the fission barrier with high angular momenta, also predicts very high equilibrium deformations for rotating nuclei in their ground states. We further show that consideration of this deformation makes substantial changes in transmission coefficients for particle emission, particularly for α particles.

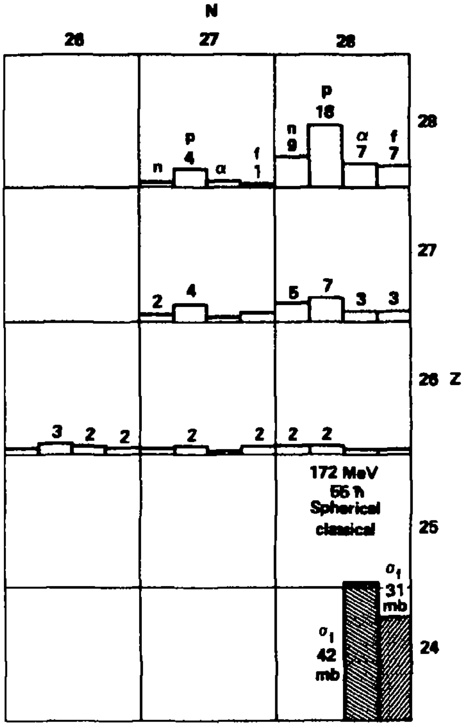

FIG. 14. Representation of branching for multiple particle emission from ^{58}Ni at 55 ħ and 172 MeV of excitation. The particle reaction cross section of 42 mb divides as shown by the histograms. Approximate emission cross sections from various nuclides are shown above the histograms. The shaded bar graphs of the lower portion of the figure indicate that 31 of 42 mb are calculated as going into fission for this example, using T_l calculated with SCO for spherical nuclei.

Since residual excitation has an exponential influence on level densities, the predicted change in T_l values for deformed nuclei leads to a strong amplification of α decay. This in turn can totally alter the predicted course of deexcitation at high angular momenta from almost pure fission to almost pure α decay, and can quantitatively alter the cross section and J distribution of ER products surviving fission.

Many of the predicted changes expected in statistical deexcitation due to including deformation effects are consistent with a broad body of experimental evidence. Many experiments which might more directly verify the model predictions are implicitly suggested, and some of these are underway. Since the deformation of nuclei at high angular momenta has been verified by a huge body of evidence, it is not so reasonable to ask for a justification of the model presented herein, as for all the previous calculations using T_l computed for spherical nuclei. While decay channels for larger clusters have not yet been explicitly included in these model calculations, it is clear that heavier cluster emission will also be very much favored by the phase space considerations

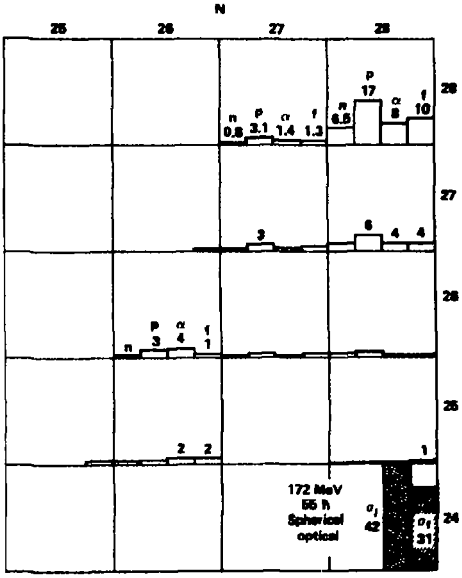

FIG. 15. As in Fig. 14, but calculated using T_l calculated with the spherical optical model.

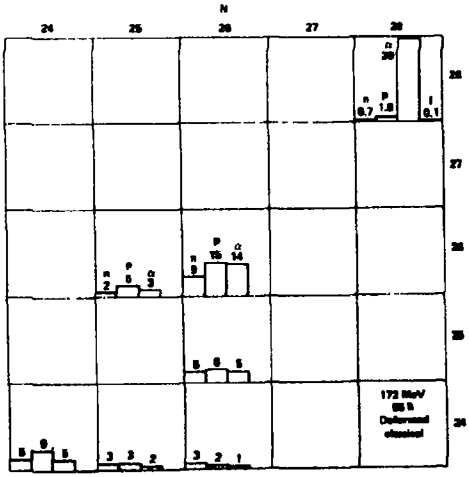

FIG. 16. As in Fig. 14, but calculated using SCO deformed nucleus T_l values. Note the virtual disappearance of fission and dominance of α emission.

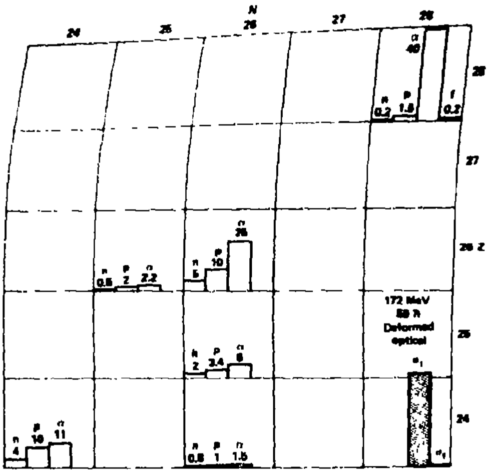

FIG. 17. As in Fig. 14, but calculated using the T_l resulting from the deformed optical model.

of superdeformed nucleus decay. Thus, a more general new mechanism of cluster emission amplification is predicted.

As there is evidence for a rapid energy equilibration in the entrance channel of heavy ion reactions,[18] the phase space considerations stressed herein may also prove valuable in addressing deexcitation of interacting heavy ion target systems prior to the attainment of equilibrium, i.e., for various possible precompound modes of deexcitation. We feel that this model, and the predicted new mechanism of α-decay amplification from superdeformed nuclei, merits further testing and exploration, as it is potentially important in understanding HI reaction mechanisms.

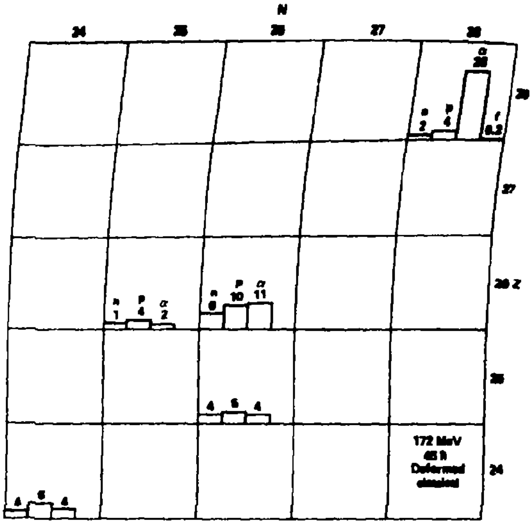

FIG. 18. As in Fig. 14 but for a ^{56}Ni compound nucleus at 45 ħ.

ACKNOWLEDGMENTS

The author has appreciated valuable discussions with Dr. W. J. Swiatecki and Dr. M. Beckerman during the course of this work. Help with the calculations by Mr. T. T. Komoto is greatly appreciated as well.

---

[1] M. Blann, A. Mignerey, and W. Scobel, Nukleonika 21, 335 (1976).

[2] M. Blann and M. Beckerman, Nukleonika 23, 1 (1978).

[3] M. Beckerman and M. Blann, Phys. Rev. Lett. 42, 156 (1979); M. Blann, Phys. Lett. 88B, 5 (1979).

[4] S. Cohen, F. Plasil, and W. J. Swiatecki, Ann. Phys. (N.Y.) 82, 557 (1974); Lawrence-Berkeley Laboratory Report No. LBL 1502 (1972).

[5] M. Beckerman and M. Blann, University of Rochester Report No. UR-NSRL-135A (unpublished).

[6] M. Blann and F. Plasil, Report No. COO-3494-10 (unpublished); M. Blann, Report No. COO-3494-29 (unpublished). F. Plasil, Oak Ridge National Laboratory ORNL/TM-6054 (unpublished).

[7] W. D. Myers and W. J. Swiatecki, Ark. Fys. 36, 343 (1967).

[8] V. F. Weisskopf, Phys. Rev. 53, 295 (1937).

[9] T. D. Thomas, Phys. Rev. 116, 703 (1959).

[10] D. W. Lang, Nucl. Phys. 77, 545 (1966).

[11] M. Blann, Phys. Rev. 157, 860 (1967).

[12] D. Wilmore and P. E. Hodgson, Nucl. Phys. 55, 673 (1964); F. G. Perey and B. Buck, *ibid.* 32, 353 (1962); F. G. Perey, Phys. Rev. 131, 745 (1963); G. R. Satchler, Nucl. Phys. 70, 177 (1965).

[13] W. J. Swiatecki (private communication).

[14] S. E. Vigdor *et al.*, Phys. Rev. C 20, 2147 (1979).

[15] H. C. Britt *et al.*, Phys. Rev. C 13, 1483 (1976).

[16] H. C. Britt *et al.*, Phys. Rev. Lett. 39, 1458 (1977).

[17] F. Plasil *et al.*, Phys. Rev. C 18, 2603 (1978); F. Pühlhofer *et al.*, Phys. Rev. C 16, 1010 (1977).

[18] M. Blann *et al.*, Phys. Rev. C 19, 1288 (1979); F. Plasil *et al.*, Phys. Rev. Lett. 40, 1164 (1978).

PHYSICAL REVIEW C VOLUME 21, NUMBER 5 MAY 1980

Target residues from the reaction of 8 GeV ^{20}Ne with ^{181}Ta and ^{197}Au

D. J. Morrissey, W. Loveland,* M. de Saint Simon,† and G. T. Seaborg
Lawrence Berkeley Laboratory, University of California, Berkeley, California 94720

(Received 14 June 1979)

The cross sections for the production of 99 different target fragments from reactions of 8.0 GeV ^{20}Ne with ^{181}Ta and ^{197}Au were measured. The target fragment radioactivities were measured by off-line gamma-ray spectroscopy. Details of the measurement as well as the calculation of the independent isotopic production cross sections and the integrated mass yields are given. Comparisons of these data to previously reported data for proton induced reactions show that the target residue production cross sections scale with the total projectile kinetic energy, not velocity. The total cross section for residue production indicates that some products result from collisions with significant overlap of the central densities of the two nuclei, in contrast to results obtained with low mass targets. Comparisons of the data with a Monte Carlo cascade calculation and an abrasion-ablation calculation verify the importance of ground state correlations of the neutrons and protons on the fragmentation isotopic cross sections.

NUCLEAR REACTIONS ^{181}Ta(^{20}Ne, spallation), ^{197}Au (^{20}Ne, spallation), $E = 8.0$ GeV; measured radionuclide production cross sections and isobaric yields; comparison to proton induced spallation of ^{181}Ta and ^{197}Au; comparison to abrasion-ablation and Monte Carlo cascade models for residue production; Ge(Li) spectroscopy, radioanalytical mass and charge distributions; relativistic heavy ion nuclear reactions.

I. INTRODUCTION

Currently the highest kinetic energy available for the laboratory study of heavy ion induced reactions is 2.1*A* GeV.[1] Reactions induced by these heavy ions were thought to hold great promise for the observation of many exotic collective phenomena not observable in proton induced reactions.[2] A large body of data now exists from the study of 25 GeV ^{12}C ions interacting with targets ranging from hydrogen to uranium.[3-8] Both radiochemical and on-line counter techniques have been successfully employed in these studies. The experimental observables have been found to separate into three major categories according to the rapidity of the products: projectile fragments tightly correlated with the beam rapidity[3] from large impact parameter peripheral collisions, light products, such as protons, alphas, and pi mesons, moving with intermediate rapidities and showing evidence of thermalization[4] from central collisions, and large target residues that do not escape the target materials and thus have low rapidities[5-8] from peripheral and near central collisions. These studies have shown no evidence for the predicted exotic phenomena that spurred them on, and now the suggestion is that still higher energies are necessary for the observation of such phenomena.[9] Such energies are not presently available; however, many facets of the reaction mechanisms at the currently available heavy ion energies are not well known. And so, attention is now being turned toward understanding the relationship of heavy ion reactions at a few GeV per nucleon to the well explored fields of low energy heavy ion reactions and relativistic proton induced reactions.

The previous studies of relativistic heavy ion (RHI) induced reactions have shown the production, in large amounts, of "heavy" target residues.[5-8,10] These residues range in mass from essentially that of the target down to a few selected light nuclei observable with the radiochemical methods employed, e.g., ^{7}Be, ^{24}Na. The residue production cross section has been found to be ~70% of the geometrical reaction cross section for both low and high mass targets. An important aspect of these studies will be to determine if the number of central collisions, i.e., collisions resulting in the complete annihilation of the target nucleus, is dependent on the projectile velocity. Due to the extreme velocity of the RHI projectiles the total reaction cross section does not vary significantly over this energy region. Up to the present only one study of target residue production in RHI reactions at an energy lower than 2.1 GeV/nucleon has been reported,[11] that for the reaction of 280 MeV/nucleon ^{14}N with copper. However, only relative yields for target residue products were reported for this system. Thus, the assumption of straight line trajectories that forms the basis of the fireball[4] and firestreak[12] models remains untested over a wide energy region of its assumed applicability.[4,13]

A second question of basic interest in RHI induced reactions is how such reactions compare with relativistic proton induced reactions. It has become common when discussing the projectile-like and intermediate products from RHI induced reactions to describe the experiments in terms of the projectile velocity (i.e., 2.1 GeV/nucleon, etc.).[3,4,13] Relative yield measurements by Cumming *et al.*[5,11] have shown that the target residue isotope production cross sections for the interaction of 3.9 GeV ^{14}N and 25.2 GeV ^{12}C with copper targets compare most favorably with isotope production cross sections from reactions induced by protons of equivalent total kinetic energy. However, another study by Cumming *et al.*[10] showed that the target residue isotope production cross sections from the reaction of 80 GeV ^{40}Ar with copper also compared very favorably with those from the reaction of 28 GeV protons with copper. In view of the observed difference between 25 GeV ^{12}C induced reactions on high mass (Ref. 8) (^{238}U) and low mass (Ref. 5) (Cu) targets and the larger volume to surface ratio in high mass targets, we felt it was important to study the relative importance of projectile velocity and total kinetic energy in RHI interactions with heavy nuclei. A particularly good target nucleus for this comparison is ^{181}Ta. Previous studies of the reaction of 340 MeV protons with ^{181}Ta by Nervik and Seaborg,[14] and the reaction of 5.7 GeV protons with ^{181}Ta by Grover[15] showed large differences between the product mass distributions for these two reactions (see Fig. 1). The comparison between the mass distribution from the reaction of 8 GeV ^{20}Ne with ^{181}Ta with these distributions should allow differentiation between the velocity and total energy dependence of RHI induced reactions with a ^{181}Ta target.

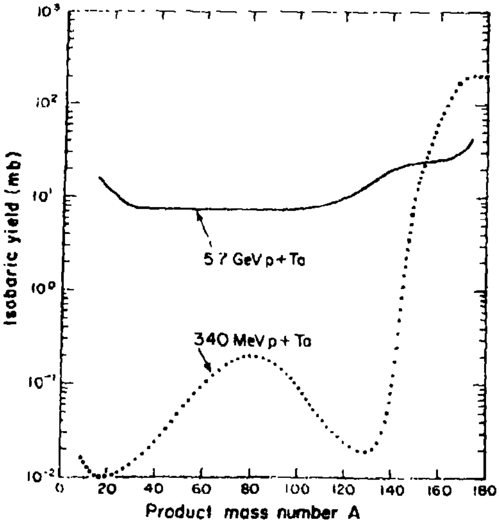

FIG. 1. Large differences in the product mass yield $\sigma(A)$ obtained as a function of incident proton energy are shown by the work of Nervik and Seaborg (Ref. 14) (340 MeV) and Grover (Ref. 15) (5.7 GeV).

In this paper we report the study of the reaction of 400 MeV/A ^{20}Ne projectiles (8.0 GeV total kinetic energy) with ^{181}Ta and ^{197}Au targets. As discussed above the choice of this projectile and energy allows us to make the comparison with the earlier studies of the proton induced reactions and also allows us to study the interaction of RHI at an energy lower than the previously reported studies. In Sec. II we present the details of the experimental procedure used in this work and in Sec. III we present the results. The results are compared to abrasion-ablation model calculations[16-18] from which we are able to draw conclusions on the ability to observe the predicted ground state correlations of nuclear matter.[18,19] Part of this work was published previously in a preliminary form.[20]

II. EXPERIMENTAL

A. Cross section measurement

As in previously reported radioanalytical measurements of the target residue products from RHI reactions,[6-8,14] these products are observed through gamma-ray spectroscopy of the target materials subsequent to the irradiation. A detailed review of the reproducibility and sources of error in such measurements has been made by Orth *et al.*,[21] and the considerations of Cumming[22] for proton induced reactions certainly apply here. The ^{197}Au targets consisted of two foils, 12.5 cm by 10.2 cm each, with thicknesses of 49.3 mg/cm^2 and 242.0 mg/cm^2, each surrounded by 6.6 mg/cm^2 Al catcher foils. These two targets, differing by a factor of approximately 5 in thickness, allowed us to evaluate the contribution from secondary particle induced reactions to the RHI reaction products. The ^{181}Ta target consisted of a single foil, 13.6 cm by 10.2 cm, of thickness 154.1 mg/cm^2, also surrounded by 6.6 mg/cm^2 Al foils. An external beam of ^{20}Ne was delivered to a 1 m air gap by the BEVALAC at the Lawrence Berkeley Laboratory. Two separate irradiations were performed, one of the gold foils and one of the tantalum foil. The average beam fluxes and durations of these irradiations are given in Table I. The beam intensity was monitored on a pulse by pulse basis with an Ar-CO$_2$ ion chamber (80% Ar, 20% CO$_2$) that was developed and calibrated for use at

TABLE I. Irradiation conditions, target thickness, and approximate values of the beam degradation by the target foils.

Target	Foil thickness (mg/cm^2)	Average flux (particles/min)	Length of bombardment (min)	Energy loss in target MeV (percent)	Nuclear reaction attenuation ϕ'/ϕ
Au-I	49.3	7.19×10^9	612	<15(<0.2)	~0.9994
Au-II	242.0			<60(<0.7)	~0.997
Ta	154.1	1.64×10^{10}	247	<40(<0.5)	~0.998

the BEVALAC facility.[23] In order to check the reproducibility of the ion chamber calibration and to facilitate absolute normalization of the calibration, aluminum monitor foils were irradiated in series with the primary target foils and the ionization chamber. These aluminum monitor foils were 20.3 mg/cm^2 thick and were surrounded by 5.6 mg/cm^2 Mylar catcher foils. A schematic diagram of the arrangement of the target foils, monitor foils, and ion chamber in the air gap irradiation facility is shown in Fig. 2. The beam enters from the left and passes through the ion chamber, the primary target materials, and then through the Al monitor foil. Approximately 30 m ahead of the targets the beam is bent ~5° clockwise and approximately 2 m ahead of the targets it is bent ~10° further clockwise to remove contaminants from the beam.

Approximate values for the energy loss of the 8.0 GeV ^{20}Ne beam in each of the primary targets are given in Table I. The ^{20}Ne^{10+} ions are near minimum ionizing at this energy[24] and approximate values of the energy loss can be obtained from the Bethe formula.[24,25] As one can see from Table I the energy lost by the ^{20}Ne beam in all the targets is quite small and for the purposes of this work can be ignored. Estimates of the attenuation of the beam by nuclear reactions are also given in Table I. These values of ϕ'/ϕ, the emergent flux divided by the incident flux, were calculated from the total reaction cross sections of Heckman *et al.*[26] Again, these estimates show that the beam is only slightly degraded by passage through the target materials, and therefore nuclear attenuation of the beam also can be ignored.

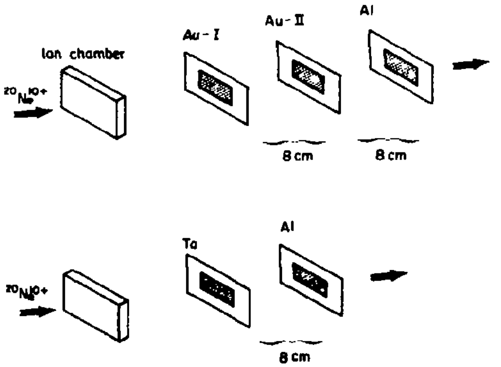

FIG. 2. A schematic diagram of the target arrangement used in the bombardment with ^{20}Ne projectiles at the BEVALAC is shown.

Gamma-ray spectrometric measurements were made with a single Ge(Li) detector on ~5–10 cm^2 area pieces cut from the irradiated target foils, which were centered on the beam spot. These measurements began 20 min after the end of bombardment (EOB) for the gold targets, 14 h after EOB for the tantalum target, and continued essentially uninterrupted for ~40 d. The irradiated target materials provided strong radioactive sources which allowed measurement in low geometries where gamma-gamma summing losses had been measured to be small.[27] The identification of the product radioactivities and the calculation of their production cross sections has been described in detail elsewhere[27] and will only be described briefly here. After the gamma-ray measurements were completed the spectra were analyzed with an automatic version of SAMPO.[27,28] This code performs a peak find, a peak fit, and then an energy calculation and a full energy peak efficiency correction for each spectrum. Decay curves are then automatically constructed with the sorting routine TAU1. These decay curves are then identified interactively by their gamma-ray energy and half-life with the code TAU2. Multiple assignments are made to the decay curves at this point if the assignment based on the combination of half-life and gamma-ray energy is ambiguous. Off line, all the assignments are screened to remove multiple assignments and ensure that the gamma rays for each isotope were observed with the proper abundances (i.e., no transition stronger than the observed transition can be missing). The cross section is then calculated from the statistically weighted average of the observed gamma-ray transitions for each isotope.

TABLE II. Cross sections (in mb) observed in this work.

Nuclide	Type ^{a}	Target 49.3 mg/cm^2 Au	 242 mg/cm^2 Au	 154 mg/cm^2 Ta
^{28}Mg	*C*	7.5 ± 2.0		5.7 ± 0.75
^{42}K	*I*		9.04 ± 0.9	7.4 ± 0.7
^{44}Sc	*I*		1.9 ± 1.5	
^{44}Sc^{m}	*I*			3.2 ± 0.3
^{46}Sc	*I*		9.3 ± 0.9	14.8 ± 3.2
^{48}Sc	*I*	2.8 ± 0.4	2.8 ± 0.1	2.4 ± 0.4
^{48}V	*C*		3.1 ± 0.3	3.1 ± 0.3
^{51}Cr	*C*			6.9 ± 2.8
^{52}Mn	*C*			1.66 ± 0.11
^{54}Mn	*I*		9.0 ± 1.3	10.6 ± 1.4
^{56}Co	*I*		5.7 ± 1.4	8.7 ± 0.9
^{59}Fe	*C*		2.8 ± 0.2	2.3 ± 0.2
^{65}Zn	*C*		7.0 ± 1.4	
^{72}Ga	*C*			3.1 ± 1.8
^{72}As	*C*	6.7 ± 0.6	7.6 ± 1.2	
^{73}Se	*C*	3.6 ± 2.0		1.8 ± 0.1
^{74}As	*I*	5.2 ± 0.9		4.8 ± 0.8
^{75}Se	*C*		6.4 ± 0.4	7.7 ± 6.1
^{76}As	*I*			9.0 ± 0.9
^{77}Br	*C*		4.3 ± 0.8	
^{82}Rb^{m}	*I*		6.4 ± 0.8	
^{83}Rb	*C*		8.5 ± 1.2	8.7 ± 0.9
^{84}Rb	*I*	3.8 ± 1.4	4.1 ± 0.3	2.2 ± 0.3
^{86}Y	*C*			8.1 ± 1.8
^{86}Zr	*C*			4.8 ± 1.1
^{87}Y	*C*		8.1 ± 0.8	
^{87}Y^{m}	*C*			9.8 ± 0.9
^{88}Y	*C*		5.4 ± 0.5	
^{88}Zr	*C*		7.7 ± 0.7	8.7 ± 0.5
^{89}Zr	*C*	8.3 ± 0.8	9.2 ± 0.9	8.4 ± 0.8
^{90}Nb	*C*	7.2 ± 0.7	6.7 ± 0.7	
^{92}Nb^{m}	*I*		1.6 ± 0.1	
^{93}Mo^{m}	*I*	4.1 ± 0.4		2.9 ± 0.2
^{95}Tc	*C*		9.0 ± 1.2	10.4 ± 1.3
^{96}Tc	*I*		3.6 ± 1.3	2.8 ± 0.3
^{97}Ru	*C*	4.0 ± 0.3	4.4 ± 0.3	5.8 ± 0.4
^{101}Rh^{m}	*C*	6.1 ± 0.8		
^{104}Ag	*C*		5.8 ± 3.0	
^{106}Ag^{m}	*I*		3.9 ± 1.2	
^{110}In^{m}	*C*			7.4 ± 1.8
^{111}In	*C*		5.3 ± 0.3	6.5 ± 0.4
^{118}Sb^{m}	*I*		8.6 ± 0.8	
^{119}Te^{m}	*C*			2.1 ± 0.4
^{121}Te	*C*	8.5 ± 0.5		12.2 ± 0.7
^{121}I	*C*		10.6 ± 2.3	
^{122}Xe	*C*		7.2 ± 0.7	10.1 ± 0.7
^{123}I	*C*	9.1 ± 1.1	8.2 ± 0.7	8.1 ± 0.9
^{125}Xe	*C*			8.6 ± 0.8
^{127}Xe	*C*		7.7 ± 0.7	11.5 ± 1.1
^{128}Ba	*C*			11.5 ± 2.4
^{129}Cs	*C*			16.7 ± 0.9
^{131}Ba	*C*	20.4 ± 1.0	19.5 ± 2.4	21.8 ± 5.1
^{135}Ce	*C*			14.7 ± 0.6
^{138}Pr^{m}	*I*		2.5 ± 0.9	
^{145}Eu	*C*	16.1 ± 1.6		29.8 ± 3.6
^{146}Eu	*C*			21.4 ± 2.1
^{147}Eu	*C*		22.7 ± 3.8	17.0 ± 4.6
^{147}Gd	*C*			24.5 ± 2.5
^{149}Gd	*C*	12.1 ± 2.4		12.7 ± 8.6

TABLE II. (*Continued.*)

Nuclide	Type[a]	Target 49.3 mg/cm^2 Au	242 mg/cm^2 Au	154 mg/cm^2 Ta
^{150}Tb[a]	*C*		4.7 ± 0.8	
^{151}Tb	*C*		10.9 ± 7.3	21.0 ± 16.0
^{152}Tb	*C*	13.6 ± 6.3	12.0 ± 6.1	36.6 ± 7.5
^{153}Tb	*C*			15.9 ± 5.3
^{153}Dy	*C*			9.7 ± 2.1
^{155}Tb	*C*			6.8 ± 0.6
^{155}Dy	*C*	13.6 ± 1.4	12.2 ± 1.2	
^{157}Dy	*C*			28.3 ± 1.9
^{160}Er	*C*	9.0 ± 3.8	12.3 ± 2.9	19.4 ± 3.1
^{161}Er	*C*	36.0 ± 3.6	30.8 ± 1.7	38.0 ± 22.0
^{165}Tm	*C*			41.0 + 16.0
^{166}Yb	*C*	29.9 ± 4.1	28.6 ± 2.9	63.0 ± 6.2
^{167}Tm	*C*	17.0 ± 6.7	15.4 ± 4.9	33.0 ± 1.3
^{169}Yb	*C*		7.4 ± 2.2	
^{169}Lu	*C*		29.1 ± 2.1	36.0 ± 11.0
^{170}Lu	*C*		27.9 ± 2.1	57.3 ± 1.1
^{170}Hf	*C*	16.5 ± 8.1		36.4 ± 7.2
^{171}Lu	*C*	19.0 ± 1.9	26.2 ± 5.0	46.7 ± 2.1
^{171}Hf	*C*			41.4 ± 3.0
^{172}Lu	*I*			11.1 ± 1.4
^{172}Hf	*C*		24.5 ± 2.7	
^{173}Hf	*C*			32.8 ± 8.6
^{173}Ta	*C*	12.0 ± 7.0	9.0 ± 2.8	
^{174}Ta	*C*		21.1 ± 6.4	
^{175}Hf	*C*			59.5 ± 5.7
^{176}Ta	*C*	52.0 ± 25.0	53.0 ± 20.0	55.4 ± 2.2
^{177}Ta	*C*			16.8 ± 1.7
^{181}Re	*C*	42.4 ± 8.0	39.1 ± 3.8	
^{182}Re	*C*		53.0 ± 18.0	
^{184}Ir	*C*	18.9 ± 7.0	13.0 ± 4.5	
^{185}Ir	*C*	29.2 ± 3.0		
^{187}Ir	*C*		58.0 ± 17.0	
^{188}Ir	*C*	42.6 ± 4.1	41.3 ± 3.6	
^{190}Ir	*I*	5.5 ± 0.9	5.0 ± 0.46	
^{188}Pt	*C*	32.4 ± 3.0	29.8 ± 2.8	
^{191}Pt	*C*		60.6 ± 9.2	
^{191}Au	*C*	31.7 ± 2.8		
^{194}Au	*I*		56.0 ± 3.8	
^{196}Au	*I*	174.0 ± 25.0	181.9 ± 14.4	
^{198}Au	*I*	43.1 ± 3.8	16.6 ± 0.8	

[a] Nuclides are typed *I* or *C* to indicate either independent yield or partial cumulative yield, respectively. This distinction is discussed in the text.

The cross section calculation includes corrections for a nonuniform beam level during the irradiation. During the bombardment of the ^{197}Au targets 2.4% of the beam was delivered in the first 175 min, and the second 97.6% was delivered in the final 416 min, with a 21 min interruption in between. A constant beam level was maintained during the bombardment of the ^{181}Ta target. The production cross sections for all the activities observed in this work are given in Table II. The cross sections and their uncertainties due to counting statistics are given in mb for each nuclide observed in each of the three targets. The nuclide type, *I* or *C*, indicates whether the cross section is an independent yield or a partial cumulative yield, respectively. Seventy-three different radioactivities were observed in the two gold targets (35 in the thinner target and 62 in the thicker target which includes those observed in both) and 65 radioactivities were identified as reaction products in the tantalum target. In all, 99 different radioactivities were identified.

The contribution of secondary particle induced reactions to the measured cross sections can be estimated from a comparison of the production cross sections measured with the thin 49.3 mg/

cm^2 ^{197}Au target to those simultaneously measured with the thicker 242.0 mg/cm^2 ^{197}Au target. Cumming *et al.* have previously reported a study of the secondary reaction contributions to the products from the reaction of the 28 GeV protons and 25 GeV ^{12}C ions with copper[5] while Porile *et al.*[43] report the results of a similar study for the interaction of 25 GeV ^{12}C with a silver target. In the study by Cumming *et al.* they found that the secondary contributions to cross sections measured using two targets of total thickness 154 mg/cm^2 and 1158 mg/cm^2 differed by factors that ranged from no contribution to 23% with the proton projectiles (the highest contributions were to near-target products) with the average secondary correction being 1.3%/100 mg/cm^2. (Upper limit estimates of the increase in secondary contributions with the ^{12}C projectiles over the protons ranges from a factor of ~1 to 3 when measured with only the thicker copper target.[5]) Novel arguments were used also by Cumming *et al.* to conclude that secondary contributions for 80 GeV ^{40}Ar projectiles, for all but the lightest products, were proportional to those found from proton reactions.[11] The thin target used in the present study was nearly a factor of 3 thinner than the thinnest targets used in obtaining the previously reported estimates of Cumming *et al.*,[5,11] and secondary contributions in this foil should be negligible (≈ 23%/3 ~ 8%). Porile[43] reported secondary contributions of 2.5–2.8%/100 mg/cm^2 for the reaction of 25 GeV ^{12}C with a silver target which would again suggest negligible corrections be applied to the thin target cross sections.

A simple way to obtain a feeling for the variation and importance of secondary reaction contributions to the cross sections measured with the thicker ^{197}Au foil is to plot the ratio of these measurements to the thin target cross sections versus product mass number. This has been done in Fig. 3 (uncertainties represent one standard deviation), and the values of the ratios are given in Table III for the 24 products observed in both foils. Figure 3 shows that no dramatic variation of the ratio of the measured cross sections can be seen as a function of product mass number. A least squares analysis shows that the linear function $R = 1.044 - 6.0\times10^{-4} A$ gives a slightly better description of the data than a straight line at $R = 1$. This function is shown by the dashed line in Fig. 3. (This function is in good agreement with the value of 1.05 ± 0.03 obtained by Porile *et al.*[43] in a similar treatment of their data.) The statistical F test of the inclusion of the mass number dependence of the ratio yields a value of $F_x = 9.2$, which also indicates that such a dependence may be justified by the data.[29] However, because all the data points (save two) are within one standard deviation of $R = 1$, contributions from secondary reactions to the production cross sections were ignored.

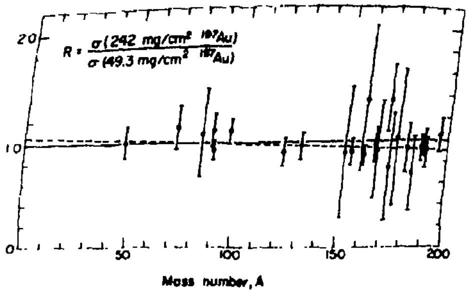

FIG. 3. The ratio of the production cross sections measured with the thick ^{197}Au target to those measured with the thin ^{197}Au are plotted versus the radionuclides' mass number. The solid line at $R = 1$ represents the value of this ratio that would be expected if there was no contribution from secondary particle induced reactions. The dashed curve is discussed in the text.

These results, and this neglect of secondary corrections, do differ somewhat from the previously cited work of Cumming *et al.*[5] and Porile *et al.* who found some significant contribution to near-target activities from secondary induced reactions. However, as Fig. 3 shows, there apparently is no such effect for the reaction of 8.0 GeV

TABLE III. Thick to thin target cross section ratio from the ^{197}Au targets.

Nuclide	Ratio $\frac{\sigma(242.0\ \mathrm{mg/cm^2}\ ^{197}\mathrm{Au})}{\sigma(49.3\ \mathrm{mg/cm^2}\ ^{197}\mathrm{Au})}$
^{48}Sc	1.00 ± 0.15
^{72}As	1.13 ± 0.21
^{84}Rb	1.08 ± 0.41
^{89}Zr	1.11 ± 0.15
^{90}Nb	0.93 ± 0.09
^{97}Ru	1.10 ± 0.11
^{123}I	0.90 ± 0.13
^{131}Ba	0.96 ± 0.13
^{152}Tb	0.88 ± 0.61
^{156}Dy	0.90 ± 0.13
^{160}Er	1.37 ± 0.66
^{161}Er	0.86 ± 0.10
^{166}Yb	0.96 ± 0.16
^{167}Tm	0.91 ± 0.46
^{171}Lu	1.38 ± 0.30
^{173}Ta	0.75 ± 0.50
^{176}Ta	1.02 ± 0.62
^{181}Re	0.92 ± 0.23
^{186}Ir	0.69 ± 0.35
^{189}Ir	0.97 ± 0.13
^{190}Ir	0.91 ± 0.17
^{188}Pt	0.92 ± 0.12
^{196}Au	1.05 ± 0.16

^{20}Ne with gold. Also, some individuals may object to our attempt to evaluate the effect of secondary induced reactions by simultaneously irradiating the thick and thin targets since, in principle, the possibility exists that for at least some of the secondaries, the two targets will act as a single thick target. With respect to this latter point, the difficulty of obtaining experimental time to check such effects already noted as being small, would indicate that further study of these phenomena is not indicated at this stage of our understanding of RHI reactions.

B. Charge and mass distributions

The radioanalytical cross sections, whose measurement was described above, represent post neutron and charged particle evaporation, post "fast" beta decay production cross sections. Thus, in order to obtain true production cross sections one needs to correct radioanalytically measured cross sections for beta decay, when possible, that occurs between the time of their production in the nuclear reaction and the time at which they are detected through their own beta decay. Once corrected, these values of the independent production cross sections can be used to calculate the mass or charge yield, and also to estimate the total cross section for target residue production.

In order to make the correction for precursor decay to each measured cross section and in order to calculate the total isobaric or mass yield, we have used the assumption of Gaussian charge dispersions; that is, the independent yield cross sections can be represented by a histogram that lies along a Gaussian curve, at constant mass number. This is written

$$\sigma(Z,A)=\sigma(A)\left\{[2\Pi s_z^2(A)]^{-1/2}\exp\left[\frac{[Z-Z_p(A)]^2}{-2s_z^2(A)}\right]\right\} \tag{1}$$

with the three parameters: $\sigma(A)$ the total isobaric yield, $s_z(A)$ the Gaussian width parameter, and $Z_p(A)$ the most probable Z value for that isobar. Given the assumption of Gaussian charge dispersions, the beta decay feeding correction factors for cumulative yield isobaric members can be calculated once the centroid and width of the Gaussian are known.

In order to uniquely specify these three variables $\sigma(A)$, $s_p(A)$, and $Z_p(A)$ one would need to measure three independent yield cross sections for each isobar. In fact, the nature of radioanalytical studies such as this one does not, in general, lend itself to the measurement of isobaric members. Rather, a wide assortment of radioactivities are observed which span the entire range of the periodic table that is accessible in the nuclear reaction. As a result relatively few isobaric pairs are observed.[5-8,10,11] A further assumption needs to be introduced in order to apply the Gaussian charge distributions to the measured data. The assumption is that the value of $\sigma(A)$ varies smoothly and slowly as a function of mass number A and is roughly constant within any A range considered when determining $Z_p(A)$ and $S_z(A)$. This assumption is not as severe as the assumption that the production cross sections for RHI reactions follow an exponential Rudstam equation[30] that has been used in the analysis of data from low mass targets by Cumming *et al.*[6,10,11] Another statement of the former, less stringent assumption is that the charge dispersion curves for neighboring isobaric chains should be similar; thus radionuclide yields from a limited mass range can be used to determine a single charge dispersion curve. The two Gaussian parameters that specify the width $s_z(A)$ and the center $Z_p(A)$ of the charge distributions are iteratively fit to the measured data over limited mass regions. The width parameter has been found, in general, to be approximately independent of mass number over small ranges of A. The center of the charge dispersions were adequately represented by linear functions in A, over small ranges of A. The width parameters and the coefficients of the $Z_p(A)$ function are given in Table IV. These parameters should not be considered as absolutes but rather as a consistent set. The values of $S_z(A)$ are uncertain to 0.1 Z

TABLE IV. Charge dispersion parameters.

Mass number range	Target	S_z	$Z_p(A)=a+bA$ a	 b
28–48	Ta, Au	0.5	0.1	0.456
51–59	Ta	0.475	1.2	0.436
54–65	Au	0.475	1.1	0.436
72–76	Ta	1.2	−2.3	0.48
72–77	Au	0.8	−3.8	0.51
83–89	Ta	0.8	−4.7	0.51
82–89	Au	1.2	−4.7	0.51
93–97	Ta	0.8	−4.7	0.51
90–111	Au	0.45	5.95	0.391
110–139	Ta	0.8	4.76	0.40
118–131	Au	0.45	4.76	0.40
145–149	Ta	0.40	13.7	0.337
138–155	Au	0.45	13.7	0.337
151–157	Ta	0.3	13.7	0.337
160–166	Ta	0.45	−1.4	0.43
160–169	Au	0.45	−1.4	0.43
169–177	Ta	0.60	−1.4	0.43
169–176	Au	0.60	−1.4	0.43
181–191	Au	0.45	13.07	0.349

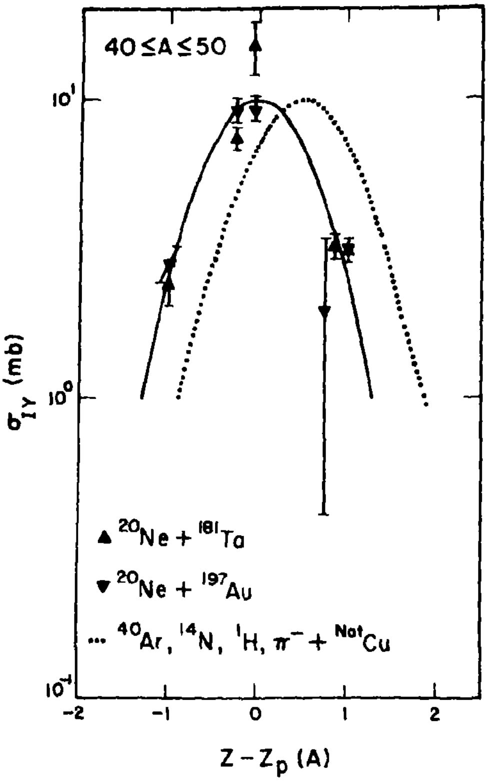

FIG. 4. A comparison of the charge dispersion curve for the low mass products $40 \le A \le 50$ observed in this work (solid curve) with the charge dispersion curve previously measured for products in the same mass range produced in the reaction of 80 GeV ^{40}Ar, 3.9 GeV ^{14}N, 3.9 GeV ^{1}H, and 1.57 GeV π—with copper (Refs. 10, 11, 31) (dotted curve). The latter curve has been arbitrarily normalized to convert the reported values of fractional chain yields into isotopic production cross sections.

units while the values of $Z_p(A)$ are believed to be known, in general, to ~$0.3S_z(A)$.

The results of this procedure can be seen in Figs. 4 and 5, where the calculated isotopic production cross sections are plotted versus $Z - Z_p(A)$, the distance in Z units from the center of the isobaric charge dispersion. Also shown in Figs. 4 and 5 are the Gaussian curves that are specified by Eq. (1) with the parameters in Table IV appropriately calculated for histogram distributions in Z. The data from the reactions of ^{20}Ne with ^{181}Ta and ^{197}Au are found to lie along the same charge dispersion curves for low mass products, but show some differences in mass regions where fission fragments are present. An interesting feature of this comparison is that, as shown in

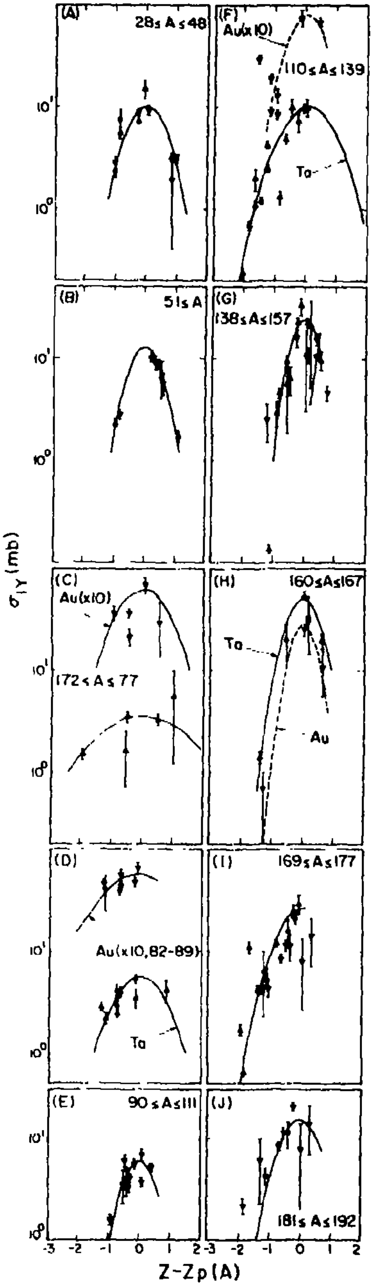

FIG. 5. The charge dispersion curves obtained in this work are shown as a function of mass region of the products. The parameters that describe the center and width of the individual curves are given in Table IV. As in Fig. 4 data from the ^{181}Ta target are shown by the triangles (Δ) and data from the ^{197}Au target are shown by the inverted triangles (∇).

Fig. 4, the low mass products from this reaction have the same charge dispersion width as the same products from RHI reactions with copper targets,[10,11,31] but in this work as shifted towards the neutron excessive side of the valley of beta stability. Such comparisons will be discussed in the next section.

The value of the isobaric or mass yield is obtained for each data point through the assumption of Gaussian charge dispersions and the set of parameters in Table IV. The measured production cross sections are adjusted to remove precursor feeding, where necessary, and a set of independent yield production cross sections, seen in Figs. 4 and 5, is generated. The mass yield is then calculated as the independent yield cross section divided by the fractional chain yield. The mass yields obtained in this manner are shown as the solid circular points in Figs. 6 and 7. When measured independent yields for two isobars exist, the resulting mass yields were averaged to give the final mass yield. The uncertainties in each solid circular point in Figs. 6 and 7 simply represent the fractional uncertainty in the measured isotopic cross section leading to that point and not any systematic uncertainty introduced by the charge dispersion analysis. The magnitude of this latter uncertainty depends on the extent to which each independent radionuclide yield is well described by a Gaussian charge dispersion (see Fig. 5), the position of the measured radionuclide Z relative to Z_p (points far from Z_p have large uncertainties compared to points near Z_p), uncertainties in $Z_p(A)$ and $S_z(A)$, and the extent to which the mass yield curve is a slow, smoothly varying function of A whose general magnitude and shape is to be determined [rapid variations of $\sigma(A)$ are poorly determined by our procedure]. Using a propagation of errors treatment, one estimates that on the average, individual points in the mass yield curve have a systematic uncertainty of $\sim\pm 30\%$ which would be added quadratically to the error in the measured value. However the average mass yield within each small A region used in the charge dispersion analysis is known to $\pm 15\%$ in general, assuming a constant or slowly varying of $\sigma(A)$ over each small mass region.

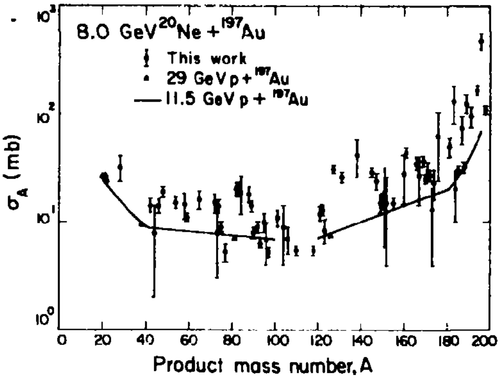

FIG. 7. Similar to Fig. 6, the mass distribution obtained for the reaction of 8 GeV ^{20}Ne with ^{197}Au target is plotted. For comparison, the data of Kaufman *et al.* (Ref. 32) for the reaction of 11.5 GeV protons (represented as a solid line) with ^{197}Au and the data of Hudis *et al.* (Ref. 33) for the reaction of 29 GeV protons with ^{197}Au (solid triangles) are also shown.

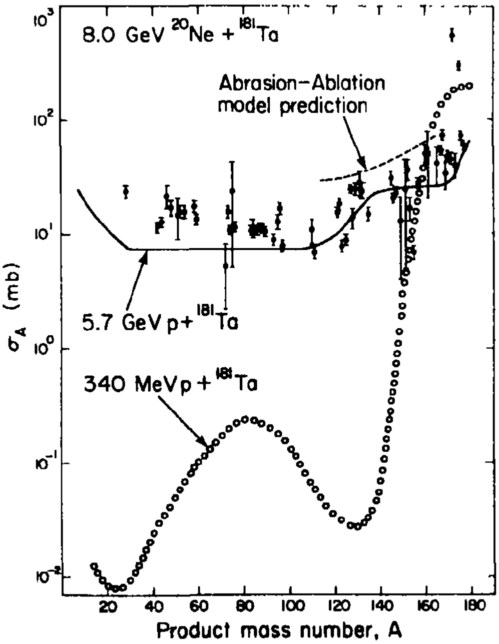

FIG. 6. The target residue mass distribution, $\sigma(A)$ obtained for the reaction of relativistic projectiles with a ^{181}Ta target is shown. For comparison the data presented in Fig. 1 are also reproduced.

III. RESULTS AND DISCUSSION

It is convenient to divide the presentation of the results into two parts. In the first part the mass distribution results are presented and discussed in terms of their implications for limiting fragmentation and their relation to the total reaction cross section. In the second part comparisons of the predictions of different models of RHI reactions are compared to the detailed isotopic production cross sections for near target residues. These comparisons will shed light on the question of correlations of neutrons and protons in the nuclear ground state.

A. Mass yield results

Comparison of the mass distribution from the reaction of 8.0 GeV ^{20}Ne with ^{181}Ta with the previous studies of proton induced reactions,[14,15] seen in Fig. 6, shows the striking agreement of the RHI results with those from proton induced reactions of the (approximately) equivalent total projectile kinetic energy. The fact that the results from the ^{20}Ne induced reaction are close in absolute value to those from the proton induced reaction, instead of being approximately twice as large according to the factorization hypothesis, may be due to changes in decay scheme information during the intervening years. This agreement is confirmed by the comparison of the ^{20}Ne + ^{197}Au mass distribution with the results of Kaufman *et al.*[32] for the reaction of 11.5 GeV protons with ^{197}Au and the sparser results of Hudis *et al.*[33] for gaseous products from the reaction of 29 GeV protons with ^{197}Au. This comparison can be seen in Fig. 7. Although no complete study of the reaction of 400 MeV protons with ^{197}Au exists, the mass distribution is expected to be similar to that obtained with ^{181}Ta targets.[34]

The agreement of the ^{20}Ne + ^{181}Ta and ^{197}Au mass distributions with those produced by high energy protons might be viewed as a manifestation of limiting fragmentation, as the studies with copper targets have been viewed.[10] This process whose origins stem from high energy physics[35] has been extensively invoked and verified in studies of projectile fragments in RHI ractions.[26,36] The fact that the general features of the mass distributions from the reaction of 8.0 GeV ^{20}Ne and 29 GeV protons with ^{197}Au are so similar, even though differing widely in projectile energy, would also appear to lend support to the limiting fragmentation hypothesis. However, similarity of these final distribution of products does not necessitate similarity of the primary excited systems, as suggested in Ref. 10 from the study of copper fragmentation. On the contrary, Morrissey *et al.*[37] have shown that strongly divergent distributions of primary products and excitation energies can, in fact, lead to essentially the same final product distributions for light fragmenting nuclei when the excitation energies are large. This can be attributed to the dominant effect of the deexcitation process (when the primary product excitation energies are high) on the distribution of the final product cross sections in the same way as the momentum distributions of projectile fragments were shown to be dominated by the Fermi momentum.[38] However, these results should be recognized as indicating that little, if any change can be expected in the mass distribution if the projectile energy is increased from 8.0 GeV to 25 GeV.

It is important to note, however, that other properties of the target fragments, such as their momenta and angular distributions, may not be invariant over this projectile energy range. In fact, there is evidence[48] that the target fragment recoil properties change significantly when comparing the reaction of 8.0 GeV ^{20}Ne and 25 GeV ^{12}C with tantalum.

Integration of the mass yield curves over mass number gives the cross section for the production of target residues. We have chosen to integrate these curves over the interval from mass number 40 to the mass of the target. We have chosen a lower limit of 40 mass units for several reasons: (a) the multiplicity of fragments with masses smaller than ~40 is unknown, that is, these products may arise from interactions where another heavy fragment also survives. This certainly is true for fragments such as protons and ^{4}He, where the number of such fragments per event is much greater than one[4]; and (b) because in studies such as this one very little data exist for these low mass products.

The results of this integration are contained in Table V. (A correction was made in each case for fission events using the results of Katcoff and Hudis.[49]) The total cross sections for the production of heavy target residues from ^{181}Ta and ^{197}Au were found to be 2.6 ± 0.4 b and 2.9 ± 0.5 b, respectively. For comparison we have included two calculations of the total reaction cross section in Table V. The hard sphere calculation refers to the overlap form of the sharp sphere model where

TABLE V. Total cross section comparison.

	Experimental large fragment cross section (b)	Calculated cross section (b)	
		hard sphere	soft sphere
^{20}Ne + ^{181}Ta	2.6 ± 0.4	3.64	3.47
^{20}Ne + ^{197}Au	2.9 ± 0.5	3.80	3.59

the total reaction cross section is written[39]

$$\sigma_R = \pi r_0^2 (A_T^{1/3} + A_p^{1/3} - b_{Tp})^2 . \qquad (2)$$

We have taken the parameters r_0 and b_{Tp} to be 1.37 fm and 0.51 fm, respectively, from the work of Heckman *et al.* on projectile fragmentation.[28] The soft sphere calculations are those of Karol which were developed to take into account both the diffuse nuclear surface and the variation of the nucleon-nucleon cross section with energy.[40] The comparison of the hard sphere calculations with our measured heavy fragment cross sections show that approximately 74% of the reaction cross section gives rise to these products. The soft sphere calculation would indicate that these products represent approximately 78% of the reaction cross section.

A current working hypothesis is that target residues are produced in peripheral reactions.[17-19] An estimate of the impact parameter range that gives rise to these products can be made from the fraction of the total reaction cross section that they represent. Thus, 75% of the hard sphere reaction cross section would lie between the impact parameter range of $0.5\,(R_T + R_p) \le b \le (R_T + R_p)$. This indicates that heavy residues are created in collisions where the center of the projectile lies inside the radius of the target nucleus. This situation is significantly different from the reaction of ^{40}Ar with ^{nat}Cu where no target residues were inferred to arise from such central collisions.[10]

B. Comparisons with reaction model calculations

At present there are two models of the collision process that occur in RHI reactions that have been used to calculate isotopic and mass yield cross sections. They are a microscopic intranuclear cascade model of Yariv and Fraenkel[41] and the macroscopic abrasion-ablation model.[16-19] The predictions of these reaction models for the fragmentation of 213 MeV per nucleon ^{40}Ar has shown that correlations in the yields of the highly excited primary reaction products are "washed out" or obscured by the deexcitation process which yields the final product mass distributions in both calculations.[37,42] A comparison of these two calculations has also been made for the target residues produced in the reaction of 25 GeV ^{12}C with ^{nat}Ag.[42,43] In this latter comparison, as with the comparison for ^{40}Ar, the mass yield curve was well reproduced by both calculations. However, unlike the ^{40}Ar fragmentation calculations, the isotopic production cross sections from the two calculations were not at all similar. The Monte Carlo cascade calculation consistently overestimated the width of the isotopic distributions while the abrasion-ablation calculation[42] was in reasonable agreement with the data. Therefore, it is interesting to see if the disagreement between the two models increases as the mass number of the fragmenting nucleus is increased.

The collision of the RHI projectile with the target nucleus is treated as a two step process in the Monte Carlo cascade calculation, a fast step with cascading collisions of nucleons from one reaction partner inside the nucleus of the other partner, and a slow statistical evaporation step deexciting the primary fragments after the fast cascading nucleons have escaped or have been captured by the primary fragments. The calculation is made using an extension of the intranucleon cascade code[44] VEGAS for proton induced reactions which has been modified to treat two colliding nuclei.[41] The calculations were performed with step function density distributions for both nuclei and without refraction and reflection at the nuclear boundaries for the cascading particles. Fermi motion was included in the projectile as well as in the target nucleus. An infinite rearrangement time was assumed for the time necessary for the nucleus to respond to the removal of nucleons from the Fermi sea by the fast cascade. Meson production and cascades were included via the ISOBAR model.[45] The impact parameter for each collision was selected at random, and the final production cross sections were integrated over impact parameter.

The primary fragments from the fast cascade are subsequently individually deexcited using a version of the Dostrovsky, Fraenkel, and Friedlander statistical model Monte Carlo calculations.[41,46] The excitation energy of each fragment was obtained from the fast cascade code. The absolute value of mass distribution of the final products, i.e., after statistical evaporation, from the reaction of 8 GeV ^{20}Ne with ^{181}Ta is shown in Fig. 8 by the histograms. For clarity the calculated values of the mass yield have been averaged into 5 amu wide bins. The uncertainties shown reflect the uncertainties in the statistics of the calculations and not the uncertainties in the averages.

For comparison with the calculations the measured mass yield results for this system are shown by the dashed curve in Fig. 8. This curve was drawn smoothly through the data points of Fig. 6 by eye. Several features of the comparison with the cascade calculation are worth noting: (a) the absolute normalization of the cross section for the production of heavy products is approximately correct, but is ~25% too large on the average. (b) The *general* shape of the residue distribution is also approximately correct in the region above

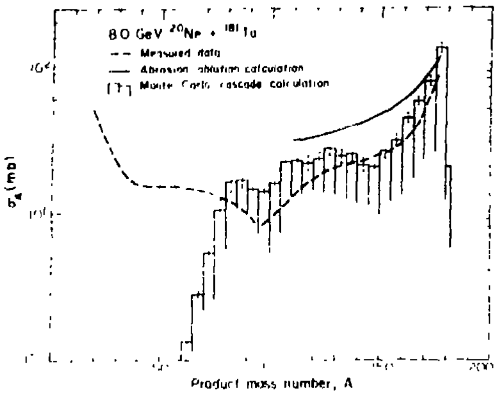

FIG. 8. A comparison of the mass yield curve measured in this work (dashed) with the predictions of the Monte Carlo cascade model (Ref. 41) (histogram) and with the predictions of the abrasion-ablation model (Ref. 42) (solid curve).

mass number 100. However, below mass number 100 the data and the calculation diverge. The cascade-evaporation calculation does not predict the production of nuclei with mass numbers less than 80 in significant amounts.

In the abrasion-ablation view of the collision of the RHI with a target nucleus[16-18] the two nuclei are taken to be hard spheres which move on straight line trajectories. Those nucleons that lie in the region of overlap of the two nuclei are sheared off in the abrasion (or fast) stage of the collision. The spectator fragments of the target (and projectile) which consist of the nucleons that were outside the region of overlap are then assigned an excitation energy that is proportional to their excess surface area. The neutron to proton ratio of the removed nucleons is taken to be equal to that of the target (or projectile) and the variance in the ratio is calculated from the zero point quantum vibrations of the giant dipole resonance (GDR).[18] The oscillator spring constant for this vibration was taken from the liquid droplet model of the GDR.[47] This calculation can be viewed as a leading term approximation to the correlated model of Bondorf *et al.*[19] in which higher order vibrations are included. The primary products are then allowed to deexcite through a statistical evaporation chain with neutron, proton, and alpha emission, and fission competition.[18]

The results of these calculations are shown in Fig. 8 by the solid line. We have arbitrarily cut off the calculations at $A \sim 110$ because products with lower mass numbers arise from collisions in which the hard sphere projectile nucleus drills a cylindrical hole through the target nucleus (removing some 40 nucleons and leaving a "donut-shaped" nucleus with some ~250 MeV of excitation energy due to its increased surface area). It is doubtful whether such nuclei are created and should be considered rather as a region outside the limitations of the original model.[16] As with the cascade calculation the absolute magnitude of the mass yield cross section is overestimated by the abrasion-ablation calculation. However, the cross section is over estimated by a factor of ~2 in the latter case, a much larger discrepancy than that for the former calculation. The *general* shape of the distribution of high mass (i.e., peripheral collision) products is reproduced.

From the comparisons shown in Fig. 8 one can see that both models can predict the general shape of the mass yield curve for high mass products but miss the absolute cross section. Neither calculation can reproduce the mass yields observed for low mass products; that is, neither calculation produces the low mass products observed in the experiment. This discrepancy was hinted at in the study of Porile *et al.*[43] with an Ag target nucleus but is dramatized in the results with the Ta target.

A more stringent test of the two reaction models can be made by comparison of the predicted isotopic production cross sections with the experimental data. A significant difference between the two calculations that is visible in the isotopic cross sections is the amount of correlation of the neutrons and protons that are removed in the fast stage of the reaction. The cascade calculation has no correlation at all as the neutron or proton nature of the cascading nucleons is selected at random in proportion to their number in the nucleus. On the other hand, the nucleons removed in the abrasion-ablation calculations are highly correlated.[18,42] The difference between the final products of the two calculations has been shown to be small for low mass nuclei[37] but should be large in high mass nuclei. Figure 9 shows the calculated final isotopic production cross sections for lutetium and hafnium products from the reaction of 8 GeV ^{20}Ne with ^{181}Ta. The details of these calculations for the abrasion-ablation model are contained in Table VI where the primary product cross sections and excitation energies are shown along with the individual cross sections after deexcitation. The irregularities in the calculated cross sections show the effects of the variation of excitation energy and irregularities in the mass surface on the statistical deexcitation process. The difference in the widths of the two distributions is dramatic, especially for these peripheral collision products. This difference stems from both the initial removal of nucleons in an uncorrelated fashion and the delivery to the target nucleus of large amounts of excitation energy with little

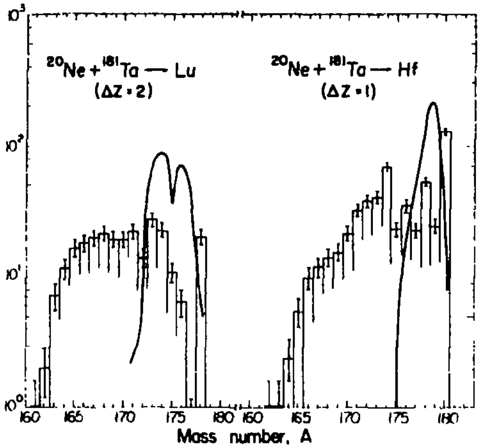

FIG. 9. Calculated final product isotopic distributions .re shown for the reaction of ^{20}Ne+^{181}Ta to produce utetium and hafnium isotopes. The solid line is from he abrasion-ablation model (Ref. 42) and the histograms rom the cascade model (Ref. 41).

emoved mass by the cascade calculation. Comarison of the calculated isotopic distributions hown in Fig. 9 with the experimental data (cf. ither Fig. 5 or Fig. 10) shows that the cascade alculation grossly overestimates the widths of the inal experimental isotopic distributions. This nust be due in part to an assumption in the calcuation that no neutron-proton correlation exists n the nuclear ground state. In fact, neither calulation is able to reproduce the measured isoopic distributions, although the abrasion-ablation alculation does describe modestly well the width f the distribution. In Fig. 10(A) we present the omparison of the abrasion-ablation calculation o the measured isotopic distributions for the ΔZ 1 and 2 products from the ^{20}Ne+^{181}Ta system. ne sees that the calculations fail to reproduce oth the absolute value and the centroid of the istributions. The difference in the absolute nornalization was seen before in the comparisons to he mass yield calculations. The difference beween the centroids of the calculated and meaured distributions may be easily understood.

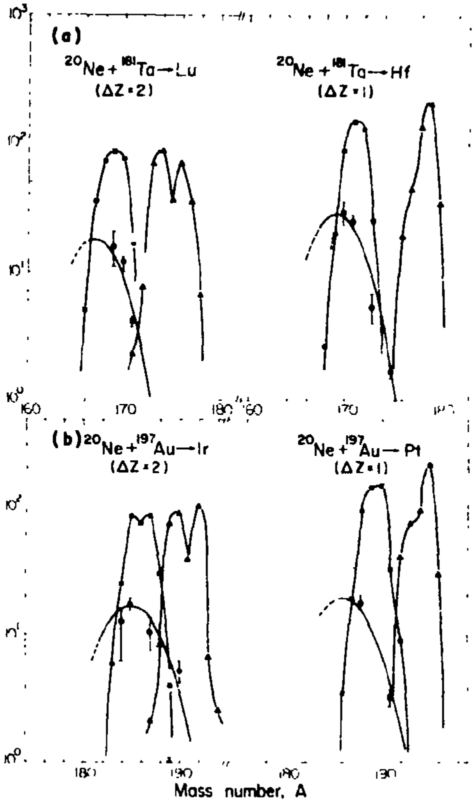

FIG. 10. The isotopic production cross section calculated from the abrasion-ablation model (triangles) are compared to the measured data (solid circles) for for the reaction of ^{20}Ne with ^{181}Ta (a) and ^{197}Au (b). The results calculated for the deexcitation of more highly excited primary products as discussed in the text are shown for both target nuclei (solid squares).

The excitation energies of the primary fragments s predicted in the abrasion-ablation model calulation are merly due to the increased surface rea of the fragments. This excitation energy learly should be viewed as a lower limit to the rue excitation energy of such fragments. Two ery likely sources of addition excitation of the spectator fragments are any frictional forces acting during the abrasion process and scattering of the participant nucleons into the spectator pieces.[17] To explore the magnitude of these excitation energies we have increased the values of the primary fragment excitation energies in 10 MeV steps until the centroids of the calculations match those of the measured products. The results of this process are shown in Fig. 10(a) by the solid squares. The excitation energies of the primary fragments were increased to the values given in Table VI. Extension of these comparisons to products with lower masses was not made because of a lack of data for these products.

In Fig. 10(b) we show the results of a similar analysis of the near-target residues from the reaction of ^{20}Ne and ^{197}Au. The features observed with the products from the ^{181}Ta target are analogously obtained with the slightly larger target nucleus. In order to match the centroids of the iridium and platinum distributions, the excita-

TABLE VI. Statistical deexcitation of abrasion-ablation fragments formed in the ^{22}Ne+^{181}Ta reaction.

Primary products Mass number	Cross section (mb)	Excitation energy (MeV)		Secondary products Cross section (mb) for each isotope of mass number given below								
(a) Hafnium products, excess surface energy only												
			Mass number			180	179	178	177	176	175	174
180	34.2	1.6				34.2						
179	206.3	4.8					206.3					
178	160.1	8.1						135	25			
177	38.0	11.6							19	19		
176	0.9	15.3									0.2	0.7
			Total production			34.2	206.3	135	44	19	0.2	0.7
(b) Hafnium products, surface energy plus 70 MeV												
			Mass number	175	174	173	172	171	170	169	168	174
180	34.2	71.6		0.2	3.5	19.1	10.7					
179	206.3	74.8			0.1	5.5	115.4	77.5	1.4			
178	160.1	78.1					5.1	71.8	73.5	1.7		
177	38.0	81.6						0.4	14.6	18.7	2.1	
176	0.9	85.3								0.2	0.55	0.05
			Total production	0.2	3.6	24.6	131.2	149.7	89.5	20.6	2.65	0.05
(c) Lutetium products, excess surface energy only												
			Mass number	178	177	176	175	174	173	172	171	170
178	6.6	8.1		6.6								
177	104.5	12.0			34.8	69.7						
176	122.7	15.5					36	86.7				
175	70.4	19.3						0.9	69.5			
174	9.8	23.2							0.1	7.6	2.2	
173	0.3	27.3									0.1	0.2
			Total production	6.6	34.8	69.7	36	87.6	69.6	7.6	2.3	0.2
(d) Lutetium products, surface energy plus 60 MeV												
			Mass number	172	171	170	169	168	167	166	165	164
178	6.6	68.1		0.75	5.0	0.7						
177	104.5	72.0		0.1	11.7	69.8	18.7					
176	122.7	75.5			0.05	5.5	66.9	42.9	0.35			
175	70.4	79.3					2.0	29.8	31.7	0.2		
174	9.8	83.2						0.1	3.2	4.8	0.4	
173	0.3	87.3								0.05	0.17	0.01
			Total production	0.85	16.75	76.0	87.6	72.8	35.25	5.05	0.57	0.01

ion energies of the primary fragments had to be aised to ~60 MeV. The difference between this alue and the value of ~70 MeV for the products rom ^{181}Ta may not be significant as it depends on he details of the deexcitation calculation. Thus, e have shown that the near-target residues from he reaction of ^{20}Ne with ^{181}Ta and ^{197}Au are not ccurately described by the Monte Carlo cascade alculation or by the abrasion-ablation calculaion. However, the abrasion-ablation calculation an be brought into closer agreement if the excitaion energies of the primary fragments are raised o ~60 to ~70 MeV.

IV. CONCLUSIONS

This study of the reaction of 8.0 GeV ^{20}Ne with ^{11}Ta and ^{197}Au has shown that several features f the reaction processes occurring in RHI colliions may be explored with high mass targets. ur results show that the total kinetic energy of he projectile is a better parameter for describing e mass yield curve than the projectile velocity r high mass targets. This is a confirmation of e results of Cumming *et al.* obtained with low ass targets.[5,10] The similarity between the mass istributions measured in this work and those reulting from the reaction of 11.5 and 29 GeV proons with a gold target may be viewed as evidence r the onset of limiting fragmentation in these rections, or perhaps the insensitivity of the mass ield curve to some important features of the priary product distributions (due to the obscuring ffect of the deexcitation of the primary products). his deexcitation can obscure large differences the distributions of highly excited primary fragents of the initial encounter.[37] Comparison of e mass yield curve to two reaction models, a onte Carlo intranuclear cascade model,[41] and an brasion-ablation model,[42] shows that neither modl predicts the existence of low mass products, although both generate approximately the correct shape for high mass product distribution. These differences are much more pronounced than those seen in the fragmentation of lighter nuclei.[37,43] Integration of the mass yields for nuclei with $A > \sim 40$ shows that ~74% of the hard sphere reaction cross section[38,39] (~78% for the soft sphere model[40] reaction cross section) is accounted for in such products. This indicates that some collisions in which the central density of the projectile lies inside the hard sphere radius of the target contribute to these products. Therefore, more central collisions give rise to heavy residues in these collisions than with lighter nuclei. Finally, neither reaction model calculation is able to reproduce the near-target isotopic production cross sections for either target. In the case of the cascade calculation this may be due to the lack of correlations of the nucleons in the nuclear ground state. The abrasion-ablation calculation fails to reproduce both the absolute values of the cross sections and the centroids of the isotopic distributions. The former problem may be an indication of the breakdown of the assumption of straight line trajectories in the model, while the latter deficiency has been shown to be due to an underestimation of the excitation energies of the primary fragments.

ACKNOWLEDGMENTS

We would like to acknowledge the efforts of Dr. R. J. Otto in the devleopment of the mass yield analysis code and helpful discussions during the course of this work. We would also like to acknowledge the staff of the BEVALAC where the irradiations were performed, especially W. Everette and F. Lothrop. This work was supported by the U. S. Department of Energy, Nuclear Physics Division, under Contract No. W-7405-ENG-48.

Permanent address: Department of Chemistry, Oregon State University, Corvallis, Oregon 97331.

Permanent address: Laboratoire René Bernas, BP1, 91406 Orsay, France.

I. A. Grunder, W. D. Hartsough, and E. J. Lofgren, Science 174, 1128 (1971).

. Stock and A. M. Poskanzer, Nucl. Part. Phys. 7, 47 (1977).

. E. Greiner, P. J. Lindstrom, H. H. Heckman, Bruce Corfa, and F. S. Bieser, Phys. Rev. Lett. 35, 152 (1975).

. Gosset, H. H. Gutbrod, W. G. Meyer, A. M. Poskanzer, A. Sandoval, R. Stock, and G. D. Westfall, Phys. Rev. C 16, 629 (1977).

. B. Cumming, R. W. Stoenner, and P. E. Haustein, hys. Rev. C 14, 1554 (1976).

[6] C. R. Rudy and N. T. Porile, Phys. Lett. 59B, 240 (1975); N. T. Porile, G. D Cole, and C. R. Rudy, Phys. Rev. C 19, 2288 (1979).

[7] W. Loveland, R. J. Otto, D. J. Morrissey, and G. T. Seaborg, Phys. Lett. 69B, 284 (1977).

[8] W. Loveland, R. J. Otto, D. J. Morrissey, and G. T. Seaborg, Phys. Rev. Lett. 39, 320 (1977).

[9] N. K. Glendenning and Y. Karant, Phys. Rev. Lett. 40, 375 (1978).

[10] J. B. Cumming, P. E. Haustein, T. J. Ruth, and G. J. Virtes, Phys. Rev. C 17, 1632 (1978).

[11] J. B. Cumming, P. E. Haustein, and R. W. Stoenner, Phys. Rev C 10, 739 (1974).

[12] W. D. Myers, Nucl. Phys. A296, 177 (1978).

[13] J. Gosset, J. I. Kapusta, and G. D. Westfall, Phys. Rev. C 18, 844 (1978).

[14] W. E. Nervik and G. T. Seaborg, Phys. Rev. 97, 1092 (1955).

[15] J. R. Grover, Phys. Rev. 126, 1540 (1957).

[16] J. D. Bowman, W. J. Swiatecki, and C. F. Tsang, Lawrence Berkeley Laboratory Report No. LBL-2908, (unpublished); J. Hufner, K. Schafer, and B. Schurman, Phys. Rev. C 12, 1888 (1975).

[17] J. O. Rasmussen, R. Donangelo, and L. F. Oliveira, in *Proceedings of the IPRC Symposium on Macroscopic Features of Heavy Ion Collisions and Pre-equilibrium Processes*, Hakone, 1977 (unpublished); L. F. Oliveira, R. Donangelo, and J. O. Rasmussen, Phys. Rev. C 19, 826 (1979).

[18] D. J. Morrissey, W. R. Marsh, R. J. Otto, W. Loveland, and G. T. Seaborg, Phys. Rev. C 18, 1267 (1978).

[19] J. P. Bondorf, G. Fai, and O. B. Nielsen, Phys. Rev. Lett. 41, 391 (1978); Nucl. Phys. A312, 149 (1978).

[20] D. J. Morrissey, W. Loveland, and G. T. Seaborg, Z. Phys. A289, 123 (1978).

[21] C. J. Orth, H. A. O'Brien, Jr., M. E. Schillaci, B. J. Dropesky, J. E. Cline, E B. Nieschmidt, and R. L. Brodzinski, J. Inorg. Nucl. Chem. 38, 13 (1976).

[22] J. B. Cumming, Annu. Rev. Nucl. Sci. 13, 261 (1963).

[23] W. L. Everette, private communication.

[24] L. C. Northcliffe and R. F. Schilling, Nucl. Data Tables 7, 233 (1970).

[25] L. C. Northcliffe, Annu. Rev. Nucl. Sci. 13, 67 (1963).

[26] H. H. Heckman, D. E. Greiner, P. J. Lindstrom, and H. Shwe, Phys. Rev. C 17, 1735 (1978).

[27] D. J. Morrissey, D. Lee, R. J. Otto, and G. T. Seaborg, Nucl. Instrum. Methods 158, 499 (1978).

[28] J. T. Routti and S. G. Prussin, Nucl. Instrum. Methods 72, 125 (1969).

[29] See, for example, P. R. Bevington, *Data Reduction and Error Analysis for the Physical Sciences* (McGraw-Hill, New York, 1969), p. 200.

[30] G. Rudstam, Z. Naturforsch. 21A, 1027 (1966).

[31] P. E. Haustein and T. J. Ruth, Phys. Rev C 18, 2241 (1978).

[32] S. B. Kaufman, M. W. Weisfield, E. P. Steinberg, B. D. Wilkins, and D. Henderson, Phys. Rev. C 14, 1121 (1976).

[33] J. Hudis, T. Kirsten, R. W. Stoenner, and O. A. Schaeffer, Phys. Rev. C 1, 2019 (1970).

[34] See, for example, V. E. Ross and K. Bachmann, J. Inorg. Nucl. Chem. 21, 13 (1974), and references therein.

[35] H. Boggild and T. Ferbel, Annu. Rev. Nucl. Sci. 24, 451 (1974).

[36] See, for example, H. H. Heckman, H. J. Crawford, D. E. Greiner, P. J. Lindstrom, and L. W. Wilson, Phys. Rev. C 17, 1651 (1978); G. D. Westfall, L. W. Wilson, P. J. Lindstrom, H. J. Crawford, D. E. Greiner, and H. H. Heckman, *ibid.* 19, 1309 (1979), and references therein.

[37] D. J. Morrissey, L. F. Oliveira, J. O. Rasmussen, G. T. Seaborg, Y. Yariv, and Z. Fraenkel, Phys. Rev. Lett. 43, 1139 (1979).

[38] H. Feshbach and K. Huang, Phys. Lett. 47B, 300 (1973).

[39] H. L. Bradt and B. Peters, Phys. Rev. 77, 54 (1950).

[40] P. J. Karol, Phys. Rev. C 11, 1203 (1975).

[41] Y. Yariv and Z. Fraenkel, Phys. Rev. C 20, 2227 (1979).

[42] The specific form of the abrasion-ablation model used in the comparison was that of Ref. 18.

[43] N. T. Porile, G. D. Cole, and C. R. Rudy, Phys. Rev. C 19, 2288 (1979).

[44] K. Chen, Z. Fraenkel, G. Friedlander, J. R. Grover, J. M. Miller, and Y. Shimamoto, Phys. Rev. 166, 949 (1968).

[45] G. D. Harp, K. Chen, G. Friedlander, Z. Fraenkel, and J. M. Miller, Phys. Rev. C 8, 851 (1973).

[46] I. Dostrovsky, Z. Fraenkel, and G. Friedlander, Phys. Rev. 116, 683 (1959).

[47] W. D. Myers, W. J. Swiatecki, T. Kodama, L. J. El-Jaick, and E. R. Hilf, Phys. Rev. C 15, 2032 (1977).

[48] W. Loveland, D. J. Morrissey, and G. T. Seaborg, Oregon State University Report No. RLO-2227-TA. 35-1 (unpublished).

[49] S. Katcoff and J. Hudis, Phys. Rev. C 14, 628 (1976).

HYSICAL REVIEW C VOLUME 21, NUMBER 5 MAY 1980

(^{7}Li,t) on 1f-2p shell nuclei

R. I. Cutler, K. W. Kemper, and A. Roy
Department of Physics, Florida State University, Tallahassee, Florida 32306

(Received 7 December 1979)

(^{7}Li,t) angular distributions have been measured on the targets ^{40}Ca, ^{44}Ca, and ^{58}Ni at $E = 34$ MeV for the ground and first excited state transitions. The results of the exact finite-range distorted-wave Born-approximation analyses of the data show a greater α spectroscopic strength for ^{62}Zn than for either ^{44}Ti or ^{48}Ti.

NUCLEAR REACTIONS ^{40}Ca, ^{44}Ca, ^{58}Ni(^{7}Li,t), $E = 34$ MeV; measured $\sigma(\theta)\theta = 3°-50°$ c.m. for 0^+ and 2^+ states in residual nuclei. Compared data to finite-range DWBA calculations; extracted relative and absolute α spectroscopic strengths.

I. INTRODUCTION

Two recent (^{6}Li, d) studies on 1f-2p shell nuclei disagree strongly as to the systematics of four particle clustering as a function of mass. A study by Fulbright *et al.*[1] finds that the largest ground state spectroscopic strength in the 1f-2p shell is n the ^{40}Ca$-$^{44}Ti system, while Hanson *et al.*[2] find the spectroscopic strength of the ^{58}Ni$-$^{62}Zn system to be twice as large as ^{44}Ti. In addition, he Ref. 2 results have a factor of 10 larger spectroscopic strength for the ^{58}Ni$-$^{62}Zn system relative to ^{44}Ti than do those of Ref. 1. Since the two analyses lead to very different conclusions about neutron blocking effects, we have measured angular distributions for the (^{7}Li, t) reaction on ^{40}Ca, ^{44}Ca, and ^{58}Ni to the ground and first excited states of the residual nuclei to resolve the discrepancy in the two previous studies. The (^{7}Li, t) reaction has been observed to selectively populate states in light nuclei,[3,4] and has a large $\alpha + t$ configuration,[5] suggesting that it might be a better reaction to extract four particle spectroscopic factors than the more commonly used (^{6}Li, d) reaction. The present results are the first published (^{7}Li, t) angular distributions on targets with $A \geqslant 40$. The spectroscopic factors for the four particle transfers were obtained by comparing the data to exact finite range distorted-wave Born approximation (DWBA) calculations that use measured optical model parameters to generate the distorted waves in the entrance and exit channels.

II. EXPERIMENTAL PROCEDURE

The 34-MeV ^{7}Li beams for the (^{7}Li, t) measurements were provided by the Florida State University Super FN tandem Van de Graaff Accelerator. Beam currents on target ranged from 100–500 nA of ^{7}Li^{+3}. The (^{7}Li, t) cross section measurements were performed using ΔE-E counter telescopes, each consisting of a 75–300 μm silicon surface barrier ΔE detector and a 4–5 mm lithium drifted silicon detector. The detectors were cooled to -30 C to improve energy resolution and stability. To eliminate the high flux of elastically scattered particles, 76 μm of Ta foil was mounted in front of each detector telescope, followed by a pair of small permanent magnets used to deflect low energy electrons produced in the foil. The (^{7}Li, t) measurements were performed in an ultrahigh vacuum (10^{-7}–10^{-8} Torr) hydrocarbon-free scattering chamber to prevent (^{7}Li, t) reactions on ^{12}C and ^{16}O contaminants, which have cross sections 1000 times larger than those of interset here, from interfering with the (^{7}Li, t) reactions from the f-p shell nuclei targets. Because of potential interference problems from ^{12}C the ^{40}Ca targets were prepared on Au backings. Both the ^{40}Ca targets and ^{58}Ni targets were prepared and transferred to the scattering chamber under vacuum to avoid ^{16}O contamination. These precautions were not necessary for the ^{44}Ca targets, because the larger Q value of the (^{7}Li, t) reaction on ^{44}Ca eliminated interference problems. The thickness of the ^{40}Ca targets was typically 350 μg/cm^2. The ^{44}Ca targets were made from isotopically separated (98.55% ^{44}Ca) ^{44}CaCO$_3$ evaporated onto 100 μg/cm^2 thick carbon backings. A typical target thickness was 360 μg/cm^2 ^{44}CaCO$_3$, or 150 μg/cm^2 ^{44}Ca. The ^{58}Ni targets were made from isotopically separated ^{58}Ni metal (99.92% ^{58}Ni) evaporated onto 60 μg/cm^2 thick carbon backings. The thickness of these targets was 350 μg/cm^2.

The (^{7}Li, t) measurements were made in 2–3°

© 1980 The American Physical Society

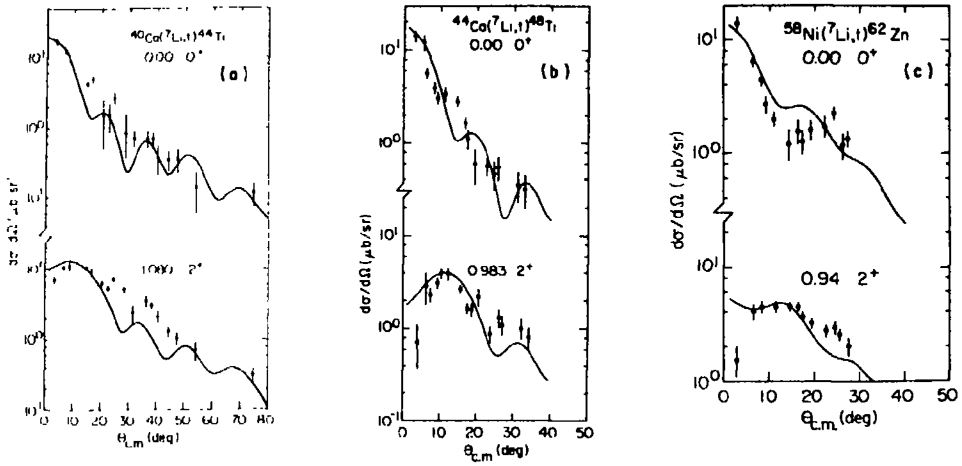

FIG. 1. (a)-(c) Experimental data for the ground and first excited state transitions from the targets indicated. The solid curves are the results of exact finite-range DWBA calculations.

steps from 2.7° (lab) to about 30° (lab), and to 70° (lab) for the ^{40}Ca target. Energy resolution was about 250 keV full width at half maximum (FWHM), which was sufficient to resolve the first two states for each target. The measured angular distributions are given in Fig. 1. The absolute cross sections are accurate to ±14% and were obtained by comparing elastic scattering measured by the counter telescopes with the stopping foils removed to previously measured scattering data.[6,7]

III. ANALYSIS AND RESULTS

To extract spectroscopic factors from the (^{7}Li, t) data, exact finite-range DWBA calculations were performed using the computer code MERCURY.[8] The ^{7}Li optical model parameters, taken from Refs. 6 and 7, had Woods-Saxon form factors with the geometrical parameters $r_r = 1.15$ fm, $r_i = 1.65$ fm, $r_c = 2.0$ fm, and $a_r = a_i = 0.83$ fm. The radius of interaction is given by $R = rA_T^{1/3}$. The real and imaginary well depths were ^{7}Li + ^{40}Ca (244 MeV, 45 MeV), ^{7}Li + ^{44}Ca (258 MeV, 33 MeV), ^{7}Li + ^{58}Ni (194 MeV, 26.7 MeV). The ^{7}Li geometry parameters used are similar to those which gave good fits to ^{7}Li induced single nucleon transfer data. The triton optical parameter sets for $t + {}^{40}$Ca and $t + {}^{62}$Ni from Table I of Ref. 9 were used for the final systems $t + {}^{44}$Ti and $t + {}^{62}$Zn, respectively. The $t + {}^{48}$Ti parameters were taken from Ref. 10. The α + target bound state parameters are given by $R = R_c = 1.23A_T^{1/3}$ fm and $a = 0.65$ fm. It was assumed that the bound α particle had $2N + L = 12$. The $\alpha + t$ bound state parameters were determined by calculating the rms radius of the $\alpha + t$ interaction radius using electron scattering measurements[11] of the α and t rms radius as

$$(\alpha + t)_{\mathrm{rms}} = [({}^7\mathrm{Li}_{\mathrm{rms}})^2 - \tfrac{3}{7}\,(t_{\mathrm{rms}})^2 - \tfrac{4}{7}(\alpha_{\mathrm{rms}})^2]^{1/2}$$

and finding Woods-Saxon well parameters which also have this rms radius. The resulting Woods-Saxon well parameters are $R = R_c = 0.79$ fm and $a = 0.23$ fm. The depth of both bound state wells was varied to give the correct separation energy. The DWBA calculations are shown in Fig. 1. The absolute alpha spectroscopic factors obtained from the DWBA calculations are listed in Table I. The

TABLE I. Absolute and relative (^{7}Li, t) and (^{6}Li, d) four particle spectroscopic factors. The relative spectroscopic factors are normalized to S (^{44}Ti g.s.) = 1.0.

Final nucleus		(^{7}Li, t) [a]			(^{6}Li, d)	
	S_{abs} (0$^+$)	S_{rel} (0$^+$)	S_{rel} (2$^+$)	S_{rel} (0$^+$) [b]	S_{rel} (2$^+$) [b]	S_{rel} (0$^+$) [c]
^{44}Ti	0.063	1.0	0.54	1.0	0.56	1.0
^{48}Ti	0.050	0.79	0.23	0.35	0.07	0.5
^{62}Zn	0.210	3.3	0.92	0.27	0.10	2.1

[a] Present work. [b] Reference 1. [c] Reference 2.

value of the spectroscopic factor for the $\alpha + t$ configuration of ^{7}Li was chosen to be 1.0.[5] It was found that the absolute spectroscopic factors were extremely sensitive to the choice of α + target bound state parameters used in the DWBA calculations. An order of magnitude change in these factors could be induced by a 20% change in bound state radius, making the absolute spectroscopic factors somewhat uncertain. However, the mass dependence of the spectroscopic factors does not vary greatly with changes in the α + target bound state radius. The relative spectroscopic factors obtained from the (^{7}Li, t) reaction and the two previous (^{6}Li, d) studies are also listed in Table I. There is good agreement between the present work and that of Hanson *et al.*[2] for the mass dependency of the ground state strength but the relative spectroscopic factors of ^{62}Zn g.s. relative to ^{40}Ca g.s. in the present work differ by an order of magnitude from the Fulbright *et al.* study. The $S(0^+)/S(2^+)$ ratios for a given target of the present work and of Fulbright *et al.*[1] are in good agreement.

The two different (^{6}Li, d) studies use very different ^{6}Li optical model parameters which is the reason for the different spectroscopic strengths reported. The Fulbright *et al.* study varied the ^{6}Li parameters until the shape of the angular distributions derived from DWBA calculations matched that of the data, while the Hanson *et al.* work used ^{6}Li parameters that fitted measured scattering data in this mass region but not necessarily that for the specific target of the (^{6}Li, d) work. We have reanalyzed the (^{6}Li, d) data of Refs. 1 and 12 with ^{6}Li parameters determined from scattering on the targets of interest. In addition, these ^{6}Li parameters were required to describe measured Li induced single nucleon transfer data. The mass trends of our spectroscopic strengths agree very well with those of Hanson *et al.*

In conclusion, the present (^{7}Li, t) results show an increase in four particle spectroscopic strength for N and $Z > 28$ in agreement with the recent (^{6}Li, d) results of Hanson *et al.*[2] These results are in agreement with neutron and proton pairing effects in this mass region.[12,13]

The authors would like to acknowledge many helpful discussions with D. Robson and D. Stanley. This work was supported in part by the National Science Foundation.

---

[1] H. W. Fulbright, C. L. Bennett, R. A. Lindgren, R. G. Markham, S. C. McGuire, G. C. Morrison, U. Strohbusch, and J. Toke, Nucl. Phys. A284, 329 (1977).

[2] D. L. Hanson, N. Stein, J. W. Sunier, C. W. Woods, and R. R. Betts, in *Clustering Aspects of Nuclear Reactions* in Proceedings of the Third International Conference on Clustering Aspects of Nuclear Structure and Nuclear Reactions, edited by W. T. H. Van Oers, J. P. Svenne, J. S. C. McKee, W. R. Falk (AIP, New York, 1978), p. 716.

[3] K. Bethge, in *Annual Review of Nuclear Science*, edited by E. Segrè, *et al.* (Annual Reviews, Palo Alto, Calif., 1970), p. 255, and references therein.

[4] M. E. Clark, K. W. Kemper, and J. D. Fox, Phys. Rev. C 18, 1262 (1978).

[5] M. E. Cobern, D J. Pisano, and P. D. Parker, Phys. Rev. C 14, 491 (1976).

[6] R. I. Cutler, M. J. Nadworny, and K. W. Kemper, Phys. Rev. C 15, 1318 (1977); *ibid.* 16, 1692(E) (1977).

[7] C. W. Glover, R. I. Cutler, and K. W. Kemper, Nucl. Phys. (to be published).

[8] L. A. Charlton and D. Robson, Florida State University Technical Report No. 5, 1973 (unpublished).

[9] E. R. Flynn, D. D. Armstrong, J. G. Beery, and A. G. Blair, Phys. Rev. 182, 1113 (1969).

[10] C. M. Perey and F. G. Perey, At. Data Nucl. Data Tables 17, 65 (1976).

[11] H. R Collard, L. R. B. Elton, and R. Hofstadter, in *Landolt-Börnstein*, edited by K.-H. Helwege (Springer, Berlin, 1967), Vol. 2.

[12] R. R. Betts, N. Stein, J. W. Sunier, and C. W. Woods, Phys. Lett. 76B, 47 (1978).

[13] D. R. Bes, R. A. Broglia, O. Hansen, and O. Nathan, Phys. Rep. 34C, 1 (1977).

PHYSICAL REVIEW C VOLUME 21, NUMBER 5 MAY 1980

^{24}Mg(^{16}O,^{12}C)^{28}Si and ^{24}Mg(^{16}O,^{16}O)^{24}Mg reactions at backward angles

M. Paul, S. J Sanders, D. F. Geesaman, W. Henning, D. G. Kovar, C. Olmer,* and J. P. Schiffer
Argonne National Laboratory, Argonne, Illinois 60439

J. Barrette and M. J. LeVine
Brookhaven National Laboratory, Upton, New York 11973

(Received 29 October 1979)

Excitation functions of the ^{24}Mg(^{16}O,^{12}C)^{28}Si and ^{24}Mg(^{16}O,^{16}O)^{24}Mg reactions to the ground states and first-excited 2^+ states in ^{28}Si and ^{24}Mg have been measured at $\theta_{c.m.} = 180°$ over the energy range $24 \leq E_{c.m.} \leq 40$ MeV, where the ^{24}Mg(^{16}O,^{12}C)^{28}Si reaction is known to exhibit a strong resonant behavior at forward angles. The four measured excitation functions show prominent structures, about 1 MeV wide, strongly correlated in the elastic and inelastic channels. Angular distributions in the range $110° \leq \theta_{c.m.} \leq 180°$ were measured at $E_{c.m.} = 27.8$, 30.8, and 36.2 MeV. At 27.8 and 36.2 MeV, where prominent peaks exist in the (^{16}O,^{12}C) backward-angle excitation function, the angular distributions of the transfer to the 0^+ ground state are strongly rising toward 180° and have an oscillatory shape. The partial waves $L = (20,22)$ and 26, respectively, are predominant at these two energies. At 30.8 MeV the data indicate the interference between odd and even partial waves.

[NUCLEAR REACTIONS ^{24}Mg(^{16}O,^{12}C), ^{24}Mg(^{16}O,^{16}O) $E_{c.m.} = 24-40$ MeV; measured $\sigma(E,\theta)$; correlation analysis; DWBA and P_L^2 analyses; deduced J values.]

I. INTRODUCTION

The resonance-like behavior observed in heavy-ion systems involving *s-d* shell nuclei has raised much interest as to its origin and the possible new physical insight it may provide. The elastic and inelastic scattering cross sections for the systems ^{16}O+^{28}Si and ^{12}C+^{28}Si,[1] for example, show pronounced structures in their excitation functions at backward angles; at maxima of the excitation functions, the cross sections are strongly enhanced above the values expected from conventional optical-model calculations and have oscillatory angular distributions. The angular momenta of the dominant partial waves, as deduced from the shapes of the angular distributions, are close to the values obtained for the grazing partial waves in optical-model calculations. Lee *et al.*[2] have observed the same phenomena in a study of the ^{24}Mg(^{16}O,^{12}C)^{28}Si reaction at backward angles.

In the forward-angle region, resonant behavior has been observed in transfer reactions involving similar heavy-ion systems.[3-6] The excitation function of the reaction ^{24}Mg(^{16}O,^{12}C)^{28}Si at forward angles[3] in the range $23 \leq E_{c.m.} \leq 38$ MeV shows four evenly spaced structures. Direct transfer calculations, which can reproduce the shapes of the angular distributions at forward angles, do not account for the experimental energy dependence of the cross sections.

The physical origin of the observed phenomena is not yet understood. Several interpretations[1,7] have been proposed for the backward-angle behavior of the elastic scattering in the systems mentioned above, primarily based on the occurrence of shape resonances in the heavy-ion potentials. No such model as yet is capable of explaining or reproducing the resonant behavior observed at forward angles. If resonance mechanisms are responsible for these phenomena, they should be dominant in the backward-angle region where the direct-transfer processes are expected to be weak. The motivation of the present work was to study the behavior of the ^{24}Mg(^{16}O,^{12}C)^{28}Si reaction as well as that of the ^{24}Mg+^{16}O elastic and inelastic scattering at backward angles in the energy region where resonances were seen at forward angles. Such a study will explore the correlations between the forward- and backward-angle reaction excitation functions as well as the possible correlations among the reaction and elastic channel excitation functions. Taken together these data may provide an insight into the reaction mechanism.

Excitation functions of the ^{24}Mg(^{16}O,^{12}C)^{28}Si reaction to the ground state and 1.78-MeV, 2^+ state in ^{28}Si and of the ^{24}Mg(^{16}O,^{16}O)^{24}Mg elastic scattering and inelastic scattering to the 1.37-MeV, 2^+ state in ^{24}Mg were measured at $\theta_{c.m.} = 180°$ between $E_{c.m.} = 24$ and 40 MeV.[8] At $E_{c.m.} = 27.8$, 30.8, and 36.2 MeV, angular distributions for the same reactions were obtained over the angular range $130° \leq \theta_{c.m.} \leq 180°$ and used to establish limits on the angular momenta of the dominant partial waves. In the following paper,[10] the ground-state

© 1980 The American Physical Society

ransfer data are discussed within the framework f resonant amplitudes added to a direct reaction ackground.

II. EXPERIMENTAL METHOD AND RESULTS

In order to measure the excitation functions and angular distributions for the ^{24}Mg(^{16}O, ^{12}C)^{28}Si and ^{24}Mg(^{16}O, ^{16}O)^{24}Mg reactions at backward angles, the kinematically reversed reactions were studied with ^{24}Mg as the projectile and the lighter outgoing ions detected at forward angles. Beams of ^{24}Mg in the energy range of 60–100 MeV were obtained from the Brookhaven National Laboratory (BNL) tandem Van de Graaff facility. Self-supporting Al_2O_3 targets, about 70 μg/cm^2 thick, were used. The outgoing ions were momentum analyzed at forward angles in the BNL quadrupole-triple-dipole (QDDD) magnetic spectrometer. The focal-plane detection system, described in Ref. 1, consisted of a double-wire proportional counter. The ions were stopped in the gas counter and generated signals for position, differential energy loss, and residual energy; unambiguous identification of ^{12}C or ^{16}O ions was possible.

For measurements at and near $\theta_{lab} = 0°$, the detector was shielded from the primary ^{24}Mg beam by metallic gold and Havar absorber foils. The thickness of the absorber was varied over the range 3–25 mg/cm^2 so that the ^{12}C or ^{16}O ions retained sufficient energy to be identified in the counter. For the detection of ^{16}O ions, an additional nickel foil of 1.7 mg/cm^2 thickness was placed at the entrance aperture of the spectrograph. This foil removed the degeneracy in magnetic rigidity between elastically scattered ^{16}O ions and one of the charge states of the primary ^{24}Mg beam and reduced the background contribution. In all these measurements, the ^{12}C or ^{16}O groups corresponding to the ground- and first-excited states in ^{28}Si or ^{24}Mg were well resolved. Figure 1 shows the ^{12}C and ^{16}O energy spectra taken at $\theta_{lab} = 0°$ with an incident ^{24}Mg beam energy of 90.0 MeV.

For relative normalization purposes, a thin layer of gold (~5 μg/cm^2) was evaporated onto the Al_2O_3 targets. ^{24}Mg nuclei elastically scattered from gold were counted in two out-of-plane monitor detectors symmetrically located at 18° with respect to the beam. The ratio of the yields in the two detectors was used to monitor the incident beam direction. Absolute cross sections were obtained by normalizing the spectrometer yields to the Rutherford elastic scattering of ^{24}Mg y the oxygen target at $E_{lab} = 60.0$ MeV over laboratory angles from 13° to 19°. Charge state correcions to the ^{16}O yields, extrapolated from measurements at incident laboratory energies of 70 and 86 MeV, were applied to the data. The estimated errors in the relative normalizations are included in the figures; the error on the absolute scale is about 25%.

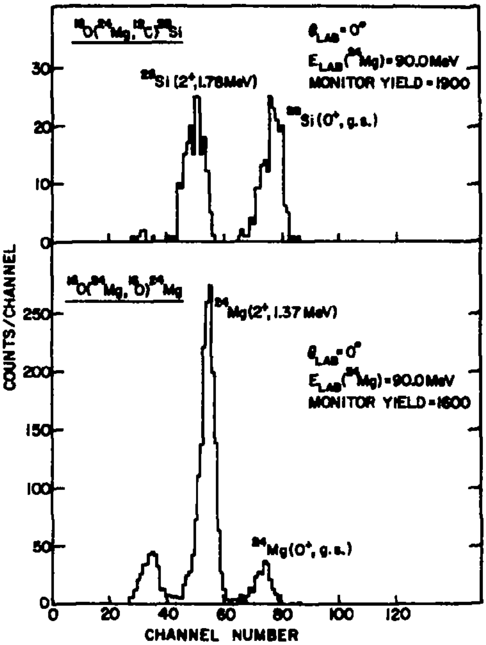

FIG. 1. Position spectra of the ^{12}C and ^{16}O groups from the ^{16}O(^{24}Mg, ^{12}C)^{28}Si and ^{16}O(^{24}Mg, ^{16}O)^{24}Mg reactions, respectively, measured in the focal plane of the BNL-QDDD spectrometer at 0° and an incident laboratory energy of 90.0 MeV.

Excitation functions for the ^{12}C and ^{16}O groups corresponding to the ground- and first-excited states in ^{28}Si and ^{24}Mg were measured at $\theta_{lab} = 0°$ with beam energies from 60 to 100 MeV in steps of 0.750 MeV. The square-shaped spectrometer aperture subtended in-plane angles of ±3°, corresponding to center-of-mass angles for the ^{24}Mg(^{16}O, ^{12}C)^{28}Si and ^{24}Mg(^{16}O, ^{16}O)^{24}Mg reactions of 180° ± 5° and 180° ± 6°, respectively. The experimental excitation functions are plotted in Fig. 2. They show a series of strong maxima about 1 MeV wide with peak-to-valley ratios as large as 10.

At $E_{c.m.} = 27.8$, 30.8, and 36.2 MeV, angular distributions of the ^{12}C groups leading to the ground state and first-excited 2$^+$ state in ^{28}Si were measured over the range $145° \leq \theta_{c.m.} \leq 180°$. At 30.8 MeV, the yield of the reaction is low and the above aperture (±3°) was used; at other energies, angular distributions were measured with a rectangular aperture subtending ±0.5°. The reaction angle was

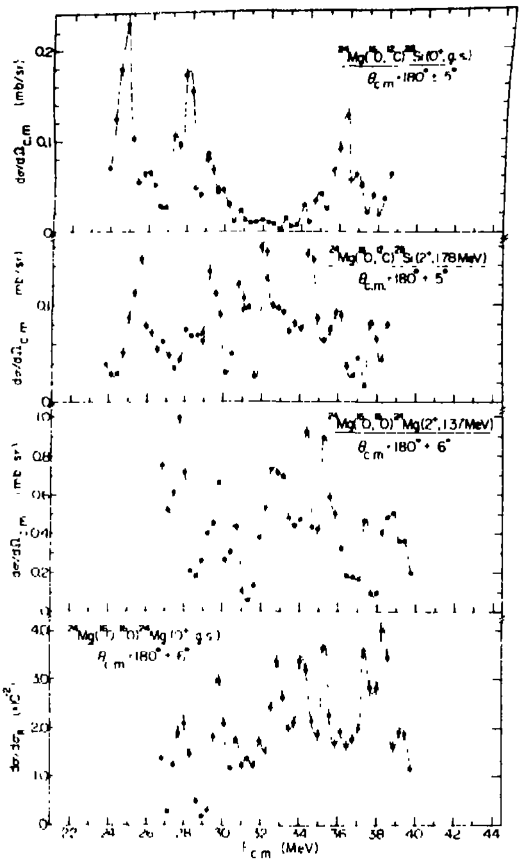

FIG. 2. Excitation functions for the indicated reactions at $\theta_{c.m.} \approx 180°$. The solid lines connect smoothly the experimental points.

determined with an accuracy of ±0.07° by performing left and right measurements of the spectrometer yields. The experimental results for the (^{16}O, ^{12}C) reaction are shown in Fig. 3; in this figure, the vertical bars indicate the relative errors in the cross sections and, for the large-aperture measurements, the horizontal bars indicate the center-of-mass aperture angles.

Elastic and inelastic scattering angular distributions were measured in the backward hemisphere at $E_{c.m.}$ = 27.8 MeV and $E_{c.m.}$ = 36.2 MeV. At $E_{c.m.}$ = 27.8 MeV, additional measurements were performed to establish the angular distribution over the full angular range. In these measurements, a self-supporting ^{24}Mg target of 120 μg/cm^2 thickness was bombarded by an ^{16}O beam from the Argonne National Laboratory FN tandem Van de Graaff. Depending on the scattering angle, ^{24}Mg

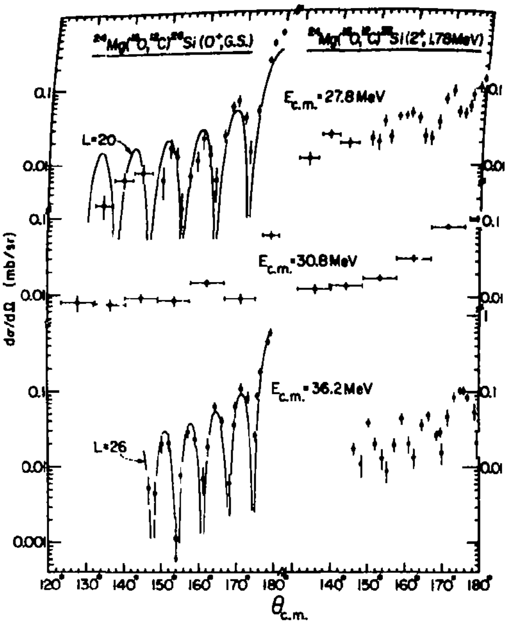

FIG. 3. Backward angular distributions of the ^{24}Mg(^{16}O, ^{12}C)^{28}Si(0$^+$,g.s.) and ^{24}Mg(^{16}O, ^{12}C)^{28}Si(2$^+$, 1.78 MeV) reactions at the indicated energies. Vertical bars show the relative errors. Horizontal bars, where shown, represent the experimental angular aperture. The solid lines represent squared Legendre polynomials with the *L* values shown, normalized to fit the data.

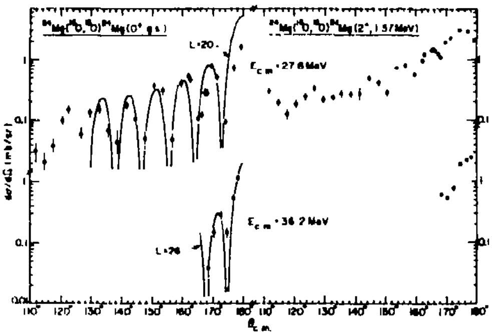

FIG. 4. Backward angular distributions of the ^{24}Mg(^{16}O, ^{16}O)^{24}Mg(0$^+$,g.s.) and ^{24}Mg(^{16}O, ^{16}O)^{24}Mg(2$^+$, 1.37 MeV) reactions at the indicated energies. The cross sections were obtained from the ^{16}O(^{24}Mg, ^{16}O)^{24}Mg reaction for 160° ≤ $\theta_{c.m.}$ ≤ 180° and the ^{24}Mg(^{16}O, ^{24}Mg)^{16}O reaction for 110° ≤ $\theta_{c.m.}$ ≤ 170°. Vertical bars show the relative errors. The solid lines represent squared Legendre polynomials with the *L* values shown, normalized to fit the data.

nuclei recoiling in the forward direction, or elastically scattered ^{16}O nuclei were analyzed in an Enge split-pole spectrograph. A resistive-wire ionization chamber[9] was used as focal-plane detector, providing position measurement and unambiguous particle identification. The backward-angle elastic and inelastic scattering angular distributions are shown in Fig. 4. In Fig. 5, the full angular distribution for the ^{16}O+ ^{24}Mg elastic scattering at $E_{c.m.}$ = 27.8 MeV is presented. Also shown in Fig. 5 are angular distributions of the ^{24}Mg(^{16}O, ^{12}C)^{28}Si reaction to the ground- and first-excited states in ^{28}Si; these curves were obtained by combining the backward-angle data obtained here with the data from Refs. 3 and 10.

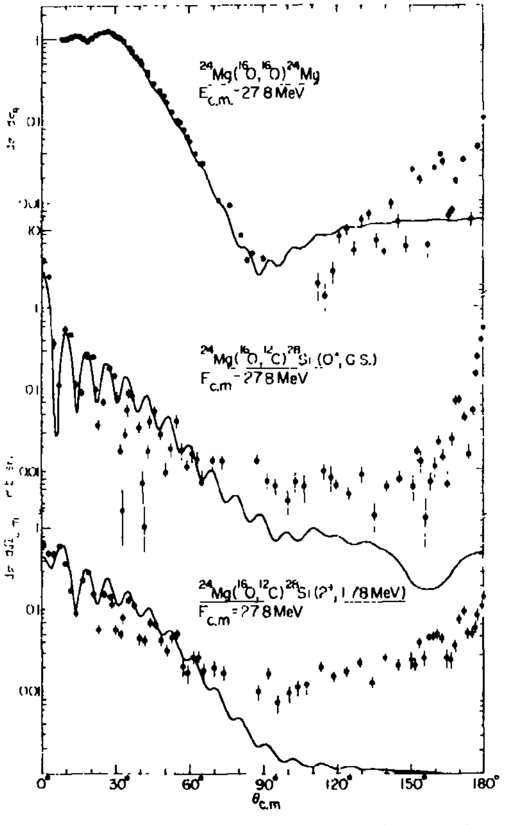

FIG. 5. Full angular distributions of the ^{24}Mg(^{16}O, ^{16}O)^{24}Mg elastic scattering and the ^{24}Mg(^{16}O, ^{12}C)^{28}Si (0$^+$, g.s.) and ^{24}Mg(^{16}O, ^{12}C)^{28}Si (2$^+$, 1.78 MeV) reactions. The elastic cross sections were measured using the ^{24}Mg(^{16}O, ^{16}O)^{24}Mg reaction for 8° ≤ $\theta_{c.m.}$ ≤ 90°, the ^{24}Mg(^{16}O, ^{24}Mg)^{16}O reaction for 110° ≤ $\theta_{c.m.}$ ≤ 170°, and the ^{16}O(^{24}Mg, ^{16}O)^{24}Mg reaction for 160° ≤ $\theta_{c.m.}$ ≤ 180°. Data at 0° ≤ $\theta_{c.m.}$ ≤ 35° and at 35° ≤ $\theta_{c.m.}$ ≤ 110° for the ^{24}Mg(^{16}O, ^{12}C)^{28}Si (0$^+$, 2$^+$) reactions are taken from Refs. 3 and 9, respectively. The solid lines are results of optical-model and DWBA calculations (see text).

Figure 5 shows the strong rise of the backward-angle yields of both the elastic and the transfer reactions. The ^{24}Mg(^{16}O, ^{16}O)^{24}Mg elastic cross section at $\theta_{c.m.}$ = 180° is about 10% of the Rutherford value. At back angles, angular distributions for transitions to the ground states of ^{28}Si and ^{24}Mg are strongly oscillatory. The angular distributions corresponding to the 2$^+$ states are somewhat smoother; some have a minimum at $\theta_{c.m.}$ = 180° (see Fig. 4).

III. DISCUSSION

The excitation functions shown in Fig. 2 for the ^{24}Mg(^{16}O, ^{12}C)^{28}Si and ^{24}Mg(^{16}O, ^{16}O)^{24}Mg reactions at 180° are similar in character to the recent results of Lee *et al.*[2] and Clover *et al.*[11] for 17 ≤ $E_{c.m.}$ ≤ 31 MeV; in the energy range of overlap, the positions of the maxima agree with our results. It has been noted previously[1] that excitation functions for the ^{12}C + ^{28}Si elastic and inelastic channels exhibit a pronounced fine structure on the scale of 250 keV. In the present results, for both the (^{16}O, ^{12}C) and (^{16}O, ^{16}O) reactions, the width of the observed structures is about 1 MeV in the center-of-mass system. However, the energy spread due to the target thickness, $\Delta E_{c.m.} \simeq 300$ keV, may have masked possible fine-structure effects.

The excitation functions for the elastic and inelastic channels (Fig. 2) show a very strong correlation in the position of their maxima. Such strong correlations have been observed previously in the elastic and inelastic scattering of ^{16}O on ^{28}Si[1] and more recently on ^{29,30}Si.[12] These correlations have been taken as an indication[1] of the existence of simple resonance mechanisms dominating the backward-angle scattering. In the present results, however, the structures in the ^{16}O+ ^{24}Mg elastic and inelastic scattering excitation functions are not obviously correlated with those seen for the (^{16}O, ^{12}C) channels, except perhaps for the peak observed near $E_{c.m.}$ = 27.8 MeV. In Table I, cross-correlation coefficients are given for the excitation functions of the ^{24}Mg(^{16}O, ^{12}C)^{28}Si reaction and of the ^{16}O+ ^{24}Mg and ^{12}C + ^{28}Si elastic and inelastic scattering. The data for the ^{12}C + ^{28}Si system were taken from Refs. 1 and 13. The coefficients were calculated using the expressions

$$S_{ij} = \frac{\langle d_i d_j \rangle}{\langle d_i^2 \rangle^{1/2} \langle d_j^2 \rangle^{1/2}},$$
$$d_i = \frac{\sigma_i(E)}{\langle \sigma_i(E) \rangle_\Delta} - 1, \qquad (1)$$

where $\langle \sigma_i(E) \rangle_\Delta$ denotes the energy dependent average cross section[14] for the channel i, calculated

TABLE I. Cross-correlation coefficients (see text) for the 180° excitation functions of the ^{24}Mg(^{16}O, ^{12}C)^{28}Si reaction to the 0$^+$ ground state and 2$^+$ first-excited state in ^{28}Si and the ^{16}O+^{24}Mg and ^{12}C+^{28}Si elastic and inelastic scattering.

	^{24}Mg(^{16}O, ^{16}O)^{24}Mg(2$^+$)	^{24}Mg(^{16}O, ^{12}C)^{28}Si(0$^+$)	^{24}Mg(^{16}O, ^{12}C)^{28}Si(2$^+$)	^{28}Si(^{12}C, ^{12}C)^{28}Si(0$^+$)	^{28}Si(^{12}C, ^{12}C)^{28}Si(2$^+$)
^{24}Mg(^{16}O, ^{16}O)^{24}Mg(0$^+$)	0.61	0.12	−0.08	−0.39	0.15
^{24}Mg(^{16}O, ^{16}O)^{24}Mg(2$^+$)		0.32	0.23	−0.11	0.05
^{24}Mg(^{16}O, ^{12}C)^{28}Si(0$^+$)			0.38	0.06	0.21
^{24}Mg(^{16}O, ^{12}C)^{28}Si(2$^+$)				0.18	−0.05
^{28}Si(^{12}C, ^{12}C)^{28}Si(0$^+$)					−0.11

by averaging $\sigma(E)$ over an energy interval Δ; $\langle\ \rangle$ denotes the averaging over the whole energy range considered, $26.9 \leq E_{c.m.} \leq 38.6$ MeV. Each excitation function consisted of 40 equally spaced data points (300 keV steps); where necessary, an interpolation procedure was employed to obtain the equal spacing. The averaging interval Δ was taken as 1.8 MeV; the results are not sensitive to this value. An additional smoothing was applied to attenuate the effect of the fine structure apparent in the excitation functions, especially prominent for the ^{12}C+^{28}Si elastic and inelastic channels; the experimental cross sections were averaged over an interval of 0.9 MeV:

$$\sigma(E)=\frac{1}{0.9}\int_{E-0.45}^{E+0.45}\sigma_{exp}(E)dE$$

in Eq. (1). From an analysis of generated random spectra, it was determined that the 70% confidence level of a true correlation corresponds to a correlation coefficient of 0.25.

It appears from Table I that only the correlation coefficient between the elastic and inelastic ^{16}O+^{24}Mg channels is appreciable. The correlations between the (^{16}O, ^{12}C) reaction channels and either the ^{16}O+^{24}Mg or the ^{12}C+^{28}Si elastic channels are weak and, in contrast with the conclusion of Ref. 2, the present results do not seem to indicate that the ^{24}Mg(^{16}O, ^{12}C)^{28}Si resonant structures are governed by the entrance channel. In this context, it should be remembered that the existence of correlations between the structures seen in a reaction and the relevant elastic channels is not a necessary feature of a simple resonant process. Since the cross section of a pure resonant reaction is $\sigma \propto \Gamma_\alpha \Gamma_\beta$, where Γ_α and Γ_β are the partial widths of the resonant state in the entrance and exit channels, the dominant structures are determined by the overlap between the resonances in the two channels. For the two elastic channels, the cross sections for the same resonance are $\sigma_\alpha \propto \Gamma_\alpha^2$ and $\sigma_\beta \propto \Gamma_\beta^2$. The resonances seen strongly in the reaction must also contribute to the elastic cross sections, but they do not have to be the dominant structures.

Figure 6 shows a comparison between the experimental excitation functions of the (^{16}O, ^{12}C) reaction to the 0$^+$ and 2$^+$ states in ^{28}Si at forward angles[3] and the present data at backward angles. The forward-angle data of Ref. 3 have been corrected for the mean energy loss in the target, which was estimated to be ~800 keV in a reanalysis of these data. The backward-angle excitation curves were obtained by averaging the cross sections, as described previously, over an interval of 0.9 MeV to match approximately the energy averaging due to the target thickness in the for-

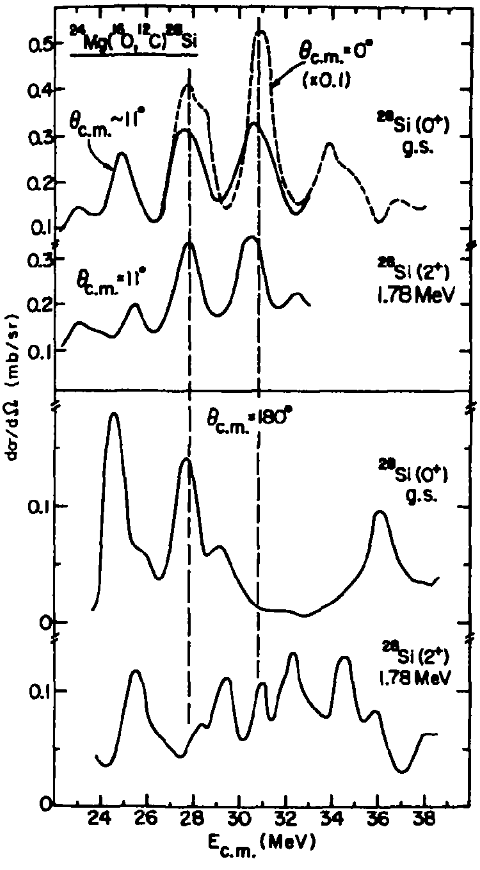

FIG. 6. Experimental excitation functions of the ^{24}Mg(^{16}O,^{12}C)^{28}Si reactions to the ground and first-excited states in ^{28}Si at forward angles (Ref. 3; upper part) and at $\theta_{c.m.}=180°$ (present work; lower part). The 180° excitation curves were obtained by averaging the data of Fig. 2 over three adjacent energy steps, i.e., over a center-of-mass energy range of ~1 MeV to match the energy spread of the forward-angle data.

ward-angle measurement. It is noted in Fig. 6 that while the correlation between the 0$^+$ and 2$^+$ excitation functions is quite strong at forward angles, at backward-angles a correlation is not apparent. The strong peak in the forward-angle excitation functions at $E_{c.m.}\approx 28$ MeV also appears at backward angles for the (^{16}O,^{12}C) reaction and the ^{16}O+^{24}Mg elastic and inelastic scattering excitation functions (Figs. 2 and 6). At $E_{c.m.}\simeq 31$ MeV, the forward-angle cross sections for the transfer reaction show a strong maximum which is not observed at 180°. This may be explained by an interference between close resonances, requiring the contribution of at least one even-J and one odd-J resonance, interfering constructively at 0° and destructively at 180°. The assumption of interfering partial waves is confirmed by the behavior of the angular distribution of the (^{16}O,^{12}C) reaction at $E_{c.m.}=30.8$ MeV, as shown below.

The presence of a resonance structure around $E_{c.m.}\approx 27.8$ MeV, as indicated both by the forward- and backward-angle data, is supported by the strong rise and the oscillatory behavior of the angular distributions of the various reactions at backward angles. In the forward-angle region, Erskine *et al.*[15] showed that the ^{24}Mg(^{16}O,^{12}C)^{28}Si angular distribution at $E_{c.m.}=33.6$ MeV is fairly well described by distorted-wave Born-approximation (DWBA) calculations using the optical-model parameters ANL1 (see Table II). Although these parameters reproduce the shapes of the (^{16}O,^{12}C) angular distributions over a wide energy range, a fit to the present forward-angle elastic data at $E_{c.m.}=27.8$ MeV (see Fig. 5) was made, using the ANL1 parameters as starting values and adjusting the real and imaginary potential geometry. The resulting parameters are listed in Table II as ANL1A. The DWBA calculations shown in Fig. 5 were performed with the code PTOLEMY[16] using the set ANL1A in both the entrance and exit channels. The calculated curves show some rise at backward angles, but neither the yield nor the oscillatory character of the data is reproduced. Some success was achieved recently[7] in reproducing the angular distributions and excitation functions in the backward-angle region for the ^{16}O+^{28}Si elastic scattering, using a surface-transparent potential with a parity-dependent absorption term. However, it is not yet clear how successful this approach is for other systems nor how it should be used in transfer calculations.

In Figs. 3 and 4, the angular distributions corresponding to the 0$^+$ state in ^{28}Si and ^{24}Mg are analyzed in terms of squared Legendre polynom-

TABLE II. Optical potential parameter sets for the system ^{16}O+^{24}Mg as discussed in the text. The optical potential $V(r)$ of Woods-Saxon shape is given in terms of the listed parameters by the following expressions:

$$V(r)=-V_0 f(r,R_r,a_r)-iW_0 f(r,R_i,a_i),$$
$$R_r=r_{0r}(A_1^{1/3}+A_2^{1/3}),$$
$$R_i=r_{0i}(A_1^{1/3}+A_2^{1/3}),$$
$$f(r,R,a)=\{1+\exp[(r-R)/a]\}^{-1}.$$

	V_0 (MeV)	r_{0r} (fm)	a_r (fm)	W_0 (MeV)	r_{0i} (fm)	a_i (fm)
ANL1	37	1.35	0.404	78	1.29	0.174
ANL1A	37	1.37	0.394	78	1.32	0.208

ials. At $E_{c.m.} = 27.8$ MeV, both the elastic and the transfer angular distributions are reasonably well fitted by $P_{20}^2(\cos\theta)$ or $P_{21}^2(\cos\theta)$, but the quality of the fits suggests that more than a single partial wave contributes to the reactions. Also, it seems impossible from these fits alone to determine the main L value better than within $\pm 1\ \hbar$. This is illustrated in Fig. 7 where the χ^2 values of the fits of $P_L^2(\cos\theta)$ to the angular distributions are plotted as a function of the L value. While the partial waves contributing to these transitions are obviously close to each other, the fits do not determine whether, indeed, the same partial wave is dominant in the transfer reaction and in the elastic scattering. From their backward-angle measurement of the ^{24}Mg(^{16}O, ^{12}C)^{28}Si(g.s.) reaction at $E_{c.m.} \simeq 28$ MeV, Lee *et al.*[2] give a value of $L \simeq 21$. Clover *et al.*[11] assign a value $L = 20$ to the $E_{c.m.} = 27.9$ MeV angular distribution of the ^{16}O + ^{24}Mg elastic scattering at backward angles. Both these values are consistent with the present work; however, it should be noted that the excitation function of the ^{24}Mg(^{16}O, ^{12}C)^{28}Si(g.s.) reaction measured at $\theta_{c.m.} \simeq 90°$ (Ref. 10) shows a maximum around $E_{c.m.} \simeq 28$ MeV and thus suggests that an even partial wave resonates at that energy, favoring a value of $L \simeq 20$ or 22.

At $E_{c.m.} = 36.2$ MeV, which corresponds to a strong maximum in the back-angle (^{16}O, ^{12}C) excitation function, the fit of $P_{28}^2(\cos\theta)$ to the 0^+-transfer angular distribution is excellent (Fig. 3) and the dependence of χ^2 upon the L value is much sharper as attested by Fig. 7. The data on the elastic angular distribution at that energy, although limited, are consistent with an L value of 26.

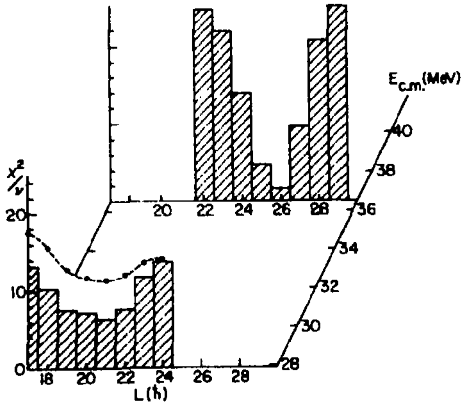

FIG. 7. Plot of the χ^2/(degree of freedom) of the fit of experimental angular distributions to $P_L^2(\cos\theta)$ as a function of L at $E_{c.m.} = 27.8$ and 36.2 MeV. The histograms correspond to the ^{24}Mg(^{16}O, ^{12}C)^{28}Si(0^+, g.s.) reaction; the points correspond to the ^{16}O+^{24}Mg elastic scattering.

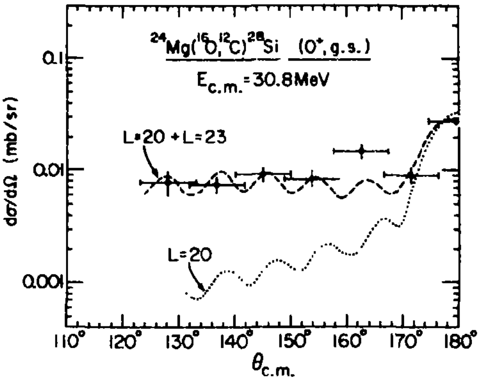

FIG. 8. Angular distributions of the ^{24}Mg(^{16}O, ^{12}C)^{28}Si(0^+) reaction in the backward-angle region measured at $E_{c.m.} = 30.8$ MeV. Horizontal bars represent the experimental angular aperture. The dashed line was obtained from the expression $|aP_{20}(\cos\theta) + bP_{23}(\cos\theta)|^2$, using $a = 0.445$ and $b - 0.216$, by averaging over the experimental angular aperture $\Delta\theta \simeq 10°$. The dotted line represents $P_{20}^2(\cos\theta)$ similarly averaged.

At $E_{c.m.} = 30.8$ MeV, the shape of the (^{16}O, ^{12}C) angular distribution (Figs. 3 and 8) differs from that of the previous cases. Although an oscillatory behavior may be masked by the averaging over the large angular aperture, the envelope to the true distribution is well defined by the data and differs drastically from the typical falloff of a P_L^2-like angular distribution, as exhibited at $E_{c.m.} = 27.8$ and 36.2 MeV. This, together with the behavior of the excitation function discussed above, suggests the existence of a strong interference between different partial waves, as is qualitatively illustrated in Fig. 8. The dashed line shows an example of the angular distribution obtained by assuming the contribution of two partial waves with opposite parity, $L = 20$ and $L = 23$, as discussed for the excitation functions. The shapes obtained are rather insensitive to the actual values of the even and odd partial waves in the range $20 \leq L \leq 25$ and to small changes in the relative phase of their amplitudes. In Fig. 8, the shape of a pure $L = 20$ angular distribution is drawn for comparison of the falloff. Both lines were calculated by averaging over the range of angles ($\Delta\theta \simeq 10°$) corresponding to the experimental aperture.

IV. SUMMARY AND CONCLUSIONS

The 180° excitation functions of the ^{24}Mg(^{16}O, ^{12}C)^{28}Si and ^{24}Mg(^{16}O, ^{16}O)^{24}Mg reactions to the ground states and first-excited 2^+ states in

^{28}Si and ^{24}Mg reveal pronounced structures and a series of strong maxima, about 1 MeV wide, in the range $24 \leq E_{c.m.} \leq 40$ MeV. A cross-correlation analysis shows a high degree of correlation between the ^{16}O+^{24}Mg elastic and inelastic scattering. The correlations between the (^{16}O,^{12}C) reaction channels and either the ^{16}O+^{24}Mg or ^{12}C+^{28}Si elastic channels are weak. At $E_{c.m.} = 27.8$ MeV, a strong peak is seen in the ^{16}O+^{24}Mg elastic, inelastic, and ^{24}Mg(^{16}O,^{12}C)^{28}Si(g.s.) excitation functions at backward angles.

The angular distributions at $E_{c.m.} = 27.8$ and 36.2 MeV show a strong rise and an oscillatory shape at backward angles. At $E_{c.m.} = 27.8$ MeV, the main partial wave contributing to the backward-angle cross sections in the (^{16}O,^{12}C) and (^{16}O,^{16}O) reactions is $L = 20$ or 22. At $E_{c.m.} = 36.2$ MeV, $L = 26$ is predominant. At $E_{c.m.} = 30.8$ MeV, the excitation function and the angular distribution of the (^{16}O,^{12}C) reaction suggest the existence of a strong interference between an even and odd partial wave.

In conclusion, the excitation functions and angular distributions of the ^{24}Mg(^{16}O,^{12}C)^{28}Si reactions both at forward and backward angles show evidence for resonant structures. However, the backward-angle data presented in this work point to a complex situation where several resonances interfere. It is not possible, on the basis of the backward angle data only, to make unique assignments of J values.

ACKNOWLEDGMENTS

The operating crew of the BNL tandem Van de Graaff is gratefully acknowledged for their assistance during experiments performed there. This research was performed under the auspices of the U. S. Department of Energy.

---

*Present address: Dept. of Physics, Indiana Univ., Bloomington, Ind. 47401.

[1] J. Barrette, M. J. LeVine, P. Braun-Munzinger, G. M. Berkowitz, M. Gai, J. W. Harris, and C. M. Jachcinski, Phys. Rev. Lett. 40, 445 (1978).

[2] S. M. Lee, J. C. Adloff, P. Chevallier, D. Disdier, V. Rauch, and F. Scheibling, Phys. Rev. Lett. 42, 429 (1979).

[3] M. Paul, S. J. Sanders, J. Cseh, D. F. Geesaman, W. Henning, D. G. Kovar, C. Olmer, and J. P. Schiffer, Phys. Rev. Lett. 40, 1310 (1978).

[4] C. K. Gelbke, T. Awes, U. E. P. Berg, J. Barrette, M. J. LeVine, and P. Braun-Munzinger, Phys. Rev. Lett. 41, 1778 (1978).

[5] J. C. Peng, D. L. Hanson, J. D. Moses, O. W. B. Schult, Nelson Stein, J. W. Sunier, and N. Cindro, Phys. Rev. Lett. 42, 1458 (1979).

[6] J. Barrette, P. D. Bond, M. J. LeVine, and I. Tserruya, Bull. Am. Phys. Soc. 24, 570 (1979).

[7] D. Dehnhard, V. Shkolnik, and M. A. Franey, Phys. Rev. Lett. 40, 1549 (1978).

[8] See AIP document No. PAPS PRVCA-21-1802-22 for 22 pages of tabulations of the cross sections measured in the present work and in Ref. 10. Order by PAPS number and journal reference from American Institute of Physics, Physics Auxiliary Publication Service, 335 E. 45th Street, New York, N. Y. 10017. The price is $1.50 for microfiche, or $5 for photocopies. Airmail additional. Make checks payable to the American Institute of Physics. This material also appears in *Current Physics Microfilm*, the monthly microfilm edition of the complete set of journals published by AIP, on the frames immediately following this journal article.

[9] J. R. Erskine, T. H. Braid, and J. C. Stoltzfus, Nucl. Instrum. Methods 135, 67 (1976).

[10] S. J. Sanders, M. Paul, J. Cseh, D. F. Geesaman, W. Henning, D. G. Kovar, C. Olmer, and J. P. Schiffer, Phys. Rev. C 21, 1810(1980), following paper.

[11] M. R. Clover, B. R. Fulton, R. Ost, and R. M. DeVries, J. Phys. G 5, L63 (1979).

[12] P. Braun-Munzinger, G. M. Berkowitz, M. Gai, C. M. Jachcinski, T. Renner, C. D. Uhlhorn, J. Barrette, and M. J. LeVine, Bull. Am. Phys. Soc. 24, 571 (1979).

[13] P. Braun-Munzinger, G. M. Berkowitz, M. Gai, J. W. Harris, C. M. Jachcinski, C. D. Uhlhorn, J. Barrette, and M. J. LeVine (unpublished).

[14] G. Pappalardo, Phys. Lett. 13, 320 (1964).

[15] J. R. Erskine, W. Henning, D. G. Kovar, L. R. Greenwood, and R. M. DeVries, Phys. Rev. Lett. 34, 680 (1975).

[16] Code PTOLEMY, M. H. Macfarlane and S. C. Pieper, Argonne National Laboratory Informal Report No. ANL-76-11 Rev 1 (unpublished).

PHYSICAL REVIEW C VOLUME 21, NUMBER 5 MAY 1980

Resonant behavior of the ^{24}Mg(^{16}O,^{12}C)^{28}Si reaction

S. J. Sanders, M. Paul, J. Cseh,* D. F. Geesaman, W. Henning, D. G. Kovar, R. Kozub,† C. Olmer,‡ and J. P. Schiffer

Argonne National Laboratory, Argonne, Illinois 60439

(Received 29 October 1979)

The ^{24}Mg(^{16}O,^{12}C)^{28}Si reaction has been studied over the energy range $26.3 < E_{c.m.} < 32.4$ MeV. Angular distributions with $4.5° \leq \theta_{c.m.} \leq 50°$ were measured at nine different energies in this range and an excitation function was measured over a wider range at $\theta_{c.m.} \simeq 90°$. The results of the present measurements, together with previously measured excitation functions at 0° and 180°, are analyzed within the framework of two resonances, at 27.6 and 30.8 MeV, added to a direct reaction background. Probable spin assignments for the two resonances are $J = 20$ (27.6 MeV) and $J = 23$ (30.8 MeV).

[NUCLEAR REACTIONS ^{24}Mg(^{16}O,^{12}C)^{28}Si (g.s.); measured $\sigma(E,\theta)$; resonance analysis; deduced spins, reduced widths.]

I. INTRODUCTION

Unexpectedly, resonancelike behavior has been observed in the interactions of medium-heavy nuclei. The systems ^{16}O+^{28}Si,[1,2] ^{12}C+^{28}Si,[1,3] and ^{16}O+^{24}Mg,[4,5] are found to have elastic scattering yields at $\theta_{c.m.} = 180°$ of between one and ten percent of the Rutherford value, and excitation functions containing resonancelike structures with widths between 300 keV and 1 MeV. Resonances are also observed at both forward and backward angles for the transfer reactions ^{24}Mg(^{16}O,^{12}C)^{28}Si (Refs. 4–6) and ^{28}Si(^{16}O,^{12}C)^{32}S[7]. In the 0° yield of the ^{24}Mg(^{16}O,^{12}C)^{28}Si(g.s.) transfer reaction, for instance, strong modulations (peak-to-valley ratios as large as 5:1) are observed at excitations energies up to 50 MeV in the ^{40}Ca compound system.

Several observations suggest a simple explanation for the rapid energy variations in the ^{24}Mg(^{16}O,^{12}C)^{28}Si reaction yield. The excitation functions for transitions to the ground state, first excited state,[6] and several more highly excited states[7] in ^{28}Si are found to be correlated. In addition, angular distributions measured in the backward hemisphere for the ground-state transition at energies corresponding to maxima in the 180° excitation function are found to have approximately $|P_l(\cos\theta)|^2$ angular dependences.[4,5] This behavior would be expected for isolated resonances populated in a reaction involving spin-zero particles in both the incoming and outgoing channels.

Attempts to explain the origin of these structures have been hindered by insufficient knowledge of the resonance parameters. We have now completed an extensive series of measurements on the ^{24}Mg(^{16}O,^{12}C)^{28}Si reaction concentrating on the energy range $26.3 \leq E_{c.m.} \leq 32.4$ MeV. Within this energy range are two, apparently isolated, resonances in the 0° excitation function. An attempt is made to establish, in a model independent a manner as possible, the properties of these resonances. The analysis is based on new measurements, which will be discussed in the next section, as well as previously published measurements[6] of the 0° excitation function for this reaction. The 180° data included in this analysis are presented in the preceding paper,[5] together with ^{16}O+^{24}Mg elastic scattering measurements.

II. EXPERIMENT AND DATA PRESENTATION

The new data to be presented consist, in part, of angular distributions for the ^{24}Mg(^{16}O,^{12}C)^{28}Si (g.s.) reaction with $4.5° \leq \theta_{lab} \leq 34°$ at $E_{c.m.} = 26.3$, 26.9, 28.6, 29.4, 30.1, 31.6, and 32.4 MeV. An excitation function for the reaction at $\theta_{c.m.} \approx 90°$ in the range $24 \leq E_{c.m.} \leq 37.8$ MeV was also measured.[8] These measurements were performed at the Argonne National Laboratory FN tandem Van de Graaff facility using an Enge split-pole magnetic spectrometer with a gas-ionization-chamber, focal-plane detector for particle detection and identification. The angular distributions were measured with a laboratory angular acceptance of ±0.8° ($\Omega \approx 1$ msr), and the 90° excitation function was measured with a ±1.4° acceptance ($\Omega \approx 2$ msr). We have also reanalyzed earlier measurements of the 0° excitation function and angular distributions at $E_{c.m.} = 27.8$ and 30.8 MeV (Ref. 6) using a better value of the target thickness to estimate the energy-loss corrections. The 0° and 90° excitation functions, together with the 180° excitation function of Ref. 5, are shown plotted in Fig. 1 and the angular distributions are shown plotted in Fig. 2.

Self-supporting ^{24}Mg foils, of 99.9% enrichment and areal densities between 150 and 250 μg/cm^2, were used for these measurements. Target thicknesses were determined by measuring the energy degradation of oxygen scattered elastically

© 1980 The American Physical Society

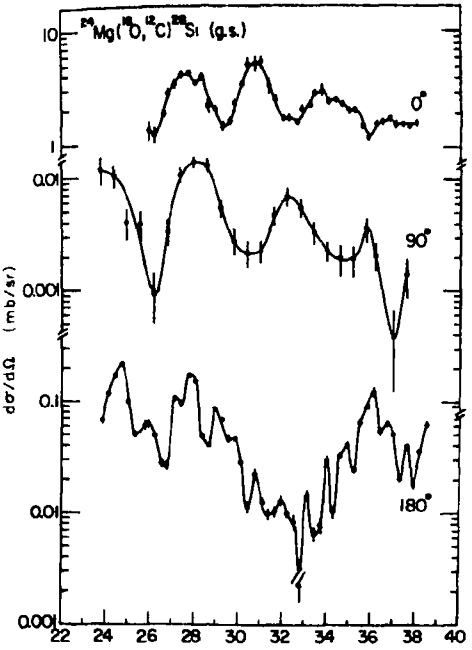

FIG. 1. Excitation functions for the ^{24}Mg(^{16}O,^{12}C)^{28}Si (g.s.) reaction at $\theta_{c.m.} = 0°$, 90°, and 180°. Indicated are the statistical errors. The curves are to guide the eye.

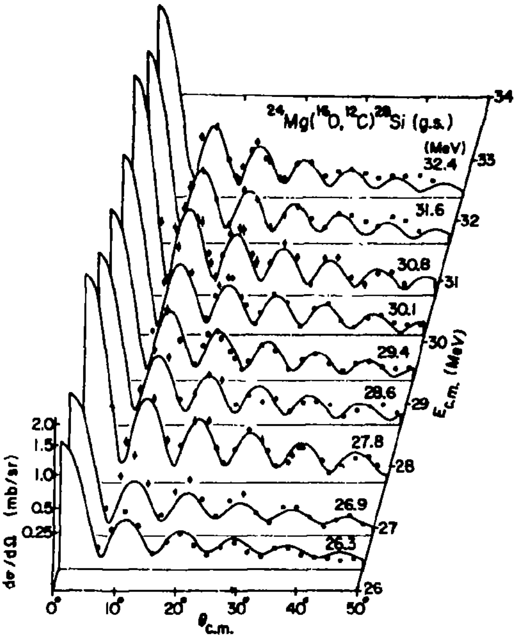

FIG. 2. Angular distributions for the ^{24}Mg(^{16}O,^{12}C)^{28}Si (g.s.) reaction. Indicated are the statistical errors. The curves, as discussed in the text, are the result of a fit to the data assuming two Breit-Wigner resonances of $l = 20$ and 23, added to a direct-reaction background which varies smoothly with energy (the background was computed using the ANL1 potential). The cross sections are plotted on a square-root scale.

from the ^{24}Mg foils. Using this technique, the uncertainty in the target areal densities is approximately ±40 μg/cm^2, which corresponds to an uncertainty of the mean beam energy of ~200 keV. In reanalyzing the 0° excitation function of Ref. 6, the target areal density was estimated to be 325 ± 75 μg/cm^2. The angle calibration of the spectrograph was checked by measuring ^{16}O elastic scattering angular distributions from gold targets at both positive and negative angles. The uncertainties in angles are estimated to be ±0.07°.

The data were normalized using the elastic scattering yields measured in a monitor detector located at $\theta_{lab} = 17.3°$. The absolute normalization of the spectrograph yields was obtained by fitting the cross section predictions of an optical-model calculation (using the potential parameters of Erskine *et al.*[9]) to an elastic scattering angular distribution measured with the spectrograph. This optical potential, whose parameters are tabulated as ANL1 in Table I, was found to reproduce the measured forward-angle, elastic scattering angular distributions in the energy range of current interest. After an absolute normalization was obtained at one energy, the normalizations for other energies were obtained by scaling the monitor yield with optical-model calculations of the elastic cross section. Two possible sources of systematic errors can be identified when using this technique: (1) the uncertainty in the calculated

TABLE I. Optical-model potentials.

	V (MeV)	r_0 (fm)	a_0 (fm)	W (MeV)	r_{i0} (fm)	a_{i0} (fm)	r_{c0} (fm)	Ref.
ANL1	37	1.35	0.404	78	1.290	0.174	1.2	11
ANL2	10	1.452	0.345	23	1.272	0.376	1.2	12

cross section at the monitor angle, and (2) since the monitor detector was located fairly close to the target (~11 cm), small displacements of the beam on target result in changes in the effective monitor angle and consequent changes in the elastic yield. The absolute normalization uncertainty is estimated to be approximately 20%.

For the present analysis we have added in quadrature a 10% error to the statistical error of each data point (15% for the 0° yields) in order to allow for possible normalization errors in the different experimental runs. For all fits to the data, the fitting function is averaged over the angular range subtended by the detector.

III. OUTLINE OF ANALYSIS

To determine the properties of the resonant structures observed in the transfer reaction, the assumption is made that the reaction amplitude for the resonant partial wave can be decomposed into a sum of a direct part, which varies slowly with energy, and a resonant part. The cross section for a reaction involving spin-zero particles in both the incoming and outgoing channels is then given by

$$\frac{d\sigma}{d\Omega} \quad \left| \sum_l \frac{1}{2ik_{\mathrm{in}}} (2l+1) f_l^{\mathrm{tot}} P_l(\cos\theta) \right|^2 , \tag{1}$$

where

$$f_l^{\mathrm{tot}} \quad f_l^{\mathrm{res}} + f_l^{\mathrm{dir}} . \tag{2}$$

The resonance term in Eq. (2) vanishes for $l \neq l_{\mathrm{res}}$. The direct part of the amplitude f_l^{dir} can be approximated by a calculated distorted wave amplitude f_l^{DWBA}, although, as will be discussed further below, there are some uncertainties in this approximation due to ambiguities in the optical-model parameters of the distorted-wave Born approximation (DWBA) calculation. It should also be realized that in the approximation of Eq. (2) the unitarity limit on the amplitudes is not guaranteed,[10] although the small size of the amplitudes as determined by the present analysis suggests that this is not a serious problem.

The behavior of the resonance amplitude f_l^{res} was investigated both in terms of requiring that it have a Breit-Wigner energy dependence and also by allowing it to be a free parameter in fits to individual angular distributions. For a Breit-Wigner resonance (see, for instance, Ref. 11),

$$f_l^{\mathrm{res}} = i \exp[i(\phi_{\mathrm{nucl}} + \sigma_{\mathrm{in}} + \sigma_{\mathrm{out}} + \phi)] \times \frac{\sqrt{\Gamma_{\mathrm{in}}}\sqrt{\Gamma_{\mathrm{out}}}}{E_0 - E - i\Gamma/2} , \tag{3}$$

where the overall phases include the DWBA nuclear phase ϕ_{nucl} and the incoming and outgoing Coulomb phases σ_{in} and σ_{out}. The additional phase ϕ was kept fixed over the full energy range and was treated as an adjustable parameter. The incoming and outgoing partial widths Γ_{in} and Γ_{out} are expressed in terms of energy independent reduced widths by factoring out the Coulomb and centrifugal-barrier penetrabilities:

$$\Gamma^l_{\mathrm{in(out)}} = 2P_l^{\mathrm{in(out)}} \gamma_{\mathrm{in(out)}}{}^2 , \tag{4}$$

where the penetrability factor can be expressed in terms of the regular and irregular Coulomb wave functions as

$$P_l = \frac{kR}{F_l{}^2 + G_l{}^2} . \tag{5}$$

For the present analysis the radius parameter R was taken as $1.6 \times (A_1{}^{1/3} + A_2{}^{1/3})$ fm. The contribution of each Breit-Wigner resonance to the cross section is therefore determined by five parameters: the resonance angular momentum l, the resonance energy E_0, the full width Γ, the product of reduced widths $\gamma_{\mathrm{in}}\gamma_{\mathrm{out}}$, and, finally, an overall phase ϕ, determined with respect to the phase of the direct amplitude. It is important to realize in applying this analysis that ϕ_{nucl}, σ_{in}, σ_{out}, $\sqrt{\Gamma_{\mathrm{in}}}$, $\sqrt{\Gamma_{\mathrm{out}}}$, and the full width Γ are all energy dependent quantities. The energy dependence of the penetrabilities can be especially significant by extending the contribution of a resonance to higher energies. Although the full width Γ has an energy dependence (through the penetrability factors for the partial widths), in the present analysis the value of Γ was fixed at 800 keV for both resonances. Allowing the full width to have the same energy dependence as the partial-width product $\sqrt{\Gamma_{\mathrm{in}}}\sqrt{\Gamma_{\mathrm{out}}}$, does not significantly alter our conclusions.

The parametrization of the direct reaction background using distorted wave amplitudes f_l^{DWBA} poses the problem of finding optical-model parameters which do not introduce resonance behavior into the transfer calculations. The substantial backward-angle yield measured in both elastic scattering channels of the ^{24}Mg(^{16}O,^{12}C)^{28}Si reaction indicates that substantial resonance strength is manifested in these channels. Ideally the optical potentials used in the analysis should fit the observed elastic data at forward angles, but not produce resonance effects at backward angles. Clearly this cannot be done in an entirely self-consistent fashion.

In the present study the analysis was carried out using two different optical potentials. The first potential, used by Erskine *et al.*[9] and herein referred to as ANL1 (Table I), was obtained from a fit to forward-angle ^{16}O+^{24}Mg elastic scattering data at $E_{\mathrm{c.m.}} = 33.6$ MeV. This potential is found to reproduce quite well the shapes of the

^{24}Mg(^{16}O,^{12}C)^{28}Si reaction angular distributions at forward angles when used in both elastic channels for a DWBA calculation although, of course, the normalizations, or spectroscopic factors, obtained at different energies vary greatly. A second potential, referred to as ANL2 (Table I) was obtained by Tabor *et al.*[12] by fitting elastic scattering data at four energies between $19.2 \leq E_{c.m.} \leq 43.2$ MeV. Four parameters (r_0, a, r_{I0}, and a_I) were varied, with the well depths fixed at $V = 10$ MeV and $W = 23$ MeV. Figure 3 shows the predictions of the two potentials for the ^{24}Mg(^{16}O,^{12}C)^{28}Si(g.s.) reaction at $E_{c.m.} = 29.4$ MeV. Here the ANL1 potential is found to provide a better fit to the data. Other potentials which predict less oscillatory transfer distributions have been found to be unsuitable for the present analysis since, even with a substantial resonance term, they do not fit the forward-angle transfer data. The potential 2 of Peng *et al.*[13] was found to yield results similar to those obtained with ANL2.

IV. DISCUSSION

Although an analysis such as the one outlined in the previous section is necessary to establish resonance parameters, it is interesting to first inspect a more naive characterization of the data. Foward-angle angular distributions measured at energies corresponding to maxima in the 0° yields of the ^{24}Mg(^{16}O,^{12}C)^{28}Si(g.s.) reaction are found to be well reproduced by a $|P_l(\cos\theta)|^2$ angular dependence. Angular distributions measured at energies corresponding to minima in the 0° excitation function are also highly oscillatory but with attenuated peak-to-valley ratios. To further explore the simple $|P_l(\cos\theta)|^2$ parametrization of these data, each of the nine forward-angle angular distributions between 26.3 and 32.4 MeV was fitted by the function $F(\theta) = A|P_l(\cos\theta)|^2$, where l was allowed to be a noninteger real number. [The function $F(\theta)$ was evaluated for noninteger l by a four-point bivariate interpolation of Legendre polynomials at integer l values.] The resulting values for l are plotted in Fig. 4 as a function of center-of-mass energy [the ordinate has been scaled as $l(l+1)$] along with the corresponding values of χ^2/(degree of freedom). As expected, this procedure best describes the data at energies corresponding to the observed maxima in the 0° yields (near 27.6 and 30.8 MeV). In addition, we note for the angular distributions taken near the 27.6 MeV resonance that the fitted value of l remains fairly constant at ≈20. A flat l dependence might be expected if an isolated resonance is dominating the structure observed in the angular distribution. For a direct-reaction mechanism, where many partial waves contribute and the dominant l has a smooth energy dependence, it would be surprising to find a plateau in the energy dependence of l. That no such plateau is found for the higher structure near 30.8 MeV may be interpreted as a consequence of the resonance amplitude competing

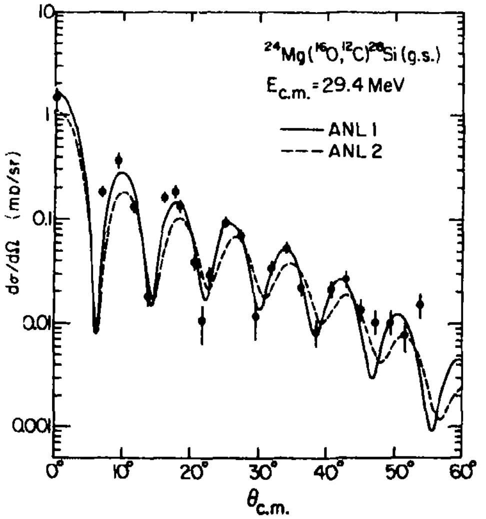

FIG. 3. Angular distributions at $E_{c.m.} = 29.4$ MeV for the ^{24}Mg(^{16}O,^{12}C)^{28}Si(g.s.) reaction. The curves are the results of DWBA calculations which have been normalized with respect to the data. The solid and dashed curves were calculated using the ANL1 and ANL2 potentials, respectively.

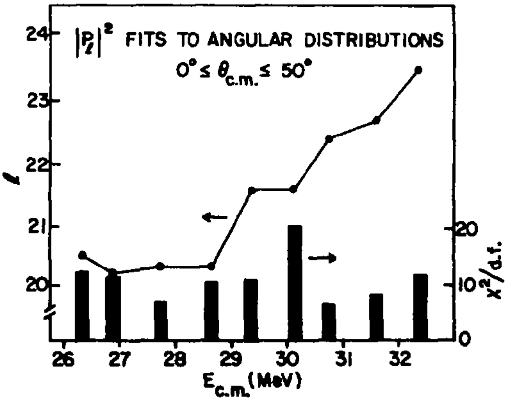

FIG. 4. Legendre polynomial fits to the forward-angle angular distributions. The polynomials were continued to noninteger values of l by interpolation from integer l values. Shown are the optimal values of l at energies where angular distributions were measured. The resulting values of χ^2/(degree of freedom) for the polynomial fits are also indicated.

less favorably with the direct amplitude at this energy.

When considering data over the full angular range, a $|P_l(\cos\theta)|^2$ parametrization is clearly not appropriate and a resonance parametrization such as discussed in the previous section becomes important. The data for the 27.8-MeV angular distribution ($0° \leq \theta_{c.m.} \leq 180°$) of Ref. 5 are shown in Fig. 5 with a fit to this angular distribution using Eq. (1). At this energy there are correlated maxima in the 0°, 90°, and 180° excitation functions (see Fig. 1). The fit to the full angular distribution has two free parameters for the complex resonance amplitude. The direct-reaction amplitudes f_l^{DWBA} were calculated with the code PTOLEMY[14] using the potential ANL1 in both the entrance and exit channels. The normalization of the direct term was fixed at the value obtained by fitting the data between 26.3 and 32.4 MeV with a Breit-Wigner parametrization of the resonance amplitudes as discussed below. The values of χ^2/d.f. for fits to the 27.8-MeV angular distribution, as well as the corresponding values of $\sqrt{\Gamma_{\mathrm{in}}}\sqrt{\Gamma_{\mathrm{out}}}$, are shown in Fig. 6 for different l assignments and using both the ANL1 and ANL2 potentials to determine the direct-reaction backgrounds. (To obtain $\sqrt{\Gamma_{\mathrm{in}}}\sqrt{\Gamma_{\mathrm{out}}}$, a fixed direct term normalization, a resonance energy of 27.6 MeV and full width Γ of 800 keV were assumed; changing the direct-amplitude normalization by 20% was found not to significantly alter the trend found for the dependence of χ^2 on l assignment.) Also shown in Fig. 6 are the resulting values of χ^2 from fits of the squares of Legendre polynomials to the backward-angle data ($120° \leq \theta_{c.m.} \leq 180°$), where the direct-reaction contribution to the observed yield is assumed to be negligible.

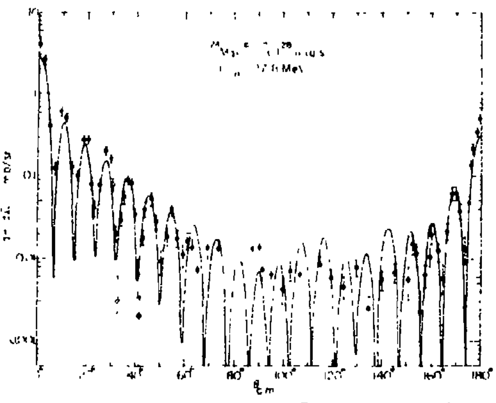

FIG. 5. Angular distribution at $E_{\mathrm{c.m.}} = 27.8$ MeV for the ^{24}Mg(^{16}O,^{12}C)^{28}Si(g.s.) reaction. The curve represents a fit to the data assuming an $l = 20$ resonance interfering with a direct-reaction DWBA amplitude as discussed in the text. The errors indicate the actual weighting of the data used in the calculated fits.

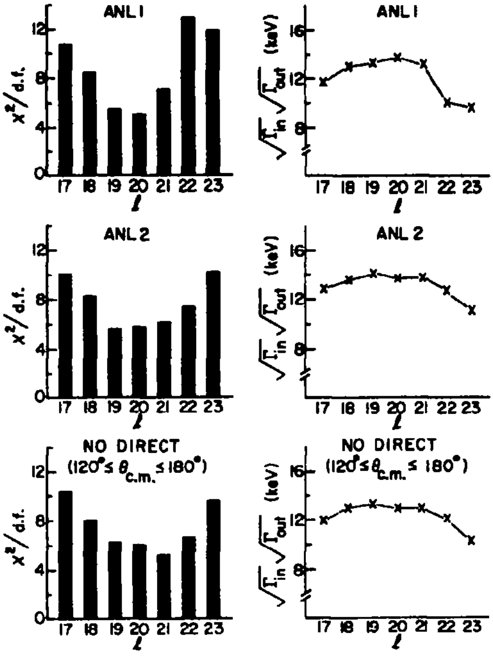

FIG. 6. Goodness-of-fit analysis and partial-width products from fits to the $E_{\mathrm{c.m.}} = 27.8$-MeV angular distribution. The partial widths were obtained assuming $E_0 = 27.6$ MeV and $\Gamma = 800$ keV.

For the analysis of the backward-angle yields there is a weak minimum in χ^2 for resonance l assignments between 19 and 21. The analyses of the full angular distribution shows a better defined minimum in χ^2 for l assignments of 19 and 20 (true for both of the background potentials used). However, the strong maximum in the 90° excitation function near 28 MeV supports an even l assignment ($P_l[\cos(\pi/2)] = 0$ for l odd). Combining this information with the results of the overall fits to the angular distribution leads us to an $l = 20$ assignment for this resonance. The best fit obtained to the full angular distribution for the $l = 20$ assignment using the ANL1 potential is the curve shown in Fig. 5.

Within the energy range of current interest a second strong maximum near 30.8 MeV is found in the 0° yield. Here it is much more difficult to make a unique l assignment: there is a minimum in the 90° excitation function at this energy—which is consistent with an odd l assignment—but there is also a relative minimum in the 180° excitation function. This low backward-angle yield prevented a precise measurement of a backward-angle angular distribution at 30.8 MeV (although an angular distribution taken with a wide aperture was obtained, see Ref. 5). From the forward-angle data alone, which are dominated by the direct process, it is not possible to rule out angular momentum assignments between $l = 20$ and $l = 26$.

To study the possible role of interference among resonances as a contributing cause for the observed 30.8-MeV angular distribution, the energy dependence of the resonance amplitudes was parametrized with a Breit-Wigner form as in Eq. (3). At least two resonances must be included to reproduce the 0° excitation function of Fig. 1 for $26.3 \leq E_{c.m.} \leq 32.4$ MeV (one of which is the 27.6-MeV resonance discussed above). The results of a two-resonance fit to the ground-state data are shown as the solid curves in Figs. 2 and 7. The two-resonance model is found to be able to reproduce the qualitative features of the data surprisingly well. In particular, the high-energy tail of the $l = 20$ resonance at 27.6 MeV, amplified by rapidly increasing penetrabilities, is found to be sufficient to destructively interfere with the 30.8-MeV resonance and result in a relative minimum in the 180° yield at the higher energy.

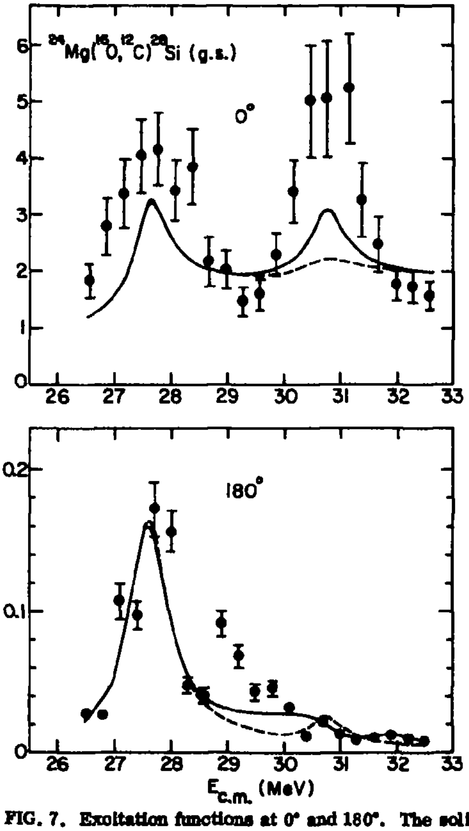

FIG. 7. Excitation functions at 0° and 180°. The solid and dashed curves are the results of $l = 20+23$ and $l = 20+22$ fits to the data, respectively. The errors indicate the actual weighting of the data used in the calculated fits. The curves have been averaged over the angular acceptance of each detector.

Unfortunately, the parameters for this two-resonance fit are not determined unambiguously; it is possible to find several different pairs of spin assignments which result in essentially equivalent fits to the data. This is seen in Fig. 8 where the value of χ^2/d.f. is plotted for several fits of the type shown in Figs. 2 and 7. In each case, an $l = 20$ assignment is assumed for the 27.6-MeV resonance, and full widths of $\Gamma = 800$ keV are assumed for both resonances. Also plotted in Fig. 8 are the fitted values of the partial width products $\sqrt{\Gamma_{in}}\sqrt{\Gamma_{out}}$ for the higher energy resonance. It is clear that the second resonance must be of opposite (odd) parity to obtain both a forward-angle maximum and a backward-angle minimum in the excitation functions near 30.8 MeV $[P_l(\cos 0°) = 1;$

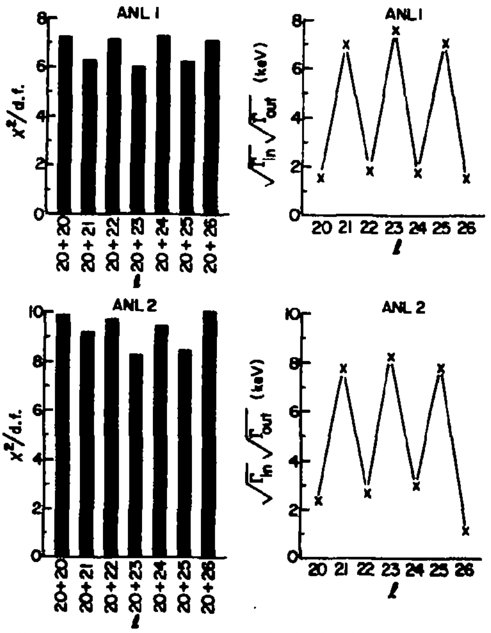

FIG. 8. Goodness-of-fit analysis for two-resonance fits to data between 26.3 and 32.4 MeV using the ANL1 and ANL2 potentials to compute the direct-reaction backgrounds. Also shown are the partial-width products determined for the higher-energy resonance near 30.8 MeV.

$P_l(\cos\pi)=(-1)^l$]. This is particularly evident in Fig. 7 where the $l=20+22$ and $l=20+23$ fits to the data are compared at 0° and 180°. It is not possible, however, to distinguish between resonance spin pairs of 20+21, 20+23, and 20+25 from Fig. 8.

Assuming that the fits should be most sensitive to the choice of spin assignments at the resonance energies, in Fig. 9 the data at $E_{\mathrm{c.m.}}=30.8$ MeV are plotted with the curves obtained for various spin-assignment parameter sets. In this figure the plotted functions are averaged over the angular acceptance for the different detectors used at forward and backward angles ($\Delta\bar{\theta}_{\mathrm{c.m.}}\approx 2.4°$ and 10° for the forward and backward angles, respectively). By inspection of the forward-angle data it is found that for the $l=25$ assignment the fit becomes out of phase with the data beyond $\theta_{\mathrm{c.m.}}\approx 25°$, at backward angles there appears to be a clear preference for the $l=23$ assignment over the $l=21$ assignment. These results suggest a spin of 23 for the 30.8-MeV resonance. In Table II the parameters associated with the Breit-Wigner fit assuming an $l=20$ resonance near 27.6 MeV and an $l=23$ resonance near 30.8 MeV are tabulated.

By imposing a Breit-Wigner energy dependence it has been possible to determine resonance parameters; however, there are several shortcomings of the analysis which become clear with closer inspection of Figs. 2 and 7. Certainly the fine structure observed at 180° in Fig. 7 cannot be reproduced by this simple model. The failure to reproduce the forward-angle peak-to-valley ratio is probably a consequence of the choice of optical-model parameters for the DWBA calculation. To loosen the assumption of a particular energy dependence, and hence to be able to check that assumption, the data for each of the angular distributions near the strong 27.6-MeV resonance were individually fitted with a complex resonance term $f^{\mathrm{res}}_{l=20}$. The direct amplitudes were computed using the ANL1 potential and normalized by the factor which gave the best fit in the Breit-Wigner analysis. The results of the Breit-Wigner analysis

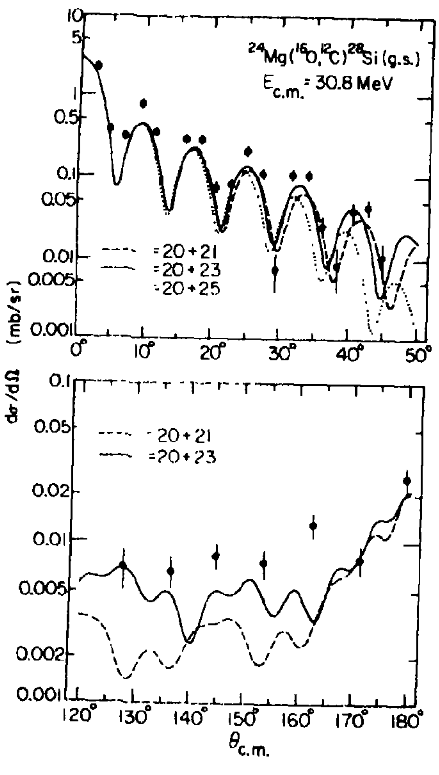

FIG. 9. Angular distribution at $E_{\mathrm{c.m.}}=30.8$ MeV. At forward angles the dashed, solid, and dotted curves correspond to the $l=20+21$, $l=20+23$, and $l=20+25$ fits to the data, respectively. At backward angles, the $l=20+21$ and $l=20+23$ fits are shown by the dashed and solid curves, respectively. The curves are averaged over the mean angular acceptance of each detector. The parameters for these curves were obtained by fitting the full range of data between 26.3 and 32.4 MeV using the ANL1 potential.

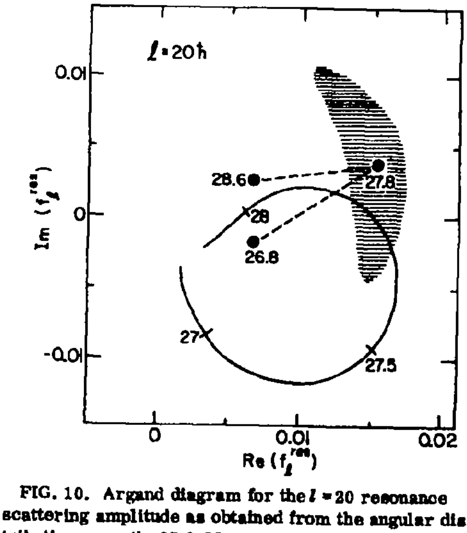

FIG. 10. Argand diagram for the $l=20$ resonance scattering amplitude as obtained from the angular distributions near the 27.6-MeV resonance. The shaded region corresponds to the loci of points where $\chi^2>1.1\times\chi_{\mathrm{min}}^2$. The solid curve is the calculated behavior assuming a Breit-Wigner energy dependence (using the parameters of Table II). The numbers are center-of-mass energies in MeV.

TABLE II. Resonance parameters.

$$f_l^{\mathrm{res}} = i\exp[i(\phi_{\mathrm{nucl}}+\sigma_{\mathrm{in}}+\sigma_{\mathrm{out}}+\phi)]\,\frac{\sqrt{\Gamma_{\mathrm{in}}}\sqrt{\Gamma_{\mathrm{out}}}}{E_0-E-i\Gamma/2}$$

$$\theta^2=\frac{3}{2}\,\frac{\hbar^2}{\mu R^2}$$

l	E_0 (MeV)	$\gamma_{\mathrm{in}}\gamma_{\mathrm{out}}$ (MeV)	$\frac{\gamma_{\mathrm{in}}\gamma_{\mathrm{out}}}{\theta_{\mathrm{in}}\theta_{\mathrm{out}}}$	$\sqrt{\Gamma_{\mathrm{in}}}\sqrt{\Gamma_{\mathrm{out}}}$ (MeV)	Γ (MeV)	ϕ
20	27.6	0.0010	0.011	0.015	0.8	176°
23	30.8	0.0006	0.006	0.008	0.8	195°

were also used as a guide in subtracting the contributions from the higher-energy resonance (generally a small correction). The resulting complex resonance amplitudes are indicated in Fig. 10 on an Argand diagram. For comparison, the Breit-Wigner behavior of the resonance amplitude using the parameters of Table II is also indicated in this figure. The resonance amplitudes for the three energies closest to the resonance energy are found to have roughly the appropriate behavior, but an estimate of the errors on the fitted amplitudes indicates the limitations of such an analysis. The shaded region in Fig. 10 surrounding the 27.8-MeV amplitude was found by mapping out a region in the χ^2 space of the complex amplitude corresponding to a 10% increase in χ^2 above its smallest value. The phase uncertainty in the amplitude is found to be about ±30%. The large uncertainties in the fitted parameters preclude any conclusions from this last analysis other than that the energy dependence is consistent with a resonance interpretation.

From these and our earlier considerations we conclude that while the simple model of parametrizing the energy dependence of the resonances with two Breit-Wigner shapes is not valid in detail, it does indicate with reasonable certainty the partial waves responsible for the dominant resonant structures.

V. CONCLUSIONS

The main features of both the forward- and backward-angle excitation functions for the $^{24}Mg(^{16}O,^{12}C)^{28}Si$(g.s.) reaction in the range 26.3 $\leq E_{\mathrm{c.m.}} \leq 32.6$ MeV have been found to be explained reasonably well by assuming two resonances near 27.6 and 30.8 MeV of probable spins 20 and 23, respectively. Both the full widths and reduced widths for these two resonances are comparable. The very selective nature of this reaction in exciting the particular resonances is seen by considering that the predicted density of spin-20 states near the 27.6-MeV resonance (corresponding to $E_x \sim 44$ MeV in the ^{40}Ca compound system) is found to be close to 5×10^4 levels/MeV using the conventional Fermi gas formula. From simple shell-model considerations the lowest energy spin-20 state should be at a ^{40}Ca excitation energy of about 27 MeV. Clearly the observed resonances are not part of the yrast band, but rather have structures more closely tied to the entrance and exit channels.

In Fig. 11 these two spin assignments as well as an $l = 26$ assignment from Ref. 5 are plotted on an energy vs $l(l+1)$ plot. Also indicated on this plot

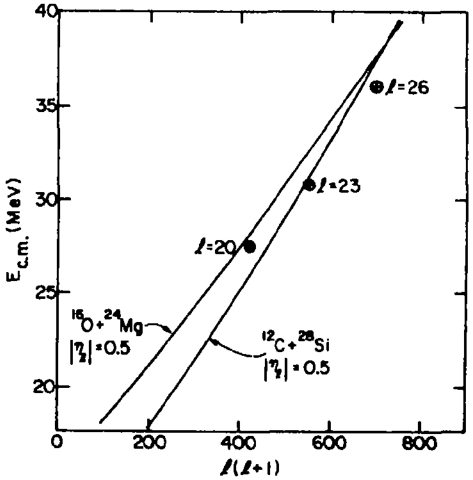

FIG. 11. Plot of l (l +1) vs energy for resonance assignments of the present work as well as a previous l = 26 assignment from Ref. 5. Also indicated are the trajectories followed by the entrance and exit channel grazing partial waves, which were calculated using the ANL1 potential, and taking as the grazing angular momenta the values where $|\eta_l| = 0.5$.

are the trajectories followed by the entrance and exit channel grazing partial waves calculated using the ANL1 potential. Here the grazing angular momentum was taken as the value where the amplitude of the elastic scattering S matrix $|\eta_l|$ equals 0.5. Even though the spins are found to follow roughly a grazing trajectory, the observed spin sequence is inconsistent with any simple band picture where the resonances are assumed to have the same principal quantum number. This situation may be compared to the backward-angle elastic scattering measurements for the $^{16}O+^{28}Si$ system where similar irregular spin sequences are found.[2,3] For the elastic case it has been suggested[1] that these spin sequences might be understood as resulting from a series of shape resonances in the ion-ion potential having different principle quantum numbers, and centered about a grazing trajectory window. Of course the strict optical-model shape resonances in the entrance and exit channels will not have a common origin. However, in the real nuclear system, there may well be simple structures, related to shape resonances in both channels, which will appear as resonances in the reaction connecting the two channels. A search for correlated resonances in other channels is in progress.

This work was performed under the auspices of the U. S. Department of Energy.

---

*Present address: Institute of Nuclear Research, Debrecen, Hungary.

†Present address: Tennessee Tech. Univ., Cookville, Tenn. 38501.

‡Present address: Dept. of Physics, Indiana Univ., Bloomington, Ind. 47401.

[1] J. Barrette, M. J. LeVine, P. Braun-Munzinger, G. M. Berkowitz, M. Gai, J. W. Harris, and C. M. Jachcinski, Phys. Rev. Lett. 40, 445 (1978).

[2] C. K. Gelbke, T. Awes, U. E. P. Berg, J. Barrette, M. J. LeVine, and P. Braun-Munzinger, Phys. Rev. Lett. 41, 1778 (1978).

[3] M. R. Clover, R. M. DeVries, R. Ost, N. J. A. Rust, R. N. Cherry, Jr., and H. E. Gove, Phys. Rev. Lett. 40, 1008 (1978).

[4] S. M. Lee, J. C. Adloof, P. Chevallier, D. Disdier, V. Rauch, and F. Scheibling, Phys. Rev. Lett. 42, 429 (1979).

[5] M. Paul, S. J. Sanders, D. F. Geesaman, W. Henning, D. G. Kovar, C. Olmer, J. P. Schiffer, J. Barrette, and M. J. LeVine, Phys. Rev. C 21, 1802 (1980), preceding paper.

[6] M. Paul, S. J. Sanders, J. Cseh, D. F. Geesaman, W. Henning, D. G. Kovar, C. Olmer, and J. P. Schiffer, Phys. Rev. Lett. 40, 1310 (1978).

[7] S. J. Sanders, D. F. Geesaman, W. Henning, D. G. Kovar, C. Olmer, M. Paul, and J. P. Schiffer, Bull. Am. Phys. Soc. 24, 571 (1979).

[8] See AIP document No. PAPS PRVCA-21-1810-22 for 22 pages of tabulations of the cross sections measured in the present work and in Ref. 6. Order by PAPS number and journal reference from American Institute of Physics, Physics Auxiliary Publication Service, 335 E. 45th Street, New York, N.Y. 10017. The price is $1.50 for microfiche, or $5 for photocopies. Airmail additional. Make checks payable to the American Institute of Physics. This material also appears in *Current Physics Microfilm*, the monthly microfilm edition of the complete set of journals published by AIP, on the frames immediately following this journal article.

[9] J. R. Erskine, W. Henning, D. G. Kovar, L. R. Greenwood, and R. M. DeVries, Phys. Rev. Lett. 34, 680 (1975).

[10] R. G. Thomas, Phys. Rev. 100, 25 (1955).

[11] J. M. Blatt and L. S. Biedenharn, Rev. Mod. Phys. 24, 258 (1952).

[12] S. L. Tabor, D. F. Geesaman, W. Henning, D. G. Kovar, K. E. Rehm, and F. W. Prosser, Jr., Phys. Rev. C 17, 2136 (1978).

[13] J. C. Peng, J. V. Maher, W. Oelert, D. A. Sink, C. M. Chong, and H. S. Song, Nucl. Phys. A264, 312 (1976).

[14] Code PTOLEMY, M. H. Macfarlane and S. P. Pieper, Argonne National Laboratory Informal Report No. ANL-76-11 Rev. 1, 1978 (unpublished).

PHYSICAL REVIEW C VOLUME 21, NUMBER 5 MAY 1980

Complete fusion of ^{15}N+^{27}Al

F. W. Prosser, Jr.
Argonne National Laboratory, Argonne, Illinois 60439
and University of Kansas, Lawrence, Kansas 66045

R. A. Racca
University of Kansas, Lawrence, Kansas 66045

K. Daneshvar, D. F. Geesaman, W. Henning, D. G. Kovar, K. E. Rehm,* and S. L. Tabor†
Argonne National Laboratory, Argonne, Illinois 60439

(Received 22 October 1979)

The total fusion cross section for the system ^{15}N + ^{27}Al has been measured over an energy range 27 MeV $\leq E_{\rm lab} \leq$ 70 MeV by detection of the fusion-evaporation residues. In addition elastic scattering was measured at six energies and fitted by optical model calculations. The fusion cross section for the system saturates at 1150±50 mb. The data can be well described by the model of Glas and Mosel, using a reasonable set of parameters. The model of Horn and Ferguson also describes the data well if an appropriate charge radius is used. Comparison is made between these results and the fusion cross sections for ^{16}O + ^{26}Mg and ^{18}O + ^{24}Mg, which lead to the same compound nucleus. The results for ^{15}N + ^{27}Al are quite similar to those for ^{18}O + ^{24}Mg, and the differences between the fusion cross sections for these two systems and those for ^{16}O + ^{26}Mg may be evidence for an entrance channel effect.

[NUCLEAR REACTIONS ^{15}N+^{27}Al, $E_{\rm lab}$=27–70 MeV; measured $\sigma_{\rm fusion}(E)$; measured $d\sigma/d\Omega$ elastic scattering; data fitted with Glas and Mosel model, Horn and Ferguson model.]

I. INTRODUCTION

As an extension to recent measurements[1] of the total fusion cross sections for the ^{16}O+^{26}Mg and ^{18}O+^{24}Mg systems, measurements of the fusion excitation function have been made for the system ^{15}N+^{27}Al. The motivations for this study were as follows: Since ^{15}N+^{27}Al forms the same compound nucleus, ^{42}Ca, as ^{16}O+^{26}Mg and ^{18}O+^{24}Mg, a comparison of the fusion excitation functions provides a test for entrance channel effects. In particular, at the time this study was undertaken no other systems had been reported in this mass region whose constituents are both odd-A nuclei, and there is the possibility that transfer reactions involving the unpaired nucleons might affect the fusion process. Since then, some results for the system ^{19}F+^{23}Na, which also forms the compound nucleus ^{42}Ca, have been presented.[2] Because the Q values for these systems differ by only a few MeV, it is expected that effects caused by different energies of the compound system are small. Also, previous measurements[3-6] of the fusion cross section for several systems indicated an abrupt change in the maximum fusion cross sections ($\sigma_{\rm fus}^{\rm max}$) in going from reactions involving only 1p-shell nuclei ($\sigma_{\rm fus}^{\rm max}$ ~ 950 mb) to reactions involving 1p- and 2s1d-shell systems ($\sigma_{\rm fus}^{\rm max}$ ~ 1200 mb). The only evidence which existed at that time contrary to the interpretation of this difference as a shell effect was the ^{15}N+^{12}C system.[7] An investigation of the ^{15}N+^{27}Al system might help in understanding whether this anomaly is due to the specific participation of the ^{15}N projectile. However, several recent measurements of other 1p-shell systems have also shown larger values of $\sigma_{\rm fus}^{\rm max}$ (e.g., $\sigma_{\rm fus}^{\rm max}$ ~ 1200 mb for the ^{10}B+^{16}O system).[8] This gives further evidence that the differences in $\sigma_{\rm fus}^{\rm max}$ between various light systems are due to the structures of the interacting nuclei, but that they cannot be ascribed to a simple shell effect alone.

II. EXPERIMENTAL PROCEDURE AND RESULTS

Evaporation residues were measured with a ΔE-E counter telescope similar to that of Fowler and Jared.[9] This counter consists of a gas-ionization chamber backed by an Si surface-barrier detector. The total fusion cross sections were established by measuring complete angular distributions at $E_{\rm lab}$=27, 33, 39, 48, 62, and 70 MeV. All particles with $Z > 13$ were identified as fusion residues. Three monitor detectors, positioned in and out of the reaction plane as described in Ref. 1, provided the relative normalization and detected changes in the incident beam

© 1980 The American Physical Society

direction. The total fusion cross sections at other energies were extracted from single angle measurements ($\Theta_{lab} = 8^\circ$). A detailed description of the experimental techniques is given elsewhere.[1,3]

The aluminum targets used in the experiment were found to contain a significant amount of oxygen contamination. Since the ^{15}N+^{27}Al residues overlap with those from ^{15}N+^{16}O, it was necessary to subtract the oxygen contribution to the total fusion yield. Two methods were used to do this. In the earlier runs, fusion residues were measured alternately for Al and WO_3 targets at several energies and angles in the mid-energy range. Since tungsten does not contribute to σ_{fus} at the bombarding energies used here (because of the higher Coulomb barrier), the ^{15}N+^{16}O fusion yield was determined with the WO_3 targets and used as a basis for subtraction from the N+Al spectra. Fusion yields of ^{15}N+^{16}O at other energies and angles were obtained by interpolation and extrapolation from the mid-energy data. In later runs, the fusion yields were alternately measured for both Al and Al_2O_3 targets at each angle and energy. An analytical subtraction procedure was then used to obtain the ^{15}N+^{27}Al fusion yield, based on the relative amounts of elastic scattering observed from Al and O. Total fusion cross sections at several energies were obtained using both methods and the results agreed to within the statistical uncertainties. Therefore the weighted average has been used at repeated points. The energy associated with each cross section is that of the target center; i.e., the energy loss in the target has been taken into account.

A plot of the total fusion cross section vs $1/E_{c.m.}$ is shown in Fig. 1. The present data are not sufficient to establish the presence of any structure in the excitation function such as that seen in several other systems.[3,5,10-12] The saturation of $\sigma_{fus}(E)$ at the highest energies does appear to be established by the present data at ~1150 mb.

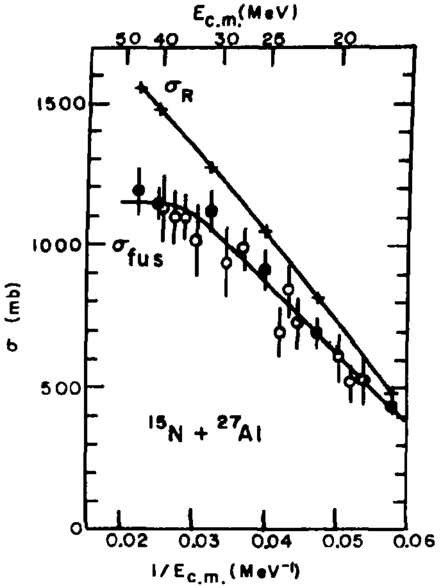

FIG. 1. Fusion and total reaction cross sections for the ^{15}N+^{27}Al system. The values of σ_{fus} obtained from complete angular distributions are shown as solid circles, while those obtained from single angle measurements are shown as open circles. The error bars indicate the estimated absolute errors. The curve denoted σ_{fus} is the fit to the fusion data with the model of Glas and Mosel. The curve denoted σ_R is the total reaction cross section predicted by the optical model, with the crosses indicating the energies where optical model fits were made to the elastic scattering data.

Elastic scattering of ^{15}N was measured simultaneously with the fusion residues at the six energies previously mentioned. Optical model analyses of the elastic scattering were performed to predict the total reaction cross sections and to help establish the absolute normalization of the fusion cross sections. The optical model analysis was done with the program PTOLEMY.[13] The depths of the real and imaginary potential wells were fixed at 10 and 23 MeV, respectively, and only the geometry of the potentials was allowed to vary, to permit comparison with the values for ^{16}O+^{28}Mg and ^{18}O+^{24}Mg from Ref. 1. The total reaction cross sections based on these calculations are shown in Fig. 1. The optical model parameters obtained are listed in Table I together with those previously determined for the O+Mg systems. The elastic scattering angular distributions and the optical model fits obtained are shown in Fig. 2 for several energies. The data were also fitted with fixed values of V and W equal to 30 and 15 MeV and to 5 and 7 MeV, respectively. These led to equally good fits,

TABLE I. Energy-independent optical model parameters obtained in a fit to the elastic scattering data. The well depths were held fixed and only the geometry of the potentials was allowed to vary. The parameters are defined in Ref. 1, from which the values for the O+Mg systems were taken.

System	V (MeV)	r (fm)	a (fm)	W (MeV)	r_I (fm)	a_I (fm)
^{15}N+^{27}Al	10	1.416	0.533	23	1.338	0.342
^{16}O+^{28}Mg	10	1.390	0.473	23	1.200	0.528
^{18}O+^{24}Mg	10	1.421	0.356	23	1.200	0.524

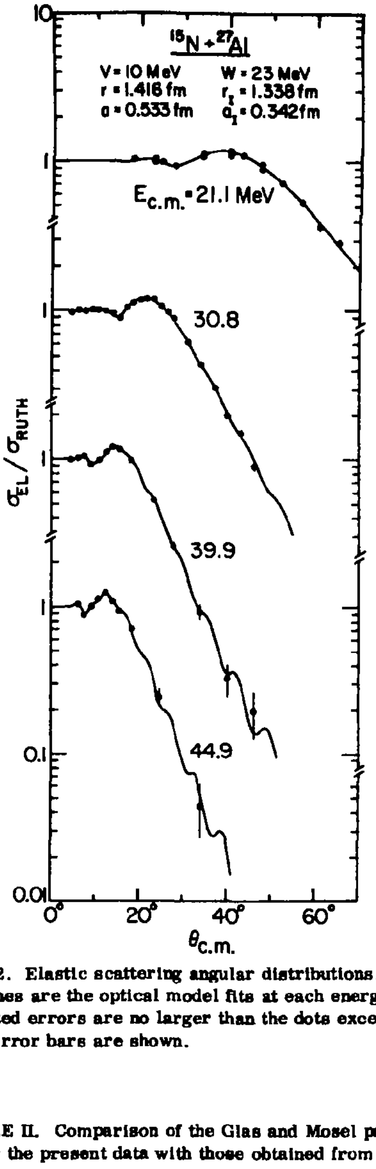

FIG. 2. Elastic scattering angular distributions. The solid lines are the optical model fits at each energy. Estimated errors are no larger than the dots except where error bars are shown.

TABLE II. Comparison of the Glas and Mosel parameters for the present data with those obtained from Ref. 1, corrected to center-of-target energies. The values of V_C and $\hbar\omega$ were fixed at 0 and 5 MeV, respectively. The value of V_B in parentheses is that for $^{15}N+^{27}Al$ adjusted for Coulomb effects (see text).

System	r_B (fm)	R_B (fm)	V_B (MeV)	r_C (fm)	R_C (fm)
$^{15}N+^{27}Al$	1.41	7.70±0.35	13.3±0.5 (14.1)	1.10	6.02
$^{16}O+^{26}Mg$	1.59	8.70±0.30	16.1±0.4	1.12	6.14
$^{18}O+^{24}Mg$	1.40	7.72±0.30	14.5±0.04	1.15	6.33

based on the final values of chi squared, and caused changes in the predicted reaction cross sections of less than 2%.

III. DISCUSSION

The fusion cross sections were fit with the model of Glas and Mosel,[14] where the criterion for fusion is that the colliding nuclei must reach a certain critical distance of separation. At low energies the fusion process is determined by the barrier potential (V_B) and the barrier radius (R_B). At high energies the important parameters are the critical distance of separation (R_C) and the potential (V_C) at this radius. As pointed out in Ref. 1, the O+Mg data were not sufficient to determine all the parameters reliably. Hence, for the purpose of comparison, the values used in Ref. 1 of $V_C = 0$ MeV and $\hbar\omega = 5$ MeV were held fixed and the other parameters varied. The Glas and Mosel fit to the data is shown in Fig. 1 and the general smooth increase and eventual saturation of σ_{fus} with increasing energy are well represented. The fitted parameters are listed in Table II, together with those of Ref. 1. All three systems agree well in the value of R_C, essentially a result of the almost identical values of σ_{fus}^{max} and the choice $V_C = 0$.

For comparison with the barrier parameters of the O+Mg systems, the value of V_B for $^{15}N+^{27}Al$ (because of the dominance of the Coulomb barrier contribution) must be multiplied by the ratio of the charge product factors. The resulting value for V_B is included in Table II in parentheses. We note that the barrier parameters agree well with those of the $^{18}O+^{24}Mg$ system and differ from those of the $^{16}O+^{26}Mg$ system. This difference is shown in Fig. 3, where the function $\pi R_B^2(1-V_B/E_{c.m.})$, which represents well the low-energy fusion cross sections, is plotted for the three systems, using the charge corrected value of V_B for $^{15}N+^{27}Al$. While the uncertainties in the individual data are sufficiently large that the data for all three systems overlap when plotted vs $Z_1Z_2/E_{c.m.}$, the general trend of the ^{15}N and ^{18}O induced fusion cross sections seems to differ from the ^{16}O induced cross sections. Thus these data appear to show evidence of an entrance channel dependence. In fact it is at the lowest energies in the present data for the three systems where these differences become most apparent, and further studies of the distributions of reaction strength for $E_{c.m.} < 20$ MeV would be of interest. Unfortunately for present purposes, the other investigation[8] of entrance channel effects in the $A = 42$ system concentrated on the higher energy region and yielded no information

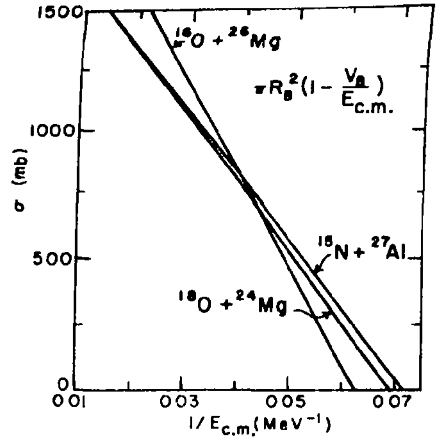

FIG. 3. Low-energy behavior of the fusion cross sections for the $^{15}N + {}^{27}Al$, $^{16}O + {}^{26}Mg$, and $^{18}O + {}^{24}Mg$ systems. The barrier parameters used are those obtained in Glas and Mosel fits to the data and listed in Table II, with the Coulomb adjusted value of V_B for N+Al (see text).

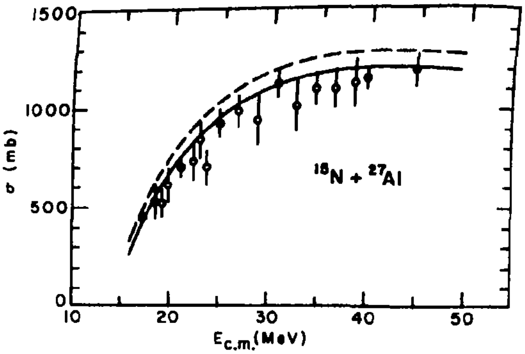

FIG. 4. Fusion cross sections for the $^{15}N + {}^{27}Al$ system. The curves were calculated with the model of Ref. 16. A radius of 4.495 fm at 1.35% charge density was used for the solid curve, while a radius of 4.696 fm was used for the dashed curve.

about the barrier dominated region. Recently, however, Rascher *et al.*[15] have noted a similar difference between ^{16}O- and ^{18}O-induced fusion with targets of ^{27}Al and natural Si.

Horn and Ferguson[16] have suggested that the difference in σ_{fus}^{max} between the $^{14}N + {}^{12}C$ and $^{15}N + {}^{12}C$ systems can be explained in terms of the measured ^{14}N and ^{15}N charge distributions. The radius parameter which they use is the sum of the radii of target and projectile at which their charge densities reach 1.35% of their central densities. Unfortunately, it appears that the electron scattering data do not determine this radius well, since the most recent compilation[17] lists fits using three different shape models for ^{15}N and the extreme values for the 1.35% radius differ by 0.2 fm. Fits to the present fusion cross sections using the two extreme values (4.696 fm for a three parameter Fermi distribution and 4.495 fm for a harmonic oscillator distribution) are shown in Fig. 4. It can be seen that the use of the smaller radius leads to a satisfactory fit to the data, while the use of the larger radius overestimates the cross sections by about 100 mb. However, use of this smaller radius predicts only a 50 mb increase for σ_{fus}^{max} in the $^{15}N + {}^{12}C$ system over that for the $^{14}N + {}^{12}C$ system, whereas the experimental difference is observed to be $\gtrsim 150$ mb.[18] Thus our present data suggest that the observed difference in these two systems is not a simple size effect.

IV. SUMMARY

In this paper, we have reported measurements of the total fusion cross sections for the $^{15}N + {}^{27}Al$ systems. A comparison of these data with those of the previously reported O+Mg systems, which lead to the same compound nucleus, suggests that the energy dependence of the low-energy fusion cross section shows evidence of entrance channel effects. The barrier parameters extracted for the $^{15}N + {}^{27}Al$ system are quite similar to those obtained for the $^{18}O + {}^{24}Mg$ system, once simple Coulomb effects are removed, while both appear to be distinct from those of the $^{16}O + {}^{26}Mg$ system. The maximum fusion cross section for $^{15}N + {}^{27}Al$ is 1150± 50 mb, typical of other systems involving a 1*p*-shell nucleus and a 2*s*1*d*-shell nucleus. Our analysis suggests that the large maximum fusion cross section for the $^{15}N + {}^{12}C$ system is not a simple size effect.

This research was conducted under the auspices of the Department of Energy. It was also supported in part (F.W.P. and R.A.R.) by the General Research Fund of the University of Kansas and by a grant from the Department of Energy. The assistance of J. Maher and W. Jordan during a portion of the data taking is gratefully acknowledged.

[*] Present address: Technische Hochschule München, 3046 Garching, West Germany.

[†] Present address: Department of Physics and Astronomy, University of Maryland, College Park, Maryland 20742.

S. L. Tabor, D. F. Geesaman, W. Henning, D. G. Kovar, K. E. Rehm, and F. W. Prosser, Jr., Phys. Rev. C 17, 2136 (1978). The energy values used in this paper were those of the beam at the front of the target. All values cited in the present paper have been corrected to center-of-target energies.

D. Horn, A. J. Ferguson, and O. Haüser, Nucl. Phys. A311, 238 (1978).

P. Sperr, S. Vigdor, Y. Eisen, W. Henning, D. G. Kovar, T. R. Ophel, and B. Zeidman, Phys. Rev. Lett. 36, 405 (1976).

R. G. Stokstad, J. Gomez del Campo, J. A. Biggerstaff, A. H. Snell, and P. H. Stelson, Proceedings of the Symposium on Macroscopic Features of Heavy-Ion Collisions, Argonne National Laboratory, Report No. ANL/PHY-76-2, 1976, Vol. II, p. 795; J. Gomez del Campo, R. G. Stokstad, J. A. Biggerstaff, R. A. Dayras, A. H. Snell, and P. H. Stelson, Phys. Rev. C 19, 2170 (1979).

[5] P. Sperr, T. H. Braid, Y. Eisen, D. G. Kovar, F. W. Prosser, Jr., J. P. Schiffer, S. L. Tabor, and S. Vigdor, Phys. Rev. Lett. 37, 321 (1976).

[6] D. F. Geesaman, C. N. Davids, W. Henning, D. G. Kovar, K. E. Rehm, J. P. Schiffer, S. L. Tabor, and F. W. Prosser, Jr., Phys. Rev. C 18, 284 (1978).

[7] S. Harar, in *Proceedings of the Colloque Franco-Japonais de Spectroscopie Nucleaire et Reaction Nucleaire*, edited by Y. Shida (Institute for Nuclear Study, Tokyo, 1976), p. 191.

[8] J. Gomez del Campo, R. A. Dayras, J. A. Biggerstaff, D. Shapiro, A. H. Snell, P. H. Stelson, and R. G. Stokstad, Phys. Rev. Lett. 43, 26 (1979).

[9] M. M. Fowler and R. C. Jared, Nucl. Instrum. Methods 124, 341 (1975).

[10] S. L. Tabor, Y. Eisen, D. G. Kovar, and Y. Vager, Phys. Rev. C 16, 673 (1977).

[11] J. J. Kolata, R. M. Freeman, F. Haas, B. Hersch, and J. Gallman, Phys. Lett. 65B, 333 (1976).

[12] Z. E. Switkowski, H. Winkler, and P. R. Christensen, Phys. Rev. C. 15, 449 (1977).

[13] D. H. Gloeckner, M. H. Macfarlane, and S. C. Pieper, Argonne National Laboratory Report No. ANL-76-11.

[14] D. Glas and U. Mosel, Phys. Rev. C 10, 2620 (1974).

[15] R. Rascher, W. F. J. Müller, and K. P. Lieb, Phys. Rev. C 20, 1028 (1979).

[16] D. Horn and A. J. Ferguson, Phys. Rev. Lett. 41, 1529 (1978).

[17] C. W. de Jager, H. de Vries, and C. de Vries, At. Data Nucl. Data Tables 14, 479 (1974).

[18] It would, of course, be preferable to use the nuclear matter distribution rather than the charge distribution. However, it is clear from the present data that no single choice of radius for ^{15}N can simultaneously explain the ^{15}N+^{12}C and ^{15}N+^{27}Al fusion cross sections with the model of Ref. 16. The problem could lie with the radius of ^{27}Al. Reference 17 gives two fits for different momentum transfer ranges, both to a two-parameter Fermi distribution, for ^{27}Al. These differ, at the 1.35% radius, by less than 0.02 fm and the choice will have a negligible effect on the conclusion.

PHYSICAL REVIEW C VOLUME 21, NUMBER 5 MAY 198

Backward angle cross sections for ^{27}Al+^{16}O reaction products

D. Shapira, J. L. C. Ford, Jr., J. Gomez del Campo, and P. H. Stelson
Oak Ridge National Laboratory, Oak Ridge, Tennessee 37830

(Received 10 December 1979)

Reactions induced by bombarding a ^{16}O gas target with ^{27}Al ions were studied. Evaporation residues as well as target-like recoils were measured over a wide range of Q values. The yield of particles with $6 \leq Z \leq 9$ was found to be forward peaked in the laboratory frame. These target-like particles emerge with center-of-mass kinetic energies that, on the average, are independent of the reaction angle. Their combined cross section has a $1/\sin\theta_{c.m.}$ angular dependence. If this cross section is assumed to be symmetric about 90° (c.m.) the integrated cross section is about 10% of the measured evaporation residue cross section at a center-of-mass energy of 54 MeV.

[NUCLEAR REACTIONS ^{27}Al+^{16}O, $E_{^{27}\mathrm{Al}} = 105$, 145 MeV; measured $d\sigma/d\Omega$ for reaction products with $6 \leq Z \leq 9$ and $Z > 13$ for $2.5° \leq \theta_L \leq 15°$. Extracted σ for evaporation residues and damped events.]

I. INTRODUCTION

The ^{16}O+^{27}Al system has been the subject of numerous studies.[1-5] The evaporation residue cross sections have been measured by bombarding ^{27}Al targets with ^{16}O beams at many different bombarding energies,[1,3,4] and some features have emerged that set it apart from other systems with similar mass. The resulting energy dependence, when analyzed in the framework suggested by Glas and Mosel,[6] yields values for the critical radius and critical potential[1] ($r_{cr} \simeq 0.79$ fm and $V_{cr} = -40$ MeV) which deviate significantly from the values one would expect on the basis of systematic trends in this mass region ($r_{cr} = 1.0$ to 1.1 fm and $V_{cr} \sim 0$ MeV).[7] Furthermore, a large component of strongly damped events with masses and charges near that of the beam (^{16}O) has been observed.[2] These events are forward peaked and have been identified[2] as deep inelastic reaction products.

In the present measurements on the ^{16}O+^{27}Al system the target and projectile were interchanged. By having the lighter particle as the target, we were able to simultaneously detect evaporation residues as well as the forward scattered target-like particles. Use of a gas target of ^{16}O enabled the identification of reaction processes over a wide range of energy loss, mass, and Z without the confusion often due to light contaminants. In this measurement we detected strongly damped-target-like products at forward angles. In this way we were able to extend the earlier measurements of damped events, done with ^{16}O as the beam, to the backward hemisphere. The angular distribution measured for these "deep inelastic" events shows a backward angle rise and follows on the average a $1/\sin\theta_{c.m.}$ angular distribution in the backward hemisphere.

II. EXPERIMENTAL PROCEDURE AND RESULTS

A natural oxygen gas target[8] was bombarded with 120- and 160-MeV ^{27}Al beams from the Brookhaven National Laboratory MP tandem accelerator. The experimental setup is shown in Fig. 1. The beam was tightly collimated by two slits, C_1 and C_2, which were about one meter apart. The target cell was constructed in a way that allowed simultaneous measurement of reaction products emerging on both sides of the beam. By detecting reaction products on both sides of the beam it was possible to monitor the average position and angle of incidence of the beam. The reaction products were identified using two ΔE-E counter telescopes. A gas ionization chamber backed by a solid state detector[9] provided energy loss and residual energy signals for each event. The solid angles of both detectors were determined from the measured dimensions by geometric calculations[8] and with a calibrated α-particle source. The absolute norm-

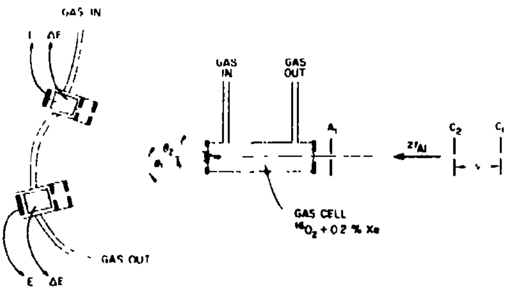

FIG. 1. A schematic of the experimental setup.

© 1980 The American Physical Society

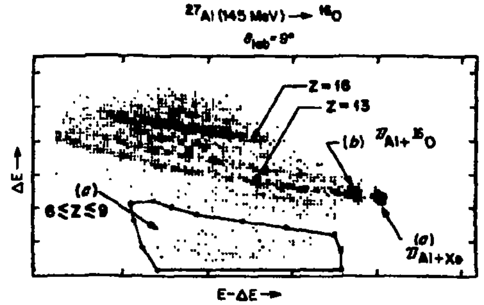

FIG. 2. A two-dimensional spectrum for ^{27}Al+^{16}O reaction products. (a) *is the peak corresponding to* ^{27}Al+Xe elastic scattering. (b) is the ^{27}Al+^{16}O elastic scattering peak. (c) damped-target-like events.

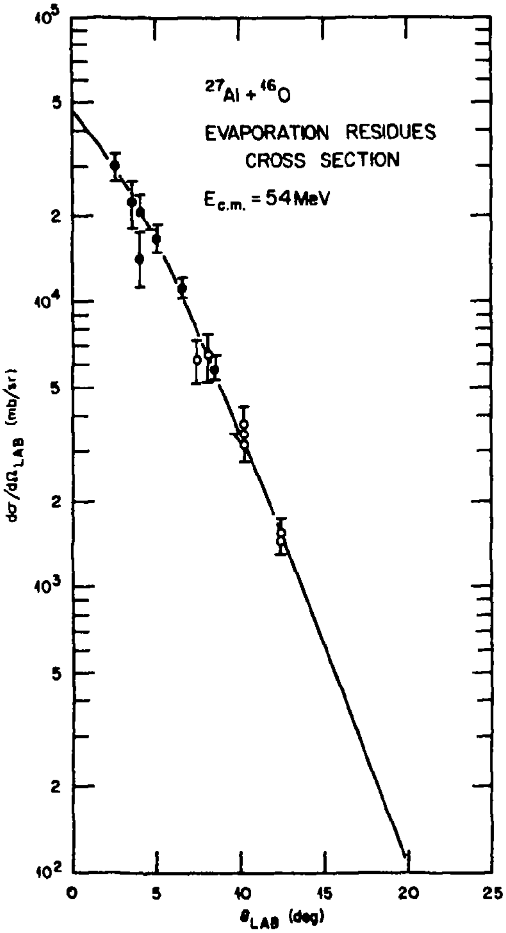

FIG. 3. Angular distribution for evaporation residues measured at a center-of-mass energy of 54 MeV. The open and closed circles correspond to measurements on opposite sides of the beam (see Fig. 1).

alization of the data was obtained from scattering of the ^{27}Al beam by Xe gas mixed with the target gas at a 0.2%±0.004% molar ratio. More details on the geometric corrections and normalization procedure are available from Ref. 8. A typical two-dimensional E vs ΔE spectrum is shown in Fig. 2. The two elastic peaks resulting from ^{16}O+^{27}Al and Xe+^{27}Al elastic scattering are indicated, as is the two-dimensional gate drawn around the events which we designate as recoiling target-like nuclei ($Z\sim8$). The evaporation residues are clustered around the strong $Z=16$ line located above the ^{27}Al line. At more forward angles the yield from evaporation residues became much more intense and was shifted toward higher Z values. Measurements were performed at eleven angles spanning 2.5° to 15° in the laboratory system. Figure 3 displays an angular distribution for evaporation residues with $Z>13$ measured at $E_{c.m.}=54$ MeV.[10] The resulting integrated evaporation residue cross section is 1260±220 mb. A comparison was made with mass and charge distributions from previous measurements at similar energies[1-3] and with the elemental distributions predicted by a Hauser-Feshbach multiparticle evaporation code.[11] As a result, we believe that by summing evaporation residues with $Z>13$ we obtain more than 96% of the total evaporation residue yield. The large uncertainties are mainly a result of low counting statistics in the Xe+^{27}Al elastic scattering peak.

We now focus our attention on the reaction products encircled by the two-dimensional mask shown

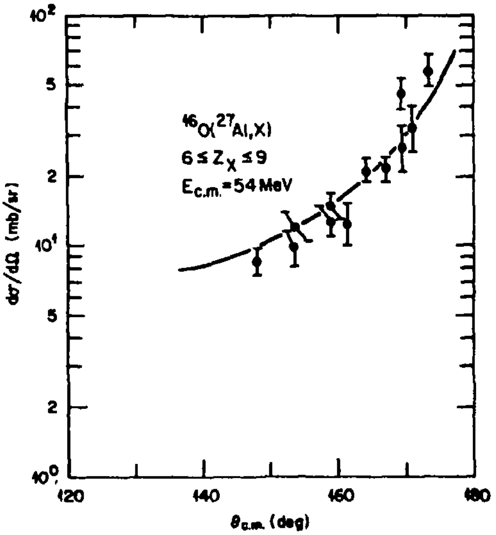

FIG. 4. Center-of-mass angular distribution for damped events at large angles and $E_{c.m.}=54$ MeV.

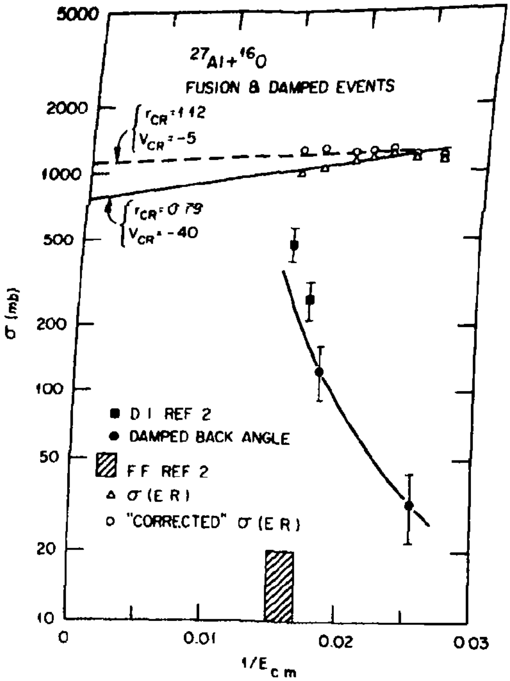

FIG. 5. Evaporation residue cross sections from Ref. 1 are shown by triangles; the open circles are the same but corrected for fission (see text). Damped back angle cross sections due to $^{27}Al + ^{16}O$ collisions are shown by solid circles. Also shown are the damped events identified as deep inelastic scattering in Ref. 2 (solid squares). The error bars are not shown for the fusion and the evaporation residue cross sections. The uncertainties are the same as given in Ref. 2. The shaded bar indicates the upper limit on fusion-fission events suggested in Ref. 2. The hyperbolic curve drawn through our data points for damped events at backward angles corresponds to an exponential energy dependence.

in Fig. 2. Assuming two-body kinematics, it was found that events with $6 \leq Z \leq 9$ could be associated with a range of Q values whose average is approximately the same at all angles studied, ($6° \leq \theta_{c.m.} \leq 40°$); $\bar{Q} = -22$ and -32 MeV for $E_{c.m.} = 39$ and 54 MeV. Using the average Q value for all the events in this group yields the center-of-mass angular distribution shown in Fig. 4. The solid curve is proportional to $1/\sin\theta_{c.m.}$. Assuming that the angular distribution for this process is symmetric about 90°, the total cross section for these events can be obtained (120 ± 25 mb at 54 MeV, Fig. 4). The total cross section deduced for this process, at the two energies studied, is shown in Fig. 5 (the solid circles). Also appearing in the same plot are the assigned total deep inelastic cross sections quoted in Ref. 2. While the present data and those of Ref. 2 were measured at slightly different energies, it is interesting to note that their cross sections lie close to the extrapolated curve through our data.

III. DISCUSSION

Our measurements show the presence of strongly damped-target-like events which have a $1/\sin\theta_{c.m.}$ angular distribution in the backward hemisphere. These events have Q values and Z distributions which are similar to those reported as deep inelastic scattering by Cormier *et al.*[2] at slightly higher energies and at scattering angles in the forward hemisphere. The angular distribution in Fig. 4 shows that the present data are due to a mechanism having a long interaction time; however, the degree of equilibration of the composite system is yet an open question.

The yield observed here could be the backward angle part of the deep inelastic process previously observed at forward angles.[2] One can view, then, the $1/\sin\theta_{c.m.}$ angular distribution in the backward hemisphere as yet another confirmation that deep inelastic scattering is an orbiting phenomenon.[12-14] The relaxed events seen here could originate also from a completely equilibrated system. The factor limiting large fragment emission could be the level density at the saddle-point configuration,[15] or the phase space available for the two fragments at infinite separation.[16] Estimating the fission with the code ALICE[17] results in very low $\Gamma_{fission}/\Gamma_{total}$ values. No attempt has been made to estimate the rate of large fragment evaporation using the second approach mentioned above, since for such a calculation the excitation energy and spin of both outgoing fragments has to be taken into account and such a code does not yet exist. It should be noted, however, that a 10% fission yield due to fission evaporation competition would be surprisingly large for a compound nucleus with mass number 42 and excitation energy of 70 MeV.[18]

One possible means of determining the degree of equilibration is to measure the full angular distribution. Symmetry about 90° would indicate that the events originate from a fusion-fission process. Unfortunately, the counting statistics of the data observed in our forward angle counters is inadequate to obtain meaningful separation of strongly damped and quasi-elastic cross sections at these angles. A comparison with the results obtained by Cormier *et al.*[2] is also difficult because our data were measured at slightly lower energies and these cross sections depend very strongly on energy (Fig. 5). However, the upper limit placed on fusion-fission events in Ref. 2 (where presumably only symmetric fission was considered) is much lower than the trend indicated by our data (see

Fig. 5).

Although it is still an open question as to whether the oxygen-like damped events observed in the present experiment originate from fusion-fission or orbiting, it is interesting to examine the consequences of an assumed fusion-fission process. If this were indeed the reaction mechanism producing these damped-target-like products, then the measured evaporation residue cross section would no longer account for the entire fusion cross section. In this case, the fusion-fission contribution must also be added to the evaporation residue cross section. The evaporation residue cross sections of Ref. 1 (open triangles in Fig. 5) "corrected" in this manner, are indicated by the open circles in the figure. The anomalous behavior reported for the ^{27}Al+^{16}O system[1] compared to the systematic trend of fusion cross sections for light systems then disappears; the new r_{cr} and V_{cr} values extracted are 1.1 fm and 5 MeV, respectively.

In conclusion, our data show the presence of a pronounced backward angle yield of strongly damped events, with an angular distribution characteristic of a long interaction time. However, the degree of equilibration of the composite system that produces this yield remains uncertain.

ACKNOWLEDGMENTS

We thank G. Hummer of BNL for his help throughout the experiment. Discussions with and critical comments by R. G. Stokstad and F. Plasil are gratefully acknowledged. This research was supported by the Department of Energy under Contract No. W-7405-eng-26 with Union Carbide Corporation.

---

[1] B. B. Back, R. R. Betts, C. Gaarde, J. S. Larson, E. Michelson, and Tai Kuang-Hsi, Nucl. Phys. A285, 317 (1977).

[2] T. M. Cormier, A. J. Lazzarini, M. A. Neuhausen, A. Sperduto, K. Van-Bibber, F. Videback, G. Young, E. B. Blum, L. Herreid, and W. Thoms, Phys. Rev. C 13, 682 (1976).

[3] R. L. Kozub, N. H. Lu, J. M. Miller, D. Logan, T. W. Debiak, and L. Kowalski, Phys. Rev. C 11, 1497 (1975).

[4] Y. Eisen, I. Tserruya, Y. Eyal, Z. Fraenkel, and M. Hillman, Nucl. Phys. A291, 459 (1977).

[5] J. Dauk, K. P. Lieb, and A. M. Kleinfeld, Nucl. Phys. A241, 270 (1975).

[6] D. Glas and U. Mosel, Nucl. Phys. A275, 429 (1975).

[7] D. Horn, A. J. Ferguson, and O. Hausser, Nucl. Phys. A311, 238 (1978).

[8] D. Shapira, R. Dayras, J. L. C. Ford, Jr., J. Gomez del Campo, A. H. Snell, P. H. Stelson, and R. G. Stokstad, Nucl. Instrum. Methods 163, 325 (1979).

[9] We thank J. Barrette and C. Thorn for providing the two detector systems.

[10] The center-of-mass energy quoted here already takes into account the energy lost by the projectile in the target gas cell. The resulting uncertainty in energy is ±1 MeV in the center of mass.

[11] LILITA, a Hauser-Feshbach Monte Carlo Evaporation Code, J. Gomez del Campo and R. G. Stokstad.

[12] D. Shapira, J. L. C. Ford, Jr., J. Gomez del Campo, R. G. Stokstad, and R. M. DeVries, Phys. Rev. Lett. 43, 1781 (1979).

[13] J. Wylcinski, Phys. Lett. 47B, 484 (1973).

[14] P. Dyer, R. J. Puigh, R. Vandenbosch, T. D. Thomas, and M. S. Zisman, Phys. Rev. Lett. 39, 392 (1977); W. Trautman, J. de Boer, W. Dunnweber, G. Graw, R. Kopp, C. Lauterbach, H. Puchta, and U. Lynen, *ibid.* 39, 1062 (1977).

[15] F. Plasil and M. Blann, Phys. Rev. C 11, 5081 (1973).

[16] L. G. Moretto, Nucl. Phys. A247, 211 (1975).

[17] F. Plasil, ORNL ALICE, Oak Ridge National Laboratory Report No. ORNL/TM-6054.

[18] C. K. Gelbke, P. Braun-Munzinger, J. Barrette, B. Zeidman, M. J. Levine, A. Gamp, H. L. Harney, and Th. Walcher, Nucl. Phys. A269, 460 (1976) and references therein.

PHYSICAL REVIEW C VOLUME 21, NUMBER 5 MAY 1980

Velocity dependence of the dynamic magnetic field acting on swift O and Sm ions

N. K. B. Shu, D. Melnik,* J. M. Brennan,† W. Semmler,‡ and N. Benczer-Koller
Department of Physics, Rutgers University, New Brunswick, New Jersey 08903

(Received 25 October 1979)

The hyperfine dynamic field acting on fast ions traversing polarized iron foils has been measured as a function of the ion velocity in the region $0.03 < v/Zv_0 < 0.06$ for Sm ions. The dynamic field increases with velocity but not linearly. The same conclusions were obtained from measurements on oxygen ions traversing thin iron foils or stopping in thick iron foils. All available data on dynamic-field measurements at ions with $8 < Z < 62$ traversing thin foils were examined and fitted to a single general form for the dynamic field. The region of validity of this parametrization of the dynamic field, as well as possible explanations of its origin, are discussed.

NUCLEAR REACTIONS $^{150,152}\mathrm{Sm}(^{16}\mathrm{O},{}^{16}\mathrm{O}')^{150,152}\mathrm{Sm}(2_1^+)$, $^{150,152}\mathrm{Sm}(^{32}\mathrm{S},{}^{32}\mathrm{S}')^{150,152}\mathrm{Sm}(2_1^+)$, and $^{16}\mathrm{O}(\alpha,\alpha')^{16}\mathrm{O}(3_1^-)$: $E_0 \sim 40$ MeV, $E_s \sim 70$–80 MeV, $E_\alpha = 17.55$ MeV; measured $W(\theta, B, \infty)$ through polarized iron; deduced $B_{\mathrm{DYNAMIC}}(v)$; compiled existing data to obtain general parametrization for $B_{\mathrm{DYNAMIC}}(v, Z)$.

INTRODUCTION

It has been known for many years that excited nuclei within ionized atoms traversing magnetic materials are subject to strong hyperfine interactions.[1] In order to obtain a consistent description of these interactions, it is helpful to separate the results of the various experiments according to the ion velocity through the solid.

Experiments on slow moving ions ($v/c < 0.01$) which eventually stop in polarized magnetic materials have shown that the ions experience a large magnetic interaction which results from the coupling between the magnetic moment of the nucleus and the magnetic field which acts on the moving ion.[2] This field was given the name of "transient field," and in the formulation of Lindhard and Winther[3] was thought to vary inversely with the ion velocity. Many excited states nuclear magnetic moments were measured by this technique, but agreement with the model could only be obtained by arbitrary adjustment of parameters.[3] In addition, these early experiments were subject to systematic uncertainties that were difficult to ascertain.

At very high velocities, ($v/Zv_0 \gg 1$ where $v_0 = e^2/\hbar$ is the Bohr velocity, and Z the atomic number of the ion), the ions can be assumed to be completely stripped and the interaction between the fast moving charge and the magnetized medium can be treated analytically in perturbation theory. The enhancement of the polarized electrons density around the moving ion was calculated classically by Sak and Bruno.[5] They obtain the following expression for the magnetic field at the position of the moving ion:

$$B = 4\pi Z \frac{v_0}{v} \mu_B N_p , \tag{1}$$

where μ_B is the Bohr magneton and N_p the number of polarized electrons/cm^3. Experiments on ^{12}C (Refs. 6 and 7) and ^{13}C (Ref. 8) nuclei and on fast polarized positive muons[9] traversing iron plates, indicate that indeed at very high velocities the hyperfine field becomes vanishingly small. It must be emphasized here that even though the velocity dependence of the field at high velocities is the same as that predicted by the Lindhard-Winther theory, the magnitude of the interactions and the actual physical mechanisms responsible for them are very different.

At intermediate velocities the moving ion will be accompanied by bound atomic electrons and the nature of the interaction is considerably more complex as several competing mechanisms can in principle be responsible for the magnetic interactions between the ion and the solid. Recent studies[1,6-8,10-13] have shown that excited nuclei traversing magnetic materials at relatively large velocities, $v/c > 0.01$, experience in fact a very much larger magnetic interaction than that predicted by the Lindhard-Winther model and that the magnetic field increases almost linearly with the velocity v of the ion. The Rutgers group developed a sensitive technique to test the velocity dependence of the hyperfine field.[14] The moving ion is allowed to *traverse* a thin magnetic foil and made to stop in an interaction free environment. Thus the magnetic interaction acts only for the well-defined time during which the ion traverses the foil and by adjusting the foil thickness, the incoming and outgoing ion velocities

© 1980 The American Physical Society

can be controlled. The thin foil idea was actually suggested in 1968 by Grodzins[15] but had not been tested because it was believed at that time that the "transient field" was proportional to $1/v$ and therefore its magnitude would only be large enough for measurements to be carried out at the end of the ion trajectory.

The following expression for the field was proposed[15,17] and generally used for practical purposes even though it had not been thoroughly tested:

$$B(v,Z)=a\left(\frac{v}{v_0}\right)^{p_v}(Z)^{p_Z}\mu_B N_p\,, \tag{2}$$

where a is a constant and $p_v \simeq p_Z \simeq 1$ are parameters that best fitted the early data for ions with $10<Z<48$. The field acting on fast ions was given the name of "dynamic field" to distinguish it from the interactions acting on very slow ions described by Lindhard and Winther. As the existence of the large dynamic field acting on *high* velocity ions was established, the advantages of the "thin magnetic foil technique" were fully realized.

The thin foil technique is particularly suited to the study of the ion-solid interaction because the results that emerge are essentially independent of the excited nucleus lifetime, of radiation damage in the stopping material which might affect the hyperfine interaction, and of a precise knowledge of the low energy ion stopping power. The last point is particularly relevant as the stopping powers of ions near the end of their range are not well known. In fact, strong oscillations have been observed both in the stopping powers of various ions from $Z=6$ to $Z=36$ in amorphous carbon[18] and a similar ion-solid interaction has affected the measurement by the Doppler shift attenuation method of nuclear lifetimes[19] of a particular ion (^{23}Na in the 3.34 MeV excited state) stopping in a complete range of stopping materials from $Z=6$ to $Z=83$. These oscillations have been generally attributed to atomic shell structure effects either in the slowing ion or in the stopping material. Van Middelkoop[1] has suggested a mechanism based on the creation of polarized holes in the s shells of the moving ion to explain the variations in the hyperfine interactions observed when light ions ($Z<14$) stop in thick iron foils. They have analyzed the experimental data available in terms of the hyperfine field[20] due to the presence of an uncoupled but polarized 1s electron in C, N, and O ions, a 2s electron in Ne, Mg, and Si ions, and a 3s electron in Fe ions. They were able to fit all the above data with a single parameter thus strongly supporting the hypothesis that the dynamic fields are of an atomic structure origin. In this work, they assume, however, that the dynamic field is linear in the velocity down to zero velocity. They caution therefore that this approach may have to be revised if the velocity dependence of the field is found to be different from linear.

The first systematic results on intermediate weight ions ($Z>14$) were obtained in fast Se ions[14] traversing *thin* iron and gadolinium foils and on fast Fe ions[13] traversing iron foils; these data suggested that the parameters p_Z and p_v in the expression for the dynamic field given by Eq. (2) differ from unity, and the best fits to the data yielded the somewhat crude results, $p_Z=1.5\pm0.5$ and $p_v=0.5\pm1.0$.

Following these studies, "thin" target measurements were carried out on Pd and Cd isotopes[21] in order to establish the Z dependence of the dynamic field for heavier ions. Furthermore, some of the data on the light ion experiments could also be used for this analysis even though the actual measurements were made with thick iron foils. The measurements had been carried out on ions entering the magnetic foil at a variety of initial velocities. The data were reanalyzed by subtracting the contribution obtained for the slowest ions from the effect measured for the faster ones. The analysis of these data seemed to suggest that the dynamic field dependence on the charge and velocity of the ion is indeed consistent with a linear behavior. However, later higher precision measurements on Pd ions and low velocity data on Sm ions contradicted this trend and suggested that if a unique field were to be responsible for the data observed for all isotopes for $6<Z<62$ and in the velocity range $0.02<v/Zv_0<0.80$, then the dynamic field must be proportional to a lower power of the velocity.

It is clear that data with higher precision are required within a narrow velocity range, and for many Z before a correct description of the dynamic field can be proposed and therefore we undertook the measurement of the dynamic field acting on Sm and O ions as they traverse thin iron foils at varying but well-defined velocities.

EXPERIMENTAL PROCEDURES

The measurement of the dynamic field acting on fast moving ions traversing ferromagnetic materials is accomplished by observing in coincidence with back-scattered beam particles the precession of the angular correlation of gamma rays emitted in the decay of an aligned nuclear excited state whose magnetic moment is affected by the presence of the dynamic field (Fig. 1). The type of targets used and details of the technique

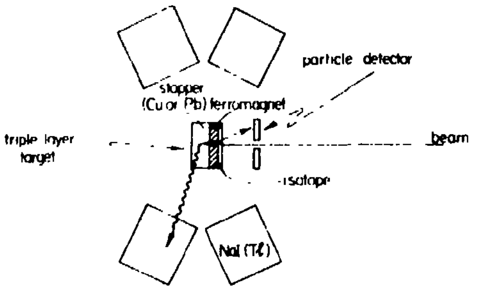

FIG. 1. Schematic of the experimental arrangement (not to scale) displaying the triple layer target and the γ-ray detectors. The recoiling ions traverse the ferromagnetic foil and stop in the interaction-free Cu or Pb backing.

have been extensively described in previous publications from this laboratory.[13,14] The target consists of three layers: a relatively thin layer of the isotope under investigation (between 200 and 800 $\mu g/cm^2$ thick) evaporated on an iron foil (between 0.5 and 2.0 mg/cm^2) backed by a thick (>10 mg/cm^2) copper (or lead) foil. The target is placed between the pole pieces of a magnet which produces an external magnetic field of 0.03–0.05 T, which is used to polarize the iron foils either up or down perpendicular to the scattering plane. The direction of the external magnetic field is reversed periodically (every three to five minutes), according to a preset count in the particle detector window.

The exciting beam is scattered backward into an annular particle detector and the decay gamma radiation is detected in four 12.7 cm × 12.7 cm NaI (Tl) detectors located 16.7 cm away from the target at the maximum slope angles of the particle-gamma angular correlation.

A. Sm ions

The first 2^+ states of both ^{150}Sm and ^{152}Sm at 335 and 122 keV, respectively, were Coulomb excited with oxygen and sulfur beams. The magnetic moment of the long-lived, $\tau = 2050$ psec state of ^{152}Sm, $\mu = 0.832 \pm 0.050$ n.m., was measured by Mössbauer spectroscopy.[22] The magnetic moment $\mu = 0.78 \pm 0.07$ n.m. of the short-lived $\tau = 69.1 \pm 1.6$ psec state of ^{150}Sm was derived from the ratio $\mu(150)/\mu(152) = 0.936 \pm 0.060$ obtained by Ben Zvi *et al.*[23] from experiments on Sm ions recoiling in gas and the magnetic moment of ^{152}Sm derived from Mössbauer experiments.

The experiments on the Sm isotopes were carried out at a variety of initial velocities and for several thicknesses of the iron foil.

The long lifetime of the ^{152}Sm state had an important effect on the angular correlation in this experiment. Instead of the full angular correlation which was found for all states with picosecond mean lives, the correlation for ^{152}Sm ions stopping in copper was attenuated. A significant weaker attenuation in the angular correlation was obtained by using lead as a stopping material. It is assumed that the electric field gradients induced by radiation damage are responsible for the attenuation of the correlation, and that the radiation damage is different for copper and lead. The measured correlations for copper and lead backings are shown in Fig. 2. The result for the lead backing is very close to that which would be expected for complete alignment of the state after correction for the finite solid angle of the detectors. The normalized slope of the angular correlation at the angle of measurement $\theta_\gamma = \pm 67.5^\circ$ and $\pm 112.5^\circ$ was $|S| = (1/W)dW/d\theta|_{\theta_\gamma} = 2.86 \pm 0.10$ for the lead backing, and $|S| = 1.39 \pm 0.05$ for the copper backing. This effect was not observed for ^{150}Sm, and copper-backed targets were used for which $|S| = 3.03 \pm 0.10$.

It is interesting to note that even though the lifetimes of the two states vary by two orders of magnitude, the observed precession of the gamma-ray angular correlation in the dynamic field is comparable within statistical errors for the two nuclei when they move at the same average velocity through the magnetic foil and stop in an environment free of radiation damage, and more important, free of static magnetic hyperfine interactions. These would in fact be larger than the dynamic-field interaction for the long-lived ^{152}Sm state. This effect demonstrates vividly the power of the thin foil technique.

A beam-bending correction of $\Delta\theta = -0.09 \pm 0.06$ mrad corresponding to the effect of the 0.03 T external field on the incident and scattered beams

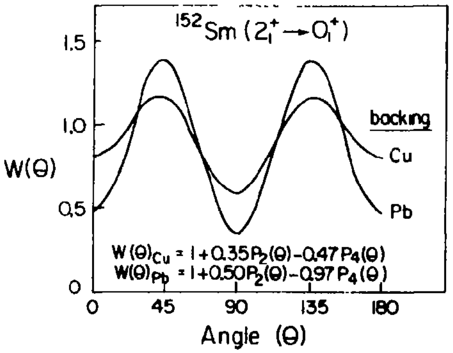

FIG. 2. Typical particle-γ angular correlation of ^{152}Sm ions for Cu and Pb backings. The four NaI(Tl) detectors were placed at angles $\theta = \pm 67.5^\circ$ and $\pm 112.5^\circ$.

was measured on a ^{150}Sm target evaporated on a Pb backing. The correction for the paramagnetic reduction[22] of the applied field was neglected because it is uncertain, and in any case amounts to no more than 10–20% of the beam-bending correction. In the case of ^{152}Sm, the precession data were corrected for an additional angular shift of −1.2 mrad due to the precession of the moment of the long-lived 2_1^+ state in the external 0.03 T field.

The summary of all the data obtained on Sm isotopes is displayed in Table I.

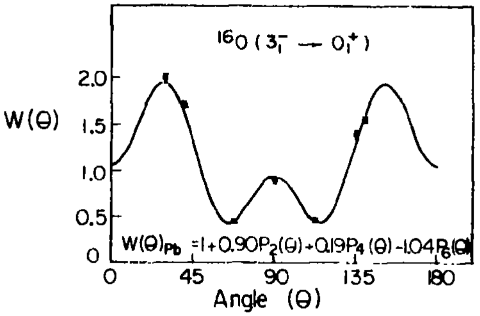

FIG. 3. Typical particle-γ angular correlation of ^{16}O for the $0^+ \rightarrow 3_1^- \rightarrow 0^+$ transition. The four NaI(Tl) detectors were placed at ± 45° and ± 135°.

B. O ions

The 6.131 MeV $J^\pi = 3^-$, $\tau = 26$ psec, $g = 0.55$ state[24] of ^{16}O was excited by inelastic α-particle scattering at a bombarding energy of 17.55 MeV. The scattered α particles were detected in an annular Si(Li) surface barrier detector at an angle $\theta_\alpha \simeq 165°–172°$. The excited nuclei traversed the ferromagnetic layer and stopped in an adjoining nonferromagnetic backing where they decayed. The de-excitation gamma-rays were detected in coincidence with the back-scattered α particles by the four 12.7 cm × 12.7 cm NaI (Tl) detectors located at angles $\theta_\gamma = \pm 45°$ and $\pm 135°$ at which the measured angular correlation had its greatest slope $|S| = (1/W)(dW/d\theta) = 2.9$. The angular correlation was consistent with an 83% $m = 0$ magnetic substate population for the particular geometry involved (Fig. 3). The solid angle correction factors for the NaI (Tl) detectors were taken from the work of Little,[25] who calculated the relevant Q_k geometrical factors by the procedure developed by Black and Gruhle.[26]

Several experiments were carried out. In the first series, targets of either 200 μg/cm² WO$_3$ or 150 μg/cm² SiO$_2$ were deposited on a 1.0 mg/cm² iron layer backed by 6 mg/cm² of Pb. For the second type of measurements, targets of 200 μg/cm² WO$_3$ evaporated on a 6 mg/cm² iron backing thick enough to stop all recoiling oxygen ions were prepared.

A third type of experiment was necessary to determine the effect on the angular correlation due to the bending of the beam. This form of beam bending cannot be calculated from purely geometrical considerations when all the parameters of the nuclear reaction are not known.[27] In contrast to excitation by Coulomb excitation, in a nuclear reaction at energies much above the Coulomb barrier, the symmetry axis of the γ-ray angular correlation need not coincide with the recoil direction of the excited nucleus. Consequently the beam-bending effect was measured by observing the precession of the angular cor-

TABLE I. Summary of the experimental net precession angles Δθ observed for ^{150}Sm and ^{152}Sm isotopes. The parameter a_{lin} was calculated using Eq. (3). E_{in}, E_{out}, $(v/v_0)_{\text{in}}$, and $(v/v_0)_{\text{out}}$ are the energies and velocities of the moving ions as they enter and leave the ferromagnetic foil. L is the thickness of the foil and T is the time spent by the ion in the ferromagnetic foil.

	E_{in} (MeV)	E_{out} (MeV)	$(v/v_0)_{\text{in}}$	$(v/v_0)_{\text{out}}$	$L\left(\frac{\text{mg}}{\text{cm}^2}\right)$	T (psec)	Δθ (mrad)	a_{lin}[a]
^{150}Sm	44.00	36.20	3.44	3.12	0.36	0.064	3.8(7)	88.6± 16.3
τ = 69.1(1.6) psec	44.21	32.81	3.45	2.97	0.55	0.100	4.9(4)	75.2± 6.5
g = 0.390(35)	34.19	24.59	3.03	2.58	0.55	0.115	5.1(4)	78.5± 6.6
	33.68	25.29	3.01	2.61	0.48	0.100	3.3(9)	57.1± 15.6
	33.38	11.73	3.00	1.78	1.50	0.375	17.8(9)	101.4± 5.4
	13.70	8.24	1.92	1.50	0.55	0.184	7.4(4)	115.0± 6.3
	13.19	9.39	1.88	1.60	0.36	0.124	3.9(5)	89.5± 11.5
^{152}Sm	39.3	14.3	3.13	1.86	1.58	0.384	20.5(8)	101.9± 4.0
τ = 2050 psec g = 0.416 (25)	34.8	11.8	3.04	1.78	1.58	0.393	19.2(7)	95.4± 3.4

[a] a_{lin} was obtained by analyzing the data with the assumption that the dynamic field is given by $B(v, Z) = a_{\text{lin}} Z (v/v_0) \mu_B N_p$.

TABLE II. Summary of the net experimental precession angles $\Delta\theta$ for ^{16}O and ^{18}O isotopes and values of a_{lin} obtained as described in Table I.

Data	Ion	E_{in} (MeV)	E_{out} (MeV)	$\left(\frac{v}{v_0}\right)_{\text{in}}$	$\left(\frac{v}{v_0}\right)_{\text{out}}$	L (mg/cm^2)	T (psec)	$\Delta\theta$ (mrad)	$\Delta\theta/g$ (mrad)	a_{lin}[a]	Ref.
I	^{16}O	8.07	3.17	4.51	2.87	1.0	0.160	−2.15(58)	−3.91(1.06)	100(27)	This work
II	^{16}O	8.07	0	4.51	0	2.24[b]		−8.4(10)	−15.3(19)	168(22)	This work
III	^{18}O	3.78	0	2.90	0	1.5[b]		−2.7(2)	9.3(9)	160(14)	11,12
IV	^{16}O	1.597	0	2.14	0	0.91[b]		−6.76(27)	−12.2(5)	346(19)	7
II-I	^{16}O	3.17	0	2.83	0	1.24			−11.4(21)		This work

[a] a_{lin} was obtained by analyzing the data with the assumption that the dynamic field is given by $B(v, Z) = a_{\text{lin}} Z(v/v_0) \mu_B N_p$.

[b] In the cases where the O ions stopped in the iron foil the active thickness is the actual range of the ion.

relation with a target of 200 $\mu g/cm^2$ WO_3 on a 50 mg/cm^2 Pb backing. The beam bending was measured for external fields of 0.03 and 0.05 T. Whereas the purely geometric bending of the beam was calculated to be about −0.4 mrad, the actual beam bending turned out to be $\Delta\theta = -2.03 \pm 0.34$ mrad and $\Delta\theta = -3.05 \pm 0.44$ mrad for $B_{\text{ext}} = 0.03$ and 0.05 T, respectively.

The results of all the measurements on "thin" and "thick" iron targets are presented in Table II, and are compared to the data of Goldberg *et al.*[7] on ^{16}O and by Forterre *et al.*[11] and Van Hienen[12] in a similar experiment on ^{18}O. In this latter work the 1.90 MeV $J^\pi = 2^+$, $\tau = 3.1$ psec[28] $g = -0.31$ (Refs. 11, 12, and 29) state of ^{18}O was also excited by inelastic alpha particle scattering but at lower energies, $E_\alpha = 7.4$ MeV, and the oxygen recoils *stopped* in the iron backing.

RESULTS

A. Sm ions

In the case where the dynamic field is assumed proportional to the first power of the velocity and atomic number of the ion [Eq. (2) with $p_v = p_z = 1$] $\Delta\theta$, the precession of the γ-ray angular correlation, is directly proportional to the thickness L of the magnetic foil as $\Delta\theta$ is given by

$$\begin{aligned}\Delta\theta &= -\frac{\mu_N}{\hbar} g \int B\, dl \\ &= -a_{\text{lin}} Z \frac{\mu_N g}{\hbar} (\mu_B N_p) \int_0^L \frac{v}{v_0} \frac{dx}{v} \\ &= -a_{\text{lin}} Z \frac{\mu_N g}{\hbar v_0} (\mu_B N_p) L \,. \qquad (3)\end{aligned}$$

Figure 4 shows the value of the constant a_{lin} determined under the above constrictions for Sm ions plotted versus the average velocity of the ion as it traverses the iron foil. The horizontal error bar indicates the range of velocities corresponding to the thickness of the foil. It is clear that a_{lin} is indeed not a constant, but decreases with the ion velocity suggesting that the simplified expression with $p_v \simeq 1$ is not valid. Therefore, the data were fitted with a dynamic field described by Eq. (2) and the best values of the parameters p_v and p_z were obtained. For this analysis a precession angle $\Delta\theta$ is calculated taking into account the slowing down of each particular ion in the magnetic foil as well as the nuclear decays that might occur within the foil. The electronic stopping powers were taken from the tabulation of Northcliffe and Shilling[30] and a polynomial interpolation scheme was used in the analysis. The simple universal fit formula

$$\sum_n = \frac{1.7\epsilon^{1/2}\ln(\epsilon + e)}{1 + 6.8\epsilon + 3.4\epsilon^{3/2}}$$

in Lindhardt, Scharff, and Schiøtt units[31] was

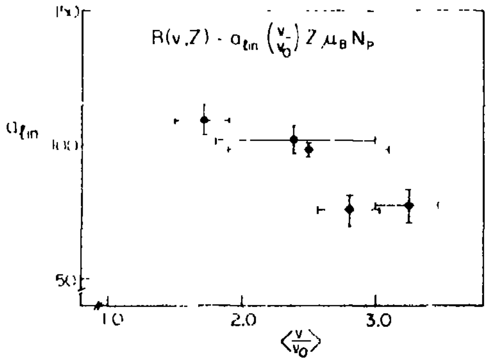

FIG. 4. Plot of the value of the constant a_{lin}, determined from Eq. (3), versus the average velocity of the Sm ion as it traverses the iron foil.

used for the nuclear stopping powers. The following integral was thus computed:

$$\frac{\Delta\theta}{g} = -\frac{\mu_N}{\hbar}\int_0^T B(v,Z)e^{-t/\tau}dt$$

$$= -\frac{\mu_N}{\hbar}\int_{E_i}^{E_f} B(v,Z)e^{-t/\tau}\left(\frac{1}{v}\,\frac{dE}{dE/dx}\right),$$

where T is the time the ion spends in the magnetic material, E_i is its initial velocity, and E_f is its energy as it leaves the magnetic foil. The actual calculation takes into account the thickness of the target, decays in flight, and the kinematic spread due to the finite solid angle subtended by the detector recording the exciting beam particles. The minimum chi square was searched and the best value for various parameters thus established. The best fit to the Sm data yielded $p_v = 0.50$ and $\chi^2 = 1.876$, but, of course, provides no information on p_z.

Several of the runs were performed in targets mounted on very thin iron foils. Under these circumstances one can assume that the ion velocity remains approximately constant through the foil and one may extract an average value for the dynamic field for that particular velocity

$$\langle B\rangle \simeq \frac{\Delta\theta}{(\mu_N/\hbar)gT}\,.$$

Figure 5 shows the results obtained for Sm ions. The solid line represents the best fit to all existing data, and was obtained by the procedure described in subsection C below. A very similar study was done by King and Clark[32] on ^{106}Pd. Their results are consistent with those obtained here.

B. O ions

Several conclusions can be drawn from the results presented in Table II. The most striking is the observation that the constants $a_{\rm lin}$ obtained from a fit to the data for the parametrization of the dynamic field with $p_v = 1$ are different by almost a factor of 2 for the thin (data I) and thick (data II and III) experiments. Since the dynamic field was found not to vary linearly with the velocity of the ion for Sm ions, it is no surprise that the same effect is observed for oxygen ions.

A rough estimate of the static hyperfine field acting on oxygen ions stopped in the iron foil can be obtained from the combined data on all oxygen isotopes. In the case of ^{18}O the precession of the angular correlation due to interaction with the static field is negligible in view of the short mean life of the 2_1^+ state. The long mean life of the 3^- state in ^{16}O, on the other hand, makes the precession of experiment II in the thick iron foil susceptible to both the influence of the dynamic and static hyperfine fields. If the precession corresponding to the high velocity portion (data I) of the range of the ion through the iron foil is subtracted from the data II, the resulting precession for ^{16}O $(\Delta\theta/g|_{\rm II} - \Delta\theta/g|_{\rm I})$ can be compared with the precession $\Delta\theta/g|_{\rm III}$ obtained for ^{18}O for the same initial $v_i/v_0 = 2.9$ and final $v_f/v_0 = 0$ velocities. The precession of the angular correlation in just the static hyperfine field is given by

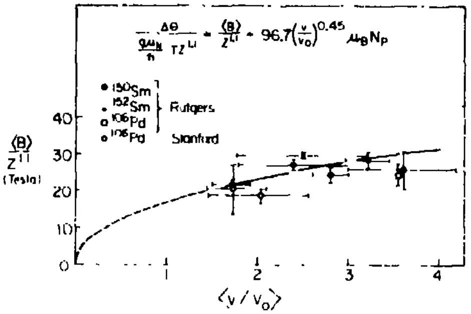

FIG. 5. Plot of the average value of the dynamic field $\langle B\rangle$ versus the transit velocity of Sm ions traversing iron foils. The solid line is a representation of the dynamic field according to Eq. (4) and the dotted line indicates the region where the formulation for Eq. (4) need not apply as no experimental data are available.

$$\Delta\theta = -\frac{\mu_N}{\hbar}g\tau B_{\rm static}e^{-t_s/\tau}\,,$$

where τ is the mean life of the state and t_s the time elapsed after creation of that state, or for the case of the thin foil experiments, the transit time of the ion in the iron layer before it stops.

An upper limit on the static field on ^{16}O ions stopping in iron can thus be extracted from

$$\left[\left(\frac{\Delta\theta}{g}\right)_{\rm I} - \left(\frac{\Delta\theta}{g}\right)_{\rm II}\right] - \left(\frac{\Delta\theta}{g}\right)_{\rm III} = \frac{\mu_N}{\hbar}g\tau B_{\rm static}e^{-t_s/\tau}$$

$$= (2.1 \pm 2.2)\ {\rm mrad},$$

giving $B_{\rm static}$ (oxygen) < 3.5 T. A similar analysis carried out by Gerber *et al.*[33] yielded $B_{\rm static} < 9.0$ T. Data IV lists additional data obtained from a low velocity experiment on ^{16}O excited by the ^{19}F$(p,\alpha)^{16}$O reaction.[33] The effect observed in this experiment is even larger than that observed for the ^{18}O experiment at comparable velocities.

C. Other ions: Generalized formulation of the dynamic field

In order to obtain the best estimate of the dynamic-field dependence on the velocity and charge

TABLE III. Summary of the net experimental precession angles $\Delta\theta$ for ^{20}Ne, ^{24}Mg, ^{28}Si, ^{56}Fe, ^{82}Se, ^{106}Pd, ^{110}Cd, ^{194}Pt, and ^{148}Nd ions traversing thin iron foils and ^{82}Se ions traversing thin gadolinium foils. The original data for Ne, Mg, Si, and Ba ions were reanalyzed differentially as described in the text in order to simulate a "thin foil" experimental situation. For these data, L represents the effective target thickness corresponding to the chosen initial and final velocities of the ion, and T is the effective time spent by the ion at these velocities.

Ion	E_{in} (MeV)	E_{out} (MeV)	$(v/v_0)_{in}$	$(v/v_0)_{out}$	L (mg/cm^2)	T (psec)	$\Delta\theta$ (mrad)	Ref.
Ions traversing iron foils								
^{20}Ne	30.4	17.9	7.83	6.02	1.85	0.155	3.8(17)	34
$\tau = 1.0$ psec	30.4	13.9	7.83	5.31	2.42	0.214	5.0(15)	
$g = 0.54(4)$								
^{24}Mg	35.57	15.1	7.73	5.06	2.36	0.216	5.2(23)	34, 27
$\tau = 2.0$ psec	35.57	7.8	7.73	3.63	3.31	0.343	8.5(35)	
$g = 0.51(2)$	35.57	2.9	7.73	2.23	4.13	0.507	10.7(18)	
^{28}Si								
$\tau = 0.68$ psec	31.4	8.7	6.72	3.56	2.4	0.275	5.3(18)	35, 16
$g = 0.53(2)$	31.4	2.8	6.72	2.04	3.3	0.468	7.2(17)	
	31.4	0.8	6.72	1.13	3.85	0.675	8.0(18)	
^{56}Fe	65.0	23.7	6.83	4.14	2.3	0.247	8.9(17)	13
$\tau = 10$ psec	56.0	32.3	6.35	4.82	1.3	0.136	4.9(11)	
$g = 0.60(8)$	56.0	17.5	6.35	3.56	2.3	0.276	8.2(16)	
^{82}Se	53.0	42.5	5.10	4.57	0.5	0.060	1.6(14)	14
$\tau = 16.3$ psec	53.0	31.4	5.10	3.93	1.1	0.142	4.8(16)	
$g = 0.42$	53.0	24.3	5.10	3.46	1.54	0.212	6.8(16)	
	53.0	19.2	5.10	3.08	1.9	0.276	10.9(16)	
	53.0	11.0	5.10	2.33	2.6	0.429	13.7(15)	
^{106}Pd	47.4	21.5	4.24	2.86	1.36	0.226	7.3(8)	21
$\tau = 16.9(9)$ psec	42.0	18.1	4.00	2.63	1.36	0.244	8.3(12)	21
$g = 0.40(2)$	45.9	23.7	4.18	3.01	1.15	0.188	6.5(9)	31
	17.3	5.9	2.56	1.50	1.15	0.339	8.4(8)	31
	11.6	5.6	2.10	1.47	0.70	0.234	6.4(20)	31
^{110}Cd	45.0	16.7	4.06	2.48	1.6	0.291	7.5(20)	21
$\tau = 7.7(6)$ psec	45.0	12.0	4.06	2.10	2.0	0.394	11.7(20)	21
$g = 0.28(5)$								
^{134}Ba	12.1	7.4	1.91	1.50	0.49	0.171	5.4(18)	36
$\tau = 7.0$ psec	43.6	14.7	3.62	2.11	1.74	0.364	15.2(38)	36
$g = 0.43(5)$[21]								
^{148}Nd	30.0	9.4	2.86	1.61	1.57	0.422	15.9(11)	37
$\tau = 123(3)$ psec								
$g = 0.33(4)$								
^{194}Pt	133.93	11.95	5.27	1.57	4.1	0.81	27.7(2.2)	38
$\tau = 60(4)$ psec	58.29	16.71	3.48	1.86	1.95	0.45	12.4(8)	38
$g = 0.274(25)$	35.72	13.62	2.72	1.69	1.44	0.389	9.2(8)	39
Ions traversing gadolinium foils								
^{82}Se	53.0	41.5	5.10	4.52	1.0	0.212	4.0(14)	14
	53.0	31.5	5.10	3.94	2.0	0.258	7.6(16)	
	53.0	18.7	5.10	3.04	3.6	0.526	20.4(44)	
	53.0	13.8	5.10	2.61	4.4	0.690	21.2(24)	

of the ion, all the existing data from this and other laboratories were collected (Table III) and analyzed. Only data obtained with "thin" iron foils were used. In the cases of Ne, Mg, Si, and Ba, however, the measurements were actually carried out on targets deposited on thick iron backings in which the ions stopped. However, several data were obtained with ions at various initial energies. In order to evaluate the effects of the dynamic field acting on fast ions only, the data were analyzed differentially as discussed in the Introduction.

The magnetic moments of all nuclear states used in the analysis are known from direct experiments such as measurements with radioactive sources in external fields or in known internal static hyperfine fields, with the exception of ^{28}Si where the theoretical value of $g(d_{5/2}^{-1}s_{1/2})$ was used.[34]

In Fig. 6, the parameters $a_{\rm lin}$ obtained from these data analyzed in the context of a dynamic-field linear in the ion velocity are plotted. It is clear that with the exception of the Pt data, $a_{\rm lin}$ decreases with the increasing ion velocity for all ions, and increases slightly with the ion atomic number, in good agreement with the conclusions obtained from the O and Sm data.

The expression (2) for the dynamic field was simultaneously fitted to all tabulated "thin target" or equivalent data in order to evaluate the parameters a, p_v, and p_z. The best fit ($\chi^2 = 1.2$) yielded

$$B(v,Z) = (96.7 \pm 1.6)\left(\frac{v}{v_0}\right)^{0.45\pm0.18} Z^{1.1\pm0.2}\mu_B N_p\,. \qquad (4)$$

Because $a_{\rm lin}$ for Pt appears to be much smaller than warranted by the trend displayed in Fig. 6, the Pt data were omitted from this fit. The solid line in Fig. 5 is a representation of this equation applied to the Sm data. The physical processes occurring at velocities $v/v_0 \gtrsim 1.5$ are not well known and the above formulation need not apply (dotted line).

There is one glaring exception to the above fit: ^{194}Pt (Refs. 38 and 39) for which the observed angular precession is much smaller than the effect which would be predicted from the above parametrization of the field. No explanation of this anomaly can be offered yet. Recent ^{134}Ba measurements[36] in thick iron foils appear to be consistent with the assumption of a dynamic-field linear in the ion velocity. However, a differential analysis of these same data yield results compatible within statistical errors with the parametrization of the field given by Eq. (4) (Fig. 6).

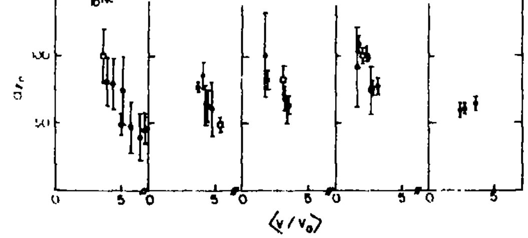

FIG. 6. Plot of the constant $a_{\rm lin}$ versus the average transit velocity for the data listed in Tables I, II, and III.

DISCUSSION

The approach used in the data analysis involved fitting all available data displayed in Tables I, II, and III by a unique field $B(v,Z)$. This approach may be erroneous insofar as it is conveivable that light ions in which atomic structure effects are dominant would be subject to a different magnetic hyperfine interaction than the heavy ions where more complex electronic configurations might average out the sharp atomic features. Nevertheless, the Sm and O data confirm that the dynamic field is not simply proportional to the ion velocity.

Under these circumstances the very elegant analysis of the light nuclei by van Middelkoop *et al.*,[1] which exhibits clear atomic structure effects, ought to be revised even though the underlying ideas are undoubtedly correct. Furthermore, when the field is proportional to a complicated function of either velocity or atomic number, it is no longer possible to exhibit the features of the dynamic field by plotting the experimental data versus some common parameter; these can only be obtained from an analysis of the least square fit to a hypothetical model for the field. In fact, it may not even be possible to write $B(v,Z)$ as a product of two separable functions of v and Z. Nevertheless, the surprising results that all 40 independent experimental data points from $Z = 8$ to $Z = 62$ obtained in many laboratories can in fact be simultaneously fitted suggest that the dynamic field could indeed be described for practical purposes by a "universal" expression and hence could be used to measure the magnetic moments of other nuclei. However, as long as the microscopic origin of the field is not quantitatively described, the above fit of a generalized expression to the data should be considered more an accident than an accurate description.

A more physical approach leading to a parametrization of $B(v,Z)$ arises from the recent results of Dybdal *et al.*[40] They have measured the K vacancy fraction for Si ions moving in nickel foils and for O and F ions in iron and nickel foils. They have shown that the K vacancy fraction indeed increases with velocity, and that the dynamic magnetic field at the moving ion can be produced by a combination of spin exchange interactions between the moving ion and the magnetic material and capture-loss processes involving polarized electrons. Furthermore, they have observed that the *K* vacancy production for O ions, contrary to that observed for other nearby ions such as F, does not remain proportional to the velocity as the velocity of the ion is reduced but stays approximately constant to very low velocity. This result is completely consistent with the present observations on the behavior of the dynamic field at O ions moving at very low velocity.

More quantitative *K* and higher shell vacancy production and dynamic-field data over the whole periodic table will be necessary to obtain a universal microscopic formulation for the dynamic field.

The "thin foil" technique is not the only approach to the study of the velocity dependence of the dynamic field. De Raedt *et al.*[11] have recently made use of the line shape of the Doppler broadened gamma-ray line profile of ^{28}Si ions slowing down in magnetized iron foil. Their preliminary results indicate a dynamic-field proportional to the ion velocity. However, within the given statistical uncertainties in the measurements, the same data can be fitted equally well with the parametrization of Eq. (3). Another method which has been used to determine the velocity dependence of the magnetic field but is of limited scope involves the measurement of the interaction on very short-lived nuclei, and the recent experiment[8] on ^{12}C ions has confirmed the medium and high velocity behavior of the dynamic field. However, this technique is by its nature limited to the higher velocities. The "thin foil" technique, on the other hand, is more readily applicable to the measurement of magnetic moments. Its advantages have been extensively described in the Introduction and in previous publications, but its limitations should not be overlooked. Since neither the dependence of the dynamic field on velocity nor on atomic number is yet completely understood from basic principles, the dynamic field should be applied with caution to absolute measurements of magnetic moments of excited levels:

(1) in ions which have no isotope with a known magnetic moment which could be used to calibrate the magnetic field,

(2) in a velocity range different from that used to calibrate the field in the case where a level with known magnetic moment is available.

It is interesting to note further that whatever parametrization of the dynamic field is chosen to reasonably fit the data for at least nearby nuclei, the best fit for each parametrization will yield the same magnetic moments for the unknown species to within 5%.[21]

One may conclude from these observations that whereas limited measurements of magnetic moments in well-chosen isotopes are possible, the greatest onus remains to establish the nature, or at least the behavior, of the dynamic magnetic field, either from basic principles or from semiempirical analysis. The observation that the dynamic field is large and correlated with the velocity dependence of *K*-shell vacancy production does suggest that single polarized electrons play an important role and therefore that atomic structure effects must be taken into consideration. On the other hand, the fact that it is possible to fit all available data ranging over one order of magnitude in atomic number with a single expression for the dynamic magnetic field, and the expectation that ions moving through solids must occur with a broad charge distribution, suggest in turn that some average over many atomic configurations could be considered.

This work was supported in part by the National Science Foundation.

---

*Present address: Bell Laboratories, Murray Hill, New Jersey 07974.

†Present address: Nuclear Structure Laboratory, State University of New York, Stony Brook, New York, 11794.

‡Present address: Hahn-Meitner Institut, Berlin, West Germany.

[1] G. Van Middelkoop, Hyp. Int. 4, 238 (1978); this paper is a review of all the recent data and contains an extensive list of references.

[2] R. R. Borchers, J. D. Bronson, D. E. Murnick, and L. Grodzins, Phys. Rev. Lett. 17, 1099 (1966); R. R. Borchers, B. Herskind, J. D. Bronson, L. Grodzins, R. Kalish, and D. E. Murnick, *ibid.* 20, 424 (1968).

[3] J. Lindhard and A. Winther, Nucl. Phys. A166, 413 (1971).

[4] G. Hubler, H. W. Kugel, and D. E. Murnick, Phys. Rev. C 9, 1954 (1974).

[5] J. Šak and J. Bruno, Phys. Rev. B 18, 3437 (1978); J. Bruno and J. Sak, Phys. Lett. A68, 463 (1978); J. Bruno and J. Sak, Phys. Rev. B 19, 3427 (1979).

[6] M. B. Goldberg, G. J. Kumbartzki, K.-H. Speidel, M. Forterre, and J. Gerber, Hyp. Int. 1, 429 (1976); M. B. Goldberg, E. Konejung, W. Knauer, G. J. Kumbartzki, P. Meyer, K.-H. Speidel, and J. Gerber, Phys. Lett. 58A, 269 (1976).

[7] M. B. Goldberg, W. Knauer, G. J. Kumbartzki, K.-H. Speidel, J. C. Adloff, and J. Gerber, Hyp. Int. 4, 262 (1978).

[8] K. Dybdal, J. L. Eberhardt, and N. Rud, Phys. Lett.

64B, 414 (1976); K. Dybdal, J. L. Eberhardt, and N. Rud, Hyp. Int. 7, 29 (1979).

[9] J. M. Brennan, N. Benczer-Koller, M. Hass, W. J. Kossler, J. Lindemuth, A. T. Flory, D. E. Murnick, R. P. Minnich, W. F. Lankford, and C. E. Stronach, Phys. Rev. B 18, 3430 (1978).

[10] M. Forterre, J. Gerber, J. P. Vivien, M. B. Goldberg, H.-K. Speidel, and P. N. Tandon, Phys. Rev. C 11, 1976 (1975).

[11] M. Forterre, J. Gerber, J. P. Vivien, M. B. Goldberg, and H.-K. Speidel, Phys. Lett. 55B, 56 (1975).

[12] J. F. A. Van Hienen, Ph.D. thesis, Utrecht University, 1975 (unpublished).

[13] M. Hass, J. M. Brennan, H. T. King, T. K. Saylor, and R. Kalish, Phys. Rev. C 14, 2119 (1976); J. M. Brennan, N. Benczer-Koller, M. Hass, and H. T. King, *ibid.* 16, 899 (1977).

[14] J. M. Brennan, N. Benczer-Koller, M. Hass, and H. T. King, Hyp. Int. 4, 268 (1978).

[15] L. Grodzins, *Hyperfine Structure and Nuclear Radiations*, edited by E. Matthias and D. A. Shirley (North-Holland, Amsterdam, 1968), p. 607.

[16] J. L. Eberhardt, R. E. Horstman, P. C. Zalm, H. A. Doubt, and G. van Middelkoop, Hyp. Int. 3, 195 (1977).

[17] In the early publications a relativistic factor $R = 1 + (Z/84)^{2.5}$ was occasionally included in Eq. (2). However, as no fundamental argument supports its existence and it was often dropped from the equation when convenient, it will not be used here.

[18] C. P. Bhalla and J. N. Bradford, Phys. Lett. 27A, 318 (1968).

[19] C. Broude, P. Engelstein, M. Popp, and P. N. Tandon, Phys. Lett. 39B, 185 (1972).

[20] H. Kopferman, *Nuclear Moments* (Academic, New York, 1958), p. 131.

[21] J. M. Brennan, M. Hass, N. K. B. Shu, and N. Benczer-Koller, Phys. Rev. C 21, 574 (1980).

[22] U. Atzmony, E. R. Bauminger, D. Froindlick, and S. Ofer, Phys. Lett. 26B, 81 (1967).

[23] I. Ben-Zvi, P. Gilad, M. B. Goldberg, G. Goldring, K.-H. Speidel, and A. Sprinzak, Nucl. Phys. A151, 401 (1970).

[24] C. Broude, M. B. Goldberg, G. Goldring, M. Hass, M. J. Renan, B. Sharon, Z. Shkedi, and D. F. H. Start, Nucl. Phys. A215, 617 (1973).

[25] W. A. Little, Ph.D. thesis, Stanford University, 1976 (unpublished).

[26] J. L. Black and W. Gruhle, Nucl. Instrum. Methods 46, 213 (1967).

[27] J. L. Eberhardt, R. E. Horstman, H. W. Heeman, and G. van Middelkoop, Nucl. Phys. A229, 162 (1974).

[28] Adopted average value quoted by A. M. Kleinfeld, K. P. Lieb, D. Werdecker, and U. Smilansky, Phys. Rev. Lett. 35, 1329 (1975).

[29] W. L. Randolph, N. Ayres de Campos, J. R. Beene, J. Burde, M. A. Grace, D. F. H. Start, and R. E. Wagner, Phys. Lett. 44B, 36 (1973).

[30] L. C. Northcliffe and R. F. Schilling, Nucl. Data A7, 233 (1970).

[31] J. Lindhard, M. Scharff, and H. E. Schiøtt, K. Dan. Vidensk. Selsk. Mat. Fys. Medd. 33, 14 (1963).

[32] H. T. King and D. L. Clark, Bull. Am. Phys. Soc. 23, 961 (1978) and private communication.

[33] J. Gerber, M. B. Goldberg, and K.-H. Speidel, Phys. Lett. 60B, 338 (1976).

[34] P. C. Zalm, A. Holthuizen, J. A. G. DeRaedt, and G. van Middelkoop, Hyp. Int. 4, 347 (1978).

[35] J. L. Eberhardt, G. van Middelkoop, R. E. Horstman, and H. A. Doubt, Phys. Lett. 56B, 329 (1975).

[36] J. L. Eberhardt and K. Dybdal, Hyp. Int. 7, 387 (1980).

[37] R. Kalish, J. A. G. DeRaedt, A. Holthuizen, W. A. Sterrenburg, and G. van Middelkoop, Nucl. Phys. A311, 3 (1978).

[38] O. Häusser, B. Haas, D. Ward, and H. R. Andrews, Nucl. Phys. A314, 161 (1979).

[39] R. Kalish, N. K. B. Shu, N. Benczer-Koller, A. Holthuisen, A. J. Rutten, and G. van Middelkoop, Hyp. Int. (to be published).

[40] K. Dybdal, J. S. Forster, and N. Rud, Phys. Rev. Lett. 43, 23 (1979).

[41] J. A. G. DeRaedt, A. Holthuizen, A. J. Rutten, W. A. Sterrenburg, and G. van Middelkoop, Hyp. Int. (to be published).

PHYSICAL REVIEW C VOLUME 21, NUMBER 5 MAY 1980

Spectroscopy of ^{213}At, ^{212}Po, and ^{210}Pb following ^{208}Pb+^{7}Li

T. P. Sjoreen,* U. Garg,† and D. B. Fossan
Department of Physics, State University of New York, Stony Brook, New York 11794

(Received 9 July 1979)

The bombardment of ^{208}Pb by ^{7}Li ions has been used to study the properties of excited states in ^{213}At, ^{212}Po, and ^{210}Pb In-beam measurements with Ge(Li), intrinsic Ge, and Si surface barrier detectors of α-decay excitation functions, α-γ coincidences, γ-γ coincidences, γ-ray angular distributions, and pulsed-beam-γ timing were made to establish decay schemes, level energies, γ-ray multipolarities, spin-parity assignments, and isomeric lifetimes. Excited states with spins up to 19/2 $\hbar$ in ^{213}At and 6 $\hbar$ in ^{212}Po were identified. The mean lifetimes of the 1272-keV 8^+ and 1193-keV 6^+ states in ^{210}Pb were measured to be 225(22) and 30(10) nsec, respectively. These lifetimes imply $B(E2)$ values of 51(12) e^2fm^4 for the 8^+ state and 308(115) e^2fm^4 for the 6^+ state. The ^{213}At decay scheme and the ^{210}Pb $B(E2)$ values are compared with shell model calculations.

NUCLEAR REACTIONS ^{208}Pb(^{7}Li, $2n$)^{213}At, ^{208}Pb(^{7}Li, t)^{212}Po, ^{208}Pb(^{7}Li, αp)^{210}Pb, $E_{\mathrm{Li}}=30$–34 MeV; measured α-decay excitations, α-γ coincidences, γ-γ coincidences, γ-$W(\theta)$, pulsed-beam-γ timing; deduced level schemes, γ multipolarities, J^{π}, $T_{1/2}$, $B(E2)$.

I. INTRODUCTION

The shell model has been very successful in describing the properties of nuclei near the doubly closed ^{208}Pb core ($N=126$, $Z=82$). As a result there has been considerable experimental and theoretical interest in this region. For nuclei with $Z>82$ and $N>126$, there is a lack of experimental spectroscopic information because it is difficult to populate these nuclei. However, the bombardment of ^{208}Pb by ^{7}Li has proved to be very useful in studying such nuclei. It has been used to study ^{212}At (Ref. 1) and ^{210}Bi,[2] as well as the closed neutron shell ($N=126$) nuclei of ^{209}Bi (Ref. 3) and ^{211}At.[4] In the present study, ^{7}Li + ^{208}Pb has also been used along with in-beam γ-ray methods to investigate the $N=128$ nuclei ^{213}At ($Z=85$), ^{212}Po($Z=84$), and ^{210}Pb($Z=82$).

The nucleus ^{213}At is composed of five valence particles, three protons and two neutrons, outside of the ^{208}Pb core, while the nucleus ^{212}Po has four valence particles, two protons and two neutrons. The low-lying high-spin states in these nuclei are expected to involve primarily neutrons in the $g_{9/2}$, $i_{11/2}$, and $j_{15/2}$ orbitals and protons in the $h_{9/2}$, $f_{7/2}$, and $i_{13/2}$ orbitals. Spectroscopic information for these nuclei would be useful in the study of the neutron-proton effective interaction. The nucleus ^{210}Pb is somewhat simpler than ^{212}Po and ^{213}At, since it is composed of just two neutrons outside of ^{208}Pb. In this nucleus it would be particularly interesting to acquire lifetime information, which could be used to extract neutron $E2$ effective charges. The purpose of the present study is to experimentally determine the properties of low-lying high-spin states in ^{213}At, ^{212}Po, and ^{210}Pb and to interpret the results in terms of the shell model.

At the beginning of the present study, the only available information for ^{213}At was the study[5] of the α decay of the ground state [$T_{1/2}=110(20)$ nsec], which was observed to decay via a 9.08-MeV α particle to the ^{209}Bi ground state. For ^{212}Po, the available experimental information included studies[6,7] of the α decay of the ground state [$T_{1/2}=0.296(2)$ μsec] to ^{208}Pb and the β decay of ^{212}Bi to low-spin states ($J\leq 2$) in ^{212}Po. For ^{210}Pb, available experimental information included transfer reaction and β-decay measurements.[8] With these measurements, many levels in ^{210}Pb were identified, including the 8^+, 6^+, 4^+, 2^+ yrast states.

In the present study, excited states in ^{213}At, ^{212}Po, and ^{210}Pb were populated via the ^{208}Pb(^{7}Li,$2n$), ^{208}Pb(^{7}Li,t), and ^{208}Pb(^{7}Li,αp) reactions, respectively. To extract the required information, several in-beam measurements were carried out. α-decay excitation measurements were made to investigate the (^{7}Li,$2n$) and (^{7}Li,t) yields near the Coulomb barrier; an α-γ coincidence measurement was carried out to identify γ rays from ^{213}At and γ-γ coincidence, γ-ray angular distribution, and pulsed-beam-γ timing measurements were made to determine level energies, spin and parity assignments, γ-ray multipolarities, and isomeric lifetimes. The experimental techniques used in the α-decay excitation and α-γ coincidence measurements are described in Sec. II. The techniques for the γ-γ coincidence, γ-ray angular distributions, and pulsed-beam-γ timing measure-

© 1980 The American Physical Society

ments are discussed in detail in Ref. 9, and are also briefly reviewed in Sec. II. The experimental results for ^{213}At and ^{210}Pb are presented in Sec. III, and discussed in terms of the shell model in Sec. IV. The ^{212}Po results are presented in Sec. III, and are also compared in Ref. 10 with a complete ^{212}Po shell model calculation. Preliminary results of these measurements have been reported previously.[11] An independent study of ^{212}Po employing the ^{209}Bi(α,p) reaction has also been recently performed to investigate high-spin states.[12]

II. EXPERIMENTAL PROCEDURE

Levels in ^{213}At, ^{212}Po, and ^{210}Pb were populated via the ^{208}Pb(^{7}Li,2n), ^{208}Pb(^{7}Li,t), and ^{208}Pb(^{7}Li,αp) reaction, respectively. For these measurements, 30–34-MeV ^{7}Li^{3+} beams, obtained from the Stony Brook tandem van de Graff accelerator were incident on enriched (>99%) ^{208}Pb foils with thicknesses of 0.5, 1.1, and 250 mg/cm^2. The deexcitation γ rays were detected by large coaxial Ge(Li) detectors with energy resolutions of ~2.0 keV full width at half maximum (FWHM) at 1.3 MeV. For weak low-energy γ rays (<400 keV), a planar type Ge detector, with an energy resolution of 0.8 keV FWHM at 122 keV, was utilized in several measurements. The α particles were detected by silicon surface barrier detectors, including one of annular geometry, which were typically 150 μg/cm^2 thick and 100–150 mm^2 in area.

The α-decay excitation study was carried out to determine the relative cross sections for the population of ^{212}At, ^{213}At, and ^{212}Po near the ^{7}Li + ^{208}Pb Coulomb barrier. This was done by measuring the α-decay yields at ^{7}Li beam energies of 30, 32, and 34 MeV with the 0.5 mg/cm^2 ^{208}Pb target. The energies of the α-particle groups for these nuclei are 9.08 MeV for ^{213}At;[5] 8.78 MeV for ^{212}Po,[7] and primarily 7.62, 7.68, 7.84, and 7.90 for ^{212}At.[13] All other expected α-particle groups have energies less than 7.45 MeV. The α particles were detected at 160° relative to the beam direction with a silicon detector (see Fig. 1). An in-beam resolution of 150 keV FWHM, which was limited by the target thickness, was sufficient to resolve the α-particle groups. The yield for each α-particle group was determined by fitting to the data a Gaussian distribution with a quadratic background. The yield for ^{212}At was obtained by summing the 7.62-, 7.68-, 7.84-, and 7.90-MeV α-particle group yields. Normalization was achieved by current integration. On the basis of these yields, the beam energies for the subsequent ^{7}Li + ^{208}Pb measurements were selected.

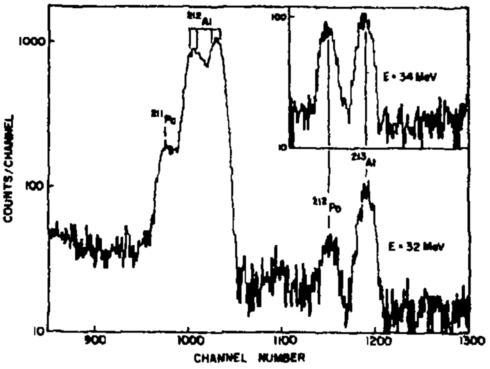

FIG. 1. The α-particle energy spectrum observed with a 0.5 mg/cm^2 ^{208}Pb target at a ^{7}Li beam energy of 32 MeV. The energies of the α-particle groups are 9.08 MeV for ^{213}At; 8.78 MeV for ^{212}Po; primarily 7.62, 7.68, 7.84, and 7.90 MeV for ^{212}At; and 7.45 MeV for ^{211}Po. The insert in the upper right corner contains the relative yield of the ^{212}Po and ^{213}At groups at 34 MeV.

A coincidence measurement between γ rays and the ground state α decay of ^{213}At was made to identify those γ rays originating from the decay of excited states in ^{213}At. Care had to be exercised because of the considerably larger yield of the (^{7}Li,3n) channel to ^{212}At (see Sec. III). In order to achieve a reasonable coincidence event rate for this measurement, large detector solid angles, an optimal ^{213}At yield, and a thick target were required. The large detector solid angles were obtained by using a target chamber which was designed to allow an annular surface barrier detector and a Ge(Li) detector to be placed as close as 3 cm from the target when the detectors are positioned at 180° and 90° to the beam, respectively. The optimal ^{213}At yield was achieved by carrying out the experiment at a 30-MeV beam energy. This energy was selected on the basis of the α-decay excitation measurements, which showed that for the range of energies studied, the yield of ^{213}At was a maximum at 30 MeV and that for ^{212}At was at a minimum. Below 30 MeV the Coulomb barrier reduced all the channels. In addition, since the yield of ^{212}Po at 30 MeV is down by about an order of magnitude relative to that for ^{213}At, it was not necessary to resolve the ^{212}Po and ^{213}At decay α particles, which are separated by only 300 keV. Thus a thick 1.1 mg/cm^2 target could be used to increase the coincidence α-γ event rate for ^{213}At. The α energy resolution with this target thickness was adequate to discriminate against the ^{212}At α groups. For the α-γ coincidence measurement, standard fast-slow electronics were employed; this was possible because the mean lifetime, $\tau = 159(29)$ nsec, of the ^{213}At ground state is sufficiently short that the true-to-random ratio is acceptable. Coincident γ-ray spectra were collected on-line by setting digital gates on the 9.08-MeV α particles from ^{213}At.

The γ-γ coincidence, γ-ray angular distribution, and pulsed-beam-γ timing measurements were carried out using 33-MeV ^{7}Li ion beams and the thick 250 mg/cm^2 target. The increased energy was chosen to increase the population of high-spin states and at this energy the ^{213}At yield relative to ^{212}At is still reasonable. The yield for ^{212}Po is also large enough that spectroscopic information could be obtained. The γ-γ coincidence measurements were carried out to identify the γ-ray decay schemes. To obtain information on the γ-anisotropies, as well as the relative γ-ray intensities I_γ, γ-angular distributions were measured at 5 angles between 0° and 90°. The extracted photopeak areas were fitted to $W(\theta)=I_\gamma(1+A_2P_2+A_4P_4)$, where P_k are the Legendre polynomials. The time differential pulsed-beam-γ measurements were made to identify delayed transitions and to obtain lifetime results for isomeric states. For the time differential measurements, the ^{7}Li beam was pulsed with repetition periods of 1 and 2 μsec and an overall time resolution of about 8 nsec was achieved with the Ge(Li) detectors.

III. EXPERIMENTAL RESULTS

A. ^{213}At and ^{212}Po

The results of the α-decay excitation measurement (see Fig. 2) show that the ^{208}Pb(^{7}Li,3n)^{212}At reaction is much stronger than that of ^{208}Pb(^{7}Li, 2n)^{213}At. These results are consistent with the cross-section estimates which are expected[14] to peak at 41.8 and 29.5 MeV for the (^{7}Li,3n) and (^{7}Li,2n) reactions, respectively. The yield of the (^{7}Li, 2n) reaction at its peak energy is significantly limited by the Coulomb barrier (≈30 MeV). The measurement also shows that the ^{208}Pb(^{7}Li,t)^{212}Po reaction has a strong energy dependence between 30–34 MeV. At 30 MeV this reaction is very weak, but increases rapidly, becoming nearly equal to the ^{208}Pb(^{7}Li,2n)^{213}At reaction at 34 MeV. The (^{7}Li,t) reaction is expected[15] to involve both direct transfer and breakup plus capture processes. Calculations with a standard equilibrium evaporation code[16] indicate that the contributions to the ^{212}Po yield from (^{7}Li,p2n) should be very small compared to the observed yields. Since these results showed that the yield of ^{213}At was largest at 30 MeV for the range of energies studied and that for ^{212}At and ^{212}Po was a minimum, this energy was chosen for the α-γ coincidence measurement in order to optimize the event rate.

From the α-γ coincidence measurement, the 341-, 387-, 405-, and 725-keV γ rays were assigned to ^{213}At. These four γ rays are seen in the coincidence spectrum for the 9.08-MeV α particles of the ground state decay of ^{213}At, which is shown in Fig. 3. The 511-keV γ ray was also observed in coincidence; however, this γ ray is most probably annihilation radiation.

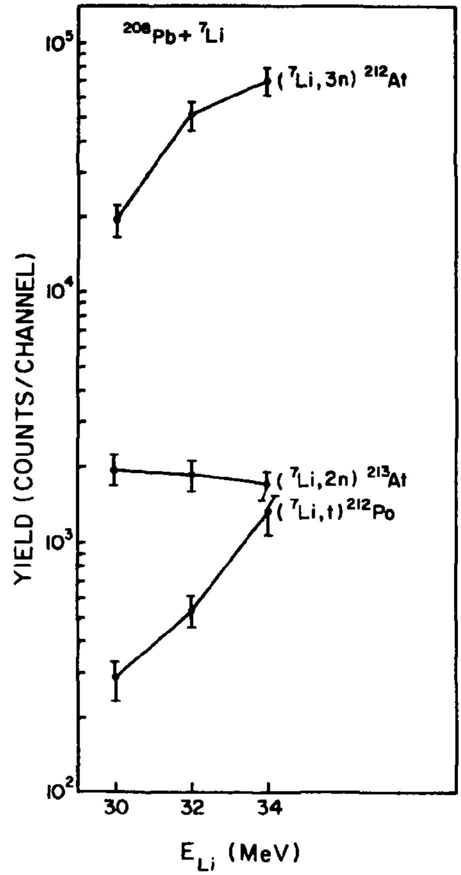

FIG. 2. Relative α-decay yields for ^{212}At, ^{212}Po, and ^{213}At during the bombardment of a 0.5 mg/cm^2 ^{208}Pb target with ^{7}Li ions at energies of 30, 32, and 34 MeV. The yield for ^{212}At was obtained by summing the 7.62-, 7.68-, 7.84-, and 7.90-MeV α-particle groups.

The results of the γ-γ coincidence and angular distribution measurements for ^{213}At and ^{212}Po are summarized in Table I. The 387-, 405-, and 725-keV γ rays assigned to ^{213}At on the basis of the α-γ coincidence measurement are also observed in coincidence with a 188-keV γ ray. These four γ rays are shown in the total γ-γ coincidence spectrum at the top of Fig. 4. The strong γ rays in this spectrum, which are not labeled in the figure, have been identified previously as γ rays from ^{212}At,[1] ^{210}Bi,[2] and ^{209}Bi.[3] In addition to the ^{213}At γ rays, γ rays with energies of 727, 405, and 222

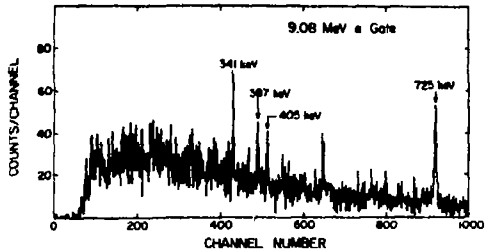

FIG. 3. γ-ray spectrum obtained in coincidence with 9.08-MeV α particles from the decay of the ^{213}At ground state during the bombardment of a 1.1 mg/cm^2 ^{208}Pb target with 30-MeV ^{7}Li ions.

keV were assigned to ^{212}Po. This assignment was made with the assumed identification of the 727-keV γ ray with the $2^+ - 0^+$ transition in ^{212}Po, which had been observed previously in β-decay studies[7] of ^{212}Bi. This identification is strengthened by the fact that the ratio of the intensity of the 725-keV transition in ^{213}At to the 727-keV transition (see Table I) is comparable to the ratio of the ^{213}At to ^{212}Po α-decay yields observed at 33 MeV, which is the energy at which the γ-γ coincidence measurements were carried out (see Fig. 2). Also the 727-keV γ ray has not been observed[1-3] in coincidence with any of the γ rays from ^{212}At, ^{209}Bi, and ^{210}Bi. Both the ^{213}At and ^{212}Po level schemes involve a 405-keV transition. The existence of two 405-keV γ rays was determined by the γ-γ coincidence measurement which showed that the 725-keV transition in ^{213}At and the 727-keV transition in ^{212}Po were both in coincidence with a 405-keV γ ray (see Fig. 4). Conversely, the 405-keV transition is observed in coincidence with both the 725- and 727-keV γ rays.

From the γ-γ coincidence results and the γ-ray intensities I_γ, level schemes for ^{213}At and ^{212}Po were constructed. The level scheme for ^{213}At is shown on the left side of Fig. 5. The main feature of the decay scheme is the γ-ray cascade from the 1318-keV level to the ground state involving the 18-, 188-, 387-, 405-, and 725-keV γ rays. The 18-keV transition between the 1130- and 1112-keV levels was not observed, but its existence is confirmed by the coincidence between the 188- and 387-keV γ rays. The 341-keV γ ray is also included in the ^{213}At level scheme, on the basis of the α-γ coincidence measurement. No γ ray was observed in coincidence with this transition, indicating that it decays to the ground state.

For ^{212}Po, the 222- and 405-keV γ rays were observed to cascade to the 727-keV 2^+ state, defining levels at 1132- and 1354-keV (see Fig. 6). The present ^{212}Po results agree with the recent ^{209}Bi$(\alpha,p)^{212}$Po study,[12] which observed 727-, 405-, and 222-keV γ rays in coincidence with the ^{212}Po decay α particles. In addition, the present γ-γ coincidence and angular distribution measurements remove any ambiguities in the placement of the 405-, and 222-keV γ rays in the ^{212}Po level scheme.

Evidence for isomerism in both ^{213}At and ^{212}Po was found in the pulsed-beam-γ timing data. All the γ rays listed in Table I had delayed components, except the 341-keV γ ray. The 387-, 405-, 725-, and 727-keV γ rays also showed prompt peaks in their time spectra. Since the 405-keV line is actually two γ rays, it could not be determined definitely whether or not either of the components lacked a prompt peak. However, since both the ^{213}At 188-keV and ^{212}Po 222-keV γ rays are delayed, it is most probable that the 1130-keV level in ^{213}At and the 1132-keV level in ^{212}Po, which

TABLE I. Results of the γ-γ coincidence and angular distribution measurements for ^{212}Po and ^{213}At.

E_γ(keV)[a]	Nucleus	I_γ[b]	A_2[c]	γ rays coincident with E_γ[d]
188.4	^{213}At	13	-0.21 ± 0.07	(386.7), (405.1), 724.6
221.5	^{212}Po	16	0.05 ± 0.06	405.1, 727.4
340.5	^{213}At	40	0.14 ± 0.04	
386.7	^{213}At	27	-0.35 ± 0.06	188.4, 724.6
405.1	^{212}Po, ^{213}At	58[e]	0.21 ± 0.05	188.4, 221.5, 724.6, 727.4
724.6	^{213}At	100	0.28 ± 0.05	188.4, 386.7, 405.1
727.4	^{212}Po	80	-0.01 ± 0.03	221.5, 405.1

[a] γ-ray energies are accurate to ±0.3 keV.

[b] γ-ray intensities are normalized to the 724.6-keV yield; intensities are accurate to 10% unless otherwise noted.

[c] The A_4 coefficients are not quoted; all the A_4 coefficients are consistent with 0.00 ± 0.08.

[d] Parentheses around γ-ray energy indicate weak coincidence.

[e] The intensities (accurate to 25%) of the ^{213}At and ^{212}Po components of this γ ray are estimated from the γ-γ coincidence measurement to be 33 and 25, respectively.

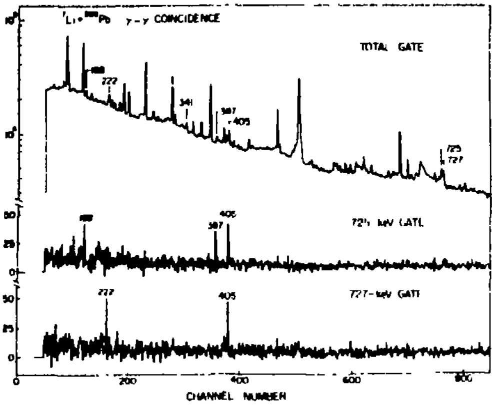

FIG. 4. γ-γ coincidence spectra from the ^{208}Pb+^{7}Li reaction at $E_{\mathrm{Li}}=33$ MeV. The total gate spectrum is coincident with all γ rays from 50 to 1000 keV. The strong γ rays in this spectrum have been identified previously in ^{208}Pb+^{7}Li studies of ^{212}At (Ref. 1), ^{210}Bi (Ref. 2), and ^{209}Bi (Ref. 3). The 725- and 727-keV gates are from the (^{7}Li, 2n)^{213}At and (^{7}Li, t)^{212}Po reactions, respectively.

decay via the 405-keV γ rays, are not isomeric. From this timing data it was impossible to exclude the existence of prompt components in the 188- and 220-keV γ rays because the prompt Compton background was very large at these energies and the delayed intensity very weak. Based on the above information, isomeric states exist at or above 1318 keV in ^{213}At and 1354 keV in ^{212}Po.

The 387- and 405-keV γ rays were the only transitions from which lifetime information could be extracted. A fit of a single lifetime to the 387-keV time differential data yielded a mean lifetime $\tau=159(25)$ nsec for the ^{213}At isomer. For the 405-keV transition, which involves two γ rays, the best fit to the time differential spectrum was obtained with a function involving two independent lifetimes, that yielded $\tau=163(14)$ and $\tau=25(9)$ nsec. These results suggest that the isomer with the shorter lifetime is in ^{212}Po and that with the longer lifetime in ^{213}At. All the other levels have lifetime upper limits of $\tau\leqslant 8$ nsec. *The observed $\tau=25$ nsec lifetime in ^{212}Po at or above 1354 keV is consistent with a recent independent ^{209}Bi(α,p)^{212}Po measurement*[12] which identified an isomeric state at 1423(30) keV with a mean lifetime of 20.5(3.5) nsec.

γ-ray multipolarities and, hence, J^π assignments were deduced from the γ-angular distributions with the assumptions that the states are aligned in low-*m* substates and that the dominant γ-ray decay proceeds via yrast levels by stretched

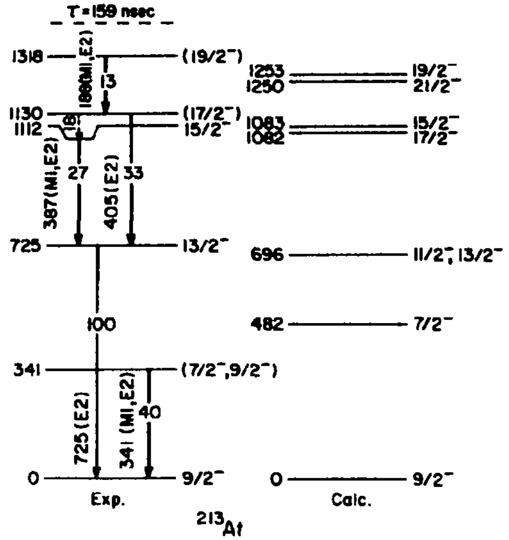

FIG. 5. The experimental and calculated energy level schemes for ^{213}At. The experimental level scheme that was determined from the present ^{208}Pb(^{7}Li, 2n) γ-ray measurements is shown on the left side. The energies of the levels and the γ rays are given in units of keV. The γ-ray intensities are normalized to the 725-keV γ-ray yield (=100). The results of the shell model calculation for the $(\pi h_{9/2})^3(\nu g_{9/2})^2$ model space are shown on the right side for several selected levels.

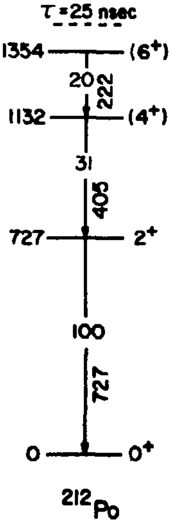

FIG. 6. The energy level scheme for ^{212}Po determined from the present ^{208}Pb(^{7}Li, t) γ-ray measurements. The 727-keV {2⁺→ 0⁺} transition was taken from Ref. 7.

$J \rightarrow J-L$ transitions,[14] where yrast levels are the lowest energy levels for a given spin J and L is the γ-ray multipolarity. Lifetime information also aided in these assignments by eliminating higher multipolarities.

The deduced γ-ray multipolarities and J^π assignments for ^{213}At are included in the level scheme of Fig. 5. Based on the angular distribution coefficients and lifetime limit, the 725-keV γ ray is identified as a stretched $E2$ transition. Assuming $J^\pi = \frac{9}{2}^-$ for the ground state of ^{213}At,[5] this multipolarity implies a $J^\pi = \frac{13}{2}^-$ for the 725-keV level. Since there are two 405-keV γ rays, the A_2 and A_4 coefficients for each separate γ ray are uncertain. However, since the angular distributions of the 222- and 727-keV γ rays in ^{212}Po were observed to be isotropic ($A_2 \approx 0$ and $A_4 \approx 0$), the ^{212}Po component of the 405-keV angular distribution is also most likely isotropic. The observed A_K thus suggest that the ^{213}At component for the 405-keV γ ray is a stretched $E2$ transition. This implies a $J^\pi = (\frac{17}{2}^-)$ for the 1130-keV level in ^{213}At; the bracket denotes the tentative nature of this assignment. For the 387-keV γ ray, the angular distribution and lifetime information strongly suggest a mixed $M1/E2$ multipolarity with a negative mixing ratio. This implies a $J^\pi = \frac{15}{2}^-$ for the 1112-keV level. Similarly, the 188-keV γ ray is consistent with a mixed $M1/E2$ transition. However, the possibility of $E1$ multipolarity cannot be ruled out for this γ ray because of the uncertainty in the A_2 coefficient. Thus, the 1318-keV level is tentatively given an assignment of $(\frac{19}{2}^-)$. For the prompt 341-keV γ ray, the small positive $A_2 = 0.14$ is suggestive of a nonstretched mixed $M1/E2$ transition. The most probable spin and parity for the 341-keV level is $(\frac{7}{2}^-, \frac{9}{2}^-)$.

For the ^{212}Po γ rays, the angular distributions are nearly isotropic (see Table I). However, the 727-keV $2^+ - 0^+$ transition is known to be a stretched $E2$. This indicates that the (^{7}Li,t) reaction is populating a broad distribution of m substates or that dealignment is occurring. Thus, strong J^π assignments cannot be made. However, because ^{212}Po is an even-even nucleus, it is most probable that the yrast decay is proceeding via the usual $6^+ \rightarrow 4^+ \rightarrow 2^+ \rightarrow 0^+$ sequence of levels. For this reason, the 1132- and 1354-keV levels are tentatively given J^π assignments of (4^+) and (6^+), respectively.

B. ^{210}Pb

The γ-γ coincidence measurements showed that levels in ^{210}Pb were being weakly populated during the bombardment of ^{208}Pb with 33-MeV ^{7}Li ions. Since the energies of the 8^+, 6^+, 4^+, and 2^+ levels in ^{210}Pb were known from previous charged particle studies,[8] the coincidence between the 297- and 799-keV γ rays observed in the present experiment identified these two γ rays as the $4^+ - 2^+$ and $2^+ - 0^+$ transitions in ^{210}Pb, respectively (see Fig. 7). These ^{210}Pb levels were being weakly populated most probably via the ^{208}Pb(^{7}Li,αp) reaction.

Evidence for two isomeric states in ^{210}Pb was found in the time differential data, which showed that both the 297- and 799-keV γ rays had delayed components. The results of the time differential measurement of the 297-keV γ ray are shown in Fig. 7. A least-squares fit to the data yielded mean lifetimes of 225(22) nsec and 30(10) nsec. The time differential spectrum of the 799-keV γ ray, which had poor statistics, also yielded lifetimes consistent with these values. Since the time differential spectra of both γ rays also include prompt components, they indicated that the isomeric levels lie above the 1096-keV 4^+ level and decay most probably via unobserved highly converted transitions. This assumption is consistent with the $8^+ \rightarrow 6^+$ and $6^+ \rightarrow 4^+$ transition energies in ^{210}Pb, which are known[8] to be 79- and 99-keV, respectively. Such $E2$ transitions have internal conversion coefficients of about 23 and 8, respectively, and would not be observed in the present γ-ray measurements. Thus, the present experimental data suggests that ^{210}Pb is similar to ^{210}Po, where the 8^+ and 6^+ states are known[17] to be isomeric with mean lifetimes of 139 and 61 nsec, respectively. Assuming the same situa-

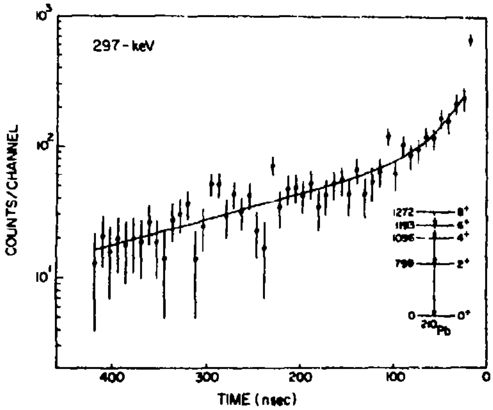

FIG. 7. Results of the time differential measurement of the 1272-keV 8^+ and 1193-keV 6^+ states in ^{210}Pb obtained from the time spectrum of the 297-keV γ ray for the bombardment of a thick ^{208}Pb target with a pulsed 33-MeV ^{7}Li beam. The solid line is a least squares fit to the data which yielded mean lifetimes of 225(22) and 30(10) nsec. The assignment of these lifetimes to the 8^+ and 6^+ states, respectively in ^{210}Pb is discussed in the text.

tion in ^{210}Pb implies that the 8^+ and 6^+ states have mean lifetimes of 225 and 30 nsec, respectively.

The decay of the recently discovered[3] 2986-keV $\frac{19}{2}^+$ isomeric state in ^{209}Bi was also observed in the present experiment. This level was strongly populated via the ^{208}Pb(^{7}Li,$\alpha 2n$) reaction. From the time differential measurements, the mean lifetime of this state was determined to be $\tau = 25(2)$ nsec, which is in excellent agreement with the previously measured value of $\tau = 26.0 \pm 1.4$ nsec.[3] The observed decay scheme for this isomer also agrees with that of Ref. 3.

IV. DISCUSSION

^{213}At

The experimental results obtained for ^{213}At from the present ^{208}Pb(^{7}Li,$2n$) γ-ray measurements are summarized in Table I and on the left side of Fig. 5. The structure of the low-lying states is expected to involve primarily the $h_{9/2}$ protons and the $g_{9/2}$ neutrons. Comparison of the ^{213}At level scheme with those for ^{211}At and ^{210}Pb suggests that the observed states in ^{213}At can be described reasonably well as the $(\pi)^3$ yrast levels in ^{211}At coupled to the $(\nu)^2$ levels of ^{210}Pb.

To check this, a shell model calculation of the energies of the $(\pi h_{9/2})^3(\nu_{9/2})^2$ structure was made using two-body empirical matrix elements extracted from ^{210}Pb, ^{210}Bi, and ^{211}At.[18] The results of the calculation for the yrast levels $J^\pi = \frac{7}{2}^-, \ldots, \frac{21}{2}^-$ are shown on the right side of Fig. 5, where they are compared with the experimental level scheme. The agreement is good. All the calculated levels are within 65 keV of the experimental levels, except for the 341-keV level, which is 142 keV below the calculated $\frac{7}{2}^-$ state. This indicates that, except for the 341-keV level, the observed levels in ^{213}At dominantly involve the $(\pi h_{9/2})^3(\nu g_{9/2})^2$ structure. Furthermore, the calculation shows that the configurations for these levels are primarily the ^{211}At ground state coupled to the $(\nu g_{9/2})^2$ excitations in ^{210}Pb.

In regard to the 341-keV $(\frac{7}{2}^-, \frac{9}{2}^-)$ level, no $\frac{7}{2}^-$ or $\frac{9}{2}^-$ levels are predicted near this energy by the calculation for the $(\pi h_{9/2})^3(\nu g_{9/2})^2$ configuration. This suggests that the 341-keV wave function involves additional orbitals. The orbital most likely involved is $\pi f_{7/2}$ through the

$$|(\pi h_{9/2})^2 0^+ (\pi f_{7/2})_{\frac{7}{2}^-}, (\nu g_{9/2})^2 0^+; \tfrac{7}{2}^-\rangle$$

configuration. This is supported by ^{211}Bi, where the first excited state, known[19] to have a large component of $|(\pi f_{7/2}), (\nu g_{9/2})^2 0^+; \frac{7}{2}^-\rangle$, is at 410 keV. This energy is considerably lower than the lowest $|(\pi h_{9/2}), (\nu g_{9/2})^2; \frac{7}{2}^-\rangle$ level in ^{211}Bi observed at 765 keV.[20]

It is interesting to conjecture as to the nature of the $\tau = 159$ nsec isomeric state in ^{213}At. Based on the $(\pi h_{9/2})^3(\nu g_{9/2})^2$ calculation and the experimental information, it is possible that the $|(\pi h_{9/2})^3\ \frac{9}{2}^-, (\nu g_{9/2})^2 8^+; \frac{25}{2}^-\rangle$ state would be isomeric, decaying via an unobserved low-energy $E2$ transition $(20 < E_\gamma < 100$ keV) to the $|(\pi h_{9/2})^3\ \frac{9}{2}^-, (\nu g_{9/2})^2 6^+; \frac{21}{2}^-\rangle$ state. This $\frac{21}{2}^-$ level would then decay promptly ($\tau \leq 8$ nsec) to the observed $(\frac{19}{2}^-)$ level at 1318 keV by an unobserved low-energy $E1$ transition. According to the $(\pi h_{9/2})^3(\nu g_{9/2})^2$ calculation, the unobserved $\frac{25}{2}^- \rightarrow \frac{21}{2}^-$ $E2$ transition should have an energy of about 60 keV. The isomeric mean lifetime, $\tau = 159$ nsec, then implies a $B(E2) \approx 76\ e^2\,\mathrm{fm}^4$ using an internal conversion coefficient ≈ 86. To zeroth order, this $B(E2)$ value should be identical to that for the $8^+ \rightarrow 6^+$ transition of the $(\nu g_{9/2})^2$ neutrons in ^{210}Pb. This value, which is discussed below, is 51(12) $e^2\,\mathrm{fm}^4$ and is somewhat smaller than that suggested for the $\frac{25}{2}^- \rightarrow \frac{21}{2}^-$ $E2$ transition in ^{213}At.

^{212}Po

The results of the ^{208}Pb(^{7}Li,t)^{212}Po measurements are summarized in Fig. 6 and Table I. These results are compared in a previous paper[10] by D. Strottman with a ^{212}Po shell model calculation, which uses realistic matrix elements and a complete shell model space.

^{210}Pb

The results of the ^{210}Pb lifetime measurements are summarized in Table II. In the present experimental investigation mean lifetimes of 225(22)and 30(10) nsec have been measured in ^{210}Pb for unobserved levels above 1096 keV. Based on the arguments described in Sec. III, these lifetimes were assigned to the 1272-keV 8^+ and 1193-keV 6^+ states, respectively. With these lifetimes, the extracted $B(E2)$ values are 51(12) $e^2\,\mathrm{fm}^4$ for the $8^+ \rightarrow 6^+$ transition and 308(115) $e^2\,\mathrm{fm}^4$ for the $6^+ \rightarrow 4^+$ transition.

The results of a calculation of the effective neutron charges in ^{210}Pb are also included in Table II. Theoretical $B(E2)$ values were calculated using the wave functions of Kuo and Herling[21] and harmonic oscillator radial wave functions with $\hbar\omega = 41A^{-1/3}$. The calculation yielded $B(E2)$ values of 48 $e^2\,\mathrm{fm}^4$ for $8^+ \rightarrow 6^+$ transition and 187 $e^2\,\mathrm{fm}^4$ for the $6^+ \rightarrow 4^+$ transition; these values imply neutron effective charges of $1.03(12)e$ and $1.28(24)e$, respectively.

It is interesting to compare the neutron effective charges of ^{210}Pb with those extracted from ^{210}Bi.[22] In ^{210}Bi, neutron effective charges of 0.81(8) and 0.89(16) were obtained from the 9^-

TABLE II. Neutron transitions and effective charges involving the $\nu(2g_{9/2})$ orbitals.

Nucleus	$J_i \rightarrow J_f$	E_γ (keV)	τ (nsec)	α	$B_{\mathrm{exp}}(E2)$ e^2 fm^4	$B_{\mathrm{th}}(E2)$ $e_{\mathrm{eff}}{}^2$ fm^4	e_{eff}/e
^{210}Pb	$8^+ \rightarrow 6^+$	79 ± 7 [a]	225 ± 22	22.3 [b]	51 ± 12	48	1.03 ± 0.12
^{210}Pb	$6^+ \rightarrow 4^+$	99 ± 7 [a]	30 ± 10	8.3 [b]	308 ± 115	187	1.28 ± 0.24
^{210}Bi [c]	$9^- \rightarrow 7^-$	162.3	84 ± 9	0.98	44 ± 5		0.81 ± 0.08
^{210}Bi [c]	$5^- \rightarrow 3^-$	90.4	55 ± 9	10.4	190 ± 30		0.89 ± 0.16

[a] The transition energy was taken from Ref. 8.

[b] The internal conversion coefficients were taken from R. S. Hager and C. E. Seltzer, Nucl. Data A4, 1 (1968) and O. Dragoun, Z. Plajner, and F. Schmatzler, *ibid.* A9, 119 (1971).

[c] Reference 21.

$\rightarrow 7^-$ and $5^- \rightarrow 3^-$ $E2$ transitions, respectively. Since the dominant configuration for these levels is $|\pi h_{9/2})(\nu g_{9/2}); J)$, an effective proton charge of 1.53e was used in order to extract the $\nu g_{9/2}$ effective charge. The ^{210}Bi values are slightly smaller than the present ^{210}Pb values, although almost consistent within the uncertainties.

ACKNOWLEDGMENTS

The authors acknowledge Dr. B. A. Brown for contributions which aided in the theoretical interpretation of the experimental results. This study was supported in part by the National Science Foundation.

---

*Present address: Indiana University Cyclotron Facility, Bloomington, Ind. 47405.

†Present address: Cyclotron Institute, Texas A & M University, College Station, Tex. 77843.

[1] T. P. Sjoreen, U. Garg, D. B. Fossan, J. R. Beene, T. K. Alexander, E. D. Earle, O. Häusser, and A. B. McDonald, Phys. Rev. C 20, 960 (1979).

[2] C. V. K. Baba, T. Faestermann, D. B. Fossan, and D. Proetel, Phys. Rev. Lett. 29, 496 (1972).

[3] J. R. Beene, O. Häusser, T. K. Alexander, and A. B. McDonald, Phys. Rev. C 17, 1359 (1978).

[4] K. H. Maier, J. R. Leigh, F. Puhlhofer, and R. M. Diamond, Phys. Lett. 35B, 401 (1971).

[5] Jørn Borggreen, Kalevi Valli, and Earl K. Hyde, Phys. Rev. C 2, 1841 (1970).

[6] Suvra Sangul, R. K. Garg, S. D. Chauhan, S. L. Gupta, and S. C. Pancholi, Phys. Rev. C 12, 318 (1975).

[7] S. C. Pancholi and M. J. Martin, Nucl. Data B8, 165 (1972).

[8] E. R. Flynn, G. J. Igo, R. A. Broglia, S. Landowne, V. Paar, and B. Nilsson, Nucl. Phys. A195, 97 (1972), and references therein; E. R. Flynn (private communication).

[9] T. P. Sjoreen, G. Schatz, S. K. Bhattacherjee, B. A. Brown, D. B. Fossan, and P. M. S. Lesser, Phys. Rev. C 14, 1023 (1976).

[10] D. Strottman, Phys. Rev. C 20, 1150 (1979).

[11] T. P. Sjoreen, U. Garg, and D. B. Fossan, Bull. Am. Phys. Soc. 22, 643 (1977).

[12] R. M. Lieder, J. P. Didelez, H. Beuscher, D. R. Haenni, M. Müller-Veggian, A. Neskakis, and C. Mayer-Böricke, Phys. Rev. Lett. 41, 742 (1978).

[13] Paul L. Reeder, Phys. Rev. C 1, 721 (1970); W. B. Jones, Phys. Rev. 130, 2042 (1963).

[14] J. O. Newton, in *Nuclear Spectroscopy and Reactions, Part C*, edited by J. Cerny (Academic, New York, 1974), p. 185.

[15] H. Freiesleben, H. C. Britt, J. Birkelund, and J. R. Huizenga, Phys. Rev. C 10, 245 (1974).

[16] M. Blann, Code ALICE, U.S.A.E.C. Report No. COO-3494-29 (unpublished).

[17] O. Häusser, T. K. Alexander, J. R. Beene, E. D. Earle, A. B. McDonald, F. C. Khanna, and I. S. Towner, Nucl. Phys. A273, 253 (1976).

[18] J. P. Schiffer and W. W. True, Rev. Mod. Phys. 48, 191 (1976).

[19] E. R. Flynn, R. E. Anderson, N. J. DiGiacomo, R. J. Peterson, and G. R. Smith, Phys. Rev. C 16, 139 (1977).

[20] E. R. Flynn, D. G. Burke, J. D. Sherman, and J. W. Sunier, Nucl. Phys. A263, 365 (1976).

[21] T. T. S. Kuo and G. H. Herling, NRL Memorandum Report No. 2258, 1971 (unpublished).

[22] G. Astner, I. Bergström, J. Blomqvist, B. Fant, and K. Wikström, Nucl. Phys. A182, 219 (1972).

tion in ^{210}Pb implies that the 8^+ and 6^+ states have mean lifetimes of 225 and 30 nsec, respectively.

The decay of the recently discovered[3] 2986-keV $\frac{19}{2}^+$ isomeric state in ^{209}Bi was also observed in the present experiment. This level was strongly populated via the ^{208}Pb(^{7}Li,$\alpha 2n$) reaction. From the time differential measurements, the mean lifetime of this state was determined to be $\tau = 25(2)$ nsec, which is in excellent agreement with the previously measured value of $\tau = 26.0 \pm 1.4$ nsec.[3] The observed decay scheme for this isomer also agrees with that of Ref. 3.

IV. DISCUSSION

^{213}At

The experimental results obtained for ^{213}At from the present ^{208}Pb(^{7}Li,$2n$) γ-ray measurements are summarized in Table I and on the left side of Fig. 5. The structure of the low-lying states is expected to involve primarily the $h_{9/2}$ protons and the $g_{9/2}$ neutrons. Comparison of the ^{213}At level scheme with those for ^{211}At and ^{210}Pb suggests that the observed states in ^{213}At can be described reasonably well as the $(\pi)^3$ yrast levels in ^{211}At coupled to the $(\nu)^2$ levels of ^{210}Pb.

To check this, a shell model calculation of the energies of the $(\pi h_{9/2})^3(\nu_{9/2})^2$ structure was made using two-body empirical matrix elements extracted from ^{210}Pb, ^{210}Bi, and ^{211}At.[18] The results of the calculation for the yrast levels $J^\pi = \frac{7}{2}^-, \ldots, \frac{21}{2}^-$ are shown on the right side of Fig. 5, where they are compared with the experimental level scheme. The agreement is good. All the calculated levels are within 65 keV of the experimental levels, except for the 341-keV level, which is 142 keV below the calculated $\frac{7}{2}^-$ state. This indicates that, except for the 341-keV level, the observed levels in ^{213}At dominantly involve the $(\pi h_{9/2})^3(\nu g_{9/2})^2$ structure. Furthermore, the calculation shows that the configurations for these levels are primarily the ^{211}At ground state coupled to the $(\nu g_{9/2})^2$ excitations in ^{210}Pb.

In regard to the 341-keV $(\frac{7}{2}^-, \frac{9}{2}^-)$ level, no $\frac{7}{2}^-$ or $\frac{9}{2}^-$ levels are predicted near this energy by the calculation for the $(\pi h_{9/2})^3(\nu g_{9/2})^2$ configuration. This suggests that the 341-keV wave function involves additional orbitals. The orbital most likely involved is $\pi f_{7/2}$ through the

$$|(\pi h_{9/2})^2 0^+ (\pi f_{7/2})\tfrac{7}{2}^-, (\nu g_{9/2})^2 0^+; \tfrac{7}{2}^-\rangle$$

configuration. This is supported by ^{211}Bi, where the first excited state, known[19] to have a large component of $|(\pi f_{7/2}), (\nu g_{9/2})^2 0^+; \frac{7}{2}^-\rangle$, is at 410 keV. This energy is considerably lower than the lowest $|(\pi h_{9/2}), (\nu g_{9/2})^2; \frac{7}{2}^-\rangle$ level in ^{211}Bi observed at 765 keV.[20]

It is interesting to conjecture as to the nature of the $\tau = 159$ nsec isomeric state in ^{213}At. Based on the $(\pi h_{9/2})^3(\nu g_{9/2})^2$ calculation and the experimental information, it is possible that the $|(\pi h_{9/2})^3\, \frac{9}{2}^-, (\nu g_{9/2})^2 8^+; \frac{25}{2}^-\rangle$ state would be isomeric, decaying via an unobserved low-energy $E2$ transition $(20 < E_\gamma < 100$ keV) to the $|(\pi h_{9/2})^3\, \frac{9}{2}^-, (\nu g_{9/2})^2 6^+; \frac{21}{2}^-\rangle$ state. This $\frac{21}{2}^-$ level would then decay promptly ($\tau \leq 8$ nsec) to the observed $(\frac{19}{2}^-)$ level at 1318 keV by an unobserved low-energy $E1$ transition. According to the $(\pi h_{9/2})^3(\nu g_{9/2})^2$ calculation, the unobserved $\frac{25}{2}^- \to \frac{21}{2}^-$ $E2$ transition should have an energy of about 60 keV. The isomeric mean lifetime, $\tau = 159$ nsec, then implies a $B(E2) \approx 76\ e^2\,\mathrm{fm}^4$ using an internal conversion coefficient ≈ 86. To zeroth order, this $B(E2)$ value should be identical to that for the $8^+ \to 6^+$ transition of the $(\nu g_{9/2})^2$ neutrons in ^{210}Pb. This value, which is discussed below, is 51(12) $e^2\,\mathrm{fm}^4$ and is somewhat smaller than that suggested for the $\frac{25}{2}^- \to \frac{21}{2}^-$ $E2$ transition in ^{213}At.

^{212}Po

The results of the ^{208}Pb(^{7}Li,t)^{212}Po measurements are summarized in Fig. 6 and Table I. These results are compared in a previous paper[10] by D. Strottman with a ^{212}Po shell model calculation, which uses realistic matrix elements and a complete shell model space.

^{210}Pb

The results of the ^{210}Pb lifetime measurements are summarized in Table II. In the present experimental investigation mean lifetimes of 225(22) and 30(10) nsec have been measured in ^{210}Pb for unobserved levels above 1096 keV. Based on the arguments described in Sec. III, these lifetimes were assigned to the 1272-keV 8^+ and 1193-keV 6^+ states, respectively. With these lifetimes, the extracted $B(E2)$ values are 51(12) $e^2\,\mathrm{fm}^4$ for the $8^+ - 6^+$ transition and 308(115) $e^2\,\mathrm{fm}^4$ for the $6^+ - 4^+$ transition.

The results of a calculation of the effective neutron charges in ^{210}Pb are also included in Table II. Theoretical $B(E2)$ values were calculated using the wave functions of Kuo and Herling[21] and harmonic oscillator radial wave functions with $\hbar\omega = 41A^{-1/3}$. The calculation yielded $B(E2)$ values of 48 $e^2\,\mathrm{fm}^4$ for $8^+ - 6^+$ transition and 187 $e^2\,\mathrm{fm}^4$ for the $6^+ \to 4^+$ transition; these values imply neutron effective charges of $1.03(12)e$ and $1.28(24)e$, respectively.

It is interesting to compare the neutron effective charges of ^{210}Pb with those extracted from ^{210}Bi.[22] In ^{210}Bi, neutron effective charges of 0.81(8) and 0.89(16) were obtained from the 9^-

TABLE II. Neutron transitions and effective charges involving the $\nu(2g_{9/2})$ orbitals.

Nucleus	$J_i \to J_f$	E_γ (keV)	τ (nsec)	α	$B_{\text{exp}}(E2)$ e^2 fm^4	$B_{\text{th}}(E2)$ e_{eff}^2 fm^4	$e_{\text{eff}/e}$
^{210}Pb	$8^+ \to 6^+$	79 ± 7[a]	225 ± 22	22.3[b]	51 ± 12	48	1.03 ± 0.12
^{210}Pb	$6^+ \to 4^+$	99 ± 7[a]	30 ± 10	8.3[b]	308 ± 115	187	1.28 ± 0.24
^{210}Bi[c]	$9^- \to 7^-$	162.3	84 ± 9	0.98	44 ± 5		0.81 ± 0.08
^{210}Bi[c]	$5^- \to 3^-$	90.4	55 ± 9	10.4	190 ± 30		0.89 ± 0.16

[a] The transition energy was taken from Ref. 8.

[b] The internal conversion coefficients were taken from R. S. Hager and C. E. Seltzer, Nucl. Data A4, 1 (1968) and O. Dragoun, Z. Plajner, and F. Schmatzler, *ibid.* A9, 119 (1971).

[c] Reference 21.

$\to 7^-$ and $5^- \to 3^-$ $E2$ transitions, respectively.

Since the dominant configuration for these levels is $|\pi h_{9/2})(\nu g_{9/2})J\rangle$, an effective proton charge of $1.53e$ was used in order to extract the $\nu g_{9/2}$ effective charge. The ^{210}Bi values are slightly smaller than the present ^{210}Pb values, although almost consistent within the uncertainties.

ACKNOWLEDGMENTS

The authors acknowledge Dr. B. A. Brown for contributions which aided in the theoretical interpretation of the experimental results. This study was supported in part by the National Science Foundation.

---

*Present address: Indiana University Cyclotron Facility, Bloomington, Ind. 47405.

†Present address: Cyclotron Institute, Texas A & M University, College Station, Tex. 77843.

[1] T. P. Sjoreen, U. Garg, D. B. Fossan, J. R. Beene, T. K. Alexander, E. D. Earle, O. Häusser, and A. B. McDonald, Phys. Rev. C 20, 960 (1979).

[2] C. V. K. Baba, T. Faestermann, D. B. Fossan, and D. Proetel, Phys. Rev. Lett. 29, 496 (1972).

[3] J. R. Beene, O. Häusser, T. K. Alexander, and A. B. McDonald, Phys. Rev. C 17, 1359 (1978).

[4] K. H. Maier, J. R. Leigh, F. Puhlhofer, and R. M. Diamond, Phys. Lett. 35B, 401 (1971).

[5] Jørn Borggreen, Kalevi Valli, and Earl K. Hyde, Phys. Rev. C 2, 1841 (1970).

[6] Suvra Sangul, R. K. Garg, S. D. Chauhan, S. L. Gupta, and S. C. Pancholi, Phys. Rev. C 12, 318 (1975).

[7] S. C. Pancholi and M. J. Martin, Nucl. Data B8, 165 (1972).

[8] E. R. Flynn, G. J. Igo, R. A. Broglia, S. Landowne, V. Paar, and B. Nilsson, Nucl. Phys. A195, 97 (1972), and references therein; E. R. Flynn (private communication).

[9] T. P. Sjoreen, G. Schatz, S. K. Bhattacherjee, B. A. Brown, D. B. Fossan, and P. M. S. Lesser, Phys. Rev. C 14, 1023 (1976).

[10] D. Strottman, Phys. Rev. C 20, 1150 (1979).

[11] T. P. Sjoreen, U. Garg, and D. B. Fossan, Bull. Am. Phys. Soc. 22, 643 (1977).

[12] R. M. Lieder, J. P. Didelez, H. Beuscher, D. R. Haenni, M. Müller-Veggian, A. Neskakis, and C. Mayer-Böricke, Phys. Rev. Lett. 41, 742 (1978).

[13] Paul L. Reeder, Phys. Rev. C 1, 721 (1970); W. B. Jones, Phys. Rev. 130, 2042 (1963).

[14] J. O. Newton, in *Nuclear Spectroscopy and Reactions, Part C*, edited by J. Cerny (Academic, New York, 1974), p. 185.

[15] H. Freiesleben, H. C. Britt, J. Birkelund, and J. R. Huizenga, Phys. Rev. C 10, 245 (1974).

[16] M. Blann, Code ALICE, U.S.A.E.C. Report No. COO-3494-29 (unpublished).

[17] O. Häusser, T. K. Alexander, J. R. Beene, E. D. Earle, A. B. McDonald, F. C. Khanna, and I. S. Towner, Nucl. Phys. A273, 253 (1976).

[18] J. P. Schiffer and W. W. True, Rev. Mod. Phys. 48, 191 (1976).

[19] E. R. Flynn, R. E. Anderson, N. J. DiGiacomo, R. J. Peterson, and G. R. Smith, Phys. Rev. C 16, 139 (1977).

[20] E. R. Flynn, D. G. Burke, J. D. Sherman, and J. W. Sunier, Nucl. Phys. A263, 365 (1976).

[21] T. T. S. Kuo and G. H. Herling, NRL Memorandum Report No. 2258, 1971 (unpublished).

[22] G. Astner, I. Bergström, J. Blomqvist, B. Fant, and K. Wikström, Nucl. Phys. A182, 219 (1972).

PHYSICAL REVIEW C VOLUME 21, NUMBER 5 MAY 1980

Exactly central heavy-ion collisions by nuclear hydrodynamics

Henry H. K. Tang*
A. W Wright Nuclear Structure Laboratory, Yale University, New Haven, Connecticut 06520

Cheuk-Yin Wong
Physics Division, Oak Ridge National Laboratory, Oak Ridge, Tennessee 37830

(Received 17 September 1979)

We study the dynamics of heavy-ion collisions using the hydrodynamical description and focus our attention on the head-on collisions which provide the most favorable case for such a description. Angular distributions and energy distributions were obtained for various combinations of projectiles and targets of equal and unequal masses in the energy range from 50 to 400 MeV per projectile nucleon. It is found that regions of high density (the shock regions) are formed during the collisions and that the angular and energy distributions for many of these collisions have prominent features. In the collision of a small projectile with a heavy target, there is the forward angular peak of slow dissociated particles which represent much of the projectile nuclear matter stopped in the larger target nucleus, in addition to the nucleons from the expansions of the shock region There is the side angular peak corresponding to the sidesplash of the target nuclear matter due to the impact of the projectile. There is also the backward angular peak due to the expansion of the shock region into the backward direction. In the collision of two equal nuclei, there are only the forward angular peak and the side angular peak. The effects of viscosity and thermal conductivity are investigated and found to affect the angular and energy distributions of the reaction products.

NUCLEAR REACTIONS Heavy-ion reactions, nuclear hydrodynamics, ^{20}Ne + ^{197}Au and ^{208}Pb + ^{208}Pb at 50, 100, 250, and 400 MeV per projectile nucleon. Nuclear viscosity and thermal conductivity.

I. INTRODUCTION

Our recent interest in high-energy, heavy-ion reactions stems in part from the possibility of probing the equation of state of nulcear matter, both with regard to its behavior at zero temperature and at high temperatures. Many exotic phenomena such as the pion condensation and density isomers manifest themselves in peculiar shapes of the equation of state.[1] As the equation of state enters prominently in the hydrodynamical description of the reaction process, it is desirable to ascertain to what degree the heavy-ion collision process can be described by hydrodynamics. Although much discussion and investigation has been made on the theoretical foundation of nuclear hydrodynamics,[2-6] in the final analysis, it is a direct confrontation of the results of hydrodynamical calculations with experiments which will validate or negate the hydrodynamical description. The recent observations by Gutbrod and collaborators[7] that many features of the heavy-ion collisions at intermediate energies may have hydrodynamical origin gives additional impetus to the treatment of heavy-ion collision in terms of nuclear hydrodynamics.

The advantages of a hydrodynamical treatment of the reaction process, if successful, are manifold. As different energy heavy ions lead to different compressed densities, the equation of state can, in principle, be traced by using projectiles of different energies. Furthermore, one may also obtain the transport coefficients of nuclear matter which otherwise cannot be obtained by other means. For these reasons, one may wish to push the hydrodynamical description as far as possible and see how it could perhaps describe some aspects of heavy-ion collisions.

It is clear from the outset that not all the nuclear collisions can be described properly by nuclear hydrodynamics. For example, peripheral and transfer reactions are unlikely to be described well by nuclear hydrodynamics as the interaction time involved is short compared with the time necessary to bring the system into local equilibrium. It is necessary to be selective in choosing the proper case for treatment. The interaction time increases as the impact parameter decreases. Head-on collisions involving large nuclei present favorable cases where nuclear hydrodynamics may perhaps be a valid description. For this reason, we focus our attention on head-on collisions, with the hope of exploring only the region around $l=0$ at a later time.

Past treatments of numerical nuclear hydrodynamics[5,8,8] centered on the comparison of theoretical results with the experimental single-particle inclusive data.[9] The objective is to ob-

© 1980 The American Physical Society

ain the angular distribution after a summation ver all the impact parameters. Earlier work eals with the case of head-on collisions.[10] The umerical technique used is the PIC (particle-n-cell) method. As no long-range interaction s used, the nuclear surface is given as a sharp urface which introduces the problem of negative ressure. Furthermore, viscosity and thermal onductivity are not taken into account. Another reatment of the hydrodynamical problem made se of the assumption of irrotational flow[11] and a ualitative representation of the mach cone conept.[12] Conjectures based on the latter are, owever, not substantiated by the detailed calcuations of Amsden *et al.*[10] Still another treatment y Wong, Tang, and collaborators[13-17] discussed hock waves in supersonic heavy-ion collisions nd later introduced the long-range interaction o describe the nuclear surface. The numerical ethod is based on the FCT (flux-corrected-ransport) method of Boris and Book[18] which llows simple incorporation of viscosity and hermal conductivity. One-dimensional hydroynamical calculations based on such a model ave been reported previously.[14] Two-dimenional calculations for the collision of one infinite ylinder of nuclear matter with another were also erformed and will be reported elsewhere.[16] his paper deals with three-dimensional head-on collisions. A preliminary report, based on the work of Wong, Welton, and Maruhn, was presented previously.[17]

This paper is organized as follows. In Sec. II he basic equations of nuclear hydrodynamics are resented. A brief description of the genealogy f nuclear hydrodynamics and its connection with he many-body theory is given. A criterion of ts validity in terms of the thermal relaxation ime is also discussed. In Sec. III an estimate f the nuclear transport coefficients is made. The shear viscosity and the thermal conductivity re estimated from the Landau-Fermi liquid heory and the compressional viscosity from the width of the giant monopole resonance. In Sec. V we discuss our choice of the equation of state nd other parameters for the nulear fluid. Section V presents a detailed description and discussion f the results. They are the calculations for ead-on collisions of ^{20}Ne + ^{197}Au and ^{208}Pb + ^{208}Pb t the bombarding energies of 50, 100, 250, and 400 MeV per projectile nucleon, both with and without viscosity and thermal conductivity. Special features of the hydrodynamical descripion and the significance of dissipation in the dyamics are emphasized in order to facilitate uture confrontations with experiments. Finally, Sec. VI summarizes the main results and remarks on future investigations along this line. An appendix is attached in which some technical aspects of the numerical problem are discussed.

A very important parameter in the present discussion is the initial kinetic energy of the colliding nuclei. For simplicity, we shall adopt the convention of measuring the energy in terms of the kinetic energy of the projectile per projectile nucleon while the target is at rest. Furthermore, in the collision of unequal nuclei we shall take the lighter nucleus as the projectile. The energy parameter is then expressed as E_{lab}/A_p, where E_{lab} is the laboratory kinetic energy of the projectile and A_p is the projectile mass. For simplicity, this quantity is sometimes expressed as simply as E/A.

II. BASIC EQUATIONS OF NUCLEAR HYDRODYNAMICS

The connection between nuclear hydrodynamics and a more fundamental quantum many-body theory has been extensively studied by various workers.[1-6,19-21] We shall briefly discuss the results of Refs. 20 and 21 with regard to the connection between nuclear hydrodynamics and the many-body theory. This connection can be depicted in Fig. 1. One can start with the exact many-body theory and obtain the extended time-dependent Hartree-Fock (ETDHF) approximation.[20] In this approximation, both the effect of the mean-field and particle collisions are considered. Next, one goes to a classical transcription[21] by interpreting the Wigner function in the ETDHF approximation as the classical distribution function. The resultant approximate Vlasov-Boltzmann equation forms the basis from which much statistical dynamics can be extracted. One can introduce the quantity of local entropy field and prove with the Vlasov-Boltzmann equation that the total time derivative of the local entropy never decreases. It is natural to speak of the situation when the local entropy is stationary as the state of local (thermal) equilibrium. One can prove[21] further that when local equilibrium is attained, the local momentum distribution is characterized by a Fermi-Dirac distribution. The parameters in the distribution are (1) the local temperature, (2) the local Fermi energy which is related to the local density, and (3) the displacement of the Fermi-Dirac spherical distribution from the origin which is related to the local velocity field. Thus, when there is local equilibrium, the local stress tensor, as obtained from the momentum distribution, depends only on the local temperature, the local density, and the local velocity field. Then, by using the well-known Enskog-Chapman procedure, one can ap-

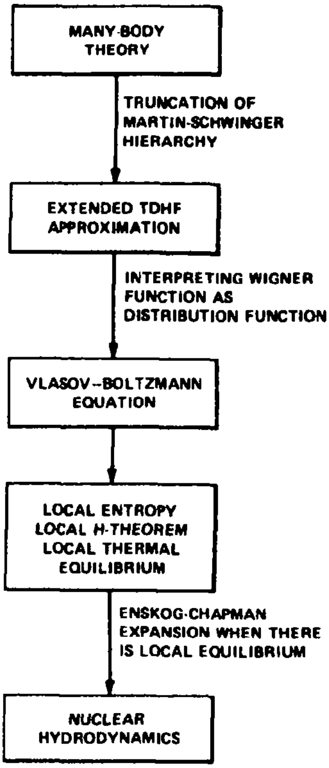
MANY-BODY THEORY
TRUNCATION OF MARTIN-SCHWINGER HIERARCHY
EXTENDED TDHF APPROXIMATION
INTERPRETING WIGNER FUNCTION AS DISTRIBUTION FUNCTION
VLASOV-BOLTZMANN EQUATION
LOCAL ENTROPY
LOCAL H-THEOREM
LOCAL THERMAL EQUILIBRIUM
ENSKOG-CHAPMAN EXPANSION WHEN THERE IS LOCAL EQUILIBRIUM
NUCLEAR HYDRODYNAMICS

FIG. 1. Genealogy of nuclear hydrodynamics and its connection with the many-body theory.

proximate the Vlasov-Boltzmann equation by those of hydrodynamics,[22] namely the continuity equation

$$\frac{\partial n}{\partial t}+\nabla\cdot(n\vec{u})=0\,, \tag{2.1}$$

the Navier-Stokes equations

$$\frac{\partial(nu_i)}{\partial t}+\sum_{j=1}^{3}\nabla_j\left[nu_iu_j+\frac{1}{m}(p\delta_{ij}+p'_{ij})\right]$$
$$=-\frac{n}{m}\nabla_i\int d^3r'n(\vec{r}\,',t)V_L(\vec{r},\vec{r}\,')\,, \tag{2.2}$$

and the thermal energy density equation

$$\frac{\partial(nE_T)}{\partial t}+\nabla\cdot(nE_T\vec{u})=-p_T\nabla\cdot\vec{u}+\nabla\cdot(\kappa\nabla T)$$
$$-\sum_{ij}p'_{ij}\frac{\partial u_i}{\partial x_j}\,. \tag{2.3}$$

Here, in the hydrodynamical picture, the basic dynamical variables are the number density field n, the velocity field $\vec{u}$, and the thermal energy field E_T. The continuity equation (2.1) describes the time evolution of the density field. The Navier-Stokes equations (2.2) are equations for the current density. In Eq. (2.2), m is the nucleonic mass and p is the total pressure which can be obtained from the equation of state of the nuclear fluid. The dissipative behavior of the system is accounted for by the viscosity stress tensor p'_{ij} which is defined as

$$p'_{ij}\equiv-\left\{\eta\left[\left(\frac{\partial u_i}{\partial x_j}+\frac{\partial u_j}{\partial x_i}\right)-\tfrac{2}{3}\delta_{ij}\nabla\cdot\vec{u}\right]\right.$$
$$\left.+\delta_{ij}\zeta\nabla\cdot\vec{u}\right\}, \tag{2.4}$$

where η and ζ are the transport coefficients of shear and compressional viscosity, respectively. The force-density term on the right hand side of Eq. (2.2) is due to the long-range part of the nucleon-nucleon interaction. In the thermal energy density equation (2.3), p_T is the thermal pressure which can be related to the equation of state, κ is the coefficient of thermal conductivity, and T, the temperature field of the nuclear fluid. The choice of the transport coefficients η, ζ, and κ, the parametrizations of the equation of state and the auxiliary quantities p, p_T, and T will be subjects of discussion in the later sections.

As the establishment of local equilibrium is necessary for the reduction of the Vlasov-Boltzmann equation to nuclear hydrodynamics, the crucial question becomes whether the relaxation time leading to local equilibrium is short compared with the total time involved in the interaction. The magntiude of this relaxation time is yet to be firmly established, although attempts are being made to calculate it for some model cases.[23-25] We can, however, make a rough estimate of the magnitude. Previously, in connection with the ETDHF approximation,[20] we argued from the magnitude of the level densities and of the two-body matrix elements that (global) thermal equilibrium for a slightly excited nucleus of mass number A could be established within a time of

$$\tau_{\text{relaxation}}\approx\frac{4000}{A}\,\text{fm}/c\,. \tag{2.5}$$

Indeed, recent experimental studies[26] of the spectrum of evaporated neutrons from the deep-inelastic collision fragments indicate that the relaxation time for thermal equilibrium of the composite system is approximately 10^{-22} sec (~30 fm/c). The estimate of Eq. (2.5) agrees with these experimental results. A model calculation[23] of the approach to equilibrium of an irregular momentum distribution leading to a temperature of 8.5 MeV also gives a relaxation time of 40 fm/c.

In heavy-ion collisions, the momentum distribuion of the nucleons in the colliding region is aproximately a Fermi bisphere whose centers are eparated by the relative momentum determined y the kinetic energy per projectile nucleon. As e blocking due to the Pauli principle becomes ess inhibitive when the separation of the centers the Fermi bi-sphere increases, the fraction of ucleons capable of making a two-body collision nd the phase space of the final states increase ith bombarding energy. One expects that the elaxation time decreases with increasing bomarding energy until the energy is so high that the isphere separates into two disjointed Fermi pheres. Thereafter, the relaxation time becomes ess sensitive to the change of bombarding enery.[24] Thus, for the bombardment energy in the ange of 250 MeV per nucleon to 2.1 GeV per ucleon (where the Fermi bi-sphere becomes isjointed) the relaxation time was found to be f the order of 5 fm/c.[24] This result agrees with e estimate of Bertsch[25] based on the moment of e collision integral for low-energy heavy-ion ollisions

$$\tau \sim \frac{1000\ \mathrm{MeV\,fm}/c}{(E_{\mathrm{lab}}/A_p)}, \tag{2.6}$$

where A_p is the projectile mass number. The relaxation time in the intermediate energy range is therefore roughly 50 fm/c for an energy of $E_{\mathrm{lab}}/A_p = 20$ MeV per nucleon and 4 fm/c for $E_{\mathrm{lab}}/A_p = 250$ MeV per nucleon.

Hydrodynamical description will be a proper approximation if the interaction time for the reaction process is large compared with the thermal relaxation time. The interaction time for a head-on collision of ^{20}Ne on ^{197}Au is about 200 fm/c for a collision with an energy of $E_{\mathrm{lab}}/A_p = 50$ MeV per nucleon, 130 fm/c for a collision with an energy of $E_{\mathrm{lab}}/A_p = 100$ MeV per nucleon, and 100 fm/c for a collision with energy of $E_{\mathrm{lab}}/A_p = 250$ MeV per nucleon. Therefore, it appears that at least for these collisions involving large nuclei, the hydrodynamical description may be appropriate. Of course, one is reminded that these estimates of relaxation time are based on a nuclear matter equilibration. There are effects due to finite sizes, nuclear surface, and shell structure which may affect these estimates. In the final analysis, a direct confrontation between experimental and theoretical results is needed to establish or reject nuclear hydrodynamics for some aspects of heavy-ion collisions.

III. TRANSPORT COEFFICIENTS

Not much is known about the transport coefficients of the nuclear fluid. At the present, they can only be estimated from the theories. Direct comparison of the predictions by assuming different sets of transport coefficients and confrontation with experimental results will eventually allow one to determine these transport coefficients.

We shall estimate the shear viscosity and thermal conductivity from the Vlasov-Boltzmann equation which is embodied in the Landau-Fermi liquid theory. We shall estimate the compressional viscosity from the width of the giant monopole resonance. Using the Born approximation and a procedure developed by Baym and Pethick[27] which was suggested earlier by Sykes and Brooker,[28] we obtain the thermal conductivity as

$$\frac{\kappa}{k_B} = \frac{1}{3\pi}\frac{p_f^3}{m^2 k_B T\langle d\sigma/d\Omega\rangle} \times \sum_{\nu=2,4,6\ldots}\frac{(2\nu+1)}{\nu(\nu+1)[\nu(\nu+1)-2\lambda_\kappa]} \tag{3.1}$$

where

$$\left\langle\frac{d\sigma}{d\Omega}\right\rangle = \int\frac{d\Omega(\theta,\phi)}{4\pi}\left\{g\frac{d\sigma}{d\Omega}(\Theta_{13}(\theta,\phi))]\right\}\bigg/ 2\cos\frac{\theta}{2} \tag{3.2}$$

and

$$\lambda_\kappa\left\langle\frac{d\sigma}{d\Omega}\right\rangle = \int\frac{d\Omega(\theta,\phi)}{4\pi}\left\{g\frac{d\sigma}{d\Omega}[\Theta_{13}(\theta,\phi)]\right\} \times(1+2\cos\theta)\bigg/ 2\cos\frac{\theta}{2}. \tag{3.3}$$

In the above expressions, θ is the angle between $\vec{p}_1$ and $\vec{p}_2$, while ϕ is the dihedral angle between the planes $\vec{p}_1\times\vec{p}_2$ and $\vec{p}_3\times\vec{p}_4$, Θ_{13} is the angle between $\vec{p}_1$ and $\vec{p}_3$, and g is the degeneracy of the nuclear fluid which is 4 in this case. Upon taking a constant value of 1.0 fm^2/sr from (p,p) scattering[29] at a relative kinetic energy of $\epsilon_f \sim 40$ MeV for $d\sigma/d\Omega$, we obtain

$$\frac{\kappa}{k_B} = \frac{0.4224\ \mathrm{MeV}\ c/\mathrm{fm}^2}{k_B T}, \tag{3.4}$$

where $k_B T$ is given in MeV. One can follow the same procedure of Baym and Pethick[27] to obtain the shear viscosity coefficient

$$\eta = \frac{1}{15\pi^3}\frac{p_f^5}{m^3(k_B T)^2}\frac{1}{\langle d\sigma/d\Omega\rangle} \times \sum_{\nu=1,3,5,\ldots}\frac{2\nu+1}{\nu(\nu+1)[\nu(\nu+1)-2\lambda_\eta]}, \tag{3.5}$$

where $\langle d\sigma/d\Omega\rangle$ is as given before and

$$\lambda_\eta\left\langle\frac{d\sigma}{d\Omega}\right\rangle = \int\frac{d\Omega(\theta,\phi)}{4\pi}\left\{g\frac{d\sigma}{d\Omega}[\Theta_{13}(\theta,\phi)]\right\}\left(-1+3\sin^4\frac{\theta}{2}\sin^2\phi\right)\bigg/ 2\cos\frac{\theta}{2}. \tag{3.6}$$

Again, upon using a constant value of 1.0 $\mathrm{fm}^2/\mathrm{sr}$ for $d\sigma/d\Omega$, we obtain

$$\eta = \frac{675.39\ (\mathrm{MeV})^3}{(k_B T)^2\ \mathrm{fm}^2 \cdot c}. \tag{3.7}$$

The transport coefficients are therefore sensitive functions of the local temperature. It is known, however, that the temperature reached in the collision of heavy ions with a few hundred MeV per nucleon is about 30 MeV.[30] So, for our first estimate of an average transport coefficient, we use 30 MeV as the temperature parameter to obtain

$$\kappa = 0.014\ c/\mathrm{fm}^2, \tag{3.8}$$

and

$$\eta = 0.75\ \mathrm{MeV}/(\mathrm{fm}^2 c). \tag{3.9}$$

To estimate the compressional viscosity coefficient from the width of the giant monopole resonance, we consider the equation of motion for small amplitude oscillations

$$\frac{\partial n}{\partial t} + \nabla \cdot (n\vec{u}) = 0 \tag{3.10}$$

and

$$\frac{\partial}{\partial t} n\vec{u} + 0(\vec{n}^2) = -a^2 \nabla n + (\zeta - \tfrac{2}{3}\eta)\nabla(\nabla \cdot \vec{u}), \tag{3.11}$$

where a is the speed of sound related to the incompressibility K by

$$a = (K/9m)^{1/2}. \tag{3.12}$$

From this set of equations, the monopole oscillation frequency becomes complex and is given by

$$\omega = \omega_0\left(1 - \frac{i(\zeta - \frac{2}{3}\eta)\pi^2}{2mn_0\omega_0 R^2}\right), \tag{3.13}$$

where $\hbar\omega_0 = (\hbar\pi/R)(K/9m)^{1/2}$ is the eigenenergy of the monopole oscillation in the absence of compressional viscosity, R is the radius of the nucleus, and n_0 the normal density of nculear matter. Identifying the imaginary part of the frequency with the width Γ of the giant monopole resonance, we have

$$\Gamma = h\frac{(\zeta - \frac{2}{3}\eta)\pi^2 R^2}{2mn_0}. \tag{3.14}$$

For $^{208}\mathrm{Pb}$ the width of the giant monopole resonance is 2.5 MeV.[31] Thus, the compressional coefficient is

$$\zeta = 18.76\ \mathrm{MeV}/(\mathrm{fm}^2 c). \tag{3.15}$$

IV. EQUATION OF STATE AND OTHER PARAMETERS

A. Energy density of the nuclear fluid

The use of an equation of state is a characteristic of nuclear hydrodynamics. In the present investigation, the internal energy per nucleon of the nuclear fluid assumes a mathematically simple, but physically plausible, form

$$E_{in}(n,\sigma) = E_0(n) + E_T(n,\sigma), \tag{4.1}$$

where E_0 is the zero-temperature part of the internal energy per nucleon, depending only on the local density field, and E_T the thermal part which depends on the local density field as well as the specific entropy σ (or temperature T). The zero-temperature part is taken to be of the form[32]

$$E_0(n) = b_0 n^{2/3} + b_1 n^{3/3} + b_2 n^{4/3} + b_3 n^{5/3} \tag{4.2}$$

and the thermal part is parametrized by the Fermi gas model

$$E_T(n,\sigma) = \frac{1}{2}\frac{\hbar^2}{m}\left(\frac{6}{4\pi}\right)^{2/3}\sigma^2 n^{2/3}, \tag{4.3}$$

which can also be re-expressed in terms of the temperature as

$$E_T(n,\sigma) = \frac{1}{2}\frac{m}{\hbar^2}\left(\frac{4\pi}{6}\right)^{2/3} n^{-2/3} T^2, \tag{4.4}$$

With this form of the internal energy function, the coefficients b_i's in Eq. (4.2) can be uniquely determined as follows. The leading coefficient b_0 is taken to be the same as the corresponding one in the Fermi gas model

$$b_0 = 75.01\ \mathrm{MeV\,fm}^2. \tag{4.5}$$

The other coefficients can then be determined by three known bulk properties of nuclei. They are the normal density at equilibrium

$$n_0 = 0.17\ \mathrm{fm}^{-3}, \tag{4.6}$$

the binding energy per particle

$$E_B = -16.5\ \mathrm{MeV} \tag{4.7}$$

and the coefficient of nuclear incompressibility at equilibrium density [estimated from giant monopole resonance of $^{208}\mathrm{Pb}$ (Ref. 33)]

$$K(n_0) = 186\ \mathrm{MeV}. \tag{4.8}$$

With the equation of state given, the pressure terms can now be obtained from standard thermodynamic relations. The total pressure of the nuclear fluid is of the form

$$p(n,\sigma) = p_0(n) + p_T(n,\sigma), \tag{4.9}$$

where the zero-temperature part is now given by

$$p_0 = n^{5/3}(\tfrac{2}{3}b_0 + b_1 n^{1/3} + \tfrac{4}{3}b_2 n^{2/3} + \tfrac{5}{3}b_3 n^{3/3})$$

and the thermal part is given by

$$p_T = \tfrac{2}{3} n E_T \,. \tag{4.10}$$

B. Interaction parameters

For the effective nucleon-nucleon interaction we adopt a parametrization similar to that used in microscopic theories such as the time-dependent Hartree-Fock theory.[14] This interaction is taken to contain a short-range part V_S and a long-range part V_L. The short-range component can be characterized by a delta function with density dependence. This, however, can be incorporated into the internal energy, while the long-range component can be taken to be the sum of a Yukawa interaction and the Coulomb interaction. The Yukawa interaction is

$$V_Y(\vec{r}, \vec{r}\,') = \beta \frac{e^{-\alpha|\vec{r}-\vec{r}\,'|}}{|\vec{r}-\vec{r}\,'|}, \tag{4.11}$$

with

$$\beta = -85 \text{ MeV fm} \tag{4.12}$$

and

$$\alpha = 1.5 \text{ fm}^{-1} \,. \tag{4.13}$$

These parameters, β and α, are chosen to fit the binding energies and root-mean-squared radii of nuclei along the β-stability line. The Coulomb interaction is given as

$$V_c(\vec{r}, \vec{r}\,') = \left(\frac{Z_P + Z_T}{A_P + A_T}\right)^2 \frac{e^2}{|\vec{r}-\vec{r}\,'|}, \tag{4.14}$$

where (Z_P, A_P) and (Z_T, A_T) are the atomic and mass numbers of the projectile and target nuclei, respectively, and e the charge of an electron.

V. RESULTS OF CALCULATIONS AND DISCUSSIONS

We shall discuss the specific features of several exactly central collisions which we have studied in the energy range from 50 MeV up to 400 MeV per nucleon. Here and henceforth, the bombarding energy is given in terms of the energy per projectile nucleon with the target at rest. Systematic studies of the other cases of non-head-on collisions will be reported elsewhere.[16] Our discussions will concentrate on the bombarding of ^{20}Ne on ^{197}Au targets and also that of ^{208}Pb on ^{208}Pb at various energies. In the subsequent discussion, we shall also refer to the case of equal projectile and target as the symmetric collision (or system) and the unequal projectile and target as asymmetric collision (or system).

To study the effects of dissipation on the dynamics, we shall compare calculations using two different sets of transport coefficients. They are

$$\eta, \zeta = 10^{-4} \text{ MeV/fm}^2 c$$

and (5.1)

$$\kappa = 10^{-4}\ c/\text{fm}^2 ,$$

which will be referred to as the "small" viscosity or simply the nonviscous or inviscid case in the text, and the values estimated in Sec. III

$$\eta = 0.75 \text{ MeV/(fm}^2 c) ,$$

$$\zeta = 18.76 \text{ MeV/(fm}^2 c) , \tag{5.2}$$

and

$$\kappa = 0.014\ c/\text{fm}^2 ,$$

which, for simplicity, will be referred to as the "large" viscosity or simply the viscous case in the text.

Each calculation is started with the nuclear surface of the projectile and target nuclei barely touching. The density distribution of each nucleus is obtained individually in a self-consistent manner as the distribution leading to static equilibrium. The nuclei are given velocity fields corresponding to the bombarding energy in question. With the initial conditions established, the complete set of hydrodynamical equations (2.1)–(2.3) is then solved for the subsequent times. Some numerical aspects of this problem will be discussed in the Appendix.

A. ^{20}Ne on ^{197}Au at 250 MeV per nucleon

Figure 2 depicts the time evolution of the density field in the center-of-mass system for the collision for 250 MeV per projectile (^{20}Ne) nucleon on ^{197}Au. The plots shown are the cuts of density contours in the reaction plane, graded in levels of 0.025 fm^{-3}. To standardize our notations in subsequent discussions, we take the value 0.15 fm^{-3} to be the "normal nuclear density." The calculation shown in Fig. 2 is done with the small values of transport coefficients given in Eq. (5.1). At about 10 fm/c, a region of compressed nuclear matter is formed and has attained a density of about 1.5 times the normal value. The density continues rising in this region until a maximum value of 0.35 fm^{-3} is reached at about 25 fm/c. During the stage of compression, the density profile of this region has a very sharp jump as one goes from this region to the rest of the system or normal density. The thickness of the shock front is only slightly greater than the mesh size of 0.6 fm. The compressed region undergoes a forward displacement to the right as a whole as time proceeds. At about 25 fm/c, the Ne nucleus is entirely embedded in the target system and the maximum density of 0.35 fm^{-3} is also reached.

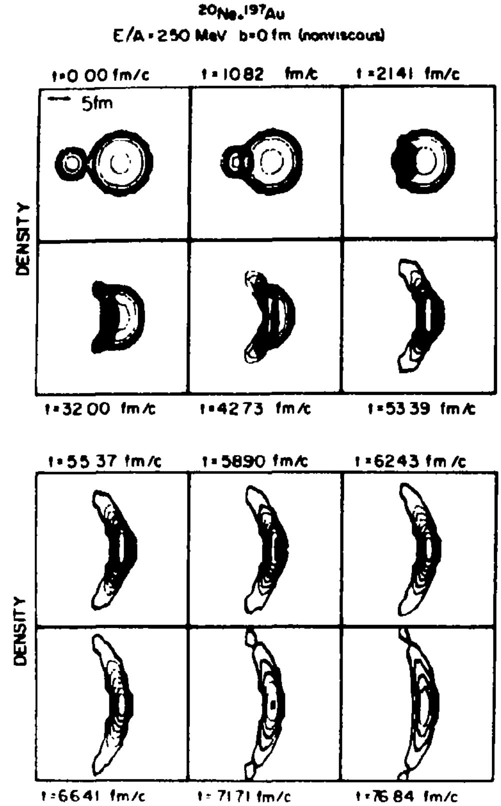

FIG. 2. Time evolution of the density field for ^{20}Ne + ^{197}Au at 250 MeV per nucleon with small viscosity.

The compressed region maintains this maximum density for a few fm/c and then begins to relax. At 32 fm/c, due to the size of the target and the consequent time delay in transmitting the impulse of the collision, roughly half of the target system is still unperturbed. There are currents going into the compressed region directed from the target. However, this current encounters the forward propagation of the shock region and gives rise to an ejection of nuclear matter along a "side-wing" direction which is approximately 120° in the center-of-mass system. This side-wing expands outwards as the density in the compressed region drops from the maximum values. After 60 fm/c, the central density of the composite system drops back to the normal value and continues to decrease monotonically in time, while the volume of the system expands outwards irretrievably. This feature in the collision is similar to what was obtained previously.[10] To determine the angular and energy distributions, we adopt the operational criteria that for such a case, the calculation is to be terminated once the maximum density drops to below 50% of the normal nuclear matter density. This is a reasonable operational criterion. For, when the maximum density drops below 50% of the normal matter density, the shortest separations between nucleons increase by 26% of the equilibrium separation. The average separation between nucleons increases even more than this value of 26% for the shortest separations. As nuclear interaction is a short-range interaction, the separation between nucleons in this dilute gas is probably too large for the nuclear interaction to become effective. The dilute gas can therefore be approximately described as a free fermion gas subject only to the Coulomb interaction. The final result of this reaction is interpreted as a complete dissociation into single particles. The knowledge of the density field and the volocity field at the end of the calculation allows us to compute both the angular and energy distributions of the outgoing nucleons. For our present calculations of angular and energy distributions, we even neglect the final state Coulom interaction and the thermal velocities of the particles. They will probably shift and broaden the peaks in the angular and energy distributions slightly, but will not change the main features of the distributions. We hope to include these effects in the future.

Figure 3(a) shows the angular distribution $dN/d\Omega$ in the center-of-mass system. The main structure has prominent forward and backward peaks which are, respectively, one and two orders of magnitude higher than the rest of the distribution. There is also a peak at 90° with a width of about 10° and a rather broad peak which extends from 100° to 120° and centers at about 110°. The corresponding angular distribution in the laboratory system is given in Fig. 3(b). Here, apart from the prominent peaks in the forward and bakcward directions (which are, respectively, two and one orders of magnitude higher than the rest), there is a rather broad peak which extends from 66° to 100° and peaks at 85°. The underlying components of this distribution can be further analyzed in greater detail from the energy distributions $d^2N/dEd\Omega$.

The forward peak comes from very slow particles of less than 5 MeV. They arise as a consequence of the stopping of the small projectile nucleus by a much larger target. The backward peak in the laboratory system consists mainly of low-energy particles of below 10 MeV and also some slightly more energetic particles of about 15 MeV. This arises from the expansion of the shock region to the backward direction. As the

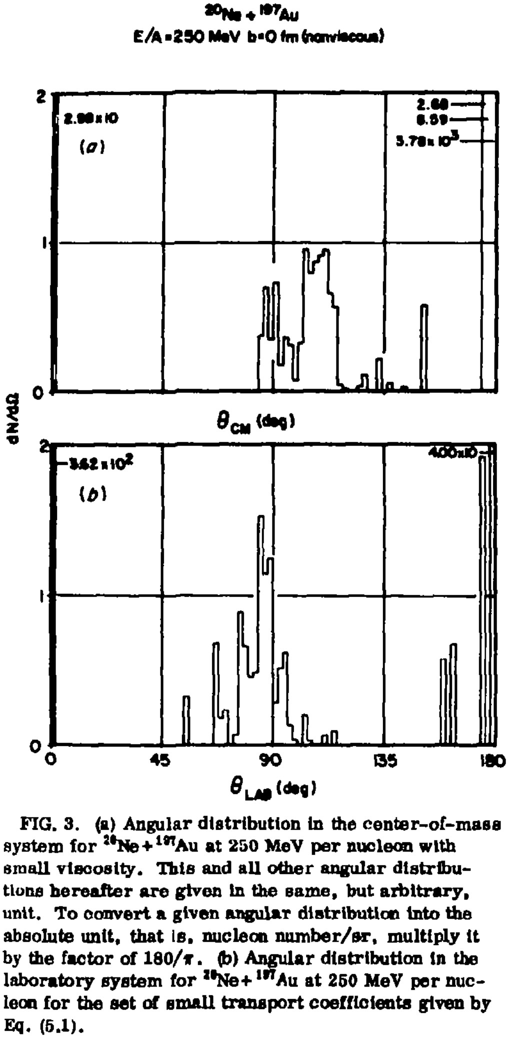

FIG. 3. (a) Angular distribution in the center-of-mass system for ^{20}Ne+^{197}Au at 250 MeV per nucleon with small viscosity. This and all other angular distributions hereafter are given in the same, but arbitrary, unit. To convert a given angular distribution into the absolute unit, that is, nucleon number/sr, multiply it by the factor of $180/\pi$. (b) Angular distribution in the laboratory system for ^{20}Ne+^{197}Au at 250 MeV per nucleon for the set of small transport coefficients given by Eq. (5.1).

expansion of the shock region at the early stage (~25 fm/c) is unhindered in this direction in contrast to the forward direction, slightly more energetic particles of about 15 MeV up to 30 MeV are also found in the backward direction, whereas the forward peak is restricted to particles below 5 MeV. The spectrum of particles in the side peak between 60° and 100° falls into roughly two groups. There is a large group of particles which peaks at about 19 and 31 MeV and a much smaller group of particles which peaks at about 65 MeV. The mean energy and standard deviation for different angular ranges are given in Table I(a).

To study the effects of the viscosity and thermal conductivity on the dynamics, the calculation for ^{20}Ne on ^{197}Au at 250 MeV per nucleon is repeated with the larger values of the transport coefficients given in Eq. (5.2). The time evolution of the density field for this calculation is depicted in Fig. 4. In this case, though some features appear to be similar to the small viscosity case, there are, in fact, several distinct differences. First, in the small viscosity case, the thermal energy remains negligible (about 1 MeV at the most) throughout the entire reaction. In contrast, the larger viscosity and thermal conductivity lead to the generation of considerable thermal energy during the compression stage, with a maximum value of about 1400 MeV. The second difference lies in the density field. With large viscosity, the density profile is smoother and the maximum density reached (0.23 fm^{-3}) is smaller. That this is a viscosity effect can be understood as a consequence of the Navier-Stokes equations. There, the compressional viscosity gives a diffusion term associated with the current density field. Therefore, the greater the compressional viscosity, the greater is the rate of diffusion of the current density field. It is clear that when the compressional viscosity is large, any effect of density accumulation in a region, due to the influx of nuclear matter from the outside, will be reduced due to a competing diffusion process.

With small viscosity, the central density begins to drop below 0.075 fm^{-3} at about 81.79 fm/c, while with large viscosity, it begins to drop below this value at about 96.87 fm/c. These are the times at which the angular and energy distributions are extrapolated from the corresponding calculations. Detailed comparisons of these distributions for the nonviscous and viscous cases provide some interesting insight. For the large viscosity case, the angular distribution in the center-of-mass system is given in Fig. 5(a). This distribution has pronounced and narrow peaks in the forward and backward directions with a width of about 2°. There is also a peak at 90° with a width of about 15°. This is a simpler structure than the corresponding distribution in the small viscosity case (Fig. 3) for which there is a broad spectrum between 90° and 135°. The laboratory distribution $dN/d\Omega$, given in Fig. 5(b), has peaks at the forward and backward directions, and also a broad distribution between 50° and 90° with a peak at about 67°. In fact, except for the positions of the various peaks which are shifted by about 18°, this is very similar in shape to the corresponding distribution between 60° and 100° of the "small" viscosity calculation. (Compare Figs. 3 and 5.) Accordingly, the effect of viscosity in this case appears to given an over-

TABLE I. The angular distribution, mean energy, and energy width for collision of ^{20}Ne + ^{197}Au at an energy of 250 MeV per nucleon. Table I(a) is for the case $\eta = \zeta = 10^{-4}$ MeV/(fm^2c) and $\kappa = 10^{-4}$ c/fm^2 and Table I(b) for $\eta = 0.75$ MeV/(fm^2c), $\zeta = 18.76$ MeV/(fm^2c), and $\kappa = 0.014$ c/fm^2. The quantity $\bar{E}$ is the average energy within the angular bin and σ_E is the root-mean-squared energy within the bin.

	(a) $\eta = \zeta = 10^{-4}$ MeV/(fm^2c) $\kappa = 10^{-4}$ c/fm^2			(b) $\eta = 0.75$ MeV(fm^2c) $\zeta = 18.76$ MeV/(fm^2c) $\kappa = 0.014$ c/fm^2		
$\theta_{\rm lab}$ (deg)	$dN/d\Omega$	$\bar{E}$ (MeV)	σ_E (MeV)	$dN/d\Omega$	$\bar{E}$ (MeV)	σ_E (MeV)
0–20	181.0	1.16	0.55	206.6	1.13	0.50
20–40	0			0.184	3.18	1.06
40–60	0.16	7.00	0.50	0.908	6.30	2.68
60–80	1.35	21.2	11.6	4.19	27.0	13.5
80–100	3.52	23.7	16.4	0.60	38.3	16.4
100–120	0.22	16.3	13.7	0.04	24.7	13.3
120–140	0			0.002	9.0	0.50
140–160	0.29	1.00	0.50	0		
160–180	21.6	1.63	3.11	3.38	1.0	0.5

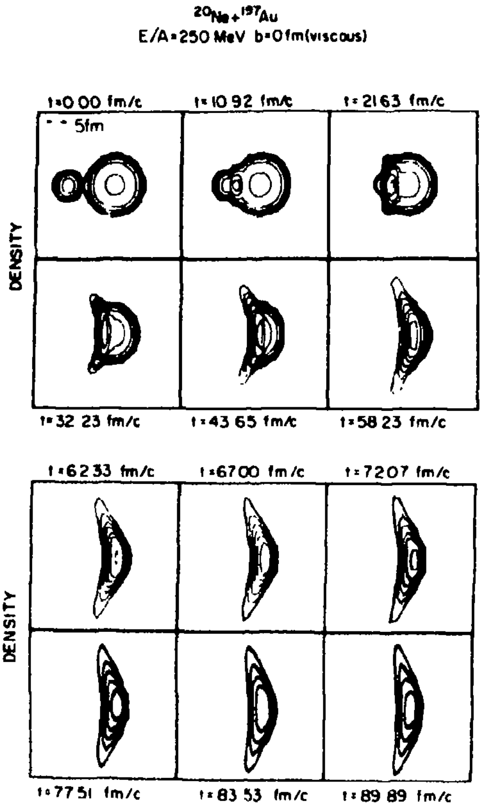

FIG. 4. Time evolution of the density field for ^{20}Ne + ^{197}Au at 250 MeV per nucleon with large transport coefficients given by Eq. (5.2).

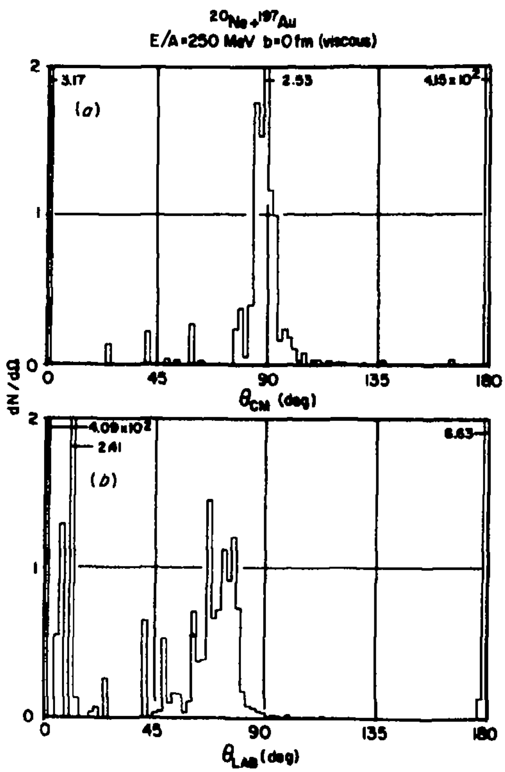

FIG. 5. (a) Angular distribution in the center-of-mass system for ^{20}Ne + ^{197}Au at 250 MeV per nucleon with large viscosity [Eq. (5.2)]. (b) Angular distribution in the laboratory system for ^{20}Ne + ^{197}Au at 250 MeV per nucleon with large viscosity [Eq. (5.2)].

all shift of the side angle peak toward smaller angles. This effect of dissipation will be systematically examined at the other energies and will be discussed again below. The mena energy and standard deviation for different angular ranges are given in Table I(b). The energy distributions in the laboratory system for the forward and backward peaks come from slow particles of below 5 and 10 MeV, respectively. This is a broad spectrum which first peaks at about 15 MeV, but drops slowly after that in an approximately exponential manner and extends to about 70 MeV. In the peak at the angular range 60°–80°, the mean energy is 27 MeV with a standard deviation of 16 MeV. These quantities are greater than the corresponding quantities in the small viscosity case. The effect of viscosity is to shift the energy of the side peak to a higher energy and also to increase the energy width.

B. ^{208}Pb + ^{208}Pb at 100 MeV per nucleon

Figure 6 depicts the reaction of ^{208}Pb + ^{208}Pb at 100 MeV per projectile nucleon and for the small values of viscosity and thermal conductivity. At 18.24 fm/c, a central region of compressed nuclear matter is formed (~0.25 fm^{-3}). This is only the beginning of the compression stage. The rest of the projectile and target nuclei are essentially unperturbed. They continue to come toward each other and maintain a constant influx of nuclear matter into the central compressed region. The maximum density reached in this reaction is 0.30 fm^{-3}. Similar to the nonviscous case of ^{20}Ne + ^{197}Au discussed earlier (Fig. 2), the density profile of the shock region also has very sharp edges. A detailed study of the intermediate steps between 18.24 fm/c and 81.58 fm/c shows that the diffuseness of the "edge" of this shock region actually undergoes oscillation. (A hint of such an oscillation can be found by comparing the level spacing of the contours from time steps 35.76 fm/c to 107.06 fm/c in Fig. 6.) This is due to the tendency of the central region to expand outward even during the compression stage. Beginning at about 36 fm/c, there is ejection of nuclear matter in the 90° direction and eventually the composite system becomes disclike before the final overall expansion. The angular distribution $dN/d\Omega$ in the center-of-mass system is given in Fig. 7(a). It has peaks at the forward and backward directions and at 90°. The angular distribution in the laboratory system is given in Fig. 7(b). Its main structure has peaks at the forward direction at 7° and at 39°. The forward peak consists of a group of particles of between 12 and 38 MeV, with a peak at about 23 MeV. The angular peak in the range between 35° and 55° consists of a broad spectrum of particles from 30 MeV up to 60 MeV, with a peak at about 39 MeV. The mean energy and standard deviation for different angular ranges are given in Table II(a). The mean energy and standard deviation increase as the angle increases until there is no cross section for $\theta_{\text{lab}} \geqslant 60°$.

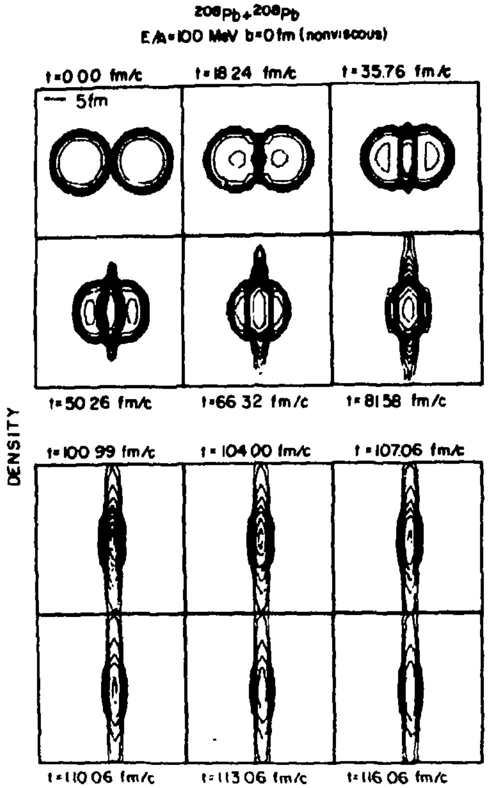

FIG. 6. Time evolution of the density field for ^{208}Pb + ^{208}Pb at 100 MeV per nucleon with small viscosity [Eq. (5.1)].

Figure 8 depicts the reaction ^{208}Pb + ^{208}Pb at 100 MeV per nucleon with the set of large coefficients of viscosity and thermal conductivity [Eq. (5.2)]. The thermal energy generated during the compression stage (~20–70 fm/c) reaches a maximum of about 1300 MeV. The maximum density attained in this reaction is 0.23 fm^{-3}. A comparison of the density plots with those of the small viscosity case (Fig. 7) reveals some differences. With large viscosity, the density profile remains very smooth during the entire compression stage. The maximum density is smaller than the small

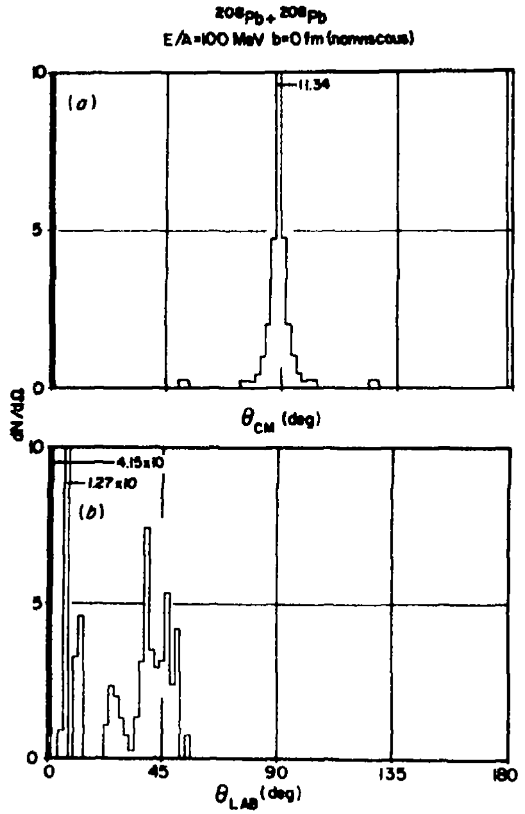

FIG. 7. (a) Angular distribution in the center-of-mass system for ^{208}Pb + ^{208}Pb at 100 MeV per nucleon with small viscosity. (b) Angular distribution in the laboratory system for ^{208}Pb + ^{208}Pb at 100 MeV per nucleon with small viscosity.

viscosity case. But once the maximum density is reached at about 36 fm/c, the system sustains this density for a longer period (~36–~68 fm/c). The center-of-mass angular distribution is very similar to the small viscosity case, that is, sharp peaks at 90°, 0°, and 180°. However, the laboratory angular distribution (Fig. 9) displays some small differences. The distribution between 30° and 70° has a shape which is roughly the same as that between 20° and 60° for the small viscosity case, with the exception that the position of the peaks are all shifted to a slightly larger angle. The mean energy and standard deviation for different angular ranges are given in Table II(b). The forward peak comes from a relatively narrow spectrum of particles which peaks at 23 MeV with a width of about 5 MeV. In the angular range between 24° and 44°. the particles have kinetic energies between 25 and 50 MeV, with the energy spectrum peaking at about 31 MeV. The energy distribution for the angular range between 44° and 64° is a broad spectrum extending from 30 MeV up to 100 MeV, peaking at about 55 MeV. There is also a small group of energetic particles of 90–100 MeV. This broad distribution is in contrast to the relatively narrower distribution for the small viscosity case for the angular range between 35° and 55°.

C. Viscosity and energy dependence of angular distributions

In the detailed study of ^{20}Ne + ^{197}Au at 250 MeV per nucleon and ^{208}Pb + ^{208}Pb at 100 MeV per nucleon, we have seen how the angular distributions of the reaction products can be sensitive to the presence of dissipation. To firmly establish this dependence as a feature of the hydrodynamical description and also to study further the energy dependence of the angular distributions, we extend our calculations also to other energies.

Figures 10(a) and 10(b) show the angular distributions for the reaction ^{20}Ne + ^{197}Au at 100 MeV

TABLE II. Same as Table I but for the case of ^{20}Ne + ^{197}Au at an energy of 100 MeV per nucleon.

	(a)			(b)		
	$\eta = \zeta = 10^{-4}$ MeV/(fm^2c) $\kappa = 10^{-4}$ c/fm^2			$\eta = 0.75$ MeV(fm^2c) $\zeta = 18.76$ MeV/(fm^2c) $\kappa = 0.014$ c/fm^2		
θ_{lab} (deg)	$dN/d\Omega$	$\bar{E}$ (MeV)	σ_E (MeV)	$dN/d\Omega$	$\bar{E}$ (MeV)	σ_E (MeV)
0–20	31.5	23.7	5.21	66.29	23.4	4.67
20–40	9.81	35.8	5.65	3.39	35.4	5.98
40–60	14.8	47.43	8.26	13.7	60.2	11.8
60–80	0			0.90	90.0	10.2
80–180	0			0		

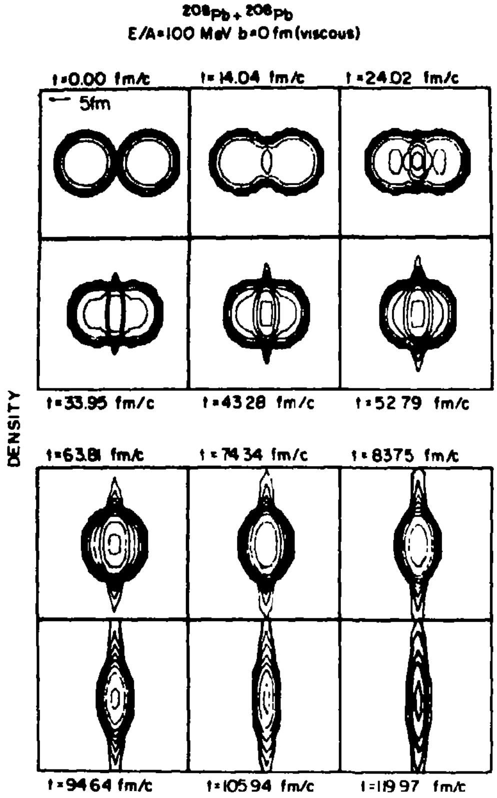

FIG. 8. Time evolution of the density field for ^{208}Pb + ^{208}Pb at 100 MeV per nucleon with large viscosity.

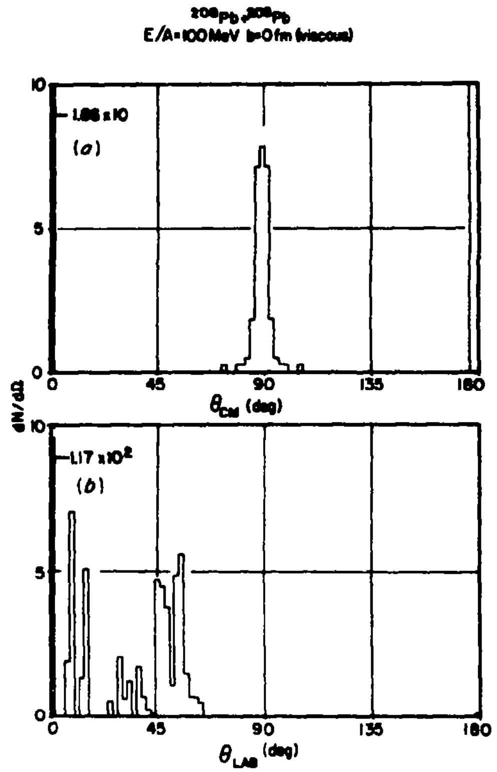

FIG. 9. (a) Angular distribution in the center-of-mass system for ^{208}Pb + ^{208}Pb at 100 MeV per nucleon with large viscosity. (b) Angular distribution in the laboratory system for ^{208}Pb + ^{208}Pb at 100 MeV per nucleon with large viscosity.

per nucleon for small and large transport coefficients, respectively. In the small viscosity case [Fig. 10(a)], there are forward peaks, and the distribution between ~50° and ~100° is approximately symmetrical and peaks at about 73°. In the large viscosity case [Fig. 10(b)], apart from forward and backward peaks, there is a broad

TABLE III. Same as Table I but for the case of ^{20}Ne + ^{197}Au at an energy of 400 MeV per nucleon.

	(a)			(b)		
				$\eta = 0.75$ MeV(fm^2c)		
	$\eta = \zeta = 10^{-4}$ MeV/(fm^2c)			$\zeta = 18.76$ MeV/(fm^2c)		
	$\kappa = 10^{-4}$ c/fm^2			$\kappa = 0.014$ c/fm^2		
$\theta_{\rm lab}$ (deg)	$dN/d\Omega$	$\bar{E}$ (MeV)	σ_E (MeV)	$dN/d\Omega$	$\bar{E}$ (MeV)	σ_E (MeV)
0–20	115.2	1.17	0.55	210	1.41	0.082
20–40	0			0.48	5.31	2.06
40–60	0			0.519	9.66	3.00
60–80	0.561	36.6	7.47	3.66	48.5	22.4
80–100	2.87	32.5	18.0	1.21	71.68	25.5
100–120	1.65	29.0	13.4	0.10	45.2	32.1
120–140	0.21	3.95	2.07	0		
140–160	0.28	1.0	0.5	0		
160–180	79.6	1.83	3.94	4.88	1.25	0.086

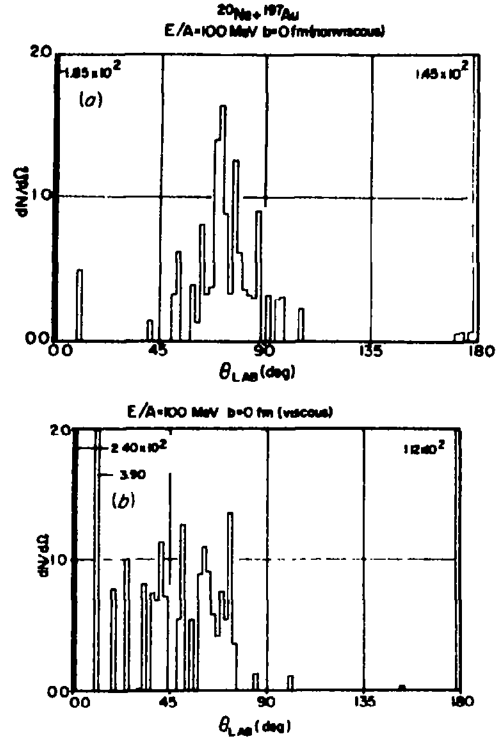

FIG. 10. (a) Angular distribution in the laboratory system for ^{20}Ne+^{197}Au at 100 MeV per nucleon with small viscosity. (b) Angular distribution in the laboratory system for ^{28}Ne+^{197}Au at 100 MeV per nucleon with large viscosity.

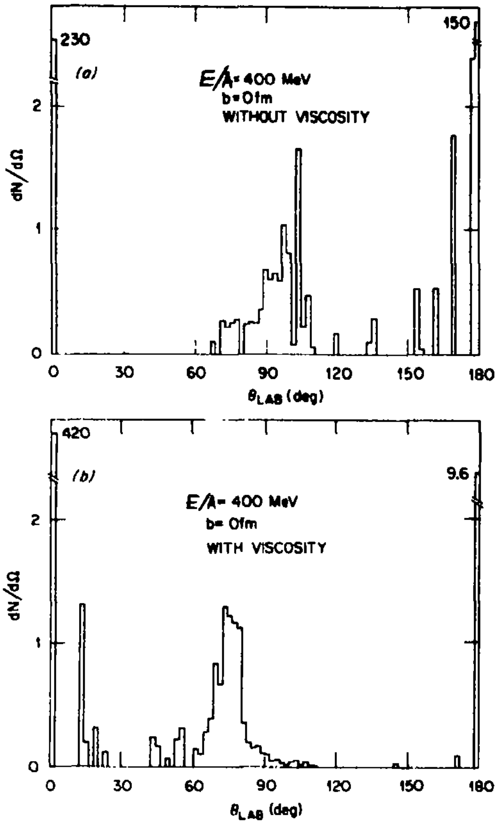

FIG. 11. (a) Angular distribution in the laboratory system for ^{20}Ne+^{197}Au at 400 MeV per nucleon with small viscosity. (b) Angular distribution in the laboratory system for ^{20}Ne+^{197}Au at 400 MeV per nucleon with large viscosity.

distribution extending from about 10° up to about 75°, and this distribution is distinctly different from that in the nonviscous case.

Figures 11(a) and 11(b) show the laboratory angular distributions of ^{20}Ne + ^{197}Au at 400 MeV per nucleon for small and large viscosity, respectively. In both cases, apart from the forward and backward peaks, there is a peak at 103° for the small viscosity case and at 73° for the large viscosity case. With respect to the angular distribution, the effect of the presence of viscosity is to shift the side peak due to the backsplash of nuclear matter from 103° to 73°. The mean energy and standard deviation for different angular ranges in the collision of ^{20}Ne + ^{197}Au at 400 MeV per nucleon is given in Table III. One finds that the forward and backward peaks consist of nucleons with small kinetic energies. For the side peak, the mean energy is about 33 MeV and the standard deviation is 18 MeV for the small viscosity case. The mean energy increases to 49 MeV and the standard deviation to 22 MeV for the large viscosity case. We hope to compare our results with the relevant high-multiplicity data of Gutbrod *et al.*[7] which is still being analyzed. Preliminary results[7] indicate the presence of sidesplash which is a feature of the hydrodynamical result.

Figures 12(a) and 12(b) are the angular distributions of ^{208}Pb + ^{208}Pb at 50 MeV per nucleon for the nonviscous and viscous cases, respectively. Figures 13 and 14 are the angular distributions for the same reaction, but at 250 MeV per nucleon and Fig. 14, at 400 MeV per nucleon. There are some differences in the detailed shapes and heights of the peaks and small shifts in these distributions due to viscosity. The energy distributions also show some differences for the two cases, and the presence of viscosity tends to

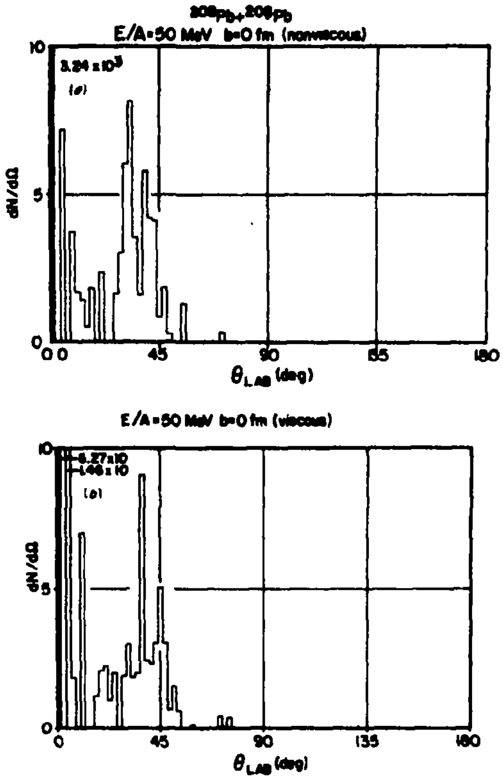

FIG. 12. (a) Angular distribution in the laboratory system for ^{208}Pb+^{208}Pb at 50 MeV per nucleon with small viscosity. (b) Angular distribution in the laboratory system for ^{208}Pb+^{208}Pb at 50 MeV per nucleon with large viscosity.

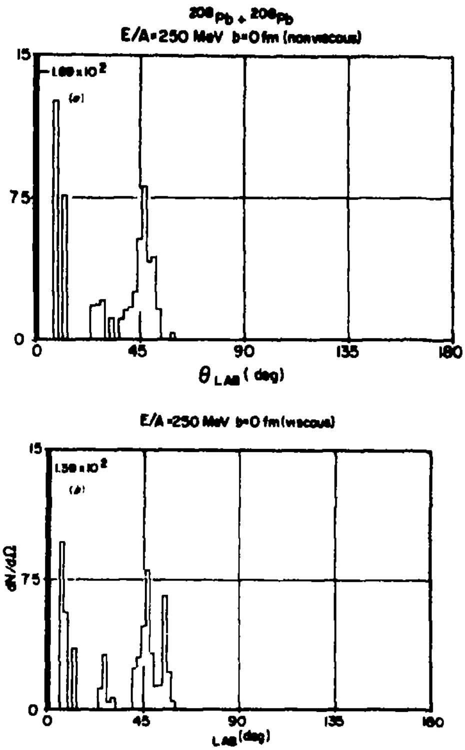

FIG. 13. (a) Angular distribution in the laboratory system for ^{208}Pb+^{208}Pb at 250 MeV per nucleon with small viscosity. (b) Angular distribution in the laboratory system for ^{208}Pb+^{208}Pb at 250 MeV per nucleon with large viscosity.

broaden the spectra. From the comparison of these results, one observes that the angular and energy distributions of the reaction products are sensitive to the presence of viscosity.

D. Compression ratio

Since the formation of compressed nuclear matter and its consequences are among the most important motivations for high-energy, heavy-ion physics, we shall study some of our results with these questions in mind. The main results of various calculations are compactly presented in Fig. 15. The curves are the compression ratios (maximum density/normal density) achieved in the ^{20}Ne + ^{197}Au and ^{208}Pb + ^{208}Pb reactions, plotted against bombarding energy. Each curve corresponds to one set of transport coefficients. It is clear from the figures that the compression ratio increases monotonically with increasing energy. Also, it appears that a high compression ratio is favored more by large projectile-target systems.

The role played by the transport coefficient is rather significant. Large viscosity and thermal conductivity results in the generation of considerable thermal energy. Not only is the density profile smoothed out by a large viscosity, but the maximum density reached is also substantially reduced.

E. Other features

Though we are mainly concerned with high-energy reactions in this paper, it is noteworthy to remark that there are also many other special features of nuclear hydrodynamics which manifest themselves, particularly at lower energies.[18] A notable example is that for an expanding composite system, there is a tendency in the density field to form clusters when the colliding energy

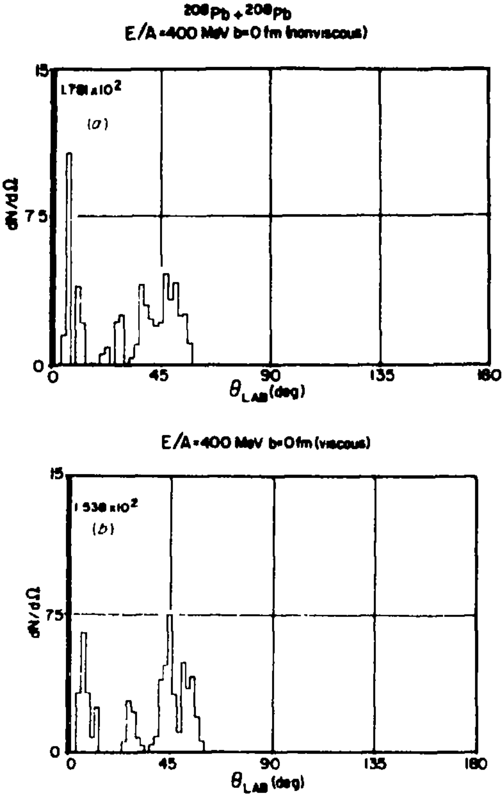

FIG. 14. (a) Angular distribution in the laboratory system for ^{208}Pb + ^{208}Pb at 400 MeV per nucleon with small viscosity. (b) Angular distribution in the laboratory system for ^{208}Pb + ^{208}Pb at 400 MeV per nucleon with large viscosity.

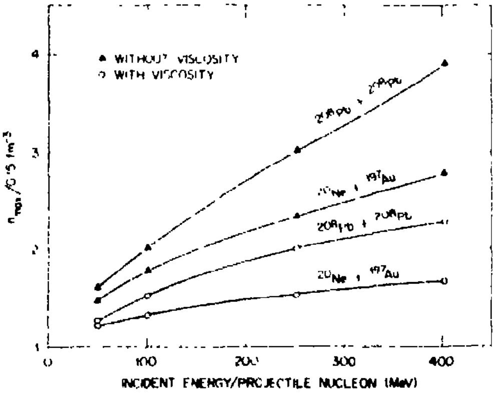

FIG. 15. Compression ratio attained in the collision of ^{20}Ne + ^{197}Au and ^{208}Pb + ^{208}Pb, with and without viscosity, as a function of bombarding energy.

is less than a certain limit. Above this energy, the nuclear matter is so much compressed in the shock region that when it expands, it keeps on expanding without collapsing back into clusters with normal nuclear matter density. This kind of behavior can be understood in terms of the shape of the equation of state $E(n)$. For small deviations of the density from equilibrium value, $E(n)$ is approximately a parabola. However, for large values of deviation, it is a high wall for large densities but an open and relatively flat region for low densities. A highly compressed nuclear matter, after relaxing to the equilibrium density and going to the low density region, will have too high a kinetic energy in the density degree of freedom to come to a turning point.

Systematic studies of two-dimensional model collisions of columns of nuclear matter indicate that asymmetric collisions at an energy of $E \geqslant 60$ MeV per nucleon lead to a complete dissociation of the composite system, while collisions at $E \geqslant 40$ MeV per nucleon lead to self-bound clusters. In the three-dimensional head-on collisions, a clustering in the direction of the collision axis corresponds to a fissionlike behavior, while a clustering perpendicular to the collision axis corresponds to the formation of a ring of nuclear matter. In order to investigate this aspect, we perform calculations for ^{20}Ne + ^{197}Au at 50 MeV with zero impact parameter. Figure 16 depicts the results for the small viscosity case. At about 70 fm/c, the composite system relaxes in response to the compression of nuclear matter. At 114.13 fm/c, we begin to see some clustering effect in the radial direction. At 198.70 fm/c, this eventually leads to the formation of a vortex ring of nuclear matter, with density of about 0.075 fm^{-3}. The central cluster has

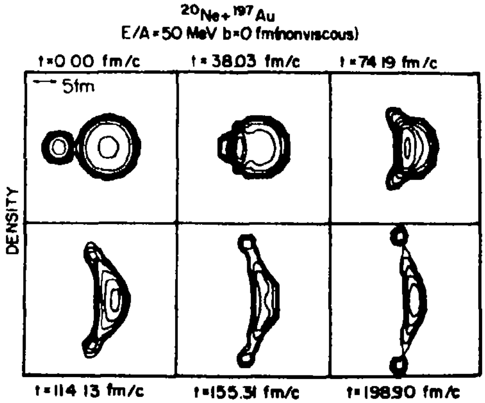

FIG. 16. Time evolution of the density field for ^{20}Ne + ^{197}Au at 50 MeV per nucleon with small viscosity.

a normal density. At the end of the calculation, this ring goes toward to the right, while the central cluster goes in the opposite direction. The calculation is terminated here, since we do not know whether this configuration is a stable one. Nonaxial sausage-type instability is a very important mode.[34] Future calculations for very small but nonzero impact parameters will help to determine more firmly the detailed dynamics beyond this stage. The same calculation but with large viscosity shows that at the comparable time scale, the "clustering effect" and the ring formation are much less pronounced.

When we increase the energy of the projectile ^{20}Ne to 100 MeV per nucleon, the density contour indicates that the density of the composite system keeps on decreasing after the shock region relaxes. There is no restriction of the nuclear matter density back to the equilibrium value, as was the case for the central cluster in the case of 50 MeV per nucleon (Fig. 16). One infers that 100 MeV per projectile nucleon is approximately the energy above which a head-on collision of the projectile ^{20}Ne with ^{197}Au will lead to a complete dissociation of the composite system. For the collision of ^{208}Pb on ^{208}Pb, one finds that a head-on collision with an energy above 50 MeV per nucleon will lead to a complete dissociation of the composite system.

F. Comparison with other results

Despite the difference of the emphasis in the present studies and the previous hydrodynamical calculations[5-7] which apply to the PIC method, it is still of interest to compare the two types of results whenever possible. Figure 3 of Ref. 8 presents the proton energy distribution for the reation ^{20}Ne + ^{238}U at 250 MeV per nucleon at zero impact parameter and for the laboratory angles 30°, 60°, 90°, and 120°. This can be compared with our calculation of ^{20}Ne + ^{197}Au at the same bombarding energy and with small viscosity.

The general features of the energy distributions at 60°, 90°, and 120°, predicted by the PIC method and the FCT method, agree well. In order to make some more quantitative comparisons, we reconstruct the four points in the angular distribution for the PIC energy distributions by a summation over the energy, taking into account that the proton spectrum is only $\frac{102}{258}$ of the whole. We found that the two types of calculations using the PIC and FCT methods agree very well in the nonviscous case.

VI. SUMMARY AND CONCLUSION

Our systematic studies of ^{20}Ne + ^{197}Au and ^{208}Pb + ^{208}Pb at different energies have revealed several interesting features of the hydrodynamical description. The angular distributions of the reaction products have prominent structures. Apart from sharp peaks in the forward and backward directions, there are distinct side peaks. The positions of the peak in this angular range tend to move toward larger angles with increasing bombarding energies. This is true in both the symmetric and asymmetric systems. The presence of dissipation also displays significant effects on the dynamics, in particular, on the maximum density in the intermediate steps of the reaction and also in the angular and energy distribution of the final reaction products. The viscosity dependence of the angular distribution is much more prominent in the asymmetric than the symmetric collisions. In the former case, the presence of viscosity can lead to a difference of as much as 10° to 20° in the positions of the angular peaks. The underlying energy distributions also show differences for the viscous and nonviscous cases. In general, they tend to be broadened by dissipation. Accordingly, future detailed comparisons with experimental distributions will provide a useful means to obtain the transport coefficients.

However, head-on collisions are rare events in heavy-ion reactions. In order to substantiate the present results, it is also necessary to extend the calculations to collisions with small, but nonzero impact parameters. Investigations of the three-dimensional calculations for near-head-on collisions which exploit axial symmetry, are now in progress (see Appendix) and the results will be available in the near future.

Even though head-on and near-head-on collisions are of special interest as a testing ground for nuclear hydrodynamics, these cases cannot be of much use if there were no way to select these events for scrutiny. Recently, a method for selecting these events was proposed[35] by one of us (C. Y. W.). This was based on the introduction of the concept of centrality as a measure of the deviation of the reaction products from the azumithal symmetry. It is hoped that the method can be well developed and supplement the usual selection based on multiplicity, so that a direct confrontation of the present results with experiments can be made to provide the critical test on the validity of the hydrodynamical description for heavy-ion collisions.

Finally, it should be remarked that the studies reported here are done with a particular choice of the equation of state for the nuclear field. It is clear that to further our investigation, other functional forms can be attempted. It will be of great interest to compare various theoretical predictions based on different forms of the equation of state. Final confrontations with experimental results will provide a unique probe into the details of this and also other properties of nuclear matter.

ACKNOWLEDGMENTS

The authors wish to thank Professor S. E. Koonin, Dr. M. R. Strayer, Dr. K. R. Sandhya Devi, Professor R. Y. Cusson, Dr. D. L. Book, Dr. D. K. Scott, Dr. H. H. Gutbrod, and the Theory Group at Oak Ridge for their helpful communications and suggestions during various states of this work. One of us (H.H.K.T.) wishes to thank Professor D. A. Bromley for his kind encouragement and valuable discussions, and Dr. P. H. Stelson and Dr. J. B. McGrory for their kind hospitality at Oak Ridge National Laboratory where this work was carried out. This research was sponsored by the U. S. Department of Energy under Contract Nos. EY-76-C-023074 with Yale University and W-7405-eng-26 with the Union Carbide Corporation. H. H. K. Tang is grateful for the support of an F. W. Heyl and Elsie L. Heyl Predoctoral Fellowship. Much of the work reported here is based on part of a thesis submitted by H. H. K. Tang to Yale University in partial fulfillment of the requirements of the Ph.D. degree.

APPENDIX. NUMERICAL METHODS OF NUCLEAR HYDRODYNAMICS

The numerical algorithms to solve the hydrodynamical equations (2.1)–(2.3), are based on the flux-corrected-transport (FCT) method and the time-step-splitting (TSS) method of Boris and Book.[18]

These methods lead to a class of Eulerian finite-difference schemes which are found to be numerically stable and accurate. The FCT algorithm solves a one-dimensional generalized continuity equation (i.e., with source term) in the following manner. The propagation of a dynamical variable over a time step is achieved in two stages. In the convection stage the dynamical variable is followed in time in a Lagrangian manner. The transient profile of the variable is then extrapolated back onto the original Eulerian grid points in such a way that the conservation of total mass is enforced and the positivity of the mass density and energy density guaranteed. This, however, introduces inherent errors due to diffusion. These are corrected in the antidiffusion stage which leads to the final solution.

The multidimensional problem is solved by means of the TSS method in the following way. Each time step is divided into two halves. A dynamical variable is propagated (by an operator from the FCT algorithm) in one direction through the first half step. The velocity along this direction is estimated. Then the variable is propagated through the entire time step using this velocity and the initial values at the beginning of the time cycle. This procedure is then repeated to the other directions.

Various details of the implementation of the FCT and TSS methods have been discussed previously[18] and will not be repeated here.

In computations which treat the three-dimensional geometry exactly, there are unavoidable problems of storage and speed. However, since we are mostly interested in head-on and near-head-on collisions in nuclear hydrodynamics, such computational problems may be circumvented. The results discussed here are obtained from a special 3D code which solves the problem as follows. In near-head-on collisions, the configuration of the density field is approximately symmetric. Hence, at each time step, we search for an approximate symmetry axis about which the density field is then axially symmetrized. All the dynamical variables are solved on the reaction plane. In this way, the three-dimensional problem is treated by a set of two-dimensional equations which include additional terms to take into account the other degree of freedom in an approximate way. In the limit of zero impact parameters, however, this method is exact for both collisions of symmetric and asymmetric systems.

As a consequence of these special considerations, this 3D code achieves a speed comparable to a 2D code but requires no additional storage. For a typical configuration of 64×64 grid points, with a grid size of 0.6 to 1.2 fm and a time step interval of 0.6 to 1.5 fm/c, depending on the actual input, output, and other special implementations, this 3D code requires only 3 to 3.5 cpu second per time step on the 360/91 computer at Oak Ridge National Laboratory.

This can easily accommodate studies of heavy systems such as ^{208}Pb + ^{208}Pb. For low energies ($E/A \leq 50$ MeV), a typical reaction requires 400 to 600 time steps. For energies over 100 MeV/nucleon, however, it takes only about 100 to 200 time steps. Hence, from a practical point of view, such hydrodynamical calculations are well within the realm of possibilities of present computing facilities.

*Present address: Center for Theoretical Physics, Massachusetts Institute of Technology, Cambridge, Mass. 02139.

[1] See, e.g., review article by A. S. Goldhaber and H. H. Heckman, Annu. Rev. Nucl. Sci. 28, 161 (1978).

[2] G. F. Bertsch, Nucl. Phys. A249, 253 (1978).

[3] C. Y. Wong, J. A. Maruhn, and T. A. Welton, Nucl. Phys. A253, 469 (1975).

[4] C. Y. Wong and J. A. McDonald, Phys Rev. C 16, 1196 (1977).

[5] A. A. Amsden, F. H. Harlow, and J. R. Nix, Phys. Rev. C 15, 2059 (1977).

[6] A. A. Amsden, A. G. Goldhaber, F. H. Harlow, and J. R. Nix, Phys. Rev. C 17, 2080 (1978).

[7] H. H. Gutbrod, in *Proceedings of the Fourth High Energy Heavy-Ion Summer Study*, Berkeley, 1978, Report No. LBL-7766.

[8] A. A. Amsden, J. N. Ginocchio, F. H. Harlow, J. R. Nix, M. Danos, E. C. Halbert, and R. K. Smith, Jr., Phys. Rev. Lett. 38, 1055 (1977).

[9] G. D. Westfall, J. Gosset, P. J. Johansen, A. M. Poskanzer, W. G. Meyer, H. H. Gutbrod, A. Sandoval, and R. Stock, Phys. Rev. Lett. 37, 1202 (1976).

[10] A. A. Amsden, G. F. Bertsch, F. H. Harlow, and J. R. Nix, Phys. Rev. Lett. 35, 905 (1975).

[11] W. Scheid, H. Müller, and W. Greiner, Phys. Rev. Lett. 32, 741 (1974).

[12] H. G. Baumgardt, J. U. Schott, Y. Sakamoto, E. Schopper, H. Stöcker, J. Hofmann, W. Scheid, and W. Greiner, Z. Phys. A273, 359 (1975).

[13] C. Y. Wong and T. A. Welton, Phys. Lett. 49B, 2431 (1974).

[14] C. Y. Wong, J. A. Maruhn, and T. A. Welton, Phys. Lett. 66B, 19 (1977).

[15] H. H. K. Tang and C. Y. Wong, ORNL Physics Division Annual Progress Report No. ORNL-5306, 1977, pp. 138–142; Bull. Am. Phys. Soc. 22, 645 (1977); C. Y. Wong and H. H. K. Tang, *ibid.* 23, 586 (1978).

[16] H. H. K. Tang, Ph.D. thesis, Yale University, 1979 (unpublished).

[17] J. A. Maruhn, in *Proceedings Topical Conference on Heavy-Ion Collisions*, Fall Creek Falls State Park, Pikeville, Tenn., June 1977, Report No. CONF-770602.

[18] J. P. Boris and D. L. Book, J. Comput. Phys. 11, 38 (1973); D. L. Book, J. P. Boris, and K. Hain, *ibid.* 18, 248 (1975); J. P. Boris and D. L. Book, *ibid.* 20, 397 (1976).

[19] M. I. Sobel, P. J. Siemens, J. P. Bondorf, and H. A. Bethe, Nucl. Phys. A251, 502 (1975).

[20] C. Y. Wong and H. H. K. Tang, Phys. Rev. Lett. 40, 1070 (1978); Phys. Rev. C 20, 1419 (1979).

[21] C. Y. Wong, ORNL report (unpublished).

[22] K. Huang, *Statistical Mechanics* (Wiley, New York, 1963), Chap. 6.

[23] C. Y. Wong and C. Toepffer in Proceedings of Topical Conference on Large Amplitude Collective Nuclear Motions, Keszthely, Hungary, June, 1979, p. 400.

[24] J. Randrup, Nucl. Phys. A314, 429 (1979).

[25] G. Bertsch, Z. Phys. A289, 103 (1978).

[26] B. Tamain, R. Cechik, H. Fuchs, F. Hanappe, M. Morjean, C. Ngô, J. Peter, M. Dakowski, B. Lucas, C. Mazur, M. Ribrag, and C. Signarbieux, Orsay report, 1979.

[27] G. Baym and C. Pethick, in *Physics of Liquid and Solid Helium*, Part II, edited by K. H. Bennemann and J. B. Ketterson (Wiley, New York, 1978).

[28] J. Sykes and G. A. Brooker, Ann. Phys. (N.Y.) 56, 1 (1970).

[29] M. A. Preston, *Physics of the Nucleus* (Addison-Wesley, Reading, Mass., 1962), p. 93.

[30] S. Nagamiya, in *Proceedings of Fourth High Energy Heavy-Ion Summer Study*, Berkeley, 1978, Report No. LBL-7766, Fig. 2.17.

[31] M. N. Harekeh *et al.*, Phys. Rev. Lett. 38, 676 (1977).

[32] K. A. Brueckner, J. R. Buchler, R. C Clark, and R. J. Lombard, Phys. Rev. 187, 1543 (1969); H. A. Bethe, Annu. Rev. Nucl. Sci. 21, 93 (1971).

[33] C. Y. Wong, Phys. Rev. C 17, 1832 (1978).

[34] C. Y. Wong, Ann. Phys. (N.Y.) 77, 279 (1973).

[35] C. Y. Wong, Phys. Lett. 88B, 39 (1979).

PHYSICAL REVIEW C VOLUME 21, NUMBER 5 MAY 1980

Complete fusion of ^{12}C with ^{20}Ne

I. Tserruya
Brookhaven National Laboratory, Upton, New York 11973
and The Weizmann Institute of Science, Rehovot, Israel

J. Barrette and S. Kubono
Brookhaven National Laboratory, Upton, New York 11973

P. Braun-Munzinger, M. Gai, and C. D. Uhlhorn*
State University of New York, Stony Brook, New York 11794

(Received 22 October 1979)

Total fusion cross sections σ_F have been measured for ^{12}C + ^{20}Ne in the energy range $24 < E_{c.m.} < 42$ MeV using the ΔE-E technique. The excitation function of σ_F shows only two structures at $E_{c.m.} = 29$ and 38 MeV which seem of different origin than those observed in the ^{16}O + ^{16}O system. The saturation value of the measured fusion cross section agrees with that obtained for other systems with nucleons in the s-d shell.

[NUCLEAR REACTIONS ^{12}C + ^{20}Ne, $24 < E_{c.m.} < 42$ MeV; measured fusion excitation function.]

I. INTRODUCTION

The fusion cross section involving nuclei in the 1p shell or in the beginning of the sd shell has focused considerable attention in the last years. Of particular interest are the resonances observed in the excitation function of fusion between "α nuclei" such as ^{12}C + ^{12}C,[1] ^{12}C + ^{16}O,[2] or ^{16}O + ^{16}O,[3-5] whereas neighboring systems such as ^{12}C + ^{14}N,[6] ^{12}C + ^{18}O,[1] ^{12}C + ^{19}F,[1] or heavier ones such as ^{16}O + ^{24,26}Mg (Ref. 7) or ^{16}O + ^{40}Ca (Ref. 8) show a smooth behavior with energy. These resonances have an almost regular spacing of 3 to 5 MeV in the center-of-mass system; they represent deviations of 10–20% from the average fusion cross section and appear most pronounced in the evaporation residues produced by the decay of high spin states in the compound nucleus[3,4] (i.e., high partial waves in the entrance channel).

These structures are explained as an entrance channel effect; they are produced by the surface transparent potentials which are required to describe the entrance channel elastic scattering. This type of potential reflects the availability of only very few direct reaction channels for the incoming grazing partial waves.

In order to check further this interpretation we have performed a study of the fusion cross section σ_F for the system ^{12}C + ^{20}Ne, forming the same compound nucleus ^{32}S as in the ^{16}O + ^{16}O reaction. The main aim was to search for structure in the excitation function of fusion, and to study the influence of transparency of the ^{12}C + ^{20}Ne optical potential.

II. EXPERIMENTAL PROCEDURE AND RESULTS

The measurements were carried out at the Brookhaven National Laboratory using the ^{12}C beam of the MP tandem accelerator. The ^{12}C + ^{20}Ne fusion excitation function was measured in the energy range $40 \leq E_{lab} \leq 69$ MeV in steps of 1 MeV. The experimental arrangement is shown schematically in Fig. 1(a). Evaporation residues were detected using a ΔE-E telescope,[9] the ΔE detector being an ionization chamber that was operated at pressures of 20 Torr with a gas mixture of 90% argon and 10% methane. The residual energy was measured with a solid state surface barrier detector placed inside the ionization chamber. The target consisted of a closed gas cell with a steady flow of natural Ne. The gas pressure was ~5 Torr (corresponding to a density of 6 μg/cm^3). Ni foils of approximately 0.6 mg/cm^2 thickness were used as windows for the entrance and exit of the beam, and polypropylene foils of 70–100 μg/cm^2 thickness were used as windows on the side opening of the cell in the direction of detection of reaction products. With this gas cell we could measure as far forward as 5°. The bombarding energy has to be corrected for the energy loss in the entrance Ni foil and in the path through the Ne gas from the Ni foil to the center of the target. The effective bombarding energy was determined from the energy loss in the Ni foil measured at several ^{12}C energies and from tabulated electronic stopping powers[10] of ^{12}C in ^{20}Ne. This effective bombarding energy differed from the incident energy by 1.1 to 1.6 MeV in the energy

© 1980 The American Physical Society

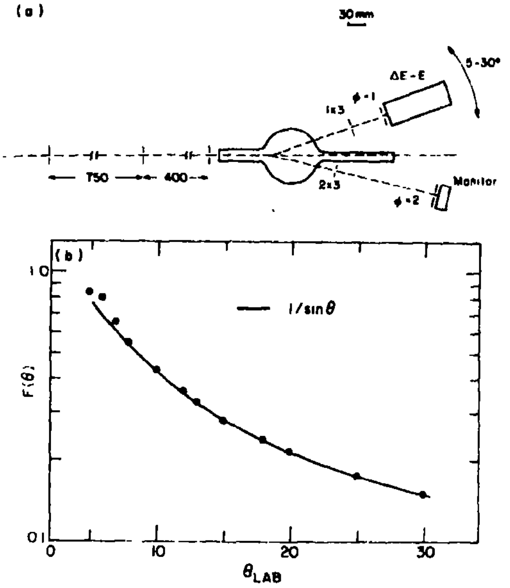

FIG. 1. (a) Schematic view of the experimental arrangement. All dimensions are in millimeters. (b) The dependence of the geometrical factor F on the angle θ of the telescope. The factor F is the ratio of the solid-angle × target length between the telescope and the monitor.

range studied, with an uncertainty smaller than 200 keV.

The beam was collimated to a spot of 1 mm^2 in the target with a divergence of ~0.1°. With this tight collimation the position and direction of the beam on target were held constant. A monitor detector was placed at 13° with respect to the beam direction. Both the monitor and the telescope were collimated in order to limit the effective target length of the gas cell.

Figure 2 shows a contour plot of (E-ΔE) vs ΔE taken at $E_{\text{lab}} = 58$ MeV and $\theta_{\text{lab}} = 10°$. Some of the evaporation residues have kinetic energies close to or below the Bragg maximum and thus for these energies the different elements cannot be completely resolved with the ΔE-E technique. However, the total yield of evaporation residues is clearly and unambiguously identified. All events with $z \geq 8$ (events enclosed by the solid line in Fig. 2) were considered as evaporation products and defined the fusion yield. Particles which were stopped in the ΔE counter or whose energies fell below the energy threshold of the E counter were also recorded and are displayed in the lowest (E-ΔE) channel in Fig. 2. These events were also considered evaporation residues when located below the whole group of fusion yield; they represent 2–6% of the total fusion yield. From the projection of the spectrum on the ΔE axis (see Fig. 2) we estimate that less than 3% of the fusion yield is tailing into the ^{12}C band and therefore outside the contour defining the fusion events Discrete transitions (which appear as sharp lines) mainly in the oxygen spectrum were attributed to direct processes and were not included in the fusion yield. It should be noticed that at the lower energies the oxygen yield contributes a very small fraction to the total fusion yield. It increases with bombarding energy and amounts to nearly 10% at 68 MeV. This fraction is in good agreement with the results of statistical model calculations (see below). The statistical accuracy of the fusion yield was generally better than 3%.

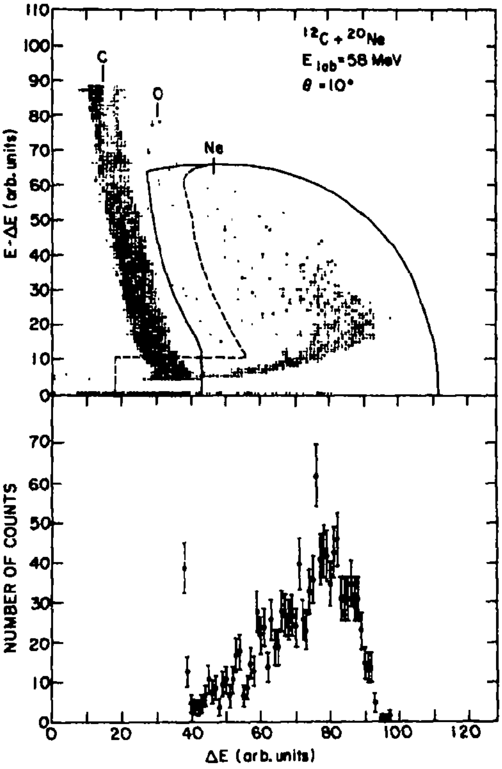

FIG. 2. Contour plot of ΔE vs (E-ΔE) for ^{12}C+ ^{20}Ne at E_{lab}= 58 MeV and θ_{lab} = 10° (upper part). The events encircled by the solid line are taken to be the evaporation residues. The bottom part presents a projected ΔE spectrum of the events encircled by the dashed line. It illustrates that only a negligible part of the fusion yield is in the tail of the ^{12}C distribution.

The fusion yield was normalized to the elastic scattering in the monitor. The geometrical factor

F (corresponding to the ratio of solid-angle × target length between the telescope and the monitor) was determined from measurements of the elastic scattering of ^{12}C on Xe at 40 MeV which follows the Rutherford law. The dependence of this quantity on the angle of the telescope is shown in Fig. 1(b). It is seen that at large angles F behaves as $1/\sin\theta$, reflecting the expected change of the target length with scattering angle. At very forward angles the measured factor used to normalize the data deviates, as expected, from the $1/\sin\theta$ curve. The absolute differential fusion cross section was obtained from the elastic scattering cross section of ^{12}C on ^{20}Ne that was measured from 22 to 68 MeV in an independent measurement using the same geometry. As target, a continuous flow of premixed ^{20}Ne and Xe gases was used at a pressure of 3 Torr. In this energy range the elastic scattering of ^{12}C on Xe at 13° obeys the Rutherford law. The relative amount of Xe and Ne in the mixture was determined assuming that the ^{12}C-^{20}Ne elastic scattering follows the Rutherford formula in the energy range 22–28 MeV. It was checked that this relative amount stayed constant by repeating several points during the measurements. The results of the elastic scattering excitation function are shown in Fig. 3.

Complete angular distributions of the fusion cross section consisting of 8–9 points in the angular range $5° \leq \theta_{\text{lab}} \leq 30°$ were measured every 5 MeV. For the intermediate energies only three angles, $\theta_{\text{lab}} = 7$, 10, and 13°, were measured, since it is well known that the shape of the angular distribution changes very little with incident energy. The angular distributions are shown in Fig. 4. The fusion cross section at a given energy was obtained by integration of the angular distribution. The amount of cross section not measured (the forward angles 0–5° and the backward angles $\theta_{\text{lab}} > 30°$) was taken from statistical model calculations. The two fractions are nearly independent of incident energy and amount to ~10% (forward angles) and ~2% (backward angles). At energies where only a few angles were measured, the fusion cross section was obtained assuming the same shape of the angular distribution as for the closest bombarding energy for which data over a complete angular range were measured.

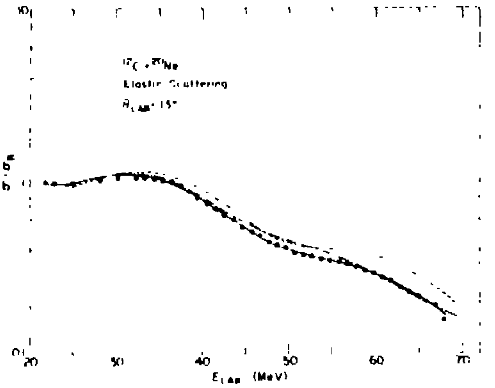

FIG. 3. Excitation function for ^{12}C+ ^{20}Ne elastic scattering measured at $\theta_{\text{lab}} = 13°$. The statistical errors are smaller than the size of the points. The dashed and dot-dashed lines are optical model calculations using the parameters of Ref. 12 and Ref. 13, respectively. The solid line was obtained from a fit to the data. All optical potential parameters are listed in Table I.

III. ANALYSIS AND DISCUSSION

The measured elastic scattering excitation function is shown in Fig. 3 together with optical model calculations performed with the code PTOLEMY.[11]

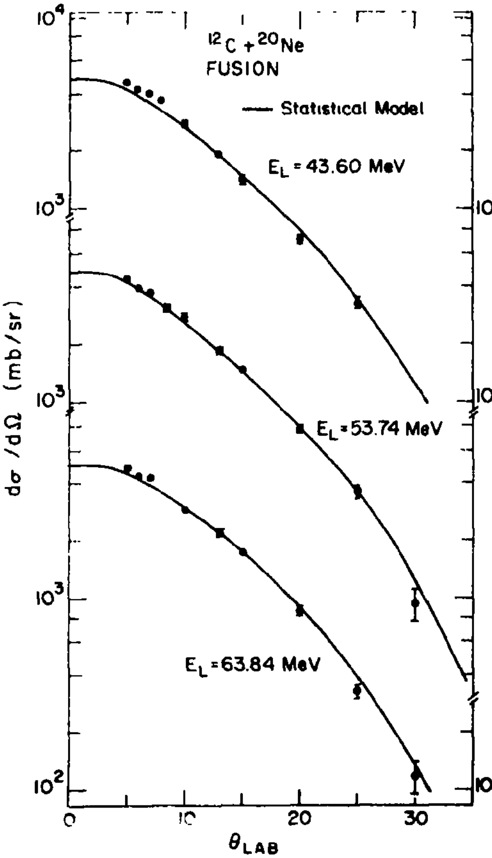

FIG. 4. Angular distributions of the ^{12}C+ ^{20}Ne fusion cross sections at the indicated incident energies. The lines are statistical model calculations.

Calculations using previously reported optical potential parameters do not reproduce the measurements well. The dashed line in Fig. 3 was obtained with the parameters of Osterfeld *et al.*[12] and the dot-dashed line with the parameters of Vandenbosch *et al.*[13] (see Table I). The solid line is the result of a fit using the parameters listed in Table I. Equally good fits could also be obtained with somewhat different parameters.

Angular distributions of the fusion cross section are shown in Fig. 4. They are forward peaked but with a considerably smaller falloff as compared to ^{16}O+ ^{16}O (Ref. 4) (the cross section falls approximately by a factor of 15 between 5–25° compared to a factor of 50 in the ^{16}O+ ^{16}O case) due to the smaller recoil momentum of the compound nucleus in the more asymmetric system ^{12}C + ^{20}Ne.

The angular distributions are well reproduced by statistical model calculations using the code JULIAN[14] as shown in Fig. 4 by the solid lines. The code includes neutron, proton, and α particle evaporations, and γ decay, and takes explicitly into account the angular momentum of the compound nucleus and of the emitted particles. The initial spin distribution of the compound nucleus was calculated as in Ref. 15. The transmission coefficients in the entrance channel was calculated using the optical potential parameters obtained from the fitting of the elastic scattering excitation function shown in Fig. 3. Level densities were generated using the expression of Gilbert and Cameron.[16]

The total fusion excitation function is shown in Fig. 5 as a function of the center-of-mass energy. An error of 5% has been assigned to each experimental point. This represents an upper limit of the total uncertainty calculated from the different factors discussed above (statistical accuracy, normalization procedure, and missing cross section). It does not include the uncertainty in the determination of the elastic scattering cross section due to beam shifts which is probably the largest source of error in σ_F. The upper limit of this uncertainty is estimated to be 10% from the maximum spread of experimental values of the same point measured in different runs. It is seen that σ_F has a quite smooth behavior with incident energy. Broad humps are observed at only $E_{c.m.} = 29$ and 38 MeV. This behavior is different from the ^{16}O+ ^{16}O system where regular structure with a significantly smaller spacing of 3–4 MeV is observed.[20] It should be pointed out that in ^{12}C + ^{20}Ne even and odd partial waves contribute to the cross section resulting in more closely spaced shape resonances. Assuming similar widths for the resonances than in the system ^{16}O + ^{16}O and in the absence of a mechanism to enhance even or odd partial waves, the structure due to shape resonances should be strongly suppressed. Note, however, that contrary to the system studied here, the system ^{12}C + ^{16}O (Ref. 2) exhibits structures of similar spacing than observed for ^{16}O+ ^{16}O even though both odd and even partial waves participate in the reaction.

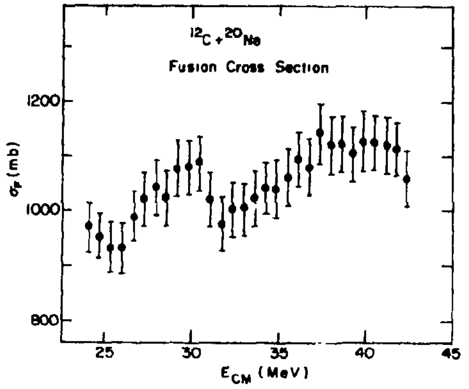

FIG. 5. Total fusion cross section σ_F of ^{12}C+ ^{20}Ne as a function of the center-of-mass energy.

Furthermore, the damping of the resonances in the fusion of ^{12}C + ^{20}Ne is also consistent with the fact that the optical potentials (of Refs. 12–14, 17, 18 and of this work) required to fit the elastic scattering data are less surface transparent than the optical potential of ^{16}O+ ^{16}O.[19] All the optical potentials listed in Table I have a rather strong absorption in the region of the nuclear surface compared to the potential of Ref. 19 and result in completely structureless variation of the total reaction cross section with energy. The differ-

TABLE I. Optical model parameters for elastic scattering of ^{12}C + ^{20}Ne.

V (MeV)	r_{0R} (fm)	a_R (fm)	W (MeV)	r_{0I} (fm)	a_I (fm)	(Ref.)
13.5	1.37	0.59	7	1.40	0.68	This work
17	1.35	0.49	$0.8 + 0.2E_{c.m.}$	1.35	0.49	12
17	1.35	0.57	$0.98 + 0.54E_{c.m.}$	1.35	0.57	13

ence in the optical potential of these two systems may be related[13] to the fact that in the $^{16}O+^{16}O$ case only very few direct reaction channels are able to carry away the high angular momentum brought in by the incoming grazing partial waves, whereas for the $^{12}C+^{20}Ne$ case the Q values for direct reactions are most favorable (particularly for inelastic scattering) and therefore more channels are available (see also Ref. 12).

From the present data, one obtains the saturation value of the fusion cross section. It has been observed[20] that for systems involving ^{12}C or ^{16}O there is a strong difference [with the exceptions of $^{12}C+^{15}N$ (Ref. 21) and $^{10}B+^{16}O$ (Ref. 22)] depending on whether both nuclei occupied only the $1p$ shell or whether one of the nuclei has nucleons in the s-d shell. In the former case the fusion cross section saturates near 950 mb while in the latter case it saturates between 1150 and 1200 mb. In good agreement with these systematics, the maximum value of the fusion cross section observed in the present work is ~1140 mb. Static deformation of nuclei such as ^{20}Ne and ^{24}Mg plays an important role in the fusion cross section at energies near or below the Coulomb barrier, where the barrier penetrability is sensitive to deformation effects. However, it is not expected to affect the cross sections at high energies[23] where the fusion cross section reaches its maximum.

The fusion of $^{12}C+^{20}Ne$ has also been measured by Menet *et al.*[24] at $E_{c.m.}=41.25$ MeV. Their value of $\sigma_F=1270\pm150$ mb is in agreement with our result of $\sigma_F=1125\pm60$ mb at the same energy. The cross sections measured by Saint-Laurent *et al.*[25] at several energies are also consistent with the results of the present work.

IV. SUMMARY

We have measured the fusion excitation function of $^{12}C+^{20}Ne$ in the energy range $24<E_{c.m.}<42$ MeV using the ΔE-E technique. The fusion cross section varies smoothly as a function of energy and shows only two broad structures at $E_{c.m.}=29$ and 38 MeV. There is no evidence for resonances similar to those observed in the $^{16}O+^{16}O$ and $^{16}O+^{12}C$ systems. The saturation value of the fusion cross section is similar to that of neighboring systems involving nuclei in the sd shell.

ACKNOWLEDGMENTS

We are particularly indebted to Mr. M. Manni and Mr. G. Hummer for their assistance in preparing the gas cell and the experimental apparatus. One of us (I.T.) would like to thank Dr. A. Schwarzschild for the friendly hospitality he enjoyed during his stay at the Brookhaven National Laboratory as a summer visitor. This work was supported in part by the Division of Basic Energy Sciences, Department of Energy, under Contract No. DE-AC02-76CH00016 and in part by the National Science Foundation.

---

*Present address: Ruhr University, Bochum, West Germany.

[1] P. Sperr, T. H. Braid, Y. Eisen, D. G. Kovar, F. W. Prosser, Jr., J. P. Schiffer, S. L. Tabor, and S. Vigdor, Phys. Rev. Lett. 37, 321 (1976).

[2] P. Sperr, S. Vigdor, Y. Eisen, W. Henning, D. G. Kovar, T. R. Ophel, and B. Zeidman, Phys. Rev. Lett. 36, 405 (1976).

[3] J. J. Kolata, R. C. Fuller, R. M. Freeman, F. Haas, B. Heusch, and A. Gallmann, Phys. Rev. C 16, 891 (1977).

[4] I. Tserruya, Y. Eisen, D. Pelte, A. Gavron, H. Oeschler, D. Berndt, and H. L. Harney, Phys. Rev. C 18, 1688 (1978).

[5] V. K. C. Cheng, A. Little, H. C. Yuen, S. M. Lazarus, and S. S. Hanna, Nucl. Phys. A322, 168 (1979).

[6] R. G. Stokstad, Z. E. Zwitkowski, R. A. Dayras, and M. M. Wieland, Phys. Rev. Lett. 37, 888 (1976).

[7] S. L. Tabor, D. F. Geesaman, W. Henning, D. G. Kovar, K. E. Rehm, and F. W. Prosser, Jr., Phys. Rev. C 17, 2136 (1978).

[8] D. F. Geesaman, C. N. Davids, W. Henning, D. G. Kovar, K. E. Rehm, J. P. Schiffer, S. L. Tabor, and F. W. Prosser, Jr., Phys. Rev. C 18, 284 (1978).

[9] M. M. Fowler and R. C. Jared, Nucl. Instrum. Methods 124, 341 (1975).

[10] L. C. Northcliffe and R. F. Schilling, Nucl. Data A7, 233 (1970).

[11] D. H. Gloeckner, M. H. Macfarlane, and S. C. Pieper, Argonne National Laboratory Report No. ANL-76-11, 1976 (unpublished).

[12] F. Osterfeld, V. Hnizdo, and C. Toepffer, Phys. Lett. 68B, 319 (1977).

[13] R. Vandenbosch, M. P. Webb, and M. S. Zisman, Phys. Rev. Lett. 33, 842 (1974).

[14] M. Hillman and Y. Eyal (unpublished).

[15] Y. Eisen, I. Tserruya, Y. Eyal, Z. Fraenkel, and M. Hillman, Nucl. Phys. A291, 459 (1977).

[16] A. Gilbert and A. G. W. Cameron, Can. J. Phys. 43, 1446 (1965).

[17] H. Doubre, J. C. Roynette, E. Plagnol, J. M. Loiseaux, P. Martin, and P. deSaintignon, Phys. Rev. C 17, 131 (1978).

[18] R. Vandenbosch and K. G. Bernhardt, J. Phys. (Paris) Lett. 37, L161 (1976).

[19] A. Gobbi, R. Wieland, L. Chua, D. Shapira, and D. A.

Bromley, Phys. Rev. C **7**, 30 (1973); J. V. Maher, M. W. Sachs, R. H. Siemmsen, A. Weidinger, and D. A. Bromley, Phys. Rev. **188**, 1665 (1969).

[20] D. G. Kovar, D. F. Geesaman, T. B. Braid, Y. Eisen, W. Henning, T. R. Ophel, M. Paul, K. E. Rehm, S. J. Sanders, P. Sperr, J. P. Schiffer, S. L. Tabor, S. Vigdor, and B. Zeidman, Phys. Rev. C **20**, 1305 (1979) and references therein.

[21] M. Conjeaud, S. Gary, S. Harar, and J. P. Wieleczko, Nucl. Phys. **A309**, 515 (1978).

[22] J. Gomez del Campo, R. A. Dayras, J. A. Biggerstaff, D. Shapira, A. H. Snell, P. H. Stelson, and R. G. Stokstad, Phys. Rev. Lett. **43**, 26 (1979).

[23] R. G. Stokstad, Y. Eisen, S. Kaplanis, D. Pelte, U. Smilansky, and I. Tserruya, Phys. Rev. Lett. **41**, 465 (1978).

[24] J. Menet, A. J. Cole, N. Longequeue, J. J. Lucas, G. Mariolopoulos, J. B. Viano, J. C. Saulnier, and D. H. Koang, J. Phys. (Paris) **38**, 1051 (1977).

[25] F. Saint-Laurent, M. Conjeaud, S. Harar, J. M. Loiseaus, J. Menet, and J. B. Viano, Nucl. Phys. **A327**, 517 (1979).

PHYSICAL REVIEW C VOLUME 21, NUMBER 5 MAY 1980

Closed-form description of heavy-ion transfer reactions based on distorted-waves theory

W. E. Frahn

Gesellschaft für Schwerionenforschung, 6100 Darmstadt, Germany
and Physics Department, University of Cape Town, Rondebosch (Cape) 7700, South Africa

(Received 5 September 1979)

The transition amplitude for quasielastic transfer reactions between heavy ions, given by distorted-waves theory, is evaluated in closed form. By means of suitable approximations the transfer partial-wave amplitude is expressed in terms of the elastic S matrix elements in the initial and final channels and of known functions defined by the Coulomb radial integrals of the transfer form factor. The partial-wave summation is performed by using the Poisson sum formula in conjunction with Fourier-Bessel transform techniques for evaluating integrals over localized functions in l space. The resulting expressions cover uniformly the whole angular range including forward and backward directions. The general structure of the excitation functions at 0° and 180° is discussed, including possible backward-angle enhancements of the transfer cross section. A crucial step in the derivation is the introduction of a mean elastic S-matrix, whose dependence on the initial and final angular momenta allows the display in detail of the magnetic quantum number and Q-value dependences of the smooth and oscillatory parts of the cross section. Applications and extensions of the present formalism will be given in subsequent papers.

[NUCLEAR REACTIONS Closed-form S-matrix theory of heavy-ion transfer reactions based on DWBA. Uniform approximation for transfer angular distributions, 0° and 180° excitation functions. Explicit form of magnetic quantum number and Q-value dependences.]

I. INTRODUCTION

In this paper we give an analytic description of "quasi-elastic" (as distinct from "deeply-inelastic") transfer reactions between heavy ions, based on distorted-waves theory. The purpose is to display explicitly all significant features of the transition amplitude, including the finer details of the dependence on magnetic quantum numbers, l matching, Q values, etc.

The earliest closed-form treatments of heavy-ion transfer reactions above the Coulomb barrier[1,2] assumed simple phenomenological forms of the partial-wave amplitude and were restricted to $L=0$ transfer. Though grossly oversimplified, these descriptions emphasized the predominantly diffractive nature of the transfer process and were the first to predict the existence of regular oscillations in the transfer cross section at small angles, even though the data known at the time showed smooth "bell-shaped" angular distributions only. Also, the systematic variations of the main cross section characteristics with energy, charge, and mass numbers were at least qualitatively described. At first, however, the diffraction oscillations were not found at the predicted energies, which was attributed[3] to the neglect of recoil effects. Not before early in the present decade was the oscillatory structure of many transfer angular distributions firmly established by experiment.[4-8]

Closed-form descriptions based on the distorted-wave Born approximation were first developed by Dar and his co-workers,[9-11] using for the mean elastic S matrix the parametric form of the strong absorption model.[12] This formulation was extended[13] by employing a more general technique for the partial-wave summation.

A different approach, with emphasis on the classical-refractive rather than the quantal-diffractive aspects of heavy-ion reactions, was followed in the early semiclassical theory.[14] This was later amended to account more appropriately for the effects of strong absorption by the use of complex trajectories and saddle-point methods.[15,16] The most recent semiclassical treatment,[17] though similar in concept to that of Ref. 15, takes a significant step towards a closed-form representation by performing analytically the main partial-wave summation in the distorted-waves transition amplitude.

Much of the recent advance in a more detailed understanding of heavy-ion transfer reactions is due to the experimental and theoretical work of Kahana and his co-workers.[18-20] These authors have interpreted several significant features of the distorted-waves amplitude that were not accounted for in the earlier closed-form descriptions, by means of an extended version of the phenomenological transfer S matrix[2] in which the localization with respect to the difference between the initial and final orbital angular momenta is incorporated explicitly. A clear and useful presentation of these developments is given in the review by Kahana and Baltz.[21]

In the present paper we employ analytic techniques developed previously for elastic[22,23] and inelastic[24] heavy-ion scattering to evaluate the partial-wave representation of the transfer transition amplitude. Particular attention is given to a more accurate treatment of the small- and large-angle regions, and to show how the specific properties pointed out by Kahana *et al.* can be derived from the transfer S matrix of distorted-waves theory.

II. SMALL-ANGLE REPRESENTATION

A. Angular distribution

We assume that the reaction

$$A_i+B_i=(A_f+c)+B_i\to A_f+(B_i+c)=A_f+B_f\,, \tag{2.1}$$

in which a nucleon or cluster c is transferred between the (heavy) nuclei A_i and B_i, can be described in distorted-wave Born approximation (DWBA). In view of excellent accounts of basic distorted-waves theory[25,21] we may start directly from the partial-wave representation of the DWBA transfer amplitude. With all due reservations, especially for heavy ions, we adopt the no-recoil approximation for simplicity, leaving recoil corrections for consideration at a later stage. Then the differential cross section for angular momentum transfer L can be written

$$\sigma_L^{(T)}(\theta)=A\,\frac{\mu_i\mu_f}{(2\pi\hbar^2)^2}\,\frac{k_f}{k_i}\sum_{M=-L}^{L}\left|\beta_{LM}(\theta)\right|^2\,, \tag{2.2}$$

where μ_i, μ_f are the reduced masses, and k_i, k_f are the relative wave numbers in the initial and final channels. Disregarding spin effects, we have lumped all spin and spectroscopic factors together in the constant A. Then the reduced transition amplitude for multipolarity (L,M) is given by

$$\beta_{LM}(\theta)=\sum_{l_il_f} i^{l_i-l_f-L}\langle l_fL;00|l_i0\rangle\langle l_fL;-MM|l_i0\rangle(2l_f+1)^{1/2}R^L_{l_fl_i}(k_f,k_i)\exp\{i[\sigma_{l_f}(k_f)+\sigma_{l_i}(k_i)]\}\,Y_{l_f,-M}(\theta,0)\,. \tag{2.3}$$

Here we have chosen a coordinate frame with z axis in the direction of $\vec{k}_i$ and y axis in the direction of $\hat{k}_i\times\hat{k}_f$. The radial integrals are defined as

$$R^L_{l_fl_i}(k_f,k_i)=\frac{4\pi}{\zeta k_fk_i}\int_0^\infty dr\,f^{(f)}_{l_f}(k_f,\zeta r)\times F^{(\kappa)}_L(r)f^{(i)}_{l_i}(k_i,r)\,, \tag{2.4}$$

where $f_l^{(i,f)}$ are the radial parts of the distorted-wave functions, and

$$F^{(\kappa)}_L(r)=-i^Lh^{(1)}_L(i\kappa r)\cong\frac{e^{-\kappa r}}{\kappa r} \tag{2.5}$$

is the transfer form factor, $\kappa=(2\mu_r\epsilon_B)^{1/2}/\hbar$ being the imaginary wave number associated with the binding energy ϵ_B of the transferred cluster in the final nucleus. The scale factor ζ arises from the no-recoil approximation and can vary between $\zeta=B_i/B_f$ and $\zeta=(B_i/B_f)[1+(c/\mu_i)]$ depending on the range of the interaction[21] (where the symbols of the particles stand for their masses), and $\sigma_l(k)$ denote the Rutherford phase shifts.

Our purpose is to evaluate the summations over the orbital angular momenta l_i, l_f in explicit analytic form by utilizing the characteristic simplifying features of heavy-ion interactions above the Coulomb barrier. These are (i) large grazing angular momenta $l_i^{(0)}$, $l_f^{(0)}$, (ii) strong Coulomb interaction indicated by high values of the Sommerfeld parameters n_i, n_f, and (iii) strong absorption of low-l partial waves.

Under these conditions we may replace the spherical harmonics in (2.3) by their asymptotic forms for large l_f. In this section we use the "small-angle asymptotics"

$$Y_{l_f,-M}(\theta,0)\cong\left(\frac{\lambda_f}{2\pi}\right)^{1/2}\left(\frac{\theta}{\sin\theta}\right)^{1/2}J_M(\lambda_f\theta)\,, \tag{2.6}$$

where $\lambda_f=l_f+\frac{1}{2}$, which is valid for $0\leq\theta\lesssim\pi-|M|/\lambda_f$ and exact in the forward direction $\theta=0$. For $L\ll l_i$, l_f we may then also use the asymptotic form of the Clebsch-Gordan coefficients

$$\langle l_fL;-MM|l_i0\rangle\cong d^L_{MK}(\tfrac{1}{2}\pi) \tag{2.7}$$

in terms of reduced rotation matrix elements, where

$$K=l_i-l_f\,. \tag{2.8}$$

With the definitions

$$R^{L}_{l_f, l_f+K}(k_f, k_i) \equiv R_{LK}(\lambda_f),$$
$$\sigma_{l_{f,i}}(k_{f,i}) \equiv \sigma^{(f,i)}(\lambda_{f,i}), \qquad (2.9)$$

and

$$b^{L}_{KM} = i^{K} d^{L}_{0K}(\tfrac{1}{2}\pi) d^{L}_{MK}(\tfrac{1}{2}\pi), \qquad (2.10)$$

we replace the summation over l_f in (2.3) by the Poisson series of integrals over λ_f with the result

$$\beta_{LM}(\theta) = \frac{i^{-L}}{\pi^{1/2}}\left(\frac{\theta}{\sin\theta}\right)^{1/2} \sum_{K} b^{L}_{KM} \sum_{m=-\infty}^{\infty} e^{-im\pi} \int_0^{\infty} d\lambda_f \lambda_f R_{LK}(\lambda_f) \exp\{i[\sigma^{(f)}(\lambda_f) + \sigma^{(i)}(\lambda_f + K)]\} e^{i2m\pi\lambda_f} J_M(\lambda_f \theta). \qquad (2.11)$$

Now we take the crucial step by making a suitable approximation for the functions $R_{LK}(\lambda_f)$. First, we assume that the nuclear part of the distorting interaction in the initial and final channels is contained in these functions through the complex nuclear phases only, so that we can write

$$R_{LK}(\lambda_f) \approx [S^{(N)}_{l_f}(k_f)]^{1/2} \mathcal{R}^{L}_{l_f l_i}(k_f, k_i) [S^{(N)}_{l_i}(k_i)]^{1/2}, \qquad (2.12)$$

where $S^{(N)}_{l}(k)$ is the nuclear part of the total elastic S matrix

$$S_l(k) = S^{(N)}_l(k) e^{i2\sigma_l(k)} = \eta_l(k) \exp\{i2[\delta^{(N)}_l(k) + \sigma_l(k)]\}$$
$$= \eta_l(k) e^{i2\delta_l(k)}, \qquad (2.13)$$

and

$$\mathcal{R}^{L}_{l_f l_i}(k_f, k_i) = \frac{4\pi}{k_i k'_f} \int_0^{\infty} dr\, \mathcal{F}_{l_f}(k'_f r) F^{(\kappa)}_{L}(r) \mathcal{F}_{l_i}(k_i r), \qquad (2.14)$$

where $k'_f = \zeta k_f$, are the transfer radial integrals with *Coulomb* radial wave functions $\mathcal{F}_l(kr)$ only. Approximations similar to (2.12), which is known as the "Sopkovich prescription,"[26] are usually made in semiclassical approaches[14,15,17]; the same device was used in our description of inelastic heavy-ion scattering[24] to approximate the Coulomb excitation part of the inelastic radial integrals.

Second, we replace the square root of the product of the nuclear S matrices by an average S matrix which may be regarded as the "geometrical mean" of $S^{(N)}_{l_i}$ and $S^{(N)}_{l_f}$. Assuming that $S_{l_{i,f}}(k_{i,f})$ may be interpolated by smooth functions $S(\lambda_{i,f})$ of the continuous variables $\lambda_{i,f} = l_{i,f} + \frac{1}{2}$, characterized by critical angular momentum parameters $\Lambda_{i,f} = l^{(0)}_{i,f} + \frac{1}{2}$ and l-window parameters $\Delta_{i,f}$ on which they depend through the combinations $\mu_{i,f} = (\lambda_{i,f} - \Lambda_{i,f})/\Delta_{i,f}$, we show in Appendix A that

$$[S^{(N)}_{l_f}(k_f) S^{(N)}_{l_i}(k_i)]^{1/2} \to [S^{(f)}_{N}(\lambda_f) S^{(i)}_{N}(\lambda_i)]^{1/2}$$
$$\approx S^{(K)}_{N}(\bar{\lambda}), \qquad (2.15)$$

where

$$S^{(K)}_{N}(\bar{\lambda}) = \eta_K(\bar{\lambda}) e^{i2\delta^{(K)}_{N}(\bar{\lambda})}, \quad \bar{\lambda} = \tfrac{1}{2}(\lambda_i + \lambda_f) \qquad (2.16)$$

with

$$2\delta^{(K)}_{N}(\bar{\lambda}) = \delta^{(i)}_{N}(\lambda_i) + \delta^{(f)}_{N}(\lambda_f)$$
$$= \delta^{(i)}_{N}(\bar{\lambda} + \tfrac{1}{2}K) + \delta^{(f)}_{N}(\bar{\lambda} - \tfrac{1}{2}K) \qquad (2.17)$$

and

$$\eta_K(\bar{\lambda}) \equiv \hat{\eta}(\bar{\mu}_K), \quad \bar{\mu}_K = \frac{\bar{\lambda} - \Lambda_K}{\Delta}. \qquad (2.18)$$

Here the critical angular momentum of the mean reflection function is given by

$$\Lambda_K = \bar{\Lambda} + \Delta_K,$$
$$\Delta_K = \Delta \ln\left\{\frac{1}{2}\left[\exp\left(\frac{K - K_0}{2\Delta_f}\right) + \exp\left(-\frac{K - K_0}{2\Delta_i}\right)\right]\right\}, \qquad (2.19)$$

where

$$\bar{\Lambda} = \tfrac{1}{2}(\Lambda_i + \Lambda_f), \quad K_0 = \Lambda_i - \Lambda_f, \qquad (2.20)$$

and Δ is the geometrical mean of the l-window parameters of the initial- and final-channel S matrices,

$$\Delta = \frac{2\Delta_i \Delta_f}{\Delta_i + \Delta_f}. \qquad (2.21)$$

It will be seen later on that the K and K_0 dependences of the mean S matrix described by (2.18)–(2.20) determine the magnetic substate population, the l matching, and most of the Q-window effects in the transfer cross section.

Third, although the Coulomb radial integrals (2.14) can be expressed in terms of generalized hypergeometric functions of two variables known as Appell functions,[27] for practical purposes we use an approximation obtained by replacing the Coulomb radial wave functions $\mathcal{F}_l(kr)$ by their WKB forms. Then we can write

$$\mathcal{R}^{L}_{l_f l_i}(k_f, k_i) = \frac{2\pi}{k_i k'_f \kappa} I^{(\kappa)}_{L-K}(\alpha, \xi), \qquad (2.22)$$

where the $I^{(\kappa)}_{L-K}$ are functions of the mean asymptotic Rutherford deflection function α and of the adiabaticity parameter ξ,

$$\alpha = \Theta_R(\bar{\lambda}) = 2\arctan(n/\bar{\lambda}), \quad \xi = n_f - n_i \qquad (2.23)$$

where

$$n = \tfrac{1}{2}(n_i + n_f), \qquad (2.24)$$

$$n_i = \frac{\mu_i Z_{A_i} Z_{B_i} e^2}{\hbar^2 k_i}, \quad n_f = \frac{\mu_f Z_{A_f} Z_{B_f} e^2}{\hbar^2 k_f}. \qquad (2.25)$$

The main properties of the functions $I_{L-K}^{(K)}$ and some further approximations are given in Appendix B.

Now we can write our approximation for the functions $R_{LK}(\lambda_f)$ as

$$R_{LK}(\lambda_f)=\frac{2\pi}{k_i k_f' \kappa} I_{L-K}^{(\kappa)}(\alpha,\xi)\,\eta_K(\lambda_f+\tfrac{1}{2}K)\times\exp[i2\delta_N^{(K)}(\lambda_f+\tfrac{1}{2}K)]\,, \tag{2.26}$$

and the amplitude (2.11) becomes

$$\beta_{LM}(\theta)=i^{-L}\frac{2\pi^{1/2}}{k_i k_f' \kappa}\left(\frac{\theta}{\sin\theta}\right)^{1/2}\sum_K b_{KM}^L \sum_{m=-\infty}^{\infty} e^{-im\pi}\int_0^\infty d\lambda_f \lambda_f I_{L-K}^{(\kappa)}(\alpha,\xi)\eta_K(\lambda_f+\tfrac{1}{2}K)\times\exp\{i[2\delta_K(\lambda_f+\tfrac{1}{2}K)+2m\pi\lambda_f]\}J_M(\lambda_f\theta)\,, \tag{2.27}$$

where we have defined the mean total phase shift

$$2\delta_K(\bar{\lambda})=\delta_N^{(i)}(\lambda_i)+\sigma^{(i)}(\lambda_i)+\delta_N^{(f)}(\lambda_f)+\sigma^{(f)}(\lambda_f)=2\delta_N^{(K)}(\lambda_f+\tfrac{1}{2}K)+2\sigma^{(K)}(\lambda_f+\tfrac{1}{2}K)\,. \tag{2.28}$$

To evaluate the integrals over λ_f in (2.27), we first note that the nonoscillatory parts of the integrands are localized in l space. This is because the reflection functions η_K for heavy ions have a strong-absorption profile with very small values for low-l partial waves, and because the functions $I_{L-K}^{(\kappa)}$ fall off exponentially at large l with a rate determined by the binding parameter κ. Thus the "transfer partial-wave amplitude functions"

$$c_{LK}(\bar{\lambda})=I_{L-K}^{(\kappa)}(\alpha,\xi)\eta_K(\bar{\lambda})\,, \tag{2.29}$$

whose general shape is sketched in Fig. 1, have maxima at $\bar{\lambda}=\bar{\Lambda}_K^T$. We note that, in contrast to the simple parametric forms assumed in Refs. 1, 2, 18, and 20, the functions $c_{LK}(\bar{\lambda})$ derived from distorted-waves theory are *essentially asymmetric* about their maximum positions, the asymmetry being determined by the difference between the binding parameter κ/k and the mean elastic window parameter Δ, in other words, by the difference between the range R_B of the bound state wave function of the transferred cluster and the mean surface diffuseness $\bar{a}$ semiclassically associated with Δ.

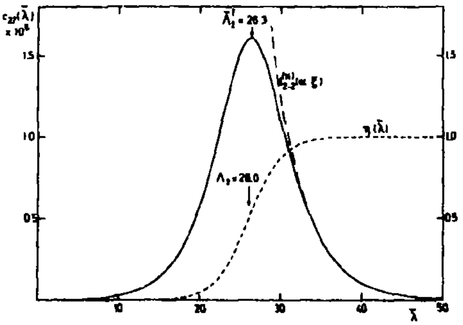

FIG. 1. Typical shape of the transfer partial-wave amplitude function $c_{LK}(\bar{\lambda})$, defined by Eq. (2.29), as a function of the mean orbital angular momentum variable $\bar{\lambda}=\frac{1}{2}(\lambda_i+\lambda_f)$, for $L=K=2$ (solid curve). The example shown pertains to the reaction ^{48}Ca(^{16}O, ^{12}C)^{50}Ti at $E_{\text{lab}}=56$ MeV. Also shown are the functions $I_{L-K}^{(\kappa)}(\alpha,\xi)$ and $\eta_K(\bar{\lambda})$ of which $c_{LK}(\bar{\lambda})$ is the product: $I_{2-2}^{(\kappa)}(\alpha,\xi)$ with $\xi=-2.79$, $\kappa=1.172$ and $\gamma=0.2667$ (long-dashed curve), and $\eta_K(\bar{\lambda})$ with $\Lambda_2=26.0$ and $\Delta=2$ (short-dashed curve; note different scale on right-hand side).

From Appendix B it is seen that we can write

$$I_{L-K}^{(\kappa)}(\alpha,\xi)\approx\bar{I}_{L-K}^{(\kappa)}(\alpha,\xi)e^{-\gamma\bar{\lambda}}=\bar{I}_{L-K}^{(\kappa)}(\alpha,\xi)e^{-\gamma K/2}e^{-\gamma\lambda_f}\,, \tag{2.30}$$

where $\bar{I}_{L-K}^{(\kappa)}(\alpha,\xi)$ is a slowly varying function of $\bar{\lambda}$, and where

$$\gamma=(\rho^2+\xi'^2)^{1/2}/n \tag{2.31}$$

with

$$\rho=\frac{\kappa}{k}n\,,\quad k=\tfrac{1}{2}(k_i+k_f)\,,\quad \xi'=\frac{k_i-k_f'}{k}n\,. \tag{2.32}$$

In terms of λ_f, the maximum of $c_K(\bar{\lambda})=c_K(\lambda_f+\frac{1}{2}K)$ is at $\lambda_f=\Lambda_K^T=\bar{\Lambda}_K^T-\frac{1}{2}K$. Its value may be calculated approximately by determining the maximum of

$$\tau_K(\lambda_f)=\eta_K(\lambda_f+\tfrac{1}{2}K)e^{-\gamma\lambda_f}\,, \tag{2.33}$$

which yields

$$\Lambda_K^T=\Lambda_K-\tfrac{1}{2}K+\delta_T\,,\quad \bar{\Lambda}_K^T=\Lambda_K+\delta_T\,, \tag{2.34}$$

where Λ_K is given by (2.19) and δ_T is obtained by solving the equation

$$\frac{\hat{D}(\delta_T/\Delta)}{\hat{\eta}(\delta_T/\Delta)}=\gamma\Delta\,, \tag{2.35}$$

with the definition $\hat{D}(\mu)=d\hat{\eta}(\mu)/d\mu$. As an example, for the convenient parametric form $\hat{\eta}(\mu)=(1+e^{-\mu})^{-1}$ we obtain

$$\delta_T=\Delta\ln\left(\frac{1}{\gamma\Delta}-1\right), \tag{2.36}$$

under the condition $\gamma\Delta<1$. Notice that, quite generally, the shift δ_T is independent of K.

Now we write

$$c_{LK}(\bar{\lambda})=\bar{c}_{LK}(\lambda_f)\tau_K(\lambda_f)=\bar{I}_{L-K}^{(\kappa)}(\alpha,\xi)e^{-\gamma K/2}\eta_K(\lambda_f+\tfrac{1}{2}K)e^{-\gamma\lambda_f}\,, \tag{2.37}$$

and expand the phase functions in (2.27) linearly about $\lambda_f=\Lambda_K^T$,

$$2\delta_K(\lambda_f+\tfrac{1}{2}K)\approx 2\delta_K(\Lambda_K^T+\tfrac{1}{2}K)+(\lambda_f-\Lambda_K^T)\theta_K^T$$
$$=2\delta_K(\bar{\Lambda}_K^T)+(\lambda_f-\Lambda_K^T)\theta_K^T\,, \tag{2.38}$$

where

$$\theta_K^T=\Theta(\bar{\Lambda}_K^T)\approx\left[\frac{2\delta_K(\bar{\lambda})}{d\lambda}\right]_{\bar{\lambda}=\bar{\Lambda}_K^T} \tag{2.39}$$

are the critical angles associated with the characteristic angular momenta $\bar{\Lambda}_K^T$. After taking the slowly varying functions $\tilde{c}_{LK}(\lambda_f)$ from under the integrals at the points $\lambda_f=\Lambda_K^T$, we obtain from (2.27)

$$\beta_{LM}(\theta)=i^{-L}\frac{2\pi^{1/2}}{k_i k_f'\kappa}\left(\frac{\theta}{\sin\theta}\right)^{1/2}$$
$$\times\sum_K b_{KM}^L\tilde{c}_{LK}(\Lambda_K^T)e^{i2\delta_K(\bar{\Lambda}_K^T)}$$
$$\times\sum_{m=-\infty}^{\infty}\exp[i2m\pi(\Lambda_K^T-\tfrac{1}{2})]T_{KM}(\theta_K^T+2m\pi)\,, \tag{2.40}$$

where

$$T_{KM}(x)=\int_0^\infty d\lambda\,\lambda\tau_K(\lambda)e^{i(\lambda-\Lambda_K^T)x}J_M(\lambda\theta)\,. \tag{2.41}$$

These integrals are of the type of combined Fourier and Bessel transforms that have been evaluated in Appendix A of Ref. 28 with the result

$$T_{KM}(x)=\tfrac{1}{2}\Lambda_K^T\{H_K^{(T)}(x-\theta)[J_M(\Lambda_K^T\theta)-iJ_{M+1}(\Lambda_K^T\theta)]$$
$$+H_K^{(T)}(x+\theta)[J_M(\Lambda_K^T\theta)+iJ_{M+1}(\Lambda_K^T\theta)]\}\,, \tag{2.42}$$

where $H_K^{(T)}(z)$ is the Fourier transform of $\tau_K(\lambda)$,

$$H_K^{(T)}(z)=\int_{-\infty}^\infty d\lambda\,\tau_K(\lambda)e^{i(\lambda-\Lambda_K^T)z}\,. \tag{2.43}$$

With (2.33) we obtain

$$H_K^{(T)}(z)=\int_{-\infty}^\infty d\lambda\,\eta_K(\lambda+\tfrac{1}{2}K)e^{-\gamma\lambda}e^{i(\lambda-\Lambda_K^T)z}$$
$$=e^{-\gamma\Lambda_K^T}\int_{-\infty}^\infty d\bar{\lambda}\,\eta_K(\bar{\lambda})e^{i(\bar{\lambda}-\bar{\Lambda}_K^T)(z+i\gamma)}$$
$$=e^{-\gamma\Lambda_K^T}e^{i(\Lambda_K-\bar{\Lambda}_K^T)(z+i\gamma)}\int_{-\infty}^\infty d\bar{\lambda}\,\eta_K(\bar{\lambda})e^{i(\bar{\lambda}-\Lambda_K)(z+i\gamma)}$$
$$=ie^{\gamma K/2}e^{-\gamma\Lambda_K}e^{-i\delta_T z}\frac{F(\Delta(z+i\gamma))}{z+i\gamma}\,, \tag{2.44}$$

where

$$F(\Delta x)=\int_{-\infty}^\infty d\lambda\,\frac{d\eta_K(\lambda)}{d\lambda}e^{i(\lambda-\Lambda_K)x} \tag{2.45}$$

is the Fourier transform of the derivative of the mean reflection function.

Noting from (2.38) that

$$2\delta_K(\bar{\Lambda}_K^T)-\delta_T\theta_K^T\approx 2\delta_K(\Lambda_K)\,, \tag{2.46}$$

and from (2.30) and (2.37) that

$$\tilde{c}_{LK}(\Lambda_K^T)e^{\gamma K/2}e^{-\gamma\Lambda_K}=I_{L-K}^{(\kappa)}(\theta_{R,K}^T,\xi)e^{\gamma\delta_T}\,, \tag{2.47}$$

where

$$\theta_{R,K}^T=2\arctan(n/\bar{\Lambda}_K^T)\,; \tag{2.48}$$

we can write the final result as

$$\beta_{LM}(\theta)=i^{1-L}\frac{\pi^{1/2}}{k_i k_f'\kappa}\left(\frac{\theta}{\sin\theta}\right)^{1/2}\sum_K b_{KM}^L\Lambda_K^T I_{L-K}^{(\kappa)}(\theta_{R,K}^T,\xi)e^{\gamma\delta_T}e^{i2\delta_K(\Lambda_K)}\{\mathcal{K}_K^{(SA)}(\theta)[J_M(\Lambda_K^T\theta)-iJ_{M+1}(\Lambda_K^T\theta)]$$
$$+\mathcal{K}_K^{(SA)}(-\theta)[J_M(\Lambda_K^T\theta)+iJ_{M+1}(\Lambda_K^T\theta)]\}\,, \tag{2.49}$$

where

$$\mathcal{K}_K^{(SA)}(\pm\theta)=e^{\mp i\delta_T\theta}\sum_{m=-\infty}^{\infty}\exp\{i2m\pi[\Lambda_K-\tfrac{1}{2}(K+1)]\}$$
$$\times\frac{F(\Delta(\theta_K^T+2m\pi+i\gamma\mp\theta))}{\theta_K^T+2m\pi+i\gamma\mp\theta}\,. \tag{2.50}$$

Close to the forward direction we have approximately

$$\beta_{LM}(\theta)\approx i^{1-L}\frac{2\pi^{1/2}}{k_i k_f'\kappa}\sum_K b_{KM}^L\Lambda_K^T I_{L-K}^{(\kappa)}(\theta_{R,K}^T,\xi)e^{\gamma\delta_T}$$
$$\times e^{i2\delta_K(\Lambda_K)}\mathcal{K}_K^{(SA)}(0)J_M(\Lambda_K^T\theta)\,,$$
$$\theta\approx 0 \tag{2.51}$$

so that the near-forward cross section behaves like

$$\sigma_{LM}^{(T)}(\theta)\propto[J_M(\Lambda_K^T\theta)]^2\propto\theta^{2|M|}\,,\quad\theta\approx 0\,. \tag{2.52}$$

B. Forward-angle excitation function

In the forward direction $\theta=0$ only the $M=0$ substate contributes, and we find

$$\beta_{LM}(0)=\beta_{L0}(0)\delta_{M0}\,,$$
$$\beta_{L0}(0)=\frac{2\pi^{1/2}}{k_i k_f'\kappa}\sum_K i^{K-L+1}[d_{0K}^L(\tfrac{1}{2}\pi)]^2\Lambda_K^T I_{L-K}^{(\kappa)}(\theta_{R,K}^T,\xi)$$
$$\times e^{\gamma\delta_T}e^{i2\delta_K(\Lambda_K)}\mathcal{K}_K^{(SA)}(0)\,, \tag{2.53}$$

with

$$\mathcal{K}_K^{(SA)}(0)=\sum_{m=-\infty}^{\infty}\exp\{i2m\pi[\Lambda_K-\tfrac{1}{2}(K+1)]\}$$
$$\times\frac{F(\Delta(\theta_K^T+2m\pi+i\gamma))}{\theta_K^T+2m\pi+i\gamma}\,. \tag{2.54}$$

To discuss the energy dependence we consider

$L=0$ transfer only. Then the forward-angle cross section becomes

$$\sigma_0^{(T)}(0)=A\,\frac{\mu_i\mu_f}{\pi\hbar^4\zeta^2k_i^3k_f\kappa^2}(\Lambda_0^T)^2[I_{00}^{(\kappa)}(\theta_R^T,\xi)]^2\times e^{2\gamma\delta_T}|\mathcal{K}_0^{(SA)}(0)|^2. \tag{2.55}$$

From the expression for $I_{00}^{(\kappa)}$ given in Appendix B it is seen that for $\Lambda_0^T\gg n$,

$$\begin{aligned}I_{00}^{(\kappa)}(\theta_R^T,\xi)&\approx\left(\frac{\pi}{2\gamma\Lambda_0^T}\right)^{1/2}\exp[-(\rho+\xi\arctan\xi'/\rho)]e^{-\gamma\Lambda_0^T}\\&\approx\left(\frac{\pi k}{2\kappa\Lambda_0^T}\right)^{1/2}e^{-\gamma\Lambda_0^T},\end{aligned} \tag{2.56}$$

so that

$$\sigma_0^{(T)}(0)\approx A\,\frac{\mu_i\mu_f}{2\hbar^4\zeta^2\kappa^2k^3}\Lambda_0^Te^{-(2\kappa\Lambda_0/k)}|\mathcal{K}_0^{(SA)}(0)|^2, \tag{2.57}$$

with

$$\Lambda_0=\bar{\Lambda}+\Delta\ln\left[\cosh\left(\frac{K_0}{2\Delta}\right)\right], \tag{2.58}$$

where for simplicity we have assumed $\Delta_i=\Delta_f=\Delta$. Since well above the Coulomb barrier Λ_0/k depends only weakly on energy, the main energy dependence is described by $|\mathcal{K}_0^{(SA)}(0)/k|^2$.

Normally only the $m=0$ term gives a significant contribution to the Poisson sum (2.54) so that

$$\mathcal{K}_0^{(SA)}(0)=\frac{F(\Delta(\theta_0^T+i\gamma))}{\theta_0^T+i\gamma}. \tag{2.59}$$

As a typical example, for the parametric form $\hat{\eta}(\mu)=(1+e^{-\mu})^{-1}$ we have $F(z)=\pi z/\sinh(\pi z)$, so that

$$|\mathcal{K}_0^{(SA)}(0)/k|^2=\frac{(\pi\Delta/k)^2}{[\sinh(\pi\Delta\theta_0^T)]^2+[\sin(\pi\Delta\gamma)]^2}. \tag{2.60}$$

Since $\Delta\gamma\approx\kappa(\Delta/k)\approx$ const, the main energy dependence comes from $\Delta\theta_0^T\approx n(\Delta/\Lambda_0^T)$ and is thus chiefly determined by the energy variation of the Sommerfeld parameter n, a feature similar to what has been found for elastic and inelastic heavy-ion scattering.[22-24] In general, the structure of Eqs. (2.53) and (2.54) shows that as long as only a single ($m=0$) Poisson term is significant, the forward-angle transfer excitation function is smooth or at least not strongly oscillatory.

III. LARGE-ANGLE REPRESENTATION

A. Angular distribution

To evaluate the transfer amplitude for large angles θ we use instead of (2.6) the large-angle asymptotic form of the spherical harmonics,

$$Y_{l_f,-M}(\theta,0)\cong(-)^{l_f+M}\left(\frac{\lambda_f}{2\pi}\right)^{1/2}\left(\frac{\vartheta}{\sin\vartheta}\right)^{1/2}J_M(\lambda_f\vartheta), \tag{3.1}$$

where $\vartheta=\pi-\theta$, which is valid for $0\leqslant\vartheta<\pi-|M|/\lambda_f$ and exact in the backward direction $\theta=\pi$. Then the Poisson representation becomes

$$\begin{aligned}\beta_{LM}(\theta)=\frac{i^{-L}}{\pi^{1/2}}(-)^M\left(\frac{\vartheta}{\sin\vartheta}\right)^{1/2}\sum_K b_{KM}^L\sum_{m=-\infty}^{\infty}e^{-i(m+1/2)\pi}\\\times\int_0^\infty d\lambda_f\lambda_fR_{LK}(\lambda_f)\exp\{i[\sigma^{(f)}(\lambda_f)+\sigma^{(i)}(\lambda_f+K)]\}e^{i(2m+1)\pi\lambda_f}J_M(\lambda_f\vartheta).\end{aligned} \tag{3.2}$$

With the same approximations as in the previous section we obtain

$$\begin{aligned}\beta_{LM}(\theta)=i^{1-L}(-)^M\frac{\pi^{1/2}}{k_ik_f'\kappa}\left(\frac{\vartheta}{\sin\vartheta}\right)^{1/2}\sum_Kb_{KM}^L\Lambda_K^TI_{L-K}^{(\kappa)}(\theta_{R,K}^T,\xi)e^{\gamma\delta_T}e^{i2\delta_K(\Lambda_K)}\\\times\{\mathcal{K}_K^{(LA)}(\vartheta)[J_M(\Lambda_K^T\vartheta)-iJ_{M+1}(\Lambda_K^T\vartheta)]+\mathcal{K}_K^{(LA)}(-\vartheta)[J_M(\Lambda_K^T\vartheta)+iJ_{M+1}(\Lambda_K^T\vartheta)]\},\end{aligned} \tag{3.3}$$

where

$$\mathcal{K}_K^{(LA)}(\pm\vartheta)=e^{\pm i\delta_T\vartheta}\sum_{m=-\infty}^{\infty}\exp\{i(2m+1)\pi[\Lambda_K-\tfrac{1}{2}(K+1)]\}\frac{F(\Delta(\theta_K^T+(2m+1)\pi+i\gamma\mp\vartheta))}{\theta_K^T+(2m+1)\pi+i\gamma\mp\vartheta}. \tag{3.4}$$

For later use we note the relations, obtained by comparing (3.4) with (2.50),

$$\mathcal{K}_K^{(LA)}(\pm\vartheta)=e^{\pm i\pi(\Lambda_K^T-1/2)}\mathcal{K}_K^{(SA)}(\mp\theta). \tag{3.5}$$

Close to the backward direction we have approximately

$$\beta_{LM}(\theta)\approx i^{1-L}(-)^M\frac{2\pi^{1/2}}{k_i k_f'\kappa}\sum_K b_{KM}^L\Lambda_K^T I_{L-K}^{(\kappa)}(\theta_{R,K}^T,\xi)e^{i\delta_T}e^{i2\sigma_K(\Lambda_K)}\mathcal{K}_K^{(LA)}(0)J_M[\Lambda_K^T(\pi-\theta)],\quad\theta\approx\pi \tag{3.6}$$

so that the near-backward cross section behaves like

$$\sigma_{LM}^{(T)}(\theta)\propto\{J_M[\Lambda_K^T(\pi-\theta)]\}^2$$

$$\propto(\pi-\theta)^{2|M|},\quad\theta\approx\pi. \tag{3.7}$$

B. Backward-angle excitation function

In the backward direction $\theta=\pi$ again only the $M=0$ substate contributes, and (3.6) reduces to

$$\beta_{LM}(\pi)=\beta_{L0}(\pi)\delta_{M0},$$

$$\beta_{L0}(\pi)=\frac{2\pi^{1/2}}{k_i k_f'\kappa}\sum_K i^{K-L+1}|d_{0K}^L(\tfrac{1}{2}\pi)|^2\Lambda_K^T I_{L-K}^{(\kappa)}(\theta_{R,K}^T,\xi)$$

$$\times e^{i\delta_T}e^{i2\sigma_K(\Lambda_K)}\mathcal{K}_K^{(LA)}(0). \tag{3.8}$$

Comparison with (2.53) and using relation (3.5) shows that the relative magnitude of $\beta_{L0}(\pi)$ and $\beta_{L0}(0)$ is determined by the ratio $\mathcal{K}_K^{(SA)}(-\pi)/\mathcal{K}_K^{(SA)}(0)$. If, as is normally the case, the $m=0$ term dominates in the Poisson sum, this becomes

$$\left|\frac{\mathcal{K}_K^{(SA)}(-\pi)}{\mathcal{K}_K^{(SA)}(0)}\right|=\left(\frac{(\theta_K^T)^2+\gamma^2}{(\theta_K^T+\pi)^2+\gamma^2}\right)^{1/2}\left|\frac{F(\Delta(\theta_K^T+\pi+i\gamma))}{F(\Delta(\theta_K^T+i\gamma))}\right|\ll 1. \tag{3.9}$$

For example, with $F(z)=\pi z/\sinh(\pi z)$ we have for the $L=0$ backward-to-forward cross section ratio

$$\frac{\sigma_0^{(T)}(\pi)}{\sigma_0^{(T)}(0)}=\left|\frac{\mathcal{K}_0^{(SA)}(-\pi)}{\mathcal{K}_0^{(SA)}(0)}\right|^2$$

$$\approx\frac{4e^{-2\pi^2\Delta}}{|1+\coth[\pi\Delta(\theta_0^T+i\gamma)]|^2}. \tag{3.10}$$

This shows that the backward-angle transfer excitation function has an additional energy dependence: The ratio (3.10) decreases rapidly with increasing energy since $\Delta\propto E^{1/2}$.

C. Enhancement effects

In our discussion so far we have assumed that the elastic S matrices in the initial and final channels have "normal strong-absorption profile," in the terminology of Ref. 28. As described there for elastic and inelastic scattering, backward-angle enhancement can occur if $\eta_K(\bar\lambda)$ contains rapidly varying deviations from the normal $\bar\lambda$ profile. If we write

$$\eta_K(\lambda)=\bar\eta_K(\bar\lambda)+\tilde\eta_K(\bar\lambda), \tag{3.11}$$

then the transfer amplitude has an additional contribution $\tilde\beta(\theta)$ of a form similar to (3.3), but with the functions $\mathcal{K}_K^{(LA)}(\pm\vartheta)$ replaced by

$$\tilde{\mathcal{K}}_K^{(LA)}(\pm\vartheta)=-ie^{\pm i\delta_T}\sum_{m=-\infty}^{\infty}\exp\{i(2m+1)\pi[\Lambda_K-\tfrac{1}{2}(K+1)]\}$$

$$\times G[\theta_K^T+(2m+1)\pi+i\gamma\mp\vartheta], \tag{3.12}$$

where

$$G(x)=\int_{-\infty}^{\infty}d\lambda\,\tilde\eta_K(\lambda)e^{i(\lambda-\Lambda_K)x}, \tag{3.13}$$

and where we have assumed for simplicity that the deviation $\tilde\eta_K(\bar\lambda)$ is centered at $\bar\lambda=\Lambda_K$. Then the condition for backward-angle enhancement is

$$\left|\frac{\tilde{\mathcal{K}}_K^{(LA)}(0)}{\mathcal{K}_K^{(LA)}(0)}\right|^2\approx\left|\frac{\theta_K^T-\pi+i\gamma}{F(\Delta(\theta_K^T-\pi+i\gamma))}G(\theta_K^T-\pi+i\gamma)\right|^2\gg 1, \tag{3.14}$$

if the $m=-1$ contributions to the Poisson sums in (3.12) and (3.4) are dominant. Thus, except for the effects of the transfer parameters γ and δ_T, the enhancement conditions are much the same as for elastic and inelastic scattering described in Ref. 28.

Interference between the $m=-1$ and $m=0$ terms in (3.12) gives rise to oscillations in the backward-angle excitation function. Assuming $L=0$ transfer for simplicity, we obtain

$$\tilde\sigma_0(\pi)=\tilde\sigma_0^{(0)}(\pi)\left|1-\frac{G(\theta_0^T+\pi+i\gamma)}{G(\theta_0^T-\pi+i\gamma)}e^{i2\pi\Lambda_0}\right|^2, \tag{3.15}$$

which shows that, aside from more slowly varying modulations due to γ and δ_T, the dominant oscillations are of period $\delta\Lambda_0=1$, as in the case of elastic and inelastic scattering. [Odd-even staggering effects in $\tilde\eta(\bar\lambda)$ would cause an additional modulation of period $\delta\Lambda_0=2$; see Ref. 28.]

IV. INTERMEDIATE ANGLES

A. Angular distribution

In this section we consider the intermediate-angle region for which we may use the asymptotic expressions

$$J_M(x)\pm iJ_{M+1}(x)\cong\left(\frac{2}{\pi x}\right)^{1/2}\exp[\pm i(x-\tfrac{1}{4}\pi-\tfrac{1}{2}M\pi)]. \tag{4.1}$$

Then (2.49) becomes

$$\beta_{LM}(\theta)=\frac{1}{(\sin\theta)^{1/2}}\sum_K B^L_{KM}[\mathcal{K}^{(SA)}_K(\theta)e^{-i[\Lambda^T_K\theta-(1/4)\pi]}+(-)^M\mathcal{K}^{(SA)}_K(-\theta)e^{i[\Lambda^T_K\theta-(1/4)\pi]}],\tag{4.2}$$

where

$$B^L_{KM}=\frac{i^{M-L+1}}{k_ik'_f\kappa}b^L_{KM}(2\Lambda^T_K)^{1/2}\Gamma^{(\kappa)}_{L-K}(\theta^T_{R,K},\xi)e^{\gamma\delta_T}e^{i2\delta_K(\Lambda_K)}.\tag{4.3}$$

Similarly, from (3.3) we obtain

$$\beta_{LM}(\theta)=\frac{1}{(\sin\theta)^{1/2}}\sum_K B^L_{KM}[\mathcal{K}^{(LA)}_K(-\vartheta)e^{i\pi(\Lambda^T_K-1/2)}e^{-i[\Lambda^T_K-(1/4)\pi]}+(-)^M\mathcal{K}^{(LA)}_K(\vartheta)e^{-i\pi(\Lambda^T_K-1/2)}\times e^{i[\Lambda^T_K-(1/4)\pi]}],\tag{4.4}$$

which is the same as (4.2) by virtue of the relations (3.5). Thus the expressions (2.49) and (3.3) cover the full angular range, with the common simplified formula (4.2) for the intermediate region.

Now it is convenient to change coordinate axes by transformation to a frame with the z axis in the direction of $\vec{k}_i\times\vec{k}_f$ and the x axis in the direction of $\vec{k}_i$. This rotation is performed by

$$\hat{\beta}_{LM}(\theta)=(-)^M\sum_{M'}i^{M'}d^L_{M'M}(\tfrac{1}{2}\pi)\beta_{LM'}(\theta).\tag{4.5}$$

Then the summations over M' and K can be carried out by using the symmetry and orthogonality relations of the rotation matrices

$$\sum_{M'}d^L_{M'M}(\tfrac{1}{2}\pi)d^L_{M'K}(\tfrac{1}{2}\pi)=\delta_{MK},\tag{4.6}$$

$$\sum_{M'}(-)^{M'}d^L_{M'M}(\tfrac{1}{3}\pi)d^L_{M'K}(\tfrac{1}{2}\pi)=(-)^L\delta_{M,-K}.\tag{4.7}$$

The resulting amplitude can be written

$$\hat{\beta}_{LM}(\theta)=\beta^{(+)}_{LM}(\theta)+(-)^M\beta^{(-)}_{LM}(\theta),\quad L+M\text{ even}\tag{4.8}$$

(on the understanding that M from now on refers to the normal of the scattering plane as quantization axis), where

$$\beta^{(\pm)}_{LM}(\theta)=y_{LM}(\theta)B^{(\pm)}_{LM}\mathcal{K}^{(\pm)}_M(\theta)e^{\mp i[\Lambda_{\mp M}\theta-(1/4)\pi]},\tag{4.9}$$

with

$$y_{LM}(\theta)=\frac{d^L_{0M}(\frac{1}{2}\pi)e^{i(1/2)M(\pi-\theta)}}{(4\pi\sin\theta)^{1/2}}=\frac{Y_{LM}(\frac{1}{2}\pi,0)}{(2L+1)^{1/2}}\frac{e^{i(1/2)M(\pi-\theta)}}{(\sin\theta)^{1/2}},\tag{4.10}$$

$$B^{(\pm)}_{LM}=i^{1-L}\frac{(8\pi)^{1/2}}{k_ik'_f\kappa}(\Lambda^T_{\mp M})^{1/2}\Gamma^{(\kappa)}_{L,\pm M}(\theta^T_{R,\mp M},\xi)e^{\gamma\delta_T}e^{i2\delta_{\mp M}(\Lambda_{\mp M})},\tag{4.11}$$

$$\mathcal{K}^{(\pm)}_M(\theta)=\sum_{m=-\infty}^{\infty}(-)^{m(M+1)}e^{i2m\pi\Lambda_{\mp M}}\frac{F(\Delta(\theta^T_{\mp M}+2m\pi+i\gamma\mp\theta))}{\theta^T_{\mp M}+2m\pi+i\gamma\mp\theta}.\tag{4.12}$$

Thus the transfer cross section for multipolarity (L,M) can be written as

$$\sigma^{(T)}_{LM}(\theta)=\bar{\sigma}^{(T)}_{LM}(\theta)\{1+|t_{LM}(\theta)|^2+(-)^M2\,\mathrm{Im}[t_{LM}(\theta)e^{i2\bar{\Lambda}_M\theta}]\},\tag{4.13}$$

where

$$\bar{\sigma}^{(T)}_{LM}(\theta)=A\frac{\mu_i\mu_f}{2\pi^2\hbar^4\zeta^2k_0{}^3k_f\kappa^2}[d^L_{0M}(\tfrac{1}{2}\pi)]^2\Lambda^T_{-M}[\Gamma^{(\kappa)}_{LM}(\theta^T_{R,-M},\xi)]^2\times e^{2\gamma\delta_T}\frac{|\mathcal{K}^{(+)}_M(\theta)|^2}{\sin\theta},\tag{4.14}$$

$$t_{LM}(\theta)=\left(\frac{\Lambda^T_M}{\Lambda^T_{-M}}\right)^{1/2}\frac{\Gamma^{(\kappa)}_{L-M}(\theta^T_{R,M},\xi)}{\Gamma^{(\kappa)}_{LM}(\theta^T_{R,-M},\xi)}e^{i(\Delta_M-\Delta_{-M})\theta}\frac{\mathcal{K}^{(-)}_M(\theta)}{\mathcal{K}^{(+)}_M(\theta)},\tag{4.15}$$

and

$$\bar{\Lambda}_M=\tfrac{1}{2}(\Lambda_M+\Lambda_{-M})=\bar{\Lambda}+\tfrac{1}{2}(\Delta_M+\Delta_{-M}).\tag{4.16}$$

In (4.15) we have used

$$2[\delta_M(\Lambda_M)-\delta_{-M}(\Lambda_{-M})]\approx(\Delta_M-\Delta_{-M})\bar{\theta},\tag{4.17}$$

where $\bar{\theta}=\Theta(\bar{\Lambda})$.

Equations (4.13)–(4.15) show that the transfer angular distribution has a smooth (bell-shaped) part determined by

$$\frac{1}{\sin\theta}(|\mathcal{K}^{(+)}_M(\theta)|^2+|\mathcal{K}^{(-)}_M(\theta)|^2),\tag{4.18}$$

and an oscillatory part described by the last term in the curly brackets. Under normal conditions only the $m=0$ term in the Poisson sum (4.12) is significant, so that

$$\mathcal{K}^{(+)}_M(\theta)\approx\frac{F(\Delta(\theta^T_{-M}-\theta+i\gamma))}{\theta^T_{-M}-\theta+i\gamma},\tag{4.19}$$

and for intermediate angles $|\mathcal{K}^{(-)}_M(\theta)|$ is much smaller than $|\mathcal{K}^{(+)}_M(\theta)|$. The maximum of the angular distribution is at $\theta=\theta^T_{-M}$, where the value of the cross section is

$$\sigma^{(T)}_{LM}(\max)=A\frac{\mu_i\mu_f}{2\pi^2\hbar^4\zeta^2k_i{}^3k_f\kappa^2}[d^L_{0M}(\tfrac{1}{2}\pi)]^2\frac{\Lambda^T_{-M}}{\sin\theta^T_{-M}}\times[\Gamma^{(\kappa)}_{LM}(\theta^T_{R,-M},\xi)]^2e^{2\gamma\delta_T}\frac{|F(i\Delta\gamma)|^2}{\gamma^2}.\tag{4.20}$$

If for example $F(z)=\pi z/\sinh(\pi z)$, we get

$$\frac{|F(i\Delta\gamma)|^2}{\gamma^2}=\left(\frac{\pi\Delta}{\sin(\pi\Delta\gamma)}\right)^2.\tag{4.21}$$

With the same parametric form we have

$$\frac{\mathcal{K}_M^{(-)}(\theta)}{\mathcal{K}_M^{(+)}(\theta)}=\frac{\sinh[\pi\Delta(\theta_M^T-\theta+i\gamma)]}{\sinh[\pi\Delta(\theta_M^T+\theta+i\gamma)]}$$
$$\approx e^{-\pi\Delta(\theta_M^T-\theta_{-M}^T)}e^{-2\pi\Delta\theta}. \qquad (4.22)$$

This shows that the oscillations in the transfer cross section are most pronounced at smaller angles and become strongly damped with increasing θ. It is also seen that at a given angle the damping is controlled by the window parameter Δ. Thus if Δ is relatively small, as in the case of "surface transparency," the oscillations are enhanced. This is the effect first discovered by the Brookhaven group.[21]

Since the radial integrals for the asymptotic form of the transfer form factor (2.5) are real functions, we may write the cross section (4.13) more explicitly as

$$\sigma_{LM}^{(T)}(\theta)=\bar{\sigma}_{LM}^{(T)}(\theta)\{1+[\tilde{I}_{LM}(\theta)]^2$$
$$+(-)^M 2\tilde{I}_{LM}(\theta)\sin[2\bar{\Lambda}_M\theta+(\Delta_M-\Delta_{-M})\bar{\theta}]\}, \qquad (4.23)$$

with

$$\tilde{I}_{LM}(\theta)\approx\left(\frac{\Lambda_M^T}{\Lambda_{-M}^T}\right)^{1/2}\frac{I_{L-M}^{(\kappa)}(\theta_{R,M}^T,\xi)}{I_{LM}^{(\kappa)}(\theta_{R,-M}^T,\xi)}e^{-\pi\Delta(\theta_M^T-\theta_{-M}^T)}e^{-2\pi\Delta\theta}. \qquad (4.24)$$

This shows that the diffraction oscillations have the angular period $\pi/\bar{\Lambda}_M$, which is M dependent because of

$$\tfrac{1}{2}(\Delta_M+\Delta_{-M})\approx\tfrac{1}{2}\Delta\ln\left(\tfrac{1}{4}\left[\exp\left(\frac{K_0}{\Delta_i}\right)+\exp\left(-\frac{K_0}{\Delta_f}\right)\right.\right.$$
$$\left.\left.+2\exp\left(\frac{\Delta_f-\Delta_i}{2\Delta_i\Delta_f}K_0\right)\cosh\left(\frac{M}{\Delta}\right)\right]\right)$$
$$\to\tfrac{1}{2}\Delta\ln\left(\tfrac{1}{2}\left[\cosh\left(\frac{K_0}{\Delta}\right)+\cosh\left(\frac{M}{\Delta}\right)\right]\right), \qquad (4.25)$$

with the latter expression for $\Delta_i\approx\Delta_f$. The M dependence of the relative phase in (4.23) is given by

$$\Delta_M-\Delta_{-M}\quad\Delta\ln\left[\frac{\exp\left(\frac{K_0-M}{2\Delta_i}\right)+\exp\left(-\frac{K_0-M}{2\Delta_f}\right)}{\exp\left(\frac{K_0+M}{2\Delta_i}\right)+\exp\left(-\frac{K_0+M}{2\Delta_f}\right)}\right]$$
$$\to\Delta\ln\left[\frac{\cosh\left(\frac{M-K_0}{2\Delta}\right)}{\cosh\left(\frac{M+K_0}{2\Delta}\right)}\right]$$
$$\approx\tfrac{1}{2}(|M-K_0|-|M+K_0|). \qquad (4.26)$$

This can modify the transfer analog of the Blair phase rule which would otherwise hold because of the factor $(-)^M$ in (4.23).

B. Magnetic substates and Q-value dependence

The dependence on the kinematic conditions of the transfer reaction can best be seen from the transfer partial-wave amplitudes (2.29),

$$c_{LK}(\bar{\lambda})=\eta_K(\bar{\lambda})I_{L-K}^{(\kappa)}(\alpha,\xi)=\eta_K(\bar{\lambda})\tilde{I}_{L-K}^{(\kappa)}(\alpha,\xi)e^{-\gamma\bar{\lambda}}, \qquad (4.27)$$

which describe the localization in $\bar{\lambda}$ space. As we have remarked earlier, these functions are essentially asymmetric about their maxima at $\bar{\lambda}=\bar{\Lambda}_K^T$: the falloff rate at large $\bar{\lambda}$ values is determined by γ and thus by the binding parameter κ, while the rate of decrease at low $\bar{\lambda}$ values is determined by the absorption and measured by Δ^{-1}.

The maximum of $c_{LK}(\bar{\lambda})$ is given (approximately) by

$$c_{LK}(\max)\approx c_{LK}(\bar{\Lambda}_K^T)=\eta_K(\bar{\Lambda}_K^T)I_{L-K}^{(\kappa)}(\theta_{R,K}^T,\xi)$$
$$=\hat{\eta}\left(\frac{\delta_T}{\Delta}\right)e^{-\gamma\delta_T}\tilde{I}_{L-K}^{(\kappa)}(\theta_{R,K}^T,\xi)e^{-\gamma\Lambda_K}. \qquad (4.28)$$

Using expression (2.19) for Λ_K yields

$$c_{LK}(\max)=\frac{\hat{\eta}\left(\frac{\delta_T}{\Delta}\right)e^{-\gamma(\bar{\Lambda}+\delta_T)}\tilde{I}_{L-K}^{(\kappa)}(\theta_{R,K}^T,\xi)}{\left\{\frac{1}{2}\left[\exp\left(\frac{K-K_0}{2\Delta_f}\right)+\exp\left(-\frac{K-K_0}{2\Delta_i}\right)\right]\right\}^{\gamma\Delta}}$$
$$\approx 2^{\gamma\Delta}\hat{\eta}\left(\frac{\delta_T}{\Delta}\right)e^{-\gamma(\bar{\Lambda}+\delta_T)}\tilde{I}_{L-K}^{(\kappa)}(\theta_{R,K}^T,\xi)e^{-|K-K_0|/g^*}, \qquad (4.29)$$

where

$$g^*=\frac{\Delta_i+\Delta_f}{\gamma\Delta_{i,f}} \qquad (4.30)$$

with index i or f depending on whether $K-K_0$ is positive or negative.

It is instructive to compare the $\bar{\lambda}$ and K dependence of $c_{LK}(\bar{\lambda})$ with the phenomenological ansatz used by Kahana *et al.*,[20] who assume the Gaussian form

$$c_{LK}^{\text{phen}}(\bar{\lambda})=I_L\exp\left[-\left(\frac{\lambda_i-\Lambda_i}{\Gamma_i}\right)^2-\left(\frac{\lambda_f-\Lambda_f}{\Gamma_f}\right)^2\right.$$
$$\left.-\left(\frac{K-K_0}{g_0}\right)^2\right] \qquad (4.31)$$
$$\approx I_L\exp\left[-2\left(\frac{\bar{\lambda}-\bar{\Lambda}}{\Gamma}\right)^2-\left(\frac{K-K_0}{g}\right)^2\right],$$

where the second expression is obtained for $\Gamma_i\approx\Gamma_f\approx\Gamma$ and where

$$g=\frac{2^{1/2}g_0\Gamma}{(g_0^2+2\Gamma^2)^{1/2}}. \qquad (4.32)$$

Although in our $c_{LK}(\bar{\lambda})$ the asymptotic dependence on $\bar{\lambda}$ and K is exponential rather than Gaussian, there is a correspondence between the parameter g and our $g^*\approx 2/\gamma$, while the parameter Γ corresponds to $\sqrt{2}/\gamma$ for large $\bar{\lambda}$ and to $\sqrt{2}\Delta$ for small $\bar{\lambda}$, or rather to the harmonic mean $\Gamma^* = \sqrt{2}\Delta/(1+\gamma\Delta)$.

Since the DWBA-based expression (4.27) has qualitatively similar features as the phenomenological form (4.31), we have in the present treatment removed the shortcomings of our earlier transfer formalism[13] which were rightly criticized in Refs. 20 and 21 for ignoring the significant K dependence of the partial-wave amplitude. The salient point where this is brought out here is the determination of the mean S matrix (2.16) by the method described in Appendix A. Most of the properties of transfer reactions discussed in Ref. 21 by means of (4.31) are described by the present formulation.

To display the M dependence of the transfer cross section (in the coordinate frame with quantization axis perpendicular to the reaction plane), we consider the maximum value (4.20) written as

$$\sigma_{LM}^{T}(\max) = \hat{A}[d_{0M}^{L}(\tfrac{1}{2}\pi)]^2 \frac{\Lambda_{-M}^{T}}{\sin\theta_{-M}^{T}} [I_{LM}^{(\kappa)}(\theta_{R,-M}^{T}, \xi)]^2 e^{2\gamma\theta_T}$$
$$= \hat{A}[d_{0M}^{L}(\tfrac{1}{2}\pi)]^2 \frac{\Lambda_{-M}^{T}}{\sin\theta_{-M}^{T}} [\bar{I}_{LM}^{(\kappa)}(\theta_{R,-M}^{T}, \xi)]^2 e^{-2\gamma\Lambda_{-M}}, \tag{4.33}$$

where

$$\hat{A} = A \frac{\mu_i \mu_f}{2\pi^2\hbar^4\zeta^2 k_i^{\,3} k_f \kappa^2} \frac{|F(i\Delta\gamma)|^2}{\gamma^2}. \tag{4.34}$$

The M- and Q-value dependence of the functions $\bar{I}_{LM}^{(\kappa)}$ is described by the expressions given in Appendix B. As discussed there, it is contained mainly in a factor $\exp(-b_{-M}^{\;2}/2\rho\epsilon_{-M})$, where

$$b_{-M} = \xi'\epsilon_{-M} + \xi + M\left(\frac{\epsilon_{-M}-1}{\epsilon_{-M}+1}\right)^{1/2},$$
$$\epsilon_{-M} = [(\Lambda_{-M}^{T}/n)^2 + 1]^{1/2}. \tag{4.35}$$

However, the most significant factor in (4.33) is

$$e^{-2\gamma\Lambda_{-M}} = e^{-2\gamma\bar{\Lambda}} e^{-2\gamma\Delta_{-M}}$$
$$= \frac{e^{-2\gamma\bar{\Lambda}}}{\left\{\frac{1}{2}\left[\exp\left(\frac{M-M_0}{2\Delta_i}\right) + \exp\left(-\frac{M-M_0}{2\Delta_f}\right)\right]\right\}^{2\gamma\Delta}}$$
$$\approx 4^{\gamma\Delta} e^{-2\gamma\Delta} \exp\left(-2\frac{|M-M_0|}{g^*}\right), \tag{4.36}$$

where $M_0 = -K_0 = \Lambda_f - \Lambda_i$, and g^* is defined by (4.30) with index i or f depending on whether $M > M_0$ or $M < M_0$. For $\Delta_i = \Delta_f$ the M dependence has the simple form $\exp(-\gamma|M-M_0|)$, showing that the cross section is largest for $M = M_0$.

Finally we consider the M dependence of the amplitude (4.24) of the diffraction oscillations, which can be written as

$$\bar{t}_{LM}(\theta) = \left(\frac{\Lambda_{M}^{T}}{\Lambda_{-M}^{T}}\right)^{1/2} \frac{\bar{I}_{L-M}^{(\kappa)}(\theta_{R,M}^{T}, \xi)}{\bar{I}_{LM}^{(\kappa)}(\theta_{R,-M}^{T}, \xi)}$$
$$\times e^{-\gamma(\bar{\Lambda}_{M}^{T} - \bar{\Lambda}_{-M}^{T})} e^{-\pi\Delta(\theta_{M}^{T} - \theta_{-M}^{T})} e^{-2\pi\Delta\theta}. \tag{4.37}$$

Since $\Delta_{\pm M} \mp \frac{1}{2}M + \delta_T \ll \bar{\Lambda}$, and $\bar{\Lambda}_{M}^{T} - \bar{\Lambda}_{-M}^{T} = \Delta_M - \Delta_{-M}$, and further

$$\theta_{M}^{T} - \theta_{-M}^{T} = \Theta(\bar{\Lambda}_{M}^{T}) - \Theta(\Lambda_{-M}^{T}) \approx (\Delta_M - \Delta_{-M})\Theta'(\bar{\Lambda}), \tag{4.38}$$

this becomes

$$\bar{t}_{LM}(\theta) \approx \frac{\bar{I}_{L-M}^{(\kappa)}(\theta_{R,M}^{T}, \xi)}{\bar{I}_{LM}^{(\kappa)}(\theta_{R,-M}^{T}, \xi)} \exp\{-[\gamma + \pi\Delta\Theta'(\bar{\Lambda})](\Delta_M - \Delta_{-M})\}$$
$$\times e^{-2\pi\Delta\theta}, \tag{4.39}$$

where $\Delta_M - \Delta_{-M}$ is given by (4.26). Aside from this difference, because of $\Theta'(\bar{\Lambda}) < 0$ the sign of the exponential depends on the relative magnitude of γ and $\pi\Delta|\Theta'(\bar{\Lambda})|$. An estimate of the latter quantity is given by the Rutherford value $\pi(\Delta/\Lambda)\sin\bar{\theta}_R$ which under strong-absorption conditions is small compared to γ. Thus the amplitudes are largest for good l matching (small K_0) in which case $\Delta_M - \Delta_{-M}$ is nearly independent of M, and the main M dependence of $t_{LM}(\theta)$ is given by the ratio of the functions $I_{LM}^{(\kappa)}$. Since from Appendix B we know that these are largest for $M = -L$ and smallest for $M = L$, the amplitude is maximal for $M = L$. Further the magnitude of $t_{LL}(\theta)$ decreases with increasing L, so that the strongest diffraction oscillations occur for $L = 0$ transfer and are weaker for higher multipolarities.

V. CONCLUSION AND OUTLOOK

The expressions derived in this paper give, in closed analytic form, a rather detailed description of the significant wave-mechanical aspects of heavy-ion transfer reactions as embodied implicitly in (first-order, no-recoil) DWBA calculations. By accounting for the important kinematical and dynamical effects of magnetic substate, angular momentum matching, and Q-value dependences, a considerable improvement is achieved over earlier closed-form evaluations of the DWBA amplitude which glossed over many subtle features by taking too rough averages over initial and final state energies and angular momentum projections. The main improving device is the introduction of the mean S matrix, which leads to an explicit representation of the partial-wave transfer amplitude that is more realistic than the *ad hoc* forms assumed in phenomenological treatments.

Of course, the formalism presented so far still has many shortcomings because of the simplifying assumptions made at the outset: (i) the no-recoil approximation, (ii) omission of higher-order and multi-step processes, and (ii) the neglect of spin and polarization effects. In subsequent work we endeavor to remove or remedy these limitations by suitable extensions of our method. One of several ways to account for recoil effects is a Taylor expansion of the final-channel distorted-wave function,[29,30] which results in the no-recoil transfer amplitude being amended by a linear combination of amplitudes pertaining to different values L_R of the transferred angular momentum and containing radial integrals with modified transfer form factors. The additional amplitudes can then be evaluated in closed form using similar approximations as for the no-recoil term. Further, the contributions of higher-order processes, such as inelastic scattering of the initial and final nuclei before and after the transfer takes place, can be taken into account by replacing the initial and final S matrices with the modified expressions derived recently[31] from a coupled-channels extension of the closed-formalism for elastic and inelastic heavy-ion scattering. Earlier, Udagawa and Tamura[32] gave a qualitative description by using a phenomenological form of the partial-wave transfer amplitude. Similar extensions are possible for multi-step, successive, or sequential transfers and will be treated in subsequent papers. Lastly, spin and polarization effects can be described by including spin-orbit interaction in the initial and final S matrices and taking the spin dependence of the bound-state wave function into account.

ACKNOWLEDGMENTS

A preliminary version of this paper was privately communicated, and test analyses with the formalism given therein have been carried out by Dr. K. E. Rehm at the Technische Universität München. Much of the present extended version was written during my stay as a guest scientist at GSI, Darmstadt and I thank Professor R. Bock, Professor C. Schmelzer, Dr. A. Gobbi, and Professor W. Nörenberg for their kind hospitality. Financial support by GSI and the Council for Scientific and Industrial Research (CSIR) is gratefully acknowledged.

APPENDIX A: DETERMINATION OF MEAN S MATRIX

Here we address the question of how to replace the product of square roots of the S matrices in the initial and final channels by a single mean S matrix. Assuming that $S_l(k)=\eta_l(k)\exp[i2\delta_l(k)]$ can be interpolated by a function of the continuous variable $\lambda=l+\frac{1}{2}$, with the reflection function $\eta_l(k)\to\eta(\lambda)=\hat{\eta}(\mu)$ characterized by the parameters Λ and Δ in the combination $\mu=(\lambda-\Lambda)/\Delta$, we require

$$[S_{l_f}(k_f)S_{l_i}(k_i)]^{1/2}\to[S^{(f)}(\lambda_f)S^{(i)}(\lambda_i)]^{1/2}$$
$$\hat{=}S^{(K)}(\bar{\lambda})=\eta_K(\bar{\lambda})e^{i2\delta_K(\bar{\lambda})}, \quad (A.1)$$

where $\bar{\lambda}=\frac{1}{2}(\lambda_i+\lambda_f)$ and $K=\lambda_i-\lambda_f$. Here and in the following equations, $a\hat{=}b$ means "a is required to equal b." Then

$$2\delta_K(\bar{\lambda})=\delta^{(i)}(\lambda_i)+\delta^{(f)}(\lambda_f)$$
$$=\delta^{(i)}(\bar{\lambda}+\tfrac{1}{2}K)+\delta^{(f)}(\bar{\lambda}-\tfrac{1}{2}K)\,, \quad (A.2)$$

and our requirement for the reflection functions is

$$[\eta^{(f)}(\lambda_f)\eta^{(i)}(\lambda_i)]^{1/2}=\left[\hat{\eta}\left(\frac{\lambda_f-\Lambda_f}{\Delta_f}\right)\hat{\eta}\left(\frac{\lambda_i-\Lambda_i}{\Delta_i}\right)\right]^{1/2}$$
$$\hat{=}\eta_K(\bar{\lambda})=\hat{\eta}\left(\frac{\bar{\lambda}-\Lambda_K}{\Delta}\right), \quad (A.3)$$

with Λ_K and Δ determined as functions of $\Lambda_i,\Lambda_f,\Delta_i,\Delta_f$ such that (A3) is optimally satisfied for functions $\hat{\eta}(\mu)$ of general "strong-absorption profile."

This is of course trivial in the sharp-cutoff limit where $\hat{\eta}(\mu)$ is a unit step function; then

$$\Lambda_K=\bar{\Lambda}+\tfrac{1}{2}|K-K_0| \quad \text{(sharp cutoff)}, \quad (A.4)$$

where $\bar{\Lambda}=\frac{1}{2}(\Lambda_i+\Lambda_f)$ and $K_0=\Lambda_i-\Lambda_f$.

For smooth profiles we first solve the problem by choosing a particular functional form of $\hat{\eta}(\mu)$ for which (A3) can be satisfied exactly, and then use the result in the general case. If $\Delta_i=\Delta_f=\Delta$, this can be done with Kauffmann's function[33]

$$\hat{\eta}(\mu)=\exp(-e^{-\mu})\,. \quad (A.5)$$

Then

$$\frac{1}{2}\left[\exp\left(-\frac{\lambda_f-\Lambda_f}{\Delta}\right)+\exp\left(-\frac{\lambda_i-\Lambda_i}{\Delta}\right)\right]=\exp\left(-\frac{\bar{\lambda}-\Lambda_K}{\Delta}\right) \quad (A.6)$$

yields

$$\Lambda_K=\bar{\Lambda}+\Delta\ln\left[\cosh\left(\frac{K-K_0}{2\Delta}\right)\right]. \quad (A.7)$$

For $\Delta_i\neq\Delta_f$ we obtain

$$\frac{1}{2}\left[\exp\left(\frac{K-K_0}{2\Delta_f}\right)\exp\left(-\frac{\bar{\lambda}-\bar{\Lambda}}{\Delta_f}\right)\right.$$
$$\left.+\exp\left(-\frac{K-K_0}{2\Delta_i}\right)\exp\left(-\frac{\bar{\lambda}-\bar{\Lambda}}{\Delta_i}\right)\right]\hat{=}\exp\left(-\frac{\bar{\lambda}-\bar{\Lambda}}{\Delta}\right), \quad (A.8)$$

which can no longer be satisfied exactly. However, we can determine optimal values of Λ_K and Δ by the following requirements: First, (A8) should hold exactly at $\bar{\lambda}=\Lambda_K$. This yields

$$\Lambda_K=\bar{\Lambda}+\Delta\ln\left\{\frac{1}{2}\left[\exp\left(\frac{K-K_0}{2\Delta_f}\right)+\exp\left(-\frac{K-K_0}{2\Delta_i}\right)\right]\right\}. \tag{A.9}$$

Then we determine Δ such that in the case of K matching, $K=K_0$, where (A8) becomes

$$\frac{1}{2}\left\{\exp\left[\left(\frac{1}{\Delta}-\frac{1}{\Delta_f}\right)(\bar{\lambda}-\bar{\Lambda})\right]+\exp\left[\left(\frac{1}{\Delta}-\frac{1}{\Delta_i}\right)(\bar{\lambda}-\bar{\Lambda})\right]\right\}\hat{=}1\,, \tag{A.10}$$

it minimizes the difference between the exponentials,

$$\left(\frac{1}{\Delta}-\frac{1}{\Delta_f}\right)^2+\left(\frac{1}{\Delta}-\frac{1}{\Delta_i}\right)^2=\text{minimum}\,, \tag{A.11}$$

$$\Delta=\frac{2\Delta_i\Delta_f}{\Delta_i+\Delta_f}. \tag{A.12}$$

Clearly, for $\Delta_i=\Delta_f$, (A.9) reduces to (A.7), and both expressions reduce to (A.4) in the sharp-cutoff limit.

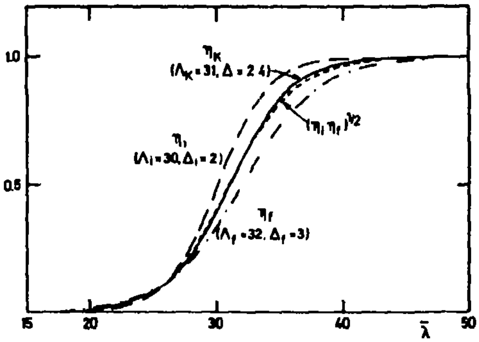

FIG. 2. Mean reflection function $\eta_K(\bar{\lambda})$ of Fermi function profile (solid curve), calculated from the initial-channel reflection function $\eta_i(\bar{\lambda})$ with $\Lambda_i=30$, $\Delta_i=2$ (long-dashed curve) and the final-channel reflection function $\eta_f(\bar{\lambda})$ with $\Lambda_f=32$, $\Delta_f=3$ (dot-dashed curve). $\eta_K(\bar{\lambda})$ represents the optimum symmetric approximation [Eq. (A3)] to the asymmetric function $[\eta_i(\bar{\lambda})\eta_f(\bar{\lambda})]^{1/2}$ (short-dashed curve), with parameters $\Lambda_K=31$ and $\Delta=2.4$ calculated from Eqs. (A9) and (A12), respectively.

An example of how relation (A.3) with (A.9) and (A.12) works for reflection functions of Fermi function profile $\hat{\eta}(\mu)=(1+e^{-\mu})^{-1}$ is shown in Fig. 2.

APPENDIX B: THE FUNCTIONS $I_{LM}^{(\kappa)}(\alpha,\xi)$

The functions $I_{LM}^{(\kappa)}(\alpha,\xi)$, defined in (2.22) as the WKB approximation to the Coulomb radial integrals (2.14) for the transfer form factor (2.5), have the integral representation

$$I_{LM}^{(\kappa)}(\alpha,\xi)=\int_0^\infty dw(-i^L)h_L^{(1)}[i\rho(1+\epsilon\cosh w)]\rho(1+\epsilon\cosh w)\cos\left\{\xi'\epsilon\sinh w+\xi w+M\arctan\left[\frac{(\epsilon^2-1)^{1/2}\sinh w}{\epsilon+\cosh w}\right]\right\}, \tag{B1}$$

where

$$\epsilon=(\sin\tfrac{1}{2}\alpha)^{-1}=[(\bar{\lambda}/n)^2+1]^{1/2}\,, \tag{B.2}$$

and ρ,ξ,ξ' are defined in (2.23) and (2.32). An approximate expansion, with an accuracy of about 10% for $|\xi'|<1.5$, is given in Ref. 14 as

$$I_{LM}^{(\kappa)}(\alpha,\xi)=\left(\frac{\pi}{2}\right)^{1/2}e^{-\rho(1+\epsilon)}\times\sum_{m=0}^{L}\frac{(L+m)!}{(L-m)!\,m!}\,\frac{1}{[2\rho(1+\epsilon)]^m}\,\frac{e^{-b^2/2a_m}}{a_m^{1/2}}\,, \tag{B.3}$$

with

$$a_m=\rho\epsilon+m\frac{\epsilon}{1+\epsilon},\quad b=\xi'\epsilon+\xi+M\left(\frac{\epsilon-1}{\epsilon+1}\right)^{1/2}. \tag{B.4}$$

For $\rho(1+\epsilon)>1$ and $b\lesssim1$, the sum in (B.3) may be approximated by the $m=0$ term,

$$I_{LM}^{(\kappa)}(\alpha,\xi)\approx\left(\frac{\pi}{2\rho\epsilon}\right)^{1/2}\exp\left[-\frac{b^2}{2\rho\epsilon}-\rho(1+\epsilon)\right]. \tag{B.5}$$

As discussed in Ref. 14, this expression shows the Q value and M dependence of $I_{LM}^{(\kappa)}$ by the exponential of $b^2/2\rho\epsilon$. For a given angle α, the optimum Q value is determined by the adiabaticity parameters, giving maximum $I_{LM}^{(\kappa)}$ for $b=0$, or

$$\frac{\xi'}{\sin\frac{1}{2}\alpha}+\xi=-M\tan\tfrac{1}{2}(\pi-\alpha)\,, \tag{B.6}$$

and the steepness with which $I_{LM}^{(\kappa)}$ decreases for increasing $|Q-Q_{\rm opt}|$ is controlled by the binding parameter κ through $\rho\epsilon=\kappa n/k\sin\frac{1}{2}\alpha$ such that the falloff is faster for weakly than for strongly bound particles. The same relation shows that for positive Q values, $I_{LM}^{(\kappa)}$ is largest for $M=-L$ and smallest for $M=L$, and that the difference is more pronounced at smaller than at larger angles α.

For $L=0$, (B.1) can be evaluated exactly in terms of a modified Hankel function of imaginary order,[27]

$$I_{00}^{(\kappa)}(\alpha,\xi)=\exp\left[-\left(\rho+\xi\arctan\frac{\xi'}{\rho}\right)\right]K_{i\xi}(n\gamma\epsilon)$$

$$\cong\left(\frac{\pi}{2n\gamma\epsilon}\right)^{1/2}\exp\left[-\left(\rho+\xi\arctan\frac{\xi'}{\rho}+n\gamma\epsilon\right)\right],\qquad\text{(B.7)}$$

where $\gamma=(\rho^2+\xi'^2)^{1/2}/n$, with the asymptotic form of (B.7) obtained for $n\gamma\epsilon\gg|\xi|$.

The main dependence of $I_{LM}^{(\kappa)}$ on $\bar{\lambda}$ is given by the factor $\exp(-n\gamma\epsilon)$, which becomes $\exp(-\gamma\bar{\lambda})$ for $\bar{\lambda}\gg n$. This enables us to define

$$I_{LM}^{(\kappa)}(\alpha,\xi)\equiv\bar{I}_{LM}^{(\kappa)}(\alpha,\xi)e^{-\gamma\bar{\lambda}},\qquad\text{(B.8)}$$

where $\bar{I}_{LM}^{(\kappa)}(\alpha,\xi)$ varies relatively slowly with $\bar{\lambda}$. Finally, using an amended notation, we note from (B.1) the symmetry relation

$$I_{L-M}^{(\kappa)}(\alpha,\xi,\xi')=I_{LM}^{(\kappa)}(\alpha,-\xi,-\xi').\qquad\text{(B.9)}$$

---

[1] W. E. Frahn and R. H. Venter, Nucl. Phys. 59, 651 (1964).

[2] V. M. Strutinsky, Zh. Eksp. Teor. Fiz. 46, 2078 (1964) [Sov. Phys.—JETP 19, 1401 (1964)]; Phys. Lett. 44B, 245 (1973).

[3] L. R. Dodd and K. R. Greider, Phys. Rev. Lett. 14, 959 (1965); Phys. Rev. 180, 1187 (1969).

[4] P. R. Christensen, O. Hansen, J. S. Larsen, D. Sinclair, and F. Videbaek, Phys. Lett. 45B, 107 (1973).

[5] P. D. Bond, J. D. Garrett, O. Hansen, S. Kahana, M. J. LeVine, and A. Z. Schwarzschild, Phys. Lett. 47B, 231 (1973).

[6] M. C. Lemaire, M. C. Mermaz, H. Sztark, and A. Cunsolo, Phys. Rev. C 10, 1103 (1974).

[7] M. J. LeVine, A. J. Baltz, P. D. Bond, J. D. Garrett, S. Kahana, and C. E. Thorn, Phys. Rev. C 10, 1602 (1974).

[8] W. Henning, D. G. Kovar, B. Zeidman, and J. R. Erskine, Phys. Rev. Lett. 32, 1015 (1974).

[9] A. Dar, Phys. Rev. 139, B1193 (1965); Nucl. Phys. 82, 354 (1966).

[10] A. Dar and B. Kozlowsky, Phys. Rev. Lett. 15, 1036 (1965).

[11] S. Varma, Nucl. Phys. A106, 233 (1968).

[12] W. E. Frahn and R. H. Venter, Ann. Phys. (N.Y.) 24, 243 (1963).

[13] W. E. Frahn and M. A. Sharaf, Nucl. Phys. A133, 593 (1969).

[14] R. A. Broglia and Aa. Winther, Phys. Rep. 4C, 153 (1972).

[15] S. Landowne, C. H. Dasso, B. S. Nilsson, R. A. Broglia, and Aa. Winther, Nucl. Phys. A259, 99 (1976).

[16] J. Knoll and R. Schaeffer, Phys. Rep. 31C, 159 (1977).

[17] H. Hasan and D. M. Brink, J. Phys. G 4, 1573 (1978).

[18] C. Chasman, S. Kahana, and M. Schneider, Phys. Rev. Lett. 31, 1074 (1973).

[19] M. Schneider, C. Chasman, S. Kahana, A. J. Baltz, and E. H. Auerbach, Phys. Rev. Lett. 31, 320 (1973).

[20] S. Kahana, P. D. Bond, and C. Chasman, Phys. Lett. 50B, 199 (1974).

[21] S. Kahana and A. J. Baltz, in *Advances in Nuclear Physics*, edited by M. Baranger and E. Vogt (Plenum, New York, 1977), Vol. 9, p. 1.

[22] W. E. Frahn, in *Heavy-Ion, High-Spin States and Nuclear Structure* (IAEA, Vienna, 1975), Vol. 1, p. 157.

[23] W. E. Frahn, in *Classical and Quantum Mechanical Aspects of Heavy Ion Collisions*, Lecture Notes in Physics (Springer, Heidelberg, 1975), Vol. 33, p. 102.

[24] W. E. Frahn, Nucl. Phys. A272, 413 (1976).

[25] N. Austern, *Direct Nuclear Reaction Theories* (Wiley, New York, 1970).

[26] M. J. Sopkovich, Nuovo Cimento 26, 186 (1962); K. Gottfried and J. D. Jackson, *ibid.* 34, 735 (1964).

[27] D. Trautmann and K. Alder, Helv. Phys. Acta 43, 363 (1970); K. Alder and D. Trautmann, Ann. Phys. (N.Y.) 66, 884 (1971); K. Alder, R. Morf, M. Pauli, and D. Trautmann, Nucl. Phys. A191, 399 (1972).

[28] W. E. Frahn, Nucl. Phys. A337, 324 (1980).

[29] M. A. Nagarajan, Nucl. Phys. A196, 34 (1972).

[30] A. J. Baltz and S. Kahana, Phys. Rev. C 9, 2243 (1974).

[31] W. E. Frahn and M. S. Hussein in *Proceedings of the Symposium on Heavy Ion Physics from 10 to 200 MeV/amu* (Brookhaven National Laboratory, N.Y., 1979), Vol. 2, p. 779.

[32] T. Udagawa and T. Tamura, Phys. Lett. 57B, 135 (1975).

[33] S. K. Kauffmann, Z. Phys. A282, 163 (1977).

PHYSICAL REVIEW C VOLUME 21, NUMBER 5 MAY 1980

Imaginary part of the ion-ion interaction potential

B. Behera, K. C. Panda, and R. K. Satpathy

Department of Physics, Sambalpur University, Jyotivihar-768017, Sambalpur, Orissa, India

(Received 16 August 1979)

The energy density formalism of Brueckner is extended to the complex domain with the use of a complex two-body effective interaction, so as to generate simultaneously the real and imaginary part of the ion-ion interaction potential. A simple effective interaction consisting of a density dependent delta function repulsion and a Gaussian attraction is chosen for the real part of the complex effective interaction, whereas the imaginary component is derived by using the forward scattering amplitude approximation. In using this approximation, emphasis has been given to use the complex two-body matrix τ, where the propagator has the nuclear many-body Hamiltonian rather than the free two-body matrix t. For the average nucleon-nucleon cross section $\langle\sigma\rangle$, required in constructing the complex effective interaction, a modified version of the relation suggested by Bohr and Mottelson is used which compares quite well with that of Clemental and Villi. The real part of the ion-ion interaction potential calculated in this model has already been reported in an earlier work and the present work deals with the calculation of the imaginary part of the potential for five pairs of spherical nuclei. The region of the potential beyond the surface is parametrized into a Woods-Saxon shape. The calculated imaginary potential for the system ^{40}Ca-^{16}O is compared with the phenomenological one of Becchetti *et al*. and the agreement between the two sets of potentials is found to be quite good in the region beyond the strong absorption radius.

[NUCLEAR REACTIONS Complex two-body effective interaction, forward scattering amplitude approximation, imaginary part of ion-ion interaction potential.]

I. INTRODUCTION

In a previous work[1] we had proposed a simple parametrization of the energy density functionals derived from a two-body effective interaction by expanding them in a Taylor series about the saturation density. It was pointed out there that such a parametrization of the density functionals allows one a simple analytic approximation of the energy density of a nucleus which has the advantage of being computationally quite simple, similar to the energy density derived from Skyrme-type effective interactions.[2,3] The resulting simple energy density was used to calculate the real part of the ion-ion interaction potentials for several pairs of spherical nuclei in the framework of Brueckner's[4] energy density formalism, and it was observed that the positions and heights of the calculated interaction barriers for all pairs of nuclei were in good agreement with those referred to in the literature. The aim of the present work is to extend the energy density formalism of Brueckner[4] to the complex domain with the use of a complex effective interaction, so as to simultaneously generate the real and imaginary part of the ion-ion interaction potential. The model, as will be shown in what follows, does not rely upon the microscopic structure of the level density, but derives its essentials from a somewhat macroscopic point of view, the primary ingredients being the density distributions of the interacting nuclei and an effective two-body interaction.

The first application of a complex two-body effective interaction to calculate the real and imaginary part of the ion-ion interaction potential was carried out by Vary and Dover.[5] A suitable complex effective interaction with an adjustable complex depth parameter to fit data accurately was folded in with the density distributions of the two colliding nuclei, and good fits were obtained for the ^{16}O + ^{58}Ni system. The saturation and antisymmetrization effects which are ignored in such a double folding procedure are taken into account rather arbitrarily through the adjustable complex depth parameter in the effective interaction. Another approach, similar to the present one but not directly based on a complex effective interaction was taken by Gupta and Kailas[6] who extended the energy density formalism of Brueckner[4] to the complex domain. However, the authors in Ref. 6 have identified the complex potential energy density with the complex nucleon-nucleus optical potential and have used the complex optical potential experienced by a nucleon in uniform nuclear matter calculated by Jeukenne *et al.*[7] using the Reid soft core potential.[8] This choice of the potential energy density is not justified in the sense that the real part of the nucleon-nucleus optical potential integrated over the density of the nucleus does not give the total nuclear potential energy. Besides, the complex nucleon-nuclear-matter optical potential needs corrections for the finite size of the nucleus which may be quite significant for nucleus-nucleus collisions. Love *et al.*[9] and Baltz *et al.*[10] on the other hand have computed the imaginary part of the nucleus-nucleus interaction potential recently by considering coupling to specific inelastic channels.

As mentioned earlier, in the present work we have calculated the real and imaginary part of the ion-ion interaction potential in the framework of Brueckner's energy density formalism using a complex two-body effective interaction. For the real part of the complex effective interaction, we have used a simple two-body effective interaction[11] consisting of a density dependent delta function repulsion and a single Gaussian attraction. On the other hand the imaginary component of the complex effective interaction is derived by using the forward scattering amplitude approximation. Saloner *et al.*[12] have already used this approximation in a detailed calculation of the imaginary part of the interaction potential for two colliding nuclei taking proper account of the Pauli principle. The validity of the approximation has been tested by the authors in Ref. 12 by solving the Brueckner-Goldstone equation in momentum space. Sinha[13] has also calculated the imaginary part of the ion-ion interaction potential by using the forward scattering amplitude approximation and folding in with the density distributions of the two colliding nuclei. However, using the forward scattering amplitude approximation, it has already been observed by Sinha and Duggan[14] that at least for incident nucleons it is more appropriate to use the complex two-body matrix $\mathcal{T}$, where the propagator has the nuclear many-body Hamiltonian rather than the free two-body matrix t, where only the free two-body Hamiltonian is used in the Green function. It is worthwhile to mention here that in the calculation of the imaginary part of the ion-ion interaction potentials in Refs. 12 and 13, the free two-body matrix t has been used rather than the matrix $\mathcal{T}$. Recently, Schery *et al.*[15] have also demonstrated the success of using the matrix $\mathcal{T}$ instead of the free two-body matrix t for the analysis of (p,n) cross sections. One of the motivations of the present work is therefore to use the matrix $\mathcal{T}$ instead of the free two-body matrix t in deriving the imaginary component of the complex two-body effective interaction in the forward scattering amplitude approximation. The real part of the ion-ion interaction potential being already reported in our earlier paper,[1] in the present work we mainly concentrate on computing the imaginary potential. The region of the potential beyond the surface is parametrized by a Woods-Saxon shape and is also compared with the phenomenological potentials.

In Sec. II we briefly consider the construction of the complex effective interaction used in the present work. Section III deals with the calculation of the ion-ion interaction potential in the energy density formalism, and the results and discussions are given in the last section.

II. THE COMPLEX TWO-BODY EFFECTIVE INTERACTION

It is well known that for a single nucleon of wave number k incident on a nucleus of density ρ_1, the imaginary potential W_1 in the forward scattering amplitude approximation is given by

$$W_1 = -\frac{\hbar^2 k}{2m}\langle\sigma\rangle\rho_1 , \tag{1}$$

where m is the nucleon mass and $\langle\sigma\rangle$ is the average total nucleon-nucleon cross section averaged over the relative momenta so as not to violate the Pauli exclusion principle. For an incident nucleus of density ρ_2, the total imaginary potential can be approximated in the simplest way as

$$W = \int W_1\rho_2 d^3r , \tag{2}$$

where the integration is carried over the density distribution ρ_2 of the incident nucleus.

The implication of replacing the free two-body matrix t by the matrix $\mathcal{T}$ in the forward scattering amplitude approximation is to replace $\rho\langle\sigma\rangle$ in Eq. (1) by $\rho_{\text{eff}}\langle\sigma\rangle$, where

$$\rho_{\text{eff}} = \frac{\int \rho V_{\text{eff}}(r)d^3r}{J_{\text{eff}}} \tag{3}$$

and J_{eff} is the volume integral of the real part of the two-body effective interaction V_{eff}. Ray and Coker[16] and also Sinha[17] have already shown how to extract a complex effective interaction V_c such that its Fourier transform is given by $\mathcal{T}(q^2)$. When $\mathcal{T}$ is not approximated by the free two-body matrix t, the derivation of V_c also follows naturally from the work of Kerman *et al.*[18] We follow the procedure of Refs. 16 and 17 so that for a two-body effective interaction we can have the following ansatz for V_c:

$$V_c = (1+i\gamma)V_{\text{eff}}(r) . \tag{4}$$

To determine γ, we apply the optical theorem for the two-body scattering amplitude $M(\vec{q})$ corresponding to $\mathcal{T}$, and in the limit $q\to 0$ we have

$$\frac{k\langle\sigma\rangle}{4\pi} = I_m[M(0)] , \tag{5}$$

and

$$I_m[M(0)] = -\frac{m}{2\pi\hbar^2}\int I_m(V_c)d^3r . \tag{6}$$

From the ansatz in Eq. (4), we see that the integral on the right hand side of Eq. (6) is $\gamma J_{\rm eff}$. Thus we get the following expression for γ:

$$\gamma = -\frac{\hbar^2 k}{2m}\frac{\langle\sigma\rangle}{J_{\rm eff}}\,. \tag{7}$$

On the other hand for a free two-body matrix t, the imaginary component of the effective interaction $i\gamma V_{\rm eff}$ in Eq. (4) reduces to $-i(\hbar k/2m)\langle\sigma\rangle$, and we get back the relations for W_1 and W in Eqs. (1) and (2) in the simplest approximation.

Since in our present case we are concerned with the nucleus-nucleus collision, each nucleon is a constituent particle of either of the two nuclei, and hence in the WKB approximation, the wave number k of a nucleon in Eq. (7) can be given by[17]

$$k^2 = \frac{2m}{\hbar^2}[E + E_{FT} - U] \tag{8}$$

where E and E_{FT} are, respectively, the pure translational energy and the average internal kinetic energy of the nucleon, and U is the real part of the optical potential experienced by the nucleon. For the sake of simplicity we use a Fermi gas model to determine E_{FT} so that

$$E_{FT} = 3\hbar^2 k_F{}^2/(10m)\,,$$

where k_F is the local Fermi momentum. The derivation of U in Eq. (8) and the computation of the average total nucleon-nucleon cross section will be considered in the next section.

For the two-body effective interaction $V_{\rm eff}$ we have used a simple density dependent effective interaction constructed by us in an earlier work.[11] The interaction has the form

$$V_{\rm eff}(\vec r_1 - \vec r_2) = C k_F{}^{1/2}(\vec R)\delta(\vec r_1 - \vec r_2) - \tfrac{1}{2}V_0(1+P)e^{-|\vec r_1 - \vec r_2|^2/\mu^2}\,, \tag{9}$$

where k_F is the Fermi momentum evaluated at the center of mass point $\vec R = (\vec r_1 + \vec r_2)/2$, and P is the Majorana exchange operator. It should be noted that in the expression for the complex effective interaction V_c in Eq. (4), γ is to be evaluated at the center of mass coordinate $\vec R$, whereas $V_{\rm eff}$ is to be evaluated at the relative coordinate $\vec r = \vec r_1 - \vec r_2$. The three parameters of the effective interaction C, V_0, and μ are determined by requiring that the interaction reproduces the correct binding energy per particle at the correct density of nuclear matter and the ground state energy of ^{16}O. It has already been shown in Ref. 11 that this effective interaction gives a satisfactory account of different properties of nuclear matter and ground state properties of three closed-shell nuclei ^{4}He, ^{16}O, and ^{40}Ca.

III. CALCULATION OF THE REAL AND IMAGINARY PART OF THE ION-ION INTERACTION POTENTIAL

The nuclear part of the ion-ion interaction potential as a function of the separation distance R between the centers of the two colliding ions is given by

$$V(R) + iW(R) = \int [H(\rho,\tau) - H(\rho_1,\tau_1) - H(\rho_2,\tau_2)]d^3r\,, \tag{10}$$

where $V(R)$ and $W(R)$ are respectively the real and imaginary part of the potential. Here $H(\rho,\tau)$ is the complex energy density of the composite system, and $H(\rho_1,\tau_1)$ and $H(\rho_2,\tau_2)$ are the same for the two separate nuclei, and ρ and τ are the particle density and kinetic energy density, respectively. We use the complex two-body effective interaction V_c in Eq. (4) with γ given by the relation in Eq. (7) to compute the complex energy density of a nuclear system. Using the prescription of Negele and Vautherin[19] for the expansion of the density matrix and the product of two densities in powers of the relative coordinate and remembering that γ is to be evaluated at the center of mass coordinate of the two interacting nucleons, we get the following expression for the complex energy density:

$$H(\rho,\tau) = \frac{\hbar^2}{2m}\tau + (1+i\gamma)[A(\rho) + B(\rho)\tau + P(\rho)(\nabla\rho)^2 + Q(\rho)\nabla^2\rho]\,. \tag{11}$$

For the simple two-body effective interaction $V_{\rm eff}$ in Eq. (9) it is possible to evaluate the density functionals $A(\rho)$, $B(\rho)$, $P(\rho)$, and $Q(\rho)$ analytically.[1,11] The results are

$$A(\rho) = \frac{Ck_F^{6.5}}{6\pi^4} - \frac{2V_0}{3\pi^{5/2}\mu^3}\left[\left(\frac{\kappa^6}{8} + \frac{27\kappa^2}{2} + 96 - \frac{63}{\kappa^2}\right) + \left(\frac{3\kappa^2}{4} - 33 + \frac{63}{\kappa^2}\right)e^{-\kappa^2} - \left(\frac{315\kappa}{4} - \frac{3\kappa^3}{2}\right)\int_0^\kappa e^{-t^2}dt\right], \tag{12}$$

$$B(\rho) = \frac{105V_0\mu^2}{4\pi^{1/2}}\left[\left(\frac{1}{\kappa^3} + \frac{6}{\kappa^5} - \frac{4}{\kappa^7}\right) - \left(\frac{2}{\kappa^5} - \frac{4}{\kappa^7}\right)e^{-\kappa^2} - \frac{5}{\kappa^4}\int_0^\kappa e^{-t^2}dt\right], \tag{13}$$

$$P(\rho) = \frac{105V_0\pi^{3/2}\mu^5}{32}\left[\left(\frac{15}{\kappa^6} + \frac{1}{\kappa^4}\right)e^{-\kappa^2/4} + \left(\frac{3}{\kappa^5} - \frac{30}{\kappa^7}\right)\int_0^{\kappa/2} e^{-t^2}dt\right], \tag{14}$$

and

$$Q(\rho)=\frac{105V_0\mu^2}{16\pi^{1/2}}\left[\left(\frac{4}{\kappa^7}-\frac{6}{\kappa^5}-\frac{1}{\kappa^3}\right)+\left(\frac{2}{\kappa^5}-\frac{4}{\kappa^7}\right)e^{-\kappa^2}+\frac{5}{\kappa^4}\int_0^{\kappa}e^{-t^2}dt+\left(\frac{5}{\kappa^6}+\frac{1}{3\kappa^4}\right)e^{-\kappa^2/4}+\left(\frac{1}{\kappa^5}-\frac{10}{\kappa^7}\right)\int_0^{\kappa/2}e^{-t^2}dt\right], \tag{15}$$

where $\kappa=\mu k_F$. In Refs. 11 and 19 it is shown that an integration by parts of the $\nabla^2\rho$ term in the energy density allows one to replace the term $P(\rho)(\nabla\rho)^2+Q(\rho)\nabla^2\rho$ by $C(\rho)(\nabla\rho)^2$, where

$$C(\rho)=P(\rho)-\frac{dQ(\rho)}{d\rho}. \tag{16}$$

However, in the present work such a reduction will involve the differentiation of $\gamma Q(\rho)$ with respect to ρ. Because of the complicated dependence of γ on ρ through $\langle\sigma\rangle$ and k, we refrain from doing this and use the energy density as given by Eq. (11).

In our earlier work[1] we had shown how one can get simple analytic approximations for the density functionals by expanding them in a Taylor series about saturation density and retaining terms up to quadratic in density in these expansions. The validity and advantage of using such parametrized versions of the density functionals instead of the exact ones in calculating the ion-ion interaction potential have been discussed in detail in Ref. 1. Since the density functionals $A(\rho)$, $B(\rho)$, and $C(\rho)$ have already been parametrized in Ref. 1, we consider here the parametrization of $P(\rho)$ and $Q(\rho)$. For this purpose, we note that $P(\rho)$ behaves as a constant as $\rho\to 0$ whereas $Q(\rho)$ behaves as ρ in the same limit. Thus we expand $P(\rho)$ and $Q(\rho)/\rho$ in Taylor series about saturation density and retain terms up to quadratic in density. With this the density functionals $P(\rho)$ and $Q(\rho)$ assume the form

$$\begin{aligned}P(\rho)&=(p_0+p_1\rho+p_2\rho^2),\\ Q(\rho)&=(q_0+q_1\rho+q_2\rho^2)\rho,\end{aligned} \tag{17}$$

where the various expansion coefficients p_i and q_i are related to the values of the corresponding density functionals and their first and second derivatives at saturation density. The values of these coefficients are given in Table I. The exact density functionals $P(\rho)$ and $Q(\rho)$ are also compared with their parametrized versions in Figs. 1 and 2, respectively, where these functions are plotted against ρ. It is seen that the parametrized functions correctly reproduce the exact functions over a wide range of density except that in the region $\rho\to 0$ there is a small discrepancy of the order of 1.5% for $P(\rho)$.

TABLE I. Values of the coefficients in the expansion of the energy density functionals.

i	p_i	q_i
0	27.87	−53.85
1	−19.70	65.88
2	17.72	−70.32

The real part of the optical potential U, experienced by a nucleon in a nuclear medium and required in computing k in Eq. (8), can be expressed[19] in terms of the density functionals $A(\rho)$, $B(\rho)$, and $C(\rho)$ as

$$U=\frac{dA(\rho)}{d\rho}+\frac{dB(\rho)}{d\rho}\tau-\frac{dC(\rho)}{d\rho}(\nabla\rho)^2-2C(\rho)\nabla^2\rho+\frac{2m}{\hbar^2}B(\rho)E, \tag{18}$$

where E is the energy of the nucleon, and in the field of the nuclear medium this will be modified

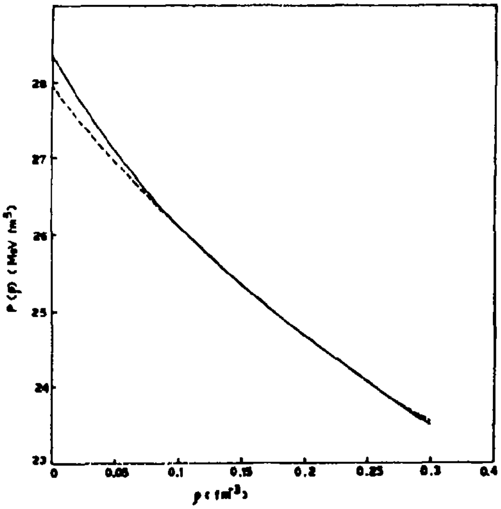

FIG. 1. Plot of exact (——) and parametrized (---) version of $P(\rho)$ as a function of density ρ.

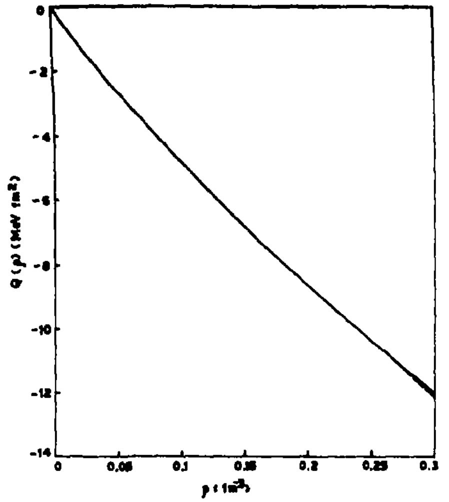

FIG. 2. Plot of exact (——) and parametrized (---) version of $Q(\rho)$ as a function of density ρ.

as $E \rightarrow E - U$. Thus from Eq. (18) we get the following relation for U:

$$U=\left[1+\frac{2m}{\hbar^2}B(\rho)\right]^{-1}\left[\frac{dA(\rho)}{d\rho}+\frac{dB(\rho)}{d\rho}\tau-\frac{dC(\rho)}{d\rho}(\nabla\rho)^2 -2C(\rho)\nabla^2\rho+\frac{2m}{\hbar^2}B(\rho)E\right]. \quad (19)$$

Since in the present case each nucleon is a constituent particle of either of the two nuclei, there will be an additional contribution to E from its internal motion[17] and E will be replaced by $E+E_{FT}$ in accordance with Eq. (8).

In calculating the imaginary part of the ion-ion interaction potential according to Eq. (10), one has to compute the average nucleon-nucleon cross section $\langle\sigma\rangle$ appearing in the expression for γ, for the two separate ions as well as for the composite system of both the ions. For the composite system the computation of $\langle\sigma\rangle$ is very complicated[13] due to the complexity of the overlap of the phase spaces of the two colliding nuclei. Even for the case of a single nucleus, the expression for $\langle\sigma\rangle$, derived by Clemental and Villi,[20] involves a complicated integral which incorporates the role of the Pauli principle, and its use in calculating the ion-ion imaginary potential W as a function of the distance of separation R between the centers of the two nuclei according to Eq. (10) will make the numerical works involved quite complicated. For this reason, in the present work we have used a modified version of the simple expression for $\langle\sigma\rangle$ given by Bohr and Mottelson,[21]

$$\langle\sigma\rangle=\sigma_0\left[1-\frac{7k_F{}^2}{5k^2}+\frac{2k_F{}^2}{5k^2}\left(2-\frac{k^2}{k_F{}^2}\right)^{3/2}\right] \text{ when } k^2<2k_F{}^2,$$
$$\langle\sigma\rangle=\sigma_0\left[1-\frac{7k_F{}^2}{5k^2}\right] \text{ when } k^2>2k_F{}^2. \quad (20)$$

Here k_F is the Fermi momentum, and k is the wave number of the nucleon defined earlier. In Ref. 21, σ_0 is referred to as the free nucleon-nucleon cross section and is assumed to be independent of energy. However, it is well known from experiments that σ_0 is roughly inversely proportional to the energy. In view of this, we have here used the following relation for σ_0,

$$\sigma_0=\frac{A}{B+\frac{\hbar^2k^2}{2m}}, \quad (21)$$

where the constant factors A and B have been obtained by taking an average of the constants associated with proton-proton and neutron-proton total cross sections given in the work of Greenlees *et al.*[22] For the case of a single nucleus it was observed by us that $\langle\sigma\rangle$ given by Eqs. (20) and (21) compares with that of Clemental and Villi[20] quite well. In Fig. 3 this comparison is shown for ^{40}Ca for three different energies $E=10$, 20, and 40 MeV, where we have shown $\langle\sigma\rangle$ as a func-

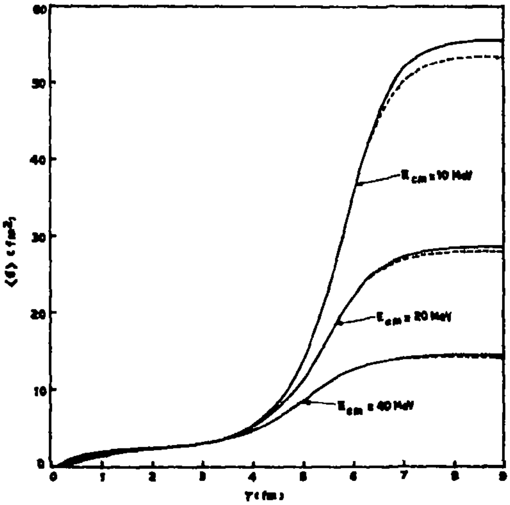

FIG. 3. Average nucleon-nucleon cross section $\langle\sigma\rangle$ for ^{40}Ca at different center of mass energy $E_{\text{c.m.}}$ as a function of separation distance r. The dotted lines correspond to $\langle\sigma\rangle$ obtained from Eqs. (20) and (21), whereas the solid lines are obtained by using the relation given in Ref. 20.

tion of the distance r of the nucleon from the center of the nucleus. From Fig. 3 it is seen that there is a small discrepancy between the two sets of values for $\langle\sigma\rangle$ at very low and high values of r, and this decreases as E increases. Since most of the contributions to W will come from the surface region of the nucleus, these discrepancies will have a negligible effect on the calculated imaginary part of the potential.

The calculation of the potentials V and W in Eq. (10) requires the knowledge of the densities ρ and τ of the composite system and ρ_i and τ_i $(i=1, 2)$ of the two separate nuclei. For the sake of simplicity we use the sudden approximation in our calculation so that $\rho=\rho_1+\rho_2$. In Ref. 1 we used the Thomas-Fermi approximation for the kinetic energy density. The advantage of this approximation is that the evaluation of the potentials from Eq. (10) reduces simply to the knowledge of the densities of the separated nuclei. Moreover, Brink and Stancu[23,24] have already shown that such a simple approach is capable of including more than 75% of the exchange effects due to antisymmetrization for distances larger than the sum of the rms radii of the interacting nuclei. However, as pointed out by Brink and Stancu,[23,24] the Thomas-Fermi approximation is most accurate when the kinetic energy density τ' is defined by

$$\tau' = -\sum_i \psi_i^* \nabla^2 \psi_i \,. \tag{22}$$

Since the kinetic energy density in Eq. (11) is defined as

$$\tau = \sum_i \nabla\psi_i^* \cdot \nabla\psi_i \,, \tag{23}$$

we used the relation

$$\tau = \tau' + \tfrac{1}{2}\nabla^2\rho \tag{24}$$

and made a Thomas Fermi approximation for τ' in Ref. 1. However, in the present work we have made use of the approximation of Kirzhnits.[25] This approximation consists of adding correction terms to the Thomas-Fermi approximation τ_{TF},

$$\tau' = \tau_{\mathrm{TF}} + \tfrac{1}{36}(\nabla\rho)^2/\rho - \tfrac{1}{6}\nabla^2\rho \,. \tag{25}$$

The second term represents the Weizsacker correction.[26] This approximation for τ' has been examined by Brink and Stancu[27] and also by one of the present authors,[28] and it has been shown that this gives a better description of the real part of ion-ion interaction potential in the tail region then the simple Thomas-Fermi approximation.

It is to be noted that unlike the case of Ref. 1, in the present work there is a relative motion between the two ions and in principle, one should compute the densities and kinetic energy densities of the two separate nuclei and the composite system taking proper account of this relative motion. However, a detailed account of this effect is very complicated,[23] and in this work we refrain from doing this. Thus the energy density in Eq. (11), which does not incorporate the effect of relative motion, is expected to be valid only for very low relative energies between the two nuclei.

Using Eqs. (10) and (11), one can separate the real and imaginary parts of the total interaction potential as

$$V(R) = \int [H_R(\rho,\tau) - H_R(\rho_1,\tau_1) - H_R(\rho_2,\tau_2)]d^3r \,, \tag{26}$$

$$W(R) = \int [H_I(\rho,\tau) - H_I(\rho_1,\tau_1) - H_I(\rho_2,\tau_2)]d^3r \,, \tag{27}$$

where H_R and H_I are the real and imaginary parts of the complex energy density $H(\rho,\tau)$ given in Eq. (11). Since in our earlier work[1,28] we have already calculated the real potential $V(R)$ for several pairs of spherical nuclei, in the present work we concentrate on calculating $W(R)$ only. The evaluation of W in Eq. (27) requires the computation of γ for the composite system and also for the two separate nuclei. In principle, $\langle\sigma\rangle$ and k appearing in γ should be evaluated for the composite system by considering the overlap of the phase spaces of both the nuclei, and as stated earlier this is much too complicated.[12] Therefore, for simplicity, we have used here, in the spirit of sudden approximation, the relation $\rho=\rho_1+\rho_2$ to evaluate $\langle\sigma\rangle$ and k for the composite system. The density distributions of the different nuclei used in this calculation have been taken from our earlier work.[1,11]

IV. RESULTS AND DISCUSSIONS

Using the complex two-body effective interaction constructed in Sec. II and the formalism of Sec. III, we have calculated the imaginary part of the ion-ion interaction potential for five pairs of spherical nuclei listed in Table II. These poten-

TABLE II. Woods-Saxon parameters of the surface region of the imaginary part of the ion-ion interaction potential.

Pairs	W_0 (MeV)	R_0 (fm)	a_0 (fm)	$V(R_D)/W(R_D)$
^{16}O-^{16}O	10.98	6.25	0.575	2.16
^{16}O-^{40}Ca	13.73	7.30	0.625	2.19
^{16}O-^{56}Ni	13.90	7.775	0.61	2.22
^{40}Ca-^{40}Ca	16.83	8.40	0.64	2.27
^{40}Ca-^{56}Ni	17.51	8.85	0.635	2.25

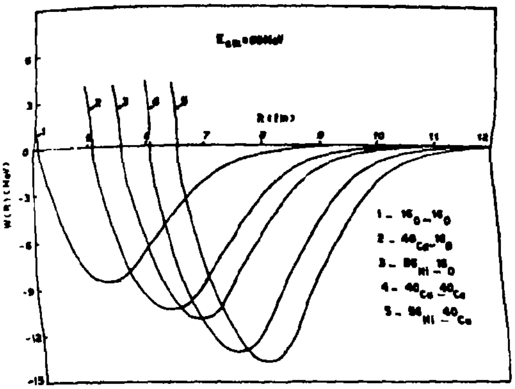

FIG. 4. Imaginary part of ion-ion interaction potential $W(R)$ as a function of the separation distance R between the two ions.

tials (for $E_{c.m.} = 60$ MeV) are also shown in Fig. 4. All the potentials have a common shape with a repulsive core at short distances followed by an attractive part. The repulsive core of these potentials is a consequence of the sudden approximation which neglects any possible distortion of the single particle wave functions of the colliding nuclei. A comparison of the positions of the minima of these potentials with those for the real parts in Refs. 1 and 28 shows that they are shifted towards larger values of R.

Following the procedure of Ref. 1, we have parametrized the region of the potentials beyond the surface by a Woods-Saxon shape. The values of the parameters W_0, R_0, and a_0 are given in Table II which fit the calculated potentials very well beyond R_0. An example of this Woods-Saxon shape for the ^{40}Ca-^{16}O system is shown in Fig. 5. The parameter R_0 is very well approximated by the formula

$$R_0 \simeq 1.23(A_1^{1/3}+A_2^{1/3}) .$$

However, we did not observe any such relation for W_0 and a_0, although it was noted that they increase with the increase in the mass number of the interacting nuclei. A comparison of the values of these parameters with those for the real part of the interaction potential given in Ref. 28 [where the same approximation for τ' in Eq. (25) has been used] shows that V_0/W_0 is roughly equal to 4 for all the pairs of nuclei listed in Table II. In addition, the half radius R_0 for the imaginary potential is found to be greater than that for the real part. However, the diffusivity a_0 for the imaginary part is smaller than that for the real part. These findings are in conformity with the observations of Becchetti *et al.*[29] in connection with the phenomenological ion-ion potentials.

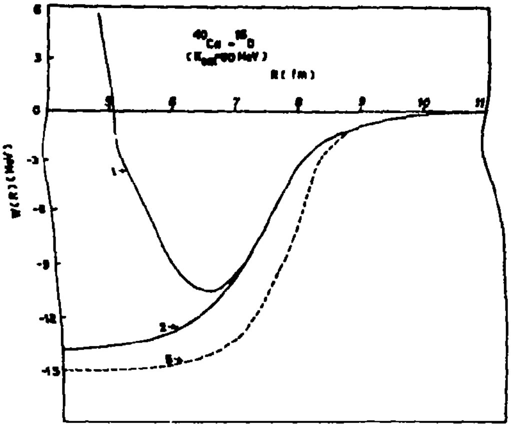

FIG. 5. The calculated imaginary potential for the system ^{40}Ca-^{16}O (curve 1) along with its Woods-Saxon form (curve 2) compared with the phenomenological potential (curve 3) of Ref. 29.

We have also compared the calculated imaginary potential for the pair ^{40}Ca-^{16}O ($E_{c.m} = 60$ MeV) with the phenomenological one of Ref. 29 in Fig. 5. It is interesting to note that our potential agrees with that of Ref. 29 quite well in the region beyond the strong absorption radius ($R_D = 8.9$ fm). In view of the fact that for elastic scattering and one or two particle transfer reaction, the imaginary potential in the region of strong absorption radius is only important; this agreement of the calculated potential with that of Ref. 29 is quite impressive. The ratio $V(R_D)/W(R_D)$ which is given in Table II is roughly 2.2 for all pairs. This is in accordance with the result of Becchetti *et al.*[29] who give a value of 2.5 for this ratio in the region of R_D. However, this observation contradicts the transition character of the ratio $V(R_D)/W(R_D)$ with projectile mass.[30]

To see how the calculated potential W depends on the relative center of mass energy $E_{c.m.}$, we calculated $W(R)$ for the pair ^{16}O-^{16}O at different values of $E_{c.m.}$. It was observed that although the strength of $W(R)$ increases with energy, this change is very small. For example, at $E_{c.m.} = 16$ and 80 MeV, the minimum values of $W(R)$ are respectively -8.24 and -8.58 MeV. This is due to the fact that the energy density used in our calculation does not incorporate the effects of relative motion between the two nuclei. We propose to investigate this aspect in a future publication.

ACKNOWLEDGMENTS

We are thankful to Dr. Bikash Sinha of Bhabha Atomic Research Centre, Bombay for many useful discussions during the progress of this work. We are also thankful to the Computer Centre, Utkal University, for providing computational facilities. Two of us (B.B. and R.K.S.) acknowledge with thanks the financial assistance provided by the University Grants Commission and Department of Atomic Energy, Government of India, respectively.

---

[1] B. Behera, K. C Panda, and R. K. Satpathy, Phys. Rev. C 20, 683 (1979).

[2] T. H. R. Skyrme, Nucl. Phys. 6, 615 (1959).

[3] S. A. Moszkowski, Phys. Rev. C 2, 402 (1970).

[4] K. A. Brueckner, J. R. Bucher, and M. M. Kelly, Phys. Rev. 173, 944 (1968).

[5] J. P. Vary and C. B. Dover, Phys. Rev. Lett. 331, 1610 (1973).

[6] S. K. Gutpa and S. Kailas, Phys. Lett. 73B, 398 (1978).

[7] J. P. Jeukenne, A. Lejeune, and C. Mahaux, Phys. Rev. C 16, 80 (1977).

[8] R. V. Reid, Ann. Phys. (N.Y.) 50, 411 (1968).

[9] W. G. Love, T. Terasawa, and G. R. Satchler, Phys. Rev. Lett. 39, 6 (1977).

[10] A. J. Baltz, S. K. Kauffmann, N. K. Glendenning, and K. Pruess, Phys. Rev. Lett. 40, 20 (1978).

[11] B. Behera and R. K. Satpathy, J. Phys. G 5, 85 (1979).

[12] D. A. Saloner, C. Toepffer, and B. Fink, Nucl. Phys. A283, 131 (1977).

[13] B. Sinha, Phys. Rev. C 11, 1546 (1975).

[14] B. Sinha and F. Duggan, Nucl. Phys. A226, 31 (1974).

[15] S. D. Sahery, S. M. Austin, A. Galonsky, L. E. Young, and U. E. P. Berg, Phys. Lett. 79B, 30 (1978).

[16] R. L. Ray and W. R. Coker, Phys. Rev. C 16, 340 (1977); R. L. Ray and W. R. Coker (unpublished report).

[17] B. Sinha, Phys. Rep. 20C, 1 (1975); B. Sinha, Proc. Nucl. Phys. Solid State Phys. (India) 21B, 66 (1978).

[18] A. K. Kerman, H. McManus, and R. M. Thaler, Ann. Phys. (N.Y.) 8, 551 (1959).

[19] J. W. Negele and D. Vautherin, Phys. Rev. C 5, 1472 (1972).

[20] E. Clemental and C. Villi, Nuovo Cimento 1, 176 (1955).

[21] A. Bohr and B. R. Mottelson, *Nuclear Structure* (Benjamin, New York, 1969), Vol. I, p. 261.

[22] G. W. Greenless, G. J. Pyle, and Y. C. Tang, Phys. Rev. 171, 1115 (1968).

[23] D. M. Brink and Fl. Stancu, Nucl. Phys. A243, 175 (1975).

[24] Fl. Stancu and D. M. Brink, Nucl. Phys. A270, 236 (1976).

[25] D. A. Kirzhnits, *Field Theoretical Methods in Many-Body Systems*, translated by A. J. Meadows (Pergamon, Oxford, 1967), p. 52.

[26] C. F. V. Weizsacker, Z. Phys. 96, 421 (1935).

[27] D. M. Brink and Fl. Stancu, Nucl. Phys. A299, 321 (1978).

[28] B. Behera, Ph.D. thesis, Sambalpur University, 1979 (unpublished).

[29] F. D. Becchetti, P. R. Christensen, V. I. Manko, and R. J. Nickles, Nucl. Phys. A203, 1 (1973).

[30] R. M. DeVries, D. A. Goldberg, J. W. Watson, M. S. Zisman, and J. G. Cramer, Phys. Rev. Lett. 39, 450 (1977); R. M. DeVries, Proceedings of the Symposium on Heavy Ion Elastic Scattering, University of Rochester, 1977 (unpublished).

PHYSICAL REVIEW C VOLUME 21, NUMBER 5 MAY 1980

Parametrization of exact-finite-range distorted-wave Born approximation overlap integral for reactions induced by heavy ions

T. Udagawa, T. Tamura, and D. Price
Department of Physics, University of Texas, Austin, Texas 78712

(Received 21 September 1979)

In a few recent publications, which utilized exact-finite-range distorted-wave Born approximation, we successfully fitted continuum spectra observed in a variety of heavy-ion reactions. In making it feasible to carry out the numerical calculations involved, we found the use of properly parametrized transition amplitudes was very powerful and almost indispensable. In the present article, methods used for this parametrization are explained in detail.

NUCLEAR REACTIONS Distorted-wave Born approximation; exact-finite-range form factors; parametrization of overlap integrals; recoil effects; heavy-ion reactions; continuum spectra.

I. INTRODUCTION

The direct reaction (DR) theories have been used very successfully and extensively in recent years, in order to analyze data of reactions leading to discrete nuclear states. More recently attempts have been made to extend these theories to analyze data of reactions leading to the continuum. This extension was first carried out successfully for the analyses of light-ion induced reactions,[1] and then later for heavy-ion induced reactions.[2-5] There are two sets of key quantities that are to be calculated in applying DR theory to continuum data, the DR cross sections and the spectroscopic densities.[1] When light-ion induced continuum reactions are studied, the DR cross sections can be evaluated in very much the same way as they are for discrete state transitions. To do the same for heavy-ion induced reactions is, however, often too involved and practically impossible. The obvious reason for this is that for heavy-ion processes we have to use the exact-finite-range distorted-wave Born approximation (EFR-DWBA) and also have to consider a huge number of partial waves and transferred angular momenta.

Fortunately, however, for heavy-ion reactions, the transition amplitudes, or equivalently the overlap integrals of the DWBA theory, admit a very simple parametrization,[6,7] even when an EFR approach is used. They are rather accurately expressed in terms of a very simple analytic function, which involves only a few parameters, as well as quantum numbers. One thus needs to perform accurate evaluation of the overlap integrals only for selected sets of quantum numbers and energies, and the results are used to fix the parameters in the assumed analytic function. Once this parametrization is done, the DR cross section can be generated rather quickly.

The first successful application[2] of this parametrization technique was made to the analysis of the (^{20}Ne, ^{16}O) and (^{20}Ne, ^{12}C) reactions on an ^{27}Al target with $E_{\text{lab}}(^{20}\text{Ne}) = 120$ MeV.[8] It was assumed that the (^{20}Ne, ^{16}O) reaction proceeded as a one-step transfer of an alpha particle, while the (^{20}Ne, ^{12}C) reaction was a successive transfer of two alpha particles. It was found that we were able to fit rather nicely, not only the spectral shapes, but also the relative magnitudes of the ^{16}O and ^{12}C cross sections.

The same technique was then found[3] to be extremely powerful in explaining the spectrum and the polarization of ^{12}B observed in the ^{100}Mo (^{14}N, ^{12}B) ^{102}Ru reaction.[9] As explained in some detail in Ref. 3, we went one step further there in carrying out the calculations analytically. Thus after the overlap integrals were expressed analytically, several geometrical factors involved in the transition amplitude were also expressed analytically, by using their asymptotic forms. This made it possible to perform the summations over quantum numbers analytically also, bringing the transition amplitude into a closed analytic form. We were then able to obtain a good physical insight into what was taking place in the reaction, in particular demonstrating very clearly the crucial role played by the so-called recoil effect.

The work of Refs. 2 and 3 was further extended more recently to somewhat more complicated processes,[4,5] again very successfully. We have thus been convinced that the method we have developed indeed has a wide applicability. In our previous publications,[2-5] however, not much detail has been presented of how the parametrization procedure was carried out. To discuss this useful approach in detail is the purpose of the present article.

For the sake of clarity of presentation, we shall restrict ourselves in the present paper, for the

© 1980 The American Physical Society

most part, to the (^{14}N, ^{12}B) reaction of Ref. 9, which was studied in Ref. 3. In Sec. II, we first present the analytic form for the overlap integrals, which is a product of four factors. We then explain, step by step, how each of these factors emerged and how the parameters involved were fixed. Two of the four factors have Gaussian forms, representing the rather well known l-window effects. Another factor, called N_0, had not been investigated in the past, however, and we found that its behavior was fairly complicated.

We thus take up this N_0 factor anew in Sec. III, and investigate the origin of its peculiar behavior. The answer we have found is that N_0 copies rather faithfully the behavior of the form factors. In other words, what we found is that, once the behavior of the form factor is known, which is a comparatively easy thing to achieve, one can predict the behavior of the N_0 factor. Since the fourth factor in the analytic expression of the overlap integral is nothing but a phase factor coming from the two distorted waves involved, we thus have a complete knowledge of what functional form should be adopted to parametrizing the overlap integrals.

A few final remarks will be presented in Sec. IV.

II. PARAMETRIZATION OF THE DWBA OVERLAP INTEGRALS

The DWBA overlap integrals which we are to evaluate may be written using the notation, e.g., of Ref. 12, as

$$I_{l_b l l_a}^{l_1 l_2}(E_b, E_a) = (k_a k_b)^{-1} \times \int \lambda_{l_b}(r_b) F_{l_b l l_a}^{l_1 l_2}(r_b, r_a) \chi_{l_a}(r_a) dr_a dr_b \,. \tag{1}$$

Here χ_{l_a} and χ_{l_b} are the distorted waves in the incident and exit channels, respectively, while $F_{l_b l l_a}^{l_1 l_2}(r_b, r_a)$ is the EFR form factor.

The above overlap integrals depend, among other things, on the orbital angular momenta l_a and l_b of the partial waves. They also depend on the channel energies E_a and E_b, but we are normally concerned with a fixed incident energy E_a, thus making (1) depend more directly on the reaction Q value, $Q = E_b - E_a$.

The overlap integrals further depend on l_1 and l_2, the orbital angular momenta which, in the specific example of the ^{100}Mo(^{14}N, ^{12}B)^{102}Ru reaction, the center of mass of the two transferred protons has, respectively, in ^{102}Ru and ^{14}N, relative to the cores ^{100}Mo and ^{12}B. It was shown in Ref. 3 that we can treat the above process by assuming that the two protons are coupled to an internal spin equal to zero, and that we can fix $l_2 = 2$. As for l_1, let the spin of a final state of ^{102}Ru be denoted by I_B. Since the internal spin of the two protons vanishes, and the target ^{100}Mo has $I_A = 0$, we have $l_1 = I_B$. The transferred orbital angular momentum l, which must satisfy the triangular condition $\vec{l} = \vec{l}_1 + \vec{l}_2$, then takes five values for fixed l_1: $l = l_1 \pm 2$, $l_1 \pm 1$, and l_1. Among them, $l = l_1 \pm 2$ and l_1 are of normal parity since $l + l_1 + l_2$ = even, while $l = l_1 \pm 1$ are of non-normal parity since $l + l_1 + l_2 =$ odd.

It is important to remark here that the radial part of the wave function, describing the motion of the center of mass of transferred nucleons in the recipient nucleus, and consequently the form factors, may in general depend on the reaction Q value, as well as on l_1. Normally, however, we ignore this Q dependence, and construct the above radial wave function once and for all corresponding to a Q value appropriate for the ground-state to ground-state transition. [See Ref. 1 for an argument justifying this treatment.] To remove this assumption of the Q independence, however, does not make our procedure tremendously more complicated than it is with this assumption. It is true that we then have to reconstruct the form factor at each Q. However, as seen below, we actually construct the overlap integral (1) for a very restricted number of Q values anyway, even when a Q-independent form factor is used.

We now claim that the above overlap integral can be represented, to a good approximation, by an analytic function of the form

$$I_{l_b l l_a}(E_b, E_a) = N_0(l_1 l_2 l l_a l_b) \exp[-(l_b - l_b^{(0)})^2/\Gamma_b^2] \times \exp[-(l_d - l_d^{(0)})^2/\Gamma_d^2] \exp(i\delta) \,, \tag{2a}$$

with

$$l_d = l_b - l_a \,, \tag{2b}$$

$$\Gamma_i = \alpha_i + \beta_i Q \quad (i = b \text{ or } d) \,, \tag{2c}$$

$$l_i^{(0)} = \gamma_i + \epsilon_i Q \quad (i = b \text{ or } d) \,, \tag{2d}$$

$$\delta = \delta_{l_a} + \delta_{l_b} \simeq \psi_0 + (l_b - l_b^{(0)}) \psi_1(Q) \,. \tag{2e}$$

The quantity δ_{l_a} in (2e) is the real part of the phase shift of the elastic scattering in the incident channel, and similarity δ_{l_b} is that for the exit channel.

A feature to be noted in (2a) is that I is characterized by two l localizations, introducing two windows in the l space. We refer to them as l_b and l_d windows henceforth. The origin of these windows has been discussed in the literature; see e.g., Ref. 7. In short, it is the peripheral nature of the direct reactions which enforces a good kinematic matching, in order for the cross sections to have significant values. The centers $l_i^{(0)}$ and the widths Γ_i ($i = b$ or d) of these windows generally depend on Q, and as seen in (2c) and (2d), we have assumed linear forms. The validity of this choice will soon be demonstrated.

The right-hand side of (2a) includes in it another real factor N_0, and we shall later discuss in detail its dependence on various angular momenta. The last factor of (2a) has a unit magnitude and is the only complex factor in (2a). The choice of δ as a sum of two phase shifts, as given in the first equality of (2e), is very reasonable because of the following facts.

As seen in (1), the origin of the complex nature of I is the two distorted waves in the integrand. Since the heavy ions are strongly absorptive, each distorted wave consists (in the peripheral region) predominantly of the outgoing wave, whose phase is given closely by the real part of the phase shift of the elastic scattering. The phase factors which the two distorted waves thus acquire are then maintained as they are, even after the integration in (1) is carried out, making it imperative for I to have the phase factor it is seen to have in (2a). That the phase δ can be expanded linearly in l_b, introducing in the course of expansion the deflection angle ϕ_1, as seen by the second equality of (2e), is rather well known,[7] and we shall not discuss this feature further here.

Once the phase factor of (2a) has been understood in this way, we may concentrate our interest and discussion on the magnitude of I, i.e., on how the functional forms of the first three factors of (2a) were chosen and how the parameters involved were fixed. This process of parametrization must of course be preceded by that of the EFR-DWBA evaluation of I, for a large but nevertheless limited number of sets of values of Q, l_a, l_b and l. [In the example of the (^{14}N,^{12}B) reaction,[3] this number was about 3000.] Somewhat crudely, it is proportional to the number of different l's (for a fixed l_1), i.e., to $(2l_2 \pm 1)$. Therefore, it can be much smaller if, e.g., $l_2 = 0$. Once a sufficient number of the $|I|$ values, which we shall henceforth call "data," are accumulated, their parametrization proceeds as follows.

The first step is to fit the magnitude of the data, i.e., $|I|$, as close as possible by a function of the form

$$|I| = N_1 \exp[-(l_b - l_b^{(0)})^2/\Gamma_b^2]. \tag{3}$$

Clearly this function has l_b as its only independent variable. In this fitting procedure, the values of the parameters $l_b^{(0)}$, Γ_b, and N_1 are obtained as functions of Q, as well as of the quantum numbers l_a, l_1, and l. It was found, however, that, although $l_b^{(0)}$ and Γ_b did depend on Q, their dependence on l_a, l_1, and l was rather weak. We thus decided to ignore the latter dependence entirely.

In order to show the situation more explicitly, we plot in Fig. 1 the χ^2-fitted values of $l_b^{(0)}$ and Γ_b, calculated for four choices of the Q values. In this figure, these values of $l_b^{(0)}$ and Γ_b are represented by open circles, each circle corresponding to a given set of l_a, l_1, and l. It is seen that these circles are nicely clustered together for each Q, showing the fairly weak dependence on the three quantum numbers.

Figure 1 further shows that the centers of the clusters of the circles lie very nicely on straight lines, justifying the choice of the linear dependence of $l_b^{(0)}$ and Γ_b on Q in Eqs. (2c) and (2d). The straight lines drawn in Fig. 1 have coefficients α_b, β_b, γ_b, and ϵ_b determined so that these lines represent best, in the sense of χ^2, the centers of the clusters of the circles, as functions of Q.

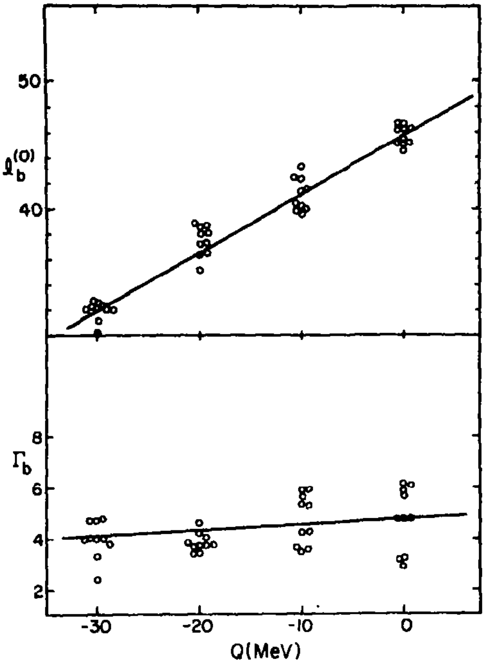

FIG. 1. χ^2-fit determined values of $l_b^{(0)}$ and Γ_b, based on (3). Circles represent as example the values calculated for $(l_1, l) = (10,10)$ and $(10,12)$ with $l_a = -4(-2)-12$. To be precise, all circles should appear on vertical lines corresponding to appropriate Q values, horizontal displacement being employed simply to avoid overlapping. As discussed in the text χ^2-fitting yields $l_b^{(0)} = 50.2 + 0.458Q$ and $\Gamma_b = 4.9 + 0.2Q$.

The second step of the parametrization begins by first expressing the coefficient N_1, whose values have been derived in the above first step of fitting, as

$$N_1 = N_0 \exp[-(Q - Q_0)^2/\Gamma_Q^2]. \tag{4}$$

The reader may wonder why a Gaussian function of Q, rather than of l_d, as was the case in (2a), is introduced here. The reason is that $|l_d|$ cannot exceed a given value of l, making it impossible to obtain enough sampling of the N_1 for a sufficiently wide range of the values of l_d. With the form of (4), this difficulty can be avoided.

By using (4), the values of N_0, Q_0, and Γ_Q can be fixed as functions of l_d, l_1, and l. It was first found that Q_0 in practice depended only on l_d, and that this dependence was linear:

$$Q_0 = q_0 + q_1 l_d , \qquad (5)$$

the coefficients q_0 and q_1 being fixed again by a χ^2 fit. It was further found that Γ_Q could be taken simply as a constant. Therefore, Eq. (4) can now be replaced by

$$N_1 = N_0 \exp[-(l_d - l_d^{(0)})^2/\Gamma_d^2] , \qquad (6)$$

recovering the coveted Gaussian factor that depends on l_d. Obviously the following relations hold, to express the parameters in (2) in terms of Γ_Q, q_0 and q_1:

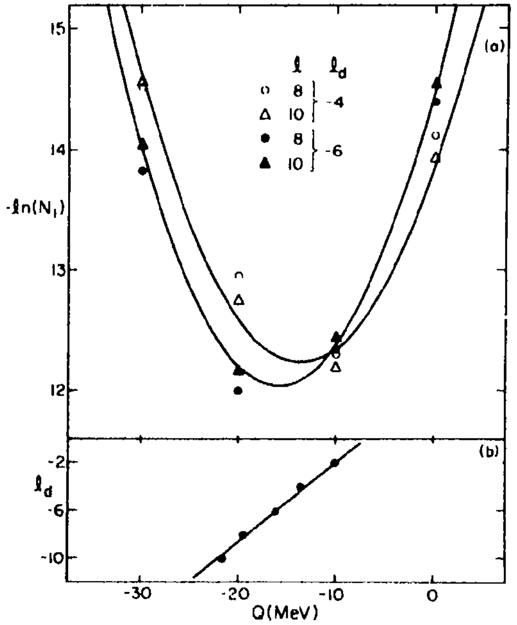

FIG. 2. (a) χ^2-fit values of $-\ln(N_1)$ determined for $(l_1, l) = (10, 8)$ and $(10, 10)$, and for $l_d = -4$ and -6. Curves drawn are represented by $-\ln(N_1) = 0.01\,(Q - Q_0)^2 + C$ with $Q_0 = -13.6$ and -15.9 (MeV) and $C = 12.24$ and 12.04, respectively, for $l_d = -4$ and -6: (b) l_d as function of Q_0. Straight line represents χ^2 fit as given by $l_d = 0.667 Q_0 + 4.67$.

$$\begin{aligned} l_d^{(0)} &= -(q_0/q_1) + Q/q_1 , \quad \Gamma_d = \Gamma_Q/q_1 , \\ \alpha_d &= \Gamma_Q/q_1 , \quad \beta_d = 0 , \quad \gamma_d = -q_0/q_1 \end{aligned} \qquad (7)$$

and

$$\epsilon_d = 1/q_1 .$$

In order to show how good this parametrization really is, we have plotted in Fig. 2(a) the values of N_1 [actually of $-\ln(N_1)$] obtained in the above first step of parametrization, for four chosen sets of l_d and l_1 values, and four different Q values. They are to be compared with the solid lines representing the N_1 values obtained from the use of Eq. (6), and the agreement is seen to be good. In Fig. 2(b), on the other hand, comparison is made between the values of calculated l_d, as a function of Q_0, and the l_d expressed in terms of (5). They agree very nicely with one another, justifying the linear dependence chosen in (5).

The second procedure for parametrization also yields the values of N_0, obtained as a function of Q, l_d, l_1, and l. A nice feature found was that N_0 was in practice independent of Q, indicating that the Q dependence of $|I|$, i.e., the dependence of $|I|$ on the reaction dynamics, has been well incorporated into the two Gaussian factors that were derived above.

In order to illustrate the dependence of N_0 on the angular momentum quantum numbers, we show in Fig. 3(a) its values plotted as functions of l_d, for all the possible five values of l $(= l_1 - 2 \sim l_1 + 2)$ and for two choices of l_1, $l_1 = 6$ and 10.

A number of interesting features are seen in this figure. First of all, we observe that two curves with different l_1 but the same $\Delta(= l - l_1)$ behave

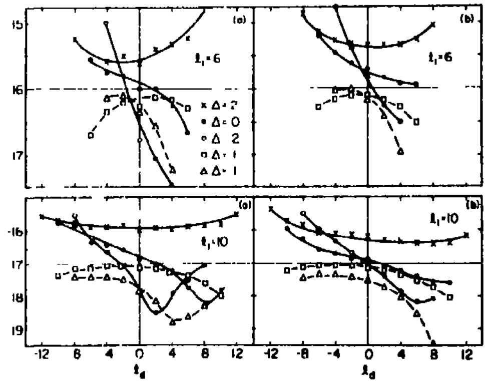

FIG. 3. (a) $\ln(N_0) - 4.4$ as determined by χ^2-fit. (b) $\ln(F)$ plotted as function of l_d. In (a), a subtraction of 4.4 has been made in order to facilitate the comparison of the two sets of quantities. In (b), the values of F as determined by (9) have not been altered. The curves were drawn simply as guides.

TABLE I. Parameters that appear in Eq. (8).

Δ	κ_1	κ_2	$\kappa_3 \times 10^2$	$\kappa_4 \times 10^2$	$\kappa_5 \times 10^2$	$\kappa_6 \times 10^2$
2	−13.9	−0.225	4.69	−0.80	0.90	−0.059
1	−14.6	−0.250	−0.25	−0.38	−1.26	0.071
0	−14.7	−0.225	−1.50	−1.00	0.0	0.0
−1	−14.3	−0.325	−9.38	−0.31	−4.61	0.353
−2	−15.2	−0.075	−7.30	0.40	0.0	0.0

very similarly. The curves with $\Delta = 2$ depend on l_4 weakly but quadratically. Those with $\Delta = 0$ and -2 are approximately linear in l_4, the latter having a gradient steeper than the former. All these three curves with even Δ, i.e., those with normal parity, share a common feature in that they increase as $|l_4|$ increases with $l_4 < 0$. Compared with them, those with odd $\Delta (= \pm 1)$ decrease with increasing $|l_4|$, the dependence being approximately quadratic.

Similar features were seen for other values of l_1 also, and combining these results, we found that the following expression gives a good description of the angular momentum dependence of N_0:

$$N_0 = \exp[\kappa_1 + \kappa_2 l_1 + (\kappa_3 + \kappa_4 l_1) l_4 + (\kappa_5 + \kappa_6 l_1) l_4^2] . \quad (8)$$

The parameters $\kappa_1 \sim \kappa_6$ are dependent on Δ. Their values are summarized in Table I.

Equation (8) with the parameter values of Table I was actually used in the calculation made in Ref. 3. As seen, the angular momentum dependence of N_0 is somewhat complicated. This has, however, to a large extent been brought about because we have chosen as an example the reaction (^{14}N, ^{12}B) for which $l_2 = 2$, allowing Δ to take five different values. In the case, e.g., of an α-transfer reaction leading a 0^+ projectile to a 0^+ ejectile, we have $l_2 = 0$. This then allows a single Δ (=0), making N_0 be given by (8) with a single set of $\kappa_1 \sim \kappa_6$ parameters. Then the factor N_0 is not much more complicated than are the other factors of (2a). In practice the use of (8) is not so tedious, however, even when several Δ's are permissible.

III. ORIGIN OF THE ANGULAR MOMENTUM DEPENDENCE OF N_0

The physical origin of the l window is well known,[7] and thus the appearance of the two Gaussian factors in (2a) was not unexpected. The rather complicated dependence of the factor N_0 on angular momenta, as found towards the end of the last section, was on the other hand somewhat unexpected. Unless the origin of this peculiar behavior of N_0 is found, our task of fully understanding the behavior of the DWBA overlap integrals remains incomplete, and the significance of the parametrization we have achieved might remain suspect. We thus attempted to find the physical origin of Eq. (8), and it appears that we have succeeded. Because of this, we now feel that the choice of the functional form of (8) has a good physical justification, and a rather universal validity.

The key step which helped to find the origin we sought for was to recognize a surprisingly close similarity between the behaviors of N_0 and of the form factors. This can be seen, e.g., by comparing the curves in Fig. 3(a) with those in Fig. 3(b), which represent peak values (in the peripheral region) of the form factors associated with various sets of three angular momenta. The choice of these sets was made in the same way as in Fig. 3(a), and the similarity of the corresponding curves in these two figures is evident. (To be more precise, the stated similarity gets somewhat poorer for large positive l_4's. For practical purposes, however, this causes no serious problem, because as we emphasized, particularly in Ref. 3, it is the large negative l_4's that contribute dominantly to most continuum spectra.)

Once the above similarity is found, it is clear that the behavior of N_0 is understood, if that of the form factor is understood. In the rest of this section, we shall thus concentrate on the latter.

For this purpose, we find it very convenient to use the following expression for the EFR form factor, which was derived in our recent reformulation[10]:

$$F^{l_1 l_2}_{l_b l l_a}(r_b, r_a) = \tfrac{1}{2}[(4\pi)^{3/2}/(2l+1)]\hat{l}_b i^{l_a+l_b+l_1+l_2}$$

$$\times \sum_{m_l m_1 m_2} (l_a m_l l_b 0 | l m_l)(l_1 m_1 l_2 m_2 | l - m_l)(-)^{l+m_l}[2/(1+\delta_{m_l,0})] \int W_{l_1}(r_1) W_{l_2}(r_2) Y_{l_a m_l}(\theta) Y_{l_1 m_1}(\theta_1)$$

$$\times Y_{l_2 m_2}(\theta_2) d\mu . \quad (9)$$

Here $\mu = \cos(\theta)$, and the angles θ, θ_1, and θ_2 are defined as $\theta = \hat{r}_a \wedge \hat{r}_b$ and $\theta_i = \hat{r}_b \wedge \hat{r}_i$ ($i = 1$ and 2). See Ref. 10 for other notation.

The use of the form (9), rather than that of Austern *et al.*[11,12] not only helps to make the following argument much more transparent, but also has been vital in making the calculations of Refs. 2–5 possible. As emphasized in Ref. 10, the Austern form becomes very inconvenient to use if l exceeds a certain value which is rather small, say 5, because a very difficult problem of truncation error emerges. With the form of (9), we do not encounter this numerical problem, and so this form is in fact used in the step of evaluating the EFR-DWBA overlap integrals, from which our parametrization procedure starts. Since we are concerned with transitions to the continuum, we encounter very large l values, which may easily go beyond 20.

Returning to the main subject of the present section, we first note that the integrand of the integral over μ, appearing in (9), is peaked very sharply in the extreme neighborhood of $\mu = 1$. In the present example of the (^{14}N,^{12}B) reaction, it is not difficult to show that the range of μ over which the above integration must be carried out is given by $\mu = 0.9995 \sim 1$. The reason why such an extremely narrow range of integration is encountered is the same as is given for a similar integral that appeared in the Austern form of the form factor, explained in detail in Ref. 12.

The fact that μ remains very close to unity results in another localization: that the integral in (9) can have significant values only when $|m_l|$ is very small, $|m_l| = 0$, and possibly $= 1$. This is because l_a is normally large, and thus $|Y_{l_a m_l \pm 1}(\mu)| \ll |Y_{l_a m_l}(\mu)|$, if $\mu \approx 1$. Thus the summation over m_l is very limited. The summation over m_2 is also limited because $|m_2| \leq l_2 = 2$. Because of the second Clebsch-Gordan (CG) coefficient in (9), which requires that $m_1 + m_2 = m_l$, the allowed range of m_1 is also narrow. We may remark further that the factor $Y_{l_1 m_1}(\theta_1)$ in the integrand in (9) also has a tendency to make the integral smaller as $|m_1|$ gets larger.

Having in mind the restriction of $|m_l|$ to 0 and 1, we may now remark that the $m_l = 0$ term in (9) gives the no-recoil part of the form factor, while that with $m_l = 1$ contributes the recoil correction. Note that we mean by "recoil" only the so-called *transverse* part of recoil. The *longitudinal* recoil is included in both the $|m_l| = 0$ and 1 terms.

We shall now rewrite the expression of (9) somewhat, by taking particular advantage of the severely restricted sum over the magnetic quantum numbers. For simplicity, we shall henceforth denote the integral factor in (9) simply by $i(m_l, m_1, m_2)$, and then introduce further the ratios $P_0 = i(0,1,-1)/i(0,0,0)$, $P_1 = i(1,0,-1)/i(0,0,0)$, $P_2 = i(1,-1,0)/i(0,0,0)$, and $P_3 = i(1,1,-2)/i(0,0,0)$. It is then a straightforward matter to find that (9) can be replaced by

$$F^{l_1 l_2}_{l_b l l_a}(r_b, r_a) \simeq \tfrac{1}{2}[(4\pi)^{3/2}/(2l+1)]\hat{l}_b i^{l_a+l_b+l_1+l_2}(-)^l i(0,0,0)$$
$$\times \{(l_a 0 l_b 0|l 0)[(l_1 0 l_2 0|l 0) + 2(l_1 1 l_2 -1|l 0)P_0]$$
$$-2(l_a 1 l_b 0|l 1)[(l_1 0 l_2 -1|l -1)P_1 - (l_1 -1 l_2 0|l -1)P_2 + (l_1 1 l_2 -2|l -1)P_3]\}. \tag{10}$$

It is clear that the terms involving P_1, P_2, and P_3 factors are the recoil terms. We also remark here that the ratios $P_0 \sim P_3$ are all positive. Keep in mind that they are the ratios of the integrals of (9) taken at the values of r_a and r_b where the form factors take their maximum values.

The expression of (10) can be brought further into a much more transparent form. To do this, we first mention the approximate relations

$$(l_a 1 l_b 0|l 1) \simeq \begin{cases} -(l_a/2l)(l_a 0 l_b 0|l 0) & (l_a + l_b + l = \text{even}), \\ [1-(l_a/l)^2]^{1/2}(l_a 0 l_b 0|l+1 0) & (l_a + l_b + l = \text{odd}), \end{cases} \tag{11}$$

which are derived by using recursion relations between CG coefficients.[13] We may also note the relation

$$(l_a 0 l_b 0|l 0) \simeq (4e/\pi)^{1/2}\hat{l}_b^{-1}[1 + (l_a/2l)^2]i^{l_a+l_b-l}, \tag{12}$$

which is obtained by using Stirling's formula to evaluate the factorials in terms of which the parity-conserving CG coefficients are expressed.

Using (11) and (12), and the explicit forms of the CG coefficients involving $l_2 = 2$, we can now rewrite (10) as

$$F^{l_1 l_2}_{l_b l l_a}(r_b, r_a) \simeq \tfrac{1}{2}[(4\pi)^{3/2}/(2l+1)][(4e/\pi)]^{1/2}$$
$$\times i(0,0,0)[1 + (l_a/2l)^2]\chi_\Delta, \tag{13a}$$

where

$$\chi_\Delta = \begin{cases} \tfrac{3}{8}[1 \pm \tfrac{8}{3}P_0 - (l_a/l)(P_1 \pm \tfrac{2}{3}P_3)] & (\Delta = \pm 2), \\ \tfrac{1}{2}[1 - \tfrac{1}{2}(l_a/l)^2](P_2 \pm P_3) & (\Delta = \pm 1), \\ \tfrac{1}{2}[1 - (l_a/l)P_1] & (\Delta = 0). \end{cases} \tag{13b}$$

This is the final expression of the form factor we wanted to derive. We shall now show that this expression does contain in it every feature which the curves given in Fig. 3(b) reveal in themselves.

For simplicity of presentation, let us denote by $F(\Delta)$ the five expressions on the right-hand side of (13). As we noted above, all the P's are positive. We further note here that P_0, P_1, and P_2 are of the same order of magnitude, being close but somewhat smaller than unity, while P_3 is much smaller. From these properties of the P's, one may easily deduce the following properties of the $F(\Delta)$.

(i) At $l_d = 0$, an inequality $F(2) > F(0) > F(-2) > F(1) > F(-1)$ should hold. (ii) For all l_d, an inequality $F(1) > F(-1)$ should hold, although the difference between $F(1)$ and $F(-1)$ is small (since $P_3 < P_2$). (iii) For all l_d, $F(1)$ and $F(-1)$ should both depend on l_d like $[1 - \frac{1}{4}(l_d/l)^2]$. (iv) For all l_d, $F(2)$ should depend on l_d as does $[1 + (l_d/l)^2]$, if (and in fact since) $P_1 - \frac{2}{3}P_2 \approx 0$. (v) $F(-2)$ and $F(0)$ should decrease almost linearly, as l_d increases, the former having a slope steeper than that in the latter. [This is seen from the last terms of $F(-2)$ and $F(0)$, and the fact that $P_1 + \frac{2}{3}P_2 > P_1$.] (vi) The l_d dependence discussed in the last three of the above items should get weaker as l_1 is increased. [This is because l_d appears in (13) always in the form of l_d/l, and because $l = l_1 + \Delta$.]

All the expectations enumerated in the above items (i)–(vi) are seen to be fulfilled by the curves given in Fig. 3(b), at least qualitatively, and in many cases even quantitatively, with possibly only one exception, namely that (ii) is violated slightly when $l_1 = 6$ and $l_d < 0$. We may thus say that we now have a nearly perfect understanding of the behavior of (the peak values of) the form factor. We may emphasize here that the complicated Δ dependence of $F(\Delta)$ is almost entirely due to the recoil effect, and we have now succeeded in understanding very clearly this Δ dependence of the recoil effect.

In the item (vi) above, we referred very briefly to the l_1 dependence of the form factor. There remains, however, one more very important l_1 dependence to be pointed out and to be explained. It is that the overall magnitude of the form factor decreases as l_1 is increased, which can be seen by comparing the two sets of curves in Fig. 3b, one for $l_1 = 6$ and the other for $l_1 = 10$. This l_1 dependence of the form factor can be traced back to that of the factor $i(0,0,0)$ in (13), and is explained as follows.

The factor $i(0,0,0)$ is nothing but the integral in (9), when all the magnetic quantum numbers there are set equal to zero. The factor $Y_{l_d 0}(\mu)$ in the integrand has its maximum value at $\mu = 1$, and decreases very rapidly as μ deviates from 1. Since $\cos\theta_1 = 1$, when $\mu = 1$, (see Ref. 10) the factor $Y_{l_1 0}(\theta_1)$ is also peaked at $\mu = 1$, and decreases as μ is decreased. When l_1 is small, however, $Y_{l_1 0}(\theta_1)$ remains essentially unchanged within the very narrow range of the μ integral, which we discussed above. However, if l_1 is large, the deviation of $Y_{l_1 0}(\theta_1)$ from its peak value becomes non-negligible, making the integrand smaller than it is otherwise. This is the reason why $i(0,0,0)$ decreases as l_1 increases. In this way the last remaining l_1 dependence of the form factor is understood.

Since the behavior of the form factor has now been well understood, so is that of the factor N_0. After all, the similarity of the behaviors of the form factor and of N_0 are also easy to understand. As can be seen from (2a), N_0 is nothing but the magnitude of the overlap integral itself, when the latter is obtained under the restriction that both l_b and l_d have their respective window values, i.e., that the best conceivable kinematic matching is established. The overlap integrals that are selected under such severe restrictions will have to depend on nothing other than the peak values of the underlying form factors.

IV. FINAL REMARKS

We have shown that the EFR-DWBA overlap integrals can be represented rather well by a fairly simple analytic function, with a few parameters in it. Once this parametrization is carried out, the calculation of the DWBA cross section can be done in a well known way; it is the same irrespective of whether the overlap integrals are given in a parametrized form or not. This cross section, which we may simply denote as σ_{DW}, is a function of Q, l_B $(=l_1)$ and l. In order to use this σ_{DW} to obtain the continuum cross section σ, it must further be combined with another function which we call[1-5] the spectroscopic density and denote by ρ_s. This function ρ_s depends on l_B, as well as on E_x, the excitation energy of the residual nucleus, which is given by $E_x = Q_{gr} - Q$, where Q_{gr} is the Q value corresponding to the ground-state-to-ground-state transition. More explicitly we may get

$$\sigma(Q,\theta) = \sum_{l_B} \left\{ \sum_{l} \sigma_{DW}(l_B, Q, l, \theta) \right\} \rho_s(E_x, l_B). \quad (14)$$

As is clear from (14), the explanation of how to use the direct reaction theory to fit the continuum cross sections remains incomplete, until the way to construct ρ_s is explained. This has been done, however, in our previous publications, though it was somewhat cursory.[1-5] We shall not repeat it here, but intend to rediscuss it in a somewhat more systematic way in a forthcoming paper,[14] in which the calculations made in Refs. 2–5 will be reviewed in detail.

As we emphasized above, the behavior of the factor N_0 was fairly complicated, largely because we chose, as an example, the case which has $l_2 = 2$. In the very simple case with $l_2 = 0$, the peak values of the form factor are simply given by (13) retaining only the term with $\Delta = 0$, after replacing P_1 there by P_2. Thus the reader will find it very easy to apply our method, if his interest is limited to the case with $l_2 = 0$.

We finally want to remark that our discussions given in the present paper have been limited to the use of the *one-step* DWBA theory. We have seen in Refs. 2–5 that a variety of data could be explained, even if this restriction was made. We also saw, however, in these same works, that (part of) the data indicated the necessity of considering higher-order contributions as well. In Ref. 2, an example was given of how to use the parametrized form of the one-step DWBA overlap integrals, in order to obtain the amplitudes of the two-step processes. Although it was found[8] that this method worked rather well also, it was also clear that the calculations involved were rather tedious. It is thus very desirable to find a method to parametrize the two- (and possibly still higher-) step amplitudes in a much more direct way. An investigation of such a possibility is under way.

We are very much indebted to Dr. B. T. Kim for his participation in the early stage of the present work. We thank Dr. W. R. Coker for editing our original manuscript. The present work was supported in part by the U.S. Department of Energy.

---

[1] T. Tamura, T. Udagawa, D. H. Feng, and K. K. Kan, Phys. Lett. 66B, 109 (1977). T. Tamura and T. Udagawa, *ibid.* 71B, 273 (1977); 78B, 189 (1978).

[2] T. Udagawa, T. Tamura, and B. T. Kim, Phys. Lett. 82B, 349 (1978).

[3] T. Udagawa and T. Tamura, Phys. Rev. Lett. 41, 1770 (1978); 42, 1501 (1979).

[4] H. Frolich, T. Shimoda, M. Ishihara, K. Nagatani, T. Udagawa, and T. Tamura, Phys. Rev. Lett. 42, 1518 (1979).

[5] M. Ishihara, T. Shimoda, H. Frolich, H. Kamitsubo, K. Nagatani, T. Udagawa, and T. Tamura, Phys. Rev. Lett. 43, 111 (1979).

[6] V. Strutinsky, Zh. Eksp. Teor. Fiz. 46, 2078 (1964) [Soviet Phys.—JETP 19, 1401 (1964)].

[7] S. Kahana and A. J. Baltz, *Advances in Nuclear Physics*, edited by M. Barangor and E. Vogt (Plenum, New York, 1977), Vol. 9, p. 1.

[8] J. B. Natowitz, N. M. Namboodiri, I. Eggers, P. Gonthier, K. Goeffroy, R. Hanus, C. Towsley, and K. Das, Nucl. Phys. A277, 477 (1977).

[9] K. Sugimoto, N. Takahashi, A. Mizobuchi, Y. Nojiri, T. Minamisono, M. Ishihara, K. Tanaka, and H. Kamitsubo, Phys. Rev. Lett. 39, 323 (1977).

[10] T. Tamura, T. Udagawa, and H. Amakawa, Prog. Theor. Phys. 60, 1238 (1978). T. Tamura, T. Udagawa, K. E. Wood, and H. Amakawa, Comp. Phys. Commun. 18, 163 (1979).

[11] N. Austern, R. M. Drisco, E. C. Halbert, and G. R. Satchler, Phys. Rev. 133, B3 (1964).

[12] T. Tamura, Phys. Rep. 14C, 59 (1974).

[13] D. M. Brink and G. R. Satchler, *Angular momentum* (Oxford University Press, London, 1968).

[14] T. Udagawa, T. Tamura, and K. Nagatani (unpublished).

PHYSICAL REVIEW C VOLUME 21, NUMBER 5 MAY 1980

Diffraction structure in back angle p-^{4}He elastic scattering

L. G. Arnold and B. C. Clark
Department of Physics, The Ohio State University, Columbus, Ohio 43210

R. L. Mercer
Thomas J. Watson Research Center, International Business Machines Corporation, Yorktown Heights, New York 10598

(Received 7 August 1979)

A Dirac equation optical model calculation with a relativistic Majorana exchange potential is used to represent the large angle diffraction structure observed in the 788 MeV p-^{4}He cross section data.

[NUCLEAR REACTIONS ^{4}He(p,p), E=788 MeV; calculated $\sigma(\theta)$, $A(\theta)$, and $Q(\theta)$ from relativistic optical model. Relativistic Majorana exchange potential, large angle scattering.]

In this paper we present a Dirac equation optical model calculation of p-^{4}He elastic scattering at 788 MeV and a comparison with cross section measurements[1] taken at LAMPF. The cross section data are an essentially complete angular distribution which shows the familiar forward angle diffraction pattern due to the direct amplitude and the back angle rise in cross section identified with exchange amplitudes. A remarkable feature of the data, not previously observed, is a diffractionlike structure at large angles that looks like a scaled and distorted mirror image of the forward angle diffraction pattern. We account for this structure in the cross section with a relativistic Majorana exchange potential that is analogous to the nonrelativistic Majorana exchange potential used previously in studies[2,3] of p-^{4}He elastic scattering at lower energies. We also find the analyzing power at large angles to be sensitive to the inclusion of the relativistic exchange potential. Diffraction structure at back angles is a natural consequence of a Majorana exchange potential under kinematic conditions which are fulfilled for p-^{4}He elastic scattering near 800 MeV.

The Dirac equation optical model is described in Refs. 4 and 5. Because the Dirac equation is a relativistic equation, it is necessary to specify the Lorentz transformation character of the optical potential. This is a macroscopic aspect of models based on relativistic wave equations. Previously, we have considered a nucleon-nucleus optical potential which consists of two parts: one part, a potential U_s, transforms as a Lorentz scalar; the other, a potential U_0, transforms as the timelike component of a Lorentz four-vector. This choice is based on elementary meson exchange considerations[6] which allow the four-vector part to be identified with the exchange of vector mesons and the scalar part to be identified with scalar mesons and scalar two pion exchange processes. The latter are often treated as a single scalar-isoscalar meson with a mass of about 550 MeV in the one boson exchange model of the two-nucleon interaction. As specified in this way, the Dirac equation optical model shares common features with recent work on relativistic descriptions of nuclear matter[7] and the ground state structure of finite nuclei.[8-9] We have found that the model is in good correspondence with the real central and spin-orbit parts of the empirical nonrelativistic optical model at low energies.[5] An extrapolation to low energies of the mixture of U_s and U_0 potentials determined from an analysis[4] of the p-^{4}He elastic scattering cross section and analyzing power data[10] for energies above 500 MeV is in good agreement with independent results.[5,7-9] The transition region from the vicinity of the pion production threshold to about 500 MeV, above which the absorption tends to stabilize, is particularly important for the development of the Dirac equation optical model. The change in the real central part of the empirical optical potential from attraction to repulsion in this energy range is dominated by a kinematic feature of the model that is due to the cancellation of U_s (attraction) and U_0 (repulsion) potentials expected from meson exchange consideration. The effect of this delicate kinematic balance on the radial shape of the real central part of the empirical potential in the transition region has been discussed recently by Jaminon, Mahaux, and Rochus.[11]

The Dirac equation with a mixture of U_s and U_0 potentials may be written

$$\{c\vec{\alpha}\cdot\vec{p}+\beta[mc^2+U_s(r)]+[U_0(r)+V_c(r)]\}\psi(\vec{r})=E\psi(\vec{r}), \tag{1}$$

where E is the total energy of the proton in the

© 1980 The American Physical Society

c.m. frame, V_C is the Coulomb potential, and m is the proton mass. The determination of the potential mixtures for p-^{4}He scattering from 560 to 1730 MeV is described in Ref. 4. Here the mixture obtained from the 800 MeV data set is used to calculate the angular distribution of cross section, analyzing power, and spin-rotation function[12] at 788 MeV. Figure 1 shows a comparison of this calculated cross section (dashed curve) with the 788 MeV LAMPF data. There is good agreement out to $-t \cong 3.4$ GeV$^2/c^2$ beyond which a back angle diffractionlike structure emerges and rises well above the calculated cross section. Figure 2 shows a more detailed comparison for the large angle region. In both Figs. 1 and 2 the solid curves are the result of including the exchange potential discussed later. Since the potential mixture was determined from data for $-t \lesssim 1$ GeV$^2/c^2$, the agreement over the seven decade decrease in the measured cross section is strong evidence that the direct amplitude obtained from the model is realistic and that the observed structure at back angles is associated with exchange amplitudes. Note that the calculated direct cross section in the vicinity of the minimum near 4 GeV$^2/c^2$ is an order of magnitude smaller than the measured cross section and that the analyzing power for the direct potential is also very small in this large angle region. While there have been no analyzing power measurements at 788 MeV, experiments[13] at TRIUMF for proton energies between 185 and 500 MeV have revealed that the p-^{4}He analyzing power in the large angle region is systematically large and negative. These results indicate that inclusion of spin dependent exchange amplitudes is important for an understanding of back angle processes. The calculated values for the spin-rotation function are also shown in Figs. 1 and 2. Measurement of this observable could provide additional constraints on the relativistic model.

There are several methods of treating antisymmetrization in descriptions of back angle p-^{4}He scattering at intermediate energies. In the work of Gurvitz, Alexander, and Rinat[14] and Alexander and Landau[15] the exchange is included in the elementary nucleon-nucleon amplitudes. An alternative approach for ^{4}He is the triton exchange model used by Leśniak, Leśniak, and Tekou.[16] The latter is more closely related to the resonating group formulation[2] developed for lower energies. As discussed in Ref. 2, a local spherically symmetric Majorana exchange potential is an approximate local equivalent of the nonlocal resonating group potential identified with heavy-particle pickup processes. Such approximate local $(-1)^l$ type exchange potentials have been used in Schrödinger equation optical model analyses[2,3,17] of back angle scattering.

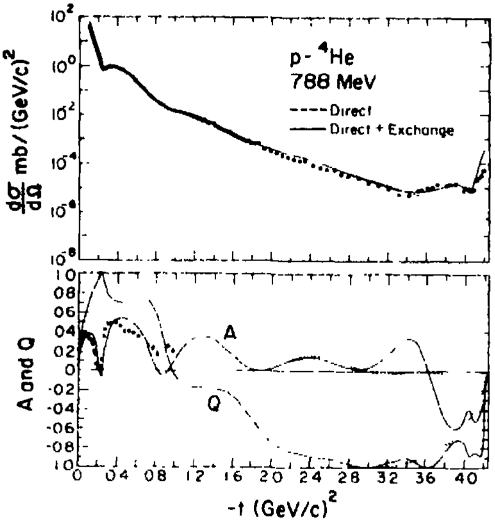

FIG. 1. Calculated 788 MeV p-^{4}He elastic scattering cross section, analyzing power (A), and spin-rotation function (Q) for the direct potential only (dashed curve) and the direct plus the exchange potential with $\lambda = -0.003$ (smooth curve) as described in the text. The cross section data are from Ref. 1 and the analyzing power data are from Ref. 10.

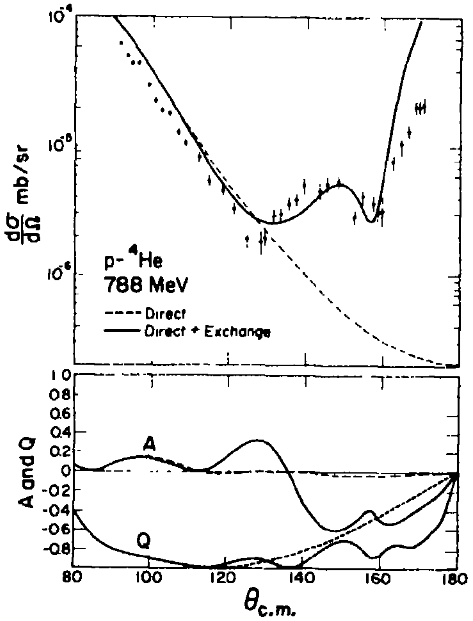

FIG. 2. Same as Fig. 1 for the angular range from 80 to 180 degrees.

An extension of the Majorana exchange potential for use in the Dirac equation is straightforward. We use the relativistic Majorana exchange operator given by

$$P_R = \gamma_0 P_{NR} , \tag{2}$$

where P_{NR} is the nonrelativistic parity operator. The scalar and vector potentials are modified by simply adding an exchange potential to the direct potential in each case. This results in potentials in the radial Dirac equation which have the form

$$U_0(r) = U_0^D(r) + U_0^E(r)(-1)^l \tag{3}$$

and

$$U_s(r) = U_s^D(r) + U_s^E(r)(-1)^l . \tag{4}$$

There is a basic difference between the relativistic and nonrelativistic treatments in that l dependence occurs in both the central and spin-orbit effective potentials obtained from a reduction of the Dirac equation to an equivalent Schrödinger equation form.[4] Thus, the relativistic exchange potentials considered here can be expected to have an effect on the analyzing powers at large angles. This feature, due to the spin dependence implicit in the Dirac equation, is absent in nonrelativistic treatments that ignore spin dependent exchange effects.

We have chosen to parametrize the exchange potentials for the Dirac equation in a manner analogous to the treatment of Ref. 2 for the Schrödinger equation. We take U_0^E and U_s^E to be proportional, respectively, to the real parts of U_0^D and U_s^D. This fixes the ratio $R_E = U_0^E/U_s^E$ to be the same as the ratio of the real parts of the direct potentials. The exchange potentials are then given by

$$U_0E = \lambda \,\mathrm{Re}(U_0^D) \tag{5}$$

and

$$U_s^E = \lambda \,\mathrm{Re}(U_s^D), \tag{6}$$

where λ, the only new parameter introduced in the model, is adjusted to give the magnitude of the cross section in the back angle diffraction region. The solid curves in Figs. 1 and 2 are the results of a calculation with $\lambda = -0.003$. Although we have not attempted a detailed fit, it is apparent that inclusion of the exchange potentials in this way reproduces the general features of the back angle diffraction structure. The exchange potentials also have a significant effect on the analyzing power in the large angle region. The analyzing power exhibits a diffraction structure complementary to the cross section and, in contrast to the analyzing power from the direct potential alone, is large in magnitude.

The model exchange potentials given by Eqs. (3) and (4) contain considerably more flexibility than the constrained single parameter form given by Eqs. (5) and (6). Preliminary calculations with the more general form reveal that the cross section and analyzing power at large angles are sensitive to a number of variables including the radial shape of the exchange potentials, the ratio R_E, and the addition of absorption. We are investigating these features and have begun a systematic analysis at other energies.

In conclusion, the calculations given in this paper show that a relativistic Majorana exchange potential can give diffraction structure in the large angle cross section. This exchange potential, which leads to a $(-1)^l$ dependence in the effective spin-orbit potential, also produces substantial changes in the calculated analyzing power at large angles. Finally, the calculations support the view that heavy-particle pickup processes are a relevant mechanism in the description of large angle cross sections and analyzing powers.

We thank B. Mulligan and H. S. Sherif for helpful discussions, C. Mahaux for useful correspondence, C. A. Whitten, Jr. for providing tables of the 788 MeV data and related information, G. Roy and H. A. Thiessen for discussions on measurement of the spin-rotation function. This work was supported in part by the National Science Foundation under Grant No. PHY-7825532.

---

[1] J. Fong, T. S. Bauer, G. J. Igo, G. Pauletta, R. Ridge, R. Rolfe, J. Soukup, C. A. Whitten, Jr., G. W. Hoffmann, N. Hintz, M. Oothoudt, G. Blanpied, R. L. Liljestrand, and T. Kozlowski, Phys. Lett. 78B, 205 (1978).

[2] G. W. Greenlees and Y. C. Tang, Phys. Lett. 34B, 359 (1971); D. R. Thompson and Y. C. Tang, Phys. Rev. C 4, 306 (1971); D. R. Thompson, R. E. Brown, M. LeMere, and Y. C. Tang, *ibid.* 16, 1 (1977).

[3] S. W-L. Leung and H. S. Sherif, Can. J. Phys. 56, 1116 (1978), and references therein.

[4] L. G. Arnold, B. C. Clark, and R. L. Mercer, Phys. Rev. C 19, 917 (1979), and references therein.

[5] L. G. Arnold and B. C. Clark, Phys. Lett. 84B, 46 (1979).

[6] G. E. Brown and A. D. Jackson, *The Nucleon-Nucleon Interaction* (North-Holland, Amsterdam, 1976), Chap. 10, Appendix B.

[7] J. D. Walecka, Ann. Phys. (N.Y.) 83, 491 (1974); S. A. Chin, *ibid.* 108, 301 (1977); F. E. Serr and J. D. Walecka, Phys. Lett. 79B, 10 (1978).

[8] L. D. Miller and A. E. S. Green, Phys. Rev. C 5, 241 (1972); L. D. Miller, Ann. Phys. (N.Y.) 91, 40 (1975), and references therein.

c.m. tra
is the pro
tential mb
1730 MeV
ture obtai
to calcu
tion,
at 7

[9]R. Brockmann and W. Weise, Phys. Rev. C 16, 1282 (1977); R. Brockmann, *ibid.* 19, 1510 (1978).

[10]H. Courant, K. Einsweiler, T. Joyce, H. Kagan, Y. I. Makdisi, M. L. Marshak, B. Mossberg, E. A. Peterson, K. Ruddick, T. Walsh, G. J. Igo, R. Talaga, A. Wriekat, and R. Klem, Phys. Rev. C 19, 104 (1979); see also, Phys. Rev. Lett. 38, 1272 (1977); Phys. Lett. 73B, 155 (1977).

[11]M. Jaminon, C. Mahaux, and P. Rochus, Phys. Rev. Lett. 43, 1097 (1979).

[12]R. J. Glauber and P. Osland, Phys. Lett. 60B, 401 (1979).

[13]R. H. McCamis, J. M. Cameron, L. G. Greeniaus,

D. A. [illegible], C. A. Miller, G. A. Moss, G. R
M. S. de Jong, R. T. [illegible], W. T. H. van O
J. G. Rogers, and A. W. Stetz, Nucl. Phys. A
(1978).

[14]S. A. Gurvitz, Y. Alexander, and A. S. Rinat, Phys. (N.Y.) 93, 152 (1975); 98, 346 (1976).

[15]Y. Alexander and R. H. Landau, Phys. Lett. 8
(1979).

[16]H. [illegible], L. [illegible], and A. Tekou, Nucl. Ph
A267, 503 (1976).

[17]R. Dymarz and A. Malecki, in *Proceedings of the In*
ternational Conference on High Energy Physics and
Nuclear Structure, Zurich (1977), contributions, p. 1

YSICAL REVIEW C VOLUME 21, NUMBER 5 MAY 1980

Systematic features of the pion-nucleus interaction

R. S. Bhalerao, L. C. Liu, and C. M. Shakin
nt of Physics and Institute for Nuclear Theory, Brooklyn College of the City University of New York, Brooklyn, New York 11210

(Received 20 June 1979)

We analyze pion elastic-scattering data for ^{40}Ca and ^{48}Ca using a covariant theory of the optical potential developed previously. Combining these results with the information obtained from the analysis of pion scattering from ^{12}C and ^{16}O reported earlier, we are able to discuss the systematics of the pion-nucleus optical potential. Our model contains a first-order optical potential which is obtained from a parameter-free calculation. The parameters of a second-order potential are determined by requiring that the sum of the first- and second-order potentials provides a fit to the elastic-scattering data. The parameters of the second-order potential exhibit a smooth dependence on energy and target mass number. These parameters have a marked resonance behavior. We find that the maximum value of the magnitude of the imaginary part of the second-order potential occurs at about 150 MeV while the first-order potential has a maximum for the magnitude of the imaginary part at about 240 MeV. The imaginary part of the first-order potential has a width at half maximum of about 200 MeV. This corresponds to a kinematic broadening of the (3,3) resonance due to the effects of the Fermi motion of the target nucleons. (This increased width is unrelated to the effects of the true absorption process or of collision broadening.) We also find a significant isospin violation in the second-order potential. For example the imaginary part of the second-order potential for π^- scattering is found to be systematically larger than that for π^+ scattering for nuclei with $N > Z$. An explanation for this feature of the optical potential is presented.

[NUCLEAR REACTIONS Elastic scattering of pions from ^{40}Ca (40–241 MeV) and ^{48}Ca (130 MeV). Systematics of first- and second-order optical potentials.]

I. INTRODUCTION

Pion elastic-scattering data for some light nuclei (^{4}He, ^{12}C, and ^{16}O) were analyzed successfully[1] using a covariant scattering theory.[2] In these calculations a complete integration over the Fermi motion of the target nucleons was carried out and the off-shell effects related to nuclear binding were treated carefully.[3] The first-order optical potential is parameter-free and is believed to be quite accurate. Parameters of the second-order phenomenological potential were determined by fitting the experimentally determined differential cross sections for elastic scattering. In general, the parameters for ^{12}C and ^{16}O varied smoothly with pion energy and exhibited a marked resonance behavior.[1]

In the present work we have tested the validity of the aforementioned parametrization in the medium-mass region. In particular, we have studied the importance of the first- and second-order optical potentials for pion scattering on ^{40}Ca and ^{48}Ca at all the energies for which experimental data are available. The systematics of the variation of the optical potential with pion energy and target mass are investigated. With some exceptions, parameters for ^{12}C and ^{16}O were found to be similar in the earlier work.[1] Hence, exploring the possibility of a universal parametrization of the optical potential was one of the motivations of the present work.

The problem of determining the neutron matter distribution in the calcium isotopes has received some attention. Information may be obtained from the conventional methods of α-nucleus[4] or proton-nucleus scattering.[5] Recently measurements of π-nucleus scattering cross sections near the (3,3) resonance have been made to study the neutron-matter radii in the calcium isotopes.[6] Another aim of our work was to study the utility of pion-nucleus scattering for the determination of neutron-matter radii. We conclude, however, that there does not seem to be much possibility of learning about the neutron-matter distribution from the studies reported here.

We believe that our studies do provide significant insight concerning the interaction of pions with nuclei. In particular, the pion-nucleus optical potential is found to exhibit some extremely interesting systematic features. We believe our analysis should stimulate further microscopic studies of pion-nucleus dynamics.

II. STRUCTURE OF THE SECOND-ORDER POTENTIAL

Pion-nucleus optical potential can be written as

$$\langle \mathbf{k}' | V_C | \mathbf{k} \rangle + \langle \mathbf{k}' | V^{(1)}(W) | \mathbf{k} \rangle + \langle \mathbf{k}' | V^{(2)}(W) | \mathbf{k} \rangle ,$$

where V_C is the Coulomb potential and $V^{(1)}$ and

© 1980 The American Physical Society

$V^{(2)}$ are the first- and second-order optical potentials, respectively. The calculation of the first-order potential has been extensively discussed previously.[3] *We note that we have used a (spherical) Hartree-Fock code to calculate the* neutron and proton wave functions which are required in the calculation of the first-order potential. (The charge density constructed from these wave functions is consistent with electron scattering data.) Experimental separation energies are used for the least bound nucleons.

In the absence of a microscopic calculation of the second-order potential we have introduced a phenomenological model by writing[1,7]

$$\langle \vec{k}' | V^{(2)}(W) | \vec{k} \rangle = R^{1/2}(\vec{k}') 2M_A A(A-1) \overline{G}(\vec{k}-\vec{k}') \times [B(W) + C(W) \vec{k}\cdot\vec{k}'] R^{1/2}(\vec{k}) . \tag{2.1}$$

Here R is a kinematical factor defined as[1]

$$R(\vec{k}) = \frac{E_\pi(\vec{k}_0) + E_A(\vec{k}_0)}{4E_\pi(\vec{k}_0) E_A(\vec{k}_0)} \cdot \frac{1}{E_\pi(\vec{k}) + E_A(\vec{k})} \tag{2.2}$$

Further,

$$W = (\vec{k}_0^{\,2} + m_\pi^{\,2})^{1/2} + (\vec{k}_0^{\,2} + M_A^{\,2})^{1/2} \tag{2.3}$$

and

$$\overline{G}(\vec{k}-\vec{k}') = (2\pi)^3 \int \exp[i(\vec{k}-\vec{k}')\cdot\vec{r}] \rho^2(\vec{r}) d\vec{r} . \tag{2.4}$$

Here $\vec{k}_0$ is the pion momentum in the π-nucleus center-of-mass frame and $\rho(\vec{r})$ is the nuclear matter density. In Eq. (2.1), B and C are complex parameters to be determined at each energy by performing a χ^2 fit to the experimental differential cross sections. The parameters B and C are determined in what may be termed an energy-

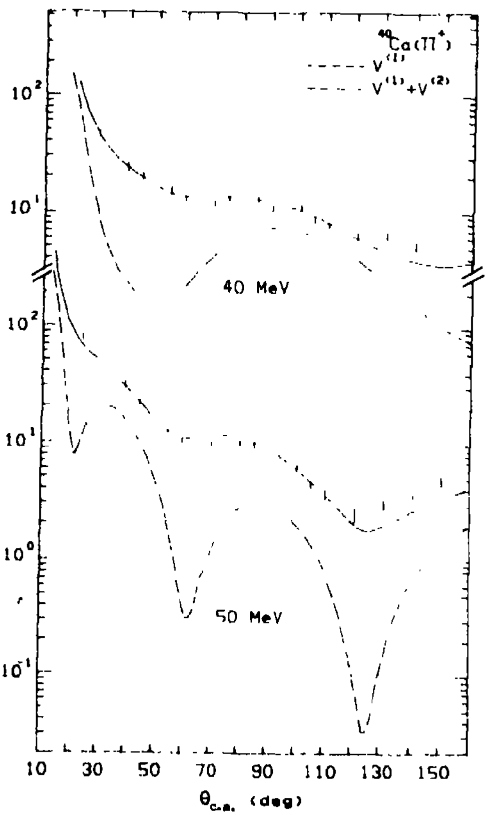

FIG. 1. Differential cross sections for π^+-^{40}Ca elastic scattering at 40 and 50 MeV. The data are taken from Ref. 9. Dashed curve: first-order potential only; solid curve: first- and second-order potentials included.

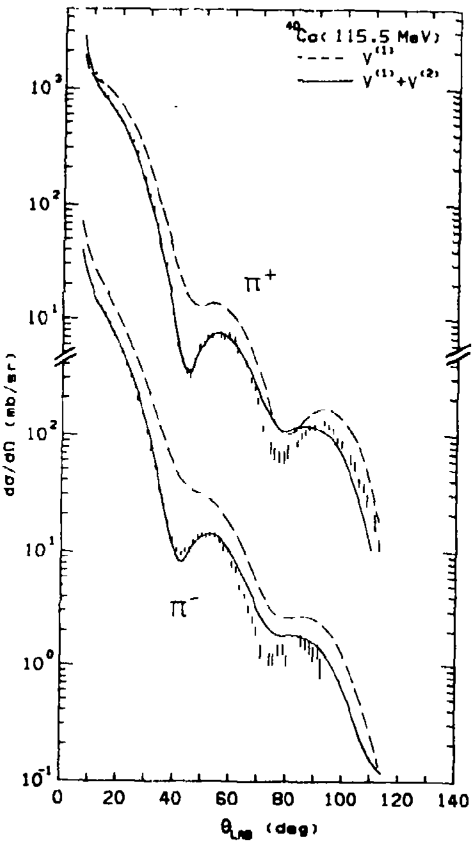

FIG. 2. Differential cross sections for $\pi^\pm$-^{40}Ca elastic scattering at 115.5 MeV. The data are taken from Ref. 8. Dashed and solid curves have the same meaning as in Fig. 1.

dependent manner; that is, no smooth energy dependence of these parameters is assumed before a χ^2 analysis is carried out. We also remark that the data for the total cross sections have not been used in the χ^2-fitting procedure. Details of similar calculations may be found in Ref. 1.

III. RESULTS AND DISCUSSION

Calculated cross sections are presented and compared with the experimental data in Figs. 1–6. The ^{40}Ca($\pi^{\pm}$) data at 115.5, 163.5, and 241 MeV are from Ref. 8. Uncertainty in the absolute normalization of these data is estimated to be $\lesssim 15\%$.[8] Similarly, the ^{40}Ca (130 MeV) and ^{48}Ca (130 MeV) data[9] have absolute normalization errors of ±5%. In Figs. 1–6 the dashed curves represent cross sections calculated with $V^{(1)}$ only and the solid curves represent calculations with $V^{(1)} + V^{(2)}$. (The Coulomb potential is included in all these calculations.)

As can be seen from Figs. 1–6, the second-order optical potential is quite important for the two nuclei studied. This result is consistent with the earlier calculations[1] for lighter nuclei (^{4}He, ^{12}C, and ^{16}O). The relative importance of the second-order potential varies with scattering angle and with pion energy. The former dependence is understandable because of the different radial shapes of the Coulomb, the first-order potential ($\sim\rho$), and the second-order potential ($\sim\rho^2$).

In Figs. 7 and 8 we have presented the real and imaginary parts of $k_0^2 C$, for various pion energies, for the nuclei ^{12}C, ^{16}O, and ^{40}Ca. Table I gives the values of the complex parameters B and $k_0^2 C$. In general, the imaginary part of B is very

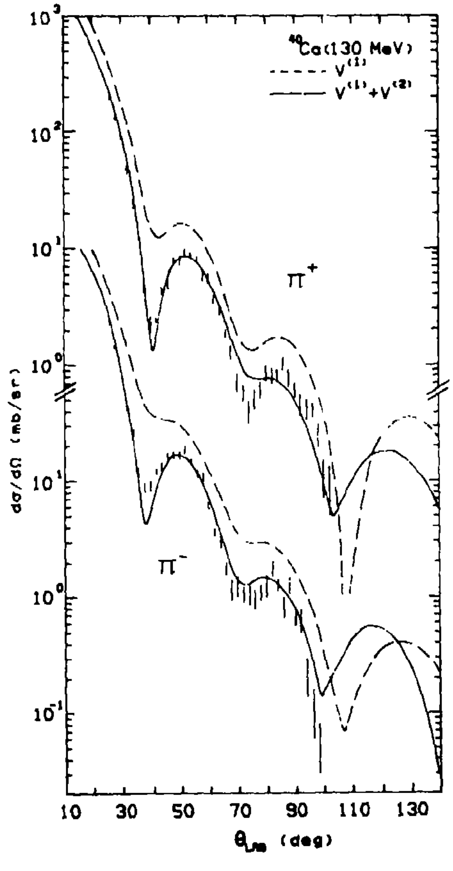

FIG. 3. Same as Fig. 2 with $T_\pi = 130$ MeV, however, the data are taken from Ref. 9.

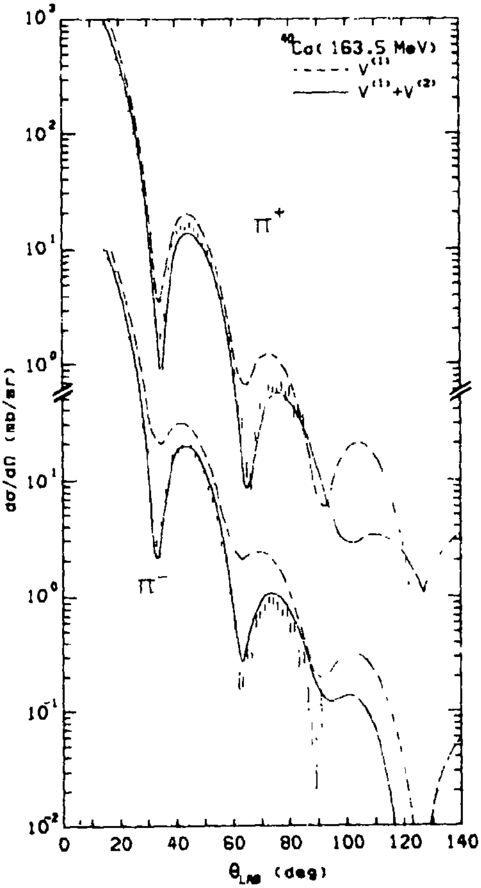

FIG. 4. Same as Fig. 2 with $T_\pi = 163.5$ MeV.

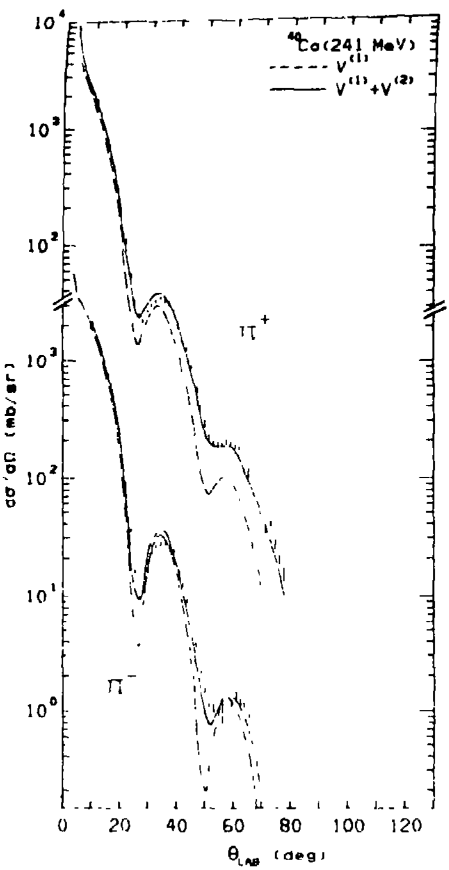

FIG. 5. Same as Fig. 2 with T_π 241 MeV.

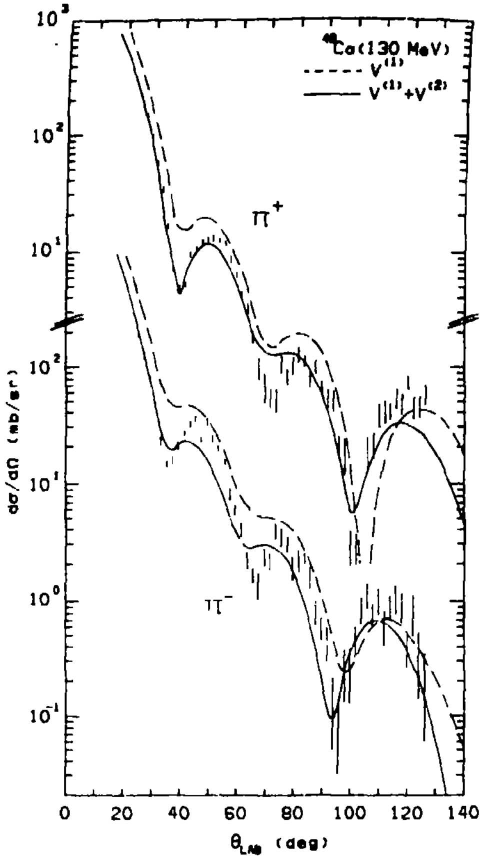

FIG. 6. Differential cross sections for $\pi^\pm$-^{48}Ca elastic scattering at 130 MeV. The data are taken from Ref. 9. Dashed and solid curves have the same meaning as in Fig. 1.

small compared to the imaginary part of k_0^2C, hence a graph of $\text{Im}(B)+\text{Im}(k_0^2C)$ would be very similar to that of Fig. 8. Except for the lowest energies, ReB is smaller than Rek_0^2C. The fit for π^- scattering from ^{48}Ca (Fig. 6) is not very good and therefore we believe the numbers given in the last row of Table I are subject to modification. Since we only have data for ^{48}Ca at a single energy (130 MeV) we have not been able to study the systematic behavior of the potential parameters for this nucleus. We believe that more data are required before we can fully understand the optical potential for such nuclei with $N\neq Z$.

Some interesting trends emerge from Figs. 7 and 8. First of all, all the curves show a marked resonance behavior, a feature probably related to the resonance in the true-pion-absorption (TPA) process. [Landau and Thomas have used the knowledge of the cross section for the reaction $\sigma_{\text{tot}}(\pi^+d\rightarrow pp)$ to estimate the magnitude of the potential describing the TPA process.[7] Other authors have performed microscopic calculation of of the absorption process.[10] The description of TPA is also an essential aspect of isobar-hole calculations[11] and gives rise to an important contribution to the Δ isobar self-energy.] In the absence of a fully microscopic calculation for finite nuclei, it is not certain whether processes other than TPA which contribute to $V^{(2)}$ would also exhibit a resonancelike behavior. (See, however, Ref. 1 for a discussion of this point.) Again referring to Figs. 7 and 8 we see that the magnitudes of both $\text{Re}(k_0^2C)$ and $\text{Im}(k_0^2C)$ generally decrease with increasing nuclear mass. Exceptions to this trend, e.g., the curve for ^{40}Ca(π^-) which lies between the curves for ^{16}O(π^-) and ^{12}C(π^-) in Fig. 8, may be thought of as

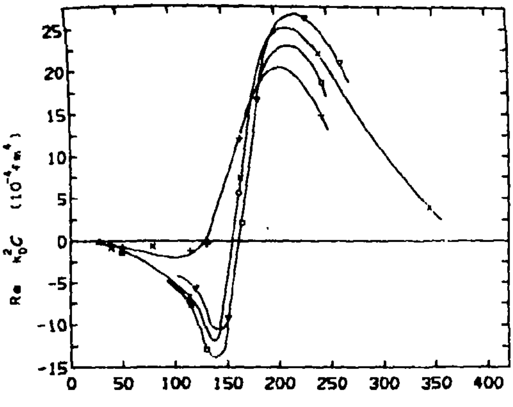

FIG. 7. Re(k_0^2C) as a function of pion kinetic energy for various nuclei. Curves are drawn only as a guide to the eye. Δ: $^{12}C(\pi^+)$, ∇: $^{12}C(\pi^-)$, ×: $^{16}O(\pi^+)$, ○: $^{16}O(\pi^-)$, +: $^{40}Ca(\pi^+)$, □: $^{40}Ca(\pi^-)$.

arising due to the "splitting" of a single ^{40}Ca curve into two curves, one corresponding to π^+ and the other to π^- (see below). We note that the positions of the minima in Fig. 8 seem to be shifting toward lower energies as A increases. Similar behavior is observed in Fig. 7 also, where the point at which a curve crosses the axis seems to move to smaller energy as A increases. In Fig. 8 the curves for $^{16}O(\pi^-)$ and $^{40}Ca(\pi^-)$ lie below those for $^{16}O(\pi^+)$ and $^{40}Ca(\pi^+)$, respectively.

It is somewhat more instructive to directly consider the potential $V^{(2)}$ rather than the parameters B and k_0^2C. Therefore we proceed to discuss the matrix elements of the first- and second-order optical potentials. The real and imaginary parts of the (on-shell) matrix elements $\langle \vec{k}|V^{(1)}|\vec{k}\rangle$ and $\langle \vec{k}|V^{(2)}|\vec{k}\rangle$ are shown in Figs. 9–12 for both ^{16}O and ^{40}Ca. It is evident from these figures that both the real and imaginary parts of $\langle \vec{k}|V^{(1)}|\vec{k}\rangle$ and $\langle \vec{k}|V^{(2)}|\vec{k}\rangle$ vary smoothly with energy. This is remarkable since no such energy dependence was presumed before the χ^2 analysis was made. The first-order potential is nearly the same for π^+ and π^-, the small differences arising from differences in the binding energies of the proton and neutron orbits. As might be expected, the matrix elements of $V^{(1)}$ are proportional to the mass number of the target. The value of $|\text{Im}\langle \vec{k}|V^{(1)}|\vec{k}\rangle|$ has a maximum at about 240 MeV and the width at half maximum (Fig. 10) is about 200 MeV for ^{16}O and

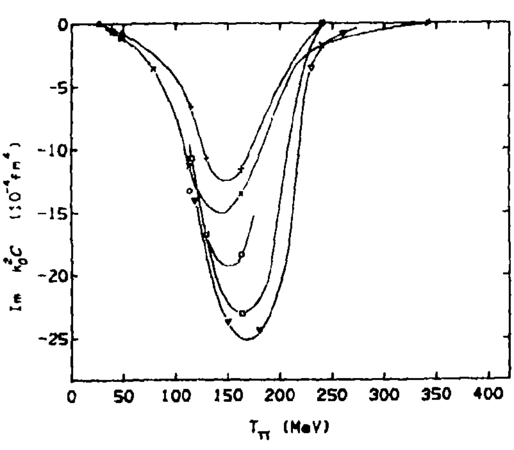

FIG. 8. Same as Fig. 7 for Im(k_0^2C).

TABLE I. Parameters of the second-order potential for $\pi^\pm$ scattering on ^{40}Ca and ^{48}Ca (in units of 10^{-4} fm^4).

	T_π (MeV)	ReB	ImB	Rek_0^2C	Imk_0^2C
$^{40}Ca, \pi^+$	40	0.837	−0.294	−0.457	−0.503
$^{40}Ca, \pi^+$	50	1.06	−0.280	−0.727	−0.839
$^{40}Ca, \pi^+$	115.5	0.571	~0	−1.19	−6.74
$^{40}Ca, \pi^-$	115.5	2.36	−0.002	−7.47	−10.7
$^{40}Ca, \pi^+$	130	0.766	~0	−0.149	−10.7
$^{40}Ca, \pi^-$	130	5.14	−0.007	−12.8	−16.7
$^{40}Ca, \pi^+$	163.5	−4.18	−0.012	11.7	−11.7
$^{40}Ca, \pi^-$	163.5	2.56	~0	2.16	−22.9
$^{40}Ca, \pi^+$	241	1.15	−0.949	14.7	~0
$^{40}Ca, \pi^-$	241	−1.88	~0	16.5	~0
$^{48}Ca, \pi^+$	130	0.242	−0.530	0.713	−4.11
$^{48}Ca, \pi^-$	130	0.559	−0.001	4.00	−0.596

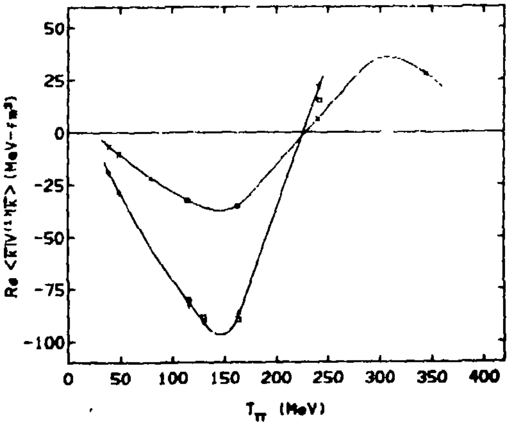

FIG. 9. Real part of $\langle \vec{k}|V^{(1)}|\vec{k}\rangle$ vs pion energy. ×: $^{16}O(\pi^+)$, ○: $^{16}O(\pi^-)$, +: $^{40}Ca(\pi^+)$, □: $^{40}Ca(\pi^-)$. Curves are drawn only as a guide to the eye.

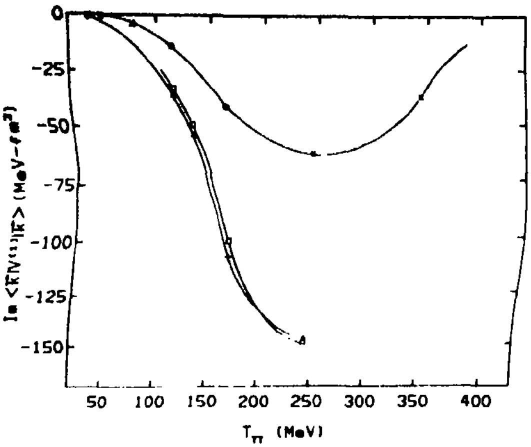

FIG. 10. Same as Fig. 9 for $\mathrm{Im}\langle\vec{k}|V^{(1)}|\vec{k}\rangle$.

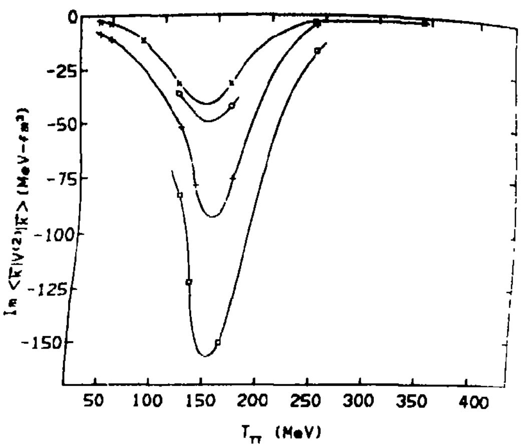

FIG. 12. Same as Fig. 9 for $\mathrm{Im}\langle\vec{k}|V^{(2)}|\vec{k}\rangle$.

^{40}Ca. (See Sec. IV.) The maximum appears at 240 MeV since the effect of Fermi motion of the target nucleons and binding effects cause the π-N T matrix to be evaluated at energies which are significantly below the fixed-scatterer value.[12] This aspect of our calculation of the first-order potential has been discussed previously.[1]

Figures 11 and 12 exhibit the real and imaginary parts of the matrix element $\langle\vec{k}|V^{(2)}|\vec{k}\rangle$. First we note that the maximum value of $|\mathrm{Im}\langle\vec{k}|V^{(2)}|\vec{k}\rangle|$ *is at about 140–150 MeV for* ^{16}O and ^{40}Ca (see Sec. IV). Most remarkable, however, is the large violation of isospin symmetry exhibited by the second-order potential. We see that the second-order potential is significantly more absorptive for π^- mesons that for π^+ mesons. [Large differences are also to be noted for the real parts of $V^{(2)}$ for π^+ and π^- mesons—see Fig. 11.]

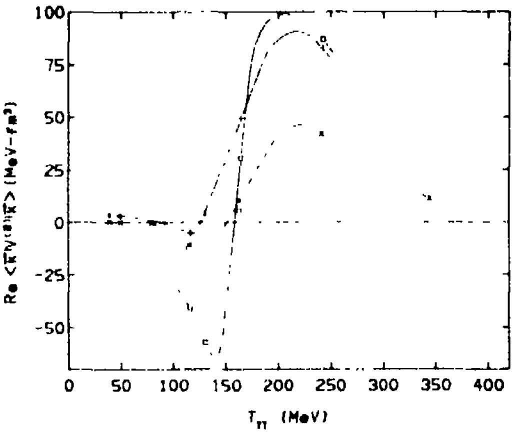

FIG. 11. Same as Fig. 9 for $\mathrm{Re}\langle\vec{k}|V^{(2)}|\vec{k}\rangle$.

To some degree the difference in the values of $V^{(2)}$ for π^- and π^+ mesons provide some further support for the conjecture that $V^{(2)}$ mainly describes the effects of the true pion absorption: We note that in the resonance region the absorption of a π^- meson on a nucleon pair would predominantly result in having two *neutrons* in the final state, while the absorption of π^+ mesons on a pair *would predominantly result in final-state proton* pairs. (The conventional model for pion absorption on a nucleon pair, which involves a rescattering on one nucleon before absorption on the other, can be called upon to support the above observation.) It follows that π^- absorption is enhanced over π^+ absorption because of the Coulomb-barrier penetration factors present in the wave functions of the final-state protons. These observations lead one to expect that the second-order potential will be more absorptive for π^- mesons, as is indicated by our phenomenological analysis. These observations may have interesting implications for the branching ratios $\sigma(\pi^+,pp)/\sigma(\pi^+,pn)$, $\sigma(\pi^-,nn)/\sigma(\pi^-,np)$, and $\sigma(\pi^+,pp)/\sigma(\pi^-,nn)$ for pions absorbed in flight. Of course, the connection between the cross sections for particular final states in pion induced reactions and the details of the optical potential which describes elastic scattering is not a simple matter in general.

The study of differences in the angular distributions of π^+ and π^- scattering cross sections has been suggested as a means to extract information about the neutron-matter radii of the Ca isotopes. However, as can be seen from Figs. 1–6, the second-order (ρ^2-dependent) potential is quite important in the resonance region. Even at 241 MeV the first- and second-order cross sections are not quite the same. Since at pion energies above about 300 MeV the true pion absorption contribution to $V^{(2)}$ is expected to be much reduced, it may be useful to have data in that energy region. At high energies, however, other processes may make appreciable contributions to $V^{(2)}$. At this time, however, it does not appear possible to extract useful information concerning the neutron-matter distribution from the study of pion-nucleus scattering.

It is possible to define several scattering amplitudes, some of which are related to measurements of the total cross section for pion-nucleus scattering. The amplitude $F_N(\theta)$ is that which results upon neglecting the Coulomb interaction $\langle \vec{k}'|V_C|\vec{k}\rangle$. We note, however, that the strong interaction potential $\langle \vec{k}'|V^{(2)}(W)|\vec{k}\rangle$ is significantly different for π^+ and π^- mesons. [We recall that $\langle \vec{k}'|V^{(1)}(W)|\vec{k}\rangle$ also exhibits some differences for π^+ and π^- mesons; however, these differences are quite small.] The amplitude $F_N(0)$ is shown in Figs. 13(a) [$V^{(1)}$ only] and Fig. 13(b) [$V^{(1)}+V^{(2)}$]. The small difference in $F_N(0)$ for π^+ and π^- mesons exhibited in Fig. 13(b) reflects the above-mentioned isospin violation in $V^{(2)}$ (see Table II).

The nuclear amplitude which includes the effects of the Coulomb interaction,

$$f_N(0)=\frac{1}{2ik_0}\sum_{l=0}^{\infty}(2l+1)e^{2i\sigma_l}(\eta_l^c e^{2i\delta_l^c}-1), \qquad (3.1)$$

is presented in Table II and in Fig. 13. Figure 13(c) exhibits the amplitude $f_N(0)$ calculated with $V^{(1)}$ only while Fig. 13(d) exhibits the result of a

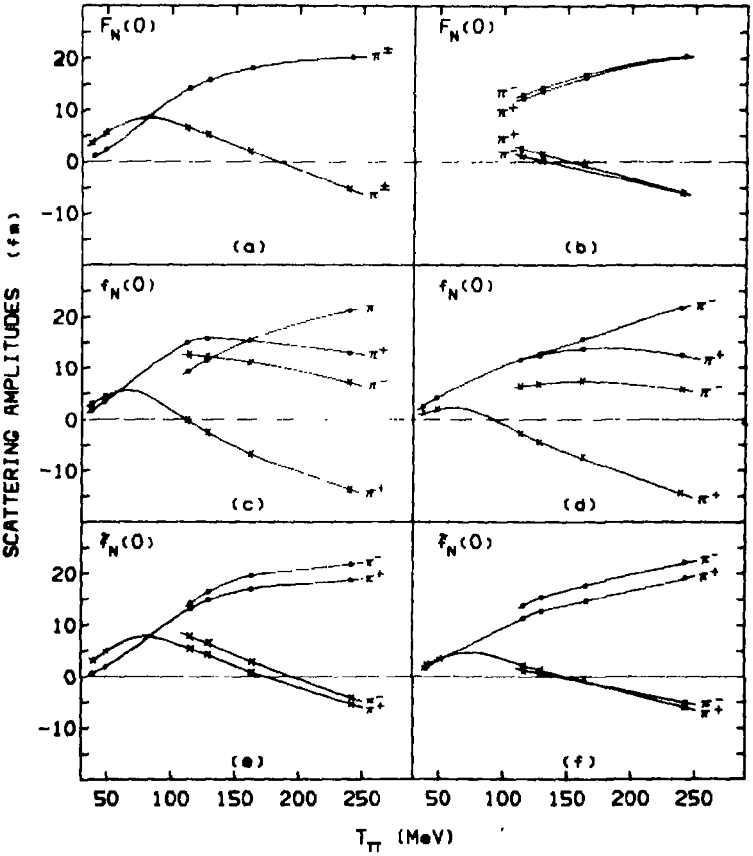

FIG. 13. Real (×) and imaginary (●) parts of the nuclear forward scattering amplitudes for ^{40}Ca vs incident π energy. (a), (c), and (e): with $V^{(1)}$; (b), (d), and (f): with $V^{(1)}+V^{(2)}$. Definitions of $F_N(0)$, $f_N(0)$, and $\bar{f}_N(0)$ are given in the text. The curves are drawn only as a guide to the eye.

TABLE II. Calculated forward nuclear scattering amplitudes $f_N(0)$ and $\tilde{f}_N(0)$ (a) without and (b) with the second-order π-nucleus potential.

	T_π (MeV)	$f_N(0)$ (fm) (a)	$f_N(0)$ (fm) (b)	$\tilde{f}_N(0)$ (fm) (a)	$\tilde{f}_N(0)$ (fm) (b)
^{40}Ca, π^+	40	$2.78+i1.81$	$1.60+i2.74$	$3.23+i0.776$	$2.22+i1.74$
^{40}Ca, π^+	50	$4.14+i3.38$	$2.04+i4.27$	$4.90+i1.98$	$3.15+i3.02$
^{40}Ca, π^+	115.5	$-0.174+i15.0$	$-2.64+i11.7$	$5.41+i13.3$	$2.19+i11.4$
^{40}Ca, π^-	115.5	$12.3+i9.33$	$6.63+i11.5$	$7.97+i14.3$	$1.35+i13.8$
^{40}Ca, π^+	130	$-2.29+i15.7$	$-4.15+i12.1$	$4.17+i14.7$	$1.22+i12.6$
^{40}Ca, π^-	130	$12.2+i11.4$	$6.91+i13.1$	$6.67+i16.3$	$0.629+i15.3$
^{40}Ca, π^+	163.5	$-6.71+i15.9$	$-6.92+i13.3$	$1.06+i16.9$	$-0.278+i15.0$
^{40}Ca, π^-	163.5	$11.0+i15.3$	$7.51+i15.5$	$3.06+i19.4$	$-0.337+i17.6$
^{40}Ca, π^+	241	$-13.5+i13.0$	$-14.3+i12.4$	$-5.47+i18.4$	$-6.45+i18.4$
^{40}Ca, π^-	241	$7.17+i21.1$	$6.05+i21.7$	$-4.26+i21.8$	$-5.40+i21.6$
^{48}Ca, π^+	130	$-1.99+i17.1$	$-3.23+i13.8$	$5.09+i15.8$	$2.83+i13.6$
^{48}Ca, π^-	130	$13.7+i14.2$	$11.9+i9.62$	$6.34+i19.8$	$6.61+i14.6$

calculation with $V^{(1)}+V^{(2)}$.

It is useful to define an additional amplitude,[13]

$$\tilde{f}_N(0)=\frac{1}{2ik_0}\sum_{l=0}^{\infty}(2l+1)(\eta_l^c e^{2i\delta_l^c}-1)\,. \tag{3.2}$$

The amplitudes of Eqs. (3.1) and (3.2) may be used to define total cross sections[13]

$$\hat{\sigma}_{\mathrm{tot}}=\frac{4\pi}{k_0}\mathrm{Im}f_N(\theta=0) \tag{3.3}$$

and

$$\sigma_{\mathrm{tot}}=\frac{4\pi}{k_0}\mathrm{Im}\tilde{f}_N(\theta=0)\,. \tag{3.4}$$

The relation of the cross sections defined in Eqs. (3.3) and (3.4) to experimental observations is discussed in Ref. 13. In this reference σ_{tot} [Eq. (3.4)] is denoted as σ_R and $\hat{\sigma}_{\mathrm{tot}}$ [Eq. (3.3)] is called σ_N. In Table III we present values for σ_{tot} [Eq. (3.4)], the elastic-scattering cross section σ_{el} and the reaction cross section σ_r calculated with and without the second-order potential. These quantities are exhibited in Fig. 14. In Fig. 14(a) (π^+) and Fig. 14(c) (π^-) we show the results of our calculations of the various cross sections including only the effects of $V^{(1)}$. Figures 14(b) (π^+) and 14(d) (π^-) are the results of a calculation including both $V^{(1)}$ and $V^{(2)}$.

IV. SUMMARY OF SALIENT FEATURES

We summarize some of our observations at this point:

(a) The first-order potential $V^{(1)}$ varies smoothly with energy with a maximum value for the matrix element $|\mathrm{Im}\langle\vec{k}|V^{(1)}|\vec{k}\rangle|$ at ~240 MeV.

TABLE III. Calculated cross sections (a) without and (b) with the second-order π-nucleus potential σ_{el}: elastic scattering cross section $=\int|f_N|^2 d\Omega=(\pi/k^2)\sum_{l=0}^{\infty}(2l+1)|\eta_l^c e^{2i\delta_l^c}-1|^2$, σ_r: reaction cross section $=(\pi/k^2)\sum_{l=0}^{\infty}(2l+1)[1-(\eta_l^c)^2]$, σ_{tot}: total cross section $=\sigma_{\mathrm{el}}+\sigma_r=(4\pi/k)\times\mathrm{Im}\,\tilde{f}_N(\theta=0)$.

	T_π (MeV)	(a) σ_{el} (mb)	(a) σ_r (mb)	(a) σ_{tot} (mb)	(b) σ_{el} (mb)	(b) σ_r (mb)	(b) σ_{tot} (mb)
^{40}Ca, π^+	40	115.7	55.44	171.1	123.3	260.6	383.9
^{40}Ca, π^+	50	266.1	119.3	385.4	202.0	384.9	586.9
^{40}Ca, π^+	115.5	893.5	659.7	1553	526.1	812.4	1339
^{40}Ca, π^-	115.5	1028	646.1	1674	659.6	949.4	1609
^{40}Ca, π^+	130	844.3	750.2	1594	523.2	835.8	1359
^{40}Ca, π^-	130	1011	750.3	1761	690.5	966.5	1657
^{40}Ca, π^+	163.5	705.2	867.3	1572	540.5	852.3	1393
^{40}Ca, π^-	163.5	892.9	906.9	1800	697.6	941.8	1639
^{40}Ca, π^+	241	548.4	754.8	1303	588.1	714.4	1302
^{40}Ca, π^-	241	707.5	836.7	1544	742.2	788.1	1530
^{48}Ca, π^+	130	949.3	755.7	1705	615.2	852.0	1467
^{48}Ca, π^-	130	1239	902.2	2141	686.4	894.1	1580

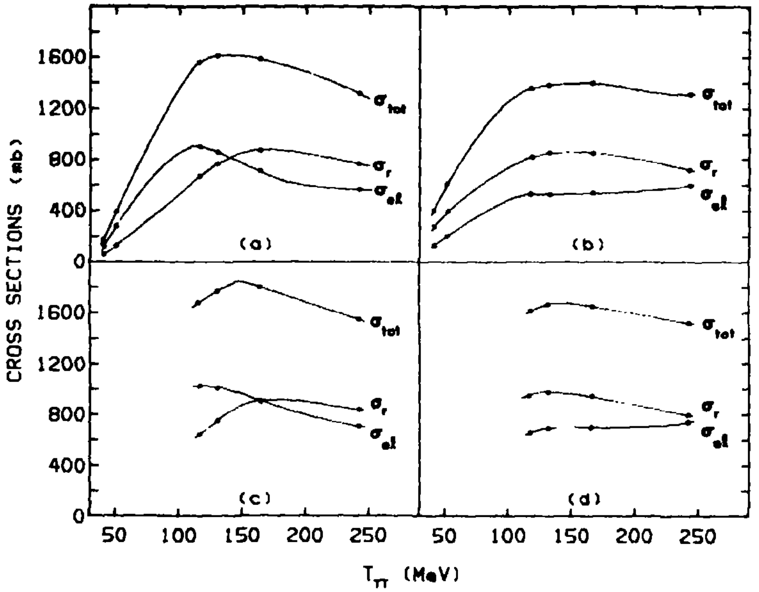

FIG. 14. Calculated total cross section (σ_{tot}), reaction cross section (σ_r), and elastic cross section (σ_{el}) vs pion energy. (a) $^{40}Ca(\pi^+)$ with $V^{(1)}$ only; (b) $^{40}Ca(\pi^+)$ with $V^{(1)}+V^{(2)}$; (c) $^{40}Ca(\pi^-)$ with $V^{(1)}$ only; (d) $^{40}Ca(\pi^-)$ with $V^{(1)}+V^{(2)}$. Curves are only drawn as a guide for the eye.

This maximum is at a greater energy than that which would be expected from the use of the fixed-scatterer approximation (FSA). The position of the maximum is determined in our calculation by nuclear binding and other off-shell effects[12] which are absent in FSA calculations.

(b) Inspection of Fig. 10 shows that the width at half maximum of $|\mathrm{Im}\langle\bar{k}|V^{(1)}|\bar{k}\rangle|$ is approximately 200 MeV for ^{16}O and ^{40}Ca. Again this is larger than the width that would be expected in the FSA and reflects the *effects of a proper treatment of Fermi motion of the target particles.* We remark that extraction of the spreading width Γ^s of the Δ via an isobar-doorway calculation[11] of pion-nucleus scattering is made exceedingly difficult since simple kinematic considerations in the calculation of the first-order potential already provide a significant *apparent* broadening of the (3, 3) resonance.[14]

(c) The parameters of the second-order potential $V^{(2)}$ are determined phenomenologically and exhibit some notable features. The maximum of the value of $|\mathrm{Im}\langle\bar{k}|V^{(2)}|\bar{k}\rangle|$ appears at about 140–150 MeV for ^{16}O and ^{40}Ca (see Fig. 12). The value of the width at half maximum of this quantity is about 90 MeV. It is interesting to note that the cross section for the reaction $\pi+d\rightarrow p+p$ has a maximum value at approximately 140 MeV. The coincidence in energy of the maxima of the $\pi+d\rightarrow p+p$ cross section and the matrix element $|\mathrm{Im}\langle\bar{k}|V^{(2)}|\bar{k}\rangle|$ may provide some further support for the conjecture that $V^{(2)}$ describes, in the main, the effects of true pion absorption.[15]

(d) As may be seen from Fig. 12, the imaginary part of the second-order potential is significantly stronger for π^- scattering than for π^+ scattering at the same energy. An explanation for this behavior has been given in Sec. III. This explanation is consistent with our interpretation of the role of the second-order potential as describing *the effects of true pion absorption.*

V. CONCLUSIONS

Our studies of pion scattering from ^{12}C, ^{16}O, and ^{40}Ca have allowed us to discuss the systematic features of the pion-nucleus optical potential. This potential is composed of first- and second-order potentials which have different geometries. They also differ markedly in their energy dependence, which is a further indication that these potentials describe different physical processes. The analysis reported here should stimulate attempts to understand the second-order potential from a more fundamental point of view. Further, the development of a simple phenomenological form to represent the first-order potential should be facilitated. (A simple representation of the entire optical potential would be useful for the rapid calculation of optical-model wave functions.)

We believe our analysis indicates the great importance of the proper treatment of off-shell effects and the effects of Fermi motion of the target nucleons. Before any investigation of true pion absorption effects or collision broadening is made, one finds a significant upward shift of the resonance position and a remarkable increase in the apparent width of the resonance due to the aforementioned effects.

ACKNOWLEDGMENT

This work was supported in part by the National Science Foundation and the PAC-BHE Faculty Award Program of the City University of New York. We wish to thank John Negele for providing us with a computer code for the calculation of Hartree-Fock wave functions.

---

[1] L. C. Liu, Phys. Rev. C 17, 1787 (1978); L. C. Liu and C. M. Shakin, *ibid.* 19, 129 (1979).

[2] L. Colenza, L. C. Liu, and C. M. Shakin, Phys. Rev. C 11, 1593 (1975); 12, 721(E) (1975).

[3] Calculations which are similar to ours are reported in J. P. Maillet, J. P. Dedonder, and C. Schmitt, Nucl. Phys. A316, 267 (1979).

[4] E. Friedman, H. J. Gils, H. Rebel, and Z. Majka, Phys. Rev. Lett. 41, 1220 (1978) and references therein.

[5] A. Chaumeaux, V. Layly, and R. Schaeffer, Phys. Lett. 72B, 33 (1977) and references therein.

[6] M. J. Jakobson, G. R. Burleson, J. R. Calarco, M. D. Cooper, D. C. Hagerman, I. Halpern, R. H. Jeppeson, K. F. Johnson, L. D. Knutson, R. E. Marrs, H. O. Meyer, and R. P. Redwine, Phys. Rev. Lett. 38, 1201 (1977).

[7] Similar phenomenological forms are used in the momentum-space calculations of R. H. Landau and A. W. Thomas, Nucl. Phys. A302, 461 (1978). For a review of the most recent coordinate-space calculations of the Michigan State University group see, H. McManus, Invited talk at Second International Conference on Meson-Nuclear Physics, Houston, Texas, 1979 (unpublished).

[8] Q. Ingram, E. Boschitz, L. Pflug, J. Zichy, J. P. Albanèse, and J. Arvieux, Phys. Lett. 76B, 173 (1978).

[9] J. P. Egger, R. Corfu, P. Gretillat, C. Lunke, J. Piffaretti, E. Schwarz, C. Perrin, J. Jansen, and B. M. Preedom, Phys. Rev. Lett. 39, 1608 (1977); B. M. Preedom, in *Proceedings of the Seventh International Conference on High-Energy Physics and Nuclear Structure, Zurich, 1977,* edited by M. P. Locher (Birkhauser, Basel, 1977), p. 119.

[10] C. M. Ko and D. O. Riska, Nucl. Phys. A312, 217 (1978); J. Chai and D. O. Riska, Phys. Rev. C 19, 1425 (1979); G. F. Bertsch and D. O. Riska, Phys. Rev. C 18, 317 (1978) and references therein. See also, F. Hachenberg, H. J. Pirner, and J. Hüfner, Phys. Lett. 66B, 425 (1977).

[11] F. Lenz, Ann. Phys. (N.Y.) 95, 348 (1975); M. Hirata, F. Lenz, and K. Yazaki, *ibid.* 108, 16 (1977); M. Hirata, J. H. Koch, F. Lenz, and E. J. Moniz, Phys. Lett. 70B, 281 (1977); W. Weise, Nucl. Phys. A278, 402 (1977); E. Oset and W. Weise, Phys. Lett. 77B, 159 (1978); E. Oset and W. Weise, Nucl. Phys. A319, 477 (1979); K. Klingenbeck, M. Dillig, and M. G. Huber, Phys. Rev. Lett. 41, 387 (1978); M. G. Huber and K. Klingenbeck, Lectures at the Massurian Summer School, Mikolajki, 1978 (unpublished); G. E. Brown and W. Weise, Phys. Rep. 22C, 280 (1975).

[12] Other authors use different prescriptions in the specification of the energy which appears in the pion-nucleon T matrix. For example, see Refs. 3 and 7.

[13] M. D. Cooper and M. B. Johnson, Nucl. Phys. A260, 352 (1976).

[14] A careful treatment of this effect appears in the work of Oset and Weise (Ref. 11); however, this kinematic broadening of the resonance is not discussed in their published work.

[15] We refer the reader to Ref. 7 for a recent discussion of TPA and the quasideuteron model.

PHYSICAL REVIEW C VOLUME 21, NUMBER 5 MAY 1980

Probing inclusive production mechanisms with the $(p,2p)$ reaction

David H. Boal

Theoretical Science Institute, Department of Chemistry, Simon Fraser University, Burnaby, British Columbia V5A 1S6, Canada

(Received 9 October 1979)

Several models for the inclusive production of protons at backward angles are reviewed. From the model amplitudes, predictions for the $(p,2p)$ differential cross section in which one of the protons is emitted in the backward direction are calculated. It is found that the magnitudes and angle dependence of the predicted cross sections vary significantly from one model to the next.

[NUCLEAR REACTIONS Inclusive production mechanisms at intermediate energies, effective momentum distributions, predictions for $(p,2p)$ reaction.]

I. INTRODUCTION

Since Frankel *et al.*[1] first measured the backward inclusive differential cross section of protons produced in proton-nucleus collisions at intermediate energies, there have been several models[2-6] put forward to explain the data. These models differ considerably in their microscopic detail, but they can each generally fit the data for emitted proton angles in the 160° to 180° range. While recent (p,p') data at more forward angles has begun to place limits on the range of validity of some of the models, it does not appear likely that further (p,p') data will be able to distinguish between them. The purpose of this paper is to consider some reactions related to (p,p'), in particular the $(p,2p)$ reaction, in an effort to find a means of testing these models.

It will be useful to have some sort of categorization of the models for our purposes. The models usually involve some sort of primary interaction, for example elastic scattering of the incident proton off a cluster of nucleons inside the nucleus. Because the clusters or residual nuclei can carry excitation energy which may lead to their breakup, the few-body intermediate state very likely leads to a many-body final state. It is assumed in all of these models that the protons emitted in the de-excitation of the residual nucleus are of such low energy as not to contribute to the 100–400 MeV protons observed by Frankel *et al.* Hence we will categorize the reactions by the number of particles or clusters there are in the intermediate state following the primary interaction.

We see immediately that two-body intermediate states are unlikely to contribute significantly to the high energy backward events looked at by Frankel since the residual nucleus would have to be carrying off an enormous amount of excitation energy. We will therefore concentrate our attention on three- and four-body intermediate states.

By far the largest number of models fall into the three-body intermediate state catagory. One of the first models proposed in this group involves the incident proton elastically scattering in the forward direction off a target proton, putting the latter on the mass shell. It is this target proton which is observed in the backward direction. The residual nucleus is then simply a spectator. This model was used by Amado and Woloshyn[3] for describing inclusive proton production at backward angles, and by Boal and Woloshyn[7] for describing the inclusive production of alpha particles at backward angles.[8] We shall call this the direct knockout (DK) model.

A simplification of this model was proposed by Frankel[2]: the quasi-two-body scaling hypothesis (QTBS). In this model, the phase space integral of the transition matrix element is set equal to a product of one function varying rapidly with and depending only on the minimum momentum of the recoiling nucleus, and a second function which varies slowly with the other kinematical variables. This approximation is not unreasonable for pp scattering and QTBS successfully describes the inclusive proton data. However, the approximation fails for p-alpha scattering, and indeed QTBS has been shown to be inadequate as a description of the inclusive alpha data. Since QTBS by itself will not allow the prediction of less inclusive processes than (p,p'), it will not be considered further here.

A model in some respects similar to the DK model is the multiparticle exchange (MPE) model proposed by Weber and Miller.[4] Here, though, the observed proton is the spectator and the primary interaction is between the incident proton and the remaining $A-1$ nucleons of the target nucleus (of mass number A). The need for detailed knowledge of the $p+(A-1)$ collision is avoided because of the inclusive nature of the (p,p') experiment.

© 1980 The American Physical Society

The other three-body intermediate state model which we wish to discuss is the correlated cluster (CC) model of Fujita.[5] In some sense the CC model incorporates both the DK and MPE models in that the incident proton scatters off everything from a single proton in the nucleus to an $(A-1)$ nucleon cluster. However, the observed proton is now assumed to be the incident proton, scattered through a very large momentum transfer.

Lastly, we take note of a four-body intermediate state model, the cluster recoil (CR) model proposed by Woloshyn.[6] As in the DK model, the primary interaction is pp scattering. However, whereas the residual nucleus carries off momentum $\vec{k}$ (where the target proton has momentum $-\vec{k}$ in the nucleus) in the DK model, in the CR model $\vec{k}$ is carried off by a "jet" of n nucleons, the remaining $A-1-n$ nucleons remaining roughly at rest in the lab. Although one has to model the relative probability of the nuclear proton with momentum $-\vec{k}$ recoiling against the n-nucleon jet with momentum $\vec{k}$ both as a function of k and n, the overall normalization is fixed by the (p,p') data.

We have outlined above four models for the (p,p') reaction (DK, MPE, CC, CR) which we feel are significantly different from one another that they should be able to be distinguished experimentally. There are other likely models of which we are aware, and doubtless others of which we are not aware, which we have excluded for brevity. In the following sections, the DK, MPE, and CC models will be reviewed in turn (concentrating most heavily on the DK model) and their $(p,2p)$ predictions will be discussed. Unfortunately, the normalization conventions of the various authors are not uniform, nor, of course are their parametrizations of the data which are put into the models. The approach taken in this paper will be to use the same data parametrization (e.g. for pp scattering) in every model to facilitate comparison, but to leave the normalization conventions intact as much as possible, for easier reference to the original works.

II. DIRECT KNOCKOUT MODEL

The kinematic labels attached to each participant are shown in Fig. 1. The incident proton has an energy and momentum of E_i and p_i in the lab system, and leaves the reaction with E_f and p_f. The struck nucleon has momentum $-\vec{k}$ before the collision, and energy and momentum E_q and q after. We will use $E_k = \bar{\mathcal{E}}^* + (k^2 + M_{A'}^2)^{1/2}$ (where $M_{A'}$ is the mass of the residual nucleus and $\mathcal{E}^*$ its average excitation energy) to denote the energy of the residual nucleus, and ϵ_k to mean $(k^2+M_p^2)^{1/2}$, where M_p is the proton mass.

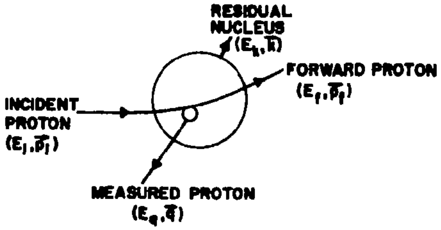
RESIDUAL NUCLEUS $(E_k, \vec{k})$
FORWARD PROTON $(E_f, \vec{p}_f)$
INCIDENT PROTON $(E_i, \vec{p}_i)$
MEASURED PROTON $(E_q, \vec{q})$

FIG. 1. Energy-momentum labels for direct knockout model.

Using the phase space normalization conventions of Bjorken and Drell,[9] and using the closure approximation to replace the sum over final nuclear states by a final state with an excitation energy $\bar{\mathcal{E}}^*$, Amado and Woloshyn[3] write the (p,p') differential cross section for a target of A nucleons in the form

$$\frac{d^2\sigma}{d\Omega_q dE_q} = \frac{M_p^4}{2(2\pi)^5}\frac{q}{p_i}\int\frac{d^3p_f}{E_f\epsilon_k}[n_p(k)|T_{pp}|^2 + n_n(k)|T_{pn}|^2] \times \delta(E_i + M_A - E_f - E_q - E_k), \quad (1)$$

where the probability of finding a proton with momentum k in a nucleus with Z protons, $n_p(k)$, is normalized by

$$2\int\frac{M_p}{\epsilon_k}n_p(k)\frac{d^3k}{(2\pi)^3} = Z, \quad (2)$$

and similarly for the neutron momentum distribution $n_n(k)$. The collision between the incident proton and the off-mass-shell proton in the nucleus is assumed to be dominated by elastic scattering, the matrix element for which, T_{pp}, is normalized to

$$\frac{d\sigma}{dt} = \frac{M_p^2}{16\pi p_{\text{lab}}^2}|T_{pp}|^2, \quad (3)$$

where t is the square of the four-momentum transfer. No effort is made to include off-mass-shell effects.

The parametrization for the pp scattering cross section chosen here is to assume that the integrated cross section is constant (as a function of energy) at 24 mb,[10] and that $d\sigma/dt$ has the form

$$\frac{d\sigma}{dt} = Ae^{bt}. \quad (4)$$

The parameter b has the rough energy dependence over the range of interest, of

$$b = 14.39T_{\text{lab}} - 6.13\ \text{GeV}^{-2}, \quad (5)$$

where T_{lab} is the lab kinetic energy of the incident proton in GeV. At the limits of applicability of this formula, b was restricted to be greater than 0.7 GeV^{-2} and less than 7.0 GeV^{-2}. Knowing b for a particular $T_{\rm lab}$, the integrated version of Eq. (4) can be solved or A. To determine the appropriate $T_{\rm lab}$ for the reaction, the momenta of p_f and q were used to define the Mandelstam variable s, for which the corresponding lab energy was then calculated.

The parametrization of $|T_{pn}|^2$ is somewhat more cumbersome. Over the energy range of interest, $|T_{pn}|^2$ at $u=0$ (backward scattering) was approximated by (in units of mb/GeV^2)

$$|T_{pn}|_{u=0}^2=\begin{cases}-1.369\times 10^4 T_{\rm lab}+1.686\times 10^4, \\ \qquad\qquad T_{\rm lab}<0.7\ {\rm GeV} \\ 0.709\times 10^4, \quad T_{\rm lab}>0.7\ {\rm GeV}.\end{cases} \tag{6}$$

The parameter b' appearing in

$$\frac{d\sigma}{du}=A'e^{b'u} \tag{7}$$

was fitted with (in GeV^{-2})

$$b'=\begin{cases}-94.34T_{\rm lab}+115.7, \quad T_{\rm lab}<0.876\ {\rm GeV} \\ 33.0, \quad T_{\rm lab}>0.876\ {\rm GeV}.\end{cases} \tag{8}$$

In general, it was found that scattering from neutrons contributed no more than a few percent of the predicted cross section, so the parametrization chosen is not terribly crucial to the results presented here. The last ingredient required for the calculation is the form of the momentum distribution. Theoretical understanding of the high momentum components of the momentum distribution is still far from complete, but some recent work by Zabolitzky and Ey,[11] as well as most fits to data, point to an approximately exponential shape in the 300–900 MeV/c range. Following Amado and Woloshyn, we try

$$n(k)=\frac{C}{[2\cosh(k/2k_0)]^2}, \tag{9}$$

where k_0 is treated as a parameter and C is determined by the normalization condition, Eq. (2). The same form is used for both protons and neutrons. Hence, the model contains only one free parameter, k_0.

Shown in Figs. 2–4 are the predictions of this model with $k_0 = 88$ MeV for a variety of targets, the bombarding energy being 800 MeV. In the original paper of Amado and Woloshyn,[3] k_0 was fixed by an analysis of (e,e') data, and Eq. (1) was not evaluated exactly. Thus, the agreement was not as good as is shown in these figures. It is clear that the agreement is good for Li and Be,

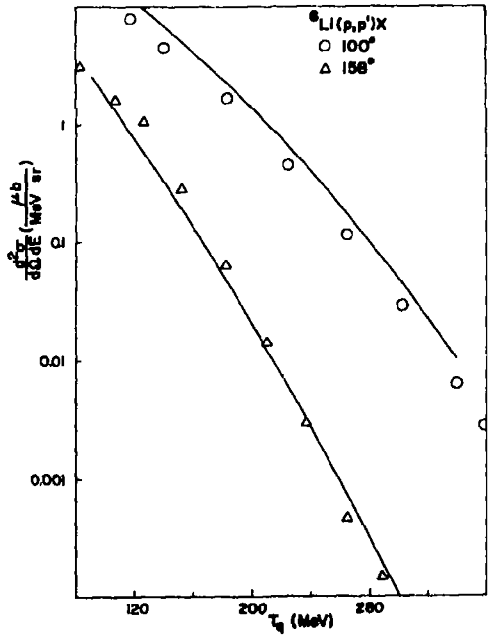

FIG. 2. Comparison of direct knockout model predictions with experiment for the reaction ^{6}Li$(p,p')X$ at incident proton energy of 800 MeV, and observed proton angle of 100° and 158°. Data from Ref. 2.

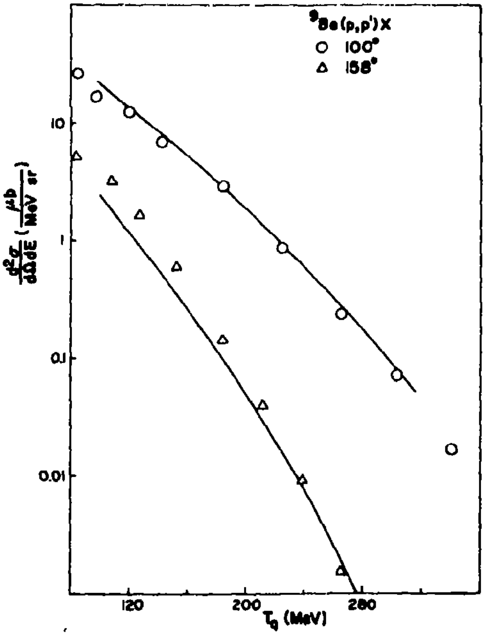

FIG. 3. Comparison of direct knockout model predictions with experiment for the reaction ^{9}Be$(p,p')X$ at incident proton energy of 800 MeV and observed proton angle of 100° and 158°. Data from Ref. 2.

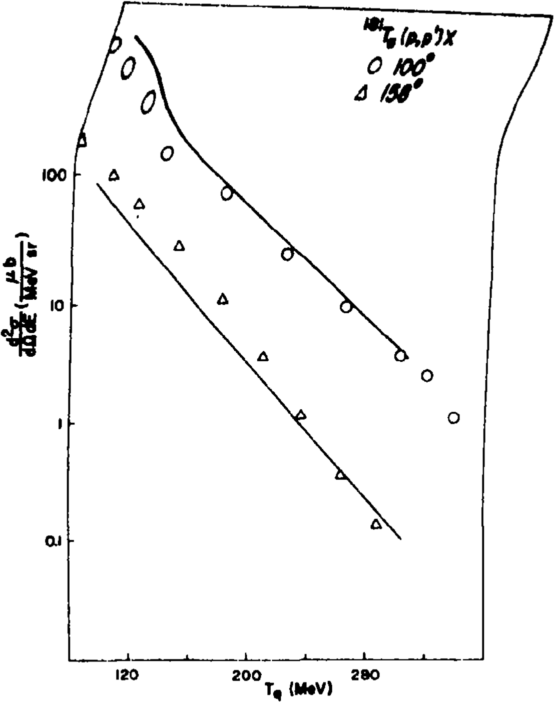

FIG. 4. Comparison of direct knockout model predictions with experiment for the reaction ^{181}Ta$(p,p')X$ at incident proton energy of 800 MeV and observed proton angle of 100° and 158°. Data from Ref. 2.

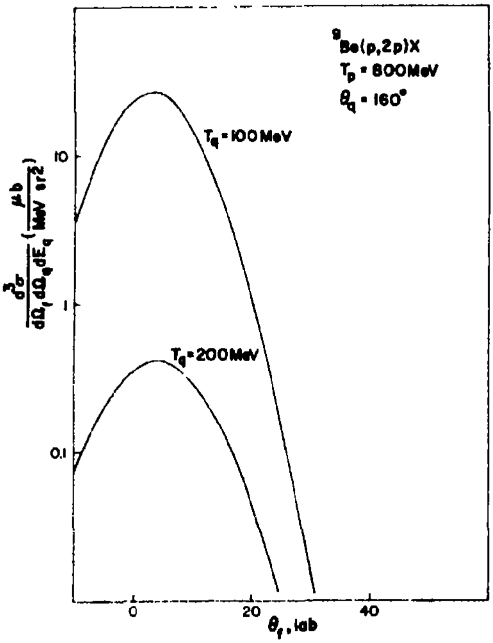

FIG. 5. DK predictions for ^{9}Be$(p,2p)X$ with $\theta_q = 160°$ and 800 MeV incident proton kinetic energy.

but has begun to deteriorate slightly for Ta. Had the simple exponential been used instead of Eq. (9) for $n(k)$, the predicted results would have been roughly 20% lower. $\bar{\delta}^*$ was set equal to zero for these calculations.

In this model, multiple scattering effects have been neglected, and it is important to find out just how significant they are. A recent experiment at TRIUMF[12] tried to address this question by using ^{4}He as a target. While the data have not yet been finalized for publication, the preliminary results are in good agreement with the DK predictions.

To test this model further, one would have to go to a less inclusive process than (p,p'). Since the DK model assumes that the incident proton is scattered forward without large momentum transfer, one can easily calculate the DK predictions for the $(p,2p)$ reaction. A comparison of light vs heavy target could then be used to investigate the importance of multiple scattering.

The differential cross section for two proton coincidence reactions is given by

$$\frac{d^3\sigma}{d\Omega_f d\Omega_q dE_q}$$

$$= \frac{M_p^4}{2(2\pi)^5}\frac{q}{p_i}\frac{E_k}{\epsilon_k}\left[\frac{p_f^2}{p_f(E_k+E_f) - |\vec{p}_i - \vec{q}|E_f\cos\theta_f}\right]$$

$$\times n(k)\,|T_{pp}|^2\,, \tag{10}$$

where θ_f refers to the angle between $\vec{p}_f$ and $\vec{p}_i - \vec{q}$. For this and other models, ^{9}Be has been chosen as the target nucleus. Shown in Fig. 5 is the DK prediction for the backward proton being observed at 160°. As expected, the peak in the distribution of the forward proton is near 0° ($\theta_{f,\text{lab}}$ is the angle between p_f and the beam axis, a positive $\theta_{f,\text{lab}}$ being on the opposite side of the beam from θ_q). For $\theta_q = 90°$, shown in Fig. 6, the peak shifts out to about 15°. In both of these calculations, $\vec{p}_f$ has been chosen to lie in the plane formed by $\vec{p}_i$ and $\vec{q}$. The cross section decreases as $\vec{p}_f$ moves out of the plane. The incident proton kinetic energy in both these results is 800 MeV.

III. MULTIPARTICLE EXCHANGE MODEL

The particle labels used for this model will be the same as those used in the previous section. In order to be able to make the $(p,2p)$ predictions for this model, we will have to go beyond the model of Weber and Miller[4] and actually construct a matrix element for the p-residual nucleus collision. Thus, the $(p,2p)$ predictions generated here are going to have significantly more model dependence than that proposed by Weber and Mil-

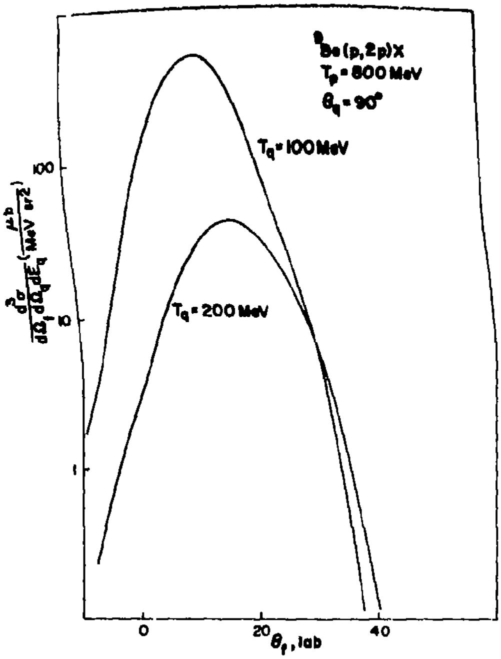

FIG. 6. DK predictions for ^{9}Be$(p,2p)X$ with $\theta_q = 90°$ and 800 MeV incident proton kinetic energy.

ler.

The normalization for the cross section chosen here will be that of Bjorken and Drell[9] for spinless particles. This is the same normalization taken in our previous work on (p,α) reactions. Denoting the p-residual nucleus matrix element by T_{pR}, the differential cross section for inclusive proton production is given by

$$\frac{d^2\sigma}{d\Omega_e dE_e}=\frac{C}{2^5(2\pi)^6 M_A M_{A'} p_i}\frac{q}{}M_{A'}F(q)$$
$$\times\int\frac{d^3p_f}{E_f E_k}|T_{pR}|^2\delta(E_i+M_A-E_e-E_f-E_k)\,. \qquad (11)$$

The function $F(q)$ is proportional to $n(k)$ of the direct knockout model. The constant C will be determined by fitting the inclusive date.[2] Now if the kinematic limits for the p_f integration were close to those of the free p-R reaction, then the integral would simply be proportional to the p-R cross section. That means that for fixed E_e and $|\vec{q}|$, the inclusive differential cross section should vary only slowly with θ_e. Experiment shows a fairly rapid variation as one goes to forward values of θ_e, so the particular version of the MPE model under investigation here is probably limited to large θ_e. To get an idea of the effect of shifting the integration limits as a function of $\vec{q}$, the following parametrization is chosen.

(i) $F(q)$ is simply set equal to e^{-q/k_0}. As in the DK model, a value of k_0 of 88 MeV adequately describes the large θ_e data.

(ii) The total p-R cross section is assumed to have the same form as given in Weber and Miller, i.e.,

$$\sigma = 86(A-1)^{2/3}\ \text{mb}\,, \qquad (12)$$

independent of energy in this region.

(iii) The differential cross section for p-R collisions is assumed to have the same t dependence as Eq. (4), and b is chosen by a rough fit to the slope parameters of elastic p-R scattering at intermediate energy[13]

$$b = 5.5A^{1.08}\ \text{GeV}^{-2}\,. \qquad (13)$$

Lastly, with this normalization, the p-R differential cross section is given by

$$\frac{d\sigma}{dt}=\frac{|T_{pR}|^2}{64\pi M_R^2 p_{\text{lab}}^2}\,. \qquad (14)$$

While this is admittedly not the best parametrization available, it will do for the purpose of this paper.

The results for ^{9}Be$(p,p')X$ at incident proton energy of 800 MeV are shown in Fig. 7. The con-

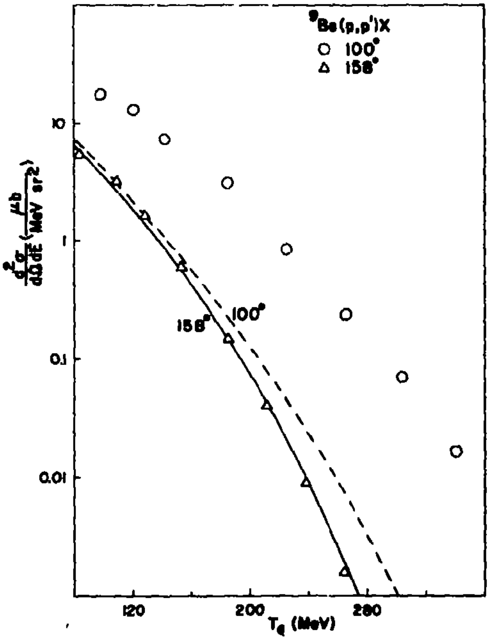

FIG. 7. Comparison of MPE model with experiment for the reaction ^{9}Be$(p,p')X$ at incident proton energy of 800 MeV and observed proton angle of 100° and 158°. Data from Ref. 2.

stant C is fixed by the 158° data, and one can see that the cross section predicted for 100° is indeed not too much different.

The $(p, 2p)$ predictions are given by Eq. (11) with the $|\vec{p}_f|$ integration performed to take care of energy conservation. The results for a Be target are shown in Figs. 8 and 9. In contrast to the DK model, the peak in the distributions of the MPE model does not shift significantly with θ_q.

IV. CORRELATED CLUSTER MODEL

The last model which we wish to treat in detail is the correlated cluster model of Fujita.[5] In this model, p_f is replaced by a cluster of N nucleons of energy E_{cc}. The differential cross section then consists of A terms:

$$\frac{d^3\sigma}{d^3q} = \sum_N G_N \int \frac{1}{E_q E_{cc}} |T_{p\text{-}cc}|^2 w_N(k) \frac{d^3p_f}{(2\pi)^3} \frac{1}{(8\pi)^2 F} \times \delta(E_i + NM_p - E_q - E_{cc} - \bar{\mathcal{E}}^*) , \tag{15}$$

where

$$F = NM_p p_i , \tag{16}$$

$$G_N = \frac{A}{N} \frac{1}{A^{N-1}} \left(\frac{V_c}{V}\right)^{N-1} \xi_N , \tag{17}$$

$$w_N(k) = \left(\frac{4\pi}{N\nu}\right)^{3/2} e^{-k^2/N\nu} . \tag{18}$$

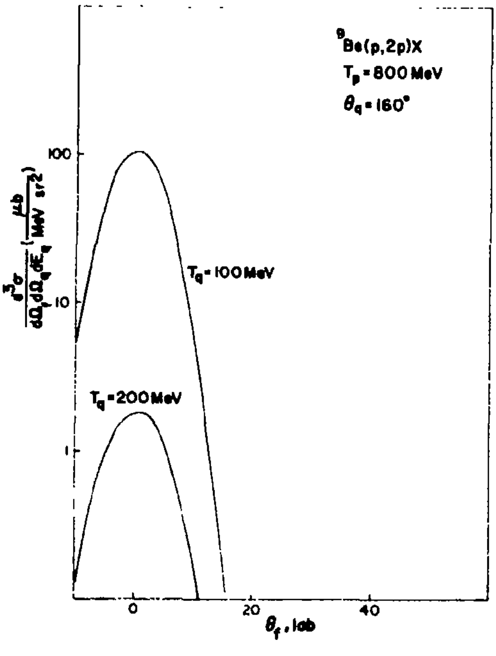

FIG. 8. MPE predictions for ^{9}Be$(p, 2p)X$ with $\theta_q = 160°$ and 800 MeV incident proton energy.

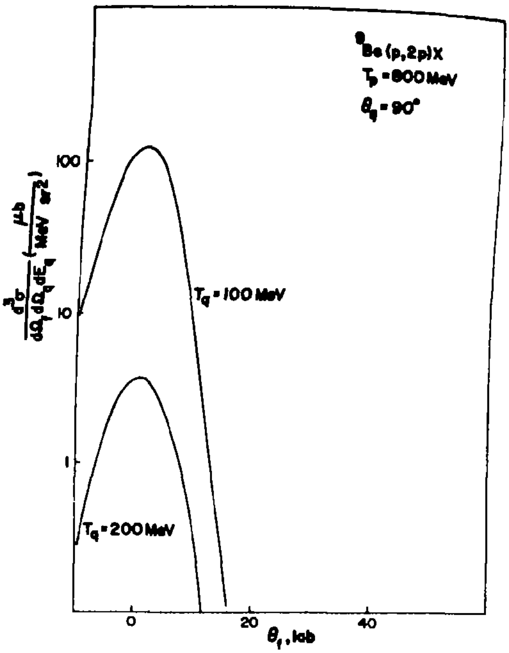

FIG. 9. MPE predictions for ^{9}Be$(p, 2p)X$ with $\theta_q = 90°$ and 800 MeV incident proton energy.

The reader is referred to the original paper of Fujita for a detailed discussion of the values of the parameters involved. The values of these parameters which Fujita found to give an acceptable fit to the inclusive data were

$$\nu = 32\,500 \text{ MeV}^2 , \tag{19}$$

$$V_c/V = 0.07 , \tag{20}$$

$$\xi_N \sim 1 . \tag{21}$$

The p-cluster cross section was replaced by the pp cross section by Fujita,[5] and the amplitude normalized as in Eq. (14). The same criteria for selecting the appropriate s and t and the same pp cross section parametrization as were used in the DK calculations are used in the results discussed below.

We are interested mainly in the $N = 1$ term of Eq. (15), as the recoiling clusters in Fujita's model do not break up, by and large. Evaluation of Eq. (15) then shows that, depending on E_q, scattering off a single nucleon contributes only $\sim 10^{-4}$ to 10^{-5} of the predicted inclusive cross section. It comes as no surprise then that when the $|\vec{p}_f|$ integration only is performed in Eq. (15) to give the $(p, 2p)$ prediction, the results are substantially lower than those found in the DK or MPE calculations. The ^{9}Be $(p, 2p)X$ cross sections for one proton at 160° are shown in Fig. 10.

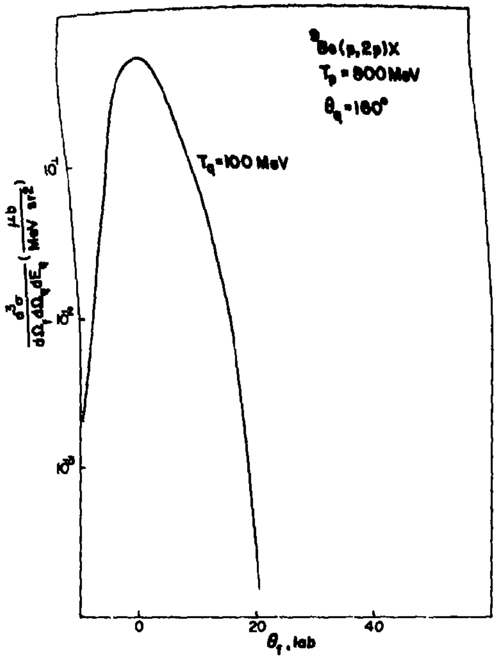

FIG. 10. CC predictions for ^{9}Be$(p,2p)X$ with $\theta_q = 160°$ and 800 MeV incident proton energy.

V. DISCUSSION

In the above, we have calculated some $(p,2p)$ predictions for a variety of models. Each model has its own characteristic spectrum which should allow experiment to rule at least one of them out. For example, although the peak in the cross section for the DK and MPE models is grossly the same, the peak should shift as θ_q is varied in the DK model, but remain roughly centered at the beam axis in the MPE model. The reason that the peak is approximately stationary in the MPE model is that the amplitude assumed here for p-R scattering falls off very rapidly with momentum transfer of the incident proton to the residual nucleus. If the amplitude did not in fact fall as fast with momentum transfer as has been assumed here, then the forward protons would not be so sharply peaked, although the position of the peak would still change only slowly with θ_q. In contrasting both of these models to the CC model, the predicted cross section of the CC model is several orders of magnitude lower than the other two.

It should be pointed out that the particular differential cross section used for comparison in these calculations, $d^3\sigma/d\Omega_f d\Omega_q dE_q$, involves only those forward protons which result from three-body kinematics as in Fig. 1. Hence, T_f is uniquely determined by energy and momentum conservation at a given Ω_f, Ω_q, T_q, and $\overline{\delta}^*$ and is roughly $T_i - T_q - \overline{\delta}^*$. These calculations then are restricted to those forward protons with T_f greater than about $\frac{1}{2}T_i$. If the coincidence trigger were defined to be any forward proton at fixed Ω_f in coincidence with a high energy proton in the backward hemisphere at fixed Ω_q and E_q (including the low energy protons resulting from evaporation of the residual nucleus) then the predicted angular distributions would look substantially different.

This point is particularly important for any discussion of the CR model. Because the CR model was not broken down into elementary amplitudes, it was not used in the above to predict the $(p,2p)$ differential cross sections. However, as described in the Introduction, one can evaluate the contribution to the (p,p') predictions of the term in which the "jet" comprises all of the residual nucleus. This would then give a rough measure of the scale factor which could be applied to the DK model results to approximate what would be the CR results at the T_f corresponding to coherent recoil of the residual nucleus. The $n = A - 1$ contribution to the ^{9}Be$(p,p')X$ cross section at incident proton energy of 800 MeV is shown in Fig. 11. As with the CC model, it is observed

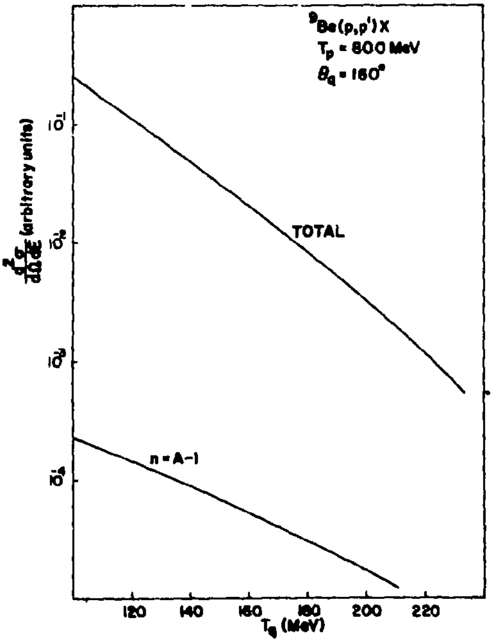

FIG. 11. Comparison of $n = A - 1$ contribution in CR model with total predicted cross section for ^{9}Be$(p,p')X$ at $\theta_q = 160°$, $T_p = 800$ MeV.

that the predicted cross section should be much smaller than the DK predictions. However, if one were to measure $d^4\sigma/d\Omega_f dE_f d\Omega_e dE_e$ as a function of E_f at fixed Ω_f, Ω_e, and E_e, then rather than observing events at a narrow band of energies centered around $T_i - T_e - \bar{\mathcal{E}}^*$ (the spreading caused by the $\bar{\mathcal{E}}^*$ distribution) as predicted by the DK model, the CR model would predict that the maximum in the cross section would be shifted to lower E_f (corresponding to lighter recoiling jets), the numerical value of the shift depending on the details of the excitation energy and momentum distributions involved.

In all of the above calculations, the average excitation energy of the residual nucleus has been set equal to zero. A more realistic calculation would have a nonzero value, but would introduce extra model dependence into the results, a situation we have tried to avoid. Green and Korteling,[14] using heavy fragment yields as constraints on an evaporation calculation, have estimated that at the beginning of the evaporation cascade, the distribution of excitation energies has an average value in the 20–40 MeV range for an incident proton in the 200–500 MeV range. While this is not necessarily the same distribution that one would expect here, it provides us with a rough value for $\bar{\mathcal{E}}^*$. This would manifest itself in the DK model by a downward shift of an amount $\bar{\mathcal{E}}^*$ in T_f from the $\bar{\mathcal{E}}^* = 0$ value of roughly $T_i - T_e$.

In performing these calculations, protons with energy 800 MeV and a ^{9}Be target were chosen to illustrate the results. ^{9}Be was chosen as it is a readily available and easily manipulated target. The proton energy was chosen to be 800 MeV because an energetic backward moving proton is required for a trigger. This should not imply that the correlation measurement could be done only at this energy. The requirement that the backward moving proton be energetic was made so that one would be measuring (within the context of these models) the high momentum part of the single particle effective momentum distribution, where the distribution seems to be adequately described by an exponential falloff. While there is no reason why the experiment could not be run at lower energy, certainly once the incident proton energy fell much below, say, 200 MeV, it is unlikely that the simple exponential would adequately describe the distribution in the momentum range required for the calculations and they would have to be done with a more appropriate distribution.

ACKNOWLEDGMENTS

The author wishes to express his gratitude to D. Hutcheon of the p-^{16}O elastic scattering experiment, and G. Roy *et al.* of the inclusive proton production experiment, all at the University of Alberta, for making their data available to him prior to publication. He also wishes to thank R. M. Woloshyn for many useful discussions. Lastly, he is grateful to the Natural Sciences and Engineering Research Council of Canada and to Simon Fraser University for financial support.

---

[1] S. Frankel *et al.*, Phys. Rev. Lett. 36, 642 (1976).

[2] S. Frankel, Phys. Rev. Lett. 38, 1338 (1977); Phys. Rev. C 17, 694 (1978); S. Frankel *et al.*, *ibid.* 18, 1375 (1978).

[3] R. D. Amado and R. M. Woloshyn, Phys. Rev. Lett. 36, 1435 (1976).

[4] H. J. Weber and L. D. Miller, Phys. Rev. C 16, 726 (1977).

[5] T. Fujita, Phys. Rev. Lett. 39, 174 (1977).

[6] R. M. Woloshyn, Nucl. Phys. A306, 333 (1978).

[7] D. H. Boal and R. M. Woloshyn, Phys. Rev. C 20, 1878 (1979).

[8] R. E. L. Green and R. G. Korteling, TRIUMF Report No. TRI-PP-79-29.

[9] J. D. Bjorken and S. D. Drell, *Relativistic Quantum Mechanics* (McGraw-Hill, New York, 1964).

[10] Particle Data Group, *NN and ND Interactions (Above 0.5 GeV/c)—A compilation*, Lawrence Radiation Laboratory, Berkeley, 1970.

[11] J. G. Zabolitzky and W. Ey, Phys. Lett. 76B, 527 (1978).

[12] G. Roy *et al.*, private communication.

[13] Data taken from the following references: O. Chamberlain *et al.*, Phys. Rev. 102, 1659 (1956); L. Ray *et al.*, Phys. Rev. C 18, 1756 (1978); H. Courant *et al.*, *ibid.* 19, 104 (1979); D. Hutcheon, private communication.

[14] R. E. L. Green and R. G. Korteling, TRIUMF Report No. TRI-PP-79-30.

PHYSICAL REVIEW C VOLUME 21, NUMBER 5 MAY 1980

Consistency between pion exchange currents and N-N potential in doubly radiative n-p capture

A. Cambi
Istituto Nazionale di Fisica Nucleare, Sezione di Firenze, Italy

B. Mosconi
Istituto Nazionale di Fisica Nucleare, Sezione di Firenze, Italy and Istituto di Fisica Teorica dell'Università di Firenze, Firenze, Italy

P. Ricci
Istituto Nazionale di Fisica Nucleare, Sezione di Firenze, Italy

(Received 22 October 1979)

The consistency between the exchange currents in the pionic range and the Reid soft-core potential, which has an asymptotic behavior like V_{OPE}, is studied in the doubly radiative n-p capture process. The cross section is evaluated using the interaction Hamiltonian expressed by means of the nuclear current, that includes the two-body terms deriving from one-pion exchange. The gauge invariance is preserved by the generalized contact term. This cross section is compared to that obtained with the Siegert form of the interaction Hamiltonian. The difference between the values of the cross section, which is of the order of 24%, constitutes a quantitative estimate of the lack of consistency between pion exchange currents and the nuclear potential considered. The use of purely phenomenological wave functions leads to a great disagreement. Finally, the existence of an exchange effect of the order of 30% is pointed out in the process under examination, which occurs via the emission of two $E1$ photons.

[NUCLEAR REACTIONS Meson exchange currents, Reid soft-core potential and Siegert's theorem; $^1\mathrm{H}(n,\gamma\gamma)$, thermal n, calculated $\sigma_{2\gamma}$.]

I. INTRODUCTION

The principal aim of this work is to give a quantitative estimate of the consistency between pion exchange currents (MEC) and N-N potential, taking the process of the doubly radiative n-p capture into consideration. To this end we compare the value of the cross section obtained using the nuclear current operator with that obtained using the charge density operator, which are connected through Siegert's theorem.[1] This last value will be assumed as the "comparison one," being model independent, as it will be shown in the following.

This reaction seems to be a convenient one because the use of Siegert's theorem is valid, being a low-energy process. At the same time, as it is a second order process, it involves off-shell matrix elements and, thus, it allows us to investigate the short range behavior of MEC and N-N potential. MEC operators are of course consistent with the long range part of an N-N potential, as the Reid soft-core potential[2] (RSC), since its asymptotic part is given by one-pion-exchange potential V_{OPE}. Their lack of consistency at short range can be pointed out in the reaction chosen because the virtual intermediate states have unlimited momenta. A similar investigation in single photon processes requires high momentum transfer, so that Siegert's theorem is no longer applicable.

The experimental and theoretical situation about the reaction $n+d\rightarrow d+2\gamma$ is briefly as follows. The most recent experimental result, which lowers considerably the first one obtained by Dress *et al.*,[3] is that of Wüst *et al.*,[4] and gives a value $\sigma_{2\gamma}=(-5.2\pm6.4)$ μb for photons in the energy range 330–1890 keV. Moreover, lowering the photon threshold to 233 keV, these authors find that the energy spectrum agrees with that expected for an $E1$-$E1$ emission mode. In agreement with this result, Earle and McDonald[5] have obtained an upper limit of 1.6 μb, for photons in the energy range 700–1520 keV.

In the meantime the problem has been studied in detail, from the theoretical point of view, in the framework of the usual electromagnetic interaction theory, i.e., without Adler's[6] conjecture about the amount of the nonorthogonality between ^3S bound and continuum wave functions. Grechukhin[7] demonstrated in 1971 that the electric dipole is the fundamental emission mode. Then the cross section for the $E1$-$E1$ mode has been calculated by several authors[8-11] still more carefully up to the value (0.1176 ± 0.0003) μb given by Blomqvist and Ericson.[12]

Emission mechanisms different from the domi-

© 1980 The American Physical Society

nant $E1$-$E1$, have been also evaluated. Bernabeu and Tarrach[13] have studied the emission of an $M1$ photon followed by a bremsstrahlung photon. The present authors[14] have calculated the influence of the exchange currents on the cross section for the $M1$-$M1$ mode. All these processes give negligible contributions to the dominant $E1$-$E1$ mode.

It is well known that for low-energy transitions, like those which come into play in this process, the continuity equation for the current allows the interaction Hamiltonian H_I to be expressed in two equivalent forms: one the "current operator" H_J by means of the current density, and the other, the "charge operator" H_ρ by means of the charge density. The mathematical formulation of the equivalence between these two operators is Siegert's theorem.[1] H_ρ is commonly used to calculate low-energy $E1$ transition amplitudes, neglecting retardation effects, relativistic corrections, and two-body exchange contributions to the charge density. With these approximations the charge operator assumes the Siegert form (3).

The results obtained with the two equivalent forms of H_I should be identical in principle in the long wavelength approximation. It is clear that this occurs only as one uses wave functions which are eigenfunctions of the nuclear Hamiltonian H. Furthermore, H must have eigenvalues coincident with the experimental values of the energies to be utilized. In general these conditions are never satisfied because, commonly, use is made of nuclear potentials, which only approximately give the experimental energies, and of wave functions which are approximations of the true eigenfunctions of H.

A simplification occurs in the case of the nuclear two-body problem where the wave functions can be exactly calculated once the N-N potential is given. Then, in order to have equivalence between the two approaches, it is necessary to use a nuclear current consistent with the potential, so that the continuity equation is satisfied.

In the low-energy processes, like the one under examination, it is usually assumed that a nuclear potential with the correct behavior at large r is sufficient. This behavior is determined by the exchange of one pion and the corresponding exchange potential is V_{OPE}.

It has been demonstrated by several authors, see for example Thompson and Heller,[15] that, up to terms M^{-1} in the nonrelativistic expansion in the inverse of the nucleon mass, the continuity equation is satisfied with V_{OPE}, if the exchange currents, commonly labeled pion current and pair current,[16] are added to the one-body current, while the charge density keeps its one-body form.

As regards the Δ_{33}-isobar excitation current, which has the same range as the pionic currents, we remember that it is not connected to the nuclear potential by the continuity equation, being divergenceless.[17] However, this current need not be considered in our case because the corresponding $E1$ operator vanishes as k^2 in the limit $k\rightarrow 0$.

At this point the outline of potential and electromagnetic operators appears consistent, but it is not so because any realistic potential must be modified from its correct OPE tail to reproduce the properties of the n-p system. In the RSC potential, as well as in many other potentials widely used in the literature, the part at intermediate and short range, which takes into account the exchange of mesons heavier than the pion, is determined in a phenomenological way. The corresponding terms are missing in the expression of the exchange current commonly used in the low-energy processes. The problem of the consistency between MEC and N-N potential, which is the object of our work, arises just from the absence of these terms.

A partial comparison between the results with H_ρ and H_J for the total cross section of this reaction has been made by Lee and Khanna,[10] considering only the convective current and the S part of the deuteron state.

A last consideration concerns the exchange effect in this reaction which occurs essentially with a double $E1$ emission. At first sight it can appear surprising that such an effect exists because Siegert's theorem, which allows us to replace the two body current density with the one-body charge density, is sometimes interpreted as demonstrating that there are no exchange effects in the low-energy $E1$ transitions. Formally, this interpretation immediately breaks down because the charge density also acquires two-body contributions[18] beginning with the second order terms in the nonrelativistic expansion in $1/M$ of the same OPE processes leading to the exchange currents. But just because of their dependence on the nuclear mass, we can neglect these two-body terms[19,20] and assume the usual one-body form of the charge density. Nevertheless, the matrix elements of the Siegert operator include the effects of the total (impulse and exchange) current because the meson exchange between the nucleons determines not only the electromagnetic operators but also the nuclear Hamiltonian and, thus, the wave functions. Comparing the cross section obtained with H_ρ and with H_J, we shall be able to distinguish the contributions of the one-body transition operators from the two-body ones, it being understood that the influence of mesons on the wave functions makes a clear distinction between one-body and two-body effects ultimately impossible.

Finally, we recall that an analogous comparison has been made by Bassani *et al.*[21] for the process of two photon absorption from the 1*s* to the 2*s* state of the atomic hydrogen. Their starting point was the problem of the choice of the electric dipole interaction $\vec{E}\cdot\vec{r}$ or $\vec{A}\cdot\vec{p}$, which are related by a gauge transformation of the electromagnetic potentials, in connection with the proper choice of the eigenstates of the unperturbed Hamiltonian. These authors have shown that both forms of H_I give the same transition amplitude for the considered process, using the same unperturbed wave functions. Hence their numerical problem is equivalent to ours, with the double advantage that the electron current is purely convective and the eigenstates of the unperturbed Hamiltonian are exactly known. In fact, the numerical results are the same, but the sum over the intermediate states converges to the final result in a very different way in the two cases. With the $\vec{E}\cdot\vec{r}$ operator, an excellent approximation is obtained considering just a few intermediate states of the discrete spectrum, the continuum giving negligible effects. On the contrary, when $\vec{p}\cdot\vec{A}$ is used, the continuum states give more than half the total value.

In Sec. II we have calculated $\sigma_{2\gamma}(E1\text{-}E1)$ for the *n*-*p* capture independently of the form of the interaction Hamiltonian. In Sec. III the calculation with H_ρ is outlined and in Sec. IV, that with H_J is more extensively reported. In Sec. V we have reported the numerical results obtained with H_J and we have discussed them in comparison with that obtained with H_ρ. In Sec. VI we have stated our conclusions.

II. *E*1-*E*1 CROSS SECTION

As is well known the interaction Hamiltonian for the emission of a photon with momentum $\vec{k}$, energy ω, and polarization λ, which is given in Coulomb gauge by

$$H_I(\vec{k}) = -\left(\frac{2\pi}{\omega}\right)^{1/2}\int d^3x\,\vec{j}(\vec{x})\cdot\vec{\epsilon}_{\vec{k},\lambda}\,e^{-i\vec{k}\cdot\vec{x}}\,, \tag{1}$$

where $\vec{\epsilon}_{\vec{k},\lambda}$ is the polarization vector and $\vec{j}(\vec{x})$ is the nuclear electromagnetic current density, gives rise to transition amplitudes for second order processes which are not gauge invariant. In order to preserve the gauge invariance, a gauge (or contact) term must be added to the dispersive part of the amplitude coming from H_I in the second order perturbation expansion. Therefore, the amplitude for the transition from the initial state $|i\rangle$ to the final state $|f\rangle$ with emission of two photons has the form

$$M_{fi} = \sum_n (1+P_{12})\,\frac{\langle f|H_I(\vec{k}_2)|n\rangle\langle n|H_I(\vec{k}_1)|i\rangle}{E_i - E_n - \omega_1} + M^{c}_{fi}\,, \tag{2}$$

where the summation over n means sum over the discrete quantum numbers and integration over the continuous ones of the intermediate state $|n\rangle$; E_i and E_n are the energies of the state $|i\rangle$ and $|n\rangle$, respectively, and the operator P_{12} changes photon 1 into photon 2. Since we are considering the *E*1-*E*1 transitions in thermal *n*-*p* capture, the energies of the emitted photons are low ($\omega_1+\omega_2=B$, if we neglect nuclear recoil, where B is the deuteron binding energy). Therefore, we can take the long wavelength limit of the theory. When $k\to 0$ H_I can be transformed by means of the continuity equation so that the current density is replaced by the charge density $\rho(\vec{x})$. This is the content of Seigert's theorem,[1] while the *E*1 interaction Hamiltonian assumes the Siegert form

$$H_\rho = -i\left(\frac{2\pi}{\omega}\right)^{1/2}[H,\vec{\epsilon}_{\vec{k},\lambda}\cdot\vec{D}]\,, \tag{3}$$

where H is the nuclear Hamiltonian and $\vec{D}$ the nuclear electric-dipole momentum

$$\vec{D} = \int d^3x\,\vec{x}\rho(\vec{x})\,, \tag{4}$$

which, in the case of point nucleons of coordinate $\vec{r}_j$, become

$$\vec{D} = e\sum_j \frac{1+\tau_3(j)}{2}\vec{r}_j\,. \tag{5}$$

The current form H_J of the *E*1 interaction Hamiltonian in the limit $k\to 0$ follows simply from (1) as

$$H_J = -\left(\frac{2\pi}{\omega}\right)^{1/2}\vec{\epsilon}_{\vec{k},\lambda}\cdot\vec{J}\,, \tag{6}$$

where $\vec{J}$ is the Fourier transform of $\vec{j}(\vec{x})$ evaluated at $\vec{k}=0$. As said in the Introduction, the aim of this work is to compare the numerical results obtained with these two equivalent forms of H_I, when the nuclear potential contains V_{OPE} as exchange potential. Therefore, the nuclear current density in (6) must include, besides the convective current, the exchange current which is the sum of the two-body currents corresponding to the processes of pion exchange and pair excitation.[16] In fact, the magnetization part of the one-body current, as well as the two-body current corresponding to the excitation of the Δ_{33} resonance, goes to zero as k^2 in the limit $k\to 0$.

Explicitly we have for our two-body problem

$$\vec{J}_c = -i\,\frac{e}{4M}(\vec{\tau}_1-\vec{\tau}_2)_3(\overrightarrow{\nabla}-\overleftarrow{\nabla})\,, \tag{7a}$$

$$\vec{J}_{ex} = \frac{2}{3} e f^2_{\pi NN}\sqrt{\pi}(\vec{\tau}_1 \times \vec{\tau}_2)_3$$

$$\times\left[e^{-\mu r}\Omega^{(1)}_{1,0} + \phi_2(\mu r)\sum_L (2\hat{L})^{1/2}\begin{pmatrix} 2 & 1 & L \\ 0 & 0 & 0 \end{pmatrix}\Omega^{(1)}_{L,2}\right], \tag{7b}$$

where $\hat{L} = 2L+1$, $\vec{r}$ is the relative coordinate, M and μ are the nucleon and pion masses, $f_{\pi NN}$ is the π-N coupling constant ($f^2_{\pi NN} \simeq 0.08$), the tensors $\Omega^{(j)}_{L,s}$ are defined by

$$\Omega^{(j)}_{L,s} = [Y^{(L)}(\hat{r}) \otimes (\vec{\sigma}_1 \otimes \vec{\sigma}_2)^{(s)}]^{(j)}, \tag{8}$$

$Y^{(L)}(\hat{r})$ being the spherical harmonics, $\hat{r} = \vec{r}/r$, and

$$\phi_2(x) = e^{-x}\left(1 + \frac{3}{x} + \frac{3}{x^2}\right). \tag{9}$$

As far as the gauge amplitude is concerned, its complete expression generalized to the case in which the exchange currents are considered, and valid for any value of the photon momenta, has been obtained by Friar.[22] In the $E1$-$E1$ long wavelength limit, it reduces to the form given by Sachs and Austern[23]

$$M^G_{fi} = \langle f\,|[[H, \vec{\epsilon}_{\vec{k}_1\lambda_1}\cdot\vec{D}], \vec{\epsilon}_{\vec{k}_2\lambda_2}\cdot\vec{D}]|\,i\rangle, \tag{10}$$

if the nuclear Hamiltonian contains V_{OPE} as exchange potential.

Because the exchange current has a complicated dependence on nuclear variables, it is convenient for the calculation of the cross section to express the transition amplitude by means of the $E1$-$E1$ generalized polarizabilities[24] $\langle f\,|P_{jm}|\,i\rangle$ defined by

$$M_{fi} = \sum_{jmM_1M_2}(-)^m\sqrt{\hat{j}}\begin{pmatrix} 1 & 1 & j \\ M_1 & M_2 & -m \end{pmatrix}D^{(1)}_{M_1\lambda_1}(R_1)$$

$$\times D^{(2)}_{M_2\lambda_2}(R_2)\langle f\,|P_{jm}|\,i\rangle, \tag{11}$$

where R_i is the rotation which makes the z axis coincident with the $\vec{k}_i$ direction, and $D^{(1)}(R_i)$ is the corresponding rotation matrix. The advantage is that $\langle f|P_{jm}|i\rangle$ are the matrix elements of irreducible tensors of rank j. Therefore we can use the standard procedure, based on the Wigner-Eckart theorem, to factorize the dependence on geometrical factors while all the dependence on dynamics is included in the reduced matrix elements. Then we can easily perform the sum and the average over the magnetic quantum numbers of the nuclear states, and the sum over the polarization of the photons, by means of the Clebsch-*Gordan series for the rotation matrices and the sum rules for the Racah coefficients.* It follows for the total cross section, the expression

$$\sigma_{2\gamma} = \frac{1}{36\pi^3 v}\int_0^B d\omega_1(\omega_1\omega_2)^2\sum_j |\langle f\,||P_j||\,i\rangle|^2, \tag{12}$$

where v is the n-p relative velocity in the initial state.

Before concluding this general discussion which is independent of the form chosen for H_I, we have to remember that in the thermal n-p capture the initial state can be a spin singlet or triplet $l=0$ state, but only the triplet one can have $E1$-$E1$ transitions to the final deuteron state. Therefore, following a standard notation for the deuteron wave function and denoting with $z(r)$ the reduced radial wave function of the continuum ${}^3S_1$ state, the initial and final states are

$$|i\rangle = \frac{z(r)}{r}\mathcal{Y}^M_{011}\eta_0,$$

$$|f\rangle = \sum_{l=0,2}\frac{u_l(r)}{r}\mathcal{Y}^M_{l11}\eta_0, \tag{13}$$

where η_0 is the singlet isospinor and $\mathcal{Y}^M_{LSJ}$ are the usual spin-angle functions.

For the sake of clarity, we must divide our treatment into two parts corresponding to the Siegert and "current" form of the $E1$ operator, because several details of the calculation are different in the two cases. We begin with the Siegert operator in order to obtain, shortly, in our formalism the results of Blomqvist and Ericson[12] and Lee and Khanna.[10] The numerical value of the cross section so obtained will be the comparison value in the next section where the cross section is evaluated with the "current" operator.

III. SIEGERT OPERATOR

When one works with the Siegert form of H_I, the dispersive part of the transition amplitude can be transformed, as noted by several authors,[8,10,12] in such a way that the gauge part is exactly canceled. It follows that the total amplitude is given by

$$M_{fi} = -2\pi(\omega_1\omega_2)^{1/2}$$

$$\times\sum_n (1+P_{12})\frac{\langle f\,|\vec{\epsilon}_{\vec{k}_2\lambda_2}\cdot\vec{D}\,|\,n\rangle\langle n\,|\vec{\epsilon}_{\vec{k}_1\lambda_1}\cdot\vec{D}\,|\,i\rangle}{E_i - E_n - \omega_1} \tag{14}$$

and the corresponding reduced polarizabilities by

$$\langle f\,||P_j||\,i\rangle = (-)^{1+J_i+J_f}2\pi(\omega_1\omega_2)^{1/2}\sum_n[1+(-)^jP_{12}]\sqrt{\hat{j}}\begin{Bmatrix} 1 & 1 & j \\ J_i & J_f & J_n \end{Bmatrix}\frac{\langle f\,||\vec{D}||\,n\rangle\langle n\,||\vec{D}||\,i\rangle}{E_i - E_n - \omega_1}. \tag{15}$$

Here J_i, J_f, and J_π are the total angular momentum of the initial, final, and intermediate states. Since for the two-body system the $\vec{\mathrm{D}}$ operator is a part the isospin factor, the relative coordinate, the possible intermediate states are spin triplet $l=1$ states. Assuming the effect of the interaction in these $|{}^3P_{J_\pi}\rangle$ states to be negligible, their wave functions become

$$|{}^3P_{J_\pi}\rangle = \sqrt{4\pi}\, j_1(pr)\mathcal{Y}^{M}_{11J_\pi}(\hat{r})\eta_{1,m}, \tag{16}$$

$\vec{\mathrm{p}}$ being the n-p relative momentum. In this approximation the radial matrix elements in (15) are independent of the angular momentum J_π, so that the sum over J_π can be easily performed with the result

$$\langle f \| P_j \| i\rangle = Me^2(\omega_1\omega_2)^{1/2}(1+P_{12}) \times[\delta_{j,0}K_0(\omega_1)+(\tfrac{2}{5})^{1/2}\delta_{j,2}K_2(\omega_1)], \tag{17}$$

where $\delta_{i,j}$ is the Kronecker symbol. The functions $K_l(\omega)$, with $l=0, 2$, are defined by

$$K_l(\omega) = \int dp \frac{p^2}{p^2+M\omega} I_{u_l}(p) I_z(p) \tag{18}$$

with

$$I_f(p) = \int dr\, r^2 j_1(pr) f(r)\,. \tag{19}$$

From the expression (17) of the reduced matrix elements of $P_{j m}$ it is clear that the total cross section is the incoherent sum of $\sigma^S_{2\gamma}$ and $\sigma^D_{2\gamma}$ which correspond to the $l=0$ and $l=2$ parts of the deuteron state. When we take the asymptotic form of the wave functions

$$\begin{aligned} u_0(r) &= Ne^{-\alpha r}\,, \\ u_2(r) &= N\rho\phi_2(\alpha r)\,, \\ z(r) &= \sqrt{4\pi}\,(r-a_t)\,, \end{aligned} \tag{20}$$

where $\alpha=\sqrt{MB}$, N is the normalization constant, ρ the asymptotic D to S ratio in the deuteron wave function, and a_t the triplet scattering length, we obtain

$$\sigma^S_{2\gamma} = \bar{\sigma}_{2\gamma}\left[\frac{191}{10}+\pi-32\ln 2-\frac{3}{5}\frac{1}{\alpha a_t}+\frac{3}{2}\frac{1}{(\alpha a_t)^2}\right], \tag{21}$$

$$\sigma^D_{2\gamma} = \frac{\rho^2}{10}\bar{\sigma}_{2\gamma}\left[54+\frac{187}{16}\pi-128\ln 2 -\frac{120}{7}\frac{1}{\alpha a_t}+\frac{75}{2}\frac{1}{(\alpha a_t)^2}\right], \tag{22}$$

where

$$\bar{\sigma}_{2\gamma} = \frac{e^4}{v}\,\frac{N^2}{9\alpha}\left(\frac{B}{M}\right)^{5/2} {a_t}^2\,. \tag{23}$$

$\sigma^S_{2\gamma}$ reproduces the result given by Blomqvist and Ericson[11] and by Lee and Khanna,[10] while $\sigma^D_{2\gamma}$ is slightly different from the expression obtainable from formula (30) in Ref. 10. Because of the factor $\rho^2 \simeq 7\times 10^{-4}$ in $\sigma^D_{2\gamma}$, the value of the total cross section evaluated with the Siegert operator is determined by $\sigma^S_{2\gamma}$, and also by its model independent expression (21). In fact, as shown in Refs. 12 and 10, both the regularization of the wave functions at the origin and the n-p interaction in the intermediate states give an effect of the order of one part in 10^3. For all these reasons the cross section obtained with H_ρ can be considered the correct one. As for its numerical value, Blomqvist and Ericson,[12] using the best values[25] for the low-energy n-p parameters entering in (21), obtain the very accurate value quoted in the Introduction.

In the next section, in order to make the comparison with the value of the cross section calculated with H_J, we can assume $\sigma_{2\gamma}=0.118$ μb as that corresponding to H_ρ.

IV. "CURRENT" OPERATOR

The partial cancellation between the dispersive and the gauge part of the transition amplitude leading to (14) does not occur when the "current" form of H_I is used in (2). Therefore, also the generalized polarizabilities are composed of two terms

$$\langle f|P_{jm}|i\rangle = \langle f|P^D_{jm}|i\rangle + \langle f|P^G_{jm}|i\rangle\,. \tag{24}$$

The reduced matrix element of the first one, corresponding to the dispersive amplitude, derives from (15) with the substitution

$$\vec{\mathrm{D}} \to i\,\frac{\vec{\mathrm{J}}}{(\omega_1\omega_2)^{1/2}}\,, \tag{25}$$

and so we can avoid writing it explicitly. In order to have the generalized polarizabilities corresponding to the gauge amplitude (10) we must express the polarization vectors of the photons by means of the rotation matrices and develop the double commutator, recalling the working hypothesis that the nuclear potential contains V_{OPE}. Then with the standard recoupling techniques, the terms can be rearranged in irreducible tensors, dividing the angular from the spin variables, with the result

$$\langle f\|P^G_j\|i\rangle = \frac{4\pi^{3/2}e^2f^2_{\pi NN}}{(3\omega_1\omega_2)^{1/2}}(\tau_{1x}\tau_{2x}+\tau_{1y}\tau_{2y})\begin{pmatrix}1&1&j\\0&0&0\end{pmatrix} \times\langle f\|re^{-\mu r}\Omega^{(j)}_{j,0} -\sum_\lambda(2\hat{\lambda})^{1/2}\begin{pmatrix}2&j&\lambda\\0&0&0\end{pmatrix}r\phi_2(\mu r)\Omega^{(j)}_{\lambda,2}\|i\rangle\,. \tag{26}$$

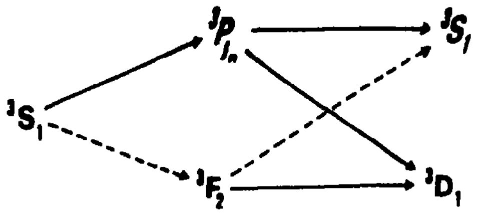

FIG. 1. $E1$-$E1$ transitions in $n+p\rightarrow d+2\gamma$. A full line indicates the transitions due to $\vec{j}_{ex}$ and $\vec{j}_c$, while a dashed line indicates those due to $\vec{j}_{ex}$ only.

We have not reported the term relative to the Thompson amplitude, which derives from the kinetic energy (and corresponding to the gauge term $A^2/2m$ of the atomic Hamiltonian), because it vanishes owing to the orthogonality between the wave functions of the initial and final states.

With respect to the calculation with H_p, another complication arises concerning the dispersive part in the amplitude, in addition to the need to consider the gauge term separately. The summation over the intermediate states extends to the $^3F_2$ channel besides the $^3P_{J_n}$ channels. In fact, the operator $\Omega^{(1)}_{3,2}$, included in the exchange current, allows the transition with $\Delta J=3$ from the initial $^3S_1$ state to the $^3F_2$ state, from which the S part of the deuteron can be reached through the same operator and the D part also through $\Omega^{(1)}_{1,0}$, $\Omega^{(1)}_{1,}$ and the gradient operator.

In conclusion, the possible $E1$-$E1$ transitions we must take into account in this case are reported in Fig. 1, where we have indicated with a dashed line the transitions due to $\vec{j}_{ex}$ and with a full line those possible with both $\vec{j}_{ex}$ and $\vec{j}_c$.

As far as the wave functions of the intermediate states are concerned, we remember that Lee and Khanna[10] have evaluated the effect of the n-p interaction in the $^3P_{J_n}$ states using only the convective part of the nuclear current. The enhancement of the cross section, which was unappreciable in the calculation with H_p, becomes about 5%, which is a small effect even if not completely negligible. Because it seems reasonable to assume that the interaction effect maintains this order of magnitude when the exchange current is added, we have considered noninteracting intermediate states only. With this hypothesis the reduced matrix elements of the nuclear current for the possible transitions become

$$\langle {}^3P_{J_n}\|\vec{j}\|{}^3S_1\rangle = i(-)^{1+J_n}\frac{e}{M}\left(\frac{\hat{J}_n\pi}{3}\right)^{1/2}\left[A^1_s(p)+12(-)^{J_n}\begin{Bmatrix}2&1&1\\J_n&1&1\end{Bmatrix}B^1_s(p)\right], \tag{27a}$$

$$\langle d\|\vec{j}\|{}^3P_{J_n}\rangle = -i\frac{e}{M}\left(\frac{\hat{J}_n\pi}{3}\right)^{1/2}\left\{A^1_{u_0}(p)+12(-)^{J_n}\begin{Bmatrix}2&1&1\\J_n&1&1\end{Bmatrix}B^1_{u_0}(p)-(-)^{J_n}3\sqrt{2}\right.$$
$$\left.\times\left[\begin{Bmatrix}2&1&1\\J_n&1&1\end{Bmatrix}A^1_{u_2}(p)+30\sum_L \hat{L}\begin{pmatrix}1&2&L\\0&0&0\end{pmatrix}^2\begin{Bmatrix}2&L&1\\1&2&1\\1&1&J_n\end{Bmatrix}B^1_{u_2}(p)\right]\right\}, \tag{27b}$$

$$\langle {}^3F_2\|\vec{j}\|{}^3S_1\rangle = 6i\left(\frac{2\pi}{5}\right)^{1/2}\frac{e}{M}B^3_s(p), \tag{27c}$$

$$\langle d\|\vec{j}\|{}^3F_2\rangle = 6i\left(\frac{2\pi}{5}\right)^{1/2}\frac{e}{M}\left[B^3_{u_0}(p)-\frac{1}{\sqrt{8}}[A^3_{u_2}(p)+2B^3_{u_2}(p)]\right]. \tag{27d}$$

The radial matrix element $B^l_f(p)$ is defined as

$$B^l_f(p)=\tfrac{4}{3}Mf^2_{\pi NN}\int dr\, rj_1(pr)\phi_2(\mu r)f(r), \tag{28}$$

while $A_f{}^l(p)$ is given by

$$A_f{}^l(p)=I_f{}^l(p)-J_f{}^l(p) \tag{29}$$

with

$$J_f{}^l(p)=\tfrac{4}{3}Mf^2_{\pi NN}\int dr\, rj_1(pr)e^{-\mu r}f(r),$$
$$I_f{}^l(p)=\int dr\left[rj_1(pr)\frac{df(r)}{dr}-f(r)\frac{d}{dr}[rj_1(pr)]+(3l_f-2)j_1(pr)f(r)\right], \tag{30}$$

where l_f indicates the orbital angular momentum of the state whose radial wave function is $f(r)$.

For the gauge term we obtain

$$\langle d\|P^G_j\|{}^3S_1\rangle=-\frac{4e^2\pi f^2_{\pi NN}}{3(\omega_1\omega_2)^{1/2}}\left[\delta_{j,0}(R_0+\sqrt{8}S_2)-\delta_{j,2}\frac{4}{\sqrt{5}}\left(S_0+\frac{1}{\sqrt{8}}(R_2-2S_2)\right)\right], \tag{31}$$

with the definitions

$$R_l=\int dr\, u_l(r)re^{-\mu r}z(r),$$
$$S_l=\int dr\, u_l(r)\phi_2(\mu r)z(r). \tag{32}$$

Since the radial wave functions of the intermediate states have been considered spin independent, all the dependence on the angular momentum J_n is contained in the (6-j) and (9-j) coefficients. Then by means of their sum rules we can make the summation over J_n in the dispersive part of the reduced generalized polarizabilities which transforms into the sum of three terms relative to the values of $j=0,1,2$:

$$\langle d\|P_j\|i\rangle=\frac{e^2}{(\omega_1\omega_2)^{1/2}}\frac{[1+(-)^j P_{12}]}{12\pi M}$$
$$\times\{\delta_{j,0}[M_0(\omega_1)+2N(\omega_1)]$$
$$+\delta_{j,1}[M_1(\omega_1)+\sqrt{3}N(\omega_1)]$$
$$+\delta_{j,2}[M_2(\omega_1)+(1/\sqrt{5})N(\omega_1)]\}\,. \qquad (33)$$

The quantity $N(\omega_1)$ corresponding to the intermediate states ${}^3F_2$ is given by

$$N(\omega_1)=\tfrac{36}{5}\sqrt{4\pi}\int dp\frac{p^2}{p^2+M\omega_1}B^1_s(p)$$
$$\times\left[B^1_{u_0}(p)-\frac{1}{\sqrt{8}}[A^1_{u_2}(p)+2B^1_{u_2}(p)]\right] \qquad (34)$$

and the $M(\omega_1)$, corresponding to the intermediate state ${}^3P_{J_n}$, are expressible as, omitting the dependence from ω_1,

$$M_0=3F_0+\tfrac{48}{5}K_0-\frac{24}{\sqrt{8}}(G_2+\tfrac{2}{5}H_2+\tfrac{4}{5}K_2)\,,$$
$$M_1=-\sqrt{3}\,\frac{36}{5}\left[K_0-\frac{1}{\sqrt{8}}(H_2+2K_2)\right], \qquad (35)$$
$$M_2=\frac{12}{\sqrt{5}}\left[G_0+H_0+\tfrac{7}{5}K_0\right.$$
$$\left.-\frac{1}{\sqrt{8}}(F_2+2G_2+\tfrac{7}{5}H_2+\tfrac{14}{5}K_2)\right],$$

by means of the functions

$$F_l(\omega)=4\pi\int dp\frac{p^2}{p^2+M\omega}A^1_{u_l}(p)A^1_s(p)\,,$$
$$G_l(\omega)=4\pi\int dp\frac{p^2}{p^2+M\omega}B^1_{u_l}(p)A^1_s(p)\,,$$
$$H_l(\omega)=4\pi\int dp\frac{p^2}{p^2+M\omega}A^1_{u_l}(p)B^1_s(p)\,, \qquad (36)$$
$$K_l(\omega)=4\pi\int dp\frac{p^2}{p^2+M\omega}B^1_{u_l}(p)B^1_s(p)\,,$$

where the index $l=0,2$ means transitions to the S,D part of the deuteron. From expressions (33) and (35) we can immediately observe that these transitions contribute simultaneously to the different j components of the generalized polarizabilities. Therefore the cross section has terms from S-D interference, unlike the Siegert operator. Furthermore, we note that because of the behavior of the operator $\vec{J}_{ex}$ for $r\to 0$, the use of the wave functions in their asymptotic form leads to divergent matrix elements. Therefore, we must consider wave functions with the correct behavior at the origin. With the aim of making as many calculations as possible analytically, we have assumed the deuteron wave functions to have the form

$$u_0(r)=N\sum_i c_i e^{-\alpha_i r}\,,$$
$$w_2(r)=N\rho\sum_i d_i\phi_2(\beta_i r)\,, \qquad (37)$$

which is the analytic form derived by Gourdin *et al.*[28] from the dispersive analysis of the π-p-d vertex in the nonrelativistic limit. The coefficients must satisfy the following sum rules:

$$\sum_i c_i=\sum_i d_i=\sum_i d_i\beta_i^2=\sum_i\frac{d_i}{\beta_i^2}=0\,. \qquad (38)$$

As for the continuum ${}^3S_1$ state we have taken the parametrization

$$z(r)=\left(1+\sum_i g_i e^{-\gamma_i r}\right)(4\pi)^{1/2}(r-a_t) \qquad (39)$$

with the condition $1+\sum_i g_i=0$.

V. NUMERICAL RESULTS

The N-N potential considered in this work is the Reid soft-core potential.[2] Therefore, we have made a fit with the expression (37) to the deuteron wave function tabulated by the author, and with the form (39) to the scattering wave function obtained by numerical integration of the system of Schrödinger equations for the ${}^3S$-${}^3D$ coupled channels at zero energy. We remember that the triplet scattering length given by the RSC potential is $a_t=5.39$ fm, the D-state probability is $P_D=6.47\%$ and the asymptotic D- to S-wave ratio is $\rho=0.026\,223$. In Tables I and II we report the value

TABLE I. Parameters of the fit in expression (37) for the RSC deuteron wave function.

i	c_i	α_i (fm^{-1})	d_i	β_i (fm^{-1})
1	1.000	0.2316	1.000	0.2316
2	1115.640	4.6677	−11 686.137	3.2179
3	−101.330	4.3700	−399.674	4.7240
4	−42.167	4.1703	−81.167	1.4294
5	−0.366	1.2344	12 389.894	3.4068
6	−941.277	4.6854	82.495	7.1600
7	−142.490	6.6890	−1 382.949	4.2093
8	110.990	6.9821	1 076.538	2.4697

TABLE II. Parameters of the fit in expression (39) for the RSC $^3S_1$ scattering state.

i	g_i	γ_i (fm^{-1})
1	−3.388	2.125
2	2307.684	8.753
3	−2412.369	8.822
4	247.455	11.050
5	−140.382	11.720

of the other parameters of our fit to the Reid set of wave functions.

Because we are interested in seeing how much the results change with phenomenological wave functions, we have also used the wave functions existing in the literature and parametrized with the form (37) and (39). While the parametrization (37) of $u_0(r)$ as the sum of exponentials is nearly of general use and so would allow many different choices, that of $u_2(r)$ drastically reduces their number. In fact, besides the various sets of parameters of Gourdin *et al.*,[26] among which we have chosen No. 1, that provide a good fit to the Garthenaus wave function, we have found only the fit of McGee[27] to the Hamada-Johnston wave function, modified so that it vanishes at $r=0$, rather than at the hard-core radius. Since we must change the asymptotic behavior of the McGee fit in order to have the correct deuteron binding energy, we are really dealing with a phenomenological wave function in this case too. Moreover, the $^3S_1$-continuum wave function, which we must add to complete the set, is partially arbitrary because the condition of orthogonality with the $^3S_1$-bound wave function is not sufficient to define it completely. A satisfactory solution to this problem for the modified McGee wave function has been given by Lee and Khanna,[10] with the triplet scattering length fixed at the value $a_t=5.41$ fm, which is very close to the best experimental value.[25] We refer to their Table II for the values of the other parameters. From now on we will call this set of deuteron and $^3S_1$-continuum wave functions the "McGee set." To complete the "Gourdin set" we have used in (39) the set of parameters obtained by Durand,[28] which gives a $z(r)$ orthogonal to the $u_0(r)$ of Gourdin *et al.* with $a_t=5.406$ fm. The phenomenological wave functions chosen have a soft-core behavior at the origin and predict deuteron properties similar to those predicted by the Reid potential. In fact, the D-state probability corresponding to the Gourdin and McGee wave function is $P_D=6.5\%$ and 7%, whereas the asymptotic D- to S-wave ratio is $\rho=0.0265$ and 0.0269, respectively.

Our numerical results for the total cross section are reported in Table III for these three sets of wave functions, considering both the ^3S part of the deuteron state (normalized to $1-P_D$) and the complete $^3S+{}^3D$ state.

The values in the first column correspond to the contributions of the convective current alone, those in the other columns to the total (impulse + exchange) current. Furthermore, in the second column only the transitions through the $^3P_{J_\pi}$ states are considered, while in the last one those through the $^3F_2$ channel are also taken into account. In both cases we have included the contribution of the generalized gauge term which vanishes when the exchange currents are not considered. Before making any comment on the results in Table III, we recall that a comparison between the total cross section calculated with the Siegert operator and the "current" operator has been made by Lee and Khanna,[10] but neglecting the exchange currents and the deuteron D state. Their results

TABLE III. Total cross section in $n+p\to d+2\gamma$ reaction evaluated with the three sets of wave functions (Gourdin, McGee, Reid). The label ^3S indicates that only the S part of the deuteron wave function has been considered, and the label $^3S+{}^3D$ indicates that the D part is included. The values in the column headed ^3P correspond to transitions through the intermediate channels $^3P_{0,1,2}$ only, while those in the column $^3P+{}^3F$ include the $^3F_2$ intermediate state too.

		Total cross sections in μb		
	Deuteron	Without exchange	With exchange currents	
Wave functions	state	currents	^3P	$^3P+{}^3F$
Gourdin set	^3S	0.0876	0.266	0.339
	$^3S+{}^3D$	0.0878	0.206	0.273
McGee set	^3S	0.0902	0.216	0.269
	$^3S+{}^3D$	0.0906	0.153	0.195
Reid set	^3S	0.0830	0.155	0.183
	$^3S+{}^3D$	0.0831	0.118	0.146

are then equivalent to ours in the first column and, more precisely, to that labeled ^3S for every set of wave functions. In the common case of the McGee set we reproduce their value. From the other values in the first column we can see that the cross section changes very little when the deuteron D state also is taken into account, because there is not S-D interference when only the impulse current is considered and the corresponding contributions are in the same ratio $1/\rho^2$ as in the calculation with H_ρ.

Unlike the Siegert operator, the "current" operator produces a large model dependence of the cross section. In Ref. 10 the considerable variation between the value obtained with hard-core and soft-core wave functions was pointed out. Our results in the first column emphasize the model dependence of the cross section for different soft-core wave functions, and those in the other columns show that even more pronounced variations arise when the exchange currents are included in the calculation.

The second feature of the calculation with the Siegert operator we have to compare is the dependence of the result on the short range behavior of the wave functions. We think that a meaningful evaluation of this effect on the cross section calculated with the "current" operator is not possible. The reason is that any determination of the asymptotic cross section is in this case highly questionable. In fact, with the choice of the experimental values of the parameters the asymptotic cross section (0.21 μb) is grossly overestimated if at the same time the gauge term is neglected, as in Ref. 10. If, instead, the spurious contribution of the gauge term is considered, the asymptotic cross section drops to 0.05 μb. Since on the other hand it is also not sensible, in our opinion, to take $a_t = \alpha^{-1} = 4.31$ fm in order to preserve the orthogonality of the wave functions, we must conclude that there is not any acceptable way for calculating the asymptotic cross section. Furthermore, we want to point out that all we have said regards the convective current, because the matrix elements of the exchange currents are divergent with the asymptotic wave functions. We think rather that the values of the cross section obtained with the impulse current alone are interesting because they allow us to make an evaluation of the exchange effect in the process under examination which occurs with a double $E1$ emission. In analogy with the interaction effect in the single photon n-p capture, which has been explained with the contributions of the pionic exchange currents and the Δ_{33}-resonance excitation current,[19,30] we call here exchange effect the percentage difference between the total cross section and the contribution of the one-body current. This value follows obviously from the difference between the cross section calculated with the Siegert operator and the convective current alone. Therefore, the exchange effect exists also in this $E1$-$E1$ process and is about 30%, a value higher than the 10% of the single photon n-p capture, which occurs with an $M1$ emission.

If we observe the values reported in the last two columns of Table III, we note that the effect produced by the inclusion of the pionic exchange currents is extremely model dependent. The percentage variations among the three cases considered, which are less than 10% in the calculation with the impulse current, become 30% in the comparison between σ (Reid) and σ (McGee), 40% between σ (McGee) and σ (Gourdin), and even 80% between σ (Reid) and σ (Gourdin). Evidently the short range behavior of the exchange operators produces considerable differences in the cross section, even if the soft-core wave functions used give very similar properties of the two-body system.

Inside every set of wave functions we can observe the importance of the D part of the deuteron. In fact, because of the negative interference between the transition amplitudes to the S and D part of the deuteron, the cross section drops, on the average, more than 20%.

From the second column in Table III, which corresponds to transitions through the intermediate channels $^3P_{J_\pi}$, we see that with the complete deuteron wave function the cross section becomes 0.206 μb with the Gourdin set, 0.153 μb with the McGee set, and 0.118 μb with the Reid set. That is, with the wave functions derived from the Reid soft-core potential, we obtain again the value of 0.118 μb which is the model independent result of the calculation made with the Siegert operator.

As we can see from the third column, the inclusion of the intermediate state $^3F_2$ reduces the agreement between the values of the cross section calculated in the two different ways. In fact, $\sigma_{\rm Reid}$ changes from 0.118 to 0.146 μb and proportionally the cross section increases in the other two cases.

These values are the final result of our calculations and we think they can allow us to reach a quantitative conclusion on the consistency between the nuclear potential and the pionic exchange currents. In fact, the only effect we have neglected is the N-N interaction in the intermediate states that, as pointed out above, we can consider to be of the order of a few percent.

As regards the dependence of our results on the wave functions, we can observe that the value most different from the comparison one is that of the Gourdin set, which has purely phenomenological wave functions. A closer value is obtained with the McGee set where the ^3S scattering wave function is purely phenomenological, while the deuteron wave function corresponds to the Hamada-Johnston potential. The best value corresponds to the Reid set, where the ^3S scattering wave function has also been calculated by integrating the system of Schrödinger equations for the Reid soft-core potential.

It seems reasonable to conclude that the agreement is increasingly better as the wave functions are less independent of the nuclear Hamiltonian and the current density operators. In fact, we have a complete equivalence between the calculations made with the Siegert operator and those made with the two-body currents used, only if the exchange part of the N-N potential is $V_{\rm OPE}$. On one hand this explains the better agreement obtained with the Reid set, on the other hand, it justifies the residual difference which can be ascribed to the medium and short range part of the interaction, owing to the exchange of heavier mesons. This part is taken into account in a phenomenological way by the Reid potential, but it is not contained in the exchange currents considered, which are those usually employed in low-energy processes. We must conclude that these short range effects are not negligible in the case under examination, because we must ascribe to them the residual difference of 20%.

VI. CONCLUSIONS

We have calculated the $E1$-$E1$ cross section for the doubly radiative n-p capture reaction, using the current operator, and taking into account the meson exchange currents in the pionic range and the generalized contact term, so that the transition amplitude is gauge invariant.

The principal aim of this work is to give a quantitative estimate of the consistency between exchange currents in the pionic range and N-N potential with the correct $V_{\rm OPE}$ behavior at large distances. To this end we compare the results obtained with H_J to that obtained with H_ρ. We have also briefly reported the calculation with H_ρ in the framework of our formalism to get a clear view of the principal differences between the two approaches. In the case of H_ρ the main feature is surely the model independence of the result $\sigma_{2\gamma} = 0.118$ μb, which is assumed to be the comparison value for that obtained with H_J.

In the calculation with the current operator, besides the wave functions deriving from the Reid soft-core potential, we have also used two essentially phenomenological sets of wave functions (Gourdin, McGee) in order to evaluate the importance of the fact that the wave functions are eigenstates of the nuclear Hamiltonian. The total cross section has a value which is extremely dependent on the kind of wave functions used. With the Reid set we obtain $\sigma_{2\gamma} = 0.146$ μb which is a value near the comparison one. In the other two cases the total cross section comes out to be 0.273 μb for the Gourdin set and 0.195 μb for the McGee set. Of particular interest is the fact that the phenomenological wave functions, which predict deuteron properties very similar to the Reid ones, give such a different value of the cross section. This is due to the short range behavior of the exchange operators which gives importance to the differences in the intermediate and short range of the wave functions. In the Reid set we have just eigenfunctions of the nuclear Hamiltonian, so that the residual difference between the cross sections calculated with H_J and with H_ρ must be ascribed to the fact that the exchange current considered does not contain the heavier meson exchange contributions and thus corresponds only to the asymptotic part of the Reid soft-core potential. In this potential $V_{\rm OPE}$ is in fact modified in a phenomenological way at intermediate and short range to take into account the meson exchange effect which differs from the OPE effects. In conclusion, we have an estimate of 24% for the lack of consistency at short range between the RSC potential and the pion exchange currents.

The use of the current operator places importance on the contributions coming from the D part of the deuteron wave function and from the intermediate channel $^3F_2$, which is now open because of the tensorial structure of the transition exchange operator. Furthermore, it is interesting to note that the contributions of the exchange currents are of the same order of magnitude as those of the impulse current. Therefore, if we express the interaction Hamiltonian by means of the current operators, it is impossible to distinguish a dominant contribution to the total cross section, as *a priori* one could be tempted to do, limiting the calculation to the impulse current and to the S part of the deuteron wave function.

Finally, comparing the value of the total cross section obtained with the impulse current ($\sigma_{2\gamma} \simeq 0.083$ μb for the Reid set) to that obtained with the Siegert operator, we can estimate the overall effect of the exchange currents in the two-photons n-p capture, which occurs mainly via two $E1$ transitions. This effect is about 30% and thus greater than the 10% effect in the single photon capture which occurs via an $M1$ transition.

[1] A. J. F. Siegert, Phys. Rev. 52, 787 (1937).

[2] R. V. Reid, Jr., Ann. Phys. (N. Y.) 50, 411 (1968).

[3] W. B. Dress, C. Guet, P. Perrin, and P. D. Miller, Phys. Rev. Lett. 34, 7 (1975).

[4] N. Wüst, H. Seyfarth, and L. Aldea, Phys. Rev. C 19, 1153 (1979).

[5] E. D. Earle and A. B. McDonald, contribution to the Third International Symposium on Neutron Capture Gamma Ray Spectroscopy and Related Topics, BNL, Upton, N. Y., 1978 (unpublished).

[6] R. J. Adler, Phys. Rev. C 6, 1964 (1972).

[7] D. P. Grechukhin, Yad. Fiz. 14, 109 (1971) [Sov. J. Nucl. Phys. 14, 62 (1972)].

[8] H. Hyuga and M. Gari, Phys. Lett. 57B, 330 (1975).

[9] H. C. Lee and F. C. Khanna, Phys. Lett. 61B, 216 (1976).

[10] H. C. Lee and F. C. Khanna, Phys. Rev. C 14, 1306 (1976).

[11] J. Blomqvist and T. Ericson, Phys. Lett. 57B, 117 (1975).

[12] J. Blomqvist and T. Ericson, Phys. Lett. 61B, 219 (1976).

[13] J. Bernabeu and R. Tarrach, Phys. Lett. 58B, 1 (1975).

[14] A. Cambi, S. Craparo, B. Mosconi, and P. Ricci, Nuovo Cimento 47A, 421 (1978).

[15] R. H. Thompson and L. Heller, Phys. Rev. C 7, 2355 (1973).

[16] M. Chemtob and M. Rho, Nucl. Phys. A163, 1 (1971).

[17] J. A. Lock and L. L. Foldy, Ann. Phys. (N. Y.) 93, 276 (1975).

[18] J. L. Friar, Ann. Phys. (N. Y.) 104, 380 (1977); W. M. Kloet and J. A. Tjon, Phys. Lett. 61B, 356 (1976); E. Hadjimichael, Nucl. Phys. A294, 513 (1978); M. Gari and H. Hyuga, *ibid.* A278, 372 (1977).

[19] The two-body charge density gives, in fact, an appreciable contribution to the electromagnetic transitions only at photon energies higher than 20 MeV [see Ref. 18 and also M. Gari and B. Sommer, Phys. Rev. Lett. 41, 226 (1978); and E. Hadjimichael, Phys. Lett. 85B, 17 (1979)]. We have checked that the pair process, which is the dominant two-body term, gives a quite negligible contribution to the cross section of the doubly radiative thermal neutron capture by hydrogen (Ref. 20).

[20] A. Cambi, B. Mosconi, and P. Ricci (unpublished).

[21] F. Bassani, J. J. Forney, and A. Quattropani, Phys. Rev. Lett. 39, 1070 (1977).

[22] J. L. Friar, Phys. Rev. Lett. 36, 510 (1976).

[23] R. G. Sachs and N. Austern, Phys. Rev. 81, 705 (1951).

[24] J. M. Eisenberg and W. Greiner, *Excitation Mechanisms of the Nucleus* (North-Holland, Amsterdam, 1970), Nuclear Theory, Vol. II.

[25] H. P. Noyes, Annu. Rev. Nucl. Sci. 22, 465 (1972).

[26] M. Gourdin, M. Le Bellac, F. Renard, and J. Tran Thanh Van, Nuovo Cimento 37, 524 (1965).

[27] I. J. McGee, Phys. Rev. 151, 772 (1966).

[28] L. Durand, Phys. Rev. 123, 1393 (1961).

[29] D. O. Riska and G. E. Brown, Phys. Lett. 38B, 193 (1972).

[30] M. Colocci, B. Mosconi, and P. Ricci, Phys. Lett. 45B, 224 (1973); M. Gari and A. H. Huffman, Phys. Rev. C 7, 994 (1973); J. Thakur and L. L. Foldy, *ibid.* 8, 1957 (1973); E. T. Dressler and F. Gross, Nucl. Phys. A262, 516 (1976).

PHYSICAL REVIEW C VOLUME 21, NUMBER 5 MAY 198

Proton-^{4}He elastic scattering at intermediate energies

G. A. Moss, L. G. Greeniaus, J. M. Cameron, D. A. Hutcheon, R. L. Liljestrand, C. A. Miller, and G. Roy
Department of Physics, The University of Alberta, Edmonton, Canada T6G 2N5

B. K. S. Koene* and W. T. H. van Oers
Department of Physics, The University of Manitoba, Winnipeg, Canada R3T 2N2

A. W. Stetz
Department of Physics, Oregon State University, Corvallis, Oregon 97331

A. Willis and N. Willis
Institut de Physique Nucléaire, 91406 Orsay, France

(Received 21 September 1979)

The differential cross section and analyzing power for p-^{4}He elastic scattering at 200, 350, and 500 MeV incident proton energy in the laboratory angle range from 4° to 168° are presented. Comparisons to theoretical calculations at 200 and 350 MeV have been made.

[NUCLEAR REACTIONS Proton-^{4}He elastic scattering 200, 350, 500 MeV measured differential cross section and analyzing power, $4° \lesssim \theta_{\rm lab} \lesssim 168°$.]

I. INTRODUCTION

Proton-nucleus scattering at intermediate energies has received considerable attention with the advent of accelerators capable of producing high-intensity, variable-energy polarized beams with good energy resolution. Extensive data for differential cross sections and analyzing powers have been obtained, which should provide a stimulus to the search for a successful microscopic description of the processes involved.

The elastic scattering of protons from ^{4}He is an unusually good case to investigate thoroughly for several reasons: The initial and final states are well defined theoretically, the target nucleus has spin zero, minimizing the complications that arise in some spin-dependent calculations, and inelastic processes are easily distinguishable, which reduces experimental demands on energy resolution.

It has become apparent that analyzing power (polarization) angular distributions are very important in the evaluation of the validity of theoretical models. In the energy range of the present experiment, 200 to 500 MeV, the analyzing power exhibits a rich and variable structure. Although a proper description of the differential cross section has established the need for spin-dependent terms, far more stringent demands are established when analyzing power data are to be explained as well.

The present experiment represents the last phase of a three-part study of p-^{4}He elastic scattering at TRIUMF. The first part[1] examined $d\sigma(\theta)/d\Omega$ and $A_y(\theta)$ in the small angle region (4°–16° in the laboratory). This measurement was made with a gas target which had a well-defined density and thickness. The cross section results of this first phase have been used as a normalization benchmark for the remaining two parts of the study.

The second part of the investigation[2] involved measurement of $d\sigma(\theta)/d\Omega$ and $A_y(\theta)$ at backward angles (144° – 168° in the laboratory) for several incident proton energies between 185 and 500 MeV. One of the goals of the experiment was a careful search for energy-dependent backward peaking of the differential cross section. The analyzing power measurements made at the same time were intended to aid in a more complete understanding of the reaction process.

In the present experiment we have completed the cross section and analyzing power angular distributions at 200, 350, and 500 MeV with measurements in the intermediate angle region. At these three energies, data sets spanning the laboratory angle range from 4° to 168° are now available.

Section II of this report discusses the experiment while Sec. III describes the analysis procedures. Results and discussion are presented in Sec. IV and conclusions are summarized in Sec. V.

II. THE EXPERIMENT

The experiment was performed using the externa 4B proton beam line at the TRIUMF cyclotron.

© 1980 The American Physical Society

Most of the features of the apparatus have been described elsewhere[1-3] so that only aspects specific to the present experiment will be discussed in detail.

The target-detector apparatus is represented schematically in Figs. 1(a) and 1(b). Some important characteristics of the system are also summarized in Table I. The liquid ^{4}He target[4,5] had a thickness of 0.77 cm (97 mg/cm^2) with a 5 cm^2 aperture. The target cell could be raised and lowered remotely. This permitted the normal ^{4}He cell to be replaced in the beam by an empty target cell of equivalent thickness in order to correct for background coming from material around the liquid ^{4}He. The target could also be rotated to ensure that none of the scattered particles would strike the side frames of the cell. The scattered particles were detected in counter telescopes consisting of 12.5 cm^2 multiwire proportional chambers (MWPC) with horizontal and vertical coordinates, plastic scintillation detectors, copper energy degraders, and NaI(Tl) detectors. The telescopes were mounted on four independently movable booms which could be remotely positioned about the target center to an accuracy of 0.1°. The efficiencies of the telescopes have been carefully measured[6] so that proper corrections for losses due to nuclear interactions in the copper and NaI could be made.

Two modes of operation were employed: a singles mode shown in Fig. 1(a) when only the scattered proton could be detected, and a coincidence setup as shown in Fig. 1(b) when the ^{4}He recoil could be detected in coincidence with the proton. Events with protons scattered to the left and to the right of the beam could be detected if the paths of the scattered particles were not obscured by the target frames. Both "left" and "right" events were collected concurrently when the target geometry permitted. A left or right event was ways defined by the side to which the proton wa scattered. In the angular range from 60° to 12 events were detected on only one side of the be

In the coincidence mode, the proton was detec in one of the back detector telescopes while the recoil ^{4}He was detected in the forward telescop on the opposite side of the beam. A trigger $(\Delta E_F \cdot E_B \cdot \Delta E_B)$ was required to define an event. The copper degrader thickness in the back telescopes was varied depending on the energy of t scattered protons so as to keep the proton ener at the entrance to the NaI detector in the range between 80 and 130 MeV. The coincidence mod gave excellent discrimination in the selection of elastic events so that the data were essentially free of any background.

The singles mode was used when the recoil ^{4} did not have sufficient energy to penetrate the target and the material before the ΔE detectors In this case the protons were detected in the fr telescopes, the trigger defining the event being $(P \cdot \Delta E_F \cdot E_F)$. Here an additional counter (P) w placed about 50 cm from the target and operate coincidence with the other counters in the telesco It served as an active collimator to eliminate protons that did not scatter from the immediate region of the liquid ^{4}He target. Again copper degraders were used to limit the proton energy in the NaI detectors. Data collected in the singles mode were composed of p-^{4}He elastic and inela scattering events, and background events from target walls and thermal insulation.

The calculated rms multiple scattering of the protons in singles mode was always less than 0.3° and effects on the measured differential cr sections have been ignored. In the coincidence mode, the distribution of recoil ^{4}He particles w observed with the FL and FR wire chambers; t

TABLE I. Properties of the system.

	Incident proton energy 200 MeV	350 MeV	500 MeV
Angular range covered (laboratory angle)			
Singles mode	13°–105°	15°–91°	13°–61°
Coincidence mode	105°–143°	91°–143°	61°–143°
Horizontal angular acceptance			
Singles mode	2.14°	1.57°	1.40°
Coincidence mode	3.48°	3.99°	2.33°
Solid angle acceptance[a]			
Singles mode	1.55 msr	0.755 msr	0.600 msr
Coincidence mode	3.27 msr	4.93 msr	1.816 msr
p-p analyzing power used for beam polarization	0.305	0.435	0.501

[a] Used in off-line analysis.

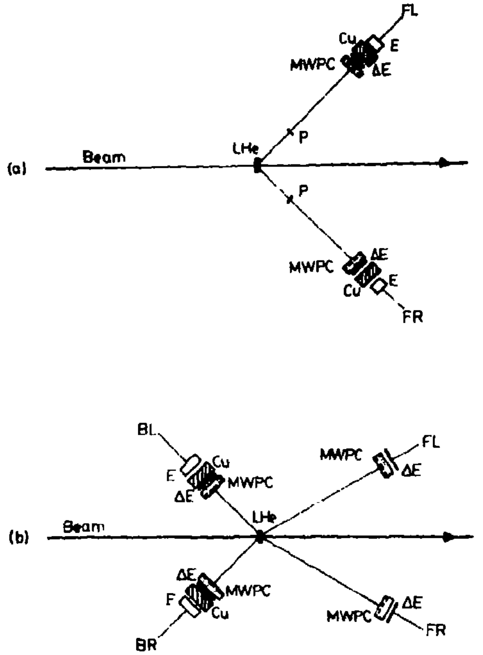

FIG. 1. (a) Setup for the singles mode data. The thin counters (*P*) served as active collimators to reduce the number of protons scattered in the entrance or exit of the scattering chamber from being detected. (b) A schematic drawing of the target-detector arrangement for the coincidence mode measurements. The protons were detected in the back telescopes and the ^{4}He recoils in the forward telescopes. The copper degraders were used to reduce the proton energies to 80–130 MeV at the entrance to the NaI detectors.

cuts on the proton solid angle were chosen so that losses due to multiple scattering of the recoil particles were negligible.

A polarized proton beam was used for all measurements. The beam intensities ranged from 0.2 to 10 nA with typical polarizations between 65% and 75%. The polarization direction, which could be reversed at the ion source, could also be set equal to zero to provide unpolarized beam for control purposes. The beam spot size on target was approximately 0.5 cm in diameter; its position was monitored regularly by observing the spot on a scintillator at the target station and by removable beam line wire scanners upstream and downstream of the target. The polarization of the beam was monitored continuously during data collection by a polarimeter[3] upstream of the ^{4}He target. The polarization was determined from the asymmetry in proton-proton scattering from a thin, 5 mg/cm^2, CH$_2$ target. The statistical uncertainty in the determination of the beam polarization during a given run was less than 1%. Corrections due to contributions from the carbon in the target were made as discussed in Ref. 3.

Data acquisition was accomplished via a CAMAC system interfaced to a Honeywell 316 computer. Data were recorded event by event on magnetic tape with left and right events appropriately identified. The acquisition program also allowed a rudimentary analysis of the data to be made on-line so that their quality could be checked.

Two independent beam flux monitors were used to provide an independent determination of the absolute scale of the cross sections and to permit the correct combination of data collected with different beam polarizations. These monitors were (1) the beam polarimeter, where the number of p-p elastic scattering events was monitored throughout each run, and (2) an ionization chamber situated downstream of the helium target. Both the polarimeter target foil and the ionization chamber had been previously calibrated at each energy by using a Faraday cup installed in the beam line. Although these monitors were used only for relative normalizations, the values of the cross sections extracted by using them agreed with those of Ref. 1 to better than 10% in all cases. The final data presented here were normalized to the results of Ref. 1 in the regions of angle overlap.

III. ANALYSIS PROCEDURES

Data collected in the two modes of operation were treated separately in the off-line analysis. For the singles data, horizontal and vertical MWPC cuts were made to select only those events in the central region of the NaI detector where the detection efficiency was uniform (see Table I). A "worst case" spectrum at a proton energy of 500 MeV is shown in Fig. 2(a). The spectrum after the background from the target walls has been subtracted is also presented. The two arrows in the figure show the final cuts around the well-defined elastic scattering peak. In the cross section calculation, corrections were made for events lost due to wire chamber inefficiencies (about 6%), for nuclear interactions of the protons while stopping in the total energy telescope,[6] and for the dead time of the system. The interaction correction was dependent on the mean energy incident on the telescope and varied between 10% and 70% depending on the beam energy and the angle setting. It should be pointed out that only the energy-dependent shape of the interaction correction is a potential source of error since the absolute magnitude of the cross section is deter-

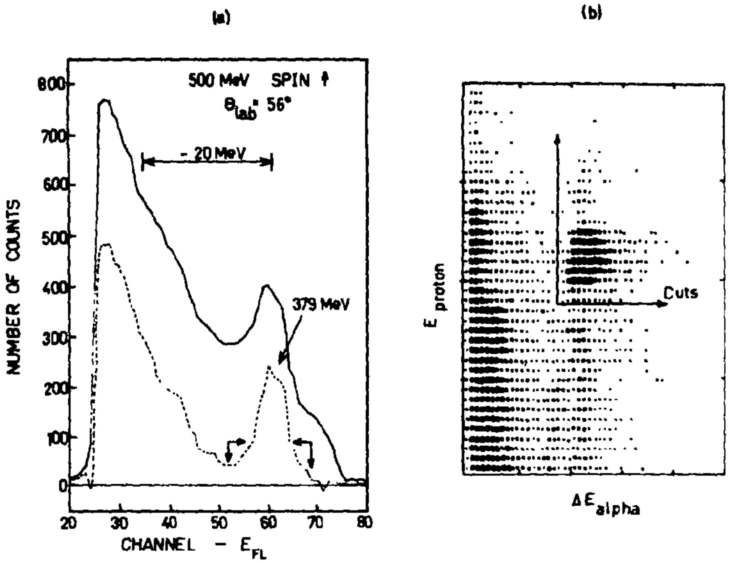

FIG. 2. (a) A "worst case" spectrum in the NaI detector for singles data in the intermediate angle region at 500 MeV. The upper curve is the target full data before background subtraction. The lower curve is the net contribution from the helium alone. The arrows indicate the cuts defining the good events. (b) A typical spectrum showing the correlation between the proton energy and the ^{4}He dE/dx for the coincidence data. The clean separation from any background events is clear. The lines indicate the cuts placed on the data.

mined by normalizing to the data of Ref. 1 where no such correction is needed. The shape of the interaction correction is very nearly linear over the relevant energies; uncertainties associated with a linear fit to the data are 1.5% of the correction or less.

The dead time of the system was dominated by the computer data acquisition and the on-line calculations. Dead-time corrections were calculated in two ways. The ratio of events detected in the electronics and the number actually accepted and written on magnetic tape was used in the final analysis. Artificial "events" created using a pulser and light-emitting diodes on each of the detectors showed that the electronic dead times were totally negligible in the experiment. The size of the dead-time correction was dependent on the beam flux, with typical values being about 15%. In several cases, data were collected at a given angle and beam polarization orientation but with different beam flux in order to check for possible systematic effects when dead-time corrections were large. Even in cases where the dead-time adjustment was larger than a factor of 2, excellent agreement was obtained with cross sections from data with more typical corrections.

The compensation for the wire chamber efficiencies was determined by observing the events corresponding to the elastic proton peak in the NaI spectra, and then finding the fraction of events that had any combination of multiple tracks or misses in the individual coordinate planes used to define the trajectory of the particle. Since the areas of the NaI detectors were smaller than those of the wire chambers, this provided a good estimate of inefficiencies in the region of interest. Losses were typically around 4% due to multiple tracks and around 2% for misses.

In the coincidence mode, the correlation of the proton energy in the NaI detector with the energy deposited in the ΔE counter by the associated ^{4}He recoil allowed the desired events to be identified unambiguously. An example is shown in Fig. 2(b). With the addition of time-of-flight cuts, all background was eliminated from this type of data. The wire chambers in the FL and FR telescopes were used only to verify that all the ^{4}He recoils were well within the limits of the ΔE counter. Corrections for proton MWPC efficiencies, system dead time, and nuclear interactions in the counter telescopes were made in a manner similar to those for the singles data.

In coincidence or singles mode, when both left and right events were observed, the background-corrected differential cross sections were calculated independently for each side (σ_L and σ_R). The differential cross section for an unpolarized beam was then found by taking the simple average

$$\sigma_0 = \frac{\sigma_L + \sigma_R}{2}\,. \tag{1}$$

Similar values were available for polarization up (+), polarization down (−), and for the unpolarized beam. The final result at a given angle was taken as the weighted average of the results for the different beam polarizations. The individual statistical errors were used as the weighting factors. The analyzing power was calculated from

$$A_y(\theta) = \frac{\sigma_L^+ + \sigma_R^- - \sigma_L^- - \sigma_R^+}{\sigma_L^+ + \sigma_R^+ + \sigma_L^- + \sigma_R^-}\,\frac{2}{(P^+ + P^-)}\,, \tag{2}$$

where the superscripts denote the direction of the beam polarization. Any instrumental asymmetries cancel to first order using this expression.

When events were detected on only one side of the beam (left in this example), more care had to be taken in extracting the equivalent unpolarized cross sections. Writing the observed cross sections with polarization up and down as

$$\sigma_L^+ = \sigma_0(1 + P^+ A_y) \tag{3}$$

and

$$\sigma_L^- = \sigma_0(1 - P^- A_y)\,, \tag{4}$$

one obtains for the unpolarized cross section

$$\sigma_0 = \frac{1}{2}\left(\sigma_L^+ + \sigma_L^- - (\sigma_L^+ - \sigma_L^-)\,\frac{P^+ - P^-}{P^+ + P^-}\right). \tag{5}$$

Here P^+ and P^- are the magnitudes of the incident beam polarization for spin up and spin down, and A_y is the analyzing power of the target at the angle being considered.

The analyzing power at the same angle is calculated from the expression

$$A_y(\theta) = \frac{\sigma_L^+ - \sigma_L^-}{\sigma_0\,(P^+ + P^-)}\,, \tag{6}$$

which can also be written as

$$A_y(\theta) = \frac{\sigma_L^+ - \sigma_L^-}{P^+\sigma_L^- + P^-\sigma_L^+}\,. \tag{7}$$

Instrumental asymmetries cancel in this case only if they remain constant for the spin up and spin down measurements. Particular care was taken to ensure that the beam position did not change.

IV. RESULTS AND DISCUSSION

The results of this experiment are presented in Table II and shown in Figs. 3 and 4. In addition, we have included in the tabulation the data from Stetz *et al.*[1] averaged over the same angular acceptance as the present experiment, and the data from McCamis *et al.*[2] which were obtained under very similar conditions to those used here. Figure 3 shows the complete angular distributions for $d\sigma/dt$ at all three energies. The data from the present experiment have been normalized to the results of Ref. 1 in the angular range near 13°–15°. The normalization uncertainty in the data of Stetz *et al.* was 5% and the combined additional statistical uncertainty in the region of overlap of the two experiments is 2%. Almost the entire allowed range of four-momentum transfer $-t$ has been covered at each energy in the combined data from the three measurements.

At 500 MeV the cross section has the expected behavior with a minimum at $-t = 0.28$ (GeV/c)^2. A quantitative comparison can be made with the results of Klem *et al.*[7,8] at 560 MeV, except in the region of the first minimum and secondary maximum where strong energy dependence in the magnitude of the cross section is known to exist[8] (see Fig. 5). The average difference between our results at 500 MeV and the data of Klem is 7.4%. For our data, the ratio of the magnitude of the differential cross section at the second maximum to that at the minimum is 1.26, which is consistent with the energy dependence obtained from other experiments.[8] There is a noticeable change in the slope of the cross section around $-t = 1.0$ (GeV/c)^2, the region where one expects to observe the onset of the triple scattering contribution in a simple Glauber model.

The results at 350 MeV are in agreement with the previous data of Aslanides *et al.*[9] where there is overlap in the angular ranges (see Fig. 5). In the overlap region the average difference between the data of the two experiments is 6.8%, which is within the range of the estimated normalization uncertainties. There is, as well, no systematic difference in the shape of the cross sections. The minimum seen at 500 MeV is replaced at 350 MeV by a "shoulder" at $-t = 0.32$ (GeV/c)^2 and again a change in slope occurs at larger values of $-t$, this time around $-t = 1.2$ (GeV/c)^2.

The 200 MeV data show a smooth decrease as a function of $-t$ with a small shoulder near $-t = 0.45$ (GeV/c)^2 except at large values of $-t$ where there is an abrupt rise. The agreement with the unpublished results of Gotow[10] is not as good as the comparisons at 350 and 500 MeV.

The analyzing power results are illustrated in Fig. 4. Once again, the angular distributions include the data from Refs. 1 and 2. Their values have been adjusted slightly as indicated in Table II by using more recent values of the p-p analyzing powers.[11,12] The uncertainty in the normalization of the analyzing power at each energy is dominated by the uncertainty in the value of the p-p analyzing power used (1.0–1.5%) and the systematic error introduced by the carbon background subtraction in the beam polarimeter (0.5%). Unlike data at

TABLE II. Proton-^{4}He elastic scattering cross sections and analyzing power.

$\theta_{\rm lab}$(deg)	$\frac{d\sigma}{d\Omega_{\rm lab}}$ (mb/sr)	$-t$ (GeV^2/c)	$\frac{d\sigma}{dt}\frac{\rm mb}{({\rm GeV}^2/c)}$	Cross section error (%)	Analyzing power	Error
T_p = 200 MeV						
4.7[a]	87.5	0.0028	663	5.8		
6.3[a]	84.7	0.0050	643	3.1		
7.9[a]	89.0	0.0079	677	2.6		
9.5[a]	77.4	0.011	589	2.3		
11.1[a]	64.8	0.016	495	1.8		
12.8[a]	52.9	0.020	405	1.6		
13.0	50.8	0.021	389	0.8	0.816	0.015
14.4[a]	41.9	0.026	322	1.5		
15.0	39.2	0.028	302	1.0	0.899	0.018
17.0	30.0	0.036	232	0.9	0.993	0.019
19.0	23.1	0.045	180	0.9	1.008	0.021
21.0	17.2	0.054	135.2	1.0	1.003	0.022
23.0	13.1	0.065	103.2	1.0	0.883	0.021
25.0	9.73	0.076	77.5	1.0	0.752	0.021
27.0	7.82	0.088	62.8	1.1	0.583	0.019
29.0	6.23	0.101	50.5	1.1	0.390	0.019
31.0	4.81	0.114	39.4	1.0	0.208	0.018
33.0	3.93	0.128	32.5	1.1	−0.013	0.019
35.0	3.08	0.143	25.8	1.1	−0.184	0.020
37.0	2.38	0.158	20.1	1.1	−0.304	0.021
39.0	1.83	0.174	15.6	1.1	−0.455	0.019
41.0	1.44	0.191	12.4	1.1	−0.597	0.021
43.0	1.08	0.207	9.48	1.2	−0.680	0.022
45.0	0.782	0.225	6.95	1.3	−0.783	0.024
49.0	0.442	0.260	4.04	1.2	−0.927	0.027
53.0	0.249	0.297	2.35	1.5	−1.029	0.035
57.0	0.156	0.334	1.52	1.4	−0.957	0.030
61.0	0.102	0.372	1.02	1.6	−0.703	0.040
65.0	0.079 1	0.410	0.826	2.5	−0.320	0.026
73.0	0.055 9	0.486	0.628	1.9	−0.042	0.019
77.0	0.047 3	0.523	0.553	1.9	0.025	0.018
80.0	0.043 1	0.550	0.519	1.7	0.076	0.016
85.0	0.034 8	0.594	0.440	1.5	0.118	0.015
90.0	0.026 7	0.636	0.356	1.1	0.065	0.018
95.0	0.019 6	0.676	0.275	1.5	−0.057	0.014
100.0	0.014 2	0.714	0.210	1.5	−0.104	0.014
105.0	0.009 34	0.750	0.145	1.5	−0.204	0.035
115.0	0.004 00	0.813	0.068 3	0.4	−0.592	0.012
125.0	0.002 04	0.866	0.038 1	0.8	−0.897	0.015
135.0	0.001 58	0.909	0.032 1	3.0	−0.632	0.017
140.0	0.001 62	0.927	0.034 0	0.9	−0.479	0.018
144.0[b]	0.001 66	0.938	0.035 8	1.4	−0.408	0.017
146.0	0.001 65	0.943	0.035 7	0.9	−0.358	0.017
152.0[b]	0.001 76	0.961	0.039 6	1.3	−0.385	0.014
158.0[b]	0.001 70	0.973	0.039 2	1.6	−0.375	0.020
163.0[b]	0.001 64	0.981	0.038 6	1.6	−0.359	0.020
168.0[b]	0.001 52	0.987	0.036 2	1.7	−0.305	0.022
T_p = 350 MeV						
3.9[a]		0.0036			0.265	0.027
4.6[a]	166	0.0051	669	3.3		
5.5[a]		0.0072			0.439	0.021
6.3[a]	122	0.0093	494	2.2		
7.1[a]		0.012			0.586	0.014
7.9[a]	99.9	0.015	405	1.5		
8.8[a]		0.018			0.649	0.014
9.5[a]	82.8	0.021	337	1.4		

TABLE II. *(Continued.)*

$\theta_{\rm lab}$(deg)	$\frac{d\sigma}{d\Omega_{\rm lab}}$ (mb/sr)	$-t$ (GeV^2/c)	$\frac{d\sigma}{dt}$ $\frac{\rm mb}{({\rm GeV}^2/c)}$	Cross section error (%)	Analyzing power	Error
$T_p = 350$ MeV						
10.4[a]		0.025			0.712	0.015
11.1[a]	68.6	0.029	280	1.1		
12.0[a]		0.034			0.746	0.012
12.8[a]	54.8	0.038	224	0.9		
13.7[a]		0.044			0.748	0.011
14.4[a]	42.7	0.048	175.5	0.9		
15.0	39.2	0.053	161.3	0.8	0.750	0.014
15.3[a]		0.055			0.717	0.017
19.0	19.8	0.083	82.8	1.0	0.568	0.016
23.0	8.64	0.121	36.6	0.8	0.303	0.012
27.0	3.21	0.164	13.9	0.9	−0.082	0.012
31.0	0.972	0.213	4.28	1.0	−0.561	0.019
33.0	0.526	0.239	2.35	1.6	−0.822	0.026
35.0	0.300	0.266	1.36	1.4	−0.863	0.030
37.0	0.206	0.295	0.942	1.7	−0.614	0.026
39.0	0.164	0.324	0.760	1.8	−0.227	0.025
41.0	0.154	0.354	0.725	1.6	0.161	0.023
46.0	0.138	0.433	0.674	1.5	0.454	0.022
51.0	0.094 1	0.516	0.479	1.6	0.374	0.025
56.0	0.053 4	0.600	0.284	1.2	0.199	0.021
61.0	0.027 8	0.686	0.155	1.0	0.023	0.013
66.0	0.013 0	0.772	0.076 1	2.3	−0.211	0.019
71.0	0.006 88	0.857	0.042 3	3.1	−0.465	0.028
76.0	0.003 79	0.941	0.024 5	3.4	−0.671	0.034
81.0	0.002 40	1.02	0.016 4	4.8	−0.802	0.053
86.0	0.001 71	1.10	0.012 3	6.0	−0.757	0.066
91.0	0.001 21	1.17	0.009 26	1.7	−0.713	0.015
96.0	9.88×10^{-4}	1.24	0.007 96	1.6	−0.524	0.012
106.0	8.44×10^{-4}	1.37	0.007 57	1.7	−0.139	0.013
116.0	6.96×10^{-4}	1.48	0.006 91	1.5	0.035	0.010
126.0	6.05×10^{-4}	1.57	0.006 60	3.0	−0.085	0.011
136.0	4.97×10^{-4}	1.64	0.005 90	1.2	−0.349	0.017
143.0	4.30×10^{-4}	1.68	0.005 36	1.5	−0.552	0.024
146.0[b]	4.34×10^{-4}	1.70	0.005 52	2.4	−0.695	0.029
152.0[b]	3.91×10^{-4}	1.72	0.005 14	2.5	−0.744	0.028
157.0[b]	3.58×10^{-4}	1.74	0.004 82	2.5	−0.791	0.028
163.0[b]	3.51×10^{-4}	1.76	0.004 83	2.3	−0.763	0.030
168.0[b]	3.17×10^{-4}	1.77	0.004 42	2.7	−0.547	0.032
$T_p = 500$ MeV						
3.9[a]		0.0055			0.283	0.018
4.7[a]	263	0.0078	697	2.4		
5.6[a]		0.011			0.386	0.015
6.3[a]	213	0.014	566	2.1		
7.2[a]		0.018			0.453	0.013
7.9[a]	163	0.022	433	1.4		
8.8[a]		0.028			0.530	0.012
9.5[a]	130	0.033	348	1.4		
10.4[a]		0.039			0.543	0.014
11.1[a]	93.7	0.044	251	1.5		
12.0[a]		0.051			0.565	0.013
12.7[a]	63.3	0.058	170.2	1.2		
13.0	61.0	0.060	164.2	0.9	0.508	0.020
13.6[a]		0.066			0.545	0.013
14.4[a]	42.9	0.074	115.9	1.1		
15.0	38.1	0.080	103.2	1.0	0.507	0.020
15.2[a]		0.082			0.488	0.017
17.0	21.7	0.102	59.1	1.0	0.403	0.019

TABLE II. *(Continued.)*

θ_{1ab}(deg)	$\frac{d\sigma}{d\Omega_{1ab}}$ (mb/sr)	$-t$ (GeV$^2/c$)	$\frac{d\sigma}{dt}\frac{\text{mb}}{(\text{GeV}^2/c)}$	Cross section error (%)	Analyzing power	Error
$T_p = 500$ MeV						
19.0	11.2	0.127	30.7	0.9	0.314	0.015
21.0	5.52	0.154	15.3	0.9	0.164	0.015
23.0	2.40	0.184	6.72	0.9	−0.134	0.016
25.0	0.851	0.215	2.404	1.4	−0.452	0.026
27.0	0.350	0.249	0.998	1.6	−0.613	0.035
29.0	0.285	0.285	0.824	1.2	−0.076	0.026
31.0	0.330	0.323	0.963	0.9	0.397	0.018
33.0	0.351	0.362	1.039	1.0	0.503	0.017
35.0	0.341	0.404	1.023	1.0	0.488	0.018
37.0	0.308	0.446	0.939	0.9	0.468	0.018
39.0	0.256	0.490	0.792	1.0	0.374	0.017
41.0	0.196	0.535	0.615	1.0	0.345	0.018
46.0	0.0805	0.653	0.263	1.1	0.162	0.019
51.0	0.0260	0.776	0.0889	1.5	−0.078	0.025
56.0	0.00737	0.901	0.0265	2.2	−0.166	0.057
61.0	0.00228	1.03	0.00862	1.5	0.037	0.013
66.0	0.00141	1.15	0.00563	1.6	0.408	0.015
71.0	0.00111	1.28	0.00467	3.4	0.484	0.037
76.0	6.29×10^{-4}	1.40	0.00281	3.7	0.470	0.040
81.0	3.86×10^{-4}	1.52	0.00182	3.7	0.318	0.039
86.0	2.75×10^{-4}	1.63	0.00138	2.6	−0.026	0.026
91.0	2.44×10^{-4}	1.74	0.00130	2.9	−0.326	0.031
96.0	1.93×10^{-4}	1.84	0.00109	3.7	−0.561	0.042
101.0	1.97×10^{-4}	1.93	0.00117	3.6	−0.670	0.044
106.0	1.83×10^{-4}	2.02	0.00115	3.8	−0.677	0.047
116.0	1.49×10^{-4}	2.17	0.00105	4.7	−0.495	0.054
126.0	1.30×10^{-4}	2.30	0.00101	3.1	−0.144	0.058
136.0	1.45×10^{-4}	2.40	0.00123	4.8	−0.303	0.052
143.0	1.53×10^{-4}	2.46	0.00136	4.0	−0.482	0.051
145.0[b]	1.66×10^{-4}	2.47	0.00150	2.6	−0.531	0.024
151.0[b]	1.57×10^{-4}	2.51	0.00147	2.6	−0.580	0.036
154.0[b]	1.48×10^{-4}	2.53	0.00140	2.8	−0.625	0.034
160.0[b]	1.46×10^{-4}	2.55	0.00142	2.8	−0.695	0.046
165.0[b]		2.57			−0.578	0.035
168.0[b]	1.17×10^{-4}	2.58	0.00117	3.3	−0.482	0.047

[a] Data from Ref. 1 averaged over the same angular acceptance as this experiment.

[b] Data from Ref. 2. For 200 MeV the analyzing power of Ref. 2 has been adjusted by using 0.305 as the p-p analyzing power.

energies below 100 MeV,[11] a great deal of structure is apparent in the present data over the whole angular range. A variation from +1.0 to −1.0 in an angle change of only 30° is seen at 200 MeV. In fact our data at this energy yield extrema that are slightly larger in magnitude than 1.0 (although within errors), indicating that the phase shift predictions of the p-p analyzing power may be slighty high. A second large negative excursion in the analyzing power is also observed at $-t = 0.85$ (GeV/c)^2 (see Table II). As the incident energy s increased above 200 MeV the extrema of the analyzing powers are reduced but additional oscillations in A_y appear.

The trend of smaller magnitudes in the oscillations of $A_y(\theta)$ which is seen as one proceeds from 200 to 500 MeV in the present experiment is continued at higher energies.[7] While one finds large positive and negative excursions in the analyzing power at 200 MeV, as the energy increases the minima fill in and the structure smooths out. This behavior is represented in Fig. 6 where the values of the analyzing power at the first maximum and the first minimum are plotted against incident proton energy. It is of interest to try to understand this behavior inasmuch as it may be a

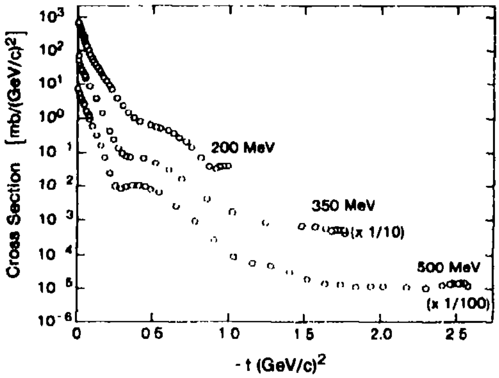

FIG. 3. The differential cross section at 200, 350, and 500 MeV as a function of the four-momentum transfer $-t$. The data from Refs. 1 and 2 are included here. The normalization uncertainty is about 5% at all energies.

manifestation of the phase differences between the spin-dependent and the spin-independent amplitudes used in multiple scattering models.

Figure 7 is a contour diagram of the analyzing power as a function of incident proton energy from 130 to 1800 MeV. The vertical lines are located at the energies and angles where data exist. The contours are drawn in a manner which assumes a systematic behavior as the energy changes. The increase in structure in the analyzing power as the energy increases is once again illustrated here. An unusual structure in $A_y(\theta)$ can be observed at large angles between 200 and 500 MeV. One should note that in this energy and angle domain there is no backward peaking in the differential cross section,[2] in contrast with the behavior at both higher and lower energies.

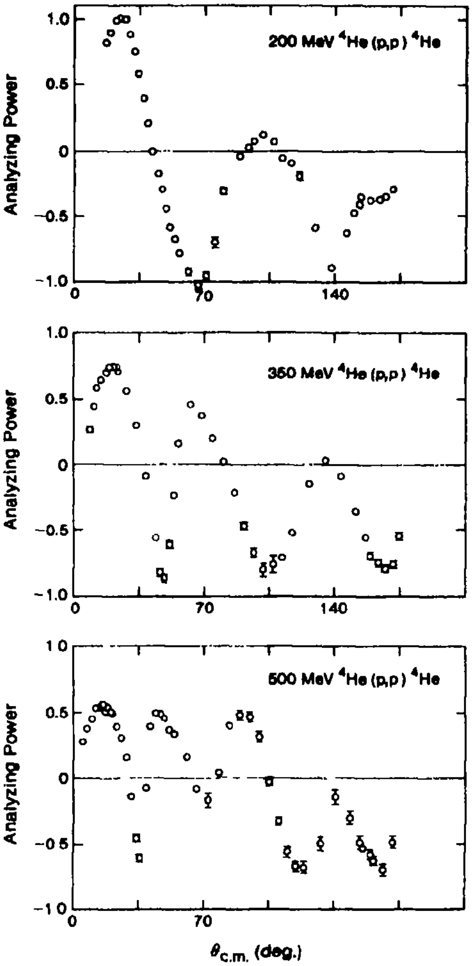

FIG. 4. The p-^{4}He analyzing power as a function of $\theta_{c.m.}$ at 200, 350, and 500 MeV. The scale uncertainty is about 1–1.5% at all energies.

V. CONCLUSIONS

Generally, existing theoretical calculations have been of two types: Glauber multiple scattering theory predictions or optical potential model calculations (see Ref. 14 for a summary). The Glauber model (and extensions thereto) is reasonably successful in describing proton-nucleus scattering at small angles with some differences between experiment and theory appearing at large scattering angles and near diffraction minima. Optical model calculations based on the procedures of Kerman, McManus, and Thaler[15] have been limited by the inexact knowledge of the nucleon-nucleon interaction. Relativistic treatments of the optical model potential based on the Dirac equation such as those of Arnold, Clark, and Mercer[16] have investigated the possibility of achieving a successful systematic description of the experimental data, including polarization results, over a wide energy range.

We have compared our results at 200 and 350 MeV with two different calculations. At 200 MeV Alexander and Landau[17] have extended to proton scattering a microscopic, momentum space, optical potential theory which has been applied with some success to pion interactions with light nuclei.[18] Figure 8 illustrates their results along

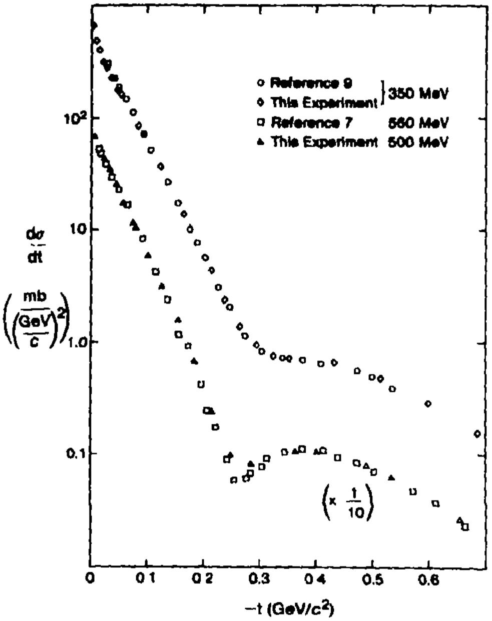

FIG. 5. Comparison of differential cross section results from the present experiment with those of Ref. 7 and Ref. 9 over regions of common $-t$. For clarity only some of the data points from Refs. 7 and 9 are shown.

with our experimental data. The agreement for the differential cross section at large angles is encouraging, although overall quantitative agreement is only fair. It is significant that the theory employed is derived from first principles and contains no free parameters.

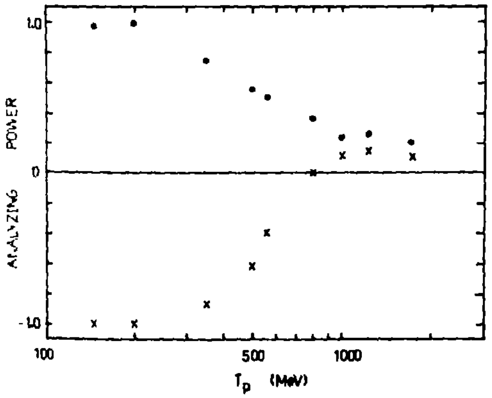

FIG. 6. The magnitude of the analyzing power at the first maximum and at the first minimum as a function of incident proton energy.

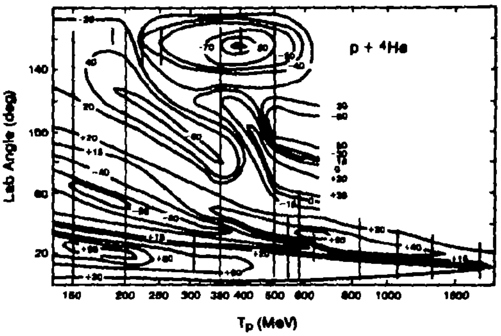

FIG. 7. An analyzing power contour diagram representing existing data between 130 and 1800 MeV.

Dymarz and Malecki[19] have used an optical potential, derived from the Glauber model of multiple collisions, in a solution of the Schrödinger equation. The scattering profile function is calculated analytically having postulated a form for the single particle density and for a correlation function which serves to describe the nature of the interaction. A spherically symmetric potential is then evaluated from the profile function and is used in a numerical solution of the Schrödinger equation. Their method accounts for center of mass and short-range correlations and includes all terms in the Glauber series through the use of the effective potential they calculate. It is limited by present knowledge of the nucleon-nucleon parameters and omits possible exchange effects between the projectile and the target which might be important at large angles for some energies. A comparison of our data and the calculation at 350 MeV is shown in Fig. 9. The solid curve is the result of their potential calculation

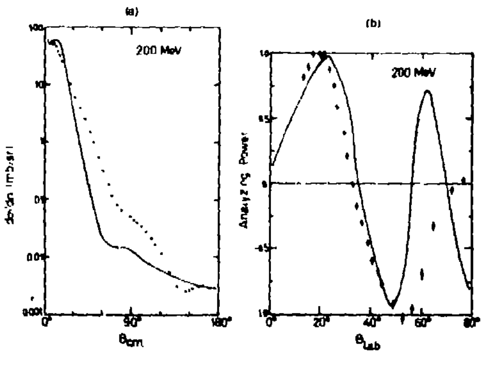

FIG. 8. The calculations of Ref. 17 along with a sample of the data of this experiment and that of (1) and (2).

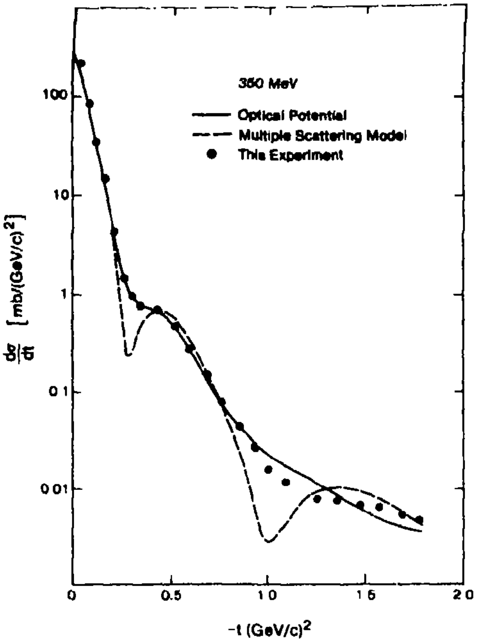

FIG. 9. The calculations of Ref. 19 along with a sample of the data of this experiment and that of (1) and (2). The nucleon parameters of the calculation of Ref. 19 are $\sigma_{pp}=23.5$ mb, $\sigma_{pn}=32.5$ mb, $\alpha_{pp}=\alpha_{pn}=-0.45$, $a_{pp}=a_{pn}=1.5$ (GeV)$^{-2}$.

using the parameters given in the figure caption. They refer to the dashed curve as the standard Glauber model, although the details of the explicit nature of this calculation are not given.

An examination of Fig. 7 reveals that measurements near 275 and 425 MeV could be useful in clearing up the energy-dependent behavior of the analyzing power. As well, larger angle measurements of $d\sigma/d\Omega$ and $A_y(\theta)$ at and above 600 MeV would be welcome additional information.

Satisfactory tests of theoretical models of proton ^{4}He elastic scattering have been restricted by the limitations in available experimental data. The extensive measurements of $d\sigma/d\Omega$ and $A_y(\theta)$ provided by this experiment as well as those of Stetz *et al.*[1] and McCamis *et al.*[2] in the energy range of 200 to 500 MeV should aid in the resolution of this problem.

ACKNOWLEDGMENTS

We would like to express our thanks to R. Abegg, A. Bishop, D. K. Hasell, D. Healy, and B. T. Murdoch, who provided valuable assistance in the operation of the liquid helium target, and to H. Coombes, who helped with the electronics during the experiment. This work was supported by the Natural Sciences and Engineering Research Council of Canada.

---

*Present address: NIKHEF, Amsterdam, The Netherlands.

[1] A. W. Stetz, J. M. Cameron, D. A. Hutcheon, R. H. McCamis, C. A. Miller, G. A. Moss, G. Roy, J. G. Rogers, C. A. Goulding, and W. T. H. van Oers, Nucl. Phys. A290, 285 (1977).

[2] R. H. McCamis, J. M. Cameron, L. G. Greeniaus, D. A. Hutcheon, C. A. Miller, G. A. Moss, G. Roy, M. S. de Jong, B. T. Murdoch, W. T. H. van Oers, J. G. Rogers, and A. W. Stets, Nucl. Phys. A302, 388 (1978).

[3] L. G. Greeniaus, D. A. Hutcheon, C. A. Miller, G. A. Moss, G. Roy, R. Dubois, C. Amsler, B. K. S. Koene, and B. T. Murdoch, Nucl. Phys. A322, 308 (1979).

[4] C. A. Goulding, B. T. Murdoch, M. S. de Jong, W. T. H. van Oers, and R. H. McCamis, Nucl. Instrum. Meth. 148, 11 (1978).

[5] R. H. McCamis, Ph.D. thesis, University of Alberta, 1977 (unpublished).

[6] J. M. Cameron, P. Kitching, R. H. McCamis, C. A. Miller, G. A. Moss, J. G. Rogers, G. Roy, A. W. Stetz, C. A. Goulding, and W. T. H. van Oers, Nucl. Instrum. Meth. 143, 399 (1977).

[7] R. Klem, G. Igo, R. Talaga, A. Wriekat, H. Courant, K. Einsweiler, T. Joyce, H. Kagan, Y. Makdisi, M. Marshak, B. Mossberg, E. Peterson, K. Ruddick, and T. Walsh, Phys. Rev. Lett. 38, 1272 (1977).

[8] R. Klem, G. Igo, R. Talaga, A. Wriekat, H. Courant, K. Einsweiler, T. Joyce, H. Kagan, Y. Makdisi, M. Marshak, B. Mossberg, E. Peterson, K. Ruddick, and T. Walsh, Phys. Lett. 70B, 155 (1977).

[9] E. Aslanides, T. Bauer, R. Bertini, R. Beurtey, A. Boudand, F. Brochard, G. Bruge, A. Chaumeaux, H. Catz, J. M. Fontaine, R. Frascaria, D. Garreta, P. Gorodetzky, J. Guyot, F. Hibou, D. Legrand, M Matoba, Y. Terrien, J. Thirion, and E. Lambert, Phys. Lett. 68B, 221 (1977).

[10] K. Gotow, University of Rochester Report No. NYO-2532, 1959 (unpublished).

[11] J. Bystricky and F. Lehar, in *Proceedings of the Fourth International Symposium on Polarization Phenomena in Nuclear Reactions, Zurich, 1975*, edited by W. Grüebler and V. Konig (Birkhauser, Basel, 1976). We thank F. Lehar and C. Lechanoine for providing us with the most up-to-date predictions of the SACLAY analysis.

[12] D. V. Bugg, J. A. Edgington, C. Amsler, R. C. Brown, C. J. Oram, K. Shakarchi, N. M. Stewart, G. A.

Ludgate, A. S. Clough, D. Axen, S. Jaccard, and J. Vávra, J. Phys. G 7, 1025 (1978). We thank D. V. Bugg for providing us with their most up-to-date results.

[13] A. Houdayer, N. E. Davison, S. A. Elbakr, A. M. Sourkes, W. T. H. van Oers, and A. D. Bacher, Phys. Rev. C 18, 1985 (1978).

[14] G. J. Igo, Rev. Mod. Phys. 50, 523 (1978).

[15] A. K. Kerman, H. McManus, and R. M. Thaler, Ann. Phys. (N.Y.) 8, 551 (1959).

[16] L. G. Arnold, B. C. Clark, and R. L. Mercer, Phys. Rev. C 19, 917 (1979).

[17] Y. Alexander and R. H. Landau, Phys. Lett. 84B, 292 (1979).

[18] R. H. Landau, Phys. Rev. C 15, 2127 (1977); R. H. Landau and A. W. Thomas, Nucl. Phys. A302, 461 (1978); R. H. Landau, S. C. Phatak, and F. Tabakin, Ann. Phys. (N.Y.) 78, 299 (1973).

[19] R. Dymarz and A. Malecki, Phys. Lett. 66B, 413 (1977).

PHYSICAL REVIEW C VOLUME 21, NUMBER 5 MAY 198

Extraction of the πNN form factor from charged pion photoproduction

C. A. Dominguez* and Robert Beck Clark
Department of Physics, Texas A&M University, College Station, Texas 77843

(Received 3 December 1979)

The πNN form factor $F_{\pi NN}(t)$, at small values of the momentum transfer, $0<|t|\lesssim 0.3$ (GeV/c)^2, has been determined from an analysis of the experimental data on $\gamma p\to\pi^+ n$ for incident photon energies in the range 3.4–18 GeV. A total of 104 unpolarized differential cross sections and 22 asymmetries have been fitted with a Reggeized one-pion-exchange model. The best fits give for a monopole vertex function a range $\Lambda\simeq 1000$ MeV and for a dual model type of form factor, an asymptotic rate parameter $\beta\simeq 2.3$–2.5. These results are consistent with those of a recent analysis of NN charge exchange scattering data at high energy and the same range of momentum transfers. The contribution of non-one-pion exchanges to the photoproduction amplitudes has been found to be negligible and does not affect the χ^2, thus leading to an essentially model independent extraction of $F_{\pi NN}(t)$. The implications of these results for the construction of one-pion-exchange potentials in nuclear physics is briefly discussed.

NUCLEAR REACTIONS Pion photoproduction on nucleons at high energies; extraction of the πNN form factor at small momentum transfers; the one-pion-exchange potential.

I. INTRODUCTION

The pionic form factor of the nucleon, i.e., the πNN three-point function $F_{\pi NN}$ is known to play an important role in the NN interaction and considerable effort has been devoted in the past to the study of its analytic structure.[1] In fact, knowledge of the πNN form factor is crucial for the construction of NN potentials for low and intermediate energy scattering, and calculations of NN phase shifts through the iteration of one-pion exchange (OPE) are known to be sensitive to the range[2] as well as to the off-shell structure of $F_{\pi NN}$.[3] The three body force, some two to three body reactions such as $NN\to\pi NN$ and OPE in nuclear physics are also examples of processes that depend strongly on the πNN vertex function. On the other hand, the value of $F_{\pi NN}$ at zero momentum transfer is an important quantity related to the strength of chiral SU(2) × SU(2) symmetry breaking through the Goldberger-Treiman discrepancy.[4]

It has been customary to parametrize the πNN form factor by a monopole form[5] involving a single free parameter Λ, i.e.,

$$F_{\pi NN}(t) = \frac{\Lambda^2-\mu_\pi^2}{\Lambda^2-t}. \tag{1}$$

However, except for its simplicity, there has been little basis for such a choice. A much more general and physically motivated form that was suggested some time ago is that based on the dual model for three-point functions.[6,7] In this framework the πNN form factor is

$$F_{\pi NN}(t) = \Gamma(\beta)\frac{\Gamma[1-\alpha_\pi(t)]}{\Gamma[\beta-\alpha_\pi(t)]}, \tag{2}$$

where

$$\alpha_\pi(t) = \alpha'(t-\mu_\pi^2), \tag{3}$$

is the pion Regge trajectory with universal slope $\alpha' = \frac{1}{2}M_\rho^{-2} \approx 0.83$ GeV^{-2} and β is a free parameter that governs the asymptotic behavior of $F_{\pi NN}$ in the spacelike region. Although as it stands Eq. (2) has poles on the real axis, it can be easily unitarized[7] without the undesirable implications that afflict the dual model for scattering amplitudes. Also, Eq. (2) can be generalized to describe any hadronic vertex with one, two or three particles off the mass shell.[3]

Another parametrization of $F_{\pi NN}$ that has been popular in Regge fits to high energy reactions is the exponential form factor.[8] However, large angle scattering data seem to indicate that form factors exhibit power rather than exponential asymptotic behavior in the momentum transfer, a feature predicted by the dual model[3] and also by the constituent interchange quark model (CIM).[9] In addition, an exponential form factor would imply exact SU(2) × SU(2) symmetry, and hence, the existence of zero mass pseudoscalar mesons (Goldstone bosons).

In any case, once a model or a parametrization of $F_{\pi NN}$ is adopted, e.g., Eqs. (1) or (2), the problem then becomes how to determine the range of the form factor, i.e., Λ or β, in the least model dependent fashion. One possibility, suggested by Chew[10] many years ago, is to extract $F_{\pi NN}(t)$ from

© 1980 The American Physical Society

an analysis of NN scattering data at high energy and small values of the momentum transfer, the idea being that in this kinematic region one expects the OPE contribution to dominate. In this spirit, a fit to the average of the differential cross sections for $\bar{p}p \to \bar{n}n$ and $np \to pn$ at $P_{lab} = 8$ GeV/c has been carried out by Bongardt, Pilkuhn, and Schlaile.[11] The reaction average is taken in order to eliminate ρ-A_2 interference thus leaving basically two contributions, viz., the pion-Pomeron cut and the OPE. If the form factor is parametrized as in Eq. (1) the result of this analysis gives $\Lambda \sim 600$ MeV. More recently, Cass and McKellar[12] have reanalyzed the NN charge exchange data at $P_{lab} = 8$ and 23.5 GeV/c using the dual model form Eq. (2) and have found $\beta \approx 6.5$. If Eq. (2) is expanded in power series near $t = 0$ and approximated by a monopole form Eq. (1) this value of β implies a range compatible with the previous analysis. The problem is, however, that such a small value of Λ disagrees with results of dispersion theory calculations ($\Lambda \sim 1$ GeV) (Ref. 13) and such a large value of β is in contradiction with the asymptotic behavior of $F_{\pi NN}$ to be expected from the power counting rules of the CIM ($\beta \sim 3$).[3] There is also a contradiction with an analysis of NN pion production[14] although here the evidence is perhaps not as conclusive due to a higher degree of model dependence.

It was pointed out recently[15] that the reason for this discrepancy is the inadequate Regge behavior of the OPE contribution used in Refs. 11 and 12. In fact, when the pion pole is allowed to become a moving rather than a fixed pole at high energy according to the prescriptions of the orthodox Regge model, which is amply supported by experiment, then fits to NN charge exchange scattering data at $P_{lab} = 5$, 8, and 25 GeV/c give[15] $\Lambda \approx 900$ MeV or $\beta \approx 3$ for Eqs. (1) and (2), respectively. It should be noted that if $\beta > 2$ Eq. (2) predicts that $F_{\pi NN}$ will have a faster asymptotic fall off than that given by the monopole form Eq. (1). For small values of the momentum transfer, however, Eq. (1) provides an excellent approximation to Eq. (2) and, in fact, the fits mentioned above give basically the same χ^2 for both models.

Due to the key role played by the πNN vertex function in intermediate energy, as well as in nuclear physics, it is essential to corroborate these results through the study of additional reactions where the OPE contribution dominates and where the extraction of $F_{\pi NN}$ involves the minimum amount of model dependency. One such reaction, to which we address ourselves in this paper, is charged pion photoproduction, i.e., $\gamma p \to \pi^+ n$. This process exhibits striking similarities with NN charge exchange since it is known[16,17] to be dominated at high energy and small momentum transfers by the pion pole and a slowly varying background (e.g., π-Pomeron cut). At first sight, though, it seems that $F_{\pi NN}$ would have to appear only once in the OPE amplitude for $\gamma p \to \pi^+ n$ in contrast with NN scattering where it contributes to both vertices in the crossed channel. However, since the exchanged pion is off the mass shell one would expect, *a priori*, some structure on both the $\gamma\pi\pi$ and πnp vertices (see Fig. 1). In fact, it has been shown in Ref. 3 that in the framework of the dual model any three-point function $F(P_1^2, P_2^2, P_3^2)$ factorizes, i.e.,

$$F(p_1^2, p_2^2, p_3^2) = g \prod_{i=1}^{3} \Gamma(\beta_i - s_i) \times \frac{\Gamma[1 - \alpha'(p_i^2 - M_i^2)]}{\Gamma[\beta_i - s_i - \alpha'(p_i^2 - M_i^2)]}, \tag{4}$$

where s_i is the spin of the particle with four momentum P_i and mass M_i, the β_i are three free parameters (one for each distinct leg), and g is an overall normalization or coupling constant fixed at the fully on-shell point, i.e.,

$$g = F(P_1^2 = M_1^2, P_2^2 = M_2^2, P_3^2 = M_3^2). \tag{5}$$

As a consequence of these considerations the form factor $F_{\gamma\pi\pi}$ ($k^2 = 0, q^2 = \mu_\pi^2, t$) should be the same as the πNN form factor $F_{\pi NN}(P_i^2 = M^2, P_f^2 = M^2, t)$ except for an overall normalization constant defined at the fully on-shell point (the electric charge for $F_{\gamma\pi\pi}$ and the strong coupling constant for $F_{\pi NN}$). This result then enhances the similarities be-

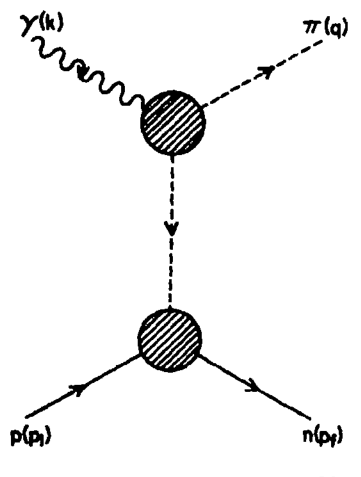

FIG. 1. The one-pion exchange (OPE) and kinematics for $\gamma p \to \pi^+ n$. The blobs at each vertex indicate the presence of a form factor due to the off-shell nature of the exchanged pion (see text).

tween pion photoproduction and *NN* charge exchange scattering.

In addition, there are two other advantages for the $\gamma p \to \pi^+ n$ reaction when compared with *NN*. First, a very large number of differential cross section measurements for unpolarized photons over a wide range of energies and second, the availability of experimental data for the asymmetry found in $\gamma p \to \pi^+ n$ with the incident photons linearly polarized parallel and perpendicular to the plane of πN production. This second feature allows a separation of the natural and unnatural parity exchange contributions in the t channel[18] and thus the isolation of the OPE. Furthermore, it is known from this as well as from other reactions that asymmetry information places stringent constraints on theoretical models, i.e., a model that gives a reasonable fit to unpolarized cross sections might fail completely to account for the polarization data.

Another well known constraint in pion photoproduction is that imposed by gauge invariance which leads to constraint theorems in all channels having a Born term.[10] An example of a model that satisfies this constraint is the so called electric Born approximation which takes into account the t-channel pion pole together with those contributions from the s- and u-channel nucleon poles required for gauge invariance but without any form factor at the vertices.[17] Since our extraction of $F_{\pi NN}$ will be based on a fully Reggeized one-pion exchange with form factors, it will be important to verify that the constraints imposed by gauge invariance[10] are still satisfied. It is easy to see that this will be the case due to (i) the factorization property of the dual model for three-point functions and (ii) the fact that once the overall coupling constant has been extracted from the form factor the remainder is normalized to one at the pole [see Eq. (4)]. Thus, the residues of the Born terms in the various channels are not affected by dressing the one particle exchanges and therefore the relations among these residues imposed by gauge invariance will not be modified.

In Sec. II we define the helicity amplitudes, cross sections, and asymmetry and, by means of the evasive constraint,[17] identify the amplitudes to which the OPE and the slowly varying background contribute. Since our purpose here is not to make a Regge fit to the data, *per se*, to add to a by now extensive list,[20] but rather to extract the πNN form factor we shall keep the parametrization of this background as simple as possible. In fact, we shall avoid any detailed dynamical model for the cut and simply assume a modified "poor man's" absorption model[16] where the background is parametrized as an exponential. This has been a standard procedure in this type of analysis and will establish a one to one correspondence with the results already obtained from *NN* charge exchange scattering.

In Sec. III we discuss the results of simultaneous fits to the unpolarized differential cross sections and asymmetries at various photon energies in the range 3.4–18 GeV and momentum transfers $0 < |t| < 0.3$ $(\text{GeV}/c)^2$. Our results give $\Lambda = 1003 \pm 66$ MeV for a monopole form factor Eq. (1), or $\beta = 2.34 \pm 0.23$ for the dual model Eq. (2), with an identical $\chi^2 = 289$ for a total of 126 data points. The sensitivity of the data to the presence of a πNN form factor has been established by attempting fits with $F_{\pi NN} = 1$ in which case the best fit χ^2 is increased to $\chi^2 = 411$ for the same number of data points. On the other hand, the presence of contributions other than the OPE and the pion cut has been studied by adding a Reggeized ρ-A_2 exchange with electric and magnetic residue functions. The results of the search show that this extra contribution is negligible in the range of momentum transfers covered by the fit and does not affect the form factor or the χ^2, i.e., $\Lambda = 1023 \pm 65$ MeV and $\chi^2 = 287$. These results are compatible with those obtained from *NN* charge exchange scattering and provide an important independent confirmation of theoretical expectations pointing to a range of the πNN vertex function of the order of 1000 MeV or an asymptotic rate parameter $\beta \approx 2$–3.

In the conclusion we discuss briefly the implications of these results for the Goldberger-Treiman discrepancy.

II. KINEMATICS AND REGGEIZATION

In the direct or s channel for $\gamma p \to \pi^+ n$ there are four independent center of mass helicity amplitudes[21] $g_i(s,t) = g_{\lambda_N';\lambda_\gamma \lambda_N}$, where $i = 1, 2, 3, 4$ stands for the photon, initial nucleon, and final nucleon helicities

$$(\lambda_\gamma, \lambda_N; \lambda_N') = (-1, -\tfrac{1}{2}; \tfrac{1}{2}), (1, -\tfrac{1}{2}; -\tfrac{1}{2}), (1, \tfrac{1}{2}; \tfrac{1}{2}), (1, -\tfrac{1}{2}; \tfrac{1}{2}),$$

respectively. In terms of these amplitudes the cross sections can be written as[21]

$$(s - M^2)^2 \frac{d\sigma_\parallel}{dt} = \frac{1}{32\pi}\left(|g_2 - g_3|^2 + |g_1 - g_4|^2\right), \qquad (6)$$

for photons polarized parallel to the reaction plane, and

$$(s - M^2)^2 \frac{d\sigma_\perp}{dt} = \frac{1}{32\pi}\left(|g_2 + g_3|^2 + |g_1 + g_4|^2\right), \qquad (7)$$

for photons polarized perpendicular to the reaction plane. The unpolarized cross section is just the average of the preceding two, i.e.,

$$\frac{d\sigma}{dt}=\frac{1}{2}\left(\frac{d\sigma_\parallel}{dt}+\frac{d\sigma_\perp}{dt}\right),$$

or in its normal form,

$$(s-M^2)^2\frac{d\sigma}{dt}=\frac{1}{32\pi}\sum_{i=1}^{4}|g_i|^2\,. \tag{8}$$

In Eqs. (6)–(8), $s=(k+p_i)^2$ is the square of the center of mass energy in the direct channel and $t=(q-k)^2$ is the square of the momentum transfer. The asymmetry in pion photoproduction with linearly polarized photons is defined as

$$\Sigma=\frac{\dfrac{d\sigma_\perp}{dt}-\dfrac{d\sigma_\parallel}{dt}}{\dfrac{d\sigma_\perp}{dt}+\dfrac{d\sigma_\parallel}{dt}}\,. \tag{9}$$

The relation between the s-channel helicity amplitudes and the traditional Chew-Goldberger-Low-Nambu (CGLN) invariant amplitudes[22] $F_i(s,t)$ is given by

$$g_1=\frac{\nu}{\sqrt{2}}\left(\frac{t}{2M}F_1-\frac{2M}{\mu_\pi^2-t}F_2+F_3\right), \tag{10}$$

$$g_2=\frac{\nu}{\sqrt{2}}\left(\sqrt{-t}\,F_1+\frac{\sqrt{-t}}{2M}F_3+2M\sqrt{-t}\,F_4\right), \tag{11}$$

$$g_3=\frac{\nu}{\sqrt{2}}\left(-\sqrt{-t}\,F_1+\frac{\sqrt{-t}}{2M}F_3-2M\sqrt{-t}\,F_4\right), \tag{12}$$

$$g_4=\frac{\nu}{\sqrt{2}}\left(\frac{t}{2M}F_1+\frac{2M}{\mu_\pi^2-t}F_2+F_3\right), \tag{13}$$

where $\nu\approx(s-M^2)/2M$ is the laboratory photon energy. Since the invariant amplitudes $F_i(s,t)$ are free of kinematic singularities Eqs. (11) and (12) imply that g_2 and g_3 vanish identically at $t=0$. Furthermore, from the "conspiracy relation"[17] for pion photoproduction, i.e.,

$$F_2(t=0)=-\frac{\mu_\pi^2}{2M}F_3(t=0) \tag{14}$$

it follows that g_4 also vanishes at $t=0$. Therefore, the pion-Pomeron cut (or slowly varying background), which clearly does not vanish at $t=0$ where it is responsible for all of the cross section, can contribute only to the amplitude g_1. On the other hand, F_1 and F_3 contain natural spin-parity exchange while F_2 and F_4 have unnatural spin-parity exchanges. Neglecting A_1 exchange gives $F_4=0$ and therefore $g_2=g_3$ so that finally one has

$$g_1(s,t)=g_\pi(s,t)-g_A(s,t)-C_\pi(t), \tag{15}$$

$$g_2(s,t)=g_3(s,t)=h_A(s,t), \tag{16}$$

$$g_4(s,t)=-g_\pi(s,t)-g_A(s,t), \tag{17}$$

where $C_\pi(t)$ is the slowly varying background, g_π the OPE, and g_A and h_A the ρ-A_2 exchange amplitudes. The Reggeized expression for the dressed OPE amplitude is[21]

$$g_\pi(s,t)=-eg_{\pi NN}\frac{t}{\mu_\pi^2-t}\{1+\exp[-i\pi\alpha_\pi(t)]\}\times\left(\frac{s}{s_0}\right)^{\alpha_\pi(t)}F_{\pi NN}^2(t), \tag{18}$$

where $e=(4\pi/137)^{1/2}$, $g^2_{\pi NN}/4\pi=14.28$, $\alpha_\pi(t)$ the pion Regge trajectory Eq. (3), $s_0\approx1$ GeV^2 a scale factor, and $F_{\pi NN}(t)$ the πNN form factor which appears squared according to the discussion in Sec. I. Similar expressions can be written for $h_A(s,t)$ and $g_A(s,t)$ including electric and magnetic couplings although we would expect their contributions to be negligible at small t due to their nonleading behavior. In fact, the effect of the pole will be less important and the A_2NN form factor will provide further damping. This expectation has been fully confirmed by the results of our fits to be discussed in the next section.

Parametrizing the background amplitude with an exponential form and using Eq. (18), the differential cross sections for OPE plus pion cut become

$$(s-M^2)^2\frac{d\sigma_\parallel}{dt}=\frac{e^2}{2}\frac{(g_{\pi NN}^2)}{4\pi}\left|Ae^{bt}+\frac{t}{\mu_\pi^2-t}\{1+\exp[-i\pi\alpha_\pi(t)]\}\left(\frac{s}{s_0}\right)^{\alpha_\pi(t)}F_{\pi NN}^2(t)\right|^2, \tag{19}$$

$$(s-M^2)^2\frac{d\sigma_\perp}{dt}=\frac{e^2}{2}\frac{(g_{\pi NN}^2)}{4\pi}\left|Ae^{bt}\right|^2. \tag{20}$$

For $A=1$ and $b=0$ Eqs. (19) and (20) reduce to the "poor man's" absorption model of Ref. 16. The parametrization of the cut was given no energy dependence beyond the overall factor of $(s-M^2)$ since the experimental cross sections in the forward direction obey the $1/s^2$ scaling law. At $t=0$ the unpolarized differential cross section is

$$(s-M^2)^2\frac{d\sigma}{dt}\bigg|_{t=0}=255A^2\ \mu\text{b GeV}^2, \tag{21}$$

and at the pion pole it becomes

$$(\mu_\pi^2-t)^2(s-M^2)^2\frac{d\sigma}{dt}\bigg|_{t=\mu_\pi^2}=255(2\mu_\pi^4)\ \mu\text{b GeV}^2, \tag{22}$$

which, except for the presence of A in Eq. (21), are the same results one obtains from the electric Born model. Since this model is known to predict roughly the correct value of the forward cross section, we would expect A to be close to one. Away from $t = 0$, however, the Reggeized and dressed OPE model with absorption that we are considering should provide an improved description of the data. For values of t very near the forward direction, e.g., $|t| \lesssim 0.05 - 0.1\ (\mathrm{GeV}/c)^2$, the interplay between the cut and the pion pole will be responsible for the forward spike in $d\sigma/dt$ and the rapid rise in the asymmetry with $F_{\pi NN}$ playing almost no role. At higher values of the momentum transfer, however, the data should be more sensitive to the range of the πNN form factor.

In summary, there are three free parameters in this model, i.e., A, b, and β (or Λ) and two independent sets of experimental data, viz., the unpolarized differential cross sections and the asymmetry. As mentioned previously, though, the presence of other non-OPE terms in the amplitudes, e.g., ρ-A_2 exchange, should also be tested in which case there will be two additional parameters; these additions should increase in importance as the value of $|t|$ increases.

III FITS

We have used all the available data[23] above $\nu = 3.4$ GeV measured at SLAC, DESY, and Cambridge Electron Accelerator (CEA), i.e., unpolarized differential cross sections[24-29] between $\nu = 3.4$ and 18 GeV and asymmetries[29, 30-32] in the range $\nu = 3.4$–16 GeV. Restricting ourselves to the interval $0 < |t| \lesssim 0.3\ (\mathrm{GeV}/c)^2$ we have used a total of 126 data points of which 104 were differential cross sections and 22 were asymmetries. The results of the fits with the OPE model with absorption are listed in Table I. As expected, the addition of non-OPE contributions to the amplitudes, e.g., ρ-A_2 exchange, did not change the results; we found $A = 1.104 \pm 0.004$, $b = 1.29 \pm 0.04\ (\mathrm{GeV}/c)^{-2}$, and $\Lambda = 1023 \pm 65$ MeV with a $\chi^2 = 287$. In this case the strength of the ρ-A_2 contribution at the highest energy and highest momentum transfer (where it should be largest) was suppressed relative to OPE by roughly two orders of magnitude.

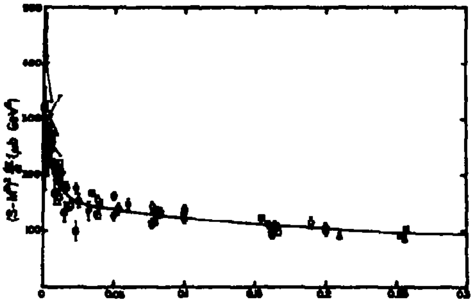

FIG. 2. Unpolarized differential cross sections for various incident photon energies. ● DESY, 3.4 GeV (Ref. 24); ○ SLAC, 5 GeV (Refs. 27 and 28); ▲ DESY, 6 GeV (Refs. 24–26); △ SLAC, 8 GeV (Refs. 27 and 28); □ SLAC, 11 GeV (Refs. 27 and 28); ■ SLAC, 16 GeV (Refs. 27–29); ▽ SLAC, 18 GeV (Ref. 28). Only a part of the data is shown. The solid curve represents the best fit with the Reggized OPE model with absorption and form factors (see Table I).

The sensitivity of the parameters A, b, and β (or Λ) to the range of momentum transfers covered by the fits was analyzed by refitting the data in different intervals, with the result that the values listed in Table I ($0 < |t| < 0.3\ (\mathrm{GeV}/c)^2$) gave essentially the lowest χ^2. For instance, for a range $0 < |t| < 0.2\ (\mathrm{GeV}/c)^2$ we found $A = 1.090 \pm 0.004$, $b = 1.19 \pm 0.01\ (\mathrm{GeV}/c)^{-2}$, and $\Lambda = 848 \pm 12$ MeV with a $\chi^2 = 298$ for 117 degrees of freedom, while for $0 < |t| < 0.45\ (\mathrm{GeV}/c)^2$ we found $A = 1.109 \pm 0.004$, $b = 1.43 \pm 0.02\ (\mathrm{GeV}/c)^{-2}$, and $\Lambda = 1790 \pm 180$ MeV with a $\chi^2 = 449$ for 139 degrees of freedom.

Since the number of experimental differential cross sections is much larger than the number of asymmetries and most of the measurements of the latter have been done at $\nu = 3.4$ and 16 GeV, we have also run fits to $d\sigma/dt$ and Σ at these two energies and $|t| < 0.3\ (\mathrm{GeV}/c)^2$ in order to check the stability of the results. We found in this case that $A = 1.118 \pm 0.009$, $b = 1.33 \pm 0.06\ (\mathrm{GeV}/c)^{-2}$, and $\Lambda = 1210 \pm 160$ MeV with a $\chi^2 = 131$ for 45 degrees

TABLE I. Parameter values from fits to pion photoproduction differential cross sections and asymmetries. 126 data points − 3 parameters = 123 degrees of freedom.

Form factor	χ^2	Λ (MeV)	β	A	b $[(\mathrm{GeV}/c)^{-2}]$
Monopole	289	1003 ± 66		1.103 ± 0.004	1.34 ± 0.03
Dual model	289		2.34 ± 0.23	1.104 ± 0.004	1.35 ± 0.03
No form factor	411	∞	2	1.105 ± 0.005	1.43 ± 0.05

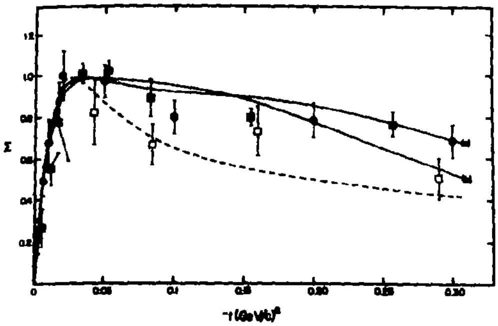

FIG. 3. Asymmetries at various incident photon energies. ● DESY, 3.4 GeV (Refs. 30 and 31); □ SLAC, 12 GeV (Ref. 32); ■ SLAC, 16 GeV (Ref. 29). Only part of the data is shown. Solid curves represent the best fit with the Reggeized OPE model with absorption and form factors. Curve (a) is for $\nu = 3.4$ GeV and curve (b) is for $\nu = 16$ GeV showing the energy dependence of the Reggeized OPE. The dotted curve is the best fit with no form factors ($\Lambda = \infty$ or $\beta = 2$) at $\nu = 3.4$ GeV (see Table I).

of freedom.

Our predictions from Table I are illustrated in Figs. 2 and 3 where only part of the data has been shown due to the high degree of overlap and clustering especially near the forward direction. The Reggeized OPE model has some energy dependence besides the overall $(s - M^2)$ factor which is much more pronounced in Σ as seen in Fig. 3; the dif- rential cross section curves for the different ergies cannot be resolved with the scales used Fig. 2. The impact of the πNN form factor is est seen in the prediction for the asymmetry ith $\Lambda = \infty$ or $\beta = 2$ (dotted curve) at $\nu = 3.4$ GeV, though the value of χ^2 in this case speaks for self.

In summary, our results point to a range of the NN vertex function $\Lambda \approx 1000$ MeV or $\beta \approx 2.3$–2.5 agreement with the recent fit to NN charge ex- ange scattering[15] as well as with other more odel dependent extractions[2,14] and theoretical pectations.[5,7,13]

IV. CONCLUSIONS

The similarities between NN charge exchange cattering and pion photoproduction provide us ith the opportunity of verifying the overall con- istency of the πNN form factor extraction. More- ver, the availability of two independent sets of xperimental data, i.e., unpolarized cross sec- ons and asymmetries, places more constraints n the parametrization of the $\gamma p \rightarrow \pi^+ n$ reaction lving us a more stringent test. On the other and, at small momentum transfers the slowly varying background amplitude can be easily parametrized and all other non-OPE contributions are expected to be negligible, making the determination of $F_{\pi NN}$ essentially model independent.

Our results indicate a range of the πNN form factor $\Lambda \approx 1000$ MeV for a monopole parametrization Eq. (1), or an asymptotic rate parameter $\beta \approx 2.3$–2.5 for the dual model, consistent with the results of a recent NN charge exchange analysis.[15]

Although the χ^2 was identical for both models, it should be realized that they predict different asymptotic behaviors in the spacelike region; the monopole form behaves like t^{-1} while the dual model behaves like $t^{1-\beta}$ as $t \rightarrow -\infty$. The question then becomes which model should be trusted more in applications where a knowledge of $F_{\pi NN}$ in a wider range of t is needed, e.g., in the iteration of OPE in the Blankenbecler-Sugar equation for NN scattering. We argue in favor of the dual model due to its sound physical motivation based on the most successful features of the Regge and dual models, e.g., correct asymptotic power behavior and mass spectra. It should also be added that when used to describe electromagnetic and weak vertices[33] this model is in excellent agreement with experimental data in a very wide range of momentum transfers, e.g., up to $t \approx -30$ $(\mathrm{GeV}/c)^2$ for the magnetic form factor of the nucleon.

As a final point we wish to comment on the implications of our results for the Goldberger-Treiman discrepancy, i.e.,

$$\Delta_\pi = 1 - \frac{(M_p + M_n) g_A}{2 f_\pi g_{\pi NN}},$$

where g_A and f_π are the β decay and pion decay constants, respectively. This quantity is of great theoretical interest since it is a direct measure of the strength of chiral SU(2) × SU(2) symmetry breaking, i.e., the mechanism that explains the smallness of the pion mass on a hadronic scale.[4] The πNN form factor at zero momentum transfer is related to Δ_π through[4]

$$F_{\pi NN}(t = 0) \approx 1 - \Delta_\pi .$$

One of the arguments invoked in the past in favor of a very short range πNN interaction was based precisely on this equation. In fact, the experimental value of Δ_π used to be $\approx 15\%$ implying a range $\Lambda \approx 400$ MeV for a monopole form factor. However, the actual value of Δ_π is far from settled and has been gradually decreasing as new determinations of $g_{\pi NN}$ and g_A become available. Using the latest compilation of coupling constants[34] one has at the present time: $f_\pi = 93.24 \pm 0.09$ MeV, $g_{\pi NN}{}^2/4\pi = 14.28 \pm 0.18$, and $g_A = 1.260 \pm 0.012$, giving for Δ_π

$$\Delta_\pi = 0.05 + 0.01 ,$$

where the error should be handled with extreme care in view of the historic evolution of Δ_π. Using $\Lambda \approx 1000$ MeV or $\beta \approx 2.3$–2.5 from Table I we find $\Delta_\pi \approx 0.02$ in both cases. This result agrees with independent estimates based on dispersion theory calculations of the matrix elements of the divergence of the axial-vector current in β decay[35] as well as with various other theoretical estimates.[6,7,36] In order to obtain $\Delta_\pi \approx 0.05$ we would need a range $\Lambda \approx 600$ MeV or an asymptotic rate parameter $\beta \approx 10$, which are ruled out by the present analysis of pion photoproduction and by the *NN* charge exchange results.[15] Moreover, if $\beta = 10$ then the πNN form factor would behave like t^{-9} as $t \to -\infty$, clearly an inconceivable situation.

ACKNOWLEDGMENTS

This work was supported in part by the United States Department of Energy under Contract No. DE-AS05-76ER05223. The authors wish to thank Bruce J. VerWest for valuable discussions.

---

*On leave of absence from Centro de Investigacion y de Estudios Avanzados, Mexico.

[1] G. E. Brown and A. D. Jackson, *The Nucleon-Nucleon Interaction* (North-Holland, Amsterdam, 1976); J. J. de Swart and M. M. Nagels, Fortschr. Phys. 28, 215 (1978).

[2] R. A. Bryan and B. Scott, Phys. Rev. 177, 1435 (1969); K. Erkelenz, Phys. Rep. 13C, 191 (1974); K. Holinde and R. Machleidt, Nucl. Phys. A256, 479 (1976).

[3] R. A. Bryan, C. A. Dominguez, and B. J. VerWest, Texas A&M University Report No. ORO-5223-16 (unpublished).

[4] H. Pagels, Phys. Rep. 16C, 219 (1975).

[5] E. Ferrari and F. Selleri, Nuovo Cimento 24, 453 (1962).

[6] C. A. Dominguez, Phys. Rev. D 7, 1252 (1973).

[7] C. A. Dominguez, Phys. Rev. D 16, 2320 (1977).

[8] P. D. B. Collins, *An Introduction to Regge Theory and High Energy Physics* (Cambridge University Press, Cambridge, 1977).

[9] D. Sivers, S. J. Brodsky, and R. Blankenbecler, Phys. Rep. 23C, 1 (1976); J. F. Gunion in *Topics in High Energy Physics*, edited by H. Moreno, Mexico, 1978.

[10] G. F. Chew, Phys. Rev. 112, 1380 (1958).

[11] K. Bongardt, H. Pilkuhn, and H. G. Schlaile, Phys. Lett. 52B, 271 (1974).

[12] A. Cass and B. H. J. McKellar, Phys. Rev. D 18, 3269 (1978).

[13] J. W. Durso, A. D. Jackson, and B. J. VerWest, Nucl. Phys. A282, 404 (1977); M. Dillig and M. Brack, J. Phys. G 5, 223 (1979).

[14] B. J. VerWest, Phys. Lett. 83B, 161 (1979).

[15] C. A. Dominguez and B. J. VerWest, Phys. Lett. 89B, 333 (1980).

[16] G. C. Fox and C. Quigg, Annu. Rev. Nucl. Sci. 23, 219 (1973); see also the contributions by F. Berends and by R. Worden, in *Proceedings of the Pion Exchange Meeting*, edited by G. A. Winbow (Daresbury Nuclear Physics Laboratory, Daresbury, England, 1973). For a recent review on the status of Reggeized pion exchange, see L. M. Jones, University of Illinois Report No. ILL-(TH)-79-7 (1979).

[17] F. J. Gilman, Phys. Rep. 4C, 95 (1972); J. K. Storrow in *Electromagnetic Interactions of Hadrons*, edited by A. Donnachie and G. Shaw (Plenum, New York, 1978).

[18] P. Stichel, Z. Phys. 180, 170 (1964).

[19] J. A. Campbell, R. B. Clark, and D. Horn, Phys. Rev. D 2, 217 (1970).

[20] P. D. B. Collins and F. D. Gault, *A Bibliography of Regge Phenomenology* (University of Durham, Durham, England, 1976); M. Fukugita and K. Igi, Phys. Rep. 31C, 237 (1977).

[21] J. D. Jackson and C. Quigg, Nucl. Phys. B22, 301 (1970).

[22] G. F. Chew, M. L. Goldberger, F. E. Low, and Y. Nambu, Phys. Rev. 106, 1345 (1957).

[23] For a compilation see D. Menze, W. Pfeil, and R. Wilcke, Phys. Data, 7-1 (1977).

[24] P. Heide *et al.*, Phys. Rev Lett. 21, 248 (1968).

[25] J. P. Dowd *et al.*, Phys. Rev. Lett. 18, 414 (1967).

[26] G. Buschhorn *et al.*, Phys. Lett. B25, 622 (1967).

[27] A. M. Boyarski *et al.*, Phys. Rev. Lett. 20, 300 (1967).

[28] A. M. Boyarski *et al.*, *Proceedings of the Fourteenth International Conference on High Energy Physics, Vienna, 1968*, edited by J. Prentki and J. Steinberger (CERN, Geneva, 1968).

[29] D. J. Quinn *et al.*, Phys. Rev. D 20, 1553 (1979).

[30] H. Burfeindt *et al.*, Phys. Lett. B33, 509 (1970).

[31] C. Geweniger *et al.*, Phys. Lett. B29, 41 (1969).

[32] R. F. Schwitters *et al.*, Phys. Rev. Lett. 27, 120 (1971).

[33] The dual model for weak and electromagnetic form factors of on-shell hadrons was first discussed by M. Ademollo and E. Del Giudice, Nuovo Cimento 63A, 639 (1969), and by Y. Oyanagi, Nucl. Phys. B14, 375 (1969). For fits to the data and for references to related work see, e.g., P. Di Vecchia and F. Drago, Lett. Nuovo Cimento 1, 917 (1969); P. Gensini, *ibid.* 2, 791 (1969); P. H. Frampton, Phys. Rev. D 1, 3141 (1970); C. A. Dominguez and O. Zandron, Nucl. Phys. B33, 303 (1971); T. C. Chia, Can. J. Phys. 50, 1652 (1972); C. A. Dominguez, Phys. Rev. D 8, 980 (1973); P. Felst, DESY Report No. DESY 73/56, 1973 (unpublished); L. F. Urrutia, Phys. Rev. D 9, 3213 (1974).

[34] M. M. Nagels *et al.*, Nucl. Phys. B147, 189 (1979).

[35] H. Pagels, Phys. Rev. 179, 1337 (1969); 182, 1913 (1969); H. Pagels and A. Zepeda, Phys. Rev. D 5, 3262 (1972); H. J. Braathen, Nucl. Phys. B44, 93 (1972); H. F. Jones and J. D. Scadron, Phys. Rev. D 11, 174 (1975).

[36] B. de Wit, R. Maciejko, and J. Smith, Phys. Rev. D 16, 1840 (1977).

PHYSICAL REVIEW C VOLUME 21, NUMBER 5 MAY 1980

Relativistic calculation of radiative muon capture in hydrogen and ^{3}He

Harold W. Fearing
TRIUMF, Vancouver, B. C., Canada V6T 1W5
(Received 31 October 1979)

In view of the fundamental importance of radiative muon capture, particularly in light nuclei, and of the somewhat confused theoretical situation, a new calculation of radiative muon capture on the proton and on ^{3}He has been made. This calculation is based on the standard set of diagrams but, unlike previous calculations, has been performed without making nonrelativistic approximations. Results are given for the rate and photon spectrum for both ^{1}H and ^{3}He. A detailed comparison of this calculation is made with the approach developed by Hwang and Primakoff which is based on general constraints of conserved vector current, partially conserved axial vector current, and gauge invariance and on a special linearity hypothesis to try to understand why the Hwang-Primakoff results differ markedly from all previous results. It is shown that this calculation, as well as other standard ones, satisfy the general constraints of Hwang and Primakoff and that the differences arise because of their linearity hypothesis and other approximations. These differences are examined in detail, and it is shown that the numerically most important one arises because the linearity hypothesis has been used in such a way that it leads to a Hwang-Primakoff amplitude which violates the Low soft photon theorem.

[RADIOACTIVITY $\mu^- p \rightarrow \nu n \gamma$ and $\mu^{-3}\mathrm{He} \rightarrow \nu^3\mathrm{H}\gamma$; relativistic calculations of rate and photon spectrum.]

I. INTRODUCTION

Radiative muon capture (RMC) has long been recognized as one of the fundamental weak interaction processes which is particularly sensitive to g_P, the induced pseudoscalar coupling of the weak hadronic current. Several experiments have been performed in nuclei,[1-4] particularly ^{40}Ca, but more recently in ^{16}O,[4] to measure the photon spectrum and in some cases the photon asymmetry with the aim of extracting g_P. A number of theoretical calculations have also addressed the question of RMC in nuclei.[5-11] However, in a nucleus there are a number of uncertainties which make interpretation of the results in terms of g_P difficult.[5,6,12] These uncertainties arise in part because of the lack of knowledge of the nuclear structure or particularly lack of knowledge of the excitation spectrum of the final nucleus, which usually forces use of the closure approximation.

It is thus very important to look at the very light nuclei, e.g., the proton, deuteron, or ^{3}He, where the nuclear physics is well understood and where the final state is clearly defined so that closure is not necessary. Such experiments are quite difficult because of the low rate for RMC in light nuclei relative to the decay rate. Howver, higher muon fluxes available at the new meson facilities have made some such experiments feasible, and in particular an RMC experiment in He has been proposed at LAMPF.[13]

Somewhat surprisingly the theoretical situation for such very light nuclei is confused. Older calculations for the proton exist, e.g., that of Opat,[14] and Beder[15] has calculated some specific correlations in both ^{1}H and ^{3}He. More recently Hwang and Primakoff[16] (HP) have made a new calculation of RMC in ^{1}H and ^{3}He, later applied also to ^{12}C,[11] using an approach which starts with a very general amplitude constrained by the conserved vector current (CVC), partially conserved axial current (PCAC), and current conservation or gauge invariance (GI) conditions plus a special "linearity hypothesis" rather than with a set of Feynman diagrams as used in essentially all other calculations of RMC in both light and heavy nuclei. Their results differ dramatically from the older calculations[14,15] for ^{1}H and ^{3}He and also from a new calculation[9] for ^{12}C (see Table I), which is somewhat surprising since the standard diagram approach seemingly also builds in currents satisfying CVC, PCAC, and GI, and contains roughly the same physics as the calculations of HP.

In view of the fundamental significance of these very simple reactions, and the implications they may have for understanding RMC in more complicated nuclear systems, it is extremely important to understand the reasons for the quite different results in the two approaches. Such understanding is the first purpose of this paper. The second is to provide some numerical results for ^{1}H and ^{3}He which may be useful in current[13] or future experiments.

To begin, the standard diagrammatic approach

© 1980 The American Physical Society

TABLE I. Comparison of the results of Hwang and Primakoff with those of Opat (Ref. 14), Beder (Ref. 15), and Wullschleger and Scheck (Ref. 9). Listed are the RMC rates for capture from various spin states on the proton, the photon spectrum *d*Γ/*dk* for several values of *k* for RMC on ^{3}He, and the ratio of total radiative to ordinary rates for capture on ^{12}C leading to the ground state of ^{12}B.

		HP	Others	Ref.
^{1}H:	Singlet rate	0.0180	0.0050	14
	Triplet rate	0.0377	0.0900	14
	Statistical rate	0.0328	0.0687	14
^{3}He:	$\frac{d\Gamma}{dk}$(70 MeV)	2.53×10^{-3}	4.58×10^{-3}	15
	$\frac{d\Gamma}{dk}$(80 MeV)	1.46×10^{-3}	2.65×10^{-3}	15
	$\frac{d\Gamma}{dk}$(90 MeV)	6.10×10^{-4}	1.07×10^{-3}	15
^{12}C:	Relative rate (to ^{12}B$_{\rm g.s.}$)	2.08×10^{-4}	3.09×10^{-4}	9

is reviewed and some details of our "standard" calculation (which differs from previous ones in that no nonrelativistic approximations are made) are described. The HP approach is then discussed and the explicit ways in which the final amplitude differs from the standard result and the numerical significance of these differences shown. The next step is to understand the origin of these differences in terms of the approximations and assumptions made by HP. Finally some numerical results are given for the proton and, after some discussion, for ^{3}He.

II. REVIEW OF STANDARD AND HP APPROACHES

The "standard" theory of radiative muon capture (see, e.g., Ref. 5) begins with a particular set of Feynman diagrams or equivalently a relativistic Hamiltonian which reproduces these diagrams.[7] A relativistic amplitude for RMC on the proton is constructed and an expansion of this amplitude in powers of $1/m$ leads to an effective nonrelativistic Hamiltonian which can be evaluated between the appropriate nuclear states or two-component spinors in the case of the free proton. This approach has been used for essentially all previous calculations of RMC except those of HP.

Five diagrams (Fig. 1) are usually used. The leading ones are the usual external radiation diagrams [Figs. 1(a), 1(b), 1(c)] in which the muon, proton, and neutron radiate. These are just the diagrams which are necessary to obtain the $1/k$ and k/k terms in an expansion of the radiative amplitude in powers of the photon momentum k and thus to satisfy the Low soft photon theorem.[17] To these are added two additional diagrams. Figure 1(d) corresponds to radiation from the internal pion in the diagram responsible for g_P. It is analogous to the type of contribution one would obtain by the minimal substitution $p\to p-eA$ in the momentum dependence of g_P. The final term, Fig. 1(e), is a gauge term obtained by letting $p\to p-eA$ in the explicit momentum-dependent terms in the weak hadronic current. Neglected are a number of additional terms such as gauge terms coming from the structure of form factors other than g_P, various structure terms, higher-order terms generated by PCAC, etc. Some of these were considered by Manacher and Wolfenstein[18] and by Adler and Dothan[19] and seem generally to be small.

From this set of diagrams one obtains a relativistic amplitude for RMC on a proton of the form

$$M_{fi}=M_a+M_b+M_c+M_d+M_e\,, \tag{1}$$

where[20]

$$M_a=\epsilon_\beta\bar u_n\Gamma^\alpha(q_L)u_p\bar u_\nu\gamma_\alpha(1-\gamma_5)\frac{(\mu\cdot\gamma-k\cdot\gamma+m_\mu)}{2k\cdot\mu}\gamma^\beta u_\mu\,,$$

$$M_b=\epsilon_\beta L_\alpha\bar u_n\Gamma^\alpha(q_N)\frac{(p\cdot\gamma-k\cdot\gamma+m_p)}{-2k\cdot p}\times\left(Q_p\gamma^\beta-i\kappa_p\frac{\sigma^{\beta\delta}}{2m_p}k_\delta\right)u_p\,,$$

$$M_c=\epsilon_\beta L_\alpha\bar u_n\left(Q_n\gamma^\beta-i\kappa_n\frac{\sigma^{\beta\delta}}{2m_n}k_\delta\right)\times\frac{(n\cdot\gamma+k\cdot\gamma+m_n)}{2k\cdot n}\Gamma^\alpha(q_N)u_p\,,$$

$$M_d=-\epsilon_\beta L_\alpha\bar u_n\frac{[2q_L^\beta+k^\beta]}{q_L{}^2-m_\pi{}^2}\frac{g_P^N}{m_\mu}q_N^\alpha\gamma_5u_p\,,$$

$$M_e=\epsilon_\beta L_\alpha\bar u_n\left(\frac{ig_M}{2m}\sigma^{\alpha\beta}+\frac{g_S}{m_\mu}g^{\alpha\beta}+\frac{g_P^L}{m_\mu}\gamma_5g^{\alpha\beta}+\frac{ig_T}{2m}\sigma^{\alpha\beta}\gamma_5\right)u_p$$

$$\Gamma^\alpha(q)=g_V\gamma^\alpha+\frac{ig_M}{2m}\sigma^{\alpha\beta}q_\beta+\frac{g_S}{m_\mu}q^\alpha+g_A\gamma^\alpha\gamma_5+\frac{g_P(q^2)}{m_\mu}q^\alpha\gamma_5+\frac{ig_T}{2m}\sigma^{\alpha\beta}q_\beta\gamma_5\,,$$

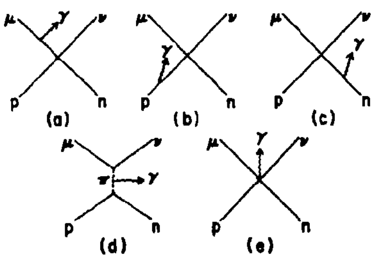

FIG. 1. Standard diagrams contributing to radiative muon capture on a proton.

$L_\alpha = \bar{u}_\nu \gamma_\alpha (1-\gamma_5) u_\mu$, $g_P^N = g_P(q_N^2)$, $g_P^L = g_P(q_L^2)$, and where the weak and electromagnetic couplings $Ge/\sqrt{2}$ have been extracted. In these expressions the four-momenta satisfy $\mu + p = n + \nu + k$, ϵ is the photon polarization vector, Q_p, κ_p, m_p, and Q_n, κ_n, m_n are, respectively, the initial and final nuclear charges, anomalous magnetic moments and masses, and m is the nucleon mass. The second-class terms g_S and g_T will be neglected from now on. The momentum dependence of $g_P(q^2)$ will be taken as $g_P(q^2) = g_P(m_\pi^2 + m_\mu^2)/(m_\pi^2 - q^2)$ with $g_P = m_\mu(m_p + m_n)g_A/(m_\pi^2 + m_\mu^2) \approx 6.6\, g_A$ being the Goldberger-Treiman[21] value. Unless otherwise noted, $g_V = 1.0$, $g_A = -1.25$, $g_M = 3.71$, $\kappa_p = 1.79$, and $\kappa_n = -1.91$.

Observe that there are two different momentum transfers in this expression: $q_L \equiv n - p$ and $q_N \equiv n - p + k$. Figures 1(a) and 1(d) depend on q_L, Figs. 1(b) and 1(c) depend on q_N, and Fig. 1(e) contains both. In the region of interest corresponding to large k, $q_L^2 \simeq -m_\mu^2$ whereas q_N^2 can approach $+m_\mu^2$. Thus g_P^N is evaluated nearly at the pion pole and hence is enhanced for large k by almost a factor of four over g_P^L.

In the usual approach, used by essentially all authors except Beder,[15] this amplitude is expanded in powers of p/m to obtain an effective Hamiltonian. Matrix elements of this Hamiltonian are taken and squared and multiplied by phase space which has also often been taken in some nonrelativistic approximation. The end result is a rate which is good through $O(1/m)$ but which generally contains only part of the $O(1/m^2)$ terms. (See, however, Ref. 7.)

Our approach, which was used to generate all numerical results given below, differs somewhat n that no nonrelativistic approximations or expansions in powers of $1/m$ were made. Instead the amplitude of Eq. (1) was evaluated numerically by direct multiplication of the various factors, squared and summed on spins, and used in the fully relativistic formula for the rate

$$\Gamma_{\rm rad} = \frac{\alpha G^2 |\phi_\mu|^2 m_n}{2(2\pi)^4} \int_0^{k_{\rm max}} k\,dk\, d\Omega_k\, d\Omega_\nu \frac{E_\nu^{\,2}}{W_0 - k(1-\nu)} \times \tfrac{1}{4} \sum_{\rm spins} |M_{fi}|^2 , \qquad (2)$$

where $\nu = \hat{k}\cdot\hat{\nu}$, $k_{\rm max} = (W_0^2 - m_n^2)/2W_0$, $W_0 = m_p + m_\mu$ - (binding energy of muon), $E_\nu = W_0(k_{\rm max} - k)/W_0 - k(1-\nu)]$ and $|\phi_\mu|^2$ is the muon wave function averaged over the initial nucleus and is taken for he proton as the point Coulomb result at $r = 0$. The $\frac{1}{4}\sum_{\rm spins}$ is for the statistical spin mixture and must be replaced appropriately if singlet or tripet rates are desired.

Since no nonrelativistic approximations have been made here, the numerical results will contain all orders in powers of $1/m$ both in the phase space and matrix element and so may differ somewhat from previous calculations which have variously dropped terms of $O(1/m^2)$, often terms of $O(p/m)$ and even sometimes other $O(1/m)$ terms. In nuclei the size of these $O(1/m^2)$ terms has been investigated recently,[7] and it was found for ^{40}Ca that all $O(1/m^2)$ terms together contribute up to 20% of the rate, though the most important of these are obtained from the square of the usual $O(1/m)$ Hamiltonian. The $O(1/m)$ terms contribute 40–50%, depending on k. The velocity terms, which explicitly contain the momentum p and contribute in a nucleus as a result of the nonzero Fermi momentum of the initial proton, give roughly 10%. Thus there may be residual differences between the present results for which all terms have been kept and those of others in which some of these terms have been dropped. It has been verified that the present calculations, using comparable form factors and for HP the changes discussed below, agree in the $m \to \infty$ limit with results of both Opat[14] and of HP to a few percent. For finite mass these results agree with Opat[14] at the 10% level, the difference being presumedly due to these additional relativistic corrections. Numerical work has also been checked against analytic results in the $m \to \infty$ and in the $|M_{fi}|^2 = 1$ limits.

This standard approach can be contrasted with that of Hwang and Primakoff,[16] who attempt to go as far as possible in deriving the RMC amplitude using only very general properties such as CVC, PCAC, and GI. Their approach thus may potentially provide a quite useful framework for looking at corrections not given by the usual perturbation theory diagrams.

To begin, HP expand the hadronic part of the RMC amplitude in terms of the most general set of structures which can be formed from the available vectors. Each structure is multiplied by a form factor which can be a function of the available invariants and couplings. The leptonic part Fig. 1(a) is evaluated as in the standard theory, using the usual definitions of the hadronic weak current.

Next the general conditions CVC, PCAC, and GI are imposed on the full amplitude, thus generating a set of constraint equations among the general form factors and the weak form factors from the muon radiating diagram, Fig. 1(a). These constraints are not sufficient to determine all unknown form factors, so it is necessary to make an additional "linearity hypothesis." This hypothesis requires that the form factors be linear in the various couplings, which is just a reflection of the first order electromagnetic-first order weak nature of the process, but more importantly that each form factor have the specific form

$$\frac{R^{+}(q_L^{2})}{k\cdot n}+\frac{R^{-}(q_L^{2})}{k\cdot p}+R^{0}(q_L^{2}). \qquad (3)$$

This form is motivated by the expressions obtained in perturbation theory from diagrams 1(b) and 1(c). It involves two crucial assumptions, namely that the only denominators allowed are those which would be obtained from neutron or proton propagators as in Figs. 1(b) and 1(c) and that there is dependence on q_L^2 but not on q_N^2. Thus contributions such as M_π from the pion radiating diagram are ruled out by assumption, and g_P^N either cannot appear or is approximated by g_P^L.

Finally, it is still necessary to assume that some of the form factors have their perturbation theory values as obtained from Figs. 1(b) and 1(c). Then with the linearity hypothesis and the constraint equations derived from general principles it is possible to solve for all of the unknown form factors and obtain an amplitude analogous to that of Eq. (1). This amplitude is then expanded in powers of $1/m$ and all $O(1)$ terms, which all contain g_V or g_A, are kept but only those $O(1/m)$ terms involving g_M or g_P. Thus fewer terms are kept than in the usual nuclear calculations. This amplitude is then squared and the cross section obtained in the usual nonrelativistic manner.

III. COMPARISON OF STANDARD AND HP APPROACHES

Having reviewed the two different approaches the next step is to examine the differences to try to understand the reason for the large difference in numerical results. This comparison will be done in three stages, first by examining the explicit differences, then looking at the numerical effect of each of these differences, and then understanding the physics, i.e., the assumptions and approximations which lead to these differences.

It is perfectly straightforward, though tedious since the metric and coupling constant definitions are different, to compare directly the amplitude of HP, Eqs. (3)–(5), (26), and (33) with the result of Eq. (1) above. The conclusion is that to get the result of HP Eq. (1) must be modified in the following three ways:

(1) Drop the contribution M_π corresponding to the radiation from the intermediate pion.

(2) Neglect the difference between q_L and q_N in the form factors and evaluate all form factors at q_L^2 (actually at an average value of q_L^2). Thus the difference between g_P^L and g_P^N and the enhancement due to g_P^N is neglected everywhere.

(3) Change the sign of some of the g_P terms appearing in the hadronic amplitude, in particular

$$\begin{aligned}
&\frac{g_P^N(n-p+k)^\alpha}{-2k\cdot p}\rightarrow\frac{g_P^L(n-p-k)^\alpha}{-2k\cdot p}\ \text{in } M_s,\\
&\frac{g_P^N(n-p+k)^\alpha}{2k\cdot n}\rightarrow\frac{g_P^L(n-p-k)^\alpha}{2k\cdot n}\ \text{in } M_e,\\
&g_P^L\rightarrow -g_P^L\ \text{in } M_\pi.
\end{aligned} \qquad (4)$$

The set of changes (1) and (2) together or the set (1), (2), and (3) both lead to an amplitude which is gauge invariant so that it makes sense to look at the numerical differences brought about by these changes. Such results for the proton are shown in Table II. Observe first that the approxi-

TABLE II. Effect of the differences (1), (2), and (3) between standard and HP theories, as described in the text, on the singlet (Γ_s), triplet (Γ_t), statistical ($\frac{1}{4}\Gamma_s+\frac{3}{4}\Gamma_t$), and ortho $p\mu p$ molecular ($\frac{3}{4}\Gamma_s+\frac{1}{4}\Gamma_t$) rates for RMC on a proton. Case (a) is the standard result from Eqs. (1), (2) with $g_V=1$, $g_A=-1.25$, $g_M=3.71$, and $g_P=6.6g_A$. Case (b) is (a) with the pion radiating diagram Fig. 1(d) dropped and $q_N\rightarrow q_L$ corresponding to the modifications (1) and (2) of the text. Case (c) is the same as (b) but with the sign changes in certain g_P terms corresponding to modifications (3) of the text and thus has the same matrix element as HP. Case (d) is the same as (c) except that the slightly different form factors of HP have been used. Case (e) is the $m\rightarrow\infty$ limit of (a) and thus corresponds to neglecting all $O(1/m)$ and higher terms in the matrix element and phase space.

Case	Radiative rate Singlet	Triplet	Statistical	Ortho $p\mu p$
(a) Standard theory—using Eqs. (1), (2)	3.23×10^{-3}	9.98×10^{-2}	7.56×10^{-2}	2.74×10^{-2}
(b) As (a), but with changes (1) and (2), i.e., no π radiation and $q_N\rightarrow q_L$	1.80×10^{-3}	9.69×10^{-2}	7.32×10^{-2}	2.56×10^{-2}
(c) As (b), but with change (3) in addition, i.e., sign change in some g_P terms	19.97×10^{-3}	5.36×10^{-2}	4.52×10^{-2}	2.84×10^{-2}
(d) As (c) but using same couplings and form factors as HP	19.22×10^{-3}	5.14×10^{-2}	4.34×10^{-2}	2.73×10^{-2}
(e) As (a), but with $m\rightarrow\infty$ everywhere except in $\lvert\phi_\mu(0)\rvert^2$	0.426×10^{-3}	5.18×10^{-2}	3.90×10^{-2}	1.33×10^{-2}

mations (1) + (2) do not change the statistical or triplet rates very much, but do reduce the singlet rate by almost a factor of 2. Thus the pion radiating diagram seems to be relatively small and the enhancement coming from g_P^N also is much less important than might be expected. This probably just reflects the fact that the muon radiating diagram dominates. When the change (3) is made, however, both the statistical and triplet rates are reduced by a factor of almost 2, and the singlet rate is increased by more than an order of magnitude. Clearly it is the change in sign of some of the g_P terms which has the most important numerical effect.

Shown also are the results obtained with the changes (1), (2), and (3) and in addition the form factors and couplings taken as nearly as possible to be the same as used by HP. The changes resulting from the slightly different choice of couplings are small. There still seem, however, to be some residual differences between these results and those actually quoted by HP, particularly for the triplet rate. Our results for the triplet rate are, however, in agreement with those of Opat[14] to within about 10% when evaluated at the appropriate values of the couplings. It may be that this residual difference with HP (and the smaller difference with Opat) is due to the higher-order relativistic corrections to both phase space and matrix element which are included in our result. Unfortunately as a result of the numerical evaluation of the amplitude used here it is impossible to sort out the contributions of each individual power of m. The $O(1)$ terms can be extracted numerically, however, by taking $m \rightarrow \infty$ everywhere except in $|\phi_\mu(0)|^2$. Such results are shown also in the table and agree in this limit with HP's results as calculated from Eq. (46a). Clearly the $O(1/m)$ and higher contributions are important, contributing almost half of the triplet rate and nearly all of the singlet rate. One further estimate can be made, albeit for the nucleus ^{40}Ca rather than for a proton, by using the work of Ref. 7 where terms in the matrix element were separated into various powers of m. Using a simple shell model-harmonic oscillator wave function approach one can test the approximation of HP of keeping only $g_V, g_A, g_M/m, g_P/m$ terms in the Hamiltonian. For ^{40}Ca this approximation misses 20–30% of the photon spectrum for larger k and even more for small k. Thus it appears that these approximations may not be as good as was assumed, and it is at least possible that these higher-order corrections could account for the residual differences mentioned above.

Having seen that the differences between HP and the standard approach are numerically significant, it is important to understand the physics of the assumptions which lead to these differences so as to make some choice between the two approaches. Several important observations can be made.

(A) It is straightforward to show that *the standard theory of Eq. (1) satisfies all of the general constraint equations arising from CVC, PCAC, and GI* which were derived in HP. This is perhaps not unexpected as both approaches begin with the same basic weak currents which satisfy CVC and PCAC.

(B) Both approaches lead to amplitudes which are gauge invariant. Hence *they differ by terms which are by themselves explicitly gauge invariant.* This just reflects the nonuniqueness of amplitudes fixed by gauge invariance; it is always possible to add pieces which are separately gauge invariant.

(C) Since the standard result satisfies the same general constraints as the HP result *the differences must be traceable to the extra linearity hypothesis used by HP.*

It is clear, and in fact already has been mentioned, that the differences (1) and (2) are direct results of the linearity hypothesis since by assumption the form factors are functions of q_L^2 only and since the assumed form of the form factors does not admit a contribution from the pion radiating diagram which has a different denominator than those assumed.

The way in which difference (3), which is the numerically important one, arises from the linearity hypothesis is somewhat more subtle. Observe from Eqs. (1) and (4) that the effect of the sign change in these g_P terms is to add to the standard result a gauge-invariant piece which contains terms of the form $k/k \cdot p$ and $k/k \cdot n$, i.e., terms which are of $O(k^0)$ but which are not independent of k. Recall, however, the usual derivation of the Low soft photon theorem[17,19] which applies to any radiative process. There the amplitude is first expanded in powers of k. All $O(1/k)$ terms must arise from the external radiation diagrams, Figs. 1(a), 1(b), 1(c) in the present case, and all terms having $k \cdot p$ or $k \cdot n$ in the denominator must arise from the nucleon propagators appearing in these same external radiation diagrams. Terms which are of $O(k^0)$ and *independent of k* are then added to make the result gauge invariant. Thus in the context of the Low theorem the terms of the form $k/k \cdot p$ and $k/k \cdot n$ are *uniquely* determined by the perturbation theory diagrams Figs. 1(b), 1(c) and thus correspond to the standard result. HP's result contains different $k/k \cdot p$ and $k/k \cdot n$ terms and hence, even though it is a gauge invariant expansion containing $O(1/k)$ and $O(k^0)$ pieces, the $O(k^0)$ terms and the result violate the Low soft photon theorem.[22]

Again we can trace this difficulty to the linearity hypothesis. The form chosen is too general since it allows $1/k \cdot p$ and $1/k \cdot n$ terms in all form factors. The Low theorem, via the argument that such terms come only from external radiation diagrams, provides an additional constraint not used by HP which uniquely determines the R^i coefficients in the linearity hypothesis. Had this constraint been used, the standard result would have been obtained for these $g_P k/k \cdot p$ and $g_P k/k \cdot n$ terms.

Thus to summarize this section, the HP results differ from results of the standard approach not because of any different use of the constraints deriving from the general principles of CVC, PCAC, and GI, but because of the specific assumptions made via the linearity hypothesis. In particular the pion radiating diagram and the dependence on q_H^2 are dropped by assumption, and the amplitude is made gauge invariant by adding terms which cause the result to violate the Low soft photon theorem. These differences are numerically significant for the rates, as was seen in Table II. They are important also for the photon spectrum, an example of which is given in Fig. 2. Since the Low theorem must be satisfied by any radiative process, and since the aspect being violated by the HP result essentially just expresses the requirement that the amplitude be obtainable from some set of field-theory-like interactions, it would seem that the standard result is the correct one and should be adopted. However, it should be relatively easy to impose the required additional constraint from the Low theorem on the HP form factors, and then the HP approach, since it is quite general up to the point at which the linearity hypothesis is imposed, may be quite powerful and useful for including a variety of corrections or improvements in the theory, such as contributions from additional diagrams, which do not arise in the standard approach.

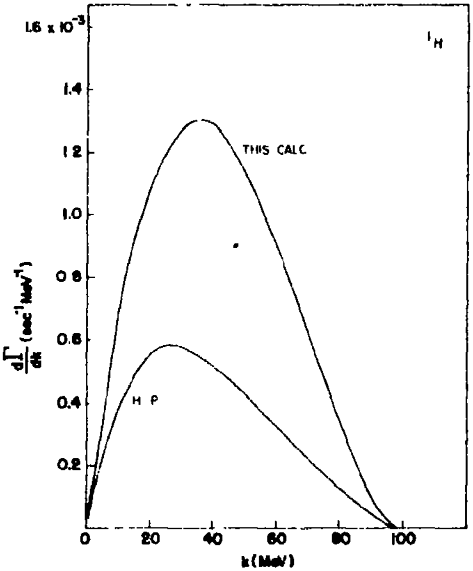

FIG. 2. Photon spectrum for radiative muon capture on a proton in the standard theory of this calculation and from HP, Eq. (48c).

IV. RMC IN ^{3}He

From an experimental point of view RMC in ^{3}He is somewhat easier than on a proton since the rate is $\sim Z^4$ and thus significantly higher. RMC in ^{3}He seems currently feasible and an experiment is planned.[13] It is thus important to have good theoretical estimates of the spectrum. Except for the work of HP and some results for specific correlations and for the upper tip of the photon spectrum by Beder,[15] such calculations in ^{3}He seem not to have been made.

However, if one uses the elementary particle picture, following for example Kim and Primakoff,[23] then it is very easy to adapt this calculation for the proton to the ^{3}He-^{3}H system, or for that matter to any spin $\frac{1}{2} \to \frac{1}{2}$ transition. The rate is thus evaluated in the standard approach using the formula obtained from Eqs. (1), (2) with the replacements $m_p \to$ mass of ^{3}He, $m_n \to$ mass of ^{3}H, $Q_p \to 2$, $Q_n \to 1$, and $\kappa_p \to -8.368$, $\kappa_n \to 7.918$. The weak couplings, as taken from Ref. 23, are $g_V = 1$ $g_M = -5.44$, $g_A = 1.22$, $g_P \approx 19.4 g_A$. Observe that g_A, and hence g_P, has the opposite sign for ^{3}He than for the proton. Note also that the nuclear mass has been retained in the denominator in the definitions of the anomalous moments, but the nucleon mass is used for g_M. Finally, for ^{3}He averaging over the nuclear volume introduces a factor so that[23] $|\phi_\mu|^2 \to 0.965 |\phi_\mu|^2$.

For a nucleus it may be necessary to include form factors in the g_V, g_A, and g_M couplings as well as g_P. This leads to a dilemma, however, since the two different momentum transfers involved will give different values of the form factors, e.g., $g_V(q_L^2)$ and $g_V(q_H^2)$, for the different diagrams and thus destroy gauge invariance unles some additional diagrams are added, analogous to Fig. 1(d), corresponding to radiation from the internal exchanged particles which generate the phenomenological form factor. In practice, however, such contributions are probably suppressed by the propagators of the (presumedly heavy) exchanged particles. Also the muon radiating dia-

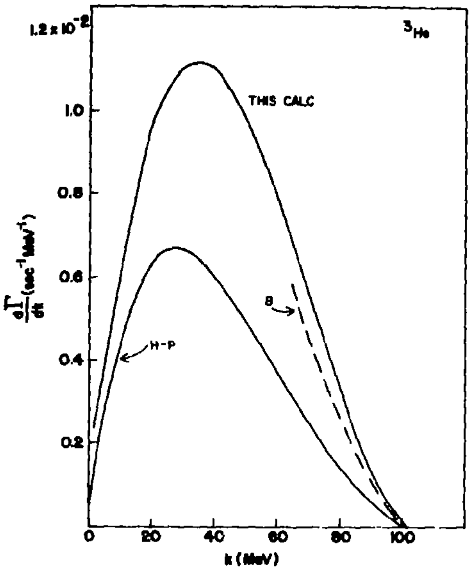

FIG. 3. Photon spectrum for radiative muon capture on ^{3}He in the standard theory of this calculation and from HP, Eq. (49q). Beder's result (perhaps with the wrong sign for g_P) is also shown. Reversing the sign of g_P would increase his result to be about 10% above the result of this calculation.

gram dominates. Thus it is probably a reasonable approximation to simply evaluate all form factors in the same way and take those values appropriate for the muon radiating diagram. Thus a simple linear interpolation of the form factors of Kim and Primakoff[23] was used for g_V, g_A, and g_M and evaluated at $q_L{}^2$, as appropriate for the muon radiating diagram. This is essentially the procedure of HP, except that they used an average value of $q_L{}^2$, independent of k.

Results for the photon spectrum as calculated in this model are shown in Fig. 3 as are the results of HP and Beder.[15] These spectra correspond to a total radiative rate of $\Lambda = 0.676$ sec^{-1} for the standard calculation vs $\Lambda = 0.373$ sec^{-1} from HP. Qualitatively the effects of the three differences in the amplitudes which arise from the linearity hypothesis of HP are the same for ^{3}He as for the proton, though for ^{3}He sensitivity to the spin state is not as great. The important effect is again (3), the change in sign of some g_P terms which cause the HP results to violate the Low theorem, which gives almost a factor of 2 reduction from the present results.

As a numerical check our results using the coupling constants and form factors of HP and the changes (1), (2), and (3) were compared with those quoted in HP. Agreement is at the 10–15% level, and hence if the higher-order terms are responsible for the differences in the proton triplet rate then they seem not to be as large here. Comparison was also made with results of Beder in the appropriate limit with the result that the standard theory seems to be about 20% higher than Beder's quoted results. If g_P is given the wrong sign, however, as we have been informed[24] may have been the case in Ref. 15, agreement is at the 10% level.

Finally, perhaps the most useful result with regard to ^{3}He is the larger rate, by a factor of 2, obtained in the standard theory, which may help make a difficult experiment somewhat easier.

ACKNOWLEDGMENTS

This work was supported in part by the Natural Sciences and Engineering Research Council of Canada. The author would like to thank W. Y. P. Hwang for a number of useful conversations regarding his work, H. Primakoff and W. Y. P. Hwang for reading a preliminary version of the manuscript, G. Dugan and C. S. Wu for information about their planned experiment, and D. Beder, A. Fujii, J. Ng, and other TRIUMF colleagues for helpful comments.

---

[1] M. Conversi, R. Diebold, and L. DiLella, Phys. Rev. 136, B1077 (1964).

[2] L. M. Rosenstein and I. S. Hammerman, Phys. Rev. C 8, 603 (1973); L. DiLella, I. Hammerman, and L. M. Rosenstein, Phys. Rev. Lett. 27, 830 (1971).

[3] R. D. Hart *et al.*, Phys. Rev. Lett. 39, 399 (1977); R. D. Hart, Ph.D. thesis, College of William and Mary, 1977.

[4] J. C. Adler *et al.*, contribution to the Eighth International Conference on High Energy Physics and Nuclear Structure, Vancouver, 1979; P. Truöl and W. Dahme (private communication).

[5] H. P. C. Rood and H. A. Tolhoek, Nucl. Phys. 70, 658 (1965).

[6] H. P. C. Rood, A. F. Yano, and F. B. Yano, Nucl. Phys. A228, 333 (1974); H. P. C. Rood and A. F. Yano, Phys. Lett. 35B, 59 (1971); A. F. Yano, F. B. Yano, and H. P. C. Rood, Phys. Lett. 37B, 189 (1971).

[7] R. S. Sloboda and H. W. Fearing, Nucl. Phys. (to be published); R. S. Sloboda, Ph.D. thesis, University of Alberta, 1979.

[8] R. S. Sloboda and H. W. Fearing, Phys. Rev. C 18, 2265 (1978).

[9] A. Wullschleger, Phys. Rev. Lett. 40, 638 (1978); A. Wullschleger and F. Scheck, Nucl. Phys. A326, 325 (1979).

[10] P. Christillin, M. Rosa-Clot, and S. Servadio, CERN Report No. Th-2659 (1979).

[11] W. Y. P. Hwang and H. Primakoff, Phys. Rev. C 18,

used to include the small πN channels. Section III is devoted to the description of the πN and NN interactions used as input. Our results are presented and discussed in Sec. IV, and we conclude the paper in Sec. V.

II. PRACTICAL CALCULATION

A. Basic equations

We use the three-body equations described by Rinat and Thomas[1] which satisfy two and three-body unitarity and covariance. In operator form, the equations read, with the notation of Ref. 1:

$$\begin{aligned} X_{nm} &= \sum_{\alpha} Z_{n\alpha} R_{\alpha} X_{\alpha m}, \\ X_{\alpha m} &= Z_{\alpha m} + \sum_{\beta} Z_{\alpha\beta} R_{\beta} X_{\beta m} + \sum_{n} Z_{\alpha n} R_{n} X_{nm}, \end{aligned} \tag{1}$$

where the α, β and n, m labels refer respectively to $N(\pi N)$ and $\pi(NN)$ three-body channels. In our case, the α, β labels do not contain the N-P_{11} channel. The driving terms Z and the propagators R are defined in terms of the form factors of the separable interactions, and for the relative momenta of the interacting pairs, we take the choice (a) of Ref. 4 corresponding to the exchanged particle on its mass shell.

The scattering amplitudes $2X_{dd}$ are obtained by solving the system of coupled one-dimensional integral equations which result from angular momentum reduction of Eq. (1). The singularities of the kernel are treated by contour rotation and the system is solved by the Padé approximant technique. The coupling of πd channels with $l, l' = J \pm 1$ orbital angular momentum is included exactly.

Compared with the RPK case, the FR calculation is much more time consuming because of the intricate coefficients which appear in the relative momenta [see Eqs. (2.20) and (2.21a) in Ref. 4]. In order to save computing time, we have (i) reduced the number of mesh points in the $[0, +\infty]$ domain, and (ii) treated perturbatively the small πN channels.

B. Numerical integration

In order to preserve the numerical accuracy when energy goes up to 300 MeV, without increasing too much the number of mesh points, we split the $[0, +\infty]$ domain of integration for the integral equation into two intervals $[0, k_c]$, $[k_c, +\infty]$. The energy-dependent parameter k_c is chosen to be in the middle of the interval delimited by the pole of the propagator and the extreme position of the logarithmic singularity in the driving term. In each interval, we use Gaussian quadratures mapped onto $[0, k_c]$ and $[k_c, +\infty]$ with, respectively, N_1 and N_2 mesh points. Because of the structure of the kernel, the convergence in the $[k_c, +\infty]$ domain is faster than in the $[0, k_c]$ region, and we take usually $N_2 = N_1/2$. The two main advantages of the method are (i) the number of mesh points is large in the region around k_c where the kernel is rapidly varying, and (ii) we have observed that the convergence of the scattering amplitudes is monotonic when N_1 and N_2 increases. Therefore, the stability of the results can be obtained with a total number of mesh points appreciably lower than in the case where the Gaussian quadrature mapped directly onto $[0, +\infty]$ is used. We estimate the accuracy to be within 2% with $N_1 = 16$ and $N_2 = 8$ at 256 MeV, while 32 points are necessary if the interval is not split.

C. Perturbation scheme

In order to treat the small πN channels, we choose the first order Alt-Grassberger-Sandhas (AGS) approximation which was applied successfully in the n-d elastic scattering problem some years ago.[9] In this method, the kernel is split into a dominant part which is treated exactly and a weak part treated approximately. In Ref. 9, it is shown that the convergence condition for the AGS perturbation theory can be formulated entirely in terms of the weak part of the kernel. From a practical point of view, the first order AGS approximation is obtained when the weak part of the kernel is taken to be zero.

In our case, the dominant part corresponds to the π-d and N-Δ channels, and the weak part involves all the N-(πN) channels with the πN pair in the S or P states (except P_{11}) other than Δ. We therefore set equal to zero all the overlapping terms between these weak channels in the three-body kernel, i.e., we set $Z_{\alpha\beta} = 0$ for α and β not equal to d or Δ. So, a large amount of computing time (~30%) is saved compared with the exact calculation.

Of course, the full advantage of this method can be exploited only in the case where the system of equations is solved by means of the Padé approximant technique. We give in Table I the comparison between the exact and AGS results for two dominant scattering amplitudes T^J_{11}, calculated at 142, 180, and 256 MeV with the $SF(6.7)$-$SP(S)$ interactions described hereafter in Sec. III. Clearly the AGS approximation is very good, the accuracy being of about 2%.

A different approximation is used in Ref. 3 where the small πN channels are introduced one at a time after the dominant part has been solved exactly. The choice of this method is imposed by the fact that the system of equations is solved by

TABLE I. Comparison of the first order AGS approximation with the exact calculation (in brackets) for two dominant scattering amplitudes. The T are dimensionless.

T_π (MeV)	T^{2+}_{33}	T^{2+}_{11}
142	$-12.976-i28.190$ $(-12.999-i28.172)$	$-865.39-i1138.4$ $(-856.72-i1142.7)$
180	$5.657-i56.747$ $(5.630-i56.733)$	$-275.36-i1421.0$ $(-268.42-i1420.4)$
256	$56.251-i52.286$ $(56.245-i52.261)$	$459.17-i869.80$ $(460.53-i869.32)$

matrix inversion, so that the storage problems are crucial. The accuracy was determined to be at the 5% level for the dominant scattering amplitudes.

In what follows, all the calculations including the small πN channels (SP scheme) are done with the AGS approximation.

III. TWO-BODY INTERACTIONS

We describe in this section the relativistic πN and NN separable interactions used as input in our calculations.

A. Pion-nucleon interactions

For the S_{11}, S_{31}, P_{13}, P_{31}, and P_{33} πN channels, we use two sets of parametrizations constructed by Rinat *et al.*[3] (denoted hereafter R) and by Schwarz *et al.*[10] (denoted S).

In the R case, the parameters are fitted in each channel to the experimental phase shifts taken from the recent analysis of Rowe *et al.*[11] which provides a smooth "best" fit to all modern πN phase shifts determined by various groups for energies below 400 MeV.

In the S case, the parameters are fitted to the "experimental" phase shifts and scattering lengths. These values are rather old and correspond to the data chosen by Thomas[2] for fitting the πN interactions in the RPK calculations. We note that in the P_{33} channel, the position of the resonance is imposed as an additional constraint in the fitting procedure.

The fits to the data are excellent as one can see in Fig. 3 of Ref. 3, and in Figs. 1 and 2 and Tables I–III of Ref. 10. We have recalculated the phase shifts and the scattering lengths for each set. The results are quite similar, the most apparent differences occurring in the P_{33} channel. This is illustrated in Table II where we give the scattering lengths for the two sets compared with the experimental values.

B. Nucleon-nucleon tensor forces

The simplest ${}^3S_1$-${}^3D_1$ parametrizations are the relativistic generalizations of Yamaguchi-type interactions described in Ref. 3, with P_D values 4 and 6.7% (denoted hereafter $Y4$ and $Y6.7$). The parameters are fitted to the ${}^3S_1$ phase shift only, without any constraint on the low energy parameters a_t (scattering length) and Q (quadrupole moment). We have calculated these quantities, which are found to be far from the correct values. For $Y4$ and $Y7$ we get, respectively, $a_t=5.63$ and 5.79 fm (accepted value 5.40 fm), and $Q=0.37$ and 0.40 fm^2 (accepted value 0.280 to 0.286 fm^2).

In order to improve the situation, we have constructed three sets of rank-1 interactions (denoted YL, S, and SF), using more elaborate form factors, and introducing in the fitting procedure more and more constraints.

For the YL potentials, we take the usual Yamaguchi form factors:

$$g_L(p)=C_L p^L/(p^2+\beta_L{}^2)^{(L+2)/2}\,. \qquad (2)$$

For the S and SF potentials we define the form factors as a ratio of polynomials:

$$g_L(p)=C_L p^L(1+\gamma_L p^2)\Big/\prod_{i=0}^{L+2}(1+\beta_{Li}p^2)\,. \qquad (3)$$

The parameters are adjusted to fit the following

TABLE II. πN scattering lengths (in m_π^{-1} for S waves) and scattering volumes (in m_π^{-3} for P waves) for the Rinat (Ref. 4) and Schwarz (Ref. 10) parametrizations. The "new" experimental data are from Ref. 11, and the "old" are given in Refs. 9–11 of the Schwarz paper.

Parametrizations	Scattering length or volume				
	S_{11}	S_{31}	P_{13}	P_{31}	P_{33}
R	0.172	−0.092	−0.013	−0.039	0.170
S	0.170	−0.091	−0.016	−0.036	0.211
Exp. (old)	0.174	−0.092	−0.016	−0.037	0.220
Exp. (new)	0.185 ±0.008	−0.098 ±0.003	−0.013 ±0.002	−0.029 ±0.002	0.205 ±0.050

quantities

(i) For the YL potentials, we impose only the static parameters, namely the deuteron binding energy $E_D = 2.2245$ MeV, the triplet scattering length $a_t = 5.40$ fm, the quadrupole moment $Q = 0.285$ fm^2, the D-state probability P_D, and the ratio of the D to S asymptotic deuteron wave functions $\eta = 0.026$.

(ii) For the S parametrizations, the $^3S_1$ phase shift up to 200 MeV is added to the foregoing constraints.

(iii) For the SF interactions, we impose one more constraint, namely the monopole form factor of the deuteron $F_0(q^2)$ up to $q \sim 6$ fm^{-1}. We choose to fit the Reid soft-core (RSC) form factor which has a minimum at $q \sim 4.5$ fm^{-1}.

In each set, two parametrizations are constructed with $P_D = 4$ and 6.7%. The parameters for the S and SF interactions are given in Table III. For the YL potentials, the values of $(C_0, \beta_0; C_2, \beta_2)$ are (124.707, 1.329; 220.795, 1.559) for $YL4$, and (98.941, 1.261; 446.940, 1.970) for $YL7$ (the C are in fm^{-2} and β in fm^{-1}).

We show in Fig. 1 the $^3S_1$ phase shift for the various interactions with $P_D = 6.7\%$, and in Table IV we give the monopole form factors compared with the Reid soft-core values. The phase shift for the SF interaction is not as good as for the S interaction above 100 MeV, but the form factor is much better for $q > 2$ fm^{-1}. We think that the SF interactions are therefore more "realistic" in the sense that the fitting procedure to $F_0(q)$ ensures the correct behavior of the deuteron wave function. Let us point out that the $SF6.7$ potential is the relativistic equivalent to the Pieper rank-1 potential used in our RPK calculations.[1]

IV. RESULTS AND DISCUSSIONS

We have performed detailed calculations at 142, 180, 230, and 256 MeV in order to investigate the sensitivity of πd observables to the NN and πN input. There are three subsections devoted, respectively, to the differential cross sections (A), the total cross sections (B), and the polarization parameters (C).

TABLE III. Parameters for the S and SF tensor forces. The C_L are in fm^L and the β are in fm^2.

	$S4$	$S6.7$	$SF4$	$SF6.7$
C_0	76.832	64.530	66.508	58.659
γ_0	−0.0404	−0.0381	−0.231	−0.240
β_{01}	0.227	0.351	0.121	0.0494
β_{02}	0.252	0.190	0.118	0.241
C_2	37.038	31.362	33.057	27.562
γ_2	1.299	0.340	0.813	0.688
β_{21}	0.364	0.0217	0.216	0.0268
β_{22}	0.503	0.428	0.414	0.580
β_{23}	0.468	0.384	0.301	0.254
β_{24}	0.271	0.0794	0.424	0.262

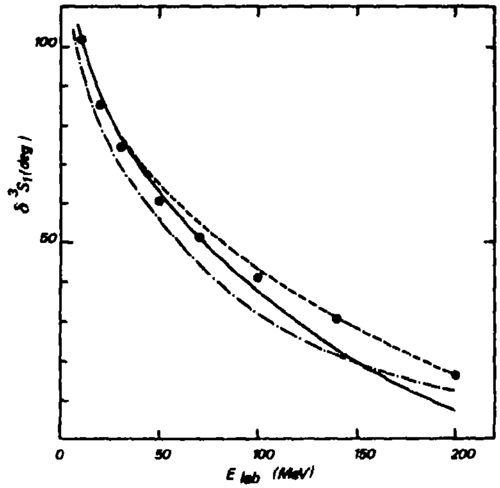

FIG. 1. Theoretical $^3S_1$ phase shifts given by the Y (— · —), YL (– – –), S (identical to YL), and SF (——) parametrizations for $P_D = 6.7\%$. The experimental data are from Ref. 12.

In what follows, each calculation is specified by two labels: The first one denotes the NN tensor force, and the second one refers to the πN channels which are retained (P_{33} or SP) and to the parametrization.

A. Differential cross sections

1. Effect of the small πN partial waves

The SP scheme consists in introducing with the AGS perturbation method the small πN channels S_{11}, S_{31}, P_{13}, and P_{31} in addition to P_{33}. As stated

TABLE IV. Monopole charge form factor of the deuteron $F_0(q)$ for the new tensor forces SF, S, and YL with $P_D = 6.7\%$, compared with the Reid soft-core values.

q (fm^{-1})	RSC	SF	S	YL
0.2	0.975	0.975	0.975	0.975
1	0.616	0.614	0.618	0.623
2	0.257	0.254	0.269	0.283
3	0.0875	0.0877	0.112	0.129
4	0.0151	0.0190	0.0453	0.0614
5	−0.0120	−0.0600	0.0177	0.0308
6	−0.0188	−0.0127	0.0064	0.0163

in the Introduction, we omit completely the P_{11} channel. The reason is that the formalism we use here does not include the effect of pion absorption, so that the nucleon pole part which is the dominant part cannot be introduced. On the other hand, the P_{11} phase shift is very small up to 150 MeV, and it seems reasonable to neglect its background contribution. The latter assumption was checked at 142 and 256 MeV. Using a separable parametrization adjusted only to the P_{11} phase shift, the πd observables calculated in the *SP* scheme with and without the nonpole P_{11} contribution were found to be almost identical.

We compare in Fig. 2 the differential cross sections calculated at 142, 180, 230, and 256 MeV in the *SP* and P_{33} schemes, with the *SF*6.7 tensor force and the *S* parametrizations of the πN channels. The forward part of $d\sigma/d\Omega$ is lowered by the *SP* scheme at energies below the resonance, and is enhanced above the resonance, while the backward part is systematically lowered. The effect is very small at 180 MeV which is close to the resonance. At all energies the *SP* scheme improves significantly the agreement with experimental data[13-16] throughout the angular range, except at forward angles for $T_\pi = 230$ MeV. Nevertheless, the situation at 230 and 256 MeV is not satisfactory, especially for $\theta_{\text{c.m.}} > 80°$, where the broad minimum observed in the experiments is not reproduced by the theory, which remains too high. However, we do not understand the discrepancy at forward angles with the experiment of Cole *et al.*[15] at 230 MeV, since our theory describes correctly, in this angular range, the "old" data at 142, 180, and 256 MeV as well as the preliminary data of Gabathuler *et al.*[5] for $T_\pi = 140$ to 300 MeV. We can thus consider the possibility of an incorrect normalization. In fact, if we enhance Cole's results by a factor of 1.4, the theory becomes quite good. On the other hand, the recent experiments of Ref. 5 seem to indicate that the minimum at 256 MeV is not so deep, but the theory still remains higher than experiment.

Let us briefly compare these results with the RPK calculations using the Pieper tensor force at 142 and 180 MeV [see Figs. 3(b) and 4(b) of Ref. 1]. The FR and RPK differential cross sections look quite similar, demonstrating that relativistic effects are moderate at these energies. We also note that the interference effects from the small πN channels are smaller in the FR theory than in RPK.

2. Sensitivity to the πN parametrizations

We compare in Table V the values of $d\sigma/d\Omega$ obtained in the *SP* scheme with the *S* and *R* parametrizations of the πN channels and the *SF*6.7 tensor force, at $T_\pi = 180$ and 256 MeV. The *R* values are slightly higher than the *S* results throughout the angular range. However, the maximum variation does not exceed 13% at backward angles, reflecting that the two sets are nearly equivalent as shown in Sec. III A.

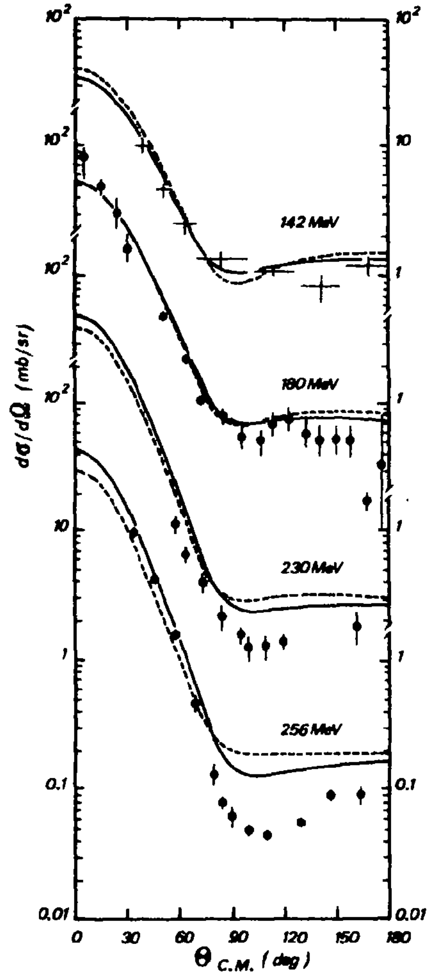

FIG. 2. πd elastic differential cross section at $T_\pi = 142$ (Ref. 13), 180 (Ref. 14), 230 (Ref. 15), and 256 (Ref. 16) MeV calculated with the *SF* 6.7 tensor force and the *S* parametrizations of the πN channels. – – – only P_{33}, —— P_{33} + small πN waves, except P_{11}.

3. Sensitivity to the NN tensor force

Now, the calculations are done in the *SP* scheme with the *S* parametrizations of the πN channels.

TABLE V. Sensitivity of the differential cross section to the πN parametrizations. The numbers in each case are the values of $d\sigma/d\Omega$ in mb/sr, at $\theta_{c.m.} = 0°$, 90°, and 180°.

T_π (MeV)	S	R
180	53.6	53.9
	0.74	0.77
	0.73	0.77
256	41.9	44.7
	0.15	0.17
	0.16	0.18

First, we consider the influence of D-state probability. In order to study a genuine effect of P_D, we use our parametrizations which, in a given set (YL, S, or SF), differ only by their P_D values as explained in Sec. III B. The differential cross sections calculated at 180 and 256 MeV with the $SF4$ and $SF6.7$ interactions are given in Table VI. When P_D goes from 4 to 6.7%, the forward part of $d\sigma/d\Omega$ decreases by about 3%, and the backward part increases by 4% at 180 MeV and by 14% at 256 MeV. Similar conclusions hold with the $S4$ and $S6.7$ interactions, and also with the $YL4$ and $YL6.7$ potentials. These results show that the overall effect of P_D is rather small, while the large variation at backward angles found in Ref. 4 is not a genuine effect, but is due to the fact that the $Y4$ and $Y6.7$ interactions give different values for the low energy parameters as mentioned in Sec. III B.

Next, we investigate the sensitivity to the description of the deuteron wave function for a fixed P_D value. We use the YL, S, and SF interactions with $P_D = 6.7\%$. The variation of $d\sigma/d\Omega$ at forward angles is very small (~2%), but the backward part exhibits large variations (up to 25%). For example, the values of $d\sigma/d\Omega$ (180°) at 180 MeV are 0.97, 0.86, and 0.73 mb/sr for the YL, S, and SF tensor forces, respectively. Similar effects are observed at the other energies. If we remember how we have constructed the YL, S, and SF interactions in Sec. III B, we see that the agreement of theory with experimental data at backward angles becomes better as we improve the description of the $^3S_1$-$^3D_1$ channel, namely with regard to the deuteron wave function. These considerations justify the systematic use throughout this paper of the SF interactions, even if they fail to reproduce the minimum for $T_\pi = 230$ and 256 MeV.

TABLE VI. Sensitivity of the differential cross section to the D-state probability. The numbers are ordered as in Table V.

T_π (MeV)	$SF4$	$SF6.7$
180	54.9	53.60
	0.78	0.74
	0.70	0.73
256	43.3	41.9
	0.16	0.15
	0.14	0.16

B. Elastic, reaction, and total cross sections

We have calculated the elastic (σ_{el}), reaction (σ_R), and total ($\sigma_T = \sigma_{el} + \sigma_R$) cross sections in the energy range 70 to 320 MeV with the $SF6.7$-$SP(S)$ interactions. In Fig. 3 we show our results and we compare the total cross section with the recent experimental data of Pedroni *et al.*[17] The agreement is fairly good, especially in the resonance region 140 MeV < T_π < 260 MeV where the theoretical curve goes through experiment. Outside this domain, the theoretical values are lower than experimental data, and the deviation increases when energy decreases from $T_\pi = 120$ MeV or increases from $T_\pi = 260$ MeV.

Compared with the RPK results (Fig. 5 or Ref. 1), the FR values of σ_T are better in a wider energy range. We also note a very good agreement with the calculations of Rinat *et al.*[3] without absorption. Our values for σ_T with the $SF6.7$-$SP(S)$ interactions at 142, 180, and 256 MeV are respectively 174, 230, and 135 mb, while the values of Rinat for $P_D = 6.7\%$ are 176, 239, and 146 mb. In fact, we have observed that the total cross section is rather insensitive to the two-body input.

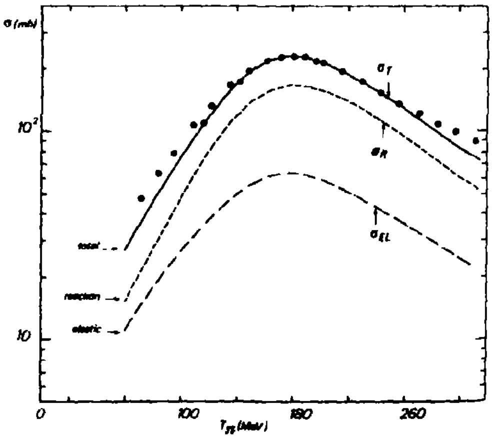

FIG. 3. Elastic (—·—), reaction (– – –), and total (——) cross sections calculated with the SF 6.7-$SP(S)$ interactions. The experimental results are from Pedroni *et al.* (Ref. 17).

C. Polarization parameters

The vector polarization it_{11} and the tensor polarizations t_{20}, t_{21}, and t_{22} for $\pi+d\to\pi+\vec{d}$ elastic scattering are easily calculated from the scattering amplitudes. The qualitative effects noted in the RPK approach are also observed in the FR calculations, only the numbers change more or less. We limit thus the present discussion to the most important aspects.

The complete change in structure of it_{11} due to the inclusion of the small πN partial waves in addition to P_{33} is observed at all energies. The FR curves look similar to the RPK curves shown in Fig. 6 of Ref. 1. The vector polarizations calculated in the *SP* scheme have a pronounced maximum which has the following characteristics: (i) the position is nearly independent of energy and of the two-body input and corresponds to $\theta_{c m}=80°$, and (ii) the magnitude is practically independent of the πN and NN input, but varies with energy; namely, it is maximum around $T_\pi=180$ MeV. For example, the values of it_{11} (80°) obtained with the *SF*6.7-*SP*(*S*) interactions at 142, 180, 230, and 256 MeV are respectively 0.43, 0.45, 0.40, and 0.36.

In contrast with it_{11}, the tensor polarizations are only slightly affected when we include the small πN channels (the difference between the *SP* and P_{33} results is less than 5%) or when we change the πN parametrizations from *S* to *R* (the effect is ~2%). Of course, the most important variations in the tensor polarizations are due to the *NN* tensor force. We discuss only the quantity t_{20} which presents an immediate interest. The angular distributions of t_{20} have the same aspect as in the RPK theory (see Fig. 7 of Ref. 1), and the values of t_{20} (180°) calculated with the *SF*6.7-*SP*(*S*) interactions at 142, 180, 230, and 256 MeV are respectively −0.74, −1.08, −1.26, and −1.27. The polarization t_{20}(180°) behaves as follows. (i) It decreases with increasing *D*-state probability; we give in Table VII the values obtained with the *SF*4 and *SF*6.7 tensor forces at 142, 180, and 256 MeV. (ii) It depends on the description of the deuteron wave function; for instance, the results at $T_\pi=180$ MeV corresponding to the *SF*, *S*, and *YL* interactions with the same P_D value (6.7%) are respectively −1.08, −0.96, and −0.90. These variations are therefore of the same order as the variations coming from different P_D values. Recently, t_{20} (180°) was observed for the first time at $T_\pi=140$ MeV by Holt *et al.*,[7] the value being -0.24 ± 0.15. The theoretical values obtained with the most elaborate tensor forces, namely the *SF* interactions, still remain far from this result since we find −0.74 for $P_D=6.7\%$ and −0.61 for $P_D=4\%$.

TABLE VII. Sensitivity of t_{20} (180°) to the *D*-state probability.

T_π (MeV)	*SF*4	*SF*6.7
142	−0.63	−0.74
180	−0.92	−1.08
256	−1.17	−1.27

V. CONCLUDING REMARKS

We have presented an extensive analysis of πd elastic scattering observables in the resonance region within a fully relativistic three-body theory. The small πN channels have been included to an excellent degree of accuracy through the AGS perturbation method, and the numerical integration has been refined in order to save computing time without losing accuracy. Since the theory we used did not include the effects of pion absorption, the P_{11} πN channel was completely omitted.

The great sensitivity of πd observables (namely the differential cross section and the t_{20} polarization at large angles) to the details of the two-body input that was demonstrated in previous RPK calculations[1] is still observed in the FR approach. The agreement between the theoretical and experimental differential cross sections is significantly improved when the small πN channels are included and when a tensor force giving a realistic deuteron wave function is used.

Let us note here that the differences between the present calculations and those of Rinat *et al.*,[3] without absorption, are moderate. Seeing that the two sets of πN interactions used in each calculation are nearly equivalent, it is clear that the differences must be attributed to the tensor forces. Figure 6 of Ref. 3 gives a spectacular illustration of the model dependence of $d\sigma/d\Omega$ at backward angles relative to the deuteron wave function. The variations corresponding to different tensor forces are found to be as important as the variations due to the inclusion of absorption effects. Our main effort in the present work was to produce pure three-body calculations based on a tensor force having the maximum degree of quality. So, we have now a sound reference for further theoretical investigations. We think that the *SF* parametrizations that we have constructed represent a real improvement compared with the tensor forces used up to now. Of course, they have some defects deriving from their structure: The *SF* interactions are of rank 1, and therefore the $^3S_1$ phase shift remains positive and the $^3D_1$ phase shift has the wrong sign. These difficulties should be removed by considering rank 2 parametrizations. However, from our experience in the RPK approach with the Pieper rank-1 and rank-2 interactions (they have the same deuteron wave function but differ by their $^{3}D_{1}$ phase shifts, and they give nearly the same πd observables), we think that this step is not essential.

None of our calculations do reproduce the minimum in the differential cross sections which is observed in the experiments at 230 and 256 MeV, and it seems now clear that the two-body input is not responsible for this discrepancy. Besides the apparent need to reconfirm the experimental data, we have now to consider further theoretical investigations. At first, we must include the effects of absorption. Detailed calculations have been recently performed in this direction by Rinat *et al.*[3] within a field-theoretical formulation including genuine pion absorption and ρ-meson exchange. The effects of absorption induce significant changes in the large angle differential cross section, but they do not produce the deep minimum at 256 MeV. On the other hand, absorption has a tremendous influence on all polarization parameters; for example, t_{20} (180°) becomes small positive at 142 MeV. An independent calculation of πd elastic scattering including π absorption is now in progress in our group, based on the approach to the theory of coupled πNN-NN systems recently developed by Avishai and Mizutani.[18] Also the effects of inelasticity in the πN partial waves may be important[19] (mainly in the P_{11} channel) in accounting for the minimum in the cross section at 256 MeV. Another direction concerns the inclusion of dibaryon resonances, but here the situation is not clear. For some people,[20] the resonant amplitude (the $^{3}F_{3}$ NN for instance) must be added to the πd elastic scattering amplitude, while for others[21] the πNN system itself is resonant and the inclusion of the NN ($^{3}P_{2}$) and πN (P_{11} and P_{33}) leads to a resonant $^{3}F_{3}$ wave.

Finally, we think that the new experimental data which ought to appear in the near future will be decisive for further theoretical work.

ACKNOWLEDGMENTS

We would like to thank A. S. Rinat and A. W. Thomas for very helpful discussions and correspondence. It is a pleasure to thank F. Myhrer for his stimulating remarks. The constant interest of E. Elbaz in the achievement of the present work is highly appreciated.

---

[1] N. Giraud, Y. Avishai, C. Fayard, and G. H. Lamot, Phys. Rev. C 19, 465 (1979); Phys. Lett. 77B, 141 (1978); N. Giraud, G. H. Lamot, and C. Fayard, Phys. Rev. Lett. 40, 438 (1978).

[2] A. W. Thomas, Nucl. Phys. A258, 417 (1976).

[3] A. S. Rinat, Y. Starkand, E. Hammel, and A. W. Thomas, Phys. Lett. 80B, 166 (1979); Nucl. Phys. A329, 285 (1979).

[4] A. S. Rinat and A. W. Thomas, Nucl. Phys. A282, 365 (1977).

[5] K. Gabathuler *et al.* (private communication).

[6] W. Grüebler *et al.*, SIN proposal R-73-01.1.

[7] R. J. Holt, J. R. Specht, E. J. Stephenson, B. Zeidman, R. L. Burman, J. S. Frank, M. J. Leitch, J. D. Moses, M. A. Yates-Williams, R. M. Laszewski, and R. P. Redwine, LAMPF report, 1979.

[8] A. Stanovnik *et al.*, in *Proceedings of the 2nd Conference on Meson-Nuclear Physics, Houston, 1979.*

[9] G. Bencze and P. Doleschall, Phys. Lett. 44B, 235 (1973).

[10] K. Schwarz, H. Zingl, and L. Mathelitsch, Phys. Lett. 83B, 297 (1979).

[11] G. Rowe, M. Salomon, and R. H. Landau, Phys. Rev. C 18, 584 (1978).

[12] M. H. MacGregor, R. A. Arndt, and R. M. Wright, Phys. Rev. 182, 1714 (1969).

[13] E. G. Pewitt, T. H. Fields, G. B. Yodth, J. G. Fetkovich, and M. Derrick, Phys. Rev. 131, 1826 (1963).

[14] J. H. Norem, Nucl. Phys. B33, 512 (1971).

[15] R. H. Cole, J. S. MacCarthy, R. C. Minehardt, and E. A. Wadlinger, Phys. Rev. C 17, 681 (1978).

[16] K. Gabathuler, C. R. Cox, J. J. Domingo, J. Rohlin, N. W. Tanner, and C. Wilkin, Nucl. Phys. B55, 397 (1973).

[17] E. Pedroni, K. Gabathuler, J. J. Domingo, W. Hirt, P. Schwaller, J. Arvieux, C. H. Q. Ingram, P. Gretillat, J. Piffaretti, N. W. Tanner, and C. Wilkin, Nucl. Phys. A300, 321 (1978).

[18] Y. Avishai and T. Mizutani, Nucl. Phys. A326, 352 (1979), and Saclay report, 1979.

[19] J. T. Londergan, K. W. McVoy, and E. J. Moniz, Ann. Phys. (N.Y.) 86, 147 (1974).

[20] K. Kubodera, M. P. Locher, F. Myhrer, and A. W. Thomas, in *Proceedings of the 8th International Conference on High Energy Physics and Nuclear Structure, Vancouver, 1979.*

[21] M. Araki, Y. Koike, and T. Ueda, Osaka University Report No. 79-9-6 (unpublished).

PHYSICAL REVIEW C VOLUME 21, NUMBER 5 MAY 1980

Nuclear disintegration of some complex nuclei by 60-MeV muons

C. J. Orth, J. D. Knight, and K. Wolfsberg
Los Alamos Scientific Laboratory, Los Alamos, New Mexico 87545

M. W. Johnson*
Department of Chemistry, University of Rochester, Rochester, New York 14627

(Received 24 October 1979)

Cross sections for muodisintegration reactions $(\mu^{\pm},\mu^{\pm}xN)$ at $T_\mu = 60$ MeV on eight nuclei from ^{12}C to ^{203}Tl have been measured by activation techniques. The cross sections, like those for comparable electron reactions, increase with target mass number. An additional measurement with 30-MeV μ^+ on ^{12}C shows a positive energy dependence. The observation that $\sigma(\mu^+,\mu^+xn) < \sigma(\mu^-,\mu^-xn)$ for heavy nuclei implies the presence of Coulomb distortion of the muon trajectories. Calculations employing the virtual photon method in the plane-wave Born approximation, together with reported photonuclear cross sections, give good agreement with the ^{12}C$(\mu,\mu'n)^{11}$C results, but not with those for higher-Z nuclei.

[NUCLEAR REACTIONS Muon scattering, 60-MeV $(\mu^{\pm},\mu^{\pm\prime}xN)$ cross sections in ^{12}C, ^{46,48}Ti, ^{58}Ni, ^{63}Cu, ^{174}Yb, ^{197}Au, ^{203}Tl; 30-MeV μ^+ on ^{12}C; 60-MeV μ^- on ^{12}C, ^{63}Cu, ^{197}Au, and ^{203}Tl. Activation method, natural targets, enriched ^{203}Tl. Comparison with plane-wave Born approximation (PWBA) virtual photon calculations.]

I. INTRODUCTION

One of the well known, but less commonly employed, modes of nuclear excitation and reaction is the direct interaction of the electromagnetic field of a fast electron with nuclear charges and currents leading to electrodisintegration (for a review see Ref. 1). Typically, electrons of a few tens of MeV kinetic energy are directed at thin-foil targets and measurements are made of the nuclear particles emitted or of the radioactive heavy products, care being taken to correct the observations for contributions from photonuclear reactions caused by bremsstrahlung generated in the target.

Theoretical treatments of electrodisintegration are usually carried out in terms of production of virtual photons (from the passing electron), which then interact with the nucleus by way of the photonuclear process.[2-4] The electrodisintegration cross section is calculated by folding the calculated virtual photon spectrum with the photonuclear excitation function:

$$\sigma_e(E_0)=\int_0^{E_0}\sum_{\lambda L} N^{\lambda L}(E_0,\omega)\,\sigma_\gamma(\omega)\frac{d\omega}{\omega}, \qquad (1)$$

where λ is the label E or M for electric or magnetic transitions, L is the multipole order, and $\sigma_\gamma(\omega)$ is the photonuclear cross section as a function of photon energy ω. E_0 is the incident electron kinetic energy and $N^{\lambda L}(E_0,\omega)$ is the virtual photon power spectrum. Many of the cross sections $\sigma_\gamma(\omega)$ have been determined experimentally using monoenergetic photons. The virtual photon spectrum is usually derived for lower-Z target nuclei using Born approximation calculations which assume a point nucleus and plane waves (PW) for the incoming and outgoing electrons; with higher-Z nuclei a distorted-wave (DW) treatment is required in order to account for the effects of nuclear size and of the differences in e^+ and e^- trajectories and therefore in the differences in the corresponding virtual photon spectra (Coulomb distortion). Plane-wave expressions for $N^{\lambda L}(E_0,\omega)$ have been derived for $E1$, $M1$, and $E2$ transitions by Thie *et al.*[5] More recently Cutler[6] and Onley and co-workers[7,8] have developed distorted-wave Born approximation (DWBA) equations and computer codes for the electron virtual photon spectra. These PW and DW calculations and their possible adaptation for muons will be discussed later.

From a nuclear standpoint, the muon may be regarded as a heavy electron with $M_\mu/M_e \approx 207$. No differences, apart from mass effects, have been found between electron-proton and muon-proton elastic scattering,[9] and the form factor for muon-nucleus scattering is thus considered to be identical to that for electron-nucleus scattering. There have been extensive experimental and theoretical investigations of high-energy ($\gtrsim$GeV) muon scattering, but these studies have been concerned primarily with the penetration of cosmic rays through matter[10,11]; to our knowledge no one has yet reported either measured or calculated cross sections for the formation of nucleon-out products below 100 MeV.

The primary incentive for this survey study was to provide "muodisintegration" data to test the validity of the virtual photon concept for these relatively slow moving leptons. This problem is complex, because the velocity of a 60-MeV muon is the same as that of a 0.29-MeV electron while its de Broglie wavelength is about the radius of a heavy nucleus, and therefore its trajectory is sensitive to the nuclear charge distribution. Further incentive for this work was provided by the desire to establish a systematics for the muodisintegration process spanning most of the nuclidic chart and to compare the results with those of similar electrodisintegration experiments, particularly the work of Kuhl and Kneissl,[12] who measured $(e,e'n)$ cross sections between 26 and 31 MeV for several targets also studied here.

In this work we have measured muodisintegration cross sections for 60-MeV muons on a selection of targets between $Z = 6$ and 81 using activation methods. A ^{12}C target was irradiated also with 30-MeV μ^+ for comparison. We compare our results with some simple plane-wave Born approximation (PWBA) calculations assuming only electric dipole transitions. These calculations show good agreement with our experimental results for ^{12}C, but as would be expected, the PW treatment is inadequate for higher-Z targets.

II. EXPERIMENTAL

The muon exposures were performed at the stopped muon channel of the Clinton P. Anderson Los Alamos Meson Physics Facility (LAMPF). The beam channel magnets were generally tuned to deliver 133-MeV/c (62-MeV) muons, plus or minus, from backward decay of the initial pion beam; the momentum bite $\Delta p/p$ averaged about 5%. Measurements have shown that these muon beams at 133 MeV/c (the maximum momentum available in the downstream part of the channel) contain ≈10 n/sec, at normal operation, with an average energy about 1 MeV, <1% electrons of the same charge sign, and no detectable pions (<0.1%) or other charged particles.[13] The targets were placed at the rather diffuse focus of the beam, where the horizontal and vertical dimensions of the beam spot were 12 and 4 cm full width at half maximum (FWHM), respectively. Muon beam profile and intensity were measured with a coincident pair of miniature plastic scintillators which were mounted on a remotely controlled assembly arranged to scan in the horizontal and vertical directions normal to the beam. At normal operation ($I_p = 0.4$ mA, duty factor = 7%) the average μ^+ flux through the targets at 133 MeV/c was 1.5×10^7 sec^{-1}, derived from a very high instantaneous rate of 3.7×10^8 coincidences per sec in the miniature scintillators; the μ^- flux was about 5-fold lower. The targets, consisting of either 5-cm square natural metal foils (Ti, Ni, Cu, Yb, and Au), 5-cm disks of Pilot B plastic scintillator[14] (composition $CH_{1.1}$), or 5-cm disks of powdered, 92.4% enriched $^{203}Tl_2O_3$, were 0.5 to 2 g cm^{-2} thick and were irradiated for periods of time ranging from a few minutes to 16 hours depending on the half-lives of the products to be counted.

Following the irradiations the targets were removed to a low background environment and counted with detector systems appropriate for the product(s) being studied. For most of the targets NaI(Tl) and Ge(Li) γ-ray systems were used; in the $^{12}C(\mu,\mu'n)^{11}C$ measurements a β^+-$\gamma^{\pm}$ self-coincidence system, which has been described previously,[15] was employed. Decays of the products were followed over several half-lives and a regression was performed to determine the activity level at the end of irradiation; cross sections were determined from these values. By this technique all of the radionuclides expected from the reactions could be studied except ^{195}Au from $^{197}Au(\mu,\mu'2n)$, where the combination of long half-life and weak, low energy γ rays precluded its detection.

A potential source of error in measurements of this kind is the contribution of bremsstrahlung and secondary-particle reactions to the yields of the muodisintegration products of interest. We assessed the bremsstrahlung effect by comparing product yields as a function of target thickness for three of the reactions: $^{12}C(\mu^+,\mu^+n)^{11}C$, $^{63}Cu(\mu^+,\mu^+n)^{62}Cu$, and $^{197}Au(\mu^+,\mu^+n)^{196}Au$. The resulting corrections ranged from zero for ^{12}C to (20 ± 5)% for ^{197}Au.

Possible contributions from fast neutrons coming down the channel, scattering from the muon beam stop, and surviving the shielding around various accelerator-associated sources were also evaluated. Conventional targets were placed below the primary targets but out of the main muon beam, and after exposure were measured like the primary targets. The fast neutron contribution was found to be <5%.

III. RESULTS AND DISCUSSION

The cross sections determined for the reactions studied in this work are given in Table I. The quoted errors (2σ) are primarily systematic in nature for most reactions, being dominated by the uncertainty in the determination of the muon flux, which is viewed as being ±12%. Statistical errors are significant mainly for the multinucleon-out cross sections.

TABLE I. Muodisintegration ($\mu, \mu' xN$) cross sections at 60 MeV.

Target	Product (xN out)	Cross section (μb) Measured[a]	Calculated[b]
μ^+ reactions			
^{12}C	^{11}C(n)	21 ± 3	20[c]
^{12}C(30 MeV)	^{11}C(n)	13 ± 4	13[c]
^{46}Ti	^{45}Ti(n)	200 ± 50	
^{48}Ti	^{47}Sc(p)	70 ± 20	
^{58}Ni	^{57}Ni(n)	108 ± 28	181[d]
^{58}Ni	^{57}Co(p)	405 ± 65	418[e]
^{63}Cu	^{62}Cu(n)	257 ± 40	419[f]
^{63}Cu	^{61}Cu($2n$)	13 ± 10	45[f]
^{174}Yb	^{173}Tm(p)	20 ± 8	
^{197}Au	^{196}Au(n)	1930 ± 400	3300[g]
^{197}Au	^{194}Au($3n$)	110 ± 25	64[g]
^{203}Tl	^{202}Tl(n)	2140 ± 380	
^{203}Tl	^{201}Tl($2n$)	409 ± 80	
^{203}Tl	^{200}Tl($3n$)	90 ± 16	
^{203}Tl	^{199}Tl($4n$)	34 ±13	
μ^- reactions			
^{12}C	^{11}C(n)	20 ± 3	20[c]
^{63}Cu	^{62}Cu(n)	305 ± 50	419[f]
^{197}Au	^{196}Au(n)	2300 ± 450	3300[g]
^{203}Tl	^{202}Tl(n)	3010 ± 650	
^{203}Tl	^{201}Tl($2n$)	590 ± 95	
^{203}Tl	^{200}Tl($3n$)	203 ± 34	
^{203}Tl	^{199}Tl($4n$)	125 ± 27	

[a] All experimental uncertainties shown are 2σ.

[b] An uncertainty of ±5% is estimated for the calculated cross sections on the basis of our ability to read published graphical displays of the appropriate photonuclear cross sections. The blanks are given where photonuclear cross sections are not available in the literature.

[c] Photoneutron cross sections taken from Ref. 24.

[d] Photoneutron cross sections taken from Ref. 19.

[e] Photoproton cross sections taken from Ref. 21.

[f] Photoneutron cross sections taken from Ref. 25.

[g] Photoneutron cross sections taken from Ref. 23.

The calculated cross sections listed in Tables I and II have been derived by folding previously reported photonuclear cross sections with $E1$ virtual photon spectra using a simple PWBA treatment of the scattered leptons that will be discussed in the following section.

The targets used in this study were chosen to provide for the establishment of general systematics for the ($\mu, \mu' xN$) reaction and possibly to test the validity of the virtual photon concept for

TABLE II. A comparison of muon and electron cross sections (μb) at 30 and 60 MeV.

	Lepton projectile and energy (MeV)[a]					
Reaction[b]	μ^+(30)[c]	μ^+(60)[c]	μ^-(60)[c]	e^+(30)[d]	e^-(30)[d]	e^-(30)[e]
^{12}C($l, l'n$)^{11}C	13 ± 4 (13)	21 ± 3 (20)	20 ± 4 (20)	12.5 (12)	12.5 (12)	11.9 ± 0.2 (12)
^{63}Cu($l, l'n$)^{62}Cu		257 ± 40 (419)	305 ± 50 (419)	280 (309)	320 (309)	

[a] Calculated cross sections are listed in parentheses under the measured cross sections.

[b] Here l denotes lepton.

[c] Cross sections determined in this work.

[d] Cross sections interpolated from the data of Ref. 12.

[e] Cross section reported in Ref. 26.

these relatively slow muons ($\beta = 0.7$), whose kinetic energy is approximately half the rest-mass energy. For the light target ^{12}C, the primary interest lies in the comparison of ($\mu,\mu' n$) cross sections with similar ($e,e'n$) data, and also with PWBA calculations, which are expected to be most satisfactory for light nuclei. In the intermediate mass region it is possible to compare cross sections for proton-out and neutron-out reactions. Finally, muodisintegration of heavy nuclei is expected to exhibit Coulomb distortion and thus the results of PW calculations should diverge considerably from the measured cross sections. In this mass region more rigorous DW calculations are required, and their current status will be discussed in Sec. III D.

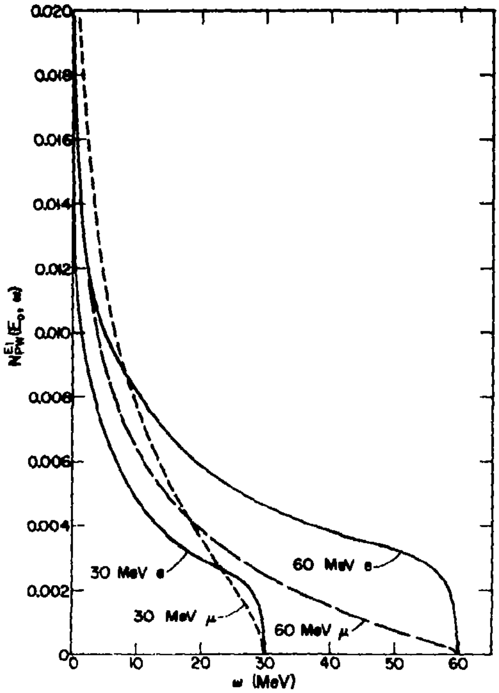

FIG. 1. Virtual photon power spectra for 30- and 60-MeV electrons and muons, calculated in *E*1 PWBA with Eq. (2).

A. ($\mu,\mu' xN$) systematics

The general picture presented by the data indicates a trend toward increasing cross sections with increasing target mass, and in the case of ^{12}C, with increasing muon kinetic energy. Such a trend with mass number is reasonable to the extent that Eq. (1) is valid because photonuclear cross sections increase with A. The increase in the ^{12}C($\mu,\mu' n$)^{11}C cross section with increase in muon kinetic energy from 30 to 60 MeV is attributed to the increase in the fraction of the virtual photon spectrum lying above the ^{12}C neutron separation energy. Figure 1 shows the virtual photon power spectra calculated with the PW approximation for 30- and 60-MeV electrons and muons, using the analytical expression of Wolynec *et al.*[16] for electric dipole transitions:

$$N^{E1}(E_0,\omega) = \frac{\alpha}{\pi}\left[\left(\frac{E_1{}^2 + E_2{}^2}{E_1{}^2 - m^2}\right)\ln\left(\frac{E_1E_2 + (E_1{}^2 - m^2)^{1/2}(E_2{}^2 - m^2)^{1/2} - m^2}{m\omega}\right) - 2\left(\frac{E_2{}^2 - m^2}{E_1{}^2 - m^2}\right)^{1/2}\right]. \tag{2}$$

Here, $N^{E1}(E_0,\omega)/\omega$ is the number of virtual photons of energy ω resulting from a lepton of initial energy E_0. The lepton rest mass m is 0.511 and 105.66 MeV for electrons and muons, respectively. Also, $E_1 = E_0 - m$ and $E_2 = E_1 - \omega$. It is important to note that the distributions plotted in Fig. 1 represent power spectra rather than photon intensity spectra.

By folding the virtual photon power spectra in Fig. 1 with published photonuclear cross sections, according to Eq. (1), one obtains the calculated muodisintegration cross sections listed in Tables I and II. The overall agreement between the experimental results and the calculations suggests that the PW approach is a reasonable starting point for modeling the muodisintegration process.

B. ^{12}C($\mu,\mu' n$)^{11}C

The most important feature of the ^{12}C($\mu,\mu' n$)^{11}C measurement is the apparent absence of Coulomb distortion at a statistically meaningful level; the ($\mu^+,\mu^+ n$) and ($\mu^-,\mu^- n$) cross sections at 60 MeV are approximately equal within experimental erro A comparison with the ($e^+,e^+ n$) and ($e^-,e^- n$) studies of Kuhl and Kneissl,[12] given in Table II reveals that here too no Coulomb distortion is seen. In fact, the overall correspondence between ($e,e'n$) and ($\mu,\mu' n$) cross sections suggests that, for the lightest nuclei, the mechanisms of the electrodisintegration and muodisintegration reactions are essentially identical. This situation does not clearly hold for heavier nuclei, as will be seen later.

The fact that PW calculations appear to be adequate to describe both $(e,e'n)$ and $(\mu,\mu'n)$ reactions in ^{12}C is not surprising in view of the established, strong Z dependence of the difference in virtual photon spectra calculated with PW and DW approaches. Nascimento *et al.*[17] obtained an analytical, semiempirical expression for the differences $\Delta N_e^{\pm}(E_0,W,Z)$ between PW and DW treatments of electron virtual photon spectra. In particular they give the formulas

$$\Delta N_{e^-}^{E1}(E_0,\omega,Z)=\omega[1.29\times10^{-5}\exp(1.245Z^{1/3}-0.052E_1)\times(E_2+m_e)/(E_1+m_e)], \qquad (3)$$

$$\Delta N_{e^+}^{E1}(E_0,\omega,Z)=-3\times10^{-5}\exp(0.675Z^{1/3}-0.06135\omega)\times(E_2-m_e)-T(E_2,Z), \qquad (4)$$

where the energies are given in MeV, and $T(E_2,Z)$ is a function which modifies the e^+ virtual photon spectra near the end point. The use of these formulas reveals that, for both positive and negative electrons, the difference between PW and DW calculations is nowhere greater than about 1% for nuclei as light as ^{12}C. Although no formulations similar to Eqs. (3) and (4) exist for muons, it is probable that the Coulomb distortion effect is also Z dependent.

C. Muon reactions in medium-mass nuclei

The targets Ti and Ni are of special interest due to the detectability of both neutron-out and proton-out products using activation techniques. In the case of Ti one can observe the neutron-out product from ^{46}Ti and the proton-out product from ^{48}Ti in a single irradiation of natural titanium; ^{58}Ni offers a special case where both the n-out and p-out products from the same nucleus can be compared from a single irradiation of normal nickel. Although no p-out species are detectable from the copper target, the $2n$-out product is measurable, leading to information on the high-energy region of the virtual photon spectrum.

The ^{58}Ni$(\mu,\mu'n)$ and $(\mu,\mu'p)$ reactions are partiularly rewarding to study due to the existence of oth photoneutron and photoproton data. The reults given in Table I indicate that with 60-MeV μ^+ the proton-out reaction is considerably more probable than the neutron-out reaction, in agreement with the photonuclear studies of Min and White[18] and Fultz *et al.*,[19] both of which report anomalously low photoneutron cross sections. The latter give a photoneutron cross section integral of 286-MeV mb over the photon energy range 0–33.5 MeV, compared to the photoproton integral of 738-MeV mb over a similar energy range reported by Wolynec *et al.*[20] The results of Fultz *et al.* were used in the calculation of the $(\mu,\mu'n)$ cross sections in Table I, while those of Ishkanov *et al.*[21] were used for calculating the $(\mu,\mu'p)$ cross section. We note that the cross sections reported by Fultz *et al.* were obtained by neutron counting and thus contain some (γ,pn) contribution, which may be responsible for some of the excess calculated $(\mu,\mu n)$ cross section.

A plausible explanation for the anomalously low $(\mu,\mu'n)$ cross section may be found in the work of Ishkanov *et al.*,[21] who suggest that the low photoneutron cross section is due to isospin splitting ($T_>$ and $T_<$) of the giant dipole resonance (GDR) and to the relatively strong population by $E1$ transitions of the $T_>$ component of the GDR in ^{58}Ni. (Here $T_>=T_0+1$ and $T_<=T_0$, where T_0 is the isospin of the nuclear ground state.) The $T_>$ component in ^{58}Ni deexcites mainly by proton emission, while the $T_<$ component deexcites about equally by emission of protons and of neutrons. Fallieros *et al.*[22] give a ratio for dipole excitation of the two resonance components as $T_>/T_<=0.82$ for ^{58}Ni; this relatively large ratio, combined with the preferred deexcitation modes for the two components, suggests that proton emission following transitions to the GDR should dominate neutron emission by a factor of greater than 2, in qualitative agreement with the present results.

The first possible indications of the inadequacy of the PW treatment of virtual photon spectra begin to appear in this mass region. For ^{62}Cu the ratio σ_-/σ_+ of (μ^-,μ^-n) to (μ^+,μ^+n) cross sections is $1.20\pm0.12(1\sigma)$. As the PW treatment gives $\sigma_-/\sigma_+=1$, it appears that even for this relatively light nucleus a more rigorous DW calculation is required. This has been shown by Kuhl and Kneissl[12] also to be the case for the corresponding electrodisintegration reactions. Their data are compared with our muon results in Table II.

D. Muon reactions in heavy nuclei

The ^{197}Au and enriched ^{203}Tl targets are particularly useful for determining the magnitude of Coulomb distortion of the muons trajectories. As in the case of electrodisintegration, Coulomb distortion is indicated by $\sigma_-/\sigma_+>1$. For 60-MeV muons on ^{203}Tl, we observe $\sigma_-/\sigma_+=1.4\pm0.2$ for both the one- and two-neutron-out products. For the three- and four-neutron-out products which require increasingly higher-energy virtual photons, this ratio is 2.3 and 3.7, respectively.

Another indication of the Coulomb distortion effect, that is, of the relatively deeper penetration of the nucleus by μ^- compared to μ^+, is the ratio of $3n$-out to n-out cross sections for each charge sign. To make this comparison, $R_-(\sigma_{3n}/\sigma_n)$ is defined as the ratio of the cross sections for

$\sigma(\mu^-,\mu^- 3n)/\sigma(\mu^-,\mu^- n)$ and $R_+(\sigma_{3n}/\sigma_n)$ as the corresponding ratio of μ^+ cross sections. Both ratios are flux independent since σ_{3n} and σ_n are obtained from the same irradiation. For ^{203}Tl, $R_-/R_+ = 1.61 \pm 0.08$ and for ^{197}Au, $R_-/R_+ = 1.63 \pm 0.13$.

Experimental electrodisintegration cross sections for ^{197}Au are not available for comparison, but it is of interest to consider calculated cross sections derived from Eqs. (3) and (4) and the experimental (γ,n) cross sections of Veyssiere *et al.*[23] For 30-MeV electrons the results are $\sigma(e^-,e^- n) = 3120$ μb and $\sigma(e^+,e^+ n) = 2165$ μb, from which it may be seen that, for electrons, Coulomb distortion is very significant.

Unfortunately, neither the rigorous DW calculations performed for electrodisintegration by Onley and co-workers,[7,8] nor the DW corrections to PW calculations embodied in Eqs. (3) and (4), have been duplicated for muodisintegration. The calculations for muons are complicated by the finite size effect; at $T_\mu = 60$ MeV, the de Broglie wavelength of the muon is about equal to the nuclear radius at $A \approx 200$.

The proton- (or other charged particle-) out channels should not be important at high Z; we see in Table I that $\sigma[^{174}\mathrm{Yb}(\mu,\mu' p)^{173}\mathrm{Tm}]$ is about 1% of the $(\mu,\mu' xn)$ cross sections.

Finally, we note the observation of the $^{203}\mathrm{Tl}(\mu^-,\mu^- xn)$ reaction for $x = 5$ at $(T_\mu = 60$ MeV), based on the detection of a weak γ ray corresponding to the decay of ^{198}Tl. The energy required to remove 5 neutrons in this case is 35.1 MeV. While the counting statistics were inadequate for determination of a meaningful cross section, this observation may be a starting point for future experiments aimed at the study of the shapes of virtual photon spectra at energies near the end point for muons in this energy range.

IV. CONCLUSIONS

The present study represents the first systematic cross section measurements of the muodisintegration reaction $(\mu,\mu' xN)$ below 100 MeV. The virtual photon method using simple PW calculations is a reasonable starting point, especially for low-Z targets, for modeling the muodisintegration process. However, the results clearly indicate that a more rigorous DW calculation is required for the evaluation of the Coulomb distortion effects which appear in muon reactions with medium- and heavy-mass nuclei. The DW modeling problem is complicated by the need to consider nuclear size, in contrast to the electrodisintegration DW calculation. A theoretical treatment of this problem might be rewarding in terms of a better understanding of these nuclear size and charge distribution effects.

ACKNOWLEDGMENTS

We express our gratitude to the LAMPF technical staff and operating crews for enabling us to carry out these irradiations, and we thank Dr. D. S. Onley for his comments and insights on the problems involved in the modeling of the muodisintegration process. This work was performed under the auspices of the U. S. Department of Energy.

---

*Present address: Department of Chemistry, University of Maryland, College Park, Md. 20742.

[1] W. C. Barber, Annu. Rev. Nucl. Sci. 12, 1 (1962).

[2] C. F von Weizsäcker, Z Phys. 88, 612 (1934).

[3] E T. Williams, Phys. Rev. 45, 769 (1934).

[4] R. H. Dalitz and D. R. Yennie, Phys. Rev. 105, 1598 (1957).

[5] J. A Thie, C. J. Mullin, and E. Guth, Phys. Rev. B 7, 962 (1952).

[6] L. S. Cutler, Phys. Rev. 157, 885 (1967).

[7] W. W. Gargaro and D. S. Onley, Phys. Rev. C 4, 1032 (1971).

[8] C. W. Soto Vargas, D. S. Onley, and L. E. Wright, Nucl. Phys. A288, 45 (1977).

[9] G. E. Masek, L. O. Heggie, Y. B. Kim, and R. W. Williams, Phys. Rev. 122, 937 (1961).

[10] G. N. Fowler and A. W. Wolfendale, Prog. Elem. Part. Cosmic Ray Phys. 4, 107 (1958).

[11] M. G. K. Menon and P. V. Ramana Murthy, Prog. Elem. Part. Cosmic Ray Phys. 9, 161 (1967).

[12] G. Kuhl and U. Kneissl, Nucl. Phys. A195, 559 (1972).

[13] P. A. Thompson (private communication).

[14] Formerly produced by Pilot Chemicals Division, New England Nuclear Corp., Watertown, Massachusetts, but currently manufactured by Nuclear Enterprises, Inc., San Carlos, California.

[15] B. J. Dropesky, G. W. Butler, C. J. Orth, R. A. Williams, G. Friedlander, M. A. Yates, and S. Kaufman, Phys. Rev. Lett. 34, 821 (1975).

[16] E. Wolynec, G. Moscati, J. R. Moreira, O. D. Goncalves, and M. N. Martins, Phys Rev. C 11, 1083 (1975).

[17] I. C. Nascimento, E. Wolynec, and D. S. Onley, Nucl. Phys. A246, 210 (1975).

[18] K. Min and T. A. White, Phys. Rev. Lett. 21, 1200 (1968).

[19] S. C. Fultz, R. A. Alvarez, B. L. Berman, and P. Meyer, in Proceedings of the International Conference on Photonuclear Reactions and Applications, 1973, Pacific Grove, California, p. 5B7-1, p. 5B7-2.

[20] E. Wolynec, W. R. Dodge, and E. Hayward, Phys. Rev. Lett. 42, 27 (1979).

[21] B. S. Ishkanov, I. M. Kapitonov, I. M. Piskarev, J. G. Shevchenko, and O. P. Shevchenko, Yad. Fiz. 11,

485 (1970) [Sov. J. Nucl. Phys. **11**, 272 (1970)].

[22] S. Fallieros, B. Goulard, and R. M. Ventor, Phys. Lett. **19**, 398 (1966). B. Goulard and S. Fallieros, Can. J. Phys. **45**, 322 (1967).

[23] A. Veyssiere, H. Beil, R. Bergere, P. Carlos, and A. Lepretre, Nucl. Phys. **A159**, 561 (1970).

[24] S. C. Fultz, J. T. Caldwell, B. L. Berman, R. L. Bramblett, and R. R. Harvey, Phys Rev. **133**, 143 (1966).

[25] S. C. Fultz, R. L. Bramblett, J. T. Caldwell, and R. R. Harvey, Phys. Rev. **133**, 1150 (1964).

[26] F. J. Kline and E. Hayward, Phys. Rev. C **17**, 1531 (1978).

PHYSICAL REVIEW C VOLUME 21, NUMBER 5 MAY 198

Interpretation of quasielastic pion scattering coincidence experiments

Morton M. Sternheim
Department of Physics and Astronomy, University of Massachusetts, Amherst, Massachusetts 01003

Richard R. Silbar
Theoretical Division, Los Alamos Scientific Laboratory, Los Alamos, New Mexico 87545

(Received 13 November 1979)

The energy dependence of the np charge exchange cross section, the angular dependence of the free $\pi^{\pm}p$ cross section ratio, and nucleon "absorption" due to quasielastic scattering are significant in predicting $(\pi^{\pm},\pi^{\pm}N)$ ratios. When these effects are taken into account, recent $(\pi,\pi N)$ coincidence data can be understood in the impulse approximation picture, with the recoil nucleon subject to charge exchange on leaving the nucleus.

[NUCLEAR REACTIONS Ratios of $\sigma(\pi,\pi N)$ when final π and/or N observed: ^{12}C, ^{27}Al, ^{208}Pb at T_π 180, 190, 255 MeV. Differences from radiochemical experiments.]

I. INTRODUCTION

The quasielastic scattering of pions by nucleons bound in nuclei is interesting for several reasons. It offers a way to study the πN amplitude in the nuclear medium,[1] complements $(e,e'p)$ and $(p,2p)$ studies of single particle energies, and provides a potential probe of the nuclear surface. With the pion intensities now available at the meson factories, it is feasible to do $(\pi,\pi N)$ coincidence experiments, and the first such experiments have recently been completed.[2-4] Here we will show that simple models of quasielastic scattering are in qualitative agreement with observations when the kinematics is appropriate.

In $(\pi,\pi N)$ experiments π^+/π^- ratios should be predictable if the scattering is indeed quasielastic, i.e., almost the same as free πN scattering. In the impulse approximation (IA), these ratios are trivially related to the free πN cross section ratios. Radiochemistry neutron removal ratios,[5] however, differ substantially from the IA predictions. This can be explained with a simple, semiclassical model[6] which modifies the π^-/π^+ total knockout cross section from the IA value of 3 at the (3,3) resonance. If P is the probability the outgoing nucleon undergoes charge exchange on leaving the nucleus, then[6]

$$R_n=\frac{\sigma(\pi^-,\pi^-n)}{\sigma(\pi^+,\pi^+n+\pi^0p)}=\frac{9-8P}{3+6P}. \tag{1}$$

This formula and its generalization to energies away from the (3,3) resonance have been quite successful in explaining the departure of R_n from the IA for all light nuclei studied[6,7,8] with not unreasonable values of the charge exchange probability ($P\simeq 20\%$).

Subsequently, this model, developed originally for radiochemical measurements which detect the presence of the residual nucleus, was extended to apply to counter experiments which detect the outgoing nucleon[9] or, in coincidence, both the pion and nucleon.[10] In this latter case, let $P_\pm$ be the probability that a neutron struck by a $\pi^\pm$ will emerge as a proton, and let $Q_\pm$ be the probability a struck proton will emerge as a proton. Because the incoming and outgoing fluxes are attenuated by quasielastic scattering, $(P_\pm+Q_\pm)<1$. Then, for example, the proton knockout ratio appropriate for a coincidence experiment is

$$R_p=\frac{\sigma(\pi^+,\pi^+p)}{\sigma(\pi^-,\pi^-p)}=\frac{ZrQ_++NP_+}{ZQ_-+NrP_-}, \tag{2}$$

where r is the ratio of the π^+p to π^-p free cross sections. For an $N=Z$ nucleus, $P_+=P_-\equiv P$, $Q_+=Q_-\equiv Q$. If, near the resonance, $r=9$, then Eq. (2) would reduce in this case to

$$\begin{aligned}R_p&=\frac{9+x}{1+9x}\simeq\frac{9-8P}{1+8P},\\ x&=P/Q,\end{aligned} \tag{3}$$

where the last approximate equality would hold only if $Q\simeq 1-P$. We give that form of the equation only to show the connection with Eq. (1). The denominators differ because the πN charge exchange process does not contribute when an outgoing charged pion is detected.

To calculate the P's and Q's in our semiclassical model, we assume that particles travel in straight line paths except at the point where the πN collision occurs. The assumption of incoherence the leads to simple differential equations for the particle fluxes. Their solution gives the P's and Q's as definite integrals over the nuclear volume. Details are given in Refs. 4, 9, and 10. This procedure is a semiclassical (and far simpler) representation of the distortion of the scattering waves that would be calculated in a distorted-wave impulse approximation (DWIA) approach—such as that outlined in Ref. 1—modified to include an isospin-dependent nucleon optical potential to account for the nucleon charge exchange.

Naive application of Eq. (2) to the recent coincidence data is dangerous, however, and that is the main thrust of this paper. There are a number of points of difference, not well recognized, between coincidence and radiochemistry experiments. We discuss these in Sec. II. With these differences in mind, we then go on to discuss each of the three new experiments[2-4] in some detail in Sec. III. A short summary concludes the paper.

II. DIFFERENCES BETWEEN COINCIDENCE AND RADIOCHEMICAL EXPERIMENTS

If we wish to apply Eq. (1) to the new experiments, we must take note of four simple but essential points which have been somewhat overlooked:

1. Kinematic limitations. If the struck nucleon does not recoil with an energy considerably larger than the minimum removal energy, multiple-step processes will swamp quasielastic scattering. (The NN cross section is large at very low energies.) Also, the Fermi motion of the struck nucleons will always smear the energies of the emerging particles. Hence the detectors must be able to observe particles with energies above and below the nominal quasielastic values.

2. Angular dependence of r. Unlike radiochemistry experiments, counter experiments observe outgoing pions and nucleons emerging at specific angles. Thus one should use *differential* cross section ratios for r. Despite the dominance of the (3,3) phase shift in the total cross sections over a large energy range, interference with other partial waves makes $r(\theta_\pi)$ strongly dependent on the scattering angle. In Fig. 1 we have plotted $r(\theta_\pi)$ for a number of incident pion energies, using a convenient energy-dependent representation of the πN experimental data.[11] There are big deviations from the naive ratio $r = 9$ even at energies quite near the (3,3) resonance. Clearly (3,3) dominance is a good approximation for the total cross section ratio for a wide range of energies, but a bad approximation for the differential cross section ratio at all energies.

3. Energy dependence. Since the nucleon charge exchange cross section $\sigma_{N,ex}$ varies rapidly with energy, so does P. For small values of $\sigma_{N,ex}$,[6]

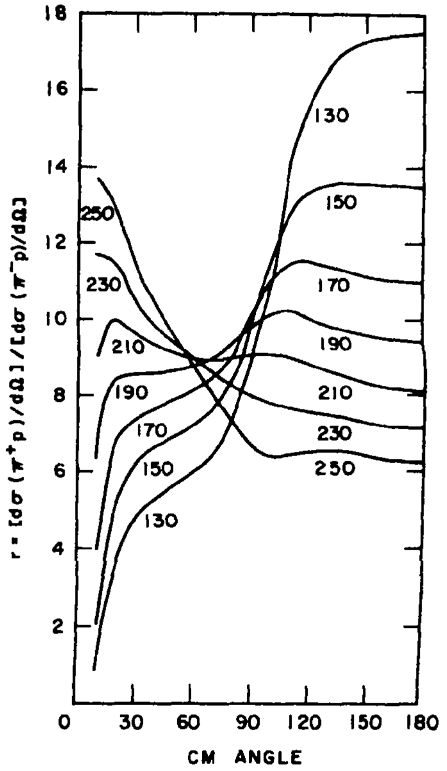

FIG. 1. The ratio of π^+p and π^-p differential cross sections as a function of the center of mass scattering angle. The laboratory energy in MeV is given next to each curve. The corresponding total cross section ratios change gradually from 9.8 at 130 MeV to 7.9 at 250 MeV.

$$x = P/Q \simeq (Z/A)\sigma_{N,ex}\rho d$$

$$\simeq \beta_N (Z/A) T_N^{-1.9} \rho d . \qquad (4)$$

Here d is the mean distance traveled by the nucleon in the nucleus, ρ is the average nuclear density normalized to $\int \rho d\tau = A$, and $\beta_N = 7.06 \times 10^4$ mb $\times$ (MeV)$^{1.9}$ is a parameter representing the somewhat poorly determined Pauli exclusion principle inhibition on the charge exchange process. Its value was determined by fitting (within a restricted range) the ratio R_π in the ^{12}C radiochemistry experiment[5] at 180 MeV. The energy dependence of x (or P) is crucial in understanding the energy variation of R_π in that and other experiments.[5-7] For a coincidence experiment, which has the advantage of a better determination of the nucleon energy T_N, it is also important to take this energy dependence of x into account when comparing predictions with experiments.

4. *Absorption effects*. As noted above, quasielastic scattering reduces the fluxes. Nucleon "absorption" has a particularly large effect on the magnitude of R_p and on its A dependence. If the nucleon absorption cross section $\sigma_{N,\mathrm{abs}}$ is large, d is essentially independent of A, while Z/A decreases with A; hence, by Eq. (4), P also *decreases* with A. On the other hand, if $\sigma_{N,\mathrm{abs}} \simeq 0$, d scales with $A^{1/3}$, and P *increases* with A.

There are some ambiguities regarding this last point which deserve further comment. It is not obvious, for instance, what to use for $\sigma_{N,\mathrm{abs}}$, since small angle scattering is inhibited by the Pauli principle, and large angle np scattering is already counted as charge exchange. In coincidence experiments, absorption refers to scatterings which deflect the outgoing particles from the detectors, i.e., which appreciably increase the angular spread of the outgoing flux over that due to Fermi motion. We elected to write $\sigma_{N,\mathrm{ex}}$ as the integral of the Pauli corrected np cross section from a minimum angle $\pi-\theta_m$ to π, and took over from the radiochemistry experiments the fitted value of β_N. (One could argue for a smaller value.) This gave us a value of θ_m at each nucleon energy T_N. We then integrated the average of the pp and np cross sections from θ_m to $\pi-\theta_m$ to obtain $\sigma_{N,\mathrm{abs}}$. We found a nearly constant $\sigma_{N,\mathrm{abs}} = 35$ mb for T_N between 60 and 90 MeV, the energy range of interest.

In a radiochemistry experiment, on the other hand, nucleon absorption corresponds to NN scatterings which eject an additional nucleon. The energy of an outgoing nucleon is estimated[6] to average about $T_\pi/3$, but it varies over a large range. The slow nucleons, for which the nucleon charge exchange process is very large, have little or no phase space for ejection of a second nucleon. Thus $\sigma_{N,\mathrm{abs}}$ is probably significantly less in a radiochemistry experiment as compared with a coincidence experiment. In Ref. 6 we made the convenient, albeit arbitrary, assumption that $\sigma_{N,\mathrm{abs}} = 0$. As indicated in the previous paragraph, such a choice would be inappropriate for a coincidence experiment.

To conclude these remarks, we note that a DWIA description of the $(\pi,\pi N)$ process using an isospin dependent optical potential would account for nucleon "absorption" in a self-consistent way. However, we now believe that a Lane-type potential (having a term $\vec{t}_\pi \cdot \vec{T}$), such as was used by Hewson,[6] would probably not be sufficient, since *non*isobaric analog charge exchange transitions appear to be very important.[12]

III. DISCUSSION OF THREE RECENT COINCIDENCE EXPERIMENTS

A. $^{12}\mathrm{C}(\pi^\pm,\pi^\pm p)^{11}\mathrm{B}$ with energy resolution

The Virginia-SIN experiment[3] used 180 MeV π^+ and π^- incident on a ^{12}C target. Pions at 100° and 110° were detected in coincidence with protons at 30°. The proton spectrum was centered near 60 MeV, the free proton value of 76 MeV less the 16 MeV proton removal energy. Thus the kinematic requirements (point 1 of Sec. II) are satisfied. Using *all* events, these authors obtained $R_p^A(\mathrm{exp}) = 5.27 \pm 0.45$. (We have taken a weighted average of the data at the two angles.) They note this is less than the IA value obtained from the free πp total cross sections, $R_p(\mathrm{IA}) = r = 9$, but more than the 2.7 they anticipated from Eq. (3), using $r = 9$ and a value of x appropriate to the ^{12}C radiochemistry results.[5]

However, from Fig. 1, for pions which scatter through 100° or 110° in the lab (115° or 125° in the πN c.m. frame), r is 11 at 180 MeV (point 2). Furthermore, the spectrum shows that the average total energy of the final πN system is less than that of the incoming pion by about 35 MeV, suggesting the need to extrapolate the πN cross sections off-shell. Since the final pion and nucleon energies are measured, it is reasonable to evaluate the cross sections using the "final energy prescription", i.e., at $180-35=145$ MeV; then $r=14$. Also, as mentioned above, in a radiochemistry experiment $\langle T_N \rangle \simeq T_\pi/3$, or 60 MeV in the present case. This is somewhat less than the 76 MeV peak quasielastic energy (point 3). Scaling the radiochemistry result according to Eq. (4) gives somewhat larger predictions, $R_p = 3.6$ ($r=9$) or $R_p = 4.2$ ($r=14$).

To study the effects of absorption (point 4), we must go beyond scaling arguments and calculate P and Q. We did this in our semiclassical model using the code QUASEX written by Varghese.[10] With $r=14$ and $\sigma_{N,\mathrm{abs}} = 35$ mb, we obtained $R_p^A(\mathrm{calc}) = 6.0$, in good agreement with $R_p^A(\mathrm{exp})$.

Ellis *et al.* also reported separate values of R_p for those events leaving the residual nucleus in relatively low states of excitation (<10 MeV) or in higher energy states:

$$R_p^L(\mathrm{exp}) = 14.0 \pm 2.6, \quad R_p^H(\mathrm{exp}) = 2.80 \pm 0.35 .$$

The first of these numbers is surprisingly large. However, proton energies in the R_p^L data average about 15 MeV higher than in R_p^A, and energies in R_p^H average 15 MeV lower. With nucleon energies of 76 ± 15 MeV, we find using QUASEX,

$$R_p^L(\mathrm{calc}) = 7.1, \quad R_p^H(\mathrm{calc}) = 4.8 .$$

Our result for R_p^H is reasonable, but R_p^L is still too small. Note that even a small value of P can greatly reduce the ratio R_p from $r = 14$, since the product rP occurs in the denominator of Eq. (2).

B. $(\pi^\pm,\pi^\pm p)$ on ^{27}Al in coincidence with nuclear γ rays

The Utah-Florida-LASL experiment[3] involved 190 MeV $\pi^\pm$ incident on ^{27}Al, and detected pions or protons at 35° in coincidence with a gamma ray. Free kinematics yields a proton energy at this angle of 74 MeV, very close to that in Ellis *et al.*[2] The observed proton spectrum is centered slightly *above* this energy, the part below 40 MeV being cut off. Thus the kinematic conditions for quasielastic scattering are moderately well satisfied when the *proton* is detected. For a proton in coincidence with the ^{26}Mg(I → 0) gamma ray, $R_p(\text{exp}) = 5.0 \pm 1.0$. Using $r = 11$ and $\sigma_{N,\text{abs}} = 35$ mb, we obtained with QUASEX $R_p = 5.3$, which agrees very well.

When a *pion* is detected at 35°, free kinematics implies a nucleon recoil energy of only 15 MeV, not much more than the binding energy. Hence the assumption of quasielastic scattering is likely to fail (point 1). Here coincidence with ^{26}Mg(I → 0) gamma rays gives $R_p(\text{exp}) = 0.93 \pm 0.14$, which would require in Eq. (1) that $P/Q \simeq 1$, a rather extreme value. By contrast, the π^-/π^+ neutron removal ratio obtained with coincidence with ^{26}Al(II → 0) gamma rays is $R_n(\text{exp}) = 3.23 \pm 0.82$, which would require a quite different P/Q, if the quasielastic scattering assumption and Eq. (2) were valid.

Further internal evidence exists for the non-quasielastic nature of the π-coincidence data. The ratio of the laboratory frame free π^+p cross section for a π^+ scattered at 35° to that for a proton recoiling at 35° (the π^+ going off at 95°) is 3.5. In coincidence with the ^{26}Mg(I → 0) gammas, the ratio of the 35° π^+ and p cross sections is 0.38 ± 0.04, an order of magnitude smaller. To make another comparison, let $\sigma_p(\pi^+)$ be the cross section for proton removal when a π^+ is detected, etc. From the ^{26}Mg and ^{26}Al data, $\sigma_p(\pi^+)/\sigma_n(\pi^-) = 5.1 \pm 0.7$, which is comparable to the spectroscopic factor ratio[13]; however, $\sigma_p(\pi^-)/\sigma_n(\pi^+) = 18.3 \pm 4.7$. In the impulse approximation, neglecting Coulomb effects, both ratios are the same.

Clearly the impulse approximation and quasielastic scattering are not relevant when pions are detected at such forward angles. Similar conclusions have been reached concerning small angle (π^+,π^0) data.[14]

C. ^{27}Al$(\pi^\pm,\pi^\pm p)X$ and ^{208}Pb$(\pi^\pm,\pi^\pm p)X$ above the resonance

The Oregon State-Oregon-LASL-Florida-Texas experiment[4] had 255 MeV π^+ and π^- incident on ^{27}Al and ^{208}Pb targets. In their paper, they also report a preliminary ^{12}C result from another collaboration. For protons at 55° in coincidence with pions at 50°, they give

$$R_p(C) = 7.9 \pm 1.0, \quad R_p(\text{Al}) = 6.9 \pm 0.7),$$

$$R_p(\text{Pb}) = 4.6 \pm 0.5 .$$

Similar results were obtained with $\theta_p = 64°$ and $\theta_\pi = 37°$ for Al and Pb.

Using QUASEX, they were able to reproduce the measured R_p values if they assumed $\sigma_{N,\text{abs}} = 0$ and an outgoing proton momentum of 650 MeV/c (204 MeV). However, if one uses the quasifree proton energies (50 MeV at $\theta_p = 55°$, 28 MeV at 64°), the calculated ratios are much too low, since $\sigma_{N,\text{ex}}$ and hence P/Q increase by large factors. Furthermore, with reasonable values of $\sigma_{N,\text{abs}}$, the A dependence reverses, with R_p smallest for carbon. Thus, with $r = 9$ (seen from Fig. 1 to correspond to this kinematical situation) and with $\sigma_{N,\text{abs}} = 35$ mb we obtained for protons at 55°,

$$R_p(C) = 4.2, \quad R_p(\text{Al}) = 4.2, \quad R_p(\text{Pb}) = 4.5 .$$

One possible explanation for this disagreement between the calculations and the data is provided by the published spectra for Al. They start at 50 MeV and have tails extending beyond 125 MeV. Allowing for the 8 MeV binding energies, the quasielastic peaks should appear at about 42 and 20 MeV, both below the experimental cutoff. On the other hand, the fastest protons detected can be produced in quasielastic collisions only if the struck proton has a momentum greater than the Fermi momentum. Thus most of the quasielastic events are not observed, while some events far from the quasielastic peak are. Perhaps we should not be too surprised at the inapplicability of the quasielastic picture for this choice of kinematics and geometry.

IV. CONCLUSION

To summarize, we see that the energy dependence of the nucleon charge exchange cross section, the angular dependence of the impulse approximation ratio, and the absorption of nucleons due to quasielastic processes are all significant in predicting $(\pi,\pi N)$ ratios. Using plausible but uncertain estimates of various parameters, we can account for most of the data involving nucleons with enough energy for quasielastic scattering to apply. An exception is R_p^L of Ref. 2. As in the data of Ref. 4, this ratio involves protons with energies extending well above the nominal quasielastic value. Even with this taken into account, however, the ratio preducted by Eq. (1) is substantially smaller than observed. A large correction to the free πN amplitude may well be required to achieve agreement with the experimental data, but based on the work of Ref. 1, a large off-shell correction is not expected.

The general features of quasielastic $(\pi,\pi N)$ scattering appear to be understood, but the four points discussed here can only be sorted out by experiments with good energy resolution covering more angles and incident energies. It is also desirable now to carry out quantum mechanical calculations using DWBA codes which include *pn* charge exchange potentials.

We wish to thank D. C. Dodder for his pion-nucleon cross sections, P. Varghese for the QUASEX code, and R. J. Ellis, V. G. Lind, C. Wilkin, and K. O. H. Ziock for discussions. This research was supported by the Department of Energy (R.R.S.) and the National Science Foundation (M.M.S.).

---

[1] D. F. Jackson, A. A. Ioannides, and A. W. Thomas, Nucl. Phys. A322, 493 (1979).

[2] R. J. Ellis *et al.*, *Meson-Nuclear Physics—1979*, Proceedings of the Second International Topical Conference on Meson-Nuclear Physics, Houston, 1979, edited by E. V. Hungerford III (AIP, New York, 1979), p. 274; H. J. Ziock *et al.*, Phys. Rev. Lett. 43, 1919 (1979). In this paper we use the experimental values as reported in the latter references.

[3] V. G. Lind *et al.*, Phys. Rev. Lett. 41, 1023 (1978); O. H. Otteson *et al.*, *Meson-Nuclear Physics—1979*, Proceedings of the Second International Conference on Meson-Nuclear Physics, Houston, 1979, edited by E. V. Hungerford III (AIP, New York, 1979), p. 282.

[4] L. W. Swenson *et al.*, Phys. Rev. Lett. 40, 10 (1978); T. C. Sharma *et al.*, Nucl. Phys. A333, 461 (1980).

[5] B. F. Dropesky *et al.*, Phys. Rev. Lett. 34, 821 (1975); Phys. Rev. C 20, 1844 (1979); L. H. Batist *et al.*, Nucl. Phys. A254, 480 (1975).

[6] M. M. Sternheim and R. R. Silbar, Phys. Rev. Lett. 34, 824 (1975). See also P. W. Hewson, Nucl. Phys. A133, 659 (1969).

[7] N. P. Jacob and S. S. Markowitz, Phys. Rev. C 13, 754 (1976).

[8] S. B. Kaufman, E. P. Steinberg, and G. W. Butler, Phys. Rev. C 20, 248 (1979).

[9] P. Varghese, R. R. Silbar, and M. M. Sternheim, Phys. Rev. C 14, 1893 (1976).

[10] P. Varghese, Ph.D. thesis, University of Oregon, 1978 (LASL Report No. LA-7453-T, 1978). A short description of the model is included in Ref. 4.

[11] The πN differential cross sections were obtained from D. C. Dodder's energy-dependent *R*-matrix analysis (private communication).

[12] R. R. Silbar, J. N. Ginocchio, and M. M. Sternheim, Phys. Rev. C 18, 2785 (1978).

[13] P. M. Endt and C. van der Leun, Nucl. Phys. A310, 1 (1978).

[14] T. Bowles *et al.*, Phys. Rev. Lett. 40, 97 (1978).

PHYSICAL REVIEW C VOLUME 21, NUMBER 5 MAY 1980

Analysis of quasi-free scattering data in the impulse approximation

Albert W. Stetz
Physics Department, Oregon State University, Corvallis, Oregon 97331

(Received 5 November 1979)

We propose a set of variables to be used in place of the customary energies and angles in the analysis of quasi-free scattering data. In terms of these variables one can reduce the usual fivefold differential cross section to a threefold differential including the effects of experimental acceptance without resorting to Monte Carlo techniques. In this form the dependence of the data on nuclear and two-particle variables is clearly separated. Finally, two simple tests of the impulse approximation, the Treiman-Yang test and the Chew-Low extrapolation, can be applied directly to the data in particularly simple form.

[NUCLEAR REACTIONS Impulse approximation, relativistic analysis.]

I. INTRODUCTION

Quasi-free scattering data are usually presented in terms of the fivefold differential

$$\frac{d^3\sigma}{d\Omega_0 d\Omega_1 dT}\,. \tag{1.1}$$

Ω_0 and Ω_1 refer to the laboratory solid angles of the two detected particles, and T is the kinetic energy of one of them. Since it is usually out of the question to populate a five dimensional space with meaningful data, some reduction in dimensionality must be carried out. This is done, in effect, by comparing the data with the results of the impulse approximation[1] in the form

$$\frac{d^3\sigma}{d\Omega_0 d\Omega_1 dT} = N\left(\frac{d\sigma}{d\Omega}\right)^{fr} G(\vec{Q})\,, \tag{1.2}$$

where N is a kinematic factor, $(d\sigma/d\Omega)^{fr}$ is the differential cross section for the free scattering of particles 0 and 1, and $G(\vec{Q})$ is a function of the nuclear recoil momentum $\vec{Q}$ containing all the specifically nuclear details. This reduces the problem of analyzing a fivefold distribution to that of analyzing the function G of at most three independent parameters.

Common as this procedure is, it suffers from two serious inconveniences: (a) The significance of the data does not become apparent until after a detailed theoretical calculation has been done; (b) since the relationship between $\vec{Q}$ and the laboratory variables is quite complicated, it is difficult to interpret the behavior of the cross section in terms of specific physical processes.

Some experimenters have tried to circumvent these difficulties by presenting their cross sections in terms of Q and θ_Q.[2] When this is done, however, a new difficulty arises; the limitations in momentum and solid angle acceptance of the experimental apparatus impose complicated boundaries in the new variable space. (One can get a feeling for the complexity of this problem by looking at Fig. 5 in Ref. 2.) The dimensionality of the cross section can only be reduced with the help of a detailed acceptance calculation. These calculations, in addition to being difficult to check, introduce an element of uncertainty into the interpretation of the data. Any acceptance calculation must make some assumptions about the variation of the cross section as a function of those variables that are being integrated away. Usually it is assumed that the cross section is independent of some pair of azimuthal angles defined in the laboratory system. The physical content of this assumption (in terms of the basic reaction mechanisms) and its range of validity, however, are far from clear.

In Sec. II we point out an alternate procedure, which avoids most of these difficulties. Rather than analyzing the data using the directly measured variables, we recommend using a set of derived variables in terms of which the impulse approximation takes a particularly simple form. We then turn to the general subject of calculating experimental acceptance, and in Sec. V we show a way in which the acceptance of most quasi-free scattering experiments can be written in closed form based on the behavior of the cross section in the impulse approximation. Finally, in Sec. VI we formulate in terms of the proposed set of variables two well known tests of the impulse approximation, the Chew-Low extrapolation scheme and the Trieman-Yang test for single-particle exchange.

II. THE IMPULSE APPROXIMATION

Consider a reaction in which a particle of mass m_0 scatters from a nucleus of mass M_0 knocking out a particle of mass m_1 and leaving behind a

© 1980 The American Physical Society

nucleus in a discrete state of mass M. We represent this with the four-momenta

$$p_0 + P = Q + q_0 + q_1 , \tag{2.1}$$

where p_0 and q_0 are the momenta of the projectile before and after scattering respectively, P and Q are the initial and final nuclear momenta, and q_1 is the momentum of the particle that is scattered from the nucleus. (See Fig. 1 for a summary of the notation used.) Where no confusion can occur we will use these symbols to refer to the particles themselves as well as their four-momenta.

In the impulse approximation the reaction (2.1) is presumed to proceed by means of the exchange of a single intermediate particle with momentum $p_1 = P - Q = q_0 + q_1 - p_0$ as shown in Fig. 2. One can readily write the amplitude for this process using Feynman's rules. If the intermediate particle spin is zero, the amplitude corresponding to the graph of Fig. 1 can be written

$$M = \frac{\Gamma_N(P,Q,p_1)\Gamma_p(p_0,p_1,q_0,q_1)}{p_1^2 - m_1^2 + i\epsilon} , \tag{2.2}$$

where $\Gamma_N(P,Q,p_1)$ is the vertex function for the reaction $P \to Q + p_1$ with particles P and Q on their respective mass shells, and $\Gamma_p(p_0,p_1,q_0,q_1)$ is the vertex function for the reaction $p_0 + p_1 \to q_0 + q_1$ in which p_0, q_0, and q_1 have their physical masses.

The function $\Gamma_N(P,Q,p_1)$ can depend on at most one Lorentz scalar invariant (in addition to the physical masses), which we will call t:

$$t \equiv p_1^2 = (P-Q)^2 . \tag{2.3}$$

The "four-tailed" function $\Gamma_p(p_0,p_1,q_0,q_1)$ is in general a function of three scalar invariants: t, the invariant mass squared of particle p_1, and two other variables, which we define as

$$s \equiv (P + p_0 - Q)^2 = (q_0 + q_1)^2 , \tag{2.4}$$

the total energy squared, and

$$u = (p_0 - q_0)^2 , \tag{2.5}$$

the momentum transfer. The impulse approximation, however, usually involves another assumption in addition to those implicit in Fig. 2, that is, that the two-particle scattering amplitude can be evaluated with all four legs on their mass shells. This means that $\Gamma_p(p_0,p_1,q_0,q_1)$ can be taken as a function of only two independent variables, s and u. We may summarize this by writing

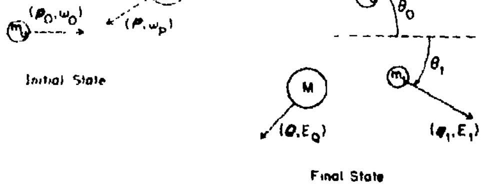

FIG. 1. The notation used in the text.

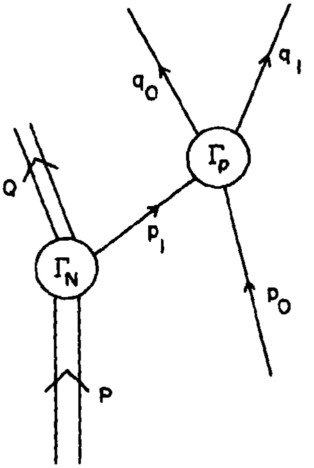

FIG. 2. Feynman diagram for quasi-free scattering in the impulse approximation.

$$M_N(t) = \frac{\Gamma_N(P,Q,p_1)}{p_1^2 - m_1^2 + i\epsilon} \tag{2.6}$$

and

$$M_p(s,u) \equiv \Gamma_p(p_1,p_0,q_0,q_1) , \tag{2.7}$$

with the understanding that whenever p_1^2 appears in Eq. (2.7) it is replaced with m_1^2 to obtain M_p. Equation (2.2) then becomes

$$M = M_N(t) M_p(s,u) . \tag{2.8}$$

Equation (2.8) illustrates the simplifying features of the impulse approximation. First, the amplitude depends on only three independent kinematic variables rather than the five required to completely specify the final state; and second, the amplitude factors into a part corresponding to two-particle elastic scattering (which can be treated phenomenologically) and a term containing the nuclear part of the interaction alone. Furthermore, this unknown nuclear amplitude, M_N, is a function of only one variable. If M_p is regarded as a known function calculated, say, from experimental phase shifts, then at least to the extent that the impulse approximation is valid, all quasi-free data for a given set of nuclear states should be reducible to a universal curve in one parameter, the invariant mass of the exchanged particle. Unfortunately, the usual practice of presenting data in terms of the laboratory energies and angles deeply obscures this underlying simplicity. The reasons for this will emerge presently. The remedy, of course, is to present data in terms of t, u, and s. The choice of the remaining two "superfluous" variables, however, is not obvious. It is tied up with the problem of calculating the acceptance of the experimental apparatus, to which we turn in Sec. III.

If the exchanged particle p_1 has nonzero spin, Eqs. (2.2) and (2.6) through (2.8) must be modified. The two amplitudes M_N and M_p become sums over form factors (which depend only on t, u, and s) multiplied by spin and direction-dependent terms. Equation (2.8) must be modified to include a summation over the polarization of the exchanged particle. It is well known, however, that if the exchanged particle has spin $\frac{1}{2}$ and the target nucleus is unpolarized, the combined effect of these sums is to produce a cross section that factors into nuclear and two-body terms as if the fundamental amplitude were of the form (2.8).[1] Since this is by far the most important case and since we are concerned here with the kinematics of quasi-free scattering rather than its detailed dynamics, we will not display the spin structure of these amplitudes. This has been done for arbitrary spin by several authors.[3,4] We will only mention in passing where the complications of higher spin affect our analysis.

Finally we should point out that the impulse approximation in the form (2.8) is not strictly valid if there are multiple scattering or distortion effects. Equation (2.8) is still a useful starting point for discussing the analysis of quasi-free scattering data, however, for several reasons: (a) If the impulse approximation is to be meaningful, the distortions must represent corrections that are in some sense "small." It is then still potentially useful to present data in a way that makes the "zeroth-order" symmetries of the interaction apparent. (b) It is frequently interesting to know the way and the extent to which the impulse approximation is violated. The largest effect is usually a constant renormalization of the cross section, which will have no effect on the analysis presented here; but there are other, more subtle effects that appear as deviations from the functional form predicted by (2.8). The mechanisms responsible for these deviations can often be inferred from the variables in which they appear. Some examples are given in subsequent sections.

III. ON CALCULATING THE ACCEPTANCE OF EXPERIMENTAL APPARATUS

It is frequently the case in studying multiparticle reactions that some set of kinematic variables are required to completely specify a reaction, while the physical interest centers about some subset of them. For example, in the simplest case of unpolarized elastic scattering, two variables are required to specify the final state kinematics. These are usually chosen as the center of mass scattering angle and the azimuthal orientation of the scattering plane about the beam axis. The scattering angle is an "interesting" variable in the sense that the object of an elastic scattering experiment is to measure the cross section *as a function of* $\theta_{\text{c.m.}}$. The azimuthal angle ϕ is "superfluous" since the cross section is expected on fundamental grounds to be axially uniform. We will say that a variable is interesting in this special sense if the object of the analysis is to extract some information from the behavior of the cross section as a function of this variable. Otherwise we will say that it is superfluous. In more complicated cases the decision to regard a variable as interesting or superfluous is often a subjective decision based on the purpose of the experiment, the level of sophistication of the theory, and the completeness of the data. Nevertheless, it is a decision that is always made, either explicitly or implicitly, when presenting data in terms of fewer variables than are required to completely specify the final state.

In the case of elastic scattering the superfluous variable enters into the cross section in a trivial way; and the experimenter usually tabulates his data as $d\sigma/d\Omega$ in spite of the fact that the cross section does not depend on ϕ. In other words, the cross section is kept in its original (twofold) dimensionality, and the distinction between interesting and superfluous variables is only implicit. In more complicated cases, however, a variable may be superfluous and still affect the magnitude of the cross section or the acceptance of the experimental apparatus or both. For practical reasons one usually integrates the data over the superfluous variables and compares it with theoretical cross sections that have been similarly reduced in dimensionality. This is clearly the case in quasi-free scattering, but we will discuss the problem in more generality first and later specialize it to reactions of the form (2.1).

Let us say that of n independent kinematic variables in a given experiment $x_1 \cdots x_{n_1}$ are interesting in the sense defined above and $y_1 \cdots y_{n_2}$ are superfluous. We wish to compare the data with a reduced theoretical cross section

$$\frac{d^{n_1}\sigma(\mathrm{th})}{dx_1\cdots dx_{n_1}}=\int_R \frac{d^n\sigma(\mathrm{th})}{dx_1\cdots dx_{n_1}dv_1\cdots dy_{n_2}}\,dv_1\cdots dy_{n_2} \tag{3.1}$$

formed by integrating the superfluous variables over the region R, the total phase space available to them. In reducing the measured cross section, however, two new problems arise. First, we are not able to evaluate the integral in (3.1) over the entire region R, but only over some smaller region, say E, limited by acceptance of the apparatus and the cuts placed on the data; and second, even within E the probability of detecting an event with a given set of x's and v's may be less than unity. In other words, when the experimenter bins his data in the n_1 interesting variables he is in effect evaluating the integral

$$\frac{d^{n_1}\sigma(\mathrm{ex})}{dx_1\cdots dx_{n_1}}=\int_{E(x)} \frac{d^n\sigma\epsilon(x,y)}{dx_1\cdots dx_{n_1}dv_1\cdots dy_{n_2}}\,dy_1\cdots dv_{n_2}, \tag{3.2}$$

where $d^n\sigma$ is the "real" cross section, $d^{n_1}\sigma(\mathrm{ex})$ is the uncorrected observed cross section in n_1 variables, and $\epsilon(x,y)$ is the efficiency for detecting a particle with the set of variables (x,v). The experimenter confronts the theory either by folding the experimental acceptance and efficiency into the theoretical expression for the cross section or by correcting his data. In the first case he calculates the modified theoretical cross section given by

$$\frac{d^{n_1}\sigma(\mathrm{mod})}{dx_1\cdots dx_{n_1}}=\int_{E(x)} \frac{d^n\sigma(\mathrm{th})\epsilon(x,v)}{dx_1\cdots dx_{n_1}dv_1\cdots dv_{n_2}}\,dv_1\cdots dv_{n_2}. \tag{3.3}$$

In the second case he corrects his data by multiplying it by a weighting factor $w(x)$ where

$$w(x)=\frac{\displaystyle\int_R \frac{d^n\sigma(\mathrm{th})}{dx_1\cdots dx_{n_1}dv_1\cdots dy_{n_2}}\,dv_1\cdots dv_{n_2}}{\displaystyle\int_{E(x)} \frac{d^n\sigma(\mathrm{th})}{dx_1\cdots dx_{n_1}dv_1\cdots dy_{n_2}}\,\epsilon(x,v)dv_1\cdots dv_{n_2}}. \tag{3.4}$$

In either case it is necessary to evaluate a difficult integral over E. This is the integral that is evaluated, in effect, in an efficiency calculation. Usually it must be evaluated with Monte Carlo techniques.

In this light it is evident why Eq. (1.1) represents an awkward choice of variables. Apart from one azimuthal angle there are no superfluous variables, or to put it more accurately, the interesting and superfluous variables are mixed so that an explicit separation as in Eqs. (3.1) to (3.4) is not possible. The origin of this difficulty and its solution are discussed in Sec. IV.

IV. CALCULATING THE CROSS SECTION

In order to disentangle the interesting and superfluous variables we must re-evaluate the cross section for quasi-free scattering in a different coordinate system from the laboratory frame used in Eq. (1.1). In terms of the momenta illustrated in Fig. 1 the invariant differential cross section has the form

$$\begin{aligned} d^3\sigma={}&\frac{(2\pi)^2\mathfrak{F}|M|^2}{(2\omega_0)(2\omega_p)}\frac{d\vec{Q}}{2E_Q}\frac{d\vec{q}_0}{2E_0}\frac{d\vec{q}_1}{2E_1}\\ &\times\delta(\vec{Q}+\vec{q}_0+\vec{q}_0-\vec{P}-\vec{p}_0)\\ &\times\delta(E_Q+E_0+E_1-\omega_0-\omega_p). \end{aligned} \tag{4.1}$$

The ω's denote the total energies of the particles in the initial state and the E's represent the total energies of the respective particles in the final state. The incident flux factor $\mathfrak{F}$ for (4.1) in a general frame is

$$\mathfrak{F}=\omega_0\omega_p[(p_{0\mu}p_\mu)^2-m_0{}^2M_0{}^2]^{-1/2}. \tag{4.2}$$

Let us count the variables that enter into a description of the reaction. The three final state vector momenta are specified by nine coordinates, but the momentum conserving δ function reduces this number to six. In most experiments the energies E_0 and E_1 are measured so that the total recoil energy E_Q and hence the invariant mass of the recoil nucleus can be calculated. One is usually interested in reactions leading to a definite nuclear state so that the data, which normally cover a wide continuum in M, are selected to correspond to some definite mass. For this "cut" data the energy conserving δ function in (4.1) reduces the number of independent variables to five.

In order to preserve the simplicity inherent in the impulse approximation we begin by evaluating (4.1) in the center of mass system of the $p_0+p_1\rightarrow q_0+q_1$ reaction, that is, in a system where

$$R\equiv P-Q+p_0 \tag{4.3}$$

lies along the time axis. (See Fig. 3.) The phase space element becomes

$$d^3\rho=\frac{d\vec{Q}}{2E_Q}\frac{d\vec{q}_0}{2E_0}\frac{d\vec{q}_1}{2E_1}\delta^{(4)}(q_0+q_1-R). \tag{4.4}$$

The last three factors constitute ordinary two-body phase space with total four-momentum R. As is well known

$$d^2\rho_2=\frac{d\phi du}{8\sqrt{s}\,|\vec{q}|}, \tag{4.5}$$

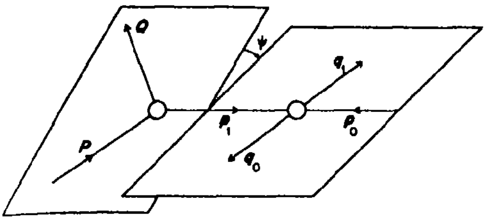

FIG. 3. Quasi-free scattering in the center of mass system.

where $d^2\rho_2$ is the two-body phase space element and ψ is the azimuthal coordinate of the scattering plane, u is the invariant momentum transfer squared from (2.5), $|\vec{q}|$ is the absolute magnitude of the center of mass three-momentum given by

$$|\vec{q}|^2=\frac{[s-(m_0+m_1)^2][s-(m_0-m_1)^2]}{4s}\,, \tag{4.6}$$

and s is the total center of mass energy squared from (2.4).

The Lorentz transformation from the laboratory to this center of mass frame is defined by the relative velocity of the two systems

$$\vec{\beta}=\frac{\vec{q}_0{}'+\vec{q}_1{}'}{E_0{}'+E_1{}'}\,; \tag{4.7}$$

the primes on this and subsequent expressions indicate that the variables are taken in the laboratory system. It is evident that $\vec{\beta}$ is not in general parallel to the beam axis, and, furthermore, its magnitude and direction depend on the *final state* momenta. This is the source of the kinematic complexity of quasi-free scattering. Each event defines its own c.m. system; or to put it another way, changing any one laboratory variable (with the exception of one allover azimuthal angle) changes all of the center of mass momenta shown in Fig. 3. This difficulty can be partly circumvented by using the Lorentz invariant variables u and s to describe the two-body scattering. The superfluous variables still present a problem, however. For example, the azimuthal variable ψ in Eq. (4.5) is usually defined as a rotation of the scattering plane about an axis taken along the direction of the incident particles in the c.m. frame. The Lorentz transformation to the laboratory, however, rotates this axis, so the azimuthal distribution of events in the laboratory will differ from that in the center of mass frame in a complicated way depending on $\vec{\beta}$. It will be argued later on that the distribution of events in the c.m. system should be axially uniform in most cases of interest, so this complexity only affects the calculation of the experimental acceptance. We will return to this problem in Sec. V.

The remaining factor in (4.4), $d\vec{Q}/2E_Q$, is separately Lorentz invariant, and it is more convenient to evaluate it in the laboratory. We first introduce the polar coordinate system

$$\frac{d\vec{Q}}{2E_Q}=\frac{Q^2dQ}{2E_Q}\,d(\cos\theta_Q)d\phi\,, \tag{4.8}$$

where θ_Q is the polar, and ϕ the azimuthal angle. Normally one would choose the incident beam direction as the polar axis; however, the Lorentz transformation between the laboratory and center of mass frames is usually not parallel to the beam, so that ϕ would transform in a complicated way. It turns out to be more convenient to take the direction of $\vec{\beta}$ as the polar axis as shown in Fig. 4. Then ϕ retains the same value in both systems. Furthermore, in the center of mass system

$$\vec{P}=-M_0\gamma\vec{\beta} \tag{4.9}$$

[as usual, $\gamma=(1-\beta^2)^{-1/2}$], so that ϕ represents the azimuthal orientation of the scattering event around an axis parallel to the momentum of the incident target nucleus. Since quasi-free scattering experiments are invariably done on unpolarized nuclear targets, there is no preferred direction around this axis, and the distribution of events must be axially uniform.

The remaining variables in Eq. (4.8) are more conveniently expressed in terms of two Lorentz scalars, s and t, defined previously. Then

$$\frac{d\vec{Q}}{2E_Q}=\frac{Q^2}{2E_Q}\,\frac{\partial(Q,\cos\theta_Q)}{\partial(s,t)}\,dsdtd\phi\,, \tag{4.10}$$

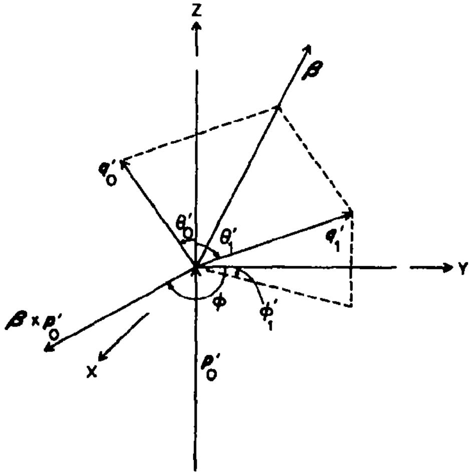

FIG. 4. The definition of ϕ in terms of laboratory coordinates.

where the Jacobian

$$\frac{Q^2}{2E_Q}\,\frac{\partial(Q,\cos\theta_Q)}{\partial(s,t)}=\frac{1}{8M_0\,|\vec{q}_0{}'+\vec{q}_1{}'|} \qquad (4.11)$$

must be separately Lorentz invariant (since it connects two Lorentz invariant volume elements). It has a particularly simple form when expressed in terms of the laboratory momenta, but can be written as a function of scalar invariants using Eqs. (A1) and (A2) from the Appendix. Finally combining (4.4), (4.5), (4.10), and (4.11) yields

$$d^5\rho=\frac{dt\,ds\,du\,d\psi\,d\phi}{64M_0\sqrt{s}\,|\vec{q}\,|\,|\vec{q}_0{}'+\vec{q}_1{}'|}\,. \qquad (4.12)$$

The flux factor appearing in (4.2) is

$$\frac{\mathfrak{F}}{\omega_0\omega_p}=\frac{1}{M_0\,|\vec{p}_0{}'|}$$

in the lab. Hence,

$$d^5\sigma=\frac{\pi^2}{64}\,|M_N(t)M_p(s,u)|^2\,\frac{dt\,ds\,du\,d\phi\,d\psi}{M_0{}^2\,|\vec{q}\,|\sqrt{s}\,|\vec{p}_0{}'|\,|\vec{q}_0{}'+\vec{q}_1{}'|}\,. \qquad (4.13)$$

The amplitude M_p represents the scattering event $p_0+p_1\to q_0+q_1$ in terms of two invariants, s the total energy and u the momentum transfer squared. In the spirit of the impulse approximation we replace this with the elastic scattering amplitude for a physical particle with mass m_1 and momentum $\vec{P}-\vec{Q}$. With the same normalization used in (4.1),

$$\frac{d\sigma}{du}(p_0p_1\to q_0q_1)=\frac{\pi^3}{4s\,|\vec{q}\,|^2}\,|M_p(s,u)|^2\,. \qquad (4.14)$$

With this substitution (4.13) becomes

$$d^5\sigma=\frac{\sqrt{s}\,|\vec{q}\,|}{16\pi M_0{}^2\,|\vec{p}_0{}'|\,|\vec{q}_0{}'+\vec{q}_1{}'|}\left(\frac{d\sigma}{du}\right)^{fr}|M_N(t)|^2\,.$$
$$\times\,dt\,ds\,du\,d\phi\,d\psi\,. \qquad (4.15)$$

In deriving (4.15) we have implicitly assumed that the exchanged particle was spinless; however, as was stated in connection with Eq. (2.8), the result is still valid for spin $\frac{1}{2}$ if the target nucleus is unpolarized. In this case $(d\sigma/du)^{fr}$ is the cross section for the scattering of the incident beam particle from a free, unpolarized nucleon target evaluated at those values of u and s given by Eqs. (2.4) and (2.5).

Equation (4.15) is the point of departure for subsequent analysis. The variables in the differential fall into three categories: t, which controls the specifically nuclear part of the interaction; u and s, which determine the elastic scattering cross section; and ψ and ϕ, which will be integrated out reducing (4.15) to a threefold differential. The kinematic factor can be expressed entirely in terms of the "interesting" variables (see Appendix) and is independent of ϕ and ψ. The fact that the cross section in Eq. (4.15) is independent of ϕ is due to our assumption that the nuclear target is unpolarized. The fact that it is independent of ψ is a consequence of the impulse approximation. This is just a restatement of the familiar Trieman-Yang criterion for one particle exchange, which is discussed further in Sec. VI. But there are several ways in which Eq. (4.15) can fail to represent the actual cross section, and these failures can induce ψ dependence which potentially carries information about the reaction mechanism.

The first of these interesting failures can come about if the exchanged particle p_1 is a nuclear cluster with spin $j\geq 1$. In this case the interference among the various terms in the sum over the polarization of the exchanged particle prevents the factorization of the two-particle cross section as in (4.15). The way in which ψ then enters into the expression for the cross section depends on the spin of the incident particle and the orbital state of the target cluster. A catalog of possibilities has been worked out by Shapiro *et al.*,[3] but so far these effects have not been investigated experimentally.

The second interesting failure comes about when the simple impulse approximation shown in Fig. 2 is violated. This, of course, is always the case when rescattering effects are present. However, it is well known that when these effects are treated in the usual distorted wave approximation the net result is only to modify the allover normalization and the effective momentum distribution of the target nucleon or nuclear cluster in the nucleus. In our terminology Eq. (4.15) is still valid if the nuclear amplitude M_N is regarded as a function of u and s as well as t. If spin-dependent distortions are included, on the other hand, this simple result cannot be proved, Eq. (4.15) is no longer valid, and the cross section becomes dependent on ψ. These spin-orbit distortions are usually neglected but have been analyzed recently by Jackson.[5] It is not currently known whether or not they are important.

For the usual coplanar, quasi-free scattering experiment these considerations are probably irrelevant. As will be shown later, the coplanar geometry tends to suppress any ψ dependence inherent in the cross section. This is another way of stating the commonplace that Trieman-Yang tests must be done with noncoplanar apparatus. In Sec. V we will study the acceptance integrals for quasi-free experiments assuming (4.15) is valid. The results should be true for any geometry subject to the two exceptions noted above, and should be accurate for coplanar geometry regardless of whether the cross section is strictly ψ independent.

V. CALCULATING THE ACCEPTANCE

If it were not for the limited acceptance of experimental apparatus we could simply eliminate ϕ and ψ in Eq. (4.15) by integrating them over 2π rad. However, to compare theory with real data we must integrate ϕ and ψ over the limits imposed by the apparatus (with t, u, and s held constant) as shown in Eqs. (3.3) and (3.4). Furthermore, Eq. (4.15) is only valid in the center of mass system (since d^2p_2 was evaluated in this system and ψ is not invariant), and even the simplest limits in the laboratory become very complicated when transformed into the center of mass. For this reason we evaluate the acceptance integrals in the laboratory system (where the limits are trivial) in terms of the measured azimuthal angles, ϕ_0' and ϕ_1'. The acceptance, $e(t,u,s)$, is defined as follows:

$$e(t,u,s)=\frac{\int_E \frac{d^5\sigma}{dt\,du\,ds\,d\phi\,d\psi}\frac{\partial(\phi,\psi)}{\partial(\phi_0',\phi_1')}\epsilon(t,u,s)\,d\phi_0'\,d\phi_1'}{\int_R \frac{d^5\sigma}{dt\,du\,ds\,d\phi\,d\psi}\,d\phi\,d\psi}\,. \tag{5.1}$$

In most experiments the detection efficiency ϵ is a slowly varying function of energy, in other words not a function of the azimuthal variables. Factoring it out of the integral and using Eq. (4.15) for the cross section yields

$$e(t,u,s)=(2\pi)^{-2}\epsilon(t,u,s)\int_E \frac{\partial(\phi,\psi)}{\partial(\phi_0',\phi_1')}\,d\phi_0'\,d\phi_1'\,. \tag{5.2}$$

The subscript E on the integral represents the limits on ϕ_0' and ϕ_1' imposed by the apparatus. In general E will depend on the scattering angles and energies of particles q_0 and q_1 and thus on the variables t, u, and s.

The way in which Eq. (5.2) is used to analyze data depends on whether the acceptance is used to modify the theoretical cross section as in Eq. (3.3) or to weight the data as in Eq. (3.4). In either case the data are binned in the variables t, u, and s. In the first case the uncorrected theoretical cross section $d^3\sigma(\mathrm{th})/dt\,du\,ds$ is multiplied by e and compared with the data. In the second procedure the experimental cross sections are multiplied by the weighting factor e^{-1} and compared with the unmodified theoretical cross section.

In order to calculate the Jacobian in Eq. (5.2) it is necessary to express ψ and ϕ as explicit functions of ϕ_0' and ϕ_1'. The function for ϕ can be found as follows: Take any vector perpendicular to the $\vec{P}-\vec{Q}-\vec{p}_1$ scattering plane. (Because of momentum conservation these three vectors are coplanar in any coordinate system.) From Eq. (4.9) such a vector will also be perpendicular to $\vec{\beta}$, the polar axis about which ϕ is defined. It will also be invariant under the Lorentz transformation defined by $\vec{\beta}$. For example, if we take the normal vector to be $\vec{Q}\times\vec{P}$, then

$$\vec{Q}\times\vec{P}=M_0\gamma\vec{\beta}\times\vec{p}_0=M_0\gamma\vec{\beta}\times\vec{p}_0'\,. \tag{5.3}$$

We now define ϕ to be the angle between this normal vector and some reference direction in the laboratory (e.g., the vertical direction). Using the coordinate system pictured in Fig. 4 we have

$$\tan\phi=\frac{(\vec{\beta}\times\vec{p}_0')_x}{(\vec{\beta}\times\vec{p}_0')_y}=\frac{|\vec{q}_0'|\sin\theta_0'\sin\phi_0'+|\vec{q}_1'|\sin\theta_1'\sin\phi_1'}{|\vec{q}_0'|\sin\theta_0'\cos\phi_0'+|\vec{q}_1'|\sin\theta_1'\cos\phi_1'}\,. \tag{5.4}$$

The angle ψ can be taken as the azimuthal orientation of the $\vec{P}-\vec{Q}-\vec{p}_1$ plane with respect to the $\vec{p}_0-\vec{q}_0-\vec{q}_1$ plane as measured around an axis defined by $\vec{p}_0$ (see Fig. 3.), i.e.,

$$\cos\psi=\frac{\vec{p}_0\times\vec{P}}{|\vec{p}_0\times\vec{P}|}\cdot\frac{\vec{p}_0\times\vec{q}_0}{|\vec{p}_0\times\vec{q}_0|}\,. \tag{5.5}$$

Using (4.7) $\vec{p}_0$, $\vec{P}$, and $\vec{q}_0$ can be rewritten in terms of the two measured laboratory momenta $\vec{q}_0'$ and $\vec{q}_1'$. A long calculation yields

$$\cos\psi=-\frac{\vec{p}_0'\times\vec{\beta}}{|\vec{p}_0'\times\vec{\beta}|}\cdot\frac{[\vec{p}_0'\times(E_1'\vec{q}_0'-E_0'\vec{q}_1')+\omega_0'\vec{q}_0'\times\vec{q}_1']}{\{[\vec{p}_0'\times(E_1'\vec{q}_0'-E_0'\vec{q}_1')+\omega_0'\vec{q}_0'\times\vec{q}_1']^2-[\vec{p}_0'\cdot(\vec{q}_0'\times\vec{q}_1')]^2\}^{1/2}}\,. \tag{5.6}$$

For a perfectly coplanar event ψ is either 0° or 180° depending on whether $\vec{\beta}$ points to the right or the left of the beam axis. The function jumps discontinuously between these two values when $\vec{p}_0'\times\vec{\beta}=0$. Figure 5 shows the behavior of ψ for symmetric but slightly noncoplanar events. The scattering angles, θ_0' and θ_1', are presumed to be held constant while E_0' and E_1' are varied along the energy sharing locus. The angle ψ varies smoothly between the two limits passing through 90° when $E_0'=E_1'$. In an asymmetric configuration this crossover point is shifted so that it occurs where

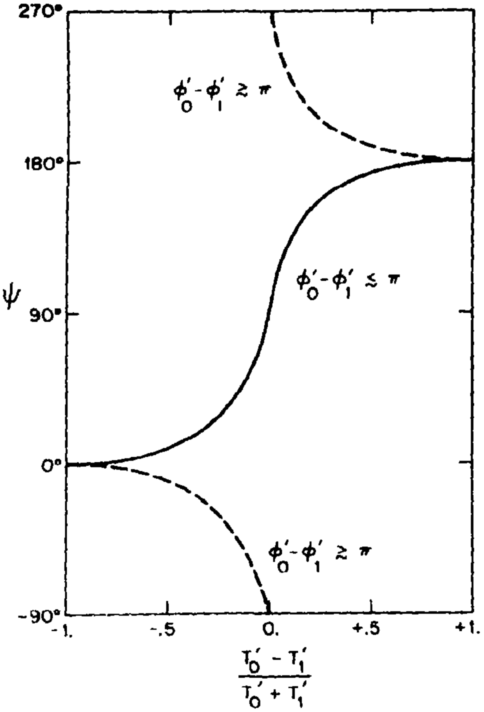

FIG. 5. Typical behavior of ψ as a function of energy sharing for a symmetric, coplanar experiment with a finite coplanarity acceptance. T_0' and T_1' are the kinetic energies of the two detected particles.

$|\vec{q}_0'|\sin\theta_0' = |\vec{q}_1'|\sin\theta_1'$.

Equations (5.4) and (5.6) could now be differentiated to evaluate the Jacobian in (5.2). Fortunately it is not necessary to do this explicitly. It is easy to show that ϕ_0' and ϕ_1' only enter into Eq. (5.6) in the combination $(\phi_0' - \phi_1')$, so that $\psi = \psi(\phi_0' - \phi_1')$ and $\partial\psi/\partial\phi_0' = -\partial\psi/\partial\phi_1'$. By differentiating (5.5) we find $\partial\phi/\partial\phi_0' + \partial\phi/\partial\phi_1' = 1$ so

$$\frac{\partial(\psi,\phi)}{\partial(\phi_0',\phi_1')} = \frac{\partial\psi}{\partial\phi_0'} .$$

The experimental acceptance is then given by the integral

$$e = (2\pi)^{-2}\int_g \frac{\partial\psi}{\partial\phi_0'}\, d\phi_0' d\phi_1' , \tag{5.7}$$

where the limits of integration are imposed either by the azimuthal acceptance of the particle detection devices or by cuts which are later made on the data. Suppose, for example, that the detector for particle 1 is centered at $\phi_1' = 0$ and the detector for particle 0 is centered at $\phi_0' = \pi$. If the smaller of the two detectors, say detector 1, subtends a range of angles $|\phi_1'| \leqslant \Delta\phi_1'$ and limits are placed on the data's coplanarity

$$\pi - \Delta\phi' \leqslant (\phi_0' - \phi_1') \leqslant \pi + \Delta\phi' ,$$

the integral in Eq. (5.7) can be evaluated exactly yielding

$$e = \frac{2\Delta\phi_1'}{(2\pi)^2}\,[\psi(\pi + \Delta\phi') - \psi(\pi - \Delta\phi')] . \tag{5.8}$$

The quantity in square brackets can be thought of as the vertical distance between the solid and dotted curves in Fig. 5. The acceptance evidently pinches out to zero when the kinetic energy of either particle goes to zero, and it rapidly passes through its maximum at the symmetry point. In some cases one may wish not to cut on coplanarity but rather to include all events accepted by the detectors. The limits of integration then are

$$|\phi_1'| \leqslant \Delta\phi_1' ,$$
$$|\phi_0' - \pi| \leqslant \Delta\phi_0' .$$

The integral can no longer be evaluated exactly, but since particle detectors usually subtend a small fraction of the total solid angle, Eq. (5.7) can be approximated easily:

$$e \approx \frac{\Delta\phi_1'}{(2\pi)^2}\,[\psi(\pi + \Delta\phi_0' - \Delta\phi_1') + \psi(\pi + \Delta\phi_0' + \Delta\phi_1') - \psi(\pi - \Delta\phi_0' - \Delta\phi_1') - \psi(\pi - \Delta\phi_0' + \Delta\phi_1')] . \tag{5.9}$$

This Simpson's rule integration is adequate except near the symmetry point where the acceptance goes through its maximum. There one must resort to numerical integration.

Equations (5.7) to (5.9) together with the expression (5.6) for ψ in terms of laboratory variables give the integral required to reduce the cross section, Eq. (4.15), to a threefold differential. A small technical difficulty arises, however, due to the fact that Eq. (5.6) is written in terms of laboratory variables, whereas the data are binned in t, u, and s. If e is used to weight the data on an event-by-event basis, then the appropriate laboratory energies and angles will be available to calculate ψ from Eq. (5.6). If the data are weighted bin by bin or if the procedure implied by Eq. (3.3) is used to correct the theoretical cross section, then E_0', E_1', θ_0', and θ_1' must be calculated from t, u, and s using the formulas in the Appendix. This is easy enough, but it is possible to choose the t, u, s bins inappropriately large so that e varies widely over the bin width. This is particularly a problem near the symmetry point where ψ and thus e are changing rapidly. It should be pointed out, incidentally, that this pathology is not unique to our formalism; it is only obscured in the customary way of doing the calculations.

Finally it should be noted that there is a slight approximation inherent in our procedure for calculating e. This comes about as follows: Eq. (5.1) implies that t, s, and u are held constant while integrating over the azimuthal angles. In fact, there is a weak azimuthal dependence in s, since in the laboratory

$$s = m_0{}^2 + m_1{}^2 + 2E_0' E_1' - 2\vec{q}_0' \cdot \vec{q}_1'$$

and $\vec{q}_0' \cdot \vec{q}_1'$ contains a term proportional to $\cos(\phi_0' - \phi_1')$. Thus to keep t, s, and u constant over the range of integration in ϕ_0' and ϕ_0', the other laboratory variables appearing in (5.6) must vary slightly, whereas (5.8) and (5.9) assume that they are constant. This effect has been investigated numerically for various experimental configurations and appears to be negligible.

VI. TESTS OF THE IMPULSE APPROXIMATION

Any scheme for reducing the dimensionality of experimental data must make assumptions regarding the behavior of the cross section as a function of those variables that are integrated away. The approach advocated here is clearly predicated on single-particle exchange. In this section we briefly describe two tests, which are well known in other contexts, for checking this assumption. The tests can be applied more or less directly to the data if they are tabulated in terms of the variables we are recommending.

The key simplifying feature of the impulse approximation is that the two vertices are independent of each other except inasmuch as they both depend on the momentum and spin of the exchanged particle. For example, if the exchanged particle is spinless and the beam unpolarized, the cross section must be independent of the variable ψ. (The center of mass coordinate system used here differs from the usual "anti-lab" system by a Lorentz boost along the direction of the polar axis of ψ, which, of course, leaves ψ invariant.) This was first proposed by Trieman and Yang[6] as a test of one-pion exchange, and has been generalized for arbitrary spin by Shapiro *et al.*[3]

Such tests are customarily made with arrays of noncoplanar detectors. However, as can be seen from Eq. (5.6) and Fig. 5, even the normal coplanar geometry takes in the complete range of ψ from 0 to 2π. This is because the vector $\vec{\beta}$, depending on the momentum sharing of the two detected particles, can point either to the right or left of the beam and (for events that are not perfectly coplanar) can point above or below the scattering plane as well. Thus the vector $\vec{p}_0' \times \vec{\beta}$ rotates through 180° (again assuming a slightly noncoplanar event) as $q_0' \sin\theta_0'$ becomes much greater or less than $q_1' \sin\theta_1'$. This makes it possible to do a limited Trieman-Yang test even with a coplanar experiment. This, in fact, is the idea behind the suggestion of Jacob, Maris, Schneider, and Teodoro[7] that asymmetries in energy sharing spectra should appear in reactions of the type $(\vec{p}, 2p)$ with polarized incident protons. They arise because distortions, i.e., departures from pure single-particle exchange, have the effect of polarizing the target nucleon. This in turn produces an ordinary $\cos^2\psi$ dependence in the center of mass cross section for the scattering of the two protons; and it is this ψ dependence that appears as an energy asymmetry in the laboratory variables.

Without polarized beam, however, the coplanar experiment is of very limited usefulness in doing Trieman-Yang tests. The reason is that for this geometry ψ passes through 90° near the point on the energy sharing locus where the nuclear recoil momentum, the target nucleon, and the incident beam are collinear. In this limit the ψ dependence must vanish regardless of the reaction mechanism, so one does not expect to observe a violation of the Trieman-Yang criterion in a coplanar experiment except possibly at the two points $\psi = 0°$ and 180°.

There is another useful test of the impulse approximation that depends on the fact that only a single particle is exchanged. This is the so-called Chew-Low extrapolation scheme.[8] Applied to quasi-free scattering experiments it can be formulated as follows: Since the upper and lower vertices in Fig. 2 are connected by a single particle of mass m_1, the scattering amplitude and hence the function $M_N(t)$ in Eq. (2.6) must have a pole at a value of t equal to $m_1{}^2$. This value is not physically accessible, nor does the pole represent the total t dependence of M, but for values of $t - m_1{}^2$ close to the minimum, one may reasonably expect the cross section to be dominated by this term. To exhibit this it is customary[9] to factor out the pole leaving a "coupling constant" or vertex function which varies more slowly with t. In our formalism

$$M_N(t) = \frac{\Gamma(t)}{t - m_1{}^2}\,. \tag{6.1}$$

If one plots t versus the variable Y defined by

$$Y = \left[K\left(\frac{d\sigma}{du}\right)^{fr}\right]^{1/2} \left(\frac{d^3\sigma}{dt\,ds\,du}\right)^{-1/2}, \tag{6.2}$$

where K is the kinematic factor

$$K = \frac{\sqrt{s}\,|\vec{q}|}{4M_0{}^2\,|\vec{p}_0'|\,|\vec{q}_0' + \vec{q}_1'|}\,, \tag{6.3}$$

the resulting plot should be a straight line with slope Γ passing through $Y=0$ at $t=m_1{}^2$. The constant Γ can be related to the effective cluster number in the usual formalism. Deviations from the straight line behavior of the t-Y plot or variations in the slope of the straight line with changes in u or s indicate a breakdown of the single-particle exchange approximation.

VII. CONCLUSION

We have proposed a set of variables to be used in place of the customary energies and angles in the analysis of quasi-elastic scattering data. Three of these variables are familiar Lorentz scalars frequently used in the analysis of high energy scattering experiments. The other two variables are azimuthal angles defined in the center of mass system of the two detected outgoing particles. In terms of these variables one can reduce the usual fivefold differential cross section to a threefold differential, including the effects of experimental acceptance, without resorting to Monte Carlo techniques. Moreover, in this form the dependence of the data on nuclear and two-particle variables is clearly separated. Finally, two simple tests of the impulse approximation, the Trieman-Yang test and the Chew-Low extrapolation, can be applied directly to the data in particularly simple form.

APPENDIX

It is a simple matter to calculate the invariants t, u, and s, given the momenta in a specific coordinate system. Occasionally, however, one needs to reverse this procedure, e.g. to evaluate the kinematic factors in (4.15) or to correct a theoretical cross section for experimental acceptance. The following sequence of equations is sufficient to reconstruct all the c.m. and lab momenta given ψ, ϕ, and the three scalar invariants. As in the text, all unprimed momenta and energies refer to the c.m. system, primed variables to the lab.

Define $E_T' = E_0' + E_1'$ then

$$E_T' = \omega_0' + \frac{M_0{}^2 - M^2 + t}{2M_0}\,, \tag{A1}$$

$$|\vec{q}_0{}' + \vec{q}_1{}'|^2 = E_T'^2 - s\,, \tag{A2}$$

$$|\vec{\beta}|^2 = 1 - s/E_T'^2\,, \tag{A3}$$

$$|\vec{p}_0|^2 = |\vec{p}_1|^2 = \frac{[s-(m_0+\sqrt{t}\,)^2][s-(m_0-\sqrt{t}\,)^2]}{4s}\,, \tag{A4}$$

$$|\vec{q}_0|^2 = |\vec{q}_1|^2 = \frac{[s-(m_0+m_1)^2][s-(m_0-m_1)^2]}{4s}\,, \tag{A5}$$

$$\omega_0 = \frac{s - t + m_0{}^2}{2\sqrt{s}}\,, \tag{A6}$$

$$E_0 = \frac{s - m_1{}^2 + m_0{}^2}{2\sqrt{s}}\,, \tag{A7}$$

$$\cos\theta_{\text{c.m.}} = \frac{u + 2\omega_0 E_0 - 2m^2}{2|\vec{p}_0||\vec{q}_0|}\,, \tag{A8}$$

where $\theta_{\text{c.m.}}$ is the c.m. angle between $\vec{p}_0$ and $\vec{q}_0$. With this information and ϕ and ψ one can reconstruct the c.m. momenta $\vec{q}_0$ and $\vec{q}_1$. The final step is to transform these momenta to the laboratory system. This requires one additional parameter, the angle between $\vec{\beta}$ and $\vec{p}_0$, which can be calculated from

$$\vec{\beta}\cdot\vec{p}_0 = \omega_0'/\gamma - \omega_0\,. \tag{A9}$$

---

[1] G. Jacob and Th. A. J. Maris, Rev. Mod. Phys. 38, 121 (1966).

[2] S. Kullander, F. Lemeilleur, P. U. Renberg, G. Landaud, J. Yonnet, B. Fagerstron, A. Johansson, and G. Tibell, Nucl. Phys. A173, 357 (1971).

[3] I. S. Shapiro, V. M. Kolybasov, and G. R. Augst, Nucl. Phys. 61, 353 (1965).

[4] N. S. Chant and P. G. Roos, Phys. Rev. C 15, 57 (1977).

[5] D. F. Jackson, Nucl. Phys. A257, 221 (1976).

[6] C. N. Yang and S. Treiman, Phys. Rev. Lett. 8, 140 (1962).

[7] G. Jacob, Th. A. J. Maris, C. Schneider, and M. R. Teodoro, Phys. Lett. 45B, 181 (1973).

[8] G. F. Chew and F. E. Low, Phys. Rev. 113, 1640 (1959).

[9] W. Dollhopf, C. F. Perdrisat, P. Kitching, and W. C. Olsen, Phys. Lett. 58B, 425 (1975). See also F. Prats, A. Ghovanlou, and D. R. Lehman, Proceedings of the International Conference on Clustering Phenomena in Nuclei, College Park, Maryland, 1975, edited by D. A. Goldberg, J. B. Marion, and S. J. Wallace (National Technical Information Service, Springfield, Virginia, 1975).

PHYSICAL REVIEW C VOLUME 21, NUMBER 5 MAY 1980

Proton-proton correlations, the fireball model, and inclusive pion spectrum

E. Forest, S. Das Gupta, and C. S. Lam
Physics Department, McGill University, 3600 University Street, Montreal, H3A 2T8 Quebec, Canada

(Received 14 September 1979)

Two proton correlations seen in the reaction ^{12}C on ^{12}C are calculated in the framework of the two fireball model. Substantial correlation is obtained. It is necessary to do the calculation in phase space, i.e., to use the microcanonical ensemble rather than the grand canonical ensemble. A model calculation shows that the latter will also overestimate pion production in the high energy tail compared to an energy and momentum conserving phase space calculation.

[NUCLEAR REACTIONS Relativistic ion-ion collisions; fireball model; phase space; pion spectrum; two proton correlations.]

I. INTRODUCTION

In the simplest version of the fireball model, the overlapping parts of the target and the projectile fuse together; the ordered kinetic energy of the collision is then dumped as random thermal energy; the energy is so high that all the nucleons are liberated.[1] Pions are also produced.[2] It is possible to include the production of composites.[3,4]

One is tempted to assume that the emission of protons from such a fireball will be uncorrelated, that is, in the fireball frame the probability of having simultaneously a proton of momentum $\vec{p}_1$ and another of momentum $\vec{p}_2$ is a function $f(p_1, p_2)$, independent of the angle between them. Recent experiments by Nagamiya *et al.*[5-7] show that this is not so. We will describe the results of these experiments later. The fact that preferential emission was seen in the Berkeley experiment was advanced as a signature of the inadequacies of the thermal type models.

In this paper we calculate two proton correlations in the fireball model. We find that the lack of correlation is dictated not so much by the basic assumption of the thermal models as by the use of the grand cannonical ensemble. If the number of the participating nucleons is small, then it is better to do a phase-space calculation, i.e., the microcanonical ensemble. Exact imposition of energy and momentum conservation then leads to a correlation like the one seen in the experiments.

As a by-product, we also do a model calculation for the inclusive spectrum of pions in the microcanonical ensemble. The reason for this exercise is the following. For C on C or Ne on NaF at 800 MeV/N in the lab the pion inclusive spectrum has been measured for pions with kinetic energy up to 500 MeV. Calculations using fireball type pictures usually overestimate[8,9] pion spectrum. Again the use of the grand canonical ensemble needs to be looked at here since the number of pions is small, and in any event one is looking at the high energy tail of the spectrum where energy and momentum conservation may play a significant role. For pions, the calculations done here are undoubtedly simplistic. We have left out effects known to be important. To do a realistic computation for a pion inclusive spectrum using phase-space calculation would be prohibitively lengthy. But the model calculation done here suggests that at least a significant part of the overestimation of the pion spectrum obtained in previous calculations may have its origin in the use of the grand canonical ensemble and not so much in the basic assumption of the fireball model.

II. THE FIREBALL MODEL AND PHASE-SPACE CALCULATIONS

At each impact parameter the overlapping parts of the projectile and the target fuse together and all the available energy is converted into random motion. Such a conversion can happen if the fireball loses the memory of how it was formed. In any event, if the number of open channels is very large then just the sheer number of these channels may play a more important role than the individual s-matrix elements leading to each of these channels, at least for inclusive reactions.

We thus consider at each impact parameter only the following information: a given relativistic energy E_{tot}, a given baryon number B, a given charge Q, a given volume V, and a net momentum P which is zero in the c.m. of the fireball. If there are many particles then instead of a fixed energy E we can introduce a fixed temperature (whose value corresponds to the correct average energy). We can also use the concept of chemical potentials to obtain the average number of particles. This is the grand canonical ensemble.

© 1980 The American Physical Society

We will, however, deal with cases where the number of particles is not large. We then use the microcanonical ensemble. To fix our ideas, let us consider a model in which only nucleons (of mass m) and pions (of mass m_π) are considered. The probability of having n_1 protons, n_2 neutrons, n_3 positive pions, n_4 negative pions, and n_5 neutral pions is given by

$$P_{n_1n_2n_3n_4n_5}=\frac{g_{n_1n_2n_3n_4n_5}}{\sum g_{n_1n_2n_3n_4n_5}},$$

$$g_{n_1n_2n_3n_4n_5}=\frac{V^N}{h^{3N}\prod_i n_i!}\int\delta\left(E-\sum_1^{N_1}\frac{p_i^2}{2m}-\sum_1^{N_2}\frac{p_i^2}{2m_\pi}\right)\delta\left(\sum_{i=1}^{N}p_i\right)\prod_{i=1}^{N}d^3p_i\,. \tag{1}$$

Here

$N_1=n_1+n_2,$

$N_2=n_3+n_4+n_5,$

$N=N_1+N_2,$

$E=E_{\text{tot}}-N_1mc^2-N_2m_\pi c^2.$

The partitions $n_1, n_2 \ldots$ must obey the law of baryon and charge conservation

$n_1+n_3-n_4=Q,$

$n_1+n_2=B\,.$

Equation (1) is a nonrelativistic approximation. We will be concerned with equal ion collision with lab energy 800 MeV/N which corresponds to 182 MeV per nucleon in the c.m. Thus for nucleons, the nonrelativistic approximation is reasonable. It is less reliable for pions. The integral of Eq. (1) can be evaluated formally. The relativistic generalization of Eq. (1) for an arbitrary number of particles can not be evaluated in a closed form.

For a given impact parameter the inclusive spectrum of say, negative pions at p in the rest frame of the fireball, is given by

$$\frac{d^3n}{d^3p}=\sum\frac{n_4\int\delta\left(E-\frac{p^2}{2m}-\sum_{i=1}^{N_1}\frac{p_i^2}{2m}-\sum_{i=1}^{N_2-1}\frac{p_i^2}{2m_\pi}\right)\delta\left(\vec{p}+\sum_{i=1}^{N_1}p_i+\sum_{i=1}^{N_2-1}\vec{p}_i\right)\prod_{i=1}^{N-1}d^3p_i}{\int\delta\left(E-\sum_{i=1}^{N_1}\frac{p_i^2}{2m}-\sum_{i=1}^{N_2}\frac{p_i^2}{2m_\pi}\right)\delta\left(\sum_{i=1}^{N}\vec{p}_i\right)\prod_{i=1}^{N}d^3p_i}\,P_{n_1n_2n_3n_4n_5}\,. \tag{2}$$

Equations (1) and (2) are straightforward applications of the microcanonical ensemble. The integrals appearing in this section are evaluated in the Appendix. It is obvious that an equation similar to Eq. (2) can be written down for the proton inclusive spectrum.

III. TWO PROTON CORRELATIONS

Let us consider the following two proton correlations in the rest frame of the fireball. Let the fireball have n_p protons, n_n neutrons ($n_p+n_n=n$), and nonrelativistic energy E. Consider a Gedankenexperiment in which a proton in the x direction with a fixed momentum $\vec{p}_1$ is measured in coincidence with another proton n the opposite direction (180° direction) but having any magnitude p_2. Let the number of counts be N_1. Consider also a second configuration in which the first counter still measures protons in fixed momentum $\vec{p}_1$ in the x direction but the second counter is in the y direction (90°). Let the number of counts be N_2. We define the ratio of these two numbers as the correlation

$C=N(180°)/N(90°).$

It is given by the ratio of two numbers each of which is given by

$$N=\frac{n_p(n_p-1)d^3p_1d\Omega_2\int\delta\left(E-\frac{p_1^2}{2m}-\frac{p_2^2}{2m}-\sum_{i=3}^{n}\epsilon_i\right)\delta\left(\vec{p}_1+\vec{p}_2+\sum_{i=3}^{n}p_i\right)p_2^2dp_2\prod_{i=3}^{n}d^3p_i}{\int\delta\left(E-\sum_{i=1}^{n}\epsilon_i\right)\delta\left(\sum_{i=1}^{n}\vec{p}_i\right)\prod_{i=1}^{n}d^3p_i}\,. \tag{3}$$

For the first configuration, $\mathbf{p}_2$ is in the 180° direction; for the second it is in the 90° direction.

Actual experiments are different from the above case. Experiments are done in the lab frame and the fireball is moving in the lab frame; for light ion collisions a two fireball description is more pertinent. An important fact is that each impact parameter defines fireballs with given n and the impact parameters ought to be summed over before taking the ratio. Nonetheless, it is instructive to study the simple case first as it can be readily generalized to handle more complicated cases.

For $n>3$, the integral in the numerator of Eq. (3) reduces to (see Appendix)

$$\frac{(2m\pi)^{3(n-3)/2}}{(n-2)^{3/2}\Gamma(3(n-3)/2)}\int \hat{E}^{3(n-3)/2-1}p_2^{2}dp_2,$$

where

$$\hat{E}=E-\frac{1}{2m}p_1^{2}\left(2-\frac{n-3}{n-2}\right)-\frac{1}{2m}p_2^{2}\left(2-\frac{n-3}{n-2}\right)$$
$$-2\frac{1}{2m}\mathbf{p}_1\cdot\mathbf{p}_2\left(1-\frac{n-3}{n-2}\right).$$

The limits on $\mathbf{p}_1$ and $\mathbf{p}_2$ are set by the condition that $\hat{E}>0$. For a given E, $\mathbf{p}_1$, and $\mathbf{p}_2$ the correlation decreases as n increases. For large n we will simply set the grand canonical ensemble result.

For $n=3$, the integral of the numerator in Eq. (3) is given by

$$\sum_i \frac{p_i^{2}}{\left|\frac{\partial f}{\partial p_2}\right|_i},$$

where p_i is a positive value of p_2 that satisfies

$$f=E-\frac{p_1^{2}}{m}-\frac{p_2^{2}}{m}-\frac{1}{m}\mathbf{p}_1\cdot\mathbf{p}_2=0.$$

In Eq. (3) we will not be concerned with $n=2$. We consider equal light ion collisions. For $n=2$, the most probable constituents of the fireball will be one proton and one neutron, thus precluding the possibility of two proton correlations. For n even, we will take $n_p=n/2$, and for odd n there is equal probability of having $(n-1)/2$ protons or $(n+1)/2$ protons.

As mentioned earlier, the actual $N(180°)/N(90°)$ is found after summing over impact parameters:

$$C=\frac{N(180°)}{N(90°)}=\frac{\sum N_n(b,180°)b\Delta b}{\sum N_n(b,90°)b\Delta b}. \qquad (4)$$

The subscript n in Eq. (4) refers to the number of nucleons in the fireball for a given impact parameter b. For any b, the ratio $N_n(b,180°)/N_n(b,90°)$ is an increasing function of p_1, yet because of the summation involved [Eq. (4)] the quantity C can have local maxima. We illustrate this in a simple case; in Fig. 1 we show a plot of

$$A_1=N_3(180°)/N_3(90°), \qquad (5)$$

$$A_3=N_{12}(180°)/N_{12}(90°), \qquad (6)$$

and a plot of

$$A_2=\frac{\frac{1}{3}N_3(180°)+\frac{2}{3}N_{12}(180°)}{\frac{1}{3}N_3(90°)+\frac{2}{3}N_{12}(90°)}. \qquad (7)$$

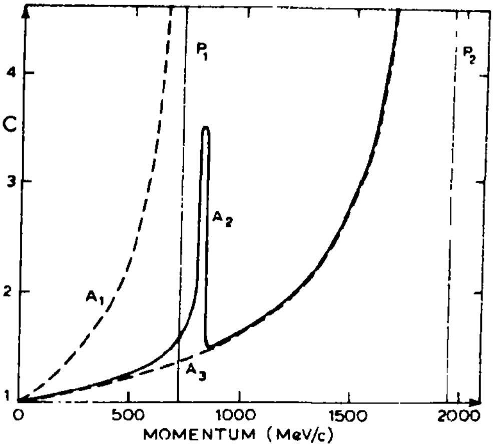

FIG. 1. Two proton correlations in the fireball frame when the fireball has 3 nucleons (A1), has 12 nucleons (A3) and $\frac{1}{3}$rd probability of having 3 nucleons and $\frac{2}{3}$rd probability of having 12 nucleons (A2) [see Eqs. (5), (6), and (7)]. The average kinetic energy per nucleon in the fireball frame is 182 MeV. To the right of the line P_1, N_3 (90°) is zero; to the right of the line P_2, N_{12} (90°) is zero.

The kinetic energy per nucleon is taken to be 182 MeV in the fireball. The quantity $N_3(90°)$ goes to zero at $p_1=716$ MeV/c, whereas $N_3(180°)$ goes to zero at $p_1=827$ MeV/c. In between these two limits one gets a peak whose magnitude is related to the relative weighting of N_3 and N_{12} but whose position is only energy dependent.

Two proton correlations have been measured[5,6] for the reaction ^{12}C on ^{12}C. The incident energy was 800 MeV/N. The proton spectrometer was set at $\theta=40°$ to the beam; the spectrometer measures protons with a given momentum p_1. The counter telescope, in coincidence with the spectrometer, was also set at $\theta=40°$ but once in plane with the proton spectrometer and the beam at $\phi=180°$ and then out of plane ($\phi=90°$). Proton energy is not measured in the telescope. The experimental results[5,6] for the correlation as a function of p_1 are shown in Fig. 2. A broad peak is seen around 1000 MeV/c. It is usually referred to as

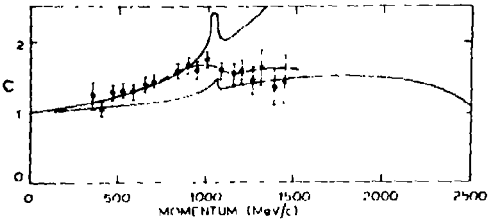

FIG. 2. The correlation curve as a function of the measured proton momentum in the spectrometer. The broken curve is through data points; the maximum has a value 1.7. The theoretical curve A is obtained when only the contribution of correlated events (both the protons must come from the same fireball) is considered. Curve C is the full calculation and also contains the events when the two protons come from two different fireballs. The calculated maximum has a value 1.5.

a quasielastic peak as kinematically its position roughly corresponds to elastic scattering of one proton in the projectile off another proton in the target.

We now use the fireball model to calculate the correlation. We recall that the proton inclusive spectrum showed that for such light ion collisions, a two fireball description is more valid than the one fireball model. The transparency factor for the two fireball model can be calculated from experimental data of p-p collisions or p-nucleus collisions.[9] The relevant details of the two fireball calculation are given in the table.[10] The transformation from the lab frame to the fireball frame was done relativistically, but, as before, the phase-space calculation in each fireball was done nonrelativistically. Since the average nucleon kinetic energy in each fireball is about 150 MeV the approximation is reasonable. For this calculation we neglect pion production; the average number of pions ≈0.25 and most of them come from central collisions where the number of nucleons is of the order 10; thus our calculated correlation curve would change very little. We also use clean cut; if for an impact parameter the volume cut out for one of the fireballs is V and the nucleon density in each nucleon density in each nucleus is ρ, then the quantity ρV is usually a noninteger. To be able to do a phase-space calculation we replace this noninteger by its nearest integer. There is an approximation involved here; even for a clean cut, the number of nucleons swept out is not unique; there will be fluctuations in this number due to quantum mechanics but it is difficult to calculate this distribution precisely.[11] In the following section where we compare results with the grand canonical ensemble, of course, the same approximation will be made for the average number of nucleons in the grand canonical ensemble. We also take the density for each nucleus to be constant throughout its volume.

The results of the calculation are shown in Fig. 2. If both the protons originate from the same fireball we get correlation. In fact, if these were the only events the theory would predict too much correlation. But one proton may come from one fireball and the second one from the other fireball. Such events are uncorrelated. When the contributions due to each of the processes are included the gross features of the experimental curve are reproduced.

These calculations lend further support to the two fireball model for C on C. The fall off towards the value unity for correlation, seen experi-

TABLE I. Relevant details of the two fireball model for ^{12}C on ^{12}C at 800 MeV/N in the lab (Ref. 9). The velocity of one fireball in the c.m., the number of nucleons in it (rounded to the nearest integer number), and the kinetic energy per particle in the fireball frame are given for each impact parameter. The same numbers apply to the other fireball except for the velocity which is opposite. In the lab the velocity of the c.m. is 0.548 c.

Impact parameter (fm)	Numbers of nucleons in each fireball	Velocity of the fireball in the c.m. in units of c	Kinetic energy in MeV per nucleon in the fireball
0.183	12	0.178	156
0.549	11	0.178	156
0.916	10	0.179	156
1.282	9	0.180	156
1.648	8	0.183	155
2.015	7	0.187	155
2.381	6	0.192	154
2.747	5	0.198	152
3.114	4	0.205	151
3.480	3	0.214	148
3.846	2	0.226	145

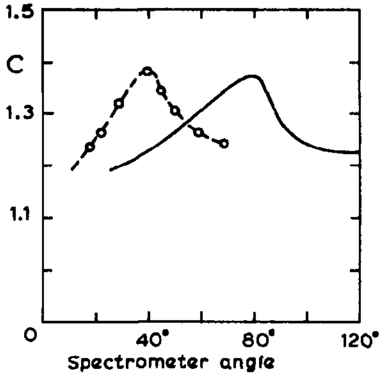

FIG. 3. Correlation as a function of θ_{sp}, the spectrometer setting with the counter telescope fixed at $\theta = 40°$.

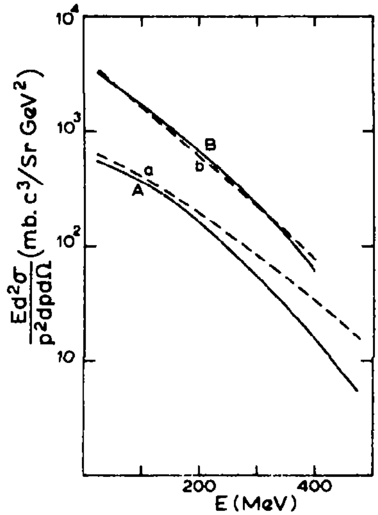

FIG. 4. Model calculation for pion and proton spectra (A,B) at 90° in the c.m. using the microcanonical ensemble (phase space) and the grand canonical ensemble (a,b). The example above is for ^{12}C on ^{12}C at 800 MeV/N in the lab. Note that at the high energy tail, the grand canonical ensemble considerably overestimates the pion spectrum over the more exact phase space calculation.

mentally, would not emerge in a one fireball calculation. This is because in the one fireball model all coincidence events are correlated, i.e., they come from the same fireball. In the two fireball model, for large p_1 in the spectrometer, the phase space for uncorrelated events is much larger than the phase space for correlated events. Hence the value of C falls towards unity.

A different version of this correlation experiment has also been reported.[7] Suppose the spectrometer of the previous experiment is used just like a telescope, i.e., is triggered by a proton of any momentum. We still take the ratio of the counts at $\phi = 180°$ and $\phi = 90°$ but repeat this for various values θ_{sp} of the spectrometer setting, still keeping θ for the counter telescope at 40°. In the experiment one sees a maximum at the setting $\theta_{sp} = 40°$. The two fireball calculations for this experiment are shown in Fig. 3. We also get a maximum as a function of θ_{sp} but it is shifted to higher value, about 80°.

The reason for this shift is difficult to unravel but in our calculations the phase space is maximum in the region of p_1 between 500 MeV/c and 1000 MeV/c (Fig. 2), and the fact that we do not fit the data very well in this region for the first xperiment is likely to have a large effect in the econd calculation.

IV. PION INCLUSIVE SPECTRUM

We now return to the pion spectrum calculation Refs. 8 and 9. Although the calculation was lly relativistic and included the production and ecay of Δ's, the fit with experiment was less an ideal. The major difficulty was that the theoetical calculation overestimated pion production, is discrepancy increasing with increasing pion ergy. We want to find out if a significant part of the discrepancy arises solely from the use of the grand canonical ensemble.

We can use the two fireball model and the formalism of Sec. II to calculate the pion inclusive spectrum. As mentioned before, a relativistic calculation is desirable here. But probably more important is the inclusion of Δ's since past experiences have shown that the slope of the pion spectrum changes significantly when Δ's are included. In principle, we can include Δ's in the formulation of Sec. II; in practice, it is prohibitively long. Thus the motivation of the calculation presented in this section is solely to estimate the error involved in the use of the grand canonical ensemble. Of course, when making the comparison we must also use a nonrelativistic grand canonical ensemble in which Δ's are not included.

The comparison is presented in Fig. 4. We find that the use of the microcanonical ensemble does indeed significantly reduce the pion inclusive spectrum in the high energy tail. By comparison, the use of the microcanonical ensemble changes the proton inclusive spectrum very little. It is thus possible that if a complete phase-space calculation could be done in the fireball model, better agreement with the experimental pion spectra could be obtained without destroying the good fit to the proton spectrum.

V. ACKNOWLEDGMENTS

We thank Dr. N. de Takacsy and Dr. Y Afek for discussions. This research was supported in part by the NSERC of Canada and in part by the Quebec Department of Education.

APPENDIX

In the integral [Eq. (1)]

$$\int \delta\left(E-\sum_{i=1}^{N_1}\frac{p_i^2}{2m}-\sum_{i=1}^{N_2}\frac{p_i^2}{2m_\pi}\right)\delta\left(\sum_{i=1}^{N}\vec{p}_i\right)\prod_{i=1}^{N}d^3p_i\,, \tag{A1}$$

where $N_1+N_2=N$, perform the integration over the N_1th nucleon to give

$$\int \delta\left[E-\sum_{i=1}^{N_1-1}\frac{p_i^2}{2m}-\sum_{i=1}^{N_2}\frac{p_i^2}{2m_\pi}-\frac{1}{2m}\left(-\sum_{i=1}^{N-1}\vec{p}_i\right)^2\right]\prod_{i=1}^{N-1}d^3p_i$$

$$=\int \delta\left(E-\frac{1}{2m}\vec{p}_i\cdot a_{ij}\vec{p}_j\right)\prod_{i=1}^{N-1}d^3p_i\,. \tag{A2}$$

Here a_{ij} is a real symmetric matrix of dimension $N-1$ whose matrix elements are

$a_{ii}=2,\quad i=\text{nucleon}$

$\quad\;=1+\dfrac{m}{m_\pi},\quad i=\text{pion}$

$a_{ij}=1,\quad i\neq j\,.$

Defining $\alpha=m/m_\pi$, the structure of the matrix is as shown.

$$a_{ij}=\left|\begin{array}{cccccccc}
2 & 1 & 1 & & & & & \\
1 & 2 & 1 & & & & & \\
1 & 1 & 2 & 1 & & & & \\
 & & 1 & & & & & \\
 & & & & \cdots & & & \\
 & & & & & 1+\alpha & 1 & 1 \\
 & & & & & 1 & 1+\alpha & 1 \\
 & & & & & 1 & 1 & 1+\alpha
\end{array}\right|\,. \tag{A3}$$

Going to a diagonal basis, the integral (A2) becomes

$$\int \delta\left(E-\frac{1}{2m}\sum_{i=1}^{N-1}\lambda_i p_i'^2\right)\prod_{i=1}^{N-1}d^3p_i'$$

$$=\frac{1}{\left(\prod_i\lambda_i\right)^{3/2}}\int \delta\left(E-\frac{1}{2m}\sum_{i=1}^{N-1}q_i^2\right)\prod_{i=1}^{N-1}d^3q_i\,. \tag{A4}$$

The integral (A4) is the surface of a hypersphere in $3(N-1)$ dimensions which is done in many textbooks.[12] To find $\prod_i\lambda_i$, the product of the eigenvalues, we note that the matrix "a" has two eigenvectors of the form

$$e_\pm=\begin{pmatrix}1\\1\\1\\\vdots\\\delta_\pm\\\delta_\pm\\\vdots\end{pmatrix}, \tag{A5}$$

with eigenvalues given by

$$\lambda_\pm=\frac{(N_1+N_2+\alpha)\pm[(N_1+N_2+\alpha)^2-4(N_1\alpha+N_2)]^{1/2}}{2}$$

and

$$\delta_\pm=\frac{N_1-1}{\lambda_\pm-N_2-\alpha}\,.$$

In addition there are N_1-2 eigenvectors with eigenvalue 1 and N_2-1 eigenvectors with eigenvalue α. The structures of these eigenvectors are, respectively,

$$\begin{pmatrix}0\\0\\\vdots\\1\\-1\\0\\\vdots\\0\\0\\0\end{pmatrix}\quad\text{and}\quad\begin{pmatrix}0\\\vdots\\0\\0\\1\\-1\\0\\\vdots\end{pmatrix}\,.$$

Finally then

$$\prod\lambda_i=\alpha^{N_2-1}(N_1\alpha+N_2),$$

and the integral (A1) gives

$$\frac{1}{\left(\prod\lambda_i\right)^{3/2}}\frac{(2m\pi)^{3(N-1)/2}}{\Gamma(3(N-1)/2)}E^{3(N-1)/2-1}.$$

Equations (A6) and (A7) hold also when $N_2=$

For pion inclusive spectrum [Eq. (2)] we need to evaluate

$$\int \delta\left(E-\frac{p^2}{2m_\pi}-\sum_{i=1}^{N_1}\frac{p_i^2}{2m}-\sum_{i=1}^{N_2-1}\frac{p_i^2}{2m_\pi}\right)\delta\left(\vec{p}+\sum_{i=1}^{N_1}\vec{p}_i+\sum_{i=1}^{N_2-1}\vec{p}_i\right)\prod_{i=1}^{N-1}d^3p_i\,. \tag{A8}$$

Performing the integration over the N_1th nucleon one obtains

$$\int \delta\left[E-\frac{p^2}{2m_\pi}-\sum_{i=1}^{N_1-1}\frac{p_i^2}{2m}-\sum_{i=1}^{N_2-1}\frac{p_i^2}{2m_\pi}-\frac{1}{2m}\left(-\vec{p}-\sum_{i=1}^{N-2}\vec{p}_i\right)^2\right]\prod_{i=1}^{N-2}d^3p_i$$

$$=\int \delta\left[E-\frac{p^2}{2m}(1+\alpha)-\frac{1}{2m}\vec{p}_i\cdot a_{ij}\vec{p}_j-\frac{2}{2m}\vec{p}\cdot\sum_{i=1}^{N-2}\vec{p}_i\right]\prod_{i=1}^{N-2}d^3p_i\,. \tag{A9}$$

Here the matrix "a" has the same structure as before. The integral (A9) is very similar (A2) with E replaced by $\hat{E}=E-(p^2/2m)(1+\alpha)$ and the additional term $(1/m)\vec{p}\cdot\sum\vec{p}_i$. By substituting $\vec{1}_i=\vec{p}_i+\vec{p}\sum_k(a^{-1})_{ik}$, (A8) reduces to

$$\int \delta\left(\hat{E}-\vec{1}_i a_{ij}\vec{1}_j-\frac{p^2}{2m}\sum_{i,k}(a^{-1})_{ik}\right)\prod_{i=1}^{N-2}d^3p_i\,. \tag{A10}$$

(A9) is now of the form (A2), although we still have to evaluate $\sum(a^{-1})_{ik}$.

$$\sum(a^{-1})_{ik}=(1a^{-1}1)$$

$$=\langle b_+e_++b_-e_-|a^{-1}|b_+e_++b_-e_-\rangle$$

$$=b_+^2e_+^2\lambda_+^{-1}+b_-^2e_-^2\lambda_-^{-1}. \tag{A11}$$

Here e_+,e_-, are the special eigenvectors of Eq. (A5) and $b_\pm$ are the coefficients which satisfy

$$b_++b_-=1,$$

$$b_+\delta_++b_-\delta_-=1.$$

---

[1] J. Gosset, H. H. Gutbrod, W. G. Meyer, A. M. Poskanzer, A. Sandoval, R. Stock, and G. D. Westfall, Phys. Rev. C 16, 629 (1977).

[2] J. I. Kapusta, Phys. Rev. C 16, 1493 (1977).

[3] A. J. Mekjian, Phys. Rev. Lett. 38, 640 (1977).

[4] J. Gosset, J. I. Kapusta, and G. D. Westfall, Phys. Rev. C 18, 844 (1978); G. Cecil, S. Das Gupta, and A. J. Mekjian, Phys. Rev. C 20, 1021 (1979).

[5] S. Nagamiya, I. Tanihata, S. R. Schnetzer, W. Brückner, L. Anderson, G. Shapiro, H. Steiner, and O. Chamberlain, J. Phys. Soc. Jpn. Suppl. 44, 378 (1978).

[6] S. Nagamiya in the Fourth High Energy Heavy Ion Summer Study, 1978, Report No. LBL 7766 (unpublished).

[7] S. Nagamiya, L. Anderson, W. Brückner, O. Chamberlain, M. C. Lemaire, S. Schnetzer, G. Shapiro, H. Steiner, and I. Tanihata, Phys. Lett. 81B, 147 (1979).

[8] S. Das Gupta, Phys. Rev. Lett. 41, 1450 (1978).

[9] S. Das Gupta and C. S. Lam, Phys. Rev. C 20, 1192 (1979).

[10] *We take this opportunity to correct a typographical* error in Ref. 9. The numerator of the right-hand side of Eq. (2) in Ref. 9 should read

$$2\int_0^{(R^2-b^2/4)^{1/2}}dy\int_{b-R_y}^{R_y}[R_y^2-(b-x)]^{1/2}(R_y^2-x^2)^{1/2}dx.$$

[11] G. Bertsch and J. Borisowicz, Phys. Rev. C 19, 533 (1979).

[12] P. M. Morse, *Thermal Physics*, 2nd ed. (Benjamin, New York, 1969), p. 260; C. Kittel, *Elementary Statistical Physics* (Wiley, New York, 1958), p. 37.

PHYSICAL REVIEW C VOLUME 21, NUMBER 5 MAY 1980

Local field corrections in π-nucleus scattering

M. K. Banerjee and S. J. Wallace
Department of Physics and Astronomy, University of Maryland, College Park, Maryland 20742

(Received 28 June 1979)

The local field correction to the π-nucleus optical potential is calculated taking recoil into account. The correction arises from the triple scattering matrix element $\langle 0;\vec{k}|\tau_1 G\tau_2 G\tau_1|0;\vec{k}'\rangle$, where τ_i are πN amplitudes. The recoil energy of nucleon 1 affects the pion Green's function G and the intermediate scattering amplitude τ_2. The recoil of nucleon 2 affects only τ_2 and has not been included to save computational time. Effects of antisymmetry of the two nucleons, spin flip, and charge exchange have been included, but not those of pair correlation and Pauli blocking. Inclusion of recoil is found to reduce the local field correction by a factor of 7 from the result of fixed scatterer calculations. Nevertheless, the local field correction remains sizable. In the π-^{16}O case it represents a correction 2/3 as large as the first order optical potential near the πN resonant energy. Nucleon 1 typically recoils through ~ 1 fm while in terms of the internucleon separation r_{12} the effect is very long ranged. Thus the P-wave nature of the πN interaction which enhances the reflection of the pion from nucleon 2 back to nucleon 1 is the main reason why the local field correction is so important in π-nucleus scattering. The imaginary part of the local field correction part of the optical potential is analyzed and its reactive content is shown to arise from two competing mechanisms. The first, and dominant, mechanism is a reduction of the single nucleon knockout contribution that is overestimated in the first order optical potential while the second mechanism is the two-nucleon knockout. The analysis suggests very slow convergence of multiple scattering expansions near the πN resonance energy.

[NUCLEAR REACTIONS Pion optical potential, local field corrections, reactive content of optical potential.]

I. INTRODUCTION

Nuclear pion scattering has the unique feature that the mean separation of nucleons, $d \sim 2$ fm, is comparable to the resonant πN scattering radius: $r_s \approx (\sigma/2\pi)^{1/2} \sim 1.8$ fm. The scattering radius is defined so that a black disk of radius r_s produces the same total cross section as is observed in the $J=\frac{3}{2}$, $I=\frac{3}{2}$, πN scattering state at resonance. The scattering radius is quite distinct from, and much larger than, the interaction range $r_{\pi N} \sim 0.3$ fm, within which the πN interaction is large. The consequence of a large scattering radius is that pion waves reaching a nucleon inside a nucleus are strongly modified by the presence of other nucleons. The rescattered pion wave a distance d from a nucleon is approximately $(f/d)\cos\theta\, e^{ikd}$, where f is the P-wave scattering amplitude, θ is the polar angle measured from the beam direction, and k is the pion's wave number. Because $f/d \simeq i\, r_s/d$ has magnitude comparable to unity at resonance, rescattered waves are as important as incident waves reaching a nucleon.

A substantial part of this multiple scattering effect is summed into the first order optical potential because the small angle ($\theta \sim 0$) pion multiple scattering tends to leave the nucleus in its ground state between scatterings. However, there is a correspondingly large amplitude for pion reflections ($\theta \sim \pi$). The reflections involve large momentum transfer and they preferentially populate excited nuclear states between scatterings. Thus, the effects of reflections come in as higher order terms of the standard optical potential expansions.[1] With few exceptions, analyses of π-nucleus scattering have been performed by omitting the higher order terms on grounds that they are thought to be small.[2] Generally calculations are based on a πN off-shell amplitude that is only kinematically modified in the nuclear medium.

By way of contrast, isobar hole theories of pion-nucleus scattering[3] describe the same physics in a fashion that emphasizes the local field corrections to the πN scattering in the (3, 3) isobar state. The pion scattering is viewed as a sequence of Δ-hole states with pion propagation between the annihilation of one Δ-h state and creation of the next. Often rather substantial local potentials are used to represent the effect of the nuclear field on the isobar self-energy and these effective interactions modify both the mass and width of the isobar in the nuclear medium.

The effects of the nuclear medium on the πN interaction are organized into higher order terms in the multiple scattering optical potential, terms which have been called local field correction by Foldy and Walecka.[4] The simplest multiple scattering model in which the local field correction

© 1980 The American Physical Society

has been studied consists of pion waves scattering from fixed, nonoverlapping potentials. Even though a local potential model is not adequate to describe pion scattering, the results of Agassi and Gal[5] are instructive by way of showing how a projectile's interaction with any one nucleon can be strongly modified by the presence of others nearby. In this simple model, the local field corrections arise from multiple reflections of the incident pion from the neighboring nucleons, a feature which is relevant to pion-nucleus scattering due to the large back-scattering πN amplitude.

In more recent fixed scatterer estimates for nuclear matter,[6] very large effects due to the local field correction have been found based on the Goldstone diagrams of Fig. 1. The importance of these diagrams is that they are the first terms in the multiple scattering series which have the reflection property, and thus the local field correction is small or large depending on their contribution to the optical potential. In the triple scattering process of Fig. 1, the pion wave scattering from nucleon 1 is modified by an intermediate scattering from nucleon 2. At resonance, this local field correction, calculated in fixed scatterer approximation, is about three times as large as the "leading" $t\rho$ term of the optical potential, indicating a severe divergence of the multiple scattering description. It has been argued[7,8] that self-consistent treatments of the multiple scattering process, which approximately sum many-body effects, ultimately regulate the local field correction to $\sim\frac{1}{3}t\rho$. However, this argument relies on a fixed scatterer analysis for infinite nuclear matter and it is recognized[7] that effects neglected in such analyses may regulate, or quench, the local field correction. Three-body analyses of π-d scattering[9] have shown that the fixed scatterer approximation overestimates the local field correction. In nuclei, however, the local field correction is long ranged[6,8] because the pion propagates at positive energy from one nucleon to another. The effect is thus proportional to $A(A-1)\langle 1/r^2\rangle$, i.e., to the number of pairs of nucleons and the mean value of r^{-2}. Clearly the deuteron case is not a decisive test of the local field effect since $\langle 1/r^2\rangle$ is not much different than for nuclei but the number of pairs is small. Because neither fixed scatterer nor three-body analyses have settled this issue, a detailed calculation of the diagrams in Fig. 1 is presented in this paper.

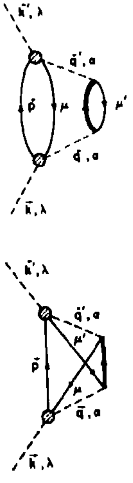

FIG. 1. Goldstone diagrams for local field correction due to triple scattering process. The contribution of the direct diagram (top) is divided into direct and spin-flip parts as discussed in the text. The contribution of the exchange diagram (bottom) is not divided. Heavy lines represent the isobar excitation.

Because the pion twice scatters from nucleon 1 in Fig. 1, an internal loop exists through which large momentum flow is supported by the P-wave coupling of the pion to nucleons. The associated recoil energy of nucleon 1 is neglected in fixed scatterer analyses, and we shall show in this paper that omission of recoil causes serious overestimates of the leading local field correction. Nevertheless, the inclusion of recoil is not sufficient to quench the local field effect in nuclei such as ^{16}O, although it does suggest a more convergent multiple scattering analysis.

The strategy of this paper is to separate the local field correction from true pion absorption effects, which we do not consider here. This is done by excising the nucleon-pole part of the πN interaction with nucleon 2 in Fig. 1, thereby omitting the intermediate state where the pion is absent and two nucleons are excited. The analysis is described in detail in Sec. II and numerical results for the local field correction with and without recoil are presented in Sec. III. Section III also examines the reactive content of the local field correction to explicitly display the origin of the large effects. Conclusions are presented in Sec. IV.

II. RESCATTERING WITH RECOIL

The Goldstone diagrams of Fig. 1 can be evaluated using the rules for a pion propagator in a nucleus.[10] One may also derive the same result using the triple scattering term of Watson's multiple scattering expansion

$$\mathcal{T}^{(3)} = A(A-1)\langle 0;\vec{k}',\lambda|\tau_1 G\tau_2 G\tau_1|0;\vec{k},\lambda\rangle\cdots, \qquad \text{(1a)}$$

where $\vec{k}$ and $\vec{k}'$ are the initial and final pion momenta and $\lambda(=1,2,3)$ the pion isospin. The ket $|0;\vec{k},\lambda\rangle$ is the product of a pion plane wave state and the target-nucleus ground state. The pion-nucleon scattering operator τ and the pion propagator G will be described later.

It should be noted that $\tilde{T}^{(3)}$ is not the matrix element of a part of the Klein-Gordon optical potential. In fact, $\tilde{T}^{(3)}$ does not even have the appropriate dimension. The discussions of Ref. 11 show that the contribution to the Klein-Gordon optical potential is given by

$$\begin{aligned} T^{(3)} &= \sqrt{2\omega_{k'}}\,\tilde{T}^{(3)}\sqrt{2\omega_k} \\ &\quad - A(A-1)\sqrt{2\omega_{k'}} \\ &\quad \times \langle 0;\vec{k}',\lambda|\tau_1 G\tau_2 G\tau_1|0;\vec{k},\lambda\rangle\sqrt{2\omega_k}\,. \end{aligned} \tag{1b}$$

Equation (1) is a generalization of the usual Watson potential theory in that the pion propagator G and the πN amplitudes have appropriate relativistic properties. The full reduction of the relativistic amplitude to the form (1) is omitted as only minimal changes from the usual Watson multiple scattering theory arise. The scattering matrices τ_i are t matrices for pion scattering from nucleon i, wherein the energy variable is $\omega + H_T$, H_T being the Hamiltonian of the target nucleus and ω the pion's asymptotic energy. In this work, we approximate H_T by a constant average binding energy ($H_T \simeq -B$) in which case the τ_i are simply related to the πN t matrix at a shifted energy, $\omega - B$.

The nuclear wave function is assumed to be a determinant of single particle wave functions ϕ_μ, and thus (1) reduces to standard two-nucleon forms which we expand as follows:

$$T^{(3)} = T_D^{(3)} + T_{SF}^{(3)} - T_{EX}^{(3)}\,, \tag{2}$$

where direct plus spin flip and exchange terms are defined via

$$T_D^{(3)} + T_{SF}^{(3)} = \sqrt{2\omega_{k'}}\sum_{\mu}\sum_{\mu'}\langle\phi_\mu(1)\phi_{\mu'}(2);\vec{k}',\lambda|\tau_1 G\tau_2 G\tau_1|\phi_\mu(1)\phi_{\mu'}(2);\vec{k},\lambda\rangle\sqrt{2\omega_k}\,, \tag{3}$$

$$T_{EX}^{(3)} = \sqrt{2\omega_{k'}}\sum_{\mu}\sum_{\mu'}\langle\phi_{\mu'}(1)\phi_\mu(2);\vec{k}',\lambda|\tau_1 G\tau_2 G\tau_1|\phi_\mu(1)\phi_{\mu'}(2);\vec{k},\lambda\rangle\sqrt{2\omega_k}\,. \tag{4}$$

In each of these expressions, the πN scattering matrices τ_1 and τ_2 are fully off energy shell. The πN matrix, τ_1, is evaluated at the shifted pion energy $\omega - B$. Expressed as a single nucleon operator, it has the form

$$\langle\vec{q}',\alpha'|\tau_1(\vec{r}_1;\omega)|\vec{q},\alpha\rangle = -4\pi\sum_{I,J} h_{2I,2J}(\omega)\Omega_{2J}(\vec{q}',\vec{q})\Lambda_{2I}(\alpha',\alpha)e^{i(\vec{q}-\vec{q}')\cdot\vec{r}_1}\frac{v(q')}{\sqrt{2\omega_{q'}}}\frac{v(q)}{\sqrt{2\omega_q}}\,. \tag{5}$$

In order to separate the local field correction from true pion absorption effects, the off-shell amplitude τ_2 is written in a form which omits the nucleon pole term, as follows:

$$\langle\vec{q}',\alpha'|\tau_2(\vec{r}_2;\omega')|\vec{q},\alpha\rangle = -4\pi\sum_{I,J}\tilde{h}_{2I,2J}(\omega')\Omega_{2J}(\vec{q}',\vec{q})\Lambda_{2I}(\alpha',\alpha)e^{i(\vec{q}-\vec{q}')\cdot\vec{r}_2}\frac{v(q')}{\sqrt{2\omega_{q'}}}\frac{v(q)}{\sqrt{2\omega_q}}\,. \tag{6}$$

The energy dependence of the off-shell amplitude is expressed as a dispersion integral, without crossing, as follows:

$$\tilde{h}_{2I,2J}(\omega') = -\frac{1}{\pi}\int_{m_\pi}^{\infty} dz\,\frac{\mathrm{Im}[h_{2I,2J}(z)]}{\omega' - z + i\eta}\,, \tag{7}$$

which is just the right-hand cut term of the Chew-Low form for the πN amplitude. The relationship of the energy variable ω' with the initial pion energy, ω, is discussed later. In these expressions, both the isospin (I) and spin (J) indices are understood to be summed over $\frac{1}{2}$ and $\frac{3}{2}$ values and the projection operators for spins $J=\frac{1}{2}$ and $\frac{3}{2}$ are

$$\Omega_1(\vec{q}',\vec{q}) = \vec{q}'\cdot\vec{q} + i\vec{\sigma}\cdot\vec{q}'\times\vec{q} = \vec{\sigma}\cdot\vec{q}'\vec{\sigma}\cdot\vec{q}\,, \tag{8a}$$

$$\Omega_3(\vec{q}',\vec{q}) = 2\vec{q}'\cdot\vec{q} - i\vec{\sigma}\cdot\vec{q}'\times\vec{q}\,, \tag{8b}$$

while those for isospins $I=\frac{1}{2}$ and $\frac{3}{2}$ are

$$\Lambda_1(\beta,\alpha) = \tfrac{1}{3}\tau_\beta\tau_\alpha\,, \tag{9a}$$

$$\Lambda_3(\beta,\alpha) = \delta_{\beta\alpha} - \tfrac{1}{3}\tau_\beta\tau_\alpha\,. \tag{9b}$$

Here $\beta, \vec{q}'$ denote the final state isospin and momentum while $\alpha, \vec{q}$ are similar labels of the initial state quantities. The πN energy dependent amplitudes, $h_{2I,2J}(\omega)$, are related to the phase shifts as follows:

$$h_{2I,2J}(\omega) = \frac{M+\omega}{M}\,\frac{\eta_{2I,2J}\exp(2i\delta_{2I,2J}) - 1}{2ik^3}\,. \tag{10}$$

The phase shift values used in the present calculations are based on Salomon's parametrization[12] up to 250 MeV pion kinetic energy. For the calculation of the right-hand cut amplitude, $\tilde{h}_{2I,2J}(\omega)$

based on Eq. (7), we employ in addition the CERN theoretical phase shifts[13] to extend the integration to 4 GeV πN center-of-mass total energy. The form factor $v(q)$ is specified later in Eq. (25).

The remaining ingredients of the triple scattering amplitude are the π-nucleus intermediate state Green's functions, $G=(E-\omega_q-H_T+i\eta)^{-1}$, where $E=\omega-E_0$ is the total energy of the external pion plus nuclear ground state. The first scattering of Fig. 1 excites the nucleon from an occupied (hole) state, ϕ_μ, to an unoccupied (particle) state which is approximated as a plane wave state of momentum $\vec{p}$. The energy of this one particle-one hole state is approximately represented as $E_0+B+p^2/(2M)$, where M is the nucleon mass, and $-B$ is the average hole state energy. Thus, the Green's function for momentum $\vec{q}$ of the pion takes the form $G=[\omega-\omega_q-p^2/(2M)-B]^{-1}$. A similar Green's function applies to the pion line of momentum $\vec{q}\,'$ in Fig. 1. The recoil effect in the pion Green's functions forces the propagation energy $\omega-p^2/(2M)-B$ negative for $p\gtrsim\sqrt{2M\omega}$. This causes two natural cutoffs for high momentum values which are not present in fixed scatterer analyses.

The off-shell πN amplitude, τ_2, may be viewed as an isobar-hole state with a continuous mass spectrum $M+z\geqslant M+m_\pi$. The energy denominator internal to this amplitude is thus $(\omega-p^2/2M-2B-z+i\eta)$, where $p^2/(2M)$ is the recoil energy of nucleon 1 and $2B$ represents the energy shift due to the two-hole states in the nucleus. The effect of the nucleon recoil energy is to cause a downward shift of the energy at which the off-shell πN amplitude is evaluated via Eq. (7). Because the πN amplitude, τ_2, is resonant with a width of $\Gamma\sim100$ MeV, the recoil effect is to force τ_2 away from resonance except in a momentum range $\Delta p\sim\sqrt{2M\Gamma}\sim2$ fm^{-1}. In the fixed scatterer analysis, the recoil energy is omitted permitting the τ_2 amplitude to remain large for an infinite range of momentum values.

In this analysis, the isobar recoil is neglected in order to keep the number of integrations manageable. The nucleon recoil affects both the pion propagators and the amplitude τ_2, while Δ-recoil affects only τ_2. Thus, it appears that the nucleon recoil provides the bulk of the recoil effect and omission of Δ recoil is a reasonable approximation, particularly considering the enormous amount of computational time required to take account of it. However, we recognize the possibility that isobar recoil could alter our results to some extent. If a nonzero momentum, say, $\vec{p}\,'$, were assigned to the isobar, then there would be an extra recoil energy, $-p'^2/2M_\Delta$, in the energy denominator. Note that the effect would be a further downward shift of the energy at which τ_2 is evaluated. The effect is qualitatively the same as that due to the nucleon recoil and in the same direction. When expressions (5) and (6) are substituted into (3), we find

$$\begin{aligned}T_{\mathrm{D}}^{(3)}+T_{\mathrm{SY}}^{(3)}=\sum_{\mu,\mu'}\sum_{\alpha,\beta}(-4\pi)^3\int\frac{d^3p}{(2\pi)^9}\int\frac{d^3q}{2\omega_q}\int\frac{d^3q'}{2\omega_{q'}}\\ \times\Big\langle\phi_\mu(1)\phi_{\mu'}(2)\Big|\Big[\sum_{I',J'}h_{2I',2J'}(\omega-B)\Omega_{2J'}(\vec{k}\,',\vec{q}\,')\Lambda_{2I'}(\lambda,\beta)e^{i(\vec{q}\,'-\vec{k}\,'-\vec{p})\cdot\vec{r}_1}\frac{v(k')v^2(q')}{\omega_{q'}-\omega-B-p^2/2M+i\eta}\\ \times\sum_{I,J}\bar{h}_{2I,2J}(\omega-2B-p^2/2M)\Omega_{2J}(\vec{q}\,',\vec{q})\Lambda_{2I}(\beta,\alpha)e^{i(\vec{q}-\vec{q}\,')\cdot\vec{r}_2}\frac{v^2(q)v(k)}{\omega_q-\omega-B-p^2/2M+i\eta}\\ \times\sum_{I'',J''}h_{2I'',2J''}(\omega-B)\Omega_{2J''}(q,k)\Lambda_{2I''}(\alpha,\lambda)e^{i(\vec{k}-\vec{q}-\vec{p})\cdot\vec{r}_1}\Big]\Big|\phi_\mu(1)\phi_{\mu'}(2)\Big\rangle.\end{aligned}\tag{11}$$

The nucleon recoil effect resides in the $p^2/(2M)$ energy shifts and the $\vec{p}$ integration. In the $M\to\infty$ (fixed scatterer) limit, the $\vec{p}$ integration can be carried out to yield $(2\pi)^3\delta^{(3)}(\vec{r}_1-\vec{r}_1\,')$, which expresses the static nucleon propagation. In the recoil case, both $\vec{p}$ and $\vec{r}=\vec{r}_1-\vec{r}_1\,'$ vector variables must be integrated. For a spin and isospin saturated nucleus, the following simplification holds [see Eq. (54)]:

$$-4\pi\sum_{\mu'}\Big\langle\phi_{\mu'}(2)\Big|\sum_{I,J}\bar{h}_{2I,2J}(w)\Omega_{2J}(\vec{q}\,',\vec{q})\Lambda_{2I}(\beta,\alpha)\Big|\phi_{\mu'}(2)\Big\rangle=-4\pi\bar{h}^{(+)}(w)4\rho_0(\vec{r}_2,\vec{r}_2)\delta_{\alpha\beta}\vec{q}\,'\cdot\vec{q}\,.\tag{12}$$

The sums over single particle states have been expressed in term of nuclear density matrices, $\rho_0(\vec{r},\vec{r}\,')$ normalized according to

$$\int d^3r\,\rho_0(\vec{r},\vec{r})=16\,,\tag{13}$$

the mass number for ^{16}O. The isospin sums simplify due to

$$\sum_{\alpha} \Lambda_{3j}(\lambda, \alpha)\Lambda_{3j''}(\alpha, \lambda) = \delta_{j', j''}\Lambda_{3j'}(\lambda, \lambda). \tag{14}$$

When the remaining spin and isospin sums are carried out, the result simplifies as follows:

$$T_D^{(3)} + T_{SF}^{(3)} = v(k)v(k')(2\pi)^{-3}\int d^3p\,[-4\pi\bar{h}^{(+)}(w)]\int d^3r_1\int d^3r_1'\int d^3r_2\,e^{i(\vec{k}\cdot\vec{r}_1-\vec{k}'\cdot\vec{r}_1')}e^{i\vec{p}\cdot(\vec{r}_1-\vec{r}_1')}$$
$$\times 4\rho_0(\vec{r}_1, \vec{r}_1')4\rho_0(\vec{r}_2, \vec{r}_2)[\mathcal{F}_D(\omega-B)K_D(\vec{k}', \vec{k}, \vec{r}', \vec{r}, w) - \mathcal{F}_{SF}(\omega-B)K_{SF}(\vec{k}', \vec{k}, \vec{r}', \vec{r}, w)], \tag{15a}$$

where

$$\vec{r} \equiv \vec{r}_1 - \vec{r}_2, \quad \vec{r}' \equiv \vec{r}_1' - \vec{r}_2, \quad w \equiv \omega - B - p^2/2M, \tag{15b}$$

$$K_i(\vec{k}', \vec{k}, \vec{r}', \vec{r}, w) = \frac{1}{(2\pi)^6}\int \frac{d^3q'}{2\omega_{q'}}\frac{v^2(q')e^{i\vec{q}'\cdot\vec{r}}}{\omega_{q'} - w + i\eta}\int \frac{d^3q\,e^{-i\vec{q}\cdot\vec{r}'}v^2(q)}{2\omega_q(\omega_q - w + i\eta)}N_i(\vec{k}', \vec{k}, \vec{q}', \vec{q}), \tag{15c}$$

$$N_D(\vec{k}', \vec{k}, \vec{q}', \vec{q}) = \vec{k}'\cdot\vec{q}'\vec{q}'\cdot\vec{q}\vec{q}\cdot\vec{k}, \tag{15d}$$

$$N_{SF}(\vec{k}', \vec{k}, \vec{q}', \vec{q}) = \vec{q}'\cdot\vec{q}(\vec{k}'\cdot\vec{q}\vec{q}'\cdot\vec{k} - \vec{q}'\cdot\vec{q}\vec{k}'\cdot\vec{k}), \tag{15e}$$

and

$$\mathcal{F}_D(\omega) = \tfrac{1}{3}(-4\pi)^2\{[h_{11}(\omega) + 2h_{13}(\omega)]^2 + 2[h_{31}(\omega) + 2h_{33}(\omega)]^2\}, \tag{16a}$$

$$\mathcal{F}_{SF}(\omega) = \tfrac{1}{3}(-4\pi)^2\{[h_{11}(\omega) - h_{13}(\omega)]^2 + 2[h_{31}(\omega) - h_{33}(\omega)]^2\}. \tag{16b}$$

The term $\mathcal{F}_D$ is due to scatterings without spin-flip and it produces the direct contribution, $T_D^{(3)}$, in (15). The term $\mathcal{F}_{SF}$ is due to double spin-flip scatterings and it produces the spin-flip contribution, $T_{SF}^{(3)}$, in (15). In both (16a) and (16b), the possibility of charge exchange in the first and the last scatterings is included. Thus, when we define a pion propagation function by

$$G(r; w) \equiv \frac{1}{(2\pi)^3}\int \frac{d^3q}{2\omega_q}\frac{e^{i\vec{q}\cdot\vec{r}}v^2(q)}{\omega_q - w + i\eta}, \tag{17}$$

it is possible to reduce the kernel K to the sum of the following direct and spin-flip terms:

$$K_D(\vec{k}', \vec{k}, \vec{r}', \vec{r}, w) = [\vec{k}'\cdot\vec{\nabla}\vec{\nabla}G(r; w)]\cdot[\vec{k}\cdot\vec{\nabla}'\vec{\nabla}'G(r'; w)], \tag{18}$$

$$K_{SF}(\vec{k}', \vec{k}, \vec{r}', \vec{r}, w) = [\vec{k}\cdot\vec{\nabla}\vec{\nabla}G(\vec{r}, w)]\cdot[\vec{k}'\cdot\vec{\nabla}'\vec{\nabla}'G(r', w)] - \vec{k}'\cdot\vec{k}\nabla_i\nabla_jG(r; w)\nabla_i'\nabla_j'G(r'; w). \tag{19}$$

Note that our form factor $v(q)$ does not absorb the $(2\omega_q)^{-1/2}$ factor and thus a hard form factor $v(q)$ is used in this paper, but there is no disagreement with "soft" form factors which do absorb the $(2\omega_q)^{-1/2}$ into $v(q)$. Further defining three pion propagation functions as follows:

$$G_0(r; w) = \nabla_r^2G(r; w), \tag{20}$$

$$G_1(r; w) \equiv r^{-1}(d/dr)G(r; w), \tag{21}$$

$$G_2(r; w) \equiv G_0(r; w) - 3G_1(r; w), \tag{22}$$

the direct and spin-flip kernels can rewritten as

$$K_D(\vec{k}', \vec{k}, \vec{r}', \vec{r}, w) = \vec{k}\cdot\vec{k}'G_1(r)G_1(r') + \vec{k}'\cdot\hat{r}'\vec{k}\cdot\hat{r}'G_1(r)G_2(r')$$
$$+ \vec{k}\cdot\hat{r}\vec{k}'\cdot\hat{r}G_2(r)G_1(r') + \vec{k}'\cdot\hat{r}\vec{k}\cdot\hat{r}'\,\hat{r}\cdot\hat{r}'G_2(r)G_2(r'), \tag{23}$$

$$K_{SF}(\vec{k}', \vec{k}, \vec{r}', \vec{r}, w) = \vec{k}\cdot\vec{k}'G_1(r)G_1(r') + \vec{k}'\cdot\hat{r}'\vec{k}\cdot\hat{r}'G_1(r)G_2(r') + \vec{k}\cdot\hat{r}\vec{k}'\cdot\hat{r}G_2(r)G_1(r')$$
$$+ \vec{k}\cdot\hat{r}'\hat{r}\cdot\hat{r}'\vec{k}'\cdot\hat{r}G_2(r)G_2(r') - \vec{k}\cdot\vec{k}'[3G_1(r)G_1(r') + G_1(r)G_2(r')$$
$$+ G_2(r)G_1(r') + G_2(r)G_2(r')]. \tag{24}$$

Here the parametric dependence of G_1 and G_2 on the recoil energy via $w = \omega - p^2/2M - B$ is implicit.

In order to permit some analytical reduction of the propagation functions, it is convenient to express the πN form factor in a monopole form

$$v(q) = (1 + k^2/\alpha^2)/(1 + q^2/\alpha^2), \qquad (2$$

where k is the on-shell momentum. The cutoff parameter α is equal to 940 MeV/c in this work,[14] however, the sensitivity of our results to other values of α is tested (see Fig. 7).

Now employing the identity

$$\frac{1}{2\omega_q(w-\omega_q+i\eta)}=\frac{\theta(w)}{w^2-m_\pi^2-q^2+i\eta}+\frac{1}{\pi}\int_0^\infty\frac{dyw}{y^2+w^2}\,\frac{1}{y^2+m_\pi^2+q^2}, \tag{26}$$

we find the pion propagation function can be reduced to a quadrature of an analytic function as follows:

$$G(r;w)=\theta(w)g(r;Q)-\frac{1}{\pi}\int_0^\infty dy\frac{w}{y^2+w^2}g[r;i(y^2+m^2)^{1/2}], \tag{27}$$

where

$$g(r;Q)=\int\frac{d^3q}{(2\pi)^3}\,\frac{e^{i\vec{q}\cdot\vec{r}}}{Q^2-q^2+i\eta}\,\frac{(\alpha^2+k^2)^2}{(\alpha^2+q^2)^2} \tag{28a}$$

takes the analytic form

$$g(r;Q)=\frac{(\alpha^2+k^2)^2e^{-\alpha r}}{8\pi\alpha(Q^2+\alpha^2)}-\frac{(\alpha^2+k^2)^2}{4\pi(Q^2+\alpha^2)^2}\left(\frac{e^{iQr}-e^{-\alpha r}}{r}\right). \tag{28b}$$

In similar fashion, the propagation functions G_0, G_1, and G_2 are also expressed in the form of Eq. (27) through use of Eqs. (20)–(22). The explicit forms used in the calculations of this paper involve Eq. (27) with

$$g_0(r;Q)=\frac{\alpha(\alpha^2+k^2)^2e^{-\alpha r}}{8\pi(Q^2+\alpha^2)}[1-2/(\alpha r)]+\frac{(\alpha^2+k^2)^2}{4\pi(Q^2+\alpha^2)^2}\,\frac{Q^2e^{iQr}+\alpha^2e^{-\alpha r}}{r} \tag{29}$$

and

$$g_1(r;Q)=-\frac{\alpha(\alpha^2+k^2)^2}{8\pi(Q^2+\alpha^2)}\,\frac{e^{-\alpha r}}{\alpha r}+\frac{(\alpha^2+k^2)^2}{4\pi(Q^2+\alpha^2)^2}\left[\frac{e^{iQr}-e^{-\alpha r}}{r^3}-\frac{iQe^{iQr}+\alpha e^{-\alpha r}}{r^2}\right]. \tag{30}$$

We note in passing that the numerical evaluation of (27) requires some care near y values satisfying $i(y^2+m_\pi^2)^{1/2}\sim i\alpha$; however, straightforward analysis shows that the propagation functions $g_0(r;Q)$ and $g_1(r;Q)$ are not singular as $Q\to i\alpha$ or as $r\to 0$.

The next steps in the reduction of (15) to a tractable calculation consist of introducing new variables $\vec{r}\equiv\vec{r}_1-\vec{r}_2$; $\vec{r}'\equiv\vec{r}_1'-\vec{r}_2'$ and carrying out the $\vec{r}_2$ integration using a harmonic oscillator shell model density for ^{16}O. To this end we define

$$D(\vec{r},\vec{r}')=\int d^3r_2e^{i(\vec{k}-\vec{k}')\cdot\vec{r}_2}\rho_0(\vec{r}+\vec{r}_2,\vec{r}'+\vec{r}_2)\rho_0(\vec{r}_2,\vec{r}_2), \tag{31}$$

and consider the shell model density matrix

$$\rho_0(\vec{r}_1,\vec{r}_1')=\frac{4}{\pi^{3/2}b^3}(1+2\vec{r}_1\cdot\vec{r}_1'/b^2)\exp[-\tfrac{1}{2}(r_1^2+r_1'^2)/b^2], \tag{32}$$

with $b=1.786$ fm. When the momentum transfer, $\vec{k}-\vec{k}'$, of the pion is neglected, the following expression emerges:

$$\begin{aligned}D(\vec{r},\vec{r}')=&\frac{4\sqrt{2}}{\pi^{3/2}b^3}\exp[-\tfrac{3}{8}(r^2+r'^2)/b^2+\tfrac{1}{4}\vec{r}\cdot\vec{r}'/b^2]\\&\times\left\{\left[1+\frac{(\vec{r}+\vec{r}')^2}{8b^2}\right]\left[1-\frac{3}{8}\,\frac{(\vec{r}+\vec{r}')^2}{b^2}+\frac{2\vec{r}\cdot\vec{r}'}{b^2}\right]+\frac{27}{4}-\frac{5}{8}\,\frac{(\vec{r}+\vec{r}')^2}{b^2}+\frac{3\vec{r}\cdot\vec{r}'}{b^2}\right\}.\end{aligned} \tag{33}$$

Further specializing the analysis to the $\vec{k}=\vec{k}'$ (zero-momentum transfer) limit, it is observed that the scattering matrix element becomes a scalar function of a single vector, $\vec{k}$. The result is invariant with respect to rotations of $\vec{k}$ and we use this fact to simplify the expression by averaging over directions of $\vec{k}$. The results are expressed as follows:

$$\begin{aligned}T_D^{(3)}=&k^2\bar{\sigma}_D(\omega-B)(2\pi^2)^{-1}\int_0^\infty dp\,p^2\left[-4\pi\bar{h}^{(+)}\left(\omega-2B-\frac{p^2}{2M}\right)\right]\\&\times\int d^3r\int d^3r'j_0(ps)D(\vec{r},\vec{r}')\left(j_0(ks)\mathcal{G}_{D0}(\vec{r},\vec{r}';p)+\frac{j_2(ks)}{s^2}\mathcal{G}_{D2}(\vec{r},\vec{r}';p)\right),\end{aligned} \tag{34}$$

$$T^{(3)}_{SF} = k^2 \mathfrak{F}_{SF}(\omega - B)(2\pi^2)^{-1}\int_0^\infty dp\,p^2\left[-4\pi\bar{h}^{(+)}\left(\omega - 2B - \frac{p^2}{2M}\right)\right]$$
$$\times\int d^3r\int d^3r'\,j_0(ps)D(\vec{r},\vec{r}\,')\left(j_0(ks)\mathcal{G}_{S0}(\vec{r},\vec{r}\,';p) + \frac{j_2(ks)}{s^2}\mathcal{G}_{S2}(\vec{r},\vec{r}\,';p)\right), \tag{35}$$

where

$$\mathcal{G}_{D0}(\vec{r},\vec{r}\,';p) = \tfrac{1}{3}G_0(r)G_0(r') + \tfrac{2}{3}G_2(r)G_2(r')P_2(\cos\theta), \tag{36}$$

$$\mathcal{G}_{D2}(\vec{r},\vec{r}\,';p) = -\tfrac{1}{3}(2r^2 - r'^2)G_2(r)G_1(r') - \tfrac{1}{3}(2r'^2 - r^2)G_1(r)G_2(r')$$
$$+ \tfrac{1}{3}rr'\cos\theta[4G_1(r)G_2(r') + 4G_2(r)G_1(r') + 3G_2(r)G_2(r')]$$
$$- \cos^2\theta[r^2G_1(r)G_2(r') + r'^2G_2(r)G_1(r') + \tfrac{2}{3}(r^2 + r'^2)G_2(r)G_2(r')] + \tfrac{1}{3}\cos^3\theta\, rr'G_2(r)G_2(r'), \tag{37}$$

$$\mathcal{G}_{S0}(\vec{r},\vec{r}\,';p) = \tfrac{2}{3}G_0(r)G_0(r'), \tag{38}$$

$$\mathcal{G}_{S2}(\vec{r},\vec{r}\,';p) = -G_0(r)G_2(r')[r^2\cos^2\theta + \tfrac{1}{3}(2r'^2 - r^2) - \tfrac{4}{3}rr'\cos\theta]$$
$$-G_2(r)G_0(r')[r'^2\cos^2\theta + \tfrac{1}{3}(2r^2 - r'^2) - \tfrac{4}{3}rr'\cos\theta], \tag{39}$$

and

$$\cos\theta = \hat{r}\cdot\hat{r}', \quad s = |\vec{r} - \vec{r}\,'|. \tag{40}$$

The p dependence of the pion propagation functions, G_l, is implicit. The final forms (34) and (35) involve four integrations which are performed numerically, namely, p, r, r', and $\cos\theta$ integrations.

The exchange contribution is given by Eq. (11) with particle labels 1, 2 interchanged in the final (or initial) state. However, this interchange gives rise to a more complicated spin-isospin sum, e.g., (14) no longer applies in a direct fashion. Consider the spin-isospin sums of Eq. (11) with final state particles exchanged in the following condensed notation:

$$\mathrm{SI} = \sum_{\mu,\mu'}\sum_{\alpha,\beta}(-4\pi)^3\left\langle\mu'\left|\sum_{I',J'}h_{2I',2J'}\Omega_{2J'}\Lambda_{2I'}(\lambda,\beta)\sum_{I'',J''}h_{2I'',2J''}\Omega_{2J''}\Lambda_{2I''}(\alpha,\lambda)\right|\mu\right\rangle$$
$$\times\left\langle\mu\left|\sum_{I,J}\bar{h}_{2I,2J}\Omega_{2J}\Lambda_{2I}(\beta,\alpha)\right|\mu'\right\rangle. \tag{41}$$

The projectors $\Omega_{2J''}$ and $\Lambda_{2I''}$ depend on spin and isospin operators of nucleon 1, in the notation of (11). Thus they have been commuted with the projectors Ω_{2J} and Λ_{2I} projectors that depend on nucleon 2 operators. The state $|\mu\rangle$, $|\mu'\rangle$ represent spin-isospin nucleon states that are summed for a closed shell nucleus. Thus, (41) involves a trace over nucleon spins and isospins and cannot depend on the external pion isospin projection, λ. If we average over the possible λ values, the spin-iosspin sums are rendered to the form

$$\Gamma = \tfrac{1}{3}\,\mathrm{Tr}\sum_{\alpha,\beta,\lambda}Q(\lambda,\beta)Q(\alpha,\lambda)\bar{Q}(\beta,\alpha), \tag{42}$$

where

$$Q(\lambda,\beta) = -4\pi\sum_{I',J'}h_{2I',2J'}\Omega_{2J'}\Lambda_{2I'}(\lambda,\beta), \tag{43}$$

and $\bar{Q}$ is a similar form involving the amplitudes $\bar{h}$ in place of h. The projection property of Λ, namely

$$\sum_\beta\Lambda_{2I}(\lambda,\beta)\Lambda_{2I'}(\beta,\alpha) = \delta_{I,I'}\Lambda_{2I}(\lambda,\alpha), \tag{44}$$

can be used to evaluate the sums in (42) *provided* we first use the crossing matrix $C_{I',I''}$ to rearrange the order of indices as follows:

$$Q(\lambda,\beta) = -4\pi\sum_{I',J'}h_{2I',2J'}\Omega_{2J'}\sum_{I''}C_{I',I''}\Lambda_{2I''}(\beta,\lambda)$$
$$= H_1\Lambda_1(\beta,\lambda) + H_3\Lambda_3(\beta,\lambda), \tag{45a}$$

where

$$H_{2I} = H^{(+)}_{2I}\vec{k}'\cdot\vec{q}\,' + H^{(-)}_{2I}i\vec{\sigma}\cdot\vec{k}'\times\vec{q}\,' \tag{45b}$$

and

$$H^{(+)}_1 = -\tfrac{4}{3}\pi(-h_{11} + 4h_{31} - 2h_{13} + 8h_{33}), \qquad \text{(45c}$$

$$H^{(-)}_1 = -\tfrac{4}{3}\pi(-h_{11} + 4h_{31} + h_{13} - 4h_{33}), \qquad \text{(45d}$$

$$H^{(+)}_3 = -\tfrac{4}{3}\pi(2h_{11} + h_{31} + 4h_{13} + 2h_{33}), \qquad \text{(45}$$

$$H^{(-)}_3 = -\tfrac{4}{3}\pi(2h_{11} + h_{31} - 2h_{13} - h_{33}). \qquad \text{(4}$$

Results similar to (45) hold for the $\bar{Q}$ as well. In this fashion, we obtain from Eqs. (42), (44), and (45).

$$\Gamma = \tfrac{1}{3}\mathrm{Tr}\sum_{\beta} H_1 H_1 \bar{H}_1 \Lambda_1(\beta,\beta) + H_3 H_3 \bar{H}_3 \Lambda_3(\beta,\beta)\,, \tag{46}$$

where $\bar{H}_1$ and $\bar{H}_3$ are defined as in (45b) in terms of the $\bar{h}_{2I,2J}$ pion-nucleon amplitudes with pole terms excised. The remaining trace in (46) is over the spin and it yields

$$\begin{aligned}\Gamma = \tfrac{4}{3}[&\mathcal{F}_1(\omega,p)\vec{\mathrm{k}}'\cdot\vec{\mathrm{q}}'\vec{\mathrm{q}}'\cdot\vec{\mathrm{q}}\vec{\mathrm{q}}\cdot\vec{\mathrm{k}}\\ &+\mathcal{F}_2(\omega,p)(\vec{\mathrm{k}}'\cdot\vec{\mathrm{q}}'\,\vec{\mathrm{q}}'\cdot\vec{\mathrm{k}}q^2+\vec{\mathrm{k}}'\cdot\vec{\mathrm{q}}\vec{\mathrm{q}}\cdot\vec{\mathrm{k}}q'^2)\\ &+\mathcal{F}_3(\omega,p)\vec{\mathrm{k}}'\cdot\vec{\mathrm{k}}(\vec{\mathrm{q}}'\cdot\vec{\mathrm{q}})^2]\,,\end{aligned} \tag{47a}$$

where

$$\begin{aligned}\mathcal{F}_1(\omega,p) = {}&(H_1^{(+)}H_1^{(+)} - H_1^{(-)}H_1^{(-)})\bar{H}_1^{(+)}\\ &+2(H_3^{(+)}H_3^{(+)} - H_3^{(-)}H_3^{(-)})\bar{H}_3^{(+)}\\ &-2H_1^{(+)}H_1^{(-)}\bar{H}_1^{(-)} - 4H_3^{(+)}H_3^{(-)}\bar{H}_3^{(-)}\,,\end{aligned} \tag{47b}$$

$$\mathcal{F}_2(\omega,p) = H_1^{(+)}H_1^{(-)}\bar{H}_1^{(-)} + 2H_3^{(+)}H_3^{(-)}\bar{H}_3^{(-)}\,, \tag{47c}$$

$$\mathcal{F}_3(\omega,p) = H_1^{(-)}H_1^{(-)}\bar{H}_1^{(+)} + 2H_3^{(-)}H_3^{(-)}\bar{H}_3^{(+)}\,. \tag{47d}$$

In Eqs.(47), the amplitudes $H_{2I}^{(\pm)}$ are evaluated via (45) in terms of $h_{2I,2J}(\omega - B)$. The amplitudes $\bar{H}_{2I}^{(\pm)}$ are evaluated in a similar fashion in terms of $\bar{h}_{2I,2J}(\omega - 2B - p^2/2M)$, i.e., at the recoil shifted energy.

The remainder of the analysis proceeds in a straightforward fashion, rather similar to the analysis leading up to (34). For brevity, we omit the details and present the results in the following form in the $\vec{\mathrm{k}}' = \vec{\mathrm{k}}$ limit:

$$\begin{aligned}T_{EX}^{(3)} = k^2(2\pi^2)^{-1}\int_0^\infty dpp^2\int d^3r\int d^3r' j_0(ps)D_{EX}(\vec{\mathrm{r}},\vec{\mathrm{r}}')\frac{1}{12}\Big\{&\mathcal{F}_1(\omega,p)\Big[j_0(ks)\mathcal{G}_{D0}(\vec{\mathrm{r}},\vec{\mathrm{r}}';p) + \frac{j_2(ks)}{s^2}\mathcal{G}_{D2}(\vec{\mathrm{r}},\vec{\mathrm{r}}';p)\Big]\\ &+\mathcal{F}_2(\omega,p)\Big[j_0(ks)\mathcal{G}_{S0}(\vec{\mathrm{r}},\vec{\mathrm{r}}';p) + \frac{j_2(ks)}{s^2}\mathcal{G}_{S2}(\vec{\mathrm{r}},\vec{\mathrm{r}}';p)\Big]\\ &+\mathcal{F}_3(\omega,p)[3j_0(ks)\mathcal{G}_{D0}(\vec{\mathrm{r}},\vec{\mathrm{r}}';p)]\Big\}\,,\end{aligned} \tag{48}$$

where

$$s = |\vec{\mathrm{r}} - \vec{\mathrm{r}}'|\,,$$

and

$$D_{EX}(\vec{\mathrm{r}},\vec{\mathrm{r}}') = \int d^3r_2\, 16\rho_0(\vec{\mathrm{r}}' + \vec{\mathrm{r}}_2, \vec{\mathrm{r}}_2)\rho_0(\vec{\mathrm{r}} + \vec{\mathrm{r}}_2, \vec{\mathrm{r}}_2)\,. \tag{49}$$

Employing the shell model density matrix of (32), we find

$$\begin{aligned}D_{EX}(\vec{\mathrm{r}},\vec{\mathrm{r}}') = {}&\frac{4\sqrt{2}}{\pi^{3/2}b^3}\exp[-\tfrac{3}{8}(r^2+r'^2)/b^2 + \tfrac{1}{4}\vec{\mathrm{r}}\cdot\vec{\mathrm{r}}'/b^2]\\ &\times\{[1+\tfrac{1}{8}s^2/b^2 - \tfrac{1}{4}(r^2+r'^2)/b^2]^2 - \tfrac{1}{16}(r^2-r'^2)^2/b^4 + \tfrac{27}{4} - \tfrac{3}{4}(r^2+r'^2)/b^2 + \tfrac{1}{8}s^2/b^2\}\,.\end{aligned} \tag{50}$$

Equations (34), (35), and (48) have been numerically evaluated. As the calculation is nontrivial, two entirely independent computer codes were written, each employing different integration variables and numerical methods. The codes were checked against each other and thus a high degree of confidence in placed on the resulting numerical evaluations.

III. RESULTS AND DISCUSSION

The size of the leading order local field corrections,

$$U^{(3)} = T^{(3)} = T_D^{(3)} + T_{SF}^{(3)} - T_{EX}^{(3)}\cdots \tag{51}$$

can be discussed best in relation to the first order potential,

$$U^{(1)} = (2\omega_k')^{1/2}\Big\langle 0;\vec{\mathrm{k}}',\lambda\Big|\sum_i \tau_i\Big|0;\vec{\mathrm{k}},\lambda\Big\rangle(2\omega_k)^{1/2}\cdots. \tag{52}$$

We do this by comparing the $\vec{\mathrm{k}} = \vec{\mathrm{k}}'$ (diagonal) matrix elements $U^{(1)}$ and $U^{(3)}$. For $\pi - {}^{16}\mathrm{O}$ scattering the $\vec{\mathrm{k}} = \vec{\mathrm{k}}'$ element of the first order optical potential is

$$U^{(1)} = 16k^2[-4\pi h^{(+)}(\omega - B)]\cdots, \tag{53}$$

where

$$h^{(+)}(\omega)=\tfrac{1}{3}[h_{11}(\omega)+2h_{31}(\omega)$$
$$+2h_{31}(\omega)+4h_{33}(\omega)]\cdots. \qquad (54)$$

The three parameters of the calculations are the binding shift $B=21$ MeV, the πN form factor cutoff $\alpha=940$ MeV/c of Eq. (25) and the ^{16}O oscillator parameter $b=1.786$ fm of Eqs. (33) and (50).

Figure 2 shows the real and imaginary parts of $U^{(1)}$ and $U^{(3)}$ as functions of the kinetic energy of the pion in the laboratory frame. Below 100 MeV, the local field correction embodied by $U^{(3)}$ is seen to be a modest correction to the first order optical potential. However, in the range 120 to 240 MeV, the local field correction can be nearly as big as $U^{(1)}$. Both the real and imaginary parts of the optical potential are affected.

The local field correction $U^{(3)}$ is composed of direct, spin-slip, and exchange contributions as shown in Fig. 3. A notable coincidence is the near cancellation of spin-flip and exchange contributions. Thus the total $U^{(3)}$ is nearly equal to just the direct contribution $T_D^{(3)}$ of Eq. (34) as is seen by comparing the solid and dashed lines of Fig. 3.

An objective of this work was to test the validity of fixed scatterer estimates of the local field correction. In the fixed scatterer case, the nucleon mass $M\to\infty$, causing the nucleon recoil energy $p^2/(2M)\to 0$. In this event, the local field correction can be much more simply evaluated since the $\vec{p}$ integration produces $\delta^{(3)}(\vec{r}_1-\vec{r}_1')$, i.e., the recoil distance is zero. For example, the direct contribution from Eq. (34) produces

$$U_{\rm FSA}^{(3)}=k^2\mathcal{F}_D(\omega-B)[-4\pi\bar{h}^{(+)}(\omega-2B)]$$
$$\times\int d^3r_{12}D(\vec{r}_{12},\vec{r}_{12})\mathcal{G}_{D0}(\vec{r}_{12},\vec{r}_{12},0). \qquad (55)$$

The function $\mathcal{G}_{D2}$ of (34) vanishes when $r=r'$ and thus does not contribute. Because of rotational invariance, a one-dimensional r_{12} integration suffices to evaluate this expression as opposed to the four-dimensional one needed when recoil is included. In the fixed scatterer calculation, the resonant amplitude $\bar{h}^{(+)}$ is unaffected by recoil energy and the pion Green's functions become free of recoil energy shifts.

The ratio R defined by

$$R\equiv U^{(3)}/U^{(1)} \qquad (56)$$

is the complex ratio of local field correction to first order optical potential. The magnitude of the ratio with recoil effects included and for the fixed scatterer approximation (FSA) (55) are compared in Fig. 4. The inclusion of recoil typically reduces the local field correction by a factor 6 to 7. Nevertheless, the peak value $|R|=0.66$ at 150 MeV shows that the local field correction remains sizeable compared to the first order optical potential. Because the resonant energy dependence of $U^{(1)}$ is divided out in the ratio R, Fig. 4 clearly shows the additional energy dependence due to the leading local field correction. Local field effects are most pronounced near the πN resonance energy and the fixed scat-

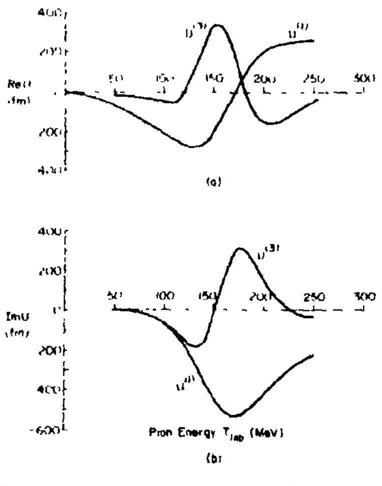

FIG. 2. Real and imaginary parts of the first order optical potential, $U^{(1)}$, and of the local field correction, $U^{(3)}$, both evaluated at $\vec{k}=\vec{k}'$, for π-^{16}O scattering.

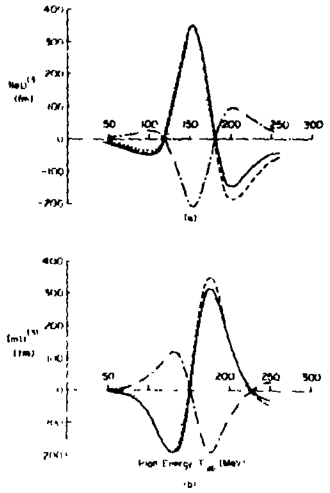

FIG. 3. Contributions to the real and imaginary parts of the local field correction due to direct (— — —), spin-flip (••••••), and exchange (—•—•—) terms for π-^{16}O scattering. The solid line shows the total which is approximately equal to just the direct contribution.

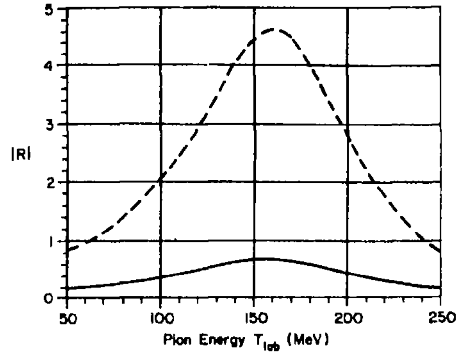

FIG. 4. Magnitude of the ratio R of $U^{(3)}$ to $U^{(1)}$ for π-^{16}O scattering. Solid line shows the recoil calculation and dashed line shows the fixed scatterer calculation.

terer limit is not a resonable approximation to them.

Figure 5 shows the ratio R as a function of M_N/M, where M is a variable nucleon mass and M_N is the physical nucleon mass. Results are shown for the local field correction with variable mass M at 150 MeV pion energy. There are two points to be noted. First, the ratio R drops rapidly in size as one moves away from the static limit, i.e., as M_N/M increases from zero. Second, the real and imaginary parts of R change differently as M_N/M goes from zero to unity, which corresponds to the physical case.

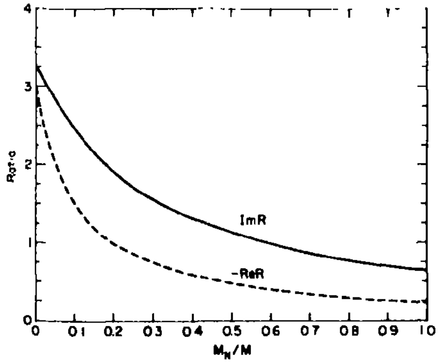

FIG. 5. Real and imaginary parts of ratio R are plotted versus inverse recoil mass, M for 150 MeV π-^{16}O scattering. (M_N is the physical nucleon mass.) Fixed scatterer results ($M_N/M=0$) are approached very slowly as the mass M increases.

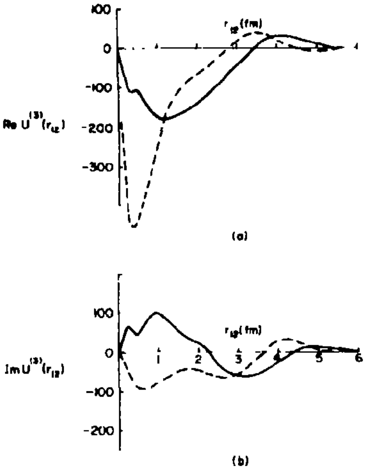

FIG. 6. Contributions to the local field correction, $U^{(3)}$, from different internucleon separations for 150 MeV π-^{16}O scattering. Solid line shows the recoil results and dashed line show one-fifth of the fixed scatterer results.

Figure 6 compares the fixed scatterer and recoil calculations as functions of the typical internucleon separations,

$$r_{12} = \left|\frac{\vec{r}+\vec{r}\,'}{2}\right| = \left|\frac{\vec{r}_1+\vec{r}_1\,'}{2} - r_2\right| ,$$

which give rise to the local field correction. The integrand of the r_{12} integration for $U^{(3)}$, other integrations having been done, is plotted versus r_{12} and it is immediately clear that the local field correction is a very long range effect. Most of the local field correction arises from nucleons 1 to 3 fm away from the subject nucleon, with non-negligible contributions arising from nucleons up to 5 fm away (i.e., on the other side of the nucleus). The failure of the fixed scatterer approximation, which is shown at one-fifth actual magnitude is Fig. 6, is most pronounced for small internucleon separations ($\lesssim 1.5$ fm). The recoil effects tend to increase the range of the local field correction.

A simple interpretation of the long range of the local field correction is made in terms of the resonant scattering amplitude mentioned in the Introduction. Pion scattered waves originating at nucleon 1 can freely propagate a substantial distance to a second nucleon, backscatter, and return to scatter once again from nucleon 1 with probability amplitude of order unity. Thus, the interaction of the pion with any nucleon is influenced by essentially all the other nucleons in the nucleus near the πN resonance energy.

It is also apparent that higher order effects will modify the local field correction. In a self-consistent treatment, the pion would not freely propagate large distances without experiencing scattering and absorption through its interaction with the surrounding nucleons.[6] Our results motivate a self-consistent description of the pion-nucleus scattering, however, that is beyond the scope of the present paper.

Because the local field correction is long range, there is not a great sensitivity to short range correlations or to πN form factor cutoffs. The dependence of the ratio R on the πN form factor parameter α of Eq. (25) is shown in Fig. 7. At 150 MeV pion energy, the ratio R reduces from 0.62 to 0.5 when the πN cutoff is reduced from 940 MeV/c to 600 MeV/c. Because of the complex interplay of direct, spin-flip, and exchange contributions, we find that further reduction of α has little effect on the local field correction.

The relative insensitivity to the πN form factor deserves some explanation. If one approximates the pion propagation functions by neglecting the tensor coupling [dropping $G_2(r)$ terms in Eqs. (36) and (37), for example], then the local field correction is found to be much shorter ranged and more sensitive to πN form factor cutoff. The long range of the actual effect is in the tensor coupling term,[18] which accounts for four-fifths of the local field correction. Thus, we find that an angular average over pion directions, such as is customarily used in derivations of the Lorentz-Lorenz correction, fails in the local field correction since it omits the tensor coupling.

Figure 8 shows the dependence of the local field correction on the recoil momentum variable, p, which is the momentum of the plane wave excited states. The integrand of the p integration for 150 MeV pion energy is plotted versus momentum p including direct, spin-flip, and exchange contributions and with all other integrations carried out. Owing to recoil effects, the contributions typically arise from excited nucleon states of momentum 0.5 to 3 fm^{-1}. We have tested the sensitivity of the calculation to Pauli exclusion of nucleon momenta in the range 0 to 1.4 fm^{-1} by excluding that range of p integration. As Fig. 8 suggests, it is found that the imaginary part of $U^{(3)}$ increases in magnitude while the real part of $U^{(3)}$ decreases in magnitude. At 150 MeV pion laboratory energy, the absolute magnitude of the ratio R does not change much due to Pauli blocking.

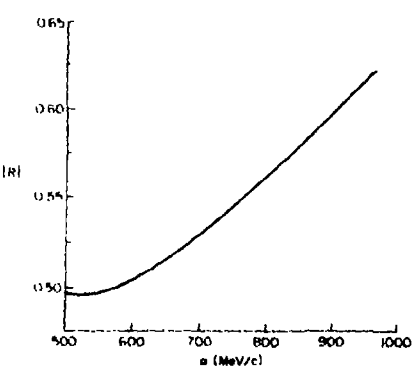

FIG. 7. Dependence of the ratio R on the πN off-shell form factor parameter [see Eq. (25)] for 150 MeV π-^{16}O scattering.

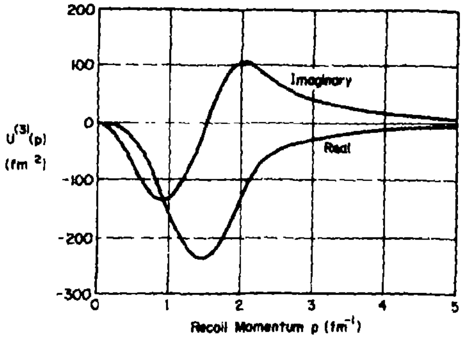

FIG. 8. Dependence of the local field correction on the nucleon recoil momentum p for 150 MeV π-^{16}O scattering.

Figure 9 shows that the excited nucleon typically recoils a distance 0.5 to 1 fm as opposed to the zero recoil distance of the fixed scatterer approximation. Thus, it is seen that the local field correction mainly arises from backward angle scatterings in the intermediate nucleon interaction and the usual interpretation in terms of multiple reflections is verified.

Because the local field corrections substantially change the imaginary part of the optical

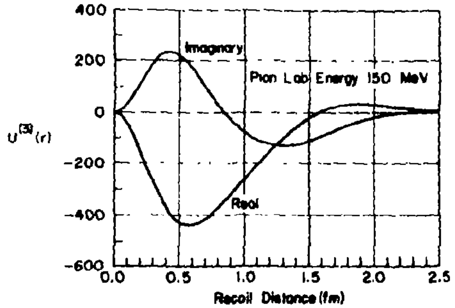

FIG. 9. Dependence of the local field correction on th nucleon recoil distance, $|\vec{r}_1 - \vec{r}_1'|$, for 150 MeV π-^{16}O scattering.

potential, it is important to identify the physical processes which are responsible. The reactive content of the optical potential is considered along the lines of the work of Tandy, Redish, and Bollé.[16] The discontinuity operator

$$\Delta U(\omega)\equiv U(\omega+i\epsilon)-U(\omega-i\epsilon) \tag{57}$$

is useful in this regard since

$$\lim_{\epsilon\to 0}\Delta U(\omega)=2i\,\mathrm{Im}U(\omega)\,. \tag{58}$$

Multiple scattering expansions generally involve operator strings of the form

$$\Gamma=ABABA\cdots, \tag{59}$$

where $A\equiv A(\omega+i\epsilon)$ and $B\equiv B(\omega+i\epsilon)$ depend on the energy variable ω and ϵ is an infinitesimal imaginary part. The discontinuity of such operator strings is given by the following theorem:

$$\begin{aligned}\Delta\Gamma=&(\Delta A)BABA\cdots+A^*(\Delta B)ABA\cdots\\&+A^*B^*(\Delta A)BA\cdots+A^*B^*A^*(\Delta B)A\cdots\\&+A^*B^*A^*B^*(\Delta A)\cdots+\cdots,\end{aligned} \tag{60}$$

where $A^*\equiv A(\omega-i\epsilon)$ and $B^*=B(\omega-i\epsilon)$. A deductive proof can readily be constructed. The discontinuity operator Δ obeys a chain rule with the exception that it conjugates the complex energy variable of all operators to its left.

The imaginary part of the triple scattering optical potential $U^{(3)}$, or of the T matrix $T^{(3)}$ of Eq. (1), arises from five separate discontinuities as follows:

$$\begin{aligned}\Delta U^{(3)}=\langle 0;\hat{k},\lambda|[&\Delta\tau_1G\tau_2G\tau_1+\tau_1^*\Delta G\tau_2G\tau_1\\&+\tau_1^*G^*\Delta\tau_2G\tau_1+\tau_1^*G^*\tau_2^*\Delta G\tau_1\\&+\tau_1^*G^*\tau_2^*G^*\Delta\tau_1]|0;\hat{k},\lambda\rangle\,.\end{aligned} \tag{61}$$

Figure 10 indicates the five cuts corresponding to this equation. The notation τ_1^* designates $\tau_1(\omega-i\eta)$, which differs from the Hermitian conjugate of $\tau_1(\omega+i\eta)$ due to the spin and isospin projections of Eqs. (5) and (6). When the spin and isospin sums are evaluated as in Sec. II, the various contributions to the discontinuity, $\Delta U^{(3)}$, can be shown to involve Hermitian forms, however, those details are omitted. For the present, we note that the third term of Eq. (61) represents the cut corresponding to a nucleon, a Δ and two hole states in the residual nucleus in the intermediate state. Because the Δ mass is greater than M_N+m_π, this discontinuity corresponds to production of πNN intermediate states and must contribute a negative imaginary part to the optical potential. Note that omission of the pole term from τ_2 in this work means that the true pion absorption cut corresponding to NN intermediate states is not present. A complete analysis, of course, must include the true absorption; however, the present focus is on the local field effect which we logically consider as a separate issue.

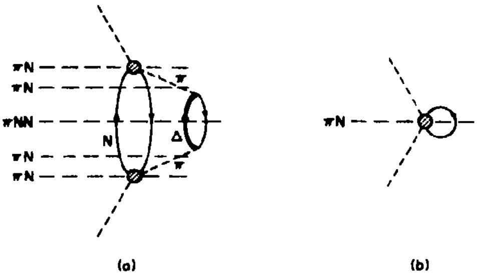

FIG. 10. Absorptive cuts of the local field correction (a) and the first order optical potential (b). The imaginary part of $U^{(1)}$ arises from plane wave impulse approximation of the quasifree knockout process $(\pi,\pi N)$. The four πN cuts of the local field correction serve to modify the absorption of the first order optical potential by inclusion of initial and final state distortions to the quasifree knockout.

The remaining four cuts of Fig. 10 and Eq. (61) correspond to intermediate πN states. These cuts are corrections to the absorptive cut of the first order optical potential,[17]

$$U^{(1)}=A\langle 0;k,\lambda|\Delta\tau_1|0;k,\lambda\rangle\,,$$

which also corresponds to πN intermediate states as indicated in Fig. 10. However, the nucleon knockout to πN intermediate states is overestimated in the first order optical potential because its discontinuity corresponds to plane wave knockout. The corrections to this discontinuity present in $\Delta U^{(3)}$ are distortion effects of the medium on the outgoing pion which generally cause a reduction of the πN reaction cross section. For this reason, the πN distortion cuts of $U^{(3)}$ tend to be emissive in that they act to reduce to absorption present in $U^{(1)}$. The imaginary part of $U^{(3)}$ can thus be either positive or negative depending on the predominance of the πN or πNN cuts.

Figure 11 shows a comparison of the various contributions to the imaginary part of the optical potential as functions of the pion energy. The imaginary part of $U^{(3)}$ is seen to consist of a large emissive part due to πN cuts and an absorptive part due to the πNN cut. The figure reemphasizes the slow convergence of the multiple scattering expansion of the optical potential in the vicinity of the πN resonance energy. It should be noted, however, that Pauli exclusion effects that are not included here will reduce the absorptive parts significantly.

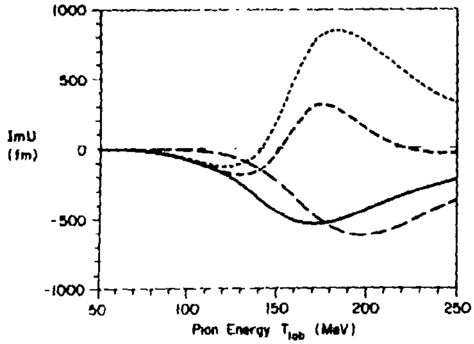

FIG. 11. Imaginary part of first order optical potential Im$U^{(1)}$ (——) is compared to the imaginary part of the local field correction Im$U^{(3)}$ (- — — —). The πNN cut contribution to Im$U^{(3)}$ (— — —) is purely absorptive, but is conterbalanced by the sum of the four πN cut contributions (- - - -), which tend to be emissive.

IV. CONCLUSIONS

The leading order local field corrections in pion-nucleus scattering are quite large near the πN resonant energy. The conventional multiple scattering theories thus converge, at best, quite slowly. The previous work on the local field corrections employing the fixed scatterer approximation seriously overestimates the effect; however, the present analysis including recoil effects basically points to the same conclusion. The pion-nucleus interaction involves very high order multiple scattering processes which may be better organized into the theory if one insists on a self-consistent optical potential theory in which the pion propagation between scatterings is modified by the effects of the medium. Inclusion of the pion absorption mechanism is not likely to alter this conclusion.

Recent papers by Oset and Weise[18] considered several higher order corrections to the optical potential in an isobar-hole model. The isobar self-energy in the nucleus was shown to be substantially altered by the isobar-nucleus Hartree potential, by Pauli blocking effects, and by pion absorption and reflection contributions. Of these effects, the pion reflection contribution to the isobar self-energy is the agent for the local field correction considered in this paper. Many differences in the approaches deter any simple numerical comparison of our results for the local field correction with the isobar self-energy results of Ref. 18. However, several remarks are in order. An important conclusion of Ref. 18 was that partial cancellation between various corrections takes place in the calculation of total cross sections for π-nucleus scattering. Furthermore, the results show that all of the above-mentioned medium corrections are large and they must be incorporated in an equal footing. Our results for the local field correction also argue strongly for its inclusion into microscopic theories of π-nucleus scattering.

We further emphasize that the local field effect should be incorporated in all orders and in a self-consistent manner. Incorporation in all orders requires that all internal pion propagators contain the pion optical potential. Self-consistency requires that the π-nucleon t matrix, so modified, be able to reproduce the pion optical potential in the relevant energy range. This conclusion is based on the very large, and opposite in sign, contributions to the imaginary part of the local-field correction discussed in relation to Figure 11. The quasifree reactive content of the optical potential is incorrect if the intermediate state pions are not distorted by the optical potential.

Because the pion-nucleus elastic scattering is nearly black-disk scattering near the πN resonance energy, the inclusion of local field corrections is not expected to induce dramatic changes in forward angle elastic scattering predictions. Back angle scattering is expected to be sensitive to the local field correction. However, the chief importance of the local field corrections may lie in their implications for distorted wave calculations for reactions. Local field corrections tend to increase the nuclear transparency. The anomaly in predictions of single pion, charge-exchange cross sections[19] when standard optical potentials are used in DWIA calculations may be an experimental indication of increased transparency of the nucleus to pions. A second pion application which may be sensitive to knowledge of the local field correction is the extraction of matter radii from pion-nucleus elastic scattering. Although the data very precisely determine a strong absorption radius for "the optical potential," it is a difficult problem to relate this information to matter radii using a microscopic theory of pion multiple scattering. Local field corrections are expected to further complicate such attempts.

As noted previously, the predominance of the first order optical potential implies that the pion-nucleus reaction cross section is strongly dominated by quasifree knockout of nucleons which is a single nucleon process. The presence of large local field corrections suggests increased importance of multinucleon processes. As shown by Morris *et al.*,[20] there are data which support this view. The ratio of nucleon knockout by π^+ and π^- beams, when the nucleus is left in a definite final state, is found to differ significantly from prediction based on quasifree scattering.

A principal conclusion of this work is that pion multiple scattering requires a self-consistent treatment of the pion self-energy in the nucleus. It is reasonable to expect that local field correction will be reduced by the self-consistency as has already been shown in the fixed scatterer case by Johnson and Bethe.[7]

ACKNOWLEDGMENT

The authors wish to acknowledge the support of the U. S. Department of Energy and the University of Maryland Computer Science Center for this work. B. D. Keister was associated with this work in its initial stages and the authors thank him for many valuable discussions and helpful suggestions.

---

[1] K. M. Watson, Phys. Rev. 89, 575 (1953); M. L. Goldberger and K. M. Watson, *Collision Theory* (Wiley, New York, 1964), p. 749; A. K. Kerman, H. McManus, and R. M. Thaler, Ann. Phys. (N.Y.) 8, 551 (1959).

[2] R. H. Landau, S. C. Phatak, and F. Tabakin, Ann. Phys. (N.Y.) 78, 299 (1973); L. C. Liu and C. M. Shakin, Phys. Rev. C 16, 333 (1977); 16, 1963 (1977); R. H. Landau and A. W. Thomas, Nucl. Phys. A302, 461 (1978); N. J. DiGiacomo, A. S. Rosenthal, E. Rost, and D. Sparrow, Phys. Lett. 66B, 421 (1977).

[3] L. Kisslinger and W. Wang, Ann. Phys. (N.Y.) 99, 374 (1976); F. Lenz, *ibid.* 95, 348 (1976); E. Moniz, in *Meson-Nuclear Physics—1976* (A.I.P. Conf. Proc. No. 33) (Carnegie-Mellon Conference), edited by P. D. Barnes, R. A. Eisenstein, and L. S. Kisslinger, p. 105.

[4] L. L. Foldy and J. D. Walecka, Ann. Phys. (N.Y.) 54, 447 (1969).

[5] D. Agassi and A. Gal, Ann. Phys. (N.Y.) 75, 56 (1973); 91, 194 (1975); 94, 184 (1975).

[6] B. D. Keister, Nucl. Phys. A271, 342 (1976).

[7] M. B. Johnson and H. A. Bethe, Nucl. Phys. A305, 418 (1978).

[8] M. B. Johnson and B. D. Keister, Nucl. Phys. A305, 461 (1978).

[9] J. M. Rivera and H. Garcilazo, Nucl. Phys. A285, 505 (1977); R. Woloshyn, E. J. Moniz, and R. Aaron, Phys. Rev. C 13, 286 (1976).

[10] J. B. Cammarata and M. K. Banerjee, Phys. Rev. C 13, 299 (1976).

[11] J. B. Cammarata and M. K. Banerjee, Phys. Rev. Lett. 31, 610 (1973).

[12] M. Salomon, TRIUMF Report No. TRI-74-2 (unpublished).

[13] R. C. Herndon *et al.*, Report No. UCRL-20030, 1970 (unpublished).

[14] This choice is compatible with the form factor $[1+q^2/(1400\ \mathrm{MeV}/c)^2]^{5/2}$ which Banerjee and Cammarata [Phys. Rev. D 18, 4078 (1978)] obtained by fitting the amplitudes $\bar{C}^{(+)}$ ($\nu = 0$, $t \leqslant 0$) determined by dispersion relations.

[15] Mikkel Johnson, private communication.

[16] P. C. Tandy, E. F. Redish, and D. Bollé, Phys. Rev. C 16, 1924 (1977).

[17] This point has been discussed by D. S. Kolton and D. M. Schneider, Phys. Rev. Lett. 42, 211 (1979).

[18] E. Oset and W. Weise, Nucl. Phys. A319, 477 (1979).

[19] J. Warszawski, A. Gal, and J. M. Eisenberg, Nucl. Phys. A294, 321 (1978).

[20] C. L. Morris *et al.*, Phys. Rev. C 17, 227 (1978).

PHYSICAL REVIEW C VOLUME 21, NUMBER 5 MAY 198

Photoproduction of pions from deuterons at medium energies

J. D. Anand, V. S. Bhasin, and V. K. Gupta
Department of Physics and Astrophysics, University of Delhi, Delhi-110007, India

(Received 29 May 1979)

We study, within the framework of impulse approximation, photoproduction of pions by deuterons leading to two final protons at incident photon energy varying from 210 to about 700 MeV. Employing for the two-body processes $\gamma N \to \pi N$ a dispersion theoretic model by Chew *et al.* and taking spin, isospin, and the identity of the two outgoing particles explicitly into account, the present investigation is primarily directed towards studying (i) the effect of the deuteron wave functions used (including the tensor force and hard core), and (ii) the effect of inserting the $\gamma N \to \pi N$ amplitude in different reference frames thereby introducing off-shell corrections to the physical amplitude. We find that the tensor force and hard core terms play only a marginal role in improving the agreement with experimental data. On the other hand, different forms of the wave function, e.g., Yamaguchi versus Gaussian, involving relatively small momentum components do affect the results considerably. The effect of off-shell corrections to the two-body amplitude is found to be significant at medium energies and large angles. The results obtained for the total cross section as well as the differential cross section for the produced pions in the entire angular region are compared with the experimental data.

[NUCLEAR REACTIONS Photopion production, total and differential cross sections, impulse approximation, effect of reference frames, deuteron wave functions.]

I. INTRODUCTION

Deuterons have since long been used as probes to extract the information on the two-body processes which are not directly accessible to experimentation. An example is the process $\gamma d \to \pi^- pp$ which has been extensively studied to derive the information about $\gamma n \to \pi^- p$. Obviously, the proton in the deuteron, except for sharing its Fermi momentum with the neutron, plays here only the role of a spectator: The incident photon knocks on the neutron producing a π^- and a proton. The two well-known methods used to analyze such a process are (i) the spectator model and (ii) the impulse approximation using closure property.[1] The basic idea in both these approaches is to express the cross section for the two-body subprocess in terms of the experimentally measured cross sections. Identifying the two-body amplitude thus deduced as that for the free two-body process, in fact, amounts to ignoring the off-shell effects. Indeed, in recent studies[2] there have been attempts to determine experimentally the kinematical region where the errors due to off-shell effects could be minimized.

We have, in the present work, analyzed within the framework of the impulse approximation the process $\gamma d \to \pi^- pp$ at photon incident energies from 210 to 700 MeV by taking the two-body amplitude $\gamma n \to \pi^- p$ from the dispersion theoretic result of Chew *et al.*[3] (henceforth referred to as CGLN). Recently, Blomqvist and Laget[4] studied this process using a model where the pion photoproduction on a nucleon is described by the Born terms and the s-channel (3, 3) resonance. The basic difference between this rather simplified model and the CGLN approach lies in the fact that the pion nucleon continuum in the latter has been truncated by the s-channel (3, 3) resonance and nucleon pole terms. From the point of view of confronting these models with experimental results, we find that both of these reproduce the data reasonably well (within about 10%). In a recent series of papers,[5] Laget and Bosted have studied the effect of various rescattering terms in $\gamma d \to \pi^- pp$ employing the above model for $\gamma n \to \pi^- p$ and investigated, within the framework of spectator model, the kinematical regions where such terms could be significant. The main thrust there has been to check the validity of the spectator model.

Here we are interested in checking the sensitivity of the results over the details of the various ingredients used and the approximations incurred. It would thus be interesting to study the effect of the details of deuteron wave functions used which could be significant especially if its large momentum components are involved. In addition, in the impulse approximation or more generally in an eikonal approach one generally employs an on-shell two-body amplitude whose kinematics are essentially determined by those of the main process. Now so long as the incident momentum of the impinging particle is sufficiently high compared to the Fermi momentum carried by the constituents

© 1980 The American Physical Societ

of the target nucleus, such an approximation is known to be reasonably good for small momentum transfers.

The present study has been devoted primarily to unfolding the effect of such approximations, i.e., to critically investigate (i) the effect of the details of the deuteron wave functions used and (ii) the effect of inserting the $\gamma n \to \pi^- p$ amplitude in different reference frames. The latter provides us, in a natural fashion, with a handle to make an estimate of the off-shell effects incurred in the two-body process.

In Sec. II, we outline the steps necessary to write the differential cross section for the breakup process leading to three particles, incorporating spin, isospin, and the effect of the identity of the two particles. The full CGLN amplitudes for $\gamma N \to \pi N$ are recorded in the Appendix. As for the s- and p-wave phase shifts for the amplitudes we adopt the parametrization obtained by Donnachie and Shaw.[6] In Sec. III, we present the results and discuss the various features comparing them with the experimental data.

II. FORMALISM

We start with the standard expression[7] for the cross section of a breakup process leading to three free particles, i.e.,

$$\sigma = \frac{1}{(2\pi)^5} \int \frac{d\vec{k}_1 d\vec{k}_2 d\vec{k}_3}{|\vec{v}_1 - \vec{v}_2|} \,|\langle \vec{k}_1 \vec{k}_2 \vec{k}_3 | T | \vec{k}_\gamma \vec{k}_d \rangle|^2 \delta(\vec{k}' - \vec{k}) \times \delta(E' - E) . \quad (2.1)$$

In the overall c.m. system, where

$$\vec{K}' = \vec{k}_1 + \vec{k}_2 + \vec{k}_3 = 0 ; \quad \vec{k} = \frac{\vec{k}_2 - \vec{k}_3}{2} ,$$

$$\vec{K} = \vec{k}_\gamma + \vec{k}_d = 0; \quad \vec{k}_\pi = \frac{2m\vec{k}_1 - \mu(\vec{k}_2 + \vec{k}_3)}{(2m + \mu)} = \vec{k}_1 \quad (2.2)$$

and $\vec{k}_\gamma (= \vec{k}_i)$ is the c.m. momentum of the incident particle, the above expression is simplified to

$$\sigma = \frac{1}{(2\pi)^5 (1 + E_\gamma / E_d)} \int d\vec{k}_\pi d\vec{k} \,\delta(E_\pi + k_\pi{}^2/4m + k^2/m - E_\gamma - E_\gamma{}^2/2M_d + \epsilon_d) \,|\langle \vec{k}, \vec{k}_\pi | T | \vec{k}_i \rangle|^2 , \quad (2.3)$$

where E_γ is the energy of the incident particle (photon) and E_d of the target (deuteron), M_d its mass, and E_d its binding energy. The integration vectors $\vec{k}_\pi, \vec{k}$ are, respectively, the momentum of the outgoing pion and the relative momentum of the other two nucleons. The matrix element corresponding to the process (see Fig. 1) is written explicitly as

$$\langle \vec{k}, \vec{k}_\pi | T | \vec{k}_i \rangle = \int d\vec{p} \,\Phi_f (\vec{p} + \tfrac{1}{2}\vec{k}_\pi) \langle -\vec{p} - \vec{k}_\pi ; \vec{k}_\pi | T_{\gamma N} | -\vec{p} - \vec{k}_i ; \vec{k}_i \rangle \phi_d (\vec{p} + \tfrac{1}{2}\vec{k}_i) , \quad (2.4)$$

where ϕ_d is the deuteron wave function, the T matrix in the integral is now an off-shell two particle amplitude, and Φ_f is the final state representing the plane wave plus the final state scattering of the two final particles, i.e.,

$$\Phi_f = \delta(\vec{p} + \tfrac{1}{2}\vec{k}_\pi - \vec{k}) + \frac{\langle \vec{k} | t_{NN} | \vec{p} + \frac{1}{2}\vec{k}_\pi \rangle}{(\vec{p} + \frac{1}{2}\vec{k}_\pi)^2 - k^2 - i\epsilon} \quad (2.5)$$

Now, using only the plane wave part, thereby neglecting, for the present, the final state scattering effect[5] in (2.5), Eq. (2.4) is simplified to

$$\langle \vec{k}, \vec{k}_\pi | T | \vec{k}_i \rangle = T_{\gamma N} (\vec{q}, k_i{}^2, k_\pi{}^2) \phi_d (+\vec{k} + \tfrac{1}{2}\vec{q}) , \quad (2.6)$$

where $\vec{q} = \vec{k}_\pi - \vec{k}_i$, is the momentum transferred between the initial photon and the final pion in the overall c.m. system. The on-shell $\gamma N \to \pi N$ T matrix is related to the differential cross section by the relation

$$\frac{d\sigma}{d\Omega} = \frac{E_\gamma' E_N' E_{N'}' E_\pi'}{(2\pi)^2 E_{\mathrm{c.m.}}^2} \frac{k_\pi'}{k_i'} |T|^2 , \quad (2.7)$$

while the more familiar expression is

$$\frac{d\sigma}{d\Omega} = \frac{k_\pi'}{k_i'} |f|^2 . \quad (2.8)$$

In (2.7) and (2.8) $E_\gamma', E_N', E_{N'}', E_\pi'$ are the total energies of the photon, incident nucleon, final nucleon, and the pion, and k_π', k_i' are the momenta of the pion and the photon—all in γN c.m. system. A comparison of (2.7) and (2.8) establishes the relation

$$f = \frac{1}{(2\pi) E_{\mathrm{c.m.}}} (E_\gamma' E_N' E_{N'}' E_\pi')^{1/2} T . \quad (2.9)$$

At this stage it is perhaps worthwhile to clarify the way and the extent to which we shall be exploring, in the following, the possibility of simulating the off-shell effects by inserting $\gamma N \to \pi N$ amplitude in different reference frames. As is evident, the $\gamma N \to \pi N$ T matrix defined through (2.7) is essentially on shell, being a function of the variables q'^2, k_π', and k_i' in the γN c.m. sys-

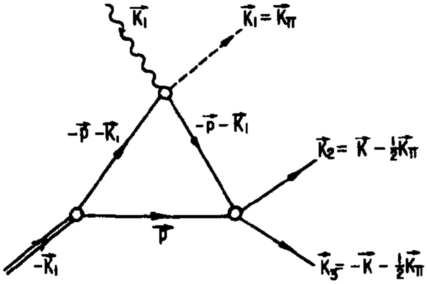
$\vec{K}_1$
$\vec{K}_1 = \vec{K}_\pi$
$-\vec{p} - \vec{K}_1$
$-\vec{p} - \vec{K}_1$
$\vec{K}_2 = \vec{K} - \frac{1}{2}\vec{K}_\pi$
$\vec{p}$
$-\vec{K}_1$
$\vec{K}_3 = -\vec{K} - \frac{1}{2}\vec{K}_\pi$

FIG. 1. The Feynman diagram for the process $\gamma d \to \pi^- pp$ evaluated in the impulse approximation.

tem. On substituting it in the expression (2.3) for σ, we find that it essentially gets decoupled, in the spirit of the impulse approximation, from the phase-space integration variable k_π especially in regard to the pion energy E_π' $[=(k_\pi'^2+\mu^2)^{1/2}]$. On the other hand, the T matrix in (2.6) involving the variables q^2, k_i, and k_π defined in the γ-d c.m. system becomes off-the-energy-shell as it is integrated, on inserting it in (2.3), over the final pion momentum k_π for a given incident photon energy. Thus, e.g., for the photon laboratory energy 210 MeV while the pion momentum k_π' is fixed at 120 MeV/c, the corresponding momentum k_π in the γd c.m. system varies from zero to 133 MeV/c. Similarly, for photon laboratory energy 300 MeV, the pion momentum k_π' is 182 MeV/c whereas k_π varies from 0 to 225 MeV/c.

The expression (2.6) for the T matrix is now generalized so as to incorporate the spin, isospin structure of the $\gamma N\to\pi N$ amplitude and to include the effect of identity of the two outgoing nucleons. We designate the charge state of the emitted pion by the index β $(=+,0,-)$ so that

$$T_{\gamma N}^{(\beta)}=f^{(+)}g_\beta^{(+)}+f^{(-)}g_\beta^{(-)}+f^{(0)}g_\beta^{(0)}, \qquad (2.10)$$

where

$$\begin{aligned}g_\beta^{(+)}&=\tfrac12(\tau_\beta\tau_3+\tau_3\tau_\beta)=\delta_{\beta3},\\ g_\beta^{(-)}&=\tfrac12(\tau_\beta\tau_3-\tau_3\tau_\beta)=\tfrac12[\tau_\beta,\tau_3], \qquad (2.11)\\ g_\beta^{(0)}&=\tau_\beta,\end{aligned}$$

where $f^{(+)}, f^{(-)}, f^{(0)}$ in (2.10) are the components of the photopion production amplitude as originally given by CGLN[3] in the static model. The spin structure of these f's can be given as

$$f^{(\alpha)}=a^{(\alpha)}+i\vec\sigma\cdot\vec b^{(\alpha)}. \qquad (2.12)$$

Thus for the process

$$\gamma d\to\pi^- pp$$

using the complete antisymmetric wave function of the final protons in the combined spin, isospin, and momentum space, the corresponding matrix element (2.6) is

$$\langle{}^3\tau_1({}^1\chi_0\Phi^{(s)}+{}^3\chi_1\Phi^{(a)})\,|\,T_{\gamma N}\,|{}^3\chi_1{}^1\tau_0\Phi_i\rangle. \qquad (2.13)$$

Here ${}^3\chi_1({}^3\tau_1)$ is the spin (isospin) triplet and ${}^1\chi_0$ $({}^1\tau_0)$ is the spin (isospin) singlet wave function of the two nucleons, and

$$\Phi^{(\substack{s\\a})}=[\delta(\vec p+\tfrac12\vec k_\pi-\vec k)\pm\delta(\vec p+\tfrac12\vec k_\pi+\vec k)] \qquad (2.14)$$

are the symmetric (+) and antisymmetric (−) plane wave states of the final protons. The isospin part of the T matrix in (2.13) can be easily worked out with the help of (2.10) and (2.11) and the final expression, after using (2.9), reduces to

$$\langle{}^3\tau_1({}^1\chi_0\Phi^{(s)}+{}^3\chi_1\Phi^{(a)})\,|\,T_{\gamma N}\,|{}^3\chi_1{}^1\tau_0\Phi_i\rangle\equiv T_{s-t}+T_{t-t}, \qquad (2.15)$$

where

$$T_{s-t}=\langle{}^1\chi_0\,|i\vec\sigma\cdot(\vec b^{(0)}-\vec b^{(-)})\,|\,[\varphi_d(-)+\varphi_d(+)]{}^3\chi_1\rangle, \qquad (2.16)$$

$$\begin{aligned}T_{t-t}=\langle{}^3\chi_1\,|(a^{(0)}-a^{(-)})&\\ +i\vec\sigma\cdot(\vec b^{(0)}-\vec b^{(-)})&\,|\,[\varphi_d(-)-\varphi_d(+)]{}^3\chi_1\rangle, \qquad (2.17)\end{aligned}$$

where

$$\varphi_d(-)=\varphi_d(-\vec k+\tfrac12\vec q), \quad \varphi_d(+)=\varphi_d(\vec k+\tfrac12\vec q)$$

are the deuteron wave functions, wherein the momenta of the protons are interchanged. These functions may still involve the spin operators particularly if the d-state component of the deuteron is to be included. T_{s-t}, T_{t-t} which refer to the spin triplet-singlet and triplet-triplet transitions are now the generalized expressions replacing (2.6).

The square of the matrix element (2.15) after summing over the final and averaging over the initial spin states is what actually appears in (2.3) to be computed for the differential cross section.

III. RESULTS AND DISCUSSION

As remarked earlier, this work has two main objectives in view: (a) To study the effect of different frames of reference on the differential and total cross section of the produced pions and (b) to investigate the effect of the details of the deuteron wave functions used. As for the former there is, in principle, hardly any choice on the reference frames to be used provided one abandons the impulse approximation and knows the off-shell two-body amplitude ($\gamma N\to\pi N$) unambiguously. It is this lack of knowledge which has been exploited to see how far one can simulate such effects by introducing different frames. Secondly, in the high energy eikonal approximation[9] one generally uses for the two-body amplitude the same kinematic variables which are determined in the overall c.m. system, implying that in this approximation the two-body subprocess is essentially on shell. Thus, it would be interesting to check the validity of such assumptions through the variants of different reference frames.

The three different frames studied here are the following.

(i) $\gamma N-\gamma d$ frame in which the kinematics of the process $\gamma d\to\pi NN$ is expressed in the γd c.m. system while the $\gamma N\to\pi N$ is described in the γN c.m. system. Thus, e.g., momentum transfer squared q'^2 in the γN c.m. system is related to the corresponding quantity q^2 in γd system by

$$\begin{aligned}q'^2&=(\vec k_\pi{}'-\vec k_i{}')^2\\ &=q^2+(E_\pi{}'-E_\gamma{}')^2-(E_\pi-E_\gamma)^2,\\ \vec q\,'\cdot\vec k_\pi{}'&=\vec q\cdot\vec k_\pi+\tfrac12[(E_\pi{}'-E_\gamma{}')^2-(E_\pi-E_\gamma)^2]\\ &\quad+\tfrac12[(k_\pi{}^2-k_\pi{}'^2)-(k_\gamma{}^2-k_\gamma{}'^2)],\end{aligned}$$

and

$$k_\pi'^2 = [(E_{\text{c.m.}}{}^2 - m^2 - \mu^2)^2 - 4m^2\mu^2]/4E_{\text{c.m.}}{}^2 ,$$

$$k_\gamma'^2 = mE_{\gamma L}{}^2/[m + 2E_{\gamma L}] .$$

(ii) γ-*d frame*, where all the kinematic factors [including those appearing in (2.7)], as well as the $\gamma N \to \pi N$ amplitude, are described in the γd c.m. system. Thus, e.g., $k_\pi' \to k_\pi$, $k_\gamma' \to k_\gamma$. As a result πN phase shifts in the process now become explicitly a function of k_π—the integration variable in (2.3). In other words, the off-shell effect of the $\gamma N \to \pi N$ amplitude is being introduced by assuming it to be the function of k_π, in addition to its on-shell variables q^2, k_γ, etc.

(iii) *Mixed frame*, here the kinematics of the γN-γd frame are retained except that $q'^2 \to q^2$, $\vec{q}\,'\cdot\vec{k}_i'\to\vec{q}\cdot\vec{k}_i$. The choice of this frame is intermediate of the two referred to above and is made with a view to see how sensitive the results are in keeping a distinction between the two.

For the deuteron wave function, we used the standard Yamaguchi form[10]

$$\varphi_d(p) = Ng(p)(p^2 + \alpha^2)^{-1} .$$

This rather simple form was generalized sometime ago[11] to incorporate the tensor force and hard core[12] effects. Thus, following closely Ref. 11,

$$Ng(\vec{p}) \to N_1\left[C(p) + \frac{1}{\sqrt{8}}\, S(\hat{p})T(p)\right] - N_2 h(p) ,$$

where the tensor operator

$$S(\hat{p}) = 3(\vec{\sigma}_1\cdot\hat{p})(\vec{\sigma}_2\cdot\hat{p}) - \vec{\sigma}_1\cdot\vec{\sigma}_2$$

and the various vertex functions are

$$C(p) = (p^2 + \beta_1{}^2)^{-1} , \quad h(p) = np^2(p^2 + \beta_2{}^2)^{-2} ,$$

$$T(p) = -tp^2(p^2 + \gamma^2)^{-2} .$$

Here N_1 and N_2 (which, in fact, are not independent) are the normalization constants as defined in Ref. 11 and the various parameters are given in Table I. This mathematically simple representation was found to be quite realistic as it not only explains the triplet n-p scattering data and the static properties of the deuteron, but also reproduces exceedingly well the fit of the deuteron electromagnetic form factors obtained from e-d scattering data over a wide range of momentum transfers (viz., from $q^2 = 0$ to $\simeq 25$ fm^{-2}).[11] However, it should be pointed out that what appears in the present analysis is directly the wave function and not these form factors (which reproduce an overall integrated effect of the wave function). Thus it is essentially the details of the deuteron vertex function (i.e., the momentum dependent shape factor) which is being subject to scrutiny in this investigation, especially for internal deuteron momenta lying between 70 and 200 MeV/c.

TABLE I. Values of the parameters used in Yamaguchi deuteron wave function. (C, T, and H stand for central, tensor, and hard core terms, respectively.)

Wave function	β_1/α	β_2/α	γ/α	n	t	λ/α^3
C	6.255	···	···	···	···	33.43
$C+T$	5.8	···	6.771	···	1.784	20.18
$C+H$	7.8	10.7	···	3.75	···	78.6
$C+H+T$	7.5	10.5	6.5	5.47	0.7348	61.5

We studied the effect of pure s state (symbolically represented as C in the figures), s state + hard core ($C+H$), s state + tensor force ($C+T$), and s state + hard core + tensor force ($C+T+H$) on the differential cross section for the pion production.

We in addition, also employed a Gaussian wave function of the form

$$\varphi_d(p) = \left(\frac{2\beta}{\pi}\right)^{3/4} \exp(-\beta p^2) ,$$

where the value of β is found in the literature to vary from $\beta = 26$ (GeV/c)$^{-2}$ obtained[13] by matching the behavior of the deuteron's electromagnetic form factor, to $\beta = 67$ (GeV/c)$^{-2}$ required[14] to reproduce the deuteron mean radius ~2.3 F. We, however, tried a set of four different values, viz.

$$\beta = 25\,(\text{GeV}/c)^{-2}, \quad \beta = 37\ (\text{GeV}/c)^{-2},$$

$$\beta = 50\,(\text{GeV}/c)^{-2}, \quad \beta = 67\ (\text{GeV}/c)^{-2}$$

to study their effect on the cross section and found that $\beta = 67$ (GeV/c)$^{-2}$ gives results in reasonably good agreement with experiment (henceforth, we shall therefore be referring to this particular value only).

We present the results for the differential and total cross section for $\gamma d \to \pi^- pp$ in the energy range $E_{\text{lab}} = 200$ to 700 MeV and in the entire angular range of the produced pion. In Fig. 2 we depict the behavior of $(d\sigma/d\Omega)_{\theta_{\text{lab}}=90°}$ versus E_{lab} employing different forms of the deuteron wave function. In view of the fact that the averaged momentum transfer in this process is typically of the order of 200 MeV/c one should expect that large momentum components of deuteron wave function contribute significantly. On the contrary, we find that the effect of including hard core and tensor terms gives only a marginal improvement (up to ~5%) in the results compared to the s-state part. This is, in fact, true not only at $\theta_{\text{lab}} = 90°$, but at all the other angles also. The main reason for this is the restricted region for phase-space integration. In the energy region we are consider-

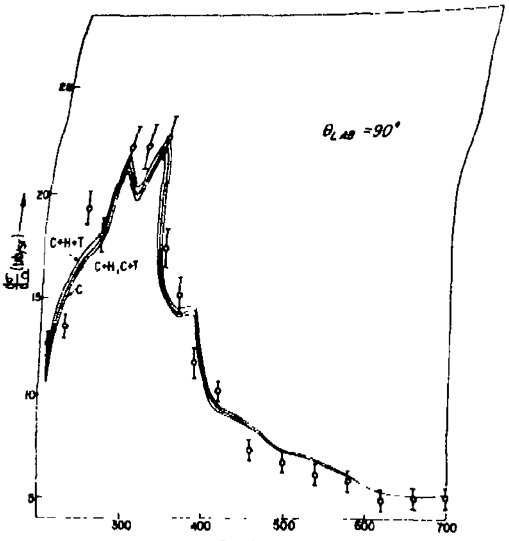

FIG. 2. Plot of differential cross section at $\theta_{\rm lab}=90°$ versus $E_{\rm lab}$ using various deuteron wave functions including central (C), hard core (H), and tensor force (T) terms. Experimental points in this and subsequent figures are taken from Ref. 1.

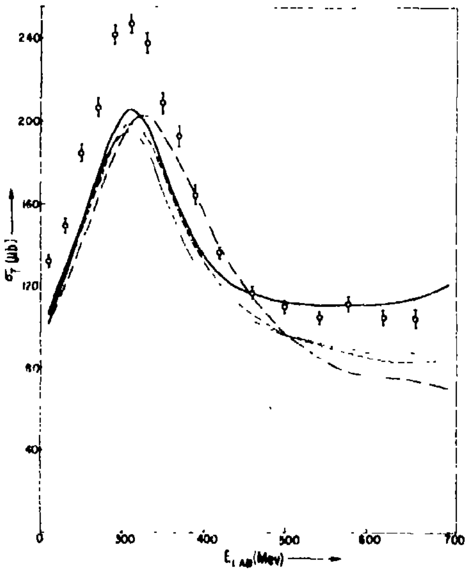

FIG. 3. Plot of total cross section versus $E_{\rm lab}$ for (I) Gaussian wave function (bold-face line) in γN-γd frame, (II) Yamaguchi wave function ($C+T+H$) in γN-γd frame (thin line), in mixed frame (dashed line), and in γd frame (dot-dashed line).

ing, the part of the wave function corresponding to its internal momenta lying between 70 to 200 MeV/c is found to play a rather significant role. From a comparative study of the behavior of Yamaguchi and Gaussian deuteron wave functions, it becomes clear that while initially, i.e., for internal momenta from 70 to 90 MeV/c the Yamaguchi form is slightly higher, at about 90 MeV/c it crosses the Gaussian wave function and then starts falling faster so that for higher internal momenta, viz., from 100 to 210 MeV/c the Gaussian wave function is distinctly higher despite the fact that it has poor asymptotic momentum dependence. This explains why a rather simplified form (with one parameter only) of the deuteron wave function gives better results compared to various Yamaguchi forms especially at higher energies, while at energies near 210 MeV, the Yamaguchi form is somewhat better. This can be seen from Fig. 3 where we plot the total cross section versus $E_{\rm lab}$ using Gaussian (bold line) as well as Yamaguchi wave functions (thin line). This point is further substantiated from a study of the differential cross section in Figs. 4 and 5 where the Yamaguchi wave function is found slightly better in the near forward direction (which again correspond to low internal momenta), while at large angles and

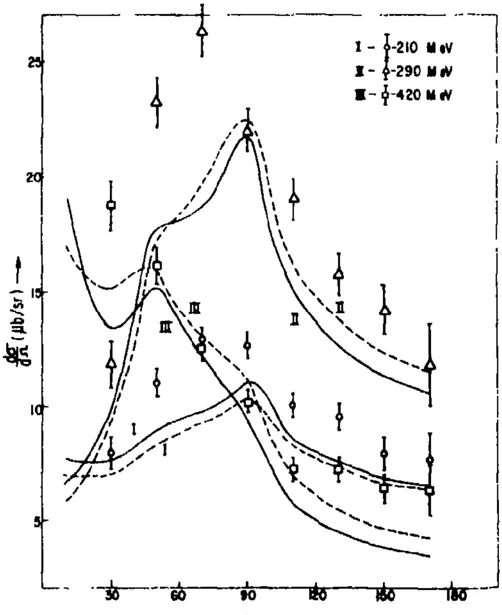

FIG. 4. Plot of differential cross-section versus $\theta_{\rm lab}$ at various incident energies, comparing the Yamaguchi wave function ($C+T+H$) (thick line) and Gaussian wave function (dashed line).

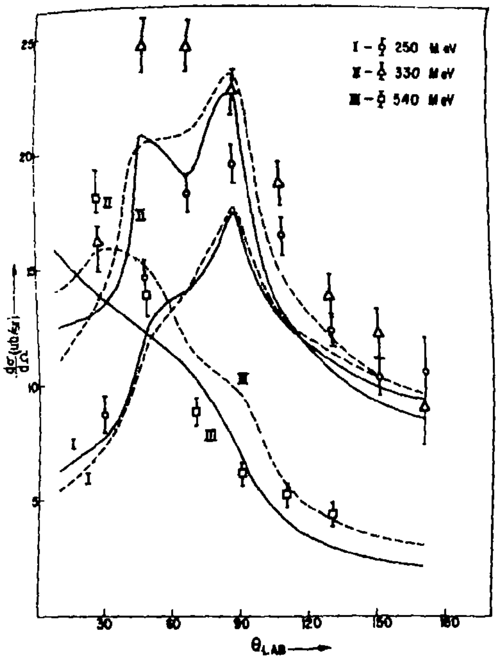

FIG. 5. Same as Fig. 4.

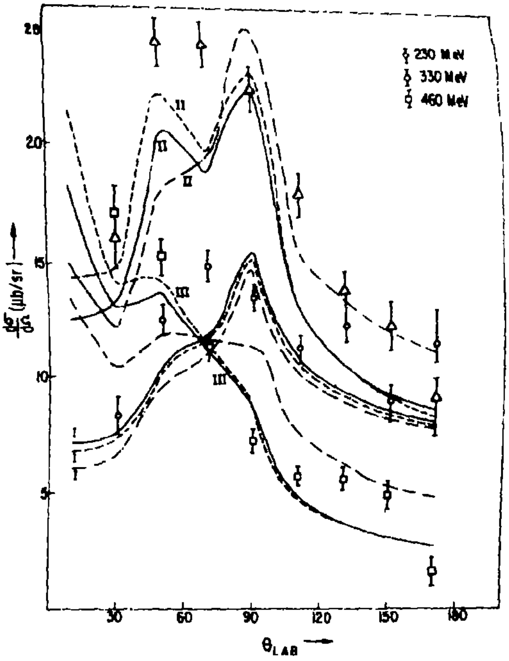

FIG. 6. Plot of differential cross section versus θ_{lab} at various incident energies showing the effect of different reference frames: (I) γN-γd frame (thick line), (II) mixed frame (dashed line), and (III) γd frame (dot-dashed line).

at higher energies the Gaussian wave function gives better agreement with experimental results.

As regards the rapid variation, including a minimum around $E_{lab} \simeq 300$ MeV shown in the calculations in Fig. 2, we find it becomes too complex to analyze this structure, especially in view of the two-dimensional phase-space integration. Even so, we tried to "read" the two variable integrand in order to arrive at some definite conclusion. We observe that in this kinematical region there is a close competition between the magnitudes of the components of $\gamma N \rightarrow \pi N$ amplitude and of those corresponding to the respective coefficients contributed by the wave function and the phase-space parts. It thus appears that this structure is rather "accidental"—more of a kinematical nature than having any dynamical content.

To investigate the effect of different frames of reference we plot in Fig. 6 the differential cross section at three typical energies, viz., 230, 330, and 460 MeV, while in Fig. 3 is shown the total cross section in the three different frames. We first compare the mixed frame with the γN-γd frame and find that in the forward direction the difference is quite appreciable especially at higher energies, whereas at large angles ($\theta_{lab} > 90°$) the difference is quite small. In the total cross section the mixed frame gives results in slightly better agreement in the intermediate energy region (270–500 MeV) whereas, on either side, the γN-γd frame is in closer agreement. The overall difference remains below 10%. It may be recalled that these two frames differ only in their kinematic variables q^2 etc., used in the two-body subsystem. This difference thus brings out clearly and in quantitative terms the sensitivity of the results on the two reference frames used.

Comparing the γ-d reference frame with γN-γd frame, we note the two essential points of difference: (i) the kinematical factor and (ii) the $\gamma N \rightarrow \pi N$ amplitude. In the γ-d frame both the factors appear within the phase-space integral while for γN-γd they are replaced by their appropriate values in that frame. As for the kinematical factors, we have studied their effect by keeping these within and outside the integral and found the difference to be almost negligible ($\lesssim 2\%$). Thus the main difference arises due to the effect of the $\gamma N \rightarrow \pi N$ amplitude. Since this amplitude has a sharp resonance structure, its effect is rather complicated to analyze. Qualitatively, however, one can see the effect in the following way. Symbolically, the amplitude in the γ-d frame which can be written as

$$\int_0^{K_{\max}} (\text{phase space}) \times (\text{deuteron wave function}) \times T_{\gamma N\to\pi N}$$

is replaced in the γN-γd frame by

$$T_{\gamma N\to\pi N}(k_\pi') \int_0^{K_{\max}} (\text{phase space}) \times (\text{deuteron wave function}),$$

where $K_{\max}$ is the maximum value of the pion momentum in the γd c.m. system. Now since this value happens to be somewhat higher than K_π', for photon laboratory energies less than the resonance energy, the contribution in the γN-γd frame is higher than the corresponding value in the γ-d frame. For incident energies higher than the resonance, the amplitude in the γN-γd frame contributes less than in the γ-d frame. For higher energies, the integration range being so large, the overall effect depends on the detailed behavior of the other functions involved and is thus too complex to analyze in this manner.

To compare the results with experiment, it may be in order to recall that the present calculations involve no free parameter. Assuming the impulse approximation to be valid in the energy region considered here, it is thus possible to bring about the limitations of the ingredients used. For instance, from Fig. 3 it is clear that a reasonably good agreement of the total cross section at energies below and above resonance indicates that the CGLN model for input process is fairly realistic. However, just at resonance energy it predicts the value of the total cross section about 25% less, which may possibly be due to inadequate $\gamma N\to\pi N$ input near resonance. This difference could not be improved even with a Gaussian deuteron wave function which has done a surprisingly good job, especially at higher energies, compared to the Yamaguchi wave function, including tensor force and hard core.

The study of inserting the $\gamma N\to\pi N$ amplitude in different reference frames vis a vis experimental results reveals that for $\theta_{\text{lab}}\simeq 90°$, the γN-γd frame is in better agreement at almost all energies. At large angles and at medium energies (say, up to 400 MeV) γ-d reference frame predicts results closer to experiment. It is probably in this kinematical region where the validity of an on-shell amplitude breaks down and the off-shell effects show up significantly. In other words the assumption underlying impulse approximation, viz., factorization of the two-body amplitude from the phase space including the deuteron wave function may no longer be true. However, the γN-γd frame produces results for the differential cross section at $\theta_{\text{lab}}= 90°$ (Fig. 2) in surprisingly good agreement with experiment.

In conclusion we have here made an attempt to analyze critically the various assumptions involved in the impulse approximation while studying $\gamma d\to\pi^- pp$ at incident photon energies starting from 210 to about 700 MeV in the entire angular range of the pion produced. The study depicts a sensitive role of the component of deuteron wave function with internal momenta lying between 70 and 210 MeV/c, while the effect of including tensor force and soft core (repulsive) terms gives only a marginal improvement in the results. This analysis also brings out the kinematical region where off-energy-shell effects in the $\gamma n\to\pi^- p$ amplitude could be significant in describing the process $\gamma d\to\pi^- pp$. Another kinematical region, viz., just above threshold for photopion production where the final state effect of the interaction of the two outgoing nucleons could be significant has not been dealt with here and would be a subject for future communication.

APPENDIX

For the sake of completeness, we write down the amplitudes $a^{(\alpha)}$ and $\vec{b}^{(\alpha)}$ defined in Eq. (2.12)[3]:

$$a^{(+)}=(ef/4\pi)(\hat{k}_\pi\cdot\hat{k}_i\times\hat{\epsilon})(\lambda h^{(++)}+\tfrac{4}{9}ie^{i\delta_{33}}\sin\delta_{33}F_M),$$

$$a^{(-)}=(ef/4\pi)(\hat{k}_\pi\cdot\hat{k}_i\times\hat{\epsilon})(\lambda h^{(-+)}-\tfrac{2}{9}ie^{i\delta_{33}}\sin\delta_{33}F_M),$$

$$a^{(0)}=0,$$

$$\vec{b}^{(+)}=(ef/4\pi)\Big\{-\hat{\epsilon}\{\tfrac{2}{3}(\delta_1-\delta_3)F_s+i(\hat{k}_\pi\cdot\hat{k}_i)[\lambda h^{(+-)}+\tfrac{2}{3}ie^{i\delta_{33}}\sin\delta_{33}(F_e-\tfrac{1}{3}F_M)]\}+i\hat{k}_i(\hat{k}_\pi\cdot\hat{\epsilon})$$
$$\times[\lambda h^{(+-)}-\tfrac{2}{3}ie^{i\delta_{33}}\sin\delta_{33}(F_e+\tfrac{1}{3}F_M)]+i\hat{k}_\pi(\hat{k}_\pi\cdot\hat{\epsilon})\frac{1}{2m\omega}\Big\},$$

$$\vec{b}^{(-)}=\left(\frac{ef}{4\pi}\right)\Bigg(-\hat{\epsilon}\left\{-\frac{i}{(1+\omega/m)}+\tfrac{1}{3}(2\delta_1+\delta_3)F_s+i(\vec{k}_\pi\cdot\vec{k}_l)\left[\lambda h^{(--)}-\tfrac{1}{3}ie^{i\delta_{33}}\sin\delta_{33}(F_q-\tfrac{1}{3}F_M)\right]\right\}+i\vec{k}_l(\vec{k}_\pi\cdot\hat{\epsilon})$$
$$\times\left\{\frac{2}{(1+\omega/m)[(k_l-k_\pi)^2+1]}+\left[\lambda h^{(--)}+\tfrac{1}{3}ie^{i\delta_{33}}\sin\delta_{33}(F_q+\tfrac{1}{3}F_M)\right]\right\}-i\vec{k}_\pi(\vec{k}_\pi\cdot\hat{\epsilon})$$
$$\times\left\{\frac{2}{(1+\omega/m)[(k_l-k_\pi)^2+1]}+\frac{1}{2m\omega}\right\}\Bigg),$$

$$\vec{b}^{(0)}=-\left(\frac{ef}{4\pi}\right)i\left[\hat{\epsilon}\,\frac{g_p+g_n}{2m}\,\omega+\vec{k}_\pi\times(\vec{k}_l\times\hat{\epsilon})\,\frac{g_p+g_n}{2m\omega}-\vec{k}_\pi(\vec{k}_\pi\cdot\hat{\epsilon})\frac{1}{2m\omega}\right].$$

In these expressions $e^2/4\pi=\frac{1}{137}$, $f^2/4\pi=0.08$, $g_p=1.78$, $g_n=-1.91$, $\lambda=(g_p-g_n)(f^2/4\pi)^{-1}/4m$, and $\omega=W-m$, where W is the total center of mass energy. The form factors F_s, F_q, and F_M are given by

$$F_s=1-\tfrac{1}{2}\left(1+\frac{1-v^2}{2v}\ln\frac{1-v}{1+v}\right),$$

$$F_q=\frac{1}{\omega^2}\left(1-\frac{3}{2v^2}(1-F_s)\right),$$

$$F_M=\frac{3}{2k_\pi^{\,2}}(1-F_s),$$

where v is the velocity of the produced pion (in units of c).

The spin-isospin amplitudes $h^{(++)}$, $h^{(+-)}$, $h^{(-+)}$, and $h^{(--)}$ are related to the p-wave shifts δ_{ij} through the following relations:

$$h^{(++)}=\tfrac{1}{3}(h_{11}+2h_{13}+2h_{31}+4h_{33}),$$

$$h^{(+-)}=\tfrac{1}{3}(h_{11}-h_{13}+2h_{31}-2h_{33}),$$

$$h^{(-+)}=\tfrac{1}{3}(h_{11}+2h_{13}-h_{31}-2h_{33}),$$

$$h^{(--)}=\tfrac{1}{3}(h_{11}-h_{13}-h_{31}+h_{33}),$$

where

$$h_{ij}=e^{i\delta_{ij}}\sin\delta_{ij}/k_\pi^{\,3}.$$

For the isosinglet and isotriplet s-wave phase shifts δ_1 and δ_3 and the various p-wave phase shifts δ_{ij} we have taken the Donnachie and Shaw parametrization,[6] viz.,

$$K_\pi\cot\delta_1=5.848+5.482K_\pi^{\,2}-3.830K_\pi^{\,4}+1.004K_\pi^{\,6}-0.1076K_\pi^{\,8}+0.003\,977K_\pi^{\,10},$$

$$K_\pi\cot\delta_3=-11.364+3.697K_\pi^{\,2}-0.8014K_\pi^{\,4}+0.0776K_\pi^{\,6}-0.002\,85K_\pi^{\,8},$$

$$K_\pi^{\,3}\cot\delta_{13}=-34.48-71.85K_\pi^{\,2}+36.70K_\pi^{\,4}-9.623K_\pi^{\,6}+0.968K_\pi^{\,8}-0.0330K_\pi^{\,10},$$

$$K_\pi^{\,3}\cot\delta_{13}=-26.30+8.479K_\pi^{\,2}-15.35K_\pi^{\,4}+3.834K_\pi^{\,6}-0.3560K_\pi^{\,8}+0.0115K_\pi^{\,10},$$

$$K_\pi^{\,3}\cot\delta_{33}=4.6512-0.6207K_\pi^{\,2}-0.1473K_\pi^{\,4}-0.0829K_\pi^{\,6},$$

up to 250 MeV laboratory energy, and

$$K_\pi^{\,3}\cot\delta_{33}=4.6512-1.236K_\pi^{\,2}+0.713K_\pi^{\,4}-0.495K_\pi^{\,6}+0.0788K_\pi^{\,8}-0.0048K_\pi^{\,10}$$

beyond 250 MeV laboratory energy.

---

[1] P. Benz *et al.*, Nucl. Phys. B65, 158 (1973). Earlier references are given therein.

[2] P. E. Argan *et al.*, Nucl. Phys. A 296, 373 (1978).

[3] G. F. Chew *et al.*, Phys. Rev. 106, 1345 (1957). See also K. Nishijima, *Fundamental Particles* (Benjamin, New York, 1965), p. 184.

[4] I. Blomqvist and J. M. Laget, Nucl. Phys. A280, 405 (1977).

[5] J. M. Laget (I), Nucl. Phys. A296 388 (1978); P. Bosted and J. M. Laget (II), *ibid.* A296, 413 (1978).

[6] A. Donnachie and G. Shaw, Ann. Phys. (N.Y.) 37, 333 (1966).

[7] See, e.g., M. L. Goldberger and K. M. Watson, *Collision Theory* (Wiley, New York, 1964).

[8] The final state effect of the scattering of the two outgoing nucleons is known to be significant just near the threshold (see, e.g., J. V. Noble, Phys. Lett. 67B, 39 1977). The work in this direction is in progress and will be reported elsewhere.

[9] R. J. Glauber, *Lectures in Theoretical Physics*, edited by W. E. Brittin and L. G. Dunham (Interscience, New York, 1955), Vol. 1, p. 315.

[10] Y. Yamaguchi, Phys. Rev. 95, 1628 (1954); 95, 1635 (1954).

[11] R. Mehrotra and K. Sengupta, Phys. Rev. D 1, 3459 (1970).

[12] Strictly speaking this is only a repulsive core to account for the observed change in the sign of triplet phase shifts around 240 MeV.

[13] M. Verde, Helv. Phys. Acta. 22, 339 (1949).

[14] V. V. Anisovich *et al.*, Phys. Lett. 42B, 224 (1972).

[15] Note the rapid variations giving rise to a minimum around $\theta_{1ab} = 70°$ especially in curve II (solid line) in Figs. 5 and 6. Presumably this effect also has the same kinematical origin as was attributed to the structure appearing in Fig. 2 (see the discussion on p. 2015).

PHYSICAL REVIEW C VOLUME 21, NUMBER 5 MAY 1980

Actinide muonic atom lifetimes deduced from muon-induced fission

W. W. Wilcke, M. W. Johnson, W. U. Schröder, D. Hilscher, J. R. Birkelund, and J. R. Huizenga
Departments of Physics and Chemistry and Nuclear Structure Research Laboratory, University of Rochester, Rochester, New York 14627

J. C. Browne and D. G. Perry
Los Alamos Scientific Laboratory, Los Alamos, New Mexico 87544

(Received 20 November 1979)

Time distributions of fragments from delayed fission after muon capture have been measured for muonic ^{235}U, ^{238}U, ^{237}Np, ^{239}Pu, and ^{242}Pu. Comparison of these data with previously measured lifetimes using muon decay electrons, neutrons, and γ rays emitted after muon capture indicates that the observed systematic discrepancies are due to atomic muon capture by fission fragments after prompt fission induced by radiationless muonic transitions. The deduced capture rates are compared with theoretical models, and very good agreement is found with a giant-resonance excitation model.

RADIOACTIVITY Muonic atoms ^{235}U, ^{238}U, ^{237}Np, ^{239}Pu, and ^{242}Pu. Measured fission fragment time distributions, deduced total muon-capture rates and isotopic effect, present data compared to lifetimes based on all other decay channels.

I. INTRODUCTION

The interaction of negative muons with actinide nuclei has been studied by numerous experiments[1-12] in recent years. These heavy muonic atoms are of particular interest because theories on muon-capture rates, which have been applied successfully for lighter nuclei, can be tested more stringently with very neutron-rich, heavy nuclei.

Experiments designed to determine the capture rate usually measure the time difference between the arrival of a muon in the target and the appearance of any reaction product associated with the capture of the muon by the nucleus. Since muon capture excites a heavy nucleus on the average to approximately 15 MeV, various reaction products including neutrons, fission fragments, and γ rays can be observed. In addition, it is possible to infer the muon-capture rate from the time distribution of electrons emitted in the leptonic decay of muons in the 1s state of a muonic atom. It was generally assumed that all these methods yield the same lifetimes for a particular muonic atom, but it soon became obvious that lifetimes measured by detecting fission fragments emitted after muon capture were consistently slightly shorter than lifetimes determined with any other method. Hadermann[13] pointed out the likely cause of this discrepancy: It is well known that "prompt fission" may occur during the atomic cascade of a muon to its ground state due to a radiationless transfer of the muonic transition energy to the nucleus. In the course of such a prompt fission process, the muon may become bound in an atomic orbital of one of the fission fragments and may later be captured by the fragment or undergo leptonic decay. In a singles experiment as described above, electrons, neutrons, and γ rays resulting from muonic fission fragments cannot be distinguished from those stemming from muon capture by the actinide nuclei. Hence, the time distributions of electrons, neutrons, and γ rays consist of a superposition of two exponential components. The characteristic lifetimes are 70–80 nsec for muonic actinides and about 130 nsec[14,15] for heavy muonic fission fragments. The capture of muons by the light fission fragment does occur only with low probability.[14,15] However, the statistics of most experiments is not sufficient to allow a distinction of the various components of the measured time distributions such that least-square fits assuming a simple exponential decay law for these distributions will yield lifetimes that are too long.

In contrast, because muon capture by a fission fragment cannot induce fission of this fragment, time distributions of delayed fission fragments produced by muon capture are not disturbed by prompt fission events. There are, however, two secondary effects that lead to insignificant contamination of these time distributions: The radiationless atomic transition of a muon can cause the emission of one neutron from the target nucleus before subsequent fission of the daughter nucleus occurs after muon capture. This process has a probability similar to prompt fission, but since the lifetime difference between two neighboring isotopes is only about 1.5 nsec for actinide nuclei (as estimated from a study[11] of ^{235,238}U and ^{239,242}Pu), the effect of this admixture on the lifetimes deduced is more than one order of magnitude smaller

© 1980 The American Physical Society

than the effect of prompt fission on measurements of electrons, neutrons, and γ rays described above, and is well within the statistical uncertainties of all experiments performed so far. The second mechanism that may affect the time distribution of fission fragments is the possible excitation of shape-isomeric nuclear states during the muonic cascade, as suggested by Bloom.[16] A quantitative discussion[11] shows, however, that the influence of this effect on the measured lifetime is very small.

Muon capture by fission fragments as proposed by Hadermann[13] and delayed fission after prompt neutron emission, however, have been observed directly in coincidence experiments, where the emission of fission fragments in coincidence with decay electrons[14] and neutrons[15] was measured. In addition, a measurement[11] with very good statistics confirmed the presence of a long-lifetime component in the singles time spectrum of neutrons emitted from muonic ^{239}Pu. Therefore, it *is concluded that measurements employing the* experimentally rather unambiguous fission technique are required to provide meaningful data on muon-capture rates for actinides that can be compared to theoretical models of muon capture. Coincidence experiments would be even better, but their statistical accuracy is inherently lower than that of singles measurements. Since the effects of prompt neutron emission and isomeric-state excitation on fission time distributions are negligible, the present study of singles fission measurements was initiated with the aim of obtaining data of high statistical accuracy.

II. EXPERIMENTAL PROCEDURE

The experiments were performed using the stopped-muon channel of the Los Alamos Meson Physics Facility (LAMPF). Muons from the channel passed through a three-element plastic scintillator telescope and were stopped in a fission chamber containing nine Ti foils, on which the actinide targets (^{235,238}U, ^{237}Np, and ^{239,242}Pu) were deposited as 0.5 mg/cm^2 thick oxide layers. Since inspection of previous experiments[1-12] indicated that systematical errors are frequently more important than statistical ones, care was taken to minimize the former by measuring three isotopes simultaneously. As shown in Fig. 1, three foils carrying one particular isotope formed an ionization chamber, and three such chambers constituted the whole fission chamber. All timing signals were processed in the same time-to-pulse-height converter and the same analog-to-digital converter (ADC), using routing signals to distinguish the ionization chamber that had fired. Time calibrations were performed frequently with several independent methods. In addition, only two isotopes were replaced at a time, so that the third isotope remaining in the chamber served as an additional

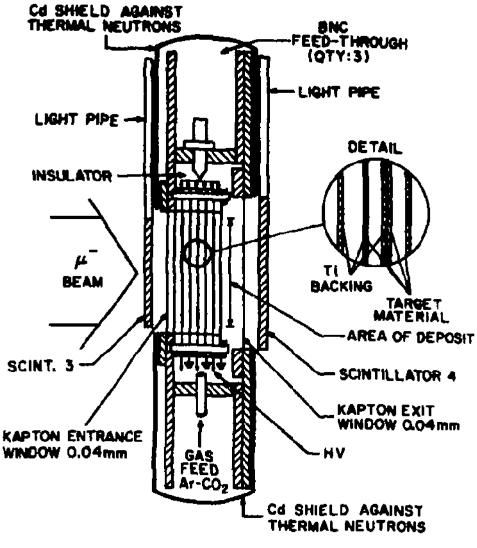

FIG. 1. Schematic drawing of the fission ionization chamber. The insert shows the arrangement of the target foils used to avoid cross talk between different sets of foils: The foil on the left is part of the adjacent electrically decoupled chamber which uses the same gas volume

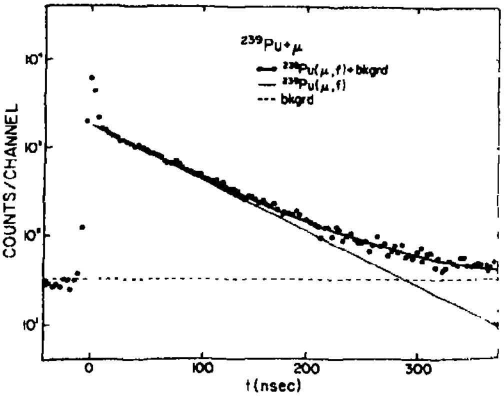

FIG. 2. The experimental fission-fragment time distribution for muonic ^{239}Pu. The peak in the region near $t=0$ corresponds to prompt fission events caused by radiationless muonic transitions. The horizontal dashed line represents a fit to the background to negative and large positive times. The curve drawn through the data points represents the sum of the exponential and the background distributions.

cross check for the consistency of the results for different runs. A typical time spectrum is shown in Fig. 2. The data were analyzed with a least-squares code and a fitting function representing an exponential distribution on a constant background. A trial fit assuming two exponentials failed to find a second lifetime component in the spectra, as was to be expected.

III. EXPERIMENTAL RESULTS AND DISCUSSION

The experimental results are compiled in Table I along with all previously published data on muonic actinide lifetimes τ_i. The indices e, n, γ, and f refer to electron-, neutron-, γ-ray-, and fission fragment measurements, respectively. The weighted averages $\bar{\tau}\pm\sigma$ have been calculated[17] by weighting the data τ_i according to the published error $\tau_i\pm\sigma_i$ using the following equations:

$$\bar{\tau}=\frac{\sum(\tau_i/\sigma_i^2)}{\sum(1/\sigma_i^2)}, \tag{1}$$

$$\sigma_A=\left[\frac{\sum(\tau_i-\bar{\tau})^2/\sigma_i^2}{(n-1)\sum(1/\sigma_i^2)}\right]^{1/2}, \tag{2}$$

$$\sigma_B=\left[\sum(1/\sigma_i^2)\right]^{-1/2}, \tag{3}$$

$$\sigma=\max(\sigma_A,\sigma_B). \tag{4}$$

Equation (2) for the error σ_A of the weighted mean can yield unphysical values for very small samples. Therefore, σ_B was introduced which sets a lower limit for σ based on the published errors. Inspection of Table I shows that for all isotopes the averaged lifetime $\bar{\tau}_f$ is shorter than either τ_n, $\bar{\tau}_\gamma$, or $\bar{\tau}_e$.

Although there is no question about the occurrence of muon capture by fission fragments, it has not been shown that this mechanism is the only one responsible for the differences between measured lifetimes. A systematical study of all muonic actinides may be helpful to shed light on this question, since a monotonic increase of the (positive) difference $\tau_n-\bar{\tau}_f$ is expected with increasing probability for prompt fission, if muon capture by fission fragments were the dominant contribution to these differences. It is possible to define a characteristic parameter allowing a systematic classification of muonic actinides. Such a suitable parameter is represented by the product of the proba-

TABLE I. Experimental lifetimes in nsec of muonic actinides deduced from measurements of decay electrons (τ_e), neutrons (τ_n), capture γ rays (τ_γ), and fission fragments (τ_f). As discussed in the text, the electron, neutron, and γ-ray lifetime measurements yield values systematically too high, because these three measurements are sensitive to contributions from muon capture by fission fragments after prompt fission. The lifetimes τ_f deduced from a detection of delayed fission fragments, however, are not affected by this effect. The weighted average $\bar{\tau}_f$ of the fission lifetimes is therefore believed to represent the best values for the true muonic actinide lifetimes.

Isotope	τ_e	$\bar{\tau}_e$	τ_n	τ_γ	τ_f	$\bar{\tau}_f$
^{232}Th	80.4 ± 2.0[2] 79.2 ± 2.0[3]	79.8 ± 1.4	80.1 ± 0.6[11]		74.2 ± 5.6[5] 87.0 ± 4.0[6] 77.3 ± 0.3[12]	77.4 ± 0.5
^{233}U					61.7 ± 3.8[4]	61.7 ± 3.8
^{235}U	78 ± 4[2] 75.4 ± 1.9[3]	75.9 ± 1.7	75.0 ± 0.7[11]		65.3 ± 2.8[4] 66.5 ± 4.2[5] 75.6 ± 2.3[6] 72.9 ± 0.9[a]	72.6 ± 1.5
^{238}U	88 ± 4[1] 81.5 ± 2.0[2] 73.5 ± 2.0[3]	78.7 ± 3.5	78.3 ± 1.0[11]	78.6 ± 1.5[9] 79.1 ± 0.5[10] $\bar{\tau}_\gamma$: 79.0 ± 0.5	74.1 ± 2.8[4] 75.6 ± 2.9[5] 76.0 ± 1.0[6] 77.1 ± 0.2[12] 77.9 ± 0.5[a]	77.2 ± 0.2
^{237}Np			73.5 ± 1.4[11]		72 ± 2[8] 71.3 ± 0.9[a]	71.4 ± 0.8
^{239}Pu	77.5 ± 2.0[2] 73.4 ± 2.8[3]	76.1 ± 1.9	74.5 ± 0.5[11]		74 ± 14[7] 70 ± 3[8] 70.1 ± 0.7[a]	70.1 ± 0.7
^{242}Pu			81.1 ± 0.7[11]		79 ± 5[8] 75.4 ± 0.9[a]	75.5 ± 0.9

[a] Present study.

bility of a radiationless muonic transition and the fissility of the target nucleus. As has been shown by Zaretski and Novikov,[18] the ratio of radiationless to radiative transition probabilities is given approximately by

$$\frac{\Gamma_{rl}}{\Gamma_r} \approx Z\alpha , \tag{5}$$

where $\alpha = e^2/\hbar c$ is the fine-structure constant. The probability of fission after a radiationless transition depends in a complicated way on the detailed shape of the double-humped fission barrier, which is augmented in the presence of the muon. It is assumed, however, that the general trend of the fissility be still given by the liquid-drop expression for the fissility[19] $X \sim Z^2/A$. Combining X with Eq. (5), one obtains a suitable scale $p(Z,A)$ for discussing the lifetimes:

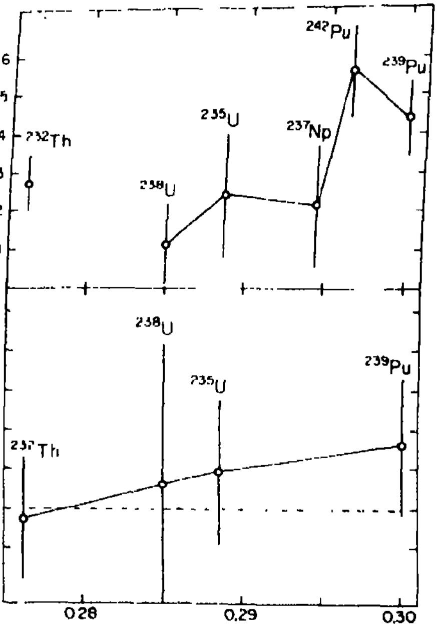

FIG. 3 The upper part shows the difference $\tau_n - \bar{\tau}_f$ of the lifetimes measured by detecting neutrons and fission fragments, respectively, after muon capture, plotted versus the product p of liquid-drop fissility and probability for radiationless transitions. Large values of this quantity, which is an approximate measure for the prompt fission probability, are correlated with large lifetime differences. The lower part shows the lifetime difference $\bar{\tau}_e - \tau_n$ between results of experiments detecting electrons and neutrons, respectively. Since $\bar{\tau}_e$ is more sensitive to contributions from muonic fission fragments than τ_n, this difference is also weakly correlated with p.

$$p = X \frac{\Gamma_{rl}}{\Gamma_{rl} + \Gamma_r} = \frac{\alpha Z^3}{50.13A(1+Z\alpha)} . \tag{6}$$

In the upper part of Fig. 3 the difference $\tau_n - \bar{\tau}_f$ of lifetimes is plotted versus p. Except for ^{232}Th, the difference $\tau_n - \bar{\tau}_f$ is seen to increase with increasing values of p as expected, if muon capture by fission fragments were the dominant cause of the lifetime differences. It is known,[8] however, that the prompt fission probability of muonic ^{242}Pu is very large, even larger than that for ^{239}Pu. Hence, the high value of $\tau_n - \bar{\tau}_f$ for ^{242}Pu is understandable, but the result for ^{232}Th is puzzling. It is known[9] that ^{232}Th has a very low probability (5×10^{-4}) for prompt fission, which is consistent with its low p value. Therefore, muon capture after prompt fission cannot explain the large difference of the lifetimes. It should be pointed out, however, that the weighted average of $\bar{\tau}_f$ for ^{232}Th is dominated by one measurement.[12] More data are needed to firmly establish the abnormal behavior for ^{232}Th shown in Fig. 3(a).

As has been discussed in the introduction, both electron and neutron measurements are influenced by the occurrence of prompt fission, whence the difference of lifetimes $\bar{\tau}_e - \tau_n$ should be small. This difference may be nonzero, however, since the two methods are of different sensitivity to the admixture of events resulting from muon capture by a fission fragment: The multiplicity M_n of neutrons emitted after muon capture in a β-stable nucleus of mass A is approximately given[20] by

$$M_n \approx 0.3A^{1/3} . \tag{7}$$

In addition, the muon-capture rate decreases rapidly with decreasing atomic mass, whereas the muon decay rate remains essentially constant. Thus the ratio of electron-to-neutron multiplicity is about twice as high for heavy muonic fission fragments as compared to muonic actinides. Therefore, the difference $\bar{\tau}_e - \tau_n$ should increase slightly with p, consistent with experimental results shown in the lower part of Fig. 3. With the possible exception of ^{232}Th, the systematic comparison of the data indicates that muon capture by fission fragments is the dominant contribution to the differences in lifetime. Therefore, $\bar{\tau}_f$ represents the best approximation to the true lifetime of a muonic actinide.

The experimental results may be compared to existing theories for muon-capture rates λ that are related to the measured lifetimes $\bar{\tau}_f$ by

$$\frac{1}{\bar{\tau}_f} = \lambda^{\exp} + R\lambda_0 . \tag{8}$$

Here λ_0 is the free-muon decay rate, and R (~0.85) accounts for the reduction of the decay rate due to effects of atomic binding.[3] Two theoretical approaches have been applied to the study of muon-capture rates in the actinide region. The well-known Goulard-Primakoff formalism[21] has been proved useful in predicting muon-capture rates over a wide range[22] of isotopes and provides a closed-form equation for the total muon-capture rate λ^{GP}:

$$\lambda^{GP} = kZ_{eff}{}^{4}\left(1-\frac{\epsilon_\mu}{m_\mu}\right)^{2}\left(1-\frac{m_\mu\epsilon_\mu}{m_N}\right) \times\left[1-0.03\frac{A}{2Z}+0.25\frac{A-2Z}{2Z} -3.24\left(\frac{A-Z}{2A}+\frac{|A-2Z|}{8ZA}\right)\right]. \tag{9}$$

The notation is that of Ref. 11. A comparison of the Goulard-Primakoff predictions to the experimentally observed capture rates is given in Table II. The predicted rates are systematically smaller than the measured ones. The Goulard-Primakoff capture rates are proportional to the value of $Z_{eff}{}^{4}$, which has to be calculated independently, but a comparison of several isotopes of the same element, which nearly eliminates the dependence on $Z_{eff}{}^{4}$, indicates that this theory consistently overrates the sensitivity of the capture rate to the neutron excess. In the alternate model[23] of Kozłowski and Zgliński the capture mechanism proceeds solely via the excitation of giant-resonance states. The transition amplitude M_V is given by the overlap integral of Pustovalov's muon wave function[24] and the neutrino wave function within the nuclear volume with an isovector transition operator and nuclear wave functions taken from the hydrodynamical model.[25] Multipolarities L from monopole to octupole are taken into account, and the total muon-capture rate λ^{KZ} is the sum of the rates for each multipolarity:

$$\lambda^{KZ} = \frac{m_\mu{}^{2}}{2\pi}G_\mu{}^{2}\sum_{L=0}^{3}|(M_V)_L|^{2}. \tag{10}$$

TABLE II. Comparison of experimentally determined muon-capture rates λ^{exp} with the predictions of the Goulard-Primakoff (λ^{GP}) and Kozłowski-Zgliński (λ^{KZ}) theories. Units are 10^5 sec^{-1}.

Isotope	λ^{exp}	λ^{GP}	λ^{KZ}
^{232}Th	125 ± 1	110	124
^{233}U	158 ± 9	131	
^{235}U	134 ± 1	122	134
^{238}U	125 ± 1	108	122
^{237}Np	137 ± 1	123	138
^{239}Pu	139 ± 2	129	139
^{242}Pu	129 ± 2	116	128

This model has been applied[26] to the nuclei under investigation (Table II), and the agreement between theory and experiment is excellent. It has been shown[27] that for light nuclei (e.g. ^{16}O) the giant resonances are very effective doorway states for muon capture. In heavy nuclei, however, numerous noncollective states at 15–20 MeV excitation energy are expected to exist, which also fulfill the spin and isospin selection rules of the operators describing muon capture. Therefore, it is rather surprising that a model which incorporates only giant-resonance states describes the capture rates so well. It appears important to check other consequences of the proposed capture mechanisms by experiment. Measurements of the neutron multiplicity and energy spectra after muon capture in actinides currently under way will yield information on the excitation energy spectrum and can be compared to this model.

ACKNOWLEDGMENTS

This work was supported by the U.S. Department of Energy. We would like to thank the technical staff of the Los Alamos Meson Physics Facility and especially L.E. Agnew and B.R. Rector for their hospitality and assistance, and J.G. Povelites for preparing the targets.

---

[1] J. C. Sens, Phys. Rev. 113, 679 (1959).

[2] O. Hashimoto, S. Nagamiya, K. Nagamine, and T. Yamazaki, Phys. Lett. 62B, 233 (1976).

[3] M. W. Johnson, W. U. Schröder, J. R. Huizenga, W. K. Hensley, D. G. Perry, and J. C. Browne, Phys. Rev. C 15, 2169 (1977).

[4] B. Budick, S. C. Cheng, E. R. Macagno, A. M. Rushton, and C. S. Wu, Phys. Rev. Lett. 24, 604 (1970).

[5] J. A. Diaz, S. N. Kaplan, and P. V. Pyle, Nucl. Phys. 40, 54 (1963).

[6] D. Chultem, V. Cojocaru, Dz. Ganzorig, Kim Si Chwan, T. Krogulski, V. C. Kuznetsov, H. G. Ortlepp, S. M. Polikanov, B. M. Sabirov, V. Schmidt, and W. Wagner, Nucl. Phys. A247, 452 (1975).

[7] V. Cojocaru, L. Marinescu, M. Petrascu, G. Voiculescu, A. Ignatenko, and M. Omelianenko, Phys. Lett. 20, 53 (1966).

[8] B. M. Aleksandrov, G. V. Buklanov, W. D. Fromm, Dz. Ganzorig, A. S. Krivokhatski, T. Krogulski, S. M. Polikanov, and B. M. Sabirov, Phys. Lett. 57B, 238 (1975).

[9] W. D. Fromm, H. G. Ortlepp, S. M. Polikanov, U. Schmidt, G. N. Zorin, R. Arlt, and G. Musiol, Nucl. Phys. A278, 387 (1977).

[10] S. N. Kaplan, J. A. Monard, and S. Nagamiya, Phys. Lett. 64B, 217 (1976).

[11] W. W. Wilcke, M. W. Johnson, W. U. Schröder, J. R. Huizenga, and D. G. Perry, Phys. Rev. C 18, 1452 (1978).

[12] Dz. Ganzorig, P. G. Hansen, T. Johansson, B. Jonson, J. Konijn, T. Krogulski, V. D. Kuznetsov, S. M. Polikanov, G. Tibell, and L. Westgaard, Phys. Lett. 78B, 41 (1978).

[13] J. Hadermann, Phys. Lett. 67B, 35 (1977).

[14] Dz. Ganzorig, P. G. Hansen, T. Johansson, B. Jonson, J. Konijn, T. Krogulski, V. D. Kuznetsov, S. M. Polikanov, G. Tibell, and L. Westgaard, Phys. Lett. 77B, 257 (1978).

[15] W. U. Schröder, W. W. Wilcke, M. W. Johnson, D. Hilscher, J. R. Huizenga, J. C. Browne, and D. G. Perry, Phys. Rev. Lett. 43, 672 (1978).

[16] S. D. Bloom, Phys. Lett. 48B, 470 (1974).

[17] P. R. Bevington, *Data Reduction and Error Analysis for the Physical Sciences* (McGraw-Hill, New York, 1969), Chap. 5

[18] D. F. Zaretsky and V. M. Novikov, Nucl. Phys. 28, 177 (1961).

[19] R. Vandenbosch and J. R. Huizenga, *Nuclear Fission* (Academic, New York, 1973), Chap. 2.

[20] P. Singer, *Springer Tracts in Modern Physics* (Springer, Berlin, 1974), Vol. 71, p. 39.

[21] B. Goulard and H. Primakoff, Phys. Rev. C 10, 2034 (1974).

[22] M. Eckhause, R. T. Siegel, R. T. Welsh, and T. A. Fillippas, Nucl. Phys. 81, 525 (1966). The Primakoff fit performed in this study corresponds to a theory preceding Ref. 21 as described in H. Primakoff, Rev. Mod. Phys. 31, 802 (1959).

[23] T. Kozłowski and A. Zgliński, Nucl. Phys. A305, 368 (1978).

[24] G. E. Pustovalov, Zh. Eksp. Teor. Fiz. 36, 1288 (1959) [Sov. Phys.—JETP 36, 1806 (1959)].

[25] A. Bohr and B. R. Mottelson, *Nuclear Structure* (Benjamin, New York, 1975), Vol. 2.

[26] A. Zgliński and T. Kozłowski, private communication.

[27] J. D. Walecka, *Muon Physics*, edited by V. W. Hughes and C. S. Wu (Academic, New York, 1975), Vol. 2.

PHYSICAL REVIEW C VOLUME 21, NUMBER 5 MAY 1980

$L_{2,3}$-subshell x-ray fluorescence and Coster-Kronig yields at $Z=64$ and 67

B. E. Gnade, R. A. Braga, and R. W. Fink
School of Chemistry, Georgia Institute of Technology, Atlanta, Georgia 30332

(Received 10 October 1979)

The total Coster-Kronig transition probability f_{23} for the L_2-L_3 transition and the L_2 and L_3 subshell x-ray fluorescence yields ω_2 and ω_3 were measured utilizing resolved L-K x-ray coincidence techniques for $Z=64$ and 67 with radioactive sources of 4.68 yr ^{155}Eu and 10.4 h ^{165}Er, respectively. Improved accuracy in the results is achieved by advances in the experimental method. The values of f_{23} are 0.130 ± 0.012 and 0.115 ± 0.011 at $Z=64$ and 67, respectively, and of ω_2 and ω_3 are 0.165 ± 0.022 and 0.161 ± 0.019 at $Z=64$, and 0.186 ± 0.023 and 0.180 ± 0.020 at $Z=67$, respectively. The quoted uncertainties are twice the average deviation from the mean of 12 values of f_{23} and two values each of ω_2 and ω_3, and arise predominantly from systematic errors.

[RADIOACTIVITY ^{155}Eu; ^{165}Er; measured ω_2, ω_3, f_{23} in $L_{2,3}$ subshells; $XX\cdot t$ coin; Ge(HP)-Si(Li) detectors.]

I. INTRODUCTION

This investigation of the $L_{2,3}$ subshell x-ray fluorescence yields and Coster-Kronig total transition probability at $Z=64$ and 67 was carried out to provide a test of theory and improved values for experimental applications. Recently, some new relativistic calculations of radiationless transition rates to L-subshell vacancy states have been performed[1] for selected elements with $Z=70$ to 96. In this region, these calculated relativistic L-subshell widths agree with experimental values better than previous nonrelativistic calculations.[2-4] Relativistic calculations for lower-Z elements, however, are not yet available, but they are of interest in the light of the new experimental results reported here and our current effort to extend the measurements to $Z=54$.

Accurate experimental values of L-subshell fluorescence and Coster-Kronig yields also are important in many practical applications, ranging from elemental analysis by x-ray emission techniques to basic studies of nuclear and atomic processes leading to emission of x rays and Auger electrons, such as electron capture, internal conversion, and ionization cross section measurements.

Previous measurements of the total L_2-L_3 Coster-Kronig transition probability f_{23} at $Z=65$ (Ref. 5) and (Refs. 6 and 7) resulted in higher values than those found in the present work, whereas the discrepancies between previous and present values of the L-subshell x-ray fluorescence yields ω_2 and ω_3 are small. The present work is based on significant improvements in the experimental technique and in data evaluation. These advances include (1) an improved electronics system and the use of much faster coincidence timing (made possible by using a three-parameter multichannel $XX\cdot t$ coincidence configuration); (2) much better resolution and spectral quality of the K x rays through the use of a new, state-of-the-art ion-implanted Ge(HP) detector; (3) collimation to drastically reduce Compton backscattering from one detector to the other in the 180° coincidence geometry used; and (4) application of a new method[8] for the direct experimental determination of the absolute correction for tailing of $K\alpha_1$ events into the $K\alpha_2$ x-ray peak.

II. BASIS OF THE EXPERIMENTAL METHOD

The basic physical relationships among the L subshells involved in the determination of ω_2, ω_3, and f_{23} can be found in the 1972 review by Bambynek *et al.*,[9] but the working equations containing the detailed experimental corrections are not included. They appear in various forms scattered throughout the literature with occasional unfortunate errors. For this reason, we consolidate and present here in a standardized form all of the necessary working experimental equations for the determination of ω_2, ω_3, and f_{23}. Where applicable, the notation follows that of Rao *et al.*[10]

The present experiment measures the quantities ω_3, f_{23}, and ν_2, the latter representing the total number of L-shell x rays (from all shells and not just from the radiative filling of an L_2-subshell vacancy) that result per primary vacancy in the L_2 subshell.[8,10] Measurement of ν_2, f_{23}, and ω_3 proceeds directly from the relationships

$$\nu_2=\frac{C_{L(K\alpha_2)}}{I_{K\alpha_2}\epsilon_L\epsilon_e}\,, \tag{1}$$

© 1980 The American Physical Society

$$f_{23} = \frac{C_{L_3X(K\alpha_2)}C_{(K\alpha_1)}}{C_{L_3X(K\alpha_1)}(\theta)C_{(K\alpha_2)}}\,, \tag{2}$$

$$\omega_3 = \frac{C_{L(K\alpha_1)}(\theta)}{I_{K\alpha_1}\epsilon_L\epsilon_c}\,, \tag{3}$$

from which the value of ω_2 is obtained through the relationship

$$\omega_2 = \nu_2 - f_{23}\omega_3\,. \tag{4}$$

In Eqs. (1)-(4), $C_{L(K\alpha_2)}$ is the total number of L x-ray counts gated by $K\alpha_2$ x rays (after correction for continuum, nuclear cascading if present, chance coincidences, and for L x-ray coincidences arising from $K\alpha_1$ tailing events falling within the $K\alpha_2$ gate $G2$). Coincidence gates $G1$ through $G5$ and $G(K_\beta)$ are shown in Fig. 1. $I_{K\alpha_2}$ is the intensity (counts) of $K\alpha_2$ *singles* events falling within the energy region defined by $G2$ (corrected for background and *singles* $K\alpha_1$ tail events). (Note that $I_{K\alpha_1}$ and $I_{K\alpha_2}$ are the intensities of $K\alpha_1$ and $K\alpha_2$ *singles* events falling within the energy region of the *singles* spectrum defined by $G1$ and $G2$, respectively, Fig. 1, and are *not* coincidence intensities.) ϵ_L is the overall L x-ray detection efficiency averaged over the L x-ray energy region of interest and incorporates geometry and air-window attenuation, etc., and ϵ_c is the coincidence efficiency determined experimentally. $C_{L_3X(K\alpha_2)}$ represents the total number of L x-ray coincidence counts gated by $K\alpha_2$ x rays (corrected for background, nuclear cascading if present, chance coincidences, and for $K\alpha_1$ coincidence tail events in gate $G2$). The quantity $C_{L_3X(K\alpha_2)}$ arises from L_3-X shell transitions, where X represents the $M, N, \cdots$ higher shells, which give rise to the $L_l + L\alpha_{1,2} + L\beta_{2,15}$ components of the L x-ray spectrum at $Z = 64$ and 67. The factor $C_{(K\alpha_1)}$ is the number of coincident $K\alpha_1$ x-ray counts in the $K\alpha_1$ gate $G1$, corrected for background. (The use of parentheses is to indicate a *coincidence* intensity, to distinguish the *singles* intensity $I_{K\alpha_1}$ in the spectrum defined by gate $G1$.)

The factor $C_{L_3X(K\alpha_1)}(\theta)$ is the total number of L x-ray counts, gated by $K\alpha_1$ x rays arising from L_3-X transitions and corrected for background, nuclear cascading if present, chance coincidences, and for the directional correlation[9] in the 180° coincidence geometry used. $C_{(K\alpha_2)}$ is the number of coincident $K\alpha_2$ counts in gate $G2$, corrected for background and for the number of coincident $K\alpha_1$ tail events falling in gate $G2$. $C_{L(K\alpha_1)}(\theta)$ is the total number of L x-ray counts gated by $K\alpha_1$ x rays, corrected for background, nuclear cascading if present, chance events, and directional correlation.[9]

The correction for nuclear cascading and chance coincidences follows the method developed by McGeorge *et al.*[11] and is based on the fact that detection of $K\beta$ x rays indicates K-shell vacancies which have been shifted to shells higher than the L shell, the only sources of L x rays in coincidence with a $K\beta$ x-ray gate then being nuclear cascading if present and chance events. Unfortunately, in Ref. 11 an error in the equations led to an erroneous result for f_{23} at $Z = 65$, although the principle of the method was correct. The L x-ray coincidence spectra corrected properly for nuclear cascading and chance events are the differences

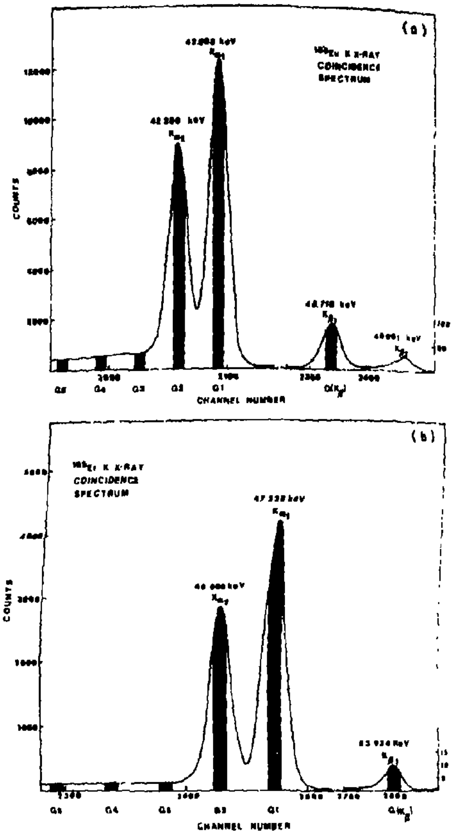

FIG. 1. (a) K x rays from 4.68-y ^{155}Eu in coincidence with L x rays. (b) K x rays from 10.4-h ^{165}Er in coincidence with L x rays. The coincidence gates $G1$, $G2$, $G3$, $G4$, $G5$, and $G(K\beta)$, indicated by the shaded areas, are set in the process of data analysis, since the three-parameter $XX \cdot t$ system stores all coincidences event by event on magnetic tape.

$$C_{L(G1)} - C_{L(K\beta)}\,(I_{K\alpha_1}/I_{K\beta})$$

and

$$C_{L(G2)} - C_{L(K\beta)}(I_{K\alpha_2}/I_{K\beta}) ,$$

where $C_{L(G1)}$ and $C_{L(G2)}$ are the gross L x-ray coincidence spectra, corrected for background, gated by $K\alpha_1$ and $K\alpha_2$ gates $G1$ and $G2$, respectively, and $I_{K\beta}$, $I_{K\alpha_1}$, and $I_{K\alpha_2}$ are the respective *singles* intensities, corrected for background, in gates $G(K_\beta)$, $G1$, and $G2$, respectively, as shown n Fig. 1. The ratios $(I_{K\alpha_1}/I_{K\beta})$ and $(I_{K\alpha_2}/I_{K\beta})$ are normalization factors needed to correct for the difference in the emission probabilities of $K\alpha_1$ and $K\beta$ and of $K\alpha_2$ and $K\beta$ x rays. These ratios are determined in the experiment and agree well with he theoretical values of Scofield.[12]

As indicated above, it is necessary to determine and correct for the number of $K\alpha_1$ tail events falling in the $K\alpha_2$ peak gate $G2$ in coincidence with the L x-ray spectrum. In all previous work reported in the literature, this correction has been made by normalizing a singles γ-ray line shape to the $K\alpha_1$ peak and then subtracting its tail from the $K\alpha_2$ peak. In the lower regions of Z where the $K\alpha_1$ and $K\alpha_2$ x rays exhibit appreciable overlap due to inadequate resolution, this procedure has been shown by us to overcorrect for the tailing,[8] because the tail from a singles peak is somewhat higher than that from a coincidence peak.

The working equation for determining the number of $K\alpha_1$ tail events in the $K\alpha_2$ gate in coincidence with L x rays, as applied in the present determination, is given by

$$N_2(2) = N_2 - N_3\left[\frac{N_1}{N_2(2)}\right] + N_4\left[\frac{N_1}{N_2(2)}\right]^2 - N_5\left[\frac{N_1}{N_2(2)}\right]^3\left[\frac{N_2(2)}{N_1 + N_2(2)}\right] , \qquad (5)$$

where N_1, N_2, N_3, N_4, and N_5 are the total numbers of $K\alpha_{(1+2)}$ events in gates $G1$, $G2$, $G3$, $G4$, and $G5$ shown in Fig. 1, respectively, and set in accordance with the exact procedure developed in Ref. 8. The quantity $N_2(2)$ is the net number of coincident $K\alpha_2$ events, after correction for $K\alpha_1$ tailing, in gate $G2$, which is the one set at the $K\alpha_2$ peak; i.e., $N_2(2) = N_2 - N_2(1)$, where $N_2(1)$ is the number of coincident $K\alpha_1$ tail events falling in the $K\alpha_2$ coincidence gate $G2$ and is the sum of the second, third, and fourth terms in Eq. (5).

Having thus determined the net number of pure $K\alpha_2$ coincident events in the $K\alpha_2$ gate $G2$, $N_2(2)$, the coincident L x-ray spectrum is then corrected for the presence of $L_1 + L\alpha_{1,2} + L\beta_{2,15}$ x-ray components arising from coincidences with $K\alpha_1$ tail events in the $K\alpha_2$ gate. The remaining $L_1 + L\alpha_{1,2} + L\beta_{2,15}$ x rays then must arise from L_3 subshell vacancies produced only from Coster-Kronig transitions shifting L_1 and L_2 vacancies into the L_3 subshell. These remaining $L_1 + L\alpha_{1,2} + L\beta_{2,15}$ x rays are the difference

$$C_{L_3X(G2)} - N_2(1)\left[\frac{C_{L_3X(K\alpha_1)}(\theta)}{N_1}\right] .$$

Quantities that involve the L_3-K transition must also be corrected for directional correlation effects, whereas the L_2-K transition is isotropic.[9] For our 180° coincidence geometry, the corrected value of the number of L x-ray counts, gated by $K\alpha_1$ x rays, arising from L_3-X transitions is

$$C_{L_3X(K\alpha_1)}(\theta) = \frac{C_{L_3X(K\alpha_1)}}{(1 + \bar{A}_{22} f_\Omega)} , \qquad (6)$$

where $C_{L_3X(K\alpha_1)}$ is the experimental value uncorrected for directional correlation. $\bar{A}_{22}$ is the average directional coefficient,[9] the numerical value of which is given theoretically by Scofield,[13] and f_Ω is the finite solid angle[9] given by

$$f_\Omega = \tfrac{1}{2}\cos\theta_m(1 + \cos\theta_m) , \qquad (7)$$

where θ_m is the half angle subtended by the detector.

The final correction to be made arises from the unresolved $L\eta$ x ray, which falls in the $L\alpha$ x-ray peak, for which the method of McGeorge *et al.*[14] is applied. On the assumption that the detection efficiencies $\epsilon_{L\alpha} \approx \epsilon_{L\eta}$, the correct value of f_{23} may be calculated from the formula

$$f_{23} = f'_{23} - \left[\frac{(L\eta/L_2)(\omega_3/\omega_2)}{(L\alpha/L_3)}\right] k , \qquad (8)$$

where f'_{23} is the uncorrected value, $(L\eta/L_2)$ is the intensity ratio of the $L\eta$ component to all x rays emitted in transitions to the L_2 subshell, $(L\alpha/L_3)$ is the intensity ratio of the $L\alpha$ component to all x-rays emitted in transitions to the L_3 subshell, and k is the fraction of $L\eta$ x rays included in the $L\alpha$ x-ray peak. The value of k depends on the detector resolution, the energy separation between the $L\eta$ and the $L\alpha$ x-ray peaks (increasing with Z), and the method used to evaluate the $L\alpha$ x-ray intensity. For $Z \lessdot 70$, with modern Si(Li) L x-ray detectors, the value $k \approx 1$. The theoretical values of Scofield[15] are used for the ratios $(L\eta/L_2)$ and $(L\alpha/L_3)$ and are in good agreement with experiment.

Two additional very small corrections to be considered are (1) subtraction of the continuum under the peaks and (2) subtraction of $L\beta$ and $L\gamma$ tail events from the $L\alpha$ x-ray peak. (In the present work these corrections are negligible, e.g., $\lessdot 0.4\%$ and $\lessdot 0.1\%$, respectively, for both nuclides.)

III. EXPERIMENTAL

The radioactive sources used were carrier-free 4.68 y ^{155}Eu and high specific activity 10.4 h ^{165}Er. The latter was prepared by irradiating 2 mg of 67% enriched $^{164}Er_2O_3$ for 4 h at 10^{13} *n*/cm^2 sec in the Georgia Tech Research Reactor. The irradiated sample was then dissolved in 1 ml of hot 3*M* HNO_3, and 5 to 10 μl aliquots were drop evaporated onto 0.25 mm thick Mylar discs, which were then lightly sealed with Krylon spray. The radioactive side was positioned to face the *L* x-ray detector in order to minimize attentuation of *L* x rays. While counting the ^{155}Eu source, a 100 mg/cm^2 plastic absorber was placed between the source and the *K* x-ray detector to remove most of the beta particles, to reduce the β^- continuum. This was unnecessary for ^{165}Er, which decays purely by electron capture to the ground state of ^{165}Ho.

The electronic block diagram is shown in Fig. 2. The dashed portion is used to acquire simultaneous singles spectra for measurements of ω_2 and ω_3, and the solid lines in the diagram represent the three-parameter coincidence experiment for determination of f_{23}. The logic gate width typically is 2 μsec, and the system resolving time is 50 to 70 nsec (full width at half amplitude). The multiparameter analyzer is a computer-based Nuclear Data ND-4420 system that requires all input signals to arrive within an interval of 2 μsec in order to be stored as coincidences, which is done event by event on magnetic tape. By using an *XX*·*t* three-parameter arrangement, a broad TAC spectrum of approximately 500 nsec can be acquired, and then a narrow, prompt portion of the TAC spectrum can be selected in the data analysis The ratio of the counts in the narrow, prompt TAC gate to those in the broad TAC spectrum is used to determine the coincidence efficiency, which is typically in the range of 60 to 65% for the narrow TAC gate, assuming the coincidence efficiency to be unity for the broad TAC spectrum.

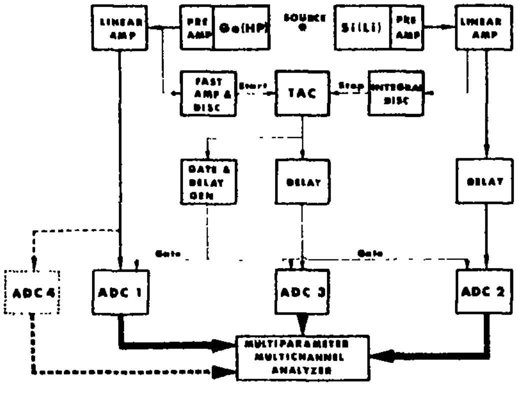

FIG. 2. The electronic block diagram for the three-parameter *XX*·*t* coincidence system. The heavy lines indicate the path of the digital signals, the medium lines represent analog signals, and the fine lines carry the logic pulses. The dashed portion is used to acquire simultaneous singles spectra for measurement of ω_2 and ω_3. The parameters of the system are described in the text.

A very narrow TAC window (50–70 nsec FWHA), was used, in spite of the fact that this produced a coincidence efficiency of only 60 to 65%. This sacrifice of some coincidence efficiency was made in order to achieve a significant reduction in tailing in the *K* and *L* x-ray spectra, where rejection of slow pulses is achieved by using the very narrow TAC window.[8]

The *K* x-ray detector is a ruggedized ion-implanted planar ORTEC Ge(HP) (which exhibits a resolution under the coincidence conditions described above of 340 eV FWHM at 46 keV and a peak/tail ratio of 70:1) and the *L* x-ray detector is a planar Kevex Si(Li) (coincidence resolution of 240-eV FWHM at 5.9 keV), using a 1.5-μsec amplifier time constant for each detector. Both detectors are fitted with 5-ml (0.125-mm) Be windows and were used in 180° coincidence geometry. In the experimental setup, collimation was employed to reduce drastically the Compton backscattering. This especially benefitted the *L* x-ray spectrum, almost completely removing the Compton continuum. The graded collimator consisted of 1.8-mm Pb, 0.6-mm Cd, 0.9-mm Cu, and 1-mm Al, placed back to back on each side of the radioactive source. The center hole was approximately 5.5 mm in diameter. An example of the *K* spectrum is shown in Fig. 1 and the *L* spectra in Figs. 3 and 4.

In order to determine ω_2 and ω_3, it is necessary to establish the detection efficiency of the *L* x-ray detector. This was done by using calibration standards of ^{57}Co, from the Laboratoire de Métrologie des Rayonnements Ionisants, Gif-sur-Yvette, France, and ^{54}Mn from the Physikalisch-Technische Bundesanstalt, Braunschweig, West Germany. Campbell *et al.*[16] have demonstrated that the use of drop-evaporated radioactive sources as standards, calibrated as γ-ray standards, can result in the determination of efficiency points in the 5- to 40-keV region that may be as much as 3 to 16% too low, owing to self-absorption and the use of X/γ ray intensity ratios, the self-absorption being negligible for the much higher energy γ ray for which the calibration was done. Another major source of error in the efficiency calibration is the presence of small variations in

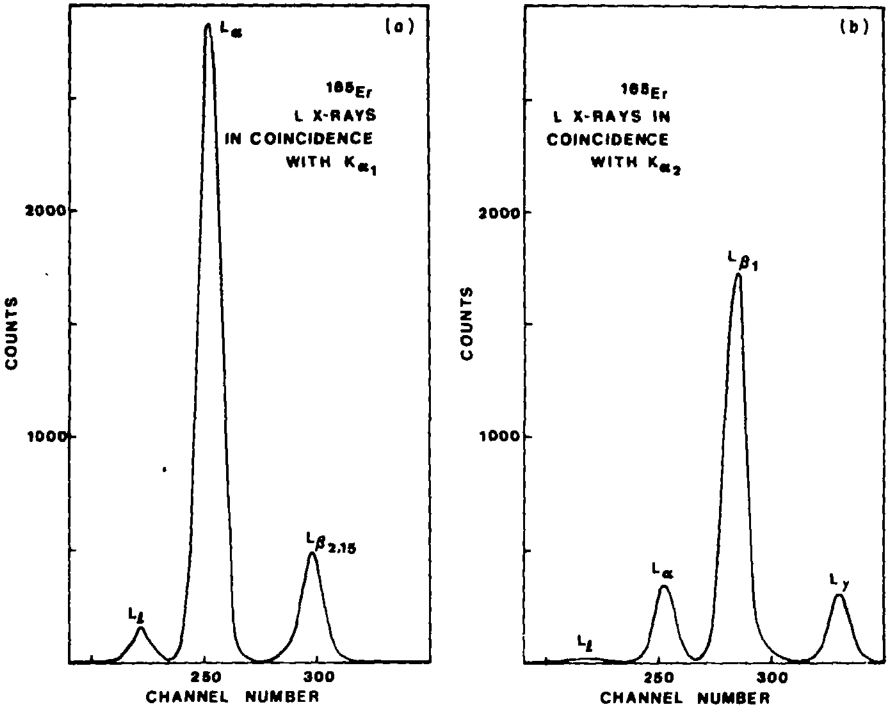

FIG. 3. (a) The L x-ray spectrum gated by $K\alpha_1$ x rays at $Z=64$ from decay of 4.68-y ^{155}Eu. (b) Similar L x-ray spectrum, but gated by $K\alpha_2$ x rays.

source position, not only in distance from the detector, but also in lateral deviation from the axial center.[17] A 5% variation in a 2-cm source-to-detector distance for a 20-mm diameter × 3-mm thick detector can cause a shift in the efficiency by as much as 8%.[18] It is due to possible systematic errors of this magnitude that inherent errors of up to 11% in the efficiency calibration of the L x-ray detector may be present, and it is this uncertainty that is the major contribution to the un-

TABLE I. Corrections applied to the K x-ray gates and the gated L x-ray spectra.[a]

	^{155}Eu				^{165}Er			
Component	$G1$ (%)	$G2$ (%)	$L_{(K\alpha_1)}$ (%)	$L_{(K\alpha_2)}$ (%)	$G1$ (%)	$G2$ (%)	$L_{(K\alpha_1)}$ (%)	$L_{(K\alpha_2)}$ (%)
Continuum	0.3	0.4			$\leqslant 0.1$	0.18		
Chance coincidences and nuclear cascades			17.9	13.8			0.5	0.4
Tailing of $K\alpha_1$ events into the $K\alpha_2$ gate		5.0				3.8		
Directional correlations			2.5				2.5	
$Ll + L\alpha_{1,2} + L\beta_{2,15}$ (i.e., L_3X) counts in gate $G2$ caused by $K\alpha_1$ tail events				23.0				21.7
Tailing of $L\beta + L\gamma$ events into the $L\alpha$ peak			$\leqslant 1.0$	2.0			≈ 0	≈ 0
Percentage of net true coincidence events	99.7	94.6	$\geqslant 78.6$	61.2	$\geqslant 99.9$	96.0	97.0	77.7

[a] $G1$ is the $K\alpha_1$ gate and $G2$ is the $K\alpha_2$ gate; $L_{(K\alpha_1)}$ and $L_{(K\alpha_2)}$ are the total L x-ray spectra produced by gates $G1$ and $G2$, respectively.

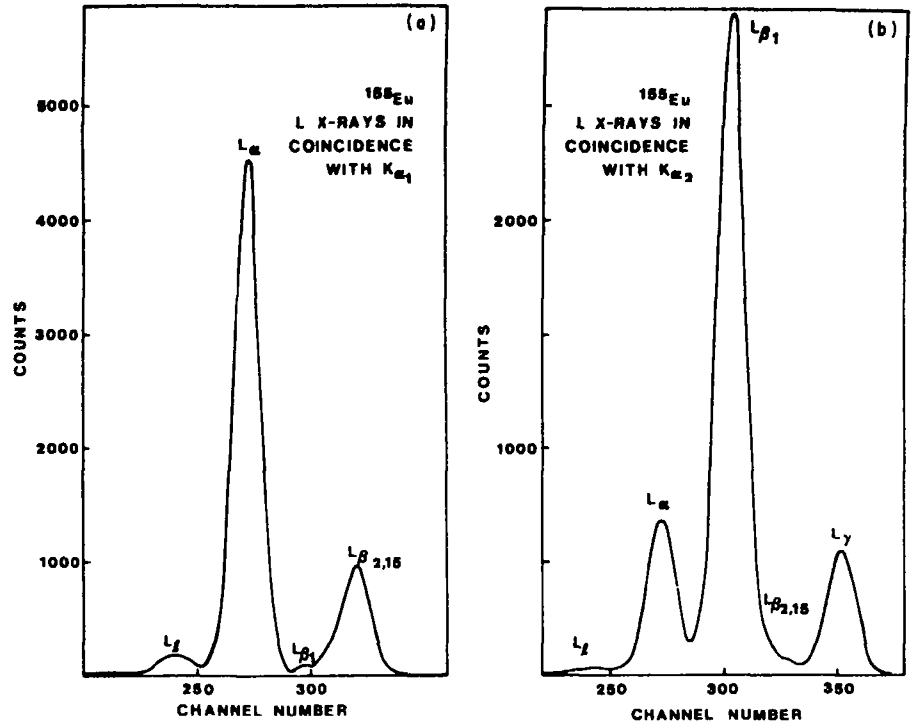

FIG. 4. (a) The L x-ray spectrum gated by $K\alpha_1$ x-rays at $Z=67$ from decay of 10.4-h ^{165}Er. (b) Similar L x-ray spectrum, but gated by $K\alpha_2$ x rays.

certainty limits placed on the determination of ω_2 and ω_3 in the present work. Since the detection efficiencies are not involved in the determination of f_{23}, these systematic errors are absent in the measurement of f_{23}.

The coincidence experiment to determine f_{23} was repeated for each nuclide four times, the last two of which included the measurements of ν_2 and ω_3. Each run required approximately one week of counting time in order to reduce the statistical errors in counting to less than 1% in the coincidence gates and coincidence spectra.

IV. RESULTS AND ANALYSIS OF ERRORS

The data were evaluated according to the procedure given in Sec. II and the various contribu-

TABLE II. Quantities used to evaluate ν_2, f_{23}, and ω_3.

	$Z=64$			
Quantity [a]	Value	% error	Value	% error
$C_{L(K\alpha_2)}$	78 000	0.4%	54 850	0.4%
$I_{K\alpha_2}$	8.91×10^7	0.1%	5.05×10^7	0.1%
ϵ_L	7.52×10^{-3}	11%	8.75×10^{-3}	11%
ϵ_c	0.6276	0.15%	0.6059	0.15%
$C_{L_3X(K\alpha_2)}$	9 037	2.5%	3 475	2.7%
$C_{(K\alpha_1)}$	104 150	0.3%	42 350	0.5%
$C_{L_3X(K\alpha_1)(\theta)}$	78 860	1.0%	39 990	1.0%
$C_{(K\alpha_2)}$	71 770	2.4%	27 925	2.6%
$C_{L(K\alpha_1)(\theta)}$	122 900	1.0%	86 510	1.1%
$I_{K\alpha_1}$	1.62×10^8	0.08%	9.06×10^7	0.1%

[a] See Eqs. (1)–(3) in the text. These values represent results and error limits from a typical run on each nuclide.

tions to the coincidence gates and coincidence L x-ray spectra are listed in Table I in the order in which the corrections are applied. The quantities needed for determining ν_2, f_{23}, and ω_3 from Eqs. 1, 2, and 3 are listed in Table II, with numerical results and percent errors for a typical run for each nuclide. Details of the error evaluations are given below.

In order to establish the independence of the values determined for ν_2, f_{23}, and ω_3 with respect to the location of the K x-ray gates $G1$ and $G2$, in each run $G1$ and $G2$ were analyzed for positions immediately below, at, and above the peak centroids. The resulting values exhibited a random distribution about the mean, thus assuring the validity of the tailing correction for $K\alpha_1$ events in gate $G2$. However, tailing in the coincident L x-ray spectra was at a minimum when gates $G1$ and $G2$ were chosen at the centroids of the K x-ray peaks. The percent errors listed in Table II from a typical run on each nuclide are purely statistical, except for ϵ_L, $C_{L_3x(K\alpha_2)}$, and $C_{(K\alpha_2)}$, which are dominated by the presence of systematic uncertainty.

From the four runs, a total of 12 values of f_{23} was obtained, and their mean value is listed in Table III with an uncertainty of twice the average deviation from the mean, arising primarily from systematic error. All previous determinations of f_{23} contained estimated systematic errors that are two to three times larger than those in the present work. The uncertainty limits on ω_2 and ω_3 values are completely dominated by the systematic error arising in the L x-ray detection efficiency ϵ_L (see Table II).

Previous measurements[5,6] of the L-subshell fluorescence yields, ω_2 and ω_3, are in approximate agreement with the present results within the error limits. However, the previous values[5,7] of f_{23} lie significantly above the present ones and are outside experimental error limits. High values can result from the following experimental difficulties[5,7]: lack of sufficient energy resolution in the K and L x-ray detectors required to reduce the tailing correction to a minimum, use of a singles γ-ray line shape to estimate the tailing of $K\alpha_1$ events in the $K\alpha_2$ peak, apparent lack of correction for $L\beta$ tailing into the $L\alpha$ peak, lack of sufficiently narrow prompt time gating in the two-parameter coincidence technique used,[5,7] and lack of collimation to reduce the Compton continuum from backscattered events.

TABLE III. Final values of ν_2, f_{23}, ω_3 and ω_2 from the present work.

Quantity	$Z=64$	$Z=67$
ν_2	0.184 ± 0.022	0.204 ± 0.023
f_{23}	0.130 ± 0.012	0.115 ± 0.011
ω_3	0.161 ± 0.019	0.180 ± 0.020
ω_2	0.165 ± 0.022	0.186 ± 0.023

V. DISCUSSION

The nonrelativistic theoretical calculation of McGuire[2] at $Z=67$ predicts $\omega_2=0.203$, $\omega_3=0.201$, and $f_{23}=0.138$, all of which lie considerably above the present experimental values. Chen and Crasemann[3] predict from a nonrelativistic independent-particle model values at $Z=67$ of $\omega_2=0.190$ and $f_{23}=0.147$. Although the predicted value of ω_2 agrees well with the present experiment, the value of f_{23} is much too large, as has been found by Nix and Fink[19] in a systematic comparison of theory and experiment for f_{23} vs Z. The 1971 nonrelativistic calculations of Chen, Crasemann, and Kostroun[4] also predict values of f_{23} which exceed the trend of experimental results, although the theoretical predictions of ω_2 and ω_3 agree with the present results.

The 1979 relativistic calculations of Chen *et al.*,[1] do not extend below $Z=70$. However, a linear extrapolation to $Z=64$ indicates good agreement with the present experimental values of ω_2. Extrapolation to $Z<70$ for f_{23} is not feasible, but it would appear to result in values much larger than the present experimental ones. We are extending the present measurement technique to $Z=54$ and to $Z=82$ to provide a more general critical test of theory.

The origin of the rather serious disagreement between theory and experiment for f_{23} can no longer be ascribed to error in the experiments, nor can it arise from the small admixture of double vacancies from K-LL and K-LM Auger transitions, since this effect has been shown at $Z=49$,[20] 73,[21] and 82 (Ref. 22) to be less than about 10% on L-fluorescence yields and is probably altogether negligible for f_{23}.

ACKNOWLEDGMENTS

We thank Mr. R. C. McFarland and Mr. R. S. Kirkland of the Georgia Tech Research Reactor for irradiations.

[1] M. H. Chen, E. Laiman, B. Crasemann, M. Aoyagi, and Hans Mark, Phys. Rev. A 19, 2053 (1979); Bull. Am. Phys. Soc. 24, 624 (1979).

[2] E. J. McGuire, Phys. Rev. A 3, 587 (1971).

[3] M. H. Chen and B. Crasemann, in *Inner Shell Ionization Phenomena and Future Applications*, edited by R. W. Fink, S. T. Manson, J. M. Palms, and P. V. Rao (U.S. Atomic Energy Commission, 1973), p. 43.

[4] M. H. Chen, B. Crasemann, and V. O. Kostroun, Phys. Rev. A 4, 1 (1971).

[5] D. G. Douglas, Can. J. Phys. 50, 1697 (1972).

[6] C. P. Holmes and V. O. Kostroun, Bull. Am. Phys. Soc. 15, 561 (1970).

[7] D. G. Douglas, Can. J. Phys. 54, 1124 (1976).

[8] B. E. Gnade, R. A. Braga, W. R. Western, J. L. Wood, and R. W. Fink, Nucl. Instrum. Methods 164, 163 (1979).

[9] W Bambynek, B. Crasemann, R. W. Fink, H. U. Freund, Hans Mark, C. D. Swift, R. E. Price, and P. V. Rao, Rev. Mod. Phys. 44, 716 (1972).

[10] P. V. Rao, R. E. Wood, J. M. Palms, and R. W. Fink, Phys. Rev. 178, 1997 (1969).

[11] J. C McGeorge, H. U. Freund, and R. W. Fink, Nucl. Phys. A154, 526 (1970).

[12] J. H. Scofield, At. Data Nucl. Data Tables 14, 121 (1974).

[13] J. H. Scofield, Lawrence Livermore Laboratory Report UCRL-51231, 1972 (unpublished).

[14] J. C. McGeorge, S. Mohan, and R. W. Fink, Phys. Rev. A 4, 1317 (1971).

[15] J. H. Scofield, Phys. Rev. 179, 9 (1969).

[16] J. L. Campbell, H. H. Jorch, and J. A. Thompson, Nucl. Instrum. Methods 140, 167 (1977); 143, 551 (1977).

[17] Z. B. Alfassi and R. Nothman, Nucl. Instrum. Methods 143, 57 (1977).

[18] G. Bertolini and G. Restelli, in *Atomic Inner-Shell Processes*, edited by B. Crasemann (Academic, New York, 1975), Vol. 2, p. 123.

[19] D. W. Nix and R. W. Fink, Z. Phys. A273, 305 (1975).

[20] P. A. Indira, I. J. Unus, P. V. Rao, and R. W. Fink, J. Phys. Atom. Molec. Phys. (London) B12, 1351 (1979).

[21] J. L. Campbell, L. A. McNelles, J. S. Geiger, J. S. Merritt, and R. L. Graham, Can. J. Phys. 55, 868 (1977).

[22] P. V. Rao, R. E. Wood, and V. R. Veluri, J. Phys. Atom. Molec. Phys. (London) B10, 399 (1977).

PHYSICAL REVIEW C VOLUME 21, NUMBER 5 MAY 1980

Half-life of ^{241}Pu

S. K. Aggarwal and H. C. Jain
Radiochemistry Division, Bhabha Atomic Research Centre, Trombay, Bombay 400085, India

(Received 22 August 1979)

The half-life of ^{241}Pu was determined by studying the ingrowth of ^{241}Am by α spectrometry. A synthetic mixture was prepared by mixing different isotopes of plutonium so as to obtain a ^{238}Pu/(^{239}Pu + ^{240}Pu) α activity ratio of nearly 0.1 and an increase in the α activity ratio due to the ingrowth of ^{241}Am of about 0.1 after a period of 30 days. This was done to get a desired change periodically in the α activity ratio and to measure this change with high precision and accuracy. The initial values of ^{239}Pu/^{241}Pu and ^{240}Pu/^{241}Pu atom ratios in the mixture were obtained by mass spectrometry. The ingrowth of ^{241}Am was measured periodically by α spectrometry on electrodeposited sources using a silicon surface barrier detector. From the 80 α spectrometric measurements carried out on five electrodeposited sources over a period of 457 days, a value of 14.42 ± 0.09 yr is obtained for the half-life of ^{241}Pu using a value of 432.6 yr for the half-life of ^{241}Am. The uncertainty quoted on the value is a combination of one standard deviation on the average value and the error evaluated from the estimate on various error components. The half-life obtained in this work is in good agreement with the preliminary results reported recently by CBNM (Geel), NBS (Washington), and AERE (Harwell) using different methods.

[RADIOACTIVITY ^{241}Pu half-life; measured: ^{241}Am ingrowth by α spectrometry, ^{239}Pu/^{241}Pu and ^{240}Pu/^{241}Pu atom ratios by mass spectrometry.]

I. INTRODUCTION

The work presented here was motivated by a large discrepancy[1] between the various published values of ^{241}Pu half-life. The half-life of ^{241}Pu in the studies reported earlier has been determined mainly by the two methods: (i) by observing the decay of ^{241}Pu relative to other isotopes of plutonium using a mass spectrometer and (ii) by measuring the ingrowth of ^{241}Am by α or γ counting. The first method, though absolute, has led to half-life values ranging from 14.6 yr to 15.1 yr[2-5] while the measurements reported by the ^{241}Am ingrowth method have yielded a half-life value of about 14.0 ± 0.2 yr[6-9] based on the half-life of ^{241}Am as 432.6 yr. There were two other measurements reported by the reactivity method[10] and by calorimetry[11] which led to the half-life values as 14.63 ± 0.27 yr and 14.355 ± 0.007 yr respectively. In view of the great importance of the half-life of ^{241}Pu in nuclear technology, it was considered worthwhile to utilize the expertise developed in the fields of α spectrometry and mass spectrometry for determining the half-life of ^{241}Pu.

In the mass spectrometric method, there is a problem of measuring accurately the small change (about 1% in 3 months) in the atom ratio of ^{241}Pu relative to other isotopes of plutonium unless the measurements are carried out under strictly controlled conditions. Further, most of the measurements reported have involved the measurement of isotopic ratios much different from unity. These may be responsible for a large variation in the half-life values reported by studying the change in the isotopic ratios mass spectrometrically. This is evident from the half-life of ^{241}Pu reported by Zeigler and Ferris[4] in which six different laboratories from the USA participated in a sample exchange program and the half-life values calculated from the data reported by these laboratories varied from 14.50 yr to 15.06 yr.

The α or γ counting methods used earlier for determining the ingrowth of ^{241}Am require a knowledge of the efficiency of the detector which should be known accurately over the period of experiment. Further, the measurements have not been performed on replicate samples to observe the ingrowth of ^{241}Am periodically to confirm the reproducibility of the experimental data.

With a view to eliminating the need for the efficiency of the detector, the ingrowth of ^{241}Am in the present work was determined by α spectrometry relative to the α activity due to ^{239}Pu + ^{240}Pu which remained practically constant during the course of investigations. Further, the measurements were carried out periodically over a period of 1.25 yr on 5 electrodeposited sources prepared from a synthetic mixture of plutonium isotopes. The synthetic mixture was prepared so as to have ^{238}Pu/(^{239}Pu + ^{240}Pu) α activity ratio nearly 0.1 and an increase in the α activity ratio due to the ingrowth of ^{241}Am by about 0.1 (i.e., 100% change in the α activity ratio) after a period of 30 days. This was done with the objective of obtaining the desired change periodically in the α activity ratio and measure this change with high precision and accuracy. The initial α activity ratio was kept as 0.1 and the measurements were performed up to

© 1980 The American Physical Society

TABLE I. Isotopic composition of the synthetic mixture of plutonium used for the determination of the half-life of ^{241}Pu.

Mass number	Atom percent
238	0.025 02 ± 0.000 25 [a]
239	49.057 7 ± 0.057
240	8.368 7 ± 0.017
241	40.020 3 ± 0.024
242	2.528 3 ± 0.025

[a] Determined by α spectrometry.

an activity ratio of about 2 so that the tail contribution due to energy degradation from the high energy ^{238}Pu + ^{241}Am peak (5.50 MeV) to the low energy ^{239}Pu + ^{240}Pu peak (5.17 MeV) was small and could be accounted for accurately.

II. PRINCIPLE OF THE METHOD

The method involved the measurement of (^{238}Pu + ^{241}Am)/(^{239}Pu + ^{240}Pu) α activity ratio periodically by α spectrometry. If R_α denotes the increase in the α activity ratio due to the ingrowth of ^{241}Am after a time t, then

$$R_\alpha = \frac{A(^{241}\mathrm{Am})_t}{A(^{239}\mathrm{Pu})_t + A(^{240}\mathrm{Pu})_t}$$

$$= \frac{N(^{241}\mathrm{Am})_t\,\lambda(^{241}\mathrm{Am})}{N(^{239}\mathrm{Pu})_t\,\lambda(^{239}\mathrm{Pu}) + N(^{240}\mathrm{Pu})_t\,\lambda(^{240}\mathrm{Pu})}\,, \tag{1}$$

where A's denote the α activities, N's stand for the number of atoms, λ's are the decay constants, the symbols in the parentheses denote the isotope, and the subscripts to the parentheses denote the ingrowth period for ^{241}Am.

The number of atoms of ^{241}Am formed from the decay of ^{241}Pu after a time t is given by

$$N(^{241}\mathrm{Am})_t = \frac{N(^{241}\mathrm{Pu})_0}{1 - \lambda(^{241}\mathrm{Am})/\lambda(^{241}\mathrm{Pu})}$$

$$\times \left[e^{-\lambda(^{241}\mathrm{Am})\,t} - e^{-\lambda(^{241}\mathrm{Pu})\,t}\right], \tag{2}$$

where $N(^{241}\mathrm{Pu})_0$ denotes the number of atoms of ^{241}Pu at zero time. Substituting the value of $N(^{241}\mathrm{Am})_t$ from Eq. (2) in Eq. (1) we get

$$R_\alpha = XY\left[e^{-\lambda(^{241}\mathrm{Am})t} - e^{-\lambda(^{241}\mathrm{Pu})t}\right], \tag{3}$$

where

$$X = \frac{\lambda(^{241}\mathrm{Am})}{R^{9/1}\lambda(^{239}\mathrm{Pu}) + R^{0/1}\lambda(^{240}\mathrm{Pu})}\,, \tag{4}$$

$$Y = \frac{1}{1 - \lambda(^{241}\mathrm{Am})/\lambda(^{241}\mathrm{Pu})}\,, \tag{5}$$

Here $R^{9/1}$ and $R^{0/1}$ denote the initial values of ^{239}Pu/^{241}Pu and ^{240}Pu/^{241}Pu atom ratios in the synthetic mixture [as t is very small compared to the half-lives of ^{239}Pu and ^{240}Pu; therefore $N(^{239}\mathrm{Pu})_t = N(^{239}\mathrm{Pu})_0$ and $N(^{240}\mathrm{Pu})_t = N(^{240}\mathrm{Pu})_0$]. Thus, knowing the values of X, Y, R_α, t and the half-life of ^{241}Am, the half-life of ^{241}Pu can be calculated using Eq. (3). It may be mentioned that an approximate value of $\lambda(^{241}\mathrm{Pu})$ suffices for calculating Y from Eq. (5).

As is seen from Eq. (3), the accuracy in the measurement of ^{241}Pu half-life by the method reported here depends on three factors: (a) change in the α activity ratio, (b) the atom ratios $R^{9/1}$ and $R^{0/1}$, and (c) the half-life values of ^{239}Pu, ^{240}Pu, and ^{241}Am. In the present work, as will be seen later, the atom ratios and the change in the α activity ratios were measured with high precision and accuracy. Further, the half-life values of the reference isotopes ^{239}Pu, ^{240}Pu, and ^{241}Am are now known accurately.

III. EXPERIMENTAL

A. Preparation and purification of synthetic mixture

A synthetic mixture of plutonium isotopes was prepared by using ^{241}Pu (enriched) and ^{239}Pu containing small amounts of other isotopes. Enriched ^{241}Pu used in this work was obtained from Oak Ridge National Laboratory, USA in 1969.

TABLE II. Illustration of tail correction factor due to energy degradation.

Sample	Counts in ^{238}Pu or ^{241}Am region (A)	Counts in ^{239}Pu + ^{240}Pu region (B)	Tail correction factor A/B
^{238}Pu-I	112 508	882	127.56
^{238}Pu-II	100 935	791	127.60
^{241}Am-I	133 007	1012	131.43
^{241}Am-II	131 926	1207	109.30
		Average =	123.97 ± 4.97 [a]

[a] Standard error of the mean calculated as $s/\sqrt{n}$, where $s^2 = \sum_{i=1}^{n}(x_i - \bar{x})^2/(n-1)$ with $n = 4$.

TABLE III. Illustration of α energy pulse height analysis.

Disk Number	1	2	3	4	5
Total counts in (^{238}Pu + ^{241}Am) region	303 555	249 777	396 137	915 465	257 136
Total counts in (^{239}Pu + ^{240}Pu) region	202 121	164 916	263 869	607 940	170 551
Tail correction[a]	−2 448	−2 015	−3 195	−7 384	−2 074
Net counts in (^{239}Pu + ^{240}Pu) region	199 672	162 901	260 674	600 556	168 477
$\left(\frac{^{238}\text{Pu} + ^{241}\text{Am}}{^{239}\text{Pu} + ^{240}\text{Pu}}\right)_\alpha$ activity ratio	1.520 27	1.533 30	1.519 66	1.524 36	1.526 24
Average = 1.524 77 ± 0.002 4[b]					

[a] Based on the tail correction factor given in Table II.

[b] Standard error of the mean calculated as $s/\sqrt{n}$, where $s^2 = \sum_{i=1}^{n} (x_i - \bar{x})^2/(n-1)$ with $n = 5$.

Precalculated and known aliquots from the solutions of ^{239}Pu and ^{241}Pu were mixed to obtain ^{238}Pu/(^{239}Pu + ^{240}Pu) α activity ratio nearly 0.1 and an increase of about 0.1 in the α activity ratio after a period of 30 days due to the ingrowth of ^{241}Am. The chemical exchange between the plutonium isotopes was ensured by using freshly prepared solutions of ferrous ammonium sulphate and sodium nitrite as the reductant and oxidant, respectively. The plutonium solution was evaporated to near dryness, treated with concentrated HNO_3 twice to break the polymer, if any, and was finally taken in 7 *M* HNO_3. It was subjected to a redox cycle once more and purified from ^{241}Am by using a double stage anion exchange procedure.

The plutonium solution in 7 *M* HNO_3 was loaded onto the jacketed column containing Dowex 1×8 resin (200–400 mesh) and operating the column at 60 °C. Americium was washed down with 3 *M* HNO_3 and plutonium was eluted with 0.35 *M* HNO_3. The purified plutonium solution (referred to as synthetic mixture) was transferred to a clean and dry volumetric flask using 1 *M* HNO_3. The radiochemical purity of the synthetic mixture was checked by α spectrometry and γ spectrometry. It was found to be free from ^{241}Am (by checking for the 60 keV peak on an intrinsic germanium detector) and only three α energy peaks corresponding to ^{241}Pu + ^{242}Pu (4.90 MeV), ^{239}Pu + ^{240}Pu (5.17 MeV) and ^{238}Pu (5.50 MeV) were observed.

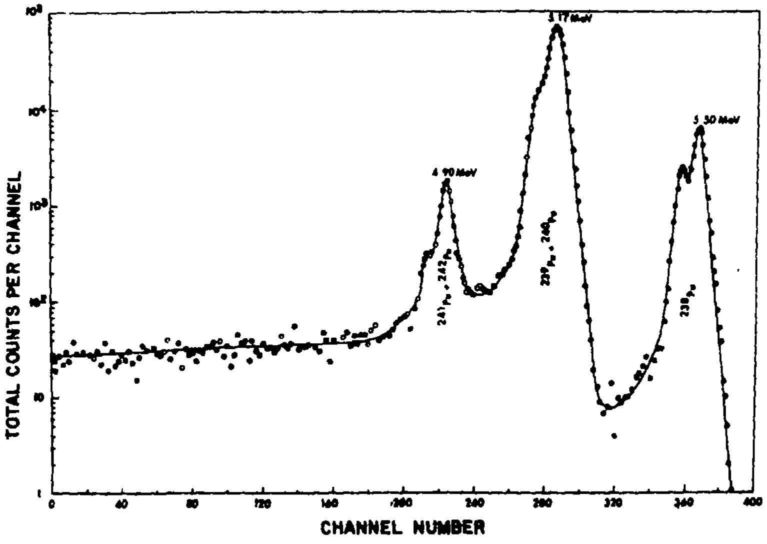

FIG. 1. The alpha particle energy spectrum of SM-241-III Pu sample (at zero time).

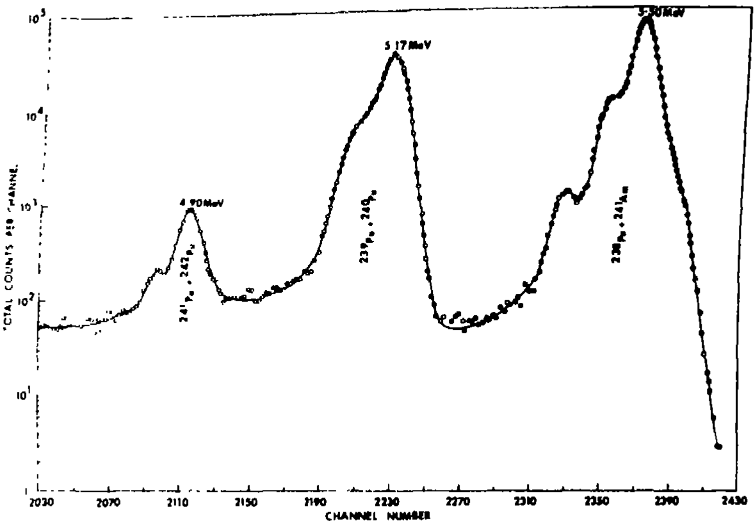

FIG. 2. The alpha particle energy spectrum of SM-241-III Pu sample (after 457 days).

B. Mass spectrometry

The isotopic composition of the synthetic mixture was determined by using a Varian MAT CH-5 mass spectrometer with a thermionic source. The instrument has a resolution of 425 (at 10% valley definition) measured at around mass 238 and an abundance sensitivity greater than 10^5. Rhenium ribbons (0.04 × 0.7 × 8 mm) were used as the sample and ionization filaments in the double filament assembly. The ionizing filament was heated to a current of about 6 A and the sample filament to a current of about 2 A. Mass spectrum was obtained by scanning the magnetic field and the output was fed to a strip chart recorder as well as to a TDC-312 computer coupled to the mass spectrometer.

The mass discrimination factor was calibrated by analyzing the isotopic standards of uranium and plutonium obtained from National Bureau of Standards. It was found to be 0.0036 per mass unit and used in the present work.

TABLE IV. Summary of ^{241}Pu half-life measurements.

Counting No.	Growth period (days)	$(^{238}Pu + ^{241}Am)/(^{239}Pu + ^{240}Pu)$ α activity ratio	Half-life of ^{241}Pu (yr)[a]
1	Taken as zero time	0.086 12 ± 0.000 16	
2	15.0	0.141 15 ± 0.000 32	14.433
3	30.0	0.196 09 ± 0.000 43	14.430
4	58.0	0.298 24 ± 0.000 06	14.435
5	90.0	0.414 99 ± 0.000 45	14.416
6	117.0	0.513 29 ± 0.000 49	14.403
7	156.0	0.653 64 ± 0.000 71	14.407
8	193.0	0.786 30 ± 0.000 68	14.389
9	218.0	0.876 34 ± 0.000 75	14.437
10	253.0	0.998 55 ± 0.001 6	14.406
11	278.0	1.087 73 ± 0.001 2	14.444
12	315.0	1.216 98 ± 0.001 1	14.445
13	350.0	1.340 10 ± 0.001 9	14.425
14	371.0	1.413 18 ± 0.001 3	14.467
15	401.0	1.524 77 ± 0.002 4	14.375
16	457.0	1.720 38 ± 0.001 2	14.353

Mean = 14.42 ± 0.03[b]

---

[a] Half-lives of ^{239}Pu, ^{240}Pu, and ^{241}Am used are 24110 yr, 6553 yr, and 432.6 yr, respectively, Ref. 14 (1978).

[b] Standard deviation s computed from $s^2 = \sum_{i=1}^{n} (x_i - \bar{x})^2/(n-1)$ with $n = 15$.

The synthetic mixture was analyzed for ^{239}Pu/ ^{41}Pu and ^{240}Pu/^{241}Pu atom ratios within 24 h from he time of purification. Three filament loadings vere carried out. Five runs, each consisting of 10–12 scans, were taken during each mass spectrometric determination. Table I presents the lata on the isotopic composition of the synthetic nixture.

C. Alpha spectrometry

Sources for α spectrometry were prepared from he synthetic mixture by electrodeposition in iqueous HNO_3 medium (pH about 2). Platinum lisks were used as the cathode and a platinum tirrer as the anode. A current density of about .00 mA/cm^2 and a voltage of 8–10 V was used. he electrodeposition was continued for about an our. A few drops of dilute ammonia solution were dded to the solution in the electrodeposition cell efore stopping the electrodeposition. The electroeposited source was washed with water, acetone, ried under an infrared lamp and ignited. Five ources were prepared from the synthetic mixure. Duplicate sources were also prepared from ^{41}Am solution and from ^{238}Pu solution on platinum lanchets.

A 50 mm^2 silicon surface barrier detector nounted in a vacuum chamber (pressure $<10^{-2}$ orr) and coupled to a 4 K analyzer (TN-1700) was sed for recording the α spectra. The system has resolution of 20 keV full width at half maximum FWHM) at 5.50 MeV. The initial activity on each ource was about 2×10^5 dpm so as to eliminate the istortion and pileup effects. The source to detecor geometry was such that about 3% of the α articles emitted (in 4π) by the source entered he detector. The sources were counted for a time ong enough to accumulate more than 10^5 counts nder each of the two peaks at 5.50 MeV and 5.17 MeV.

The α spectra from the five sources prepared rom the synthetic mixture were recorded periodcally for studying the ingrowth of ^{241}Am over a eriod of about 1.25 yr. Alpha spectra were also recorded from ^{238}Pu and ^{241}Am sources each time under the identical conditions. All the sources were kept in a perspex planchet box and handled with extreme care. The (^{238}Pu + ^{241}Am)/(^{239}Pu + ^{240}Pu) α activity ratios were computed by taking the equal number of channels for ^{239}Pu + ^{240}Pu and ^{238}Pu + ^{241}Am peaks. The tail correction due to energy degradation from the high energy ^{238}Pu + ^{241}Am peak (5.50 MeV) to the low energy ^{239}Pu + ^{240}Pu peak (5.17 MeV) was applied based on the contribution calculated from α spectra recorded on ^{238}Pu and ^{241}Am sources. The tail contribution varied from about 0.1% of the α activity ratio at the beginning of the experiment to about 1% at the end of the experiment. An illustration of the tail correction factor due to energy degradation and the results of α energy pulse height analysis are given in Tables II and III, respectively. Figures 1 and 2 show the typical α spectra recorded from one of the sources at zero time and after the growth period of 457 days, respectively.

Our experience[12] in the field of α spectrometry shows that the accuracy in computing the α activity ratio from an α spectrum on weightless electrodeposited source is mainly dependent upon the ratio of counts in the high energy peak to those in the low energy peak and as this ratio increases, the tail contribution also goes on increasing. It was therefore considered essential to maintain the initial ^{238}Pu/(^{239}Pu + ^{240}Pu) α activity ratio in the synthetic mixture at nearly 0.1 and carry out the measurements up to (^{238}Pu + ^{241}Am)/(^{239}Pu + ^{240}Pu) α activity ratio nearly 2 so that the change in the α activity ratio due to the ingrowth of ^{241}Am could be obtained with high precision and accuracy while still keeping the tail contribution low. In order to determine the precision and accuracy achievable in the measurement of α activity ratios, synthetic mixtures having a wide range of ^{238}Pu/(^{239}Pu + ^{240}Pu) α activity ratios were prepared from solutions of ^{238}Pu and ^{239}Pu isotopes. It was found[13] that following the conditions described above, an accuracy of 0.5% or better can be achieved while the precision is ±0.2%.

IV. RESULTS AND DISCUSSION

Table IV summarizes the results on the α activity ratios obtained after different growth periods and the half-life values calculated from the data. It is worth noting that the half-life values of ^{241}Pu obtained by the α spectrometric method after different growth periods (15 days to 457 days) are in good agreement with each other, which enhances the confidence in the α spectrometric measurements. The growth interval was obtained by taking the midtime of the pulse height analysis.

TABLE V. Constants used in the calculation of the ^{41}Pu half-life.

One year	=	365.24 d
Half-life of ^{238}Pu	=	87.74 ± 0.09 yr [a]
Half-life of ^{239}Pu	=	24 110 ± 30 yr [a]
Half-life of ^{240}Pu	=	6 553 ± 8 yr [a]
Half-life of ^{241}Am	=	432.6 ± 0.6 yr [a]
Half-life of ^{241}Pu	=	14.5 ± 0.5 yr [b]

[a] Reference 14 (1978).
[b] Reference 1 (1974).

The values of various constants used in the calculation of ^{241}Pu half-life are given in Table V. A small correction was applied to the initial ^{238}Pu/(^{239}Pu + ^{240}Pu) α activity ratio to account for the decay of ^{238}Pu during the period allowed for the growth of ^{241}Am. The correction varied from 0.05% after 15 days to about 1% after 457 days. As an example, the half-life of ^{241}Pu is calculated using the α spectrometric data obtained after a growth period of 401 days.

From Table IV,

$$R_\alpha = 1.524\,77 - 0.086\,12\, e^{-\lambda(^{238}\mathrm{Pu})t} = 1.439\,39\,,$$

where

$$t = 1.098\,56\ \mathrm{yr}\,.$$

From Table I,

$$R^{9/1} = 1.225\,82,\ R^{0/1} = 0.209\,11\,,$$

so

$$X = \frac{0.693\,145/432.6}{1.225\,82(0.693\,145/24\,110) + 0.209\,11(0.693\,145/6553)}$$

$$= 27.933\,58\,,$$

$$Y = \frac{1}{1-(0.693\,145/432.6)(14.5/0.693\,145)}$$

$$= 1.034\,68\,,$$

$$1.439\,39 = 27.933\,58 \times 1.034\,68\,[e^{-0.693\,145/432.6 \times 1.098\,56} - e^{-0.693\,145/T_{1/2} \times 1.098\,56}]$$

$$= 28.902\,32\,[e^{-0.001\,760\,2} - e^{-0.761\,46/T_{1/2}}]\,,$$

$$T_{1/2} = 14.375\ \mathrm{yr}.$$

TABLE VI. Estimates of errors (1σ).

S.No.	Quantity	Approximate value	Error (%)	Remarks
1	R_α	0.1 to 1.6	0.50	Evaluated by experiments conducted on synthetic mixtures
2		$X = \frac{\lambda(^{241}\mathrm{Am})}{R^{9/1}\cdot\lambda(^{239}\mathrm{Pu}) + R^{0/1}\cdot\lambda(^{240}\mathrm{Pu})}$		
(a)	$R^{9/1}$	1.225 82	0.10	Evaluated experimentally
(b)	$R^{0/1}$	0.209 11	0.20	-do-
(c)	$\lambda(^{239}\mathrm{Pu})$	$\frac{0.693\,145}{24\,110}\ \mathrm{yr}^{-1}$	0.12	Ref. 14
(d)	$\lambda(^{240}\mathrm{Pu})$	$\frac{0.693\,145}{6553}\ \mathrm{yr}^{-1}$	0.12	-do-
(e)	$\lambda(^{241}\mathrm{Am})$	$\frac{0.693\,145}{432.6}\ \mathrm{yr}^{-1}$	0.14	-do-
	X	27.938	0.19	Computed by error propagation in Eq. (4)
3		$Y = \frac{1}{1-\frac{\lambda(^{241}\mathrm{Am})}{\lambda(^{241}\mathrm{Pu})}}$		
(a)	$\lambda(^{241}\mathrm{Am})$	$\frac{0.693\,145}{432.6}\ \mathrm{yr}^{-1}$	0.14	Ref. 14
(b)	$\lambda(^{241}\mathrm{Pu})$	$\frac{0.693\,145}{14.5}\ \mathrm{yr}^{-1}$	3.44	Ref. 1
	Y	1.034 68	0.12	Computed by error propagation in Eq. (5)
4	Growth period t	15 d to 457 d	0.10	Evaluated experimentally
	Combined error		0.55%	Computed by error propagation in Eq. (3)

TABLE VII. Comparison of various ^{241}Pu half-life values.

S.No.	Authors	Year	Method	Half-life value (yr)
1	Seaborg *et al.* (Ref. 19)	1949		10
2	Thompson *et al.* (Ref. 20)	1950	Ingrowth of ^{241}Am	15.37 [a]
3	Mackenzie *et al.* (Ref. 6)	1953	Ingrowth of ^{241}Am by α counting	14.12 ± 0.2 [a]
4	Rose *et al.* (Ref. 7)	1956	Ingrowth of ^{241}Am by γ counting	13.87 ± 0.28 [a]
5	Brown *et al.* (Ref. 8)	1960	Ingrowth of ^{241}Am by α counting	14.12 ± 0.24 [a]
6	Smith (Ref. 9)	1961	α/β Branching ratio	13.3 ± 0.3
7	French *et al.* (Ref. 2)	1966	Change in isotopic ratios by mass spectrometry	13.59 ± 0.46
8	Nisle and Stepan (Ref. 10)	1970	Change in reactivity	14.63 ± 0.27
9	Shields (Ref. 3)	1970	Change in isotopic ratios by mass spectrometry	14.6 ± 0.4
10	Whitehead *et al.* (Ref. 21)	1972	Ingrowth of ^{241}Am	14.96 ± 0.15 [a]
11	Zeiglor and Ferris (Ref. 4)	1973	Change in isotopic ratios by mass spectrometry (mean of 6 laboratories)	14.89 ± 0.11
12	Strohm and Jordan (Ref. 11)	1974	Calorimetric determination of power decay	14.355 ± 0.007
13	Wilkins (Ref. 5)	1974	Change in isotopic ratios by mass spectrometry	15.02 ± 0.10
14	Whitehead (Ref. 15)	1977	Ingrowth of ^{241}Am	14.56 ± 0.10
15	Crouch (Ref. 16)	1978	Change in isotopic ratios by mass spectrometry on different samples	14.24 to 14.53
16	Garner (Ref. 17)	1978	Change in isotopic ratios by mass spectrometry on different samples	14.38 ± 0.07
17	Vaninbroukx (Ref. 18)	1978	a) Change in isotopic ratios by mass spectrometry	14.30 ± 0.14
			b) Ingrowth of ^{241}Am by α and γ counting	14.60 ± 0.10
18	Present work	1979	Ingrowth of ^{241}Am by α spectrometry	14.42 ± 0.09 [b]

[a] Half-life of ^{241}Pu recalculated using $T_{1/2}$ for ^{241}Am = 432.6 yr, Ref. 14 (1978).

[b] Combination of the one standard deviation on the average value in Table IV and the estimated error given in Table VI.

The half-life of ^{241}Pu obtained in the present work is 14.42 ± 0.09 yr. The uncertainty given here is a combination of one standard deviation on the average value given in Table IV and the combined error evaluated from various error components listed in Table VI.

The various published values for the half-life of ^{241}Pu are given in Table VII. The half-life of ^{241}Pu has been recalculated for various measurements reported earlier by ^{241}Am ingrowth method using the recommended[14] half-life value (432.6 yr) of ^{241}Am. The errors reported are as those given in the original papers. As is seen from data in Table VII, the half-life of ^{241}Pu obtained in this work by an independent method is in good agreement with the measurements reported recently[15-17] by other methods during the course of these investigations.

The authors are thankful to Dr. M. V. Ramaniah, Director, Radiological Group for his keen interest in this work.

---

[1] R. Vaninbroukx, European Atomic Energy Report No. EUR-5194e, 1974.

[2] R. J. French, F. L. Langford, Jr., W. D. Leggett, and R. J. Nodvik, WCAP-6082, Yankee Core Evaluation Program Quarterly Progress Report for the period ending 30 September 1966.

[3] W. R. Shields, National Bureau of Standards Technical Note 546, 25 (1970).

[4] R. K. Zeigler and Y. Ferris, J. Inorg. Nucl. Chem. 35, 3417 (1973).

[5] M. Wilkins, AERE-R 7906 (1974).

[6] D. R. Mackenzie, M. Lounsbury, and A. W. Boyd, Phys. Rev. 90, 327 (1953).

[7] B. Rose and J. Milsted, J. Nucl. Energy 2, 264 (1956).

[8] F. Brown, G. G. George, D. E. Green, and D. E. Watt, J. Inorg. Nucl. Chem. 13, 192 (1960).

[9] H. L. Smith, J. Inorg. Nucl. Chem. 17, 178 (1961).

[10] R. G. Nisle and I. E. Stepan, Nucl. Sci. Eng. 39, 257 (1970).

[11] W. W. Strohm and K. C. Jordan, Trans. Am. Nucl. Soc. 18, 185 (1974).

[12] S. K. Aggarwal, H. C. Jain, C. K. Mathews, and M. V. Ramaniah, BARC Report, BARC-824 (1975).

[13] Unpublished results from this laboratory.

[14] A. Lorenz, summary report of the first coordinated research meeting on the measurement of Transactinium Isotope Nuclear Data, Vienna, 1978, Report No. INDC(NDS)-96/N.

[15] C. Whitehead, U. K. Nuclear Data Progress Report UKNDC(76) P86, 41 (1977).

[16] E. A. Crouch, U. K. Nuclear Data Progress Report, UKNDC(78) P88, 97 (1978).

[17] E. L. Garner's private communication to P. DeBievre cited in Ref. 18.

[18] R. Vaninbroukx, International Conference on Neutron Physics and Nuclear Data for Reactors and other Applied Purposes, Harwell, 1978.

[19] G. T. Seaborg, R. A. James, and L. O. Morgan, *The Transuranium Elements: Research Papers* (McGraw-Hill, New York, 1949), p. 22.1; National Nuclear Energy Series, Plutonium Project Record, Div. IV, Vol. 14B (1949).

[20] S. G. Thompson, K. Street, A. Ghiorso, and F. L. Reynolds, Phys. Rev. 80, 1108 (1950).

[21] C. Whitehead, A. C. Sherwood, and B. Rose, AERE Report, AERE-PR/NP 18 (1972).

Levels of ^{230}Ac and ^{230}Th populated by decay of ^{230}Ra and ^{230}Ac

J. Gilat,* S. Katcoff, and L. K. Peker
Brookhaven National Laboratory, Upton, New York 11973

(Received 2 October 1979)

Decay schemes, based on γ-ray and β-ray spectroscopy, are proposed for 93-min ^{230}Ra and 122-sec ^{230}Ac. Of 48 observed γ transitions following decay of ^{230}Ra, 39 are accommodated among 19 levels in ^{230}Ac. For decay of the ^{230}Ac, 135 γ transitions were observed and 98 are accounted for among 46 levels (22 known previously) in ^{230}Th. The ground state of $^{230}_{89}\mathrm{Ac}_{141}$ is assigned $I^{\pi} = K^{\pi} = 1^{+}$. A number of levels are discussed in terms of Nilsson orbital assignments. $Q_{\beta^-} \simeq 0.71$ MeV for ^{230}Ra and $Q_{\beta^-} = 2.70$ MeV for ^{230}Ac.

[RADIOACTIVITY ^{230}Ra, ^{230}Ac from $^{232}\mathrm{Th}(n,2pn)^{230}\mathrm{Ra} \xrightarrow{\beta^-} {}^{230}\mathrm{Ac}$; radiochemistry, Ge(Li) and plastic detectors. Measured $T_{1/2}$, E_γ, I_γ, E_{β^-}; deduced I_{β^-}, log*ft*, decay schemes, *J*, π, Nilsson assignments.]

I. INTRODUCTION

As part of a program to investigate the level structure of selected neutron-rich heavy nuclei, we recently studied the radioactive decay of both ^{230}Ra and its ^{230}Ac decay product.[1] The ^{230}Ra was produced by the $^{232}\mathrm{Th}(n,2pn)$ reaction at the Brookhaven Medium Energy Intense Neutron facility, MEIN.[2] After thorough chemical separations (some of which involved continuous "milking" of the Ac from its Ra parent) γ-ray spectra were obtained with Ge(Li) detectors. The half-life of ^{230}Ra was determined to be 93 ± 2 min, and that of ^{230}Ac, 122 ± 3 sec. From a preliminary analysis of the data, energies and relative intensities were listed[1] for 35 γ rays from ^{230}Ra decay and 93 γ rays from ^{230}Ac decay. Source strength was insufficient for γ-γ coincidence studies but some measurements were made with plastic scintillators of β-ray spectra in coincidence with selected γ rays detected in Ge(Li) crystals. From these data it was estimated that Q_{β^-} is ~0.80 MeV for ^{230}Ra and 2.70 MeV for ^{230}Ac. No decay schemes, based on the preliminary analysis, were proposed.

In the present paper, decay schemes for both ^{230}Ra and ^{230}Ac are presented; they were derived from a more complete analysis of the original data.

II. RESULTS

By a process of continuous chemical separation of 122-sec ^{230}Ac from its 93-min ^{230}Ra parent it was possible to obtain a γ-ray spectrum of each nuclide separately. Typical spectra are shown in the earlier publication.[1] The newly evaluated γ-ray energies and relative intensities (with their associated errors) are given here in Tables I and II. Possible effects of coincidence summing were taken into account when evaluating the intensities and their uncertainties. In general, each datum is an average value derived from several runs. About 40% more γ rays are tabulated here than in the first paper; nearly all of the energies and intensities given before are in reasonable agreement with the newly evaluated results. Some of the weakest γ-ray peaks were observed only in the mixed ^{230}Ra-Ac sources which were more intense than the separated ^{230}Ra and ^{230}Ac sources.

Some of the excited levels in ^{230}Th had previously been established[3] from studies of the electron capture decay[4-6] of 17.4-d ^{230}Pa, of the Cou-

TABLE I. Gamma-ray energies (keV) and relative intensities from decay of ^{230}Ra, compared to 100 for the 454.9-keV γ ray of the daughter ^{230}Ac.

E_γ	I_γ	E_γ	I_γ
49.2 ± 0.1	2.6 ± 0.5	251.5 ± 0.1	9.9 ± 0.5
63.0 ± 0.1	40 ± 2	255.7 ± 0.2	1.6 ± 0.4
72.0 ± 0.1	113 ± 6	259.9 ± 0.2	3.4 ± 0.5
92.1 ± 0.1	21 ± 5	274.6 ± 0.2	1.0 ± 0.3
101.0 ± 0.1	16 ± 3	285.2 ± 0.1	18.2 ± 0.7
110.7 ± 0.1	3.1 ± 0.3	288.2 ± 0.2	1.0 ± 0.3
117.8 ± 0.3 [a]	<0.3	292.9 ± 0.1	4.3 ± 0.6
125.3 ± 0.3 [a]	<0.3	296.1 ± 0.2	1.2 ± 0.2
132.7 ± 0.3	<0.3	297.6 ± 0.2 [a]	0.5 ± 0.2
134.3 ± 0.1	4.5 ± 0.5	316.4 ± 0.1	1.0 ± 0.2
138.7 ± 0.2 [a]	0.6 ± 0.2	363.9 ± 0.3 [a]	0.6 ± 0.2
141.4 ± 0.2	0.7 ± 0.2	375.8 ± 0.2	0.3 ± 0.1
147.9 ± 0.1	5.6 ± 0.3	412.9 ± 0.1 [a]	0.9 ± 0.2
151.5 ± 0.1	2.0 ± 0.2	437.7 ± 0.3	0.3 ± 0.1
177.5 ± 0.3	0.6 ± 0.2	440.0 ± 0.3	0.3 ± 0.1
184.1 ± 0.1	11.5 ± 0.3	448.9 ± 0.1	15.0 ± 0.5
189.2 ± 0.1	16.7 ± 0.5	457.9 ± 0.1	18.5 ± 0.6
192.6 ± 0.1	1.4 ± 0.3	469.7 ± 0.1	29.3 ± 1.0
197.1 ± 0.2	1.3 ± 0.2	473.5 ± 0.3 [a]	<0.3
198.2 ± 0.1	3.4 ± 0.4	478.7 ± 0.1	24.2 ± 1.0
202.8 ± 0.1	30.8 ± 1.0	484.2 ± 0.2	1.9 ± 0.4
211.8 ± 0.1	11.3 ± 0.3	490.5 ± 0.1	4.3 ± 0.8
236.3 ± 0.3 [a]	<0.3	509.4 ± 0.2	6.5 ± 0.6
247.4 ± 0.3 [a]	<0.3	536.9 ± 0.2	1.2 ± 0.2

[a] Not placed in level scheme.

TABLE II. Gamma-ray energies (keV) and relative intensities from decay of ^{230}Ac.

E_γ	I_γ	E_γ	I_γ
53.2 ± 0.1	2.4 ± 0.6	1198.9 ± 0.2	1.8 ± 0.4
120.8 ± 0.1	4.0 ± 0.4	1212.0 ± 0.2[a]	1.8 ± 0.4
363.9 ± 0.3	0.5 ± 0.2	1226.7 ± 0.1	11.7 ± 0.6
388.3 ± 0.1	1.2 ± 0.1	1243.9 ± 0.1	42.7 ± 1.0
397.7 ± 0.1	5.0 ± 0.5	1252.5 ± 0.3	0.8 ± 0.2
423.2 ± 0.1	1.1 ± 0.2	1267.1 ± 0.2	5.0 ± 0.5
443.9 ± 0.1	2.2 ± 0.4	1268.2 ± 0.3[a]	2.5 ± 0.5
448.9 ± 0.1	1.5 ± 0.3	1302.6 ± 0.1	6.6 ± 0.3
454.9 ± 0.1	100	1306.2 ± 0.4[a]	1.4 ± 0.4
503.5 ± 0.2	2.1 ± 0.4	1311.5 ± 0.2	1.8 ± 0.4
508.2 ± 0.1	62.8 ± 2.0	1322.1 ± 0.1	8.6 ± 0.5
518.5 ± 0.1	5.1 ± 0.5	1347.7 ± 0.1	19.1 ± 0.5
571.1 ± 0.2	1.3 ± 0.3	1375.4 ± 0.1	14.8 ± 0.5
581.7 ± 0.1	6.5 ± 0.5	1394.5 ± 0.2	2.0 ± 0.5
600.7 ± 0.2[a]	1.0 ± 0.3	1401.0 ± 0.1	4.0 ± 0.4
624.4 ± 0.1	1.8 ± 0.2	1432.4 ± 0.1	2.4 ± 0.2
628.8 ± 0.1	2.9 ± 0.3	1455.5 ± 0.2	1.8 ± 0.5
635.6 ± 0.3[a]	1.0 ± 0.4	1524.6 ± 0.3[a]	1.0 ± 0.4
671.4 ± 0.2[a]	2.2 ± 0.4	1536.6 ± 0.3	0.8 ± 0.3
677.6 ± 0.1	2.2 ± 0.2	1573.5 ± 0.2	2.3 ± 0.2
728.0 ± 0.1	5.7 ± 0.6	1585.4 ± 0.2	2.1 ± 0.2
735.1 ± 0.2	1.2 ± 0.3	1597.2 ± 0.2[a]	1.6 ± 0.3
750.7 ± 0.3	1.8 ± 0.3	1625.1 ± 0.3	1.4 ± 0.3
772.6 ± 0.1	2.9 ± 0.5	1636.8 ± 0.2	1.9 ± 0.4
781.5 ± 0.1	4.6 ± 0.5	1642.5 ± 0.2	1.1 ± 0.2
789.0 ± 0.1	6.5 ± 0.3	1675.4 ± 0.3	1.0 ± 0.2
798.0 ± 0.1[a]	1.4 ± 0.2	1691.7 ± 0.1	7.3 ± 0.4
816.7 ± 0.1[a]	3.9 ± 0.2	1695.7 ± 0.1	2.9 ± 0.3
839.9 ± 0.1	2.2 ± 0.2	1717.5 ± 0.1	7.8 ± 0.4
867.1 ± 0.3	5.7 ± 0.3	1721.9 ± 0.1	8.0 ± 0.4
878.0 ± 0.2	1.0 ± 0.1	1728.0 ± 1.0[a]	<0.3
892.7 ± 0.1	8.4 ± 0.4	1732.0 ± 1.0[a]	<0.3
898.5 ± 0.1	3.1 ± 0.3	1757.5 ± 0.1	10.6 ± 0.3
913.7 ± 0.2	1.2 ± 0.3	1770.5 ± 1.0	1.2 ± 0.3
918.6 ± 0.1	3.5 ± 0.3	1775.3 ± 0.1	13.6 ± 0.5
939.2 ± 0.2[a]	1.0 ± 0.4	1787.1 ± 0.5[a]	0.3 ± 0.1
946.3 ± 0.2[a]	1.0 ± 0.4	1789.4 ± 0.5	0.3 ± 0.1
952.0 ± 0.1	10.1 ± 0.3	1797.2 ± 0.3	1.0 ± 0.2
956.5 ± 0.1	5.3 ± 0.3	1800.4 ± 0.3[a]	0.8 ± 0.2
959.1 ± 0.2	2.3 ± 0.2	1805.0 ± 0.5	0.6 ± 0.2
963.0 ± 0.2[a]	1.3 ± 0.5	1810.7 ± 0.1	2.1 ± 0.2
968.0 ± 0.2	1.2 ± 0.5	1817.7 ± 0.3[a]	0.7 ± 0.2
973.5 ± 0.2[a]	1.4 ± 0.5	1839.6 ± 0.2	1.1 ± 0.2
977.6 ± 0.2	0.7 ± 0.3	1853.8 ± 0.5[a]	0.6 ± 0.2
982.0 ± 0.5[a]	<0.3	1869.0 ± 0.3[a]	2.0 ± 0.3
987.0 ± 0.5[a]	<0.3	1896.7 ± 0.1	6.4 ± 0.3
991.2 ± 0.1	1.2 ± 0.3	1902.7 ± 0.1	9.1 ± 0.3
999.1 ± 0.1	2.7 ± 0.5	1913.8 ± 0.1	6.8 ± 0.3
1009.7 ± 0.1	3.0 ± 0.3	1920.2 ± 0.1	5.2 ± 0.2
1026.3 ± 0.1	2.0 ± 0.2	1949.8 ± 0.1	15.3 ± 0.3
1043.2 ± 0.3	1.0 ± 0.3	1956.9 ± 0.1	5.3 ± 0.3
1045.3 ± 0.3[a]	0.6 ± 0.3	1966.7 ± 0.3	1.0 ± 0.2
1053.1 ± 0.2	1.8 ± 0.4	1971.3 ± 0.5	0.5 ± 0.2
1065.5 ± 0.3[a]	0.5 ± 0.2	1973.5 ± 0.5	0.5 ± 0.2
1068.7 ± 0.3	0.8 ± 0.3	2000.9 ± 0.1	4.4 ± 0.4
1093.8 ± 0.4[a]	1.8 ± 0.5	2010.1 ± 0.2	0.9 ± 0.2
1106.2 ± 0.3[a]	0.7 ± 0.2	2024.6 ± 0.3	0.6 ± 0.2
1147.9 ± 0.1	4.8 ± 0.3	2069.5 ± 0.2	3.6 ± 0.3
1187.5 ± 0.3	1.3 ± 0.3	2084.9 ± 0.2[a]	3.1 ± 0.3
2098.6 ± 0.1	6.4 ± 0.3	2263.0 ± 1.0[a]	0.2 ± 0.1
2122.8 ± 0.1	7.1 ± 0.3	2277.0 ± 0.5[a]	0.5 ± 0.2
2150.0 ± 1.0[a]	0.4 ± 0.1	2282.5 ± 0.3	1.4 ± 0.1
2152.0 ± 1.0	0.4 ± 0.1	2298.6 ± 0.3	0.7 ± 0.1
2187.7 ± 0.3[a]	0.8 ± 0.2	2314.0 ± 1.0	0.5 ± 0.1
2203.0 ± 0.5[a]	0.6 ± 0.2	2330.5 ± 0.5[a]	0.7 ± 0.1
2229.5 ± 0.5	1.1 ± 0.2	2356.8 ± 0.5[a]	0.2 ± 0.1
2233.0 ± 0.5[a]	0.6 ± 0.2	2517.0 ± 1.0[a]	0.1 ± 0.1
2245.4 ± 1.0	0.4 ± 0.2		

[a] Not placed in level scheme.

lomb excitation[7] of ^{230}Th, of the ^{232}Th(p,t) reaction,[8,9] and of the ^{230}Th(d,d') reaction.[10] About 32 of the ^{230}Ac γ rays matched energy differences of 21 known levels in ^{230}Th, and thus a framework was provided for addition of new levels. By means of energy sums and differences, and by taking intensity balances into account, 24 new levels are proposed for ^{230}Th (Fig. 1). About 73% of the γ transitions (98 of 135), which account for nearly all the γ-ray intensity, are placed in this level scheme. All γ-ray intensities are shown relative to 100 for the 454.9-keV γ ray. When calculating the balance of intensities of the β- and γ-ray transitions, it was important to take into account internal conversion only for three strongly converted transitions[3]: 53.2 keV ($2^+ \to 0^+$; $E2$; $\alpha_{\text{total}} = 233$), 120.8 keV ($4^+ \to 2^+$; $E2$; $\alpha_{\text{total}} = 5.04$), and 624.4 keV ($0^+, 2^+ \to 0^+, 2^+$; $E0 + E2 + M1$; $\alpha_{\text{total}} = 5.1$). Since there was no direct measurement of the β-ray intensity to the 0^+ ground state, this was estimated by comparison with the β intensity to the 2^+ level at 53.2 keV according to the Alaga rules for β transitions.[11] The β-ray branchings to the ground state (0.42 ± 0.17) and to the 53.2-keV level (0.21 ± 0.08) are approximate, mainly because of the relatively low accuracy of the 53.2-keV γ-ray intensity measurement and the somewhat uncertain accuracy of the Alaga rule. The sum of β branching to all other levels is thus about 37%. However, these uncertainties can affect the logft values by only ± 0.2 unit. $Q_{\beta^-} = 2700 \pm 100$ keV was determined from the β-γ coincidence measurements[1] which showed that β rays of $E_{\max} = 1400$ keV were coincident with 1243.9-keV γ rays that are emitted from the 1297.1-keV level.

A level scheme for ^{230}Ac is proposed in Fig. 2; in this case there were no previously determined levels in the literature. Thus, the suggested scheme was deduced mainly from γ-ray energy loops and γ-transition intensity balances.[12] Some information on the extent of internal conversion was obtained from measurements of the K_α and K_β x-ray intensities associated with decay of the 93-min ^{230}Ra. These showed that about 250 K shell vacancies were formed in ^{230}Ac, relative to 100 units for the 454.9-keV γ ray. Table III shows the number of K shell vacancies I_K expected from individual transitions for $E1$ and $M1$ multipolarity assignments. The corresponding total conversion coefficients[13] and total transition intensities are also listed. Underlined numbers show the selected multipolarities; the sum of these I_K values (236) is consistent with the observed value (250). The suggested decay scheme (Fig. 2), which is discussed in more detail below, contains 18 excited levels, accounts for nearly all of the γ-ray intensity, and accommodates 39 of the 48 observed γ rays. When calculating the β-ray branches, account was taken of the Ra-Ac genetic relationship; the intensity of β decay to the ground state and to the 9-keV level (0.44 ± 0.30) is of low accuracy because of the uncertainties mentioned above. The value of $Q_{\beta^-} \approx 710$ keV was derived from the measurements which showed that 500-keV β rays were

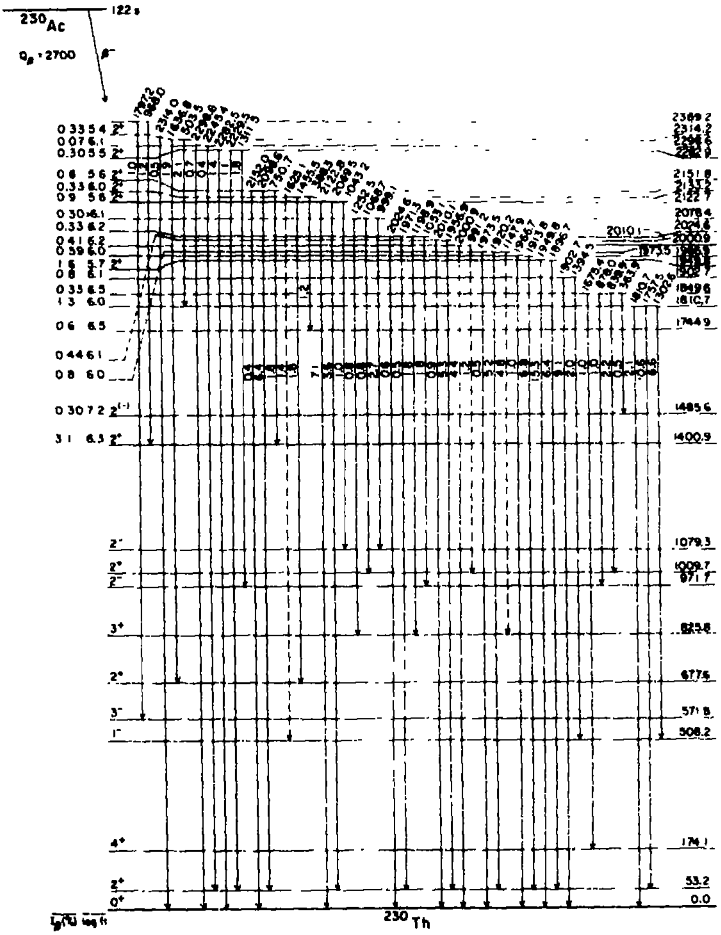

FIG. 1. (a) Decay of ^{230}Ac and proposed level scheme of ^{230}Th [continued in (b)]. Intensities of γ rays are relative to 100 for the 454.9-keV transition. I_β to the ground state and to the 53.2-keV level are (42 ± 17)% and (21 ± 8)%, respectively. The highly converted 635-keV $E0$ transition to the ground state (Ref. 3) is not shown because it was not observed in the γ-ray spectra. If it were included, then I_β to the 635-keV level would be 1.1% (instead of 0.5%) and the corresponding logft would be 7.4 (instead of 7.7). Supporting evidence for levels shown to de-excite by only a single γ ray comes mainly from observations made in the (d,d') reaction study (Ref. 10). (b) Level scheme of ^{230}Th continued from (a). Some levels are repeated.

coincident with 202.8-keV γ rays that are assumed to decay from a level at 211.8 keV. The earlier estimate[1] of $Q_{\beta^-} \approx 800$ keV was based on a preliminary decay scheme.

III. DISCUSSION

The ground state spin of the parent nucleus ${}^{230}_{89}\mathrm{Ac}_{141}$ can be deduced from the following observations: (1) There is strong β-ray branching to the well known[3] 508.2-keV octupole vibrational level with $K^\pi = 0^-$ and $I^\pi = 1^-$. This limits the assignment to $I = K \leq 1$, for otherwise the β transition would be K-forbidden. (2) A β transition is observed ($\log ft = 7.5$) to populate the γ-vibrational state at 781.4 keV with $K^\pi = 2^+$; therefore $K = 0$ is excluded. (3) There are also some allowed β-ray transitions with small $\log ft$ (≈ 5.5) to high-lying $I^\pi = 2^+$ levels. This further restricts the possible spins of the ${}^{230}\mathrm{Ac}$ ground state, and thus $I = K = 1$. Assignment of positive parity follows from consideration of possible Nilsson orbitals which are discussed below.

One of the interesting features of the decay scheme (Fig. 1) is the existence of several β transitions to high-lying levels with $\log ft \approx 5.7$. These low values of $\log ft$ indicate allowed unhindered β transitions which are possible in strongly deformed nuclei if the changes in Nilsson quantum numbers for the β-decaying nucleon, from initial to final states, are $\Delta N = 0$, $\Delta n_z = 0$, $\Delta\Lambda = 0$, and $\Delta\Omega = 1$. Inspection of the relevant parts of the Nilsson diagrams for $Z \approx 90$ and $N \approx 140$ shows that this condition is satisfied only for the transition $\frac{5}{2}^+[633]_n \to \frac{7}{2}^+[633]_p$. Thus we deduce that the ground state of the odd-odd nucleus ${}^{230}_{89}\mathrm{Ac}_{141}$ contains a $\frac{5}{2}^+[633]$ neutron and that these high-lying two quasi-particle states of ${}^{230}_{90}\mathrm{Th}_{140}$ contain a $\frac{7}{2}^+[633]$ proton. It should be noted that a $\frac{5}{2}^+[633]_n$ configuration has also been assigned[14] to the ground states of ${}^{231}_{90}\mathrm{Th}$ and ${}^{233}_{92}\mathrm{U}$, both of which also contain 141 neutrons. Because the γ transitions from most of these two quasi-particle states to the lowest levels $I^\pi = 0^+$ and $I^\pi = 2^+$ in ${}^{230}\mathrm{Th}$ have comparable intensity, they should have similar multipolarity ($E1$, $M1$, or $E2$). Thus I^π for these states is 2^+, 1^+, or 1^-. In ${}^{230}_{89}\mathrm{Ac}_{141}$, Ω_p for the odd proton should be $\frac{3}{2}$ or $\frac{7}{2}$ in order to be compatible with $K = I = 1$ and $\frac{5}{2}^+[633]$ for the odd neutron. Inspection of the Nilsson diagram for protons in the region $Z \approx 90$ excluded the $\Omega_p = \frac{7}{2}$ possibility and showed two possible configurations for $\Omega_p = \frac{3}{2}$. One is $\frac{3}{2}^+[651]_p$ and the other is $\frac{3}{2}^-[532]_p$. Only the first satisfies the con-

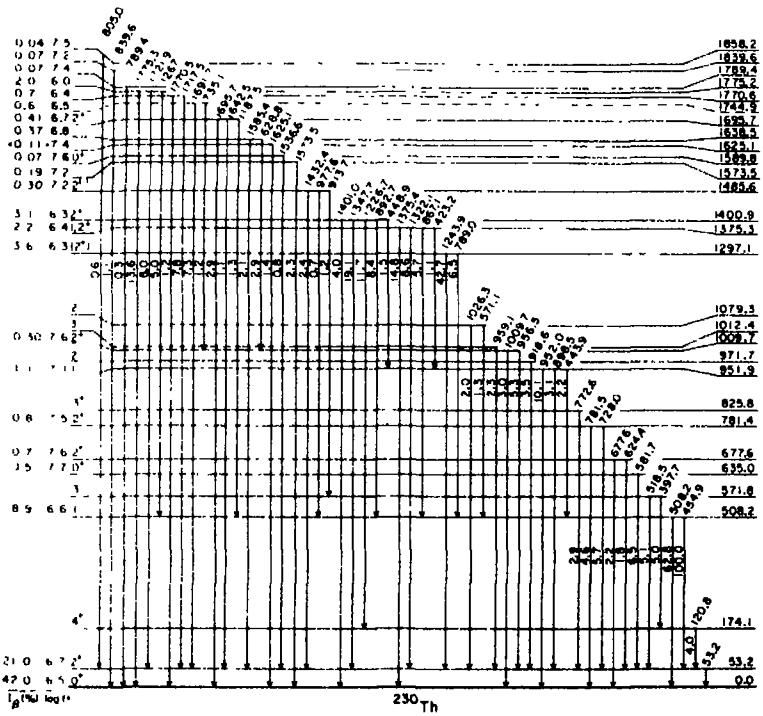

FIG. 1. (*Continued*).

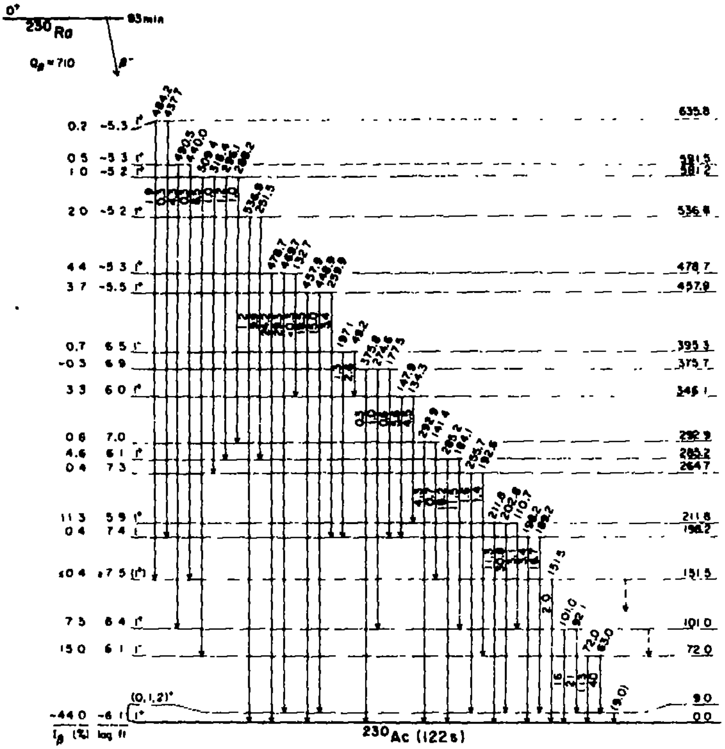

FIG. 2. Decay of ^{230}Ra and proposed level scheme of ^{230}Ac. Intensities of γ rays are relative to 100 for the 454.9-keV γ ray from ^{230}Ac decay. The combined I_β to the 0.0- and 9.0-keV levels is (44 ± 30)%.

dition that the two-proton states of ^{230}*Th have* $I^\pi = 2^+, 1^+$, or 1^-. Thus these states have the configuration $\frac{3}{2}^+[651]_p$, $\frac{1}{2}^+[633]_p$ with $I^\pi = K^\pi = 2^+$, and the ground state of $^{230}_{89}\mathrm{Ac}_{141}$ has the configuration $\frac{3}{2}^+[651]_p$, $\frac{5}{2}^+[633]_n$ with $I^\pi = K^\pi = 1^+$.

Direct β decay to the ground state $I^\pi = 0^+$ and to the first rotational state $I^\pi = 2^+$ of ^{230}Th involves the transformation $\frac{5}{2}^+[633]_n \rightarrow \frac{3}{2}^+[651]_p$ and is allowed by spin-parity selection rules, but retarded by the Nilsson selection rules because $\Delta n_z = 2$ and $\Delta\Lambda = 2$. Usually for such β transitions $\log ft > 6.0$, and this agrees with the observed values of 6.5 and 6.7, respectively [Fig. 1(b)].

We now consider the β transitions to the collective states of ^{230}Th, the octupole vibrational state at 508.2 keV ($K^\pi = 0^-$, $I^\pi = 1^-$) and the γ-vibrational state at 781.4 keV ($K^\pi = 2^+$, $I^\pi = 2^+$). The relatively intense β-ray branch, 8.9%, is to the $K^\pi = 0^-$, $I^\pi = 1^-$ octupole state. To understand why this first forbidden transition ($1^+ \rightarrow 1^-$) is so strong and has a $\log ft$ as small as 6.6, it is necessary to consider the microscopic structure of the $K^\pi = 0^-$ level. The wave function of a vibrational state can be considered as a superposition of the wave functions *of many strongly correlated particle-hole (p-h) configurations:*

$$\psi_{\mathrm{vibr}}(K) = \sum_i \alpha_i \psi_i^{(\mathrm{p-h})}(K) .$$

Unless they are retarded, only β transitions to the major components of such an expansion have the smallest values of $\log ft$ for their class (allowed, first forbidden, etc.). The major component corresponds to a (p-h) configuration in the Nilsson orbitals closest to the Fermi level F: p($F+1$), h($F-1$). In $^{230}_{90}\mathrm{Th}_{140}$ the $K^\pi = 0^-$ neutron configuration $\frac{5}{2}^-[752]_{n_1}$, $\frac{5}{2}^+[633]_{n_2}$ is the closest to the Fermi surface. Therefore, it is expected to the be major (p-h) configuration in the $K^\pi = 0^-$ octupole vibrational state. Semimicroscopic calculations[15] showed that its weight is ~54%, whereas other possible configurations have weight ≲5%. Thus in the β decay to the 1^- octupole level the major contribution comes from the transition $\frac{3}{2}^+[651]_p$, $\frac{5}{2}^+[633]_n \rightarrow \frac{5}{2}^-[752]_{n_1}$, $\frac{5}{2}^+[633]_{n_2}$. Since $\Delta\Omega = 1$, yes, $\Delta N = 1$, $\Delta n_z = 0$, and $\Delta\Lambda = 1$, the transition is first forbidden, unhindered. According to systematics the observed $\log ft = 6.6$ is typical for such β transitions.

TABLE III. Total transition intensities ($I_{\gamma+e}$) in ^{230}Ac, following β decay of ^{230}Ra, calculated from I_γ (Table I) and the theoretical total conversion coefficients (α_{total}) for $E1$ and $M1$ multipolarities. Corresponding K-shell conversion from each transition is given as I_K. The units are relative to 100 for the 454.9-keV γ ray. Underlined numbers show the multipolarities selected for the decay scheme (Fig. 2).

Level (keV)	E_γ	α_{total} $E1$	α_{total} $M1$	$I_{\gamma+e}$ $E1$	$I_{\gamma+e}$ $M1$	I_K $E1$	I_K $M1$
72.0	63.0	0.394	13.97	55.7	598		
	72.0	0.276	9.47	144	1183		
101.0	92.1	0.144	4.63	24.1	118		
	101.0	0.112	3.55	17.9	73		
151.5	151.5	0.181	5.53	3.8	12.7	0.3	8.8
198.2	189.2	0.106	2.95	18.4	66	1.4	39
	198.2	0.095	2.58	3.8	12.3	0.3	7.0
211.8	110.7	0.388	13.53	4.2	42.0	0.9	33
	202.8	0.090	2.42	33.5	105	2.3	58
	211.8	0.081	2.15	12.3	35.4	0.8	19
264.7	192.6	0.102	2.80	1.51	5.2	0.1	3.1
	255.7	0.052	1.28	1.65	3.8	0.1	1.7
285.2	184.1	0.113	3.18	12.7	48.2	1.0	29
	285.2	0.041	0.94	18.9	35.4	0.6	13.3
292.9	141.4	0.214	6.73	0.9	5.2	0.1	3.8
	292.9	0.038	0.87	4.2	8.0	0.1	2.8
346.1	134.3	0.242	7.79	5.7	39.7	0.9	28
	147.9	0.192	5.92	6.6	38.7	0.8	26
375.7	177.5	0.124	3.53	0.66	2.69	0.1	1.7
	274.6	0.045	1.05	1.04	2.03	<0.1	0.9
	375.8	0.022	0.44	0.33	0.42		0.1
395.3	49.2	0.76	28.7	4.6	77		
	197.1	0.096	2.62	1.42	4.7	0.1	2.7
457.9	259.9	0.051	1.22	3.5	7.5	0.1	3.6
	448.9	0.015	0.27	15.2	19.0	0.2	3.3
	457.9	0.015	0.26	18.7	23.2	0.2	3.7
478.7	132.7	0.250	8.61	<0.4	<3	<0.1	<1.9
	469.7	0.014	0.24	29.6	36.2	0.3	5.6
	478.7	0.013	0.23	24.4	29.7	0.3	4.4
536.8	251.5	0.054	1.34	10.4	23.1	0.4	12.4
	536.9	0.011	0.17	1.23	1.42	<0.1	0.2
581.2	288.2	0.039	0.91	1.04	1.89	<0.1	0.7
	296.1	0.038	0.85	1.23	2.22	<0.1	0.7
	316.4	0.032	0.71	1.04	1.70	<0.1	0.5
	509.4	0.012	0.20	6.6	7.8	<0.1	1.0
591.5	440.0	0.015	0.29	0.30	0.39	<0.1	0.1
	490.5	0.013	0.22	4.3	5.2	<0.1	0.8
635.8	437.7	0.016	0.29	0.30	0.39	<0.1	0.1
	484.2	0.013	0.22	1.94	2.31	<0.1	0.3

The 781.4-keV state of $^{230}_{90}\mathrm{Th}_{140}$ ($K^\pi = I^\pi = 2^+$) has two major (p-h) components: (1) $\frac{5}{2}^+[633]_{n_1}$, $\frac{1}{2}^+[631]_{n_2}$ corresponding to p($F+1$), h($F+3$) and (2) $\frac{3}{2}^+[631]_{n_1}$, $\frac{1}{2}^+[631]_{n_2}$ corresponding to p(F), h($F+3$). The β decay from $\frac{1}{2}^+[651]_p$, $\frac{5}{2}^+[633]_n$ of $^{230}_{89}\mathrm{Ac}_{141}$ to (1) is strongly hindered by Nilsson selection rules because $\Delta n_z = 2$; the β decay to (2) involves a two-particle transition and therefore it is forbidden. Thus we can expect that the β transition to the γ-vibrational state of ^{230}Th would be allowed but stronlgy retarded by Nilsson selection rules; this corresponds to the observed low β branching of 0.8% and the logft of 7.5. Similar reasons are responsible for weak population of $K = 2^+$ γ-vibrational levels in the β decay of other $I^\pi = 1^+$ heavy odd-odd nuclei.[16,17]

Although the β transition $\frac{5}{2}^+[633]_n \rightarrow \frac{1}{2}^+[651]_p$ from the 0^+ ground state of $^{230}_{88}\mathrm{Ra}_{142}$ to the 1^+ ground state of $^{230}_{89}\mathrm{Ac}_{141}$ (Fig. 2) is expected to be allowed, it should be somewhat retarded by the Nilsson selection rules (since $\Delta n_z = 2$ and $\Delta\Lambda = 2$). All of the β transitions to ^{230}Ac levels above 400 keV have low values of logft (~5.3). Therefore these transitions are allowed unhindered with $\Delta\Omega = 1$,

$\Delta N = \Delta n_z = \Delta\Lambda = 0$, and I^π of these levels must be 1^+. From inspection of the relevant Nilsson diagrams it follows that the most probable β transition is $\frac{5}{2}^+[633]_n \rightarrow \frac{7}{2}^+[633]_p$ and therefore these higher lying levels in ^{230}Ac include a large admixture of the two particle configuration $\frac{7}{2}^+[633]_p$, $\frac{5}{2}^+[633]_n$.

This research was performed under contract with the U.S. Department of Energy and supported by its Office of Basic Energy Sciences.

---

*Present address: Soreq Nuclear Research Center, Yavne, Israel.

[1] J. Gilat and S. Katcoff, J. Inorg. Nucl. Chem. 40, 369 (1978).

[2] S. Katcoff, J. B. Cumming, J. Godel, V. J. Buchanan, H. Susskind, and C. J. Hsu, Nucl. Instrum. Methods 129, 473 (1975).

[3] Y. A. Ellis, Nucl. Data Sheets 20, 139 (1977).

[4] T. Valkeapää, J. Heinonen, and G. Graeffe, Phys. Scr. 5, 119 (1972).

[5] W. Kurcewicz, K. Stryczniewicz, J. Zylich, S. Chojnacki, T. Morek, and I. Yutlandov, Acta Phys. Pol. B2, 393 (1971).

[6] W. Lourens, B. O. ten Brink, and A. H. Wapstra, Nucl. Phys. A152, 463 (1970).

[7] F. K. McGowan, C. E. Bemis, Jr., W. T. Milner, J. L. C. Ford, Jr., R. L. Robinson, and P. H. Stelson, Phys. Rev. C 10, 1146 (1974).

[8] E. Takekoshi, Y. Ishizaki, H. Orihara, M. Kanazawa, J. Kasagi, K. Koyama, N. Matsuoka, and T. Takemasa, J. Phys. Soc. Jpn. 36, 336 (1974).

[9] J. V. Maher, J. R. Erskine, A. M. Friedman, R. H. Siemssen, and J. P. Schiffer, Phys. Rev. C 5, 1380 (1972).

[10] R. C. Thompson, J. R. Huizenga, and T. W. Elze, Phys. Rev. C 12, 1227 (1975).

[11] G. Alaga, K. Alder, A. Bohr, and B. R. Mottelson, Kgl. Danske Videnskab. Selskab Mat. Fys. Medd. 29, No. 9 (1955).

[12] This decay scheme is the most likely one although it is not unique. A modified version is possible where the first excited level is placed at 63.0 keV and the 9.0-keV transition is from the 72.0-keV level. A few alternative spin assignments may also be considered and some of the β branching might be slightly different, but there would be no appreciable changes in the logft values.

[13] R. S. Hager and E. C. Seltzer, Nucl. Data A4, 1 (1968).

[14] R. R. Chasman, I. Ahmad, A. M. Friedman, and J. R. Erskine, Rev. Mod. Phys. 49, 833 (1977).

[15] S. P. Ivanova, A. L. Komov, L. A. Malov, and V. G. Solov'ev, Sov. J. Part. Nucl. 7, 175 (1976).

[16] P. E. Haustein, H. -C. Hseuh, R. L. Klobuchar, E. -M. Franz, S. Katcoff, and L. K. Peker, Phys. Rev. C 19, 2332 (1979).

[17] Y. A. Ellis, Nucl. Data Sheets 21, 549 (1977).

PHYSICAL REVIEW C VOLUME 21, NUMBER 5 MAY 1980

Sturmian expansion method for bound state problems

A. Deloff* and J. Law

Department of Physics, University of Guelph, Guelph, Ontario N1G 2W1, Canada

(Received 9 July 1979)

A novel precision method is developed to solve a two-body bound state problem where the interaction may be an arbitrary relativistic, complex, nonlocal operator and, in particular, may contain also the Coulomb potential. The method is based on the expansion of the Green's function (free or Coulomb modified) in terms of a discrete set of Coulomb Sturm functions which have equally simple forms in x or p space representation. The method should be particularly useful for hadronic atom problems. Other applications are also suggested.

[NUCLEAR STRUCTURE Sturmian expansion, bound states.]

I. INTRODUCTION

The purpose of this paper is to present an extremely versatile method for solving a bound state problem. The method is applicable whether the interaction considered is local or nonlocal, real or complex (non-Hermitian), with or without the addition of the Coulomb interaction. It works equally well in coordinate or momentum space.

The motivation for this investigation originates from the hadronic atom problem, where besides the dominant Coulomb potential, one has to cope with the strong hadron-nucleus interaction, the latter being usually a rather complicated nonlocal and non-Hermitian operator. In order to extract the information about the hadron-nucleus interaction, one has to solve the relevant bound state problem. However, since the purely Coulomb levels are shifted by a very small amount (typically, the observable strong interaction effects are of order 10^{-2}–10^{-3} of the Coulomb energy), precise numerical techniques are required.[1] One possible method[2] involves solving the associated scattering problem to find the pole of the scattering matrix (T matrix). Since the level energies are usually not larger than several hundred keV, the continuation of the scattering matrix below threshold can be carried through easily using the effective range expansion. This procedure leads to a simple linear relation between the level shift and the hadron-nucleus Coulomb corrected scattering length, so that it is sufficient to evaluate the latter to obtain the level shift. Indeed, for a local potential this method has proved to be very effective because a single numerical integration of the differential equation gives the level shift. On the other hand, when the potential is nonlocal, the evaluation of the Coulomb corrected scattering length is not much simpler than solving the bound state problem directly, besides which, for problems where the binding energy is large, the effective range expansion becomes insufficient, and a knowledge of the full K matrix is needed to locate the position of the pole of the T matrix. Thus, it appears that in the case of nonlocal potentials it might be simpler to solve the bound state problem directly. Nonlocal potentials are most conveniently treated in momentum space, where the problem reduces to solving an integral equation, rather than an integro-differential equation in configuration space. The Coulomb potential V_C, however, leads to difficulties in momentum space, because the appropriate partial wave projection of $\langle \vec{k}' | V_C | \vec{k} \rangle$ is proportional to a Legendre function of the second kind $Q_l[(k^2 + k'^2)/2kk']$ and this function has a logarithmic singularity for $k = k'$. Although the existence of an exact solution of the Coulomb bound state problem in momentum space indicates that this difficulty cannot be very serious, it has only recently been shown that the singularity can indeed be removed by applying a suitable subtraction technique, after which the numerical solution of the integral equation becomes possible, as has been shown explicitly by Kwon and Tabakin.[3] Undoubtedly, the elegant subtraction technique[3] solves the problem completely, but the knowledge of the exact analytic solution of the Coulomb problem is of no help in simplifying the calculations. On the other hand, it is not easy to exploit the knowledge of the exact Coulomb solution. One possibility is to solve the wave equation numerically in the region where the short range strong interaction potential is present together with the Coulomb potential (modified by any charge distribution) and match the solution to the pointlike Coulomb solutions outside the range of the strong

© 1980 The American Physical Society

force to obtain the level shifts.[4] A second possibility is to make a systematic expansion in Coulomb wave functions with the inherent difficulty of including the continuum functions. Finally, a third possibility is to use the Coulomb Green's function to eliminate the Coulomb potential completely leaving only the strong interaction potential to be dealt with explicitly. Although the Coulomb Green's function is well known[5] with exact representations in both coordinate and momentum space, their rather complicated natures have discouraged most people from using them in bound state problems. A form of the Coulomb Green's function which is particularly useful for practical applications is an expansion in Coulomb Sturm functions.[6] The latter form a complete discrete set, have very simple forms in both coordinate and momentum representations, and are known analytically for all partial waves. With this set of functions, both the Coulomb and free Green's function are given as separable expansions with coefficients which are simple algebraic functions of energy.[6]

In this paper, we make use of these properties of the Green's function to solve for the bound states when a strong interaction potential is present. Since the Coulomb potential is eliminated, we do not have to worry about its singular behavior on-shell. Further, the purely Coulomb bound states appear as poles of the Green's function. It is also noted that calculations may be performed in either coordinate or momentum space, the choice being dictated by convenience. Although the method to be presented has been originally designed for a study of hadronic atoms, it may profitably be applied to any other bound state problem. In particular, it may be useful for studying relativistic wave equations (e.g., Bethe-Salpeter equation) where one encounters highly nonlocal operators, heavy-ion, or cluster interactions where the Pauli principle introduces nonlocality, atom-atom interactions, etc.

Our presentation is as follows. In Sec. II, we give a brief review of the properties of the Sturm functions (or Sturmians) together with a compilation of useful formulas for use in practical calculations. Section III contains the derivation of the equation for calculation of bound state energies when Sturmians are used, and numerical examples are given in Sec. IV, to illustrate the effectiveness of the method.

II. STURMIANS

Sturmians or Sturm functions are eigenfunctions of the kernel of the Lippmann-Schwinger (LS) equation. They have been well known to mathematicians for a long time, but the first study of Sturmians within the context of the LS equation seems to have been made by Meetz,[6] who showed that they form a complete biorthonormal system in the complex energy plane cut along the positive real axis. Denoting the energy, the free Hamiltonian, and the interaction potential by E, H_0, and V respectively, the Sturmians $\Psi_n(E)$ are solutions of the eigenvalue problem

$$K(E)\Psi_n(E)=\eta_n(E)\Psi_n(E), \tag{1}$$

where

$$K(E)=G_0(E)V\equiv(E-H_0)^{-1}V$$

is the kernel of the LS equation and $\eta_n(E)$ is the appropriate energy dependent eigenvalue. If V is chosen to be a local, central potential, the eigenvalues $\eta_n(E)$ and eigenfunctions can be determined by solving the differential equation

$$\left[p^2-\frac{d^2}{dr^2}+\frac{l(l+1)}{r^2}+\frac{2\mu V(r)}{\eta_{nl}(E)}\right]s_{nl}(p,r)=0, \tag{2}$$

where $p=(-2\mu E)^{1/2}$ and $\Psi_n(E)=[s_{nl}(p,r)/r]Y_{lm}(\theta,\phi)$, μ being the reduced mass and hereafter $\hbar=c=1$. The radial functions $s_{nl}(p,r)$ vanish at $r\to 0$ and $r\to\infty$ according to the superimposed boundary conditions

$$s_{nl}(p,r)\to r^{l+1}\ (r\to 0),$$

$$s_{nl}(p,r)\to e^{-pr}\ (r\to\infty),\quad \mathrm{Re}(p)>0.$$

It should be emphasized that the functions $s_{nl}(p,r)$ are in general not eigenfunctions of a physical system even though they are obtained by solving Eq. (2), which is closely related to the Schrödinger equation, form a complete set without a continuum, regardless of the nature of the potential $V(r)$ as long as $K(E)$ is a completely continuous operator. The main difference between (2) and the Schrödinger equation is that E is kept constant, and in order to solve the eigenvalue problem, $\eta_n(E)$ is varied instead. The latter may be looked upon as a coupling constant, or a scaling factor which has to be adjusted to bring states of higher number of nodes down in order to keep E constant. Thus if V is an attractive potential, by increasing the depth of V [by adjusting $\eta_n(E)$], we make the bound state level sink deeper, but in order to maintain a constant total energy E, the kinetic energy must also increase causing the functions $s_{nl}(p,r)$ to show more and more nodes.

Because the Sturmians form a discrete set, they are particularly useful as a basis for various expansions. Rotenberg[7,8] who applied Sturmians in a calculation of positron-hydrogen atom scattering, seems to be the first to stress their importance in this context. More extensive applications of Sturmians, however, began with the work of

Weinberg[9] in which he suggests expansion of the t matrix in terms of these functions and since then, the expansion in Sturmians has often been referred to in many papers as the "Weinberg expansion." These expansions have been particularly useful in various three-body calculations,[10] but we are not aware of any attempt to use them for solving a two-body bound state problem.

Once the solutions to (2) are known, the Sturmians in momentum space $\phi_{nl}(p,k)$ are obtained by taking a Fourier transform of $s_{nl}(p,r)$,

$$(k^2/2\mu+p^2/2\mu)^{-1}\phi_{nl}(p,k)=\int_0^\infty s_{nl}(p,r)j_l(kr)r\,dr\,. \tag{3}$$

The appropriate normalization conditions are

$$\int_0^\infty s_{nl}(p,r)[\eta_n^{-1}(E)V(r)]s_{n'l}(p,r)\,dr=-\delta_{nn'} \tag{4}$$

$$(2/\pi)\int_0^\infty \phi_{nl}(p,k)(k^2/2\mu+p^2/2\mu)^{-1}\phi_{n'l}(p,k)k^2dk = \delta_{nn'}\,, \tag{5}$$

and the completeness relationships take the form

$$\sum_n s_{nl}(p,r_1)[\eta_n^{-1}(E)V(r_1)]s_{nl}(p,r_2)=-\delta(r_1-r_2)\,, \tag{6}$$

$$\sum_n \phi_{nl}(p,k_1)[k_1^2/2\mu+p^2/2\mu]^{-1}\phi_{nl}(p_1,k_2) = (\pi/2k_1^2)\delta(k_1-k_2)\,. \tag{7}$$

The free Green's function $G_0(E)$ expansion in Sturmians may be readily derived from (7). Writing $G_0(E)$ in momentum space

$$\langle\vec{\mathbf{k}}_2|G_0(E)|\vec{\mathbf{k}}_1\rangle=\sum_{lm} Y^*_{lm}(\hat{k}_2)G_0^{(l)}(E;k_2,k_1)Y_{lm}(\hat{k}_1)\,, \tag{8}$$

where

$$G_0^{(l)}(E;k_2,k_1)=-\delta(k_1-k_2)k_1^{-2}(k_1^2/2\mu+p^2/2\mu)^{-1}\,, \tag{9}$$

a comparison of (9) and (7) gives

$$\begin{aligned}G_0^{(l)}(E;k_2,k_1)=-(2/\pi)\sum_n (k_2^2/2\mu+p^2/2\mu)^{-1}\\ \times\phi_{nl}(p,k_2)(k_1^2/2\mu+p^2/2\mu)^{-1}\\ \times\phi_{nl}(p,k_1)\,.\end{aligned} \tag{10}$$

Transforming (10) to coordinate space yields

$$\begin{aligned}G_0^{(l)}(E;r_2,r_1)&=-(4\mu p/\pi)i_l(pr_<)k_l(pr_>)\\ &=-\sum_n r_2^{-1}s_{nl}(p,r_2)r_1^{-1}s_{nl}(p,r_1)\,,\end{aligned} \tag{11}$$

where $i_l(x)$ and $k_l(x)$ are spherical Bessel functions of the second and third kind, respectively. It is also a simple matter to obtain the Green's function $G(E)$ which incorporates the interaction V, defined as

$$G(E)=(E-H_0-V)^{-1}\,. \tag{12}$$

Now the operator $G(E)$ may be related to the kernel $K(E)$ by

$$1-K(E)=1-(E-H_0)^{-1}V=G_0(E)[G(E)]^{-1} \tag{13}$$

so that

$$G(E)=[1-K(E)]^{-1}G_0(E)\,. \tag{14}$$

Since the Sturmians are eigenfunctions of $K(E)$, using (10) and (11), we can immediately write the corresponding expansions for the partial wave Green's function:

$$\begin{aligned}G^{(l)}(E;k_2,k_1)\\ =-(2/\pi)\sum_n[1-\eta_{nl}(E)]^{-1}\\ \times[k_1^2/2\mu+p^2/2\mu]^{-1}\phi_{nl}(p,k_1)\\ \times[k_2^2/2\mu+p^2/2\mu]^{-1}\phi_{nl}(p,k_2)\,,\end{aligned} \tag{15}$$

$$\begin{aligned}G^{(l)}(E;r_2,r_1)=-\sum_n[1-\eta_{nl}(E)]^{-1}r_2^{-1}\\ \times s_{nl}(p,r_2)r_1^{-1}s_{nl}(p,r_1)\,.\end{aligned} \tag{16}$$

For completeness, we give also the spherical Bessel function expansion in Sturmians:

$$rj_l(kr)=\sum_n s_{nl}(p,r)\phi_{nl}(p,k)\,.$$

Although any potential may be taken for $V(r)$, practicality dictates the choice of $V(r)$ to be the Coulombic potential

$$V_C(r)=Z\alpha/r\,, \tag{17}$$

where α is the fine structure constant with the convention that $Z<0$ correspond to an attractive potential. In this case the eigenvalues are

$$\eta_{nl}(E)=-(\mu Z\alpha/np)\,,\quad n=1,2,3,\ldots \tag{18}$$

and the Sturmians take the well known form

$$s_{nl}(p,r)=N_{nl}e^{-pr}(2pr)^{l+1}L^{2l+1}_{n-l-1}(2pr)\,, \tag{19}$$

where $L^{\alpha}_{\beta}(x)$ is the Laguerre polynomial and the normalization constant is

$$N_{nl}^{2}=(\mu/np)\Gamma(n-l)[\Gamma(n+l+1)]^{-3}. \quad (20)$$

The corresponding momentum representations of Sturmians are in terms of Gegenbauer polynomials $C^{l+1}_{n-l-1}(x)$, viz,

$$\begin{aligned}\phi_{nl}(p,k)=&\,2^{2l+2}[n\Gamma(n-l)/\mu\Gamma(n+l)]^{1/2}\Gamma(l+1)\\ &\times k^{l}p^{l+3/2}(k^{2}+p^{2})^{-l-1}C^{l+1}_{n-l-1}\\ &\times([k^{2}-p^{2}]/[k^{2}+p^{2}]). \quad (21)\end{aligned}$$

In actual calculations of hadronic atoms level shifts and widths, one has to include relativistic effects by solving the Klein-Gordon rather than the Schrödinger equation, namely

$$[\nabla^{2}+(E-V_{c})^{2}-\mu^{2}]\Psi=2EV\Psi. \quad (22)$$

To adapt our scheme presented above to account for relativistic effects, it is sufficient to replace l by $\lambda=[(l+1/2)^{2}-(Z\alpha)^{2}]^{1/2}-\frac{1}{2}$, μ by the total energy $E=(\mu^{2}-p^{2})^{1/2}$, and n by $\nu=n-l+\lambda$. Equations (18)–(21) will then go over into Sturmians for the Klein-Gordon equation. Equation (22) is not the only relativistic equation that has been considered as a generalization of the Schrödinger equation (e.g. the strong potential V may also be regarded as a Lorentz scalar, whence it should be added to the mass μ). Usually, higher order terms such as $2V_{C}V$ and V^{2} may be present and can easily be allowed for. The above method may similarly be modified to accommodate the Dirac equation.

III. BOUND STATE PROBLEM

As stated at the end of the preceding section, relativistic effects can be trivially incorporated, so in this section, for clarity of presentation, we will solve the bound state problem of a sum of Coulomb V_{C} and strong interaction potential V inserted in the Schrödinger equation. Using the Coulomb Green's function $G_{c}(E)=(E-H_{0}-V_{C})^{-1}$, the Schrödinger equation to be solved can be written as

$$|\Psi(E)\rangle=G_{c}(E)V|\Psi(E)\rangle. \quad (23)$$

The only assumption we need to make about V is that $G_{c}(E)V$ is a completely continuous operator. Expanding $G_{c}(E)$ in a complete set of Sturmians $\{|\beta\rangle\equiv|nlm\rangle\}$, we have

$$G_{c}(E)=-\sum_{\beta}[1-\eta_{\beta}(E)]^{-1}|\beta\rangle\langle\beta|, \quad (24)$$

where $\eta_{\beta}(E)\equiv\eta_{nl}(E)$ are given by (18). Inserting (24) in (23), and multiplying (23) by $\langle\alpha|V$, we obtain

$$\sum_{\beta}\{[1-\eta_{\alpha}(E)]\delta_{\alpha\beta}+\langle\alpha|V|\beta\rangle\}\langle\beta|V|\Psi\rangle=0. \quad (25)$$

If the coefficients $\langle\beta|V|\Psi\rangle$ in (25) are not to vanish identically, we have to set equal to zero the determinant

$$\det\|[1-\eta_{\alpha}(E)]\delta_{\alpha\beta}+\langle\alpha|V|\beta\rangle\|=0. \quad (26)$$

Equation (26) can be readily solved by standard methods and the roots are the desired energy eigenvalues. It should be emphasized that the matrix elements $\langle\alpha|V|\beta\rangle$ are also functions of E and therefore Eq. (26) is not a secular equation. Clearly, the above scheme still remains valid if the Coulomb potential vanishes, in which case $\eta_{\alpha}\to 0$. On the other hand, if we set $V=0$, Eq. (26) yields an infinite set of conditions $\eta_{n}(E)=1$ for $n=1, 2, \ldots$ which, using (18), leads to a not unfamiliar energy level sequence,

$$E_{n}=-\mu(Z\alpha)^{2}/(2n^{2}).$$

Strictly speaking, Eq. (26) is an infinite dimension determinant which in practical applications has to be truncated. The rate of convergence of the method depends of course on the nature of V and the required precision of the eigenvalue E. Furthermore, the derivation of (26) is independent of representation, therefore the matrix element $\langle\alpha|V|\beta\rangle$ may be evaluated in either coordinate or momentum space, whichever is more convenient. Since the Sturmians (19) and (20) have simple analytic form, the evaluation of $\langle\alpha|V|\beta\rangle$ is usually straightforward.

IV. EXAMPLES

We shall demonstrate the effectiveness of the scheme developed in the previous section with three examples. For the first one, we consider solving the Schrödinger equation with a Hulthén potential, given by

$$V(r)=-(s/2\mu a^{2})(e^{r/a}-1)^{-1}, \quad (27)$$

where s is a dimensionless strength parameter and a is the potential range. For this case, we switch off the Coulomb potential, so that $\eta_{\alpha}=0$ in (26). The energy levels for $l=0$ states in the potential (27) are

$$E_{n}=-(s-n^{2})^{2}/(8\mu a^{2}n^{2}), \quad n=1,2,\ldots \quad (28)$$

and have been used to test the accuracy of the computations. In Table I, we present the results of our computations for the 1s level using a complex strength parameter $s=(1.5, 0.15)$, and a range $a=0.5$ fm, and have truncated the determinant (26) at different ranks $N=5, 10, \ldots$. We observe that the rate of convergence is quite rapid,

TABLE I. Solution for the 1s level for Hulthén's potential. We take a complex strength parameter $s=(1.5, 0.15)$ and a range parameter $a=0.5$ fm. The exact energy in units of $(8\mu a^2)^{-1}$ from Eq. (28) is $(-0.2275, -0.15)$.

Rank N	$(8\mu a^2E)$
5	(−0.209 808, −0.164 793)
10	(−0.227 506, −0.150 394)
15	(−0.227 506, −0.150 004)
20	(−0.227 500, −0.150 000)

and the converged result is stable against adding more terms in the expansion.

As a second example, we considered a case where V_C is nonzero and V is a realistic phenomenological kaon-nucleus potential of the form[11]

$$2\mu V(r)=-\bar{a}4\pi A(1+m_K/m_N)\rho(r)\,, \tag{29}$$

where m_K, m_N are kaon and nucleon masses, A is the mass number, $\rho(r)$ is the nuclear density (taken to be of Fermi shape), and $\bar{a}$ is a complex strength parameter of dimension of length. The Klein-Gordon equation (22) may be solved directly as well as using our expansion method. In Table II we compare the calculated complex energy shifts for the 2p level of ^{12}C and the 3d level of ^{32}S with the results obtained by other authors. In these calculations, we wanted to reproduce six significant digits in the total energy, and in order to attain such precision, the determinant (26) has to be truncated at N not less than about 60. In practical applications, the accuracy is determined essentially by the experimental error which is not less than 10%. Thus if one wants to make the theoretical calculations to be accurate within 5%, it is sufficient to take the rank N to be about 50. In the case of the results shown in Table II, final convergence appears at rank 120, after a few strongly damped oscillations.

As a final example, we consider the case of Coulomb plus a nonlocal separable potential of rank one. For this case, it should be noted that using the direct momentum space method,[3] one has still to solve an integral equation because the Coulomb potential is not separable. In contrast, the Sturmian expansion method preserves all the simplifying features of a separable potential. The partial wave integral equation to be solved is

$$|\Psi_l\rangle=G_c^l(E)V_l|\Psi_l\rangle\,, \tag{30}$$

where

$$V_l=-(\lambda_l/2\mu)|v\rangle\langle v| \tag{31}$$

is the separable potential with strength parameter λ_l and form factor v. Multiplying (3) by $\langle v|$ and simplifying gives

$$1=-(\lambda_l/2\mu)\langle v|G_c^l(E)|v\rangle\,. \tag{32}$$

Expanding $G_0^l(E)$ in Sturmians, we obtain an algebraic equation which determines the binding energy

$$1=(\lambda_l/2\mu)\sum_n[1-\eta_{nl}(E)]^{-1}\Gamma_{nl}^{\,2}(E)\,, \tag{33}$$

where

$$\Gamma_{nl}(E)=\langle v|nl\rangle=\int_0^\infty v(r)s_{nl}(r)r\,dr\,. \tag{34}$$

For $l=0$ and a Yamaguchi form factor[12]

$$v(r)=(2\pi^2)^{1/2}\exp(-\beta r)/r\,, \tag{35}$$

where β is the range parameter, (34) gives

$$\Gamma_{n0}(E)=(2\mu/p)^{1/2}(2\pi p)(\beta^2-p^2)^{n-1}(\beta+p)^{-2n} \tag{36}$$

and (33) reduces to

$$\lambda_0^{-1}=\pi^2\beta^{-1}(\beta+p)^{-2}$$
$$\times\left\{(1-\xi)\xi^{-1}\sum_n[1-\eta_{n0}(E)]^{-1}\xi^n\right\} \tag{37}$$

with $\xi=(\beta-p)^2/(\beta+p)^2$. When the Coulomb potential vanishes, the expression in the parenthesis { } reduces to unity and we recover the well known formula for a bound state in a Yamaguchi potential. The expression in parenthesis thus constitutes the modification due to the Coulomb potential. Writing $\eta_{n0}(E)$ as

$$\eta_{n0}(E)=-(\alpha Z\mu/p)/n\equiv-\eta/n \tag{38}$$

the sum in (37) can be recast into the form

TABLE II. Comparison of various methods for calculating the level shifts of ^{12}C(2p) and ^{32}S(3d) kaonic atoms. The parameters for the potential (29) are from Koch-Sternheim (Ref. 11). Our values correspond to rank 60. Units are keV.

	^{12}C(2p) (ϵ,Γ)	^{32}S(3d) (ϵ,Γ)
Koch-Sternheim, Ref. 11	(−0.632, 1.571)	(−0.516, 2.346)
Kwon-Tabakin, Ref. 3	(−0.620, 1.551)	(−0.503, 2.317)
This work	(−0.637, 1.579)	(−0.509, 2.354)

TABLE III. Solution for 1s level for Yamaguchi potential plus Coulomb. We take a complex strength $s=\lambda\pi^2/\beta^3=(1.494, 0.181)$, a range parameter $\beta = 3.14\ \mathrm{fm}^{-1}$, and an attractive Coulomb potential $Z=-10$. The converged nergy in units of $-0.5\,\mu(Z\alpha)^2$ is (0.674 518, 0.027 672).

Rank N	Energy
5	(0.693 480, 0.024 331)
15	(0.675 606, 0.027 443)
25	(0.674 651, 0.027 641)
35	(0.674 539, 0.027 667)
45	(0.674 522, 0.027 671)

$$\begin{aligned}(1-\xi)\xi^{-1}\sum_{n=1}^{\infty} n(n+\eta)^{-1}\xi^n &= (1+\eta)^{-1}+\sum_{n=1}^{\infty}\eta(n+\eta)^{-1}(n+1+\eta)^{-1}\xi^n\\ &= (1+\eta)^{-1}{}_2F_1(1,\eta,2+\eta,\xi)\,, \qquad (39)\end{aligned}$$

where ${}_2F_1$ is the usual hypergeometric function, so that Eq. (37) reduces to

$$\begin{aligned}\lambda_0^{-1} &= \pi^2\beta^{-1}(\beta+p)^{-2}(1+\eta)^{-1}\\ &\quad\times {}_2F_1(1,\eta,2+\eta,\xi)\,. \qquad (40)\end{aligned}$$

The above equation has also been derived by other methods.[13] To find the actual bound states, Eq. (40) has to be solved numerically. If the separable potential (31) has more than one term, say is of rank M, then the resulting equation for the bound state has, as in the Coulomb-free case, a form of a rank M determinant equated to zero. A numerical example for the Coulomb plus a rank one separable potential with complex strength is shown in Table III.

The work was supported by a grant from the Natural Sciences and Engineering Research Council of Canada.

---

[*] Permanent address: Institute for Nuclear Physics, Warsaw, Poland.

[1] For a review see G. Backenstoss, Ann. Phys. Nucl. Sci. 20, 467 (1970); R. Seki and C. E. Wiegand, *ibid.* 25, 241 (1975).

[2] A. Deloff, Phys. Rev. C 13, 730 (1976) and the references therein.

[3] Y. R. Kwon and F. Tabakin, Phys. Rev. C 18, 932 (1978).

[4] This method for scattering problems has been used in C. M. Vincent and S. C. Phatak, Phys. Rev. C 10, 391 (1974).

[5] For a review see J. C. Y. Chen and A. C. Chen, *Advances in Atomic and Molecular Physics*, edited by D. R. Bates and I. Estermann (Academic, New York, 1972), Vol. 8.

[6] K. Meetz, J. Math. Phys. 3, 690 (1961).

[7] M. Rotenberg, Ann. Phys. (N.Y.) 19, 262 (1962). See also a review article by the same author (Ref. 8) where he dubbed the Sturm function as Sturmians.

[8] M. Rotenberg, *Advances in Atomic and Molecular Physics*, edited by D. R. Bates (Academic, New York, 1970), Vol. 6.

[9] S. Weinberg, Phys. Rev. 131, 440 (1963); 133, B232 (1964).

[10] See, e.g., D. Sprung and M. K. Srivastava, *Advances in Nuclear Physics* (Academic, New York, 1974), Vol. 8.

[11] J. H. Koch and M. M. Sternheim, Phys. Rev. Lett. 28, 1061 (1972).

[12] Y. Yamaguchi, Phys. Rev. 95, 1628 (1954).

[13] W. W. Zachary, J. Math. Phys. 12, 1379 (1971); 14, 2018 (1973). See also a discussion on the number of bound states in the Coulomb plus Yamaguchi potential in H. van Haeringen *et al.*, J. Math. Phys. 18, 941 (1975).

PHYSICAL REVIEW C VOLUME 21, NUMBER 5 MAY 1980

Alternative methods for the solution of static Hartree-Fock and related problems

M. Di Toro and G. Russo
Istituto di Fisica dell'Università, Catania, Italy

F. Duggan
Institut de Physique Nucléaire, Orsay, France

(Received 30 July 1979)

Alternative ways to the usual diagonalization procedures to solve the self-consistent nuclear Hartree-Fock problem are discussed. It is shown that they are much faster than the conventional approach and computationally much simpler. It is shown how they can be further improved. Finally all these new methods are unified within the framework of a direct minimization of the total energy in the subspace of Slater determinants. Results are given for medium-light deformed nuclei.

[NUCLEAR STRUCTURE Alternative Hartree-Fock solutions.]

I. INTRODUCTION

Certainly the Hartree-Fock (HF) approximation represents a starting point for any microscopic attempt to describe nuclear structure. In addition, with the introduction of schematic density-dependent interactions, this approach has recently shown its validity in reproducing static ground state properties of a wide range of nuclei.[1] Constrained HF calculations, coupled to an evaluation of the collective mass parameter in an adiabatic time evolution, seem to give very promising results in describing large amplitude oscillations far away from the stability region (fission modes, yrast states, and so on).[1] Therefore it seems worthwhile to improve the numerical methods for solving the HF problem in order to obtain faster convergence and more reliable solutions, particularly for the case of heavy deformed nuclei.

The usual approach is based on a linearization of the HF equation which leads to a self-consistent diagonalization of the HF Hamiltonian

$$h_F(\rho)=T+\mathrm{Tr}\bar{V}\rho+\tfrac{1}{2}\,\mathrm{Tr}\,\mathrm{Tr}\,\rho\frac{\partial\bar{V}}{\partial\rho}\rho\,, \qquad (1.1)$$

where T is the kinetic energy $\bar{V}$ is the antisymmetrized interaction, and ρ is the one-body density matrix of the nuclear system. The third term has to be included when one uses density-dependent forces.

The diagonalization method is actually a quite lengthy procedure for heavy elements where huge matrices are involved. On the other hand this approach is based on a particular linearization of a problem which is highly nonlinear, especially for density-dependent interactions. This means that a different linearization can lead to much faster convergence. Finally, the reduction of the problem to the solution of a Schrödinger equation raises some mathematical uncertainties in constrained cases because of the unboundedness which occurs for certain values of the Lagrange multipliers in the Hamiltonian.[2,3]

Recently two methods have been proposed to overcome such difficulties which make no use of diagonalization procedures. One, the "direct density" approach, is based on a minimization of the total energy through a steepest descent procedure in the space of one-body density matrices.[4] The other, the "imaginary time" approach, is based on a transformation of single particle wave functions which resembles a time evolution with imaginary time and which ensures a decreasing total energy towards the minimum value.[5]

In this paper we show that the two approaches are closely related in a general framework of a direct minimization problem for the total energy functional with different linearization options which lead to different convergence rates, also connected to the density dependence of the used schematic interaction. We shall focus our attention on the HF problem, but the extension of these methods and of our conclusions to constrained cases and to the Hartree-Fock-Bogoliubov problem is straightforward.[6]

II. DIRECT ENERGY MINIMIZATION METHOD

Here we briefly discuss the method, and demonstrate the possibility of including higher order terms in the variation of the energy functional with respect to the density matrix. The problem is to minimize the total energy in the HF approximation

$$E(\rho)=\mathrm{Tr}T\rho+\tfrac{1}{2}\,\mathrm{Tr}\,\mathrm{Tr}\rho\bar{V}\rho \qquad (2.1)$$

in the space of the one-body density matrices with

© 1980 The American Physical Society

e constraints

$$\rho^{\dagger}=\rho\,,\qquad \rho^2=\rho\,,\qquad \mathrm{Tr}\rho=A\,. \tag{2.2}$$

This means that if we start with a density matrix ρ_0 which satisfies the HF conditions [Eqs. (2.2)] and if we operate with a unitary transformation

$$\rho=e^{i\chi}\rho_0 e^{-i\chi}\,, \tag{2.3}$$

our problem reduces to a search for an Hermitian operator χ which secures a maximum energy decrease at each step.

We can introduce an expansion for the energy variation

$$\Delta E=\left\langle\frac{\partial E}{\partial\rho}\middle|\Delta\rho\right\rangle+\frac{1}{2}\left\langle\frac{\partial^2 E}{\partial\rho^2}\cdot\Delta\rho\middle|\Delta\rho\right\rangle+\frac{1}{6}\left\langle\left(\frac{\partial^3 E}{\partial\rho^3}\cdot\Delta\rho\right)\cdot\Delta\rho\middle|\Delta\rho\right\rangle+\cdots \tag{2.4}$$

in a matrix space with scalar product

$$A\cdot B=\langle A|B\rangle\equiv\mathrm{Tr}A^{+}B\,. \tag{2.5}$$

Because of the very general result

$$\frac{\partial E}{\partial\rho}=h_F(\rho)\,, \tag{2.6}$$

where $h_F(\rho)$ is the HF Hamiltonian, Eq. (2.4) may be rewritten as

$$\begin{aligned}\Delta E&=\mathrm{Tr}\left[h_F(\rho)+\frac{1}{2}\,\frac{\partial h_F}{\partial\rho}\cdot\Delta\rho+\frac{1}{6}\left(\frac{\partial^2 h_F}{\partial\rho^2}\cdot\Delta\rho\right)\cdot(\Delta\rho)\right]\Delta\rho+\cdots\\&\equiv\mathrm{Tr}h_{\mathrm{eff}}(\rho)\Delta\rho+\cdots\,.\end{aligned} \tag{2.7}$$

We remark that no further terms are needed for inearly density-dependent forces (e.g., of Skyrme type). In any case, we have a definite way to consider higher order terms.

Assuming the trial density matrix ρ_0 is not far away from the solution, we can approximate

$$\delta\rho\sim i[\chi,\rho_0]\,. \tag{2.8}$$

We finally get

$$\Delta E=-i\,\mathrm{Tr}[h_{\mathrm{eff}},\rho_0]\chi \tag{2.9}$$

and the choice[4]

$$\chi=i\lambda[h_{\mathrm{eff}},\rho_0]\,, \tag{2.10}$$

with λ real positive, ensures a maximum energy decrease of the truncated energy at each step. The result is actually related to the approximation equation (2.8). In this respect the choice of the λ parameters requires some attention. In order to secure the validity of the approximation equation (2.8), where we neglect higher order terms in the χ operator, we must keep

$$\|\chi_n\|\ll 1\,,\quad n=0,1,\ldots\,.$$

In our metric this means

$$\lambda_n\ll\frac{1}{\|[h_{\mathrm{eff}}^{(n)},\rho_n]\|}=\frac{1}{(-\mathrm{Tr}[h_{\mathrm{eff}}^{(n)},\rho_n]^2)^{1/2}}\,, \tag{2.11}$$

which implies a large range of acceptable values if we start with a density matrix corresponding to a good trial mean field. Actually we have no problems in nuclear theory where spherical potentials, with standard choices of depth and radius, give the bulk of the self-consistent field. In any case, from the inequality equation (2.11) it seems to be safe to choose *small values of* λ. *A good prescription is* to take the smallest real positive solution of the nonlinear equation

$$\frac{\partial E[\rho(\lambda)]}{\partial\lambda}=0\,. \tag{2.12}$$

Expanding $\rho(\lambda)$ to the second order in λ we get a definite expression for the best value of λ (see Appendix A)

$$\lambda_{\mathrm{opt}}^{(n)}=\frac{\mathrm{Tr}(D_n{}^2)}{\mathrm{Tr}\{[D_n,h_{\mathrm{eff}}^{(n)}][D_n,\rho_n]\}}\,, \tag{2.13}$$

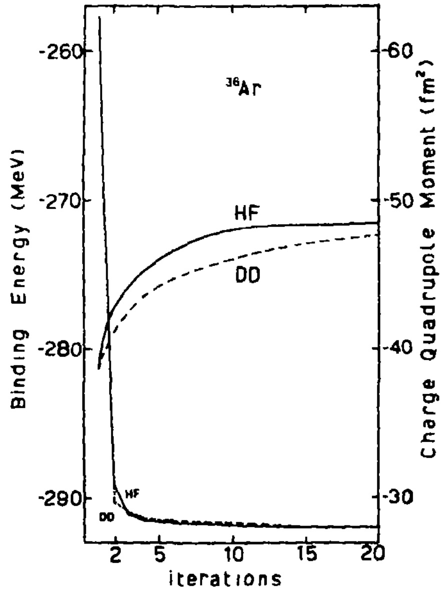

FIG. 1. Total energy (lower curves) and charge quadrupole moment (upper curves) of ^{36}Ar as a function of iteration number. HF lines are obtained with the usual procedure, DD lines refer to the method described in the text with the approximation equation (2.14).

where $D_n \equiv [h_{\text{eff}}^{(n)}, \rho_n]$, with ρ_n the density matrix at the nth iteration. The approach has been proven successful for a quite wide choice of the starting density ρ_0.

In Fig. 1 we show results of this method compared to the usual HF diagonalization procedure for the energy and quadrupole moment of the ground state of ^{36}Ar. In effecting the comparison, we have used the simple DD approximation

$$h_{\text{eff}}(\rho) \simeq h_F(\rho), \tag{2.14}$$

i.e., we have neglected higher order terms in the energy variation ("direct density" method of Ref. 4). The interaction used is of Skyrme II type. The starting density matrix ρ_0 is computed from a spherical Woods-Saxon potential with radius $R = 1.35\, A^{1/3}$ fm, diffuseness $a = 0.6$ fm, and depth $V = -70$ MeV.[4,7] The DD method seems to be slower than standard HF, but this is not a serious difficulty because it is computationally much faster.

The introduction of second and third order terms, with a Skyrme force, significantly improves the convergence rate. This can be seen in Figs. 2, 3, and 4 for the ^{20}Ne and ^{24}Mg cases (DDH curves), where a suitable extrapolation has been used to compute the shift (see Appendix B)

$$\Delta\rho = \rho_{n+1} - \rho_n. \tag{2.15}$$

All the results have been obtained with a deformed harmonic oscillator basis,[7] but of course the method is not dependent on the choice of the representation.

In contrast to the HF case, both the binding energy and the charge quadrupole moment converge at about the same iteration in the DDH method. In terms of computation time the DD and DDH methods are very similar (the former being fractionally faster) because of the two intermediate estimates of the density being required in the DDH case. However, the DDH method is much more stable since an almost simultaneous convergence of the binding energy and the nuclear shape is obtained. Moreover, the DDH method is about a factor 4 faster than the usual HF.

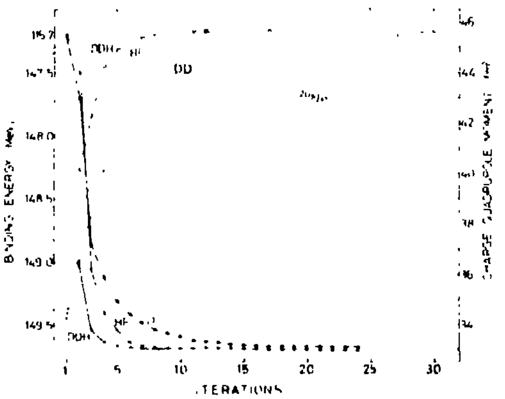

FIG. 2. Total energy (lower curves) and charge quadrupole moment (upper curves) of ^{20}Ne as a function of iteration number. The DDH lines correspond to the inclusion of higher order terms.

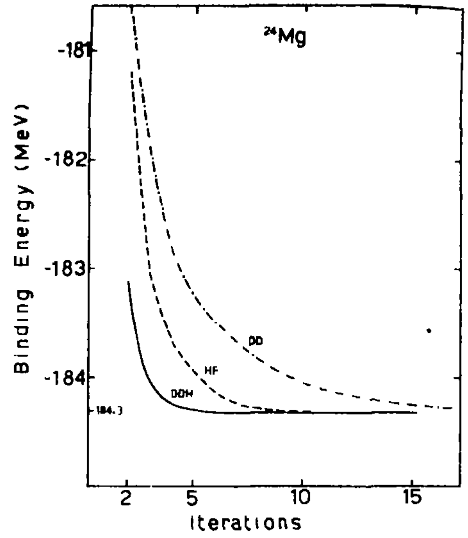

FIG. 3. Total energy of ^{24}Mg as a function of iteration number with also the results obtained with higher order terms (DDH line).

At the end of this section we would like to make two more points which are important in order to

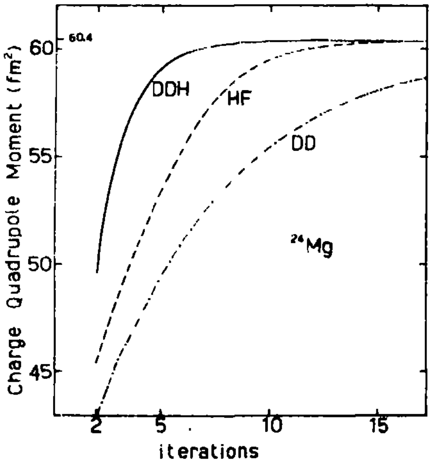

FIG. 4. The same as Fig. 2 for the charge quadrupole moment.

make connection with the imaginary time method described in the next paragraph. First of all, let us consider the changes of the single particle wave functions during the iteration procedure. If we introduce at each step the eigenstates of the one-body density matrix

$$\rho_n = \sum_i^{1,A} |\psi_i^{(n)}\rangle\langle\psi_i^{(n)}| , \tag{2.16}$$

with the same unitary transformation as discussed previously, we can construct the eigenstates of the (n+1)st density matrix

$$\begin{aligned}|\psi_i^{(n+1)}\rangle &= \exp(i\chi^{(n)})|\psi_i^{(n)}\rangle \\ &= \exp\{-\lambda[h_{\text{eff}}^{(n)}, \rho_n]\}|\psi_i^{(n)}\rangle .\end{aligned} \tag{2.17}$$

Moreover, while we do not keep track of the single particle energies, which have no direct physical meaning, we can easily compute the variation of the total energy at each iteration

$$E^{n+1} - E^n \equiv \Delta E = -\lambda \operatorname{Tr}(D_n D_n^+) , \tag{2.18}$$

with D_n defined in Eq. (2.13).

III. IMAGINARY TIME APPROACH

This method has been originally introduced as a byproduct of time-dependent–Hartree-Fock (TDHF) calculations and it is actually based on an "evolution" method similar to that used to describe a real time-evolving system.[5]

In the "true" TDHF we have a unitary transformation acting on single particle wave functions

$$|\psi_j^{(n+1)}\rangle = U|\psi_j^{(n)}\rangle , \tag{3.1}$$

with

$$U = \exp\left(-i\frac{\Delta t}{\hbar} h^{(n+1/2)}\right) , \tag{3.2}$$

where $h^{(n+1/2)}$ is an effective Hamiltonian chosen to conserve exactly the total energy in a real evolution (Appendix B of Ref. 5).

Introducing imaginary time intervals

$$\Delta T \to -i\Delta t \tag{3.3}$$

and a suitable orthonormalization of the single particle wave functions after every "time" step, we get a fast convergence to the static solution, provided we make a "small" choice of the magnitude of Δt, actually chosen on empirical grounds. This can be clearly seen from the total energy variation shown in Eqs. (3.6)–(3.8).

From a first order expansion of the U operator we can get a precise idea of the connection with the previously described "direct energy minimization method."

At the first order we act on the single particle wave function with an operator which has the form $[1-\mu h^{(n+1/2)}]$ with $\mu = \Delta t/\hbar$ a real positive parameter. If we add the orthonormalization procedure, we finish with the transformation,[5] valid for small values of μ only,

$$\begin{aligned}|\psi_j^{(n+1)}\rangle &= (1-\mu h^{(n+1/2)})|\psi_j^{(n)}\rangle \\ &\quad + \mu \sum_k^{1,A} \langle\psi_k^{(n)}|h^{(n+1/2)}|\psi_j^{(n)}\rangle|\psi_k^{(n)}\rangle ,\end{aligned} \tag{3.4}$$

that in the density matrix formalism becomes

$$|\psi_j^{(n+1)}\rangle = [1-\mu(1-\rho_n)h^{(n+1/2)}]|\psi_j^{(n)}\rangle . \tag{3.5}$$

On the other hand, the variation of the total energy at each iteration step is given by[5]

$$\begin{aligned}E^{(n+1)} - E^{(n)} &= \sum_j^{1,A} (\langle\psi_j^{(n+1)}|h^{(n+1/2)}|\psi_j^{(n+1)}\rangle \\ &\qquad - \langle\psi_j^{(n)}|h^{(n+1/2)}|\psi_j^{(n)}\rangle) \\ &= -2\mu \operatorname{Tr}(AA^+) \le 0 ,\end{aligned} \tag{3.6}$$

with

$$A \equiv \rho_n h^{(n+1/2)}(1-\rho_n) . \tag{3.7}$$

The result is a nonpositive definite variation which goes to zero at convergence, where

$$A = 0 \text{ and hence } [h^{(n+1/2)}, \rho_n] = 0 . \tag{3.8}$$

IV. CONNECTION BETWEEN THE TWO APPROACHES

It is easy to show that we obtain very similar results, in fact identical in form, within the direct energy minimization (DEM) framework. Indeed the first order expansion of the unitary transformation equation (2.17) gives

$$|\psi_j^{n+1}\rangle \simeq [1-\lambda(1-\rho_n)h_{\text{eff}}]|\psi_j^n\rangle . \tag{4.1}$$

For the total energy variation we get from Eq. (2.18), using the cyclic property of the trace and the idempotency $\rho_n^2 = \rho_n$,

$$E^{n+1} - E^n = \Delta E = -2\lambda \operatorname{Tr}(BB^+) \le 0 , \tag{4.2}$$

where

$$B = \rho_n h_{\text{eff}}(1-\rho_n) , \tag{4.3}$$

so that at convergence

$$[h_{\text{eff}}(\rho_n), \rho_n] = 0 . \tag{4.4}$$

If we compare Eqs. (4.1), (4.2), and (4.4) with the relations (3.5), (3.6), and (3.8) we see a striking similarity between the two approaches. The similarity can be strengthened by demonstrating the equivalence of the Hamiltonians $h^{(n+1/2)}$ and h_{eff}, as we now show for the case with the simplified density-dependent two-body interaction,[5]

$$v_2 = t_0\delta(\vec{r}_1 - \vec{r}_2) + \frac{t_3}{6}\rho\left(\frac{\vec{r}_1+\vec{r}_2}{2}\right)\delta(\vec{r}_1 - \vec{r}_2) , \tag{4.5}$$

with which imaginary time calculations have been extensively done.

Now the Hartree-Fock Hamiltonian becomes

$$h_F^{(n)} = -\frac{\hbar^2}{2m}\Delta + \tfrac{3}{4} t_0 \rho_n + \tfrac{3}{16} t_3 \rho_n^2 , \tag{4.6}$$

where ρ_n is the *local* density at the nth iteration. In Ref. 5 it is shown that in this case the $h^{n+1/2}$ operator to be used in the imaginary time-step formalism is given by

$$h^{n+1/2} = \tfrac{1}{2}(h_F^{(n)} + h_F^{(n+1)}) - \frac{t_3}{32}(\rho_{n+1} - \rho_n)^2 . \tag{4.7}$$

We can compare now with the h_{eff} operator used in the DEM method

$$h_{\text{eff}}^{(n)} = h_F^{(n)} + \frac{1}{2}\,\frac{\partial h_F^{(n)}}{\partial \rho}\cdot\Delta\rho + \frac{1}{2}\,\frac{\partial^2 h_F^{(n)}}{\partial^2 \rho}\cdot(\Delta\rho)^2 . \tag{4.8}$$

Because the HF Hamiltonian now is a function of the local density only, and introducing

$$\Delta\rho = \rho_{n+1} - \rho_n ,$$

we get

$$\begin{aligned} h_{\text{eff}} &= h_F^{(n)} + \tfrac{1}{2}(\tfrac{3}{4} t_0 + \tfrac{3}{8} t_3 \rho_n)(\rho_{n+1} - \rho_n) \\ &\quad + \tfrac{1}{16} t_3 (\rho_{n+1} - \rho_n)^2 \\ &= \tfrac{1}{2}(h_F^{(n)} + h_F^{(n+1)}) - \frac{t_3}{32}(\rho_{n+1} - \rho_n)^2 \\ &= h^{(n+1/2)} . \end{aligned} \tag{4.9}$$

The two Hamiltonians are exactly the same, order by order, in the density shift $\Delta\rho$. Indeed we can easily show that the term $\frac{1}{16} t_3(\rho_{n+1} - \rho_n)^2$ in $h^{n+1/2}$ comes from third order contributions in $\Delta\rho$ to the total energy variation.[5] Actually if we expand

$$\begin{aligned} \rho_{n+1}^3 &= \rho_n^3 + \Delta\rho(\rho_{n+1}^2 + \rho_n\rho_{n+1} + \rho_n^2) \\ &= \rho_n^3 + \Delta\rho[3\rho_n\rho_{n+1} + (\rho_{n+1} - \rho_n)^2] \\ &= \rho_n^3 + 3\rho_n\rho_{n+1}\Delta\rho + (\Delta\rho)^3 \end{aligned} \tag{4.10}$$

and if we neglect $(\Delta\rho)^3$ terms in the variation $E^{n+1} - E^n$, we get again a relation [Eq. (3.2)] with a

$$h^{(n+1/2)} = h_F^{(n)} + \tfrac{1}{2}(\tfrac{3}{4} t_0 + \tfrac{3}{8} t_3 \rho_n)(\rho_{n+1} - \rho_n) , \tag{4.11}$$

i.e., with a second order h_{eff} only.

In conclusion we can say that there is a perfect equivalence between the two methods in the limit of small values of λ. However, we remark that in the DEM approach we are not bound to choose very small values of this parameter, the only condition being Eq. (2.11), which can allow a wide range of choices. Moreover, we get a definite prescription *for finding the best parameter* λ *at each iteration* step [see Eq. (2.12)]. All that, as expected from general grounds, can improve the velocity of convergence. However, we must remark that there is a "numerical" price to pay: at each iteration we need the construction of the whole density matrix.

We would like to close this section with a remark related to the empirical observation[9] of obtaining a faster convergence using an average HF Hamiltonian

$$h_{\text{AV}} = \tfrac{1}{2}(h_F^{(n)} + h_F^{(n+1)}) \tag{4.12}$$

in the conventional HF method, with density independent interactions. In this case, which corresponds to $t_3 = 0$, the operator h_{eff} is just the average Eq. (4.12), as can be clearly seen from Eq. (4.9). This means that one is actually solving the equation

$$[h_{\text{eff}}(\rho), \rho] = 0 ,$$

which, from the previous analysis, corresponds to a minimization of the total energy with a better linearization procedure.

V. CONCLUSION

In this paper we showed that the "direct density" (DD or DDH) and the imaginary time approaches to solve static HF problems can be seen as two sides of a general method based on a direct minimization of the total energy in the space of the one-body density matrices.

Many advantages can follow from this connection and in general from the development of nondiagonalizing procedures to solve HF-type problems:

(i) We have now available methods which are much faster than the conventional HF procedures. In addition, for axially symmetric nuclei, charge quadrupole moments and binding energies are found to converge simultaneously at about the same iteration.

(ii) We have a definite way to generalize the approach to any density-dependent nuclear interaction.

(iii) We can get a precise prescription on the *choice of the length of the "time step" following* Eq. (2.12).

(iv) We can easily extend the method to the Hartree-Fock-Bogoliubov problem, which can be seen as a minimum problem for the energy functional in a generalized density matrix space.[6]

(v) In this framework of a general minimum problem we can make use of several mathematical tools to study constrained situations (shape, angular momentum, and so on).

ACKNOWLEDGMENTS

We are grateful to D. M. Brink, H. Flocard, and D. Vautherin for helpful suggestions and useful discussions. F. D. would like to thank Professor R. Vinh Mau for his kind hospitality at Orsay and the CNRS for a research fellowship. The work of

M. D. T. and G. R. was supported in part by INFN, Sezione di Catania, and by CSFNSM.

APPENDIX A: SEARCH FOR THE BEST λ

With our choice of the χ operator [Eq. (2.10)] the λ-dependence of the density matrix is given by

$$\begin{aligned}\rho_{n+1}^{(\lambda)} &= e^{-\lambda D_n}\rho_n e^{\lambda D_n}\\ &= \rho_n - \lambda[D_n,\rho_n] + \frac{\lambda^2}{2}[D_n,[D_n,\rho_n]]\\ &\quad - \frac{\lambda^3}{6}[D_n,[D_n,[D_n,\rho_n]]] + \cdots\end{aligned}$$

with

$$D_n = [h_{\mathrm{eff}}^{(n)},\rho_n]\,.$$

Neglecting third order terms, the variation with respect to λ is

$$\Delta\rho = \frac{\partial\rho}{\partial\lambda}\Delta\lambda \simeq -[D_n,\rho_n]\Delta\lambda + \lambda[D_n,[D_n,\rho_n]]\Delta\lambda\,.$$

Our nonlinear equation (2.12) becomes

$$\begin{aligned}\frac{\Delta E}{\Delta\lambda} &= \mathrm{Tr}\,h_{\mathrm{eff}}^{(n)}\frac{\Delta\rho}{\Delta\lambda}\\ &\simeq \mathrm{Tr}\,h_{\mathrm{eff}}^{(n)}\{-[D_n,\rho_n] + \lambda[D_n[D_n,\rho_n]]\} = 0\,,\end{aligned}$$

with solution

$$\lambda_{\mathrm{opt}}^{(n)} = \frac{\mathrm{Tr}(D_n{}^2)}{\mathrm{Tr}\{[D_n,h_{\mathrm{eff}}^{(n)}][D_n,\rho_n]\}} > 0\,, \tag{A2}$$

which can be shown to be positive in the region of validity of the whole method.

We can easily consider higher order terms in Eq. (A1). In this way we get higher order equations in λ. The prescription is to choose the smallest real positive solution. Condition equation (A2) ensures the existence of a solution of this kind.

APPENDIX B: EXTRAPOLATION OF THE DENSITY MATRIX

Since h_{eff}^{n} is dependent on $\Delta\rho = \rho_{n+1} - \rho_n$ we must evaluate the $(n+1)$-th density matrix through some extrapolation procedure. We can follow several ways to do it (Lagrangian, exponential, and also linear), always obtaining convergence rates faster than HF.

We get the best results, reported as DDH curves in Figs. 2, 3, and 4 using a more involved predictor-corrector method. $\Delta\rho$ is estimated introducing successively higher order terms during each iteration as follows:

$$\begin{aligned}\rho_n - h_F(\rho_n) &\to \rho_{n+1}^{(0)} \to h_F(\rho_n) + \tfrac{1}{2}h_F'(\rho_n)(\rho_{n+1}^{(0)} - \rho_n)\\ &\to \rho_{n+1}^{(1)} \to h_F(\rho_n) + \tfrac{1}{2}h_F'(\rho_{n+1}^{(1)} - \rho_n)\\ &\quad + \tfrac{1}{6}h_F''(\rho_n)(\rho_{n+1}^{(1)} - \rho_n) \to \rho_{n+1}\,.\end{aligned}$$

Thus we make two intermediate guesses $\rho_{n+1}^{(0)}$ and $\rho_{n+1}^{(1)}$ for the new density matrix before obtaining its best evaluation ρ_{n+1}.

---

[1] P. Quentin and H. Flocard, Annu. Rev. Nucl. Sci. 28, 523 (1978) and references therein.

[2] G. Fonte and G. Schiffrer, Nucl. Phys. A259, 20 (1976).

[3] W. H. Bassichis, M. R. Strayer, and M. T. Vaughn, Nucl. Phys. A263, 379 (1976).

[4] A. Bonaccorso, M. Di Toro, and G. Russo, Phys. Lett. 72B, 27 (1977).

[5] H. Flocard, S. E. Koonin, and M. S. Weiss, Phys. Rev. C 17, 1682 (1978).

[6] M. Di Toro, Nucl. Phys. A328, 537 (1979).

[7] D. Vautherin, Phys. Rev. C 7, 296 (1973).

[8] H. J. Flocard, K. T. R. Davies, S. J. Krieger, and M. S. Weiss (unpublished).

[9] D. Vautherin and M. Vénéroni, Phys. Lett. 25B, 175 (1967).

PHYSICAL REVIEW C VOLUME 21, NUMBER 5 MAY 1980

Mass parameters in the adiabatic time-dependent Hartree-Fock approximation. I. Theoretical aspects; the case of a single collective variable

M. J. Giannoni and P. Quentin*

Division de Physique Théorique, Institut de Physique Nucléaire, 91406 Orsay-Cedex, France

(Received 2 August 1979)

A self-consistent method for evaluation of mass parameters is presented in the framework of the adiabatic limit of the time-dependent Hartree-Fock approximation, reduced to a single collective variable. The corresponding collective path is assumed to be given either by solving a constrained Hartree-Fock problem with a given time-even constraining operator Q, or by scaling a static Hartree-Fock equilibrium solution. In the former case, once the path is given, a method for solving the equation of motion (of the Hamilton type) is provided, which reduces to a double-constrained Hartree-Fock problem with the time-even constraint Q and with a time-odd constraining operator P. In the case of the scaling path, an analytical solution of the Hamilton equation is discussed and the adiabatic mass for the particular case of an isoscalar quadrupole Q_{20} mode is given. The operator P, which is uniquely determined from the knowledge of Q, has the physical meaning of a momentum operator; it satisfies, together with Q, a weak quantal conjugation relation. Finally, the connection between the two paths is discussed in terms of generalized random-phase approximation sum rules.

NUCLEAR STRUCTURE Evaluation of mass parameters within time-dependent Hartree-Fock approximation in adiabatic limit for single collective variable motion. Discussion and comparison of constrained Hartree-Fock and scaling paths. Expression as a doubly constrained Hartree-Fock problem with momentum operator uniquely defined from coordinate operator. Connection with sum rule and Inglis cranking approaches.

I. INTRODUCTION

During the last few years, significant progress has been made in the theoretical description of collective phenomena in nuclei. Most of the work in this direction had the same purpose: to find a coherent microscopic foundation for the Copenhagen phenomenological collective model,[1] and at the same time to get free of several too restrictive hypotheses underlying the existing microscopic theories [random phase approximation (RPA), cranking model, ...]. Reaching this goal would also considerably increase the predictive character of the collective model by allowing one to calculate, from the nucleon-nucleon interaction, the values of its adjustable parameters. The Inglis cranking model[2] was a first attempt in this respect; however, it suffers from a lack of self-consistency. Thouless and Valatin[3] gave a self-consistent version of the cranking formula in the particular case of a slowly rotating nucleus. For a long time, one has had at one's disposal another microscopic formalism, the RPA; this approximation can be very efficient for the description of several collective properties (especially of giant resonances), but it is clearly not adequate for large amplitude motions, such as fusion, fission, and other nonharmonic nuclear phenomena such as those encountered, for instance, in soft nuclei.

The time-dependent Hartree-Fock approximation, with the additional hypothesis of small collective velocities (compared to some characteristic single-particle velocities), has been the foundation of recent theoretical formulation. The main interest of the adiabatic approximation, besides its physical content, is to allow a connection with the phenomenological collective model. The Villars approach[4] deals with a single collective variable; the collective path is formally defined by an iterative procedure, with some "reasonable" guess for the starting point. Baranger and Vénéroni[5] have obtained two sets of coupled equations of motion which, in the adiabatic limit, are equivalent to the time-dependent Hartree-Fock (TDHF) equation. As shown in Ref. 6, these equations are equivalent to Hamilton-like equations derived from a variational principle similar to a classical least action condition. The solution of these equations would in principle provide both the mass parameters and the collective paths for the collective degrees of freedom. It is clear, however, that the practical implementation of this problem would require a considerable amount of numerical effort.

To bypass some of these difficulties, one may decide in a first step to make an ansatz for the collective trajectories. It then becomes possible to solve the first set of Hamilton equations of motion providing the mass parameters. This is the ap-

© 1980 The American Physical Society

proach adopted in the present paper, the formal framework being the adiabatic time-dependent Hartree-Fock (ATDHF) formalism as presented in Refs. 5 and 6, reduced to a single collective variable. This approach lies between the exact ATDHF solution and phenomenological calculations such as those using Nilsson single-particle wave functions to compute inertial parameters by the Inglis cranking formula. In other words, we shall compute in a consistent way the inertial parameters. We shall not study the dynamical validity of the path, which will be chosen *a priori*. We shall, however, compare the properties of two different choices for this path. Moreover, we shall present a method for the computation of the masses which we believe to be particularly convenient and accurate.

All the matter is presented at a very general level. In an accompanying paper[7] (hereafter referred as II), we specialize to the isoscalar Q_{20} quadrupole mode, and give results obtained for large and small amplitude motions for the corresponding mass parameters, calculated with several Skyrme interactions. We would like to emphasize that the present work has been carried out entirely in the line of Refs. 5 and 6, and that the quotations of other work which will be found here constitutes a step towards a better understanding of the connections between different formulations of collective theories[4,8-10] and towards their unification.

II. THE ADIABATIC TIME-DEPENDENT HARTREE-FOCK APPROXIMATION

In the independent particle approximation, one describes the physical system only in terms of its one-body reduced density operator ρ. For a pure A-body state, the operator ρ writes

$$\rho=\sum_{i=1}^{A}|i\rangle\langle i|\,, \tag{2.1}$$

where $\{|i\rangle;\, i=1,\ldots,A\}$ is an orthonormal set of single-particle (SP) states. The projector character of ρ,

$$\rho^2=\rho\,, \tag{2.2}$$

clearly follows from Eq. (2.1). In other words, the corresponding wave function Ψ is a Slater determinant built with the A single-particle states $|i\rangle$.

Given a Hamiltonian H composed of a kinetic energy operator T and a two-body interaction V,[11] the dynamical evolution of ρ is governed, in terms of $W(\rho)$, the so-called Hartree-Fock Hamiltonian (which is the one-body reduction of H with respect to Ψ)

$$W(\rho)=T+\mathrm{Tr}_2\tilde{V}(1,2)\rho(2)\,, \tag{2.3}$$

by the TDHF equation[12]:

$$i\hbar\dot{\rho}=[W(\rho),\rho]\,, \tag{2.4}$$

which is the one-body reduction of the Liouville-Von Neumann equation.

The total TDHF energy, easily shown to be a constant of the motion, is given by

$$\langle\Psi|H|\Psi\rangle=E[\rho]=\mathrm{Tr}(T\rho)+\tfrac{1}{2}\,\mathrm{Tr}\,\mathrm{Tr}\rho\tilde{V}\rho\,. \tag{2.5}$$

The notation of Eqs. (2.3) and (2.5) is standard (see, e.g., Ref. 5).

The TDHF equation (2.4) can be derived in various ways, and, in particular, from the stationarity principle:

$$\delta\int_{t_1}^{t_2}\left\langle\Psi\left|i\hbar\frac{\partial}{\partial t}-H\right|\Psi\right\rangle dt=0\,, \tag{2.6}$$

where Ψ and Ψ^*, restricted to be Slater determinants, should be varied independently, with fixed end points for Ψ.

The adiabaticity assumptions. To give a simple formulation of the ATDHF formalism, Baranger and Vénéroni have introduced the following decomposition of the density operator ρ:

$$\rho=e^{i\chi}\rho_0e^{-i\chi}\,. \tag{2.7}$$

The justification for such a decomposition is given by the following theorem, studied in Ref. 5, and further investigated in Refs. 13–15.

Decomposition theorem.[16] Given a Hermitian projection operator ρ and its time-reversal conjugate ρ_T,

(i) *There exists* a projection operator ρ_0 and an operator χ, both Hermitian and time-even:

$$\rho_0=\rho_0^\dagger=(\rho_0)_T=\rho_0^2\,, \tag{2.8}$$

$$\chi=\chi^\dagger=\chi_T \tag{2.9}$$

such as Eq. (2.7) is fulfilled, *provided* ρ and ρ_T do not have any common eigenvector corresponding to different eigenvalues of ρ and ρ_T.

(ii) In addition to the requirements (2.8) and (2.9), *the supplementary conditions*

$$\rho_0\chi+\chi\rho_0=\chi\,, \tag{2.10}$$

$$\lambda_i\in\left]-\frac{\pi}{4},\frac{\pi}{4}\right[\,, \tag{2.11}$$

where λ_i is any eigenvalue of χ, *ensure the uniqueness* of the decomposition (2.7).

One can easily show that there cannot exist any decomposition (2.7) satisfying (2.8) and (2.9) for the one-body reduced density operator of an odd system of fermions; consequently, the ATDHF formalism as presented in Refs. 5 and 6 is restricted to even-even nuclei. When dealing with a sp density operator built from states $|i\rangle$ [see Eq.

(2.1)] which are eigenstates of the spin projection s_z, the (sufficient) condition for the existence of the decomposition to be satisfied by ρ and its time-reversed ρ_T requires the same number of spin-up and spin-down occupied states $\{|i\rangle;\, i=1,\ldots,A\}$.[14,15] This sufficient condition formulated in the decomposition theorem will be satisfied in all physical situations considered in this work (see also II); this allows us to make use of the decomposition (2.7) without any further justification.

Following Baranger and Vénéroni, we call "natural" the particular decomposition unequivocally defined by Eqs. (2.7), (2.8), (2.9), and by the additional conditions (2.10) and (2.11). Notice that the condition (2.10) can be written equivalently (see Appendix A) as

$$\rho_0\chi\rho_0=\sigma_0\chi\sigma_0=0\,, \tag{2.12}$$

where $\sigma_0=1-\rho_0$. Defining the hole (or particle) states as eigenvectors of ρ_0 (or σ_0) associated with the eigenvalue 1, it appears from Eq. (2.12) that the operator χ of the "natural" decomposition has only particle-hole and hole-particle matrix elements.

In the summary of the ATDHF formalism which follows we will make use of the natural decomposition of ρ. The apparent lack of generality due to this peculiar choice of the decomposition (2.7) will be discussed below.

The hypothesis of slow motion is introduced by the assumption that χ and its time derivative $\dot{\chi}$ are small.[17] Leaving for a moment the physical content of such conditions, we expand the exponential operators in Eq. (2.7) and truncate the resulting expression of ρ at second order in χ:

$$\rho(t)=\rho_0(t)+\rho_1(t)+\rho_2(t)\,, \tag{2.13}$$

with

$$\rho_1=i[\chi,\rho_0]\,, \tag{2.14}$$

$$\rho_2=-\tfrac{1}{2}[\chi,[\chi,\rho_0]]\,. \tag{2.15}$$

It is worth recalling here that the zero-order term ρ_0 depends on time, and may deviate considerably from a static Hartree-Fock solution, allowing thus the description of large amplitude motions. In this respect, the ATDHF expansion (2.13) differs basically from the one usually made in the derivation of RPA equations around the static Hartree-Fock (HF) equilibrium (see, e.g., Ref. 18).

Classical Hamiltonian formulation

By inserting the expansion (2.13) into the expression (2.5) for the TDHF energy, Baranger and Vénéroni have obtained a division of the adiabatic energy into a potential and a kinetic part. The corresponding Lagrange equations have then been shown to be equivalent to the equations obtained directly by inserting the expansion (2.13) into the time-even and time-odd parts of the TDHF equation (2.4). Adopting the alternative point of view of a Hamiltonian formulation, Brink, Giannoni, and Vénéroni[8] have directly introduced the expansion (2.13) into the variational principle (2.6) source of the TDHF equation. As a result, they have found

$$\delta\int_{t_1}^{t_2}\{\mathrm{Tr}(\hbar\chi\dot{\rho}_0)-E_a[\rho_0,\chi]\}\,dt=0\,, \tag{2.16}$$

where $E_a[\rho_0,\chi]$, which is a functional of ρ_0 and χ, is the total energy of the system in the adiabatic approximation, i.e., is obtained by replacing ρ in (2.5) by its adiabatic expansion (2.13). This allows us to write the adiabatic energy E_a as

$$E_a=E_0+E_2\,, \tag{2.17}$$

where the term E_2 is quadratic in χ, and where the zero-order part E_0 is the energy for the time-dependent determinant ϕ_0 associated with the density operator ρ_0:

$$E_0=\langle\phi_0|H|\phi_0\rangle=E[\rho_0]\,. \tag{2.18}$$

The integrand in Eq. (2.16) has therefore the same structure as the Lagrangian of a classical system, with a kinetic energy quadratic in the momenta and a coordinate-dependent metric tensor:

$$\mathfrak{L}_{\mathrm{cl}}=\sum_i p_i\dot{q}_i-\tfrac{1}{2}\sum_{i,j}[\mathfrak{M}^{-1}(q_k)]_{ij}\,p_ip_j-V(q_k)\,. \tag{2.19}$$

In this analogy, the matrix elements of ρ_0 and $\hbar\chi$ in a time-independent basis play respectively the roles of the coordinate and their conjugate momenta. As is well known, the condition of stationarity for the classical action $\int_{t_1}^{t_2}\mathfrak{L}_{\mathrm{cl}}dt$ with respect to independent variations of the p's and q's leads to Hamilton's equations.[19] Therefore, Hamilton-like equations should emerge from the stationarity equation (2.16) if the coordinates and the conjugate momenta are taken as independent variables. The situation is, however, complicated by the existence of two constraints to be taken into account during the variation. The first is the holonomic constraint expressing the projector character of ρ_0. The second is the algebraic relation (2.12) between coordinates and momenta. A complete discussion of these constraints would exceed the scope of this paper, and can be found in Ref. 20. It should be noted, however, that these constraints can be satisfied implicitly, i.e., without the introduction of Lagrange multipliers. The two sets of Hamilton quations read

$$i\hbar\sigma_0\dot{\rho}_0\rho_0=\sigma_0\{[W_0^D,\rho_1]+[W_1,\rho_0]\}\rho_0, \qquad (2.20a)$$

$$\hbar\sigma_0\dot{\chi}\rho_0=\sigma_0\{-W_0-iW_1\sigma_0\chi+i\chi\rho_0W_1-W_2\}\rho_0, \qquad (2.20b)$$

where W_0, W_1, and W_2 are the three first terms of the expansion of the Hartree-Fock Hamiltonian in powers of χ:

$$W_0=T+\mathrm{Tr}\,\tilde{V}\rho_0 \qquad (2.21)$$

its diagonal part W_0^D is defined in Eq. (2.30)],

$$W_1=\mathrm{Tr}\,\tilde{V}\rho_1, \qquad (2.22)$$

$$W_2=\mathrm{Tr}\,\tilde{V}\rho_2. \qquad (2.23)$$

Notice[11] that W_0 and W_2, like ρ_0 and ρ_2, are time-even, whereas W_1, like ρ_1, is time-odd.

One sees that the two Hamilton equations (2.20a) and (2.20b) have only particle-hole matrix elements. This reduction of the number of dynamical equations results from the constraint $\rho_0^2=\rho_0$. The advantage of the choice of the natural decomposiion is now understandable, since its operator χ, whose matrix elements are the momenta, contains he right number of degrees of freedom.

One can also write the first Hamilton equation as

$$i\hbar\dot{\rho}_0=[\rho_0W_0\rho_0+\sigma_0W_0\sigma_0,\rho_1]+[W_1,\rho_0]. \qquad (2.24)$$

Equation (2.24) [or (2.20a)], which provides a inear relation between the velocities and the momenta similar to the corresponding classical equaion,

$$\dot{q}_i=\sum_j[\mathcal{M}^{-1}(q_k)]_{ij}p_j, \qquad (2.25)$$

can be rewritten in form

$$\hbar\begin{pmatrix}\dot{\underline{\rho}}_0\\ \dot{\underline{\rho}}_0^*\end{pmatrix}=\mathcal{M}^{-1}\begin{pmatrix}\underline{\chi}\\ \underline{\chi}^*\end{pmatrix}, \qquad (2.26)$$

where $\dot{\underline{\rho}}_0$ and $\underline{\chi}$ stand for vectors whose components are the particle-hole matrix elements of $\dot{\rho}_0$ and χ n the time-dependent basis defined by the eigenvectors of ρ_0. The inertia matrix is defined by

$$\mathcal{M}=\begin{pmatrix}A[\rho_0] & -B[\rho_0]\\ -B^*[\rho_0] & A^*[\rho_0]\end{pmatrix}^{-1}, \qquad (2.27)$$

with

$$A_{ph,p'h'}=(\epsilon_p-\epsilon_h)\delta_{pp'}\delta_{hh'}+\frac{\delta^2E[\rho_0]}{\delta\rho_{hp}\delta_{p'h'}}, \qquad (2.28)$$

$$B_{ph,p'h'}=\frac{\delta^2E[\rho_0]}{\delta\rho_{hp}\delta_{h'p'}} \qquad (2.29)$$

(where there is no possible confusion between the Kronecker and functional derivative symbols).

The energy functional $E[\rho_0]$ in (2.28) and (2.29) is given by Eq. (2.5); the single-particle states, labeled by p, p' (particle) and h, h' (hole), are defined as the common eigenvectors of ρ_0 and of the diagonal part of W_0 (see below the discussion of Inglis cranking):

$$W_0^D=\rho_0W_0\rho_0+\sigma_0W_0\sigma_0, \qquad (2.30)$$

and the single-particle energies ϵ_p, ϵ_h are the eigenvalues of W_0^D. One can notice that the submatrices A and B have the same formal definition as in the RPA theory, but they are represented in a time-dependent particle-hole basis defined by ρ_0 instead of the static equilibrium operator ρ_{st}. Moreover, one should not confuse the matrix $\mathcal{M}^{-1}$, which is Hermitian, with the matrix giving the RPA eigensolutions [see Eq. (6.3)].

For the purpose of the present paper we need not discuss in great details the second Hamiltonian equation (2.20b), although its role is crucial since, when solved together with the first Hamilton equation, it determines the collective path $\rho_0(t)$. It allows also to give a different formulation of the second adiabaticity condition ($\hbar\dot{\chi}$ small). Indeed, Eq. (2.20b) shows that if the motion if adiabatic, the commutator $[W_0,\rho_0]$ (or equivalently the antidiagonal part of W_0: see Appendix A) should be small, at least of first order in χ. This condition means that at all times the system is in a "quasistatic" equilibrium since the static Hartree-Fock equation

$$[W_{st},\rho_{st}]=0 \qquad (2.31)$$

is nearly satisfied. The meaning of the assumptions on χ and $\dot{\chi}$ can now be formulated as follows: Since χ is the "conjugate momentum" of the "coordinate" ρ_0, the first hypothesis (smallness of χ) expresses simply a condition of small velocities; the second assumption (smallness of $\hbar\dot{\chi}$) prevents the system from getting large accelerations, and therefore preserves the slow character of the motion along the whole path.

At this point one should distinguish between two limiting cases according to whether $[W_0,\rho_0]$ is of first or second order in χ. The first case corresponds to the RPA, i.e., to the small amplitude limit. The second corresponds to the large amplitude limit. Let us note in this respect that, as in Ref. 5, we use the term adiabaticity in a somewhat misleading way since with our definition (χ and $\hbar\dot{\chi}$ small) it encompasses these two limiting cases, whereas traditionally[21] it is only attached to the second situation.

By use of the first Hamilton equation, it can be shown that the collective kinetic energy, which is the quadratic part in χ of $E_s[\rho_0,\chi]$, can be expressed as

$$\mathcal{K}=\tfrac{1}{2}\hbar\,\mathrm{Tr}(\chi\dot{\rho}_0)=\tfrac{1}{2}\hbar^2(\underline{\dot{\rho}}_0^*,\underline{\dot{\rho}}_0)\mathcal{M}\begin{bmatrix}\underline{\dot{\rho}}_0\\ \underline{\dot{\rho}}_0^*\end{bmatrix}. \qquad (2.32)$$

It is useful to give another expression for $\mathcal{K}$, in terms of the conjugate momentum χ. By expanding at order two the average value of the full Hamiltonian H:

$$\langle\Psi|H|\Psi\rangle=\langle\phi_0|e^{-i\chi}He^{i\chi}|\phi_0\rangle, \qquad (2.33)$$

one gets

$$E_s[\rho_0,\chi]=E[\rho_0]+\tfrac{1}{2}\langle\phi_0|[\chi,[H,\chi]]|\phi_0\rangle, \qquad (2.34)$$

and Eq. (2.17) leads to

$$E_2[\rho_0,\chi]=\tfrac{1}{2}\langle\phi_0|[\chi,[H,\chi]]|\phi_0\rangle=\mathcal{K}. \qquad (2.35)$$

As for the potential energy

$$\mathcal{V}=E_s[\rho_0,\chi]-\mathcal{K}, \qquad (2.36)$$

which is only a function of the coordinate ρ_0, it is simply

$$\mathcal{V}=E[\rho_0]. \qquad (2.37)$$

In the preceding, we have thus put the total energy in a classical Hamiltonian form:

$$\mathcal{H}=\mathcal{K}+\mathcal{V}, \qquad (2.38)$$

which will allow us to make the connection between this TDHF approach and the Bohr collective Hamiltonian approach.[1]

As already mentioned, the variational approach to ATDHF formalism presented here has been obtained in the case where the natural decomposition of ρ into ρ_0 and χ is chosen. For the more general case of any other choice for the decomposition (2.7), Hamiltonlike equations can still be derived. but with some more difficulties[20]; all the equations (2.17) to (2.20a) and (2.21) to (2.38) remain valid. The only equation affected by a different choice of ρ_0 and χ is the second Hamilton equation (2.20b). Since this equation is supposed to define the adiabatic path, it may be argued that the natural choice for χ brings some arbitrariness into the whole approach. [Indeed, it is well known in some particular cases[5] that ρ may be decomposed as in Eqs. (2.7), (2.8), and (2.9) without fulfillment of Eq. (2.10)]. In this respect, it is worth recalling the important result of Ref. 5: *In the adiabatic limit*, all decompositions fulfilling Eq. (2.7) with ρ_0 and χ Hermitian and time-even are dynamically equivalent.

"Constrained forms" for the TDHF and first ATDHF equations. As an immediate consequence of the projector character of ρ [see Appendix A, Eq. (A18)], one can write[22] the TDHF equation (2.4) as

$$[W-i\hbar[\dot{\rho},\rho],\rho]=0. \qquad (2.39)$$

This is formally a constrained Hartree-Fock equation for the external field $F=-i\hbar[\dot{\rho},\rho]$.

Inserting the expansion (2.13) into Eq. (2.39), one gets for the time-odd part of the adiabatic limit of (2.39)

$$i\hbar[[\dot{\rho}_0,\rho_0],\rho_0]=[W_0,\rho_1]+[W_1,\rho_0]. \qquad (2.40)$$

The left-hand side and the last right-hand side terms in Eq. (2.40) have clearly vanishing diagonal (particle-particle and hole-hole) matrix elements. The diagonal part of the second term is $[W_0^A,\rho_1]$, which, due to the smallness of $[W_0,\rho_0]$, is at least of second order in χ (see Appendix A). Neglecting this term in the first order equation (2.40) leads to

$$i\hbar[[\dot{\rho}_0,\rho_0],\rho_0]=[W_0^D,\rho_1]+[W_1,\rho_0]. \qquad (2.41)$$

Eq. (2.41) is nothing but the first Hamilton equation (2.24) in which the operator $\dot{\rho}_0$ has been written under its double commutator form.

This equation can also be viewed as the time-odd part[23] of the following constrained Hartree-Fock (CHF) equation:

$$[W_0^D+W_1-i\hbar[\dot{\rho}_0,\rho_0],\rho_0+\rho_1]=0. \qquad (2.42)$$

In Eq. (2.42), the term which generates the time-odd part ρ_1 of the density is the time-odd external field:

$$-F_0=-i\hbar[\dot{\rho}_0,\rho_0]. \qquad (2.43)$$

Therefore, the operator F_0 has the physical content of a "momentum" operator, times a velocity. Let us consider its mean value in the time-dependent state:

$$\langle F_0\rangle=\mathrm{Tr}\,F_0\rho. \qquad (2.44)$$

By noticing that the only part of ρ contributing to the trace is *time-odd* (due to the property of the product of two Hermitian operators having opposite parities under time reversal to have a vanishing trace), one obtains

$$\langle F_0\rangle=\mathrm{Tr}F_0\rho_1=\hbar\,\mathrm{Tr}[\dot{\rho}_0,\rho_0][\chi,\rho_0]. \qquad (2.45)$$

A straightforward handling of Eq. (2.45) leads to

$$\langle F_0\rangle=\hbar\,\mathrm{Tr}\,\chi\dot{\rho}_0=2\mathcal{K}, \qquad (2.46)$$

which further supports the interpretation of F_0 as the product of a momentum by a velocity.

The interest of the "constrained form" (2.42) of the first Hamilton equation and the reason for introducing the operator F_0 will appear in the next two sections.

The Inglis cranking. To close this section, we make some comments about the cranking model and its relation with the ATDHF approximation. The Inglis cranking approach[2] may be defined as a non-self-consistent solution of Eq. (2.24). More precisely, one neglects the effect of the time-odd self-consistent field W_1 on the time-odd density ρ_1. The corresponding approximate equation of motion reads

$$i\hbar\dot{\rho}_0=[W_0^D,\rho_1], \tag{2.47}$$

whose inversion provides ρ_1 in terms of $\dot{\rho}_0$.

The Inglis formula can be deduced from (2.47) once a proper choice of the single-particle basis is made. A reasonable choice would consist in common eigenvectors of ρ_0 and of an "energy operator" commuting with ρ_0, as in the static Hartree-Fock case. Such an operator cannot be exactly the Hartree-Fock field W_0 constructed from ρ_0, which in general does not commute with ρ_0. However, the adiabaticity condition requires that $[W_0,\rho_0]$ should be small compared to some characteristic single-particle excitation energy; therefore, the eigenvectors of the diagonal part W_0^D of ρ_0 [see Eq. (2.30)] are "nearly" eigenvectors of W_0. Since the operator W_0^D clearly commutes with ρ_0, we can define the single-particle basis $\{|h\rangle, |p\rangle\}$ by

$$\rho_0|h\rangle=|h\rangle\,,\quad W_0^D|h\rangle=\epsilon_h|h\rangle\,, \tag{2.48}$$

$$\rho_0|p\rangle=0\,,\quad W_0^D|p\rangle=\epsilon_p|p\rangle\,. \tag{2.49}$$

Taking the matrix elements of Eq. (2.47) leads to

$$i\hbar\langle h|\dot{\rho}_0|p\rangle=(\epsilon_h-\epsilon_p)\langle h|\rho_1|p\rangle\,, \tag{2.50}$$

which gives, in terms of χ [see Eq. (2.14)],

$$\langle h|\chi|p\rangle=\frac{\hbar}{\epsilon_p-\epsilon_h}\langle h|\dot{\rho}_0|p\rangle\,. \tag{2.51}$$

The kinetic energy, given by Eq. (2.32), can then be written as

$$\mathcal{K}=\hbar^2\sum_{p,h}\frac{|\langle h|\dot{\rho}_0|p\rangle|^2}{\epsilon_p-\epsilon_h}\,, \tag{2.52}$$

which is the cranking formula.

III. REDUCTION OF THE NUMBER OF DYNAMICAL VARIABLES

From now on, we will restrict the number of dynamical variables by assuming that the operator ρ_0 depends on time only through a few number of dynamical variables q_i. This implies in particular that

$$\dot{\rho}_0=\sum_i\dot{q}_i\frac{\partial\rho_0}{\partial q_i}\,. \tag{3.1}$$

For the sake of simplicity, we will consider the case of a single variable q. The generalization to several variables is straightforward.

From Eqs. (2.20a) and (2.22) one sees that ρ_1 (or equivalently χ) is linear in $\dot{q}$, and therefore the kinetic energy $\mathcal{K}$ [see Eqs. (2.32)], such that

$$\mathcal{K}=\tfrac{1}{2}\dot{q}\,\mathrm{Tr}\left(\hbar\chi\frac{\partial\rho_0}{\partial q}\right), \tag{3.2}$$

is, as it should be, quadratic in $\dot{q}$. Equation (3.2) tells us that p defined as

$$p=\hbar\,\mathrm{Tr}\,\chi\frac{\partial\rho_0}{\partial q}=\frac{\partial\mathcal{L}}{\partial\dot{q}}=2\frac{\partial\mathcal{K}}{\partial\dot{q}} \tag{3.3}$$

is the conjugate momentum of the coordinate q. This has also been checked directly in Ref. 6 by varying the adiabatic action. Since they are classical canonical variables, p and q satisfy the Poisson bracket relations:

$$\{q,p\}=1\,, \tag{3.4}$$

$$\dot{q}=\{q,\mathcal{K}\}\,, \tag{3.5}$$

$$\dot{p}=\{p,\mathcal{K}\}\,. \tag{3.6}$$

From Eq. (3.3) [or Eq. (3.2)], one defines an adiabatic mass $M(q)$ by

$$M(q)=\frac{p}{\dot{q}}=\frac{2\mathcal{K}}{\dot{q}^2}=\mathrm{Tr}\;\frac{\hbar\chi}{\dot{q}}\frac{\partial\rho_0}{\partial q}\;, \tag{3.7}$$

which is of course independent of $\dot{q}$.

Let us now consider the time-odd Hermitian operator:

$$P=i\hbar\left[\frac{\partial\rho_0}{\partial q},\rho_0\right], \tag{3.8}$$

which is just [see Eq. (2.43)]

$$P=F_0/\dot{q}\,. \tag{3.9}$$

From Eq. (2.46) and the definition (3.3) of p, we deduce that the expectation value of the operator P in the time-dependent state Ψ is the conjugate momentum p of q:

$$\langle P\rangle=\frac{1}{\dot{q}}\langle F_0\rangle=\frac{2\mathcal{K}}{\dot{q}}=p\,. \tag{3.10}$$

It happens frequently that the coordinate q is chosen to be the expectation value of some time-even observable Q:

$$q=\langle Q\rangle=\mathrm{Tr}\rho Q\simeq\mathrm{Tr}\rho_0 Q\,. \tag{3.11}$$

(The last equality has been obtained by using time-reversal properties of the operators under the trace, and by neglecting terms of second order in χ.) Whereas we have just seen that the expectation values of P and Q are classical conjugate variables, it can be proved that P and Q, as quantal variables, are canonically conjugate in a weak sense precised below. To show this, we compute the mean value of their commutator:

$$\langle\Psi|[Q,P]|\Psi\rangle=\mathrm{Tr}\rho[Q,P]\,. \tag{3.12}$$

Using again well known properties of the trace and neglecting second order terms in χ, we get

$$\mathrm{Tr}\rho[Q,P]\simeq\mathrm{Tr}\rho_0[Q,P]=\mathrm{Tr}Q[P,\rho_0]\,. \tag{3.13}$$

After inserting the definition (3.8) of P and the expression (A18) of Appendix A transposed to $\partial\rho_0/\partial q$, Eq. (3.13) leads to

$$\mathrm{Tr}\rho[Q,P]=i\hbar\,\mathrm{Tr}Q\frac{\partial\rho_0}{\partial q}=i\hbar\frac{\partial}{\partial q}\mathrm{Tr}Q\rho_0=i\hbar\frac{\partial}{\partial q}\langle Q\rangle\,, \tag{3.14}$$

which provides the canonical relation

$$\langle\Psi|[Q,P]|\Psi\rangle=i\hbar\,. \tag{3.15}$$

Of course, such a relation is valid for any time-even Hermitian operator Q; therefore, it does not provide any criterion for the choice of a "good" collective path. This is not surprising, since it is valid whether the second Hamilton equation (2.20b) is satisfied or not. Nevertheless, once a choice for Q has been made, the weak conjugation relation (3.15) does support the definition (3.8) for P.

Some authors (see, e.g., Refs. 4 and 10) define the conjugate momentum $\hat{P}$ of Q as:

$$\hat{P}\Psi(q)=i\hbar(\partial/\partial q)\Psi(q)\,. \tag{3.16}$$

Such a $\hat{P}$ is clearly not equal to the operator P considered in the present work, which has only particle-hole matrix elements in the sp basis of ρ_0 [see Appendix A, Eq. (A16)], whereas $\hat{P}$ can have nonvanishing diagonal matrix elements. Indeed, one can easily see that

$$P|h\rangle=\sigma_0P|h\rangle=\sigma_0\hat{P}|h\rangle\neq\hat{P}|h\rangle\,, \tag{3.17}$$

$$P|p\rangle=\rho_0P|p\rangle=\rho_0\hat{P}|p\rangle\neq\hat{P}|p\rangle\,. \tag{3.18}$$

However, if one considers the time-dependent state $(|\psi\rangle=e^{i\chi}|\phi_0\rangle)$ built from the natural decomposition[24] one can show that these two operators have the same expectation value:

$$\langle\hat{P}\rangle=\langle P\rangle\,. \tag{3.19}$$

Let us finally comment about the evolution with time of $\langle P\rangle$ and $\langle Q\rangle$. As for the expectation value of any one-body operator G (having no explicit dependence on time), their TDHF equations of motion are of the general form

$$\frac{d}{dt}\langle G\rangle=\frac{i}{\hbar}\langle\Psi|[H,G]|\Psi\rangle\,. \tag{3.20}$$

The latter is easily demonstrated as follows: Since

$$\frac{d}{dt}\langle G\rangle=\mathrm{Tr}\dot{\rho}G\,, \tag{3.21}$$

one gets from the TDHF equation of motion (2.4)

$$\frac{d}{dt}\langle G\rangle=-\frac{i}{\hbar}\{G[W(\rho),\rho]\}\,, \tag{3.22}$$

where $W(\rho)$ is the one-body reduction with respect *to ρ of the one-body plus two-body operator H.* From the general property of one-body reductions $\mathcal{O}(\rho)$ of many-body operators $\mathcal{O}$,[26]

$$\langle\Psi|[\mathcal{O},C_m^\dagger C_n]|\Psi\rangle=-\langle m|[\mathcal{O}(\rho),\rho]|n\rangle \tag{3.23}$$

(where ρ is the density matrix defining the independent particle state $|\Psi\rangle$, and $C_i^\dagger$ are creation operators on the single-particle states $|i\rangle$), one gets readily Eq. (3.20). Using Eqs. (3.5) and (3.6), together with Eq. (3.20) applied to $G=Q$ and $G=P$ leads to

$$\{q,\mathcal{H}\}=\langle\Psi|\frac{1}{i\hbar}[Q,H]|\Psi\rangle\,, \tag{3.24}$$

$$\{p,\mathcal{H}\}=\langle\Psi|\frac{1}{i\hbar}[P,H]|\Psi\rangle\,. \tag{3.25}$$

The approximation consisting in reducing the number of dynamical variables, together with the preceding ones (existence of a mean field, adiabaticity of the motion), are the basis for the unified model description of low energy nuclear excitations.[1] However, a further approximation is generally associated to this approach. One decides *a priori*, i.e., without solving the equations of motion, what the dynamical variables should be. In other words, one chooses a special family $\rho_0(q)$. Possible choices for such families will be discussed in Secs. IV and V.

In this case, one has only to solve the first Hamilton equation, providing the pass parameter $M(q)$

$$i\hbar\dot{q}\frac{\partial\rho_0}{\partial q}=[W_0^D,\rho_1]+[W_1,\rho_0]\,. \tag{3.26}$$

It is worth noticing that this equation is not capable of determining the diagonal part of χ in terms of $\partial\rho_0/\partial q$. In other words, the mass parameter $M(q)$ does not depend on the diagonal part $(\rho_0\chi\rho_0+\sigma_0\chi\sigma_0)$ of χ. This can also be seen directly on the expression (3.7) of $M(q)$. Since the operator $\partial\rho_0/\partial q$ has only particle-hole matrix elements, the particle-particle and hole-hole parts of χ do not contribute to the trace.

Let us finally deduce, from the Inglis formula (2.52) for the kinetic energy, the usual cranking formulae for the mass parameter $M(q)$. The first one is obtained by replacing $\dot{\rho}_0$ by $\dot{q}\,\partial\rho_0/\partial q$ in Eq. (2.52):

$$M(q)=2\hbar^2\sum_{p,h}\frac{|\langle h|\partial\rho_0/\partial q|p\rangle|^2}{\epsilon_p-\epsilon_h} \tag{3.27}$$

$$=2\hbar^2\sum_{p,h}\frac{|\langle h|\partial/\partial q|p\rangle|^2}{\epsilon_p-\epsilon_h}\,. \tag{3.28}$$

By use of

$$(\partial/\partial q)[W_0^D,\rho_0]=0\,, \tag{3.29}$$

one can also express the mass parameter as

$$M(q)=2\hbar^2\sum_{p,h}\frac{|\langle h|\partial W_0^D/\partial q|p\rangle|^2}{(\epsilon_p-\epsilon_h)^3}\,, \qquad (3.30)$$

which is an alternative form for the cranking formula.

IV. CONSTRAINED HARTREE-FOCK PATHS

As a possible prescription, the trajectory $\rho_0(q)$ is assumed to be given by the solution of a CHF equation

$$\delta\langle\phi_0|H-\lambda Q|\phi_0\rangle=0\,, \qquad (4.1)$$

where ϕ_0 is a Slater determinant minimizing the total energy of the system under the action of the time-even external field $(-\lambda Q)$. In terms of the density operator $\rho_0(q)$, Eq. (4.1) can be written equivalently as

$$[W_0-\lambda Q,\,\rho_0(q)]=0\,. \qquad (4.2)$$

The operator W_0 is the Hartree-Fock Hamiltonian built from the density matrix ρ_0, and the collective coordinate q is the expectation value of the constraining operator

$$q=\langle Q\rangle=\mathrm{Tr}\rho_0 Q\,. \qquad (4.3)$$

The equations of motion form, as noticed before, a linear homogeneous system [see the matrix formulation (2.26) of the first ATDHF equation (2.20a)], and could be solved by a matrix inversion. For technical reasons, we prefer to proceed in a rather different way, i.e., take advantage of the "constrained form" (2.42) of the first Hamilton equation:

$$[W_0^D+W_1-\dot{q}P,\,\rho_0+\rho_1]=0\,, \qquad (4.4)$$

with P defined by

$$P=i\hbar\left[\frac{\partial\rho_0}{\partial q},\rho_0\right]\,. \qquad (4.5)$$

As a consequence of Eq. (4.2), the operators W_0 and λQ have identical particle-hole (and hole-particle) matrix elements:

$$\sigma_0 W_0\rho_0=\sigma_0(\lambda Q)\rho_0\,, \qquad (4.6)$$

$$\rho_0 W_0\sigma_0=\rho_0(\lambda Q)\sigma_0\,. \qquad (4.7)$$

Denoting by Q^A the antidiagonal (off-diagonal) part of Q,

$$Q^A=\sigma_0 Q\rho_0+\rho_0 Q\sigma_0\,,$$

we deduce from (4.6) and (4.7) the following expression of W_0^D:

$$W_0^D(=W_0-W_0^A)=W_0-\lambda Q^A\,. \qquad (4.8)$$

Inserted into (4.4), Eq. (4.8) leads to

$$[W_0+W_1-\lambda Q^A-\dot{q}P,\ \rho_0+\rho_1]=0\,, \qquad (4.9)$$

which is the doubly constrained Hartree-Fock equation:

$$\delta\langle\Psi|H-\lambda Q^A-\dot{q}P|\Psi\rangle=0\,. \qquad (4.10)$$

The determinant Ψ built from the occupied states of the density operator $\rho=\rho_0+\rho_1$ is not time-reversal invariant, due to the presence in the external field of the time-odd part $(-\dot{q}P)$. In the limiting case of small velocities $\dot{q}$, the time-odd part ρ_1 of ρ is, as it should be [see Eq. (3.26)], proportional to $\dot{q}$ [linear response in Eq. (4.10)]. Since the adiabatic mass parameter $M(q)$ has no dependence on $\dot{q}$, its knowledge require only the computation of $\rho_1/\dot{q}$, or equivalently of $\chi/\dot{q}$, as seen in Eq. (3.7). The determination of $\rho_1/\dot{q}$ as given by Eq. (3.26) can thus be performed by solving Eq. (4.10) with an arbitrary value of $\dot{q}$, small enough to fulfill the linear response condition.

Equation (4.10) is composed, of course, of two distinct equations. The time-odd part

$$i\hbar\dot{q}\frac{\partial\rho_0}{\partial q}=[W_0^D,\rho_1]+[W_1,\rho_0]=\dot{q}[P,\rho_0] \qquad (4.11)$$

is the equation which we actually want to solve. The time-even part is

$$[W_0-\lambda Q^A,\rho_0]+[W_1-\dot{q}P,\rho_1]=0\,, \qquad (4.12)$$

and is therefore automatically satisfied up to first order in the doubly constrained Hartree-Fock process. This equation does not coincide exactly with Eq. (4.2), and it induces thus a slight change in the path $\rho_0(q)$. However, by choosing a sufficiently small $\dot{q}$ value, the second term of Eq. (4.12) responsible for this modification of the path is negligible. A quantitative discussion concerning the range of the choice of $\dot{q}$ in numerical applications will be given in II.

We have already noticed that the smallness of $\dot{q}$ is a necessary condition to ensure a linear response. Since this implies also the smallness of ρ_1, it is related to the first adiabaticity condition (smallness of χ). On the other hand, the second adiabaticity assumption ($\hbar\dot{\chi}$ small) constrains the Lagrange multiplier λ to be small; indeed, the smallness of $\hbar\dot{\chi}$ corresponds to the smallness of the commutator $[W_0,\rho_0]$, as mentioned in Sec. II. Using the definition (4.2) of the path ρ_0

$$[W_0,\rho_0]=\lambda[Q,\rho_0]\,,$$

one sees how the smallness of λ is imposed by the second adiabaticity assumption. Thus in our double CHF approach for which the external field is $(-\lambda Q^A-\dot{q}P)$, *both* λ and $\dot{q}$ should be small. These conditions are connected to the adiabaticity assumptions, but *they clearly do not imply any small amplitude hypothesis*. A simple example of cases where λ is small but where a large amplitude motion occurs is given by nuclei having a soft behavior with respect to deformations. Their potential energy curve is very flat in a large region around the HF minimum, corresponding to a small value of the slope $\lambda(q)$ (see, e.g., Fig. 7 of II). The authors of Ref. 26 identify the limiting case $\lambda \to 0$ with small amplitude motion, which is in contradiction with the previous statement; it is likely that they have in mind a definition of small vibrations different from the usual RPA hypothesis ($\|\rho - \rho_{st}\| \ll 1$).

The method of computation of mass parameters described in the present section has been first proposed in Ref. 22, where the first numerical applications were also presented. Up to now, it has been applied to the calculation of mass parameters for quadrupole vibrations[7,28] and for heavy ion collisions.[27]

To conclude this presentation of the CHF path, we will discuss briefly the connection of the preceding with different approaches of the same problem.

(i) The Inglis cranking formula is obtained, as seen in Sec. II, by neglecting W_1 in the first ATDHF equation of motion. Starting from a solution ρ_0 of the time-even CHF problem, one gets simply the Inglis cranking value of ρ_1 from the solution $(\rho_0+\rho_1)^1$ of the first iteration of the CHF equation (4.10) (i.e., the solution of the Schrödinger equation for the one-body Hamiltonian $W_0 - \lambda Q^A - \dot{q}P$). The Inglis adiabatic mass is thus obtained very easily as a byproduct of the full solution of the ATDHF problem.

(ii) In the particular case of rotational collective motion (rotations of the nucleus as a whole), Thouless and Valatin[3] have already shown that the solution of the TDHF equation could be cast into the form of a CHF problem, with the time-odd constraining field $(-\omega\hat{n}\cdot\vec{\mathrm{J}})$ (ω being the angular velocity, $\hat{n}$ the unit vector defining the rotation axis, and $\vec{\mathrm{J}}$ the angular momentum operator). This result can be easily deduced from our more general formalism, since in this case the family $\rho_0(\theta)$ (where θ is the collective coordinate specifying the angular position) is simply given by

$$\rho_0(\theta) = \exp(-i\theta\hat{n}\cdot\vec{\mathrm{J}}/\hbar)\rho_{st}\exp(i\theta\hat{n}\cdot\vec{\mathrm{J}}/\hbar)\,, \qquad (4.13)$$

where ρ_{st} correspond to a static HF solution. From the definition (4.5) of P, one gets readily

$$P = (\hat{n}\cdot\vec{\mathrm{J}})^A\,. \qquad (4.14)$$

Our time-odd constraining field P is therefore the antidiagonal part of the Thouless-Valatin's time-odd field; however, it is easily seen that the moments of inertia obtained by these two methods are equal. Indeed, one could add to the "momentum operator" P in the time-odd equation (4.11) any particle-particle plus hole-hole part P^D without any change in the result, since any diagonal operator commutes with ρ_0. Thus the value of ρ_1 would not be affected by such a change of P. Moreover, the mean value of $P' = P + P^D$ would remain unchanged, since

$$\begin{aligned}\langle P'\rangle &= i\hbar\,\mathrm{Tr}\rho P' = i\hbar\,\mathrm{Tr}\rho_1(P+P^D)\\ &= i\hbar\,\mathrm{Tr}\rho_1 P = \langle P\rangle\,.\end{aligned} \qquad (4.15)$$

In the above equalities, we have used the property $\mathrm{Tr}\rho_1 P^D = 0$, which comes from the antidiagonal character of ρ_1 (see Appendix A). Of course, a similar result is available for uniform translational motion, and one gets for the mass parameter the nucleus mass, as in the Thouless-Valatin method.

(iii) The present approach bears some similarities with a formalism presented by Villars in Ref. 8. In this paper, the author considers also a doubly constrained Hartree-Fock equation of the type of our Eq. (4.10), where the operators P and Q satisfy the canonical relation (3.15). However, once the choice of Q is made, we do have a prescription to determine P, while in Ref. 8 an ambiguity in the choice of P is explicitly acknowledged. This ambiguity stems from the fact that P is only subject to the weak canonical relation (3.15). It may be noted that in our case it is the adiabatic approximation (via the first Hamiltonian equation) which leads to the unequivocal determination of P.

Rowe and Bassermann[9] have also proposed a double CHF approach to nuclear dynamics, giving explicit expressions for the P and Q operators in terms of a set of local normal coordinates and momenta. Such a general formalism does not assume any adiabaticity.

In fact, these approaches,[8,9] and several other attempts[4,10,28] to derive the collective path (problem which we do not touch in the present contribution) do correspond in practice to a tremendous numerical effort which, to the best of our knowledge, has not yet been mastered in nontrivial cases.

V. SCALING PATH

The choice of a dynamical path defined by a scaling of equilibrium wave functions has been recently considered by several authors either in the framework of the ATDHF formalism[28,29] or within a slightly different context.[30-34] Our aim here is to study is some detail the scaling hypothesis as a possible prescription for the ATDHF path $\rho_0(q)$.

The scaling approximation consists in constructing from a static equilibrium HF solution defined by its density matrix ρ_{st} a family of density operators $\rho_0(\beta)$ by

$$\rho_0(\beta) = e^{i\beta\hat{\theta}} \rho_{st} e^{-i\beta\hat{\theta}}, \tag{5.1}$$

where $\hat{\theta}$ is a local time-odd Hermitian spin-independent one-body operator whose $\vec{r}$ representation is such that

$$\forall f(\vec{r}), \quad 2i\hat{\theta} f(\vec{r}) = 2\vec{\nabla}\theta(\vec{r}) \cdot \vec{\nabla} f(\vec{r}) + f(\vec{r})\vec{\nabla}^2\theta(\vec{r}). \tag{5.2}$$

In Eqs. (5.1) and (5.2), β is a small number (compared to one) and $\theta(\vec{r})$ is a given real function of the space coordinate chosen to reproduce the studied collective motion. One may consider, for instance,

$$\theta = r^2 \quad \text{(isoscalar monopole vibrations)}, \tag{5.3}$$

$$\theta = 2z^2 - x^2 - y^2 \quad \text{(isoscalar quadrupole vibrations)}, \tag{5.4}$$

$$\theta = \hat{n} \cdot \vec{r} \quad \text{(translations defined by the unit vecor } \hat{n}\text{)}. \tag{5.5}$$

The well known example of translations, studied extensively in Ref. 5, suggests to try as a solution of the first ATDHF equation (2.24) for the most general mode.

$$\chi = -(m/\hbar)\dot{\beta}\theta(\vec{r}). \tag{5.6}$$

In fact, it is shown in Appendix B that the operators ρ_0 and χ defined in Eqs. (5.1) and (5.6) do satisfy Eq. (2.24) provided the two-body interaction V is gauge invariant with respect to $\theta(\vec{r})$:

$$[V, \theta(\vec{r})] = 0. \tag{5.7}$$

This gauge invariance property is trivially fulfilled for velocity-independent interactions. For velocity-dependent forces of the Skyrme type, it can be shown (see Appendix A of II) that the gauge invariance is ensured, even for the spin-orbit part, but *only for isoscalar modes*.

From now on we will restrict ourselves to isoscalar modes and assume the gauge invariance property. In this case, we may write a continuity equation

$$\dot{\rho}_0(\vec{r}) + (\hbar/m)\vec{\nabla} \cdot \vec{j}(\vec{r}) = 0, \tag{5.8}$$

where the current vector $\vec{j}$ is given by

$$\vec{j}(\vec{r}) = \rho_0(\vec{r})\vec{\nabla}\chi(\vec{r}). \tag{5.9}$$

In order to get it, one can, for instance, represent the first Hamilton equation (2.24) in configuration space and take its limit when $\vec{r}' \to \vec{r}$.[35] Consider now the classical adiabatic kinetic energy

$$\mathcal{K} = \tfrac{1}{2}\hbar \operatorname{Tr} \chi \dot{\rho}_0 . \tag{5.10}$$

Using the continuity equation, we get for $\mathcal{K}$

$$\mathcal{K} = -\frac{\hbar^2}{2m} \int \chi(\vec{r})\vec{\nabla} \cdot \vec{j}(\vec{r}) d^3r \tag{5.11}$$

$$= \frac{\hbar^2}{2m} \int \rho_0(\vec{r})[\vec{\nabla}\chi(\vec{r})]^2 d^3r, \tag{5.12}$$

after integration by parts. From the definition (5.6) for χ one obtains finally

$$\mathcal{K} = \tfrac{1}{2} M_{sc}(\beta)\dot{\beta}^2, \tag{5.13}$$

where the scaling mass parameter $M_{sc}(\beta)$ is given by

$$M_{sc}(\beta) = m \int \rho_0(\vec{r})[\vec{\nabla}\theta(\vec{r})]^2 d^3r. \tag{5.14}$$

To illustrate the preceding we will now concentrate on a specific isoscalar collective mode, namely the quadrupole motion. In this case since

$$(\vec{\nabla}\theta)^2 = 4(x^2 + y^2 + 4z^2), \tag{5.15}$$

one gets for the mass parameter $M_{sc}(\beta)$

$$M_{sc}(\beta) = 4m(2\langle r^2 \rangle + \langle Q_{20} \rangle), \tag{5.16}$$

where r^2 and Q_{20} are the operators:

$$r^2 = x^2 + y^2 + z^2, \tag{5.17}$$

$$Q_{20} = 2z^2 - x^2 - y^2. \tag{5.18}$$

Since we would like to compare the scaling path with the CHF one, we must choose the same collective variable $q = \langle Q_{20} \rangle$ in the two cases. For this purpose we expand each orbital $\psi_i^0(\beta; x, y, z)$ of ρ_0 around the corresponding orbital ψ_i^{st} of ρ_{st} to first order in β, which leads to

$$\psi_i^0(\beta; x, y, z) \simeq (1 + i\beta\hat{\theta})\psi_i^{st}(x, y, z). \tag{5.19}$$

For $\theta(\vec{r})$ given by Eq. (5.4),

$$\vec{\nabla}^2\theta(\vec{r}) = 0, \tag{5.20}$$

and thus one gets from Eq. (5.19)

$$\begin{aligned} \psi_i^0(\beta; x, y, z) &= \psi_i^{st}(x, y, z) + \beta\vec{\nabla}\theta \cdot \vec{\nabla}\psi_i^{st}(x, y, z) \\ &= \psi_i^{st}\left\{x(1 - 2\beta), y(1 - 2\beta), z\frac{1}{(1 - 2\beta)^2}\right\}. \end{aligned} \tag{5.21}$$

It is clear from the preceeding that the operator $\beta\hat{\theta}$ acts as a scaling operator *only for small values of* β, that is, for small amplitude motions. The quadrupole moment $q(\beta)$ of $\psi_i^0(\beta; x, y, z)$ can be easily expressed as

$$\begin{aligned} \langle Q_{20} \rangle = q(\beta) &= \frac{(1 - 2\beta)^2}{3}(q_{st} - 2Ar_{st}^2) \\ &\quad + \frac{2}{3(1 - 2\beta)^4}(Ar_{st}^2 + q_{st}), \end{aligned} \tag{5.22}$$

where q_{st} and Ar_{st}^2 are the expectation values of Q_{20} and r^2 for the equilibrium state ρ_{st}, a being the number of particles. Similarly, one gets for the radius $r(\beta)$ the expression

$$\langle r^2\rangle = Ar^2(\beta) = -\frac{(1-2\beta)^2}{3}(q_{st} - 2Ar_{st}^2) + \frac{1}{3(1-2\beta)^4}(Ar_{st}^2 + q_{st}) . \quad (5.23)$$

Therefore, the mass $M_{sc}(\beta)$ is given by

$$M_{sc}(\beta) = 4m\left[-\frac{(1-2\beta)^2}{3}(q_{st} - 2Ar_{st}^2) + \frac{4}{3(1-2\beta)^4}(Ar_{st}^2 + q_{st})\right] \quad (5.24)$$

$$= m(1-2\beta)\frac{dq}{d\beta} , \quad (5.25)$$

which for small values of β leads to

$$dq/d\beta \simeq M_{sc}(\beta)/m . \quad (5.26)$$

Now the mass $M_{sc}(q)$ can be deduced from the mass $M_{sc}(\beta)$ as

$$M_{sc}(q) = M_{sc}(\beta)\left(\frac{d\beta}{dq}\right)^2 , \quad (5.27)$$

that is, in the small β limit,

$$M_{sc}(q) = \frac{m^2}{M_{sc}(\beta)} = \frac{m}{4(2\langle r^2\rangle + \langle Q_{20}\rangle)} . \quad (5.28)$$

One may note incidentally that the operator P defined in Eq. (3.8) writes

$$P - i\hbar\left[\frac{\partial\rho_0}{\partial q}, \rho_0\right] \simeq -\hbar\frac{dq}{d\beta}\hat{\theta}^A . \quad (5.29)$$

We have heuristically used the result obtained for translations to find a solution to the first ATDHF equation in the most general scaling case. However, the latter is significantly different from the translational case. Indeed, the second ATDHF equation is exactly fulfilled for uniform translational motion as a consequence of the Galilean invariance.[6] Such a fulfillment is not achieved *a priori* for an arbitrary scaling transformation.

The operator χ considered in this section is *not* the natural one since it has obviously nonvanishing p-p and h-h matrix elements. (In this respect it has been shown that the natural χ cannot be local.[14]) We recall that the expressions (2.20a) for the first Hamilton equation and (3.7) for the mass parameter are valid for any (natural or non-natural) decomposition (2.7). Therefore, it was legitimate to calculate the scaling mass parameter from a local χ solution of Eq. (2.20a). Whereas the p-h representation is most convenient to derive the general ATDHF formalism, the $\vec{r}$ representation is undoubtedly more appropriate when χ is local. In this case, most of the mechanical properties will pertain more to classical fluid dynamics than to point particle Hamiltonian mechanics.

We have presented the cases of scaling variables and of CHF variables in separate sections. It should be noticed, however, that the scaling path for a multipole operator Q can also be given by a CHF equation[28]:

$$\delta\langle H - \lambda[H,[H,Q]']' = 0 . \quad (5.30)$$

In Eq. (5.30), the prime indicates one-body reductions of operators. According to the prescription given in Sec. IV, the definition of the collective coordinate q corresponding to the path provided by (5.30) would be

$$q = \langle [H,[H,Q]']'\rangle , \quad (5.31)$$

which is proportional to the variable β considered in the present section (see, e.g., Ref. 33). The definition (5.30) for the collective path has of course a purely formal interest, since mass and stiffness parameters can be numerically calculated in a much simpler way.

VI. SUM RULES

During the last few years, the language of sum rules has been extensively used (see, e.g., Ref. 31) for the description of collective states. In this section, we briefly recall some results which can be of some help to better understand our study, and discuss the physical content of the two kinds of paths presented before.

The energy-weighted moments of any one-body operator Q are defined by

$$m_k(Q) = \sum_{n>0} |\langle n|Q|0\rangle|^2(\epsilon_n - \epsilon_0)^k , \quad (6.1)$$

where k is integer, and n (or 0) labels excited (or ground) states.

These moments are often evaluated within the RPA approximation for the excitation energies $(\epsilon_n - \epsilon_0)$ and for the transition matrix elements $\langle n|Q|0\rangle$ defined as

$$\langle n|Q|0\rangle = \sum_{ph}\{(\underline{X_n})^*_{ph}Q_{ph} + (\underline{Y_n})^*_{ph}Q_{hp}\} , \quad (6.2)$$

where the Q_{ph}'s are the particle-hole matrix elements of Q in the static Hartree-Fock basis, and the vectors $\underline{X_n}$ and $\underline{Y_n}$ [whose components are $(\underline{X_n})_{ph}$ and $(\underline{Y_n})_{ph}$] satisfy the RPA eigenvalue equation

$$\begin{pmatrix} A & B \\ -B^* & -A^* \end{pmatrix}\begin{pmatrix} \underline{X_n} \\ \underline{Y_n} \end{pmatrix} = (\epsilon_n - \epsilon_0)\begin{pmatrix} \underline{X_n} \\ \underline{Y_n} \end{pmatrix} . \quad (6.3)$$

In Eq. (6.3), A and B are the standard RPA matrices defined by (2.28) and (2.29) in the static

Hartree-Fock basis.

When the Hartree-Fock solution is a true local minimum of the total energy, the stability RPA condition[37] ensures that the excitation energies $(\epsilon_n - \epsilon_0)$ are real; this leads to positive moments m_k.[38]

By straightforward use of Schwarz inequality, one can deduce various inequalities for the moments,[30,31] in particular,

$$E_k \leqslant E_{k+1}\,, \tag{6.4}$$

$$E_1 \leqslant \bar{E} = \frac{m_1}{m_0} \leqslant E_2\,, \tag{6.5}$$

where the energies E_k are defined by

$$E_k = \left(\frac{m_k}{m_{k-2}}\right)^{1/2}. \tag{6.6}$$

Moments evaluated according to RPA prescriptions can be expressed, at least for odd k, in the following form[26]:

$$m_{2n+1}(Q) = \tfrac{1}{2}(\underline{\tilde{Q}}^*\underline{\tilde{Q}}) \begin{bmatrix} A & B \\ -B^* & -A^* \end{bmatrix}^{2n+1} \begin{bmatrix} \underline{Q} \\ -\underline{Q}^* \end{bmatrix}, \tag{6.7}$$

where the components of the vector $\underline{Q}$ are the particle-hole matrix elements of the operator Q in the static Hartree-Fock basis. Formula (6.7) holds for positive or negative n.

If one does no longer consider a static Hartree-Fock solution ρ_{st}, but instead some point of an "adiabatic path" $\rho_0(q)$, one can still define "generalized local RPA moments" by Eq. (6.7). But now, while the matrices A and B keep the same formal expressions (2.28) and (2.29) as previously, they are expressed in the ATDHF particle-hole basis composed of common eigenvectors of ρ_0 and $(W_0)^D$ [as in Eq. (2.27)]. Since these generalized matrices A and B are not related to the static HF equilibrium, they do not *a priori* satisfy the stability condition. Therefore, the positiveness of m_k and the inequalities (6.4) and (6.5) are no longer guaranteed in this case. However, sum rules can still be obtained by standard procedures; in particular, the adiabatic mass parameters $M_{\rm CHF}(q)$ and $M_{\rm sc}(q)$ calculated respectively for a "constrained Hartree-Fock" coordinate and for a scaling coordinate can be expressed in terms of generalized moments along the whole path $q(t)$. In both cases, the adiabatic mass is the nuclear polarizability with respect to the momentum operator P generating the motion $[M = 2m_{-1}(P)]$. Let us now express M in terms of generalized moments of the operator Q defining the path.

(a) Scaling path. To get a sum rule for the scaling mass parameter, we introduce the expression (5.6) of χ into Eq. (2.35) for the kinetic energy. This leads to

$$\mathcal{K} = \tfrac{1}{2}\dot{\beta}^2\left(\frac{m}{\hbar}\right)^2 \langle \phi_0 | [\theta,[H,\theta]] | \phi_0 \rangle\,. \tag{6.8}$$

As is well known, the expectation value of the double commutator $[\theta,[H,\theta]]$ in the static Hartree-Fock state ϕ_{st} is related to the first RPA moment, provided θ is a one-body operator:

$$m_1(\theta) = \tfrac{1}{2}\langle \phi_{st} | [\theta,[H,\theta]] | \phi_{st} \rangle\,. \tag{6.9}$$

This linear energy-weighted sum rule studied by Thouless[30] has been recently extended to density-dependent interactions.[31] Similarly, it can be shown that the generalized first moment satisfies the relation

$$m_1(\theta,\beta) = \tfrac{1}{2}\langle \phi_0(\beta) | [\theta,[H,\theta]] | \phi_0(\beta) \rangle \tag{6.10}$$

along the whole path $\rho_0(\beta)$. For multipole modes, θ is the corresponding multipole operator Q [see Eqs. (5.3), (5.4), and (5.5)], and the scaling mass parameter writes

$$M_{\rm sc}(\beta) = 2\left(\frac{m}{\hbar}\right)^2 m_1(Q,\beta)\,, \tag{6.11}$$

or, in terms of the coordinate $q = \langle Q \rangle$,

$$M_{\rm sc}(q) = \frac{\hbar^2}{2}\,\frac{1}{m_1(Q,q)}\,. \tag{6.12}$$

To evaluate the excitation energy in the small amplitude limit, one needs the stiffness parameter at the static Hartree-Fock equilibrium point q_{st}:

$$K_{\rm sc} = \left.\frac{\partial^2 \mathcal{V}_{\rm sc}}{\partial q^2}\right]_{q_{st}} = \left.\frac{\partial^2 E[\rho_0(q)]}{\partial q^2}\right]_{q_{st}}. \tag{6.13}$$

From the expansion of the potential energy

$$E[\rho_0] = \langle \phi_0 | H | \phi_0 \rangle = \langle \phi_{st} | e^{-i\beta\hat{\theta}} H e^{i\beta\hat{\theta}} | \phi_{st} \rangle \tag{6.14}$$

to leading order in β, one gets

$$\begin{aligned} \left.\frac{\partial^2 \mathcal{V}_{\rm sc}}{\partial \beta^2}\right]_{st} &= \langle \phi_{st} | [\hat{\theta},[H,\hat{\theta}]] | \phi_{st} \rangle \\ &= 2m_1(\hat{\theta}) = 2m_3(Q)\,. \end{aligned} \tag{6.15}$$

The demonstration of the last equality in Eq. (6.15) can be found in Ref. 30. This leads for the stiffness parameter $K_{\rm sc}$ to the value

$$K_{\rm sc} = \frac{m_3(Q)}{[m_1(Q)]^2}\,, \tag{6.16}$$

and for the ATDHF excitation energy corresponding to a scaling path $\rho_{\rm sc}(q)$ in the small amplitude limit:

$$E_{\rm sc} = \hbar\left(\frac{K_{\rm sc}}{M_{\rm sc}(q_{st})}\right)^{1/2} = \left(\frac{m_3(Q)}{m_1(Q)}\right)^{1/2} = E_3\,. \tag{6.17}$$

The latter expression for the excitation energy has already been considered by several authors. In

Ref. 30, it is used as a prescription for an estimation of the isoscalar resonance energy, the operator Q being the corresponding multipole operator. As mentioned in these references, the evaluation of E_{SC} through formula (6.17) involves only a static Hartree-Fock calculation at the equilibrium point. The authors of Ref. 33 get the same expression of the excitation energy by a method offering some similarity with the ATDHF approach. They also use a scaling hypothesis for the wave function, and they construct a collective Hamiltonian in the small amplitude limit of TDHF approximation.

(b) Constrained Hartree-Fock path. The mass parameter obtained by solving the first ATDHF equation for a path $\rho_0(q)$ solution of Eq. (4.2) can also be expressed in terms of the previously defined generalized moments as[26,40]

$$M_{CHF}(q)=\tfrac{1}{2}\hbar^2\frac{m_{-3}(Q,q)}{[m_{-1}(Q,q)]^2}\,. \tag{6.18}$$

Although it would be meaningless to make the small amplitude approximation if the ATDHF motion is found to be anharmonic, let us give the expression of the excitation energy in this very restrictive hypothesis. As is well known, the stiffness of the deformation energy curve at the static HF minimum is related to the polarizability sum rule:

$$\begin{aligned}K_{CHF}&=\frac{\partial^2\mathcal{V}_{CHF}}{\partial q^2}\bigg]_{q_{st}}=\frac{\partial^2E[\rho_0(q)]}{\partial q^2}\bigg]_{q_{st}}\\&=\frac{\partial^2E_0}{\partial\lambda^2}\bigg]_{\lambda_{st}}^{-1}=\frac{1}{2m_{-1}(Q)}\,.\end{aligned} \tag{6.19}$$

Therefore, *in the small amplitude limit*, the excitation energy writes

$$E_{CHF}=\hbar\left(\frac{K_{CHF}}{M_{CHF}(q_{st})}\right)^{1/2}=\left(\frac{m_{-1}(Q)}{m_{-3}(Q)}\right)^{1/2}=E_{-1}\,. \tag{6.20}$$

It should be emphasized that the latter expression *for the excitation energy is given only for indication*, and does not represent, in general, the true ATDHF result for a constrained path. Indeed, it can happen that such a path corresponds to a large amplitude motion, as illustrated in II. In this case, the calculation of the ATDHF excitation energy would require a quantization of the collective Hamiltonian:

$$\mathcal{H}=\frac{p^2}{2M_{CHF}(q)}+\mathcal{V}_{CHF}(q)\,, \tag{6.21}$$

which may be very different from an harmonic oscillator Hamiltonian.

The expressions (6.12) and (6.18) of $M_{SC}(q)$ and $M_{CHF}(q)$ already allow us to draw some conclusions. Let us consider for the discussion the example of isoscalar quadrupole modes, and make for the operator Q the choice $Q=Q_{20}$. As a first important remark, we note that the presence of negative moments in the CHF path gives more weight to low energy particle-hole excitations, whereas the linear sum rule of Eq. (6.12) for $M_{SC}(q)$ favors $2\text{-}\hbar\omega$ excitations. As a consequence, we expect significant differences between the two paths for non-spin-saturated nuclei.

To develop the preceding comment, let us restrict the comparison to the static Hartree-Fock equilibrium point, where the two mass parameters can be expressed in terms of the usual RPA moments

$$\begin{aligned}M_{CHF}(q_{st})&=\tfrac{1}{2}\hbar^2\frac{m_{-3}(Q)}{[m_{-1}(Q)]^2}\,,\\M_{SC}(q_{st})&=\tfrac{1}{2}\hbar^2\frac{1}{m_1(Q)}\,.\end{aligned} \tag{6.22}$$

By use of Eqs. (6.4), (6.6), and (6.22), one gets the following property for the ratio of the two mass parameters:

$$\frac{M_{CHF}(q_{st})}{M_{SC}(q_{st})}=\frac{E_1}{E_{-1}}\geq 1\,. \tag{6.23}$$

Moreover, one knows that the inequalities (6.4) are reduced to equalities only in the case where the whole strength of the excitation operator Q is concentrated in one collective state. Equation (6.23) thus means that the two paths considered here lead to the same mass parameter at the equilibrium Hartree-Fock point if and only if the RPA sum rules are exhausted by a single excited state; otherwise, the CHF mass is always greater than the scaling mass.

The fact that the CHF path takes into account low energy excitations, whereas the scaling path is completely dominated by the giant resonance, is confirmed by the values E_{-1}(CHF) and E_3 (scaling) of the excitation energies in the small amplitude limit.

All the preceding arguments will be illustrated and supported in II, but henceforth it is possible to conclude that these two paths are adapted to different physical situations. The scaling path, as is well known, is convenient for the description of giant resonances, whereas the CHF path with the constraint $(-\lambda Q_{20})$ seems appropriate to the study of *low lying collective states*. The discussion of the matter presented here will be completed by the calculations reported in II to which we reserve general conclusions.

ACKNOWLEDGMENTS

At an early stage of this work, we benefited from the collaboration of D. M. Brink, D. Vautherin, and M. Vénéroni, which was an inspiration for the present study. Illuminating discussions with O. Bohigas, J. Martorell, and S. Stringari are gratefully acknowledged. M. Vénéroni was at the origin of our interest in the field; his continuous stimulation through numerous constructive discussions has been a decisive help in carrying out this work. This work was performed at the *Division de Physique Théorique* (*Institut de Physique Nucléaire*), which is *Laboratoire associé au C. N. R. S.*

APPENDIX A: PARTICLE-HOLE ALGEBRA

In this Appendix, we derive some useful properties resulting from the idempotency of ρ_0 (or of the TDHF density operator ρ):

$$\rho_0^2 = \rho_0 . \tag{A1}$$

We introduce the projector $\sigma_0 = 1 - \rho_0$ orthogonal to ρ_0

$$\sigma_0 \rho_0 = 0 , \tag{A2}$$

and recall that the hole and particle states are defined, with respect to ρ_0, as

$$\rho_0 |h\rangle = |h\rangle \quad (\text{thus } \sigma_0 |h\rangle = 0) , \tag{A3}$$

$$\rho_0 |p\rangle = 0 \quad (\text{thus } \sigma_0 |p\rangle = |p\rangle) . \tag{A4}$$

Let us decompose any one-body operator R as

$$R = (\rho_0 + \sigma_0) R (\rho_0 + \sigma_0) \tag{A5}$$

or

$$R = R^A + R^D , \tag{A6}$$

with

$$R^A = \sigma_0 R \rho_0 + \rho_0 R \sigma_0 , \tag{A7}$$

$$R^D = \rho_0 R \rho_0 + \sigma_0 R \sigma_0 . \tag{A8}$$

It is clear from (A3) and (A4) that the operator R^A is antidiagonal in the particle-hole basis (it has vanishing p-p and h-h matrix elements), whereas the operator R^D is diagonal (it has vanishing p-h and h-p matrix elements).

Many operators involved in the present work are antidiagonal. Let us consider, for instance, an operator R such that

$$\rho_0 R + R \rho_0 = R . \tag{A9}$$

Writing (A9) as

$$\rho_0 R(\rho_0 + \sigma_0) + (\rho_0 + \sigma_0) R \rho_0 = (\rho_0 + \sigma_0) R (\rho_0 + \sigma_0) \tag{A10}$$

leads immediately to

$$\rho_0 R \rho_0 = \sigma_0 R \sigma_0 = 0 , \tag{A11}$$

which means that

$$R = R^A . \tag{A12}$$

As examples of operators satisfying (A9), we know

(i) the natural χ [see Eq. (2.10)], which therefore fulfills Eq. (2.12), and

(ii) any first derivative of the density ρ_0. For instance,

$$\frac{\partial}{\partial \alpha} \rho_0 = \frac{\partial}{\partial \alpha} (\rho_0^2) = \rho_0 \frac{\partial \rho_0}{\partial \alpha} + \frac{\partial \rho_0}{\partial \alpha} \rho_0 . \tag{A13}$$

Consequently, the operator $\dot{\rho}_0$ has only p-h and h-p matrix elements

$$\dot{\rho}_0 = \sigma_0 \dot{\rho}_0 \rho_0 + \rho_0 \dot{\rho}_0 \sigma_0 , \tag{A14}$$

and the same property holds for $\partial \rho_0 / \partial q$.

Let us consider the commutator of any operator R with ρ_0

$$[R, \rho_0] = [R^D + R^A, \rho_0] = [R^A, \rho_0] , \tag{A15}$$

since the diagonal operator R^D commutes with ρ_0. Making (A15) explicit leads to

$$\begin{aligned} [R, \rho_0] &= [R^A, \rho_0] = [\rho_0 R \sigma_0 + \sigma_0 R \rho_0, \rho_0] \\ &= \sigma_0 R \rho_0 - \rho_0 R \sigma_0 . \end{aligned} \tag{A16}$$

From (A16), we see that the commutator of any operator with ρ_0 has only p-h and h-p matrix elements. This is the case for $\rho_1 = i[\chi, \rho_0]$, $F_0 = i\hbar[\dot{\rho}_0, \rho_0]$, $P = F_0/\dot{q}$. and $[W_0, \rho_0]$. Notice also [see Eq. (A15)] that the antidiagonal part of R is the only one contributing to the commutator. We have used this property for the operator χ, which enters into the first Hamilton equation (2.24) only through ρ_1; therefore, this equation gives access only to the antidiagonal part χ^A of χ. As another consequence of Eq. (A15), the second adiabaticity hypothesis (small acceleration) can be formulated equivalently by the smallness of $[W_0, \rho_0]$ or by the smallness of W_0^A.

In the same way followed to obtain Eq. (A16), we get

$$\begin{aligned} [[R^A, \rho_0], \rho_0] &= [\sigma_0 R \rho_0 - \rho_0 R \sigma_0, \rho_0] \\ &= \sigma_0 R \rho_0 + \rho_0 R \sigma_0 , \end{aligned} \tag{A17}$$

that is,

$$[[R^A, \rho_0], \rho_0] = R^A . \tag{A18}$$

This latter property has been used for the antidiagonal operators $\dot{\rho}$ and $\dot{\rho}_0$ to derive the "constrained forms" of the TDHF and first ATDHF equations.

We finally remark that the product of a diagonal operator with a diagonal one is antidiagonal,

$$(\rho_0 R \rho_0 + \sigma_0 R \sigma_0)(\rho_0 S \sigma_0 + \sigma_0 S \rho_0) = \rho_0 R S \sigma_0 + \sigma_0 R S \rho_0 , \tag{A19}$$

and therefore has a vanishing trace

$$\mathrm{Tr}\, R^D S^A = 0\,. \tag{A20}$$

In particular, this applies to the product of ρ_1 with a diagonal operator P^D [see Eq. (4.15)], and also for the product of χ with $\dot\rho_0$,

$$\mathrm{Tr}\,\chi\dot\rho_0 = \mathrm{Tr}\,\chi^A\dot\rho_0\,,$$

since $\dot\rho_0 = (\dot\rho_0)^A$. Therefore, the only part of χ contributing to the collective kinetic energy is its antidiagonal part.

APPENDIX B: THE FIRST HAMILTON EQUATION FOR THE SCALING PATH

Here we show explicitly that the operators

$$\rho_0(\beta) = e^{i\beta\hat\theta}\rho_{st}e^{-i\beta\hat\theta} \tag{5.1}$$

and

$$\chi = -(m/\hbar)\dot\beta\theta(\vec{r}) \tag{5.6}$$

satisfy the first Hamilton equation

$$\hbar\dot\rho_0 + i[W_0^D, \rho_1] + i[W_1, \rho_0] = 0\,, \tag{B1}$$

provided the gauge invariance

$$[V, \theta(\vec{r})] = 0 \tag{B2}$$

is fullfilled.

The operators θ and $\hat\theta$ are defined in Sec. V, and V is the two-body interaction.

First, we will use Eq. (B2) to find a new expression for W_1. To explicit the gauge invariance, we expand the two-body force as a sum of tensor products

$$V(1,2) = \sum_i V_1^i(1) \otimes V_2^i(2) \tag{B3}$$

and define

$$\chi(1) = \chi \otimes \underline{1}\,, \tag{B4}$$

$$\chi(2) = \underline{1} \otimes \chi\,. \tag{B5}$$

Equation (B2) can also be written as

$$[V(1,2), \chi(1) + \chi(2)] = 0\,, \tag{B6}$$

which leads to

$$\sum_i [V_1^i, \chi] \otimes V_2^i + \sum_i V_1^i \otimes [V_2^i, \chi] = 0\,. \tag{B7}$$

By right-multiplying this equation by $\underline{1}\otimes\rho_0$, one gets

$$\sum_i [V_1^i, \chi] \otimes V_2^i\rho_0 + \sum_i V_1^i \otimes [V_2^i, \chi]\rho_0 = 0\,. \tag{B8}$$

We now consider the definition of W_1 (Ref. 41)

$$W_1 = i\,\mathrm{Tr}_2 V(1,2)[\chi(2), \rho_0(2)]\,, \tag{B9}$$

which leads to

$$W_1 = i\,\mathrm{Tr}_2 \sum_i V_1^i \otimes V_2^i[\chi, \rho_0]\,, \tag{B10}$$

by inserting the definition (B5) of $\chi(2)$ and the expansion (B3) of $V(1,2)$. By use of the cyclic property of the trace, this equation writes

$$W_1 = i\,\mathrm{Tr}_2 \sum_i V_1^i \otimes [V_2^i, \chi]\rho_0\,. \tag{B11}$$

From Eq. (B8), we get

$$W_1 = -i\,\mathrm{Tr}_2 \sum_i [V_1^i, \chi] \otimes V_2^i\rho_0 \tag{B12}$$

$$= -i\,\mathrm{Tr}_2 \left[\sum_i V_1^i \otimes V_2^i\rho_0, \chi\otimes\underline{1}\right], \tag{B13}$$

which gives

$$W_1 = -i[W_0 - T, \chi]\,. \tag{B14}$$

Using the definition (5.6) of χ, we easily obtain

$$[T, \chi] = i\hbar\dot\beta\hat\theta\,. \tag{B15}$$

Equations (B14) and (B15) lead finally to

$$-iW_1 = [\chi, W_0] + i\hbar\dot\beta\hat\theta\,. \tag{B16}$$

This equation will be used to transform the particle-hole matrix elements of Eq. (B1):

$$\sigma_0\{i[W_0^D, \rho_1] + i[W_1, \rho_0]\}\rho_0$$

$$= \sigma_0\chi W_0^D\rho_0 - \sigma_0 W_0^D\chi\rho_0 + i\sigma_0 W_1\rho_0 \tag{B17}$$

$$= \sigma_0\chi W_0^D\rho_0 - \sigma_0 W_0^D\chi\rho_0 - \sigma_0[\chi, W_0^A + W_0^D]\rho_0 - i\hbar\dot\beta\sigma_0\hat\theta\rho_0 \tag{B18}$$

$$= -\sigma_0\chi W_0^A\rho_0 + \sigma_0 W_0^A\chi\rho_0 - i\hbar\dot\beta\sigma_0\hat\theta\rho_0\,. \tag{B19}$$

Since the operator W_0^A (or equivalently the commutator $[W_0, \rho_0]$) is at least of first order in χ, we obtain, by keeping only terms of first order in Eq. (B19),

$$\sigma_0\{i[W_0^D, \rho_1] + i[W_1, \rho_0]\}\rho_0 = -i\hbar\dot\beta\sigma_0\hat\theta\rho_0\,. \tag{B20}$$

Now since

$$\sigma_0(\hbar\dot\rho_0)\rho_0 = i\hbar\dot\beta\sigma_0\hat\theta\rho_0\,, \tag{B21}$$

[which is a trivial consequence of Eq. (5.1)], all the particle-hole matrix elements of Eq. (B1) vanish, at least as far as we neglect second order terms in χ. Since all terms of this equation have trivially vanishing particle-particle and hole-hole matrix elements, the fulfilling of the first Hamilton equation by ρ_0 and χ given by Eqs. (5.1) and (5.6) is established.

*Present address: Institut Laue-Langevin, BP 156X, 38042 Grenoble-Cedex, France.

[1] Å. Bohr, Mat. Fys. Medd. Danske Vid. Selsk. 26, No. 14 (1952); 27, No. 16 (1953); Å. Bohr and B. R. Mottelson, *Nuclear Structure* (Benjamin, New York, 1975), Vol. 2.

[2] D. R. Inglis, Phys. Rev. 96, 1059 (1954); 103, 1786 (1956).

[3] D. J. Thouless and J. G. Valatin, Nucl. Phys. 31, 211 (1962).

[4] F. M. H. Villars, Nucl. Phys. A285, 269 (1977).

[5] M. Baranger and M. Vénéroni, Ann. Phys. (N.Y.) 114, 123 (1978).

[6] D. M. Brink, M. J. Giannoni, and M. Vénéroni, Nucl. Phys. A258, 237 (1976).

[7] M. J. Giannoni and P. Quentin, Phys. Rev. C 21, 2076 (1980).

[8] F. M. H. Villars, in *Dynamical Structure of Nuclear States* edited by D. J. Rowe, L. E. H. Trainor, S. S. M. Wong, and T. W. Donelly (University of Toronto Press, Toronto, 1975), p. 3.

[9] D. J. Rowe and R. Basserman, Can. J. Phys. 54, 1941 (1976).

[10] K. Goeke and P. G. Reinhard, Ann. Phys. (N.Y.) 112, 328 (1978); P. G. Reinhard and K. Goeke, Nucl. Phys. A312, 121 (1978).

[11] For the sake of conciseness, we will assume that V is a density-independent two-body force. A generalization to Skyrme-like density-dependent forces is straightforward (see II). Besides, V is assumed to be even under time reversal.

[12] P. A. M. Dirac, Proc. Camb. Phil. Soc. 26, 376 (1930).

[13] P. Ring and P. Schuck, Nucl. Phys. A292, 20 (1977).

[14] P. Bonche and P. Quentin, Phys. Rev. C 18, 1891 (1978).

[15] M. J. Giannoni, J. Math. Phys. (to be published); and in *Time-dependent Hartree-Fock Method*, edited by P. Bonche, B. Giraud, and P. Quentin (Editions de Physique, Orsay, 1979), p. 251.

[16] Notice incidentally that this decomposition theorem (in spite of our notation) applies to more general density operators than our operator ρ (which describes a system of independent fermions). Moreover, a sharper form of this theorem has been given in Ref. 15.

[17] All assumptions on smallness of operators require some mathematical cautions which we skip here, and which are developed in Ref. 5. We simply mention that the smallness of $\hbar\dot{\chi}$ must be understood as by comparison with some typical single particle energy.

[18] M. Baranger, in *Cargese Lectures in Theoretical Physics*, edited by M. Lévy (Benjamin, New York, 1963), Sect. V.

[19] H. Goldstein, *Classical Mechanics* (Addison-Wesley, Reading, 1956); C. Lanczôs, *The Varitional Principles of Quantum Mechanics*, Fourth edition (University of Toronto Press, Toronto, 1977).

[20] M. J. Giannoni, Report No. IPNO/TH 79-65, 1979.

[21] L. D. Landau and E. M. Lifshitz, *Course of Theoretical Physics, Vol. 1: Mechanics* (Pergamon, Oxford 1960).

[22] M. J. Giannoni, F. Moreau, P. Quentin, D. Vautherin, M. Vénéroni, and D. M. Brink, Phys. Lett. B65, 305 (1976).

[23] The reasons for introducing this CHF equation will be clarified in the following sections. It should be stressed that, in general, its *time-even* part is not equivalent to the adiabatic limit of the time-even part of the TDHF equation.

[24] The authors defining $\hat{P}$ as in Eq. (3.16) have also a definite prescription for the time-dependent state which leads to a unique value for $\langle \hat{P} \rangle$. In our case, the arbitrariness in the particle-particle and hole-hole matrix elements of χ leads to an ambiguity in $\langle \hat{P} \rangle$. It should be emphasized however that our prescription for the momentum operator (which has been imposed by the first ATDHF equation of motion) leads to a unequivocal definition of the adiabatic mass parameter.

[25] M. Gaudin, Nucl. Phys. 15, 89 (1960); J. des Cloiseaux, in *Many-Body Physics*, edited by C. de Witt and R. Balian (Gordon and Breach, New York, 1968), p. 1.

[26] K. Goeke, A. M. Lane, and J. Martorell, Nucl. Phys. A296, 109 (1978).

[27] H. Flocard, P. H. Heenen, and D. Vautherin, Nucl. Phys. (to be published); and in *Time-dependent Hartree-Fock Method*, edited by P. Bonche, B. Giraud, and P. Quentin (Editions de Physique, Orsay, 1979), p. 50.

[28] G. Holzwarth and T. Yukawa, Nucl. Phys. A219, 125 (1974); F. M. H. Villars, in *Nuclear Self-Consistent Fields*, edited by G. Ripka and M. Porneuf (North-Holland, Amsterdam, 1975), p. 3; T. Marumori, in *Selected Topics in Nuclear Structure* (JINR, Dubna, 1976), Vol. II, p. 412; B. G. Giraud and J. Letourneux, Report No. D Ph-T 78/52, 1978; B. G. Giraud and D. J. Rowe, J. Phys. Lett. 8, 177 (1979); Nucl. Phys. A330, 352 (1979).

[29] Y. M. Engel, D. M. Brink, K. Goeke, S. J. Krieger, and D. Vautherin, Nucl. Phys. A249, 215 (1975); D. Vautherin, Phys. Lett. 57B, 425 (1975).

[30] J. Martorell, O. Bohigas, S. Fallieros, and A. M. Lane, Phys. Lett. 60B, 313 (1976).

[31] O. Bohigas, A. M. Lane, and J. Martorell, Phys. Rep. 51, 269 (1979).

[32] D. M. Brink and R. Leonardi, Nucl. Phys. A258, 285 (1976).

[33] S. Stringari, E. Lipparini, G. Orlandini, M. Traini, and R. Leonardi, Nucl. Phys. A309, 177 (1978); A309, 189 (1978).

[34] G. Holzwarth and G. Eckart, Z. Phys. A284, 291 (1978); and Nucl. Phys. A325, 1 (1979).

[35] This equation has been demonstrated in Ref. 36 under more general assumptions. Indeed, provided there exists a decomposition of ρ into ρ_0 and a *local* operator χ (both Hermitian and time even), and assuming a weak gauge invariance property ($[\chi,[\chi,V]]=0$) but without assuming adiabaticity, one gets Eq. (5.8).

[36] M. J. Giannoni, D. Vautherin, M. Vénéroni, and D. M. Brink, Phys. Lett. 63B, 8 (1976).

[37] D. J. Thouless, Nucl. Phys. 21, 225 (1960).

[38] Solutions of (6.3) occur by pairs $\pm(\epsilon_n-\epsilon_0)$. The sum in Eq. (6.1) is restricted to positive values of $(\epsilon_n-\epsilon_0)$.

[39] D. J. Thouless, Nucl. Phys. 22, 78 (1961).

[40] D. Vautherin, Phys. Lett. 69B, 393 (1977).

[41] For the sake of simplicity, we neglect the antisymmetrization of V, but exchange terms can be treated in the same way.

$$\mathrm{Tr}\, R^D S^A = 0\,. \tag{A20}$$

In particular, this applies to the product of ρ_1 with diagonal operator P^D [see Eq. (4.15)], and also for the product of χ with $\dot{\rho}_0$,

$$\mathrm{Tr}\, \chi\dot{\rho}_0 = \mathrm{Tr}\, \chi^A \dot{\rho}_0\,,$$

since $\dot{\rho}_0 = (\dot{\rho}_0)^A$. Therefore, the only part of χ contributing to the collective kinetic energy is its antidiagonal part.

APPENDIX B THE FIRST HAMILTON EQUATION FOR THE SCALING PATH

Here we show explicitly that the operators

$$\rho_0(\beta) = e^{i\beta\hat{\theta}} \rho_{st} e^{-i\beta\hat{\theta}} \tag{5.1}$$

and

$$\chi = -(m/\hbar)\dot{\beta}\theta(\vec{r}) \tag{5.6}$$

satisfy the first Hamilton equation

$$\hbar\dot{\rho}_0 + i[W_0^D, \rho_1] + i[W_1, \rho_0] = 0\,, \tag{B1}$$

provided the gauge invariance

$$[V, \theta(\vec{r})] = 0 \tag{B2}$$

is fullfilled.

The operators θ and $\hat{\theta}$ are defined in Sec. V, and V is the two-body interaction.

First, we will use Eq. (B2) to find a new expression for W_1. To explicit the gauge invariance, we expand the two-body force as a sum of tensor products

$$V(1,2) = \sum_i V_1^i(1) \otimes V_2^i(2) \tag{B3}$$

and define

$$\chi(1) = \chi \otimes \underline{1}\,, \tag{B4}$$

$$\chi(2) = \underline{1} \otimes \chi\,. \tag{B5}$$

Equation (B2) can also be written as

$$[V(1,2), \chi(1) + \chi(2)] = 0\,, \tag{B6}$$

which leads to

$$\sum_i [V_1^i, \chi] \otimes V_2^i + \sum_i V_1^i \otimes [V_2^i, \chi] = 0\,. \tag{B7}$$

By right-multiplying this equation by $\underline{1} \otimes \rho_0$, one gets

$$\sum_i [V_1^i, \chi] \otimes V_2^i \rho_0 + \sum_i V_1^i \otimes [V_2^i, \chi] \rho_0 = 0\,. \tag{B8}$$

We now consider the definition of W_1 (Ref. 41)

$$W_1 = i\,\mathrm{Tr}_2 V(1,2) [\chi(2), \rho_0(2)]\,, \tag{B9}$$

which leads to

$$W_1 = i\,\mathrm{Tr}_2 \sum_i V_1^i \otimes V_2^i [\chi, \rho_0]\,, \tag{B10}$$

by inserting the definition (B5) of $\chi(2)$ and the expansion (B3) of $V(1,2)$. By use of the cyclic property of the trace, this equation writes

$$W_1 = i\,\mathrm{Tr}_2 \sum_i V_1^i \otimes [V_2^i, \chi] \rho_0\,. \tag{B11}$$

From Eq. (B8), we get

$$W_1 = -i\,\mathrm{Tr}_2 \sum_i [V_1^i, \chi] \otimes V_2^i \rho_0 \tag{B12}$$

$$= -i\,\mathrm{Tr}_2 \left[\sum_i V_1^i \otimes V_2^i \rho_0, \chi \otimes \underline{1} \right], \tag{B13}$$

which gives

$$W_1 = -i[W_0 - T, \chi]\,. \tag{B14}$$

Using the definition (5.6) of χ, we easily obtain

$$[T, \chi] = i\hbar\dot{\beta}\hat{\theta}\,. \tag{B15}$$

Equations (B14) and (B15) lead finally to

$$-iW_1 = [\chi, W_0] + i\hbar\dot{\beta}\hat{\theta}\,. \tag{B16}$$

This equation will be used to transform the particle-hole matrix elements of Eq. (B1):

$$\sigma_0\{i[W_0^D, \rho_1] + i[W_1, \rho_0]\}\rho_0$$

$$= \sigma_0 \chi W_0^D \rho_0 - \sigma_0 W_0^D \chi \rho_0 + i\sigma_0 W_1 \rho_0 \tag{B17}$$

$$\begin{aligned} &= \sigma_0 \chi W_0^D \rho_0 - \sigma_0 W_0^D \chi \rho_0 \\ &\quad - \sigma_0 [\chi, W_0^A + W_0^D] \rho_0 - i\hbar\dot{\beta}\sigma_0\hat{\theta}\rho_0 \end{aligned} \tag{B18}$$

$$= -\sigma_0 \chi W_0^A \rho_0 + \sigma_0 W_0^A \chi \rho_0 - i\hbar\dot{\beta}\sigma_0\hat{\theta}\rho_0\,. \tag{B19}$$

Since the operator W_0^A (or equivalently the commutator $[W_0, \rho_0]$) is at least of first order in χ, we obtain, by keeping only terms of first order in Eq. (B19),

$$\sigma_0\{i[W_0^D, \rho_1] + i[W_1, \rho_0]\}\rho_0 = -i\hbar\dot{\beta}\sigma_0\hat{\theta}\rho_0\,. \tag{B20}$$

Now since

$$\sigma_0(\hbar\dot{\rho}_0)\rho_0 = i\hbar\dot{\beta}\sigma_0\hat{\theta}\rho_0\,, \tag{B21}$$

[which is a trivial consequence of Eq. (5.1)], all the particle-hole matrix elements of Eq. (B1) vanish, at least as far as we neglect second order terms in χ. Since all terms of this equation have trivially vanishing particle-particle and hole-hole matrix elements, the fulfilling of the first Hamilton equation by ρ_0 and χ given by Eqs. (5.1) and (5.6) is established.

[*] Present address: Institut Laue-Langevin, BP 156X, 38042 Grenoble-Cedex, France.

[1] Å. Bohr, Mat. Fys. Medd. Danske Vid. Selsk. 26, No. 14 (1952); 27, No. 16 (1953); Å. Bohr and B. R. Mottelson, *Nuclear Structure* (Benjamin, New York, 1975), Vol. 2.

[2] D. R. Inglis, Phys. Rev. 96, 1059 (1954); 103, 1796 (1956).

[3] D. J. Thouless and J. G. Valatin, Nucl. Phys. 31, 211 (1962).

[4] F. M. H. Villars, Nucl. Phys. A285, 269 (1977).

[5] M. Baranger and M. Vénéroni, Ann. Phys. (N.Y.) 114, 123 (1978).

[6] D. M. Brink, M. J. Giannoni, and M. Vénéroni, Nucl. Phys. A258, 237 (1976).

[7] M. J. Giannoni and P. Quentin, Phys. Rev. C 21, 2076 (1980).

[8] F. M. H. Villars, in *Dynamical Structure of Nuclear States* edited by D. J. Rowe, L. E. H. Trainor, S. S. M. Wong, and T. W. Donelly (University of Toronto Press, Toronto, 1975), p. 3.

[9] D. J. Rowe and R. Basserman, Can. J. Phys. 54, 1941 (1976).

[10] K. Goeke and P. G. Reinhard, Ann. Phys. (N.Y.) 112, 328 (1978); P. G. Reinhard and K. Goeke, Nucl. Phys. A312, 121 (1978).

[11] For the sake of conciseness, we will assume that V is a density-independent two-body force. A generalization to Skyrme-like density-dependent forces is straightforward (see II). Besides, V is assumed to be even under time reversal.

[12] P. A. M. Dirac, Proc. Camb. Phil. Soc. 26, 376 (1930).

[13] P. Ring and P. Schuck, Nucl. Phys. A292, 20 (1977).

[14] P. Bonche and P. Quentin, Phys. Rev. C 18, 1891 (1978).

[15] M. J. Giannoni, J. Math. Phys. (to be published); and in *Time-dependent Hartree-Fock Method*, edited by P. Bonche, B. Giraud, and P. Quentin (Editions de Physique, Orsay, 1979), p. 251.

[16] Notice incidentally that this decomposition theorem (in spite of our notation) applies to more general density operators than our operator ρ (which describes a system of independent fermions). Moreover, a sharper form of this theorem has been given in Ref. 15.

[17] All assumptions on smallness of operators require some mathematical cautions which we skip here, and which are developed in Ref. 5. We simply mention that the smallness of $\hbar\dot{\chi}$ must be understood as by comparison with some typical single particle energy.

[18] M. Baranger, in *Cargese Lectures in Theoretical Physics*, edited by M. Lévy (Benjamin, New York, 1963), Sect. V.

[19] H. Goldstein, *Classical Mechanics* (Addison-Wesley, Reading, 1956); C. Lanczös, *The Varitional Principles of Quantum Mechanics*, Fourth edition (University of Toronto Press, Toronto, 1977).

[20] M. J. Giannoni, Report No. IPNO/TH 79-65, 1979.

[21] L. D. Landau and E. M. Lifshitz, *Course of Theoretical Physics, Vol. 1: Mechanics* (Pergamon, Oxford 1960).

[22] M. J. Giannoni, F. Moreau, P. Quentin, D. Vautherin, M. Vénéroni, and D. M. Brink, Phys. Lett. B65, 305 (1976).

[23] The reasons for introducing this CHF equation will be clarified in the following sections. It should be stressed that, in general, its *time-even* part is not equivalent to the adiabatic limit of the time-even part of the TDHF equation.

[24] The authors defining $\hat{P}$ as in Eq. (3.16) have also a definite prescription for the time-dependent state which leads to a unique value for $\langle\hat{P}\rangle$. In our case, the arbitrariness in the particle-particle and hole-hole matrix elements of χ leads to an ambiguity in $\langle\hat{P}\rangle$. It should be emphasized however that our prescription for the momentum operator (which has been imposed by the first ATDHF equation of motion) leads to a unequivocal definition of the adiabatic mass parameter.

[25] M. Gaudin, Nucl. Phys. 15, 89 (1960); J. des Cloiseaux, in *Many-Body Physics*, edited by C. de Witt and R. Balian (Gordon and Breach, New York, 1968), p. 1.

[26] K. Goeke, A. M. Lane, and J. Martorell, Nucl. Phys. A296, 109 (1978).

[27] H. Flocard, P. H. Heenen, and D. Vautherin, Nucl. Phys. (to be published); and in *Time-dependent Hartree-Fock Method*, edited by P. Bonche, B. Giraud, and P. Quentin (Editions de Physique, Orsay, 1979), p. 50.

[28] G. Holzwarth and T. Yukawa, Nucl. Phys. A219, 125 (1974); F. M. H. Villars, in *Nuclear Self-Consistent Fields*, edited by G. Ripka and M. Porneuf (North-Holland, Amsterdam, 1975), p. 3; T. Marumori, in *Selected Topics in Nuclear Structure* (JINR, Dubna, 1976), Vol. II, p. 412; B. G. Giraud and J. Letourneux, Report No. D Ph-T 78/52, 1978; B. G. Giraud and D. J. Rowe, J. Phys. Lett. 8, 177 (1979); Nucl. Phys. A330, 352 (1979).

[29] Y. M. Engel, D. M. Brink, K. Goeke, S. J. Krieger, and D. Vautherin, Nucl. Phys. A249, 215 (1975); D. Vautherin, Phys. Lett. 57B, 425 (1975).

[30] J. Martorell, O. Bohigas, S. Fallieros, and A. M. Lane, Phys. Lett. 60B, 313 (1976).

[31] O. Bohigas, A. M. Lane, and J. Martorell, Phys. Rep. 51, 269 (1979).

[32] D. M. Brink and R. Leonardi, Nucl. Phys. A258, 285 (1976).

[33] S. Stringari, E. Lipparini, G. Orlandini, M. Traini, and R. Leonardi, Nucl. Phys. A309, 177 (1978); A309, 189 (1978).

[34] G. Holzwarth and G. Eckart, Z. Phys. A284, 291 (1978); and Nucl. Phys. A325, 1 (1979).

[35] This equation has been demonstrated in Ref. 36 under more general assumptions. Indeed, provided there exists a decomposition of ρ into ρ_0 and a *local* operator χ (both Hermitian and time even), and assuming a weak gauge invariance property ($[\chi,[\chi,V]]=0$) but without assuming adiabaticity, one gets Eq. (5.8).

[36] M. J. Giannoni, D. Vautherin, M. Vénéroni, and D. M. Brink, Phys. Lett. 63B, 8 (1976).

[37] D. J. Thouless, Nucl. Phys. 21, 225 (1960).

[38] Solutions of (6.3) occur by pairs $\pm(\epsilon_n-\epsilon_0)$. The sum in Eq. (6.1) is restricted to positive values of $(\epsilon_n-\epsilon_0)$.

[39] D. J. Thouless, Nucl. Phys. 22, 78 (1961).

[40] D. Vautherin, Phys. Lett. 69B, 393 (1977).

[41] For the sake of simplicity, we neglect the antisymmetrization of V, but exchange terms can be treated in the same way.

PHYSICAL REVIEW C VOLUME 21, NUMBER 5 MAY 198

Mass parameters in the adiabatic time-dependent Hartree-Fock approximation. II. Results for the isoscalar quadrupole mode

M. J. Giannoni and P. Quentin[*]
Division de Physique Théorique, Institut de Physique Nucléaire, 91406 Orsay-Cedex, France

(Received 2 August 1979)

The formalism presented in the preceding paper is used to compute self-consistent adiabatic mass parameters for the isoscalar quadrupole modes. Skyrme-like effective forces have been used. A detailed study of the practical methods of calculation is made. A special attention is devoted to the problem of numerical accuracy. Results are presented for both scaling and constrained Hartree-Fock paths. A comparative discussion of the two corresponding sets of results is made. The method used to calculate self-consistent mass parameters for the constrained Hartree-Fock path provides, as a byproduct, the non-self-consistent cranking mass. This method (for self-consistent as well as cranking masses) is free of continuum problems inherent to the application of the usual cranking formula. The effect of self-consistency is extensively studied by use of a large set of Skyrme-like forces.

NUCLEAR STRUCTURE ^{12}C, ^{16}O, ^{40}Ca, ^{48}Ca, ^{56}Ni, ^{90}Zr, ^{140}Ce, ^{208}Pb; mass parameters for isoscalar quadrupole collective motion calculated within time-dependent Hartree-Fock approximation in adiabatic limit. Skyrme-like forces used. Numerical accuracy discussed. Self-consistent results for both scaling and constrained Hartree-Fock paths discussed. Validity of Inglis cranking masses assessed. Influence of forces studied.

I. INTRODUCTION

In an accompanying paper,[1] hereafter referred to as I, a theoretical study of the adiabatic time-dependent Hartree-Fock (ATDHF) approximation was presented, where attention was focused on the particular case of a collective path parametrized by a single collective variable. The ATDHF formalism allows then the calculation of the corresponding mass parameter through the solution of the first set of Hamilton-like equations of motion.

Two choices for the parametrization of the path were discussed in detail. In the first choice, the trajectory is given by the solution of a constrained Hartree-Fock (CHF) problem, i.e., is fixed by the guess of a constraining operator. In the second choice, the path is obtained by scaling a static Hartree-Fock wave function. In this second case, the computation of the mass is straightforward. In the former case we have shown that the inversion of the first set of Hamilton equations providing the mass parameter can be advantageously replaced by the solution of a double CHF problem.

The content of paper I was rather general. No particular form was assumed for the effective nucleon-nucleon interaction and, except for the illustration of some specific points, no explicit mention was made of particular excitation modes. In the present paper, we apply the formalism of I to the study of isoscalar quadrupole Q_{20} vibrations. As effective interactions, we shall use Skyrme forces, which have been quite successful for the description of many static nuclear properties.[2-6]

In Sec. II we summarize the method of the calculation, and give some of the necessary formulas for the case where Skyrme forces are used and some symmetries assumed for the ATDHF solutions. Section III is devoted to the discussion of several numerical problems, including the convergence of the mass parameters with respect to the size of the truncated basis on which we expand the CHF orbitals. The results of our calculations are presented, and their physical significance discussed in Sec. IV.

II. CALCULATION OF QUADRUPOLE ADIABATIC MASSES WITH SKYRME-LIKE FORCES

A. General outline of the calculations

For the two choices of the path we have considered, we present the practical method of calculation of the mass parameter.

The quadrupole scaling path. In this case, we perform a static Hartree-Fock (HF) calculation, providing an equilibrium one-body reduced density operator ρ_{st}. The corresponding radius and quadrupole moment are called r_{st} and q_{st}. If the effective interaction is gauge invariant with respect to the isoscalar excitation operator Q_{20} (we will see in Sec. II B that it is so for the Skyrme forces in use in this work), the scaling mass

© 1980 The American Physical Societ

parameter is given as a function of the quadrupole moment $q=\langle Q_{20}\rangle$ by

$$M_{SC}(q)=\frac{m}{8Ar^2+4q}\,, \tag{2.1}$$

where r is deduced from q through the following equations up to first order in the scaling parameter β:

$$Ar^2=\frac{(1-2\beta)^2}{3}(2A{r_{st}}^2-q_{st}) + \frac{1}{3(1-2\beta)^4}(A{r_{st}}^2+q_{st})\,, \tag{2.2}$$

$$q=\frac{(1-2\beta)^2}{3}(q_{st}-2A{r_{st}}^2) + \frac{2}{3(1-2\beta)^4}(A{r_{st}}^2+q_{st})\,. \tag{2.3}$$

The CHF path with the external field Q_{20}. The calculations are performed in two steps. We first get the adiabatic path $\rho_0(q)$ from a CHF calculation for the time-even constraining field $(-\lambda Q_{20})$

$$[W_0-\lambda Q_{20},\rho_0]=0\,, \tag{2.4}$$

where W_0 is the Hartree-Fock Hamiltonian built from ρ_0. The path $\rho_0(q)$ is parametrized by the variable $q=\mathrm{Tr}Q_{20}\rho_0$ corresponding to the Lagrange multiplier λ.

When this is achieved, one can compute numerically the matrix $\partial\rho_0/\partial q$, and therefore calculate the "momentum" operator P generating the dynamics [see in I Eq. (4.5) and the related discussion). This time-odd operator enters in the double CHF equation, equivalent to the first ATDHF equation [see Eq. (2.24) of I]:

$$[W_0+W_1-\lambda Q_{20}^A-\dot{q}P,\rho_0+\rho_1]=0\,, \tag{2.5}$$

where Q_{20}^A is the antidiagonal part of Q_{20} $[Q_{20}^A=\rho_0 Q_{20}(1-\rho_0)+(1-\rho_0)Q_{20}\rho_0]$, and where the velocity parameter $\dot{q}$ must be chosen small enough to ensure the linear response.

This CHF equation is solved iteratively by taking as a first guess for the solution the time-even density ρ_0 obtained by solving Eq. (2.4) with the same value of the Lagrange multiplier λ. At the first iteration, we get a time-odd density ${\rho_1}^1$ which is the non-self-consistent response of the system to the time-odd perturbating field $(-\dot{q}P)$; this ${\rho_1}^1$ is therefore calculated in the *Inglis cranking* approximation.

Once ρ_1 is determined, the mass parameter is given by

$$M(q)=\mathrm{Tr}(P\rho_1)/\dot{q}\,. \tag{2.6}$$

This formula is of course valid for a self-consistent as well as for a non-self consistent (Inglis cranking) operator ρ_1.

B. The effective forces

As for phenomenological effective forces we use Skyrme-like forces which, in the $\vec{r}$ representation, write

$$\begin{aligned}V_{sk}(\vec{r}_1,\vec{r}_2)={}&t_0(1+x_0P_\sigma)\delta(\vec{r})+\tfrac{1}{2}t_1(1+x_1P_\sigma)\{\vec{P}'^2\delta(\vec{r})+\delta(\vec{r})\vec{P}^2\}\\&+t_2(1+x_2P_\sigma)\vec{P}'\cdot\delta(\vec{r})\vec{P}+iw_0\vec{\sigma}\cdot\{\vec{P}'\times\delta(\vec{r})\vec{P}\}+\tfrac{1}{6}t_3(1+x_3P_\sigma)\{\rho(\vec{R})\}^\alpha\delta(\vec{r})\end{aligned} \tag{2.7}$$

with

$\vec{r}=\vec{r}_1-\vec{r}_2\,,$

$\vec{R}=(\vec{r}_1+\vec{r}_2)/2\,,$

$\vec{P}=(\vec{\nabla}_1-\vec{\nabla}_2)/2i$ ($\vec{P}'$ being the complex conjugate of $\vec{P}$ acting on its left-hand side)

$\vec{\sigma}=\vec{\sigma}_1+\vec{\sigma}_2$ ($\vec{\sigma}_i$ being a Pauli spin matrix acting in the i subspace)

$P_\sigma=(1+\vec{\sigma}_1\cdot\vec{\sigma}_2)/2\,.$

Notice that, due to the presence in $V_{sk}(\vec{r}_1,\vec{r}_2)$ of $\delta(\vec{r}_1-\vec{r}_2)$, there is no need to introduce other exchange operators than P_σ.

These forces depend on 10 parameters. Most of the time we consider in this work forces such that $x_1=x_2=0$ and $x_3=\alpha=1$. For this class of forces an extensive study of the parameter adjustment has been done in Ref. 5. It has been found that imposing only a good reproduction of nuclear matter (or equivalently magic nuclei) saturation properties is not sufficient for a complete determination of the parameter set. The remaining freedom is associated with the well known fact that nuclear matter saturation can be obtained either by a velocity-dependent interaction, or by a density-dependent interaction, or by a mixture of these two types of forces. One may thus characterize saturating Skyrme forces by their effective mass m^* in nuclear matter, i.e., by their velocity dependence. By adjusting the parameters to static properties of nonmagic nuclei, one obtains a small range of acceptable values for m^*. The SIII force, for which m^*

$=0.76$ (in units of the nucleonic mass m), gives a particularly good fit to a large number of experimental data.[6]

For a Slater determinant $|\phi\rangle$ the expectation value of the Hamiltonian H:

$$H = T + V_{\mathrm{sk}} + V_{\mathrm{coul}}, \qquad (2.8)$$

where T is the kinetic energy operator and V_{coul} the Coulomb interaction, can be written as the integral of a Hamiltonian density

$$\langle\phi|H|\phi\rangle = \int \mathcal{H}(\vec{r})d^3r\,. \qquad (2.9)$$

The Hamiltonian density $\mathcal{H}$ is defined by[7,8]

$$\begin{aligned}
\mathcal{H}(\vec{r}) = {}& \frac{\hbar^2}{2m}\tau + \tfrac{1}{2}t_0\Big((1+\tfrac{1}{2}x_0)\rho^2 - (x_0+\tfrac{1}{2})\sum_q(\rho^q)^2 + \tfrac{1}{2}x_0\vec{\rho}^{\,2} - \tfrac{1}{2}\sum_q(\vec{\rho}^{\,q})^2\Big)\\
&+ \tfrac{1}{4}t_1\Big((1+\tfrac{1}{2}x_1)[\rho\tau - \vec{j}^{\,2} + \tfrac{3}{4}(\vec{\nabla}\rho)^2] - (x_1+\tfrac{1}{2})\sum_q[\rho^q\tau^q - (\vec{j}^{\,q})^2 + \tfrac{3}{4}(\vec{\nabla}\rho^q)^2]\\
&\qquad + \tfrac{1}{2}x_1[\vec{\rho}\cdot\vec{\tau} - ((J_{\mu\nu}))^2 + \tfrac{3}{4}((\nabla_\mu\rho_\nu))^2] - \tfrac{1}{2}\sum_q[\vec{\rho}^{\,q}\cdot\vec{\tau}^{\,q} - ((J^q_{\mu\nu}))^2 + \tfrac{3}{4}((\nabla_\mu\rho^q_\nu))^2]\Big)\\
&+ \tfrac{1}{4}t_2\Big((1+\tfrac{1}{2}x_2)[\rho\tau - \vec{j}^{\,2} - \tfrac{1}{4}(\vec{\nabla}\rho)^2] + (x_2+\tfrac{1}{2})\sum_q[\rho^q\tau^q - (\vec{j}^{\,q})^2 - \tfrac{1}{4}(\vec{\nabla}\rho^q)^2]\\
&\qquad + \tfrac{1}{2}x_2[\vec{\rho}\cdot\vec{\tau} - ((J_{\mu\nu}))^2 - \tfrac{1}{4}((\nabla_\mu\rho_\nu))^2] + \tfrac{1}{2}\sum_q[\vec{\rho}^{\,q}\cdot\vec{\tau}^{\,q} - ((J^q_{\mu\nu}))^2 - \tfrac{1}{4}((\nabla_\mu\rho^q_\nu))^2]\Big)\\
&+ \tfrac{1}{12}t_3\rho^\alpha\Big((1+\tfrac{1}{2}x_3)\rho^2 - \sum_q[(x_3+\tfrac{1}{2})(\rho^q)^2] + \tfrac{1}{2}x_3\vec{\rho}^{\,2} - \tfrac{1}{2}\sum_q(\vec{\rho}^{\,q})^2\Big)\\
&- \frac{W_0}{2}\Big(i\sqrt{2}[\vec{J}\cdot\vec{\nabla}\rho + \sum_q(\vec{J}^q\cdot\vec{\nabla}\rho^q)] + \vec{\nabla}\times\vec{\rho}\cdot\vec{j} + \sum_q(\vec{\nabla}\times\vec{\rho}^{\,q}\cdot\vec{j}^{\,q})\Big) + \mathcal{H}_{\mathrm{coul}}\,.
\end{aligned} \qquad (2.10)$$

The six density functions[9] appearing in Eq. (2.10) are defined in terms of the one-body density matrix ρ,

$$\rho(\vec{r},\sigma;\vec{r}\,',\sigma') = \sum_i \psi_i^*(\vec{r}\,',\sigma')\psi_i(\vec{r},\sigma)\,, \qquad (2.11)$$

(where the ψ_i's are occupied orbitals) by

$$\begin{aligned}
\rho(\vec{r}) &= \sum_\sigma \rho(\vec{r},\sigma;\vec{r},\sigma)\,,\\
\vec{\rho}(\vec{r}) &= \sum_{\sigma,\sigma'}\rho(\vec{r},\sigma;\vec{r},\sigma')\langle\sigma'|\vec{\sigma}|\sigma\rangle\,,\\
\tau(\vec{r}) &= \sum_\sigma \vec{\nabla}\cdot\vec{\nabla}'\rho(\vec{r},\sigma;\vec{r}\,',\sigma)|_{\vec{r}=\vec{r}\,'}\,,\\
\vec{\tau}(\vec{r}) &= \sum_{\sigma,\sigma'}\vec{\nabla}\cdot\vec{\nabla}'\rho(\vec{r},\sigma;\vec{r}\,',\sigma')|_{\vec{r}=\vec{r}\,'}\langle\sigma'|\vec{\sigma}|\sigma\rangle\,,\\
\vec{j}(\vec{r}) &= \frac{1}{2i}\sum_\sigma(\vec{\nabla}-\vec{\nabla}')\rho(\vec{r},\sigma;\vec{r}\,',\sigma)|_{\vec{r}=\vec{r}\,'}\,,\\
J_{\mu\nu}(\vec{r}) &= \frac{1}{2i}\sum_{\sigma,\sigma'}(\nabla_\mu - \nabla'_\mu)\rho(\vec{r},\sigma;\vec{r}\,',\sigma')|_{\vec{r}=\vec{r}\,'}\\
&\qquad\times\langle\sigma'|\sigma_\nu|\sigma\rangle\,,
\end{aligned} \qquad (2.12)$$

where the indices μ, ν label the spherical components of the vectors $\vec{\rho}$, $\vec{\nabla}$ and $\vec{\sigma}$. The Hamiltonian density (2.10) involves two tensorial products,

$$\begin{aligned}
((J_{\mu\nu}))^2 &= \sum_{\mu\nu}(-)^{\mu+\nu}J_{\mu\nu}J_{-\mu-\nu}\\
&= (J^{(0)})^2 - (J^{(1)})^2 + (J^{(2)})^2
\end{aligned} \qquad (2.13)$$

and

$$\begin{aligned}
((\nabla_\mu\rho_\nu))^2 &= ([\vec{\nabla}\otimes\vec{\rho}]^{(0)})^2 - ([\vec{\nabla}\otimes\vec{\rho}]^{(1)})^2\\
&\qquad + ([\vec{\nabla}\otimes\vec{\rho}]^{(2)})^2\\
&= \tfrac{1}{3}(\vec{\nabla}\cdot\vec{\rho})^2 + \tfrac{1}{2}(\vec{\nabla}\times\vec{\rho})^2\\
&\qquad + ([\vec{\nabla}\otimes\vec{\rho}]^{(2)})^2\,,
\end{aligned} \qquad (2.14)$$

where $J^{(i)}$ and $[\vec{\nabla}\otimes\vec{\rho}]^{(i)}$ are the irreducible components of rank i of the tensors J and $\vec{\nabla}\otimes\vec{\rho}$. In Eq. (2.10) the vector component $J^{(1)}$ of J has been noted $\vec{J}$ [it is $i/\sqrt{2}$ times the spin-density $\vec{J}$ of Eq. (11) in Ref. 2]. To be consistent with the phenomenological determination of the force parameters made in Ref. 5 we shall neglect in $\mathcal{H}(\vec{r})$ the contribution of the tensors of rank 1 and 2 to $((J_{\mu\nu}))^2$. The superscript q in Eq. (2.10) indicates the charge state (which cannot be confused with the collective variable q); the total (neutron + proton) densities (2.12) are therefore given by

$$\rho(\vec{r}) = \sum_q \rho^q(\vec{r}) \qquad (2.15$$

and by similar formulas. Finally, the Coulomb energy density is written in terms of the proton density $\rho^p(\vec{r})$ as

$$\mathcal{H}_{\text{coul}}(\vec{r})=\frac{e^2}{2}\rho^p(\vec{r})\left\{\int\frac{\rho^p(\vec{r}\,')}{|\vec{r}-\vec{r}\,'|}d^3r' - \frac{3}{2}\left(\frac{3}{\pi}\right)^{1/3}[\rho^p(\vec{r})]^{1/3}\right\}, \quad (2.16)$$

where the last term is a local approximation, due to Gombàs,[10] of the Coulomb exchange contribution.

In relation with the discussion made in I about the scaling path, we notice that the central *and* the spin-orbit parts of the Skyrme force are invariant for isoscalar gauge transformations (see Appendix A). This holds in particular for the description of isoscalar quadrupole modes with Skyrme forces presented in Sec. IV.

C. Symmetries

Let us associate to a particular collective mode, an operator Q which possesses some symmetries. It is reasonable to assume that the ATDHF solution shares the same symmetries. Because the numerical calculations of Sec. IV correspond to the isoscalar operator $Q=Q_{20}$, we shall now assume that ρ has the following symmetries:

(i) the axial symmetries

$$R_3^s(\theta)=e^{i\theta s_3}\,,$$
$$R_3^x(\theta)=e^{i\theta l_3}\,, \quad (2.17)$$

for both spin and space variables,

(ii) the parity symmetry P_0,

(iii) the reflection symmetry

$$U_2=P_0e^{i\pi(l_2+s_2)} \quad (2.18)$$

with respect to the 1-3 coordinate plane.

Notice that if one defines the operators U_1 and U_3 as in Eq. (2.18), the symmetries (i) and (ii) imply the symmetry under U_3. Since

$$U_1U_2U_3=P_0\,, \quad (2.19)$$

the symmetries (i), (ii), and (iii) imply the symmetry under U_1. If one assumes that the symmetries (i) and (ii) are satisfied and that ρ is time even (e.g., ρ_0 in our case), one can show (see Appendix B) that ρ commutes also then with U_2, and therefore with U_1.

Let us now investigate the implications of the symmetries (i), (ii), and (iii) on the two step determination of ρ_0 and $\rho_0+\rho_1$. We first prove that the equations

$$[V,R_3^x]=[V,R_3^s]=[V,P_0]=0 \quad (2.20)$$

and

$$[Q_{20},R_3^x]=[Q_{20},R_3^s]=[Q_{20},P_0]=0\,, \quad (2.21)$$

imply the existence of a solution of the ATDHF equations such that

$$[\rho_0,R_3^x]=[\rho_0,R_3^s]=[\rho_0,P_0]=0 \quad (2.22)$$

and

$$[\rho_1,R_3^x]=[\rho_1,R_3^s]=[\rho_1,P_0]=0\,. \quad (2.23)$$

Indeed, Eq. (2.22) follows from the symmetry assumptions and from the well known theorem on consistent symmetries (see, e.g., Ref. 11) applied to the Hamiltonian $H-\lambda Q_{20}$. Furthermore, from the definition of the operator P [see Eq. (4.5) of I], we have

$$[P,R_3^x]=[P,R_3^s]=[P,P_0]=0\,. \quad (2.24)$$

This is because P, being an algebraic function of ρ_0 and $\partial\rho_0/\partial q$, has the same symmetries (2.22). If we now apply the theorem on consistent symmetries to the Hamiltonian $H-\lambda Q_{20}^A-\dot{q}P$ we obtain

$$[\rho,R_3^x]=[\rho,R_3^s]=[\rho,P_0]=0 \quad (2.25)$$

and then Eq. (2.23).

The symmetry properties of ρ greatly simplify the numerical calculations. Indeed, it can be shown (see Appendix C) that Eqs. (2.22) and (2.23) imply

$$\vec{\rho}=\vec{\tau}=J_{\mu\nu}^{(0)}=j_\theta=0\,, \quad (2.26)$$

where j_θ is the θ component of the current $\vec{j}$ in cylindrical coordinates. The vanishing of $J_{\mu\nu}^{(0)}$, combined with the dropping of $J_{\mu\nu}^{(1)}$ and $J_{\mu\nu}^{(2)}$, suppresses any contribution of $((J_{\mu\nu}))^2$ to $\mathcal{H}$.

As a consequence of Eq. (2.26), the introduction of a time-odd constraint P requires only two new density functions j_r and j_z to those needed in the "ordinary" static CHF calculations of the type discussed in Refs. 3 and 4. This illustrates the considerable simplification brought in by the symmetry requirements.

D. The Hartree-Fock Hamiltonian

The doubly constrained HF equations are obtained by the minimization of the quantity

$$F=\int\mathcal{H}(\vec{r})d^3r-\lambda\langle Q_{20}^A\rangle-\dot{q}\langle P\rangle-\sum_i e_i\int|\phi_i(\vec{r})|^2d^3r \quad (2.27)$$

with respect to the variations of the occupied orbitals ϕ_i. The expression (2.27) contains the total energy defined by Eq. (2.10), the energies corresponding to the external fields Q_{20}^A and P, and constraining terms ensuring the norm conservation of each occupied orbital. Considering only the CHF solutions with the symmetries which have just been discussed, one obtains[7] the following equation for an orbital ψ_j of charge q:

$$\left[-\vec{\nabla}\cdot\frac{\hbar^2}{2m_q^*(\vec{r})}\vec{\nabla}+U^q(\vec{r})-i\vec{W}^q(r)\cdot(\vec{\nabla}\times\vec{\sigma})+\vec{W}_1^q(\vec{r})-e_j\right]\psi_j(\vec{r})+\int U^{ext}(\vec{r},\vec{r}\,')\psi_j(\vec{r}\,')d^3r'=0\,. \tag{2.28}$$

In Eq. (2.28), the effective mass $m_q^*(\vec{r})$ is given by

$$\frac{\hbar^2}{2m_q^*(\vec{r})}=\frac{\hbar^2}{2m}+\tfrac{1}{4}[t_1(1+\tfrac{1}{2}x_1)+t_2(1+\tfrac{1}{2}x_2)]\rho-\tfrac{1}{4}[t_1(\tfrac{1}{2}+x_1)-t_2(\tfrac{1}{2}+x_2)]\rho^q\,, \tag{2.29}$$

the central field $U^q(\vec{r})$ is

$$\begin{aligned}U^q(\vec{r})=\;&t_0[(1+\tfrac{1}{2}x_0)\rho-(x_0+\tfrac{1}{2})\rho^q]+\tfrac{1}{8}[3(1+\tfrac{1}{2}x_1)t_1-(1+\tfrac{1}{2}x_2)t_2]\vec{\nabla}^2\rho\\&+\tfrac{1}{8}[3(\tfrac{1}{2}+x_1)t_1+(\tfrac{1}{2}+x_2)t_2]\vec{\nabla}^2\rho^q+\tfrac{1}{4}[(1+\tfrac{1}{2}x_1)t_1+(1+\tfrac{1}{2}x_2)t_2]\tau\\&-\tfrac{1}{4}[(\tfrac{1}{2}+x_1)t_1-(\tfrac{1}{2}+x_2)t_2]\tau^q+\tfrac{1}{12}t_3\{(1+\tfrac{1}{2}x_3)(2+\alpha)(\rho)^{\alpha+1}-(x_3+\tfrac{1}{2})[\alpha(\rho)^{\alpha+1}(\rho^q)^2+2(\rho)^\alpha\rho^q]\}\\&+\frac{i}{\sqrt{2}}w_0(\vec{\nabla}\cdot\vec{J}+\vec{\nabla}\cdot\vec{J}^q)+\delta_{q,\mathrm{proton}}\tfrac{1}{2}e^2\left\{\int\frac{\rho^q(\vec{r}\,')}{|\vec{r}-\vec{r}\,'|}d^3r'-2\left[\frac{3}{\pi}\rho^q(\vec{r})\right]^{1/3}\right\},\end{aligned} \tag{2.30}$$

the spin-orbit field $\vec{W}^q(\vec{r})$ is

$$\vec{W}^q(r)=\tfrac{1}{2}w_0(\vec{\nabla}\rho+\vec{\nabla}\rho^q)\,, \tag{2.31}$$

the time-odd field $W_1^q(\vec{r})$ is

$$W_1^q(\vec{r})=\frac{1}{2i}[\vec{I}^q(\vec{r})\cdot\vec{\nabla}+\vec{\nabla}\cdot\vec{I}^q(\vec{r})] \tag{2.32}$$

with

$$\begin{aligned}\vec{I}^q(\vec{r})\;=\;&\tfrac{1}{2}[t_1(1+\tfrac{1}{2}x_1)+t_2(1+\tfrac{1}{2}x_2)]\vec{j}(\vec{r})\\&+\tfrac{1}{2}[t_1(\tfrac{1}{2}+x_1)-t_2(\tfrac{1}{2}+x_2)]\vec{j}^q(\vec{r})\,,\end{aligned} \tag{2.33}$$

and the external (non local) field $U_{ext}(\vec{r},\vec{r}\,')$ is

$$U^{ext}(\vec{r},\vec{r}\,')=-\langle\vec{r}|\lambda Q_{20}^A+\dot{q}P|\vec{r}\,\rangle\,. \tag{2.34}$$

To solve the set of coupled equations (2.28), we expand each orbital ψ_i on a truncated set of eigenfunctions of the axially symmetric harmonic oscillator. We shall discuss in Sec. III the numerical problems related to this truncation. Notice that these basis states fulfill the symmetry requirements of Sec. II C. The expansion of the ψ_i's converts the solution of Eqs. (2.28) into the diagonalization of a Hermitian complex matrix which is performed by the usual Jacobi method.[12] To construct the Hamiltonian matrix, we perform a numerical integration for the kinetic energy, U^q and $\vec{W}^q$, following the methods of Ref. 3. These methods have been extended to include the time-odd field W_1^q (see Appendix D). For the contribution of the external field U^{ext}, due to its nonlocality, we have computed its matrix elements in the harmonic oscillator basis. This is easy for P since we know how to express ρ_0 and $\partial\rho_0/\partial q$ on this basis. For Q_{20}^A, we need to compute the matrix elements of Q_{20} in the expansion basis which is readily performed according to the methods developed in Ref. 13.

Notice that even though the HF states belonging to a subspace Ω^π (Ω being the third component of the total angular momentum and π the parity) are *not* complex conjugates of the states belonging to the subspace $-\Omega^\pi$, their respective contributions to the different density functions are equal. Thi is due to the imposed symmetries, as shown in Appendix B, and leads to an important simplific tion, in the computation of the various terms of Eq. (2.28). It may be also worth recalling that the formalism has been developed in I for two-body density-independent forces; introducing th most general two body density-dependent or thr body forces would result in a more involved expression for the operator W_1. However, the density-dependent part of the Skyrme interactio contributes only to W_0 once the symmetries wh we have imposed are properly taken into accoun For this reason, the expression (2.22) of paper for W_1 remains correct for Skyrme-like forces.

III. SOME COMMENTS ON NUMERICAL PROBLEMS

For both choices of the adiabatic path, one ha first to solve a static HF equation (with, or wit out a time-even constraint). In the case of the CHF collective trajectory, one must solve a second CHF equation, with a double (time-even plus time-odd) constraint. This is done, as already indicated in Sec. II D, by expanding the CHF orbitals on a truncated basis of axially symmetrical harmonic oscillator states. We would like to discuss the numerical checks wh have been performed to test the stability of ou results with respect to the choice of the truncated basis.

For "ordinary" (time-even) HF calculations of equilibrium states, such a study consists mostly in making sure that the HF energy, the rms and the first multipole moments are reasonably well converged. For spherical nuclei, the "exact" calculation (in the coordinate space) allows us to know the degree of accuracy obtained for a given basis size, and to choose accordingly the number of oscillator shells. Let us notice that for spherical nuclei the scaling mass $M_{sc}(q)$, completely determined by the values of r_{st} [see Eqs. (2.1) to (2.3)], can be obtained from the exact $\vec{r}$ code for spherical nuclei, and is therefore given with an excellent accuracy. In CHF calculations of deformation energy curves, the physical energies to be considered are relative energies. The convergence therefore is ensured whenever increasing the basis size results roughly in a shift of the *deformation energy curve as a whole*. This is illustrated by Fig. 1 which shows for the ^{12}C nucleus a reasonable convergence with nine oscillator shells, the truncation error for the equilibrium energy being only 300 keV.

All the previous check do not ensure the convergence of the operator $\partial\rho_0/\partial q$ entering the time-odd constraining operator P. In this respect we have carefully studied the influence of the choice of the basis on the resulting mass parameters. The variation of the ^{12}C mass parameter at $q=0$ with respect to the basis size is shown on Fig. 2. One sees that between 9 and 11 harmonic oscillator shells, both the self-consistent M_{CHF} and the Inglis cranking M_{ICR} mass parameters do not change more than by 1%. This study has been carried out with the same oscillator length for all basis sizes. Let us now investigate the combined effects on M_{CHF} of the oscillator parameter *and* the basis size. As is well known,[4] the optimal basis parameters (i.e., those minimizing the potential energy $E[\rho_0]$), may significantly change with the basis size. That is why on Figs. 3–5 we have plotted over a wide range of oscillator lengths the ^{16}O, ^{40}Ca, and ^{56}Ni mass parameters obtained at $q=0$ for basis including 5, 7, 9, and 11 oscillator shells. It has been found, for 9 or 11 oscillator shells, that the mass parameters are almost constant in a rather large interval of oscillator lengths around the optimal values. Moreover, the results obtained with 7, 9, or 11 oscillator shells are found to be very close, as already seen in the case of ^{12}C presented on Fig. 2.

One could think that all of this lengthy numerical

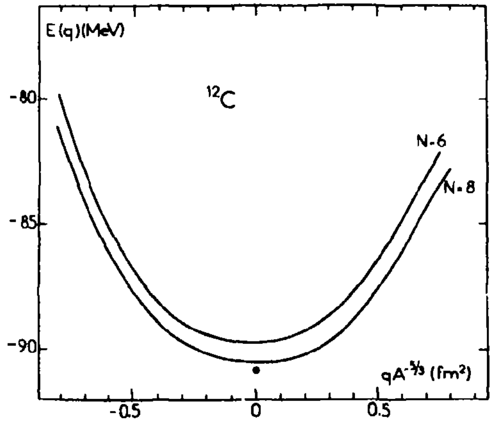

FIG. 1. Deformation energy curves of ^{12}C calculated with SIII for 7 and 9 oscillator shell basis. The "exact" result (obtained with an $\vec{r}$-space code) for the spherical configuration is represented by a dot. It is to be noted that in this figure, as in the following, N denotes the maximum total number of quanta in the harmonic oscillator basis.

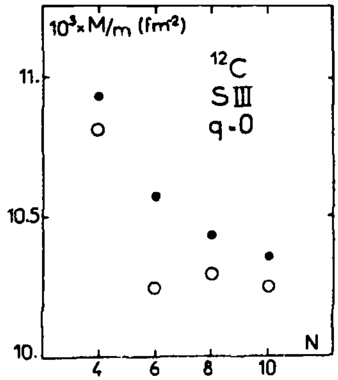

FIG. 2. Mass parameters of ^{12}C at spherical equilibrium, as functions of N. The dots represent self-consistent masses M_{CHF}, and the open circles correspond to cranking masses M_{ICR}.

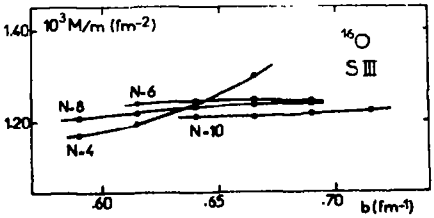

FIG. 3. Variations of the adiabatic mass M_{CHF} of ^{16}O with the oscillator constant $b=(m\omega/\hbar)^{1/2}$, for different basis sizes.

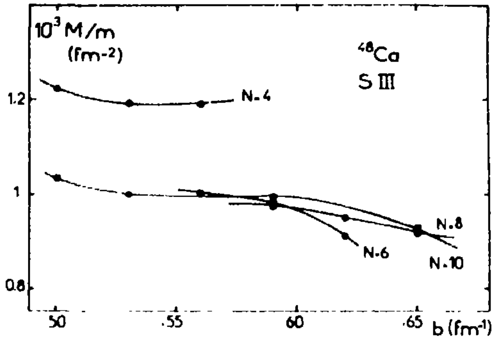

FIG. 4. Same as Fig. 3, for ^{48}Ca.

analysis could have been avoided by directly solving the double CHF equation in configuration space, as was done in Ref. 14. It must be remarked, however, that, in the present state of the art, such a solution in $\vec{r}$ space has only been achieved for a simplified Skyrme-like force without spin-orbit and without velocity-dependent parts. The first simplification prohibits a detailed description of dynamical properties for spin-unsaturated nuclei as ^{12}C and ^{56}Ni. The second restriction has the important consequence that the ATDHF mass reduces in this case to the Inglis cranking mass. Indeed, as shown by Eqs. (2.32) and (2.33), the time-odd HF potential W_1 arises for the Skyrme force only from its velocity-dependent part.

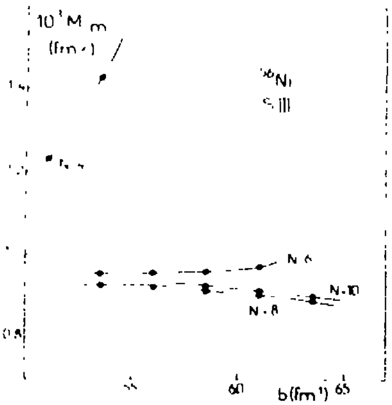

FIG. 5. Same as Fig. 3, for ^{56}Ni.

Let us now discuss the numerical evaluation of the operator $\partial\rho_0/\partial q$ for a given basis size. It has been computed from three CHF calculations of ρ_0 corresponding to the values $q_0 - dq$, q_0, $q_0 + dq'$ of the collective variable. For this purpose we have used a standard 3-points Lagrange formula:

$$\left.\frac{\partial\rho_0}{\partial q}\right]_{q_0} = \frac{-dq'}{dq(dq+dq')}\rho_0(q_0 - dq) + \frac{dq'-dq}{dq\,dq'}\rho_0(q_0) + \frac{dq}{dq'(dq+dq')}\rho_0(q_0+dq') . \tag{3.1}$$

In order to get reliable estimates for $\partial\rho_0/\partial q$ one must choose the magnitude of the differences dq, dq' in the collective variable not too small to yield significant numerical differences and not too large to guarantee the validity of the local quadratic behavior. The reliability of our choice for dq, dq' has been check by computations where these differences have been multiplied by 2 and $\frac{1}{2}$. In all cases the adiabatic mass parameters were found equal up to insignificant numerical differences.

The value of the collective velocity $\dot{q}$ should not be chosen too large (large enough though to secure numerical reliability) in order to ensure the linear response character of the solution. In Fig. 6 we have shown some quadrupole mass parameters as functions of the ratio of the adiabatic collective kinetic energy $\mathcal{K}$ [Eq. (2.32) of I] to the absolute value E of the ATDHF energy [Eq. (2.38) of I]. One sees that the linear response is obtained for a large range of collective velocities $\dot{q}$. In this figure, the arrows correspond to a crude estimate of the maximum collective velocities obtained in the nuclear ground state due to the quadrupole zero point motion. It is seen that for such maximum collective velocities, the linear response approximation is roughly valid.

It can also be noted that the smallness of $\dot{q}$ is

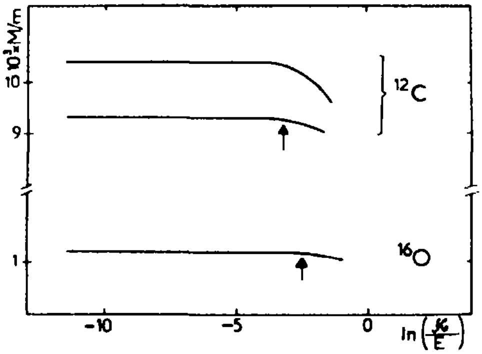

FIG. 6. Variation of the adiabatic mass M_{CHF} of ^{12}C and of ^{16}O with the collective velocity $\dot{q}$. The lower (upper) curve of ^{12}C corresponds to $A^{-5/3} = -0.56$ (0) fm^2 whereas for ^{16}O the calculation has been performed at $q = 0$. The choice of the abscissa (corresponding in fact to a linear plot in $\dot{q}$) is discussed in the text together with the meaning of the arrows.

TABLE I. Parameters of the SIII* and SVII forces. For both interactions, $x_3 = 1$ and $\alpha = 1$.

	t_0 (MeV fm^3)	t_1 (MeV fm^5)	t_2 (MeV fm^5)	t_3 (MeV fm^6)	x_0	x_1	x_2	W_0 (MeV fm^5)
SIII*	−1121	400	−533.33	14 000	0.432 25	0.35	−0.9875	120
SVII	−1096.8	246.2	−148	17 626	0.62	0	0	112

necessary for another reason; solving the double CHF problem does perturb the path given in Eq. (2.4) by terms of *second order in* $\dot{q}$. This comes from the effect of ρ_1 in the time-even part of Eq. (2.5) (see the discussion in Sec. IV of I). In the ^{40}Ca nucleus and for $\hbar\dot{q} = 0.1$ MeV fm^2 for instance, this modification of the path leads to relative variations of ATDHF energies, radii, and quadrupole moments smaller than 10^{-4}, 10^{-3}, and 10^{-2}, respectively, over a wide range of deformations.

The preceding discussion leads to the conclusion that our method is capable of yielding mass parameters with a very good accuracy. This is not surprising, since we calculate a nuclear polarizability (linear response to the external field P) by solving a Schrödinger equation only *for occupied states*. Computing mass parameters by perturbation techniques would require a description of unbound states, which are poorly represented in the oscillator basis.[15]

IV. RESULTS

In this section we present numerical results for the isoscalar axial quadrupole mode. Various effective forces have been used: (i) the SII*, SIII, SIV, and SV forces proposed in Ref. 5, (ii) a force called SVII, linearly extrapolated from the preceding to give a nuclear effective mass m^* equal to the nucleonic mass m, (iii) a force called SIII* with the same m^*/m ratio as SIII but where spin-stability properties have been slightly modified to improve some spectroscopic properties of the interaction,[16] and (iiii) the two forces *SG*0 [with the exponent α of Eq. (2.7) equal to either $\frac{1}{3}$ or to 1] proposed in Ref. 17. The parameters of all these forces can be found in Refs. 5 and 17, except for those of SIII* and SVII which are given in Table I.

Deformation energy curves obtained by CHF calculations in the vicinity of the spherical configuration are displayed on Fig. 7. The SIII force has been used for ^{12}C, ^{16}O, ^{40}Ca, and ^{56}Ni, and the SIV force also for ^{12}C and ^{16}O. In the ^{56}Ni case we have repeated the calculation with SIII* but the resulting energy curve cannot be distinguished from the SIII curve. To facilitate the comparison of curves corresponding to different nucleonic numbers A, we have plotted in abscissa throughout this paper, a "reduced" quadrupole moment $qA^{-5/3}$ in order to remove the trivial A dependence. In our HF (i.e., without pairing correlations) calculations, the range of deformation has been extended as far as the occurence of single-particle level crossings has permitted.

Figure 7 shows that ^{40}Ca is much stiffer against quadrupole deformation than ^{16}O and ^{56}Ni, whereas the ^{12}C nucleus appears to be very soft. Indeed, the distortion needed to gain 1 MeV is four times larger in ^{12}C than in ^{40}Ca. Notice the existence of a spherical equilibrium configuration for ^{12}C with SIII, while a very shallow valley centered around a negative q value is obtained with SIV. Therefore, by mere inspection of the *static deformation energy curve* one would infer a strong dependence of the ^{12}C ground state intrinsic deformation on the effective force. We will

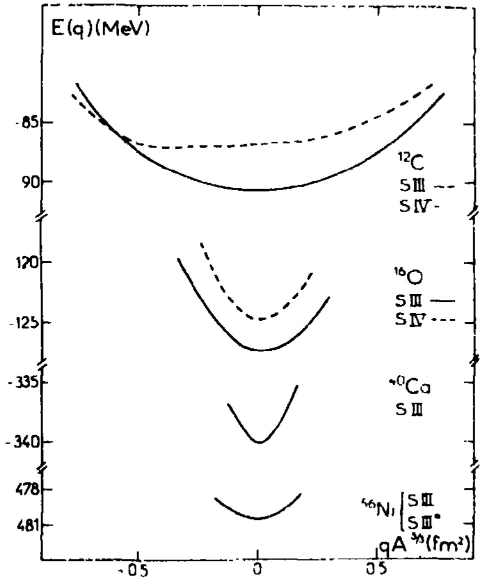

FIG. 7. Deformation energy curves of ^{12}C, ^{16}O, ^{40}Ca, and ^{56}Ni. SIV results are represented by dashed lines, and SIII results by solid lines. The SIII and SIII* forces lead, for ^{56}Ni, to the same curve.

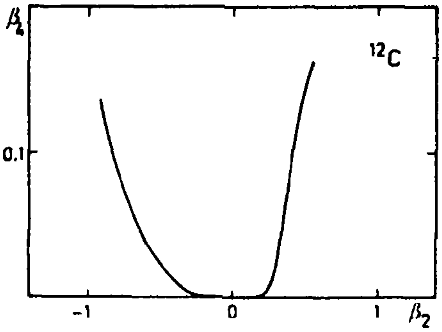

FIG. 8. Bohr and Mottelson standard deformation parameters of ^{12}C, calculated from SIII results for the CHF path.

see below that the (usually neglected) consideration of the associated adiabatic mass parameter can lead to a different conclusion.

It is interesting to analyze, in the ^{12}C case, the adiabatic path obtained from the solution of the CHF Eq. (2.4) with Q_{20} as constraining operator, in terms of quadrupole and hexadecapole surface distortions. For this purpose we have deduced the Bohr-Mottelson standard deformation parameters β_2 and β_4 from the calculated expectation values of the operators Q_{20} and Q_{40}. This has been done by assimilating the nuclear density with a sharply cut liquid-drop density. The result presented in Fig. 8 shows that for small quadrupol distortions ($|\beta_2| \leq 0.2$) the adiabatic path is well described in terms of Q_{20} surface deformation while this seems[18] not to be the case for larger $|\beta_2|$ values.

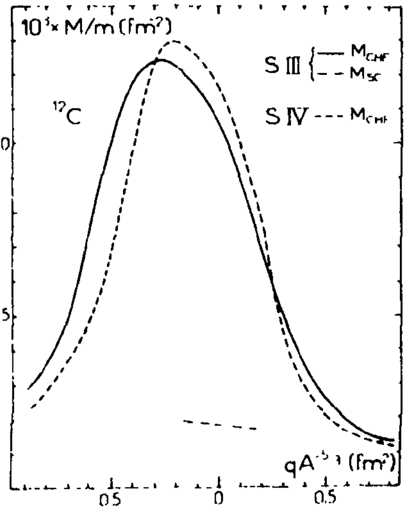

FIG. 9. Adiabatic mass parameters of ^{12}C, as functions of the collective variable. M_{CHF} is obtained from the CHF path with the constraint Q_{20}; M_{SC} is obtained from the scaling path (scaling with Q_{20} of a static HF solution).

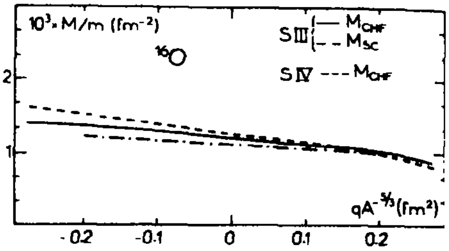

FIG. 10. Same as Fig. 9, for ^{16}O.

On Figs. 9–12 we show, for ^{12}C, ^{16}O, ^{40}Ca, a ^{56}Ni, the variation, with respect to the deformation, of the adiabatic mass for the CHF and sca ing paths. For the latter we have limited (see the discussion of Sec. V in I) the range of $qA^{-5/}$ to the interval (−0.2, 0.2) corresponding to a ma mum variation of the scaling parameter β of ±1 As expected from Eq. (2.1), the scaling mass parameters for all nuclei are smooth functions of q.

The mass parameters for CHF paths behave quite differently, their q variation has not the same features for spin-saturated nuclei (^{16}O, ^{40}Ca) as for spin-unsaturated nuclei (^{12}C, ^{56}Ni). For ^{16}O and ^{40}Ca, the HF masses are roughly constant with the deformation whereas for ^{12}C and ^{56}Ni they change dramatically. Such a well marked structure is a clear-cut signature of an harmonic motion. Of particular significance is the bump in the mass of ^{12}C already reported in an earlier publication.[19] Recently, a very similar situation[14] has been encountered in the calcu lation of the quadrupole Inglis cranking mass associated with two colliding ^{12}C nuclei; a shar peak has been found for a separation distance

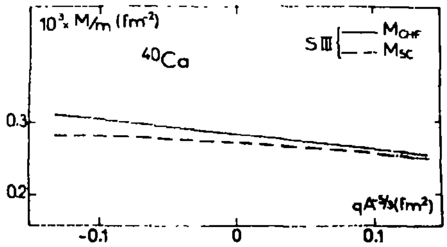

FIG. 11. Same as Fig. 9, for ^{40}Ca.

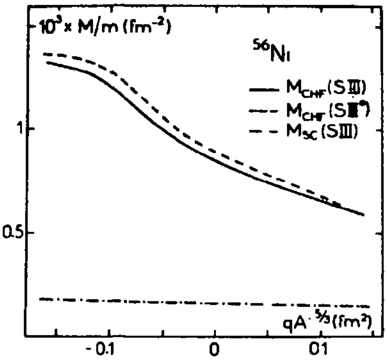

FIG. 12. Same as Fig. 9, for ^{56}Ni.

smaller than the barrier radius. In our case the behavior of the mass parameter can easily be explained. We first mention that in this case the Inglis cranking and self-consistent masses closely follow each other with an almost constant discrepancy of ~1–2% with the SIII force, and of ~3–4% with the SIV force. This allows us to restrict the discussion to the Inglis cranking mass:

$$M_{\mathrm{ICR}}(q)=\sum_{ph}\frac{|\langle p|\partial W_0/\partial q|h\rangle|^2}{\epsilon_{ph}{}^3}. \tag{4.1}$$

The main contribution to Eq. (4.1) comes from the particle-hole excitation between the two $\Omega^{\pi} = \frac{1}{2}^-$ states stemming from the $1p^{3/2}$ and $1p^{1/2}$ spherical subshells as seen on Fig. 13. The minimum value of the corresponding particle-hole energy ϵ_{ph} occurs roughly at the same deformation as the bump in M_{ICR}. Moreover, the quantity $1/\epsilon_{ph}{}^3$ roughly behaves, as a function of q, like M_{ICR} which implies that the matrix element in the numerator of Eq. (4.1) does not depend strongly on q.

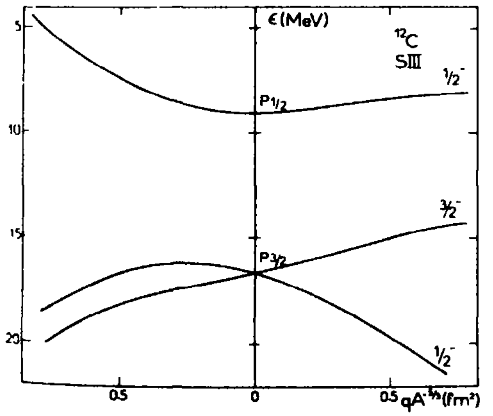

FIG. 13. Single-particle HF levels of ^{12}C around the Fermi surface as functions of the collective variable.

The spin-orbit splitting of the p shell results in an exchange (on the oblate deformation side of Fig. 13) of the two "asymptotic" [110] and [101] Nilsson $\Omega^{\pi}=\frac{1}{2}^-$ states, which is responsible, as we have seen, for the structure of the mass parameter. This kind of effect can thus be expected for all closed sub-shell nuclei which are not spin saturated. This is indeed the case for ^{56}Ni as seen on Fig. 12 where a similar structure as in ^{12}C takes shape. Unfortunately, due to the presence of level crossings, it has been impossible in this case to span the same range of deformation.

When requantizing the collective Hamiltonian with some quantization prescription one would therefore expect a concentration of the collective wave function around the deformation where the mass exhibits a maximum. This generates in the ^{12}C ground state an oblate deformation of purely dynamical origin. For ^{12}C and ^{56}Ni, the Bohr Hamiltonian is far from an harmonic oscillator one, which invalidates any small amplitude approximation.

As seen from Figs. 9 and 10, the mass parameters calculated for ^{12}C and ^{16}O with SIII and SIV, respectively, are very close. In particular the, same ground-state deformation of ^{12}C is found for both forces. In ^{56}Ni, SIII and SIII* yield also adiabatic masses in very good agreement (one expects, however, more important differences for *isovector* modes).

On Table II we present the quadrupole mass parameters calculated[30] at $q=0$ with SIII for both scaling and CHF paths. To facilitate the comparison between different nuclei we have multiplied the mass parameters by $A^{5/3}$. As expected, the "reduced" scaling masses are found almost constant with A. Indeed, since they correspond to an irrotational flow motion, their variation with A must go as $A^{-5/3}$. In contrast, the "reduced" CHF masses display a significant A dependence. For magic light (i.e., spin-saturated) nuclei they are equal to (or slightly larger than) the corresponding scaling values; for nonmagic nuclei they are much larger. This is easily understood in terms of random phase approximation (RPA) sum rules (see Sec. VI of I). For nuclei with static equilibrium at $q=0$, we know for the scaling mass $M_{\mathrm{SC}}(q=0)$ that

$$M_{\mathrm{SC}}(q=0)=\frac{\hbar^2}{2}\frac{1}{m_1(Q_{20})}, \tag{4.2}$$

whereas for the CHF mass $M_{\mathrm{CHF}}(q=0)$,

$$M_{\mathrm{CHF}}(q=0)=\frac{\hbar^2}{2}\frac{m_{-3}(Q_{20})}{[m_{-1}(Q_{20})]^2}. \tag{4.3}$$

TABLE II. Mass parameters of various nuclei at spherical equilibrium, in reduced units $MA^{5/3}$, for the CHF and scaling paths, calculated with SIII.

	^{12}C	^{16}O	^{40}Ca	^{48}Ca	^{56}Ni	^{90}Zr	^{140}Ce	^{208}Pb
$\frac{M_{CHF}\ (q=0)}{m} \times A^{5/3}$ (fm^{-2})	0.65	0.13	0.13	0.60	0.72	0.32	0.17	0.25
$\frac{M_{SC}\ (q=0)}{m} \times A^{5/3}$ (fm^{-2})	0.13	0.12	0.13	0.13	0.14	0.14	0.14	0.14

As mentioned in I these masses satisfy

$$M_{CHF}\ (q=0) \geq M_{SC}(q=0)\,, \tag{4.4}$$

which is verified in our calculations (see Table II). Moreover, the large discrepancies between M_{CHF} and M_{SC}, when they occur, are clearly related to a distribution of the quadrupole strength between "0-$\hbar\omega$" and "2-$\hbar\omega$" particle-hole excitations. This is obviously the case for open-shell nuclei. For heavy magic nuclei, the spin-orbit coupling, as is well known, introduces in the hole states, intruder orbitals from the next shell (which gives rise to low-lying states in the RPA spectrum). On the contrary, the two masses are roughly equal for light magic nuclei, where 0-$\hbar\omega$ excitations are forbidden by the Pauli principle.

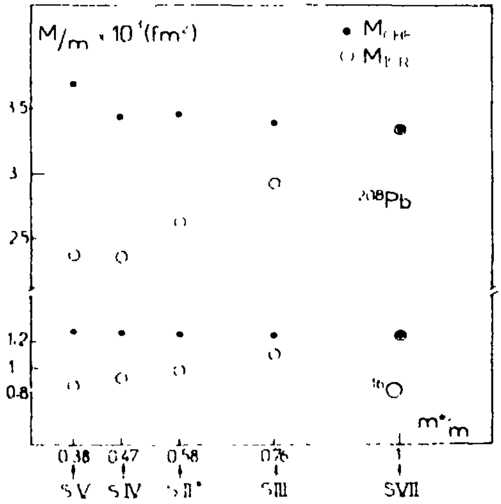

FIG. 14. Mass parameters of ^{208}Pb and ^{16}O (at spherical equilibrium) as functions of the interactions characterized by their effective mass. The dots represent self-consistent masses M_{CHF}, and the open circles correspond to cranking masses M_{ICR}.

Restricting ourselves from now on to the CHF path, we shall compare the exact adiabatic mass M_{CHF} with its non-self-consistent (Inglis cranking) approximation M_{ICR}. In fact, it is mainly for this purpose that various Skyrme forces all yielding the same saturation properties but having different effective masses m^* have been used. By inspection of Eq. (2.29) defining m^* and Eqs. (2.32) and (2.33) defining $W_1(\vec{r})$, one sees that for isoscalar modes (assuming moreover that $\rho^q = \rho/2$ and $\vec{j}^q = \vec{j}/2$) the time-odd self-consistent field $W_1(\vec{r})$ is proportional to $(m/m^* - 1)$. One expects therefore the difference ΔM

$$\Delta M = M_{CHF} - M_{ICR} \tag{4.5}$$

to be a monotonous function of $(m/m^* - 1)$. This is illustrated in Fig. 14. ΔM decreases with m^*/m for ^{16}O and ^{208}Pb; one notices also that $\Delta M = 0$ for SVII, for which $m^* = m$. As seen on Fig. 15 for ^{16}O, $\Delta M/M_{ICR}$ is also an increasing function of $(m/m^* - 1)$ and varies between 0 and 50% for all considered Skyrme forces. Since the ef-

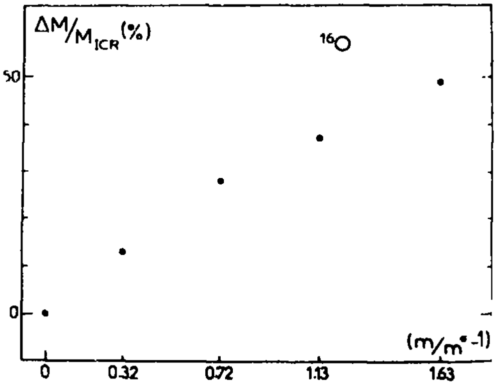

FIG. 15. Relative discrepancy between self-consistent (M_{CHF}) and cranking (M_{ICR}) mass parameters, as function of the interactions [characterized by the function $(m/m^* - 1)$ of their effective mass m^*], for ^{16}O at spherical equilibrium.

TABLE III. Relative discrepancy between self-consistent (M_{CHF}) and cranking (M_{ICR}) mass parameters for various nuclei at spherical equilibrium, calculated with SIII.

	^{12}C	^{16}O	^{40}Ca	^{48}Ca	^{56}Ni	^{90}Zr	^{140}Ce	^{208}Pb
$\Delta M/M_{ICR}$ $(q=0)$ (%)	1	11	8	7	13	11	10	16

fective mass in nuclear matter is expected[6,21] to be of the order of $(0.6-0.8)m$, one is led to assess a validity of ~15–30% to the mass parameters calculated with the Inglis cranking formula (at least for the isoscalar quadrupole mode). This is illustrated by Table III where $\Delta M/M_{ICR}$ is given for various nuclei calculated (at $q=0$) with SIII.

For ^{16}O, we have calculated M_{CHF} and M_{ICR} with the two forces SG0 of Ref. 17, corresponding to different powers of ρ ($\alpha=1$ and $\frac{1}{6}$) in the density-dependent force, both having the same effective mass $m^*/m=0.64$. Results displayed in Table IV show that $\Delta M/M_{ICR}$ is the same for the two forces. Moreover, these interactions lead, for M_{CHF}, to the same value as the other Skyrme forces (see Fig. 14); also, the result for M_{ICR} would take place in Fig. 14, on the straight line joining the points. These results and the result in ^{56}Ni with SIII* show that the value of m^* is the relevant parameter to characterize the degree of validity of the Inglis cranking formula. {Indeed, in this respect, the dependence of the path ρ_0 and of the currents $\vec{j}^s$ [see Eqs. (2.32) and (2.33)] on the choice of the interaction does not seem to play any role.}

It has been found in extensive calculations (with SIII and SIV for ^{12}C, ^{16}O, and ^{40}Ca) that ΔM is roughly constant with q. This seems to indicate that, at least for the isoscalar quadrupole mode, the effect of self-consistency is merely to shift upwards the curve $M_{ICR}(q)$.

We come now to an interesting feature which can be observed for ^{16}O on Fig. 14 and which is the quasiconstancy of $M_{CHF}(q=0)$ with respect to m^*, in contrast to the strong variation of M_{ICR}. Indeed, why M_{ICR} is an increasing function of m^* is easy to explain, since to increase m^* amounts to contract the single-particle spectrum, and hence to decrease the energy denominators in Eq. (4.1). The explanation of the quasiconstancy of $M_{CHF}(q=0)$ is somewhat more subtle. Take the magic ^{16}O nucleus; in this case the quadrupole strength is concentrated in the narrow giant resonance and the sum rule inequalities [Eq. (6.4)] of I become

$$\frac{m_3(Q_{20})}{m_1(Q_{20})}\propto\frac{m_1(Q_{20})}{m_{-1}(Q_{20})}\propto\frac{m_{-1}(Q_{20})}{m_{-3}(Q_{20})}. \tag{4.6}$$

On the other hand, it is known[22] that for Skyrme forces

$$m_3(Q_{20})\propto(m^*)^{-1}, \tag{4.7}$$

and also that $m_1(Q_{20})$ is almost constant with m^* (which comes from the force parameter adjustment to a correct saturation density). Therefore, Eq. (4.6) leads to

$$\begin{aligned}&m_{-1}(Q_{20})\propto m^*,\\&m_{-3}(Q_{20})\propto(m^*)^3,\end{aligned} \tag{4.8}$$

which shows, according to Eq. (4.3), the independence of M_{CHF} on m^*.

This argument, which was developed for ^{16}O, cannot be applied to ^{208}Pb where the quadrupole strength is more fragmented and indeed a slight but significant dependence of M_{CHF} on m^* is found in this case (see Fig. 14).

TABLE IV. Self-consistent (M_{CHF}) and cranking (M_{ICR}) mass parameters of ^{16}O at spherical equilibrium, calculated with the SG0 forces (characterized by the exponent α of ρ in the density-dependent term).

α	$10^3 M_{ICR}/m$ (fm^{-4})	$10^3 M_{CHF}/m$ (fm^{-4})	$\Delta M/M_{ICR}$
1	1.06	1.28	21%
$\frac{1}{6}$	1.01	1.22	21%

V. CONCLUSION

In the present works (papers I and II), we have carried out a theoretical study of the ATDHF formalism when it is restricted to a single collective trajectory, assumed to be known, together with a practical application to a specified collective motion, the quadrupole mode.

Two possible choices for the adiabatic paths have been considered. For the standard scaling path, we have found an analytical solution of the first set of Hamilton equations, which directly provides the mass parameter. To be able to compare the scaling mass with the CHF one, we have chosen the same collective variable in the two cases, which restricts the scaling transformation to small amplitude motions. In the CHF path case, we have developed a method to calculate the mass parameter, which reduces to a doubly constrained HF problem. This method avoids difficulties in dealing explicitly with the continuum part of the HF spectrum (as encountered in perturbation series), since it is equivalent to the solution of the Schrödinger equation for bound states. As shown by our numerical applications, the resulting values of the mass parameters are quite reliable, even if the solution is performed in a truncated harmonic oscillator basis.

This doubly constrained HF form of the first ATDHF equation is reminiscent of the starting points of other approaches to collective motion. In some of these, one chooses a time-even constraining operator Q defining the path (as we do), but there is no unique prescription to define the time-odd constraint P generating the dynamics. In our case, the operator P is unequivocally defined (except for irrelevant diagonal matrix elements) by the first Hamilton equation of motion. For any kind of path, the "coordinate" Q and the "momentum" P satisfy weak quantal canonical relations and their expectation values with respect to the time-dependent wave function are classically conjugate.

Numerical calculations of mass parameters have been performed for the two paths, with Q_{20} as scaling or constraining operator. Several interactions of the Skyrme type have been used. We have in particular focused our attention on four points: (i) distinction between small and large amplitude motions, (ii) comparison of the two choices of the path, (iii) for the CHF path, comparison between the ATDHF and the Inglis cranking masses, and (iv) influence on the results of the choice of the interaction (among a family of saturating Skyrme forces).

As is well known, the scaling path leads to the irrotational hydrodynamical value for the mass parameter. In reduced units ($MA^{5/3}$), this mass at equilibrium has almost the same value for all spherical nuclei (indeed, it is proportional to the inverse square of the nucleus radius). The scaling path is appropriate for the description of giant resonances, since it provides the excitation energy $E_3=(m_3/m_1)^{1/2}$, which is almost insensitive to the low-lying part of the spectrum. On the contrary, the CHF path does contain information on the shell structure; this is illustrated by the value $\frac{1}{2}\hbar^2 m_{-3}/(m_{-1})^2$ of the inertial parameter, which is dominated by the low energy states. Consequently, the CHF path, with Q_{20} as the constraint, is more appropriate to describe low energy collective excitations. For doubly closed shell nuclei it happens, however, that this path is capable of describing the giant resonance. In this case, which is a case of RPA harmonic vibrations, the CHF mass parameter is roughly constant with respect to the deformation, and very close to the scaling mass.

For non-spin-saturated nuclei (see the results for ^{12}C and ^{56}Ni), the CHF mass parameter exhibits a strong structure with respect to the deformation. This is incompatible with a small amplitude motion, and is a signature of the occurrence of anharmonic effects.

A systematic study of the results at the equilibrium spherical state shows that the ATDHF mass parameter is nearly independent of the choice of the Skyrme interaction. For light doubly closed shell nuclei, this quasiconsistancy can be proved analytically in terms of sum rules. On the contrary, the cranking mass is very sentitive to the interaction, and this sensitivity appears therefore to be a spurious effect due to the lack of self-consistency. In this respect, all the tests carried out with a large variety of Skyrme-like forces lead to the conclusion that the relevant parameter is the effective mass m^* in nuclear matter. For "reasonable" values of m^* (as in SIII), the self-consistent and cranking inertial parameter differ by 15–30%.

However, one should not extrapolate these results to other kinds of collective excitations, and, in particular, to rotational spectra. Relaxing some symmetries would give rise to new terms in the time-odd field W_1, leading possibly to a quite different value of the ratio $(M_{\mathrm{CHF}}-M_{\mathrm{ICR}})/M_{\mathrm{ICR}}$. Moreover, it would remain to investigate the effects of the other parametrizations of the effective interactions.

In the present work we have ignored the question of determining microscopically the adiabatic path. To solve this problem one would encounter as in "exact" TDHF calculations, the difficulty of finding (or even averaging over) initial conditions Some attempts to determine the collective paths have been proposed.[23-25] But in practice, they involve a considerable amount of difficulties. In our opinion it is not clear that such approaches are more valuable than extracting the path from TDHF solutions in the adiabatic limit.[26] It shoul also be stressed that, up to now, the numerical applications of all these methods are restricted to effective forces which are not as elaborate as those used in this paper. (In particular, the inc. sion of the spin-orbit force is needed to describ low energy collective motion).

The method presented here and illustrated by lot of numerical calculations is both practicable and microscopically well founded. In many respects however (the choice of the path, the absence of pairing correlations, the single collective variable reduction, etc.) there is room for further improvements.

ACKNOWLEDGMENTS

This work would not have been completed without constant and fruitful interaction with M. Vénéroni. We would like to express our gratitude to him and to D. Vautherin, for stimulating discussions and a critical reading of the manuscript. For the question of symmetries we have benefitted from the help of D. Vautherin and from a constructive criticism of J. Dobaczewski and A. Sobiczewski. We are indebted to X. Campi and H. Flocard for valuable discussions. We thank also D. Vautherin and F. Moreau for their contribution to the first stage of the numerical calculations. Finally, the Bureau de Calcul (IPN, Orsay) is gratefully acknowledged for extended computing facilities. This work has been performed at the Division de Physique Théorique (Institut de Physique Nucléaire), which is Laboratoire associé au C. N. R. S.

APPENDIX A: GAUGE INVARIANCE OF THE SKYRME FORCE WITH RESPECT TO ISOSCALAR SPIN-INDEPENDENT OPERATORS

(1) *Definition.* Given any wave function $|\phi_0\rangle$ and a Hermitian operator Q defining a new wave function $|\phi\rangle$ by

$$|\phi\rangle = e^{iQ}|\phi_0\rangle\,, \tag{A1}$$

the interaction V is said to be gauge invariant with respect to Q if

$$\langle\phi_0|V|\phi_0\rangle = \langle\phi|V|\phi\rangle = \langle\phi_0|e^{-iQ}Ve^{iQ}|\phi_0\rangle\,. \tag{A2}$$

A sufficient condition for that is

$$[V,Q]=0\,, \tag{A3}$$

as can be readily seen by expanding the exponentials. It may be noted that if $|\phi_0\rangle$, V, and Q are all time-even objects, the less restrictive condition[27]

$$[Q,[Q,V]]=0 \tag{A4}$$

is sufficient, the expectation value of time-odd operators vanishing for time-even states.

(2) *The Central Skyrme force.* Let us restrict ourselves for the moment to the central part of the two-body Skyrme force. If the spin-independent operator Q commutes with the spatial part of the central force, the whole central force is obviously gauge invariant (including the exchange terms). That is why we can limit ourselves to the gauge invariance property of the spatial part of the central force, the following proof being partially borrowed from Refs. 21 and 28.

The velocity-independent part

$$V_0(\vec{r}_1,\vec{r}_2)=\left[C+Df\left(\frac{\vec{r}_1+\vec{r}_2}{2}\right)\right]\delta(\vec{r}_1-\vec{r}_2) \tag{A5}$$

of the Skyrme force fulfills obviously the condition (A3). We are then left with two interaction terms

$$V_1=\sum_{ij}(\vec{P}_{ij}{}^2\delta_{ij}+\delta_{ij}\vec{P}_{ij}{}^2) \tag{A6}$$

and

$$V_2=\sum_{ij}(\vec{P}_{ij}\cdot\delta_{ij}\vec{P}_{ij}) \tag{A7}$$

with the notation

$$\begin{aligned}&\delta_{ij}=\delta(\vec{r}_i-\vec{r}_j)\,,\\&\vec{P}_{ij}=\vec{P}_i-\vec{P}_j\,,\\&\vec{P}_j=\frac{\hbar}{i}\vec{\nabla}_j\,.\end{aligned} \tag{A8}$$

The definitions (A6) and (A7) of the velocity-dependent parts of the Skyrme force differ from Eq. (2.7) by the replacement of $\vec{P}'$ by $\vec{P}$, which is irrelevant for our purpose here [the same remark holds for Eq. (A17) below].

From now on we will restrict ourselves to a one-dimensional problem since V_1 and V_2 involve only scalar products. It is easily seen that

$$[P_{ij},\delta_{ij}^{(n)}]=\frac{2\hbar}{i}\delta_{ij}^{(n+1)}\,, \tag{A9}$$

where $\delta^{(n)}$ is the nth derivative of δ. Moreover, upon defining

$$Q=\sum_{k=1}^{A}q(\vec{r}_k)=\sum_{k=1}^{A}q_k\,, \tag{A10}$$

one gets readily

$$[q_k,\delta_{ij}^{(n)}]=0\,. \tag{A11}$$

It is now possible to prove that if V_2 commutes with Q, V_1 does it also, since

$$\begin{aligned}[P_{ij}{}^2\delta_{ij}+\delta_{ij}P_{ij}{}^2,q_k]&=\left[2P_{ij}\delta_{ij}P_{ij}+\frac{2\hbar}{i}[P_{ij},\delta_{ij}^{(1)}],q_k\right]\\&=2[P_{ij}\delta_{ij}P_{ij},q_k]-(2\hbar)^2[\delta_{ij}^{(2)},q_k]\\&=2[P_{ij}\delta_{ij}P_{ij},q_k]\,.\end{aligned} \tag{A12}$$

To demonstrate that V_2 commutes with Q, one first notes, using Eqs. (A9) and (A11), that

$$[P_{ij}\delta_{ij}P_{ij},q_k]=[P_{ij},[P_{ij},q_k]\delta_{ij}]_+\,. \tag{A13}$$

Now since

$$[P_{ij}, q_k] = \begin{cases} \frac{2\hbar}{i} q_k^{(1)} & \text{if } i = k \\ -\frac{2\hbar}{i} q_k^{(1)} & \text{if } j = k \\ 0 & \text{otherwise,} \end{cases} \tag{A14}$$

one gets

$$[V_2, Q] = \frac{4\hbar}{i} \sum_{jk} [P_{kj}, q_k^{(1)} \delta_{kj}]_+ . \tag{A15}$$

Partially resumming the (j, k) and (k, j) contributions, one sees that $[V_2, Q]$ vanishes since $P_{kj} = -P_{jk}$ and $q_k^{(1)}\delta_{kj} = q_j^{(1)}\delta_{jk}$. As seen in Eq. (A10), we have considered an *isoscalar* operator Q. An *isovector* operator Q would have been defined as

$$Q = \sum_k \epsilon_k q_k \tag{A16}$$

with, e.g., $\epsilon_k = 1$ for protons, $\epsilon_k = -1$ for neutrons, and the previous proof could have been repeated up to Eq. (A15), the cancellation of the (j, k) and (k, j) contributions occuring only for $\epsilon_k = \epsilon_j$. As a result, the velocity-dependent Skyrme force is generally not gauge invariant with respect to isovector operators Q, as already noted in Refs. 7, 21, and 29.

(3) *The spin orbit force.* Let us consider the interaction

$$V_{so} = \sum_{ij} (\vec{P}_{ij} \times \delta_{ij} \vec{P}_{ij}) \cdot (\vec{\sigma}_i + \vec{\sigma}_j) . \tag{A17}$$

Using Eq. (A9), the x component of $\vec{P}_{ij} \times \delta_{ij} \vec{P}_{ij}$ writes

$$(\vec{P}_{ij} \times \delta_{ij} \vec{P}_{ij})^x = \frac{2\hbar}{i} (P_{ij}^z \delta_{ij}^{\prime y} - P_{ij}^y \delta_{ij}^{\prime z}) , \tag{A18}$$

where P_{ij}^z is the z component of P_{ij} and $\delta_{ij}^{\prime y}$ the first partial derivative of δ_{ij} with respect to y. From Eqs. (A14) and (A18) one gets

$$\sum_{ijk} [(\vec{P}_{ij} \times \delta_{ij} \vec{P}_{ij})^x, q_k] = -4\hbar^2 \sum_{jk} (\delta_{kj}^{\prime y} q_k^{\prime z} + \delta_{jk}^{\prime z} q_k^{\prime y}) , \tag{A19}$$

where $q_k^{\prime z}$ is the first partial derivative of q_k with respect to z. Collecting the contributions from the pairs (k, j) and (j, k) leads to the vanishing of the commutator (A19). A similar demonstration for the y and z components would achieve the proof of the gauge invariance of V_{so} with respect to isoscalar operators Q.

(4) *The Coulomb force.* Since the Coulomb force is velocity independent, it is gauge invariant with respect to isoscalar operators. It is trivial to show that this is also true for isovector operators.

APPENDIX B: WAVE FUNCTIONS AND IMPOSED SYMMETRIES

Consider a one-body reduced density matrix ρ commuting with J_3 and P_0, and define occupied states of ρ which are eigenstates of J_3 and P_0 with eigenvalues Ω and π. Their wave function in cylindrical coordinates can be written as

$$\varphi(\vec{r}, \vec{\sigma}) = \phi^-(r, z) e^{i\Lambda^+\theta} |-\rangle + \phi^+(r, z) e^{i\Lambda^-\theta} |+\rangle , \tag{B1}$$

where

$$\Lambda^\pm = \Omega \pm \tfrac{1}{2} , \tag{B2}$$

and where the kets $|\pm\rangle$ are the eigenstates of s_3.

Let us define for each φ, a state $\tilde{\varphi} = U_2 \varphi$ which is another occupied state of ρ with the wave function[30]

$$\tilde{\varphi}(\vec{r}, \vec{\sigma}) = \phi^-(r, z) e^{-i\Lambda^+\theta} |+\rangle - \phi^+(r, z) e^{-i\Lambda^-\theta} |-\rangle . \tag{B3}$$

It is an eigenstate of J_3 and P_0 with eigenvalues $-\Omega$ and π.

Let us introduce also the state $\bar{\varphi}$ deduced from φ by time-reversal conjugation $\mathcal{C}$:

$$\bar{\varphi}(\vec{r}, \vec{\sigma}) = -\phi^-(r, z)^* e^{-i\Lambda^+\theta} |-\rangle + \phi^+(r, z)^* e^{-i\Lambda^-\theta} |+\rangle . \tag{B4}$$

Time-even densities. If in addition to the J_3 and P_0 symmetries we assume that ρ is even under time reversal, there exists a representtion which is such that the functions ϕ^- and ϕ^+ are real and therefore

$$\tilde{\varphi} = -\bar{\varphi} . \tag{B5}$$

Hence, since ρ commutes with $\mathcal{C}$ it commutes also with U_2.

Consequence of the U_2 symmetry on density functions. It is easy to check that the wave functions φ and $\tilde{\varphi}$ and defined in Eqs. (B1) and (B3) give the same contribution to the spin-scalar density functions ρ, τ, j_r, j_z, and $\vec{\nabla} \cdot \vec{J}$.

APPENDIX C: THE SYMMETRIES OF THE SOLUTIONS INDUCE THE VANISHING OF SOME DENSITIES

First we show that the spin-vector density matrix $\vec{\rho}$ vanishes when the symmetries (i), (ii), and (iii) defined in Sec. II C are assumed. Any vector $\vec{V}$ will be represented by its *cylindrical* coordinates V_k $(k = r, \theta, z)$ defined from the Cartesian representation V_1, V_2, V_3 by

$$V_r=\tfrac{1}{2}(V_+e^{-i\theta}+V_-e^{i\theta}),$$
$$V_\theta=\tfrac{1}{2}i(-V_+e^{-i\theta}+V_-e^{i\theta}), \tag{C1}$$
$$V_z=V_3,$$

where

$$V_\pm=V_1\pm iV_2 . \tag{C2}$$

Let us denote by $\rho^{(l)}$ the density matrix

$$\rho^{(l)}=U_l\rho . \tag{C3}$$

From the symmetry properties

$$[\vec{\rho},U_l]=0, \tag{C4}$$

and therefore

$$\rho_k^{(l)}=\rho_k,\quad k=r,\theta,z . \tag{C5}$$

To prove the vanishing of $\vec{\rho}$ we will show by explicit action of a suitably chosen U_l transformation that

$$\rho_k^{(l)}=-\rho_k,\quad k=r,\theta,z . \tag{C6}$$

r component. Let us consider the action of U_3 on ρ_r

$$\rho_r^{(3)}(\vec{x},\vec{x}')=\sum_{\sigma\sigma'}\langle r,z,\theta,\sigma|U_3^{+}\rho U_3|r',z',\theta',\sigma'\rangle \times\langle\sigma'|\sigma_r|\sigma\rangle , \tag{C7}$$

where

$$U_3=P_0e^{i\pi l_3}i\sigma_3$$

and

$\vec{x}(\vec{x}')$ stands for $r,z,\theta(r',z',\theta')$.

The $P_0e^{i\pi l_3}$ operator transforms (r,z,θ) into $(r,-z,\theta)$. Since the density matrix is invariant under this transformation, its radial part is even with respect to z and therefore

$$\rho_r^{(3)}(\vec{x},\vec{x}')=\sum_{\sigma\sigma'}\langle\vec{x},\sigma|\sigma_3\rho\sigma_3|\vec{x}',\sigma'\rangle\langle\sigma'|\sigma_r|\sigma\rangle . \tag{C8}$$

Defining

$$|\bar{\sigma}\rangle=\sigma_3|\sigma\rangle \tag{C9}$$

and similarly

$$|\bar{\sigma}'\rangle=\sigma_3|\sigma'\rangle \tag{C10}$$

leads to

$$\rho_r^{(3)}(\vec{x},\vec{x}')=\sum_{\sigma\sigma'}\langle\vec{x},\bar{\sigma}|\rho|\vec{x}',\bar{\sigma}'\rangle\langle\bar{\sigma}'|\sigma_3\sigma_r\sigma_3|\bar{\sigma}\rangle . \tag{C11}$$

Since

$$\sigma_3\sigma_r\sigma_3=-\sigma_r , \tag{C12}$$

one easily gets

$$\rho_r^{(3)}(\vec{x},\vec{x}')=-\rho_r(\vec{x},\vec{x}') . \tag{C13}$$

θ component. A similar proof for ρ_θ gives

$$\rho_\theta^{(3)}(\vec{x},\vec{x}')=-\rho_\theta(\vec{x},\vec{x}') . \tag{C14}$$

z component. In this case we consider the action of U_2 on ρ_z. The operator $P_0e^{i\pi l_2}$ transforms (r,z,θ) into $(r,z,-\theta)$. Due to the axial symmetry the radial part of ρ_z does not depend on θ and therefore

$$\rho_z^{(2)}(\vec{x},\vec{x}')=\sum_{\sigma\sigma'}\langle\vec{x},\sigma|\sigma_2\rho\sigma_2|\vec{x}',\sigma'\rangle\langle\sigma'|\sigma_z|\sigma\rangle . \tag{C15}$$

From

$$\sigma_2\sigma_z\sigma_2=-\sigma_z , \tag{C16}$$

one gets readily

$$\rho_z^{(2)}(\vec{x},\vec{x}')=-\rho_z(\vec{x},\vec{x}') . \tag{C17}$$

Extension to other density functions. The preceding arguments can easily be extended to demonstrate the vanishing of the kinetic energy spin-vector density $\vec{T}$, the scalar part of the $J_{\mu\nu}$ tensor, and the j_θ component of the current vector $\vec{j}$.

APPENDIX D: THE MATRIX ELEMENTS OF W_1 IN THE HARMONIC OSCILLATOR BASIS

(1) *Notation.* A normalized basis vector is defined by two oscillator constants $c_\perp$ and c_z and by a set of 4 quantum numbers n_z, $n_\perp$, Λ,Σ, eigenvalues of the numbers of quanta in the z direction and in the $x0y$ plane, the z component of the orbital and spin angular momenta (divided by $\hbar$), respectively. One generally introduces

$$n=\tfrac{1}{2}(n_\perp-|\Lambda|) \tag{D1}$$

and defines the current basis vector by $\alpha\equiv\{n_z,n,\Lambda,\Sigma\}$. In cylindrical coordinates (r,θ,z) the corresponding normalized spatial wave function can be expressed as the product of three wave functions:

$$\varphi_{n_z n,\Lambda}(\vec{r})=\psi_n^\Lambda(r)\psi_{n_z}(z)\psi_\Lambda(\theta) . \tag{D2}$$

The radial wave function (for $\Lambda>0$) writes

$$\psi_n^\Lambda=N_n^\Lambda c_\perp\sqrt{2}\,\eta^{\Lambda/2}e^{-\eta/2}L_n^\Lambda(\eta) , \tag{D3}$$

with

$$N_n^\Lambda=\left[\frac{n!}{(n+\Lambda)!}\right]^{1/2} \tag{D4}$$

and

$$\eta=c_\perp^2r^2 , \tag{D5}$$

$L_n^\Lambda(x)$ being the usual Laguerre polynomial.[31] The longitudinal wave function writes

$$\psi_{n_z} = M_{n_z}\sqrt{c_z}\,e^{-\zeta^2/2}H_{n_z}(\zeta), \tag{D6}$$

where

$$M_{n_z} = (\sqrt{\pi}\,2^{n_z}n_z!)^{-1/2} \tag{D7}$$

and

$$\zeta = c_z z, \tag{D8}$$

$H_{n_z}(x)$ being the usual Hermite polynomial.[31] The angular wave function writes

$$\psi_\Lambda = \frac{1}{\sqrt{2\pi}}e^{i\Lambda\theta}. \tag{D9}$$

To deal with first derivatives of the ψ's we introduce as in Ref. 3 new polynomials $\bar{H}_{n_z}$ and $\bar{L}_n^\Lambda$ defined by

$$\nabla_z\psi_{n_z}(\zeta) = M_{n_z}c_z^{3/2}e^{-\zeta^2/2}\bar{H}_{n_z}(\zeta), \tag{D10}$$

$$\nabla_r\psi_n^\Lambda(r) = N_n^\Lambda c_\perp^2\sqrt{2}\,\eta^{(\Lambda-1)/2}\bar{L}_n^\Lambda(\eta). \tag{D11}$$

Using standard relations for H and L polynomials leads to

$$\bar{H}_{n_z}(\zeta) = \zeta H_{n_z}(\zeta) - H_{n_z+1}(\zeta), \tag{D12}$$

$$\bar{L}_n^\Lambda(\eta) = 2(n+1)L_{n+1}^\Lambda(\eta) - (2n+\Lambda+2-\eta)L_n^\Lambda(\eta). \tag{D13}$$

(2) *Current.* The k component of the current vector $\vec{j}$ can be written in terms of the basis wave functions φ_α and $\varphi_{\alpha'}$ as

$$j_k(\vec{r}) = \frac{1}{2i}\sum_{\alpha\alpha'}[\rho_{\alpha\alpha'}\nabla_k\varphi_\alpha(\vec{r})\varphi^*_{\alpha'}(\vec{r}) - \varphi_\alpha(\vec{r})\nabla_k\varphi^*_{\alpha'}(\vec{r})]. \tag{D14}$$

Using the Hermiticity of ρ and the reality of $\nabla_k\varphi_\alpha(\vec{r})\varphi^*_{\alpha'}(\vec{r})$ ($\Lambda_\alpha = \Lambda_{\alpha'}$ due to the axial symmetry and the spin scalar character of ρ) one gets

$$j_k(\vec{r}) = \tfrac{1}{2}\sum_{\alpha\alpha'}\mathrm{Im}(\rho_{\alpha\alpha'})[\nabla_k\varphi_\alpha(\vec{r})\varphi^*_{\alpha'}(\vec{r}) - \varphi_\alpha(\vec{r})\nabla_k\varphi^*_{\alpha'}(\vec{r})]. \tag{D15}$$

From the definition relations (D10) and (D11) one obtains

$$j_r(\zeta,\eta) = \frac{c_z c_\perp^3}{2\pi}e^{-(\zeta^2+\eta)}\sum_{\alpha\alpha'}\{\mathrm{Im}(\rho_{\alpha\alpha'})M_{n_z}M_{n_z'}N_n^\Lambda N_{n'}^{\Lambda'}\delta_{\Lambda\Lambda'}\eta^{(\Lambda-1)/2}H_{n_z}(\zeta)H_{n_z'}(\zeta)[\bar{L}_n^\Lambda(\eta)L_{n'}^{\Lambda'}(\eta) - L_n^\Lambda(\eta)\bar{L}_{n'}^{\Lambda'}(\eta)]\} \tag{D16}$$

and

$$j_z(\zeta,\eta) = \frac{c_z^2 c_\perp^2}{2\pi}e^{-(\zeta^2+\eta)}\sum_{\alpha\alpha'}\{\mathrm{Im}(\rho_{\alpha\alpha'})M_{n_z}M_{n_z'}N_n^\Lambda N_{n'}^{\Lambda'}\delta_{\Lambda\Lambda'}\eta^\Lambda L_n^\Lambda(\eta)L_{n'}^{\Lambda}(\eta)[\bar{H}_{n_z}(\zeta)H_{n_z'}(\zeta) - H_{n_z}(\zeta)\bar{H}_{n_z'}(\zeta)]\}. \tag{D17}$$

(3) *The matrix elements.* From the preceding expressions for j_r^q and j_z^q one gets, according to Eq. (2.33), the components I_r^q and I_z^q of the fields $\vec{I}^q(\vec{r})$. Now, integrating by parts the second term of

$$\langle\alpha|W_1|\alpha'\rangle = \frac{1}{2i}\langle\alpha|\vec{I}^q\cdot\vec{\nabla} + \vec{\nabla}\cdot\vec{I}^q|\alpha'\rangle, \tag{D18}$$

the matrix element to be computed becomes

$$\langle\alpha|W_1|\alpha'\rangle = \frac{1}{2i}\int\{\varphi^*_\alpha(\vec{r})\vec{I}^q(\vec{r})\cdot\vec{\nabla}\varphi_{\alpha'}(\vec{r}) - [\vec{\nabla}\varphi^*_\alpha(\vec{r})\cdot\vec{I}^q(\vec{r})\varphi_{\alpha'}(\vec{r})]\}d^3r, \tag{D19}$$

that is, with our notation,

$$\begin{aligned}\langle\alpha|W_1|\alpha'\rangle = {}& -i\delta_{\Omega\Omega'}\delta_{\Lambda\Lambda'}M_{n_z}M_{n_z'}N_n^\Lambda N_{n'}^{\Lambda'}c_\perp^2 c_z \\ &\times\int_0^\infty e^{-\eta}\eta^\Lambda d\eta\int_{-\infty}^{\infty}e^{-\zeta^2}d\zeta \\ &\times\{c_\perp H_n(\zeta)H_{n'}(\zeta)I_r(\eta,\zeta)\eta^{-1/2}[L_n^\Lambda(\eta)\bar{L}_{n'}^{\Lambda'}(\eta) - \bar{L}_n^\Lambda(\eta)L_{n'}^{\Lambda'}(\eta)] \\ &+ c_z L_n^\Lambda(\eta)L_{n'}^{\Lambda'}(\eta)I_z(\eta,\zeta)[H_n(\zeta)\bar{H}_{n'}(\zeta) - \bar{H}_n(\zeta)H_{n'}(\zeta)]\}.\end{aligned} \tag{D20}$$

*Present address: Institut Laue-Langevin, BP 156X, 38042 Grenoble-Cedex, France.

[1] M. J. Giannoni and P. Quentin, Phys. Rev. C 21, 2060 (1980).

[2] D. Vautherin and D. M. Brink, Phys. Rev. C 5, 626 (1972).

[3] D. Vautherin, Phys. Rev. C 7, 296 (1973).

[4] H. Flocard, P. Quentin, A. K. Kerman, and D. Vautherin, Nucl. Phys. A203, 433 (1973).

[5] M. Beiner, H. Flocard, Nguyen Van Giai, and P. Quentin, Nucl. Phys. A238, 29 (1975).

[6] See, e.g., P. Quentin and H. Flocard, Ann. Rev. Nucl. Part. Sci. 28, 523 (1978).

[7] Y. M. Engel, D. M. Brink, K. Goeke, S. J. Krieger, and D. Vautherin, Nucl. Phys. A249, 215 (1975).

[8] See also H. Flocard, Nukleonika 24, 19 (1979).

[9] Their $\vec{r}$ dependence has been omitted for the sake of conciseness.

[10] P. Gombás, Ann. Phys. (Leipzig) 10, 253 (1952).

[11] G. Ripka, Adv. Nucl. Phys. 1, 189 (1968).

[12] In this respect, we are indebted to P. Gara (Bureau de Calcul, IPN Orsay) for having provided us with a very efficient routine.

[13] P. Quentin and R. Babinet, Nucl. Phys. A156, 365 (1970).

[14] H. Flocard, P. H. Heenen, and D. Vautherin, in *Time-dependent Hartree-Fock Method*, edited by P. Bonche, B. Giraud, and P. Quentin (Editions de Physique, Orsay, 1979), p. 50; Nucl. Phys. (to be published).

[15] In a recent paper K. Goeke [Phys. Rev. Lett. 38, 212 (1977)] has solved the first Hamilton equation for isoscalar monopole vibrations in $\vec{r}$ representation. The comparison of his "exact" results with those obtained by perturbation techniques shows indeed a very poor convergence of the latter.

[16] H. Flocard, thèse d'Etat, Université Paris-Sud, 1975 (unpublished).

[17] J. Treiner and H. Krivine, J. Phys. G 2, 285 (1976).

[18] It is clear that for very large $|\beta_2|$ values, higher multipole moments should be included in the analysis, which has not been done here.

[19] M. J. Giannoni, F. Moreau, P. Quentin, D. Vautherin, M. Véneroni, and D. M. Brink, Phys. Lett. B65, 305 (1976).

[20] We have used a 9 oscillator shell basis for nuclei with $A \leq 90$ and an 11 oscillator shell basis for $A > 90$.

[21] O. Bohigas, A. M. Lane, and J. Martorell, Phys. Rep. 51, 267 (1979).

[22] D. M. Brink and R. Leonardi, Nucl. Phys. A258, 285 (1976).

[23] M. Baranger and M. Véneroni, Ann. Phys. (N.Y.) 114, 123 (1978); D. M. Brink, M. J. Giannoni, and M. Véneroni, Nucl. Phys. A258, 237 (1976).

[24] F. M. H. Villars, Nucl. Phys. A285, 269 (1977).

[25] K. Goeke and P. G. Reinhard, Ann. Phys. (N.Y.) 112, 328 (1978); P. G. Reinhard and K. Goeke, Nucl. Phys. A312, 121 (1978).

[26] P. Bonche and P. Quentin, Phys. Rev. C 18, 1891 (1978). P. Bonche, H. Doubre, and P. Quentin, Phys. Lett. 82B, 5 (1979).

[27] M. J. Giannoni, D. Vautherin, M. Véneroni, and D. M. Brink, Phys. Lett. B63, 8 (1976).

[28] S. Fallieros, Lecture Notes, Orsay, 1975 (unpublished).

[29] H. Krivine, J. Treiner and O. Bohigas, Nucl. Phys. (to be published); J. Treiner and H. Krivine, in *Time-dependent Hartree-Fock Method*, edited by P. Bonche, B. Giraud, and P. Quentin (Editions de Physique, Orsay, 1979), p. 194.

[30] Since $U_2 = P_0 e^{i\pi/2} i\sigma_2$, the U_2 transformation amounts for the space variables only to a change of (r, z, θ) into $(r, z, -\theta)$.

[31] The Bateman Manuscript Project, *Higher Transcendental Functions*, edited by A. Erdelyi (McGraw-Hill, New York, 1953), Vol. II.

PHYSICAL REVIEW C VOLUME 21, NUMBER 5 MAY 19

Comments

The Comments section is for short papers which comment on papers previously published in **The Physical Review**. *Manuscripts intend for this section must be accompanied by a brief abstract for information retrieval purposes and a keyword abstract*

Pion-nucleus optical potential including the nuclear Hamiltonian

Humberto Garcilazo*
Escuela Superior de Física y Matemáticas, Instituto Politécnico Nacional, México 14 D. F., México

(Received 6 November 1979)

We use the fact that the mass of the pion is much smaller than the mass of the nucleon to derive an expression for the first-order pion-nucleus optical potential that includes the effect of the nuclear Hamiltonian through a single-particle model. We apply this potential to calculate the total and reaction cross sections of ^{12}C and the charge-exchange cross section to the isobaric analog state in ^{13}C for energies between 0 and 300 MeV, obtaining qualitative agreement with experiment.

[NUCLEAR REACTIONS $^{13}\mathrm{C}(\pi^+,\pi^0)$, $^{12}\mathrm{C}(\pi^+,\pi^+)$, $E=0-300$ MeV; calculated $\sigma_{\rm tot}(E)$, $\sigma_{\rm reac}(E)$, and $\sigma_{\rm cex}(E)$.]

Recently, Tandy, Redish, and Bollé[1] have proposed a three-body model for the first-order optical potential of Kerman, McManus, and Thaler,[2] which in the case of pion-nucleus scattering takes the form

$$\langle \vec{k}'|V_{\rm opt}(E)|\vec{k}\rangle = \frac{(A-1)}{A}\sum_{i=1}^{A}\langle \vec{k}'\phi_0|\bar{t}^{(i)}_{\pi N}(E)|\vec{k}\phi_0\rangle\,, \tag{1}$$

where A is the number of nucleons, ϕ_0 is the ground-state wave function of the nucleus, and the operator $\bar{t}^{(i)}_{\pi N}(E)$ is the pion-nucleon amplitude in the nuclear medium, which obeys the integral equation

$$\bar{t}^{(i)}_{\pi N}(E) = V^{(i)}_{\pi N} + V^{(i)}_{\pi N}\frac{1}{E-T_\pi - H_N + i\epsilon}\bar{t}^{(i)}_{\pi N}(E)\,, \tag{2}$$

where $V^{(i)}_{\pi N}$ is the potential between the pion and nucleon i, T_π is the kinetic energy operator of the pion, and H_N is the nuclear Hamiltonian. The simplest approximation to Eq. (2), which is known as the closure approximation,[3] consists in replacing the nuclear Hamiltonian H_N by a constant effective excitation $\bar{E}$, which is usually taken to be zero, so that the operator $\bar{t}^{(i)}_{\pi N}$ becomes the free pion-nucleon T matrix. Tandy, Redish, and Bollé[1] have proposed a systematic way to improve the description of Eq. (2) by taking for the nuclear Hamiltonian H_N the single-particle Hamiltonian $H_N=\sum_{i=1}^{A}T_N^{(i)}+V_N^{(i)}$, where $T_N^{(i)}$ is the kinetic energy operator of nucleon i, and $V_N^{(i)}$ is the potential of that nucleon in the nuclear well. This corresponds to the first term of an expansion in which the residual interaction appears only in second- and higher-order terms.[1] If we use the eigenstates of H_N to evaluate Eqs. (1) and (2), the when we introduce a complete set of these states in the propagator, the part of the wave functions describing all nucleons other than i collapses with the corresponding one in ϕ_0, so that ϕ_0 is left only with the part describing nucleon i, and the nuclear Hamiltonian H_N can effectively be taken to be $H_N=T_N^{(i)}+V_N^{(i)}$, so that if we now drop the index i, Eq. (2) can be written in the form

$$\begin{aligned}\bar{t}_{\pi N}(E) &= V_{\pi N}+V_{\pi N}\frac{1}{E-T_\pi-T_N-V_N+i\epsilon}\bar{t}_{\pi N}(E)\\ &= V_{\pi N}+V_{\pi N}\frac{1}{E-T_\pi-T_N-V_N-V_{\pi N}+i\epsilon}V_{\pi N}\,.\end{aligned} \tag{3}$$

If we now reexpress the kinetic energy operators in terms of relative and center of mass variables, we can write

$$\begin{aligned}T_\pi+T_N+V_N+V_{\pi N} &= T^{\rm rel}+T^{\rm c.m.}+V_N+V_{\pi N}\\ &= H^{\rm rel}_{\pi N}+T^{\rm c.m.}+V_N\\ &\simeq H^{\rm rel}_{\pi N}+H^{\rm c.m.}_N\,,\end{aligned} \tag{4}$$

where we have made the approximation that the single-nucleon potential V_N is a function of the pion-nucleon center of mass coordinate; that is, if we call μ the mass of the pion and M the mass of the nucleon, then

© 1980 The American Physical Society

$$\vec{R}^{\text{c.m.}}=\frac{1}{M+\mu}(M\vec{r}_N+\mu\vec{r}_\pi)\simeq\vec{r}_N\,,\ \text{since}\,\frac{\mu}{M}\ll 1\,. \tag{5}$$

Substituting Eq. (4) into Eq. (3), we get the approximate expression

$$\bar{t}_{\pi N}(E)\simeq V_{\pi N}+V_{\pi N}\frac{1}{E-H_{\pi N}^{\text{rel}}-H_N^{\text{c.m.}}+i\epsilon}V_{\pi N}\,, \tag{6}$$

where $H_{\pi N}^{\text{rel}}$ is the Hamiltonian of the relative motion of the pion-nucleon system which depends on the relative variables, and $H_N^{\text{c.m.}}$ is the Hamiltonian of the nucleon which depends here on the pion-nucleon center of mass variables.

The free pion-nucleon amplitude $t_{\pi N}$ differs from the amplitude $\bar{t}_{\pi N}$ by not containing the nuclear Hamiltonian, so that it is given in the language of Eq. (6) as

$$t_{\pi N}(E)=V_{\pi N}+V_{\pi N}\frac{1}{E-H_{\pi N}^{\text{rel}}+i\epsilon}V_{\pi N}\,. \tag{7}$$

Using Eq. (6), we can write the matrix elements of the operator $\bar{t}_{\pi N}$ that are needed in Eq. (1), as

$$\begin{aligned}\langle\vec{k}'\phi_0|\bar{t}_{\pi N}(E)|\vec{k}\phi_0\rangle&=\langle\vec{k}'\phi_0|V_{\pi N}|\vec{k}\phi_0\rangle\\&\quad+\sum_{\alpha n}\sum\langle\vec{k}'\phi_0|V_{\pi N}|\chi_\alpha\phi_n\rangle\\&\qquad\times\frac{1}{E-E_\alpha-E_n+i\epsilon}\\&\qquad\times\langle\chi_\alpha\phi_n|V_{\pi N}|\vec{k}\phi_0\rangle\,,\end{aligned} \tag{8}$$

where χ_α are relative pion-nucleon wave functions of energy eigenvalue E_α and ϕ_n are single-nucleon wave functions of energy eigenvalue E_n, considered here as functions of the pion-nucleon center of mass variable. Similarly, the free pion-nucleon T matrix given by Eq. (7) can be written as

$$\begin{aligned}\langle\vec{q}'|t_{\pi N}(E)|\vec{q}\rangle&=\langle\vec{q}'|V_{\pi N}|\vec{q}\rangle\\&\quad+\sum_\alpha\langle\vec{q}'|V_{\pi N}|\chi_\alpha\rangle\frac{1}{E-E_\alpha+i\epsilon}\\&\qquad\times\langle\chi_\alpha|V_{\pi N}|\vec{q}\rangle\,,\end{aligned} \tag{9}$$

where $\vec{q}$ is the relative momentum of the pion-nucleon system which is given in terms of the pion and nucleon momenta $\vec{k}$ and $\vec{p}$ as

$$\vec{q}=\frac{1}{M+\mu}(M\vec{k}-\mu\vec{p})\simeq\vec{k}\,. \tag{10}$$

Using the separation into relative and center of mass components for the intermediate wave functions that enter in Eq. (8), we can write the term that appears there,

$$\begin{aligned}\langle\chi_\alpha\phi_n|V_{\pi N}|\vec{k}\phi_0\rangle&=\int d\vec{p}\langle\chi_\alpha\phi_n|V_{\pi N}|\vec{k}\vec{p}\rangle\langle\vec{p}|\phi_0\rangle\\&=\int d\vec{p}\langle\chi_\alpha|V_{\pi N}|\vec{q}\rangle\langle\phi_n|\vec{k}+\vec{p}\rangle\langle\vec{p}|\phi_0\rangle\\&\simeq\langle\chi_\alpha|V_{\pi N}|\vec{k}\rangle\Lambda_n(\vec{k})\,,\end{aligned} \tag{11}$$

where we have used Eq. (10), and we are defining

$$\begin{aligned}\Lambda_n(\vec{k})&\equiv\int d\vec{p}\langle\phi_n|\vec{k}+\vec{p}\rangle\langle\vec{p}|\phi_0\rangle\\&=\int d\vec{p}\,\phi_n^*(\vec{k}+\vec{p})\phi_0(\vec{p})\,.\end{aligned} \tag{12}$$

If we substitute Eq. (11) into Eq. (8), then using Eqs. (9) and (10) to recognize the free pion-nucleon T matrix, and the fact that the functions ϕ_n form a complete set, we get the expression

$$\langle\vec{k}'\phi_0|\bar{t}_{\pi N}(E)|\vec{k}\phi_0\rangle=\sum_n\langle\vec{k}'|t_{\pi N}(E-E_n)|\vec{k}\rangle\Lambda_n^*(\vec{k}')\Lambda_n(\vec{k})\,, \tag{13}$$

which together with Eqs. (1) and (12), is our result for the pion-nucleus optical potential including the effect of the nuclear Hamiltonian. Equations (12) and (13) provide a simple way to construct the matrix elements of the operator $\bar{t}_{\pi N}$ in terms of the free pion-nucleon T matrix $t_{\pi N}$ and the single-nucleon wave functions ϕ_n. Equation (13) represents also the solution to the problem of the first-order optical potential as formulated by Tandy, Redish, and Bollé, where one has to solve the three-body problem defined by the pion, the nucleon, and the residual nucleus, assuming that there is no interaction between the pion and the residual nucleus. If we call M_{res} the mass of the residual nucleus, then in the limit $M_{\text{res}}\gg M\gg\mu$, Eq. (13) is the solution of that simple three-body problem.

As we will show below, Eq. (13) reduces to the standard expression of the optical potential based in the closure approximation if we neglect the single-nucleon energies E_n in the argument of $t_{\pi N}$, since using the fact that the single-nucleon wave functions ϕ_n form a complete set,

$$\begin{aligned}\langle\vec{k}'\phi_0|\bar{t}_{\pi N}(E)|\vec{k}\phi_0\rangle&\simeq\langle\vec{k}'|t_{\pi N}(E)|\vec{k}\rangle\sum_n\Lambda_n^*(\vec{k}')\Lambda_n(\vec{k})\\&=\langle\vec{k}'|t_{\pi N}(E)|\vec{k}\rangle\sum_n\int d\vec{p}'d\vec{p}\langle\phi_0|\vec{p}'\rangle\langle\vec{k}'+\vec{p}'|\phi_n\rangle\langle\phi_n|\vec{k}+\vec{p}\rangle\langle\vec{p}|\phi_0\rangle\\&=\langle\vec{k}'|t_{\pi N}(E)|\vec{k}\rangle\int d\vec{p}'d\vec{p}\,\phi_0^*(\vec{p}')\delta(\vec{k}'+\vec{p}'-\vec{k}-\vec{p})\phi_0(\vec{p})\\&=\langle\vec{k}'|t_{\pi N}(E)|\vec{k}\rangle\int d\vec{r}\,e^{i(\vec{k}-\vec{k}')\cdot\vec{r}}|\phi_0(\vec{r})|^2\,,\end{aligned} \tag{14}$$

which is recognized as the standard expression of the first-order optical potential.[1-5]

As an example, we applied our expressions (1), (12), and (13) to calculate the total and reaction cross sections of ^{12}C up to 300 MeV. We can also apply our Eq. (13) to calculate the charge exchange reaction to the isobaric analog state ^{13}C$(\pi^+,\pi^0)^{13}$N, since in this process the wave function of the valence nucleon is the same in the initial and final state except that its isospin projection has been flipped from $-\frac{1}{2}$ to $\frac{1}{2}$, so that using the distorted wave impulse approximation,[6,7] we can write

$$T^{\mathrm{cex}}(E)=\int d\vec{\mathrm{k}}'d\vec{\mathrm{k}}\,\chi^{(+)*}(\vec{\mathrm{k}}')\langle\vec{\mathrm{k}}'\phi_0|t^{\mathrm{cex}}_{\pi N}(E)|\vec{\mathrm{k}}\phi_0\rangle\chi^{(-)}(\vec{\mathrm{k}})\,, \tag{15}$$

where $\bar{t}^{\mathrm{cex}}_{\pi N}$ is the elementary pion-nucleon charge exchange amplitude in the nuclear medium, ϕ_0 is the wave function of the valence nucleon, and $\chi^{(-)}$ and $\chi^{(+)}$ are the incoming and outgoing distorted pion waves.

In order to construct the optical potential given by Eqs. (1), (12), and (13), we need to know the free pion-nucleon T matrix $t_{\pi N}$, and the complete set of single-nucleon wave functions ϕ_n. We used for the free pion-nucleon T matrix the separable form with s and p waves,

$$\langle\vec{\mathrm{k}}'|t_{\pi N}(E)|\vec{\mathrm{k}}\rangle=\frac{\alpha^2+k_0{}^2}{\alpha^2+k'^2}\,[b_0(E)+b_1(E)\vec{\mathrm{k}}'\cdot\vec{\mathrm{k}}]\times\frac{\alpha^2+k_0{}^2}{\alpha^2+k^2}\,, \tag{16}$$

where k_0 is the on-shell momentum corresponding to the energy E, and the parameters $b_l(E)$ are given in terms of phase shifts.[4] We used the analytic parametrization of the phase shifts given in Ref. 8.

We constructed the single-nucleon wave functions ϕ_n using a square well potential of radius $R=2.9$ fm and depth $V_0=48$ MeV, which has only two bound states, one for $l=0$ with energy -32.21 MeV and one for $l=1$ with energy -16.57 MeV, so that they correspond approximately to the experimental single-particle energies of carbon.[9] The continuum wave functions can be expressed analytically in terms of spherical Bessel and Neumann functions.[10] We tested our integration routines by checking that using these wave functions in Eq. (13), together with a pion-nucleon T matrix that is independent of energy, gives indeed the closure result (14).

In order to calculate our results, we solved the Lippmann-Schwinger equation in momentum space[8] with the optical potential given by Eqs. (1), (12), and (13). We assumed that the ground-state wave function of ^{12}C consists of four particles in the s shell and eighth particles in the p shell, and evaluated the expression (13) separately for each shell, defining the energy parameter E in Eq. (13), as the external kinetic energy of the pion minus the binding energy of the nucleon. Fo the contribution of the bound states in Eq. (13), we included all possible transitions without regard of the Pauli principle in the case of closed shells. For the ^{13}C nucleus, we used the same well as for ^{12}C, with the wave function of the valence neutron being given as a p-wave bound state wave function.

We show our results in Fig. 1, where we also show for comparison the results of the closure approximation potential (14) for three different values of the off-shell parameter α in the pion-nucleon amplitude (16). We see that the predictions of the two models in the case of the total and reaction cross sections are not very differe *from each other or from the data, nor do they*

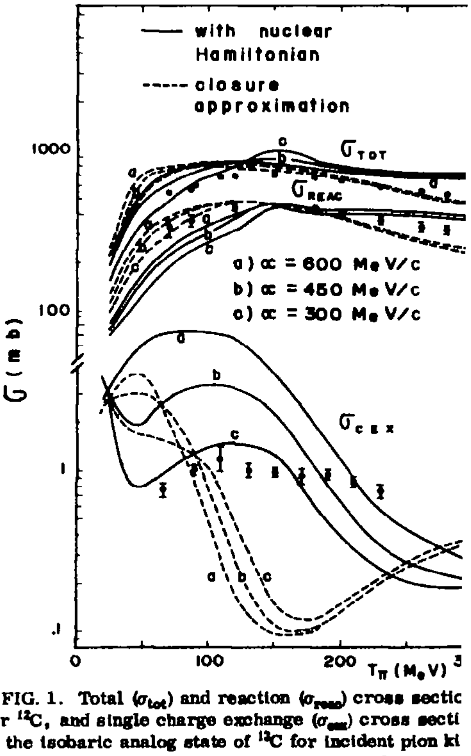

FIG. 1. Total (σ_{tot}) and reaction (σ_{reac}) cross sectic for ^{12}C, and single charge exchange (σ_{cex}) cross secti to the isobaric analog state of ^{12}C for incident pion ki netic energies from 0 to 300 MeV. The solid curves the results of the potential containing the nuclear Har tonian (13), and the dashed curves are the results of closure approximation potential (14). The experimen points are from Refs. 11 and 12.

depend very strongly on which off-shell extension of the pion-nucleon amplitude is used. The situation, however, is completely different for the charge exchange reaction, where first of all the results of the two models are very different both in shape and magnitude, and for the potential which includes the nuclear Hamiltonian very dependent on the value of α. In the case of the charge exchange reaction we observe the well-known result[6,7,13,14] that is practically impossible to fit the data with a model based in the closure approximation, while by including the nuclear Hamiltonian a great improvement is noticed. We see that we can explain the data reasonably well up to $T_\pi = 170$ MeV, with a value of α of 300 MeV/c, which is in striking agreement with the value of this parameter obtained by Goplen, Gibbs, and Lomon[15] in their analysis of the $\pi^+ + d \rightarrow p + p$ reaction. We interpret the disagreement at high energies as giving the range of validity of the theory, since relativistic effects will produce large corrections to the approximate result (13); we can see this roughly by replacing the mass of the pion by its relativistic energy $\omega = (\mu^2 + k_0^2)^{1/2}$, and noticing that while at low energies the condition (5) $\mu/M \simeq \frac{1}{7} \ll 1$ is satisfied, for a 300 MeV pion $\omega/M \simeq \frac{1}{2}$, so that the approximation is very bad, and in this case Eq. (3) must be treated exactly as a relativistic three-body problem.

This work was supported by Comisión de Operación y Fomento de Actividades Académicas del I.P.N. and by a computer grant from Centro Nacional de Cálculo.

---

*Present address: Department of Physics, Texas A & M University, College Station, Texas 77843.

[1] P. C. Tandy, E. F. Redish, and D. B. Bollé, Phys. Rev. C 16, 1924 (1977); Phys. Rev. Lett. 35, 921 (1975).

[2] A. K. Kerman, H. McManus, and R. M. Thaler, Ann. Phys. (N.Y.) 8, 551 (1959).

[3] D. J. Ernst, C. M. Shakin, and R. M. Thaler, Phys. Rev. C 9, 1374 (1974).

[4] E. Auerbach, M. Sternheim, and D. Fleming, Phys. Rev. 162, 49 (1970).

[5] H. Garcilazo, Nucl. Phys. A302, 493 (1978).

[6] N. Auerbach and J. Warszawski, Phys. Lett. 45B, 171 (1973).

[7] H. Garcilazo, Phys. Rev. C 13, 1753 (1976).

[8] G. Rowe, M. Salomon, and R. H. Landau, Phys. Rev. C 18, 584 (1978).

[9] V. Gillet and N. Vinh Mau, Nucl. Phys. 54, 321 (1964); 57, 698 (1964).

[10] E. Merzbacher, *Quantum Mechanics* (Wiley, New York, 1961), pp. 231–235.

[11] F. Binon *et al.*, Nucl. Phys. B17, 168 (1970).

[12] Y. Shamai *et al.*, Phys. Rev. Lett. 36, 82 (1976).

[13] K. P. Lohs and A. Gal, Nucl. Phys. A292, 375 (1977).

[14] J. Warszawski, A. Gal, and J. M. Eisenberg, Nucl. Phys. A294, 321 (1978).

[15] B. Goplen, W. R. Gibbs, and E. Lomon, Phys. Rev. Lett. 32, 1012 (1974).

PHYSICAL REVIEW C VOLUME 21, NUMBER 5 MAY 1980

Communications

The Communications section is for brief reports on completed research. A Communication may be no longer than the equivalent of 2800 words, i.e., the length to which a **Physical Review Letter** *is limited. (See the editorial in the 21 December 1970 issue of* **Physical Review Letters**.*) Manuscripts intended for this section must be accompanied by a brief abstract for information retrieval purposes and a keyword abstract.*

Glauber theory and N-N inelasticity

William A. Friedman
Physics Department, University of Wisconsin, Madison, Wisconsin 53706

Alvin M. Saperstein
Physics Department, Wayne State University, Detroit, Michigan 48202

(Received 19 October 1979)

A shortcoming of standard Glauber theory which becomes important in considering nucleon-nucleus reaction cross sections above the inelastic nucleon-nucleon threshold is discussed.

[NUCLEAR REACTIONS Inelastic nucleon-nucleus cross sections; multiple scattering theory; Glauber theory.]

We wish to point out an interesting shortcoming of standard Glauber theory with respect to the question of unitarity. We shall show how this deficiency may be physically understood and what remedy is necessary to remove it.

In any fixed scattering formulation one develops an operator $F(q, r_1, \ldots, r_A)$ which is used to find scattering amplitudes $F_{n'n}(q)$ by

$$F_{n'n}(q) = \int \psi^*_{n'}(r_1, \ldots, r_A) F(q, r_1, \ldots, r_A) \times \psi_n(r_1, \ldots, r_A) \prod_i dr_i . \tag{1}$$

In the standard Glauber formulation[1] of scattering of a nucleon from a nucleus

$$F(\vec{q}, \vec{r}_1, \ldots, \vec{r}_A) = \frac{ik}{2\pi} \int d^2b\, e^{-i\vec{b}\cdot\vec{q}} \left\{ 1 - \prod_j [1 - \Gamma(\vec{b} - \vec{s}_j)] \right\}, \tag{2}$$

where $\vec{s}_j$ is that component of the coordinate vector $\vec{r}_j$ for particle j which is in the plane perpendicular to the beam direction (z axis), and where $\Gamma(\vec{b})$, the profile function, is given by

$$\Gamma(\vec{b}) = \frac{1}{2\pi ik} \int d^2q\, e^{i\vec{b}\cdot\vec{q}} f_{NN}(\vec{q}), \tag{3}$$

with $f_{NN}(\vec{q})$ the nucleon-nucleon elastic scattering amplitude. If one makes the simplifying assumption that the ground state of the target is $\psi_0 = \prod_j \phi(z_j, \vec{s}_j)$ with $|\phi|^2 = \rho(\vec{r})/A$, then the elastic scattering amplitude becomes

$$F_{00}(\vec{q}) = \frac{ik}{2\pi} \int d^2b\, e^{-i\vec{b}\cdot\vec{q}} \left\{ 1 - \left[1 - \int d^3r\, \Gamma(\vec{b} - \vec{s}) \frac{\rho(\vec{r})}{A} \right]^A \right\}. \tag{4}$$

Further assuming that Γ is much more rapidly varying than $\rho(z, \vec{b})$ one obtains

$$F_{00}(q) = \frac{ik}{2\pi} \int d^2b\, e^{-i\vec{b}\cdot\vec{q}} \left\{ 1 - \left[1 - \frac{T(\vec{b})}{A} \frac{2\pi}{ik} f_{NN}(0) \right]^A \right\}, \tag{5}$$

with

$$T(\vec{b}) = \int_{-\infty}^{\infty} dz\, \rho(\vec{b}, z) \quad \text{and} \quad \int d^2s\, \Gamma(\vec{s}) = \frac{2\pi}{ik} f_{NN}(0).$$

Finally for large A, Eq. (5) leads to

$$F_{00}(\vec{q}) = \frac{ik}{2\pi} \int d^2b\, e^{-i\vec{b}\cdot\vec{q}} \left\{ 1 - \exp\left[-T(\vec{b}) \frac{2\pi}{ik} f_{NN}(0) \right] \right\}. \tag{6}$$

Using the optical theorem we obtain the following total cross section, from $F_{00}(q = 0)$:

$$\sigma_T = \mathrm{Re}\, 2 \int d^2b \left\{ 1 - \exp\left[-T(\vec{b}) \frac{2\pi}{ik} f_{NN}(0) \right] \right\} \tag{7}$$

and the integrated elastic cross section

$$\sigma_{el} = \int db^2 \left| 1 - \exp\left[-\frac{2\pi}{ik} T(\vec{b}) f_{NN}(0) \right] \right|^2 . \tag{8}$$

We now define the nucleon-nucleus reaction cross section σ_r as the difference $\sigma_T - \sigma_{el}$, so that

© 1980 The American Physical Society

$$\sigma_r = \int d^2b\,(1 - e^{-\sigma_T^{NN} T(b)})\,, \qquad (9)$$

where σ_T^{NN}, the NN cross section, enters through the use of the nucleon-nucleon optical theorem.

The expressions above are well known and analogous to the standard partial-wave expressions where we associate b with $(l+\frac{1}{2})/k$ and $e^{-T(b)(2\pi/ik)f_{NN}(0)}$ with S_l.

Let us now calculate the reaction cross section by summing the Glauber inelastic amplitudes[2] derived from Eqs. (1) and (2):

$$\sigma_r^G = \int \frac{d^2q}{k^2} \sum_{n\neq 0}^{\infty} |F_{n0}(q)|^2\,,$$

$$= \int \frac{d^2q}{k^2} \left(\sum_{n=0}^{\infty} F_{n0}^*(q) F_{n0}(q) - |F_{00}(q)|^2 \right). \qquad (10)$$

With closure and Eq. (1) σ_r^G becomes

$$\sigma_r^G = \int \frac{d^2q}{k^2} \int \prod_j d^3r_j\, |\psi_0(\vec{r}_1, \ldots, \vec{r}_A)|^2 |F(\vec{q}, \vec{s}_1, \ldots, \vec{s}_A|^2$$

$$- \int \frac{d^2q}{k^2} \left| \int \prod_j d^3r\, |\psi_0(\vec{r}_1, \ldots, \vec{r}_A)|^2 F(\vec{q}, \vec{s}_1, \ldots, \vec{s}_A) \right|^2. \qquad (11)$$

With the simplified ψ_0 assumed above,

$$\sigma_r^G = \int d^2b \left[1 - 2 \int \mathrm{Re}\,\Gamma(\vec{b} - \vec{s}) \frac{\rho(\vec{r})}{A} d^3r + \int |\Gamma(\vec{b} - \vec{s})|^2 \frac{\rho(\vec{r})}{A} d^3r \right]^A$$

$$- \int d^2b \left| \left[1 - \int \Gamma(\vec{b} - \vec{s}) \frac{\rho(\vec{r})}{A} d^3r \right] \right|^{2A}, \qquad (12)$$

with

$$2\,\mathrm{Re} \int \Gamma(s)\, d^2s \equiv \sigma_T^{NN}$$

and

$$\int |\Gamma(s)|^2 d^2s = \sigma_{el}^{NN}\,.$$

We obtain, following the steps leading to Eq. (5),

$$\sigma_r^G = \int d^2b \left\{ \left[1 - (\sigma_T^{NN} - \sigma_{el}^{NN}) \frac{T(b)}{A} \right]^A - \left[1 - \sigma_{Tot}^{NN} \frac{T(b)}{A} + \frac{1}{A^2} \left| \frac{2\pi T(b)}{k} f_{NN}(0) \right|^2 \right]^A \right\}. \qquad (13)$$

For large A we find

$$\sigma_r^G = \int d^2b\,(e^{-(\sigma_T^{NN} - \sigma_{el}^{NN}) T(b)} - e^{-\sigma_T^{NN} T(b)})\,. \qquad (14)$$

When $\sigma_T^{NN} = \sigma_{el}^{NN}$ the reaction cross section in Eq. (14) becomes identical with σ_r derived from the optical theorem. When the NN inelastic reaction cross section $\sigma_{in}^{NN} \equiv (\sigma_T^{NN} - \sigma_{el}^{NN})$ is nonzero, however,

$$\sigma_r^G = \int d^2b\,(e^{-\sigma_{in}^{NN} T(b)} - e^{-\sigma_T^{NN} T(b)})\,, \qquad (15)$$

and there is a difference between the optical and the summed reaction cross sections, $\Delta\sigma_r$,

$$\Delta\sigma_r = \int d^2b\,(1 - e^{-\sigma_{in}^{NN} T(b)})\,, \qquad (16)$$

which is significant for nucleon energies near 1 GeV where $\sigma_{in}^{NN} \approx \frac{3}{4}\sigma_T^{NN}$.

The difference in reaction cross sections has a simple physical origin. The inelastic amplitudes $F_{n'n}$ obtained from the Glauber operators cannot describe transitions to states in which new particles are produced or isobars excited. The reaction cross section obtained by summing the Glauber amplitudes is thus short by this amount.

The deficiency obviously vanishes below the inelastic NN threshold as we have seen. We can recast $\Delta\sigma_r$ in a form which explicitly shows that the differences arise from inelastic NN effects. For this purpose we decompose the reaction cross section into contributions from terms in which $m = 1, 2, 3$, etc. of the original target nucleons are excited from their ground state configurations. It is not necessary that the particles be knocked out but only that their final orbits differ from their initial ones.

The sum on m from 1 to A represents the reaction cross section while $m = 0$ represents the elastic cross section. Dropping the $1/A^2$ term in Eq. (13) we can write

$$\sigma_{r,m}^G = \int d^2b \binom{A}{m} \left[\sigma_{el}^{NN} \frac{T(b)}{A} \right]^m \left[1 - \sigma_T^{NN} \frac{T(b)}{A} \right]^{A-m},$$

with

$$\sigma_r^G = \sum_{m=1}^{A} \sigma_{r,m}^G\,. \qquad (17)$$

The expression in Eq. (17) has a simple intuitive interpretation. If we associate $\sigma_{el}^{NN} T(b)/A$, and

$\sigma_T^{NN}T(b)/A$ with the probability for an elastic NN or a total NN collision, $\sigma_{r,m}^{G}$ then gives the probability that m particles have been involved in elastic collisions while $A-m$ have been involved in no collisions at all. Since the Glauber operator F can only describe elastic N-N collisions this result is all that σ_r^G can provide. One would expect that for physical processes some of the collisions will be inelastic in the sense of particle production. These interactions contribute to the full reaction cross section $\sigma_{r,m}$. The expression for $\Delta\sigma_r$ can be decomposed into contributions from reactions in which m nucleons are involved: $\Delta\sigma_r = \sum_{m=1}^{A} \Delta\sigma_{r,m}$. Then one obtains

$$\Delta\sigma_{r,m} = \int d^2b \sum_{\nu=1}^{m} [\sigma_{el}^{NN}T(b)]^{m-\nu}[\sigma_{in}^{NN}T(b)]^{\nu} \times \left[1-\sigma_T^{NN}\frac{T(b)}{A}\right]^{A-m}\binom{m}{\nu}\binom{A}{m}. \tag{18}$$

This difference represents a process in which, of the m particles colliding, ν inelastically collide, where ν ranges from 1 to m; the remaining $m-\nu$ collisions are elastic.

Clearly if one wishes to include all types of reactions for situations in which $\sigma_{in}^{NN} > 0$ one should go beyond the Glauber model and replace σ_{el}^{NN} in Eq. (17) by σ_T^{NN} to obtain

$$\sigma_{r,m} = \int d^2b \binom{A}{m}\left[\sigma_T\frac{T(b)}{A}\right]^{m}\left[1-\sigma_T\frac{T(b)}{A}\right]^{A-m}. \tag{19}$$

This sums to the optical result, Eq. (9), and includes all NN processes that can occur between the projectile and target. This substitution has frequently been made in papers, i.e., Hufner *et al.*[3] without specific discussion. We wish to emphasize that a sum of purely Glauber amplitudes provides $\sigma_{r,m}^{G}$ and that

$$\sigma_{r,m}^{G}/\sigma_{r,m} = (\sigma_{el}/\sigma_T)^m, \tag{20}$$

so that at 1 GeV $\sigma_{r,m}^{G}$ will in fact give a very small part of the full reaction cross section.

We wish to express our appreciation to the organizers of the 1979 University of Washington Theoretical Topical Conference on Nucleus-Nucleus Interactions where much of this work was done. This work was supported in part by funds from the National Science Foundation.

---

[1] R. J. Glauber, *Lectures in Theoretical Physics*, edited by W. E. Brittin (Interscience, N.Y., 1959), Vol. I, p. 315.

[2] R. J. Glauber and G. Matthiae, Nucl. Phys. B21, 135 (1970).

[3] J. Hufner *et al.*, Phys. Rev. C 12, 1888 (1975); J. Hufner, Ann. Phys. (N.Y.) 115, 43 (1978).

PHYSICAL REVIEW C VOLUME 21, NUMBER 5 MAY 1980

New isotope ^{199}Rn and evidence for an isomeric state ^{199}Rn^m

A. C. DiRienzo, H. A. Enge, S. B. Gazes, M. K. Salomaa, and A. Sperduto
Laboratory for Nuclear Science, Massachusetts Institute of Technology, Cambridge, Massachusetts 02139

W. Schier
Department of Physics, University of Lowell, Lowell, Massachusetts 01854

H. E. Wegner
Department of Physics, Brookhaven National Laboratory, Upton, New York 11973

(Received 28 December 1979)

The nuclide ^{199}Rn has been produced in the ^{169}Tm(^{35}Cl,5n) ^{199}Rn reaction. The recoiling ^{199}Rn nuclei were separated from the beam at zero degrees by a recoil-separator arrangement utilizing electric and magnetic fields, and detected by their alpha decay signatures in a surface-barrier detector. Two alpha lines were found with energies 6.990±0.015 MeV and 7.060±0.015 MeV. Alpha decay of the known daughter ^{195}Po was also observed.

[RADIOACTIVITY ^{199}Rn and ^{199}Rn^m; measured excitation functions ^{169}Tm(^{35}Cl,5n) ^{199}Rn and E_α's.]

The three-stage Tandem Accelerator at Brookhaven National Laboratory provides ^{35,37}Cl ions with energies up to about 200 MeV, suitable for studies of fusion reactions producing heavy elements as evaporation residues. Elements of the energy-mass spectrograph designed by the M.I.T. heavy-ion group to study these reactions are used in this work for the single purpose of separating the recoiling evaporation residues from the beam at zero degree.[1,2] The present apparatus produces neither mass nor velocity dispersion of any significance at the point of collection of the recoils.

Figure 1 shows a diagram of the equipment. The velocity selector described in Ref. 2 has been modified to provide better rejection of beam particles. A 20-cm long section has been cut from the electrostatic deflector plates and mounted separately closer to the target. The evaporation residues are deflected upwards by, typically, 7 deg, while the beam in this experiment is deflected by less than 1.5 deg. A region of magnetic fields bends the trajectories of the evaporation residues back to the horizontal before they enter the velocity selector proper (Wien filter). The beam is collected in a Faraday cup as shown in Fig. 1. A pair of magnetic quadrupoles close to the target produces an image of the target spot roughly in the middle of the velocity selector and another quadrupole pair reimages this on the detector.

The detector is a ΔE-E telescope consisting of a gas, proportional ΔE counter followed by a 450 mm^2 surface barrier E detector. Evaporation residues in this experiment have energies of, typically, 30 MeV. They pass through the gas counter and embed themselves in the surface barrier detector. If they decay by alpha emission the decay is observed with 100% efficiency although some alpha's emitted in the backward direction escape through the surface of the detector and therefore do not give rise to full energy peaks. Typically, 42% of the alpha's fall into this category. Since only the events in the full-energy peaks could be identified, the efficiency of the detector was in reality only 58%. Some ^{35}Cl particles scattered from the various parts of the separation system with energy degraded to about 5 MeV have the correct velocity to pass through the velocity selector. They are rejected from the alpha spectrum by an anticoincidence signal from the ΔE gas detector.

Figure 2 shows an excitation function of some of the alpha lines produced in these reactions. The 6.77-MeV line and the 6.91-MeV line are well known lines from ^{201}Rn and ^{200}Rn produced in the $3n$ and $4n$ reactions, respectively. Four weak lines, all peaking at a beam energy of about 175 MeV, are seen in the spectra. In Fig. 2 the

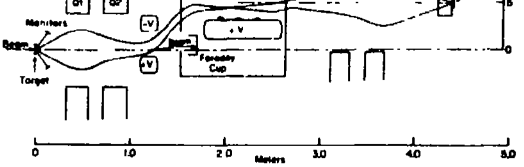

FIG. 1. Apparatus used to separate recoiling evaporation residues from the beam at zero degree.

© 1980 The American Physical Society

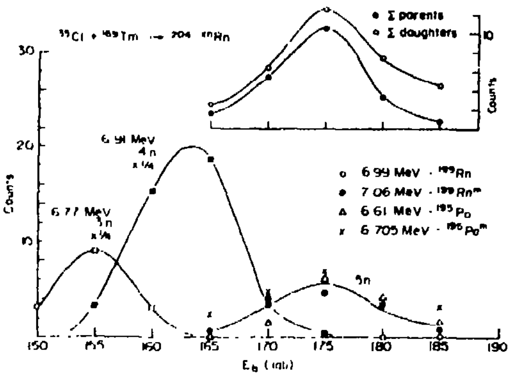

FIG. 2. Excitation function for alpha lines arising from recoils produced in the $3n$, $4n$, and $5n$ reactions. Only the lines from the parent nuclei are shown except for $5n$ case. *The true number of counts has been multiplied* by a normalizing factor (close to unity) to more closely represent relative cross section. E_B is the energy of the incident ^{35}Cl.

yields of these four lines have been plotted, but only one curve, representing the average, is shown in the lower part. Two of the four alpha lines have been identified as arising from the decay of the known isotope ^{195}Po. The other two lines at 6.990 ± 0.015 MeV and 7.060 ± 0.015 MeV are assigned to a new isotope ^{199}Rn. This assignment is based on the following three observations:

(1) The excitation functions for these lines ($5n$) peak at the energy expected from extrapolation of the $3n$ and $4n$ data (Fig. 2).

(2) The excitation functions coincide with those for the alpha lines of ^{195}Po, the presumed daughter.

(3) The alpha energies observed are close to what is expected for ^{199}Rn by extrapolation from heavier radon isotopes (see below).

In the upper part of Fig. 2 is shown the sum of the yields of the two lines assigned to the parent ^{199}Rn and the sum assigned to the daughter ^{195}Po. The total yields for the daughter lines appear to be higher than those for the parent lines. This may be due to the fact that the daughter lines bracketed a much stronger peak—that from the $4n,p$ residue ^{199}At at 6.64 MeV. Therefore, some of the counts on the wings of this peak may have been included in the counts for the daughter lines.

The cross section for the production of ^{199}Rn via the ^{35}Cl + ^{169}Tm reaction was not measured accurately, but is of the order of $\sigma = 1$ μb at the peak (175 MeV). The total evaporation residue cross section at this energy, close to the maximum, was about 30 times larger. The most intense alpha line was the one mentioned above at 6.64 MeV assigned to ^{199}At.

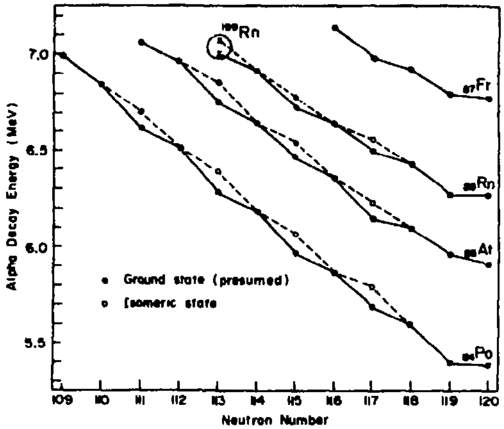

FIG. 3. Alpha-energy systematics for francium, radon, astatine, and polonium isotopes. The encircled points represent the alpha lines associated with the new isotope ^{199}Rn.

Figure 3 is a plot of the alpha-particle energies of some of the previously known isotopes[3] of radon and three of its neighbor elements and of the new isotope ^{199}Rn. The nuclides ^{201}Rn and ^{203}Rn both have isomeric states demonstrated by the fact that they emit two alpha lines with two different associated half-lives. In the case of ^{199}Rn two lines are again observed and the systematics of the energies shown in Fig. 3 strongly hint that ^{199}Rn has decay modes similar to ^{201}Rn and ^{203}Rn, i.e., that one of the observed lines is produced by an isomeric state. Presumably, because of strong hindrance factors, a high (low) spin state in ^{199}Rn decays to a high (low) spin state in ^{195}Po. Assuming that the difference in alpha energies of the daughter lines, corrected for recoils, reflects the excitation energy of ^{195}Po^m, this level is at 97 keV. The corrected difference for the two new alpha lines observed in this work is 71 keV. The excitation energy of ^{199}Rn^m is therefore 97 ± 71 keV, i.e., either 168 or 26 keV. Our data do not allow us to determine which of the two energies is the correct one.

This work was supported in part by the U. S. Department of Energy under Contract No. EY-76-C-02-3069.

---

[1] H. A. Enge and D. Horn, Nucl. Instrum. Methods 145, 271 (1977).

[2] M. Salomaa and H. A. Enge, Nucl. Instrum. Methods 145, 279 (1977).

[3] *Table of Isotopes, 7th ed.*, edited by C. M. Lederer and V. S. Shirley (Wiley-Interscience, New York, 1978).

PHYSICAL REVIEW C VOLUME 21, NUMBER 5 MAY 1980

Self-energy of the Δ resonance in finite nuclei and Fermi broadening

R. S Bhalerao, L. C. Liu, and C. M. Shakin

Department of Physics and Institute for Nuclear Theory, Brooklyn College of the City University of New York, Brooklyn, New York 11210

(Received 20 June 1979)

It is shown that because of the Fermi motion of the target nucleons the Δ resonance exhibits a large kinematic broadening in nuclei. This broadening is unrelated to the coupling of the isobar to inelastic channels and is neglected in some of the calculations of pion-nucleus scattering based upon the isobar-hole model.

[NUCLEAR REACTIONS Effects of Fermi motions; self-energy of the Δ isobar; pion-nucleus optical potential.]

It is convenient in many calculations to treat the (3,3) resonance of the πN system as an elementary particle, the Δ isobar. In the attempt to understand the interaction of pions with nuclei, extensive use has been made of the isobar-doorway[1] or isobar-hole[2-8] model. In these models the Δ self-energy in the nuclear medium plays an essential role. In some works this quantity is treated in a phenomenological manner and is adjusted in order to fit the experimental data.[1,3,4,7,8] Other authors have reported microscopic calculations of some parts of the Δ self-energy.[5,6] In this work we wish to describe an important kinematical effect which has not been previously discussed in the literature and which we will term *Fermi broadening*. (While the authors of Refs. 5 and 6 discuss a large number of effects which govern the dynamics of isobar propagation, Pauli correlations, broadening due to absorption channels, binding effects, etc., they have not discussed Fermi broadening. The calculations reported in Refs. 5 and 6, however, do correctly incorporate terms in the Δ propagator which give rise to Fermi broadening.)

We recall the expression obtained for the pion-nucleus transition operator when use is made of the doorway approximation and the projection-operator formalism,[3]

$$T_{PP}=H_{PD}(E-\mathcal{H}_{DD})^{-1}H_{DP}$$

$$=H_{PD}(E-H_{DD}-H^{\uparrow}_{DD}-H^{\downarrow}_{DD}+i\epsilon)^{-1}H_{DP}\,, \qquad (1)$$

$$H^{\uparrow}_{DD}=H_{DP}(E-H_{PP}+i\epsilon)^{-1}H_{PD}\,, \qquad (2)$$

$$H^{\downarrow}_{DD}=H_{DQ}(E-H_{QQ}+i\epsilon)^{-1}H_{QD}\,. \qquad (3)$$

Here, the P channel contains the pion plus the nucleus in its ground state, the D space contains the isobar-hole states, and the Q space consists of more complicated states. Let us first consider the isobar-hole interaction with the Q space, $H^{\downarrow}_{DD}$. In some works this interaction is replaced by a potential having the shape of the nuclear density and a complex strength which is treated as a free parameter.[3,7] (Some results for the energy dependence of this parameter have been given in Ref. 7.) Explicit calculation of $H^{\downarrow}_{DD}$ requires evaluation of diagrams such as those of Fig. 1.[5,6] These diagrams represent the coupling of the Δ to inelastic channels. For example, Fig. 1(b) represents the coupling to the channel with no pions; specifically, the Δ-hole state is coupled to the 2p-2h states of the nucleus. [See Fig. 1(d).] We remark that the potentials used to represent $H^{\downarrow}_{DD}$ are quite large,[3,7] having a typical strength parameter of about (−60 −*i*70) MeV.[3] In more recent work,[7] the real part of the interaction is somewhat smaller in magnitude and exhibits a marked energy dependence. The spreading potentials used to represent $H^{\downarrow}_{DD}$ give rise to an absorption width for the isobar, $\Gamma_{\text{abs}}\sim 140$ MeV. This is in part compensated by a Pauli correction[5-8] to the decay width of $\Gamma_P\sim -40$ MeV. Combining these effects we see that some calculations using the isobar-hole model suggest an increase of the Δ width in the nuclear medium of about 100 MeV.[7]

In this work we wish to raise some questions as to the proper interpretation of these *phenomenological* parameters. Specifically, we wish to point out that *apparent* "self-energies" of the magnitude noted above already are present when proper consideration is given to the Fermi motion and nuclear binding of the target particles. These effects are present before one considers the coupling of the resonance to more complicated modes of excitation—processes such as those depicted in Fig. 1.

We now contrast the analysis of the isobar-hole model with a covariant multiple-scattering theory which has been extensively developed.[9-11] In the latter theory one constructs a first-order optical

© 1980 The American Physical Society

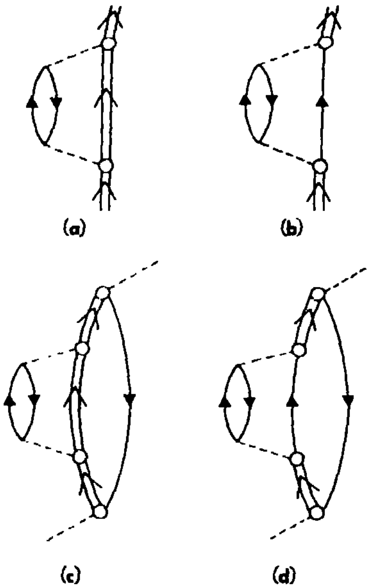

FIG. 1. Some contributions to the isobar self-energy in nuclei. The isobar is represented as a double line, the pion as a dashed line, and nucleons as single lines. (a) Coupling of the isobar to a state consisting of a Δ and a particle-hole excitation. (b) Coupling of the isobar to a 2p-1h state. The dashed line may also be taken to represent the exchange of a ρ meson. (c) The portion of the self-energy of the Δ shown in (a) is included in the calculation of the pion optical potential. (d) The self-energy term of (b) is shown as modifying the propagator of the Δ in the calculation of the pion optical potential.

potential by evaluating the "triangle diagram" shown in Fig. 2.[12] In this figure the dashed line denotes a pion and the solid circle is a πN T matrix. The heavy lines denote (on-mass-shell) nuclei of A or $(A-1)$ nucleons. An integral is evaluated over the momentum $\vec{Q}$ of the spectator nucleus. The fourth component of the momentum vector of the struck nucleon is $E_A(\vec{k}) - E_{A-1}(\vec{Q})$. Therefore, if W denotes the energy in the center of mass of the pion-*nucleus* system, the energy in the center of mass for the pion-*nucleon* collision is $\sqrt{s} = \{[W - E_{A-1}(\vec{Q})]^2 - \vec{Q}^2\}^{1/2}$.

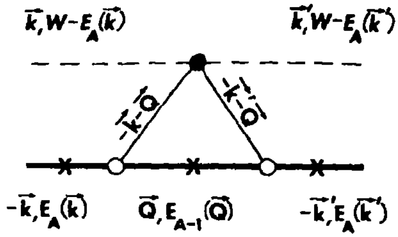
$\vec{k}, W-E_A(\vec{k})$
$\vec{k}', W-E_A(\vec{k}')$
$-\vec{k}-\vec{Q}$
$-\vec{k}'-\vec{Q}$
$-\vec{k}, E_A(\vec{k})$
$\vec{Q}, E_{A-1}(\vec{Q})$
$-\vec{k}', E_A(\vec{k}')$

FIG. 2. Diagrammatic representation of the process which determines the first-order optical potential. The dashed line is a pion, the solid circle is a πN T matrix, and the open circles are nuclear vertex functions. The heavy lines represent nuclei which are kept on their mass shell in the calculation; for example, $E_A(\vec{k}) = (k^2+M_A^2)^{1/2}$.

Let us consider the evaluation of the diagram of Fig. 2 for the on-shell matrix element of the first-order optical potential. In carrying out the integration over $\vec{Q}$, the πN T matrix (see Fig. 2) is evaluated over a range of values of $\sqrt{s}$ and of $\vec{k}_c$, the relative momentum of the pion and nucleon. A typical situation is depicted in Fig. 3, where the shaded region indicates the values of $k_c = |\vec{k}_c|$ and $\sqrt{s}$ that contribute most significantly to the integral. The black dot denotes the point at which the T matrix would be evaluated if use were made of the fixed-scatterer approximation (FSA). Further, $\bar{k}_c$ is the relative momentum for the collision of the pion with a nucleon at rest, and the solid line represents the equation $\sqrt{s} = (k_c^2 + m_N^2)^{1/2} + (k_c^2 + m_\pi^2)^{1/2}$. The size and location of the shaded region in Fig. 3 can be understood if one gives some thought to the role of nuclear binding and Fermi motion in modifying the FSA kinematics.[11,13]

The evaluation of the diagram of Fig. 2 yields a first-order optical potential $\langle \vec{k}' | V^{(1)}(W) | \vec{k} \rangle$. On-shell values of this quantity [$k = k'$ and $W = (k^2 + m_\pi^2)^{1/2} + (k^2 + m_A^2)^{1/2}$] are shown in Fig. 4.[14] As may be seen from this figure, the maximum magnitude of the imaginary part of the first-order potential is calculated to be at $T_\pi \sim 240$ MeV for ^{16}O and ^{40}Ca targets. The width at half maximum is about 200 MeV. Therefore we see that the effects of Fermi motion and nuclear binding cause an upward shift of the resonance position of about 40 MeV and an increased width of about 80 MeV with respect to FSA values. This increased width may

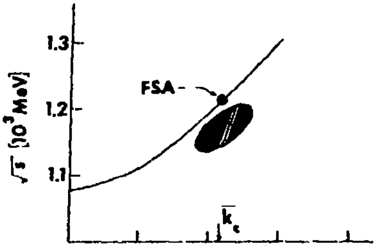

FIG. 3. Kinematical region that is important for the evaluation of the first-order optical potential when $k_\pi^{\rm LAB} \sim 220$ MeV/c. (See text.)

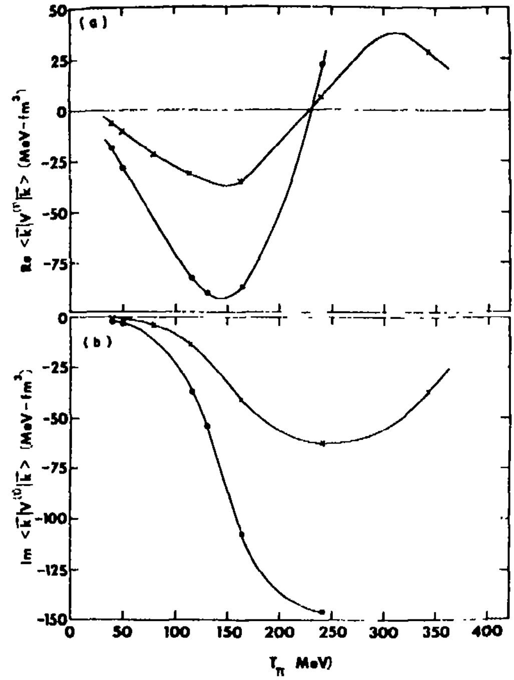

FIG. 4. Real and imaginary parts of the matrix element of the (on-shell) first-order optical potential. (a) Real part for ^{16}O[×], ^{40}Ca[●]. (b) Imaginary part for ^{16}O[×] and ^{40}Ca[●]. The potentials shown in the figures are averages of the potentials for π^+ and π^- mesons, which differ slightly because of Coulomb effects on the binding energy of the target nucleons.

be termed "Fermi broadening" since it has its origin in the Fermi motion of the target nucleons.

The distinction between the physical processes that are important for the calculation of the self-energy and of Fermi broadening can be clarified by noting that in the multiple-scattering approach[9-11] the incident pion encounters nucleons having a range of momenta. Correspondingly, the isobar is not formed with a definite energy and momentum. This feature of the dynamics ultimately leads to a large broadening of the resonance. This broadening is not representative of the true self-energy of the isobar since it is unrelated to the coupling of the Δ to other channels.

The part of the isobar Hamiltonian which would give rise to the broadening effects mentioned above is treated rather crudely in some isobar-hole calculations. For example, consider the quantity $\hat{G}_D(E) \equiv [E - H_{DD} - H^{\dagger}_{DD}(E)]^{-1}$ with $H^{\dagger}_{DD}(E) \equiv \Delta_R(E) - i\Gamma^{\dagger}_R(E)/2$ [see Eq. (2)], and $H_{DD} \equiv E_R + H_\Delta \equiv E_R + T_\Delta + V_\Delta + H_{A-1}$.[4,7] In performing calculations, the following approximation has often been used[4,7]:

$$\hat{G}_D^{-1}(E) \equiv G_D^{-1}(E - H_\Delta) = E - [E_R + \Delta_R(E)] + \frac{i\Gamma^{\dagger}_R(E)}{2} - H_\Delta \tag{4}$$

$$\simeq G_D^{-1}(E) - \left[\frac{\partial}{\partial E} G_D^{-1}(E)\right] H_\Delta \tag{5}$$

$$\equiv D(E) - \gamma(E) H_\Delta . \tag{6}$$

Furthermore, H_Δ is treated as a parameter. This approximation has led to the suppression of the Fermi broadening effect in some isobar-hole calculations and the introduction of phenomenological spreading widths whose interpretation is obscure.

We have shown that the kinematic broadening of the isobar resonance is very large. We believe that it is important to extend some of the isobar-hole models to include a better treatment of this effect. Such developments will allow for an improved understanding of the relation between the optical model analysis[9-11] and the isobar-hole[2-8] or isobar-doorway[1] theories. Further, general agreement as to the magnitude of the isobar self-energy can only be achieved if the various isobar-hole calculations are consistent in the details of their treatment of Fermi broadening.

---

[1] L. S. Kisslinger and W. L. Wang, Phys. Rev. Lett. 30, 1071 (1973); Ann. Phys. (N.Y.) 99, 374 (1976).

[2] F. Lenz, Ann. Phys. (N.Y.) 95, 348 (1975).

[3] M. Hirata, J. H. Koch, F. Lenz, and E. J. Moniz, Phys. Lett. 70B, 281 (1977).

[4] M. Hirata, F. Lenz, and K. Yazaki, Ann. Phys. (N.Y.) 108, 116 (1977).

[5] W. Weise, Nucl. Phys. A278, 402 (1977).

[6] E. Oset and W. Weise, Phys. Lett. 77B, 159 (1978); Nucl. Phys. A319, 477 (1979).

[7] M. Hirata, J. H. Koch, F. Lenz, and E. J. Moniz, report (unpublished).

[8] K. Klingenbeck, M. Dillig, and M. G. Huber, Phys. Rev. Lett. 41, 387 (1978); K. Klingenbeck, University of Erlangen report; M. G. Huber and K. Klingenbeck, lectures delivered at the Massurian Summer School, Mikolajki, 1978 (unpublished).

[9] L. Celenza, L. C. Liu, and C. M. Shakin, Phys. Rev. C 11, 1593 (1975); 12, 721(E) (1975).

[10] L. C. Liu, Phys. Rev. C 17, 1787 (1978).

[11] L. C. Liu and C. M. Shakin, Phys. Rev. C 16, 333 (1977); 16, 1963 (1977); 19, 129 (1979); Phys. Lett. 78B, 389 (1978); R. S. Bhalerao, L. C. Liu, and C. M. Shakin, Phys. Rev. C 21, 1903 (1980).

[12] The *first-order* optical potential is the same in the multiple-scattering theory of Refs. 9–11 and in a the-

ory of the optical potential based upon unitarity and analyticity considerations: L. C. Liu and C. M. Shakin, Phys. Rev. C **20**, 2339 (1979).

[13] Calculations which are most similar to ours with respect to the treatment of the motion of the target nucleons are reported in J. P. Maillet, J. P. Dedonder, and C. Schmitt, Nucl. Phys. **A271**, 253 (1976); **A316**, 267 (1979), where extensive references to the work of other researchers in this field may be found.

[14] The ratio of the momentum space matrix elements for ^{16}O and ^{40}Ca is approximately the ratio of the mass numbers (~16/40) which is as expected for potentials that have the *same strengths in coordinate space*.

PHYSICAL REVIEW C VOLUME 21, NUMBER 5 MAY 1980

Relative importance of neutron and proton components of nuclear transitions and comparative π^-/π^+ inelastic scattering

B. A. Brown
Nuclear Physics Laboratory, University of Oxford, Oxford OX1 3RH, England

B. H. Wildenthal
Nuclear Physics Laboratory, University of Oxford, Oxford OX1 3RH, England and Cyclotron Laboratory, Michigan State University, East Lansing, Michigan 48824

(Received 14 September 1979)

Shell-model calculations for ^{18}O and ^{26}Mg yield predictions of strong state dependence of the isovector component of nuclear transition strengths, with results for ^{18}O being consistent with recent measurements of π^-/π^+ inelastic scattering ratios.

[NUCLEAR STRUCTURE ^{18}O, ^{26}Mg; calculated neutron and proton components of inelastic scattering excitations; estimates of π^-/π^+ cross section ratios: shell model.]

For a complete understanding of nuclear structure it is necessary to be able to distinguish between the neutron and proton components of nuclear transitions. This problem has been addressed with conventional nuclear probes by comparing the reduced electromagnetic strength of a transition in a stable ($N > Z$) nucleus to the strength of the corresponding transition in the analog ($Z > N$) nucleus[1,2] or, alternatively, to the reduced strengths of the same transition in the ($N > Z$) nucleus as induced by hadronic probes such as protons or alphas.[3] The first of these approaches is complicated[1] by the necessity of dealing with the (often significant) differences[4] in the radial wave functions of the protons and neutrons in the two different nuclear systems. The second approach faces the problem of quantitatively relating the reduced strengths of a transition induced by completely different types of probes.

The new "meson factories" offer a fresh alternative approach to this problem via the measurement of the relative cross sections for excitation of a given nuclear level by the inelastic scattering of π^+ and π^- projectiles. The sensitivity of this measurement to the differences in the neutron and proton components of the transition comes from the fact that the resonant cross sections for the interactions of π^+ with protons and π^- with neutrons are about nine times larger than for the corresponding interactions of π^+ with neutrons and π^- with protons. Experimental results of studies on ^{18}O which employ this technique have recently been published.[5,6]

We present here some shell-model predictions for the isoscalar and isovector, or in other terms the neutron and proton, components of nuclear transitions in ^{18}O and ^{26}Mg. These shell-model predictions are used, together with the simplest possible assumptions about the π-nucleus reaction mechanism, to predict the results of π^-/π^+ inelastic scattering cross section ratios. The results for ^{18}O seem consistent with existing data and suggest that measurement of additional transitions in this system should prove very interesting. The results for ^{26}Mg explain the anomaly of the phase of the isovector term of the 0_1^+-2_1^+ transition noted in Ref. 1 and predict a striking difference between the relative neutron-proton structures of the 0_1^+-2_1^+ and 0_1^+-2_2^+ transitions.

The shell-model wave functions employed in the present analysis are obtained from calculations in which the space of basis vectors is generated either by the $0p_{1/2}$, $1s_{1/2}$, and $0d_{5/2}$ single-nucleon orbits[7] (a "^{12}C-core model") or by the $0d_{5/2}$, $1s_{1/2}$, and $0d_{3/2}$ orbits[8] (an "^{16}O-core model"). For $A = 18$, the ^{16}O-core model provides only a schematic accounting of the observed level structure. Accordingly, while such results are presented for ^{18}O, attention is principally focused upon the results of the ^{12}C-core model for this system. For ^{26}Mg, the ^{16}O-core model provides the appropriate degrees of freedom.

Our procedure is to condense the information contained in the nuclear wave functions which is relevant to a transition of angular momentum and isospin rank ΔJ and ΔT into the one-body-transition densities

$$D_{\Delta J,\Delta T}^{N,JT,J'T'}(j,j')=\frac{\langle\psi^{NJT}|||(a_j^\dagger\otimes\tilde{a}_{j'})_{\Delta J,\Delta T}|||\psi^{NJ'T'}\rangle}{(2\Delta J+1)^{1/2}(2\Delta T+1)^{1/2}}, \qquad (1)$$

© 1980 The American Physical Society

where $a_{j'}$ annihilates a nucleon in shell-model orbit j' and $a_j^\dagger$ creates a nucleon in orbit j. These matrix elements constitute the many-body component for analyses of transition strengths which employ any desired complexity of formulation of the nucleonic operators and reaction mechanisms by which the transition is effected, so long as the process is one-body in nature. For simplicity and uniformity, in our present application we combine the isovector and isoscalar D values into neutron and proton strength amplitudes A_p and A_n by taking the appropriate sums and differences and multiplying the resulting $D_{n,p}$ values by the single-particle matrix elements of $r^L Y^L$, assuming harmonic oscillator radial dependence for the single nucleon states. (The harmonic oscillator parameters used for ^{18}O and ^{26}Mg were chosen to reproduce their respective charge radii, taking into account the orbit occupations in the model spaces and making the conventional corrections for finite nucleon size and relativistic and center-of-mass effects.)

In terms of the model-space matrix elements A_p and A_n, the full proton and neutron matrix elements M_p and M_n are given[9] by

$$\begin{aligned} M_p &= A_p + A_p\delta_{pp} + A_n\delta_{pn}, \\ M_n &= A_n + A_n\delta_{nn} + A_p\delta_{np}, \end{aligned} \tag{2}$$

where the δ_{ab} account for the coupling of the nucleons b of the model space to the virtual excitations of the core nucleons a. The strength of a transition induced by a probe which couples to protons and neutrons, respectively, with strengths C_p and C_n is given by

$$B(\Delta J) = (2J' + 1)^{-1}(C_p M_p + C_n M_n)^2. \tag{3}$$

For electromagnetic transitions, $C_p = 1$ and $C_n = 0$ in units of e. We are concerned here with the *relative* differences in the strengths of a given transition as it is excited by probes with differing *relative* values of C_p and C_n. To emphasize this, as opposed to becoming involved with the probe-specific details of *absolute* transition strengths, we deal with normalized strengths such that $C_p' + C_n' = 1$, that is, such that a purely isoscalar transition (one in an $N = Z$ nucleus) would have the same strength value (equal to the electromagnetic strength) independent of the probe which induced it. The relevant characteristics of different probes are then represented solely by the difference $C_p' - C_n'$. For electromagnetic excitation or decay, $C_p' - C_n' = 1$, for alpha-induced excitation $C_p' - C_n' = 0$, and for $\pi^\pm$ excitation $C_p' - C_n' = \pm 0.5$.

Since the model cores have $N = Z$, $\delta_{pn} = \delta_{np}$ and $\delta_{pp} = \delta_{nn}$ up to order $(N - Z)/A$. Hence the complete structure of the core-valence coupling can be expressed in terms of the conventional model-space total effective charges $e_p = 1 + \delta_{pp}$ and $e_n = \delta_{pn}$. The isoscalar effective charge can be easily established from electromagnetic transition rates and it is found that $\delta_{pp} + \delta_{pn} = 0.7 \pm 0.1$ serves quite well for strong $E2$ and $E4$ transitions in this region with these model spaces.[10] There is very little known, on the other hand, about the empirical value of the isovector effective change, as is implied, of course, by the focus of the present work. Previous comparison[4] of experimental and calculated $B(E2)$ values and quadrupole moments has shown that $\delta_{pp} \ll \delta_{pn}$. The results to be presented here have been calculated with the values $\delta_{pp} = \delta_{pn} = 0.35$, although the empirical foundation of this choice of the ratio is weak. Ultimately, the study of data such as are treated here should provide a clearer picture of the empirically correct ratio δ_{pp}/δ_{pn}.

Our calculations for ^{18}O and ^{26}Mg are presented in Table I. They are based on the shell-model values of A_p and A_n as therein listed, Eqs. (2) and (3), and the values of C_p', C_n', and δ_{ab} just noted. We show results for the total electromagnetic strengths $B(E^L)$ and the ratios of the π^- to π^+ strengths, $B(\pi^-)/B(\pi^+)$, of the alpha-induced to electromagnetically-induced strengths, $B(\alpha)/B(\gamma)$, and of the ratio of total neutron to total proton transition strengths, $(M_n/M_p)^2$. Other quantities bearing on the central problem of the relative importance of neutron and proton components in nuclear transitions can be calculated from the A_p and A_n in a similar fashion. We emphasize that the various predictions of transition strength ratios depend not only upon A_p and A_n but also upon δ_{pp} and δ_{pn}.

The ^{12}C-core calculations for ^{18}O predict dominant neutron components for the 0_1^+-2_1^+ and 0_1^+-4_1^+ transitions which, while differing in details, are consistent with the naive ^{16}O-core picture. The predicted ratios of excitation strengths are reasonably consistent with the various measured values. The 0_1^+-$2_{2,3}^+$ and 0_1^+-3_1^- transitions are predicted to be dominated by proton excitations, with the calculated 0_1^+-3_1^- $B(\pi^-)/B(\pi^+)$ ratio being close to that observed. The large differences in the $B(\pi^-)/B(\pi^+)$ values calculated for these five states suggest that extending the present experimental results to include the neighboring states would be of great interest.

Our calculations predict that the 0_1^+-2_1^+ and 0_1^+-4_1^+ transitions in ^{26}Mg have larger proton than neutron components. The corollary of this result is that the electromagnetic strengths of these transitions in ^{26}Mg are larger than in the proton-rich mirror nucleus of ^{26}Mg, ^{26}Si. While this might seem surprising at first glance, it is, of

TABLE I. Matrix elements and transition rates in ^{18}O and ^{26}Mg.

Transition	A_p	A_n	Excitation (MeV) th	Excitation (MeV) exp	$B(E^L)(e^2\ \mathrm{fm}^{2L})$ th	$B(E^L)(e^2\ \mathrm{fm}^{2L})$ exp	$B(\pi^-)/B(\pi^+)$ th	$B(\pi^-)/B(\pi^+)$ exp[d]	$B(\alpha)/B(\gamma)$ th	$B(\alpha)/B(\gamma)$ exp[e]	$(M_n/M_p)^2$ th	$(M_n/M_p)^2$ exp[f]
^{18}O(^{12}C core, $\hbar\omega = 13.24$ MeV)												
$0^+ \to 2_1^+$	2.12	8.57	1.80	1.98	34.4	45 ± 5[a]	2.05	1.67 ± 0.08	2.40	1.46 ± 0.45	4.41	5.5 ± 0.9
$0^+ \to 2_2^+$	1.58	−0.01	4.18	3.92	4.5	27 ± 10[a]	0.29		0.40	0.72 ± 0.33	0.06	0.35 ± 0.21
$0^+ \to 2_3^+$	3.95	0.02	5.10	5.26	28.5	8 ± 2[a]	0.30		0.40		0.07	
$0^+ \to 3_1^-$	17.5	10.0	4.90	5.10	736	1120 ± 100[a]	0.72	0.89 ± 0.05	0.74		0.52	
$0^+ \to 4_1^+$	1.7	−65.3	3.89	3.56	423		3.60		6.91		18.1	
^{18}O(^{16}O core, $\hbar\omega = 12.65$ MeV)											14.9	
$0^+ \to 2_1^+$	0	9.41	2.00	1.99	10.8	45 ± 5[a]	3.36	1.67 ± 0.08	5.89	1.46 ± 0.45	14.9	
$0^+ \to 4_1^+$	0	104.6	3.52	3.56	1340		3.36		5.89			
^{26}Mg(^{16}O core, $\hbar\omega = 12.86$ MeV)												
$0^+ \to 2_1^+$	10.57	7.22	2.05	1.81	282	301 ± 13[b]	0.80		0.81	1.00 ± 0.14	0.64	0.54 ± 0.25
$0^+ \to 2_2^+$	1.16	7.00	3.25	2.94	16	9 ± 2[b]	2.35		2.99	6.0 ± 1.8	6.02	8.00 ± 6.00
$0^+ \to 4_1^+$	70.6	44.7	4.59	4.32	12311		0.77		0.79		0.59	
$0^+ \to 4_2^+$	53.0	75.1	5.41	4.90	9572	$(26 \pm 7) \times 10^3$[c]	1.23		1.24		1.50	

[a] Reference 11.

[b] Reference 2.

[c] Reference 12.

[d] Cross section ratios from average of measurements at bombarding energies of 164, 180, and 230 MeV, Ref. 5.

[e] Based on the values of $\bar{B}(IS)$ given in Ref. 3; $B(\alpha) = (A/2Z)^2\bar{B}(IS)$.

[f] Extracted from $B(E2)$ values of the mirror transitions as described in Ref. 1, but without corrections for Coulomb effects upon the single-particle wave functions.

course, consistent with the simplest shell-model expectations, in which the lowest 0^+, 2^+, and 4^+ states of ^{26}Mg are formed by the two *proton* $0d_{5/2}$ holes in ^{28}Si and the analogs in ^{26}Si by the corresponding two *neutron* holes. In contrast to the 0_1^+-2_1^+ transition, the 0_1^+-2_2^+ transition in ^{26}Mg is predicted to be dominated by neutron excitations, with a $B(\pi^-)/B(\pi^+)$ ratio three times bigger than that of the 0_1^+-2_1^+ transition. Since ^{26}Mg should present no target difficulties and these lowest two 2^+ states are well isolated in energy, the experimental test of our predictions should be precise.

We have illustrated in these calculations for ^{18}O and ^{26}Mg that current theory for the many-body aspects of nuclear structure predicts ratios of the neutron and proton components of nuclear transitions which differ markedly from state to state and that the analyses of these differences can yield revealing insight into the natures of the various different excitations. Comparison with some of the few existing relevant data suggests that our theoretical interpretation is correctly focused, even though at present the empirical foundation of our assumption for the isovector effective charge is quite weak. Calculations for the ratios for inelastic scattering strengths for π^- and π^+ show variations between different excited states which should be clearly identifiable with current experimental techniques and pursuit of this type of experiment should, therefore, prove very rewarding.

This material is based upon work supported in part by the U. S. National Science Foundation under Grant No. Phy-7822696. One of the authors (B. H. Wildenthal) wishes to thank Professor K. A. Allen and Dr. P. E. Hodgson for their hospitality during his stay in Oxford.

---

[1] A. M. Bernstein, V. R. Brown, and V. A. Madsen, Phys. Rev. Lett. 42, 425 (1979).

[2] P. M. Endt and C. van der Leun, Nucl. Phys. A235, 27 (1974).

[3] A. M. Bernstein, *Advances in Nuclear Physics*, edited by M. Baranger and E. Vogt (Plenum, New York, 1969).

[4] B. A. Brown *et al.*, Nucl. Phys. A277, 77 (1977).

[5] S. Iverson *et al.*, Phys. Lett. 82B, 51 (1979).

[6] S. Iverson *et al.*, Phys. Rev. Lett. 40, 17 (1978); J. Jansen, Phys. Lett. 77B, 359 (1978), C. Lunke *et al.*, *ibid.* 78B, 201 (1978).

[7] B. S. Reehal and B. H. Wildenthal, Part. Nucl. 6, 137 (1973).

[8] W. Chung, thesis, Michigan State University, 1976 (unpublished); B. H. Wildenthal, *Elementary Modes of Excitation in Nuclei*, edited by A. Bohr and R. Broglia (North-Holland, Amsterdam, 1977).

[9] V. R. Brown and V. A. Madsen, Phys. Rev. C 11, 1298 (1975).

[10] D. Schwalm *et al.*, Nucl. Phys. A293, 425 (1977); B. A. Brown *et al.* (unpublished).

[11] F. Ajzenberg-Selove, Nucl. Phys. A300, 1 (1978).

[12] E. W. Lees *et al.*, J. Phys. A 7, 936 (1974).

$^{12}C+^{12}C$ intermediate structures correlated among elastic and reaction channels

E. R. Cosman, R. Ledoux, and A. J. Lazzarini*
Department of Physics and Laboratory for Nuclear Science, Massachusetts Institute of Technology, Cambridge, Massachusetts 02139

(Received 24 October 1979)

Prominent intermediate structure correlations are suggested between $^{12}C + ^{12}C$ elastic and reaction channel excitation functions over a wide range of energies above the Coulomb barrier. The associated resonant states in ^{24}Mg would have large partial widths to elastic, inelastic, and $\alpha + ^{20}Ne^*$ channels.

[NUCLEAR REACTIONS Correlation analysis on $^{12}C+^{12}C$ resonance channels. Deduced positions of intermediate structure states in ^{24}Mg and ^{12}C, $\Gamma(^{12}C+^{12}C)$ strength function.]

The $^{12}C+^{12}C$ elastic and reaction channels show exceptionally dramatic intermediate structures.[1] The relationship of this to the demonstration of quasimolecular states has been unclear because of the uncertain role of statistical fluctuations. Several analyses have indicated that the pronounced intermediate structures in the $^{12}C+^{12}C$ elastic and the $^{12}C(^{12}C,\alpha)^{20}Ne^*$ reactions are consistent with statistical compound-nucleus fluctuations.[2-4] Other analyses have interpreted the elastic structures as arising from coupling to resonant inelastic channels, which would make them of nonstatistical origin.[5] In none of these studies has an explicit correlation between elastic and reaction intermediate structures been made.

Here we suggest that a strong correlation exists between nearly all $^{12}C+^{12}C$ intermediate structures seen in elastic channels above the Coulomb barrier and resonances seen in other reaction channels, particularly the inelastic and $\alpha+^{20}Ne^*$ channels.

Figure 1 shows excitation functions for the $^{12}C+^{12}C$ elastic scattering at 90° c.m. and for the total reaction,[6] the $^{12}C+^{12}C^*$ inelastic,[7,8] and $\alpha+^{20}Ne^*$ reaction channels.[6,9] The dashed lines indicate apparent correlations of intermediate structures among these channels. The maxima in the 90° c.m. elastic channel correlate well to nearly all reaction intermediate structures, suggesting that they do not arise from interference effects and fluctuations, but rather are nearly isolated resonances in ^{24}Mg. Comparison to 90° c.m. elastic data only is restrictive, however, it is most likely to reveal such correlated states because the ratio of resonance to background amplitude is a maximum at that angle.

Figure 2 shows further details of this comparison near $E_{c.m.}=20$ MeV using data taken at several laboratories.[1,3,6,7,10] Major structures at $E_{c.m.}\cong 18.4$, 19.3, 20.4, and 21.0 MeV appear in the elastic, $\alpha+^{20}Ne^*$, $^{12}C+^{12}C^*(2_1^+)$, and $p+^{23}Na^*$ channels. Shifts in the positions of maxima are, in some cases, up to half a peak width, as may be expected from background interference and overlap of resonance tails. Kolata *et al.*[9] have noted that the $^{16}O(3_1^- \rightarrow 0_1^+)$ yield is dominated by the $^{12}C(^{12}C,\alpha)^{20}Ne^* \rightarrow \alpha+^{16}O^*$ reaction above $E_{c.m.}\cong 20$ MeV with little from $^{12}C(^{12}C,^{8}Be)^{16}O^*$ directly in that region. Also the $^{12}C(^{12}C,^{8}Be)^{16}O(g.s.)$ yield[11] is relatively small and shows no resonant structure that is clearly correlated with that mentioned here over the range of $E_{c.m.}\cong 9$ to 20 MeV.

Figure 3 shows correlation functions of the data of Fig. 1. Relatively strong effects are seen, in most cases, near $E_{c.m.}=19.3$, 20.3, MeV, and from 24 to 28 MeV, supporting the above suggestion. Shifts in peak positions from background interference make difficult any more exact interpretation of Fig. 3.

These correlations imply that the intermediate structures in the elastic and other channels represent a fairly sparse population of $^{12}C+^{12}C$ doorway states, and thus their properties may be learned in detail. More complete elastic cross sections should yield $\Gamma(^{12}C)$ and J^π values directly. More complete reaction channel data could be analyzed with the elastic data to provide all partial decay widths and background phase shifts.

With the present data, the observation of discrete, correlated intermediate structures implies that they have unusually large carbon widths, and, in that sense, are of quasimolecular character. Figure 4 shows a comparison of the 90° elastic data with a calculated curve using an optical background plus resonances added at the energies suggested by Figs. 1 and 2. The calculation is not intended to be a careful fit since many important aspects of doing such a fit, mentioned in the Fig. 4 caption, are ignored. However, it illustrates

© 1980 The American Physical Society

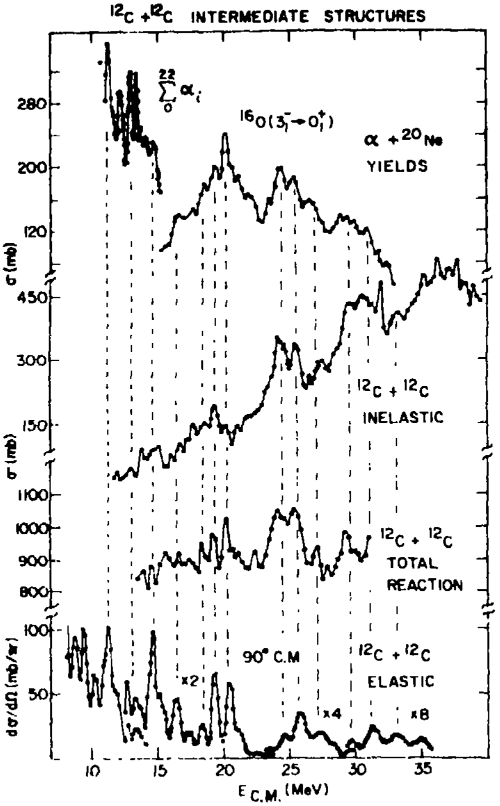

FIG. 1. Comparison of ^{12}C + ^{12}C intermediate structures. From top to bottom the data is from: top left, summed alpha yield, Ref. 9; top right, ^{16}O($3^- \to 0^+$) gamma yield corresponding mostly to 2α emission through ^{20}Ne* states, Ref. 6; ^{12}C + ^{12}C inelastic, meaning the total ^{12}C($2^+ \to 0^+$) gamma yield, Ref. 7; ^{12}C + ^{12}C total reaction cross section, Ref. 6; and, ^{12}C + ^{12}C elastic at 90° c.m., Ref. 1. Dashed lines show correlated resonances.

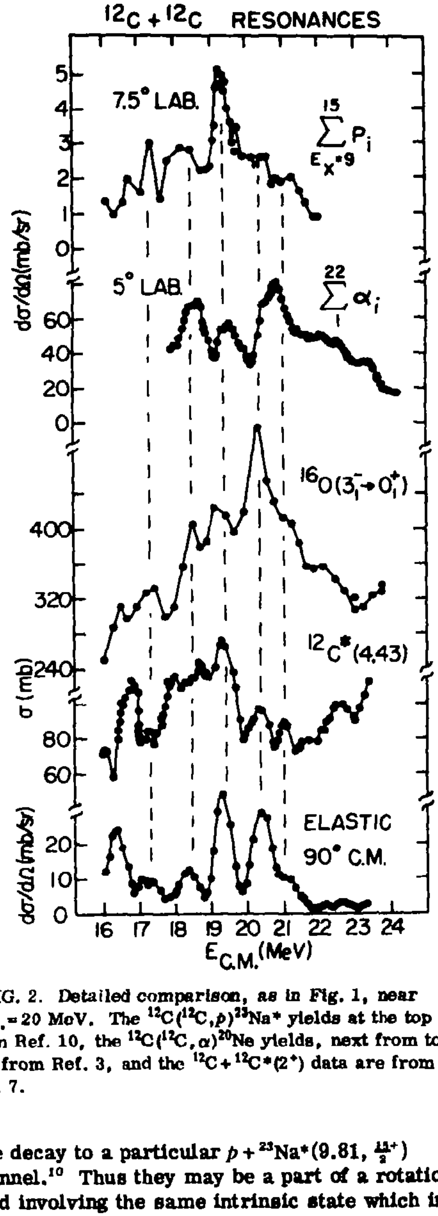

FIG. 2. Detailed comparison, as in Fig. 1, near $E_{c.m.} = 20$ MeV. The ^{12}C(^{12}C,p)^{23}Na* yields at the top are from Ref. 10, the ^{12}C(^{12}C,α)^{20}Ne yields, next from top, are from Ref. 3, and the ^{12}C + ^{12}C*(2^+) data are from Ref. 7.

that to match the amplitude of the intermediate structures at 90°, the values of $\Gamma(^{12}\mathrm{C})/\Gamma_{\mathrm{total}}$ must all be in the range of 10 to 50%. This range of $\Gamma(^{12}\mathrm{C})/\Gamma_{\mathrm{total}}$ is also consistent with the strength of resonances in the total reaction cross section, Fig. 1.

The origin of these intermediate structure resonances is an interesting question. Their decays are simple and seem to depend on specific final state structures rather than statistical selection rules, and so their wave functions and quantum numbers may be learned in detail. It has been pointed out that the resonances at $E_{c.m.} \cong 11.4$, 14.3, and 19.3 MeV probably have $J^\pi = 8^+$, 10^+, and 12^+, respectively, and show the same selective decay to a particular $p + {}^{23}\mathrm{Na}^*(9.81, \frac{11}{2}^+)$ channel.[10] Thus they may be a part of a rotational band involving the same intrinsic state which includes a specific $p + {}^{23}\mathrm{Na}^*(\frac{11}{2}^+)$ particle-core component. The limited available α-spectra data indicate that specific $\alpha + {}^{20}\mathrm{Ne}^*$ particle-core configurations may play a major role in the explanation of the ^{12}C + ^{12}C intermediate structures. We note from Fig. 1 that, for each intermediate structure, the resonant $\alpha + {}^{20}\mathrm{Ne}^*$ decay is comparable to and often stronger than the prominent resonant inelastic decay, and thus it represents a major

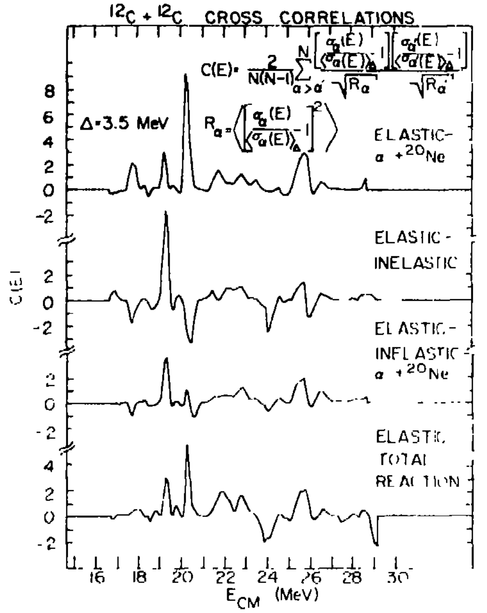

FIG. 3. Correlation functions between cross sections of pairs of channels shown in Fig. 1. In the second graph from the bottom, we summed the $\alpha + ^{20}Ne$ and elastic correlation function with the inelastic and elastic correlation functions. Correlation functions were similar for averaging intervals Δ between 2 to 3.5 MeV.

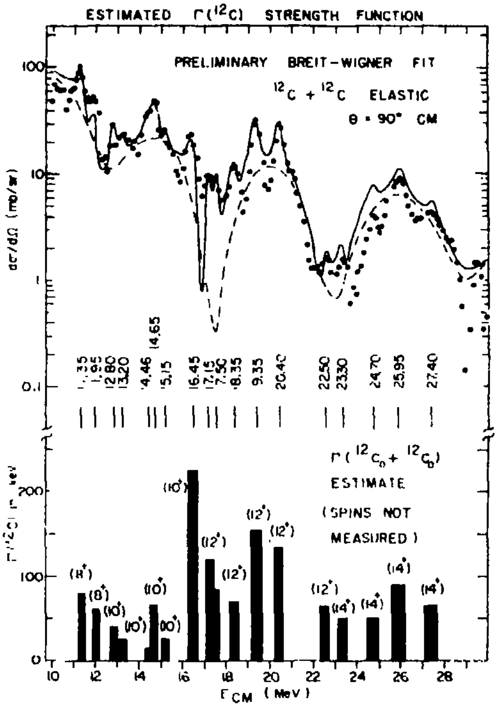

FIG. 4. The $^{12}C+^{12}C$ 90° c.m. elastic data is compared to the solid curve calculated crudely by adding independent Breit-Wigner resonances to the S matrix. No attention has been paid to overlapping resonance conditions, resonance background phases (taken as zero), unitarity, and other important points. Spins, which are largely unknown, were assumed to be the values in parenthesis. The comparison at other angles is comparable in quality. The background, dashed curve, is calculated using parameters in Ref. 12, except for an increased absorption. The lower graph shows the resulting $\Gamma(^{12}C)$ strength function. Width of each histogram equals Γ_{total} and runs between 200 and 400 keV. The assumed resonance energies are indicated.

fraction of the resonant total reaction cross section. Moreover, there is evidence that a large fraction of the $\alpha + ^{20}Ne^*$ decay itself populates only a few selected states in ^{20}Ne. For example, the $E_{c.m.} = 11.4$ MeV resonance decays primarily to the $E_x = 0$ MeV, 0^+ and $E_x = 5.62$ MeV, 3^- states[4]; the $E_{c.m.} \cong 18.5$, 19.3, and 20.3 MeV resonances decay to a selected group of high spin states[3] between $E_x = 8$ and 20 MeV in ^{20}Ne. These resonances are seen in the $^{12}C(0^+) + ^{12}C^*(2^+)$ channel, the $E_{c.m.} \cong 19.3$ MeV resonance being most prominent, and are at most weakly visible in the $^{12}C^*(2^+) + ^{12}C^*(2^+)$ channel.[7] They are also probably weak in the $^8Be + ^{16}O$ and $^8Be + ^{16}O^*(3^-)$ channels.

The band crossing model involving elastic coupling to resonances in the inelastic channels has been proposed by Nogami, Imanishi, and others[5] for describing the $^{12}C + ^{12}C$ elastic and inelastic intermediate structure. The present observation of intermediate structure correlations between elastic, inelastic, and reaction channels should provide further basis for comparison to calculations with this model. The prominent resonances in the $\alpha + ^{20}Ne^*$ channel and the selective decays to $p + ^{23}Na^*$ suggest that these degrees of freedom also may have to be included directly in the band crossing model for a complete explanation of the data. In this connection, the extraordinarily prolate shapes of ^{20}Ne and ^{23}Na may play a role in enabling a favorable mixing of the above particle-core configurations with the $^{12}C + ^{12}C$ quasimolecular states. The apparent nonadmixture at $E_{c.m.} \sim 20$ MeV of the $^{12}C + ^{12}C$ states with $^8Be + ^{16}O$ configurations is yet further evidence for specific structure effects, possibly related to dissimilar shapes of the two systems.

The existence of gross structures, such as shape resonances,[13] fragmented by the doorway states as discussed by Feshbach[14] finds support in the present observation. Hints of broad groups of states near $E_{\mathrm{c.m.}}=15$, 20, and 25 MeV are seen in the channels of Fig. 1, in elastic deviation functions,[15] and perhaps in the $\Gamma(^{12}C)$ strength of Fig. 4. Again, spin measurements for the elastic resonances is an obvious next step in this problem. The gross structures in the inelastic scattering have been cited as support of the picture,[7] but Phillips *et al.*[16] have shown that such features can be reproduced, in part, by nonresonant diffraction. The grouping of spins measured by $^{12}C(^{12}C,{}^{8}Be)^{16}O$ reaction may be governed by the exit channel and indicative of different states in ^{24}Mg. This conclusion is confirmed over a limited range by the work of Eberhard *et al.*[17]

In summary, the present observation of correlated, discrete intermediate structures in the $^{12}C+{}^{12}C$ elastic and reaction channels demonstrates directly the appearance of quasimolecular states in the elastic scattering, provides a tractable indication of how to measure the spins and partial widths for these states, and indicates the large admixture of $\alpha+{}^{20}Ne^{*}$ configurations into the $^{12}C+{}^{12}C$ quasimolecular states.

The authors are grateful to J. J. Kolata and H. Voit for receiving their data prior to its publication, and to H. Feshbach for helpful discussions. This work has been supported in part by the U.S. Department of Energy Contract No. EY-76-C-02-3069.

---

[*] Present address: University of Washington, Seattle, Washington.

[1] D. A. Bromley *et al.*, Phys. Rev. Lett. 4, 365 (1960); W. Reilly *et al.*, Nuovo Cimento A13, 897 (1973); M. L. Halbert *et al.*, Phys. Lett. 51B, 341 (1974).

[2] D. Shapira, R. G. Stokstad, and D. A. Bromley, Phys. Rev. C 10, 1063 (1974); J. P. Bondorf, Nucl. Phys. A202, 30 (1973).

[3] L. R. Greenwood *et al.*, Phys. Rev. C 12, 156 (1975).

[4] E. Almqvist *et al.*, Phys. Rev. 13, 384 (1964).

[5] B. Imanishi, Nucl. Phys. A125, 33 (1969); J. H. Fink, W. Scheid, and W. Griener, *ibid.* A188, 259 (1972); Y. Abe, T. Matsuse, and Y. Kondo, Yale Report No. 3074-503 (unpublished).

[6] J. J. Kolata, R. M. Freeman, F. Haas, B. Heusch, and A. Gallmann (unpublished).

[7] T. M. Cormier *et al.*, Phys. Rev. Lett. 40, 924 (1978); T. M. Cormier *et al.*, *ibid.* 38, 940 (1977).

[8] H. Emling *et al.*, Nucl. Phys. A211, 600 (1973).

[9] H. Voit *et al.*, Phys. Lett. 67B, 399 (1977); W. True *et al.* (unpublished).

[10] E. R. Cosman *et al.*, Phys. Rev. Lett. 35, 265 (1975); Van Bibber *et al.*, Phys. Rev. Lett. 32, 687 (1974).

[11] N. R. Fletcher *et al.*, Phys. Rev. C 13, 1173 (1976).

[12] A. Gobbi *et al.*, Phys. Rev. C 7, 30 (1973).

[13] A. Arima, G. Scharff-Goldhaber, and K. W. McVoy, Phys. Rev. Lett. 40B, 7 (1972).

[14] H. Feshbach, J. Phys. (Paris), Colloq. 37, C5-177 (1976).

[15] A. J. Lazzarini *et al.*, Phys. Rev. Lett. 40, 1426 (1978).

[16] R. L. Phillips *et al.*, Phys. Rev. Lett. 42, 566 (1979).

[17] K. A. Eberhard and K. G. Bernhardt, Phys. Rev. C 13, 440 (1976).

PHYSICAL REVIEW C VOLUME 21, NUMBER 5 MAY 1980

Interior probing capability in kaon-nucleus inelastic scattering

Stephen R. Cotanch
Department of Physics, North Carolina State University, Raleigh, North Carolina 27607

(Received 10 December 1979)

Results from a nuclear structure form factor study are presented to investigate the extent of surface localization and volume sensitivity in K^+-nucleus inelastic scattering. Using wave functions from a macroscopic collective model and the microscopic particle-hole model of Gillet and Vinh Mau, form factors (transition densities) and cross sections are independently calculated and then compared for low-lying excited states in ^{12}C. Unlike strongly absorbed projectiles (including the pion), which have dominant surface localized reaction mechanisms, the interior differences between model form factors are clearly reflected (measurably distinct) at *all* scattering angles.

[NUCLEAR REACTIONS kaon-nucleus inelastic scattering. DWIA, KMT, and RPA. Calculated $\sigma(\theta, E)$ for ^{12}C. Comparative form factor study.]

One of the conclusions reached in an earlier study[1] of K^+-nucleus inelastic scattering was that the inelastic process was localized ($\pm\frac{1}{2}$ fm) near the nuclear surface. This study[1] also confirmed that the K^+ meson was, as previously noted by Dover,[2] quite weakly absorbed. These developments would appear "anomalous" as surface dominating processes are normally associated with strongly absorbed particles. Because of the potential ramifications from a growing interest in kaon-nucleus phenomena,[3-10] it is important at this time to fully understand this surface localization behavior and to determine the extent of volume probing sensitivity of the K^+ meson. In particular, it is essential to further document the improved and new nuclear structure information which can be uniquely obtained through kaon induced reactions. The purpose of the present communication is to address these issues by reporting results from a comparative form factor study for K^+-nucleus inelastic scattering. The comparison is between inelastic form factors obtained using a macroscopic collective model and the microscopic particle-hole model of Gillet and Vinh Mau.[11] The results indicate that the surface localization is directly attributable to the surface peaking of the collective form factor and that the kaon is indeed sensitive to details of the nuclear interior.

This theoretical study, which parallels a previous pion investigation,[12] compares microscopic and macroscopic form factors (transition densities) for the $J^\pi = 2^+$ ($E_x = 4.43$ MeV) and 3^- ($E_x = 9.64$ MeV) states in ^{12}C. The calculations are based on the distorted-wave impulse approximation (DWIA) to the exact multiple scattering transition amplitude and are further detailed in Refs. 1, 8, and 13. The necessary information entering the analysis are the phenomenological kaon-nucleon amplitudes and nuclear structure (model) wave functions. All calculations reported in this work use Martin[14] kaon-nucleon amplitudes and Fermi motion effects are neglected (no Fermi averaging). These amplitudes are used to construct the elastic (distorting) and inelastic kaon-nucleus interactions as a function of bombarding energy (see Ref. 8). To study surface localization two different wave functions were used to generate form factors: a macroscopic collective rotational model, in which the density is deformed, and the microscopic particle-hole model of Gillet and Vinh Mau (GV).[11]

The GV model, which used the random phase approximation (RPA), includes all 1 particle-1 hole excitations involving $1s$, $2s$, $1p$, $2p$, $1d$, and $1f$ single-particle orbitals. Since two particle-two hole contributions are important for the low-lying collective states in ^{12}C, the GV wave functions fail to provide sufficient collectivity. However, because the phenomenological effective nucleon-nucleon interaction entering the RPA calculation was determined in part by properties of the first 2^+ state in ^{12}C, the results presented below, while perhaps not completely physically correct, should remain representative. For the collective model the ground state density, as determined by electron scattering, was deformed with deformation parameter β_J. To ensure consistent, meaningful form factor comparisons the collective model was constrained[12] to provide electric transition rates ($BE2$ and $BE3$ values) identical to those obtained using the GV wave functions. This yielded $\beta_2 \simeq \beta_3 = 0.56$. Finally, consistency also required the omission of all spin-flip inelastic amplitudes (magnetic transitions) in the microscopic form factor. The latter effect was found small for

© 1980 The American Physical Society

pions[12] involving natural parity excitations and should be even smaller for kaons since the kaon-nucleon amplitude is predominantly s wave for the energies used in the present calculation.

The microscopic and macroscopic ($BE2$ normalized) radial transition densities (inelastic form factors) for the ground to 2^+ (4.43 MeV) transition in ^{12}C are plotted in Fig. 1. The form factors differ appreciably in the interior but are similar near the nuclear surface (about 2.3 fm for ^{12}C). Accordingly, strongly absorbed particles, which predominantly probe the nuclear surface, should not provide sensitive means for distinguishing between these two different radial shapes. This is particularly true for the pion at energies near the (3,3) resonance and has been discussed in Ref. 12 where calculations demonstrate that only at back angles (large momentum transfer) can theoretical pion inelastic cross sections predict measurable differences.

Of central importance in this work is the interior probing capability of the weakly absorbed kaon. Figure 2 compares the predicted angular distributions for K^+ inelastic scattering at 100 MeV lab kinetic energy. There is a clear, measurable distinction between the particle-hole and collective models. The cross section difference is as much as 50% at forward angles, including a 10° maxima shift, and grows to an order of magnitude at back angles. Figure 3 demonstrates a similar sensitivity at 300 MeV where the minimum predicted by the collective model near 40° is completely missing in the particle-hole picture. Form factor and cross section calculations were also performed for the 3^- (9.64 MeV) state and similar differences were found (not shown).

A cursory examination of Fig. 1 immediately suggests that in the collective model the dominant inelastic contributions should come from the nuclear surface. The particle-hole model, however, peaks somewhat inside the surface (about 1.6 fm). To further determine the extent to which the kaon can resolve this difference, radial cutoff calculations, identical to the study in Ref. 1, were performed. The results are shown in Fig. 4 where the total inelastic cross section is plotted as a function of the cutoff radius R_c. For comparison, both the collective and particle-hole DWIA cross sections are presented along with corresponding plane-wave impulse approximation (PWIA) calculations. To effectively illustrate the differences, the curves have been renormalized to produce identical cross sections at $R_c=0$. Notice that the kaon is indeed sensitive to the interior tail of both model form factors (see Fig. 1) and clearly reflects the radial peak shift of the GV form factor relative to the collective form factor.[15] Further-

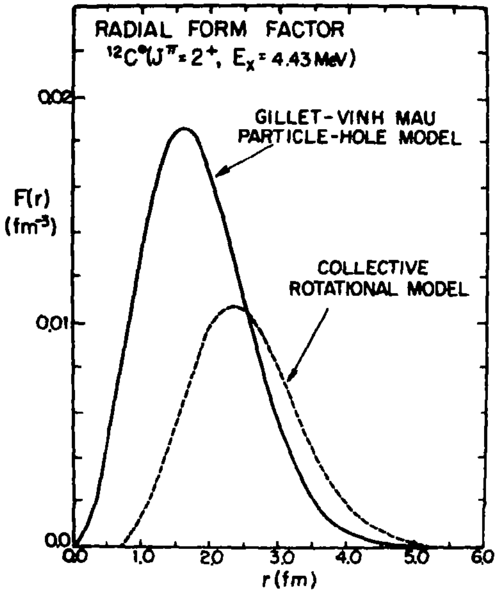

FIG. 1. Radial transition densities, $F(r)$ (form factors), computed for ground state to 2^+, 4.43 MeV state transition using microscopic particle-hole (solid curve) and collective macroscopic (dashed curve) models.

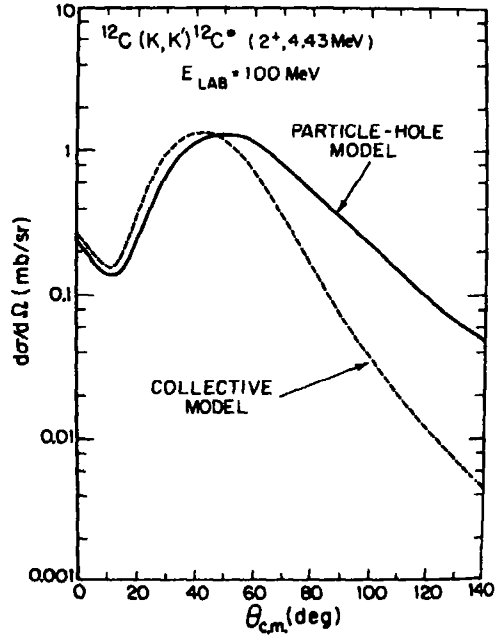

FIG. 2. Differential inelastic cross section for kaon inelastic scattering using the particle-hole (solid curve) and collective (dashed curve) form factors plotted in Fig. 1.

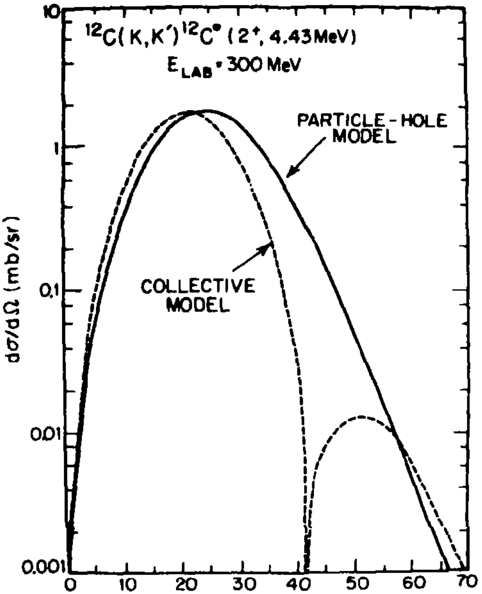

FIG. 3. Same as Fig. 2 for E_{LAB} 300 MeV.

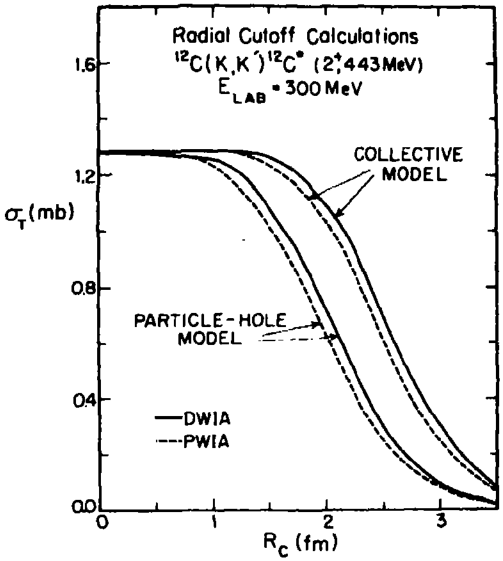

FIG. 4. Microscopic and macroscopic total inelastic cross section as a function of cutoff radius R_c. Solid curves represent DWIA, dashed curves PWIA. For visual comparison the curves have been renormalized to give equal cross sections at R_c - 0.

more, the small radial difference between DWIA and PWIA (no absorption) convincingly demonstrates that kaon distortion effects are small and do not significantly affect the probing sensitivity. In essence, the kaon appears to "see" whatever is available to be seen.

In summary, the weakly absorbed K^+ meson is predicted to be sensitive to details concerning the interior structure of the nucleus. Further, the kaon appears to have the rare capability of distinguishing between microscopic and macroscopic structure models. Although the microscopic particle-hole model used in this work may be incomplete for the low-lying collective states in ^{12}C, these conclusions should be valid for studies involving improved models. In particular, for high spin (stretched configuration) natural and unnatural parity states, the kaon should provide a powerful tool for probing particle-hole excitations.[3,7] Likewise for giant resonance studies, the kaon should prove invaluable in assessing the 1 particle-1 hole $T_<$ component of the resonance.[2,3,7,8] Finally, in the active area of kaon-nucleus elastic scattering, where experiments have recently been performed,[16,17] the kaon should provide a unique means for determining the ground state neutron distribution as well as neutron-proton density differences using neighboring isotope measurements (e.g., $^{40}Ca-^{48}Ca$). These studies focus on both volume (interior) and surface structure and are now in progress.[18]

The author wishes to acknowledge invaluable discussions with T. S. Lee. Support has been provided by grants from the U. S. Department of Energy, the N. C. Science and Technology Committee, and the Research Corporation.

---

[1] S. R. Cotanch and F. Tabakin, Phys. Rev. C 15, 1379 (1977).

[2] C. B. Dover and P. J. Moffa, Phys. Rev. C 16, 1087 (1977); see also C. B. Dover, Brookhaven Summer Study on Kaon Physics and Facilities, BNL, 1976.

[3] G. E. Walker, Bull. Am. Phys. Soc. 21, 646 (1976).

[4] R. D. Koshel, P. J. Moffa, and E. F. Redish, Phys. Rev. Lett. 39, 1319 (1977).

[5] Y. Alexander and P. J. Moffa, Phys. Rev. C 17, 676 (1978).

[6] S. R. Cotanch, Phys. Rev. C 18, 1941 (1978).

[7] C. B. Dover and G. E. Walker, Bull. Am. Phys. Soc. 23, 554 (1978); Phys. Rev. C 19, 1393 (1979).

[8] S. R. Cotanch, Nucl. Phys. A308, 253 (1978).

[9] S. R. Cotanch, in The (p,π) Reaction and the Nucleon-Nucleon Force Conference, Telluride, Colorado, 1979 (Plenum, New York, to be published).

[10] B. F. Gibson, 2nd International Conference on Meson-Nuclear Physics, University of Houston, Houston, Texas, 1979.

[11] V. Gillet and N. Vinh Mau, Nucl. Phys. **54**, 321 (1964).

[12] T. S. Lee and F. Tabakin, Nucl. Phys. **A226**, 253 (1974).

[13] R. A. Eisenstein and G. A. Miller, Comput. Phys. Commun. **11**, 95 (1976).

[14] B. R. Martin, Nucl. Phys. **B94**, 413 (1975).

[15] The conclusion concerning surface localization may have been overstated in Ref. 1 since a larger density radius parameter was used in that work.

[16] D. Marlow, P. Barnes, S. Dytman, R. Eisenstein, W. Wharton, F. Takeutchi, S. Bart, D. Hancock, R. Hackenberg, E. Hungerford, L. Pinsky, T. Williams, R. Chrien, H. Palevsky, and R. Sutter, in *Meson-Nuclear Physics—1979*, Proceedings of the 2nd International Topical Conference on Meson-Nuclear Physics, Houston, edited by E. V. Hungerford III (AIP, New York, 1979).

[17] R. A. Eisenstein, in *Proceedings of the Kaon Factory Workshop, Vancouver, 1979*, edited by M. K. Craddock (TRIUMF, Vancouver, 1979), p. 75.

[18] S. R. Cotanch, in *Proceedings of the Kaon Factory Workshop, Vancouver, 1979*, edited by M. K. Craddock (TRIUMF, Vancouver, 1979), p. 92.

PHYSICAL REVIEW C VOLUME 21, NUMBER 5 MAY 1980

Pion electroproduction from the nucleon near threshold

E. T. Dressler
Department of Physics, Ogontz Campus, The Pennsylvania State University, Abington, Pennsylvania 19001

N. Freed and H. B. Miska
Department of Physics, 104 Davey Laboratory, The Pennsylvania State University, University Park, Pennsylvania 16802

(Received 5 September 1979)

We investigate the dependence on production amplitude of the low energy scattering cross section for positive pion electroproduction from the nucleon. Calculations based on the threshold approximation to the full amplitudes of Dombey and Read are illustrated and compared to results for the full amplitudes. Inclusion of the momentum-dependent terms yields differential cross sections in the near-threshold region differing from those given by the threshold approximation by no more than 15% at any angle.

[NUCLEAR REACTIONS Dependence of $\sigma(\theta)$ for electron scattering on nucleon upon production amplitudes.]

It has long been realized that electromagnetic probes of the nucleus can be particularly sensitive to details of nuclear structure. This sensitivity persists at energies over pion production threshold where it becomes possible additionally to investigate the dynamics of the π-nucleus interaction over a broad energy range. This is particularly important in the near-threshold region ($5 \leq T_\pi \leq 25$ MeV) where little useful information can be obtained from elastic pion scattering experiments.

Calculations on threshold and near-threshold pion photoproduction and electroproduction are typically carried out in the framework of the distorted wave impulse approximation (DWIA), incorporating various models for the nuclear structure, single-particle $\gamma\pi N$ amplitudes, and π-nucleus optical potentials. Clearly, the reliability of the structure and particle production input determines the reliability of the conclusions that can be drawn from these processes regarding the π-nucleus interaction. In many cases, the nuclear matrix elements can be determined independently from analysis of related experiments.[1] For charged pion photoproduction, the single-particle amplitudes are likewise well determined from analysis of the reaction $\gamma N \to \pi N$ on a free nucleon.[2] Consequently, one is often able to make for photoproduction fairly unequivocal statements regarding the form of the pion optical potential and its relation to the basic πN interaction. The situation with respect to electroproduction is quite different. Here the greater complexity of the full dispersion-theoretic single-particle amplitudes has resulted in the uniform use[3-5,10] of threshold reductions in calculations on electroproduction from nuclei. In the course of carrying out detailed calculations on electropion production from nuclei in the threshold and near-threshold regions, we found that predictions for the electroproduction process on a single nucleon based on the full amplitudes can differ by 15% from those based on threshold approximations even at low energy. We think it important to present these intermediate results here because of the need to have accurate single nucleon input for the analysis of recent and projected nuclear electroproduction measurements, several of which are to be carried out at energies far above threshold.

The differential cross section for meson production in electron-nucleon collisions may be written

$$\frac{d^4\sigma}{ds_2\,dp\,d\Omega_2\,d\Omega_\pi} = (2\pi)^{-2} s_2{}^2 p^2 \delta(\epsilon_1 - \epsilon_2 - \omega_\pi + m - E_f) \left| T_{fi} \right|^2 , \quad (1)$$

where the initial and final electron four-momenta are $(\vec{s}_1, \epsilon_1)$ and $(\vec{s}_2, \epsilon_2)$ respectively; the pion momentum is $[\vec{p}, \omega_\pi = (p^2 + \mu^2)^{1/2}]$; the nucleon recoil momentum is $[\vec{q}, E_f = (q^2 + m^2)^{1/2}]$. All angles are measured with respect to the z axis, here taken to lie in the direction of propagation of the virtual photon of four-momentum $k = s_1 - s_2$, polarization $e_\mu = e\bar{u}(s_2)\gamma_\mu u(s_1)/k^2$. This choice of frame[6] explicitly separates the single-particle amplitudes from the nuclear physics, thereby allowing easy incorporation of the latter into calculations of nuclear electroproduction.

The transition matrix T_{fi} is proportional to the product of the leptonic and hadronic currents. The spatial part of the hadronic current can be written down from invariance requirements in the form[2]

© 1980 The American Physical Society

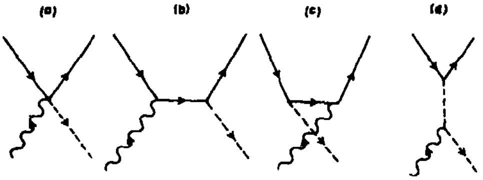

FIG. 1. Born diagrams included in present calculation: (a) contact term; (b) nucleon pole term; (c) crossed nucleon pole term; (d) pion current term. Solid lines are nucleons, dashed lines are pions, and wiggly lines are photons.

$$\vec{H} = i\vec{\sigma}F_1 + (\vec{\sigma}\cdot\hat{p})(\vec{\sigma}\times\hat{k})F_2 + i(\vec{\sigma}\cdot\hat{k})\hat{p}F_3 + i(\vec{\sigma}\cdot\hat{p})\hat{p}F_4 + i(\vec{\sigma}\cdot\hat{k})\hat{k}F_5 + i(\vec{\sigma}\cdot\hat{p})\hat{k}F_6, \qquad (2)$$

where the F_i are the single-particle amplitudes and $\hat{p}(\hat{k})$ are unit vectors for the pion (photon). The time component can be obtained from the continuity equation $k_\mu H_\mu = 0$; its inclusion leads to a redefinition of F_5 and F_6. We may then write for the transition matrix ($\hbar = c = 1$)

$$|T_{fi}|^2 = |\epsilon_\mu H_\mu|^2 = \frac{8\alpha^2 f^2 m}{\mu^2 \omega_\pi k^4 E_f}\,(M_{00}^{00} + M_{00}^{11} + 2M_{11}^{11}). \qquad (3)$$

Here

$$M_{00}^{00} = A\,|2F_2 \sin\theta_\pi|^2, \qquad (4a)$$

$$M_{00}^{11} = A\,|\sin\theta_\pi(F_2 + F_3 + F_4\cos\theta_\pi)|^2 + B\,|(F_1 + F_5) + (F_3 + F_6)\cos\theta_\pi + F_4\cos^2\theta_\pi|^2, \qquad (4b)$$

$$M_{11}^{11} = M_{-1-1}^{11} = A[\,|\tfrac{1}{2}\sin^2\theta_\pi F_4|^2 + |F_1 - F_2\cos\theta_\pi + \tfrac{1}{2}\sin^2\theta_\pi F_4|^2] + B(\tfrac{1}{2}\sin^2\theta_\pi)\,|F_4\cos\theta_\pi + F_6|^2. \qquad (4c)$$

The terms in $A = \frac{1}{2}\{1 - \cos\theta_2[1 - (s_2/s_1)^2\sin^2\theta_2]^{1/2}\}$ and $B = \frac{1}{2}[1 + \cos\theta_2(1 - (s_2/s_1)^2\sin^2\theta_2)^{1/2} - s_2/s_1\sin^2\theta_2]$ correspond to transverse and longitudinal photons, respectively.[7] Again, all angles are measured with respect to the virtual photon. To include the four component of the current, we make the following replacements:

$$F_5 \to F_5 - \frac{k^2}{\omega_k^2}(F_1 + \hat{p}\cdot\hat{k}F_3 + F_5), \qquad (5a)$$

$$F_6 \to F_6 - \frac{k^2}{\omega_k^2}(F_4\hat{p}\cdot\hat{k} + F_6). \qquad (5b)$$

It remains only to insert expressions for the F_i. We have used the "full model" proposed for electroproduction by Dombey and Read.[8] This consists of a contact (seagull) term, two nucleon pole terms, and a pion pole term (Fig. 1), all calculated in pseudovector coupling, together with a $\Delta(1236)$ resonance contribution. It was shown[8] that this model was consistent with both partial conservation of axial-vector current (PCAC) and existing data 100 MeV above threshold. Nonrelativistic limits of the Born terms were used, retaining *all* terms[9] to order m^{-1}.

The cross sections we are interested in are those for which ω_π and the orientation of the pion with respect to the direction of the incident electron are measured. The integrals in Eq. (1) are carried out in the forward peaking approximation (FPA) in which matrix elements of the elementary amplitudes are evaluated[5,10] at $\theta_2 \sim 0°$. The resulting cross sections are completely dominated by the transverse component of the amplitude with the various form factors replaced by their $k^2 = 0$ values.

In Fig. 2 we illustrate our results for π^+ production using the parameters ($E_e = 280$ MeV, $T_\pi = 21.6$ MeV) of the recent Mainz experiment[4] on threshold electroproduction from ^{12}C and ^{16}O. Curve (a) is the result using the threshold reduction[3-5,10] of the operators [$\vec{H} = \vec{\sigma}\cdot\vec{\epsilon}(1 - \mu/2m)$], corresponding to the $\vec{p} = 0$ limit of all diagrams in Fig. 1. Curve (b) contains the contact term and both nucleon pole terms. Curve (c) uses the

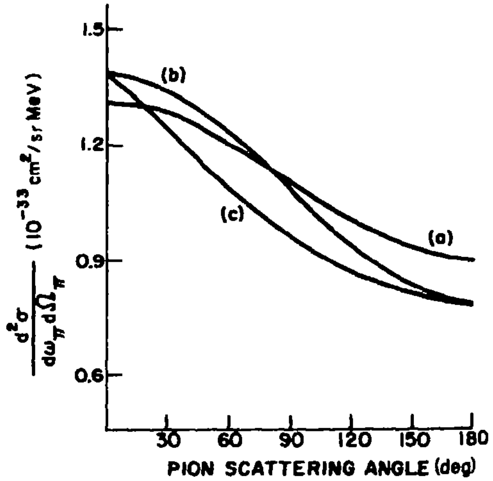

FIG. 2. Double-differential cross sections for positive pion production by 280 MeV electrons. Pion kinetic energy is 21.6 MeV. Curve (a) is for the threshold amplitudes (Refs. 3–5, 10); (b), for the contact and both nucleon pole terms [diagrams (a), (b), and (c) of Fig. 1]; (c), for the full amplitudes (all diagrams in Fig. 1 plus Δ resonance).

full form, consisting of all the Born terms and the Δ term (the latter contributes less than 1% at these energies).

The cross sections are dominated by the term proportional to $|F_1 - F_2 \cos\theta_\pi + \frac{1}{2}\sin^2\theta_\pi F_4|^2$ in M_{11}^{11} and M_{-1-1}^{11} [Eq. (4c)]. The nucleon pole contributions (all of which are momentum dependent), entering through F_1 and F_2, yield in this region ~10% corrections to the momentum-independent terms and vary with $\vec{p}\cdot\vec{k}/2m\omega_k$. The $\cos\theta_\pi$ dependence leads to a rotation of the threshold curve $(F_1 \sim 1 - \mu/2m)$ about $\theta_\pi = 90°$. A comparison of curves (b) and (c) illustrates the importance of the pion pole contribution. This term enters through $F_4 \sim -\vec{p}^2/(\omega_\pi\omega_k - \vec{p}\cdot\vec{k})$ and yields a 15–20% contribution. In the threshold approximation, all of the above momentum-dependent terms vanish identically. There is an additional pion pole term that does not vanish even at threshold. However, it enters only through the longitudinal amplitude F_5 and contributes little to the cross section. It should be noted in passing that although the F_5 term is negligible, its presence is formally required to maintain overall gauge invariance.

The chief conclusion to be drawn from this work is that the commonly made threshold approximation to the full electroproduction amplitudes leads to results for π^+ electroproduction on a free nucleon that can differ by ~15% from the predictions given by the full amplitudes. This finding is consistent with a recent result[11] on pion photoproduction from ^{7}Li and ^{12}C, a reaction equivalent to $(e,e'\pi)$ in the peaking approximation, where it was found that adding the momentum-dependent terms to the threshold operator yielded ~10% corrections for pion energies less than 50 MeV. Those electroproduction calculations on nuclei which employ threshold amplitudes within the framework of fairly sophisticated models of nuclear structure and final state interactions should include the correction terms, both for consistency of approach and for purposes of comparison with the accurate experimental data now becoming available.

---

[1] E.g., J. C. Bergstrom, I. P. Auer, and R. S. Hicks, Nucl. Phys. A251, 401 (1975).

[2] F. A. Berends, A. Donnachie, and D. L. Weaver, Nucl. Phys. B4, 1 (1967); B4, 54 (1967).

[3] E. Borie, H. Chandra, and D. Drechsel, Phys. Lett. 47B, 291 (1973); Nucl. Phys. A226, 58 (1974).

[4] F. Borkowski, Ch. Schmitt, G. G. Simon, V. Walther, D. Drechsel, W. Haxton, and R. Rosenfelder, Phys. Rev. Lett. 38, 742 (1977); R. Rosenfelder, in *Photopion Nuclear Physics*, edited by P. Stoler (Plenum, New York, 1979), p. 57.

[5] J. Asai and E. L. Tomusiak, Can. J. Phys. 55, 2066 (1977).

[6] L. M. Saunders, Nucl. Phys. B7, 293 (1968).

[7] T. deForest, Jr. and J. D. Walecka, Adv. Phys. 15, 1 (1966).

[8] Norman Dombey and B. J. Read, Nucl. Phys. B60, 65 (1973).

[9] E. T. Dressler, National Bureau of Standards Technical Note 957 (unpublished).

[10] W. C. Haxton, Nucl. Phys. A306, 429 (1978).

[11] F. Tabakin, in *Photopion Nuclear Physics*, edited by P. Stoler (Plenum, New York, 1979), p. 301; M. K. Singham, G. N. Epstein, and F. Tabakin (unpublished).

PHYSICAL REVIEW C VOLUME 21, NUMBER 5 MAY 1980

Truncated pion-nucleon amplitudes and pion-nucleus interactions

K. L. Kowalski
Department of Physics, Case Western Reserve University, Cleveland, Ohio 44106

(Received 23 July 1979)

It is pointed out that there are considerable structural differences among the various types of truncated pion-nucleon amplitudes which have been proposed in order to avoid overcounting ambiguities in pion-nucleus interactions. A previously proposed prescription is shown to yield truncated amplitudes which are free of the usual problems involved with the proper representation of the nucleon-pole term. It is shown that these truncated amplitudes can also possess ghost pole singularities arising from the πNN vertex function. Some problems caused by the appearance of such ghost poles in approximations to pion-nucleus amplitudes are discussed.

[NUCLEAR REACTIONS Pion-nucleon amplitudes without nucleon propagator terms. Overcounting in pion-nucleus interactions. Pion-nucleon vertex function ghost poles in approximate pion-nucleus amplitudes.]

The possibility of pionic absorption on nuclei, whether real or virtual, significantly alters the picture of interactive processes familiar in potential scattering. For example, departures from the potential scattering picture are certainly required if one is to maintain a dynamical distinction between the interactive processes associated with the external pion(s) and the pionic processes involved in the formation of nuclear bound states, for instance. Such a distinction is of considerable calculational importance since independent information concerning these nuclear states can then be utilized. A clean separation of the description of the interactive process from the characterization of the initial and final nuclear states is obtained straightforwardly in potential scattering. Such a separation can also be obtained for a fully relativistic field-theoretic description of pionic interactions.[1] A crucial aspect of any theoretical description of pionic interactions is an unambiguous specification of the nuclear bound state. Only then can one avoid the ambiguities which can arise from including pionic interactions already accounted for in the dynamics of the nuclear bound states or perhaps in the initial and final distorted waves if these are employed.[1-6]

In this article we are concerned with elaboration of the analysis in Ref. 1 of a particular type of ambiguity which arises from an improper identification of the complete interaction of a pion with a nucleon in the nucleus under certain circumstances. What is required here in order to avoid overcounting is the subtraction of one or both parts of the off-mass-shell pion-nucleon amplitude which contain nucleon poles.[1,5,6] We show in detail here that the prescriptions of Ref. 1 for doing this differ in several significant respects from those proposed in Refs. 5 and 6 despite some superficial resemblances.[2] These differences highlight the importance of the characterization of the bound state as part of any such subtraction algorithm. We also show how practical questions, which are inherent in the prescriptions of Refs. 3–6, relating to the choice between the pseudoscalar and pseudovector (PV) representation of the nucleon-pole terms can be circumvented. Finally, we demonstrate how the structural aspects of the πNN vertex function enter into the subtraction prescriptions of Ref. 1, in contrast to those of Refs. 3–5, and we comment on their possible influence upon the transition amplitudes. The differences among these alternative subtraction methods may or may not be of quantitative importance in calculations of pion-nucleus interactions. However, in order to assess this it is first necessary to understand in detail what these differences are and what they do entail in the way of calculation and this is our objective at this time.[7,8]

In order to illustrate the essential aspects of the sort of overcounting ambiguity we have referred to in the preceding paragraph we review some of Ref. 1 for the specific example of pion absorption on deuterium:

$$\pi + d \to N + N . \tag{1}$$

The pion-rescattering mechanism (Fig. 1) makes an important contribution to the reaction (1). In Fig. 2 we show the detailed structure of the final-state nucleon-nucleon interaction. The central question in regard to Fig. 1 concerns the proper identification of the effective pion-nucleon scattering amplitude t_R. There is no *a priori* reason to expect that t_R can be identified, consistently, with the full πN amplitude and in fact it cannot be.[1] In

© 1980 The American Physical Society

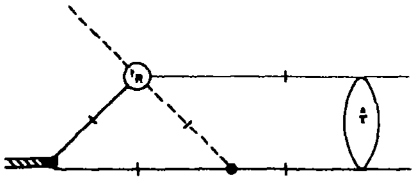

FIG. 1. Pion rescattering process where t_R represents the effective pion-nucleon scattering amplitude. The crossed solid internal lines represent full nucleon propagators S_F' while the crossed dashed internal line represents the full pion propagator Δ_F'. The final-state nucleon-nucleon interaction is denoted by $\hat{\tau}$. The dashed, solid, and cross-hatched external lines refer to the pion, nucleon, and deuteron, respectively. The dark circle corresponds to the proper πNN vertex function while the dark triangle represents the proper dNN vertex function. We follow these notational conventions in the other figures.

Ref. 1 it is shown that with a representation of the dNN vertex appropriate to the description of the deuteron bound state

$$t_R = t_{\pi N} - B_D - B_C\,. \tag{2}$$

Here $t_{\pi N}$ is the full πN amplitude and B_D and B_C comprise the sum of all connected $\pi + N \to \pi + N$ Feynman graphs which can be disconnected by cutting a single internal nucleon line. Such graphs consist of a single bare internal nucleon line with two external pion lines at its end points plus arbitrary self-energy insertions onto the nucleon lines and arbitrary (proper) vertex insertions at its end points.[9] The graphs which contribute to B_C and B_D are distinguished from each other as to whether their external pion lines are crossed or not, respectively (Fig. 3).

The analytic structure of B_D includes an s-channel nucleon pole while B_C has a u-channel nucleon pole and thus they are often referred to as the nucleon-pole or Born terms of $t_{\pi N}$.[10] These nucleon poles arise from the nucleon propagator S_F' which appears in the analytical expressions for B_D and B_C (Fig. 3):

$$B_D = \Gamma_{\pi NN}(k, k+p) S_F'(k+p) \Gamma_{\pi NN}(k', p')\,, \tag{3a}$$

$$B_C = \Gamma_{\pi NN}(k', p-k') S_F'(p-k') \Gamma_{\pi NN}(k, p')\,. \tag{3b}$$

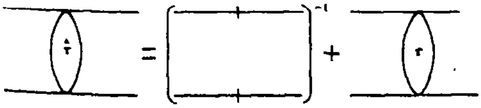

FIG. 2. Final-state nucleon-nucleon interaction. τ refers to the off-mass-shell nucleon-nucleon scattering amplitude.

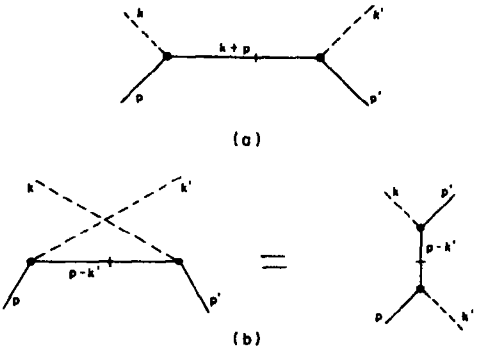

FIG. 3. (a) The full (direct) nucleon propagator term B_D. The internal nucleon line includes all self-energy corrections and the vertices (dark circles) represent fully dressed proper vertex functions. B_D contains the s-channel nucleon pole. (b) Two equivalent graphical representations for the full (crossed) nucleon propagator term B_C with the same internal nucleon line and vertex properties as in (a). B_C contains the u-channel nucleon pole.

We have suppressed in Eqs. (3) all inessential kinematical, isospin, and spinor features of B_D and B_C; the proper vertex function[11] is represented by $\Gamma_{\pi NN}$. It is important to keep in mind that $S_F'(p)$ possesses not only a pole at $p^2 = m_N^2$ but also a branch cut from $p^2 = (m_N + m_\pi)^2$ to $p^2 = +\infty$ which results from the multiparticle contributions to the nucleon two-point function.[12] The vertex function has a more complicated structure.[13-18]

If in Fig. 1 we were to use $t_{\pi N}$ instead of t_R, then Fig. 1 would include a contribution from B_C which is represented in Fig. 4. The internal pion line in Fig. 4 then gives rise to an ambiguous contribution to the reaction (1).[19] One can question the extent to which the internal pion exchange in Fig. 4 reproduces dynamical effects already included in the dNN vertex. In this regard, it is unclear to what degree Fig. 4 reproduces dynamics already included in the impulse term of Fig. 5 which combines coherently with the graph of Fig. 1 in its contribution to the reaction (1).

The conclusion of Ref. 1 is that Fig. 4 is ruled out as a legitimate contribution to the reaction (1)

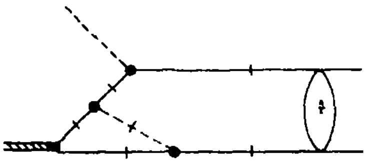

FIG. 4. Ambiguous contribution of B_C to the pion rescattering process.

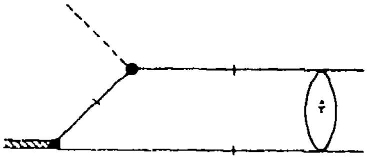

FIG. 5. Impulse graph for pion absorption with a final-state interaction.

and so is a similar graph generated by B_D in which the internal pion has its upper insertion to the right of the external pion's attachment vertex. The essential point is that it is the *full* contribution of both B_D and B_C as given by Eqs. (3) which must be subtracted from $t_{\pi N}$ to obtain the correct t_R.[20] It is exactly in this respect that Ref. 1 differs from the prescriptions of Refs. 5 and 6 for choosing t_R which involve subtracting off only the s-channel and u-channel *pole* terms from $t_{\pi N}$. These pole terms are then represented by PV coupling[21] with point vertices and a free nucleon propagator so that t_R is identified with the background term studied elsewhere by Liu and Shakin.[22]

Evidently one can decompose $t_{\pi N}$ in a variety of ways into a sum of "Born terms" which include the s- and u-channel poles plus a background term analogous to t_R.[21-23] The essential constraint upon any of these choices for the Born terms is that the residues of the poles be properly described. The conventional PV-coupling choice for the representation of the Born terms is motivated by the good approximation they provide to the threshold amplitudes.[21] However, because one has then lost the Feynman graph correspondence there is no compelling justification for identifying these Born terms with the sum of Feynman graphs which B_D and B_C represent and therefore the model proposed by Liu and Shakin[5, 6, 22] for the background amplitude should not be identified with t_R. There may be circumstances where this identification is adequate, e.g., in the neighborhood of the nucleon poles or when the ultimate effects of any of the various subtractions are small.

However, it is possible that the behavior of B_D and B_C is markedly different from that of say the Born terms resulting from PV-coupling with point vertices and a free nucleon propagator. We refer here, for example, to the fact that the vertex functions $\Gamma_{\pi NN}$ may possess ghost poles.[14, 18, 26] These are poles of $\Gamma_{\pi NN}$ coupled to the zeros of the full nucleon propagator S'_F. These ghost poles appear in B_D and B_C by Eqs. (3); however, they must be canceled by compensating poles in t_R in order to yield a $t_{\pi N}$ without these unphysical singularities. This can be shown to be the case.[14, 26] In a situation where, e.g., only t_R enters into an amplitude (Fig. 1) the compensating ghost poles in t_R will *not* be canceled *explicitly* and this may produce effects of importance under certain kinematical conditions and in an approximation where, e.g., only the amplitude corresponding to Fig. 1 is retained. We remark that the calculation of Mizutani and Rochus of $\Gamma_{\pi NN}$ with only one nucleon off its mass shell has yielded two ghost poles at unphysical energies.[18]

In Ref. 18 it is conjectured that it may be possible to observe the effects of these poles in pion-nucleus interactions, although no specific examples are proposed there nor are any reasons given why it should be possible to observe such effects. The pion rescattering process as represented by Fig. 1 may constitute such an example. However, in order that this be the case it is necessary to show that no other collection of graphs which also contributes to the process (1), such as those represented by Fig. 5, will cancel the effects of the poles in t_R. If such a cancellation does occur, analogous to what happens for free $t_{\pi N}$ amplitudes,[14, 25] then under circumstances where ghost poles appear in t_R consistent approximations to (1) would consist of such "ghost-free" combinations of amplitudes. We remark that any poles in t_R will be converted into branch singularities of the amplitude represented in Fig. 1, e.g., as a consequence of the integration over the loop momenta.

According to the prescriptions of Ref. 1 truncated pion-nucleus amplitudes appear in the contributions to an arbitrary pion-nucleus amplitude even those for elastic scattering.[20] It is not at all clear how the presence of ghost poles would alter the formulation of consistent approximations for these processes. These points deserve further investigation.

This work was supported in part by the National Science Foundation under Grant No. PHY 78-26595.

---

[1] K. L. Kowalski, E. R. Siciliano, and R. M. Thaler, Phys. Rev. C 19, 1843 (1979).

[2] A rather large literature exists concerning some of these overcounting ambiguities which predates Ref. 1. (We remark that the receipt date of Ref. 1 is misprinted and was actually 2 January 1979.) Most of the published works are cited in Ref. 1. Three unpublished works also warrant mention, namely Refs. 3–5; these

investigations have been cited frequently in connection with one or another overcounting ambiguity. The work of Liu and Shakin (Ref. 5) bears considerable resemblance to some aspects of Ref. 1, especially to those parts concerned with nucleon-pole-term subtractions from the constituent pion-nucleon amplitudes. However, Ref. 5, along with several other previous studies (including Refs. 3 and 4), does not contain an unambiguous specification of the nuclear bound state and as a consequence the subtraction prescriptions advocated there do not necessarily resolve the overcounting problems.

[3] A. W. Thomas, Ph.D. thesis, Flinders University, 1973 (unpublished).

[4] T. Mizutani, Ph.D. thesis, University of Rochester, 1976 (unpublished).

[5] L. C. Liu and C. M. Shakin, Brooklyn College Report No. B.C.I.N.T.-77/121, 1977 (unpublished).

[6] The prescriptions of Ref. 5 concerning overcounting are proposed again by R. S. Bhalerao, L. C. Liu, and C. M. Shakin, Brooklyn College-C.U.N.Y. Report No. B.C.I.N.T.-79/041/93, (unpublished).

[7] Reference 8 contains a preliminary calculation of the quantitative effects of nucleon-pole-term subtractions. The exact nature of the subtractions actually employed in this work is unclear, but it appears to be more in accord with the prescription of Refs. 5 and 6 rather than those of Ref. 1.

[8] D. R. Giebink, W. R. Gibbs, and E. R. Siciliano, *Meson-Nuclear Physics—Houston, 1979*, Proceedings of the 2nd International Topical Conference on Meson-Nuclear Physics, edited by E. V. Hungerford III (AIP, New York, 1979), p. 205.

[9] We keep in mind the nucleon propagator, πNN vertex, and external line renormalizations in connection with these graphical designations.

[10] Unfortunately, these appellations are not very precise. With the momentum labels of Fig. 3, $s=(k+p)^2$ and $u=(p-k')^2$.

[11] By this we mean that $\Gamma_{\pi NN}$ represents the sum of all connected graphs with two external nucleon lines and one external pion line which cannot be made disconnected by cutting either a single internal nucleon line or a single internal pion line.

[12] J. B. Bjorken and S. D. Drell, *Relativistic Quantum Fields* (McGraw-Hill, New York, 1965), p. 151. See also M. Gell-Mann and F. E. Low, Phys. Rev. 97, 1300 (1954).

[13] M. Ida, Phys. Rev. 135, B449 (1964); 136, B1767 (1964).

[14] Y. S. Jin and S. W. MacDowell, Phys. Rev. 137, B688 (1965).

[15] W. Nutt and B. Loiseau, Nucl. Phys. B104, 98 (1976).

[16] W. T. Nutt and C. M. Shakin, Phys. Rev. C 16, 1107 (1977).

[17] G. N. Epstein, Phys. Lett. 79B, 195 (1978).

[18] T. Mizutani and P. Rochus, Phys. Rev. C 19, 958 (1979).

[19] It may be thought that the internal pion in Fig. 4, for example, can somehow be distinguished kinematically from the pion exchanges which contribute to the *dNN* vertex function Γ_{dNN} which in the nonrelativistic limit is related to the deuteron wave function. This appears to be an ill-defined expectation; fortunately, it also appears to be an irrelevant one. The correct way to phrase these questions is to begin from a consistent description of the scattering process which includes a precise characterization of the composite nuclear state. When this is done diagrams such as Fig. 4 are simply ruled out from consideration at the start and the question of kinematic distinction never arises. It is also relevant to keep in mind that for appreciable momentum transfers carried by the internal pion in Fig. 1, Γ_{dNN} will not necessarily be represented adequately in terms of a nonrelativistic wave function.

[20] Other types of graphs contributing to (1) which involve effective pion-nucleon scattering insertions may require the subtraction of one or the other, or neither, of B_D and B_C from $t_{\pi N}$ to obtain proper amplitude. Several examples are explored in Ref. 1. See also Ref. 5.

[21] B. H. Bransden and R. G. Moorhouse, *The Pion-Nucleon System* (Princeton University Press, Princeton, New Jersey, 1973), p. 286.

[22] L. C. Liu and C. M. Shakin, Phys. Rev. C 18, 604 (1978).

[23] M. G. Olsson and E. T. Osypowski, Nucl. Phys. B101, 136 (1975).

[24] B. H. Wilde, S. A. Coon, and M. D. Scadron, Phys. Rev. D 18, 4489 (1978).

[25] C. J. Goebel and B. Sakita, Phys. Rev. Lett. 11, 293 (1963).

PHYSICAL REVIEW C VOLUME 21, NUMBER 5 MAY 1980

Projection operator method for heavy ion reactions and application to $^{12}C+^{12}C$

Thomas L. Larry and William P. Beres
Department of Physics, Wayne State University, Detroit, Michigan 48202

(Received 25 September 1979)

A projection operator formalism based on the Feshbach doorway approach is developed for low energy heavy ion scattering. An application to $^{12}C+^{12}C$ is made with doorways taken as quasibound or virtual states of the reduced mass coupled to 2^+ and 3^- vibrations. The elastic differential cross section at 90° is calculated and agrees rather well with experiment by producing both the gross and intermediate molecular structure.

[NUCLEAR REACTIONS $^{12}C+^{12}C$ elastic scattering, $E\sim 10$–30 MeV c.m., projection operator intermediate structure theory, calculated $\sigma(90°)$.]

The experimental study of nonrelativistic heavy ion reactions involving ions in the mass region up to about $A=18$ has shown that there are remarkably simple modes of excitation in energy regions where one would expect considerable complexity. Especially interesting is the discovery of certain resonances that appear to be attributable to nuclear molecule formation. While the gross structure can be reproduced with optical potentials[1] or diffraction models[2] there is still the need for a theoretical microscopic description that *not* only reproduces the broad resonances but also yields the underlying observed intermediate structure. In fact, Ref. 2 stresses the need for such a description in order to establish the existence of nuclear molecular phenomena. In this paper we present a unified theory of low energy heavy ion reactions using a projection operator formalism based on the Feshbach doorway approach.[3]

This technique, while seemingly akin to coupled channel methods,[4,5] is better suited to consistently take into account both microscopic and compound nuclear effects. The expressions obtained enable one to trace in a clear way the development of the different stages of complexity. For clarity the usual Feshbach notation is used. As an example the differential scattering cross section for $^{12}C+^{12}C$ in the energy region of 10–30 MeV c.m. is calculated and compared to the experimental results of Bromley and collaborators at Chalk River and Yale.[6]

We divide the Hilbert space into two orthogonal subspaces $\{P\}$ and $\{Q\}$ representing, respectively, the shape elastic continuum space of the reduced mass and the rest of the Hilbert space, the projection operators P and Q satisfy

$$P+Q=1.$$

Each of the subspaces associated with these operators can be further subdivided by introducing the mutually orthogonal operators p, R, d, and q so that

$$p+R=P, \tag{2a}$$

$$d+q=Q. \tag{2b}$$

The subdivision into p and R follows the procedure of Lev and Beres,[7] where R produces the subspace of shape elastic continuum resonances of the reduced mass projectile, and p produces the orthogonal nonresonance subspace. The operator d produces the subspace that contains the doorways, i.e., states which involve a nuclear interaction in addition to an optical potential, and are one step more complex than $\{R\}$. The operator q produces the states more complicated than d. Letting $\mathcal{H}$ be the total Hamiltonian and $\Psi^{(+)}$ the scattering wave function, the Schrödinger equation is

$$(E-\mathcal{H})\Psi^{(+)}=0. \tag{3}$$

We now make the usual doorway assumption that $\mathcal{H}_{Pq}$ is zero and, hence, does *not* contribute to our calculation. We introduce the effective Hamiltonian H via,

$$H=\mathcal{H}_{(P+d)(P+d)}+\mathcal{H}_{dq}\frac{1}{E-H_{qq}}\mathcal{H}_{qd}, \tag{4}$$

and obtain the coupled equations,

$$(E-H_{pp})p\Psi^{(+)}=H_{pR}R\Psi^{(+)}+H_{pd}d\Psi^{(+)}, \tag{5a}$$

$$(E-H_{RR})R\Psi^{(+)}=H_{Rp}p\Psi^{(+)}+H_{Rd}d\Psi^{(+)}, \tag{5b}$$

and

$$(E-H_{dd})d\Psi^{(+)}=H_{dp}p\Psi^{(+)}+H_{dR}R\Psi^{(+)}. \tag{5c}$$

By construction, the deviation of the scattering from pure shape elastic develops entirely from the coupling of R to d, i.e., $H_{pd}=0$. The solutions for the different portions of the scattering wave function can be obtained from Eqs. (5) and are

© 1980 The American Physical Society

$$p\Psi^{(+)}=\bar{\psi}^{(+)}+\bar{G}_p^{(+)}h_{pR}\frac{1}{E-h_{RR}-h_{Rp}\bar{G}_p^{(+)}h_{pR}}h_{Rp}\bar{\psi}^{(+)}, \tag{6a}$$

$$R\Psi^{(+)}=\frac{1}{E-h_{RR}-h_{Rp}\bar{G}_p^{(+)}h_{pR}}h_{Rp}\bar{\psi}^{(+)}, \tag{6b}$$

and

$$d\Psi^{(+)}=\frac{1}{E-H_{dd}}H_{dR}R\Psi^{(+)}, \tag{6c}$$

where h is a one body Hamiltonian given by,

$$h=H_{PP}+H_{Pd}\frac{1}{E-H_{dd}}H_{dP}, \tag{7}$$

$^{(+)}$ satisfies

$$(E-h_{pp})\bar{\psi}^{(+)}=0, \tag{8}$$

nd $\bar{G}_p^{(+)}$ is the Green's function given by

$$\bar{G}_p^{(+)}=(E^+-h_{pp})^{-1}. \tag{9}$$

The complete set of eigenstates $\{\Phi_R^i\}$ is obtained s solutions of

$$(\epsilon_R^i-h_{RR})\Phi_R^i=0, \tag{10}$$

here the eigenvalues ϵ_R^i are given in terms of heir real and imaginary parts as

$$\epsilon_R^i=E_R^i-i\frac{\Gamma_R^{\downarrow}}{2}. \tag{11}$$

he resonances are at energies E_R^i. The notaon $\Gamma_R^{\downarrow}$ indicates the spreading width of Φ_R^i and is btained in terms of the resonance and doorway tates and their coupling as in Ref. 6.

Assuming isolated gross (shape) resonances, he T matrix may be written in the vicinity of any esonance Φ_R as

$$T=T_1+T_2+T_3+T_4, \tag{12}$$

here the superscript i has been dropped for ease, nd

$$T_1=\langle\chi_f|H_I|\bar{\psi}^{(+)}\rangle, \tag{13a}$$

$$T_2=\langle\chi_f|H_I\bar{G}_p^{(+)}h_{pR}|\Phi_R\rangle\frac{\langle\Phi_R|h_{Rp}|\bar{\psi}^{(+)}\rangle}{E-E_R-\Delta_R+i\Gamma_R/2}, \tag{13b}$$

$$T_3=\langle\chi_f|H_I|\Phi_R\rangle\frac{\langle\Phi_R|h_{Rp}|\bar{\psi}^{(+)}\rangle}{E-E_R-\Delta_R+i\Gamma_R/2}, \tag{13c}$$

$$T_4=\left\langle\chi_f\middle|H_I\frac{1}{E-H_{dd}}H_{dR}\middle|\Phi_R\right\rangle\frac{\langle\Phi_R|h_{Rp}|\bar{\psi}^{(+)}\rangle}{E-E_R-\Delta_R+i\Gamma_R/2}, \tag{13d}$$

ith

$$\Delta_R=\mathrm{Re}\langle\Phi_R|h_{Rp}\bar{G}_p^{(+)}h_{pR}|\Phi_R\rangle, \tag{14a}$$

$$\Gamma_R=\Gamma_R^{\uparrow}+\Gamma_R^{\downarrow}, \tag{14b}$$

and

$$\Gamma_R^{\uparrow}=-2\,\mathrm{Im}\,\langle\Phi_R|h_{Rp}\bar{G}_p^{(+)}h_{pR}|\Phi_R\rangle. \tag{14c}$$

The final state wave function is χ_f.

The total effective Hamiltonian H Eq. (4) can be taken to be of the form

$$H=-\frac{\hbar^2}{2m}\nabla^2+H_1+H_2+V(r)+iW+H_{12} \tag{15}$$

where, respectively, H_1 and H_2 represent the internal Hamiltonians of each separate ion, $V(r)$ is an effective average well, W represents the absorption into $\{q\}$, and H_{12} couples the relative motion to the internal degrees of freedom of each ion. The interaction H_I in Eqs. (13) is

$$H_I=V(r)+H_{12}-V_C(r). \tag{16}$$

The quantity $V_C(r)$ is a Coulomb potential chosen in a two potential formulation to generate χ_f, and $\bar{\psi}^{(+)}$ is a distorted wave obtained from Eqs. (7) and (8).

For our test case the real optical potential $V(r)$ is taken to be a local Woods-Saxon well with a linear energy dependence in the depth plus an effective Coulomb potential obtained from a Fermi charge distribution, while $V_C(r)$ is taken as $(Ze)^2/r$. The imaginary part W in principle involves the many degrees of freedom but, as is customary, is taken to be a constant energy averaging interval representing the spreading of the doorways into the space $\{q\}$. In contrast we use the single particle resonance spreading width $\Gamma_R{\downarrow}$ to derive the imaginary part[6] of the Hamiltonian h which is used in obtaining $\bar{\psi}^{(+)}$ and Φ_R. The eigenstates of H_1 and H_2 are assumed to be internal nuclear vibrations and H_{12} is a first order particle-vibration interaction of the standard form which takes into account the identity of the interacting ions. Since it is well known that there are strong low lying vibrations in ^{12}C, the states in $\{d\}$ are taken to be reduced mass particle-vibration doorways. The two phonon states are of second order and are not considered here. The radial wave functions for these states are obtained from the well by solving the Schrödinger equation at the energies E_R of the quasibound or virtual resonances. In Eq. (13d) the matrix elements H_{dd} and H_{dR} become, via Eq. (15),

$$H_{dd}=\langle d|H-H_{12}|d\rangle \tag{17a}$$

and

$$H_{dR}=\langle d|H_{12}|R\rangle. \tag{17b}$$

The only available parameters that might be varied in our calculations are (i) the depth, range, and diffuseness of the Woods-Saxon well and the strength of its assumed linear energy dependence

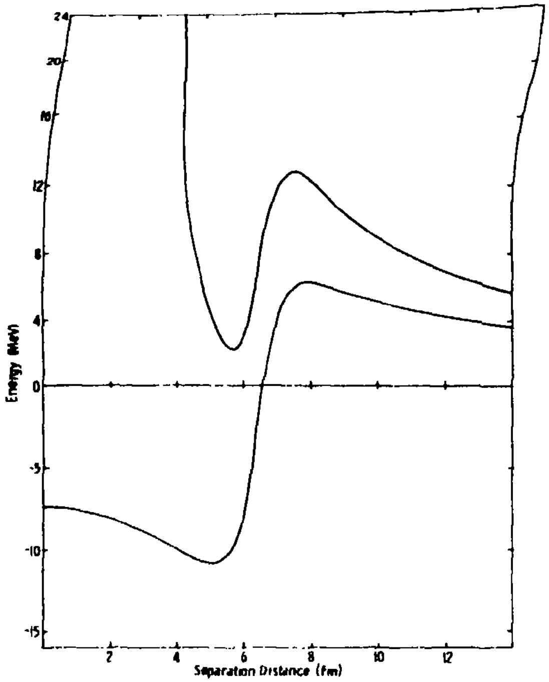

FIG. 1. Real well $V(r)$ (bottom curve) and real well plus centrifugal potential (top curve) are shown for $E = 15$ MeV c.m. and $J = 10$. For our calculation $V(r) = (V_0+\alpha E) f_{WS}(r) + V_{Fermi}(r)$. The diffuseness and range of f_{WS} were $0.35f$ and $6.4f$ respectively, $V_0 = 17.45$ MeV and $\alpha = 0.402$. The diffuseness and range of V_{Fermi} were $0.91f$ and $4.8f$ respectively.

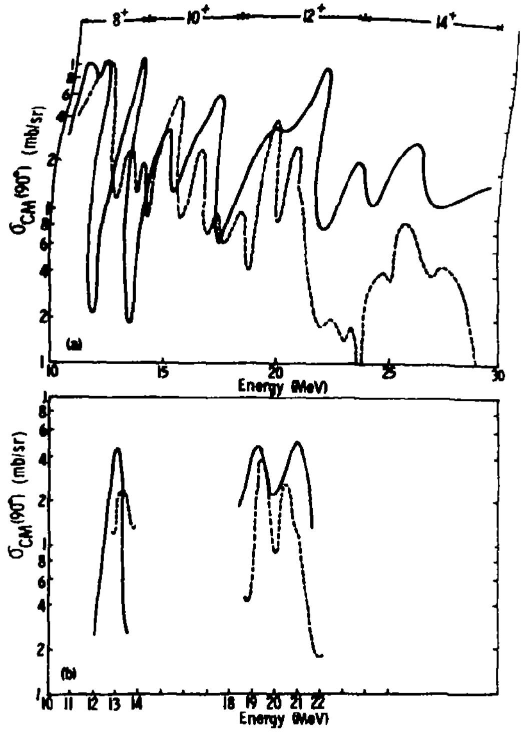

FIG. 2. (a) Comparison of calculated and experimental differential cross sections for $^{12}C+^{12}C$ elastic scattering at $\theta_{c.m.} = 90°$ in the energy range 10–29 MeV c.m. The solid line shows the calculated results and the dashed line the experimental. The associated total angular momentum is also indicated. (b) Differential cross section in vicinity of resonances at 13.1 MeV, 19.3 MeV, and 21.0 MeV after altering their continuum widths from 0.005 MeV, 1.438 MeV, and 0.316 MeV to 0.204 MeV, 0.700 MeV, and 0.700 MeV, respectively. The solid line shows the calculated result and the dashed line the experimental.

in the depth, (ii) the diffuseness and range of the Fermi charge distribution, and (iii) the averaging interval W. This interval was given the reasonable value of 200 keV. The strength of the particle-vibration coupling is obtained in the standard way from the experimental gamma transition probabilities[8] of the internal nuclear vibrational states to the ground state. We considered both the 2^+ (4.43 MeV) and 3^- (9.64 MeV) vibrations in ^{12}C.

The procedure in determining the well parameters was to use the reasonable values of Gobbi[9] *et al.*, for the range and diffuseness of the Woods-Saxon well and to adjust the depth to produce the experimental gross resonances using the projection operator method of Lev and Beres[10] which approximates the resonances in a well as harmonic oscillator states. The Fermi-Coulomb parameters (ii) were given reasonable values consistent with the nuclei studied. The values of the potential parameters are given in the caption for Fig. 1. The figure depicts $V(r)$ and also for comparison $V(r)$ plus the centrifugal potential at a certain total angular momentum; in this case $J = 10$. The resulting peak positions of the gross resonances of total angular momenta $J = 8$, 10, 12, 14, are at 10.5 MeV, 15.0 MeV, 19.5 MeV, and 26.0 MeV. They have, respectively, 5, 6, 4, and 5 associated doorways of the correct angular momentum within the resonance width.

The calculated differential cross section at 90° c.m. is given in Fig. 2(a) and is compared to experiment. Note the correspondence between the prominent experimental peaks and those that we calculate. The overwhelmingly dominant total angular momentum at 13.1 MeV is 8^+ and that at 16.9 MeV is 10^+. The intermediate structure in the figure comes mainly from T_4 [Eq. (13d)] and is essentially due to the doorways of 2^+ origin. The 3^- doorways provide no new structure but reduce the overall cross section somewhat. The term T_3[Eq. (13c)] is very important in providing the gross structure envelope. While the agreement is quite good as to the number and positions of resonances, the widths and shapes were found to be sensitive to the details of the calculation For example, certain theoretical peaks changed when the escape widths of the corresponding states were varied slightly, and these widths were in turn sensitive to slight changes in the real potential. In Fig. 2(b) we show as an example the results of varying these widths for the states at $E_{c.m.}=13.1$ MeV, 19.3 MeV, and 21.0 MeV. The resulting changes in real well depth were small enough so as not to shift significantly the peak energies of the calculated resonances.

This work was supported in part by the National Science Foundation Grant No. Phy 78-00925.

---

[1] R. M. Wieland, R. G. Stokstad, G. R. Satchler, and L. D. Rickersten, Phys. Rev. Lett. 37, 1458 (1976).

[2] R. L. Phillips, K. A. Erb, D. A. Bromley, and J. Weneser, Phys. Rev. Lett. 42, 566 (1979).

[3] H. Feshbach, A. K. Kerman, and R. H. Lemmer, Ann. Phys. (N. Y.) 41, 230 (1967).

[4] J. Y. Park, W. Greiner, and W. Scheid, Phys. Rev. C 16, 2276 (1977).

[5] O. Tanimura, Nucl. Phys. A309, 233 (1978).

[6] D. A. Bromley, in *Proceedings of the International Conference on Nuclear Reactions Induced by Heavy Ions, Heidelberg 1969*, edited by R. Bock and W. R. Hering (North-Holland, Amsterdam, 1970).

[7] A. Lev and W. P. Beres, Phys. Lett. 58B, 263 (1975).

[8] S. J. Skorka, J. Hertel, and T. W. Retz-Shmidt, Nucl. Data Sect. A2, 369 (1966).

[9] A. Gobbi, in Proceedings of the Symposium on Heavy Ion Scattering held at Argonne, Illinois, 1971, edited by R. H. Siemssen *et al.*, ANL Report No. ANL-7837 (unpublished).

[10] A. Lev and W. P. Beres, Phys. Rev. C 14, 354 (1976).

PHYSICAL REVIEW C VOLUME 21, NUMBER 5 MAY 1980

Existence of strongly bound states of pions in nuclei

Javier Sesma*
Nuclear Physics Laboratory, Oxford, United Kingdom

(Received 27 February 1979; revised manuscript received 21 December 1979)

References are given to mostly unknown work on velocity-dependent potentials of the kind used in optical pion-nucleus models for which the possibility of an infinity of strongly bound states has been recently suggested.

[NUCLEAR REACTIONS Pion-nucleus optical potential; nuclear bound states of pions in nuclei; complex velocity-dependent potential.]

Recently, Friedman, Gal, and Mandelzweig[1] (FGM) have studied the possible existence of strongly bound states of pions in nuclei. This possibility was first suggested by Ericson and Myhrer[2] (EM) and has been reconsidered by FGM in view of the new data on levels in pionic atoms.[3] It seems that some comments on that question would be worthwhile, in order to clarify the situation.

At low energies, the pion-nucleus optical potential is usually taken as

$$2\mu V(r,p) = 2\mu V_1(r) + 2\mu V_2(r,p)\,, \tag{1}$$

sum of a "static" weakly repulsive term

$$2\mu V_1(r) = q(r)\,, \tag{2}$$

and a velocity-dependent attractive term

$$2\mu V_2(r,p) = -\vec{p}\cdot\alpha(r)\vec{p}\,. \tag{3}$$

Here, μ represents the reduced mass of the pion-nucleus system. The intensity parameters[1] entering the expressions of $q(r)$ and $\alpha(r)$ are taken to be complex, to account for the absorption of pions in nuclei.

Assuming, in a simplified model, a real square well shape for $\alpha(r)$ in Eq. (3), EM show that a velocity-dependent potential can produce an infinity of bound states of indefinitely high binding energy. This result, rediscovered by EM in the context of the pion-nucleus system, had been reported earlier.[4] Besides this, EM note that, for general shape $\alpha(r)$, the wave equation and the wave function present a singularity when $\alpha(r) = 1$. This fact was quoted and thoroughly discussed a long time ago.[5] Provided $\alpha(r)$ passes linearly through the value 1, the wave function is physically acceptable, in spite of its logarithmic singularity, as it is square integrable.

It is a pleasure to acknowledge Professor P. E. Hodgson for hospitality at the Oxford Physics Laboratory and for drawing the attention of the author to the problem discussed above. Financial support of Instituto de Estudios Nucleares is also acknowledged.

---

*Permanent address: Departamento de Fisica Teorica, Facultad de Ciencias, Universidad de Zaragoza, Zaragoza, Spain.

[1] E. Friedman, A. Gal, and V. B. Mandelzweig, Phys. Rev. Lett. 41, 794 (1978).

[2] T. E. O. Ericson and F. Myhrer, Phys. Lett. 74B, 163 (1978).

[3] C. J. Batty, S. F. Biagi, E. Friedman, S. D. Hoath, J. D. Davies, G. J. Pyle, and G. T. A. Squier, Phys. Rev. Lett. 40, 931 (1978).

[4] E. M. Ferreira, N. Guillen, and J. Sesma, J. Math. Phys. 9, 1210 (1968); E. M. Ferreira, R. Meri, and J. Sesma, *ibid.* 18, 944 (1977).

[5] E. M. Ferreira, N. Guillen, and J. Sesma, J. Math. Phys. 8, 2243 (1967).

© 1980 The American Physical Society

PHYSICAL REVIEW C VOLUME 21, NUMBER 5 MAY 1980

Bremsstrahlung from $^{12}C+p$ near the 1.7-MeV resonance

C. C. Trail, P. M. S. Lesser, A. H. Bond, Jr., M. K. Liou, and C. K. Liu
Department of Physics, Brooklyn College of the City University of New York, Brooklyn, New York 11210

(Received 20 August 1979)

The spectrum of bremsstrahlung radiation emitted by the scattering of protons by ^{12}C near the 1.7-MeV resonance has been studied at bombarding energies 76 and 146 keV above the resonance and 140 keV below the resonance. The spectra are in very good agreement with a complete calculation using the Feshbach-Yennie approximation which includes both the principal term and correction term.

[NUCLEAR REACTION Measurement of bremsstrahlung spectrum from $p+^{12}C$ near $E_p = 1.7$ MeV.]

It was suggested by Eisberg, Yennie, and Wilkinson[1] that the observation of low energy bremsstrahlung radiation produced in the scattering by a nucleus of a nucleon or nucleus would be a good technique for measuring the time delay between the beginning and the end of a nuclear reaction, important information which would allow an unambiguous separation between compound nuclear reactions and direct interactions. Their classical treatment of the bremsstrahlung process was extended with a quantum mechanical treatment by Feshbach and Yennie,[2] whose method differs from the conventional treatment of the bremsstrahlung process first introduced by Low.[3] The Feshbach-Yennie approximation uses the scattering amplitudes evaluated at two different energies, the initial and final scattering energies, for calculating bremsstrahlung cross sections, whereas the soft-photon approximation of Low uses the elastic scattering amplitude evaluated at a fixed on-shell energy. The latter approximation gives the well-known $1/E_\gamma$ dependence for the photon spectrum whereas the former approximation would predict structure in the region of a resonance.

Since the cross section for proton-carbon bremsstrahlung is roughly 10^{-8} the elastic scattering cross section, no one has been able until recently to get good data on the process. In a series of three pioneering papers[4-6] a group from Bologna reported observing bremsstrahlung radiation in coincidence with protons scattered by ^{12}C near the 1734-keV resonance. Among the bremsstrahlung spectra measured by this group, the spectrum obtained at a bombarding energy of 1795 keV is the only one which has structure clearly exhibited at a photon energy corresponding to the difference between the incident proton energy E_p and the resonance energy E_R. The Bologna group, however, was unable to obtain quantitative agreement between the measured bremsstrahlung spectrum and the spectrum calculated from the principal term of the Feshbach-Yennie approximation if the parameters of the resonance obtained from elastic scattering data[7,8] were used. They were able to fit the 1795-keV experimental data only by introducing *ad hoc* a new set of resonance parameters.

This new set of parameters was studied by Jan *et al.*[9] They found that these parameters give poor agreement with the elastic scattering cross sections near the resonance for some scattering angles. Furthermore, they show that the bremsstrahlung spectrum obtained at 1795 keV is inconsistent with the elastic scattering data of Refs. 7 and 8, if the theory of Feshbach and Yennie is correct. Conversely, if the elastic scattering data and the bremsstrahlung data are consistent, then the bremsstrahlung data at 1795 keV cannot be described by the principal term of the Feshbach-Yennie approximation.

A further ambiguity in the theoretical interpretation of bremsstrahlung data arises from the pion-proton bremsstrahlung process reported by a UCLA group[10,11] at incident energies of 269 MeV and 298 MeV, just above the (3, 3) resonance at 195 MeV. In an analysis of this experiment, Liou and Nutt[12] show that the bremsstrahlung spectrum agrees well with the soft-photon approximation with little contribution from the resonance. Thus the validity of the Feshbach-Yennie approximation for describing bremsstrahlung emission near a resonance has not been established, warranting further experimental and theoretical studies.

We have extended the measurement of the bremsstrahlung cross section for $p+^{12}C$ near the 1734-keV resonance with the hope of confirming the findings of the resonance structure first reported by the Bologna group, of resolving the possible

© 1980 The American Physical Society

inconsistency between the elastic scattering data and the bremsstrahlung data obtained at 1795 keV by the Bologna group, and of clarifying the theoretical picture. Three bremsstrahlung spectra were measured at bombarding energies of 76 keV and 146 keV above the 1734-keV resonance and 140 keV below the resonance. In order to obtain spectra which possibly contain structure due to the resonance, we have expanded the measured range of the photon energy to 200 keV.

The experimental measurements involved the detection of scattered protons in coincidence with bremsstrahlung radiation. Protons from the Brooklyn College Dynamitron accelerator bombarded a 50-μg/cm^2 carbon target mounted on a lucite holder which was tilted 45° with respect to the beam. Protons scattered at a laboratory angle of 155° were stopped in a surface barrier detector subtending a solid angle of 4 msr. Bremsstrahlung photons were detected by a NaI crystal 76 mm in diameter and 6 mm thick, located 28 mm above and normal to the scattering plane. The beam, about 2 mm in diameter, was stopped in a Faraday cup 2 m from the target. The measured beam current was typically 400 na.

Figure 1 is a plot of the yield of elastically scattered protons at a laboratory angle of 155° as a function of incident bombarding energy E_p. The solid line drawn through the data points is for guiding the reader's eye and does not represent a fit to the data. This curve clearly shows a peak at $E_p \simeq 1734$ keV $= E_R$, and a minimum just below the peak. The structure results from interference effects between two closely spaced levels of $\frac{5}{2}^+$ and $\frac{3}{2}^-$ in the compound nucleus ^{13}N.

Coincident events between bremsstrahlung photons and scattered protons were identified using standard fast-slow coincidence electronics with a time resolution of 12 ns full width at half maximum (FWHM). For each coincident event, photon and proton energies were recorded in a two dimensional pulse-height analyzer. In the analyzer display, real coincidences corresponding to bremsstrahlung events could be seen along a diagonal line in the E_γ, $E_{p'}$ plane, where $E_{p'}$ is the energy of the scattered proton. The diagonal line is defined by the kinematic restriction that the sum of the proton and photon energies ($E_{p'} + E_\gamma$) must be constant and equal to the energy E_{el} of an elastically scattered proton, apart from a slight variation in the ^{12}C recoil energy. The number of elastically scattered protons was recorded independently for normalization.

Figure 2 shows the events in the E_γ, $E_{p'}$ plane at $E_p = E_R + 146$ keV. Each dot in Fig. 2 represents a coincident event. Because of the resolution of the detectors, the kinematic line becomes a kinematic band which is clearly visible in Fig. 2. Events below the kinematic band correspond to real coincident events in which photons did not deposit their full energies in the NaI crystal. The large number of events

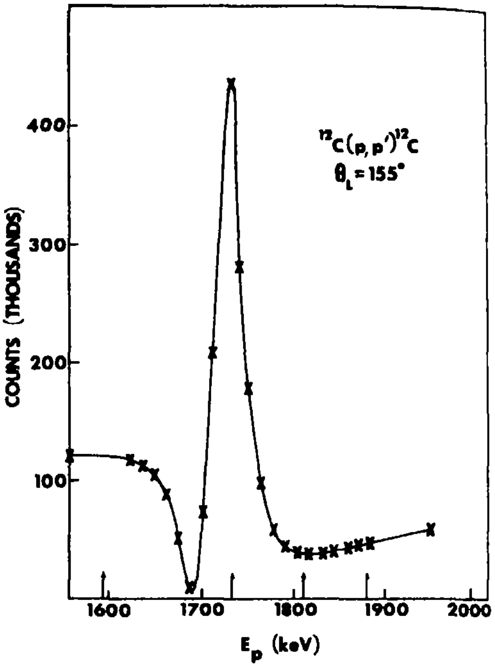

FIG. 1. Yield of elastically scattered protons from a 50-μg/cm^2 carbon foil at a laboratory angle of 155° as a function of the incident energy E_p. The arrows along the energy axis indicate the position of the 1734-keV resonance and energies 76 keV and 146 keV above the resonance, 140 keV below the resonance.

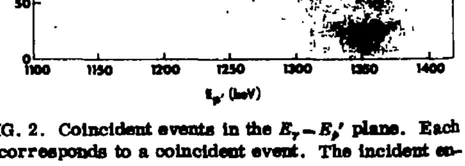

FIG. 2. Coincident events in the $E_\gamma - E_p'$ plane. Each dot corresponds to a coincident event. The incident energy was $E_R + 146$ keV.

at $E_{p'} = 1350$ keV $= E_{el}$ is due to accidental coincidences between photons and elastically scattered protons. Outside of this region, the number of accidental coincidences is negligible, as can be seen from the absence of counts above the kinematic band. An independent check of the accidental rate revealed its contribution to the final cross section to be less than 1%.

In analyzing the data, we projected onto the $E_{p'}$ axis, for $E_{p'}$ less then $E_{el} - 30$ keV, all events for which E_γ was in or below the kinematic band. We have thus included real coincident events in which the photons did not deposit their full energies in the NaI crystal. An independent check showed that these Compton-scattered events were consistent with the expected full-energy peak to Compton ratio. The projected spectra, as a function of $E_{p'}$, were replotted as a function of the corresponding photon energy E_γ, where $E_\gamma = E_{el} - E_{p'} - E$ (^{12}C recoil). These spectra were then corrected for NaI detector efficiency and detector housing attenuation. The corrections for detector efficiency varied from 40% at 250 keV down to 1% at 30 keV, while corrections for attenuation increased in the same interval from 3% to 20%. Near 100 keV the total correction was only about 5%. The resulting bremsstrahlung cross section, at each of the three bombarding energies, was divided by the corresponding elastic scattering cross section at 155°. The result

$$\sigma_{rel} = \frac{d^3\sigma}{d\Omega_\gamma d\Omega_{p'} dE_\gamma} \bigg/ \frac{d\sigma_{el}}{d\Omega_{p'}}$$

is plotted in Fig. 3 as a function of E_γ, corresponding to $E_{el} - E_{p'}$, for each of the bombarding energies. The error bars in Fig. 3 include both statistical errors and uncertainties in the systematic corrections for NaI detector efficiency and photon attenuation. Uncertainties due to counting statistics were typically about 30% while uncertainties in the systematic corrections were at most about 10%. These uncertainties were combined in quadrature to determine the final error bars.

The cross sections measured at the two bombarding energies above E_R clearly show structure, in the form of peaks, while the cross section measured below the resonance exhibits a simple $1/E_\gamma$ behavior. It is also clear that the position of the peak in photon energy approximately corresponds to the difference between the bombarding energy and the resonant energy, for both bombarding energies above E_R.

The solid curves in Fig. 3 represent the theoretical predictions of the Feshbach-Yennie approximation, averaged over the solid angle of the photon detector. Our calculations[13] include both the principal term and the correction term discussed by Feshbach and Yennie.

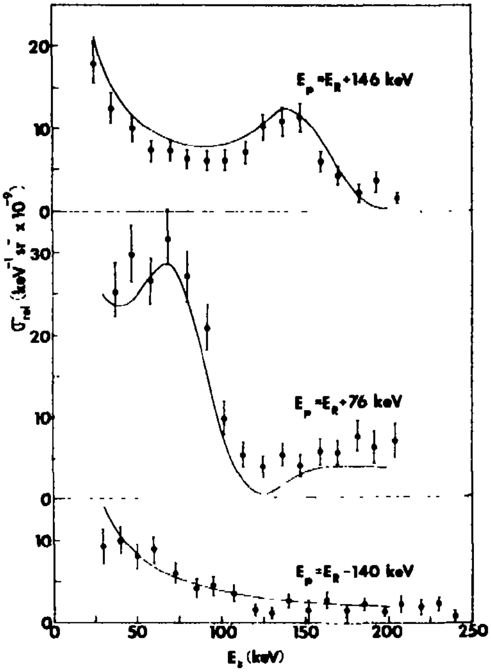

FIG. 3. The bremsstrahlung cross section relative to the elastic scattering cross section. The solid curve is the result of a complete calculation of the Feshbach-Yennie approximation with resonance parameters from elastic scattering data.

We calculated these terms in the form

$$\sigma_{rel} = \frac{\sigma_{-1}}{E_\gamma} + \sigma_0 ,$$

where the principal term σ_{-1}/E_γ depends upon the elastic scattering amplitude, and the correction term σ_0 depends upon the derivatives of the scattering amplitudes. We have found that the correction term, which is negligible at energies far from resonance, becomes significant in the region of a resonance. By including this term, we are able to achieve a satisfactory fit to the data, as shown in Fig. 3, using the elastic scattering resonance parameters from Ref. 8 without modification.

In conclusion, we have measured the proton-carbon bremsstrahlung cross sections near the 1.7-MeV resonance at three bombarding energies. The structure due to resonance effects which is clearly observed in two of our bremsstrahlung spectra can be successfully described by the Feshbach-Yennie approximation. Our work represents the first quantitative experimental confirmation of the Feshbach-Yennie approximation. We have achieved this confirmation by extending the range of previous measurements both in terms of bombarding energies and measured photon energies, and by including in our theoretical calculations a term which had been previously ignored in comparing theory with experiment. There is no inconsistency between our bremsstrahlung data and the elastic data.

We wish to thank Dr. William Nutt for many helpful discussions; Dr. Richard Yen, Taun-Ran Yeh, and Beartron Lin for assistance in collecting and analyzing the data. This work was supported in part by grants from the National Science Foundation and the Professional Staff Congress—Board of Higher Education Research Award Program of the City University of New York.

---

[1] R. M. Eisberg, D. R. Yennie, and D. H. Wilkinson, Nucl. Phys. 18, 338 (1960).

[2] H. Feshbach and D. R. Yennie, Nucl. Phys. 37, 150 (1962).

[3] F. E. Low, Phys. Rev. 110, 974 (1958).

[4] C. Maroni, I. Massa, and G. Vannini, Phys. Lett. 60B, 344 (1976).

[5] A. Cristallini, C. Maroni, I. Massa, and G. Vannini, Phys. Lett. 56B, 245 (1975).

[6] C. Maroni, I. Massa, and G. Vannini, Nucl. Phys. A273, 429 (1976).

[7] H. L. Jackson and A. Galonsky, Phys. Rev. 89, 370 (1953); H. L. Jackson, A. I. Galonsky, F. J. Eppling, R. W. Hill, E. Goldberg, and J. R. Cameron, *ibid.* 89, 365 (1953).

[8] J. C. Armstrong, M. J. Baggett, W. R. Harris, and V. A. Latonne, Phys. Rev. 144, 823 (1966).

[9] G. J. Jan, C. C. Perng, and M. K. Liou, Phys. Lett. 85B, 25 (1979).

[10] D. I. Sober, M. Arman, D. J. Blasberg, R. P. Haddock, K. C. Leung, B. M. K. Nefkens, B. L. Schrock, and J. M. Sperinde, Phys. Rev. D 11, 1017 (1975).

[11] M. Arman, D. J. Blasberg, R. P. Haddock, K. C. Leung, B. M. K. Nefkens, B. L. Schrock, D. I. Sober, and J. M. Sperinde, Phys. Rev. Lett. 29, 962 (1972).

[12] M. K. Liou and W. T. Nutt, Phys. Rev. D 16, 2176 (1977); Nuovo Cimento 46A, 365 (1978).

[13] M. K. Liou, C. K. Liu, P. M. S. Lesser, and C. C. Trail, Phys. Rev. C 21, 518 (1980).

PHYSICAL REVIEW C VOLUME 21, NUMBER 5 MAY 1980

Levels in ^{44}K via the ^{48}Ca(p,αn) reaction

P. A. Mandò and G. Poggi
Istituto di Fisica dell'Università, Firenze, Italy
and Istituto Nazionale di Fisica Nucleare, Sezione di Firenze, Italy

G. Lo Bianco and N. Molho
Istituto di Scienze Fisiche dell'Università, Milano, Italy
and Istituto Nazionale di Fisica Nucleare, Sezione di Milano, Italy

(Received 1 August 1979)

Excited levels in ^{44}K have been populated via the ^{48}Ca(p,αn) reaction. From γ-γ coincidence measurements, the level and decay schemes have been obtained for ^{44}K, up to $E_x = 1368$ keV, including several so far unobserved levels and transitions. No lifetime $> \sim 1$ ns has been detected for any of these levels. A comparison is done with the neighboring even-A ^{44}K isotope and with a simple shell model calculation to give a set of possible J^π assignments.

NUCLEAR REACTIONS ^{48}Ca($p,\alpha n$)^{44}K, E=18–45 MeV; measured E_γ, $\sigma(E,E_\gamma)$, γ-γ coin, pulsed beam electronic timing; deduced ^{44}K levels and transitions, lifetime limits. Enriched target, Ge(Li) coax. and HP Ge.

A decay scheme of ^{44}K, obtained observing γ rays following the β^- emission of ^{44}Ar, has been recently published.[1] Only a few of the levels and transitions of this decay scheme coincide with the ones we had previously observed "in-beam" using the ^{48}Ca($p,\alpha n$)^{44}K reaction.[2] This fact is probably due to the different selectivity of the two excitation modes with respect to the population of high-spin states in ^{44}K. In our measurements in fact, the ^{48}Ca($p,\alpha n$) reaction at E_p=18–45 MeV probably populates ^{44}K states of relatively high angular momentum, contrary to the case of ^{44}Ar β^- decay.

A detailed description and discussion of our results is hereafter reported, for a more complete and consistent picture of the available spectroscopic information on ^{44}K.

A powder target of ^{48}CaCO$_3$ (enriched to 97.2% in ^{48}Ca), sandwiched between two thin foils of polythene, was bombarded by the proton beam of the cyclotron in Milano at energies ranging from 18 to 45 MeV. Single spectra were recorded using a Ge(Li) coaxial detector [~35 cm^3, full width at half maximum (FWHM) at 1.33 MeV: ~3 keV] placed at 90° to the beam direction, and a Ge(Li) low energy photon spectrometer (LEPS) (~0.5 cm^3, FWHM at 122 keV: 700 eV). A γ spectrum recorded at 28 MeV proton energy is shown in Fig. 1. The most intense unattributed γ lines were the ones of 126.9, 137.2, and 382.7 keV, which also showed a very similar excitation function (Fig. 2). The assignment of these transitions to ^{44}K was initially based on the fact that 137 and 383 keV corresponded in that nucleus to the energy differences between the known levels at 520 and 383 keV[3] and between the latter and the ground state, respectively.[4] The population of ^{44}K via the ($p,\alpha n$) reaction, on the other hand, was confirmed by the presence, in the activity spectra, of γ rays from ^{44}Ca, as expected from ^{44}K β^- decay.

To check this attribution, γ-γ coincidences were measured at 28 MeV proton energy, using either two Ge(Li) large volume coaxial detectors, or a

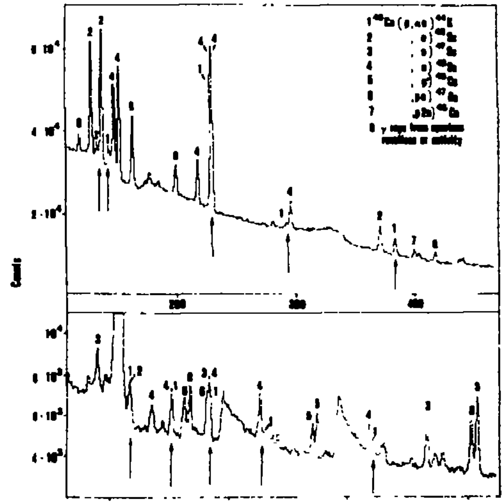

FIG. 1. Spectrum of γ rays following the bombardment of ^{48}Ca by 28 MeV protons [Ge(Li) coaxial detector]. Attributions of the prominent lines are reported.

© 1980 The American Physical Society

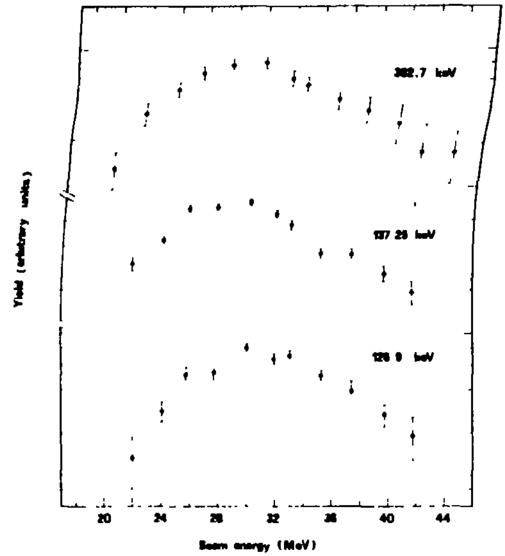

FIG. 2. Experimental yields as a function of beam energy. The LEPS was used for the 126.9 and 137.2 keV lines; the coaxial Ge(Li) for the 382.7 keV line. The three yields are not normalized to one another.

Ge(Li) coaxial versus a high resolution high puri Ge LEPS. The most significant results are show in Fig. 3 and summarized below, while the proposed level scheme is reported in Fig. 4(b).

The 382.7 keV transition clearly shows in coincidence, besides the 137.2 keV line, γ rays of 126.9, 227.4, 291.6, 556.3, 586.1, 630.7, and 721.2 keV. Of these, the 291.6 keV line, which is also prominent in the spectrum gated by the 137.2 keV peak, is easily identified with a transition in ^{44}K connecting the known levels at 811 and 520 keV.[3] From the presence of the 586.1 keV line, a state at 969.8 keV, decaying by such a transition, may tentatively be established. (This level is probably to be identified with the one at 966 ± 20 reported in Ref. 3.)

The γ rays of 630.7, 227.4, and 126.9 keV, instead, belong to a cascade feeding the 382.7 keV level and proceeding via so far unobserved states in ^{44}K, at 1367.7, 1240.8, and 1013.4 keV excitation energy. The assignment of this cascade to ^{44}K is based on the presence of the cross transitions of 721.2 keV (which is in coincidence with the 382.7, 137.2, and 126.9 keV transitions), and

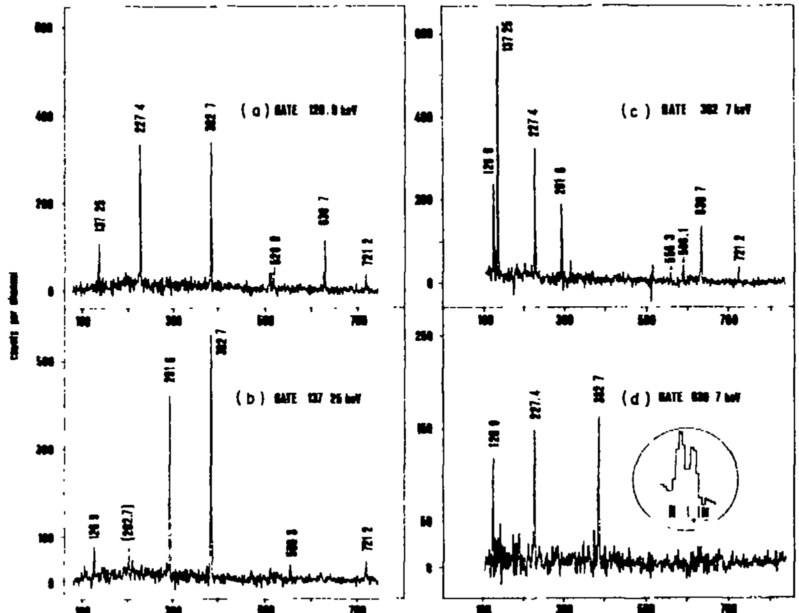

FIG. 3. Relevant spectra from γ-γ measurements. Background and randoms have been subtracted. Gates (a) and (b), from Ge(Li)-LEPS coincidences, are set on the LEPS spectrum, where the peaks at 126.9 and 137.25 keV are well resolved from the neighboring ones. Gates (c) and (d) refer to the Ge(Li)-Ge(Li) coincidences. As to the gate (d), even if the doublet at 627–631 keV is much better resolved in the total γ-γ coincidence spectrum (see detail) then in the singles, particular care was nevertheless necessary for background subtraction. Gate setting was chosen as shown, on the basis of a channel-by-channel analysis.

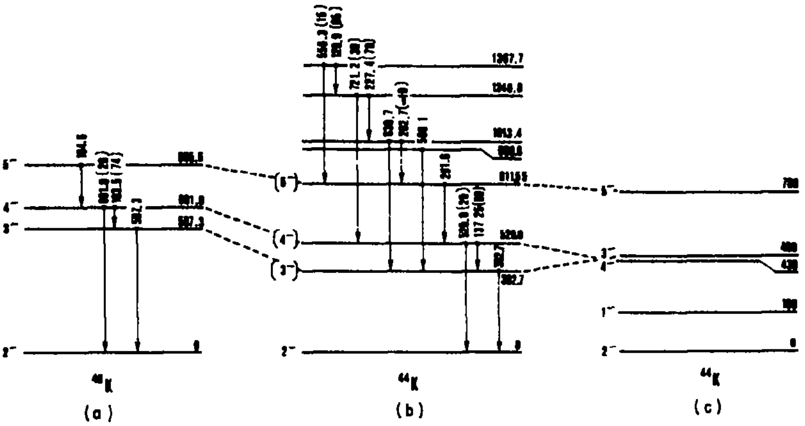

FIG. 4. (a) and (b). Experimental decay schemes of low-lying levels in ^{46}K (from Ref. 5) and ^{44}K (from this work); the branching ratios given in (b) are based on our coincidence data. (c) Theoretical calculation (from Ref. 6). The calculated level at 180 keV very probably corresponds to the 182.6 keV level observed by Huck *et al.* (Ref. 1).

556.3 keV (which is in coincidence with the 382.7, 137.2, 291.6 keV γ rays). A further, though much weaker, cross transition of 202.7 keV probably connects levels at 1013.4 and 811.6 keV, as resulting more clearly from the gates on the 137.2 and 291.6 keV peaks. The existence of such a transition would support the proposed order of the 227.4 → 630.7 keV cascade, which was established on the basis of the observed intensities in the coincidence spectra gated by the 382.7, 227.4, and 630.7 keV lines.

The fact that the energy sums of the cross cascades are equal well within the experimental errors is to be emphasized (see Table I).

Time delay spectra of different γ rays with respect to the beam bunches have also been obtained, using both a Ge(Li) coaxial detector and a Ge(Li) LEPS. From these measurements, we can only state an upper limit of ~1 ns for the lifetime of the levels at 382.7, 520.0, and 1367.7 keV (gates on γ rays of 382.7, 137.2, and 126.9 keV, respectively).

TABLE I. γ rays attributed to ^{44}K.

126.9 ±0.1 keV
137.25±0.05 keV
202.7 ±1 keV
227.4 ±0.15 keV
291.6 ±0.1 keV
382.7 ±0.15 keV
520.0 ±1 keV
556.3 ±0.3 keV
586.1 ±0.3 keV
630.7 ±0.1 keV
721.2 ±0.4 keV

The absence in our coincidence spectra of any sizable transition to the $J=1$ first excited level at $E_x=182$ keV (Ref. 1) suggests that all the ^{44}K levels we have populated via the ^{48}Ca($p,\alpha n$) reaction should be assigned to $J \geq 3$. Furthermore, since the 137.2 and 382.7 keV γ rays are observed in fast coincidence with the beam pulse, multipolarities other than $M1$ or $E1$ may be excluded for the former transition and appear to be unlikely for the latter one.

Taking this experimental evidence into account, the comparison of the decay scheme for the low-lying levels in ^{44}K with the one for the neighboring even-A ^{46}K isotope[5] [Fig. 4(a)] suggests the following set of possible J^π assignments: $3^-, 4^-, 5^-$ for the 382.7, 520.0, and 811.6 keV states, respectively.

This assumption is also in agreement with a simple calculation made by Johnstone,[6] based on a ^{45}Ca $\otimes (d_{3/2})^{-1}$ configuration, using the ^{40}K spectrum to deduce the $(f_{7/2})\,(d_{3/2})^{-1}$ interaction matrix elements [Fig. 4(a)]. Because of the observed branching ratio of the 520.0 keV level and the lifetime limit of the 382.7 keV state, however, the sequence of the 4^- and 3^- levels is, actually, very probably reversed.

The authors wish to thank Professor P. G. Bizzeti for many stimulating discussions and Miss Rita Lippi for help in data taking and reduction.

[1] A. Huck, G. Klotz, A. Knipper, C. Miehe, G. Walter, and C. Richard-Serre, Phys. Rev. C 18, 1803 (1978).

[2] P. G. Bizzeti, P. A. Mandò, G. Poggi, G. Lo Bianco, and N. Molho, in *Proceedings of the EPS International Conference on Physics of Medium-Light Nuclei, Firenze, 1977*, edited by P. Blasi and R. A. Ricci (Compositori, Bologna, 1977), p. 538.

[3] P. M. Endt and C. Van der Leun, Nucl. Phys. A310, 1 (1978).

[4] Transitions of 137.3 and 382.9 keV have been successively observed by Huck *et al*. in the ^{44}Ar β^- decay experiment quoted in Ref. 1.

[5] W. W. Daehnick, J. H. Orloff, T. Canada, and T. S. Bhatia, Phys. Rev. C 10, 136 (1974).

[6] I. P. Johnstone (private communication).

PHYSICAL REVIEW C VOLUME 21, NUMBER 5 MAY 1980

Erratum: Neutron capture cross sections on ^{138}Ba, ^{140,142}Ce, ^{175,176}Lu, and ^{181}Ta at 30 keV: Prerequisite for investigation of the ^{176}Lu cosmic clock

[Phys. Rev. C 21, 534 (1980)]

H. Beer and F. Käppeler

Concerning the solar Hf and Zr abundances we are indebted to Professor Anders who drew our attention to his revised values contained in the review article of V. Trimble, Rev. Mod. Phys. 47, 877 (1975). For Hf he quotes 0.15 atoms/10^6 Si which is still larger by a factor of 1.67 than the present value. Renormalizing his Zr abundance by this factor (provided the Zr/Hf abundance ratio is correct) one obtains $N(\mathrm{Zr}) = (9 \pm 5)$ atoms/10^6 Si which is in excellent agreement with his best current estimate of 9.6 atoms/10^6 Si (E. Anders, private communication).

Reference 23 should be read: B. J. Allen and D. D. Cohen, Aust. J. Phys. 32, 447 (1979).

Erratum: Intranuclear cascade calculation of high-energy heavy-ion interactions

[Phys. Rev. C 20, 2227 (1979)]

Y. Yariv and Z. Fraenkel

Figure 13 as shown in the paper was calculated assuming an experimental efficiency of 60% as mentioned in the text. The "Note added in proof" which appears on page 2241 should be ignored.

Reference 3 should read: T. D. Lee and G. C. Wick, Phys. Rev. D 9, 2291 (1974).

© 1980 The American Physical Society

Cumulative Author Index

All authors of papers published so far in the current volume are listed alphabetically with the issue and page numbers following the dash. A more complete index, with the full title and authors listed with each first author's name, is published in the last issue of the volume. A cumulative author and subject index covering **Physical Review A** *through* **D** *and* **Physical Review Letters** *is published annually under separate cover.*

Abbas, Afsar—(2) 738
Abegg, R —(5) 1687
Abou-Zeid, O A —(5) 1687
Adams, G S —(2) 757, (4) 1488
Adhikari, Sadhan K —(1) 54
Adler, I. —(4) 1680(E)
Aggarwal, S K —(5) 2033
Ahmad, I —(3) 874
Alburger, D E —(2) 705
Alexander, John M —(3) 940, (4) 1261
Alford, W P —(4) 1203
Alt, E O —(5) 1733
Alvarez, R A —(4) 1215
Amado, R D —(2) 647
Amann, J F —(1) 254, (4) 1488
Amsler, C —(3) 988, 998, 1004
Anand, J D —(5) 2010
Anderson, A N —(2) 675
Anderson, R E —(2) 757
Andreozzi, F —(3) 1094
Andritsopoulos, G —(4) 1648
Ansari, A —(4) 1674
Anttila, A —(4) 1196
Apagyi, B —(2) 779
Argan, P —(2) 662, (4) 1416
Arnold, L G —(5) 1899
Arnold, Raymond G —(4) 1426
Asai, J —(2) 469, (5) 1746
Aslanoglou, X —(4) 1648
Audit, G —(2) 662 (4) 1416
Auerbach, N —(2) 744
Austern, N —(1) 272
Austin, Sam M —(4) 1133
Axen, D —(3) 988, 998, 1004

Badelek, B —(1) 306
Bagchi, B —(1) 1
Bakoyeorgos, P —(4) 1648
Baktash, C —(3) 933
Balagna, J P —(2) 637
Banerjee, M K —(5) 1996
Barbarino, S —(3) 1104
Bargholtz, Chr —(3) 1078
Barlett, M —(4) 1488
Barrette, J —(5) 1802, 1864
Bass, R —(4) 1377
Bates, G M —(1) 147
Bauer, T S.—(2) 757, (3) 1014
Bazzacco, D.—(1) 222
Beachy, J S.—(1) 147
Becchetti, F D —(1) 444
Bechtold, G.—(4) 1239
Becker, J —(3) 1078
Beckerman, M.—(2) 614
Beene, J. R —(1) 167
Beer, H —(2) 534, (5) 2139(E)
Behera, B —(5) 1883
Belehrad, R. H —(4) 1626
Bellicard, J B —(4) 1652
Benczer-Koller, N —(2) 574, (5) 1828
Bendel, W L —(4) 1162
Benenson, W.—(1) 462
Beres, William P —(5) 2126
Berman, B. L —(2) 503, (4) 1215
Bernard, V —(2) 744
Berrier-Ronsin, G —(1) 124, (4) 1232
Berthot, J —(1) 306
Bertrand, F E.—(2) 768
Beshai, S —(3) 1078
Betts, R R —(1) 175
Beveridge, J L —(2) 675, (3) 988
Bhalerao, R S —(5) 1903, 2103
Bhasin, V S —(5) 2010
Bini, M —(1) 116
Birkelund, J R —(5) 2019
Bisplinghoff, J —(2) 614
Bizzeti-Sona, A. M —(1) 116
Bland, L —(1) 11
Blann, Marshall—(2) 614, (5) 1770
Blanpied, G S —(4) 1452, 1488
Blasi, P —(1) 116
Blatt, S L —(3) 791
Bloch, A —(2) 662, (4) 1416
Boal, David H.—(5) 1913
Bock, R —(4) 1377
Bond, A H , Jr —(5) 2131
Bond, P. D —(1) 459
Bonetti, R —(3) 816
Borner, H G —(1) 65
Boudrie, R L.—(1) 254, (2) 757, (3) 1030, (4) 1488
Bounin, P —(4) 1652
Bowman, C. D —(1) 58
Boyd, R N —(4) 1203
Brady, F P.—(4) 1149, 1185, 1190
Braga, R A.—(5) 2025
Braithwaite, W. J.—(3) 1030
Braun-Munzinger, P.—(5) 1864
Breitig, D —(1) 65
Brennan, J. M —(2) 574, (5) 1828
Briscoe, W. J.—(4) 1495
Britt, H. C.—(2) 761
Bronson, J D —(4) 1252
Brown, B A —(5) 2107
Browne, J C.—(5) 2019
Buenerd, M.—(3) 879
Bugg, D V —(3) 988, 998, 1004
Bülow, B —(4) 1460
Burg, J. P —(1) 306
Burleson, G R.—(1) 254, (4) 1452
Burt, P. E —(4) 1495
Buschmann, J —(4) 1239
Buskirk, F. R —(1) 28, 147

Caffrey, A J —(2) 603
Caldwell, J T —(4) 1215
Cambi, A.—(5) 1921
Cameron, J M —(5) 1932
Canto, L F —(2) 772
Canty, M J —(1) 361
Caretto, A A. , Jr.—(1) 246
Carey, T. A —(3) 799, (5) 1705
Carlson, Carl E.—(4) 1426
Cassidy-Aaquist, Denise—(4) 1538
Castaneda, C. M.—(1) 179
Castel, Boris—(4) 1538
Casten, R. F —(1) 65
Catchen, Gary L.—(3) 940
Cerruti, C —(4) 1680(F)
Cha, D —(4) 1672
Chakravarti, S —(1) 254
Chant, N. S —(3) 799, (5) 1705
Chasman, R. R.—(1) 456
Chauvin, J.—(3) 879
Cheifetz, F —(2) 761
Chemarin, M.—(1) 306
Cheng, W K.—(1) 374
Chéry, R.—(1) 405
Chevallier, M.—(1) 306
Chisholm, A.—(4) 1653
Chrien, R E.—(2) 498, (3) 1014
Church, L. B.—(1) 246
Ciofi degli Atti, C.—(3) 805
Cizewski, J. A.—(1) 65

Clark, B. C.—(4) 1652; (5) 1899
Clark, H. W.—(2) 475
Clark, Robert Beck—(5) 1944
Cleary, T. P.—(2) 764
Clements, J. S.—(4) 1285
Clough, A. S.—(3) 988, 998, 1004
Clover, M. R.—(1) 167
Colli Milazzo, L—(3) 816
Collins, M. T.—(3) 799
Conzett, H. E.—(1) 44
Cormier, T. M.—(1) 198
Cosman, E. R.—(5) 2111
Cotanch, Stephen R.—(5) 2115
Côté, J.—(3) 861
Cotte, P.—(1) 306
Cottingame, W B.—(4) 1452
Courtemanche, A. N—(3) 1128(E)
Courtney, L. H—(1) 217
Covello, A.—(3) 1094
Crannell, Hall—(4) 1495
Cseh, J—(5) 1810
Cunsolo, A.—(3) 952
Cutler, R I.—(5) 1799
Cwiok, S.—(1) 448

Dahlgren, S—(1) 306
Dally, F. B.—(1) 147
Daneshvar, K.—(5) 1819
Dange, S. P.—(4) 1411
Daniels, W. R.—(3) 972
Das Gupta, S—(5) 1989
Datta, S K.—(5) 1687
Datta, Tarun—(4) 1411
Davidson, W F—(1) 65
Davis, J.—(4) 1452
Davis, S—(2) 776
Debevec, P T—(1) 25
e Botton, N.—(2) 662; (4) 1416
DeCarlo, V.—(4) 1460
Dechargé, J.—(4) 1568
De Clercq, A.—(1) 237, (2) 629; (3) 963
Dedonder, J.-P.—(2) 647
De Frenne, D—(1) 237; (2) 629; (3) 963
De Gelder, P.—(1) 237, (2) 629; (3) 963
el Campo, J. Gomez—(5) 1824
De Leo, R—(3) 830, 844
e Lima, A. P.—(4) 1311
Deloff, A.—(4) 1516; (5) 2048
e Passos, E. J. V.—(1) 425
D'Erasmo, G—(3) 830, 844
er Mateosian, E.—(3) 933
De Rosa, A.—(3) 816
Deruytter, A. J.—(1) 237; (2) 629; 3) 963
e Saint Simon, M.—(5) 1783
e Saussure, G.—(4) 1400
e Toledo Piza, A. F. R.—(1) 425
etomo, R., Jr.—(2) 475
e Tourreil, R.—(3) 861
Deutsch, J—(2) 662; (4) 1416
Devereux, M. J—(1) 254
DeVries, R. M.—(1) 167
DeYoung, P A.—(2) 776
D'hondt, P.—(1) 237, (2) 629; (3) 963
DiCenzo, S B—(1) 175
Didelez, J. P—(3) 879
Dietrich, F. S.—(4) 1153, 1158
Dietzsch, O—(4) 1667
Difilippo, F. C—(4) 1400
DiGiacomo, N J.—(2) 757
DiRienzo, A C—(5) 2101
Di Toro, M.—(5) 2054
Dodd, L. R.—(5) 1724
Dominguez, C. A—(5) 1944
Donangelo, R.—(2) 772
Donoghue, T R—(2) 475
Doré, C.—(1) 306
Dover, Carl B—(4) 1466
Dowdy, E J.—(4) 1215
Dracoulis, G D—(1) 464
Drake, D. M.—(3) 902
Dressler, E. T—(5) 2119
Dries, L J.—(2) 475
Drosg, M.—(3) 902
Dubois, D. H—(1) 147
Dubois, R.—(3) 988, 998
Dudek, J—(1) 448
Duder, J. C.—(4) 1653
Duggan, F.—(5) 2054
Duhamel, G—(1) 124, (3) 879
Dumbrajs, Olgierd—(4) 1677
Dupzyk, R. J—(2) 761, (3) 972
Dworzecka, Maria—(3) 1098; (4) 1351
Dyer, J N.—(1) 147

Edgington, J A—(3) 988, 998, 1004
Eggers, R—(4) 1680(E)
Eisen, Y—(4) 1377
Ekelöf, T.—(1) 306
El Hage, Y—(1) 98
El-khoshi, M—(3) 1078
Elwyn, A J.—(4) 1290
Enge, H. A—(5) 2101
Ernst, D J.—(4) 1472
Escudié, J L.—(3) 830
Eyal, Y—(4) 1377

Fabrici, E—(3) 830, 844
Fagg, L. W.—(4) 1162
Fäldt, G.—(1) 306
Falk, W. R.—(5) 1687
Faul, D. D.—(2) 503
Faure, J.-L.—(2) 662; (4) 1416
Favart, D.—(2) 662; (4) 1416
Fayard, C.—(5) 1959
Fearing, Harold W.—(5) 1951
Felawka, L.—(3) 988
Filevich, A.—(3) 933
Fink, R. W.—(5) 2025
Fitzgerald, D. H.—(4) 1149, 1185, 1190
Fliessbach, Torsten—(3) 919
Flynn, D S.—(3) 896
Flynn, E. R.—(4) 1203
Fodor, I—(3) 787
Ford, G. P—(2) 637
Ford, J. L C., Jr.—(2) 764, (5) 1824
Forest, E.—(5) 1989
Fortier, S.—(1) 98
Fortney, D R.—(2) 664
Fortune, H. T—(1) 11
Fossan, D. B.—(5) 1838
Foti, A.—(3) 952
Fox, S. H.—(4) 1133
Fraenkel, Z—(4) 1377; (5) 2139(E)
Frahn, W. E—(5) 1870
Fransson, K—(3) 1078
Freed, N—(4) 1460, (5) 2119
Freedman, M. S—(1) 348
Freeman, R. M—(2) 579
Friedman, A M—(3) 874
Friedman, E—(4) 1239, 1245
Friedman, William A.—(5) 2098
Frisbee, P. E.—(3) 799
Frosch, R F.—(4) 1652
Fry, L. H, Jr.—(4) 1285
Fuda, Michael G—(1) 18, (4) 1480
Fulton, B. R.—(1) 198
Funk, E. G.—(2) 595
Furuno, Kohei—(4) 1387
Fuschini, E—(4) 1646

Gabbard, F.—(3) 896
Gai, M.—(5) 1864
Galès, S—(1) 98, 124
Gallmann, A.—(2) 579
Galloway, R. B—(1) 453
Galonsky, A.—(4) 1344
Gambhir, Y K.—(3) 1124; (4) 1637
García Bermúdez, G—(3) 933
Garcilazo, Humberto—(5) 2094
Garg, U—(4) 1252
Garg, U.—(5) 1838
Garrett, R.—(4) 1149, 1190, 1653
Gavron, A.—(1) 230, (4) 1377
Gazes, S. B.—(5) 2101
Geerts, R.—(1) 439
Geesaman, D F—(1) 254, (5) 1802, 1810, 1819
Gerlic, E.—(1) 124; (3) 879
Giai, Nguyen Van—(2) 744
Giannoni, M. J.—(5) 2060, 2076
Gibson, D R—(3) 988
Gibson, W. R.—(3) 998, 1004
Gilat, J.—(5) 2041
Gils, H. J.—(4) 1239, 1245
Ginocchio, Joseph N.—(3) 1056
Girard, B. A—(1) 18
Giraud, B. G.—(1) 391
Giraud, N.—(5) 1959
Glashausser, C.—(4) 1488
Gleeson, A. M.—(3) 1065
Glendenning, Norman K.—(4) 1501
Glöckle, W.—(1) 54
Gnade, B. E.—(5) 2025

Gobbi, A.—(4) 1377
Gogny, D.—(4) 1568
Goldflam, R.—(2) 483
Gomez del Campo, J.—(2) 764
Gonthier, P.—(4) 1680(E)
Gosset, J.—(4) 1321
Goulard, B.—(1) 374
Gould, C. R —(4) 1377
Goulding, C.—(4) 1452
Grafström, P.—(1) 306
Grammaticos, B —(1) 391
Greene, S.—(4) 1452
Greeniaus, L. G.—(5) 1932
Greenwood, R C.—(2) 498
Greiner, Walter—(3) 958
Griffin, James J.—(3) 1098, (4) 1351
Griffin, P. J.—(3) 799
Gronemeyer, S A —(4) 1290
Gross, Franz—(4) 1426
Gugelot, P. C.—(1) 306
Guillot, J.—(3) 879
Günther, C.—(4) 1670
Gupta, Raj K —(4) 1278
Gupta, V. K.—(5) 2010
Guthrod, H H.—(4) 1321

Haas, F.—(2) 579
Hagberg, E —(1) 306
Haglund, R F. , Jr —(3) 906
Hall, A S —(1) 453
Hallgren, A —(1) 306
Halperin, J.—(2) 545, 563
Hamilton, J. H —(2) 603, (4) 1311
Hanashima, Susumu—(4) 1387
Hanson, D L —(4) 1203
Haq, S.—(3) 1124
Haque, A M. I —(1) 222
Harakeh, M. N.—(2) 768
Hardekopf, R A —(3) 906
Hardie, G —(4) 1290
Hass, M —(2) 574
Hecht, K T —(1) 444
Heikkinen, D. W —(4) 1153
Heisenberg, J.—(3) 1128(E)
Henderson, D J —(3) 1048
Henning, W.—(5) 1802, 1810, 1819
Hensley, D C.—(2) 764
Herman, B. J —(1) 198
Herman, R —(4) 1652
Hernandez, E S —(3) 929
Hershberger, R L —(3) 896
Heusch, B —(2) 579
Heyde, K —(1) 405, 419
Higashi, Y —(2) 620
Hill, John C.—(1) 384
Hilscher, D —(5) 2019
Hindi, M. M —(1) 175
Hintz, N M.—(4) 1488
Hirooka, M.—(5) 1758
Hoffman, Darleane C —(2) 637, 761,
(3) 966, 972
Hoffmann, G. W —(2) 757; (4) 1488
Hofstadter, R.—(4) 1652
Holt, R. J.—(5) 1699
Horn, D.—(1) 459
Houk, W. A.—(1) 28
Hourani, E.—(1) 124
Howell, R. H.—(4) 1153, 1158
Hübel, H.—(4) 1670
Huck, A.—(2) 712
Huffman, R.—(4) 1344
Huizenga, J. R.—(5) 2019
Hulet, E. K.—(3) 966, 972
Hummel, Paul C.—(2) 723
Hussein, M. S.—(2) 772
Hutcheon, D. A.—(2) 675; (5) 1932
Hwang, W-Y. P.—(3) 1086

Igo, G. J.—(2) 757, (4) 1488
Ille, B.—(1) 306
Immè, G.—(3) 952
Ingle, R W.—(4) 1400
Inglima, G.—(3) 816
Irom, F.—(4) 1488

Jackson, H. E.—(5) 1699
Jacobs, E.—(1) 237, (2) 629, (3) 963
Jacobs, W W.—(4) 1656
Jahnel, Lucia C —(4) 1531
Jain, H. C —(5) 2033
Jänecke, J.—(1) 444
Johnsen, S. W.—(4) 1190
Johnson, C. H.—(2) 545, (3) 896
Johnson, M W.—(5) 1967, 2019
Johnson, Mikkel B.—(3) 1056
Johnston, A —(1) 464
Jones, E. C ,Jr.—(4) 1162
Jonsson, G. G.—(4) 1460
Jonsson, S —(1) 306
Jourdain, J -C —(4) 1321
Jury, J W —(2) 503

Kaczarowski, R —(2) 595
Kailas, S.—(4) 1656
Kaitchuck, M D —(4) 1656
Kakiuchi, S.—(1) 344
Kalifa, J.—(4) 1232
Källne, Jan—(2) 675
Kan, K -K.—(3) 1098
Kane, W R.—(1) 65
Kaplan, Morton—(3) 940
Kapoor, S. S.—(2) 752
Käppeler, F —(2) 534; (5) 2139(E)
Kapusta, Joseph I.—(4) 1301
Karant, Yasha J —(4) 1501
Karwowski, H.—(1) 179
Kashy, E —(1) 462
Kasiraj, P.—(4) 1680(E)
Katcoff, S —(5) 2041
Katori, Kenji—(4) 1387
Kaufman, S. B.—(3) 1048
Kawakami, H.—(4) 1311
Keeler, R.—(3) 988, 998
Keinonen, J.—(4) 1196
Kekelis, G.—(1) 444
Kemper, K. W.—(1) 217; (5) 1799
Kim, H. J.—(2) 603; (4) 1311
King, C. H.—(4) 1321
King, G.—(4) 1321
King, N. S. P.—(3) 1030; (4) 1185
Klein, Jeffrey—(4) 1664
Kleinrahm, A.—(4) 1670
Klewe-Nebenius, H.—(4) 1239
Klotz, G.—(2) 712
Knight, J. D.—(5) 1967
Knipper, A.—(2) 712
Koene, B. K. S.—(5) 1932
Kok, L. P.—(2) 512
Kolata, J. J.—(2) 579, 776
Koshel, R. D.—(3) 799
Kovar, D. G.—(5) 1802, 1810, 1819
Kowalick, S. J.—(1) 147
Kowalski, K. L.—(2) 483; (5) 2122
Kozlowski, T.—(3) 1014
Kozub, R.—(5) 1810
Kraus, L.—(3) 791
Krause, T. O.—(1) 1
Kraushaar, J. J.—(2) 757; (3) 1030
Kreiner, A. J —(3) 933
Kreyling, G.—(4) 1377
Krieger, T. J —(3) 1014
Ku, T H.—(2) 705
Kubono, S.—(1) 459, (5) 1864
Kuehner, J. A —(3) 1116
Kullander, S —(1) 306
Kurath, D.—(1) 293
Kusuhara, M —(4) 1165
Kwan, S. P —(5) 1687
Kyle, G. S —(4) 1488

Lacombe, M —(3) 861
Lagu, A V.—(3) 1120
Laird, C. E.—(2) 723
Lakshminarayana, S.—(2) 728
Lam, C S —(5) 1989
Lambert, M.—(1) 306
Lamot, G. H.—(5) 1959
Landrum, J. H.—(3) 966, 972
Landsberger, S —(2) 588
Langevin-Joliot, H.—(1) 124,
(3) 879
Larimer, R. M.—(1) 44
Larry, Thomas L.—(5) 2126
Laszewski, R. M.—(5) 1699
Lattuada, M.—(3) 1104
Laurent, H.—(1) 98
Law, J.—(5) 2048
Lawson, R. D.—(2) 679
Lazzarini, A. J.—(5) 2111
Lecomte, R.—(2) 588
Ledoux, R.—(5) 2111
Lee, M. A.—(1) 328
Lee, T. -S. H.—(1) 254, 293; (2) 679
Leemann, B. T.—(1) 44
Lejeune, A.—(3) 1107
LeMere, M.—(4) 1170
Lenz, F.—(2) 647
Lesser, P. M. S.—(2) 518; (5) 2131
LeVine, M. J.—(5) 1802

Levit, S.—(4) 1594, 1603
Lichtenstadt, J.—(3) 1128(E)
Lichtner, Peter C.—(3) 1098; (4) 1351
Liljestrand, R. L.—(5) 1932
Linck, I —(3) 791
Lindgren, K.—(4) 1460
Lindgren, R. A.—(4) 1162
Lindholm, A.—(3) 902
Liou, M K.—(2) 518; (5) 2131
Liu, C K.—(2) 518; (5) 2131
Liu, Hsing-Chung—(2) 723
Liu, L. C.—(5) 1903, 2103
Lo Bianco, G.—(5) 2135
Logan, B A.—(4) 1525
Loiseau, B —(3) 861
Lorazo, B —(1) 374
Lorini, M.—(1) 116
Lougheed, R. W.—(2) 761; (3) 966, 972
Love, W G.—(5) 1718
Loveland, W —(5) 1783
Ludgate, G. A —(3) 988, 998, 1004
Luhn, R —(2) 776
Lui, Y. -W.—(4) 1252
Lukner, Ch —(4) 1321
Lynen, U.—(4) 1377

MacDonald, William M.—(4) 1642
Macklin, R. L —(2) 545, 563
Macphail, M. R.—(1) 65
Mahaux, C —(4) 1546
Maheshwari, C.—(3) 1120
Maison, J. M —(1) 98
Majka, Z.—(4) 1245
Malaguti, F —(4) 1646
Malmin, R E —(2) 776
Mandò, P A.—(5) 2135
Manohar, S. B.—(4) 1411
Mariscotti, M A. J —(3) 933
Markham, R.—(4) 1344
Matsui, M.—(1) 344
May, M —(3) 1014
Mazaki, H.—(1) 344
McCarthy, J. S —(3) 1128(E); (4) 1452, 1652
McCarthy, R. J.—(4) 1626, (5) 1718
McDonald, W. J.—(2) 675
McGill, J —(4) 1488
McMahan, M. A.—(4) 1261
Medsker, L. R.—(4) 1285
Melnik, D.—(5) 1828
Mennenga, G.—(1) 361
Mercer, R. L —(5) 1899
Meritet, L —(1) 306
Meyer, P.—(2) 503; (4) 1215
Meyer, W. G.—(4) 1321
Meyer-Schützmeister, L.—(4) 1290
Micheletti, S.—(3) 830, 844
Miehé, C.—(2) 712
Mihelich, J. W.—(2) 595
Mikumo, T.—(2) 620
Miller, C. A.—(5) 1932
Miller, Gerald A.—(4) 1472
Milner, W. T.—(2) 603
Minehart, R. C.—(4) 1452
Miska, H. B —(5) 2119
Moake, G. L.—(1) 25
Molho, N.—(5) 2135
Monahan, J. E.—(5) 1699
Monaro, S.—(2) 588
Moore, C. F.—(3) 1030; (4) 1452
Moore, R. W.—(1) 28
Moretto, Luciano G.—(1) 204
Morris, C L.—(1) 254; (3) 1030; (4) 1452
Morrissey, D. J.—(5) 1783
Morsch, H. P.—(2) 768
Mosconi, B —(5) 1921
Moss, G A —(5) 1932
Moszkowski, S A —(3) 929
Mughabghab, S F —(1) 65
Mukoyama, Takeshi—(1) 344, (5) 1753
Mulligan, B.—(1) 1
Murphy, J. J. , II—(2) 469, (5) 1746

Nadasen, A.—(3) 799; (5) 1705
Nagashima, Y.—(2) 620
Nair, A. G C —(4) 1411
Nair, S C K —(4) 1674
Namboodiri, M. N —(4) 1680(E)
Nassalski, J.—(1) 306
Natowitz, J. B —(4) 1680(E)
Nazarewicz, W —(1) 448
Negele, J. W —(4) 1603
Neumann, B —(4) 1239
Nieukerke, K. J —(5) 1724
Nigam, B P.—(4) 1177
Nilsson, L.—(3) 902
Nix, J Rayford—(1) 396, (3) 982
Norman, Eric B —(3) 1109
Nuytten, C —(1) 439

O'Brien, J. T.—(4) 1495
Ohlsen, G. G.—(3) 906
Olmer, C.—(1) 254, (5) 1802, 1810
Olsen, D. K.—(4) 1400
Ooi, Takao—(2) 620, (4) 1387
Oram, C. J.—(3) 988, 998, 1004
Orth, C. J —(5) 1967
Overway, D.—(1) 444

Pace, E.—(3) 805
Palevsky, H.—(3) 1014
Paltiel, Z —(4) 1603
Panda, K. C —(5) 1883
Pantaleo, A.—(3) 830, 844
Papanicolas, C N —(3) 1128(E)
Pappalardo, G.—(3) 952
Paradis, P.—(2) 588
Pardo, R. C.—(1) 462
Park, Jae Y.—(3) 958
Parker, P. D.—(1) 175
Parks, L. A.—(1) 217
Parthasarathy, R.—(4) 1637
Pašagić, V.—(4) 1525
Paul, M.—(5) 1802, 1810
Pauletta, G.—(2) 757
Payne, Gerald L.—(4) 1177
Peker, L. K.—(4) 1311; (5) 2041
Perez, R. B.—(4) 1400
Perillo, E.—(3) 816
Perrin, G.—(3) 879
Perry, D G.—(5) 2019
Pesl, R.—(4) 1239
Peterson, R. J.—(2) 757; (3) 1030
Petrovich, F.—(4) 1153, 1158; (5) 1718
Petry, R. F.—(1) 384
Pettersson, R.—(4) 1460
Piercey, R. B.—(2) 603
Piffaretti, J —(3) 1030
Pignanelli, M.—(3) 830, 844
Pilt, A A —(3) 1116
Pirès, P —(3) 861
Pisk, K.—(4) 1525
Pitthan, R.—(1) 28, 147
Ploughe, W —(4) 1656
Poggi, G —(5) 2135
Poletti, J. L —(4) 1653
Porile, N T.—(2) 664
Porrino, A —(3) 1094
Poskanzer, A M —(4) 1321
Postma, H —(1) 361
Prakash, M —(2) 752
Prakash, Satya—(4) 1411
Price, D —(5) 1891
Priedels, R —(2) 662; (4) 1416
Priyadarsini, D K —(2) 728
Prosser, F. W , Jr —(5) 1819
Protop, C —(1) 222
Pugh, H. G.—(3) 799

Quentin, P —(5) 2060, 2076
Querrou, M —(1) 306

Racca, R A.—(5) 1819
Raciti, G.—(3) 952
Raha, S.—(3) 1065
Rakel, D. A —(2) 595
Ramamurthy, V S.—(2) 752
Ramaniah, M. V —(4) 1411
Ramayya, A. V.—(2) 603, (4) 1311
Ray, L —(4) 1488
Rebel, H —(4) 1239, 1245
Reber, J. D —(4) 1185
Regner, J L.—(2) 475
Rehm, K. E.—(5) 1819
Renfordt, R —(4) 1377
Renner, T. R.—(1) 459
Resmini, F G.—(3) 830, 844
Rhodes, W.—(4) 1460
Ricci, P.—(5) 1921
Richard, J M —(3) 861; (4) 1466
Richards, P —(2) 705
Richard-Serre, C —(2) 712
Richardson, J R —(3) 988, 1004
Riggi, F.—(3) 1104
Rinat, A. S.—(1) 324
Ristinen, R. A.—(3) 1030

Rivet, M F —(3) 940
Rizzo, F —(3) 952
Roberson, N R.—(2) 525
Robertson, L P —(3) 988, 998, 1004
Robinson, L W —(1) 462
Robinson, R L.—(2) 603, (4) 1311
Rode, I —(4) 1377
Rogers, J.—(2) 675
Romero, J L.—(4) 1149, 1185, 1190
Ronningen, R M —(1) 462, (4) 1311
Roos, P G —(3) 799, (5) 1705
Rosina, M —(1) 391
Rotbard, G —(4) 1232
Roy, A.—(5) 1799
Roy, G —(5) 1932
Roy, R —(1) 44
Rozsa, C M —(4) 1252
Russo, G —(5) 2054

Saharia, A N.—(3) 1111
Salmè, G — (3) 805
Salomaa, M K —(5) 2101
Sanders, S J —(5) 1802, 1810
Sandhas, W —(5) 1733
Sandoli, M —(3) 816
Sandoval, A —(4) 1321
Saperstein, Alvin M —(5) 2098
Sargent, C P —(3) 1128(E)
Sartor, R —(4) 1546
Sasagase, M — (2) 620
Sastry, D I —(2) 728
Sato, M —(2) 620
Satpathy, R K —(5) 1883
Sau, J —(1) 405, 419
Saunier, N —(3) 952
Saxena, R N — (4) 1531
Sayer, R O —(2) 603
Schapira, J P — (1) 98
Scheid, Werner—(3) 958
Schier, W —(5) 2101
Schiffer, J P —(5) 1802, 1810
Schmid, I W — (2) 691
Schmitt, Richard P —(1) 204
Schoeters, I —(1) 439
Schrack, R A —(1) 58
Schreckenbach, K —(1) 65
Schroder, W U —(5) 2019
Schuhl, C —(2) 662, (4) 1416
Schultheis, H —(2) 755
Schultheis, R — (2) 755
Schupp, G —(1) 348
Schwandt, P.—(4) 1656
Scobel, W —(2) 614
Seaborg, G T —(5) 1783
Segel, R E.—(1) 254
Semmler, W —(5) 1828
Sen, Nguven Van—(4) 1321
Seshagiri Rao, V —(2) 728
Sesma, Javier—(5) 2130
Shahabuddin, M A. M —(3) 1116
Shahin, F —(3) 816
Shakin, C M —(5) 1903, 2103
Shapira, D.—(1) 167; (2) 764; (5) 1824
Sheline, R. K.—(4) 1232, 1660
Shepard, J. R.—(2) 757; (3) 1030
Shimizu, Sakae—(5) 1753
Shu, N. K B.—(2) 574; (5) 1828
Siemssen, R. H.—(1) 254
Sierk, Arnold J —(1) 396; (3) 982
Sikora, B.—(2) 614
Silbar, Richard R.—(5) 1974
Silver, M.—(1) 272
Silverans, R.—(1) 439
Simon, S —(4) 1680(E)
Singh, P P —(1) 179, (4) 1656
Singham, M K.—(3) 1039
Sjoreen, T P —(5) 1838
Skopik, D M —(2) 469; (5) 1746
Smith, G J —(1) 65
Smith, G R.—(2) 757, (3) 1030
Smith, H. A , Jr.—(1) 179
Sober, D I.—(4) 1495
Sood, P C —(3) 1120
Spanhoff, R —(1) 361
Specht, J R.—(5) 1699
Sperduto, A —(5) 2101
Spitaleri, C —(3) 1104
Srinivasa Rao, M —(2) 728
Stanley, D P —(1) 217
Stapor, W J —(4) 1495
Starkand, Y —(1) 324
Stearns, R L —(3) 1014
Steinberg, E P —(3) 1048
Stelson, P H —(5) 1824
Stelts, M L —(1) 65
Stelzer, H —(4) 1377
Stelzer, K —(4) 1377
Stephens, William—(4) 1664
Stephenson, F J —(1) 44
Sternheim, Morton M —(5) 1974
Stetz, Albert W —(5) 1932, 1979
Stewart, N M —(3) 988, 998, 1004
Stock, R —(4) 1321
Subramanian, T S —(4) 1185, 1190
Sugarbaker, E —(4) 1203
Sugawara, M —(5) 1758
Sundstrom, B.—(3) 1078
Suri, J K —(3) 1124
Sutter, R J —(3) 1014
Swenson, L W —(1) 254
Sziklai, J —(3) 787
Szymański, Z —(1) 448

Tabakin, F —(3) 1039
Tabor, S L —(5) 1819
Taccetti, N —(1) 116
Takagui, E. M —(4) 1667
Talbert, W L. , Jr —(1) 328
Tamae, T —(5) 1758
Tamas, G —(2) 662, (4) 1416
Tamura, T —(4) 1271, (5) 1891
Tang, Henry H K.—(5) 1846
Tang, Y. C.—(4) 1170
Tarrats, A —(3) 830
Theisen, L. V.—(4) 1285
Thieberger, P —(3) 933
Thierens, H.—(1) 237; (2) 629; (3) 963
Thiessen, H. A.—(1) 254; (3) 1030; (4) 1452
Th Leeman, B.—(3) 799
Thompson, W J —(3) 906
Tilley, D R.—(2) 525
Toth, K S.—(2) 764
Trail, C. C —(2) 518, (5) 2131
Tserruya, I.—(4) 1377, (5) 1864
Turner, J D —(2) 525
Tzara, C —(2) 662, (4) 1416

Udagawa, T —(4) 1271, (5) 1891
Uguzzoni, A —(4) 1646
Uhlhorn, C D —(5) 1864
Uhrhane, F J.—(4) 1652
Ullah, Nazakat—(1) 466
Ullmann, J. L —(4) 1149, 1185, 1190
Urano, T.—(5) 1758
Urbon, J A.—(3) 1048

van der Weg, K —(2) 768
van der Woude, A.—(2) 768
Van de Wiele, J.—(1) 124, (3) 879
van Haeringen, H —(2) 512
Vanneste, L —(1) 439
van Oers, W T H.—(5) 1932
Van Oystaeyen, B —(2) 662, (4) 1416
Vary, J P —(4) 1626
Vazeille, F.—(1) 306
Veeser, L. R —(2) 637, (3) 906
Vergnes, M —(1) 124, (4) 1232
Vernotte, J —(4) 1232
Verondini, E —(4) 1646
Vertse, T —(2) 779
Vincent, F —(2) 662, (4) 1416
Vinciguerra, D —(3) 1104
Vinh Mau, R.—(3) 861
von Brentano, P.—(1) 222
von Rossen, P —(1) 44
Vourvopoulos, G.—(4) 1648

Wald, S —(4) 1377
Walker, P M —(1) 464
Wallace, S J —(5) 1996
Walter, G —(2) 712
Wang, A. T M.—(4) 1488
Wang, C W.—(5) 1705
Wang, K. H.—(1) 384
Watanabe, Yoshihisa—(5) 1753
Watson, J W.—(4) 1149, 1190
Weber, J.—(3) 966, 972
Wegner, H. E.—(5) 2101
Weller, H. R.—(2) 525
Wells, J C. , Jr.—(2) 603
Wender, S. A.—(2) 525
Westfall, G. D.—(4) 1321
Whiting, J. S.—(1) 18
Whitten, C. A. , Jr —(2) 757; (4) 1488
Wilcke, W. W.—(5) 2019
Wild, J. F.—(3) 966, 972

ldenthal, B. H.—(5) 2107
lhelmy, J. B.—(2) 761; (3) 966, 972
lliamson, C.—(4) 1344
llis, A —(5) 1932
llis, N.—(5) 1932
nters, R. R.—(2) 545, 563
olf, K. L.—(4) 1321
olfsberg, K.—(5) 1967
oloshyn, R. M.—(3) 1111
Wong, Cheuk-Yin—(5) 1846
Woodworth, J. G —(2) 503
Wright, N.—(3) 998, 1004

Yamanouchi, M.—(2) 620
Yariv, Y.—(5) 2139(E)
Yates, S. W —(3) 874
Youngblood, D. H.—(4) 1252
Zagromski, S —(4) 1239
Zamick, Larry—(2) 738
Zanelli, C —(4) 1149
Zawislak, F. C.—(4) 1531
Zeidman, B.—(1) 254
Zell, K. O.—(1) 222
Zitzmann, R.—(4) 1377
Zurmühle, Robert—(4) 1664

CONTENTS—*Continued*

Mass parameters in the adiabatic time-dependent Hartree-Fock approximation. I. Theoretical aspects; the case of a single collective variable . . . . **M. J. Giannoni and P. Quentin** 2060

Mass parameters in the adiabatic time-dependent Hartree-Fock approximation. II. Results for the isoscalar quadrupole mode . . . . **M. J. Giannoni and P. Quentin** 2076

Comments

Pion-nucleus optical potential including the nuclear Hamiltonian . . . . Humberto Garcilazo 2094

Communications

Glauber theory and *N-N* inelasticity . . . . William A. Friedman and Alvin M. Saperstein 2098

New isotope ^{199}Rn and evidence for an isomeric state ^{199}Rn^{m} . . . A. C. DiRienzo, H. A. Enge, S. B. Gazes, M. K. Salomaa, A. Sperduto, W. Schier, and H. E. Wegner 2101

Self-energy of the Δ resonance in finite nuclei and Fermi broadening . . . . R. S. Bhalerao, L. C. Liu, and C. M. Shakin 2103

Relative importance of neutron and proton components of nuclear transitions and comparative π^{-}/π^{+} inelastic scattering . . . . B. A. Brown and B. H. Wildenthal 2107

^{12}C + ^{12}C intermediate structures correlated among elastic and reaction channels . . . . E. R. Cosman, R. Ledoux, and A. J. Lazzarini 2111

Interior probing capability in kaon-nucleus inelastic scattering . . . . Stephen R. Cotanch 2115

Pion electroproduction from the nucleon near threshold . . . . . . E. T. Dressler, N. Freed, and H. B. Miska 2119

Truncated pion-nucleon amplitudes and pion-nucleus interactions . . . . K. L. Kowalski 2122

Projection operator method for heavy ion reactions and application to ^{12}C + ^{12}C . . . . Thomas L. Larry and William P. Beres 2126

Existence of strongly bound states of pions in nuclei . . . . Javier Sesma 2130

Bremsstrahlung from ^{12}C + p near the 1.7-MeV resonance . . . . C. C. Trail, P. M. S. Lesser, A. H. Bond, Jr., M. K. Liou, and C. K. Liu 2131

Levels in ^{44}K via the ^{48}Ca(p,αn) reaction . . . . P. A. Mandò, G. Poggi, G. Lo Bianco, and N. Molho 2135

Errata

Erratum: Neutron capture cross sections on ^{138}Ba, ^{140,142}Ce, ^{175,176}Lu, and ^{181}Ta at 30 keV: Prerequisite for investigation of the ^{176}Lu cosmic clock [Phys. Rev. C 21, 534 (1980)] . . . . H. Beer and F. Käppeler 2139

Erratum: Intranuclear cascade calculation of high-energy heavy-ion interactions [Phys. Rev. C 20, 2227 (1979)] . . . . Y. Yariv and Z. Fraenkel 2139

Cumulative Author Index 2140

PHYSICAL REVIEW C VOLUME 21, NUMBER 6 JUNE 1980

Inelastic excitation of ^{12}C and ^{14}N by 122 MeV protons and implications for the effective nucleon-nucleon interaction

J. R. Comfort
Department of Physics and Astronomy, University of Pittsburgh, Pittsburgh, Pennsylvania 15260

Sam M. Austin
Cyclotron Laboratory and Physics Department, Michigan State University, East Lansing, Michigan 48824

P. T. Debevec
Department of Physics, University of Illinois, Urbana, Illinois 61801

G. L. Moake*
Department of Physics, Purdue University, West Lafayette, Indiana 47907

R. W. Finlay
Department of Physics, Ohio University, Athens, Ohio 45701

W. G. Love
Department of Physics, University of Georgia, Athens, Georgia 30602

(Received 1 October 1979)

Cross sections for the ^{12}C$(p,p')^{12}$C and ^{14}N$(p,p')^{14}$N reactions have been measured at $E_p = 122$ MeV. Scattered protons were momentum analyzed in a dispersion-matched magnetic spectrograph and detected in a helical-cathode position-sensitive proportional counter. Transitions to states in ^{12}C at 4.44 MeV $(2^+, T=0)$, 12.71 MeV $(1^+,0)$, 15.11 MeV $(1^+,1)$, 16.11 MeV $(2^+,1)$, and in ^{14}N at 2.31 MeV $(0^+,1)$ and 3.95 MeV $(1^+,0)$, are very useful for studying the spin-isospin dependence of the effective two-nucleon interaction. Cross sections for these states from the present experiment and from earlier measurements at 185 MeV have been analyzed in the distorted-wave impulse approximation. Simultaneous consideration of (e,e') data for the same transitions helped to disentangle some nuclear-structure and reaction-mechanism effects. The distorted-wave impulse approximation provides a good description of those transitions in ^{12}C mediated predominantly by the $S=T=1$ part of the effective interaction and also gives a reasonable description of the $S=T=0$ transitions in both nuclei. The mechanisms for excitation of the 12.71-MeV state in ^{12}C $(S=1, T=0)$ and the 2.31-MeV state in ^{14}N $(S=1, T=1)$ remain a puzzle.

[NUCLEAR REACTIONS ^{12}C, ^{14}N(p,p), (p,p'), $E=122$ MeV; measured $\sigma(E_p,\theta)$; resolution 100 keV; $\theta = 6-60°$. ^{12}C 2^+ states deduced β_2 DWIA analysis; microscopic effective interaction with $\vec{L}\cdot\vec{S}$, tensor, and exchange terms.]

I. INTRODUCTION

A fundamental goal of nuclear physics is to relate nuclear structure and reaction dynamics to the underlying nucleon-nucleon (N-N) interaction. Since this interaction is complicated and has other awkward features such as a strong short-range repulsion, it is necessary in practice to represent it by an effective interaction V^{eff}. This in turn must be tested and understood before nucleon-nucleus scattering can be used as a detailed probe of nuclear structure.

One approach to this might be the construction of complex optical-model potentials from realistic internucleon interactions and the comparison of predicted cross sections with the extensive body of elastic-scattering data. Although these procedures have received considerable impetus recently from the work of several groups,[1,2] they have the limitation that elastic scattering is not selectively sensitive to each individual spin and isospin component of the effective interaction.

On the other hand, inelastic-scattering and charge-exchange reactions have the advantage, particularly on light nuclei, that selection rules and reaction dynamics often isolate a very few components of V^{eff}. Bertsch *et al.*[3] have constructed a V^{eff} based on the shell-model G matrix and this has been applied with generally satisfactory results to nucleon data for energies less than 65 MeV.[3,4] Since the effective interaction is energy dependent,[4] complementary studies at different energies or for different ranges of momentum transfer will therefore enrich our understanding of its components and also of nuclear structure.

In many ways intermediate energies such as 100–200 MeV seem superior for such studies. Resolution is still sufficient to permit separation of many states of interest. The reaction dynamics should also be considerably simpler since the im-

© 1980 The American Physical Society

portance of multistep processes[5] and resonances[6] should be reduced and sensitivity to optical distortions will be smaller. It is unfortunate that little is known about the effective interaction in this energy range.

To the extent that the distorted-wave impulse approximation (DWIA) is applicable, $V^{\rm eff}$ is related simply to the free nucleon-nucleon interaction.[7] But the DWIA is not unquestionably valid near 100 MeV and only a few tests of its adequacy have been made. Moreover, as we shall see, empirical procedures for fixing $V^{\rm eff}$ are not useful at these energies. The present study attempts to delineate the range of validity of the impulse approximation and to test a microscopic effective interaction constructed for this energy range.

Inelastic nucleon scattering from ^{12}C and ^{14}N provides an excellent situation for studying these issues. States are available which isolate most individual combinations of spin and isospin transfer and some which are also particularly sensitive to the tensor force. Moreover, shell-model wave functions are available for these states which reproduce many of the known properties quite well. Since isospin is a rather good quantum number for these light nuclei, the charge form factor, which is determined rather well from high-quality (e, e') data, is a good measure of both proton and neutron transition densities. Although the large oblate deformation of ^{12}C is often thought to create unusual difficulties in interpretations of data, it is found here that the problems are not very severe and that ^{12}C is indeed a tractable nucleus.

This paper reports measurements of (p, p') reactions on ^{12}C and ^{14}N at an energy of 122 MeV. Attention is focused on transitions to states that correspond to rearrangements of the $1p$-shell nucleons. In ^{12}C these are the 2^+ state at 4.44 MeV $(T=0)$ and 16.11 MeV $(T=1)$, and the 1^+ states at 12.71 MeV $(T=0)$ and 15.11 MeV $(T=1)$. In ^{14}N the transitions are from the 1^+ $(T=0)$ ground state to the 0^+ $(T=1)$ state at 2.31 MeV and the 1^+ $(T=0)$ state at 3.95 MeV. This selection spans the full range of terms in $V^{\rm eff}$, often with strong constraints on the number of significant components. For example, the 15.11-MeV transition $(S=T=1)$ can be expected to be particularly sensitive to the one-pion-exchange (OPE) part of the N-N interaction. The direct contributions to the other transitions in ^{12}C might be more sensitive to the exchange of mesons of larger mass and other aspects of the short-range N-N interaction.

After a brief phenomenological interpretation of the data, analysis will be made in terms of a thoroughgoing treatment of an effective interaction derived from elastic N-N data at 140 MeV and applied in the DWIA. In order to study the energy dependent of $V^{\rm eff}$, analysis is also made of data near 185 MeV taken from the literature.[8,9]

Studies similar to this have been carried out in the past.[10-13] Our approach is somewhat more *a priori*. We take the wave functions, the effective interaction, and reaction dynamics as known and inquire how well the data are reproduced. Auxiliary studies on some of these items allow us to reach specific conclusions regarding the components of $V^{\rm eff}$.

II. EXPERIMENTAL PROCEDURES

A. Data acquisition

A beam of 122-MeV protons from the Indiana University cyclotron bombarded targets of ^{12}C and ^{14}N placed in a 61-cm-diameter scattering chamber. The ^{12}C target was of natural graphite with a thickness of 11.3 mg/cm^2, while the ^{14}N target consisted of about 5.8 mg/cm^2 of melamine evaporated onto backings of formvar and carbon with a thickness of 25 μg/cm^2. A thick BN target (26.9 mg/cm^2) was used to check the normalization of the ^{14}N data.

Emerging protons were momentum analyzed in a quadrupole-dipole-dipole-multipole magnetic spectrograph operating in a dispersion-matched mode and were detected in a helical-cathode, position-sensitive proportional chamber.[14] This chamber was followed by two plastic scintillator detectors of thicknesses 0.63 and 1.27 cm which were used for particle identification. The solid angle of the spectrograph was about 1.5 msr (±0.5° horizontally) at forward angles and 2.58 msr (±1.0°) for larger angles. For some of the elastic scattering data, solid angles a factor of 10 smaller were used at the forward angles.

The position of a particle in the focal plane was determined from the time difference of signals from the two ends of the helical-cathode wire. Upon a triple coincidence between the helix and the two scintillators, the position signal and the signals from the scintillators E_1 and E_2 were passed through an ADC system and processed by the program DERIVE[15] in an on-line computer. Protons were selected digitally by imposing a contour on a two-dimensional E_1 vs E_2 display. The dead time of the system was monitored by feeding pulser signals triggered from the current integrator through the entire system. Event rates were kept to a few hundred per second and the corresponding dead times were only a few percent. The relative efficiency of the helix across its length was checked and monitored. The overall energy resolution was typically 80–100 keV.

Special care was taken with the data acquisition for ^{14}N. The state of principal interest lies low in excitation energy at 2.31 MeV and has a very small cross section. Backgrounds were consequently a severe problem for small angles. Background from a small beam halo was eliminated by stacking several empty frames to the rear of the target, thus degrading the halo protons below the energy range of interest. At forward angles, it was not feasible to have the elastic and 2.31-MeV peaks on the detector simultaneously. Yet moving the elastic group off the end of the detector produced additional backgrounds. A thick lead block placed in front of the focal plane at the position of the elastic group generated no spurious events and, together with the thick target holder, allowed reliable data to be taken at angles as small as 6°. An additional problem was the fragility of the melamine target. Beams were therefore kept low and possible target deterioration was monitored by numerous measurements at 14°.

B. Data reduction for ^{12}C

Because of the small energy bite of the spectrograph, it was necessary to take data at two different magnetic field settings. One group included elastic scattering and inelastic scattering to the 4.44-MeV state, and the other spanned the region of exciation from about 10 to 17 MeV. Spectra for the two groups at a laboratory angle of 39° are shown in Fig. 1. Data were not obtained for the states at 7.65 and 9.64 MeV.

Analysis of the data in the first group was straightforward. In the higher excitation-energy group, the narrow states of interest sat upon a continuum resulting from both three-body breakup and other broad states. Yields were determined by representing the continuum under them by smooth curves. After they were subsequently removed from the data, the resultant spectra were compressed. This enhanced the visibility of broader states, which were similarly extracted. Figure 2 shows the compressed spectrum at 39° and the assumed "backgrounds."

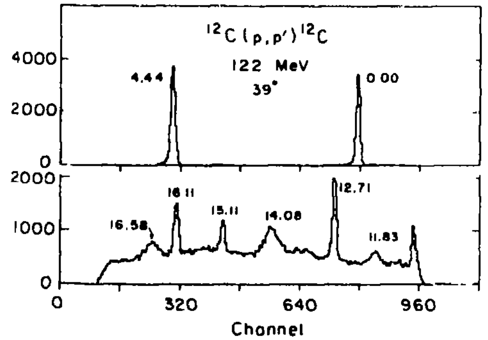

FIG. 1. Representative spectra of the ^{12}C(p,p')^{12}C reaction at two separate field strengths of the magnetic spectrograph. Peaks are labeled with their excitation energies.

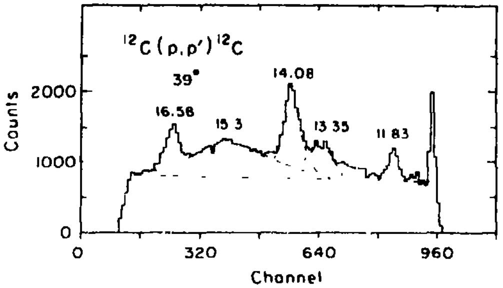

FIG. 2. Compressed spectrum of ^{12}C for the excitation-energy range 11–17 MeV. Three narrow peaks have been removed (see Fig. 1). The dotted lines indicate the "backgrounds" assumed for the remaining peaks.

The center-of-mass differential cross sections (relativistic kinematics) for all states are shown in Figs. 3 and 4. The elastic cross sections in Fig. 3 have been corrected for the approximate 1.5% unresolved contribution from ^{13}C at forward angles. Data were obtained on two separate occasions. The absolute cross sections for several repeat runs reproduced very well within statistics, apart from an overall scale change of about 4%. This was attributed to a change in Faraday cups. The final cross sections for ^{12}C were normalized according to the experience at IUCF, for which 1–2% agreement with the absolute cross sections

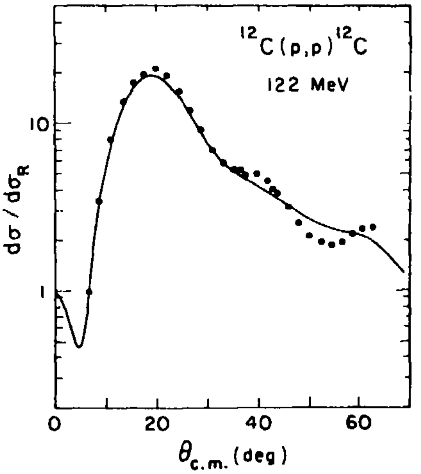

FIG. 3. The angular distribution for the scattering of 122-MeV protons from ^{12}C, in ratio to the Rutherford cross section (relativistic kinematics only).

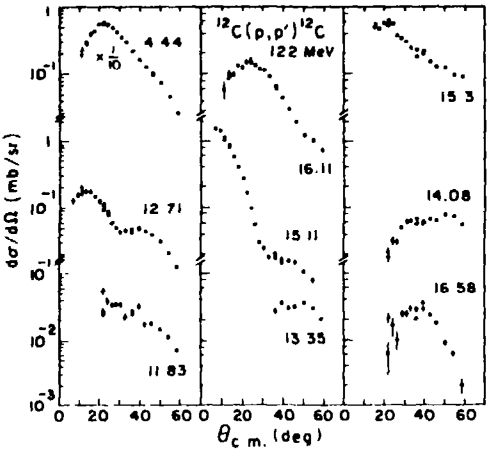

FIG. 4. Differential cross sections for the states of ^{12}C seen in the (p,p') reaction. The excitation energy of each state is indicated. Error bars are shown when they exceed the size of the data points.

of calibration reactions is normally obtained.[16] The absolute scale is believed to be reliable to better than 4%.

No effort has been made to interpret the data for states other than those enumerated earlier. Most have known J^π assignments.[17] The broad state at 15.3 MeV has been reported previously and interpreted[18,19] as having $J^\pi = 2^+$, $T = 0$.

C. Data reduction for ^{14}N

A representative spectrum for $^{14}N(p,p')^{14}N$ is shown in Fig. 5. Angular distributions were extracted for the ground state and the excited states at 2.31 and 3.95 MeV. States at higher excitation energies are obscured by impurity peaks at many angles. The angular distributions for scattering from ^{14}N, shown in Fig. 6, were normalized to the cross sections for $^{12}C(p,p')^{12}C$ (4.44 MeV) by using the data of Fig. 4. The yields for this state were observed simultaneously with that for the ^{14}N states upon bombardment of the melamine target. The normalization constant was compared at 28° to an absolute cross-section scale determined by use of a thick BN target. The two normalizations agreed to within 2%. Effects of deterioration of the melamine target were less than ±3%. The overall cross-section scale is believed accurate to within ±5%. A tabulation of all the cross sections has been deposited in the Physics Auxiliary Publications Service.[20]

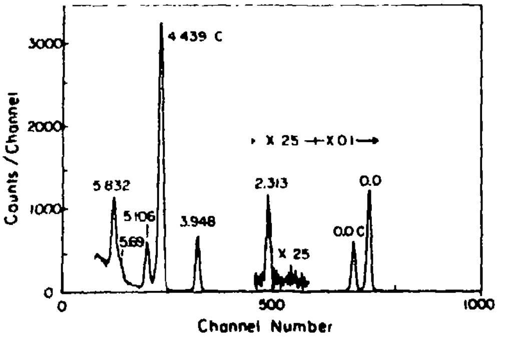

FIG. 5. Composite spectrum of protons scattered from a melamine target at 26°. Peaks labeled C are from the ^{12}C component of the target and the remainder are from ^{14}N.

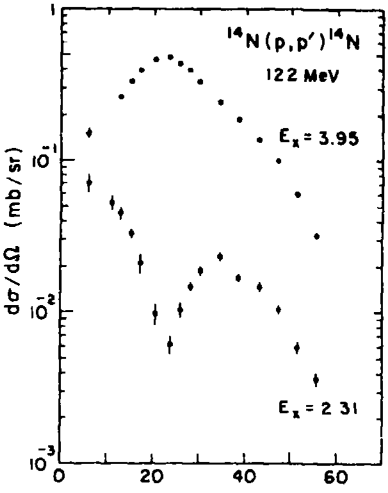

FIG. 6. Differential cross sections for (p,p') reactions to excited states of ^{14}N.

III. COLLECTIVE MODEL INTERPRETATION

Since collective models have been applied frequently to the excitation of ^{12}C, it is useful for orientation purposes to make brief comparisons with the data here. Although the focus of our study is on microscopic interpretations, the underlying intent of this section is to help gauge the relative importance of various contributions. The parameters for the optical-model potential describing 122-MeV proton scattering from ^{12}C were obtained in a companion study[21] and are listed in Table I. The fit to the elastic-scattering data is shown in Fig. 3.

A direct application of the conventional collective model to the excitation of the 2^+ $T=0$ state at 4.44 MeV gave agreement with the maximum cross section near 20° for a deformation parameter $|\beta_2|$

TABLE I. The optical potentials used in the calculations. The potentials are defined by $U(r) = V_C(r) + Vf_R(r) + iWf_I(r) + V_{so}(1/r)(d/dr)f_{so}(r)\vec{l}\cdot\vec{s}$, where V_C is the coulomb potential for a uniformly charged sphere $f_i(r) = 1/(1+e^{x_i})$ and $x_i = (r-R_i)/a_i$ with $R_i = r_iA^{1/3}$. Energies have units MeV and lengths have units fm. The potentials are defined for use with relativistic kinematics (see Ref. 21).

Particle	Energy	V	r_R	a_R	W	r_I	a_I	V_{so}	r_{so}	a_{so}	r_c
p	122	−18.3	1.20	0.65	−10.6	1.30	0.64	−18.3	0.90	0.50	1.2
p	183	−12.5	1.20	0.68	−13.1	1.20	0.61	−16.4	0.90	0.49	1.2
d	110	−68.0	1.20	0.62	−14.4	1.40	0.67	−11.0	0.90	0.50	1.2

0.55. At larger angles the calculated curve fell ff much too steeply. When corrections for Cou- omb excitation and the deformation of the spin- rbit potential were included, the value was re- ucedto $|\beta_2| \simeq 0.45$. The deformed spin-orbit poten- ial also enhances the cross sections at the larger ngles. It is interesting to note that when the oods-Saxon potentials themselves were deformed nd the monopole part projected out, the best fit o the elastic-scattering data was achieved for a alue $\beta_2 = -0.44$.

We may thus anticipate that at 122 MeV the oulomb and spin-orbit interactions may each ake about 10% corrections to the 2^+ $T=0$ transi- on intensities and that the latter interaction may e quite important for producing correct shapes t large angles. In the same model, but without e corrections, the transition to the 2^+ $T=1$ state t 16.11 MeV requires a value $|\beta_2| = 0.085$.

The transitions to the 1^+ states may proceed by $=0$ and 2. The collective model allows the $L=0$ art to have both volume and surface-derivative rms.[22] Satchler found that the $L=2$ parts were ominant for both the 12.71- and 15.11-MeV transi- ons in ^{12}C induced by 46-MeV protons.[22] This ould raise serious problems in the present study. ince the central terms of the microscopic effec- ve interaction produce negligible $L=2$ contribu- ons, their dominance would have to result from e tensor interaction. The sensitivity to the im- ortant central terms then might well be lost.

We find, however, that the situation is not so isturbing at 122 MeV. In fact, both the 12.71- nd the 15.11-MeV states may be fitted (out to out 30°) with combinations of only the volume nd surface $L=0$ terms. The combinations did not reserve the volume integral of the potential, but scillations of the diffuseness parameters[22] were ot included. The situation is ambiguous since ternative combinations with $L=2$ contributions ere also possible. However, in all cases, the $=0$ terms were the dominant ones, especially or the 15.11-MeV transition. Some reasons re- ting to reaction dynamics are offered in the ompanion article[21] for the difficulties at 46 MeV.

IV. MICROSCOPIC DWIA CALCULATIONS

A. The effective interaction

It has been suggested[10] that above ~100-MeV proton bombarding energy, the distorted-wave impulse approximation might be appropriate for interpreting nucleon-nucleus scattering. In the DWIA, V^{eff} is taken to be the free N-N t matrix. When valid, the appeal of this appraoch is evident; V^{eff} may be regarded as known and attention can be focused directly on extracting nuclear structure information. The objective of this section is to assess empirically the validitiy of this approach for a variety of nuclear transitions.

The use of the DWIA implies that the effects of multiple scattering and multistep contributions are either negligible or are well described by the distorted waves. In a companion study[21] it was found that, for relatively strong transitions, the effects of a number of strong multistep processes are accurately included in one-step calculations provided that one uses optical-model parameters that reproduce the elastic scattering in a single-channel approximation. Additional discussion of multistep processes is given in Sec. V B.

The two-nucleon interaction may be written

$$V_{12}^{\mathrm{eff}} = V_{12}^{\mathrm{central}} + V_{12}^{\mathrm{spin\text{-}orbit}} + V_{12}^{\mathrm{tensor}}, \tag{1}$$

where in more detail

$$V_{12}^{\mathrm{cent}} = V_0 + V_\sigma\vec{\sigma}_1\cdot\vec{\sigma}_2 + V_\tau\vec{\tau}_1\cdot\vec{\tau}_2 + V_{\sigma\tau}(\vec{\sigma}_1\cdot\vec{\sigma}_2)(\vec{\tau}_1\cdot\vec{\tau}_2), \tag{2a}$$

$$V_{12}^{\mathrm{so}} = (V_{LS} + V_{LS\tau}\vec{\tau}_1\cdot\vec{\tau}_2)\vec{\mathrm{L}}\cdot\vec{\mathrm{S}}, \tag{2b}$$

$$V_{12}^{\mathrm{ten}} = (V_T + V_{T\tau}\vec{\tau}_1\cdot\vec{\tau}_2)S_{12}. \tag{2c}$$

S_{12} is the tensor operator

$$S_{12} = 3(\vec{\sigma}_1\cdot\hat{r}_{12})(\vec{\sigma}_2\cdot\hat{r}_{12}) - \vec{\sigma}_1\cdot\vec{\sigma}_2. \tag{3}$$

All interaction strengths are functions of the relative coordinate $\vec{r}_{12}$. For these we use the complex local coordinate-space representation of the antisymmetrized on-shell t matrix reported in Refs. 4 and 23. This V^{eff} basically consists of a sum of Yukawa terms with the three ranges

(0.25, 0.4, and 1.414 fm) chosen to reflect the exchange of various mesons. The tensor part of V^{eff} has an $r^2 \times$ Yukawa form and the maximum (third) range is 0.7 fm. The specific interaction was constructed from the N-N scattering phase shifts at 140 MeV,[24] an energy that is intermediate to the two cases considered here. The constraint was imposed that only the $V_{\sigma\tau}$ interaction has a term with the longest range, corresponding to one-pion exchange. This and the limitation on the number of ranges are the main differences between this interaction and that of Picklesimer and Walker.[25]

A rough criterion for neglecting knockon exchange terms is that $kR \gg 1$ where k is the incident momentum in fm^{-1} and R denotes each of the ranges. When this condition is met, V^{eff} is incapable of transferring the required momentum with appreciable amplitude. For the bombarding energies considered here, $k \sim 2$–3 fm^{-1} so that exchange terms may be expected to be important for the short-range parts of V^{eff}. The exchange contributions were calculated exactly with a modified version of the code DWBA70.[26] Relativistic kinematics was also used. The appropriate optical potentials are given in Table I.

The remainder of this section describes the calculations based on shell-model wave functions and the effective interaction in the DWIA. The single-particle wave functions for the bound particles were of harmonic-oscillator form with an oscillator parameter chosen to match the prominent maxima of the longitudinal and transverse form factors $F_L(q)$ and $F_T(q)$, respectively, obtained from (e, e') experiments.[27] The parameters for the various transitions are listed in Table II. Wave functions constructed from Woods-Saxon potentials may also be used. The results are generally rather insensitive to this choice, as well as to reasonable variations of the Woods-Saxon parameters and binding energies.

B. Shell-model wave functions

One of the best shell-model descriptions for the states of ^{12}C and ^{14}N is provided by the effective 1p-shell interaction of Cohen and Kurath (CKWF).[28] The wave functions for ^{12}C and ^{14}N were constructed from the (8–16) POT and (8–16)2BME two-body matrix elements, respectively. For the 2.31-MeV transition in ^{14}N we considered as an alternative the wave functions determined by Ensslin *et al.*[29] directly from (e, e') form factors and other experimental data.

TABLE II. The parameters for the harmonic-oscillator bound-state wave functions, where the $l = 0$ radial dependence is given by $\sim\exp(-\frac{1}{2}\mu^2 r^2)$.

Nucleus	Final state	μ (fm^{-1})
^{12}C	4.44	0.568
	12.71	0.609
	15.11	0.613
	16.11	0.610
^{14}N	2.31	0.588
	3.95	0.595

The most simple view of ^{12}C is that the $p_{3/2}$ orbit is entirely filled and that the 2^+ and 1^+ states with $T = 0$ and 1 are formed by promoting a single nucleon to the $p_{1/2}$ orbit. However, for the CKWF, the ground state has a population probability of about 6.5 $p_{3/2}$ particles, as do also the excited states (the 16.11-MeV state actually contains about 6.7 $p_{3/2}$ particles). The main components of the transition amplitudes involve both $p_{3/2} \to p_{1/2}$ and $p_{1/2} \to p_{3/2}$ transitions. The effect on the (p, p') cross sections is illustrated in Fig. 7. These were calculated for a simple Yukawa interaction of 1 fm range. It is clear that a good description of the wave functions is essential. The main limitation of the CKWF is the truncation to the 1p shell so that the collective effects on the transitions will be underestimated.

C. The $T = 1$ states of ^{12}C

1. The 1^+ state at 15.11 MeV

Since this state has unnatural parity and $T = 1$, its excitation is mediated primarily by the $V_{\sigma\tau}$ part of V^{eff} whose origin is largely the OPE interaction. Figure 8 shows a comparison of the experimental data at 122 MeV and the DWIA calculations. Since both the peak value of $|F_T(q)|^2$ and the ground-state $M1$ radiative width[17] are under-

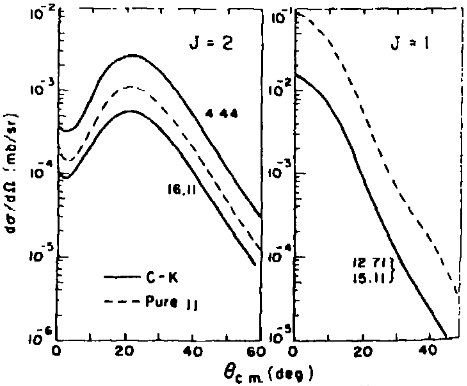

FIG. 7. Cross sections of four states in ^{12}C for the (p,p') reaction at 122 MeV resulting from pure single-particle $p_{3/2} \to p_{1/2}$ transitions and from the Cohen-Kurath wave functions. The dashed curves for each J apply to both transitions and the CK curves for $J = 1$ agree.

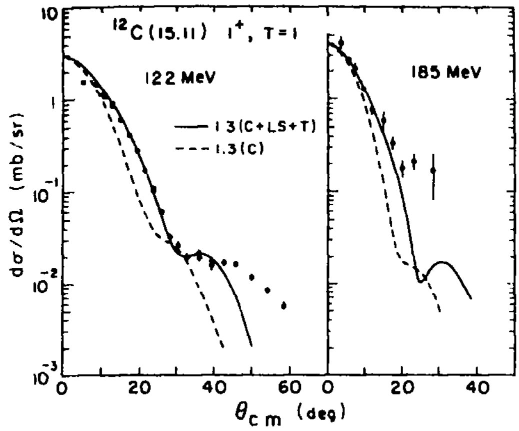

FIG. 8. DWIA calculations for the 15.11-MeV transition in ^{12}C at two proton energies in comparison with the data. The calculations include central (*C*), spin-orbit (*LS*), and tensor (*T*) contributions and are renormalized by a multiplicative factor of 1.3.

estimated by a factor of about 1.3 by the CKWF, the calculated cross sections have been multiplied by 1.3. It may be noted, however, that the CKWF give the correct value of the *ft* value from β decay which, like the (p,p') reaction, is dominated by the spin contribution. The dashed curve is for the central part of the force only; the solid curve includes contributions from central, spin-orbit, and tensor terms. The two-body spin-orbit interaction has a weak isovector part and is therefore unimportant for this cross section. When the tensor force is included the results are quite satisfactory; without it, the shape of the calculated cross section is in much poorer agreement with the data.

The results are especially significant when one notes that the transverse from factor given by the CKWF agrees well in shape with that inferred from (e,e') measurements[27] out to momentum transfers of $q \sim 1.5$ fm^{-1}, which for 122-MeV protons corresponds to ~37°. A second peak[27] in $|F_T(q)|^2$ near 2 fm^{-1} is very poorly described by these wave functions and this deficiency shows up in the predicted (p,p') results. It seems fairly clear that the $S = T = 1$ part of V^{eff} is given reliably by the free *N-N* *t* matrix as represented in Refs. 4 and 23, at least out to $q \sim 1.5$ fm^{-1}.

Analogous calculations have been made at 185 MeV and these are compared with experimental data from Ref. 8 in Fig. 8. As at 122 MeV, the tensor force significantly improves the shape of the calculated cross section. It is somewhat disturbing that the shape is correctly predicted out to only $q \sim 0.8$ fm^{-1}. Modern and more complete data for this OPE dominated transition would be desirable. The disagreement at 185 MeV might also reflect the greater departure in energy from that of the 140-MeV *t* matrix being used.

2. *The 2$^+$ state in ^{12}C at 16.11 MeV*

Excitation of this state is in principle more complicated than for the 1$^+$ state since both the V_τ and $V_{\sigma\tau}$ terms may contribute, in addition to the $V_{LS\tau}$ and $V_{T\tau}$ terms. The isovector part of the spin-orbit force is small and thus $V_{LS\tau}$ contributes relatively little. Also, at intermediate energies, $V_{\sigma\tau}$ is more important than V_τ so that the $S = 1$ contributions are at least as large as those for $S = 0$. Since the tensor contributions remain large, we are sensitive mainly to the same terms of V^{eff} as for the 1$^+$ state.

The wave function for this state is somewhat uncertain. The $S = 1$ part of the transition density is sampled by $F_T(q)$ in (e,e') experiments. Unfortunately the shape of $|F_T(q)|^2$ is not reproduced in detail by the CKWF.[27] While the magnitude is properly given for small q, the theoretical result must be reduced by a factor ~0.7 in order to match the experimental value at the peak. The relationship of the experimental and theoretical ground-state widths of this state is also unclear. The CKWF estimate is in reasonable agreement with one recent measurement[30] and a factor of 2 larger than another.[31] In any case, such a discrepancy would not be as serious as it might initially appear because the radiative decay is isovector $E2$ whereas the (p,p') reaction proceeds mainly by the $S = T = 1$ terms.

Figure 9 shows a comparison of the 122-MeV data and the DWIA calculations, the latter scaled

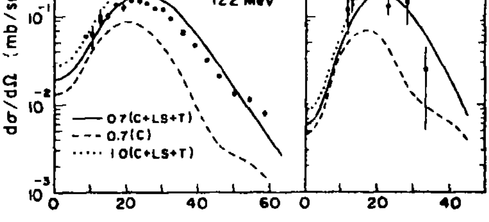

FIG. 9. Comparison of DWIA calculations with data for the 16.11-MeV transition in ^{12}C. See also the caption for Fig. 8. The curves have been renormalized by 0.7 except for the dotted curves where unit normalization for low momentum transfer is also shown.

down by a factor 0.7 corresponding to use of the CKWF for large q. Again the tensor part is very important in establishing the proper magnitude and the spin-orbit part improves the shape at larger angles.

Similar calculations have been made at 185 MeV and are compared with experimental data[8] in Fig. 9. The data at this energy are much less definitive than those at 122 MeV due to the larger errors and the much smaller range of momentum transfers. The calculated cross sections would appear to need no renormalization, corresponding to the predictions of the CKWF at low q.[27] At both energies the general agreement of theory with experiment for this transition is quite reasonable in view of the somewhat imprecisely described transition density.

D. The $T = 0$ states of ^{12}C

1. *The 2^+ state at 4.44 MeV*

The CKWF reproduce the shape of the longitudinal (e, e') form factor[27] $F_L(q)$ out to $q \sim 2$ fm^{-1} but the magnitude of the calculated $|F_L|^2$ requires an enhancement factor of 2 to match the data. The calculated $B(E2)$ for this transition requires an enhancement factor of about 1.6. On the basis of the (e, e') results the spin-independent part of the transition density should be reliable out to $q \sim 2$ fm^{-1}, which for (p, p') at $E_p = 122$ (185) MeV corresponds to $\theta_{c.m.} \sim 50°$ (45°).

As can be seen in Fig. 10 the calculated cross sections at each bombarding energy are overestimated with use of the average renormalization factor of 1.8. The spin-orbit part of V^{eff} is important at the larger angles and increases the integrated cross section by ~60%(~100%) at $E_p = 122$ (185) MeV. The cross sections at these larger angles are still considerably underestimated relative to the forward peak.

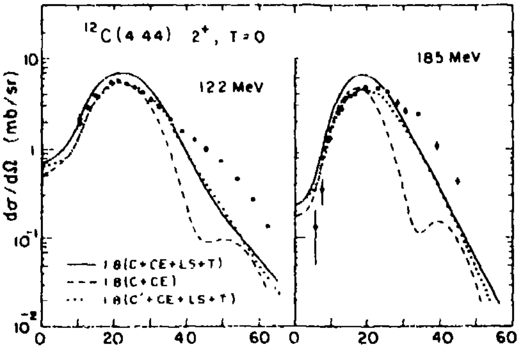

FIG. 10. Comparison of DWIA calculations with data for the 4.44-MeV transition in ^{12}C. See also the caption of Fig. 8. Coulomb excitation (CE) is included. The dotted curves are for a calculation in which the imaginary part of the central interaction was reduced by a factor of 2 (C'). The renormalization of 1.8 accounts for known core-polarization effects.

Indirect but independent information is available on the scalar-isoscalar part of V^{eff} from folding-model estimates of the central part of the optical potential.[4] The real part of the volume integral (per nucleon) of the phenomenological optical potential agrees reasonably well with that of V^{eff} while the imaginary part is overestimated by about a factor of 2. For this reason calculations were also made in which the overall strength of the imaginary part of V^{eff} was reduced by a factor of 2. The shape of the calculated cross section is only slightly altered but a renormalization of it by a factor of ~1.8 is now required, in good agreement with the electromagnetic results. Expansion of the shell-model basis space has been found to produce good agreement for cross sections at 61 MeV without any renormalization.[32]

The relatively poor shape of the calculated cross section for $q \gtrsim 1.2$ fm^{-1} may indicate the need for a larger $S = 1$ component in the transition density. (It may be noted that the shapes of the experimental cross sections for this state and for the 16.11-MeV state, which is dominated by $S = 1$, are quite similar.) The CKWF do not represent the shape of the relevant transition density $|F_T(q)|^2$ from (e, e') experiments very well and the calculated magnitude is low by a factor of 3.[27] Another possibility is that coupled-channels effects are beginning to show up at larger angles.[21]

2. *The 1^+ state at 12.71 MeV*

With an oscillator parameter chosen to reproduce the peak positions of the (e, e') transverse form factor, the CKWF underestimates $|F_T(q)|^2$ by roughly a factor of 4. An earlier (e, e') measurement of the electromagnetic width reported[33] a value of 0.35 eV which is also much larger than the value 0.113 eV given by the CKWF. The very small calculated width and form factor are due to isoscalar $M1$ suppression in self-conjugate nuclei and in addition to a cancellation of spin and orbital contributions. It makes these transitions very sensitive to isovector impurities in the wave functions.[30] The (p, p') reaction may be less sensitive to such impurities since the relative contributions from spin and current densities may be quite different, even though the ratio of central isovector to isoscalar coupling strengths is large and comparable to (for small momentum transfers) the analogous ratio for the (e, e') reaction. Explicit calculations based on the mixing coefficients proposed in Refs. 30 and 33 showed that the effects of isospin mixing were entirely negligible, changing the 1^+ (p,p') cross sections by 5% or less.

The CKWF are not only clearly inadequate for a satisfactory description of the electromagnetic excitation of this state, but are also inadequately tested by (e,e') data with respect to their reliability for use in (p,p') calculations. This is to be contrasted with the excitation of the $T=1$ state at 15.1 MeV which has a large $S=1$ isovector transition density (and a weak current term) so that (e,e') experiments yield a relatively reliable measure of the transition density sampled by (p,p').

Figure 11 shows a comparison between the calculated and measured (p,p') cross sections at $E_p = 122$ MeV. The experimental cross sections are not well described in the DWIA. The large and predominantly isovector tensor force, which was derived from the Sussex oscillator matrix elements and which also describes the N-N t matrix reasonably well, overestimates the cross sections at small angles without reproducing the shoulder in the experimental cross section near 40°. Figure 11 also illustrates the strong sensitivity of this transition (unlike most $T=1$ transitions) to the particular representation of the tensor part of the t matrix. In particular the curve labeled $C+LS+T'$, for which the tensor interaction was obtained from a detailed fit[4] to the momentum components ($q \lesssim 2$ fm^{-1}) of the t matrix, describes the shape of the experimental cross section quite well forward of 30°. This angle corresponds to $q \sim 1.2$ fm^{-1}, just where $|F_T(q)|^2$ has a strong minimum. The magnitude of the calculated cross section forward of 30° is, however, still too large by 50–60%.

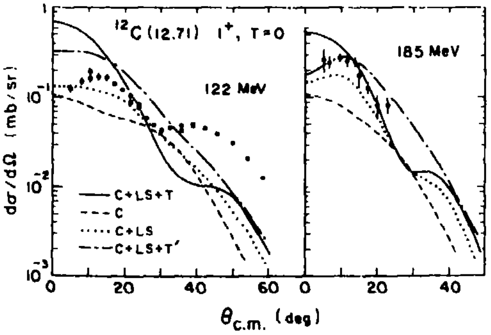

FIG. 11. Comparison of DWIA calculations and data for the 12.71-MeV transition in ^{12}C. See also the caption for Fig. 8. The dash-dot curve shows the result of a calculation that used the "detailed-fit" tensor interaction (T'). Renormalization of that curve by 0.64 would cause it to pass through most data points out to 30°.

Since the tensor force contributes primarily through the exchange terms for this state, the difference between the two tensor forces considered is likely due to their differences near $q \sim 2.2$ fm^{-1} where the Sussex-based ("detailed fit") tensor force is larger (smaller) than the actual N-N t matrix. Except for the 2.31-MeV transition in ^{14}N, none of the other transitions considered here are particularly sensitive to the choice of tensor force in this range of momentum transfer.

Analogous calculations have been made at 185 MeV and these are compared with experimental data in Fig. 11. At this energy, where only forward angle data are available, a reasonable description of the data is obtained without renormalization. The shape of the cross section is also reasonably well reproduced, with a preference for the Sussex-based tensor force for $\theta_{c.m.} \gtrsim 15°$. At smaller angles ($\theta_{c.m.} \lesssim 10°$) the "detailed fit" tensor force is clearly preferred. As is seen in Fig. 11, the *shape* of the experimental cross section is given best with no tensor force; in this case the magnitude is 50% too small. The difference in normalizations required at the two energies studied here is not understood but may reflect the decreasing importance of multistep processes with increasing bombarding energy. This is discussed further in Sec. V B. The predicted asymmetries for each of the tensor forces considered here are relatively large and good data should discriminate between them.

E. The states of ^{14}N

1. The 0^+ state at 2.31 MeV

At first glance the transition to this state should be rather like that for the 15.11-MeV state in ^{12}C since the transfer quantum numbers ($S=T=1$) are the same and the same parts of V^{eff} can contribute. However, this transition is known[14,35] to be quite sensitive to the isovector part of the tensor force and is therefore especially suitable for testing that portion of V^{eff}.

The sensitivity arises from the extremely small transition density at small momentum transfers, where the central part of V^{eff} dominates, together with the relatively greater importance of the tensor part of V^{eff} at larger momentum transfers.[4,36] This is an essential property of any wave function that is consistent with the strongly inhibited Gamow-Teller matrix element for the analogous β decay of ^{14}C.

This property is illustrated in Fig. 12 where the quantity

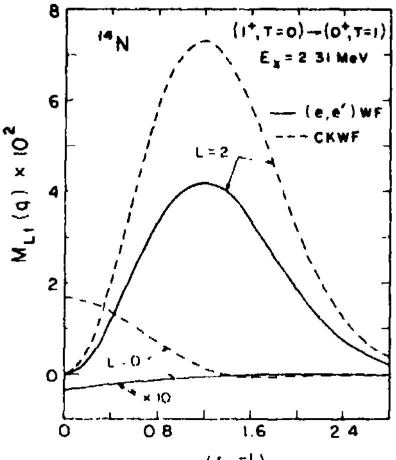

FIG. 12. The transition density in momentum space for the 2.31-MeV transition in ^{14}N. Shown are $L=0$ and 2 components for the CKWF and the wave functions given in Ref. 19. The $L=0$ component of the latter has been multiplied by an extra factor of 10.

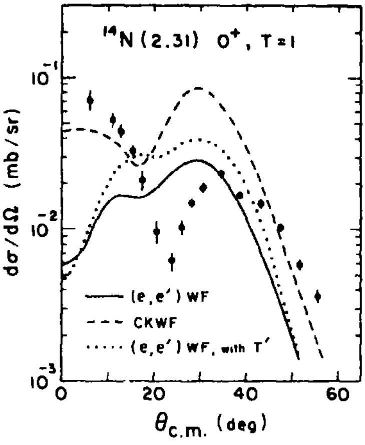

FIG. 13. Comparison of DWIA calculations and data for the 2.31-MeV transition in ^{14}N. See also the captions for Figs. 8, 11, and 12.

$$M_{LJ}(q)=\left\langle J_f \left\| \sum_i j_L(qr_i)T_{L1J}(\Omega_i,\vec{\sigma}_i)\tau_{iz}\right\| J_i\right\rangle \quad (4)$$

is plotted in arbitrary units for both the CKWF and the more recent wave functions deduced from electron scattering.[20] The oscillator parameter of 0.588 fm^{-1} is not well determined. The tensor T_{L1J} is constructed from a spherical harmonic of rank L and a Pauli spin operator. M_{LJ} is proportional to that part of the transverse-magnetic form factor for electron scattering which may be attributed to the spin density. The amplitude for each orbital (L) and total (J) angular momentum transfer to the target in the (p,p') reaction is proportional to M_{LJ}. Here $J=1$ with $L=0, 2$. The wave functions deduced from electron scattering[20] (and other constraints) are seen to yield $L=0$ and $L=2$ transition densities that are considerably weaker than those of the CKWF. The latter are known to overestimate both the (e,e') cross section and the $L=0$ β-decay rate.

In Fig. 13 the (p,p') cross sections at $E_p = 122$ MeV are compared with DWIA calculations for each set of wave functions described above. Auxiliary calculations show that the central exchange contributions cancel about 95% of the central direct cross section and the $L=2$ transfers to the projectile[36] are rather small. The angular distribution at this stage is relatively flat out to about 30-35°. Interference with the tensor force produces the minimum in the 15–20° region. Near $\theta_{c.m.} \sim 30°$ ($q \simeq 1.3$ fm^{-1}) the contribution of the tensor force is roughly 5 times that of the central force. Although none of the results are very satisfactory, the magnitude of the second peak is only given correctly when the wave functions constrained by (e,e') are used. This is a direct consequence of the relative sizes of $M_{21}(q)$ for the two sets of wave functions.

At this point it should be stressed that the (e,e') data[20] on which the (e,e') wave functions are based only cover momentum transfers corresponding (in the plane-wave approximation) to scattering angles between ~15° and ~30°, a region where, on the basis of the above calculation for the 1^+ state ^{12}C at 15.11 MeV, the N-N effective interaction used here appears adequate. Unlike the transition in ^{12}C which is dominated at small q by a relatively large $L=0, S=1$ transition density, contributions from multistep processes cannot be ruled out for this weak transition in ^{14}N, particularly for small q where matrix elements involving the nuclear current dominate. That this may in fact be so is discussed in Sec. V B.

There is also noticeable sensitivity to the tensor terms as is shown by the curve in Fig. 13 for the (e,e') wave functions and the "detailed fit" tensor interaction. Unfortunately, the possible interference with multistep processes makes a preferred choice here somewhat difficult.

The inhibition of small-momentum transfers suggests that in using this reaction to test effective forces, relatively greater emphasis should be placed on describing the second maximum. It is worth noting that this maximum appears at a constant momentum transfer 1.5 ± 0.1 fm^{-1} and has a constant cross section 22 ± 2 μb/sr over the range of bombarding energies 30–122 MeV.[37] One may suggest the need for additional (e, e') data for this state out to somewhat larger momentum transfers ($q \gtrsim 2$ fm^{-1}) in order to define the magnitude of the transition density over the peak more precisely.

Effects of admixtures from the $2s$-$1d$ shell were studied by using the extended CKWF (CKSD) given in Tables I and III of Ref. 38. The vanishing Gamow-Teller β-decay matrix element is achieved with these wave functions by strong cancellation between the p-shell and sd-shell contributions so that $M_{01}(q)$ is much smaller for small q than given by the CKWF; the $M_{21}(q)$ for the CKSD is, however, very similar in shape but 0.86 times the size of that for the CKWF. The calculated (p,p') cross section using the CKSD is almost identical in shape to that obtained by using the (e, e') wave functions but is ~2.3 times as large at the peak. This accurately reflects the peak values of the corresponding $M_{21}(q)$ but still yields a poor description of the data.

2. The 1⁺ state at 3.95 MeV

This transition is perhaps the most complicated of all. Since it is between two 1^+ states, three J transfers are allowed. However, the $J=2$ contribution is much larger than that for $J=1$ and the $J=0$ contribution is negligible. Both the V_0 and V_σ parts of the V^{eff} can contribute, as well as the V_{LS} and $V_{T_{\text{e}}}$ terms.

The $J=2$ transition density is roughly 30% larger for $S=1$ than for $S=0$. This is in sharp contrast with the excitation of the 2^+ $T=0$ state in ^{12}C at 4.44 MeV where the CKWF give an $S=1$ transition density that is negligible compared to that for $S=0$. The situation is reminiscent of the 16.11-MeV transition in ^{12}C. An important difference, however, is that the ^{14}N transition is isoscalar and V_σ is much weaker than V_0 so that sensitivity to the $S=1$ transition density is not very large. In summary, then, the 3.95-MeV transition in ^{14}N might be expected to be reasonably similar to the 4.44-MeV transition in ^{12}C.

Empirically, the peak cross sections for these two states imply $B(E2)\uparrow \approx 3.5\ e^2$ fm^4 for the ^{14}N transition, based on a value[17] $B(E2)\uparrow = 39\ e^2$ fm^4 for the 4.44-MeV transition in ^{12}C. The recent (e, e') experiment of Ensslin *et al.*[29] yielded $B(E2)\uparrow = 3.4 \pm 0.3\ e^2$ fm^4 for ^{14}N. An independent lifetime measurement,[39] together with known $M1/E2$ mixing ratios and branching ratios,[40] resulted in a value $3.3 \pm 0.2\ e^2$ fm^4. The CKWF used here give $B(E2)\uparrow = 1.7\ e^2$ fm^4 so that an upward renormalization of the (p,p') calculations by a value of about 2 is expected.

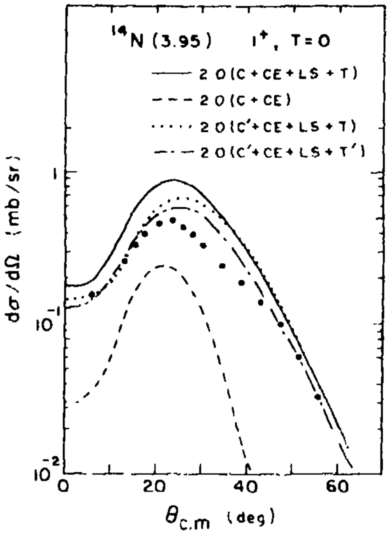

FIG. 14. Comparison of DWIA calculations and data for the 3.95-MeV transition in ^{14}N. See also the captions for Figs. 8, 10, and 11.

In Fig. 14 an enhancement of the calculated cross section (solid curve) by only 10% would have been required to match the experimental cross section. The shape of the angular distribution is reasonably well reproduced. Just as for the 4.44-MeV state in ^{12}C, calculations have also been made in which the imaginary coupling was reduced by a factor of 2. The shape of the calculated cross section is slightly worse, but the magnitude is in better agreement with the data.

The dashed curve in Fig. 14 shows the calculated cross section when the "detailed fit" tensor force is used and the imaginary coupling is also reduced by a factor of 2. This gives the best agreement of all. Until the $S=1, J=2$ part of the transition density and the large-momentum components of the tensor force are better understood it is difficult to draw more definitive conclusions. An (e, e') measurement of the transverse $E2$ form factor could in principle give more precise information on the $S=1$ part of the transition density, but this would likely be dominated by the $M1$ component.

V. ADDITIONAL CONSIDERATIONS

A. Simpler approaches

The magnitude and complexity of the calculations in Sec. IV raise the question whether a simpler approach might be possible. It has already been made clear that accurate wave functions are essential. Indeed it is the purpose of such studies eventually to learn more details about nuclear wave functions. Since the exact treatment of knockon exchange is the most time-consuming part of these calculations, it might be hoped that an appropriate pseudopotential for use in conventional computer programs might be sufficiently accurate. Such approaches are also necessary for investigating the importance of more complex reaction mechanisms.

Following Austin,[34] it is attractive to consider a simple N-N interaction consisting of a real, central interaction with a Yukawa radial dependence having a range of 1 fm. The strengths and volume integrals needed to fit the cross sections of the four states of ^{12}C discussed in Sec. IV are listed in Table III. The CK wave functions were used. The calculated curves were normalized to the data for the best overall visual agreement for angles less than about 35°. The fits are quite satisfactory in this range for all but the 12.71-MeV state. The calculated curve for this resembles the solid curve in Fig. 11 and it was normalized similarly.

For comparison a Gaussian radial dependence $\sim\exp(-r^2/b^2)$ with b 1.8 fm was also tried. This value of the range parameter produces about the same mean-square radii as the Yukawa interaction. The calculated angular distributions for the 2^+ states peak at 20° and fall off more rapidly than for the Yukawa case so the fitting was confined to smaller angles. The interaction strengths are again listed in Table III.

Unfortunately, while this approach is useful at lower energies, it is of dubious validity here. It has been shown that the spin-orbit and tensor parts of the N-N interaction are quite important at intermediate energies for most of these transitions so that the phenomenological extraction of strengths is subject to much uncertainty. Furthermore, no Yukawa or Gaussian form with a single range can come close to reproducing the shape of the 12.71-MeV transition. Even in zero range, the calculated curve decreased much too steeply at forward angles. Sophisticated treatments of the radial dependence are therefore essential.

TABLE III. Strengths (MeV) of a simple 1-fm Yukawa or 1.8-fm Gaussian interaction for inelastic proton scattering to states of ^{12}C. Volume integrals in units MeV fm^3 are given in parentheses. Core-polarization enhancement factors (see Sec. IV) have not been factored from the numbers.

Term	Excitation energy	Yukawa	Gaussian
V_0	4.44	45 (570)	18 (580)
V_σ	12.71	~14 (180)	~6 (190)
V_τ	16.11	17 (210)	6.7 (210)
$V_{\sigma\tau}$	15.11	14 (180)	6.0 (190)

It might be possible, however, to use the microscopic interaction described in Sec. IV in computer codes that do not evaluate the exchange contributions exactly and to use an appropriate pseudopotential[4,41,42] for these. To explore this issue many of the above calculations were repeated with the programs DWUCK4 and CHUCK3.[43] The exchange pseudopotential was available only for the central part of V^{eff}. The tensor interaction was also slightly different from that in Sec. IV since these programs use a regularized OPEP form. Neither program has a microscopic $\vec{L}\cdot\vec{S}$ interaction, although DWUCK4 had been modified to handle a deformed-spin-orbit coupling potential in the Oak Ridge form.[44]

In general this approach was moderately successful. It became clear though that no shortcuts were possible. Both the even and odd parts of the two-body interaction were necessary, as were also the exchange pseudopotential, the imaginary parts of the form factors, the tensor interaction, and all L and S transfers. In specific cases some of these ingredients were not too important, but it is hard to know these cases in advance.

The best representation was for the 15.11-MeV transition in ^{12}C. Here the imaginary form factor was small. The exchange terms reduced the cross section due to the central direct terms by about an order of magnitude, reflecting the inclusion of odd-state forces. The tensor terms fine tuned the shape by allowing projectile $L=2$ amplitudes to contribute slightly. With everything included the calculations were nearly identical to the results of the DWBA70 program. It thus seems that such an approach may be feasible for transitions dominated by the OPE process. Even the 2.31-MeV transition in ^{14}N was reproduced nearly perfectly for angles >20°. At smaller angles, the dip near 15° was deeper and the 0° cross section was larger.

The situation was not so good for the 2^+ excitations in ^{12}C. Also, the worst case was the 12.71-MeV isoscalar spin-flip transition. Here the final cross sections were an order of magnitude below the DWBA70 calculations, although the angular dependence was similar. It is difficult to assess the reasons for the difficulties. It is known, however, that the exchange contributions of the tensor interaction are frequently very important. They could not be included in these alternate calculations.

Since a microscopic $\vec{L}\cdot\vec{S}$ interaction was not available in these programs, consideration was given to the use of a collective spin-orbit coupling potential. Figure 15 shows a comparison of central and spin-orbit cross sections for the 2^+ $T=0$ state of ^{12}C as calculated with the collective and microscopic models. The deformed spin-orbit potential

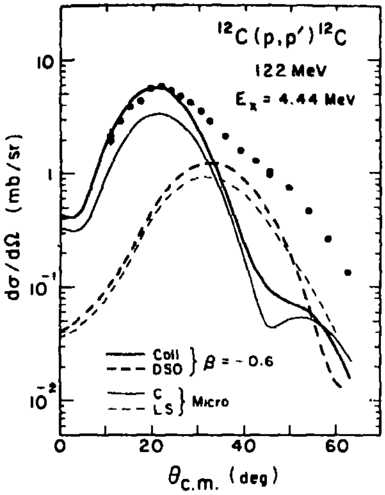

FIG. 15. Results of collective-model and microscopic-model calculations of the cross sections for the central and spin-orbit contributions to the excitation of the 4.44-MeV state in ^{12}C. A deformation parameter $\beta = -0.6$ was used for the collective model.

was of the full Thomas form. The Oak Ridge form[44] produced a distinctively different shape and the combined result was rather less satisfactory.

It should be stressed that all comparisons were made with respect to cross sections. The moderate success in this regard does not extend to polarizations. For these the full treatment, with the $\vec{L}\cdot\vec{S}$ interaction, is essential.

B. Multistep processes

A final concern in the comparison of theory with experiment is the possibility of multistep processes. It is argued in Ref. 21 that, at intermediate energies, an optical potential that fits proton elastic-scattering data embodies many effects of the couplings to other channels. Nevertheless, individual features of some multistep processes may still remain.

Two types of multistep processes were considered. In the first case, cross sections for the 1^+ states in ^{12}C were computed for excitations that proceeded through the strong 2^+ $T=0$ state. The CKWF were used throughout and the amplitude for the 0^+-2^+ step was renormalized in order to match the experimental cross sections. Also, the V_σ interaction for the $2^+\rightarrow 1^+$ $(T=0)$ step was adjusted to increase the cross sections by compensating for the deficiency noted in Sec. V A. These calculations produced at most 4 and 2 μb/sr at 0° for the 12.71- and 15.11-MeV states, respectively, several orders of magnitude below the data.

The second case dealt with pickup-stripping processes through the states of ^{11}C or ^{13}N. The CKWF were used for all spectroscopic amplitudes. A folded potential of the Johnson-Soper type[45] was used for the deuteron channels, with parameters based on the energy systematics[21] of proton scattering from ^{12}C. These zero-range calculations included the common correction terms for nonlocality and finite range with parameters selected in accordance with exact finite-range calculations of the ^{12}C$(p,d)^{11}$C ground-state transition. Even though experimental cross sections[46] for the (p,d) reaction were reproduced well, there is no assurance that the two-step calculations have the correct magnitude. Quite possibly they are overestimated due to finite-range and nonorthogonality effects.[47]

The shapes of the (p,d,p) two-step cross sections at 122 MeV were typically peaked at 0° and fell off fairly rapidly with angle, much like one-step (p,d) cross sections. There was generally a fair amount of cancellation among the paths through different intermediate states (three states in ^{11}C and five in ^{13}N). Maximum cross sections of about 60, 100, and 70 μb/sr were found for the states at 12.71, 15.11, and 16.11 MeV in ^{12}C, respectively, with these being at 0° for the 1^+ states and 23° for the 2^+ state. For ^{14}N the maximum two-step cross section was about 15 μb/sr for angles less than 20°.

It is clear that while the two-step cross sections are not large, they could be important for the 12.71- and 2.31-MeV transitions. These are the ones described least well by the DWIA calculations. Even the 2^+ $T=1$ state in ^{12}C may not be free of concern. Since the transition amplitudes computed by the DWBA70 program are in a different (i.e., helicity) convention from that of CHUCK3, interference effects have not been explored in detail. Preliminary studies with the one-step amplitudes as represented by CHUCK3 indicate that some improvements in fitting the data are possible. Uncertainties about the details of the (p,d,p) calculations as well as about the accuracy of the complex phases in the CHUCK3 representation of the one-step paths preclude further conclusions at this time.

VI. SUMMARY AND CONCLUSIONS

The DWIA calculations of the ^{12}C$(p,p')^{12}$C cross sections are based on several implicit experimental constraints: (a) The effective t matrix is taken from phase-shift fits to N-N scattering data; (b) the shell-model effective interaction is determined by fitting to experimental energy levels; (c) the optical-model parameters are determined by fitting proton elastic-scattering data; (d) bound-state harmonic-oscillator parameters are determined from (e, e') data of longitudinal and transverse form factors; and (e) renormalizations have been made to correct for known deficiencies of the shell-model wave functions. Within this environment the calculations have no adjustable parameters. The comparisons with data are remarkably good and satisfying, particularly over the range of momentum transfer where the wave functions are in good accord with electron-scattering form factors. Apart from known deficiencies (see Sec. IVD1), the impulse approximation seems to work rather well.

The best agreement occurs for the $V_{\sigma\tau}$ part of $V^{\rm eff}$, which is dominated by the OPE process, at least for momentum transfers $q \lesssim 1.5$ fm^{-1}. The V_0 and tensor parts also seem to be described fairly well. The enhancement factor required to match the data for the 2^+ $T = 0$ state of ^{12}C is related primarily to the truncation of the shell-model space to the 1p shell,[32] although there is good reason to believe that the imaginary part of V_0 is too large. The tensor terms of the effective interaction plays an important role in the excitation of the 16.11-MeV state in ^{12}C and the 2.31-MeV state in ^{14}N. In both cases there are also important contributions from other terms and some uncertainty about the precise wave functions.

The study here does not shed much light on the V_τ and V_σ interactions. The former might be expected to be most important for the 16.11-MeV transition, but it turns out that, with the CKWF, the $S = 1$ transition density and $V_{\sigma\tau}$ terms dominate. It appears, however, not to be far from correct. The coordinate-space representation of the $S = 1$, $T = 0$ two-body interaction is poorly determined and is quite noisy. The volume integral of the real part is quite small and its mean square radius is negative.[4] The calculations for the 12.71-MeV state in ^{12}C are not very satisfactory, although there is substantial sensitivity to the tensor force and probably also to (p, d, p) multistep contributions.

It is unfortunate that knockon exchange is still an important consideration at these energies. Calculations that use a pseudopotential were moderately successful for cross sections but not for polarization quantities. The exchange contributions should decrease at higher energies and it is possible that the tensor and spin-orbit terms may eventually decrease also.

Additional (e, e') data for large q would be very beneficial in order to provide a more thorough foundation for the (p, p') calculations. Also (p, p') data on ^{12}C and ^{14}N in the 200–400 MeV range would provide a basis for useful extensions of techniques described here. There is some reason to hope that multistep processes[21] and exchange terms will be less important there and that the sensitivity to the ingredients of $V^{\rm eff}$ will be more direct. If so, our knowledge and understanding of effective interactions should be enriched considerably.

ACKNOWLEDGMENTS

This work was supported in part by the National Science Foundation under Grants Nos. PHY76-84033, PHY76-23468, PHY77-24134, and PHY78-22696. Additional support for computations was provided by the University of Georgia, the University of Pittsburgh, and Oak Ridge National Laboratory. We are indebted to F. Petrovich for helpful discussions regarding the electron scattering, to the University of Massachusetts electron-scattering group for providing numerical values of the (e, e') form factors, and to J. B. McGrory for providing the CKWF in a convenient form.

---

[*] Present address: Indiana University Cyclotron Facility, Bloomington, Ind. 47401.

[1] J. P. Jeukenne, A. Lejeune, and C. Mahaux, Phys. Rep. 25C, 83 (1976); Phys. Rev. C 16, 80 (1977).

[2] F. A. Brieva and J. R. Rook, Nucl. Phys. A291, 299, 317 (1977); A297, 206 (1978); A307, 493 (1978).

[3] G. Bertsch, J. Borysowicz, H. McManus, and W. G. Love, Nucl. Phys. A284, 399 (1977).

[4] W. G. Love, in *Proceedings of the Conference on (p, n) Reactions and the Nucleon-Nucleon Force, Telluride, Colorado, 1979*, edited by C. D. Goodman, S. M. Austin, S. T. Bloom, J. R. Rapaport, and G. R. Satchler (Plenum, New York, 1980), p. 23.

[5] J. R. Comfort, in *Proceedings of INS International Symposium on Nuclear Direct Reaction Mechanism, Fukuoka, Japan, 1978*, edited by M. Tanifuji and K. Yazaki (INS, University of Tokyo, 1979), p. 118.

[6] K. A. Amos, H. V. Geramb, R. Sprickmann, J. Arvieux, M. Buenerd, and G. Perrin, Phys. Lett. 52B, 138 (1974).

[7] A. K. Kerman, H. McManus, and R. M. Thaler, Ann. Phys. (N.Y.) 8, 551 (1959).

[8] D. Hasselgren, P. U. Renberg, O. Sundberg, and G. Tibell, Nucl. Phys. 69, 81 (1965).

[9] A. Ingemarsson, O. Jonsson, and A. Hallgren, Nucl. Phys. A319, 377 (1979).

[10] R. M. Haybron and H. McManus, Phys. Rev. 136, B1730 (1964).

[11] R. M. Haybron, M. B. Johnson, and R. J. Metzger, Phys. Rev. 156, 1136 (1967).

[12] H. K. Lee and H. McManus, Phys. Rev. 161, 1087 (1967).

[13] M. Buenerd, Phys. Rev. C 13, 444 (1976).

[14] V. C. Officer, R. S. Henderson, and I. D. Svalbe, Bull. Am. Phys. Soc. 20, 1169 (1975).

[15] R. Kouzes and A. Broad, I.U.C.F. Internal Report No. 75-6 (unpublished).

[16] P. Schwandt, private communication.

[17] F. Ajzenberg-Selove, Nucl. Phys. A248, 1 (1975).

[18] M. Buenerd, P. Martin, P. deSaintignon, and J. M. Loiseaux, Nucl. Phys. A286, 377 (1977).

[19] K. T. Knöpfle, G. J. Wagner, A. Kiss, M. Rogge, C. Mayer-Böricke, and Th. Bauer, Phys. Lett. 64B, 263 (1976).

[20] See AIP document No. PAPS PRVCA 21-2147-20 for 20 pages of differential cross-section data. Order by PAPS number and journal reference from American Institute of Physics, Physics Auxiliary Publications Service, 335 East 45th Street, New York, New York 10017. The price is $1.50 for microfiche or $5.00 for photocopies. Airmail is additional. Make checks payable to the American Institute of Physics.

[21] J. R. Comfort and B. C. Karp, Phys. Rev. C 21, 2162 (1980).

[22] G. R. Satchler, Nucl. Phys. A100, 481 497 (1967).

[23] W. G. Love, A. Scott, F. T. Baker, W. P. Jones, and J. D. Wiggins, Jr., Phys. Letters 73B, 277 (1978).

[24] M. H. MacGregor, R. A. Arndt, and R. M. Wright, Phys. Rev. 182, 1714 (1969).

[25] A. Picklesimer and G. E. Walker, Phys. Rev. C 17, 237 (1978).

[26] R. Schaeffer and J. Raynal (unpublished).

[27] J. B. Flanz, R. S. Hicks, R. A. Lindgren, G. A. Peterson, A. Hotta, B. Parker, and R. C. York, Phys. Rev. Lett. 41, 1642 (1978) and references therein; G. A. Peterson and R. A. Lindgren, private communication.

[28] S. Cohen and D. Kurath, Nucl. Phys. 73, 1 (1965).

[29] N. Ensslin, W. Bertozzi, S. Kowalski, C. P. Sargent, W. Turchinetz, C. F. Williamson, S. P. Fivozinsky, J. W. Lightbody, Jr., and S. Penner, Phys. Rev. C 9, 1705 (1974).

[30] E. G. Adelberger, R. E. Marrs, K. A. Snover, and J. E. Bussoletti, Phys. Rev. C 15, 484 (1977).

[31] A. Friebel, P. Manakos, A. Richter, E. Spamer, W. Stock, and O. Titze, Nucl. Phys. A294, 129 (1978).

[32] K. Amos and I. Morrison, Phys. Rev. C19, 2108 (1979).

[33] F. E. Cecil, L. W. Fagg, W. L. Bendel, and E. C. Jones, Jr., Phys. Rev. C 9, 798 (1974).

[34] S. M. Austin, in *The Two-Body Force in Nuclei*, edited by S. M. Austin and G. M. Crawley (Plenum, New York, 1972), p. 285. See also Ref. 4, p. 203.

[35] G. M. Crawley, S. M. Austin, W. Benenson, V. A. Madsen, F. A. Schmittroth, and M. J. Stomp, Phys. Lett. 32B, 92 (1970).

[36] W. G. Love and L. J. Parish, Nucl. Phys. A157, 625 (1970).

[37] Sam M. Austin and S. H. Fox, in *Proceedings of the International Conference on Nuclear Physics, Munich, Germany*, edited by J. deBoer and H. J. Mang (North-Holland, Amsterdam, 1973), Vol. I, p. 388.

[38] H. J. Rose, O. Häusser, and E. K. Warburton, Rev. Mod. Phys. 40, 591 (1968).

[39] M. Bister, A. Anttila, and J. Keinonen, Phys. Rev. C 16, 1303 (1977).

[40] J. W. Olness, A. R. Poletti, and E. K. Warburton, Phys. Rev. 154, 971 (1967).

[41] F. Petrovich, H. McManus, V. A. Madsen, and J. Atkinson, Phys. Rev. Lett. 22, 895 (1969).

[42] W. G. Love, Nucl. Phys. A312, 160 (1978).

[43] P. D. Kunz (unpublished); extended versions of J. R. Comfort.

[44] M. P. Fricke, R. M. Drisko, R. H. Bassel, E. E. Gross, B. J. Morton, and A. Zucker, Phys. Rev. Lett. 16, 746 (1966).

[45] R. C. Johnson and P. J. R. Soper, Phys. Rev. C 1, 976 (1970).

[46] J. R. Shepard, R. E. Anderson, J. J. Kraushaar, and J. R. Comfort (unpublished).

[47] P. D. Kunz and L. A. Charlton, Phys. Lett. 61B, 1 (1976).

PHYSICAL REVIEW C VOLUME 21, NUMBER 6 JUNE 1980

Scattering and reaction dynamics for the ^{12}C+p system

J. R. Comfort and B. C. Karp

Department of Physics and Astronomy, University of Pittsburgh, Pittsburgh, Pennsylvania 15260

(Received 1 October 1979)

Elastic scattering data for proton scattering from ^{12}C are analyzed phenomenologically by use of local, complex, one-channel optical-model potentials and in an extended coupled-reaction-channel environment. Although the back-coupling amplitudes in the elastic channel from pickup-stripping paths through ^{11}C intermediate states are found to be quite sizable, the optical-model potential is able to simulate most of the effects quite well for both scattering and reaction processes at energies greater than about 60 MeV. The parameters of the optical-model potential and the residual optical-model potential of the coupled-reaction-channel environment are found to vary smoothly with energy. Below 60 MeV, these parameters have quite different trends and the ability of the one-channel optical-model potential to simulate the singular effects of strong couplings is much reduced.

NUCLEAR REACTIONS ^{12}C+p system, energies up to 185 MeV; optical-model phenomenological analysis; coupled-reaction-channel analysis; comparison with DWBA calculations.

I. INTRODUCTION

The recent extension of high-quality nuclear reaction experiments to intermediate energies raises many issues regarding the reaction mechanisms. For convenience it is hoped that many of the tools and techniques developed for low-energy applications, such as local, phenomenological, optical-model potentials (OMP), partial-wave expansions, and coordinate-space representations, might be readily extended to the higher energies. Conversely, one might also hope that certain difficulties such as exchange contributions and coupled-channels effects might be reduced so that the data will be more sensitive to the nuclear-structure information inherent in reaction processes at higher momentum transfers. Since it is known, for example, that deuteron D-state contributions for (p,d) or (d,p) reactions are beginning to become important at these energies,[1] the hopes can never be fully realized. Careful studies of the significant ingredients to the reaction dynamics are therefore required.

Reactions on ^{12}C can provide an excellent opportunity for such studies. The number of states in this nucleus and its neighbors is small enough to make many calculations feasible and much information is available about the wave functions. The extensive and very satisfying analysis of 122-MeV (p,p') data from ^{12}C and ^{14}N in the preceding article[2] illustrates quite well the possibilities that are available here. Indeed, the present article arose out of the need for a reliable treatment of the reaction dynamics in that analysis of effective interactions.

It has often been argued, of course, that the large permanent deformation of ^{12}C and the consequent strong couplings to excited states in inelastic scattering processes makes reaction analyses unreliable. We find, however, that these couplings are by far not the most important ones. Yet, as the energy increases, the disturbing effects of all the couplings decrease and, at intermediate energies, ^{12}C is as tractable for study as other nuclei.

At issue here is the ability of the local, one-channel, phenomenological OMP to represent the implicit effects of couplings between the elastic and reaction channels on scattering and reaction cross sections. This, of course, is the principal role of the imaginary part of the complex OMP, although the real part must make some contributions as well.[3,4] An understanding of this role will enhance our knowledge of the OMP itself, particularly with respect to its microscopic foundations. It should also enhance our confidence in calculations of reaction dynamics and in the inferences of nuclear properties based on parametrizations of empirical potentials.

Remarkable progress has been made recently[5,6] on the microscopic foundations of the OMP and this has elucidated many of the features of the phenomenological potentials. In these works both the real and imaginary parts arise naturally from the construction of the complex two-nucleon t matrix (or G matrix) in nuclear matter. This *a priori* approach has been unusually successful in reproducing elastic scattering data, but the relationship of the OMP so constructed to channel couplings is not at all transparent.

An alternative approach, particularly for the

© 1980 The American Physical Society

imaginary part, might be the direct calculation of the ingredients of the OMP from a realistic treatment of reaction processes.[7] This would involve specific assumptions regarding the detailed structure of the nucleus of interest and its neighbors, as well as a thorough calculation of the reaction dynamics, possibly with an exact solution of the coupled equations. Since the channel space must necessarily be truncated, the remaining OMP must still be adjusted to fit empirical data and will remain complex. We shall refer to this as a residual OMP (ROMP). It is defined for use in an extended mutichannel environment.

A one-channel OMP might be said to be equivalent to a ROMP (each with its appropriate environment) if they reproduce elastic scattering data equally well. The use of one-channel OMP's in distorted-wave Born-approximation (DWBA) calculations of particular reactions is an extension of this equivalence and the general success of this approach provides support for it. Nevertheless, it is entirely possible that, due to their strengths, certain individual channel couplings may have a singular influence on elastic scattering and/or reaction cross sections and that this cannot be simulated reliably by an average local OMP. The frequent use of multistep and coupled-channel (CC) calculations for reactions attests to these singular influences in many instances.

It is not easy to obtain information on such questions. Mackintosh has made extensive studies on heavier nuclei and at energies below 50 MeV.[3,4,8] He has considered environments in which the elastic channel is strongly coupled to both inelastic scattering and pickup channels. Valuable insights have come from the demand that the ROMP's give the same elastic scattering as a conventional OMP. The present article is similar in approach. Although much of the work was developed independently, and benefited from the use of automatic search procedures,[9] many of the general conclusions are the same.

The present work is devoted to an intensive and systematic study of the dynamics of proton induced reactions on ^{12}C at intermediate energies. Elastic scattering data are taken from the literature for energies up to 185 MeV, with the primary emphasis in the range 60–185 MeV. Although there are considerable data at lower energies, they have been given little attention here. The concern is mainly for intermediate energies. As will become clear in Secs. IV and V, numerous difficulties are also encountered in the lower range.

After a conventional analysis in terms of the conventional one-channel optical model (OM), attention is given to a vigorous treatment of a coupled-channel environment within the framework of a specific model. The scattering data are refitted in this environment. Conclusions may be reached regarding the energy dependence of the parameters of the OMP and ROMP as well as for the specific importance of the coupled channels. Reports on portions of this work have already been given.[10-12]

II. DATA SELECTION

A. General considerations

Examination of the literature reveals that data for proton scattering from ^{12}C are available at a number of energies between 60 and 185 MeV, but are of diverse vintage and quality. Our interest was not in making a global analysis of all the data, but rather in more detailed studies at selected energies spread smoothly across the range. Preliminary inspections suggested that the best data were available near 60, 120, and 180 MeV. Data at some values more closely spaced were also desired.

In the literature it is not always unambiguously clear whether the data are presented in laboratory or center-of-mass frames and, if the latter, whether relativistic or nonrelativistic kinematics were used for the conversion. The questions could usually be resolved by detailed numerical inspection. We adopted the policy of tabulating absolute center-of-mass cross sections with nonrelativistic kinematics used for the conversion for energies below 80 MeV, and relativistic kinematics above 80 MeV. This corresponds to common historical practice, but necessitated adjustments of some of the data sets.

In order to gauge the reliability of the available data, the absolute cross sections for the various data sets were plotted against momentum transfer q. The data thought to be the most reliable then revealed a systematic pattern, particularly in the range $50 \leq q \leq 150$ MeV/c. (For orientation, the first maximum in the ratio-to-Rutherford cross section occurs at $q = 155 \pm 5$ MeV/c for all energies above 40 MeV). This pattern allowed judgments to be formed about the other data, as will be indicated in Sec. II B.

Since studies of optical-model parameters normally benefit from polarization data, an effort was made to find energies where both cross-section and polarization data existed. There have been few polarization measurements at intermediate energies and they are often at energies where the differential cross sections seem less reliable. Since the search program[9] required identical energies for simultaneous fitting, the polarization data at some energies were used for other energies by changing the angle scale according to the relation $\theta\sqrt{E}$ = constant. Test calculations indicated that this assumption was reasonable for the individual cases. In practice, the polarization data were not a strong constraint on the results of the search procedures.

Since the model space for the CC calculations included inelastic scattering and pickup channels, data for (p,p') and (p,d) reactions on ^{12}C were also obtained whenever possible. Tabulations were often not available, but the cross sections could be read from graphs with sufficient accuracy.

Apart from the above considerations, the data were taken as given in the literature. In particular, no adjustments were made to the errors so as to take into account the uncertainties in scattering angles. Absolute values for the goodness-of-fit parameter χ^2 may therefore not have much significance. The emphasis of the present study is on systematic trends. At each energy an effort was made to minimize χ^2.

B. Individual choices

Although our principal interest was in energies above 60 MeV, a partial study was also made at 40 MeV. Following is a brief discussion of the data and adjustments made to them.

1. 12.07 and 21.65 MeV

Since the CC analyses also required proton OMP's at substantially lower energies, data for 12.07 and 21.65 MeV were selected specifically for this purpose. The systematic study of differential cross sections by Nagahara[13] was used for 12.07 MeV. Cross sections have been measured at 21.6 MeV (Ref. 14) and polarizations at 21.7 MeV.[15]

2. 40.0 MeV

Both differential cross sections and polarizations have been measured by Blumberg *et al.* for several nuclei at 40 MeV.[16] The data are closely spaced and extend over the full angular range.

3. 61.4 MeV

Elastic scattering cross sections out to about 110° have been reported by Fulmer *et al.* at 61.4 MeV.[17] Although polarization data were not available, (d,p) data have been published for 65 MeV.[18]

4. 96 MeV

Cross-section data at 96 MeV (Ref. 19) are mainly concentrated at angles $\leq 30°$, but numerous data points extend to almost 90°. Nonrelativistic kinematics had originally been used for the center-of-mass tabulation,[19] which was also given in ratio to the Rutherford cross section. Comparisons with the 95-MeV data of Dickson and Salter[20] indicate that their cross sections are consistently low by about 15%. Data at 100 MeV[21] are untabulated. Neither set of data was used.

5. 122 MeV

Differential cross sections for elastic scattering were reported in Ref. 2. Polarization angular distributions are in the process of being measured[22] and the data of Dickson and Salter[20] for 135-MeV protons were extrapolated to this energy. Measurements of the (p,d) and (p,p') cross sections are also available.[2,23]

6. 135 MeV

The systematic trends of the q-space plots suggested that the 135-MeV differential cross sections of Dickson and Salter[20] were low by 15–20%, as was also the case for their 95-MeV data. This exceeds their quoted uncertainty of 7%. Since the angles were tabulated for the laboratory reference frame, it was assumed that the cross sections were also, although the Jacobian for the center-of-mass transformation could account for the discrepancy. When multiplied by 1.15, the cross sections gave good agreement with systematic trends. Since the polarization data seemed valuable to have, the data were used in this modified form.

7. 144 MeV

Very accurate differential cross sections are available for $\theta < 20°$ at 144 MeV.[24] Data also exist for $\theta > 20°$ at 145 MeV,[25] but the errors are substantial and the cross sections do not extrapolate smoothly from the 144-MeV results. Since the 145-MeV data extend to quite large angles, and polarization measurements were also reported,[25] it is unfortunate that they could not be used for more than a qualitative check on the systematics.

8. 150–156 MeV

The systematics of the q-space plots indicate clearly that the 150-MeV differential cross sections of Rolland *et al.*[26] are low by up to 20%, depending on the angle. The measurements of Comparat *et al.*[27] at 156 MeV are untabulated. Again the inability to use the cross sections is regretted since polarization data are available at these energies.[26,28]

9. 183 MeV

Excellent data for elastic scattering cross sections are available at 183 MeV, with a few extra data points for large angles at 177 MeV.[29] A companion paper[30] gives data for total reaction cross sections at the same energy and has a useful graph of their energy dependence. Polarization data were extrapolated from 155 MeV (Ref. 28) since the very recent data at 185 MeV (Ref. 31) were not available at the time of this study. There is very little difference with the extrapolated data. Data for the (p,p') reaction[32] and the (p,d) reaction,[33] both at 185 MeV, are also available.

III. OPTICAL-MODEL ANALYSIS

In this section we consider a conventional analysis in terms of the one-channel optical model. Attention is directed to systematic trends.

A. Optical model

Representing the scattering wave function by a partial-wave expansion in the usual manner, the radial Schrödinger equation to be integrated is

$$\frac{d^2\chi_{lj}(r)}{dr^2}+\left[k^2-\frac{2\mu}{\hbar^2}U(r)-\frac{l(l+1)}{r^2}\right]\chi_{lj}(r)=0\,. \tag{1}$$

$U(r)$ is the local optical potential

$$\begin{aligned}U(r)=V_c(r)+Vf(r)+iWf'(r)+iW'a\frac{d}{dr}f'(r)\\+\frac{1}{r}\left[V_{so}\frac{d}{dr}f_{so}(r)+iW_{so}\frac{d}{dr}f_{so}(r)\right]\vec{l}\cdot\vec{s}\,.\end{aligned} \tag{2}$$

The Coulomb potential

$$V_c(r)=\begin{cases}\dfrac{\eta k}{R_c}(3-r^2/R_c^2) & \text{for } r<R_c\,,\\[2ex] 2\eta k/r & \text{for } r\geq R_c\end{cases} \tag{3}$$

corresponds to a uniformly charged sphere, with $R_c=r_cA^{1/3}$. The complex nuclear potential may contain volume Woods-Saxon potentials of strengths V and W and with radial shapes

$$f(r)=1/(1+e^x)\,,\quad x=(r-R)/a\,,\quad R=r_0A^{1/3}\,, \tag{4a}$$

$$f'(r)=1/(1+e^{x'})\,,\quad x'=(r-R')/a'\,,\quad R'=r'A^{1/3}\,. \tag{4b}$$

Optionally, the imaginary part may have a surface term with strength W' and radial dependence $-e^{x'}/(1+e^{x'})^2$. The radial form $f_{so}(r)$ of the spin-orbit potentials is the same as in Eq. (4) and the usual $(\hbar/m_\pi c)^2$ factor is included in the strengths.

In the automatic parameter search procedures, the program CUPID[9] attempts to minimize χ^2, the measure of goodness of fit defined by

$$\chi^2=\sum_{i=1}^{N}\left(\frac{y_i^{\rm exp}-y_i^{\rm th}}{\Delta y_i^{\rm exp}}\right)^2\,, \tag{5}$$

where $y_i^{\rm exp}$ is the experimental value with error $\Delta y_i^{\rm exp}$ and $y_i^{\rm th}$ is the theoretical value. These may be differential cross sections or polarizations. It is common to report χ^2/N separately for these quantities.

B. Kinematics

As projectile energies increase, relativistic effects become more important. For convenience the nonrelativistic Schrödinger equation may still be used, but it is common to calculate the kinematic quantities k, μ, and η with relativistic expressions.

Convenient relationships are easily found.[34] We let a projectile of mass m and with kinetic energy E be incident on a target with mass M and set $\hbar=c=1$. The total energy of the system is

$$T=[(m+M)^2+2ME]^{1/2} \tag{6}$$

and the center-of-mass wave number is

$$k=(E^2+2Em)^{1/2}M/T\,. \tag{7}$$

The total energies of the particles in the center-of-mass frame are

$$w=(m^2+mM+ME)/T\,, \tag{8a}$$

and

$$W=(M^2+mM+ME)/T\,. \tag{8b}$$

The reduced mass μ is appropriately replaced with the reduced energy

$$\mu=wW/(w+W)\,. \tag{9}$$

Finally, for both forms of the kinematics, the Coulomb parameter is

$$\eta=zZe^2\mu/k\,, \tag{10}$$

where z and Z are the charges of the colliding nuclei and μ has units of energy.

Since the Coulomb cross section is proportional to $(\eta/k)^2$, among other factors, the choice of kinematics affects the ratio-to-Rutherford values. It also affects the conversion between laboratory and center-of-mass frames. Relativistic kinematics were used for all energies above 80 MeV.

One should note that the potentials extracted from the data are defined with respect to the chosen kinematics. They should not be used with the other choice. There are no extra factors and the approximations of a commonly used alternative[35] are avoided.

C. Search procedures

Parameter studies were carried out for each energy separately. These included numerous calculations with different starting values, varying choices of the parameters to be searched, and some calculations with constraints between parameter pairs. When trends and systematic features were noted, these were then adopted and searches were made with fewer parameters. Thus, the final results partly reflect the systematic features and partly the individual characteristics.

Early efforts were devoted to eliminating unnecessary parameters. In order to avoid family ambiguities, the radius of the real potential was fixed at $r_0 = 1.20$ fm (except at 12.07 MeV). This seemed to be the best value at 21 MeV and the data at all higher energies were not very sensitive to it, although some improvements in χ^2 could sometimes be obtained with a slight increase.

Volume absorption seemed reasonable and acceptable at all energies. At 21 MeV, pure surface absorption gave inferior results and mixed surface and volume forms were no improvement over pure volume absorption. Systematic parametrizations for heavier nuclei indicate that volume absorption should dominate at higher energies and be negligible near 12 MeV.[30] For this reason pure surface absorption was used only for the 12.07 MeV data.

The spin-orbit potentials were particularly interesting. All the data above 60 MeV required significantly smaller values of the geometrical parameters than those at lower energies. The χ^2 minima in parameter space were exceedingly narrow and changes of 0.01–0.02 fm in r_{so} or a_{so} could have quite deleterious effects. Some studies were also made of the imaginary spin-orbit potential. The data seemed not to be very sensitive to it. Searches begun with either sign of W'_{so} usually terminated with the same sign or near zero with little improvement in the final χ^2. Hence we have taken $W'_{so} = 0$ in all cases.

D. Results

The final OM fits to the differential cross sections are shown by solid curves in Figs. 1–5 and for polarizations in Figs. 6 and 7. Figure 8 presents the volume integrals per nucleon for the real, imaginary, and spin-orbit parts of the potential. The geometrical parameters are plotted as solid lines in Fig. 9. Values are listed in Table I.

It is apparent from the trends in Figs. 8 and 9 that the parametrization seems smooth at energies above 60 MeV, but is irregular below that. This is our first indication of a qualitative difference in the scattering of protons from ^{12}C above and below 60 MeV. We may discuss individual features in these regions separately.

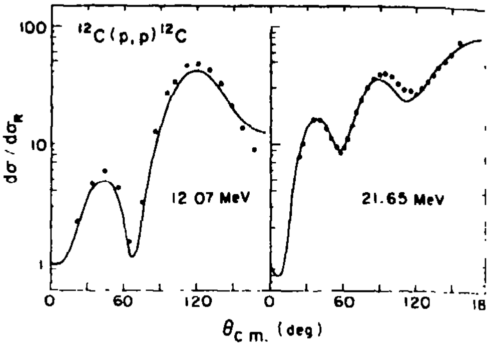

FIG. 1. One-channel optical-model calculations for proton elastic scattering from ^{12}C, in ratio to the Rutherford cross sections.

1. $E < 60$ MeV

The fit to the 12.07-MeV data in Fig. 1 is good. It is a little worse than in a previous analysis,[37] due mainly to our desire to keep the diffuseness parameters from becoming too small. Okai and Tamura showed[38] that broad resonances brought about by the couplings to other channels might be present in this energy range. It is possible that the unusual parameters at this energy are reflecting these couplings.

Although resonances have been alleged to play an important role near 20–25 MeV,[39] our pure OM results in Figs. 1 and 6 with reasonable parameters are superior to other parametrizations.[15,34,4]

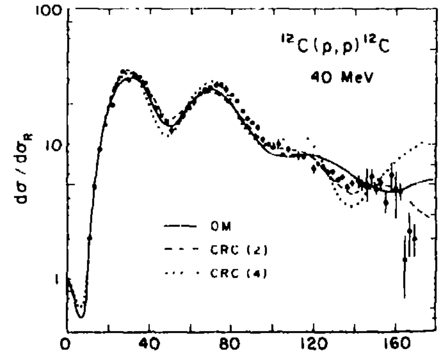

FIG. 2. Proton elastic scattering from ^{12}C in ratio to the Rutherford cross sections. The solid curve is a pu optical-model calculation. The dash and dotted curves result from CRC calculations after two and four iterations, respectively, of the search procedures.

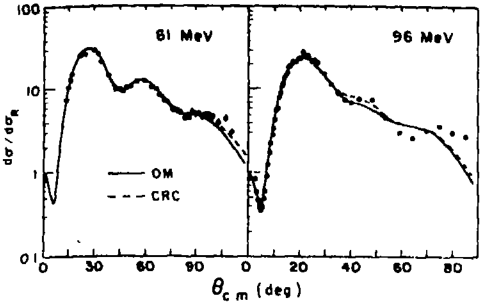

FIG. 3. Optical-model and CRC calculations of proton elastic scattering from ^{12}C, in ratio to the Rutherford cross sections.

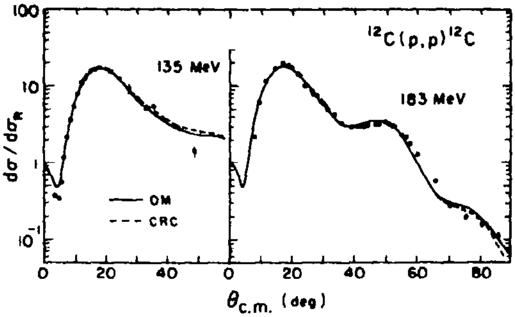

FIG. 5. Optical-model and CRC calculations of proton elastic scattering from ^{12}C, in ratio to the Rutherford cross sections.

At 40 MeV the fits in Figs. 2 and 6 are comparable to previous ones.[16] The fit to the polarization data is appreciably worse than at 21 MeV. It seems to be exceedingly difficult to obtain good fits to both cross-section and polarization data in this energy range with reasonable parameters.[41] We shall return to this point in Sec. IV. The most characteristic feature of the parameter systematics in Fig. 9 for this energy range is the rise in the spin-orbit radius to values comparable with the real central radius, and steep changes in the diffuseness parameters.

2. *E* > *60 MeV*

Generally, the fits to the data were quite satisfactory in this higher-energy range and the parameters varied smoothly with energy. The fit to the 135-MeV polarization is not impressive and the χ^2 values for the cross-section data (also at 122 and 183 MeV) could be significantly reduced if the polarization data were ignored. However, there are numerous correlations among the parameters, especially between the imaginary and spin-orbit parameters, and it was difficult to establish systematic trends with only the cross-section data. The constraints of the polarization data seemed useful to have, although the experimental situation needs to be vastly improved. A recent article illustrates the value of such data at 183 MeV.[31]

Unlike Ref. 17, we had no difficulty in fitting the 61-MeV data with excellent χ^2 values and total reaction cross sections and with very reasonable parameters. Although data on reaction cross sections are scant,[30] they are useful for rejecting

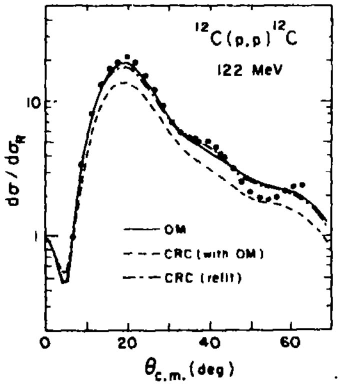

FIG. 4. Proton elastic scattering from ^{12}C at 122 MeV in ratio to the Rutherford cross sections. The solid curve is for the one-channel optical model. The dashed curve resulted from use of the same OM potential in full CRC calculations, while the dash-dot curve shows the result when the diagonal potential is adjusted for best fit to the data.

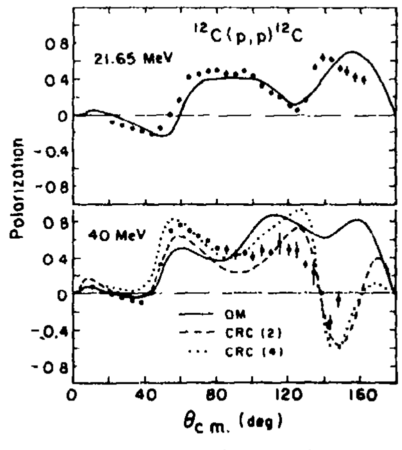

FIG. 6. The polarizations of proton elastic scattering from ^{12}C. See also the caption for Fig. 2.

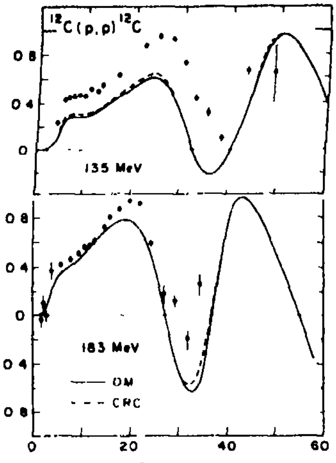

FIG. 7. The polarizations for proton elastic scattering from ^{12}C in comparison with optical-model and CRC calculations.

alternative parameter sets and trends.

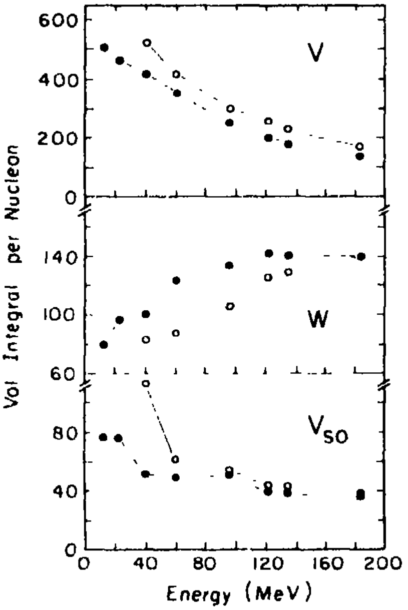

FIG. 8. Energy dependence of the volume integrals per nucleon of the real, imaginary, and spin-orbit potentials. The solid data are for the one-channel OMP and the open circles are for the ROMP of the CRC environment.

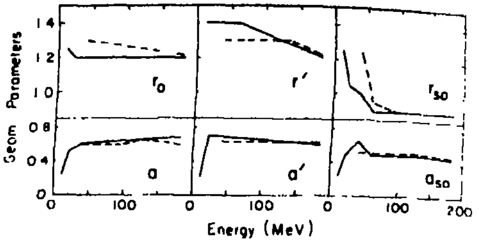

FIG. 9. Energy dependence of the geometrical parameters of the optical-model potentials. The solid lines are for the one-channel OMP and the dashed lines are for the ROMP of the CRC environment.

The data at 96 and 122 MeV indicate more structure than is provided by the calculations in Figs. 3 and 4. The situation can be improved considerably by allowing higher-order terms due to the permanent deformation of ^{12}C to appear in the optical potential. The radius parameter R in Eq. (4a) was replaced by $R_0[1+\beta_2 Y_2^0(\theta,\phi)]$, the resulting potential was averaged over all angles, and a search was carried out for β_2. We obtained $\beta_2 = -0.44$ with a reduction in χ^2 by a factor of 2 and with almost no change in the potential depths. The shape was improved considerably in the 30–60° range. There was little effect on the polarizations.

IV. COUPLED-CHANNEL ANALYSIS

There is little need to justify an exploration of coupled-channel effects on scattering from ^{12}C since it is well known that the strong coupling to the collective 2^+ state at 4.44 MeV is very important. In a pioneering work, Okai and Tamura demonstrated[38] that this coupling could produce resonancelike effects.

What is at stake, rather, is the number and type of channels that must be coupled. Rawitscher has shown the importance of strong couplings on both (d,p) cross sections and deuteron elastic scattering.[12] More recently, Mackintosh has investigated the effects of the coupling to pickup channels on proton scattering and reactions.[3,4,8]

The situation for ^{12}C is readily investigated. Using the CC program CHUCK2,[43] cross sections in the elastic channel were computed for pure two-step transitions proceeding through the 2^+ state of ^{12}C or the $\frac{1}{2}^-$ ground state in ^{11}C. The surprising results are shown in Fig. 10. At 135 MeV, the (p,d,p) cross sections are more than two orders of magnitude larger than the (p,p',p) cross sections. An almost identical situation holds at 180 MeV, while at 60 MeV the back coupling from the inelastic path is beginning to increase in importance. The two-step (p,d,p') cross sections to the 2^+ state (not shown) are an order of magnitude lower than the one-step yield at the first maximum, but become increasingly important at larger angles.

TABLE I. Parameters of the local, proton optical-model potential for use in one-channel calculations. The strengths have units MeV and lengths have units fm. Also listed are the total reaction cross sections (mb) and χ^2 per point for cross-section and polarization data.

E	V	r_0	a	W	r'	a'	V_{so}	r_{so}	a_{so}	σ_R	χ_σ^2/N	χ_p^2/N
12.1	−57.8	1.25	0.248	+32.6[a]	1.40	0.223	−26.0	1.25	0.248	309	48	
21.6	−47.6	1.20	0.517	−5.76	1.40	0.70	−30.4	1.05	0.50	445	4.7	17
40	−39.3	1.20	0.61	−6.23	1.40	0.69	−21.5	1.00	0.65	343	8.8	136
61.4	−32.8	1.20	0.62	−7.54	1.40	0.67	−22.5	0.90	0.50	317	1.7	
96	−23.0	1.20	0.635	−9.00	1.35	0.655	−23.3	0.90	0.50	282	18	
122	−18.3	1.20	0.65	−10.6	1.30	0.64	−18.3	0.90	0.50	264	53	156
135	−16.2	1.20	0.66	−11.1	1.28	0.63	−17.8	0.90	0.50	252	10	114
183	−12.5	1.20	0.68	−13.1	1.20	0.61	−16.4	0.90	0.47	222	12	22

[a] Surface-derivative absorption, W is W' in Eq. (2).

It is not easy to understand the reasons for this behavior. The one-step (p,p') and (p,d) cross sections are comparable (the integrated cross sections differ by factors of 2–3). Although the cross-section ratio is also reflected in the magnitudes of the two-step transition amplitudes, those for the (p,d,p) path peak at lower l values and are more localized in l space. The (p,p') form factor peaks more than 1 fm beyond that of the (p,d) form factor. Mackintosh has given arguments regarding the significance of this.[8] Whatever the reason, the CC effects for proton scattering from ^{12}C are far more serious than had been previously thought.

This last statement does not imply that CC calculations must inevitably be done since the normal OMP might very well simulate their effects. But it is necessary to investigate this issue. Since it is impossible to incorporate all channels in detail, further effort must proceed within the framework of a model.

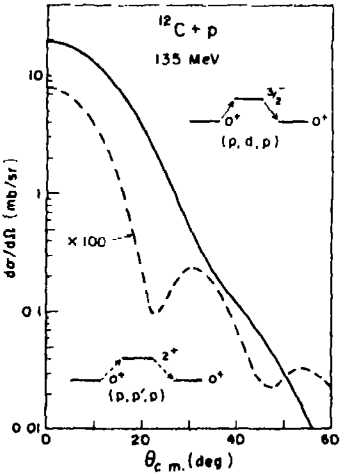

FIG. 10. Cross sections in the elastic channel of proton scattering from ^{12}C resulting from pure two-step paths for which the ground state of ^{11}C (solid curve) or the first-excited 2^+ state of ^{12}C (dashed curve) is the intermediate state.

A. CC environment

The environment we shall consider consists of proton scattering from the lowest two states of ^{12}C and (p,d) reactions to the lowest two states of ^{11}C. These states and the transfer couplings between them are shown in Fig. 11. Inelastic couplings in ^{11}C are not considered at this time.

The 2.0-MeV state of ^{11}C has almost no influence on the proton elastic cross sections, but was retained because it had a rather significant influence (destructive) on the 2^+ state of ^{12}C. A second $\frac{3}{2}^-$ level at 4.79 MeV in ^{11}C was ignored. At 122 MeV the (p,d) cross sections[23] for this state are a factor of 6 below the ground-state cross sections. The back-coupling effect on the elastic scattering is related approximately to the square of this ratio, although the influence on the 2^+ state is probably more important. It is hoped that the effects of all neglected channels are sat-

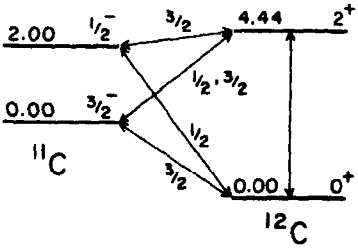

FIG. 11. The environment of the coupled-reaction-channel calculations. The states of ^{11}C and ^{12}C are labeled with their excitation energies and spin-parity values. The double-headed arrows denote two-way coupling and they are labeled also with the total angular momentum transfer j.

isfactorily taken into account in the residual ROMP.

Within this framework, which may be denoted the coupled-reaction-channel (CRC) environment,[44] the homogeneous Schrödinger Eq. (1) is replaced with a set of coupled inhomogeneous equations

$$\frac{d^2\chi_i(r)}{dr^2}+\left[k^2-\frac{2\mu_i}{\hbar^2}U_i(r)-\frac{l(l+1)}{r^2}\right]\chi_i(r) = \sum_{j\neq i}\frac{2\mu_i}{\hbar^2}V_{ij}\chi_j(r)\,. \quad (11)$$

Although there were only four separate mass-energy channels, angular momentum considerations resulted in as many as 15 coupled equations. These were solved exactly (infinite order) with the code CHUCK2.[43]

The off-diagonal coupling potentials $V_{ij}(r)$ for the (p,p') reaction to the 2^+ state were treated according to the collective model. The higher-order terms due to the $\beta_2 Y_2^0$ contribution to R (see Sec. III D. 2) were included, but here $\beta_2 = -0.6$ gave better agreement with experimental (p,p') cross sections. The parameters of the coupling potentials were kept equal to those of the central part of the proton ROMP during search procedures. Wave functions of Cohen and Kurath[45] were used to compute the spectroscopic amplitudes for the (p,d) reactions.

B. Deuteron potentials and form factors

A serious problem in the CRC calculations is the choice of deuteron potentials for the intermediate pickup channels. This has been discussed extensively elsewhere.[10] At first thought one might expect to use a phenomenological deuteron OMP that reproduces elastic scattering data. But if the diagonal proton OMP must be modified in a CC environment, so must also the deuteron OMP.[42] Furthermore, deuteron breakup and the general treatment of the p-n continuum are known to be very important for elastic scattering and stripping processes.[46,47] The observed failure of a conventional deuteron OMP in our calculations[10] may be related to this.

Although several detailed investigations of breakup effects have appeared in the literature,[47,48] such calculations were prohibitively large for us to incorporate. Instead we relied on the simulation provided by folded deuteron potentials. These were constructed from proton OMP's at half the deuteron energy needed in the CRC calculations. Hence, for the CRC calculations at 40, 61, 96, 122, 135, and 183 MeV, OM proton potentials were required at 12.1, 21.6, 40, 55, 61, and 80 MeV, respectively. These were determined either by direct fitting to data or from the systematics found in Sec. III. Neutron OMP's were taken to be the same as for protons.

The adiabatic model of Johnson and Soper[46] was used for this folding. Since this model contains an approximation in which the neutron and proton wave functions were treated at coincidence, it is possibly the most appropriate for our zero-range calculations. Approximate formulas for the folding have been given.[49] However, it was found sufficient merely to multiply the proton potential strengths by two (with proper adjustments for the spin-orbit portion). The Watanabe folding procedure[50] was also tried, although it may not be appropriate for simulating breakup effects. Numerical folding methods had to be adopted here. The results were sometimes sensitive to the choice of methods, an issue that will be discussed further in Sec. V.

The CRC calculations were rather insensitive to the choice of bound-state geometrical parameters, particularly with regard to the elastic scattering cross sections. The radius parameter was taken to be 1.20 fm in accordance with the proton OMP's. The diffuseness parameter varied from 0.65 fm for the Johnson-Soper calculations to 0.70 fm for those of Watanabe and the spin-orbit parameter had the conventional value $\lambda = 25$.

C. Additional factors

It is common in stripping and pickup calculations to make approximate corrections for nonlocality and finite range. These present certain theoretical difficulties in the present calculations. First of all the back feeding in the CRC calculations brings in some nonlocality directly, and secondly there are various arguments to suggest that the back feeding will be reduced considerabl with an exact finite-range treatment.[51,52]

Although finite-range corrections to one-step (p,d) reactions are normally small, due to energ conservation and good well matching, off-energy-shell contributions can become very sizable in pickup-stripping processes. Coulter and Satchle indicate,[7] however, that they should be unimportant for the imaginary parts. Their effect on the real parts will be compensated in the ROMP whe the elastic scattering data are refitted.

Irrespective of these difficulties, we have adopted the more conventional procedures in our model. From examination of exact finite-range calculations it was determined that calculations with nonlocality parameters $\beta = 0.85$ for protons and 0.43 for deuterons, and a finite-range parameter $R = 0.77$ (all as used in CHUCK2) gave (p,d) differential cross sections in reasonable accord with experiment at all energies.

One additional problem also could not be exumined. The inclusion of both $p+{}^{12}$C and $d+{}^{11}$C nass partitions introduces a degree of nonrthogonality to the system. One might hope that he restriction of the model space to only the owest two states in each partition would alleviate nost of the difficulty since, physically, the different arrangements are very dissimilar and hould have little overlap. It has also been rgued[53] that the nonorthogonality effects are aproximately canceled in pickup-stripping proesses by the usual procedure of dropping the emnant terms of the interaction, thus generating post-prior asymmetry. Explicit studies have ndicated that the nonorthogonality corrections hould be small.[54,55]

D. Elastic scattering results

The refitting of the elastic scattering data in the :RC environment as defined in Sec. IV. A–C ras carried out with the programs CHUCK2[43] and :UPID[9] according to the iterative procedures decribed elsewhere.[9] Except for a partial study t 40 MeV, the calculations were limited to the nergy range above 60 MeV. The most extensive earches used the Watanabe-folded deuteron poential. The results are shown in Figs. 2–7 and ıe parameters of the ROMP's are presented in 'able II.

One might hope that this more rigorous treatient of reaction dynamics might result in imroved agreement with data. In fact, the χ^2 values or both cross-section and polarization data are nproved slightly, except possibly at 40 MeV. 'isually the changes seem to be in the right laces. However, the effects are relatively small, ven for the polarization data, and we do not beieve that too much significance should be atiched to the improvements at this time.

The more interesting aspects are in the systematics of the parameters. Again, these systematics are partly a result of the trends that became apparent during the search procedures and partly a result of their explicit adoption. In Fig. 8 we find that the volume integral of the imaginary potential has decreased significantly at most energies, as expected. However, those for the real central and spin-orbit potentials have increased, indicating that the effects of the back couplings are repulsive.[4] It is not known whether this applies for both the (p,d,p) and (p,p') processes or what the relative energy dependence of each might be.[7]

The systematics of the geometrical parameters were also modified somewhat. There was a clear indication that, at low energies, the real radius parameters r_0 and r_{so} are significantly larger than the OM case, while the imaginary radius r' is smaller. At the high end of the energy scale the OMP and ROMP seemed to be very similar, suggesting that the CC effects were becoming less important with increasing energy.

An important consideration here is the degree to which optical-model parameters might simulate the effects of channel couplings and whether the "bare" potential might be distorted thereby. Answers are very difficult to obtain, in large part because of cross correlations between various parzmeter groups. Nevertheless, there may very well be substantial effects, especially on radius parameters at low energies and particularly for r_{so}.

E. The 40-MeV case

The calculations at 40 MeV gave a special problem. Unlike the situation at higher energies, where the search procedures converged after two

TABLE II. Parameters of the proton residual optical-model potential for use in the CRC environment described in Sec. IV. See also the caption of Table I.

E	V	r_0	a	W	r'	a'	V_{so}	r_{so}	a_{so}	σ_r	χ_σ^2/N	χ_p^2/N
Watanabe-folded deuteron potential												
40	−40.8	1.30	0.60	−6.14	1.30	0.63	−37.8	1.25	0.52	395	34	75
61.4	−33.7	1.29	0.57	−6.56	1.30	0.63	−27.1	0.95	0.52	299	1.0	
96	−24.8	1.275	0.60	−8.00	1.30	0.63	−25.1	0.90	0.52	261	14	
122	−20.9	1.26	0.65	−9.47	1.30	0.63	−19.3	0.90	0.52	261	55	119
135	−18.9	1.25	0.65	−9.69	1.30	0.63	−19.9	0.90	0.52	252	8	91
183	−15.2	1.23	0.60	−11.6	1.23	0.63	−17.2	0.90	0.48	227	11	21
Johnson–Soper folded deuteron												
61.4	−32.6	1.29	0.60	−6.06	1.30	0.63	−25.0	0.95	0.52	281	1.2	
96	−24.5	1.275	0.60	−8.00	1.30	0.63	−25.1	0.90	0.52	263	15	
122	−20.9	1.26	0.65	−9.49	1.30	0.63	−19.0	0.90	0.52	260	49	120
135	−19.2	1.25	0.65	−9.47	1.30	0.63	−19.2	0.90	0.52	248	6	95
183	−15.4	1.23	0.60	−11.8	1.30	0.63	−16.8	0.90	0.48	230	10	22

or three iterations, the cycle between successive CHUCK2 and CUPID calculations seemed unstable. The best results from the optical-model search program were obtained with the ROMP in Table II used in conjunction with the back couplings from the second iteration through CHUCK2. The χ^2 for the cross sections was about the same as for the OM parameters of Table I, while that for the polarization data was very substantially improved.

Unfortunately, what initially seemed like a convergent process became a slightly divergent one. After four iterations the parameters of the ROMP had settled down to fairly stable values, but the χ^2 values had increased significantly, particularly for the cross sections. The results of both iterations are shown in Figs. 2 and 6 and in Table II.

The main difficulty seemed to be at back angles. The back-coupling amplitudes had a strong tendency to put a sharp rise in the elastic cross sections beyond 140° and changes in the geometrical parameters of the ROMP were necessary to bring it back down. The most significant changes were a sharpening of the edge of the spin-orbit potential and its shift to larger radii.

In spite of the difficulties, one conclusion seems clear. The CRC environment has resulted in very substantial improvement of the fit to the polarization data, with not much change in the fit to the cross-section data. Qualitatively, the ratio of the polarizations at the 60° and 120° humps has been nearly inverted and a dip near 140° has been formed, which is in much better agreement with the experimental patterns. Satchler has reported much difficulty in fitting simultaneously both cross-section and polarization data in this energy range.[41] We suggest that the problems may be intimately associated with the influence of strongly coupled pickup channels. The difficulties with the convergence here are possibly related to ambiguities regarding calculational procedures, some of which are discussed in the next section.

V. DWBA or CRC?

Although there was a general and systematic improvement in χ^2 values in the CRC environment, this was not very large. This suggests that, at intermediate energies, the local, complex OMP might be doing an excellent job of representing all the complications of proton elastic scattering from ^{12}C. The question naturally arises whether this simulation ability also extends to proton-induced reactions.

It should be understood that this favorable state of affairs is not a consequence of very small back-coupling amplitudes. This is made clear in Fig. 4 where the dashed curve represents the elastic scattering cross section in the full CRC environment, but with the normal OMP from Table I used for the proton channels. The cross section has dropped by up to 30–40% compared with the pure one-channel OM result. It is only when the proton potential is replaced with the ROMP from Table II that the CRC calculations give the proper result.

The situation for reactions is very similar. This is illustrated in Fig. 12 for the (p,p') reaction to the lowest 2^+ state in ^{12}C and the (p,d) reaction to the ground state of ^{11}C, both at 122 MeV. The solid lines are the results of conventional DWBA calculations (pure one-way transitions from the ^{12}C ground state to the final states). When the one-channel proton OMP is used in the CRC calculations there is again a decrease in the cross sections, although this is not very large for the (p,d) reaction. After the elastic scattering data had been refitted, the final CRC results at the first maxima were very much like the original DWBA calculations. For the 2^+ state, however, there is some enhancement at large angles, a result anticipated in the exploratory calculation of Sec. IV. (The failure to reproduce the data very well beyond the first maximum is believed to be due primarily to the neglect of the deformed spin-orbit coupling interaction.[2])

This pattern of behavior was similar for both choices of folded deuteron potentials and there was little distinction between the choices at the higher energies. The (p,p') cross sections were insensitive to this, even at the lower energies. However, as illustrated in Fig. 13, the (p,d) ground-state cross sections were distinctively different for the Johnson-Soper or Watanabe po-

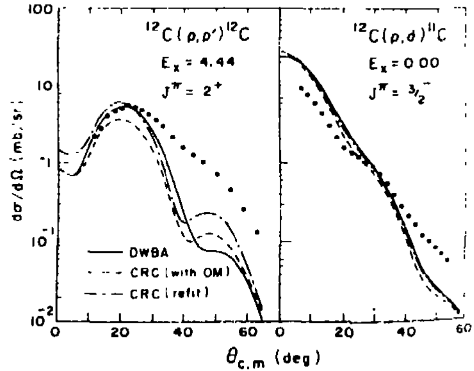

FIG. 12. Calculations of cross sections for the (p,p') reaction to the lowest 2^+ state of ^{12}C and the (p,d) reaction to the ^{11}C ground state, in comparison with data at 122 MeV. See also the caption for Fig. 4.

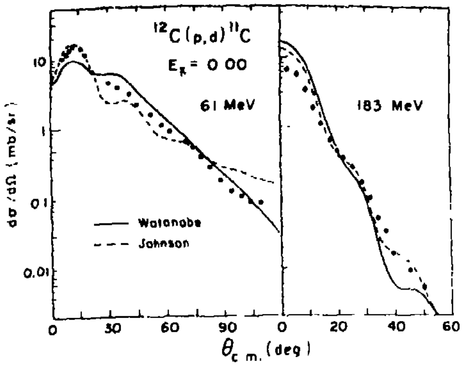

FIG. 13. Calculations of (p,d) cross sections to the ^{11}C ground state at two energies in comparison with data. The solid curve represents use of the Watanabe-folded deuteron potential, while the dashed curve corresponds to Johnson-Soper folding.

tentials. There is some preference for the results with the Johnson-Soper adiabatic potential (even a slight preference at 183 MeV). However, it seems that the (p,d) calculations do not exactly fit the slope of the data at any energy. Certainly the choice of deuteron potential is a very important consideration, but it is difficult at this time to reach specific conclusions regarding it.

A possible consideration here is the effects of inelastic excitations in ^{11}C. The Cohen-Kurath wave functions[45] predict that there should be many important couplings between the states of ^{11}C and that $\Delta J = 1$ transitions ($\Delta L = 0$ and 2, $\Delta S = 1$) may be quite important. Unfortunately, these will increase the complexity of the CRC calculations very substantially. Macroscopically, the $\Delta L = 2$ parts might be handled (along with $\Delta J = 2$ transitions) with the usual collective model, but the $\Delta L = 0$ terms are also likely to be significant at intermediate energies. Microscopically, the spin-flip portions of the isoscalar excitations may not be well described.[2]

A test calculation at 122 MeV with a single inelastic coupling in ^{11}C indicated that the ground-state (p,d) cross sections could be reduced slightly at forward angles, in better agreement with the data. Although the CRC environment is now different from that in Sec. IV, it is unlikely that this improvement would be eliminated completely when the proton ROMP is readjusted since the influence on the elastic channel is of higher order.

Thus, although the DWBA calculations seem to be entirely adequate for describing the main features of the transitions, many details also seem to depend on the singular effects brought about by individual channel couplings. Since the full apparatus of CRC calculations makes very large demands on computer resources, one might hope that certain approximations would allow these singular features to be described with sufficient accuracy. Calculations of two-step contributions (second-order DWBA) has been a common approach and this has the advantage that the amplitudes from several paths leading to the same final state may be calculated separately and added together.

In testing this approach, calculations were made of the 122-MeV pickup-stripping (p,d,p') cross sections to the 1^+ states of ^{12}C at 12.71 and 15.11 MeV. In the first approach the full CRC environment of Fig. 11 was used, but with one-way transitions from both ^{11}C states to the 1^+ states of ^{12}C also included. The ROMP from Table II was used for all proton channels. In the second approach only the one-way transitions from the ^{12}C ground state to both ^{11}C states were specified, followed by the same one-way transitions up to the 1^+ states. The OMP from Table I was used for all proton channels here. The cross sections for the 1^+ states from both approaches were identical out to about 30°, while the pure two-step cross sections were slightly lower at larger angles.

It should be noted that three-step contributions from paths that proceed through the 2^+ state of ^{12}C were not included in the second approach. They are expected to be relatively small, particularly at forward angles. Furthermore, no distinctions have been made between the OM potentials of the entrance and exit channels.[56] The calculations here seem to work best when these are the same, but the issue needs more exploration.

The most important result of the investigation in this section is that the particular effects of the CRC environment appear to decrease with energy. Not only was the convergence of the iterated search procedures better, but the differences between the ROMP and OMP decreased and the results were also less sensitive to uncertainties regarding details, such as the choice of deuteron potentials. Thus, it appears that the DWBA methods become more suitable as the energy increases and that the complexities of the CRC calculations are less necessary.

This result is of course reflected in the magnitudes of the back-coupling amplitudes in the elastic channel. A way to express this is illustrated in Fig. 14. For three energies we have plotted the ratios of the S-matrix elements $S_{lj} = \exp(2i\delta_{lj})$ obtained from the ROMP's of Table II and OMP's of Table I and also the changes in the nuclear

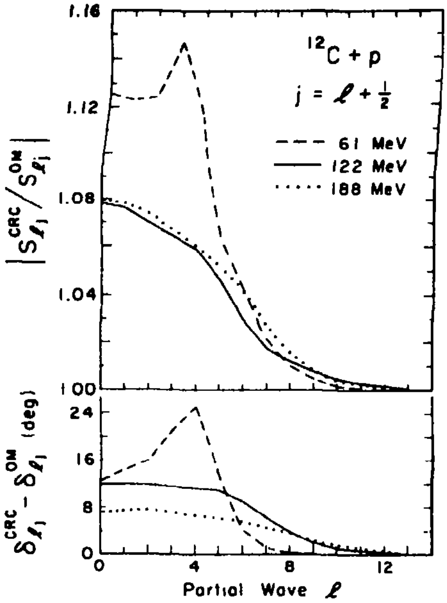

FIG. 14. Ratios of the amplitudes of the S-matrix elements and the differences in phase for the OMP's and ROMP's from Tables I and II at three energies.

phase shifts δ_{lj}. As the energy increases, the ratios of the S-matrix elements and the differences in phase shifts tend to decrease. The principal effects are in the lowest partial waves where the S-matrix amplitudes of the ROMP are several percent larger and are shifted in phase to larger angles. For the partial waves with $j = l - \frac{1}{2}$, the ratios of S-matrix amplitudes are essentially the same as those shown in Fig. 14. The changes in the phases are a little smaller at 183 MeV, but considerably smaller at 61 MeV.

The behavior of the ratios and shifts is smooth at the higher energies, but shows some irregularities at 61 MeV. The situation is reminiscent of patterns found in the scattering of protons from ^{16}O and ^{40}Ca, where phenomenological l-dependent potentials were included in the analysis.[57,58] The l-dependent effects were similarly concentrated in the lowest partial waves and it was suggested that the phenomenological l dependence was related to couplings to pickup channels.[58,59] Additional explorations of this question would be interesting.

VI. DISCUSSION AND CONCLUSIONS

The phenomenological analysis of proton scattering from ^{12}C in both the optical-model and coupled-channel approaches has revealed numerous systematic features. It has also shown clearly that ^{12}C is quite suitable for the study of nuclear reactions and scattering and that calculations for these processes can be reliable. The situation is best at intermediate energies, say $E > 100$ MeV, and seems adequate for energies as low as about 60 MeV. Below that the effects of strong couplings to other channels become particularly important in a manner that requires attention to all details.

This dichotomy about an energy near 60 MeV is revealed in many ways. The volume integrals and geometrical parameters shown in Figs. 8 and 9 seem to have smooth and regular trends above that energy. The trends are distinctively different below 60 MeV, particularly for the spin-orbit geometrical parameters and the other diffuseness parameters. At the higher energies the effects of the back couplings are not very substantial, while at lower energies they can have a dramatic impact on cross sections and polarizations. This was becoming apparent in the analysis of the 61-MeV data, where the (p, d) angular distributions showed greater sensitivity to the choice of the deuteron optical-model potential. At 40 MeV the effects were quite severe. Undoubtedly the calculations here are being hurt by the approximations used: the zero-range assumption, the neglect of nonorthogonality corrections, and the incomplete treatment of deuteron breakup and the p-n continuum.

An important conclusion here is that the local, complex OMP is able to simulate the effects of channel couplings quite well in many instances, a feature that improves with increasing energy. Furthermore, the use of this OMP in DWBA calculations of reactions appears to be realistic and justified even from a more detailed approach. The important criterion is that the elastic scattering data should be reproduced well. Some features of a more encompassing CRC model may yet remain to be included, but it appears feasible to evaluate these by use of the second-order DWBA.

It must be stressed that this study has focused attention almost exclusively on transitions that have large spectroscopic couplings with the elastic channel. In terms of past experience one expects these to be primarily single-step processes. Transitions that are inhibited in terms of direct couplings, such as the excitation of the 4^+ state of ^{12}C, will still require appropriate treatment of multistep contributions. Second-order DWBA may be adequate for some of these, while the full CRC environment may be needed for others. The CRC may also be necessary for details of the uninhibited transitions.

One may thus conclude that the DWBA calculations of the $^{12}C(p, p')^{12}C$ reaction at 122 MeV in the preceding article[3] are entirely adequate. This has much significance since the contributions from knockon exchange are very considerable and no codes exist which can calculate them exactly in the CRC model described in Sec. IV. Thus, the focus of Ref. 2 was properly directed towards the microscopic effective interaction. Although some effects from two-step processes may be present, as was discussed in Ref. 2, the treatment of the reaction dynamics is not a serious limitation on the conclusions.

There are no major surprises in the conclusions expressed so far. Indeed they are implicit in much of current practice. More explicitly they may be considered to be an extension into the CRC environment of the tendency to equivalence between DWBA and CC calculations previously noted[60] for strong inelastic couplings, under the constraint that elastic scattering data be fit equally well. Nevertheless, it is gratifying to have them emerge directly front the phenomenological analyses in the present study.

Again the reader is cautioned that the favorable state of affairs expressed here does not extend to lower energies, such as below 60 MeV. As the back-coupling amplitudes take on greater importance (e.g., as the inelastic coupling parameter β increases),[60] the equivalence between DWBA and coupled-channel approaches breaks down. Although resonances of various types may produce significant effects at the lower energies,[38,39,61] we concur with Mackintosh that couplings to pickup channels are probably the most important ones for light nuclei. Similar conclusions were also reached for low-energy nucleon scattering from molybdenum isotopes.[62]

Unfortunately, one item of considerable interest could not be illuminated very clearly in the present work. The strengths and geometrical parameters of one-channel OMP's resulting from phenomenological analyses of elastic scattering data are often used to infer features of microscopic effective interactions and geometrical properties of nuclei. It is important to determine the extent to which these parameters have become distorted from their more intrinsic values in order to compensate for and to simulate channel-coupling effects. The sharp decrease in the diffuseness parameters at low energies in Fig. 9 is surely an indication of this. However, in view of the difficulties even at 40 MeV it became impractical to extend the analysis to these low energies.

The cross correlations between parameter groups also precluded specific conclusions from being drawn regarding such simulation effects. While it is difficult to make general statements, there appeared to be various compensations between the parameters of the imaginary and the spin-orbit potentials. Furthermore, the differences of the proton OMP's and ROMP's, as discussed in Sec. V, are asymmetric with respect to the spin-orbit components of the partial waves. What implications this may have for phenomenological imaginary spin-orbit potentials is not clear since the data considered here were not especially sensitive to them.

It is felt that greater insight into the issues raised here would come if the experimental situation were improved. A well-designed program of the elastic scattering of nucleons and other light projectiles at intermediate energies from several targets would be beneficial. It is especially important that cross-section and polarization data span large angular ranges and that data for the predominant reactions also be available. The energies should span a range such that back-coupling effects are significant at one end and relatively unimportant at the other. It is not known how this energy range depends on mass number. As the mass increases, the averaging effects of more open channels should probably keep the range from being higher than that considered for ^{12}C here.

Finally, although substantial and excellent progress has been made in recent years in terms of theoretical techniques, some difficult problems remain to be examined in more detail. Probably the most important for the type of analyses discussed here is the handling of the intermediate channels. Since large-scale CRC calculations are impractical and simple adiabatic potentials[44] may be inadequate,[48] realistic approximation techniques need to be devised. In combination with new experimental data, these techniques may reasonably be expected to lead to great enrichment in our understanding of effective nucleon-nucleus interactions.

ACKNOWLEDGMENTS

This work was supported in part by the National Science Foundation. Many of the computer calculations were also carried out with internal support. We also gratefully acknowledge many fruitful discussions on all aspects of this work with Dr. C. M. Vincent.

[1] R. E. Anderson, J. J. Kraushaar, J. R. Shepard, and J. R. Comfort, Nucl. Phys. A311, 93 (1978).

[2] J. R. Comfort, S. M. Austin, P. T. Debevec, G. L. Moake, R. W. Finlay, and W. G. Love, Phys. Rev. C 21, 2147 (1980), preceding paper.

[3] R. S. Mackintosh, Nucl. Phys. A164, 398 (1971).

[4] R. S. Mackintosh and A. M. Kobos, Phys. Lett. 62B, 127 (1976).

[5] J. P. Jeukenne, A. Lejeune, and C. Mahaux, Phys. Rep. 25C, 83 (1976); Phys. Rev. C 16, 80 (1977).

[6] F. A. Brieva and J. R. Rook, Nucl. Phys. A291, 299 (1977); A291, 317 (1977); A297, 206 (1978); A307, 493 (1978).

[7] P. W. Coulter and G. R. Satchler, Nucl. Phys. A293, 269 (1977).

[8] R. S. Mackintosh, Nucl. Phys. A209, 91 (1973); A230, 195 (1974).

[9] J. R. Comfort, Comput. Phys. Commun. 16, 35 (1978).

[10] J. R. Comfort and B. C. Karp, Phys. Lett. 80B, 1 (1978).

[11] J. R. Comfort, in *Proceedings of INS International Symposium on Nuclear Direct Reaction Mechanisms, Fukuoka, Japan, 1978*, edited by M. Tanifuji and K. Yazaki (INS, University of Tokyo, 1978), p. 118.

[12] J. R. Comfort in *Proceedings of the Conference on (p, n) Reactions and the Nucleon-Nucleon Force, Telluride, Colorado, 1979*, edited by C. D. Goodman, S. M. Austin, S. T. Bloom, J. R. Ropaport, and G. R. Satchler (Plenum, New York, 1980), p. 303.

[13] Y. Nagahara, J. Phys. Soc. Jpn. 16, 133 (1961).

[14] J. K. Dickens, D. A. Haner, and C. N. Waddell, Phys. Rev. 132, 2159 (1963).

[15] R. M. Craig, J. C. Dore, G. W. Greenlees, J. Lowe, and D. L. Watson, Nucl. Phys. 79, 177 (1966).

[16] L. N. Blumberg, E. E. Gross, A. van der Woude, A. Zucker, and R. H. Bassel, Phys. Rev. 147, 812 (1966).

[17] C. B. Fulmer, J. B. Ball, A. Scott, and M. L. Whiten, Phys. Rev. 181, 1565 (1969).

[18] P. G. Roos, S. M. Smith, V. K. C. Cheng, G. Tibell, A. A. Cowley, and R. A. J. Riddle, Nucl. Phys. A255, 187 (1975).

[19] G. Gerstein, J. Niederer, and K. Strauch, Phys. Rev. 108, 427 (1957). Data are tabulated by H. J. Kim, W. T. Milner, and F. K. McGowan, Nucl. Data A2, 1 (1966).

[20] J. M. Dickson and D. C. Salter, Nuovo Cimento 6, 235 (1957).

[21] S. K. Mark, P. M. Portner, and R. B. Moore, Can. J. Phys. 44, 2961 (1966).

[22] J. R. Comfort, G. Moake, C. Foster, J. Rapaport, and C. Goodman, Bull. Am. Phys. Soc. 24, 829 (1979).

[23] R. E. Anderson, J. R. Shepard, and J. R. Comfort, Bull. Am. Phys. Soc. 21, 979 (1976).

[24] O. N. Jarvis, M. Shah, and C. Whitehead, Harwell Report No. AERE-R6769, 1971 (unpublished).

[25] J. McL. Emmerson, J. C. W. Madden, C. M. P. Johnson, N. Middlemas, A. B. Clegg, and W. S. C. Williams, Nucl. Phys. 77, 305 (1966).

[26] C. Rolland, B. Geoffrion, N. Marty, M. Morlet, B. Tatischeff, and A. Willis, Nucl. Phys. 80, 625 (1966).

[27] V. Comparat, R. Frascaria, N. Marty, M. Morlet, and A. Willis, Nucl. Phys. A221, 403 (1974).

[28] R. Alphonce, A. Johansson, and G. Tibell, Nucl. Phys. 4, 672 (1957).

[29] A. Johansson, U. Svanberg, and P. E. Hodgson, Ark. Fys. 19, 541 (1961).

[30] A. Johansson, U. Svanberg, and O. Sundberg, Ark. Fys. 19, 527 (1961).

[31] A. Ingemarsson, O. Jonsson, and A. Hallgren, Nucl. Phys. A319, 377 (1979).

[32] D. Hasselgren, P. U. Renberg, O. Sundberg, and G. Tibell, Nucl. Phys. 69, 81 (1965).

[33] J. Källne and E. Hagberg, Phys. Scr. 4, 151 (1971).

[34] W. S. C. Williams, *An Introduction to Elementary Particles* (Academic, New York, 1961), Appen. A.

[35] M. Goldberger and K. M. Watson, *Collision Theory* (Wiley, New York, 1964), Sec. 6.8.

[36] F. D. Becchetti, Jr., and G. W. Greenlees, Phys. Rev. 182, 1190 (1969).

[37] J. S. Nodvik, C. B. Duke, and M. A. Melkanoff, Phys. Rev. 125, 975 (1962).

[38] S. Okai and T. Tamura, Nucl. Phys. 31, 185 (1962).

[39] T. Tamura and T. Terasawa, Phys. Lett. 8, 41 (1964).

[40] J. J. Kolata and A. Galonsky, Phys. Rev. 182, 1073 (1969).

[41] G. R. Satchler, Nucl. Phys. A100, 497 (1967).

[42] G. H. Rawitscher, Phys. Rev. 163, 1223 (1967).

[43] P. D. Kunz (unpublished); extended version of J. Comfort.

[44] W. R. Coker, T. Udagawa, and H. H. Wolter, Phys. Rev. C 7, 1154 (1973).

[45] S. Cohen and D. Kurath, Nucl. Phys. 73, 1 (1965).

[46] R. C. Johnson and P. J. R. Soper, Phys. Rev. C 1, 976 (1970).

[47] G. H. Rawitscher, Phys. Rev. C 9, 2210 (1974); 11, 1152 (1975).

[48] J. P. Farrell, C. M. Vincent, and N. Austern, Ann. Phys. (N.Y.) 96, 333 (1976); 114, 93 (1978).

[49] G. L. Wales and R. C. Johnson, Nucl. Phys. A274, 168 (1976).

[50] S. Watanabe, Nucl. Phys. 8, 484 (1958).

[51] P. D. Kunz and L. A. Charlton, Phys. Lett. 61B, 1 (1976).

[52] P. D. Kunz, in Ref. 12.

[53] T. Udagawa, H. H. Wolter, and W. R. Coker, Phys. Rev. Lett. 31, 1507 (1973).

[54] S. R. Cotanch and C. M. Vincent, Phys. Rev. Lett. 36, 21 (1976).

[55] S. R. Cotanch and C. M. Vincent, Phys. Rev. C 14, 1739 (1976).

[56] R. J. Ascuitto, J. F. Petersen, and E. A. Seglie, Phys. Rev. Lett. 41, 1159 (1978).

[57] A. M. Kobos and R. S. Mackintosh, J. Phys. G 5, 97 (1979).

[58] R. S. Mackintosh and A. M. Kobos, J. Phys. G 5, 359 (1979).

[59] R. S. Mackintosh and L. A. Cordero-L., Phys. Lett. 68B, 213 (1977).

[60] F. Perey and G. R. Satchler, Phys. Lett. 5, 212 (1963).

[61] K. A. Amos, H. V. Geramb, R. Sprickmann, J. Arvieux, M. Buenerd, and G. Perrin, Phys. Lett. 52B, 138 (1974).

[62] J. R. Comfort, Phys. Rev. Lett. 42, 30 (1979).

PHYSICAL REVIEW C VOLUME 21, NUMBER 6 JUNE 1980

Electroexcitation of odd-parity states in ^{27}Al

R. S. Hicks, A. Hotta,[*] J. B. Flanz,[†] and H. deVries[‡]
University of Massachusetts, Amherst, Massachusetts 01003

(Received 13 September 1979)

Inelastic electron scattering form factors were measured for the low-lying odd-parity states of ^{27}Al over a momentum transfer range of 0.57 to 2.41 fm^{-1}. Reduced ground-state transition probabilities were deduced for states at 4.055 MeV($1/2^-$), 5.156 MeV(3/2), 6.159 MeV($3/2^-$), 6.477 MeV($7/2^-$), 6.605 MeV(1/2 or $3/2^-$), 6.651 MeV($5/2^-$), 6.993 MeV($3/2^-$), and 7.228 MeV(9/2). In addition, the results support odd-parity assignments for the 5.827 MeV($3/2^-$ or $5/2^+$) and 7.477 MeV(7/2) levels. Attempts have been made to interpret the results in terms of the weak-coupling and strong-coupling models. The measurements confirm the apparent high concentration of 1*p*-shell proton hole strength in the 4.055 MeV,$1/2^-$ and 5.156 MeV,$3/2^-$ states. To satisfactorily account for the observed properties of these two levels using the weak-coupling model requires an anomalously small value of 1.35 MeV for the spin-orbit splitting of the 1*p* shell. The structure of levels in the 6 to 7.5 MeV region is shown to be based on the excitation of 1*d*-shell nucleons into the 1*f* shell.

[NUCLEAR REACTIONS ^{27}Al(e,e'), $E-70$–340 MeV; measured $\sigma(E;\theta)$, DWBA analysis. $\pi=-1$ levels, deduced $B(\lambda)$, δ. Strong-coupling model, weak-coupling model.]

I. INTRODUCTION

In contrast to the even-parity states, the low-lying odd-parity states of the 2*s*-1*d* shell nuclei have received relatively little attention, either experimental or theoretical. For example, whereas reasonably successful shell-model calculations of the even-parity spectra can be made by considering only the *sd*-shell configuration space,[1-3] any realistic calculation of the negative-parity levels would have to include active 1*p* and 2*p*-1*f* shells. In the absence of such theoretical work, approaches to the understanding of the structure of odd-parity states are usually based upon more collective descriptions.

The 2*s*-1*d* shell nucleus considered here, ^{27}Al, is frequently regarded as transitional in shape, intermediate between lower-*Z*, prolate rotational nuclei (^{25}Mg, ^{25}Al, and ^{26}Mg), and heavier nuclei of oblate deformation (^{28}Si and ^{29}Si). Nevertheless, available experimental evidence seems to suggest a clearly prolate character for ^{27}Al: The sign of the observed ground-state quadrupole moment is positive (+0.140*e*b),[4] and a Nilsson-model interpretation[5] of the low-lying level scheme favors a prolate deformation corresponding to $\eta=3$. On the other hand, a simple rotational description of ^{27}Al is not nearly as convincing as it is for the $A=21$–25 nuclei. More satisfactory interpretations invoke appreciable band mixing,[6] the coupling of rotational and vibrational motions,[7] the strong interaction of particles in different Nilsson-model orbits,[8] or the weak coupling of a proton hole to the collective rotational levels of a ^{28}Si core.[9-13] Even so, insofar as the even-parity states are concerned, none of these models is as comprehensively successful as the shell model calculations of Cole *et al.*[2] or Wildenthal and McGrory.[1]

Recent (p,γ) measurements by Maas and collaborators[14] have done much to clarify the spin-parity assignments of low-lying levels in ^{27}Al. The odd-parity spectrum shown in Fig. 1 is principally based upon two different configurations, one represented by the excitation of an *sd*-shell nucleon into the *pf* shell, and the other by the creation of a 1*p*-shell proton hole in the ground state of ^{28}Si. A comparison of data from pickup and stripping reactions[15] indicates that the 4.055 MeV, $J^\pi=\frac{1}{2}^-$ and the 5.156 MeV, $\frac{3}{2}^-$ levels are hole states, and that the 6.159 MeV, $\frac{3}{2}^-$ and 6.477 MeV, $\frac{7}{2}^-$ states arise from particle excitation into the *pf* shell. In the framework of the Nilsson[16] model, Ropke *et al.* identified the latter pair of states as the lowest two members of the $K^\pi=\frac{1}{2}^-$, [330] rotational band.[15] This identification is supported by observed similarities with negative-parity states in neighboring nuclei.

Presented in this paper are electron scattering form factors for most of the odd-parity states identified in ^{27}Al up to an excitation energy of 7.5 MeV. The availability of these form factors permits further tests to be made of the various models proposed for the structure of this nucleus. Previous electron scattering experiments[6,9,17,18] have not defined the form factors of the odd-parity spectrum, primarily because these experiments lacked the resolution to cope with the increasing level density at excitations in excess of 4 MeV.

© 1980 The American Physical Society

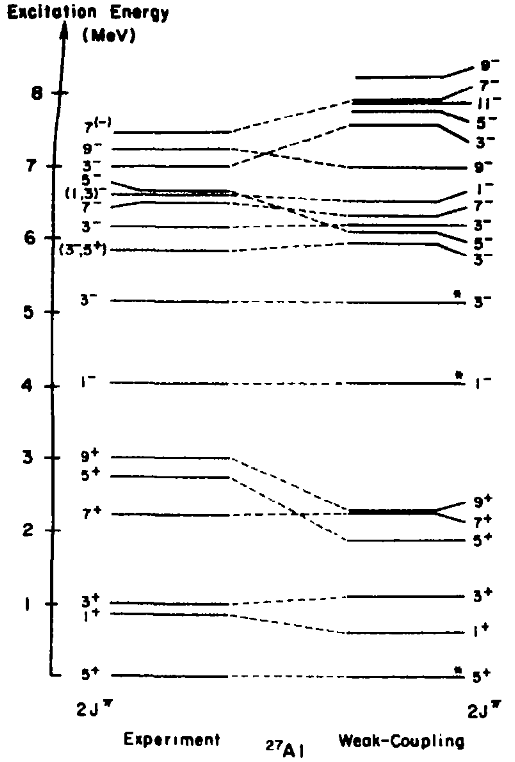

FIG. 1. Experimental and weak-coupling level schemes for ^{27}Al. Only the lowest-lying even-parity states are shown. An asterisk denotes that the corresponding weak-coupling level was fitted exactly to the energy of an observed state.

II. EXPERIMENTAL DETAILS

The measurements were performed using the 22-section linear accelerator of the Bates Laboratory in Middleton, Massachusetts. This S-band device can accelerate electrons to energies of 350 MeV or more with a duty factor of about 0.5%. The energy-analyzed beam emerges from the beam switchyard with a horizontal momentum dispersion which is rotated to the vertical plane by a system of five quadrupole lenses. When the beam is subsequently intercepted by the target it has a momentum dispersion of 10 cm/% and usual beam-spot dimensions of approximately 1 mm wide by 30 mm high.

For the experiment reported here, average on-target beam currents of up to 55 μA were delivered within a momentum spread of ±0.15%. Beam currents were monitored by means of two identical ferrite toroids,[19] the calibration of which had been previously established using the Faraday cup at the National Bureau of Standards Laboratories in Maryland. Further details of the Bates electron accelerator and beam-handling system are given in Refs. 20 and 21.

Scattered electrons were momentum analyzed in a *900 MeV/c, split-pole magnetic* spectrometer[22] having a 2.23 m mean bending radius and a total deflection angle of 90°. The maximum spectrometer aperture subtended at the target was 26.8 × 130.9 mrad, corresponding to an acceptance solid angle of 3.514 msr.

The spectrometer focal plane instrumentation[23] consists of a pair of multiwire drift chambers and two Čerenkov counters. The Čerenkov counters fulfill three separate functions: They assist in the rejection of stray room background, provide information for the assessment of counting losses due to the wire-chamber dead time, and supply the timing start pulse for the delay-line circuit which measures the trajectory of incoming electrons. In the first wire chamber, the positions of the electrons in the momentum-dispersion direction are determined with a spatial resolution of 0.12 mm. Further trajectory information, from both chambers, is used to correct for focal-plane curvature and other spectrometer aberrations.[23] In the course of the present experiment, momentum resolutions as fine as 26 keV were obtained operating in the dispersion-matching mode.[22] The useful momentum bite spanned by the focal-plane detection system is approximately 5%.

Measurements were performed at three scattering angles: 90°, 160°, and 180°. The 180° data were collected as an adjunct to a separate experiment to determine the cross section for elastic magnetic scattering.[24] When 180° scattering is being measured, an additional four-magnet system is employed to deflect backscattered electrons into the spectrometer.[25] The targets used in this experiment were high-impurity aluminum foils of thickness 6.62 to 30.6 mg cm^{-2}.

III. ANALYSIS OF DATA

A preliminary step in the analysis procedure was to determine the spectrometer momentum calibration. In the momentum-dispersion direction of the focal plane, the position x of an electron, momentum k_2, can be parametrized by[22]

$$x = x_s + (x|\delta)\left(\frac{k_2 - k_s}{k_s}\right) + (x|\delta\delta)\left(\frac{k_2 - k_s}{k_s}\right)^2 , \qquad (1)$$

where $(x|\delta)$ and $(x|\delta\delta)$ are first and second order spectrometer dispersion coefficients, and x_s and $k_s = 66.85\ B$ MeV/c correspond to the central trajectory for a spectrometer field of B kG. From the reaction kinematics,[26] an electron scattering from a level of excitation energy ω_i will have momentum

$$k_2 = \frac{k_1 - \omega_i - \frac{\omega_i^2}{2M}}{1 + \frac{2k_1}{M}\sin^2\frac{\theta}{2}} - \epsilon , \qquad (2)$$

where k_1 is the incoming electron momentum, θ the scattering angle, M the mass of the target nucleus, and ϵ is the ionization energy loss.

By observing the focal-plane positions of several well-known peaks in the spectra of electrons scattered from targets of at least two different masses, the values of the unknowns, $(x|\delta)$, $(x|\delta\delta)$, x_s, and k_1, can be accurately determined.

Corrections were applied for wire-chamber counting losses and the raw data were bin sorted. No corrections were applied for variation in the relative detection efficiency along the length of the chamber, since measurements have repeatedly shown the response to be flat, within a percent or so, across a broad range.[27] A representative bin-sorted spectrum is shown in Fig. 2.

Notwithstanding the fine momentum resolution of this experiment, the density of states at higher excitation energies necessitated the use of a line-shape fitting procedure to extract the integrated counts for each peak. The excitation spectra were divided up into convenient 1–3 MeV regions, each of which was individually fitted by an empirical polynomial background and a set of resonant peak functions $\phi_i(\omega, \omega_i)$ centered at various excitation energies ω_i:

$$\text{Counts/(Coulomb MeV)} = A + B\omega^{+1} + C\omega^{+2} + \Sigma_i a_i \phi_i(\omega, \omega_i) . \qquad (3)$$

The background coefficients A, B, and C are free parameters, determined in the fit.

The line-shape function $\phi_i(\omega, \omega_i)$ is defined by several different processes which take place in the measured target. Most important of these are the emission of soft and virtual photons during scattering, hard-photon bremsstrahlung, and radiation and ionization straggling. The observed line shape is obtained by convoluting the distributions for these processes, together with an empirical function which characterizes not only the strength distribution of the measured nuclear state, but also the response of the particular experimental system, which is dependent upon the finite spatial resolution of the detector system and upon optical uncertainties in the accelerator, beam-handling system, and spectrometer. A detailed examination of the total electron scattering line-shape function has been made by Bergstrom.[28]

From our point of view, an important aspect of the line shape is that the dependence of the so-called "radiative tail"[28] be given accurately, especially in the region close to the associated spectrum peak. This importance stems from our method of computing the differential cross sections. The total number of counts in a particular peak is determined by integrating the fitted curve out towards the low-energy scattered electron side. The integration is continued until some specified cutoff energy Δ below the energy of the peak E_2 and corrections for the previously mentioned radiative and ionization processes are then applied. If the shape of the tail is appropriate, corrected areas obtained to various integration cutoffs should closely agree.

Insofar as the complete calculation of the line-shape function is rather time consuming, we have used an alternative, approximate method to gene-

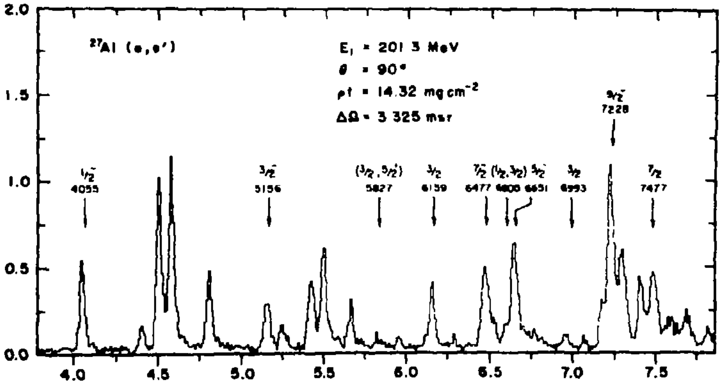

FIG. 2. Identification of ^{27}Al odd-parity states in a representative bin-sorted spectrum. A target of thickness 14.3 mg cm^{-2} was used in transmission geometry.

rate the line shape.[29] This derives from the functional form of the predominant Schwinger correction factor,[28]

$$S(\Delta)=\exp[-\delta_s(\Delta)], \tag{4a}$$

where

$$\delta_s(\Delta)=\kappa\left[\ln\left(\frac{E_1^{1/2}E_2^{1/2}}{\Delta}\right)-\frac{13}{12}\right] + (2\alpha/\pi)\left\{\frac{17}{36}+\frac{1}{4}\ln^2\left(\frac{E_1}{E_2}\right)+\frac{1}{2}\left[\frac{\pi^2}{6}-L_2\left(\cos^2\frac{\theta}{2}\right)\right]\right\}, \tag{4b}$$

E_1 being the incident electron energy, and L_2 the Euler dilogarithm. The parameter κ, given by

$$\kappa=(2\alpha/\pi)[\ln(q^2/m_e^2)-1], \tag{4c}$$

may be altered slightly to incorporate contributions from radiation and ionization straggling corrections. Given the dependence of Eq. (4b), it may then be shown that the proper line-shape function can be well approximated by[29]

$$\phi(E)=\kappa\frac{\int_{E+d}^{\infty}\phi_0(E')dE'}{\int_{E+d}^{\infty}(E'-E)\phi_0(E')dE'} \times\int_{E+d}^{\infty}\phi(E')dE'+\phi_0\left(E+\frac{d}{2}\right)S(d), \tag{5}$$

where d is the bin-sort channel width and ϕ_0 describes the peak shape in the absence of radiation and ionization effects. Proceeding from the high-energy scattered electron side, the line-shape function for a particular peak may then be calculated.

The choice of the function ϕ_0 is somewhat arbitrary. We have used asymmetric Gaussian parametrizations, Lorentzians, and Fermi-type functions for cases of relatively thick targets in reflection geometry. In any case, the particular form of ϕ_0 is important only within approximately 2 full width at half maximum (FWHM) of the peak position. At lower scattered electron energies, the shape of the radiative tail is strongly determined by calculable parameters entering into the equations for the radiation correction factors. It has been found that this method of calculating the line-shape function is quite amenable to interactive analysis carried out on small computers, such as the PDP 11/40 used in the present case.

An example of a line-shape fitted spectrum is shown in Fig. 3. The absolute scale of the deduced differential cross sections was established by normalizing a set of ^{12}C elastic scattering measurements, taken concurrently during the course of the Al experiment, to the ^{12}C cross section of Sick and McCarthy.[30] At 180°, where scattering from the spinless ^{12}C nucleus is much reduced, the data were normalized to the proton cross sections.[31]

A more explicit and convenient comparison with theory can be obtained by transforming the measured cross sections into electron scattering form factors[32]:

$$\sigma(E,\theta)=\frac{2Z^2\alpha^2}{q_\mu{}^4}\frac{k_2}{k_1}\frac{V_L}{1+(2k_1/M)\sin^2\theta/2}|F(k_1,\theta)|^2, \tag{6}$$

where k_1 and k_2 are the initial and final electron momenta and q_μ is the four-momentum transfer,

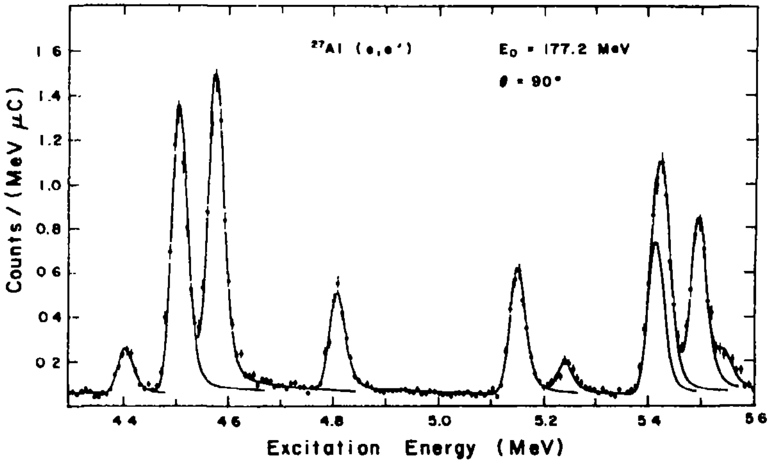

FIG. 3. Example of line-shape fitting analysis. The peak positions are fixed to tabulated excitation energies, and all peak widths are assumed equal.

given to good approximation by

$$q_\mu^2 \approx 4k_1k_2\sin^2\theta/2\,. \tag{7}$$

In the plane-wave Born approximation, the form factor separates into longitudinal and transverse components, dependent only upon the three-momentum transfer q:

$$|F(q)|^2 = |F_L(q)|^2 + \frac{V_T}{V_L}|F_T(q)|^2\,, \tag{8}$$

$$q^2 = (\vec{k}_1 - \vec{k}_2)^2\,. \tag{9}$$

For our purposes, the coefficients V_L and V_T are given sufficiently well by

$$V_L = \frac{1}{2}\frac{q_\mu^4}{q^4}\left[4k_1k_2\cos^2\theta/2 + m_e^2\left(2 + \frac{k_1}{k_2} + \frac{k_2}{k_1}\right)\right] \tag{10a}$$

and

$$V_T = \frac{1}{2}\frac{q_\mu^2}{q^2}\left[(k_1+k_2)^2 - 2k_1k_2\cos^2\theta/2\right], \tag{10b}$$

where m_e is the electron rest mass.

For the present data, obtained using many different incident electron energies, comparison with theoretical models would normally be a tedious procedure in that each different energy requires a separate distorted-wave calculation. However, tests showed that it was adequate to compare the data with a single distorted-wave result calculated for one incident energy (250 MeV), provided that both the data and the calculated curve are plotted against an "effective" momentum transfer,[33] given by

$$q_{\text{eff}} = q\left(1 + \frac{3Z\alpha}{2k_1R}\right). \tag{11}$$

The parameter R represents the "uniform-density" charge radius, 3.94 fm for ^{27}Al.

In the course of the experiment inelastic form factors were obtained for both odd- and even-parity levels up to 8 MeV excitation energy. Of the levels tabulated by Endt and van der Leun,[4] only the 5.752 MeV, $\frac{1}{2}^+$ state remained unobserved below 6 MeV. In the entire measured spectrum, the only established odd-parity state not to be observed was the $\frac{3}{2}^-$ state at 6.993 MeV. The data span a momentum transfer range of 0.57 to 2.41 fm^{-1}, with low-q measurements being sparse for the higher excited states. Although the focus of this paper is constrained to the odd-parity spectrum, a large quantity of data was also collected on even-parity levels. This will be presented at a later date.[34] Complete tables of cross sections and form factors are available from the authors.

IV. RESULTS

Theoretical C3 form factors for the most likely single-particle transitions are shown in Fig. 4.

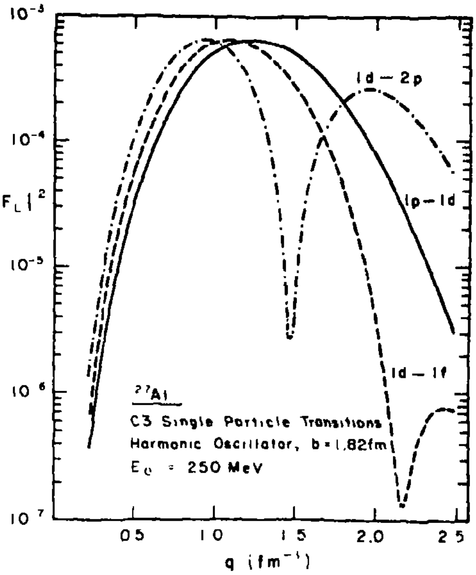

FIG. 4. Comparison of $C3(e,e')$ form factors for single-particle, odd-parity transitions in ^{27}Al. The form factors were computed in the distorted-wave Born approximation using harmonic oscillator radial wave functions with a range parameter b equal to 1.82 fm. The magnitudes of the form factors have been arbitrarily normalized to emphasize the different q dependences.

These have been computed in the harmonic oscillator model, with a value of 1.82 fm for the oscillator size parameter b. Although a small degree of freedom is commonly permitted in this parameter, meaningful theoretical interpretations require it to lie within 5–10% of the value determined from the ground-state rms charge radius. For ^{27}Al this value is 1.815 ± 0.030 fm.[35,36]

In view of the recognized collective nature of the ^{27}Al inelastic spectrum, we might not expect to observe the pure transition q dependences shown in Fig. 4; at least some degree of configuration mixing is anticipated. Nonetheless, a comparison of these calculations with the observed form factors should permit identification of the essential underlying character of the various odd-parity states. A detailed examination of the various measured form factors now follows.

The measured longitudinal form factors were predominantly of C3 character. Except for the form factor of the 5.156 MeV, $\frac{3}{2}^-$ state, evidence for C1 strength was minimal. Form factors deduced for the 4.055, 5.156, and 5.827 states are shown in Fig. 5. The observed momentum transfer dependence identifies these levels as proton-hole states, rather than states involving the pro-

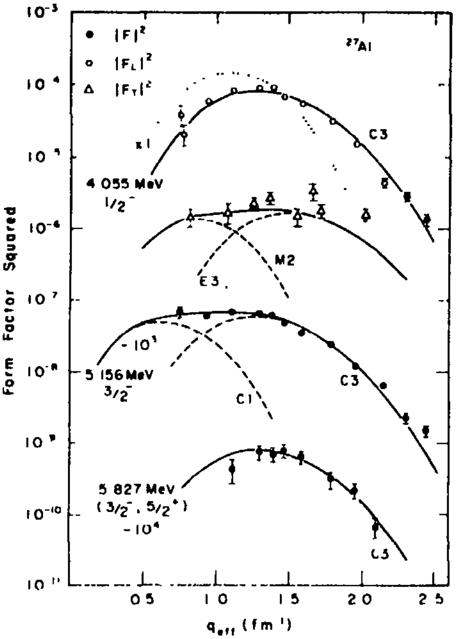

FIG. 5. Inelastic form factors measured for 1p-hole states in ^{27}Al, and comparison with best-fit theoretical curves. The calculated longitudinal form factors were obtained in the distorted-wave Born approximation using the single-particle, harmonic oscillator model with b 1.85 fm. The q dependence of the data differs markedly from that expected for the $C3$ multipole of a $1d \rightarrow 1f$ transition, which is represented by a dotted curve at the top of the figure.

motion of a $d_{5/2}$ nucleon into the pf shell. This is in accord with the structure indicated by particle transfer reactions.[16] The enhancement of the 5.156 MeV longitudinal form factor at low q discloses the existence of a measurable $C1$ component. No such enhancement is observed in the form factor of the 4.055 MeV level. The experimental form factors are therefore consistent with the respective assignments of $\frac{3}{2}^-$ and $\frac{1}{2}^-$ made recently by Maas *et al.*[14] The spin and parity of the 5.827 MeV level are currently restricted to two possibilities: $\frac{3}{2}^-$ or $\frac{5}{2}^+$. Our results for this state, although of relatively poor statistical precision, lend support to the odd-parity assignment.

The value of the harmonic oscillator parameter which best describes the momentum transfer dependence of the 1p-hole form factors is 1.85 ± 0.09 fm. The deduced $C1$ and $C3$ transition probabilities are listed in Table I. It is noted that the combined $C3$ strength of the 4.055 and 5.156 MeV states amounts to (58 ± 29)% of the total single-particle strength allowed for excitation to 1p-shell proton-hole states.

By comparing the 90° data with the measurements made at backward scattering angles, we were able to determine the transverse form factor of the 4.055 MeV state. This form factor is also shown in Fig. 5. The shapes of the constituent $M2$ and $E3$ multipole components were again computed using the harmonic oscillator, single-particle model with $b = 1.85$ fm and the normalization of the $E3$ form factor was fixed to the $B(C3)$ value established previously, as required by Siegert's theorem. Adjusting the magnitude of the $M2$ component to give a best fit to the experimental form factor leads then to a deduced multipole mixing ratio for the decay to the ground state of

$$|\delta| = \left[\frac{\Gamma(E3)}{\Gamma(M2)}\right]^{1/2} = 0.11 \pm 0.03\,,$$

where the error includes a component corresponding to a ±5% variation in the parameter b.

Figure 6 shows 90° form factors deduced for odd-parity states in the 6 to 7.5 MeV region. The q dependence of these form factors is charac-

TABLE I. Transition probabilities for excitations from ground state of ^{27}Al, deduced from harmonic oscillator model fits.

E_x[a] (MeV)	$2J^\pi$	$B(C1\uparrow)$ (e^2 fm^2)	$B(C3\uparrow)$ (e^2 fm^6)	$B(C5\uparrow)$ (e^2 fm^{10})	$B(M2\uparrow)$ (e^2 fm^4)
4.055	1^-		60 ± 25		0.034 ± 0.011
5.156	3^-	0.041 ± 0.011	41 ± 17		
5.827	$(3^-, 5^+)$		5.5 ± 2		
6.159	3^-		207 ± 44		
6.477	7^-		217 ± 32	$(8.0 \pm 3.0) \times 10^4$	
6.605	$(1, 3)^-$		86 ± 21		
6.651	5^-		367 ± 55	$(2.3 \pm 1.1) \times 10^4$	
6.993	3^-		<15		
7.228	9^-		604 ± 91	$(1.7 \pm 1.2) \times 10^4$	
7.477	7		281 ± 42	$(3.3 \pm 2.0) \times 10^4$	

[a] Excitation energies and spin assignments taken from Ref. 4.

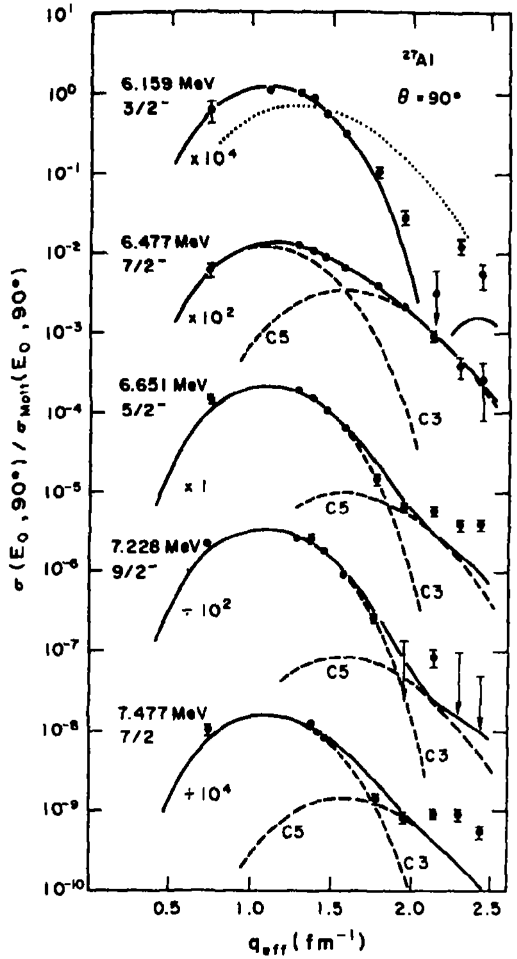

FIG. 6. Measured (e,e') form factors for ^{27}Al odd-parity states characterized, in large part, by the excitation of a 1d-shell nucleon into the 1f shell. For comparison, the q dependence expected for a $C3$ excitation to a 1p-hole state is shown by the dotted line at the top of the figure. The best-fit DWBA curves were calculated using the single-particle harmonic oscillator model with $b = 1.94$ fm. Transverse components were assumed to be small and are excluded from the calculated curves.

teristic of 1d − 1f particle excitation, differing markedly from the dependence observed for the 1p-hole states. The best-fit value of the parameter b was 1.94± 0.05 fm, which represents a slight increase over the value obtained from the ground-state charge radius. This enhancement may reflect the presence of weak admixtures of other particle-hole configurations in the excited states, most probably configurations containing a nucleon in the 2p-shell. Note, however, that in order to fit the observed form factors with the q dependences calculated for either the 1d − 2p or 1p − 1d transitions, respective b values close to 1.48 and 2.27 fm are required, values unacceptable for ^{27}Al. We conclude that the $C3$ excitation strength in the 6 to 7.5 MeV region originates mainly from 1d − 1f particle transitions.

At a scattering angle of 90°, longitudinal strength is expected to dominate these form factors, except in the $q > 2$ fm^{-1} region above the first maximum of the $C3$ multipole component, where the transverse contributions may be appreciable. The fitted $B(C5)$ values that are listed in Table I are therefore rather uncertain. In any case, only the $\frac{7}{2}^-$, 6.477 MeV level shows evidence of strong $C5$ excitation.

Three levels deserve individual mention. Two or three statistically imprecise data points, not shown in Fig. 6, were obtained on the $(\frac{1}{2}, \frac{3}{2})^-$, 6.605 MeV level. Based on these points we were able to make a crude estimate for the strength of $C3$ excitation to this state. On the other hand, the failure to observe the $\frac{3}{2}^-$ state at 6.993 MeV meant that only an upper limit could be set for the C3 transition probability to this level. In order to do this, the form factor was assumed to have a q dependence similar to that of neighboring negative-parity states. Finally, although the parity of the $\frac{7}{2}$, 7.477 MeV state has yet to be identified, the close similarity of its form factor with those of established odd-parity states in the vicinity suggests that this state also belongs to the odd-parity spectrum.

V. STRONG-COUPLING MODEL

In the preceding section, the extreme single-particle model has been utilized to establish the underlying character of each observed odd-parity state. By following this procedure, we have been able to discriminate between the hole states and the particle states, and the conclusions reached are in accord with those indicated by data from pickup and stripping reactions. Moreover, by adjusting the single-particle parameters to fit the experimental form factors, reduced ground-state transition probabilities have also been deduced. It is clear, however, that the extreme single-particle model is unable to account for the large number of observed odd-parity states. The single-particle excitations are evidently coupled to more collective modes. In this section, and the one that follows, we therefore attempt to interpret the odd-parity states in terms of two collective models, the strong- and weak-coupling models.

The $\frac{3}{2}^-$ and $\frac{7}{2}^-$ levels at 6.159 and 6.477 MeV have been identified as the lowest two members of the

$K^\pi = \frac{1}{2}^-$, [330] rotational band which is based on the $1f_{7/2}$ subshell.[18] It has long been recognized that strong decoupling inverts the ordering of this band, displacing the $J^\pi = \frac{3}{2}^-$ member to the position of lowest excitation energy.[37] This is followed by the $\frac{7}{2}^-$ and $\frac{1}{2}^-$ members. Although the odd-parity state at 6.605 MeV still bears an ambiguous spin assignment of $\frac{1}{2}^-$ or $\frac{3}{2}^-$, it is tempting to identify this as the $\frac{1}{2}^-$, third member of the [330] band, and to further assume that states at 6.651 and 7.228 MeV represent the $J^\pi = \frac{5}{2}^-$ and $\frac{9}{2}^-$ members. In the rotational model, the probable second $\frac{7}{2}^-$ state at 7.477 MeV and unobserved $\frac{3}{2}^-$, 6.993 MeV level must belong to a different band or bands.

The reduced transition probability for electromagnetic transitions of multipolarity λ between bands of angular momentum projections K and K' is given by[16]

$$\begin{aligned} B(E\lambda; JK \rightarrow J'K') = e^2\left(\frac{\hbar}{M\omega_0}\right)^\lambda \frac{2\lambda+1}{4\pi} G_{E\lambda}{}^2 \\ \times \lvert C(J\lambda J'; K\,K'-K\,K') \\ + b_{E\lambda}(-1)^{J+K'} \\ \times C(J\lambda J'; K\,-K'-K\,-K')\rvert^2, \quad (12) \end{aligned}$$

where the second term contributes only for cases in which $\lambda \geq K+K'$.

C3 transition rates computed using theoretical values[16] of the coefficients $b_{E\lambda}$ and $G_{E\lambda}$ (which depend upon the nuclear deformation) unfortunately lie in poor agreement with the rates observed experimentally. In particular, the measured rates are not obtained unless the parameter G_{E3} is approximately doubled. We have therefore chosen to fit the values of b_{E3} and G_{E3} to the excitation strengths observed for two low-spin band members. The results presented in Table II correspond to

$$b_{E3} = -0.04$$

and

$$\lvert G_{E3}\rvert = 5.484\,.$$

With the solitary exception of the $\frac{9}{2}^-$ state, excellent agreement is obtained with the experimental $B(C3\uparrow)$ values. It is possible, of course, that the 7.228 MeV $\frac{9}{2}^-$ state in fact belongs to a different band. The true $\frac{9}{2}^-$ member of the [330] band is expected to be excited only weakly, and hence may have remained unobserved in this region of relatively high level density. The failure to locate a possible $\frac{11}{2}^-$ band member is scarcely surprising, in view of the very weak excitation strength pre-

TABLE II. Comparison of experimental excitation energies and transition probabilities with predictions of weak- and strong-coupling models.

		Experiment			Weak coupling			Strong coupling
$2J^\pi$	L	E_x[a] (MeV)	$B(CL\uparrow)$ ($e^2\,\mathrm{fm}^{2L}$)		E_x (MeV)	$B(CL\uparrow)$ ($e^2\,\mathrm{fm}^{2L}$)		$B(CL\uparrow)$ ($e^2\,\mathrm{fm}^{2L}$)
1^+	2	0.843	13.5 ± 1.0[b]		0.62	37		
3^+	2	1.013	27 ± 2[b]		1.11	43		
7^+	2	2.211	95 ± 10[b]		2.27	65		
5^+	2	2.734	8 ± 3[b,d]		1.89	29		
9^+	2	3.001	57 ± 3[b]		2.30	129		
1^-	3	4.055	60 ± 25		4.06[c]	69		
3^-	3	5.156	41 ± 17		5.16[c]	39		
3^-	3	5.827[e]	5.5 ± 2		5.96	12.8		
5^-	3				6.01	4.2		
1^-	3	6.605[e]	86 ± 21		6.52	74		55
3^-	3	6.159	207 ± 44	207 ±47	6.20	156	251	207[c]
3^-	3	6.993	<15		7.55	95		
5^-	3	6.651	367 ± 55		6.09	398		367[c]
5^-	3				7.73	200		
7^-	3	6.477	217 ± 32	498 ±53	6.32	898	1049	232
7^-	3	7.477[e]	281 ± 42		7.87	151		
9^-	3	7.228	604 ± 91		6.92	1282	1286	90
9^-	3				8.20	4		
11^-	3				7.83	446		12
11^-	3				9.12	405		

[a] Reference 4.

[b] References 4, 9, 34.

[c] Parameter fitted specifically to measured value.

[d] Assuming C0 excitation strength can be neglected.

[e] Observed state has uncertain spin-parity assignment.

dicted for this state.

The existence of $K^\pi=\frac{1}{2}^-$ rotational bands based on 1p-hole states has long been recognized in the mass 21 and 23 nuclei. For example, band members up to $J^\pi=\frac{11}{2}^-$ have been identified in ^{21}Ne and ^{23}Na.[38] From the spectroscopic factors observed for proton pickup it is apparent, however, that the lowest-excited odd-parity states of ^{27}Al cannot similarly be interpreted as members of a single rotational band. The respective spectroscopic factors measured for the 4.055 MeV, $\frac{1}{2}^-$ and 5.516 MeV, $\frac{3}{2}^-$ states are 2.9 and 2.3,[4] and since each Nilsson level can contain just two particles, the involvement of several different rotational bands is implied. That such bands may be strongly mixed is not unexpected, inasmuch as it is well known that the Coriolis interaction in *sd*-shell nuclei results in appreciable mixing of bands whose angular momentum projections K differ by $1\hbar$. (Such band mixing may also account for the necessity of having to increase the parameter G_{E3} in order to generate the appropriate strength for excitation of members of the [330] band.[39]) Furthermore, the sizable $C1$ multipole component in the form factor of the $\frac{3}{2}^-$, 5.156 MeV state also points to this level having a somewhat different structure from that of the $\frac{1}{2}^-$, 4.055 MeV state.

VI. WEAK-COUPLING MODEL

During the decades of the sixties and seventies, numerous attempts were made to describe the lowest-excited even-parity levels of ^{27}Al as resulting from the weak coupling of a $1d_{5/2}$ proton hole to the first excited 2^+ state of ^{28}Si (Refs. 9–13). Support for this interpretation came not only from the fact that the center of gravity of the relavant ^{27}Al levels lies close to the 1.779 MeV excitation energy of the ^{28}Si core state, as expected in the weak-coupling limit, but also from the measured inelastic scattering cross sections,[12,13] which appeared to follow the predicted $(2J+1)$ strength rule. As both the range and precision of nuclear data have been progressively improved, several deficiencies have become apparent in the weak-coupling interpretation of these levels.[9] For example, in the mid-sixties Thankappan[10] and Evers *et al.*[11] independently obtained good fits to the observed energy levels and electromagnetic properties using the then unknown quadrupole moment of the ^{28}Si first 2^+ state as a free parameter. Their respective best-fit values of 0.035 and 0.017 eb were later shown to be in substantial disagreement with the experimentally observed moment, $+0.16\pm0.04$ *e*b (Ref. 40). Subsequent recalculations using the measured value experienced some difficulty in reproducing the observed properties of the even-parity ^{27}Al levels, even when the weak-coupling basis was extended to include higher-excited ^{28}Si core states.[9]

Notwithstanding these problems, we elected to recompute the weak-coupling model once again, with particular emphasis on the negative-parity states. For the mid-*sd*-shell nuclei the weak-coupling model can be expected to provide a better description of the unnatural-parity $1\hbar\omega$ states than it does for states of $0\hbar\omega$ character. The lowest even-parity levels were retained in the calculation primarily for the sake of achieving reasonable self-consistency.

In the weak-coupling model, odd-parity states in the 6–8 MeV region of the ^{27}Al excitation spectrum can be constructed by coupling a $1d_{5/2}$ proton hole to the strongly collective 3^- state of ^{28}Si at 6.878 MeV. This representation is lent weight by the closely similar q dependences observed for the respective (e,e') form factors.[41,42] However, as pointed out by Brain *et al.*[43] the 4^- core state at 8.413 MeV should also be included, since this is observed to be connected to the 3^- state by an appreciable $E2$ matrix element.

Following the formalism of Thankappan and True,[44] the core-hole interaction was assumed to consist of dipole and quadrupole terms:

$$H_{ch}=-\xi(J_c\cdot j_h)-\eta(Q_c\cdot Q_h)\,, \tag{13}$$

where J_c and Q_c are the angular momentum and mass quadrupole operators for the core, and j_h and Q_h are the corresponding operators for the hole. The required core matrix elements were determined from measured electromagnetic transition rates and quadrupole moments or, where experimental data were lacking, were computed using the rigid rotor model.[45] $C2$ matrix elements for the $1d_{5/2}$ proton hole were calculated using harmonic oscillator radial wave functions with a size parameter of 1.815 fm. To perform the actual weak-coupling calculation, the program INTER[45] was used, with the strength parameters ξ and η being varied until a reasonable compromise solution was found for both the energy levels and the electromagnetic properties. The results summarized in Tables II and III correspond to the values $\xi=-0.113$ and $\eta=0.008\,54$.

Before discussing these results, mention should be made of the basis chosen for the calculation of the lowest-lying odd-parity states at 4.055 and 5.156 MeV. These states were assumed to be given by the coupling of $1p_{3/2}$ and $1p_{1/2}$ proton holes to the 0^+ ground state and 2^+ first excited state of the ^{28}Si core nucleus. A similar construction has been used by Benson and Flowers[46] to compute the low-lying negative-parity spectrum of ^{19}F. Two additional parameters entering into the calculation

TABLE III. Weak-coupling eigenvalues and eigenvectors for low-lying states of ^{27}Al. Listed at the head of each column is the weak-coupling basis state, $|J_C j_h\rangle$.

E_x (MeV)	$2J$	$\|0^+\frac{5}{2}\rangle$	$\|2^+\frac{5}{2}\rangle$	$\|3^-\frac{5}{2}\rangle$	$\|4^-\frac{5}{2}\rangle$	$\|0^+\frac{1}{2}\rangle$	$\|2^+\frac{1}{2}\rangle$	$\|0^+\frac{3}{2}\rangle$	$\|2^+\frac{3}{2}\rangle$
0.00	5^+	0.9642	−0.2651						
0.62	1^+		1.0000						
1.11	3^+		1.0000						
1.89	5^+	−0.2651	−0.9642						
2.27	7^+		1.0000						
2.30	9^+		1.0000						
4.06	1^-					0.9823			0.1875
5.16	3^-						−0.5578	0.7934	−0.2438
5.96	3^-						−0.8065	−0.5875	−0.0666
6.01	5^-						0.9930		−0.1178
6.09	5^-			0.9292	0.3696				
6.20	3^-			0.9210	0.3897				
6.32	7^-			0.9686	0.2484				
6.52	1^-			1.0000					
6.92	9^-			0.9992	−0.0393				
7.55	3^-			0.3897	−0.9210				
7.73	5^-			0.3696	−0.9292				
7.83	11^-			0.8822	−0.4708				
7.87	7^-			0.2484	−0.9686				
8.20	9^-			−0.0393	−0.9992				
9.12	11^-			−0.4708	−0.8822				
9.78	13^-				1.0000				

f these states are $\epsilon_{p_{3/2}}$ and $\epsilon_{p_{1/2}}$, the energies of he 1p-shell proton holes relative to the 1$d_{5/2}$ hole.

A comparison of the calculated and experimental[4] evel schemes is shown in Fig. 1. Only the lowest ven-parity states are depicted. Given that the ulk of the theoretical spectrum is computed using nly two free parameters, ξ and η, the level of greement is generally quite fair. The calculations re seen to support the $\frac{1}{2}^-$ and $\frac{7}{2}^-$ assignments pre-iously suggested for the states observed at 5.827 nd 7.477 MeV.

The most notable deficiency of the model is the ocating of the first excited $\frac{1}{2}^+$ state 0.85 MeV be-ow the measured excitation energy. This has een a persistent problem in the weak-coupling nterpretation of ^{27}Al.[9,10] Moreover, as indicated n Table II, the predicted $B(C2\uparrow)$ strength leading o this state exceeds the experimental value by a actor of approximately 3. With the exception of he 2.211 MeV $\frac{7}{2}^+$ state, the $B(C2\uparrow)$ values for the ven-parity states are also overestimated, al-hough the calculated ground-state quadrupole mo-nent of 0.136 eb lies in good agreement with the bserved value, 0.140 ± 0.002 eb.[4] Proton pickup neasurements give rise to further misgivings in he weak-coupling description of the low-lying ositive-parity spectrum. The pickup angular dis-ribution for the $\frac{1}{2}^+$ 0.843 MeV state is character-stic of an $l = 0$ angular momentum transfer, indi-ating that this level has a somewhat different structure to that of the neighboring even-parity states, which are observed to have $l = 2$ distributions.[47,48]

Turning to the odd-parity states, measured $B(C3\uparrow)$ values for the $\frac{1}{2}^-$, $\frac{3}{2}^-$, and $\frac{5}{2}^-$ levels in the 6–8 MeV excitation range are seen to be reasonably well described by the weak-coupling calculation. On the other hand, the strengths of the neighboring $\frac{7}{2}^-$ and $\frac{9}{2}^-$ states are substantially overestimated. To some extent this disagreement can be rectified by assuming greater mixing of the two sets of basis states; those formed by coupling to the 3^- 6.878 MeV state of the ^{28}Si core, and those constructed by coupling to the 4^- level at 8.413 MeV. However, the corresponding $E2$ matrix element appears to be reasonably well fixed by experiment,[49] and, in any case, any *ad hoc* increase in the magnitude of the matrix element leads to a rapid deterioration in the agreement between the observed and calculated energy level schemes.

The properties of the lowest-excited odd-parity states, those formed by coupling a 1p proton hole to the ^{28}Si core, prove to be rather sensitive to the values chosen for the proton-hole energies $\epsilon_{p_{3/2}}$ and $\epsilon_{p_{1/2}}$. For nuclei in this region, $(p,2p)$ and $(e,e'p)$ reactions suggest[50]

$$\epsilon_{p_{1/2}} \simeq 11 \text{ MeV and } \epsilon_{p_{3/2}} \simeq 15.5 \text{ MeV}.$$

However, in ^{27}Al the proton promoted from the 1p-shell is strongly attracted by the configuration that has a single hole in the $d_{5/2}$ shell, and the energies $\epsilon_{p_{1/2}}$ and $\epsilon_{p_{3/2}}$ are greatly reduced.[51] In our first calculation of these states, the 4.055 MeV excitation energy of the first $\frac{1}{2}^-$ level was fitted, at the same time retaining the 4.5 MeV indicated as appropriate for the $1p$-shell spin-orbit splitting. This calculation left the $\frac{3}{2}^-$ state 0.5 MeV above its observed excitation, but more seriously, underestimated the $C3$ excitation strength leading to the state by a factor of 12.

In order to generate the missing strength in this transition it was found necessary to introduce appreciable $1p_{3/2}^{-1}$ admixtures into the wave function of the first $\frac{3}{2}^-$ state. The observed excitation energies of the 4.055 and 5.156 MeV levels can be fitted exactly with

$$\epsilon_{p_{1/2}} = 4.01 \text{ MeV and } \epsilon_{p_{3/2}} = 5.35 \text{ MeV},$$

values corresponding to a $1p$-shell spin-orbit splitting of only 1.35 MeV. Nevertheless, using these values we obtain the results listed in Tables II and III. It is somewhat remarkable to note that not only is excellent agreement obtained for both the excitation energies and the $B(C3\uparrow)$ values of the $\frac{1}{2}^-$, 4.055 MeV and $\frac{3}{2}^-$, 5.156 MeV levels, but the calculation also provides a good prediction of the excitation energy and weak transition strength to the probable second $\frac{3}{2}^-$ state at 5.827 MeV.

In an attempt to improve the overall level of agreement between the weak-coupling predictions and the experimental observations, we investigated the effect of assigning to the proton hole an effective charge of 1.5 e. The improvement was only marginal. At the same time, we have refrained from extending the core-hole interaction [Eq. (13)] to higher order than quadrupole in the belief that, if the weak-coupling interpretation is to be credible, it should be able to reasonably reproduce the observed properties without the introduction of multiple free parameters. Furthermore, the introduction by Singhal[9] of terms to fourth order yields little improvement in the $B(C2)$ values calculated for low-lying even-parity states.

VII. CONCLUDING DISCUSSION

The simple strong- and weak-coupling models are seen to provide only partial explanations for the data presented on the odd-parity spectrum of ²⁷Al. In the 6–8 MeV excitation range, the strong-coupling model can account for the $C3$ excitation strengths to the lowest $\frac{1}{2}^-$, $\frac{3}{2}^-$, $\frac{5}{2}^-$, and $\frac{7}{2}^-$ states, but only at the cost of approximately doubling the Nilsson coefficient G_{E3}. Furthermore, not only is the strength of the $\frac{5}{2}^-$, 7.228 MeV poorly given, but the model also fails to account for the probable existence of a second $\frac{7}{2}^-$ state at 7.477 MeV. In part, these problems may reflect the existence o band mixing, which is readily apparent in the properties observed for the 1p-hole states at 4.055 and 5.156 MeV. Moreover, as pointed out t Bhatt[5] and others,[52] the single-particle Nilsson model is fundamentally incapable of explaining th rich detail of the ²⁷Al inelastic spectrum; the energy required to recouple a pair of $d_{5/2}$ nucleons may be less than that required to promote the unpaired nucleon. Such coupling effects have been noted in the even-parity spectrum.[53] In this regard, it would therefore be worthwhile to have available a calculation which represented ²⁷Al as three sd-shell particles moving in Nilsson orbitals about a deformed $A = 24$ core.

It has been shown that the weak-coupling model can provide a reasonable description of the odd-parity level scheme. However, although $C3$ excitation strengths to states in the 6–8 MeV excitation region are less satisfactorily given, perhaps the greatest difficulty is encountered in the interpretation of the lowest-lying even-parity states.

In large part, these problems are attributable t fundamental defects which become apparent in the weak-coupling model when it is examined from a microscopic viewpoint. Some of these weaknesse lie in the nature of the $1d_{5/2}$ hole states, in which the hole is coupled into a subshell that is already actively depopulated in the formation of the excited ²⁸Si core states.[54] For example, the core states undoubtedly contain strong components wit two holes in the $d_{5/2}$ shell.[1] When another $d_{5/2}$ hole is coupled to such a configuration the pairing energy will make it much easier for a nucleon pr moted into the $2s_{1/2}$ or $1d_{3/2}$ subshells to drop bac to the $d_{5/2}$ shell. To some extent, such componen could be included in the calculation by coupling $2s_{1/2}$ and $1d_{3/2}$ holes to the ²⁶Si core states, however, care must be taken to ensure that the orthogonality of the basis states is not jeopardized.[54]

This objection is less easily applied to the case of the 1p-hole states, so perhaps it is not surpri ing that this is where the weak-coupling model seems to enjoy its greatest success. However, ir order to account for the excitation energy and observed transition strength of the $\frac{3}{2}^-$, 5.156 MeV state, it is necessary that the $1p$-shell spin-orbit splitting be set equal to 1.35 MeV, in contrast to the 4.5 MeV indicated by experimental measurements,[50] and the 4.25 MeV used by Benson and Flowers[46] in their calculation of low-lying odd-parity states in the ¹⁹F spectrum. The reasons for this discrepancy are unclear.

ACKNOWLEDGMENTS

We are indebted to the many people who assiste

in the data taking during the long course of this experiment: Dr. K. Itoh, Dr. F. J. Kline, Dr. S. Kowalski, Dr. R. A. Lindgren, Dr. G. A. Peterson, Dr. D. V. Webb, Dr. C. F. Williamson, and Dr. R. C. York. Helpful communications from Dr. L. W. Fagg and Dr. R. P. Singhal are gratefully acknowledged. The continued encouragement given throughout this project by Professor G. A. Peterson and our other colleagues at the University of Massachusetts is deeply appreciated. Special thanks are due to Lyman Stinson. This work was financially supported by the U. S. Department of Energy.

---

[*] Present address: School of Physics, Shizuoka University, Shizuoka 422, Japan.

[†] Present address: Bates Linear Accelerator, P.O. Box 95, Middleton, Mass. 01949.

[‡] Present address: I.K.O., Postbus 4395, Amsterdam 1006, Netherlands.

[1] B. H. Wildenthal and J. B. McGrory, Phys. Rev. C 7, 714 (1973).

[2] B. J. Cole, A. Watt, and R. R. Whitehead, J. Phys. G 1, 935 (1975).

[3] M. J. A. de Voigt, P. W. M. Glaudemans, J. de Boer, and B. H. Wildenthal, Nucl. Phys. A186, 365 (1972).

[4] P. M. Endt and C. van der Leun, Nucl. Phys. A310, 1 (1978).

[5] K. H. Bhatt, Nucl. Phys. 39, 375 (1962).

[6] C. L. Lin and F. J. Kline, Proceedings of the Sendai Conference on Electro- and Photoexcitations. Supp. to Research Report of Lab. of Nucl. Sci., Tohoku University 10, 181 (1977).

[7] H. Röpke, V. Glattes, and G. Hammel, Nucl. Phys. A156, 477 (1970).

[8] H. G. Price, P. J. Twin, A. N. James, and J. F. Sharpey-Schafer, J. Phys. A 7, 1151 (1974).

[9] R. P. Singhal, A. Johnston, W. A. Gillespie, and E. W. Lees, Nucl. Phys. A279, 29 (1977).

[10] V. K. Thankappan, Phys. Rev. 141, 957 (1966).

[11] D. Evers, J. Hertel, T. W. Retz-Schmidt, S. J. Skorka, Nucl. Phys. A91, 472 (1967).

[12] R. M. Lombard and G. R. Bishop, Nucl. Phys. A101, 625 (1967).

[13] G. M. Crawley and G. T. Garvey, Phys. Lett. 19, 228 (1965).

[14] J. W. Maas, A. J. C. D. Holvast, A. Baghus, H. J. M. Aarts, and P. M. Endt, Nucl. Phys. A301, 237 (1978).

[15] H. Röpke, V. Glattes, and G. Hammel, Nucl. Phys. A172, 506 (1971).

[16] S. G. Nilsson, K. Dan. Vidensk. Selsk. Mat. Fys. Medd. 29, No. 16 (1955).

[17] R. M. Lombard and G. R. Bishop, Nucl. Phys. A101, 601 (1967).

[18] T. Terasawa, K. Nakahara, M. Oyamada, H. Saito, and E. Tanaka, Kakuriken Kenkyu Hokoku 4, 27 (1972).

[19] P. C. Dunn, Nucl. Instrum. 165, 163 (1979).

[20] S. Kowalski, W. Bertozzi, and C. P. Sargent, in 1967 MIT Summer Study: Medium Energy Nuclear Physics with Electron Linear Accelerators. L.N.S. Report TID-24667, USAEC, 1967 (unpublished), p. 39.

[21] J. Haimson, IEEE Trans. Nucl. Sci. 20, 914 (1973).

[22] W. Bertozzi, M. V. Hynes, C. P. Sargent, W. Turchinetz, and C. F. Williamson, Nucl. Instrum. 162, 211 (1979).

[23] W. Bertozzi, M. V. Hynes, C. P. Sargent, C. Creswell, P. C. Dunn, A. Hirsch, M. Leitch, B. E. Norum, F. N. Rad, and T. Sasanuma, Nucl. Instrum. 141, 457 (1977).

[24] R. S. Hicks, private communication.

[25] G. A. Peterson, J. B. Flanz, D. V. Webb, H. deVries, and C. F. Williamson, Nucl. Instrum. Methods 160, 375 (1979).

[26] H. Überall, *Electron Scattering from Complex Nuclei* (Academic, New York, London, 1971).

[27] H. Crannell, internal report, Catholic University, Washington D.C. (1977).

[28] J. C. Bergstrom, in 1967 MIT Summer Study: Medium Energy Nuclear Physics with Electron Linear Accelerators, L.N.S. Report No. TID-24667, USAEC, 1967 (unpublished), p. 251.

[29] I. P. Auer and J. C. Bergstrom, FORTRAN program IPA, unpublished notes (1975).

[30] I. Sick and J. S. McCarthy, Nucl. Phys. A150, 631 (1970).

[31] F. Borkowski, P. Peuser, G. G. Simon, V. H. Walther, and R. D. Wendling, Nucl. Phys. A222, 269 (1974).

[32] T de Forest and J. Walecka, Adv. Phys. 15, 1 (1966).

[33] D. G. Ravenhall and D. R. Yennie, Proc. Phys. Soc. London A70, 857 (1957).

[34] R. S. Hicks and A. Hotta, private communication.

[35] T. Stovall, D. Vinciguerra, and M. Bernheim, Nucl. Phys. A91, 513 (1967).

[36] C. W. deJager, H. deVries, and C. deVries, At. Data Nucl. Data Tables 14, 479 (1974).

[37] A. E. Litherland, H. McManus, E. B. Paul, D. A. Bromley, and H. E. Gove, Can. J. Phys. 36, 378 (1958).

[38] A. A. Pilt, Z. Naturforsch 32A, 73 (1977).

[39] D. A. Bromley, H. E. Gove, and A. E. Litherland, Can. J. Phys. 35, 1057 (1957).

[40] A. Christy and O. Häusser, Nucl. Data Tables 11, 281 (1972).

[41] G. Mulhaupt, Ph.D. thesis, Universität Mainz, 1970 (unpublished).

[42] K. Whitner and C. F. Williamson, private communication (1979).

[43] S. W. Brain, A. Johnston, W. A. Gillespie, E. W. Lees, and R. P. Singhal, J. Phys. G 3, 681 (1977).

[44] V. K. Thankappan and W. W. True, Phys. Rev. 137, B793 (1965).

[45] A. Johnston, Internal Report, Kelvin Laboratory, University of Glasgow (1975).

[46] H. G. Benson and B. H. Flowers, Nucl. Phys. A126, 305 (1969).

[47] B. H. Wildenthal and E. Newman, Phys. Rev. 167, 1027 (1968).

[48]H. Mackh, G. Mairle and G. J. Wagner, Z. Phys. 269, 353 (1974).

[49]J. D. MacArthur, Bull. Am. Phys. Soc. 17, 90 (1972).

[50]R. C. Barrett and D. F. Jackson, *Nuclear Sizes and Structure* (Clarendon, Oxford, 1977), p. 370.

[51]G. J. Wagner, Phys. Lett. 26B, 429 (1968).

[52]D. M. Brink and A. K. Kerman, Nucl. Phys. 12, 314 (1959).

[53]H. Röpke, P. Betz, G. Bender, V. Glattes, G. Hammel, and W. Brondler, Z. Phys. 268, 391 (1974).

[54]M. H. Macfarlane and J. B. French, Rev. Mod. Phys. 32, 567 (1960).

PHYSICAL REVIEW C VOLUME 21, NUMBER 6 JUNE 1980

Neutron total cross section of sulfur: Single level to multilevel to optical model

C. H. Johnson and R. R. Winters*
Oak Ridge National Laboratory, Oak Ridge, Tennessee 37830

(Received 6 February 1980)

This paper is a further analysis of the high resolution total cross section of sulfur for 25–1100 keV neutrons that previously were measured by Halperin, Johnson, Winters, and Macklin and evaluated by single-level analysis. The usual procedure in reporting the results of high resolution neutron cross sections has been to present the data and resonance parameters with corresponding neutron strength functions resulting from some type of R-matrix analysis. Often the important nonresonant phase shifts are not reported. In this paper, making use of both strength functions and phase shifts, we extend the analysis to include an average nuclear potential (a spherical optical model). An optical model analysis not only facilitates comparison with a broad spectrum of other nucleon-nucleus experiments, but also may provide an incentive for microstructure calculations. Six average empirical functions, two each for $s_{1/2}$, $p_{1/2}$, and $p_{3/2}$ partial waves, are derived from the R-matrix analysis. From these we deduce optical model parameters, the real and imaginary well depths for s- and p-wave neutrons, and the spin-orbit well depth for p waves. The resulting real well is deeper for p waves than for s waves and for averages over partial waves at higher energies. The depth of the imaginary wells are about half those deduced at higher energies. An interesting feature of the analysis is that the multilevel curve including interference effects is produced from single-level parameters including the phase shifts.

[NUCLEAR REACTIONS ^{32}S(n,n), $E_n = 25$–1100 keV, multilevel analysis of $\sigma_{n,\mathrm{tot}}(E)$, deduced R', strength functions for $l = 0$ and 1, optical model parameters for $l = 0$ and 1.]

I. INTRODUCTION

The continued importance of the optical model potential (OMP) as a link between experimental and theoretical neutron physics is demonstrated by the microscopic optical potential calculations appearing in the recent literature, e.g., Bernard and van Giai[1] (^{208}Pb), Brieva and Rook[2] (^{40}Ca), Jeukenne, Lejeune, and Mahaux[3] (^{12}C, ^{16}O, ^{27}Al, ^{40}Ca, ^{58}Ni, ^{120}Sn, and ^{208}Pb), Mau and Bouyssy[4] (^{40}Ca), and O'Dwyer, Kawai, and Brown[5] (^{58}Ni). As noted by O'Dwyer *et al.*,[5] the imaginary part of the OMP describes particle-core excitations which can be strongly dependent on the incident particle energy. In this paper we present a spherical OMP analysis of the low energy neutron total cross section for ^{32}S$+n$. Using the cross sections and "single-level" resonance parameters reported by Halperin, Johnson, Winters, and Macklin,[6] we produce an R-matrix multilevel curve which describes the ^{32}S$+n$ total cross section in detail from 0.025 to 1.1 MeV. From this multilevel curve we deduce the depths of the real and imaginary OMP wells for scattering of s- and p-wave neutrons.

Two results from this work seem to indicate a need for microstructure calculations. Firstly, our absorptive (imaginary) potentials are approximately half as deep as required[7] for sulfur at higher energies. This may be an indication that few particle-core excitations are available at low energies for ^{32}S$+n$. Secondly, for the assumed spherical OMP the real well depths are found to be l dependent, perhaps an indication of nuclear deformation and associated collective state excitations.

Section II includes the essential formulas for the single-level description and for the multilevel conversion. Most of these are from standard references on the R-matrix formalism. Using this conversion and the level parameters[6] for those resonances for which definite J^{π} assignments were made, we calculate a multilevel curve which gives a very good description of the neutron total cross section of sulfur. The procedure does require that a nonresonant phase shift $\phi'_{\lambda l}$ be one of the single-level parameters reported for each resonance. This phase contains information relative not only to the conversion to multilevel parameters for the given resonance but also to the interference of the resonance with others of the same J^{π}, both those observed and those outside of the energy region of the measurements. It is in connection with the outer levels that we introduce a linear smoothed R function $\bar{R}$, which is not familiar in high resolution work but is a standard concept[8] for an OMP.

Section III is an interpretation of the data in terms of an OMP. An OMP, being an average potential, describes averages rather than individual resonances. Most published data relative to the OMP consist of averages over resonances, but high resolution data are needed if one wishes to

© 1980 The American Physical Society

study the effects of specific partial waves. Historically[9,10] the most significant high resolution cross section data have been at low neutron energies where s-wave scattering is dominant. From such total cross sections on a given target one can extract two average quantities; the s-wave strength function is found from the average neutron resonance widths and spacings while the scattering radius, usually designated R', is found from the phase shifts observed between resonances. At low energies the s-wave scattering radius is defined as $R' = a_c(1 - \bar{R})$, where a_c is the chosen R-matrix boundary radius. In turn, two OMP quantities can be deduced,[11] e.g., the depths of the real and imaginary wells for an OMP of given geometry.

In this paper, these familiar concepts for low energy s waves are extended to a broader energy region and to higher partial waves. The extension of the strength function is straightforward and familiar; the broader region improves our knowledge of the strength because more levels are included in the average and the higher energies allow higher partial waves to be investigated. The extension of the analog for the scattering radius is more subtle but has been discussed in the literature, e.g., Lane and Thomas.[8] It involves a second average function which accounts for the phase shift which would be observed if all the levels in the energy region under investigation were removed. That phase shift, which could be called "phase-external," is related in the R-matrix formalism to a function "R-external," which is a sum over all outer levels, both *nearby* and *far away*. In the literature the R-external has usually been designated R-infinity R^{∞}_{Jl}, with the implication that only far away states contribute. That notation is appropriate if the measured interval is small such that the effects of levels immediately above and below tend to cancel, leaving only the distant contributions. An extension of measurements to a broader energy region with more levels allows a better determination of R-infinity, which is R-external near the center of the interval. This follows since in the construction of R-external, the truly nearby levels *within* the region are subtracted exactly and the remaining levels just outside the region are less important for the cancellation. However, as the energy is moved away from the center of the interval, the R-external is changed by the imbalance of the contributions of nearby outer levels. Thus, R-external must increase continuously within the interval. This energy dependence contains important information[12]; in fact, it leads to our conclusion that the s-wave absorptive potential is relatively small for ^{32}S.

II. ANALYSIS OF TOTAL CROSS SECTIONS

A. R-matrix formalism

Only elastic neutron scattering is included in the following R-matrix analysis of the neutron total cross section of sulfur (95% ^{32}S) because the energies are below the inelastic threshold and the absorption widths are small relative to the neutron widths of the prominent resonances that enter into the analysis. Also, ^{32}S has zero spin. Thus, the R-matrix for ^{32}S reduces to a single-channel function R_{Jl} for each partial wave. The corresponding total cross section is given by[8]

$$\sigma_{Jl} = 4\pi k^{-2}(J + \tfrac{1}{2})\sin^2\phi_{Jl}\,, \tag{1}$$

where

$$\phi_{Jl} = \phi_l + \tan^{-1}(P_l R_{Jl})\,. \tag{2}$$

Here ϕ_l and P_l are the usual hard sphere phase shift and penetrability for l-wave neutrons at the chosen boundary radius. [For simplicity in Eq. (1) we have set the boundary condition B_l equal to the shift factor S_l at all energies.]

The R function is a sum over all levels of the given J^{π}:

$$R_{Jl}(E) = \sum_{\lambda=1}^{\infty} \gamma_{\lambda Jl}{}^2/(E_{\lambda Jl} - E)\,, \tag{3}$$

where $\gamma_{\lambda Jl}{}^2$ and $E_{\lambda Jl}$ are the reduced width and eigenenergy, respectively, for the λth level. We replace this infinite sum by a finite sum over the levels observed in the interval "I" of our measurements plus an R-external for the outer region:

$$R_{Jl}(E) = R^{e}_{Jl}(E) + \sum_{I} \gamma_{\lambda Jl}{}^2/(E_{\lambda Jl} - E)\,. \tag{4}$$

The above expressions, corrected for experimental resolution and Doppler broadening, could be used with the aid of a sophisticated search routine to produce a detailed multilevel fit to our measurements from 0.025 to 1.1 MeV. An alternate procedure is first to fit each resonance separately and then to convert to the multilevel description. For this purpose Eq. (2) can be rewritten[8] near a level λJl as

$$\phi_{Jl} = \phi'_{Jl} + \tan^{-1}\frac{\Gamma_n/2}{E_0 - E}\,, \tag{5}$$

where the "non-resonant" phase shift is given by

$$\phi'_{Jl} = \phi_l + \tan^{-1}(P_l R^0_{Jl})\,, \tag{6}$$

and where

$$\Gamma_n = 2P_l\gamma_{\lambda Jl}{}^2/d_{Jl}\,, \tag{7}$$

$$E_0 = E_{\lambda Jl} + P_l R^0_{Jl}\Gamma_n/2\,, \tag{8}$$

$$R^0_{Jl}(E) = R_{Jl}(E) - \gamma_{\lambda Jl}{}^2/(E_{\lambda Jl} - E)\,, \tag{9}$$

and

$$d_{Jl} = 1 + (P_l R^0_{Jl})^2 . \tag{10}$$

The R^0_{Jl} is the R function for all but the λJl level. These equations are exactly equivalent to the original multilevel phase in Eq. (2).

B. Single-level analysis

The fitting by Halperin *et al.*[6] of each resonance involved Eqs. (1) and (5) without detailed reference to other resonances as contained in Eqs. (6)–(10). Each level was fit by least-squares adjustment of five parameters: Γ_n, E_0, ϕ'_{Jl}, plus two parameters for a linear background. In a few cases two overlapping levels of different J^π were fit simultaneously. The J and l assignments were discussed.

Some approximations of R^0_{Jl} for other levels are implicit in the fitting procedure. Firstly, the energy dependences of Γ_n and E_0 through R^0_{Jl} are neglected. Secondly, substitution of Eq. (5) into Eq. (1) yields three terms involving the energy dependence of R^0_{Jl}: a Breit-Wigner term, an interference term, and a background term. For the first two terms the R^0_{Jl} is in effect held constant, equal to the value at E_0. But the latter term, which is proportional to $\sin^2\phi'_{Jl}$ and is the partial cross section that would occur if the given resonance were missing, is included in the linear background. Hence an important energy dependence for R^0_{Jl} is effectively included.

C. Multilevel description

The conversion from single to multilevel parameters requires a choice of boundary radius which is essentially arbitrary but, according to the R-matrix formalism, must be outside the polarizing forces. We choose $a_c = 6.4$ fm or $2.016\,A^{1/3}$, a radius at which the real potential for the OMP assumed in Sec. III is 2% of its central value. Table I lists the multilevel parameters $E_{\lambda Jl}$ and $\gamma_{\lambda Jl}{}^2$ calculated for this boundary radius using Eqs. (6)–(10) and the reported[6] parameters for levels of known Jl. Clearly, $E_\lambda = E_0$ and $\gamma_\lambda{}^2 = \Gamma_n/2P_l$ whenever $P_l R^0_{Jl} \ll 1$.

TABLE I. Multilevel R-matrix parameters and compound excitation energies for $^{32}S + n$ resonances of definite J^π for boundary radius $a_c = 6.4$ fm.

J^π	E_λ (keV lab)	$\gamma_\lambda{}^2$ (keV lab)	$E_{\rm exc}$ (keV)
$\frac{1}{2}^-$	30.38	2.50	8671.7
$\frac{3}{2}^-$	97.50	0.90	8736.7
$\frac{1}{2}^+$	101.37	17.72	8740.5
$\frac{3}{2}^-$	112.18	3.54	8751.0
$\frac{1}{2}^-$	202.63	9.09	8838.6
$\frac{1}{2}^-$	272.09	3.48	8906.0
$\frac{3}{2}^-$	288.36	2.20	8921.7
$\frac{1}{2}^+$	375.32	5.16	9006.0
$\frac{3}{2}^-$	412.33	0.10	9041.9
$\frac{6}{2}^+$	462.76	0.73	9090.8
$\frac{5}{2}^+$	586.87	6.80	9211.1
$\frac{6}{2}^+$	649.24	2.09	9271.6
$\frac{5}{2}^+$	675.37	1.07	9296.9
$\frac{1}{2}^+$	693.21	6.38	9314.2
$\frac{1}{2}^-$	724.74	3.38	9344.8
$\frac{3}{2}^-$	740.78	0.84	9360.3
$\frac{3}{2}^-$	778.58	1.02	9397.0
$\frac{5}{2}^+$	818.71	1.57	9435.9
$\frac{5}{2}^+$	919.85	1.80	9533.9
$\frac{3}{2}^-$	920.66	1.72	9534.7
$\frac{5}{2}^+$	947.23	2.19	9560.5
$\frac{1}{2}^-$	984.58	4.74	9596.7
$\frac{1}{2}^-$	1007.84	0.87	9619.2
$\frac{1}{2}^+$	1045.97	1.10	9656.2
$\frac{1}{2}^-$	1048.50	1.36	9658.7
$\frac{6}{2}^+$	1055.28	2.27	9665.2
$\frac{1}{2}^+$	1064.78	0.13	9674.4
$\frac{3}{2}^-$	1091.39	0.23	9700.2

To complete the calculations of the multilevel R function in Eq. (4) we require R-external, $R^e_{Jl}(E)$. At each resonance, we first calculate R^0_{Jl} from the phase shift ϕ'_{Jl} in Eq. (6). That R function includes all but the level at E_0. We then use the level parameters to subtract the contributions of the remaining levels of the same Jl in the interval. The remainders are plotted in Fig. 1. Although the points show fluctuations due to experimental uncertainties, the actual $R^e_{Jl}(E)$ must increase continuously with energy. This behavior is in contrast to the deviations of ϕ'_{Jl} from a smooth curve, which result from nuclear level fluctuations. (Plots of ϕ'_{Jl} were useful for parity assignments.[6]) One could visually draw a smooth curve for $R^e_{Jl}(E)$ to fit the points in Fig. 1 and then adjust this curve to achieve a final multilevel fit to the data. However, our procedure is to introduce a form factor for least-squares fitting of the points and to show that the resulting multilevel curve gives a good description of the cross sections. The chosen form factor serves also to introduce the OMP.

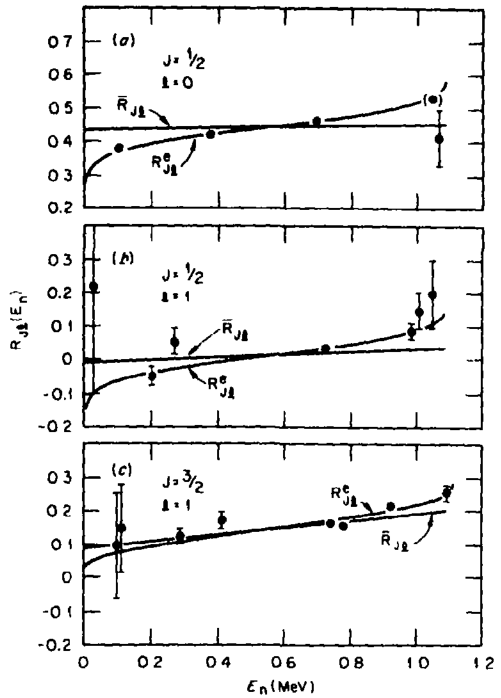

FIG. 1. Experimental and empirical external R functions and corresponding smoothed $\bar{R}$. The points show the experimental $R^e_{J\ell}$; the point in parenthesis represents one member of a close doublet (see Ref. 6) that was not included for fitting $R_{J\ell}$. The curves are the empirical best fits to $R^e_{J\ell}$ and corresponding linear $\bar{R}_{J\ell}$ deduced with the internal strengths equal to the observed values from Fig. 1. Parameters are listed in Table II.

An analytic form factor is needed. If the actual discrete levels are replaced by a continuous density of reduced width, i.e., the strength function $s_{J\ell}(E)$, then a smoothed real R function can be defined:

$$\bar{R}_{J\ell}(E) = \mathrm{Pr} \int_{-\infty}^{+\infty} s_{J\ell}(E')dE'/(E'-E), \tag{11}$$

where Pr signifies the "principle part." The external R function is then

$$R^e_{J\ell}(E) = \bar{R}_{J\ell}(E) - \mathrm{Pr} \int_I s_{J\ell}(E')dE'/(E'-E), \tag{12}$$

where the integral is over the measured interval I.

In Sec. III we use an OMP to generate $\bar{R}_{J\ell}(E)$ and $s_{J\ell}(E)$ but in this section we use a more empirical approach. To evaluate the integral in Eq. (12) we need the average experimental strength function, $\langle\gamma^2/D\rangle \approx s_{J\ell}(E)$. Figure 2 shows conventional step plots of the summed reduced widths versus energy for partial waves, $s_{1/2}$, $p_{1/2}$, and $p_{3/2}$. Also shown are linear least-squares fits obtained using weighting factors discussed by Halperin[6] and in Sec. III. The strength functions, which are the slopes of the curves, are listed in Table II and are used to evaluate the above integral. We then fit $R^e_{J\ell}(E)$ from Eq. (12) by least squares to the data of Fig. 1, under the assumption that $\bar{R}_{J\ell}(E)$ is linear with two adjustable parameters, i.e.,

$$\bar{R}_{J\ell}(E) = \alpha_{J\ell} + \beta_{J\ell}E\,. \tag{13}$$

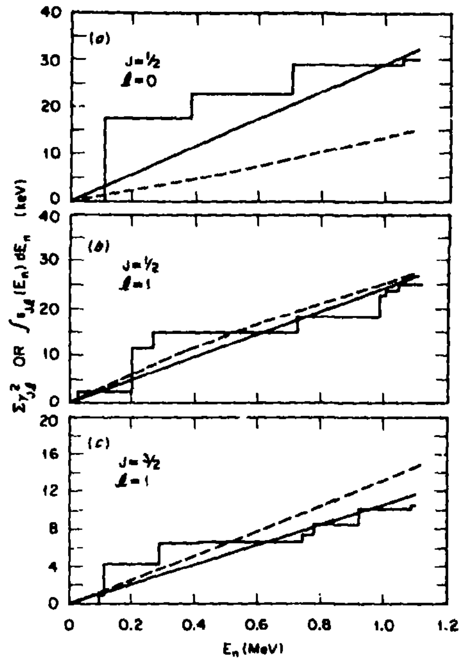

FIG. 2. Integrated reduced widths for s- and p-wave resonances. The step plots show the summations of observed reduced widths and the solid straight lines are best-fit curves. The strength functions of slopes of these curves are listed in Table II. The dashed curves are for the best-fit optical model potentials; the corresponding fits to R-external are shown in Fig. 5.

TABLE II. Parameters for the empirical external R function.[a]

$J\ell$	$s_{J\ell}$	$\alpha_{J\ell}$	$\beta_{J\ell}$ (MeV^{-1})
$s_{1/2}$	0.029	0.43	0.018
$p_{1/2}$	0.025	−0.010	0.041
$p_{3/2}$	0.011	0.088	0.11

[a] Equations (12) and (13) with integral limits 0 to 1.1 MeV.

Figure 1 shows the fitted R^{e}_{Jl} curves with corresponding $\bar{R}_{Jl}$, and Table II lists the best-fit parameters.

Figures 3 and 4 show the resulting multilevel curves for natural sulfur (0.95% ^{32}S) calculated from the equation

$$\sigma_{n,\text{tot}} = \sum_{Jl} (0.95\sigma_{Jl} + 0.05\bar{\sigma}_{Jl}), \qquad (14)$$

where σ_{Jl} is calculated for ^{32}S from Eqs. (1), (2), (4), (12), and (13) with parameters from Tables I and II, and $\bar{\sigma}_{Jl}$ is an average approximation for the minor isotopes for which R_{Jl} is replaced by $\bar{R}_{Jl}$. Eight *d*-wave resonances[6] are included; the nonresonant *d*-wave cross sections are negligible. Excluded from this curve are the minor resonances of uncertain J^{π}, the effects of Doppler and resolution broadening, and all resonances for minor isotopes. The small broad peaks near energies of 0.3, 0.36, 0.4, 0.8, and 0.85 MeV are attributed to ^{34}S. The multilevel curve gives a good description of the data, including the broad interfering resonances.

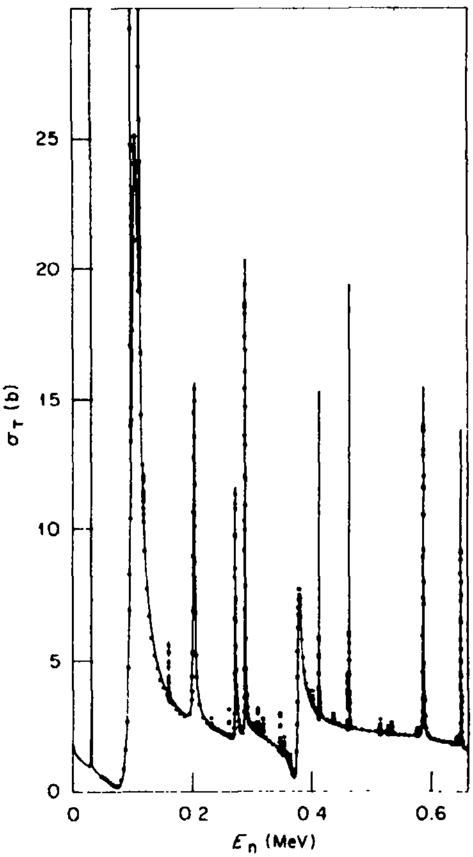

FIG. 3. Experimental cross sections and multilevel curve for neutrons on sulfur. The data from Ref. 6 have been averaged over many energy channels wherever no resonances were observed. The multilevel curve was deduced from the single-level analyses of Ref. 6. It does not include the effects of Doppler or resolution broadening, the minor resonances in ^{32}S, and all resonances in the minor isotopes.

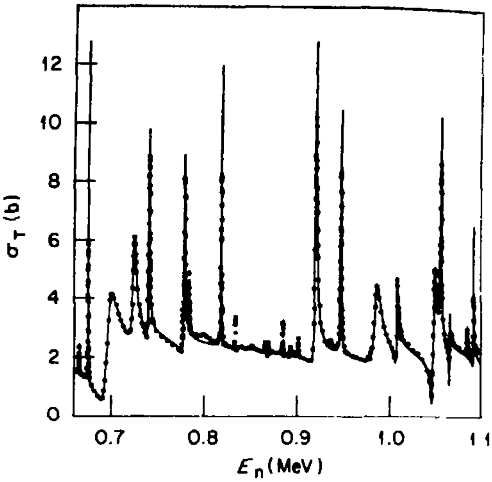

FIG. 4. Continuation of Fig. 3.

If for some reason a different boundary radius were desired, it would be necessary to regenerate Tables I and II from the single-level parameters.[6] Essentially the same multilevel curve should result.

We emphasize that, even though the use of the single-level formalism with the subsequent multilevel conversion gives considerable insight and is often convenient (as it was in the present study), a direct multilevel least-squares fit to the data would certainly be feasible and would give the same parameters. Suitable search parameters for the *R*-external of Eqs. (12)–(13) would be the α_{Jl} and β_{Jl} for the smoothed *R* function. The strength s_{Jl} for the integral would be fixed at a reasonable value deduced either from a preliminary analysis of the resonances or from the literature. Generally the exact value for s_{Jl} is not critical because it is highly correlated with β_{Jl}.

III. OPTICAL MODEL ANALYSIS

If an average neutron-nucleus potential is assumed, the neutron scattering matrix elements $\bar{U}_{Jl}$ can be calculated. If only elastic neutron scattering is allowed, the matrix elements can be expanded in terms of average complex *R* functions[8]:

$$\bar{U}_{Jl} = e^{2i\phi_l}\frac{1-L_l^*R_{Jl}}{1-L_lR_{Jl}}, \tag{15}$$

where $L_l = S_l - B_l + iP_l$, S_l is the shift factor evaluated at the boundary radius, and B_l is the boundary condition. The boundary conditions must be the same as used for the R-matrix analysis, namely $B_l = S_l$ at all energies and $a_c = 6.4$ fm. Also the assumed OMP must be negligible for $r > a_c$.

The complex R functions can be written

$$R_{Jl} = \bar{R}_{Jl} + i\pi s_{Jl}, \tag{16}$$

where, as shown by Lane and Thomas,[8] the s_{Jl} corresponds to the strength function of the actual fine structure averaged over many levels and $\bar{R}_{Jl}$ is the smoothed R function defined by Eq. (11).

For the average potential we use for each J^π a spherical optical model consisting of real Woods-Saxon and spin-orbit terms plus an imaginary surface term. In order to satisfy the requirement of the R-matrix formalism, i.e., that our channel radius a_c be truly outside the range of the nuclear forces, we cut off the potential at a radius $r_c = 2.01A^{1/3}$ which is slightly smaller than a_c. Thus, our potential has the form, for $r < r_c$,

$$V^l(r) = V_0^l f(r) + V_{s0}\frac{\vec{\sigma}\cdot\vec{l}}{r}\left(\frac{\hbar}{m_\pi c}\right)^2\frac{d}{dr}f(r) + i4a_D W_D^{Jl}\frac{d}{dr}g(r)$$

and

$$V^l(r) = 0 \quad \text{for } r \geq r_c,$$

where

$$f(r) = \{1 + \exp[(r - R_0)/a_0]\}^{-1},$$
$$g(r) = \{1 + \exp[(r - R_D)/a_D]\}^{-1}, \tag{17}$$
$$R_0 = r_0 A^{1/3} \text{ and } R_D = r_D A^{1/3}.$$

Since the model with its seven parameters for ach l value is overparametrized for the present tudy, we must fix some values at the outset. Our hoice is to fix all four geometric parameters at he values deduced by Holmqvist[7] from a systematic tudy of neutron elastic scattering in the energy egion of 1.5 to 8.1 MeV. These values are similar o others in the literature[13] and are listed in Table II. Our OMP calculations were done using the omputer code SCAT.[14]

With this model we fit the observed R external nd strength functions by least-squares adjustments of V_0^l and W_D^l for $s_{1/2}$ waves and of V_0^l, V_{s0}, nd W_D^{Jl} for $p_{1/2}$ and $p_{3/2}$. The criterion for the OMP best fits for each l value was the minimization of the chi-squared statistic

$$\chi_\nu^2 = \chi_\nu^2(R_{Jl}^e) + \chi_\nu^2(s_{Jl}), \tag{18}$$

where $\chi_\nu^2(R_{Jl}^e)$ and $\chi_\nu^2(s_{Jl})$ are the usual reduced chi-squared estimators for fits to the R external and strength function, respectively. The weights for the fits to R external were the reciprocal of the variances deriving from the variances for the single-level phase shifts. However, the relatively small experimental variances associated with the reduced widths underestimate the uncertainty in the estimate of s_{Jl}. Liou and Rainwater[15] discuss this problem and provide estimates of the uncertainty for s_{Jl}. The OMP and empirical least-squares (Sec. II) fits to the integrated strengths were weighted with the variance estimators of Liou and Rainwater. For the OMP fitting, this weighting largely removed the bias toward minimizing $\chi_\nu^2(s_{Jl}^1)$ which would result if the experimental variances of the reduced widths had been used. The best-fit values are listed in Table III. The corresponding curves for the strengths are shown by the dashed lines in Fig. 2. Figure 5 shows the $R_{Jl}^e(E)$ and corresponding $\bar{R}_{Jl}(E)$. The multilevel curves resulting from the OMP analysis are almost indistinguishable from those plotted in Figs. 3 and 4. The $R_{Jl}^e(E)$ in Fig. 5 are essentially the

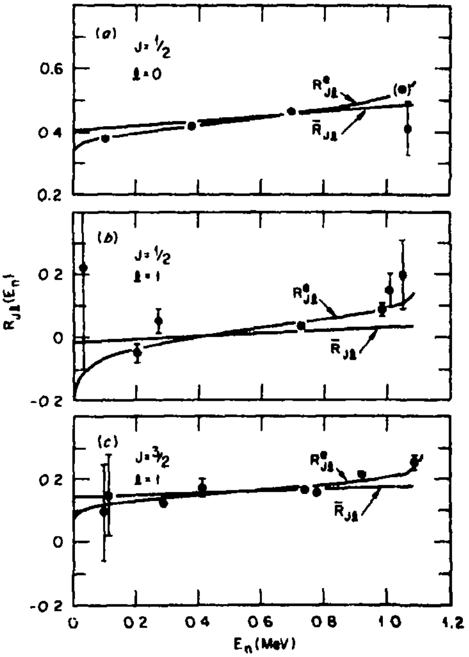

FIG. 5. Optical model fits to the external R functions. The figure is similar to Fig. 1 except that the curves are deduced from the optical model potential.

TABLE III. Fixed and best-fit optical model parameters.

Fixed geometries (fm)	Best-fit depths (MeV)	
	s waves	p waves
$r_0 = 1.21$	$V_0 = 53.8 \pm 0.4$	$V_0 = 62.4 \pm 1.1$
$a_0 = 0.66$	$W_D = 3.0 \pm 1.3$	$V_{s0} = 13 \pm 3$
$r_D = 1.21$		$W_D(p_{1/2}) = 2.6 \pm 1.1$
$a_D = 0.48$		$W_D(p_{3/2}) = 4.5 \pm 1.8$

same as in Fig. 1 but the $\bar{R}_{Jl}(E)$ are different, particularly for s waves, as discussed below.

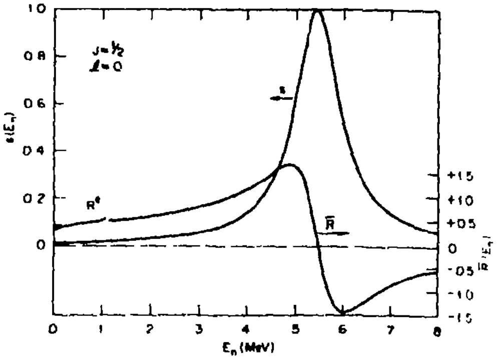

FIG. 6. Predictions of $\bar{R}(E_n)$ and $s(E_n)$ for the best fit s-wave potential. The well depths are held constant with $V_0 = 53.8$ MeV and $W_D = 3.0$ MeV. The resonance energy of 5.45 MeV for the 3s state depends on the 6.4 fm boundary radius as well as the volume of the real well. The interval of the measurement is only 0 to 1.1 MeV and the external function R^e shown for the interval is the same as in Fig. 5.

IV. DISCUSSION OF THE OPTICAL MODEL

A. A possible nonstatistical component for the 101-keV resonance

The resonance at 101 keV contains more than half of the total reduced width for the five s-wave resonances and its width is about 1% of the 3s single particle width. Moreover, Halperin *et al.*[8] report that it has a non-negligible valency capture component. If that one level were a nonstatistical state, the observed average strength with this level included would not properly represent the strength function. Further information on the correct strength function is contained in the R external because it depends partly on the strength just outside the measured region. Furthermore, the R external has a relatively small uncertainty, particularly for s waves for which a small change in $R^e(E)$ would produce an obvious misfit to the cross sections. For the empirical s-wave fit in Sec. II the nearly constant $\bar{R}$ requires that the external strengths above and below the measured interval be the same as the observed internal average. In contrast, the OMP analysis in Sec. III requires, as indicated by the dashed curve in Fig. 2, that the outer strengths be about half of the internal average. Since the observed strength could be reduced to the OMP value if the 101-keV resonance were omitted, this OMP analysis indicates that the resonance is nonstatistical.

This prediction from the OMP is clarified by Fig. 6, which shows $s(E)$ and $\bar{R}(E)$ for s waves calculated up to 8 MeV using constant well depths from Table III. The energy of the 3s resonance is a function of the assumed boundary radius, 6.4 fm, and of the parameters of the real well; the spreading width is a function of the imaginary potential. Also shown is the fitted $R^e(E)$ from Fig. 5(a). It deviates from $\bar{R}(E)$ towards both ends of the interval, but the deviations are small because $s(E)$ is small, i.e., only about half of the observed average. The OMP $s(E)$ can be increased to equal the observed average, *without* disturbing the average $\bar{R}$, by increasing W_D about a factor of 2 and making a slight adjustment in V_0. But the $R^e(E)$ then deviates more strongly from $\bar{R}(E)$ and the multilevel curve is a poor description of the cross sections.

B. Real well *l* dependence

The real well depths are determined primarily from the phase-external or corresponding R external. A particularly interesting result of this study is that the real well for p waves is deeper than for s waves by about 16%. The s-wave depth of 53.8 MeV is about as expected from other OMP studies. For example, if our s-wave potential depth is used with the isospin term[16] $24(N-Z)/A$ MeV subtracted, it predicts the peak of the 3s size resonance at $A = 52$, in good agreement with the observed[10] maximum near $A = 55$. At higher energies (6, 7, and 8 MeV) Holmqvist[7] scattered neutrons from sulfur and, using the present OMP geometry, deduced a 50-MeV depth. (This represents an average for all partial waves.) The difference from our 53.8-MeV for s waves could be attributed to a linear term in an energy dependent real well depth with coefficient 0.58 MeV^{-1}, a reasonable value[17,18] for ^{32}S.

These comparisons suggest that our p-wave well depth is unusually deep. But if the p-wave depth were reduced to the s-wave value, the 2$p_{1/2}$ single particle state would become unbound by about 500 keV and the strength would be much larger than observed. In other words, the 2p size resonance would be near $A = 32$. The deeper well binds the p-states and, although this may not agree with other OMP studies, it is consistent with (d,p) stripping measurements, which have shown that most of the $2p$ strength is in the bound region. Mermaz *et al*[19] measured $^{32}S(d,p)$ stripping for 18-MeV deuterons and deduced spectroscopic factors, some tentative, for four $p_{1/2}$ levels and six $p_{3/2}$ levels. The summed spectroscopic factors were nearly unity, 1.01 for $p_{1/2}$ and 0.91 for $p_{3/2}$, and the energy centroids weighted by the spectroscopic factors were −2.4 MeV for $p_{1/2}$ and −4.0 MeV for $p_{3/2}$. (These quantities may have large uncertainties.) It is of interest to compare these centroids with the eigenenergies for our p-wave OMP. The real part of our OMP binds the $2p_{1/2}$ state at −2.0 MeV and the $2p_{3/2}$ at −5.7 MeV.

If the s-wave well were increased to the p-wave depth of 62.4 MeV, the 3s resonance in Fig. 6 would move down to 2.5 MeV. Both $\bar{R}(E)$ and $s(E)$ would then be too large relative to the experiment.

It is reasonable to believe that another model, say a nonspherical OMP, could remove the l dependence in the real well. Given the 6.4 fm R-matrix boundary, the model would be required to reproduce the average strengths and external R functions reported here.

C. Small absorptive potentials

The imaginary well depths of about 3 MeV for both s and p waves are a factor of 2 or 3 smaller than usually found in OMP studies. For example, Holmqvist[7] found $W_D = 6$ to 10 MeV for neutron scattering from sulfur at 6, 7, and 8 MeV. But a small well depth may be reasonable at low energies if particle-core states are not easily reached. In the theory[1-5] of the OMP the absorptive or imaginary potential arises from processes in which the incident particle excites the core to states in which the energy of the excited core-plus-particle is approximately equal to the incident energy of the particle. A likely candidate for $\frac{1}{2}^+$ particle-core states near the energy region studied here would be a $d_{3/2}$ particle coupled to the 1^+ excited ^{32}S core consisting of a $d_{3/2}$ particle and $d_{5/2}$ hole. The 1^+ or $M1$ strengths in the ^{32}S core have been observed[20] at 8.13, 10.82, 11.14, and 11.62 MeV with $M1$ strengths 2.8, 2.9, 18.9, and 9.7 eV, respectively. Since very little of the reported $M1$ strength is contained in the range of excitation energies 8.6–9.7 MeV of our work, a small W_D might be expected if states which de-excite by $M1$ transitions dominate. More detailed microstructure calculations of these and other particle-core excitations should be made. Even without such detailed calculations, we expect that the s-wave imaginary well depth would increase significantly over the next 2 MeV of excitation as the bulk of the $M1$ strength is encountered.

D. R-matrix boundary radius invariance

It is emphasized that the optical model parameters are expected to be independent of the assumed R-matrix boundary radius, providing the radius is outside the potential. We investigated this by repeating the analysis using the same model form factors but with the boundary radius a_c increased to 7.4 fm. The best fit OMP well depths were unchanged.

F. Scattering radius

A real potential phase shift can be defined

$$\phi^{\rm pot}_{Jl} = \phi_l + \tan^{-1}(P_l \bar{R}_{Jl}). \tag{19}$$

In general this differs from the real part $\phi^{\rm real}_{Jl}$ of the complex phase shift for the OMP. However, at low energies where $P_l s_{Jl}$ is negligible and with the boundary conditions $B_l = S_l$, these two real phases become equal. It follows from the foregoing discussion that the low energy potential phase is independent of the assumed boundary radius a_c. The scattering radius is then given by

$$R' = k^{-1}\phi^{\rm real}_{l=0} \simeq a_c(1 - \bar{R}_{l=0}). \tag{20}$$

For the s-wave OMP we find in the limit $E \to 0$, $R' = 3.80$ fm. A compilation of low energy data[10] gives $R' = (4.1 \pm 0.2)$ fm, in good agreement with our result.

ACKNOWLEDGMENTS

We are grateful to Dr. D. J. Horen and Dr. R. L. Macklin for many helpful discussions. We are also indebted to Dr. J. A. Harvey and Dr. E. G. Perey for careful and critical reading of this manuscript.

This work was sponsored by the Division of Basic Energy Sciences, U. S. Department of Energy under Contract No. W-7405-eng-26 with the Union Carbide Corporation and Contract No. EY-76-5-02-2696 with Denison University.

---

[*] Present address: Denison University, Granville, Ohio 43203.

[1] V Bernard and Nguyen van Giai, Nucl. Phys. A327, 397 (1979).

[2] F. A. Brieva and J. R. Rook, Nucl. Phys. A291, 317 (1977).

[3] N.-P. Jeukenne, A. Lejeune, and C. Mahaux, Phys. Rev. C 16, 80 (1977).

[4] N. Vinh Mau and A. Bouyssy, Nucl. Phys. A257, 189 (1976).

[5] T. F. O'Dwyer, M. Kawai, and G. E. Brown, Phys. Lett. 41B, 259 (1972).

[6] J. Halperin, C. H. Johnson, R. R. Winters, and R. L. Macklin, Phys. Rev. C 21, 545 (1980).

[7] B. Holmqvist, Ark. Fys. 38, 403 (1968).

[8] A. M. Lane and R. G. Thomas, Rev. Mod. Phys. 30, 257 (1958).

[9] *Experimental Neutron Resonance Spectroscopy*, edited by J. A. Harvey (Academic, New York, 1970).

[10] *Resonance Parameters*, 3rd ed., compiled by S. F. Mughabghab and D. I. Garber, BNL Report No. 325 (National Technical Information Service, Springfield, Virginia, 1973), Vol. 1.

[11] J. E. Lynn, *Theory of Neutron Resonance Reactions* (Clarendon, Oxford, 1968).

[12] F. W. K. Firk, J. E. Lynn, and M. C. Moxon, Proc. Phys. Soc. (London) 82, 477 (1963).

[13] C. M. Perey and F. G. Perey, At. Data and Nucl. Data Tables 17, 1 (1976).

[14] W. R. Smith, Comput. Phys. Commun. 1, 106 (1969).

[15] H. I. Liou and J. Rainwater, Phys. Rev. C 6, 435 (1972).

[16] G. R. Satchler, in *Isospin in Nuclear Physics*, edited by D. H. Wilkinson (North-Holland, Amsterdam, 1969), Chap. 9.

[17] F. G. Perey, Phys. Rev. 131, 745 (1963).

[18] P. H. Stelson and L. Grodzins, Nucl. Data Sect. A 1, 21 (1965).

[19] M. C. Mermaz, C. A. Whitten, Jr., J. W. Champlin, A. J. Howard, and D. A. Bromley, Phys. Rev. C 4, 1778 (1971).

[20] L. W. Fagg, Rev. Mod. Phys. 47, 683 (1975).

PHYSICAL REVIEW C VOLUME 21, NUMBER 6 JUNE 1980

Wave-function formalisms in the channel coupling array theory of many-body scattering

F. S. Levin*
Physikalisches Institut der Universität Bonn, D 5300, Bonn, West Germany

(Received 20 September 1979)

Wave-function formalisms corresponding to different channel coupling array transition operators of many-body scattering theory are derived and discussed. The Kouri-Levin transition operators are seen to be in typical Lippmann-Schwinger form and allow for the introduction of wave-function components in a particularly straightforward way. The Baer-Kouri transition operators are not in the Lippmann-Schwinger form and an alternate procedure is used to derive their corresponding wave-function components. In the three-body case, the Kouri-Levin operators $\hat{T}_{jk}$ obtained from the Faddeev-Lovelace choice of channel coupling array are seen to lead to precisely the Faddeev wave-function components. The Baer-Kouri operators are shown to lead to wave-function components obeying inhomogeneous equations. These inhomogeneous equations are used to give an alternate explanation of the nonunitary amplitudes obtained in recent calculations based on approximate forms of the Baer-Kouri operators.

NUCLEAR REACTIONS Many-body scattering theory, channel coupling array wave-function formalisms, aspects of the bound-state type of approximation method, explanation of some nonunitary numerical results of Baer and Kouri and of Lewanski and Tobocman.

I. INTRODUCTION

In this paper we investigate wave-function formalisms for some of the channel coupling array[1] (CCA) theories of many-body scattering.[2-8] Our work is in part complementary to that of Vanzani, who has discussed this topic for a number of n-particle scattering theories not based on the CCA method.[9] In contrast to the approaches reviewed by Vanzani, some of the CCA types of scattering equations for transition operators are in matrix Lippmann-Schwinger (LS) form,[10] which allows for the introduction of wave-function equations in a particularly transparent manner, and we discuss examples of this case in some detail.

For those CCA types of equations not in LS form, we introduce an alternate procedure for introducing wave-function equations. This latter procedure is found to lead to *inhomogeneous* differential equations for the wave-function components, rather than to homogeneous ones, as in the LS case. The existence of such inhomogeneous equations provides an alternate explanation to the one given previously[11] for the occurrence of the nonunitary results found in the recent numerical calculations of Baer and Kouri[1] and of Lewanski and Tobocman,[12] as we discuss in detail below.

The organization of this paper is as follows. In Sec. II we introduce our notation. Transition operator equations are stated in Sec. III. Wave-function equations are derived in Sec. IV, and approximations are discussed in Sec. V. Section VI summarizes our work.

II. NOTATION

Our notation mostly follows that of earlier work,[2-6] and we provide only a brief summary here. We consider a scattering system consisting of n, nonrelativistic, distinguishable particles labeled $1\ldots n$, governed by a Hamiltonian H and obeying the Schrödinger equation

$$(E-H)|\Psi\rangle=0\,. \tag{2.1}$$

The particles can be observed in a variety of m-cluster channels or partitions, $1\le m\le n$. Corresponding to these channels are partitions of H into a channel Hamiltonian H_j, governing the motion of the noninteracting clusters in channel j, and a channel interaction V^j, which goes to zero as the separations between all clusters in channel j become asymptotic:

$$H=H_j+V^j,\quad 0\le j\le N\,. \tag{2.2}$$

H_0 is the total kinetic energy operator, and $V^0=V$ is the sum of all interactions; $j=0$ thus refers to the n-particle breakup channel.

The asymptotic states $|\Phi_j(E)\rangle\!\rangle$ of the system are eigenstates of H_j with total binding plus kinetic energy equal to E:

$$(E-H_j)|\Phi_j(E)\rangle\!\rangle=0\,. \tag{2.3}$$

The $|\Phi_j(E)\rangle\!\rangle$ are products of a bound state for each cluster in the channel times plane wave states describing the intercluster motion.

Resolvent operators $G(z)$ and $G_j(z)$ are defined

© 1980 The American Physical Society

hat $n=3$ here)

$$U_{jk}(z)=\bar{\delta}_{jk}G_0^{-1}(z)+\sum_m \bar{\delta}_{jm}t_m(z)G_0(z)U_{mk}(z) \tag{3.14a}$$

$$=\bar{\delta}_{jk}G_0^{-1}(z)+\sum_m U_{jm}(z)G_0(z)t_m(z)\bar{\delta}_{mk}\,. \tag{3.14b}$$

Jse of (2.12a) and (2.12b) in (3.14a) and (3.14b) llows one to express the latter equations in terms f $V_mG_m(z)$ or $G_m(z)V_m$ rather than $t_m(z)$ and $G_0(z)$. lthough it is straightforward to express (3.14a) nd (3.14b) as matrix equations, it is unnecessary) do so in order to see that they are not in standard LS form. Nevertheless, they do possess an quivalent wave-function formalism, viz., the 'addeev wave-function component equations, as oted, for example, by Vanzani.[22]

Alt, Grassberger, and Sandhas have shown that ıeir operators U_{jk} are related to those defined y Lovelace, i.e., the X_{jk} and $\hat{X}_{jk}$:

$$U_{jk}(z)=\bar{\delta}_{jk}G_k^{-1}(z)+X_{jk}(z) \tag{3.15a}$$

nd

$$U_{jk}(z)=\bar{\delta}_{jk}G_j^{-1}+\hat{X}_{jk}(z)\,. \tag{3.15b}$$

he relation between the U_{jk} and T_{jk} of Eq. (3.9a) : given in Ref. 5:

$$\lim_{\epsilon\to 0+} T_{jk}(E+i\epsilon)=\lim_{\epsilon\to 0+} U_{jk}(E+i\epsilon)G_0(E+i\epsilon)V_k\,. \tag{3.16a}$$

he analogous relation for $\hat{T}_{jk}$ of (3.9b) is

$$\lim_{\epsilon\to 0+} \hat{T}_{jk}(E+i\epsilon)=\lim_{\epsilon\to 0+} V_jG_0(E+i\epsilon)U_{jk}(E+i\epsilon)\,. \tag{3.16b}$$

These last four equations show that on-shell, the :act matrix elements of these various operators re phase equivalent. Nevertheless, the corres- ɔnding wave-function formalisms need not be ıd are not the same. Furthermore, use of an ɔproximation in one of the wave-function formasms will, in general, not lead to the same form ır each of the approximate transition operator ıuations to which the wave-function equation ɔrresponds. This is, of course, not surprising, nce approximations can be viewed as off-shell ·ansformations. What may be surprising, how'er, are the particular approximate equations emselves, a point discussed in Sec. V.

IV. WAVE-FUNCTION FORMALISMS

A. Methods

The resemblance of Eqs. (3.6a) and (3.7b) to the S equation (2.10a) suggests that at least for the KL operators it will be simple to obtain wave-function components. This is indeed the case and we first review the relevant procedure for the LS equation $n=2$. The analog of (2.10a) for $n=2$ is

$$t(z)=v+v(z-H_0)^{-1}t(z)\,, \tag{4.1}$$

where $H=H_0+v$, with H_0 the relative-motion kinetic-energy operator and v the interparticle interaction. The LS equation for the state vector $|\Psi\rangle=\lim|\Psi^{(+)}\rangle$ (i.e., the LS wave-function equation) is obtained from Eq. (4.1) by means of the definition

$$v|\Psi^{(+)}\rangle\equiv t(E+i\epsilon)|\Phi(E)\rangle\,, \tag{4.2}$$

where $|\Phi(E)\rangle$ is a plane wave state with energy E, the $n=2$ analog of $|\Phi_j(E)\rangle$ of Eq. (2.3).

Applying both sides of (4.1) to $|\Phi(E)\rangle$ for $z=E+i\epsilon$ and using (4.2) yields

$$|\Psi^{(+)}\rangle=|\Phi(E)\rangle+(E+i\epsilon-H_0)^{-1}v|\Psi^{(+)}\rangle\,, \tag{4.3}$$

the well-known LS equation.[10] That a similar procedure can be applied to the T and $\hat{T}$ matrix equations[4] is a consequence of the occurrence of $\mathrm{v}(\hat{\mathrm{v}})$ in both the driving term and the kernel term of these equations. However, since the X and $\hat{X}$ equations (3.11a) and (3.11b) are not of this form, we may anticipate possible problems using the LS type of method for these latter operators.

We shall consider in detail only the right-hand form of the various operator equations, since in left-hand form, e.g., Eq. (3.6b)—one obtains equations for the components $\langle\overleftrightarrow{\psi}|$ rather than $|\overleftrightarrow{\psi}\rangle$. For the case of arbitrary particle number n, the various matrix operator equations take the form

$$O(z)=B(z)+K(z)O(z)\,, \tag{4.4}$$

where O stands for any of the transition operators, B is the Born or driving term, and K is the kernel term.

Of particular interest is the situation wherein $K(z)$ factorizes as

$$K(z)=B(z)\mathcal{G}(z)\,, \tag{4.5}$$

where $\mathcal{G}(z)$ contains outgoing wave Green's functions (in limit $z\to E+i0$). Equations (3.6a), (3.7b), and (3.14a) are all of this form. If K does not factorize or if instead of (4.5), one finds

$$K(z)=C(z)\mathcal{G}(z)\,, \tag{4.6}$$

with $C^{-1}B\neq I\neq B^{-1}C$, I being the unit matrix, then, in general, other methods for obtaining wave-function equations must be sought.

Thus when (4.5) holds, then analogously to (4.2), we define a column vector of state-vector components $|\overleftrightarrow{\psi}\rangle$ via

$$B(E+i0)|\vec{\psi}\rangle = O(E+i0)|\vec{\Phi}\rangle, \tag{4.7}$$

where for future notational simplicity we have omitted the necessary intermediate step of first setting $z=E+i\epsilon$ and writing $|\vec{\psi}^{(\epsilon)}\rangle$, and then taking the limit $\epsilon\to 0^+$. The vector $|\vec{\Phi}\rangle$ is defined by

$$(|\vec{\Phi}\rangle)_j = \delta_{jk}|\Phi_k(E)\rangle, \tag{4.8}$$

where k is arbitrarily taken to be the incident channel (assumed to be a two-cluster channel unless otherwise stated). Correspondingly, we have

$$(|\vec{\psi}\rangle)_j = |\psi_j\rangle \tag{4.9}$$

and the dependence of $|\psi_j\rangle$ on both E and the incident channel index k is suppressed.

From Eqs. (4.4), (4.5), and (4.7) we easily find

$$|\vec{\psi}\rangle = |\vec{\Phi}\rangle + \mathcal{G}(E+i0)B(E+i0)|\vec{\psi}\rangle, \tag{4.10}$$

the desired result in general form. The definition (4.7) immediately allows one to determine the transition amplitudes from the asymptotic form of (4.10) in a coordinate (wave-function) representation.

When $K(z)$ does not factorize, or (4.6) holds, one must seek other procedures for introducing wave-function components. The method we follow here is to define components $|\vec{\chi}\rangle$ by

$$|\vec{\chi}\rangle = |\vec{\Phi}\rangle + \mathfrak{g}(E+i0)O(E+i0)|\vec{\Phi}\rangle, \tag{4.11}$$

where $\mathfrak{g}$ is given by (3.5). Substituting (4.4) into (4.11) gives

$$|\vec{\chi}\rangle = [I+\mathfrak{g}(E+i0)B(E+i0)]|\vec{\Phi}\rangle + \mathfrak{g}(E+i0)K(E+i0)O(E+i0)|\vec{\Phi}\rangle. \tag{4.12}$$

From (4.12) one can try to construct an integral equation for $|\vec{\chi}\rangle$. We apply this procedure below to the operators $\hat{X}$.

Once equations for $|\vec{\psi}\rangle$ or $|\vec{\chi}\rangle$ have been determined, the next step is to relate the components to the Schrödinger state $|\Psi\rangle$. [One is, after all, trying to solve the Schrödinger equation (2.1).] Finally, one may introduce approximations and examine their consequences, a point we consider in Sec. V. We now apply the procedures just outlined to the operators of Sec. III.

B. KL case

We examine these operators first because they are defined by Eqs. (3.6a) and (3.7b), which are precisely in the form of Eq. (4.4). Hence their corresponding wave-function components will obey equations of the form (4.10). Thus for (3.6a) ave

$$\vec{\psi}\rangle = |\vec{\Phi}\rangle + \mathfrak{g}\,\mathcal{U}|\vec{\psi}\rangle,$$

or (3.7b) we find

$$|\hat{\vec{\psi}}\rangle = |\vec{\Phi}\rangle + \mathfrak{g}\,\hat{\mathcal{U}}|\hat{\vec{\psi}}\rangle.$$

The components corresponding to different choices of W will be distinguished by superscripts.

1. FL choice of W

We begin with this $n=3$ choice of W, Eqs. (3.9a) and (3.9b), because of the interesting properties of the corresponding sets of components.

(*a*) *The operators* $\hat{T}$. From Eqs. (3.9b) and (4.7) one easily finds that the components $|\hat{\psi}_j^F\rangle$ corresponding to the $\hat{T}_{jk}$ obey[3,6]

$$|\hat{\psi}_j^F\rangle = |\Phi_k(E)\rangle\delta_{jk} + G_j^{(+)}V_j\sum_{m=1}^{3}\bar{\delta}_{jm}|\hat{\psi}_m^F\rangle, \tag{4.13}$$

which are the Faddeev wave-function component equations;[23] hence the superscript F. In addition, (4.13) also defines the set of components corresponding to the AGS operators.[22] That this is true even though $\mathcal{G}(z)$ for the AGS equations is not equal to $\mathfrak{g}(z)$ is shown by an easy calculation using Eqs. (3.14a) and (4.7). Such a result might be expected, given the multiplicative relationship (3.16b). Notice, however, that (4.13) follows only from the right-hand equation (3.16) for $\hat{T}_{jk}$. Had the left-hand form been used, the result would have been equations defining the Hermitian conjugate to the components corresponding to T_{jk} of (3.9a). These latter components have quite different properties from the $|\hat{\psi}_j^F\rangle$, despite the fact that both the $\hat{T}_{jk}$ and the T_{jk} are each multiplicatively related to the U_{jk}. We enlarge on this point in subsection (b) below.

Equation (4.13) has two well-known properties[23]:

$$(E-H)\sum_j|\psi_j^F\rangle = 0 \tag{4.14}$$

and

$$|\psi_j^F\rangle = G_0V_j|\Psi\rangle. \tag{4.15}$$

Taken together these imply

$$\sum_j|\psi_j^F\rangle \equiv |\Psi\rangle, \tag{4.16}$$

illustrating the well-known fact that in integral form the Faddeev wave-function component equations do not admit spurious solutions,[24] i.e., $\sum_j|\hat{\psi}_j^F\rangle \neq 0$.

(*b*) *The operators* T. From Eq. (3.9a) we see that B_{jk} of (4.7) is just $\bar{\delta}_{jk}V_k$, so that the components corresponding to the T_{jk} obey

$$|\psi_j^{FL}\rangle = \delta_{jk}|\Phi_k\rangle + G_j^{(+)}\sum_{m=1}^{3}\bar{\delta}_{jm}V_m|\psi_m^{FL}\rangle. \tag{4.17}$$

Despite the great similarity in structure between Eqs. (3.9a) and (3.9b), their equivalent wave-function components, given by Eqs. (4.13) and

(4.17), are totally dissimilar. As first pointed out by Sandhas,[25] these latter components are each identical to the full Schrödinger state $|\Psi\rangle$. To prove this, one simply operates on both sides of (4.17) by $[G_j^{(+)}]^{-1}$; a little rearranging then yields $(E-H_0)|\psi_j^{FL}\rangle=\sum_m V_m|\psi_m^{FL}\rangle$, showing that $|\psi_j^{FL}\rangle$ is independent of j. The equation that results from utilizing this is the Schrödinger equation. A similar result holds for the components corresponding to the T defined by a CPA (see below).

We thus see that in (4.17), the channel indices on the $|\psi_j^{FL}\rangle$ act essentially as a bookkeeping device: They remind us that $G_j^{(+)}$ governs the asymptotic behavior of $|\psi_j^{FL}\rangle$. Unlike the $|\hat{\psi}_j^{F}\rangle$ of Eq. (4.13), which do depend on the channel index and have as bound-state sources only contributions from the "tube" defined by the relative coordinate in channel j becoming large,[26] the $|\psi_j^{FL}\rangle=|\Psi\rangle$ of (4.17) receive contributions from all asymptotic channels, and hence yield amplitudes for scattering into all channels, not only j.

2 *Channel permuting choice of W*

(*a*) *The $\hat{T}$ operators.* In this case, the operators are defined through Eq. (3.8b) and lead to components obeying

$$|\hat{\psi}_j^{(+)}\rangle=|\Phi_1(E)\rangle\delta_{j1}+G_j^{(+)}V^{j+1}|\hat{\psi}_{j+1}^{(+)}\rangle\,, \tag{4.18}$$

where the incident wave is in channel 1. As with the components of Eq. (4.13), those of (4.18) also obey

$$(E-H)\sum_j|\hat{\psi}_j^{(+)}\rangle=0\,, \tag{4.19}$$

but now in addition to $\sum|\hat{\psi}_j^{(+)}\rangle=|\Psi\rangle$, one can have a spurious bound-state solution[24] of the form $\sum|\hat{\psi}_j^{(+)}\rangle=0$. This has not proved to be a serious drawback for the bound-state applications for which (4.18) has been used.[27] In addition, Eq. (4.18) has the advantage over Eq. (4.13), for example, in that it not only applies to an arbitrary number of channels, but this set can also be truncated in a simple fashion, thus permitting a variety of approximations to be studied.[28] Both sets, Eqs. (4.13) and (4.18), have been used for numerical studies of model nuclear reactions.[17] Each of these sets of equations has the "in-principle" advantage that only the jth component yields the amplitude for scattering from an initial two-cluster state in channel k to a final two-cluster (bound) state in channel j: Components $|\hat{\psi}_m\rangle$, $m\neq j$, do not contribute to this amplitude,[6] in contrast to the components, i.e., channel scattering states,[2-4] of Eqs. (4.17) and (4.20) below.

(*b*) *The T operators.* These operators, which are defined by Eq. (3.8a), yield components superficially similar to those of (4.19), viz.,

$$|\psi_j^{(+)}\rangle=|\Phi_1(E)\rangle\delta_{j1}+G_j^{(+)}V^j|\psi_{j+1}^{(+)}\rangle\,. \tag{4.20}$$

The similarity ends here, however, since (4.20) defines channel scattering states having the same properties as those of Eq. (4.17), i.e., they are independent of the subscript j and are each equal to the Schrödinger state $|\Phi\rangle$. This feature has been discussed in Ref. 4; we now present a much simpler demonstration of it.[29]

First, we note that in the present case, Eq. (4.7) takes the simple form

$$T_{j1}(E+i0)|\Phi_1(E)\rangle=V^j|\psi_{j+1}^{(+)}\rangle\,, \tag{4.21}$$

where $|\Phi_1(E)\rangle$ is now specifically assumed to be an incident two-cluster state. From this latter assumption, it follows that if both sides of (3.3) are applied to $|\Phi_1(E)\rangle$ $(k=1)$, we get

$$\begin{aligned}U_{j1}^{(+)}(E+i0)|\Phi_1(E)\rangle&=T_{j1}(E+i0)|\Phi_1(E)\rangle\\&=V^j|\psi_{j+1}^{(+)}\rangle\,,\end{aligned} \tag{4.22}$$

the second line being a result of (4.21). But Eq. (2.7) may be written as $U_{j1}^{(+)}=V^jGG_1^{-1}$, while $|\Psi\rangle$ is given by

$$|\Psi\rangle=\lim G(E+i\epsilon)G_1^{-1}(E+i\epsilon)|\Phi_1(E)\rangle\,.$$

Putting these results into (4.22) thus yields

$$V^j|\Psi\rangle=V^j|\psi_{j+1}^{(+)}\rangle\,, \tag{4.23}$$

i.e.,

$$|\psi_{j+1}^{(+)}\rangle=|\Psi\rangle\,, \tag{4.24}$$

a result that obviously holds for all j and is thus independent of j.

That components based on the T operators are in fact equal to $|\Psi\rangle$ is essentially the reason for the more complicated derivation presented in Ref. 26 of the "true" wave-function components for the BRS transition operators. It is also this same fact that renders the $|\psi_j^{(+)}\rangle$ of (4.20) less useful than those based on the $\hat{T}$ operators, should one introduce approximations which include breakup, rather than keeping strictly to bound-state approximations. However, we do note that since $|\psi_j^{(+)}\rangle=|\Psi\rangle$, Eq. (4.20) is just the set uniquely defining $|\Psi\rangle$.[30]

C. BK case

We have presented the results in the previous section in some detail, as they illustrate the ease with which one can derive wave-function equations when the transition operators obey equations of LS type, e.g., (3.7). In contrast to this, (3.11b) is not in standard LS form, and thus one encounters difficulties in deriving associated wave functions.

We shall illustrate this using Eq. (3.12b), the CPA version of (3.11b).

The matrix equation (3.11b) can be written as

$$\hat{X}(z)=B(z)+C(z)g(z)\hat{X}(z)\,, \tag{4.25}$$

where $B=NV$ and $C=\mathcal{V}$. In seeking to apply relation (4.7), we may try to define components $|\hat{\psi}\rangle$ via either

$$NV|\hat{\psi}\rangle=\hat{X}|\hat{\Phi}\rangle \tag{4.26a}$$

or

$$V|\hat{\psi}\rangle=\hat{X}|\hat{\Phi}\rangle\,. \tag{4.26b}$$

Neither of these definitions leads to a satisfactory equation for $|\hat{\psi}\rangle$, in the first instance because N^{-1} does not exist and in the second because a proper plane wave term $|\Phi\rangle$ does not occur. To remedy this, we shall derive components using Eqs. (4.11) and (4.12) for which it suffices to work out the two-channel case. Before doing so, we establish the validity of such a procedure by applying it to Eq. (3.8b) for $\hat{T}$, for which we have already derived components.

In the two-channel case (3.8b) becomes

$$\hat{T}_{11}=V^2G_2\hat{T}_{21} \tag{4.27a}$$

and

$$\hat{T}_{21}=V^1+V^1G_1\hat{T}_{11}\,, \tag{4.27b}$$

where the dependence on $E+i0$ is suppressed.

Now "define" components $|\hat{\psi}_1^{C}\rangle\!\rangle$ and $|\hat{\psi}_2^{C}\rangle\!\rangle$ via

$$|\hat{\psi}_j^{C}\rangle\!\rangle=\delta_{j1}|\Phi_1\rangle+G_j^{(+)}\hat{T}_{j1}|\Phi_1\rangle\,, \tag{4.28}$$

following (4.11). Substituting (4.27) into (4.28) and then using (4.28) on the right-hand sides of the resulting equations yields Eq. (4.18) for the two-channel case, just as predicted. Hence the procedure is a proper one to follow, although in the present instance it does not emphasize the essential LS structure of the equations.

We now turn to the operators of interest, defined by Eq. (3.11b). For the two-channel case they are

$$\hat{X}_{11}=V^1+V^1G_2\hat{X}_{21} \tag{4.29a}$$

and

$$\hat{X}_{21}=V^1+V^2G_1\hat{X}_{11}\,. \tag{4.29b}$$

The equations defining the corresponding "components" $|\hat{\chi}_j^{C}\rangle\!\rangle$ are

$$|\hat{\chi}_1^{C}\rangle\!\rangle=|\Phi_1(E)\rangle+G_1^{(+)}\hat{X}_{11}|\Phi_1(E)\rangle \tag{4.30a}$$

and

$$|\hat{\chi}_2^{C}\rangle\!\rangle=G_2^{(+)}\hat{X}_{21}|\Phi_1(E)\rangle\,. \tag{4.30b}$$

Substituting (4.29) into (4.30) and using (4.30) in the resulting equations leads to

$$\begin{aligned}|\hat{\chi}_1^{C}\rangle\!\rangle=|\Phi_1(E)\rangle&+G_1^{(+)}V^1|\Phi_1(E)\rangle\\&+G_1^{(+)}V^1|\hat{\chi}_2^{C}\rangle\!\rangle\end{aligned} \tag{4.31}$$

and

$$\begin{aligned}|\hat{\chi}_2^{C}\rangle\!\rangle=G_2^{(+)}&(V^1-V^2)|\Phi_1(E)\rangle\\&+G_2^{(+)}V^2|\hat{\chi}_1^{C}\rangle\!\rangle\,.\end{aligned} \tag{4.32a}$$

Equation (4.32a) can be simplified by using in it Lippmann's identity,[14]

$$G_2^{(+)}(V^1-V^2)|\Phi_1(E)\rangle=-|\Phi_1(E)\rangle\,.$$

This gives

$$|\hat{\chi}_2^{C}\rangle\!\rangle=-|\Phi_1(E)\rangle+G_2^{(+)}V^2|\hat{\chi}_1^{C}\rangle\!\rangle\,. \tag{4.32b}$$

The presence of $-|\Phi_1(E)\rangle$ in (4.32b) and the resulting implication that $|\hat{\chi}_1^{C}\rangle\!\rangle+|\hat{\chi}_2^{C}\rangle\!\rangle$ cannot be equal to $|\Psi\rangle$ because of the apparent lack in this sum of a plane wave term suggests that the $|\hat{\chi}_j^{C}\rangle\!\rangle$ cannot be components in the same sense as the $|\hat{\psi}_j^{C}\rangle\!\rangle$ of (4.18). They are, however, very closely related to the $|\psi_j^{C}\rangle\!\rangle$ of Eq. (4.20) in that $|\hat{\chi}_j^{C}\rangle\!\rangle$ is related to $|\Psi\rangle$ additively [recall Eq. (4.24)]. To see this, we first display the equations uniquely defining $|\Psi\rangle$ (Ref. 30); in the two-channel case, those are, from (4.20) with $N_2=2$ and $|\psi_j^{C}\rangle\!\rangle=|\Psi\rangle$,

$$|\Psi\rangle=|\Phi_1(E)\rangle+G_1^{(+)}V^1|\Psi\rangle \tag{4.33a}$$

and

$$|\Psi\rangle=G_2^{(+)}V^2|\Psi\rangle\,. \tag{4.33b}$$

Next consider Eq. (4.32b). As an equation for the sum $|\hat{\chi}_2^{C}\rangle\!\rangle+|\Phi_1(E)\rangle$, it becomes similar to (4.20), i.e., similar to (4.33b). We therefore form this combination in each of Eqs. (4.32a) and (4.32b), yielding

$$|\hat{\chi}_1^{C}\rangle\!\rangle=|\Phi_1(E)\rangle+G_1^{(+)}V^1[|\hat{\chi}_2^{C}\rangle\!\rangle+|\Phi_1(E)\rangle] \tag{4.34a}$$

and

$$[|\hat{\chi}_2^{C}\rangle\!\rangle+|\Phi_1(E)\rangle]=G_2^{(+)}V^2|\hat{\chi}_1^{C}\rangle\!\rangle\,. \tag{4.34b}$$

The identifications

$$|\hat{\chi}_1^{C}\rangle\!\rangle=|\Psi\rangle \tag{4.35a}$$

and

$$|\hat{\chi}_2^{C}\rangle\!\rangle=|\Psi\rangle-|\Phi_1(E)\rangle \tag{4.35b}$$

immediately follow on comparison of Eqs. (4.33) and (4.34); (4.35) and (4.35b) are the desired relations.

These identifications notwithstanding, (4.33) and (4.34) differ not only directly in their approaches to solving the Schrödinger equation, but more importantly in their response to approximations. We examine this point in detail in the next section.

We end this section by remarking that the results just obtained [Eqs. (4.35a) and (4.35b)] are easily generalized beyond the case $N_2=2$. For an arbitrary number of channels N and incident channel $k=1$, one finds

$$|\hat{\chi}_1^{c}\rangle=|\Psi\rangle \tag{4.36a}$$

and

$$|\hat{\chi}_j^{c}\rangle=|\Psi\rangle-|\Phi_1(E)\rangle,\ \ j\neq 1\,. \tag{4.36b}$$

This result arises from the cyclic nature of the coupling in Eq. (3.11b), the $N_2=2$ example of which is (4.30).

V. APPROXIMATIONS

Analyses of collision data usually rely on some form of empirical procedure such as the distorted wave Born approximation, the impulse approximation, or a coupled channel approximation. The successful application of such methods has made their justification one of the several goals of many-body scattering theory. Since some of these empirical methods are based on wave-function approaches, the need for approximate wave-function versions of many-body scattering theory is obvious. We consider the Faddeev wave-function components as an example.

In addition to their use in possible attempts to justify empirical approximations, many-body wave-function formalisms may also play the important role of elucidating the results of approximate transition operator calculations. To the extent that they can provide insights into such calculations, they provide a description of multiparticle scattering complementary to that of transition operator formalisms. We show in Sec. V B how the BK wave function components $|\hat{\chi}_j^{c}\rangle$ can be used to understand certain nonunitary numerical results based on approximations to the BK transition operators $\hat{X}_{jk}$.

A. Faddeev wave-function components

The AGS operators U_{jk} defined, e.g., by Eq. (3.14a) are probably the most widely used transition operators for analyses of three-body problems. They have the advantage over the Lovelace and CCA operators of being symmetric and reducing to relatively simple form when separable two-body potentials or t-operator approximations are used. Corresponding to the U_{jk} are the Faddeev wave-function components $|\hat{\psi}_j^F\rangle$. Nevertheless, while the path transition operator → wave function leads to $U_{jk}\to|\hat{\psi}_j^F\rangle$, the reverse process is $|\hat{\psi}_j^F\rangle\to\hat{T}_{jk}$ and not $|\hat{\psi}_j^F\rangle\to U_{jk}$.

At first glance, this may seem to be a trivial distinction to emphasize, since on-shell matrix elements of $\hat{T}_{jk}$ and U_{jk} are equal. The aspect of this which we stress is that under identical approximations, $\hat{T}_{jk}$ and U_{jk} will most likely differ on-shell, and under any such approximation, the $|\hat{\psi}_j^F\rangle$ equations will yield the approximate $\hat{T}_{jk}$ amplitudes and not approximate U_{jk} amplitudes. This point is pertinent for the traditional analyses of atomic, molecular, or nuclear collisions when three-body models are used, since such analyses are, as noted above, based on wave-function methods.

We illustrate this by using a particular bound-state approximation which is often referred to as the coupled reaction channel (CRC) method in nuclear physics,[17,31] and as the coupled states (CS) method in molecular physics[32] and in atomic physics[33] (without the additional use of pseudostates).

The approximation procedure is as follows. Consider only two-cluster partitions. Then the channel Hamiltonian H_j can be expressed as

$$H_j=T_j+h_j\,, \tag{5.1}$$

where T_j is the relative-motion kinetic-energy operator and h_j is the Hamiltonian for the internal states of the clusters.

The eigenstates $|\phi_j(\gamma)\rangle$ of h_j obey

$$[\epsilon_j(\gamma)-h_j]\,|\phi_j(\gamma)\rangle=0\,, \tag{5.2}$$

where $\epsilon_j(\gamma)$ is the energy of the state and γ denotes the set of relevant quantum numbers. Let $\{|\phi_j(\gamma_b)\rangle\}$ denote the subset of the $\{|\phi_j(\gamma)\rangle\}$ which consist of bound internal states only [the former are the states which occur in the $|\Phi_j(E)\rangle$ of Eq. (2.3)]. Now form the projection operators $P_j(\gamma_b)$ and P_j:

$$P_j(\gamma_b)=|\phi_j(\gamma_b)\rangle\langle\phi_j(\gamma_b)| \tag{5.3}$$

and

$$P_j=\sum_{\gamma_b}{}'\,P_j(\gamma_b)\,, \tag{5.4}$$

where the prime on the γ_b sum in (5.4) means that not all the bound states in channel j need be included in the sum.

The CRC or CS approximation to the solution $|\Psi\rangle$ of the Schrödinger equation (2.1) consists in replacing $|\Psi\rangle$ in Eq. (2.1) by

$$|\bar{\Psi}\rangle=\sum_j P_j|\Psi\rangle\simeq|\Psi\rangle\,, \tag{5.5}$$

projecting the result onto each $\langle\phi(\gamma_b)|$ in turn, and then solving the resulting set of coupled equations for the unknown scattering coefficients $\langle\phi_j(\gamma_b)|\Psi\rangle$, according to the usual outgoing wave boundary conditions.

The corresponding approximations for the Faddeev components $|\hat{\psi}_j^F\rangle$, the CCA operators $\hat{T}_{jk}$, and the AGS operators U_{jk} are obtained as follows. In the Faddeev equations (4.13), one first replaces $|\hat{\psi}_j^F\rangle$ by $P_j|\hat{\psi}_j^F\rangle$ and $G_j^{(+)}$ by $\bar{G}_j^{(+)}\equiv P_jG_j^{(+)}$;

then one solves for the unknown scattering coefficients $\langle\phi_j(\gamma_b)|\hat{\psi}_j^P\rangle$ from

$$\langle\phi_j(\gamma_b)|\hat{\psi}_j^P\rangle=\langle\phi_j(\gamma_b)|\Phi_k(E)\rangle\delta_{jk}+\langle\phi_j(\gamma_b)|\bar{G}_j^{(+)}V_j\sum_{m=1}^{3}\bar{\delta}_{jm}P_m|\hat{\psi}_m^P\rangle\,. \tag{5.6}$$

The analogous approximations used in (3.9b) for $\hat{T}_{jk}$ lead to

$$\langle\phi_j(\gamma_b)|\hat{T}_{jk}(z)|\phi_k(\alpha_b)\rangle=\langle\phi_j(\gamma_b)|V_j|\phi_k(\alpha_b)\rangle\bar{\delta}_{jk}+\langle\phi_j(\gamma_b)|V_j\sum_m\bar{\delta}_{jm}P_m\bar{G}_m(z)\hat{T}_{mk}(z)|\phi_k(\alpha_b)\rangle, \tag{5.7}$$

while the same approximations inserted into (3.14a) for U_{jk} yield

$$\langle\phi_j(\gamma_b)|U_{jk}(z)|\phi_k(\alpha_b)\rangle=\langle\phi_j(\gamma_b)|G_0^{-1}(z)|\phi_k(\alpha_b)\rangle\bar{\delta}_{jk}+\langle\phi_j(\gamma_b)|\sum_m\bar{\delta}_{jm}V_m\bar{G}_m(z)P_mU_{mk}(z)|\phi_k(\alpha_b)\rangle\,. \tag{5.8}$$

It is straightforward to verify our earlier remark that Eqs. (5.6) and (5.7) produce the same on-shell amplitude approximations, which are *not* equal to the approximate on-shell amplitudes arising from the AGS operators U_{jk}. This should not be unexpected, since it is only in left-hand form that the approximate $\hat{T}$ operators would be phase equivalent to the approximate operators U_{jk}.

B. The CCA wave-function components

One of the interesting aspects of the CRC or CS approximation (discussed in Sec. V A) is that it is unitary. This follows essentially from the fact that the coupled equations of the method are flux conserving, i.e., there are no sources of or sinks for the incident flux outside of the channels and states coupled to the initial one. In general, however, one does not expect approximations to transition operators to yield transition amplitudes (and thus S matrix elements) which are unitary, the simple Born approximation being a well-known example.

Let us now consider the CCA transition operators defined by Eqs. (3.8) and (3.12) in light of the these comments. Although they and their corresponding wave-function components, defined, e.g., by (4.18) and (4.32), do obey coupled equations, these coupled equations contain asymmetric coupling terms rather than symmetric ones such as occur in the CRC approximation. This suggests that approximations to these CCA equations may not yield unitary amplitudes. The fact that ap-roximations to the KL equations *have* led to uniary results while approximations to the BK quation have not, thus requires explanation.

Before using the BK wave-function components o analyze this, we first review the relevant calulations and the original Kouri, Levin, Craigie, nd Secrest analysis.[11] Baer and Kouri[1] found onunitary elastic scattering amplitudes for $+H$ scattering at energies below the $n=2$ hreshold using a symmetrized form of the two-channel BK transition operator equations in the approximation of Sec. V A, in which the P_j are formed from the 1s hydrogenic ground state only. Subsequent calculations based on a symmetrized form of the KL transition operator equations using the same approximation yielded a unitary amplitude, i.e., one of the form $\exp(i\delta)\sin\delta$. The phase of the BK amplitude was found to be the same as for the KL amplitude, viz., δ.

Earlier work of Kouri and Levin had established the existence of K or reaction operators related to the KL transition operators by a Heitler damping equation[2]; by contrast, no such relation exists for the BK transition and reaction operators. This fact was used to prove that in the one-state approximation for the P_j, the ratio of the BK and KL amplitudes would be a real number, i.e., that the amplitudes would have the same phase.[11] Lack of unitarity of the BK amplitude was shown to be a consequence of the bound-state approximation for the P_j. In effect, this means that use of P_2 in channel 2 is not the same as (equivalent to) use of P_1 in channel 1: To achieve the effect in channel 2 of P_1 in channel 1, continuum states must be used in P_2. The cause of this behavior of the BK operators is the fact that in Eq. (3.11b), for example, the inhomogeneity NV is not repeated in the kernel term $\mathcal{V}\mathcal{G}$, in contrast to the KL equations; the latter, of course, did yield unitary amplitudes. An analogous incompatibility in apparently equivalent approximations will be seen to be the basis of our alternate explanation, using the inhomogeneous equations obeyed by the components $|\hat{\chi}_j^{CCA}\rangle$ discussed below.

The Lewanski-Tobocman calculations[12] involve approximations using projection-operator expansions applied to collisions in a system consisting of two light and one infinitely massive particle, the Hulburt-Hirschfelder model.[34] Three sets of calculations were done: those based on a boundary matching procedure employing the Schrödinger equation, those based on BK equations, and those based on KL equations. The first of the three provided the benchmark against which the other two could be measured. In addition, parameters were changed to allow the two light particles to be identical fermions, thus introducing Pauli principle effects. A maximum of seven expansion states were used in the calculations.

We consider the nonidentical-particle case first. Within this case there are two subcases: all three interactions either not equal or equal. When they are not equal, the KL-based results are found to converge more or less to the same results as those based on the boundary matching procedure, and also to be unitary. For this *same case of the three interactions not being* equal, the BK-based results are not only nonunitary, they also do not converge to the same numbers to which the other two sets of calculations tend to converge. The other distinguishable particle subcase, that of all three interactions being equal, leads to the opposite results for the BK based calculations: They are not only unitary, but converge to the same numbers as the other two sets of calculations do. This apparently paradoxical situation is easily understood as soon as one realizes that when all three interactions are equal, the matrix elements of each of the channel interactions V^j appearing in the BK equations, when taken betweeen the same initial and the same final states, are *equal*. Hence in this particular situation, the BK equations become a set for which one may expect unitary results, as in the KL case.

The second interesting case examined by Lewanski and Tobocman is that where the two light particles are identical. In this case all three interactions are equal, the three sets of calculations are all unitary (when the seven expansion states are used), and all three converge to the same limits. These results are easily understood in terms of the preceding remarks.

More generally, one can apply the same arguments as used in Ref. 11 to explain the nonunitarity of the Lewanski-Tobocman BK results. Since theirs was a two-channel calculation using equations without a repeated driving term, the inequivalence between the P_1 and P_2 approximations remarked on in connection with the Baer-Kouri results similarly affects the BK results of Ref. 12. Although the latter statement is correct, it is perhaps not as straightforward to apply to the Lewanski-Tobocman computations as to those of Ref. 1. The alternate explanation based on the $|\hat{\chi}_j^{C}\rangle$ is, however, much simpler to apply, and we examine it in the following.

In the two-channel case the $|\hat{\chi}_j^{C}\rangle$ obey Eqs. (4.32). These are easily converted into the differential equations

$$(E-H_1)|\hat{\chi}_1^{C}\rangle - V^1|\hat{\chi}_2^{C}\rangle = V^1|\Phi_1(E)\rangle \tag{5.9a}$$

and

$$(E-H_2)|\hat{\chi}_2^{C}\rangle - V^2|\hat{\chi}_1^{C}\rangle = (V^2-V^1)|\Phi_1(E)\rangle\,. \tag{5.9b}$$

Equations (5.9) are inhomogeneous differential equations. Subject to the boundary conditions of (4.32), they will yield on-shell matrix elements of the operators $\hat{X}_{jk}$, while if standing wave boundary conditions are imposed, they will yield K matrix elements.

Exact solutions of (5.9) will lead to unitary amplitudes. Suppose, however, that one introduces bound-state approximations via the projection operators P_j of Sec. V A. One then wants to determine the $P_j|\hat{\chi}_j^{C}\rangle$ rather than the entire component $|\hat{\chi}_j^{C}\rangle$. Since (5.9a) and (5.9b) are equations for the channel 1 and 2 components, respectively, the equations one apparently should solve are the projections of (5.9a) and (5.9b) onto P_1 and P_2:

$$(E-H_1)P_1|\hat{\chi}_1^{C}\rangle - P_1V^1P_2|\hat{\chi}_2^{C}\rangle = P_1V^1|\Phi_1(E)\rangle \tag{5.10a}$$

and

$$(E-H_2)P_2|\hat{\chi}_2^{C}\rangle - P_2V^2P_1|\hat{\chi}_1^{C}\rangle = P_2(V^2-V^1)|\Phi_1(E)\rangle\,, \tag{5.10b}$$

where we have used $[P_j,H_j]=0$.

The solutions to (5.9) and (5.10) are each a sum of two terms: the complementary function, which satisfies the homogeneous equations and the "particular integral," which involves the inhomogeneities. Although the sum of these two terms will yield a unitary amplitude for (5.9), i.e., when each $P_j=1$, there is no way to guarantee that under the actual projection approximation the sum of the two terms forming the solution of (5.10) will also give a unitary amplitude. That is, one can always postulate an approximation of the form

$$(E-H_1)P_1|\hat{\chi}_1^{C}\rangle - P_1V^1P_2|\hat{\chi}_2^{C}\rangle = P_1\eta_1 \tag{5.11a}$$

and

$$(E-H_2)P_2|\hat{\chi}_2^{C}\rangle - P_2V^2P_1|\hat{\chi}_1^{C}\rangle = P_2\eta_2\,, \tag{5.11b}$$

such that the sum of the complementary function and the particular integral of (5.11) produces a unitary amplitude, but then we cannot expect that the right-hand sides of (5.10a), (5.10b), and (5.11a), (5.11b) will be equal. In general, they will be unequal, leading to nonunitary amplitudes resulting from (5.10).

The reason for this behavior is the inequivalence in approximating the left- and right-hand sides of an inhomogeneous equation. In other words, while the set (5.9) denotes an equality, the set (5.10) does not form a consistent approximation to it. The consistent approximation comes from first projecting (5.9) to yield

$$(E-H_1)P_1|\hat{\chi}_1^{CCA}\rangle - P_1V^1|\hat{\chi}_2^{CCA}\rangle = P_1V^1|\Phi_1(E)\rangle \tag{5.12a}$$

and

$$(E-H_2)P_2|\hat{\chi}_2^{CCA}\rangle - P_2V^2|\hat{\chi}_1^{CCA}\rangle = P_2(V^2-V^1)|\Phi_1(E)\rangle\,. \tag{5.12b}$$

Equations (5.12) are not yet in the desired form since the entire term $|\hat{\chi}_j^{CCA}\rangle$ still appears in the second term on the left-hand sides. The next step of the approximation is obtained by defining $Q_j = 1 - P_j$ and putting the Q_j terms in the right-hand sides:

$$\begin{aligned}(E-H_1)P_1|\hat{\chi}_1^{CCA}\rangle - P_1V^1P_2|\hat{\chi}_2^{CCA}\rangle \\ = P_2V^1|\Phi_1(E)\rangle + P_1V^1Q_2|\hat{\chi}_2^{CCA}\rangle\end{aligned} \tag{5.13a}$$

and

$$\begin{aligned}(E-H_2)P_2|\hat{\chi}_2^{CCA}\rangle - P_2V^2P_1|\hat{\chi}_1^{CCA}\rangle \\ = P_2(V^2-V^1)|\Phi_1(E)\rangle + P_2V^2Q_1|\hat{\chi}_1^{CCA}\rangle\,.\end{aligned} \tag{5.13b}$$

Equations (5.10) are obtained from (5.13) by neglecting the terms containing the operators Q_j. But since the inhomogeneous terms also occur on the right-hand side of (5.13), retaining them in full while neglecting the Q_j terms cannot be expected to lead to unitary results. This is the heart of the inconsistency. Thus the final step leading to a consistent, i.e., a unitary, approximation will involve modifying the inhomogeneous terms as well. Doing so will lead in principle to equations of the form of (5.11), not (5.10). Unfortunately, there is in practice no specific procedure available for determining any such modification which is guaranteed to lead to unitary amplitudes. Because the approximate BK transition operator equations used by Baer and Kouri and by Lewanski and Tobocman have corresponding wave-function components obeying equations of the form (5.10) and not (5.11), we immediately see that the amplitudes obtained from such approximate equations cannot be expected to be unitary.

The lack of unitarity of the approximate BK amplitudes of Refs. 1 and 12 illustrate these remarks quite concretely. Similar nonunitarities and an acausal resonance behavior were found in an entirely different $e^- + H$ calculation also based on an approximate inhomogeneous equation.[35] As noted in Ref. 35, caution is obviously called for when using inhomogeneous equations as the basis for approximations.

We have noted above that the approximate KL operators did yield unitary results for $e^- + H$ scattering below the $n = 2$ threshold. It is thus interesting to compare the approximate KL wave-function component equations, viz.,

$$(E-H_j)P_j|\hat{\psi}_j^{CCA}\rangle = P_jV^{j+1}P_{j+1}|\hat{\psi}_{j+1}^{CCA}\rangle\,, \tag{5.14}$$

with the inconsistent ones for the $P_j|\hat{\chi}_j^{CCA}\rangle$, Eq. (5.10). Since (5.14) contains no inhomogeneities, it contains no sources of or sinks for flux, immediately leading to the conclusion that these are flux-conserving equations, i.e., the resulting amplitudes will indeed be unitary. However, since the channels are coupled asymmetrically, one also expects time-reversal noninvariant amplitudes, as found numerically.[17]

VI. SUMMARY

We have derived wave-function component equations for the CCA transition operators and discussed their properties in detail. In particular, we have shown that the amplitudes arising from an approximate solution of the Faddeev wave-function component equations are the matrix elements of the KL operators $\hat{T}_{jk}$ and not the AGS operators U_{jk}. We have also shown that in differential form, the BK wave-function component equations are inhomogeneous, and we have used this to give an alternate explanation of the nonunitary character of amplitudes determined from approximate solution of the BK operator equations.

ACKNOWLEDGMENT

A portion of this work was done under the auspices of the Alexander von Humboldt-Stiftung, to whom the author gratefully acknowledges the receipt of a Senior U. S. Scientist Award. He also thanks Professor W. Sandhas for his hospitality at the Physikalisches Institut der Universität Bonn and Professor K. Kowalski for a number of helpful comments on an earlier version of this article. This work was supported in part by the U. S. Department of Energy.

---

*Permanent address: Physics Department, Brown University, Providence, R. I. 02912.

[1] M. Baer and D. J. Kouri, J. Math. Phys. 14, 1637 (1973).

[2] D. J. Kouri and F. S. Levin, Phys. Lett. 50B, 421 (1974); Phys. Rev. A 10, 1616 (1974); Nucl. Phys. A250, 127 (1975).

[3] Y. Hahn, D. J. Kouri, and F. S. Levin, Phys. Rev. C 10, 1615 (1974).

[4] D. J. Kouri and F. S. Levin, Nucl. Phys. A253, 395 (1975); Phys. Rev. C 16, 556 (1977).

[5] D. J. Kouri, F. S. Levin, and W. Sandhas, Phys. Rev.

C 13, 1825 (1976).

[6] D. J. Kouri, H. Krüger, and F. S. Levin, Phys. Rev. D 15, 1156 (1977).

[7] W. Tobocman, Phys. Rev. C 9, 2466 (1974); 11, 43 (1975); 12, 1146 (1975).

[8] R. Goldflam and W. Tobocman, Phys. Rev. C 17, 1914 (1978); C 20, 904 (1979).

[9] V. Vanzani, in *Few-Body Nuclear Physics*, edited by G. Pisent, V. Vanzani, and L. Fonda (IAEA, Vienna, 1978), p. 57; and in *Few-Body Systems and Nuclear Forces*, edited by H. Zingl, M. Haftel, and H. Zankel (Springer, Berlin, 1978), p. 360.

[10] B. A. Lippmann and J. Schwinger, Phys. Rev. 79, 469 (1950).

[11] D. J. Kouri, F. S. Levin, M. Craigie, and D. Secrest, J. Chem. Phys. 61, 17 (1974).

[12] A. J. Lewanski and W. Tobocman, Phys. Rev. C 17, 423 (1978).

[13] R. G. Newton, *Scattering Theory of Waves and Particles* (Wiley, New York, 1966).

[14] B. A. Lippmann, Phys. Rev. 102, 264 (1956); P. Benoist-Gueutal, Phys. Lett. 56B, 413 (1975); P. Benoist-Gueutal, M. L'Huillier, E. F. Redish, and P. C. Tandy, Phys. Rev. C 17, 1924 (1978).

[15] E. F. Redish, Nucl. Phys. A225, 16 (1974).

[16] Gy. Bencze and P. C. Tandy, Phys. Rev. C 16, 564 (1977); K. L. Kowalski, *ibid.*, 16, 7 (1977).

[17] J. M. Greben and F. S. Levin, Phys. Lett. 71B, 252 (1977) and Nucl. Phys. A325, 145 (1979); F. S. Levin and J. M. Greben, Phys. Rev. Lett. 41, 1447 (1978); Phys. Rev. C 20, 437 (1979).

[18] E. O. Alt., P. Grassberger, and W. Sandhas, Nucl. Phys. B2, 167 (1967).

[19] R. Goldflam and D. J. Kouri, Chem. Phys. Lett. 34, 595 (1975).

[20] D. J. Kouri, M. Craigie, and D. Secrest, J. Chem. Phys. 60, 1851 (1974).

[21] C. Lovelace, Phys. Rev. 135, B1225 (1964); and in *Strong Interactions and High-Energy Physics*, edited by R. G. Moorhouse (Oliver and Boyd, London, 1964), p. 437.

[22] V. Vanzani, Lett. Nuovo Cimento 10, 610 (1974).

[23] L. D. Faddeev, Zh. Eksp. Teor. Fiz. 39, 1459 (1960) [Sov. Phys. JETP 12, 1014 (1961)]; *Mathematical Aspects of the Three-Body Problem in the Quantum Scattering Theory* (Davey, New York, 1965).

[24] C. Chandler, Nucl. Phys. A301, 1 (1978); V. Vanzani, Ref. 9 and unpublished; S. K. Adhikari and W. Glöckle, Phys. Rev. C 19, 616 (1979). See, however, J. W. Evans and D. K. Hoffman (unpublished) who show that in differential equation form, the Faddeev equations do admit nonphysical spurious solutions.

[25] W. Sandhas, in *Few-Body Dynamics*, edited by A. N. Mitra, I. Slaus, V. S. Bhasin, and V. K. Gupta (North-Holland, Amsterdam, 1976), p. 540.

[26] M. L'Huillier, E. F. Redish, and P. C. Tandy, J. Math. Phys. 19, 1276 (1978).

[27] F. S. Levin and H. Krüger, Phys. Rev. A 15, 2147 (1977); 16, 836 (1977); F. S. Levin, Int. J. Quantum Chem. Quant. Chem. Symp. 12, 109 (1978).

[28] Additional studies for simple atoms and molecules are being carried out with W. Ford; results will be discussed elsewhere.

[29] This demonstration closely follows an analysis used by L'Huillier *et al.*, Ref. 26.

[30] W. Glöckle, Nucl. Phys. A141, 620 (1970); W. Sandhas, in *Few-Body Nuclear Physics*, edited by G. Pisent, V. Vanzani, and L. Fonda (IAEA, Vienna, 1978), p. 3; V. Vanzani, in *Few-Body Nuclear Physics* (Ref. 9).

[31] See, e.g., T. Udagawa, H. H. Wolter, and W. R. Coker, Phys. Rev. Lett. 31, 1507 (1973), and references cited therein.

[32] See, e.g., the articles by A. Kupperman and by K. Takayanagi in *Physics of Electronic and Atomic Collisions*, edited by J. S. Risley and R. Geballe (Univ. of Washington Press, Seattle, 1976).

[33] See, e.g., G. Drukarev, *The Theory of Electron-Atom Collisions* (Academic, New York, 1965); or P. G. Burke, United Kingdom Atomic Energy Authority Report No. AERE-L 170 (unpublished), available from H. M. Stationery Office.

[34] H. Hulbert and J. O. Hirschfelder, J. Chem. Phys. 11, 276 (1943).

[35] P. W. Dahlgren and F. S. Levin, J. Phys. B 10, 471 (1977).

PHYSICAL REVIEW C VOLUME 21, NUMBER 6 JUNE 1980

Proton-nucleus charge exchange measurements at 144 MeV as a test of one-pion exchange and the partially conserved axial vector current

G. L. Moake,* L. J. Gutay, and R. P. Scharenberg
Department of Physics, Purdue University, West Lafayette, Indiana 47907

P. T. Debevec†
Department of Physics, Indiana University, Bloomington, Indiana 47405

P. A. Quin
Department of Physics, University of Wisconsin, Madison, Wisconsin 53706

(Received 29 October 1979)

We have measured the differential cross sections of the (p,n) reaction on ^{6}Li, ^{12}C, and ^{14}N to the ground state of the final nucleus ($\Delta J = 1$, $\Delta T = 1$, $\Delta\pi = 0$) and to the 7.77 MeV excited state of ^{14}O at $E_p = 144$ MeV and $0° < \theta_{lab} < 20°$. For the ground state cases, we treat the nuclei as elementary particles, which are assigned the initial nucleus-pion-final nucleus coupling constants predicted using the partially conserved axial vector current. The Born helicity amplitudes for one-pion exchange are presented along with a method for including distortions in momentum space. The calculations which have no free parameters agree with the data for ^{6}Li and ^{12}C, but not for ^{14}N.

NUCLEAR REACTIONS ^{6}Li(p,n), ^{12}C(p,n), and ^{14}N(p,n) at $E_p = 144$ MeV. Differential cross sections measured between 0° and 20° (lab). Initial nucleus-pion-final nucleus coupling constants extracted.

I. INTRODUCTION

In nuclear physics we have become accustomed to the concept of a nucleon-nucleon potential which has its fundamental foundations in the theoretical premise of meson exchange. Our understanding of this potential, while by no means complete, is rather advanced. It is well known, for example, that a realistic potential must contain both central and noncentral components and must be momentum dependent. There cannot be a simple correspondence between components of this potential and individual meson exchanges. However, since the pion is the least massive meson, one-pion exchange must become dominant at large distances. In fact, a comparison of the one-pion exchange potential to a phenomenological force which reproduces the nucleon-nucleon phase shifts, e.g., the Hamada-Johnston potential, shows that one-pion exchange is dominant in the spin-isospin component and the isovector tensor component at distances as small as the Compton wavelength of the pion.[1] Yet at these intermediate ranges, it is necessary to introduce the exchange of scalar mesons, both isoscalar and isovector, which represent the effective contribution of nonresonant two-pion exchange. In order to account for the other components of the central interaction at shorter distances and to characterize the short range repulsion, even the most sophisticated calculations must become phenomenological at small distances. The understanding of the nucleon-nucleon interaction in terms of meson exchange is then largely successful, especially at large distances or equivalently, at high partial waves.

When one considers the scattering of nucleons from a nucleus, the complexity of the many-body problem makes the *ab initio* description of the nuclear force in terms of meson exchange unfeasible. However, the transition of the nucleus from one state of definite spin, parity, and isospin to another imposes definite limitations on the meson exchanges that can occur (assuming a single interaction which may be valid at intermediate energies). For nuclear transitions of $J=0 \rightarrow J=1$, $T=0 \rightarrow T=1$, and $\pi=1 \rightarrow \pi=1$, the meson exchange must transfer one unit of angular momentum and isospin without changing the parity. Thus, for interactions of medium and long range, which correspond to scattering in the forward direction, the reaction may be dominated by one-pion exchange. One-pion exchange is known to contribute to $n+p \rightarrow p+n$ charge exchange scattering where the quantum number restrictions are not so severe. There, one-pion exchange manifests itself in a large forward peak.[2] This peak is not reflected in most nuclear inelastic scatterings, however, but the quantum numbers of most transitions are inconsistent with one-pion exchange. For the transitions with quantum numbers listed above, we

(c) 1980 The American Physical Society

C 13, 1825 (1976).

[6] D. J. Kouri, H. Krüger, and F. S. Levin, Phys. Rev. D 15, 1156 (1977).

[7] W. Tobocman, Phys. Rev. C 9, 2466 (1974); 11, 43 (1975); 12, 1146 (1975).

[8] R. Goldflam and W. Tobocman, Phys. Rev. C 17, 1914 (1978); C 20, 904 (1979).

[9] V. Vanzani, in *Few-Body Nuclear Physics*, edited by G. Pisent, V. Vanzani, and L. Fonda (IAEA, Vienna, 1978), p. 57; and in *Few-Body Systems and Nuclear Forces*, edited by H. Zingl, M. Haftel, and H. Zankel (Springer, Berlin, 1978), p. 360.

[10] B. A. Lippmann and J. Schwinger, Phys. Rev. 79, 469 (1950).

[11] D. J. Kouri, F. S. Levin, M. Craigie, and D. Secrest, J. Chem. Phys. 61, 17 (1974).

[12] A. J. Lewanski and W. Tobocman, Phys. Rev. C 17, 423 (1978).

[13] R. G. Newton, *Scattering Theory of Waves and Particles* (Wiley, New York, 1966).

[14] B. A. Lippmann, Phys. Rev. 102, 264 (1956); P. Benoist-Gueutal, Phys. Lett. 56B, 413 (1975); P. Benoist-Gueutal, M. L'Huillier, E. F. Redish, and P. C. Tandy, Phys. Rev. C 17, 1924 (1978).

[15] E. F. Redish, Nucl. Phys. A225, 16 (1974).

[16] Gy. Bencze and P. C. Tandy, Phys. Rev. C 16, 564 (1977); K. L. Kowalski, *ibid.*, 16, 7 (1977).

[17] J. M. Greben and F. S. Levin, Phys. Lett. 71B, 252 (1977) and Nucl. Phys. A325, 145 (1979); F. S. Levin and J. M. Greben, Phys. Rev. Lett. 41, 1447 (1978); Phys. Rev. C 20, 437 (1979).

[18] E. O. Alt., P. Grassberger, and W. Sandhas, Nucl. Phys. B2, 167 (1967).

[19] R. Goldflam and D. J. Kouri, Chem. Phys. Lett. 34, 595 (1975).

[20] D. J. Kouri, M. Craigie, and D. Secrest, J. Chem. Phys. 60, 1851 (1974).

[21] C. Lovelace, Phys. Rev. 135, B1225 (1964); and in *Strong Interactions and High-Energy Physics*, edited by R. G. Moorhouse (Oliver and Boyd, London, 1964), p. 437.

[22] V. Vanzani, Lett. Nuovo Cimento 10, 610 (1974).

[23] L. D. Faddeev, Zh. Eksp. Teor. Fiz. 39, 1459 (1960) [Sov. Phys. JETP 12, 1014 (1961)]; *Mathematical Aspects of the Three-Body Problem in the Quantum Scattering Theory* (Davey, New York, 1965).

[24] C. Chandler, Nucl. Phys. A301, 1 (1978); V. Vanzani, Ref. 9 and unpublished; S. K. Adhikari and W. Glöckle, Phys. Rev. C 19, 616 (1979). See, however, J. W. Evans and D. K. Hoffman (unpublished) who show that in differential equation form, the Faddeev equations do admit nonphysical spurious solutions.

[25] W. Sandhas, in *Few-Body Dynamics*, edited by A. N. Mitra, I. Slaus, V. S. Bhasin, and V. K. Gupta (North-Holland, Amsterdam, 1976), p. 540.

[26] M. L'Huillier, E. F. Redish, and P. C. Tandy, J. Math. Phys. 19, 1276 (1978).

[27] F. S. Levin and H. Krüger, Phys. Rev. A 15, 2147 (1977); 16, 836 (1977); F. S. Levin, Int. J. Quantum Chem. Quant. Chem. Symp. 12, 109 (1978).

[28] Additional studies for simple atoms and molecules are being carried out with W. Ford; results will be discussed elsewhere.

[29] This demonstration closely follows an analysis used by L'Huillier *et al.*, Ref. 26.

[30] W. Glöckle, Nucl. Phys. A141, 620 (1970); W. Sandhas, in *Few-Body Nuclear Physics*, edited by G. Pisent, V. Vanzani, and L. Fonda (IAEA, Vienna, 1978), p. 3; V. Vanzani, in *Few-Body Nuclear Physics* (Ref. 9).

[31] See, e.g., T. Udagawa, H. H. Wolter, and W. R. Coker, Phys. Rev. Lett. 31, 1507 (1973), and references cited therein.

[32] See, e.g., the articles by A. Kupperman and by K. Takayanagi in *Physics of Electronic and Atomic Collisions*, edited by J. S. Risley and R. Geballe (Univ. of Washington Press, Seattle, 1976).

[33] See, e.g., G. Drukarev, *The Theory of Electron-Atom Collisions* (Academic, New York, 1965); or P. G. Burke, United Kingdom Atomic Energy Authority Report No. AERE-L 170 (unpublished), available from H. M. Stationery Office.

[34] H. Hulbert and J. O. Hirschfelder, J. Chem. Phys. 11, 276 (1943).

[35] P. W. Dahlgren and F. S. Levin, J. Phys. B 10, 471 (1977).

PHYSICAL REVIEW C VOLUME 21, NUMBER 6 JUNE 1980

Proton-nucleus charge exchange measurements at 144 MeV as a test of one-pion exchange and the partially conserved axial vector current

G. L. Moake,* L. J. Gutay, and R. P. Scharenberg
Department of Physics, Purdue University, West Lafayette, Indiana 47907

P. T. Debevec†
Department of Physics, Indiana University, Bloomington, Indiana 47405

P. A. Quin
Department of Physics, University of Wisconsin, Madison, Wisconsin 53706

(Received 29 October 1979)

We have measured the differential cross sections of the (p,n) reaction on ^{6}Li, ^{12}C, and ^{14}N to the ground state of the final nucleus ($\Delta J = 1$, $\Delta T = 1$, $\Delta\pi = 0$) and to the 7.77 MeV excited state of ^{14}O at $E_p = 144$ MeV and $0^\circ < \theta_{\text{lab}} < 20^\circ$. For the ground state cases, we treat the nuclei as elementary particles, which are assigned the initial nucleus-pion-final nucleus coupling constants predicted using the partially conserved axial vector current. The Born helicity amplitudes for one-pion exchange are presented along with a method for including distortions in momentum space. The calculations which have no free parameters agree with the data for ^{6}Li and ^{12}C, but not for ^{14}N.

[NUCLEAR REACTIONS ^{6}Li(p,n), ^{12}C(p,n), and ^{14}N(p,n) at $E_p = 144$ MeV. Differential cross sections measured between 0° and 20° (lab). Initial nucleus-pion-final nucleus coupling constants extracted.]

I. INTRODUCTION

In nuclear physics we have become accustomed to the concept of a nucleon-nucleon potential which has its fundamental foundations in the theoretical premise of meson exchange. Our understanding of this potential, while by no means complete, is rather advanced. It is well known, for example, that a realistic potential must contain both central and noncentral components and must be momentum dependent. There cannot be a simple correspondence between components of this potential and individual meson exchanges. However, since the pion is the least massive meson, one-pion exchange must become dominant at large distances. In fact, a comparison of the one-pion exchange potential to a phenomenological force which reproduces the nucleon-nucleon phase shifts, e.g., the Hamada-Johnston potential, shows that one-pion exchange is dominant in the spin-isospin component and the isovector tensor component at distances as small as the Compton wavelength of the pion.[1] Yet at these intermediate ranges, it is necessary to introduce the exchange of scalar mesons, both isoscalar and isovector, which represent the effective contribution of nonresonant two-pion exchange. In order to account for the other components of the central interaction at shorter distances and to characterize the short range repulsion, even the most sophisticated calculations must become phenomenological at small distances. The understanding of the nucleon-nucleon interaction in terms of meson exchange is then largely successful, especially at large distances or equivalently, at high partial waves.

When one considers the scattering of nucleons from a nucleus, the complexity of the many-body problem makes the *ab initio* description of the nuclear force in terms of meson exchange unfeasible. However, the transition of the nucleus from one state of definite spin, parity, and isospin to another imposes definite limitations on the meson exchanges that can occur (assuming a single interaction which may be valid at intermediate energies). For nuclear transitions of $J=0 \to J=1$, $T=0 \to T=1$, and $\pi=1 \to \pi=1$, the meson exchange must transfer one unit of angular momentum and isospin without changing the parity. Thus, for interactions of medium and long range, which correspond to scattering in the forward direction, the reaction may be dominated by one-pion exchange. One-pion exchange is known to contribute to $n+p \to p+n$ charge exchange scattering where the quantum number restrictions are not so severe. There, one-pion exchange manifests itself in a large forward peak.[2] This peak is not reflected in most nuclear inelastic scatterings, however, but the quantum numbers of most transitions are inconsistent with one-pion exchange. For the transitions with quantum numbers listed above, we

© 1980 The American Physical Society

may expect one-pion exchange in the forward direction, producing a forward peak. In order to test this hypothesis, we have measured the forward angle cross sections for the (p,n) reaction on ^{6}Li, ^{12}C, and ^{14}N to the resulting ground states; these transitions all have $\Delta J = 1$, $\Delta T = 1$, $\Delta\pi = 0$.

If the reaction at forward angles is dominated by one-pion exchange, then one has an opportunity to test the application of the partially conserved axial vector current hypothesis (PCAC) to nuclei in a novel way, as first suggested by Kim and Primakoff.[3] The proposal is to consider the initial and final nuclear states as elementary particles, specifying only the mass, spin, parity, and isospin, and to introduce a vertex function which characterizes the coupling of the initial nucleus, a pion, and the final nucleus. By application of PCAC, one can derive a relation similar to the Goldberger-Treiman relation,[4] which relates the initial nucleus-pion-final nucleus coupling for a virtual pion to the matrix element of the axial vector current $\langle N'|A_\alpha(x)|N\rangle$. This matrix element is known from the β decay of the final nucleus N' to the initial nucleus N. In a similar manner, PCAC can be used to relate the momentum transfer dependence of the vertex function $g_{N\pi N'}(q^2)$ to that of an inelastic electron scattering form factor. Since the axial vector matrix elements for the cases considered herein are known (assuming ^{6}Be $-$ ^{6}Li has the same matrix element as ^{6}He $-$ ^{6}Li), and since the required inelastic electron scattering form factors have been measured, then in principle the one-pion exchange differential cross section for $p+N \to n+N'$ can be calculated.

It is useful to make a comparison between this proposal and the more conventional procedure. Present day nuclear inelastic scattering calculations in the intermediate energy range are typically made with an effective interaction in the distorted wave impulse approximation (DWIA).[5,6] The effective interaction is chosen to have (on-shell) matrix elements which reproduce the nucleon-nucleon scattering amplitudes in the intermediate energy range. The functional form of the interaction is usually taken to be a sum of Yukawa functions $e^{-\mu r}/\mu r$; a slightly different functional form is used for the tensor force. Generally there is one term in the effective interaction with the range and strength appropriate for one-pion exchange, with other terms representing interactions of shorter range. The interaction is folded over the entire nucleus using nuclear wave functions, which reflect the structure of the states involved, to produce an inelastic scattering form factor. In certain cases the transition density measured in inelastic electron scattering can be used directly. The scattering waves in the initial and final states are generated from an optical potential which reproduces the measured elastic scattering. The transition amplitude then is the integral of the inelastic scattering form factor and the two distorted waves. Although this method incorporates one-pion exchange, the exchange is only between individual nucleons, and there is no means of introducing the initial nucleus-pion-final nucleus vertex function. Thus, it is not possible to test the application of the PCAC hypothesis to nuclei.

We have chosen to use the one-particle exchange model developed for particle physics applications[7-9] known as the absorption model to incorporate initial and final state distortions. Since the Born amplitudes for meson exchange are most naturally expressed in momentum space, the absorption model modifies the Born amplitudes to account for initial and final state distortions in momentum space. Since at high energy the elastic scattering potential is primarily absorptive, the inclusion of distortions merely reduces the magnitude of each partial wave of the Born amplitudes. Hence, the method is known as the absorption model.

Our calculational procedure, then, was to begin with the Born helicity amplitudes for one-pion exchange represented by the Feynman diagram shown in Fig. 1. The proton-pion-neutron vertex is known from pion-nucleon scattering, and the initial nucleus-pion-final nucleus vertex function at zero momentum transfer $g_{N\pi N'}(0)$ was obtained from PCAC. The dependence of the two vertices on momentum transfer was obtained from PCAC using in the nuclear case the inelastic electron scattering form factor. Thus, the Born amplitudes

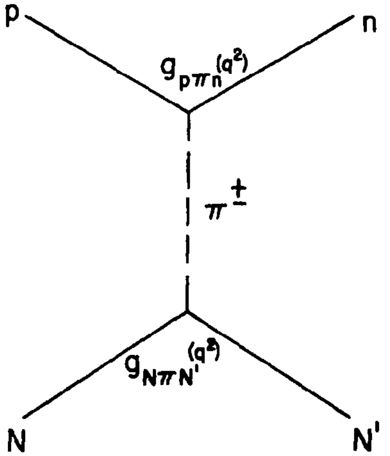

FIG. 1. One-pion exchange diagram for the reaction $p+N \to n+N'$ in the Born approximation.

were completely determined. Initial and final state interactions were inserted through the absorption model, although changes in the model were made to make it more applicable to scattering from a nucleus. Neglected in our calculations are explicit two-step processes and exchange erms arising from antisymmetrization between he projectile and the target nucleons. Multistep processes, however, are probably well accounted for by use of an optical potential which reproduces elastic scattering.[10] The exchange term may be neglected for forward scattering at intermediate energy for these transitions of low multipolarity. It is easy to see in impulse approximation that the exchange term is proportional to $v(|\vec{k}+\vec{k}'|)$, which s much smaller than the direct term which is proportional to $v(|\vec{k}-\vec{k}'|)$.[11] It is also the case that we neglect all contributions from other meson exchanges (or equivalently, other components of the effective interaction which would contribute upon antisymmetrization). Again, for transitions of ow multipolarity and for forward scattering this neglect should not be serious. One-pion exchange does include the tensor component.

As our calculations are performed in momentum space, they appear radically different from the raditional nuclear physics calculations. In fact, hey are actually quite similar to the effective nteraction calculations of Petrovich,[12] which are also formulated in momentum space. Petrovich argues that the momentum space calculations are useful as they can make direct use of information obtained on the momentum components of the transition density from inelastic electron scattering. The argument is persuasive even though electron scattering does not provide all of the transition densities required for nucleon scattering.) When he traditional calculation is written in momentum space, the parallel to our calculation becomes lear. Our Born amplitudes with the nuclear verex function removed corresponds to the effective nteraction, and our nuclear vertex function corresponds to the transition density. The distortions due to initial and final state interactions are nserted in each method. The difference between he two methods is simply that the traditional calulation performs an integral over momentum to ccount for the spatial extent of the nucleus, while we approximate the integration by choosing a mean alue. It is shown below that our approximation should be adequate; it does in fact produce a very similar reduction in the differential cross section compared to the Born amplitudes, as does the disorted wave impulse approximation when compared o the plane wave impulse approximation.[13]

It should be noted that our application of PCAC o nuclei is rather different than its usual application to elementary particles.[7] There, the differences between the coupling to nucleons of virtual pions and real pions can be ignored. We make no statement from our analysis, from which we obtain $g_{N\pi N'}(0)$, on the coupling of the nucleus to real pions, $g_{N\pi N'}(-m_\pi^2)$. This question has been raised in other applications of PCAC to nuclei, namely, muon capture,[14,15] radiative pion capture,[14,16] and pion scattering.[17] In our application we assume that PCAC is exact, or rather the Goldberger-Treiman relation (as stated) is exact, and compare our calculation to the measured differential cross sections. Our proposal also differs from the original suggestion of Kim and Primakoff,[3] who suggested an extrapolation of the measured (p,n) differential cross section into the unphysical region, the pion pole. This procedure has its difficulties even in application to nucleon charge exchange. Similarly, extraction of one-pion exchange from the higher partial waves of the (p,n) differential cross section would be extremely difficult. At the very least, a rather complete angular distribution would be required for a partial wave analysis; and although the forward scattering appears to have a large component from one-pion exchange, many other processes may contribute to the scattering at larger momentum transfers.[18] We find rather good agreement between our assumptions of one-pion exchange and the applicability of PCAC and our measured differential cross sections. Although this agreement does not uniquely justify our assumptions, it does give them a certain amount of credence.

II EXPERIMENTAL PROCEDURE AND RESULTS

A. Apparatus

The experiment was carried out at the Indiana University Cyclotron Facilty (IUCF). The experimental area is shown in Fig. 2. The target assembly was placed inside the chamber and just before the pole faces. Steel cylinders were placed inside and outside of the entrance beam pipe to prevent the beam from being bent in the magnetic field before it hit the target. The main proton beam was swept by the magnetic field into a Faraday cup buried in the wall, whereas the forward scattering neutrons emerged from the chamber through a 0.076 mm thick kapton window. Neutrons destined to reach the detector had to pass through very restrictive collimation, as shown in Fig. 3. The vertical collimation was supplied by stacked lead and concrete blocks, and the horizontal collimation was provided by lead bricks stacked on carts. This allowed the detector to view only the target. The scattering angle was changed by moving the detector, which was placed on a mobile hut. Angles

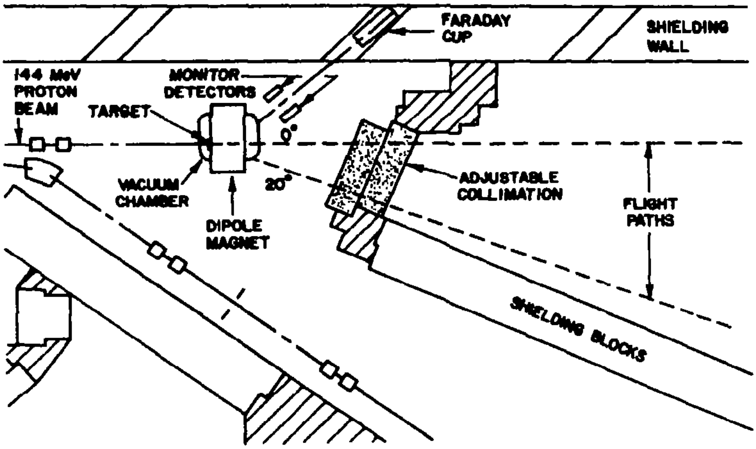

FIG. 2. Floor plan of the experimental area.

from 4° beam left to 25° beam right could be obtained and flight paths of 20 and 25 m were employed. A beam energy of 144 MeV was chosen because it was one of the maximum energies available at IUCF at that time and because good elastic scattering data for the ^{6}Li and ^{12}C existed at that energy.[19]

The detector used is shown in Fig. 4. It consisted of a sheet of plastic scintillator (charged particle identifier) followed by two NE 102 plastic scintillator timing rods (45.7 cm long and 4.44 cm in diameter), which in turn were followed by a vat of NE 213 liquid scintillator (50.8 cm long, 25.4 cm high, and 15.2 cm deep). The rods and vat were viewed at both ends by phototubes. Timing signals from each end of a rod were used to start a TAC, which was stopped by the subsequent rf pulse. The signals from the two ends of a rod were then added in the computer. Since the rod was thin, the resulting spectrum represented the time between the projectile leaving the target and the time it interacted in the rod. Pulse height signals from both ends of each rod and both ends of the vat were summed individually in hardware and were also stored. Timing signals from the charged particle identifier and the rods were used to produce an analog routing signal, whose magnitude depended on whether the detected particle was charged or not (interacted in the charged particle identifier or not), and on the rod with which it had interacted. In this way, both neutron and proton pulse height and time-of-flight spectra could be observed. (Although the bending magnet turned the main proton beam into the beam dump, it also bent elastically scattered protons toward the detector. The horizontal collimation could usually be arranged to block these particles, but some were always allowed to pass, providing a useful diagnostic tool.) Wrap-around, the contribution to

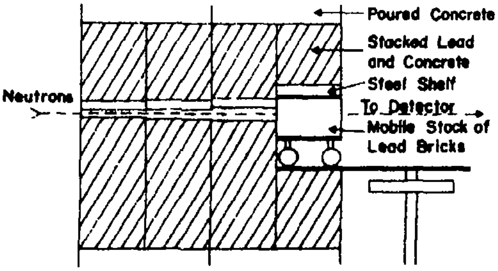

FIG. 3. Schematic drawing of the neutron collimator.

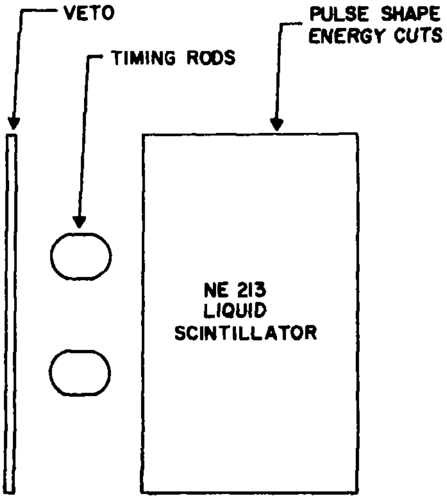

FIG. 4. Drawing of the neutron detector.

he time spectrum originating from neutrons that vere so slow that they would reach the detector at he same time as a faster neutron from a later urst, was always eliminated by setting a software threshold on the vat energy. The threshold equired to eliminate wrap-around depends on the eam repetition rate (~30 MHz), as well as the light path. Since the higher the pulse height hreshold detection, the lower the efficiency, the eam repetition rate was reduced by pulse selecting one out of four beam bunches (4×32 nsec) beore main stage acceleration. Because of low eam currents during the initial phase of the experiment, the ^{6}Li data were taken with no pulse election.

Two monitor counters, a plastic scintillator, and n NaI crystal, were placed outside of the vacuum hamber, downstream from the target, on either ide of the exit beam line. Kapton windows in the hamber allowed protons elastically scattered at bout 7° to reach these detectors relatively unindered. The plastic scintillator was used as a nonitor of the target thickness, while the NaI rystal was used to monitor the beam arrival time elative to the cyclotron rf phase. Owing to instabilities in the cyclotron, the time at which the beam was extracted relative to a signal generated from an rf crossing would drift. By stopping the protons in the NaI crystal, measuring their time of flight against the rf, and using the energy signal to choose only elastically scattered protons, the beam arrival time fluctuations were measured in an average way by observing the shifts in the flight time of the elastically scattered protons.

The signals that were monitored on-line and stored in event mode were the time of flight of both sides of the rods, the rod energy, the vat energy, the router, and the time of flight from the NaI monitor. The latter was recorded asynchronously to allow off-line corrections for beam arrival time variations.

The targets used were natural carbon and 98.5% enriched ^{6}Li; they were about 55 mg/cm^2 thick and presented a 300 keV loss to the proton beam. The full energy loss of the proton in the target is reflected in the resolution of the scattered neutrons. A nitrogen target was obtained by using melamine ($N_6C_3H_6$); the Q value for (p,n) on carbon is high enough so that reactions on carbon do not interfere with the ^{14}O ground state. The melamine target was about 70 mg/cm^2 thick, causing a 350 keV loss to the proton beam.

B. Data reduction

The first step in the data reduction was to correct the time-of-flight spectra for beam arrival time drifts. This correction was done by calculating for each 100 events recorded in the NaI monitor the centroid of their time of flight. This centroid was compared to an arbitrary time reference. The corresponding events in the neutron detector (which occurred in real time over the same period of time as the monitor signal) were then shifted in the opposite direction by the appropriate amount. Depending on the mood of the accelerator, this would give a 6% to 25% reduction in the FWHM.

The pulse height spectrum of the vat was calibrated from the position of the elastically scattered proton peak using the known light output for protons in NE 213. Thus the threshold required to eliminate wrap-around could be determined, and events with vat pulse heights below this threshold were ignored. Using the router signal, the data were then sorted into four time-of-flight arrays, representing protons and neutrons in each rod. Peak areas were then extracted by fitting Gaussian curves on a quadratic background to the data. For the ^{6}Li and melamine targets, the resolution was sufficient to easily distinguish the ground state peak from the first excited state. For the carbon target, however, the first excited state was only six-tenths of a FWHM away. Although better resolution is desired, this resolution should give reasonable results. Actually, there was no indication of the first several excited states being present, and chi-squares/degrees of freedom near one were obtained by assuming that they were absent. Statistical errors were calculated by finding the area for which the total chi-square was increased by one. The results from the two rods were then averaged.

Dead time corrections for the computer and TAC's were made. The router pulses were scaled as well as stored by the computer, so that the computer dead time could be obtained. Dead time in only one of the TAC's manifested itself in a poor resolution time spectrum superimposed on the principal one. The ratio of these two was then obtained from the proton spectra to determine the TAC dead time. The total of these corrections was always less than 10%.

The magnetic shielding before the target could not totally prevent the incident beam from bending before hitting the target, so the true beam direction θ_0 had to be determined. Consequently, cross sections for ^{6}Li were measured at the nominal angles of 0, ±1, and ±2°. A function quadratic in $|\theta - \theta_0|$ was then fitted to the data, yielding $\theta_0 = -0.3 \pm 0.3°$. Thus, all nominal angles were increased by 0.3°.

C. Normalization

The detector efficiency and solid angle were calibrated by normalizing the carbon data to data taken with a liquid scintillator detector measuring 12.7 cm deep and 12.7 cm in diameter. This detector was calibrated for 130 MeV neutrons in an independent experiment,[20] in which a tagged neutron beam was produced using the reaction $p+{}^7\mathrm{Li}\to n+{}^7\mathrm{Be}$. A small correction for the neutron absorption by air was also made. We estimate that the normalization of all the data, including the efficiency and target thickness, is ±7%; the errors indicated are statistical. Our final differential cross sections for ^{6}Li are in excellent agreement with the (n,p) data of Measday and Palmieri obtained at 152 MeV.[21] From charge symmetry the two differential cross sections should be equal.

D. Results

The forward angle spectra for the three targets are shown in Fig. 5. For the case of mass 6 and 12, the ground state clearly dominates the spectrum, but this is certainly not true for the case of mass 14. Indeed, in this case, the ground state is extremely small, and the spectrum is dominated by the 7.77 MeV $(2^+;1)$ excited state of ^{14}O. After corrections for the beam arrival time, the time resolution varied from 0.85 to 1.0 nsec. From the proton spectra we inferred that the time resolution was mainly limited by the beam itself. The corresponding energy resolution was between 1.7 and 2.0 MeV.

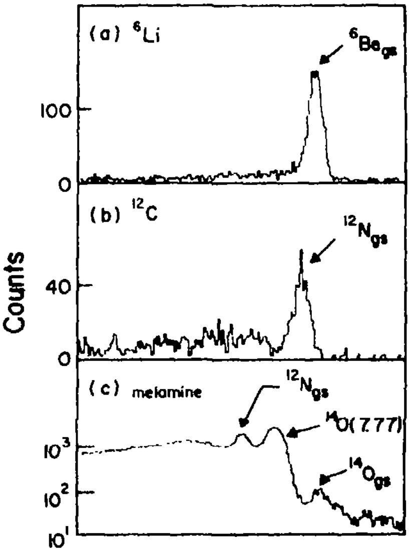

FIG. 5. The 0.3° time-of-flight spectrum for (a) $p+{}^6\mathrm{Li}\to n+{}^6\mathrm{Be}$, (b) $p+{}^{12}\mathrm{C}\to n+{}^{12}\mathrm{N}$, and (c) $p+$ melamine $\to n+X$.

The measured cross sections for the ground states and oxygen excited state are shown in Fig. 6. They are all forward peaked, but the ^{14}O ground state is much flatter than the others. The excited state of ^{14}O is almost identical to the mass 12 case, indicating that they may be produced by the same mechanism.

III. THEORETICAL ANALYSIS

A. Scattering amplitudes

We first start by writing down the general form of the Born amplitudes corresponding to the Feynman diagram shown in Fig. 1,

$$T^{\kappa}_{\lambda'\lambda}=2g_{N\pi N'}(q^2)g_{p\pi n}(q^2)\frac{\bar u^{\lambda'}(\vec p\,')\gamma_5 u^{\lambda}(\vec p)}{q^2+m_\pi^2}\xi_\nu^{(\kappa)}(\vec p\,')q_\nu . \quad (1)$$

The indices of the helicity amplitude $T^{\kappa}_{\lambda'\lambda}$ denote the helicity of the spin-1 nucleus κ and the initial and final nucleon helicities (λ and λ'). The proton-pion-neutron and initial nucleus-pion-final nucleus vertex functions are represented by $g_{p\pi n}(q^2)$ and $g_{N\pi N'}(q^2)$, respectively, and are functions of the four-momentum transfer squared, q^2. Also, $u^{\lambda}(\vec p)$ is the Dirac spinor with helicity λ and momentum $\vec p$, $\xi_\nu^{(\kappa)}(\vec p\,')$ is the spin-1 function (polarization vector) with helicity κ and momentum $\vec p\,'$, ξ_ν is the four-momentum transfer, and γ_5 is the usual Dirac operator. There are twelve different amplitudes $T^{\kappa}_{\lambda'\lambda}$, but space reflection can be used to relate six of them to the other six by[7]

$$T^{-\kappa}_{-\lambda'-\lambda}=(-1)^{\kappa+\lambda+\lambda'}T^{\kappa}_{\lambda'\lambda} . \quad (2)$$

A set of six independent amplitudes are written below in a form in which the angular dependence and momentum transfer dependence are explicitly denoted:

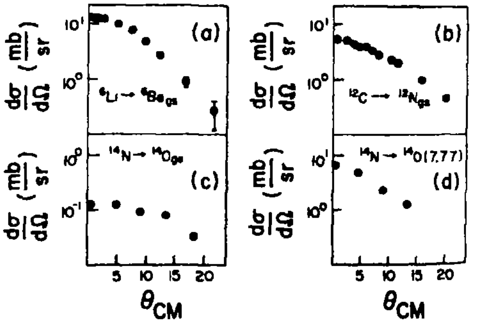

FIG. 6. The differential charge exchange cross section for (a) $p+{}^6\mathrm{Li}\to n+{}^6\mathrm{Be}$ (ground state), (b) $p+{}^{12}\mathrm{C}\to n+{}^{12}\mathrm{N}$ (ground state), (c) $p+{}^{14}\mathrm{N}\to n+{}^{14}\mathrm{O}$ (ground state), and (d) $p+{}^{14}\mathrm{N}\to n+{}^{14}\mathrm{O}$ (7.77 MeV, 2^+ state).

$$T^0_{++}=g_{p\pi n}(q^2)g_{N\pi N'}(q^2)b\xi_-\frac{E_1}{M_1}\left\{-d^{1/2}_{1/2,1/2}(\theta)+(z-\gamma)\frac{\cos(\theta/2)}{z-\cos\theta}\right\}, \tag{3a}$$

$$T^0_{+-}=g_{p\pi n}(q^2)g_{N\pi N'}(q^2)b\xi_+\frac{E_1}{M_1}\left\{d_{-1/2,1/2}(\theta)+(z-\gamma)\frac{\sin(\theta/2)}{z-\cos\theta}\right\}, \tag{3b}$$

$$T^1_{++}=g_{p\pi n}(q^2)g_{N\pi N'}(q^2)\frac{b}{\sqrt{2}}\xi_-\left\{-d^{1/2}_{-1/2,1/2}(\theta)+(z+1)\frac{\sin(\theta/2)}{z-\cos\theta}\right\}, \tag{3c}$$

$$T^1_{--}=-g_{p\pi n}(q^2)g_{N\pi N'}(q^2)\sqrt{2}\,b\xi_-\frac{\sin(\theta/2)\cos^2(\theta/2)}{z-\cos\theta}, \tag{3d}$$

$$T^1_{+-}=g_{p\pi n}(q^2)g_{N\pi N'}(q^2)\frac{b}{\sqrt{2}}\xi_+\left\{d^{1/2}_{1/2,1/2}(\theta)-(z-1)\frac{\cos(\theta/2)}{z-\cos\theta}\right\}, \tag{3e}$$

$$T^1_{-+}=g_{p\pi n}(q^2)g_{N\pi N'}(q^2)\sqrt{2}\,b\xi_+\frac{\sin^2(\theta/2)\cos(\theta/2)}{z-\cos\theta}. \tag{3f}$$

Our notation is similar to that of Refs. 7–9, which consider $\pi+p\to p+n$, which has the same spin sequence and is described by one-pion exchange. The angle θ denotes the center of mass angle of the neutron, and $d^{1/2}_{\lambda'\lambda}(\theta)$ denotes the rotation function of order $\frac{1}{2}$. The rest of the symbols are defined in Table I. These helicity amplitudes then represent the one-pion exchange Born approximation to the (p,n) reaction for $0^+\to1^+$ transitions.

B. Extraordinary terms

It is seen from Eqs. (3) that four of the Born amplitudes contain an s-wave contribution in the form of $d^{1/2}_{\lambda'\lambda}$. These terms are referred to as the "extraordinary" terms in the literature and must be removed from the Born amplitudes before a comparison can be made to experimental data. The appearance of extraordinary terms is quite general in one-boson exchange Born amplitudes, and they are often removed.[22] There does not appear to be a universal consensus on the justification for this procedure. The fact that these terms are troublesome is easily seen by plotting the contribution to the Born amplitudes of each partial wave, as is done in Fig. 7. Without the extraordinary terms, the amplitudes are seen to be continuous functions of the angular momentum. However, if the extraordinary terms are included, then the s-wave ($j=\frac{1}{2}$) amplitudes become negative while all other partial waves are unmodified, causing a

TABLE I. Variables of Eq. (3) not defined in the text.

Variable	Definition
b	$1/p'$ for $J=0\to1$ transitions and $1/p$ for $J=1\to0$ transitions
$\chi_\pm$	$\{(E+m_p)(E'+m_n)\}^{1/2}\{p/(E+m_p)\pm p'/(E'+m_n)\}$
$\xi_\pm$	χ for $J=0\to1$ transitions and $-\chi$ for $J=1\to0$ transitions
z	$(2EE'+m_\pi{}^2-m_n{}^2-m_p{}^2)/2pp'$
γ	$p'E_N/pE_{N'}$ for $J=0\to1$ and $pE_{N'}/p'E_N$ for $J=1\to0$
E_1	Center of mass energy of the nucleus with spin 1
M_1	Mass of the nucleus with spin 1
m_n	Neutron mass
m_p	Proton mass
m_π	Charged pion mass

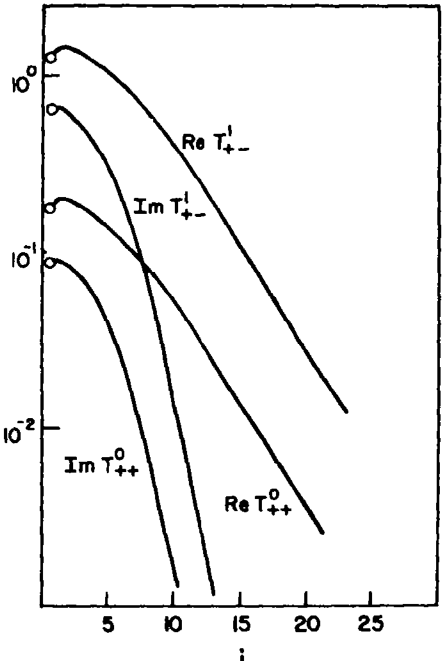

FIG. 7. Plot of the partial waves of the nonzero one-pion exchange amplitudes at 0°, including the distorted wave modification. A curve has been drawn through the discrete half-integer points to guide the eye. If the extraordinary terms were to be included, then the only difference would be that the $j=\frac{1}{2}$ points would become negative.

discontinuity. In the elementary particle literature it is noted that the extraordinary terms will violate s-wave unitarity, an absolute constraint, and thus their removal is justified.[8,23] The argument is also formulated with reference to the peripheral (high partial wave) nature of one-particle exchange processes that the Born amplitudes are simply inadequate for the lower partial waves. If one transforms the Born amplitudes to coordinate space, then the extraordinary terms become a δ function in the relative coordinate. In the one-pion exchange potential, this δ function is called a "contact" term. As one would expect, this term is traditionally discarded in the coordinate space formulation as well.[24] With respect to the nucleon-nucleon one-boson exchange potential, the argument is put forth that the short range repulsion prevents the contact term from contributing. More complicated arguments also have been formulated.[25] Although it is certainly the case that one-pion exchange cannot be the dominant contribution at small distances, the removal of the contact term has a rather simple justification for the Born approximation. A repulsive δ function can cause no contribution to the scattering amplitude because the boundary condition on the wave function requires that it vanish identically for $r=0$. Thus, if only Born approximation is considered and not the solution to the Schrödinger equation, it is more correct to neglect the δ function completely.

It is perhaps worthwhile to digress and to mention the relevance of these considerations for the historical determination of the pion-nucleon coupling constant from nucleon-nucleon scattering. Two rather different methods have been applied. Recognizing that one-pion exchange becomes dominant at large distances, the phase shifts for the high partial waves of intermediate energy scattering ($\lesssim$ 450 MeV) should be totally determined by the one-pion exchange potential. Thus, the magnitude of the coupling constant can be fixed by a best fit of the one-pion exchange potential to the $L \gtrsim 4$ partial waves.[26] In this manner the well-known number $g^2/4\pi = 14.6$ is obtained. We have argued that an analogous procedure would probably fail in the nuclear application. The second method follows the observation of Chew that the singularity in the scattering amplitude (the pion pole)[27] lies close to the physical region. The suggestion was made that a rather modest extrapolation of the differential cross section into the unphysical region would provide the pion-nucleon coupling constant. However, the Born amplitude for one-pion exchange in $n+p\rightarrow p+n$ vanishes at zero degrees (the effect of the extraordinary or the contact term) and the ubiquitous charge exchange peak in $n+p\rightarrow p+n$ was obtained through the interference of the one-pion exchange Born amplitude and smooth background terms. It is surprising then that the extrapolation procedure applied by Ashmore *et al.*[28] could obtain approximately the pion-nucleon coupling constant, a result which may be ascribed to a rather judicious choice of the data set and the order of the extrapolated polynomial. It is seen in the extrapolation performed by Cziffra and Moravcsik[29] that nonsensical results are obtained if the polynomial is either of too low or too high an order. The suggestion has been made that more optimal extrapolation procedures can be employed[30]; we do not feel competent to comment on this suggestion. Instead, we continue with the method described in the Introduction: Having introduced the Born amplitudes, we modified them to account for distortions introduced by the initial and final state interactions, and chose vertex functions consistent with the PCAC hypothesis.

Once the extraordinary term has been removed, it is easy to see which of the amplitudes in Eq. (3) is dominant. Since ξ_- is essentially zero, only T^0_{+-}, T^1_{+-}, and T^1_{-+} need be considered. These are the amplitudes corresponding to the projectile flipping its helicity. Of them, T^1_{+-} is dominant at forward angles, which is easily seen by examining their angular dependence.

C. Absorption model

It is not surprising that a method for doing distorted wave calculations in momentum space was developed in elementary particle physics, as almost all of their calculations are done in momentum space. The method was developed because of the discrepancy between one-pion exchange Born approximation calculations and various experiments in which one-pion exchange was firmly believed to dominate the reaction. Historically, in the first attempt to remove this discrepancy, arbitrary vertex functions were introduced. However, in order to fit the data, these phenomenological functions had to be much stronger than was thought reasonable. It was realized that the effect of these form factors was to reduce the contribution of the lower partial waves to the scattering amplitude. Consequently, a more natural way of doing this was sought. With the realization that the existence of scattering channels other than the one being observed would reduce the amplitudes of the lower partial waves and with the concurrent application of distorted wave techniques in nuclear physics, the absorption model was born.[7,8]

The absorption model includes distortions by modifying each partial wave of the Born amplitudes by a factor accounting for the effect of the elastic scattering on that partial wave. A rather simple form can be derived under the assumptions that (1) the particle wavelengths are small compared to the characteristic ranges of the interactions, (2) the entrance and exit channels are strongly coupled to many inelastic channels, and (3) the range of the exchange interaction is small compared to that of other interactions.[a] It must be admitted that these assumptions are invalid in nuclear physics; they are also of questionable validity in particle applications. The form of the modification in our calculation is

$$T^{\kappa,J}_{\lambda',\lambda} = \tfrac{1}{4}\{(S_i^{l,J+1/2})^{1/2} + (S_i^{l,J-1/2})^{1/2} + (S_f^{l,J+1/2})^{1/2} + (S_f^{l,J-1/2})^{1/2}\}\, T^{\kappa,J}_{\lambda',\lambda}(\text{Born})\,, \tag{4}$$

where $S_i^{l,J}(S_f^{l,J})$ is the elastic scattering S matrix element for the incident (scattered) particle and $T^{\kappa J}_{\lambda'\lambda}$(Born) is the Jth partial wave Born helicity amplitude, which is obtained from $T^{\kappa}_{\lambda',\lambda}$(Born) by the technique of Hogaasen and Hogassen.[9] The justification of Eq. (4) is given in the Appendix and holds only for forward angles. It will be noted that Eq. (4) differs from that used in elementary particle physics in two ways. One way is that S is taken to depend on the orbital angular momentum l as well as J. The primary difference, however, is that S is raised to the one-half power instead of the first power, which accounts for the range of the elastic and inelastic potentials being comparable in a nucleus.

The S matrix elements were calculated from the optical potentials for the target nuclei at 144 MeV,[31] using the optical model code SNOOPY.[32] The potential for the final nucleus was assumed to be that of the target, so the final S matrix elements were calculated for a neutron with the appropriate energy. The sensitivity of the (p,n) cross section to uncertainties in the S matrix elements was estimated for ^{12}C by calculating it for a potential optimized to the differential cross section and to a potential optimized to polarization data. The results differed by only 5%. The sensitivity could be greater for ^{6}Li, however, since the potential is not as well determined.

D. Vertex functions

As pointed out by Kim and Primakoff,[3] the magnitude of an initial nucleus-pion-final nucleus vertex function at zero momentum transfer can be obtained by applying PCAC to the nuclear states to obtain a nuclear Goldberger-Treiman relation. The original Goldberger-Treiman relation[4] was a proportionality between the proton-pion-neutron coupling constant $g_{p\pi n}(-m_\pi^2)$ and the axial vector coupling constant measured in neutron β decay $g_A(0)$. The nuclear relation, which we derive below, is a proportionality at $q^2=0$ between the initial nucleus-pion-final nucleus vertex function $g_{N\pi N'}(q^2=0)$ and the weak axial vector coupling constant $F_A(q^2=0)$, for the $N'\to N+e^+ +\nu$ decay. In this approach the nucleus is treated as an elementary particle in the sense that only the spin, parity, isospin, and mass of the nuclear states are explicitly specified. It has also been shown by Kim[33] that the dependence of the nuclear vertex function $g_{N\pi N'}(q^2)$ for transitions dominated by no change of orbital angular momentum can be obtained from the inelastic electron scattering form factor $\mu(q^2)$. Kim also shows that the corrected Goldberger-Treiman relation for nucleons can be used to estimate the dependence on momentum transfer of the pion-nucleon vertex function $g_{p\pi n}(q^2)$. The arguments go as follows.

PCAC, in the formulation of Gell-Mann and Levy,[34] states that

$$\partial_\alpha A_\alpha(x) = a_\pi m_\pi^3 \phi(x)\,, \tag{5}$$

where $A_\alpha(x)$ is the weak axial vector current, $\phi(x)$ is the pion field operator that creates or destroys a pion, m_π is the pion mass, and $a_\pi = 0.939$ is the pion decay constant, determined from $\pi\to\mu+\nu$. If one treats the nucleus as an elementary particle, then $A_\alpha(x)$ can only be constructed from vector quantities pertaining to the nucleus as a whole.

For $0^+\to 1^+$ transitions, one has

$$\langle N'_\kappa | A_\alpha(x) | N\rangle = 2(M_N M_{N'})^{1/2}\left\{\xi_\alpha^{(\kappa)} F_A(q^2) + q_\alpha \xi_\mu^{(\kappa)} q_\mu \frac{F_P(q^2)}{m_\pi^2} + (P_\alpha^N + P_\alpha^{N'})\xi_\mu^{(\kappa)} q_\mu \frac{F_T(q^2)}{m_\pi^2}\right\} e^{-iq_\nu x_\nu}\,. \tag{6}$$

The symbols M_N and $M_{N'}$ stand for the masses of the nuclei N and N'; $\xi_\alpha^{(\kappa)}$ is the usual spin-1 function with helicity κ; $F_A(q^2)$, $F_P(q^2)$, and $F_T(q^2)$ are, respectively, the axial vector, induced pseudoscalar, and induced tensor weak nuclear form factors; P_α^N and $P_\alpha^{N'}$ are the momenta of N and N' with the momentum transfer $q_\alpha = P_\alpha^N - P_\alpha^{N'}$; and x_ν is the position at which the current is evaluated. The matrix element of the pion field, $\langle N'_\kappa|\phi|N\rangle$, can be broken into an expansion of terms represented by the diagrams shown in Fig. 8. Evaluating only the first term in the expansion gives

$$\langle N'_\kappa|\phi|N\rangle = -2i\,\frac{\xi_\alpha^{(\kappa)} q_\alpha}{q^2+m_\pi^2}\, g_{N\pi N'}(q^2)\,. \tag{7}$$

With the PCAC choice of the pion field, Eqs.

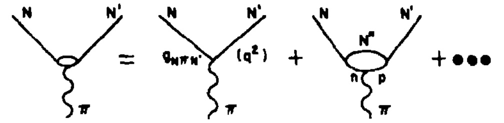

FIG. 8. Diagramatic representation of the two lowest order terms of the pion field matrix element $\langle N'|\,\phi\,|N\rangle$ in covariant perturbation theory.

(5)–(7) can be combined to give

$$F_A(q^2)+\frac{q^2}{m_\pi^2}F_P(q^2)+\frac{M_N^2-M_{N'}^2}{m_\pi^2}F_T(q^2)=\frac{a_\pi m_\pi^3}{(M_NM_{N'})^{1/2}}\,\frac{g_{N\pi N'}(q^2)}{(q^2+m_\pi^2)}. \tag{8}$$

As there is no evidence for the induced tensor term,[35] it may be neglected. Evaluating Eq. (8) at $q^2=0$ then gives the nuclear Goldberger-Treiman relation

$$g_{N\pi N'}(0)=\frac{(M_NM_{N'})^{1/2}}{a_\pi m_\pi}F_A(0). \tag{9}$$

Finally, the value of $g_{N\pi N'}(0)$ can be obtained from the ft value for the β decay of $N'\to N$,[36] since

$$|F_A(0)|^2=\frac{2\pi^3\ln 2(2J_{N'}+1)}{3G^2\cos^2\theta_C m_e^5\{ft\}}, \tag{10}$$

where the weak interaction coupling constant $G=1.026\times10^{-5}/m_p^2$, the Cabibbo angle $\theta_C=0.257$, m_e is the electron mass, and $J_{N'}$ is the spin of the nucleus N'.

A similar procedure can be applied to the nucleon β decay. In this case, one obtains for nucleons that

$$g_A(q^2)+\frac{q^2}{m_\pi^2}g_P(q^2)=\frac{a_\pi m_\pi^3}{(m_n+m_p)}\,\frac{g_{p\pi n}(q^2)}{q^2+m_\pi^2}. \tag{11}$$

Evaluating this expression at $q^2=0$, one obtains a modified Goldberger-Treiman relation, namely

$$g_{p\pi n}(0)=\frac{(m_n+m_p)}{a_\pi m_\pi}g_A(0). \tag{12}$$

Here and in the following, the weak nucleon form factors have been denoted by g_A and g_P, and the weak nuclear form factors have been denoted by F_A and F_P. From the neutron β decay,[37] we obtain $g_A(0)=1.239$,[38] and thus

$$g_{p\pi n}(0)=17.8. \tag{13}$$

From a dispersion theoretical analysis of pion-nucleon scattering, it is known that the physical coupling constant is[39]

$$g_{p\pi n}(-m_\pi^2)=19.3. \tag{14}$$

Thus, choosing a simple functional form for $g_{p\pi n}(q^2)$ expected to be valid for $-m_\pi^2\leq q^2\leq m_\pi^2$, we find that

$$g_{p\pi n}(q^2)=g_{p\pi n}(0)/[1+q^2/(4.92m_\pi)^2]^2. \tag{15}$$

The dependence of the nuclear vertex function $g_{N\pi N'}(q^2)$ could be determined from Eq. (8) if the two form factors, $F_A(q^2)$ and $F_P(q^2)$, were known. The pseudoscalar form factor may be estimated from the axial vector form factor. One has from the impulse approximation[13,40]

$$\frac{F_P(q^2)}{F_A(q^2)}=\frac{g_P(q^2)}{g_A(q^2)}. \tag{16}$$

With this expression for $F_P(q^2)$, it is then necessary to know only the ratio $g_P(q^2)/g_A(q^2)$ and $F_A(q^2)$. If the dependence on momentum transfer of $g_A(q^2)$ and $g_{p\pi n}(q^2)$ were identical, then we would obtain directly from (11)

$$\frac{g_P(q^2)}{g_A(q^2)}=\frac{-m_\pi^2}{m_\pi^2+q^2}. \tag{17}$$

However, from an analysis of neutrino scattering, Kim[33] finds

$$g_A(q^2)=g_A(0)/(1+q^2/45.8m_\pi^2)^2. \tag{18}$$

This difference increases the ratio of $g_P(q^2)/g_A(q^2)$ by a factor of 1.04.[41] For $|q^2|\approx m_\pi^2$ this modification and corrections to the impulse approximation [Eq. (16)] are rather insignificant.[33]

The dependence on momentum transfer of the axial vector form factor may be obtained from the inelastic electron scattering form factor. In this approximation we first note that from the impulse approximation[16]

$$F_M(q^2)\cong\{F_M(q^2)\}_{\text{orbital}}+\{F_M(q^2)\}_{\text{spin}}$$

$$\cong\{F_M(q^2)\}_{\text{orbital}}+\frac{g_V+g_M}{g_A}F_A(q^2), \tag{19}$$

where $F_M(q^2)$ is a weak magnetism nuclear form factor that contributes to the vector current in the decay $N'\to N+e+\nu$, and $(g_V+g_M)/g_A$ may be taken to be independent of momentum transfer $[=(1+3.7)/1.24]$. For nucleon transitions in which the initial and final states have no orbital angular momentum, which is approximately the situation for the cases of masses 6 and 12 considered here, the orbital contribution vanishes. Thus, Eq. (19) yields, for nuclei in which the spin contribution is dominant,

$$\frac{F_A(q^2)}{F_A(0)}\cong\frac{F_M(q^2)}{F_M(0)}. \tag{20}$$

Now the weak magnetism form factor can be related to the transverse inelastic electron scattering form factor $\mu(q^2)$ measured in the scattering to the analog state of N'. Using CVC[33] Kim shows that

$$\frac{F_M(q^2)}{F_M(0)}=\frac{\mu(q^2)}{\mu(0)}\,. \tag{21}$$

For $q^2 \lesssim m_\pi^2$ the inelastic electron scattering form factor can be fitted by the dipole form, from which Kim[33] obtains

$$\frac{F_A(q^2)}{F_A(0)}=\frac{1}{(1+q^2/M_N^2)^2}\,,\quad q^2 \lesssim m_\pi^2 \tag{22a}$$

where

$$M_N^2=2.0m_\pi^2 \;\text{ for } {}^6\text{Li}\rightarrow{}^6\text{Be} \tag{22b}$$

and

$$M_N^2=2.6m_\pi^2 \;\text{ for } {}^{12}\text{C}\leftarrow{}^{12}\text{N}\,. \tag{22c}$$

Now, taking Eqs. (8), (9), (16), (17), and (22), we obtain for $g_{N\pi N'}(q^2)$

$$\frac{g_{N\pi N'}(q^2)}{g_{N\pi N'}(0)}=\frac{1-q^2/25m_\pi^2}{(1+q^2/M_A^2)^2}\,. \tag{23}$$

Without too much reflection one will recognize that the important assumption in this argument is that the nuclear vertex functions and the weak form factors all have dependence on momentum transfer similar to $\langle N'|\vec{\sigma}\tau\, e^{iq\cdot x}|N\rangle$.

Although the assumptions that were introduced to arrive at Eq. (23) are justified for ^{6}Li and ^{12}C, the justification is not so evident for ^{14}N. The difficulty lies in the fact that although ^{14}N is a 1^+ nucleus, its total orbital angular momentum is dominantly $L=2$ (see Ref. 15). Thus, in Eq. (19) the orbital term $\{F_M(q^2)\}_{\text{orbital}}$ is not negligible. In fact, Goulard *et al.* take the extreme position that the spin contribution $\{F_M(q^2)\}_{\text{spin}}$ is negligible in obtaining the dependence of $g_{N\pi N'}(q^2)$ on momentum transfer. However, their analysis was intended for use at larger q^2 than we are considering since they assume that $\{F_M(0)\}_{\text{spin}}=0$, which is probably not exact. With no other guide to the separation of $\{F_M(q^2)\}_{\text{spin}}$ and $\{F_M(q^2)\}_{\text{orbital}}$, we use Eq. (20) for F_A, along with the functional form of Goulard *et al.*[15] for $F_M(q^2)/F_M(0)$. We then obtain for mass 14

$$\frac{g_{N\pi N'}(q^2)}{g_{N\pi N'}(0)}=(1-q^2/25m_\pi^2)(1+q^2/m_\pi^2)\,e^{-0.38q^2/m_\pi^2}\,. \tag{24}$$

If we were to follow the argument of Goulard *et al.*, the factor $1+q^2/m_\pi^2$ would be changed to q^2/m_π^2, with the consequence that the $p+{}^{14}\text{N}\rightarrow n+{}^{14}\text{O}$ cross section would vanish in the forward direction.

It should be noted that Eqs. (8) and (11), from which the magnitude of the vertex functions at $q^2=0$ and their dependence on momentum transfer were obtained, were derived by neglecting the higher order terms in $\langle N'|\phi|N\rangle$ and $\langle n|\phi|p\rangle$. However, it is the case that for $p+N\rightarrow n+N'$ we also neglect higher order contributions. Thus, to the extent that higher order contributions are similar, the vertex function $g_{N\pi N'}(q^2)$, as derived, is actually an effective coupling for the initial nucleus changing to the final nucleus with a pion somehow being produced. Thus, the cross sections predicted with this vertex function should be more accurate than one might initially expect. If one were to attempt to determine from the $p+N\rightarrow n+N'$ data the physical coupling constant $g_{N\pi N'}(-m_\pi^2)$, then it would be necessary to understand the differences in the higher order contributions, both in the charge exchange reaction itself and the PCAC application.

E. Results

The comparisons between the predicted and experimental cross sections at 0° are especially important since they are independent of the form factors. The momentum transfer is approximately zero, so that the magnitude of the cross section is determined solely by the values of $g_{p\pi n}(0)$ and $g_{N\pi N'}(0)$, which are obtained from PCAC. [See Eqs. (9) and (12).] In Table II the predicted values of $g_{N\pi N'}(0)$ and those extracted from the data are shown, while in Fig. 9, the predicted cross sections are displayed with the data.

The sensitivity of the theoretical predictions to variations in the ingredients of the calculation is shown in Fig. 10. It is clear that absorption is a significant, yet not an overwhelming, modification of the Born amplitudes. Furthermore, the traditional prescription for the absorption correction yields results that are only half as large as those obtained with our prescription, and they are much lower than the mass 6 and 12 data. Our treatment of distortions yields a reduction in the Born cross sections similar to that given by a traditional

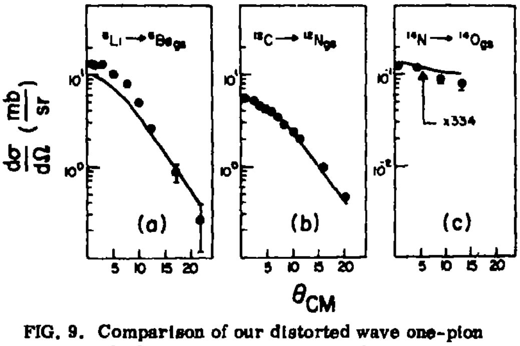

FIG. 9. Comparison of our distorted wave one-pion exchange calculation to the measured differential cross sections in the reaction (a) $p+{}^6\text{Li}\rightarrow n+{}^6\text{Be}$ (ground state), (b) $p+{}^{12}\text{C}\rightarrow n+{}^{12}\text{N}$ (ground state), and (c) $p+{}^{14}\text{N}\rightarrow n+{}^{14}\text{O}$ (ground state).

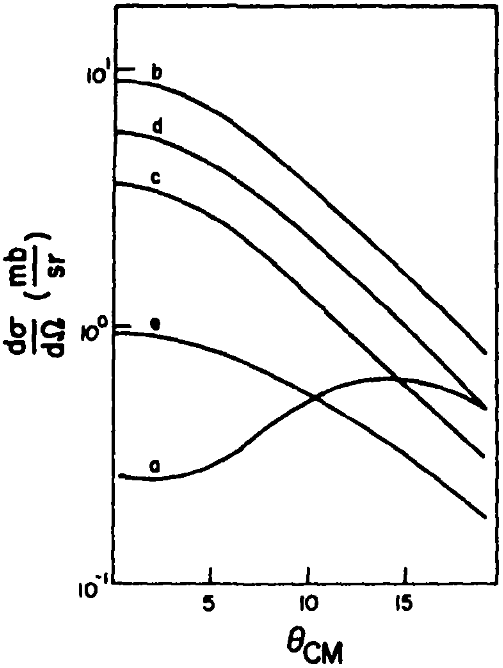

FIG. 10. Various calculations of the ^{12}C differential cross sections. Detailed descriptions of the calculations appear in the text. The curves represent: (a) Born approximation, including the extraordinary terms, (b) Born approximation, excluding the extraordinary terms, (c) DWBA, excluding the extraordinary terms, with the distortion modifications made with the $(S_i^J$ $(S_i^J)^{1/2}T^J(S_f^J)^{1/2}$ prescription used in elementary particle physics (Refs. 7 and 8), and (d) DWBA, excluding the extraordinary terms, with the distortion modifications introduced by the authors. Curve (e) represents the θ or q^2 dependence of the form factor product

$$g_{p\pi n}(q^2)g_{N\pi N'}(q^2)/\{g_{p\pi n}(0)g_{N\pi N'}(0)\}.$$

DWIA calculation.[13] The validity of our approximation is discussed in the Appendix. The shapes of the cross sections are seen to be rapidly falling with angle; about one-half of this decline is due to the form factor, with the rest being due to the pion propagator. Finally, one sees that if the extraordinary terms are left in the Born amplitudes, then the results bear no resemblance to the data.

IV. DISCUSSION AND CONCLUSIONS

As seen in Table II and Fig. 8, the agreement between the theory and experiment is fair for ^6Li and ^{12}C. The 30% disagreement for ^6Li (15% is the amplitudes) could be largely due to the fact that $g_{N\pi N'}(0)$ was determined from the $F_A(0)$ value of the ^6He β decay, since the $F_A(0)$ value for the unstable ^6Be is unknown. Other contributions to the discrepancy could come from the 7% normalization error, uncertainties in the S matrix, and inadequacies of the absorption model. It is also possible that there are small contributions from interactions other than one-pion exchange. At any rate, the agreement that is achieved for ^6Li and ^{12}C is good evidence that these reactions are dominated by one-pion exchange.

The ^{14}N case is much different, however. Here, the measured cross sections are a factor of 100 lower than for ^6Li, but they are still a factor of 300 larger than the values predicted from one-pion exchange and PCAC. This is not a failure of the model, however, as the model predicts one-pion exchange amplitudes, which in this case are expected to be extremely small. These amplitudes are so small, in fact, that other mechanism which are normally small effects, such as two-step process and rho exchange, are no longer negligible. Thus, the model is predicting that

TABLE II. The initial nucleus (N), pion (π), final nucleus (N') vertex function $g_{N\pi N'}(0)$ as calculated from nuclear β decay, assuming the validity of the modified Goldberger-Treiman relation. It is compared to $g_{N\pi N'}(0)$ extracted from our 0.3° differential cross sections using our absorption modified one-pion exchange model, assuming one-pion exchange dominance.

Target	$N' \to N$ ft (sec)	{Ref.}	$g_{N\pi N'}(0)$ {PCAC}	$g_{N\pi N'}(0)$ {experiment}	$(d\sigma/d\Omega)/0°$ (mb/sr)
n	1.076×10^3	{42}	17.8		13 [a]
^6Li	8.157×10^2 [b]		69.2	60.9	13.1
^{12}C	1.315×10^4	{44}	59.5	59.9	5.56
^{14}N	2.14×10^7	{15}	0.994	18.0	0.13

[a] Extrapolation of 152 MeV data from Ref. 43.

[b] The ^6He ft value (Ref. 45) was actually used, since the value for the short lived ^6Be was not known.

these are the processes that will be measured. In that sense, the fact that the cross sections are so much smaller than the mass 6 and 12 cases is a success of the model. Since this case is a measurement of reactions such as two-step processes and rho exchange, it provides an estimate of the magnitude of such processes in light nuclei and indicates the limits of one-pion exchange dominance.

The inhibition of one-pion exchange in the $p+{}^{14}\mathrm{N}_{\mathrm{g.s.}}\to n+{}^{14}\mathrm{O}_{\mathrm{g.s.}}$ reaction is due to the structure of the two nuclei. The ${}^{14}\mathrm{N}_{\mathrm{g.s.}}$ nucleus is predominantly a ${}^{3}D_{1}$ state, whereas the ${}^{14}\mathrm{O}_{\mathrm{g.s.}}$ nucleus is a combination of ${}^{1}S_{0}$ and ${}^{3}P_{0}$ states.[15] The ${}^{14}\mathrm{O}$ (7.77 MeV) state, however, is a $J^{\pi}=2^{+}$ state, so it may be ${}^{1}D_{2}$. Such a state could be obtained from ${}^{14}\mathrm{N}_{\mathrm{g.s.}}$ by a spin-flip transition, so one would expect it to be dominated by one-pion exchange. Therefore, the similarity of the experimental differential cross sections for the $p+{}^{14}\mathrm{N}\to n+{}^{14}\mathrm{O}$ (7.77 MeV) transition to those for the mass 12 case suggests that it is dominated by one-pion exchange and that the 7.77 MeV state of ${}^{14}\mathrm{O}$ is predominantly a ${}^{1}D_{0}$ state.

If the differential cross sections for ${}^{6}\mathrm{Li}$ and ${}^{12}\mathrm{C}$ were due exclusively to one-pion exchange, then they would provide a definitive test of the application of PCAC to nuclei. However, if the ${}^{14}\mathrm{N}$ cross sections are interpreted as interactions other than one-pion exchange, which could also occur in the ${}^{6}\mathrm{Li}$ and ${}^{12}\mathrm{C}$ transitions, then the test is obscured. One can estimate the maximum effect that this background could have on the one-pion exchange amplitudes by assuming only one independent helicity amplitude for ${}^{14}\mathrm{N}$ and that this amplitude interferes coherently with the primary amplitude of one-pion exchange at 0°. Using

$$\frac{d\sigma}{d\Omega}=\frac{1}{(2J_{i}+1)}\,|f|^{2}\,, \tag{25}$$

this gives $|f_{{}^{6}\mathrm{Li}}(0)|=6.27$, $|f_{{}^{12}\mathrm{C}}(0)|=2.36$, and $|f_{{}^{14}\mathrm{N}}(0)|=0.62$. Thus, the measured cross sections may deviate from those of one-pion exchange and, hence, those predicted by PCAC, by up to 20% for ${}^{6}\mathrm{Li}$ and 50% for ${}^{12}\mathrm{C}$. If the applicability of PCAC to nuclei is to be tested better than this with the data measured here, then the background contributions will actually have to be calculated.

Since PCAC predicts amplitudes, we have found it to be valid at the 25% level. Based on what one has learned about PCAC in particle physics, was this expected? Well, even if one firmly believes in the validity of PCAC when applied to elementary particles such as a pion, one could imagine various complications that could arise when it is applied to a compound system as a whole. The fact that these complications are so small is remarkable. Furthermore, there have so far been only two impressive tests of PCAC in the particle physics domain, other than the Goldgerger-Treiman relation for which PCAC was created to explain. These are the Adler consistency condition, which is a relation between the nuclear coupling constant and the pi-nucleon off-mass shell scattering amplitude,[46] and the Adler-Weisberger sum rule, which predicts the weak axial vector coupling constant in terms of off-mass shell pion-proton total cross sections.[47] Both relations are derived using PCAC, and they appear to be valid to 10% and 5%, respectively. The test that we have made lends further credence to PCAC.

Since PCAC seems to be valid for nuclei, what are its applications? Perhaps its most important use would be to help unravel the nuclear force. In most nuclear transitions, there are more pieces to the interaction than one-pion exchange, and it is a complex problem to disentangle and identify the pieces. However, for transitions in which the final state β decay to the initial state is allowed and measurable, the pion contribution can be predicted from PCAC, thereby simplifying the problem.

In conclusion, we find that there are certain types of nuclear reactions in which the nucleus acts as a filter for the nuclear force, allowing only one-pion exchange and reactions which are usually a very small component of nucleon-nucleus scattering in the forward direction at intermediate energies. Of the three cases studied here, ${}^{6}\mathrm{Li}$ and ${}^{12}\mathrm{C}$ had large, sharply forward-peaked angular distributions, whereas that for $p+{}^{14}\mathrm{N}\to n+{}^{14}\mathrm{O}_{\mathrm{g.s.}}$ was extremely small and gently forward peaked. One-pion exchange calculations were made by treating the nucleus as an elementary particle. When the initial nucleus-pion-final nucleus coupling constant was assigned the value predicted by PCAC, the results were in fair and good agreement with ${}^{6}\mathrm{Li}$ and ${}^{12}\mathrm{C}$, respectively, but they were a factor of 300 lower than the ${}^{14}\mathrm{N}$ data. If the ${}^{14}\mathrm{N}$ data are taken as a background level to one-pion exchange for ${}^{6}\mathrm{Li}$ and ${}^{12}\mathrm{C}$, then we have tested the applicability of PCAC to nuclei at the 25% level and found it to be valid.

V. ACKNOWLEDGMENTS

It is a pleasure to acknowledge the assistance of Dr. C. C. Foster in the design and construction of the neutron beam line and shielding arrangements. The support of Professor R. E. Pollock and Professor G. T. Emery throughout this work has been appreciated. We would like to thank Professor K. Vasavada for his theoretical assistance during the proposal and analysis stage. Professor

H. Primakoff, Professor B. Goulard, and Professor F. Petrovich were kind enough to elucidate the problems in ^{14}N. Finally, we thank Dr. H. Foelsche of the BNL Accelerator Division for arranging the loan of the sweeping magnet, without which our experiment would not have been possible. This work was supported in part by the National Science Foundation and the Department of Energy.

APPENDIX: DWBA IN MOMENTUM SPACE

The goal of this appendix is to find a method of modifying the Born amplitudes for inelastic scattering to account for the distortions of elastic scattering, without the need of complex calculations. It is hoped that the success of the absorption model in elementary particle physics means that this is possible, although we realize that the absorption model must be modified before it can be applied to a nucleus. The form we use for including distortions will be derived in the eikonal approximation, and the final form is by no means exact. Although the derivation will be done in coordinate space, the final result will be written in terms that are easily transposed to momentum space.

The general form of the scattering amplitude for scattering from a potential V is given by[48]

$$T_{\beta\alpha}=\int u_\beta^*(\vec{r})V(\vec{r})\chi_\alpha^+(\vec{r})d^3r\,, \tag{A1}$$

where u_β is a plane wave representing the final state and χ_α^+ is the solution of the Schrödinger equation with potential V representing the initial state. We wish to consider the case

$$V=V_1+V_2\,, \tag{A2}$$

where V is the total nuclear potential and V_2 is the potential corresponding to the inelastic transition in question. We will make the DWBA approximation that the *effect of* V_2 on χ_α^+ can be ignored.

In the eikonal approximation, one writes[49]

$$\chi_\alpha^+(\vec{r})=u_\alpha(\vec{r})\exp-\frac{i}{v}\int_{-\infty}^{z}V_1(b,z')dz'\,, \tag{A3}$$

where V has been taken as being spherically symmetric, v is the velocity of the projectile, and cylindrical coordinates have been used. If one defines

$$E(b)=\left\langle\exp-\frac{i}{v}\int_{-\infty}^{z}V_1(b,z')dz'\right\rangle_{\text{Average over }z}\,, \tag{A4}$$

then Eqs. (A1) and (A3) give

$$\begin{aligned}T_{\beta\alpha}&=\int u_\beta^*(\vec{r})[V_1(r)+V_2(r)]u_\alpha(\vec{r})\left\{\exp-\frac{i}{v}\int_{-\infty}^{z}V_1(b,z')dz'\right\}dz\,d^2b\\&\simeq\int E(b)u_\beta^*(\vec{b},z)[V_1(b,z)+V_2(b,z)]u_\alpha(\vec{b},z)dz\,d^2b\,.\end{aligned} \tag{A5}$$

Since V_1 does not contribute to the inelastic scattering, and since it is of no longer range than V, it will not contribute to the last expression of Eq. (A5). (If V were of longer range than V_2, then its effects would be seen after the inelastic scattering had occurred, so they would have to be dealt with. The absence of this effect is the major difference between our calculation and those of traditional nuclear physics and is a result of treating the nucleus as an elementary particle.) Thus, Eq. (A5) becomes

$$T_{\beta\alpha}\simeq\int E(b)T_{\beta\alpha}^{\text{Born}}(\vec{b})d^2b\,, \tag{A6}$$

where $T_{\beta\alpha}^{\text{Born}}(\vec{b})$ is the Born scattering amplitude defined by

$$T_{\beta\alpha}^{\text{Born}}=\int T_{\beta\alpha}^{\text{Born}}(\vec{b})d^2b\,. \tag{A7}$$

It would be useful if $E(b)$ could be replaced by something simpler than (A4). Since the value of the integral over V_1 in Eq. (A4) for $z=0$ is one-half of its value for $z=\infty$, it seems reasonable to use

$$E(b)\sim D(b)^{1/2}\,, \tag{A8a}$$

$$D(b)\equiv\exp-\frac{i}{v}\int_{-\infty}^{\infty}V_1(b,z')dz'\,. \tag{A8b}$$

However, the integral in Eq. (A8b) can be identified as twice the elastic scattering phase shift for the angular momentum corresponding to the impac parameter b. This is seen by calculating the elastic scattering S matrix from Eq. (A3), using Eq. (A8b):

$$\begin{aligned}\langle\beta|S|\alpha\rangle&=\int u_\beta^*(\vec{b},z)\chi_\alpha^+(\vec{b},z=\infty)dz\,d^2b\\&=\int u_\alpha^*(\vec{b},z)u_\alpha(\vec{b},z)D(b)dz\,d^2b\\&=\langle\beta|\alpha\rangle+\int u_\beta^*(\vec{b},z)u_\alpha(\vec{b},z)[D(b)-1]dz\,d^2b\,.\end{aligned}$$

(A

Now, for small scattering angles,

$$(\vec{k}-\vec{k}')\cdot\vec{r} = kz - \vec{k}'\cdot\vec{r}$$
$$= kz - k'z\cos\theta - k'\sin\theta\hat{x}\cdot\vec{b}$$
$$\simeq (k-k')z - k'b\sin\theta\cos\phi\,, \tag{A10}$$

and from Ref. 50,

$$J_0(l\cos\theta)\simeq P_l(\cos\theta)\,. \tag{A11}$$

Equation (A9) then gives

$$\langle\beta|S-1|\alpha\rangle = 2\pi\delta(k-k')\int e^{-k'b\sin\theta\cos\phi}$$
$$\times[D(b)-1]b\,db\,d\phi$$
$$=4\pi^2\delta(k-k')\int J_0(k'b\sin\theta)[D(b)-1]b\,db\,. \tag{A12}$$

Letting $b\to l/k$ and $\int l\to\sum_l$, Eqs. (A11) and (A12) give

$$\langle\beta|S-1|\alpha\rangle = 4\pi^2\delta(k-k')\sum_l P_l(\cos\theta)[D(b)-1]l/k^2$$
$$\simeq\frac{2\pi^2\delta(k-k')}{k^2}\sum_l(2l+1)P_l(\cos\theta)$$
$$\times[D(l/k)-1]\,. \tag{A13}$$

Equation (A13), however, is the expression relating the S matrix to the phase shifts if one takes $D(l/k)=e^{2i\delta_l}=S_l$.

Thus, transforming Eq. (A6) to angular momentum space and using Eq. (A8a), one has

$$T_{\beta\alpha}=\sum_l S_l^{1/2}T^{\text{Born}}_{\beta\alpha,l}\,. \tag{A14}$$

Actually, the S matrix depends on the total angular momentum j as well. Furthermore, Eq. (A14) was derived assuming that the elastic scattering potential was the same before and after the inelastic reaction. Since this is not true for (p,n) scattering, one must take an average of the two potentials. However, since the resultant S matrices are very similar, the exact method of averaging is unimportant. Also, the Born amplitudes are easier to decompose in terms of j, whereas the S matrices depend on j and l. An exact calculation would decompose the jth partial wave into $l=j+\frac{1}{2}$ and $l=j-\frac{1}{2}$ components, but an unweighted average should be sufficient. Thus, we write the scattering amplitudes as

$$T_{\beta\alpha}=\sum_j S_j^{1/2}T^{\text{Born}}_{\beta\alpha,j}\,, \tag{A15a}$$

$$S_j^{1/2}=\tfrac{1}{4}[(S_i^{l,j+1/2})^{1/2}+(S_i^{l,j-1/2})^{1/2}$$
$$+(S_f^{l,j+1/2})^{1/2}+(S_f^{l,j-1/2})^{1/2}]\,, \tag{A15b}$$

where $S_i^{l,j}$ ($S_f^{l,j}$) is the elastic scattering matrix for the potential corresponding to the incident (outgoing) projectile.

In order to get an idea of how accurate Eq. (A8a) is, consider the case with the largest absorption, $l=0$. If Eq. (A4) is considered as an average of a sum of terms where z ranges from $-R$ to R, and the terms are grouped into pairs of $\pm z$, then the largest deviation from the average would be expected to occur for the pair $z=\pm R$. For $z=-R$, the term is 1, and for $z=R$, the term is S_l. A typical value for $S_{1/2\,0}$ is $e^{-0.5+1.0i}$. Using this, one has

$$\tfrac{1}{2}(1+S_{1/2\,0})=0.664+i0.255\,, \tag{A16a}$$
$$(S_{1/2\,0})^{1/2}=0.684+i0.373\,. \tag{A16b}$$

These terms differ in magnitude by about 13%. Since they represent the worst case of the worst case, the error in replacing (A4) by $\sqrt{S_l}$ may only incur an error of 5% or less.

It is not clear, however, how much error one makes in using the second relation in Eq. (A5). It should be a reasonable approximation if V_1R/v is not too large.

One would also expect to have to satisfy the conditions under which the eikonal approximation is valid,[51]

$$\frac{k^2}{2m}\gg\frac{|V(r)|}{4}\,,\quad |V(r)|\gg\frac{\lambda}{4\pi}\left|\frac{dV(r)}{dz}\right|\,. \tag{A17}$$

For the cases considered here, this translates to

$$130\text{ MeV}\gg 4.2\text{ MeV}\,,\quad 17\text{ MeV}\gg 1.4\text{ MeV}\,, \tag{A18}$$

so the eikonal approximation is a reasonable one.

---

*Present address: Indiana University Cyclotron Facility, Milo B. Sampson Lane, Bloomington, Indiana 47405.

†Present address: Department of Physics, University of Illinois, Champaign, Illinois 61820.

[1] A. Bohr and B. Mottelson, *Nuclear Structure* (Benjamin, New York, 1969), Vol. I.

[2] L. Durand and Y. T. Chiu, Phys. Rev. B 137, 1530 (1965).

[3] C. W. Kim and H. Primakoff, Phys. Rev. B 139, 1447 (1965).

[4] M. L. Goldberger and S. B. Treiman, Phys. Rev. 110, 1178 (1958).

[5] W. G. Love, A. Scott, F. T. Baker, W. P. Jones, and J. D. Wiggens, Phys. Lett. 73B, 277 (1978).

[6] A. Pickelesimer and G. E. Walker, Phys. Rev. C 17,

237 (1978).

[7] K. Gottfried and J. D. Jackson, Nuovo Cimento 34, 735 (1964).

[8] L. Durand and Y. T Chiu, Phys. Rev. B 139, 646 (1965).

[9] H. Hogaasen and J. Hogaasen, Nuovo Cimento 39, 941 (1965).

[10] J. R Comfort, Proceedings from the Conference on (p,n) Reactions and the Nucleon-Nucleon Force, Telluride, Colorado, 1979.

[11] R. Schaeffer, in *Two Body Force in Nuclei*, proceedings of the Gull Lake Conference on the two body force in nuclei, 1971, edited by S. M. Austin and G. Crawley (Plenum, New York, 1972).

[12] F. Petrovich, Nucl. Phys. A251, 143 (1975).

[13] R. M. Haybron and H. McManus, Phys. Rev. B 136, 1730 (1964).

[14] J. Delorme, Nucl. Phys. B19, 573 (1970).

[15] B. Goulard, B. Lorazo, H. Primakoff, and J. D. Vergados, Phys. C 16, 1999 (1977).

[16] M. Ericson and A. Figureau, Nucl. Phys. B3, 609 (1967).

[17] T. E O. Ericson and M. P. Locher, Nucl. Phys. A148, 1 (1970).

[18] H. Toki and W Weise, Phys. Rev. Lett. 42, 1034 (1979).

[19] O. N. Jarvis, C. Whitehead, and M. Shah, Nucl. Phys. A184, 615 (1974).

[20] P. T. Debevec, G. L. Moake, and P. A. Quin, Nucl. Inst. Methods 166, 467 (1979).

[21] D F. Measday and J. N. Polmieri, Phys. Rev. 161, 1071 (1967).

[22] K. Erkelenz, Phys. Rev. 23, 191 (1974).

[23] P. K. Williams, Phys. Rev. 181, 1963 (1969).

[24] G. Breit and R. D. Horacz, in *High Energy Physics*, edited by E. H. S. Burhop (Academic, New York, 1967), Vol. I.

[25] G. E. Brown and A. D. Jackson, *The Nucleon-Nucleon Interaction* (North-Holland, Amsterdam, 1976).

[26] M. H. MacGregor, R. A. Arndt, and R. M. Wright, Phys. Rev. 182, 1714 (1969).

[27] G. F. Chew, Phys. Rev. 112, 1380 (1958).

[28] A. Ashmore, W. H. Range, R. T. Taylor, M. B. Townes, L. Castillejo, and R. F. Peierls, Nucl. Phys. 36, 258 (1962).

[29] P. Cziffra and M. F. Moravcsik, Phys. Rev. 116, 226 (1959).

[30] O. Dumbrajs, Ann. Phys. (N.Y.) 118, 249 (1979).

[31] G. L. Moake and P. T. Debevec, Phys. Rev. C 21, 25 (1980).

[32] P. Schwandt, Indiana University Cyclotron Facility Internal Report No. 77-8.

[33] C. W. Kim, Riv. Nuovo Cimento 4, 189 (1974).

[34] M. Gell-Mann and M. Levy, Nuovo Cimento 16, 705 (1960).

[35] H. Brandle, L. Grenacs, J. Lang, L. Ph. Roesch, V. L. Telegdi, P. Truttmann, A. Weiss, and A. Zehndev, Phys. Rev. Lett. 40, 306 (1978).

[36] G. L. Moake, Indiana University Cyclotron Facility Internal Report No. 79-2.

[37] C. J. Christensen, A. Nielsen, A. Bahnsen, W. K. Brown, and B. M. Rustad, Phys. Rev. D 5, 1628 (1972).

[38] R. J. Blin-Stoyle, *Fundamental Interactions and the Nucleus* (North-Holland, Amsterdam, 1973).

[39] M. L. Perl, *High Energy Hadron Physics* (Wiley, New York, 1974).

[40] Y-W. P. Hwang and H. Primakoff, Phys. Rev. C 16, 397 (1977).

[41] C. W. Kim and J. S. Townsend, Phys. Rev. D 11, 656 (1975).

[42] Reference 37; the f function was calculated by J. N. Bahcall, Nucl. Phys. 75, 10 (1966).

[43] J. N. Palmieri and J. P. Wolfe, Phys. Rev. C 3, 144 (1971).

[44] R. E. McDonald, J. A. Becker, R. A. Chalmers, and D. H. Wilkinson, Phys. Rev. C 10, 333 (1974).

[45] D. H. Wilkinson and D. E. Alburger, Phys. Rev. C 10, 1993 (1974).

[46] S. L. Adler, Phys. Rev. B 137, 1022 (1965); 139, 1638 (1965).

[47] S. L. Adler, Phys. Rev. B 140, 736 (1965); W. I. Weisberger, Phys. Rev. 143, 1302 (1966).

[48] L. I. Schiff, *Quantum Mechanics* (McGraw-Hill, New York, 1968).

[49] See Ref. 39, p. 42.

[50] See Ref. 39, p. 60.

[51] See Ref. 39, p. 44.

PHYSICAL REVIEW C VOLUME 21, NUMBER 6 JUNE 1980

Reaction ^{27}Al(α,d)^{29}Si at 27.2 MeV

L. C. Bland and H. T. Fortune
Physics Department, University of Pennsylvania, Philadelphia, Pennsylvania 19104

O. K. Gorpinich, Yu S. Stryuk, and V. N. Shcherbin
Institute of Nuclear Research, Academy of Science of the Ukrainian SSR, Kiev, Union of Soviet Socialist Republic

V. V. Tokarevski*
Physics Department, Swarthmore College, Swarthmore, Pennsylvania 19081

(Received 26 July 1979)

At a bombarding energy of 27.2 MeV, complete angular distributions have been measured for the reaction ^{27}Al(α,d)^{29}Si, populating the seven lowest states of ^{29}Si. Data have been analyzed in distorted-wave Born approximation, using both cluster and microscopic formalisms. For the latter, transfer amplitudes were taken from shell-model and weak-coupling calculations.

[NUCLEAR REACTION ^{27}Al(α,d); $E=27.2$ MeV; measured $\sigma(E_d,\theta)$, $\theta=3-169°$ ^{29}Si levels. DWBA analysis, microscopic and macroscopic.]

I. INTRODUCTION

The reaction ^{27}Al(α,d)^{29}Si has previously been studied at bombarding energies of 28.4 MeV[1] and 18.7 MeV,[2] but data are sparse. At the higher energy, measurements were performed for only four angles in the range 23°–55° (lab). In Ref. 2, the angular range was large enough but data were obtained for only the ground and first excited state.

The present report concerns an investigation of this reaction at a bombarding energy of 27.2 MeV and includes data for the first seven states of ^{29}Si for an angular range of 9°–169°, with additional measurements at more forward angles for a few states. A spectrum is displayed in Fig. 1. Preliminary experimental results have been published elsewhere[3]; differential cross sections are tabulated in Ref. 4. Data have been analyzed in the framework of distorted-wave Born approximation (DWBA) using both microscopic and macroscopic formalisms.

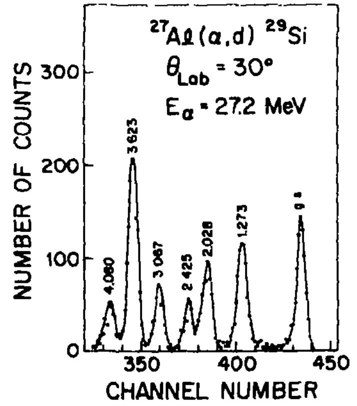

FIG. 1. Spectrum of the reaction ^{27}Al(α,d)^{29}Si, at a bombarding energy of 27.2 MeV and a laboratory angle of 30°.

II. EXPERIMENTAL PROCEDURE AND RESULTS

The measurement of the differential cross sections was carried out at the R-7 cyclotron of the Institute of Nuclear Research in Kiev. The geometry of the experiment, monitoring technique of the incident beam, and the method of absolute cross

TABLE I. Results of ^{27}Al(α,d)^{29}Si.

E_x (MeV)	J^π	σ (mb) 10°–90°(c.m.)	σ (mb) 90°–160°(c.m.)	L	S_L [a]
0	$\frac{1}{2}^+$	0.33	0.084	2	4.3
				4	~0
1.27	$\frac{3}{2}^+$	0.41	0.091	0	0.90
				2	1.6
				4	0.44
2.03	$\frac{5}{2}^+$	0.28	0.099	2	0.48
				4	2.8
2.43	$\frac{3}{2}^+$	0.19	0.058	2	0.7
				4	2.7
3.07	$\frac{5}{2}^+$	0.12	0.075	0	0.41
				2	0.89
				4	0.31
3.62	$\frac{7}{2}^-$	0.60	0.25	1	0.25
				3	0.10
				5	0.48
4.08	$\frac{7}{2}^+$	0.20	0.13	0	~0
				2	0.70
				4	1.2

[a] $S_L \propto \sigma_{exp}/\sigma_{calc}$, with bound-state parameters $r_0=1.175$, $a=0.40$.

© 1980 The American Physical Society

section determination are identical to those which were published earlier.[5] The deuterons from the reaction ^{27}Al$(\alpha,d)^{29}$Si were detected by a set o ΔE-E Si(Li) counter telescopes. The thickness o the ΔE detectors was about 200 μm and the thickness of the E detectors about 1500 μm. At angle less than 60° (lab) Ta or Mo absorbers were plac before the ΔE detectors to cut off the elastically scattered alphas.

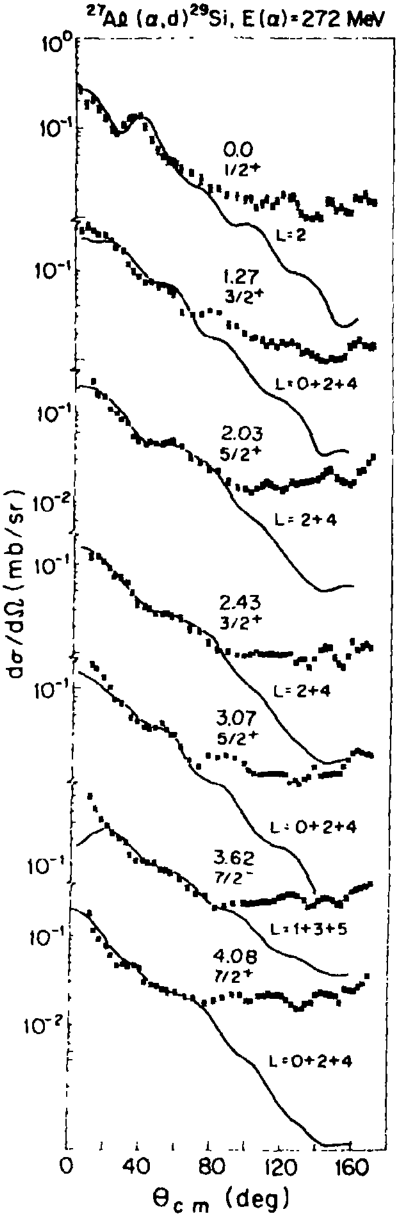

FIG. 2 Experimental angular distributions for ^{27}Al$(\alpha,d)^{29}$Si compared with cluster-transfer DWBA curves calculated using optical-model and bound-state parameter set *K* listed in Table II. Admixtures of different *L* values are listed in Table I.

Angular distributions were measured in 3° step in the angular range of 3°–169° (lab) for the grou state and first excited state, and from 9°–169° fc other levels. Spins and parities of these states a listed in Table I. Experimental angular distributions are displayed in Fig. 2. The experimental errors are the weighted mean values of the statis tical errors of several measurements. The unce tainty in the absolute cross section is ≈7%.

Two features of the experimental angular distributions are immediately apparent. All angula distributions are forward peaked, indicative of a direct reaction mechanism. However, with increasing excitation energy the ratio of backward forward angle cross sections increases as illustrated by comparing the angle-integrated cross sections from 10 –90° (c.m.) and 90°–160° (c.m.) (Table I). Another feature of the angular distributio is their rather smooth oscillatory structure at bo forward and back angles.

III. ANALYSIS

Experimental angular distributions were first analyzed with the assumption that the (α,d) reaction proceeds by the transfer of a proton-neutron correlated pair, i.e., a quasideuteron cluste Neglecting the spin-orbit interaction in the exit channel the theoretical cross section may be wri ten as[6]

$$\frac{d\sigma}{d\Omega}=\frac{2J_B+1}{2J_A+1}\sum_{LSJ}|A_{LSJ}|^2\sigma_{LSJ}(\theta)\,, \qquad (1$$

where J_A and J_B are the spins of the target and r sidual nuclei respectively; L, S, J, are the orbital, spin, and total angular momentum transferred to the target nucleus, and $\sigma_{LSJ}(\theta)$ is the DWBA cross section. All angular momenta are related by the obvious selection rules for one-st "single-particle" transfer. If both ^{27}Al and ^{29}Si are deformed in their ground states an additiona selection rule is present:

$$J \geq \Omega\,, \quad \Omega=|k_B-k_A|\,, \qquad ($$

where Ω, k_B, and k_A are the projections of J, J and J_A on the symmetry axis of the correspondi nuclei. This restriction will suppress some al-

TABLE II. Optical-model parameters used in analysis of $^{27}Al(\alpha,d)^{29}Si$ [strengths in MeV, lengths in (fm)].

Label	Channel	V	r_0	a	W	$W' = 4W_d$	r_0'	a'
K^a	$^{27}Al + \alpha$	196.5	1.30	0.630	24.3	0	1.30	0.63
K^b	$^{29}Si + d$	102.5	1.175	0.585	0	88.0	1.25	0.68
K	d bound state	varied	1.175	0.400				
$A5^c$	$^{27}Al + \alpha$	228.0	1.366	0.557	23.3	0	1.242	0.557
$D1^c$	$^{29}Si + d$	98.1	1.127	0.848	0	59.5	1.394	0.655
	bound state^d	varied	1.260	0.600				

[a] Reference 10.
[b] Reference 11.
[c] Reference 12.
[d] Included Thomas spin orbit with $\lambda = 25$.

lowed L transfers if the strong-coupling model is important for the description of the excited states of ^{28}Si. It has been suggested[7] that the low-lying levels of ^{29}Si may be explained as members of three rotational bands: (1) $K^\pi = \frac{1}{2}^+$ band (Nilsson orbital 9) containing the g.s.$(\frac{1}{2}^+)$, 2.028-MeV$(\frac{5}{2}^+)$ and 2.425-MeV$(\frac{3}{2}^+)$ states; (2) $K^\pi = \frac{3}{2}^+$ band (Nilsson orbital 8) containing the 1.273-MeV$(\frac{3}{2}^+)$, 3.067-MeV $(\frac{5}{2}^+)$ and 4.080-MeV$(\frac{7}{2}^+)$ states; and (3) $K^\pi = \frac{7}{2}^-$ band (Nilsson orbital 10) containing the 3.623-MeV$(\frac{7}{2}^-)$ level. Under these assumptions, $L = 0$ transfer is prohibited for the 2.028-MeV$(\frac{5}{2}^+)$ and the 2.425-MeV $(\frac{3}{2}^+)$ states if we assume $K^\pi = \frac{5}{2}^+$ for the ground state of ^{27}Al.

TABLE III. Two-nucleon transfer amplitudes for $^{27}Al \rightarrow ^{29}Si$ (Ref. 13). The symbols d, s, d' denote $1d_{5/2}$, $2s_{1/2}$, and $1d_{3/2}$, respectively.

E_x	J^π	J	d^2	s^2	d'^2	ds	dd'	sd'
0.0	$\frac{1}{2}^+$	2	0	0	0	+0.7532	0.0327	+0.1780
		3	0.3549	0	−0.0359	−0.7481	0.0798	0.0
1.27	$\frac{3}{2}^+$	1	−0.1766	−0.3600	0.0752	0	0.3704	−0.0515
		2	0	0	0	+0.0485	−0.5136	+0.1474
		3	−0.0613	0	−0.0416	+0.0371	0.6107	0
		4	0	0	0	0	−0.7022	0
2.03	$\frac{5}{2}^+$	1	−0.1267	0.3287	−0.0568	0	0.0047	+0.0121
		2	0	0	0	−0.1623	0.0459	−0.1146
		3	−0.1819	0	0.0050	+0.0178	0.0023	0
		4	0	0	0	0	0.0027	0
		5	−0.3436	0	0	0	0	0
2.43	$\frac{3}{2}^+$	1	−0.0890	−0.4918	0.0600	0	−0.0697	+0.1517
		2	0	0	0	−0.0306	0.1345	−0.3153
		3	0.0165	0	0.0227	+0.0729	−0.2076	0
		4	0	0	0	0	0.0765	0
3.07	$\frac{5}{2}^+$	1	0.0132	0.2834	−0.0599	0	0.1022	−0.2207
		2	0	0	0	−0.0630	−0.0534	+0.3063
		3	−0.0921	0	−0.0464	−0.0513	0.0406	0
		4	0	0	0	0	0.0948	0
		5	−0.1169	0	0	0	0	0
4.08	$\frac{7}{2}^+$	1	−0.0166	0.0144	0.0750	0	0.0429	+0.1463
		2	0	0	0	−0.0366	−0.0762	−0.2449
		3	−0.0180	0	0.0986	+0.0160	0.0773	0
		4	0	0	0	0	−0.1107	0
		5	0.0168	0	0	0	0	0

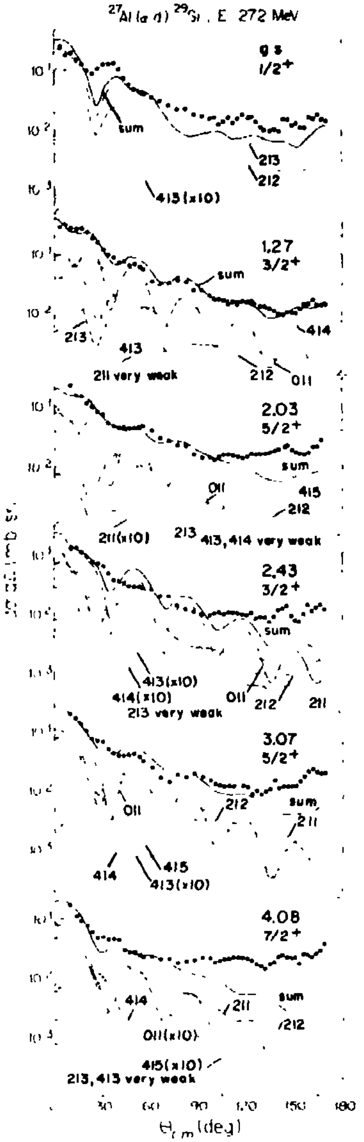

FIG. 3. Same as Fig. 2 but compared with microscopic DWBA curves calculated with potential set *A*5, *D*1 of Table II. Curves are labeled with *LSJ* values.

The reduced differential cross section $\sigma_{LSJ}(\theta)$ was computed with a computer code.[8] The factors A_{LSJ} in Eq. (1) are related to the "spectroscopic" factors S_{LJ} of the quasideuteron states in the final nucleus: $|A_{LSJ}|^2 \propto S_{LJ}$.

Initially, the sensitivity of the DWBA calculation to the choice of parameters was studied. These parameters are the geometrical parameters of the bound state of the quasideuteron in the residual nucleus and the optical potentials in the entrance and exit channels. The ground state transition is most favorable for this investigation: (1) The oscillatory pattern is more pronounced than in the other states, and (2) the number of different angular momentum transfers allowed is smaller than for the other states (Table I). The bound-state wave function was calculated in a Woods-Saxon potential well with the assumption that the transferred neutron and proton are moving as a single body (quasideuteron) with principle quantum number N and orbital angular momentum L. These quantities are related by $N=\frac{1}{2}(4-L)$ if we consider only the $2s$-$1d$ orbitals in ^{29}Si.[9]

The depth of the bound state potential well was found by requiring that the binding energy ϵ_d of the quasideuteron in the state of excitation energy E^*_f be equal to the separation energy B_c of a deuteron from that state of ^{29}Si. This requirement is not sufficient to determine a unique set of parameters V, r_0, and a, but rather defines an infinite set of bound-state potentials. The depth of the potential V_0 is strongly dependent on r_0 and weakly related to a. The choice of these parameters substantially influences the shape of the theoretical angular distributions. This fact was used to determine empirically r_0 and a. The best fit to the ground state angular distribution was found for $r_0=1.175$ fm and $a=0.40$ fm. The angluar distributions for the other states were then analyzed with the same bound-state geometry.

A four-parameter Woods-Saxon potential, with volume absorption, was used for the entrance channel. The parameters V, W, r_0, and a were found from an analysis[10] of the elastic scattering of 27.2 MeV alpha particles on ^{27}Al and are listed in Table II. The deuteron potential is from Ref. 11 Results of these DWBA calculations are shown in

TABLE IV. *Normalization factors from microscopic DWBA calculations.*

E_x (MeV)	J^π	$N(\times 10^{-3})$ Shell model	Weak coupling
0.00	$\frac{1}{2}^+$	8.4	8.4
1.27	$\frac{3}{2}^+$	11	27
2.03	$\frac{5}{2}^+$	20	6.6
2.43	$\frac{3}{2}^+$	10	4.5
3.07	$\frac{5}{2}^+$	23	7.8
4.08	$\frac{7}{2}^+$	39	13

TABLE V. Weak coupling amplitudes for ^{27}Al $\rightarrow$ ^{29}Si.

E_x (MeV)	J^π	Assumed configuration	J	Amplitudes
0	$\frac{1}{2}^+$	$0^+\otimes 2s_{1/2}$	2	$-0.6455(1d_{5/2})(2s_{1/2})$
			3	$0.7638(1d_{5/2})(2s_{1/2})$
1.27	$\frac{3}{2}^+$	$0^+\otimes 1d_{3/2}$	1	$-0.3536(1d_{5/2})(1d_{3/2})$
			2	0.4564
			3	-0.5401
			4	0.6124
2.03	$\frac{5}{2}^+$	$2^+\otimes 2s_{1/2}$	1	$0.6416(2s_{1/2})^2 - 0.3118(1d_{3/2})(2s_{1/2})$
			2	$0.4409(1d_{3/2})(2s_{1/2})$
2.43	$\frac{3}{2}^+$	$2^+\otimes 2s_{1/2}$	1	$0.8400(2s_{1/2})^2 + 0.3572(1d_{3/2})(2s_{1/2})$
			2	$0.4050(1d_{3/2})(2s_{1/2})$
3.07	$\frac{5}{2}^+$	$2^+\otimes 1d_{3/2}$	1	$-0.4850(2s_{1/2})(1d_{3/2}) - 0.2422(1d_{3/2})^2$
			2	$0.6859(2s_{1/2})(1d_{3/2}) - 0.0589(1d_{3/2})^2$
			3	$0.4107(1d_{3/2})^2$
4.08	$\frac{7}{2}^+$	$2^+\otimes 1d_{3/2}$	1	$0.0(2s_{1/2})(1d_{3/2}) + 0.2041(1d_{3/2})^2$
			2	$0.5144(2s_{1/2})(1d_{3/2}) - 0.3535(1d_{3/2})^2$
			3	$0.0(2s_{1/2})(1d_{3/2}) + 0.3535(1d_{3/2})^2$

Fig. 2.

The macroscopic selection rules for the ground state permit the transfer of two values of angular momentum, $L=2$ and $L=4$. However, the contribution of $L=4$ to this transition is found to be negligible and the ground state can be fitted by a pure $L=2$ distribution.

In contrast to the ground state, the excited states can be fitted only by mixing different L values. The theoretical distributions for $L=0$ and $L=4$ have oscillations which are out of phase with the $L=2$ distribution so that their mixing produces a relatively smooth curve in accordance with the data (Fig. 2). For angles $< 70°$ (c.m.) the fit is good for levels of the supposed ground state rotational band ($K=\frac{1}{2}$). The transitions corresponding to the $K=\frac{3}{2}$ band [1.273($\frac{3}{2}^+$), 3.067($\frac{5}{2}^+$), and 4.080($\frac{7}{2}^+$)] are not fitted as well at forward angles, possibly indicating a different bound-state geometry for each rotational band. The back angles are consistently underpredicted by DWBA with the difference in-
asing with increasing angle. If one assumes
this is due to compound nucleus contributions
lusively, then the compound reaction contri-
ion for the ground state and six excited states
ıld be 41%, 36%, 52%, 47%, 54%, 58%, and
%, respectively. This very crude estimate from
integrated cross sections should be regarded
an upper limit only.

mong all of the excited states studied only the
23 MeV level has negative parity ($\frac{7}{2}^-$). The ang-
r distribution of this state looks very similar to the data for the $\frac{7}{2}^+$ 4.08 MeV state. This may be partially explained as the consequence of similarities in the forward angles of $L=2$ and 3 and L mixing. For the mixing of $L=1$, 3, and 5 there is considerable discrepancy between the DWBA predictions and the experimental data for angles θ(c.m.) $> 20°$.

For the microscopic analysis, we have used the well-matched set of optical model parameters *D1-A5* from Ref. 12 (in order to minimize finite-range effects), and two nucleon transfer amplitudes from a shell-model calculation. These amplitudes (Table III) have given a reasonable account of data for the ^{27}Al(^{3}He,p)^{29}Si reaction.[11] Cross sections were calculated with the two nucleon transfer options of the code DWUCK,[14] using the half-separation energy technique for binding energies. Experimental cross sections were related to theoretical ones through the expression

$$\sigma_{\exp}(\theta)=N\frac{2J_f+1}{2J_i+1}\sum_{LJ}\frac{\sigma_{\mathrm{DWBA}}(\theta)}{2J_x+1}\,.$$

Theoretical curves for different LJ transfer were added together in the ratio required by the shell-model amplitudes, and the summed cross section then arbitrarily normalized to the data (Fig. 3) to get the normalization factors, N, listed in Table IV. The fits are generally quite good. They underestimate the back-angle cross sections, but not to such an extent as the cluster calcula-

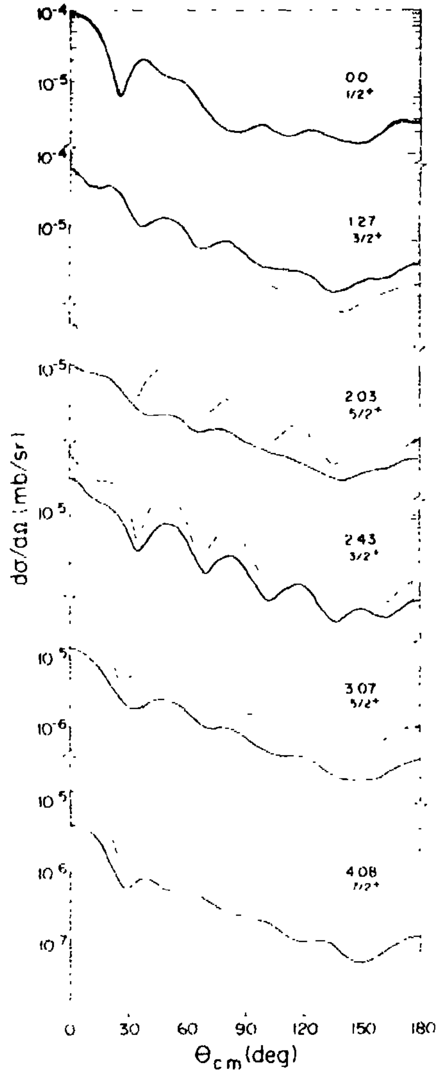

FIG. 4. Theoretical angular distributions for ^{27}Al(α,d), using two-nucleon transfer amplitudes from shell model (solid) and weak coupling (dashed).

tions.

TABLE VI. Cluster-transfer amplitudes.

J	$(nlj)_1(nlj)_2$	Amplitude $L=0$, $S=1$	$L=2$, $S=1$	$L=4$, $S=$
1	$(1d_{5/2})^2$	0.353	−0.189	0
	$(1d_{3/2})^2$	−0.189	0.353	0
	$(1d_{5/2})(1d_{3/2})$	−0.533	−0.249	0
	$(2s_{1/2})(1d_{3/2})$	0	−0.882	0
	$(2s_{1/2})^2$	0.745	0	0
2	$(1d_{5/2})(2s_{1/2})$	0	0.558	0
	$(2s_{1/2})(1d_{3/2})$	0	0.683	0
	$(1d_{5/2})(1d_{3/2})$	0	0.471	0
3	$(1d_{5/2})^2$	0	0.370	−0.151
	$(1d_{3/2})^2$	0	−0.062	0.907
	$(1d_{5/2})(1d_{3/2})$	0	−0.285	−0.393
	$(1d_{5/2})(2s_{1/2})$	0	0.882	0
4	$(1d_{5/2})(1d_{3/2})$	0	0	1.0
5	$(1d_{5/2})^2$	0	0	1.0

We have also calculated transfer amplitudes in a weak-coupling picture, in which states of ^{29}Si are considered to be neutron single-particle states weakly coupled to the ground and first excited states of ^{28}Si. For ^{27}Al → ^{28}Si(0$^+$), the amplitude is pure $1d_{5/2}$, whereas for ^{27}Al → ^{28}Si(2$^+$), it is a mixture of $l=0(2s_{1/2})$ and $l=2$ (assumed $1d_{3/2}$). For these amplitudes we use the ratio of $l=0$ to $l=2$ spectroscopic factors measured[15] in ^{27}Al(d,n)^{28}Si(2

$$\frac{S(l=0)}{S(l=2)}=2.4\ ,$$

giving $A(2s_{1/2})=0.84$, $A(1d_{3/2})=0.54$. Resulting two-nucleon amplitudes are displayed in Table V.

This is probably not a good description of the states of ^{28}Si. In fact, the transfer amplitudes calculated from weak coupling (Table V) show marked differences from the shell-model ones (Table III). Nevertheless, the calculated cross sections for the two sets of amplitudes are remarkably similar (Fig. 4). It thus appears that a weak coupling description contains most of the essential features.

Finally we have computed cluster transfer spectroscopic factors from the microscopic two-nucleon amplitudes using SU(3) coefficients[16] listed in Table VI. These cluster spectroscopic factors are compared with those extracted from the cluster-transfer analysis in Table VII. Except for certain $L=4$ transfers, the ratio of experimenta to theoretical spectroscopic factors is roughly constant at about 8 plus or minus about a factor o two. The large deviations for $L=4$ may be connected with the fact that this shell-model calculation does not correctly reproduce the degree of a $1d_{5/2}$ shell closure at ^{28}Si.

Finally, in Fig. 5, we display the experimenta angular distribution for the $\frac{7}{2}^-$ state at 3.62 MeV and microscopic DWBA curves for $L=1$, 3, an

TABLE VII. Comparison of theoretical and experimental cluster spectroscopic factors for ^{27}Al(α,d)^{29}Si.

E_x	J^π	L	S	J	S_{LSJ}(th)[a]	S_L(th)[b]	S_L(exp)[c]	R[d]
0.0	$\frac{1}{2}^+$	2	1	2	0.2776	0.8715	4.28	4.91
		2	1	3	0.5939			
		4	1	3	0.0138	0.0138	0.0	
1.27	$\frac{3}{2}^+$	0	1	1	0.2940	0.2940	0.90	3.06
		2	1	1	0.0061			
		2	1	2	0.1368	0.1944	1.62	8.33
		2	1	3	0.0515			
		4	1	3	0.0720			
		4	1	4	0.4931	0.5651	0.44	0.78
2.03	$\frac{5}{2}^+$	0	1	1	0.0435	0.0435		
		2	1	1	0.0002			
		2	1	2	0.0363	0.0436	0.48	11.01
		2	1	3	0.0071			
		4	1	3	0.0010			
		4	1	4	0.0	0.1191	2.76	23.17
		4	1	5	0.1181			
2.43	$\frac{3}{2}^+$	0	1	1	0.1385	0.1385		
		2	1	1	0.0358			
		2	1	2	0.0875	0.1233	0.71	5.76
		2	1	3	0.0			
		4	1	3	0.0099			
		4	1	4	0.0059	0.0158	2.70	171
3.07	$\frac{5}{2}^+$	0	1	1	0.0302	0.0302	0.41	13.58
		2	1	1	0.0592			
		2	1	2	0.0397	0.0989	0.89	9.00
		2	1	3	0.0			
		4	1	3	0.0019			
		4	1	4	0.0090	0.0246	0.31	12.6
		4	1	5	0.0137			
4.08	$\frac{7}{2}^+$	0	1	1	0.0010	0.001	0.0	
		2	1	1	0.0219			
		2	1	2	0.0230	0.043	0.70	14.80
		2	1	3	0.0024			
		4	1	3	0.0038			
		4	1	4	0.0123	0.0164	1.16	70.7
		4	1	5	0.0003			

[a] $S_{LSJ}(\mathrm{th}) = \left| \sum_{(j_1 j_2)} C_{(j_1 j_2)-LSJ}\, a_{(j_1 j_2)} \right|^2$.

[b] $S_L(\mathrm{th}) = \sum_J S_{LSJ}(\mathrm{th})$.

[c] From Table I.

[d] $R = S_L(\mathrm{exp})/S_L(\mathrm{th})$.

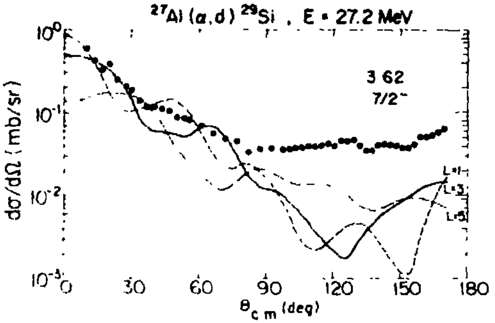

FIG. 5. Experimental angular distributions for the $\frac{7}{2}^-$ state at 3.62 MeV compared with microscopic DWBA curves for $L = 1$, 3, and 5.

5. A combination of the allowed L values can give a good account of the data up to about 90°, but for larger angles the DWBA curves fall below the data, as was the case for positive-parity states.

In conclusion, both cluster and microscopic DWBA calculations give reasonable accounts of the data for the reaction ^{27}Al(α,d), although both fail to account for all the measured back-angle cross sections. Two-nucleon transfer amplitudes calculated in weak coupling give results similar to those obtained from a shell-model calculation.

We wish to acknowledge financial support of the National Science Foundation. One of the authors (V. V. T.) is grateful for the support of a Fulbright-Hayes scholarship.

---

*On leave from Institute of Nuclear Research, Academy of Science of the Ukrainian SSR, Kiev, USSR.

[1] S. Kakigi, J Phys. Soc. Jpn. 20, 1967 (1965).

[2] B. B. Srivastava and O. E. Johnson, Phys. Rev. 166, 1083 (1968).

[3] O. K. Gorpinich, Yu S. Stryuk, and V. V. Tokarevski, in *The Program and Abstracts of XXIII Meeting on Nuclear Spectroscopy and Atomic Nucleus Structure*, *Nauka*, *1973*, p. 307.

[4] O. K. Gorpinich, Yu S. Stryuk, V. V. Tokarevski, and V. N. Shcherbin, Institute of Nuclear Research of the Academy of Science, Ukrainian Soviet Socialist Republic, Report No. KIYaI-76-37.

[5] V. V. Alekseev *et al.*, Izv. Akad. Nauk SSSR Ser. Fiz. 32, 1726 (1968).

[6] G. R. Satchler, Nucl. Phys. 55, 1 (1968).

[7] A. A. Pilt, R. H. Sper, R. V Elliott, and J. A. Kuehner, Can. J. Phys. 49, 1263 (1971).

[8] V. V. Alekseev, V. N. Polanski, K. O. Terenetski *et al*, Sizvestia AN USSR, Ser. Fiz. 34, 194 (1970).

[9] T. A. Brody and M. Moshinsky, Tables of Transformation Brackets, Mexico, 1960.

[10] Yu S. Stryuk and V. V. Tokarevski, in the Program an Abstracts of XXI Meeting of Nuclear Spectroscopy and Atomic Nucleus Structure, VII, Nauka, Leningrad, 1971, p. 85.

[11] Report of IF AN UKRSSR, Kiev, 1970, O. F. Nemets, editor.

[12] J. R. Comfort, H. T. Fortune, J. V. Maher, and G. C Morrison, Phys. Rev. C 10, 2399 (1974).

[13] H. Nann, T Mozgovoy, R. Bass, and B. H. Wildenthal Nucl. Phys. A192, 417 (1972).

[14] P. D. Kunz (private communication).

[15] W Bohne *et al.*, Nucl. Phys. A131, 273 (1969).

[16] M. De Llano *et al.*, Nucl. Phys. A72, 379 (1965).

PHYSICAL REVIEW C VOLUME 21, NUMBER 6 JUNE 1980

Finite range distorted-wave Born approximation analysis of (p,t) reactions with a realistic triton wave function

M. F. Werby and M. R. Strayer*
Department of Physics, Texas A & M University, College Station, Texas 77843

M. A. Nagarajan
Daresbury Laboratory, Daresbury, Warrington WA4 4AD, England

(Received 23 July 1979)

Exact finite range distorted-wave Born approximation analysis of the ground state reactions ^{208}Pb$(p,t)^{206}$Pb and ^{18}O$(p,t)^{16}$O are presented. The calculations are carried out using a realistic triton wave function comprising a spatially symmetric S and mixed symmetric S' and D states. The transfer interaction is treated consistently with the interaction used in obtaining the triton wave function. The use of a realistic wave function and transfer potential yields improved agreement between experimental and theoretical angular distributions. Calculations using the wave function of the transferred neutron pair suggest it is possible to explain both the absolute magnitude and shape of the angular distribution for these transitions.

[NUCLEAR REACTIONS (p,t), distorted-wave Born approximation analyses.]

I. INTRODUCTION

The two nucleon transfer reactions (p,t) and (t,p) are enormously rich and useful processes for the understanding of nuclei as is demonstrated by the vast amount of experimental work in the area.[1] Despite the great amount of experimental work, the theoretical development is far from complete. The zero-range distorted-wave Born approximation (DWBA) is usually employed[2,3] in analyzing data of angular distributions. Unfortunately zero-range analyses can only predict
ipes of angular distributions with arbitrary
rmalization introduced to fit absolute magnitudes
data. Although these analyses can often suggest
orbital angular momentum being transferred,
y are not a useful tool in studying nuclear wave
ictions which differ by two neutrons. Such wave
ictions are seldom made up of pure configura-
ns but are composed of linear combinations of
mentary configurations whose amplitudes add
ierently in yielding angular distributions. The
me superposition of elementary configurations
duces the strong correlations responsible for
ermining the collective properties of the nuclear
ve functions. For most cases studied[4] the
apes of angular distributions are not sensitive
the individual configurations employed. Thus
order to properly assess nuclear collectivity
m (p,t) and (t,p) processes one must use a
ory which can predict absolute magnitudes of
gular distributions.

Ve present exact finite-range DWBA calcula-
ns[5,6] which predict both absolute magnitudes
d shapes of angular distributions. Our work differs from earlier finite-range (p,t) studies[7-10] in several important ways. A fully realistic triton wave function is employed comprising a state of symmetric orbital permutation symmetry and total orbital angular momentum zero (S state) and two states of mixed orbital permutation symmetry having total orbital angular momentum zero and two respectively (S' and D states). A type of consistency is maintained wherein the realistic two-body potential used in calculating the triton ground state is also the interaction causing the transfer. This feature is essential for reliable predictions[11] of absolute magnitudes of angular distributions. Our method employs a modification of the half-separation energy method for obtaining neutron pair wave functions, but can easily be extended to include wave functions derived from any method. Preliminary results[12,13] of our theory demonstrate a systematic agreement between theory and experiment for the ground state transitions ^{18}O$(p,t)^{16}$O, ^{208}Pb$(p,t)^{206}$Pb, and ^{92}Zr$(t,p)^{90}$Zr which is a significant improvement on the previous finite-range calculations.

It should be emphasized that the spatial part of the two-neutron wave function employed throughout is a modification of the standard half-separation energy method. Our endeavor has been to focus on the development and improvement of the transition interactions and the three-body wave functions. However, our formalism, as described below, is sufficiently general to accommodate any neutron pair wave function.

In Sec. II we briefly outline the conventions followed in obtaining the exact finite-range DWBA amplitude, the form factor, and the three nucleon

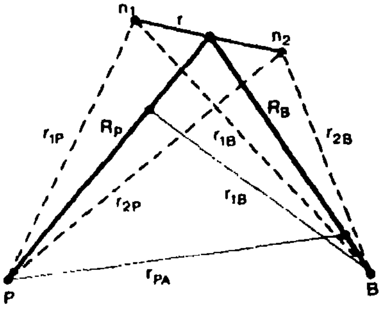

FIG. 1. The coordinate system for the reaction $A(p,t)B$. The three linearly independent vector coordinates appearing in the DWBA amplitude are $\vec{r}_{pA}$, $\vec{r}_{tB}$, and $\vec{r}$. The form factor is a function of the two vector coordinates $\vec{R}_p$ and $\vec{R}_B$.

wave functions. General selection rules for both natural and unnatural parity transitions are given in Sec. III. Results are reported for the reactions $^{18}O(p,t)^{16}O(0^+ g.s.)$ and $^{208}Pb(p,t)^{206}Pb(0^+ g.s.)$ in Sec. IV. Section V summarizes the major conclusions of this work.

II. EXACT FINITE-RANGE DWBA AMPLITUDE

Consider a reaction $A(p,t)B$ with coordinates as shown in Fig. 1. Following the usual convention in finite-range DWBA,[14] we chose the vectors $\vec{r}_{pA}$, $\vec{r}_{tB}$, and $\vec{r}$ as the three linearly independent vectors. $\vec{r}_{pA}$ and $\vec{r}_{tB}$ are the initial and final channel vectors designating, respectively, the position of the proton relative to the target and the position of the triton relative to the residual nucleus. $\vec{r}$ is the relative separation of the two neutrons transferred in the reaction. The finite-range amplitude is obtained by evaluating a nine-dimensional integral over the above three vectors. Usually, this task is separated into two parts. A form factor is first evaluated by integrating over the vector $\vec{r}$ yielding a function of the vectors $\vec{R}_p$ and $\vec{R}_B$, and is characterized by several angular momenta some of which contribute coherently and the others incoherently to the cross section. The method of Austern *et al.*[15] is used to transform the form factor to a function of the channel vectors $\vec{r}_{pA}$ and $\vec{r}_{tB}$ and the remaining six-dimensional integration is then carried out using a suitably modified finite-range single particle transfer computer code.

The DWBA transition amplitude is

$$T(\vec{k}_t,\vec{k}_p)=\left[\binom{3}{2}\binom{A}{2}\right]^{1/2}\mathcal{J}\int d\vec{r}_{pA}\int d\vec{r}_{tB}\,\Phi_{\vec{k}_t}^{(-)*}(\vec{r}_{tB})$$

$$\times\langle J_B T_B M_B M_{T_B};\, J_t T_t M_t M_{T_t}|V|J_A T_A M_A M_{T_A};\,\sigma_p\tau_p\rangle\Phi_{\vec{k}_p}^{(+)}(\vec{r}_{pA})\,, \qquad (1)$$

where $\Phi_{\vec{k}_p}^{(+)}$ and $\Phi_{\vec{k}_t}^{(-)}$ are the elastic scattering wave functions in the initial and final channels, respectively. $\vec{k}_p$ and $\vec{k}_t$ are the initial and final channel momenta. The quantum numbers J,T,M,M_T with the appropriate suffixes denote the total angular momentum, the isospin, and their respective z-components of the corresponding nuclei A, B or triton. σ_p and τ_p are the z-components of the spin and isospin of the proton. $\mathcal{J}$ is the Jacobian of the transformation to the coordinates $\vec{r}$, $\vec{r}_{tB}$ and $\vec{r}_{pA}$, i.e.,

$$\mathcal{J}=(A/A+1)^3(\tfrac{3}{2})^{3/2}\,.$$

The constant $[(^3_2)(^A_2)]^{1/2}$ is a normalization factor for the direct (p,t) amplitude arising from the antisymmetrization of the initial and final states of the system.

Following Satchler,[16] we express the nuclear matrix element in (1) as

$$\left[\binom{3}{2}\binom{A}{2}\right]^{1/2}\mathcal{J}\langle J_B T_B M_B M_{T_B};J_t T_t M_t T_{M_t}|V|J_A T_A M_A M_{T_A};\sigma_p\tau_p\rangle$$

$$=\sum_{\substack{LSJ\\M_L M_S M_J}}(-i)^L\langle J_B M_B J M_J|J_A M_A\rangle\langle T_B M_{T_B}1-1|T_A M_{T_A}\rangle(-1)^{1/2-\sigma_p}\langle J_t M_t \tfrac{1}{2}-\sigma_p|SM_s$$

$$\times\langle LM_L SM_s|JM_J\rangle G_{LSJM_L}(\vec{R}_p,\vec{R}_B)\,, \qquad (2$$

where we have assumed that the transfer interaction is spin independent. $G_{LSJM_L}(\vec{R}_p,\vec{R}_B)$ is the two-neutron transfer form factor characterized by the orbital, spin, and total transfer angular momenta L, S, and J which contribute incoherently to the cross section. M_L is the z-component of L

In the analyses presented in this paper, the transfer interaction which in the prior form is given by

$$V = V_{1p} + V_{2p} , \tag{3}$$

i.e.; the sum of the interactions of the proton with the two neutrons being transferred is replaced by $(\epsilon_t - K - V_{12})$, where ϵ_t is the triton binding energy, K the triton kinetic energy operator, and V_{12} the neutron-neutron interaction. One should note that for a realistic interaction $V_{1p} + V_{2p}$ includes partial waves from the triplet even channels and hence have contributions from the short range N-N tensor force. These terms are in principle more complicated to evaluate. Whereas, V_{12}, the neutron-neutron interaction, is diagonal for all the two-body channels considered and much simpler in structure. The above replacement is justifiable provided one uses the same interaction to calculate the internal state of the triton. We have used the triton wave function of Strayer and Sauer,[17] who obtained it as a variational eigenfunction of a three-body Hamiltonian with the Reid[18] soft core potential. We use the variational binding energy for ϵ_t and the Reid soft core potential for V_{12}. The triton wave function of Strayer and Sauer[17] primarily consists of a spatially symmetric S state, and mixed symmetric S' and D states. The other components of the triton wave function have negligible amplitude. The classification of the states used in the description of the triton wave function is given in Table I, along with the variational binding energy and the rms charge radius. The wave function is obtained variationally as a linear combination of harmonic oscillator functions which refer to the internal coordinates of the triton $r/\sqrt{2}$, $\sqrt{2/3}\, R_p$. The details of the wave function are contained in the paper of Strayer and Sauer[17] as well as in Ref. 4.

TABLE I. Classification of basis states and ground state properties of the triton using the wave function of Ref. 17.

State	Percent wave function	L_t	S_t	$[\lambda_{L_t}]$	(r_L)
S	89.8	0	$\frac{1}{2}$	[3]	(111)
S'	1.4	0	$\frac{1}{2}$	[21]	(211) (121)
D	8.8	2	$\frac{1}{2}$	[21]	(211) (121)
E_t	−6.7 MeV		$\langle r_{ch}^2\rangle^{1/2} = 1.85$ fm		

Following Glendenning,[19] we define the generalized two particle fractional parentage coefficients

$$\beta([l_1 j_1 l_2 j_2]J) = \binom{A}{2}^{1/2} \langle [(J_B T_B)(l_1 j_1 l_2 j_2)T = 1J] \times J_A T_A M_A M_{T_A} | J_A T_A M_A M_{T_A} \rangle , \tag{4}$$

and expand the two-neutron pair wave function in a complete set of antisymmetrized product of single neutron wave functions. In the actual calculation, we used the two-neutron amplitudes $\beta([l_1 j_1 l_2 j_2]J)$ obtained by shell model calculations and used the half-separation energy method[19] for the radial wave functions of the two neutrons.

The final expression of the form factor is

$$G_{LSJM_L}(\vec{R}_p, \vec{R}_B) = (i)^L \sum_{\substack{L_p L_B \\ M_p M_B}} \sum_{L_t [\lambda_{L_t}] S_t} \langle L_p M_p L_B M_B | L M_L \rangle \times g^{L_t [\lambda_{L_t}] S_t}_{L_p L_B ; LSJ} (R_p, R_B) Y_{L_p M_p} \times (\hat{R}_p) Y_{L_B M_B}(\hat{R}_B) , \tag{5}$$

where L_t, $[\lambda_{L_t}]$, and S_t are, respectively, the orbital angular momentum, orbital permutation symmetry, and spin of the triton. L_p and L_B are, respectively, the orbital angular momentum of the proton relative to the c.m. of the two neutrons and that of the residual nucleus B relative to the c.m. of the two neutrons. The angular momenta L_p, L_B, L_t, and S_t contribute coherently to the cross section. Hence, it is easier to sum over their contributions as in (5). In reality, Eq. (5) contains an additional sum over l, the relative orbital angular momentum of the two neutrons. This sum has already been performed and is implicit in (5). The detailed expression for $g^{L_t [\lambda_{L_t}] S_t}_{L_p L_B ; LSJ}$ can be obtained from Ref. 4.

The differential cross section is given by

$$\frac{d\sigma}{d\Omega} = \frac{\mu_p \mu_t}{(2\pi \hbar^2)^2} \frac{k_p}{k_t} \sum_{LSJM_L} \left| \sum_{L_p L_B} B^{L_p L_B}_{LSJM_L}(\vec{k}_t, \vec{k}_p) \right|^2 \cdots , \tag{6}$$

where the reduced amplitude $B^{L_p L_B}_{LSJM_L}$ is defined as

$$(i)^L(2L+1)^{1/2} B^{L_p L_B}_{LSJM_L}(k_t, k_p) = \sum_{\substack{L_t[\lambda_{L_t}]S_t \\ M_p M_B}} \sum_{L_p M_p L_B M_B L M_L} \int dr_{pA} \int dr_{tB} \Phi^{(-)*}_{k_t}(r_{tB})\, g^{L_t[\lambda_{L_t}]S_t}_{L_p L_B; LSJ} \times (R_p, R_B) Y_{L_p M_p}(R_p) Y_{L_B M_B}(R_B) \Phi^{(+)}_{k_p}(r_{pA}) . \quad (7)$$

The amplitudes $B^{L_p L_B}_{LSJM_L}$ are computed for fixed values of L, S, J, M_L, L_p, L_B and the allowed components are summed in the appropriate manner to compute the cross section.

III. SELECTION RULES

The selection rules for (p,t) reactions using realistic triton wave functions that include mixed symmetry components have been reported in Ref. 20 and may be derived from the form factor. An additional constraint on the selection rules is that $l+S_{12}$ is even as a consequence of the antisymmetry of the two transferred neutrons where l is the relative orbital angular momentum and S_{12} the total spin of the two-neutron sybsystem. For a triton wave function composed of only a symmetric S state one has $S_{12}=0$ and l even. Most simple wave functions allow only $l=0$. For triton wave functions that contain mixed symmetry components it is possible for $S_{12}=1$ and for l to have odd values.

If π_A and π_B designate the intrinsic parities of the states of the target and residual nuclei A and B, respectively, then natural parity transitions are those which satisfy the condition

$$\pi_A \pi_B = (-1)^J ,$$

while unnatural parity transitions satisfy the condition

$$\pi_A \pi_B = -(-1)^J .$$

The selection rules for each component of the triton can be obtained from the following equations and are given below.

$$\begin{aligned} \vec{S}_{12} &= \vec{I}_t + \vec{S} , \\ (-1)^{l+S_{12}} &= 1 , \\ \vec{J} &= \vec{L} + \vec{S}_{12}, \\ \vec{L} &= \vec{L}_B + \vec{L}_p , \\ \vec{L}_p &= \vec{L}_t + \vec{l} , \\ \vec{S}_t &= \vec{S}_{12} + \vec{\tfrac{1}{2}} . \end{aligned} \quad (8)$$

A. Symmetric *S* state

For this state we have $L_t=0$, $S_t=\frac{1}{2}$, and $S_{12}=0$. From Eq. (8) we therefore have $S=0$, $l=L_p$, and $L=J$. The parity change is given by the relation

$$\Delta\pi = \pi_A \pi_B = (-1)^{l+L_B} .$$

However, since l is even for this case, then $\Delta\pi = (-1)^{L_B}$. Now for $l=0$ we have that $L_p=0$, $L=L_B=J$. Thus $\Delta\pi=(-1)^J$ and for $l=0$ one can only have natural parity transitions. However, if $l\neq 0$ one has $\Delta\pi = (-1)^{|\vec{J}+\vec{l}|}$ and unnatural parity transitions can occur with a leading term corresponding to $l=2$.

B. Mixed symmetry *S* state

The mixed symmetry component of the triton can have $S_{12}=0, 1$. For $S_{12}=0$ the selection rules are the same as for the symmetric state. For the $S_{12}=1$ component, one has $l=$odd, and $\Delta\pi = -(-1)^{L_B}$. Thus unnatural parity transitions are possible with a leading term corresponding to $l=1$.

C. Mixed symmetry *D* state

Here the total intrinsic and orbital angular momentum of the triton are $S_t=\frac{1}{2}$ and $L_t=2$, respectively. Thus $S_{12}=1$ and l will always be odd. Therefore, this term can contribute to both natural and unnatural parity transitions with the leading component corresponding to $l=1$.

For a fixed angular momentum transfer J one can have values of orbital angular momentum transfer subject to the following conditions:

$$|J-S_{12}| \leq L \leq |J+S_{12}|$$

and

$$|L_B - L_p| \leq L \leq |L_B + L_p| .$$

The conditions on L_B are

$$|l_{n_1} - l_{n_2}| \leq L_B \leq |l_{n_1} + l_{n_2}| ,$$

where l_{n_1} and l_{n_2} are the relative orbital angular momenta of the single particle states of neutrons n_1 and n_2 used in constructing the two particle states. Conditions on L_p are that $L_p \geq 0$ for natural parity transitions and $L_p \geq 1$ for unnatural parity transitions.

TABLE II. Optical parameters used in this study.

Target	Projectile	V_0	r_0	a_0	W	$4W_D$	r_I	a_I
^{18}O	p	56.0	1.17	0.75	1.70	0.0	1.32	0.588
^{18}O	t	146.0	1.40	0.44	14.70	0.0	1.40	0.551
^{208}Pb	p	47.9	1.25	0.65	0.0	40.0	1.25	0.750
^{208}Pb	t	149.8	1.24	0.68	12.0	0.0	1.43	0.870

IV. RESULTS

In this section we discuss details of the finite-range DWBA analysis of the reactions $^{18}O(p,t)^{16}O(0^+_{g.s.})$ and $^{208}Pb(p,t)^{206}Pb(0^+_{g.s.})$. These reactions are natural parity transitions and have been considered by other authors.[8] The particular target ^{208}Pb and ^{16}O were chosen since both the ^{208}Pb target and the ^{16}O residual nucleus are thought to be very good closed shell nuclei and thus are systems for which one would expect a shell model description to be valid.

The optical model potentials used to generate the distorted waves have the usual form

$$V(r)=V_c(r)-V_0f_V(r)$$

$$-iW_Vf_w(r)+4ia_sW_sf_s'(r)\ ,$$

where

$$f_\lambda(r)=[1+\exp(r-R_\lambda)/a_\lambda]^{-1}\ ,$$

and where $V_c(r)$ is the Coulomb potential due to a uniformly charged sphere of radius $r_cA^{1/3}$. The radius R is often taken to have the form $R_\lambda = r_\lambda A_T{}^{1/3}$ or $R_\lambda = r_\lambda (A_T{}^{1/3}+A_p{}^{1/3})$, where A_T and A_p are the mass numbers of the target nucleus and projectile, respectively. In our analysis we employ the former of the two prescriptions since most of the optical model analyses with light projectiles utilize this form. The optical parameters are illustrated in Table II and were obtained from the literature. One should note that there is some sensitivity to the choice of these parameters for reactions in light nuclei. For reactions on ^{208}Pb, various combinations were employed with virtually no difference in the results obtained. However, for the reaction on ^{18}O, both the absolute magnitude and shape of the predicted angular distribution changed when different optical model parameters were employed. In this work, we chose that particular set which gave the best comparison between the theoretical and experimental angular distributions.

The two-neutron configurations were assumed to be identical to those predicted by shell model calculations[21, 22] except that the radial wave functions were replaced by the eigenfunctions of a Woods-Saxon potential adjusted to yield eigenvalues equal to half the two-neutron separation energy. The radius and diffuseness parameters of these potentials are

$$R=1.25A^{1/3},$$

$$a_0=0.65\ \text{fm}\ .$$

The two-neutron spectroscopic amplitudes for all of the reactions studied are given in Table III. For the $^{18}O(p,t)^{16}O$ transition the spectroscopic amplitudes were obtained from ^{18}O wave functions computed by Kahana[21] and are linear combinations of $[0d_{5/2}]^2$ and $[1S_{1/2}]^2$ configurations. Those for the reactions on ^{208}Pb are taken from the work of True[22] and are linear combinations of products of $2p$ and $1f$ hole states in the closed ^{208}Pb core.

Form factors for the reactions $^{18}O(p,t)^{16}O$ and $^{208}Pb(p,t)^{206}Pb$ are shown for oxygen in Figs. 2 and 3, and for lead in Figs. 4 and 5 for the ground state transitions. In Figs. 2 and 4 the fully two-dimensional form factors are shown while in Figs. 3 and 5 one-dimensional "slices" along the zero-range line $R_p=0$ are given.

For the ground state transitions, the allowed values of the various angular momenta based on the previously discussed selection rules are given in Table IV. We find that *only* the component having $l=S=0$ contributes in any significant way to the form factor. The corresponding form factors

TABLE III. Spectroscopic amplitudes defined in Eq. (4) and used in obtaining form factors in Figs. 2–5.

Reaction	Ref.	$[0d_{5/2}]^2$	$[1S_{1/2}]^2$	$[2P_{1/2}]^{-2}$	$[2P_{3/2}]^{-2}$	$[1f_{5/2}]^{-2}$
$^{18}O(p,t)^{16}O(0^+_{g.s.})$	21	0.893	0.450			
$^{208}Pb(p,t)^{206}Pb(0^+_{g.s.})$	22			0.822	0.363	0.401

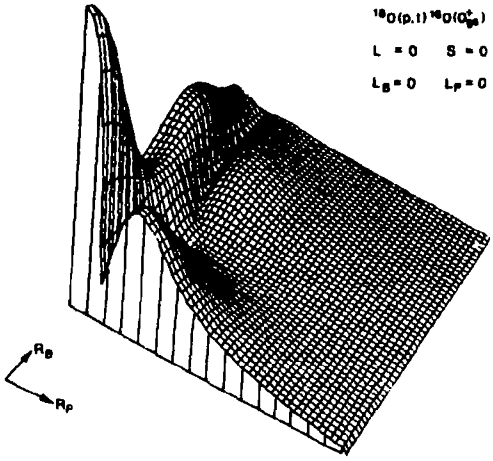

FIG. 2. The form factor $\mathcal{F}^{LSJ}_{L_p L_B}(R_p, R_B)$, for the reaction $^{18}\mathrm{O}(p,t)^{16}\mathrm{O}(0^+_{g.s.})$, in arbitrary units, as a function of R_p and R_B, shown over the range 0 to 5 fm for R_p and R_B, respectively.

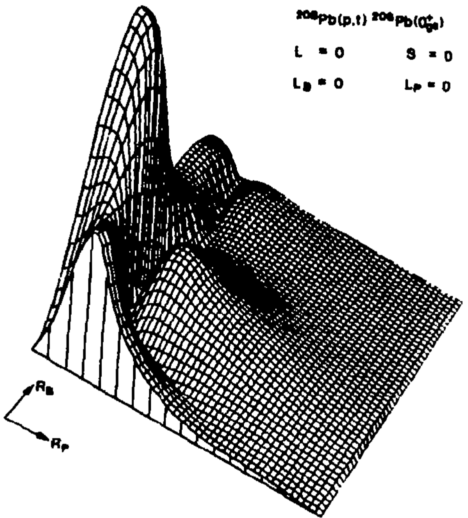

FIG. 4. The form factor $\mathcal{F}^{LSJ}_{L_p L_B}(R_p, R_B)$, for the reaction $^{208}\mathrm{Pb}(p,t)^{206}\mathrm{Pb}(0^+_{g.s.})$ in arbitrary units, as a function of R_p and R_B, shown over the range 0 to 5 fm for R_p and R_B, respectively.

are shown in Figs. 2 and 4, respectively, for oxygen and lead. Both of these form factors comprise S and S' components and are extremely nonlocal, nonseparable functions. The form factors along the zero-range line in Figs. 3 and 5, respectively, for oxygen and lead display a structure significantly different from that away from the

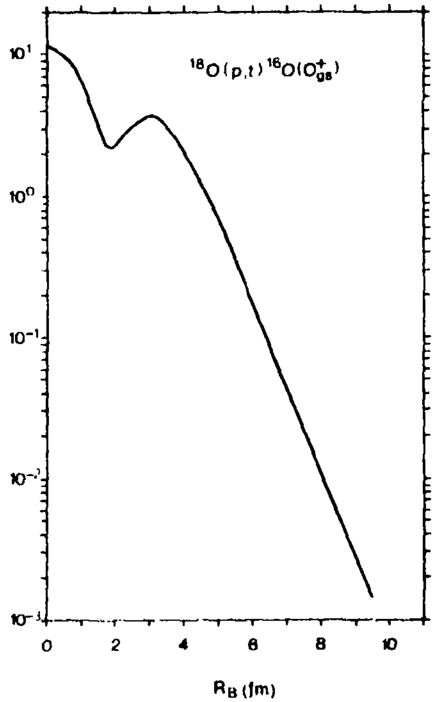

FIG. 3. The form factor in Fig. 2 plotted along the zero-range line $R_p = 0$ in units MeV fm^{-3}.

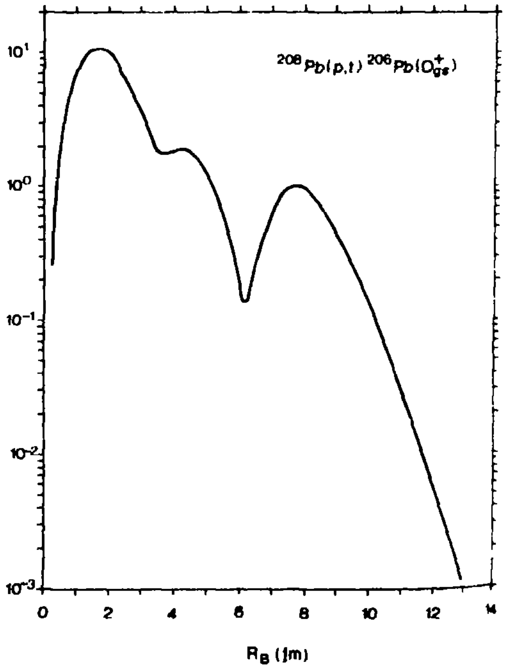

FIG. 5. The form factor in Fig. 4 plotted along the zero-range line $R_p = 0$ in units MeV fm^{-3}.

TABLE IV. Allowed values of the angular momentum quantum numbers for the ground state transitions in this work.

L	S	L_B	L_P	Triton and neutron pair components
0	0	0	0	S and S' states
		2	2	$S_{12}=S,\ l=L_P$
1	1	1	1	S' and D states
		3	3	$S_{12}=S,\ l=L_P\pm 2, L_P$

zero-range line in Figs. 2 and 4. The zero-range form factors (Figs. 3 and 5) differ in the interior from those obtained by Ibarra, Feng, and Vallieres[23-27] using extended shell model basis techniques to account for the correlation of the neutrons being transferred. The half-separation energy method assumes that the neutrons act independently in a potential well and share the total separation energy equally. Any correlation between the two particles is introduced subsequently in the spectroscopic amplitudes.

In Fig. 6 a comparison is made between the finite-range DWBA prediction and the experimental data for the $^{18}\mathrm{O}(p,t)^{16}\mathrm{O}$ reaction at a proton energy of 20 MeV. The figure displays two sets of experimental data covering a wide range of angles. The theoretical calculation has been normalized by the factor

$$n=\sigma_{\mathrm{expt}}/\sigma_{\mathrm{cal}}=1.63\ .$$

An exact finite-range calculation of this reaction has been performed by Charlton.[8] In his analysis, Charlton uses two different optical model parameter sets and obtains results for one case which are comparable with those presented in this study. However, our calculation differs from Charlton's in the following respects: The triton wave function and transfer interaction are treated consistently in this work. The two-body interaction was the Reid soft core potential and the triton wave function was obtained variationally as given in Ref. 17. In Charlton's calculations the transfer interaction was *not* consistent with that used to obtain the triton wave function. The geometrical parameters of the bound neutron wave functions employed here are larger than those of Charlton and we have omitted spin-orbit terms from the potentials used to obtain these states. This omission has little effect on the wave function, however.

In Fig. 7, the theoretical and experimental angular distributions are compared for the reaction $^{208}\mathrm{Pb}(p,t)^{206}\mathrm{Pb}(0^+_{g.s.})$. The two-neutron spectroscopic factors are obtained from the shell model wave function of True. The normalization factor for this reaction is

$$n=\sigma_{\mathrm{expt}}/\sigma_{\mathrm{cal}}=1.23\ .$$

This reaction was also analyzed by Charlton[8] and although he found good agreement with the shape of the angular distribution, his calculation underpredicted the absolute magnitude by a factor of 1.6. In calculations presented here, both the symmetric and mixed symmetry triton S states contribute, and in Fig. 8, we compare the angular distributions calculated with and without the S' state. The difference between the two is never more than 5% except at the minimum near $\theta_{c.m}$

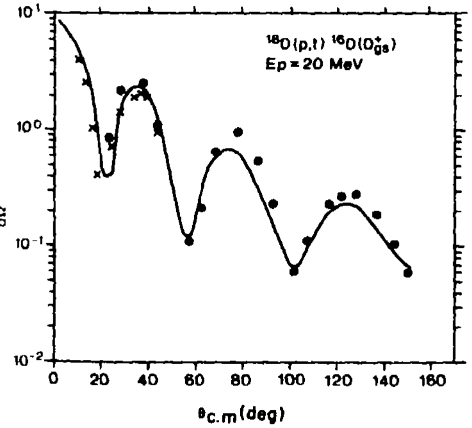

FIG. 6. The comparison of the theoretical and experimental angular distribution for the reaction $^{18}\mathrm{O}(p,t)^{16}\mathrm{O}(0^+_{g.s.})$ at the proton energy of 20 MeV. The experimental points (x, 0) are taken from Refs. 28, 29, respectively.

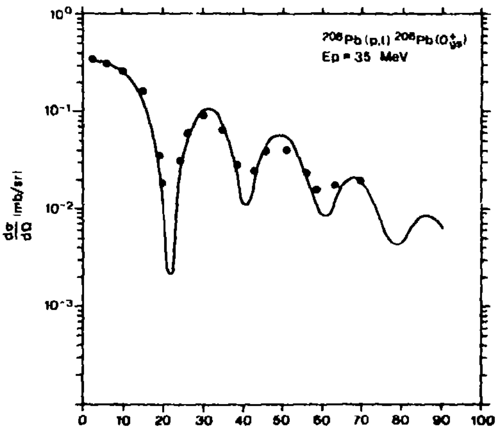

FIG. 7. The comparison of the theoretical and experimental angular distributions for the reaction $^{208}\mathrm{Pb}(p,t)^{206}\mathrm{Pb}(0^+_{g.s.})$ at a proton energy of 35 MeV. The experimental points are taken from Ref. 30.

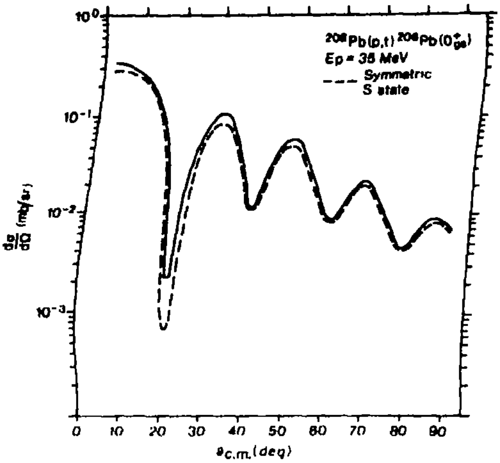

FIG. 8. The comparison of the total ($S+S'$) and S contributions to the reaction in Fig. 9.

= 23°, where the influence of the mixed symmetry S state is to fill in the minimum.

One uncertainty in fitting the absolute magnitude of these angular distributions can be ascribed to our use of the half-separation energy method. The half-separation energy method assumes that the transferred neutrons move independently in a potential well and share the removal energy equally. From the work of Ibarra *et al.*[23, 24] we know that this is not the case, and that treating the correlated neutron pair more precisely enhances the magnitude of the form factor in the surface of the nucleus. Accordingly, we can "effect" this enhancement within the framework of the half-separation energy method by determining larger geometrical parameters for the bound particles. One believes this kind of prescription only insofar as absorption and phase averaging of the distorted waves cause the reaction to be surface peaked. This procedure was used successfully for the reactions studied in Refs. 10–13, 20, with the geometrical parameters

$$R = 1.2(A^{1/3} + 1)\ \text{fm},$$

$$a_0 = 0.65\ \text{fm},$$

and produces the necessary enhancement needed to fit the reactions presented in this study.

V. SUMMARY AND CONCLUSIONS

We have presented a finite-range DWBA analysis of the reactions $^{208}Pb(p,t)^{206}Pb(0^+_{g.s.})$ and $^{18}O(p,t)^{16}O(0^+_{g.s.})$ and corresponding calculations of the two-neutron transfer form factor employing a realistic triton wave function. The transfer interaction in the prior formulation of DWBA is eliminated in favor of the binding energy, the internal kinetic energy, and the interaction between the neutron pair in the triton. Form factors calculated for these reactions demonstrate the importance of maintaining a manifestly finite-range theory.

Our work differs significantly from earlier finite-range calculations in our treatment of the triton wave function and of the transfer interaction. We have employed a variational triton wave function having a totally symmetric S state, and mixed symmetry S and D state components obtained using a realistic nucleon-nucleon potential. The same potential is used to construct the transfer interaction thereby maintaining a consistency between the interactions involving the transferred neutrons and the interaction between nucleons in the triton.

Selection rules are obtained from these form factors which have the following properties:

(i) For two-neutron states in nuclei which have uniquely $S_{12} = 0$ *only* the S and S' states can contribute, whereas for states with $S_{12} = 1$ *only* the S' and D states contribute.

(ii) The importance of the mixed symmetry states is enhanced in the two cases when the two-neutron configuration has natural parity and a dominant $S_{12} = 1$ component, or the two-neutron configuration has unnatural parity. For the above reactions the spatially symmetric S state of the triton contributes more than 90% of the differential cross section.

Our analysis of the ground state transitions has demonstrated very good agreement between the theoretical and experimental angular distribution shapes but absolute magnitudes which are too small by 60% and 23%, respectively, for the $^{18}O(p,t)^{16}O$ and $^{208}Pb(p,t)^{206}Pb$ reactions. However, as has already been discussed, we can expect enhancements of this order from the use of more tightly correlated wave functions.[31]

The results of our calculations indicate the importance of the use of realistic triton wave functions and consistent transfer interactions in the determination of the absolute magnitude of (p,t) or (t,p) cross sections.

We have recently received a report on similar analyses by Takemasa, Tamura, and Udgawa. We thank the authors for sending us the report.

ACKNOWLEDGMENTS

We wish to acknowledge valuable discussions with Dr. G. R. Satchler and Dr. D. Robson. This work was supported in part by National Science Foundation Grant No. PH7 78-11577.

[*] Present address, W. W. Wright Nuclear Structure Lab., Yale University, 260 Whitney Avenue, New Haven, Connecticut 06520.

H. Feshbach, in *Proceedings of the Symposium on Two-Nucleon Transfer and Pairing Excitation*, Argonne National Laboratory, 1972. (Argonne National Laboratory Informal Report No. PHY-172H, 1972).

[2] N. K. Glendenning, *Nuclear Spectroscopy and Reactions, Part D*, edited by J. Cerny (Academic, New York, 1974).

[3] N. Austern, *Direct Nuclear Reaction Theories* (Wiley, New York, 1970).

[4] M. R. Strayer, M. F. Werby, and M. A. Nagarajan, Daresbury Laboratory Report No. DLNSF P52 (1977).

[5] M. R. Strayer, M. F. Werby, and M. A. Nagarajan, Daresbury Laboratory Report No. DLNSF P53 (1977).

[6] B. F. Bayman, Nucl. Phys. A168, 1 (1971).

[7] B. F. Bayman and D. H. Feng, Nucl. Phys. A205, 513 (1973).

[8] L. A. Charlton, Phys. Rev. C 12, 351 (1975).

[9] T. Takemasa, Nucl. Phys. A220, 31 (1974).

[10] M. R. Strayer and M. F. Werby, J. Phys. G 3, L179 (1977).

[11] M. F. Werby, M. R. Strayer, and M. A. Nagarajan, Bull. Am. Phys. Soc. 22, 597 (1977).

[12] M. R. Strayer, M. F. Werby, and M. A. Nagarajan, International Conference on Medium Light Nuclei, Florence, Italy, 1977.

[13] M. F. Werby and M. A. Strayer, J. Phys. G 3, L179 (1977).

[14] I. S. Towner and J. C. Hardy, Adv. Phys. 18, 401 (1969).

[15] N. Austern, R. M. Drisko, E. Halbert, and G. R. Satchler, Phys. Rev. B 3 133 (1964).

[16] G. R. Satchler, Nucl Phys. 55, 1 (1964).

[17] M. R. Strayer and P. U. Sauer, Nucl. Phys. A231 1 (1974).

[18] R. V. Reid, Ann. Phys. (N.Y.) 50, 41 (1968).

[19] N. K. Glendenning, Phys. Rev. 137B, 102 (1965).

[20] M. A. Nagarajan, M.R. Strayer, and M. F. Werby, Phys. Lett. 67B, 141 (1971).

[21] S. Kahana, Phys. Rev. C 5, 1388 (1968).

[22] W. W. True, Phys. Rev. 168, 1388 (1968).

[23] D. H. Feng, R. H. Ibarra, and M. Vallieres, Phys Lett. 76B, 37 (1973).

[24] R. H. Ibarra, M. Vallieres, and D. H. Feng, Nucl. Phys. A241, 386 (1975).

[25] W. T. Pinkston, Nucl. Phys. A269, 281 (1976).

[26] R. H. Ibarra, N. Austern, M. Vallieres, and D. H. Feng, Nucl. Phys. A288, 397 (1977).

[27] M. Vallieres, D. H. Feng, and R. H. Ibarra, Nucl. Phys. A265, 21 (1976).

[28] M. Pignanelli, S. Micheletti, I. Iori, O. Guazonni, F. G. Resmini, and J. L. Escudie, Phys. Rev. C 10, 445 (1974).

[29] D. G. Fleming, A. Arima, H. W. Fulbright, and M. Blaum, Phys. Rev. C 10, 1350 (1974).

[30] W. A. Lanford and J. B. McGrory, Phys. Lett. 45B, 238 (1973).

[31] D. H. Feng *et al*. (unpublished).

PHYSICAL REVIEW C VOLUME 21, NUMBER 6 JUNE 198

^{210}Bi$^{m}(d,t)$ reaction; ^{210}Bi(9$^-$) parentage of states in ^{209}Bi

T. P. Cleary* and W. D. Callender†
Wright Nuclear Structure Laboratory, Yale University, New Haven, Connecticut 06520

R. K. Sheline
Florida State University, Tallahassee, Florida 32306

(Received 9 July 1979)

Configuration assignments and spectroscopic factors are deduced from angular distribution data on 22 levels or level groupings in ^{209}Bi using the reaction ^{210}Bi$^{m}(d,t)^{209}$Bi at $E_d = 17$ MeV. Transitions to levels in ^{209}Bi between 2.6 and 6.0 MeV are observed and these levels are interpreted in terms of the coupling of the pure $|h^{\pi}_{9/2},g^{\nu}_{9/2}\rangle_{9^-}$ target state with neutron holes in ^{207}Pb. The *j* values of the transferred neutron are determined through comparison of the measured angular distributions and energies with angular distributions and energies for the corresponding single-hole states in ^{207}Pb. Levels below 5.0 MeV are assigned $p_{1/2}$, $p_{3/2}$, or $f_{5/2}$ neutron hole parentage while the levels above 5.0 MeV all have $f_{7/2}$ neutron hole parentage. The results complement and extend previous inelastic scattering and analog resonance studies on levels below 4.0 MeV excitation in ^{209}Bi. In particular, the summed spectroscopic strength for the $p_{1/2}$ neutron hole parentage states agrees well with the theoretical sum rule limit and measured single-hole strength in ^{207}Pb. The microscopic shell model (in contrast to the weak-coupling model) successfully predicts the observed splitting of spectroscopic strength among the members of the $(|h^{\pi}_{9/2},g^{\nu}_{9/2}\rangle_{9^-} \otimes p^{-1\nu}_{1/2})$ multiplet.

[NUCLEAR REACTIONS ^{210}Bi$^{m}(d,t)^{209}$Bi, $E_d = 17$ MeV. $\theta_{\text{lab}} = 12.5°, 20°, 27.5°, 35°, 42.5°, 50°, 57.5°, 72.5°, 87.5°, 100°, 115°$. Measured $\sigma(\theta)$ for $E^*(^{209}\text{Bi})$ 2700–6000 keV. Deduced $l_j^{-1\nu}$, spectroscopic factors.]

I. INTRODUCTION

The single-particle structure of ^{209}Bi, with one proton beyond the double closed shell nucleus ^{208}Pb, has been studied[1,2] extensively. These studies demonstrated that the ^{209}Bi levels can be almost completely described in terms of the simple shell model. More recent experimental efforts[3-5] have investigated the next level of shell model structure in ^{209}Bi—the two particle–one hole configuration. In this paper we report on results obtained from a study of the ^{210}Bi$^{m}(d,t)$ reaction. This reaction is highly selective in the states that can be excited and this has permitted the 2p-1h structure of many levels in ^{209}Bi to be identified.

States of 2p-1h character are excited in direct inelastic scattering on ^{209}Bi; however, these reactions are most sensitive to the collective excitations of the ^{208}Pb core and thus emphasize the particle-vibration structure of ^{209}Bi. Through studies of this type[6] a multiplet of levels near an excitation energy of 2.6 MeV in ^{209}Bi has been associated with the weak coupling of an $h_{9/2}$ proton to the 3$^-$ state of ^{208}Pb. The success of this weak-coupling or particle-vibration model[7-12] in describing these states has led several groups[4,13-16] to search for multiplets built on other excitations of the ^{208}Pb core. While experimental evidence does exist for structure in ^{209}Bi based upon couplings to the higher excited states of ^{208}Pb, it was pointed out[17] that, for levels in the energy region from 2.8 to 3.6 MeV in ^{209}Bi, an alternate description in term of the coupling of a neutron hole to the low-lying states of ^{210}Bi provides an equally valid account of the experimental data. The properties of the levels in this energy region were more fully examined by means of isobaric analog studies involving the ^{209}Bi(p,p') reaction,[3] and it was shown that a consideration of the underlying microscopic 2p-1h structure provides a rather complete description of the observed properties of these levels.

The existence of a ^{210}Bi^{m} target[18] provides a means of testing in a definitive way the microscopic model[3] proposed for the levels in ^{209}Bi from 2.8 to 3.6 MeV and of extending our knowledge of the microscopic structure of levels associated with a particular class of 2p-1h configurations. Since the target exists in the 9$^-$ metastable state at an excitation energy of 0.271 MeV, the (d,t) reactions should populate states in ^{209}Bi that can be described as a neutron hole coupled to a 9$^-$ ^{210}Bi core state. Moreover, abundant theoretical[19-21] and experimental[22-27] evidence strongly suggests that this 9$^-$ state is a very pure two particle state whose wave function is dominated by the $|h^{\pi}_{9/2},g^{\nu}_{9/2}\rangle$ component. Thus the present experiment explores states in ^{209}Bi with the $|h^{\pi}_{9/2},$

© 1980 The American Physical Society

$g^{\nu}_{9/2}|_{9^-}\otimes(l_j)^{-1\nu}$ configuration in their structure where $(l_j)^{-1\nu}$ specifies the neutron hole orbital. These neutron hole orbitals are determined for many transitions observed in the ^{210}Bi^m(d,t) reaction from both the measured triton angular distributions and the regions of the triton spectra at which single-hole transition strength is expected based upon results from a ^{208}Pb(d,t) reaction study.[28] Since this latter reaction on ^{208}Pb was performed at the same incident deuteron energy as the present measurement, a detailed comparison of the single-hole transition strength is presented. The present results are employed in a critical evaluation of the microscopic 2p-1h and weak-coupling descriptions of levels in ^{209}Bi below 3.5 MeV excitation.

II. EXPERIMENTAL PROCEDURES

The fabrication of the ^{210}Bi^m target was carried out using the Florida State University Isotope Separator and has been described in detail in Ref. 18. Briefly, an ultrapure sample of ^{209}Bi was exposed to a high flux of neutrons at the Savannah River Laboratories of the U. S. DOE. After the five-day ground state of ^{210}Bi had decayed out, the 2.6 $\times 10^6$ year 9$^-$ isomer was initially separated at the Oak Ridge Calutron. The resulting separated material consisted of 1.39 mg of ^{210}Bi^m with an isotopic abundance of 2.5 at.% in ^{209}Bi. This material was then placed in the ion source of the Florida State University Isotope Separator which had been designed[18] to accomodate extremely small amounts of material. Following retardation, the target (with 99% isotopic purity) was deposited on a 60 μg/cm^2 carbon backing with a maximum density of material in an oval spot 4 mm × 2 mm.

In the present experiment the ^{210}Bi^m target was bombarded by a 17 MeV deuteron beam from the Yale MP tandem accelerator and the reaction prolcts analyzed by a multigap spectrograph. The chnical aspects of this magnet are discussed in ef. 29. Data were recorded at 22 angles on Ilford μm thick nuclear emulsion plates with the exosure lasting for approximately 50 000 μC of colcted charge. A surface barrier detector, located a laboratory angle of 75°, was used to monitor uterons elastically scattered from the target d this provided a means of locating the position maximum ^{210}Bi^m thickness on the target. The eld of the spectrograph was selected in order to llow tritons and deuterons associated with tranitions to levels from 2.5 to 6.0 MeV in ^{209}Bi and om 0.0 to 3.0 MeV in ^{210}Bi, respectively, to fall the focal plane of the magnet.

Data for 11 angles from 12.5° to 115° were anazed in detail. The plates were scanned in 0.5 mm steps in the vicinity of the peaks and in 1.0 mm steps over the background region. Since the magnetic field varies slightly from gap to gap in the spectrograph, a peak in each spectrum which could be identified with the 2.987 MeV transition in ^{209}Bi was used to compute the effective field for each gap. The 2.987 MeV transition therefore served as a reference energy[4] for the calibration of the spectra. The effective fields and experimentally measured calibration curves[29] which relate the distance along the plate to the radius of curvature of the magnet were then used to convert plate distance into Q value.

A typical spectrum from the ^{210}Bi^m(d,t) measurement is shown in Fig. 1. For ease of presentation, the spectrum is plotted in ΔQ steps of ~6 keV although the data were actually analyzed in steps of ~3 keV. The full width at half maximum (FWHM) for peaks in the spectra varies from ~15 keV at more forward angles to ~30 keV at more backward angles. However, for any given spectrum the resolution was relatively constant over the entire energy range of interest. Excitation energies were obtained from the positions of the $\frac{1}{2}$ heights of the peaks and intensities were extracted by summing the counts over the appropriate ΔQ interval and separating overlapping peaks by making use of the peak shape for the 2.987 MeV transition. Reproducibility of the level energies from angle to angle and the reasonableness of the angular distributions give us confidence in the results in spite of the very thin target. The energies of many transitions in ^{209}Bi have already been measured in inelastic scattering experiments[4] with an uncertainty of less than 5 keV and transitions measured in the present experiment can readily be identified with those derived from the

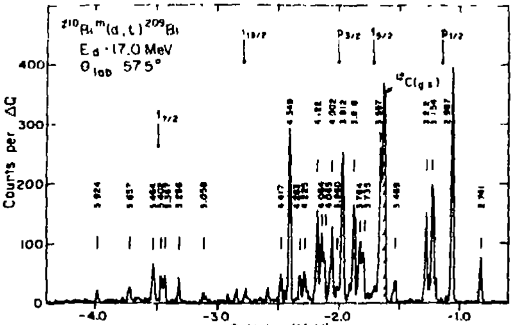

FIG. 1. Triton spectrum from ^{210}Bi^m(d,t) measurement. Excitation energies of corresponding states in ^{209}Bi are indicated and arrows show the locations of the unperturbed single-hole transition strength based upon the states of ^{207}Pb.

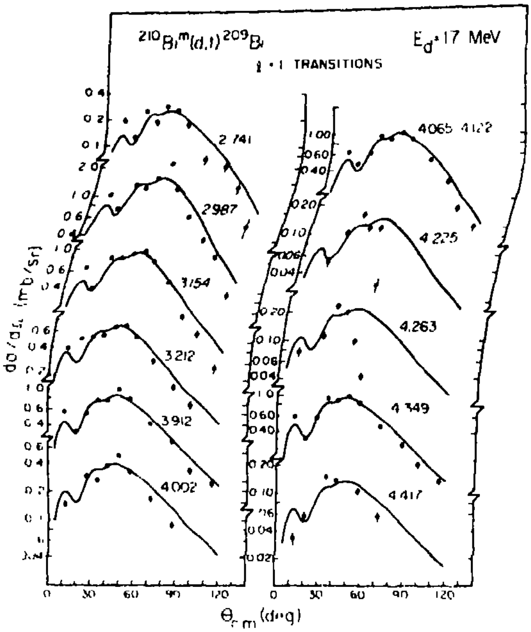

FIG. 2. Triton angular distributions for $l=1$ transitions in ^{209}Bi.

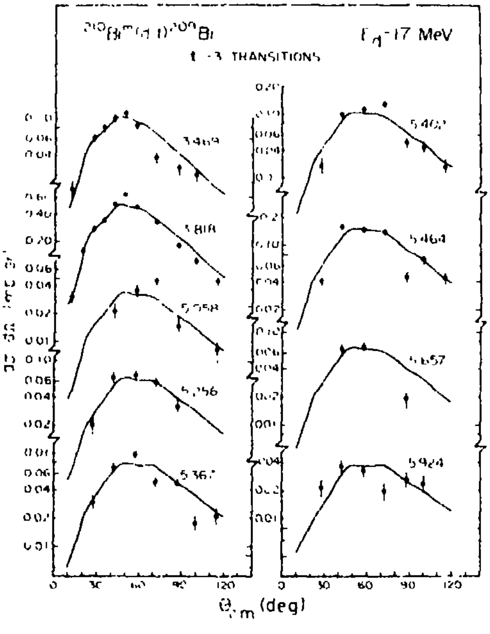

FIG. 3. Triton angular distributions for $l=3$ transitions in ^{209}Bi.

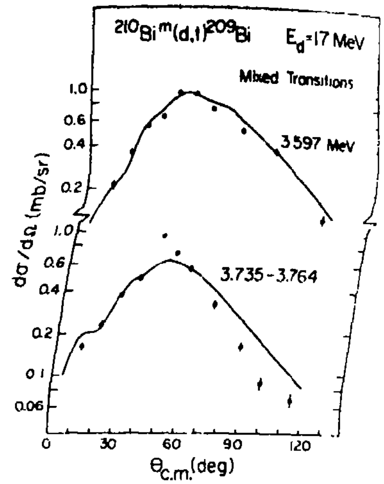

FIG. 4. Triton angular distributions for mixed transi tions in ^{209}Bi. See text for discussion.

previous work.

Since the amount of target material relative to the carbon backing foil was quite small, reaction products from the foil and the impurities containe in the foil could give rise to rather large peaks in the spectra. While every attempt was made to identify each of these contaminant peaks, it is possible that not all were identified and some of the large deviations in certain isolated data point in the angular distributions could be a reflection of this problem. The measured angular distributions for the ^{210}Bi(d,t) reaction are shown in Figs 2-4.

Data for ^{210}Bi(d,d) scattering could only be extracted for angles greater than 110°. However, by comparing the results obtained at these angles with similar data from elastic deuteron scatterin on ^{208}Pb and ^{209}Bi, an absolute cross-section normalization was established. As an additional chec on the normalization, the elastic deuteron counts obtained with the monitor detector were compare with values for the differential cross section calculated from the deuteron optical potential of Ref. 30. The two methods yielded a consistent value for the target thickness of 3.0±0.3 μg/cm^2 at the beam spot used in this experiment. An uncertaint of 10% is therefore assumed for the absolute cross-section normalization in this work.

III. ANALYSIS

The solid curves in Figs. 2-4 are distorted-wave Born approximation (DWBA) calculations based upon the optical potential used in Ref. 30 and corrected for Q-value dependence. These ame parameters were used in the analysis of the ^{08}Pb(d,t) data of Moyer *et al.*[28] The DWBA code WUCK[31] was used in the present calculations.

Since the shapes of the angular distributions inolving spin transfers of $j=l+\frac{1}{2}$ and $j=l-\frac{1}{2}$ are ndistinguishable, the angular distributions alone o not permit the identification of the orbital from hich the transferred neutron has been picked up. he triton spectrum in Fig. 1 is displayed as a unction of reaction Q value and corresponds to an xcitation energy region from 2.6 to 6.0 MeV in ^{9}Bi. The arrows along the upper part of the figre indicate the expected location of single-hole transition strength based upon the energies of the single-hole states of ^{207}Pb. If the fragmentation of single-hole strength caused by the presence of the extra-core neutron and proton in the ^{210}Bi^m(d,t) reaction does not spread out the population over too great an energy range, then the single-hole strength should lie close to the unperturbed positions and thus identification of both the l and j of the transferred neutron should be possible.

The energy separation of the $f_{5/2}$ and $f_{7/2}$ neutron hole states is quite large, approximately 2 MeV, and therefore multiplets in ^{209}Bi associated with these two orbitals should be well separated. In the case of the $p_{1/2}$ and $p_{3/2}$ orbitals, though, the *energy separation is small (0.85 MeV) and the* corresponding multiplets in ^{209}Bi could overlap in energy and indeed by admixed thus causing difficulty in assignment. Fortunately, however, resonance studies[3] of the ^{209}Bi(p,p') reaction have already suggested assignments for many of the levels in ^{209}Bi with structure involving the $p_{1/2}$ hole orbital; three of these levels are populated in the present experiment. These suggested assignments are discussed in terms of the present experimental results in Sec. IV.

The results of the present analysis are summarized in Table I. The l and j values for the transferred neutron have been determined from the angular distributions and the unperturbed positions of the single-hole strength. The corresponding values for the spectroscopic strength are also tabulated. The spectroscopic factors were derived using the normal definition

$$\frac{d\sigma}{d\Omega}=\frac{3.33}{(2j+1)}\,\mathcal{S}\sigma_{\rm DWBA}(\theta)\,,$$

where j is the total angular momentum of the transferred neutron. The spin assignments for the six lowest levels have been taken from Refs. 3 and 4.

Finally, the spectroscopic sums and energy centroids are compared with the values for the single-hole states obtained in the ^{208}Pb(d,t) reaction.[28] The energy centroids were calculated using the formula

$$\bar{E}_{l_j}=\frac{\sum_i \mathcal{S}^i_{l_j}E^i}{\sum_i \mathcal{S}^i_{l_j}}\,,$$

where $\mathcal{S}^i_{l_j}$ and E^i are the spectroscopic factor

TABLE I. Summary of results for the ^{210}Bi^m(d,t)^{209}Bi reaction.

Energy[a] MeV	J^π Ref. b	l	$\mathcal{S}$	l_j Ref. c
2.741	$\frac{15}{2}^+$	1	0.14	$p_{3/2}$
2.987	$\frac{13}{2}^+$	1	0.98	$p_{1/2}$
3.135	$\frac{15}{2}^+$, $\frac{11}{2}^+$			
3.154	$\frac{17}{2}^+$, $\frac{9}{2}^+$	1	0.61	$p_{1/2}$
3.212	$\frac{17}{2}^+$	1	0.48	$p_{1/2}$
3.469	$\frac{11}{2}^+$ Ref. d	3	0.27	$f_{5/2}$
3.597	$\frac{19}{2}^+$	1, 3	0.17, 1.95	$p_{3/2}$, $f_{5/2}$
3.735 3.764		1, 3	0.25, 0.94	$p_{3/2}$, $f_{5/2}$
3.818		3	1.58	$f_{5/2}$
3.912		1	0.71	$p_{3/2}$
3.960				
4.002		1	0.35	$p_{3/2}$
4.021				
4.065 4.084 4.122		1	0.92	$p_{3/2}$
4.225		1	0.14	$p_{3/2}$
4.263		1	0.21	$p_{3/2}$
4.349		1	0.97	$p_{3/2}$
4.417		1	0.14	$p_{3/2}$
5.058		3	0.15	$f_{7/2}$
5.256		3	0.32	$f_{7/2}$
5.367		3	0.41	$f_{7/2}$
5.402		3	0.56	$f_{7/2}$
5.464		3	0.83	$f_{7/2}$
5.657		3	0.43	$f_{7/2}$
5.924		3	0.28	$f_{7/2}$

[a] Energies are derived from present study with 2.987 MeV level as a reference energy. Energy uncertainties are 5 keV for levels below 3.60 MeV and 10 keV for levels above 3.60 MeV.

[b] From Table I of Ref. 4.

[c] Orbital and total angular momentum of transferred neutron.

[d] Possible doublet. See text for discussion.

and excitation energy in ^{209}Bi, respectively, corresponding to the pickup of a neutron with orbital and total angular momentum l_j.

IV. CONFIGURATION ASSIGNMENTS

A. The $|^{210}\mathrm{Bi}(9^-)\otimes p_{1/2}^{-1\nu}|$ configuration

From angular momentum coupling considerations, the $|^{210}\mathrm{Bi}(9^-)\otimes p_{1/2}^{-1\nu}|$ configuration is expected to give rise to two states of spin-parity—$\frac{19}{2}^+$ and $\frac{17}{2}^+$. Thirteen transitions with $l=1$ angular distributions are observed and these correspond to the population of states at excitation energies between 2.5 and 4.5 MeV in ^{209}Bi. The states at 2.987, 3.154, and 3.212 MeV have been identified in previous work[3] with the $|^{210}\mathrm{Bi}(9^-)\otimes p_{1/2}^{-1\nu}|$ configuration with suggested spin assignments of $\frac{19}{2}^+$, $\frac{17}{2}^+$, and $\frac{17}{2}^+$, respectively. These results have been used to separate the $p_{1/2}$ $l=1$ transitions from the $p_{3/2}$ $l=1$ transitions listed in Table I. The energy centroid position and total spectroscopic strength for these three transitions are found to be in remarkable agreement with the experimental results for the $p_{1/2}$ hole state transition derived from the ^{208}Pb(d,t) reaction[30] (see Table II). In summary, the interpretation of the 2.987, 3.154, and 3.212 MeV states in terms of the $|^{210}\mathrm{Bi}(9^-)\otimes p_{1/2}^{-1\nu}|$ configuration is strongly supported by the present results.

B. The $|^{210}\mathrm{Bi}(9^-)\otimes p_{3/2}^{-1\nu}|$ configuration

The states identified with the $|^{210}\mathrm{Bi}(9^-)\otimes p_{3/2}^{-1\nu}|$ configuration include all the levels excited by $l=1$ transitions which have not been associated with the $|^{210}\mathrm{Bi}(9^-)\otimes p_{1/2}^{-1\nu}|$ configuration. The spin-parity values expected on the basis of the $|^{210}\mathrm{Bi}(9^-)\otimes p_{3/2}^{-1\nu}|$ configuration are $\frac{15}{2}^+$, $\frac{17}{2}^+$, $\frac{19}{2}^+$, and $\frac{21}{2}^+$. Aside from the level at 2.741 MeV excitation energy, all these levels lie at energies greater than 3.450 MeV. From the angular distribution data it is found that eight of the level groupings (the 2.741, 3.912, 4.002, 4.065–4.122, 4.225, 4.263, 4.349, and 4.417 MeV levels) are excited by $l=1$ transitions while two (the 3.597 and 3.764 MeV levels) are populated by mixed $l=1$ and $l=3$ transitions. The 3.764 MeV peak could be resolved from the 3.735 MeV peak at only a few angles and they were, therefore, analyzed together. At the most forward angles, the cross section for the 3.764 MeV transition is much larger than that for the 3.735 MeV transition and this leads to the identification of the 3.764 MeV transition as the $l=1$ component of the doublet. The results are summarized in Table I. The listed levels can account for 100% of the spectroscopic strength obtained for the $p_{3/2}$ single-hole transition in ^{207}Pb and their energy centroid is only 120 keV above the unperturbed position for the $|^{210}\mathrm{Bi}(9^-)\otimes p_{3/2}^{-1\nu}|$ configuration. The angular distributions for the mixed transitions are consistent with the data and this suggests that no serious misassignment of strength has occurred.

The association of the ten groups discussed above with the $|^{210}\mathrm{Bi}(9^-)\otimes p_{3/2}^{-1\nu}|$ configuration is consistent with the total transition strength and energy centroid for these levels and provides additional support for the division of $p_{1/2}$ and $p_{3/2}$ $l=1$ transitions assumed in this analysis.

TABLE II. Comparison of single-particle transitions for the ^{208}Pb(d,t) and ^{210}Bi(d,t) reactions.

l_j	Energy centroids E_{sp} Ref. a	$\bar{E}$	Spectroscopic strengths S_{sp} Ref. a	$\sum_j \mathcal{S}_{l_j}$
$p_{1/2}$	3.080	3.088	2.1[b]	2.07
$f_{5/2}$	3.650	3.691	6.8	4.74
$p_{3/2}$	3.930	4.050	4.0	4.0
$i_{13/2}$	4.720		14.5	
$f_{7/2}$	5.420	5.467	7.1	2.98

[a] Aside from E_{sp} and S_{sp} for the $p_{1/2}$ transition, the single-particle results are from the ^{208}Pb(d,t) reaction study of Ref. 28.

[b] From study of Ref. 30.

C. The $|^{210}\mathrm{Bi}(9^-)\otimes f_{5/2}^{-1\nu}|$ configuration

Six states with spin-parities $\frac{13}{2}^+$ through $\frac{23}{2}^+$ are expected for the $|^{210}\mathrm{Bi}(9^-)\otimes f_{5/2}^{-1\nu}|$ configuration. From the angular distributions for transitions to levels below 4.5 MeV, it is found that the 3.469 and 3.818 MeV levels are excited by $l=3$ transitions and the 3.597 and 3.735 MeV levels by mixe $l=1$ and 3 transitions. The 3.735 MeV transition is the second member of the 3.735–3.764 MeV doublet discussed above and it is identified as the $l=3$ component in this unresolved transition. Th 1.770 MeV energy separation of the $f_{5/2}$ and $f_{7/2}$ single-hole states (see Fig. 1) suggests that the corresponding levels in ^{209}Bi can be associated with the $|^{210}\mathrm{Bi}(9^-)\otimes f_{5/2}^{-1\nu}|$ and $|^{210}\mathrm{Bi}(9^-)\otimes f_{7/2}^{-1\nu}|$ configurations on the basis of energetics.

For levels associated with the $|^{210}\mathrm{Bi}(9^-)\otimes f_{5/2}^{-1\nu}|$ configuration, the resulting energy centroid is 41 keV higher than the unperturbed value and the total spectroscopic strength is about 30% bel the single-hole value obtained from ^{207}Pb. From the ^{209}Bi(p,p') data of Ref. 3, the excitation func tion for a transition leading to a level at 3.465 MeV is found to exhibit resonance structure at tl 6^- analog state and much weaker resonance struc ture near the 9^-. This level can probably be ider tified with the 3.469 MeV transition observed in the present measurement. The excitation of this level at the 9^- analog state is consistent with its population in the present (d,t) experiment; however, the present assignment of the 3.469 MeV level as a member of the $|^{210}\mathrm{Bi}(9^-)\otimes f_{5/2}^{-1\nu}|$ multiplet is in conflict with the $\frac{11}{2}^+$ spin assignment derived in Ref. 3. This conflict could be resolved if this level is actually a doublet with one member associated with the $|^{210}\mathrm{Bi}(6^-)\otimes p_{1/2}^{-1\nu}|$ configuration and the other with $|^{210}\mathrm{Bi}(9^-)\otimes f_{5/2}^{-1\nu}|$.

Within the assumptions of the present analysis, the description of all the levels below 4.400 MeV excited by $l=3$ transitions in terms of the $|^{210}\mathrm{Bi}(9^-)\otimes f_{5/2}^{-1\nu}|$ configuration provides a consistent explanation of the experimental results.

D. The $|^{210}\mathrm{Bi}(9^-)\otimes f_{7/2}^{-1\nu}|$ configuration

Seven levels above an excitation energy of 5.0 MeV are identified in Table I with the $|^{210}\mathrm{Bi}(9^-)$ $\otimes f_{7/2}^{-1\nu}|$ configuration. Eight states are predicted for this configuration with spins from $\frac{11}{2}^+$ to $\frac{25}{2}^+$. The transitions associated with the configuration ccount for only 40% of the predicted single-hole trength and the energy centroid for the levels is 7 keV above the unperturbed position. These reults indicate that the $f_{7/2}$ single-hole strength is uite fragmented. Some $f_{7/2}$ strength might reside ı transitions to levels above 6.000 MeV in ^{209}Bi; owever, this region of the energy spectrum was bscured at most angles in the present measureıent by contaminant peaks.

E. The $|^{210}\mathrm{Bi}(9^-)\otimes i_{13/2}^{-1\nu}|$ configuration

Angular momentum coupling suggests that 14 tates are expected from the configuration $^{210}\mathrm{Bi}(9^-)\otimes i_{13/2}^{-1\nu}|$ with spin-parities from $\frac{5}{2}^-$ to $\frac{31}{2}^-$. ased on the location of the $i_{13/2}$ hole state in ^{7}Pb, we may expect most of the strength from ıe $|^{210}\mathrm{Bi}(9^-)\otimes i_{13/2}^{-1\nu}|$ configuration to lie in the enrgy region from 4.5 to 5.0 MeV (see Fig. 1). owever, the fragmentation of the strength into a ıinimum of 14 states combined with the intrinsiallly lower $i_{13/2}$ single-particle cross section ıakes it very difficult to observe the individual ansitions. There are a number of extremely eak fluctuations in the background in the excitaon region from 4.5 to 5.0 MeV (see Fig. 1). An ttempt was made to extract a summed angular istribution of all of these fluctuations between 4.5 nd 5.0 MeV to see if the integrated yield exhibited n $l=6$ distribution. This effort was inconclusive ossibly because of the presence of many other eak non-$i_{13/2}$ transitions in this region of the pectrum. Therefore, more sensitive experiments re required to locate the $|^{210}\mathrm{Bi}(9^-)\otimes i_{13/2}^{-1\nu}|$ conguration.

V. DISCUSSION

The configurational structure of the ^{210}Bi target state does permit the direct excitation of the $h_{9/2}$ ground state of ^{209}Bi via pickup of a $g_{9/2}$ neutron; however, only the region of excitation above 2.5 MeV in ^{209}Bi was explored in the present experiment. No other single-particle states of ^{209}Bi are expected to be strongly excited in the energy range studied in the present measurement and indeed no evidence is found for such excitations.

Since the structure of the ^{210}Bi target state is dominated by the $|h_{9/2}^{\pi},g_{9/2}^{\nu}|$ configuration, the (d,t) reaction should preferentially excite the 2p-1h states of ^{209}Bi possessing the $\{|h_{9/2}^{\pi},g_{9/2}^{\nu}|_{9^-}$ $\otimes(l_j)^{-1\nu}\}$ configuration in their wave functions. The present results, therefore, provide an extremely sensitive test of the microscopic or shell model description of ^{209}Bi.

The lowest level in ^{209}Bi excited in the present $^{210}\mathrm{Bi}^{m}$ experiment is the 2.741 MeV level. This level has been identified in several experiments[4,6-9,13-17] as the spin $\frac{15}{2}^+$ member of a septuplet of states based upon the coupling of an $h_{9/2}$ proton to the 3^- core state of ^{208}Pb at 2.615 MeV. This latter model assumes that the coupling between the valence particle and the core vibration is weak and thus neglects the microscopic structure of the core state. From the $l=1$ nature of the angular distribution shown in Fig. 2 and total angular momentum coupling considerations, the excitation of this level must proceed via pickup of a $p_{3/2}$ neutron. The spectroscopic factor associated with the transition to this level provides a measure of the amplitude of the $\{|h_{9/2}^{\pi},g_{9/2}^{\nu}|_{9^-}$ $\otimes p_{3/2}^{-1\nu}\}$ configuration in the wave function of this level. On the basis of the weak-coupling model and the random-phase approximation (RPA) wave functions for the ^{208}Pb 3^- state calculated by Gillet *et al.*,[32] it is possible to derive a theoretical value for the spectroscopic factor. With an amplitude for the $|g_{9/2}^{\nu},p_{3/2}^{-1\nu}|$ component in the ^{208}Pb 3^- wave function of 0.42 and employing Racah coefficients to recouple the microscopic orbitals (see Ref. 9), it can be shown that

$$|\langle |h_{9/2}^{\pi},g_{9/2}^{\nu}|_{9^-}\otimes p_{3/2}^{-1\nu}|^{208}\mathrm{Pb}(3^-)\otimes h_{9/2}^{\pi}\rangle_{15/2}|^2=0.147\,.$$

This overlap squared times the statistical factor of $(2J_f+1)/(2J_i+1)$, where J_i and J_f are the target and final state spins, respectively, leads to a weak-coupling model prediction of 0.123 for the spectroscopic factor for the $\frac{15}{2}^+$ state. This result is in excellent agreement with the measured value of 0.165 determined for the 2.741 MeV level.

The next three levels strongly excited in the $^{210}\mathrm{Bi}^{m}(d,t)$ experiment are identified as members of the $|^{210}\mathrm{Bi}(9^-)\otimes p_{1/2}^{-1\nu}|$ multiplet. In Ref. 3 the spin assignments for these levels (at 2.987, 3.154, and 3.212 MeV) are given as $\frac{19}{2}^+$, $\frac{17}{2}^+$, and $\frac{17}{2}^+$, respectively. These assignments are consistent with the spin-parities allowed for the $|^{210}\mathrm{Bi}(9^-) \otimes p_{1/2}^{-1\nu}|$ configuration and are supported by the present experimental results. It is important to note that these spins are in disagreement with spins derived for these same levels in several direct inelastic scattering measurements on ^{209}Bi. In these studies[13-15] a weak-coupling model based on the coupling of an $h_{9/2}$ proton to the 5^- state of ^{208}Pb was assumed. There are ambiguities inherent in this method of determining spins and the present results strongly suggest that some of the spins derived in these studies[13-15] are incorrect. The spin of $\frac{19}{2}^+$ for the 2.987 MeV level has also been confirmed by the γ-branching observed in the $^{208}\mathrm{Pb}(^6\mathrm{Li},\alpha 2n\gamma)$ reaction.[33]

The existence of two $\frac{17}{2}^+$ levels is experimentally supported by the strong excitation of each of these levels both in inelastic scattering experiments[4] and in the present $^{210}\mathrm{Bi}^m(d,t)$ measurement. Since only one $\frac{17}{2}^+$ state should be strongly populated in the present experiment via pickup from the $p_{1/2}$ orbital, the excitation of a second $\frac{17}{2}^+$ indicates admixture of the $|^{210}\mathrm{Bi}(9^-) \times p_{1/2}^{-1\nu}|$ configuration with another configuration. Indeed, the calculations of Ref. 3 predict almost complete admixture of the $|^{210}\mathrm{Bi}(9^-) \otimes p_{1/2}^{-1\nu}|_{17/2^+}$ and $|^{210}\mathrm{Bi}(8^-) \otimes p_{1/2}^{-1\nu}|_{17/2^+}$ configurations. In these calculations the microscopic 2p-1h structure of ^{209}Bi was derived for configurations involving the $g_{9/2}$, $h_{9/2}$, and $p_{1/2}$ orbitals by considering the individual two-body interactions between the various particles and holes. The theoretical energies and spectroscopic factors deduced from the calculated wave functions as expressed in the ^{210}Bi representation are compared with the experimental results for the 2.987, 3.154, and 3.212 MeV levels in Table III. In view of the restricted model space considered, the theoretical results provide a remarkable reproduction of the experimental energies and spectroscopic factors and support an interpretation of these levels in terms of their 2p-1h structure. Weak-coupling calculations have been performed by Arita and Horie[12] in which the levels in the energy region from 3.0 to 3.5 MeV in ^{209}Bi are interpreted as members of a multiplet built on the coupling of an $h_{9/2}$ proton to the 5^- state of ^{208}Pb. In marked contrast to the microscopic calculations, the weak-coupling calculations are not able to account for either the experimental energies or the fragmentation of the $\frac{17}{2}^+$ member of the multiplet. Arita and Horie also present a shell model analysis which more accurately accounts for the energies of the $\frac{19}{2}^+$ and lowest $\frac{17}{2}^+$ states but fails to predict the presence of a second $\frac{17}{2}^+$ state.

TABLE III. Comparison of theoretical and experimental results for $[^{210}\mathrm{Bi}(9^-) \otimes p_{1/2}^{-1\nu}]$ states in ^{209}Bi.

Experiment[a]			Theory[b]	
Energy (MeV)	J^π	$S_{p_{1/2}}$	Energy (MeV)	$S_{p_{1/2}}$
2.987	$\frac{19}{2}^+$	0.98	2.892	1.053
3.154	$\frac{17}{2}^+$	0.61	3.171	0.495
3.212	$\frac{17}{2}^+$	0.48	3.264	0.452
		2.07		2.000

[a] From Table I.
[b] From Cleary *et al.*, Ref. 3.

VI. CONCLUSION

The $|^{210}\mathrm{Bi}(9^-) \otimes (l_j)^{-1\nu}|$ configurational structure of ^{209}Bi was examined by means of the $^{210}\mathrm{Bi}^m(d,t)$ reaction. Twenty-eight levels from 2.7 to 6.0 MeV excitation energy in ^{209}Bi are noted as having parentage in the 9^- state of ^{210}Bi. Based on the triton angular distributions and the unperturbed energies of the single-hole states derived from ^{207}Pb, the neutron hole structure for all of the strongly excited levels was suggested. These results are summarized in Table I. A comparison of the total spectroscopic strength and the energy centroids for the various hole state transitions fo $^{210}\mathrm{Bi}^m(d,t)$ and $^{208}\mathrm{Pb}(d,t)$ reveals that most of the $p_{1/2}$, $f_{5/2}$, and $p_{3/2}$ transition strengths have been identified. The existence of a total of 20 states is predicted from coupling the ^{210}Bi 9^- state to the $p_{1/2}$, $f_{5/2}$, $p_{3/2}$, and $f_{7/2}$ neutron hole orbitals. Since experimentally only 25 levels are associate with these neutron hole transitions and because the transitions to these levels account for approximately 70% of the expected hole strength, the fragmentation of strength caused by the presence of the extra-core neutron and proton is not large.

It is of course clear from Table II that ~60% of the $f_{7/2}$ and ~30% of the $f_{5/2}$ neutron hole strength have not been observed. Some fraction of the $f_{7/2}$ strength could lie above the 6.0 MeV excitation energy which was the upper limit of this experiment. The intrinsically weaker cross section fo the $l=3$ vs $l=1$ strength could result in some mi assignment of strength through the presence of unresolved transitions and the existence of singl transitions with mixed l transfers. Within the limits of the present data, some $l=3$ strength could be present in some of the angular distributions identified as $l=1$ transitions and thus be u accounted for. While such situations would affec the total $l=3$ strength, it would have little effec on the assignment of $l=1$ strength. Since the energy centroids lie quite close to the unperturbed values, it is probable that the loss of strength through mixed or unresolved transitions is small. Finally, the missing strength could well be an indication of the breakdown of the simple description of the levels of ^{209}Bi in terms of the $|^{210}\text{Bi}(9^-) \otimes l_j^{-1\nu}|$ configuration. In this instance, the transition strength would be distributed over many more transitions than the 6 for the $f_{5/2}$ and the 8 for the $f_{7/2}$ transfers expected on the basis of angular momentum coupling. Considering the 3.0 μg/cm^2 target thickness, it is possible that such weak transitions would not be observed above the background in the present spectra. Indeed, in the light of the great density of levels in ^{209}Bi above an excitation energy of 3.0 MeV,[34] it is surprising that the description of ^{209}Bi in terms of the coupling of a neutron hole to the 9$^-$ state of ^{210}Bi works as well as it does in explaining the results from our measurements.

Transitions involving transfer of an $i_{13/2}$ neutron are not seen in the present experiment. This is consistent with the relatively weak cross section observed for this transition in the ^{208}Pb(d,t) reaction[28] and with the prediction that this small transition strength should be distributed over a minimum of 14 states arising from the $|^{210}\text{Bi}(9^-) \otimes i_{13/2}^{-1\nu}|$ configuration.

Finally, the excitations of the 2.987, 3.154, and 3.212 MeV levels in the present measurement by transfer of a $p_{1/2}$ neutron are consistent with the spin assignments of $\frac{19}{2}^+$, $\frac{17}{2}^+$, and $\frac{17}{2}^+$, respectively, given in Refs. 3 and 4, and in disagreement with the assignments of Refs. 13–15 in which a weak-coupling model was assumed in the spin determination. Indeed, a comparison of the spectroscopic factors and energies predicted by the microscopic shell model with the experimental results for these three levels strongly supports the 2p-1h description of the levels in this energy region.

ACKNOWLEDGMENTS

We would like to thank Bob Leonard for the fabrication of the ^{210}Bi^m target, Dr. Lee Ponting, Dr. Lance McVay, and Dr. Charles McGuire for assistance during the experiment, and Dr. John Philpott and Dr. Roger Griffioen for very helpful suggestions. The assistance of Dr. Karl Erb is also gratefully acknowledged. This work was supported by the U. S. Department of Energy under Contract No. EY-76-C-02-3074 and by the National Science Foundation under Grant No. PHY77-12876.

---

*Present address: Oak Ridge National Laboratory, Oak Ridge, Tenn. 37830.

†Present address: Malden Public Schools, Malden, Mass. 02148.

[1] N. Stein, in *Proceedings of the International Conference on Properties of Nuclear States, Montreal, 1969*, edited by M. Harvey, R. Y. Cusson, J. S. Geiger, and J. M. Pearson (Presses de l'Universite de Montreal, Montreal, 1969), p. 337.

[2] J. S. Lilley and N. Stein, Phys. Rev. Lett. 19, 709 (1967); B. H. Wildenthal, B. M. Preedom, E. Newman, and M. R. Cates, *ibid.* 17, 960 (1967); R. Woods, P. D. Barnes, E. R. Flynn, and G. J. Igo, *ibid.* 19, 453 (1967); J. Bardwick and R. Tickle, Phys. Rev. 171, 1305 (1968); C. Ellegaard and P. Vedelsby, Phys. Lett. 26B, 155 (1968); C. Ellegaard, B. Patnaik, and P. D. Barnes, Phys. Rev. C 2, 2450 (1970).

[3] T. P. Cleary, N. Stein, and P. R. Maurenzig, Nucl. Phys. A232, 287 (1974).

[4] T. P. Cleary, N. Stein, W. D. Callender, D. A. Bromley, J. P. Coffin, and A. Gallmann, Nucl. Phys. A232, 311 (1974).

[5] P. D. Barnes, E. Romberg, C. Ellegaard, R. F. Casten, O. Hansen, T. J. Mulligan, R. A. Broglia, and R. Liotta, Nucl. Phys. A195, 146 (1972).

[6] J. C. Hafele and R. Woods, Phys. Lett. 23, 579 (1966).

[7] J. W. Hertel, D. G. Fleming, J. P. Schiffer, and H. E. Gove, Phys. Rev. Lett. 23, 488 (1969).

[8] R. A. Broglia, J. S. Lilley, R. Perazzo, and W. R. Phillips, Phys. Rev. C 1, 1508 (1970).

[9] J. P. Coffin, N. Stein, T. P. Cleary, C. H. King, and D. A. Bromley, Nucl. Phys. A181, 337 (1972).

[10] B. R. Mottelson, in *Proceedings of the International Conference on Nuclear Structure, Tokyo, 1967*, edited by J. Sanada, J. Phys. Soc. Japan, Suppl. 24, 87 (1968).

[11] I. Hamamoto, Phys. Rep. 10, No. 2, 63 (1974).

[12] K. Arita and H. Horie, Nucl. Phys. A173, 97 (1971).

[13] G. Francillon, Y. Terrien, and G. Vallois, Phys. Lett. 33B, 216 (1970).

[14] J. Ungrin, R. M. Diamond, P. O. Tjøm, and B. Elbek, Mat. Fys. Medd. Dan. Vid. Selsk. 38, No. 1 (1971).

[15] W. T. Wagner, G. M. Crawley, and G. R. Hammerstein, Phys. Rev. C 11, 486 (1975).

[16] M. B. Lewis, C. D. Goodman, and D. C. Hensley, Phys. Rev. C 3, 2027 (1971).

[17] T. P. Cleary, W. D. Callender, N. Stein, C. H. King, D. A. Bromley, J. P. Coffin, and A. Gallmann, Phys. Rev. Lett. 28, 699 (1972).

[18] R. Leonard, R. L. Ponting, and R. K. Sheline, Nucl. Instrum. Methods 100, 459 (1972).

[19] Y. E. Kim and J. O. Rasmussen, Nucl. Phys. 47, 184 (1963).

[20] J. Vary and J. N. Ginocchio, Nucl. Phys. A166, 479 (1971).

[21] G. H. Herling and T. T. S. Kuo, Nucl. Phys. A181, 113 (1971).

[22] J. R. Erskine, W. W. Buechner, and H. A. Enge, Phys. Rev. 128, 720 (1962).

[23] J. J. Kolata and W. W. Daehnick, Phys. Rev. C 5, 568 (1972).

[24] C. H. Cline, W. P. Alford, H. E. Gove, and R. Tickle, Nucl. Phys. A186, 273 (1972).

[25] H. T. Motz, E. T. Jurney, E. B. Shera, and R. K. Sheline, Phys. Rev. Lett. 26, 854 (1971).

[26] T. R. Canada, R. A. Eisenstein, C. Ellegaard, P. D. Barnes, and J. Miller, Nucl. Phys. A205, 145 (1972).

[27] D. Proetel, F. Riess, E. Grosse, R. Ley, M. R. Maier, and P. von Brentano, Phys. Rev. C 7, 2137 (1973).

[28] R. A. Moyer, B. L. Cohen, and R. C. Diehl, Phys. Rev. C 2, 1898 (1970).

[29] D. G. Kovar, C. K. Bockelman, W. D. Callender, L. J. McVay, C. F. Maguire, and W. D. Metz, Wrigh Nuclear Structure Laboratory Internal Report No. 49, 1970 (unpublished).

[30] G. Muehllehner, A. S. Poltorak, W. C. Parkinson, and R. H. Bassel, Phys. Rev. 159, 1039 (1967).

[31] P. D. Kunz, computer code DWUCK, University of Colorado, 1969 (unpublished).

[32] V. Gillet, A. M. Green, and E. A. Sanderson, Nucl. Phys. 88, 321 (1966).

[33] J. R. Beene, O. Häusser, T. K. Alexander, and A. B McDonald, Phys. Rev. C 17, 1359 (1978).

[34] M. J. Martin, Nucl. Data Sheets 22, 545 (1977).

PHYSICAL REVIEW C VOLUME 21, NUMBER 6 JUNE 1980

Global optical model potential for elastic deuteron scattering from 12 to 90 MeV

W. W. Daehnick, J. D. Childs,* and Z. Vrcelj
Nuclear Physics Laboratory, University of Pittsburgh, Pittsburgh, Pennsylvania 15260

(Received 21 January 1980)

A set of about 4000 data points has been used in a global search for a general optical model parameter prescription. This potential for deuteron-nucleus scattering was confined to remain within the range given by folding model calculations. The data set spans the energy range from 11.8 to 90 MeV and includes many targets ranging in mass from ^{27}Al to ^{238}Th. The set includes 50 reaction cross sections, 13 angular distributions for vector polarization at and above 15 MeV, and 103 angular distributions for elastic scattering. A successful 11-parameter potential of the conventional form fits all data analyzed to about 18% rms. Two of these parameters, V_R and a_I, are functions of proton number and target mass, while five (V_R, a_o, W_S, W_D, V_{LS}) are smooth functions of bombarding energy. The remainder (r_o, r_I, r_c, r_{LS}, a_{LS}) are constants. A simple functional dependence for $a_I(A,Z)$ approximately reproduces the rapid changes in $\sigma(\theta)$ found experimentally for nuclei at or near neutron shell closure. A comparison with earlier work suggests that the optical model analyses furnish the rms radii for the real and imaginary potentials with little ambiguity. General agreement but with a somewhat larger scatter (10%) is also found for the real and the imaginary volume integrals deduced. However, little consistency is seen for the imaginary volume integral if the bombarding energy is below 15 MeV. The rms radii and volume integrals have a small but distinct energy dependence. It was found that the 11-parameter potential occasionally has difficulty delivering good simultaneous fits for cross sections and vector polarizations. This situation was improved by the addition of a small, three-parameter imaginary spin-orbit term, which in our global prescription required short range and very small diffuseness.

[NUCLEAR REACTIONS $A(d,d)A$ for $27 \leq A \leq 238$, $11.8 \leq E \leq 90$ MeV. Optical model analysis. Deduced: global optical model parameter prescriptions, real and imaginary volume integrals, and rms radii.]

I. INTRODUCTION

The understanding of deuteron-nucleus scattering has benefited greatly from the use of the folding ideas introduced by Watanabe[1] and from subsequent refinements of this approach.[2-7] More complicated effects like deuteron breakup, distortions of the internal wave functions, the Pauli principle, and nonlocality have been addressed in the more recent theoretical studies.[3-15] As a result, folding considerations have effectively removed the earlier discrete ambiguities for the real potential V_R described by Drisko and others[16,17] and have limited the ranges for the optical model parameters r_0, a_0, and r_I, which may be considered physically meaningful. This in turn greatly reduces the remaining continuous ambiguities in optical model fits to elastic scattering data. The nonlocality effects encountered, particularly in the treatment of deuteron breakup effects, indicate some energy dependence not only for the corresponding optical potential depths,[3-5] but also for such geometric parameters as radii and diffusenesses. However, the transition from he computed nonlocal folding potentials to equivalent energy dependent local ones is difficult. Some folding calculations have been compared directly to data sets for limited energy ranges,[5,6] and fair agreement has been found at low energies where Coulomb effects are important or predominate. Other studies[14,8] make a direct comparison of folding calculations with data for a specific target (^{58}Ni) for deuteron energies up to 80 MeV. The agreement is quite acceptable; however, it is not yet of a quality which is expected routinely from typical optical model fits, nor, as we wish to show in this paper, of the quality obtainable from a global optical model prescription for a wide range of target mass and deuteron energy.

The difficulties underlying folding calculations have several sources. Austern[13] points out that the results of the so-called "adiabatic three-body" approach (e.g., Ref. 3) in some cases differ appreciably from a more rigorous three-body treatment. Another uncertainty arises from the use of phenomenological nucleon-nucleus potentials in the folding integrals. Although the theoretical construction of nucleon-nucleus potentials is considerably further advanced than that for complex projectiles (e.g., Refs. 18 and 19), it has not yet reached the state where they can fully supplant empirical potentials. For instance, they still inadequately predict the energy dependence for the real volume integral for scattering of protons above 60 MeV.[20] Available phenomenological proton-nucleus po-

© 1980 The American Physical Society

tentials[30-32] are very successful in their respective energy ranges. Nevertheless, they differ in important parameters such as real radius (1.15 to 1.25 fm), imaginary radius (1.25 to 1.5 fm), spin-orbit geometry, etc. This variation will necessarily be reflected in the folded deuteron potentials.

There remain many calculations, for instance those in the distorted wave Born approximation (DWBA), where one would be inclined to turn to empirical potentials for realistic deuteron phase shifts. Often consistency in the DWBA analysis requires also that even those phase shifts poorly determined in elastic scattering (but important in other reactions) be obtained in a systematic and optimal way.[23] These requirements often have been met by a good global optical model prescription. To the extent that such potential prescriptions fit data well they also correlate and systematize large amounts of empirical knowledge. Some historical average deuteron parameter sets (e.g., those of Refs. 17, 24, 25, 6, and 26) have proven very useful for these reasons. Their major shortcoming, as we found, is that an extrapolation to energies outside their data bases is not very successful. Hence the inclusion of higher energy data in a broad based analysis is called for. Our goal has been a systematic optical model description of elastic scattering for deuteron energies above 11.8 MeV where adequate data exist, i.e., up to 90 MeV, and over as wide a mass range as experience made seem advisable. We found that in general it was not difficult to constrain our parameters to values reasonable in the light of the available folding calculations.

II. OPTICAL MODEL CALCULATIONS FOR ELASTIC DEUTERON SCATTERING

A. Prior work

A large number of deuteron scattering experiments has been reported in the literature[6,24-44] in the energy range of interest. In most of the studies listed a limited number of isotopes was investigated at one particular energy in the region from 11.8 to 90 MeV. Concurrent or subsequent optical model[45] analyses were successful in fitting subsets of the known data with reasonable parameters.[5,6,16,17,24-26,46-48] A complete compilation of (d,d) optical model work before 1976 is given in Ref. 49. Here a brief summary of the earlier results may suffice. In optical model studies it has been customary to use a complex central potential of the Woods-Saxon shape and its derivatives, a spin-orbit term of the Thomas form, and a Coulomb term. Hence the optical potential has been written as

$$V(r) = -V_R f(r, r_0, a_0) + i4a_I W_D \frac{d}{dr} f(r, r_I, a_I)$$

$$-iW_S f(r, r_I, a_I)$$

$$+V_{LS}\left(\frac{\hbar}{m_\pi c}\right)^2 (\vec{L}\cdot\vec{S})\frac{1}{r}\frac{d}{dr} f(r, r_{LS}, a_{LS}) + V_{\text{Coul}},$$

where the Woods-Saxon well f is given by

$$f(r, r_i, a_i) = \left[1 + \exp\left(\frac{r - r_i A^{1/3}}{a_i}\right)\right]^{-1};$$

A is the target mass number. The square of the pion Compton wavelength $(\hbar/m_\pi c)^2 = 2.00\ \text{fm}^2$ is a conventional normalization factor. The Coulomb term is taken as the potential for a uniformly charged sphere of radius $R_c = r_c A^{1/3}$.

The search codes can vary any specified combination of potential parameters such that χ^2, a quality of fit quantity, is optimized. This quantity is defined as

$$\chi^2 = \frac{1}{N}\sum_{i=1}^{N}\left(\frac{\sigma_i^{th} - \sigma_i^{exp}}{\Delta\sigma_i^{exp}}\right)^2 .$$

The quantities V_i, W_i, r_i, and a_i define four potential and six geometric parameters that can be varied in a fitting calculation. The Coulomb radius $R_c = r_c A^{1/3}$ is an eleventh parameter which is not very sensitive and rarely changed. More recently a tensor potential has been added to $V(r)$, and V_{LS} has been permitted to be complex (e.g., Refs. 50, 5, and 43). In most searches fewer than ten parameters are varied, and this has proved adequate to give an excellent reproduction of deuteron scattering below 90 MeV. However, a glance at the compilation of Ref. 49 shows a great diversity of "best-fit" parameters. Perey and Perey[17] in their pioneering 1963 study were able to find several equivalent families of similar best-fit parameters which gave good fits to data from 11.8 to 27 MeV. They also deduced an averaged parameter set (without spin-orbit term) which fit their entire data set to 25–30% on the average (rms deviation). In 1968 this low energy study was supplemented by Hinterberger *et al.*[24] by the analysis of their 52 MeV data. Taking into account the results of the 34 MeV study by Newman, Becker, and Preedom at Oak Ridge,[25] Hinterberger was able to propose an averaged parameter set, including a spin-orbit term which provided fits of similar quality to Perey's for the wider energy range of 12 to 52 MeV. Checking with our corresponding data set we find about 28% for the average root mean square deviation. Both studies achieved the wide range of usefulness of their parameter sets by determining and parametrizing the A and E dependence in their best-fit parameters and making this a part of their global parameter prescription. Lohr and Haeberli[6] proposed an average parameter set for their 9–13-MeV scattering and polarization data. Their prescription gave no energy dependence and proposed a different A dependence for the imaginary term. It produced very good fits to the low energy polarization measurements. We find, however, that their prescription is not very successful outside the energy range for which it was constructed. A similar restriction applies to the averaged parameter set of Perrin *et al.* for their 29-MeV scattering and polarization data,[26] and to a number of earlier studies. In 1973 we began compiling a comprehensive data set which included a wide range of bombarding energies and was meant to be analyzed with the global search code GENOA, written by Perey.[51] As a first step an attempt was made to resolve experimental discrepancies[17] for the early 15-MeV data by careful measurement of 23 angular distributions for medium weight and heavy targets at 17 MeV.[38] In the subsequent global analysis of the 17-MeV data it was found that very acceptable fits could be obtained with a single set of parameters.[52] An extension of this parameter set to higher and lower energies (12–52 MeV) also proved successful after (a linear) energy dependence in the V and W parameters was introduced.[52,53] When (d,d) scattering data in the 80–90-MeV energy range[39–41] were compared with the early prescriptions, it was found that the potentials of Refs. 52 and 53 reproduced the higher energy data in a qualitative way. Typical rms deviations were ±40%. This was better than for other available global prescriptions, but much worse than the ±25% fits obtained for the data at 52 MeV and below.

B. Data sets for a global search

listorically, optical model best-fit parameters ve shown variations with beam energy E and rget mass A. It has also been noted from the ginning that good systematic fits at low energy 30 MeV) were very difficult to find for targets th $A<40$. Even at the higher energies of 60–90 eV it has been found[40,41] that scattering from ht targets such as ^{12}C and ^{24}Mg must be anazed with a coupled channels mechanism that kes explicit account of the strong inelastic attering channel. The search code GENOA ef. 51) will handle 1000 data points at a time, d it was decided to incorporate a carefully lected subset of all available data into the data sets for our global searches. Eliminated from consideration were all data for bombarding energies below 11.8 MeV and almost all data for targets lighter than aluminum ($A=27$). An exception was made for cross sections for energies at and above 80 MeV where elastic scattering data are scarce and where compound-elastic effects are unimportant. The existence of important two-step effects[40,41] was taken into consideration by weighting the ^{12}C and ^{24}Mg entries less than other data (i.e., at 50%). A similar, reduced weighting was used for a few targets of high deformation (^{232}Th and ^{238}U) if strong low-lying excited states were not resolved experimentally. It seemed advisable to not completely ignore such data because they could expand the mass range investigated down to $A=12$ and up to $A=238$. Generally, in our selection, the more systematic and more recent studies were preferred, especially if accurate numerical data had been published or could be obtained.

Included from the beginning were 21 angular distributions at 11.8 MeV from Heidelberg,[27] 23 angular distributions at 17 MeV from Pittsburgh,[38] 16 angular distributions at 34 MeV from Oak Ridge,[25] and 18 angular distributions at 52 MeV from Karlsruhe.[24] At later dates the global search sets were expanded by the inclusion of six vector polarization angular distributions at 15 MeV from Los Alamos,[54] five at 30 MeV from Grenoble,[55] and two at 79 MeV from Indiana.[43]

Most 80–90 MeV data[39–41,44] were not available in numerical form and had to be read off the graphs in the publications cited. Although done with care, this method introduced additional errors estimated at up to 10%. It was noticed that the near duplicate data available for ^{12}C and ^{27}Al had normalizations (see Refs. 39, 40, and 44) that disagreed by factors so far outside statistical or ordinary experimental uncertainties that one or the other of these early measurements had to be in error. In the absence of more objective criteria we looked for systematic (dis)-agreement at angles below 30° with global optical model parameters for other targets at similar energies. By this criterion the absolute ^{12}C normalization of Ref. 40 appeared in error. It was increased by a factor 1.58, whereas that of Ref. 39 was left unchanged. For ^{27}Al the normalization of the more recent study of Ref. 44 seems to be correct. It was left unchanged, but the ^{27}Al cross sections of Ref. 39 were renormalized by a factor 0.55. A smaller, but less trivial, systematic error seems to exist for the ^{58}Ni curve of the same study. This cross section was remeasured as part of a recent polarization study at the same energy.[42] After finding the expected disagreements with the earlier study, we excluded the older ^{58}Ni curve from our searches and used the new one. Hence the current 80–90-MeV set contains five angular distributions at 80 MeV from Orsay,[39] six angular distributions at 85–90 MeV from Julich,[40,41,44] and four angular distributions at 79–79.5 MeV from Indiana.[43]

The distribution in A and E of the data in our search sets is illustrated in Fig. 1. Thirteen of the 106 angular distributions are for vector polarization $P(\theta)$, $[P = (2/\sqrt{3})iT_{11}]$, the remainder for elastic cross sections. The total number of data points used is slightly below 4000. This number is somewhat lower than the total number of points available for the 106 angular distributions and results from the dropping of alternate points in overdetermined cross sections with little structure, mostly for In to Th at 11.8 MeV, where fits are easy to obtain and provide little information. The statistical errors for most data points are 1–2%, but always below 5%. Hence the errors significant for the global analysis are generally of a systematic nature (errors in absolute normalization and the uncertainty in the scattering angle θ for the higher energies). It appears that most data sets have systematic errors of about 10%. For the purpose of the global searches, we assigned equal (5 or 10%) errors to all data points at a given energy and treated them as if they were random. This assumption would be poor for the analysis of one individual angular distribution. However, for the entire set of 106 angular distributions it seems reasonable to assume that the cross section normalization errors and typical angle calibration errors have a random variation from one angular distribution to the next. Because of the scarcity of data near 80 MeV the high energy data (except ^{12}C and ^{24}Mg) were weighted twice as heavily as the low energy points. This intentional bias might lead to better fits in the 80–90-MeV region and slightly poorer ones at 52 MeV than with uniform weighting. Of course, as with any limited data set, we may still have unintentional biases in our search of which we have remained unaware.

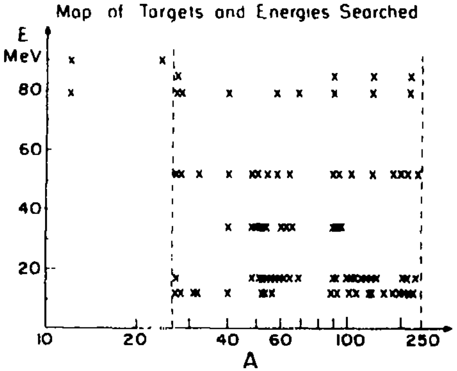

FIG. 1. Graphic display of the data set used in this study. Targets are indicated by their mass A. The E axis denotes the deuteron bombarding energy. Data with energies below 11.8 MeV were not included. The exclusion of data for targets with $A < 27$ at the lower energies is explained in the text. Of 106 angular distributions included, 13 are for vector polarization.

C. Search procedure

The typical search for our 4000 data points required five parallel GENOA runs. We tended to use five free global parameters at a time with five to six successive variations for good convergence. The CPU time at the Pittsburgh DEC1090 computers for such a search of the complete data set totals 36 min. This relatively modest cost permitted us to make many searches over a span of several years. Historically the following search procedure was followed. Starting with optical potentials closely analogous to those obtained from an adiabatic folding approach[5,2] individual best-fit parameters for all 17-MeV angular distributions were found. Generally, the variation of nine parameters was needed to obtain fits within the experimental accuracy over the full angular range (5° to 165°). Best-fit r_0 values for the 17-MeV data fell between 0.91 and 1.17. The ranges of the other best-fit parameters[38] were $92 < V_0 < 114$ MeV, $0.71 < a_0 < 0.96$, $8.7 < W_D < 16.7$, $1.27 < r_I < 1.46$, $0.64 < a_I < 0.86$, $5.63 < V_{so} < 13.5$, $0.7 < r_{so} < 1.4$, $0.3 < a_{so} < 1.85$. A similarly large variance is found for unconstrained best-fit parameters at 85 MeV, although here r_0 tends to stay above 1.15, a_0 above 0.81, and r_I below 1.30. All parameters were subject to continuous ambiguities which, however, had limited and differing ranges. We next restricted the geometric parameters to ranges consistent with the adiabatic folding models. In particular, real radius parameters below 1.1 fm and above 1.20 fm were not admitted in the searches. This restriction saved a lot of computer time and does not seem to have excluded above average fits. Similarly, only such V_R values were tried which would keep the real volume integrals within the range (300–450 MeV fm^3) predicted by folding calculations.

D. Global fits for 11.8-52-MeV differential cross section data

Because our version of GENOA cannot handle more than 30 angular distributions (or 1000 points) simultaneously for a given search, the data were first organized and searched on according to their deuteron beam energies. Each search started with a similar parameter prescription. The well converged parameter values were then plotted against energy to construct a general global formulation. Initially it was found that there was a very clear energy and A dependence in the depth of the real potential, as well as in the diffuseness of the imaginary potential. In analogy to earlier work,[17,24,6] we introduced the parametrization $V_R = V_0 - a_2 E + a_3 Z/A^{1/3}$ and $a_I = a_8 + a_9 A^x$. It was found, particularly from the analysis of the 17–52-MeV data, that with the constraint of global parameters, $x = \frac{1}{3}$ provided the best approximation.

From the beginning of the analysis it was recognized that any global fits to deuteron elastic data on a number of different targets would be hampered by target-dependent structure effects. In particular, for our 17-MeV cross section data we had observed that for a fixed real geometry the imaginary geometry parameters were noticeably affected by the fullness of the shells. With hopes of isolating the one imaginary potential parameter that could be correlated most clearly with shell effects, each of the three parameters (W_D, r_I, and a_I) was allowed to go free as the other two parameters were kept global. The only parameter of the three showing any striking and simple target structure dependence was the imaginary diffuseness a_I.

A number of attempts were made to correlate imaginary geometry behavior with known structure effects. At various times, we considered in turn the deformation parameter β, the $BE(2)$ values,[33] the ground state mass excesses, and the excitation energies of the first 2^+ state. Some systematic correlation with the imaginary potential was observed, but no single functional dependence could be used for a wide mass and energy range.

The observed behavior of a_I near closed shells ed us to the introduction of a shell structure magic number) term in the imaginary diffuseness a_I,

$$a_I = a_{I_0} - k \sum_i \exp\{-[(N - M_i)/\delta]^2\},$$

where k is the strength of the shell effect (~0.05) at closed *neutron* shells, δ is the "width" of the shell term around the closed shell in units of neutron number, and the index i designates the magic numbers (so that $M_i = 8$, 20, 28, 50, 82, and 126). This self-contained formula proved adequate in accounting for the more pronounced structure effects in our subsequent fits.

The neutron shell closure behavior was a very striking property of the 17-MeV data as well as the 11.8-MeV data and the 34-MeV data. The 52-MeV data displayed less of this kind of magic neutron shell systematics. It is plausible that such shell effects would be important at lower energies but become less prominent as the bombarding energy is raised. Attempts were made to incorporate a similar structure term which would reduce a_I at the closed proton shells. However, when the data base was expanded from 17 MeV to include the other energies, the global searches rejected such a term.

Many of our subsequent global searches were performed on three data sets organized by neutron number, i.e., one set contained only targets at all energies with magic neutron numbers, a second set included targets whose neutron numbers are "close" to a magic number ($1 \leq |N - N_{\text{magic}}| \leq 5$), and a third set included targets whose neutron numbers are "far" from a magic number ($|N - N_{\text{magic}}| > 5$).

Initially the fitting was performed with only a surface-peaked imaginary potential W_D. Since one expects volume contributions to the absorption to become more significant with increasing energy,[18] it was logical to include a volume imaginary potential which would share the same geometry as the surface term. It was further hoped that by letting these imaginary depths become energy dependent, as the folding models predict, the energy term in the imaginary diffuseness could be eliminated. In general, one would prefer that geometric parameters like a_I would be constant with energy.

Searches were made at each energy with an energy-independent a_I and fixed r_I. The resulting imaginary depths showed the expected behavior: the surface term dominated at low energies while the volume term became more important at 52 MeV and was most important at 85 MeV. Although the inclusion of energy-dependent volume and surface imaginary terms was essential for good fits over a reasonable energy range, the precise relative strengths and energy dependences were *not* well established by the data. It was observed that the change with E from surface to volume absorption could be made more or less gradual without any considerable change in the fits. The inclusion of the 80–90-MeV data helped reduce this ambiguity considerably.

Three potentials were obtained from fits to the 11.8–52-MeV differential cross section data[32] which we label A, B, and C. They are distinguished by their (fixed) real radius values of 1.1, 1.15, and 1.2 fm, respectively. They are listed in Table I, along with the other early prescriptions for global potentials. The quality of their

TABLE I. A comparison of global optical parameter prescriptions used previously. The potential names indicate the year the prescription was first available, names of authors, and energy range of the data base which was fit, or to which it was adaptable. The listing is for comparison purposes only. For most purposes these potential forms are superseded by those listed in Table III. See text and Table II. A = mass number, Z = proton number, N = neutron number, $\alpha = -(E/91.7)^2$, $\mu_i = [(M_i - N)/2]^2$, where M_i = magic number (8, 20, 28, 50, 82, 126). E = deuteron laboratory energy in MeV. CD = Ref. 52, VRC = this work.

Name	V_R (MeV)	r_0 (fm)	a_0 (fm)	W_S (MeV)	W_D (MeV)
(63) Perey 11.8–27 MeV	$81 - 0.22E$ $-2.0ZA^{-1/3}$	1.15	0.61	0	$14.4 + 0.24E$
(68) Hinterberger 34–52 MeV	$79 - 0.35E$ $-1.5ZA^{-1/3}$	1.25	0.81 $-0.024A^{1/3}$	0	13.0
(74) Lohr and Haeberli 9–13 MeV	$91.13 - 2.2ZA^{-1/3}$	1.05	0.86	0	$218A^{-2/3}$
(76) Perrin with $V(E)$ 9–34 MeV	$(88.04 - 0.26E)$ $-1.77A^{-1/3}$	1.13	0.80	0	12.0
(76) CD, 11.8–52 MeV, A	$93.4 - 0.235E$ $+1.2ZA^{-1/3}$	1.10	0.825	$0.08(E - 17)$	$14.58 - 0.07E$
(76) CD, 11.8–52 MeV, B	$89.05 - 0.23E$ $+1.0ZA^{-1/3}$	1.15	0.79	$0.063(E - 17)$	$14.9 - 0.066E$
(76) CD, 11.8–52 MeV, C	$84.0 - 0.196E$ $+0.79ZA^{-1/3}$	1.20	0.751	$0.046(E - 17)$	$15.3 - 0.062E$
(76) CD, 11.8–52 MeV, D	$89.05 - 0.23E$ $+1.0ZA^{-1/3}$	1.15	0.78	$0.063(E - 17)$	$14.9 - 0.066E$
(76) CD, 11.8–52 MeV, E	$89.05 - 0.23E$ $+1.0ZA^{-1/3}$	1.15	0.79	$0.063(E - 17)$	$14.9 - 0.066E$
(79) VRC, 11.8–90 MeV, C' (relativistic kinematics)	$86 - 0.285E$ $+0.88ZA^{-1/3}$	1.20	0.755	$15.9(1 - e^{\alpha})$	$15.0e^{\alpha}$

Name	r_I (fm)	a_I (fm)	r_C (fm)	V_{LS} (MeV)	r_{LS} (fm)	a_{LS} (fm)	Data fitted
(63) Perey 11.8–27 MeV	1.34	0.68	1.15	0			$\sigma(\theta)$, σ_R
(68) Hinterberger 34–52 MeV	1.25	$0.51 + 0.076A^{1/3}$	1.30	6.0	1.25	0.81 $-0.024A^{1/3}$	$\sigma(\theta)$
(74) Lohr and Haeberli 9–13 MeV	1.43	$0.50 + 0.013A^{2/3}$	1.30	7.0	0.75	0.50	$\sigma(\theta)$, $P(\theta)$
(76) Perrin with $V(E)$ 9–34 MeV	$1.15 - 0.75A^{-1/3}$	$0.585 + 0.05A^{1/3}$	1.30	5.2	0.85	0.475	$\sigma(\theta)$, $P(\theta)$
(76) CD, 11.8–52 MeV, A	1.36	$0.414 + 0.088A^{1/3}$ $-0.031\sum_i e^{-\mu_i}$	1.30	7.3	0.98	1.0	$\sigma(\theta)$
(76) CD, 11.8–52 MeV, B	1.33	$0.443 + 0.082A^{1/3}$ $-0.034\sum_i e^{-\mu_i}$	1.30	7.1	0.98	1.0	$\sigma(\theta)$
(76) CD, 11.8–52 MeV, C	1.31	$0.478 + 0.075A^{1/3}$ $-0.044\sum_i e^{-\mu_i}$	1.30	6.8	0.98	1.0	$\sigma(\theta)$
(76) CD, 11.8–52 MeV, D	1.33	$0.528 + 0.064A^{1/3}$ $-0.025\sum_i e^{-\mu_i}$	1.30	5.7	1.10	0.55	$P(\theta)$, $\sigma(\theta)$
(76) CD, 11.8–52 MeV, E	1.33	$0.448 + 0.082A^{1/3}$ $-0.043\sum_i e^{-\mu_i}$	1.20	5.5	1.10	0.55	$\sigma(\theta)$, $P(\theta)$, σ_R
(79) VRC, 11.8–90 MeV, C' (relativistic kinematics)	1.31	$0.495 + 0.064A^{1/3}$ $-0.052\sum_i e^{-\mu_i}$	1.30	$\frac{9.73}{(1 - 0.0095E)^2}$	1.10	0.55	$\sigma(\theta)$

its to the 11.8–52-MeV data can be assessed by comparing Table II with Figs. 2–5.

The spin-orbit geometry for these potentials was held fixed to that predicted by a folding calculation.[5] However, with each potential, V_{LS} was allowed to vary. Differential cross section data do not, by themselves, accurately determine the spin-orbit potential. Nevertheless, such a potential was needed to help fit the high angle ross sections for many targets.

E. Fits of polarization data

In order to cross check and to better determine the parameters of the spin-orbit potential it was decided to use the available vector polarization data at and above 15 MeV.

First, we fitted the polarization data by themselves starting with the ($r_0 = 1.15$) potential B which used the folding prediction for the spin-orbit geometry, $r_{LS} = 0.98$ fm and $a_{LS} = 1.0$ fm. Letting the spin-orbit depth go free, the χ^2 mproved by a factor of 2 as V_{LS} settled on very ow values of 2.1 to 2.4 MeV. When all three pin-orbit parameters were allowed to vary, ven further improvements in χ^2 were obtained about 30%) as the spin-orbit radius r_{LS} increased to 1.1 fm, the diffusivity a_{LS} halved in alue to 0.55 fm, and the depth V_{LS} settled into the range of around 5.5 MeV. Next we included both the differential cross section sets *and* the 15- and 30-MeV polarization sets in the search. The resulting potential, known as potential D, is found in Table I. Potential D represents about a 15% increase in the total χ^2 for differential cross section data with an improvement by about a factor of 2 in the total χ^2 for polarization data, compared to the fits with potential B.

Up to this point, our polarization searches were done with a spin-$\frac{1}{2}$ formalism. [Comparisons of selected 12- and 17-MeV polarization predictions between spin-$\frac{1}{2}$ and spin-1 calculations had indicated remarkably little difference, except for the rescaling (by $\frac{4}{3}$) of the spin-orbit depth V_{LS} itself.] The 30-MeV (and 80-MeV) polarization predictions, however, displayed more significant differences between the two formalisms, primarily concerning the amplitude of oscillations, particularly for the heavier nuclei.

Hence, polarization searches for the higher energies were always checked (or redone) with a spin-1 formalism. Because the search code GENOA permits only spin-$\frac{1}{2}$ calculations, it was necessary to perform the searches either by doing a series of single-shot calculations using a spin-1 code (DWUCK) or by using the search

TABLE II. The success of several popular global prescriptions in fitting the current set of data is quantified in terms f χ^2 values found. These χ^2 values are tabulated below, together with χ^2 values of potentials presented in this paper. or $\sigma(\theta)$, $\chi^2 \approx 1$ means an rms data-theory difference of 10%; $\chi^2 \approx 4$ implies an rms difference of 20% between data and redictions. The names of the parameter sets indicate year of availability, author, energy range of expected validity, nd letter A–L label. As can be seen from Tables I and III, the potentials become more complicated towards the bottom f the list. The χ_{av}^2 values for fits to the vector polarization are approximate and are based on $\Delta P_i(\theta) \approx \pm 0.05$. General-, asymmetry data are more accurate. For most potentials the 15-MeV polarizations are fit poorly. [The situation is eversed for the (74) Lohr potential. Here the fits are very good with $\chi^2 \approx 3.4$ for the 15-MeV data, but close to 48 for he 30-MeV data. We were not able to generalize the Lohr potential with a function $V_R(E)$, as proved possible for the errin potential.] $(\chi^2)_{av} = (1/N)\sum_{i=1}^{N}[(\sigma_i^{th} - \sigma_i^{exp})/\Delta\sigma_i^{exp}]^2$; $\Delta\sigma_i = 0.1\sigma_i$; $\Delta P_i = 0.05$.

Deuteron energy Parameter sets	11.8 MeV	17 MeV	34 MeV	52 MeV	85 MeV	Pol. 15, 30 MeV	Pol. 80 MeV
Historical sets							
(63) Perey and Perey 11.8–27 MeV	5.3	10.1	(47.5)	(95)	(494)	no $L \cdot S$	no $L \cdot S$
(68) Hinterberger 34–52 MeV	4.65	6.6	10.8	8.9	(82.6)	16	(75)
(74) Lohr and Haeberli 9–13 MeV	2.04	12.1	(148)	(17 667)		20	(276)
(76) Perrin with $V(E)$ 9–52 MeV	4.3	4.9	14.9	(69.8)	(99.5)	7.5	(190)
(76) CD, 11.8–52 MeV, A	2.89	2.84	6.09	5.32	11.7	10	(106)
(76) CD, 11.8–52 MeV, B	3.06	2.75	6.07	5.31	11.6	9.0	(92)
(76) CD, 11.8–52 MeV, C	3.09	2.96	6.67	5.49	15.9	9.3	(87)
(76) CD, 11.8–52 MeV, D	3.16	3.51	5.99	6.82	25.8	5.2	(80)
(76) CD, 11.8–52 MeV, E	3.35	3.36	6.06	5.87	19.9	5.9	(53)
(79) VRC, rel, 11.8–90 MeV C'	3.49	3.08	7.70	6.84	4.28	9.2	(34)
Current-this work							
(79) DCV, rel, 11.8–90 MeV, F	2.46	2.57	5.54	4.00	2.9	6.8	3.9
(79) DCV, nonrel, 11.8–90 MeV, L	2.51	2.44	5.37	3.99	3.1	7.4	3.0

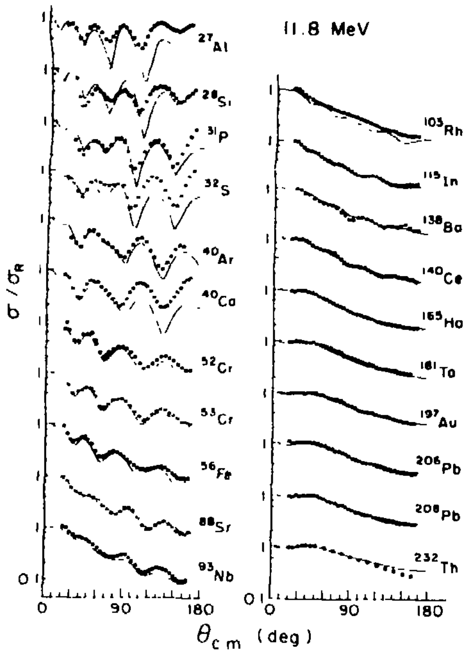

FIG. 2. *Comparison of the 11.8-MeV data* [$\sigma(\theta)_{exp}/\sigma_{Rutherford}$] of Ref. 27 with the predictions of the global potential L (Table III). Nearly identical agreement was obtained for potential F. Slightly better fits would be provided by the low energy potential of Lohr (Ref. 6) and slightly inferior fits are obtained from potentials A, B, C, D, E, and VRC. (See Table II for a quantitative comparison.) If allowance is made for the $\sigma/\sigma_{Rutherford}$ presentation it is seen that the difference between data and theory for targets up to ^{52}Cr is nearly independent of angle as might be expected from S-wave compound elastic scattering contributions. For ^{103}Rh and ^{232}Th inelastic cross sections to one or more low-lying excited states may be included in the data.

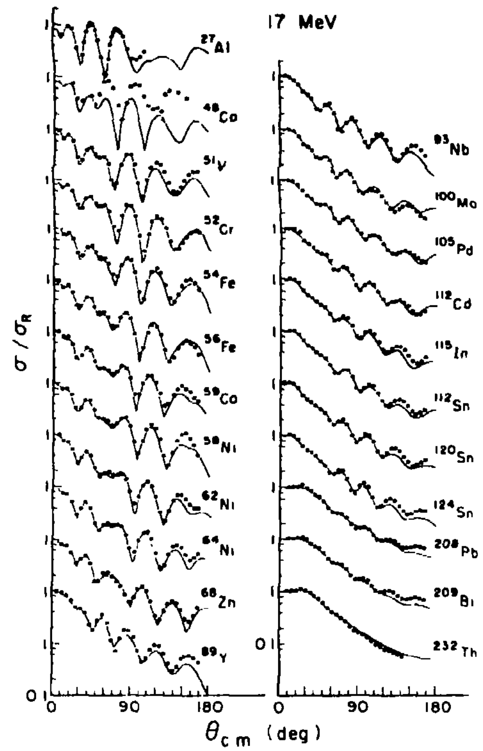

FIG. 3. Comparison of the 17-MeV elastic scattering data of Ref. 38 with the predictions of the global potential L. *Fits with potentials F and F' are nearly identical.* See Table II for a quantitative comparison of fits to these data by other global prescriptions.

code CUPID.[39] This modified global potential was then refit to the differential cross section data, which resulted in a slight readjustment of the structure term in the imaginary diffuseness a_I. In addition, setting $r_C = 1.2$ fm resulted in a slight change in the real depth V_R. This potential which fits differential cross sections and polarization data from 11.8 to 52 MeV was labeled potential E (see Table I). The quality of the polarization fits is similar to potential D, but it does a better job for the 52-MeV cross section data (see Table II).

F. Inclusion of 80–90 MeV data

An adequate set of 80–90-MeV cross sections was obtained fairly late in this study. The first 80-MeV polarization data did not become available until summer, 1979.[42] It then became apparent that none of the earlier global prescriptions produced good predictions at 80 MeV. The overview of Table II shows that our potentials A, B, and C gave agreement to within 35–45% (rms deviation), which falls far short of the quality of the fits at lower energy. A search on the "85-MeV" set starting with potentials B or C indicated the need for changes in a_0, r_I, and in the spin-orbit potential V_{LS}. As a minimum, V_{LS} had to be made energy dependent. It turned out that a reasonable extension of potential C was possible if relativistic kinematics were used in the computations. This potential has been named C' and is listed in Table I. Table II shows that potential C' extends the range of usefulness to 85 MeV at a modest cost in fit accuracy at the lower energies, but still fails to fit the 80-MeV polarization data.

Ultimately it was decided to take a second look at the energy dependence of critical parameters

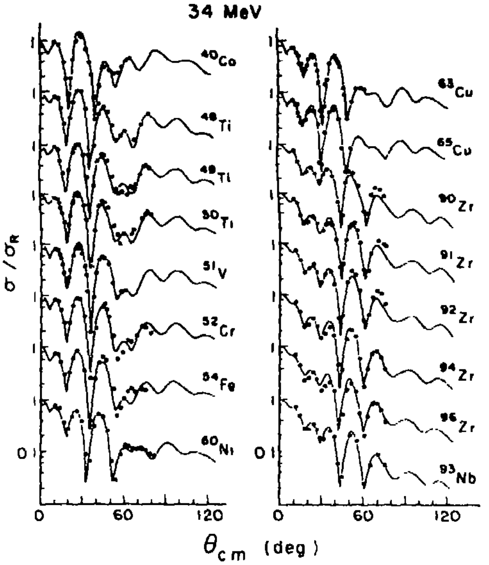

FIG. 4. Comparison of the 34-MeV data of Ref. 25 with the predictions of the global potential L. Fits with potentials F and F' are nearly identical. See Table II for a quantitative comparison with fits by other global prescriptions.

by refitting the E = const data sets at all energies, this time incorporating the polarization data from the beginning. The goal was to improve on all previous fits—admitting additional parameters if necessary. In this we retained our original criterion that additional (trial) parameters were kept only if they produced a χ^2 improvement above 10% for the total set. This last, but extensive search cycle resulted in potential F (for calculations with relativistic kinematics) and the very closely related potential L (for calculations with the nonrelativistic kinematics, which are used in most older DWBA codes). The newly introduced weak energy dependence in a_0 was essential for the significant improvement in fits over potentials A through E. The energy dependence in W (and in r_I for potential F) is somewhat less unique. The global potentials F and L are listed in Table III. The numerical χ^2 comparison with prior potentials is shown in Table II. A comparison of the predictions of potential L (in the nonrelativistic spin-1 formalism) with the experimental points of the full data set is shown in Figs. 2–8. The results of potential F would be visually almost indistinguishable from L and are not shown in the figures.

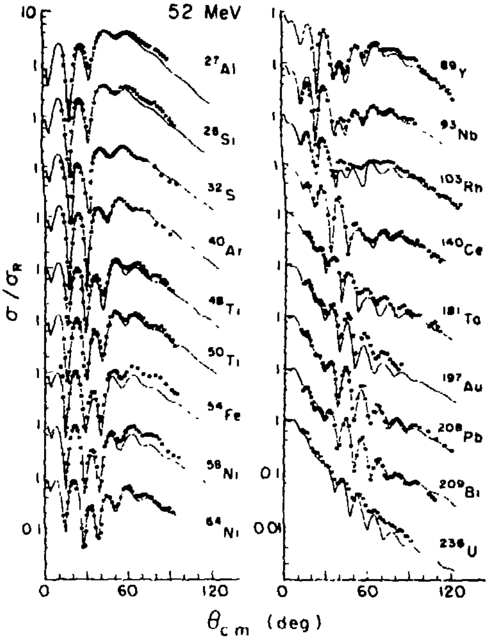

FIG. 5. Comparison of the 52-MeV data of Ref. 24 with curves from potential L. Curves from potentials F and F' are nearly identical. See Table II for comparison with other global prescriptions. For ^{103}Rh, ^{181}Ta, and ^{238}U low excited levels are included in the elastic peak and may distort the angular distributions at larger angles.

G. Unanswered questions concerning the reaction cross sections

Two comprehensive deuteron reaction cross section studies using attenuation techniques were performed at 22.4 MeV by Wilkens and Igo[57] and at 25 MeV by Mayo *et al.*[58] Predictions of potential L (which are very close to potentials A–F at 25 MeV) are shown with the σ_R data in Fig. 8.

This section outlines our unsuccessful attempt to better fit the reaction cross section data. The lettered potentials A–L give σ_R predictions for the lower energy (10–13 MeV) region which generally lie within the quoted experimental errors. (An exception is ^{12}C at 12.8 MeV, a very light target which we would not expect to fit well). However, a close look at the two surveys at 22.4 and 25 MeV indicates a systematic A dependence in the quality of fit. The predictions of potential L are good for low mass targets, but for the heavier masses there is a discrepancy between predictions and data, particularly with the 22.4-MeV data.

TABLE III. A listing of recommended global parameter prescriptions, which fit a wide range of deuteron scattering data. Potentials L and F are nearly equivalent in the range 15–85 MeV. Potential F' differs from F in having a complex spin-orbit term. The addition of the imaginary part (W_{LS}) provided a better fit primarily to polarization data. The F' parameters are tentative as only a small set of polarization data was available for this analysis. A = mass number, Z = proton number, $\beta = -(E/100)^2$, $\mu_i = [(M_i - N)/2]^2$, where M_i = magic numbers (8,20,28,50,82,126), N = neutron number, E = deuteron laboratory energy in MeV.

Potential name	V_R (MeV)	r_0 (fm)	a_0 (fm)	W_S (MeV)	W_D (MeV)	r_I (fm)
79 DCV, L (nonrelativistic kinematics only)	$88.5-0.26E$ $+0.88ZA^{-1/3}$	1.17	$0.709+0.0017E$	$(12.2+0.026E)(1-e^{\beta})$	$(12.2+0.026E)e^{\beta}$	1.325
79 DCV, F (for relativistic kinematics only)	$88.0-0.283E$ $+0.88ZA^{-1/3}$	1.17	$0.717+0.0012E$	$(12+0.031E)(1-e^{\beta})$	$(12+0.031E)e^{\beta}$	$1.376-0.01\sqrt{E}$
79 DCV, F' (for relativistic kinematics only)	$88.0-0.283E$ $+0.88ZA^{-1/3}$	1.17	$0.717+0.0012E$	$(12+0.031E)(1-e^{\beta})$	$(12+0.031E)e^{\beta}$	$1.376-0.01\sqrt{E}$
Example for ^{93}Nb F parameters at 52 MeV	81.25	1.17	0.7794	3.225	10.387	1.304

Potential name	a_I (fm)	r_C (fm)	V_{LS} (MeV)	r_{LS}	a_{LS}	W_{LS}	r_{ILS}	a_{ILS}
79 DCV, L (nonrelativistic kinematics only)	$0.53+0.07A^{1/3}$ $-0.04\sum_i e^{-\mu_i}$	1.30	$7.33-0.029E$	1.07	0.66	0	0	0
79 DCV, F (for relativistic kinematics only)	$0.52+0.07A^{1/3}$ $-0.04\sum_i e^{-\mu_i}$	1.30	$7.20-0.032E$	1.07	0.66	0	0	0
79 DCV, F' (for relativistic kinematics only)	$0.52+0.07A^{1/3}$ $-0.04\sum_i e^{-\mu_i}$	1.30	5.0	1.04	0.60	$0.37A^{1/3}$ $-0.03E$	0.80	0.25
Example for ^{93}Nb F parameters at 52 MeV	0.8223	1.30	5.744	1.07	0.66			

A data set was constructed of these two σ_R surveys, and searches were performed. By allowing only the non-structure-dependent terms of the imaginary diffuseness to vary, excellent fits ($\chi^2 \approx 1$) to σ_R were obtained with $a_I = 0.65$ fm. This value is to be compared with the potential L value of $0.53+0.07A^{1/3}$ fm, which would yield $a_I = 0.74$ to 0.95 fm for a typical target range of Al to Pb.

Thus the reaction cross section fits seemed to suggest that there should be no residual mass dependence in the imaginary diffuseness a_I, and in addition that the overall magnitude of a_I is too high. As a result, attempts were made to revamp the global potential to exclude the mass term in the imaginary diffuseness. This necessitated a steeper mass dependence of the real potential depth and also the inclusion of a mass dependent term in the real diffuseness a_0. The resulting potential we called potential T.[82] The advantage of potential T was that without the A dependence in the absorptive potential, the changes in the σ_R predictions with A reflected the changes of the 22- and 25-MeV σ_R data. Also, we observed that the differential cross section predictions for heavy targets ($A > 200$) at the low energies ($E \leq 17$ MeV) displayed more structure than potential L.

The disadvantages of potential T, however, greatly outweigh the advantages. First, although potential T fits the change in σ_R with A quite well, the magnitude of the imaginary diffuseness a_I required to fit the differential cross section data (0.82 fm) still yields too much absorption *overall* for the σ_R data. Searches on the differential cross section data using potential T with a_I fixed at 0.65 fm generates fits whose total χ^2 is eight times larger than with a_I of 0.82 fm. Consequently, even potential T overpredicts the 25-MeV σ_R data by 12% and the 22-MeV σ_R data by 20%. Secondly, potential T predicts too much structure in the heavier targets ($A > 100$) at 52 MeV, in a few cases, predicting oscillations not reflected at all in the data. Finally, the most

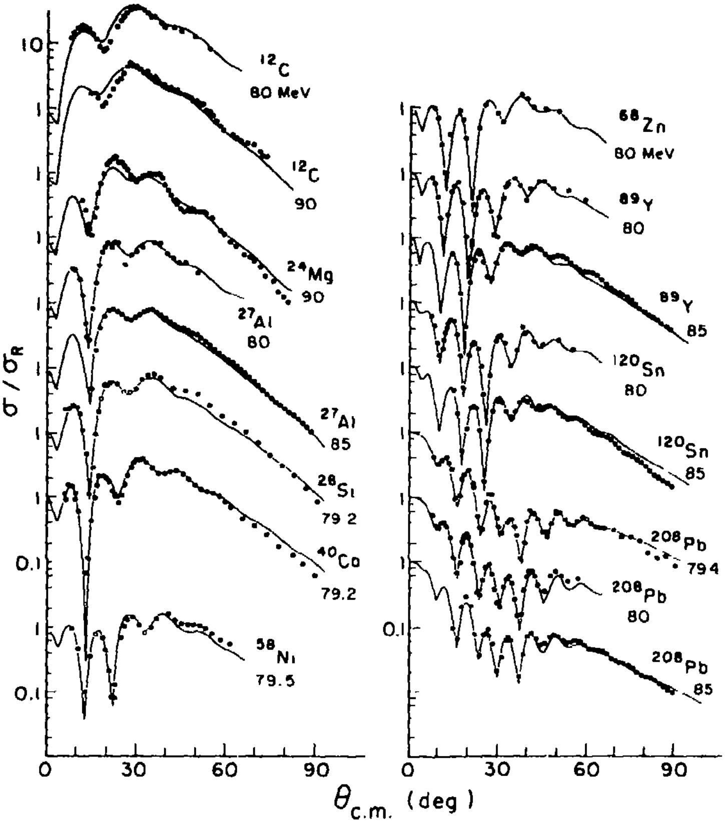

FIG. 6. Comparison of 80–90-MeV data (Refs. 39–42) with curves from potential L. Fits with potentials F and F' are marginally better. The other global prescriptions are not very useful at this energy. (Compare Table II.) It is noted that the data for 79.2 and 79.5 MeV (Ref. 42) are tentative and subject to small changes.

significant objection to potential T is the quality of its polarization predictions. The central part of potential T distorts the polarization predictions qualitatively to such an extent that it is impossible to obtain good fits with *any* values f the spin-orbit parameters.

Finally, we explored the effect of a possible symmetry in the surface of the real potential. he folding computation of the real deuteron opcal potential by Perey and Satchler[2] yielded related local potential with a near Woods-Saxon orm if the diffuseness was made asymmetric bout the half-radius point. The effective folded eal Woods-Saxon form would then have a typical ner diffuseness of $a = 0.68$ fm and an outer (tail) iffuseness of 0.82 fm varying slowly with A. his could in turn be represented by an A-deendent term in a_0. That is, for a given bombardng energy, the incident deuteron would see more f the tail region of a heavier target, where the olding model predicts a large diffuseness. An attempt was made to employ this asymmetric a_0 term with our data in GENOA, with hopes that it might replace the need for an $A^{1/3}$ dependence in the σ_R global potential. After a number of searches, the resulting fits were about 10% worse, with the two diffuseness values (a_{in} and a_{out}) tending to converge to one another. It has not yet been possible to use such an asymmetric a_0 to obtain the overall goodness of fit we ordinarily obtain, without a major reorganization of the real potential.

The failure to accurately reproduce an appreciable fraction of the total reaction cross section data is of concern. It could imply that in the global prescriptions some important phase shifts are not obtained correctly. Hence we expended considerable effort trying to overcome this difficulty, as outlined above. Our present feeling is that even individual best-fit parameters for 22.4-MeV angular distributions (if available) would give total cross sections larger than the

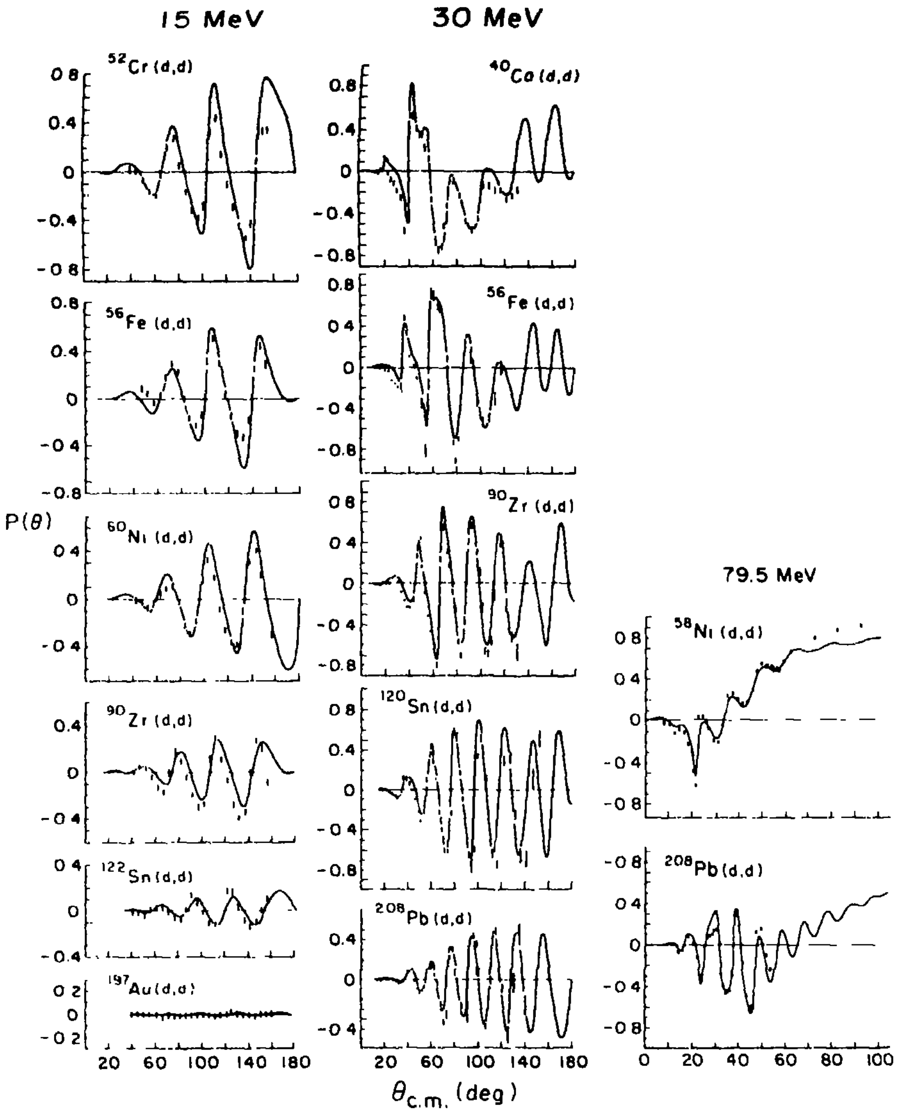

FIG. 7. Comparison of potential L predictions with vector polarization data from Refs. 54, 55, and 42. The 79.5 MeV polarizations (Ref. 42) are preliminary. Fits with potential F are marginally better, while potential F' (by virtue of the complex spin-orbit term) does noticeably better. See text and Tables II and III.

measured ones. We refer to Fig. 22 in Ref. 17(a) where best-fit parameters for 21.6-MeV angular distributions are used to predict total cross sections. These (21.6-MeV) reaction cross section predictions are about 10% larger than the measured ones at 22.4 MeV. Figure 9 shows the predictions of potential L for σ_R as function of A and E. It can be seen that, for targets with $A \geqslant 100$, σ_R grows very rapidly with E, i.e., by about 4% per MeV in the 20-MeV region. Accounting for this trend further increases the disagreement already apparent in Perey's best-fit comparison.[17] We thus may see a limitation of the optical model analysis for deuteron scattering. On the other hand, such a conclusion should probably be deferred until these early and difficult measure-

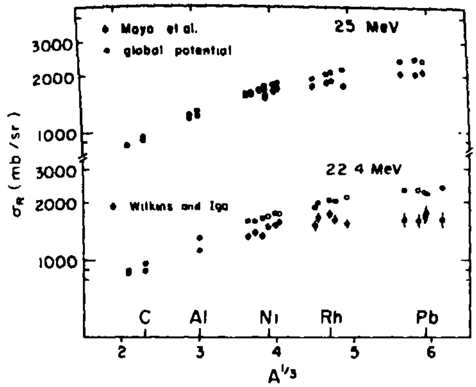

FIG. 8. Comparison of the reaction cross section data of Refs. 57 and 58 with the predictions of potential L. The low-energy data (not shown) and the data for small A give good agreement with the optical model predictions of potentials A–L. However, for the heavier targets all predictions are systematically higher than the data shown, particularly for 22.4 MeV. Forcing a fit to these reaction data produces dramatically inferior fits to the polarization data.

ments have been checked with improved experimental methods.

III. DISCUSSION

A. Comparison with experimental data

In some respects the highest energy data (80–) MeV) should be hardest to fit. There are ore and generally deeper minima than at lower nergies, and the rapid variation with θ would resent problems if measurements are uncertain y as little as 0.5°. However, a glance at Fig. 6 ows that the global approach leads to very satisfactory fits. Some cases of excellent agreeent are found at all energies investigated (Figs. –7), but we also notice a number of disagreeents. Most of them, we feel, can be understood for the reasons given below.

(a) All but the most recent experiments used deuteron beams of moderate resolution (i.e., >100 keV), and a number of the experimental cross sections are, therefore, suspect at large angles. For instance, the measured cross sections for ^{93}Nb, ^{103}Rh, ^{181}Ta, and ^{238}U contain the inelastic cross section for one or more unresolved states below 150 keV excitation. Inelastic contributions are generally out of phase and wash out the elastic structure. The angular distributions which we suspect on experimental grounds are noted in the figures. They generally lie *above* the calculated curves, as might be expected. This is especially obvious for ^{238}U at 52 MeV (Fig. 5).

(b) The cross sections for the lightest targets at 11.8 and 17 MeV show systematic disagreements with the optical model curves $[\sigma(\theta)_{\text{exp}} - \sigma(\theta)_{\text{theor}} \simeq \text{const}$ for low E, A, as for protons[22]$]$. We think this effect is meaningful and not an artifice of the data or the analysis. Its disappearance at higher energies suggests that compound-elastic scattering and/or other higher order effects are not negligible, at 11.8 and 17 MeV. The optical model is not expected to work well when such effects are important.

(c) At 11.8, 17.0, and 34.0 MeV data for $f_{7/2}$ targets show recurring differences from the calculated curves. This could be a more subtle structure effect which the optical model in its current form cannot predict (e.g., a nonuniform increase of R with A). This effect is particularly striking for ^{48}Ca in Fig. 3. $\sigma(\theta)$ for ^{48}Ca shows almost no similarity to that of the neighboring ^{51}V, which also has a closed ($N = 28$) neutron shell. In most other atypical, shell-closure correlated variations the global fits were improved considerably by the introduction of the magic shell correction term for a_I. Minor problems at large angles remain. See, for instance, $\theta > 150°$ for ^{89}Y, ^{93}Nb, ^{124}Sn, and ^{208}Pb in Fig. 3. A 50% larger magic term would better reproduce these shell effects at 17 and 34 MeV; however, it would harm the fits at higher energies. The coefficient of 0.04 given in Table III represents a compromise.

(d) A few angular distributions (e.g., ^{54}Fe and ^{197}Au at 52 MeV) disagree with our global fits by being systematically 30–50% higher everywhere, even at very small angles (Fig. 5). It is our experience that such disagreements often result from an incorrect normalization of the data. (We noted in our own measurements that ^{197}Au absolute cross sections could not be reproduced from run to run because of the nonuniformity of our commercial self-supporting

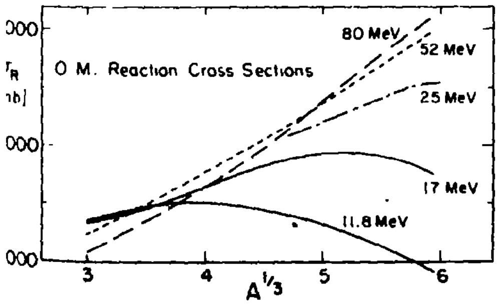

FIG. 9. Predictions of potential L for the mass and nergy dependence of the total reaction cross sections.

gold foils). A remeasurement for ^{54}Fe and ^{197}Au would be very desirable.

B. The real potential

The historically observed discrete ambiguities for the depth V_0 of the real potential[16,17] have essentially been resolved by the folding method[1-3,5] in favor of a potential characterized by a volume integral $J/2A \approx 350$ MeV fm^3. As explained above, this theoretical result was one of the boundary conditions imposed on our searches. But the familiar continuous ambiguity for r and V_R characterized by the empirical relation Vr^n = const was not resolved when this study began. Owing to the ability of empirical models to fit proton-nucleus scattering with radius parameters ranging from 1.15 to 1.25 fm (Refs. 21, 22, and 20), a range of $1.1 \lesssim r_0 \lesssim 1.2$ for the deuteron-nucleus radius parameter is consistent with the folding approach. The analysis of the lower energy data showed no striking preference for any particular r_0 value inside this range; however, by and large, the lowest energies were more easily fit for $1.1 \lesssim r_0 \lesssim 1.15$ and the highest ones (80–90 MeV) were better fit with $1.15 \lesssim r_0 \lesssim 1.20$. We have somewhat arbitrarily resolved this ambiguity by demanding that r_0 should not be energy dependent. There is no clear theoretical guide as yet on how r_0 should change with E, and r_0 = const is the simplest and a palatable option. It was found that for $r_0 = 1.17$ fm, high and low energy data could be well fit as long as a small energy dependence of a_0 was permitted. (a_0 for potential L grows linearly from 0.73 fm at 12 MeV to 0.825 fm at 90 MeV.) This energy dependence of a_0 is no longer optional if r_0 is kept at a (any) constant value. We see no unusual significance in this particular parametrization except that it works and involves reasonable values for r_0 and a_0. We note that R_{rms}, the resulting rms radius for the potential, is apparently unique for potentials of the Woods-Saxon shape and should be reproduced by a successful theoretical construction of the real potential. Figure 10 shows the values $R_{rms}(E)$ for several nuclei as predicted by potential L. A moderate but distinct increase in R_{rms} with energy is seen. This trend is supported quantitatively by independent, individual best-fit rms values which were taken (mostly) from the literature and are shown as circles in Fig. 10. The agreement of best-fit rms values with the global potential L is better than expected given the usual fitting ambiguities.

In Fig. 11 we show as solid lines the real volume integrals $J/2A$ extracted by our global fit. Again the circles are independent best-fit values. The value of $J/2A$, at least if obtained

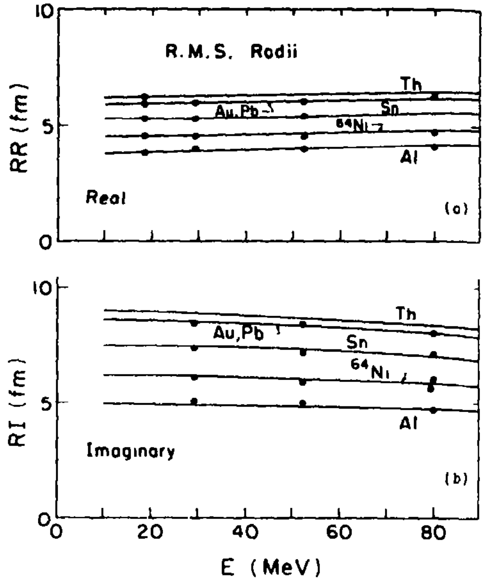

FIG. 10. The solid lines represent rms radii extracted from the global analysis of our data set. They were computed from potential L for several targets as a function of energy. We note the close agreement with corresponding real and imaginary rms radii extracted in th literature from individual best-fit analyses (e.g., Refs 38, 26, 24, 39, and 42, shown as closed circles).

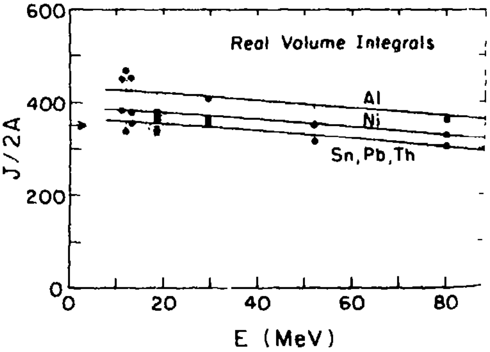

FIG. 11. The solid lines show the energy dependence of the real volume integrals for several targets as extracted by the global fit L to our data base. Correspon ing volume integrals ($J/2A$) deduced from best-fit par eters in the literature (full circles) agree with these lines to about 10% or better. We noticed that $J/2A$ depended somewhat on the r_0 values chosen in the optical model analyses. The real volume integrals decrease most linearly with energy and show a nonlinear dependence on A.

from individual best fits, seems to be less unique and more strongly dependent on the choice of the real radius parameter. Note the large scatter at 11–17 and at 52 MeV around the "global" curves. The 52-MeV points result from ($r_0 = 1.05$) best fits.[34] We believe that so small an r_0 value is unphysical at 52 MeV. The lower energy best fits use more conventional r_0 values, but do not seem to determine $J/2A$ very precisely. Our global fit indicates a distinct, nearly linear drop of $J/2A$ with energy, a feature that is also seen in proton scattering and thus expected, at least qualitatively, from folding theory.

$V(r)$ of potential L has been carefully optimized for the available data set. Given the number of variables used and potential shapes of Woods-Saxon type we find the parametrization of Table III superior to all others we have tried. This is not to say that better shapes could not be found. Even if we retain $f(r)$ some ambiguities persist. Using the notation $V_R(r) = (V_0 + K_1 Z A^{-1/3} + K_2 E) f(r)$, they can be expressed roughly by the relation $V_0 + 9K_1 \approx C = \text{const}$, where the constant C depends on the fixed real radius value r_0. Quite good fits could be maintained with ±20% variations in K_1 as long as the above relationship was satisfied. It is interesting to note that for Perey's[17] set B ($V_0 \approx 100$ MeV, $r_0 = 1.15$), $K_1 = 2.0$ and $V_0 = 81$, so that the constant $C = 99$ MeV. The global potential E ($V_0 = 89.5$ MeV, $K_1 = 1.0$) has $C = 98.5$ MeV. For our potential L ($r_0 = 1.17$, $V_0 = 88.5$ MeV, $K_1 = 0.88$) we have $C = 96.4$. Hence the divergent values for K_1 appear to be part of a long valley in χ^2 hyperspace.

The Coulomb term was originally introduced into the optical model potential in the proton studies by Perey[21] and by Becchetti and Greenlees[22] to represent an energy correction term to the real potential depth. Thus, a deuteron will
rience a Coulomb repulsion of about
$Z/A^{1/3}$ MeV at the nuclear surface. Since our
gy dependence is $0.28E$ we might then expect
t energy correction of $0.28(E - 1.38Z/A^{1/3})$
$8E - 0.39Z/A^{1/3}$. The fitted value of $0.88Z/A^{1/3}$,
g more than twice the expected value, could
ably not be explained away by corrections to
Coulomb term. It appears rather that the
lomb" term in V_R represents actually two
rate terms, the first being a contribution
entirely to Coulomb repulsion, and the sec-
being an A-dependent fitting parameter. In
the $Z/A^{1/3}$ term may be a disguised term of
form $A^{2/3}$, which behaves very similarly with
r most targets. Even our previously observed
iguity between V_0 and $K_1 Z/A^{1/3}$ does not ex-
down to the region of $0.4Z/A^{1/3}$ without con-
rable worsening of the fits.

The energy dependence of V_R is well defined for a given r_0. Whenever the potential depth V_R was plotted versus energy for best fits for a single isotope at various energies with a common real geometry, a very nearly straight line was described by the points, up to 52 MeV. Thereafter, the slope increased somewhat. It is expected that outside the incident deuteron energy range of 11.8 to 85 MeV, such a linear approximation for $V_R(E)$ would not hold. The energy dependence of V_R for nucleons should become weaker as E increases further.[59] However, for the energy range we analyzed, a linear dependence was adequate and it was not deemed advisable to employ a more complicated E dependence.

The real radius parameter r_0 was fixed to a given value for most fits performed, both single and global. Attempts were made to introduce a radius of the form $r_d + r_0 A^{1/3}$ where $r_0 A^{1/3}$ would be the nuclear radius and r_d would represent the deutron size. However, fitting with such an expression brought no improvement and the addition of such a term seemed thus unjustified. At various times the radius was allowed to go free for each target in a global fit, but no systematic variance from a constant value could be detected.

The real diffuseness a_0 was observed to be tied to the real radius, in an inverse relationship. Freeing a_0 with fixed r_0 on targets in a global fit showed a slight energy dependence. This E dependence of a_0 was found to be easily absorbed by the E dependence of the real depth V_R unless and until the 85-MeV data were included.

In general, the global fits over broad mass ranges required an A-dependent term in one of the central diffuseness parameters—in a_0 or in a_I. Putting the A dependence in a_0 rather than a_I, while improving the overall slope of the σ_R fits with mass, considerably worsened the differential cross section fits overall.

C. The imaginary potential

The simple Watanabe model[1] is not adequate for a correct prediction of the imaginary part of the optical potential.[2,3] This is mostly due to the large probability of deuteron breakup in the scattering process.[3,5,7] Extensive theoretical work in recent years[8,12,13,15] has greatly enhanced understanding of this process. The simple folding of imaginary nucleon-nucleus potentials considerably underpredicts the imaginary potential needed, and breakup is a major physical cause for the large imaginary surface term found in the phenomenological deuteron-nucleus potential.[15] The processes contributing to the absorption of the incident deuteron wave are sufficiently complex as to discourage a quantitative construction of a local, equivalent optical model term. Hence most recent theoretical calculations for deuteron scattering compute the scattering matrix elements directly. When a comparison with the matrix elements obtained from the optical model is made it is noted that theoretical refinements tend to give matrix elements which more closely agree with phenomenological values.[8]

Qualitatively, it is expected that as the deuteron energy increases, the absorption will decrease at the surface and increase in the volume region of the target.[18] Such a dependence was also found empirically by Becchetti and Greenlees[22] in their elastic nucleon optical model studies. For protons, Becchetti and Greenlees obtained $W_S = 0.22(E-12.3)$ and $W_D = 11.8 - 0.25E$ + (isospin term), i.e., the surface potential drops to 50% of its maximum value at 24 MeV per nucleon. This is about twice as steep a drop as found for our deuteron potentials A to E which employ a similar parametrization. This linear energy dependence did not work so well once the data set was extended to 90 MeV. The fits to the 85-MeV data indicated a preference for a stronger switch to an imaginary volume potential than given by potential E. The very slow drop of W_D at low energies and the faster drop at and beyond 52 MeV, which we found empirically, could be approximated by a Gaussian function of the type $W\exp[-(E/E_0)^2]$. This function also has the advantage that it will not cross zero (as any linearly decreasing function would). The least squares search fixed E_0 at 100 MeV to within about 10% (depending on geometric parameters). Hence our imaginary potentials took the form

$$W_D = W_1(E)\exp[-(E/100)^2],$$

$$W_S = W_2(E)\{1-\exp[-(E/100)^2]\},$$

where $W_1(E)$ and $W_2(E)$ showed a very weak increase with E. It was found that for all practical purposes we could set

$$W_1 = W_2 = W = 12.0 + 0.03E$$

and

$$W_D = W - W_S .$$

In this parametrization, W_D drops to 50% of its maximum at 40 MeV per nucleon, or at 80-MeV deuteron energy, faster than for the low energy potential E (which yields the half point at $E_d = 113$ MeV), but not as fast as the Becchetti-Greenlees potential for protons (which would have yielded the half point at 48-MeV deuteron energy). The Gaussian shape in our parametrization is somewhat arbitrary, but there is reasonable (χ^2) evidence for the nonlinearity in the decrease of W_D and the corresponding nonlinear increase of W_S.

The strong coupling of W_D and W_S is a consequence of the near constancy of the imaginary volume integral which is demanded by the data. Figure 12 shows the volume integrals $JI/2A$ deduced from our global fit L as function of deuteron energy. The upper five curves refer to targets of different sizes and give the total imaginary volume integrals. The lower two curves give the surface (JD) and volume (JS) components separately for ^{124}Sn. The circles represent independent best-fit results from the literature. They are connected by vertical lines to the curve to which they correspond most closely in mass ($\Delta A = \pm 2$). These best fit values scatter about the global curves, differing by 5 to 10%. They do, however, agree well with our global fit conclusion that the total imaginary volume integral per nucleon is nearly constant with energy and decreases with target mass. There is as yet no independent test for the magnitude of the volume

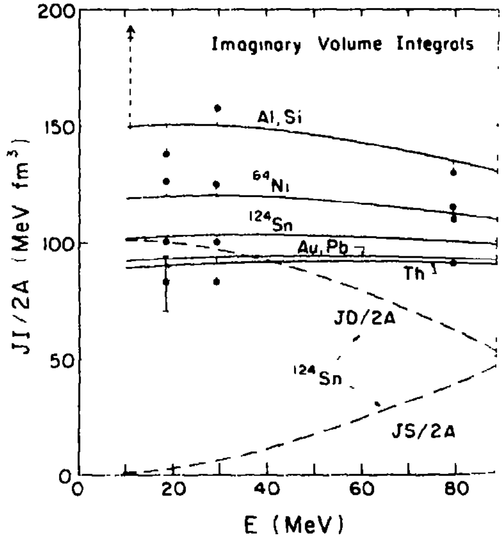

FIG. 12. Lines show imaginary volume integrals ($JI/2A$) deduced from the data through the global fit L. Corresponding individual best-fit values for $JI/2A$ are taken from the literature and shown as closed circles. Above 15 MeV deuteron energy agreement to within 10% is seen; however, individual best fit values reported at 11 MeV (arrow) disagree by 30% or more. It is noted that $JI/2A$ varies strongly with A, but only very gradually with energy. The dashed lines separately show the changing surface ($JD/2A$) and volume ($JS/2A$) components of the integral for ^{124}Sn. Both parts contribute about equally at 90 MeV.

and surface parts separately. The arrow at 11 MeV is added as a reminder that the volume integrals for <12-MeV best fits[6] are not close to our global curves, being much larger than at higher energy and showing larger scatter.

A glance at Fig. 10(b) shows that our global parameters and the independent best-fit parameters from others deduce remarkably similar imaginary rms radii $RI_{\rm rms}$, in spite of the fact that other analyses use rather different r_I, a_I parametrizations. Hence, good fits to the data over a sufficiently large angular range apparently fix the real and imaginary root mean square radii of the scattering potentials rather accurately (in contradistinction to the continuous ambiguities in the optical model parameters r_0 and r_I). The global and individual best-fit analyses agree that $RI_{\rm rms}$ for a given target *falls* slowly with deuteron energy and can be considered well known.

We return briefly to the question of volume versus surface absorption components. Figure 13 shows the radial dependence of the combined imaginary potential contributions as given by the global potential L for two nuclei of very different size. We note that the switch from surface to volume dominance automatically reduces the half point radius with increasing energy. This decrease of RI is a real effect needed to fit the data well. However, the magnitude of W at $r \approx 0$ is probably not well determined by our data. It is determined only in the following sense: Throughout our global fitting study we followed the self-imposed rule that the *minimum* requirement for the introduction of a new parameter is the improvement by 10% in χ^2 for the data set. It was known that lower energy data (~17 MeV) required no appreciable volume term but did need a surface term with $r_I \approx 1.33$. On the other hand, medium energy proton $E > 50$ and higher energy deuteron data have been fit best with a volume absorptive potential. Similarly, nucleon-nucleus folding calculations predict increased volume absorption at higher energy.[18] This led us to introduce both potential shapes. Given this additional complexity we subsequently tried to not further increase the parameter space by holding r_I and a_I to the same values at all energies *and* for both radial shapes. This constraint led to W_D and W_S values which were well fit by the Gaussian energy dependence given above. It came as a pleasant surprise that the best fits resulted in $W_1 \approx W_2$, thus eliminating the need for one of the W parameters. There are undoubtedly other and more complex $W(r, E)$ parametrizations which would fit the data equally well or better.

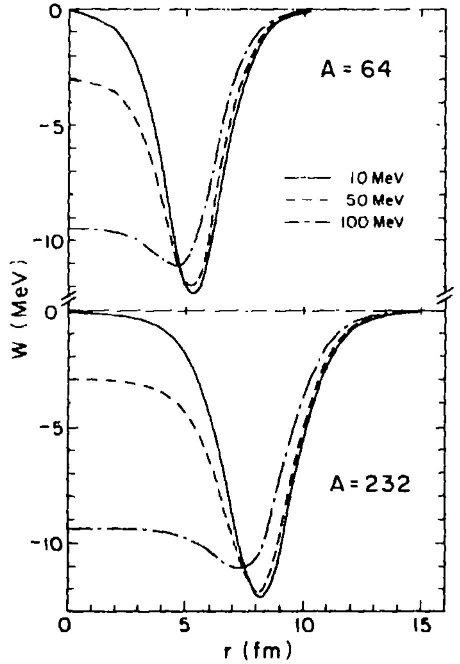

FIG. 13. Radial dependence of the imaginary parts of le optical potential L as a function of deuteron energy ır two targets. Note that the half-value radius is markdly affected by the shift from surface to volume aborption without a change in the radius parameter r_I.

For the range of our fits $W = 12.0 + 0.03E$, i.e., W grows slowly but linearly. This probably cannot be extrapolated very far beyond 100 MeV. Generally, we expect that at higher energies optical parameter energy dependences will become weaker, with the imaginary depths asymptotically approaching a constant value. Such behavior has been observed with elastic nucleon scattering, where W_S rises with increasing bombarding energy from a depth of 5 MeV to a depth of 20 MeV (at 50-MeV incident energy) (Ref. 59, p. 175, see also Ref. 20), but for incident energies from 50 through 300 MeV, W_S remains fairly constant.

The imaginary radius parameter r_I is fairly stable in the region 1.30–1.33 fm with our global fits, showing a preference for the lower value at the higher energies. $A^{-1/3}$ terms were introduced into r_I at various times, but no particular advantage was obtained. The imaginary diffuseness a_I is the parameter which we have chosen to contain the observed structure dependence. The shell correction term which is a function of closed neutron shells reduces absorption by making the imaginary diffuseness sharper near and at magic neutron numbers. Although a great deal of scatter was seen in plots of best a_I versus nearness to magic neutron shell, the distribution $a_I(N)$ could be fitted quite adequately with a Gaussian centered at the magic shell number with a half-width of about 2.0 neutron numbers. This variation of a_I has a striking resemblance to the drop of the average level spacings near and at shell closure,[60] and is, conceivably, a consequence of it.

D. The spin-orbit potential

Knutsen found that the adiabatic folding $L\cdot S$ potential is well approximated by an effective spin-orbit potential of the Thomas form with a depth of 5.63 MeV and a geometry of $r_{LS}=0.98$, $a_{LS}=1.00$ fm.[61] Our initial global fits (potentials A, B, and C) were performed with this geometry. Initially, we varied only the spin-orbit depth. Later, searching on the 15-, 30-, and 80-MeV vector polarization data, the spin-orbit geometry as well as the depth was allowed to vary. The data at the higher energies showed a definite preference for a much narrower diffuseness ($a_{LS}=0.55$ fm), with roughly the same depth and radius ($V_{LS}=5.5$ MeV, $r_{LS}\approx 1.0$ fm) as the folding results. The fits were somewhat insensitive to changes in the radius r_{LS}. However, they were very sensitive to changes in the diffuseness, and the final fits with the narrow values of 0.55 to 0.66 give about half the χ^2 of the fits with the fixed folding geometry.

For the 15-MeV data the advantage of the narrower spin-orbit diffuseness ($a_{LS}=0.55$ fm) was less visible in our analysis because the major errors arose from a phase shift between data and calculation (see Fig. 7). At 15 MeV the $P(\theta)$ curves have crossover points about 3° farther back than the data. This is not influenced much by the value of a_{LS}. This problem has been encountered before for individual fits at this and lower energies.[6,62] Goddard and Haeberli suggested that the introduction of a small imaginary spin-orbit term can remove this phase shift and also improve the fit to the tensor analyzing powers.[62] They gave five examples each at 10 and 15 MeV where a best-fit search with a complex spin-orbit potential (six free spin-orbit parameters per nucleus) gives good fits for vector and tensor polarizations, whereas omitting the imaginary spin-orbit terms increases the best possible χ^2 by about 70%. Similar conclusions have been drawn by Bürgi *et al.*[43] from an analysis of 9–12-MeV polarization data for ^{40}Ar. Both analyses use very narrow spin-orbit geometries, i.e., $r_{LS}\approx 0.8$, $a_{LS}\leq 0.50$ for the real part and $0.7\approx R_{ILS}\approx 1.1$, $0.2\leq a_{ILS}\approx 0.35$ for the imaginary part, but such extremely narrow geometries have not been found in folding studies. More recently Quin[63] has reported that similar problems for polarization data at low deuteron energy could be remedied by taking explicit account of some large stripping channels in a coupled channel analysis. Quin's approach appears promising; however, it falls outside the scope of this study.

We note that generally, but particularly at 15 MeV, *simultaneous* good fits to cross section and polarization data are difficult to obtain with just a real spin-orbit term, even if only individual targets are fit. The systematic differences between data and calculations visible in Fig. 7 and in a different perspective in Fig. 14 seem less the result of our reliance on a global parameter prescription than of a shortcoming in the (real) polarization term given in the Introduction. Although we have no theoretical guidance for the exact form of a complex spin-orbit term, the existence of a weak imaginary component is suggested by folding considerations[5] and a recent proton scattering analysis.[20] Hence we let the spin-orbit term become complex in some of our global searches. Initially the real and imaginary terms had the same geometry: $V_{LS}f(r)\to(V_{LS}+iW_{LS})f(r,r_{LS},a_{LS})$. The results of such searches were negative. W_{LS} did not converge to any particular value and the fits were not appreciably improved. In our recent searches we permitted different geometries for the real and imaginary parts, i.e., $V_{so}=V_{LS}f(r,r_{LS},a_{LS})+iW_{LS}f(r,r_{ILS},a_{ILS})$. It was found that $a_{LS}\gg a_{ILS}$

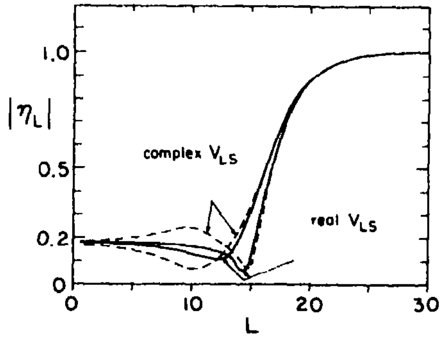

FIG. 14. Plot of S-matrix moduli η_L as a function of L for fits to ^{58}Ni at 79.5 MeV. The solid lines are derived from the global potential F. They are very similar to those from potential L and represent phase shifts for the highest and lowest couplings of $\vec{L}+\vec{I}$, respectively. The addition of an imaginary spin-orbit term in potential F' improves primarily the polarization fit, but leads to considerable changes in the phase shifts for the lower partial waves ($L\leq 12$).

≈0.25, for superior fits. Also, W_{LS} proved energy dependent and changed sign between 30 and 70 MeV. A comparison of polarization data with such an extended potential is shown in Fig. 15. The very limited number of high energy polarization measurements in our data set makes it difficult to draw firm conclusions about the imaginary spin-orbit term. However, a trial potential with a complex $L\cdot S$ term is listed in Table III as prescription F'. Further work is clearly warranted and is contemplated in connection with new measurements of vector and tensor polarizations at the Indiana cyclotron.

The results of this study support making V_{LS} energy dependent. A reduction of V_{LS} relative to the low energy data was necessary at 80 MeV. A decreasing $V_{LS}(E)$ also provided significant improvements for the vector polarizations at 30 MeV. The linear relation $V_{LS}=7.33-0.029E$ of potential L is adequate, but not unique in the 12–90-MeV range. The value $a_{LS}=0.66$ is an uncertain compromise. If greater weight were given to the elastic scattering cross sections, its value would go up by about 0.1 fm. Conversely, a much heavier weighting of the vector polarization would reduce a_{LS}. The parameter $r_{LS}=1.07$ similarly is only certain to about 0.15 fm, the reason being the differing preferences shown by polarization and (high energy) scattering data. All in all the spin-orbit parameters are the least well determined ones in our set. Changes up or down from the average values given affect different parts of the data set in opposite ways.

We tentatively conclude that these uncertainties reflect not only the scarcity of polarization data at higher energies, but possibly the inadequacy of the functional dependence of the spin-orbit term and of the imaginary central potential as traditionally used. Although not yet warranted by our ≳10%/parameter rule, a potential like potential F' may be justified as more polarization data are used in the data base.

It may be worth emphasizing that the strength of spin-orbit potential V_{LS} strongly affects the large angle ($\theta > 45°$) range of the 80–90-MeV scattering data and acts as a sensitive fitting parameter at the higher energies. This can be understood from Fig. 14 which shows the ^{58}Ni phase shifts η_L for $J=L\pm1$ couplings of the spin-1 projectile. Scattering and absorption for the surface waves is seen to depend strongly on J, even in the absence of an imaginary spin-orbit term. The strong J dependence of the phase shift may also determine the onset of the loss of structure in the angular distributions.

Similarly, the different absorption of the ($J=L\pm1$) partial waves in Fig. 14 for different deuteron spin orientation may be responsible for the observation at 80 MeV of a large polarization of the same (positive) sign for all angles past 40°. A complex spin-orbit term enhances this

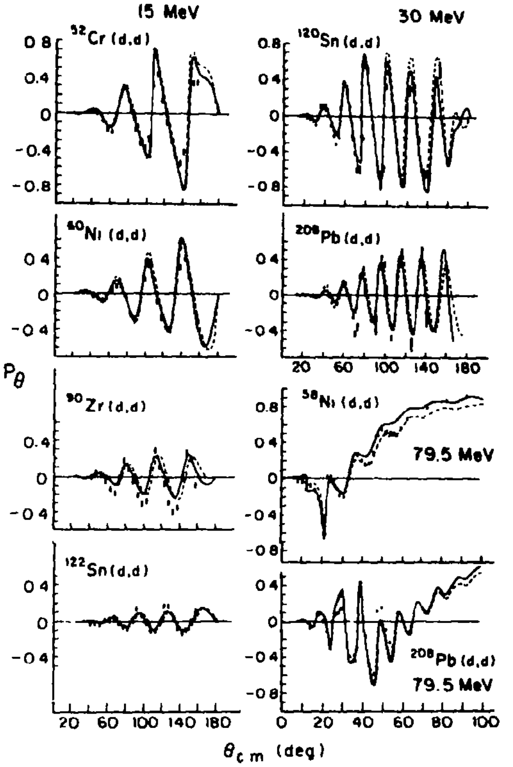

FIG. 15. The less adequately reproduced polarization data of Fig. 7 are shown here in comparison with predictions of potentials F and F' of Table III. Potential F curves are shown as dashed lines. Although not identical with those of potential L in Fig. 7, they are of similar quality and show similar shortcomings, as was seen in a detailed comparison of χ^2 values ($\chi_L^2 \approx \chi_F^2 \approx 7.4$). The use of a complex spin-orbit potential (global prescription F') results in the calculated vector polarizations shown by the solid lines. χ_w^2 for these curves is improved by a factor 0.7. The greatest changes are seen at 15 MeV. The imaginary term W_{LS} needed for better fits changes considerably and systematically with target mass and deuteron energy. The W_{LS} values for 15 MeV are close to those of Ref. 62. However, at 30 MeV W_{LS} is very small and has changed sign at 79.5 MeV. Note that the visible effects also change with energy. At 15 MeV predictions are shifted toward smaller angles, often by as much as 3°. At 30 MeV a similar but smaller shift is seen, whereas at 79.5 MeV the main effect is a 10–20% enhancement of the polarization at larger angles.

effect, through its influence on smaller L partial waves (see dotted lines in Fig. 14).

IV. CONCLUSIONS

Experience has shown that average optical parameter or "global potential" prescriptions tend to be successful within the mass and energy range of the data bases from which they were derived. Extrapolation to lower energies was quite successful for the Hinterberger[34] and Perrin[26] prescriptions, but all of the tested potentials were surprisingly unsuccessful when extrapolated into a higher energy range. Although noticeably better than the published global potentials, our early prescriptions named A through E,[58] which were derived without the consideration of data above 52 MeV, also lose a lot of their predictive power when extrapolated to 80 MeV (compare Table II).

The comparison of Table II suggests that our most recent potentials F and L are equal or superior to the others tested over the 12–90-MeV range, but there is a continuing lack of detailed theoretical guidance. Therefore, significant extrapolations, e.g., to energies above 100 MeV, probably would be of a quality just as uncertain as that which has been found for extrapolations of earlier sets.

It seems on theoretical grounds that the linear energy dependence given for V_R and $W(E)$ (Table III) is too simple; however, no quantitative theoretical estimate for the local equivalence of a current folding potential has been available. It is also unlikely that a_0 and V_{LS} should retain their linear energy dependence over a wide energy range. The linearity of most correction terms in Table III merely reflects the fact that the relatively weak energy dependences that were found could be determined only to first order. On the other hand, it is encouraging that the global prescriptions L and F are useful *and* remain simple for an energy range from 12 MeV to seven times that value.

As in most preceding studies the predictions at 11.8 MeV (Fig. 2) are poor for the light targets. (We note again that these targets deliberately were weighted less in the data sets.) The complicated behavior of the polarizations and the enhanced cross sections for backward angles at the lower energies seem to indicate that compound or higher order direct effects like coupled stripping channels make important contributions. We also noted a problem with the ^{27}Al and ^{48}Ca angular distributions at 17 MeV.

Aside from the exceptions mentioned above, satisfactory global fits have been found over a mass range $27 \leq A \leq 238$. The global prescriptions L and F encompass more cross sections for light targets as the energy approaches 90 MeV, and do well for the polarizations in the middle of the energy range. While the values of most optical model parameters depend strongly on the details of the parametrization, a few quantities appear to be deduced reliably for potentials of Woods-Saxon shape. The real and imaginary rms radii are sharply defined in the fitting and tend to agree closely with values obtained elsewhere for individual best fits. In the energy range analyzed the real rms radii grow slightly but distinctly with E, whereas the imaginary ones fall with E while still remaining larger that the real ones (Fig. 9). A slightly weaker statement can be made for the deduced real and imaginary volume integrals. Consistency of values deduced from the global analysis with those derived from best-fit potentials is good at higher energies, but variable at lower energies, and clearly dependent on the same solution to the discrete potential ambiguities. Much less consistent agreement with other work is found at energies below 15 MeV (see Figs. 11 and 12). In the range $12 \leq E \leq 90$ MeV our real volume integrals show a 16%, nearly linear falloff with E, while the imaginary volume integrals are almost constant with E for the heavier targets. Our analysis suggests a shift from nearly pure surface absorption at 12 MeV to almost equal parts of surface and volume absorption at 90 MeV; however, the details of this transition are less certain than other parameters.

In Sec. II G we discussed our partial failure to closely reproduce the 22 and 25 MeV reaction cross section data. New data at these and higher energies are greatly needed.

Owing to the scarcity of published data above 15 MeV and the limitations of time, we did not analyze or consider tensor polarization data. While the addition of a small tensor potential term to potential L or F is not expected to materially change the fits presented here, it would be essential to fit or predict such data.[5,64] It is noted that this topic and improvements in the understanding of vector polarization demand and deserve much additional work. Experimental and theoretical studies of tensor and vector polarizations at 80 MeV are planned for the near future in collaboration with the Indiana group.

Note added in proof. A recent study (unpublished) with 52 MeV vector-polarized deuterons by G. Mairle, K. T. Knöpfle, H. Riedesel, G. J. Wagner, V. Bechthold, and L. Friedrich finds good fits to their analyzing powers with $r_{LS} \approx 1.2$ fm and $a_{LS} \approx 0.4$ fm in their parameter set characterized by $r_0 = 1.15$. No imaginary $\vec{L} \cdot \vec{S}$ term was needed.

Potential *F* of our study yields predictions that fit their data with $\chi^2 = 7.2$. Potential *F′* has a very small imaginary $\vec{L}\cdot\vec{S}$ term at this energy and does only marginally better with $\chi^2 = 6.2$. χ^2 is defined as in Table II.

ACKNOWLEDGMENTS

One of us (W. W. D.) wishes to thank his Indiana collaborators (Ref. 42) for the permission to use the 79-MeV data in this analysis before publication. We owe special thanks to Dr. F. G. Perey for making his code GENOA available and providing the necessary starting help. Dr. J. R. Comfort aided us by maintaining his search code CUPID at Pittsburgh and making it readily accessible. A. Hernandez deserves great thanks for the hard and time-consuming job of digitizing many of the 80–90-MeV cross sections which had been reported only in graphical form. We also gladly acknowledge the benefit of discussions with Dr. Norman Austern, Dr. Richard Drisko, Dr. G. Rawitscher, and Dr. Martin Vincent. A large amount of computer time was needed for this study. It was provided without charge by the University of Pittsburgh Computer Center. This work was supported in part by the National Science Foundation.

---

[*] Present address: Goddard Space Flight Center, Code 681, Bldg. 21, Greenbelt, Md. 20770.

[1] S. Watanabe, Nucl. Phys. 8, 484 (1958).

[2] F. G. Perey and G. R. Satchler, Nucl. Phys. A97, 515 (1967).

[3] R. C. Johnson and P. J. R. Soper, Phys. Rev. C 1, 976 (1970).

[4] R. C. Johnson and P. J. R. Soper, Nucl. Phys. A182, 619 (1972).

[5] P. W. Keaton and D. D. Armstrong, Phys. Rev. C 8, 1692 (1973).

[6] J. M. Lohr and W. Haeberli, Nucl. Phys. A232, 381 (1974).

[7] G. H. Rawitscher, Phys. Rev. C 9, 2210 (1974).

[8] G. H. Rawitscher and S. N. Mukherjee, Phys. Rev. Lett. 40, 1486 (1978); Ann. Phys. (N.Y.) 122, 1 (1979).

[9] W. S. Pong and N. Austern, Ann. Phys. (N.Y.) 93, 369 (1975).

[10] A. A. Ioannides and R. C. Johnson, Phys. Lett. 61B, 4 (1976).

[11] N. Austern, Phys. Lett. 61B, 7 (1976).

[12] N. Austern, C. M. Vincent, and J. P. Farrell, Ann. Phys. (N.Y.) 114, 93 (1978); 96, 333 (1976).

[13] N. Austern, J. P. Farrell, K. Kabir, and C. M. Vincent, Phys. Rev. C 18, 1577 (1978).

[14] H. Amakawa *et al.*, Phys. Lett. 82B, 13 (1979).

[15] G. Baur, R. Shyam, F. Rösl, and D. Trautman (unpublished).

[16] R. M. Drisko, G. R. Satchler, and R. H. Bassel, Phys. Lett. 5, 347 (1963).

[17] C. M. Perey and F. G. Perey, Phys. Rev. 132, 755 (1963); C. M. Perey and F. G. Perey, Phys. Rev. 134, B353 (1964).

[18] F. A. Brieva and J. R. Rook, Nucl. Phys. A307, 493 (1978).

[19] J. P. Jeukenne, A. Lejeuen, and C. Mahaux, Phys. Rev. C 16, 88 (1977); C. B. Dover and N. V. Giai, Nucl. Phys. A190, 373 (1972); M. Jaminon, C. Mahaux, and P. Rochus, Phys. Rev. Lett. 43, 1097 (1979).

[20] A. Nadasen, P. Schwandt, P. P. Singh, A. D. Bacher, W. W. Jacobs, M. D. Kaitchuk, and J. T. Meek (unpublished).

[21] F. G. Perey, Phys. Rev. 131, 745 (1963).

[22] F. D. Becchetti and G. W. Greenlees, Phys. Rev. 182, 1190 (1969).

[23] W. W. Daehnick and R. M. DelVecchio, Phys. Rev. C 11, 623 (1975); R. M. DelVecchio and W. W. Daehnick, *ibid.* 6, 2095 (1972); J. R. Shepard, P. D. Kunz, and J. J. Kraushaar, Phys. Lett. 56B, 135 (1975).

[24] F. Hinterberger, G. Mairle, U. Schmidt-Rohr, and G. J. Wagner, Nucl. Phys. A111, 265 (1968).

[25] E. Newman, L. C. Becker, and B. M. Preedom, Nucl. Phys. A100, 225 (1967).

[26] G. Perrin *et al.*, Nucl. Phys. A282, 221 (1977).

[27] G. Igo, W. Lorenz, and U. Schmidt-Rohr, Phys. Rev. 124, 832 (1961).

[28] W. Fitz, J. Heger, R. Santo, and S. Wenneis, Nucl. Phys. A143, 113 (1970).

[29] M. Takeda, J. Phys. Soc. Jpn. 15, 557 (1960).

[30] P. R. Christensen, A. Berinde, I. Neamy, and N. Scintei, Nucl. Phys. A129, 337 (1969).

[31] N. Cindro and N. S. Wall, Phys. Rev. 119, 1340 (1960).

[32] A. N. Vereshchagin, O. F. Nemets, L. S. Sokolov, I. P. Chernov, and A. A. Yatts, Izv. Akad. Nauk SSSR, Ser. Fiz. 32, 1956 (1968). [Bull. Acad. Sci. USSR, Phys. Ser. 32, 1800 (1968)].

[33] S. A. Hjorth, E. K. Lin, and A. Johnson, Nucl. Phys. A116, 1 (1968).

[34] R. K. Jolly, E. K. Lin, and B. L. Cohen, Phys. Rev. 130, 2391 (1963).

[35] J. L. Yntema, Phys. Rev. 113, 261 (1959).

[36] H. R. E. Tjin a Djie, F. Udo, and L. A. Ch. Koerts, Nucl. Phys. 53, 625 (1964); Nucl. Phys. 74, 417 (1965).

[37] J. Testoni, J. Rosenblatt, and S. Mayo, Nucl. Phys. 74, 481 (1965).

[38] J. D. Childs, W. W. Daehnick, and M. J. Spisak, Phys. Rev. C 10, 217 (1974).

[39] G. Duhamel *et al.*, Nucl. Phys. A174, 485 (1971).

[40] O. Aspelund *et al.*, Nucl. Phys. A253, 263 (1975).

[41] A. Kiss *et al.*, Nucl. Phys. A262, 1 (1976).

[42] C. C. Foster, J. C. Collins, D. L. Friesel, W. W. Jacobs, W. P. Jones, S. Kailas, M. Kaitchuck, P. Schwandt, and W. W. Daehnick, Bull. Am. Phys. Soc. 24, 594 (1979); 24, 838 (1979).

[43] H. R. Bürgi *et al.*, Nucl. Phys. A247, 322 (1975); A307, 91 (1978), and A321, 445 (1979).

[44] J. Bojowald, C. Mayer-Böricke, M. Rogge, V. Schwinn, and P. Turek, Annual reports KFA Jülich, 1974, 1976, 1978 (unpublished).

[45] P. E. Hodgson, *The Optical Model of Elastic Scattering*

(Clarendon, Oxford, 1963); Adv. Phys. 15, 329 (1966); N. Austern, *Direct Nuclear Reactions Theories* (Wiley-Interscience, New York, 1970), Chap. 5.

[46] C. M. Perey and F. G. Perey, Phys. Rev. 152, 923 (1966).

[47] G. R. Satchler, Nucl. Phys. 85, 273 (1966).

[48] P. Schwandt and W. Haeberli, Nucl. Phys. A132, 401 (1969).

[49] C. M. Perey and F. G. Perey, At. Data Nucl. Data Tables 17, 1 (1976).

[50] G. R. Satchler, Nucl. Phys. 21, 116 (1960).

[51] Optical model search code GENOA, 1969, written by F. G. Perey (unpublished). The code was modified slightly to adapt it to the characteristics of the DEC 10 system at the University of Pittsburgh.

[52] J. D. Childs, Ph.D. thesis, University of Pittsburgh, 1976 (unpublished).

[53] J. Childs and W. W. Daehnick, Bull. Am. Phys. Soc. 20, 626 (1975).

[54] R. A. Hardekopf, D. D. Armstrong, L. L. Catlin, P. W. Keaton, Jr., and G. P. Lawrence, Los Alamos Report No. LA-5051 (1972).

[55] R. Roche, N. VanSen, G. Perrin, J. C. Gondrand, A. Fiore, and H. Muller, Nucl. Phys. A220, 381 (1974).

[56] Search code CUPID, written by J. R. Comfort, Univ. of Pittsburgh (unpublished). The code employs a formalism similar to DWUCK (written by P. D. Kunz, Univ. of Colorado), but has a search routine which permits simultaneous fits to polarizations and cross sections *for a single target and energy.*

[57] B. Wilkens and G. Igo, Phys. Lett. 3, 48 (1962).

[58] S. Mayo, W. Schimmerling, and M. J. Sametband, Nucl. Phys. 62, 393 (1965).

[59] L. R. B. Elton, *Introductory Nuclear Theory* (Pitman, New York, 1965).

[60] See, for instance, A. Bohr and B. R. Mottelson, *Nuclear Structure* (Benjamin, New York, 1969), Vol. I, p. 187.

[61] L. D. Knutson and W. Haeberli, Phys. Rev. Lett. 30, 986 (1973). L. D. Knutson and W. Haeberli, Phys. Rev. C 12, 1469 (1975).

[62] R. P. Goddard and W. Haeberli, Phys. Rev. Lett. 40, 701 (1978); Nucl. Phys. A316, 116 (1979).

[63] W. H. Wong and P. A. Quin, Bull. Am. Phys. Soc. 24, 846 (1979).

[64] J. R. Frick *et al.*, Phys. Rev. Lett. 44, 14 (1980).

PHYSICAL REVIEW C VOLUME 21, NUMBER 6 JUNE 1980

W(p,t) reactions. I. Even targets

M. H. Mortensen, R. R. Betts, and C. K. Bockelman
A. W. Wright Nuclear Structure Laboratory, Yale University, New Haven, Connecticut 06520

(Received 20 August 1979)

Data for two-nucleon transfer reactions on even tungsten nuclei are presented. Several systematic features emerge from the data and are discussed in detail. These include the influence of multistep processes on angular distribution shapes. The systematic behavior of excited 0^+ strengths is shown to arise from two types of excitation, one associated with a subshell gap at $N = 108$, the other being of the pairing isomer type.

[NUCLEAR REACTIONS ^{186,184,182,180}W(p,t), $E_p = 21$ MeV; measured $\sigma(E_t,\Theta)$. ^{180}W(t,p); $E_t = 15$ MeV; measured $\sigma(E_p,\Theta)$. ^{184,182,180,178}W deduced levels, L, π, J. Nuclear structure analysis.]

I. INTRODUCTION

The even tungsten nuclei are well deformed rotational nuclei with deformation parameters[1,2] which change little from isotope to isotope. It is therefore to be expected that these nuclei will be ideal for a systematic study of the influence of the underlying microscopic structure on collective rotational and vibrational states. In this, the first of two papers, we report the results of such a study in which the structure of even tungsten nuclei was probed using two-particle transfer reactions. The sensitivity of two-particle transfer to both microscopic and collective features of nuclear structure is well known, and in this paper we are able to exploit the large body of qualitative and quantitative understanding of these reactions that has been obtained over the years.[3] Specifically, the reactions studied were ^{186,184,182,180}W(p,t) and ^{180}W(t,p). The ^{183}W(p,t) reaction was also studied and will be discussed in the second of these two papers.

Previous work on light-ion induced two-particle transfer reactions between these nuclei includes investigations of the ^{186,184,182}W(p,t) reactions to states low in excitation (Ref. 4), $^{\mathrm{nat}}$W(p,t) (Ref. 5), and a detailed study[6-8] of reaction mechanism effects in the ^{186}W(p,t) reaction. Results for (t,p) reactions on ^{180,182,184,186}W have been reported,[9,10] although in the interesting case of ^{180}W, the data obtained were confined to the ground-state rotational band. In addition to these reactions, studies less related to the present work include single-particle transfer and inelastic scattering reactions on various isotopes and of course, numerous gamma-ray studies. These will be referred to specifically in the text as necessary, as will be the numerous theoretical investigations of nuclei in this mass region.

Some preliminary results of the present work have already appeared.[11,12] The ideas already presented will, however, be expanded and new supporting data presented.

II. EXPERIMENTAL METHOD

For the (p,t) reactions, targets of enriched W isotopes were bombarded with a beam of 21 MeV protons from the Yale MP Tandem accelerator. With the exception of ^{180}W, the targets were fabricated by direct vacuum deposition of a suboxide of W onto 20 μgm/cm^2 carbon backings—the details of the isotopic enrichments and thicknesses are given in Table I. The ^{180}W target was made in an isotope separator by direct deposition of ^{180}W on the carbon backing. The reaction tritons were detected using photographic emulsions after momentum analysis in a multiangle spectrograph. These plates were then scanned manually and the data reduced in the usual manner.

The cross-section scales for the reactions studied were obtained in two subsidiary experiments. In order to measure the relative ground-

TABLE I. Target thicknesses and enrichments.

Target	Thickness (μg/cm^2)	Isotopic composition (%) 180	182	183	184	186
^{180}W [a]	50	100				
^{182}W	130	<0.05	94.3	2.5	2.3	0.8
^{183}W	70	<0.10	3.5	90.0	5.6	1.1
^{184}W	160	<0.05	1.8	2.0	94.2	1.9
^{186}W	120	<0.02	0.5	0.3	2.2	97.1
$^{\mathrm{nat}}$W	60	0.13	26.3	14.3	30.7	28.5

[a] Enrichment not available. From analysis of spectrum maximum impurity content ^{182}W $\simeq 2\%$. No others detected.

© 1980 The American Physical Society

state cross sections, the (p, t) reaction was measured in the spectrograph with a natural W target —thus giving accurate relative cross sections for ^{186,184,183,182}W(p, t) reactions. The cross section for the ^{180}W(p, t) reaction could not be obtained in this manner due to the extremely small (0.13%) natural abundance of this isotope. The cross section for this reaction and also the absolute cross-section scale for the other reactions was therefore determined in a counter-telescope experiment in which the (p, t) and (p, p) reactions were measured on targets of ^{184,182,180}W. The elastic scattering angular distributions thus obtained were then compared with the results of optical model calculations, giving an absolute normalization which is believed to be accurate to within 10%.

The (t, p) experiment was performed at a bombarding energy of 15 MeV using the triton beam from the University of Pennsylvania FN Tandem accelerator and a multiangle spectrograph. The ^{180}W target used was the same one used in the (p, t) experiment. The absolute cross section for this reaction was not measured so we quote the value obtained in Ref. 9.

III. EXPERIMENTAL RESULTS

Spectra for ^{186,184,182,180}W(p, t) and ^{180}W(t, p) reactions are shown in Figs. 1–5. The overall energy resolution in each case is of the order of 20 keV. Peaks identified as belonging to the appropriate W isotope in each case are labeled by numbers, while those arising from the small admixtures of other W isotopes and from reactions on C and O are labeled according to the specific reaction. The measured excitation energies for each isotope are listed in Tables II–VI in comparison with values from the literature. Also listed is the maximum value of the differential cross section for each transition.

In general, we have refrained from making spin assignments based on L values obtained from the angular distributions[13] measured in this study. The exception to this general rule is the case of $L = 0$ transitions where the highly oscillatory angular distributions, quite unlike other L values, make unambiguous identification reasonably easy. Angular distributions so identified are shown in Fig. 6. For other L values, the featureless angular distribution shapes make such assignments unreliable—especially, as we shall see, in the face of complex reaction mechanisms.

The results for individual nuclei are discussed below.

A. Nucleus ^{184}W

Only the states up to 1.2 MeV were analyzed in detail although a complete spectrum is shown. A search was made up to an excitation energy of 3 MeV for $J^{\pi} = 0^{+}$ states excited with greater than 3% of the ground-state yield. None were observed,

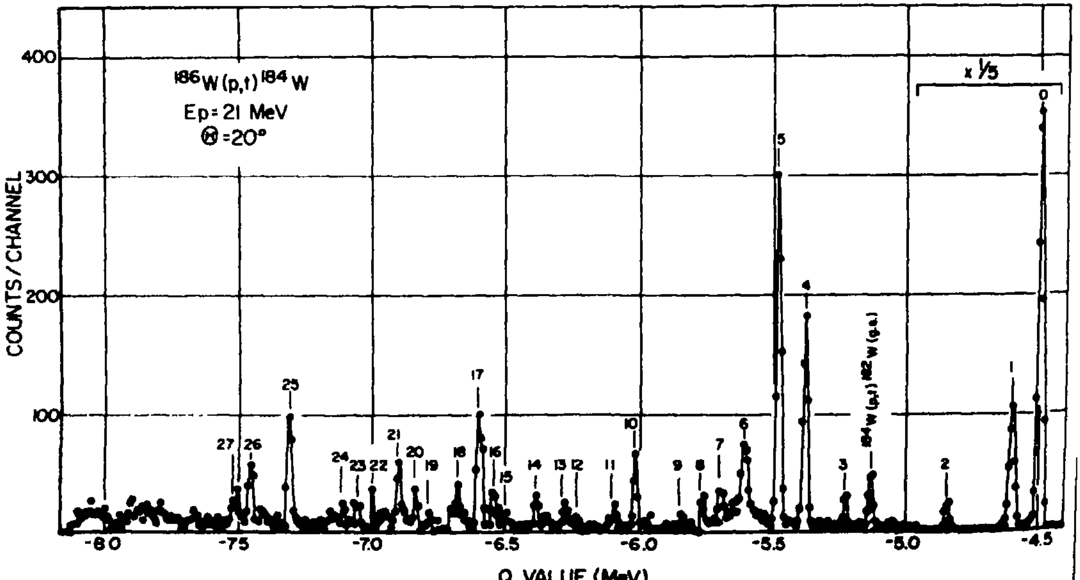

FIG. 1. Spectrum of the ^{186}W(p, t)^{184}W reaction at a proton bombarding energy of 21 MeV and a laboratory angle of 20°.

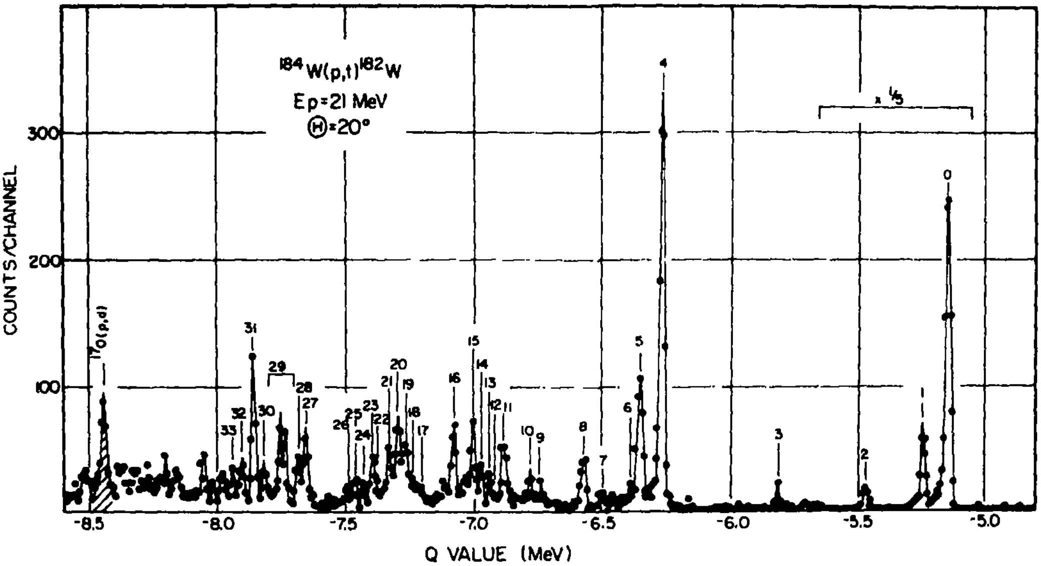

FIG. 2. Spectrum of the ^{184}W(p, t)^{182}W reaction.

except for the known 995 keV 0^+ state which is excited with 8% of the ground-state strength.

B. Nucleus ^{182}W

Angular distributions were extracted for all peaks below 3 MeV. The well-known 0^+ state at 1138 keV is strongly excited with 14% of the ground-state yield. In addition, three previously unreported 0^+ states were identified at excitation energies of 2520, 2552, and 2725 keV with 2%, 1%, and 3% of the ground-state yield, respectively. The outstanding result from the (t,p) experiment pop-

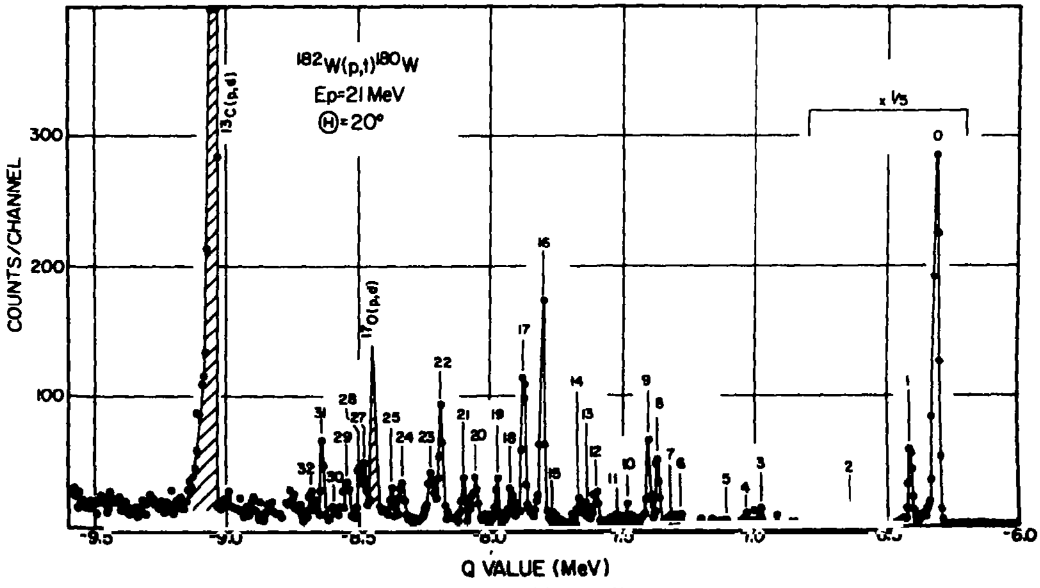

FIG. 3. Spectrum of the ^{182}W(p, t)^{180}W reaction.

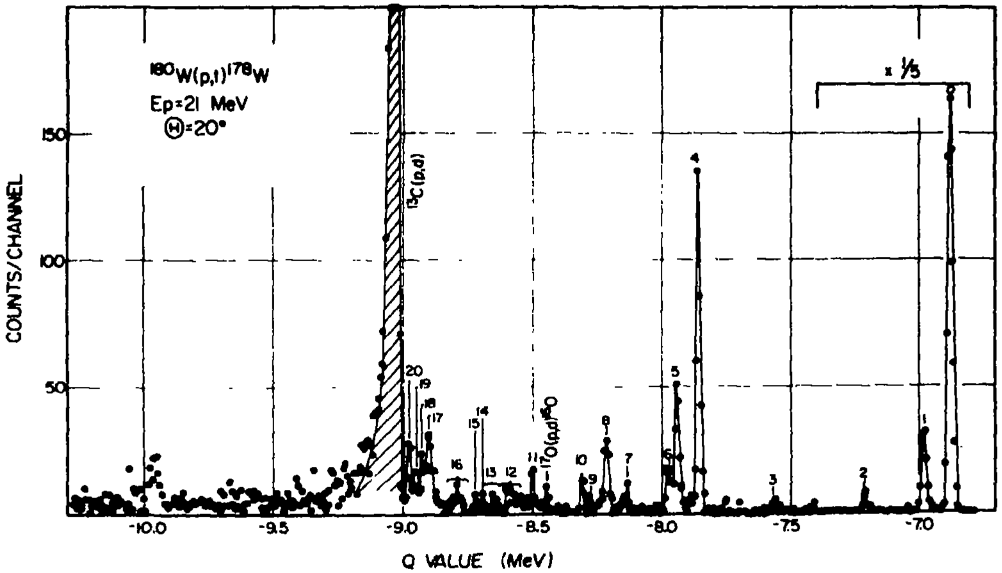

FIG. 4. Spectrum of the ^{180}W(p,t)^{178}W reaction.

ulating this nucleus is the extremely strong population of the 1138 keV 0^+ state.

C. Nucleus ^{180}W

Considerable emphasis was placed on the analysis of data for this nucleus since its structure previously had not been extensively probed with particle transfer reactions, and its level scheme not well established.[14] The $J^\pi = 2^+$ state reported at 1118 keV in a (d,d') study[15] is consistent with our observation of a state at 1120 keV with an angular distribution similar to that of the known $J^\pi = 2^+$ state in ^{182}W at 1219 keV. The state at 1321 keV is similarly identified with one member of a doublet seen in the (d,d') study at 1319 keV. The peaks labeled 4, 5, 6, and 7 are observed only at the limit of detection, so their assignment as states in ^{180}W must be considered tentative. More important, however, in this excitation region is the absence of a peak corresponding to the 908 keV $J^\pi = 0^+$ level suggested by Graetzer *et al.*[18] We do, however, observe a strong $L = 0$ transition to a state at 1516 keV excitation with an associated 2^+ state occurring at 1589 keV. One other weakly excited 0^+ state was located at 1695 keV.

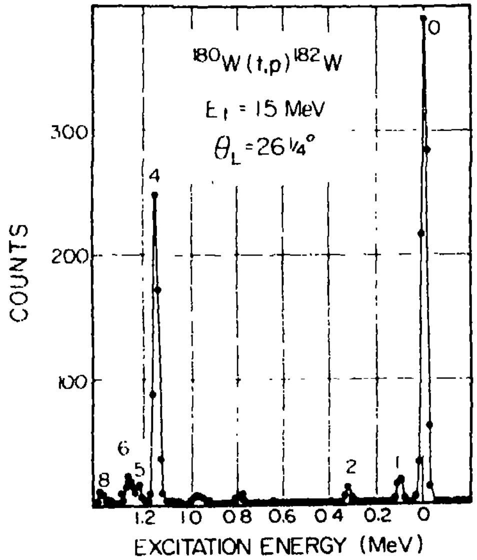

FIG. 5. Spectrum of the ^{180}W(t,p)^{182}W reaction at a triton bombarding energy of 15 MeV and a laboratory angle of $26\frac{1}{4}°$.

D. Nucleus ^{178}W

The spectrum above an excitation energy of 2 MeV is obscured by the presence of the intense ^{13}C(p,d)^{12}C(g.s.) peak. Below this excitation energy, however, three 0^+ states are identified. The lowest at 997 keV is most strongly excited with 9% of the ground-state yield. The $L = 0$ assignment for this state is consistent with the suggestion by Canty *et al.*[19] of the existence of a 0^+ state at 1001 keV. The assignments of levels at 1083 and 1278 keV, the 2^+ and 4^+ members of a band built on the 997 keV state, are also confirmed. Other 0^+

TABLE II. Levels populated in ^{186}W$(p,t)^{184}$W.

State number	J^{π} [a]	E_x (keV) Present [b]	E_x (keV) Previous [a]	$(d\sigma/d\Omega)_{max}$ (μb/sr)
0	0^+	0	0	740
1	2^+	109	111	144
2	4^+	364	364	25
3	$\left\{\begin{matrix} 6^+ \\ ^{182}\mathrm{W}(2^+) \end{matrix}\right\}$	744	748	5 [c]
4	2^+	901	903	37
5	$\left\{\begin{matrix} 0^+ \\ 3^+ \end{matrix}\right\}^{d}$	995	1002 1006	57
6	$\left\{\begin{matrix} 2^+ \\ 2^- \\ 4^+ \end{matrix}\right\}^{d}$	1122	1121 1130 1134	22
7	3^-	1214	1221	8

[a] From Ref. 8 unless otherwise indicated.

[b] Excitation energies ±10 keV.

[c] Upper limit.

[d] Strengths expected to be vanishingly small for unnatural parity states.

states at 1356 and 1643 keV are populated with 3% and 1% of the ground-state yield, respectively.

IV. DISCUSSION

A. Angular distribution shapes for members of the ground-state rotational bands

Angular distributions for (p,t) transitions to members of the ground-state rotational bands (GSRB) are shown in Fig. 7. The shapes for the ground-state transitions are in each case very similar, while the shapes of the $L=2$ transitions vary considerably, although smoothly, with mass. This result is at variance with the expectations for one-step direct transitions, which should have similar shapes for all masses. It is well known, however, that the inclusion of inelastic excitation effects is necessary in the description of angular distribution shapes and magnitudes in this mass region. The specific case of the ^{186}W$(p,t)^{184}$W reaction at 18 MeV bombarding energy has been discussed in detail in Refs. 6–8. A similar calculation was performed for the ^{182}W$(p,t)^{180}$W reaction at 21 MeV bombarding energy. The calculation was performed using the coupled-channel Born approximation (CCBA) code LISA of Ascuitto,[20] which includes inelastic couplings to all orders between the 0^+, 2^+, and 4^+ members of the GSRB, and to first order in the two-neutron transfer process. The transfer form factors were calculated[21] in the BCS framework using single-particle levels calculated in a deformed Woods-Saxon well with deformation parameters appropriate to these nuclei. The optical model parameters taken from elastic scattering studies on spherical nuclei[22,23] are listed in Table VII. The results of these calculations for members of the GSRB of ^{180}W are shown in Fig. 8. The CCBA calculations are shown as full curves; one-step distorted-wave Born approximation (DWBA) curves are shown dashed for the purposes of comparison. Only one normalization, chosen to fit the ground-state strength, was used for all of the curves.

TABLE III. Levels populated in ^{184}W$(p,t)^{182}$W. D and M indicate doublet and multiplet.

State number	J^{π} [a]	E_x (keV) Present [b]	E_x (keV) Previous [a]	$(d\sigma/d\Omega)_{max}$ (μb/sr)
0	0^+	0	0	700
1	2^+	100	100	200
2	4^+	330	329	26
3	6^+	690	680	6
4	0^+	1135	1138	100
5	2^+	1219	1221	60
6	2^+	1266	1257	12
7	3^-	1372	1374	7
8	4^+	1444	1443	12
9	$(6)^-$	1626	1621	3
10	$(5)^-$	1663 D	1660	5
11		1767 (D)		15
12	5^-	1814	1810 [d]	2
13		1824		8
14	2^+	1853	1851	6
15		1890		20
16	$\left\{\begin{matrix} (5,6,7^-) \\ (5,6) \end{matrix}\right\}$	1961	$\left\{\begin{matrix} 1960.4 \\ 1960.9 \end{matrix}\right\}$	22
17		2094		5
18		2117		3
19		2154		14
20		2175		17
21	(3^-)	2209	2209	15
22		2251		4
23		2278	2274 [d]	14
24		2311 D		13
25		2331 D		7
26		2363		34
27	0^+ [c]	2520 (D)		14
28	0^+ [c]	2552		10
29		~2625 M		30
30		2689		12
31	0^+ [c]	2725		22
32		2775		10
33		2815		5

[a] From Ref. 14 unless otherwise indicated.

[b] Excitation energies ±5 keV below 2 MeV, ±10 keV above 2 MeV.

[c] Assignment this work.

[d] From Refs. 8, 15, and 16.

The shape of the angular distribution of the ground-state transition is well reproduced by both DWBA and CCBA calculations, indicating that multistep inelastic effects for strong $L=0$ transitions are minimal. The falloff of the 2^+ angular distribution from 0° to 50° is not reproduced by the

TABLE IV. Levels populated in $^{182}W(p,t)^{180}W$. D indicates doublet.

State number	J^{π} [a]	E_x (keV) Present [b]	E_x (keV) Previous [a]	$(d\sigma/d\Omega)_{max}$ (μb/sr)
0	0^{+} [d]	0	0	500
1	2^{+}	109	104	180
2	4^{+}	332	338	22
3	6^{+}	688	689	4
4		(746) [e]		(2)
5		(831) [e]		(2)
6		(1012) [e]		(2)
7		(1034) [e]	(1036)	(3)
8	3^{-}	1083	1083	13
9	2^{+}	1120	1118	21
10		1190		3
11		1229	(1234)	2
12	$4^{+}, 5^{-}$	1321	1319	8
13		1359		4
14		1382		4
15		1470		5
16	0^{+} [c]	1516		36
17	2^{+} [c]	1589		51
18		1635		8
19	0^{+} [c]	1695		11
20		~1740 D		7
21		1824		6
22		1906		21
23		1944		17
24		2057		10
25		2095		10
26		2164		25
27		2203		8
28		2212		10
29		2265		10
30		2293		5
31		2356		18
32		2400		7

[a] From Ref. 17 unless otherwise indicated.

[b] Error ±5 keV below 2 MeV, ±10 keV above 2 MeV.

[c] Assignment this work.

[d] Doublet with $^{184}W(p,t)^{182}W$ (1135 keV).

[e] States near lower limit of observation, error ±10 keV.

TABLE V. Levels populated in $^{180}W(p,t)^{178}W$. D and M indicate doublet and multiplet.

State number	J^{π} [a]	E_x (keV) Present [b]	E_x (keV) Previous [a]	$(d\sigma/d\Omega)_{max}$ (μb/sr)
0	0^{+}	0	0	741
1	2^{+}	105	106	294
2	4^{+}	343	343	21
3	6^{+}	699	694	4
4	0^{+}	997	(1001) [d]	63
5	2^{+}	1083	1083	69
6	$\begin{Bmatrix} 2^{+} \\ 3^{-} \end{Bmatrix}$	1117 D	$\begin{Bmatrix} 1111 \\ 1120 \end{Bmatrix}$	16
7	4^{+}	1278	1276	6
8	0^{+} [c]	1356		22
9		1435		2
10		1450		6
11	0^{+} [c]	1643		9
12		~1720 D		10
13		~1790 M		3
14		~1825		1
15		~1860 M		2
16		~1960 M		6
17		2030		21
18		2060		11
19		2091		7
20		2116		11

[a] From Ref. 18 unless otherwise indicated.

[b] Excitation energies ±5 keV.

[c] Assignment this work.

[d] Suggested in Ref. 19.

DWBA, but is well described by the CCBA calculation. For the 4^{+} transition, it is hard to favor one calculation over the other. One obvious deficiency of the 2^{+} calculation is the overprediction of the magnitude. This magnitude is, however, sensitively dependent on the size of the pairing matrix element used in the BCS calculation. The value used here was chosen so that Δ, the BCS gap parameter, was equal to the experimental odd-even mass difference P_N. As we shall see later, there is a large gap in the single-particle energy spectrum at $N=108$ (^{182}W), thus perhaps making the above an unreliable choice. Further, in the absence of known deformation parameters for ^{180}W, the same values as for ^{182}W were used. The results presented here are thus considered satisfactory.

As mentioned, the shapes of the 2^{+} transitions change with mass. Studies[24] of ($^{12}C,^{14}C$) reactions on these isotopes also showed changing shapes as a function of mass. Detailed CCBA analysis of these data showed that although the magnitude of the multiple-step contributions to the total cross section remained more or less constant, the direct transfer contribution changed considerably. The

TABLE VI. Levels populated in $^{180}W(t,p)^{182}W$.

State number	J^{π} [a]	E_x (keV) Present [b]	E_x (keV) Previous [a]	$(d\sigma/d\Omega)_{max}$ (μb/sr)
0	0^{+}	0	0	283 [c]
1	2^{+}	100	100	77
2	4^{+}	330	329	33
3	6^{+}	690	680	
4	0^{+}	1135	1138	147
5	2^{+}	1219	1221	41
6	2^{+}	1266	1257	20
7	3^{-}	1372	1374	
8	4^{+}	1444	1443	10

[a] Reference 14.

[b] Values from $^{184}W(p,t)^{182}W$ experiment.

[c] Reference 9.

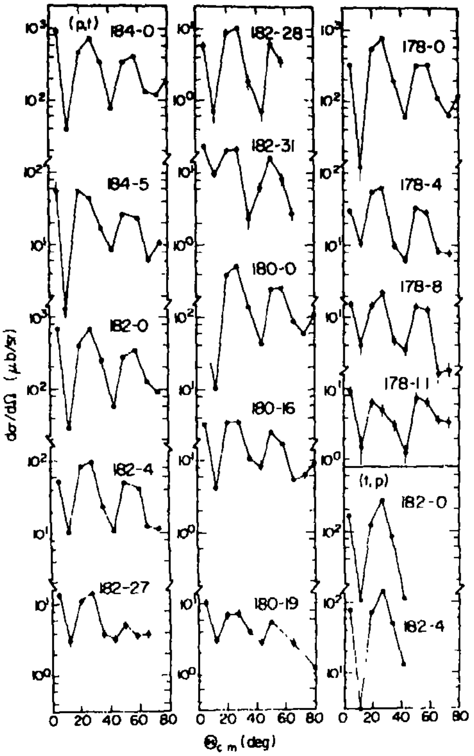

FIG. 6. Angular distributions showing characteristic $l=0$ shapes. Each distribution is identified by the mass of the final nucleus and level number as used in Figs. 1–5 and Tables II–VI.

direct route was found to be particularly weak for the $^{186}W \rightarrow {}^{184}W(2^+)$ transition, increasing with decreasing mass. The effect of this increase, added coherently to the constant multiple-step cross section, results in the changing angular distributions observed.

B. Cross-section systematics of ground states

In the pairing-rotation model,[25] the ground states of neighboring even-even superfluid nuclei are described by the same intrinsic wave function Φ_{BCS} but with different orientations in particle number space. Within this model, using the 0s approximation,[3] the (p,t) cross sections between ground states are given by

$$\sigma \sim \left(\frac{2\Delta}{G}\right)^2 f(Q),$$

where the last term contains only the kinematics of the reaction under consideration. The values of Δ used were set equal to P_N, which were calculated using the Nilsson-Prior prescription.[26] G was taken to be constant with mass. The results of these calculations are listed in Table VIII in comparison with the experimental values—normalized to the value for $^{184}W(p,t)^{182}W$. The overall agreement is good with the notable exception of $^{182}W(p,t)^{180}W$, for which the experimental cross section is only $\frac{2}{3}$ of the predicted value. This result is confirmed by the results of more detailed calculations in which form factors for each ground-state transition were generated from BCS calculations for the ground state of each isotope. The single-particle basis used was calculated in a deformed Woods-Saxon well with parameters suitable for the lead region and deformations taken from measurements for W isotopes. Mixing of up to four major shells was included in the calculations. The single-particle levels calculated in this way are shown in Fig. 9 in comparison with those deduced from experiment by Ogle *et al.*[27] The specific parameters employed in the BCS calculations are listed in Table IX together with the resulting ground-state cross sections and the appropriate experimental values. The comparison of experimental and theoretical cross sections is also shown in Fig. 10. Once again, the agreement is good with the notable exception of the $^{182}W(p,t)^{180}W$ ground-state transition. This discrepancy between these two calculations and experiment is not unexpected, due to the occurrence of the subshell closure at $N=108$ (^{182}W). The BCS calculations (and pairing-rotational model) are only expected to describe average properties of nuclei, and are thus unable to account for phenomena arising from specific nonuniformities in the underlying single-particle level scheme, which require more sophisticated approaches such as the exact diagonalization of the pairing force.

That there is a gap in the single-particle levels at $N=108$ which has a significant effect on the structure of ground states is clear from both a study of the calculated single-particle level scheme and a study of the masses of W nuclei. The discontinuity in the values of the two-neutron separation energies illustrated in Fig. 11 indicates a gap of approximately 1 MeV, comparable with that observed in Yb ($N=104$) or Sn ($N=64$). The presence of this gap reduces the effective degeneracy in the vicinity of the Fermi surface at $N=108$ resulting in a reduction in the pair transfer reaction cross sections on this target nucleus.

C. Transitions to excited $J^\pi = 0^+$ states

The conventional expectation for basically superfluid nuclei is that virtually all the $L=0$ transfer

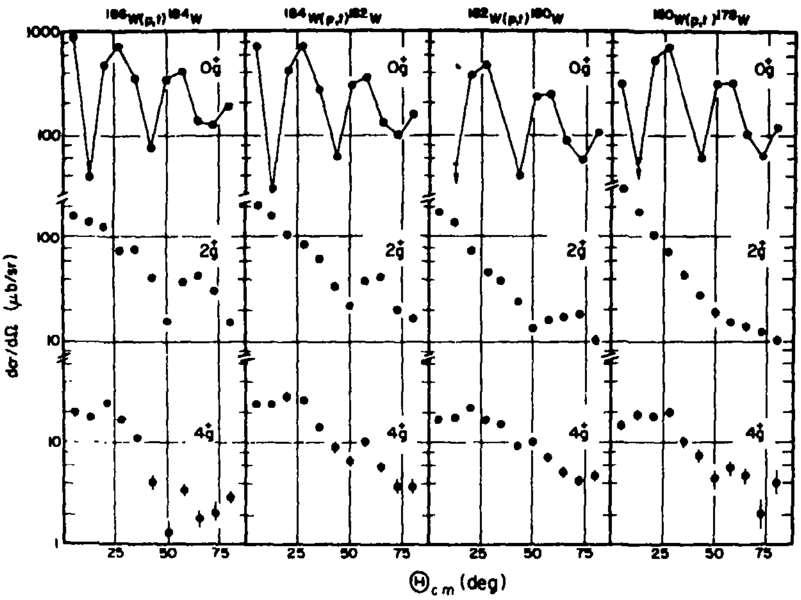

FIG. 7. Angular distributions of (*p, t*) transitions to members of the ground-state rotational bands of the even W isotopes.

strength will reside in the ground state. Thus, the observation of substantial $L=0$ transfer strength to excited states is worthy of note and merits explanation. The usual description of excited $J^\pi = 0^+$ states in deformed nuclei is the geometrical one of a mass vibration in the β_2 degree of freedom. Microscopically, such β vibrations are described as two quasiparticle collective excitations involving pairs of Nilsson orbits with the same $J^\pi K$, but otherwise different quantum numbers. Within the space of single-particle orbitals spanning a 4 MeV range about the Fermi surface of the W isotopes, only two such configurations are possible—$\frac{1}{2}|510| \otimes \frac{1}{2}|521|$ and $\frac{7}{2}|503| \otimes \frac{7}{2}|514|$. Calculations of the strengths associated with these configurations indicate, however, only extremely small cross sections when compared with typical nonbroken pair configurations. The conventional explanation is therefore excluded in the present case.

The measured strengths for excited 0^+ states, corrected for kinematic effects, are listed in Table X. Also noted, where available, are the 0^+-2^+ spacings for the bands built on these states and also the ratios of cross sections for these pairs of states. It is reasonably obvious that, of the stronger excited states, there is a division into two classes. Namely, those in the high mass isotopes with 0^+-2^+ spacings similar to those of the ground bands and with $\sigma(2^+)/\sigma(0^+)$ ranging from 0.10–0.40, and those in the lower masses with 0^+-2^+ spacings smaller than the former and with $\sigma(2^+)/\sigma(0^+)$ of the order of 1.3. We further note that one of the latter class, the 1516 keV ^{180}W state, is characterized by a totally different excitation energy than those of other first excited 0^+ states (~1000

TABLE VII. Optical model parameters used in DW calculations.

Channel	V (MeV)	r_0 (fm)	r_c (fm)	a (fm)	W (MeV)	W_D (MeV)	r_I (fm)	a_I (fm)	V_{so} (MeV)	r_{so} (fm)	a_{so} (fm)
$W+p$ [a]	−57.0	1.17	1.25	0.75	−1.9	35.2	1.32	0.64	−24.8	1.01	0.75
$W+t$ [b]	−161.4	1.20	1.25	0.72	−25.0		1.30	0.84	−10.0	1.20	0.72

[a] Reference 22.

[b] Reference 23.

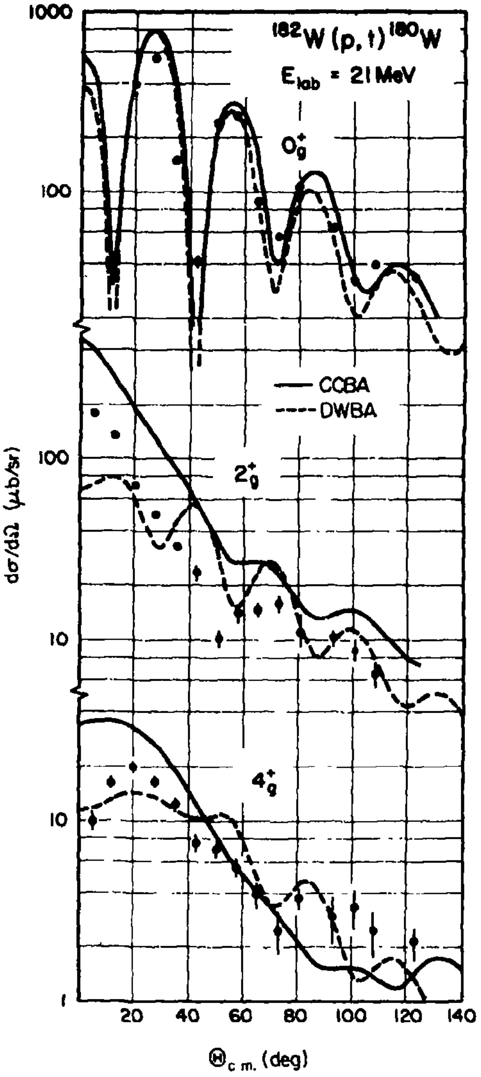

FIG. 8. Comparison of CCBA and DWBA calculations for ^{182}W$(p,t)^{180}$W transition. The details of the calculations are described in the text.

TABLE VIII. Ground-state (p,t) strengths in the pairing-rotational limit.

Mass	P_N [a]	P_N (average) [b]	$f(Q)$ [c]	$P_N^2 f(Q)$ [d]	Expt [e]
186	0.797				
184	0.720	0.758	1.05	713	740
182	0.809	0.765	1.06	720	720
180	0.805	0.807	1.00	750	500
178	0.832	0.818	0.92	698	744

[a] Calculated using the Nilsson-Prior prescription (Ref. 26).

[b] Average of two neighboring values.

[c] Kinematic factor from DWBA calculations.

[d] Pairing-rotational prediction, normalized to the ^{184}W$(p,t)^{182}$W(g.s.) transition.

[e] Taken to be the differential cross section at the second maximum ≈27½°.

keV).

A clue to the origin of this division into two classes is shown in Fig. 12 where the strengths of $L = 0$ transitions are shown plotted as a function of (p,t) Q value rather than excitation energy in the residual nucleus. It is seen that the 997 keV ^{178}W state, the 1516 keV ^{180}W state, and the group of three states near 2600 keV in ^{182}W have almost identical (p,t) Q values. This constancy of Q value can be explained if the structure of these states is such that they are populated by removal of a pair of neutrons from the same single-particle level or group of levels. This picture, while provid-

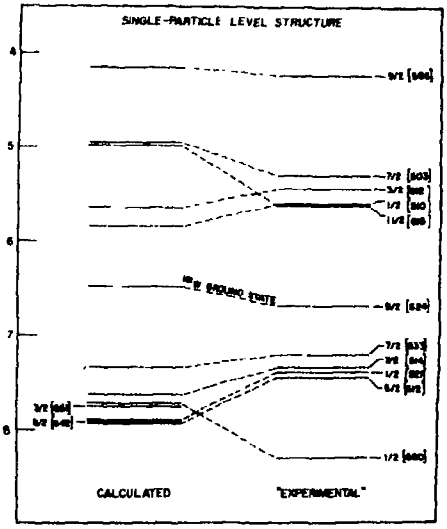

SINGLE-PARTICLE LEVEL STRUCTURE
SINGLE-PARTICLE BINDING ENERGY (MeV)
4
5
6
7
8
W GROUND STATE
CALCULATED
"EXPERIMENTAL"
7/2 [503]
1/2 [510]

FIG. 9. Single-particle levels calculated in a deformed Woods-Saxon well ($\beta_2 = 0.221$, $\beta_4 = 0.087$) compared with the level scheme extracted from experimental data (Ref. 27).

TABLE IX. Input and results for BCS form factor calculations.

Target mass	Q value (MeV)	β_2[a]	β_4[a]	G[b]	P_N	$(d\sigma/d\Omega)_{\text{second max}}$ (μb/sr)	Expt (μb/sr)
186	−4.470	0.209	−0.088	0.143	0.797	681	740 ± 75
184	−5.120	0.221	−0.087	0.140	0.720	720	720 ± 70
182	−6.271	0.219	−0.069	0.146	0.809	836	500 ± 75
180	−6.843	0.219	−0.069	0.143	0.805	855	744 ± 75
178		0.219	−0.069	0.138	0.832		

[a] ^{186,184}W deformations from Lee *et al.* (Ref. 2) scaled to $r_0 = 1.25$ fm, ^{182}W deformation from Aponick *et al.* (Ref. 28) other deformations taken to be the same as for ^{182}W.

[b] Value chosen so that Δ P_N.

[c] Normalized to ^{184}W$(p,t)^{182}$W experimental result.

ing a ready explanation of the constant Q values of these states, does not immediately provide reason for their substantial strength. The occurrence of such strength, within 2Δ of the ground states in the cases of ^{178}W and ^{180}W, also requires a specific mechanism preventing the pairing force from removing the pair transfer strength associated with these orbitals into the ground state. Such a mechanism has been proposed by Griffin, Jackson, and Volkov,[29] Bes, Broglia, and Nilsson,[30] and also by Van Rij and Kahana[31] in connection with a similar effect observed in Actinide nuclei.[4,32] The states arising from this mechanism have been termed "pairing isomers."[4,3] Specifically, the pairing matrix elements which mix pairs in prolate ($\partial\epsilon/\partial\beta_2 < 0$) and oblate ($\partial\epsilon/\partial\beta_2 > 0$) orbitals are proposed to be smaller than those connecting pairs only in prolate orbitals or only in oblate orbitals. This then provides a mechanism for partially decoupling the two sets of single-particle orbitals, resulting in the existence of two 0^+ states with substantial pair transfer strength. Examination of the calculated single-particle level scheme does indeed show a group of four prolate orbitals ($\frac{1}{2}$|521], $\frac{3}{2}$|651], $\frac{5}{2}$|512], and $\frac{5}{2}$[642]) close to a binding energy of 8 MeV, whereas the majority of levels comprising the Fermi surface are oblate. Further, the pair pickup strength associated with this group of orbitals is calculated to be approximately 10% of that for a typical ground-state transition, consistent with the experimental results. It is also worth noting that the direct 2^+ transfer strength associated with this group of orbitals is found to be considerably larger than for the oblate orbitals in the vicinity of the Fermi surface—again consistent with the experimental observations.

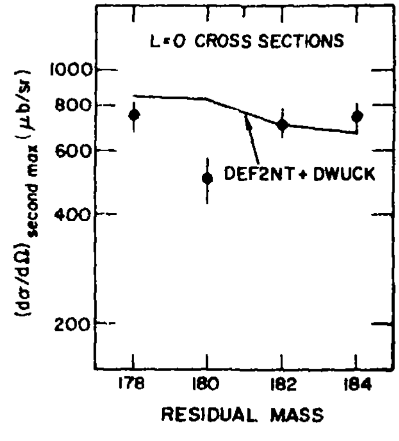

FIG. 10. Measured ground-state cross sections in comparison with the results of DWBA calculations using BCS form factors described in the text and the code DWUCK (Ref. 38).

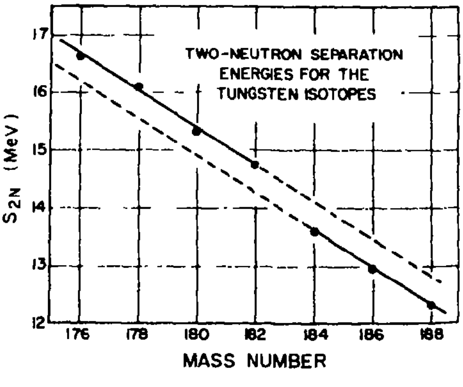

FIG. 11. Experimental values of two-neutron separation energies for even W nuclei plotted as a function of mass. The gap at ^{182}W is clearly visible.

TABLE X. $L=0$ strengths to 0^+ states.

Nucleus	Ex (keV)	S/S(g.s.)[b] (%)		$E(2^+-0^+)$ keV	$\sigma(2^+)/\sigma(0^+)$[a]	
^{184}W	0	100		109	0.19	
	1002	8		119	<0.39	
^{182}W	0	100	100[c]	100	0.29	0.27[c]
	1135	16	52	119	0.12	0.14
	2620	2				
	2552	2				
	2725	5				
^{180}W	0	100		104	0.36	
	1516	13		73	1.42	
	1695	3				
^{178}W	0	100		106	0.40	
	997	12		86	1.10	
	1356	5				
	1643	2				

[a] Ratio of maximum cross sections from Tables I–VI.
[b] (p,t) unless noted.
[c] (t,p).

Another important piece of evidence regarding the correctness of this interpretation concerns the results of the (p,t) reaction on ^{183}W in which $L=0$ transitions to states corresponding to the coupling of the odd particle to the ground and excited 0^+ state of the even core are observed. The details of that study are contained in the second of these two papers. Suffice it to say here that these results support the above interpretation.

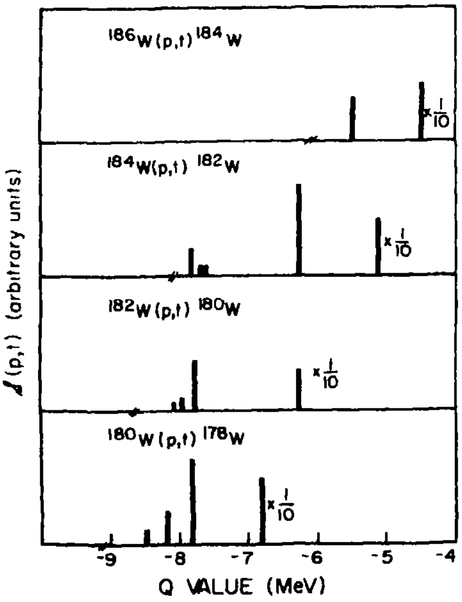

FIG. 12. Strengths for $L=0$ (p,t) transitions plotted as a function of Q value.

The other group of excited 0^+ transitions, those to the 1138 keV state in ^{182}W [(p,t) and (t,p)] and to the 995 keV state in ^{184}W can be understood in several ways. Microscopically, these arise from the previously mentioned subshell closure at $N=108$ and are therefore four quasiparticle excitations of a pairing vibrational nature. Calculations due to Mikoshiba *et al.*[34] in fact predict the 0^+ state in ^{182}W to be primarily a pair-vibrational rather than beta-vibrational state. Similarly, the random phase approximation (RPA) calculations of Ascuitto and Sorenson[20] with pairing-plus-quadrupole forces were able to correctly reproduce the (p,t) population of the 995 keV state in ^{184}W, although no identification of this state as a pair vibration was made. Discussion of these states in terms of pure pairing vibrations is, however, difficult. The data possess features of both the pairing-vibration and pairing-rotation schemes, indicating some intermediate situation between the above two extremes. To illustrate this, Fig. 13 shows the energies of the ground and excited 0^+ states plotted as suggested by Bohr.[25] These ground-state energies are well fitted by the pairing rotation expression $E=aI(I+1)$ where $I=|N-108|/2$ and $a=293$ keV and, as mentioned previously, the more or less constant ground-to-ground transition strengths are consistent with the existence of a superfluid pairing-rotational band. This picture is unable, however, to explain the excited state transitions which must be described in terms of pairing vibrations. The pairing-vi-

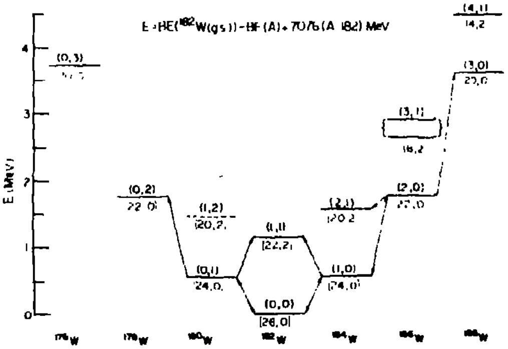

FIG. 13. Energies of ground and excited 0^+ states plotted in the manner suggested in Ref. 25. The numbers assigned to each level are the pairing vibration (n (n_π, n_ν) and SU(3) [λ, μ] quantum numbers, respectively. The excited 0^+ states in ^{182}W, ^{180}W, and ^{178}W with constant Q value are shown dotted and the unconfirmed 0^+ state in ^{180}W shown dashed.

bration scheme correctly predicts the occurrence of an excited 0^+ state in ^{182}W which should be strongly populated in both (p,t) and (t,p) reactions and further correctly predicts the occurrence of excited (p,t) strength and lack of excited (t,p) strength in the high mass isotopes. It is, however, unable to explain the ground-to-ground transition strengths which should increase linearly going away from the subshell closure and also underpredicts the ground-state energies.

These discrepancies lead us naturally to consider the interacting boson approximation (IBA) model of Arima and Iachello[35-37] which contains both of the above pairing models as limiting cases, and also introduces quadrupole pairs (d bosons) and all interactions between them. The application of this model to the present data has been recently discussed.[12] We therefore merely reiterate the conclusion of Ref. 12 that the predictions of the IBA model are in better accord with the experimental results than either the pairing-vibration or the pairing-rotational models. We further note that this model has the possibility of achieving still more detailed agreement with the data when numerical calculations are performed within this framework.

V. SUMMARY AND CONCLUSIONS

We have presented results for (p,t) reactions on all stable even W isotopes and the (t,p) reaction on ^{180}W. Besides the basic spectroscopic information, several systematic features of the data have emerged and been investigated. These are:

(1) The role of multistep processes in the shapes of members of the ground-state rotational bands.

(2) The systematics of the ground-state cross sections in the framework of both microscopic and macroscopic collective models.

(3) The division of excited 0^+ states into two groups, one with the qualitative characteristics of a pairing isomer and the other with similarities to pairing vibrations.

In all these, the stability of shape and consequent stability of the underlying single-particle structure has been important in enabling the recognition of the simplicities and origins of these phenomena. Further calculations within the framework of the IBA will surely prove rewarding.

VI. ACKNOWLEDGMENTS

The authors would like to thank R. Ascuitto and F. Iachello for many helpful theoretical discussions. The careful scanning of Mrs. M. Fitzgerald, Mrs. D. Purcell, and Mrs. M. Synder is also gratefully acknowledged. The assistance of Dr. W. D. Callender, Dr. S. B. DiCenzo, and Dr. R. L. White in the data taking is greatly appreciated. We are indebted to J. G. Tracey of Oak Ridge National Laboratory for the manufacture of the ^{180}W target.

---

[1] F. Bernthal, B. D. Jeltema, J. S. Boyno, T. L. Khoo, and R. A. Warner, Phys. Rev. Lett. 33, 915 (1974).

[2] I. Y. Lee, J. X. Saladin, J. Holden, J. O'Brien, C. Baktash, C. Bemis, P. H. Stelson, F. K. McGowan, W. T. Milner, J. L. C. Ford, R. L. Robinson, and W. Tuttle, Phys. Rev. C 12, 1483 (1975).

[3] R. A. Broglia, Ole Hansen, and C. Riedel, in *Advances in Nuclear Physics*, edited by M. Baranger and E. Vogt (Plenum, New York, 1973), Vol. 6, p. 287.

[4] J. V. Maher, J. R. Erskine, A. M. Friedman, R. H. Siemssen, and J. P. Schiffer, Phys. Rev. C 5, 1380 (1972).

[5] M. Oothoudt and N. M. Hintz, Nucl. Phys. A213, 221 (1973).

[6] R. J. Ascuitto, C. H. King, and L. J. McVay, Phys. Rev. Lett. 29, 1106 (1972).

[7] C. H. King, R. J. Ascuitto, N. Stein, and B. Sørensen, Phys. Rev. Lett. 29, 71 (1972).

[8] C. H. King, Ph.D. dissertation, Yale University, 1973 (unpublished).

[9] R. F. Casten, D. Burke, and Ole Hansen, Nucl. Phys. A261, 445 (1976).

[10] J. D. Garrett and Ole Hansen, Nucl. Phys. A276, 93 (1977).

[11] M. H. Mortensen, R. R. Betts, and C. K. Bockelman, Phys. Lett. 70B, 17 (1977).

[12] R. R. Betts and M. H. Mortensen, Phys. Rev. Lett. 43, 616 (1979).

[13] Complete angular distributions of all transitions are contained in M. H. Mortensen, Ph.D. dissertation, Yale University, 1978, copies of which are available from the authors.

[14] M. R. Schmorak, Nucl. Data Sheets 14, 559 (1975).

[15] C. Gunther, P. Kleinheinz, R. F. Casten, and B. Elbek, Nucl. Phys. A172, 273 (1971).

[16] B. D. Jeltema, F. M. Bernthal, T. L. Khoo, and C. L. Dors, Nucl. Phys. A280, 21 (1977).

[17] L. R. Greenwood, Nucl. Data Sheets 15, 559 (1975).

[18] R. Graetzer, G. B. Hagemann, K. A. Hagemann, and B. Elbek, Nucl. Phys. 76, 1 (1966).

[19] M. J. Canty, N. E. Davison, D. A. Dohan, and P. Yuen, Nucl. Phys. A265, 1 (1976).

[20] R. J. Ascuitto and B. Sørensen, Nucl. Phys. A190, 297 (1972); A190, 309 (1972).

[21] R. J. Ascuitto, Code DEF2NT (unpublished).

[22] F. D. Becchetti and G. W. Greenlees, Phys. Rev. 182, 1190 (1969).

[23] F. D. Becchetti and G. W. Greenlees, in *Polarization*

Phenomena in Nuclear Reactions, edited by H. Barschall and W. Haeberli (University of Wisconsin Press, Madison, Wisconsin, 1971), p. 682.

[24]K. A. Erb, D. L. Hanson, R. J. Ascuitto, B. Sørensen, J. S. Vaagen, and J. J. Kolata, Phys. Rev. Lett. 33, 1102 (1974).

[25]Aa. Bohr, in *Nuclear Structure* (International Atomic Energy Agency, Vienna, 1968), p. 179.

[26]S. G. Nilsson and O. Prior, Kgl. Danske Viedenskab. Selskab. Mat. Fys. Medd. 32, 16 (1961).

[27]W. Ogle, S. Wahlborn, R. Piepenbring, and S. Fredriksson, Rev. Mod. Phys. 43, 424 (1971).

[28]A. A. Aponick, C. M. Chesterfield, D. A. Bromley, and N. K. Glendenning, Nucl. Phys. A159, 367 1970).

[29]R. E. Griffin, A. D. Jackson, and A. B. Volkov, Phys. Lett. 36B, 281 (1971).

[30]D. R. Bes, R. A. Broglia, and B. Nilsson, Phys. Lett. 40B, 338 (1972).

[31]W. I. van Rij and S. H. Kahana, Phys. Rev. Lett. 28, 50 (1972).

[32]J. V. Maher, J. R. Erskine, A. M. Friedman, J. P. Schiffer, and R. H. Siemssen, Phys. Rev. Lett. 25, 302 (1970).

[33]I. Ragnarsson and R. A. Broglia, Nucl. Phys. A263, 315 (1976).

[34]O. Mikoshiba, R. K. Sheline, T. Udagawa, and S. Yoshida, Nucl. Phys. A101, 202 (1967).

[35]A. Arima and F. Iachello, Phys. Rev. Lett. 35, 1069 (1975); Ann. Phys. (N.Y.) 99, 253 (1976); 111, 201 (1978).

[36]A. Arima and F. Iachello, Phys. Rev. C 16, 2085 (1977).

[37]F. Iachello (private communication).

[38]P. D. Kunz, Code DWUCK (unpublished).

PHYSICAL REVIEW C VOLUME 21, NUMBER 6 JUNE 1980

W(p,t) reactions. II. Odd target

M. H. Mortensen, R. R. Betts, and C. K. Bockelman
A. W. Wright Nuclear Structure Laboratory, Yale University, New Haven, Connecticut 06520

(Received 20 August 1979)

Data for the ^{183}W$(p,t)^{181}$W reaction are presented. States corresponding to the coupling of the odd neutron to collective excitations of the even core are identified and used to test the microscopic structure of these collective excitations. *In particular, the proposed nature of the pairing isomers observed in the neighboring* even nuclei is confirmed. Information concerning the previously observed anomalous population of 2^+ states in this mass region is also presented.

[NUCLEAR REACTIONS ^{183}W(p,t), $E_p = 21$ MeV; measured $\sigma(E_t,\Theta)$. ^{181}W deduced levels, L, π, J. Nuclear structure analysis.]

I. INTRODUCTION

In this, the second of our papers on W(p,t) reactions, we present and discuss the results for the single stable odd W isotope ^{183}W. The spectroscopic information obtainable from two-neutron transfer reactions on odd targets is generally rather limited. However, in this particular case we are able to glean a considerable amount of structural information, particularly from the effect of the coupling of the odd neutron to collective excitations of the even core. We are thus able to test some of the hypotheses presented in the preceding paper concerning the even targets,[1] and in the case of excited 2^+ states, shed new light on the origin of some previously unexplained anomalies.

II. EXPERIMENTAL METHOD

The details of the experimental method are identical to those presented in Ref. 1. The target consisted of ~70 μgm/cm^2 of WO$_3$ enriched to 90% in ^{183}W deposited on a 20 μgm/cm^2 C backing. Other isotopes present in the target were ^{182}W (3.5%), ^{184}W (5.6%), and ^{186}W (1.1%). The absolute cross sections were obtained from the ^{184}W(p,t) experiment as described in Ref. 1.

III. EXPERIMENTAL RESULTS

A spectrum taken at a laboratory angle of 20° is shown in Fig. 1—note the reduction by a factor of 5 for peaks 3–12. The overall resolution is ~20 keV. Peaks identified as belonging to ^{181}W are numbered and also their measured excitation energies listed in Table I in comparison with previous results.[2,3] Angular distributions for some of the stronger peaks are shown in Fig. 2.

The most prominent peak in the spectrum (No. 5) has a distinct $L=0$ angular distribution. This transition presumably leads to the $J^\pi = \frac{1}{2}^-$ bandhead of the band built on the $\frac{1}{2}^-[510]$ Nilsson orbit, since the odd neutron of the ^{183}W ground state has been assigned to that single-particle state.[4] Based on published level schemes, we expect that this $\frac{1}{2}^-$ state at 458 keV would not be completely resolved from the $\frac{3}{2}^-$ state at 450 keV and barely resolved from the $\frac{7}{2}^-$ state at 476 keV. The deep minima in the angular distribution, however, unambiguously identify this transition as $L=0$ and not $L=2$ or 4, which would be required for the $\frac{3}{2}^-$ and $\frac{7}{2}^-$ states, respectively. The maximum contribution from these other states can be estimated to be 5 μb/sr of the maximum cross section of 280 μb/sr for this peak.

Besides the $L=0$ transition to the $J^\pi = \frac{1}{2}^-$ bandhead of the $K^\pi = \frac{1}{2}^-$ band, $L=2$ transitions to the $\frac{3}{2}^-$ and $\frac{5}{2}^-$ members of this band are also observed, being peaks Nos. 7 and 8, respectively.

The above three transitions correspond to the states formed by the coupling of the odd neutron to the 0^+ and 2^+ members of the ground-state rotational band of the even score. Similarly, strong transitions corresponding to the gamma-vibrational and excited 0^+ modes should also be observable. Assuming that the coupling between the $\frac{1}{2}^-$ neutron and the gamma-vibrational degree of freedom is weak, we would expect to see two transitions, to $\frac{3}{2}^-$ and $\frac{5}{2}^-$ states, corresponding to the

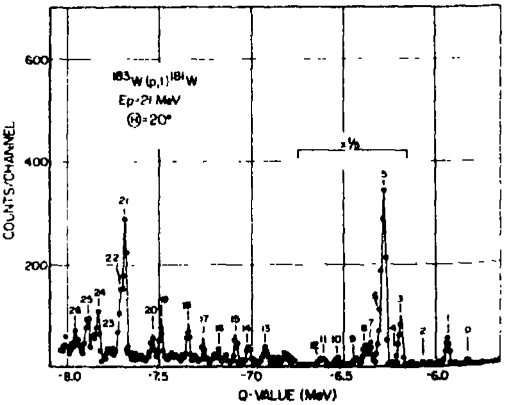

FIG. 1. Spectrum of the ^{183}W$(p,t)^{181}$W reaction at 21 MeV bombarding energy and a laboratory angle of 20°.

© 1980 The American Physical Society

TABLE I. Levels populated in ^{183}W$(p,t)^{181}$W.

State number	J^{π} [a]	Present [b]	Previous [a]	$(d\sigma/d\Omega)_{\max}$ (μb/sr)
0	$\frac{9}{2}^{+}$	0	0	
1	$\frac{11}{2}^{+}$		113	
2	$\frac{13}{2}^{+}$		250	
3	$\frac{5}{2}^{-}$	365	366	70
4	$\frac{1}{2}^{-}$ $\frac{7}{2}^{-}$	409 D	385 409	7
5	$\frac{3}{2}^{-}$ $\frac{1}{2}^{-}$	454	450 458	280
6	$\frac{7}{2}^{-}$ $\frac{5}{2}^{-}$	489	476 488	72
7	$\frac{9}{2}^{-}$ $\frac{3}{2}^{-}$	531	527 529	34
8	$\frac{5}{2}^{-}$	560	560	63
9	$\frac{9}{2}^{-}$	610	~611	11
10		714	715	13
11		784		8
12	$\frac{5}{2}^{-}$	807	807	11
13		1093		7
14		1193		8
15		1262		6
16		1377		7
17		1437		6
18		1518		8
19		1667		14
20		1712		7
21	$\frac{1}{2}^{-}$ [c]	1864		44
22		1892		35
23		1945		5
24		2015		12
25		2034		8
26		2067		17

[a] From Refs. 2, 3, and 4, unless otherwise indicated.
[b] Calculated assuming $\frac{5}{2}^{-}$ state at 365 keV excitation, error ± 5 keV.
[c] Assignment this work.
[d] Doublet.

$L=2$ strength in the even target case. These should occur at about 1 MeV above the $\frac{1}{2}^{-}[510]$ state, i.e., at an energy roughly corresponding to the excitation energy of this mode in the even nucleus. No such transitions are seen. Instead, a strong $L=2$ transition to the $\frac{5}{2}^{-}$ state at 365 keV (No. 3) is seen—the Nilsson assignment of this state being $\frac{5}{2}^{-}[512]$. The implications of this observation will be discussed in Sec. IV.

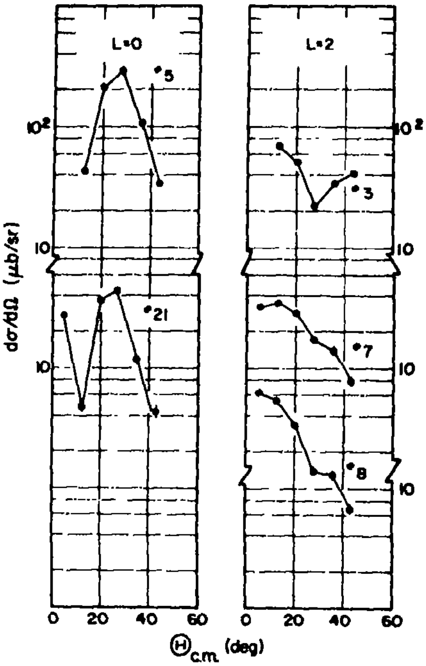

FIG. 2. Angular distributions for some of the stronger transitions.

A strong $L=0$ transition is found at an excitation energy of 1864 keV (No. 21) and is interpreted as arising from a state formed by the coupling of the odd neutron to the excited 0^{+} state in ^{180}W at 1516 keV. There is a barely resolved state (No. 22) at an excitation energy of 1892 keV, but this was easily separated by standard peak fitting procedures.

IV. DISCUSSION

A. $L=0$ transitions

As discussed above, strong $L=0$ transitions are observed to states at 454 and 1864 keV. These correspond to the strong $L=0$ transitions observed in the (p,t) reaction on the even core, but with an extra neutron in Nilsson orbit $\frac{1}{2}^{-}[510]$ coupled to the initial and final states. This supposition is strengthened by the near equality of the Q values for these two transitions and the ^{182}W$(p,t)^{180}$W(g.s.) and ^{182}W$(p,t)^{180}$W (1516 keV) transitions, respectively. These two states therefore become very important in our understanding of the underlying microstructure in the even target cases. Microscopically, the 454 keV transition corresponds identically to the $^{182}W(p,t)^{180}W$(g.s.) transition, but with one important difference. The odd particle occupies one of the orbits from which a pair of neutrons is picked up in the even case. This orbit is then said to be "blocked" and the odd target $L=0$ cross section reduced by the appropriate amount. Experimentally, the $^{182}W(p,t)^{180}W$(g.s.) transition has a maximum cross section of 500 μb/sr, whereas the present 454 keV transition has only 280 μb/sr—a 40% decrease. This number can then be used as a sensitive test of the microscopic form factors used to describe the even target ground-state strengths. A calculation to do just this was performed as follows.

The standard set of single-particle levels described in the previous paper was used to generate a BCS form factor which was then used in conjunction with the distorted-wave Born approximation (DWBA) code DWUCK[7] to calculate the strength of the $^{182}W(p,t)^{180}W$(g.s.) transition. Precisely the same calculation was then performed, except that the $\frac{1}{2}^-[510]$ level was effectively blocked by artificially respecifying its binding energy so as to place that level well above the Fermi surface. Its occupancy was then such that it contributed negligibly to the final cross section. This calculation predicts a blocking effect of 45%, in reasonable agreement with experiment. The calculated values of Δ did not, however, agree well with the experimental values of P_N for either ^{181}W or ^{183}W, reflecting not unexpected deficiencies in the single-particle spectrum used. The calculation was repeated using a value of the pairing matrix element chosen so that $\Delta = P_N$. A blocking of 36% was predicted, again in good agreement with the experimental value of 40%.

For the 1864 keV $L=0$ transition, it was proposed in Refs. 1 and 5 that the 1516 keV 0^+ state in ^{180}W as well as 0^+ states at 997 in ^{178}W and near 2600 keV in ^{182}W, arise from pair pickup from a group of orbitals below and decoupled from the Fermi surfaces of the target nuclei. An important consequence of this picture is that in the odd target case, not only should there also exist an analogous $L=0$ transition, but also that, owing to the decoupling, this transition should not exhibit blocking. As we have seen, the transition corresponding to the even ground-state transition is blocked by ≈40%—the results for the excited state transition do not show this effect. The maximum cross section for $^{182}W(p,t)^{180}W$(1516 keV) is 36 μb/sr, the 1864 keV $^{183}W(p,t)^{181}W$ transition has 44 μb/sr in agreement with expectations. These results are illustrated in Fig. 3.

B. $L=2$ transitions

Two $L=3$ transitions are observed corresponding to the $\frac{3}{2}^-$ and $\frac{5}{2}^-$ states formed by the coupling of the odd neutron to the 2^+ member of the even core ground-state rotational band. The angular distributions for these transitions, the $L=0$ transition to the 454 keV $\frac{1}{2}^-$ state and the $^{182}W(p,t)^{180}W$ transitions to the 0^+ and 2^+ members of the ground band are shown in Fig. 4. As discussed above,

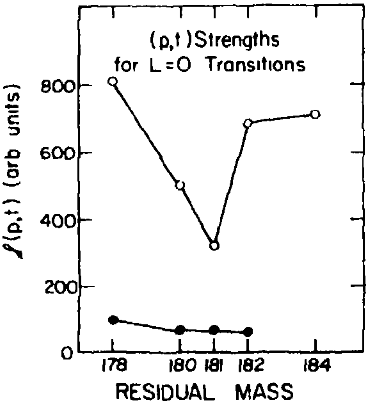

FIG. 3. Strengths for $L=0$ transitions throughout the W isotopes. This illustrates the blocking of the ground-state strength (open circles) and the constant strength for the excited $L=0$ transitions (closed circles).

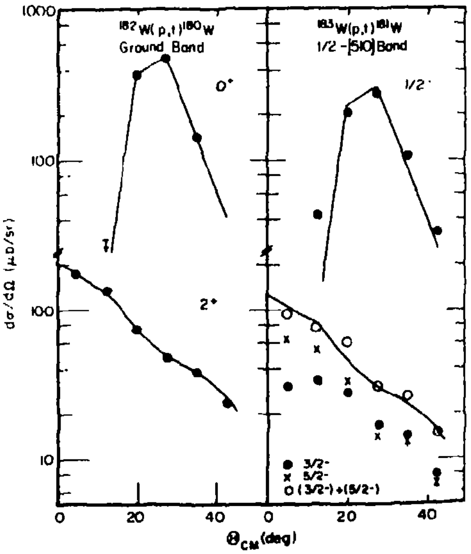

FIG. 4. Comparison of angular distributions for the transitions to members of the ground band of ^{180}W and the corresponding states in ^{181}W. The shapes of the ^{180}W transitions are shown superimposed on the ^{181}W data.

apart from the blocking effect, the $L=0$ shapes are identical and we expect a similar result for the $L=2$ transitions. We see that the summed strength of the two odd target transitions closely resembles the even target data and shows a similar reduction in strength to the $L=0$ case. The splitting of the summed strength is also of interest. In the adiabatic limit, the cross sections for the two transitions should follow the rule

$$\frac{\sigma(\theta)(\frac{3}{2}^-)}{\sigma(\theta)(\frac{5}{2}^-)}=\frac{2}{3}$$

at all angles. Experimentally we find that whereas the ratio of the integrated yields to these two states closely equals the expected value (182:184 = 2.15:3), the shapes of the two angular distributions are quite different, especially at forward angles. The origin of this discrepancy can be traced to differences between the multiple step routes populating the two states. Simply, the multiple step route involving quadrupole inelastic excitation and quadrupole pair transfer enters with different phases for the two final states—resulting in different angular distribution shapes. A detailed study of this phenomenon would surely prove rewarding.

Finally, we address the case of the $L=2$ strength corresponding to the gamma-vibrational state in the even nuclei. As mentioned above, no strength was observed in the excitation region expected. A very strong transition was, however, observed to a $\frac{5}{2}^-$ state at 365 keV. This state has been associated with the $\frac{5}{2}^-[512]$ Nilsson orbit, and calculations show that of all the single-particle orbital combinations with $J^\pi K=2^+2$ which are close to the Fermi surface, the coupling to this orbit with the $\frac{1}{2}^-[510]$ orbit has one of the stronger intrinsic two-nucleon pickup strengths. In fact, as can be seen in Table II, only for two-particle configurations have any significant gamma-vibrational strength—thus casting doubt on the collective nature of this state as seen in two-particle transfer. The amount of gamma-vibrational strength seen in any nucleus will therefore depend strongly on the position of the Fermi surface relative to these single-particle orbitals, and it is therefore perhaps not surprising that anomalies such as that reported by Casten and Garrett[8] for the ^{183}W$(t,p)^{184}$W reaction occur. What is perhaps more surprising is that these anomalies are not more frequent. We therefore understand the present result and the trend of gamma-vibrational strength in the even nuclei as arising from a sensitivity to a few single-particle configurations which carry most of the relevant two-particle transfer strength.

TABLE II. $J^\pi K=2^+2$ pickup strengths.

Configuration	$\left(\frac{d\sigma}{d\Omega}\right)^a$ 42.5° (μb/sr)
$\frac{1}{2}[510]\otimes\frac{3}{2}[512]$	660
$\otimes\frac{5}{2}[512]$	164
$\frac{1}{2}[521]\otimes\frac{3}{2}[512]$	10
$\otimes\frac{5}{2}[512]$	147
$\frac{3}{2}[512]\otimes\frac{7}{2}[503]$	334
$\otimes\frac{7}{2}[514]$	3
$\frac{5}{2}[512]\otimes\frac{9}{2}[505]$	15
$\frac{1}{2}[660]\otimes\frac{5}{2}[642]$	1
$\frac{3}{2}[651]\otimes\frac{7}{2}[633]$	1
$\frac{5}{2}[642]\otimes\frac{9}{2}[624]$	8
$\frac{7}{2}[633]\otimes\frac{11}{2}[615]$	2

[a] Calculated using Nilsson wave functions for $\beta_2=0.30$ and optical model parameters as quoted in Ref. 1.

V. SUMMARY AND CONCLUSIONS

A study of the ^{183}W$(p,t)^{181}$W reaction has led to the identification of transitions to states corresponding to the coupling of the odd neutron to collective excitations of the even core. Specifically these are $L=0$ and $L=2$ transitions corresponding to the 0^+ and 2^+ members of the ground-state rotational band and an $L=0$ transition corresponding to the lowest excited 0^+ state of the even core. The former transitions show a blocking effect while the latter does not, consistent with the assumed microscopic structure of both. The failure to observe $L=2$ strength corresponding to the gamma vibration of the even core is traced to the dominance of a few single-particle configurations in the excitation of this mode in two-particle transfer reactions. Some interesting multistep effects have also been pointed out in the case of the $L=2$ transitions corresponding to the 2^+ excitation of the core.

ACKNOWLEDGMENTS

R. Ascuitto is thanked for many helpful discussions, as are Mrs. M. Fitzgerald, Mrs. D. Purcell, and Mrs. M. Synder for their careful scanning. This work was supported by U.S.D.O.E. Contract No. EY-76-C-02-3074.

[1] M. H. Mortensen, R. R. Betts, and C. K. Bockelman, Phys. Rev. C 21, 2275 (1980) (preceding paper) and references therein.

[2] R. F. Casten, P. Kleinheinz, P. J. Daly, and B. Elbek, K. Dan. Vidensk. Selsk., Mat. Fys. Medd. 38, 13 (1972).

[3] R. F. Casten, P. Kleinheinz, P. J. Daly, and B. Elbek, Phys. Rev. C 3, 1271 (1971).

[4] Y. A. Ellis, Nucl. Data Sheets 9, 319 (1973).

[5] M. H. Mortensen, R. R. Betts, and C. K. Bockelman, Phys. Lett. 70B, 17 (1977).

[6] R. F. Casten and J. D. Garrett, Phys. Lett. 47B, 436 (1973).

[7] P. D. Kunz, Code DWUCK (unpublished).

PHYSICAL REVIEW C VOLUME 21, NUMBER 6 JUNE 1980

Neutron rich ^{73}Ga and ^{79}As isotopes via the (α,p) reaction

G. Rotbard, M. Vergnes, G. Berrier-Ronsin, and J. Vernotte
Institut de Physique Nucléaire, BP n°1, 91406 Orsay, France

(Received 20 July 1979)

The (α,p) reaction at 26 MeV has been used to study ^{73}Ga and ^{79}As with 12 keV resolution full width at half maximum. The reaction behaves like a simple proton stripping ("spectator" zero coupled neutron pair) and the characteristic shapes of the angular distributions permit assigning new spins and parities. In ^{73}Ga. 198 keV$(5/2^-)$, 1116 keV$(1/2^-)$, 1494 keV$(9/2^+)$. In ^{79}As: g.s.$(3/2^-)$, 233 keV$(5/2^-)$, 499 keV$(1/2^-)$, 777 keV$(9/2^+)$, 1806 keV$(9/2^+)$, 1891 keV$(1/2^-)$, 1964 keV$(9/2^+)$. The observed splitting of the $J^\pi = 3/2$ strength in ^{73}Ga, important as compared to the one observed in ^{71}Ga, is attributed to a change of structure between $N = 40$ and 42.

[NUCLEAR REACTION ^{64,66,68,70}Zn, ^{76}Ge(α,p), $E = 26$ MeV; measured $\sigma(\theta)$; ^{73}Ga, ^{79}As deduced levels, E, j, π.]

I. INTRODUCTION

Evidence for a change in nuclear structure between $N = 40$ and 42 has recently been reported in the Ge isotopes ($Z = 32$), both from the variation of the occupation numbers in the $2p_{3/2}$ and $1f_{5/2}$ proton orbitals [measured in the $(d,{}^3\text{He})$ reaction[1]] and from a comparison of the populations of the low-lying first 0^+ excited level in the (p,t) and (t,p) reactions.[2] The striking difference in the distribution of the $L = 0$ strength in the (t,p) reaction, between the final nuclei ^{71}Ga and ^{73}Ga, appears as evidence for a similar change[2,3] in the Ga isotopes ($Z = 31$). The concentration of the $L = 0$ strength in the ground state transition for the ^{75}As$(p,t)^{73}$As reaction[3,4] seems, however, to indicate that such a change does not occur, at least between $N = 40$ and 42, in the As isotopes ($Z = 33$). Many other discontinuities have been reported[5-7] in this region of the elements table, and systematic studies of level schemes have shown strange results (see for example, Ref. 8) among which a relatively regular and anomalous variation of the energy of the first $J^\pi = \frac{9}{2}^+$ level in the odd-Z isotopes.[9]

In this interesting region, where so many anomalies have been observed but which are not yet really understood, it appears very worthwhile to improve our knowledge of the level schemes and transfer properties of the odd-Ga and -As isotopes. The lightest are relatively well known,[10-14] both from β decay and γ ray spectroscopy and from transfer reactions (see Refs. 1-8 and 15-19), but the situation is much worse for heavier isotopes like ^{73}Ga and ^{79}As. Although many levels of the previously unknown ^{73}Ga have been recently observed in our $(d,{}^3\text{He})$ and (t,p) experiments,[1,3] and 3 γ rays have been observed[20] in the β decay of ^{73}Zn, spin values could not be unambiguously determined for an appreciable number of levels; the level scheme of ^{79}As is practically unknown, except for the excitation energies of two levels.[21] The aim of the present work was to extend our knowledge of these two neutron rich nuclei, ^{73}Ga and ^{79}As, with, respectively, $N = 42$ and 46.

These two nuclei, particularly ^{79}As, are rather difficult to reach by conventional transfer reactions; in particular, the $(^3\text{He},d)$ proton stripping reaction is impossible, due to the lack of a stable target. In order to overcome this difficulty, we have used in the present work the (α,p) reaction which, under favorable circumstances, is known to behave very much like the $(^3\text{He},d)$ reaction.[22] The (α,p) angular distributions also have the attractive feature[23,24] of being sensitive, not only to the transferred orbital angular momentum l, but also to some extent to the total transferred angular momentum j. There is, in particular, an important and reproducible difference in the angular distributions for the $l = 1$, $j = \frac{1}{2}$, and $j = \frac{3}{2}$ transfers.

The experimental procedures and the distorted-wave Born approximation (DWBA) analysis are briefly described in Sec. II and the special features of the (α,p) reaction in Sec. III. The results for ^{73}Ga and ^{79}As are presented in Secs. IV and V, and are discussed in Sec. VI.

II. EXPERIMENTAL PROCEDURE AND DWBA ANALYSIS

The experiment was performed with a beam of 26 MeV α particles from the Orsay MP tandem accelerator. The intensity was limited to 900 nA to avoid target deterioration. The outgoing particles were detected by two solid state position sensitive detectors in the focal plane of the split-pole magnetic spectrometer. The solid angle was 1.7 msr. The experimental setup and procedures have already been described.[25] Enriched metallic

© 1980 The American Physical Society

Zn targets with an areal density of 60 $\mu g/cm^2$, deposited on thin carbon backings, were used. The enrichment was ≥ 97%, except for ^{70}Zn, where it was only 86.8%. The Ge target was composed of GeO_2 evaporated on a thin carbon backing. The isotopic enrichment of ^{76}Ge was 95.5%. Proton spectra were measured, in 8° steps, between 5° and 69° laboratory angles for the ^{68,70}Zn$(\alpha,p)^{71,73}$Ga reactions, and from 5° to 45° for the ^{76}Ge$(\alpha,p)^{79}$As reaction. Spectra were measured at 13° for the ^{64,66}Zn$(\alpha,p)^{67,69}$Ga reactions. A typical proton spectrum for the ^{76}Ge$(\alpha,p)^{79}$As reaction is shown in Fig. 1. The overall energy resolution is 12 keV full width at half maximum (FWHM). The known energy levels of ^{67,69,71}Ga were used to calibrate the energy spectra and to deduce the excitation energies for the observed levels in ^{73}Ga and ^{79}As. Angular distributions relative normalizations were obtained using a solid state monitor detector positioned at an angle of 45°. The absolute cross sections have not been determined. The excitation energies and the relative yields (ratio of the counting rates in the spectrometer and in the monitor, respectively) measured at a 13° laboratory angle are reported in Tables I and II. Results obtained with other transfer reactions are summarized in the same tables.

In order to take account of the kinematics of the (α,p) reaction, a DWBA calculation has been performed using the semimicroscopic model of Smits *et al.*[26-28] The DWBA cross section is computed using standard optical model potentials[29,30] and describing the transferred triton as a cluster, bound in a Woods-Saxon well ($r = 1.16$ fm, $a = 0.7$ fm) by an energy equal to the separation energy. The number of nodes of the form factor corresponds to the transfer of the two neutrons in the $1g_{9/2}$ orbital. Typical angular distributions are compared in Fig. 2 to experimental results.

It has been shown by Kamermans *et al.*[31] that a dineutron "spectator model" (simplified version of the semimicroscopic model where the two neutrons are always coupled to zero angular momentum) can be reasonably used if the ratio of the dineutron spectroscopic amplitudes to, respectively, the 2_1^+ and $0_{g.s.}^+$, is small in the (t,p) reaction.[31] From a cluster analysis of the experimental Zn(t,p) data,[32] this ratio is found to be of the order of 0.17. It is therefore not unreasonable to neglect the neutron pairs coupled to $J^\pi = 2^+$. In the spectator model the (α,p) cross section may be written[31]

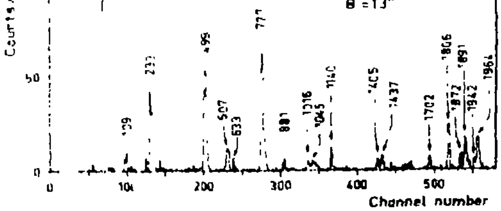

FIG. 1. A typical proton spectrum from the ^{76}Ge$(\alpha,p)^{79}$As reaction Peaks are labeled by their excitation energy in keV.

$$(d\sigma/d\Omega)_{l_p,j_p} = D \times (d\sigma/d\Omega)^{\mathrm{DW}}_{l_p,j_p} \times G_{l_p,j_p}$$

$$\times \langle N l_p 00; l_p | n_p l_p \bar{N} 0; l_p \rangle^2 ,$$

where D is a normalization factor, G_{l_p,j_p} is the proton spectroscopic strength, $(d\sigma/d\Omega)^{\mathrm{DW}}$ is the cross section computed in the DWBA cluster calculation, and the bracket $\langle\,|\,\rangle$ results from the Talmi-Moshinsky transformation. The relative values of the spectroscopic strengths have been extracted from experiments using the above formula and the brackets computed by Smits.[28] The strengths, normalized for the ground state of ^{71}Ga to the mean value of 1.95 found in the $(^3$He$,d)$ experiments, are given in Tables I and II. For ^{79}As, it should be noted that no correction has been applied for the variation in the elastic scattering cross section between a Zn and a Ge target (this could result in a global increase, up to 30%, of the proton strengths in ^{79}As).

III. SELECTIVITY AND SPECIFIC FEATURES OF THE (α,p) REACTION

The (α,p) reaction, as well as the time-reversed (p,α) reaction, are known to proceed (at high enough incident energy) as selective triton transfer reactions.[26,33] It may occur, under favorable circumstances, that the neutron pair in the triton is coupled to zero angular momentum: The triton transfer then behaves as a simple proton transfer.[22] In some cases, however, as in the ^{89}Y$(p,\alpha)^{86}$Sr reaction,[33] the transfer of a nonzero coupled neutron pair may be important, and states with neutron configurations may be populated with strengths of the same order as those observed for states with proton configurations. The selectivity of the reaction must therefore be carefully checked in the Ga-As region before using it as a spectroscopic tool.

(i) The proton spectroscopic strengths extracted (as described in Sec. II) from the (α,p) reaction are reported in Table I for the three lightest Ga isotopes and compared to those extracted from the $(^3$He$,d)$ reaction (for both reactions the very small spectroscopic strengths, or cross sections, have not been reported in the table). It is clear that the

TABLE I. Comparison of transfer results for ^{67}Ga, ^{69}Ga, and ^{71}Ga.

^{67}Ga						^{69}Ga							^{71}Ga								
E_x (keV)	J^π	(α,p)	(α,p)	(^{3}He,d)		E_x (keV)	J^π	(α,p)	(α,p)	(^{3}He,d)		(d,^{3}He)	E_x (keV)	J^π	(α,p)	(α,p)	(^{3}He,d)		(d,^{3}He)	(t,p)	
a	a	b	c	d	e	f	f	b	c	d	g	h	i	i	b	c	d	g	h	j	k
0	$\frac{3}{2}^-$	4.1	1.5	1.35	1.44	0	$\frac{3}{2}^-$	3.5	1.78	1.85	1.55	1.63	0	$\frac{3}{2}^-$	2.9	1.95	2.1	1.8	2.14	1024	0
167	$\frac{1}{2}^-$	2.8	0.95	1.0	1.27	318	$\frac{1}{2}^-$	2.2	1.02	1.3	1.27	0.49	390	$\frac{1}{2}^-$	0.35	0.22	0.21	0.16	0.04		
359	$\frac{5}{2}^-$	2.3	2.7	3.4	4.75	574	$\frac{5}{2}^-$	1.8	3.1	3.2	4.47	1.14	487	$\frac{5}{2}^-$	1.15	2.7	3.3	3.2	1.14		
828	$\frac{3}{2}^-$	1.0	0.41	0.58	0.40	872	$\frac{3}{2}^-$	0.57	0.32	0.43	0.34	0.58	511	$\frac{3}{2}^-$	(0.11)	(0.08)	0.4	0.4	0.21	23	0
911	$\frac{5}{2}^-$					1027	$\frac{1}{2}^-$	0.12	0.06	0.12	0.14	0.10	910	$\frac{1}{2}^-$						67	(0)
1082	$\frac{1}{2}^-$	0.31	0.115	0.23	0.20	1106	$\frac{5}{2}^-$					0.10	964	$\frac{5}{2}^-$					0.20	96	2
1203	$\frac{7}{2}^-$					1336	$\frac{7}{2}^-$			(0.4)	(≤0.65)	0.49	1107	$\frac{7}{2}^-$							
1413	$\frac{7}{2}^-$					1488	$\frac{7}{2}^-$					0.24	1109	$\frac{1}{2}^-$	1.5	1.05	1.1	1.4	0.39	18	(2)
1520	$\frac{3}{2}^-$					1525	($\frac{3}{2}^-$ $\frac{5}{2}^-$)						1395	$\frac{7}{2}^-$, ($\frac{5}{2}^-$)					0.52	96	2
1554	$\frac{5}{2}^-$	0.34	0.47	0.68	0.46	1723	$\frac{5}{2}^-$	0.25	0.54	0.61	0.70		1476	$\frac{5}{2}^-$, $\frac{7}{2}^-$	0.31	0.86		[l]	0.2		
1640	$\frac{3}{2}^-$					1765	$\frac{3}{2}^-$						1494	$\frac{9}{2}^+$	1.7	3.3	5.3	3	0.24	12	(3)
1810	$\frac{3}{2}^-$					1891	$\frac{3}{2}^-$	0.18	0.11			0.14	1499	$\frac{5}{2}^-$ $\frac{7}{2}^-$							
1978	$\frac{5}{2}^-$					1923	$\frac{7}{2}^-$					0.23	1631	$\frac{3}{2}^-$							
2041	$\frac{1}{2}^-$					1972	$\frac{9}{2}^+$	4.4	5.82	5.2	3.6	0.26	1702								
2074	$\frac{9}{2}^+$	6.8	7.74	5.5	3.5	1978	($\frac{1}{2}^-$, $\frac{3}{2}^-$)						1720	($\frac{5}{2}^-$, $\frac{7}{2}^-$)	0.5	1.4	0.9	1		19	(2)
						2002	($\frac{1}{2}^-$, $\frac{3}{2}^-$)														
						2022	($\frac{5}{2}^-$, $\frac{7}{2}^-$)	0.34	0.75		1.3										

[a] Excitation energies in keV and spin-parity values from Refs. 10 and 11.

[b] (α,p) cross sections at $\theta_{\rm lab} = 13°$ (arbitrary unit: see text, Sec. II).

[c] Spectroscopic strengths from the (α,p) reaction (see text).

[d] Spectroscopic strengths from Ref. 18.

[e] Spectroscopic strengths from Ref. 16.

[f] Excitation energies in keV and spin-parity values from Refs. 12 and 13.

[g] Spectroscopic strengths from Ref. 17.

[h] Spectroscopic factors from Ref. 1.

[i] Excitation energies and spin-parity values from Ref. 14.

[j] Summed cross sections of the (t,p) reaction (Ref. 3).

[k] Angular momentum transfer in the (t,p) reaction (Ref. 3).

[l] The spectroscopic strength given in Ref. 17 does not correspond to an $l = 3$ transfer.

TABLE II. Results for ^{73}Ga and ^{79}As.

		^{73}Ga							^{79}As			
E_x (keV)	J^π	(α,p)	(α,p)	$(d,{}^3\mathrm{He})$	(t,p)		E_x (keV)	J^π	(α,p)	(α,p)	E_x	$E\gamma$
a	a	b	c	d	e	f	g	g	b	c	h	i
0	$\frac{3}{2}^-$	1.63	1.47	1.33	264	0	0	$\frac{3}{2}^-$	1.25	2.2		
198 ± 3	$\frac{5}{2}^-$	0.72	2.2	1.87			109 ± 3		0.11			109
216 ± 3	$\frac{3}{2}^-$	0.54	0.51	0.07	248	0	233 ± 3	$\frac{5}{2}^-$	0.49	3	230	
495	$\frac{5}{2}^-$	(0.04)	(0.12)	0.32	55	2	499 ± 3	$\frac{1}{2}^-$	0.69	1.2		
913 ± 4	$\frac{3}{2}^-$	0.67	0.69	0.04	324	0	607 ± 4		0.17			
952	$\frac{7}{2}^-$, $(\frac{5}{2}^-)$	0.06		0.50	77	2	633 ± 4		0.05			
1119 ± 4	$\frac{1}{2}^-$	0.91	0.86	0.43	20	(2)	777 ± 4	$\frac{9}{2}^+$	0.83	3.6	773	
1237 ± 4	$\frac{9}{2}^+$	1.39	3.45	0.37			881 ± 4		0.05			
1396	$(\frac{5}{2}^-$ to $\frac{11}{2}^-)$				13	4	1016 ± 5		0.06			
1531	$\frac{7}{2}^-$			1.79			1045 ± 5	$(\frac{1}{2}^-)$	0.10	0.18		
1576 ± 6	$(\frac{5}{2}^-)$	0.31	1.1		18		1140 ± 6		0.10			
1620	$\frac{7}{2}^-$, $(\frac{5}{2}^-)$			0.50			1405 ± 6		0.05			
1700	$(\frac{1}{2}^-$ to $\frac{7}{2}^-)$				77	2	1437 ± 6		0.10			
1777	$\frac{7}{2}^-$, $(\frac{5}{2}^-)$			0.21	55	2	1702 ± 8		0.07			
1800	$\frac{3}{2}^-$				14	0	1806 ± 8	$\frac{9}{2}^+$	0.26	1.3		
1812 ± 8		0.18					1872 ± 8		0.08			
1926	$(\frac{1}{2}^-$ to $\frac{7}{2}^-)$				34	2	1891 ± 8	$\frac{1}{2}^-$	0.18	0.4		
1939 ± 8	$(\frac{5}{2}^-)$	0.23	0.9				1942 ± 8		0.05			
							1964 ± 8	$\frac{9}{2}^+$	0.23	1.2		

[a] The excitation energies with the estimated uncertainties are from the present work. For states weakly or not populated in the (α,p) reaction, the values are taken from Refs. 1 and 3. Spin and parity are from the present work and from Refs. 1 and 3.

[b] (α,p) cross sections at θ_{lab} 13° (arbitrary unit: see text, Sec. II).

[c] Spectroscopic strengths from the (α,p) reaction (see text).

[d] Spectroscopic factors from Ref. 1.

[e] Summed cross sections of the (t,p) reaction (Ref. 3).

[f] Angular momentum transfer in the (t,p) reaction (Ref. 3).

[g] Excitation energies and spin-parity values from present work.

[h] Energies of levels deduced from γ rays observed in the decay of the 42 s isomer of ^{79}Ge (Ref. 21).

[i] Energy of a γ ray observed in the decay of the 18.5 s isomer of ^{79}Ge (Ref. 40).

(^{3}He, d) and (α,p) reactions have a very similar behavior: The proton spectroscopic strengths are in an amazingly good agreement, considering the relatively rough analysis used for the (α,p) reaction.

(ii) The $\frac{5}{2}{}_2^-$ and $\frac{1}{2}{}_1^-$ levels in ^{67}Ga and ^{69}Ga are expected[11,34] to be members of the multiplet resulting from the coupling of the $\frac{3}{2}^-$ three proton cluster with the 2^+ collective excitation. These levels are therefore expected to be populated if the neutron pair in the transferred triton is coupled to 2^+; they are only very weakly populated in

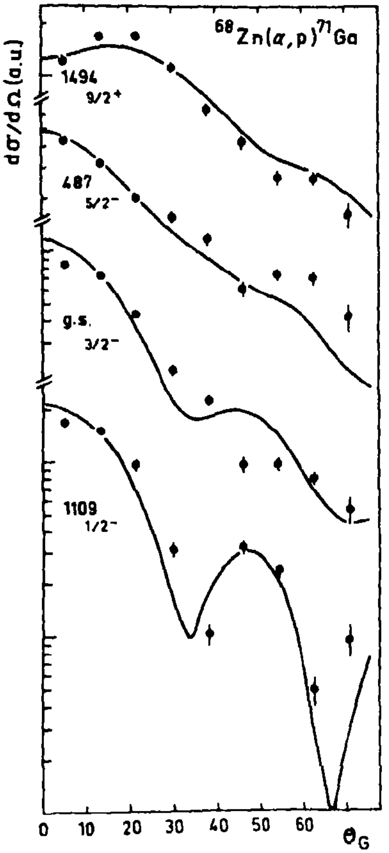

ꟻIG. 2. Comparison of experimental angular distribu-
ons for the ^{68}Zn(α,p)^{71}Ga reaction with DWBA cluster
lculations (see text).

e (α.p) reaction.

(iii) For the two heaviest Ga isotopes, the (α,p) d (t,p) results^3 can be compared and the rengths appear to be very different: The only vels strongly populated in both reactions are the $' = _2{}^-$ levels (the two ground states and the levels 216 and 913 keV in ^{73}Ga) populated by $L = 0$ ansitions in the (t,p) reaction; all the levels with rong $L = 2$ strengths in the (t,p) reaction are eakly populated in the (α,p) reaction.

From the facts summarized above, it can be ncluded that the Zn(α,p)Ga reaction behaves ry much like the (^{3}He,d) proton stripping reac- n and populates predominantly the proton states, e transferred neutron pair being coupled to zero gular momentum (spectator model). We shall sume that this is also true for the ^{76}Ge(α,p)^{79}As action.

Empirically, the shapes of the angular distributions corresponding to large (α,p) cross sections are characteristic enough to permit a classification into four groups: In Fig. 3 the angular distributions with shapes identical to that of the $\frac{3}{2}^-$ ground state of ^{71}Ga, in Fig. 4 those with shapes identical to that of the $\frac{5}{2}{}_1^-$ state of ^{71}Ga, in Fig. 5 those with shapes identical to that of the $\frac{1}{2}{}_1^-$ state of ^{71}Ga, and in Fig. 6 those with shapes identical to that of the $\frac{9}{2}{}_1^+$ state of ^{71}Ga.

The possibility of distinguishing unambiguously between final levels with $J^\pi = \frac{1}{2}^-$ and $J^\pi = \frac{3}{2}^-$ is due to the well known and very striking j effect of the (α,p) reaction. Although a j effect has also been reported^{24} between the $j = \frac{5}{2}$ and $j = \frac{7}{2}$ transfers, the differences in shape are rather weak and can-

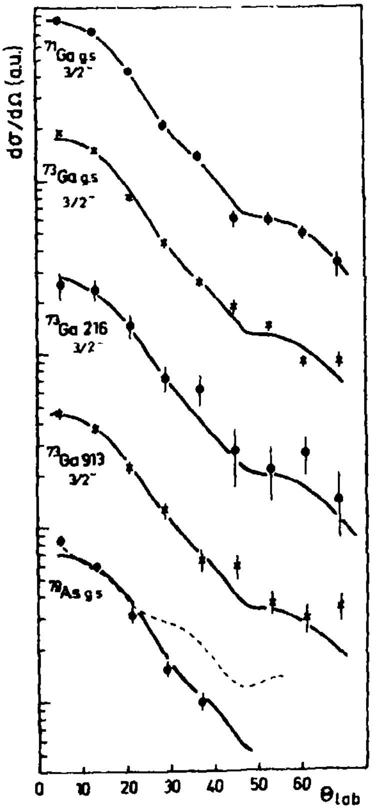

FIG. 3. (α,p) angular distributions with similar shapes, compared with the empirical curve for a $J^\pi = \frac{3}{2}^-$ final state as deduced from the ^{68}Zn(α,p)^{71}Ga$_{g.s.}$ reaction. The distributions have been arbitrarily shifted in order to save space. Relative yields are given in Tables I and II. A $J^\pi = \frac{5}{2}^-$ empirical curve is also shown for comparison (dotted line) for the ^{79}As$_{g.s.}$ where back angle data are lacking.

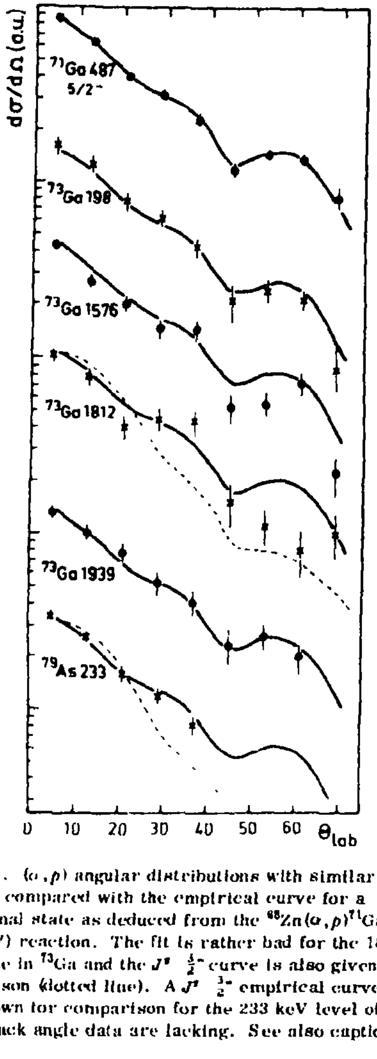

FIG. 4. (α,p) angular distributions with similar shapes, compared with the empirical curve for a $J^\pi = \frac{5}{2}^-$ final state as deduced from the ^{68}Zn$(\alpha,p)^{71}$Ga* (487 keV) reaction. The fit is rather bad for the 1812 keV state in ^{73}Ga and the J^π $\frac{3}{2}^-$ curve is also given for comparison (dotted line). A J^π $\frac{3}{2}^-$ empirical curve is also shown for comparison for the 233 keV level of ^{79}As where back angle data are lacking. See also caption for Fig. 3.

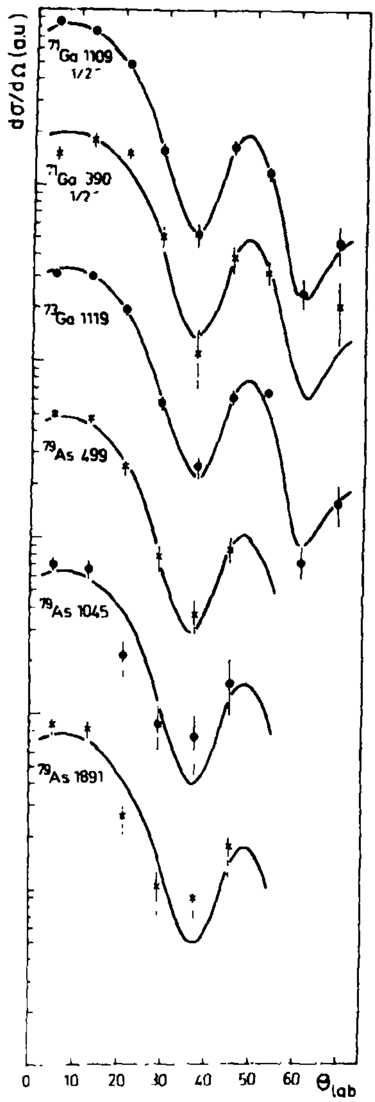

FIG. 5. (α,p) angular distributions with similar shapes, compared with the empirical curve for a $J^\pi = \frac{1}{2}^-$ final state as deduced from the ^{68}Zn$(\alpha,p)^{71}$Ga* (1109 keV) reaction. See also caption for Fig. 3.

not be used to make a choice between $J^\pi = \frac{5}{2}^-$ and $\frac{7}{2}^-$ for the final level. However, since the (α,p) reaction behaves as a proton stripping reaction, only states with spin-parity values $J^\pi = \frac{3}{2}^-$, $\frac{5}{2}^-$, $\frac{1}{2}^-$, and $\frac{9}{2}^+$, corresponding to the active (unfilled) proton shells, can be strongly populated at low excitation energy. The states with $J^\pi = \frac{7}{2}^-$ could only be weakly populated, the $1f_{7/2}$ shell being expected to be filled in the even Zn and Ge targets. This is experimentally supported by the fact that none of the known $J^\pi = \frac{7}{2}^-$ states in the lighter Ga isotopes are observed in the (α,p) reaction (see Table I). The strongly populated states of Fig. 4 can therefore be confidently assigned $J^\pi = \frac{5}{2}^-$. For similar reasons, the strongly populated states of Fig. 6 shall be assigned $J^\pi = \frac{9}{2}^+$.

IV. THE ^{73}Ga NUCLEUS

The results obtained concerning the ^{73}Ga nucleus in the present (α,p) experiment are now discussed and compared with previous results obtained using

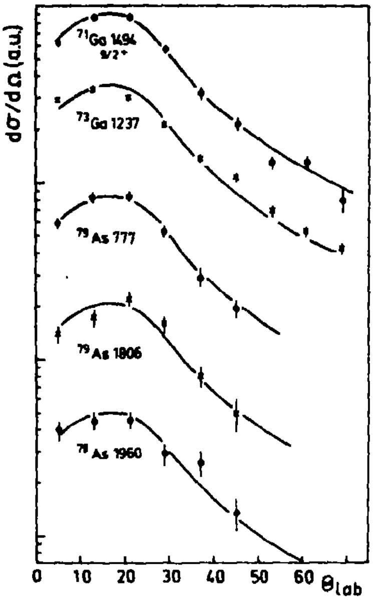

FIG. 6. (α,p) angular distributions with similar hapes, compared with the empirical curve for a $J^\pi = \frac{9}{2}^+$ inal state as deduced from the ^{68}Zn(α,p)^{71}Ga* (1494 keV) eaction. See also caption for Fig. 3.

he (d, ^{3}He) and (t,p) reactions.[1,3]

Three states at 0, 216, and 913 keV are known nambiguously as $J^\pi = \frac{3}{2}^-$ from the $L = 0$ transfer ı the (t,p) reaction. They all exhibit a $j = \frac{3}{2}$ angu- ır distribution in the (α,p) reaction (see Fig. 3). appears from a comparison of the (α,p) results ɔr the different Ga isotopes in Tables I and II that ıe $\frac{3}{2}^-$ strength is strongly split only in ^{73}Ga. This plitting can be attributed, like the one observed ɔr the $L = 0$ strength in the (t,p) reaction,[2,3] to a hange in the nuclear structure of the Ga isotopes etween $N = 40$ and 42.

The level at 1119 keV was the only one populated y an $l = 1$ transition in the (d, ^{3}He) reaction and by n $L \neq 0$ transition in the (t,p) reaction. The value $= \frac{1}{2}^-$ was preferred[1] on this basis, but $J^\pi = \frac{3}{2}^-$ ould not be excluded. The angular distribution of he (α,p) reaction permits, due to the very striking effect (see Figs. 3 and 5) a clear $J^\pi = \frac{1}{2}^-$ assign- nent. No other angular distribution with a similar hape has been observed in ^{73}Ga.

Five states at 198, 495, 952, 1534, and 1620 eV have been observed in the (d, ^{3}He) reaction, opulated by an $l = 3$ transfer and therefore with $= \frac{5}{2}^-$ or $\frac{7}{2}^-$. The value $J^\pi = \frac{5}{2}^-$ was preferred[1] or the two low-lying states from a comparison ith the level schemes of the lighter Ga isotopes nd because their spectroscopic $l = 3$ strengths, added to the total measured $l = 1$ strength, gave a value very close to the sum rule limit of 4 for the valence shells. The four higher lying levels, with large $l = 3$ spectroscopic strengths, were accordingly supposed[1] to have $J^\pi = \frac{7}{2}^-$.

The state at 198 keV, strongly populated in the (α,p) reaction, with an angular distribution identical to that of the $J^\pi = \frac{5}{2}^-$ state at 487 keV in ^{71}Ga, can be assigned (see Sec. III) $J^\pi = \frac{5}{2}^-$. The same is true for two other states, at 1576 and 1939 keV in ^{73}Ga, not observed in the (d, ^{3}He) reaction.

The strengths observed in the (α,p) reaction for the states at 954, 1534, and 1620 keV are very small; this is in agreement with the idea that these states, strongly populated in the (d, ^{3}He) reaction, have indeed $J^\pi = \frac{7}{2}^-$.

The 495 keV state is appreciably populated in the (d, ^{3}He) reaction and has been proposed[1] as $J^\pi = \frac{5}{2}^-$. As the states discussed above, it is very weakly populated in the (α,p) reaction and can on this basis have $J^\pi = \frac{7}{2}^-$. It should be remarked, however, that the strength observed in the (α,p) and in the (^{3}He, d) reaction for the $\frac{5}{2}^-_2$ state of the lighter Ga isotopes is also very small. The 495 keV state remains, therefore, as a good candidate for being the second $J^\pi = \frac{5}{2}^-$ state of ^{73}Ga.

The angular distribution observed for the strongly populated state at 1237 keV in ^{73}Ga is the same as that of the $\frac{9}{2}^+$ state at 1494 keV in ^{71}Ga. This clearly confirms the tentative assignment deduced from the (d, ^{3}He) angular distribution.[1]

V. THE ^{79}As NUCLEUS

A. Results of the (α,p) reaction

The low energy part of the ^{79}As spectrum (see Fig. 1) is dominated by four large peaks. The angular distributions (Figs. 3–6) permit assignments of $J^\pi = \frac{3}{2}^-$ to the ground state, $J^\pi = \frac{5}{2}^-$ to the 233 keV state, $J^\pi = \frac{1}{2}^-$ to the 499 keV state, and $J^\pi = \frac{9}{2}^+$ to the 777 keV state. Between 800 and 1800 keV, only weak peaks are observed. Above 1800 keV, three relatively large peaks appear, corresponding to rather strongly populated states. From the angular distributions the assignments are: $J^\pi = \frac{9}{2}^+$ for the states observed at 1806 and 1964 keV, $J^\pi = \frac{1}{2}^-$ for the state observed at 1891 keV. Angular distributions corresponding to other, weakly populated states suffer from large statistical uncertainties and appear to be relatively uncharacteristic. Only the state observed at 1045 keV may be, very tentatively, assigned $J^\pi = (\frac{1}{2}^-)$. The results obtained are summarized in Table II.

B. Comparison with (^{3}He,d) results for lighter As isotopes

The results for ^{79}As deduced from the (α,p) reaction may be compared with results obtained[19]

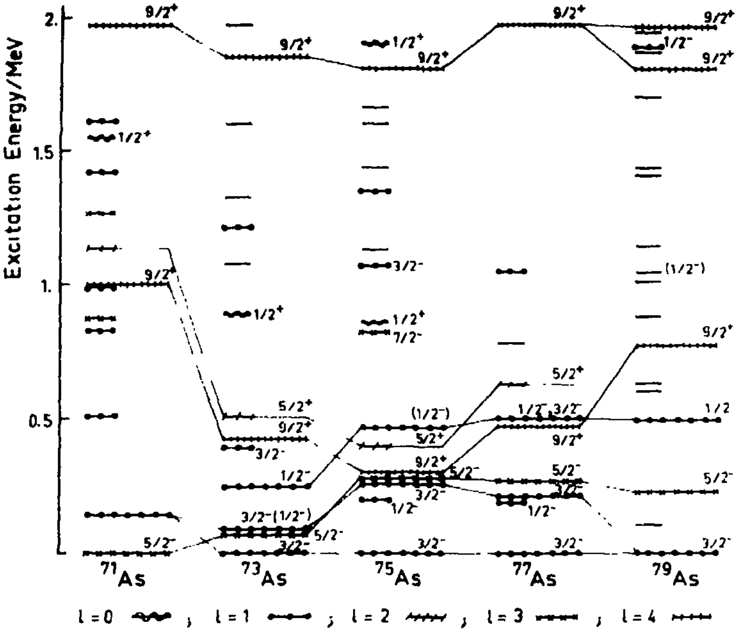

FIG. 7. Comparison of the levels of ^{79}As observed in the (α,p) reaction with the levels of the lighter As isotopes observed in the (^{3}He, d) reaction (Ref. 19). States strongly populated are represented by long lines, states observed but weakly populated by short lines. Symbols on the lines are characteristic of the transferred angular momentum l. Bare lines represent states with either no reported l values or reported l values in disagreement.

for the lighter As isotopes via the (^{3}He, d) reaction (see Fig. 7). Up to 2 MeV excitation energy, all the transferred angular momentum values $l=0$, 1, 2, 3, and 4 are observed in the (^{3}He, d) reaction, but only states with spin-parity values $J^\pi=\frac{1}{2}^-$, $\frac{3}{2}^-$, $\frac{5}{2}^-$, and $\frac{9}{2}^+$ are populated with large spectroscopic strength. We shall compare states with large spectroscopic strengths in the transfer reactions.

The major part of the $l=3$ spectroscopic strength is concentrated on the first $\frac{5}{2}^-$ state (ground state in ^{71}As, 72 keV state in ^{73}As, 279 keV in ^{75}As, 265 keV state in ^{77}As). The corresponding state is observed at 233 keV in ^{79}As. The major part of the $l=1$ spectroscopic strength, concentrated in ^{71}As on a single state observed at 146 keV is split in ^{73,75,77}As between three states.

One of these states (at 253 keV in ^{73}As, 469 keV in ^{75}As, 503 keV in ^{77}As) is, surely or presumably, $J^\pi=\frac{1}{2}^-$. The corresponding state in ^{79}As is the $J^\pi=\frac{1}{2}^-$ state observed at 499 keV. The two other states have $J^\pi=\frac{3}{2}^-$ (the ground states and the states at 84 keV in ^{73}As, 263 keV in ^{75}As, 215 keV in ^{77}As). Only the $J^\pi=\frac{3}{2}^-$ ground state of ^{79}As has a large strength in the (α,p) reaction.

The $1g_{9/2}$ spectroscopic strength is split between at least two states in the (^{3}He, d) reaction, for the light As isotopes. The energy of the first $\frac{9}{2}^+$ state goes down from 1004 keV in ^{71}As to 427 keV in ^{73}As, to a minimum energy of 304 keV in ^{75}As, then up to 475 keV in ^{77}As. The corresponding level is observed still higher, at 777 keV, in ^{79}As. A second fraction of the $l=4$ strength, observed in the lighter isotopes at an energy of about 1900 keV, is split in ^{79}As between the two $\frac{9}{2}^+$ states observed at 1806 and 1964 keV.

C. Comparison with other results

The ground state spin-parity value $J^\pi=\frac{3}{2}^-$, presently deduced from the (α,p) reaction, is in agreement with that deduced[21] from the measured $\log ft$ values in the β decay of ^{79}As. Further information about the excited states of ^{79}As may be deduced from the decay of the ^{79}Ge parent nucleus.

Two isomeric decays have been proposed for ^{79}Ge:

(i) The first decay is clearly established,[35–39] with a measured half-life lying between 40 and 50 s (it will be further referred to as 42 s). The β energy end point is close to 4 MeV and the stronges γ ray observed in the direct spectrum, at 230 ke and a 543 keV γ ray observed in coincidence, we assigned to cascade transitions from a 773 keV state to the 230 keV state, then to the ground state. The present work not only confirms the existence of these two states, but also specifies their spins and parities: $J^\pi = \frac{5}{2}^-$ for the 230 keV state, $J^\pi = \frac{9}{2}^+$ for the 773 keV state. A 781 keV γ ray has also been observed in coincidence with the 230 keV γ ray[39] and may then be assigned to a transition between the state observed in the (α,p) reaction at 1016 keV and the 230 keV state. Other γ rays have been observed in the direct spectrum.

(ii) The second decay, with a 18.5 s (or 19.1 s) half-life,[37, 40] has been considered by the Nuclear Data Sheets Compilers[21] to be only tentatively attributed to a state of ^{79}Ge. However, the energy of 109 keV for the strongest γ ray observed[40] corresponds exactly to the energy measured in the present work for the first excited state in ^{79}As. This would appear as a strong support for the attribution of the 18.5 s half-life to a state of ^{79}Ge.

It would be a great help for further spin and parity assignments to excited states in ^{79}As, to know the spins and parities of the two isomeric states discussed above. The presently known results[35-39] on the ^{79}Ge decays are not sufficient, alone, for an unambiguous J^π assignment to the parent states. However, the isotopes ^{75}Ge and ^{77}Ge are known[41, 42] to have isomeric states with $J^\pi = \frac{1}{2}^-$ and $\frac{7}{2}^+$ and the isotones with $N = 47$ are known[43-45] to have isomeric states with $J^\pi = (\frac{1}{2}^-)$ and $(\frac{7}{2}^+)$ in ^{81}Se, $J^\pi = \frac{1}{2}^-$ and $\frac{9}{2}^+$ in ^{83}Kr, $J^\pi = (\frac{1}{2}^-)$ and $(\frac{9}{2}^+)$ in ^{85}Sr. The parent isomeric states in ^{79}Ge may then reasonably be assumed to have $J^\pi = \frac{1}{2}^-$, $\frac{7}{2}^+$, or $\frac{9}{2}^+$. The strong branching observed[36, 38] through the 773 keV state, known from the present work to have $J^\pi = \frac{9}{2}^+$, eliminates the previously assumed[35] possibility $J^\pi = \frac{1}{2}^-$ for the 42 s parent state, leaving only $J^\pi = \frac{7}{2}^+$ or $\frac{9}{2}^+$. Let us see now what can be deduced for the states of ^{79}As.

The first excited state is observed at 109 keV in the (α,p) reaction, but no 109 keV γ ray has been reported in the 42 s decay of ^{79}Ge and none of the reported γ rays can be assigned to a transition from one of the excited states observed in the (α,p) reaction, to the 109 keV state. It is then very likely that the 109 keV state is not populated in the 42 s decay; its spin should then be low: $J = \frac{1}{2}$ (or $\frac{3}{2}$). The (α,p) cross section for this level is small; in the ^{75}As and ^{77}As isotopes the first excited state, $J^\pi = \frac{1}{2}^-$, is also weakly populated in the equivalent $(^3\text{He},d)$ reaction; a tentative assignment for the 109 keV state is then $J^\pi = (\frac{1}{2}^-)$.

A $J^\pi = \frac{5}{2}^+$ excited state is known in ^{71,73,75,77}As, at an excitation energy varying between 100 and 200 keV above the first excited $J^\pi = \frac{9}{2}^+$ state. The two states observed at 881 and 1016 keV in the (α,p) reaction might be candidates for this state in ^{79}As. Such a state would decay by $E1$ transitions to the $\frac{3}{2}^-$ ground state and to the $\frac{5}{2}^-$ state at 230 keV. No γ ray corresponding to the ground state transition has been reported but a 781 keV γ ray has been observed, both in the direct γ spectrum[36] and in coincidence with the 230 keV γ ray.[39] This γ ray appears to correspond to the decay from the 1016 keV state, which is therefore a good candidate for the $J^\pi = \frac{5}{2}^+$ in ^{79}As.

VI. SYSTEMATIC OF THE $J^\pi = \frac{9}{2}^+$ STATE

The spectra of many odd nuclei in the Ga, As, Br, Rb region have been calculated by Scholz and Malik[46] using a Coriolis coupling model with a pairing interaction. The occurrence at low excitation energy, in many isotopes, of a positive parity doublet, $J^\pi = \frac{9}{2}^+$ and $\frac{5}{2}^+$, is shown to indicate a prolate deformation. The minimum found at $N = 42$ for the excitation energy of the first $J^\pi = \frac{9}{2}^+$ state in the As and Br isotopes has been related[9] to a maximum value for the deformation. The relatively high excitation energy found in the present work for the first $J^\pi = \frac{9}{2}^+$ state in ^{79}As fits nicely in this scheme and confirms the minimum observed at $N = 42$ for the As isotopes. According to the interpretation of Ref. 9, this relatively high energy would imply a deformation smaller for ^{79}As than for ^{75}As.

The present work, complemented by the results of our $(d,{}^3\text{He})$ study,[1] shows that a minimum for the excitation energy of the first $J^\pi = \frac{9}{2}^+$ state also occurs at $N = 42$ in the Ga isotopes. There is no evidence, at least for the Ga, As, and Br isotopes, of a shift with Z of the N value corresponding to the minimum, as suggested for heaviest isotopes in Ref. 9. Although the minimum is observed at the same place in the Ga, As, and Br isotopes, it should be stressed that the energy of the minimum is much higher in the Ga isotopes (1237 keV) than in the As (304 keV) and Br (106 keV) isotopes, and that no "satellite" $J^\pi = \frac{5}{2}^+$ state has been observed in the Ga isotopes, close to the first $J^\pi = \frac{9}{2}^+$ state. It is therefore not clear at the present time whether the situation in the Ga isotopes is similar or not to the situation in the As and Br isotopes.

VII. SUMMARY

The study of the neutron rich isotopes ^{73}Ga and ^{79}As, by means of the (α,p) reaction at 26 MeV, has permitted a determination of a level scheme for ^{79}As and of spin values for several excited states in ^{73}Ga. The Zn(α,p) reaction appears to proceed predominantly with the transferred neutron pair coupled to zero angular momentum. The splitting of the $p_{3/2}$ strength in the ^{70}Zn$(\alpha, p)^{73}$Ga appears as an additional indication for a recently reported[2,3] structural transition between $N = 40$ and 42, in the Ga ground state wave functions. No indication for such a sudden change has been found in the As isotopes. The energies determined in the present work for the $J^\pi = \frac{9}{2}^+_1$ state allow an extension of the systematics of these states and show that the minimum in energy occurs at $N = 42$ for the Ga isotopes. Although this minimum had been observed previously, also at $N = 42$, for the As and Br isotopes, work remains to be done before a clear interpretation of these results can be proposed.

---

[1] G. Rotbard, G. La Rana, M. Vergnes, G. Berrier, J. Kalifa, F. Guilbault, and R. Tamisier, Phys. Rev. C 18, 86 (1978).

[2] M. N. Vergnes, G. Rotbard, F. Guilbault, D. Ardouin, C. Lebrun, E. R. Flynn, D. Hanson, and S. D. Orbesen, Phys. Lett. 78B, 447 (1978).

[3] M. N. Vergnes, G. Rotbard, E. R. Flynn, D. L. Hanson, S. D. Orbesen, F. Guilbault, D. Ardouin, and C. Lebrun, Phys. Rev. C 19, 1276 (1979).

[4] M. N. Vergnes, G. Rotbard, R. Seltz, F. Guilbault, D. Ardouin, R. Tamisier, and P. Avignon, Phys. Rev. C 14, 58 (1976).

[5] G. Rotbard, M. Vergnes, G. La Rana, J. Vernotte, J. Kalifa, G. Berrier, F. Guilbault, R. Tamisier, and J. F. A. Van Hienen, Phys. Rev. C 16, 1825 (1977).

[6] M. Vergnes, G. Rotbard, J. Vernotte, G. Berrier, and C. Lebrun, *Proceedings of the 6th European Physical Society Nuclear Division Conference on the Structure of Medium-Heavy Nuclei, Rhodes, 1979*, Conference Series No. 49 (Institute of Physics, London), p. 228.

[7] D. Ardouin, D. Hanson, and N. Stein, Bull. Am. Phys. Soc. 23, 941 (1978).

[8] M. Vergnes, *Proceedings of the 6th European Physical Society Nuclear Division Conference on the Structure of Medium-Heavy Nuclei, Rhodes, 1979*, Conference Series No. 49 (Institute of Physics, London), p. 25.

[9] M. Behar, A. Filevich, G. Garcia-Bermudez, and M. A. J. Mariscotti, Phys. Rev. C 17, 516 (1978).

[10] R. L. Auble, Nucl. Data Sheets 16, 417 (1975).

[11] T. Paradellis, Nucl. Phys. A279, 293 (1977).

[12] R. L. Auble, Nucl. Data Sheets 17, 193 (1976).

[13] T. Paradellis, A. Xenoulis, and C. A. Kalfas, Z. Phys. A275, 269 (1975); T. Paradellis and G. Vourvopoulos, Phys. Rev. C 18, 660 (1978).

[14] W. H. Zoller, W. B. Walters, and G. E. Gordon, Nucl. Phys. A142, 177 (1970).

[15] M. G. Betigeri, H. H. Duhm, R. Santo, R. Stock, and R. Bock, Nucl. Phys. A100, 416 (1967).

[16] M. G. Betigeri, P. David, J. Debrus, H. Mommsen, and A. Riccato, Nucl. Phys. A104, 1073 (1967).

[17] A. Riccato and P. David, Nucl. Phys. A228, 461 (1974).

[18] B. Zeidman, R. H. Siemssen, G. C. Morrison, and L. L. Lee, Jr., Phys. Rev. C 9, 409 (1974).

[19] R. R. Betts, S. Mordechai, D. J. Pullen, B. Rosner, and W. Scholz, Nucl. Phys. A230, 235 (1974); M. Schrader, H. Reiss, G. Rosner, and H. V. K. Klapdor, *ibid.* A263, 193 (1976); C. R. Ramaswamy, N. G. Puttaswamy, and N. Sarma, Phys. Rev. C 19, 1239 (1979).

[20] B. R. Erdal, L. Westgaard, J. Zylicz, E. Roeckl, and the Isolde Collaboration, Nucl. Phys. A194, 449 (1972).

[21] P. P. Urone and D. C. Kocher, Nucl. Data Sheets 15 257 (1975).

[22] D. Bucurescu, M. Ivascu, G. Semenescu, and M. Titirici, Nucl. Phys. A189, 577 (1972).

[23] L. L. Lee, Jr., A. Marinov, C. Mayer-Böricke, J. P Schiffer, R. H. Bassel, R. M. Drisko, and G. R. Satchler, Phys. Rev. Lett. 14, 261 (1965).

[24] K. A. Aniol, D. W. Gebbie, C. L. Hollas, and J. Nurzinski, Nucl. Phys. A303, 154 (1978).

[25] D. Ardouin, R. Tamisier, G. Berrier, J. Kalifa, G. Rotbard, and M. Vergnes, Phys. Rev. C 11, 1649 (1975).

[26] J. W. Smits and R. H. Siemssen, Nucl. Phys. A261, 385 (1976).

[27] J. W. Smits, Ph.D. thesis, University of Groningen, 1977.

[28] J. W. Smits, University of Groningen, Report No. K.V.I 104 (unpublished).

[29] F. D. Becchetti and G. W. Greenlees, Phys. Rev. 182, 1190 (1969).

[30] A. Budzanowski *et al.*, Nucl. Phys. A106, 21 (1967).

[31] R. Kamermans, J. W. Smits, J. Van Driel, and R. H. Siemssen, Phys. Lett. 66B, 226 (1977).

[32] F. R. Hudson and R. N. Glover, Nucl. Phys. A189, 264 (1972).

[33] M. Vergnes, G. Rotbard, J. Kalifa, and G. Berrier-Ronsin, Phys. Rev. C 10, 1156 (1974).

[34] V. Paar, Nucl. Phys. A211, 29 (1973).

[35] M. Karras, T. E. Ward, and H. Ihochi, Nucl. Phys. A147, 120 (1970).

[36] J. Van Klinken, L. M. Taff, H. T. Dijkstra, A. H. De Haan, H. Hanson, B. K. S. Koene, J. W. Maring, J. J. Schuurman, and F. B. Yano, Nucl. Phys. A157, 385 (1970).

[37] B. Grapengieser, E. Lund, and G. Rudstam, J. Inorg. Nucl. Chem. 36, 2409 (1974).

[38] P. Del Marmol and P. Fettweis, Nucl. Phys. A194, 140 (1972).

[39] J. V. Kratz, Institute für Kernchemie des Universität Mainz, Annual Report 1972, p. 18.

[40] K. Aleklett, E. Lund, G. Nyman, and G. Rudstam, Nucl. Phys. A285, 1 (1977); T. Matsushigue and L. Matsushigue, unreported results quoted in the above paper.

[41] P. J. Horen, Nucl. Data Sheets 16, 25 (1975).

[42] P. P. Urone, L. L. Lee, Jr., and S. Raman, Nucl. Data Sheets 9, 229 (1973).

[43] J. F. Lemming, Nucl. Data Sheets 15, 137 (1975).

[44] D. C. Kocher, Nucl. Data Sheets 15, 169 (1975).

[45] D. J. Horen, Nucl. Data Sheets 5, 131 (1971).

[46] W. Scholz and F. B. Malik, Phys. Rev. 176, 1355 (1968).

PHYSICAL REVIEW C VOLUME 21, NUMBER 6 JUNE 1980

Interaction of 80–164 MeV protons with nickel isotopes

M. E. Sadler,[*] P. P. Singh, and J. Jastrzebski[†]
Indiana University Cyclotron Facility, Bloomington, Indiana 47405

L. L. Rutledge, Jr.[‡] and R. E. Segel
Northwestern University, Evanston, Illinois 60204

(Received 6 June 1979; revised manuscript received 19 February 1980)

Production cross sections of various final nuclei have been determined using the in-beam gamma rays produced during the 80, 100, 136, and 164 MeV proton bombardment of ^{58}Ni, ^{60}Ni, ^{62}Ni, and ^{64}Ni targets. From the systematics of these cross sections it is concluded that (a) typically, 1–2 nucleons are emitted in the fast pre-equilibrium phase leaving a few nuclei excited over a broad range of excitation energy, (b) the bulk of the final nuclei are produced following nucleon evaporation from the excited nuclear residues of the pre-equilibrium phase, (c) the fraction of the incident energy dissipated through fast emission increases from about 1/2 to 2/3 over the above energy range, (d) the average excitation energy of the nuclear residues of the pre-equilibrium phase is estimated to increase by only 10 MeV in going from about 40 to 50 MeV over the above energy range, and (e) no evidence is found for significantly preferred removal of alpha particles from the target nucleus. Detailed comparisons of the observed cross sections are made with the cascade and hybrid models. The cascade model yields better overall agreement with the measured results. A hybrid model which includes both multiple pre-equilibrium emission and geometric surface effects is needed if it is to be equally effective.

[NUCLEAR REACTIONS ^{58,60,62,64}Ni$(p,x\gamma)$, $E_p = 80$, 100, 136, and 164 MeV; measured E_γ, σ_γ, σ production various final nuclei; results compared with cascade and hybrid exciton models including evaporation.]

I. INTRODUCTION

Historically, the mechanisms of nuclear reactions have been categorized in terms of (1) the direct processes, which occur on a time scale on the order of the time it takes the projectile to pass through the nucleus, and (2) the compound nuclear processes, which occur on a time scale many orders of magnitude greater than the direct processes and correspond to complete absorption of the projectile by the target from which a statistical decay (compound nucleus evaporation) of the system in equilibrium is assumed to ensue. The former is characterized, in particle emission spectra, by peaks near the beam energy corresponding to discrete and continuum states of the residual nucleus, and the latter by a broad hump at low energy, the shape and position of which can be described quite well by the statistical models. At the projectile energies greater than a few times the nuclear binding energies in the nucleus a third mechanism is recognized to play a significant role, namely that of "precompound" or "pre-equilibrium" emission. This is envisioned to correspond to a cascade of quasielastic nucleon-nucleon interactions in the nucleus and occurs on a time scale between those for direct and compound reactions as the projectile plus target nuclear system tends toward equilibrium.

Semiclassical models have been developed which embody few of the details of nuclear structure but employ more general properties of the interacting entities such as the mean free path of nucleons in nuclear matter derived from the free nucleon-nucleon scattering cross section suitably corrected for various effects, densities of particle-hole states at varying excitation, effects of the nuclear surface and emission rates of nucleons from a highly excited nuclear system. To some degree the existing and developing models can be categorized as "statistical" or "cascade." The former extends the statistical theory for compound nucleus emission to nonequilibrium systems and the latter considers successive intranuclear nucleon-nucleon collisions which produce a cascade of particles, using free nucleon-nucleon scattering cross sections modified to the nuclear environment. The calculated results obtained from each of these models are compared with experimentally observed quantities in this work to determine which, if any, of the models give a better description of reality and to find directions in which the models should be extended to bring them in accord with the observations.

The measurements presented here pertain to the determination of the production cross sections for residual final nuclei after targets of medium mass elements were bombarded by 80–164 MeV protons using the inclusive in-beam γ rays detected with high resolution. These measurements are the first of a continuing program to decipher the broad features of the reaction mechanisms of proton-nucleus interactions in the 80 to 200 MeV proton energy domain. A preliminary report embodying the systematic trends of the observed cross sections and their implications has been published.[1] Complementary measurements of the recoil ranges of the residual nuclei[2] of the γ-ray multiplicities of the residual nuclei[3] and of the differential cross sections of the charged particles[4] have been completed and shall be published elsewhere.

It is appropriate to list here some of the motivations which led to the initiation of this experimental program. Earlier measurements of this type,[5-11] primarily with proton and pion beams, reported enhanced production of residual nuclei which were an integral number of alpha particles removed from the target, thus focusing interest on the role of direct multiple alpha knockout in the reaction process. Furthermore, previously reported production cross sections at 100 MeV[10] with ^{58}Ni were systematically lower by a factor of 2 with respect to those reported at 200 MeV.[11] This difference was hard to understand in terms of the expected energy dependence of the cross sections. Detailed measurements in the 80–200 MeV energy range have not only helped to clear some of the above discrepancies[1] but also have provided systematic data to test the applicability of the existing models in detail.

II. EXPERIMENTAL RESULTS

This work was performed at the Indiana University Cyclotron Facility utilizing 80, 100, 136, and 164 MeV proton beams in the low-intensity target area, especially designed for in-beam γ-ray measurements. Beam intensity on the target was typically 0.5 nA. The transmitted beam was collected in a well shielded Faraday cup for current integration. Gamma rays produced produced by the proton bombardment of isotopically enriched$^{58-64}$Ni targets (about 1 mg/cm^2 in thickness) were detected by a lithium-drifted germanium Ge(Li) crystal which had an efficiency of 10% compared to a 7.6 cm × 7.6 cm NaI detector for the 1332 keV line of a ^{60}Co source placed at 25 cm. Most measurements were made with the Ge(Li) at 90°, 3 to 5 cm from the target, with varying thicknesses of lucite absorber placed between the detector and target to protect against charged particle damage to the crystal. Some measurements were made at 125° to determine anisotropy corrections to the γ-ray cross sections, for which the detector was moved back to 12 cm. For each geometry during every run an efficiency and energy calibration of the Ge(Li) detector was made by using a mixed radioactive source in the target position. The mixed source consisted of known amounts of ^{109}Cd, ^{57}Co, ^{139}Ce, ^{113}Sn, ^{137}Cs, ^{60}Co, and ^{88}Y giving calibration points over an energy range of 88 to 1836 keV.

Overall γ-ray energy resolution varied from 2.5 to 3.0 keV full width at half maximum (FWHM) during the course of the measurements. The time of production of γ rays relative to the incident beam burst (about 1 nsec wide) was also determined using conventional electronics techniques. Efforts were made to optimize the timing resolution over a large energy range and an FWHM of 5 nsec for the prompt peak in the time spectrum for higher energy γ rays (>800 keV) was typically obtained. Nevertheless, the timing resolution for lower energy γ rays grew progressively worse and was comparable to the time between the beam bursts (30 nsec) for γ rays lower than 200 keV in energy, which limited the usefulness of the timing information.

The dead time of the electronics and the data acquisition system was determined by feeding a pulser, triggered by the current integrator, into the preamplifier of the Ge(Li) detector and by comparing the number of pulser triggers to the total number of counts in the pulser peak in the Ge(Li) spectrum. Dead times averaged about 15%.

The linear energy and timing signals were digitized and routed to a computer for sorting and storage. Using software conditions three 4096 channel arrays for the prompt, delayed, and singles spectra and a 256 channel time spectrum were prepared. Each energy spectrum contained more than one hundred identifiable peaks which were fitted to Gaussian shapes by a computer program to extract peak areas. The latter were used to determine the production cross sections for each gamma ray after normalizing for the incident number of protons, the target thickness, the detection efficiency, and the dead time. Typically, adequate statistics were obtained to observe gamma rays produced with cross sections as low as 2 mb with an accuracy of about 10%. However, major uncertainty in the measured cross section was introduced by the unstripping of two or more overlapping peaks, especially when it involved one or more weak peaks. Whenever possible, contribution to the peaks in the prompt spectrum due to the decay process was determined using the corresponding delayed spectrum. However, as mentioned above, the in-beam timing information was often not adequate to allow an accurate determination of the delayed component for lower energy γ rays. For these recourse had to be made to off-line activation measurements which will be described elsewhere.[2]

Systematic uncertainties associated with the absolute cross sections due to charge integration,

TABLE I. Assignments, energies, and production cross section (and the associated percent errors) of the gamma rays observed in 164 MeV proton bombardment of ^{62}Ni.

Nucleus γ ray assigned	Gamma energy (fitted) keV	Production cross sections mb	Error in cross sections %
^{58}Mn	104.0	1.5	68
BKD (^{19}F)	110.1	7.3	13
^{58}Co	112.1	4.5	20
^{57}Fe	122.0	35.8	3
^{55}Mn	125.8	11.1	8
^{57}Fe	136.5	5.8	15
^{54}Fe	146.0	0.8	107
^{54}Mn	156.1	13.3	7
^{56}Co, ^{60}Co	158.4	8.9	10
BKG (^{19}F)	198.0	39.9	3
^{54}Mn, ^{48}V, ^{56}Mn	211.8	10.3	6
^{50}V	226.6	2.6	24
^{60}Co	229.7	4.2	16
^{51}Mn	238.3	3.6	19
^{54}Mn	252.8	2.3	36
^{60}Co	254.3	0.6	124
^{55}Fe, ^{56}Mn	273.6	5.7	12
^{60}Co	277.1	2.6	27
^{61}Ni	282.9	4.0	16
BKD?	295.6	3.3	24
^{48}V, ^{55}Mn	309.1	0.6	141
^{51}Cr, ^{56}Mn	315.6	2.4	33
^{51}V	320.1	5.1	17
^{58}Co	320.8	7.9	12
^{61}Co	333.5	4.9	20
^{59}Ni	339.4	18.5	5
BKD (^{21}Ne)	350.7	10.8	9
^{57}Fe	352.3	5.1	16
^{58}Co	365.6	5.0	14
^{53}Mn	376.8	3.5	22
^{55}Fe	384.8	1.5	50
^{60}Co	389.8	4.5	15
^{54}Fe, ^{55}Fe	411.7	6.5	12
BKD (^{26}Al)	416.9	15.7	4
^{48}V	427.8	1.0	62
^{58}Co, ^{50}Mn	432.9	4.7	16
^{60}Co	436.5	2.4	30
BKD (^{23}Na)	439.9	17.7	4
^{60}Co, ^{52}Mn	448.0	0.6	121
^{57}Co, ^{59}Ni	466.1	5.3	23
^{60}Ni	467.0	4.1	25
BKD (^{24}Ne)	472.2	9.1	13
^{55}Fe, ^{59}Fe	477.3	10.0	13
^{60}Co	482.3	3.9	33
^{60}Cu, ^{60}Ni	493.4	1.3	76
annihilation	511.0	318.5	1
^{60}Co	555.8	1.0	88
^{57}Fe	571.1	0.5	173
^{56}Co, ^{59}Co	575.7	3.6	27
BKD (^{22}Na)	584.2	20.3	6
^{56}Fe	605.0	11.6	9
^{51}V?	609.4	14.5	8
^{48}V	627.4	0.8	144
^{56}Mn?	648.9	0.5	170
^{61}Ni	656.0	1.1	92
^{50}Cr, BKD	661.8	22.0	5
^{54}Mn	704.7	3.8	27

TABLE I. *(Continued.)*

Nucleus γ ray assigned	Gamma energy (fitted) keV	Production cross sections mb	Error in corss sections %
^{58}Co, ^{60}Co, ^{53}Mn	727.6	1.6	72
^{62}Mn	731.0	0.6	177
^{52}Cr	744.3	13.1	8
^{51}Cr	749.7	4.8	22
^{50}Cr	782.6	2.6	44
^{60}Co	785.9	3.2	35
^{55}Fe	803.9	0.8	140
^{61}Cr	808.1	0.8	120
^{58}Fe	811.3	6.7	16
^{58}Co	811.4	8.7	12
^{60}Ni	826.4	12.8	10
^{56}Co, BKD (^{26}Al)	830.1	10.7	11
^{54}Cr	834.9	20.3	6
^{54}Mn, ^{50}V	839.6	8.0	16
BKD (^{27}Al)	843.9	44.6	3
^{56}Fe, ^{55}Fe, ^{52}Cr	846.9	146.5	1
^{54}Mn?, ^{57}Mn?	851.6	2.7	39
^{55}Mn	858.4	2.7	42
^{58}Fe	864.3	0.9	121
^{52}Mn	869.3	10.6	12
^{59}Ni	879.0	1.7	70
^{60}Mn, ^{46}Ti, ^{51}Ti	890.7	3.8	28
^{57}Fe	898.4	0.6	174
^{61}Ni	909.5	5.3	25
^{53}Mn	913.2	3.6	36
^{55}Fe	931.3	8.2	14
^{52}Cr	935.2	12.4	9
^{54}Co, ^{49}Cr	937.0	9.3	13
^{61}Ni	947.8	8.0	17
^{61}Cu	970.7	0.6	206
^{45}Sc?	974.7	7.0	18
^{48}Ti	983.8	13.3	10
^{54}Mn, ^{57}Mn?	991.5	4.6	34
^{59}Ni	998.5	2.4	61
^{58}Ni	1004.2	7.4	21
^{53}Cr	1006.6	5.1	27
^{56}Co	1010.5	6.7	20
BKD (^{27}Al)	1014.5	69.6	3
^{60}Ni, ^{61}Co, ^{54}Fe	1027.5	1.0	130
^{56}Fe	1038.1	14.6	10
^{58}Co	1044.4	2.0	72
^{58}Co	1051.1	6.4	24
^{57}Mn?	1062.1	5.9	26
^{59}Co, ^{50}Cr	1099.4	9.6	17
^{58}Cu?	1106.9	3.2	38
^{56}Co	1114.4	2.6	51
^{62}Ni	1129.9	6.4	24
^{54}Fe	1130.2	7.4	20
^{62}Ni	1162.4	3.9	27
^{51}Cr	1165.6	9.2	13
^{62}Ni, ^{60}Ni	1173.3	30.9	4
^{61}Ni	1185.7	2.2	54
^{59}Ni, ^{59}Co	1190.4	9.3	15
^{61}Co	1205.3	3.3	54
^{55}Fe	1223.2	10.4	21
^{57}Co	1223.7	7.2	30
^{56}Fe, ^{58}Co	1238.4	84.5	2
^{56}Fe	1265.7	2.4	57

TABLE I. (*Continued.*)

Nucleus γ ray assigned	Gamma energy (fitted) keV	Production cross sections mb	Error in cross sections %
BKD (^{22}Na)	1274.7	33.2	4
^{59}Co	1291.7	1.1	154
^{60}Ni	1293.8	3.5	41
^{56}Fe	1303.8	6.0	23
^{56}Fe, ^{48}Ti	1312.2	13.7	12
^{55}Fe	1316.6	8.4	18
^{60}Ni, ^{52}Cr	1332.8	50.0	4
^{59}Ni	1337.9	1.5	99
BKD (^{24}Mg)	1368.8	101.5	2
^{57}Co	1378.2	6.0	31
^{54}Fe, ^{55}*Fe*	1408.5	11.2	12
^{59}Ni	1428.7	7.4	19
^{52}Cr	1434.3	27.4	5
^{53}Mn	1441.1	9.2	15
^{54}Co?	1446.8	0.7	163
^{58}Ni	1454.3	13.8	11
BKD (^{40}K), ^{61}Ni	1460.7	32.2	4
^{59}Co	1462.3	1.9	83
^{51}Cr	1481.0	2.1	71
^{59}Co	1481.4	3.2	51
^{55}Mn	1529.0	6.6	26
^{61}Ni	1543.0	0.6	270
^{50}Ti	1553.2	1.4	123
^{61}Ni?	1610.5	8.6	20
^{54}Co	1614.1	1.4	95
BKD, ^{52}Cr?	1633.5	28.7	8
BKD	1731.3	4.8	30
^{57}Co, ^{60}Ni	1756.9	0.7	175
^{59}Ni?	1778.9	12.2	13
^{59}Ni?	1800.5	9.1	24
^{58}Ni	1801.4	0.7	344
BKD (^{26}Mg)	1808.7	84.6	4
^{57}Co	1898.1	3.8	67

lead time corrections, target thickness, and de-ection efficiency are estimated to be about 15%. he corresponding uncertainty for the 80 MeV mea-urements for ^{58}Ni and ^{62}Ni and 100 MeV measure-nents with a ^{64}Ni target is estimated to be 30% be-ause of a bias in charge integration due to an al-ernating current pick up in the Faraday cup for the irst case and because of poor integration at low urrents (≤0.1 nA) employed in the second case. elative uncertainties in the cross sections vary idely and depend not only on the statistics but of-en on the accuracy with which overlapping peaks ould be separated and, in a number of cases, on he precision with which the delayed components ould be subtracted.

Observed gamma rays were assigned to a partic-lar final nucleus on the basis of the measured en-rgies and the consistency of relative intensity atterns with those expected for γ-ray transitions elonging to one or more cascades for that nucleus. For this purpose a list of gamma rays assigned on the basis of in-beam measurements to nuclei with $44 \leq A \leq 65$ and their relative location in their decay schemes was prepared from the recently published literature. In Table I are listed the energies, the production cross sections (including the percent uncertainties), and the assignment to possible final nucleus (or nuclei) for each gamma ray observed in the 164 MeV proton bombardment of ^{62}Ni. The contribution of a given gamma ray to each of the many final nuclei, wherever applicable, was determined using the observed intensities of other gamma rays belonging to the same cascade and the branching ratios published in the literature. The details and reservations pertaining to individual assignments can be found elsewhere.[12]

Cross sections for the production of individual final nuclei were obtained by summing observed cross sections for gamma rays assigned to transition to the ground state and to the known isomeric

TABLE II. Production cross sections for various final nuclei from in-beam γ-ray measurements with 80, 100, 136, and 164 MeV proton bombardment of ^{58}Ni target.

Final nucleus	Production cross sections (mb) 80 MeV	100 MeV	136 MeV	164 MeV
^{58}Ni	31 ± 3	29 ± 3	17 ± 2	9 ± 2
^{57}Ni	33 ± 3	34 ± 5	31 ± 5	23 ± 9
^{57}Co	38 ± 10	35 ± 10	32 ± 10	21 ± 8
^{56}Co	70 ± 15	74 ± 15	53 ± 8	43 ± 7
^{55}Co	4 ± 2	2 ± 2	2 ± 2	2 ± 2
^{54}Co	<2	<2	<2	<2
^{56}Fe	28 ± 5	27 ± 5	25 ± 5	20 ± 8
^{55}Fe	77 ± 14	70 ± 13	53 ± 10	42 ± 8
^{54}Fe	53 ± 5	60 ± 6	47 ± 5	30 ± 4
^{53}Fe	6 ± 3	10 ± 3	8 ± 3	6 ± 2
^{52}Fe	2 ± 2	2 ± 2	2 ± 2	<3
^{56}Mn	2 ± 2	3 ± 2	2 ± 2	3 ± 2
^{54}Mn	19 ± 4	13 ± 3	14 ± 3	9 ± 3
^{53}Mn	27 ± 5	38 ± 6	34 ± 6	30 ± 6
^{52}Mn	9 ± 4	10 ± 4	14 ± 4	11 ± 4
^{51}Mn	12 ± 2	11 ± 2	10 ± 2	8 ± 2
^{54}Cr	1 ± 1	2 ± 2	4 ± 2	5 ± 3
^{53}Cr	2 ± 2	4 ± 3	7 ± 3	3 ± 3
^{52}Cr	12 ± 2	14 ± 2	19 ± 4	20 ± 6
^{51}Cr	16 ± 3	14 ± 3	13 ± 3	11 ± 3
^{50}Cr	9 ± 2	21 ± 2	23 ± 2	18 ± 4
^{49}Cr	2 ± 1	3 ± 2	5 ± 2	6 ± 2
^{48}Cr	1 ± 1	1 ± 1	1 ± 1	1 ± 1
^{50}V	2 ± 1	3 ± 2	4 ± 2	3 ± 2
^{49}V	6 ± 4	10 ± 4	17 ± 5	17 ± 5
^{48}V	4 ± 2	4 ± 2	7 ± 3	7 ± 3
^{47}V	1 ± 1	2 ± 2	3 ± 2	4 ± 2
^{50}Ti	<2	<2	<2	<2
^{49}Ti	<2	<2	<2	<2
^{48}Ti	2 ± 1	3 ± 2	6 ± 2	6 ± 4
^{46}Ti	1 ± 1	3 ± 2	5 ± 2	8 ± 2

TABLE III. Production cross section for various final nuclei from in-beam γ-ray measurements with 100 and 136 MeV proton bombardment of ^{60}Ni.

Final nucleus	Production cross section (mb) 100 MeV	136 MeV
^{60}Ni	42 ± 4	25 ± 3
^{59}Ni	89 ± 10	63 ± 8
^{58}Ni	39 ± 4	28 ± 3
^{57}Ni	8 ± 5	7 ± 5
^{59}Co	16 ± 6	12 ± 6
^{58}Co	49 ± 7	47 ± 7
^{57}Co	63 ± 10	43 ± 8
^{56}Co	27 ± 6	18 ± 5
^{55}Co	2 ± 2	2 ± 2
^{58}Fe	4 ± 2	1 ± 1
^{57}Fe	12 ± 3	18 ± 4
^{56}Fe	62 ± 8	53 ± 7
^{55}Fe	60 ± 8	45 ± 8
^{54}Fe	17 ± 4	22 ± 4
^{53}Fe	1 ± 1	5 ± 2
^{56}Mn	4 ± 3	3 ± 3
^{55}Mn	16 ± 3	12 ± 3
^{54}Mn	21 ± 3	26 ± 4
^{53}Mn	15 ± 3	19 ± 3
^{52}Mn	8 ± 6	8 ± 6
^{51}Mn	3 ± 2	3 ± 2
^{54}Cr	6 ± 4	8 ± 4
^{53}Cr	10 ± 8	14 ± 10
^{52}Cr	11 ± 3	12 ± 3
^{51}Cr	4 ± 2	11 ± 3
^{50}Cr	3 ± 2	9 ± 2
^{49}Cr	2 ± 2	3 ± 2
^{50}V	3 ± 2	4 ± 2
^{49}V	4 ± 3	8 ± 3
^{48}V	4 ± 3	5 ± 3
^{50}Ti	<2	<2
^{49}Ti	<2	<2
^{48}Ti	1 ± 1	5 ± 2
^{46}Ti	1 ± 1	1 ± 1

states of the respective nucleus. The measured in-beam cross sections for the ^{58}Ni, ^{60}Ni, and ^{64}Ni targets for different proton energies are given in Tables II to V, respectively. It should be noted that the in-beam measurements yield only a lower limit for the production cross sections for a given nucleus since weak transitions to and direct production of the ground state are not observed. This effect is expected to be particularly large for odd A and odd-odd nuclei and indeed the activation measurements often yield considerably greater cross sections for these cases than the in-beam studies. For even-even nuclei this should be a small correction since the decay is mostly funneled through the first 2^+ state.

III. MODEL CALCULATIONS

Comparisons were made between measured cross sections and those predicted by hybrid[13] and cascade models.[14-16] Both models calculate nucleon emission from the nonequilibrated nuclear system of the incident proton plus the target nucleus, the so-called pre-equilibrium phase. Once equilibrium is attained, statistical techniques are employed to determine the evaporation of nucleons and clusters such as deuterons and alpha particles. Cross sections for the production of final nuclei as the end product of both kinds of emissions are calculated and correspond to the cross sections of specific nuclei measured in this study.

The hybrid model operates in phase space and describes the change of state of the nucleus, as it proceeds toward equilibrium, by a change in the number of excitons (excited particles and holes). The cascade model follows the trajectories of the incident and struck particles in real, or geometric, space. The hybrid model follows the evolvement of the reaction until the number of excitons reaches its equilibrium value. The cascade model

TABLE IV. Production cross section for various final nuclei from in-beam γ-ray measurements with 80, 100, 136, and 164 MeV proton bombardment of ^{62}Ni.

Final nucleus	Production cross sections (mb) 80 MeV	100 MeV	136 MeV	164 MeV
^{62}Ni	30 ± 10	30 ± 10	18 ± 10	11 ± 7
^{61}Ni	76 ± 20	54 ± 20	49 ± 15	48 ± 15
^{60}Ni	77 ± 7	74 ± 7	64 ± 7	52 ± 5
^{59}Ni	52 ± 6	47 ± 6	41 ± 6	31 ± 5
^{58}Ni	23 ± 3	18 ± 2	19 ± 2	14 ± 2
^{61}Co	3 ± 2	2 ± 2	6 ± 3	4 ± 3
^{60}Co	10 ± 4	13 ± 5	14 ± 5	13 ± 5
^{59}Co	17 ± 6	17 ± 6	17 ± 6	17 ± 6
^{58}Co	41 ± 7	37 ± 7	39 ± 7	35 ± 8
^{57}Co	21 ± 5	27 ± 6	24 ± 5	19 ± 6
^{56}Co	3 ± 2	6 ± 3	7 ± 3	8 ± 4
^{58}Fe	6 ± 2	6 ± 2	9 ± 2	9 ± 4
^{57}Fe	9 ± 2	13 ± 3	17 ± 3	17 ± 6
^{56}Fe	26 ± 5	36 ± 5	44 ± 5	52 ± 12
^{55}Fe	21 ± 5	21 ± 5	25 ± 5	24 ± 4
^{54}Fe	4 ± 2	7 ± 2	9 ± 2	8 ± 2
^{56}Mn	1 ± 1	2 ± 2	4 ± 3	5 ± 3
^{55}Mn	7 ± 2	11 ± 3	13 ± 3	18 ± 4
^{54}Mn	8 ± 2	18 ± 3	20 ± 4	21 ± 4
^{53}Mn	1 ± 1	4 ± 2	9 ± 4	13 ± 4
^{51}Mn	1 ± 1	2 ± 2	2 ± 2	4 ± 2
^{54}Cr	7 ± 4	8 ± 2	11 ± 2	12 ± 8
^{53}Cr	2 ± 2	2 ± 2	2 ± 2	5 ± 3
^{52}Cr	4 ± 2	5 ± 2	11 ± 3	13 ± 8
^{51}Cr	2 ± 2	2 ± 2	4 ± 3	12 ± 6
^{50}Cr	1 ± 1	1 ± 1	2 ± 2	3 ± 2
^{50}V	1 ± 1	1 ± 1	2 ± 2	3 ± 2
^{49}V	<2	<2	2 ± 2	2 ± 2
^{48}V	<2	<2	2 ± 2	2 ± 2
^{50}Ti	<2	<2	2 ± 2	2 ± 2
^{48}Ti	1 ± 1	3 ± 2	4 ± 2	6 ± 4
^{46}Ti	1 ± 1	2 ± 2	1 ± 1	4 ± 2

TABLE V. Production cross sections for various final nuclei from in-beam γ-ray measurements with 100 and 136 MeV proton bombardment of ^{64}Ni.

Final nuclei	Production cross sections (mb) 100 MeV	136 MeV
^{64}Ni	29 ± 4	14 ± 2
^{63}Ni	59 ± 10	50 ± 10
^{62}Ni	90 ± 12	69 ± 10
^{61}Ni	62 ± 20	45 ± 15
^{60}Ni	53 ± 6	41 ± 5
^{59}Ni	32 ± 5	27 ± 5
^{58}Ni	17 ± 2	17 ± 2
^{63}Co	10[a]	10[a]
^{62}Co	22[a]	22[a]
^{61}Co	11 ± 4	10 ± 4
^{60}Co	35 ± 10	22 ± 8
^{59}Co	13 ± 6	16 ± 6
^{58}Co	29 ± 7	41 ± 8
^{57}Co	11 ± 5	15 ± 5
^{56}Co	3 ± 3	3 ± 3
^{58}Fe	10 ± 2	13 ± 2
^{57}Fe	17 ± 6	29 ± 7
^{56}Fe	31 ± 5	38 ± 5
^{55}Fe	13 ± 4	10 ± 3
^{54}Fe	<2	<2
^{56}Mn	2 ± 2	7 ± 3
^{55}Mn	14 ± 4	19 ± 4
^{54}Mn	9 ± 6	17 ± 10
^{53}Mn	3 ± 2	10 ± 4
^{54}Cr	10 ± 3	11 ± 3
^{53}Cr	<2	<2
^{52}Cr	5 ± 2	5 ± 2
^{51}Cr	<4	<4

[a] These cross sections are estimated from systematics of activity measurements for other Ni targets.

assumes the nucleus to be at equilibrium when all the cascade particles that are not emitted fall below an arbitrary cutoff energy. The hybrid model calculates the emission probability of nucleons in a statistical manner and converges to the evaporation formalism for large numbers of excitons. For the cascade model, a nucleon reaching the nuclear surface is assumed to be emitted, although provision for reflection or refraction by the changing nuclear potential is sometimes included.

In spite of these different calculational philosophies, the models incorporate many of the same ideas on the reaction mechanism. Both divide the reaction into fast (pre-equilibrium) and slow (equilibrium) components. Both use free nucleon-nucleon scattering cross sections, corrected to account for the Pauli principle, to determine the transition rates (hybrid model) or collision rates (cascade model). The hybrid model has an option to determine this information using optical model parameters which fit elastic nucleon-nucleus scattering, but this option has not been used in the present analyses since knowledge of the optical potential in this energy range is only now being obtained.

The computer codes used for the hybrid model calculations are ALICE (Refs. 17, 18) and EVAHYB (Ref. 19) which were developed at the University of Rochester. Only the geometry-dependent-hybrid (GDH) option was used in ALICE. With this option (GDH) the code calculates the reaction for each partial wave separately, increasing the mean free paths for the larger partial waves which see more of the diffuse nuclear surface, and also modifies the particle-hole level densities. EVAHYB includes a provision for multiple pre-equilibrium emission but does not include the geometric effects.

The computer code used for the cascade calculations is VEGAS (Ref. 15) which incorporates a nonconstant nuclear density distribution and potential and provides an option to treat reflection or refraction at the potential boundaries. The subsequent evaporation computations were performed using two separate computer codes: (1) DFFMH (Ref. 20) which utilizes the Monte Carlo technique to calculate evaporation of particles using the Weisskopf evaporation formula, and (2) a modified[12] ALICE calculation which sorts the VEGAS results to determine the distribution of excitation energy after the cascade for each residual nucleus and calculates the Weisskopf evaporation in the same way that was done for the hybrid model. The DFFMH code is the one generally used with VEGAS, and the modified ALICE calculation allows direct comparison of the different pre-equilibrium calculations since the same evaporation calculation could be utilized. Also, since the two evaporation codes can be used with the same pre-equilibrium calculation (VEGAS), the effect due to different treatment of the evaporation in the two codes on the final results could be directly compared.

All computer codes were adapted to the Indiana University Cyclotron Facility's Harris 6024 computers, utilizing the virtual memory VULCAN operating system. There are several possible combinations of input parameters that can be used for ALICE, EVAHYB, VEGAS, and DFFMH. The ones used in this work are listed in the Appendix.

IV. DISCUSSION OF RESULTS

A. Absolute cross section

The total observed cross section obtained by summing the production cross sections of all final nuclei (see Tables II to V) for a given target and proton energy are listed in Table VI for various cases along with those including the radioactivity results[2] for a few cases. There appears to be some tendency for the summed cross sections to decrease with increasing bombarding energy, although this effect is barely discernable and may, at any rate, merely be the result of unassigned cross section due to increasing complexity of the gamma spectra as the bombarding energy is increased. The magnitudes of the cross section reported here for ^{58}Ni target are consistent with those reported in Ref. 11 but disagree by a large factor with those reported in Ref. 10.

For comparison total reaction cross sections predicted by the optical model calculation using the code ALICE and those given by the cascade model are also listed in Table VI. The cascade model computes the reaction cross section by multiplying the geometric cross section by the ratio of the number of incident protons which interact in the nucleus to the total number of trials. The observed in-beam cross sections are typically 50–70% of the optical model reaction cross sections and 60–80% of the cascade model values. With activation results the observed values become 65–75% and 80–90% of the two predicted values, respectively.

B. Cross section distributions

In Tables VII through IX are listed the predicted cross sections for individual final nuclei for the cases of 80 and 164 MeV protons on a ^{62}Ni target and for 164 MeV protons on a ^{58}Ni target, respectively, along with the corresponding observed values (including the activation results). For an overall graphic view, the experimental cross sections are plotted in Fig. 1 for a ^{62}Ni target at two energies and the values predicted by EVAHYB and VEGAS are plotted in Fig. 2 for the case of 164 MeV protons on ^{62}Ni. Features of the observed

TABLE VI. Total observed and calculated reaction cross sections.

		Reaction cross sections (mb)				
		Observed				
Target nucleus	Proton energy (MeV)	In-beam	In-beam plus activity	Optical model	VEGAS	Geometric
^{58}Ni	80	463[a]	637	845	678	1281
	100	495		804	674	1302
	136	452		786	659	1324
	164	361	531	763	647	1334
^{60}Ni	100	597		822	696	1321
	136	534		801	657	1343
^{62}Ni	80	629[a]	772	884	717	1318
	100	465		840	710	1340
	136	481	611	816	691	1362
	164	477	606	800	683	1373
^{64}Ni	100	736[a]		858	717	1358
	136	522		830	711	1381

[a] *These cross sections are relatively more uncertain owing to reasons stated in the text.*

TABLE VII. Comparison of the observed production cross sections for final nuclei with those predicted by various models for the case of 80 MeV proton bombardment of ^{62}Ni.

Final nuclei	Observed	Production cross sections (mb)			
		GDH (MFP × 1)	EVAHYB (MFP × 2)	VEGAS + DILMH	VEGAS + ALKF
^{62}Cu	20 ± 8[a]	14	4	18	18
^{61}Cu	12.4 ± 0.6[a]	12	3	26	14
^{60}Cu	5.2 ± 1[a]	4	1	20	4
^{62}Ni	30 ± 10	23	9	29	22
^{61}Ni	76 ± 20	53	69	91	89
^{60}Ni	77 ± 7	74	102	66	77
^{59}Ni	52 ± 6	54	83	67	48
^{58}Ni	23 ± 3	27	45	69	20
^{57}Ni	2.3 ± 0.1[a]	6	8	10	6
^{56}Ni	0.8 ± 0.3[a]	0.1	0.07	0.1	0.08
^{61}Co	23 ± 2[a]	2	4	14	17
^{60}Co	32 ± 3[a]	10	16	22	23
^{59}Co	17 ± 6	31	48	29	37
^{58}Co	82 ± 4[a]	86	100	46	75
^{57}Co	52 ± 3[a]	69	77	59	64
^{56}Co	6 ± 1[a]	15	12	23	18
^{55}Co	1.5 ± 0.1[a]	5	3	4	3
^{59}Fe	2.3 ± 0.4[a]	1	1	2	2
^{58}Fe	6 ± 2	7	6	6	7
^{57}Fe	9 ± 2	22	13	9	23
^{56}Fe	26 ± 5	29	21	26	23
^{55}Fe	21 ± 5	70	36	40	34
^{54}Fe	4 ± 2	21	25	7	22
^{53}Fe	<1[a]	0.03	0.04	0.3	0.3
^{52}Fe	0.02 ± 0.005	0	0	<0.1	0
^{56}Mn	2.5 ± 0.2[a]	2	1	1	2
^{55}Mn	7 ± 2	15	5	9	8
^{54}Mn	13.0[a] ± 1[a]	36	11	10	34
^{53}Mn	1 ± 1	5	6	2	9
^{52}Mn	1.5 ± 0.2[a,b]	8	1	2	3
^{51}Mn	1 ± 1	0.3	0.05	0.1	0.6
^{54}Cr	7 ± 4	0.3	0.2	0.2	0.6
^{53}Cr	2 ± 2	2	0.4	1	0.9
^{52}Cr	4 ± 2	10	6	2	5
^{51}Cr	2.5 ± 0.3[a]	4	4	1	7
^{50}Cr	1 ± 1	0.01	0.01	0.1	0.1
^{49}Cr	<0.04	0	c	0.1	0
^{48}Cr	<0.005	0	c	0.1	0
^{50}V	1 ± 1	0.2	0.06	0.1	0.2
^{48}V	0.1 ± 0.04[a]	0.03	c	0.1	0.1
^{48}Ti	1 ± 1	0.02	0.02	0.1	0.001
^{47}Ti	1 ± 1	0	c	0.1	0.001

[a] Deduced from activation measurements, Ref. 2.

[b] Does not include isomeric state production.

[c] Outside dimensioned limits of program.

cross section, which the models are able to reproduce quite well, are: (a) nuclei farther from the target nucleus are produced with progressively smaller cross sections at a given bombarding energy, (b) at higher bombarding energies nuclei farther from the target are produced with relatively larger cross sections at the expense of those near the target mass, and (c) the production cross sections of nuclei of a given Z show a peaked distribution with centroids lying near the line of stability. The cascade model on the whole not only gives a rather satisfactory account of the absolute magnitude of the observed cross sections, but also of trends among isotopes of various nuclear species. EVAHYB systematically predicts more cross sections for Mn, Cr, and V isotopes than those either observed or predicted by the cascade model. This discrepancy along with the necessity to in-

TABLE VIII. Comparison of the observed production cross sections for final nuclei with those predicted by various models for the case of 164 MeV proton bombardment of ^{62}Ni.

Final nuclei	Production cross sections (mb) Observed	EVAHYB (MFP × 2)	VEGAS + DFFMH	VEGAS + ALICE
^{62}Cu	12 ± 6[a]	2	11	9
^{61}Cu	5.4 ± 0.2[a]	2	15	9
^{60}Cu	1.7 ± 0.2[a]	0.4	10	3
^{62}Ni	11 ± 7	4	15	12
^{61}Ni	48 ± 15	44	78	78
^{60}Ni	52 ± 5	65	46	52
^{59}Ni	31 ± 5	51	36	29
^{58}Ni	14 ± 2	20	29	11
^{57}Ni	1.3 ± 0.3[a]	5	7	3
^{56}Ni	<0.4[a]	0.5	0.4	0.2
^{61}Co	26 ± 4[a]	4	19	18
^{60}Co	35 ± 5[a]	12	18	19
^{59}Co	17 ± 6	30	26	30
^{58}Co	58 ± 2[a]	51	29	44
^{57}Co	42 ± 4[a]	57	41	33
^{56}Co	11 ± 1[a]	30	28	20
^{55}Co	1.5 ± 0.2[a]	8	6	5
^{59}Fe	3.1 ± 0.3[a]	0.9	3	2
^{58}Fe	9 ± 4	4	5	4
^{57}Fe	17 ± 6	15	11	15
^{56}Fe	52 ± 12	32	30	25
^{55}Fe	24 ± 4	47	42	36
^{54}Fe	8 ± 2	31	19	19
^{53}Fe	1.0 ± 0.4[a]	2	9	4
^{52}Fe	0.09 ± 0.02[a]	0.08	0.7	0.3
^{56}Mn	3.6 ± 0.2[a]	2	2	2
^{55}Mn	18 ± 4	8	11	7
^{54}Mn	25 ± 2[a]	17	28	26
^{53}Mn	13 ± 4	38	19	34
^{52}Mn	6.1 ± 0.7[a]	10	18	19
^{51}Mn	4 ± 2	1	4	4
^{54}Cr	12 ± 8	0.6	2	0.9
^{53}Cr	5 ± 3	3	8	5
^{52}Cr	13 ± 8	30	9	14
^{51}Cr	14 ± 1[a]	20	13	22
^{50}Cr	3 ± 2	4	6	12
^{49}Cr	0.6 ± 0.1[a]	c	2	3
^{48}Cr	0.05 ± 0.01[a]	c	0.06	0.2
^{50}Ti	2 ± 2	0.3	0.4	0.3
^{48}Ti	6 ± 4	1	1	3
^{46}Ti	4 ± 2	3	0.6	3
^{48}Sc	0.13 ± 0.02[a]	c	0.07	0.1
^{46}Sc	1.0 ± 0.3[a]	c	0.2	0.8
^{44}Sc	0.19 ± 0.03[a,b]	c	0.06	c
^{43}K	0.042 ± 0.007	c	0.03	c

[a] Deduced from activation measurements.
[b] Does not include isomeric state production.
[c] Outside dimensional limits of program.

crease the mean free path (MFP) by a factor of 2 to get reasonable comparison with the observations is expected to be corrected when the geometry-dependent effects arising from the diffuseness of the nuclear surface are incorporated, as appears to be the case for GDH predictions at 80 MeV (Table VII). As is obvious from a brief perusal of Tables VII through IX, there are a number of larg quantitative discrepancies between the observed and predicted values. Some of these arise becaus

TABLE IX. Comparison of the observed production cross sections for final nuclei with those predicted by various models for the case of 164 MeV proton bombardment of ^{58}Ni.

Final nuclei	Observed	EVAHYB (MFP × 2)	VEGAS + DFFMH	VEGAS + ALICE
	Production cross sections (mb)			
^{58}Ni	9 ± 2	4	19	10
^{57}Ni	46 ± 3[a]	36	70	57
^{56}Ni	5.0 ± 0.7[a]	8	11	8
^{57}Co	56 ± 6[a]	15	40	43
^{56}Co	60 ± 8[a]	63	67	64
^{55}Co	21 ± 2[a]	38	27	28
^{54}Co	<2	2	15	4
^{56}Fe	20 ± 8	5	8	8
^{55}Fe	42 ± 8	40	41	38
^{54}Fe	30 ± 4	75	39	47
^{53}Fe	6 ± 2	14	33	17
^{52}Fe	2.6 ± 0.3[a]	2	8	3
^{55}Mn	3 ± 2	0.3	1	0.6
^{54}Mn	18 ± 2[a]	6	13	16
^{53}Mn	30 ± 6	76	16	40
^{52}Mn	17 ± 4[a,b]	39	42	38
^{51}Mn	8 ± 2	8	22	16
^{54}Cr	5 ± 3	0.01	0.1	0.04
^{53}Cr	3 ± 3	0.4	2	1
^{52}Cr	20 ± 6	41	3	9
^{51}Cr	47 ± 7[a]	52	22	28
^{50}Cr	18 ± 4	23	25	31
^{49}Cr	8 ± 2[a]	4	19	14
^{48}Cr	1.2 ± 0.2[a]	0.4	3	2
^{50}V	3 ± 2	24	5	9
^{49}V	17 ± 5	22	7	17
^{48}V	12 ± 2[a]	10	17	22
^{47}V	4 ± 2	2	6	8
^{50}Ti	<2	0.2	0.04	0.08
^{49}Ti	<2	2	0.7	0.8
^{48}Ti	6 ± 4	8	2	3
^{47}Ti		9	6	12
^{46}Ti	8 ± 2	4	5	13
^{46}Sc	1.2 ± 0.3[a]	c	0.5	1
^{44}Sc	1.5 ± 0.3[d]	c	2	5

[a] Obtained from activation measurements.

[b] Does not include the cross section with which isomeric state is populated.

[c] There is no prediction for these cases due to limited dimensions of the mass removal variables in the program.

[d] Does not include the cross section with which ground state is populated.

the observed cross sections are only part of the total production cross sections, but in other cases, especially where activation results are available and the predicted values are smaller than the observed, these differences must be real.

C. Mass and charge removal

The average number of nucleons removed from the initially formed target plus proton system is defined to be

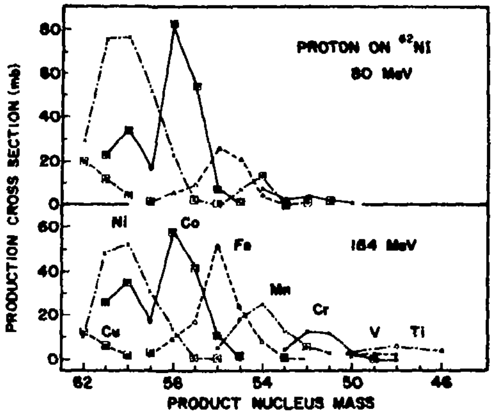

FIG. 1. Production cross sections of various final nuclei as a function of the product mass for the cases of 80 and 164 MeV proton bombardment of ^{62}Ni. Values of cross sections which are plotted with a rectangle surrounding the various symbols correspond to results obtained with activation technique.

$$\langle \Delta A \rangle = \sum_i (\Delta A_i)\sigma_i / \sum_i \sigma_i , \qquad (1)$$

where ΔA_i is the difference in mass number of the ith final nucleus from that of the initial system and σ_i is the production cross section of the ith nucleus. Values of $\langle \Delta A \rangle$ based upon the observed cross sections are plotted (solid symbols) in the top portion of Fig. 3 and listed in Table X. A straight line trend of the observed values has a

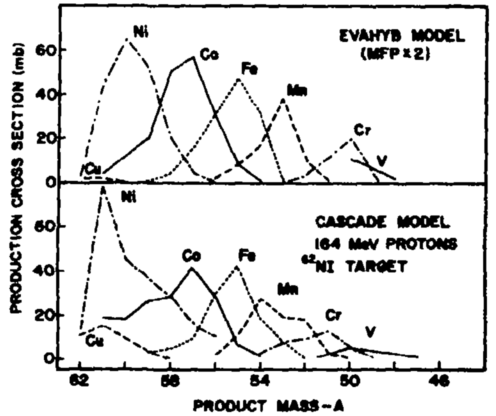

FIG. 2. Production cross sections of final nuclei as predicted by EVAHYB model using twice the mean free path given by the nucleon-nucleon cross sections (top section) and by the cascade model for the case of 164 MeV proton bombardment of ^{62}Ni (bottom section).

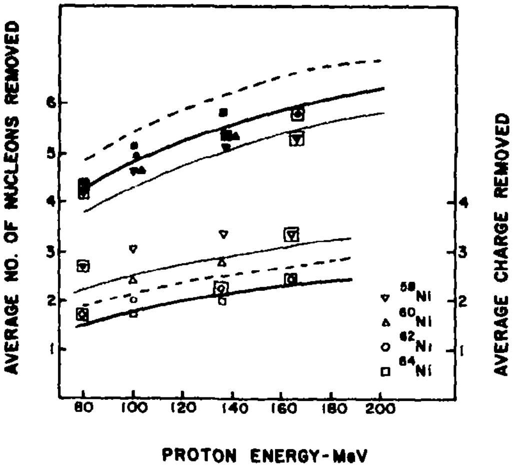

FIG. 3. Average number of nucleons removed ⟨ΔA⟩ (solid symbols in top part) and protons removed ⟨ΔZ⟩ (open symbols in lower part) from the target plus incident proton system as a function of the incident energy. The solid curves correspond to predictions by the cascade model for the cases of ^{58}Ni (thin line) and ^{62}Ni (thick line) targets. The dashed line corresponds to those of the hybrid model using the EVAHYB code and pertains to the ^{62}Ni target.

slope of 0.017 nucleons/MeV for the energy range of 80 to 164 MeV. This result immediately rules out total fusion of the incident proton with the target nucleus as a possible mechanism since this process would yield a slope of 0.1 nucleon/MeV. The single-emission hybrid model is similarly discarded because it predicts[12] a value of 0.05 nucleon/MeV. However, at 80 MeV the geometry-dependent-hybrid model (GDH) gives a value of ⟨ΔA⟩ which is only half a nucleon higher than the observed value indicating that below this energy a single pre-equilibrium emission model may be adequate. In the energy range of 80 to 164 MeV the MFP×1 (see Appendix) calculation (not shown) with EVAHYB consistently predicts emission of about 1.5 nucleons more than is observed. This difference is about the same as that between the predictions of GDH and the simple hybrid model at 80 MeV. Therefore the MFP×2 (see Appendix) option which gives better overall agreement may be viewed as a means of simulating the geometry-dependent effects. Other than higher absolute values for ⟨ΔA⟩ by about half a unit (dashed curve in Fig. 3), EVAHYB predicts ⟨ΔA⟩ to increase with energy at the rate of 0.02 nucleon per MeV as does the cascade model (solid curves in Fig. 3) although the latter predicts the absolute magnitudes of ⟨ΔA⟩ closer to those observed. Both models predict dependence of ⟨ΔA⟩ on the isotopic nature of the targets which is somewhat less than that observed (see comparison for ^{58}Ni and ^{62}Ni cases in Fig. 3).

Points (open symbols) and the set of curves in Fig. 3 correspond to the average amount of charge removal ⟨ΔZ⟩ as a function of bombarding energy. The relative ability of the two model calculations to account for the energy and isotopic (target) dependence of ⟨ΔZ⟩ is a little better than that found for ⟨ΔA⟩ (see Sec. IV D for further discussion on this point).

D. Mass and charge distribution

The total observed cross sections for production of nuclei of a certain mass A or charge Z are plotted in Figs. 4 through 8 for ^{62}Ni and ^{58}Ni targets along with the corresponding results of various model calculations. The models are able to give a

TABLE X. Average number of nucleons ⟨ΔA⟩ and protons ⟨ΔZ⟩ removed from the initial proton plus target system.

Target	Energy MeV	Experimental ⟨ΔZ⟩	⟨ΔA⟩	EVAHYB (MFP×2) ⟨ΔZ⟩	⟨ΔA⟩	VEGAS + DI FMH ⟨ΔZ⟩	⟨ΔA⟩	VEGAS + ALICE ⟨ΔZ⟩	⟨ΔA⟩
^{58}Ni	80	2.8 [a]	4.2 [a]	2.9 [b]	4.6 [b]	2.3	3.9	2.8	4.5
^{58}Ni	100	3.1	4.6	3.2	5.0	2.5	4.3	3.1	5.0
^{58}Ni	136	3.4	5.1	3.5	5.6	2.9	5.0	3.4	5.7
^{58}Ni	164	3.3 [a]	5.2 [a]	3.7	5.9	3.1	5.4	3.6	6.0
^{60}Ni	100	2.5	4.6	2.7	5.2	2.1	4.5	2.6	5.3
^{60}Ni	136	2.8	5.3	3.0	6.0	2.4	5.1	2.9	5.9
^{62}Ni	80	1.7 [a]	4.3 [a]	1.8	4.8	1.6	4.4	1.9	4.9
^{62}Ni	100	2.0	4.9	2.1	5.3	1.8	4.9	2.2	5.5
^{62}Ni	136	2.2 [a]	5.3 [a]	2.3	6.1	2.1	5.4	2.5	6.1
^{62}Ni	164	2.4 [a]	5.7 [a]	2.5	6.5	2.3	5.9	2.7	6.6
^{64}Ni	100	1.8	5.1	1.5	5.5	1.5	4.9	1.7	5.5
^{64}Ni	136	2.0	5.8	1.9	6.2	1.7	5.5	2.0	6.1

[a] These values were derived including the cross sections determined through activation measurements.

[b] GDH model predicts essentially the same values but EVAHYB (MFP×1) gives values of 3.5 and 5.6 for ⟨ΔZ⟩ and ⟨ΔA⟩, respectively, for the 80 MeV case.

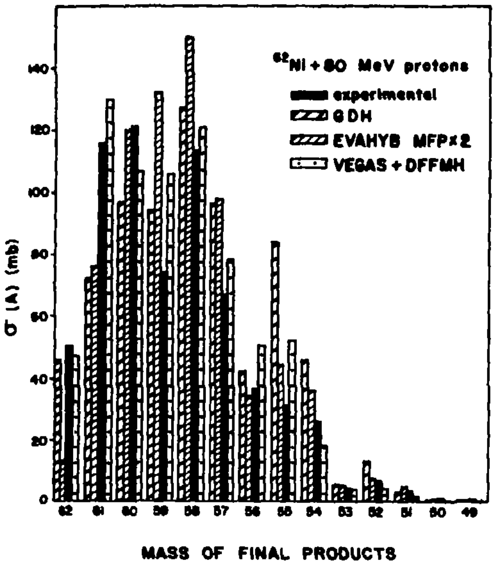

FIG. 4. Comparison of the observed cross sections (solid bars) for nuclei of various masses with those predicted by different models for 80 MeV proton bombardment of ^{62}Ni.

reasonable account of the trends in the observed distributions both with changes in the target mass and in the incident proton energy. GDH calculations seem to be in better agreement with observations at 80 MeV than those of EVAHYB, even with the MFP×2 option. EVAHYB systematically overestimates the cross sections for lighter nuclei far from the target and underestimates for the heavier ones. VEGAS plus DFFMH gives, on the whole, a better account of the observed trends with A and Z

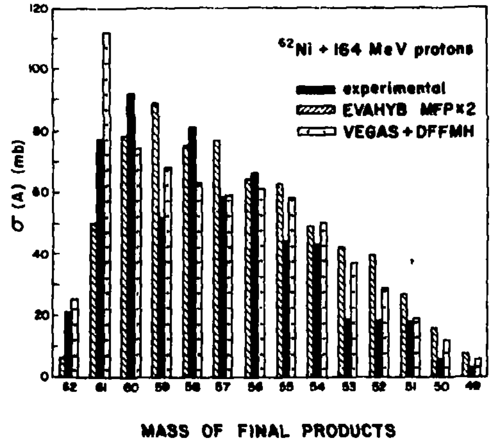

FIG. 5. Comparison of the observed cross sections (solid bars) for nuclei of various masses with those predicted by different models for 164 MeV proton bombardment of ^{58}Ni.

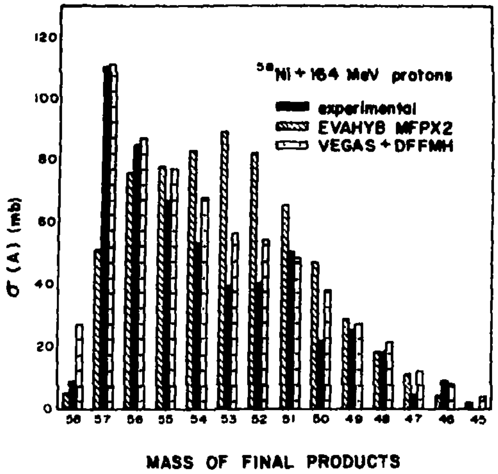

FIG. 6. Comparison of the observed cross sections (solid bars) for nuclei of various masses with those predicted by different models for 164 MeV proton bombardment of ^{62}Ni.

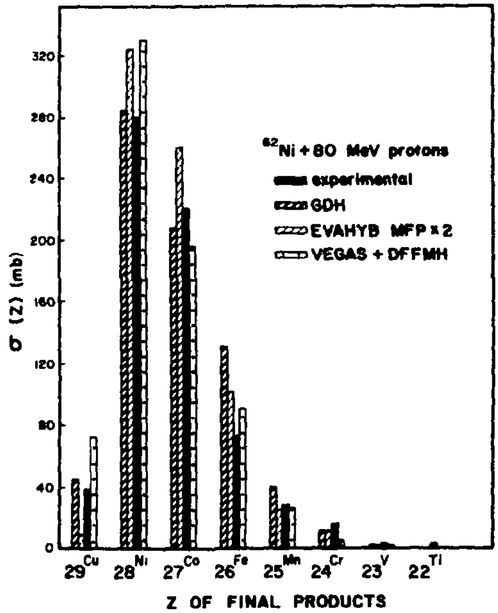

FIG. 7. Comparison of the observed cross sections (solid bars) for various nuclear species with those predicted by different models for 80 MeV proton bombardment of ^{62}Ni.

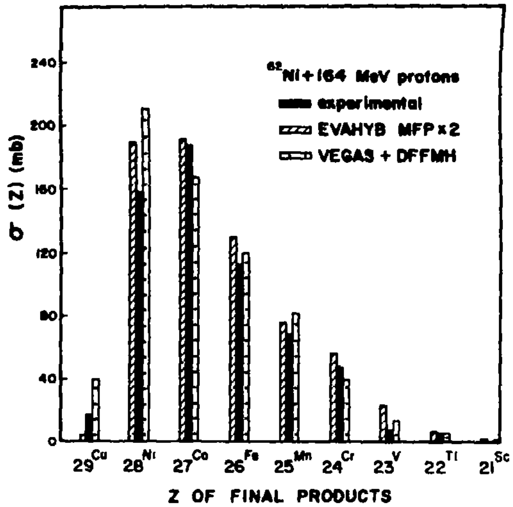

FIG. 8. Comparison of the observed cross sections (solid bars) for various nuclear species with those predicted by different models for 164 MeV proton bombardment of ^{64}Ni.

over the entire energy range for all targets, although it disagrees with the measurements for a number of product nuclei. Model predictions pertaining to the charge distributions are found to be more strongly dependent on the parameter values used in the evaporation phase of the calculation than do the mass distributions. To investigate this effect, evaporation calculations in conjuction with the output of VEGAS were performed using both DFFMH and the evaporation part of ALICE. A compliation of the average charge and mass removal for the two cases is given in Table X along with experimental values. ALICE systematically predicts about 0.6 more nucleon removed, although it reproduces the charge removed to within 0.1 unit (see Table X). On the other hand DFFMH tends to underpredict the charge removal by about 0.3 units and overpredicts the neutron removal by about the same amount, thus giving the average number of nucleons removed closer to those actually observed (see Fig. 3 and Table X). Since both codes are based upon the Weisskopf formulation[21] this difference ostensibly arises from details of how the inverse cross sections and level densities are calculated in the two codes. Since the same amount of excitation energy is dissipated through nucleon evaporation in both calculations, it implies that the average emission energies are less in ALICE than in DFFMH. Indeed for the case of 136 MeV protons on ^{58}Ni the average evaporation energies are 5.0, 8.9, 11.3, and 16.1 MeV in DFFMH for neutrons, protons, deuterons, and alpha particles, respectively, whereas the corresponding values i ALICE are 3.5, 7.0, 9.6, and 13.9 MeV. It is obvious that there is still much to be learned about evaporation from highly excited nuclei and that existing uncertainties significantly affect the conclusions that can be drawn from the observations.

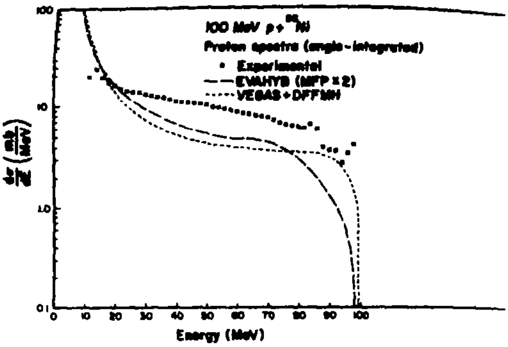

FIG. 9. Angle integrated proton energy spectrum observed (open squares) and those predicted by EVAHYB (dashed curve) and VEGAS (dotted curve) for the case of 100 MeV protons on ^{58}Ni. The experimental values wer taken from Ref. 23.

E. Energy and angular distribution of emitted protons

In Fig. 9 the observed angle integrated energy spectrum of protons following bombardment by 10 MeV protons on ^{58}Ni reported by Wu *et al.*[21] is reproduced along with corresponding predictions of EVAHYB (MFP × 2) and VEGAS plus DFFMH. Between 20 to 100 MeV there seems to be a discrepancy between the observed and the predicted cros sections, the latter being systematically lower tha the former. VEGAS reproduces the shape of the

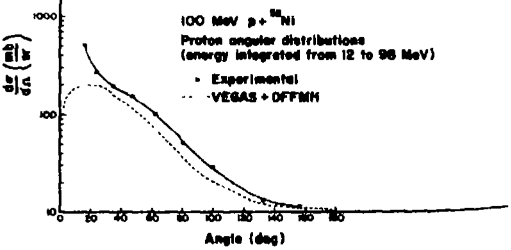

FIG. 10. Energy integrated angular distribution of protons emitted following 100 MeV proton bombardment of ^{58}Ni; solid curve is drawn through experimental point and dotted curve represents the predictions of the cascade model.

spectrum at higher energy noticeably better (not including the elastic peak) than EVAHYB. The discrepancies in shape and magnitude of the cross section for the lower (<20 MeV) end of the spectrum not being well determined because of experimental cutoffs or to inadequacies of the calculation in the equilibrium (or near-equilibrium) phase. In Fig. 10 the observed energy integrated (from 12 to 98 MeV) angular distribution of the emitted protons is compared with the predictions of VEGAS. Except at very forward angles where VEGAS predicts a peak and the observed distributions continue to rise, the calculations agree rather well with the observations in shape but are systematically lower in magnitude.

V. SUMMARY AND CONCLUSIONS

The measurements reported in this study pertain to the determination of the cross sections with which various final nuclei are produced following the bombardment of nickel isotopes by 80–164 MeV protons. The motivation was to provide a systematic set of experimental results to (a) gain insight about the characteristics of nucleon-nucleus interactions at intermediate energies, (b) test various existing models, and (c) compare results from proton-induced reactions with those for other projectiles. In particular, the earlier measurements[5-11] had highlighted the following results: (a) Nuclei which are an integral number of alpha particles removed from the target nucleus were produced with relatively larger cross section, and (b) the average number of nucleons removed from the target by pions did not vary over an incident pion energy range of 0 to 200 MeV. The first result had strong implications concerning the extent to which correlated clusters of nucleons either exist in nuclei or are dynamically formed in the course of an interaction. The second result begged for similar proton data at intermediate energy, with the hope that comparison of the results would point out similarities and differences in the reaction mechanism of these two types of projectiles. Other relevant questions regarding the reaction mechanism of medium energy nucleons with nuclei are: (a) In the pre-equilibrium phase, what are the relative roles of direct knockout, inelastic scattering, charge exchange and intranuclear cascade processes? (b) How many interactions or emissions take place in the pre-equilibrium (or fast) phase prior to attainment of equilibrium? (c) How is the incident energy shared between the fast emissions and the residual energy of the equilibrated system? (d) What are the relative roles of emission of different types of particles (p, n, d, t, ^{3}He, α, etc.) in the pre-equilibrium and evaporation phases? (e) How does the interaction vary with bombarding energy? (f) How are the measured quantities affected by the characteristics of the target nucleus, e.g., its neutron excess ($N-Z$)? (g) In what respects do the current models need to be extended to better account for the experimental results? (h) Are any physical quantities determined as a result of the comparisons with models?

The nucleon-nucleus interaction is envisaged as first proceeding through a pre-equilibrium phase in which the incident nucleon scatters off the target nucleons with the struck nucleon and the incident nucleon undergoing further scatterings or escaping from the nucleus. At the end of this phase the residual nucleus deexcites through the evaporation process. From the present data an estimate of the number of nucleons emitted in the pre-equilibrium phase can be made. The situation is most transparent in the case of ^{64}Ni as here a large fraction of the observed cross section, ~48% at 100 MeV and 50% at 136 MeV, goes into producing lighter nickel isotopes. Therefore, about half of the time only one proton is able to escape from the ^{64}Ni plus incident proton system during the pre-equilibrium phase. Noting that neutrons and protons should behave similarly in the pre-equilibrium phase, emission of one fast neutron is also quite likely. Thus, for ^{64}Ni in ~50% of the cases only one or two fast nucleons appear to be emitted, leaving the residual nuclei of ^{64}Cu, ^{64}Ni, and ^{63}Ni in a broad range of excitation from which the evaporation subsequently drives the production towards the lighter nickel isotopes lying near the line of stability. The rapid convergence toward the line of stability observed for all cases indicates that the number of pre-equilibrium nucleons emitted is of the same order for all targets. This constitutes the first time[1] that such a conclusion has been explicitly drawn from experimentally determined quantities and is one of the major results of this study.

The increase in $\langle \Delta A \rangle$ of 1 to 1.4 mass units from 80 to 164 MeV bombarding energy (see Fig. 4) shows that almost all the additional energy above 80 MeV is dissipated in the pre-equilibrium phase of the reaction. In the evaporation phase only about 10 MeV is needed for the emission of an additional nucleon. If all of the increase in $\langle \Delta A \rangle$ in going from 80 to 164 MeV were due to extra nucleons emitted in the evaporation phase, one would conclude that the average excitation energy of the residual equilibrated nuclei increased by 10–15 MeV. This number is an upper limit in the absence, as yet, of a direct measurement of the increase in the average energy of the particles in the fast phase. However, in terms of model calculations it appears that the pre-equilibrium emissions are responsible for about half of this increase, i.e., the average number of pre-equilibrium particles emitted at 164 MeV is about 0.7 more than those at 80 MeV. Thus, it is likely that the average excitation energy of the equilibrated nuclei increases less than 10 MeV for the above mentioned range of incident energies. Given the fact that at 164 MeV the total $\langle \Delta A \rangle$ is about 5.5 and of this about two nucleons are emitted in the fast phase; then about 3.5 nucleons are emitted in the evaporation phase. This number corresponds to an average excitation of the system in equilibrium of about 45 MeV (the residual nucleus after evaporation may have about 10 MeV excitation energy). Thus, on an average about $\frac{3}{4}$ of the incident energy is taken away by pre-equilibrium emissions at 164 MeV. Similar arguments lead to the result that this fraction decreases to about $\frac{1}{2}$ at 80 MeV, which, in turn, confirms that (a) the average excitation energy following the pre-equilibrium phase does not increase rapidly with bombarding energy, and (b) its magnitude is about 40–45 MeV for the proton energy range of 80–164 MeV. However, the fact that one observes production of nuclei as much as 14 (10) mass units removed from the target mass with proton bombarding energy of 164 (80) MeV implies that the range of nuclear excitation over which nuclei are left after the pre-equilibrium emissions is rather broad, extending to within 10 MeV of the bombarding energy.

Relatively large cross sections with which "1α" ($2n$, $2p$) removed nuclei are produced with ^{58}Ni and ^{60}Ni targets (12% and 11% of the total observed cross section, respectively) are believed to be a consequence of the fact that for these targets the 1α nuclei lie close to the line of stability where the cross sections for nuclei of a given Z are observed to peak, in general. In contrast, for ^{62}Ni and ^{64}Ni the 1α removed nuclei lie relatively far from the line of stability and therefore the production cross sections for these nuclei are small. Since the nucleon removal through evaporation tends to drive the system toward the line of stability, the above results are not surprising and there is no reason, as yet, to postulate enhanced alpha removal for these reactions.

Extensive comparisons of experimental results with the cascade and hybrid models have been made in this work. Overall, the cascade model (VEGAS) exhibits better agreement with the observed results. Inclusion of surface effects in the multiple pre-equilibrium emission version of the hybrid model (EVAHYB) is shown to be necessary in order to obtain an equivalent accounting of the experimental cross sections. While there are significant differences between calculated and observed production cross sections, the overall capability of the models to predict the observed cross sections for the different targets and energy range covered here is convincing evidence that the dominant features of the mechanism for these reactions are incorporated in the calculations. In particular, the fact that calculated range in mass of products nuclei and the associated cross sections agree with those observed (see Figs. 4–6) implies that the models, especially VEGAS, are predicting the range of nuclear excitations (and the corresponding cross sections) left after the pre-equilibrium emissions essentially correctly. A sizeable discrepancy in this respect would have led to either under or overprediction in the range of masses of the product nuclei.

Emission of high energy clusters (e.g., d, t, ^{3}He, and α) in the pre-equilibrium phase is not included in the hybrid and cascade models but is observed[4,22] with proton bombardment. Also, interactions which excite collective modes of various multipoles in the target nucleus through inelastic scattering are not included. However, there are indications that contributions from such processes may be significant; for example, the sharp rise in the angular distribution of the emitted protons in the forward direction in contrast to the prediction of the cascade model which predicts a peak at about 20° (Fig. 10).

A study of the model calculations (see Ref. 12 f details) reveal a few interesting results worthy o brief notice here. (1) Of a total of about five nucleons that are emitted on an average from vario nickel targets, e.g., at 136 MeV, the models predict (see Fig. 11) that about two are emitted in th pre-equilibrium phase and the remaining three a

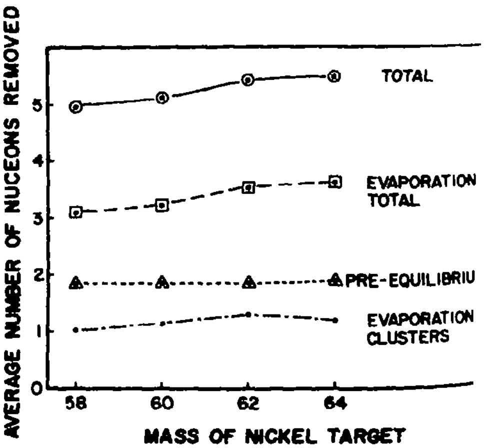

FIG. 11. Partitioning of nucleon removed between th pre-equilibrium and equilibrium phases as predicted b the cascade model for 0 proton energy of 136 MeV.

emitted in the equilibrium phase; of the latter, two are emitted as nucleons and the third is emitted in the form of clusters such as d, t, ^{3}He, and ^{4}He. (2) All of the models predict that beyond 100 MeV bombarding energy the fraction of the initial interactions which leads to emission of at least one fast nucleon is essentially 100%. At 50 MeV this fraction is still large, 60–80 %, although actual values vary with the type of model calculation. (3) The energy dependence of the average number of nucleons emitted in the pre-equilibrium phase as predicted by the cascade model, shown in Fig. 12, has a slope of 0.007 nucleons per MeV. When compared to the observed value of 0.015 nucleons per MeV one can conclude that there is a small increase in the number of nucleons emitted in the evaporation phase with energy or, in other words, the average excitation energy of the equilibrium phase slightly (~5 MeV) increases over 80–160 MeV incident proton energy. (4) Calculations reveal that the range of excitation energy that a nucleus is left in after pre-equilibrium emission is very broad, with noticeably greater probability for lower excitations; for example, for the case (see Fig. 13) of 136 MeV protons on ^{58}Ni, $A = 58$ nuclei are left excited over a range of 0–130 MeV, $A = 57$ nuclei are left with 0–120 MeV excitation, and so on. An experimental study of this phenomenon through particle-gamma coincidence studies may provide a stringent test of the models and may reveal their limitation a little more explicitly. (5) The average energy of nucleons emitted in the pre-equilibrium phase is calculated to decrease precipitously after the first emission, e.g., at 136 MeV the first nucleon is emitted with an average energy of about 50 MeV, but with two or more encounters this value drops to between 10–20 MeV. A particle multiplicity measurement may provide a good test for this aspect of the model dynamics.

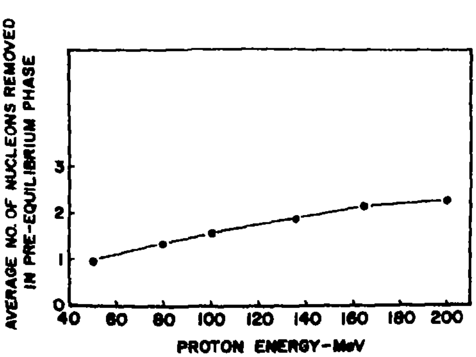

FIG. 12. Average number of nucleons emitted in the pre-equilibrium phase predicted by the cascade model as a function of the incident proton energy for ^{58}Ni.

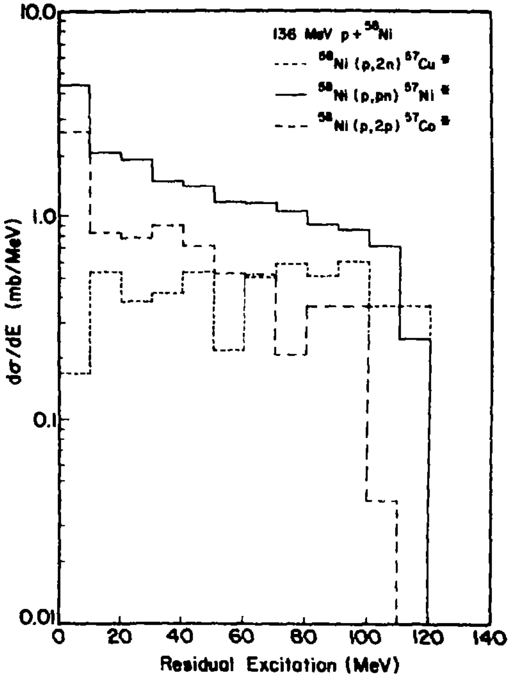

FIG. 13. The excitation energy range of nuclei which are one nucleon removed from the ^{58}Ni target nucleus predicted by the cascade model for incident proton energy of 136 MeV.

Some recent arguments in the literature pertaining to mean free paths (λ) of nucleons in nuclear matter are also worthy of some attention. In searching for answers to phenomena pertaining to the equilibrium process, Gadioli *et al.*[23,24] presented arguments that a mean free path for 20 to 100 MeV nucleons in nuclear matter of the order of 16.7 fm, instead of the value of about 4.2 fm obtained from using the free nucleon interaction cross sections in a Fermi gas model calculation, gives a better account of the energy spectra of emitted protons. On the other hand, Blann[25] claimed that an error in the formulation of Gadioli's exciton model necessitates an increase in the assumed mean free path.

The qualitatively good agreement of the calculations in terms of the hybrid model with the present results indicates that large modification of the calculated mean free path is not necessary, at least not by a factor of 4. The factor of 2 used in most EVAHYB calculations was found to be necessary to simulate the effects of the nuclear surface on the emission process. Even this factor of 2 was not found to be necessary at 80 MeV when the results of the geometry-dependent-hybrid (GDH) model, which incorporates surface effects, were compared with experiment. It is significant, though, that a drastic (factor of 2) increase in the assumed mean free path is required to change $\langle \Delta A\rangle$ by approximately the same amount that GDH changes this quantity in comparison to the simple hybrid model at 80 MeV. It is plausible that much of the increase in the mean free path in Refs. 24 and 25 is necessitated by the non-inclusion of these surface effects.

As noted above, similar studies of nuclide production have been made for medium energy pions, $E_\pi \leqslant 200$ MeV, interacting with nickel isotopes. One of the important differences between the proton-induced and pion-induced reactions is that whereas with pions, e.g., on a ^{58}Ni target, the product mass spectrum peaks[26] at $A \simeq 54-56$, with protons after the initial increase the production cross sections fall off more or less smoothly as the number of nucleons removed increases. In particular VEGAS plus evaporation calculations show[26] important qualitative deviations from the observed pion-induced mass spectra. The fact that this model satisfactorily reproduces the proton-induced spectra indicates that there is some extra physics in the pion-nucleus reaction that is not embodied in the VEGAS code.

In closing it is sufficient to say that systematic data of other kinds such as energy spectra of emitted particles, the particle multiplicities, and particle-gamma coincidence are needed in order to answer some of the questions that are raised here.

ACKNOWLEDGMENTS

This research work has been supported in part by grants from the National Science Foundation. We are thankful to Professor M. Blann of Rochester University for many discussions and for providing various hybrid model codes and to Dr. J.N. Ginocchio of the Los Alamos Scientific Laboratory for making the VEGAS code available to us.

APPENDIX: INPUT PARAMETERS FOR MODEL CALCULATIONS

There are several possible combinations of input parameters that can be used for ALICE, EVAHYB, VEGAS, and DFFMH. The ones used in this work are given below.

1. *Hybrid model calculations*

For single pre-equilibrium model calculations the GDH model in ALICE was used. All default input parameters were used, except the following:

(a) Experimental masses were used to determine the binding energies instead of the mass formula. Pairing was removed from the calculated binding energies in the same way that would be done if the option for shell corrected masses, zero pairing were used (default option).

(b) Inverse cross sections for ^{59}Co were used. These were calculated from the optical model by ALICE subroutines using the parameters given by Perey and Perey.[27]

(c) Reaction cross sections from VEGAS (see Table VI) were used so that all calculations would be normalized to the same total cross section.

(d) Weisskopf evaporation was used.

(e) Initial exciton number = 3.0. Initial excited neutron number = 0.8. Initial excited proton number = 1.2.

(f) Nucleon-nucleon mean free paths were used. The mean free path multiplier was 1.0.

For multiple pre-equilibrium calculations the computer code EVAHYB was used. Some modifications were introduced into the code. These included extension of the dimensions to obtain cross sections for nuclei farther away from the target, separate accumulations of the pre-equilibrium and evaporation particle spectra, plotting routines, and output options. All default parameters were used, with the exception of:

(a) Reaction cross sections from VEGAS were used (Table VI).

(b) Initial exciton number = 3.0. Initial excited neutron number = 0.8. Initial excited proton number = 1.2.

(c) Mean free paths derived from free nucleon-nucleon scattering were used. A mean free path multiplier of 1.0 or 2.0 was used and is so denote when an EVAHYB calculation is referenced.

(d) The same inverse cross sections as described above with GDH were used. These were also used in the VEGAS plus ALICE calculations d scribed below.

2. *Cascade model calculations*

The computer code VEGAS was used for the pr equilibrium cascade model calculations. The nu ber of cascades run was 8000–10000 for each case. Relevant input parameters for the calcula tions presented in this work are:

(a) The cutoff energies for neutrons and proto respectively, were the binding energy of the la neutron in the target and the binding energy of last proton plus the Coulomb energy. Nucleons with energies below these values are considere to be captured. The actual values of these cut were in (MeV):

Target	^{58}Ni	^{60}Ni	^{62}Ni	^{64}Ni
Neutron	12.2	11.4	10.6	9.7
Proton	14.2	15.6	17.4	19.0.

(b) No reflection or refraction was included at the potential boundaries. This option was chosen since in previous work inclusion of reflection and refraction resulted in poorer comparisons with the data, indicating that this effect is overestimated in the calculation.

(c) No restriction on the distance between successive collision sites was used.

The input parameters for DFFMH followed the suggested options. The maximum of six particles n, p, d, t, ^{3}He, and α were allowed in the evaporation phase. The parameter a in the level density expression $\rho(U)\alpha e^{2aU}$ was taken to be $A/20$ where A is the mass number of the evaporating system. Inverse cross sections are calculated internally using "continuum theory" by DFFMH with no available input parameters for modification.

ALICE calculations used inverse cross sections from a ^{59}Co evaporating system for all targets. A Co nucleus was thought to be more typical of the evaporating nuclei than a Cu nucleus. The differences between the cross sections for formation of different Co nuclei are mostly geometrical, an effect that changes the emission probabilities of all particles in the same direction and roughly preserves the relative probability of evaporating a particle of a given type. Thus, the ^{59}Co system was chosen and used for all ALICE calculations even though the nucleus cannot be formed with a ^{58}Ni target. The optical model parameters were the same as given above.

---

*Present address: LAMPF, Los Alamos Scientific Laboratory, M.S. 831, Los Alamos, N. M. 87545.

†On leave from INR, Swierk, Poland.

‡Present address: Argonne National Laboratory, Argonne, Ill.

[1] M. Sadler, J. Jastrzebski, A. Nadasen, P. P. Singh, L. L. Rutledge, Jr., T. Chen, and R. E. Segel, Phys. Rev. Lett. 38, 950 (1977).

[2] J. Jastrzebski, H. Karwowski, M. E. Sadler, and P. P. Singh, Bull. Am. Phys. Soc. 22, 634 (1977); and to be published.

[3] J. Wiggins, P. P. Singh, M. Sadler, H. Karwowski, J. Jastrzebski, and D. G. Sarantites, Bull. Am. Phys. Soc. 23, 626 (1978) and to be published.

[4] R. E. Segel, T. Chen, J. V. Maher, J. Wiggins, M. E. Sadler, P. P. Singh, and P. T. Debevec, Bull. Am. Phys. Soc. 23, 926 (1978); and to be published.

[5] P. D. Barnes, R. A. Eisenstein, W. C. Lam, J. Metler, R. B. Sutton, M. Ecklause, J. Kane, R. E. Welsh, D. A. Jenkins, R.J. Powers, R. Kunselman, R. P. Redwine, R. E. Segel, and J. P. Schiffer, Phys. Rev. Lett. 29, 230 (1972).

[6] H. E. Jackson, L. Meyer-Schutzmeister, T. P. Wangler, R. P. Redwine, R. E. Segel, J. Tonn, and J. P. Schiffer, Phys. Rev. Lett. 31, 1353 (1973).

[7] V. G. Lind, H. S. Plendl, H. O. Funsten, W. J. Kossler, B. J. Lieb, W. F. Lankford, and A. J. Buffa, Phys. Rev. Lett. 32, 479 (1974).

[8] D. Ashery, M. Zider, Y. Shamai, S. Cochavi, M. A. Moinester, A. I. Yavin, and J. Alster, Phys. Rev. Lett. 32, 943 (1974).

[9] H. Ullrich, E. T. Boschitz, H. D. Engelhardt, and C. W. Lewis, Phys. Rev. Lett. 33, 433 (1974).

[10] C. C. Chang, N. S. Wall, and Z. Fraenkel, Phys. Rev. Lett. 33, 1493 (1974).

[11] H. E. Jackson, D. G. Kovar, L. Meyer-Schutzmeister, R. E. Segel, J. P. Schiffer, S. E. Vigdor, T. P. Wangler, R. L. Burman, D. M. Drake, P. A. M. Gram, R. P. Redwine, V. C. Lind, E. N. Hatch, O. H. Otteson, R. E. McAdams, B. C. Cook, and R. B. Clark, Phys. Rev. Lett. 35, 641 (1975).

[12] M. E. Sadler, Ph.D. thesis, Indiana University, Bloomington, Indiana (1977); IUCF Internal Report No. 77-2.

[13] M. Blann, Annu. Rev. Nucl. Sci. 25, 123 (1975) and references therein.

[14] N. Metropolis, R. Bivins, M. Storm, A. Turkevich, J. M. Miller, and G. Friedlander, Phys. Rev. 110, 185 (1958).

[15] K. Chen, Z. Fraenkel, G. Friedlander, J. R. Grover, J. M. Miller, and Y. Shimamoto, Phys. Rev. 166, 949 (1968).

[16] V. S. Barashenkov, H. W. Bertini, K. Chen, G. Friedlander, G. D. Harp, A. S. Iljinov, J. M. Miller, and V. D. Toneev, Nucl. Phys. A187, 531 (1972).

[17] M. Blann, OVERLAID ALICE, Report No. COO-3494-29 (1975).

[18] M. Blann and J. Bishplinghoff, Hybrid Code Description, Report No. COO-3494-27 (1975).

[19] A. Mignerey, and M. Blann (unpublished).

[20] I. Dostrovsky, Z Fraenkel, and G. Friedlander, Phys. Rev. 116, 683 (1959).

[21] V. F. Weisskopf and D. H. Ewing, Phys. Rev. 57, 472 (1940).

[22] J. R. Wu, C. C. Chang, H. D. Holmgren, N. S. Wall, J. P. Didelez, and C. Butterfield, in *Proceedings of the Second International Conference on Clustering Phenomena in Nuclei, College Park, Maryland, 1975*, edited by D. A. Goldberg, J. B. Marion, and S. J. Wallace (National Technical Information Service, Springfield, 1975), VA. 6, p. 1.

[23] E. Gadioli, E. Gadioli Erba, G. Tagliaferri, and J. J. Hogan, Phys. Lett. 65B, 311 (1976).

[24] E. Gadioli, Nukleonika 21, 385 (1976).

[25] M. Blann, Phys. Lett. 67B, 145 (1977).

[26] H. E. Jackson, S. B. Kaufman, D. G. Kovar, L. Meyer-Schutzmeister, K. E. Rehm, J. P. Schiffer, S. L. Tabor, S. E. Vigdor, T. P. Wangler, L. L. Rutledge, Jr., R. E. Segel, R. L. Burman, P. A. M. Gram, R. P. Redwine, and M. A. Yates-Williams, Phys. Rev. C 18, 2656 (1978).

[27] F. G. Perey and C. M. Perey, At. Data Nucl. Data Tables 13, 294 (1974).

PHYSICAL REVIEW C VOLUME 21, NUMBER 6 JUNE 198

Gamma-ray lifetimes for parity doublets in ^{41}K, ^{41}Ca

S. K. Saha, M. J. Maynard, and B. C. Robertson
Queen's University, Kingston, Ontario

A. B. McDonald and E. D. Earle
Atomic Energy of Canada Limited, Chalk River Nuclear Laboratories, Chalk River, Ontario K0J 1J0

(Received 14 February 1980)

Lifetimes have been measured by direct timing for the 1582 keV, $3/2^-$ level of ^{41}K($\tau < 38$ ps) and the 2010 keV, $3/2^+$ level of ^{41}Ca($\tau = 730 \pm 18$ ps). These levels are members of closely spaced parity doublets. The sensitivity of measurements to determine the parity mixing within these doublets is discussed.

[NUCLEAR REACTIONS ^{41}K($p,p\gamma$), $E_x = 1582$ keV, measured τ; ^{40}Ca($d,p\gamma$), $E_x = 2010$ keV, measured τ. Direct timing.]

I. INTRODUCTION

The Weinberg-Salam unified model of the weak and electromagnetic interactions[1] is in excellent agreement with the results of a variety of recent high energy experiments involving lepton-lepton and lepton-quark interactions.[2] Measurements of parity violation in nuclear systems can test the predictions of this unified model for weak nucleon-nucleon (and hence quark-quark) interactions, and considerable experimental and theoretical effort has been devoted to this subject.[3]

Although measurements of parity violation in few-nucleon systems such as $p+p$ and deuterium[4-6] are easiest to relate theoretically to the basic weak nucleon-nucleon interaction, the size of parity violating effects is extremely small ($\sim 1 \times 10^{-4}\%$). Therefore, a number of experiments have been performed to search for parity mixing in energy levels of heavier nuclei, particularly in those cases where nuclear structure effects result in large enhancements in the parity violating observables. Initial experiments[7] in a number of cases in heavy nuclei produced definite results which were of the order of magnitude expected for parity violation according to the basic weak interaction models.

More recently, experimental results have been obtained[8-11] for a few cases in light nuclei where the parity mixing occurs predominantly between two closely spaced nuclear energy levels, for which the wave functions are quite well described by nuclear shell models. In these cases, experimental results can be related to the basic weak nucleon-nucleon interaction and the predictions of various weak interaction models may be tested. The particular cases studied to date are also favored experimentally because of large inhibitions in electromagnetic transition rates, resulting in relatively large parity violating observables.

The present paper described lifetime measurements for gamma decay of the long lifetime members of closely spaced parity doublets in ^{41}K and ^{41}Ca. The energy spacing in these cases is sufficiently small so that parity mixing with other nuclear levels can probably be neglected. In addition, the proximity of these nuclei to the doubly magic nucleus ^{40}Ca and the low excitation energy of the levels, implies that shell model calculation of their wave functions should be quite accurate. The purpose of the present work is to determine the electromagnetic transition rates and hence the sensitivity of possible experiments searching for parity mixing of these levels.

The low-lying energy levels of ^{41}K and ^{41}Ca are shown in Fig. 1. The doublets of interest in the present work are the $J^\pi = \frac{3}{2}^-$, $\frac{3}{2}^+$ pairs at 1582 and 1560 keV in ^{41}K, and at 1943 and 2010 keV in ^{41}Ca The lifetimes of the short-lived $\frac{3}{2}$ levels have bee measured to be about 600 fs (see Table I). Prior to the present measurement, only a lower limit w known for the lifetime of the 1582 keV, $\frac{3}{2}^-$ level of ^{41}K and the lifetime of the 2010 keV, $\frac{3}{2}^+$ level of ^{41}Ca was known to be about 800 ps.

The next section describes the measurements c the lifetimes of the long-lived $\frac{3}{2}$ levels in ^{41}K and ^{41}Ca by electronic timing, Sec. III lists the resul and in Sec. IV the results are discussed in terms of possible parity violation measurements.

II. EXPERIMENTS

The 1582 keV level in ^{41}K was populated via th ^{41}K($p,p'\gamma$)^{41}K reaction at $E_p = 3.22$ MeV with the pulsed beam facility of the Chalk River Nuclear Laboratories (CRNL) MP tandem accelerator. beam burst duration of ~0.5 ns was used with an interval of 800 ns between successive bursts an

© 1980 The American Physical Soc

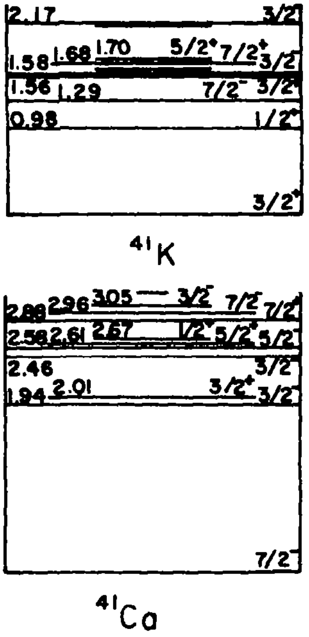

FIG. 1. Low-lying energy levels of ^{41}Ca and ^{41}K (from Ref. 15).

an average beam intensity of 20 nA. The target was a 1300 μg cm^{-2} layer of ^{41}KI (enriched to >94%) evaporated onto a thick gold backing. Gamma-ray levels were detected at 0° to the incident beam direction in an 86 cm^3 coaxial Ge(Li) detector placed with its front face 3.5 cm from the target.

The 2010 keV level in ^{41}Ca was populated via the ^{40}Ca$(d,p\gamma)^{41}$Ca reaction at $E_d = 3.0$ MeV with the pulsed beam facility of the Queen's University 4 MV Van de Graaff accelerator. A beam burst duration of ≤ 1 ns was used with an interval of 50 ns between successive bursts and an average beam intensity of 23 nA. The target consisted of a 100 μg cm^{-2} layer of natural calcium evaporated onto a thick gold backing. Oxygen buildup on the target was inhibited by evaporating a 100 μg cm^{-2} encapsulating layer of gold over the front face. Gamma rays were detected in a 48.3 cm^3 coaxial Ge(Li) crystal placed 10 cm from the target at 135° to the incident beam direction. At this angle the 2010 keV γ ray was well separated from the Doppler-shifted 2001 keV γ ray from the 3944 keV level (see Fig. 2).

In both experiments, signals from the Ge(Li) crystals were used to obtain timing as well as energy information. Gamma-ray timing signals were extracted by a timing filter amplifier and

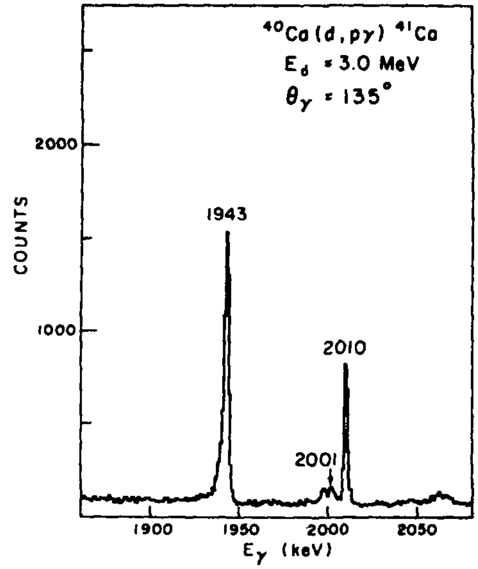

FIG. 2. Gamma-ray spectrum from the ^{40}Ca$(d,p\gamma)^{41}$Ca reaction at $E_d = 3.0$ MeV. At $\theta_\gamma = 135°$ the 2001 keV γ ray is clearly separated from the 2010 keV γ ray.

constant fraction discriminator, and provided the start signal for a time-to-amplitude convertor. The stop signal was derived from the beam pulsing system. The time and energy were stored in an event mode format for subsequent off-line analysis. Calibration of the time spectra was carried out with standard delay cables and a Tennelec TC850 time calibrator.

The performance of the constant fraction discriminator is characterized by a residual correlation between detection time and γ-ray energy, which depends explicitly on the individual setup of the discriminators. It is therefore necessary to determine this characteristic response under the conditions encountered in the actual timing experiment and in the appropriate γ-ray energy region. The prompt calibration was therefore obtained by simultaneously accumulating the time spectra for several "prompt" ($\tau < 1$ ps) γ rays produced in the same reaction and in the same energy region as the γ ray of interest. Accordingly, the time spectrum corresponding to the photopeaks of the 661, 728, 1039, 1485, 1943, 2010, 2575, and 2605 keV γ rays in ^{41}Ca, and the 1560, 1582, and 1594 keV γ rays in ^{41}K were simultaneously accumulated, and the centroid position of each time peak determined.

In addition to the systematic energy dependence, it is necessary to account for the fact that the photopeak and the underlying background arise from different production and detection mechanisms, and can have a significantly different time characteristic. The contribution of underlying background to the relevant photopeaks was accounted for by generating the time spectrum from the background under the photopeak and subtracting it from the photopeak time spectrum. The background spectra were produced by taking the time spectra of an equal number of background channels immediately adjacent to the relevant photopeak. This correction was carried out both by using background channels higher than the photopeak and two sets with half the number of channels placed symmetrically about the peak. Differences between the two methods of background subtraction were significantly smaller than the statistical errors.

III. RESULTS

The 1560 and 1594 keV γ rays from ^{41}K were used to generate the prompt calibration line for the 1582 keV ground-state decay γ ray, and a comparison of the 1582 keV γ-ray decay time and the prompt calibration curve, shown in Fig. 3, shows no measurable time centroid shift for that γ ray. This limits the lifetime of the ^{41}K 1582 keV level to $\tau < 38$ ps.

The prompt γ rays from ^{41}Ca were used to provide a calibration curve for the 2010 keV ground-state decay. In this case, a significant time centroid shift is observed, as can be seen in Fig. 4, and leads to $\tau = 730 \pm 18$ ps for the lifetime of the 2010 keV level in ^{41}Ca. This value is in good agreement with, and more accurate than, the earlier measurements of $\tau = 800 \pm 200$ ps, obtained by the electronic timing technique,[12] and $\tau = 670 \pm 70$ ps obtained by the recoil distance technique.[13]

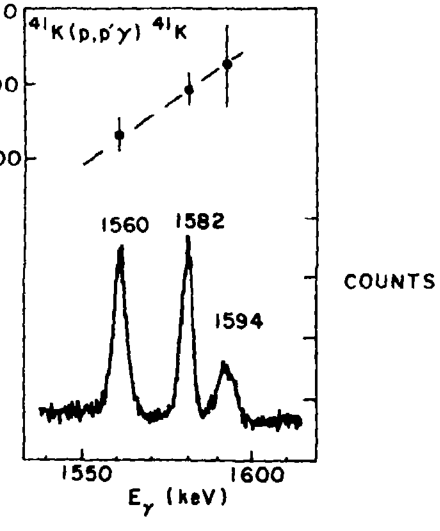

FIG. 3. Time centroids of the full energy peak as a function of γ-ray energy for the ^{41}K$(p,p'\gamma)^{41}$K reaction at $E_p = 3.22$ MeV.

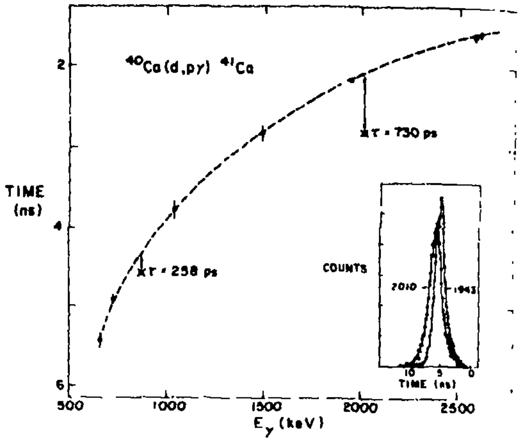

FIG. 4. Time centroids of the full energy peak as a function of γ-ray energy for the ^{40}Ca$(d,p\gamma)^{41}$Ca reaction at $E_d = 3.0$ MeV. The dashed curve is a least squares fit of a polynomial for the prompt ($\tau \lesssim 1$ ps) γ rays. The time spectra for the 1944 and 2010 keV γ rays (inset) clearly show the centroid shift for the latter transition. The delayed 871 keV γ ray is produced by the ^{16}O$(d,p\gamma)$-^{17}O reaction on the oxide layer on the target.

An independent check of the direct timing method was carried out by measuring the known lifetime of the 871 keV level in ^{17}O produced by the ^{16}O$(d,p\gamma)^{17}$O reaction on the oxygen surface layer on the Ca target. The centroid shift of the 871 keV γ ray was used to determine a lifetime of $\tau = 258 \pm 14$ ps, in excellent agreement with the average of previous measurements,[14] $\tau = 258 \pm 4$ ps.

IV. DISCUSSION

The parity mixing between these pairs of levels could be determined by measuring the circular polarization of the gamma-ray transition from the longer lifetime (unpolarized) $\frac{3}{2}$ level to the ground states. Alternatively, this $\frac{3}{2}$ level could be polarized (such as by polarization transfer from a polarized beam) and the asymmetry relative to the direction of polarization could be measured. (For a discussion, see Ref. 15.)

For either measurement, the parity violating observable is almost directly proportional to the ratio

$$\frac{\langle 1560\text{ keV},\ \frac{3}{2}^{+}\|M1\|0,\frac{3}{2}^{+}\rangle}{\langle 1582\text{ keV},\ \frac{3}{2}^{-}\|E1\|0,\frac{3}{2}^{+}\rangle}$$

in ^{41}K or

$$\frac{\langle 1943\text{ keV},\ \tfrac{3}{2}^-\|E2\|0,\ \tfrac{7}{2}^-\rangle}{\langle 2010\text{ keV},\ \tfrac{3}{2}^+\|M2\|0,\ \tfrac{7}{2}^-\rangle}$$

in ^{41}Ca.

In particular, for the circular polarization measurement,

$$P_\gamma(^{41}\text{K}, 1582\text{ keV}) = 2\langle\tfrac{3}{2}^+|H^w|\tfrac{3}{2}^-\rangle\left\langle\left\|\frac{M1}{E1}\right\|\right\rangle \frac{1+\delta_+\delta_- + B_2(\frac{3}{2})P_2(\cos\theta)[-0.400+0.775(\delta_+ + \delta_-)]}{1+\delta_-^2 + B_2(\frac{3}{2})P_2(\cos\theta)(-0.400+1.550\delta_-)}$$

and

$$P_\gamma(^{41}\text{Ca}, 1943\text{ keV}) = 2\langle\tfrac{3}{2}^+|H^w|\tfrac{3}{2}^-\rangle\frac{\langle\|E2\|\rangle}{\langle\|M2\|\rangle}$$

$$\times\frac{1+\delta_+\delta_- + B_2(\frac{3}{2})P_2(\cos\theta)[-0.143+0.500\delta_+\delta_- - 0.463(\delta_- + \delta_+)]}{1+\delta_+^2 + B_2(\frac{3}{2})P_2(\cos\theta)(-0.143+0.500\delta_+^2 - 0.926\delta_+)},$$

where H^w is the weak parity violating Hamiltonian responsible for the parity mixing, $\frac{3}{2}^+$ and $\frac{3}{2}^-$ refer to the two members of the parity doublet, and δ_+ and δ_- are mixing ratios for the transitions from the $\frac{3}{2}^+$, $\frac{3}{2}^-$ components to the ground state. The energy difference between the members of the parity doublet is denoted by ΔE; $B_2(\frac{3}{2})$ is the statistical tensor for the state being excited. The notation and phase convention of Rose and Brink[16] are used.

From the data in Table I, including the present measurements, one can conclude that for the 1582 keV level in ^{41}K 5 ps $< \tau <$ 38 ps and for the 2010 keV level in ^{41}Ca $\tau = 727 \pm 18$ ps. Using this information, together with previous measurements of mixing ratios and the lifetime of the short-lived $\frac{3}{2}$ levels, one can calculate that for a circular polarization measurement at 55°, where $P_2(\cos\theta) \approx 0$,

$$P_\gamma(^{41}\text{K}, 1582\text{ keV}) = (5.5 \pm 2.3) \times 10^{-4}\text{ eV}^{-1}\langle\tfrac{3}{2}^+|H^w|\tfrac{3}{2}^-\rangle$$

and

$$P_\gamma(^{41}\text{Ca}, 2010\text{ keV}) = (1.1 \pm 0.2) \times 10^{-3}\text{ eV}^{-1}\langle\tfrac{3}{2}^+|H^w|\tfrac{3}{2}^-\rangle.$$

Although the relatively short lifetime for the ^{41}K, 1582 keV level results in a reduced sensitivity in this case, these sensitivities to parity mixing

TABLE I. Parameters of parity doublets in ^{41}K, ^{41}Ca.

Nucleus	Initial level (J^π)	Lifetime measurements	Final level (J^π)	Branching ratio (%)	Mixing ratio
^{41}K	1560.4 ± 0.2($\frac{3}{2}^+$)	600 ± 110 fs	0.0($\frac{3}{2}^+$)	82.4 ± 0.6	+0.27 ± 0.02
		(average)[a]	980($\frac{1}{2}^+$)	17.6 ± 0.6	−0.12 ± 0.04
			1294($\frac{7}{2}^-$)	<0.4	
	1582.3 ± 0.2($\frac{3}{2}^-$)	>4.5 ps[b]	0.0($\frac{3}{2}^+$)	84.2 ± 0.7	$+0.08^{+0.02}_{-0.03}$
		>1.5 ps[c]	980($\frac{1}{2}^+$)	15.8 ± 0.7	+0.06 ± 0.03
		<38 ps[d]	1294($\frac{7}{2}^-$)	<0.7	
^{41}Ca	1942.61 ± 0.11($\frac{3}{2}^-$)	570 ± 100 fs	0.0($\frac{7}{2}^-$)	100	
		(average)			
	2009.8 ± 0.2($\frac{3}{2}^+$)	800 ± 200 ps[e]	0.0($\frac{7}{2}^-$)	100	−0.13 ± 0.03
		670 ± 70 ps[f]			
		730 ± 18 ps[d]			

[a] All information from Ref. 17 unless otherwise noted.
[b] Reference 18.
[c] Reference 19.
[d] Present work.
[e] Reference 12.
[f] Reference 13.

matrix elements compare favorably to the sensitivities of cases previously investigated[8,9] in ^{18}F

$$|P_\gamma(1082\text{ keV}\to 0)=4.9\times10^{-3}\text{ eV}^{-1}\langle 0^+|H^w|0^-\rangle|$$

and ^{19}F

$$|A_\gamma(110\text{ keV}\to 0)=1.8\times10^{-4}\text{ eV}^{-1}\langle \tfrac{1}{2}^-|H^w|\tfrac{1}{2}^+\rangle|$$

but are less favorable than the very sensitive case[10] in ^{21}Ne

$$\{P_\gamma(2789\text{ keV}\to 0)=9.5\times10^{-2}\text{ eV}^{-1}\langle \tfrac{1}{2}^-|H^w|\tfrac{1}{2}^+\rangle\}.$$

The practicability of possible measurements of parity mixing in ^{41}K and ^{41}Ca is obviously dependent on details of the reaction used to populate the levels and on the apparatus used. This is emphasized by the fact that the least sensitive case, ^{19}F, is the only one for which a statistically significant result has been obtained.[9]

However, if the parity mixing matrix elements in ^{41}K and ^{41}Ca were as large as those measured[9] for $^{19}\text{F}(\langle \tfrac{1}{2}^-|H^w|\tfrac{1}{2}^+\rangle = -0.33\pm0.18\text{ eV})$, then the expected circular polarizations would be

$$P_\gamma(^{41}\text{K}, 1582\text{ keV})\approx 2\times10^{-4}$$

and

$$P_\gamma(^{41}\text{Ca}, 2010\text{ keV})\approx 4\times10^{-4}.$$

These P_γ may be compared with those attained recently in accelerator based experiments:

$$^{18}\text{F}:\quad P_\gamma=(-7\pm20)\times10^{-4}\quad(\text{Ref. }8)$$

and

$$^{21}\text{Ne}:\quad P_\gamma=(9\pm51)\times10^{-4}\quad(\text{Ref. }10).$$

This sensitivity, and the possibility of accurate shell model calculations for these levels, suggests that these cases should be included in the short list of experiments that could provide quantitative information on the weak nucleon-nucleon interaction.

The ^{41}K case is of particular interest because the parity mixing occurs between two $T=\tfrac{3}{2}$ levels and therefore involves matrix elements in which the isospin changes by 0, 1, or 2 units. There has been some interest in isotensor ($\Delta T=2$) parity violating matrix elements because of the result[5] obtained for the circular polarization of gamma rays following the capture of thermal neutrons in hydrogen $[P_\gamma=(1.60\pm0.45)\times10^{-6}]$. The circular polarization in this case depends on mixing matrix elements with $\Delta T=0$ and 2, but the size of the $\Delta T=0$ matrix element is constrained by a measurement[11] in ^{18}O ($\Delta T=0$). The observed circular polarization in the $n+p\to d+\gamma$ case could be explained by a relatively large isotensor matrix element,[20] but this is not predicted[21] by basic calculations of the weak nucleon-nucleon interaction. Although the dependence of parity mixing on the $\Delta T=2$ matrix element has yet to be determined in the ^{41}K case, a measurement in this case might provide an additional determination of the size of isotensor parity mixing.

The ^{41}Ca case involves parity mixing of two isospin $\tfrac{1}{2}$ levels, and hence involves $\Delta T=0$, 1 matrix elements. If the Weinberg-Salam model of weak interactions is valid for quark-quark interactions, then $T=1$ matrix elements may be enhanced[21] by a factor as large as 20 over the size predicted by the previously accepted Cabibbo model without neutral currents. A measurement of parity mixing in ^{41}Ca could provide an additional test for the enhancement of $\Delta T=1$ matrix elements in a case of two state mixing with well defined wave functions.

The complete determination of the weak two-nucleon interactions responsible for the $\Delta T=0$, 1, 2 parity mixing matrix elements requires measurements for a number of cases with different isospin combinations. The experimental information available to date has been parametrized in terms of weak two-nucleon matrix elements[22] or weak meson-nucleon-nucleon vertices.[23] However, the present experimental uncertainties and theoretical nuclear structure difficulties are too large to define a possible enhancement of $\Delta T=1$ matrix elements arising from the Weinberg-Salam model.

To date, the number of experiments contributing to this information is small, and most provide only upper limits. More accurate measurements and results for new cases with well defined nuclear structure are required. Parity mixing measurements for the doublets discussed in the present work could provide valuable additional information.

---

[1] S. Weinberg, Phys. Rev. Lett. 19, 1264 (1967); A. Salam, in *Elementary Particle Theory: Relativistic Groups and Analyticity (Nobel Symposium No. 8)*, edited by N. Svartholm (Alqvist and Wiksell, Stockholm, 1968), p. 367.

[2] C. Baltay, Phys. Rep. 48, 157 (1979).

[3] E. G. Adelberger, in *Unification of Elementary Forces and Gauge Theories*, edited by D. B. Cline and F. E. Mills (Harwood, London, 1979), p. 197; D. Tadic, *ibid.*, p. 245.

[4] D. E. Nagle, see Ref. 3, p. 301.

[5] V. M. Lobashov, D. M. Kaminker, G. I. Kharevich, V. A. Kniazkov, N. A. Lozovoy, V. A. Nazarenk, L. Sayenko, L. M. Smotritsky, and A. I. Yegorov, Nucl

Phys. A197, 241 (1972).

[6] J. F. Cavaignac, B. Vignon, and R. Wilson, Phys. Lett. 67B, 148 (1977).

[7] For a review see M. Gari, Phys. Rep. 6C, 40 (1973).

[8] C. A. Barnes, M. M. Lowry, J. M. Davidson, R. E. Marrs, F. B. Morinigo, E. G. Adelberger, and H. E. Swanson, Phys. Rev. Lett. 40, 840 (1978).

[9] E. G. Adelberger, H. E. Swanson, M. D. Cooper, J. W. Tape, and T. A. Trainor, Phys. Rev. Lett. 34, 402 (1975); E. G. Adelberger, in *Unification of Elementary Forces and Gauge Theories*, edited by D. B. Cline and F. E. Mills (Harwood, London, 1978), p. 198.

[10] K. A. Snover, R. Von Lintig, E. G. Adelberger, H. E. Swanson, T. A. Trainor, A. B. McDonald, E. D. Earle, and C. A. Barnes, Phys. Lett. 41, 145 (1978).

[11] K. Neubeck, H. Schober, and H. Waffler, Phys. Rev. C 10, 320 (1974).

[12] R. E. Holland and F. J. Lynch, Phys. Rev. C 2, 1365 (1970).

[13] J. Keinonen, R. Rascher, M. Uhamacher, N. Wust, and K. P. Lieb, Phys. Rev. C 14, 160 (1976).

[14] *Table of Isotopes, 7th Edition*, edited by C. Michael Lederer and Virginia S. Shirley (Wiley-Interscience, New York, 1979), p. 23.

[15] D. J. Millener, E. K. Warburton, K. A. Snover, R. Von Lintig, and P. G. Ikossi, Phys. Rev. C 18, 1878 (1978).

[16] H. J. Rose and D. M. Brink, Rev. Mod. Phys. 39, 306 (1967).

[17] P. M. Endt and C. Van Der Leun, Nucl. Phys. A310, 1 (1978).

[18] C. J. Lister, A. J. Brown, L. L. Green, A. N. James, P. J. Nolan, and J. F. Sharpey-Schafer, J. Phys. G 2, 577 (1976); C. J. Lister, A. M. Al-Naser, A. H. Behbehani, L. L. Green, P. J. Nolan, and J. F. Sharpey-Schafer, *ibid.* 4, 907 (1978).

[19] J. C. Merdinger, A. Chevallier, L. Courdiear, B. Haas, J. Styczen, and P. Taras, Nucl. Phys. A260, 307 (1976).

[20] M. A. Box, A. J. Gabric, K. R. Lassey, and B. H. J. McKellar, J. Phys. G 2, 407 (1976).

[21] B. Desplanques, J. F. Donoghue, and B. Holstein, Ann. Phys. (N.Y.) (to be published).

[22] B. Desplanques and J. Missimer, Nucl. Phys. A300, 286 (1978).

[23] J. D. Bowman, B. F. Gibson, P. Herczeg, and E. M. Henley, Los Alamos Report No. LA-UR-79-1083 (unpublished).

PHYSICAL REVIEW C VOLUME 21, NUMBER 6 JUNE 198

Photon-absorption cross sections between 3 and 30 MeV

N. K. Sherman, C. K. Ross, and K. H. Lokan*

Division of Physics, National Research Council, Ottawa, Ontario K1A OR6, Canada

(Received 5 October 1978; revised manuscript received 19 November 1979)

Photon absorption by Al, Ta, and Bi between 3 and 30 MeV was measured using as a photon spectrometer a photoneutron time-of-flight detector and a liquid deuterium target. The atomic cross sections of Ta and Bi at the lowest energies (and of Al at higher energies) agree with calculated values appearing in published tabulations but exceed them at 25 MeV by about 2% in Ta and 3% in Bi. Calculations by others using empirical Coulomb corrections and improved screening corrections to the cross section for pair production by the nucleus agree with experiment to within (0.5 ± 0.4)%. Best experimental values of the combined correction for Bi are given.

[NUCLEAR REACTIONS ^{27}Al, ^{181}Ta, ^{209}Bi; measured total photon absorption $\sigma_\gamma(E)$; observed GDR; deduced electron pair production $\sigma_\kappa(E)$; $E=3.0$ to 30.0 MeV; resolution 500 keV; deduced experimental values for Bi of the combined Coulomb and screening correction; $^2H(\gamma,n)$ LD_2/TOF spectrometer.]

INTRODUCTION

By time-of-flight detection of photoneutrons from liquid deuterium we have measured the transmission of 3 to 30 MeV γ rays through Al, Ta, and Bi. We find that the atomic absorption cross sections exceed calculated values listed in well-known tabulations by amounts which increase with the photon energy and the atomic number of the absorber. Experimental evidence has accumulated[1-3] showing that the photon absorption cross sections of heavy elements at intermediate energies have been underestimated in the tables.[4,5] The dominant contribution to the total cross section σ for energies above a few MeV is the cross section for production of electron pairs in the Coulomb field of the nucleus σ_κ. The nuclear pair cross section as a function of photon energy ω has recently been calculated[6] using improved empirical Coulomb corrections[7] to the plane wave approximation and relativistic atomic form factors in the screening corrections. From our measured total cross sections which agree within experimental error with those measured at Mainz[3,6] (or in the case of Bi, with Pb measurements suitably scaled up) we have extracted values of $\sigma_\kappa(\omega)$ which agree very closely with the improved calculated values.[6]

METHOD

The present experiment is the first one using the $^2H(\gamma,n)$ reaction which is able to furnish high quality total absorption data, although use of the deuteron to measure γ-ray energy goes back 40 years.[8] Our innovations are the use of a liquid deuterium (LD_2) target with a time-of-flight (TOF) detector, and rapid cycling of absorbers in and out of the γ beam for precise time periods.

The Ottawa spectrometer is described schemat cally in Fig. 1. The experiment consists in measuring as a function of ω the ratio of F, the photo flux transmitted by an absorber of known mass per unit area, to the flux F_0 incident on it. Then is obtained from the relation

$$F(\omega)=F_0(\omega)\exp[-n\sigma(\omega)], \tag{1}$$

where n is the number of atoms/cm^2 in the absorber. Whereas other γ spectrometers detect electrons amidst a high electron background, in the TOF method neutrons are detected after the beam pulse at a remote quiet location. The thin-walled plastic LD_2 holder we use, which has been described before,[8] adds little background and the spectrum is free of nuclear structure present in earlier TOF measurements using the $^2H(\gamma,n)$ method—the first[9] using a deuterated polyethylene target, the second in our laboratory[10] based on ($D_2O - H_2O$) differences. Cycling the absorbers avoids normalization to a second spectrometer (as was done at Mainz[11] with Compton spectrometers). A continuous energy range is covered (an advantage over nuclear resonance absorption experiments[1] which can be performed only at certain discrete energies) without changing magnet settings as one does with pair[2] or Compton[3] spectrometers. At 6 MeV our energy resolution $\Delta\omega$ is 30 keV, comparable to that of Ge(Li) detectors which, moreover, cannot operate in a high intensity γ beam. At 2 MeV $\Delta\omega$ is 340 keV, still better than for NaI (Tl). In common with all ratio measurements of total cross section, experimental factors such as incident γ spectrum, neutron detector efficiency, photon absorption in the target chamber walls,

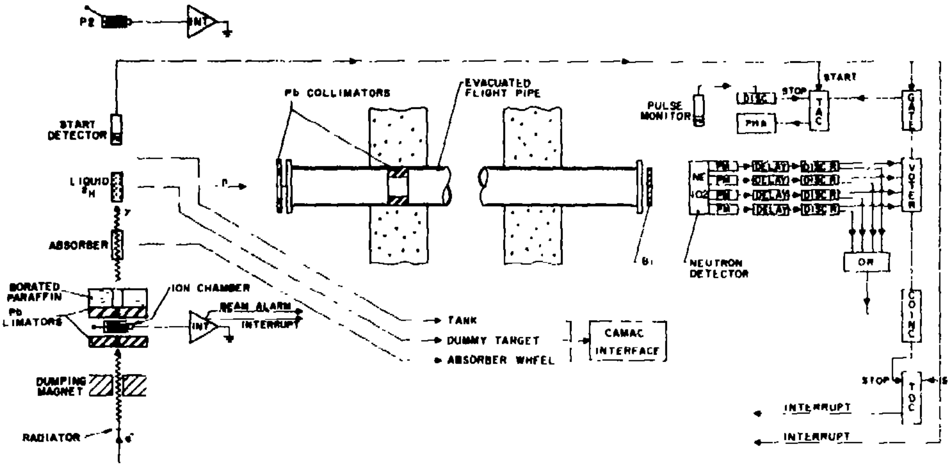

FIG. 1. Schematic diagram of the LD$_2$-TOF spectrometer. Three absorbers and a blank are mounted on a wheel ahead of the liquid deuterium (LD$_2$) target which is viewed by a TOF photoneutron detector. In the figure, e^- denotes the incident electron beam, γ the collimated photon beam, and n a photoneutron. The deuterium target is indicated by the label liquid ^{2}H, the standard ion chamber of Natl. Bur. Stand. (U.S.) design by $P2$, the bismuth γ-flash filter by Bi, and the plastic scintillator by NE 102. In the boxes representing electronic circuitry, the letters PM stand for photomultiplier tube, INT for current integrator, DISCR for discriminator, VOTER for majority-logic coincidence unit, COINC for coincidence unit, TDC for time digitizer, TAC for time-to-amplitude converter, and PHA for pulse height analyzer. The CAMAC interface permits computer-controlled cycling of the absorbers and alternation of the full target with an empty target. For background runs the vacuum tank (not shown) containing the LD$_2$ target is moved laterally and the dummy target descends into the photon beam. The pulse monitor is actually located on the flight pipe axis behind the neutron detector to record the average duration of the incident photon bursts. Photoneutron events (coincident pulses from 3 out of the 4 photomultipliers) are stored in time channels according to the interval between START and STOP pulses. The flight time reveals the neutron energy, so giving the photon energy.

and neutron absorption in the target or flight pipe windows cancel in the extraction of the experimental cross section $\sigma_{\exp}(\omega)$.

A deuteron absorbing a photon of energy greater than the binding energy B (2.2246 MeV) disintegrates into a neutron and a proton with kinetic energies T_n and T_p uniquely related—so we need measure only T_n. If the photon is of low energy and a neutron moving perpendicular to the photon direction is detected, the simple relationship

$$\omega = 2T_n + B \tag{2}$$

gives the photon energy. In the present experiment, however, neutrons with energies of up to 20 MeV were detected requiring use of a relativistic version of (2). The flight time t of a neutron traversing a distance L, represented by τ in reduced units, is

$$t = (L/c)\tau , \tag{3}$$

where c is the speed of light. The kinetic energy of the neutron is

$$T_n = m_n[(1 - \tau^{-2})^{-1/2} - 1] , \tag{4}$$

where m_n is the mass energy of the neutron. The photon energy is given by[12]

$$\omega = \frac{T_n[1 + (m_n - B)/m_p] + B[1 - (B/2m_p)]}{1 - (T_n + B)/m_p + [T_n(T_n + 2m_n)]^{1/2}\cos\theta/m_p} , \tag{5}$$

where m_p is the mass energy of the proton and θ is the laboratory angle between the photon beam direction and the direction of emission of the neutron.

EXPERIMENTAL PROCEDURE

The experimental arrangement is depicted in Fig. 1. Pulsed 42 MeV bremsstrahlung from the National Research Council of Canada (NRC) electron Linac irradiated the LD$_2$ target (47 mm diam., 15 cm long) axially. The γ beam was produced by 3A, 720 Hz electron pulses of 8 ns duration striking a 0.5 mm Ta radiator. The LD$_2$ target was suspended in a large vacuum tank at a distance of 2.5 m from the radiator. Halfway between was a 4-armed wheel carrying three 54 mm diam. absorbers whose physical characteristics are listed in Table I. The fourth position was empty. Two Pb collimators each 5 cm thick placed ahead of the wheel restricted the photons to a pencil

TABLE I. Physical characteristics of the absorbers, including atomic number Z, purity by weight, and mass per unit area m. The measured densities ρ are compared with reference densities ρ_{ref}.

Element	Z	Purity (wt %)	m (g/cm^2)	ρ(g/cm^3)	ρ_{ref} (g/cm^3)
Al	13	99.995 [a]	47.86 ± 0.10	2.680 ± 0.008	2.6985 [d]
Ta	73	>99.9 [b]	30.25 ± 0.06	16.640 ± 0.050	16.6
Bi	83	>99 [c]	19.58 ± 0.04	9.745 ± 0.029	9.747

[a] *Matrix of large single crystals:* Mg(12 ppm), Si(10 ppm), Fe(10 ppm), Cu(30 ppm).

[b] Vacuum cast: principal impurity Nb($Z = 41$).

[c] Vacuum cast: Cl(1 ppm), Fe(1 ppm), Ni(1 ppm), Cu(1 ppm), Ag(4 ppm), Sb(2 ppm), Pb(3 ppm), <1% *As* ($Z = 33$).

[d] Average of CRC Handbook value and Mainz (Ref. 3) value.

falling on the end of the LD_2 holder to prevent inscattering by those portions of the absorbers not directly shadowing the target. An empty holder suspended in the same vacuum tank as the LD_2 target was made to descend into the γ beam when the tank moved sideways to remove the LD_2 from the beam. This permitted background runs to be performed. The wheel, tank, and holder were moved by stepping motors controlled by a computer which also accumulated eight (γ,n) TOF spectra sequentially during each 6-min cycle; 1 min for each absorber position with full LD_2 target and 20 s for each position with empty holder. Data were rejected and the position remeasured if the beam intensity (measured by the first ion chamber) fell below about 85% of a set value during a cycle or if neutron events did not occur. Since the beam intensity changed with a time constant of the order of an hour, often several hours, variations were averaged over all target and absorber combinations. The number of beam pulses per cycle was constant to better than 1 in 43 200. The integrated current from the ion chamber between the collimators was independent of wheel position to within 0.03%.

Neutrons emitted at 90° were detected at the end of a 38.3 m evacuated flight path in a conventional recoil detector. A pulse from the detector signifying the arrival of a neutron stopped the rundown of a 1000-channel (4 ns/ch) time-to-digital converter (TDC) started by the photon pulse which produced the neutron. In this way the neutron flight time was measured. Figure 1 summarizes the detector electronics. No significant variations in neutron detector efficiency from cycle to cycle (monitored by the individual photomultiplier counting rates), or from run to run (monitored by the neutron detection threshold) were observed. Periodically, by inserting 7.62 cm of graphite in the TOF path, the TDC was calibrated against the 5 strongest and sharpest features in the $^{12}C(n,n')$ absorption spectrum. These are listed in Table II. The TDC calibration obtained from a linear least squares fit was then used to calculate the neutron energies for 8 features in the absorption spectrum (including the 5 used in the fit), given the time channel in which each feature was observed. Table II lists the photon energy which would be assigned to each of these time channels if the fitted calibration curve were used without further correction. The systematic error in all cases would be less than 60 keV between 6 and 18 MeV. In this energy region the photon energies have been further corrected by linear interpolation between the calibrating features, so the systematic error is estimated to be less than 30 keV. Above 18 MeV the possible systematic error is estimated to be 60 keV.

The observed full width at half maximum of the 2077 keV absorption line was 2 channels (8.8 ns) indicating that the time resolution of the TOF system was 0.23 ns/m. The photon energy resolution was therefore 38 keV at 6.3 MeV, worsening to 280 keV at 18 MeV and 484 keV at 25 MeV. In presenting the data in Tables III–V and Figs. 2 and 3, sufficient time channels have been added together to form energy bins of width approximately equal to 500 keV (2 time channels at 26 MeV).

The 2077 keV line was visible in all the neutron TOF spectra, due to neutron absorption by ^{12}C in the plastic scintillator of the TOF detector. The sharpness of the minimum provided a continuous check on the time stability of the TOF system. No drift was observed at any time. The threshold energy for neutron detection was 400 keV. This imposed a lower limit of 3 MeV on the photon energy which could be measured.

The elements studied were chosen because they are monoisotopic, span a fairly wide range of atomic number Z, can be obtained in very pure form, possess good dimensional stability, and have a well-defined, uniform density. The masses of the absorbers were measured to a precision of 0.1 mg (about 2 parts in 10^7) on a standards

TABLE II. Features in the ^{12}C(n,n') absorption cross section used to calibrate the time-of-flight system. The neutron kinetic energy T_n at which a feature appears and the neutron flight time t over a distance of 38.3 m are compared with T_f and t_f, the kinetic energy and time obtained from the fitted calibration curve. The photon energy ω assigned to photoneutrons emitted by deuterium at 90° and detected in a given channel is systematically in error by $\delta\omega$ when T_f differs from T_n. Photon energies in the other tables have been adjusted by linear interpolation to correct for this.

Channel No.	T_n (keV) [a]	t (ns)	t_f (ns)	T_f (keV)	ω (MeV)	$\delta\omega$ (MeV)
180	7758 ± 5 [b]	1000	1000	7770	17.765	+0.024
205	6293 ± 5 [b]	1109	1109	6295	14.815	+0.004
226	5366 ± 6	1200	1202	5356	12.936	−0.020
259.5	4260 ± 20	1346	1349	4247	10.718	−0.026
289	3600 ± 50	1464	1478	3533	9.290	−0.054
316	3010 ± 2 [bcd]	1600	1597	3025	8.275	+0.031
322	2950 ± 2 [b]	1616	1623	2922	8.069	−0.056
391	2077 ± 2 [b]	1925	1926	2076	6.278	−0.001

[a] S. F. Mughabghab and D. I. Garber, BNL 325, 3rd ed. (Brookhaven National Laboratory, U. S. Dept. of Commerce, Springfield, Virginia, 1973), p. 6-1.

[b] Used in best fit ($r^2 = 0.999\,967$, compared to 1.00 for a perfect fit), giving 4.388 25 ns/channel.

[c] R. B. Schwartz, R. A. Schrack, and H. T. Heaton, NBS Monograph 138 (National Bureau of Standards, U. S. Dept. of Commerce, Washington D. C., 1974), pp. 26, 27.

[d] Resonant minimum in the ^{12}C(n,n') cross section.

balance. For Al the accuracy was limited to 4 parts in 10^5 by uncertainty in the correction to the mass for air displacement. The absorber diameters were measured by micrometer to an accuracy of 0.1%. The mass per unit area was therefore uncertain to ±0.2%. As a check on the presence of appreciable voids which if distributed nonuniformly throughout the absorber volume (not all of which was traversed by photons) could lead to an error in the mass per unit area, the absorber lengths were measured by caliper to 0.1%. The densities obtained are compared in Table I with reference values. There is no reason to suspect that the Ta and Bi absorbers, which were vacuum cast, contain voids. Our measured density for Al is slightly smaller than the mean of the Mainz[3] and Chemical Rubber Company (CRC) handbook values (by about 0.6% which is only about twice our estimated measurement error). The Mainz sample, having been sawn up, is known to have been free of voids. Our sam-

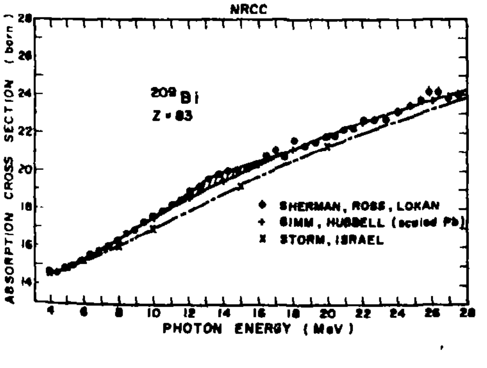

FIG. 2. The measured Bi photon absorption cross ection is plotted (solid circles) against photon energy. he bars represent statistical error. The hatched rea, the total (γ,n) cross section (Refs. 14 and 15), pproximates the total photonuclear absorption. The rosses (+) represent the calculated (Ref. 6) atomic ross section of Pb scaled up to $Z = 83$. Previous calulations (Ref. 5) are denoted by (X).

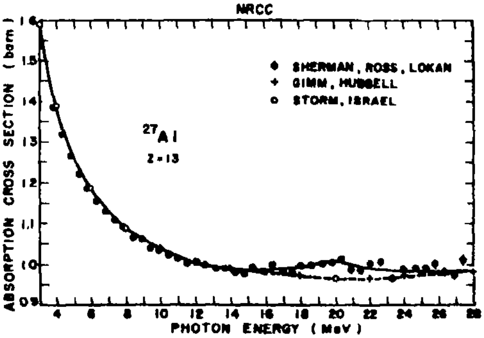

FIG. 3. The measured Al absorption cross section (solid circles) compared to the new (Ref. 6) (crosses) and old (Ref. 5) (open circles) theory. The excess above 15 MeV is photonuclear.

TABLE III. Measured values $\sigma_{\text{exp}}(\text{Ta})$ of the absorption cross section of tantalum and thei statistical errors ϵ_0 are listed against photon energy ω along with the atomic cross section $\sigma_Z(\text{Ta})$ and nuclear pair cross sections $\sigma_K(\text{Ta})$ obtained from them. Values of σ_Z interpolat from measurements made at Mainz[a] are shown for comparison. The amounts $\delta\sigma_Z$ and $\delta\sigma_K$ l which $\sigma_Z(\text{Ta})$ and $\sigma_K(\text{Ta})$ exceed the calculated[b] values $\sigma_Z(\text{calc})$ and $\sigma_K(\text{calc})$ are also given.

ω (MeV)	$\sigma_{\text{exp}}(\text{Ta})$ (b)	ϵ_0 (mb)	$\sigma_Z(\text{Ta})$[c] (b)	$\delta\sigma_Z$ (mb)	$\sigma_Z(\text{Mainz})$ (b)	$\sigma_K(\text{Ta})$ (b)	$\sigma_K(\text{calc})$ (b)	$\delta\sigma_K$ (b)
3.869	12.126	±56	12.123	−57		4.47	4.45	+0.02
4.327	12.128	30.5	12.124	−66		5.04	5.05	−0.01
4.830	12.258	23.5	12.252	+8		5.82	5.67	+0.15
5.333	12.394	21	12.386	−4		6.26	6.23	+0.03
5.837	12.561	20.5	12.551	0		6.80	6.75	+0.05
6.348	12.789	21.5	12.777	+60		7.35	7.27	+0.08
6.870	12.990	21.5	12.974	+70		7.84	7.77	+0.07
7.404	13.171	22.5	13.149	+40		8.26	8.24	+0.02
7.936	13.391	24.5	13.365	+40		8.69	8.66	+0.03
8.382	13.601	26.5	13.564	+11		9.11	9.07	+0.04
8.936	13.854	28.5	13.807	+70		9.55	9.46	+0.09
9.476	14.079	30	14.019	+70		9.92	9.84	+0.08
9.992	14.318	32	14.240	+70	14.19	10.30	10.22	+0.08
10.514	14.507	34	14.405	+30	14.40	10.61	10.56	+0.05
11.039	14.775	36.5	14.635	+60	14.58	10.98	10.90	+0.08
11.557	15.056	40	14.828	+40	14.79	11.30	11.23	+0.07
12.088	15.380	41.5	15.052	+60	14.98	11.63	11.58	+0.05
12.629	15.562	46	15.194	0	15.17	11.88	11.88	0.00
13.174	15.730	47.5	15.386	−20		12.18	12.18	0.00
13.715	15.947	54	15.605	−20		12.48	12.46	+0.02
14.253	16.124	56.5	15.764	−50	15.81	12.70	12.76	−0.06
14.780	16.303	63	15.921	−80	16.02	12.93	13.02	−0.09
15.293	16.522	64.5	16.137	−50	16.23	13.21	13.27	−0.06
15.840	16.683	67.5	16.333	−40	16.40	13.48	13.50	−0.02
16.422	16.841	68.5	16.541	−10	16.57	13.76	13.77	−0.01
16.977	16.924	78	16.684	−30		13.97	14.00	−0.03
17.500	17.093	82.5	16.895	+20		14.25	14.22	+0.03
18.078	17.188	84	17.026	−30		14.44	14.46	−0.02
18.665	17.324	86.5	17.188	−20	17.25	14.72[d]	14.66	+0.06
19.286	17.412	±90	17.294	−100	17.45	14.96[d]	14.90	+0.06
19.856	17.920	112	17.816	+260	17.62	15.17[d]	15.11	+0.06
20.370	17.850	112	17.758	+70	17.75	15.35[d]	15.28	+0.07
20.907	17.868	115	17.785	−50	17.88	15.53[d]	15.47	+0.06
21.468	17.903	117.5	17.829	−140				
22.055	18.316	124	18.252	+130				
22.670	18.362	127.5	18.306	+50				
23.314	18.380	131	18.333	−90				
23.989	18.791	136.5	18.751	+170				
24.697	18.514	137.5	18.480	−250				
25.312	18.709	176	18.679	−190				
25.825	18.658	177.5	18.632	−360				
26.355	19.156	187.5	19.132	+30				
26.903	19.300	195.5	19.277	+50				
27.470	19.408	206.5	19.387	+30				

[a] J. Ahrens *et al.* (Ref. 3). Numerical values are given in Ref. 6.

[b] Calculated atomic cross section values $\sigma_Z(\text{calc})$ were obtained by interpolation of tables compiled by J. H. Hubbell, H. A. Gimm, and I. Øverbø (private communication).

[c] Obtained by subtracting the total photoneutron cross section measured (Ref. 17) by R. Bergere *et al.* from $\sigma_{\text{exp}}(\text{Ta})$. See also Ref. 16.

[d] Using the interpolated Mainz (Ref. 6) value.

ple (consisting of 3 shorter cylinders) was cut from an ingot of such high purity that it consisted of a uniform mosaic of large single crystals. No voids were encountered on the cuts, or during the machining of the cylinders. Further evidence for uniformity of the Al density is that the measured density of each cylinder differs from the mean value by no more than 0.12%.

DATA AND DISCUSSION

The TOF spectrum for each target-absorber combination was corrected for counting losses as described in Appendix A and normalized to the number of Linac pulses which produced it. Then the empty target spectrum with or without absorber was subtracted from the corresponding full target spectrum.

For a given absorber having n atoms/cm^2 experimental values $\sigma_{\exp}$ of the cross section are obtained from the subtracted TOF spectra: The time bin corresponding to photon energy ω [see (4) and (5)] gives, using (1),

$$\sigma_{\exp}(\omega) = \{\ln[N_0(\omega)/N(\omega)]\}/n , \qquad (6)$$

where N and N_0 are the corrected, normalized numbers of events in this bin (two or more time channels added together, as mentioned earlier) with and without the absorber in the beam.

The measured cross section values and their statistical errors ϵ_σ are listed in Tables III, IV, and V. Where necessary the cross section value given by (6) was corrected for in-scattering and air displacement. The combined correction amounted to an increase of 0.2% for Al, and was negligible for Ta and Bi. In-scattering is discussed in more detail in Appendix B. Displacement of air by the absorber prevents complete cancellation in the ratio in Eq. (6) of the effect of photon absorption in the air path between radiator and LD$_2$ target. The apparent reduction in cross section is easily calculated to be 0.08% at 3 MeV for the Al absorber, decreasing to 0.04% at higher energy.

In the case of a heavy element the total photoneutron cross section σ_n at a given energy is expected to be a good approximation to σ_N, the total nuclear absorption cross section at the same energy. Since

$$\sigma_{\exp} = \sigma_z + \sigma_N , \qquad (7)$$

where σ_z is the sum of all the atomic cross sections, we can write in the case of Ta and Bi, at each energy,

$$\sigma_z = \sigma_{\exp} - \sigma_n . \qquad (8)$$

The measured values of σ_z obtained from (8) are compared to the new calculations[6] in the tables. The Ta results are compared to measurements[3,4] made at Mainz. The Bi results are compared to Pb results from Mainz scaled up by the ratio of σ_z (Bi) to σ_z (Pb) calculated by Gimm and Hubbell.[6] Figure 2 shows that σ_z for Bi agrees around 3 MeV with the tabulation by Storm and Israel[5] (which they produced by interpolating in Z and ω from Hubbell's calculations[4]). Agreement at low energy between measurements and these calculated values has been observed previously.[13] However, as ω increases our measured σ_z rises above the old calculated curves. The "scaled up Pb" points in the figure were obtained by multiplying the Rayleigh, photoelectric, Compton, triplet, and nuclear pair cross sections calculated[6] by Gimm and Hubbell for Pb by the appropriate powers of (83/82) and plotting their sum. The calculated values listed in the tables have been interpolated from an unpublished compilation by Hubbell, Gimm, and Øverbø which includes the case of $Z=83$. The hatched area in Fig. 2 represents σ_n which has been measured by two groups.[14,15] It should be noted that the data from Young's thesis[15] has been used in the tables. The Livermore (γ,n) cross section[14] is systematically smaller by several percent. This difference would be visible in Fig. 2 only in the vicinity of the giant dipole resonance (where it would be about the width of the solid lines). In the case of Bi also, two measurements of σ_n have been reported.[16,17] Again, we have used the larger[17] values to obtain σ_z.

The Al data is shown in Fig. 3, and the absorption cross section below the photonuclear giant resonance is compared to calculations in Table V. The table shows that $\sigma_{\exp}$ for Al, corrected upwards by 0.2% for in-scattering and air displacement, lies on the average about 0.35% or approximately one standard deviation (imposed by uncertainty in the absorber area) below the calculated values in the energy interval 7 to 13 MeV, and about 1% below them between 4 and 7 MeV. The discrepancy appears to decrease systematically from 1.9% below 4 MeV to about zero at 13 MeV. The theoretical uncertainty is believed to be less than 0.2% for low-Z elements. Nevertheless the discrepancy appears to be real below 9 MeV. In support of this we note that Moreh and Wand[1] obtained (1147 ± 3) mb for the total Al cross section at 6.418 MeV, compared to (1152 ± 2) mb obtained by interpolation of our results—a discrepancy of only (5 ± 5) mb, or 0.4%, between the two experiments. Above 9 MeV, however, the agreement is very good between the calculated cross sections and our measurement modified by small in-scattering corrections. This gives us confidence in the soundness of the Ta and Bi measurements where the corrections are smaller still. We are

TABLE III. Measured values $\sigma_{exp}(\mathrm{Ta})$ of the absorption cross section of tantalum and their statistical errors ϵ_σ are listed against photon energy ω along with the atomic cross sections $\sigma_Z(\mathrm{Ta})$ and nuclear pair cross sections $\sigma_\kappa(\mathrm{Ta})$ obtained from them. Values of σ_Z interpolated from measurements made at Mainz[a] are shown for comparison. The amounts $\delta\sigma_Z$ and $\delta\sigma_\kappa$ by which $\sigma_Z(\mathrm{Ta})$ and $\sigma_\kappa(\mathrm{Ta})$ exceed the calculated[b] values $\sigma_Z(\mathrm{calc})$ and $\sigma_\kappa(\mathrm{calc})$ are also given.

ω (MeV)	$\sigma_{exp}(\mathrm{Ta})$ (b)	ϵ_σ (mb)	$\sigma_Z(\mathrm{Ta})$[c] (b)	$\delta\sigma_Z$ (mb)	$\sigma_Z(\mathrm{Mainz})$ (b)	$\sigma_\kappa(\mathrm{Ta})$ (b)	$\sigma_\kappa(\mathrm{calc})$ (b)	$\delta\sigma_\kappa$ (b)
3.869	12.126	±56	12.123	−57		4.47	4.45	+0.02
4.327	12.128	30.5	12.124	−66		5.04	5.05	−0.01
4.830	12.258	23.5	12.252	+8		5.82	5.67	+0.15
5.333	12.394	21	12.386	−4		6.26	6.23	+0.03
5.837	12.561	20.5	12.551	0		6.80	6.75	+0.05
6.348	12.789	21.5	12.777	+60		7.35	7.27	+0.08
6.870	12.990	21.5	12.974	+70		7.84	7.77	+0.07
7.404	13.171	22.5	13.149	+40		8.26	8.24	+0.02
7.936	13.391	24.5	13.365	+40		8.69	8.66	+0.03
8.382	13.601	26.5	13.564	+11		9.11	9.07	+0.04
8.936	13.854	28.5	13.807	+70		9.55	9.46	+0.09
9 476	14.079	30	14.019	+70		9.92	9.84	+0.08
9.992	14.318	32	14.240	+70	14.19	10.30	10.22	+0.08
10.514	14.507	34	14.405	+30	14.40	10.61	10.56	+0.05
11.039	14.775	36.5	14.635	+60	14.58	10.98	10.90	+0.08
11.557	15.056	40	14.828	+40	14.79	11.30	11.23	+0.07
12.088	15.380	41.5	15.052	+60	14.98	11.63	11.58	+0.05
12.629	15.562	46	15.194	0	15.17	11.88	11.88	0.00
13.174	15.730	47.5	15.386	−20		12.18	12.18	0.00
13.715	15.947	54	15.605	−20		12.48	12.46	+0.02
14.253	16.124	56.5	15.764	−50	15.81	12.70	12.76	−0.06
14.780	16.303	63	15.921	−80	16.02	12.93	13.02	−0.09
15.293	16.522	64.5	16.137	−50	16.23	13.21	13.27	−0.06
15.840	16.683	67.5	16.333	−40	16.40	13.48	13.50	−0.02
16.422	16.841	68.5	16.541	−10	16.67	13.76	13.77	−0.01
16.977	16.924	78	16.684	−30		13.97	14.00	−0.03
17.500	17.093	82.5	16.895	+20		14.25	14.22	+0.03
18.078	17.188	84	17.026	−30		14.44	14.46	−0.02
18.665	17.324	86.5	17.188	−20	17.25	14.72[d]	14.66	+0.06
19.286	17.412	±90	17.294	−100	17.45	14.96[d]	14.90	+0.06
19.856	17.920	112	17.816	+260	17.62	15.17[d]	15.11	+0.06
20.370	17.850	112	17.758	+70	17.75	15.35[d]	15.28	+0.07
20.907	17.868	115	17.785	−50	17.88	15.53[d]	15.47	+0.06
21.468	17.903	117.5	17.829	−140				
22.055	18.316	124	18.252	+130				
22.670	18.362	127.5	18.306	+50				
23.314	18.380	131	18.333	−90				
23.989	18.791	136.5	18.751	+170				
24.697	18.514	137.5	18.480	−250				
25.312	18.709	176	18.679	−190				
25.825	18.658	177.5	18.632	−360				
26.355	19.156	187.5	19.132	+30				
26.903	19.300	195.5	19.277	+50				
27.470	19.408	206.5	19.387	+30				

---

[a] J. Ahrens *et al.* (Ref. 3). Numerical values are given in Ref. 6.

[b] Calculated atomic cross section values $\sigma_Z(\mathrm{calc})$ were obtained by interpolation of tables compiled by J. H. Hubbell, H. A. Gimm, and I. Øverbø (private communication).

[c] Obtained by subtracting the total photoneutron cross section measured (Ref. 17) by R. Bergere *et al.* from $\sigma_{exp}(\mathrm{Ta})$. See also Ref. 16.

[d] Using the interpolated Mainz (Ref. 6) value.

ple (consisting of 3 shorter cylinders) was cut from an ingot of such high purity that it consisted of a uniform mosaic of large single crystals. No voids were encountered on the cuts, or during the machining of the cylinders. Further evidence for uniformity of the Al density is that the measured density of each cylinder differs from the mean value by no more than 0.12%.

DATA AND DISCUSSION

The TOF spectrum for each target-absorber combination was corrected for counting losses as described in Appendix A and normalized to the number of Linac pulses which produced it. Then the empty target spectrum with or without absorber was subtracted from the corresponding full target spectrum.

For a given absorber having n atoms/cm^2 experimental values σ_{exp} of the cross section are obtained from the subtracted TOF spectra: The time bin corresponding to photon energy ω [see (4) and (5)] gives, using (1),

$$\sigma_{exp}(\omega)=\{\ln[N_0(\omega)/N(\omega)]\}/n\,, \qquad (6)$$

where N and N_0 are the corrected, normalized numbers of events in this bin (two or more time channels added together, as mentioned earlier) with and without the absorber in the beam.

The measured cross section values and their statistical errors ϵ_σ are listed in Tables III, IV, and V. Where necessary the cross section value given by (6) was corrected for in-scattering and air displacement. The combined correction amounted to an increase of 0.2% for Al, and was negligible for Ta and Bi. In-scattering is discussed in more detail in Appendix B. Displacement of air by the absorber prevents complete cancellation in the ratio in Eq. (6) of the effect of photon absorption in the air path between radiator and LD$_2$ target. The apparent reduction in cross section is easily calculated to be 0.08% at 3 MeV for the Al absorber, decreasing to 0.04% at higher energy.

In the case of a heavy element the total photoneutron cross section σ_n at a given energy is expected to be a good approximation to σ_N, the total nuclear absorption cross section at the same energy. Since

$$\sigma_{exp}=\sigma_Z+\sigma_N\,, \qquad (7)$$

where σ_Z is the sum of all the atomic cross sections, we can write in the case of Ta and Bi, at each energy,

$$\sigma_Z=\sigma_{exp}-\sigma_n\,. \qquad (8)$$

The measured values of σ_Z obtained from (8) are compared to the new calculations[6] in the tables. The Ta results are compared to measurements[3,8] made at Mainz. The Bi results are compared to Pb results from Mainz scaled up by the ratio of σ_Z (Bi) to σ_Z (Pb) calculated by Gimm and Hubbell.[6] Figure 2 shows that σ_Z for Bi agrees around 3 MeV with the tabulation by Storm and Israel[5] (which they produced by interpolating in Z and ω from Hubbell's calculations[4]). Agreement at low energy between measurements and these calculated values has been observed previously.[13] However, as ω increases our measured σ_Z rises above the old calculated curves. The "scaled up Pb" points in the figure were obtained by multiplying the Rayleigh, photoelectric, Compton, triplet, and nuclear pair cross sections calculated[6] by Gimm and Hubbell for Pb by the appropriate powers of (83/82) and plotting their sum. The calculated values listed in the tables have been interpolated from an unpublished compilation by Hubbell, Gimm, and Øverbø which includes the case of $Z=83$. The hatched area in Fig. 2 represents σ_n which has been measured by two groups.[14,15] It should be noted that the data from Young's thesis[15] has been used in the tables. The Livermore (γ,n) cross section[14] is systematically smaller by several percent. This difference would be visible in Fig. 2 only in the vicinity of the giant dipole resonance (where it would be about the width of the solid lines). In the case of Bi also, two measurements of σ_n have been reported.[16,17] Again, we have used the larger[17] values to obtain σ_Z.

The Al data is shown in Fig. 3, and the absorption cross section below the photonuclear giant resonance is compared to calculations in Table V. The table shows that σ_{exp} for Al, corrected upwards by 0.2% for in-scattering and air displacement, lies on the average about 0.35% or approximately one standard deviation (imposed by uncertainty in the absorber area) below the calculated values in the energy interval 7 to 13 MeV, and about 1% below them between 4 and 7 MeV. The discrepancy appears to decrease systematically from 1.9% below 4 MeV to about zero at 13 MeV. The theoretical uncertainty is believed to be less than 0.2% for low-Z elements. Nevertheless the discrepancy appears to be real below 9 MeV. In support of this we note that Moreh and Wand[1] obtained (1147 ± 3) mb for the total Al cross section at 6.418 MeV, compared to (1152 ± 2) mb obtained by interpolation of our results—a discrepancy of only (5 ± 5) mb, or 0.4%, between the two experiments. Above 9 MeV, however, the agreement is very good between the calculated cross sections and our measurement modified by small in-scattering corrections. This gives us confidence in the soundness of the Ta and Bi measurements where the corrections are smaller still. We are

TABLE IV. Measured values σ_{exp}(Bi) of the absorption cross section of bismuth and their statistical errors ϵ_σ are listed against photon energy ω along with the atomic cross sections σ_Z(Bi) and nuclear pair cross sections σ_K(Bi) obtained from them. The amounts $\delta\sigma_Z$ and $\delta\sigma_K$ by which σ_Z(Bi) and σ_K(Bi) exceed the calculated[a] values σ_Z(calc) and σ_K(calc) are also given.

ω (MeV)	σ_{exp}(Bi) (b)	ϵ_σ (mb)	σ_Z(Bi)[b] (b)	$\delta\sigma_Z$ (mb)	σ_K(Bi) (b)	σ_K(calc) (b)	$\delta\sigma_K$ (b)
3.869	14.846	±76.5	14.841	+103	5.854	5.80	+0.05
4.327	14.781	44.5	14.775	−25	6.500	6.52	−0.02
4.830	14.927	33.5	14.919	−6	7.282	7.30	−0.02
5.333	15.091	30.5	15.081	−54	7.961	8.00	−0.04
5.837	15.324	29.5	15.311	−39	8.649	8.70	−0.05
6.348	15.624	31	15.606	+36	9.311	9.28	+0.03
6.870	15.878	32	15.856	+44	9.919	9.85	+0.07
7.404	16.100	33.5	16.072	−15	10.422	10.42	0
7.936	16.412	37	16.377	+27	10.987	10.96	+0.03
8.382	16.810	39	16.763	+158	11.613	11.48	+0.13
8.936	17.013	42.5	16.953	+63	12.028	11.96	+0.07
9.476	17.402	45	17.324	+174	12.574	12.42	+0.15
9.992	17.673	47.5	17.571	+166	13.004	12.92	+0.08
10.514	17.945	50	17.807	+132	13.407	13.30	+0.11
11.039	18.293	54	18.105	+145	13.880	13.75	+0.13
11.557	18.583	58.5	18.316	+91	14.229	14.12	+0.11
12.088	19.137	60.5	18.770	+283	14.803	14.55	+0.25
12.629	19.244	66	18.744	−6	14.919	14.92	0
13.174	19.669	68.5	19.049	+49	15.334	15.33	0
13.715	19.861	76.5	19.219	−46	15.619	15.66	−0.04
14.253	20.095	80.5	19.575	+40	16.088	16.02	+0.07
14.780	20.165	89	19.695	−90	16.280	16.32	−0.04
15.293	20.299	90.5	19.922	−90	16.585	16.64	−0.06
15.840	20.428	93	20.143	−92	16.893	16.95	−0.06
16.422	20.738	94.5	20.523	+58	17.343	17.24	+0.10
16.977	21.082	108.5	20.910	+223	17.805	17.56	+0.24
17.500	20.972	112	20.830	−70	17.785	17.85	−0.10
18.078	21.532	116	21.413	+303	18.438	18.14	+0.30
18.665	21.395	118	21.295	−30	18.385	18.41	+0.03
19.286	21.513	122	21.428	−117	18.578	18.69	−0.11
19.856	21.905	146.5	21.833	+78	19.033	18.96	+0.07
20.370	22.147	148.5	22.086	+156	19.341	19.17	+0.17
20.907	22.286	154	22.232	+122	19.532	19.41	+0.12
21.468	22.247	157	22.198	−87	19.553	19.62	+0.07
22.055	22.589	161	22.544	+57	19.944	19.87	+0.07
22.670	22.862	167.5	22.822	+157	20.277	20.08	+0.20
23.314	22.906	170.5	22.871	+4	20.384	20.34	+0.04
23.989	23.098	173	23.067	+2	20.630	20.60	+0.03
24.697	23.348	182	23.318	+48	20.923	20.85	+0.07
25.312	23.504	229.5	23.476	+26	21.126	21.08	+0.05
25.825	24.074	239.5	24.049	+462	21.724	21.27	+0.45
26.355	24.281	242	24.258	+521	21.958	21.45	+0.50
26.903	23.803	247	23.782	−108	21.502	21.62	−0.12
27.470	24.142	251	24.122	+62	21.852	21.80	+0.05

[a] Calculated atomic cross section values σ_Z(calc) were obtained by interpolation of tables compiled by J. H. Hubbell, H. A. Gimm, and I. Øverbø (private communication).

[b] *Obtained by subtracting the total photoneutron cross section measured (Ref. 15) by L. M. Young from σ_{exp}(Bi). See also Ref. 14.*

on firm ground for asserting that discrepancies between measurement and the earlier tabulations for large Z and ω arise from assumptions made in the calculations.

Tables III and IV compare σ_Z for Ta and Bi with σ_Z (calc) obtained by interpolation of values found in Ref. 6. The discrepancy $\delta\sigma_Z$ is listed, where

$$\delta\sigma_Z = \sigma_Z - \sigma_Z(\text{calc}). \tag{9}$$

TABLE V. Values σ_A and σ_B of the Al absorption cross section obtained from different data sets A and B for photon energies ω below the photonuclear giant resonance. Data set A was accumulated in about one-quarter the time required for data set B, at an average counting rate about 4% higher. The difference $\delta_{AB}\sigma$ between the two measurements is listed, as are σ_{AB}(Al) obtained by statistically weighting both data sets, σ_{calc} interpolated from a table[a] of calculated values, and $\delta\sigma$ the difference between σ_{calc} and the experimental values σ_{exp}(Al) obtained from σ_{AB}(Al) by correcting for in-scattering and air displacement.

ω (MeV)	σ_A (b)	σ_B (b)	$\delta_{AB}\sigma$ (mb)	σ_{AB}(Al) (b)	σ_{exp}(Al) (b)	σ_{calc} (Al) (b)	$\delta\sigma$ (mb)
3.873	1.398 ± 0.0075	1.385 ± 0.007	+13	1.388 ± 0.007	1.391	1.418	27
4.327	1.338 ± 0.0075	1.323 ± 0.0035	+15	1.326 ± 0.004	1.329	1.354	25
4.830	1.272 ± 0.005	1.272 ± 0.0025	0	1.272 ± 0.003	1.274	1.293	19
5.333	1.233 ± 0.004	1.226 ± 0.002	+7	1.228 ± 0.002	1.230	1.244	14
5.837	1.187 ± 0.0035	1.186 ± 0.002	+1	1.186 ± 0.002	1.188	1.202	14
6.348	1.150 ± 0.0035	1.154 ± 0.002	−4	1.153 ± 0.002	1.155	1.167	12
6.870	1.126 ± 0.0035	1.130 ± 0.002	−4	1.129 ± 0.002	1.131	1.139	8
7.404	1.106 ± 0.004	1.107 ± 0.002	−1	1.107 ± 0.002	1.109	1.115	6
7.936	1.085 ± 0.004	1.089 ± 0.002	−4	1.088 ± 0.002	1.090	1.097	7
8.382	1.068 ± 0.0045	1.067 ± 0.002	+1	1.067 ± 0.002	1.069	1.079	10
8.936	1.059 ± 0.0045	1.058 ± 0.0025	+1	1.058 ± 0.002	1.060	1.062	2
9.476	1.045 ± 0.005	1.038 ± 0.0025	+7	1.040 ± 0.002	1.042	1.051	9
9.992	1.036 ± 0.005	1.035 ± 0.003	+1	1.035 ± 0.003	1.037	1.040	3
10.514	1.022 ± 0.005	1.023 ± 0.0025	−1	1.023 ± 0.003	1.025	1.029	4
11.039	1.019 ± 0.0055	1.015 ± 0.003	+4	1.016 ± 0.003	1.018	1.018	0
11.557	1.008 ± 0.006	1.004 ± 0.003	+4	1.005 ± 0.003	1.007	1.009	2
12.088	0.985 ± 0.006	1.003 ± 0.003	−18	0.999 ± 0.003	1.001	1.001	0
12.629	0.995 ± 0.0065	0.995 ± 0.0035	0	0.995 ± 0.004	0.997	0.995	−2

[a] J. Hubbell, H. Gimm, and I. Øverbø (private communication).

At Mainz σ_Z has been measured for Ta over three intervals of photon energy lying within the energy range studied in this experiment. Interpolation of the data of Ahrens *et al.* (given in Ref. 6) provides values of σ_Z which agree very well with the present data, as Table III shows.

Similarly if the values of the total absorption cross section for Pb measured at Mainz are scaled up according to the ratio of calculated[8] atomic cross sections (a factor of 1.020 applies over most of the photon energy range) they agree closely with our measured values where the two data sets overlap.

A set of experimental values of σ_K, the cross section for electron pair production on the nucleus, was obtained by subtracting from σ_Z the sum of the calculated atomic cross sections (photoelectric, Compton, Rayleigh, and triplet):

$$\sigma_K = \sigma_Z - (\sigma_{ph} + \sigma_C + \sigma_R + \sigma_t)\,. \qquad (10)$$

The cross sections in the parentheses in (10) have been recalculated by Hubbell, Gimm, and Øverbø.[8] The new values do not differ materially from older ones and are presumed to be accurate to better than 0.2%. The measured nuclear pair cross section σ_K is compared in Tables III and IV with σ_K(calc) obtained by Hubbell *et al.* using relativistic atomic form factors in the screening correction as well as the Øverbø estimate of the Coulomb correction. The discrepancy $\delta\sigma_K$ is tabulated, where

$$\delta\sigma_K = \sigma_K - \sigma_K(\text{calc})\,. \qquad (11)$$

Table VI compares for Bi the average $\bar{\sigma}_K$ of the Ottawa and "Mainz" (rescaled) values of σ_K with σ_K(calc). The unscreened, point nucleus, Born approximation prediction of the nuclear pair cross section at intermediate energies is[13]

$$\sigma_K = (\sigma_0\{28[\lambda - f(Z)]/9 - 218/27 + \Delta M\} + \Delta C' + \Delta S) f_{\text{rad}}\,, \qquad (12)$$

where the curly-bracket term is the Davies-Bethe-Maximon cross section σ_{DBM}. The fine structure constant α and the classical radius of the electron r_0 are contained in

$$\sigma_0 = Z^2 \alpha r_0^2\,, \qquad (13)$$

and the photon energy, expressed in terms of the electron mass energy m as

$$k = \omega/m\,, \qquad (14)$$

enters logarithmically via

$$\lambda = \ln 2k\,. \qquad (15)$$

The correction term ΔM added to the Bethe-Heitler

TABLE IV. Measured values σ_{exp}(Bi) of the absorption cross section of bismuth and their statistical errors ϵ_σ are listed against photon energy ω along with the atomic cross sections σ_Z(Bi) and nuclear pair cross sections σ_K(Bi) obtained from them. The amounts $\delta\sigma_Z$ and $\delta\sigma_K$ by which σ_Z(Bi) and σ_K(Bi) exceed the calculated[a] values σ_Z(calc) and σ_K(calc) are also given.

ω (MeV)	σ_{exp}(Bi) (b)	ϵ_σ (mb)	σ_Z(Bi)[b] (b)	$\delta\sigma_Z$ (mb)	σ_K(Bi) (b)	σ_K(calc) (b)	$\delta\sigma_K$ (b)
3.869	14.846	±76.5	14.841	+103	5.854	5.80	+0.05
4.327	14.781	44.5	14.775	−25	6.500	6.52	−0.02
4.830	14.927	33.5	14.919	−6	7.282	7.30	−0.02
5.333	15.091	30.5	15.081	−54	7.961	8.00	−0.04
5.837	15.324	29.5	15.311	−39	8.649	8.70	−0.05
6.348	15.624	31	15.606	+36	9.311	9.28	+0.03
6.870	15.878	32	15.856	+44	9.919	9.85	+0.07
7.404	16.100	33.5	16.072	−15	10.422	10.42	0
7.936	16.412	37	16.377	+27	10.987	10.96	+0.03
8.382	16.810	39	16.763	+158	11.613	11.48	+0.13
8.936	17.013	42.5	16.953	+63	12.028	11.96	+0.07
9.476	17.402	45	17.324	+174	12.574	12.42	+0.15
9.992	17.673	47.5	17.571	+166	13.004	12.92	+0.08
10.514	17.945	50	17.807	+132	13.407	13.30	+0.11
11.039	18.293	54	18.105	+145	13.880	13.75	+0.13
11.557	18.583	58.5	18.316	+91	14.229	14.12	+0.11
12.088	19.137	60.5	18.770	+283	14.803	14.55	+0.25
12.629	19.244	66	18.744	−6	14.919	14.92	0
13.174	19.669	68.5	19.049	+49	15.334	15.33	0
13.715	19.861	76.5	19.219	−46	15.619	15.66	−0.04
14.253	20.095	80.5	19.575	+40	16.088	16.02	+0.07
14.780	20.165	89	19.695	−90	16.280	16.32	−0.04
15.293	20.299	90.5	19.922	−90	16.585	16.64	−0.06
15.840	20.428	93	20.143	−92	16.893	16.95	−0.06
16.422	20.738	94.5	20.523	+58	17.343	17.24	+0.10
16.977	21.082	108.5	20.910	+223	17.805	17.56	+0.24
17.500	20.972	112	20.830	−70	17.785	17.85	−0.10
18.078	21.532	116	21.413	+303	18.438	18.14	+0.30
18.665	21.395	118	21.295	−30	18.385	18.41	+0.03
19.286	21.513	122	21.428	−117	18.578	18.69	−0.11
19.856	21.905	146.5	21.833	+78	19.033	18.96	+0.07
20.370	22.147	148.5	22.086	+156	19.341	19.17	+0.17
20.907	22.286	154	22.232	+122	19.532	19.41	+0.12
21.468	22.247	157	22.198	−87	19.553	19.62	+0.07
22.055	22.589	161	22.544	+57	19.944	19.87	+0.07
22.670	22.862	167.5	22.822	+157	20.277	20.08	+0.20
23.314	22.906	170.5	22.871	+4	20.384	20.34	+0.04
23.989	23.098	173	23.067	+2	20.630	20.60	+0.03
24.697	23.348	182	23.318	+48	20.923	20.85	+0.07
25.312	23.504	229.5	23.476	+26	21.126	21.08	+0.05
25.825	24.074	239.5	24.049	+462	21.724	21.27	+0.45
26.355	24.281	242	24.258	+521	21.958	21.45	+0.50
26.903	23.803	247	23.782	−108	21.502	21.62	−0.12
27.470	24.142	251	24.122	+62	21.852	21.80	+0.05

[a] Calculated atomic cross section values σ_Z(calc) were obtained by interpolation of tables compiled by J. H. Hubbell, H. A. Gimm, and I. Øverbø (private communication).

[b] Obtained by subtracting the total photoneutron cross section measured (Ref. 15) by L. M. Young from σ_{exp}(Bi). See also Ref. 14.

firm ground for asserting that discrepancies tween measurement and the earlier tabulations r large Z and ω arise from assumptions made the calculations.

Tables III and IV compare σ_Z for Ta and Bi with σ_Z (calc) obtained by interpolation of values found in Ref. 6. The discrepancy $\delta\sigma_Z$ is listed, where

$$\delta\sigma_Z = \sigma_Z - \sigma_Z(\text{calc}). \tag{9}$$

TABLE V. Values σ_A and σ_B of the Al absorption cross section obtained from different data sets A and B for photon energies ω below the photonuclear giant resonance. Data set A was accumulated in about one-quarter the time required for data set B, at an average counting rate about 4% higher. The difference $\delta_{AB}\sigma$ between the two measurements is listed, as are $\sigma_{AB}(\text{Al})$ obtained by statistically weighting both data sets, σ_{calc} interpolated from a table [a] of calculated values, and $\delta\sigma$ the difference between σ_{calc} and the experimental values $\sigma_{\text{exp}}(\text{Al})$ obtained from $\sigma_{AB}(\text{Al})$ by correcting for in-scattering and air displacement.

ω (MeV)	σ_A (b)	σ_B (b)	$\delta_{AB}\sigma$ (mb)	$\sigma_{AB}(\text{Al})$ (b)	$\sigma_{\text{exp}}(\text{Al})$ (b)	σ_{calc} (Al) (b)	$\delta\sigma$ (mb)
3.873	1.398 ± 0.0075	1.385 ± 0.007	+13	1.388 ± 0.007	1.391	1.418	27
4.327	1.338 ± 0.0075	1.323 ± 0.0035	+15	1.326 ± 0.004	1.329	1.354	25
4.830	1.272 ± 0.005	1.272 ± 0.0025	0	1.272 ± 0.003	1.274	1.293	19
5.333	1.233 ± 0.004	1.226 ± 0.002	+7	1.228 ± 0.002	1.230	1.244	14
5.837	1.187 ± 0.0035	1.186 ± 0.002	+1	1.186 ± 0.002	1.188	1.202	14
6.348	1.150 ± 0.0035	1.154 ± 0.002	−4	1.153 ± 0.002	1.155	1.167	12
6.870	1.126 ± 0.0035	1.130 ± 0.002	−4	1.129 ± 0.002	1.131	1.139	8
7.404	1.106 ± 0.004	1.107 ± 0.002	−1	1.107 ± 0.002	1.109	1.115	6
7.936	1.085 ± 0.004	1.089 ± 0.002	−4	1.088 ± 0.002	1.090	1.097	7
8.382	1.068 ± 0.0045	1.067 ± 0.002	+1	1.067 ± 0.002	1.069	1.079	10
8.936	1.059 ± 0.0045	1.058 ± 0.0025	+1	1.058 ± 0.002	1.060	1.062	2
9.476	1.045 ± 0.005	1.038 ± 0.0025	+7	1.040 ± 0.002	1.042	1.051	9
9.992	1.036 ± 0.005	1.035 ± 0.003	+1	1.035 ± 0.003	1.037	1.040	3
10.514	1.022 ± 0.005	1.023 ± 0.0025	−1	1.023 ± 0.003	1.025	1.029	4
11.039	1.019 ± 0.0055	1.015 ± 0.003	+4	1.016 ± 0.003	1.018	1.018	0
11.557	1.008 ± 0.006	1.004 ± 0.003	+4	1.005 ± 0.003	1.007	1.009	2
12.088	0.985 ± 0.006	1.003 ± 0.003	−18	0.999 ± 0.003	1.001	1.001	0
12.629	0.995 ± 0.0065	0.995 ± 0.0035	0	0.995 ± 0.004	0.997	0.995	−2

[a] J. Hubbell, H. Gimm, and I. Øverbø (private communication).

At Mainz σ_z has been measured for Ta over three intervals of photon energy lying within the energy range studied in this experiment. Interpolation of the data of Ahrens *et al.* (given in Ref. 6) provides values of σ_z which agree very well with the present data, as Table III shows.

Similarly if the values of the total absorption cross section for Pb measured at Mainz are scaled up according to the ratio of calculated[8] atomic cross sections (a factor of 1.020 applies over most of the photon energy range) they agree closely with our measured values where the two data sets overlap.

A set of experimental values of σ_K, the cross section for electron pair production on the nucleus, was obtained by subtracting from σ_z the sum of the calculated atomic cross sections (photoelectric, Compton, Rayleigh, and triplet):

$$\sigma_K = \sigma_z - (\sigma_{pe} + \sigma_C + \sigma_R + \sigma_t)\,. \qquad (10)$$

The cross sections in the parentheses in (10) have been recalculated by Hubbell, Gimm, and Øverbø.[8] The new values do not differ materially from older ones and are presumed to be accurate to better than 0.2%. The measured nuclear pair cross section σ_K is compared in Tables III and IV with $\sigma_K(\text{calc})$ obtained by Hubbell *et al.* using relativistic atomic form factors in the screening correction as well as the Øverbø estimate of the Coulomb correction. The discrepancy $\delta\sigma_K$ is tabulated, where

$$\delta\sigma_K = \sigma_K - \sigma_K(\text{calc})\,. \qquad (11)$$

Table VI compares for Bi the average $\bar{\sigma}_K$ of the Ottawa and "Mainz" (rescaled) values of σ_K with $\sigma_K(\text{calc})$. The unscreened, point nucleus, Born approximation prediction of the nuclear pair cross section at intermediate energies is[18]

$$\sigma_K = (\sigma_0\{28[\lambda - f(Z)]/9 - 218/27 + \Delta M\} + \Delta C' + \Delta S)\, f_{\text{rad}}\,, \qquad (12)$$

where the curly-bracket term is the Davies-Bethe-Maximon cross section σ_{DBM}. The fine structure constant α and the classical radius of the electron r_0 are contained in

$$\sigma_0 = Z^2\alpha r_0^2\,, \qquad (13)$$

and the photon energy, expressed in terms of the electron mass energy m as

$$k = \omega/m\,, \qquad (14)$$

enters logarithmically via

$$\lambda = \ln 2k\,. \qquad (15)$$

The correction term ΔM added to the Bethe-Heitler

TABLE VI. *The measured values σ_K of the electron pair cross section on the Bi nucleus (above 9.5 MeV, the mean of Ottawa values for Bi, and Mainz values for Pb rescaled and interpolated) are compared with σ_K(calc) obtained (Ref. 6) by Hubbell, Gimm, and Øverbø at each photon energy ω. Also listed are the Davies-Bethe-Maximon cross section σ_{DBM}, σ_K divided by the radiative correction f_{rad}, the experimental values of the combined correction $(\Delta C' + \Delta S)$ for the energy dependent part of the Coulomb correction plus the screening correction, and the combined correction expressed as a fraction of the Bethe-Heitler cross section σ_{BH}.*

ω (MeV)	σ_K (b)	σ_K(calc) (b)	σ_{DBM} (b)	$\sigma_K/f_{\mathrm{rad}}$ (b)	$(\Delta C' + \Delta S)$ (b)	$\frac{(\Delta C' + \Delta S)}{\sigma_{\mathrm{BH}}}$
3.869	5.854	5.80	0.9556	5.742	4.786	3.151
4.327	6.500	6.52	1.7685	6.338	4.570	1.571
4.830	7.282	7.30	2.5791	7.171	4.592	1.074
5.333	7.961	8.00	3.3111	7.856	4.544	0.8255
5.837	8.649	8.70	3.9740	8.536	4.562	0.6885
6.348	9.311	9.28	4.5825	9.191	4.608	0.6010
6.870	9.919	9.85	5.1459	9.793	4.647	0.4745
7.404	10.422	10.42	5.6690	10.291	4.622	0.4825
7.936	10.987	10.96	6.3021	10.850	4.548	0.4356
8.382	11.613	11.48	6.9274	11.470	4.543	0.4119
8.936	12.028	11.96	7.8452	11.881	4.036	0.3387
9.476	12.536	12.42	8.5986	12.384	3.785	0.2994
9.992	12.956	12.92	9.2748	12.800	3.525	0.2650
10.514	13.410	13.30	9.9206	13.248	3.327	0.2388
11.039	13.871	13.75	10.5358	13.704	3.168	0.2179
11.557	14.238	14.12	11.1125	14.067	2.954	0.1955
12.088	14.725	14.55	11.6755	14.549	2.874	0.1834
12.629	14.935	14.92	12.2226	14.758	2.535	0.1564
13.174	15.312	15.33	12.7493	15.132	2.383	0.1424
13.715	15.769	15.66	13.2500	15.496	2.246	0.1303
14.253	16.126	16.02	13.7277	15.940	2.212	0.1249
14.780	16.343	16.32	14.1778	16.155	1.977	0.1089
15.293	16.636	16.64	14.6003	16.445	1.845	0.0992
15.840	16.939	16.95	15.0350	16.745	1.710	0.0899
16.422	17.324	17.24	15.4808	17.126	1.645	0.0845
16.977	17.704	17.56	15.8910	17.503	1.612	0.0811
17.500	17.829	17.85	16.2654	17.627	1.362	0.0672
18.078	18.302	18.14	16.6659	18.095	1.429	0.0692
18.665	18.403	18.41	17.0597	18.196	1.136	0.0539
19.286	18.642	18.69	17.4627	18.432	0.969	0.0451
19.856	18.993	18.96	17.8212	18.780	0.959	0.0439
20.370	19.258	19.17	18.1358	19.042	0.906	0.0409
20.907	19.469	19.41	18.4559	19.252	0.796	0.0354
21.468	19.605	19.62	18.7816	19.386	0.604	0.0265
22.055	19.925	19.87	19.1134	19.703	0.590	0.0255
22.670	20.209	20.08	19.4515	19.984	0.532	0.0227
23.314	20.400	20.34	19.7959	20.174	0.378	0.0159
23.989	20.656	20.60	20.1467	20.427	0.280	0.0116
24.697	20.934	20.85	20.5042	20.703	0.199	0.0081
25.312	21.144	21.08	20.8066	10.911	0.104	0.0042
25.825	21.531	21.27	21.0532	21.294	0.241	0.0096
26.355	21.736	21.45	21.3029	21.497	0.194	0.0077
26.903	21.594	21.62	21.5559	21.356	−0.200	−0.0078
27.470	21.856	21.80	21.8122	21.616	−0.196	−0.0076

terms of σ_{DBM} is due to Maximon[19]:

$$\Delta M = KA - K^2B - K^3C\,, \tag{16}$$

where

$$K = (2/k)^2\,, \tag{17}$$

and the coefficients of (16) are

$$A = (\tfrac{4}{3})\lambda^3 - \lambda^2 - (\pi^2/3 - 6)\lambda + \pi^2/6 - \tfrac{7}{2} + 2\zeta(3)\,, \tag{18a}$$

$$B=(3/16)\lambda+\tfrac{1}{8}\,, \tag{18b}$$

$$C=(29/2304)\lambda-(77/13\,824)\,, \tag{18c}$$

and $\zeta(3)$ is 1.2020569. In (12), ΔS is the screening correction. The Coulomb correction ΔC contributes two terms to (12) and is given by

$$\Delta C=-(28/9)\sigma_0 f(Z)+\Delta C'\,, \tag{19}$$

where $\Delta C'$ vanishes in the extreme relativistic limit, and

$$f(Z)=a^2\sum_{n=1}^{\infty}[1/n(n^2+a^2)] \tag{20}$$

with

$$a=Z\alpha\,. \tag{21}$$

The radiative correction in (12) is given by[6]

$$f_{\rm rad}=1+0.0093(\ln 2k-1.58)/(\ln 2k-2.08)\,. \tag{22}$$

Table VI lists the experimental average cross section $\bar{\sigma}_\kappa$ for Bi alongside the values calculated by Hubbell, Gimm, and Øverbø. The agreement is excellent. However, the ΔC used in the calculations is empirical, and is uncertain by about 10% according to Maximon and Gimm.[20] It is difficult to calculate it exactly. We can usefully, therefore, obtain from $\bar{\sigma}_\kappa$ a list of experimental values of the sum of the screening correction plus the energy-dependent Coulomb correction. This sum of corrections is obtained from the experimental data by means of

$$(\Delta C'+\Delta S)=(\sigma_\kappa/f_{\rm rad}-\sigma_{\rm DBM})\,. \tag{23}$$

Its values are listed in Table VI. It has also been expressed as a fraction of the Bethe-Heitler cross section $\sigma_{\rm BH}$, where

$$\sigma_{\rm BH}=\sigma_0(28\lambda/9-218/27)\,, \tag{24}$$

in the last column of the table.

It should be noted that we have used one of Maximon's expansions,

$$\sigma_\kappa^M=(2\pi/3)\sigma_0[(k-2)/k]^3[1+\epsilon/2+23\epsilon^2/40+37\epsilon^3/210+\cdots]\,, \tag{25}$$

where

$$\epsilon=(k-2)/(k+2)\,, \tag{26}$$

to calculate $\sigma_{\rm DBM}$ at small values of k using

$$\sigma_{\rm DBM}=\sigma_\kappa^M-28\sigma_0 f(Z)/9\,. \tag{27}$$

The expansion (25) is supposed to be good for values of k less than 4. We have used it up to 7.404 MeV in order to obtain a smooth transition to values of $\sigma_{\rm DBM}$ calculated using the term contained in curly brackets in (12).

As can be seen from Table VI, the measured and measured mean values of σ_κ for Bi differ from σ_κ(calc) by less than the statistical errors. Indeed, up to 14 MeV the average discrepancy over 2 MeV intervals fluctuates between about +0.02% and −0.02%. Between 14 and 28 MeV it fluctuates between about +0.2% and −0.3%. Since the sum of the cross sections contained within the parentheses of (10) (which is about one-third as large as σ_κ) is uncertain to about 0.2% (possible systematic error) this agreement may be fortuitous. Combining the experimental statistical errors of about 0.6% we estimate an uncertainty of 0.4% in the mean measured values. The various sources of uncertainty are summarized in Table VII. We conclude that σ_κ(calc) and σ_κ agree to within about (0.5 ± 0.4)% over the range of photon energies studied in this experiment. In the region of the giant dipole resonance the uncertainty in the discrepancy increases to about ±0.6% because of a possible 10% uncertainty in the nuclear absorption cross section. Some of the local deviations from σ_κ(calc) may be significant, however. If we compare values of the pair cross section σ_κ measured only in the present experiment with σ_κ(calc), we see from Tables III and IV that between 6 and 13 MeV σ_κ is systematically the larger in both Ta and Bi. The average discrepancy is about +2Σ, where Σ is the standard deviation in a single measurement, and so is significant. For Ta between 13 and 17 MeV the average discrepancy in the cross section changes sign and decreases in magnitude to about −0.6Σ. However, the Mainz measurements for Ta are larger than σ_κ(calc) by about the same amount, so above 13 MeV an average $\bar{\sigma}_\kappa$ of the Ottawa and Mainz cross sections agrees very well with the values of Hubbell *et al.*[6], as mentioned earlier. At 6.418 MeV Moreh and Wand[1] obtained (12 777 ± 12) mb for the total cross section of Ta and (15 487 ± 15) mb for Bi. Corresponding values interpolated from our data are (12 819 ± 22) mb and (15 662 ± 32) mb. For Ta, the value of σ_κ deduced from the Negev measurements lies 33 mb above σ_κ(calc) while ours lies 75 mb above, whereas for Bi the Negev value lies 125 mb below σ_κ(calc) and ours lies 50 mb above. Hence the resonance absorption results corroborate our measurement of σ_κ for Ta, the mean of the two measured values being 0.42% larger than σ_κ(calc) at 6.418 MeV. For Bi at this energy the mean of Ottawa and Negev measured values is 0.24% less than σ_κ(calc). Indeed, all of our measured σ_κ between 4.3 and 5.8 MeV are smaller than σ_κ(calc).

SUMMARY AND CONCLUSIONS

To summarize, the experimental evidence is that σ_κ(calc) for Al, overestimated by nearly

TABLE VII. Summary of uncertainties in measured quantities caused by factors which do not cancel in the ratio of absorbed to transmitted intensity. The photon energy is denoted by ω, the total absorption cross section by σ, the atomic cross section by σ_Z, and the pair cross section by σ_K.

Measured quantity	Uncertainty	Cause	Remarks
ω	±0.5% at 6 MeV ±1.9% at 26 MeV	timing resolution	data were lumped into 500 keV bins, however
ω	$\pm(0.5+0.2)\%$	energy calibration	includes possible drift
σ	±0.2% at 6 MeV ±1.0% at 26 MeV	counting statistics	includes background uncertainty
σ	±0.03% or less	photon flux normalization	dependence on absorber position
σ	±0.1% or less	photon flux variation	
σ	±0.2%	mass/unit area of absorber	
σ	−0.18% for Al −0.08% for Bi	photon in scattering	correction applied correction not applied
σ	−0.04% to −0.08% for Al	air displacement by absorber	correction applied
σ_Z	±0.2% near GDR	10% uncertainty in photonuclear cross section	additional to uncertainties in σ
σ_K	±0.1% or less	0.2% uncertainty in $(\sigma_{pn}+\sigma_c+\sigma_R+\sigma_t)$	additional to uncertainties in σ_Z

2% at 4 MeV, reaches agreement with the data by 13 MeV; that σ_K(calc) for Ta is on the average about 0.8% too small between 6 and 13 MeV, and is correct at higher energies; and that for Bi, σ_K(calc) is about 0.3% too large between 4 and 6 MeV, about 0.7% too small between 6 and 13 MeV, and is correct at higher energies. It should be noted that for Ta between 11 and 17 MeV a possible overestimate of 10% in the total nuclear absorption cross section σ_n causes an overestimate of about 0.2% in σ_Z (and so in σ_K) and for Bi an overestimate ranging from 0.1 to 0.3% (because of its narrower giant dipole resonance). If σ_n were in fact 10% smaller than believed, the conclusion that σ_K(calc) is too small would not be changed. Presumably the empirical Coulomb correction is the cause of these discrepancies, and since it contributes about 10% to the total cross section at intermediate energies it may be as much as 8% too small between 6 and 13 MeV for Ta and 7% for Bi.

Until calculations for σ_Z are performed for heavy elements using exact Coulomb corrections between 5 and 50 MeV, values of σ_Z accurate to better than 1% will only be obtained by experiment. Nevertheless we conclude that the improved calculations[8] of the e^+-e^- pair cross sections give impressive agreement with experiment, albeit using an empirical Coulomb correction. The improved screening and Coulomb corrections used in these calculations are necessary to remove discrepancies as large as 3% in the older calculations of the pair cross section. In view of the close similarity of the matrix element for bremsstrahlung to that fo pair production, we expect that bremsstrahlung cross sections of heavy elements will also requi revision.

ACKNOWLEDGMENTS

We gratefully acknowledge a wide range of tec nical support provided by A. Nowak, M. Kosaki, and D. Kleinbub. We thank J.-P. Carlos for his collaboration during preliminary data taking. G. Hennek assisted in the engineering design of the LD_2 tank. B. Wheeler contributed to the mec anical design. Much of the mechanical construc tion was done in the NRC Physics Shop under th direction of W. Taylor, and some in the NRC Manufacturing and Technology Centre. The ma of the absorbers were measured by P. G. R. Ge dron of the Mechanical and Optical Physics section.

APPENDIX A: COUNTING LOSS CORRECTIONS

The counting system shown schematically in Fig. 1 permits one neutron event to be recorde after each Linac beam pulse. An early event stopping the time-to-digital converter (TDC) prevents observation of any later event produced by the same beam pulse. With the Linac operating at 720 Hz typically about 8000 events were recorded during each 1-min period when the full LD$_2$ target was irradiated without absorber (133 events/s). Total counting losses in this (worst) case were 3.4%, distributed over 1000 time channels. The greatest fractional counting loss (about 18%) occurred in the last channel, whereas the loss in the early channels was negligible. The TOF spectra were roughly bell shaped with a broad maximum in the counting rate per time channel occurring at a neutron energy of about 3 MeV. The region of interest corresponding to high energy neutrons lay mainly on the early side of the maximum. Counting losses in these channels were lower than at 3 MeV where the average losses were about 9% without absorber and 3% with absorber. If no ead-time correction were applied these losses ould cause the absorption cross section at a pho- on energy of 8 MeV to appear to be about 5% too ow (assuming 33% of the 8 MeV photons are ransmitted by the absorber).

The observed count O_i in the ith time channel s

$$O_i = S\exp\left(-\sum_{j=1}^{i-1} C_j/S\right)(C_i/S)\exp(-C_i/S), \qquad (A1)$$

here S is the total number of beam pulses used in e experiment. The first exponential term ex- resses the reduced probability of the TDC reach- g the ith channel because of the cumulative probability than an event will occur in an earlier jth hannel. Rewriting (A1) gives

$$C_i\exp(-C_i/S) = O_i\exp\left(\sum_{j=1}^{i-1}(C_j/S)\right). \qquad (A2)$$

he present TOF data were corrected for dead- me channel by channel starting from the earliest, ssuming that $\exp(-C_i/S)$ had the value unity, ne- lecting self-losses in the ith channel. This ap- roximation causes a negligible systematic error hich can be determined from the first-order ap- roximation. Substituting $(1 - C_i/S)$ for $\exp(-C_i/S)$ nd Y_i for the term on the right-hand side, (A2) ecomes

$$C_i - C_i^2/S = Y_i. \qquad (A3)$$

here Y_i differs little from C_i, it can replace C_i the quadratic term, so that

$$C_i = Y_i(1 + Y_i/S). \qquad (A4)$$

t the maximum point in the TOF spectrum in the orst case, Y_i/S was about 8×10^{-4}. Including e self-loss correction increases the count per channel without absorber by 0.08% and the count with absorber by 0.03% which (because the absorber cross section is proportional to the logarithm of the ratio of the two counts) represents a 0.05% increase in the cross section at low energy.

The data presented here were accumulated in 13 separate runs. All the runs were added together and then corrected for counting losses. This procedure was justified by the observation that fluctuations from the average counting rate during a single run were similar to the fluctuation in average rate from run to run. For the full LD$_2$ target without absorber the weighted sum, (8236 ± 1221) events/min, of the average counting rates during the individual runs in the Al data set (each individual rate weighted by the ratio of the number of counting cycles in the run to the total number of cycles in the complete data set) differed from the mean of all the observations of the rate during all the runs, (8013 ± 899) events/min, by less than 3%. For this analysis the average counting rate during an individual run was determined from a series of separate readings taken at random times.

To estimate the possible systematic error introduced by a global dead-time correction, we have compared the cross section for Al at low energy computed from an additional run of 885 cycles duration (about 88.5 beam hours) with the cross section obtained from the sum of the present set of runs with Al absorber, amounting to 3047 cycles, as shown in Table V.

An increase by 20% in the observed counting rate from the average rate requires dead-time corrections of 11% at the maximum of the TOF spectrum of LD$_2$ without absorber and 4% at the maximum of the spectrum with absorber, compared to 7% and $2\frac{1}{2}$% for a counting rate 20% below average. The same given ratio of "absorber-in" to "absorber-out" counts in the maximum channel, corrected for dead time according to these two different rates, would give values of the cross section differing by about ±1.5%. This figure is an upper limit to the possible error since a dead-time correction based on the average counting rate will be quite appropriate for about half of the data.

In the 885-cycle run the average neutron counting rate was (8460 ± 858) events/min where the quoted error is the average of the absolute values of the deviations from the mean of 51 readings recorded at different times during the run. This is 4% higher than the average rate of (8172 ± 947) events/min for the remaining Al runs. The absorption cross sections for Al extracted from the two different data sets are compared in Table V at low energies. We see for example that at 7.936 MeV the two values (1.085 ± 0.004) b and (1.089

±0.002) b differ by no more than 0.4%, which is less than the statistical uncertainty. One might therefore estimate that at energies as low as 8 MeV the possible error resulting from applying the dead-time correction globally to all the data could be about ±0.2%. However, the average difference between the two sets of measured cross sections over the photon energy interval 3.87 to 12.6 MeV is only +0.0013 b, which is a discrepancy of only 0.1%.

APPENDIX B: SCATTERING CORRECTIONS

At low energy the Compton scattering cross section σ_C is a large fraction of the total photon cross section σ. As the incident photon energy increases the fractional contribution of σ_C decreases. For Al, σ_C contributes 94.5% of σ at 3 MeV, and 52.5% at 15 MeV; while for Bi, σ_C is 64.3% of σ at 3 MeV, and 15.8% at 15 MeV. Some Compton-scattered photons, reduced in energy, remain within the detection solid angle causing an apparent reduction in the measured cross section at a lower energy. We can show, however, that the effect is quite small for Al, and negligible for Bi.

Because the solid angle subtended by the LD_2 target at the absorber was small, the energy ω' of photons scattered by the absorber through an angle θ_s into the target differed by only a small amount $\Delta\omega$ from the energy ω of the incident photon:

$$\Delta\omega = \omega[1 + k^{-1}(1 - \cos\theta_s)^{-1}]^{-1}, \tag{B1}$$

where $\Delta\omega = (\omega - \omega')$, $k = \omega/m$, and m is the mass energy of the electron. The bremsstrahlung entering the absorber was collimated into a cone whose apex half angle (0.55°) was slightly less than the angle subtended at the radiator by the exit end of the LD_2 target. The radiator was 1.34 m from the front face of the absorber and 2.49 m from the front face of the LD_2 target. For the Ta and Bi absorbers, each about 2.5 cm long, the maximum possible in-scattering angle $\theta_s^{\max}$ was 2.5°. For the Al absorber (about 18 cm long) $\theta_s^{\max}$ was 2.9°. Between the mid plane of the Al absorber and the center of the LD_2 target, θ_s could be no larger than 2.5°. The average solid angle for in-scattering was about 1.84 msr for the Al absorber.

Scattering by 2.5° reduces the energy of 10 MeV photons by 183 keV, of 20 MeV photons by 718 keV, and of 30 MeV photons by 1588 keV. The cross section for attenuation of a photon varies slowly with ω and is essentially the same before and after a small-angle scattering. The path length in the absorber traversed by a detected photon is very nearly the same whether or not scattering has occurred.

The differential cross section for scattering of unpolarized photons by electrons according to Klein and Nishina is

$$\frac{d\sigma_C(\omega)}{d\Omega} = (r_0^2/2)(\omega'/\omega)^2(\omega/\omega' + \omega'/\omega - \sin^2\theta_s), \tag{B2}$$

where r_0 is the classical radius of the electron. For $\theta_s \sim 2°$, so that $\sin\theta_s \sim 10^{-3}$, (B2) can be written as

$$\frac{d\sigma_C(\omega)}{d\Omega} \simeq r_0^2(\omega'/\omega)(1 - \Delta\omega/\omega) \tag{B3}$$

and hence as

$$\frac{d\sigma_C(\omega)}{d\Omega} \simeq r_0^2(1 - \Delta\omega/\omega)(1 - 2\Delta\omega/\omega). \tag{B4}$$

At 10 MeV, $d\sigma_C/d\Omega$ can fall to about 0.94 r_0^2, and at 30 MeV it can fall to about 0.84 r_0^2, when σ_C is as large as 2.5°. It is a slight overestimate therefore, for an absorber of atomic number Z, to use Z times the zero-angle differential scattering cross section for hydrogen ($r_0^2 = 79.41$ mb) as the forward-scattering differential cross section averaged over the detection solid angle:

$$\left(\frac{d\sigma_C}{d\Omega}\right)_z = 79.41Z \ (\text{mb sr}^{-1}).$$

The effect of in-scattering thought of as a (negative) cross section "σ_s" can therefore be expressed as a fraction of $\sigma(\omega)$ by

$$(\text{"}\sigma_s\text{"}/\sigma(\omega))_z \simeq \left(\frac{d\sigma_C}{d\Omega}\right)_z \Delta\Omega/\sigma(\omega). \tag{B5}$$

For Al at 10 MeV, where σ is 1.037 b, the effect is smaller than 0.18%. In the case of Bi at 10 MeV, in-scattering can reduce the cross section observed in this experiment by no more than 0.08%, and by lesser amounts at higher energies. Even at 10 MeV this correction is three times smaller than the statistical error in the experimental value, and is an even smaller fraction of it at lower or higher energies. Hence no correction has been applied to the Ta and Bi cross sections.

*Present address: Australian Radiation Laboratory, Melbourne, Australia.

[1] R. Moreh, D. Salzmann, and Y. Wand, Phys. Lett. 30B, 536 (1969); T. Bar-Noy, Internal Report, Nuclear Research Center, Negev, Beer-Sheba, Israel; R. Moreh and Y. Wand, Nucl. Phys. A252, 423 (1975).

[2] S. Sugiyama and T. Tomimasu, *Proceedings of the International Conference on Photonuclear Reactions and Applications*, edited by B. L. Berman (University of California, Livermore, 1973), Vol. I, p. 563.

[3] J. Ahrens, H. Borchert, K. H. Czock, H. B. Eppler, H. Gimm, H. Gundrum, M. Kroning, P. Riehn, G. Sita Ram, A. Zieger, and B. Ziegler, Nucl. Phys. A251, 479 (1975).

[4] J. H. Hubbell, Report No. NSRDS-NBS 29 (U. S. Government Printing Office, Washington, 1969), p. 1.

[5] E. Storm and H. I. Israel, Nucl. Data Tables A7, 565 (1970).

[6] H. A. Gimm and J. H. Hubbell, National Bureau of Standards Technical Note 968 (U.S. Government Printing Office, Washington, 1978), p. 4; and J. H. Hubbell, H. A. Gimm, and I. Øverbø (private communication).

[7] I. Øverbø, Phys. Lett. 71B, 412 (1977).

[8] For a review, see N K. Sherman, Nucl. Instrum. Methods 116, 301 (1974).

[9] C.-P. Wu, F. W. K. Firk, and B. L. Berman, Nucl. Instrum. Methods 79, 346 (1970).

[10] R. G. Jones, R. G. Johnson, J. W. Jury, J. I. Lodge, K. H. Lokan, N. K. Sherman, and R. W. Gellie, Phys. Can. 27, 59 (1971); and R. G. Jones, M.Sc thesis Trent University, 1971 (unpublished).

[11] J. Ahrens, H. Borchert, A. Zieger, and B. Ziegler, Nucl. Instrum. Methods 108, 517 (1973).

[12] N. K. Sherman, Nucl. Instrum. Methods 79, 197 (1970).

[13] L. C. Henry and T. J. Kennett, Can. J. Phys. 49, 1167 (1971).

[14] R. R. Harvey, J. T. Caldwell, R. L. Bramblett, and S. C. Fultz, Phys. Rev. 136, B126 (1964).

[15] L. M. Young, Ph.D. thesis University of Illinois, 1972 (unpublished).

[16] R. L. Bramblett, J. T. Caldwell, G. F. Archampaugh, and S. C. Fultz, Phys. Rev. 129, 2723 (1963).

[17] R. Bergère, H. Beil, and A. Veyssière, Nucl. Phys. A121, 463 (1968).

[18] For a review, see J. W. Motz, H. A. Olsen, and H. W. Koch, Rev. Mod. Phys. 41, 581 (1969).

[19] L. C. Maximon, J. Res. Natl. Bur. Stand. 72B, 79 (1968).

[20] L. C. Maximon and H. A. Gimm, National Bureau of Standards Internal Report 78-1456 (U.S. Government Printing Office, Washington, 1978), p. 9.

PHYSICAL REVIEW C VOLUME 21, NUMBER 6 JUNE 1980

Factorization in high-energy nucleus-nucleus fragmentation cross sections

J. Cugnon* and R. Sartor
Institut de Physique, Université de Liège, Sart Tilman, B-4000 Liège 1, Belgique

(Received 17 September 1979)

It is shown that the basic quantity of the abrasion-ablation model of nucleus-nucleus collisions, namely the probability of extracting a nucleon from the projectile, is a quasi-universal quantity. It can be given a form which does not depend upon the target and which depends weakly upon the projectile. It is shown how this property is related to the weak factorization of the cross sections.

[NUCLEAR REACTIONS Fragmentation in relativistic heavy ion collisions. Factorization of the cross section.]

It has been observed for a few years[1,2] that the inclusive fragmentation cross sections in the relativistic nucleus-nucleus collisions can be factorized according to the formula

$$\sigma(\mathrm{F},\mathrm{P},\mathrm{T})=\sigma_{\mathrm{P}}^{\mathrm{F}}\gamma_{\mathrm{PT}}\,, \tag{1}$$

where F, P, and T stand for the fragment, the projectile, and the target, respectively. Form (1) can be called weak factorization as opposed to the strong factorization form which reads

$$\sigma(\mathrm{F},\mathrm{P},\mathrm{T})=\sigma_{\mathrm{P}}^{\mathrm{F}}\gamma_{\mathrm{T}}\,. \tag{2}$$

The present experimental data do not allow one to draw conclusions about the validity of relation (2).

It has been shown recently[3] that the abrasion-ablation model[4-8] of relativistic heavy ion collisions predicts that weak factorization is approximately valid while strong factorization is violated. In this paper, our aim is to bring to light the exact relation between the abrasion-ablation model and the factorization and to comment about some properties of the model.

Let us call $\sigma_n(\mathrm{P},\mathrm{T})$ the abrasion cross section for removing n nucleons from the projectile. It is clear that the factorization of $\sigma_n(\mathrm{P},\mathrm{T})$ implies the one of the abrasion-ablation cross section (see Ref. 5). One has the basic relations[5]

$$\sigma_n(\mathrm{P},\mathrm{T})=\binom{A_{\mathrm{P}}}{n}\int_0^{\infty} d^2\vec{b}\,[1-P_{\mathrm{PT}}(b)]^n \times[P_{\mathrm{PT}}(b)]^{A_{\mathrm{P}}-n}\,, \tag{3}$$

where the probability function $P_{\mathrm{PT}}(b)$ is defined by

$$P_{\mathrm{PT}}(b)=\int d^2\vec{t}\,\phi_{\mathrm{P}}(\vec{t})\exp[-A_{\mathrm{T}}\sigma_{NN}\phi_{\mathrm{T}}(\vec{t}+\vec{b})] \tag{4}$$

with

$$\phi_i(\vec{t})=\int_{-\infty}^{+\infty}dz\,\rho_i(\vec{t},z),\quad i=\mathrm{P},\mathrm{T}\,. \tag{5}$$

In the above equations, σ_{NN} is the nucleon-nucleon cross section and ρ is the nuclear density. $(\vec{t},z)$ are cylindrical coordinates with z along the incident direction and $\vec{b}$ is the impact parameter.

We recall that Eqs. (3)–(5) are obtained by using the nonrelativistic Glauber multiple scattering theory[9] as applied[10-17] to a composite projectile and target. It is interesting to note that the trivial relativistic extension, namely the introduction of Lorentz contracted objects, does not change the value of $P_{\mathrm{PT}}(b)$ since the function $\phi(\vec{t})$ is not affected by a Lorentz contraction.

We have computed the quantities $\sigma_n(\mathrm{P},\mathrm{T})$ and $P_{\mathrm{PT}}(b)$ for a large number of colliding pairs. Our results confirm those of Ref. 3. Moreover, we observed that the probability function $P_{\mathrm{PT}}(b)$ can be written

$$P_{\mathrm{PT}}(b)=f_{\mathrm{P}}(b-\xi_{\mathrm{T}})\,, \tag{6}$$

where the function $f_{\mathrm{P}}(x)$ only depends upon the projectile P. In other words, the quantity $P_{\mathrm{PT}}(b)$ only depends on the target T by a translation of the coordinate. More remarkable perhaps is the fact that the amplitude ξ_{T} of the translation does not depend upon the projectile (see Table I). We show in Fig. 1 how the relation (6) is fulfilled for the ^{27}Al and ^{107}Ag projectiles. The discrepancy for $x=b-\xi_{\mathrm{T}}$ smaller than 5 fm which arises for light targets only can be disregarded in practice since

TABLE I. The translation amplitude ξ (in fm) of Eq. (6) for different projectiles (P) and targets (T). It appears that ξ is a function of T only.

		T				
	ξ	^{16}O	^{27}Al	^{63}Cu	^{107}Ag	^{208}Pb
P	^{16}O	−2.1	−1.3	0	1.1	2.6
	^{27}Al	−2	−1.3	0	1	2.5
	^{63}Cu	−2.1	−1.3	0	1	2.5
	^{107}Ag	−2.1	−1.3	0	1.1	2.6
	^{208}Pb	−2.1	−1.3	0	1.1	2.6

© 1980 The American Physical Soc

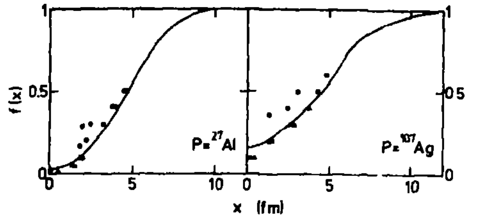

FIG. 1. The universal function $f_P(x)$ for the ^{27}Al and ^{107}Ag projectiles. $f_P(x)$ is the probability function $P_{PT}(x)$ for the ^{63}Cu target. The filled (●) and open (○) dots, the crosses (×) and the triangles (△) correspond to the translated probability functions of the ^{16}O, ^{27}Al, ^{107}Ag, and ^{208}Pb targets, respectively. For x greater than 5 fm, they all fall on the universal curve and are not shown. The computations were done at an energy of 2 GeV/nucleon with a Woods-Saxon density distribution for the targets and projectiles.

the main contribution to the integral in Eq. (3) comes from higher values of x [see Eq. (7) below]. We have set ξ_T equal to zero for the ^{63}Cu target.

Let us now show how the above mentioned quasi-universality guarantees the weak factorization property of the cross sections. By making use of (6) Eq. (3) can be written

$$\sigma_n(\mathrm{P},\mathrm{T})=\binom{A_\mathrm{P}}{n}\int_{-\xi_\mathrm{T}}^{\infty} dx(x+\xi_\mathrm{T}) \times[1-f_\mathrm{P}(x)]^n f_\mathrm{P}(x)^{A_\mathrm{P}-n}, \qquad (7)$$

where the lower limit of integration can be put equal to zero since this introduces at most a one percent error even in the less favorable cases. We write

$$\sigma_n(\mathrm{P},\mathrm{T})=\binom{A_\mathrm{P}}{n}(\langle x_{n\mathrm{P}}\rangle+\xi_\mathrm{T})N_{n\mathrm{P}}, \qquad (8)$$

where $N_{n\mathrm{P}}$ is the normalization constant relative to the distribution $[1-f_\mathrm{P}(x)]^n[f_\mathrm{P}(x)]^{A_\mathrm{P}-n}$ and where $\langle x_{n\mathrm{P}}\rangle$ is the corresponding x average.

The ratio

$$\frac{\sigma_n(\mathrm{P},\mathrm{T})}{\sigma_{n'}(\mathrm{P},\mathrm{T})}=\frac{\binom{A_\mathrm{P}}{n}}{\binom{A_\mathrm{P}}{n'}}\frac{N_{n\mathrm{P}}}{N_{n'\mathrm{P}}}\frac{\langle x_{n\mathrm{P}}\rangle+\xi_\mathrm{T}}{\langle x_{n'\mathrm{P}}\rangle+\xi_\mathrm{T}} \qquad (9)$$

should be independent of T if weak factorization is valid. This is indeed the case for either $\langle x_{n\mathrm{P}}\rangle\approx\langle x_{n'\mathrm{P}}\rangle$ or $\langle x_{n\mathrm{P}}\rangle$ and $\langle x'_{n\mathrm{P}}\rangle\gg\xi_\mathrm{T}$ as can be seen from Tables I and II. It appears that weak factorization holds within 10–15% on an average. In the least favorable case (n very different from n' and $T=$ ^{16}O) the weak factorization is broken by some 20%.

TABLE II. The average $\langle x_{n\mathrm{P}}\rangle$ (see text) for the ^{27}Al and the ^{107}Ag projectiles for different values of the number n of abraded nucleons.

P = ^{27}Al		P = ^{107}Ag	
n	$\langle x_{n\mathrm{P}}\rangle$	n	$\langle x_{n\mathrm{P}}\rangle$
1	8.4	1	11
2	7.8	2	10.7
3	7.4	3	10.3
4	7.0	4	10
5	6.7	5	9.6
6	6.4	6	9.3

We also looked at the ratio

$$\frac{\sigma_n(\mathrm{P},\mathrm{T})}{\sigma_n(\mathrm{P},\mathrm{T}')}=\frac{\langle x_{n\mathrm{P}}\rangle+\xi_\mathrm{T}}{\langle x_{n\mathrm{P}}\rangle+\xi_{\mathrm{T}'}} \qquad (10)$$

which should not depend upon n if weak factorization is valid. This is realized if $\langle x_{n\mathrm{P}}\rangle$ is much larger than ξ_T whatever n and T are. Tables I and II and Fig. 1 indicate that, once again, Eq. (10) is satisfied by 10% on an average, but this percentage becomes larger for the ^{16}O projectile when T is very different from T′.

Equation (10) and our tables tell that strong factorization is not so well satisfied as the weak one. Indeed the range of variation of $\langle x_{n\mathrm{P}}\rangle$ becomes rather large when both n and P are allowed to vary while it is much smaller when n is varied with P kept fixed [notice that relation (9) does not tell anything about the strong factorization property].

The weak and simple dependence of the fragmentation cross sections upon the details of the target can be traced back to the interplay between the exponential form of Eq. (4) and the relatively high value of σ_{NN}. Hence the projectile only "sees" the outer fringes of the target and one may consider that in the last resort the factorization arises from the relatively short mean free path of the high-energy nucleons in nuclear matter.

Helpful discussions with Professor C. Mahaux and Mr. G. Richelle are gratefully acknowledged. One of us (R.S.) would like to thank the Institut Interuniversitaire des Sciences Nucléaires for financial support.

*Present address: Kellogg Radiation Laboratory, California Institute of Technology, Pasadena, California 91125.

[1] H. H. Heckman, D. E Greiner, P. J. Lindstrom, and F. S. Bieser, Phys. Rev. Lett. 28, 926 (1972).

[2] P. J. Lindstrom, D. E. Greiner, H. H. Heckman, B. Cork, and F. S. Bieser, Lawrence Berkeley Laboratory Report No. LBL-3650 (unpublished).

[3] M. Bleszynski and C. Sander, Nucl. Phys. A326, 525 (1979).

[4] J. D. Bowman, W. J. Swiatecki, and C. F. Tsang, Lawrence Berkeley Laboratory Report No. LBL-2908 (unpublished).

[5] J. Hüfner, K. Shäfer, and B. Shürmann, Phys. Rev. C 12, 1888 (1975).

[6] A Abul-Magd, J. Hüfner, and B. Shürmann, Phys. Lett. 60B, 327 (1976).

[7] A. Abul-Magd and J. Hüfner, Z. Phys. A227, 379 (1976).

[8] J. Hüfner, C. Sander, and G. Wolschin, Phys. Lett. 73B, 289 (1978).

[9] R. J. Glauber, in *Lectures in Theoretical Physics*, edited by W. E. Brittin and L. G. Dunham (Interscience New York, 1959), Vol. 1.

[10] W. Czyż and L. C. Maximon, Ann. Phys. (N.Y.) 52, 59 (1969).

[11] O. Kofoed-Hansen, Nuovo Cimento A60, 621 (1969).

[12] J. Formánek, Nucl. Phys. B12, 441 (1969).

[13] G. Fäldt, Phys. Rev. D 2, 846 (1970).

[14] A. Tékou, Nucl. Phys. B46, 141, 152 (1972).

[15] G. Fäldt, H. Pilkuhn, and H. G. Schlaile, Ann. Phys. (N.Y.) 82, 326 (1974).

[16] P. M. Fishbane and J. S. Trefil, Phys. Rev. D 10, 300 3228 (1974); Phys. Rev. Lett. 32, 396 (1974).

[17] V. Franco, Phys. Rev. Lett. 32, 911 (1974).

PHYSICAL REVIEW C VOLUME 21, NUMBER 6 JUNE 1980

$^{12}C(^6Li,d)^{16}O \rightarrow \alpha + ^{12}C$ reaction mechanism by means of angular correlation measurements

A. Cunsolo, A. Foti, G. Immè, G. Pappalardo, and G. Raciti
Istituto Nazionale di Fisica Nucleare Sezione di Catania, Centro Siciliano di Fisica Nucleare e di Struttura della Materia, Istituto di Fisica dell'Università di Catania, Corso Italia, 57, 95129 Catania, Italy

N. Saunier
Département de Physique Nucléaire, CEN Saclay, Boîte Postale 2, 91190 Gif-sur-Yvette, France

(Received 28 September 1979)

The particle-particle angular correlation method is applied to the reaction $^{12}C(^6Li,d)^{16}O \rightarrow \alpha + ^{12}C$. Deuterons were detected at $\theta_d^{lab} = 10°$. Information on the reaction mechanism is obtained by analyzing the shape and the angular shift of the experimental data. A dominant direct transfer mechanism is found for the primary reaction. The ratios Γ_{α_0}/Γ and the α-reduced widths γ_{α_0} are deduced.

[NUCLEAR REACTIONS $^{12}C(^6Li,d)^{16}O \rightarrow \alpha + ^{12}C$. $E_{^6Li} = 34$ MeV; measured $W(\Omega_d, \Omega_\alpha)$; confirmed J^π for ^{16}O levels. Evaluated Γ_{α_0}/Γ and γ_{α_0}. EFR-DWBA and HF analysis.]

I. INTRODUCTION

It has been shown¹⁻³ that the measurement of the particle-particle angular correlation $X(a,b)Y^*_{I'} \rightarrow c + Z$ gives information on the properties of the residual nucleus levels and on the mechanism of the primary reaction $X(a,b)Y^*_{I'}$.

The sensitivity of the correlation curve to the reaction mechanism is particularly evident when the ejectile b is detected at an angle θ_b different from zero. The evolution of the correlation curve with increasing θ_b has been recently discussed under different hypotheses on the primary reaction mechanism.[1,2] For small θ_b values the shape of the whole correlation is similar to that obtained at $\theta_b = 0°$, the curve being only shifted by an angular amount δ that depends on the relative population of the magnetic substates $m_{I'}$.[1] In general, different reaction mechanisms produce different values of the populations $P_{m_{I'}}$ and, in turn, different angular shifts.

In a recent work[4] we measured the angular distributions of the deuterons emitted in the $^{12}C(^6Li,d)^{16}O$ reaction at incident energies of 28 and 34 MeV. The analysis of the data has shown that this reaction can be understood as due mainly to a direct α-transfer mechanism for the transitions leading to the ^{16}O states belonging to the rotational band $K^\pi = 0^+$ [6.05 MeV(0^+), 6.92 MeV (2^+), 10.35 MeV (4^+), and 16.3 MeV (6^+)] and to the 7.11 MeV (1^-) and the 6.13 MeV (3^-) ^{16}O levels. This result agrees with that found in two similar investigations: the first one on the same reaction done at higher incident energy[5] and the other on the $^{12}C(^7Li,t)^{16}O$ at 38 MeV.[6]

We have also recently measured[2] the $^{12}C(^6Li,d)^{16}O \rightarrow \alpha + ^{12}C$ angular correlation between deuterons and α particles at $\theta_d = 0°$ and at $E_{^6Li} = 34$ MeV. In this selected geometry the correlation curve is symmetric with respect to 90°,[7] allowing an accurate determination of the spin and parity of the involved level. This method has been also applied to the $^{12}C(^{12}C,^8Be)^{16}O \rightarrow \alpha + ^{12}C$ reaction successfully.[8] However, as mentioned before, information on the reaction mechanism is better gained if a noncollinear geometry is adopted. Then, in the present work, we have extended the previous measurements of the $^{12}C(^6Li,d)^{16}O \rightarrow \alpha + ^{12}C$ reaction by detecting the emitted deuterons at $\theta_d = 10°$. Data on this reaction have been carried out previously by Artemov *et al.*[3] at lower energy, reporting only the high energy ^{16}O states.

We have analyzed our experimental results in terms of exact finite range–distorted wave Born approximation (EFR-DWBA) and compound nucleus mechanism.

Section II of the present work concerns the experimental procedure. Section III is devoted to the analysis of the data in terms of the formalism developed by Da Silveira.[1] Some conclusions are drawn in Sec. IV.

II. EXPERIMENTAL PROCEDURE AND RESULTS

A 34 MeV $^6Li^{+++}$ beam was produced by the CEN-Saclay FN tandem Van de Graaff with intensity of the order of 65 nA. The target used was a self-supporting natural C foil, 150±20 $\mu g/cm^2$ thick.

The emitted deuterons and the α particles in coincidence were detected by means of two ΔE-E

© 1980 The American Physical Society

silicon counter telescopes: $\Delta E_d = 206$ μm, $E_d = 3000$ μm; $\Delta E_\alpha = 13.8$ μm, $E_\alpha = 300$ μm. The particles were identified by an analogical processing of the E and ΔE signals. The elementary information corresponding to identification, total energy, and time were stored on magnetic tape for off-line analysis. The overall deuteron energy resolution [full width at half maximum (FWHM)] was about 100 keV, the time resolution about 8 ns.

The deuterons were detected at $\theta_d = 10°$ ($\phi_d = 0$ azimuthal angle) and angular correlations were obtained in the angular range $35° \leq \theta \leq 95°$ ($\phi_\alpha = \pi$ azimuthal angle) in steps of 2.5°.

A single deuteron spectrum is displayed in Fig. 1; the arrows indicate the ^{16}O levels for which the d-α correlation measurements were carried out.

Figure 2 shows a two-dimensional energy spectrum of d-α coincidences obtained at $\theta^{\rm lab} = 65°$. An interesting feature of this spectrum is the presence of a strong component due to the particles corresponding to the first excited 4.43 MeV (2^+) and to the 9.6 MeV (3^-) ^{12}C levels.

Figure 3 shows the deuteron energy spectra in coincidence with α_0 particles and with the α_1 particles. It can be observed from Figs. 2 and 3 that an important contribution to the broad structure observed in the single deuteron spectrum comes from deuterons associated with alpha particles corresponding to excited states of the ^{12}C final nucleus. Then, as already proposed in Ref. 9, the continuous deuteron spectrum cannot be interpreted as due only to a ^{6}Li breakup mechanism leaving the target nucleus in its ground state.

The experimental d-α angular correlations for α particles corresponding to the decay to the ^{12}C g.s. are shown in Fig. 5.

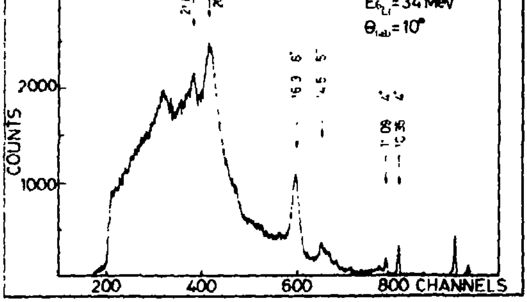

FIG. 1. Deuteron energy spectrum from the ^{6}Li induced reaction on ^{12}C.

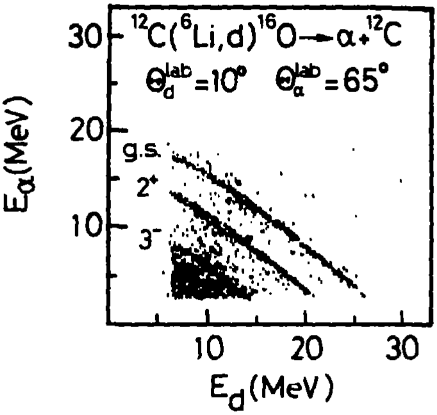

FIG. 2. Two-dimensional energy spectrum of d-α coincidences from the ^{12}C(^{6}Li,d)^{16}O$\rightarrow\alpha+{}^{12}$C reaction. Note that a large amount of d-α coincidence events are distributed along kinematic bands corresponding to the excited 4.43 MeV (2^+), 9.6 MeV (3^-) ^{12}C levels.

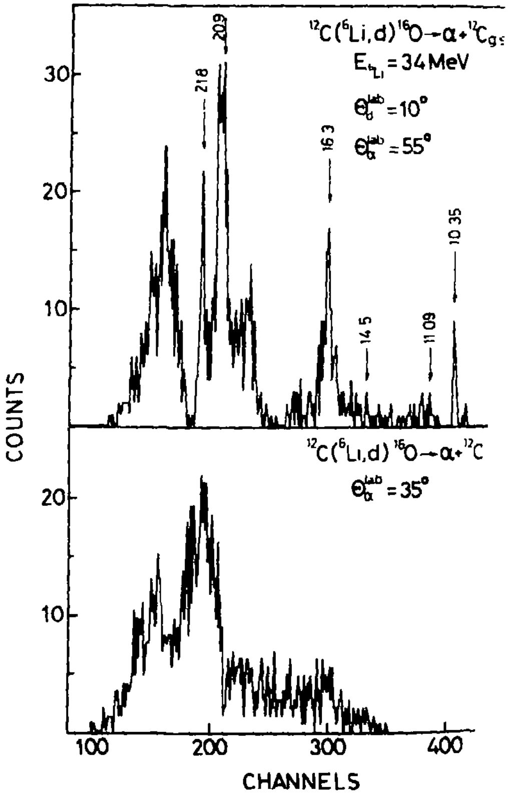

FIG. 3. Coincidence spectra from the ^{12}C(^{6}Li,d)^{1} $\rightarrow\alpha+{}^{12}$C reaction obtained from projecting the even distributed in the ground state locus or in the 4.43 (2^+) locus onto the deuteron energy axis.

III. ANALYSIS OF THE DATA

A. Reaction mechanism

The theoretical expression of the correlation function, when the formation of a well-defined state is assumed, is[1]

$$W(\Omega_1,\Omega_2)=N\sum_{\substack{m_i m_I\\ m_{i'} m_{i''} m_{I''}}}\left|\sum_{m_{I'}}\left[T^{m_i m_I}_{m_{i'} m_{I'}}(\Omega_1)T'^{m_{I'}}_{m_{i''} m_{I''}}(\Omega_2)\right]\right|^2, \tag{1}$$

where $T(\Omega_1)$ and $T'(\Omega_2)$ are the transition amplitudes of the primary reaction and of the disintegration process, respectively. For other notations see Refs. 1 and 2.

In the channel spin representation and in the case of the ^{12}C(^{6}Li,d)^{16}O$\rightarrow\alpha+^{12}$C reaction ($I=0$ then $s=I$, $i''=0$ then $s''=I''$) the expansions in partial waves for the reaction and disintegration amplitudes are[1]

$$\begin{aligned}T^{m_i}_{m_{i'} m_{I'}}(\Omega_1)=\sum_{s' m_{s'}}\sum_{\substack{J l l'\\ m_J m_{l'}}}&(2l+1)^{1/2}(l s\, 0\, m_s|J m_J)\\ &\times(l' s' m_{l'} m_{s'}|J m_J)(I' i' m_{I'} m_{i'}|s' m_{s'})\\ &\times S^{J}_{s' l' s l}Y^{m_{l'}}_{l'}(\Omega_1)\end{aligned}$$

and

$$T'^{m_{I'}}_{m_{I''}}(\Omega_2)=\sum_{l'' m_{l''}}(l'' I'' m_{l''} m_{I''}|I' m_{I'})S^{I'}_{I'' l''}Y^{m_{l''}}_{l''}(\Omega_2),$$

where the information on the reaction and disintegration mechanism is contained in the matrix elements $S^{J}_{s l' s l}$ and $S^{I'}_{I'' l''}$, respectively.

The normalization condition $\int_{4\pi}W(\Omega_1,\Omega_2)d\Omega_2=1$ defines

$$N^{-1}=\sum_{\substack{m_i m_I\\ m_{i'} m_{I'}}}|T^{m_i m_I}_{m_{i'} m_{I'}}(\Omega_1)|^2\sum_{s'' l''}\left|S^{I'}_{\alpha'' l'' s''}\right|^2 .$$

Then, expression (1) becomes

$$W(\Omega_1,\Omega_2)=\frac{\displaystyle\sum_{\substack{m_i m_{i'}\\ m_{I''}}}\left|\sum_{m_{I'}}T^{m_i}_{m_{i'} m_{I'}}(\Omega_1)T'^{m_{I'}}_{m_{I''}}(\Omega_2)\right|^2}{\displaystyle\sum_{\substack{m_i m_{i'}\\ m_{I'}}}\left|T^{m_i}_{m_{I'} m_{i'}}(\Omega_1)\right|^2\sum_{l''}\left|S^{I'}_{I'' l''}\right|^2}. \tag{2}$$

The decay amplitude $S^{I'}_{I'' l''}$ is related to the total level width $\Gamma^{I'}$ and to the partial width $\Gamma^{I'}_{I'' l''}$ for the decay into the channel $(I' l'' I'')$ by

$$|S^{I'}_{I'' l''}|^2=\Gamma^{I'}_{I'' l''}/\Gamma^{I'} .$$

Thus the differential cross section for the sequential process can be expressed in the form

$$\frac{d^2\sigma(\Omega_1,\Omega_2)}{d\Omega_1 d\Omega_2}=\frac{d\sigma(\Omega_1)}{d\Omega_1}\,\frac{\sum_{l''}\Gamma^{I'}_{I'' l''}}{\Gamma^{I'}}\,W(\Omega_1,\Omega_2). \tag{3}$$

We calculated the amplitudes $T^{m_i}_{m_{i'} m_{I'}}(\Omega_1)$ in the framework of the EFR-DWBA using the code SATURN-MARS-I of Tamura and Low,[10] assuming that the primary process is a direct α transfer without spin-orbit interaction. These amplitudes have also been calculated, in the hypothesis of a *compound nucleus statistical mechanism*, using the Hauser-Feshbach (HF) formalism.[1,11]

The optical model parameters for DWBA and HF calculations reported in Tables I and II, respectively, are the same as those in Ref. 4. Finally, the complete calculation of expression (2) has been carried out, for both the assumed reaction mechanisms, using the CORRELA code of Da Silveira.[12]

As an example, the theoretical DWBA and HF correlation curves for the 21.8 MeV (6^+) ^{16}O level are shown together with the experimental data in Fig. 4 as solid and dashed lines, respectively. We note that the angular shift and the positions of the maxima and minima predicted by both the HF and DWBA calculations reproduce the data. However, the strongly oscillating behavior of the experimental angular correlation is very well accounted for by the DWBA curve. This finding and the very smooth behavior of the HF curve indicate that the contribution from the statistical mechanism is negligible. Similar results have been found for all the transitions investigated in this work.

Therefore only the DWBA calculations are shown, as solid lines, in Fig. 5 together with the experimental data. The spins and parities of ^{16}O levels at 10.35 MeV (4^+), 16.3 MeV (6^+), 14.5

TABLE I. Optical model parameters for EFR-DWBA calculations.

Channel	V[a]	r_v	a_v	W	r_w	a_w	r_c	Ref.
^{6}Li + ^{12}C	250	1.354	0.65	30[b]	1.354	0.65	2.0	17, 18
d + ^{16}O	95	1.127	0.8	10[b]	1.332	0.8	2.0	
d-α		1.545[c]	0.65				1.545[c]	17
^{12}C-α		1.25[c]	0.65				1.25[c]	

[a] Form factor: Woods-Saxon.

[b] Form factor: Woods-Saxon derivative.

[c] $R=r(A_1^{1/3}+A_2^{1/3})$.

TABLE II. Optical model parameters for HF calculations. Potential depths are in MeV, lengths in fm, and the radii dependence is $R = r A_t^{1/3}$. For the spin-orbit potential the same radius and diffuseness were used as in the real part.

Channel	V^a	r_v	a_v	W	r_w	a_w	r_c	V_{so}^b	Ref.
$^6Li + ^{12}C$	241	1.75	0.55	14.5^a	2.27	0.23	2.5		19
$n + ^{17}F$	c	1.309	0.66	b, e	1.26	0.48	1.309		20
$p + ^{17}O$	d	1.25	0.65	7.70^b	1.25	0.47	1.25	7.5	21
$d + ^{16}O$	101.4	1.0	0.717	8.75^b	1.589	0.625	1.3		22
$t + ^{15}O$	146.8	1.4	0.551	18.4^a	1.4	0.551	1.3		23
$\alpha + ^{14}N$	195	1.28	0.654	21^a	1.28	0.654	1.3		24

[a] Form factors: Saxon-Woods.

[b] Form factors: Saxon-Woods derivative.

[c] Energy dependence: $V(E) = 47.01 - 0.267\,E - 0.00118\,E^2$.

[d] Energy dependence: $V(E) = 56.1 - 0.55\,E$.

[e] Energy dependence: $W(E) = 9.52 - 0.53\,E$.

MeV (5⁻), 20.9 MeV (7⁻), and 21.8 MeV (6⁺), previously assigned,[2,13] are confirmed. We note that both the shapes and the angular shifts are well reproduced, definitively confirming that all the above levels are populated mainly through a direct α transfer.

These levels, except the 21.8 MeV, have been also analyzed in Ref. 8, in which the $^{12}C(^{12}C,^8Be)^{16}O \rightarrow \alpha + ^{12}C$ reaction was studied. A good consistency is generally found between the two results. In effect, the energy resolutions obtained in the two cases are quite different (FWHM ~ 400 keV in that reaction) and hamper any detailed comparison, particularly at high excitation energy. However, some important differences can be remarked. In the $^{12}C(^{12}C,^8Be\alpha)^{12}C$ reaction the 11.09 MeV (4⁺) level is only noticeable and the 21.8 MeV (6⁺) level is only seen in the α_1 decay. On the other hand, a possible 8⁺ state is reported at 22.5 ± 0.5 MeV, for which, up to now, no clear evidence is found in our case. These differences probably originate from the different selectivities shown by the two (^{6}Li,d), (^{12}C,^{8}Be) primary reactions in the population of the α-decaying states.

In Fig. 4 a comparison for the 21.8 MeV level is made between the present results and the previous ones obtained at $\theta_d = 0°$.[2] It is evident that the correlation curve has the shape substantially unchanged but it is only shifted.

We note that, for small θ_d values, the angular shift has the following simplified expression[1]:

$$\delta \approx \frac{2}{l'}\left(\frac{P_1(\Omega_1)}{P_0(\Omega_1)}\right)^{1/2} \cos\xi ,$$

where ξ is the relative phase between the amplitudes corresponding to $m = 0$ and $m = 1$, and $P_\ell(\Omega_1)$,

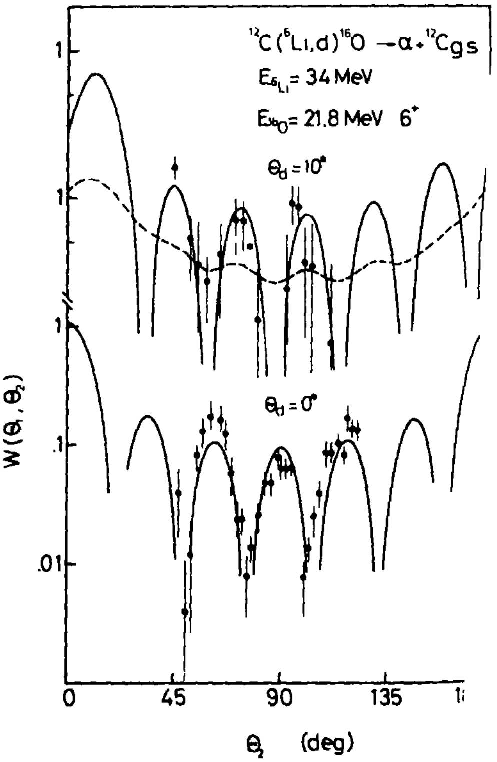

FIG. 4. Comparison of the $\theta_d = 0°$ and $\theta_d = 10°$ resu of the d–α correlation function for the 21.8 MeV (6⁺ level. Solid lines are the results of EFR-DWBA ca tions. The dashed lines are the HF predictions, ar trarly normalized. θ_2 is the α-particle angle defin the recoil nucleus center-of-mass frame, but with spect to the beam direction.

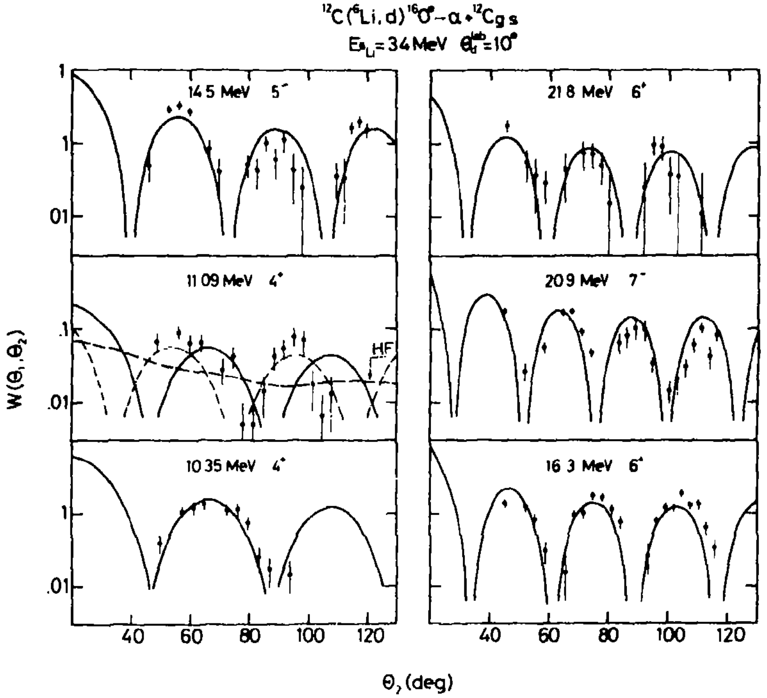

FIG. 5. d-α correlation functions for the $^{12}C(^{6}Li,d)^{16}O\rightarrow\alpha+^{12}C_{g.s.}$ reaction. Solid and dashed curves are as in Fig. 4. For the dot-dashed curve see text.

$P_1(\Omega_1)$ are the populations of the magnetic substates $m_{I'}=0$ and $m_{I'}=1$, respectively:

$$_{,}(\Omega_1)=\sum_{\substack{m_i m_I\\ m_{I'}}} |T^{m_i m_I}_{m_i m_{I'}}(\Omega_1)|^2 \Big/ \sum_{\substack{m_i m_I\\ m_i m_{I'}}} |T^{m_i m_I}_{m_i m_{I'}}(\Omega_1)|^2 .$$

e values of $P_{m_{I'}}$ and δ deduced from ERF-DWBA 1 HF calculations are listed in Table III for the estigated ^{16}O levels. From Fig. 5 and Table it appears that an overall agreement between 'BA calculations and experimental data is found the considered cases, except for the α decay m the 11.09 MeV (4^+) level. For this transition in Fig. 5 the HF prediction is also reported as a dashed curve. The clear disagreement existing between both the theoretical predictions and data, indicates that the reaction mechanism involved in the population of this level cannot be explained in terms of one-step direct α transfer or of a statistical compound nucleus. However (see the dot-dashed curve in Fig. 5), a good fit to the data is obtained by shifting the DWBA curve 12°. A possible explanation for this "anomalous" shift, previously observed,[3] relies on the hypothesis that the primary reaction proceeds through a two-step direct mechanism. This would be also

TABLE III. Angular shifts and magnetic substates populations from EFR-DWBA and HF.

Level	J^π	δ_{exp}[a]	δ_{DWBA}	P_0(%)	P_1(%)	P_2(%)	δ_{HF}	P_0(%)	P_1(%)	P_2(%)
21.8	6^+	10°	11.36°	36.6	29.5	1.6	8.5°	30.8	21.9	9.7
20.9	7^-	11°	9.5°	41.1	27.2	2.2	7.4°	30.0	21.5	10.1
16.3	6^+	14°	13.6°	25.1	33.6	3.7	10.7°	26.3	21.1	10.8
14.5	5^-	16°	15.89°	20.1	37.1	2.9	13.9°	24.9	20.9	11.0
11.09	4^+	5°	17.47°	29.8	32.9	2.1	19.0°	23.1	20.4	11.6
10.35	4^+	19°	17.8°	28.4	33.1	2.6	19.3°	20.4	18.1	10.4

[a] An indetermination of ±0.5 for δ_{exp} is expected from the applied chi-square procedure.

TABLE IV. Decay properties of some ^{16}O levels.

E (MeV)	J^π	$\Gamma_{\text{c.m.}}$ (keV)[a]	P_l[b]	Γ_{α_0}/Γ	Γ_{α_0}/Γ[c]
21.8	6^+	55	0.966	0.67 ± 20%	
20.9	7^-	650 ± 75	0.727	1.13 ± 20%	
16.3	6^+	370 ± 40	0.455	1.07 ± 10%	0.90 ± 0.10
14.5	5^-	560 ± 75	0.583	1.03 ± 10%	0.75 ± 0.15
11.09	4^+	0.28 ± 0.05	0.127	0.31 ± 10%	
10.35	4^+	27 ± 4	0.033	0.86 ± 10%	0.90 ± 0.10

[a] Reference 25.
[b] Reference 26.
[c] Reference 8.

in agreement with the suggestions[4,14] that this level has an important core excited $[^{12}\mathrm{C}_{2^+} \otimes {}^{20}\mathrm{Ne}_{2^+}]$ structure.

B. Decay properties

From the expressions (3) and (2), the ratio Γ_{α_0}/Γ corresponding to the α decay to the ground state of the ^{12}C nucleus can be deduced. The results are summarized in Table IV. This ratio, which is consistent with the results obtained in Ref. 8, for the 10,35, 14.5, 16.3, and 20.9 MeV levels, results close to unity, confirming the α structure of these levels.

A more quantitative information about the structure of these ^{16}O levels is contained in the α-reduced widths which are related, in the approximations discussed in Refs. 15 and 16, to Γ_{α_0} by

$$\Gamma_{\alpha_0} \simeq 2P_l \gamma_{\alpha_0}{}^2 .$$

Figure 6 shows the Γ_{α_0} values, for each level, compared with the respective penetrabilities P_l. The existing proportionality in the case of the *above levels indicates that the γ_{α_0} values are constant.* A similar result was found in Ref. 13 in agreement with the classification of these levels into positive $K^\pi = 0^+$ and $K^\pi = 0^-$ α-rotational bands.

IV. CONCLUSIONS

The present work extends previous evidence on the sensitivity of the particle-particle angular correlation method to the reaction mechanism the first-step process. In particular, we have shown that the EFR-DWBA reproduces the shi and the shape of the experimental data in the cases in which a direct α transfer is predomi antly expected. The previously found[4] small tribution of the compound nucleus mechanism not significantly change the position of maxim and minima of the correlation curves. When more complicated reaction mechanism contri butes, as in the 11.09 MeV (4^+) case, the corr tion data are a more sensitive tool than the s ple angular distribution.[4-6] *Finally an additio* support to the α-structure of some ^{16}O levels derived from the extracted ratios Γ_{α_0}/Γ and reduced widths γ_{α_0}.

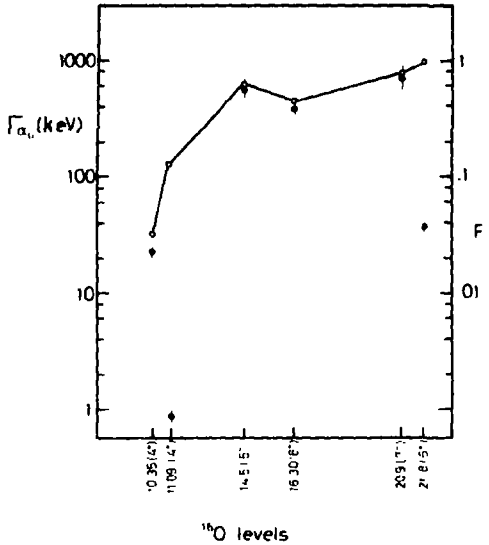

FIG. 6. Γ_{α_0} and P_l values for different ^{16}O α-deca levels.

The authors would like to thank Dr. E. F. I Silveira for the use of the code CORRELA and the enlightening discussions; they would als to thank Mr. Avril for his technical assistan

---

[1] E. F. Da Silveira, Proceedings of the Fourteenth Winter Meeting on Nuclear Physics, Bormio, 1976 (unpublished).

[2] A. Cunsolo, A. Foti, G. Pappalardo, G. Raciti, N. Saunier, and E. F. Da Silveira, Nuovo Cimento 40, 293 (1977).

[3] K. P. Artemov, V. Z. Gold'dberg, I. P. Petrov, V. P. Rudakov, I. N. Serikov, and V. A. Timofeev, Yad. Fiz. 20, 686 (1974) [Sov. J. Nucl. Phys. 20, 368 (1975)].

[4] A. Cunsolo, A. Foti, G. Pappalardo, G. Raciti, N. Saunier, Phys. Rev. C 18, 856 (1978).

[5] F. D. Becchetti, J. Janeke, and C. E. Thorn, N Phys. A305, 313 (1978).

[6] F. D. Becchetti, E. R. Flynn, D. L. Hanson, an Sunier, Nucl. Phys. A305, 293 (1978).

[7] A. E. Litherland and A. J. Fergusson, Can. J. I 39, 788 (1961).

[8] S. J. Sanders, L. M. Martz, and P. D. Parker,

Phys. Soc. Jpn. 44, 648 (1978), Suppl.; Phys. Rev. C 20, 1743 (1979).

[9] A. Cunsolo, A. Foti, G. Immè, G. Pappalardo, G. Raciti, and N. Saunier, Proceedings of the Seventeenth International Winter Meeting on Nuclear Physics, Bormio, 1979 (unpublished).

[10] T. Tamura and K. S. Low, Comput. Phys. Commun. 8, 349 (1974).

[11] W. Hauser and H. Feshbach, Phys. Rev. 87, 366 (1952).

[12] E. F. Da Silveira, private communication.

[13] K. P. Artemov, V. Z. Gold'dberg, I. P. Petrov, V. P. Rudakov, I. N. Serikov, and V. A. Timofeev, Phys. Lett. 37B, 61 (1971).

[14] P. T. Debevec, H. T. Fortune, R. E. Segel, and J. F. Tonn, Phys. Rev. C 9, 245 (1974).

[15] A. M. Lane and R. G. Thomas, Rev. Mod. Phys. 30, 257 (1958).

[16] A. Arima and S. Yoshida, Nucl. Phys. A219, 475 (1974).

[17] U. Strohbusch, G. Bauer, and H. W. Fulbright, Phys. Rev. Lett. 34, 968 (1975).

[18] G. D. Gunn, R. N. Boyd, N. Anantaraman, D. Shapira, J. Tőke, and H. E. Gove, Nucl. Phys. A275, 524 (1977).

[19] G. Bassani, N. Saunier, B. M. Traorè, J. Raynal, A. Foti, and G. Pappalardo, Nucl. Phys. A189, 353 (1972).

[20] D. Wilmore and P. E. Hodgson, Nucl. Phys. 55, 673 (1964).

[21] F. G. Perey, Phys. Rev. 131, 745 (1963).

[22] G. R. Satchler, quoted by P. E. Hodgson, Adv. Phys. 15, 329 (1966).

[23] R. N. Glover and A. D. W. Jones, Phys. Lett. 16, 69 (1965).

[24] G. C. Ball and J. Cerny, Phys. Rev. 177, 1466 (1969).

[25] F. Ajzenberg-Selove, Nucl. Phys. A281, 1 (1977).

[26] N. Baron, R. F. Leonard, and W. N. Stewart, Phys. Rev. C 4, 1159 (1971).

PHYSICAL REVIEW C VOLUME 21, NUMBER 6 JUNE 1980

Total fusion cross section for the ^{9}Be+^{28}Si system

J. S. Eck,* J. R. Leigh, T. R. Ophel, and P. D. Clark
Department of Nuclear Physics, Australian National University, Canberra, A.C.T. 2600, Australia

(Received 7 January 1979)

The total fusion cross sections for the system ^{9}Be + ^{28}Si have been measured in the ^{9}Be bombarding energy range 30–60 MeV by the detection of evaporation residues in a ΔE-E ionization-chamber surface-barrier detector telescope. Although the measured ^{9}Be + ^{28}Si fusion cross sections are similar to those in which a similar compound system is formed by heavy-ion ($A \geq 12$) interaction, the ratio of the measured fusion cross section to the total reaction cross section is much smaller than that observed for other systems and is attributed to the structure of ^{9}Be and the ease with which it breaks up into smaller fragments. This view is consistent with the anomalous ^{9}Be + ^{28}Si elastic scattering results.

[NUCLEAR REACTIONS ^{9}Be+ ^{28}Si fusion E=30–60 MeV, measured fusion product angular distributions and total fusion cross sections, calculated total reaction cross section using optical model, compared fusion cross section with total reaction cross section and with fusion cross section systematics.]

Elastic scattering measurements[1-3] and analysis[4] of the ^{9}Be +^{28}Si system in the ^{9}Be bombarding energy range 14–200 MeV have indicated that the interaction of ^{9}Be with ^{28}Si is different in some aspects from that for both lighter projectiles such as α particles, and heavier projectiles such as ^{12}C and ^{16}O. In particular, the double folding model[5,6] using a realistic nucleon-nucleon interaction, which is successful in describing the elastic α and heavy-ion scattering from such nuclei as ^{28}Si and ^{40}Ca, is not successful in describing the elastic scattering for ^{9}Be +^{28}Si unless the real double folding potential is reduced by a factor ~0.4. Furthermore, the optical model using either the calculated double folding potential or one of Woods-Saxon shape and classical considerations, indicates that the interaction separation for ^{9}Be is larger than for α and heavy-ion interactions with the same target nucleus, and that the imaginary potential necessary to describe ^{9}Be scattering is more diffuse than for α or heavy-ion ($A \geq 12$) scattering.[1-3]

In order to obtain a better understanding of the ^{9}Be +^{28}Si interaction, we have measured the total fusion cross sections for ^{9}Be +^{28}Si in the ^{9}Be bombarding energy range 30–60 MeV. Many fusion studies conducted on similar nuclei in this mass range have investigated possible resonant structures in the fusion cross sections. The goal of the present study, on the other hand, was to investigate the average behavior of the fusion cross section in order to better understand the absorption processes for the ^{9}Be +^{28}Si system. For most systems the fusion cross section is ~90–100% of the total reaction cross section at low energies, while at higher energies the fusion cross section falls well below the total reaction cross section.[7] These effects have been explained in terms of critical angular momenta and critical radii for fusion.[8] In general, whether fusion takes place or not for a particular partial wave depends critically on whether the total potential (nuclear +Coulomb +centrifugal) is attractive at the critical distance for fusion. The double folding potential which is necessary to fit ^{9}Be +^{28}Si scattering must be reduced by a factor ~0.4 from what is calculated using the same realistic nucleon-nucleon interaction that yields a suitable folding potential fit to ^{12}C +^{28}Si and ^{16}O +^{28}Si scattering cross sections, with no reduction in the calculated potential.[4] This reduced attractiveness of the ^{9}Be +^{28}Si potential may have an effect on the fusion cross section for this system.

The fusion cross sections for the ^{9}Be +^{28}Si system were measured using a ΔE-E ionization-chamber surface-barrier detector system[9] by detecting the evaporation residues (the details of the measurements will be reported elsewhere). The target consisted of an 80 μg/cm^2 self-supporting foil of ^{28}Si. The contamination of ^{16}O was less than 3%. The ^{9}Be beam was extracted from a sputter source and accelerated by the Australian National University 14UD tandem accelerator. The detector window consisted of a 30 μg/cm^2 VYNS film[9-11] and was operated using isobutane as the counting gas at a pressure between 14–18 mm of Hg depending on the incident ^{9}Be energy. The data were recorded in an event mode in which each event consisted of a ΔE signal, the E signal fed through an amplifier with high gain, and the same E signal fed through an amplifier with low gain, so as to allow the elasti

© 1980 The American Physical Soci

scattering cross section to be measured simultaneously with the total fusion cross section. The gains of the two E signal amplifiers were scaled with energy so as to maintain the same relative threshold. The high gain energy spectrum and the low oxygen contamination in the target allowed a low energy threshold to be set. There were some events for which there was a ΔE signal and no E signal. These events can arise from either extremely low energy fusion products or from multiple scattering in the detector gas and/or window. The contribution of these events to the fusion cross section is in all cases less than or equal to ~12%, and represents one of the largest sources of error in the reported measurements. Complete angular distributions were measured at 30, 46, and 60 MeV and are shown in Fig. 1. All residues with $Z \geq 14$ were summed to obtain the final yield. Because of the forward angle of e ΔE-E telescope, only ^{28}Si recoils from very .ckward scattered ^{9}Be projectiles, where the astic scattering cross section is negligible, uld enter the detector. At 40, 50, and 55 MeV, i angular distribution around the maximum was easured and the total fusion cross section was timated by the simple scaling relation[10]

$$\sigma_{\mathrm{TOT}}^{\mathrm{FUS}} = 0.345 \frac{d\sigma}{d\theta}(\theta_{\max}),$$

iere (1)

$$\frac{d\sigma^{\mathrm{FUS}}}{d\theta} = 2\pi \sin\theta \frac{d\sigma^{\mathrm{FUS}}}{d\Omega},$$

iere all quantities are in the laboratory system. was found from the three complete angular dis- ibutions that Eq. (1) was accurate to better than 5%. The relative normalization was obtained using a fixed monitor counter, and the absolute cross sections were determined by normalizing to elastic scattering cross sections, which were measured simultaneously with the fusion measurements. Because the elastic scattering is not pure Rutherford for the angles at which the maxima occur, optical model calculations using the parameter sets which fitted the elastic scattering angular distributions were used for normalization. This procedure introduces an error of about 8% in the fusion cross section determination. The error obtained by combining the above errors and the error from counting statistics (typically 2%) leads to an error in the fusion cross section measurements of the order of 20%. This error is considerably larger than those reported in similar experiments, however, because of the lower energy of the recoiling fusion products, and the inability to normalize to Rutherford scattering in the present case; errors of this magnitude are not unexpected and are an accurate estimate of the precision of the reported measurements. The measured fusion cross sections are shown in Fig. 2 as a function of $1/E_{\mathrm{c.m.}}$ The total fusion cross sections decrease in a fairly linear fashion with increasing $1/E_{\mathrm{c.m.}}$ from a value of $\sigma_{\mathrm{TOT}}^{\mathrm{FUS}}$ ~1100 mb at $1/E_{\mathrm{c.m.}} = 0.022$ ($E_L = 60$ MeV) to $\sigma_{\mathrm{TOT}}^{\mathrm{FUS}}$ ~480 mb at $1/E_{\mathrm{c.m.}} = 0.044$ ($E_L = 30$ MeV). There is an indication of possible structure in the fusion cross sections at $1/E_{\mathrm{c.m.}} = 0.033$, but more

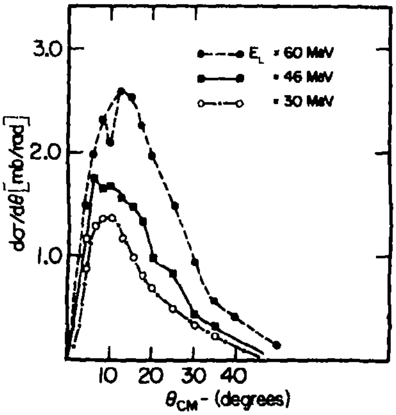

ᴦIG. 1. Angular distributions for the evaporation resiues of the ^{9}Be+ ^{28}Si system at $E_L = 30$, 46, and 60 MeV. ll products with $Z \geq 14$ have been summed. $d\sigma/d\theta$ is in e lab system of coordinates.

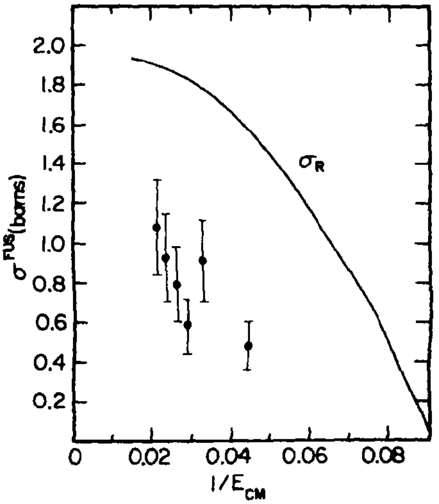

FIG. 2. Total fusion cross sections in barns for the ^{9}Be+ ^{28}Si system as a function of $1/E_{\mathrm{c.m.}}$ (MeV^{-1}). The solid curve is the total reaction cross section calculated using the optical model parameters which fitted the elastic scattering angular distributions (see text).

measurements would be required before any conclusions could be drawn regarding this point. They are similar in shape but smaller in magnitude than those observed for other systems in which a similar compound system is formed. The total reaction cross section, which is calculated from the optical model with Woods-Saxon form factor using the parameter sets which fitted the elastic scattering at 45 and 60 MeV (i.e., $U = 10.0$ MeV, $r_0 = 1.368$, $a_0 = 0.6067$, $W = 23.4$, $r_W = 1.277$, $a_W = 0.6090$, and $r_c = 1.35$; see Ref. 2 for details) is also shown. The calculated reaction cross sections agree within 10% to those obtained from the folding potential fits and those calculated using the energy independent potential for ^{9}Be +^{28}Si scattering of Balzer *et al.*[1] In all cases in which the optical model gives reasonable fits to the elastic scattering cross sections, the calculated reaction cross sections are insensitive to the particular parametrization utilized.

Fitting the relationship $\sigma_{\text{FUS}} = R_{\text{FUS}}^2(1 - V_B/E_{\text{c.m.}})$ to the cross section data of Fig. 2 yields values of $V_B = 22 \pm 4$ MeV and $r_{\text{FUS}} = 1.5 \pm 0.2$, where $R_{\text{FUS}} = r_{\text{FUS}}(9^{1/3} + 28^{1/3})$. The reaction radius R_R is related to the fusion radius by

$$\frac{\sigma_R}{\sigma_{\text{FUS}}} = \frac{R_R^2}{R_{\text{FUS}}^2} = \frac{r_R^2}{r_{\text{FUS}}^2}\,.$$

Since

$$\sigma_R/\sigma_{\text{FUS}} \approx 2.5-3$$

for the energy range investigated here, $r_R = 2.4$–2.6. The fusion radius parameter r_F, the fusion barrier V_B, and the saturation value of the fusion cross section are similar to what one would expect from fusion systematics. The total reaction cross section, however, is much greater than the measured fusion cross sections even at the lowest energies where systematics[11] based on studies of such systems as ^{12}C +^{27}Al, ^{12}C +^{24}Mg, ^{16}O +^{27}Al, etc., would predict that $\sigma_R \simeq \sigma_{\text{FUS}}$ up to values of $1/E_{\text{c.m}} \sim 0.02$. In order for two nuclei to fuse, they must penetrate to a critical radius,[8] which for the energy range considered here is $R_{cr} = r_0(A_T^{1/3} + A_P^{1/3})$, where $r_0 \simeq 1.4$. In the case of ^{9}Be +^{28}Si, the ^{9}Be has a high probability of breaking up into two α particles and a neutron, which gives rise to a large reaction cross section without particularly affecting the fusion cross sections. This picture is consistent with the elastic scattering results obtained at 45 and 60 MeV bombarding energy shown in Fig. 3, where σ/σ_C is plotted as a function of d,[12] where

$$d = \frac{D}{A_T^{1/3} + A_P^{1/3}}$$

and

$$D = \frac{Z_T Z_P e^2}{2E_{\text{c.m}}}\left(1 + \frac{1}{\sin\theta_{\text{c.m.}}}\right).$$

Also shown for comparison are heavy-ion +^{28}Si scattering elastic cross sections[3] at various energies and the ^{28}Si +^{208}Pb elastic scattering cross section measured at $E_{\text{c.m.}} = 145$ MeV. In order to avoid confusion, the cross section data for these latter cases are shown by solid lines, as they all lie on the same curve (CNO curve) for the case of ^{12}C, ^{14}N, ^{16}O, and ^{18}O projectiles at the energies reported here. For large distances of closest approach (i.e., large d) the ^{28}Si +^{208}Pb cross section falls below the CNO curve, but then merges with it again at smaller values of d. The difference at large d in the ^{28}Si +^{208}Pb cross section is due to a strong reduction in the elastic scattering cross section due to the strong long-range Coulomb excitation of the 1.78 MeV state in ^{28}Si. The ^{9}Be +^{28}Si elastic scattering cross sections at 45 and 60 MeV lie considerably lower than both the CNO curve and the ^{28}Si +^{208}Pb curve at large d. This discrepancy cannot be explained by Coulomb excitation, but is most likely due to the fact that ^{9}Be is loosely bound and has a large spatial extent; thereby direct reactions cause the ^{9}Be to break up even at large separation distances.[13] Indeed, the reaction radius parameter calculated above, $r_R = 2.4$–2.6, is consistent with what one would estimate from inspection of Fig.

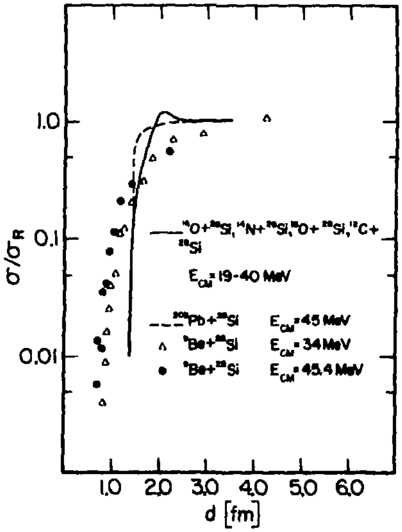

FIG. 3. Plot of σ/σ_R as a function of the reduced distance of closest approach, d, for ^{9}Be + ^{28}Si at $E_{^9\text{Be}} = 6$ MeV (solid dots), and at $E_{^9\text{Be}} = 45$ MeV (open triangle The dashed curve is σ/σ_R for ^{208}Pb + ^{28}Si at $E_{^{28}\text{Si}} = 165$ MeV, and the solid curve is σ/σ_R for assorted heavy ions ($A \geq 12$) incident on ^{28}Si targets plotted as a funct of d.

3. (i.e., for ^{9}Be + ^{28}Si scattering at $r_R = d \approx 2.5$, reactions are taking place causing a decrease in σ/σ_R from 1). For the case of ^{12}C + ^{28}Si and ^{16}O + ^{28}Si, the much stronger binding of ^{12}C and ^{16}O prevents any substantial breakup, and the fall from Rutherford does not occur until the nuclei are within the critical distance for fusion. It is postulated, therefore, that one of the essential differences between the heavy-ion ($A \geq 12$) scattering and the ^{9}Be scattering from ^{28}Si is due to the fact that the main reaction channel for the heavy-ion interactions is compound nucleus formation (i.e., fusion) which is well localized, while for ^{9}Be interactions it is the direct breakup of the projectile by the strong nuclear and Coulomb fields at large separation distances before fusion can occur. The fact that the calculated double folding potential for ^{9}Be + ^{28}Si must be reduced by a factor of 0.4 in order to fit the measured cross sections may be related to a strong coupling between elastic and breakup channels.[4]

In summary, the fusion cross sections for ^{9}Be + ^{28}Si have been measured in the range $E(^9\mathrm{Be}) = 30-60$ MeV. The fusion cross sections are considerably lower than the total reaction cross section over the whole energy range, while for systems which have similar compound nuclei such as ^{18}O + ^{24}Mg, ^{16}O + ^{27}Al, ^{12}C + ^{24}Mg, ^{12}C + ^{27}Al, $\sigma_{\mathrm{FUS}} \approx \sigma_R$ at the lowest energies. These differences can be qualitatively reconciled with each other and with the anomalous elastic scattering results for ^{9}Be + ^{28}Si by assuming that there is a large possibility for ^{9}Be breakup at large ^{9}Be and ^{28}Si separation distances. The ^{9}Be + ^{28}Si system is an interesting one to study, as apparently the nuclear structure of ^{9}Be is important in determining the details of the fusion reaction and elastic scattering cross sections, even at low energies.

This work was supported in part by the U. S. National Science Foundation under the U. S.-Australia Cooperative Science Program.

---

[1] R. Balzer, M. Hugi, B. Kamys, J. Lang, R. Miller, E. Ungricht, and J. Untermahrer, Nucl. Phys. A293, 518 (1977).

[2] J. S. Eck, T. R. Ophel, P. D. Clark, and D. C. Weisser, Nucl. Phys. A334, 519 (1980).

[3] M. S. Zisman, J. G. Cramer, R. M. DeVries, D. A. Goldberg, and J. W. Watson, *1977–1978 Nuclear Science Annual Report of the Lawrence Berkeley Laboratory*, edited by L. S. Schroeder, R. A. Gough, and M. J. Nurmia (Lawrence Berkeley Laboratory, Berkeley, 1978), p. 72.

[4] G. R. Satchler, Phys. Lett. 83B, 284 (1979).

[5] G. R. Satchler and W. G. Love, Phys. Rep. (to be published).

[6] G. R. Satchler and W. G. Love, Phys. Lett. 65B, 415 (1976).

[7] R. Bass, Nucl. Phys. A231, 45 (1974).

[8] D. Glas and U. Mosel, Nucl. Phys. A237, 429 (1975).

[9] M. M. Fowler and R. C. Jared, Nucl. Instrum. Methods 124, 341 (1975).

[10] G. F. Geesaman, C. N. Davids, W. Henning, D. G. Kovar, K. E. Rehm, J. P. Schiffer, S. L. Tabor, and F. W. Prosser, Phys. Rev. C 18, 284 (1978).

[11] D. G. Kovar, G. F. Geesaman, T. H. Braid, Y. Eisen, W. Henning, T. R. Ophel, M. Paul, K. E. Rehm, S. J. Sanders, P. Sperr, J. P. Schiffer, S. L. Tabor, S. Vigdor, B. Zeidman, and F. W. Prossen, Phys. Rev. C 20, 2147 (1979).

[12] P. R. Christensen, V. I. Manko, F. D. Becchetti, and R. J. Nickles, Nucl. Phys. A207, 33 (1973).

[13] J. Untermahrer, J. Lang, and R. Muller, Phys. Rev. Lett. 40, 1077 (1978).

PHYSICAL REVIEW C VOLUME 21, NUMBER 6 JUNE 1980

Direct transfer reaction to discrete and continuum states

M. C. Mermaz
DPh-N/BE, CEN Saclay, BP 2, 91190 Gif-sur-Yvette, France

(Received 8 October 1979)

A parametrization based on the distorted-wave Born-approximation (DWBA) formalism, using the diffractional model, is given in order to fit angular distributions and continuum energy spectra of direct transfer reactions induced by heavy ions populating continuum states at incident energy well above the Coulomb barrier. Experimental data analysis of two-proton and alpha-transfer reactions on $1f$-$2p$ shell nuclei are successful at low incident energies. On the other hand, at high incident energy, alpha stripping induced by ^{16}O beam on ^{208}Pb cannot be described by this direct surface reaction model. It turns out that fragmentation is the most likely process.

[NUCLEAR REACTIONS DWBA and diffractional model applied to direct reactions induced by heavy ions—continuum states. Analysis of ^{54}Fe(^{16}O, ^{12}C)^{58}Ni, ^{48}Ca(^{16}O, ^{14}C)^{50}Ti, ^{64}Ni(^{16}O, ^{14}C)^{66}Zn, ^{76}Ge(^{16}O, ^{14}C)^{78}Se, ^{208}Pb(^{16}O, ^{15}N)^{209}Bi, ^{208}Pb(^{16}O, ^{12}C)^{212}Po, and ^{208}Pb(^{16}O, ^{11}B)^{213}At reactions.]

I. INTRODUCTION

The populations of the first few discrete levels in heavy ion transfer reactions are rather well described by the distorted wave method formalisms such as the distorted wave Born approximation (DWBA) and/or the coupled channel Born approximation (CCBA) for two-step processes involving core excitation of target and residual nucleus and/or projectile-ejectile system.[1]

Furthermore, for heavy ion reactions occurring well above the Coulomb barrier, continuum states are also strongly populated and some authors, using the previous formalism used for discrete transitions, but with large simplifications, have already succeeded in explaining the energy spectra as well as the angular distributions of the continuum states.[2]

We want to present here a similar but more simple model assuming that the reactions proceed mainly by one-step processes. The DWBA transition matrix element is calculated on the basis of the diffractional model of Austern and Blair.[3] The DWBA parametrization is thus extremely simple and allows very fast computation. The second ingredient of the calculations for the population of the continuum states is the level density of the residual nucleus. This level density can be assumed to be similar to the usual statistical level density.

The main interest of this new formalism is to allow us to distinguish for a surface reaction between a quasielastic transfer process and a process where a large number of degrees of freedom of the projectile and target system are severely relaxed as occurs, for instance, in deep inelastic collisions.[4] In the distorted wave method formalism, these deep inelastic collisions would be treated as multistep processes.

Various examples of analysis with this model for several nucleon transfer reactions induced by ^{16}O on various targets at different incident energies will be presented in order to illustrate the previous point of view.

II. DIFFRACTIONAL MODEL

For a zero spin system, the DWBA cross section for a given transfer angular momentum can be written as

$$\sigma(\theta,E_f,J=L)=\frac{\mu_i\mu_f}{(2\pi\hbar^2)^2}\frac{k_f}{k_i}\sum_M|T_L^M|^2 \tag{1}$$

with

$$T_L^M=\tau_L\frac{4\pi}{k_ik_f}\sum_{l,l'}i^{l-l'}\beta_{ll'}e^{i(\sigma_l^i+\sigma_{l'}^f)}(2l'+1)^{1/2}\times Y_{l'}^{-M}(\theta,0)\langle l'L-MM|l0\rangle\langle l'L00|l0\rangle,$$

where the indices i and f refer, respectively, to the initial and final channels, μ is the reduced mass and k the wave number, and l and l' are, respectively, the partial wave angular momentum in the entrance and exit channels. The value τ_L is the "transfer parameter." The σ_l are the Coulomb phase shift

$$\sigma_l=\arg\Gamma(l+1+in), \tag{2}$$

where n is the Sommerfeld parameter in entrance or exit channel,

$$n=\frac{zZe^2}{\hbar v}.$$

The two brackets are the usual Clebsch-Gordan coefficients.

In the no-recoil approximation and for quasi-

© 1980 The American Physical Soc

elastic transfers, the reduced matrix elements $\beta_{ll'}$ of Eq. (1) are proportional to the product of the derivatives of the reflection coefficient η_l, respectively, in the entrance and exit channels:

$$\beta_{ll'} = \frac{1}{2i}\left\{E_i E_f \frac{\partial\eta_l}{\partial l}\frac{\partial\eta_{l'}}{\partial l'}\right\}^{1/2}, \tag{3}$$

where E_i and E_f are, respectively, the center of mass energy in the entrance and exit channels. This formula is just an extension of the Austern-Blair theory for inelastic excitation.[3] As expected, the $\beta_{ll'}$ are then peaked at the nuclear surface.

The Frahn and Venter semiclassical parametrization[5] is used to describe the coefficient of reflection η_l in the *strong absorption model*:

$$\eta_l = \{1 + \exp[(l_g - l)/\Delta]\}^{-1}, \tag{4}$$

where the grazing wave l_g and the width Δ are given by the following semiclassical relationships:

$$l_g + kR\left[1 - \frac{2n}{kR}\right]^{1/2}, \tag{5}$$

$$\Delta = kd\left[1 - \frac{n}{kR}\right]\left[1 - \frac{2n}{kR}\right]^{-1/2}, \tag{6}$$

where n is the Sommerfeld parameter and k the wave number. The values R and d are, respectively, the radius and the diffuseness parameters. These parameters are related to those determined from phase shift analysis of the elastic scattering in the entrance and exit channels. The grazing wave l_g and width Δ are obviously different in the entrance and exit channels.

The parametrization of the DWBA cross sections $\sigma(\theta, E_f, J = L)$ of formula (1) can be drastically improved by modifying the Coulomb phase shifts σ_l^i and $\sigma_{l'}^f$. Effectively, the two parameters R and d which allow the calculations of the $\beta_{ll'}$ through formulas (3)–(6) do not give the possibility of reproducing the shape of the transfer reaction angular distributions. These parameters R and d have to be strongly modified in order to focus the calculated angular distribution to the forward angles where the experimental cross section is peaked. This procedure is similar to the one which consists of modifying the optical model parameters in the entrance and exit channels in the usual DWBA analysis. Even with a strong modification of the radius R, it is, in most of the cases, impossible to obtain the correct shape of the angular distributions. Thus, in order to produce the necessary shift of the calculated angular distribution to the forward angle, we have introduced a nuclear rainbow in the pure Coulomb deflection function for a charged point:

$$\theta_l = 2\arctan\frac{n}{l}. \tag{7}$$

The new phase shift $\hat{\sigma}_l^{i,f}$, used in formula (1), is then parametrized as

$$\hat{\sigma}_l = \sigma_l\left[1 + \exp\left(\frac{l - l_g}{\Delta}\right)\right]^{-1}. \tag{8}$$

The nuclear plus Coulomb deflection function is now

$$\begin{aligned}\hat{\theta}_l &= 2\frac{\partial\hat{\sigma}_l}{\partial l}\\ &= 2\arctan\frac{n}{l} - 2\alpha\frac{\partial}{\partial l}\left[1 + \exp\left(\frac{l - lg}{\Delta}\right)\right]^{-1}.\end{aligned} \tag{9}$$

The value of the nuclear rainbow angle is then

$$\theta_{l=l_g} = 2\arctan\frac{n}{l_g} - \frac{\alpha}{2\Delta}. \tag{10}$$

This is illustrated in Fig. 1 for the elastic scattering of ^{16}O on ^{54}Fe at 46 MeV incident energy. The quantity $\Delta\theta$ written on Fig. 1 is just $\Delta\theta = -\alpha/2\Delta$. The local minimum (nuclear rainbow) around the grazing wave $l_g = 17$ produces the necessary shift to forward angle of the calculated cross section with formula (1). The cross section is then depending only on three parameters: the radius $R = r_0(A_1^{1/3} + A_2^{1/3})$, the diffusivity d, and the phase angle $\Delta\theta$. The radius r_0 is determined from the elastic scattering—for instance, using the quarter point method of J. S. Blair[6]—and is usually 1.55 fm.

The DWBA cross section $\sigma(\theta, E_f, J = L)$ is maximum for an $L = 0$ transfer when the grazing waves are equal in the entrance and exit channels. This allows us to determine the Q value of the reaction for which this condition is fulfilled by eliminating the grazing wave l_g between the center of mass energy equations of the entrance and exit channels:

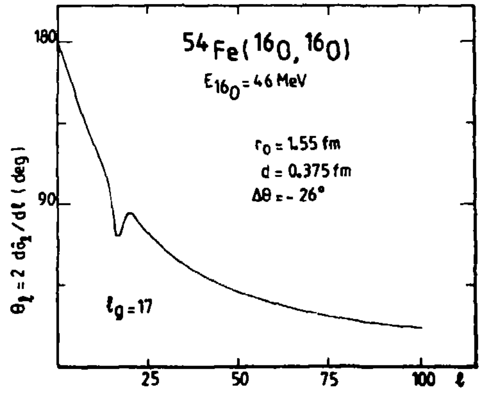

FIG. 1. Deflection function of ^{16}O elastic scattering on ^{54}Fe target [see formula (9) in the text]; $\Delta\theta = -\alpha/2\Delta = -26°$.

$$E_i = V_i^{\mathrm{Coul}} + \frac{\hbar^2}{2\mu_i R_i^2} l_g(l_g+1)$$

and (11)

$$E_i + Q = V_f^{\mathrm{Coul}} + \frac{\hbar^2}{2\mu_f R_f^2} l_g(l_g+1).$$

The cross section $\sigma(\theta, E_f, J=0)$ is then maximum for the following Q value:

$$Q_{\max} = -(E_i - V_f^{\mathrm{Coul}} + \frac{\mu_i R_i^2}{\mu_f R_f^2}(E_i - V_i^{\mathrm{Coul}}). \quad (12)$$

This quantity is very different from the usual optimum Q value quoted in the literature.[7] The behavior of the cross sections following the excitation energy in the final nucleus is plotted on Fig. 2 for the ^{54}Fe(^{16}O, ^{12}C) ^{58}Ni four nucleons stripping reaction and for three different values of transfer angular momentum L. The calculations were performed at 56 MeV ^{16}O incident energy. As expected, the cross sections decrease as the excitation energy increases.

III. POPULATION OF THE CONTINUUM STATES

For the quasielastic transfer reactions to the continuum states, the double differential cross section in the center of mass system is given by

$$\frac{d^2\sigma}{d\Omega dE_f} = \sum_J \rho(J, E^*)\sigma(\theta, E_f, J), \quad (13)$$

where $\rho(J, E^*)$ is the level density including the σ^2 spin cutoff term of the residual nucleus:

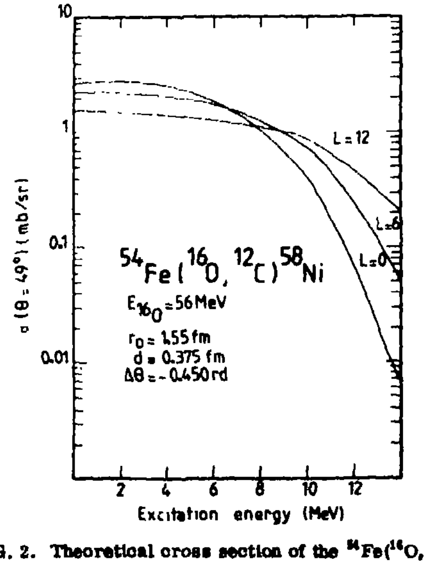

FIG. 2. Theoretical cross section of the ^{54}Fe(^{16}O, ^{12}C)-^{58}Ni reaction at the grazing angle for various L angular momentum transfer at 56 MeV ^{16}O incident energy.

$$\rho(J, E^*) = (2J+1)e^{-J(J+1)/2\sigma^2}\rho(0, E^*), \quad (14)$$

where $\rho(0, E^*)$ is the density of spin 0 level given, for instance, by the relationships of Gilbert and Cameron[8]:

$$\rho(0, E^*) = \frac{\exp(2\sqrt{aU})}{24\sqrt{2}\sigma^3} \frac{1}{a^{1/4}U^{5/4}}. \quad (15)$$

The various parameters involved in formulas (14) and (15) can be calculated, for instance, by using the table of shell correction energies and pairing energies given in Ref. 8. The quantity U is the excitation energy after subtraction of the proton and neutron pairing energies and a is the level density parameter which is roughly equal to $A/8$ outside the magic nucleus regions where strong deviations are observed.[9] Let us note that the spin law distribution [formula (14)] is bell shaped and that the most abundant spin at a given excitation energy is $J = \sigma$.

For the sake of simplicity, in our experimental data analysis, a more simple form was preferred for the spin zero level density[9]:

$$\rho(0, E) = \rho_0 \exp(E^*/T), \quad (16)$$

where ρ_0 is a constant and T is the nuclear temperature.

In formula (14) we can consider that the spin cutoff is equal to

$$\sigma^2 = \frac{\mathscr{I}T}{\hbar^2}, \quad (17)$$

where $\mathscr{I}$ is the effictive moment of inertia of the nucleus. It is well known that this moment of inertia increases with the excitation energy up to the rigid body value.

Writing formula (13), we have implicitly assumed that the excitation energy of the ejectile can be neglected and that the fragmentation of the projectile does not compete seriously with the transfer mechanism leading to continuum states of the residual nucleus. Furthermore, it is also assumed that the one-step process is the dominant mechanism. Multistep process calculations will lead to description of deep inelastic phenomena and are not presently taken into account.

The double differential cross section $d^2\sigma/d\Omega dE_f$ can be rewritten also as

$$\frac{d^2\sigma}{d\Omega dE_f} = \rho(0, E^*) \sum_J (2J+1)e^{-J(J+1)/2\sigma^2}\sigma(E_f, J). \quad (18)$$

The numerical calculations show that the summation over J is a function exponentially decreasing with the excitation energy while the level density $\rho(0, E^*)$ is exponentially increasing but most of the time with a lower rapidity. That explains the bell-shaped energy spectrum of the heavy ion reactions. The rapidity of the exponential decrease of the summation over J is inversely proportional to the value of the diffusivity parameter of the nuclei.

From formula (18) it can be seen that as the excitation energy increases, more higher spin states can be populated. Nevertheless, there is a window spin due to the spin cutoff term. Furthermore, $\sigma(E_f,J)$ decreases as the excitation energy increases (see, for instance, Fig. 2).

From the behavior of the level density $\rho(J,E^*)$ with spin and excitation energy and from the behavior of the DWBA reduced cross section, formula (1), with respect to the Q maximum value, it turns out that in few nucleon stripping reactions, bell-shaped energy spectra are obtained which correspond to population of high spin states for high excitation energy in the final nucleus. Large transfers of nucleons are inhibited due to the Q value mismatch with respect to the Q maximum, formula (12). Furthermore, for these last reactions, the ground states are not populated, because high angular momentum transfers L are required to assure the balance between the entrance channel- and exit channel-grazing waves. The weak point of this transfer reaction model are the transfer parameters τ_L which presently cannot be theoretically calculated. For fitting purposes, τ_L has to be assumed constant and independent of the L transfer for the overall range of excitation energy. This quantity τ_L, in average, is a very small number since we are populating only a given class of states: In fact, the states which have configurations made with the transferred nucleons coupled to the target nucleus on its ground state. We can hope that this class of states has, at high excitation energy, the same kind of spectroscopic factors in average and that their level density is similar to the statistical level density.

IV. RESULTS AND DISCUSSIONS

In all the present analyses the diffractional model parameters—radius $R(r_0)$, diffusivity d, and phase angle $\Delta\theta$—have been fixed by analyzing the experimental angular distributions of the heavy ion transfer reactions. The radius r_0 was kept constant to 1.55 fm, the usual value for heavy ion elastic scattering.[10] These parameters are the same in the entrance and exit channels.

We shall present first the analysis of the angular distributions of the discrete states of various energy spectra. It is important to show how powerful and accurate is the diffractional model for well known states. This analysis on discrete states allows us to determine the diffractional model parameters used later on in the analysis of the continuum spectra. The free parameters for this second analysis being ρ_0, σ^2, and T in formula (13).

A small computer code named FAST has been written to calculate the reduced differential cross sections for different L transfer and final energies which are stored on magnetic disc and used in a second step by an automatic search code FITS to determine the level density parameters ρ_0, T, and σ^2 which allow us to reproduce the experimental shape of excitation energy spectra.

A. The four-nucleon stripping reaction: ^{54}Fe(^{16}O,^{12}C)^{58}Ni

For the reaction ^{54}Fe(^{16}O,^{12}O)^{58}Ni the angular distributions for the discrete levels and the energy spectrum have been measured, respectively, at 46 and 56 MeV ^{16}O incident energy.[11] All the angular distributions have the same bell-shaped pattern independently of the final level reached by the transfer reaction. In Fig. 3 the 1.45 MeV 2^+ state angular distribution of the ^{58}Ni final nucleus is presented. This fit has been obtained with formula (1). The diffractional parameters are given in Table I: family II. The phase angle was adjusted in order to reproduce the experimental points: $\Delta\theta = -0.450$ rad (or $-26°$). The diffusivity parameter d is responsible for the width of the experimental angular distribution. The

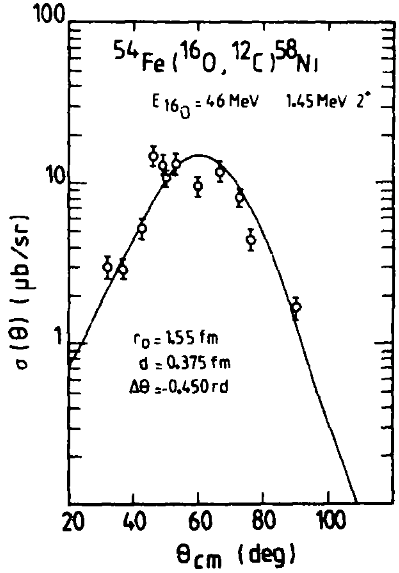

FIG. 3. Angular distribution of the ^{54}Fe(^{16}O,^{12}C)^{58}Ni reaction of the first 2^+ level of ^{58}Ni measured at 46 MeV ^{16}O incident energy. The theoretical curve has been obtained with the diffractional model [formula (1)].

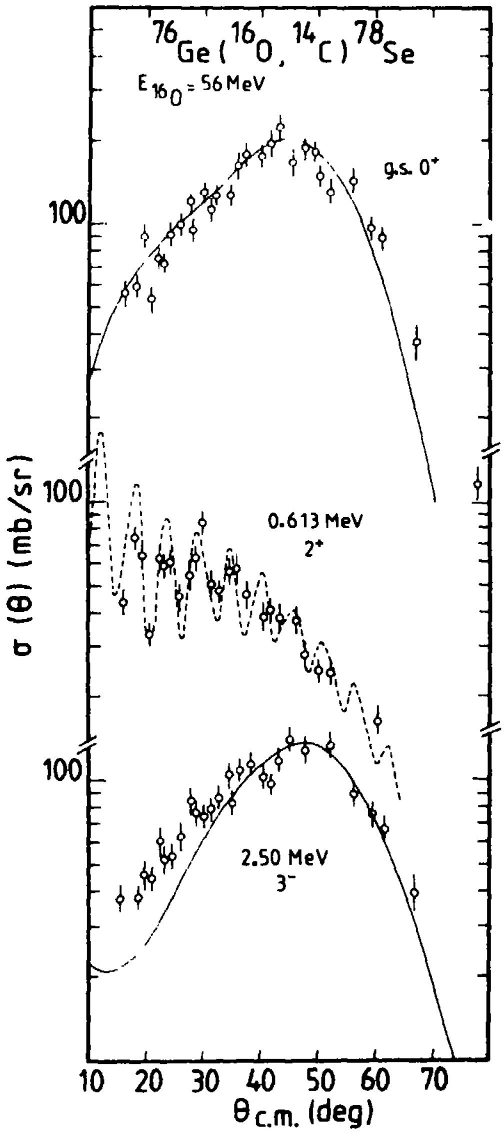

FIG. 6. Angular distributions of the ^{76}Ge(^{16}O, ^{14}C)^{78}Se reaction for the first few excited levels of ^{78}Se. The curves are obtained from the diffractional model (see text).

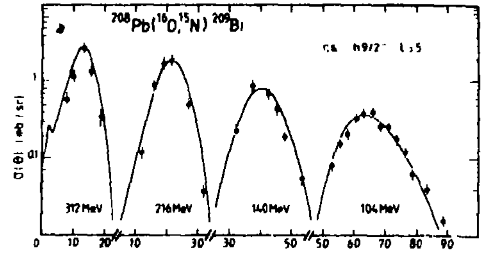

FIG. 7. Ground state angular distributions of the ^{218}Pb(^{16}O, ^{15}N)^{209}Bi one-proton transfer reaction measured at several ^{16}O incident energies.

$$\chi^2 = \frac{1}{N} \sum_{i=1} (\sigma^i_{\text{exp}} - \sigma^i_{\text{theo}})^2 ,$$

where N is the number of experimental points which define the average shape of the energy spectrum. The χ^2 is given in arbitrary units.

The quality of both fits is presently similar. The level density parameters T, $\mathcal{J}/\hbar^2$, or σ^2 extracted from this automatic search analysis are given in Table III. The level densities are not determined in all these analyses in absolute values since the transfer parameter τ_L^2 is unknown and assumed constant and independent of the L transfer. There is a certain ambiguity between the temperature T and the spin cutoff term σ^2 or the moment of inertia $\mathcal{J}(\sigma^2 = \mathcal{J}T/\hbar^2)$. Equally good fits can be obtained with different combinations of these two parameters. In Table III, the quantity labeled T_0 is the statistical level density temperature calculated at the centroid energy of the spectrum according to the systematics of Gilbert and Cameron[8] and also of Baba,[10] the quantity $\mathcal{J}_0$ is the rigid body moment of inertia for a spherical nucleus, and $\sigma_0{}^2$ is the spin cutoff parameter for the statistical level density according to the systematics of Gilbert and Cameron.[8] Since the temperature T determined in the present analysis is higher than the one of the statistical level density, the moment of inertia $\mathcal{J}$ is then much lower than the rigid body value $\mathcal{J}_0$, which is any way an upper limit. On the other hand, the quantity σ^2 is of the same order of magnitude as the σ_0^2 of Gilbert and Cameron[8] (statistical level density).

TABLE II. Transfer parameter $\tau_L{}^2$ for ^{208}Pb(^{16}O, ^{15}N)^{209}Bi ($h_{9/2^-}$, g.s.).

Incident energy (MeV)	104	140	216.6	312
$\tau_L{}^2 = 5$	0.114	0.0909	0.0562	0.0375

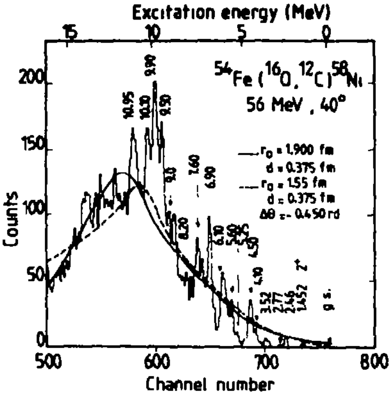

FIG. 8. Energy spectrum of the ^{54}Fe(^{16}O, ^{12}C)^{58}Ni reaction measured at 56 MeV ^{16}O incident energy and 40° lab. The two curves were obtained with the diffractional model for two different sets of parameters. The dashed curve corresponds to modified Coulomb phase shifts [see formula (9)].

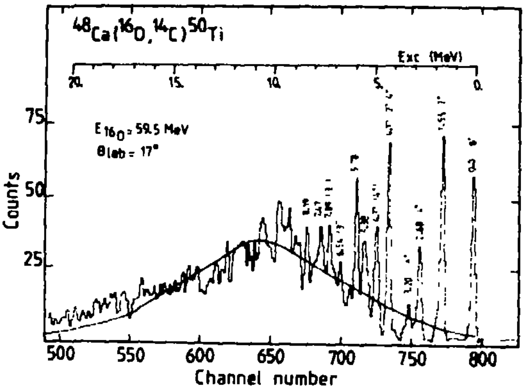

FIG. 9. Energy spectrum of the ^{48}Ca(^{16}O, ^{14}C)^{50}Ti reaction measured at 17° lab and 59.5 MeV ^{16}O incident energy. The solid line is a result of a best fit using the diffractional model.

Figure 9 presents the ^{14}C energy spectrum of the ^{48}Ca(^{16}O, ^{14}C)^{50}Ti two-proton transfer reaction measured at 59.5 MeV excitation energy and at 17° laboratory angle.[13] The fit is excellent and the corresponding parameters of the level density are given in Table III. The drawn curve has a $\chi^2 = 40$. In this analysis the temperature is also higher than the one of the statistical level density.

A similar example is given for the (^{16}O, ^{14}C) two-proton transfer reaction on ^{76}Ge target nucleus measured at 56 MeV ^{16}O incident energy and 20° laboratory angle.[14] The best fit, solid curve of Fig. 10, corresponds to the use of pure Coulomb phase shift in the DWBA calculations, family II of Table I. The dashed curve, on the other hand, corresponds to family I for the diffractional model parameters ($\chi^2 = 262$). The nuclear phase shift is then taken into account. As in the previous analysis, the temperature T is much higher than the statistical one T_0.

The ^{12}C and ^{11}B spectra[17] obtained by bombarding the ^{208}Pb target with an 140 MeV ^{16}O beam were analyzed in the same vein. Figure 11 presents the ^{12}C and ^{11}B spectra measured at the grazing angle: 40° lab. The diffractional model para-

TABLE III. Level density parameters.

Nucleus	T (MeV)	$J/\hbar^2$ (MeV^{-1})	σ^2	Spectrum centroid energy (MeV)	T_0 (MeV)	$\mathcal{J}_0$ (MeV^{-1})	σ_0^2	χ^2 a.u.	D.M. family
^{58}Ni	1.752	5.50	9.64	11	1.253	11.90	9.06	316	II
	1.766	5.50	9.72					72	I
	1.831	6.50	11.90					74	I
^{50}Ti	2.782	4.10	11.41	9	0.929	9.29	7.56	64	I
	3.171	5.50	17.44					40	I
^{78}Se	1.434	6.50	9.32	7	0.663	19.50	11.50	263	I
	1.612	8.50	13.70					262	I
	1.356	8.50	11.53					121	II
^{212}Po (140 MeV)	4.132	15.96	65.94	25	1.531	103.26	62.85	504	II
^{212}Po (312 MeV)	3.062	10.34	31.66					636	II
	8.788	1.92	16.87					59	II
^{213}At (140 MeV)	3.126	15.0	44.89	25	1.559	104.07	67.67	812	II
	3.320	20.0	66.4					483	II
	3.320	23.80	79.02					361	II

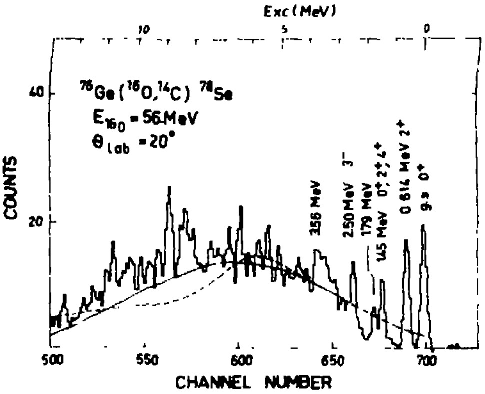

FIG. 10. Experimental energy spectrum of the ^{76}Ge(^{16}O, ^{14}C)^{78}Se reaction measured at 56 MeV ^{16}O incident energy and 20° lab. The solid curve corresponds to pure Coulomb phase shift in the diffractional model while for the dashed curve nuclear phase shifts were taken into account.

meters are those of family II of Table I. They were obtained by analyzing the one-proton transfer reactions on the ^{208}Pb target for highly excited states of ^{209}Bi.[17] The corresponding level density parameters are given in Table III. The drawn curves are for a χ^2 of 504 for the ^{12}C case and for a χ^2 of 483 for the ^{11}B case. The temperature T is still too high by a factor of 2 with respect to the statistical one T_0. On the other hand, the spin cutoff parameter σ^2 is very close to the statistical limit σ_0^2 as in the previous examples.

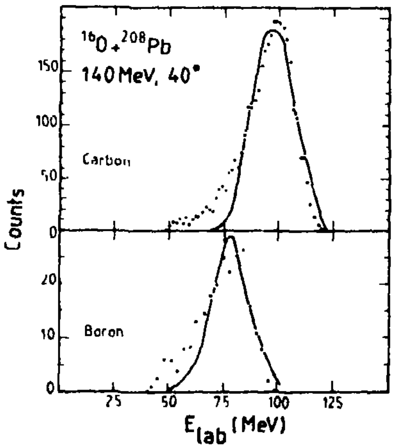

FIG. 11. Experimental energy spectra of the (^{16}O, ^{12}C) and (^{16}O, ^{11}B) reactions on ^{208}Pb target nucleus measured at 140 MeV ^{16}O incident energy. The solid curve is a best fit obtained from the diffractional model.

The spectra obtained at high incident energy, namely 312 MeV of ^{16}O, cannot be fitted with reasonable parameters. The temperature T and spin cutoff term σ^2 are, respectively, 8.8 MeV and 17. The best fit obtained with these parameters is presented in Fig. 12. It has been shown that at 20 MeV/nucleon the reaction mechanism is not any more of a quasielastic type but more likely a fragmentation process.[17] It is probably for this reason that we have obtained the level density parameters corresponding to a very light nucleus. Lukyanov and Titov[19] had established that the integrated cross section on energy for a fragmentation process is roughly proportional to the level density of the ejectile multiplied by a dynamical factor taking into account the Q matching of the fragmentation reaction.

V. SUMMARY

It has turned out that the diffractional model, using modified Coulomb phase shift, is very successful in accounting for the transfer reaction angular distributions of discrete levels. As expected, for levels populated mainly by two-step processes the diffusivity parameter has to be much smaller than in case of a one-step process and the phase angle has to be also much larger, which means that the deflection function is more peaked at forward angles.

As far as continuum states are concerned, very reasonable fits can be obtained; nevertheless, a serious discrepancy is present concerning the level density temperature. The temperatures found in this analysis are different from the statistical one but are of the same order of magnitude than the ones given by a Volkov plot for a $Q_{g.s.-g.s.}$ systematics.[18] On the other hand, the spin cutoff values σ^2 agree rather well with the systematics of Gilbert and Cameron for statistical level densities.[8]

The complete failure of the model at very high ^{16}O incident energy on ^{208}Pb target is due to the

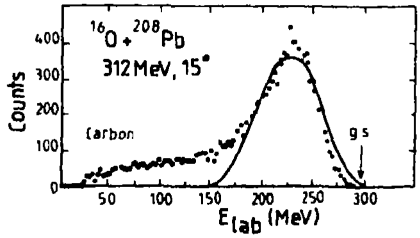

FIG. 12. Experimental energy spectrum of the (^{16}O, ^{12}C) reaction on ^{208}Pb target nucleus measured at 312 MeV ^{16}O incident energy. The solid curve is a best fit using the diffractional model.

fact that we are dealing with fragmentation processes of the projectile instead of pure direct transfer reaction.

The fact that some spectra can be fitted up to the Coulomb barrier of the ejectile is in favor of the wide excitation energy range of quasielastic transfer reactions. On the other hand, it would be impossible, with this one-step model of direct surface reaction, to reproduce the second bump observed in some spectrum in the vicinity of the Coulomb barrier of the ejectile.[4] This second bump corresponds effectively to deep inelastic collisions or, in other words, to multistep processes.

Sincere thanks are due to Dr. B. T. Kim and Dr. J. Raynal for useful discussions concerning the coding of the formulas contained in this article.

---

[1] K. S. Low, J. Phys. (Paris), Colloq. 37, C5 (1976); T. Udagawa, in *Proceedings of the International Conference on Nuclear Structure, Tokyo, 1977*, edited by T. Marumori (Physical Society of Japan, Tokyo, 1978), Vol. 44, suppl. 667; N. K. Glendenning, in *Proceedings of the International Conference on Reactions between Complex Nuclei, 1974*, edited by R. L. Robinson, F. K. Mc Govan, J. B. Ball, and J. H. Hamilton (North-Holland, Amsterdam, 1974), p. 137; R. J. Ascuitto and J. S. Vaagen, *ibid.*, p. 257.

[2] T. Udagawa, T. Tamura, and B. T. Kim, Phys. Lett. 82B, 349 (1979); T. Udagawa and T. Tamura, Phys. Rev. Lett. 41, 1770 (1978); H. Fröhlich, T. Shimoda, M. Ishihara, K. Nagatani, T. Udagawa, and T. Tamura, *ibid.* 42, 1518 (1979).

[3] N. Austern and J. S. Blair, Ann. Phys. (N.Y.) 33, 15 (1965); F. J. W. Hahne, Nucl. Phys. A104, 545 (1967).

[4] V. V. Volkov, Phys. Rep. 44, 93 (1978); M. Lefort and Ch. Ngô, Ann. Phys. (N.Y.) 3, 5 (1978).

[5] W. E. Frahn and R. H. Ventor, Ann. Phys. (N.Y.) 24, 243 (1963); Nucl. Phys. 59, 651 (1964).

[6] J. S. Blair, Phys. Rev. 95, 1218 (1954).

[7] J. P. Schiffer, H. J. Körner, R. H. Siemssen, K. W. Jones, and A. Schwarzschild, Phys. Lett. 44B, 47 (1973).

[8] A. Gilbert and A. G. W. Cameron, Can. J. Phys. 43, 1446 (1965).

[9] J. R. Huizenga and L. G. Moretto, Annu. Rev. Nucl. Sci. 22, 427 (1972).

[10] P. Bonche, B. Giraud, A. Cunsolo, M.-C. Lemaire, M. C. Mermaz, and J. L. Québert, Phys. Rev. C 6, 577 (1972).

[11] M.-C. Lemaire, Phys. Rep. 7, 279 (1973); H. Faraggi, A. Jaffrin, M.-C. Lemaire, M.-C. Mermaz, J. C. Faivre, J. C. Gastebois, B. G. Harvey, J. M. Loiseaux, and A. Papineau, Ann. Phys. (N.Y.) 66, 905 (1971).

[12] M.-C. Lemaire, M.-C. Mermaz, H. Sztark, and A. Cunsolo, Phys. Rev. C 10, 1103 (1974).

[13] P. Bonche, ANL Report No. PHY-1973B, 1973, p. 235.

[14] M. Cobern, M.-C. Lemaire, K. S. Low, M.-C. Mermaz, H. Sztark, T. Udagawa, and T. Tamura, Phys. Rev. C 13, 1200 (1976).

[15] C. Olmer, M. Mermaz, M. Buenerd, C. K. Gelbke, D. L. Hendrie, J. Mahoney, D. K. Scott, M. H. Macfarlane, and S. C. Pieper, Phys. Rev. C 18, 205 (1978).

[16] H. Baba, Nucl. Phys. A159, 625 (1970).

[17] C. K. Gelbke, C. Olmer, M. Buenerd, D. L. Hendrie, J. Mahoney, M.-C. Mermaz, and D. K. Scott, Phys. Rep. 42, 312 (1978).

[18] V. K. Lukyanov and A. I. Titov, Phys. Lett. 57B, 10 (1975).

PHYSICAL REVIEW C VOLUME 21, NUMBER 6 JUNE 1980

High-spin properties of ^{164}Er in the multiple band crossing region

S. W. Yates
University of Kentucky, Lexington, Kentucky 40506
and Oak Ridge National Laboratory, Oak Ridge, Tennessee 37830

I. Y. Lee,[*] N. R. Johnson, and E. Eichler[†]
Oak Ridge National Laboratory, Oak Ridge, Tennessee 37830

L. L. Riedinger, M. W. Guidry,[*] and A. C. Kahler[‡]
University of Tennessee, Knoxville, Tennessee 37916
and Oak Ridge National Laboratory, Oak Ridge, Tennessee 37830

D. Cline[*]
Nuclear Structure Research Laboratory, University of Rochester, Rochester, New York 14627

R. S. Simon,[§] P. A. Butler,[‖] P. Colombani,[¶] F. S. Stephens, and R. M. Diamond
Lawrence Berkeley Laboratory, University of California, Berkeley, California 94720

R. M. Ronningen,[**] R. D. Hichwa,[††] and J. H. Hamilton
Vanderbilt University, Nashville, Tennessee 37235

E. L. Robinson
University of Alabama in Birmingham, Birmingham, Alabama 35294

(Received 31 October 1979)

High-spin states in ^{164}Er have been studied by using the ^{150}Nd(^{16}O,4$n\gamma$) and ^{164}Dy(α,4$n\gamma$) reactions and by multiple Coulomb excitation with ^{136}Xe ions. Several positive-parity bands are excited, and two negative-parity bands have been identified. The previously reported backbending behavior of the yrast sequence is demonstrated to result from the intersection of the ground band (seen to spin 22^+) with an even-spin "superband" observed from spins 12^+ to 24^+. The odd-spin yrast superband and the second lowest even-spin superband also have been observed. All the superbands have moments of inertia appreciably larger than the ground band. The observed intersection of these multiple superbands with the γ band produces different backbending behavior and a staggering of the energies of the odd- and even-spin members of the γ band. $B(E2)$ values for transitions below and through the band intersection regions of both the ground band and γ bands have been deduced from multiple Coulomb excitation yields. In addition, lifetimes have been measured for the ground band by the Doppler-broadened line-shape technique. The level energies and $B(E2)$ values are consistent with weak interaction matrix elements ($\simeq 45$ keV) between the intersecting bands. The $B(E2)$ values of the unperturbed band are found to obey the simple rigid-rotor relationship. The 7^- negative-parity band exhibits a normal rotational sequence, while the 5^- band exhibits a large odd-even staggering and a larger moment of inertia. Two-quasiparticle-plus-rotor model calculations indicate strong rotation-alignment and reproduce the observed properties of the high-spin states for both the positive- and negative-parity bands in ^{164}Er

NUCLEAR REACTIONS ^{150}Nd(^{16}O,4$n\gamma$), $E=69.6$ MeV, ^{164}Dy(α,4$n\gamma$), $E=51$ MeV, ^{164}Er(^{136}Xe,^{136}Xe$'\gamma$), $E=547$, 612, 620 MeV; measured E_γ, I_γ, $\gamma\gamma$ coin, Doppler-broadened line shapes, multiple Coulomb excitation probabilities; deduced levels, J, π, τ, $B(E2)$ values from lifetimes and yields, compared levels and $B(E2)$'s to theory.

I. INTRODUCTION

The observed anomalous behavior of the moment of inertia at high spin in nuclear rotational bands (commonly referred to as backbending) is generally believed to be a result of the intersection of the ground-state rotational band with a second rotational band, i.e., the so-called yrast superband. The structure of this yrast superband, which has a moment of inertia close to the rigid-body value, has been interpreted primarily in terms of the rotation-alignment model[1,2] or the Coriolis antipairing model.[3] The rotation-alignment model attributes the structure of this superband to two high-j quasiparticles which are aligned with respect to the rotating core by the Coriolis force, while in the Coriolis antipairing formalism this band results from the collapse of

© 1980 The American Physical Soci

pairing.

Recent studies of the properties of both even- and odd-mass nuclei in the erbium region have provided an abundance of data which are in agreement with the predictions of the rotation-alignment model. Studies[4-6] of level energies and $B(E2)$ values of ^{164}Er through the backbend show behavior in reasonable agreement with the predictions of this model. The generalized calculations of Flaum and Cline[7] within the framework of the two-quasiparticle-plus-rotor model[1,2] predict not only the lowest superband, responsible for backbending, but also additional rotation-aligned bands of both positive and negative parity with similar moments of inertia at slightly higher excitation energies than the yrast superband. Experimental data relating to these additional bands and to the extension of known bands are, therefore, important to an understanding of high-spin nuclear structure. Data in the band-crossing region are particularly crucial, since they specify the interaction between the ground and γ bands with the superbands and hence, give information on the structure of the superband.

This paper details our previous studies[4-6] of ^{164}Er by the (^{18}O, $4n\gamma$), (α, $4n\gamma$), and multiple Coulomb excitation reactions and presents new information on the $E2$ properties of the ground band and γ band derived from the Coulomb excitation data and new Doppler-broadened line-shape measurements. The advantages of such a combined set of measurements is apparent, if a truly extensive characterization of the high-spin states is sought. The determination of reduced transition probabilities from multiple Coulomb excitation, which selectively excites collective bands strongly coupled to the ground state, and from lifetimes measured by the Doppler-broadened line-shape method is important, because these quantities provide rigorous tests of nuclear models. The observed properties of the high-spin states in ^{164}Er are compared with the rotation-alignment model. We point out that our results are in quite good agreement with the recent study of ^{164}Er by Kistner, Sunyar, and der Mateosian.[8]

II. EXPERIMENTAL PROCEDURES AND RESULTS

A. In-beam γ-ray measurements

Gamma-ray measurements were performed at the Lawrence Berkeley Laboratory with the ^{164}Dy (α, $4n\gamma$)^{164}Er reaction and at Oak Ridge National Laboratory with the ^{150}Nd(^{18}O, $4n\gamma$)^{164}Er reaction. While the results from the (α, $4n\gamma$) reaction were instrumental in establishing the level structure in the backbending region of ^{164}Er, the more extensive (^{18}O, $4n\gamma$) measurements were used primarily in constructing the level scheme shown in Fig. 1 and will be described in greater detail.

A 2.8 mg/cm^2 self-supporting enriched neodymium foil (96% ^{150}Nd) was bombarded with 10–20 nA beams of 69.6-MeV ^{18}O ions from the Oak Ridge Isochronous Cyclotron (ORIC). Two large-volume (10% and 18% efficient for a 1.33-MeV γ ray relative to a 7.6 × 7.6 cm NaI(Tl) detector at 25 cm distance) Ge(Li) detectors having resolutions of 2.1 and 2.4 keV, respectively, were placed at 90° to the beam direction. Absorbers consisting of 0.28 mm of copper and 0.15 mm of tin were placed between the target and the detectors to reduce the number of x rays detected. The target to detector distance was 5 cm for the smaller detector and 7 cm for the larger detector.

Both γ-ray singles and γ-γ-time coincidence data (total of 3.5×10^7 coincidence events) were recorded simultaneously using a Tennecomp TP-5000 data acquisition system. The three-parameter coincidence data were stored serially on magnetic tape and prompt coincidences were later sorted using the same data system. Figure 2 shows a portion of the γ-ray singles spectrum, while Figs. 3 and 4 display some of the γ-γ coincidence spectra which are important in making level placements in the positive-parity bands. Gamma rays resulting from the Coulomb excitation of the ^{150}Nd target and, to a much lesser degree, from the production of ^{163}Er by the (^{18}O, $5n\gamma$) reaction are also present in the singles spectrum. Table I gives the energies, intensities, and placements of transitions which have been attributed to ^{164}Er. In many cases where the γ-ray singles spectrum was complex, energies and intensities were obtained from the coincidence spectra.

Analysis of the γ-ray spectra was performed with the interactive peak fitting codes PKFT (Ref. 9) and LIZA (Ref. 10) at Oak Ridge National Laboratory. The level scheme shown in Fig. 1 was constructed from our γ-ray measurements. The established spin assignments are based primarily on previous measurements,[8,11-15] while most levels with spins shown in parentheses are assigned on the basis of our coincidence information and γ-ray intensity values.

Recently, Kistner *et al.*[8] published their study of ^{164}Er from the ^{160}Gd(^{9}Be, $5n\gamma$) reaction which includes angular distribution and linear polarization measurements. Our level schemes are in quite good agreement; and, where discrepancies exist, they will be noted in the description which follows. Moreover, to first order it can be assumed that a similar degree of alignment is achieved in both the (^{18}O, $4n$) and (^{9}Be, $5n$) reac-

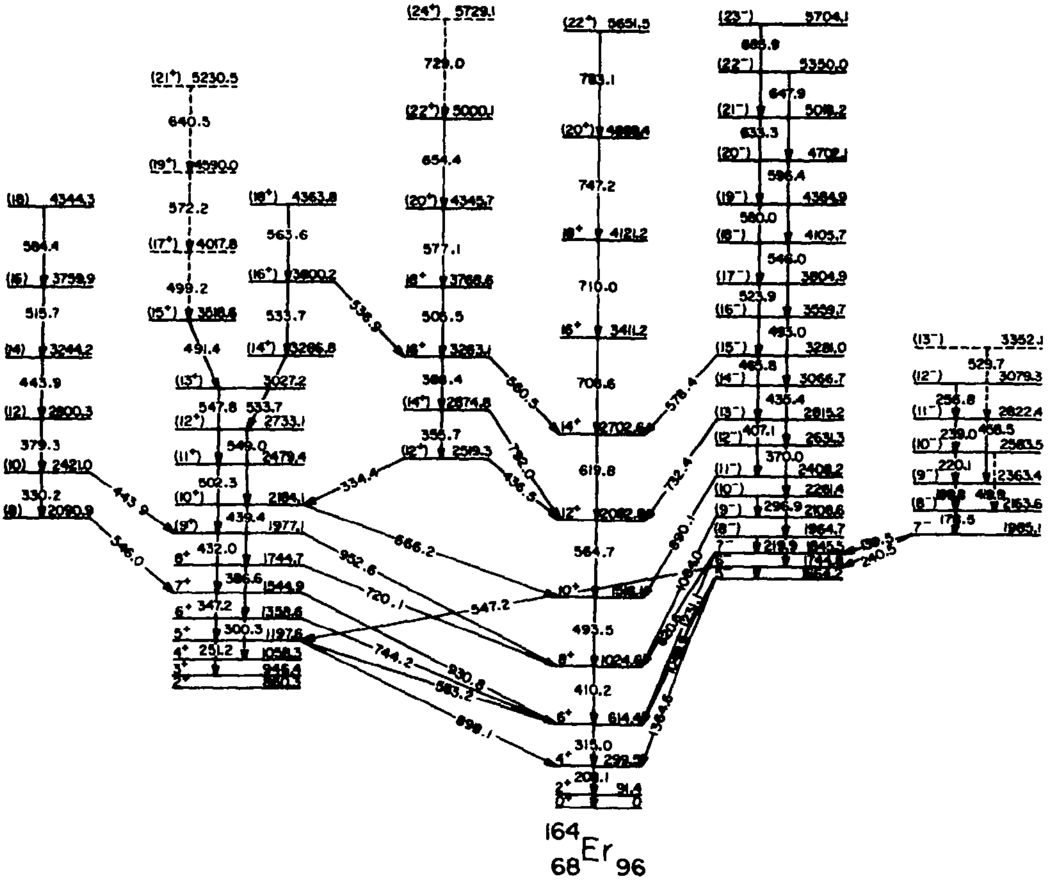

FIG. 1. Level scheme of ^{164}Er showing states populated by the ^{150}Nd(^{18}O,4n)^{164}Er reaction.

tions. This is verified by the fact that the relative intensities for the high-spin states are similar from the two reactions and, hence, the maximum angular momenta imparted in the two reactions are comparable. Thus, the γ-ray intensities listed in Table I include a $\lesssim 30\%$ correction for the angular distribution, which was calculated using the angular distribution data of Kistner *et al.*[8]

1. *The ground-state band*

Using in-beam γ-ray measurements, Jett and Lind[16] studied the levels of ^{164}Er populated by four different reactions and proposed levels in the ground-state rotational band to spin 14$^+$ on the basis of the agreement of observed with calculated γ-ray energies. Their assignments were confirmed by Banaschik *et al.*[11] who used the (α,4nγ) reaction and by Davidson *et al.*[12] who employed not only the (α,4nγ) reaction but also the (^{14}C,4nγ) reaction for population of ^{164}Er levels. The coincidence and angular distribution measurements of the latter two studies[11,12] clearly showed that the levels up to the backbend in the ground-state band of Fig. 1 are connected by stretched *E*2 transitions.

Evidence for placement of the spin 16$^+$ and 18$^+$ members of the ground-state band came first from our ^{136}Xe induced Coulomb excitation data reported earlier.[4] The yield of the 709-keV (708.6 and 710.0 keV from our latest measurements) self coincident doublet, which was placed as feeding the 14$^+$ state at 2703 keV, was observed to have 1.5 times the calculated yield for Coulomb excitation of the 16$^+$ state of the ground-state band. However, the predicted sum of the yields of the 18$^+$ → 16$^+$ and 16$^+$ → 14$^+$ transitions is in excellent agreement with the observed yield of this doublet, if rigid-rotor *B*(*E*2) values are assumed. All the

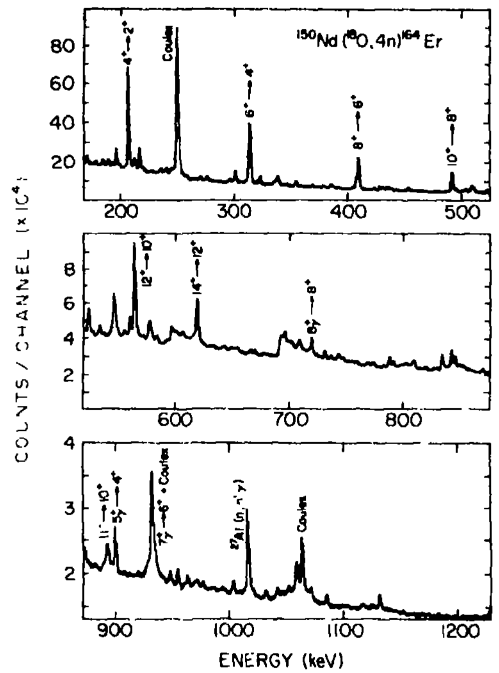

FIG. 2. Spectrum of γ rays observed following the ^{150}Nd(^{18}O,4n)^{164}Er reaction. Some of the more prominent peaks in the spectrum are labeled. Coulex refers to the Coulomb excitation of the ^{150}Nd target.

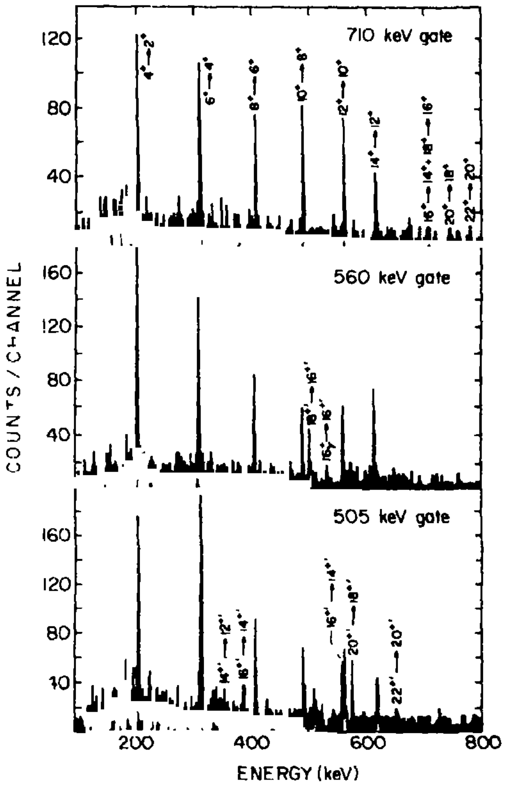

FIG. 3. Coincidence spectra from the 505-, 560-, and 710-keV gating transitions. Some of the more prominent peaks in the spectra are labeled.

available evidence, including our coincidence measurements (see Fig. 3), supports the proposed assignment.

The coincidence spectra also show transitions of 747.2 and 783.1 keV to be in coincidence with the 709-keV doublet. The energies and intensities of these γ rays suggest that they deexcite the next two members of the ground-state rotational band of ^{164}Er.

2. *The even-spin yrast superband*

The backbending of the yrast sequence in ^{164}Er was first observed by Banaschik *et al.*[11] who placed the 560.5-keV transition from the 16⁺ state in the even-spin yrast superband to the 14⁺ ground-band state. The yrast superband was extended to the 18⁺ member at 3768.6 keV by Davidson *et al.*[12] and, on the basis of our (^{18}O,4nγ) coincidence measurements, the 20⁺ and 22⁺ levels have been assigned. Kistner *et al.*[8] have suggested that the 24⁺ level is deexcited by a 729-keV γ-ray transition. This placement appears to be in agreement with our coincidence results, although the counting statistics of our coincidence data are only sufficient for us to make a tentative assignment.

The spin 14⁺ level in the yrast superband was established on the basis of the observed coincidence of the 792-keV γ ray with the 565-keV γ ray (12⁺ → 10⁺) in the ground-state band, the 388–792 keV γ-ray coincidence, and the excellent energy summation to the 3262.1-keV state via both decay paths. The branching ratio from the 16⁺ yrast state is a sensitive measure of the interaction matrix element between the superband and ground-state band. Since the 388-keV region is complex in our singles spectrum, the intensity of the 388-keV γ ray was extracted from the coincidence spectra. The 388/560-keV γ-ray intensity ratio from our work, 0.22 ± 0.07, is not in good agreement with the value of 0.40 obtained from the study by Kistner *et al.*,[8] although no uncertainties are assigned to their γ-ray intensities.

The level at 2519 keV, which is placed from the observed coincidence with γ rays deexciting the 12⁺ ground-band state, the 10⁺ member of the γ-vibrational band (see next subsection), and the 14⁺

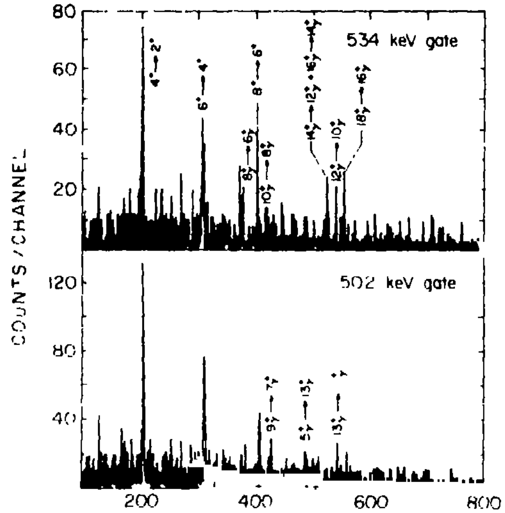

FIG. 4. Coincidence spectra from the 502- and 534-keV gating transitions. These data are from only one detector and have not been smoothed or summed. Some of the more prominent peaks in the spectra are labeled.

member of the yrast superband, is interpreted as the 12⁺ member of the yrast superband. This assignment is in agreement with Kistner *et al.*[8] and, in addition, they report a 1001-keV γ ray which deexcites this state to the 10⁺ ground-band state. A γ ray of this energy is clearly evident in our γ-ray singles spectrum, but its placement could not be made from our coincidence data. For this reason the transition from the 12⁺ yrast superband state to the 10⁺ member of the ground-state band is not included in our level scheme.

3. *The γ-vibrational band*

The γ-vibrational band of ^{164}Er has been established to spin 8⁺ from studies of the β decay of the ^{164}Tm isomers[13] and from the in-beam spectroscopic work of Graetzer *et al.*[14] and West *et al.*[15] Our data are in agreement with these assignments. Although only weak evidence exists for population of the states having spins less than 5⁺, these levels are well known and, for completeness, are shown in the level scheme. The even-spin members of the γ band are clearly seen in the Coulomb excitation data described in Sec. II B. The higher-spin levels shown in Fig. 1 were placed on the basis of our coincidence information and γ-ray intensity values.

When the backbending phenomenon was observed[6] in this γ-vibration band, considerable effort was expended in extending this band as far as possible. To this end, the coincidence gates

TABLE I. Energies, intensities, and assignments of γ rays observed in the ^{150}Nd(^{18}O, $4n\gamma$)^{164}Er reaction.

Energy[a] (keV)	Relative intensity[a,b] Exp.[c]	Corrected[d]	Transition[e] $(I^\pi_{\text{initial}} \to I^\pi_{\text{final}})$
91.37 (6)	26 (2)		$2^+ \to 0^+$
118.7 (2)	1.4 (6)		$8^- \to 7^-$
139.5 (2)	1.6 (5)		$7^{-\prime} \to 7^-$
152.70 (12)	0.9 (2)	0.8 (3)	$10^- \to 9^-$
178.48 (6)	3.6 (2)	3.4 (2)	$8^{-\prime} \to 7^{-\prime}$
199.75 (9)	3.5 (3)	3.3 (3)	$9^{-\prime} \to 8^{-\prime}$
208.10 (6)	100	100	$4^+ \to 2^+$
219.9 (2)	2.0 (8)		$8^- \to 6^-$
220.1 (2)	2.5 (6)		$10^{-\prime} \to 9^{-\prime}$
239.0 (3)	1.8 (4)	1.7 (4)	$11^{-\prime} \to 10^{-\prime}$
240.5 (1)	4.8 (3)	4.4 (3)	$7^{-\prime} \to 6^-$
251.2	<0.5		$(5_\gamma^+ \to 3_\gamma^+)$
256.8 (4)	0.6 (3)	0.6 (3)	$12^{-\prime} \to 11^{-\prime}$
296.93 (7)	4.7 (3)	4.7 (3)	$10^- \to 8^-$
300.3	<0.5		$(6_\gamma^+ \to 4_\gamma^+)$
314.95 (7)	88 (5)	88 (5)	$6^+ \to 4^+$
330.2 (2)	1.3 (2)		$10 \to 8$
334.4 (4)	2.2 (9)		$12^{+\prime} \to 10_\gamma^+$
347.2 (2)	2.2 (3)		$7_\gamma^+ \to 5_\gamma^+$
355.7 (4)	0.7 (3)		$14^{+\prime} \to 12^{+\prime}$
369.96 (6)	4.4 (2)	4.6 (3)	$12^- \to 10^-$
379.32 (7)	2.2 (2)	2.2 (2)	$12 \to 10$
386.6 (4)	2.3 (9)	2.3 (9)	$8_\gamma^+ \to 6_\gamma^+$
388.4 (3)	1.1 (3)	1.1 (3)	$16^{+\prime} \to 14^{+\prime}$
407.1 (4)	1.3 (7)	1.3 (7)	$13^- \to 11^-$
410.22 (7)	65 (5)	67 (5)	$8^+ \to 6^+$
419.9 (6)	0.2 (2)		$(10^{-\prime} \to 8^{-\prime})$
431.95 (7)	4.7 (3)	4.9 (4)	$9_\gamma^+ \to 7_\gamma^+$
435.4 (3)	3.2 (5)	3.3 (5)	$14^- \to 12^-$
436.5 (5)	2.6 (4)	2.7 (4)	$12^{+\prime} \to 12^+$
439.43 (8)	2.6 (3)	2.6 (3)	$10_\gamma^+ \to 8_\gamma^+$
443.9 (2)	2.9 (3)		$14 \to 12$ $10 \to 9_\gamma^+$
458.5 (4)	1.7 (9)		$11^{-\prime} \to 9^{-\prime}$
465.8 (1)	2.1 (2)	2.1 (2)	$15^- \to 13^-$
491.4 (4)	1.4 (6)		$15_\gamma^+ \to 13_\gamma^+$
493.0 (3)	1.3 (4)		$16^- \to 14^-$
493.46 (10)	52 (3)	54 (3)	$10^+ \to 8^+$
499.2 (4)	1.1 (6)	1.1 (6)	$(17_\gamma^+ \to 15_\gamma^+)$

TABLE I. (*Continued.*)

Energy[a] (keV)	Relative intensity[a,b] Exp.[c]	Corrected[d]	Transition[e] ($I^\pi_{\text{initial}} \to I^\pi_{\text{final}}$)
502.33 (6)	3.2 (2)	3.3 (2)	$11^+_\gamma \to 9^+_\gamma$
505.50 (6)	4.7 (3)	4.8 (4)	$18^{+\prime} \to 16^{+\prime}$
515.7 (3)	1.1 (4)	1.1 (4)	$16 \to 14$
523.9 (4)	3.8 (10)	3.9 (11)	$17^- \to 15^-$
529.7 (4)	0.9 (5)		$(13^{-\prime} \to 11^{-\prime})$
533.7 (3)	2.9 (2)		$16^+_\gamma \to 14^+_\gamma$
			$14^+_\gamma \to 12^+_\gamma$
536.9 (3)	1.8 (8)		$16^+_\gamma \to 16^{+\prime}$
546.0 (5)	1.0 (4)		$18^- \to 16^-$
546.0 (5)	1.5 (6)		$8 \to 7^+_\gamma$
547.2 (4)	5.1 (13)		$6^- \to 5^+_\gamma$
547.8 (4)	2.2 (9)		$13^+_\gamma \to 11^+_\gamma$
549.0 (4)	2.3 (8)	2.3 (8)	$12^+_\gamma \to 10^+_\gamma$
560.50 (11)	4.9 (5)	5.1 (5)	$16^{+\prime} \to 14^+$
563.6 (5)	1.7 (9)		$18^+_\gamma \to 16^+_\gamma$
564.73 (6)	32 (2)	33 (2)	$12^+ \to 10^+$
572.2 (2)	1.1 (6)		$(19^+_\gamma \to 17^+_\gamma)$
577.1 (3)	1.9 (5)	2.0 (5)	$20^{+\prime} \to 18^{+\prime}$
578.4 (6)	1.2 (6)	1.0 (6)	$15^- \to 14^+$
580.0 (2)	2.3 (6)	2.3 (7)	$19^- \to 17^-$
583.2 (2)	2.1 (3)		$5^+_\gamma \to 6^+$
584.4 (4)	1.0 (3)		$18 \to 16$
596.4 (3)	0.7 (3)	0.7 (3)	$20^- \to 18^-$
619.76 (11)	16 (2)	17 (2)	$14^+ \to 12^+$
633.3 (4)	1.7 (9)	1.7 (9)	$21^- \to 19^-$
640.5 (4)	1.1 (6)		$(21^+_\gamma \to 19^+_\gamma)$
647.9 (4)	0.7 (3)		$22^- \to 20^-$
654.4 (4)	1.6 (2)	1.6 (3)	$22^{+\prime} \to 20^{+\prime}$
666.2 (2)	1.6 (10)		$10^+_\gamma \to 10^+$
685.9 (8)	1.7 (9)		$23^- \to 21^-$
708.6 (3)	2.7 (5)	2.8 (6)	$16^+ \to 14^+$
710.0 (3)	2.5 (5)	2.6 (6)	$18^+ \to 16^+$
720.1 (2)	2.3 (10)	1.8 (9)	$8^+_\gamma \to 8^+$
729.0 (5)	0.4 (2)		$(24^{+\prime} \to 22^{+\prime})$
732.4 (1)	3.4 (4)	2.6 (4)	$13^- \to 12^+$
744.2 (3)	4.4 (15)	3.6 (13)	$6^+_\gamma \to 6^+$
747.2 (4)	1.4 (4)		$20^+ \to 18^+$
783.1 (4)	0.8 (3)		$22^+ \to 20^+$
791.98 (7)	3.0 (2)	3.1 (3)	$14^{+\prime} \to 12^+$

TABLE I. (*Continued.*)

Energy[a] (keV)	Relative intensity[a,b] Exp.[c]	Corrected[d]	Transition[e] ($I^\pi_{\text{initial}} \to I^\pi_{\text{final}}$)
820.6 (2)	1.6 (3)		$7^- \to 8^+$
890.12 (11)	3.5 (3)	2.7 (3)	$11^- \to 10^+$
898.14 (6)	7.6 (4)	6.4 (4)	$5^+_\gamma \to 4^+$
930.8 (4)	4.4 (14)	3.4 (11)	$7^+_\gamma \to 6^+$
952.60 (7)	3.3 (3)	2.5 (3)	$9^+_\gamma \to 8^+$
1049.0 (9)	1.0 (2)	0.9 (2)	$5^- \to 6^+$
1083.95 (9)	2.1 (2)	1.7 (2)	$9^- \to 8^+$
1231.10 (7)	5.0 (3)	4.2 (3)	$7^- \to 6^+$
1364.6 (3)	3.9 (5)	3.3 (5)	$5^- \to 4^+$

[a] Uncertainties in the least significant figures are indicated in parentheses.

[b] Intensities are normalized to 100 for the 208.10-keV γ ray.

[c] Experimental singles values with Ge(Li) detector located at 90° with respect to the beam direction.

[d] The intensities have been corrected for the angular distribution effect using the experimental angular distribution coefficients of Kistner *et al.* (Ref. 8).

[e] The symbols used in transition placements can readily be understood by a comparison with the band structures shown in Fig. 1. Tentative γ-ray transition placements are indicated in parentheses.

providing information on this band were scanned with gates set on the first detector, and spectra were stored for the second detector. The gating was then done on the second detector, and spectra were recorded for the first detector. After the spectra were normalized for energy, they were summed. As a final aid in making decisions on the weak coincidences, the data were smoothed.

It is convenient to discuss the even-spin levels separately from the odd-spin levels, since there are no intraband transitions between these sets of levels. The even-spin sequence was extended to spin 18^+. The 534-keV γ-ray peak in the spectrum is a selfcoincident doublet and was assigned as the transitions deexciting the 16^+ and 14^+ levels of the γ-vibrational band on the basis of intensity. The observed 537-keV transition from the 16^+ state to the 16^+ yrast superband state lends further support to these placements. No even-spin states higher than the proposed 18^+ state at 4363.8 keV could be extracted from our data.

As a result of the complexity of the γ-ray spectra, the 502-keV $(11^+_\gamma \to 9^+_\gamma)$ transition is the highest-lying γ ray which can reliably be used as a gating transition in the odd-spin sequence. This coincidence spectrum shows the 548-keV and the 491-keV γ rays in coincidence as well as γ rays at 499, 572, and 641 keV which have a coincidence intensity of ~80% of that of the 491-keV γ ray. We have suggested[6] that the latter three γ rays form a cascade into the 15^+ level. The level order is based on level systematics in the backbending region where abrupt changes have not been observed. Any order other than that shown produced a severe discontinuity in the backbending plot. Since these placements are tentative, the. are shown as dashed in the level scheme. Kistner *et al.*[8] showed that the 499.2-keV ($17^+_\gamma - 15^+_\gamma$) transition has the angular distribution of a stretched $E2$ transition, and they also observed a 571-keV γ ray, which they assigned as the ($19^+_\gamma - 17^+_\gamma$) transition.

4. *The $K^\pi = 5^-$ band*

The first three members of the rotational band built on the 5^- state at 1664.2 keV have been assigned from the decay of ^{164}Tm^m by de Boer *et al.*[13] The 80-keV γ ray which depopulates the 6^- state has been reported[13] but was not seen in our measurements because of its large internal conversion coefficient and high probability of absorption. The coincidence data suggest, however, that this transition must exist. We also did not observe the 101-keV ($7^- - 6^-$) transition. The additional members of this band shown in Fig. 1 were established from the coincidence results.

Kistner *et al.*[8] have observed this band to spin 24. Our level scheme is in excellent agreement with theirs, but we have not been able to substantiate their placement of the highest state (24^-).

5. *The $K^\pi = 7$ band*

The 7^- state at 1985.1 keV has been assigned[13] as the $\{\frac{7}{2}^+[404]\pi;\ \frac{7}{2}^-[523]\pi\}_{7^-}$ state because of the observed allowed unhindered electron capture decay to this level from the 6^- isomeric state of ^{164}Tm. The γ rays from the levels of the rotational band built on this state are observed by gating on the 240-keV γ ray which most strongly deexcites the 7^- state into the aforementioned $I^\pi = 5^-$ negative-parity band. The regular rotational sequence of level energies and the observation of both cascade and cross-over transitions leaves little doubt as to the identity of the band up to spin 12^-. The 13^- level is placed solely on the basis of the coincidence of the 530-keV γ ray with the 239-keV γ ray and the energy systematics. Kistner *et al.*[8] also report a 273-keV γ ray from this level, but this transition could not be confirmed by our spectral measurements.

6. *The rotational band based on 2090.9 keV*

A series of states which form a band of unknown parity was placed by Kistner *et al.*[8] who suggested that the lowest observed level at 2091.3 keV had a spin of 8. Our work substantiates these placements up through the sixth member ($I = 18$) of this band and their arguments about this band appear to be well based.

B. *Multiple Coulomb excitation measurements*

The nucleus ^{164}Er is one of the few stable nuclei which is known to exhibit backbending behavior. With very heavy ions such as ^{136}Xe it is possible to Coulomb excite ^{164}Er into the high angular momentum states of the backbending region with appreciable cross section. This is quite advantageous because Coulomb excitation selectively populates collective bands strongly coupled to the ground state as opposed to the γ-decay pattern following (HI,xn) reactions which is often constrained to follow the yrast sequence. Consequently, Coulomb excitation leads to much less complicated γ-ray spectra than those obtained using nuclear reactions. In addition, the γ-ray transition yields following Coulomb excitation can be used to establish the $B(E2)$ values.

The target used in the multiple Coulomb excitation measurements was a 1.34 mg/cm^2 isotopicall enriched (73.6% ^{164}Er) metallic self-supporting erbium foil. This target was bombarded with 547- and 612-MeV ^{136}Xe ions from the Lawrence Berkeley Laboratory SuperHILAC, and the deexcitation γ rays were detected by a 50-cm^3 Ge(Li) detector. Silicon detectors were used to detect scattered Xe ions at angles of 65°, 77°, a 90° (three detectors at each angle) in coincidence with γ rays observed in the Ge(Li) detector at $-30°$ to the incident beam. By placing the Ge(Li) detector in the average recoil direction, where the Doppler shift is maximum (8%) and the Doppler broadening is minimum, and by correcti for the different recoil velocities occurring at dif ferent scattering angles, γ-ray energy resolutio of $\leq 1\%$ full width at half maximum (FWHM) was achieved. A multiplicity filter consisting of four 7.6×7.6 cm NaI(Tl) detectors was used to determine the multiplicity of each γ-ray transition observed in the Ge(Li) spectrum in coincidence wit scattered ions. The dependence of the γ-ray yiel on (1) the multiplicity distribution, (2) the bombarding energy, and (3) the projectile scattering angle, provided three independent measures of t location of each deexciting γ-ray transition in th nuclear decay scheme. These confirmed the dec scheme derived from the (^{18}O, $4n\gamma$) reaction sho in Fig. 1.

A spectrum of γ rays in coincidence with scattered ^{136}Xe ions is shown in Fig. 5. A striking feature of this spectrum is that Coulomb excitation preferentially populates the extension of the ground band above the intersection with the lowest superband. Observed γ-ray transitions involving levels in both the ground-state band and γ band are indicated. Unmarked peaks are from Coulomb excitation of ^{166}Er or ^{168}Er contaminants or from excited target nuclei which recoil into the silicon detectors and exhibit a small Doppler shift. The yields for each γ-ray transition were obtained using an interactive peak fitting routine FIT.[17]

The Winther-de Boer[18] computer program, which assumes semiclassical Coulomb excitation theory, was used to calculate the γ-ray yields. The symmetric rotor model was used to calculate the $E2$ matrix elements with $\langle 0 \| M(E2) \| 2_1 \rangle = 2.341$ eb, which is taken from α-particle Coulomb excitation measurements.[19] For simplicity we have used the rigid-triaxial-rotor model with $\gamma = 12.7°$ for the γ band. The matrix elements calculated with this small value for the asymmetry parameter should closely approximate those of rotation-vibration calculations. The two-band mixing model, using a 45-keV interaction strength, was used to estimate the $B(E2)$ values coupling the ground band and yrast even-spin superbands. The weak $B(E2; 2_\gamma^+ \to 2^+)$, $B(E2; 8_\gamma^+ \to 8^+)$, and $B(E2; 10_\gamma^+ \to 10^+)$ matrix elements were adjusted slightly to ensure that the experimental branching ratios were obtained. The calculations also included $E4$ matrix elements derived assuming that $\langle 0 \| M(E4) \| 4_1 \rangle = +0.12$ eb^2 and assuming that only the Q_{40} intrinsic $E4$ moment is nonzero. The inclusion of $E4$ excitation produced $\leq 2\%$ changes in the calculated γ-ray yields. The calculations of the γ-ray yields included (1) $M1$ transition matrix elements derived from known $E2/M1$ mixing ratios[15] and systematics; (2) the deorientation effect ($\leq 20\%$ effect), calculated using the two-state model of Brenn *et al.*[20]; (3) the finite size of the Ge(Li) and summing effects in the Ge(Li) ($\propto 1\%$ correction); and (4) internal conversion. These corrections are predicted reliably and accurately and are smaller than the uncertainties involved in obtaining the yields from the γ-ray spectra. The only important systematic error occurs for a bombarding energy of 612 MeV where we expect a small Coulomb-nuclear interference effect.[21] This slightly excessive bombarding energy was chosen in order to maximize the excitation probabilities through the band intersection region which was not fully explored when these Coulomb excitation data were reported.[4] It is estimated that the Coulomb-nuclear interference will produce $\leq 5\%$ uncertainty in the $B(E2)$ values extracted from the data taken at 612 MeV and is a negligible correction for the 547-MeV data.

A comparison of the experimental and calculated sums of γ-ray yields deexciting each level is shown in Fig. 6. The sum of the $18^+ \to 16^+$ and $16^+ \to 14^+$ unresolved doublet and also the sum of the

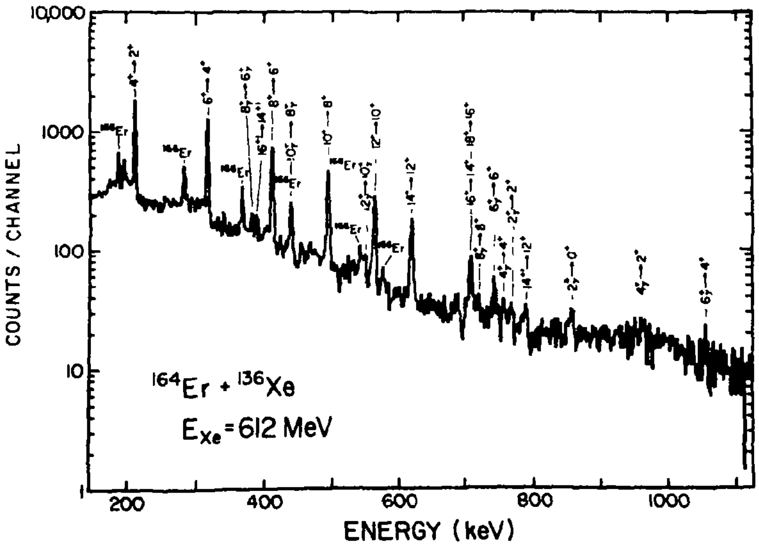

. 5. Coincidence γ-ray spectrum for the Coulomb excitation of ^{164}Er by 612-MeV ^{136}Xe ions. Transitions in ^{164}Er ibeled.

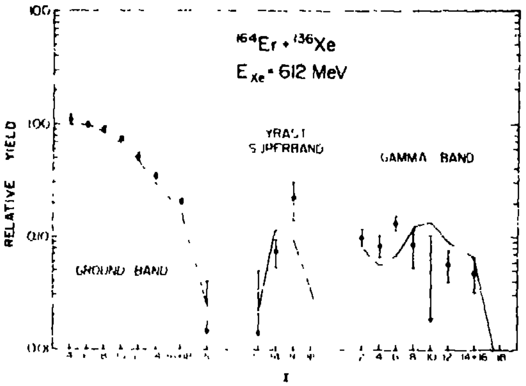

FIG. 6. Comparison of the total yield of γ rays from multiple Coulomb excitation of ^{164}Er by 612-MeV ^{136}Xe ions with Coulomb excitation calculations. The measured and calculated yield of the 16^{+} state was corrected to include the known branching ratio.

$16_\gamma^+ \rightarrow 14_\gamma^+$ and $14_\gamma^+ \rightarrow 12_\gamma^+$ unresolved doublet are compared with the sum of the calculated yields of the unresolved transitions in Fig. 6. Destructive interference occurs for multiple Coulomb excitation of the odd-spin members of the γ band with the result that they are calculated to be populated ~20 times weaker than the adjacent even-spin γ-band states. The population of these odd-spin states is not shown in Fig. 6, since they are too weakly excited to be observed in the present work. Unfortunately, the even-spin yrast superband was difficult to observe because the $16^{+} \rightarrow 14^{+}$ transition, which is the strongest branch from the 16^{+} superband state, is not resolved from the strong $12^{+} \rightarrow 10^{+}$ ground-band transition. The overall agreement between experiment and calculation is satisfactory for all three bands indicating that the assumed $E2$ properties are consistent with the data.

The extraction of individual $B(E2)$ values from the above comparison is somewhat complicated, since most states were populated by multistep excitation and thus the yield of a given state depends on several matrix elements. However, a large part of this complexity is removed by comparing the experimental and calculated ratios of γ-ray yields of successive levels connected by large $B(E2)$ values, i.e., for the ground band, the ratio $R_I = Y_I / Y_{I-2}$ where Y_I is the yield of γ rays deexciting the spin I state. The sensitivity of R_I to the $B(E2; I-2 \rightarrow I)$ can be expressed as

$$\frac{R_I^{\text{exp}} - R_I^{\text{calc}}}{R_I^{\text{calc}}} = \alpha_I \left[\frac{B(E2; I-2 \rightarrow I)_{\text{exp}} - B(E2; I-2 \rightarrow I)_{\text{calc}}}{B(E2; I-2 \rightarrow I)_{\text{calc}}}\right].$$

It can be shown[22] that the sensitivity parameter $\alpha_I \approx 1 - R_I$. The Coulomb excitation code[18] was used to calculate the coefficient α_I. The final $B(E2)$ values were obtained by an iterative procedure where the above relation was used to correct the $B(E2)$ values used in the initial calculations.

For the ground-band states up to spin 14^{+}, the experimental value of R_I is equal, within the 5–10% statistics, to the theoretical value of R_I

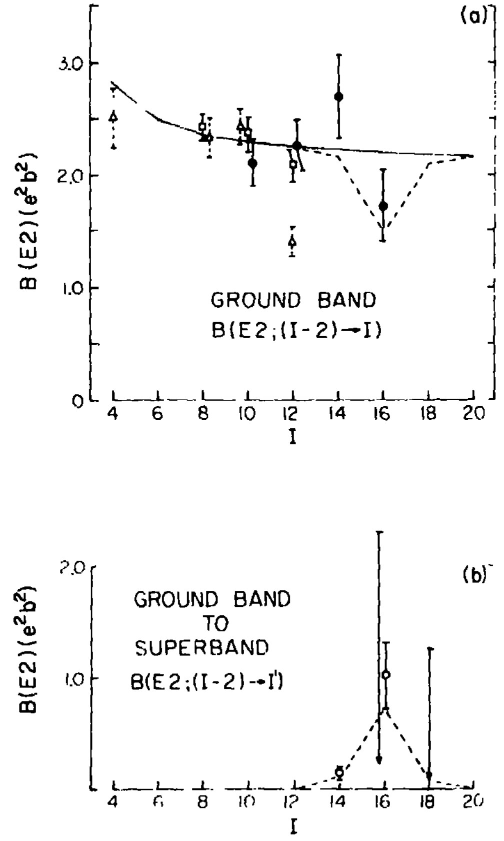

FIG. 7. $B(E2)$ values extracted for the Coulomb excitation yields (solid circles), Doppler-broadened line shape (open squares), and results from previous work (triangles). The solid line corresponds to the $B(E2)$ values derived from the $B(E2; 0^{+} \rightarrow 2^{+})$ assuming the rigid-spheroidal-rotor relation. The dashed line corresponds to the $B(E2)$ values derived assuming a 45-k interaction matrix element between the intersecting bands and assuming identical intrinsic quadrupole moments for both bands. The open circles for the superband correspond to the $B(E2)$ values derived from the measured branching ratio assuming that the superband has a constant and similar intrinsic quadrupole moment to that of the ground band.

evaluated using the spheroidal rigid-rotor relation for the $B(E2)$ values. Although this implies that on the average the experimental $B(E2)$ values are close to the values derived from the known $B(E2; 0^+ \to 2^+)$ assuming the rigid-rotor relation, it does not prove that the individual $B(E2)$ values obey this relation. Typically, α_I is less than 0.3 for transitions between ground-band states below $I^\pi = 12^+$. Consequently, the $B(E2)$ value derived from a given R_I has a fractional error magnified by a factor of more than three compared with the fractional error in R_I. Multiple Coulomb excitation data obtained with lower bombarding energies or with lighter projectiles would provide reliable $B(E2)$ values for ground-band states below spin 10^+.

The ground-band $B(E2)$ values extracted from the present multiple Coulomb excitation data are shown in Fig. 7 and listed in Table II. The individual ground-band $B(E2)$ values are consistent with the rigid-rotor relation (solid curve) amended to include band mixing (dashed curve). The ground to superband $B(E2)$ values are poorly determined by the Coulomb excitation data because, as mentioned earlier, the strongest branch from the $16^{+\prime}$ state was masked by the $(12^+ \to 10^+)$ ground-band transition. The dashed line corresponds to the $B(E2)$ values used in the Coulomb excitation calculations.

The $B(E2)$ values involving the γ band used in the Coulomb excitation calculations are indicated by the dashed lines in Fig. 8. The values are those given by the rigid-triaxial-rotor model except that the $B(E2; 2_\gamma^+ \to 2^+)$, $B(E2; 8_\gamma^+ \to 8^+)$, and $B(E2; 10_\gamma^+ \to 10^+)$ values were slightly adjusted to obtain better agreement with the known branching ratios. Both the intraband and interband $B(E2)$ values strongly influence the population of states in the γ band. This complication, coupled with the weak and uniform population of γ-band states up to spin 10^+, makes it possible to extract reliable $B(E2)$ values only for the unresolved $(16_\gamma^+ \to 14_\gamma^+)$ and $(14_\gamma^+ \to 12_\gamma^+)$ doublet and the $(12_\gamma^+ \to 10_\gamma^+)$ transition. Within the very large error, these individual $B(E2)$ values are consistent with the model values.

C. Lifetimes from Doppler-broadened line-shape analysis

Heavy-ion Coulomb excitation is ideal for measuring lifetimes of excited states by the Doppler-broadened line-shape technique, because the recoil velocities are large and the population of states is well understood. The large recoil velocity ($v/c \approx 0.08$) imparted by Xe projectiles makes this

TABLE II. Lifetimes and $B(E2)$ values for states in ^{164}Er.

Transition $I \to I-2$	Doppler-broadened line shape Meanlife τ_{exp} (ps)	Doppler-broadened line shape $B\{E2; I \to (I-2)\}$ $(e\,\mathrm{b})^2$	Multiple Coulomb excitation $B\{E2; I \to (I-2)\}$ $(e\,\mathrm{b})^2$	Previous work $B\{E2; I \to (I-2)\}$ $(e\,\mathrm{b})^2$	Rigid rotor $B\{E2; I \to (I-2)\}$ $(e\,\mathrm{b})^2$
Ground band					
$4^+ \to 2^+$				1.39 ± 0.14^{a}	1.57
$6^+ \to 4^+$					1.73
$8^+ \to 6^+$	3.69 ± 0.18	1.86 ± 0.09		1.78 ± 0.13^{b}	1.81
$10^+ \to 8^+$	1.46 ± 0.09	1.91 ± 0.12	1.70 ± 0.16	1.96 ± 0.12^{b}	1.85
$12^+ \to 10^+$	0.8 ± 0.06	1.75 ± 0.13	1.89 ± 0.19	1.19 ± 0.09^{b}	1.89
$14^+ \to 12^+$			2.33 ± 0.32		1.91
$16^+ \to 14^+$			1.52 ± 0.28^{c}		1.93
Superband					
$16^{+\prime} \to 14^+$			≤ 2.8		
Gamma band					
$12_\gamma^+ \to 10_\gamma^+$			1.5 ± 0.7		1.59
$14_\gamma^+ \to 12_\gamma^+$			1.9 ± 0.9^{c}		1.62

[a] Reference 47—lifetime measurement by a microwave technique.

[b] Reference 29—Doppler-broadened line-shape measurement.

[c] Gamma ray unresolved from weaker transition between next two higher members of the collective band. This ted $B(E2)$ value was extracted assuming that the weaker transition from the higher transition was correctly calcu- ed using a $B(E2)$ value given by the rotational model.

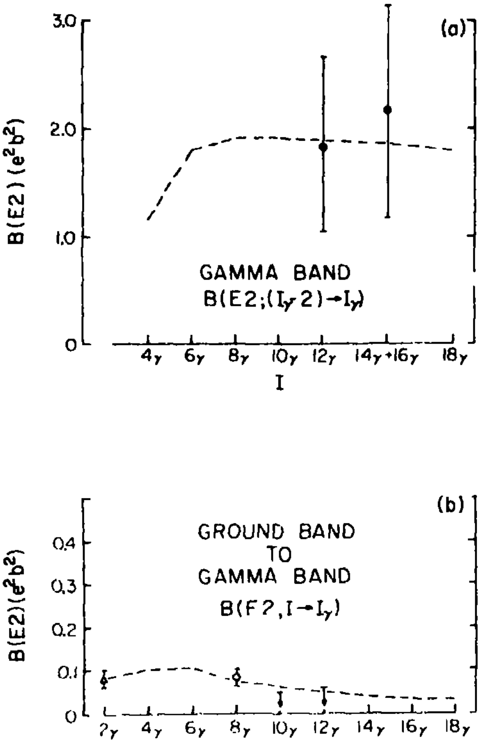

FIG. 8. The $B(E2)$ values for the γ band derived from the Coulomb excitation data. The dashed line corresponds to the values used in the calculation and was derived using the rigid-triaxial-rotor model as described in the text. The open circle for the $B(E2; 8^+ \rightarrow 8_\gamma^+)$ was derived from the branching ratio assuming that the intraband transitions were given by the rotor model.

technique a sensitive method for studying the shor lifetimes characteristic of high-spin states. This method complements the multiple Coulomb excitation method for extracting $B(E2)$ values, because the present multiple Coulomb excitation yields are insensitive to the $B(E2)$'s of those lower-spin states which are most easily studied by Doppler-broadened line-shape analysis. In addition, complications involving the complex feeding patterns and feeding times, which make it difficult to measure lifetimes of states populated following (HI,*xn*) reactions, are avoided. Using this technique, we have performed lifetime measurements of the 8^+, 10^+, and 12^+ ground-band states in ^{164}Er

A thick ~30 mg/cm^2 metallic ^{164}Er target was bombarded by a beam of 620-MeV ^{136}Xe ions from the Lawrence Berkeley Laboratory SuperHILAC. This target was of sufficient thickness to stop the beam and the recoiling ^{164}Er target nuclei. The deexcitation γ rays following Coulomb excitation were detected in a 50-cm^3 Ge(Li) detector placed at 0° to the beam. As can be seen in Fig. 9, the γ rays emitted during deceleration of the recoilin nuclei in the target are Doppler broadened. The lifetime of the state can be extracted from the shape of the γ-ray peak and a knowledge of the slowing-down time. The lineshapes of the γ rays from the $8^+ \rightarrow 6^+$, $10^+ \rightarrow 8^+$, and $12^+ \rightarrow 10^+$ transitio were analyzed using the computer code DOPCO.[23] In this code the recoil velocity and angular distribution of the target nucleus are taken together with the stopping power, and the expected lineshape for a given lifetime is calculated.

The angular distribution and the excitation func tion of the Coulomb excitation process were calculated using the program of Winther and de

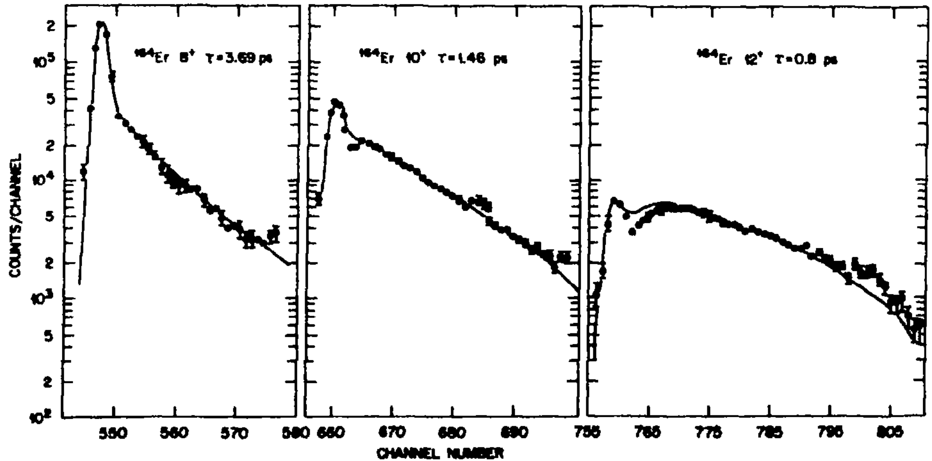

FIG. 9. Line-shape fits to transitions in ^{164}Er following excitation by 620-MeV ^{136}Xe ions. The points are the experimental data and the solid lines are the calculated fits from the program DOPCO (Ref. 23).

Boer.[18] The $E2$ and $E4$ matrix elements described in the previous section were used. Gamma-ray yields and angular distributions were calculated for center-of-mass particle scattering angles ranging from 20° to 180° in 20° steps at energies from 80 to 620 MeV in five steps to account for energy loss in the thick target.

The electronic stopping powers, taken from the table of Northcliffe and Schilling,[24] were corrected at low energies for medium dependences using the table of Ziegler and Chu[25] according to the usual procedure.[26] The maximum correction was found to be about 8%. The theory of Lindhard *et al.*[27] was used for the nuclear stopping powers, and the large-angle scattering effect was taken into account using the Blaugrund[28] prescription.

Lifetimes were obtained from a least squares fit of the calculated line shapes to the experimental data and are listed in Table II. The uncertainties include statistical contributions from the data, errors in background subtraction, and uncertainties in the stopping powers. The state of highest spin (12^+) was analyzed first; hence, the γ-ray feeding to the next lower state is treated properly by using the experimentally determined lifetime. Feeding from 14^+, 16^+, and 18^+ states were also included by assuming rotational lifetimes for these states.

The best fits to the γ-ray transitions depopulating the 8^+, 10^+, and 12^+ states are shown in Fig. 9. The region of the line shape just above the stopped component of the peak from the $12^+ \rightarrow 10^+$ transition is not well reproduced by the calculation. This may indicate that the values of the stopping power at low velocity ($v/c \sim 0.004$) are not correct in our calculations. However, the extracted lifetime is not very sensitive to this deviation because this region represents only a small fraction of the total counts. As a check of the integrity of our calculations, an analysis of this data was performed with a different computer code.[28] The results of these calculations were in excellent agreement with those presented in Table II.

The $B(E2)$ values derived from the measured lifetimes are in excellent agreement with the rigid-rotor relation and the values extracted from the multiple Coulomb excitation data. Kearns *et al.*[29] have also measured the lifetimes of rotational states in ^{164}Er by the Doppler-broadened line-shape technique using Coulomb excitation with ^{56}Fe and ^{84}Kr projectiles. They found the $B(E2)$ values for decay of the 8^+ and 10^+ states to be in good agreement with rotational values, but their value for the $B(E2; 12^+ \rightarrow 10^+)$ level is more than 32% lower than the rotational prediction and our values derived from both Doppler-broadened line shape and multiple Coulomb excitation yield measurements.

III. DISCUSSION

A. Rotational-alignment model

Since the rotation-alignment model[1] will be used extensively in interpreting the high-spin level structure of ^{164}Er, it is appropriate that we examine the qualitative predictions of this model. A characteristic feature of the rotation-alignment model is that it predicts a series of rotation-aligned bands similar to the superbands observed in ^{164}Er. Calculations within the rotation-alignment model[1,7] predict that the wave functions of the low-lying positive-parity two-quasiparticle bands in nuclei such as ^{164}Er are dominated by a single K component at low spin ($I \leq 4$) and one rotation-aligned structure for $I^\pi \geq 16^+$. The lowest yrast even-spin rotation-aligned band has only even-spin members and evolves from a $K^\pi = 0^+$ structure (at spin zero) to a structure at $I \geq 16$ which is mainly two $i_{13/2}$ quasineutrons coupled to $J = 12$ and aligned with the rotation of the core. This is presumed to be the superband observed to intersect the ground-state band at $I^\pi = 16^+$ in ^{164}Er, producing the well-known backbend in the yrast sequence. The next two lowest bands are predicted to start out as a single $K^\pi = 4^+$ band which evolves into the lowest odd-spin (yrast odd) and the second-lowest even-spin (yrare even) rotation-aligned bands. The largest components of the wave functions of these two bands for $I^\pi \sim 16^+$ have a rotation-aligned structure with two $i_{13/2}$ neutrons coupled to $J = 12$ and $J = 10$ for the odd- and even-spin bands, respectively. The odd-even splitting for the yrast superbands occurs because both R (the core rotation) and J (spin of the two coupled neutrons) are only even, whereas the total spin $\vec{I} = \vec{R} + \vec{J}$ can be both even or odd; thus the rotational energy of an odd-spin state is similar to the next higher even-spin state. The yrare even-spin superband is predicted to be slightly above the yrast odd-spin aligned band, and it has a structure for which roughly half of the wave function corresponds to the two $i_{13/2}$ neutrons coupled to $J = 10$ with maximum alignment along the rotation axis. In the extreme limit of the rotation-alignment model, the yrast even-spin (I), yrast odd-spin ($I - 1$), and yrare even-spin ($I - 2$) states would have the same rotational energy, because they have the same value of R.

The structure of these rotation-aligned superbands can be probed by studying the interaction of these bands with the ground-state band and with the β- and γ-vibrational bands. The interaction of the lowest superband with the ground and β bands has been observed previously.[30–37] The interaction matrix elements between the ground-state band and this superband lie between 8 and 80 keV, which is one to two orders of magnitude smaller than typical Coriolis matrix elements at this spin.[38] The interaction between the β band and the lowest superband is known to be weak; that is, it is around 30 keV and 55 keV for ^{154}Gd and ^{156}Dy, respectively,[32,33,38] at the band intersections. The γ band would appear to serve as a better probe of the superbands, since one can study the interactions with both even- and odd-spin states of the superbands, if the necessary intersections of these bands with the γ band can be observed. On the other hand, the ground-state and β bands can only probe the even-spin states. Prior to our previous publication[6] in which we presented evidence for the discovery of the yrast odd- and yrare even-spin superbands, only the lowest superband (yrast even-spin) had been observed and the intersection of superbands with the γ band had never been observed.

B. Backbending of positive-parity bands

The plot of the experimental energies versus spin [Fig. 10(a)] clearly shows that several intersecting bands exist in ^{164}Er. These results can be understood when compared with the predictions of the rotation-alignment model.[1] A sample calculation was performed within this model to illustrate the general features predicted by the model, but no attempt was made to fit the calculation to the experimental data. Both zero and two-quasineutron configurations within the complete $i_{13/2}$ orbit were included. The Fermi level was taken to be between the $\Omega = \frac{3}{2}$ and $\frac{5}{2}$ orbitals with the pairing parameter $\Delta = 1$ MeV. A common moment of inertia parameter $2\mathscr{J}/\hbar^2 = 78.1$ MeV^{-1} was used throughout the calculations except that the ground-band energies were allowed to follow a typical VMI (Ref. 39) behavior. The excitation energies predicted by this calculation are compared with the experimental results in Fig. 10. The γ band was not explicitly included in the calculations; however, a line corresponding to the expected position of the γ-vibrational band in ^{164}Er has been added to Fig. 10 for illustration. The overall similarity between the experimental data and the calculation is striking. The lowest two-neutron band is expected to intersect the γ band between spin 12^+ and 14^+ and the ground band near spin 16^+. The yrare even-spin and yrast odd-spin two-neutron bands are expected to intersect the γ band around spin 15^+. The yrast odd-spin two-quasineutron band is predicted to be about 0.5 MeV above the yrast even-spin rotation-aligned band and it also is predicted to fall slightly below the yrare even-spin rotation-aligned band.

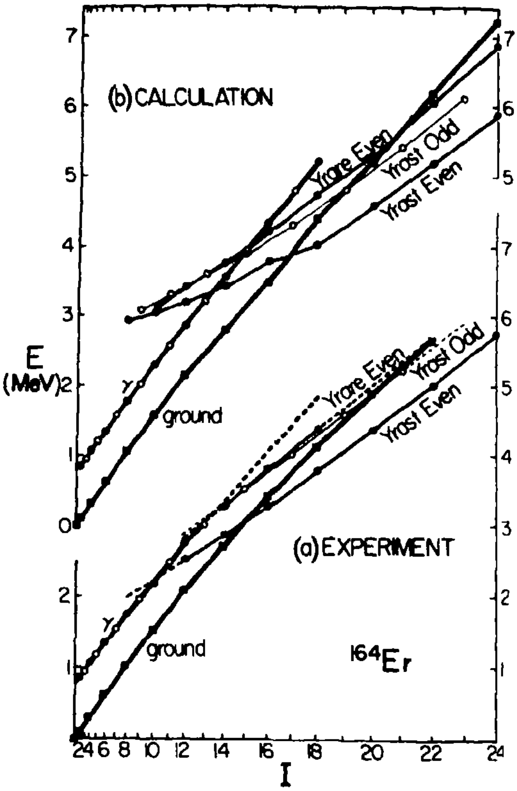

FIG. 10. Plot of the level excitation energies for various bands in ^{164}Er from (a) experiment and (b) the rotation-alignment model. The solid circles correspond to even-spin states and the open circles to odd-spin states.

All of the predicted features appear to be exhibited by the data. The calculation predicts that the ground-state band will intersect the yrare even-spin band and an extrapolation of the experimental third 16^+ and 18^+ states to higher spin suggests such an intersection with the ground band will occur experimentally near spin 24^+. A more detailed comparison shows that the calculations are inadequate in that the intersections are predicted to occur at spins which are slightly too high. In addition, even though the calculation predicts small interaction matrix elements between the intersecting bands, the predicted matrix elements appear to be around a factor of 3 larger than experimentally observed. Almberger *et al.* performed a similar calculation in which they made a least square fit to the experimental level energies to determine four parameters—the Fermi level, the pairing gap, and the magnitude and slope of the moment-of-inertia dependence of rotational frequency. Using reasonable values for these parameters, they obtained excellent fits, i.e., a rms deviation of only 4 keV, for both the ground band and the yrast superband.

The interaction between the intersecting bands is most clearly illustrated by a conventional backbending plot as shown in Fig. 11. The backbending behavior of the ground-state band of ^{164}Er is very similar to that observed[41] in the other $N=96$ isotopes ^{166}Yb, ^{168}Hf, and ^{170}W. The yrast superband displays about the same moment of inertia and excitation energy in all of these nuclei. Below the backbend the moment of inertia characteristically increases slightly with increasing spin, presumably due to the influence of Coriolis antipairing. If it is assumed that the backbending in the yrast even-spin sequence is due to the intersection of two bands with an interband interaction strength of 45 keV, then the unperturbed ground-band states lie on a smooth extension of the lines up through the 18^+ state, and the yrast even-spin superband energies vary smoothly as shown by the open circles in the left portion of Fig. 11. However, the 20^+ and 22^+ members of the ground band are affected very little by this interaction. We note that if we extrapolate the yrare-even superband, as shown by the dashed line in Fig. 10(a), and assume that the interaction between these bands is 45 keV, then the upward kink in the ground band for the 20^+ and 22^+ states is largely removed.

The ratio of the intraband and interband $B(E2)$ values at the band intersection is sensitive to the strength of the interaction between the intersecting bands. The interaction strength can be determined from the measured branching ratio, provided the level energies are known, if it is assumed that only two bands are interacting and that the bands have the same intrinsic quadrupole moments. The γ-ray branching ratio $16^{+\prime} \to 14^{+\prime}/16^{+\prime} \to 14^{+} = 0.22 \pm 0.07$ implies an interaction strength between the ground band and yrast even-spin superband of $H_e = 51^{+2}_{-6}$ keV. Kistner *et al.*[8] obtain a value of 0.40 for this branching ratio, implying an interaction strength of 43 keV. These values are consistent with the 45-keV interaction strength implied by the perturbation of the level energies. The absolute $B(E2)$ values measured by multiple Coulomb excitation also are consistent with the 45-keV interaction strength as illustrated in Fig. 7. The $B(E2; 14^{+\prime} \to 12^{+})$ can be inferred from the γ-ray branching ratio $14^{+\prime} \to 12^{+}/14^{+\prime} \to 12^{+\prime}$ assuming that the superband has a constant intrinsic quadrupole moment similar to the ground band. This $B(E2; 14^{+\prime} \to 12^{+})$, shown by an open circle in Fig. 7, is in good agreement with the value (dashed line) predicted assuming a 45-keV interaction between the intersecting bands.

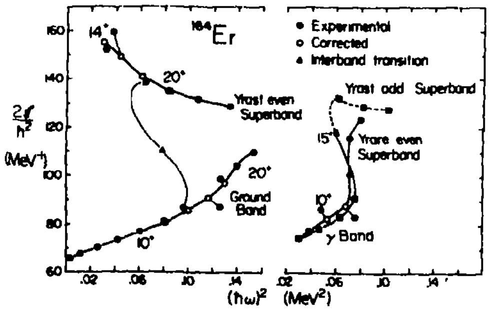

FIG. 11. Plot of $2\mathscr{I}/\hbar^2$ versus $(\hbar\omega)^2$ for members of the ground-state band, γ-vibrational band, and superbands in ^{164}Er. The open circles on the ground-state and even-yrast superbands are corrections for a 45-keV interaction matrix element. The energies of the 10^+_γ and 12^+_γ states were adjusted in accord with this interaction strength. The circles represent even-spin and the squares odd-spin states.

Gamma-ray branching ratios at the backbend have been measured[32,33] in two other nuclei, ^{154}Gd and ^{156}Dy. Average interaction matrix elements of 23.5 ± 1.5 keV for the 16^+ and 18^+ states in ^{154}Gd and 8.5 ± 1.5 keV for the 16^+ state in ^{156}Dy result from similar calculations. Band-interaction matrix elements of this size are remarkably small, i.e., they are nearly two orders of magnitude smaller than expected for Coriolis matrix elements at these spins, but are consistent with the rotation-alignment model.

Calculations[1,7] within the two-quasiparticle-plus-rotor model show that the aligned two $i_{13/2}$ neutron eigenfunctions for the yrast states become localized around $J=12$ and $R=I-12$ with increasing spin. On the other hand, the zero-quasiparticle ground band has $I=R$ for a fully paired state. The Coriolis force does not couple states with differing core rotation R, and thus the two bands interact only via the overlap of weak components in the wave functions. This overlap becomes progressively smaller with increasing spin due to the increased localization in R space of the aligned states. Calculations[1,4,7] within this model suggest that the interaction is ≤ 140 keV and is nearly constant for $10 < I < 22$. Although these calculations predict small interaction matrix elements, they are still more than a factor of 2 or 3 larger than experimental values. This implies that the assumptions made in these calculations may not be completely adequate. A more complete Hartree-Fock-Bogoliubov calculation by Mang[42] also predicts small interaction strengths.

A backbending plot for the transitions in the γ-vibrational band of ^{164}Er is shown on the right side of Fig. 11. The rotation-alignment model suggests that the interaction between the lowest rotation-aligned two-neutron bands and the ground-state, β and γ bands will be weak and of comparable strength. As a first approximation, we assumed that the three superbands have the same interaction strength of 45 keV with both the ground-state and γ bands. Furthermore, we assumed that we could estimate the positions of unobserved states by making the extrapolations shown by dashed lines in Fig. 10. The positions of the unperturbed levels were then calculated and are plotted as open circles in Fig. 11. This procedure produces a 25-keV shift in the 10_γ^+ level energy and equal but opposite shifts in the $10_\gamma^+ \rightarrow 8_\gamma^+$ and $12_\gamma^+ \rightarrow 10_\gamma^+$ transition energies. The obvious discontinuities in the backbending plot for the even-I members of the γ band are removed if the unperturbed values are used. The odd-spin state energies in the γ band are smooth in this spin region without such a shift. The behavior of the odd-spin sequence provides direct evidence that the odd-spin states in the yrast superband lie considerably higher than the even-spin states.

The abrupt backbends of both the even- and odd-spin sequences of the γ band are apparent around spins 13 and 14. Even without the placements of the tentative 17^+ and higher-spin states, it is also apparent that a marked reversal in the odd-even staggering occurs through the backbend region. This behavior becomes more obvious when the states of the γ band (and the superband continuation) are displayed as in Fig. 12, where it is clear that the odd-spin states lie low relative to the even-spin ones below the backbend and high after the backbend. There is also the possibility that the behavior in the (true) γ band below the backbend is caused by the interaction with the β band which lies 400 keV above the γ band. An interaction of about 100 keV between these bands could reproduce the observed odd-even staggering just below the backbend. However, the higher-spin states of the γ band give the best insight into this situation. Above the backbend the rotation-alignment model predicts both the behavior in the odd-even staggering and the relative moments of inertia of the yrare even-I and yrast odd-I superbands (89 and 96%, respectively, of the yrast even-I superband moment of inertia at similar spin values). The observed reversal in the staggering is the strongest evidence that these higher superbands correspond to the higher $i_{13/2}$ bands coupled to the ground band.

The γ-ray branching ratios at the band intersections with the γ band also can be used to determine the interaction strength. The absence of observed superband states below the intersection with the γ band can be understood if the interaction matrix element is 45 keV. Both the yrast and yrare even-I superbands are then predicted to decay 85% into the γ band at the intersection, while the odd-I superband is calculated to have a 77% branch into the γ band. Thus in all three cases the lower superband branch would be too weak to be observed in our work. The $B(E2; 10_\gamma^+ \rightarrow 12_\gamma^+)$ and $B(E2; 12_\gamma^+ \rightarrow 14_\gamma^+)$ values will be attenuated by about 50% assuming band mixing with a 45-keV interaction strength. The experimental $B(E2)$ values shown in Fig. 8 are of insufficient accuracy to determine whether this attenuation occurs.

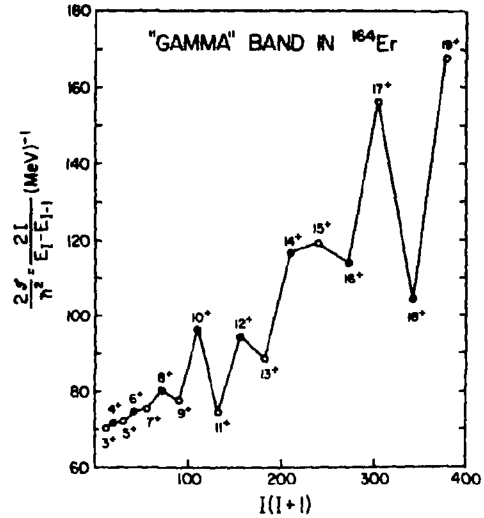

FIG. 12. Plot of $2I/(E_I - E_{I-1})$ versus $I(I+1)$ for the γ-vibrational band in ^{164}Er. The odd-even staggering as well as a change in this effect at higher spins is clearly shown.

The energy separation between the γ and ground bands is similar to the separation between the upper two superbands and the lowest superband. This suggests a second possible explanation[8,43,44] for the structure of the two upper superbands, i.e., they could be composed of the lowest $i_{13/2}$ yrast superband coupled to the γ band. However, it is not apparent to us that this model can explai the change in the odd-even staggering observed at the backbend.

The calculations show that the splitting between the yrast even-spin (I), the yrast odd-spin ($I-1$) and the yrare even-spin ($I-2$) two-quasiparticle bands is proportional to I at low spin, where a given K value dominates the wave function and then becomes constant when a rotation-aligned configuration dominates. If it is assumed that the three observed superbands are indeed two-quasiparticle rotation-aligned bands, as suggested by the present data, then the spin at which these splittings become approximately constant with I can be used as a check on the Coriolis matrix elements. Almberger *et al.*[40] used these data to determine if a Coriolis attenuation factor is required in two-quasiparticle-plus-rotor calculations. They determined the attenuation factor to be 0.97, i.e., essentially no attentuation, in agreement with the earlier conclusions of Flaum and Cline.[7] This result is to be compared with values from 0.60 to 0.76 required in one-quasiparticle-plus-rotor descriptions of positive-parity states in neighboring odd-neutron nuclei.[45-46]

C. Negative-parity bands

The yrast (5^-) and yrare (7^-) negative-parity bands have been interpreted[13] as rotational bands built on the $\{\frac{5}{2}^-[523]\nu;\frac{5}{2}^+[642]\nu\}_{5^-}$ and $\{\frac{7}{2}^+[404]\pi;\frac{7}{2}^-[523]\pi\}_{7^-}$ two-quasiparticle configurations. The moments of inertia for these bands derived from the E_I-E_{I-1} level spacing are plotted versus $I(I+1)$ in Fig. 13. The 5^- band exhibits (1) an odd-even staggering which reverses sign at spin 21^-, (2) a moment of inertia comparable to those of the positive-parity superbands, i.e., close to the rigid body value, (3) a moment of inertia which decreases with increasing spin at low-spin values, (4) intraband γ-decay paths which separate into an odd-spin sequence and an even-spin sequence, and (5) $E1$ transitions from the odd-spin states to the ground band which occur with inhibition factors of $\sim 10^4$ relative to the Weisskopf estimate. These features suggest that rotation alignment is important for this band. Similar features have been observed[30] in negative-parity bands in ^{126,128}Ba. In contrast, the 7^- band exhibits a moment of inertia which increases smoothly from 60% to 64% of the rigid-body value as the spin increases from 8^- to 13^- and $E1$ transitions are inhibited by factors of $\sim 5\times 10^9$ relative to the Weisskopf estimate. These are characteristic of a deformation-aligned band with a relatively good K quantum number.

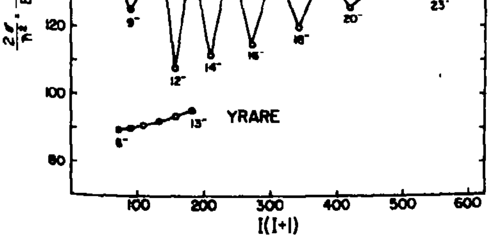

FIG. 13. Plot of $2I/(E_I-E_{I-1})$ versus $I(I+1)$ for the negative-parity states in ^{164}Er.

The behavior observed in these negative-parity bands was predicted by the two-quasiparticle-plus-rotor model calculations of Flaum and Cline.[7] These calculations, which were made for both positive- and negative-parity bands in ^{156}Er, showed that the structure of the yrast negative-parity band above spin 11^- was characterized by the $[\nu h_{9/2},\nu i_{13/2}]J^\pi=11^-$ rotation-aligned two-quasiparticle configuration. States with $I^\pi \leqslant 11^-$ were strongly influenced by collective 3^-, 5^-, etc. correlations because the residual two-quasiparticle interaction is comparable to the Coriolis interaction for these low-spin values. The rotation-aligned band was predicted[7] to exhibit a large odd-even staggering in excitation energy. The reason for this behavior is that the angular momentum of the core, R, has only even-spin values for axial symmetry. Consequently, since the total spin $\vec{I}=\vec{R}+\vec{J}$ (J is the angular momentum of the two quasiparticles), it follows that for J odd (even) the odd (even) spin, $|I|=|R|+|J|$ (fully aligned) and $I'=I-1$ (partially aligned) states will have the same value of R and hence the same rotational energy. Thus, since the $[\nu h_{9/2},\nu i_{13/2}]J^\pi=11^-$ two-quasiparticle configuration is predicted to dominate the structure of the yrast negative-parity band, then the I^-_{odd} and $I^-_{\text{odd}}-1$ states will be nearly degenerate in excitation energy when rotation alignment is complete. Flaum and Cline[7] predicted that at high-spin values the $[\nu h_{11/2},\nu i_{13/2}]J^\pi=12^-$, two-quasiparticle configurations will start to dominate the wave function and then the I^-_{even} states will be depressed in energy relative to the I^-_{odd} states. That is, a reversal in the odd-even staggering should occur at high spin.

The rotation-aligned configurations are predicted to dominate the wave function of the yrast negative-parity band in ^{156}Er because the Fermi level is close to the $\Omega=\frac{1}{2}$ orbitals based on $\nu i_{13/2}$ and $\nu h_{9/2}$ spherical shell model configurations. Two-quasiparticle-plus-rotor model calculations were not performed for the negative-parity states in ^{164}Er, but what will occur in ^{164}Er is clear by reference to the calculations[7] for ^{156}Er. The Fermi level in ^{164}Er is close to the $\Omega=\frac{5}{2}$ orbitals based on $\nu i_{13/2}$ and $\nu h_{9/2}$ spherical shell model configurations; consequently, the rotation alignment should be appreciably less complete than for ^{158}Er. This is what is observed. The I^-_{odd} states are depressed in energy relative to the I^-_{even} states, but the effect is appreciably smaller than predicted for ^{158}Er. The data also exhibit the large moments of inertia and the reversal in odd-even staggering at $I^\pi = 21^-$, both of which are expected for rotation-aligned two-quasiparticle configurations.

The calculations[7] for ^{158}Er show that rotation alignment is unimportant for the lowest two-proton negative-parity band because of the j and high Ω of the important configurations (i.e., $\frac{7}{2}^+[404]$ and $\frac{7}{2}^-[523]$). Consequently, this band should have a smaller moment of inertia and no noticeable odd-even staggering at lower-spin values. This is exactly what is observed for the 7^- band in ^{164}Er. Since K is a good quantum number, the $E1$ decay to the ground band will be strongly inhibited as is observed.

Bengtsson and Frauendorf[44] have also performed a detailed theoretical analysis of the observed bands in ^{164}Er. They analyze the energies of the bands in the rotating frame of the nucleus and compare these to the results of cranking model calculations. This comparison leads to quasiparticle assignments for the yrast (5^-) and yrare (7^-) negative-parity bands identical, at least at lower spins, to those indicated by the rotation-alignment calculations discussed in the present paper. Furthermore, Bengtsson and Frauendorf[44] suggest the $\{\frac{11}{2}^-[505]\nu;\ \frac{5}{2}^+[642]\nu\}_{8^-}$ interpretation for the band beginning with $I = 8$ at 2090.9 keV, an assignment which our rotation alignment calculations indicate may become important in the composition of the 5^- band at higher spins, as discussed above.

IV. SUMMARY

A relatively complete description of the high-spin states of ^{164}Er has emerged from the present work. Several positive-parity and two negative-parity bands have been identified. The previously reported backbending behavior of the positive-parity yrast sequence is demonstrated to result from the intersection of the ground band, seen to spin 22^+, with an even-spin "superband," having a large moment of inertia, which is observed from spins 12^+ to 24^+. The observed interaction between this yrast superband and the γ band demonstrates that this band possesses only even-spin members for $I \geq 12^+$. We have found additional even-spin (yrare even) and odd-spin (yrast odd) superbands possessing large moments of inertia which lie about 0.5 MeV above the lowest superband. The interaction of these bands with the γ band was observed. Although the evidence is weak, the data also imply that the ground-state and yrare even-spin bands intersect at $I \approx 24$. The observed level energies and γ-ray branchings are consistent with the three superbands having a constant 45 keV interaction matrix element with the ground-state and γ bands. These interaction matrix elements are more than an order of magnitude smaller than typical Coriolis matrix elements at these spin values. The level energies of the two negative-parity bands are observed to behave differently; the 7^- band behaves like a good rotor while the 5^- band exhibits an odd-even staggering characteristic of a rotation-aligned band.[1,7]

The Coulomb excitation and lifetime data are all consistent with a picture of interacting rotational bands with an interaction matrix element ≈ 45 keV. In particular, the $B(E2)$ values for the unperturbed ground band are in agreement with the rigid-rotor relation, i.e., with a constant intrinsic quadrupole moment, while the excitation of the γ band is consistent with the prediction of the rigid-triaxial-rotor model with asymmetry $\gamma = 12.7°$.

The rotation-alignment model successfully explains the available data and correctly predicts the occurrence and relative energies of the super bands when typical collective model parameters are assumed. Moreover, it gives approximately the correct spin for the intersection of these thre bands with the ground-state and γ bands. This model predicts the relative moments of inertia of all the intersecting bands and, in particular, correctly accounts for the reversal in the odd-even staggering at the backbend in the γ band. The model also reproduces the very different moment of inertia and odd-even staggering behavior of the 5^- and 7^- bands. This model is consistent with the observed $E2$ properties. The rotation-alignment model also predicts very small interaction matrix elements between the intersecting bands although not quite as small as the observed values. All of the evidence strongly supports the rotation-alignment model description of the structure of the superbands in ^{164}Er.

It should be pointed out that, although the rotation alignment and cranking models take somewha different approaches to explain the backbending phenomenon, they both predict very similar band crossing properties and represent the same underlying physics.

ACKNOWLEDGMENTS

We are indebted to the operating crew of the SuperHILAC and the ORIC operations staff for their help during these experiments. This research was supported in part by the U.S. Department of Energy, partially under contract with Union Carbide Corporation, and by the National Science Foundation. One of us (E.L.R.) wishes to thank the University of Alabama (Birmingham) Graduate Faculty Research Committee for partial support of his participation in this research.

---

[*] Also at Lawrence Berkeley Laboratory, Berkeley, California 94720.

[†] Deceased.

[‡] Present address: Cyclotron Institute, Texas A & M University, College Station, Texas 77843.

[§] Present address: Gesellschaft für Schwerionenforschung, Darmstadt, Germany.

[∥] Present address: Department of Physics, University of Liverpool, P. O. Box 147, Liverpool L69 3BX, United Kingdom.

[¶] Present address: Etudes et Productions, Schlumberger, 25 Rue de la Cavée, 92142 Clamart, France.

[**] Present address: Cyclotron Laboratory, Michigan State University, East Lansing, Michigan 48824.

[††] Present address: Department of Radiology, Medical Physics, University Hospitals, Madison, Wisconsin 53706.

[1] F. S. Stephens and R. S. Simon, Nucl. Phys. A183, 257 (1972).

[2] F. S. Stephens, Rev. Mod. Phys. 47, 43 (1975).

[3] B. R. Mottelson and J. G. Valatin, Phys. Rev. Lett. 5, 511 (1960).

[4] I. Y. Lee, D. Cline, R. S. Simon, P. A. Butler, P. Colombani, M. W. Guidry, F. S. Stephens, R. M. Diamond, N. R. Johnson, and E. Eichler, Phys. Rev. Lett. 37, 420 (1976).

[5] N. R. Johnson, S. W. Yates, R. M. Ronningen, R. D. Hichwa, L. L. Riedinger, and A. C. Kahler, Bull. Am. Phys. Soc. 21, 984 (1976) and Proceedings of the International Conference on Nuclear Structure, Tokyo, 1977, edited by T. Marumori (Physical Society of Japan, Tokyo, 1978).

[6] N. R. Johnson, D. Cline, S. W. Yates, F. S. Stephens, L. L. Riedinger, and R. M. Ronningen, Phys. Rev. Lett. 40, 151 (1978).

[7] C. Flaum and D. Cline, Phys. Rev. C 14, 1224 (1976).

[8] O. C. Kistner, A. W. Sunyar, and E. der Mateosian, Phys. Rev. C 17, 1417 (1978).

[9] M. J. Saltmarsh (unpublished).

[10] M. L. Halbert (unpublished).

[11] M. V. Banaschik, C. Günther, H. Hübel, A. C. Rester, G. Nowicki, and J. J. Pinajian, Nucl. Phys. A222, 459 (1974).

W. F. Davidson, R. M. Lieder, H. Beuscher, A. Neskakis, G. A. Varley, J. C. Willmott, F. Kearns, and J. C. Lisle, J. Phys. G 3, 199 (1976).

F. W. N. de Boer, P. F. A. Goudsmit, P. Koldewijn, and G. J. Meijer, Nucl. Phys. A169, 577 (1971).

R. Graetzer, G. B. Hagemann, K. A. Hagemann, and B. Elbek, Nucl. Phys. 76, 1 (1966).

R. L. West, E. G. Funk, A. Visvanathan, J. P. Adams, and J. W. Milhelich, Nucl. Phys. A270, 300 (1976).

J. H. Jett and D. A. Lind, Nucl. Phys. A155, 182 (1970).

D. Elmore, Ph.D. thesis, University of Rochester, 1974.

[18] A. Winther and J. de Boer, in *Coulomb Excitation*, edited by K. Adler and A. Winther (Academic, New York, 1966), p. 303.

[19] R. M. Ronningen, R. B. Piercey, J. H. Hamilton, C. F. Maguire, A. V. Ramayya, H. Kawakami, B. van Nooijen, R. S. Grantham, W. K. Dagenhart, and L. L. Riedinger, Phys. Rev. C 16, 2218 (1977).

[20] R. Brenn, H. Spehl, A. Weckerlin, H. Doubt, and G. van Middlekoop, Z. Phys. A281, 219 (1977).

[21] M. W. Guidry, P. A. Butler, R. Donagelo, E. Grosse, Y. El Masri, I. Y. Lee, F. S. Stephens, R. M. Diamond, L. L. Riedinger, C. R. Bingham, A. C. Kahler, J. A. Vrba, E. L. Robinson, and N. R. Johnson, Phys. Rev. Lett. 40, 1016 (1978).

[22] D. Cline, Nukleonika (to be published).

[23] W. T. Milner (unpublished).

[24] L. C. Northcliffe and R. F. Schilling, Nucl. Data Tables A7, 23 (1970).

[25] J. F Ziegler and W. K. Chu, At. Data Nucl. Data Tables 13, 463 (1974).

[26] M. W. Guidry, P. A. Butler, P. Colombani, I. Y. Lee, D. Ward, R. M. Diamond, F. S. Stephens, E. Eichler, N. R. Johnson, and R. Sturm, Nucl. Phys. A266, 228 (1976).

[27] J. Lindhard, M. Scharff, and H. E. Schiott, K. Dan. Vidensk. Selsk, Mat. Fys. Medd. 33, no. 14 (1963).

[28] A. E. Blaugrund, Nucl. Phys. 88, 501 (1966).

[29] F. Kearns, G. Varley, G. D. Dracoulis, T. Inamura, J. C. Lisle, and J. C. Willmott, Nucl. Phys. A278, 109 (1977).

[30] C. Flaum, D. Cline, A. W. Sunyar, and O. C. Kistner, Phys. Rev. Lett. 33, 973 (1974); Nucl. Phys. A264, 291 (1976).

[31] R. A. Warner, F. M. Bernthal, J. S. Boyno, T. L. Khoo, and G. Sletten, Phys. Rev. Lett. 31, 835 (1973).

[32] T. L. Khoo, F. M. Bernthal, J. S. Boyno, and R. A. Warner, Phys. Rev. Lett. 31, 1146 (1973).

[33] H. R. Andrews, D. Ward, R. L. Graham, and J. S. Geiger, Nucl. Phys. A219, 141 (1974).

[34] R. Lieder, H. Beuscher, W. F. Davidson, A. Neskakis, C. Mayer-Böricke, Y. El Masri, P. Monseu, J. Steyaert, and J. Vervier, Phys. Lett. 49B, 161 (1974).

[35] Y. El Masri, R. Janssens, C. Michel, P. Monseu, J. Steyaert, and J. Vervier, Z. Phys. A274, 113 (1975).

[36] M. Piiparinen, J. C. Cunnane, P. J. Daly, C. L. Dors, F. M. Bernthal, and T. L. Khoo, Phys. Rev. Lett. 34, 1110 (1975).

[37] L. Funke, P. Kemnitz, G. Winter, S. A. Hjorth, A. Johnson, and T. Lindblad, Phys. Lett. 55B, 436 (1975).

[38] D. Cline, Bull. Am. Phys. Soc. 21, 962 (1976).

[39] M. A. J. Mariscotti, G. Scharff-Goldhaber, and B. Buck, Phys. Rev. 178, 1864 (1969).

[40] J. Almburger, I. Hamamoto, and G. Leander, Nucl. Phys. A333, 184 (1980).

[41] R. O. Sayer, J. S. Smith III, and W. T. Milner, At. Data Nucl. Data Tables 15, 85 (1975).

[42] H. J. Mang, private communication, and J. L. Egido, H. J. Mang, and P. Ring, Nucl. Phys. A334, 1 (1980).

[43] L. K. Peker, private communication.

[44] R. Bengtsson and S. Frauendorf, Nucl. Phys. A314, 27 (1979).

[45] S. A. Hjorth, H. Ryde, K. A. Hagemann, G. Løvhøiden, and J. C. Waddington, Nucl. Phys. A144, 513 (1970).

[46] G. Løvhøiden, P. O. Tjom, and L. O. Edvardson, Nucl. Phys. A194, 463 (1972).

[47] I. Ben-Zvi, A. E. Blaugrund, Y. Dar, G. Goldring, J. Hess, M. W. Sachs, E. Z. Skurnik, and Y. Wolfson, Nucl. Phys. A117, 625 (1968).

PHYSICAL REVIEW C VOLUME 21, NUMBER 6 JUNE 1980

Creation and observation of a pion condensate in high-energy heavy-ion collisions

S. Krewald* and J. W. Negele
Laboratory for Nuclear Science and Department of Physics, Massachusetts Institute of Technology, Cambridge, Massachusetts 02139

(Received 4 February 1980)

Spin-isospin instabilities corresponding to the onset of π^0 condensation are investigated for the case of central collisions of high-energy heavy ions in the time-dependent mean-field approximation.

[NUCLEAR REACTIONS Calculation of pion condensation in heavy-ion collisions. Time-dependent Hartree-Fock calculation for $^{15}N+^{15}N$ and $^{39}K+^{39}K$.]

I. INTRODUCTION

The possible existence of pion condensation at densities of the order of magnitude of nuclear densities[1-6] raises a number of challenging questions and novel possibilities in nuclear physics and astrophysics. Most theoretical effort to date has concentrated on equilibrated cold matter at uniform proton and neutron density relevant to neutron stars.[1-12] Although the occurrence of pion condensation in such equilibrated dense matter would have exceedingly interesting astrophysical implications for the structure and cooling of neutron stars, direct inferences concerning the quantitative behavior of pion condensation from existing data are highly ambiguous.[13,14] Hence it is important also to consider the possibility of terrestrial production of condensates in high-energy heavy-ion collisions.

The main qualitative features of pion condensation near threshold in equilibrated nuclear matter have been understood in terms of the random phase approximation (RPA) contribution to the density-density correlation function.[1-12] As the density increases, a collective state of particle-hole and Δ-hole excitations with the quantum numbers of the pion and finite wavelength decreases in energy until it becomes a self-sustaining zero frequency mode at the critical density ρ_c. Whereas the bare πNN p-wave driving term alone would create a condensate below nuclear density, estimates of the combined effects of pion S-wave interactions, Δ propagation, N-N correlations, and Δ-N correlations suggest that the onset occurs somewhere in the region of twice nuclear density.

A. Pion condensation in the static limit

An essential observation for this present work is the fact that near threshold, all the many-body physics in terms of propagation of pions and isobars may be equally well described in terms of an instantaneous effective nucleon-nucleon interaction. At threshold, where one is dealing with a zero frequency mode, the static reduction of the pion propagator is exact. But even well away from the threshold $\omega \ll \mu$, so that the static approximation should be quite adequate. Isobar propagation and correlation corrections are also included, of course, by taking the static limit of the corresponding effective operators.

In this language, as has also been emphasized in Ref. 15, the physics of pion condensation is completely described in terms of spin-isospin fluctuations. As the density increases, spin-isospin modes of positive, neutral, and negative charge become softer and at a critical density become self-sustaining, at which point the ground state acquires spin-isospin oscillations. The analog of the finite expectation value of the pion field, or order parameter, in the condensed phase becomes the finite expectation value of the pion source term $\vec{\nabla}\cdot\langle\vec{\sigma}\tau\rangle$. [The pion field is just the convolution of this source term with a Yukawa potential as seen in Eq. (2.14).] If one neglects the charge-changing components of the interaction and works in a space in which only wave functions of a single charge are included, only the neutral mode, corresponding to a π^0 condensate, exists and has a real order parameter. In the full space of all charge states and including the charge-changing components, one has charged modes corresponding to $\pi^{\pm}$ condensates with complex order parameter. Although the π^- mode is relevant to the neutron rich matter in neutron stars, in heavy-ion collisions we will consider essentially equal neutron and proton densities for which all three modes are degenerate and we will thus restrict our attention to the technically simpler calculation of neutral condensation.

The static description is extremely important both in understanding the physics of condensation and in implementing practical calculations. Any careful nuclear structure calculation with an ef-

© 1980 The American Physical Society

TABLE I. Parameters of the energy functional, nuclear matter properties, and Landau parameters.

t_0 (MeV fm^3)	−497.73	k_F (fm^{-1})	1.29
x_0	1.464	E/A (MeV)	−15.43
t_3 (MeV fm^6)	17 270	K (MeV)	369
V_L (MeV)	−338.84	a_T (MeV)	26.0
V_U (MeV)	−378.41	k_c (fm^{-1})	1.50
a (fm)	0.459 79	q_c (fm^{-1})	1.99
t_4 (MeV fm^3)	280	f_0 (MeV fm^3)	242
t_5 (MeV fm^3)	150	f_0' (MeV fm^3)	194
(f^2/μ^2) (MeV fm^3)	28	g_0 (MeV fm^3)	280
a_r (fm)	1.41	g_0' (MeV fm^3)	150

and the indices s and q denote spin and isospin, respectively.

The values of the phenomenological force constants are shown in Table I and were selected as follows. To obtain the correct gross behavior of the shape and density of the nuclei throughout the collision, the values t_0, t_3, a, and $\frac{1}{3}(V_L+V_u)$ were taken from Ref. 17. Condensation is governed by the spin-isospin dependent interaction

$$V_0(\vec{q}) = t_5\vec{\sigma}\cdot\vec{\sigma}\,'\vec{\tau}\cdot\vec{\tau}\,' - 4\pi\left(\frac{f^2}{\mu^2}\right)\frac{1}{q^2+\mu^2}\,\vec{\sigma}\cdot\vec{q}\vec{\sigma}'\cdot\vec{q}\vec{\tau}\cdot\vec{\tau}' , \tag{2.4}$$

where t_5 and f^2/μ^2 represent effective renormalized coefficients incorporating the average effect of Lorentz-Lorenz, Δ-hole, and other corrections. The values of these coefficients were therefore adjusted to reproduce typical values of the critical density and critical momentum arising from complete pion condensation calculations. The value of $\rho_c = 1.5\ \rho_0$ was selected from the lower end of the range of possible condensation densities so as to enhance our chance of seeing anything at all in the very light collisions calculated in this work. From Fig. 8 of Ref. 21, for example, one sees that for $\rho_c \sim 1.5\ \rho_0$, $q_c \sim 1.5\ k_F$ so that our parameters are in fact consistent with the result of a full calculation. The conventional Landau parameter $g'_{\text{conventional}} = 2m_N k_F/\pi^2\ g_0' = 0.95$ should not be compared directly with values $1.1 < g_0' < 1.8$ obtained in the Pb region,[22] since the present analysis explicitly includes the OPEP. It also cannot be directly compared with the values of Ref. 21, since correction factors of the form $[1-g'\xi(h)]$ have simply been lumped into the overall constants t_5 and f^2/μ^2. Note that our value of the driving term $f^2/\mu^2 = 28$ MeV fm^3 is in fact not renormalized very much from the value 31 MeV fm^3 obtained with the bare pion-nucleon coupling constant.

All other spin-isospin channels were regarded as inessential and thus only constrained so as to avoid completely unphysical behavior. Thus, x_0 and $(V_L - V_U)$ were simply constrained to produce a sensible symmetry energy coefficient a_τ and a stable Landau parameter f_0' up to $2\rho_0$, and t_4 was defined to avoid instabilities arising from the Landau parameter g_0.

In a translationally invariant system, our energy functional yields the following RPA effective interaction:

$$V_R(\vec{q}) = \frac{t_5\vec{\sigma}\cdot\vec{\sigma}'\tau\cdot\tau'}{1-t_5 4\Pi_0(q)} - \frac{4\pi(f^2/\mu^2)\vec{\sigma}\cdot\vec{q}\vec{\sigma}'\cdot\vec{q}\vec{\tau}\cdot\vec{\tau}'}{(q^2+\mu^2)[1-t_5 4\Pi_0(q)]\left\{1-\left[t_5-\dfrac{4\pi(f^2/\mu^2)q^2}{\mu^2+q^2}\right]4\Pi_0(q)\right\}} , \tag{2.5}$$

where $\Pi_0(q)$ denotes the zero frequency Lindhardt function and the factors of 4 arise from spin-isospin sums. In the special case of nuclear matter with a Fermi momentum k_F, the zero frequency Lindhardt function is

$$\Pi_0(q,k_F) = \frac{mk_F}{\hbar^2 4\pi^2}\left\{-1+\frac{k_F}{q}\left[1-\tfrac{1}{4}(q/k_F)^2\right]\ln\left|\frac{1-\frac{1}{2}(q/k_F)}{1+\frac{1}{2}(q/k_F)}\right|\right\} . \tag{2.6}$$

In nuclear matter, the Fermi momentum corresponding to the critical density, k_c, and critical momentum transfer q_c, for pion condensation are determined by the double pole of the effective interaction:

$$D(q_c,k_c) = 1-\left[t_5-\frac{4\pi(f^2/\mu^2)q^2}{\mu^2+q^2}\right]4\Pi_0(q_c,k_c) = 0 \tag{2.7}$$

and

$$\frac{\partial}{\partial q} U(q_c, k_c) = 0 . \tag{2.8}$$

The resulting values are shown in Table I together with the Landau parameters

$$\begin{aligned} f_0 &= \tfrac{3}{4} t_0 + \tfrac{3}{8} \rho t_3 + \frac{V_L + V_U}{2} \frac{4\pi a^3}{1 + a^2 k_F^2} , \\ f_0' &= -\frac{t_0}{4} - \frac{t_0 x_0}{2} - \frac{t_3}{8} \rho + \frac{V_L - V_U}{2} \frac{4\pi a^3}{1 + a^2 k_F^2} , \end{aligned} \tag{2.9}$$

$$g_0 = t_4 ,$$

and

$$g_0' = t_5 .$$

The nuclear matter properties were derived from the equation of state

$$\frac{E}{A} = \frac{3}{5} \frac{\hbar^2}{2m} k_F^2 + [\tfrac{3}{8} t_0 + (V_L + V_U) \pi a^3] \rho + (\tfrac{1}{16} t_3) \rho^2 . \tag{2.10}$$

The static HF equations are obtained by variation of (2.1):

$$\frac{\delta}{\delta \psi_\nu^*(r)} \left[E - \sum_{\nu\nu'} e_{\nu\nu'} \int d^3 r \, \psi_\nu^*(r) \psi_{\nu'}(r) \right] = 0 \tag{2.11}$$

which yields

$$-\frac{\hbar^2}{2m} \nabla^2 \psi_\nu(\vec{r}) + [V_q(\vec{r}) + t_4 \langle \vec{\nabla}(\vec{r}) \rangle \cdot \vec{\sigma} + t_5 \langle \vec{\sigma}\tau_3(\vec{r}) \rangle \cdot \vec{\sigma}\tau_3 - \vec{\nabla} \cdot \phi(\vec{r}) \vec{\sigma}\tau_3] \psi_\nu(\vec{r}) = e_\nu \Psi_\nu(\vec{r}) , \tag{2.12}$$

where

$$\begin{aligned} V_q(\vec{r}) = {} & \tfrac{1}{2} t_0 (1 - x_0) \rho_q(\vec{r}) + \tfrac{1}{2} t_0 (2 + x_0) \rho_{-q}(\vec{r}) + \tfrac{1}{4} t_3 [2 \rho_q(\vec{r}) \rho_{-q}(\vec{r}) + \rho_{-q}^2(\vec{r})] \\ & + V_L \int d^3 r' \frac{e^{-|r - r'|/a}}{|r - r'|/a} \rho_q(r') + V_U \int d^3 r' \frac{e^{-|r - r'|/a}}{|r - r'|/a} \rho_{-q}(r') , \end{aligned} \tag{2.13}$$

$$\phi(\vec{r}) = -\left(\frac{f^2}{\mu^2} \right) \int d^3 r' \frac{e^{-|r - r'|/\mu r}}{|r - r'|} \vec{\nabla} \cdot \langle \sigma\tau_3(r') \rangle . \tag{2.14}$$

and $q = \pm 1$ denotes the two nucleon isospin states. The equation of motion is obtained by replacing the right-hand side of Eq. (2.12) by $i\hbar[\partial \psi_\nu(\vec{r}, t)/\partial t]$.

In order to render the computation practical, axially symmetric wave functions

$$\psi_\nu^q(r, z, \phi) = \sum_{\nu, s} \psi_\nu^m(r, z) \frac{e^{i m_s \phi}}{\sqrt{2\pi}} \chi_s^{1/2} \chi_q^{1/2} \tag{2.15}$$

with $m_{-1/2} = m_{+1/2} + 1$ were used where s denotes the spin state. Among the various symmetries used in previous calculations, time-reversal invariance of the HF determinant can no longer be used. A time-reversal invariant determinant has a vanishing spin density and thus, the symmetry conservation of the TDHF equations would prevent the building up of any fluctuations of the spin density. In order to bypass this difficulty, the present formalism will be applied to odd-mass nuclei.

The initial TDHF wave function consists of two spatially separated Hartree-Fock determinants, moving towards each other with a given initial velocity. Only head-on collisions were considered. Reactions with the spins of the original nuclei both aligned and antialigned were investigated.

Apart from the total density $\rho(r, t)$, the observable quantities are the different spin and isospin densities $\langle \tau_3(\vec{r}, t) \rangle$, $\langle \vec{\sigma}(\vec{r}, t) \rangle$, and $\langle \vec{\sigma}\tau_3(\vec{r}, t) \rangle$. A phase transition is signaled by the growth of fluctuations of the spin-isospin density $\langle \vec{\sigma}\tau_3(\vec{r}, t) \rangle$. Since this is a vector quantity, it is more convenient to look at the pseudoscalar source term $\vec{\nabla} \cdot \langle \vec{\sigma}\tau_3 \rangle$ of the one-pion exchange potential.

The actual calculation is based on a discretized equation of motion derived by varying the discretized energy functional. This method, as compared to discertizing Eq. (2.12), has the advantage of yielding manifestly Hermitian matrix equations. The details are presented in the Appendix.

The discretization error arises mainly from the discretized spatial derivatives occurring in the kinetic energy and pion source term. In previous investigations it was shown that mesh sizes up to $\Delta = 1$ fm gave stable results.[18,20] In the present calculation, additional numerical noise originates from the source term of the one-pion exchange potential. A seven-point differentiation formula was used in order to reduce the discretization error to the order Δ^5. In order to test the influence of the discretization error, the uniform translation of a single nucleus was investigated. Although the total energy was strictly conserved, the expectation value of the OPEP was oscillating in time with an amplitude proportional to Δ^5. A mesh size of $\Delta = 0.4$ fm was required in order to reduce the amplitude of this oscillation below 10% of the OPEP expectation value at the time $t = 0$.

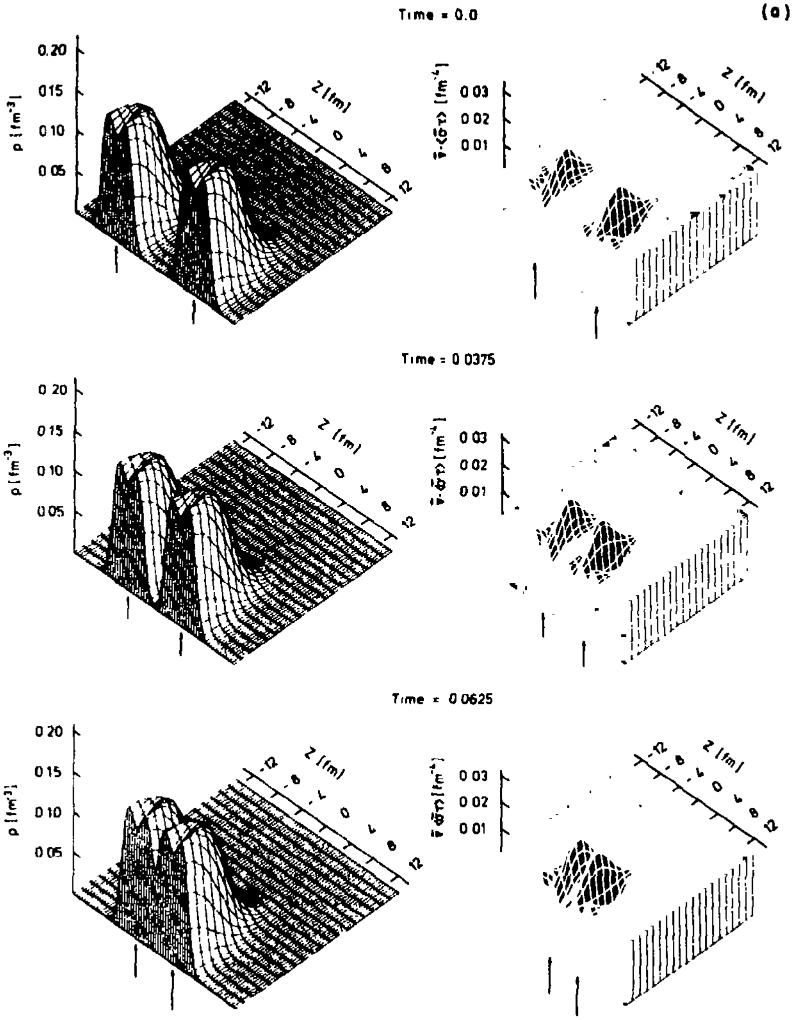

FIG. 1. (a) Density ρ (left part) and the divergence of the spin-isospin density $\vec{\nabla}\cdot\langle\vec{\sigma}\tau_3\rangle$ (right part) for a head-on $^{15}N+{}^{15}N$ collision at a cm energy of 20 MeV/nucleon. The density and the divergence of the spin-isospin density are plotted vertically above the $(r_\perp, z)$ plane. The z axis is in the beam direction. The length scale is given in fm, the time scale in 10^{-21} sec. At $t=0$, the right nucleus is given by a $K=3/2$ ground state, the left one has $K=-3/2$. The arrows indicate the positions of the centers of mass of nuclei moving with the given initial speed. (b) Similar to (a), except at later times. (c) Similar to (a), except at later times. (d) Similar to (a), except at later times.

III. RESULTS AND DISCUSSION

Figures 1(a)–1(d) show plots of the nucleon density $\rho(r,t)$ and of the divergence of the spin-isospin density $\vec{\nabla}\cdot\langle\vec{\sigma}\tau_3(r,t)\rangle$ for a head-on $^{15}N+{}^{15}N$ reaction at a center-of-mass bombarding energy per nucleon $E/A=20$ MeV, corresponding to $E_{\rm Lab}=1.20$ GeV. *The beam direction is parallel to the z axis.* The markers indicate the positions of the centers of two nuclei moving with the initial velocity. The central density in the ground state ($t=0\times10^{-21}$ sec) is $\rho=0.13$ fm^{-3}.

The spin-isospin density of the ground state is mainly determined by the unpaired nucleon. For the right nucleus which has an angular momentum projection $K=+\frac{1}{2}$ along the beam axis, the spin-up

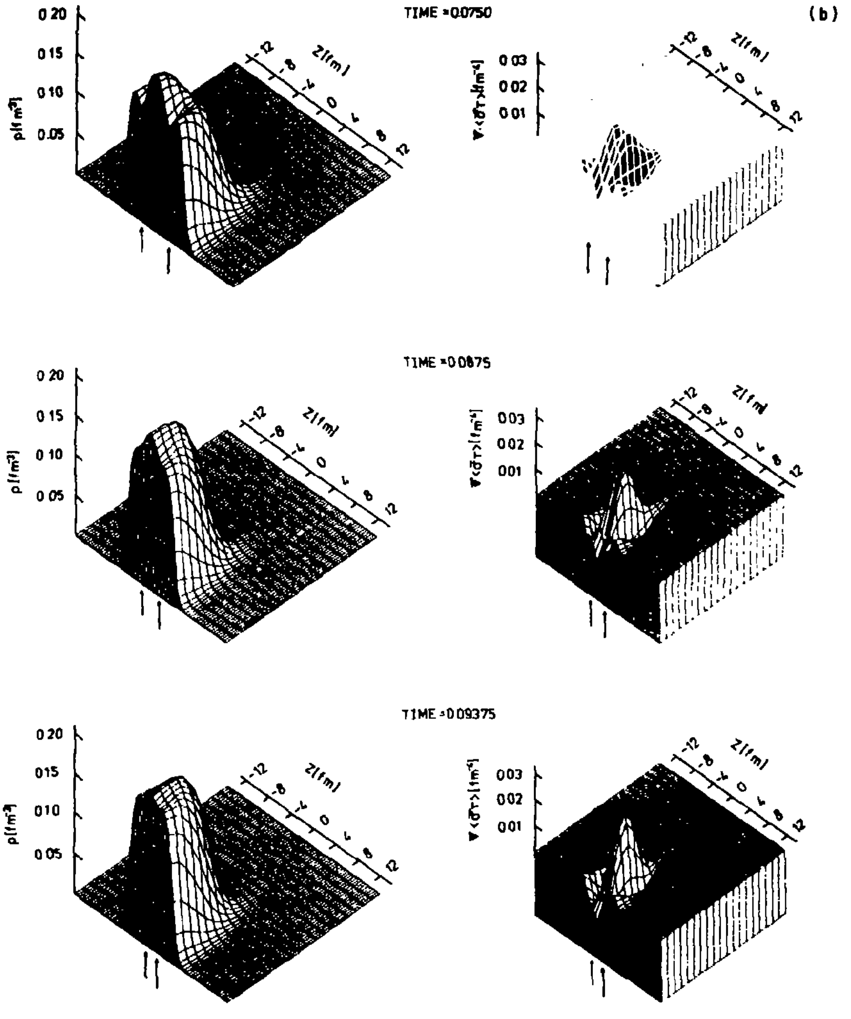

FIG. 1. *(Continued.)*

component of the corresponding wave function is approximately given by a p ($m=1$) harmonic oscillator wave function while the spin-down component is close to zero. Therefore the largest component of the spin-isospin vector density is the one in the z direction, a toroidal distribution around the beam axis. The divergence of the spin-isospin density is mainly determined by the z derivative of this component which results in the dipole-like structure in the right part of the figure.

The left nucleus has angular momentum projection $K=-\frac{1}{2}$. The ions clutch at $t\simeq 0.04\times 10^{-21}$ sec. The density in the center of the compound system now builds up rapidly. By the time $t=0.075\times 10^{-21}$ sec [Fig. 1(b)] the central density has reached a value of $\rho=0.200$ fm^{-3}. The divergence of the spin-isospin density has slightly increased in the interior. After this time, the central density does no longer increase significantly. The region of high density now spreads mainly in the direction orthogonal to the beam axis, while the divergence of the spin-isospin density continues to grow until it reaches its maximum of 0.026 fm^{-4} at $t=0.094\times 10^{-21}$ sec.

By the time $t=0.1\times 10^{-21}$ sec, only a very small region of high density ($\rho\simeq 0.2$ fm^{-3}) has remained

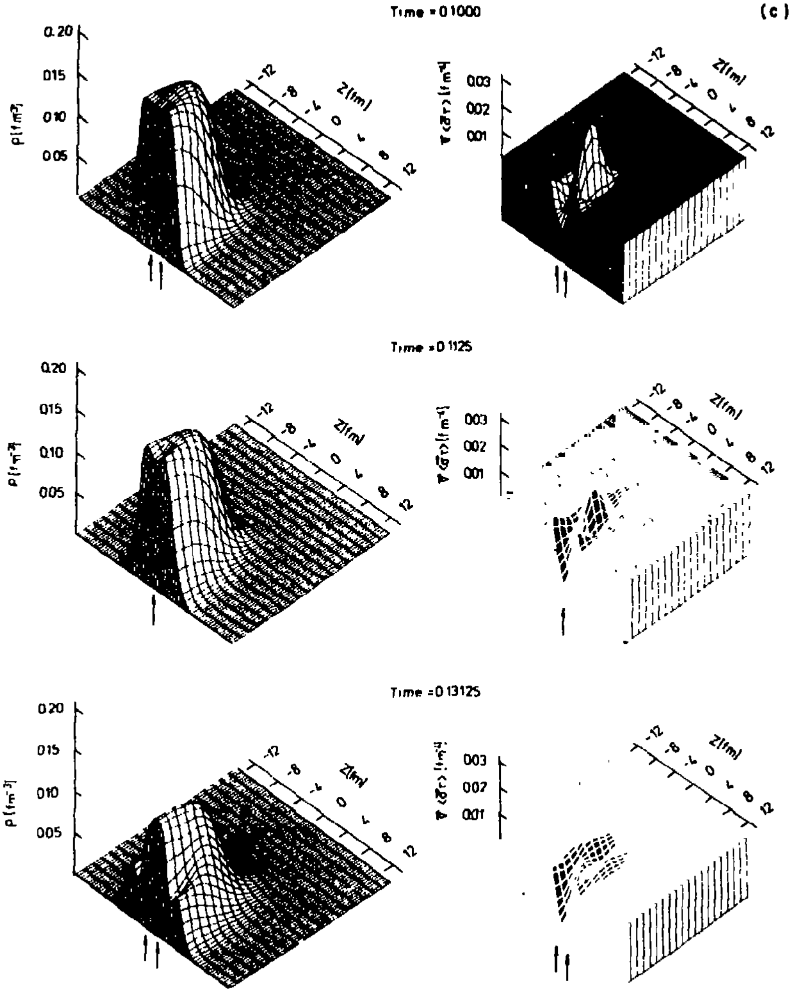

FIG. 1. *(Continued.)*

at a distance of ~ 1 fm orthogonal to the beam axis and the growth of the spin-isospin structure has stopped. At $t = 0.15\times 10^{-21}$ sec [Fig. 1(d)], individual fragments appear which finally separate.

The collision of a $K=\frac{1}{2}$ nucleon with a $K=-\frac{1}{2}$ nucleon yields a particularly clean indication of the nonlinear growth of a spin-isospin instability. Whereas linear superposition of the two initial wave functions would yield a vanishing source term at maximum overlap, one observes in Fig. 1(c) a source term at $t = 0.1125$ somewhat larger than that existing originally in either the target or projectile.

Nevertheless, the growth of the spin-isospin density falls far behind the factor of 10–20 one might have expected from the RPA estimates of Ref. 16. The lack of growth may arise from any combination of the factors that the time interval during which a high density region existed was too short, the spatial region was too small, the driving term was too weak, or the fluctuation geometry of concentric cylinders forced by axial symmetry is less favorable than that of plane layers permitted by three-dimensional geometry.

One may attempt to increase the time interval by lowering the energy. However, at a c.m. energy

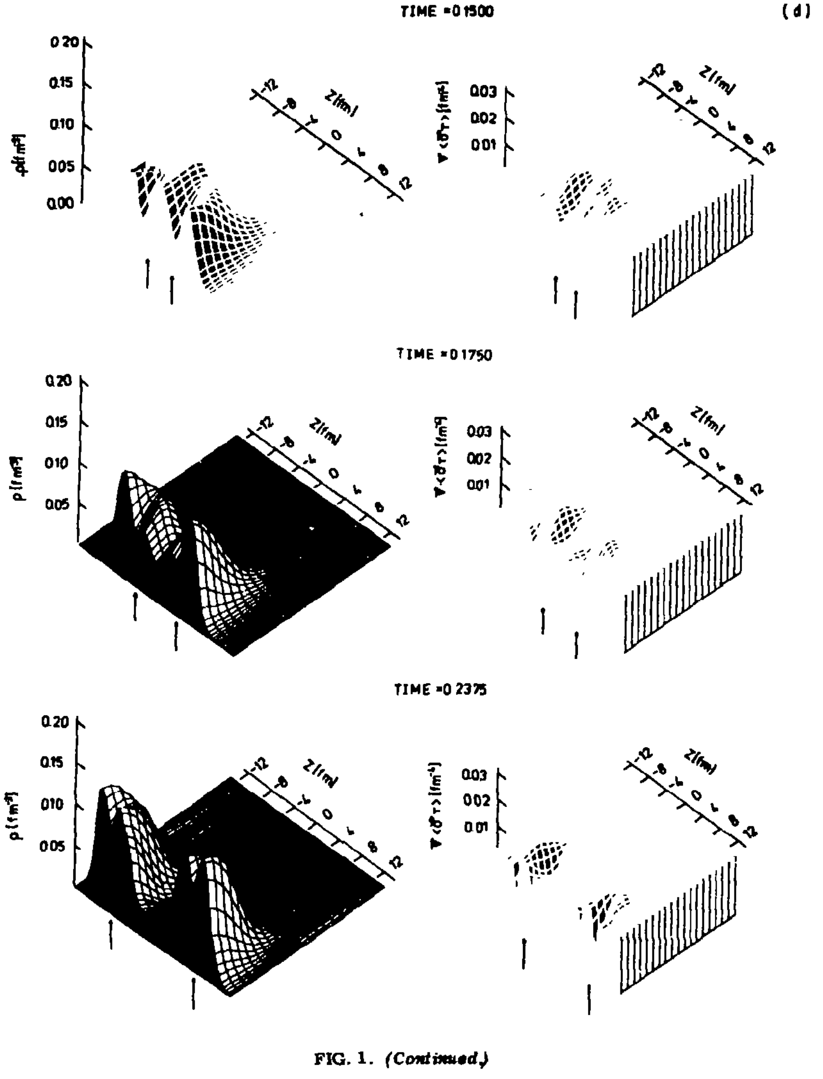

FIG. 1. *(Continued.)*

10 MeV/*A*, each Fermi sphere is displaced by
ighly $k_{F/2}$ so that some of the advantage of the
ancement of the Lindhardt function for two in-
penetrating streams is lost. Rather than in-
ease the time interval at the expense of the
ength of the driving term, a much more promis-
possibility is to increase both the size of the
h density region and the overlap time by collid-
heavier nuclei. Hence we have also investi-
ed the largest computationally feasible system
+ ^{39}K at a c.m. energy of $E/A = 20$ MeV.
igure 2 displays the results of a ^{15}N+^{15}N collision at 10 MeV/*A* and a ^{39}K+^{39}K collision at 20 MeV/*A*. In the upper part, the time dependence of the energy of the $\sigma\tau$ channel [the contribution to Eq. (2.1) proportional to t_s and f^*] is given. In the middle portion, the density in the center of the compound system is shown as a function of time. In the lower part, the fragment separation distance

$$R=\int d^3r\,|z|\,\rho(\vec{r},t) \qquad (3.1)$$

is displayed. For the $A=15$ reaction, it is found that the pionic mode is more strongly excited in the case of the higher bombarding energy. A comparison of both reactions shows that the energy in the στ channel stops growing very soon after the maximum density has been reached. By the time at which the two original nuclei overlap, given approximately by the minimum of $R(t)$, it has already substantially decreased. We have to conclude that a pionic instability is favored only during a small fraction of the total collision time. Although we were unable to evolve the $A = 39$ reaction for corresponding time intervals, the early portion of the reaction shown in Fig. 2 does not indicate substantially greater growth of an instability for this larger system.

IV. CONCLUSION

Evaluation of the one-body density matrix in the time-dependent mean-field approximation appears to provide a reasonable framework for investigation of the growth of spin-isospin instabilities in the nonequilibrium conditions encountered in heavy-ion reactions at c.m. energies of the order of 20 MeV/A. In contrast to the restrictive assumption of local equilibrium implicit in the use of an equation of state, the one-body density matrix is sufficiently general to include the strong enhancement of the Lindhart function for two interpenetrating streams of matter. At 20 MeV/A, the energy is sufficiently high that most of the advantage of the enhanced two-stream driving term is obtained and yet not so high as to invalidate a mean-field description of the reaction.

Nonlinear growth of a spin-isospin mode has been demonstrated even for the very light systems and the nonoptimal axially symmetric geometry considered in this work. Although we deliberately selected initial conditions in which linear superposition of the source term in the target and projectile at maximum overlap would have produced zero field, in fact the source term at maximum overlap was comparable to or larger than that in the original target or projectile. Although the growth observed in these small systems was far from dramatic, it is an open question as to what would occur in this theory for a full three-dimensional calculation of Pb+Pb, where the larger overlap time, larger spatial extent, and possibility of planar rather than cylindrical fluctuations are all much more conducive to the growth of an instability.

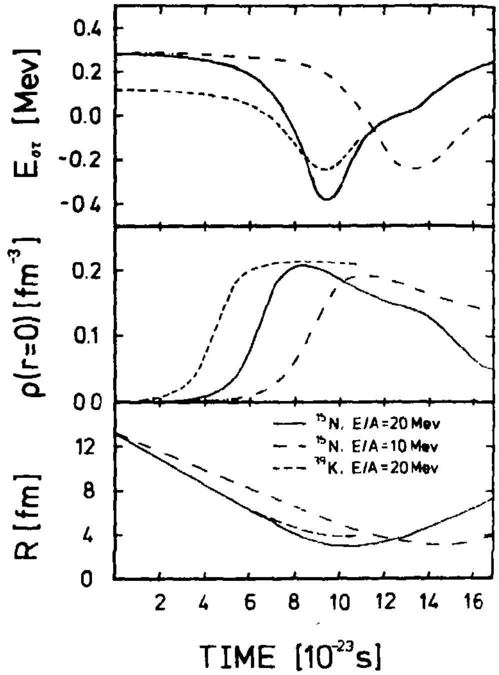

FIG. 2. Comparison of three different reactions. The energy in the στ channel [contributions proportional to f^2 and t_5 in Eq. (2.1)] as a function of time is displayed in the upper part for the reactions $^{15}N + ^{15}N$, $E/A = 20$ MeV (solid), $^{15}N + ^{15}N$, $E/A = 10$ MeV (dashed-dotted), and $^{39}K + ^{39}K$, $E/A = 20$ MeV (dashed). The corresponding densities in the origin of the center-of-mass system are given in the middle part of the figure, while the distance between the two nuclei defined by Eq. (3.1) is shown in the lower part.

A key question to be addressed in any subsequent investigation is the observable consequence of a significant condensate, or spin-isospin instability. Although in principle two-nucleon coincidence measurements are sensitive to spin-isospin correlations in the decaying compound system, it is difficult to quantitatively isolate the role of final state interactions from the structure of the decaying system. Since the condensate tends to anticorrelate neutrons and protons of like spin, one might naively hope to see a decrease in the ratio of deuterons produced to alpha particles produced, but again a quantitative calculation of the effect appears exceedingly difficult.

Pion emission is not a particularly promising candidate, since at least one hard collision with a nucleon in the two interpenetrating streams is required to knock a condensed pion on shell, thereby destroying most or all of any simple signatures associated with the perpendicular orientation of the condensate. Even should such an ephemeral state exist with pronounced spin-isospin correlations, the fact that it is not accessible to external probes such as electrons, photons, or pions renders it a nontrivial problem to unambigously verify its existence. Present theory, at least, appears far more suited to calculating such a state's existence than identifying its signature.

ACKNOWLEDGMENTS

It is a pleasure to acknowledge stimulating and helpful discussions with M. Gyulassy and E. Moniz concerning pion condensation, the two-stream problem, and effective interactions.

APPENDIX: COMPUTATIONAL TECHNIQUES

The calculations were performed in cylindrical coordinates (r, z, φ) assuming axial symmetry. Using the mesh

$$r_i = (i - 1/2)\Delta r; \quad 1 \le i \le N_r,$$

$$z_j = (j - 1)\Delta z; \quad 1 \le j \le N_z,$$

the discretized energy functional reads

$$\begin{aligned} E_D = \sum_{ij} 2\pi(\Delta r)(\Delta z)\Bigg(&\frac{\hbar^2}{2m}\sum_q\Bigg[\Bigg(r_{i+1/2}\sum_{\nu s}\left|\psi_{\nu s}^{sq}(i+1,j) - \psi_\nu^{sq}(i,j)\right|^2\frac{1}{(\Delta r)^2} + \frac{1}{r_i}\sum_{\nu s} m_{\nu s}{}^2\left|\psi_\nu^{sq}(i,j)\right|^2\Bigg) \\ &\times(1 - \tfrac{1}{2}\delta_{j,1}^s) + r_i\sum_{\nu s}\left|\psi_\nu^{sq}(i,j+1) - \psi_\nu^{sq}(i,j)\right|^2\frac{1}{(\Delta z)^2}\Bigg] \\ &+ \frac{t_0}{2}\left(\frac{1-x_0}{2}\right)[\rho_p{}^2(i,j) + \rho_n{}^2(i,j)] + \frac{t_0}{2}(2 + x_0)\rho_p(i,j)\rho_n(i,j) + \frac{t_3}{4}[\rho_p(i,j)\rho_n{}^2(i,j) + \rho_n(i,j)\rho_p{}^2(i,j)] \\ &+ \frac{V_L}{2}[\rho_p(i,j)Y_p(i,j) + \rho_n(i,j)Y_n(i,j)] + \frac{V_U}{2}[\rho_p(i,j)Y_n(i,j) + \rho_n(i,j)Y_p(i,j)] \\ &+ \frac{t_4}{2}\left|\vec{S}_p(i,j) + \vec{S}_n(i,j)\right|^2 + \frac{t_5}{2}\left|\vec{S}_p(i,j) - \vec{S}_n(i,j)\right|^2 \\ &+ \tfrac{1}{2}\phi(ij)\sum_k\Bigg\{\frac{W_k}{\Delta r}\frac{r_{i+k}}{2}(\vec{S}_1(i+k,j) + \vec{S}_{-1}(i+k,j)) - \frac{r_{i-k}}{2}(\vec{S}_1(i-k,j) + \vec{S}_{-1}(i-k,j)) \\ &+ r_i\frac{W_k}{\Delta z}(\vec{S}_0(i,j+k) - \vec{S}_0(i,j-k))\Bigg\}(1 - \tfrac{1}{2}\delta_{j1}^s)\Bigg), \end{aligned} \tag{A1}$$

$\delta_{j1}^s = 1$ for $j = 1$ and a z-symmetric mesh and $\delta_{j1}^s = 0$ elsewhere.
re $Y_q(ij)$ and $\phi(ij)$ denote the Yukawa foldings of the nuclear density ρ_q and the divergence of the spin ity $\vec{\nabla}\cdot\langle\vec{\sigma}\tau_3\rangle$. The quantities $\vec{S}_i$ stand for the following components of the spin density $\langle\sigma\tau_3\rangle$:

$$_1(ij) = 2\sum_\nu\sum_{q=-1}^{+1} q\,\psi_\nu^{+1,q}(i,j)^*\psi_\nu^{-1,q}(ij), \tag{A2}$$

$$_0(ij) = \sum_\nu\sum_{q=-1}^{+1} q(|\psi_\nu^{+1,q}(ij)|^2 - |\psi_\nu^{-1,q}(ij)|^2), \tag{A3}$$

$_{-1} = \vec{S}_1^*$ where

$$= \begin{cases}1 & \text{proton} \\ -1 & \text{neutron}\end{cases} \quad \text{and } s = \begin{cases}1 & \text{spin up} \\ -1 & \text{spin down},\end{cases} \tag{A4}$$

$W_1 = \frac{3}{4}$, $W_2 = -\frac{3}{20}$, $W_3 = \frac{1}{60}$.
e discretized Hamiltonian is obtained by varying (A1) with respect to the single-particle wave function ij). Defining

$$^{\nu s q}_{ij} = \left(\frac{r_i}{\Delta r}\right)^{1/2}\psi_\nu^{sq}(ij), \tag{A5}$$

$^{\nu s q}_{N_r,j} = 0$ and $g^{\nu s q}_{i,N_z} = 0$,

obtains

$$(Hg)_{ij}^{\nu sq}=(Ag)_{ij}^{\nu sq}+(Bg)_{ij}^{\nu sq}+(Cg)_{ij}^{\nu sq}, \tag{A6}$$

where inside the mesh and along the outer edges

$$(Ag)_{ij}^{\nu sq}=-\frac{\hbar^2}{2m}\frac{1}{(\Delta z)^2}g_{ij+1}^{\nu sq}-\frac{\hbar^2}{2m}\frac{1}{(\Delta z)^2}g_{ij-1}^{\nu sq}+n_aW_{ij}^qg_{ij}^{\nu sq} \tag{A7}$$

$$(Bg)_{ij}^{\nu sq}=-\frac{C_i}{(\Delta r)^2}\frac{\hbar^2}{2m}g_{i+1,j}^{\nu sq}-\frac{C_{i-1}}{(\Delta r)^2}\frac{\hbar^2}{2m}g_{i-1,j}^{\nu sq}+\frac{\hbar^2}{2m}\frac{m_{\nu s}}{r_i}^2g_{ij}^{\nu sq}+n_bW_{ij}^qg_{ij}^{\nu sq}, \tag{A8}$$

$$\begin{aligned}(Cg)_{ij}^{\nu sq}=&\Big(st_4[\vec{S}_{0,p}(ij)+\vec{S}_{0,n}(ij)]+sq\Big\{t_5[\vec{S}_{0,p}(ij)-\vec{S}_{0,n}(ij)]+\sum_k\Big(\frac{W_k}{\Delta z}\Big)[\phi(i,j-k)-\phi(i,j+k)]\Big\}+(1-n_a-n_b)W_{ij}^q\Big)\\&\times g_{ij}^{\nu sq}+\Big(t_1[\vec{S}_{-s,p}(ij)-\vec{S}_{-s,n}(ij)]+q\Big\{t_5[\vec{S}_{-s,p}(ij)-\vec{S}_{-s,n}(ij)]+\sum_k\Big(\frac{W_k}{\Delta r}\Big)[\phi(i-k,j)-\phi(i+k,j)]\Big\}\Big)g_{ij}^{\nu,-s,q}\end{aligned} \tag{A9}$$

with

$$\begin{aligned}W_{ij}^q=&\frac{\hbar^2}{m}\frac{1}{(\Delta r)^2}+\frac{\hbar^2}{m}\frac{1}{(\Delta z)^2}+\frac{t_0}{2}(1-x_0)\rho_q(ij)+\frac{t_0}{2}(2+x_0)\rho_{-q}(ij)\\&+\frac{t_3}{4}[2\rho_q(ij)\rho_{-q}(ij)+\rho_{-q}^2(ij)]+V_LY_q(ij)+V_UY_{-q}(ij)\end{aligned} \tag{A10}$$

and

$$C_i=\frac{i}{(i^2-\frac{1}{4})^{1/2}} \tag{A11}$$

and $n_a=n_b=\frac{1}{2}$. For $i=1$ one has, using the axial symmetry,

$$(Hg)_{ij}^{\nu sq}=-\frac{C_1}{(\Delta r)^2}\frac{\hbar^2}{2m}g_{2j}^{\nu sq}+\frac{\hbar^2}{2m}\frac{m_{\nu s}^2}{r_i^2}g_{ij}^{\nu sq}+n_bW_{ij}g_{ij}^{\nu sq}. \qquad \text{(A8}$$

The static HF calculation uses real wave functions. Since the single-particle wave functions (2.15) are reflection symmetric through the plane $z=0$, the numerical calculation can be confined to the region $z>0$. For a wave function with positive z parity, (A7) is modified as follows:

$$(Ag)_{i1}^{\nu sq}=-2\frac{\hbar^2}{2m}\frac{1}{(\Delta z)^2}g_{ij=2}^{\nu sq}+n_aW_{ij}^qg_{ij=1}^{\nu sq}. \tag{A7$'$}$$

The pion field ϕ is real, invariant under a rotation along the z axis, and has a negative z parity. In the time-dependent calculation, the single-particle wave functions are complex because of the velocity-dependent phase factor. In a collision with aligned initial spins, the initial TDHF wave function consists of the following two HF ground states:

$$\psi_{\nu,R}(r,z)=e^{i(z_0-z)k}\psi_\nu(r,z),\quad 1\le\nu\le A$$

and

$$\psi_{\nu,L}(r,z)=e^{i(z-z_0)k}\psi_\nu(r,z),\quad 1\le\nu\le A.$$

In order to antialign the initial spins, the left nucleus was taken to be the time-reversed static solutions

$$\psi_{\nu,L}(r,z)=e^{i(z-z_0)k}(-i\sigma_yk_0)\psi_\nu(r,z),$$

$$1\le\nu\le A,$$

where k_0 denotes the complex conjugation operat

Using the reflection symmetry through the plan $z=0$, the numerical work can be reduced to evol ing A single-particle wave functions on a mesh of the minimal size $(N_r,4N_z)$. The number of wav functions to be evolved is larger than that in clo shell nuclei[18-20] by a factor of 4, because now spi up and spin-down components have to be evolved and orbits with $\pm J_z$ are no longer degenerate. Th exact evolution operator $\exp(-i\hbar^{-1}\Delta tH)$ was appro mated by

$$\begin{aligned}U(\Delta t)=&\Big(1+i\frac{\Delta tC}{2\hbar}\Big)^{-1}\Big(1+i\frac{\Delta tB}{2\hbar}\Big)^{-1}\Big(1+i\frac{\Delta tA}{2\hbar}\Big)^{-1}\\&\times\Big(1-i\frac{\Delta tA}{2\hbar}\Big)\Big(1-i\frac{\Delta tB}{2\hbar}\Big)\Big(1-i\frac{\Delta tC}{2\hbar}\Big).\end{aligned} \qquad \text{(A12}$$

This approximate evolution operator agrees with the exact one and is unitary through order $(\Delta t)^2$. The potentials involve the density at the times $t_{n+1/2}$ which were obtained by evolving the wave functions with a time step $\frac{1}{2}\Delta t$. This double step ping method provides a more reliable evolution of gradients of the density $\rho(t_{n+1/2})$ than the averaging in Ref. 18.

In any subsequent investigations, one should seriously consider the alternative of using a finite number of terms in the Taylor series of the exact evolution operator. Though unstable for arbitrarily large Δt, the deviation from unitarity should be negligible for time steps of the order used in the present investigation.

---

*Permanent address: Institut für Kernphysik, Kernforschungsanlage Jülich, D-5170 Jülich, West Germany.

[1] A. B. Migdal, Zh. Eksp. Teor. Fiz. 61, 2209 (1972) [Sov. Phys.—JETP 34, 1184 (1972)]; *ibid*. 62, 1621 (1972) [*ibid*. 35, 845 (1972)]; Phys. Rev. Lett. 31, 257 (1973).

R. F. Sawyer, Phys. Rev. Lett. 29, 382 (1972).

D. J. Scalapino, Phys. Rev. Lett. 29, 386 (1972).

G. Baym and C. Pethik, Annu. Rev. Nucl. Sci. 25, 27 (1975).

G. Baym, Phys. Rev. Lett. 30, 1340 (1973).

G. Baym and E. Flowers, Nucl. Phys. A 222, 29 (1974).

W. Weise and G. E. Brown, Phys. Lett. 48B, 297 (1974).

S. O. Bäckman and W. Weise, Phys. Lett. 55B, 1 (1975).

E. Oset and W. Weise, Phys. Lett. 60B, 141 (1976).

G. E. Brown and W. Weise, Phys. Rep. C27, 1 (1976).

G. F. Bertsch and M. B. Johnson, Phys. Lett. 48B, 397 (1974).

D. K. Campbell, R. F. Dashen, and J. T. Manassah, Phys. Rev. D 12, 979 (1975).

J. Kogut and J. T. Manassah, Phys. Lett. 41A, 129 (1972).

[14] J. N. Bahcall and R. A. Wolf, Phys. Rev. 140, B 1445 (1965).

[15] T. Takatsuka and R. Tamagaki, J. Phys. Soc. Jpn. Suppl. 44 (1978), p. 495; T. Takatsuka, K. Tamiya, T. Tatsumi, and R. Tamagaki, Prog. Theor. Phys. 59, 1933 (1978).

[16] M. Gyulassy, in Symposium on Relativistic Heavy Collisions, Darmstadt, 1978 (unpublished); M. Gyulassy and W. Greiner, Ann. Phys. 109, 485 (1977).

[17] P. Bonche, S. Koonin, and J. W. Negele, Phys. Rev. C 13, 1226 (1976).

[18] S. E. Koonin, K. T. R. Davies, V. Mahrun-Rezwani, H. Feldmeier, S. J. Krieger, and J. W. Negele, Phys. Rev. C 15, 1359 (1977).

[19] J. A. Maruhn and R. Y. Cusson, Nucl. Phys. A 270, 471 (1976).

[20] J. W. Negele, S. E. Koonin, P. Möller, J. R. Nix, and A. J. Sierk, Phys. Rev. C 17, 1098 (1978).

[21] H. J. Pirner, K. Yazaki, P. Bonche, and M. Rho, Nucl. Phys. A329, 491 (1979).

[22] K. Ebert, P. Ring, W. Wild, V. Klemt, and J. Speth, Nucl. Phys. A 298, 285 (1978); R. Bauer *et al.*, Z. Phys. A274, 41 (1975); and Nucl. Phys. A 209, 535 (1973).

PHYSICAL REVIEW C VOLUME 21, NUMBER 6 JUNE 1980

Dominance of strong absorption in ^{9}Be+^{28}Si elastic scattering

M. S. Zisman
Lawrence Berkeley Laboratory, Berkeley, California 94720

J. G. Cramer
Physics Department, University of Washington, Seattle, Washington 98195

D. A. Goldberg
Cyclotron Laboratory, University of Maryland, College Park, Maryland 20742

J. W. Watson
Physics Department, Kent State University, Kent, Ohio 44242

R. M. DeVries
Los Alamos Scientific Laboratory, Los Alamos, New Mexico 87545

(Received 11 January 1980)

The elastic scattering of ^{9}Be + ^{28}Si has been measured at laboratory energies of 121.0 and 201.6 MeV. These data have been combined with existing lower energy ^{9}Be + ^{28}Si data in order to carry out a global optical model analysis. Calculations employing Woods-Saxon potentials yield good fits to the data without requiring explicitly energy-dependent parameters. In contrast, using a proximity form for the real potential requires an explicitly energy-dependent Woods-Saxon imaginary potential in order to achieve comparable quality fits. Notch perturbation calculations have been utilized to locate the radial region of the potential to which the scattering is sensitive. At all energies the imaginary potential is stronger than the real potential at the radius of maximum sensitivity. This dominance of the absorptive potential greatly limits the amount of information which can be gained about the real potential. Comparison of the ^{9}Be + ^{28}Si system with other light heavy ion systems such as ^{6}Li + ^{28}Si, ^{12}C + ^{28}Si, and ^{16}O + ^{28}Si suggests that the weak binding of ^{9}Be may be responsible for the strong absorption in this case.

NUCLEAR REACTIONS ^{28}Si(^{9}Be,^{9}Be), $E_L = 121.0$ and 201.6 MeV, measured $d\sigma/d\Omega$; optical model anaylsis; deduced Woods-Saxon and proximity model optical parameters, V/W ratios, fusion barriers. Comparison with ^{6}Li+^{28}Si and ^{16}O+^{28}Si behavior.

I. INTRODUCTION

In recent years we have been involved in a systematic study[1,2] of the elastic scattering of various light heavy ion projectiles from ^{28}Si. Our goal is to gain a better understanding of this relatively simple heavy ion interaction process. For example, we wish to learn about the energy dependence of the optical potentials, the sensitivity to the real or imaginary well depths, the "projectile dependence" of the interaction, and whether heavy ions show evidence for nuclear "rainbow" scattering (as is found[3] for light ion projectiles).

The ansatz for this study will be the same as that used in previous work: We combine our high energy measurements with existing lower energy data[4-6] in order to perform global optical model searches. In addition, we begin with a simple assumption about the interaction—that it can be described by a potential having no explicit energy dependence. The neglect of the energy dependence of the real potential (due to nonlocality of the nucleon-nucleon force) is expected to be a good approximation for heavy ion projectiles, since the nonlocality effects decrease as $1/A_p$.[7] As regards the imaginary potential, the situation is less clear. Our view is that, insofar as it is possible to describe data over a large energy range without explicit energy dependence, the approach is a reasonable one. If the data do not allow such a treatment, then more complicated parametrizations must be sought. We will see below that the question of whether or not the imaginary potential need be explicitly energy dependent depends quite strongly on the choice of the real potential. In particular, using a non-Woods-Saxon (WS) shape, such as a folded or proximity real potential, seems to require a marked energy dependence in the imaginary potential.

Based on our previous work,[1,2] we have been able to separate the characteristics of the projectiles investigated into two classifications, which we refer to as "light ion" and "heavy ion" behavior. In the case of light ion behavior, e.g., ^{4}He, it is found[3] that (a) nuclear rainbow scattering is observed at high energies; (b) the fitted potentials are dominated by the real potential, that is $V/W \sim 5$ (in the central region); and (c) the fitted potentials are energy dependent. In contrast, for heavy ions, e.g., ^{16}O, we find[1,2] (a) no evidence for nuclear rainbow scattering; (b) the fitted potentials have $V/W \sim 1$ (in the nuclear surface); and (c) it *is* possible to find energy-independent potentials which fit data over a very large energy range, provided a shallow real well ($V_0 \sim 10$ MeV) is chosen.

In Ref. 2 it was shown that the elastic scattering of ^{12}C+^{28}Si exhibits heavy ion behavior very similar to the ^{16}O+^{28}Si system.[1] In contrast, the ^{6}Li+^{28}Si system[2] behaves in a qualitatively different fashion. In particular, the ^{6}Li data at $E_L = 135.1$ MeV do exhibit the characteristic exponential falloff of nuclear rainbow scattering. As is true for α-particle elastic scattering,[3] a reasonable fit to the high energy data requires a real well depth $V_0 \gtrsim 100$ MeV. Furthermore, it has not been possible to fit ^{6}Li+^{28}Si data over a large energy range with an energy independent WS potential. For these reasons we classify the ^{6}Li+^{28}Si system as one which exhibits light ion behavior.

Because the character of the elastic scattering from a ^{28}Si target changes markedly from ^{6}Li to ^{12}C projectiles, we have undertaken a study of the intermediate ^{9}Be+^{28}Si system in order to map out the transition region. In addition, ^{9}Be shares a number of properties in common with ^{6}Li, namely, both have ground states which are not spin zero and both are quite weakly bound compared with other projectiles studied. Comparison of the ^{6}Li and ^{9}Be behavior might therefore be expected to shed some light on the question of whether or not the differences between ^{6}Li and ^{12}C elastic scattering are related to these roperties of ^{6}Li.

II. EXPERIMENTAL

The elastic scattering of ^{9}Be+^{28}Si has been tudied at laboratory energies of 121.0 and 01.6 MeV using ^{9}Be(3+) and ^{9}Be(4+) beams from ie LBL 88-inch cyclotron. Data were measured ith an array of four 2.5 mm thick Si(Li) dectors mounted in a 91 cm diameter scattering hamber. The beam spot size at the target was bout 1.5 × 3 mm; the calculated divergence is oughly 0.5°. The individual counters in the array ad an angular acceptance of 0.25° and a spacing f 2°; each had a solid angle of 0.13 msr. Measurements were made in 0.5° steps at forward ngles and 1° steps at backward angles. The angular range covered was 3° to 22° at 201.6 MeV and 3° to 34° at 121.0 MeV.

Absolute angles were determined by making comparative measurements on both sides of the beam axis. Fluctuations in the beam direction were monitored and corrected for in the analysis by means of a suitably placed monitor detector. The monitor angle was chosen to correspond to a rapidly changing region of the oscillatory forward angle elastic angular distribution. Since the inelastic angular distribution of the ^{28}Si(2$^+$) state at 1.78 MeV excitation is oscillating out of phase with the elastic, the $0^+/2^+$ ratio is an extremely sensitive measure of the scattering angle. Using this ratio easily allows detection of beam angle changes as small as ±0.05°.

The thickness of the self-supporting, enriched ^{28}Si target was 380 μg/cm^2. It was determined by comparing the elastic cross section to that of a ^{nat}Si target which was later weighed. Relative errors were obtained for each point by adding in quadrature the error due to angular uncertainty and the statistical error. The former error dominates at the forward angles and is essentially negligible thereafter. Absolute cross sections measured here are estimated to have an uncertainty of ±10%.

The data were stored in an analyzer based on a TI-960A computer and transferred to a ModComp IV/25 computer where they were written on tape for subsequent analysis.

III. RESULTS AND DISCUSSION

A. Woods-Saxon potentials

As mentioned earlier, we begin by looking for a potential which requires no explicit energy dependence. We use a WS shape for both the real and imaginary potentials:

$$V(r) = -V_0\{1+\exp[(r-R_R)/a_R]\}^{-1}, \tag{1}$$

$$W(r) = -iW_0\{1+\exp[(r-R_I)/a_I]\}^{-1}, \tag{2}$$

where

$$R_R = r_R(A_p^{1/3}+A_t^{1/3}), \tag{3a}$$

$$R_I = r_I(A_p^{1/3}+A_t^{1/3}). \tag{3b}$$

For the Coulomb potential we use the standard form

$$V_C(r) = \frac{Z_pZ_te^2}{r} \quad (r>R_C) \tag{4a}$$

$$= \frac{Z_pZ_te^2}{2R_C}\left(3-\frac{r^2}{R_C^2}\right) \quad (r<R_C), \tag{4b}$$

where

$$R_C = r_C(A_p^{1/3}+A_t^{1/3}). \tag{4c}$$

Global optical model searches were carried out using the code GENOA.[8] Generally the input data consisted of ^{9}Be + ^{28}Si elastic scattering cross sections at 13 MeV (Ref. 5) along with the 121.0 and 201.6 MeV cross sections measured here. Representative examples of the quality of fits obtained are shown in Fig. 1. Parameters for the optical potentials shown in Fig. 1, along with those for other potentials which lead to comparable quality fits, are listed in Table I.

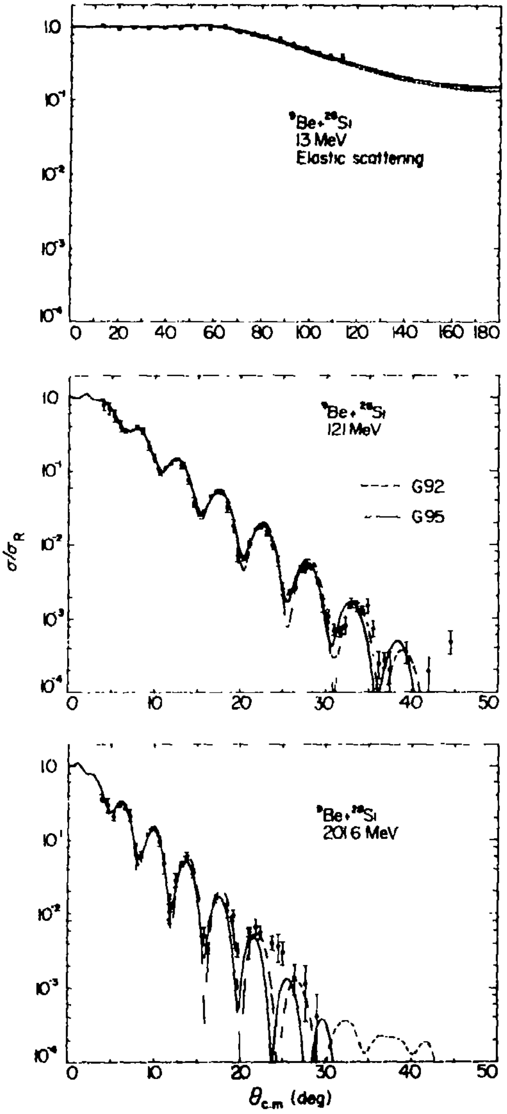

FIG. 1. ^{9}Be + ^{28}Si elastic scattering angular distributions at E_L = 13, 121.0, and 201.6 MeV. The curves are representative optical model fits using two of the WS potentials listed in Table I. Values of χ^2/N for potential G95 (G92) are 13 MeV, 1.4 (2.5); 121.0 MeV, 2.6 (5.1); 201.6 MeV, 2.7 (2.8).

It is apparent from Table I that a wide range of real well depths is allowed by the data, even with the additional constraint of demanding an energy-independent potential. For example, the two potentials shown in Fig. 1, G92 and G95, have very similar imaginary wells and yet differ by an order of magnitude in the real well depth. The close similarity of the predicted angular distributions at all three energies demonstrates clearly that in the absence of additional knowledge it will not be possible to extract information about the real well depth in this system. At first glance this does not seem surprising—heavy ions are usually assumed to behave this way. However, our previous results[1,2] with ^{16}O and ^{12}C do not show the same lack of sensitivity to the real well. In order to fit ^{16}O + ^{28}Si data over a wide energy range with an energy independent potential, it was found that only a shallow real well (set E18 in Table II) gave acceptable results. The ^{12}C + ^{28}Si system led to a similar conclusion (set H12 in Table II).

The sensitivity to the real well in the case of ^{12}C and ^{16}O scattering is related to the predicted existence of nuclear rainbow scattering for deep real potentials having moderate absorption. This is illustrated in Fig. 2 where predictions for ^{16}O + ^{28}Si elastic scattering at 215 MeV are compared for two choices of real well depth, V_0 = 10 MeV and V_0 = 100 MeV. The latter potential, which fits low energy ^{16}O + ^{28}Si elastic data ($E_{\rm lab}$ = 33–81 MeV) as well as does the shallow potential, is totally incompatible with the high energy data. (We note that it is possible, if one relaxes the requirement of energy independence, to rectify this discrepancy.[9]) However, we emphasize that in the ^{9}Be + ^{28}Si system there is *no need* to make the imaginary potential energy dependent in order to achieve reasonable agreement with the data, independent of the depth of the real potential.

There is some problem with most of the potentials listed in Table I in reproducing the trend of the larger angle data ($\theta_{c.m.} \sim 25^\circ$) in the 201.6 MeV angular distribution. This defect is improved, as shown in Fig. 3, by using a potential such as G38. (Although the parameters of potential G38 are somewhat unusual, it will be seen below that this potential is not very different from the other potentials used here in the important radial region around 5–10 fm.)

We found empirically that the fitting procedure we used tended to overemphasize the high energy data sets. Recently there have appeared[6]

TABLE I. ^{9}Be + ^{28}Si optical potentials.[a]

Set	V_0 (MeV)	r_R[b] (fm)	a_R (fm)	W_0 (MeV)	r_I[b] (fm)	a_I (fm)	θ_R[c] (deg)
G90	300.0	0.567	0.942	41.1	1.054	0.782	−81
G92	150.0	0.703	0.944	27.6	1.150	0.753	−46
G89	100.0	0.767	0.960	23.1	1.191	0.736	−31
G84	75.0	0.776	1.012	29.8	1.143	0.744	−22
G95	15.0	1.149	0.914	24.4	1.185	0.701	−2
G38	13.8	1.244	0.652	503.2	0.617	0.825	−3
G05[d]	13.8	1.232	0.729	16.9	1.232	0.729	−3
B01[e]	10.0	1.162	0.820	20.4	1.162	0.820	0
P01[f]		0.059[g]	0.078[h]	17.8	1.241	0.7145[i] (1.20×10^{-3})	−17

[a] WS form, except as noted. The Coulomb radius, Eq. (4), is $r_C = 1.0$ fm unless noted otherwise.

[b] See Eq. (3).

[c] Value of calculated rainbow angle for the real potential at $E_L = 201.6$ MeV.

[d] Four parameter fit with $r_I = r_R$ and $a_I = a_R$.

[e] Taken from Ref. 6, $r_C = 0.71$ fm.

[f] Proximity real potential, see Eqs. (5)–(12) in Sec. III B 2.

[g] Value of ΔR in Eq. (10).

[h] Value of Δb in Eq. (11).

[i] Energy-dependent imaginary diffuseness, $a = a_0 + (a_1)E_L$. The value of a_1 is shown in parentheses.

TABLE II. ^{6}Li, ^{12}C, and ^{16}O + ^{28}Si optical potentials.[a]

Ion	Set	V_0 (MeV)	r_R[b] (fm)	a_R (fm)	W_0 (MeV)	r_I[b] (fm)	a_I (fm)
^{6}Li	R22	150.0	0.727	0.877	44.4	0.904	1.060
	R27	150.0	0.682	0.828	38.8	1.020	0.889
	S01	150.0	0.725	0.874	34.2	1.019	0.904
	S02	150.0	0.725	0.874	51.6[c] (−0.18)	1.112	0.742
	S22	150.0	0.577	0.770	44.4	0.904	1.060
	S23	150.0	0.727	0.877	50.8	1.113	0.743
	P10[d]		0.107[c]	0.048[f]	45.5	0.906	1.029
	P11[d]		0.107[e]	0.048[f]	45.5	0.906	0.7620[g] (6.3×10^{-3}) $[-3.2\times10^{-5}]$
	P12[d]		−0.045[e]	−0.081[f]	45.5	0.906	1.029
	P13[d]		0.107[c]	0.048[f]	36.9	1.088	0.770
	Z8	10.0	1.340	0.809	82.1	0.955	0.727
^{12}C	H12	10.0	1.320	0.617	30.3	1.160	0.609
^{16}O	E18	10.0	1.350	0.618	23.4	1.230	0.552
	A23	100.0	0.932	0.797	165.0	0.890	0.764
	S75	100.0	1.060	0.640	42.0	1.060	0.640
	A-type[h]	100.0	0.967	0.745	44.1	1.073	0.605[g] (1.14×10^{-3})

[a] WS form, except as noted. The Coulomb radius, Eq. (4), is $r_C = 1.0$ fm unless noted otherwise. Potentials E18, A23, and S75 are from Ref. 1 and potentials R22, R27, Z8, and H12 are from Ref. 2.

[b] See Eq. (3).

[c] $W_0 = W_1 + (W_2)\, E_L$. The value of W_2 is shown in parentheses.

[d] Proximity real potential, see Eqs. (5)–(12) in Sec. III B2.

[e] Value of ΔR in Eq. (10).

[f] Value of Δb in Eq. (11).

[g] Energy-dependent imaginary diffuseness, $a = a_0 + (a_1)E_L + [a_2]E_L^2$.

[h] From Ref. 9, with $r_C = 1.3$ fm.

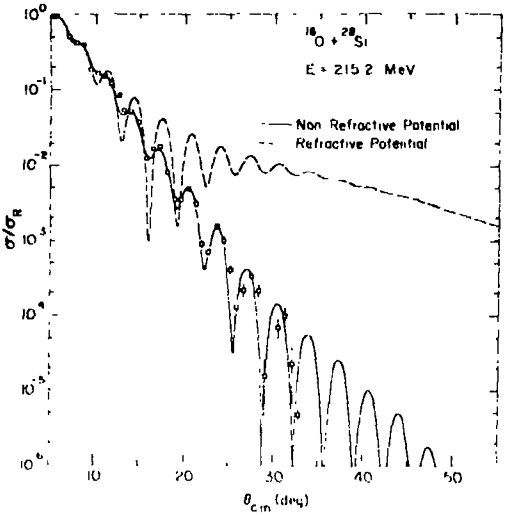

FIG. 2. $^{16}O + ^{28}Si$ elastic scattering angular distribution at $E_L = 215.2$ MeV (taken from Ref. 1). The solid curve is a fit with a shallow WS potential, E18, and the dashed curve is a prediction using the deeper potential S75 of Table II. Although the deep potential predicts a substantial enhancement of the back angle cross sections due to the existence of nuclear rainbow scattering, the data show no such effect.

some high quality $^9Be + ^{28}Si$ scattering data at low energies; it is instructive to see whether or not our potentials can reproduce these data. Figure 4 shows predictions from two of our potentials, G92 and G38, compared with the data and one of the "universal" potentials from Balzer *et al.*[6] (set B01 in Table I). It can be seen that potential G92 does not do a completely adequate job at the low energies. (This deficiency is already in evidence, albeit not too visibly, in Fig. 1.) On the other hand, the fits using potential G38 are quite comparable to those using potential B01. In contrast, Fig. 5 shows that the potential derived from the low energy data alone does not extrapolate well to the high energy data sets measured in this work.

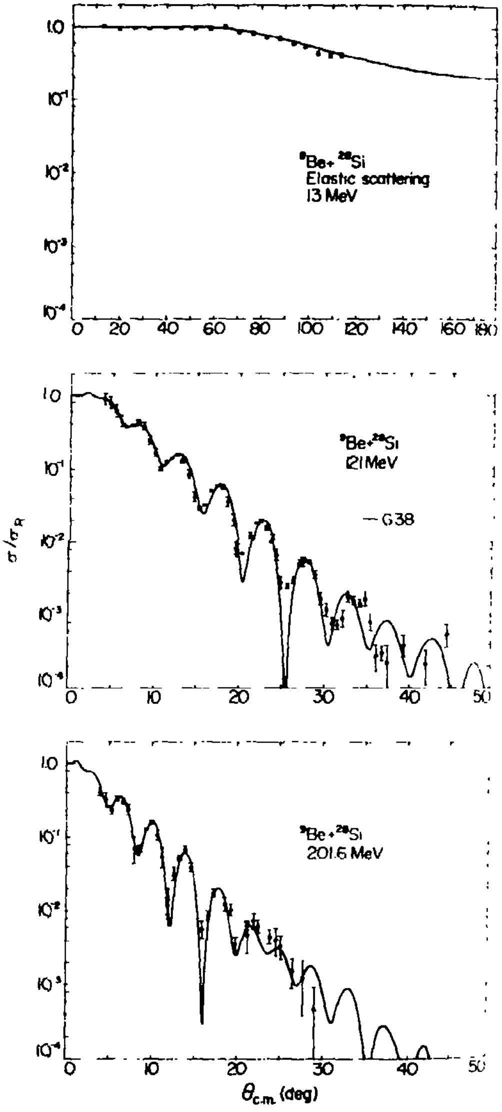

FIG. 3. $^9Be + ^{28}Si$ elastic scattering angular distributions at $E_L = 13$, 121.0, and 201.6 MeV. The solid cur is a fit to all three energies using potential G38. Values of χ^2/N for potential G38 are 13 MeV, 1.2; 121.0 MeV, 10.2; 201.6 MeV, 1.8.

One question we hope to answer in this study concerns the existence of nuclear rainbow scattering in the high energy angular distributions. We know[2,3] that high energy light ions, up to ^6Li, do show behavior which is dominated by nuclear rainbow scattering, while ^{12}C and ^{16}O projectiles (see Fig. 2) do not.[1,2] The $^9Be + ^{28}Si$ potentials listed in Table I have predicted rainbow angles θ_R ranging from −81° to −2°. Thus, one would expect to see evidence for rainbow scattering in the data if V_0 is greater than about 75 MeV, provided the absorption is not too strong. This is demonstrated in Fig. 6 which shows the behavior of potential G92 as the imaginary strength is reduced toward zero. Although the predicted value of θ_R is −46°, there is nonetheless an increase in cross section of almost two orders of magnitude in the region

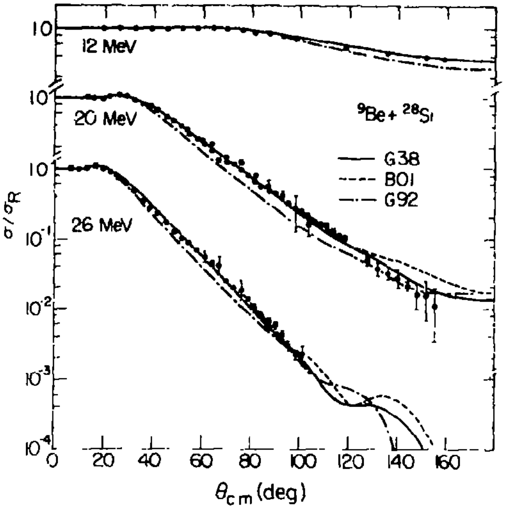

FIG. 4. ^{9}Be+^{28}Si elastic scattering angular distributions at E_L=12, 20, and 26 MeV. Data are from Ref. 6. Predicted angular distributions are shown for potentials G38 and G92 from this work, along with one of the "universal" potentials from Ref. 6, B01. Values of χ^2/N for potential G38 (G92) [B01] are 12 MeV, 0.6 (5.0)[0.2]; 20 MeV, 2.0 (25.6)[2.7]; 26 MeV, 1.9 (12.7) [1.5].

where data exist. We conclude from this that the absorption required to fit the data *is* sufficient to remove the observable effects of rainbow scattering in the calculated angular distributions. Although the calculation involving potential G38 (Fig. 3) does show some flattening out at back angles, this is not related to rainbow effects. It can be seen in Fig. 7 that for this potential a reduction of the imaginary strength by a factor of 100 (to W=5 MeV) makes essentially no change in the magnitude of the predicted cross sections, although the phase of the oscillations shifts markedly.

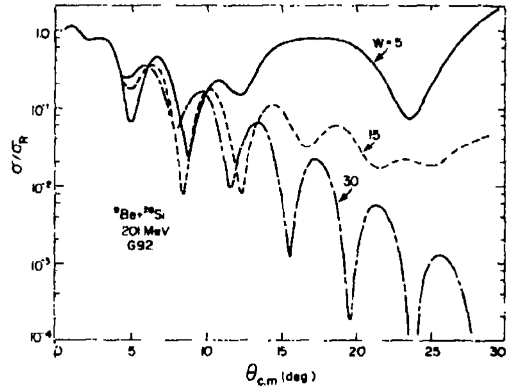

FIG. 6. Predicted angular distributions for ^{9}Be+^{28}Si elastic scattering at E_L=201.6 MeV, using the deep potential G92 with various imaginary well depths. As the imaginary strength decreases, a large enhancement in the back angle cross sections due to nuclear rainbow scattering becomes clearly visible.

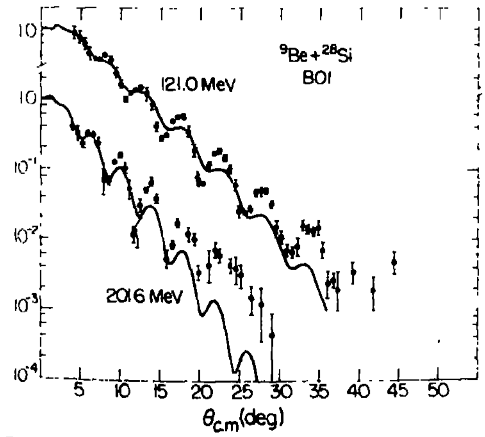

FIG. 5. Comparison between predicted and experimental angular distributions for ^{9}Be+^{28}Si elastic scattering at 121.0 and 201.6 MeV. The universal potential B01 from Ref. 6 does not do a good job of reproducing the high energy data.

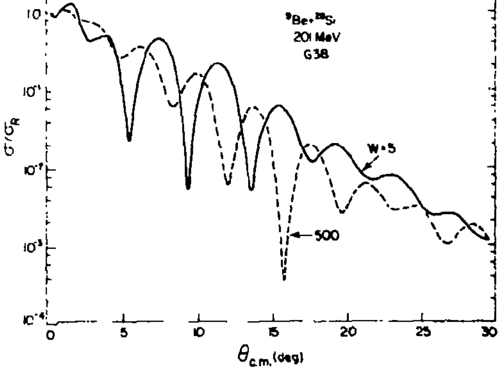

FIG. 7. Predicted angular distributions for ^{9}Be+^{28}Si elastic scattering, using the shallow potential G38 with two different imaginary well depths. In this case no evidence for a cross section enhancement due to nuclear rainbow scattering is seen because the rainbow effects are so far forward in angle they are dominated by the huge Coulomb rainbow.

Based on the classifications outlined in Sec. I, the above results clearly indicate that ^{9}Be behaves as a "heavy ion" projectile.

B. Other potential shapes

1. Folding model

Satchler[10] has performed an extensive analysis of our high energy $^9\text{Be}+{}^{28}\text{Si}$ data and also the low energy data of Balzer *et al.*[5] utilizing a double-folding model for the real part of the optical potential and a WS imaginary potential. As was true for the $^{16}\text{O}+{}^{28}\text{Si}$ system analyzed earlier,[9] the folding model fits are similar in quality to those obtained with a WS real potential. However, for the $^9\text{Be}+{}^{28}\text{Si}$ system the folding-model results are anomalous in the sense that a substantial renormalization ($N\sim 0.5$) is required. In other words, the predicted strength of the real potential must be reduced a factor of 2 from the folding model estimate in order to fit the data. Although a substantial number of projectile + target combinations have been studied,[11] only ^{9}Be and ^{6}Li (Ref. 12) appear to require such a large reduction in the predicted strength of the folding-model real potential.

In the folding-model analysis of the $^{16}\text{O}+{}^{28}\text{Si}$ data,[9] a global approach was employed. In order to get agreement with the data, however, it was essential to use a WS imaginary potential having an explicit energy dependence of the diffuseness parameter. Satchler also showed that the same sort of parametrization of the imaginary potential allowed a fit to the ^{16}O data with a deep WS real well, something which was not possible with an energy-independent imaginary potential. Unfortunately, no global analysis was performed[10] for the $^9\text{Be}+{}^{28}\text{Si}$ system so no systematic behavior of the imaginary potential is available.

2. Proximity potential

In recent years, it has become more common to analyze heavy ion elastic scattering[13] and also fusion data[14,15] by means of the proximity potential formulation. In the proximity model, the real ion-ion potential is given by[16]

$$V(\zeta)=4\pi\gamma\bar{C}b\phi(\zeta)\,, \tag{5}$$

where the dimensionless distance parameter is

$$\zeta=(r-C_t-C_p)/b\,. \tag{6}$$

In Eq. (5),

$$\bar{C}=\frac{C_pC_t}{C_p+C_t}\,, \tag{7}$$

with

$$C_x=R_x[1-(b^2/R_x^2)]\,. \tag{8}$$

In this paper we will use for the universal proximity function the analytic approximation given by Blocki *et al.*,[16]

$$\phi(\zeta)=-0.5(\zeta-2.54)^2-0.0852(\zeta-2.54)^3\,,\quad \zeta\leq 1.2511 \tag{9a}$$

$$\phi(\zeta)=-3.437\exp(-\zeta/0.75)\,,\quad \zeta\geq 1.2511\,. \tag{9b}$$

Following Vaz and Alexander,[14] we use suggested values[16] for most of the parameters but allow for some deviation from the standard proximity formulas:

$$R_x=1.28A_x^{1/3}-0.76+0.8A_x^{-1/3}+\Delta R\,, \tag{10}$$

$$b=1.0+\Delta b\,, \tag{11}$$

$$\gamma=0.9517\left[1-1.7826\left(\frac{N-Z}{A}\right)^2\right]. \tag{12}$$

In Eqs. (10) and (11), ΔR and Δb give us the ability to modify the potential slightly. For simplicity, the same ΔR value will be used for both target and projectile radii.

Satchler[9] employed a slightly different parametrization of the proximity potential in his study of the $^{16}\text{O}+{}^{28}\text{Si}$ system. He found that it was possible to get fits comparable in quality to those employing a folding-model or WS real potential, again using an energy-dependent imaginary diffuseness.

Our results, using proximity potential P01 in Table I to fit the $^9\text{Be}+{}^{28}\text{Si}$ data, are shown in Figs. 8 and 9. We found, as did Satchler,[9] that it was not possible to obtain agreement with the data if an energy-independent imaginary potential is used. However, as can be seen in Figs. 8 and 9, the agreement with the data is quite good when an energy-dependent imaginary diffuseness is employed. Other possibilities for the energy dependence (e.g., an energy-dependent value of W_0) were not investigated. In the $^{16}\text{O}+{}^{28}\text{Si}$ system,[1] even a quadratic energy dependence of W_0 was unsuccessful compared to the approach utilized here.

The optimum values for ΔR and Δb in Eqs. (10) and (11) are 0.059 and 0.078 fm, respectively. In the important radial region, these correspond to increasing the real potential by about 25–50% compared with the standard proximity potential ($\Delta R=\Delta b=0$). (Note that this modification is in the opposite sense to that required for the folding-model potential discussed earlier.) In Fig. 10 we compare the best WS real potential G38 with the folding-model potential ($N=0.5$) and the proximity potential P01. It is evident that the data define

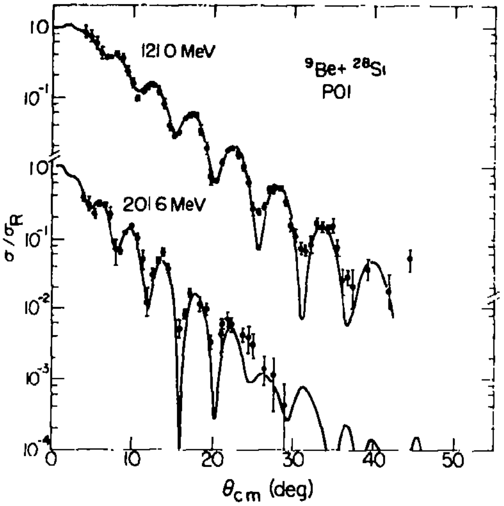

FIG. 8. Fits to high energy ^{9}Be+^{28}Si data using the proximity model (potential P01 in Table I). The fits are similar in quality to the WS potential fits shown in Figs. 1 and 3. Values of χ^2/N for potential P01 are 121.0 MeV, 4.9; 201.6 MeV, 3.1.

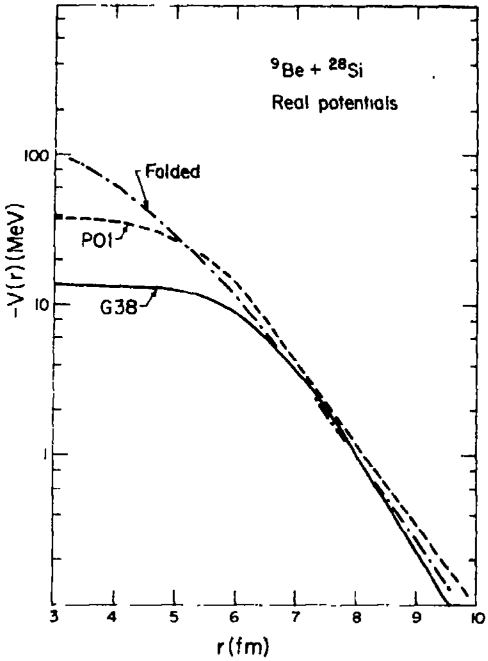

FIG. 10. Comparison of WS (G38), proximity (P01) and folding model (Ref. 10, method B, $N=0.5$) real potentials which fit ^{9}Be+^{28}Si elastic scattering. The data appear to define the potential reasonably well in the radial region around 6–9 fm.

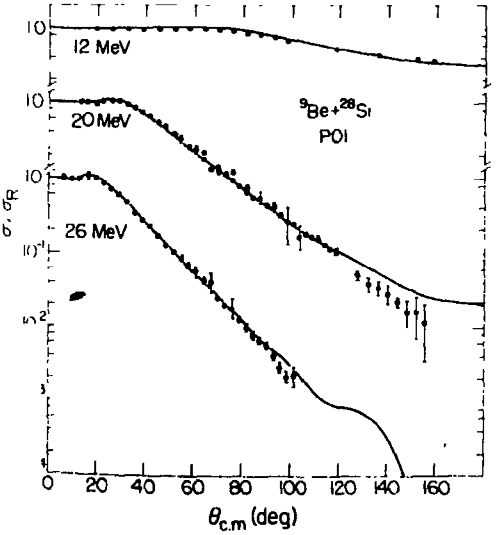

. 9. Fits to low energy ^{9}Be+^{28}Si data using the mity model (potential P01 in Table I). The fits imilar in quality to the WS potential fits shown in . Values of χ^2/N for potential P01 are 12 MeV, 0 MeV, 4.9; 26 MeV, 0.9.

the value of the real potential, at least to some extent, in the radial region around 6–9 fm.

C. Comparison with other projectiles

In order to understand why ^{9}Be behaves differently from the other projectiles, it is instructive to examine the potentials which fit the various systems. Figure 11 shows the radial form of the WS potentials for ^{6}Li, ^{9}Be, and ^{16}O elastic scattering from ^{28}Si. (The behavior and the best-fit potential for ^{12}C are so similar to ^{16}O that the latter projectile can be considered representative of both ions.) Potential parameters may be found in Table I for ^{9}Be and in Table II for the other projectiles. We see in Fig. 11 that there is evidence for a transition in behavior in going from ^{6}Li to ^{16}O. For ^{6}Li, the imaginary potential exceeds the real potential at large radii (or low energies), while for ^{16}O the real potential is stronger at large radii. The behavior of ^{9}Be is intermediate between these extremes. In this case the real and imaginary potentials are comparable throughout the tail region, with the imaginary potential somewhat stronger than the real.

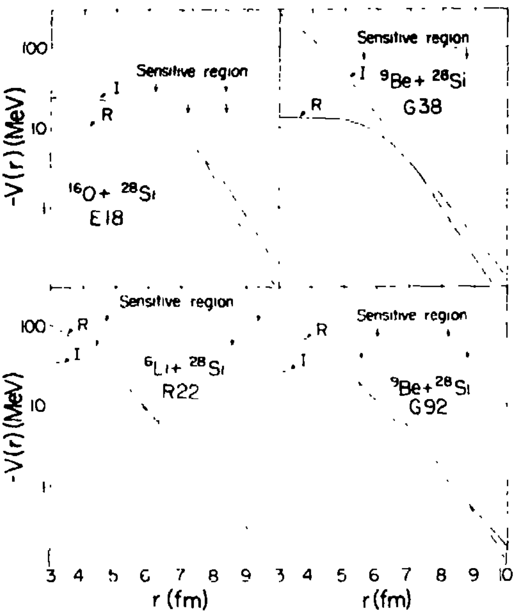

FIG. 11. Radial form of WS potentials which fit the ^{16}O, ^{9}Be, and ^{6}Li+^{28}Si systems. ^{9}Be potentials are listed in Table I; those for the other projectiles are listed in Table II. The "sensitive region" for each potential is obtained from a notch perturbation calculation and is shown separately for the real (solid lines) and imaginary (dashed lines) well unless the two regions coincide.

The sensitive regions shown in Fig. 11 were obtained from "notch perturbation" calculations.[17] As shown schematically in Fig. 12, this technique involves scanning a radial perturbation across the potential. In radial regions where there is no sensitivity, the χ^2 value of the fit remains unchanged, while in sensitive regions χ^2 worsens dramatically. Figure 13 shows the results of such a scan for the ^{9}Be+^{28}Si system at 201 MeV with potential G38. It can be seen that in this case the sensitive region is about $r = 5-9$ fm and that the radius of maximum sensitivity (for the real potential) R_{sens} is 6.7 fm. For this particular case the real and imaginary potentials have essentially the same region of sensitivity. In the other cases shown in Fig. 11, the sensitive regions for the real and imaginary potentials are indicated separately. For each projectile, the sensitive region shown in Fig. 11 is evaluated for the highest energy data set available, that is 135.1 MeV ^{6}Li, 201.6 MeV ^{9}Be, and 215.2 MeV ^{16}O.

Although the potentials we have used have no

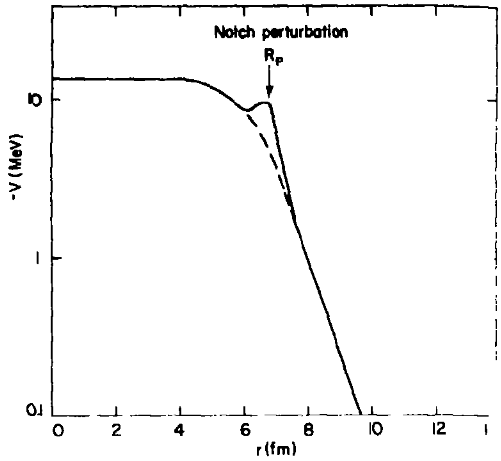

FIG. 12. Example of a WS potential which has been modified by addition of a localized radial perturbation. Varying the position of the perturbation R_p produces a sensitivity function such as that shown in Fig. 13.

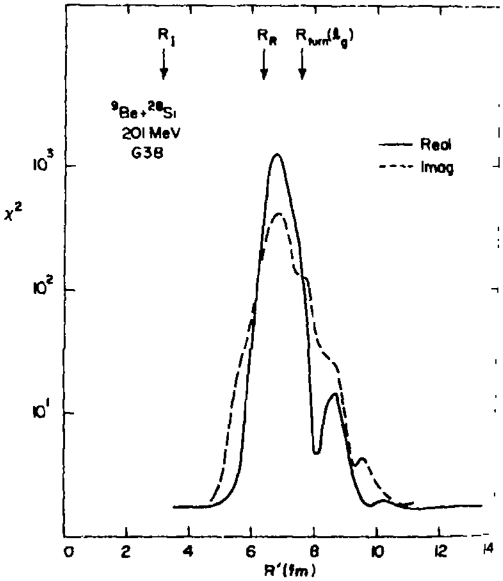

FIG. 13. Sensitivity function for a radial perturbation such as that in Fig. 12. The "baseline" corresponds to the unperturbed χ^2 value. Radii of the real and imaginary wells along with the turning point of the grazing partial wave ($T_l = 0.5$) are indicated for comparison. In this case, the scattering is sensitive to a region from about 5–9 fm, and the "radius of maximum sensitivity" R_s is about 6.7 fm. In general, R_s decreases as the energy increases and tends to be inside of the strong absorption radius ($D_{1/2}$) used by Satchler (Refs. 9–12).

explicit energy dependence, the different real and imaginary well geometries nonetheless give rise to an implicit energy dependence. This is demonstrated for the ^{16}O+^{28}Si system in Fig. 14, where we show the ratio of V/W (evaluated at the radius of maximum sensitivity from the notch perturbation calculations) as a function of energy. We see that for a potential which fits the data, such as E18, the ratio slopes downward as the energy increases, signifying a gradual increase in the strength of the imaginary compared with the real potential. The behavior of Satcher's "A-type" WS potential[9] is also shown in Fig. 14. This potential has a deep real well but has an imaginary diffuseness which increases with energy; it does about as well as potential E18 in fitting the data. Although not shown in Fig. 14, the proximity model fit to the ^{16}O+^{28}Si data obtained by Satchler[9] behaves very similarly to the "Satchler" curve. Thus, it is clear that the trend shown in Fig. 14 for potential E18 is more or less characteristic of all potentials which fit the ^{16}O+^{28}Si data over the whole energy range. It is worth commenting that the overall trend displayed here for the ^{16}O+^{28}Si system has also been reported for other systems involving this projectile, such as ^{16}O+^{40}Ca (Ref. 18) and ^{16}O+Ni (Ref. 19). For comparison, we also show in Fig. 14 the behavior of potential A23 from Ref. 1. This potential is energy independent and has a deep real well similar to the A-type potential above; it was "adjusted" to fit the high energy data by increasing the imaginary strength. (Such an increase has the effect of absorbing away the trajectories which give rise to the large rainbow cross sections generated with the deep real potential. When a shallow real potential such as E18 is used, the rainbow angle moves toward 0° and the effect gets lost in the more familiar Coulomb rainbow region.) Looking at the V/W ratios in Fig. 14, we see that potential A23 behaves very differently than E18 at low energies. We might expect, therefore, that potential A23 will work less well than E18 in this energy range, as is indeed the case.

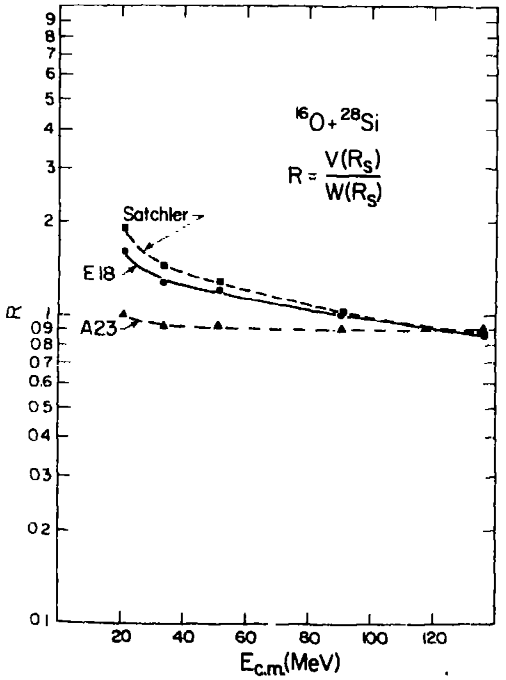

FIG. 14. Ratio of real to imaginary strength for various ^{16}O+^{28}Si potentials. The curve marked "Satchler" refers to the A-type WS potential from Ref. 9 (see Table II). At each energy the ratio is evaluated at R_s, the radius of maximum sensitivity (for the real potential) from a notch perturbation calculation. For this system, the real potential is stronger at low energies and the imaginary potential becomes more important as the energy increases.

As shown in Fig. 15, for ^{6}Li+^{28}Si just the opposite trend is observed, with the V/W ratio increasing as the energy increases. In the case of ^{6}Li, it was not possible to find an energy-independent potential which fits the high and low energy data sets simultaneously[2]; the curve marked "fits" is obtained from somewhat different potentials at each energy. We have attempted to improve this situation by including *various energy-dependent parametrizations of* both the real and imaginary potential. Thus far it has turned out to be difficult to fit the high and low energy data sets together. This is demonstrated in Fig. 16, where we show WS potential fits to ^{6}Li+^{28}Si data at a number of energies. The solid curve in Fig. 16 is representative of a six-parameter WS fit to all three energies using potential S01 of Table II. Compared with a potential such as R22 of Ref. 2, this compromise fit causes the χ^2/N value at 135.1 MeV to worsen by a factor of 2; in spite of this the fit at the lowest energy is quite poor. By allowing an explicitly energy-dependent imaginary well depth (potential S02), it is possible to improve the fit to the low energy data set with some additional worsening of the high energy fit. Unfortunately, such improvement corresponds to a substantial worsening of the fit at 46 MeV. We note that for a WS shape, an optimum energy-dependent fit leads to a *negative* energy dependence, that is, W decreases with increasing energy. This aspect is consistent with the trend evidenced in Fig. 15

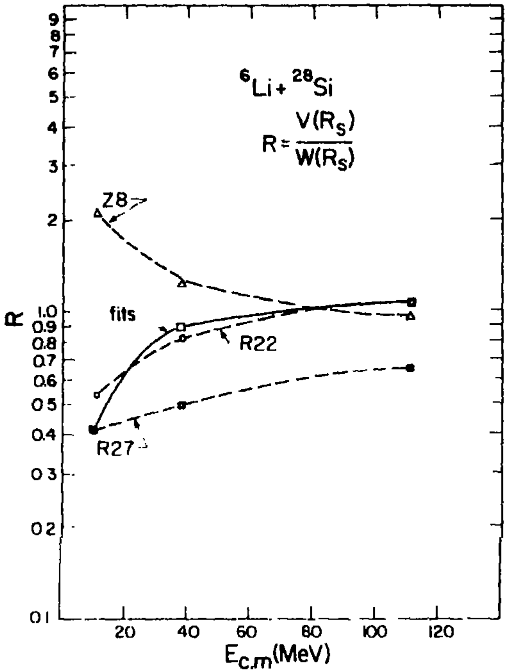

FIG. 15. Same as Fig. 14, but for ^{6}Li+^{28}Si. The curve marked "fits" refers to somewhat different potentials at each energy (see text). Potential parameters are given in Table II. For this system, the imaginary potential is stronger at low energies and the real potential becomes more important as the energy increases.

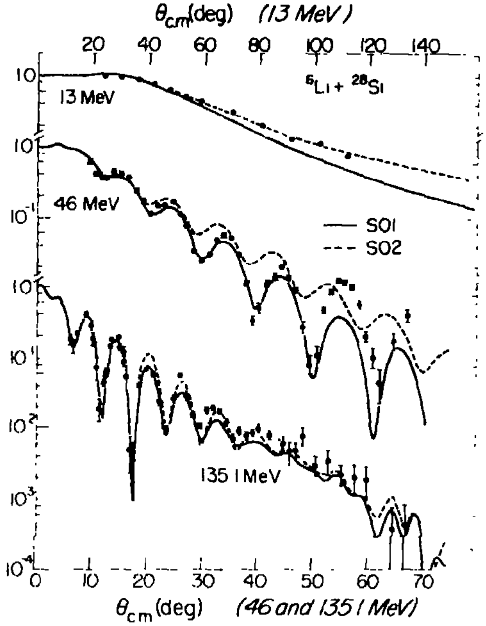

FIG. 16. Fits to ^{6}Li+^{28}Si elastic scattering at 13 MeV [data from J. E. Poling, E. Norbeck, and R. R. Carlson, Phys. Rev. C 13, 648 (1976)], 46 MeV (Ref. 5), and 135.1 MeV (Ref. 2) using an energy-independent WS potential (S01) and an energy-dependent WS potential (S02). The difficulty in fitting ^{6}Li data over a wide energy range is apparent (see text). Potential parameters are listed in Table II. Values of χ^2/N for potential S01 (S02) are 13 MeV, 21.1 (1.7); 46 MeV, 16.0 (119.5); 135.1 MeV, 5.4 (10.3). Note the different angle scales for the high and low energy data.

but is very unusual from a phenomenological point of view.[20] This point will be discussed further below.

Recently Tabor *et al.*[21] attempted to apply the proximity formalism to the scattering of light ions. They found that, while the formalism itself appeared to work, certain discrepancies were apparent. Firstly, the effective projectile radius required by the data was larger than the model prediction[16] (in agreement with the present results) and secondly, the effective ion-ion interaction $\phi(\zeta)$ was determined to be more steeply rising in both the surface and tail regions than that given by Ref. 16. It is therefore of interest to see how well a proximity potential can do on the ^{6}Li data sets we have studied here. Figure 17 shows results of using proximity potential P10. As with the WS potentials, the fit to the lowest energy data set is quite poor. In contrast to the WS potentials, however, we find that no better agreement with the 135.1 MeV data set is obtained even when it is fitted alone. The combination of a proximity real potential and a WS imaginary potential has difficulty reproducing the smooth back angle rainbow falloff. This is consistent with the results of Tabor *et al.*,[21] in essence affirming the inadequate deflecting force represented by the conventional proximity potential of Ref. 16. For the ^{6}Li+^{28}Si system, the "trick" of using an energy-dependent imaginary diffuseness to obtain global fits does not help much. As was true with a WS potential (see Fig. 16) improving the 13 MeV fit comes at the expense of the 46 MeV fit. Even the extreme of allowing independently optimized values of a_I at each energy did little to improve things. The resulting values of a_I can be parametrized with a quadratic energy dependence (potential P11). This is basically an exercise in parameter juggling and is unlikely to have any predictive power; nonetheless, the corresponding fits are sl the dashed curves in Fig. 17.

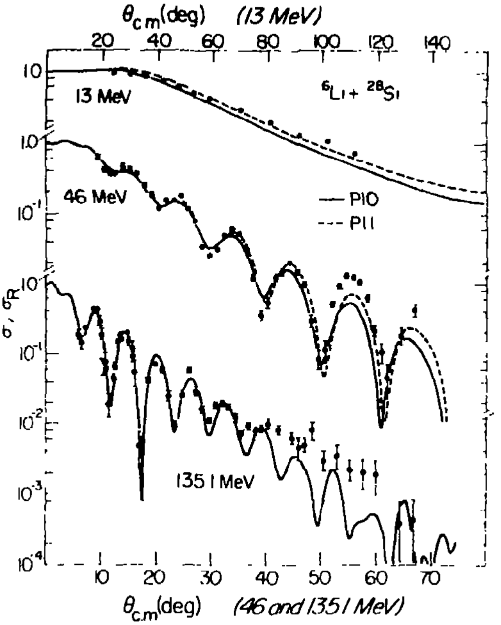

FIG. 17. Fits to ^{6}Li+^{28}Si elastic scattering using the proximity model. Parameters are listed in Table II. In contrast to the results of Ref. 2 or Ref. 12, which employed WS and folded potentials, respectively, the combination of a proximity real potential and a WS imaginary potential does not properly reproduce the smooth falloff of the data in the rainbow region. Values of χ^2/N for potential P10 (P11) are 13 MeV, 18.0 (9.0); 46 MeV, 14.9 (10.9); 135.1 MeV, 6.1 (6.1). Note the different angle scales for the high and low energy data.

The basic problem with fitting the ^{6}Li+^{28}Si data over the whole energy range can be discerned by looking at Fig. 15. The low energy data set requires a very different value of the V/W ratio than do higher energy data sets. In fact, the ratio appears to change almost discontinuously at low energies; the high energy data sets are in fair agreement with an energy-independent potential. (This statement is confirmed by comparing the potentials discussed here with existing 99 MeV ^{6}Li+^{28}Si data.[23]) Unfortunately, at low energies the real and imaginary wells are complementary to each other to a large extent. If we compare the potentials which fit the 13 MeV data with those which fit the higher energy data, we find that there are two different types of modification of the high energy potentials which are successful in achieving a fit at 13 MeV. Either the real potential can be decreased by a factor of roughly 3, with the imaginary potential kept the same (e.g., S22 or P12 in Table II), or the imaginary potential can be adjusted to have a steeper falloff at large radii with the real potential fixed (e.g., S23 or (P13). Obviously some combination of these techniques (e.g., R27) also works. In any case, it seems unambiguous that the ^{6}Li+^{28}Si optical potential is very different at 13 MeV than it is at energies above 46 MeV. Possible reasons for this behavior will be discussed below.

Returning now to the ^{9}Be+^{28}Si system, we see in Fig. 18 that the overall trend of V/W is quite flat as a function of energy, with the imaginary potential always being stronger than the real. If we stretch our faith in a representation of this type, we can infer that for this particular system a four-parameter WS potential (that is, $r_R = r_I$, $a_R = a_I$) might be adequate over the whole energy range. Figures 19 and 20 show the results of using the four-parameter potential G05 (see Table I) to fit the data. As expected, the fits are nearly the same quality as those from the six-parameter potentials. On the other hand, using the folding-model potential with a "complex normalization constant" does not yield good fits to the high energy ^{9}Be data,[23] although the optimum V/W ratio 0.77 is in good agreement with what we

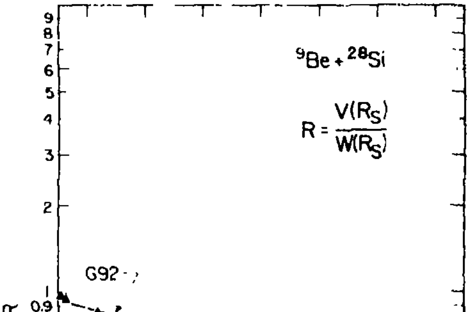

FIG. 18. Same as Fig. 14, but for ^{9}Be+^{28}Si. For this system the imaginary potential is stronger than the real potential at all energies.

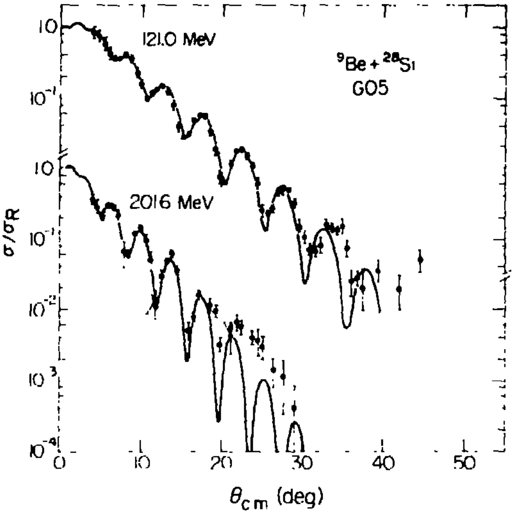

FIG. 19. Fits to the high energy ^{9}Be+ ^{28}Si data using a four-parameter WS potential G05 (see Table I). Values of χ^2/N for potential G05 are 121.0 MeV, 4.1; 201.6 MeV, 3.5.

find using WS potentials. (The preference for a phenomenological WS shape over a folded shape for the imaginary potential seems to hold for all of the systems studied up to now.[11]) Although there is no theoretical justification for doing so, as an exercise we tried a proximity form for the imaginary as well as the real potential. We found, as for the folding model, that the optimum ratio of V/W was about 0.75, but the fits were rather poor (χ^2/N for the high energy data sets increased by a factor of 5). Thus, for the ^{9}Be +^{28}Si system, an optical potential having a common geometry for the real and imaginary well is only successful if a WS form is used.

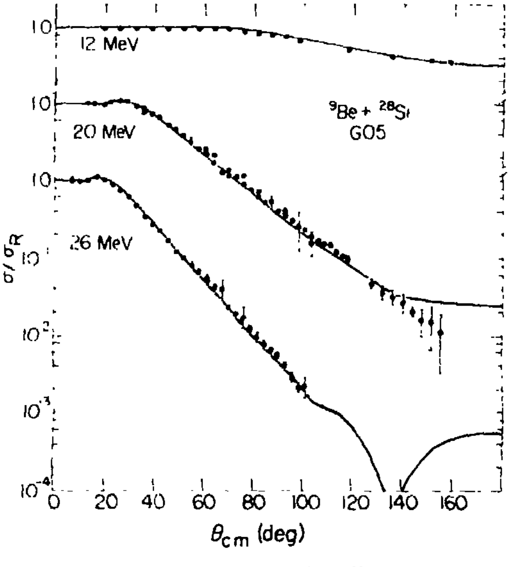

FIG. 20. Fits to the low energy ^{9}Be+^{28}Si data using a four-parameter WS potential G05 (see Table I). Values of χ^2/N for potential G05 are 12 MeV, 0.6; 20 MeV, 4.6; 26 MeV, 1.9.

D. Projectile spin effects

As mentioned earlier, one difference between the ^{6}Li and ^{9}Be projectiles and the other projectiles we have studied is that both the former have nonzero ground state spins ($J^\pi = 1^+$ and $\frac{3}{2}^-$ for ^{6}Li and ^{9}Be, respectively). In principle, this means that a spin-orbit potential, which we have not considered in our analysis, must contribute to the scattering. One must therefore ask whether ignoring the spin-orbit term leads to incorrect values of the central potential parameters. Although there is no information on this point for ^{9}Be elastic scattering, the spin-orbit effects in ^{6}Li have been investigated previously both experimentally[24,25] and theoretically.[26] The existence of a spin-orbit term in the interaction potential was demonstrated[24] in a study of ^{6}Li elastic scattering at 20 and 22.8 MeV using a vector polarized ^{6}Li beam on a number of targets, including ^{28}Si. It was shown in this work that the observed asymmetries were consistent with a folding-model estimate[26] of the spin-orbit potential. On the other hand, it was also pointed out that a "reasonable" spin-orbit potential has almost no effect on the predicted angular distributions. Chua *et al.*[25] made a study of unpolarized ^{6}Li elastic scattering on a variety of targets, but not ^{28}Si, at a higher energy of 50.6 MeV. Their conclusion, based on a standard derivative form for the spin-orbit potential, was that the data gave no unambiguous evidence for spin-orbit effects. Here, too, the addition of the spin-orbit term had very little observable effect on the angular distributions, the main one being a slight increase in the predicted structure at large angles. (Even this effect could be compensated by slight changes in the imaginary potential.) From these studies[24,25] we conclude that, in terms of angular distributions, the spin-orbit influence is likely to be negligible. Thus, the potentials we extracted from our angular distributions would not be significantly different if a spin-orbit term were explicitly considered. Similar conclusions were reached by Satchler and Love.[12]

Although there are no data from which one can get information on the spin-orbit potential in the case of ^{9}Be elastic scattering, we can use the folding model to estimate the mass dependence of the effect. Amakawa and Kubo[26] have shown that the result of folding the spin-orbit potential over the projectile volume is that the radial form of the spin-orbit term changes from its original derivative form to a volume form, and that the mass dependence is A_p^{-2}. In this case the spin-orbit effects in ^{9}Be elastic scattering would be even smaller than for ^{6}Li and would not be expected to influence our optical model analysis. (Clearly the effect of the spin-orbit potential will increase at high energies and heavier projectile masses due to the larger value of the grazing angular momentum. However, since the centrifugal potential increases much more rapidly with energy than the spin-orbit potential, even at high energies the spin-orbit effects are expected[26] to be small.)

In addition to possible spin-orbit effects, ^{6}Li and ^{9}Be might also be influenced by quadrupole terms in the optical potentials. Satchler and Fulmer[27] have shown that, in a simple coupling model, the (incoherent) contribution from the quadrupole term leads to an additional elastic cross section which is proportional to the cross section for inelastic scattering to the 2^+ state in the core. Because the 2^+ cross section is generally out of phase with the elastic, the practical ffect of this term is to damp out the structure ı the back angle elastic scattering angular disribution (where σ_{el} and σ_{inel} are more or less omparable in magnitude). Evidence for this ort of behavior has been seen in heavy ion sysems similar to the ones studied here by Parks *l al.*,[28] who investigated the elastic scattering f ^{10}B and ^{11}B from ^{27}Al at 50 MeV. They find ıat for ^{10}B + ^{27}Al there is substantial damping of ıe cross sections in the angular region beyond $_{c.m} \approx 50°$ compared with a standard optical model rediction. In the case of ^{11}B, the effect is less evere, but some filling in of the minima is visle. Parks *et al.* were able to reproduce these rends by adding the quadrupole cross section, alculated with a double-folding model, to the pherical optical model cross section. The imortance of the quadrupole term was found[28] to cale roughly as the quadrupole moment of the rojectile.

If we try to apply these results to our situaion, the following points emerge. Since ^{6}Li as a very small quadrupole moment (−0.8 e mb) (Ref. 9) compared with that for ^{10}B or ^{11}B (80 and 40 $e$mb, espectively),[30] it is unlikely that the quadrupole erm is significant in this case. On the other and, the ^{9}Be quadrupole moment (65 $e$mb) Ref. 29) is comparable to those in the boron projectiles. It seems possible, therefore, that the larger angle ^{9}Be data, particularly at 201.6 MeV (Figs. 1, 3, and 8), could contain a contribution from this effect. If this is the case, it calls into question to some extent a potential such as G38 (Fig. 3), which more or less reproduces the lack of back angle structure in the high energy ^{9}Be angular distribution. However, the fact that a potential such as G38 is capable of fitting data over such a large energy range argues at the very least that it is possible to successfully incorporate quadrupole effects, if present, into an optical potential. Although calculations such as those reported by Parks *et al.*[28] are beyond the scope of this paper, they would clearly be very interesting to perform for the ^{9}Be + ^{28}Si system. (It is unfortunate that our experiment does not allow us to observe the ^{9}Be projectile excitation, since the approach of Satchler and Fulmer[27] would then yield a direct estimate of the quadrupole contribution to the elastic scattering.)

E. Breakup

If we look at the trends for the various projectiles indicated in Figs. 14, 15, and 18, we see that ^{16}O behaves in a rather intuitive way, that is, the imaginary potential gets more important as the energy increases. On the other hand, ^{6}Li behaves in the opposite fashion and ^{9}Be shows a stronger imaginary potential at all energies. Because the binding energies of ^{6}Li and ^{9}Be (1.47 and 1.67 MeV, respectively) are very low compared with other light heavy ions, it is tempting, particularly in the case of ^{6}Li, to ascribe the low energy behavior to breakup in the Coulomb field of the target.

The Coulomb breakup mechanism for ^{6}Li has already been demonstrated[31,32] at near-barrier energies on a variety of targets. (Even very near the barrier, however, it has been shown[33] that the nuclear potential plays a role in the breakup process.) In addition, it was shown[32] that the majority of the ^{6}Li$-\alpha+d$ cross section comes from a sequential mechanism in which ^{6}Li is first inelastically excited to its 2.18 MeV, 3^+ level. At high energies, on the other hand, there is evidence[34] that the breakup changes to a direct (presumably nuclear) process which does not proceed through the ^{6}Li 2.18 MeV state.

If we assume a Coulomb excitation mechanism is dominant at low energies, it is possible to estimate what effect it might have on the ^{6}Li + ^{28}Si optical potential. Love *et al.*[35] have shown that the main effect shows up in the imaginary potential, which has a long range tail added to it characterized by a strength

$$W_p = 0.016\,76\,\frac{\mu Z_t^2}{k} B(E2) g_2 \text{ MeV fm}^5 , \qquad (13)$$

where μ is the reduced mass (in amu), k is the wave number, g_2 is a tabulated adiabaticity factor and the $B(E2)$, taken from Ref. 36, is in units of $e^2\,\text{fm}^4$. Compared with the cases listed in Ref. 35, however, the strength appropriate to $^6\text{Li}+{}^{28}\text{Si}$ is more than two orders of magnitude weaker; near the sensitive radius at 13 MeV the polarization potential is a few keV, compared with an imaginary strength of about 1 MeV. Thus, it is not clear that (sequential) Coulomb breakup is responsible for the low energy behavior.

If one considers instead a breakup process initiated by nuclear inelastic scattering, the conclusion[35] is that the imaginary potential should still be more strongly modified than the real potential. In the nuclear case, no simple expression for the polarization potential is available. Although our experimental technique does not allow us to measure the cross section for projectile excitation of the $^6\text{Li}(3^+)$ state at 2.18 MeV, it is known from light ion inelastic scattering[37] that this excited state is populated very strongly. In fact, with α particles, the integrated cross section for inelastic scattering is twice that of the elastic. It is in just this situation that channel coupling may be most important.[38] Assuming the projectile excitation in low energy $^6\text{Li}+{}^{28}\text{Si}$ scattering has a similar strength, it seems clear that either a full coupled-channels calculation, or at least an approximate calculation such as proposed by Love *et al.*[35] should be carried out. It is interesting that, for a fixed real potential, the change required in the imaginary potential at higher energies is that the tail increases (a_I increases). Qualitatively, this is just the sort of behavior which would be expected due to the addition of a polarization potential[35] at the higher energies. The rapid change in the imaginary potential as the energy increases might be related to a change in the strength of the coupling to the elastic channel when the breakup mechanism changes from a sequential to a direct one.[34] Of course, depending on the strength of the direct process, in the higher energy regime it may be inappropriate to ignore the explicit channel coupling in obtaining optical potentials. Unfortunately, there is not enough information presently available to answer this question. (As mentioned earlier, the low energy data are equally consistent with a fixed imaginary potential and a markedly weaker real potential. This could conceivably be viewed as symptomatic of the same problem that causes the folding-model real potential to require[13] a substantial reduction for ^6Li projectiles. If this were true, one might expect that a "global" folding-model fit to the 13 MeV data would require an even larger renormalization than do the higher energy fits.)

In the ^9Be case, Fig. 18 does not indicate any anomaly in the low energy region, although there is some preference here too for the imaginary to increase relative to the real potential at low energies. There are certain differences in the ^9Be breakup compared with ^6Li breakup which might explain this fact. Although ^6Li breakup at low energies goes mainly through a single state, which is populated predominantly via Coulomb excitation, the ^9Be breakup[39] goes through a number of low-lying states. One of these states is reached by an $E2$ transition with a $B(E2)$ similar[29] to that for the ^6Li excited state, but the others are not reached by $E2$ transitions and are probably excited predominantly by nuclear inelastic scattering. Depending on which states dominate the breakup process at a given energy, it is conceivable that the V/W ratio for ^9Be does not change much near the barrier. At higher energies, Stahel *et al.*[40] have shown that there is a sizable direct breakup cross section in the (^9Be, ^8Be) reaction at 50 MeV. How, or if, the breakup mechanism changes between the Coulomb barrier and 50 MeV is presently unknown.

F. Fusion

Certain groups[13,15] have recently attempted to fit both elastic and fusion cross sections with a single interaction potential, rather than treating the two types of data independently. Although there is not much information on $^9\text{Be}+{}^{28}\text{Si}$ fusion available, some data have recently been measured[41] which make it worthwhile to compare with predictions from our elastic scattering potentials.

In order to predict fusion cross sections, we must employ a model of the fusion process. Most models[15,42,43] agree that, at low energies, the fusion barrier is determined by the maximum in the real (S-wave) potential:

$$V_B = V(R_B) = V_n(R_B) + V_C(R_B) + V_{\text{cent}}(l, R_B) , \qquad (1$$

where the barrier radius R_B is defined by

$$\left.\frac{dV(r)}{dr}\right|_{r=R_B} = 0 . \qquad (15$$

In addition, there is a maximum in the fusion cross section at an energy E_{max}, which in some models[13,15] is related to the disappearance of the "pocket" in the real potential for $l > l_{cr}^{max}$ and in other models[43] is related to reaching a critical distance R_{cr}. The fusion cross section is given by

$$\sigma_f = \pi ƛ^2 \sum_{l=0}^{\infty} (2l+1) P_l \,, \tag{16}$$

where P_l is the fusion probability for partial wave l. In a sharp cutoff (SCO) model,

$$P_l = 1 \quad (l \leq l_{cr}) \tag{17a}$$

$$\quad = 0 \quad (l > l_{cr}) \tag{17b}$$

and l_{cr} is the highest partial wave for which the barrier maximum is below $E_{c.m.}$. Alternatively, the P_l values can be calculated allowing transmission through, as well as passage over, the barrier.[13] Insofar as using an SCO model, i.e., using Eq. (17), predicts essentially the same fusion cross sections except at energies very near the barrier, we have used the simpler approach. The SCO cross sections are then given by

$$\sigma_f = \pi ƛ^2 (l_{cr} + 1)^2 \quad (E \leq E_{max}) \tag{18a}$$

$$\quad = \pi ƛ^2 (l_{cr}^{max} + 1)^2 \quad (E > E_{max}) \,. \tag{18b}$$

In the critical radius picture of Glas and Mosel (GM),[43] the fusion probability P_l is calculated for transmission through a parabolic barrier. If the approximations of constant barrier curvature and constant barrier radius are made, this model leads to an analytic expression for σ_f in terms of the $l = 0$ barrier [see Eqs. (14) and (15)] and the potential at the "critical" radius for fusion:

$$R_{cr} = r_0^{cr} (A_p^{1/3} + A_t^{1/3}) \,, \tag{19}$$

$$V(R_{cr}) = V_n(R_{cr}) + V_C(R_{cr}) \,, \tag{20}$$

where empirically[43] the value for r_0^{cr} is about 1.0 fm.

igure 21 shows calculations based on both the) and GM models compared with data from . 41. The various parameters needed for the culations were taken from either potential) (solid curves) or the proximity potential shed curves) and are listed in Table III. It ears that the data are most consistent with GM calculation based on potential G38. This somewhat surprising since in other systems, h as ^{16}O+^{28}Si, a GM calculation based on a llow WS potential such as E18 predicts cross tions much lower than are observed eximentally.[13] An SCO calculation with a deep real potential, such as G92, would look fairly ilar to the proximity potential calculation wn in Fig. 21. Although a real WS well depth ween 13.8 and about 100 MeV is capable of

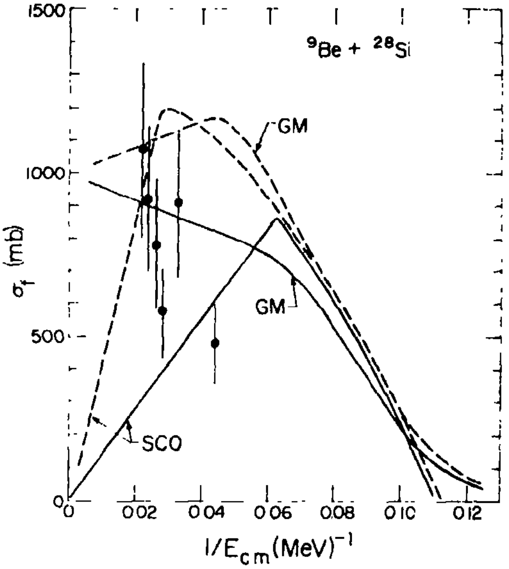

FIG. 21. Predicted complete fusion cross sections for ^{9}Be+^{28}Si, based on parameters extracted from potentials which fit the elastic scattering. The solid lines correspond to potential G38 and the dashed lines to proximity potential P01. Both sharp cutoff (SCO) and Glas-Mosel (GM) calculations (see Sec. III F) are shown for each potential. (Predictions using a deep WS potential such as G92 would look similar to the dashed lines). Data points are from Ref. 41 and the relevant barrier parameters are summarized in Table III. Note the increased cross sections predicted in the GM model compared with the SCO model at low energies due to the consideration of barrier penetrability in the former case.

TABLE III. Predicted ^{9}Be+^{28}Si fusion barriers.

Set	R_B (fm)	V_B (MeV)	R_{cr}[a] (fm)	$V(R_{cr})$[a] (MeV)
G38	8.145	9.056	5.63	3.90
G05	8.215	8.881	5.63	4.44
G92	8.193	8.699	5.63	−1.30
P01	8.165	8.897	5.63	−4.25
B01[b]	7.444	9.447	5.63	8.37
Folded[c]	8.066	9.080	5.63	−2.67
Syst.[d]	8.248	8.874		

[a] Values of critical radius and critical potential, Eqs. (19) and (20), required for Glas-Mosel calculations. A barrier curvature $\hbar\omega = 5$ MeV was also used.

[b] From Ref. 6. This potential does not reproduce the high energy data sets measured in this work.

[c] From Ref. 10, using method B and $N = 0.5$.

[d] From Eqs. (21) and (22), based on Ref. 14.

roughly matching the magnitude of the experimental cross sections, the SCO model must produce a downward sloping curve at high energies, in apparent contradiction with the experimental results.[41]

We note that our potentials suggest that the fusion data measured in Ref. 41 are high energy data, in the sense of being beyond the "bend" in the predicted fusion cross sections (see Fig. 21). In the analysis of Ref. 41, the data are assumed to be in the low energy regime of fusion cross sections. This assumption leads[41] to values for the radius and height of the fusion barrier of $R_B = 7.68 \pm 1.02$ fm and $V_B = 22 \pm 4$ MeV. Although the radius extracted from the data is in reasonable agreement with systematics,[14] the barrier height is not and will lead to very different fusion cross sections at near-barrier energies. In spite of there being no low energy data available with which to compare, the values for R_B and V_B obtained from potentials which fit the elastic data (Table III) may be compared with the results of Vaz and Alexander,[14] who made a systematic study of fusion barrier parameters over a very wide range of nuclei. Their parametrization of the barrier is[14]

$$R_B = r_B(A_p^{1/3} + A_t^{1/3}), \tag{21a}$$

$$r_B = 2.0337 - 0.2412 \log_{10}(Z_p Z_t), \tag{21b}$$

$$V_B = \frac{Z_p Z_t e^2}{r_e(A_p^{1/3} + A_t^{1/3})}, \tag{22a}$$

$$r_e = 2.301 - 0.3003 \log_{10}(Z_p Z_t). \tag{22b}$$

For ^{9}Be + ^{28}Si, this leads to the values $R_B = 8.248$ fm and $V_B = 8.874$ MeV. Agreement with the values obtained in Table III is very good and gives some hope that the potentials we have extracted from the elastic scattering will be capable of also reproducing low energy fusion cross sections. Clearly the combination of high-quality fusion data along with the available elastic data over a wide energy range will provide an important test of whether or not it is possible to fit both types of data together with a common potential.

One word of caution regarding the GM calculations is clearly in order. It is not implausible that the elastic scattering potential can give information regarding the outer S-wave barrier, but it is much less clear[11] that the optical potential is still "operative" at the smaller separations corresponding to R_{cr}. There is some hope in our case that the optical model V_{cr} is reasonable, however, since the high energy elastic data do have sensitivity into small enough radii to correspond at least roughly to the R_{cr} values.

In the ^{6}Li + ^{28}Si system, there is an ambiguity at the lowest energy about whether the required change in the fit potential should be ascribed to the real or the imaginary well. Although hardly a definitive test, it is instructive to compare the predicted fusion barriers of the various real potentials to the Vaz and Alexander systematics.[14] The results given in Table IV show that the real potentials obtained from the high energy data lead to fusion barriers consistent with systematics, while the real potentials adjusted to fit the low energy data do not. If we make the assumption that low energy ^{6}Li + ^{28}Si fusion data do not show any unusual behavior compared with systematic predictions—a fact not presently verified—we would conclude that the change in optical potential from low to high energies is most likely related to a change in the tail of the imaginary potential (possibly due to strong coupling to other channels).

IV. SUMMARY

We have measured the elastic scattering of ^{9}Be + ^{28}Si at 121.0 and 201.6 MeV and, in combination with other data, have performed a globa optical model analysis in the energy range from 12 to 201.6 MeV. In contrast to earlier studies,[1] we find that it is possible to obtain a number of energy independent WS potentials, spanning a wide range of real well depths, which fit the data rather well. Optical model calculations employing a proximity form for the real potential have also been performed. Good fits to the data can b obtained provided the parameters of the proximity potential are modified somewhat from their suggested values. In this case it is necessary to employ a WS imaginary potential having an explicit energy dependence in order to reproduce th data. At the highest energy, an examination of th various potentials indicates that there are no visible effects due to nuclear rainbow scattering.

TABLE IV. Predicted ^{6}Li + ^{28}Si fusion barriers.

Set	R_B (fm)	V_B (MeV)
R22[a]	8.099	6.654
S01[a]	8.071	6.677
P10[a]	8.018	6.803
R27[b]	7.558	7.120
P12[b]	7.314	7.489
Syst.[c]	7.971	6.871

[a] Preferred for high energy data sets.

[b] Preferred for 13 MeV data set.

[c] From Eqs. (21) and (22), based on Ref. 14.

However, the data at 201.6 MeV are suggestive of the influence of quadrupole terms in the interaction potential. A calculation of this effect would be very informative to see if this is the case.

Notch perturbation calculations have been performed for the ^{9}Be+^{28}Si potentials obtained here as well as the ^{6}Li+^{28}Si and ^{16}O+^{28}Si potentials studied earlier.[1,2] The sensitive region in ^{9}Be elastic scattering extends from about 5–10 fm, and shows that the imaginary potential is stronger than the real potential throughout. In the case of ^{6}Li elastic scattering, the data indicate that the imaginary potential exceeds the real potential at low energies with the real potential becoming increasingly important at higher energies, while for ^{16}O the reverse is true. For all systems at all energies we have shown that the ratio of V/W evaluated at the radius of maximum sensitivity is nearly the same for all potentials which fit the data. However, this ratio is not sufficient by itself to map out the potential, probably because the V/W ratio samples the potential at only one point while the scattering itself is sensitive to a fairly large region at any given energy.

Possible explanations of why the low energy ^{6}Li data, and to some extent the ^{9}Be data, are dominated by strong absorption have been considered. One possibility is related to either Coulomb or nuclear breakup at low energies. However simple estimates of this effect indicate that the expected Coulomb excitation contribution is too small to have a major influence on the ^{6}Li+^{28}Si elastic scattering. It may be that the strength of the coupling to the direct breakup channel is sufficiently large that a full coupled-channels approach will be required; this aspect should be investigated by calculations.

Using two simple models of the fusion process, we have compared our potentials to existing fusion reaction cross sections. The S-wave barrier radii and heights extracted from the various potentials agree very well with predictions from fusion systematics. It will be interesting to see how these barrier parameters compare with low energy ^{9}Be fusion data.

ACKNOWLEDGMENTS

We would like to thank D. L. Hendrie and D. K. Scott for their support of this project and R. A. Gough and the crew of the LBL 88-inch cyclotron for providing the ^{9}Be beams used in the experiment. We also thank the authors of Ref. 5 for allowing us to utilize their unpublished data, G. R. Satchler for providing information on his folding-model calculations, and J. Alexander for several informative discussions. This work was supported in part by the National Science Foundation and in part by the Division of Nuclear Physics, U. S. Department of Energy.

---

[1] J. G. Cramer, R. M. DeVries, D. A. Goldberg, M. S. Zisman, and C. F. Maguire, Phys. Rev. C 14, 2158 (1976).

[2] R. M. DeVries, D. A. Goldberg, J. W. Watson, M. S. Zisman, and J. G. Cramer, Phys. Rev. Lett. 39, 450 (1977).

[3] D. A. Goldberg and S. M. Smith, Phys. Rev. Lett. 29, 500 (1975); D. A. Goldberg, S. M. Smith, and G. F. Burdzik, Phys. Rev. C 10, 1367 (1974).

[4] J. S. Eck, T. J. Gray, and R. K. Gardner, Phys. Rev. C 16, 1873 (1977).

[5] R. M. DeVries, D. S. Shapira, N. Anantaraman, R. Cherry, M. R. Clover, and H. E. Gove (unpublished data).

[6] R. Balzer, M. Hugi, B. Kamys, J. Lang, R. Müller, E. Ungricht, and J. Unternährer, Nucl. Phys. A293, 518 (1977).

[7] D. F. Jackson and R. C. Johnson, Phys. Lett. 49B, 249 (1974).

[8] F. Perey (unpublished).

[9] G. R. Satchler, Nucl. Phys. A279, 493 (1977).

[10] G. R. Satchler, Phys. Lett. 83B, 284 (1979).

[11] G. R. Satchler and W. G. Love, Phys. Rep. 55, 183 (1979).

[12] G. R. Satchler and W. G. Love, Phys. Lett. 76B, 23 (1978).

[13] L. C. Vaz, J. M. Alexander, and E. H. Auerbach, Phys. Rev. C 18, 820 (1978); L. C. Vaz and J. M. Alexander, Phys. Rev. C 18, 833 (1978).

[14] L. C. Vaz and J. M. Alexander, Phys. Rev. C 18, 2152 (1978).

[15] J. R. Birkelund and J. R. Huizenga, Phys. Rev. C 17, 126 (1978); J. R. Birkelund, L. E. Tubbs, J. R. Huizenga, J. N. De, and D. Sperber, Phys. Rep. 56, 107 (1979).

[16] J. Blocki, J. Randrup, W. Swiatecki, and C. F. Tsang, Ann. Phys. (N.Y.) 105, 427 (1977).

[17] J. G. Cramer, University of Washington Nuclear Physics Laboratory Annual Report 1976, p. 115 (unpublished); J. G. Cramer and R. M. DeVries, Phys. Rev. C (to be published).

[18] S. E. Vigdor, D. G. Kovar, P. Sperr, J. Mahoney, A. Menchaca-Rocha, C. Olmer, and M. S. Zisman, Phys. Rev. C 20, 2147 (1979).

[19] G. R. Satchler, Phys. Lett. 58B, 408 (1975).

[20] H. T. Fortune, A. Richter, R. H. Siemssen, and J. L. Yntema, Phys. Rev. C 20, 648 (1979); R. Vandenbosch, M. P. Webb, and M. S. Zisman, Phys. Rev. Lett. 33, 842 (1974); J. V. Maher, M. W. Sachs, R. H. Siemssen, A. Weidinger, and D. A. Bromley, Phys. Rev. 188, 1665 (1969).

[21] S. L. Tabor, D. A. Goldberg, and J. R. Huizenga, Phys. Rev. Lett. 41, 1285 (1978).

[22] P. Schwandt (unpublished data).

[23] G. R. Satchler, private communication.

[24] W. Weiss, P. Egelhof, K. D. Hildenbrand, D. Kassen, M. Makowska-Rzeszutko, D. Fick, H. Ebinghaus, E. Steffens, A. Amakawa, and K. I. Kubo, Phys. Lett. 61B, 237 (1976).

[25] L. T. Chua, F. D. Becchetti, J. Jänecke, and F. L. Milder, Nucl. Phys. A273, 243 (1976).

[26] H. Amakawa and K. I. Kubo, Nucl. Phys. A266, 521 (1976).

[27] G. R. Satchler and C. B. Fulmer, Phys. Lett. 50B, 309 (1974).

[28] L. A. Parks, K. W. Kemper, A. H. Lumpkin, R. I. Cutler, L. H. Harwood, D. Stanley, P. Nagel, and F. Petrovich, Phys. Lett. 70B, 27 (1977).

[29] F. Ajzenberg-Selove and T. Lauritsen, Nucl. Phys. A227, 1 (1974).

[30] G. H. Fuller and V. W. Cohen, Nucl. Data Tables A5, 433 (1969).

[31] K. O. Pfeiffer, E. Speth, and K. Bethge, Nucl. Phys. A206, 545 (1973).

[32] D. Scholz, H. Gemmeke, L. Lassen, R. Ost, and K. Bethge, Nucl. Phys. A288, 351 (1977).

[33] H. W. Wittern, Phys. Lett. 32B, 441 (1970).

[34] R. W. Ollerhead, C. Chasman, and D. A. Bromley, Phys. Rev. 134, B74 (1964).

[35] W. G. Love, T. Terasawa, and G. R. Satchler, Nucl. Phys. A291, 183 (1977).

[36] D. L. Disdier, G. C. Ball, O. Häusser, and R. E. Warner, Phys. Rev. Lett. 27, 1391 (1971).

[37] S. Matsuki, S. Yamashita, K. Fukunaga, D. C. Nguyen, N. Fujiwara, and T. Yanabu, J. Phys. Soc. Jpn. 26, 1344 (1969).

[38] W. Henning, J. P. Schiffer, D. G. Kovar, S. Vigdor, B. Zeidman, Y. Eisen, and H. J. Körner, Phys. Lett. 58B, 129 (1975).

[39] H. Werle, L. Van der Zwan, and K. W. Geiger, Z. Physik 259, 275 (1973).

[40] D. P. Stahel, G. J. Wozniak, M. S. Zisman, B. D. Jeltema, and J. Cerny, Phys. Rev. C 16, 1456 (1977).

[41] J. S. Eck, J. R. Leigh, T. R. Ophel, and P. D. Clark (unpublished).

[42] R. Bass, Nucl. Phys. A231, 45 (1974).

[43] D. Glas and U. Mosel, Nucl. Phys. A237, 429 (197

PHYSICAL REVIEW C VOLUME 21, NUMBER 6 JUNE 1980

Techniques for heavy-ion coupled-channels calculations. I. Long-range Coulomb coupling

M. Rhoades-Brown, M. H. Macfarlane, and Steven C. Pieper
Argonne National Laboratory, Argonne, Illinois 60439

(Received 6 September 1979)

Direct-reaction calculations for heavy ions require special computational techniques that take advantage of the physical peculiarities of heavy-ion systems. This paper is the first of a series on quantum-mechanical coupled-channels calculations for heavy ions. It deals with the problems posed by the long range of the Coulomb coupling interaction. Our approach is to use the Alder-Pauli factorization whereby the channel wave functions are expressed as products of Coulomb functions and modulating amplitudes. The equations for the modulating amplitudes are used to integrate inwards from infinity to a nuclear matching radius (≈ 20 fm). To adequate accuracy, the equations for the amplitudes can be reduced to first order and solved in first Born approximation. The use of the Born approximation leads to rapid recursion relations for the solutions of the Alder-Pauli equations and hence to a great reduction in computational labor. The resulting coupled-channels Coulomb functions can then be matched in the usual way to solutions of the coupled radial equations in the interior region of r space. Numerical studies demonstrate the reliability of the various techniques introduced.

[NUCLEAR REACTIONS HI coupled-channel inelastic scattering. Treatment of long-range Coulomb potential.]

I. INTRODUCTION

Models of nuclear direct reactions are based on the identification of a few privileged reaction channels, usually the elastic channel and those particularly strongly coupled to it. The Schrödinger equation is then solved in the model space spanned by these privileged channels. The influence of channels excluded from the model space is either taken into account statistically or expressed by absorptive components in the effective interaction potentials that act within the truncated model space. In a partial-wave configuration-space representation, reaction models of the sort under consideration lead to sets of coupled integro-differential equations for radial wave functions. The number of coupled equations (N) for a given total angular momentum and parity (J,π) is usually several times as large as the number of channels in the model space because there are usually several distinct ways to couple the internal nuclear spins and the orbital angular momentum of the relative motion to a given total angular momentum.

The numerical complexity of coupled-channels calculations has severely inhibited the study of nuclear direct reactions. The standard procedure is to solve the N coupled radial equations N times with linearly independent regular starting values. The equations are integrated from the origin to a joining radius R_m at which all nuclear and coupling interactions have become insignificant. A single linear combination with the appropriate asymptotic behavior (incoming and outgoing waves in the elastic channel, outgoing waves in all others) is then constructed; in the process the desired S-matrix elements are found. This method is satisfactory for light-ion reactions but is particularly inefficient for heavy-ion reactions. The long range of the Coulomb coupling interaction, the small step size necessitated by the short wavelength, and the large number of partial waves that contribute significantly have restricted fully quantum-mechanical coupled-channels calculations for heavy ions to at most three or four reaction channels—clearly inadequate to address the key physical questions in the field.

Many-channel calculations have been possible only within the semiclassical framework pioneered by Alder and Winther[1] for multiple Coulomb excitation. This approach has a number of limitations. Its accuracy decreases steadily as the excitation energy of the reaction channels increases. Its accuracy for particle-transfer reactions is largely untested. At energies significantly above the Coulomb barrier the computational complexity of accurate semiclassical calculations increases rapidly; alternatively, the accuracy of the simplest sort of semiclassical calculation rapidly decreases. Thus, although semiclassical methods are indispensable within their natural bailiwick, their limitations are such that a fully quantum-mechanical alternative that can cope with more than three or four reaction channels is worth seeking.

This paper is the first of a series that will describe numerical methods for quantum-mechanical coupled-channels calculations for heavy ions.

The methods to be presented in this series differ from those conventionally used in light-ion studies in three significant respects.

(1) Exploitation of the semiclassical aspects of Coulomb excitation. In light-ion coupled-channels calculations, the solutions of the coupled equations in the interior region (the region wherein nuclear and coupling potentials are significant) are joined to Coulomb functions at a joining radius R_∞ (~20 fm for light ions) characteristic of the outer limit of nuclear and coupling interactions. In heavy-ion reactions the effects of Coulomb excitation are often large and produce significant channel-coupling effects out to distances of hundreds or even thousands of fm. Extension of the boundary of the interior region to the outer limit of Coulomb excitation is catastrophically inefficient. If the coupled equations for Coulomb excitation are integrated inwards from infinity to the nuclear joining radius R_N, the channel wave functions are found to be Coulomb functions modulated by factors that vary slowly with r. As first shown by Alder and Pauli,[2] the coupled equations for the modulating amplitudes can be integrated to adequate accuracy more rapidly by an order of magnitude than the original equations. The resulting coupled-channels Coulomb functions are then matched to the interior solutions at the nuclear joining radius R_N. The time taken to calculate the effects of Coulomb excitation is then at worst comparable to the time needed to generate the internal solutions.

(2) Iterative solutions of the coupled equations within the range of nuclear interactions. The wasteful conventional strategy, whereby the coupled equations are solved N times to produce the one desired solution, can be avoided either by expansion of the channel wave function in terms of a fixed basis[3] or by iterative techniques.[4] We find that the sequential-iteration method of Raynal,[4] with Padé approximants to accelerate convergence of the S-matrix elements, is ideally suited to our present purposes. In all cases considered, it yields S-matrix elements accurate to 1 or 2% in about four iterations. (This number is the average over all contributing partial waves. Five or six iterations may be needed in grazing partial waves, only two or three in others.)

(3) Extensive use of partial-wave interpolation and extrapolation. Huge numbers of partial waves typically contribute significantly to heavy-ion cross sections. On the other hand, the underlying semiclassical features of heavy-ion interactions result in S matrices that are smooth functions of the total angular momentum. It is therefore possible to calculate S-matrix elements directly at rather widely spaced angular momenta and to supplement these calculated matrix elements by interpolation and extrapolation. For example, in computing cross sections for the elastic scattering of 800 MeV ^{132}Xe ions on ^{208}Pb and for the inelastic excitation of the first 2^+ excited state of Xe, 2000 partial waves contribute significantly, but only 25 need be treated explicitly to produce cross sections accurate to 1 or 2%. The necessary interpolation techniques have already been used[5] extensively in distorted-wave Born approximation (DWBA) studies of heavy-ion induced inelastic scattering and transfer reactions.

We believe that these techniques—the Alder-Pauli method for multiple Coulomb excitation, iterative solution of coupled equations in the interior region, and partial-wave interpolation and extrapolation—will combine to accelerate heavy-ion coupled-channels calculations by factors of 10 to 100 over the previous state-of-the-art. In this paper we are concerned with the first of the above aspects, the semiclassical nature of Coulomb excitation. The other two aspects of heavy-ion coupled-channels equations will be discussed in subsequent papers.

In Sec. II the notation to be used in this series is described, and the structure of the coupled equations for the radial functions is discussed. Section III presents the Alder-Pauli factorization of the radial wave functions for multiple Coulomb excitation; coupled equations are derived for the slowly-varying factors that modulate the asymptotic Coulomb functions. We show that under certain commonly satisfied conditions it is possible to solve these equations in first Born approximation, using integrals similar to those encountered in the DWBA for inelastic scattering. Section IV presents numerical studies of the methods developed in Sec. III, and Sec. V contains our conclusions.

II. COUPLED EQUATIONS FOR INELASTIC SCATTERING

We consider inelastic collisions between nuclei a and A and ignore all processes that can occur other than elastic scattering or inelastic excitation. Let $\vec{r}$ be the relative position vector of the centers of mass of projectile a and target A and let x_a and x_A be internal nuclear coordinates. We assume that the Hamiltonian of the system has the form

$$H = H_a(x_a) + H_A(x_A) + T + V(\vec{r}, x_a, x_A), \tag{2.1}$$

where H_a, H_A are the internal Hamiltonians of projectile and target and T is the relative kinetic energy operator. The interaction potential V contains the nuclear and Coulomb components

$V_N(r)$, $V_c(r)$ of the optical potential and the nuclear and Coulomb transition potentials $V_N(\vec{r},x_a,x_A)$, $V_c(\vec{r},x_a,x_A)$ that couple internal excitations of a,A with the relative motion:

$$V(\vec{r},x_a,x_A)=V_N(r)+V_c(r)+V_N(\vec{r},x_a,x_A) + V_c(\vec{r},x_a,x_A)\,. \tag{2.2}$$

Next we construct a complete set of channel eigenstates of definite angular momentum J and parity π. The internal states of a and A are eigenstates of the internal Hamiltonians H_a and H_A:

$$\begin{aligned}(H_a-\mathcal{E}_a^{J_a})\Phi_{M_a}^{aJ_a}(x_a)&=0\,,\\ (H_A-\mathcal{E}_A^{J_A})\Phi_{M_A}^{AJ_A}(x_A)&=0\,,\end{aligned} \tag{2.3}$$

where a,A distinguish different internal states of given angular momentum and the energies are excitation energies referred to the respective ground states.

The space corresponding to a pair (aJ_a,AJ_A) of internal states of projectile and target will be referred to as a "channel." The states in this channel have a $(2J_a+1)(2J_A+1)$-fold spin degeneracy; we introduce eigenstates

$$\Phi^{aJ_a,AJ_A,S}(x_a,x_A)=[\Phi^{aJ_a}(x_a)\times\Phi^{AJ_A}(x_A)]_M^S\,, \tag{2.4}$$

of the channel spin $\vec{S}=\vec{J}_a+\vec{J}_A$, where we have ignored the effects of antisymmetry between projectile and target nucleons. A basis state α for given J,π is specified by a definite channel, a definite channel spin, and a definite relative orbital angular momentum l_α. Solutions of the Schrödinger equation can then be expressed in terms of the basis states α in the form

$$\Psi_M^{J\pi}(\vec{r},x_a,x_A)=\frac{1}{r}\sum_\alpha R_\alpha^{J\pi}(r)\psi_{\alpha M}^{J\pi}(\hat{r},x_a,x_A)\,, \tag{2.5}$$

where

$$\psi_{\alpha M}^{J\pi}(\hat{r},x_a,x_A)=[i^{l_\alpha}Y^{l_\alpha}(\hat{r})\times\Phi^{aJ_a,AJ_A,S_\alpha}(x_a,x_A)]_M^J\,.$$

In practice, only a few channels can be included in the expansion (2.5). Within the truncated model space so defined, the Schrödinger equation for each value of J,π reduces to a finite set of coupled radial equations[6]:

$$\left(\frac{d^2}{dr^2}-\frac{l_\alpha(l_\alpha+1)}{r^2}-U_\alpha^{\text{opt}}+k_\alpha{}^2\right)R_\alpha^{J\pi}(r)=\sum_{\beta=1}^{N}U_{\alpha\beta}R_\beta^{J\pi}(r)\,, \tag{2.6}$$

where the coupling matrix is

$$\begin{aligned}U_{\alpha\beta}(r)=\frac{2\mu_\alpha}{\hbar^2}\int d\hat{r}\,dx_a\,dx_A\,\psi_\alpha^{J\pi*}(\hat{r},x_a,x_A)\\ \times[V_N(\vec{r},x_a,x_A)+V_c(\vec{r},x_a,x_A)]\\ \times\psi_\beta^{J\pi}(\hat{r},x_a,x_A)\,,\end{aligned} \tag{2.7}$$

and U_α^{opt} is $2\mu_\alpha/\hbar^2$ times the optical potential. Here N is the number of coupled equations for angular momentum (J,π), and the channel wave number k_α is given by

$$k_\alpha{}^2=\frac{2\mu_\alpha}{\hbar^2}(E-\mathcal{E}_A^{J_A}-\mathcal{E}_a^{J_a})\,. \tag{2.8}$$

In these formulas, E is the center-of-mass energy in the incident channel, and μ_α is the reduced mass in channel α.

Solutions of the set (2.6) of coupled differential equations are required that are regular at the origin $[R_\alpha(0)=0]$ and have the asymptotic form

$$R_\alpha^{J\pi}(r)\underset{r\to\infty}{=}\frac{i}{2}\left[I_{\alpha_0}(r)\delta_{\alpha\alpha_0}-\left(\frac{k_{\alpha_0}}{k_\alpha}\right)^{1/2}S_{\alpha\alpha_0}^{J\pi}O_\alpha(r)\right]\,, \tag{2.9}$$

where α_0 is the incident channel and I_α, O_α are incoming and outgoing Coulomb functions. If the channel spin for the incident channel is nonzero, there will be several basis states α_0 with incoming components; we ignore this minor complication here. There are N linearly independent regular solutions of Eqs. (2.6); the asymptotic condition (2.9) uniquely defines the desired element of the N-dimensional vector space that they span, including normalization. Conventional techniques for the solution of the coupled equations involve explicit construction of a complete set of N regular solutions, each with a linearly independent choice of starting conditions (dR_α/dr at $r=0$). The coefficients of the linear combination of these solutions that has the asymptotic form (2.9) are determined, together with the N S-matrix elements $S_{\alpha\alpha_0}$, by matching at a radius $r=R_m$ sufficiently large that all the potentials except $V_c(r)$ in Eq. (2.2) are negligible. The main point of iterative solutions of Eqs. (2.6) is to eliminate the need to solve the coupled equations N times in order to construct a complete set of regular solutions.

Complete specification of the coupling matrix $U_{\alpha\beta}(r)$ requires the introduction of a detailed model for the internal nuclear states involved and specific assumptions about the nuclear interaction potential V_N. No general discussion of this complex task will be attempted here. We are concerned with techniques for the solution of the coupled equations (2.6). To test and compare various methods, we consider collisions between nuclei with 0^+ ground states and allow one of the nuclei to be excited to a single state of natural parity. We believe that the conclusions drawn from these two-channel test cases have a wide range of validity.

The nuclear part of the optical potentials will be taken to be of complex Woods-Saxon form, with the Coulomb part given by the interaction potential of a point charge with a uniform spherical charge distribution. The couplings $U_{\alpha\beta}(r)$ are calculated from the deformed optical model, with rotational eigenstates for the nuclear wave functions and the transition potential $V(\vec{r}, x_a, x_A)$ carried to first order in the deformation. Because the unexcited nucleus has spin 0, the quantity S defined in Eq. (2.4) has the value J_A for target excitation or J_a for projectile excitation, and the coupling potential $U_{\alpha\beta}(r)$ can be expressed as a sum over multipoles λ in the form

$$U^J_{s_\alpha l_\alpha, s_\beta l_\beta}(r) = \frac{2\mu_\alpha}{\hbar^2} \sum_\lambda A_\lambda(S_\alpha l_\alpha, S_\beta l_\beta, J) H_\lambda(r)\,,$$

$$A_\lambda(S_\alpha l_\alpha, S_\beta l_\beta, J) = i^{l_\beta - l_\alpha}(-1)^{J+\lambda} \frac{\hat{S}_\alpha \hat{S}_\beta \hat{l}_\alpha \hat{l}_\beta \hat{\lambda}}{(4\pi)^{1/2}} \begin{pmatrix} S_\beta & \lambda & S_\alpha \\ 0 & 0 & 0 \end{pmatrix}$$

$$\times \begin{pmatrix} l_\alpha & \lambda & l_\beta \\ 0 & 0 & 0 \end{pmatrix} \begin{Bmatrix} S_\alpha & l_\alpha & J \\ l_\beta & S_\beta & \lambda \end{Bmatrix}, \tag{2.10}$$

$$H_\lambda(r) = -(\beta^N_\lambda R_v)\frac{dV_N(r)}{dr} + \frac{3Z_A Z_a e^2}{(2\lambda+1)}(\beta^c_\lambda R^\lambda_c)\phi_c(r)\,,$$

$$\phi_c(r) = \begin{cases} \dfrac{1}{r^{\lambda+1}}, & r > R'_c \\[2ex] \dfrac{r^\lambda}{(R'_c)^{2\lambda+1}}, & r < R'_c\,. \end{cases}$$

Here the symbol $\hat{a}$ stands for $\sqrt{2a+1}$; β^N_λ, R_v, β^c_λ, and R_c are the deformation parameters and radii (nuclear and Coulomb) of the excited nucleus, and R'_c is the Coulomb radius of the optical potential (the sum of the projectile and target Coulomb radii).

III. TREATMENT OF COULOMB EXCITATION

Two distinct radii that play an important part in all subsequent discussions have been introduced. The first is the outer limit R_N of all nuclear interactions. The second is the asymptotic radius R_∞ beyond which only point-Coulomb interactions survive. Three regions are then to be distinguished:

(i) The interior region $0 < r < R_N$, to which nuclear interactions are restricted,

(ii) the intermediate region $R_N < r < R_\infty$, in which only the Coulomb components of optical-model and coupling potentials survive,

(iii) the true asymptotic region $r > R_\infty$, in which the wave function in each channel reduces to a combination [Eq. (2.9)] of pure Coulomb functions. We will find that in actual calculations it is possible to let $R_\infty \to \infty$ so that region (iii) is eliminated.

For $r > R_N$, the coupled equations (2.6) reduce to the equations that describe multiple Coulomb excitation[1]:

$$\left(\frac{d^2}{dr^2} - \frac{2\eta_\alpha k_\alpha}{r} - \frac{l_\alpha(l_\alpha+1)}{r^2} + k_\alpha{}^2\right) R^{J\pi}_\alpha(r) = \sum_\beta U^c_{\alpha\beta}(r) R^{J\pi}_\beta(r)\,, \tag{3.1}$$

where η_α is the usual Sommerfeld parameter, and from Eqs. (2.10) the Coulomb coupling potential $U^c_{\alpha\beta}$ is given by

$$U^c_{l_\alpha s_\alpha, l_\beta s_\beta}(r) = \frac{2\mu_\alpha}{\hbar^2} \sum_\lambda{}' A_\lambda(S_\alpha l_\alpha, S_\beta l_\beta, J) \frac{3Z_A Z_a e^2}{(2\lambda+1)} \frac{R^\lambda_c \beta^c_\lambda}{r^{\lambda+1}}\,. \tag{3.2}$$

In writing Eq. (3.2) we have assumed that R_N has been chosen such that $R_N > R'_c$.

Solutions of Eqs. (3.1) in the region $[R_N, \infty]$ are Coulomb functions modulated by slowly varying amplitudes that reflect the influence of the coupling potentials (3.2). Following Alder and Pauli[2] and Alder, Roesel, and Morf,[7] we solve directly for the modulating amplitudes—a much easier procedure than direct integration of the original radial equations (3.1). Our procedure, in fact, is to extend the Coulomb functions O_α, I_α for each basis state inwards from ∞ to R_N; the resulting outgoing and incoming solutions of the coupled Coulomb-excitation equations (3.1) are then matched at $r = R_N$ to iterative solutions of the original equations (2.6) in the interior region. The gain in efficiency over straightforward integration of the coupled equations (2.6) from 0 to R_∞ is enormous.

A. Introduction of modulating functions

In the intermediate region $R_N < r < \infty$, the coupled equations (3.1) have N independent outgoing and N incoming solutions. We define $\vec{O}_s(r)$ (a vector whose N components are labeled by basis states α) to be that outgoing solution obtained by starting at $r = \infty$ with an outgoing wave $O_s(k_s r)$ in basis state s, zero in all other channels, and integrating inwards to R_N. The incoming solution $\vec{I}_s(r)$ is defined in similar fashion. Clearly, $\vec{O}_s(r)$ $(s = 1, 2, \ldots, N)$ is a complete set of outgoing solutions and $\vec{I}_s(r)$ $(s = 1, 2, \ldots, N)$ a complete set of incoming solutions of Eqs. (3.1).

The Alder-Pauli[2] representation of the solutions $\vec{O}_s, \vec{I}_s$ is

$$\mathcal{O}_{s,\alpha}(r)=\frac{1}{\sqrt{k_\alpha}}\cdot a^{+}_{s,\alpha}(r)O_\alpha(k_\alpha r)\,,$$
$$\mathcal{I}_{s,\alpha}(r)=\frac{1}{\sqrt{k_\alpha}}\cdot a^{-}_{s,\alpha}(r)I_\alpha(k_\alpha r)\,, \tag{3.3}$$

where O_α, I_α are uncoupled Coulomb functions and $\mathcal{O}_{s,\alpha}$ designates the αth component of $\vec{\mathcal{O}}_s$. The modulating functions $\vec{a}^{\pm}_s$ (which are also N-component vectors) have the asymptotic behavior

$$a_{s,\alpha}(r)\underset{r\to\infty}{=}\sqrt{k_\alpha}\cdot\delta_{\alpha s}\,,$$
$$\frac{d}{dr}\vec{a}_s(r)\underset{r\to\infty}{=}0\,. \tag{3.4}$$

In terms of the coupled-channels Coulomb wave functions just introduced, the asymptotic form (2.9) of the radial wave functions is

$$R^{J\pi}_\alpha(r)\underset{r\to\infty}{=}\frac{i}{2}\left[\mathcal{I}_{\alpha_0,\alpha}(r)-\sum_\beta\left(\frac{k_{\alpha_0}}{k_\beta}\right)^{1/2}S^{J\pi}_{\beta\alpha_0}\mathcal{O}_{\beta,\alpha}(r)\right]. \tag{3.5}$$

The advantage of Eq. (3.5) is that it becomes valid at $r=R_N$ instead of the much larger radius R_∞ at which Eq. (2.9) becomes valid.

The uncoupled Coulomb functions I_α and O_α are solutions of the homogeneous part of Eqs. (3.1). Substitution of Eqs. (3.3) in Eqs. (3.1) then yields a set of coupled second-order equations for the outgoing amplitudes:

$$\frac{d^2}{dr^2}a^{+}_{s,\alpha}+\frac{2}{O_\alpha}\frac{d}{dr}O_\alpha\frac{d}{dr}a^{+}_{s,\alpha}=\sum_\beta\left(\frac{k_\alpha}{k_\beta}\right)^{1/2}\cdot U^{c}_{\alpha\beta}(r)\frac{O_\beta}{O_\alpha}a^{+}_{s,\beta}\,. \tag{3.6}$$

It is also seen that the incoming solution $\vec{\mathcal{I}}_s(r)$ is the complex conjugate of the outgoing solution $\vec{\mathcal{O}}_s(r)$,

$$\vec{\mathcal{I}}_s(r)=\vec{\mathcal{O}}^{*}_s(r)\,, \tag{3.7}$$

so that only the equations for the outgoing solutions need be considered explicitly.

B. Approximations for the modulating functions

By a sequence of approximations, Eqs. (3.6) can be considerably simplified. To state the approximations involved, we use the phase-amplitude representation,[8]

$$\begin{pmatrix}O_\alpha\\ I_\alpha\end{pmatrix}=\frac{e^{\pm i\phi_\alpha}}{\sqrt{\zeta_\alpha}}\,, \tag{3.8}$$

of the Coulomb functions. The asymptotic phase is given by

$$\phi_\alpha\underset{r\to\infty}{=}k_\alpha r-\eta_\alpha\ln 2k_\alpha r+\sigma_\alpha-\frac{l_\alpha\pi}{2}\,, \tag{3.9}$$

where σ_α is the Coulomb phase shift. Outside the Coulomb turning point, ζ_α is a very slowly varying function of r that increases monotonically towards its asymptotic value of unity

$$\zeta_\alpha\underset{r\to\infty}{=}1\,. \tag{3.10}$$

The Wronskian relation for Coulomb functions reduces to

$$\frac{d}{dr}\phi_\alpha=k_\alpha\zeta_\alpha\,. \tag{3.11}$$

In this representation, the coefficients in the coupled equations (3.6) become

$$\frac{1}{O_\alpha}\frac{dO_\alpha}{dr}=k_\alpha\left(i\zeta_\alpha-\frac{1}{2k_\alpha}\frac{d}{dr}\zeta_\alpha\right), \tag{3.12}$$

$$\frac{O_\beta}{O_\alpha}=\left(\frac{\zeta_\alpha}{\zeta_\beta}\right)^{1/2}e^{i(\phi_\beta-\phi_\alpha)}\,. \tag{3.13}$$

Two approximations can now be made to exploit the fact that the various amplitudes involved vary slowly with r. (i) Because $a^{+}_{s,\alpha}(r)$ varies slowly with r,

$$\left|\frac{d^2a^{+}_{s,\alpha}}{dr^2}\right|\ll\left|k_\alpha\frac{da^{+}_{s,\alpha}}{dr}\right|, \tag{3.14}$$

and the second-derivative terms in Eqs. (3.6) may be dropped. (ii) Because the amplitude ζ_α of the Coulomb functions varies very slowly with r,

$$\frac{d}{dr}\zeta_\alpha\ll k_\alpha\zeta_\alpha\,, \tag{3.15}$$

and $(d/dr)\zeta_\alpha$ may be neglected in Eq. (3.12), whence

$$\frac{1}{O_\alpha}\frac{dO_\alpha}{dr}\simeq ik\zeta_\alpha\,. \tag{3.16}$$

With these approximations, the coupled equations (3.6) for the modulating amplitudes reduce to the first-order matrix equation

$$\frac{d}{dr}\vec{a}^{+}_s(r)=\mathcal{M}(r)\vec{a}^{+}_s(r)\,, \tag{3.17}$$

where the matrix $\mathcal{M}$ is defined by

$$\mathcal{M}_{\alpha\beta}(r)=-\frac{i}{2(k_\alpha k_\beta)^{1/2}}I_\alpha U^{c}_{\alpha\beta}O_\beta\,. \tag{3.18}$$

Equations (3.17) and (3.18) are identical to those derived by Alder, Morf, and Roesel[7] from the integral equivalent of the coupled equations (3.1); the differential derivation given here has the merit of exhibiting the two underlying approximations more explicitly.

Note that from Eq. (3.8) we can express the elements of $\mathcal{M}$ as

$$\mathfrak{M}_{\alpha\beta} = -\frac{i}{2}\,\frac{U^{0}_{\alpha\beta}e^{-i(\phi_\alpha-\phi_\beta)}}{(k_\alpha\zeta_\alpha k_\beta\zeta_\beta)^{1/2}}\,. \tag{3.19}$$

Because from Eq. (3.9),

$$\phi_\alpha-\phi_\beta \sim (k_\alpha-k_\beta)r=\Delta k_{\alpha\beta}r\,, \tag{3.20}$$

it follows that the coupling matrix elements in Eq. (3.17) are slowly varying functions of r modulated by oscillatory functions of wavelength $2\pi/(\Delta k_{\alpha\beta})$. Thus while the quadrature step length in the original coupled equations (3.1) is proportional to some average of k_α^{-1}, that in the first-order amplitude equations is proportional to the minimum $(\Delta k_{\alpha\beta})^{-1}$. For heavy-ion reactions, $(\Delta k/k)^{-1}$ is typically of the order 10 or greater. The original set of second-order equations has thus been replaced by a first-order set that can be integrated with a much larger step length.

Yet another major simplification is possible. For the values of r of interest here $(r>R_N\gg R_c^{\prime})$, the deviations of $\vec{\mathrm{a}}_s(r)$ from $\vec{\mathrm{a}}_s(\infty)$ are small enough to permit solution of the amplitude equation (3.17) by the first term of a Born-Neumann series:

$$\vec{\mathrm{a}}_s^{+(n)}(r)=\vec{\mathrm{a}}_s^{+(n-1)}(r)+\int_\infty^r \mathfrak{M}(r')\vec{\mathrm{a}}_s^{(n-1)}(r')dr'\,, \tag{3.21}$$

where the initial guess to be used is

$$a_{s,\alpha}^{+(0)}(r)=\sqrt{k_\alpha}\,\delta_{\alpha s}\,. \tag{3.22}$$

The first iteration of Eq. (3.21) gives the DWBA contribution to Coulomb excitation from r to ∞:

$$a_{s,\alpha}^{+(1)}(r)=\sqrt{k_\alpha}\left(\delta_{\alpha s}-\int_r^\infty \mathfrak{M}_{\alpha s}(r')dr'\right). \tag{3.23}$$

C. Recursion relations

Efficient techniques for the numerical evaluation of the integral appearing in Eq. (3.23) have been used for several years in the program Ptolemy[5] for the DWBA evaluation of inelastic scattering. Following the suggestion of Belling,[9] we can evaluate the integral as an asymptotic series in the lower limit r. The use of this asymptotic series makes it unnecessary to introduce the asymptotic radius R_∞ into the calculation. Furthermore, simple recursion relations (in terms of the orbital angular momenta l_α and l_s) can be derived for the integrals. The use[5] of these recursion relations greatly accelerates the calculation. We derive the recursion relations in this subsection; similar relations have recently[10] been derived independently.

We consider integrals of the form

$$I_{l',l}^{(\lambda)}=\int_R^\infty dr\,\frac{1}{r^{\lambda+1}}\,Y_{l'}(\eta',k'r)X_l(\eta,kr)\,, \tag{3.24}$$

where Y and X designate Coulomb functions (F, G, I, or O). The lower limit of the integral may be zero if both Y and X are regular Coulomb functions. We will use the standard[11] Coulomb recursion relations:

$$l[(l+1)^2+\eta^2]^{1/2}X_{l+1}-(2l+1)\left(\eta+\frac{l(l+1)}{kr}\right)X_l$$
$$+(l+1)[l^2+\eta^2]^{1/2}X_{l-1}=0\,, \tag{3.25}$$

and

$$\frac{l}{k}\,\frac{d}{dr}X_l+\left(\eta+\frac{l^2}{kr}\right)X_l-[l^2+\eta^2]^{1/2}X_{l-1}=0\,. \tag{3.26}$$

Equation (3.26) may be used to eliminate X_{l-1} from Eq. (3.25):

$$X_{l+1}=\frac{l+1}{[(l+1)^2+\eta^2]^{1/2}}\left(\frac{\eta}{l+1}+\frac{l+1}{kr}-\frac{1}{k}\,\frac{d}{dr}\right)X_l\,. \tag{3.27}$$

This may be substituted in Eq. (3.24) for $I_{l',l+1}^{(\lambda)}$ to yield

$$I_{l',l+1}^{(\lambda)}=\frac{l+1}{[(l+1)^2+\eta^2]^{1/2}}\left(\frac{\eta}{l+1}I_{l',l}^{(\lambda)}+\frac{l+1}{k}\,I_{l',l}^{(\lambda+1)}\right.$$
$$\left.-\frac{1}{k}\int_R^\infty dr\,\frac{1}{r^{\lambda+1}}Y_{l'}\,\frac{d}{dr}X_l\right). \tag{3.28}$$

The derivative in the last integral in Eq. (3.28) may be moved to $Y_{l'}$ by integration by parts. Then using Eq. (3.26) to eliminate $(d/dr)Y_{l'}$, we obtain

$$\int_R^\infty dr\,\frac{1}{r^{\lambda+1}}\,Y_{l'}\,\frac{d}{dr}X_l=-J_{l',l}^{(\lambda)}+\frac{k'\eta'}{l'}I_{l',l}^{(\lambda)}$$
$$-\frac{k'(l'^2+\eta'^2)^{1/2}}{l'}I_{l'-1,l}^{(\lambda)}$$
$$+(\lambda+l'+1)I_{l',l}^{(\lambda+1)}\,, \tag{3.29}$$

where

$$J_{l',l}^{(\lambda)}=\frac{1}{R^{\lambda+1}}Y_{l'}(\eta',k'R)X_l(\eta,kR)\,. \tag{3.30}$$

If we substitute Eq. (3.29) in Eq. (3.28) and use Eq. (3.25) to express $I_{l',l}^{(\lambda+1)}$ in terms of $I_{l',l-1}^{(\lambda)}$, $I_{l',l}^{(\lambda)}$, and $I_{l',l+1}^{(\lambda)}$, we obtain an expression for $I_{l',l+1}^{(\lambda)}$ in terms of $I_{l'-1,l}^{(\lambda)}$, $I_{l',l-1}^{(\lambda)}$, $I_{l',l}^{(\lambda)}$, and $I_{l',l+1}^{(\lambda)}$. This may be solved for $I_{l',l+1}^{(\lambda)}$ to yield the recursion relation:

$$I^{(\lambda)}_{l',l+1}=\frac{l+1}{k(l+l'+\lambda+1)[(l+1)^2+\eta^2]^{1/2}}\Big[(2l+1)\Big(\eta k\frac{l'+\lambda}{l(l+1)}-\eta' k'\frac{1}{l'}\Big)I^{(\lambda)}_{l',l}+k'\frac{2l+1}{l'}(l'^2+\eta'^2)^{1/2}I^{(\lambda)}_{l'-1,l}$$
$$+k\frac{l-l'-\lambda}{l}(l^2+\eta^2)^{1/2}I^{(\lambda)}_{l',l-1}+(2l+1)J^{(\lambda)}_{l',l}\Big]. \qquad (3.31)$$

By symmetry we can interchange l with l', η with η', and k with k' in Eq. (3.31) to yield a recursion relation for $I^{(\lambda)}_{l'+1,l}$ in terms of the same quantities that appear in Eq. (3.31).

Consider even λ. If we have $I^{(\lambda)}_{L-\delta,L-1+\delta}$ for $\delta=-\lambda/2+1,\ -\lambda/2+2,\dots,\lambda/2$ and $I^{(\lambda)}_{L-\delta,L+\delta}$ for $\delta=-\lambda/2,\dots,\lambda/2$, then the two recursion relations may be used to generate first $I^{(\lambda)}_{L+1-\delta,L+\delta}$ for $\delta=-\lambda/2+1,\dots,\lambda/2$ and then $I^{(\lambda)}_{L+1-\delta,L+1+\delta}$ for $\delta=-\lambda/2,\dots,\lambda/2$. These may then be used to go on to $L+2$, and so forth. A similar scheme may be used for odd λ. Thus we need only $2\lambda+1$ initial values of $I^{(\lambda)}_{l',l}$ to generate all of the required $I^{(\lambda)}_{l',l}$. These initial values may be computed by numerical quadrature of Eq. (3.24) or, as previously mentioned, from an asymptotic expansion in R.

We have tested the stability of these recursion relations for many cases. Unless $R=0$, the upward recursion relations are only slightly unstable for all combinations of Coulomb functions; one or two decimal places may be lost in 1000 iterations. Downward recursion relations analogous to Eq. (3.31) may be developed for $\int_0^\infty dr F_l F_{l'}/r^{\lambda+1}$; we shall not give the results here.

D. Asymptotic expansions for coupled-channel Coulomb functions

Asymptotic series expansions in powers of $1/r$ have been given[12] for the coupled-channels Coulomb functions $\mathcal{O}_{s,\alpha}$ and $\mathcal{I}_{s,\alpha}$. In the adiabatic limit, the coupled-channels asymptotic series are straightforward matrix generalizations of the single-channel series. The coefficients are given by three-term recursion formulas. Ten-figure accuracy can still be achieved from these series at distances less than twice the turning-point radius. Inclusion of the effects of nonadiabaticity significantly complicates matters. The three-term recursion relations for the expansion coefficients are replaced by four-term recursion relations whose leading terms are proportional to the energy differences $\Delta E_{\alpha\beta}$ between channels. Such recursion formulas are numerically ill-conditioned; for extensive use it would probably be necessary to develop some form of perturbation expansion in ΔE based on the adiabatic limit as unperturbed solution. The numerical effort involved for all necessary J values is in any case considerably greater than that involved in evaluating the Alder-Pauli amplitudes by the techniques described above. This comparison depends on the accuracy of the first-order reduction of the equations for the modulating amplitudes and of the Born solution of the first-order equations. In case of failure of the Born solution of the reduced first-order equations, it would be necessary to reassess the merits of direct use of the asymptotic expansions for the coupled-channels Coulomb functions.

IV. NUMERICAL STUDIES OF THE MODULATING FUNCTIONS

A. Accuracy of approximations for the modulating functions

We now discuss the accuracy of the three approximations introduced in the previous section for the modulating functions: (1) Neglect of the second-derivative terms in the Eq. (3.6), resulting in a set of first-order equations for the amplitudes $\tilde{a}_s$; (2) neglect of the derivatives $(d/dr)\zeta_\alpha$ of the amplitudes of the single-channel Coulomb functions in computing the coupling terms in the first-order equations; and (3) use of the Born approximation to integrate the first-order equations inwards from $r=\infty$ to distances r of the order of the outer limit R_N of the "nuclear" interior region.

The following coupled channels are considered

	Channels			
	Elastic	Excited	$E_{\rm Lab}$	η
(a)	^{18}O + ^{184}W	^{18}O + ^{184}W(2$^+$, 0.111 MeV)	90	41.7
(b)	^{132}Xe + ^{208}Pb	^{132}Xe(2$^+$, 0.668 MeV) + ^{208}Pb	800	283.2
(c)	^{16}O + ^{44}Ca	^{16}O + ^{44}Ca(2$^+$, 1.156 MeV)	60	13.0

where the projectile is listed first and the values of η refer to the elastic channel. Optical-model and deformation parameters for the calculations to be reported are given in the appropriate figure captions. In all of the calculations reported in this section, reorientation effects (couplings within the excited channel) have been ignored; we have verified that their inclusion does not affect our conclusions.

To simplify notation for the modulating amplitudes and S-matrix elements, we use the following labeling for the four reaction channels for given angular momentum J (>2) in the reactions involving 2^+ excitation:

$$\begin{aligned}&\alpha=1;\ 0^+,\ l=J\\&\alpha=2;\ 2^+,\ l=J-2\\&\alpha=3;\ 2^+,\ l=J\\&\alpha=4;\ 2^+,\ l=J+2\,.\end{aligned}\tag{4.1}$$

Reaction (a), $^{18}O+^{184}W$ at $E_{lab}=90$ MeV. Figure 1 shows the modulus of the amplitude $a^+_{1,3}(J=50)$ in the critical partial wave; $a^+_{1,3}$ is the amplitude in channel 3 of the outgoing-wave solution of Eqs. (3.6) that tends asymptotically to an outgoing wave in channel 1. For comparative purposes the amplitudes have been divided by $\sqrt{k_3}$. In this reaction, the main source of error is neglect of the second-derivative terms in Eqs. (3.6); the relative error in $a_{1,3}$ is around 2% all the way in to 15 fm (the turning point for $l=50$ is at 13.5 fm). The additional approximations—neglect of $(d/dr)\zeta$ and Born approximation solution of the first-order equations—introduce negligible errors less than 0.1% for $r>15$ fm. Figure 1 also shows the modulus of the error in the Born amplitude $|a_{1,3}(\text{Born})-a_{1,3}(\text{exact})|$; this error is of the order of 1% of the magnitude of the amplitude $a_{1,1}$ [the one that according to Eqs. (3.4) approaches $\sqrt{k_1}$ as $r\to\infty$].

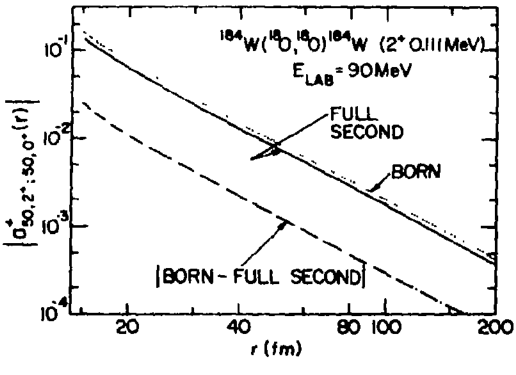

FIG. 1 A comparison of the modulus of the amplitude $a^+_{1,3}(J=50)$ calculated using the full second-order equation (3.6) and the Born approximation (3.23). The modulus of the error in the Born amplitude $|a_{1,3}(\text{Born})-a_{1,3}(\text{exact})|$ is also shown. The amplitudes have been divided by $\sqrt{k_3}$. The Coulomb coupling had $\beta_2^C=0.234$.

Reactions (b), $^{132}Xe+^{208}Pb$ at $E_{Lab}=800$ MeV. This reaction may be treated semiclassically with high accuracy. The first-order reduction of the amplitude equations introduces negligible errors; for $J=100$, neglect of second-derivative terms in Eq. (3.6) results in a relative error in $a_{1,3}$ ($J=100$) of 0.16% at $r=25$ fm. The Born approximation is the dominant source of error, yielding a 10% error in $a_{1,3}$ at 25 fm, 1% at 40 fm.

Reaction (c), $^{16}O+^{44}Ca$ at $E_{Lab}=60$ MeV. This reaction does not lend itself to a semiclassical treatment, and the neglect of the second-derivative term introduces the largest error—2% in $a_{1,3}(J=4)$ at 20 fm. Neglect of $(d/dr)\zeta$ introduces an additional relative error of 0.06%, and the Born approximation 0.2% at 20 fm. However, the departures of the a's from their asymptotic values are quite small $[|a(r=20)-a(r=\infty)|\sim0.02]$ so that these percentage errors represent negligible absolute errors.

These results illustrate our conclusions, drawn from studies of a wide variety of reactions. For very strong Coulomb fields (large η), errors due to the first-order reduction of the amplitude equations are small, the amplitudes themselves deviate strongly from their asymptotic values [Eqs. (3.4)] and the dominant source of error is the Born approximation. For reactions with small values of η, the main source of error is the neglect of second derivatives in Eqs. (3.6); the modulating amplitudes for $r>R_N$ do not deviate strongly from their asymptotic values [Eqs. (3.4)], and the errors due to the Born approximation are negligible. In such cases, because the deviations from the asymptotic values are small, the moderately large relative errors introduced by the neglect of the second-derivative terms result in very small errors in S-matrix elements and cross sections. In general, the Born approximation (3.23) to the solution of the approximate first-order equation (3.17) permits calculation of the modulating amplitudes $a^+_\alpha(r)$ in Eqs. (3.3) inwards from $r=\infty$ to typical nuclear matching radii, $R_N\sim20$ to 30 fm, with errors of a few percent.

B. Sensitivity of S-matrix elements and cross sections to errors in the modulating functions

It remains to be seen whether "few percent" errors in the modulating amplitudes lead to significant errors in computed S-matrix elements and cross sections. The modulating amplitudes are used through Eqs. (3.3) to construct a complete set of outgoing solutions $\vec{O}_s$ and an incoming solution $\vec{I}_{\alpha_0}$ of the coupled equations (3.1) for Coulomb excitation. These coupled Coulomb functions are then matched at the joining radius R_N to solutions of the original coupled Eqs. (2.6) in the interior region. The techniques used to produce interior solutions will be discussed in the second paper of this series.

Figure 2 shows the S-matrix elements S_{11} (elastic) and S_{21} (inelastic), in the $J = 50$ partial wave for reaction (a), obtained from matching procedures of the sort described using a's computed by the Born approximation. The magnitudes of the S-matrix elements obtained by matching at a variety of values R_N from 75 to around 20 fm are compared with exact values. It is clear that the modified matching procedure yields S-matrix elements of satisfactory accuracy. Figure 2 also shows the S-matrix elements obtained by matching at R_N to single-channel Coulomb functions (the traditional matching procedure). Accurate results are not obtained until $R_N > 75$ fm, with large discrepancies at values of R_N of practical interest (~30 fm). The differential cross sections for reaction (a) obtained using Born a's at various matching radii are compared in Fig. 3 with each other and with what is obtained by matching to single-channel Coulomb functions. The Born a's yield the cross section accurately for matching radii R_N as small as 20 fm; the errors in the cross sections obtained by matching to single-channel Coulomb functions are large.

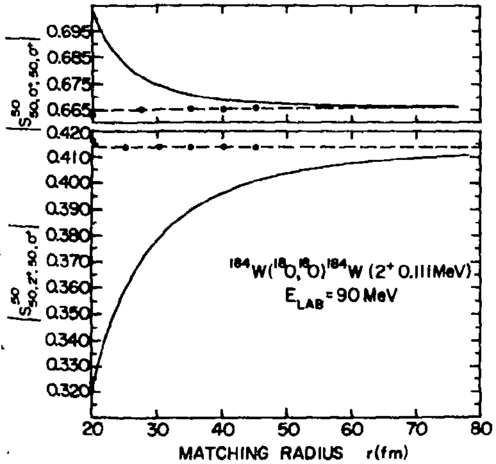

FIG. 2. The solid lines represent the modulus of the elastic and one inelastic S-matrix elements obtained by matching to single channel Coulomb functions at various radii r. The dashed lines represent the converged re-ults, and the open circles show the values obtained us-ng the Born approximation to the amplitude function with the matching equation (3.5). All calculations were erformed using complex Woods-Saxon potentials of qual geometry with the parameters $V = 40$, $W = 25$, r_0 1.29, $a = 0.508$, $r_{c0} = 1.2$, $\beta_2^N = 0.145$, and $\beta_2^C = 0.234$.

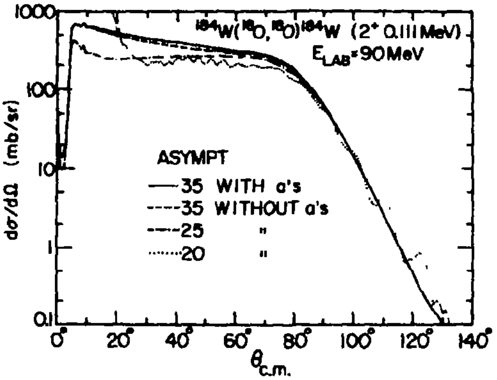

FIG. 3. A comparison of the inelastic cross sections calculated using S-matrix elements derived from the matching equations (2.9) and (3 5) at various matching radii r. The results using Eq. (3.5) are indistinguishable for matching radii ≥ 20 fm The cross sections for $\theta_{c.m.} < 15°$ are inaccurate because of the orbital angular momentum truncation ($l, l' \leq 1000$). The potential parameters are the same as for Fig. 2.

The main conclusions, confirmed by the results of many other calculations, are (i) Coulomb-coupling effects in the intermediate region ($R_N < r < R_\infty$) have a large influence on S-matrix elements and cross sections; and (ii) these effects are accounted for accurately and efficiently on the basis of the Alder-Pauli factorization (3.3) of the solutions of the coupled equations for Coulomb excitation, with the first Born approximation for the modulating amplitudes.

V. QUALITATIVE ASPECTS OF THE ALDER-PAULI PROCEDURE

The procedure established above for dealing with intermediate-range effects of Coulomb excitation involves matching interior solutions of the coupled equations to combinations of incoming and outgoing solutions $\vec{I}_s$, $\vec{O}_s$ of the coupled equations for Coulomb excitation. The matching radii R_N can then be taken to be of "nuclear" size (20 to 30 fm). The coupled-channels Coulomb functions take over the role of ordinary Coulomb functions I_α, O_α in the matching procedures of conventional optical-model and coupled-channels calculations. For this modified matching procedure to be computationally feasible it is essential that the coupled-channels Coulomb functions be computed efficiently. Direct integration of the original coupled equations from R_∞ to R_N is out of the question; indeed it was the extreme inefficiency of such integrations across the intermediate region of r space that triggered the search for modified procedures. The Alder-Pauli factorization (3.3) is the basis of our technique for construction of the coupled-channels Coulomb functions. Its great efficiency depends on the validity of three approximations for the modulating functions.

(1) Neglect of second derivatives in the coupled equations (3.8) for the modulating functions. This first-order reduction greatly enhances the value of the Alder-Pauli transformation. Direct numerical integration of the second-order equations (3.6) is a difficult numerical task, in spite of the fact that the modulating amplitudes vary slowly with r, because second-order equations that are approximately of first order are numerically awkward.

(2) Neglect of the derivatives $(d/dr)\zeta_\alpha$ of the amplitudes of the single-channel Coulomb functions. It is this approximation that permits the Born solution (3.23) to be written in terms of the DWBA matrix elements for Coulomb excitation. These integrals satisfy simple recursion formulas that enormously reduce the numerical labor involved in evaluating the coupled-channel Coulomb functions. Errors due to neglect of $(d/dr)\zeta_\alpha$ are always negligible relative to those involved in the first-order reduction of Eqs. (3.6).

(3) Use of the first Born approximation (3.23) to solve the first-order equations for a_s. The accuracy of this approximation depends on the fact that for distances of interest ($r \gtrsim 20$ fm) in a large class of reactions, the modulating amplitudes deviate in magnitude by $0.2\sqrt{k_\alpha}$ or less from their asymptotic values (3.4). When the Born approximation is reasonable, the errors involved should be of the order of the second-order correction and hence proportional to $|a_{s,\alpha}-\sqrt{k_\alpha}\delta_{s\alpha}|^2$. Thus the magnitudes of the Born amplitudes can be used as an error indicator; if any of the quantities $|a_{s,\alpha}|^2/k_\alpha$ for $\alpha \neq s$ at R_N exceed some desired accuracy, consideration should be given to increasing the matching radius. (Note that in the Born approximation $a_{s,s}=\sqrt{k_s}$.)

By using these techniques, one can compute heavy-ion coupled-channels scattering amplitudes involving strong Coulomb excitation in much the same time as if there were no long-range component to the Coulomb coupling.

ACKNOWLEDGMENTS

We thank Dr. Fritz Coester for helpful discussions and for a critical reading of the manuscript. This work was supported by the U. S. Dept. of Energy.

---

[1] K. Alder and A. Winther, K. Dan. Vidensk. Selsk., Mat. Fys. Medd. 32, No. 8 (1960).

[2] K. Alder and H. C. Pauli, Nucl. Phys. 128, 1931 (1969).

[3] L. Schlessinger and G. L. Payne, Phys. Rev. A 10, 1559 (1974).

[4] J. Raynal in *Computing as a Language of Physics*, (IAEA, Vienna, 1972), p. 281.

[5] M. H. Macfarlane and S. C. Pieper, Argonne Nat. Lab. Report No. ANL-76-11, Rev. 1, 1978 (unpublished).

[6] G. R. Satchler in *Lectures in Theoretical Physics*, Vol. VIII-C, edited by P. D. Kunz, D. A. Lind, and W. E. Britten (Univ. of Colorado Press, Boulder, 1966), p. 73

[7] K. Alder, F. Roesel, and R. Morf, Nucl. Phys. A284, 145 (1977).

[8] M. J. Seaton and G. Peach, Proc. Phys. Soc. London 79, 1296 (1962).

[9] J. A. Belling, J. Phys. B 1, 136 (1968).

[10] L. E. Wright, Phys. Rev C 20, 393 (1979).

[11] M. Abramowitz in *Handbook of Mathematical Functions*, edited by M. Abramowitz and I. A. Stegun (U.S. Government Printing Office, Washington, 1964), p. 537.

[12] F. Rösel, K. Alder, R. Morf, and J. X. Saladin, J Phys. G 3, 613 (1977).

PHYSICAL REVIEW C VOLUME 21, NUMBER 6 JUNE 1980

Fusion of ^{16}O + ^{148,150,152,154}Sm at sub-barrier energies

R. G. Stokstad
Oak Ridge National Laboratory, Oak Ridge, Tennessee 37830
and The Weizmann Institute of Science, Rehovot, Israel

Y. Eisen, S. Kaplanis, D. Pelte, U. Smilansky, and I. Tserruya
The Weizmann Institute of Science, Rehovot, Israel

(Received 19 November 1979)

Measurements of the cross section for fusion of ^{16}O with ^{148,150,152,154}Sm have been made in the range $60 \le E_{^{16}\mathrm{O}} \le 75$ MeV. Evaporation residues trapped in a carbon catcher foil were observed off line by means of the K x rays emitted by radioactive Yb nuclei and their daughters. Absolute cross sections varying in magnitude from 0.1 to 400 mb were determined with an uncertainty of $\pm 10\%$. The cross sections for individual x-n channels were also determined. At high energies, the fusion cross sections for all isotopes are similar, whereas at lower bombarding energies the cross sections for the more deformed targets are larger than those for the spherical targets.

[NUCLEAR REACTIONS Measured σ_{fusion} for ^{16}O+^{148,150,152,154}Sm, $E^{^{16}\mathrm{O}}_{\mathrm{lab}} = 60$–75 MeV. Observation of x rays from radioactive evaporation residues.]

I. INTRODUCTION

The study of subtle effects such as nuclear deformation on the cross section for fusion of complex nuclei requires experimental data of high precision at low bombarding energies, where penetrability effects are important.[1,2] We present here an experimental study of the fusion of ^{16}O with the even-even isotopes of samarium, ^{148,150,152,154}Sm, which undergo a transition from a spherical to a deformed equilibrium shape as the neutron number increases. This report considers the experimental techniques and methods of analysis leading to values of the cross section for fusion. The attainment of high precision is emphasized. The interpretation of these experimental results, as well as a discussion of related experimental and theoretical work, will appear in a subsequent article. A short account of this work has been published.[3]

II. EXPERIMENTAL CRITERIA

The choice of projectile and targets was governed by three factors. (i) The interpretation of the results is simplified if only one of the colliding uclei is deformed; thus ^{16}O was chosen as the projectile. (ii) The Sm isotopes offer a variation n nuclear deformation without an accompanying hange in atomic number. Thus the relatively arge changes in the interaction barrier associ- ed with a change of nuclear charge are elimi- ted. The equilibrium deformations for these otopes are well known.[4] (iii) The isotopes of Yb formed by the fusion of ^{16}O+Sm at energies below 70 MeV c.m. should have a negligible fission width.[5] The entire fusion cross section is thus concentrated in the yield of evaporation residues.

A number of direct experimental methods can be used to measure the cross section for production of evaporation residues. These include direct identification by $\Delta E - E$ energy loss,[6] time of flight,[7] and track detectors.[8] Of these three methods, the first is unsuitable because the energy of the Yb compound nuclei ($\lesssim$ 7 MeV) is too low. Both the first and the second methods require measurement and integration of an angular distribution which is strongly forward peaked. The residues must be detected in the presence of intense elastic scattering. The third method would not easily distinguish evaporation residues ($A \sim 170$) from elastically scattered or Coulomb-excited target recoils ($A \sim 154$).

Indirect methods involve the detection of some characteristic radiation emitted by the evaporation residue along its path back to the valley of stability. In-beam measurements of discrete γ-ray transitions following x-n reactions are effective at higher energies[9] but have a poor signal-to-noise ratio at low bombarding energies because of Coulomb excitation of the target and reactions with light contaminants, e.g., ^{12}C, ^{16}O, in the target. The detection of delayed γ rays from the radioactive nuclei formed following prompt neutron emission improves the signal-to-noise ratio, but requires (in addition to an unstable residue) an absolute normalization for the intensity of transitions in the decay scheme, i.e., the number of transitions per 100 decays. Such information is often available provided a detailed study of γ-ray and conversion electron spectra has been made.

The detection of delayed x-ray emission offers the highest signal-to-noise ratio of all the techniques which we considered. Because proton rich nuclei in the rare earth region decay predominantly by electron capture, and because there are many highly converted electromagnetic transitions, the yield of x rays per decay often exceeds unity, whereas for a given γ ray this yield is usually substantially smaller. As is the case with delayed γ rays, a knowledge of the absolute intensity of x-ray emission per decay is required. However, the large and rather regular contribution by electron capture to the number of K vacancies tends to reduce the relative uncertainty in the total intensity. A disadvantage, however, is that isotopic identification of a residue no longer follows directly from the energy of the radiation, but is only possible through an analysis of the time dependence of the decay.

We chose the detection of x rays for the present experiments primarily because it would enable us to measure small cross sections at the low bombarding energies where the relative effects of nuclear deformation are expected to be largest.

III. THE EXPERIMENTAL CONFIGURATION AND PROCEDURE

The essential features of the experiment are centered around the collection of the evaporation residues in a catcher foil and the subsequent off-line measurement of the x rays. Beams of ^{16}O produced by the 14-UD Pelletron accelerator at the Weizmann Institute were used to bombard thin, isotopically enriched targets of Sm. The catcher foil, made of carbon, was located approximately 2 mm behind the target. The beam emerged from the target and catcher foil and was stopped in a magnetically suppressed Faraday cup. Two surface barrier detectors were used to monitor the elastic scattering from the target. Following a bombardment of typically one-half to one hour, the catcher foil was removed from the scattering chamber and placed before a Ge spectrometer. X-ray spectra were then recorded at various time intervals until further activity could no longer be detected. We consider in more detail now each of the above elements of the experiment.

A. The ^{16}O beam

Energies between 60 MeV and 75 MeV were used. The energy of the beam was determined by calibrating the 90° analyzing magnet of the newly operational 14-UD Pelletron with the analyzing magnet associated with the Institute's EN Van de Graaff. This was done by comparing directly in an elastic scattering experiment the energy of beams produced by each of these accelerators. This procedure resulted in an estimated uncertainty of ± 0.15% on the absolute energy of the ^{16}O beam.

B. The targets

The targets were prepared by vacuum evaporation of samarium oxide enriched to the following percentage in the main isotope for each of the four targets: $(A,\%)$, (148, 95), (150, 95), (152, 98), and (154, 99). The target material was backed by a carbon film having a thickness typically of 20 $\mu g/cm^2$. The samarium oxide was first mixed with tantalum, and thus was reduced to elemental form during the evaporation. An amount of tantalum varying up to 20% of the total number of target nuclei was deposited on the carbon foil as a result of this procedure, however. This amount was measured for each target by using a surface-barrier detector to observe the relative number of ^{16}O nuclei scattered at 60° from Sm and from Ta. This was an important correction insofar-as the elastic scattering from the Ta impurity was not resolved by the surface-barrier detectors during an actual irradiation. In this case, the monitor detectors were at a more forward angle (40°) and viewed the target through the carbon catcher foil. Otherwise, the Ta impurity had no effect on the experiment, since the ^{16}O energy was too low to initiate nuclear reactions.

The thicknesses of the targets varied between 100 and 200 $\mu g/cm^2$ and were determined using the measured elastic scattering, the integrated charge at the Faraday cup, and the known Rutherford cross section. These measurements of the target thickness also showed that no detectable amount of Sm was lost from the target, even at the highest beam intensities. The target thickness thus determined had an uncertainty of about 5% and was used only for estimating the energy loss of the beam in the target; it did not enter directly into the determination of the cross section (see Sec. III D below).

C. The catcher foils

Carbon, rather than aluminum, was chosen as the material for the catcher foil since the compound nuclei formed in the reaction of $^{16}O+^{12}C$ have a high velocity and are not stopped in the catcher foil. It is this fact which is largely responsible for the low background and resulting high sensitivity of this measurement. Individual carbon foils of thickness ~ 250 $\mu g/cm^2$ were pre pared by vacuum evaporation. Three to four of these foils were then combined on a single target frame to form a catcher foil. A thin film of organic material, amyl acetate, was used between each carbon foil as a clamping agent. Foils so made varied in thickness from 700 to 1000 $\mu g/cm^2$. Upon a first exposure to an intense beam, some of the foils "exploded," presumably because of the presence of the organic film sandwiched between the carbon foils. Those foils which were not damaged initially (raising the beam current gradually increased the survival rate) were able to withstand particle-current densities of up to ~30 nA/mm^2 with no deterioration. Attempts to detect activity remaining in the target and in an additional carbon foil placed behind the catcher foil demonstrated that all of the evaporation residues were indeed stopped in the catcher foil. Measurements made with varying beam intensities showed that activity was not lost from the catcher foil because of beam heating.

The catcher foils developed a dimple where the beam intersected the foil. The effective displacement of the foil due to this dimple was measured for each foil with a microscope and was used to correct the efficiency for the detection of x rays from each catcher foil. The magnitude of this correction was usually less than 4%.

D. The monitor system

Surface-barrier detectors placed at ±40° and at 25 cm distance from the target were used to monitor the scattering from the Sm. These events (elastic scattering plus Coulomb excitation) were well resolved from reaction products produced by light contaminants in the target (carbon and oxygen) and by the carbon catcher foil. Since the solid angle of these detectors and the scattering angle could be measured with high precision, and since the sum of the scattered particles in the two detectors was insensitive to small variations in the angle of the beam with respect to the chamber axis, an absolute measure of the product of the time-integrated number of beam particles and target atoms could be obtained with high precision. Checks using (i) optical model calculations and (ii) the measured ratio of the elastic scattering at 40° and 60° showed that the summed cross section for elastic and inelastic scattering at 40° is given by the Rutherford formula to within ±0.2% and 0.7%, respectively. The accuracy of the above techniques is estimated at 1% for systematic errors and 2% for random errors. The random errors were estimated by an analysis of runs at different energies using the same target.

The intensity of the beam as a function of time during the irradiation was recorded by multiscaling, in one-minute intervals, the number of elastic events in the monitor counters.

E. The Ge spectrometer

The x-ray detector[10] consisted of 1.5 cm^3 of intrinsically pure Ge and employed an optically coupled feed-back loop in the preamplifier. A resolution of 350 eV (FWHM) was obtained at 50 keV. The catcher foil was positioned in front of the detector such that the photopeak efficiency in the range of 30–60 keV was 5.5%. This efficiency was determined using a variety of calibrated point sources (^{241}Am, ^{137}Cs, ^{57}Co, ^{152}Eu) mounted on frames identical to those holding the catcher foil. An empirical function[11] was then used to fit these calibration points and to determine the photopeak efficiency at any energy in the range from 20 to 150 keV to an accuracy of ±3%. The total efficiency was also measured and used, together with the known decay schemes, to estimate sum corrections for the calibrated sources. The spectrometer was shielded by 10 cm of lead.

IV. ANALYSIS OF THE X-RAY SPECTRA

The x rays and γ rays from the catcher foils were measured in the range from 10–250 keV. The portion of the spectrum including the x rays associated with the decay of Yb, Tm, and Er nuclei is shown in Figs. 1 and 2. Figure 1 presents a spectrum obtained in 5 min of counting just after a 28-min bombardment of ^{150}Sm with 70-

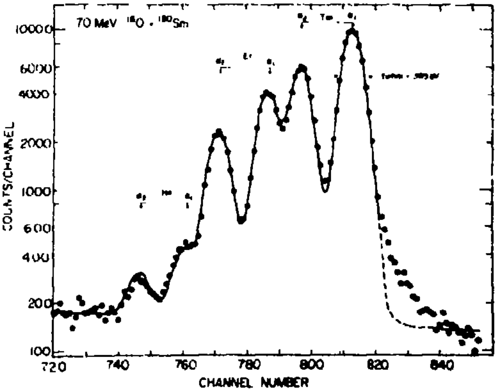

FIG. 1. Photon spectrum covering the range from 45 to 53 keV. The Tm $K_{\alpha 1}$ and $K_{\alpha 2}$ x rays are produced by the electron-capture decay of Yb and subsequent internal conversion in the Tm daughter. The full curve is a fit to the data in which each component is approximated by a Gaussian. The cross section for fusion in this case is 243 mb and the counting interval was 5 min.

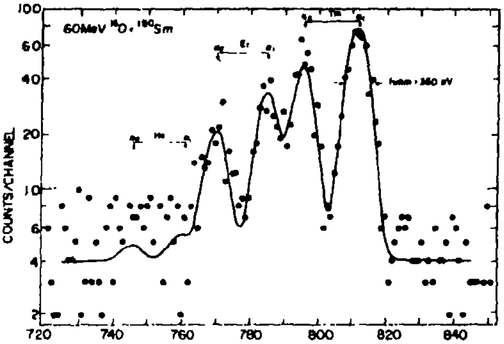

FIG. 2. Same as Fig. 1, except that the bombarding energy is lower and the fusion cross section is only 0.47 mb. The bombardment time was 1 h and the counting interval was 10 mb.

MeV ^{16}O ions. Individual $K_{\alpha 1}$ and $K_{\alpha 2}$ lines from all the decay products are resolved. The full curve is a least-squares fit of Gaussian peak shapes in which the widths, relative energy spacings, and $K_{\alpha 1}/K_{\alpha 2}$ intensity ratios are fixed quantities. The portion of the curve shown as a dashed line indicates a region of data excluded from the fit because of pile-up distortion. (Inclusion of this region has a sizable effect on χ^2 but a negligible effect on the peak areas.)

A spectrum obtained at the lowest bombarding energy, 60 MeV, for which the fusion cross section is much smaller, is shown in Fig. 2. This spectrum was obtained in 10 min of counting after a 45-min bombardment. The signal-to-noise ratio in this case was still high. Thus, the statistical uncertainty in the peak area was a negligible source of error in the determination of the cross section, even at the lowest bombarding energies. In cases where a γ-ray transition occurred in the K x-ray energy region, the γ-ray peak was analyzed simultaneously with the x rays. The K_β x rays were not analyzed. Electronic dead time was measured by evaluating the area of a peak from an electronic pulser.

V. DETERMINATION OF THE ABSOLUTE CROSS SECTION

Evaluation of the absolute cross section depends directly on the Rutherford cross section, the number of counts in the monitor, the measured intensity of the x rays, and the absolute intensity, in photons per decay, of the various radioactive products in the catcher foil. All but the last quantity have been discussed so far.

A. Absolute *K* x-ray intensities

Given a decay scheme with an absolute normalization, it is possible to calculate the number of K vacancies formed per 100 decays. Since the lifetime of a K vacancy ($\sim 10^{-17}$ sec) is short compared to typical nuclear decay times, electron capture and the internal conversion of transitions in a cascade are independent, additive sources of K x rays.

In evaluating the K vacancies produced by electron capture to each level of a daughter nucleus and K vacancies produced subsequently by each individual nuclear transition in the decay scheme, use was made of the quantities f_e/f_t from Ref. 12, ϵ_k/ϵ from Ref. 13, and α_K/α_{tot} from Ref. 14. The total number of K_α x rays was then obtained using the fluorescence yield ω_K and K_α/K_β intensity ratios from Ref. 13. Decay schemes from the Nuclear Data Sheets[15] were used. In some cases normalized decay schemes were not available from this source but had appeared in the literature subsequent to the last evaluation. An effort was made to use the most recent sources of information. For a number of nuclei with shorter half-lives and located relatively far from stability, an educated guess at the x-ray intensity was necessary. These cases, however, had a rather small influence on the overall determination of the cross section. The results of the above evaluation are given in Table I.

It is difficult to assess an error for each absolute intensity. In the few cases where an error is given in the literature for an absolute normalization, the error is of the order of 10% or less. We have therefore assumed an error of 10% for each intensity unless it is known to be larger. Since a given decay chain has at least two and sometimes up to four members before stability is reached, an internal check on the relative accuracy of the members in a given chain is possible. This check indicates that the choice of 10% for the typical error is a reasonable one.

In one case it was clear, from a lack of internal consistency in fitting the data, that an evaluated absolute intensity was in error. Examination of the decay schemes indicated a probable source of the error and led to a 15% increase in the calculated absolute intensity for the decay of ^{163}Yb. With this modification, internal consistency was obtained and the maximum effect on the deduced cross section was less than 7%.

Since the sources (catcher foils) are used in a high efficiency geometry, corrections for the simultaneous detection of more than one photon (summing) were applied. These were evaluated for each level scheme and were typically 5%, but did not exceed 13%.

TABLE I. Mean lifetimes and K_α x-ray intensities (EC denotes electron capture; IC denotes internal conversion).

Parent nucleus	t_m (min)	K vacancies/100 decays		$K_{\alpha 1}+K_{\alpha 2}$ intensity (photons/100 decays)
		EC	IC	
^{159}Yb	2.0[a]			75[a]
^{159}Tm	17.3			75[a]
^{159}Er	51.9			75[a]
^{159}Ho	47.6	83	76	118
^{160}Yb	6.9			75[a]
^{160}Tm	13.3	71	23	70
^{160}Er	2474.0	83	17	75
^{160}Ho	36.9	83	18	75
^{161}Yb	6.1	73	25	72[b]
^{161}Tm	54.8	76	138	159
^{161}Er	280.2	83	17	74
^{161}Ho	216.6	83	17	74
^{162}Yb	27.3	83	8	69[c]
^{162}Tm	31.3	75	25	74[d]
^{163}Yb	16.0	73	24	72[e]
^{163}Tm	156.7	82	55	102
^{163}Er	108.2	84	0	63
^{164}Yb	109.4	84	1	63[c]
^{164}Tm	2.9	51	9	45[c]
^{165}Yb	14.3	75	51	94
^{165}Tm	2602.0	84	17	75
^{165}Er	896.8	81	0	60
^{166}Yb	4908.0	73	70	106
^{166}Tm	667.0	83	24	80
^{167}Yb	25.2	84	116	149
^{167}Tm	19195.0	82	21	77

[a] The value is a guess, based on systematics, and is not crucial for this analysis.

[b] Assumes the decay of ^{161}Yb is similar to the decay of ^{163}Yb.

[c] An average of an experimental value and the value calculated from the level scheme.

[d] An experimental value.

[e] Assumes no appreciable capture to the ground state. The decay scheme assumed 32% capture to the ground state, but this led to an inconsistency in fitting the data.

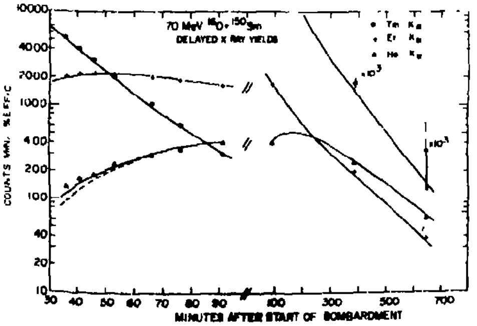

FIG. 3. The x-ray count rate as a function of time. The length of the bombardment was 28 min. The full curves are fits to the data incorporating known half-lives and absolute x-ray intensities.

B. Analysis of the time dependence of the x-ray intensity

Several isotopes, each with a different half-life, can contribute to the intensity of a given x ray. Thus, the time dependence of the intensity is complicated. Figure 3 illustrates a typical case. The growth and decay patterns associated with a parent, daughter, and granddaughter are seen, respectively, in the Tm, Er, and Ho x-ray intensities. Using the known half-lives and absolute x-ray intensities and assuming a parent-daughter relationship, it is possible to determine quite accurately the relative amounts of each isotope. The procedure was to fit all of the experimental data shown in Fig. 3 simultaneously, with the only unknowns being the activity present in each Yb isotope at the end of the bombardment.

The effect of variations in beam intensity during the irradiation and of the variation in source strength during a counting interval were treated exactly in the computer program used to fit the measured time dependence of the x-ray intensities.

Elementary statistical considerations for neutron evaporation usually limited to three the number of mass chains which needed to be included in a fit. Detailed statistical model calculations[16] showed that charged-particle emission is strongly hindered relative to neutron emission for the reactions and bombarding energies studied here. The emission of two protons, which leads to stable isotopes of Er, was predicted to be negligible. Nevertheless, it seems possible in some cases to detect charged-particle emission through a detailed examination of the time dependence of the daughter activities. The fitted yield of Ho x rays is increased from the dashed line to the full line in Fig. 3 by the inclusion of ~1% of $2p$-$1n$ emission from the compound nucleus. Deduced yields of charged-particle emission were largest for $^{16}O + ^{148}Sm$, but even in this case did not exceed 15%. The total fusion cross section was independent to within ~1–2% of whether or not the possibility of charged-particle emission was included in the fit.

The full curves in Fig. 3 are the result of a simultaneous fit of all the data shown in the figure. Figures 4 and 5 show the intensities for the parent decay and daughter decay, respectively. The contributions of the various isotopes (labeled by the number of mass units emitted from the compound nucleus) are shown. It may be seen from these two figures how the different half-lives associated with the different isotopes enable a determination of their relative contributions, provided the sources are counted over a sufficiently long time span.

The relative amounts of the various evaporation residues are listed in Table II and presented in

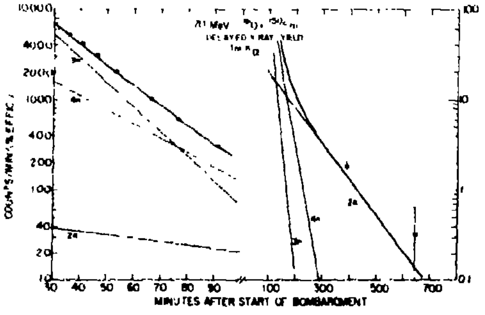

FIG. 4. The time dependence of the parent activity with the deduced contributions of the $2n$, $3n$, and $4n$ activities to the total. Note that measurements at later times effectively determine the $2n$ portion.

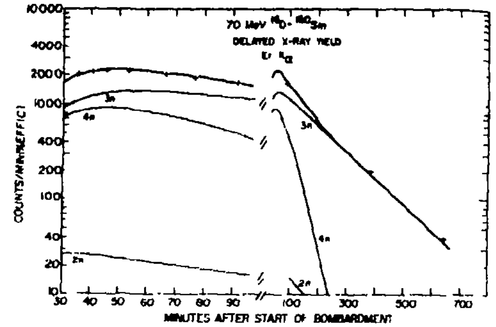

FIG. 5. Same as Fig. 4, but for the daughter activity. In this case the later times determine the $3n$ portion.

TABLE II. x-n distributions (%).

E_{lab}	Target	$1n$[a]	$2n$	$3n$	$4n$	$5n$
75.0	148		5(7)[b]	84(4)	11(8)	
	150		2(1)	43(2)	55(2)	
	152			15(2)	81(2)	4(1)
	154				66(2)	34(2)
70.0	148		14(1)	81(2)	5(3)	
	150		2(1)	72(2)	26(1)	
	152			37(1)	62(1)	1(1)
	154			8(1)	82(2)	9(1)
67.5	148		21(1)	78(1)	1(1)	
	150		5(1)	81(1)	14(3)	
	154			18(2)	82(4)	
65.0	148		39(1)	59(1)	2(2)	
	150		8(2)	86(2)	6(2)	
	152		2(1)	73(2)	25(1)	
	154			32(1)	68(2)	
63.75	148	2(2)	49(2)	49(2)		
	150		10(1)	81(2)	9(2)	
	152		1(5)	83(2)	16(1)	
	154			45(2)	55(2)	
62.5	148	3(1)	62(2)	35(2)		
	150		13(2)	80(2)	7(2)	
	152		2(1)	90(3)	8(2)	
	154			51(2)	49(2)	
61.25	148	12(6)	73(4)	15(4)		
	150		16(4)	71(3)	13(1)	
	152		5(2)	92(3)	3(1)	
	154			68(2)	32(5)	
60.0	148	9(5)	91(7)			
	150		24(3)	67(4)	9(4)	
	152		7(3)	93(3)		
	154			80(2)	20(5)	

[a] The value of n denotes the number of atomic mass units evaporated from the compound nucleus. For ^{148}Sm and $E_{lab} \geqslant 65$ MeV, charged-particle emission up to ~15% of the total is included. In all other cases, n is the number of neutrons evaporated to a very good approximation.

[b] The number in parentheses is the uncertainty on the last digit.

Fig. 6. The full curves in Fig. 6 are only to guide the eye. The value of *n* denotes the number of atomic mass units removed from the compound nucleus; since charged-particle emission is small, *n* approximates the number of neutrons evaporated. The cross section for fusion, which is the sum of the various *x-n* channels and charged-particle emission is listed in Table III and shown in Fig. 7. The laboratory bombarding energies given in Table III correspond to the energy at the center of the target. (The stopping powers of Northcliffe and Schilling[17] were used to estimate the energy loss in the target.) Figure 7 shows that the cross sections obtained for the different isotopes are nearly identical at the highest bombarding energy. As the bombarding energy is reduced, however, σ_{fus} exhibits a systematic variation, with the more deformed isotopes exhibiting progressively larger cross sections relative to the less deformed isotopes. A quantitative analysis of these data in terms of the deformation of the target nucleus will be given in a subsequent paper.

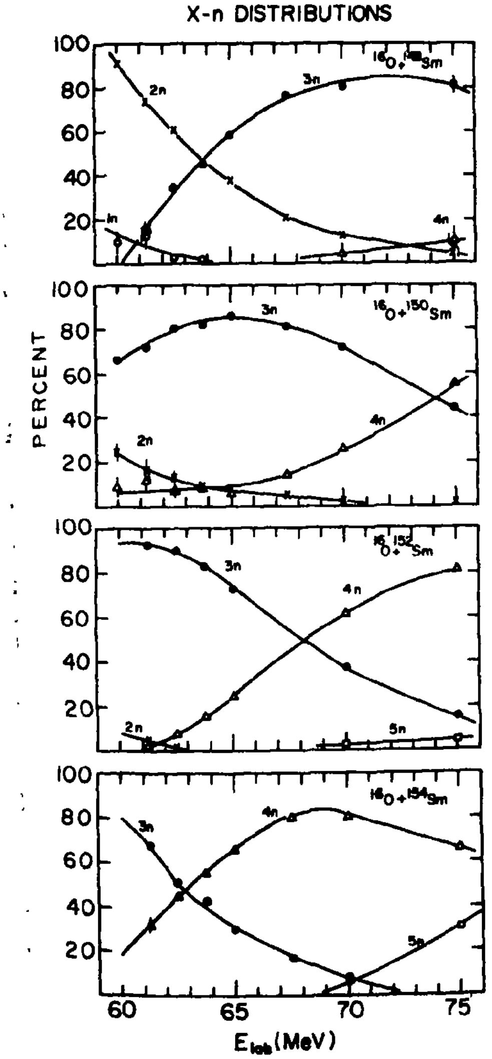

FIG. 6. The distribution of the evaporation residues s a function of bombarding energy for the four systems tudied. The value of *n* denotes the number of mass s evaporated by the compound nucleus. The yields re expressed as a percentage of the total fusion cross ction. The lines are only to guide the eye.

VI. DISCUSSION OF ERRORS

The sources of error in the present experiment can be divided into several categories. Purely systematic errors consist only of the absolute Ge-detector efficiency (± 3%) and the solid angle of the monitor detectors (± 1%). Purely random errors include the number of counts in the monitor detector and the reproducibility of the monitor system in different runs. Experimental checks show that these contribute an error of ± 2% to the cross section. An additional source of random error involves the accuracy of the correction applied to the efficiency of the Ge detector due to variations in the position of the source (± 2%).

The large value of χ^2 sometimes obtained from fitting the time decay of the sources indicated that errors other than random errors on the peak areas were present. The main additional source of error most likely was the absolute x-ray intensities. This is indicated by the fact that values of χ^2/Λ of the order of unity were routinely obtained when only a parent decay or only a daughter decay curve was fit. Nevertheless, a straightforward evaluation of the error on the total fusion cross section for a simultaneous fit of all members of the decay chains, obtained by multiplying the internal error with $(2\chi^2/\Lambda)^{1/2}$, yielded errors of typically 2% and never more than 7%.

Sources of error which are partly random and partly systematic in nature include the errors on the absolute x-ray intensities and the corrections for summing of coincidental radiations (± 3%). We have assumed that each absolute intensity is known to ± 10% and that two independent absolute intensities (a parent and a daughter) contribute to each cross section. Thus a net contribution of ± 7% to the total error is associated with the uncertainty in the absolute intensities. This is a conservative estimate since there is often a granddaughter activity present. Also, more than one mass chain contributes to the x-ray yield, which further randomizes the error from the absolute

TABLE III. Fusion cross sections for $^{16}O + ^{148,150,152,154}Sm$.[a]

E_{lab} (MeV)	^{148}Sm (mb)	^{150}Sm (mb)	E_{lab} (MeV)	^{152}Sm (mb)	E_{lab} (MeV)	^{154}Sm (mb)
75.02	404.0	440.0	74.95	462.0	75.06	430.0
70.01	183.0	243.0	69.94	213.0	70.05	235.0
67.51	89.4	117.0			67.54	134.0
65.00	27.0	38.4	64.93	43.9	65.04	55.8
63.75	10.7	20.2	63.68	24.4	63.78	29.4
62.49	3.13	7.75	62.42	11.7	62.53	15.3
61.24	0.721	2.22	61.17	4.40	61.28	6.24
59.98	0.115	0.472	59.92	1.06	60.03	2.21

[a] The uncertainty on the fusion cross sections is ±10%. The uncertainty on the beam energy is ±0.15%.

intensities.

Since the *x-n* distributions, expressed as a percentage of the fusion cross section, vary slowly with bombarding energy (see Fig. 6) it was possible to extrapolate accurately the relative amounts of 1*n*, 2*n*, and 3*n* emission at the lowest bombarding energy. Fixing these relative amounts in the fit greatly reduced the error in the cross section at the lowest bombarding energy where a low yield prohibited observing the x rays over a long time interval.

A summation in quadrature of random and partially random errors yields a standard deviation of 8.4%. The corresponding value for purely systematic errors is 3.2%. If all errors are added in quadrature, a value of 9% is obtained. We have therefore adopted an error of ± 10% for each cross section listed in Table III.

The reproducibility of the experimental method was checked by repeating selected measurements on different runs and using different targets and catcher foils. The maximum discrepancy encountered was 5.5%. In one case (70 MeV $^{16}O + ^{148}Sm$), the γ rays were analyzed to deduce cross sections for the individual mass chains. These cross sections agreed within a few percent with those deduced from the analysis of the x-ray yields.

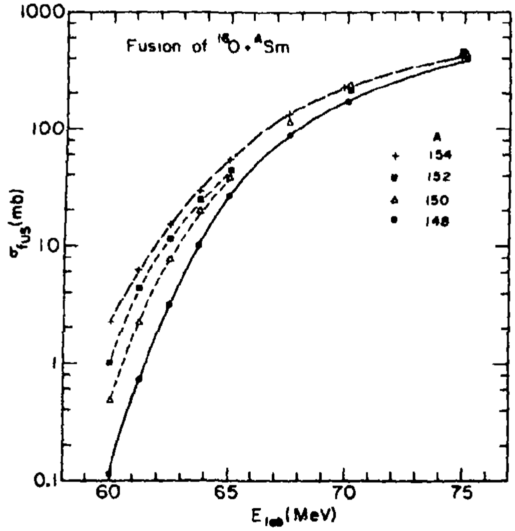

FIG. 7. The fusion cross sections as a function of bombarding energy. The total error on each point is ±10%. The fusion cross sections, similar at energies well above the fusion barrier, vary markedly at low energies with the more deformed isotopes having the larger cross sections. The lines are to guide the eye.

VII. DISCUSSION AND SUMMARY

The smallest cross section measured in this study is 0.1 mb and was done with only a one-hour-long bombardment. It appears to us that cross sections a factor three smaller could be measured by simply extending the length of the bombardment and increasing the beam intensity. Further increases in sensitivity could be obtained by studying the sources of background and taking steps to reduce them. In the case of $^{16}O + ^{154}Sm$, the 2*n* evaporation leads to a stable nucleus and thus a small correction would have to be applied for this unobserved yield at bombarding energies much below 60 MeV.

It does not appear possible for the moment to improve significantly on the precision of the method, since the largest source of error is currently associated with the absolute x-ray intensities. Computer-based calculations of the absolute intensity from the evaluated level schemes, which can be performed by the Nuclear Data Project at Oak Ridge National Laboratory, would be desirable in that they would both eliminate a lot of work and reduce the possibility of error in the evaluation of the absolute intensities from the level schemes. It might well turn out that we have overestimated the uncertainty on these values.

The above errors on the fusion cross section do not include any contribution from the uncertainty in the beam energy. For 60 MeV $^{16}O+^{148}Sm$, $d\sigma/\sigma)\cdot 1/dE$ is ~15% per 100 keV. An uncertainty of ±0.15% in the beam energy thus results in a -15% uncertainity in the cross section at this energy. However, this error on the beam energy s systematic and common to all bombardments.

Since the determination of the fusion cross section has been the goal of this study, a detailed statistical model analysis of the x-n distribution has not been undertaken. Some evaporation calculations[16] confirmed our expectation that the systematic behavior shown in Fig. 6 is reasonable and that charged-particle emission is generally small. Nevertheless, a careful analysis of the results presented here would be worthwhile, especially since the prediction of the x-n distributions is rather sensitive to the strength of the γ-ray competition. The latter quantity is of current interest in predicting the γ-ray multiplicity. Thus, the present data might be useful in calibrating statistical model calculations.

In summary, fusion cross sections for the reaction of $^{16}O+^{148,150,152,154}Sm$ have been measured by observing the delayed x rays from evaporation residues trapped in a catcher foil. This technique has enabled the determination of cross sections as small as 0.1 mb to a precision of ± 10%. The yields of individual isotopes could be determined from an analysis of the time dependence of the x-ray yield. The principle source of error in this technique has been the absolute intensities of the x rays emitted by the radioactive evaporation residues and their daughter activities. The fusion cross sections were found to be similar at energies well above the fusion barrier, but to differ markedly at energies well below the barrier.

ACKNOWLEDGMENTS

We wish to thank B. Feldman, E. Skurnik, and L. Sapir and their staffs for assistance with some technical aspects of the experiments. The help of Dr. A. Gavron in performing the statistical model calculations is acknowledged. One of us (R.G.S.) would like to thank Professor Z. Fraenkel and Professor G. Goldring for the stimulating scientific atmosphere and friendly hospitality he enjoyed during his visit at the Weizmann Institute. This research was sponsored in part by the U. S. Department of Energy under Contract No. W-7405-eng-26 with Union Carbide Corporation.

L. C. Vaz and J. M. Alexander, Phys. Rev. C 10, 464 (1974).

L. C. Vaz and J. M. Alexander, Phys. Rev. C 18, 2152 (1978).

R. G. Stokstad, Y. Eisen, S. Kaplanis, D. Pelte, U. Smilansky, and I. Tserruya, Phys. Rev. Lett. 41, 465 (1978).

D. L. Hendrie, N. K. Glendenning, B. G. Harvey, O. N. Jarvis, H. H. Duhm, J. Saudinos, and J. Mahoney, Phys. Lett. 26B, 127 (1968); N. K. Glendenning, D. L. Hendrie, and O. N. Jarvis, *ibid*. 26B, 131 (1968); W. Brückner, D. Husar, D. Pelte, K. Traxel, M. Samuel, and U. Smilansky, Nucl. Phys. A231, 159 (1974); A. H. Shaw and J. S. Greenberg, Phys. Rev. C 10, 263 (1974).

T. Sikkeland, Phys. Rev. 135, B669 (1964).

H. H. Gutbrod, W. G. Winn, and M. Blann, Nucl. Phys. A213, 267 (1973).

F. Pühlhofer, W. Pfeffer, B. Kohlmeyer, and W. F. W. Schneider, Nucl. Phys. A244, 329 (1975).

[8] J. B. Natowitz, Phys. Rev. C 1, 623 (1970).

[9] R. Broda, M. Ishihara, B. Herskind, H. Oeschler, S. Ogaza, and H. Ryde, Nucl. Phys. A248, 356 (1975).

[10] Obtained from Seforad Applied Radiation, Ltd., Emek Hayarden, Israel.

[11] R. A. Mowatt, Nucl. Instrum. Methods 70, 237 (1969).

[12] N. B. Gove and M. J. Martin, Nucl. Data Tables A10, 205 (1971).

[13] A.H. Wapstra, G. J. Nijgh, and R. Van Lieshout, *Nuclear Spectroscopy Tables* (North-Holland, Amsterdam, 1959).

[14] R. S. Hager and E. C. Seltzer, Nuclear Data Tables A4, 1 (1968).

[15] *Nuclear Data Sheets*, edited by W. B. Ewbank for the Nuclear Data Project (Academic, New York).

[16] Monte Carlo statistical model code JULIAN, M. Hillman and Y. Eyal (unpublished), as modified by A. Gavron.

[17] L. C. Northcliffe and R. F. Schilling, Nucl. Data Tables A7, 233 (1970).

PHYSICAL REVIEW C VOLUME 21, NUMBER 6 JUNE 1980

Techniques for heavy-ion coupled-channels calculations.
II. Iterative solution of the coupled radial equations

M. Rhoades-Brown, M. H. Macfarlane, and Steven C. Pieper
Argonne National Laboratory, Argonne, Illinois 60439
(Received 26 November 1979)

This paper, the second in a series on techniques for heavy-ion coupled-channels calculations, compares various iterative methods for the solution of the coupled radial equations in the interior region of configuration space. We consider the Born-Neumann series, sequential iteration, the method of moments, and Austern's modification of the Sasakawa method. The use of Padé approximants is shown to eliminate convergence problems with Born and sequential iteration. We conclude that sequential iteration with Padé acceleration is the most rapidly convergent and most efficient way of carrying out coupled-channels calculations for heavy-ion inelastic scattering; 0.5% accuracy in cross sections can be achieved with three or four iterations in each partial wave.

[NUCLEAR REACTIONS HI coupled-channels inelastic scattering. Iterative solution of radial equations.]

I. INTRODUCTION

Coupled-channels calculations for the inelastic scattering of heavy ions have been severely restricted by their computational complexity. Major souces of difficulty include (1) the long range of the Coulomb coupling potential, (2) the large number of channels that must be considered, and (3) the large number of partial waves that contribute significantly. The efficient treatment of Coulomb coupling was discussed in the first paper[1] of this series. It was shown that the Alder-Pauli[2] decomposition of the coupled-channels Coulomb wave functions allows efficient computation of incoming and outgoing solutions of the coupled radial equations in the region $r > R_N$, where R_N is a radius at which nuclear potentials are no longer important ($R_N \sim 20$–30 fm). These coupled-channels Coulomb functions replace the standard Coulomb functions in the process of extracting S-matrix elements. Thus it is possible to stop the outward integration of the interior radial equations at R_N instead of the several-hundred-fm radius that would be necessary if the Coulomb coupling were not explicitly treated.

In the present paper we discuss methods for solving the coupled equations in the region $r < R_N$, i.e., where both nuclear and Coulomb forces are important. For Coulomb-dominated reactions it is possible to avoid explicit treatment of an interior region by use of the Alder-Pauli[2] approach for all significant r values. However, in the presence of strong nuclear interactions most of the approximations used to simplify the equations of the Alder-Pauli method break down; we therefore prefer to solve the original radial equations directly.

The traditional method is to solve the N coupled equations, from $r = 0$ to $r = R_N$, N times with linearly independent starting values. A linear combination of the resulting N sets of regular solutions may then be found that has the desired boundary conditions as $r \to \infty$ (incoming and outgoing waves in the elastic channel, outgoing waves in all other channels). In this process the complete $N \times N$ S matrix can be extracted even though only one column is needed to compute the desired cross sections.

This procedure is reasonable for light-ion calculations where the number of coupled equations is usually moderate ($N \lesssim 20$). In heavy-ion studies much larger systems of coupled equations are encountered and it is no longer feasible to solve the N coupled equations N times (thus computing N^2 radial wave functions) in order to extract the single desired column of the S matrix.

A number of iterative procedures have been introduced in attempts to reduce the amount of computational labor. All involve recursive solution for a single set of radial wave functions that are constrained to have the desired boundary conditions. The aim is to construct a converged solution in a reasonable number of iterations. In this paper we compare several of these schemes and discuss their efficiency for heavy-ion reactions.

The most obvious scheme is to generate the Born-Neumann series for the wave functions and S matrices. We refer to this as "block iteration" since the wave functions in all channels are treated together in a block. Raynal[3] has sugge a variant of this method in which the radial equ tions are treated one at a time in a definite sequence rather than as a block; improvements in the solutions of the equations that occur earlier the sequence are then incorporated in the equations to be solved later in the sequence. This is referred to as "sequential iteration." We find that it has substantially better convergence properties than block iteration.

Both of these methods build up the wave functions and S matrices as power series in the coupling potential and both can diverge for physically reasonable potentials. As was suggested by Raynal[3] one can use Padé approximants to accelerate the convergence of the S matrices for both schemes. The Padé approximants to these power series are rational functions that have a larger radius of convergence and may converge when the original series diverges. Furthermore, if block iteration is used, the Padé approximants yield the S-matrix elements as rational functions of the overall coupling strength. This permits the coupling strength to be fitted to data in about the same time as it takes to do a calculation for a single coupling strength.

Other iterative techniques have been proposed that also express the S-matrix elements as rational functions of the coupling strength. One is the method of moments, recently studied for proton inelastic scattering by Griffin and Koshel.[4] It has been proved to converge for a wide class of potentials—certainly wide enough to include any potential likely to be encountered in heavy-ion studies. We find that for heavy-ion inelastic scattering, the moment method converges markedly more slowly than sequential iteration with Padé acceleration.

We also consider a variant, proposed by Austern,[5] of the Sasakawa[6,7] method. The modified procedure has no guaranteed convergence properties and fails to converge in some of our tests. While it is more reliable than straightforward block iteration, it is significantly slower than either block or sequential iteration with Padé acceleration. The multichannel implementation[8] of the original Sasakawa method, which does have proved convergence properties,[7] involves much more computational labor than the brute force solution of the original coupled equations and is therefore not practical.

In Sec. II we describe in more detail the methods of iteration outlined above. Numerical comparisons of the techniques are presented in Sec. III; iterative solution of the Alder-Pauli equations for all values of r is discussed in Sec. IV; and our conclusions are summarized in Sec. V.

II. ITERATIVE TECHNIQUES FOR THE COUPLED RADIAL EQUATIONS

The radial equations to be solved, in the notation established in paper I[1] of this series, are

$$D_\alpha(r)R_\alpha(r)=\sum_{\beta=1}^{N} U_{\alpha\beta}(r)R_\beta(r) \quad (\alpha=1,2,\ldots,N), \tag{2.1}$$

where

$$D_\alpha(r)=\frac{d^2}{dr^2}-\frac{l_\alpha(l_\alpha+1)}{r^2}-U_\alpha^{\text{opt}}(r)+k_\alpha^{\,2}. \tag{2.2}$$

These equations refer to a single value (J,π) of the total angular momentum and parity of the system; we suppress the labels (J,π). The solutions R_α of Eq. (2.1) are to be regular at the origin and have the asymptotic form

$$R_\alpha(r)\underset{r\to\infty}{=}\frac{i}{2}\left[I_{\alpha_0}(r)\delta_{\alpha\alpha_0}-\left(\frac{k_{\alpha_0}}{k_\alpha}\right)^{1/2}S_{\alpha\alpha_0}O_\alpha(r)\right], \tag{2.3}$$

where I_α and O_α are incoming and outgoing Coulomb functions and $S_{\alpha\alpha_0}$ are the desired S-matrix elements. The channel with an incoming wave is indicated by α_0.

Use of the asymptotic form (2.3) requires integration of the radial equations out to distances beyond which Coulomb coupling terms are negligible—several hundred fm for many heavy-ion reactions. As discussed in paper I, use of the modified asymptotic form

$$R_\alpha(r)\underset{r\to\infty}{=}\frac{i}{2}\left[\mathscr{I}_{\alpha_0,\alpha}(r)-\sum_\beta\left(\frac{k_{\alpha_0}}{k_\beta}\right)^{1/2}S_{\beta\alpha_0}\mathscr{O}_{\beta,\alpha}(r)\right], \tag{2.4}$$

where $\mathscr{I}_{\beta,\alpha}$ and $\mathscr{O}_{\beta,\alpha}$ are incoming and outgoing *coupled-channels* Coulomb functions, permits matching to the interior solutions at the much-smaller nuclear matching radius R_N.

We shall make frequent use of the regular solutions f_α of the homogeneous parts of Eqs. (2.1). These regular or optical-model solutions satisfy

$$D_\alpha(r)f_\alpha(r)=0, \tag{2.5}$$

with

$$f_\alpha(r)\underset{r\to\infty}{=}\tfrac{1}{2}i\left[I_\alpha(r)-S_\alpha O_\alpha(r)\right], \tag{2.6}$$

where S_α is the optical-model S-matrix element in channel α. The solutions $R_\alpha(r)$ of the coupled equations (2.1), the optical-model solutions $f_\alpha(r)$ and the S-matrix elements $S_{\alpha\alpha_0}$ and S_α, satisfy an integral identity,

$$S_{\alpha\alpha_0}=\delta_{\alpha\alpha_0}S_\alpha-\frac{2i}{(k_\alpha k_{\alpha_0})^{1/2}}\sum_\beta\int f_\alpha(r)U_{\alpha\beta}(r)R_\beta(r)dr, \tag{2.7}$$

which will be used in our discussion of some of the iterative techniques.

In this section we discuss a number of iterative techniques for the solution of Eqs. (2.1). All of them involve replacement of the system (2.1) of coupled equations by sets of uncoupled inhomogeneous equations

$$D_\alpha R_\alpha(r) = \phi_\alpha(r) \quad (\alpha = 1, 2, \ldots, N), \tag{2.8}$$

with driving terms specified by the known functions ϕ_α. The numerical solution of these equations proceeds in the following fashion. Let Z_α be a particular solution obtained by numerical integration starting with $Z_\alpha = 0$ at $r = 0$ (or at some finite value of r at which Z_α is negligibly small) and an arbitrary choice for $(d/dr)Z_\alpha$. The most general regular solution in channel α is obtained by adding an arbitrary multiple of the regular solution f_α of the homogeneous equation

$$R_\alpha(r) = Z_\alpha(r) + c_\alpha f_\alpha(r). \tag{2.9}$$

Substitution of Eq. (2.9) in the matching equations [Eqs. (2.4) and their r derivatives] yields a set of $2N$ inhomogeneous linear equations for the coefficients c_α and the S-matrix elements $S_{\alpha\alpha_0}$.

A. Block and sequential iteration

We first consider the most straightforward of iterative methods for the solution of Eqs. (2.1). Suppose that $k-1$ iterative steps have been completed, yielding a set of radial solutions $R_\alpha^{(k-1)}(r)$. These radial functions are used to construct the kth approximation to the solutions by solving the set of N uncoupled inhomogeneous equations

$$D_\alpha R_\alpha^{(k)} = \sum_\beta U_{\alpha\beta} R_\beta^{(k-1)}, \tag{2.10}$$

using the numerical procedure outlined above. The corresponding S-matrix elements $S_{\alpha\alpha_0}^{(k)}$ are obtained by solution of the matching equations. The new radial wave functions $R_\alpha^{(k)}$ are then substituted in the right-hand side of Eqs. (2.10) and the procedure iterated until convergence to a certain preassigned accuracy is achieved. As a criterion for convergence, we demand that the maximum (over channels α) of the magnitudes $|S_{\alpha\alpha_0}^{(k)} - S_{\alpha\alpha_0}^{(k-1)}|$ be less than some pre-assigned absolute error. Various initial estimates $R_\alpha^{(0)}$ may be used to start the iterative procedure. We have found that the precise choice of starting estimate is rather unimportant and therefore use the optical-model solution in the incoming channel:

$$R_\alpha^{(0)} = \delta_{\alpha\alpha_0} f_{\alpha_0}. \tag{2.11}$$

This iterative procedure, wherein at each stage all channels are treated in the same way and at the same level of approximation, we refer to as "block iteration." Each iteration generates one more term of the Born series for the S matrix and the wave functions. Because of this it is particularly ill suited for reactions in which a high-spin state can be reached only by a sequence of excitations of low multipolarity. For example in considering the population of a $J^\pi = 20^+$ state by successive 2^+ excitations, the desired S-matrix element will be zero for the first nine iterations of the block method.

Raynal[3] has proposed that the iterative scheme outlined above be carried out sequentially. The basic idea of sequential iteration is to solve the N inhomogeneous equations (2.10) in some definite order; each improved solution $R_\alpha^{(k)}(r)$ is immediately inserted in the inhomogeneous term of subsequent equations.

Each step of sequential iteration incorporates many effects absent in block iteration. Suppose that the channels α are ordered in some fashion with the elastic channel α_0 first, channels most strongly coupled to α_0 next, and so on, with channels that are strongly coupled grouped close to each other. The equations to be solved, in order, are then

$$D_\alpha R_\alpha^{(k)} = \sum_{\beta<\alpha} U_{\alpha\beta} R_\beta^{(k)} + \sum_{\beta>\alpha} U_{\alpha\beta} R_\beta^{(k-1)}, \tag{2.12}$$

for $\alpha = 2, 3, \ldots, N$, and for the elastic channel ($\alpha_0 = 1$)

$$D_1 R_1^{(k)} = \sum_{\beta=2}^{N} U_{1\beta} R_\beta^{(k)}. \tag{2.13}$$

As the iteration progresses through the channels, the initial guesses $R_\alpha^{(k-1)}$ are gradually replaced in the inhomogeneous terms by improved solutions $R_\alpha^{(k)}$. It is clear that higher-order corrections are thereby introduced that are absent from the corresponding stage of block iteration. In the example mentioned previously, the S-matrix element for the 20^+ state is nonzero in the first iteration with the appropriate ordering of channels.

The matching equations [Eq. (2.4) and its r derivative, with Eq. (2.9)] are also modified. In generating the solution $R_\alpha^{(k)}$ in channel α, the expansion coefficients $c_\beta^{(k)}$ and S-matrix elements $S_{\beta\alpha_0}^{(k)}$ in all other channels $\beta \neq \alpha$ are to be regarded as fixed; this yields a pair of simultaneous linear equations for $c_\alpha^{(k)}$, $S_{\alpha\alpha_0}^{(k)}$. Thus the $2N$ linear equations of block iteration are replaced in sequential iteration by N successively solved sets of two linear equations.

B. Padé approximants

It is found that, for heavy-ion as for light-ion reactions, sequential iteration provides significantly better convergence than block iteration; this will be shown in Sec. III. Nevertheless there are many interesting heavy-ion reactions for which sequential iteration diverges. As was suggested by Raynal,[3] the convergence problems of either block or sequential iteration can be overcome with the aid of Padé approximants. Suppose that an iterative procedure yields a sequence

$$S^{(0)}, S^{(1)}, S^{(2)}, \dots, S^{(k)} \tag{2.14}$$

of approximations to a certain S-matrix element

$$S = S_{\alpha\alpha_0}. \tag{2.15}$$

We define a set of coefficients b_r by the relations

$$\begin{aligned} b_0 &= S^{(0)}, \\ b_1 &= S^{(1)} - S^{(0)}, \\ b_2 &= S^{(2)} - S^{(1)}, \\ b_k &= S^{(k)} - S^{(k-1)}. \end{aligned} \tag{2.16}$$

By construction, the kth iterate $S^{(k)}$ is given by the sum of $k+1$ terms of the power series

$$S_k(x) = \sum_{r=0}^{k} b_r x^r, \tag{2.17}$$

evaluated at $x = 1$:

$$S^{(k)} = S_k(1). \tag{2.18}$$

A Padé approximant to the polynomial $S_k(x)$ of order k is a rational function (ratio of polynomials)

$$[L/M] = \frac{P_L(x)}{Q_M(x)} \quad (L + M = k), \tag{2.19}$$

whose coefficients are chosen such that the first k erms of its Maclaurin expansion coincide with $S_k(x)$. Techniques for evaluating the coefficients in $P_L(x)$ and $Q_M(x)$, discussions of the use of $[L/M]$ as a more accurate representative of the function approximated by S_k, and analyses of convergence will be found in textbooks on Padé theory.[9] We use the Wynn[10] algorithm to generate directly the approximants $[L/L]$ and $[L+1/L]$ for $x = 1$. The algorithm described by Patry and Gupta[11] is a reasonably stable method of computing the coefficients of the polynomials P and Q in Eq. (2.19).

Numerical studies in Sec. III will show that sequences of Padé approximants to $S_k(x)$ such as

$$\begin{matrix} [0/0] & [1/0] & [1/1] & [2/1] & [2/2] & \dots \\ (k=0) & (k=1) & (k=2) & (k=3) & (k=4) & \dots \end{matrix}, \tag{2.20}$$

evaluated of course at $x = 1$, accelerate the convergence of the original sequence (2.14) when it converges, and continue to converge rapidly under many circumstances in which the original sequence diverges, providing that the sequence was generated by either block or sequential iteration. It should be noted, however, that we have obtained only converged S-matrix elements; we do not obtain improved wave functions so our results cannot be used as input to coupled-channels Born-approximation calculations.

The Padé approximants have a very useful feature if the original sequence (2.14) was generated by block iteration. In this case the successive differences b_k are proportional to the kth power of the coupling potential. If an overall coupling parameter Λ is factored out of the coupling potential [$U \to \Lambda \bar{U}$ in Eq. (2.1)], we can regard x in Eqs. (2.17) and (2.19) as

$$x = \Lambda/\Lambda_0, \tag{2.21}$$

where Λ_0 is the value of Λ for which the sequence (2.14) was generated. Evaluating Eqs. (2.17) or (2.19) for values of x different from 1 then gives the S-matrix element as a function of Λ. With this method the S-matrix elements can easily be found for other values of Λ once they have been calculated for any single value. This could be of practical utility if it were desired to determine a deformation parameter by fitting computed cross sections to data; when the coupling potential is derived from a first order collective model of a single multipolarity with the equal nuclear and Coulomb deformations, the overall coupling parameter Λ may be identified as the deformation parameter β.

As is evident from Eq. (2.12), the successive differences b_k computed by sequential iteration are not proportional to a single power of the coupling potential. Thus in this case we cannot use Eq. (2.19) with $x \neq 1$ to evaluate S as a function of Λ. One must therefore choose between the more rapid convergence of the sequential iteration method and the advantage of being able to compute S simultaneously for more than one value of Λ.

C. Method of moments

The method of moments[12] is an iterative technique for the solution of the integral equivalent of the coupled differential equations (2.1); a finite set of basis functions is defined iteratively and at each stage the integral equations are solved in the truncated basis constructed up to that point. The linearly independent basis functions used are in fact differences of the functions $R_\alpha^{(i)}$ generated by block iteration; the basis functions are defined by

$$u_\alpha^{(0)} = R_\alpha^{(0)} = \delta_{\alpha\alpha_0} f_{\alpha_0}, \tag{2.22}$$

$$u_\alpha^{(i)} = R_\alpha^{(i)} - R_\alpha^{(i-1)} \quad (i = 1, \dots, k). \tag{2.23}$$

These basis functions are defined only on the interval $0 \leq r \leq R_N$, where R_N has previously been defined as the boundary of the interior region.

We introduce the integral operator

$$K_{\alpha\beta}(r,r')=D_\alpha^{-1}(r,r')U_{\alpha\beta}(r')\,,\quad 0\leq r,\ r'\leq R \tag{2.24}$$

where D_α^{-1} designates the (outgoing-wave) Green's function associated with the differential operator D_α of Eq. (2.1). The successive basis functions are related by application of the operator K:

$$u_\alpha^{(i)}(r)=\sum_\beta\int_0^R dr'K_{\alpha\beta}(r,r')u_\beta^{(i-1)}(r')\,. \tag{2.25}$$

For all potentials of interest here the scalar products

$$\langle u^{(j)}|u^{(i)}\rangle=\sum_\alpha\int_0^R dr\,[u_\alpha^{(j)}(r)]^*u_\alpha^{(i)}(r) \tag{2.26}$$

of the basis functions are finite. [$u^{(i)}$ is a vector with N components $u_\alpha^{(i)}$.]

We let $H^{(k-1)}$ be the space spanned by the k vectors $u^{(0)},u^{(1)},\ldots,u^{(k-1)}$ and let $P^{(k-1)}$ be a projection operator onto it. We determine a vector $\hat{R}^{(k)}$ in $H^{(k-1)}$ that is the solution of the integral equivalent of the coupled equations (2.1) restricted to the space $H^{(k-1)}$:

$$\hat{R}_\alpha^{(k)}(r)=\delta_{\alpha\alpha_0}f_{\alpha_0}(r)+\sum_\beta\int_0^R dr'\,K_{\alpha\beta}^{(k-1)}(r,r')\hat{R}_\beta^{(k)}(r')\,, \tag{2.27}$$

where

$$K^{(k-1)}=P^{(k-1)}KP^{(k-1)}\,. \tag{2.28}$$

If we express $\hat{R}^{(k)}$ as a linear combination of the basis functions that span $H^{(k-1)}$,

$$\hat{R}^{(k)}=\sum_{i=0}^{k-1}a_iu^{(i)}\,, \tag{2.29}$$

and substitute in Eq. (2.27), we obtain a set of linear equations for the expansion coefficients:

$$\sum_{i=0}^{k-1}a_iu^{(i)}(r)=u^{(0)}(r)+\sum_{i=0}^{k-2}a_iu^{(i+1)}(r)+a_{k-1}P^{(k-1)}u^{(k)}(r)\,, \tag{2.30}$$

where we have made use of

$$P^{(k)}u^{(i)}=u^{(i)}\quad(i=0,\ldots,k-1)\,. \tag{2.31}$$

For the last term of Eq. (2.30), we write

$$P^{(k-1)}u^{(k)}=\sum_{i=0}^{k-1}b_i^{(k)}u^{(i)}\,, \tag{2.32}$$

where the $b_i^{(k)}$ satisfy the linear equations

$$\sum_{j=0}^{k-1}\langle u^{(i)}|u^{(j)}\rangle b_j^{(k)}=\langle u^{(i)}|u^{(k)}\rangle\quad(i=0,\ldots,k-1)\,. \tag{2.33}$$

Inserting Eqs. (2.32) in Eq. (2.30) and equating the coefficients of each $u_\alpha^{(i)}$, we obtain

$$a_0=1-b_0/Q \tag{2.34}$$

and

$$a_i=a_{i-1}-b_i/Q\quad(i=1,\ldots,k-1)\,, \tag{2.35}$$

where

$$Q=1+\sum_{i=0}^{k-1}b_i\,. \tag{2.36}$$

The approximation $\hat{S}_{\alpha\alpha_0}^{(k)}$ to the S matrix at the kth iteration is obtained by substituting the approximate wave function $\hat{R}^{(k)}$ in the integral identity (2.7). Equation (2.25) may be rewritten in differential form:

$$D_\alpha u_\alpha^{(i+1)}=\sum_\beta U_{\alpha\beta}u_\beta^{(i)}\,. \tag{2.37}$$

Substituting the expansion (2.29) in Eq. (2.7) and using Eq. (2.37), we find

$$\hat{S}_{\alpha\alpha_0}^{(k)}=\delta_{\alpha\alpha_0}S_{\alpha_0}-\frac{2i}{(k_\alpha k_{\alpha_0})^{1/2}}\times\sum_{i=0}^{k-1}a_i\int_0^R dr\,f_\alpha(r)D_\alpha(r)u_\alpha^{(i+1)}(r)\,. \tag{2.38}$$

Integration by parts and the Wronskian relations for the Coulomb functions then give the result

$$\hat{S}_{\alpha\alpha_0}^{(k)}=\delta_{\alpha\alpha_0}S_{\alpha_0}+\sum_{i=0}^{k-1}a_i(S_{\alpha\alpha_0}^{(i+1)}-S_{\alpha\alpha_0}^{(i)})\,, \tag{2.39}$$

where $S_{\alpha\alpha_0}^{(i)}$ is the S-matrix element associated with the asymptotic form of $R_\alpha^{(i)}$ by Eq. (2.4). Thus it is not necessary to evaluate the integral in Eq. (2.7) because the $S_{\alpha\alpha_0}^{(i)}$ are available from the construction of the $R_\alpha^{(i)}$.

It should be noted that the improved wave functions $\hat{R}_\alpha^{(k)}$ and the associated S-matrix elements $\hat{S}_{\alpha\alpha_0}^{(k)}$ are not used in the next iteration of the method of moments. Rather $R_\alpha^{(k+1)}$ and $S_{\alpha\alpha_0}^{(k+1)}$ are generated by block iteration from $R_\alpha^{(k)}$ and the coupled integral equations (2.27) solved in the resulting larger space. It has been proved that the iterative process of the moment method converges for any local potential, regardless of its strength.[1]

The S-matrix elements obtained from the method of moments are rational functions of the coupling strength. If we factor out an overall coupling strength Λ from $U_{\alpha\beta}$, it is clear that $u^{(i)}$ is proportional to Λ^i. Hence, as was the case for block iteration with Padé acceleration, given the $\hat{S}_{\alpha\alpha_0}^{(k)}$ for a specific Λ, it is easy to generate S matrices for other values of Λ.

D. A simplified variant of the Sasakawa method

The original Sasakawa[6] iterative scheme has been shown[7] to converge for a class of potentials that includes all those of interest here: however, the multichannel generalization[8] of the Sasakawa method involves too much computational labor per iteration to be useful. Austern[5] and Soper[8] have studied a modification of the Sasakawa method that reduces the amount of computation to a reasonable level. The modified iteration scheme, however, does not have any of the convergence guarantees of the original method.

The basic idea is to modify the coefficient of the outgoing part of the radial wave functions obtained by solution of the inhomogeneous equations (2.10) such that at each iteration the modified radial functions $\hat{R}^{(k)}_\alpha$ and S-matrix elements $\hat{S}^{(k)}_{\alpha\alpha_0}$ satisfy the integral (2.7). In block iteration, this relation holds only after a converged solution has been obtained. Suppose, then, that a set of radial wave functions $\hat{R}^{(k-1)}_\alpha$ has been generated by $(k-1)$ iterative steps. The kth step of the Austern-Sasakawa procedure is then carried out as follows.

The radial functions $\hat{R}^{(k-1)}_\alpha$ are substituted in the right-hand side of Eqs. (2.10) and the resulting inhomogeneous equations solved for a new set of approximations $\hat{R}^{(k)}_\alpha$ and $\hat{S}^{(k)}_{\alpha\alpha_0}$. This portion of the calculation is identical to the kth step of block iteration. Auxiliary functions $J^{(k)}_\alpha$ are then defined by

$$J^{(k)}_\alpha(r)=\frac{R^{(k)}_\alpha(r)-\delta_{\alpha\alpha_0}f_\alpha(r)}{S^{(k)}_{\alpha\alpha_0}-\delta_{\alpha\alpha_0}S_\alpha}\,. \tag{2.40}$$

Corrected radial wave functions $\hat{R}^{(k)}_\alpha$ are given by

$$R^{(k)}_\alpha=\delta_{\alpha\alpha_0}f_{\alpha_0}(r)+(\hat{S}^{(k)}_{\alpha\alpha_0}-\delta_{\alpha\alpha_0}S_{\alpha_0})J^{(k)}_\alpha\,, \tag{2.41}$$

where the S-matrix elements $\hat{S}^{(k)}_{\alpha\alpha_0}$ are to be determined from the integral relation (2.7). Substitution of (2.41) in (2.7) yields the set of inhomogeneous linear equations

$$\begin{aligned}\hat{S}^{(k)}_{\alpha\alpha_0}=\delta_{\alpha\alpha_0}S_{\alpha_0}&-\frac{2i}{(k_\alpha k_{\alpha_0})^{1/2}}\int f_\alpha U_{\alpha\alpha_0}f_{\alpha_0}\\&-\frac{2i}{(k_\alpha k_{\alpha_0})^{1/2}}\sum_\beta\int f_\alpha U_{\alpha\beta}J_\beta(\hat{S}^{(k)}_{\beta\alpha_0}-\delta_{\beta\alpha_0}S_{\alpha_0})\end{aligned} \tag{2.42}$$

for the S-matrix elements. The solutions then determine the modified radial functions $\hat{R}^{(k)}_\alpha$ with the help of Eqs. (2.41).

E. Computer requirements

A complete comparison of the relative efficiency of the various methods must involve not only the number of iterations needed to achieve a desired accuracy, but also the time and storage requirements for an iteration of each technique. The convergence rates of the various iterative schemes are compared in Sec. III. Here we discuss the computer time and storage requirements. We have identified those parts of the calculations that demand the most computing time and storage and estimated the time and storage that would be needed by efficient programs implementing each method. The time required to compute Coulomb wave functions (or coupled-channels Coulomb wave functions) has not been included in these estimates.

Storage requirements are given in terms of floating point (real) numbers or "words." A complex number requires two such words. We have found that single precision (32 bits) on IBM 370 computers is adequate for all of the large arrays used in these calculations. Modern large-scale computers have the ability to overlap the processing of several operations such as accessing memory, decoding instructions, computing subscript quantities and floating-point operations. For this reason the execution times of large scientific programs depend most heavily on the number of floating-point operations (FLOP) that must be made—auxiliary computations such as subscript evaluations may be ignored. We present timing estimates in terms of the number of floating-point operations; in calculations similar to the ones described here the CDC 7600 and IBM 370/195 computers are capable of about 5×10^6 FLOP/sec, the CRAY-I computer about 50×10^6 FLOP/sec.

In the estimates we assume that the Numerov method as described in Ref. 2 is used to generate all radial functions $R^{(k)}_\alpha$. This method computes the wave function on a grid of equally spaced coordinate values and requires the potentials on the same grid. The integration starts at some value of r (not necessarily at $r=0$) for which the wave function is negligible. If the grid contains M points, then the Numerov method for inhomogeneous equations may be executed in $20M$ floating-point operations.

There are N^2 complex potential functions for N coupled equations and each of these is required at M grid points. Clearly it is impractical to store such a three-dimensional array for large N or M. Instead we will make the following assumptions that seem reasonable for heavy-ion calculations. The optical potential is the same for all channels. In addition a separate array containing r^{-2} is stored to allow rapid computation of the centrifugal term in the kinetic energy. The coupling potentials can be expressed in the form

$$U_{\alpha\beta}(r)=\sum_t X^{(t)}_{\alpha\beta}v_t(r)\,, \tag{2.43}$$

where $X^{(t)}_{\alpha\beta}$ is independent of r and contains all angular-momentum-coupling factors while $v_t(r)$ is independent of the labels α and β. There are separate v_t for each distinct function of r (each multipolarity and order of coupling) appearing in $U_{\alpha\beta}$. Since there are typically only a few v_t, separate storage of the $X^{(t)}_{\alpha\beta}$ and the $v_t(r)$ allows the potentials to be saved in a reasonable amount of core. We use N_v to designate the number of different v_t that must be stored. The $X^{(t)}_{\alpha\beta}$ may be chosen to be real. In many problems each R_α will be coupled to only a few of the N functions R_β and $X^{(t)}_{\alpha\beta}$ may have the form of a band matrix. We use N_c to designate the average number of couplings per channel basis state. Because the best way to store the matrices $X^{(t)}_{\alpha\beta}$ depends on whether or not they are band matrices, we do not include their size in the storage estimates that follow.

Table I presents our estimates of the storage and time requirement of the various iterative techniques. The first part of the table summarizes the symbols that are used in the estimates and gives their values for two extreme computations. The first is a simple two-channel calculation involving ^{16}O and ^{44}Ca. The second is sub-Coulomb $E2$ excitation of ^{154}Sm by 900 MeV ^{208}Pb ions including states up to $J=20^+$ in the ground-state rotational band. We have not yet attempted a calculation as large as this one. The wavelength for the reaction is 0.156 fm, so the 1500 steps ($M=1500$) indicated in the table correspond to ten steps per wavelength starting from 11 fm and going out to 35 fm, which is a resonable matching radius if the coupled-channels Coulomb functions are used.

The second part of Table I presents the core and time estimates as functions of the relevant parameters and for the two reactions. The time estimates are in terms of FLOP/iteration. It can be seen that an iteration of the Austern-Sasakawa method is two or three times slower than an iteration of the block method. The method of moments requires less additional time but needs much more storage to save the wave functions at each iteration. The last line of the table shows the requirements of the traditional method of solving the coupled equations (construction of N linearly independent sets of solutions of the N coupled equations). Because the time for this method varies as N^3, a solution for the second example requires the equivalent of 2100 block iterations.

Griffen and Koshel have suggested expanding the R_α in plane waves as a method of solving the inhomogeneous differential equations. Because it takes many fewer expansion coefficients than values on a coordinate grid to represent each R_α with adequate accuracy, the plane-wave method significantly reduces the storage requirements of the method of moments. Both the core and time requirements for the plane-wave method depend upon the number of plane waves needed to represent the R_α. Plane-wave matrix elements of the potentials and operators such as D_α must be computed and stored. The solution of the inhomogeneous equation is then reduced to the solution of a set of simultaneous equations; the time for this is proportional to the cube of the number of plane

TABLE I. Core and time estimates for the methods discussed in the text. The first part gives the symbols used and reasonable values for two calculations. (1) $^{16}O+{}^{44}Ca$ at 60 MeV using the 0^+ and 2^+ states of ^{44}Ca, (2) $^{208}Pb+{}^{154}Sm$ at 900 MeV using the 0^+, 2^+_1, ..., 20^+ ground-state rotational band of ^{154}Sm with quadrupole coupling. Core estimates are in floating-point words, time estimates in floating-point operations (FLOP).

Symbol	Meaning	Values Example 1	Example 2
N	Number of coupled equations	4	121
M	Number of Numerov grid points	200	1500
N_v	Number of $v_t(r)$	1	1
N_c	Number of couplings per equation	4	9
n	Number of iterations	5	5

Method	Core (Floating words)	Time/Iteration (FLOP)	Example 1 Core 10^3 words	Example 1 time 10^3 FLOP	Example 2 Core 10^6 words	Example 2 time 10^6 FLOP
Block	$M(4N+2N_v+3)$	$MN[30+N_v(4N_c+6)]$	5.0	41.6	0.74	13.4
Sequential	$M(4N+2N_v+5)$	$MN[30+N_v(4N_c+6)]$	5.0	41.8	0.74	13.4
Austern-Sasakawa	$M(6N+2N_v+3)+2N^2$	$MN[36+N_v(14N_c+12)]+\frac{8}{3}N^3$	6.2	84	1.13	53.9
Moments	$M[(2n+4)N+2N_v+3]$	$MN[40+4n+N_v(4N_c+6)]$	11.4	66.6	2.13	18.9
Conventional	$M(2N_v+3)+12N^2[+2N^2M]^a$	$M(11N^3+4N^2)[+8MN]^a$	1.6^b	154^b	0.19^b	29 000.0^b

[a] Required only if wave functions needed.

[b] Wave function computation not included.

waves. We have made a few studies of the number of plane waves needed and conclude that for example 1, 30 plane waves are necessary,[13] 60 or more for example 2. In both cases the plane-wave expansion technique requires somewhat more storage and more than thrice the time than the grid method to construct the radial functions $R_\alpha^{(n)}$.

III. COMPARISON OF ITERATIVE METHODS

We have used a rather simple coupled-channels problem to assess the convergence rates of the iterative techniques described in Sec. II. The two coupled channels are $^{16}O+{}^{44}Ca$ (g.s.) and $^{16}O+{}^{44}Ca$ $(2^+, 1.156$ MeV). Calculations were made for a bombarding energy of 60 MeV. The optical potential is of the Woods-Saxon form with identical real and imaginary radial dependence; the potential parameters are

$$V = 110\text{ MeV},\quad W = 20\text{ MeV},$$
$$r_0 = 1.2\text{ fm},\quad a = 0.5\text{ fm},\qquad (3.1)$$
$$r_{c_0} = 1.2\text{ fm},$$

where V and W are respectively the real and imaginary well depths, r_0 is the radius parameter, a is the diffuseness, and r_{c_0} is the Coulomb radius parameter. The potential radii (both Coulomb and nuclear) are related to the radius parameters by

$$R' = r_0(A_P^{1/3} + A_T^{1/3}),\qquad (3.2)$$

where A_P and A_T are the projectile and target atomic weights. The rotational model [Eq. (2.10) of Ref. 1] was used for $U_{\alpha\beta}$. In the calculations reported here only nuclear coupling was considered ($\beta_c = 0$). This represents a stringent test of the methods of solution since the sharply peaked nuclear coupling results in significantly distorted wave functions. Coulomb coupling reduces the distortion and the number of iterations necessary to achieve a given accuracy. Nuclear reorientation effects and the diagonal elements of $U_{\alpha\beta}$ are included in the calculations. Most of the calculations were made for $J = 30$ (a near-grazing partial wave) for which the elastic S matrix has the magnitude $|S^{J=30}_{30,0^+;30,0^+}| = 0.46$.

Tables II and III compare the rate of convergence of the magnitude of one of the inelastic S-matrix elements ($|S^{J=30}_{30,2^+;30,0^+}|$) for the various techniques. Table II is for a physically reasonable deformation parameter ($\beta = 0.25$) while Table III is for a much larger value ($\beta = 0.4$). The calculation for this unrealistic deformation value is of course much harder; it is of interest as a simulation of realistic calculations involving the strongly deformed rare-earth nuclei.

The tables show the convergence as a function of iteration number k; in comparing the different techniques we must take into account the time estimates given in Table I. In the Padé columns the $[M/M]$ Padé estimate is given for the even-numbered iterations, the $[M/M-1]$ estimate for the odd, as illustrated in sequence (2.17).

Table II shows that with the possible exception

TABLE II. Convergence properties of the modulus of the inelastic S-matrix element $|S^{30^+}_{30,2^+;30,0^+}|$, as a function of iteration number k, for the reaction $^{44}Ca(^{16}O,{}^{16}O)^{44}Ca(2^+ 1.156\text{ MeV})$ $E_{Lab} = 60$ MeV The numerical techniques are described in Sec. II. The potentials used are given in Sec. III. The nuclear deformation is $\beta = 0.25$.

k	Sequential	Sequential and Padé	Block	Block and Padé	Method of moments	Austern-Sasakawa
1	0.12 69	0.12 69	0.16 95	0.16 95	0.16 95	0.12 58
2	0.16 11	0.15 93	0.14 72	0.14 87	0.14 36	0.14 78
3	0.14 92	0.14 84	0.15 30	0.15 94	0.16 11	0.14 87
4	0.14 67	0.14 81	0.16 65	0.15 10	0.14 81	0.14 74
5	0.14 802	0.14 793	0.13 40	0.14 75	0.15 01	0.14 79
6	0.14 806	0.14 797	0.15 14	0.14 78	0.14 79	0.14 81
7	0.14 796	0.14 7971	0.15 35	0.14 791	0.14 788	0.14 790
8	0.14 798	0.14 7975	0.13 84	0.14 795	0.14 807	0.14 798
9	0.14 7976	0.14 7975	0.15 49	0.14 795	0.14 798	0.14 792
10	0.14 7974		0.14 76	0.14 794	0.14 796	0.14 797
11	0.14 7975		0.14 33	0.14 796	0.14 7976	0.14 798
12	0.14 7975		0.15 46	0.14 7971	0.14 7976	0.14 793
13			0.14 38	0.14 7973		0.14 796
14			0.14 74	0.14 7976		0.14 796
15			0.15 25	0.14 7976		0.14 795
16			0.14 29			
17			0.15 02			
18			0.14 99			
19			0.14 39			
20			0.15 14			

TABLE III. Convergence properties of the modulus of the inelastic *S*-matrix element $|S^{30^+}_{30,2^+;30,0^+}|$ *for the reaction* and potentials of Table II with $\beta = 0.4$.

k	Sequential	Sequential and Padé	Block	Block and Padé	Method of moments	Austern-Sasakawa
1	0.1634	0.16 32	0.2713	0.27 13	0.27 13	0.1561
2	0.2906	0.23 60	0.2157	0.22 10	0.21 03	0.2050
3	0.2540	0.20 78	0.2921	0.25 36	0.26 21	0.2067
4	0.1448	0.20 95	0.3390	0.22 20	0.21 28	0.1987
5	0.2035	0.20 81	0.0222	0.20 47	0.22 47	0.2076
6	0.2494	0.20 70	0.4046	0.20 41	0.20 54	0.2098
7	0.2125	0.20 72	0.4645	0.20 58	0.20 93	0.2043
8	0.1747	0.20 713	0.3390	0.20 63	0.20 66	0.2077
9	0.2156	0.20 717	0.9398	0.20 63	0.20 64	0.2056
10	0.2293	0.20 7173	0.9914	0.20 59	0.20 716	0.2113
11	0.1971	0.20 7170	1.481	0.20 65	0.20 716	0.2092
12	0.1950	0.20 7175	2.501	0.20 69	0.20 717	0.1995
13	0.2182	0.20 7175	3.296	0.20 69	0.20 718	0.2116
14	0.2134		5.290	0.20 713	0.20 717	0.2080
15	0.1980		8.068	0.20 717	0.20 7176	0.2013
16	0.2054		11.79	0.20 719	0.20 7175	0.2146
17	0.2142		18.26	0.20 7179	0.20 7175	0.2042
18	0.2068		27.27	0.20 7175	0.20 7175	0.2036
19	0.2023		40.80	0.20 7176	0.20 7176	0.2156
20	0.2088		61.64	0.20 7175	0.20 7175	0.2001

of the unmodified block method, all the methods converge for $\beta = 0.25$. *At $\beta = 0.4$ (Table III) both the* block and Austern-Sasakawa methods fail to converge and the sequential method is converging very slowly (we have continued the calculations to 40 iterations to verify these statements).

Sequential iteration with Padé acceleration is clearly the most rapidly convergent method for $\beta = 0.4$; it achieves an accuracy of 0.5% in five iterations while the method of moments requires eight and block iteration with Padé acceleration requires 11 iterations to achieve the same accuracy. For $\beta = 0.25$ both sequential iteration with Padé and Austern-Sasakwa require only three iterations to achieve 0.5% accuracy; block iteration with Padé and unaccelerated sequential require five iterations and the method of moments needs six iterations. For these cases, and all others studied, Padé approximants do not increase the convergence rates of either the method of moments or the Austern-Sasakawa method.

Although the Austern-Sasakawa technique converged rapidly for $\beta = 0.25$, the divergence for $\beta = 0.4$ together with the substantial computer storage and time requirements suggests that this method is not competitive for heavy-ion coupled-channels calculations.

As was described in Sec. II, both block iteration with Padé acceleration and the method of moments allow straightforward evaluation of *S*-matrix elements as a function of β, once they are computed for a single value of β. Figures 1 and 2 show the resulting curves for block iteration with Padé *acceleration and the method of moments, respectively*. The curves are labeled with the number of iterations that were used to generate them. In both cases the first iteration is just the first-order Born result. For the first nine iterations, the block method is clearly superior to the method of

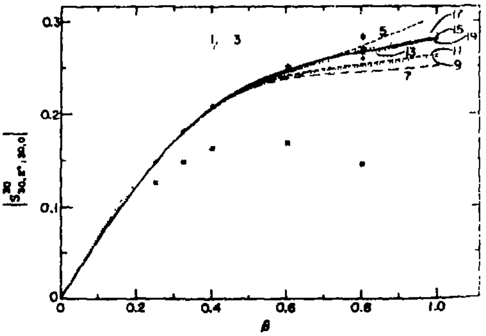

FIG. 1. The modulus of the inelastic *S*-matrix element $|S^{30}_{30,2^+;30,0}|$, plotted as a function of the nuclear deformation parameter, *for the reaction* $^{44}Ca(^{16}O, ^{16}O)^{44}Ca(2^+, 1.156$ MeV) at $E_{LAB} = 60$ MeV. The lines represent the results of block iteration with Padé approximants and are labeled by the number of iterations k. The stars represent the values obtained from sequential iteration and Padé approximants for $k = 1$. The crosses give the corresponding results obtained for k ranging from 3 to 11. The potential parameters used in this calculation are listed in Sec. III.

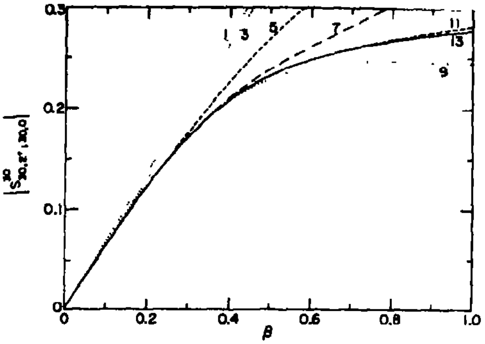

FIG. 2. The modulus of the inelastic S-matrix element shown in Fig. 1, for various numbers of iterations obtained by the method of moments.

moments. However, for $\beta > 0.6$ the convergence of block iteration with Padé acceleration significantly slows down for iterations 11 to 17 and the 19th iteration is only as good as the 11th iteration of the method of moments. This wandering of the Padé accelerant appears to be an intrinsic feature of the Padé method because several different ways of evaluating the Padé approximants (the Wynn and epsilon algorithms,[10] Patry and Gupta's method,[11] and matrix inversion[9]) produce the same results. The method of moments does not seem to exhibit this phenomenon of a temporary interruption in its march towards a fully converged result.

The points in Fig. 1 show the results of separate Padé-accelerated sequential-iteration calculations for five values of β. It is obvious that if one is not interested in results for more than one value of β, this method is far more rapidly convergent than block iteration with Padé or the method of moments.

We have also tried these six methods for the $^{16}O + ^{44}Ca$ reaction for $J = 10$ with similar conclusions. The sequential-iteration method with Padé acceleration has also been used by us for many other two-channel heavy-ion reactions such as $^{136}Xe + ^{208}Pb$ and $^{18}O + ^{184}W$. In an attempt to simulate a multichannel calculation we considered the excitation of a 16^+ state by a $\lambda = 16$ transition with $\beta_{16} = 0.5$ for which the Born series rapidly diverged; 0.1% accuracy was achieved in only nine iterations of the Padé-accelerated sequential method. Except for some extraordinarily large unphysical values of β, this method has always been found to converge, usually to 0.1% accuracy in fewer than seven iterations.

IV. INWARD-OUTWARD ITERATION METHODS

In the first paper of this series, we used the Alder-Pauli[2] transformation to solve for the Coulomb part of heavy-ion inelastic scattering. The channel wave functions in the exterior region are expressed as products of Coulomb functions and modulating amplitudes and the coupled equations for the modulating amplitudes are reduced to first order and shown to be capable of accurate solution in first Born approximation; this latter step permits the use of recursion relations in angular momentum that in turn eliminate the need to integrate explicitly in all but a few partial waves. Iterative techniques for solution of the radial equations in the interior region are the topic of the present study.

Alder, Roesel, and Morf[14] and Ichimura *et al.*[15] have proposed a different strategy. The Alder-Pauli transformation is to be used over the entire range of r values; the distinction between interior and exterior regions disappears. This involves finding not only incoming and outgoing solutions, but also the S-matrix elements. Alder *et al.* approach this combined problem of solving the coupled equations and imposing appropriate boundary conditions by an iterative procedure. A first estimate of the S-matrix elements is made and the coupled equations are integrated inwards from infinity; regularity is imposed at small r and the coupled equations integrated outwards to obtain an improved estimate of the pertinent S-matrix elements. The whole process is iterated until adequate accuracy has been achieved in the S-matrix elements. Recently Tolsma[16] has studied a variant of this procedure in which the asymptotic Coulomb functions of the Alder-Pauli transformation are replaced by Airy functions; the coupled equations for the modulating functions are solved by inward-outward iteration.

Tolsma considers Coulomb excitation only and presents impressive results, including a computation of excitation of rotational bands in deformed nuclei up to $I = 24^+$; these are by far the largest quantal Coulomb excitation calculations ever carried out. There is, however, one aspect of Tolsma's work on which we wish to comment. He compares inward-outward iteration with sequential iteration as a method of solution of the equations for the modulating amplitudes and finds that sequential iteration diverges for some cases of interest. He concludes that inward-outward integration is superior. We have shown, however, that Padé acceleration (which Tolsma does not consider) eliminates convergence problems when using sequential iteration to solve the coupled radial equations in the interior region. It appears that Tolsma's argument as to the relative merits of inward-outward and sequential iteration is incomplete.

We have not made detailed studies of the relative efficiency of inward-outward iteration and the methods discussed here. However, Tolsma implies that his method is some 30 times faster than the conventional method, for example 2 of Table I. As can be seen from the table, ten sequential iterations with Padé acceleration (which should be adequate to achieve convergence) should be some 200 times faster than the conventional method for the same problem.

V. CONCLUSIONS

Of the iterative methods considered, sequential iteration with Padé acceleration is the most reliable and rapidly convergent; typically it gives 0.5% accuracy in three or four iterations. In addition it requires considerably less storage and time per iteration than the more complicated Austern-Sasakawa and moment methods. Its principal defect in the form we have discussed is that the Padé approximants are used to improve the convergence of the S-matrix elements only. For calculations requiring converged wave functions it would be possible to apply Padé approximants point by point to each set of iterated channel wave functions. Although this would substantially increase the computer storage required, it will usually be possible to avoid storing every iterated wave function in each channel; thus even with point-by-point Padé approximation of the wave functions, sequential iteration should in practice require considerably less storage than the method of moments. Other schemes for computing the wave functions once accurate S-matrix elements are known might also be considered, but it seems to us that the Padé approximants will prove most useful when it is not necessary to obtain the scattering wave functions.

A hypothetical calculation considered in this paper is excitation of the ground-state rotational band of ^{154}Sm up to the 20^+ level by a 900 MeV ^{208}Pb projectile. We would expect sequential iteration with Padé acceleration to complete this calculation in about 0.005 of the time required by the conventional method of solving the N equations N times. This tremendous increase in speed makes such calculations fully feasible on present computers.

ACKNOWLEDGMENTS

We are indebted to Dr. Fritz Coester for many helpful comments, criticisms, and suggestions. This work was supported by the U.S. Department of Energy.

---

[1] M. Rhoades-Brown, M. H. Macfarlane, and S. C. Pieper, Phys. Rev. C 21, 2417 (1980).

[2] K. Alder and H. C. Pauli, Nucl. Phys. 128, 1931 (1969).

[3] J. Raynal, *Computing As a Language of Physics* (IAEA, Vienna, 1972), p. 281.

[4] P. J. Griffin and R. D. Koshel, Ann. Phys., to be published.

[5] N. Austern, Phys. Rev. 188, 1595 (1969).

[6] T. Sasakawa, Prog. Theor. Phys. Suppl. 27, 1 (1963).

[7] F. Coester, Phys. Rev. C 3, 525 (1970).

[8] P. Soper, Phys. Rev. C 10, 1282 (1974).

[9] G. Baker, *Essentials of Padé Approximants* (Academic, New York, 1975).

[10] P. Wynn, Numer. Math. 8, 264 (1966).

[11] J. Patry and S. Gupta, EIR-BERICHT NR247 EIDG. Institut für Reaktorforschung, Würenlingen, Switzerland, 1973.

[12] Our description of the method of moments parallels that of Ref. 4. However, our notation, in particular the meaning of the superscripts on $P^{(n)}$ and $H^{(n)}$, is somewhat different from that of Ref. 4.

[13] R. D. Koshel (private communication) also found 30 terms are necessary.

[14] K. Alder, F. Roesel, and R. Morf, Nucl. Phys. A284, 145 (1977).

[15] M. Ichimura, M. Igarashi, S. Landowne, C. H. Dasso, B. S. Nilsson, R. A. Broglia, and A. Winther, Phys. Lett. 67B, 129 (1977).

[16] L. D. Tolsma, Phys. Rev. C 20, 592 (1979).

PHYSICAL REVIEW C VOLUME 21, NUMBER 6 JUNE 1980

Angular distributions and ranges of heavy products from quasi-elastic transfer reactions induced by heavy ions in ^{209}Bi

D. Gardes, R. Bimbot, J. Maison, and M. F. Rivet
Laboratoire de Chimie Nucléaire, Institut de Physique Nucléaire, B.P. n° 1, 91406 Orsay, France

A. Fleury, F. Hubert, and Y. Llabador
Centre d'Etudes Nucléaires de Bordeaux Gradignan, Le Haut Vigneau, 33170 Gradignan, France

(Received 15 November 1979)

The projected ranges, angular distributions and range distributions at each laboratory angle have been measured for one-, two-, and three-proton transfer reactions induced in ^{209}Bi by various heavy ions from ^{14}N to ^{63}Cu. The products observed were ^{210}Po, ^{211}At, and ^{211}Rn. They were identified by their radioactive decay characteristics. Some complementary experiments have been performed using Tl and Au targets. The angular and energy distributions have been used to identify the most probable reaction paths leading to the observed isotopes. At low incident energy, these reaction paths appear to be those which correspond to the most favorable energetics, for all incident ions. At higher energies, more complex reaction channels have a significant contribution to the production of the observed isotopes. For all incident ions, the position of the angular distribution maximum θ_{max} is governed by the value of the ratio E/B of the incident energy to the interaction barrier. The variation of θ_{max} versus E/B is very similar to that of the rainbow angle corresponding to elastic scattering. This might indicate that quasi-elastic transfer and rainbow scattering occur for similar distances of closest approach between colliding nuclei.

[NUCLEAR REACTIONS ^{209}Bi(HI, x)^{210}Po, ^{211}At, ^{211}Rn, with HI = ^{14}N, ^{16}O, ^{19}F, ^{40}Ar, ^{40}Ca, ^{56}Fe, and ^{63}Cu. Measured $\sigma(\theta)$, recoil ranges. Deduced most probable reaction path.]

I. INTRODUCTION

This work is part of a systematic study of quasi-elastic transfer reactions induced by heavy ions in heavy targets. This study is centered on the evolution of the reaction characteristics when the incident mass is increased. Absolute cross sections, projected ranges (on the beam axis), and angular and energy distributions of the heavy transfer residues have been determined using recoil techniques, associated with off-line activity measurements. Such techniques are particularly fruitful for this type of study in which large quantities of data must be gathered. The resolution obtained for the energy distributions is poorer than that associated with light transfer fragments (see for example Refs. 1–3 and the review papers[4,5]), so that it is not possible to separate final levels. But such a separation is not necessary for deriving the gross features of the reaction mechanisms. Moreover, the resolution obtained for angular distributions is generally sufficient, as these distributions exhibit a single peak for the systems and energies concerned here. Finally, the main advantage of these techniques is that the final product atomic numbers and masses are unambiguously identified.

The excitation functions have been measured for several products of transfer reactions induced in ^{209}Bi by 10 ions, from ^{12}C to ^{84}Kr. These data have been published in Refs. 6–8. The influence of energetics on the threshold of these reactions was discussed qualitatively in Ref. 9 and a quantitative interpretation was proposed in Ref. 10.

The present paper concerns projected ranges, angular and energy distributions. Projected range distributions have been measured at several energies for ^{210}Po, ^{211}At, and ^{211}Rn produced through transfer reactions induced in ^{209}Bi by ^{19}F, ^{40}Ar, ^{40}Ca, ^{56}Fe, and ^{63}Cu. Angular distributions, and range distributions at all laboratory angles have been measured for the same nuclei produced by ^{14}N, ^{16}O, ^{19}F, ^{40}Ar, and ^{40}Ca induced reactions in ^{209}Bi. Similar data concerning ^{12}C induced reactions in ^{209}Bi and ^{197}Au have been already published.[6]

As several reaction channels may in principle lead to the production of a given final nucleus, the angular and energy distributions have been used to gain better assignment of the transfer reactions involved in this production. In order to remove some ambiguities which remained after this kinematic analysis, a few complementary experiments have been performed. These experiments consisted in measuring the angular distributions or ranges of transfer products from reactions induced in Au and Tl targets. Moreover, for ^{40}Ar projectiles, the cross sections and angular distributions of light transfer residues (^{42}K, ^{41}Ar, ^{39}Cl, and ^{38}S) have been measured and the data

© 1980 The American Physical Society

relative to ^{36}Cl and ^{38}S have been compared to those obtained for the complementary heavy products ^{210}Po and ^{211}At.

The experimental technique is described in Sec. II and the experimental results are given in Sec. III. The identification of the reactions leading to the observed nuclei is presented in Sec. IV, and the main features of the c.m. angular distributions and of the variation of projected ranges with incident energy are discussed in Sec. V. The experimental angular distributions presented here have been used as a basis for a quantitative interpretation using a formalism derived from the distorted-wave Born approximation (DWBA). This interpretation was published in Ref. 11.

II. EXPERIMENTAL TECHNIQUES

The experimental technique consisted of irradiations followed by off-line activity measurements.

A. Projectiles and targets

Beams of ^{14}N, ^{16}O, ^{19}F, ^{40}Ar, ^{40}Ca, ^{56}Fe, and ^{63}Cu were accelerated by the Orsay Alice facility. The incident energy was determined from the cyclotron frequency and extraction radius, and a small correction was applied to take into account the systematic deviation observed[12] between calculated and measured energies. It has been shown[12] that such a procedure leads to uncertainties of the order of ±2.5% on the energy. The low-energy ^{19}F experiments ($E < 110$ MeV) were performed using the Orsay Tandem MP Van de Graaff accelerator. For these experiments, the energy was measured with an accuracy better than ±0.1% using a calibrated magnet.

Targets of Bi, Au, and natural Tl were prepared by evaporation onto aluminum backings. The target thicknesses ranged from 50 μg/cm^2 (for the angular distributions corresponding to light projectiles) to 1 mg/cm^2 (for the projected range measurements relative to heavy projectiles).

B. Experimental devices

The projected ranges were measured simultaneously with the absolute cross sections published in Ref. 8; the target and a stack of Al catcher foils were placed in a Faraday cup [see Fig. 1(a)]. After irradiation, the catcher foils were separated and their α activity was measured in 2π ionization chambers. The projected ranges were deduced from these measurements by the method described in Ref. 13. The only improvement relative to this method concerned the correction for α self-absorption in the catcher foils. In Ref. 13, this correction was made under the assumption that for each catcher foil, all the activity was concentrated in the mid-plane of the foil (i.e., at a depth $d = e/2$, e being the catcher foil thickness). In the present work the distribution of the activity along the d axis was taken into account. This distribution was obtained from an approximate determination of the range distribution without self-absorption correction. However, this improvement led to very small changes in the projected ranges. The range straggling ρ was deduced from the full width at half maximum (FWHM) W of the projected range distribution by the relation

$$\rho = \frac{W}{2.354 R_0} \tag{1}$$

in which R_0 is the average projected range (see Ref. 14).

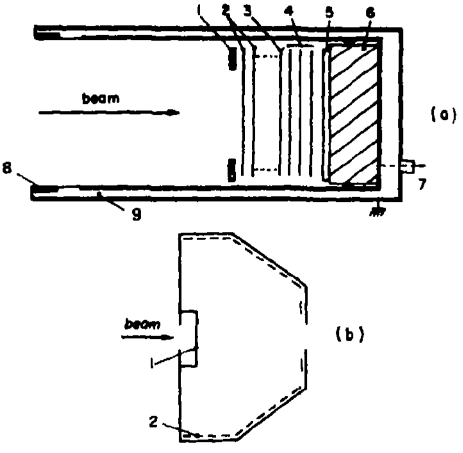

FIG. 1. Experimental set up. (a) For projected range measurements: (1) Al ring holding the stacks of foils on the Cu block. (2) Al degraders. (3) Target. (4) Al catcher foils. (5) Thick Al foil to stop all light reaction products. (6) Cu block. (7) Collected charges to beam integrator. (8) Ring shield. (9) Insulator. (b) Collection chamber: (1) Target. (2) Stacks of annular Al catcher foils.

For angular distribution measurements, the target was placed in the center of a collection chamber, and the recoil nuclei were stopped in angular catcher foils as indicated in Fig. 1(b). The target was placed either perpendicular to the beam or at 45°, according to the expected position of the angular distribution maximum. For light projectiles (up to ^{19}F), the experimental conditions were the same as in Ref. 6, while for the heaviest ions (^{40}Ar, ^{40}Ca), the conditions were similar to those of Ref. 15.

The technique used for measuring the recoil ranges at each laboratory angle depended on the incident ion. For heavy projectiles, i.e., for large range values (>1 mg/cm^2 of Al), stacks of annular catcher foils were placed at each angle θ, and the range $R(\theta)$ was determined in the same way as *the projected ranges.*[15] *For light projectiles,* i.e., for low range values, thick annular catcher foils were used, and the recoil range (the depth of the α-emitting nucleus) was deduced from the energy degradation of the emitted α particle. This technique, also used in Ref. 6, is described in Ref. 16.

Finally, special systems were designed to collect simultaneously the light and heavy products of the transfer reactions at incident energies close to the interaction barrier. (See Fig. 2.) In Fig. 2(a) is shown the device which was used to measure *the angular distribution of products for incident* energies of 203 and 212 MeV. At the highest of these energies, the angular distributions of ^{210}Po and ^{211}At were measured from 10 to 60° using stacks of Al catcher foils. Simultaneously, the *distributions of the light transfer products* ^{38}S, ^{39}Cl, ^{41}Ar, and ^{43}K were measured from 60 to 120° using 10μ Au catcher foils. The choice of this material of high atomic number was made in order to reduce the contribution of spurious reactions induced by the scattered beam in the catcher foils. At 203 MeV, the angular interval corresponding to the heavy product distribution was the same, but the light products were collected in the angular interval 90–150°. In this experiment, the activity was lower, and the angular distributions could only be measured (with a sufficient accuracy) for the esidual nuclei ^{210}Po, ^{211}At, and ^{41}Ar. The relaive yields of light and heavy products were also deived from these experiments at 212 and 203 MeV.

Two other experiments were performed to meaure the cross sections for these light and heavy roducts. A much smaller *collection chamber* was hen used [see Fig. 2(b)]. The incident energies of 90 and 194 MeV were such that the heavy transfer roducts were emitted at forward angles and the ight ones at backward angles ($\theta_{lab} > 90°$). The valls *of the collection chamber* were covered with l catcher foils in the forward hemisphere and vith Au catcher foils in the backward hemisphere. The activity caught by each hemisphere was counted as a whole, and the collection yield was assumed to be equal to 100%. The cross sections were thus measured relative to that of ^{211}At, as in the experiments at 212 and 203 MeV mentioned above. For each incident energy, the absolute cross sections for ^{211}At were measured in separate

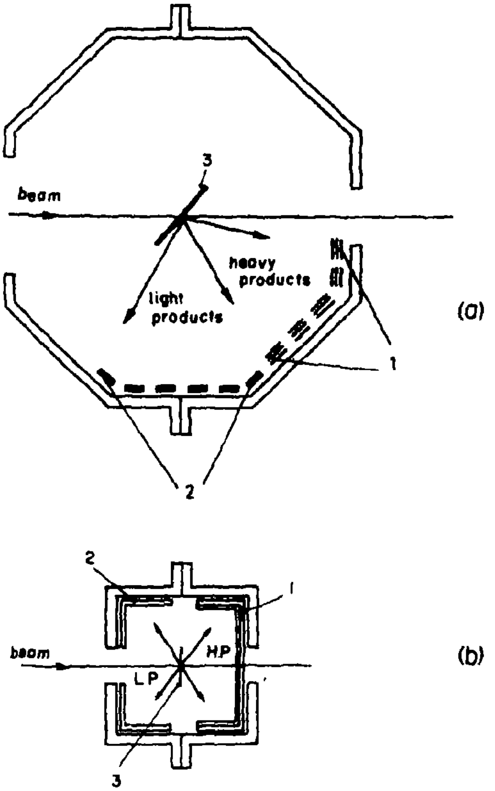

FIG. 2. Systems used for simultaneous collection of the light and heavy products. (a) For angular distribution measurements. (b) For cross section measurements. Both systems have cylindrical symmetry around the beam axis: (1) Al stacks of catcher foils for heavy products (HP). (2) Au thick catcher foils for light products (LP). (3) Target.

TABLE I. Decay characteristics of the light products of Ar induced transfer reactions (from Ref. 18).

Isotope	*Half-life*	Decay mode	E_γ (keV)	Branching ratio
^{38}S	2.83 h	β^-	1942	0.84 ±0.02
^{39}Cl	56.2 min	β^-	250	0.47 ±0.02
			1267	0.543 ±0.013
			1517	0.385 ±0.012
Ar	1.83 h	β^-	1293	0.9922 ± 0.0002
K	22.2 h	β^-	373	0.87 ±0.03

experiments in which the target was placed in the Faraday cup, as in Fig. 1(a).

C. Off-line measurements

The radionuclides were identified by their decay characteristics. These characteristics are given in Ref. 8 for heavy products and in Table I for the light ones. The activity measurements were performed using 2π ionization chambers for α spectrometry and Ge-Li detectors for γ spectrometry. The decay curves were analyzed by the least square fit method to determine the initial activity of each isotope. Details concerning the α-decay curve analysis can be found in Ref. 13.

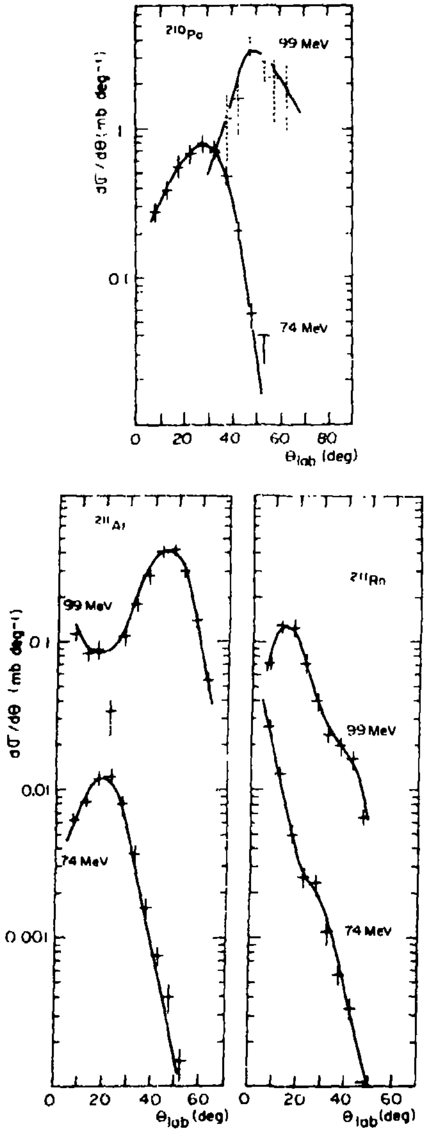

FIG. 3. Angular distributions of ^{210}Po, ^{211}At, and ^{211}Rn produced through $^{14}N+^{209}Bi$ reactions at 74 and 99 MeV. The lines are drawn to guide the eye through the experimental points.

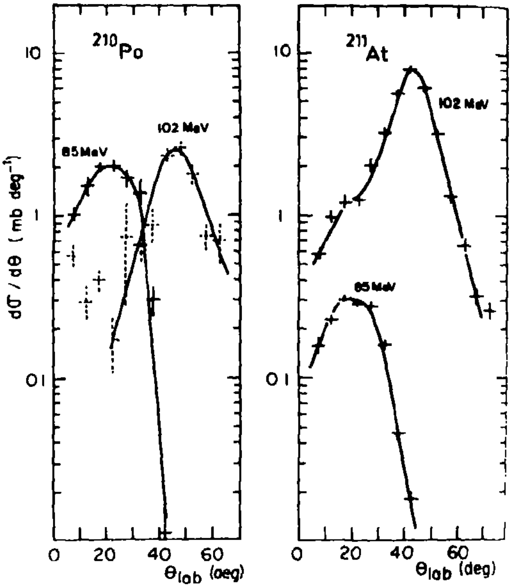

FIG. 4. Angular distributions of ^{210}Po and ^{211}At produced through $^{16}O+^{209}Bi$ reactions at 85 and 102 MeV. The lines are drawn to guide the eye through the experimental points.

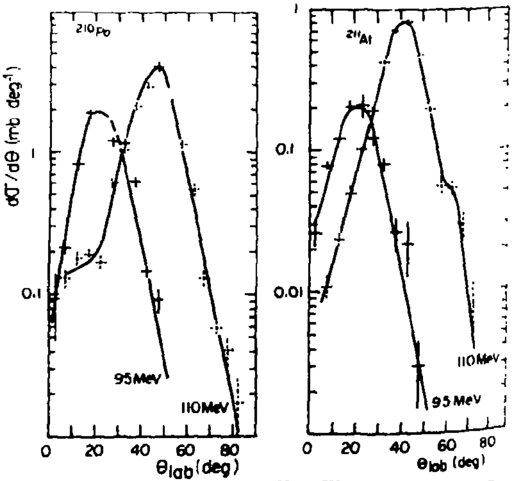

FIG. 5. Same as Fig. 4 for $^{19}F+^{209}Bi$ reactions at 95 and 110 MeV.

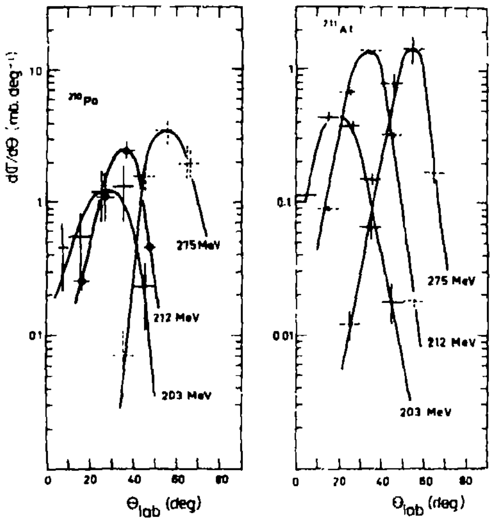

FIG. 6. Same as Fig. 4 for ^{40}Ar + ^{209}Bi reactions at 203, 212, and 275 MeV.

III. EXPERIMENTAL RESULTS

A. Angular distributions and ranges of heavy products in the laboratory system

The angular distributions obtained in the laboratory system for the nuclides ^{210}Po, ^{211}At, and ^{211}Rn produced through ^{14}N to ^{40}Ca induced reactions in ^{209}Bi are given in Figs. 3–7. Those obtained for the reactions $^{16}O + ^{197}Au \to ^{198}Tl, ^{200}Tl, ^{204}Bi$ at the incident energy $E_{lab} = 112$ MeV are given in Fig. 8. Finally, the angular distribution corresponding to the reaction $^{40}Ar + ^{nat}Tl \to ^{211}At$ at 242 MeV is given in Fig. 9.

Two remarks concerning these angular distributions can be made.

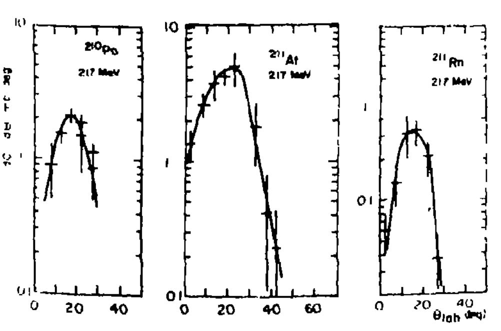

FIG. 7. Angular distributions of ^{210}Po, ^{211}At, and ^{211}Rn produced through ^{40}Ca + ^{209}Bi at 217 MeV. The lines are drawn to guide the eye through the experimental points.

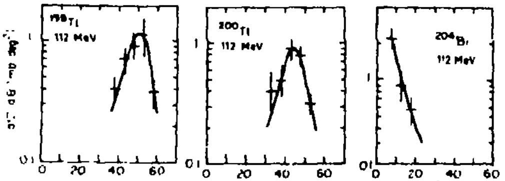

FIG. 8. Angular distributions of ^{198}Tl, ^{200}Tl, and ^{204}Bi produced through ^{16}O + ^{197}Au reactions at 112 MeV. The lines are drawn to guide the eye through the experimental points.

First it should be noted that all of them exhibit a pronounced side peaking, except for the reactions

$$^{14}N + ^{209}Bi \to ^{211}Rn \text{ at } 74 \text{ MeV}, \tag{2}$$

and

$$^{16}O + ^{197}Au \to ^{204}Bi \text{ at } 112 \text{ MeV} \tag{3}$$

for which a forward peaking is observed. Such a forward peaking is typical of a compound nucleus process.[6,17]

Therefore, from these angular distributions and the known parent-daughter relationships,[18] one can assign the productions of ^{211}Rn and ^{204}Bi to the following reactions:

$$^{14}N + ^{209}Bi \to 4n + ^{219}Th \xrightarrow{\alpha \text{ decay}} ^{215}Ra \xrightarrow{\alpha \text{ decay}} ^{211}Rn, \tag{2'}$$

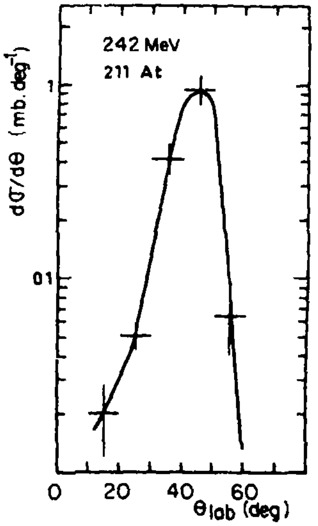

FIG. 9. Angular distribution of ^{211}At produced through the reaction $^{40}Ar + ^{nat}Tl \to ^{211}At$ at $E_{lab} = 242$ MeV. The line is drawn to guide the eye.

$$^{16}O + {}^{197}Au \rightarrow 5n + {}^{208}Fr \xrightarrow{\alpha\ decay} {}^{204}At \xrightarrow{E.C.} {}^{204}Po \xrightarrow{E.C.} {}^{204}Bi \qquad (3')$$

(the symbol E.C. denotes electron capture decay).

The intermediate nuclei were not observed because of their short half-lives (^{215}Ra, ^{204}At) or small α branching ratio (^{204}Po).

This assignment is confirmed by the range measurements, and by the excitation energies calculated for the compound nuclei ^{223}Th ($E^* = 35$ MeV) and ^{213}Fr ($E^* = 71$ MeV) at the energies considered. Note that the excitation energy of 71 MeV is also consistent with the hypothesis of (α, 5n) evaporation. This would lead to the direct production of ^{204}At, which is not excluded by the angular distribution.

The second remark concerns the angle θ_{max} which corresponds to the maximum of the angular distributions. For a given projectile, this angle seems to depend mainly on the incident energy and to be independent of the transfer reaction. In order to compare the data corresponding to different projectiles, the value θ_{max} has been plotted versus the ratio E/B of the incident energy to the strong interaction barrier (calculated according to Ref. 19).

This plot, in which the results from Ref. 6 have been included, is shown in Fig. 10. The data have been divided into two groups according to the value of the ratio a/A_p of the transferred mass to the projectile mass. (The transferred mass a is known from the analysis described in Sec. IV.) For the data corresponding to a/A_p <0.2, shown in Fig. 10(a), a strong correlation is observed between the value of θ_{max} and the ratio E/B. It will be shown in Sec. IV that this correlation may be related to the rainbow effect; the dotted line in Fig. 10(a) represents the variation of the rainbow angle, calculated for elastic scattering (See Sec. IV). This curve is independent of the system projectile target. From a phenomenological point of view, the correlation shown in Fig. 10(a) can be used to predict the position of the angular distribution maximum, in the laboratory system, for the heavy products of transfer reactions. Such predictions can be useful, either for isotope production purposes or for the identification of a reaction mechanism.

When the ratio a/A_p is larger than 0.2, the above mentioned correlation if no longer observed, as can be seen in Fig. 10(b). Moreover, the deviation from the position predicted by the systematics increases with the ratio a/A_p; this ratio is indicated for most of the points in Fig. 10(b). This property was used in Ref. 10 to distinguish between two-charge and four-charge transfers induced by ^{12}C in ^{209}Bi, both of these transfers leading finally to ^{211}At. This distinction was made by a comparison with the angular distributions relative to the same reactions for a gold target, which produced Tl and Bi isotopes, respectively. For both targets, the values of θ_{max} associated with two-charge transfers ($a/A_p = 0.25$–0.3) were about 35°, while those associated with four-charge transfers ($a/A_p = 0.67$) were found near 17.5°.

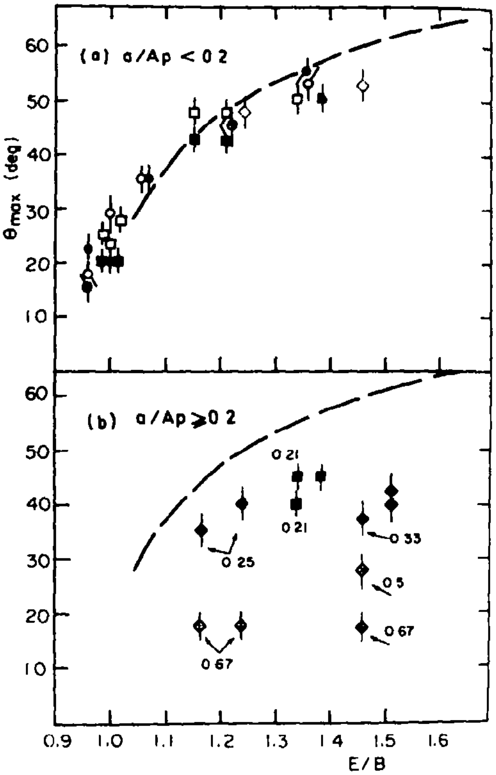

FIG. 10. Variation of the position of the angular distribution maximum θ_{max} (laboratory system) versus the ratio E/B. The shape of the symbols, which represent the experimental data, depend on the projectile: diamonds for ^{12}C, squares for ^{14}N, ^{16}O, ^{19}F, and circles for ^{40}Ar and ^{40}Ca. Open symbols represent single-proton transfer, black symbols two-charge transfer, and the symbols X and + inside circles, squares, or diamonds represent, respectively, three- and four-charge transfers. The dotted line represents the variation of the rainbow angle, calculated for elastic scattering. (a) For $a/A_p < 0.2$ a strong correlation between θ_{max} and E/B is observed, and the angle θ_{max} is close to the rainbow angle. (b) For $a/A_p \geq 0.2$, the deviation from the rainbow angle increases with increasing a/A_p. (The values of this ratio, when known, are indicated close to each point.)

Note that the angular distribution measured for the reaction $^{40}Ar + {}^{203}Tl \rightarrow {}^{211}At$, which corresponds

TABLE II. Experimental values for the range R_0 and range straggling ρ measured at given angles in the laboratory system for ^{210}Po recoil nuclei in Al. The uncertainties in ρ values are of about ±15%. The recoil energy E_0 and energy straggling ρ_E are derived from R_0 and ρ as indicated in text.

Incident ion	Energy E_{lab} (MeV)	Angle θ_{lab} (deg)	Range R_0 (mg/cm^2)	R straggling ρ	Recoil energy E_0 (MeV)	E straggling ρ_E
^{14}N	74	5	0.79 ± 0.04	0.17	13.3 ± 1.2	<0.05
		15	0.83 ± 0.04	0.16	14.2 ± 1.2	<0.05
		25	0.77 ± 0.04	0.13	12.8 ± 1.1	<0.05
		35	0.67 ± 0.03	0.12	10.8 ± 1	<0.05
		45	0.57 ± 0.03	0.18	9 ± 0.8	<0.05
	99	17.5	0.43 ± 0.04	0.24	6.7 ± 0.6	<0.05
		35	0.41 ± 0.04	0.30	6.5 ± 0.6	0.17
		45	0.35 ± 0.04	0.33	5.5 ± 0.5	0.22
^{16}O	83	5	1.05 ± 0.05	0.09	19 ± 2	<0.05
		15	1.03 ± 0.05	0.11	18.5 ± 2	0.06
		25	0.96 ± 0.05	0.09	17 ± 1.7	<0.05
		35	0.83 ± 0.05	0.19	14 ± 1.6	0.19
	102	17.5	0.46 ± 0.05		7.2 ± 0.7	
		25	0.64 ± 0.06	0.29	10.3 ± 0.9	0.14
		35	0.67 ± 0.06	0.29	11 ± 1	0.14
		45	0.55 ± 0.06	0.22	8.7 ± 0.9	<0.05
		55	0.44 ± 0.04	0.4	7 ± 0.6	0.3

to a four-charge transfer, exhibits a maximum at 45°, in good agreement with the systematics of Fig. 10(a). This indicates that the relevant parameter for this classification is the ratio a/A_p (or the corresponding charge ratio z/Z_p), and not the absolute number of transferred nucleons (charges); here $a/A_p = 0.15-0.20$.

The data concerning the range values at each angle θ_{lab} are summarized in Tables II and III. In these tables, the values measured for the mean range R_0 and the range straggling parameter ρ [defined in Ref. 14 by Eq. (1)] are given for each projectile, energy, and laboratory angle. The mean recoil energy E_0, also given in Tables II and III, is deduced from R_0 using a range energy relationship, the low-energy part of which is represented in Fig. 11 by the solid line. This curve has been obtained from the experimental data[16,20-22] available at low energies, and the calculated values of Northcliffe and Schilling[23] at high energy.

In the last column of Tables II and III, the energy straggling parameter ρ_E is given. This parameter is deduced from ρ, as in Refs. 6 and 16, by subtracting from the range straggling the contributions of the straggling due to the slowing down process itself to the neutron evaporation and to the target thickness.

These data (angular distribution, recoil energy, and energy straggling) will be used to get the angular and energy distributions in the c.m. system, and to discuss the reaction paths leading to the observed nuclei (see Sec. IV).

B. Projected ranges

The ranges projected on the beam axis and range straggling values measured for the reactions induced by ^{19}F, ^{40}Ar, ^{40}Ca, ^{56}Fe, and ^{63}Cu are given in Tables IV-IX. Some of the data relative to ^{40}Ar projectiles had been already published,[13] but since that time small corrections were applied to the incident energies and to the projected range values, as indicated in Sec. II.

It can be seen from these tables that no significant difference is observed between the ranges and range stragglings corresponding to different reactions for a given projectile and energy. The variation of the projected range $R_{\parallel}$ of ^{211}At versus incident energy is shown in Fig. 12 for ^{40}Ca projectiles, as the most significant example.

The projected range increases slightly at low energy, then decreases sharply at high energy. The excitation function from Ref. 8 is shown on the same graph. It can be seen that the projected ranges begin to decrease when the cross sections reach the value corresponding to the plateau. This happens for an incident energy (E_0) 15 MeV

TABLE III. Same as Table II, but for ^{211}At recoil nuclei.

Incident ion	Energy E_{lab} (MeV)	Angle θ_{lab} (deg)	Range R_0 (mg/cm^2)	R straggling ρ	Recoil energy E_0 (MeV)	E straggling ρ_E
^{14}N	74	5	0.78 ± 0.04	0.12	13 ± 1.3	<0.05
		15	0.78 ± 0.04	0.14	13 ± 1.3	<0.05
		25	0.71 ± 0.04	0.10	12 ± 1.2	<0.05
	99	17.5	0.34 ± 0.02	0.31	5.2 ± 0.5	0.24
		25	0.29 ± 0.02	0.32	4.3 ± 0.4	0.24
		35	0.32 ± 0.02	0.41	5.0 ± 0.5	0.37
		45	0.29 ± 0.02	0.46	4.3 ± 0.4	0.40
^{16}O	83	5	1.06 ± 0.06	0.07	19.5 ± 2	0.06
		15	1.05 ± 0.06	0.10	19.4 ± 2	0.09
		25	0.93 ± 0.05	0.11	16 ± 1.7	0.07
		35	0.83 ± 0.04	0.17	14 ± 1.4	0.15
	102	7.5	0.35 ± 0.02	0.33	5.3 ± 0.5	0.22
		17.5	0.41 ± 0.03	0.60	7.2 ± 0.7	0.57
		25	0.64 ± 0.04	0.42	10 ± 1	0.37
		35	0.57 ± 0.04	0.30	9.4 ± 0.9	0.22
		45	0.49 ± 0.03	0.28	7.7 ± 0.8	0.16
		55	0.42 ± 0.03	0.30	6.7 ± 0.7	0.21
^{19}F	95	2.5	1.43 ± 0.1	0.34	30 ± 3	0.09
		7.5	1.25 ± 0.09	0.15	25 ± 3	<0.05
		12.5	1.26 ± 0.09	0.22	25 ± 3	<0.05
		17.5	1.20 ± 0.09		23.5 ± 2.5	
		27.5	1.17 ± 0.09	0.29	22.5 ± 3	<0.05
		37.5	0.84 ± 0.08	0.17	15 ± 2	<0.05
		42.5	0.93 ± 0.08		17 ± 2	
	110	22.5	0.78 ± 0.12	0.30	14 ± 3	0.17
		27.5	0.89 ± 0.13	0.14	16 ± 3	<0.05
		32.5	0.76 ± 0.12	0.15	13 ± 2.6	<0.05
		37.5	0.76 ± 0.12	0.18	13 ± 2.6	<0.05
		42.5	0.71 ± 0.10	0.11	12.5 ± 2.5	<0.05
		47.5	0.58 ± 0.08	0.16	10 ± 2	<0.05
		52.5	0.56 ± 0.08	0.21	9 ± 1.8	<0.05
^{40}Ar	203	7.5	3.4 ± 0.3	0.14	110 ± 14	<0.05
		15	3.1 ± 0.3	0.10	95 ± 12	<0.05
		25	2.9 ± 0.3	0.08	86 ± 11	<0.05
		35	2.7 ± 0.3	0.11	75 ± 10	<0.05
		45	2.1 ± 0.2	0.15	53 ± 7	<0.05
	212	5	3.1 ± 0.3	0.10	95 ± 12	<0.05
		15	2.9 ± 0.3	0.16	86 ± 10	<0.05
		25	2.8 ± 0.3	0.14	80 ± 9	<0.05
		35	2.6 ± 0.3	0.16	70 ± 14	<0.05
		45	2.5 ± 0.3	0.27	65 ± 13	0.1
	275	45	1.53 ± 0.08	0.25	32 ± 4	0.23
		55	1.55 ± 0.10	0.21	33 ± 4	0.18
		65	1.59 ± 0.12	0.24	34 ± 4	0.22
^{40}Ca	217	2.5	3.4 ± 0.3	0.11	110 ± 10	<0.05
		7.5	3.1 ± 0.3	0.15	95 ± 10	<0.05
		12.5	2.95 ± 0.3	0.13	88 ± 9	<0.05
		17.5	2.9 ± 0.3	0.15	86 ± 10	<0.05
		22.5	2.95 ± 0.3	0.17	88 ± 10	<0.05

TABLE III. (*Continued.*)

Incident ion	Energy E_{lab} (MeV)	Angle ϑ_{lab} (deg)	Range R_0 (mg/cm^2)	R straggling ρ	Recoil energy E_0 (MeV)	E straggling ρ_E
		27.5	2.7 ±0.3	0.13	75 ± 8	<0.05
		35	2.6 ±0.7	0.30	70 ±20	0.17
		45	2.5 ±0.8	0.36	65 ±25	0.26

lower than the strong interaction barrier B, calculated according to Ref. 9, for the ^{40}Ca + ^{209}Bi reaction. One should note, however, that this energy E_0 is approximately equal to the barrier B_v which corresponds to the systematics of Vaz and Alexander[24] (i.e., a Coulomb barrier calculated with a radius parameter r_0 equal to 1.43 fm for the system considered). This seems to indicate that the use of this systematics leads to a better estimation of the strong interaction barrier than the calculation of Ref. 19 based on the energy density formalism. The decreasing behavior of projected ranges when plotted against incident energy has been observed several times[6,7,13,20,22,25,26] and is considered as typical of transfer reactions. It differs strongly from the variation expected under the assumption of a compound nucleus process (curve labeled C.N. in Fig. 12), but the increasing part of the curve $R = f(E_{lab})$ at low energy had never been observed before. This observation was possible here because of the high cross sections observed near the barrier for this reaction. Such high cross sections can be explained by a favorable energy balance for the reaction ^{40}Ca + ^{209}Bi → ^{211}At (see Refs. 8 and 9).

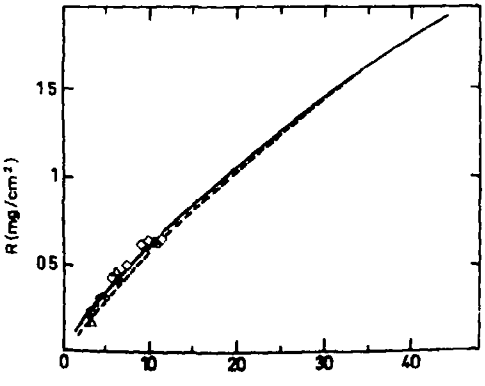

FIG. 11. Range energy relationship for ^{211}At nuclei in Al. The experimental values are represented by the following symbols: triangles (Ref. 20), squares (Ref. 21), open circles (Ref. 22), and black circles (Ref. 16). The dotted line represents the calculated values from Ref. 23, and the solid line the relationship adopted here.

The variation of the projected ranges versus E_{lab} are shown in Fig. 13 for the ions ^{19}F, ^{40}Ar, ^{56}Fe, and ^{63}Cu. These curves are similar to that observed for the ^{40}Ca induced reaction which is presented again in Fig. 13 for comparison, but the low-energy increase is less clear. Only a constant value of $R_\parallel$ is observed at low energy for projectiles other than ^{40}Ca. This behavior of the projected ranges versus incident energy will be discussed in Sec. V.

C. Light and heavy transfer products from Ar induced reactions

Angular distributions. The laboratory distributions of ^{38}S, ^{39}Cl, ^{41}Ar, and ^{43}K produced in the reaction ^{40}Ar + ^{209}Bi at 212 MeV are given in Fig. 14, together with that of ^{41}Ar obtained at 203 MeV. The heavy product distributions at the same energies have been given in Sec. III A. For E_{lab} = 212 MeV, one can observe in Fig. 14 that the position of the angular distribution maximum is approximately the same for the four reactions considered (θ_{max} = 88 ± 5°). This property was already outlined for the heavy products. The complementary aspect of the distributions relative to ^{38}S and ^{39}Cl

TABLE IV. Experimental projected ranges $R_\parallel$ and range straggling ρ for ^{210}Po, and ^{211}At produced through ^{19}F + ^{209}Bi reactions. The uncertainties in ρ values are of about ±15%.

^{19}F E_{lab} (MeV)	^{210}Po $R_\parallel$ (mg/cm^2 Al)	^{210}Po ρ	^{211}At $R_\parallel$ (mg/cm^2 Al)	^{211}At ρ
109 ±0.3	0.47 ±0.02	0.58	0.48 ±0.02	0.60
104.5 ±0.3	0.70 ±0.03	0.44	0.73 ±0.03	0.42
99 ±0.3	0.70 ±0.02	0.42	0.74 ±0.03	0.39
94 ±0.3	0.91 ±0.04	0.36	0.93 ±0.04	0.28
91.5 ±0.3	0.92 ±0.04	0.32	0.94 ±0.04	0.25
89 ±0.3	0.97 ±0.04	0.28	0.95 ±0.04	0.36
87 ±0.3	1.02 ±0.04	0.26	0.98 ±0.04	0.21
84 ±0.3	0.94 ±0.04	0.25	0.94 ±0.04	0.27
79 ±0.3			1.02 ±0.04	

TABLE V. Experimental projected ranges $R_{\parallel}$ and range straggling ρ for ^{210}Po, ^{211}At, and ^{211}Rn produced through ^{40}Ar + ^{209}Bi reactions. The uncertainties in ρ values are of about ±15%.

^{40}Ar	^{210}Po		^{211}At		^{211}Rn	
E_{lab} (MeV)	$R_{\parallel}$ (mg/cm^2 Al)	ρ	$R_{\parallel}$ (mg/cm^2 Al)	ρ	$R_{\parallel}$ (mg/cm^2 Al)	ρ
294 ± 6			0.69 ± 0.04	0.49		
286 ± 7	0.71 ± 0.04	0.49	0.71 ± 0.04	0.49	0.69 ± 0.04	0.55
280 ± 8			0.79 ± 0.04	0.45		
272 ± 9	0.84 ± 0.04	0.42	0.83 ± 0.04	0.43	0.80 ± 0.04	0.53
265 ± 10			0.91 ± 0.04			
260 ± 7[a]			0.89 ± 0.10	0.44	0.76 ± 0.10	0.45
249 ± 12			1.09 ± 0.06	0.37		
241 ± 9[a]			1.07 ± 0.10	0.44	1.09 ± 0.10	0.53
236 ± 13	1.48 ± 0.07	0.26	1.30 ± 0.07	0.34	1.27 ± 0.07	0.44
233 ± 5[a]			1.32 ± 0.10	0.32		
226 ± 11[a]			1.63 ± 0.15	0.26		
223 ± 15			1.79 ± 0.09	0.23		
221 ± 7[a]			1.50 ± 0.15	0.26	1.3 ± 0.2	0.24
217 ± 16	2.0 ± 0.1	0.23	1.9 ± 0.10	0.21	2.0 ± 0.1	0.31
215 ± 4			1.95 ± 0.10	0.31		
209 ± 17			2.3 ± 0.10	0.22		
207 ± 5			2.26 ± 0.11			
206 ± 9[a]			2.15 ± 0.20	0.27		
203 ± 6			2.6 ± 0.10			
202 ± 4			2.14 ± 0.11	0.23	2.27 ± 0.11	0.21
201 ± 4			2.53 ± 0.12	0.17		
193 ± 5			2.87 ± 0.15	0.13		
192 ± 7			2.60 ± 0.13	0.15		
191 ± 19	2.84 ± 0.15	0.08	2.82 ± 0.15	0.11		
191 ± 7[a]			3.10 ± 0.16			
190 ± 6			2.78 ± 0.14	0.19		
186 ± 8			2.93 ± 0.16			
182 ± 9			2.84 ± 0.14			
181 ± 7			2.94 ± 0.15	0.13		

[a] Data from Ref. 13 after correction (see text).

with those of ^{211}At and ^{210}Po will be discussed in Sec. IV.

Cross sections. The absolute cross sections obtained for the light and heavy reaction products at four energies (obtained with the device of Fig. 2) are given in Table X. The corresponding excitation functions are shown in Fig. 15. It is clear from Table X and Fig. 15 that the complementary products ^{39}Cl and ^{210}Po on one hand and ^{38}S and ^{211}At on the other hand are produced with the same cross sections in the energy range which has been explored (with a possible exception for ^{38}S and ^{211}At at low energy for which the difference in the cross sections exceeds slightly the calculated uncertainties).

IV. REACTIONS LEADING TO THE OBSERVED NUCLEI

As was already stated in previous papers on the same subject,[6-8] the identification of a final residue is not sufficient to specify unambiguously the nuclear reaction involved in its production. This is due to two factors: (i) the possible production of the observed nucleus from a radioactive parent, and (ii) the existence of many reaction channels leading to a given final product. For example, for ^{211}At production, one may consider the direct transfer of two protons from projectile to target followed by gamma deexcitation, a process denoted $(+2p, \gamma)$, the transfer of two protons and one neutron followed by one-neutron evaporation, a process denoted $(+2p+n, n)$, or more complex reaction paths.

In this section, an attempt will be made to specify more completely the reaction paths leading to the observed nuclei. Firstly, the question of the parent-daughter relationship will be studied. Secondly, the possible reaction paths will be tested by a kinematic analysis based on the angular and energetic distributions of heavy products. Finally, for Ar induced reactions, this study will be completed by using the results of the light product measurements.

TABLE VI. Same as Table V for ^{40}Ca + ^{209}Bi reactions.

^{40}Ca	^{210}Po		^{211}At		^{211}Rn	
E_{lab} (MeV)	$R_{\parallel}$ (mg/cm^2 Al)	ρ	$R_{\parallel}$ (mg/cm^2 Al)	ρ	$R_{\parallel}$ (mg/cm^2 Al)	ρ
275 ± 5	1.30 ± 0.06	0.31	1.17 ± 0.06	0.35	1.14 ± 0.06	0.38
249 ± 5	1.90 ± 0.09	0.22	1.66 ± 0.08	0.31	1.70 ± 0.08	0.31
226 ± 4	2.35 ± 0.12	0.20	2.17 ± 0.10	0.27	2.12 ± 0.10	0.19
225 ± 4	2.60 ± 0.12	0.19	2.37 ± 0.12	0.24	2.52 ± 0.12	0.17
218 ± 13	2.85 ± 0.14	0.18	2.79 ± 0.14	0.16	2.47 ± 0.13	
214 ± 4			2.94 ± 0.15	0.11	2.87 ± 0.15	0.10
213 ± 4	2.93 ± 0.15	0.15	3.04 ± 0.15	0.11	2.95 ± 0.15	0.15
211 ± 4			2.98 ± 0.15	0.13	2.97 ± 0.15	0.11
205 ± 7	3.05 ± 0.15	0.13	2.94 ± 0.15		2.98 ± 0.15	
204 ± 5			3.12 ± 0.16			
204 ± 5			2.91 ± 0.14			
202 ± 5			3.04 ± 0.15			
202 ± 6			2.94 ± 0.15	0.16		
199 ± 11			3.15 ± 0.16	0.16		
198 ± 6			3.06 ± 0.16	0.15		
197 ± 6			3.00 ± 0.15	0.15		
196 ± 3	3.20 ± 0.16	0.15	3.24 ± 0.16	0.09		
196 ± 3	2.93 ± 0.15	0.09	3.17 ± 0.16	0.10		
195 ± 8	3.00 ± 0.15	0.13	2.73 ± 0.14			
195 ± 6			2.80 ± 0.14			
193 ± 7			2.70 ± 0.14	0.17		
192 ± 7			2.84 ± 0.14	0.16		
187 ± 7	2.70 ± 0.14	0.20	2.69 ± 0.13	0.21		
186 ± 2	3.10 ± 0.16	0.19	2.65 ± 0.14	0.37		
180 ± 9			2.79 ± 0.14	0.21		

A. Decay of radioactive parents

The observed nuclei ^{210}Po and ^{211}At can either be produced directly or can result from the decay of radioactive parents, ^{210}Bi and ^{210}At for ^{210}Po, ^{215}Fr for ^{211}At. [The production of ^{211}At from the decay of ^{211}Rn ($T_{1/2} = 14.6$ h) is known from the decay-curve analysis and already subtracted.] For the incident ions and energies corresponding to the angular distributions measured here, the contributions of such precursors have been calculated, using the cross sections measured in Ref. 8. The

TABLE VII. Same as Table V for ^{56}Fe + ^{209}Bi reactions.

^{56}Fe	^{210}Po		^{211}At		^{211}Rn	
E_{lab} (MeV)	$R_{\parallel}$ (mg/cm^2 Al)	ρ	$R_{\parallel}$ (mg/cm^2 Al)	ρ	$R_{\parallel}$ (mg/cm^2 Al)	ρ
396 ± 8			1.73 ± 0.05	0.29		
371 ± 12			1.22 ± 0.07		1.34 ± 0.07	
328 ± 7	2.73 ± 0.14	0.30	2.80 ± 0.14	0.25	2.79 ± 0.14	0.26
317 ± 9	2.93 ± 0.15	0.20	3.08 ± 0.15	0.20	2.96 ± 0.15	0.22
308 ± 10	3.3 ± 0.2	0.26	3.4 ± 0.2	0.18	3.4 ± 0.2	0.19
304 ± 6	3.5 ± 0.2	0.18	3.5 ± 0.2	0.16	3.5 ± 0.2	0.17
298 ± 6			3.8 ± 0.2	0.17		
291 ± 7	3.9 ± 0.2	0.19	3.9 ± 0.2	0.16	4.0 ± 0.2	0.14
286 ± 8			4.2 ± 0.2	0.17		
284 ± 10	4.2 ± 0.2	0.15	4.1 ± 0.2	0.10		
282 ± 9			4.2 ± 0.2			
280 ± 8			4.1 ± 0.2	0.12		
276 ± 8	4.5 ± 0.2	0.05	4.2 ± 0.2	0.14		
273 ± 10			4.2 ± 0.2			
266 ± 10			4.1 ± 0.2			
266 ± 4			4.0 ± 0.2	0.18		
263 ± 11			4.3 ± 0.2			

TABLE VIII. Same as Table V for $^{63}Cu + ^{209}Bi$ reactions.

^{63}Cu E_{lab} (MeV)	^{210}Po $R_{\parallel}$ (mg/cm^2 Al)	ρ	^{211}At $R_{\parallel}$ (mg/cm^2 Al)	ρ	^{211}Rn $R_{\parallel}$ (mg/cm^2 Al)	ρ
410 ± 9	2.4 ± 0.1	0.25	1.60 ± 0.08	0.30	1.64 ± 0.08	0.29
377 ± 8	2.9 ± 0.1	0.20	3.77 ± 0.07	0.19	3.6 ± 0.2	0.24
355 ± 11	3.7 ± 0.2	0.23	3.8 ± 0.2			
345 ± 7			4.0 ± 0.2	0.17		
338 ± 7			4.2 ± 0.2	0.14	4.3 ± 0.2	0.10
336 ± 8			4.5 ± 0.2	0.12		
328 ± 9			4.5 ± 0.2	0.11		
324 ± 9			4.8 ± 0.2	0.12		
321 ± 16	3.6 ± 0.2	0.28	4.6 ± 0.2	0.11	4.3 ± 0.2	0.13
321 ± 10			4.6 ± 0.2	0.10		
317 ± 10			4.8 ± 0.2	0.09	4.9 ± 0.2	0.09
309 ± 12			4.6 ± 0.2	0.10		
309 ± 2			4.9 ± 0.2	0.15		
305 ± 11			4.8 ± 0.2	0.23		
301 ± 13			4.3 ± 0.2	0.21		
295 ± 3			5.0 ± 0.2	0.12		

ratios $\sigma(^{210}At)/\sigma(210)$, $\sigma(^{210}Bi)/\sigma(210)$, and $\sigma(^{215}Fr)/\sigma(211)$, in which $\sigma(210)$ and $\sigma(211)$ denote the cumulative yields for ^{210}Po and ^{211}At, respectively, are given in Table XI. The value $\sigma(^{215}Fr)$, which is the cross section for the four-charge transfer reaction $^{40}Ar + ^{209}Bi \rightarrow ^{215}Fr$, *has been taken equal to that for the similar reaction* $^{40}Ar + ^{205}Tl \rightarrow ^{211}At$ *measured* in Ref. 8.

It can be seen from Table XI that the contributions of ^{210}Bi and ^{210}At, when measured, are always less than 25% of the observed ^{210}Po production. Therefore, the corresponding reactions have not been considered in the kinematic analysis. Similarly, the four-charge transfers have been neglected in the analysis concerning ^{211}At production through $^{40}Ar + Bi$ reactions, but they have been considered for the lighter projectiles ^{14}N, ^{16}O, ^{19}F.

As far as the light products from Ar induced reactions are concerned, the accumulation of cross sections due to β^- decays can be summarized by the following equations in which $\sigma(X)$ with $X = 43$, 41, 39, 38 denotes the measured cross sections for ^{43}K, ^{41}Ar, ^{39}Cl, and ^{38}S, respectively:

TABLE IX. Experimental projected ranges for ^{211}At produced through $^{40}Ar + Tl$ reactions.

$^{40}Ar + Tl$ E_{lab} (MeV)	^{211}At $R_{\parallel}$ (mg/cm^2 Al)
280 ± 8	0.96 ± 0.07
259 ± 7	1.07 ± 0.07
215 ± 4	2.05 ± 0.12
194 ± 5	2.5 ± 0.1

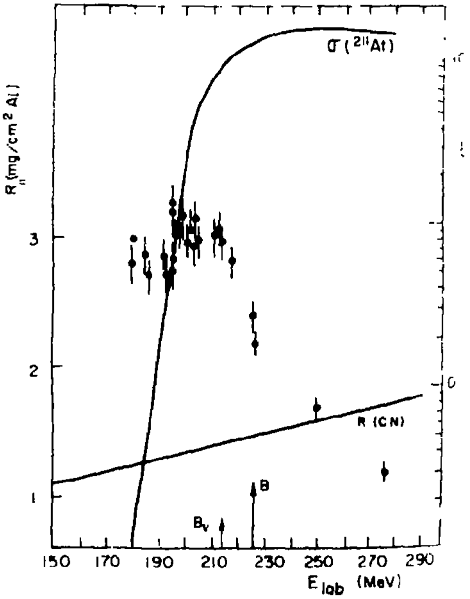

FIG. 12. Variation of the projected range $R_{\parallel}$ versus incident energy for the reaction $^{209}Bi + ^{40}Ca \rightarrow ^{211}At$. The experimental projected ranges are represented by the dots associated with error bars. The projected ranges calculated under the assumption of a compound nucleus process are represented by a curve labeled R (CN). The excitation function for ^{211}At production is represented by the curve labeled $\sigma(^{211}At)$. The arrows labeled B and B_V indicate the interaction barriers calculated according to Ref. 19 and Ref. 24, respectively.

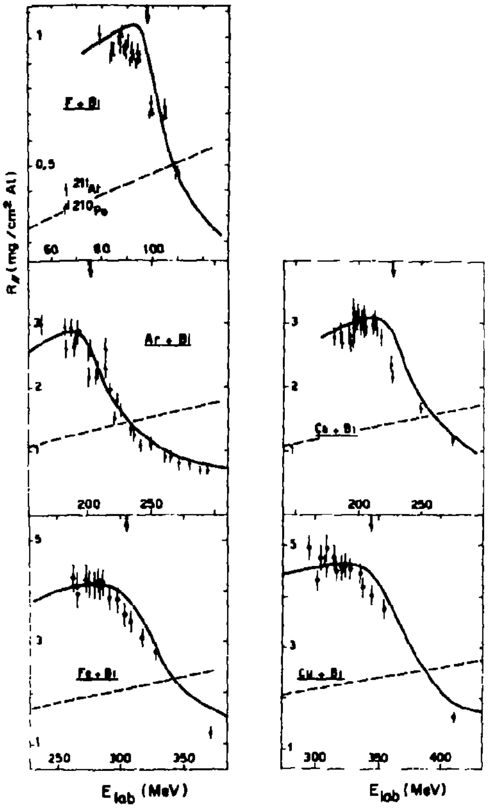

FIG. 13. Variation of the projected range $R_\parallel$ of the heavy products for reactions induced by ^{19}F, ^{40}Ar, ^{40}Ca, ^{56}Fe, and ^{63}Cu in ^{209}Bi. The arrows indicate the calculated strong interaction barriers as in Fig. 12. The solid lines are the ranges calculated for a two-proton transfer (see text). The dotted lines represent the ranges calculated under the assumption of a compound nucleus process.

$$\sigma(43)=\sigma(^{43}\mathrm{K})+\underline{\sigma(^{43}\mathrm{Ar})}+\sigma(^{43}\mathrm{Cl})+\cdots,$$

$$\sigma(41)=\underline{\sigma(^{41}\mathrm{Ar})}+\sigma(^{41}\mathrm{Cl})+\sigma(^{41}\mathrm{S})+\cdots,$$

$$\sigma(39)=\underline{\sigma(^{39}\mathrm{Cl})}+\sigma(^{39}\mathrm{S})+\sigma(^{39}\mathrm{P})+\cdots,$$

$$\sigma(38)=\underline{\sigma(^{38}\mathrm{S})}+\sigma(^{38}\mathrm{P})+\cdots.$$

In these equations, the term $\sigma(^AX)$ denotes the ross section for direct production of the isotope X. For each line, the term which has been nderlined is assumed to represent the main contribution to the observed cross section. This assumption is made because the corresponding reacon involves the transfer of the smallest number of nucleons. Moreover, for $\sigma(43)$ the contribution of ^{43}K, produced by the transfer of one proton and two neutrons towards the projectile has been assumed to be smaller than that of ^{43}Ar produced by a three-neutron transfer. This hypothesis is based on the energetic balance $Q_{gg}-\Delta B$, which is more

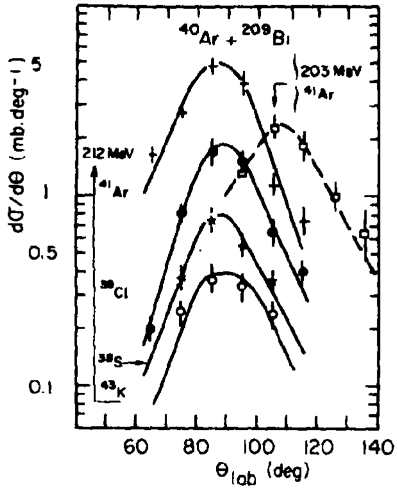

FIG. 14. Experimental angular distributions of light products from the reaction ^{40}Ar + ^{209}Bi. The lines are drawn to guide the eye.

TABLE X. Experimental cross sections for heavy and light products of Ar induced transfer reactions in ^{209}Bi. The complementary products (such as ^{211}At and ^{38}S) are found on the same horizontal line.

Energy	Heavy product		Light product	
E_{lab} (MeV)	Isotope	σ (mb)	Isotope	σ (mb)
212 ± 5	^{211}At	17 ± 3	^{38}S	17 ± 4
	^{210}At	12 ± 3		
	^{209}At	8 ± 2		
	^{210}Po	34 ± 9	^{39}Cl	36 ± 7
			^{41}Ar	106 ± 15
			^{43}K	11 ± 2
203 ± 5	^{211}At	15 ± 2	^{38}S	13 ± 4
	^{210}At	9 ± 3 [a]		
	^{210}Po	28 ± 7	^{39}Cl	27 ± 9
			^{41}Ar	75 ± 13
194 ± 5	^{211}At	7.5 ± 1	^{38}S	11 ± 2
	^{210}At	2 ± 0.5		
	^{209}At	0.9 ± 0.2		
	^{210}Po	23 ± 4	^{39}Cl	22 ± 5
			^{41}Ar	57 ± 8
190 ± 5	^{211}At	1.2 ± 0.15	^{38}S	1.9 ± 0.4
	^{210}At	<0.3 [a]		
	^{210}Po	5.7 ± 1.2	^{39}Cl	6 ± 1
			^{41}Ar	15 ± 2

[a] Estimated value.

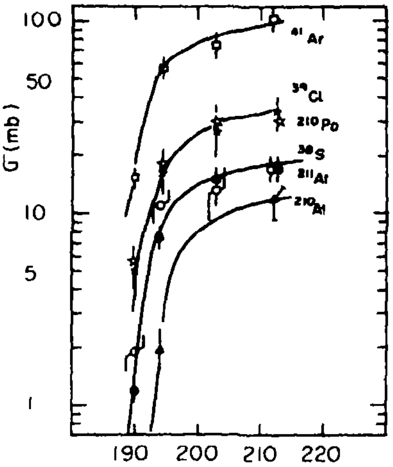

FIG. 15. Excitation functions for light and heavy products from the reaction $^{40}Ar+^{209}Bi$. Open squares: ^{41}Ar; open stars: ^{39}Cl; black stars: ^{210}Po; open circles: ^{38}S; black circles: ^{211}At; black triangles: ^{210}At. The lines are drawn to guide the eye.

TABLE XI. Contribution of the decay of radioactive parents to the production of the observed nuclei ^{210}Po and ^{211}At.

Ion	Energy (MeV)	$\frac{\sigma(^{210}At)}{\sigma(210)}$	$\frac{\sigma(^{210}Bi)}{\sigma(210)}$	$\frac{\sigma(^{215}Fr)}{\sigma(211)}$
^{14}N	74	<0.01	<0.02	
	99	<0.01	0.15	
^{16}O	83	0.01	<0.02	
	102	0.25	<0.03	
^{19}F	96	<0.01		
	110	0.1		
^{40}Ar	203	0.20		~0.1
	212	0.23		~0.1
	275	0.25		~0.1

favorable to this last reaction (for this concept and for the notations, see Ref. 9). With these assumptions, the observation of ^{41}Ar, ^{43}K, ^{39}Cl, and ^{38}S correspond, respectively, to reactions in which one neutron, or three neutrons, or one proton, or two protons are transferred from projectile to target. It can be seen in Fig. 15 that the cross sections do decrease when the number of transferred particles is increased.

B. *Kinematic analysis*

The kinematic analysis has been performed on the basis of the ranges measured at each angle, as explained in Ref. 6, for all the reactions listed in Table XII, except for the reaction $^{19}F+Bi \rightarrow ^{210}Po$. For this reaction such ranges have not been measured accurately enough. Therefore, the analysis was made using the projected ranges, with the assumption that all the nuclei are emitted at the angle θ_{max} (known from the angular distribution). Let us recall that the principle of this analysis is to compare the kinetic energy measured for a given product to the maximal value which can be calculated under the assumption of a given mechanism. Such mechanisms are defined by specifying the nature and number of the particles transferred in the first reaction step and the associated excitation energy E^*. This energy must be such that the correct number of nucleons be evaporated in a second step to produce the observed nucleus. For example, the production of ^{211}At by the process denoted $(+2p, \gamma)$ corresponds to an ex-

TABLE XII. Most probable reaction path leading to the observed heavy products ^{210}Po, ^{211}At, and ^{211}Rn.

			Most probable reaction path		
Ion	Energy (MeV)	E/B	^{210}Po	^{211}At	^{211}Rn
^{14}N	74	1.01	$(+p,\gamma)$	$(+2p,\gamma)$	$(+^{14}N, 4n)^{a}$
	99	1.34	$(+p,\gamma)$, $(+p+n,n)$	$(+2p,\gamma)$, $(+2p+n,n)$ $(+2p+2n,2n)$	$(+^{14}N, \alpha 4n)^{a}$, $(+3p,n)$
^{16}O	83	1.0	$(+p,\gamma)$, $(+p+n,n)$	$(+2p,\gamma)$	
	102	1.21	$(+p,\gamma)$, $(+p+n,n)$	$(+2p,\gamma)$, $(+2p+n,n)$ $(+^{9}Be, 2n)^{c}$, $(+^{12}C, \alpha 2n)^{c}$	
^{19}F	95	0.99	$(+p,\gamma)$, $(+p+n,n)$	$(+2p,\gamma)$	
	110	1.15	$(+p,\gamma)$, $(+p+n,n)$	$(+2p,\gamma)$, $(+2p+n,n)$	
^{40}Ar	203	1.0	$(+p,\gamma)^{d}$	$(+2p,\gamma)^{d}$	
	275	1.36	$(+p,\gamma)$, $(+p+n,n)$	two-charge transfer	
^{40}Ca	217	0.96		two-charge transfer	three-charge tran

[a] Compound nucleus process.

[b] For the shoulder at 40° (see Fig. 3).

[c] For the shoulder at 15–20° (see Fig. 4).

[d] From the measurements of light products (Sec. III C).

citation energy E_0^* less than the neutron binding energy (8 MeV), while the process denoted $(+2p+n, n)$ involves an excitation energy E_1^* of ^{212}At such that 8 MeV$< E_1^* <$15 MeV. This excitation energy E_1^* ensures the evaporation of one neutron. The maximum kinetic energy of the residue is associated to the lowest limit for E^* and corresponds to a cold light reaction product. The processes for which this maximum energy is lower than the measured value can be excluded without ambiguity.

The most probable reaction paths resulting from the analysis are given in Table XII. Several comments can be made relative to these results.

Firstly, except for ^{211}Rn production through ^{14}N induced reactions, which is due to a compound nucleus process at both energies, all the angular distributions correspond to transfer reactions.

Secondly, for 102 MeV ^{16}O ions, the shoulder observed at $\theta = 15°$ in the ^{211}At angular distribution can be explained by a four-charge (or six-charge) transfer. It is interesting to note that such a transfer of two α particles (or a ^{8}Be nucleus) was observed with a much higher probability in ^{12}C induced reactions,[8] while it is not observed for ^{14}N and ^{19}F ions. This can be interpreted as an effect of the projectile structure.

Thirdly, for ^{211}At production with light ions at the barrier energy, the only reaction path which is not excluded is the $(+2p, \gamma)$ process, i.e., the least energy consuming. This is due to the dramatic influence of the energetics on the transfer probability, which has been outlined several times.[8,10,27] When the incident energy is increased, the process $(+2p+n, n)$, which requires more energy, becomes possible. A similar behavior seems to be observed, but less clearly, for one-charge transfer reactions. These conclusions confirm the indications obtained in the early work of Croft *et al.*[35] on the same subject.

Finally, for ^{40}Ar and ^{40}Ca ions, the kinematic analysis is not precise enough to determine the number of neutrons transferred together with one proton (for ^{210}Po) or two protons (for ^{211}At). However, for incident ^{40}Ar ions, the production of these isotopes can be assigned to the processes $(+p, \gamma)$ and $(+2p, \gamma)$, respectively. Such an assignment is made on the basis of the light fragment study (similarity of the shape and amplitude of the excitation functions and complementarity of the angular distributions for the complementary residues ^{39}Cl and ^{210}Po on one hand and ^{38}S and ^{211}At on the other hand). From the above mentioned energetics arguments, one may think that these processes $(+p, \gamma)$ and $(+2p, \gamma)$ are also predominant for ^{210}Po and ^{211}At production, at least at low energy, for the heaviest projectiles ^{40}Ca, ^{56}Fe, and ^{63}Cu.

V. INTERPRETATION

A. Angular and energetic distributions of heavy residues in the c.m. system

From the laboratory angular distributions and the ranges measured at all angles θ_{lab} for the heavy reaction products, it is possible to get the angular and energetic distributions of these products in the c.m. system. This laboratory to c.m. transformation is made using the method described in Ref. 28. Examples of the c.m. distributions are given in Figs. 16–18 for the reactions

$$^{14}\mathrm{N} + {}^{209}\mathrm{Bi} \to {}^{211}\mathrm{At} \text{ at 74 and 99 MeV},$$

and

$$^{40}\mathrm{Ar} + {}^{209}\mathrm{Bi} \to {}^{211}\mathrm{At} \text{ at 212 and 275 MeV}.$$

In Figs. 16–18 are shown the c.m. angular distributions, energy distributions, and the contour plots which represent the variation of the double differential cross section versus angle and energy. Except for those relative to Ar induced reactions at 275 MeV, all the curves exhibit the shape typical of quasi-elastic transfer, with a single peak in the angular and energy distributions, and a limited extension in the $(\bar{\theta}, \bar{E})$ plane. The position of the peak in the angular distribution is always close to the grazing angle, calculated for the heavy product using the relation

$$\bar{\theta}_{gr} = \pi - 2 \arcsin\left[\frac{2r_0(A_p^{1/3} + A_t^{1/3})\ A_t E_p}{Z_p Z_t e^2 (A_t + A_p)} - 1\right]^{-1} \quad (4)$$

with $r_0 = 1.5$ fm for ^{14}N ions, and 1.45 fm for ^{40}Ar ions,[11] and indicated by an arrow in Figs. 16–18. In Eq. (4), A_t and Z_t denote the target mass and charge, and E_p is the laboratory projectile energy.

The distributions relative to ^{40}Ar induced reactions at 275 MeV differ from the previous ones (see the two-dimensional diagram in Fig. 18). In addition to the quasi-elastic peak ($\bar{\theta} = 110°$, $\bar{E} \sim 35$ MeV), they exhibit a tail towards lower energies and larger angles. Such a tail is typical of partially damped events in deeply inelastic reactions.[5,26] Therefore, for such high-energy incident Ar ions, the total production of ^{211}At cannot be assigned any more to quasi-elastic processes. One should particularly note in Fig. 18 that the most probable energy (maximum in the $d\sigma/d\bar{E}$ distribution) is now different from the quasi-elastic energy (maximum in the $d^2\sigma/d\bar{\theta}d\bar{E}$ distribution).

The kinematic analysis used in Sec. IV to identify the reactions leading to the observed isotopes can obviously be made in the c.m. system. The limits of c.m. energy calculated for three types of transfer are indicated in Figs. 16–18. The comparison of these limits with the experimental energy distributions leads us to the same conclu-

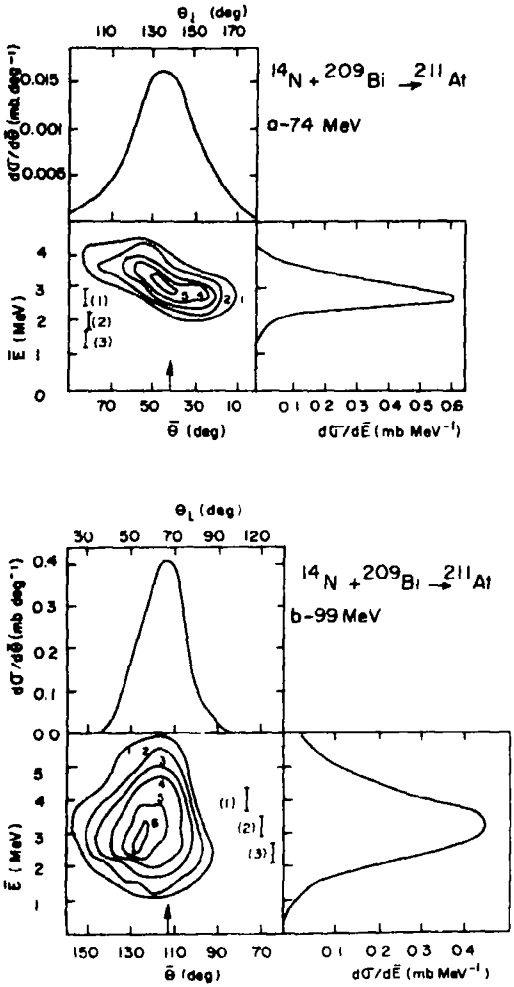

FIG. 16. Angular and energy distributions of ^{211}At produced through $^{14}N + ^{209}Bi$ reactions (a) at $E_{lab} = 74$ MeV and (b) at $E_{lab} = 99$ MeV. The scaling relative to heavy product angles $\bar{\theta}$ has been made from the right to the left in order to make easier the comparison with data concerning light fragments. The upper scale $\bar{\theta}_l = 180° - \bar{\theta}$ is relative to the associated light product. The contour plots represent lines of equal double differential cross section $d^2\sigma/d\bar{\theta}d\bar{E}$ (expressed in arbitrary units by the number written close to each line). The vertical bars labeled (1), (2), (3) represent the calculated energies for the processes $(+2p,\gamma)$, $(+2p+n,n)$, and $(+2p+2n,2n)$, respectively.

sions as in Sec. IV; for $^{14}N + Bi$ at 74 MeV, only the process $(+2p,\gamma)$ is consistent with the measured energy. For the same reaction at 99 MeV, the energy distribution is broader and the three processes considered are possible.

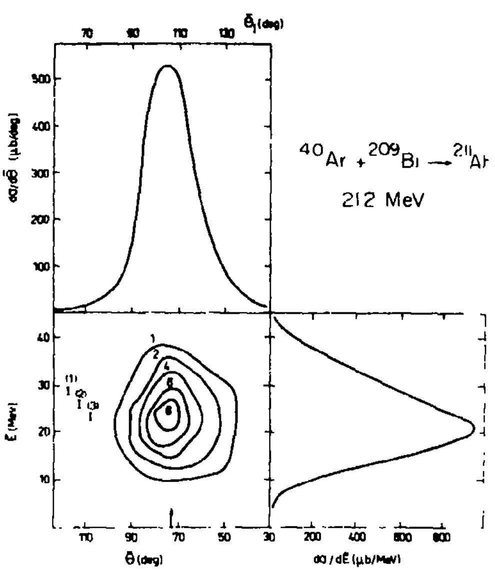

FIG. 17. Same as Fig. 16 for ^{40}Ar induced reactions at $E_{lab} = 212$ MeV.

For 212 MeV Ar projectiles, the experimental precision is not sufficient to distinguish among the three reaction paths considered, all of them being inside the FWHM of the distribution. Finally, for 275 MeV Ar ions, these reaction paths can explain the "quasi-elastic" peak, but not the tail corresponding to partially damped events. To explain

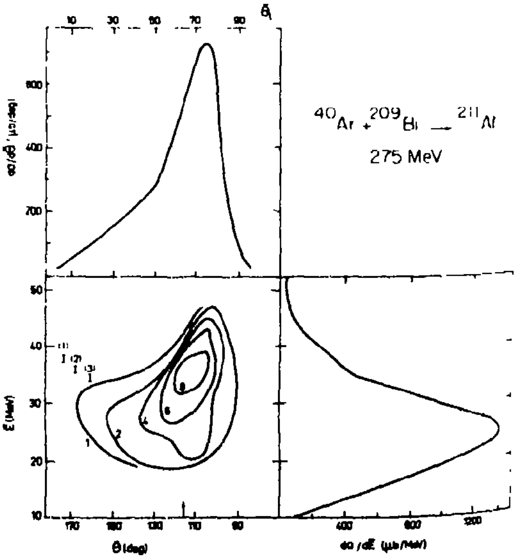

FIG. 18. Same as Fig. 16 for ^{40}Ar induced reactions at $E_{lab} = 275$ MeV.

the low kinetic energies associated with these events, one should invoke reactions in which substantial amounts of excitation energy would be given to both projectile and target, i.e., a large number of particles would be evaporated. However, the low cross section measured for the four-charge transfer reaction $^{40}Ar + ^{205}Tl \rightarrow ^{211}At$ at the same energy seems to indicate that most of the ^{211}At production must be assigned to two-charge transfer (quasi-elastic + deeply inelastic transfer).

Each angular distribution can be defined by the position of its maximum $\bar{\theta}_{max}$ and its full width at half maximum. These parameters, which have been derived from Gaussian fits to the distributions, are given in Table XIII for all the systems studied. The value of $\bar{\theta}_{max}$ depends mainly on the ratio E/B, and this point will be discussed in Sec. V C. The values of $\bar{\theta}_{max}$ and FWHM have been used in Ref. 11 for a quantitative analysis of the data. This analysis was made using a formalism derived from a general treatment of multinucleon transfer,[29] in an approach similar to that of Frahn and Venter[30] for neutron transfer reactions, i.e., in the limits of the distorted wave Born approximation. It led to the determination of the optimal distance of closest approach for the transfer reactions considered. The whole set of data was consistent with an interaction distance $d = 2.7-3$ fm between the half-density radii of the colliding nuclei. This d value is in good agreement with the distances deduced from elastic scattering analysis by Schröder and Huizenga.[31]

B. Correlation between heavy and light fragment distributions for ^{40}Ar induced reactions

For ^{40}Ar induced reactions, at an incident energy of 212 MeV, the laboratory angular distributions of ^{210}Po and ^{211}At exhibit a maximum for $\theta_{max} = 35 \pm 5°$. (See Fig. 6.) If one makes the assumption that these nuclei are produced through the processes $(+p, \gamma)$ and $(+2p, \gamma)$, respectively, the corresponding light fragments are ^{39}Cl and ^{38}S. In order to satisfy the momentum and energy conservation laws, these fragments should be emitted at the "complementary" angles $\theta'_{max}(^{39}Cl) = 96 \pm 10°$ and $\theta'_{max}(^{38}S) = 95 \pm 10°$ in the laboratory system. These calculated angles are in fair agreement with the experimental maxima observed at $88 \pm 5°$ for both distributions (see Fig. 14). Moreover, the kinetic energy calculated for ^{211}At under the same assumption is equal to 68 ± 7 MeV, i.e., very close to the measured value $E_R = 73 \pm 14$ MeV (see Table II). These numbers, together with the similarities observed between the excitation functions relative to complementary products (see Fig. 15), are a good confirmation of the inferred mechanisms.

TABLE XIII. Parameters $\bar{\theta}_{max}$ and FWHM defining the position and width of the angular distributions in the c.m. system.

Reaction	E_{lab} (MeV)	$\bar{\theta}_{max}$ (deg)	FWHM (deg)
$^{14}N + ^{209}Bi \rightarrow ^{210}Po$	74	56	40
	99	120	22
$^{14}N + ^{209}Bi \rightarrow ^{211}At$	74	48	36
	99	118	32
$^{16}O + ^{209}Bi \rightarrow ^{211}At$	83	46	40
	102	105	22
$^{19}F + ^{209}Bi \rightarrow ^{211}At$	95	44	36
	110	96	20
$^{40}Ar + ^{209}Bi \rightarrow ^{211}At$	203	50	32
	212	76	17
	275	120	14
$^{40}Ca + ^{209}Bi \rightarrow ^{211}At$	217	46	32

C. Influence of the ratio E/B on the angular distributions and correlation with the rainbow angle

As was already outlined in Sec. III, for the data in the laboratory system, the angular distributions seem to be strongly influenced by the ratio E/B of the incident energy over the interaction barrier. This is particularly clear in Fig. 19, where the angle $\bar{\theta}_{max}$ relative to two-charge transfers has been plotted versus E/B, for all the systems studied. A strong correlation is observed between $\bar{\theta}_{max}$ and E/B for all projectiles. This property is similar to that mentioned by da Silveira[32] concerning the rainbow angle $\bar{\theta}_r$ in elastic scattering. Therefore, it is interesting to compare the variation of $\bar{\theta}_{max}$ and $\bar{\theta}_r$ versus E/B. Such a comparison is shown in Fig. 19. The solid line represents the variation $\bar{\theta}_r = f(E/B)$ calculated in Ref. 32 using a Woods-Saxon nuclear potential. In order to verify that the shape of this potential does not influence the value of $\bar{\theta}_r$, provided that the height of the interaction barrier is respected, we have calculated some values of $\bar{\theta}_r$ using a nuclear potential derived from the energy density formalism.[19] These values are represented by triangles in Fig. 19, and one can see that they agree perfectly with the solid curve.

A striking similarity is observed between the curves $\bar{\theta}_{max} = f(E/B)$ and $\bar{\theta}_r = f(E/B)$, the former being slightly shifted towards low values of E/B relative to the latter. If one remembers that the calculated curve was in good agreement with the observed maxima for angular distributions relative to neutron transfer,[20] the shift observed here (which corresponds to a preferential emission of the light product at smaller angles) can be attributed to an effect of the charge transfer, which decreases the projectile charge by two units, i.e.,

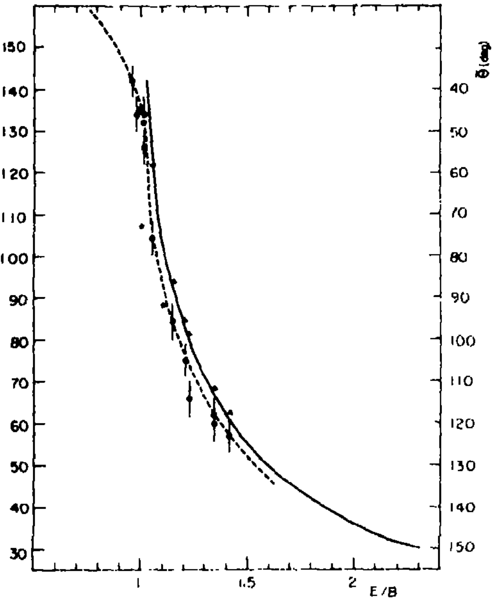

FIG. 19. Variation of $\bar{\theta}_{\max}$ and of the rainbow angle $\bar{\theta}_r$ versus the ratio E/B. The angle $\bar{\theta}_r$ is calculated with (i) a Woods-Saxon potential (Ref. 32): solid line; (ii) a potential derived from the energy density formalism (Ref. 19): triangles. The points associated with error bars represent the experimental values of $\bar{\theta}_{\max}$ relative to two-proton transfer for all projectiles but ^{40}Ca. The stars represent the same data for ^{40}Ca projectiles. The dotted line has been drawn through the experimental points and arbitrarily extrapolated at low energy.

reduces its deviation by the Coulomb field. (Note that this shift would be somewhat reduced by using strong interaction barriers from Ref. 24.) The vicinity of the two curves may thus be interpreted as an indication that the transfer reactions take place for distances of closest approach close to those corresponding to the rainbow effect. This is confirmed by the quantitative analysis made in Ref. 11, and this result is in good agreement with the conclusions of Ref. 33. Moreover, the data shown in Fig. 19 may be used to predict the position of the angular distribution maximum, in the c.m. system for one- and two-proton transfer reactions.

Let us note, finally, that the laboratory rainbow angle θ_r relative to the heavy partner of the collision can easily be calculated from the c.m. value $\bar{\theta}_r$ using the well known relation

$$\theta_r = \bar{\theta}_r/2 \tag{5}$$

This relation is valid for elastic scattering and for the nucleus initially at rest in the laboratory frame. The curve $\theta_r = f(E/B)$ obtained from this transformation is shown in Fig. 10, and gives an explanation for the correlation observed in Sec. III between $\theta_{\max}$ and E/B, for $a/A_p < 0.2$. This correlation is the result of the nearly equal values of $\bar{\theta}_{\max}$ and $\bar{\theta}_r$, associated to the quasi-elastic nature of the collision, which makes it possible to use the relation $\theta_{\max} \simeq \bar{\theta}_{\max}/2$, when the ratio a/A_p is sufficiently low. When this ratio increases, even if $\bar{\theta}_{\max}$ does not deviate strongly from θ_r, the c.m. to laboratory transformation does not correspond any more to Eq. (5), and this explains the deviations observed between $\theta_{\max}$ and θ_r for $a/A_p \geqslant 0.2$ [see Fig. 10(b)].

D. Variation of projected ranges with incident energy

The general behavior observed in Figs. 12 and 13 for the variation of projected ranges with incident energy, can be explained in the following way:

At low incident energies, the distance of closest approach of the nuclei is limited by Coulomb repulsion, and only the head-on collisions can lead to transfer reactions. This implies that the projectile residue be emitted backwards, and the target residue at small angle (in the laboratory system), with a velocity well above that which corresponds to total momentum transfer. When the incident energy is increased, but remains lower than the strong interaction barrier, the nuclei come into closer contact and the transfer probability is increased. However, the emission angle of the heavy fragment remains small, and its velocity increases (effect of the momentum conservation), so that the projected range increases. Finally, when the incident energy exceeds the strong interaction barrier, the head-on collisions lead to fusion, or deeply inelastic reactions, and the transfer reactions are governed by the well known rule of the constant distance of approach.[34] This implies a decrease of the laboratory kinetic energy of the heavy residue, associated with an increase of its emission angle. Both phenomena lead to the decreasing behavior observed for the projected range at high energy.

The evolution of the projected ranges with increasing incident energies is consistent with the above mentioned variation of $\bar{\theta}_{\max}$ versus E/B. This can be verified in the following way: For a given projectile and energy, the angle $\bar{\theta}_{\max}$ is determined using the dotted line in Fig. 19. This line has been drawn through the experimental points with an arbitrary extrapolation at low energy. (The exact position of the curve for these low energies has little influence on the projected ranges calculated as explained below.) The c.m. energy of products $\bar{E}$ is calculated assuming a $(+p,\gamma)$ or a $(+2p,\gamma)$ process. From $\bar{\theta}_{\max}$ and $\bar{E}$, the laboratory angle $\theta_{\max}$ and energy E can be calculated, and the laboratory energy is converted into recoil range $R(\theta_{max})$ according to the relation represented by the curve in Fig. 11. Then the mean projected range $R_{\parallel}$ is calculated by the relation

$$R_{\parallel} = R(\theta_{max})\cos\theta_{max}\,. \qquad (6)$$

The results of such calculations are represented by solid lines in Fig. 2. These curves are sensitive to the value adopted for the barrier B (indicated by arrows in Fig. 13). For example, for the Ca + Bi system, a change of less than 5% in B would remove the difference between the curve and the experimental points. Taking this remark into account, the agreement with the experiment is surprisingly good. As far as ^{56}Fe and ^{63}Cu projectiles are concerned, this agreement is a good indication that the variation of $\bar{\theta}_{max}$ with E/B (for which no direct measurement has been made) can be taken from Fig. 19, i.e., is the same as for lighter projectiles.

VI. CONCLUSION

Recoil techniques have been used to measure the angular distributions and ranges of ^{210}Po, ^{211}At, d ^{211}Rn produced through heavy ion reactions with Bi. These reactions involved the transfer of e, two, and three protons, respectively. The ojectiles ranged from ^{14}N to ^{63}Cu. The results tained indicate a great unity in the characteris:s of quasi-elastic transfer reactions for all the ojectiles.

At low incident energy, the reaction path which ads to the formation of the observed nucleus is always that which corresponds to the minimal energy cost. This confirms the strong influence of the reaction energetics on the transfer probability, which was previously observed in the study of the excitation function thresholds.[8,10] At higher energies, more complex reaction channels take place with significant probabilities.

The position of the angular distribution maxima, in the laboratory and c.m. frames, are strongly correlated with the ratio E/B of the incident energy to the interaction barrier. The corresponding curves are independent of the projectile and of the nature of the transferred particles if the ratio of the transferred mass a to the projectile mass A_p is low enough $(a/A_p < 0.2)$. This property can be used to predict the position of the angular distribution maximum for other transfer reactions. Moreover, the correlation appears to be very similar to that of the rainbow angle with the ratio E/B. This indicates a strong influence of the rainbow effect on the angular distribution for quasi-elastic transfer, and can be taken as an indication that the distances of closest approach corresponding to maximal transfer probabilities are not far from those corresponding to the rainbow effect. This conclusion is in agreement with the quantitative analysis of these data,[11] and with the study made by Vaz *et al.*[33] on ^{16}O + ^{208}Pb reactions.

We thank the crews of the Orsay heavy ion accelerators (ALICE and MP Tandem) for their cooperation, L. de Reilhac for helping in some of the experiments, and J. M. Alexander for a critical reading of the manuscript.

. Galin, D. Guerreau, M. Lefort, J. Péter, X. Tarrago, and R. Basile, Nucl. Phys. A159, 461 (1970).

. L. C. Ford Jr., K. S. Toth, G. R. Satchler, D. C. lensley, L. W. Owen, R. M. DeVries, R. M. Gaedke, P. J. Riley, and S. T. Thornton, Phys. Rev. C 10, 1429 (1974).

. Olmer, M. Mermaz, M. Buenerd, C. K. Gelbke,). L. Hendrie, J. Mahoney, D. K. Scott, M. M. MacFarlane, and S. C. Pieper, Phys. Rev. C 18, 205 (1978).

I. C. Lemaire, Phys. Rep. 7C, 279 (1973).

.. Fleury and J. M. Alexander, Annu. Rev. Nucl. Sci. 24, 279 (1974).

. Bimbot, D. Gardès, and M. F. Rivet, Nucl. Phys. A189, 193 (1972).

. Bimbot and M. F. Rivet, Phys. Rev. C 8, 375 (1973).

. Gardès, R. Bimbot, J. Maison, L. de Reilhac, M. F. Rivet, A. Fleury, F. Hubert, and Y. Llabador, Phys. Rev. C 18, 1298 (1978).

. Gardès, R. Bimbot, A. Fleury, F. Hubert, and M. F. Rivet, J. Phys. Lett. 36, 59 (1975).

R. Bimbot, D. Gardès, J. Cugnon, and R. da Silveira, Z. Phys. A290, 157 (1979).

[11] Y. Llabador, F. Hubert, A. Fleury, D. Gardès, M. F. Rivet, and R. Bimbot, Z. Phys. A289, 173 (1979).

[12] R. Bimbot, C. Cabot, J. Depauw, D. Gardès, H. Gauvin, L. Martial, A. Richomme, and M. F. Rivet, Report No. IPNO-RC-79-03 (unpublished).

[13] R. Bimbot, D. Gardès, and M. F. Rivet, Phys. Rev. C 4, 2180 (1971).

[14] J. M. Alexander, in *Nuclear Chemistry*, edited by L. Yaffe (Academic, New York, 1968).

[15] R. Bimbot, D. Gardès, R. L. Hahn, Y. de Moras, and M. F. Rivet, Nucl. Phys. A228, 85 (1974); and A248, 377 (1975).

[16] R. Bimbot and D. Gardès, Nucl. Instrum. Methods 109, 333 (1973).

[17] J. M. Alexander and G. N. Simonoff, Phys. Rev. 133, B93 (1964).

[18] C. M. Lederer and V. S. Shirley, *Table of Isotopes*, VIIth edition (Wiley, New York, 1978).

[19] C. Ngô, B. Tamain, J. Galin, M. Beiner, and R. J. Lombard, Nucl. Phys. A240, 353 (1975).

[20] J. M. Alexander and L. Winsberg, Phys. Rev. 121, 529 (1961).

[21] L. Winsberg and J. M. Alexander, Phys. Rev. 121,

518 (1961).

[22] P. M. Strudler, I. L. Preiss, and R. Wolfgang, Phys. Rev. 154, 1126 (1967).

[23] L. C. Northcliffe and R. F. Schilling, Nucl. Data Tables A7, 233 (1970).

[24] L. C. Vaz and J. M. Alexander, Phys. Rev. C 10, 464 (1974).

[25] P. D. Croft, J. M. Alexander, and K. Street, Phys. Rev. 165, 1380 (1968).

[26] F. Hubert, H. Delagrange, and A. Fleury, Nucl. Phys. A228, 415 (1974).

[27] R. M. Diamond, A. M. Poskanzer, F. S. Stephens, W. J. Swiatecki, and D. Ward, Phys. Rev. Lett. 20, 802 (1968).

[28] M. F. Rivet, R. Bimbot, A. Fleury, D. Gardès, and Y. Llabador, Nucl. Phys. A276, 157 (1977).

[29] C. Toepffer, Z. Phys. 253, 78 (1972).

[30] W. E. Frahn and R. H. Venter, Nucl. Phys. 59, 651 (1964).

[31] W. V. Schröder and J. R. Huizenga, Annu. Rev. Nucl. Sci. 27, 465 (1977).

[32] R. da Silveira, Phys. Lett. 50B, 237 (1974).

[33] L. C. Vaz, J. M. Alexander, and E. M. Auerbach, Phys. Rev. C 18, 820 (1978).

[34] J. A. McIntyre, T. L. Watts, and F. C. Jobes, Phys. Rev. 119, 1331 (1960).

PHYSICAL REVIEW C VOLUME 21, NUMBER 6 JUNE 1980

Scission-point configuration of ^{252}Cf

A. K. Sinha and G. K. Mehta
Indian Institute of Technology, Kanpur-208016, India

(Received 10 August 1979)

A recent experiment by Guet *et al.* indicates that the width of the α-particle angular distribution in long-range-alpha-particle accompanied fission decreases as the fission-fragment kinetic energy E_F increases Earlier trajectory calculations yielded wide distributions for initial α-particle energy E_α^0 and fragment energy E_F^0. It is found that the decreased angular width can be reproduced by trajectory calculations only if the interfragment separation at the scission point is restricted to be around 20.5 fm. This gives rise to a scission-point configuration characterized by $E_\alpha^0 = 0.5$ MeV and $E_F^0 = 1.2$ MeV and explains all the correlations observed in the asymptotic values of E_F, E_α, and the angle of the α particle.

[NUCLEAR REACTIONS, FISSION LRA-fission ^{252}Cf, trajectory calculations, scission configuration.]

I. INTRODUCTION

The configuration of a fissioning nucleus at the scission point is a controversial problem in fission physics. The long-range alpha-particle accompanied fission (LRAF) is believed to be capable of providing information about the scission-point configuration, that is, the initial kinetic energies of the three particles and their relative positions at the scission point. Several attempts have been made to reconstruct the scission configuration based on trajectory calculations of LRAF. However, no consistent picture has emerged so far.

Guet *et al.*[1] have recently measured angular distribution of alpha particles as a function of the total fission-fragment kinetic energy E_F. They found that the average angle of α-particle emission is nearly constant, whereas the angular width decreases with increasing E_F. The trajectory calculations by Krishnarajulu and Mehta[2] indicated broad distributions for the initial α-particle energy E_α^0, fragment energy E_F^0 and interfragment distance D, covering low values as predicted by statistical theory as well as high values as predicted by dynamical theory. However, reproducing the experimental anticorrelation between E_F and α-particle energy E_α demanded the initial interfragment distance to be severely restricted. We have reexamined these trajectory calculations in the light of the new results of Guet *et al.* The observed correlations in the final angle and the energy of α-particle and fragment kinetic energy are studied by restricting D within a narrow range at values varying from 19 to 27 fm.

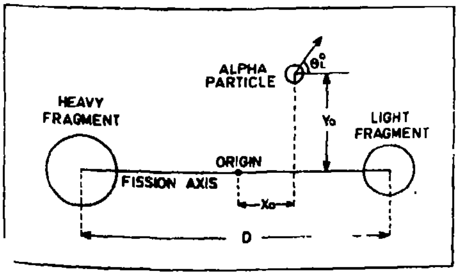

G. 1. Schematic diagram of the initial parameters of calculation.

II. PROCEDURE

The detailed procedure of trajectory calculations is essentially the same as described earlier.[2] The scission configuration is described by the following initial parameters (Fig. 1): the interfragment distance D, the distance of the α particle from the zero-field point X_0, the initial α-particle energy E_α^0, and the initial total fragment energy E_F^0. The initial distance of the α particle from the fission axis, Y_0, was assumed to be zero and the initial angle between the di-

TABLE I. Calculated angular distributions for various values of the mass ratio R and kinetic energy of the fragments.

E_F	165 ± 5 MeV		175 ± 5 MeV	
R	$\bar{\theta}_{\alpha-L}$	FWHM	$\bar{\theta}_{\alpha-L}$	FWHM
1.2	88.9°	15°	87.4°	12°
1.3	85.5°	17°	85.3°	14°
1.4	84.3°	16°	84.2°	12°

© 1980 The American Physical Society

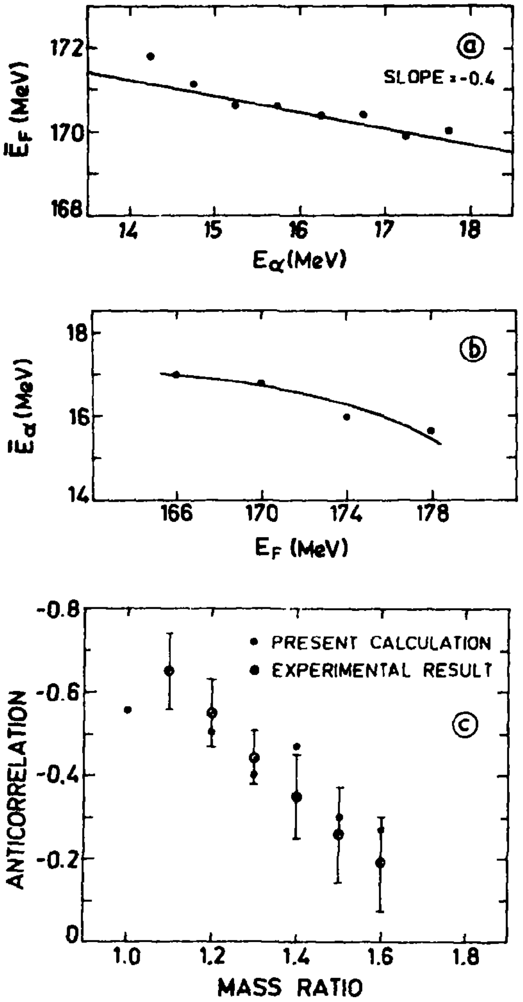

FIG. 2. (a) Variation of the mean kinetic energy of fragments $\bar{E}_F$ as a function of kinetic energy E_α of the α particle for mass ratio 1.3. (b) Variation of mean energy of α particle as a function of the fragment kinetic energy E_F for mass ratio 1.3. (c) Calculated anticorrelation in $\bar{E}_F$ and E_α as a function of mass ratio. Also shown are the experimental results of Mehta *et al.* (Ref. 3). In (a) and (b) lines are only visual fits.

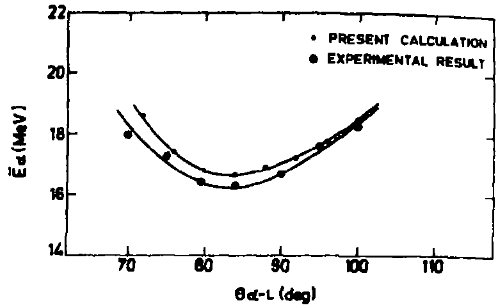

FIG. 3. Variation of the mean kinetic energy of α particle as a function of the angle of α-particle emission with respect to the light fragment $\theta_{\alpha-L}$. Experimental results of Tsuji *et al.* (Ref. 4) are also shown. Lines are only visual guides.

rection of motion of the α particle and the direction of motion of the light fragment, θ_L^0, was allowed an isotropic variation between 45° and 135°. Other input parameters were varied over a wide range. Each trajectory was computed using a set of initial values and was assigned a weight by using the experimental distributions in E_α and E_F. In the present calculations, D is restricted within a range of ±0.5 fm at values varying from 19.5 to 26.5 fm. All other parameters were allowed to have their normal statistical distributions demanded by the experimental E_F and E_α distributions used for assigning weights to the trajectories.

III. RESULTS AND DISCUSSION

The angular distribution of α particles was studied as a function of the fragment kinetic energy for various mass ratios R of the fragments. It is observed that the average angle of emission shows the correct experimental behavior for all values of D studied. However, the width of the angular distribution and its dependence on E_F for various values of R was correctly reproducible only by restricting the value of D below 21 fm. In fact calculations with other D values showed that the angular width increases with final E_F which is in contradiction with the experimental results of Guet *et al.* Table I gives the calculated results for the angular distribution for three values of mass ratio and two values of E_F. Results with other mass ratios have poor statistics.

The observed anticorrelation between $\bar{E}_F$ and E_α and its dependence on mass ratios are reproduced with D values restricted between 20 and 21 fm. It was found that if D is restricted to higher values, one gets either a positive correlation or the anticorrelation was not reproduced for all values of R. The anticorrelation condition is very sensitive to D, and this result alone demands value of D to be restricted to a narrow range around 20.5 fm. Figures 2(a) and 2(b) give the calculated relationships between E_F and E_α for a mass ratio of 1.3 and the anticorrelation $\partial \bar{E}_F/\partial E_\alpha$ as a function of mass ratio. The observed

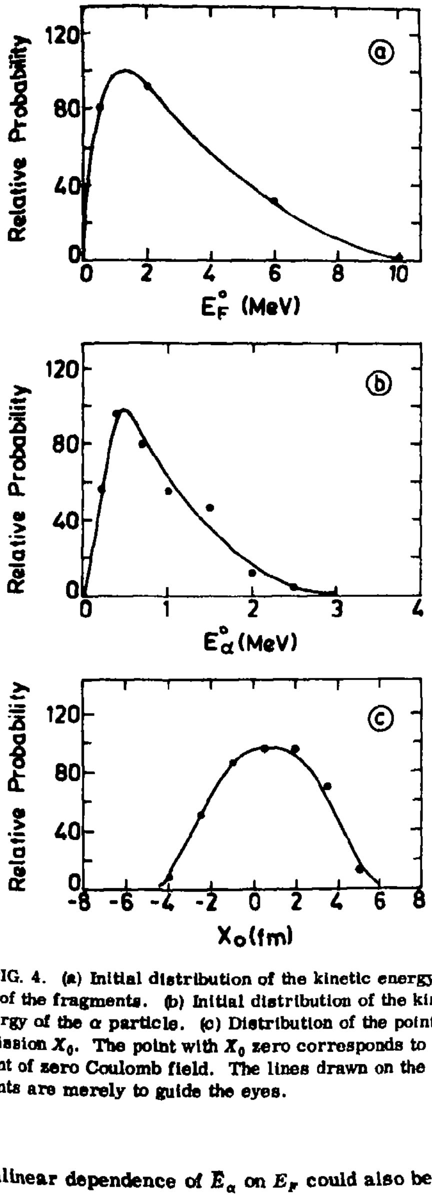

FIG. 4. (a) Initial distribution of the kinetic energy E_F^0 of the fragments. (b) Initial distribution of the kinetic energy of the α particle. (c) Distribution of the point of emission X_0. The point with X_0 zero corresponds to the int of zero Coulomb field. The lines drawn on the ints are merely to guide the eyes.

nlinear dependence of E_α on E_F could also be produced only with a value of D lying between and 21 fm [Fig. 2(c)].

The variation of E_α as a function of the angle α-particle emission with respect to the light gment is also in good agreement with experintal results for values of D less than 21 fm g. 3).

We used experimental E_F and E_α distributions assigning the weights to the trajectories. As ross check for the procedure used, we calculated final fragment energy and α-particle energy distributions with values of D below 21 fm. Mean values of E_F and E_α were quite accurately reproduced. The width of the E_F distribution agreed quite satisfactorily with the one used in assigning the weights. However, the width of the α-particle energy distribution was low (about 0.6 times the width used in assigning the weights). The reason for this is being explored further. It may, partially, be because of using a point-charge approximation and ignoring nuclear forces after scission. For values of D around 20.5 fm these effects may contribute significantly.

The distributions of initial parameters with values of D below 21 fm are shown in Fig. 4. The distributions of the initial energies of the α particle and the fragments are sharply peaked at about 0.5 and 1.2 MeV, respectively, with high-energy tails. The distribution in X_0 was found to be peaked at about 1 fm towards the light fragment from the zero field point with a full width at half-maximum (FWHM) of about 5 fm. This distribution actually represents distribution of the projection of the actual emission point on the fission axis.

There is a basic ambiguity in determining the scission point configuration using trajectory calculations. During the time evolution of the trajectory, any time along the trajectory can be taken as the scission point. However, we find that for a typical trajectory characterized by $E_\alpha^0 = 0.5$ MeV, $E_F^0 = 1.2$ MeV, $Y_0 = 0$ fm, and $D = 20.5$ fm, distance of the α particle from the fission axis exceeds 3 fm when the fragment separation becomes more than 23 fm Davies *et al.*[5] give an estimate of the neck radius of about 2 fm at scission. Taking 3 fm as a limiting value of the neck radius at scission, we see that for $D \geq 23$ fm the configuration of the three particles is nonphysical for the scission point (assuming that LRA emission coincides with the scission and occurs in the neck region). Considering the fact that the scission point parameters can be extrapolated to later times which will yield larger values for the initial kinetic energies and the fragment separation, we can get estimates of the range of variations in the initial parameters by imposing the condition that Y at the scission point should be <3 fm. We find under this restriction upper limit for the possible values of E_α^0, E_F^0, and D to be about 1.4 MeV, 16 MeV, and 23 fm, respectively.

We wish to acknowledge the financial support of the Department of Atomic Energy, Government of India in the form of a research project.

[1] C. Guet, C. Signarbieux, P. Perrin, H. Nifenecker, B. Leroux, and M. Asghar, J. Phys. Lett. 39, 213 (1978).

[2] B. Krishnarajulu and G. K. Mehta, Pramana 4, 74 (1975).

[3] G. K. Mehta, J. Poitou, M. Ribrag, and C. Signarbieux, Phys. Rev. C 7, 373 (1973).

[4] K. Tsuji, A. Kataze, Y. Yoshida, T. Katayama, F. Toyofuku, and H. Yamamoto, in *Proceedings of the Symposium on Chemistry and Physics of Fission, Rochester, 1973* (IAEA, Vienna, 1974), Vol. II, p. 405.

[5] K. T. R. Davies, R. A. Managan, J. R. Nix, and A. J. Sierk, Phys. Rev. C 16, 1890 (1977).

PHYSICAL REVIEW C VOLUME 21, NUMBER 6 JUNE 1980

Neutron angular and energy distributions from 710-MeV alphas stopping in water, carbon, steel, and lead, and 640-MeV alphas stopping in lead

R. A. Cecil, B. D. Anderson, A. R. Baldwin, and R. Madey
Department of Physics, Kent State University, Kent, Ohio 44242

A. Galonsky, P. Miller, and L. Young*
Cyclotron Laboratory, Michigan State University, East Lansing, Michigan 48824

F. M. Waterman†
Department of Radiology, University of Chicago, Chicago, Illinois 60637

(Received 22 October 1979)

We measured neutron angular and energy distributions from 710-MeV alphas stopping in targets of water, carbon, steel, and lead for neutron energies from 3 MeV to above 300 MeV. We also measured neutron spectra from 640-MeV alphas stopping in lead. These spectra are similar to the 710-MeV spectra but are reduced in magnitude by about 20 percent. The angular distributions are forward peaked and have a broad bump at about 120 MeV in the 0- and 6-degree spectra. The 710-MeV integrated yields above 10 MeV are about 0.5 neutron per incident alpha, independent of the target. The measured spectra from the water target are consistent with the calculations of an intranuclear cascade model at the forward angles, but are larger than the calculations at the backward angles.

NUCLEAR REACTIONS H_2O, C, steel, Pb(α,xn), $E = 710$ MeV; Pb(α,xn), $E = 640$ MeV. Measured unidirectional spectra and yields from thick targets. Deduced total integrated neutron yields above 10 MeV. Compared spectra with intranuclear-cascade model.

I. INTRODUCTION

We measured unidirectional neutron spectra above 3 MeV at angles ranging from 0 to 150 deg produced by 710-MeV alpha particles stopping in argets of carbon, water, steel, and lead; in addition, we report some measurements of neutron spectra produced by 640-MeV alphas stopping in ead. These measurements were made at the Space Radiation Effects Laboratory in Newport News, Virginia. They were motivated by the need or data to design shielding for the superconducting heavy-ion accelerator at Michigan State University. These data for the light targets are of interest also for estimating neutron doses produced by nuclear interactions during irradiation of cancerous tumors with alpha beams. The measured spectra from the water target are compared with those calculated from an intranuclear-cascade model.[1]

II. EXPERIMENTAL PROCEDURE

The energy of a neutron produced in the target was measured by the time-of-flight (TOF) technique. We measured the time difference between the detection of an alpha particle in a beam telescope and the detection of a neutron in one of several counters located one to five m away from the target. The neutron energy was then calculated from the TOF of the neutron measured relative to the observed prompt gamma peak. Absolute neutron yields were determined from the number of incident alphas counted in the beam telescope and from the detection efficiency for each neutron counter as calculated with the computer code of Cecil *et al.*[2]

A. Experimental arrangement

Figure 1 shows the experimental arrangement and indicates a typical placement of five neutron counters. As many as six counters were used simultaneously during the experimental run. A 710-MeV alpha beam was extracted from the cyclotron and transported to the experimental area in an evacuated beam line. During one experimental run a copper degrader was used to reduce the 710-MeV beam to 640 MeV. The external alpha beam passed through a beam telescope consisting of two 7.6 cm by 7.6 cm by 0.79 mm thick NE-102 plastic scintillators shown as $S1$ and $S2$ in Fig. 1. Signals from $S1$ and $S2$ were used in a coincidence circuit to count the absolute number of beam particles incident on the target. The duration of the data-taking runs varied from about 1 to 4 h with a typical flux of 5×10^4 alphas per second incident on the target. After traversing

© 1980 The American Physical Society

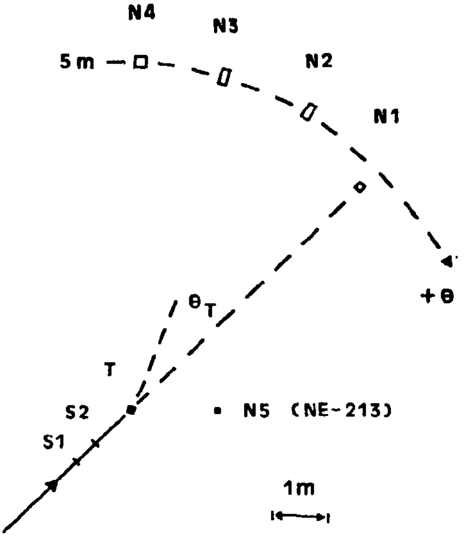

FIG. 1. The forward-angle experimental arrangement. The reference system for the target and detector angles discussed in the text is indicated.

the beam telescope, an alpha particle stopped in the target *T*. From geometric cross sections, we estimate that the alpha beam incident on the target had less than 1 percent contamination caused by nuclear reactions of the beam in the beam-telescope scintillators and exit window of the evacuated beam transport system. The beam spot size incident on the target was about 2 cm high by 3 cm wide. Neutrons produced in the target were detected by hydrocarbon scintillation counters. The detectors were arranged to equalize the counting rates and to provide better energy resolutions in the forward directions where there are larger yields of high-energy neutrons. The neutron flight paths were measured from the center of the target to the center of each neutron counter. The neutron counters and the target were supported by aluminum stands. The beam height was 1.5 m above the concrete floor of the experimental area. The detector angles are referenced to a spherical coordinate system with its origin at the center of the target and the positive *z* axis along the direction of the beam. All of the counters were in the *x*-*z* plane parallel to the floor except for the 6-deg counter which was positioned 6 deg above the beam. The NE-102 counters were deployed in two arrangements as indicated in Table I. A 5.1-cm diam by 5.1-cm thick NE-213 counter was placed at a flight path of 1 m from the target to measure the low-energy portion of the neutron spectrum; it was positioned at +45 deg in the first experimental arrangement and at either 0, −90, or +135 degrees in the second experimental arrangement. The NE-213 liquid scintillator was directly coupled to a 5.1-cm diam Amprex 56DVP photomultiplier tube (PMT); each of the 12.7-cm diam NE-102 scintillators was mounted directly on a 12.7-cm diam Amperex XP2041 PMT. Madey *et al.*[3] described the 22.9-cm diam NE-102 scintillator which was fitted with a tapered Plexiglass light pipe and mounted on a 12.7-cm diam 58AVP PMT. A 6.3-mm thick NE-102 plastic scintillation counter was placed immediately in front of each neutron counter to veto charged particles. In order to minimize neutron in-scattering, no local shielding was used near the counters.

TABLE I. NE-102 scintillator dimensions and locations.

Angle θ (deg)	Scintillator Thickness (cm)	Scintillator Diameter (cm)	Flight path (m)
Arrangement 1			
0	10.2	12.7	4.9
0 (6 up)	10.2	12.7	4.9
−15	21.6	12.7	5.0
−30	21.6	12.7	5.0
−45	20.3	23.9	5.0
Arrangement 2			
−60	10.2	12.7	3.0
−90	21.6	12.7	3.0
+120	21.6	12.7	2.0
+150	20.3	20.3	2.0

B. Target dimensions and orientations

The target thicknesses and orientations are presented in Table II. The target orientation is described by the angle θ_T of the spherical coordinate system in Fig. 1. The carbon, steel, and le targets were rectangular blocks: 15.2, 15.4, an 10.2 cm wide by 12.7, 10.2, and 10.2 cm, respectively. The water target was contained in a 22.9 cm long by 15.2-cm diam aluminum cylinder with a wall thickness of 1.4 mm. The beam entrance end of the cylinder was a 0.05 mm aluminum foil

TABLE II. Target thicknesses and orientations.

	Carbon	Water	Steel	Lead
Thickness				
(g/cm^2)	25.13	22.86	34.43	44.65
(cm)	14.73	22.86	4.445	3.937
Orientation				
θ_T (deg)	23.5	0.0	23.5	22.5

and the exit end was a 3.2-mm thick aluminum plate.

C. Data acquisition electronics

The data acquisition system included a PDP 11/15 computer, 12 bit analog-to-digital converters, commercially available electronics, and specialized electronics developed at Kent State University to provide increased count rate and dynamic range capabilities for neutron spectral measurements. As many as six neutron counters were operated simultaneously. The anode signal from each neutron counter was split into two signals with a linear fan-out module. One signal went to a constant-fraction timing discriminator (CFD) and the other, to a wide dynamic-range stretcher module.[4] This stretcher enabled reliable pulse-height measurements over a 50:1 dynamic range. All TOF information was obtained from a single time-to-amplitude converter (TAC). The TAC was started by a signal from the output of an OR module which received the timing signal from each CFD. A fast timing signal from the beam telescope stopped the TAC. The output of the stretcher module and the TAC were processed by separate analog-to-digital converters. Pulse-height and TOF information for each counter were recorded event by event on magnetic tape by the computer; in addition, TOF and pulse-height histograms were accumulated in the computer memory and displayed on-line to monitor the operation of the detectors and to provide preliminary results.

III. DATA ANALYSIS

The event-by-event list of pulse-height and TOF data recorded on magnetic tape was analyzed offline at Kent State University. Since pulse-height information was recorded for each TOF event, the data could be reanalyzed at any desired threshold above the hardware threshold set by the CFD for each counter. After choosing thresholds, TOF spectra were produced and backgrounds were subtracted as described below. The resulting TOF spectra were converted to energy spectra to obtain the yields reported here.

A. Background subtraction

Figure 2 is the TOF spectrum from a carbon target with the NE-102 counter at 15 deg. The estimated background, as represented by the dashed line, decreases from about 25% of the total spectrum at 14 MeV (about twice threshold), to 12% at 34 MeV, to about 2% from 68 MeV up to about 300 MeV, which energy represents the practical limit of our measurement of neutron yield at this angle. The spectrum shown in Fig. 2 is typical of the spectra obtained in this experiment. Because the backgrounds are relatively small, we estimated them in the following manner: In each TOF spectrum, the level of the background in the region below the discrimination threshold on the slow side of the neutron TOF spectrum was slightly higher than that on the fast side of the spectrum earlier than the gamma peak. We attributed the excess events on the slow side of the spectrum to target-induced background from room-scattered neutrons. Note that room-scattered neutron backgrounds measured by other workers[5] with shadow bars revealed similar (but larger) differences in the background levels on each side of the neutron TOF spectra. Also the magnitude of the background levels was much larger. A neutron produced in the target and scattered from the floor would have a flight time at least 1.2 times longer than a direct-path neutron of the same energy. Since such floor-scattered neutrons would dominate the room-scattered background, we estimated the background by extrapolating the flat region on the slow side of the spectrum up to a point at 1.2 times the flight time of the high-energy peak observed in the spectrum; then we extrapolated linearly down to the level observed on the fast side of the spectrum at the center of the prompt gamma-ray peak. We estimate that the (~25%) uncertainty in the background introduces an uncertainty in the extracted yields of typically less than 7%. The region of greatest

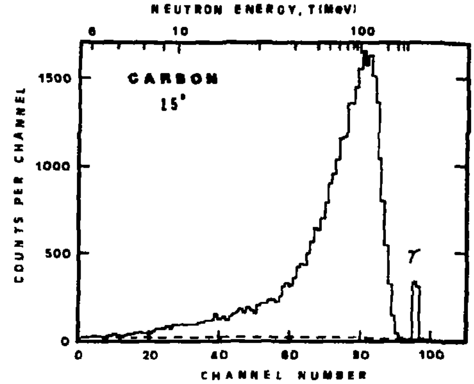

FIG. 2. The neutron time-of-flight (TOF) spectrum at 15° from 710-MeV alphas stopping in a carbon target. The dashed line represents the background that was subtracted to obtain the neutron yields. The background is a flat extrapolation from the observed background at the left of the TOF spectrum to a point at 1.2 × the most probable flight time and then sloped to the level of the background under the gamma peak. See text for discussion.

uncertainty in the background is near the assumed discontinuity where the background is always the smallest fraction (~2%) of the total spectrum.

The low-energy portions of the spectra were measured at a few angles with an NE-213 type scintillator. Although the time resolution and pulse-shape information for this detector were observed to be too poor to permit the use of n-γ discrimination for neutron spectral analysis, the pulse-shape information was used to study the γ-ray TOF spectrum. The γ-ray spectra were observed to be flat over the range from threshold to flight times corresponding to neutron energies greater than 50 MeV. Since the NE-213 detector was used to measure the spectrum only below 40 MeV, the γ-ray background was assumed to be flat and the background subtraction method described above for the NE-102 detectors was adopted also for the NE-213 data analysis. Note that γ rays from the target seen in the spectra at neutron energies above 50 MeV for the NE-213 counter at a flight path of 1 m will appear at a neutron energy above 200 MeV for an NE-102 counter at 3 m and above 500 MeV for an NE-102 counter at 5 m. Since the NE-102 counters were placed at flight paths of 3 m only for the backward angles where the neutron yield is negligible above 200 MeV, the γ-ray backgrounds for the NE-102 detectors would be expected to be flat also; moreover, the higher pulse-height thresholds adopted for the NE-102 counters (see Sec. III B below) would greatly reduce γ-ray backgrounds for these detectors.

B. Pulse-height thresholds

Before and after the experimental run, each counter was pulse-height calibrated with a series of radioactive gamma sources (viz., ^{137}Cs, ^{60}Co, ^{22}Na, and ^{228}Th); in addition, at least once every 12 h during the experimental run, each of the counters was calibrated with a ^{60}Co gamma source. The Compton peak in the gamma-ray spectrum was used as the calibration point and was associated with an equivalent-electron energy (ee) of 0.95 of the maximum Compton energy.[6] To calibrate the stretcher module and the analog-to-digital converter for large pulse heights, we used precision attenuators and a fast linear amplifier with a measured gain of 10.0 to amplify the anode signals produced in each of the neutron counters by a ^{228}Th gamma source ($E_\gamma = 2.62$ MeV). Since pulse-height information was recorded for each TOF event, the data were analyzed and compared at various pulse-height thresholds.

Yield spectra for the NE-102 counters were compared at several pulse-height thresholds ranging from 1.5 to 6.0 MeV ee. At a threshold of 1.5 MeV ee, spikes of room-scattered gammas were observed in the yield spectra. At a threshold of 3.0 MeV ee, the spikes were no longer present and the yields were consistent with the yields obtained at a 6.0-MeV ee threshold. Yield spectra were produced for the NE-213 counter over the threshold region from 0.3 MeV ee to 0.8 MeV ee. The analyses produced yield spectra which were the same for thresholds of 0.6 and 0.8 MeV ee. Pulse-height analysis thresholds for the NE-102 counters were set at 3.0 MeV ee (≈ 6.8-MeV proton energy[7]) and at 0.6 MeV ee (≈ 2.0-MeV proton energy[2]) for the NE-213 counter for the yields reported here. These thresholds provide the lowest-energy neutron spectra possible while remaining consistent with the neutron yields of the higher-threshold analyses.

C. Energy resolutions

For measurements of neutron energies by the TOF method, the fractional energy resolution $\Delta T/T$ is given by the expression

$$\frac{\Delta T}{T} = \frac{(2M+T)(M+T)}{M^2}\left[\left(\frac{\Delta t}{t}\right)^2 + \left(\frac{(1-\beta n)\Delta x}{x}\right)^2\right]^{1/2} \qquad (1)$$

with

$$t = x/\beta c\ .$$

Here T is the neutron kinetic energy, M is the neutron rest mass, Δx is the uncertainty in the neutron flight path x arising from the finite dimensions of the counter, and n is the refractive index of the scintillator material. The effective thickness of the neutron counter is reduced from the physical thickness Δx by the factor $(1-\beta n)$. The finite thickness of the counter contributes to the energy resolution only because there exists a difference between the neutron speed and the speed of light in the scintillator. The time dispersion Δt was taken as the observed full width at half maximum (FWHM) of the prompt gamma peak in each neutron TOF spectrum. The observed width includes contributions from the beam telescope, the neutron counter, and the thickness of the target. The observed (FWHM) time dispersions were 0.8 ns for the 12.7-cm diam 10.2-cm thick detectors, 1.0 ns for the 12.7-cm diam 21.6-cm thick detectors, 1.2 ns for the 22.9-cm diam 20.3-cm thick detector, and 2.3 ns for the NE-213 counter. The poor resolution of the NE-213 counter was probably the result of the age of the NE-213 scintillation liquid. The resolutions calculated from Eq. (1) were used to determine the widths of the energy bins for the yield spectra reported in Sec. IV.

D. Conversion to energy spectra

The prompt gamma peak in each spectrum provided a reference point for calculating absolute neutron flight times. The background-subtracted TOF spectra were converted to energy spectra with bin widths equal to integral and fractional multiples of the experimental energy resolution. The smallest bin widths revealed no rapidly varying structure as a function of energy; consequently, the spectra are presented at integral multiples of the experimental energy resolutions to increase the statistics in each bin. The NE-213 detector was binned at the experimental energy resolution. For the NE-102 counters at neutron energies below 50 MeV, the energy bins are twice the energy resolutions; at neutron energies above 50 MeV, the multiple is two for the 30, 45, 60, and 90 deg spectra and three for the 0 and 6 deg spectra. To produce the absolute yields, each energy spectrum was divided by the number of alphas incident on the target, the calculated neutron detector efficiency, and the detector solid angle. The mean solid angle was calculated from the measured distance from the center of the target to the center of the neutron counter. The solid angles varied from about 0.5 msr for a 12.7-cm diam counter at 5 m to 2.0 msr for the 5.1-cm diam counter at 1 m.

E. Neutron detector efficiency calculations

The neutron detection efficiency of each counter was calculated with the Monte Carlo code of Cecil *et al.*[2] Calculations with this code provide good agreement with many experimental measurements of neutron detector efficiencies for neutron energies from about 1 to 300 MeV and for detector thresholds from about 0.1 to 22 MeV ee.[2] The calculated efficiencies used for the different neutron counters of this experiment are plotted in Fig. 3.

F. Corrections

The livetime was measured directly as the ratio of the actual number of events recorded by the computer data-acquisition system to the number of scaled neutron events detected by the neutron counters. The resultant deadtime correction was typically 1 to 3 percent.

The number of alphas incident on the target was measured as the number of beam-telescope coincidences. The incident beam rate was kept below 2×10^5 particles per second to keep the calculated correction for the occurrence of two or more beam ions per observed micropulse below two percent. The correction C is

$$C=\sum_{n=2}^{\infty}\frac{(n-1)f_a(n)}{1-f_a(0)}, \qquad (2)$$

where $f_a(n)$ is the Poisson probability for the observation of n particles in one micropulse with an average probability per micropulse of a. Note that the factor $(n-1)$ in Eq. (2) corrects for miscounting of alpha particles when the micropulse contains more than two alpha particles. The average probability a is given by the 78 ns period between micropulses divided by the mean time between alpha particles. The stochastic extractor in the cylcotron was adjusted to maximize the macroscopic duty cycle, which was greater than 50 percent. Since the probability of two or more alphas per micropulse was always less than 2%, the effect on the time resolution was ignored.

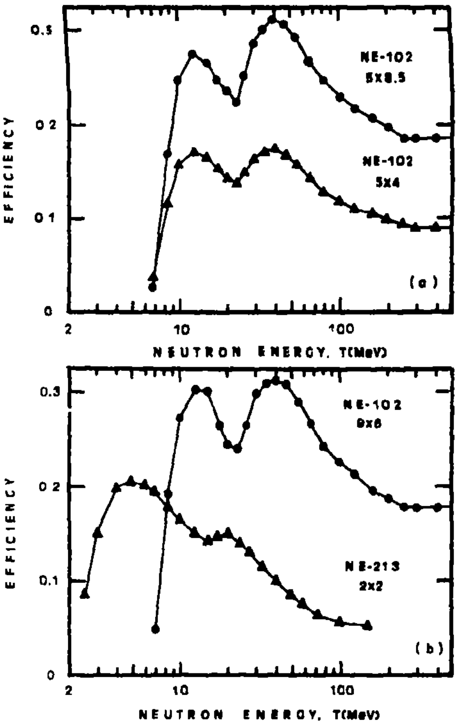

FIG. 3. Neutron detector efficiencies calculated with the Monte Carlo computer code[2]) for (a) a 12.7 cm diam by 21.6 cm thick NE-102 counter and a 12.7 cm diam by 10.2 cm thick NE-102 counter both with thresholds set at 3 MeV equivalent-electron energy, and (b) for a 22.9 cm diam by 20.9 cm thick NE-102 counter and a 5.1 cm diam by 5.1 cm thick NE-213 counter with thresholds set at 3 and 0.6 MeV equivalent-electron energies, respectively. The straight lines connecting the calculated points indicate interpolations used in the data analysis.

TABLE III. Scale uncertainties.

Source	Percent uncertainty		
Number of alphas	2		
Efficiency	5		
Background	7		
Target:	Steel/lead	Carbon	Water
Solid-angle[a]	1(3)	4(6)	6(9)
Total[a]	9(9)	10(11)	11(13)

[a] Numbers in parentheses are for the NE-213 counter.

G. Experimental uncertainties

The experimental uncertainties have been divided into two categories, those which scale an entire spectrum and those which are associated with a particular point or energy bin of the yield spectra and are primarily statistical. The statistical uncertainty is shown as a vertical error bar for each point of the reported yield spectra. The scale uncertainties are summarized in Table III. The uncertainty in the number of alphas incident on the target is composed entirely of the estimated error in the calculated beam pileup of particles in the beam telescope. The uncertainty in the Monte Carlo calculation of the efficiencies is estimated to be about 4 percent for a well-known threshold.[2] An uncertainty estimated to be about 3 percent in the pulse-height threshold results in an additional uncertainty in the efficiencies of about 3 percent at neutron energies near threshold. A net uncertainty of 5 percent in the efficiency results from the quadrature sum of these two quantities. As a percentage of the total yield, the background decreases typically from about 25 percent at a low energy (at twice threshold) to only about 2 percent at high energies. Since we estimate that the uncertainty in the background is about 25 percent, this uncertainty produces an uncertainty in the extracted yield that is typically less than 7 percent. The uncertainty in the solid angle is dominated by the uncertainty in the position of production of a neutron in the thick targets. An upper bound on the uncertainty in the solid angle is equal to the difference in solid angle for a point at the extremity of the target and the solid angle for a point at the center of the target. One-half of this calculated upper bound on the uncertainty in the solid angle is taken as the estimated uncertainty in the solid angle. The resulting uncertainties in the solid angle for the steel/lead, carbon, and water targets are 1, 4, and 6 percent, respectively, for the high-energy (NE-102) measurements and 3, 6, and 9 percent, respectively, for the low-energy (NE-213) measurements.

IV. YEILD SPECTRA

The yield spectra are presented in Tables IV through VII. The differential neutron yields from 710-MeV alphas measured with the NE-102 counters are presented in Table IV starting at about 10 MeV and extending to the highest neutron energies observed. Differential neutron yields from 710-MeV alphas measured with the NE-213 counter are presented in Tables V and VI starting at about 3 MeV and extending to about 50 MeV. The measured neutron yields from 640-MeV alphas are presented in Table VII. The statistical uncertainties in the data points are indicated following each datum. The energy corresponding to each point is the mean energy of an energy bin whose width extends halfway to the nearest neighboring data points.

The yields reported here include neutrons produced in the target by the interactions of primary neutrons and secondary charged particles. The effects of neutron scattering in the target are included also. An accurate separation of these effects to reveal the primary neutron spectra would require a Monte Carlo simulation of the neutron and charged particle transport through the target. The consequences of these finite-target size effects are estimated to be large only at low energies and are not separated in the yields reported here.

Some of the neutron spectra produced by 710-MeV incident alphas are plotted in Figs. 4 through 8. These spectra are distinctly forward peaked with the lighter (carbon and water) targets (Figs. 4 and 5) having a somewhat larger proportion of their yield in the forward direction than the heavier (steel and lead) targets (Figs. 6, 7, and 8). For angles less than 30 deg, there is a significant yield of neutrons with energies greater than the 177 MeV per nucleon of the incident alphas. The 0-deg spectra from carbon and water have a large bump in their neutron yield spectra at about 120 MeV. The 0-deg spectra from the steel and lead targets show a somewhat smaller bump in the neutron yield at about the same energy. The 6, 15, and 30-deg spectra for all the targets show progressively smaller bumps at somewhat lower neutron energies. For angles larger than 30 deg, the yield spectra decrease uniformly with increasing neutron energy and angle. Neutron yields for energies down to about 3 MeV, measured with the single NE-213 counter, are shown at 45 deg for carbon, water, and steel targets and at 0, 45, and 90 deg for the lead target. Because the targets were placed at an angle to the incoming alpha beam, the neutron attenuation was, in general, different for the NE-213 and NE-102 detector measurements performed at the same

TABLE IV. Neutron yields from 710-MeV alphas stopping in carbon, water, steel, and lead targets.

Energy (MeV)	Neutron yield (Neuts/10^6 alphas MeV sr)[a]			
	Carbon	Water	Steel	Lead
0 deg				
10.0	2250 (8.5)	2430 (10.0)	2470 (16.0)	3850 (5.4)
12.3	2380 (6.5)	2150 (8.6)	2430 (13.0)	3340 (4.9)
15.0	2480 (5.5)	1960 (7.9)	2570 (11.0)	2940 (4.6)
18.5	2210 (5.3)	1860 (7.2)	2250 (10.0)	2640 (4.4)
22.8	2780 (4.1)	2280 (5.6)	1840 (10.0)	2590 (4.0)
28.2	2740 (3.4)	2360 (4.4)	1760 (8.2)	2030 (3.7)
35.2	2850 (2.8)	2560 (3.6)	2050 (6.3)	2030 (3.2)
44.3	3180 (2.3)	2930 (2.8)	2070 (5.3)	1920 (2.8)
56.5	3920 (1.8)	3730 (2.2)	2380 (4.3)	1900 (2.5)
68.6	4720 (2.0)	4780 (2.4)	2740 (5.0)	2070 (2.9)
79.8	5740 (1.7)	5640 (2.1)	3150 (4.3)	2290 (2.6)
93.7	6340 (1.5)	6500 (1.8)	3600 (3.7)	2430 (2.3)
111.0	7190 (1.3)	7110 (1.6)	4130 (3.2)	2590 (2.0)
134.0	6900 (1.2)	6640 (1.4)	3850 (2.9)	2370 (1.9)
165.0	5260 (1.2)	4470 (1.5)	3000 (2.9)	1890 (1.8)
207.0	2370 (1.5)	1930 (2.0)	1350 (3.6)	865 (2.3)
268.0	488 (2.7)	369 (3.8)	242 (7.2)	170 (4.4)
363.0	40.2 (7.9)	29.5(12.0)	15.3(27.0)	14.7(13.0)
525.0	2.4(32.0)			
6 deg				
10.0	2610 (7.9)		3390 (11.0)	4850 (5.0)
12.3	2450 (6.6)		2770 (11.0)	3450 (5.0)
15.0	2470 (5.6)		2220 (11.0)	3210 (4.5)
18.5	2510 (5.0)		2480 (8.9)	3030 (4.1)
22.8	2890 (4.1)		2700 (7.6)	2660 (4.0)
28.2	2620 (3.5)		1930 (7.4)	2250 (3.5)
35.2	2790 (2.9)		1870 (6.4)	2040 (3.2)
44.3	2940 (2.4)		2100 (5.1)	1930 (2.7)
56.5	3300 (2.0)		2280 (4.3)	1910 (2.4)
68.6	3820 (2.3)		2270 (5.4)	2020 (2.9)
79.8	4300 (2.0)		2630 (4.7)	2020 (2.7)
93.7	4450 (1.8)		2480 (4.5)	2110 (2.5)
111.0	4470 (1.7)		2470 (3.9)	2080 (2.3)
134.0	4190 (1.5)		2540 (3.6)	1780 (2.2)
165.0	3080 (1.6)		1820 (3.7)	1350 (2.2)
207.0	1550 (1.9)		902 (4.5)	637 (2.7)
268.0	406 (3.0)		244 (7.1)	165 (4.4)
363.0	50.0 (7.0)		30.7(17.0)	18 (12.0)
525.0	2.5(29.0)			
15 deg				
11.4	2540 (4.9)	1720 (7.4)	2640 (8.7)	4240 (3.5)
14.6	2550 (3.9)	1890 (5.6)	2610 (7.4)	3250 (3.4)
18.6	2510 (3.5)	2140 (4.5)	2210 (7.0)	2520 (3.5)
23.6	2680 (3.0)	2070 (4.1)	2100 (6.4)	2460 (3.1)
29.9	2480 (2.5)	1980 (3.3)	1980 (5.2)	2010 (2.8)
37.8	2450 (2.2)	1980 (2.8)	1870 (4.6)	1820 (2.5)
47.6	2430 (1.9)	1990 (2.5)	1790 (4.1)	1690 (2.2)
56.7	2590 (2.3)	2050 (3.1)	1780 (5.2)	1640 (2.8)
64.3	2650 (2.2)	2190 (2.8)	1940 (4.7)	1560 (2.7)
72.9	2660 (2.1)	2170 (2.8)	1770 (4.8)	1500 (2.7)
83.0	2480 (2.1)	2030 (2.7)	1660 (4.7)	1360 (2.7)
94.9	2300 (2.0)	1870 (2.6)	1530 (4.5)	1290 (2.6)
109.0	1960 (2.0)	1650 (2.6)	1330 (4.5)	1010 (2.7)
126.0	1580 (2.1)	1340 (2.6)	988 (4.8)	851 (2.7)
147.0	1050 (2.3)	925 (2.9)	732 (5.1)	558 (3.0)

TABLE IV. *(Continued.)*

Energy (MeV)	Neutron yield (Neuts/10^6 alphas MeV sr)[a] Carbon	Water	Steel	Lead
		15 deg		
172.0	578 (2.9)	518 (3.5)	378 (6.5)	317 (3.7)
205.0	271 (3.7)	236 (4.6)	146 (9.3)	133 (5.2)
249.0	91.9 (5.6)	78.3 (7.2)	50.6(14.0)	46.4 (8.1)
309.0	16.3(12.0)	14.3(16.0)		5.1(30.0)
		30 deg		
11.4	2180 (5.5)	1850 (7.5)	3020 (8.2)	4330 (3.6)
14.6	2260 (4.3)	1560 (6.7)	2410 (7.7)	2840 (3.9)
18.6	2100 (4.0)	1550 (5.8)	2260 (7.1)	2320 (3.9)
23.6	2130 (3.5)	1690 (4.8)	1670 (7.5)	2150 (3.5)
29.9	1790 (3.0)	1370 (4.2)	1510 (6.2)	1790 (3.0)
37.8	1590 (2.7)	1380 (3.5)	1230 (5.9)	1360 (3.0)
47.6	1520 (2.4)	1230 (3.3)	1290 (4.9)	1220 (2.7)
56.7	1440 (3.2)	1250 (4.0)	1050 (6.9)	1040 (3.7)
64.3	1480 (3.0)	1210 (3.9)	985 (6.8)	1000 (3.5)
72.9	1340 (3.0)	1270 (3.7)	891 (6.9)	938 (3.5)
83.0	1180 (3.0)	1120 (3.7)	710 (7.3)	767 (3.6)
94.9	911 (3.3)	832 (4.0)	615 (7.3)	635 (3.7)
109.0	620 (3.7)	589 (4.5)	421 (8.3)	413 (4.4)
126.0	425 (4.1)	386 (5.1)	279 (9.5)	272 (5.0)
147.0	272 (4.7)	236 (6.0)	184 (11.0)	143 (6.6)
172.0	133 (6.2)	126 (7.6)	104 (13.0)	87.1 (7.8)
205.0	55.3 (8.8)	50.1(11.0)	38.2(21.0)	33.8(12.0)
249.0	19.2(14.0)	14.8(21.0)		
		45 deg		
11.1	1650 (3.3)	1370 (4.7)	2260 (5.1)	3270 (2.3)
14.1	1410 (3.0)	1290 (3.9)	1590 (5.2)	2320 (2.4)
17.9	1380 (2.7)	1250 (3.5)	1410 (5.0)	1720 (2.6)
22.7	1270 (2.5)	1200 (3.1)	1280 (4.7)	1530 (2.4)
28.6	1080 (2.2)	1020 (2.7)	1000 (4.3)	1210 (2.2)
36.2	893 (2.1)	875 (2.5)	842 (4.0)	944 (2.1)
45.9	791 (1.9)	780 (2.3)	696 (3.8)	712 (2.1)
54.9	683 (2.6)	682 (3.0)	549 (5.4)	568 (2.9)
62.7	582 (2.7)	588 (3.1)	573 (5.0)	516 (2.9)
71.8	510 (2.7)	485 (3.2)	460 (5.3)	411 (3.0)
82.8	426 (2.7)	401 (3.3)	326 (6.0)	335 (3.2)
96.2	327 (2.9)	299 (3.6)	275 (6.0)	255 (3.4)
113.0	219 (3.3)	210 (4.0)	162 (7.4)	154 (4.1)
133.0	131 (3.9)	126 (4.7)	99.5 (8.7)	88.9 (5.1)
159.0	59.8 (5.3)	52.4 (6.8)	40.9(13.0)	36.1 (8.0)
194.0	22.3 (7.9)	21.0(10.0)	17.3(19.0)	12.5(14.0)
239.0	6.1(15.0)	5.6(20.0)		
		60 deg		
10.5	908 (8.2)	819 (8.9)	1360 (6.5)	1930 (4.9)
13.0	765 (7.4)	799 (7.2)	1230 (5.6)	1300 (5.1)
16.2	777 (6.5)	702 (6.8)	888 (6.1)	999 (5.3)
20.3	699 (6.2)	690 (6.2)	797 (5.9)	789 (5.5)
25.5	584 (5.9)	617 (5.6)	605 (6.0)	590 (5.6)
32.3	540 (5.0)	560 (4.8)	516 (5.2)	463 (5.0)
41.3	402 (4.7)	421 (4.5)	375 (5.0)	346 (4.7)
53.5	319 (4.7)	311 (4.6)	298 (5.0)	255 (4.8)
65.8	251 (6.5)	213 (6.9)	226 (7.0)	168 (7.6)
77.2	220 (6.6)	174 (7.3)	177 (7.5)	130 (8.3)
91.7	146 (7.3)	107 (8.5)	112 (8.6)	80.8(10.0)
110.0	68.7(10.0)	74.4 (9.4)	59.8(11.0)	58.6(11.0)
135.0	37.4(12.0)	34.9(13.0)	28.8(14.0)	15.9(25.0)

TABLE IV. *(Continued.)*

Energy	Neutron yield (Neuts/10^6 alphas MeV sr) [a]			
(MeV)	Carbon	Water	Steel	Lead
		60 deg		
169.0	19.2(15.0)	13.1(19.0)	11.8(21.0)	
217.0	4.2(31.0)			
		90 deg		
13.2	574 (3.9)	550 (3.7)	964 (3.8)	1160 (2.2)
17.8	417 (4.0)	366 (4.1)	579 (4.5)	640 (2.7)
23.8	377 (3.7)	307 (3.9)	496 (4.4)	458 (2.8)
31.8	250 (3.5)	168 (4.2)	319 (4.3)	262 (2.9)
42.3	143 (3.8)	110 (4.3)	173 (4.9)	155 (3.2)
56.2	86.6 (4.4)	56.9 (5.4)	111 (5.6)	87.4 (3.9)
69.4	47.0 (7.7)	34.7 (9.0)	56.8(10.0)	49.1 (7.1)
81.6	25.6 (9.8)	20.5(11.0)	39.8(12.0)	30.6 (8.7)
96.7	12.9(14.0)	13.5(13.0)	29.9(13.0)	17.0(12.0)
115.0	6.9(18.0)	6.0(20.0)	11.9(21.0)	9.4(17.0)
139.0			4.7(33.0)	
		120 deg		
13.2	393 (4.7)	330 (4.8)	792 (3.0)	1190 (2.1)
17.8	283 (4.9)	234 (5.0)	420 (3.7)	622 (2.7)
23.8	182 (5.5)	150 (5.5)	290 (4.0)	330 (3.4)
31.8	91.1 (6.1)	68.8 (6.5)	148 (4.4)	173 (3.7)
42.3	39.6 (8.0)	32.7 (8.1)	72.8 (5.3)	74.6 (5.1)
56.2	15.3(12.0)	11.6(13.0)	28.2 (7.9)	33.5 (7.6)
69.4	11.0(18.0)	6.0(25.0)	12.9(16.0)	13.1(19.0)
81.6			6.9(21.0)	10.2(20.0)
		150 deg		
12.8	347 (2.7)	222 (3.3)	648 (1.9)	1080 (1.2)
17.1	218 (3.0)	148 (3.5)	348 (2.3)	483 (1.8)
22.8	133 (3.5)	81.3 (4.4)	192 (2.9)	255 (2.3)
30.4	55.7 (4.4)	38.5 (5.2)	83.8 (3.6)	108 (3.1)
40.7	21.7 (6.1)	15.0 (7.4)	31.8 (5.1)	40.9 (4.7)
54.7	7.5(10.0)	6.0(11.0)	9.4 (9.6)	12.0(10.0)
68.7				4.0(30.0)

[a] Percent uncertainties (in parentheses) are statistical only. The yields include neutrons produced by the interactions of primary neutrons and secondary charged particles as well as the effects of neutron scattering in the thick targets (see text).

angles, but on the opposite sides of the beam line. For purposes of comparison the NE-213 spectra were adjusted to have the same neutron attenuation in the target as the corresponding NE-102 spectra. This adjustment was approximated using the inelastic neutron cross sections for each target.[8,9] The reported yields increase at the lower energies for all of the targets but most rapidly for the lead target; in addition, the angular distribution of low-energy neutrons becomes almost isotropic for the lead target.

The basic characteristics of the spectra are consistent with the simple idea that the high-energy neutrons are produced primarily by direct-reaction processes and the low-energy neutrons by evaporation processes. For the light targets, the direct-reaction products are more likely to escape the nucleus without being absorbed to form compound nuclei. Thus, the carbon and water spectra at the most forward angles show pronounced peaks somewhat below the kinetic energy per nucleon. For the heavier targets of steel and lead, this high-energy peak is suppressed.

Neutron spectra measured at angles of 0, 45, 90, and 150 deg from 640-MeV alphas stopping in a lead target are presented in Fig. 9. These spectra are similar to the 710-MeV spectra except that they are reduced in magnitude. The spectra are forward peaked and there is a bump in the zero-degree spectrum at about 120 MeV. The yields for angles of 90 deg and larger decrease uniformly with increasing neutron energy.

TABLE V. Neutron yields at low energies from 710-MeV alphas stopping in a lead target.[a]

Energy (MeV)	Neutron yield (Neuts/10^6 alphas MeV sr) 0 deg	90 deg	135 deg
3.39	31 600(2.6)	17 800(3.2)	19000 (2.7)
3.91	23 500(2.6)	13 400(3.2)	15100 (2.6)
4.52	17 600(2.7)	9 100(3.4)	11 300 (2.7)
5.27	13 500(3.8)	6 670(3.6)	8120 (2.8)
6.18	10 200(3.0)	4 880(3.9)	6 780 (3.1)
7.32	7 900(3.1)	3 590(4.1)	4 030 (3.4)
8.79	5 750(3.7)	2 490(4.6)	2 920 (3.7)
10.6	4 230(3.8)	1 670(5.2)	1 870 (4.3)
13.1	3 470(3.8)	1 180(5.8)	1 210 (5.1)
16.3	2 510(3.8)	772(6.1)	709 (5.7)
20.9	2 080(3.3)	491(6.4)	399 (6.4)
27.3	1 700(3.2)	298(7.2)	208 (8.0)
37.1	1 690(2.7)	230(7.2)	136 (8.8)
52.9	1 690(2.3)	141(8.2)	80.1(10.0)

[a] See Table VI for yields at 45 deg. Percent uncertainties (in parentheses) are statistical only. The yields include neutrons produced by the interactions of primary neutrons and secondary charged particles as well as the effects of neutron scattering in the thick targets (see text).

V. COMPARISON WITH INTRANUCLEAR-CASCADE-MODEL CALCULATIONS

The neutron spectra from alpha bombardment of a stopping oxygen target were calculated using an intranuclear-cascade and evaporation model[1] of the nucleon interactions. The calculation was performed as a series of thin-target calculations which were then summed to obtain the neutron yields from alphas stopping in the thick target. The neutron yields from a water target are shown compared with these calculations in Fig. 5. The calculations are for a range of angles centered about the angle of the experimental measurement. There is good agreement between the calculations and the measured spectra at the forward angles. The 0- to 10-deg calculation falls midway between the measured 0- and 15-deg spectra. The agreement of the 30- to 60-deg calculation with the 45-deg measurement is excellent. The spectra measured at 90 and 120 deg have different shapes from the calculated spectra. The 90-deg calculations are significantly less than the measured yields.

The prominent bumps seen in the neutron spectra at forward angles near 120 MeV are apparently the result of peripheral reactions (with large impact parameters) between the projectile and target nuclei. These reactions often result in quasi-free elastic scattering of the target and projectile nucleons. The intranuclear-cascade calculations for a thin target show quasi-free elastic scattering peaks at the incident beam energy per nucleon minus the nuclear binding energy of a neutron. For a stopping target, the production contributions of several thin targets are added together at increasingly lower energies. The resultant quasi-free bump appears at about 120 MeV, in good agreement with the measured spectra.

The high-energy tails of the small-angle neutron spectra extend to nearly twice the energy per nucleon of the incident alphas. The magnitude of the high-energy tails of the 0- and 6-deg spectra are nearly the same. These characteristics of the measured spectra at high energies are consis-

TABLE VI. Low-energy neutron yields at 45° from 710-MeV alphas stopping in carbon, water, steel, and lead targets.

Energy (MeV)	Neutron yield (Neuts/10^6 alphas MeV sr)[a] Carbon	Water	Steel	Lead
3.39	3040(7.0)	2420(7.9)	10 100(4.6)	35 900(2.2)
3.91	2960(6.0)	2320(6.7)	7 200(4.7)	26 900(2.2)
4.52	3120(5.0)	2050(6.3)	5 930(4.6)	21 100(2.2)
5.27	2370(5.2)	1880(5.8)	4 600(4.7)	15 500(2.4)
6.18	2040(5.2)	1630(5.8)	4 040(4.5)	11 700(2.5)
7.32	1810(5.0)	1400(5.6)	3 000(4.8)	8 510(2.7)
8.79	1440(5.2)	1180(5.6)	2 490(4.9)	5 900(3.0)
10.60	1410(4.8)	1230(5.0)	2 060(5.0)	4 670(3.1)
13.10	1440(4.4)	1400(4.3)	1 620(5.2)	3 350(3.4)
16.30	1220(4.0)	1160(4.0)	1 230(5.0)	2 400(3.4)
20.90	974(3.7)	959(3.6)	1 000(4.5)	1 620(3.4)
27.30	866(3.4)	858(3.3)	760(4.5)	1 240(3.4)
37.10	760(3.2)	792(3.0)	694(4.0)	1 090(3.2)
52.90	681(3.0)	658(3.0)	601(3.8)	802(3.3)

[a] Percent uncertainties (in parentheses) are statistical only. The yields include neutrons produced by the interactions of primary neutrons and secondary charged particles as well as the effects of neutron scattering in the thick targets (see text).

TABLE VII. Neutron yields from 640-MeV alphas stopping in a lead target.

Energy (MeV)	Neutron yield[a] (Neuts/10^6 alphas MeV sr)	Energy (MeV)	Neutron yield[a] (Neuts/10^6 alphas MeV sr)
	0 deg		45 deg
10.0	3 630 (9.4)	27.30	655 (5.5)
12.3	3 500 (8.0)	37.10	505 (5.5)
15.0	2 390 (8.8)	52.90	390 (5.6)
18.5	1 910 (9.1)		
22.8	1 900 (8.3)		90 deg
28.2	1 900 (6.7)	13.2	581 (5.2)
35.2	1 520 (6.4)	17.8	381 (5.7)
44.3	1 540 (5.4)	23.8	257 (6.2)
56.5	1 530 (4.8)	31.8	141 (6.5)
68.6	1 530 (6.0)	42.3	94.4 (6.6)
79.8	1 810 (5.1)	56.2	46.7 (8.5)
93.7	1 830 (4.7)	69.4	29.5(14.0)
111.0	1 770 (4.3)	81.6	19.0(16.0)
134.0	1 620 (4.0)		
165.0	1 040 (4.4)		120 deg
207.0	332 (6.7)	13.2	953 (3.9)
268.0	62.1(13.0)	17.8	560 (4.5)
		23.8	273 (6.0)
	45 deg	31.8	141 (6.5)
3.39	18 600 (3.7)	42.3	51.7 (9.5)
3.91	12 800 (3.8)	56.2	21.7(14.0)
4.52	10 000 (3.8)	69.4	10.3(28.0)
5.27	7 270 (4.1)		
6.18	5 260 (4.4)		150 deg
7.32	4 210 (4.4)	12.8	905 (2.2)
8.79	2 880 (5.0)	17.1	416 (3.0)
10.60	2 180 (5.3)	22.8	200 (4.2)
13.10	1 620 (5.7)	30.4	87.5 (5.1)
16.30	1 080 (6.0)	40.7	24.6 (9.2)
20.90	857 (5.5)	54.7	8.2(17.0)

[a] Percent uncertainties (in parentheses) are statistical only. The yields include neutrons produced by the interactions of primary neutrons and secondary charged particles as well as the effects of neutron scattering in the thick targets (see text).

tent with the production mechanism proposed by Bertini[10] in which a free nucleon from the dissociated incident ion interacts with the tangential component of the fermi momentum of a nucleon in the target.

Calculations based on classical equations of motion[11] suggest that central collisions (with small impact parameters) of heavy ions with nuclei result in an isotropic distribution in the center-of-mass system of the emitted particles. Much of the initial kinetic energy of the heavy ion is dissipated in the prolific production of particles. This effect is observed in the measured neutron spectra which become more nearly isotropic at low energies.

In Table VIII, we list the total integrated neutron yield above 10 MeV for each of the targets. There are about 0.5 neutrons above 10 MeV per incident alpha, relatively independent of the target nucleus. The flux in the backward hemisphere increases as the atomic number of the target increases and is only 10 to 20 percent of the total flux. The NE-213 measurements on lead at angles of 0, 45, 90, and 135 deg were used in conjunction with the NE-102 measurements to obtain the angle-integrated neutron yields above 3.0, 5.0, 10.0, 20.0, and 50.0 MeV. These data are shown in Fig. 10 and are well represented by the simple

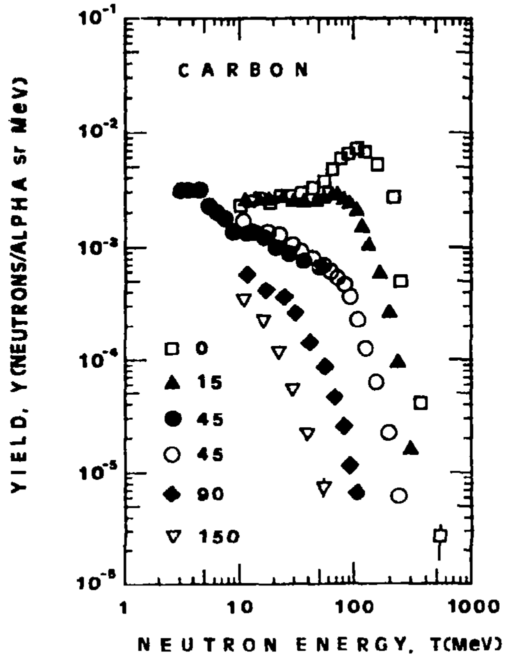

FIG. 4. Neutron yield spectra at laboratory angles of 0, 15, 45, 90, and 150 deg from 710-MeV alphas stopping in a carbon target. The data shown as solid circles are from the NE-213 detector.

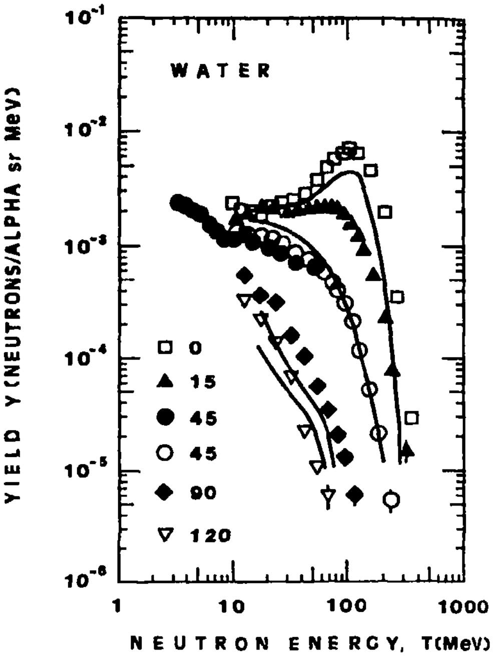

FIG. 5. Neutron yield spectra at laboratory angles of 0, 15, 45, 90, and 120 deg from 710-MeV alphas stopping in a water target compared with Monte Carlo intranuclear-cascade calculations for alphas interacting in an oxygen target. The four calculations shown as the solid lines are averaged over the angular ranges 0–10, 30–60, 80–110, and 110–130 deg, respectively. The data represented by solid circles are from the NE-213 counter.

power law

$$Y[>T\ (\text{MeV})] = 2.35T^{-0.65}\,. \tag{3}$$

The total yield of neutrons above 3.0 MeV for the lead target is about 1.2 neutrons per incident alpha.

VI. SUMMARY

We measured neutron angular and energy distributions produced by 710-MeV alphas stopping in targets of water, carbon, steel, and lead, and 640-MeV alphas stopping in a lead target. Measurements are presented for neutron energies as low as 3 MeV and up to about 300 MeV. The neutron angular distributions are forward peaked with a broad bump at about 120 MeV in the 0- and 6-deg spectra. Also the 0- and 6-deg neutron spectra have significant yields of neutrons above the kinetic energy per nucleon of the incident alpha beam. The 640-MeV spectra are similar to the 710-MeV spectra but the 640-MeV yields are reduced in magnitude by about 20 percent. The largest source of uncertainty in these measurements is associated with the contribution of room-scattered neutrons to the subtracted backgrounds. The overall uncertainty in the absolute normalization of these data is estimated to vary from about 9 to 13 percent. The statistical uncertainty of the data is typically 5 percent.

These measurements are important for the design of beam dumps and shielding for medium-energy heavy-ion accelerators. The neutron spectra from alphas stopping in carbon and water targets are of interest also for estimating neutron background doses in heavy-ion cancer radiotherapy. The calculations of an intranuclear-cascade model for an oxygen target are consistent with the measurements for the water target at forward angles but are always smaller than the measured yields at backward angles.

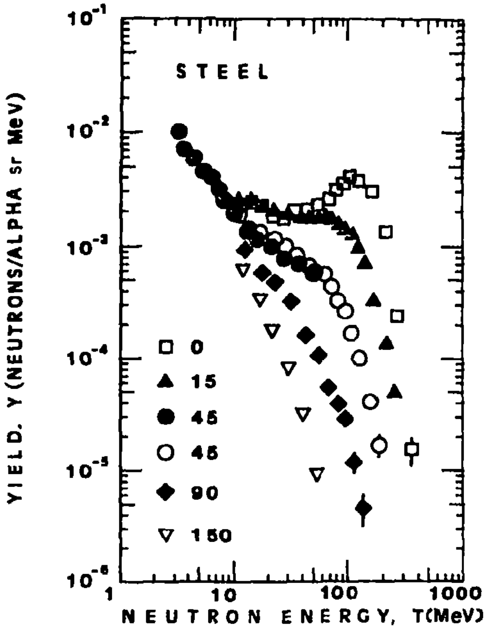

FIG. 6. Neutron yield spectra at laboratory angles of 0, 15, 45, 90, and 150 deg from 710-MeV alphas stopping in a steel target. The data shown as solid circles are from the NE-213 counter.

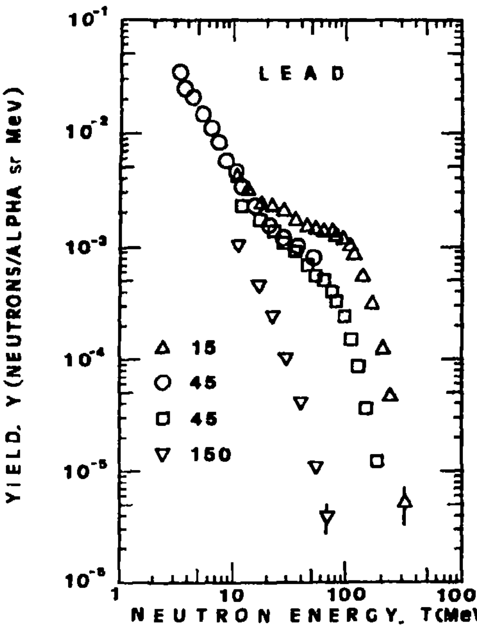

FIG. 8. Neutron yield spectra at laboratory angles of 15, 45, and 150 deg from 710-MeV alphas stopping in a lead target. The data shown as circles are from the NE-213 counter.

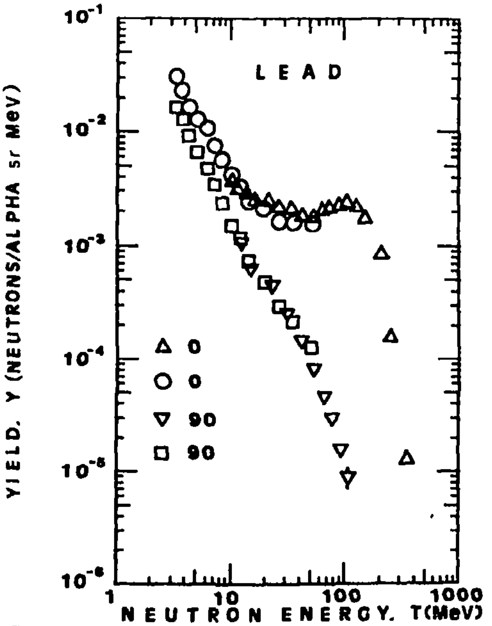

FIG. 7. Neutron yield spectra at laboratory angles of 0 and 90 deg from 710-MeV alphas stopping in a lead target. The data shown as squares and circles are from the NE-213 counter.

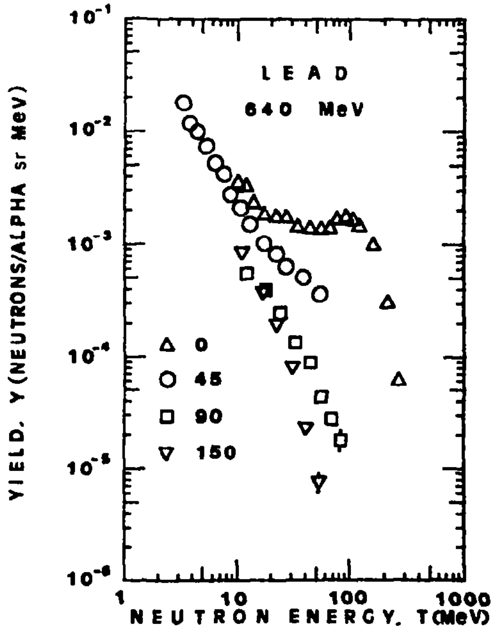

FIG. 9. Neutron yield spectra at laboratory angles of 0, 45, 90, and 150 deg from 640-MeV alphas stopping in a lead target. The data shown as circles are from the NE-213 counter.

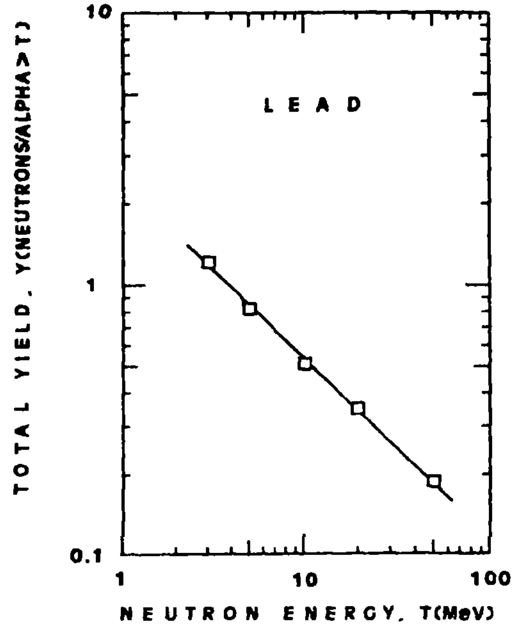

FIG. 10. The angle-integrated neutron yields above a given energy from 710 MeV alphas stopping in a lead target.

TABLE VIII. Neutrons above 10 MeV per 100 alphas.

Target	Total	Forward $(0<\theta<90)$	Backward $(90<\theta<180)$
Water	52	48	4
Carbon	58	54	4
Steel	51	44	7
Lead	51	43	8

ACKNOWLEDGMENTS

We gratefully acknowledge the support and advi of Professor N. S. Wall of the University of Maryland during the preliminary stage of this experiment and the support and assistance of the staff at the Space Radiation Effects Laboratory during the running of this experiment. We thank Dr. T. Gabriel of Oak Ridge National Laboratory for performing heavy-ion cascade calculations for us. This work was supported in part by the Department of Energy under Contract No. EY-76-S-02-2231 and the National Science Foundation under Grants Nos. PHY-75-02870, PHY-79-07790, PHY-76-02206, and PHY-78-01684.

---

*Present address: Jet Propulsion Laboratory, 4800 Oak Grove Drive, Pasadena, California 91103.

†Present address: Department of Radiation Therapy and Nuclear Medicine, Thomas Jefferson University, Philadelphia, Pennsylvania 19107.

[1] T. A. Gabriel, private communication, calculations done with the code HIC-1, described in H. W. Bertini, T. A. Gabriel, R. T. Santoro, D. W. Herman, N. M. Larson, and J. M. Hunt, ORNL/TM-4134 (1974); H. W. Bertini, T. A. Gabriel, and R. T. Santoro, Phys. Rev. C 9, 622 (1974).

[2] R. A. Cecil, B. D. Anderson, R. Madey, Nucl. Instrum. Methods 161, 439 (1979).

[3] R. Madey and F. M. Waterman, Nucl. Instrum. Methods 106, 89 (1973).

[4] A. R. Baldwin and R. Madey, Nucl. Instrum. Methods 128, 557 (1975).

[5] R. Hartmann, H. P. Isaak, R. Engfer, E. H. Hermes, H. S. Pruys, W. Dey, H. J. Pfeiffer, U. Sennhauser, H. K. Walter, and J. Morgenstern, Nucl. Phys. A308, 345 (1978).

[6] H. Knox and T. Miller, Nucl. Instrum. Methods 101, 519 (1972).

[7] R. Madey, F. M. Waterman, A. R. Baldwin, J. D. Carson, and J. Rapaport, Nucl. Instrum. Methods 151, 4 (1978).

[8] BNL 325, 3rd ed., Vol. 2, Brookhaven National Laboratories, Upton, New York, 1976.

[9] H. W. Patterson and R. H. Thomas, *Accelerator Healt Physics* (Academic, New York, 1973).

[10] H. W. Bertini, R. T. Sanforo, and O. W. Hermann, Phys. Rev. C 14, 590 (1977).

[11] A. R. Bodmer and C. N. Panos, Phys. Rev. C 15, 134 (1977).

PHYSICAL REVIEW C VOLUME 21, NUMBER 6 JUNE 1980

800-MeV inelastic proton scattering from ^{40}Ca, ^{48}Ca, and ^{54}Fe

G. S. Adams,* Th. S. Bauer,† G. Igo, G. Pauletta, C. A. Whitten, Jr., and A. Wriekat
Physics Department, University of California, Los Angeles, California 90024

G. W. Hoffmann
Physics Department, University of Texas, Austin, Texas 78712
and Los Alamos Scientific Laboratory, Los Alamos, New Mexico 87545

G. R. Smith
Physics Department, University of Colorado, Boulder, Colorado 80302

M. Gazzaly‡
Physics Department, University of Pennsylvania, Philadelphia, Pennsylvania 19174

(Received 15 November 1979)

Differential cross sections have been measured over a wide range of angles for the well resolved and/or strongly excited peaks in the inelastic proton spectra from ^{40}Ca, ^{48}Ca, and ^{54}Fe targets. Inelastic analyzing powers were also measured for the ^{54}Fe transitions. Microscopic distorted-wave impulse approximation analyses of the 2_1^+ transitions in ^{48}Ca and ^{54}Fe yield values for the ratio $B(N2)/B(E2)$. Collective-model distorted-wave Born-approximation calculations for the high-spin levels at 8.85 and 9.24 MeV in ^{40}Ca suggest spin and parity assignments of 6^+ and 5^-, respectively.

[NUCLEAR REACTIONS ^{40,48}Ca, ^{54}Fe$(\vec{p},p')$; measured $\sigma(\theta)$, $A(\theta)$; deduced optical-model parameters, $B(N2)$, DWBA analysis.]

I. INTRODUCTION

One of the primary reasons for extending pro- n-nucleus scattering measurements to inter- ediate energies is the hope that unambiguous formation about nuclear wave functions can be duced from the data. Theoretical descriptions intermediate-energy proton-nucleus scattering e much simpler than their low-energy counter- rts.[1] In particular, the effective nucleon-nu- eon (N-N) interaction more closely resembles e free N-N interaction as the projectile energy raised.[2]

Although proton-nucleus elastic scattering at termediate energies has been extensively stud- d for the purpose of extracting ground-state neu- on density distributions,[3,4] this technique has ldom been applied to the study of neutron tran- tion densities via inelastic scattering. The fact at proton inelastic scattering is sensitive to the ape of the nuclear transition density will be monstrated from the analysis of new 800-MeV $,p')$ data. Angular distributions for a variety transitions in ^{40}Ca, ^{48}Ca, and ^{54}Fe have been easured and theoretical analyses based on the storted-wave Born approximation (DWBA) have en performed. While most of these data are ell reproduced by calculations which assume a llective-model form factor, some transitions require a more microscopic treatment of the transition density.

II. EXPERIMENTAL PROCEDURE

Data were obtained using the high resolution spectrometer at the Clinton P. Anderson Meson Physics Facility. The beam energy, 800 ± 2 MeV, was determined by measuring the kinematic energy difference resulting from elastic scattering from ^{40}Ca and ^{16}O targets. Differential cross sections and analyzing powers (^{54}Fe only) were measured out to a maximum momentum transfer q of 3.4 fm^{-1}. During the analyzing power measurements the transverse beam polarization P was continuously monitored by measuring the ^{1}H$(\vec{p},p)$ analyzing power, using a thin CH$_2$ target located upstream from the scattering chamber. The average value for P was 76%.

Measurements were performed at laboratory scattering angles from 4° to about 24°. These data were sorted into 0.5° scattering angle bins (three bins per spectrometer setting) by off-line analysis. The relative uncertainty in the scattering angle points is estimated at ±0.015°. The absolute scattering angle was determined by normalizing to published ^{12}C$(\vec{p},p)$ data,[5] resulting in an absolute uncertainty of ±0.07°.

Excitation energies up to at least 15 MeV were

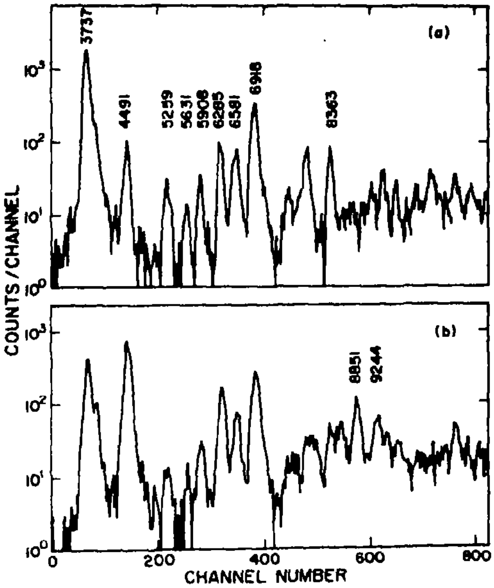

FIG. 1. Inelastic proton spectra from ^{40}Ca(p,p') at laboratory scattering angles of 8° (a) and 13.5° (b). The energy scale is approximately 10 keV per channel and the excitation energies of some of the strong peaks are given in keV.

measured in all three targets. Sample spectra are shown in Figs. 1 and 2. Typical energy resolutions for these measurements were 105, 130, and 140 keV full width at half maximum (FWHM) for ^{40}Ca, ^{48}Ca, and ^{54}Fe, respectively. Fixed lineshape peak fitting programs were used to extract peak areas for excitation energies up to 12.5, 9.0, and 6.5 MeV in these respective nuclei. Angular distributions will be presented for those peaks that are dominated by a single state, plus the 5.26 and 6.92 MeV doublets in ^{40}Ca. Cross sections for these transitions were measured relative to the count rates in two plastic-scintillator monitor telescopes which viewed the target at scattering angles of plus and minus 80°. These cross sections were normalized absolutely to the elastic cross sections of Refs. 6 and 7 at laboratory scattering angles $\lesssim 8°$, with relative uncertainties of about ±4% in each case. Adding these errors in quadrature with the ten percent uncertainties present in the published elastic scattering data[6,7] yields absolute cross section uncertainties of ±12% for ^{40}Ca and ±11% for ^{48}Ca and ^{54}Fe.

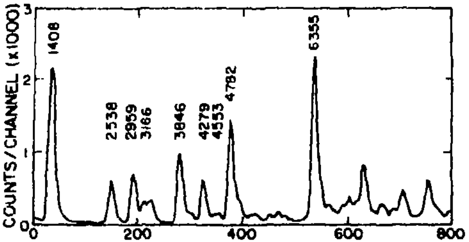

FIG. 2. Inelastic proton spectrum from ^{54}Fe($\vec{p}$,p') at 8° (laboratory). This spectrum is composed of the sum of both beam polarizations, with scattering angle bin ≈ 1.5°. The energy scale is approximately 10 keV per channel and the excitation energies of some of the strong peaks are given in keV.

Excitation energies for high-lying levels were determined relative to several well known levels in the same nucleus.[8-10] These calibration levels are indicated by parentheses in Table I.

Targets of isotopically enriched ^{40}Ca (>99.9%), ^{48}Ca (94.5%), and ^{54}Fe (97.6%) were used for the present measurements. Target thicknesses were 48, 101, and 97 mg/cm^2, respectively. A 5.3% ^{40}Ca contamination in the ^{48}Ca target was the only noteworthy contaminant in any of the targets. Substantial contributions from the 3_1^- excitation in ^{40}Ca were subtracted from the ^{48}Ca 2_1^+ data.

III. DATA AND COLLECTIVE MODEL DWBA ANALYSIS

Figures 3–8 show the differential cross sections and analyzing powers measured in this experiment. One interesting feature of these data is the variety of shapes exhibited in the angular distributions for transitions having the same orbital angular momentum transfer, L. The best examples are the 3^- transitions in ^{40}Ca and the 2^+ transitions in ^{54}Fe. This variety is not exhibited in the ^{40}Ca (α, α') data of Rutledge and Hiebert,[14] probably because the alpha particle is more strongly absorbed than an 800-MeV proton.

The solid curves in Figs. 3 through 8 are the results of collective-model DWBA calculations in which the form factors are proportional to the derivative of the elastic scattering optical potentials. The parameters of these phenomenological optical potentials, given in Table II, were fitted to the elastic differential cross section and polarization data of Refs. 6 and 7. The elastic and inelastic analyses used relativistic kinematics,[15] and the deformed spin-orbit amplitude was included in the DWBA using the full Thomas form.[16] Spin-orbit and central deformation parameters were set equal to one another. The importance of the spin-orbit amplitude for 800-MeV protons has been previously emphasized.[17,18] Program constraints limited the number of partial waves used in the DWBA calculations to 50. Because of this limitation, only the results for scattering angles less than 20° were deemed accurate. This limit was determined by calculations with a different pro-

TABLE I. Deformation lengths $\delta_L (=\beta_L R_{\mathrm{optical}})$ from collective-model DWBA analyses.

Nucleus	J^π	E_x[a] (keV)	E_x[b] (keV)	δ_L[b] (fm)	δ_L[c] (fm)
^{40}Ca	0^+	3352	(3352)		
	3^-	3737	(3737)	1.39	1.32
	2^+	3904	3915 ± 12	0.52	0.43
	5^-	4491	(4491)	0.76	0.80
	0^+	5213			
	2^+	5249	5259 ± 10		0.12
	4^+	5279			0.13
	4^-	5614			
	2^+	5630	5631 ± 5	0.15	
	1^-	5903	5908 ± 13		
	2^-	6026			
	3^+	6029			
	3^-	6285	(6285)	0.38	0.40
	4^+	6508			0.17
	4^+	6543			
	3^-	6583	6581 ± 10	0.34	0.32
	2^-	6751	6700 ± 42		
	2^+	6909	6918 + 20	0.49	0.45
		6927			
	(6^+)	6930			
		6938			
	1^-	6951			
	4^+	8373	8363 ± 13	0.35	0.33
	$(6-8)^+$	8851	8851 ± 9	$\delta_8=0.28$	$\delta_7=0.09$
	$(6-8)^-$	9237	9244 ± 9	$\delta_5=0.23$	$\delta_7=0.06$
^{48}Ca	2^+	3832	(3832)	0.64	0.70
	0^+	4284			
	(4^+)	4503			
	3^-	4507	4518 ± 20	0.87	0.81
	3^-	5370	5376 ± 25	0.41	0.46
	0^+	5461			
	5^-	5729	(5729)	0.38	0.46
^{54}Fe	2^+	1408	(1408)	0.86	0.75
	4^+	2538	(2538)	0.36	
	0^+	2561			
	6^+	2950			
	2^+	2959	(2959)	0.51[d]	0.67
	2^+	3166	(3166)	0.30	
	4^+	3295			
	3	3345			
	4^+	3834	3846 ± 15	0.43	
	(4^+)	4033			
	4^+	4047			
	3	4072			
	4^+	4263	4279 ± 18	0.35	
	(0)	4292			
	2^+	4578	4553 ± 36	0.26	
	(2^+)	4655			
	3^-	4760	4782 ± 12	0.47	0.54
	3^-	6335	6355 ± 14	0.63	0.67

[a] Excitation energies and J^π values from Refs. 8, 9, and 10.

[b] Present work. For the 800-MeV analysis $\delta_L \equiv \beta_L r_I A^{1/3}$.

[c] See Refs. 11, 12, and 13.

[d] Add these numbers in quadruture for comparison with the value on the right.

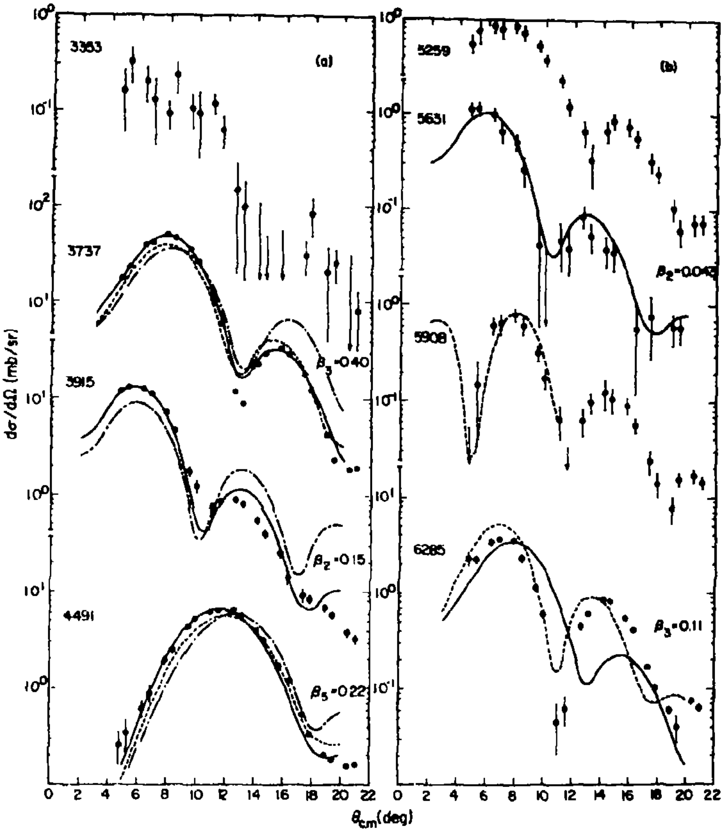

FIG. 3. Angular distributions for excitations in ^{40}Ca. Solid lines are the results of collective-model DWBA calculations with β_L indicated for each case. The remaining curves (described in the text) are the results of microscopic DWIA calculations.

gram which allowed more partial waves to be included but did not have provisions for a spin-orbit transition operator.

The DWBA results, including deformation parameters (β_L^2 = measured rate/calculated rate), are given in Figs. 3 through 8. Very good agreement was obtained between the shapes of the DWBA predictions and the measured angular distributions for most transitions. Table I summarizes the present results and compares them with the low-energy proton results of Refs. 11–13. The deformation length $\delta_L (=\beta_L R_{\text{optical}})$ was chosen as the most unambiguous parameter for comparison. For the present analysis $R_{\text{optical}} = r_i A^{1/3}$. This comparison reveals that the results of the 800-MeV analysis are in good agreement with most of the low-energy work. It should be mentioned that considerable variation exists in the published deformation lengths for the ^{54}Fe transitions.[10] Our results show better agreement with the results of Fricke and co-workers[13] than with those of some other authors (see the compilation in Ref. 10).

More interesting than this general confirmation of the distorted-wave method are those exceptional cases in which the DWBA fails to reproduce the data. The best examples are the $J_N^\pi = 2_1^+$, 4_1^+, 3_2^-, and 3_3^- transitions in ^{40}Ca, with excitation energies of 3.91, 5.26, 6.28, and 6.58 MeV, respectively. The failure in the case of the 2_1^+ state manifests itself in predicted cross sections that are too oscillatory at large angles. Note also that the present deformation length is considerably larger than the value deduced by Gruhn *et al.*[11] Based on low-energy proton scattering results,[11] the peak at 5.26 MeV is expected to have substantial contributions from both the 2_2^+ and the 4_1^+ states. It was not possible to achieve a reasonable fit to the present data using a sum of $L=2$ and $L=4$ distributions. The presence of a minimum in the measured angular distribution at 13.5° is particu-

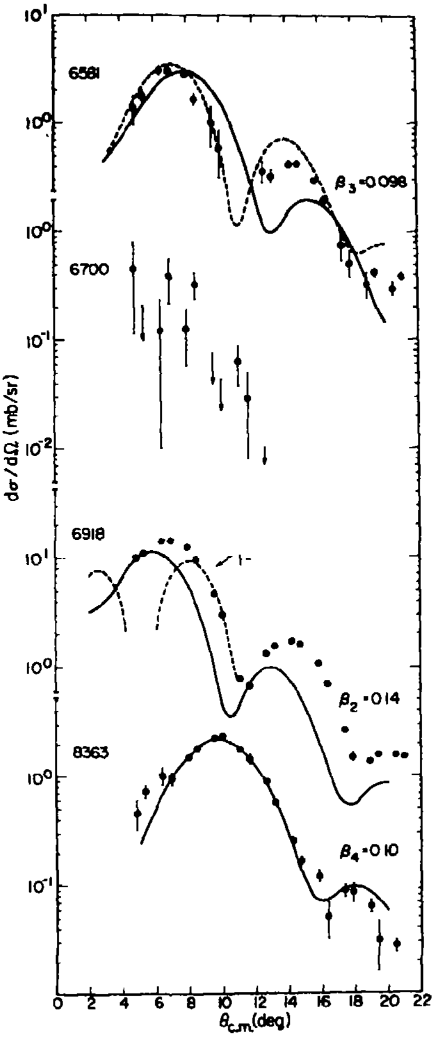

FIG. 4. Same as Fig. 3.

larly restrictive. Since a sum of $L=2$ and $L=3$ distributions with $\beta_2=0.027$ and $\beta_3=0.048$ provided a much better description of the data, we conclude that an anomalous 4^+ angular distribution is the source of difficulty. As the 2_1^+ and 4_1^+ states in ^{40}Ca are members of a $K^\pi=0^+$ rotational band,[19] it appears likely that the neglect of coupled-channels effects may be the cause of the disagreement between the DWBA and the data for these two transitions. Previous analyses of inelastic proton scattering from ^{12}C (Ref. 20) and ^{58}Ni (Ref. 21) have demonstrated the importance of such effects for 800-MeV protons. The analysis presented in

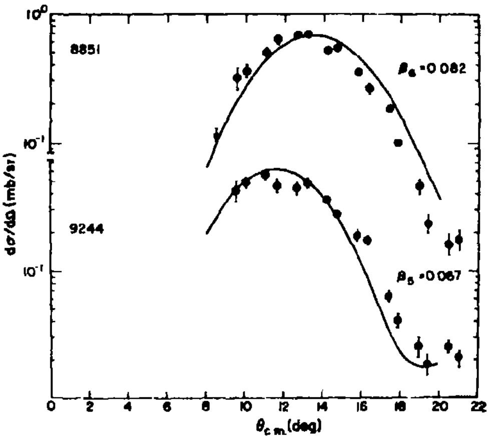

FIG. 5. Angular distributions for the high-spin states in ^{40}Ca. The theoretical curves are the best-fit DWBA results, with β_L indicated for each case.

the next section shows that the discrepancies observed between the DWBA calculations and the 3_2^- and 3_3^- data are due to the fact that these states have wave functions that are quite different from those produced by the collective model.

Other interesting features of the present data are the weak excitation of the 2^- state at 6.7 MeV in ^{40}Ca, and the strong excitation of the levels at 8.85 and 9.24 MeV (see Figs. 4 and 5). Although the 2^- peak was not resolved from the adjacent peaks at 6.58 and 6.92 MeV in any of the measured spectra, its presence was required at several angles in order to obtain good peak fitting results. In view of this fact, we assign an absolute cross section uncertainty of ±50% to the 2^- data. The levels at 8.85 and 9.24 MeV are known to have high spin; low-energy (p,p') work suggests $L=7$ for both of these levels.[11] Spin and parity assignments of 6^- have also been suggested by the low-energy work because the $(d_{3/2}^{-1},f_{7/2})$ "stretched" configuration produces the states with highest spin in a $1\text{-}\hbar\omega$ particle-hole basis. Since the corresponding 6^- states[22] are not strongly excited by 800-MeV proton scattering from ^{24}Mg and ^{28}Si,[23] this assignment is unlikely for these strong ^{40}Ca excitations. We also observe no measurable excitation of the stretched 8^- state located at 13.26 MeV in ^{54}Fe.[24] Figure 5 shows the DWBA results for the ^{40}Ca transitions. The best agreement between the DWBA and the data was obtained with $L=6$ and $L=5$ for the 8.85 and 9.24 MeV transitions, respectively. However, an $L=6$ assignment for the 9.24-MeV state cannot be ruled out. In view of these results we suggest that the states at 8.85 and 9.24 MeV have natural parity, with probable J^π assignments of 6^+ and 5^-, respec-

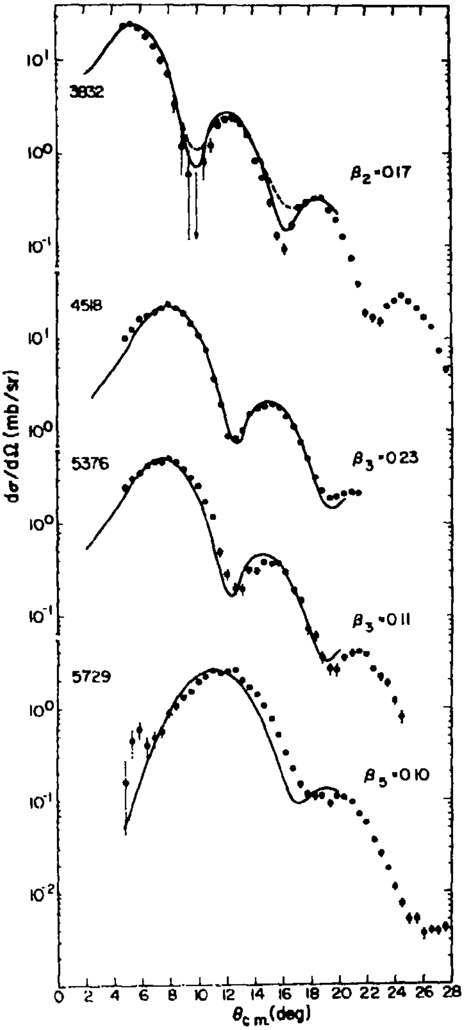

FIG. 6. Same as Fig. 3, but for ^{48}Ca.

tively. Large-angle (e,e') and (α,α') measurements coupled with the present data would provide unambiguous spin, parity, and isospin assignments for these states. Forthcoming asymmetry data should also prove interesting since, as one can see from Fig. 8, the DWBA is able to reproduce the analyzing powers for a variety of natural-parity transitions rather well.[17]

IV. DWIA ANALYSIS

Distorted-wave impulse approximation (DWIA) calculations for some natural-parity transitions were carried out following the approach of Haybron, Johnson, and Metzger.[25] Empirical proton transition densities ρ_p resulting from fits to inelastic electron scattering data were used in these calculations. The parameters of the neutron density ρ_n were either set equal to the proton ones (as for ^{40}Ca) or adjusted to fit the (p,p') data. Although this method has been applied to a number of lower-energy (p,p') studies,[26] it has received only limited application in the region of 1-GeV proton energy.[4] Similar studies of intermediate-energy proton[27] and alpha[28] inelastic scattering have been carried out in the Glauber formalism. Exchange effects were included implicitly through the use of a symmetrized N-N t matrix,[1,3,4] a procedure which is known to be valid at high energies.[1,3,4,29] Contributions from the spin-spin parts of the nucleon-nucleon t matrix were neglected,[4] as were the small S-1 spin-orbit amplitudes.[18,30] The distorted waves were again generated with the optical potentials of Table II.

A. ^{40}Ca

Analyses[3,4] of proton elastic scattering data[8,31] are consistent with the assumption that the ground-state neutron and proton distributions of ^{40}Ca are approximately equal. Therefore, in the present investigation the approximation $\rho_n = \rho_p$ was deemed sufficiently accurate for the low-lying excited states of ^{40}Ca as well. Thus the ^{40}Ca data will provide a test of the DWIA approach which is relatively insensitive to nuclear structure uncertainties. The N-N t matrix was taken from the elastic scattering analysis of Ray,[3] the spin-orbit part having been fitted to the 800-MeV $p+{}^{40}$Ca elastic scattering data, with appropriate adjustments for the $p+$ nucleus center-of-mass frame.[4] The empirical charge transition densities ρ_{ch} were also taken from the literature. Figure 3 shows the effect of assuming different shapes for ρ_{ch}. The dot-dash and dashed curves for the 3_1^- and 2_1^+ transitions used Tassie[32] and shell-model[33] shapes, respectively. The dot-dash and dashed curves for the 5_1^- transition show a similar comparison using Gaussian[34] and shell-model ($\alpha = 0$ fit in Ref. 33) shapes, respectively. Striking differences are observed, particularly at high momentum transfers, between the different calculations and between some of the calculations and the (p,p') data. The differences between the calculations are due to the differences in the shapes of the transition densities. These shape differences arise primarily from a dependence of the electron scattering analyses on the range of momentum transfer q spanned by the data. Generally only the first maximum in the momentum-space form factors is well determined. One

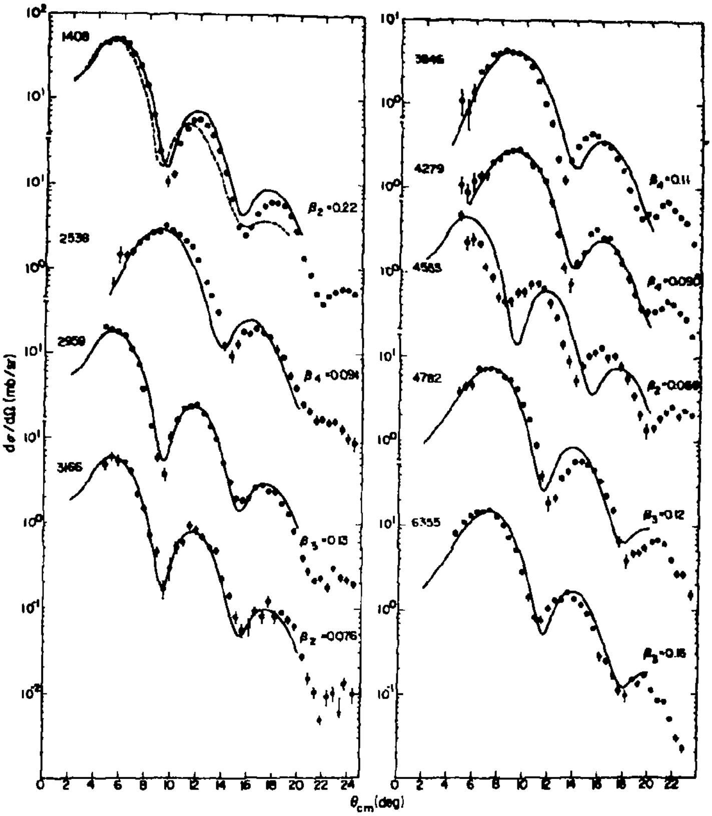

FIG. 7. Same as Fig. 3, but for ^{54}Fe.

might expect that the (p,p') distributions would not be very sensitive to the high-q parts of the transition densities because the incident and outgoing proton waves are strongly distorted by the nuclear optical potential. Obviously this is not the case for the low-lying states in ^{40}Ca. Other examples are the 3_2^- and 3_3^- states. The predictions for these transitions, shown as dashed curves in Figs. 3 and 4, also used the shell-model transition densities of Itoh, Oyamada, and Torizuka.[33] In these cases the (p,p') data clearly demonstrate the same distinctive large-q enhancement that is present in the electron scattering form factors.[33] Such features do not appear in the (α,α') angular distributions[14] for these excitations, however, they can be observed in 135-MeV (p,p') data[35] and may be discernable in the low-energy proton data of Ref. 11.

The remaining DWIA calculations were for the 1^- states at 5.91 and 6.92 MeV. For these cases ρ_{ch} had the form

$$\rho_{ch}=C\left(\frac{1}{r^2}\frac{d}{dr}(r^3\rho)\right), \tag{1}$$

where C was determined by normalizing to the maximum in the (e,e') form factors,[33] and ρ was the ground-state density of Frosch *et al.*[36] Since this shape is not well determined at large q, the proton calculations were not extended beyond 11°. From Figs. 3 and 4 we observe that these calculations are in good agreement with the data, provided the excitation of both the 2^+ (6.91 MeV) and the 1^- (6.95 MeV) states are accounted for in the 6.92 MeV peak. Unlike the ^{16}O 1_1^- excitation,[18] the predicted minimum in the angular distribution for the 5.91 MeV state is present in the data. The overall agreement between the proton data and those DWIA calculations depicted by dashed curves in Figs. 3 and 4 is very encouraging. We interpret these results as a confirmation of the validity of the DWIA method in its present (approximate) form.

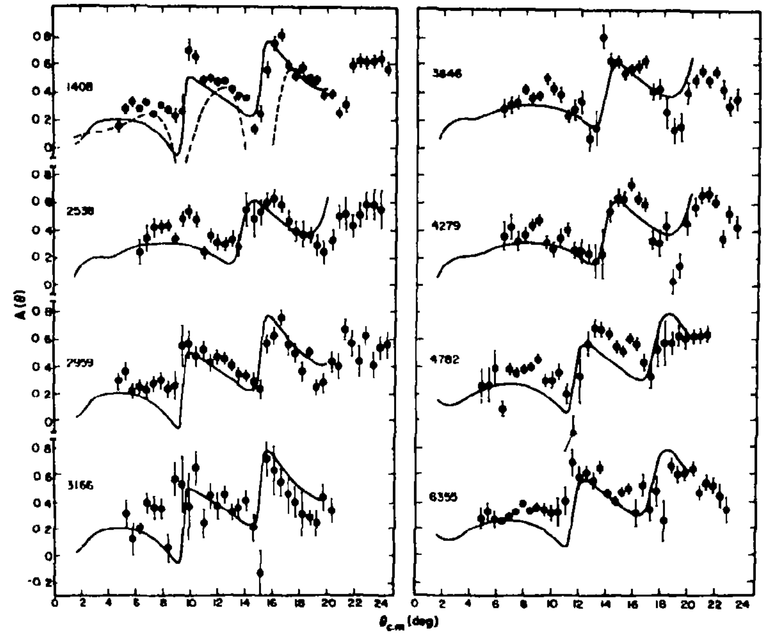

FIG. 8. Analyzing powers for excitations in ^{54}Fe. Solid lines are the results of collective-model DWBA calculations with $\beta_{so}=\beta_{central}$. The dashed curve is the result of a microscopic DWIA fit to the differential cross sections for the 2_1^+ transition.

B. ^{48}Ca

Having verified that the ^{40}Ca data are amenable to a DWIA approach, it is then possible to use the same method to study those cases for which $\rho_n \neq \rho_p$. Such a study has been carried out on a variety of nuclei by Chaumeaux, Layly, and Schaeffer[4] using 1-GeV proton scattering data.[4,31] Few electron scattering data exist for ^{48}Ca, however, Eisenstein *et al.*[37] have measured the small-q form factors of the low-lying states and fitted them with a Tassie-model shape. The resulting ρ_{ch} for the 2_1^+ state was used in the DWIA calculation of the (p,p') distribution.

Two choices for the N-N spin-orbit interaction were tried in the DWIA calculations, resulting in only minor differences in the predicted cross sections. Since the structure calculations of Ref. 38a and the results of the present analysis suggest that the isospin composition of the 2_1^+ state in ^{48}Ca could be very different from that of the ground state, the N-N parameters of "solution 1" in Ref. 3 were chosen over the isospin-averaged interaction of Ref. 6 for the analysis presented below. These parameters were fitted to the free N-N scattering data.

The Tassie-model parameters of ρ_n were adjusted to reproduce the proton data, with the final results depicted in Fig. 6. Although the overall fit to the data is reasonably good, one can observe interesting discrepancies in the regions of the minima. An important quantity which can be deduced from this fit is the neutron equivalent of the $B(E2)$ value $B(N2)$, where

TABLE II. Phenomenological optical-model parameters. The convention followed is that of Perey and Perey [At. Data Nucl. Data Tables 13, 293 (1974)]. No investigation of possible fitting ambiguities was made.

Nucleus	V (MeV)	W (MeV)	V_{so} (MeV)	W_{so} (MeV)	r_0 (fm)	a_0 (fm)	r_I (fm)	a_I (fm)	r_{so} (fm)	a_{so} (fm)	r_c (fm)
^{40}Ca	−4.40	66.6	0.64	2.34	0.89	0.69	1.01	0.61	0.98	0.65	1.05
^{48}Ca	−2.02	64.0	0.74	1.71	1.05	0.55	1.03	0.59	1.03	0.57	1.05
^{54}Fe	−3.39	65.9	0.73	1.72	0.94	0.69	1.04	0.57	1.01	0.65	1.05

$$B(NJ) \equiv (2J+1)\left| \int_0^\infty \rho_n r^{J+2} dr \right|^2 . \qquad (2)$$

This quantity is proportional to ρ_n^2 at q equal to zero. In the fit to the proton data it was most sensitive to the overall magnitude of $\rho_n(q)$ and hence to the peak cross section in the proton angular distribution. The resulting value of $B(N2) = 877\ e^2\,\mathrm{fm}^4$ is likely very model dependent. Since the final shapes for ρ_n and ρ_p are similar, a less model dependent quantity is $B(N2)/B(E2) = 10.2 \pm 3.0$.[38b] The error in this ratio is composed of a 12% uncertainty in $B(E2)$,[37] an 18% error in $B(N2)$ for proton cross section normalization uncertainty, and a 20% error in $B(N2)$ due to ambiguities in the fitted parameters of ρ_n. One further source of error that is difficult to determine is the uncertainty in the q dependence of ρ_{ch}. The electron scattering data[37] do not span the necessary range of momentum transfer to determine ρ_{ch} in the region covered by the proton data, and this results in a correlated uncertainty in the deduced value of $B(N2)$. Because of these uncertainties it is useful to compare $\rho_n(q)$ with $\rho_p(q)$ near their maxima. Such a comparison does not require large extrapolations of either the electron or proton fits. Also, multiple scattering effects are minimal near the maximum in ρ_n.[4] In fact, at $q = 0.8\ \mathrm{fm}^{-1}$ the ratio $\rho_n^2/\rho_p^2 = 6.7$ may be a better estimate of the ratio $B(N2)/B(E2)$ than the value deduced above. Contributions to the error in $B(N2)/B(E2)$ due to uncertainties in the N-N amplitudes and second order transitions have been omitted,[4] as have contributions due to model dependence.

Both of the above mentioned estimates of $B(N2)/B(E2)$ are surprisingly large results. They are considerably larger than the values deduced by the same technique for the 2_1^+ states in ^{40}Ca, ^{44}Ca, and a variety of Ni isotopes.[4] Unfortunately the present estimates are inconsistent with the DWBA analysis presented in Sec. III. Approximately equal β_2 values were deduced for the 2_1^+ transitions in both ^{40}Ca and ^{48}Ca, and the electron scattering analyses[37] yield approximately equal $B(E2)$ values as well. This implies that $B(N2)/B(E2) \simeq 1$ for the ^{48}Ca state. This inconsistency can be removed only if the DWBA method of analysis is shown to be inappropriate for the ^{40}Ca 2_1^+ transition (e.g., if coupled channels are important) or if large sources of error remain unaccounted for in the ^{48}Ca DWIA analysis. These 2_1^+ transitions warrant further theoretical study, as well as experimental investigation with electron and proton probes.

C. ^{54}Fe

Although a significant amount of ^{54}Fe (e,e') data has been published,[38] analysis of the proton data is complicated by the absence of phenomenological fits to the electron scattering data. An approximate fit to the 2_1^+ charge form factor was obtained as follows. A Tassie-model shape with the parametrization

$$\rho_{ch} = Kr \frac{d}{dr}\left(1 + e^{(r-C)/Z}\right)^{-1}$$

was assumed. The value for Z was extrapolated from the ^{56}Fe value of Ref. 34 using the results of their Ca and Ti isotopic analyses, and C and K were fitted to the small-q data of Ref. 39 in a plane-wave calculation. Thus the resulting values of $Z = 0.692$ fm, $C = 3.48$ fm, and $B(E2) = 1159\ e^2\,\mathrm{fm}^4$ are not as well determined as one would like. In particular, one should note that this $B(E2)$ value is about 60% larger than what would have been obtained by normalizing the shell-model form factor of Ref. 39 to agree with their data, and is more than twice as large as the value determined by Morrison, Smith, and Amos.[40]

Two choices for the N-N spin-orbit interaction[3,7] were again tried in the DWIA calculations, resulting in only small differences in the predicted cross sections and hence in the deduced value of $B(N2)$. The isospin-averaged interaction of Ref. 7 produced inelastic analyzing powers that were in better agreement with the 2_1^+ data of Fig. 8 than those calculated with the solution 1 interaction of Ref. 3; therefore, the former was chosen for the analysis presented below. The parameters of this interaction were fitted to the 800-MeV ^{54}Fe(p,p) cross section and asymmetry data.[7]

In view of the large uncertainties present in the parameters of ρ_{ch} for the 2_1^+ excitation, fitting the proton cross section data by varying all of the parameters of ρ_n is not very instructive. Figures 7 and 8 show the results that were obtained by adjusting only the magnitude of ρ_n, assuming the same shape for ρ_n and ρ_p. As in the previous case the resulting value for $B(N2)$, $985\ e^2\,\mathrm{fm}^4$, shows little sensitivity to small changes in C and Z provided the maximum value of the (p,p') cross section is always reproduced. Using the $B(E2)$ value given above we obtain the ratio $B(N2)/B(E2) = 0.85 \pm 0.27$. The error is composed of a 10% uncertainty in $B(N2)$ due to an uncertainty in the peak magnitude of the electron scattering form factor, 15% uncertainties in each of $B(N2)$ and $B(E2)$ due to proton and electron fitting ambiguities, respectively, and a 21% error in $B(N2)$ due to proton absolute cross section uncertainty. No model dependence was included in the error analysis.

From Fig. 8 one can easily observe that the above procedure produces only qualitative agreement between the DWIA prediction and the 2_1^+ analyzing power data. This suggests that a phenomenological approach which fits the parameters of the spin-orbit t matrix to the inelastic analyzing power, rather than the elastic analyzing power, might be more appropriate.

V. SUMMARY AND CONCLUSIONS

Angular distributions for 800-MeV proton excitation of many discrete states in ^{40}Ca, ^{48}Ca, and ^{54}Fe have been presented. These data show a variety that is not present in low-energy alpha particle distributions. While the collective-model DWBA provides a good description of most of the data, its failures are not limited to those cases in which coupled channels effects are expected to be important. DWIA calculations using empirical electron scattering transition densities resolve some of these discrepancies and show an unexpected sensitivity to the shapes of the transition densities at large q. Full exploitation of the DWIA method of analysis is hampered by the scarcity of high-resolution electron scattering data for targets of ^{48}Ca and ^{54}Fe. However, it was possible to extract values for the ratio of $B(N2)$ to $B(E2)$ for the 2_1^+ states by adjusting the parameters of ρ_n to fit the present data.

The relatively large strengths measured for the 8.85 and 9.24 MeV transitions in ^{40}Ca suggest that these are natural-parity states. Collective-model DWBA analyses of these states are consistent with $J^\pi = 6^+$ and 5^-, respectively.

ACKNOWLEDGMENTS

We wish to thank Dr. F. Petrovich for providing the distorted-wave programs and for many helpful discussions. This work was supported in part by the United States Department of Energy, the National Science Foundation, and the Robert A. Welch Foundation.

---

*Present address: Department of Physics and Laboratory for Nuclear Science, Massachusetts Institute of Technology, Cambridge, Mass. 02139.

†Present address: CEN de Saclay, Gif-sur-Yvette, France.

‡Present address: Department of Physics, University of Minnesota, Minneapolis, Minn. 55455.

[1] A. K. Kerman, H. McManus, and R. M. Thaler, Ann. Phys. (N.Y.) 8, 551 (1959); G. R Satchler, Nucl. Phys. 77, 481 (1966); R. J. Glauber, *High Energy Physics and Nuclear Structure*, edited by S. Devons (Plenum, New York, 1970), p. 207.

[2] G. Bertsch, J. Borysowicz, H. McManus, and W. G. Love, Nucl. Phys. A284, 399 (1977); W. G. Love *et al.*, Phys. Lett. 73B, 277 (1978); A. Picklesimer and G. Walker, Phys. Rev. C 17, 237 (1978).

[3] L. Ray, Phys. Rev. C 19, 1855 (1979), and references therein.

[4] A. Chaumeaux, V. Layly, and R. Schaeffer, Ann. Phys. (N.Y.) 116, 247 (1978), and references therein.

[5] G. S. Blanpied *et al.*, Phys. Rev. Lett. 39, 1447 (1977).

[6] G. Igo *et al.*, Phys. Lett. 81B, 151 (1979).

[7] G. W. Hoffmann *et al.*, Phys. Lett. 79B, 376 (1978).

[8] P. M. Endt and C. Van der Leun, Nucl. Phys. A310, 1 (1978).

[9] J. R. Beene, Nucl. Data Sheets 23, 1 (1978).

[10] H. Verheul and R. L. Auble, Nucl. Data Sheets 23, 455 (1978).

[11] C. R. Gruhn *et al.*, Phys. Rev. C 6, 915 (1972).

[12] C. R. Gruhn, T. Y. T. Kuo, C. J. Maggiore, and B. M. Preedom, Phys. Rev. C 6, 944 (1972).

[13] M. P. Fricke, E. E. Gross, and A. Zucker, Phys. Rev. 163, 1153 (1967).

[14] L. L. Rutledge, Jr. and J. C. Hiebert, Phys. Rev. C 13, 1072 (1976).

[15] M. L. Goldberger and K. M. Watson, *Collision Theory* (Wiley, New York, 1964).

[16] H. Sherif, Nucl. Phys. A131, 532 (1969); W. G. Love, *ibid.* A192, 49 (1972), and references therein.

[17] R. P. Liljestrand *et al.*, Phys. Rev. Lett. 42, 363 (1979).

[18] G. S. Adams *et al.*, Phys. Rev. Lett. 43, 421 (1979).

[19] J. J. Simpson *et al.*, Phys. Rev. Lett. 35, 23 (1975), and references therein; P. Braun-Munzinger *et al.*, *ibid.* 21, 1261 (1972).

[20] L. Ray *et al.*, Phys. Rev. Lett. 40, 1547 (1978).

[21] L. Ray *et al.*, Phys. Lett. 83B, 275 (1979).

[22] G. S. Adams *et al.*, Phys. Rev. Lett. 38, 1387 (1977), and references therein.

[23] N. Hintz, private communication.

[24] R. Lindgren, private communication.

[25] R. M. Haybron, M. B. Johnson, and R. J. Metzger, Phys. Rev. C 156, 1136 (1967).

[26] A. Scott, N. P. Mathur, and F. Petrovich, Nucl. Phys. A285, 222 (1977); Y. Terrien, *ibid.* A199, 65 (1973); G. R. Hammerstein, R. H. Howell, and F. Petrovich, *ibid.* A213, 45 (1973); R. Schaeffer, *ibid.* A135, 231 (1969); see also the references in the above.

[27] I. Amhad, Nucl. Phys. A247, 418 (1975).

[28] T. S. Bauer *et al.*, Phys. Rev. C 19, 1438 (1979), and references therein.

[29] Richard Schaffer, *The Two-Body Force in Nuclei*, edited by S. M. Austin and G. M. Crawley (Plenum, New York, 1972), p. 245; F. Petrovich, V. A. Madsen, and J. Atkinson, Phys. Rev. Lett. 22, 895 (1969).

[30] F. Petrovich *et al.*, Phys. Lett. (to be published).

[31] G. D. Alkhazov *et al.*, Nucl. Phys. A274, 443 (1976).

[32] P. L. Hallowell *et al.*, Phys. Rev. C 7, 1396 (1973).

[33] K. Itoh, M. Oyamada, and Y. Torizuka, Phys. Rev. C 2, 2181 (1970).

[34] J. Heisenberg, J. S. McCarthy, and I. Sick, Nucl. Phys. A164, 353 (1971).

[35] G. S. Adams, Ph.D. thesis, Indiana University (1977), or Indiana University Cyclotron Facility Internal Report No. 77-3.

[36] R. F. Frosch *et al.*, Phys. Rev. 174, 1380 (1968).

[37] R. A. Eisenstein *et al.*, Phys. Rev. 188, 1815 (1969).

[38a] J. B. McGrory, B. H. Wildenthal, and E. C. Halbert, Phys. Rev. C 2, 186 (1970).

[38b] This ratio is consistent with the isoscalar transition rate one deduces from (α, α') data [see A. M. Bernstein, in *Advances in Nuclear Physics*, edited by M. Baranger and E. Vogt (Plenum, New York, 1969), Vol. 3, p. 325].

[39] Phan-Xuan-Ho, J. Bellicard, and Ph. Leconte, Nucl. Phys. A210, 189 (1973).

[40] I. Morrison, R. Smith, and K. Amos, Nucl. Phys. A244, 189 (1975).

PHYSICAL REVIEW C VOLUME 21, NUMBER 6 JUNE 1980

Electroexcitation of ^{6}Li with application to the reactions ^{6}Li$(\pi^-,\gamma)_{1s}$ ^{6}He$(0^+,2^+)$

J. C. Bergstrom

Saskatchewan Accelerator Laboratory, University of Saskatchewan, Saskatoon S7N 0W0, Canada

(Received 5 September 1979)

The transverse form factor for the 5.37 MeV$(2^+,T=1)$ level of ^{6}Li is analyzed in terms of a phenomenological model to give the configuration amplitudes and transition density. Radiative pion capture rates for the $1s$ atomic orbital of ^{6}Li leading to the two lowest states of ^{6}He are estimated using the phenomenological functions. The radiative pion capture rate to ^{6}He(g.s.) agrees with experiment, but the rate to ^{6}He$(2^+$,1.8 MeV) is larger than the measured value. It is shown that if the longitudinal form factor is small at $q \approx m_\pi$, the transverse 5.37 MeV form factor gives the radiative pion capture matrix elements directly. As part of this study, the $C2$ form factor was measured near $q = m_\pi$, and its implications on the wave functions are considered.

[NUCLEAR REACTIONS ^{6}Li(e,e'), E=76–141 MeV; $\sigma(E;E_{e'},\theta)$. ^{6}Li deduced form factors, wave functions, radiative capture.]

I. INTRODUCTION

In a recent paper, Renker *et al.*[1] presented measurements of the radiative pion capture (RPC) rate from the $1s$ atomic orbital in ^{6}Li leading to the ground and first excited states of ^{6}He. By eliminating the contribution from the competitive p-state capture, interpretation of the results becomes greatly simplified. For example, the $1s$ capture, rate in the impulse approximation (neglecting nucleon Fermi motion) is primarily determined by the nuclear matrix element of $\tau^-\vec{\sigma}\cdot\vec{\epsilon}_\lambda e^{-i\vec{k}\cdot\vec{r}}$ between ^{6}Li and ^{6}He. This operator is related by isospin rotation to the spin-dependent part of the (e,e') interaction leading to the corresponding analog state in ^{6}Li. In other words, the same nuclear matrix elements occur in $1s$ radiative capture and electron scattering when the final states belong to the same isospin multiplet.

In this work, we use the information provided by the electron scattering form factors for the 3.56 MeV $(0^+,T=1)$ and 5.37 MeV $(2^+,T=1)$ levels of ^{6}Li to estimate the $(\pi^-,\gamma)_{1s}$ rates to the ground $(0^+,T=1)$ and 1.80 MeV $(2^+,T=1)$ states of ^{6}He. The transition to the 2^+ state is complicated by the fact that the transverse form factor for the 5.37 MeV state does not have a unique multipolarity, but can in principle be a mixture of $M1$, $E2$, and $M3$ components. Therefore, we have performed a phenomenological analysis of this form factor similar to that previously done for the 3.56 MeV $M1$ transition.[2,3] From this, we conclude that electroexcitation of the 5.37 MeV level is predominantly $E2+M3$ in character, with nearly equal contributions from each multipole.

For excitations involving recoupling within a $(1p)^n$ configuration, we show that the convection current matrix element vanishes for $M3$ transitions, and is negligible for $E2$ transitions providing the longitudinal (C2) form factor is small. Then only the spin-dependent magnetization density contributes, and the $(\pi^-,\gamma)_{1s}$ nuclear matrix elements may be obtained directly from the corresponding $E2$ or $M3$ form factors, assuming the simple impulse approximation is valid.

We have measured the longitudinal form factor of the 5.37 MeV state near the momentum transfer appropriate for the radiative capture reaction and verified that it is small. The capture rate to ^{6}He(2^+) derived directly from the 5.37 MeV transverse form factor is shown to be in reasonable agreement with the result derived from the phenomenological functions.

The $1s$ capture rate to ^{6}He(g.s.) is found to be in good agreement with the measurement of Renker *et al.*, but the transition to ^{6}He(2^+) is two standard deviations above the experimental value. On the other hand, our estimate of the ratio of the (γ,π^+) cross sections to the same states is in accord with the result of Audit *et al.*[4]

II. MEASUREMENT OF $F_L^2(q)$ FOR THE 5.37 MeV LEVEL

As alluded to in the Introduction, the longitudinal form factor of the 5.37 MeV level provides a measure of the convection current contribution to the transverse $E2$ form factor, and also provides a constraint on the phenomenological wave functions. In this section, we briefly discuss the present measurement of this form factor. Unfortunately, because of the natural width of this state ($\Gamma_{\text{tot}} \approx 0.55$ MeV), and its disposition relative to the much larger and broader 4.31 MeV $(2^+,T=0)$ level,

© 1980 The American Physical Society

even a crude measurement is extremely difficult and time consuming. Furthermore, the 5.37 MeV total form factor is known to be predominantly transverse in character,[5,6] so the longitudinal contribution is small even at forward electron scattering angles.

This measurement was made at the electron scattering facility of the Saskatchewan accelerator laboratory. The target was 99% isotopically enriched ^{6}Li metal rolled to a thickness of about 20 mg/cm^2. Incident beam currents were kept below 2.5 μA to avoid target melting. The total momentum resolution, as given by the elastic peak full-width at half maximum (FWHM), was about 0.15%.

The longitudinal and transverse form factors are related to the differential cross section by

$$\sigma_M^{-1}\frac{d\sigma}{d\Omega}=F_L^2(q)+\left(\frac{1}{2}+\tan^2\frac{\theta}{2}\right)F_T^2(q)$$
$$=F_{\rm tot}^2(q,\theta)\,, \qquad (1)$$

where σ_M is the Mott cross section for a point charge Ze. The form factors were separated in the usual way by measuring the angular dependence of $F_{\rm tot}^2(q,\theta)$ at a fixed momentum transfer q. In this experiment, the scattering angles and associated incident energies were 59.0° (140.9 MeV), 90.0° (99.3 MeV), and 140.0° (75.6 MeV), corresponding to $q=0.687$ fm^{-1}.

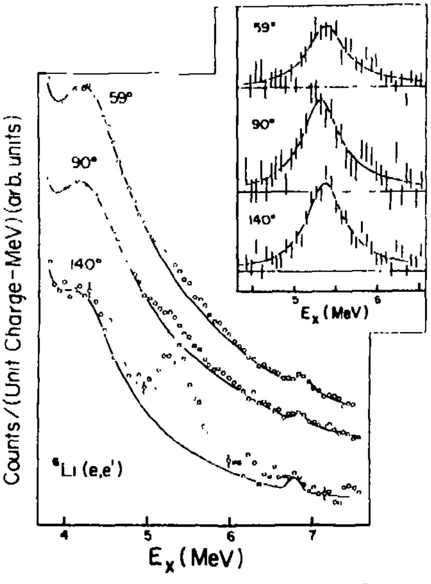

FIG. 1. Electron scattering spectra from ^{6}Li showing the 5.37 MeV peak on the flank of the broad 4.31 MeV (2$^+$) resonance. The three spectra do not have a common scale factor. The solid curve represents the total background under the 5.37 MeV resonance and the inset shows the background-subtracted spectra. The Breit-Wigner curves were fit simultaneously with the background by a least-squares procedure. The small peak near 7 MeV is the 7.66 MeV (0$^+$) state of ^{12}C, apparently introduced during target fabrication.

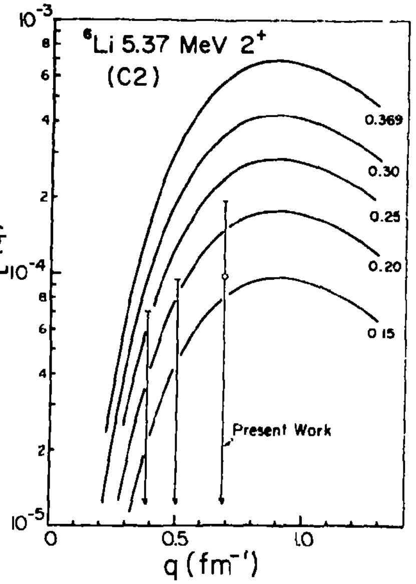

FIG. 2. Longitudinal form factors of the 5.37 MeV state based on the phenomenological densities and amplitudes determined from the experimental transverse form factor. The curves are labeled by β, the ground state $^1P_1$ amplitude. The experimental result at $q=0.69$ fm^{-1} is from the present work, the others are from Ref. 5.

The area of the 5.37 MeV peak was determined by simultaneously fitting the (e,e') spectra with a series of shape functions describing the inelastic peaks, plus a polynomial representing the elastic peak radiation tail and the various breakup continua.[3] Breit-Wigner resonances were used for the 4.31 and 5.37 MeV peaks. The position of the 5.37 MeV shape function, having been determined from the back-angle data (and previous work), was not allowed to vary during the fitting procedure, and its total natural width was fixed at $\Gamma_{\rm tot}=0.55$ MeV.

The line-shape fits in the region of the 5.37 MeV state are illustrated in Fig. 1, where the curves represent the total "background" under the resonance. When these are subtracted from the data, we obtain the spectra shown in the inset. The Breit-Wigner curves in this figure describe the fits to the 5.37 MeV peak generated during the least-squares spectrum analysis.

The area of the 5.37 MeV peak was normalized

TABLE I. Summary of the present experimental results for the 5.37 MeV ($2^+, T=1$) state of ^{6}Li. Radiative corrections and the elastic form factor were calculated as in Ref. 3. The total form factor is defined within ±0.55 MeV of the peak center. Errors do not reflect uncertainties in the position and width of the state.

E_0 (MeV)	θ (deg)	$\sigma(5.37)/\sigma(\text{el})$ ($\times 10^3$)	$F_{\text{el}}^2(q)$ (calc.)	$F_{\text{tot}}^2(q,\theta)$ ($\times 10^4$)
140.9	59.0	1.12 ± 0.20	0.364	4.08 ± 0.71
99.3	90.0	1.80 ± 0.32	0.358	6.43 ± 1.14
75.6	140.0	8.83 ± 0.79	0.352	31.1 ± 2.8

$q = 0.687$ fm^{-1}
$F_L^2(q) = (9.7 \pm 9.5) \times 10^{-5}$
$F_T^2(q) = (3.73 \pm 0.40) \times 10^{-4}$

to the elastic peak, which in turn was evaluated by phase shift analysis, and radiative corrections were made as discussed elsewhere.[3] The results are summarized in Table I, and as before, the form factor represents the strength within $\pm\Gamma_{\text{tot}}$ of the peak maximum. From a least-squares fit of $F_{\text{tot}}^2(q,\theta)$ vs $\frac{1}{2}+\tan^2\theta/2$, we obtain the separate form factors given in Table I. The present and previous[5] measurements of $F_L^2(q)$ are displayed in Fig. 2.

III. PHENOMENOLOGICAL ANALYSIS OF THE 5.37 MeV FORM FACTOR

Our purpose here is twofold. First, we require wave functions and transition densities to estimate the $(\pi^-,\gamma)_{1s}$ matrix elements. Second, we must establish the $M1$ contribution to the 5.37 MeV transverse form factor, since if it is large, one cannot expect the $(\pi^-,\gamma)_{1s}$ estimate based directly on the form factor to be reliable (the $M1$ form factor need not have a negligible convection current part).

We assume a $(1p)^2$ model space and L-S wave functions

$$\Psi_{\text{gnd}}(1^+,0) = \alpha\, {}^3S_1 + \beta\, {}^1P_1 + \gamma\, {}^3D_1\,, \tag{2}$$

$$\Psi_{5.37}(2^+,1) = G\, {}^3P_2 + H\, {}^1D_2\,, \tag{3}$$

where[2,7]

$$\alpha = 0.924\,, \quad \beta = 0.369\,, \quad \gamma = 0.102\,. \tag{4}$$

The inelastic transverse form factor in general contains $M1$, $E2$, and $M3$ terms,

$$F_T^2(q) = F_{M1}^2(q) + F_{E2}^2(q) + F_{M3}^2(q)\,, \tag{5}$$

where the individual form factors are given by

$$F_{M1}(q) = \left(\frac{q}{m}\right)\left[C_0\langle j_0(qr)\rangle + C_2\langle j_2(qr)\rangle\right] f_p f_{\text{c.m.}}\,, \tag{6}$$

$$F_{E2}(q) = \mu_v D\left(\frac{q}{m}\right)\langle j_2(qr)\rangle f_p f_{\text{c.m.}}\,, \tag{7}$$

$$F_{M3}(q) = \mu_v E\left(\frac{q}{m}\right)\langle j_2(qr)\rangle f_p f_{\text{c.m.}}\,. \tag{8}$$

Here $\mu_v = \mu_p - \mu_n = 4.706$, m is the nucleon mass, and the coefficients C_0, C_2, D, and E are functions only of the ground and excited state amplitudes. The proton and center of mass form factors, f_p and $f_{\text{c.m.}}$, and the radial matrix elements $\langle j_\lambda(qr)\rangle$ are defined in Ref. 3. As before, the radial density is expanded in a convenient series, with coefficients to be determined by the experimental data. The only difference from the procedure described in Ref. 3 is that here we do not assume the radial density $[R'(r)R(r)]$ is normalized to unity. The 5.37 MeV level is unbound to two- and three-body breakup, so the radial wave function $R'(r)$ may be more spread out than the ground state function $R(r)$.

Most of the experimental results were obtained using Breit-Wigner fits to the spectra, and $F_T^2(q)$ is defined within $\pm\Gamma_{\text{tot}}$ of the peak center. Consequently, the theoretical form factors must be renormalized downward to account for the strength not included within this limit[3]

$$[F^2(q)]_{\text{exp}} = [F^2(q)]_{\text{theor}}/1.42\,. \tag{9}$$

The transverse form factor expressed by Eqs. (5)–(8) was fitted by the method of least squares to 37 data points from Refs. 3,5,8, some unpublished Saskatoon results, and the present measurement. No corrections were made for Coulomb distortion effects, which are usually small for very light nuclei. Most of the data were obtained at large scattering angles, and in view of the upper limits on $F_L^2(q)$, are essentially transverse in character. With the ground state configuration given by Eq. (4), the fitting procedure was repeated for various excited state amplitudes (G,H) until a minimum in the chi-square per degree of freedom, χ_ν^2, was located. One finds two solutions for the 5.37 MeV amplitudes (G,H) which give comparable χ_ν^2, represented by $G>0$ and $G<0$, where H is considered positive. The $G<0$ solution is rejected for reasons discussed later.

When the wave functions and radial density which give the best fit are used to evaluate the longitudinal form factor, given by

$$F_L(q) = (1/\sqrt{6})\left[\left(\tfrac{[illegible]}{60}\right)^{1/2} G\gamma - H\beta\right]\langle j_2(qr)\rangle f_p f_{\text{c.m.}}\,, \tag{10}$$

we obtain the curve in Fig. 2 labeled $\beta = 0.369$, the ground state $^1P_1$ amplitude. Although the experimental errors are large, the discrepancy with theory is evident. The source does not likely lie in the amplitudes (G,H), since the transverse form factor is mainly determined by the product αH, and $\alpha \approx 0.9-1.0$ for most theories of ^{6}Li. We must therefore consider the possibility that β as given in Eq. (4) is too large.

In order to find a range of β values consistent with the transverse and longitudinal form factors, the fitting procedure was repeated for a series of ground state amplitudes. For a given β, the amplitudes α and γ were constrained by the quadrupole moment[2] using a $1p$-shell rms radius $\langle r^2\rangle_p^{1/2} = 3.46$ fm (Ref. 3) (the magnetic moment is somewhat less sensitive to the amplitudes). The predicted longitudinal form factors, as a function of β, are summarized in Fig. 2.

Inspection of Fig. 2 suggests $\beta \lesssim 0.20$. However, since the ground state magnetic moment deviates monotonically from the experimental value for $\beta < 0.369$, as a compromise we will adopt $\beta = 0.200$ as our alternative estimate of this amplitude. The respective magnetic moment is 5% above the experimental value, not an unreasonable difference considering we have ignored configurations higher than $(1p)^2$, as well as two-body contributions. Both sets of amplitudes are presented in Table II

The normalization of the radial density $[R'R]$, also determined by the least-squares fit, is slightly less than unity. The transition radius, defined as the rms radius of $[R'R]$, is estimated to be $\langle r_t^2\rangle^{1/2} = 3.78$ fm.

The 5.37 MeV transition density parameters (b, a_n) for $\beta = 0.200$ and $G = 0.460$ are as follows:

$$b = 2.324 \text{ fm}, \quad a_2 = 6.641\times10^{-2} \text{ fm}^{-5}$$

$$a_3 = -3.502\times10^{-2} \text{ fm}^{-6}, \quad a_4 = 7.427\times10^{-3} \text{ fm}^{-7}$$

$$a_6 = -1.668\times10^{-4} \text{ fm}^{-9}, \quad a_8 = 2.619\times10^{-6} \text{ fm}^{-11}. \quad (11)$$

Since the χ_ν^2 and corresponding (G, H) are nearly independent of b, we have arbitrarily used the value obtained from the 3.56 MeV form factor analysis.[3] According to Eq. (9) the a_n must be multiplied by $(1.42)^{1/2}$ to represent the entire resonance.

The fit to the transverse form factor with the $\beta = 0.200$ amplitudes of Table II is shown in Fig. 3, along with its multipole components. The $E2$ and $M3$ contributions are nearly equal, but the $M1$ form factor is suppressed and has a diffraction minimum at $q = 0.75$ fm^{-1}. Actually, the multipole form factors do not change significantly between the two sets of amplitudes, suggesting the decomposition shown in Fig. 3 is not strongly model dependent.

The $M1$ form factor gives the ground state $M1$ radiative width for the entire 5.37 MeV resonance:

$$\Gamma_{\gamma 0}(M1) = 0.27 \pm 0.05 \text{ eV}. \quad (12)$$

Finally, for completeness, we make a few re-

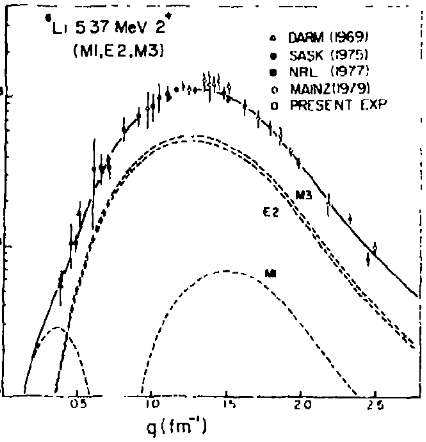

FIG. 3. Transverse form factor of the 5.37 MeV state and its multipole components compared with the data. The curves represent the least-squares fit with the $\beta = 0.200$ amplitudes of Table II. The $E2$ and $M3$ form factors have the same q dependence [see Eqs. (7) and (8)], differing only in their normalization. The peculiar change in slope of the fit above $q = 2$ fm^{-1} is caused by the absence of any constraints on the physical form factor at high momentum transfers, and should not be considered as realistic.

TABLE II. Configuration amplitudes for the ground state and excited $T = 1$ states of ^{6}Li as obtained from the phenomenological analyses. The set labeled C is preferred if the 5.37 MeV $C2$ form factor is considered an acceptable constraint. The L-S wave functions are defined by Eqs. (2), (3), and (13).

Ground $(1^+, T=0)$			5.37 MeV $(2^+, T=1)$		3.56 MeV $(0^+, T=1)$		
α	β	γ	G	H	A	B	
0.979	0.200	0.041	0.460	0.888	0.881 ± 0.018	-0.473 ± 0.034	(C)
					0.996 ± 0.004	0.087 ∓ 0.039	(D)
0.924	0.369	0.102	0.360	0.933	0.843 ± 0.022	-0.537 ± 0.034	(A)
					1.00	-0.012 ± 0.041	(B)

marks about the 3.56 MeV $M1$ form factor. The L-S wave function for the 3.56 MeV ($0^+, T=1$) state in a $(1p)^2$ configuration space is

$$\Psi_{3.56}(0^+,1)=A\,{}^1S_0+B\,{}^3P_0\,. \tag{13}$$

Previous analyses of this form factor utilized the wave functions corresponding to $\beta=0.369$. Since the present work suggests the $\beta=0.20$ ground state may be more realistic, we have reanalyzed this transition and give an alternative set of excited state amplitudes which we call sets C and D, to distinguish them from the former A and B solutions (Table II). As before, we use the ground state radiative width as a constraint, and the amplitude uncertainties reflect the experimental error on this quantity.

The new amplitudes yield a transition density virtually indistinguishable from that of Ref. 3. The β-decay $ft_{1/2}$ value for ^{6}He, and the threshold photopion cross section leading to ^{6}He(g.s.) have been recalculated with the C amplitudes in Table II. With the coupling constants employed by Cammarata and Donnelly,[7] we obtain $ft_{1/2}=789\pm 23$, compared with the "experimental" value $f_{1/2}=814$ (Ref. 9). The photopion cross section is 7 ± 4% higher than our previous estimate.[3]

IV. COMPARISON OF PHENOMENOLOGICAL AND THEORETICAL AMPLITUDES

Since the phenomenological amplitudes were generated by fitting various electromagnetic form factors with no consideration given to the nuclear potentials, residual interactions, etc., it is worthwhile comparing the present results with the amplitudes derived from more fundamental approaches. Here, we consider two examples.

The first example is obtained by diagonalizing the Hamiltonian matrix using the Kuo-Brown two-body matrix elements in a $(1p)^2$ model space. The single-particle energy difference $\epsilon=E(1p_{1/2})-E(1p_{3/2})$ is probably somewhere around 3-5 MeV for ^{6}Li, and indeed as shown in Table III, the theoretical and phenomenological amplitudes of the ground and 5.37 MeV states compare favorably for $\epsilon=3$–4 MeV. The situation with the 3.56 MeV state is not so favorable, the shell model giving a smaller $L=1$ component than the phenomenological analysis. Although the predicted 2^+-0^+ separation is 1.76 MeV, in good agreement with experiment, the excitation energies relative to the ground state are about 1.8 MeV too low.

For the second example, we consider the calculation by Barker[10] which relies on the known excitation energies to determine the exchange mixture in the effective shell model interaction. The resulting amplitudes are given in Table III.

Both calculations give wave functions that are more or less consistent with the phenomenological results. Note that the theoretical values of G are positive, which is the principal reason for rejecting the $G<0$ phenomenological solutions.

V. APPLICATION TO $^6\text{Li}(\pi^-,\gamma)_{1s}{}^6\text{He}$

The radiative capture rate from the 1s atomic orbital is given in the impulse approximation by[11]

$$\Lambda_\gamma(1s)=A^2\frac{k}{m_\pi}\left(1+\frac{m_\pi}{m}\right)^2\left(1+\frac{k}{M}\right)^{-1}\times\frac{(4\pi)^2}{2J_i+1}\,|\phi_\pi(0)|^2\langle M\rangle^2\,, \tag{14}$$

where $\hbar=c=1$, k is the photon momentum in the c.m. system, and m_π, M are the pion and nuclear masses. The constant A is the elementary dipole amplitude $E_{0+}(\pi^-)=(3.26\pm 0.04)\times 10^{-2}m_\pi^{-1}$ (Ref. 11). The transition matrix element between the states J_i and J_f is

$$\langle M\rangle^2=(4\pi)^{-2}\sum_{M_i M_f \lambda}\int\left|\langle J_f|e^{-i\vec{k}\cdot\vec{r}}(\vec{\sigma}\cdot\vec{\epsilon}_\lambda)\tau^-|J_i\rangle\right|^2 d\hat{k}\,, \tag{15}$$

where $\vec{\epsilon}_\lambda$ is the photon polarization ($\lambda=\pm1$) and τ^- is the isospin operator defined by $\tau^-|p\rangle=|n\rangle$. The operator notation implies a sum over nucleons. Since the pion wave function varies slowly over the nuclear volume, it has been removed from the nuclear matrix element and replaced by the value

TABLE III. Comparison of the theoretical and phenomenological amplitudes. The results based on the Kuo-Brown two-body matrix elements are indicated by ϵ, the single-particle $p_{1/2}-p_{3/2}$ splitting.

	Ground ($1^+, T=0$)			5.37 MeV ($2^+, T=1$)		3.56 MeV ($0^+, T=1$)	
Model	α	β	γ	G	H	A	B
$\epsilon=3$ MeV	0.984	0.149	0.010	0.452	0.892	0.960	−0.280
$\epsilon=4$ MeV	0.977	0.205	0.056	0.539	0.843	0.945	−0.328
$\epsilon=5$ MeV	0.966	0.259	0.017	0.597	0.802	0.931	−0.364
Barker	0.992	0.120	−0.028	0.553	0.833	0.934	−0.358
Phen. model	0.979	0.200	0.041	0.460	0.888	0.881	−0.473

at the nuclear center:

$$|\phi_\pi(0)|^2 = \frac{R}{\pi}(Z\alpha\mu)^3 . \tag{16}$$

Here, μ is the pion-nuclear reduced mass, and R is a distortion factor which takes into account nuclear size and strong interaction effects. This factor was obtained by computing the pion 1s atomic orbital bound by a Gaussian charge distribution ($r_{\text{rms}} = 2.56$ fm) and modified by a strong potential of the form

$$2\mu V_s(r) = -4\pi(1+m_\pi/m)b_0\rho(r) . \tag{17}$$

Nonlocal and absorptive terms have been ignored in $V_s(r)$, while the isovector (b_1) term vanishes if, as we assume, the proton and neutron distributions are identical. The density $\rho(r)$ was also assumed to be a Gaussian-type distribution.[12] We find

$$R = 0.64 \quad \text{for } b_0 = -0.030 m_\pi^{-1} . \tag{18}$$

The multipole decomposition of Eq. (15) is accomplished by expanding $(\vec{\sigma}\cdot\vec{\epsilon}_\lambda)e^{-i\vec{k}\cdot\vec{r}}$ in vector spherical harmonics [see e.g., Ref. 13 Eq. (3.30)], and with the Wigner-Eckart theorem one obtains

$$\langle M\rangle^2 = \sum_J \left\{ |\langle J_f || \vec{\mathrm{M}}_{JJ}\cdot\vec{\sigma}\tau^- || J_i\rangle|^2 + \frac{1}{k^2}|\langle J_f || \vec{\nabla}\times\vec{\mathrm{M}}_{JJ}\cdot\vec{\sigma}\tau^- || J_i\rangle|^2 \right\} . \tag{19}$$

In the notation of deForest and Walecka,[13]

$$\vec{\mathrm{M}}^M_{JL}(\vec{\mathrm{r}}) = j_L(kr)\vec{\mathrm{Y}}^M_{JL1}(\Omega) \tag{20}$$

and

$$\frac{1}{k^2}|\langle J_f || \vec{\nabla}\times\vec{\mathrm{M}}_{JJ}\cdot\vec{\sigma}\tau^- || J_i\rangle|^2 = \left| \left\langle J_f \right\| \left[-\left(\frac{J}{2J+1}\right)^{1/2}\vec{\mathrm{M}}_{JJ+1} + \left(\frac{J+1}{2J+1}\right)^{1/2}\vec{\mathrm{M}}_{JJ-1}\right]\cdot\vec{\sigma}\tau^- \left\| J_i \right\rangle \right|^2 . \tag{21}$$

The states J_f in ^{6}He and the $T = 1$ levels of ^{6}Li are presumably members of the same isospin multiplet, in which case the matrix elements in Eq. (19) and those for the analog states in ^{6}Li are related by a Clebsch-Gordan coefficient in isospin space. For $T_i = 0, T_f = 1$ we have

$$|\langle J_f || Q\tau^- || J_i\rangle|^2 = 2|\langle J_f || \tfrac{1}{2}Q\tau_3 || J_i\rangle|^2 , \tag{22}$$

where Q is the appropriate multipole operator. The right side of Eq. (22) was evaluated using the phenomenological ^{6}Li wave functions and transition densities.

The 1s radiative capture rates to the ground and first excited states of ^{6}He are summarized in Table IV. The ground state transition rate is in good agreement with the experimental results of Renker *et al.*,[1] but the capture rate to the 1.8 MeV (2^+) state is about 70%, or two standard deviations above the experimental value. For the excited state transition the multipole contributions are estimated to be in the ratio $M1/E2/M3 = 0.095/0.93/1.0$.

TABLE IV. Radiative pion capture rates from the 1s atomic orbital of ^{6}Li based on the phenomenological L-S amplitudes and transition densities.

	^{6}Li → ^{6}He (g.s., 0^+)		
β	B	$\langle M\rangle^2$	$\Lambda_\gamma(1s)$ (sec^{-1})
0.200	−0.473	4.77×10^{-2}	1.39×10^{15}
0.369	−0.537	4.48×10^{-2}	1.30×10^{15}
	Exp. value:	$(1.39\pm0.16)\times10^{15}$ (Ref. 1)	
	^{6}Li → ^{6}He (1.8 MeV, 2^+)		
β	G	$\langle M\rangle^2$	$\Lambda_\gamma(1s)$ (sec^{-1})
0.200	0.460	1.96×10^{-2}	5.64×10^{14}
0.369	0.360	1.99×10^{-2}	5.70×10^{14}
	Exp. value:	$(3.3\pm1.2)\times10^{14}$ (Ref. 1)	

VI. THE ^{6}Li → ^{6}He (1.8 MeV, 2^+) TRANSITION: MODEL INDEPENDENT CONSIDERATIONS

The difference between the predicted and experimental capture rates to the 1.8 MeV (2^+) state of ^{6}He is puzzling in view of the good agreement achieved for the ground state transition. Therefore, we will consider an alternative approach to the former transition, and show under what circumstances the nuclear matrix elements may be obtained directly from the experimental form factor.

In general, transverse form factors have contributions from both the convection and magnetization currents, while only the latter are relevant, via Eq. (22), to the radiative capture process. If the convection terms are negligible at $q = k$, then the electron scattering form factor gives $\langle M\rangle^2$ directly:

$$\langle M\rangle^2 = \frac{2}{\pi}(2J_i+1)\frac{Zm}{k\mu_v}F_T^2(k) , \tag{23}$$

where Z is the charge of the target nucleus and the other symbols have their previous meaning.

The 5.37 MeV transverse form factor has $M1$, $E2$, and $M3$ components, and all the amplitudes and transition densities considered here produce a minimum in $F_{M1}^2(q)$ in the region $q = 0.7-0.9$ fm^{-1}. (This minimum has also been suggested by others.[6]) Therefore it seems likely that $F_T^2(q)$ is dominated by the $E2$ and $M3$ terms near $q = k = 0.67$ fm^{-1}, the momentum transfer appropriate for capture to ^{6}He (2^+).

In Appendix A we show that the convection current makes no contribution to $M3$ transitions in a $(1p)^n$ space, and in Appendix B we show that the convection contribution to $F_{E2}^2(k)$ is negligible even when the initial and final state radial functions differ slightly providing $F_{C2}^2(k)$ is small. Then, since the $M1$ term is suppressed, the experimental 5.37 MeV form factor provides a *lower* limit for the sum in Eq. (19). From the experimental form factor (renormalized upward by 1.42) and Eq. (23) we obtain

$$\begin{aligned} \langle M\rangle^2 &= 1.89 \times 10^{-2}\,, \\ \Lambda_\gamma(1s) &= 5.42 \times 10^{14}\ \text{sec}^{-1}\,, \end{aligned} \tag{24}$$

which are not appreciably different from the results in Table IV.

Although we have assumed the configuration space is $(1p)^2$ (but not necessarily harmonic oscillator functions), the preceding arguments are a bit more general. The convection current part of $F_{M3}^2(q)$ vanishes if we expand the basis to include any s- or p-orbital components. Similarly, the remarks about $F_{E2}(q)$ are valid for any $E2$ transition that only involves angular momentum recoupling.

VII. PION PHOTOPRODUCTION NEAR THRESHOLD

Our estimate for the ratio of radiative capture rates to the 2^+ and 0^+ states of ^{6}He is larger than the experimental ratio. Since the pion photoproduction cross sections near threshold leading to the same states in ^{6}He depend essentially on the same nuclear matrix elements, evaluated at nearly the same momentum transfer, one would expect a similar behavior for the ratio of photopion cross sections if the source of disagreement lies in the nuclear wave functions. The predicted ^{6}Li(γ,π^+) ^{6}He(0^+) cross section has already been shown to be in reasonable accord with experiment.[4] Unfortunately, the ^{6}Li $\rightarrow$ ^{6}He(2^+) experimental data are complicated by the underlying $\alpha + 2n$ continuum.

The photopion results are usually expressed in terms of the quantities $a(i-f)$, defined in Ref. 4, which are proportional to the matrix elements $\langle M\rangle^2$, Eq. (19), at the appropriate momentum transfers (0.72–0.73 fm^{-1}). We will not deal here with the complications introduced by the distorted pion wave functions; this is discussed, for example, in Refs. 7 and 2. Our estimate of the ratio, and the experimental value, are

$$\begin{aligned} \frac{a[^6\text{Li}\rightarrow{}^6\text{He}(2^+)]}{a[^6\text{Li}\rightarrow{}^6\text{He}(0^+)]} &= 0.57\ \text{(phen. model)} \\ &= 0.70 \pm 0.24\ \text{(expt.; Ref. 4)}. \end{aligned}$$

Although well within the quoted error, the theoretical ratio is lower than experiment, in contrast to the radiative capture situation.

Note that the excited state cross section may contain a contribution from the $\alpha + 2n$ background, which we have not included in our calculation. This would serve to increase the experimental ratio above the theoretical value.

VIII. DISCUSSION

The ^{6}Li(2^+, 5.37 MeV) form factor has been used both directly and indirectly to estimate the RPC rate to ^{6}He(2^+), and the results are consistently about 70% above the experimental value of Renker *et al.*

Since our prediction is relatively model independent, the origin of the discrepancy likely lies elsewhere. Contamination of the experimental cross section by the nearby $\alpha + 2n$ continuum is not the problem, since the theoretical value is already too large. It can be argued that we are pushing the model too far in the sense that the $2^+, T = 1$ states are not true analogs, that is, they may not have identical radial functions as we assumed in applying Eq. (22). The 2^+ states have different natural widths and dispositions with respect to the two- and three-body thresholds, so some difference in the radial structure is expected, but it would have to be unreasonably large to resolve the discrepancy, and furthermore would destroy the favorable agreement we achieve with the photopion cross sections.

To summarize, the (e,e'), $(\pi^-,\gamma)_{1s}$, and (γ,π^+) cross sections to the $0^+, T = 1$ levels are consistent, but a marked disagreement of unknown origin exists among the transitions to the $2^+, T = 1$ states.

This work was supported by the Natural Sciences and Engineering Research Council of Canada.

APPENDIX A

In this appendix, we show that in a $(1p)^n$ model space, the convection part of the nuclear transition current density does not contribute to $M3$ transitions.

The $M\lambda$ matrix element is

$$\langle f|T^{\mathrm{mag}}_{\lambda\mu}(q)|i\rangle = \int d\vec{r}\,\vec{J}_{fi}\cdot[j_\lambda(qr)\vec{Y}^{\mu}_{\lambda\lambda 1}(\Omega)]\,, \qquad \text{(A1)}$$

where $\vec{J}_{fi}$ is the transition current density, and here we are concerned only with the convection part of $\vec{J}_{fi}$. In the approximation that $T^{\mathrm{mag}}_{\lambda\mu}$ is a one-body operator, Eq. (A1) may be expanded in terms of single-particle matrix elements between states ϕ_i and ϕ_f, where

$$\phi_i = R(r_j)Y_{l_i m_i}(\Omega_j) \quad \phi_f = R'(r_j)Y_{l_f m_f}(\Omega_j)\,. \qquad \text{(A2)}$$

The single-particle current, symmetrized to satisfy the continuity equation, is

$$\vec{J}_{fi}(\vec{r}_j) = \left(\frac{-ie_j}{2m}\right)[\phi_f^\dagger\vec{\nabla}\phi_i - (\vec{\nabla}\phi_f)^\dagger\phi_i]\,, \qquad \text{(A3)}$$

where $e_j = [1+\tau_3(j)]/2$ is the charge of the particle. For simplicity, the particle label will be suppressed in the following. Combining Eqs. (A3) and (A1), we obtain the general single-particle term

$$\langle R'l_f m_f|T^{\mathrm{mag}}_{\lambda\mu}(q)|Rl_i m_i\rangle$$

$$= \left(\frac{-ie}{m}\right)\langle R'l_f m_f|j_\lambda(qr)\vec{Y}^{\mu}_{\lambda\lambda 1}(\Omega)\cdot\vec{\nabla}|Rl_i m_i\rangle\,. \qquad \text{(A4)}$$

Using the definition of the vector spherical harmonics,

$$\vec{Y}^{\mu}_{\lambda\lambda 1}(\Omega) = \sum_{\nu q}(\lambda\nu 1q|\lambda 1\lambda\mu)Y_{\lambda\nu}(\Omega)\vec{e}_q \qquad \text{(A5)}$$

and the closure property of the spherical harmonics, Eq. (A4) may be written

$$\langle R'l_f m_f|T^{\mathrm{mag}}_{\lambda\mu}(q)|Rl_i m_i\rangle = \left(\frac{-ie}{m}\right)\sum_{q\nu}\sum_{lm}(\lambda\nu 1q|\lambda 1\lambda\mu)\langle l_f m_f|Y_{\lambda\nu}(\Omega)|lm\rangle\langle lmR'|j_\lambda(qr)\nabla_q|Rl_i m_i\rangle\,. \qquad \text{(A6)}$$

The sum over the projections is facilitated by the Wigner-Eckart theorem, giving

$$\langle R'l_f m_f|T^{\mathrm{mag}}_{\lambda\mu}(q)|Rl_i m_i\rangle = \left(\frac{-ie}{m}\right)(-1)^{l_f-m_f}(2\lambda+1)^{1/2}\sum_l \begin{pmatrix} l_f & \lambda & l_i \\ m_f & -\mu & -m_i \end{pmatrix} \begin{Bmatrix} l_f & \lambda & l_i \\ 1 & l & \lambda \end{Bmatrix} \langle l_f||Y_\lambda||l\rangle$$

$$\times\langle R'l||j_\lambda(qr)\vec{\nabla}||Rl_i\rangle\,, \qquad \text{(A7)}$$

which vanishes if $\lambda > l_i + l_f$. In other words, the convection part of $T^{\mathrm{mag}}_{\lambda\mu}$ is a tensor operator of rank λ in the orbital angular momentum space. Thus, the convection current does not contribute to the $M3$ transition in a model space restricted to s- and p-wave orbitals.

APPENDIX B

We wish to show that the convection current makes a negligible contribution to the 5.37 MeV transverse $E2$ form factor at momentum transfers corresponding to the radiative pion capture, $q \approx 0.67\ \mathrm{fm}^{-1}$. Actually, the argument is more general and applies to any $E2$ form factor involving recoupling within a $(1p)^n$ configuration, if the longitudinal ($C2$) form factor is known to be small.

The $E\lambda$ matrix element is

$$\langle f|T^{\mathrm{el}}_{\lambda\mu}(q)|i\rangle = \frac{1}{q}\int d\vec{r}\,\vec{J}_{fi}\cdot\vec{\nabla}\times[j_\lambda(qr)\vec{Y}^{\mu}_{\lambda\lambda 1}(\Omega)]\,, \qquad \text{(B1)}$$

where as before we retain only the convection part of $\vec{J}_{fi}$. Using various integral identities and the continuity equation, Eq. (B1) becomes

$$\langle f|T^{\mathrm{el}}_{\lambda\mu}(q)|i\rangle = -\left(\frac{\omega_{fi}}{q}\right)\left(\frac{\lambda+1}{\lambda}\right)^{1/2}$$

$$\times\int d\vec{r}\,\rho_{fi}Y_{\lambda\mu}(\Omega)\left[j_\lambda(qr) - \left(\frac{qr}{\lambda+1}\right)j_{\lambda+1}(qr)\right]$$

$$+\frac{iq}{[\lambda(\lambda+1)]^{1/2}}\int d\vec{r}\,M_{\lambda\mu}\vec{r}\cdot\vec{J}_{fi}\,, \qquad \text{(B2)}$$

where ρ_{fi} is the transition charge density, $\omega_{fi} = E_f - E_i$ is the excitation energy, and

$$M_{\lambda\mu} = j_\lambda(qr)Y_{\lambda\mu}(\Omega)\,. \qquad \text{(B3)}$$

The first term in Eq. (B2), without the $j_{\lambda+1}(qr)$ part, is the longitudinal (Coulomb) matrix element reduced by the factor $(-\omega_{fi}/q)[(\lambda+1)/\lambda]^{1/2}$, which is much less than unity. For $E2$ transitions in a harmonic oscillator $(1p)^n$ configuration, the $j_{\lambda+1}(qr)$ part reduces the first term even further providing $(qb_0)^2/6 < 1$, and this is satisfied for $q = 0.67\ \mathrm{fm}^{-1}$. Finally, we have shown that $F_L{}^2(q) < 2\times 10^{-4}$ for the 5.37 MeV state, so the contribution of the first term in Eq. (B2) to $F_{E2}{}^2(q)$ is less than 5×10^{-7} and completely negligible. Therefore, we have

$$\langle f|T^{e1}_{\lambda\mu}(q)|i\rangle \approx \frac{iq}{[\lambda(\lambda+1)]^{1/2}} \int d\vec{r}\, M_{\lambda\mu}\, \vec{r}\cdot\vec{J}_{fi}\,. \quad \text{(B4)}$$

Combining Eqs. (A3) and (B4), we obtain the single-particle matrix element

$$\langle R'l_f m_f|T^{e1}_{\lambda\mu}(q)|Rl_i m_i\rangle \approx \left(\frac{q}{2m}\right)\frac{e}{[\lambda(\lambda+1)]^{1/2}}\int d\vec{r}\, M_{\lambda\mu} r\left(\phi^\dagger_f \frac{\partial\phi_i}{\partial r} - \frac{\partial\phi^\dagger_f}{\partial r}\phi_i\right). \quad \text{(B5)}$$

For transitions involving angular momentum recoupling within the $1p$ shell, Eq. (B5) vanishes if ϕ_i and ϕ_f have identical radial functions, such as in the usual harmonic oscillator model. We may obtain an order of magnitude estimate of the form factor when the radial functions are not the same, by considering oscillator functions with different oscillator parameters in the initial and final $1p$ orbitals. If b_0 and b_0' are, respectively, the initial and final oscillator parameters, the convection current part of the $E2$ form factor which follows from Eq. (B5), relative to the total longitudinal $C2$ form factor, is given by

$$\frac{F^{\text{conv}}_{E2}(q)}{F_{C2}(q)} = \left(\frac{49}{6}\right)^{1/2}\left(\frac{q}{2m}\right)\left(\frac{1-\eta^2}{1+\eta^2}\right)\left(1-\tfrac{2}{7}y\right), \quad \text{(B6)}$$

where $\eta = b_0'/b_0$ and

$$y = \frac{2\eta^2}{1+\eta^2}\left(\frac{qb_0}{2}\right)^2. \quad \text{(B7)}$$

(This expression is independent of the j-j configuration amplitudes.) Then, with $q = 0.67\ \text{fm}^{-1}$, $\eta = 1.2$ and $F_{C2}{}^2(q) < 2\times10^{-4}$, Eq. (B6) yields $|F^{\text{conv}}_{E2}(q)|^2 < 3\times10^{-7}$. This is the same order as the result generated by the first term of Eq. (B2), and even if both contributions add constructively, the total form factor (squared) is 2×10^{-6} and therefore negligible.

---

[1] D. Renker *et al.*, Phys. Rev. Lett. 41, 1279 (1978).

[2] J. C. Bergstrom, I. P. Auer, and R. S. Hicks, Nucl. Phys. A251, 401 (1975).

[3] J. C. Bergstrom, U. Deutschmann, and R. Neuhausen, Nucl. Phys. A327, 439 (1979).

[4] G. Audit *et al.*, Phys. Rev. C 15, 1415 (1977).

[5] F. Eigenbrod, Z. Phys. 228, 337 (1969).

[6] R. Neuhausen and R. M. Hutcheon, Nucl. Phys. A164, 497 (1971).

[7] J. B. Cammarata and T. W. Donnelly, Nucl. Phys. A267, 365 (1976).

[8] L. W. Fagg, R. A. Lindgren, W. L. Bendel, and E. C. Jones, Jr., Phys. Rev. C 15, 1181 (1977).

[9] F. Ajzenberg-Selove and T. Lauritsen, Nucl. Phys. A227, 1 (1974).

[10] F. C. Barker, Nucl. Phys. 83, 418 (1966).

[11] H. W. Baer, K. M. Crowe, and P. Truöl, Adv. Nucl. Phys. 9, 177 (1977).

[12] G. C. Li, I. Sick, R. R. Whitney, and M. R. Yearian, Nucl. Phys. A162, 583 (1971).

[13] T. deForest, Jr. and J. D. Walecka, Adv. Phys. 15, 1 (1966).

PHYSICAL REVIEW C VOLUME 21, NUMBER 6 JUNE 1980

Phenomenological relativistic quantum mechanics of the *NNπ* system

M. Betz and F. Coester
Argonne National Laboratory, Argonne, Illinois 60439

(Received 7 December 1979)

The theoretical basis is given for a class of mathematically well defined *NNπ* models. They are designed to describe nucleon-nucleon scattering, pion-nucleon scattering, pion-deuteron scattering, pion production, and absorption. The elementary degrees of freedom of the models are the nucleon, the Δ isobar, and the pion. The models are relativistic and do not require renormalization.

[NUCLEAR SCATTERING Relativistic models, *N-N* scattering, *π-N* scattering, *π-d* scattering.]

I. INTRODUCTION

Traditional nuclear theory assumes that nuclei can be treated as a collection of nucleons with the effects of the other degrees of freedom absorbed in the phenomenological Hamiltonian. For a treatment of pion-nucleus reactions it is desirable to extend this scheme so that pions and Δ isobars can play an explicit role.[1,2] A relativistic treatment is indicated because of the small pion mass.

Relativistic quantum mechanics requires a unitary representation of the Poincaré group on the Hilbert space of states. Relativistic field theories satisfy the requirement; they realize the generators of the infinitesimal transformations by space integrals over the energy-momentum tensor.[3] Inevitably there are then infinitely many degrees of freedom and the one-nucleon problem is intractable. Truncation of a relativistic field theory to states with a finite number of particles necessarily destroys the relativistic invariance. This lack of invariance may imply the lack of "cluster separability"[4,5]; specifically, the pion-nucleon scattering in the *NNπ* channel with a distant nucleon spectator is not the same as the pion-nucleon scattering in the *πN* channel, unless special precautions are taken. It is reasonable in most cases to assume that real baryons move with nonrelativistic velocities, but renormalization problems and problems of internal consistency persist in this approximation. There are many models of the *NNπ* system based on truncated field theories.[6]

The purpose of this paper is to construct relativistic models of the *NNπ* system in which *π*, *N*, and Δ are the elementary degrees of freedom; the pion can be absorbed and no renormalization is required. The underlying theory is not new.[5] Relativistic quantum mechanics need not be a field theory. It is possible to construct representations of the Poincaré group for interacting particles by modifying the mass operator *M* of a system of free particles.[7,4]

The formal structure, which is not unlike that of nonrelativistic quantum mechanics, is based on the following remark. The ten generators of the Poincaré group ($\vec{P}, H$ for space and time translations, $\vec{J}$ for rotations, and $\vec{K}$ for Lorentz boosts) can be constructed as functions of operators $\vec{P}$, $\vec{X}$, $\vec{j}$, and M defined such that the total momentum $\vec{P}$ and the c.m. position $\vec{X}$ satisfy canonical commutation relations and commute with the spin operator $\vec{j}$ and the mass M. The mass operator must also commute with $\vec{j}$.

Conversely, if the ten Poincaré generators are known, then $\vec{P}$, $\vec{X}$, $\vec{j}$, and M are defined as functions of these generators and satisfy the commutation relations specified above as a consequence of the Lie algebra of the Poincaré group. For noninteracting particles the Poincaré generators are well determined. Phenomenological interactions can be introduced by retaining the operators $\vec{P}$, $\vec{X}$, and $\vec{j}$ of the noninteracting system and modifying only the mass operator M:

$$M = M^0 + V \,, \tag{1}$$

where M^0 is the noninteracting mass operator and V commutes with $\vec{P}$, $\vec{X}$, and $\vec{j}$. For two particles, the construction of V is simple.[8,9] For three particles, it is an essential requirement that the right two-body scattering is recovered if one of the particles is far away.[5]

In Sec. II we construct a model of the *NNπ* system along the following lines. Let $\mathcal{H}_N$, $\mathcal{H}_\pi$, and $\mathcal{H}_\Delta$ be one-particle Hilbert spaces of a nucleon, a pion, and a Δ isobar. We begin with a description of nucleon-nucleon scattering in the space

$$\mathcal{H}_{NN} = \mathcal{H}_N \otimes \mathcal{H}_N \,, \tag{2}$$

with the mass operator

$$M_{NN} = M_{NN}^0 + v_{NN} \,. \tag{3}$$

The interaction v_{NN} is fitted to N-N scattering data and to the properties of the deuteron.

Similarly, we have a description of the πN system in the space

$$\mathcal{H}_{N\pi}=\mathcal{H}_N\otimes\mathcal{H}_\pi\oplus\mathcal{H}_\Delta\ , \tag{4}$$

with the mass operator

$$M_{N\pi}=M^0_{N\pi}+v_{N\pi}\ . \tag{5}$$

The operator $v_{N\pi}$ includes two-body interactions in $\mathcal{H}_N\otimes\mathcal{H}_\pi$ as well as a vertex $N\pi\rightleftarrows\Delta$. For a large class of models the properties of v_{NN} and $v_{N\pi}$ assure the existence and completeness of Møller wave operators.[10]

As an intermediate step we proceed to an equivalent description of the NN system in the presence of a spectator pion, and a description of the $N\pi$ system in the presence of a spectator nucleon. The Hilbert space of states is then

$$\mathcal{H}'=\mathcal{H}_N\otimes\mathcal{H}_N\otimes\mathcal{H}_\pi\oplus\mathcal{H}_N\otimes\mathcal{H}_\Delta\ , \tag{6}$$

and the interacting mass operator is a function of v_{NN} and $v_{N\pi}$. If both NN and $N\pi$ interactions are present it is possible to construct the interacting mass operator M^0+V' in such a manner that, if one of the three particles is moved away, the remaining particles scatter correctly.

For the full model, the Hilbert space of states is $\mathcal{H}=\mathcal{H}'\oplus\mathcal{H}_N\otimes\mathcal{H}_N$, with a mass operator of the form (1) with

$$V=V_0+V'+V''\ , \tag{7}$$

where V' vanishes on states in $\mathcal{H}_N\otimes\mathcal{H}_N$. The operator V_0 is a phenomenological baryon-baryon interaction defined on the states in $\mathcal{H}_N\otimes\mathcal{H}_N\oplus\mathcal{H}_N\otimes\mathcal{H}_\Delta$. By definition V_0 vanishes on states in $\mathcal{H}_N\otimes\mathcal{H}_N\otimes\mathcal{H}_\pi$. The operator V'' is defined as a three-body interaction on states in $\mathcal{H}_N\otimes\mathcal{H}_N\otimes\mathcal{H}_\pi$ with possible off-diagonal elements to states in $\mathcal{H}_N\otimes\mathcal{H}_N$. It vanishes if any one of the particles is moved away.

The model is designed to allow pion production and absorption and the parameters of V_0 are to be determined by fits to N-N scattering data both above and below the pion threshold. Since the model does not allow inelastic N-N scattering when a pion is present, the cluster separability can be satisfied only to the extent that inelastic N-N scattering is negligible in the $NN\pi$ channel.

The scheme outlined above meets our specifications. (i) It is relativistically invariant. (ii) If all stable particles are distant from each other, then $M\to M^0$ and thus no renormalization is called for. (iii) True pion absorption is included by the mechanism $N\pi\to\Delta$, $N\Delta\to NN$, as well as the off-diagonal part of V''. To the extent that pion production is dominated by the Δ resonance, it is reasonable to consider models in which $V''=0$.

In Sec. III, the multichannel scattering theory for the $NN\pi$ system is summarized and the expressions for the scattering and reaction amplitudes are brought into a form which reflects the strategy for numerical computation that will be used in a subsequent paper.[11] The relevant properties of the Poincaré generators are listed in the Appendix.

II. CONSTRUCTION OF THE $NN\pi$ MODEL

We begin with a representation for two interacting nucleons on $\mathcal{H}_{NN}$. States $|\psi\rangle\in\mathcal{H}_{NN}$ can be represented by functions $\psi(\vec{p}_a,\vec{p}_b)$, where $\vec{p}_a$ and $\vec{p}_b$ are the nucleon momenta. We suppress the spin variables to simplify the notation. They are not important for the general structure of the model. Alternatively we may represent $|\psi\rangle$ by functions $\psi(\vec{P}_{NN},\vec{k}_a)$, where

$$\vec{P}_{NN}=\vec{p}_a+\vec{p}_b\ . \tag{8}$$

The vector $\vec{k}_a$ is defined by

$$k_a=L(\vec{Q}_{NN})\,p_a\ , \tag{9}$$

where k_a and p_a are four-vectors and $L(\vec{Q})$ is the Lorentz transformation that transforms $\{\vec{Q},(1+\vec{Q}^2)^{1/2}\}$ into $\{0,0,0,1\}$. The vector $\vec{Q}_{NN}$ is a center-of-mass velocity defined by

$$\vec{Q}_{NN}=\vec{P}_{NN}/M^0_{NN}\ . \tag{10}$$

In this representation the mass operator (3) has the kernel

$$(\vec{P}'_{NN},\vec{k}'_a|M_{NN}|\vec{k}_a,\vec{P}_{NN})=(\vec{k}'_a|\hat{M}_{NN}|\vec{k}_a)\delta(\vec{P}'_{NN}-\vec{P}_{NN})\ , \tag{11}$$

where

$$(\vec{k}'_a|\hat{M}_{NN}|\vec{k}_a)=2\omega(\vec{k}_a)\delta(\vec{k}'_a-\vec{k}_a)+(\vec{k}'_a|\hat{v}_{NN}|\vec{k}_a) \tag{12}$$

and

$$\omega(\vec{k})=(\vec{k}^2+m_N^2)^{1/2}\ . \tag{13}$$

It follows from Eq. (11) and the definition *of the* Møller wave operators $\Omega_\pm$,

$$\Omega_\pm(M,M^0)=s-\lim_{\tau\to\pm\infty}e^{iM\tau}\,e^{-iM^0\tau}\ , \tag{14}$$

that $\Omega_{NN\pm}=\Omega_\pm(M_{NN},M^0_{NN})$ has matrix elements of the form

$$(\vec{P}'_{NN},\vec{k}'_a|\Omega_{NN\pm}|\vec{k}_a,\vec{P}_{NN})=\delta(\vec{P}'_{NN}-\vec{P}_{NN})(\vec{k}'_a|\hat{\Omega}_{NN\pm}|\vec{k}_a). \tag{15}$$

From Eq. (14) and the definition

$$T=v\,\Omega_\pm\ , \tag{16}$$

it follows that the Lippmann-Schwinger equation for the nucleon-nucleon T matrix is

$$(\vec k'|\hat T_{NN}|\vec k) = (\vec k'|\hat v_{NN}|\vec k) + \int_{\omega(\vec k)} d^3k'' \frac{(\vec k'|\hat v_{NN}|\vec k'')(\vec k''|\hat T_{NN}|\vec k)}{2[\omega(\vec k - \omega(\vec k'') + i\varepsilon]}, \tag{17}$$

where the limit $\varepsilon \to +0$ is implied.

If there is a pion present, the space of states is $\mathcal{H}_{NN} \otimes \mathcal{H}_\pi$ and the operator defined as $M_{NN} \otimes 1$ on this tensor product will be denoted again by M_{NN}. Its kernel in the representation (11) is

$$(\vec p_\pi', \vec P_{NN}, \vec k_e'|M_{NN}|\vec k_e, \vec P_{NN}, \vec p_\pi) = (\vec k_e'|\hat M_{NN}|\vec k_e)\delta(\vec P_{NN}' - \vec P_{NN})\delta(\vec p_\pi' - \vec p_\pi) . \tag{18}$$

Similarly,

$$(\vec p_\pi', \vec P_{NN}', \vec k_e'|\Omega_{NN\pm}|\vec k_e, \vec P_{NN}, \vec p_\pi) = (\vec k_e'|\hat\Omega_{NN\pm}|\vec k_e)\delta(\vec P_{NN}' - \vec P_{NN})\delta(\vec p_\pi' - \vec p_\pi) . \tag{19}$$

The three-body Hamiltonian and the three-body boost operator are additive in this representation if the pion does not interact with the nucleons;

$$H_{NN,\pi} = H_{NN} + H_\pi , \tag{20}$$

$$\vec K_{NN,\pi} = \vec K_{NN} + \vec K_\pi . \tag{21}$$

Neither the mass operator (18) nor the wave operator (19) commute with the center-of-mass position $\vec X$ defined by (A7) for the noninteracting system. To implement the construction outlined in the Introduction we need a scattering equivalent mass operator M_{NN} that commutes with the noninteracting $\vec X$.

Let $\vec q_\pi$ be defined by

$$q_\pi = L(\vec P/M_{NN}^0)p_\pi . \tag{22}$$

It is possible to represent states $|\psi> \in \mathcal{H}_{NN} \otimes \mathcal{H}_\pi$ by functions $\psi(\vec P, \vec k_e, \vec q_\pi)$. We define the mass operator M_{NN} by its kernel in this representation

$$(\vec q_\pi', \vec P', \vec k_e'|\mathrm{M}_{NN}|\vec k_e, \vec P, \vec q_\pi) = (\vec k_e'|\hat M_{NN}|\vec k_e)\delta(\vec P' - \vec P)\delta(\vec q_\pi' - \vec q_\pi) . \tag{23}$$

Manifestly, the wave operators

$$\tilde\Omega_{NN\pm} = \Omega_\pm(\mathrm{M}_{NN}, M^0) , \tag{24}$$

exist and are complete. From Eqs. (23) and (24) it follows that the matrix elements of $\tilde\Omega_{NN\pm}$ are

$$(\vec q_\pi', \vec P', \vec k_e'|\tilde\Omega_{NN\pm}|\vec k_e, \vec P, \vec q_\pi) = (\vec k_e'|\hat\Omega_{NN\pm}|\vec k_e)\delta(\vec P' - \vec P)\delta(\vec q_\pi' - \vec q_\pi) . \tag{25}$$

It is clear from (19) and (25) that $\Omega_{NN\pm}$ and $\tilde\Omega_{NN\pm}$ differ. But the S matrices are identical,

$$S_{NN} = \Omega_{NN+}^\dagger \Omega_{NN-} = \tilde\Omega_{NN+}^\dagger \tilde\Omega_{NN-} , \tag{26}$$

because S commutes with M^0. (Note that $\vec q_\pi' = \vec q_\pi$ follows from $\vec p_\pi' = \vec p_\pi$ and $\vec P_{NN}' = \vec P_{NN}$ if and only if $|\vec k_e'| = |\vec k_e|$.) Since

$$M^0 = (\vec q_\pi^{\,2} + M_{NN}^{0\,2})^{1/2} + (\vec q_\pi^{\,2} + m_\pi^2)^{1/2} , \tag{27}$$

it follows from

$$\mathrm{M}_{NN}\tilde\Omega_{NN\pm} = \tilde\Omega_{NN\pm} M_{NN}^0 \tag{28}$$

that

$$\tilde\Omega_{NN\pm} M^0 = \mathrm{M}_{NN,\pi}\tilde\Omega_{NN\pm} , \tag{29}$$

where

$$\mathrm{M}_{NN,\pi} = (\vec q_\pi^{\,2} + \mathrm{M}_{NN}^2)^{1/2} + (\vec q_\pi^{\,2} + m_\pi^2)^{1/2} . \tag{30}$$

We may therefore expect the desirable result

$$\Omega_\pm(\mathrm{M}_{NN,\pi}, M^0) = \Omega_\pm(\mathrm{M}_{NN}, M_{NN}^0) . \tag{31}$$

A proof of (31) uses the Birman-Kato invariance principle[12,13] and Lebesgue's bounded convergence theorem.[14]

The Hamiltonian

$$\tilde H_{NN,\pi} = [\vec P^2 + \mathrm{M}_{NN,\pi}^2]^{1/2} \tag{32}$$

is not additive as in (20). The two-body interaction term

$$\begin{aligned} V_{NN,\pi} &= \mathrm{M}_{NN,\pi} - M^0 \\ &= (\vec q_\pi^{\,2} + \mathrm{M}_{NN}^2)^{1/2} - (\vec q_\pi^{\,2} + M_{NN}^0)^{1/2} \end{aligned} \tag{33}$$

depends parametrically on the spectator momentum $\vec q_\pi$.

The treatment of the two-body πN problem is similar to that of N-N scattering described above except that the masses are not equal and πN is coupled to a virtual Δ channel. Any state $|\psi>$ in $\mathcal{H}_{N\pi}$ has a component in $\mathcal{H}_N \otimes \mathcal{H}_\pi$ represented by a function $\psi_{N\pi}(\vec P_{N\pi}, \vec k_\pi)$ and a component in $\mathcal{H}_\Delta$ represented by a function $\psi_\Delta(\vec P_{N\pi})$, where $\vec P_{N\pi}$ denotes the total momentum and k_π is defined by

$$k_\pi = L(\vec P_{N\pi}/M_{N\pi}^0)p_\pi . \tag{34}$$

The mass operator $M_{N\pi}$ has matrix elements proportional to $\delta(\vec P_{N\pi}' - \vec P_{N\pi})$ as in (11) and the restricted matrix $\hat M_{N\pi}$ is of the form

$$(\vec k_\pi'|\hat M_{N\pi}|\vec k_\pi) = W(\vec k)\,\delta(\vec k_\pi' - \vec k_\pi) + (\vec k_\pi'|v_{N\pi}|\vec k_\pi) , \tag{35}$$

where

$$W(\vec k) = (\vec k^2 + m_N^2)^{1/2} + (\vec k^2 + m_\pi^2)^{1/2} , \tag{36}$$

$$(\Delta|\hat M_{N\pi}|\Delta) = m_\Delta , \tag{37}$$

$$(\Delta|\hat{M}_{N\pi}|\vec{k}_\pi) = (\Delta|\hat{v}_{N\pi}|\vec{k}_\pi) \ . \tag{38}$$

The parameters are such that $\hat{M}_{N\pi}$ has no point spectrum. The T matrix for πN scattering satisfies the Lippmann-Schwinger equation

$$(\vec{k}'|\hat{T}_{N\pi}|\vec{k}) = (\vec{k}'|\hat{U}(\vec{k})|\vec{k}) + \int d^3k'' \frac{(\vec{k}'|\hat{U}(\vec{k})|\vec{k})(\vec{k}''|T_{N\pi}|\vec{k})}{W(\vec{k}) - W(\vec{k}'') + i\varepsilon} \ , \tag{39}$$

where the effective potential $\hat{U}(\vec{k})$ is defined by

$$(\vec{k}')|\hat{U}(\vec{k})|\vec{k}'') = (\vec{k}'|\hat{v}_{N\pi}|\vec{k}'') + \frac{(\vec{k}'|\hat{v}_{N\pi}|\Delta)(\Delta|\hat{v}_{N\pi}|\vec{k}'')}{W(\vec{k}) - m_\Delta + i\varepsilon} \ . \tag{40}$$

The wave operators $\Omega_{N\pi}$ are known to exist and to be complete.[10]

The pion-nucleon interaction in the three-body space can be defined by the same procedure that led to Eq. (33). The result is

$$\begin{aligned} V_{a\pi,b} &= \mathrm{M}_{a\pi,b} - M^0 \\ &= (\vec{q}_b^{\,2} + M_{a\pi}^2)^{1/2} - (\vec{q}_b^{\,2} + M_{a\pi}^{02})^{1/2} \ , \end{aligned} \tag{41}$$

where a labels the nucleon that interacts with the pion and b labels the spectator.

The fully interacting mass operator is then of the form (1) with (7) and

$$V' = V_{NN,\pi} + V_{a\pi,b} + V_{b\pi,a} \ . \tag{42}$$

The Hamiltonian $H = (\vec{P}^2 + M^2)^{1/2}$ does not become additive when a particle is moved away, but the wave operators

$$\Omega_\pm = s\text{-}\lim_{\tau\to\pm\infty} e^{iM\tau} e^{-iM^0\tau} \tag{43}$$

satisfy the cluster relations[5]

$$\lim_{|\vec{d}|\to\infty} \| (\Omega_\pm - \tilde{\Omega}_{NN\pm}) e^{i\vec{q}_\pi\cdot\vec{d}} |\psi\rangle \| = 0 \ , \tag{44}$$

$$\lim_{|\vec{d}|\to\infty} \| (\Omega_\pm - \bar{\Omega}_{a\pi\pm}) e^{i\vec{q}_b\cdot\vec{d}} |\psi\rangle \| = 0 \ , \tag{45}$$

where $|\psi\rangle \in \mathcal{H}_{NN} \otimes \mathcal{H}_\pi$. The S operator has therefore the required cluster properties,

$$\lim_{|\vec{d}|\to\infty} \| (S - S_{NN} \otimes 1) e^{i\vec{p}_\pi\cdot\vec{d}} |\psi\rangle \| = 0 \tag{46}$$

and

$$\lim_{|\vec{d}|\to\infty} \| (S - S_{a\pi} \otimes 1) e^{i\vec{p}_b\cdot\vec{d}} |\psi\rangle \| = 0 \ . \tag{47}$$

This completes the proof that the models constructed above satisfy the conditions stated in the Introduction. In any concrete realization, a convenient form is assumed for the two-body interactions v_{NN}, $v_{N\pi}$, and V_0. The mass operator is then of the form (1) and (7) with V' given by (42). This mass operator together with the operators $\vec{P}$, $\vec{X}$, and $\vec{J}$ of the noninteracting system can be used to obtain the Poincaré generators using (A13)–(A15).

Contact with experiment requires equations for the relevant scattering amplitudes. The derivation of these equations from the general theory is sketched in the Sec. III.

III. SCATTERING THEORY

The complete scattering theory of the $NN\pi$ system must consider the channels NN, $NN\pi$, and πd. Since a bound state—the deuteron—is involved, it is most convenient to use a two-Hilbert-space formulation.[5,15–17] The initial and final state are described in the Hilbert space $\mathcal{H}^f$,

$$\mathcal{H}^f = \mathcal{H}^f_{NN} \oplus \mathcal{H}^f_{NN\pi} \oplus \mathcal{H}^f_{\pi d} \ . \tag{48}$$

The Poincaré generators in $\mathcal{H}^f$ are those for free particles in the three channels NN, $NN\pi$, and πd. A time dependent scattering state $\psi(t) \in \mathcal{H}$ satisfies the initial condition

$$\lim_{t\to-\infty} \|\psi(t) - \Phi\chi(t)\| = 0 \ , \tag{49}$$

where $\chi(t)$ is a state of noninteracting particles in $\mathcal{H}^f$ and the operator Φ from $\mathcal{H}^f$ into $\mathcal{H}$ maps $\mathcal{H}^f_{NN}$ and $\mathcal{H}^f_{NN\pi}$ identically into $\mathcal{H}_{NN}$ and $\mathcal{H}_{NN\pi}$. It maps $\mathcal{H}^f_{\pi d}$ into $\mathcal{H}_{NN\pi}$ according to

$$(\vec{p}_\pi{}', \vec{P}_{NN}, \vec{k}|\Phi|\vec{P}_d, \vec{p}_\pi) = \delta(\vec{p}_\pi{}' - \vec{p}_\pi)\delta(\vec{P}_d - \vec{P}_{NN})\phi_d(\vec{k}), \tag{50}$$

where $\phi_d(\vec{k})$ is the momentum space deuteron wave function. The wave operators are then defined by

$$\Omega_\pm = s\text{-}\lim_{\tau\to\pm\infty} e^{iM\tau} \Phi e^{-iM^f\tau} \ . \tag{51}$$

From the definition of Φ it follows that

$$\Phi M^f|\alpha\rangle = M^0\Phi|\alpha\rangle \tag{52}$$

if $|\alpha\rangle \in \mathcal{H}^f_{NN}$ or $|\alpha\rangle \in \mathcal{H}^f_{NN\pi}$, and that

$$\Phi M^f|\delta\rangle = (M^0 + V_{NN,\pi})\Phi|\delta\rangle \tag{53}$$

if $|\delta\rangle \in \mathcal{H}^f_{\pi d}$.

An off-shell T operator in $\mathcal{H}^f$ can be defined by[18]

$$T(z) = \Phi^\dagger \mathcal{V} + \mathcal{V}^\dagger \frac{1}{z - M} \mathcal{V} \ , \tag{54}$$

where $\mathcal{V}$ is by definition

$$\mathcal{V} = M\Phi - \Phi M^f . \tag{55}$$

It follows from Eqs. (51) and (54) and the definition of S,

$$S = \Omega_+^\dagger \Omega_- , \tag{56}$$

that

$$\langle w' | S | w \rangle = \delta(w' - w)[1 - 2\pi i \langle w' | T(w) | w \rangle] , \tag{57}$$

where w is an eigenvalue of M^f. From the definition of $\mathcal{V}$ together with (52) and (53) it follows that

$$\mathcal{V} | \alpha \rangle = V \Phi | \alpha \rangle \tag{58}$$

and

$$\mathcal{V} | \delta \rangle = V_d \Phi | \delta \rangle , \tag{59}$$

where

$$V_d = V - V_{NN,\pi} . \tag{60}$$

It is therefore possibe to express the channel projections of the operator $T(z)$ in the form $\Phi^\dagger \mathcal{T}(z) \Phi$ where $\mathcal{T}(z)$ is a different operator for different channel projections. We have

$$\langle \beta | T(z) | \alpha \rangle = \langle \beta | \Phi^\dagger \mathcal{T}(z) \Phi | \alpha \rangle , \tag{61}$$

with

$$\mathcal{T}(z) = V + V \frac{1}{z - M} V , \tag{62}$$

if $|\alpha>$ and $|\beta>$ are in the NN channel or in the $NN\pi$ channel. If $|\delta>$ and $|\delta'>$ are in the πd channel we have

$$\langle \alpha | T(z) | \delta \rangle = \langle \alpha | \Phi^\dagger \mathcal{T}_d(z) \Phi | \delta \rangle , \tag{63}$$

$$\langle \delta' | T(z) | \delta \rangle = \langle \delta' | \Phi^\dagger \mathcal{T}_{dd}(z) \Phi | \delta \rangle , \tag{64}$$

where

$$\mathcal{T}_d(z) = \left(1 + V \frac{1}{z - M}\right) V_d \tag{65}$$

and

$$\mathcal{T}_{dd}(z) = \left(1 + V_d \frac{1}{z - M}\right) V_d . \tag{66}$$

For purposes of calculations it will be convenient to project out the three-body space $\mathcal{H}_{NN} \otimes \mathcal{H}_\pi$. Let $\mathcal{P}$ be the projection operator that projects onto $\mathcal{H}_{NN} \oplus \mathcal{H}_{N\Delta}$ and $\bar{\mathcal{P}} = 1 - \mathcal{P}$. We use the following definitions:

$$R(z) = (z - M)^{-1} , \tag{67}$$

$$\bar{R}(z) = (z - \bar{\mathcal{P}} M \bar{\mathcal{P}})^{-1} \bar{\mathcal{P}} , \tag{68}$$

$$\tilde{M}(z) = \mathcal{P} M \mathcal{P} + \mathcal{P} V \bar{R}(z) V \mathcal{P} , \tag{69}$$

$$\tilde{R}(z) = [z - \tilde{M}(z)]^{-1} . \tag{70}$$

Because of the $\Delta \to N\pi$ vertex, $\tilde{M}(z)$ does not go to M^0 if the nucleon in the space $\mathcal{H}_N \otimes \mathcal{H}_\Delta$ is moved to infinity. Let $V_D(z)$ be the surviving Δ self-interaction,

$$\begin{aligned} V_D(z) &= \lim_{|\vec{d}| \to \infty} e^{i\vec{q}_N \cdot \vec{d}} \, \mathcal{P}_{N\Delta} [\tilde{M}(z) - M^0] \, \mathcal{P}_{N\Delta} \, e^{-i\vec{q}_N \cdot \vec{d}} \\ &= \lim_{|\vec{d}| \to \infty} e^{i\vec{q}_N \cdot \vec{d}} \, \mathcal{P} V \bar{R}(z) V \mathcal{P} e^{-i\vec{q}_N \cdot \vec{d}} , \end{aligned} \tag{71}$$

and define

$$\tilde{V}(z) = \tilde{M}(z) - \tilde{M}^0(z) = V_0 + \mathcal{P} V \bar{R} V \mathcal{P} - V_D(z) , \tag{72}$$

where

$$\tilde{M}^0(z) = \mathcal{P} M^0 \mathcal{P} + V_D(z) . \tag{73}$$

The following relations are simple consequences of these definitions and the identities

$$\begin{aligned} \frac{1}{z - A - B} &= \frac{1}{z - A} + \frac{1}{z - A} B \frac{1}{z - A - B} \\ &= \frac{1}{z - A} + \frac{1}{z - A - B} B \frac{1}{z - A} \end{aligned} \tag{74}$$

which hold for any z, A, and B.

$$\tilde{R}(z) = \mathcal{P} R(z) \mathcal{P} , \tag{75}$$

$$R(z) = [1 + \bar{R}(z) V] \tilde{R}(z) [V \bar{R}(z) + 1] + \bar{R}(z) . \tag{76}$$

From (65) and (74) it follows that

$$\mathcal{T}(z) = U(z) + U(z) \tilde{R}(z) U(z) , \tag{77}$$

$$\mathcal{T}_d(z) = [1 + U(z) \tilde{R}(z)] U_d(z) , \tag{78}$$

and

$$\mathcal{T}_{dd}(z) = U_{dd}(z) + U_d^\dagger(z^*) \tilde{R}(z) U_d(z) , \tag{79}$$

where

$$U(z) = V + V \bar{R}(z) V - V_D(z) , \tag{80}$$

$$U_d(z) = [1 + V \bar{R}(z)] V_d , \tag{81}$$

and

$$U_{dd}(z) = V_d + V_d \bar{R}(z) V_d . \tag{82}$$

Further reductions involve the identities

$$\tilde{R}(z) = \tilde{R}_0(z) + \tilde{R}_0(z) \tilde{T}(z) \tilde{R}_0(z) , \tag{83}$$

where

$$\tilde{R}_0(z) = [z - \tilde{M}_0(z)]^{-1} \tag{84}$$

and

$$\begin{aligned} \tilde{T}(z) &= \tilde{V}(z) + \tilde{V}(z) \tilde{R}(z) \tilde{V}(z) \\ &= \tilde{V}(z) + \tilde{V}(z) \tilde{R}_0(z) \tilde{T}(z) . \end{aligned} \tag{85}$$

Since

$$\mathcal{P}U(z)\mathcal{P}=\bar{V}(z)\,, \tag{86}$$

we have

$$\mathcal{P}\mathcal{T}(z)\mathcal{P}=\bar{T}(z) \tag{87}$$

and

$$\langle\beta|T(z)|\alpha\rangle=\langle\beta|\Phi^{\dagger}\bar{T}(z)\Phi|\alpha\rangle \tag{88}$$

if $|\alpha>$ and $|\beta>$ are in the *NN* channel.

In practice, the parameters of $v_{N\pi}$ are determined from π-N elastic scattering data using (39) and (40). The parameters of v_{NN} are obtained from (17) by fits to N-N elastic scattering data in the energy region where inelasticity is negligible. The parameters of V_0 are then determined from N-N elastic scattering data both above and below the pion production threshold. This involves using (88) and (85). The study of other processes then provides tests of the validity of the model as well as means of removing any remaining ambiguity in the interactions. The numerical implementation of this scheme will be reported elsewhere.[11]

We wish to thank T.-S. H. Lee for helpful discussions. This work was performed under the auspices of the U.S. Dept. of Energy.

APPENDIX

The Poincaré generators $\vec{P}$, H, $\vec{J}$, $\vec{K}$ satisfy the commutation relations

$$[P_i,P_j]=[P_i,H]=0\,, \tag{A1}$$

$$[J_p,J_q]=i\sum_r \varepsilon_{pqr}J_r\,, \tag{A2}$$

$$[J_p,P_q]=i\sum_r \varepsilon_{pqr}P_r,\quad [J_i,H]=0\,, \tag{A3}$$

$$[J_p,K_q]=i\sum_r \varepsilon_{pqr}K_r\,, \tag{A4}$$

$$[K_p,K_q]=-i\sum_r \varepsilon_{pqr}J_r\,, \tag{A5}$$

$$[K_p,P_q]=i\,\delta_{pq}H,\quad [K_r,H]=i\,P_r\,. \tag{A6}$$

The Newton Wigner position operator[19] $\vec{X}$ is defined by

$$\vec{X}=\tfrac{1}{2}\,(H^{-1}\,\vec{K}+\vec{K}H^{-1})-\frac{\vec{P}\times(H\vec{J}+\vec{P}\times\vec{K})}{MH(M+H)} \tag{A7}$$

and the canonical spin $\vec{j}$ is

$$\vec{j}=\vec{J}-\vec{X}\times\vec{P}\,. \tag{A8}$$

It follows from (A1)–(A8) that

$$[X_r,X_s]=0\,, \tag{A9}$$

$$[X_r,P_s]=i\delta_{rs}\,, \tag{A10}$$

and

$$[X_r,j_s]=[P_r,j_s]=0\,. \tag{A11}$$

Since M commutes with all the generators, it follows that

$$[M,\vec{j}]=[M,\vec{X}]=[M,\vec{P}]=0\,. \tag{A12}$$

Conversely if $\vec{X}$, $\vec{P}$, $\vec{j}$, and M satisfy (A1)–(A12), then the generators H, $\vec{J}$, $\vec{K}$ defined by

$$H=(\vec{P}^2+M^2)^{1/2}\,, \tag{A13}$$

$$\vec{J}=\vec{X}\times\vec{P}+\vec{j}\,, \tag{A14}$$

and

$$\vec{K}=\tfrac{1}{2}\,(H\vec{X}+\vec{X}H)-\vec{j}\times\vec{P}\,(M+H)^{-1} \tag{A15}$$

satisfy the commutation relations (A1)–(A6).

---

[1] G. E. Brown and W. Weise, Phys. Rep. 22C, 279 (1975).

[2] L. S. Kisslinger and W. L. Wang, Ann. Phys. (N.Y.) 99, 374 (1976).

[3] J. Schwinger, Phys. Rev. 127, 324 (1962).

[4] L. L. Foldy, Phys. Rev. 122, 275 (1961).

[5] F. Coester, Helv. Phys. Acta 38, 7 (1965).

[6] See A. W. Thomas and A. S. Rinat, Phys. Rev. C 20, 216 (1979) and references therein.

[7] B. Bakamjian and L. H. Thomas, Phys. Rev. 92, 1300 (1953).

[8] R. Fong and J. Sucher, J. Math. Phys. 5, 956 (1964).

[9] F. Coester, S. C. Pieper, and F. J. D. Serduke, Phys. Rev. C 11, 1 (1975), Secs. II and III.

[10] M. Reed and B. Simon, *Methods of Modern Mathematical Physics* (Academic, New York, 1979), Vol. III, Theorem XI. 9, p. 27.

[11] M. Betz and T.-S. H. Lee (unpublished).

[12] J. Kato, *Perturbation Theory for Linear Operators* (Springer, Berlin-Heidelberg, 1966), Chap. X.4.

[13] Reference 10, Vol. I, Theorem XI.4, p. 30 and Appendix 3 to Chap. XI.3, p. 49ff.

[14] Reference 10, Vol. I, Theorem I.11.

[15] T. Kato, J. Funct. Anal. 1, 342 (1967).

[16] Reference 10, Vol. III, Chap. XI.3.

[17] F. Coester, Proceedings of the Conference on Mathematical Methods and Applications of Scattering Theory, May, 1979, Catholic University, Washington, D. C.

[18] F. Coester and L. Schlessinger, Ann. Phys. (N.Y.) 78, 90 (1973), see Appendix, p. 128.

[19] M. H. L. Pryce, Proc. R. Soc. London A195, 62 (1949), definition (e); T. D. Newton and E. P. Wigner, Rev. Mod. Phys. 21, 400 (1949).

PHYSICAL REVIEW C VOLUME 21, NUMBER 6 JUNE 1980

Angular distributions of Sc fragments from the interaction of ^{238}U with 0.8–400 GeV protons

D. R. Fortney* and N. T. Porile
Department of Chemistry, Purdue University, West Lafayette, Indiana 47907

(Received 14 January 1980)

Angular distributions of ^{44}Sc^m, ^{46}Sc, ^{47}Sc, and ^{48}Sc emitted in the interaction of ^{238}U with 0.8, 3.0, 11.5, and 400 GeV protons have been measured. The angular distributions peak at forward angles at 0.8 and 3 GeV but are sideward-peaked at 11.5 and 400 GeV. At 400 GeV, fewer fragments are emitted at forward than at backward angles. Isotopic differences were found to be small. The data were fitted with the function $F_L(\theta_L) = 1 + A_1\cos\theta_L + A_2\cos^2\theta_L$ and were also analyzed in terms of the two-step model. The values of A_1 peak at 3 GeV, go through zero at 11.5 GeV, and become negative at 400 GeV. The values of A_2 are zero at 0.8 GeV and become increasingly negative with increasing proton energy. A qualitative explanation in terms of a possible change in the nature of proton-nucleus interactions at high energies is presented.

[NUCLEAR REACTIONS ^{238}U(p,x) ^{44}Sc^m, ^{46}Sc, ^{47}Sc, ^{48}Sc. T_p = 0.8, 3.0, 11.5, 400 GeV. Measured angular distributions.]

I. INTRODUCTION

Considerable evidence has accumulated in recent years indicating that a profound change in the mechanism for the formation of light fragments and deep spallation products from the interaction of heavy elements with high-energy protons occurs at energies below 10 GeV. Beg and Porile[1] thus discovered that the ratio of forward-to-backward emission (F/B) of several deep spallation products from the interaction of ^{238}U with protons peaked sharply in the vicinity of 3 GeV while the ranges decreased by about a factor of 2 between 1 and 4 GeV. Similar results were later reported for a broad range of products from the interaction of both uranium and gold with protons.[2-6] These results have been interpreted[5,7] in terms of a change in the initial proton-nucleus interaction from an intranuclear cascade to a coherent interaction with part of the nucleus.[8]

Angular distribution measurements also reveal a striking change in the production of these nuclides at multi-GeV energies. Remsberg and Perry[9] measured the angular distributions of light fragments emitted in the interaction of heavy elements with 28 GeV protons. Sideward peaking was observed for fragments such as sodium in contrast to the forward peaking previously observed at 2.9 GeV.[10] Porile *et al.*[11] similarly observed that the angular distributions of deep spallation products resulting from the interaction of ^{238}U with 11.5 GeV protons peaked at sideward angles. By contrast, forward peaking had been observed for these products at a bombarding energy of 2.2 GeV.[12,13] In a recent report Porile *et al.*[14] measured the angular distributions of a number of products resulting from 400 GeV proton bombardment of uranium. In addition to sideward peaking, these authors also observed several instances of a novel effect, namely, preferential emission at backward angles. This result indicates that measurements at the highest available energies are of special interest.

The present work is one of a series of studies of the variation with proton energy between 0.8 and 400 GeV of the properties of scandium fragments emitted in the breakup of uranium. These products are apparently formed in near-central collisions and a study of their properties may be used to probe nuclear matter under fairly extreme conditions. Previous papers in this series have dealt with the excitation functions and thick-target recoil properties,[3] and with the differential ranges of fragments emitted at 90° to the beam.[15] The excitation functions were found to rise steeply with energy up to ~10 GeV and the recoil properties exhibited the behavior described above. The spectra derived from the differential ranges broadened with increasing proton energy while the peaks shifted to lower values suggesting that extensive mass dissipation occurred prior to breakup for proton energies of 10 GeV and above. We report here the results of angular distribution measurements on ^{44}Sc^m, ^{46}Sc, ^{47}Sc, and ^{48}Sc performed at 0.8, 3.0, 11.5, and 400 GeV. The first three of these energies span the region of the peak in F/B as well as the sharp dropoff in range, while the 400 GeV experiments focus on the unusual enhancement at backward angles.[14] The existence of four measurable isotopes makes it possible to investigate the effect of fragment composition. Preliminary reports of this work have been published.[14,16]

© 1980 The American Physical Society

II. EXPERIMENTAL

The experimental procedure has been described in detail in previous reports from our laboratory.[11,15] We emphasize here only those details unique to the present work.

The experiments at 400 GeV were performed in the Neutrino Hall beam line at Fermilab, those at 11.5 and 3.0 GeV in the internal beam of the zero-gradient synchroton (ZGS), and those at 0.8 GeV in line *B* of LAMPF. The experiments involved the irradiation in vacuum of thin UF_4 targets and the collection of the emitted fragments in aluminum. The targets consisted of 0.1–0.3 mg/cm^2 UF_4 evaporated onto high-purity aluminum (99.999%) and were inclined at 30° and 150° (ZGS) or 45° and 135° to the beam. The catchers consisted of 50 μm thick 99.999% pure aluminum and were sufficiently thick to stop all the Sc fragments. An additional 25 μm foil backed up the catchers in order to protect them from the possibility of contamination by recoils originating in the catcher holder. The catchers intercepted the angular range of 15°–105° and 75°–165° relative to the beam direction (5°–105° and 75°–175° at Fermilab). In a single ZGS irradiation either the forward or backward half of the angular distribution could be determined. By contrast, at LAMPF and Fermilab measurements over the entire angular range could be performed in a single exposure. This was accomplished by placing two targets back to back with enough aluminum between them to prevent any cross contamination of recoils.

The catcher foils were cut into 15° wide strips (a 10° wide strip was cut at the most forward and backward angles at Fermilab). Because of the low counting rates, the catcher foils subtended a large fraction of the available solid angle. The resulting mismatch between the spherical reaction coordinates and the cylindrical catcher angles dictated that the foils be cut along curves of constant recoil angle for a point source of recoils.[17] The solid angle subtended by each catcher as well as the average recoil angle were evaluated with a code[18] which, in addition to the target-catcher geometry, took into account the beam profile at the target location. This profile was determined from the distribution of the ^{24}Na activity in the target backing. The beam spot varied in full width at half-maximum from ~0.3 cm at Fermilab to 1.0 ×2.2 cm at LAMPF. The solid angles subtended by the catcher segments were approximately 0.3 sr at all energies. This value applies with relatively little variation over most of the angular range excepting the most forward and backward angles, for which much smaller solid angles were available.

The irradiations were performed for periods ranging from ~1 hr (ZGS) to ~1 week (Fermilab). Following bombardment, the Al foils were cut and dissolved and scandium separated by a previously described[3] radiochemical procedure. The samples were assayed with Ge(Li) detectors and results obtained for ^{44}Sc^m, ^{46}Sc, ^{47}Sc, and ^{48}Sc on the basis of the γ rays emitted by these nuclides.[3] The angular distributions were obtained by extrapolation of the counting rates to end of bombardment and correction for chemical yield and solid angle. The forward and backward halves of each angular distribution were combined by normalizing them to each other at their common intervals.

As a check on the forward-backward normalization a number of experiments were performed with the catcher foils in a 2π geometry. The target stack in these experiments consisted of two Al foils in contact, with one foil having ~0.3 mg/cm^2 UF_4 evaporated onto it. Two such sets of foils, with the target facing forward and backward, respectively, were irradiated in a single experiment. This combination permitted a correction to be made for the small (1–3%) amount of Sc activity retained in the target.

In order to ensure the validity of the results, two subsidiary types of experiments were performed. The possible contribution to the Sc activities from extraneous sources was investigated in blank experiments performed at each accelerator and upper limits of 1% were placed in all cases. In a different experiment, the effect of target thickness on the angular distribution was investigated at 11.5 GeV. The results obtained for 100 μg/cm^2 and 300 μg/cm^2 thick targets yielded essentially identical results indicating that scattering effects could be neglected at these thicknesses.

III. RESULTS

The angular distributions of ^{44}Sc^m, ^{47}Sc, and ^{48}Sc are displayed in Figs. 1–3, respectively. The results for ^{46}Sc are very similar to those obtained for the other isotopes but, due to the long half-life of this nuclide, are subject to greater statistical uncertainty. Either two or three complete angular distributions were measured at each energy and the separate results are displayed. The plotted points are the differential cross sections at the average laboratory angle θ_L normalized to unity at 90°. Typical error bars are shown; these are based on the statistical uncertainties in the counting rates (1–5%), estimated errors in the determination of solid angles and their dispersion due to finite target size (2–5%), uncertainty in forward-backward normalization (2%), and error in

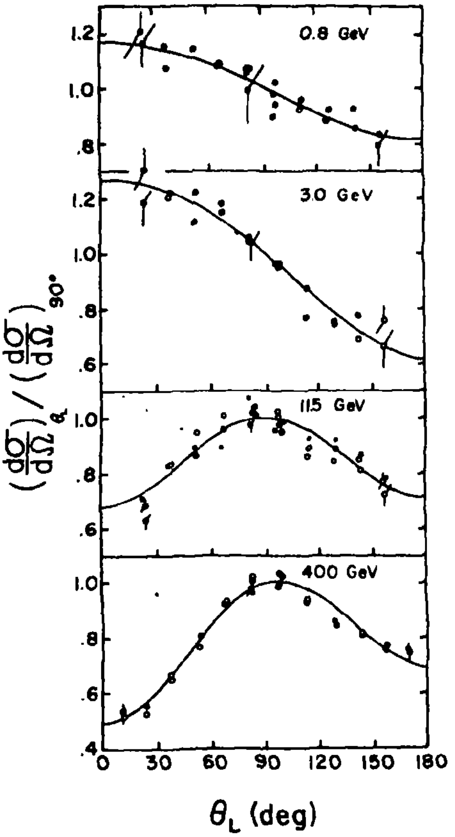

FIG. 1. Angular distributions of ^{44}Sc^m from the interaction of ^{238}U with 0.8-400 GeV protons. The various points at each angle represent the results of replicate experiments. The solid points at 11.5 GeV show the results obtained for a "thin" (100 μg/cm^2) target. Typical error bars are shown at each energy. The curves constitute a least-squares fit of Eq. (1). The differential cross sections are normalized to unity at 90°.

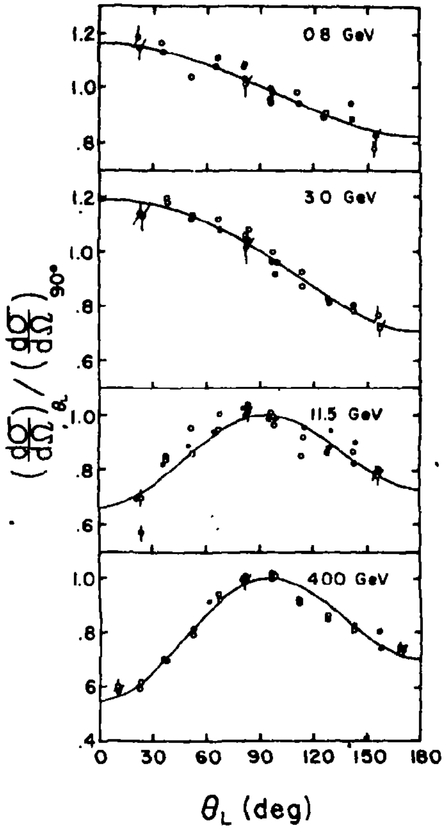

FIG. 2. Angular distributions of ^{47}Sc. See Fig. 1 for details.

chemical yield determination (2%).

In order to systematize the rather large body of data obtained in this study it is useful to fit the laboratory angular distributions with some simple function containing relatively few parameters. It was found that the following two-parameter equation gave a reasonable fit to the data:

$$F_L(\theta_L)=1+A_1\cos\theta_L+A_2\cos^2\theta_L\,. \qquad (1)$$

Similar functions, including forms with additional terms in the series, were also tried and found to be less satisfactory. The curves in Figs. 1–3 represent least-squares fits of Eq. (1) to the data points. The resulting values of A_1 and A_2 are summarized in Table I. It is seen that the points generally scatter about the curves in a fairly random way. Note, however, that at 400 GeV, where the greatest precision was obtained, the curves appear to systematically overestimate the values of the differential cross sections in the vicinity of 120° by somewhat more than one standard deviation. The significance, if any, of this discrepancy is unclear at this time.

A useful measure of the asymmetry in the angular distribution is the ratio of forward-to-backward emission, $(F/B)_{\theta_L}$. This quantity may be conveniently obtained by integrating the fitted angular distributions over the forward and backward hemispheres, i.e.,

$$(F/B)_{\theta_L}=\frac{\int_0^{\pi/2}F_L(\theta_L)\sin\theta_L d\theta_L}{\int_{\pi/2}^{\pi}F_L(\theta_L)\sin\theta_L d\theta_L}\,. \qquad (2)$$

The resulting values are summarized in Table I.

As indicated above, several experiments in which the catchers were in a 2π geometry were

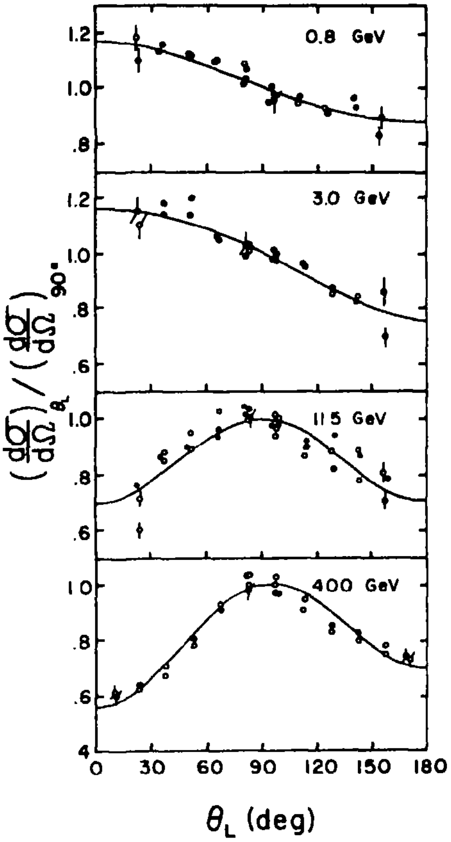

FIG. 3. Angular distributions of ^{46}Sc. See Fig. 1 for details.

performed to check on the forward-backward normalization and recoil retention in the target. These experiments may be used to derive values of the forward-to-backward emission ratio, designated $(F/B)_{2\pi}$, by use of the relation

$$(F/B)_{2\pi}=R_B(R_F+1)/(R_B+1)\,, \tag{3}$$

where R_B and R_F are the experimental forward-to-backward ratios obtained with the target material evaporated onto the backward and forward catchers, respectively. A single experiment of this type was performed at 3 GeV and replicates were run at 11.5 and 400 GeV. The results are summarized in Table I. It is seen that both types of F/B determinations yield essentially the same values, confirming the validity of the forward-backward normalization. In particular, the values of $(F/B)_{2\pi}$ obtained at 400 GeV are significantly less than unity confirming the rather unusual result derived from the angular distributions at this energy.

IV. DISCUSSION

A. Variation of angular distributions with proton energy and product composition

The results displayed in Figs. 1–3 clearly show that some unusual changes in the nature of highly inelastic interactions occur at multi-GeV energies. The angular distributions thus are forward peaked at 0.8 and 3 GeV, with the asymmetry increasing with proton energy in this regime. This trend is indicative of increasing forward momentum transfer to the struck nucleus, consistent with the high excitation energy transfer implied by the steeply rising excitation functions.[3,19,20] Between 3 and

TABLE I. Parametrization of the angular distribution of Sc fragments from the interaction of ^{238}U with protons.

T_p (GeV)	Nuclide	A_1	A_2	$(F/B)_{\theta_L}$	$(F/B)_{2\pi}$
0.8	^{44}Sc^m	0.178 ± 0.035	-0.010 ± 0.045	1.20 ± 0.04	
	^{46}Sc	0.126 ± 0.044	-0.024 ± 0.064	1.14 ± 0.05	
	^{47}Sc	0.172 ± 0.018	-0.010 ± 0.020	1.19 ± 0.02	
	^{48}Sc	0.152 ± 0.014	0.020 ± 0.017	1.16 ± 0.02	
3.0	^{44}Sc^m	0.324 ± 0.023	-0.062 ± 0.026	1.40 ± 0.03	1.40 ± 0.10
	^{46}Sc	0.220 ± 0.035	-0.152 ± 0.039	1.26 ± 0.04	
	^{47}Sc	0.243 ± 0.015	-0.059 ± 0.018	1.28 ± 0.02	1.46 ± 0.03
	^{48}Sc	0.202 ± 0.018	-0.046 ± 0.020	1.23 ± 0.02	1.16 ± 0.04
11.5	^{44}Sc^m	-0.013 ± 0.019	-0.310 ± 0.026	0.99 ± 0.02	1.00 ± 0.01
	^{46}Sc	-0.041 ± 0.011	-0.239 ± 0.017	0.96 ± 0.01	0.96 ± 0.01
	^{47}Sc	-0.033 ± 0.027	-0.307 ± 0.037	0.96 ± 0.03	1.00 ± 0.01
	^{48}Sc	-0.003 ± 0.029	-0.300 ± 0.039	1.00 ± 0.03	1.01 ± 0.01
400	^{44}Sc^m	-0.100 ± 0.007	-0.411 ± 0.010	0.89 ± 0.01	0.91 ± 0.01
	^{46}Sc	-0.066 ± 0.011	-0.356 ± 0.012	0.94 ± 0.01	0.95 ± 0.02
	^{47}Sc	-0.072 ± 0.008	-0.377 ± 0.011	0.92 ± 0.01	0.95 ± 0.01
	^{48}Sc	-0.064 ± 0.011	-0.374 ± 0.014	0.93 ± 0.01	0.95 ± 0.01

11.5 GeV the angular distributions undergo a major change: Forward peaking gives way to sideward peaking and the angular distributions become symmetric about 90° in the laboratory. This may be indicative of a process in which the energy and momentum of the incident proton are carried off by an ensemble of participant nucleons, with the fragments being formed from the spectator remnant.[5,7] At 400 GeV, the angular distributions retain the prominent peak at 90° but, in addition, show that emission at backward angles is more likely than that at forward angles.[14]

A somewhat different perspective on these trends is provided in Fig. 4, which shows the energy dependence of the parameters A_1 and A_2, as well as that of the forward-to-backward ratio, for each of the Sc fragments. The parameter A_1, which is a measure of the forward-backward asymmetry, initially increases with proton energy, peaks at 3 GeV, and becomes negative at 400 GeV. There is a small but significant difference between the value of A_1 for neutron-deficient ^{44}Sc^m and those for the three neutron-excess fragments. The former thus is larger than the latter up to 3 GeV indicating that the angular distribution is more forward peaked. On the other hand, A_1 for ^{44}Sc^m is more negative at 400 GeV, reflecting the greater degree of backward enhancement for this fragment. The parameter A_2 is a measure of the anisotropy and decreases monotonically with bombarding energy, reflecting the increasing importance of sideward relative to forward-backward emission. Within the limits of error, there is no isotope effect in A_2.

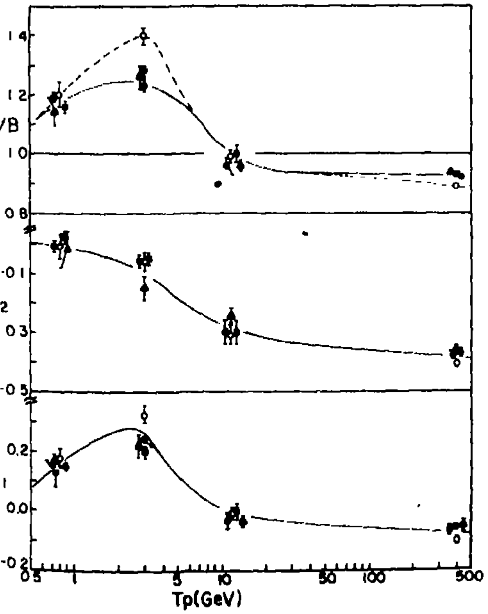

FIG. 4. Energy dependence of angular distribution parameters A_1, A_2, and F/B for ^{44}Sc^m (○), ^{46}Sc (△), ^{47}Sc (●), and ^{48}Sc (■). The curves show the trends in the data.

The energy dependence of F/B is similar to that previously obtained in thick-target experiments[3] but the present values are uniformly lower. This difference is a consequence of the fact that the thick-target values are range weighted while the present results are independent of range. As is already apparent in the angular distribution plots, the F/B ratios are less than unity at 400 GeV. The difference in A_1 values between ^{44}Sc^m and the other isotopes results in a corresponding difference in F/B, as indicated.

The previously measured excitation functions for the formation of Sc nuclides from ^{238}U (Ref. 3) may be used to convert the angular distributions to differential cross sections (mb/sr). As an example of this procedure we display the values of $d\sigma/d\Omega$ for ^{47}Sc in Fig. 5. It is apparent that the transition from forward to sideward peaking occurs only once the production cross section is close to its maximum value. In order to compare the changes in shape in detail it is more convenient to normalize the differential cross sections to the same value of the integrated cross section at all energies. The results obtained in this fashion for ^{47}Sc are displayed in Fig. 6. It is of interest to note that the angular distributions at backward angles are similar in shape, particularly at the higher energies. The large change in the shapes occurs at forward angles, where the normalized differential cross sections decrease sharply between 3 and 11.5 GeV. The decrease in F/B to

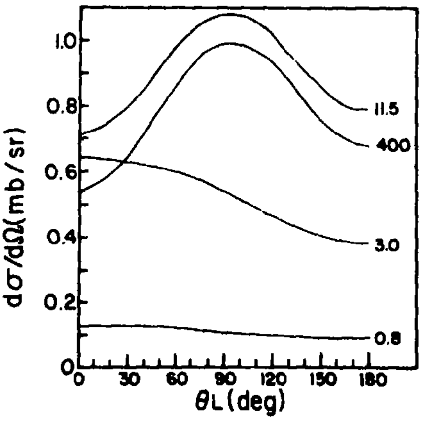

FIG. 5. Differential cross sections (mb/sr) of ^{47}Sc at the indicated proton energies.

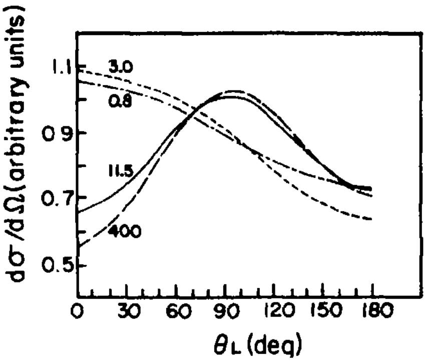

FIG. 6. Differential cross sections of ^{47}Sc normalized to the same value of the integrated cross section. The numbers near the curves represent the bombarding energies.

below unity at 400 GeV may thus be viewed as a natural continuation of this trend. The differential ranges of Sc fragments[15] indicate that an increasing amount of mass dissipation occurs with increasing proton energy. Recent coincidence experiments performed on fragments emitted in the interaction of ^{238}U with 11.5 GeV protons also show that extensive mass loss occurs prior to fragment emission.[7] An explanation of the backward enhancement may thus be sought in a possible connection between these two trends. If the loss of close to half the mass of the target at 400 GeV (Ref. 15) occurs primarily at forward angles, the nuclear density in the forward cone will be sharply reduced. Furthermore, if fragment emission occurs prior to either equilibration or rotation, the occurrence of such a process at forward angles must be hindered, thereby leading to the observed relative enhancement at backward angles.

B. Two-step vector model analysis

The angular distributions may be analyzed in terms of the two-step vector model commonly used to interpret high-energy nuclear reactions. Although the general validity of this model above 3 GeV is questionable, it is nonetheless of interest to examine the dependence on energy and isotopic mass of the parameters in the model in view of the large body of data that has been analyzed in this fashion.

Let $\vec{v}$ be the velocity acquired by the struck nucleus as a result of the initial interaction. The components of v along and at right angles to the beam direction are designated $v_\parallel$ and $v_\perp$, respectively. The effect of $v_\perp$ on the angular distributions is small and unduly complicates the analysis.[11,21] We have therefore not incorporated this variable in the present version of the two-step model. The mean velocity acquired by the fragment in the breakup step is denoted as $\vec{V}$ and its angular distribution in the moving frame obeys the relation

$$F(\theta)=\frac{1+(b/a)\cos^2\theta}{1+b/3a}, \qquad (4)$$

where b/a is the anisotropy parameter. Note that the angular distribution is symmetric about 90° as required by the temporal separation between the two steps. The ratio $\eta_\parallel=v_\parallel/V$ is a measure of the relative velocity imparted in the two steps and is one of the important parameters derived from the analysis. The laboratory angular distribution may be expressed in terms of $\eta_\parallel$ and b/a by the equa-

TABLE II. Two-step model parameters derived from angular distributions of Sc fragments.

T_p (GeV)	Nuclide	$\eta_\parallel$	b/a	$1000\beta_\parallel$
0.8	^{44}Sc^m	0.089 ± 0.018	−0.023 ± 0.040	5.8 ± 1.2
	^{46}Sc	0.063 ± 0.024	−0.026 ± 0.054	3.9 ± 1.4
	^{47}Sc	0.086 ± 0.008	−0.019 ± 0.022	5.4 ± 0.6
	^{48}Sc	0.076 ± 0.007	0.010 ± 0.017	4.7 ± 0.5
3.0	^{44}Sc^m	0.163 ± 0.010	−0.115 ± 0.028	10.2 ± 0.8
	^{46}Sc	0.111 ± 0.015	−0.214 ± 0.046	6.6 ± 1.0
	^{47}Sc	0.123 ± 0.007	−0.087 ± 0.018	7.4 ± 0.6
	^{48}Sc	0.102 ± 0.008	−0.060 ± 0.021	6.0 ± 0.6
11.5	^{44}Sc^m	−0.003 ± 0.012	−0.311 ± 0.026	−0.2 ± 0.7
	^{46}Sc	−0.021 ± 0.008	−0.240 ± 0.014	−1.1 ± 0.4
	^{47}Sc	−0.013 ± 0.015	−0.308 ± 0.038	−0.7 ± 0.8
	^{48}Sc	0.002 ± 0.014	−0.301 ± 0.036	0.1 ± 0.7
400	^{44}Sc^m	−0.057 ± 0.008	−0.421 ± 0.016	−3.0 ± 0.4
	^{46}Sc	−0.030 ± 0.007	−0.365 ± 0.013	−1.6 ± 0.4
	^{47}Sc	−0.040 ± 0.008	−0.383 ± 0.014	−2.0 ± 0.4
	^{48}Sc	−0.036 ± 0.008	−0.378 ± 0.016	−1.8 ± 0.4

tion[22]

$$F_L(\theta_L)=\frac{1+(b/a)\cos^2[\theta_L+\sin^{-1}(\eta_\parallel\sin\theta_L)]}{1+b/3a}\times\frac{[\eta_\parallel\cos\theta_L+(1-\eta_\parallel^2\sin^2\theta_L)^{1/2}]^2}{(1-\eta_\parallel^2\sin^2\theta_L)^{1/2}}\,. \qquad (5)$$

This equation assumes that $\eta_\parallel \ll 1$ not only on the average, but for each interaction. The effect of overlapping distributions of $v_\parallel$ and V has been discussed elsewhere[23] and does not affect the present analysis.

The parameters obtained from a least-squares fit of Eq. (5) to the data are summarized in Table II. The resulting angular distributions are virtually indistinguishable from the curves in Figs. 1–3 provided that the same normalization is used. This is not surprising since for $\eta_\parallel \ll 1$ Eq. (5) reduces to Eq. (1) with $A_1 \simeq 2\eta_\parallel$ and $A_2 \simeq b/a$. Table II also lists the mean values of $v_\parallel$ (designated $\beta_\parallel$ and expressed in units of c) obtained by combining the values of $\eta_\parallel$ with the mean velocities derived from the 90° differential range spectra for the same reactions.[15] This procedure assumes that the velocities derived from these spectra can be exclusively associated with the breakup step, an assumption that is approximately valid for small $v_\perp$.

The energy dependence of b/a and $\beta_\parallel$ is displayed in Fig. 7. The values of b/a show that, within the context of the two-step model, the angular distributions are isotropic in the moving system at 0.8 GeV and become increasingly sideward peaked at higher energies. Within the limits of error, all the Sc fragments display the same values of b/a.

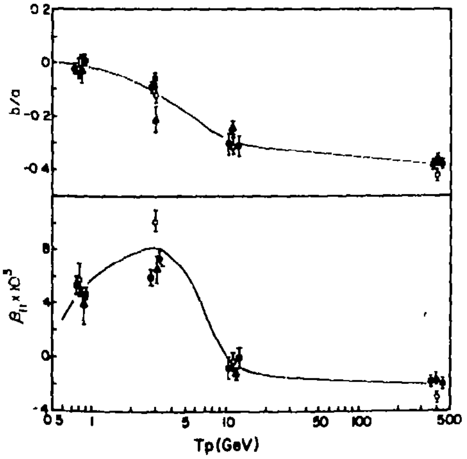

FIG. 7. Energy dependence of two-step model paramters $\beta_\parallel$ and b/a for Sc fragments. See Fig. 4 for symbols.

The values of $\beta_\parallel$ increase between 0.8 and 3 GeV, drop sharply to zero at 11.5 GeV, and become negative at 400 GeV. According to the two-step model, the residual nucleus resulting from the initial proton-nucleus interaction thus is at rest in the laboratory for a proton energy of 11.5 GeV, and actually recoils backward when the bombarding energy is increased to 400 GeV. These observations are difficult to reconcile with the high excitation energies that appear to be required to form Sc fragments from uranium[3,15] and suggest that the two-step model may not be applicable in these cases. A comparison of the energy spectra of fragments emitted at forward and backward angles would provide a more rigorous test of the consistency of the angular distributions with the two-step model.[10]

V. CONCLUSIONS

The angular distributions of Sc fragments emitted in the interaction of ^{238}U with 0.8–400 GeV protons have been measured. The distributions become increasingly forward peaked between 0.8 and 3 GeV. This trend does not continue at higher energies; instead, the 11.5 GeV curves are sideward peaked and symmetric about 90°. At 400 GeV, the peaking at sideward angles becomes even more pronounced and, in addition, emission at forward angles is less probable than that at backward angles. These features are displayed by both neutron-excess and neutron-deficient fragments.

The results appear to be consistent with a model advanced to explain some related high-energy results.[5,7] In a near-central collision at highly relativistic energies, the Lorentz contraction results in a coherent interaction between the incident proton and the nucleons lying in its path.[8] Owing to relativistic time dilation the resulting multiparticle state is ejected from the nucleus in the forward direction prior to decay. Additional mass loss occurs from the zone adjacent to the ejected tube due to final state interactions, frictional effects, etc. The resulting nucleus is highly unstable and rapidly breaks apart. The fast time scale of the process, which is attested to by the anomalous results obtained from an analysis based on the two-step model, leads to preferential emission at 90° to the beam. Since practically all the momentum of the proton is carried off by the ejected participants, the spectator fragments show little evidence of momentum transfer and so display a forward-to-backward ratio close to unity. A quantitive formulation of this model has been recently published.[24] The backward enhancement observed at 400 GeV can be explained as a consequence of the very extensive mass dissipation observed at this energy.[15] If this process primarily depletes a cone-shaped region of the nucleus opening at forward angles, a rapid breakup will inhibit the emission of fragments at these angles. Since the back side of the nucleus is not depleted, backward emission is not reduced and so is enhanced relative to emission at forward angles. By contrast, the forward peaking seen up to 3 GeV is understandable as the result of the transfer of both momentum and excitation energy to the struck nucleus by the intranuclear cascade.

ACKNOWLEDGMENTS

The cooperation and assistance of E. P. Steinberg and S. Kaufman with the ZGS irradiations, and that of B. J. Dropesky with the LAMPF experiments, are gratefully acknowledged. The Fermilab experiments were performed in conjunction with similar studies by a group from the University of Chicago and we wish to acknowledge the cooperation of N. Sugarman and R. A. Johns. This work was financially supported by the U. S. Department of Energy.

---

*Present address: Sandia Corporation, Albuquerque, New Mexico.

[1] K. Beg and N. T. Porile, Phys. Rev. C 3, 1631 (1971).

[2] S. B. Kaufman and M. W. Weisfield, Phys. Rev. C 11, 1258 (1975).

[3] Ø. Scheidemann and N. T. Porile, Phys. Rev. C 14, 1534 (1976).

[4] S. B. Kaufman, E. P. Steinberg, and M. W. Weisfield, Phys. Rev. C 18, 1349 (1978).

[5] S. Biswas and N. T. Porile, Phys. Rev. C 20, 1467 (1979).

[6] D. R. Fortney and N. T. Porile, Phys. Rev. C 14, 1652 (1976).

[7] B. D. Wilkins, S. B. Kaufman, E. P. Steinberg, J. A. Urbon, and D. J. Henderson, Phys. Rev. Lett. 43, 1080 (1979).

[8] G. Berlad, A. Dar, and G. Eilam, Phys. Rev. D 13, 161 (1976); Meng Ta-chung, *ibid.* 15, 197 (1977); Meng Ta-chung and E. Moeller, Phys. Rev. Lett. 41, 1352 (1978).

[9] L. P. Remsberg and D. G. Perry, Phys. Rev. Lett. 35, 361 (1975).

[10] J. B. Cumming, R. J. Cross, J. Hudis, and A. M. Poskanzer, Phys. Rev. 134, B167 (1964).

[11] N. T. Porile, S. Pandian, H. Klonk, C. R. Rudy, and E. P. Steinberg, Phys. Rev. C 19, 1832 (1979).

[12] V. P. Crespo, J. B. Cumming, and A. M. Poskanzer, Phys. Rev. 174, 1455 (1968).

[13] K. Bächmann and J. B. Cumming, Phys. Rev. C 5, 210 (1972).

[14] N. T. Porile, D. R. Fortney, S. Pandian, R. A. Johns, T. Kaiser, K. Wielgoz, T. S. K. Chang, N. Sugarman, J. A. Urbon, D. J. Henderson, S. B. Kaufman, and E. P. Steinberg, Phys. Rev. Lett. 43, 918 (1979).

[15] D. R. Fortney and N. T. Porile, Phys. Rev. C. 21, 664 (1980).

[16] D. R. Fortney and N. T. Porile, Phys. Lett. 76B, 553 (1978).

[17] C. R. Rudy, N. T. Porile, and S. B. Kaufman, Nucl. Instrum. Methods 138, 19 (1976).

[18] D. R. Fortney, Ph.D. thesis, Purdue University, 1979 (unpublished).

[19] N. T. Porile, Phys. Rev. 120, 572 (1960).

[20] N. T. Porile and N. Sugarman, Phys. Rev. 107, 1422 (1957).

[21] A. M. Poskanzer, J. B. Cumming, and R. Wolfgang, Phys. Rev. 129, 374 (1963).

[22] J. B. Marion, T. I. Arnette, and H. C. Owens, Oak Ridge National Laboratory Report No. ORNL-2574, 1959 (unpublished).

[23] N. T. Porile, Phys. Rev. 185, 1371 (1969); V. P. Crespo, J. B. Cumming, and J. M. Alexander, Phys. Rev. C 2, 1777 (1970); L. Winsberg, Nucl. Instrum. Methods 150, 1465 (1978).

[24] J. B. Cumming, Phys. Rev. Lett. 44, 17 (1980).

PHYSICAL REVIEW C VOLUME 21, NUMBER 6 JUNE 1980

Low-energy absorption of pions on nuclei and the real $\rho^2(r)$ potential

Gerald A. Miller and J. V. Noble*

Department of Physics, University of Washington, Seattle, Washington 98195

(Received 28 September 1979; revised manuscript received 5 February 1980)

A Wick-formalism treatment of the $\sigma+\omega$ model dynamics is used to obtain the real and imaginary parts of the π-nucleus optical resulting from the true absorption of "s-wave" pions. Good agreement is obtained with the empirical value of the imaginary potential at threshold. The corresponding (dispersive) real potential is attractive. All parameters are taken from other experiments.

NUCLEAR REACTIONS $A(\pi^-, NN)B$; imaginary part of π-A optical potential calculated in $\sigma+\omega$ model using Fermi-gas wave functions. Off-shell absorptive amplitude used to calculate corresponding real part from unsubtracted dispersion relation.

The $\sigma+\omega$ model is a relativistic quantum field theory of interacting pions and nucleons (as well as the σ and ω mesons) which is renormalizable, satisfies PCAC, and gives a good description of low-energy NN, πN, and $\pi\pi$ dynamics. Various aspects of the dynamics of pions interacting with nuclei have recently been explored within the framework of this model, including near-threshold pion production and low-energy elastic scattering of pions.[1,2]

In this paper we investigate the predictions of the $\sigma+\omega$ model for "true" pion absorption. This process is usually represented by a term of the phenomenological pion-nucleus optical potential which is quadratic in the nuclear density (because true absorption is dominated by the emission of *two* nucleons):

$$2k^0 v = -4\pi i\,\mathrm{Im}(B_0)\rho^2(r)\,. \qquad (1)$$

The folklore of absorption rate calculations has been that the amplitude is dominated by terms representing off-shell elastic scattering of the incident pion from one active nucleon, followed by its absorption on a second nucleon, as illustrated in Fig. 1.[3] In order to calculate this diagram, one needs the off-shell πN scattering matrix, the πNN absorption vertex, and the initial and final nucleonic wave functions. Several authors have recently calculated true pion absorption in this manner, using phenomenological models of varying sophistication to represent the πN scattering matrix.[4-6] These calculations have been unable to account for more than about 70–75% of the low-energy absorptive cross section. Our calculation of the absorptive amplitude differs from those of other authors primarily in that it is based on evaluation of the leading terms in the $\sigma+\omega$ model through third order in the coupling constant. We find that the missing strength is provided by short-range terms arising from the exchange of the heavy mesons included in this theory. (There are also some differences in technical details of the handling of Fermi-gas wave functions and the avoidance of unitarity-violating unphysical singularities.)

In addition to the imaginary part of the pion-nucleus potential arising from true pion absorption, Eq. (1), we expect a real contribution to B_0 arising from dispersion. The expected analytic properties of the amplitudes imply that $\mathrm{Re}(B_0)$ satisfies a dispersion relation; the expected rapid decrease with energy of the imaginary part, for large energy, implies that the dispersion relation will be unsubtracted. Thus, the algebraic sign of the real part near threshold is determined by the energy dependence of the imaginary part. All microscopic calculations of the absorptive part[5-8] have found it to be peaked at energies well above threshold, so that the resulting dispersive real part is attractive. Our calculation is no exception.

We now describe our calculation. The elastic T matrix for π^--nucleus scattering is given exactly by the Wick formalism in the $\sigma+\omega$ model[2]

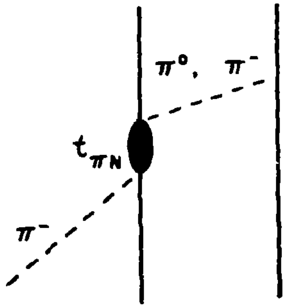

FIG. 1. Rescattering model of $A(\pi, NN)B$ reaction.

© 1980 The American Physical Society

$$T_{\vec{k}'\vec{k}}(k^0)=\int\frac{d^3x}{(2\pi)^3 2k^0}e^{i(\vec{k}-\vec{k}')\cdot\vec{x}}\langle\text{g.s.}|\left\{\frac{8M\lambda}{G}\sigma(\vec{x})+4\lambda[\sigma^2(\vec{x})+\vec{\pi}(\vec{x})\cdot\vec{\pi}(\vec{x})]+8\lambda\pi_+(\vec{x})\pi_-(\vec{x})\right\}|\text{g.s.}\rangle$$
$$+\langle\text{g.s.}|J^\dagger_{\vec{k}'}(E_{\text{g.s.}}+k^0+i\eta-H)^{-1}J_{\vec{k}}|\text{g.s.}\rangle+\langle\text{g.s.}|J_{\vec{k}}(E_{\text{g.s.}}-k_0+i\eta-H)^{-1}J^\dagger_{\vec{k}'}|\text{g.s.}\rangle\,, \tag{2}$$

where $8\lambda M^2/G^2=m_\sigma{}^2-m_\pi{}^2$, M is the nucleon mass, $\sigma(\vec{x})$ and $\vec{\pi}(\vec{x})$ are the nuclear σ-meson and pion fields, and $J_{\vec{k}}$ is the Fourier transform of the source term in the Klein-Gordon equation

$$\left(\nabla^2-m^2-\frac{\partial^2}{\partial t^2}\right)\pi_-(\vec{x})=J(\vec{x})\,,$$
$$J_{\vec{k}}=\int\frac{d^3x}{(2\pi)^{3/2}\sqrt{2k^0}}e^{i\vec{k}\cdot\vec{x}}J(\vec{x})$$
$$=\int\frac{d^3x}{(2\pi)^{3/2}\sqrt{2k^0}}e^{i\vec{k}\cdot\vec{x}}$$
$$\times\left\{iGN^\dagger(\vec{x})\gamma^0\gamma^5\tau_-N(\vec{x})+\frac{8M\lambda}{G}\sigma(\vec{x})\pi_-(\vec{x})\right.$$
$$\left.+4\lambda\pi_-(\vec{x})[\sigma^2(\vec{x})+\vec{\pi}(\vec{x})\cdot\vec{\pi}(\vec{x})]\right\}. \tag{3}$$

As noted in Ref. 2, the field operators in (3) include interactions, hence include terms of all orders in G. Here we shall concentrate on terms through $O(G^3)$, which arise in the expansion of the $N^\dagger N$ and $\sigma\pi$ terms. The $\lambda\pi(\sigma^2+\pi^2)$ term is $O(G^5)$ (at least), so is dropped.

The first term of Eq. (2) contains the effects of pion interactions with the fluctuating meson fields of the target nucleus. The next two terms are handled by using those states containing zero or one asymptotic mesons to spectrally represent the energy denominators in which H appears. The zero meson states of low energy give a contribution which is the sum over nucleons of the driving terms of the (free) π-nucleon Low equation, and which leads to the impulse contribution to the optical potential.[9] The zero-meson states of higher energies (2p-2h states not reached by matrix elements of $J_{\vec{k}}$ involving single nucleons only) lead to an imaginary part of T (true pion absorption) which is physically distinct from that arising from elastic and inelastic unitarity. This absorptive part is given by the imaginary parts of the terms of Eq. (2) involving J's, in which the intermediate states have no free pions. In fact, we know from experiment that the dominant process in low-energy pion absorption is the emission of two high-energy nucleons, so we shall write

$$\text{Im}[T^{0\prime}_{\vec{k}'\vec{k}}(k^0)]\simeq-\pi\sum_{2p\text{-}2h}\langle\text{2p-2h}|J_{\vec{k}'}|\text{g.s.}\rangle^*$$
$$\times\langle\text{2p-2h}|J_{\vec{k}}|\text{g.s.}\rangle$$
$$\times[\delta(E_x-k^0)+\delta(E_x+k^0)]\,, \tag{4}$$

where E_x is the energy difference between the 2p-2h and ground states, and where we have assumed $N=Z$. Note that Eq. (4) is strictly correct only for $k^0\approx m_\pi$. At such low energies, neither pion-nucleus inelastic scattering nor meson production can occur. At higher energies both inelastic scattering and meson production represent an important part of Im(T) which is omitted deliberately from Eq. (4). Note that the spectral function [negative imaginary part of $T_{\vec{k}'\vec{k}}$ from Eq. (2)] is a positive operator in the sense that, for arbitrary functions ψ,

$$\int d\vec{k}'\int d\vec{k}\,\psi^*(\vec{k}')[-\text{Im}(T_{\vec{k}'\vec{k}}(k^0)]\psi(\vec{k})\geq 0\,.$$

(It is this property which guarantees that the imaginary part of the optical potential is absorptive, rather than emissive, even when it is nonlocal.)

We are interested in calculating the optical potential v, but Eqs. (2) and (4) involve $T(k^0)$. Liu and Shakin[10] have shown that in order to obtain formal expressions for v from those involving $T(k^0)$, one need merely remove from $T(k^0)$ all terms involving intermediate π-nuclear eigenstates, in which the nucleus remains in its ground state. Clearly, no terms involving the pion plus nuclear ground state appear in the right-hand side of Eq. (4). Thus we may write, ignoring nonlocality which is clearly present in Eq. (4),

$$\text{Im}[T^{0\prime}_{\vec{k}'\vec{k}}(k^0)]\simeq\text{Im}\int\frac{d^3x}{(2\pi)^3}e^{i(\vec{k}-\vec{k}')\cdot\vec{x}}v(\vec{x},k^0)\,. \tag{5}$$

[*It will be reasonable to ignore nonlocal effects* since they have a range smaller than $\sim(2m_\pi)^{-1}$, and for low-energy pions, $T_\pi\leq 50$ MeV, both k and k' $<m_\pi$.]

To simplify the calculation we treat the nucleus as a Fermi gas and ignore surface effects. Then for small momenta $\vec{k}$ and $\vec{k}'$,

$$\text{Im}[V(k^0)]\simeq-\frac{(2\pi)^3\pi}{\Omega}\sum_{2p\text{-}2h}|\langle\text{2p-2h}|J_0|\text{g.s.}\rangle|^2$$
$$\times[\delta(E_x-k^0)+\delta(E_x+k^0)] \tag{6}$$

and

$$\text{Re}[V(k^0)]=-\frac{P}{\pi}\int_{-\infty}^{\infty}d\nu\frac{\text{Im}[V(\nu)]}{k^0-\nu}\,, \tag{7a}$$

or

$$\text{Re}[V(k^0)]=\frac{2}{\pi}P\int_0^{\infty}\frac{d\nu\,\nu}{(k^0)^2-\nu^2}(-\text{Im}[V(\nu)])\,, \tag{7b}$$

where $V(\nu)=v(x=0,\nu)$ and Ω is the nuclear volume. In obtaining Eq. (6) we have replaced the left-hand side of Eq. (5) by Eq. (4) and then taken an inverse Fourier transform. The result, (7a), is essentially the dispersive part of Eq. (2)—Eq. (7b) is obtained from (7a) via Eq. (6) (crossing symmetry for a $T=0$ target). Thus, $-\mathrm{Im}V(\nu)$ defined in (6) approximates the spectral function of the true absorption contribution to the pion-nucleus scattering amplitude.

The off-shell dynamics specified by the Low equation are exhibited in Eqs. (6) and (7). To calculate $V(k^0)$ one must first obtain the absorptive transition matrix for incident pions of four-momentum $k \approx (k^0,\vec{0})$. Contributions to $\mathrm{Re}V(k^0)$ occur for values of ν ranging from 0 to ∞, so the incident pions are, in general, far off the mass-shell $[k^2=(k^0)^2 \neq m_\pi^2]$. This specification has not been used by previous authors.

An important difference between this calculation and that of Hachenberg and Pirner[5] is that our spectral function, Eq. (6), is positive definite, whereas theirs is of indefinite sign. [This would remain true even had we kept the nonlocal part of the optical potential (arising from the nuclear surface), in the sense that the spectral function would be a positive-definite integral kernel.]

The matrix elements $\langle 2\text{p-}2\text{h}|J_0|\text{g.s.}\rangle$ are obtained from covariant perturbation theory, and the diagrams of lowest order (G^3) in the $\sigma+\omega$ model are displayed in Fig. 2. To this order no terms involving the pion plus nuclear ground state appear. The single nucleon term, proportional to $\vec{\sigma}_1\cdot\vec{k}$, is expected to provide negligible contributions here, so is not included.

The approximate evaluation of the diagrams of Fig. 2 leads to the following two-nucleon absorption operator

$$J_0=\frac{G\sqrt{2}}{(2\pi)^{3/2}}\frac{1}{\sqrt{2k^0}}\frac{1}{\Omega}\,\delta_{\vec{P}_f,\vec{P}_i}u^2(q)$$

$$\times\{-\vec{\sigma}_1\cdot\vec{q}A-\vec{\sigma}_1\cdot[\vec{p}_2+\vec{p}_2{}'+i\vec{\sigma}_2\times(\vec{p}_2{}'-\vec{p}_2)]B$$

$$+\tau_3(2)(\vec{\sigma}_1-\vec{\sigma}_2)\cdot\vec{q}C\} \tag{8}$$

with

$$A=\frac{G^2}{q^2+m_\sigma{}^2}-\frac{G_\omega{}^2}{q^2+m_\omega{}^2}-C\,,$$

$$B=\frac{G_\omega{}^2}{q^2+m_\omega{}^2}\frac{k^0}{2M+k^0}\,, \tag{9}$$

$$C=\frac{1}{2}\frac{G^2}{q^2+m_\pi{}^2}\frac{k^0}{2M+k^0}\,,$$

and where $\vec{q}=\vec{p}_2{}'-\vec{p}_2$. Our convention is always that the proton absorbing the negative charge is labeled "1", and the other nucleon is labeled "2". (See Fig. 2.) The meson-nucleon vertex function $u(\vec{q}^2)$ is taken to be

$$u(q^2)=(1+q^2/M^2)^{-1}\,. \tag{10}$$

For simplicity we have assumed that the vertex function is the same for all meson-nucleon couplings. (Although the dispersion integral would converge with point vertex functions, as in other calculations extended vertices are required to cut off the integral at a physically reasonable energy, since what happens above $\nu\sim 1$ GeV clearly cannot influence the threshold pion-nucleus scattering significantly.) In our evaluations of Eqs. (8) and (9) we use empirically determined values $G^2/4\pi \simeq 14.2$, $G_\omega{}^2/4\pi \simeq 12.9$, and $m_\sigma \simeq 700$ MeV.[11]

To obtain $\mathrm{Im}[V(k^0)]$, we square the matrix element of J_0 (between the ground and 2p-2h states) and perform the sum over all such intermediate states. We assume in common with other authors[4-8] that the sum is dominated by those terms in which each final nucleon has energy $k^0/2$. For $k^0 \sim m_\pi$ the momentum of each final nucleon is much greater than the momenta of the initial nucleons in the ground state. Hence, we neglect in (8) the momenta of the initial nucleons. This approximation, made also in Refs. 4–8, gives the simple result $q^2 \simeq Mk^0$. In order to obtain $\mathrm{Re}V(k^0)$ we need $\mathrm{Im}[V(\nu)]$ for small values of ν for which the preceding approximation fails. However, $-\mathrm{Im}[V(\nu)]$ peaks at (as we shall show, Fig. 3) $\nu \approx 250$ MeV, so that our approximation is quite good for the energy interval which dominates the integral representation of $\mathrm{Re}V(k^0)$.

With the use of the above approximations, the evaluation of $\langle 2\text{p-}2\text{h}|J_0|\text{g.s.}\rangle$ is straightforward except for the consequences of the antisymmetry of the ground and 2p-2h wave functions. If the

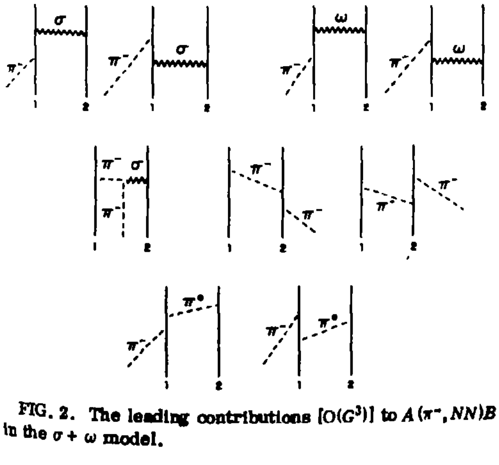

FIG. 2. The leading contributions $[O(G^3)]$ to $A(\pi^-,NN)B$ in the $\sigma+\omega$ model.

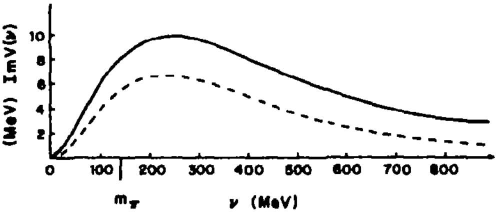

FIG. 3. The imaginary *s*-wave part of the pion-nucleus optical potential arising from true pion absorption, Fig. 2. (See text for details.)

intermediate state contains two neutrons, this state must be antisymmetrized. If the intermediate state contains a neutron-proton pair, the ground state contains a proton-proton pair which must be antisymmetrized. Using Eqs. (8)–(10) to evaluate Eq. (6), we find

$$\operatorname{Im}[V(k^0)] = -\frac{G^2\rho^2}{256\pi}(Mk^0)^{1/2}(\hbar c)^6 u^2(Mk^0)F(Mk^0/k_F{}^2)$$

$$\times[(A+B)^2+(A+3B)^2+4C^2]\,. \qquad (11)$$

In Eq. (11) ρ is the density of nuclear matter (0.166 fm^{-3}), k_F is the Fermi momentum, and F is a factor which results from the requirements that the two initial momenta lie within, and the two intermediate momenta lie outside, the Fermi sphere. The function F is displayed in Fig. 4 and given by

$$F(Mk^0/k_F{}^2)=\left\{\frac{M}{2}\left(\frac{4\pi}{3}k_F{}^3\right)^2(Mk^0)^{1/2}\right\}^{-1}$$

$$\times\left\{\int d\vec{p}_1{}'\int d\vec{p}_2{}'\int d\vec{p}_1\int d\vec{p}_2\,\theta(p_1'-k_F)\theta(p_2'-k_F)\theta(k_F-p_1)\theta(k_F-p_2)\delta\left(\frac{p_1'^2+p_2'^2-p_1{}^2-p_2{}^2}{2M}-k^0\right)\right\}. \qquad (12)$$

The numerical evaluation of Eq. (11) is displayed in Fig. 3. The low-energy cutoff is provided by the function F, since the phase space for producing a 2p-2h excitation by absorbing energy k^0 decreases rapidly as k^0 approaches zero. At threshold, $\operatorname{Im}[V]=-8.0$ MeV, in excellent agreement with the experimental value.[12] (This value of $\operatorname{Im}[V]$ corresponds to $\operatorname{Im}[B_0]=0.042m_\pi{}^{-4}$.) In the energy region of current interest for π-nuclear scattering ($m_\pi < k^0 < 3m_\pi$) $\operatorname{Im}[V(k^0)]$ is relatively constant in magnitude, never deviating by more than 10% from its mean value of about 9 MeV. About one-third of $\operatorname{Im}[V(k^0)]$ arises from the inclusion of heavy meson exchange.

The function $-\operatorname{Im}[V(\nu)]$ peaks at about 250 MeV and falls off slowly at high energies. This falloff results both from the large-$\vec{q}^{\,2}$ behavior of the mesonic propagators appearing in Eq. (9), as well as from the meson-nucleon vertex functions.

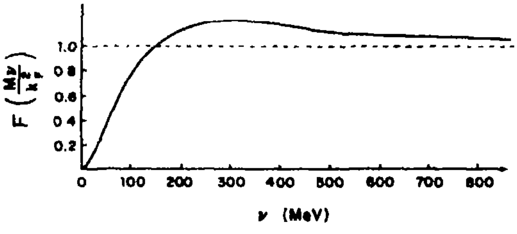

FIG. 4. The phase-space factor for 2p-2h excitations of energy k^0, using Fermi-gas wave functions, relative to its asymptotic (large k^0) form.

Given $\operatorname{Im}[V(\nu)]$ from Fig. 3 and Eq. (7), we expect $\operatorname{Re}V(k^0)$ to be negative (attractive) near threshold and to decrease with increasing energy. This behavior is shown in Fig. 5. The real potential has the value −12 MeV at threshold and decreases monotonically to −4 MeV at 310 MeV.

Our attractive potential (at threshold) is about 60% smaller than that obtained in Ref. 5. Pionic atom data have required a real *repulsive* term about equal in magnitude to the imaginary potential.[12,13] The present work yields an attractive dispersive potential in qualitative agreement with all

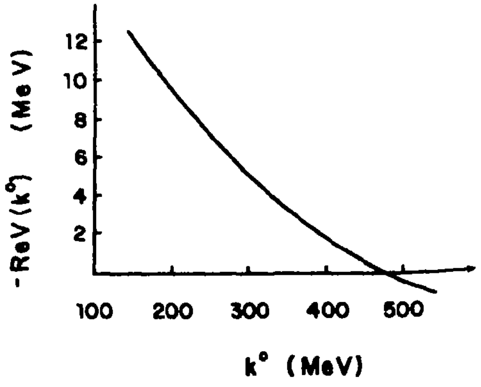

FIG. 5. The dispersive real part of the *s*-wave pion nucleus optical, arising from the substitution of Im $V(\nu)$ (from Fig. 3) into Eq. (7b).

other microscopic calculations of the dispersive real part, and in disagreement both with the early work of Brueckner[14] and of Thouless,[15] as well as with the more recent discussion of Hüfner.[13] In other words, the dispersive real part of B_0 cannot account for the definitely repulsive effect required by experiment.

Finally, we note that Mizutani and Koltun,[16] and Rinat[17] have proposed formalisms alternative to Eq. (2)ff, based on amalgamating multiple scattering theory and field theory. We feel that the application of the $\sigma + \omega$ model is more transparently expressed in terms of Eq. (2), however.

This work was supported in part by DOE and by NSF. One of us (J. V. N.) wishes to thank the Physics Department of the University of Washington for its hospitality during the 1978–79 academic year.

---

*Present address: Department of Physics, University of Virginia, Charlottesville, Va. 22901.

[1] J. V. Noble, Phys. Rev. Lett. 43, 100 (1979).

[2] J. V. Noble, Phys. Rev. C 20, 225 (1979).

[3] D. S. Koltun and A. Reitan, Nucl. Phys. B4, 629 (1968).

[4] G. F. Bertsch and D. O. Riska, Phys. Rev. C 18, 317 (1978).

[5] F. Hachenberg and H. J. Pirner, Ann. Phys. (N.Y.) 112, 401 (1978).

[6] J. Chai and D. O. Riska, Phys. Rev. C 19, 1425 (1979); Nucl. Phys. A329, 429 (1979).

[7] C. B. Dover, J. C. Ballot, and R. H. Lemmer, Lett. Nuovo Cimento 2, 715 (1971).

[8] D. Beder, Nucl. Phys. B14, 586 (1969).

[9] G. A. Miller, Phys. Rev. C 16, 2325 (1977).

[10] L. C. Liu and C. M. Shakin, Phys. Rev. C 19, 129 (1979).

[11] M. M. Nagels, J. J. de Swart, H. Nielson, G. C. Oades, J. L. Paterson, B. Tromborg, G. Gustafson, A. C. Irving, C. Jarlskog, W. Pfiel, H. Pilkuhn, F. Steiner, and L. Tauscher, Nucl. Phys. B109, 1 (1976).

[12] K. Stricker, H. McManus, and J. A. Carr, Phys. Rev. C 19, 928 (1978).

[13] J. Hüfner, Phys. Rep. 21C, 1 (1975).

[14] K. Brueckner, Phys. Rev. 98, 769 (1955).

[15] D. J. Thouless, Proc. R. Phys. Soc. London 69, 280 (1956).

[16] T. Mizutani and D. S. Koltun, Ann. Phys. (N.Y.) 109, 1 (1977).

[17] A. Rinat, Ann. Phys. (N.Y.) (to be published), and Weizmann Institute of Science Report No. WIS-78/46 Ph.

PHYSICAL REVIEW C VOLUME 21, NUMBER 6 JUNE 1980

Products of stopped-pion interactions with Cu and Ta

C. J. Orth, W. R. Daniels, B. J. Dropesky, R. A. Williams, and G. C. Giesler
Los Alamos Scientific Laboratory, Los Alamos, New Mexico 87545

J. N. Ginocchio
Theoretical Division, Los Alamos Scientific Laboratory, Los Alamos, New Mexico 87545

(Received 9 January 1980)

Yields of radioactive products from the interactions of stopped π^- with Cu and Ta have been measured. Absolute yields of products ranging down to 10^{-5} per stop were determined. The experimental yields are compared with yields calculated with a model that was developed in this work for the stopped-π interaction The calculations give excellent agreement with measured total mass yields for Ta, but some discrepancies exist for the independent yields of Hf, Er, and Tm isotopes; in the case of Cu, most independent yields, except for Co and Sc, are in good agreement. Measurements were also made with both stopped π^- and 20-MeV π^+ on Cu and Fe to determine the shift in the centroids of the isotopic yields with pion charge.

[NUCLEAR REACTIONS Stopped-negative-pion interactions with Cu and Ta. Measured yields of residual radioactive products. Calculated yields from model for the interactions.]

I. INTRODUCTION

The process of stopped-pion absorption begins with the capture of a low-kinetic-energy π^- by the Coulombic potential of the nucleus. The capturing Bohr orbit is presumed to have a large principal quantum number n of about 20.[1] The resultant pionic atom deexcites by x-ray and Auger-electron emission until it reaches a lower n state with sufficient overlap of its wave function with the nuclear volume so that the nucleus captures the pion, due to the strong pion-nucleon interaction. In order to conserve momentum and energy the pion is presumed to be absorbed on at least a correlated pair of pp or np nucleons.

Absorption of the π^- converts a proton into a neutron, and the pion imparts its 140-MeV rest mass into kinetic energy of the absorbing pair, each nucleon of the pair recoiling in the center-of-mass system with about 70 MeV plus the original kinetic energy of the pair of nucleons. Depending on the point of absorption and the direction of motion of these recoiling nucleons, they can either escape without interaction or undergo collisions with other nucleons in the nucleus and thereby initiate an intranuclear cascade.

Early studies of the yields of radioactive products from the interactions of π^- with N, O, Zn, As, Br, I, and Hg targets have been reported by investigators at the University of Chicago.[2-7] Negative pions with initial kinetic energies of 30 to 70 MeV were stopped in very thick targets (~30 g/cm^2). Following irradiation, the different elemental products were chemically separated from the target material and the radioactivities were measured.

Gadioli and Gadioli-Erba[8] used an exciton model with fair success to fit the data of the Chicago authors. In this treatment the two nucleons that share the pion rest mass are assumed to give rise to two (parallel) intranuclear cascades, each characterized by a one-particle–one-hole initial configuration.

A rather sophisticated treatment of the stopped π^- process is reported by Iljinov, Nazaruk, and Chigrinov.[9] These authors assume a Gaussian form for the probability density of pion absorption with the nuclear radius corresponding to the center of the Gaussian as a variable parameter. The resultant intranuclear cascade is treated by a Monte Carlo method developed by Bertini[10] and the subsequent evaporation on the part of the excited nucleus is calculated by the method developed by Dostrovsky *et al.*[11] These authors[9] are able to duplicate the residual yields reported by the Chicago group[2-7] rather well. In addition, they reproduced measured neutron and charged-particle spectra.

A team at Dubna has measured the residual products from stopped-π^- interactions with some heavy targets ranging from Ta to Bi.[12,13] These researchers stress their observation of the production of high-spin products; however, most of their yields are reported on a qualitative basis.

A group at CERN has recently measured yields[14] from stopped-pion reactions in ^{9}Be, ^{10}B, ^{16}O, ^{31}P, Ca, and ^{93}Nb. Also, a team at SIN has reported[15] on measurements of residual product yields using in-beam spectroscopy and activation methods on targets of ^{59}Co, ^{75}As, ^{197}Au, and ^{209}Bi.

Another recent investigation relevant to our study has been reported by a group[16] working at CERN on absolute yield measurements of high-spin states in Hf and Pb nuclei following pion capture in ^{181}Ta and ^{208}Pb. They measured prompt and delayed γ rays following the interaction and give absolute yields for quadrupole transitions in the even-even Hf isotopes from $A = 166$ to 178 with nuclear spins of the initial states as high as 16.

A primary aim of the present study was to provide information about the average depth of absorption of the pion and, possibly, about the mechanism of absorption, such as preference for absorption on pp, np, or either of these in clusters. We did this by measuring the yields of radioactive products from the interaction of stopped π^- with Cu and Ta targets and by comparing these data with model calculations. We measured about two dozen yields from each target, ranging from 10 to 10^{-3} percent per pion stop, thereby providing a rather stringent test of the calculations. In the model, the radial location of absorption is established by wave mechanical cascade calculations through use of an optical potential obtained from pionic x-ray measurements. To first order, the probability of absorption on np to pp pairs is equal to $2N/(Z-1)$. Upon absorption, the resulting intranuclear cascade is treated with the Monte Carlo code VEGAS[17,18]. The deexcitation of the residual nucleus following the cascade is calculated with the Dostrovsky, Fraenkel and Friedlander (DFF) evaporation code.[11]

II. EXPERIMENTAL

Stopped-π^- target exposures were performed at the low-energy pion channel (LEP) of the Clinton P. Anderson Los Alamos Meson Physics Facility (LAMPF). The channel was tuned for 170 MeV/c (80 MeV) π^- and the resultant beam composition, determined by dE/dx measurements, was 60% π^-, 36% e^-, and ~4% μ^-. The pions were slowed down to stop in the targets by degrading their energy with graphite plates. The exact thickness of graphite required to establish the maximum number of stops in the target foils was achieved by using a three-element $(12\bar{3})$ scintillator telescope coupled to conventional fast electronics. The differential range curves showed full width at half maximum (FWHM) = 2.4 g/cm^2 of graphite at any momentum bite $\Delta p/p$ between 0.2 and 2% due to pion straggle in traversing the ~12-cm thickness of degraders.

The targets were 3.8-cm diam disks of thin Cu or Ta stacked to a total thickness of ~1 g/cm^2. By using multiple-disk targets, we could apportion certain foils for various chemical procedures and direct counting, and by gross γ counting of each foil, we could also confirm the exact location of maximum pion stops per unit density. All counting was done in a low-background environment. The Cu targets were counted directly, while for the Ta targets, both direct counting and radiochemical separations before counting were performed. In the latter, Hf and four rare earth fractions (Er, Tm, Yb, and Lu) were separated. Most of the products emit γ rays which were measured with one of three different Ge(Li) detector systems. Photopeak intensities of the γ rays in the spectra were determined with the GAMANAL[19] computer code. Spectra were measured over a period of six months. The photopeak efficiencies of the detectors were determined with National Bureau of Standards ^{241}Am, ^{228}Th, and multiple-species sources. Two β-emitting products from Ta, ^{169}Er, and ^{170}Tm, were measured in a low-background proportional counter.

The absolute yields (atoms/pion stop) of several high-yield "monitor products" were determined for Cu and Ta from short-duration, low-intensity irradiations. The intensity was reduced by closing the momentum slits to $\Delta p/p \sim 0.1\%$ and the number of pion stops in each target was established by the use of the three-element $(12\bar{3})$ scintillator telescope. Under these conditions and with 225 μA on the 3-cm thick graphite pion production target, the stop rate was 7×10^4 sec^{-1}. In subsequent high-intensity pion irradiations, product yields down to 10^{-3}% were determined; the relative yields were converted to absolute values by normalization to the monitor products.

The contributions to product yields from secondary nucleon reactions (chiefly from neutrons) were estimated from measurements on secondary targets placed downstream of the primary targets. To ensure that the secondary target was beyond the range of the pions, a graphite absorber, 2 cm thick, was interposed between the primary and secondary targets.

Stopped muons can also contribute to the yields of products near the target via (μ^-, xn) and to a lesser extent via (μ^-, pxn) reactions. On the basis of reported stopped muon yields,[20,21] the larger range of muons than pions, and the 4% muon contamination in our pion beam, we estimate the muon contributions to ^{60,61}Co from Cu, and ^{179}Hf^m and ^{179}Lu from Ta to be less than 5% of the reported yields.

III. MODEL DESCRIPTION

The model used for calculating the yields of residual-spallation-product nuclei, resulting when stopped negative pions are absorbed in a target nucleus, has three steps. The initial step assumes that the pion is absorbed on two nucleons, thus transferring the pion rest energy to the two nucleons. In the next step these two recoiling nucleons can either escape or scatter from other nucleons and thereby transfer excitation energy to the nucleus. The third step involves particle evaporation from the heated nucleus, which yields the observed residual products.

The location of the pion absorption in the nucleus is calculated from pionic-atom data.[22] The wave function for each pionic orbit is determined by solving the Klein-Gordon equation with a pion-nuclear optical potential. This pion optical potential[23] has an imaginary part which is proportional to the square of the nuclear density due to the pion absorption on two nucleons. The strength of this absorptive potential is determined by fitting pionic x-ray transition strengths. The nuclear densities used in the pionic optical potential are taken from electron scattering.[24]

The resulting pion wave function has the form

$$\psi_l = \phi_l e^{iEt/\hbar}, \tag{1}$$

where ϕ_l is the radial wave function, E is the complex pion energy, and t is the time coordinate. The probability for absorption of the pion from each orbit is then calculated from the equation of continuity which determines that the pion is absorbed in a volume element, $dV = 4\pi r^2 dr$, where r is the distance from the center of the nucleus. We define the differential probability dP_l/dr for absorption of the pion from an orbit l along the radius r as

$$dP_l/dr = \frac{2\pi r^2 h}{\mathrm{Im}E}\left(\vec{\nabla}\cdot\vec{j} - \frac{2\mathrm{Im}E\,|\phi_l|^2}{h}\right), \tag{2}$$

where h is Planck's constant, $\vec{\nabla}$ is the gradient operator, and j_l is the pion current defined as

$$\vec{j}_l = \frac{i\hbar}{2m}(\phi_l \vec{\nabla}\phi_l^\dagger - \phi_l^\dagger \vec{\nabla}\phi_l)\,. \tag{3}$$

In order to calculate the total pion absorption probability, the relative weight W_l, with which a particular orbit l will be populated in the pionic-atom cascade must be estimated. This weighting was calculated by assuming that the pion was Coulomb captured in the atom with some initial distribution in angular momentum l_0 and then a Monte Carlo technique was used to follow the pion down through the pionic levels in order to determine the population of the final orbits.[25] Two simple distributions of initial angular momenta were used, a uniform distribution and one proportional to the angular momentum degeneracy, $2l_0 + 1$. The total differential probability is then given by

$$dP/dr = \sum W_l\, dP_l/dr\,. \tag{4}$$

In Figs. 1 and 2, the absorption probability dP/dr is plotted for ^{63}Cu and ^{181}Ta for the initial distribution proportional to $2l_0 + 1$; the uniform initial distribution gives almost identical results. The capture probability shows a rapid rise from the

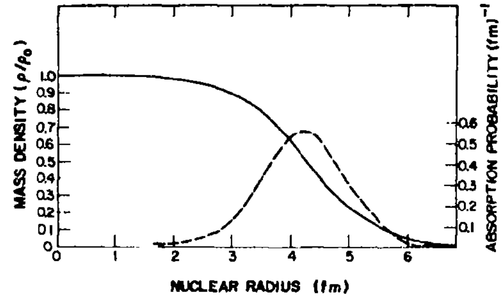

FIG. 1. The mass density for ^{63}Cu (solid line, left-hand scale) in units of the central density ρ_0 versus the nuclear radius. The mass density is from Ref. 24 and corresponds to a Fermi distribution with half radius = 4.2 fm and to a diffuseness = 0.59 fm. The absorption probability is plotted (right-hand scale) versus the radius.

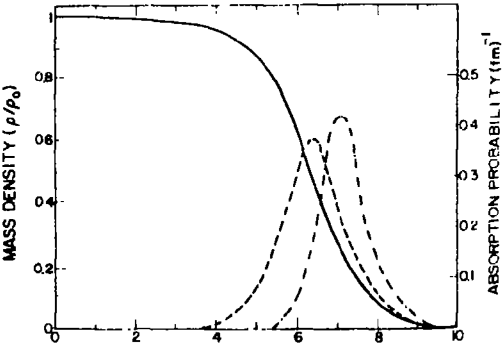

FIG. 2. The mass density for ^{181}Ta (solid line, left-hand scale) in units of the central density ρ_0 versus the nuclear radius. The mass density is from Ref. 24 and corresponds to a Fermi distribution with half radius = 6.4 fm and to a diffuseness = 0.64 fm. The absorption probability, calculated from the pionic-atom cascade code is shown dashed ($\rho/\rho_0 = 0.5$), while an arbitrarily chosen absorption distribution that peaks closer to the nuclear surface ($\rho/\rho_0 = 0.25$) is shown by the dash-dot curve.

edge of the nucleus, reaches a maximum at the half-central-density radius of the nucleus, and then slowly decreases to zero inside the nucleus. An arbitrarily chosen distribution for ^{181}Ta centered at the quarter-central-density radius is also shown in Fig. 2. This distribution is used to test the sensitivity of the model to the location of the pion absorption.

The negative pion can be absorbed on either a neutron-proton pair or a proton-proton pair. The probability that it will absorb on the neutron-proton pair will be proportional to the number of neutron-proton pairs in the nucleus NZ. The probability that it will absorb on a proton-proton pair will be proportional to the number of proton-proton pairs, $Z(Z-1)/2$. We define the ratio of these probabilities as the quantity R which then will be

$$R = 2k\frac{NZ}{Z(Z-1)} = R_0\frac{N}{(Z-1)}, \tag{5}$$

where k is the proportionality constant. For convenience we have defined R_0 as

$$R_0 = 2k \tag{6}$$

so that $R \simeq R_0$ for $N = Z$ nuclei. From Eq. (5) we see that for absorption that is equally probable on neutron-proton pairs as well as on proton-proton pairs, $k = 1$ or $R_0 = 2$.

The value of R_0 depends on the details of the pion absorption mechanism. For delta dominance, that is, absorption through a pion-nucleon isospin $\frac{3}{2}$ partial wave only, R_0 has a unique value of 5, independent of the magnitude of the absorption.[26] For absorption through a pion-nucleon partial wave with isospin $\frac{1}{2}$, R_0 can vary between 0 and 2. When both partial waves are contributing, there are no *a priori* bounds on R_0.

The quantity R_0 has a direct physical significance in that it represents the extent to which neutron-neutron pairs are ejected from the nucleus compared to neutron-proton pairs. As R_0 increases, π^- absorption will tend to produce more neutron-deficient isotopes because n-n out will result in a lower N/Z than for n-p out.

However, R_0 is not very well known. The experimental ratio of neutron-neutron pairs to neutron-proton pairs ejected from the nucleus, which we denote by R_e, has been measured for a number of nuclei.[27] If there were no charge-exchange scattering of the two nucleons as they leave the nucleus, R_e would be identical to R. However, charge-exchange scattering of the

TABLE I. Yields of products from stopped-π^- interaction with Cu.

Nuclide		Yield type	E_γ (keV)	γ/dis	Measured yield (%)	Calculated yield (%)
6.1 -d	^{56}Ni	*I*	751	0.474	0.0074 ± 0.0030	0.008 ± 0.008
36-h	^{57}Ni	*I*	1377	0.78	0.119 ± 0.014	0.232 ± 0.068
17.9-h	^{55}Co	*C*	931	0.73	0.115 ± 0.014	0.156 ± 0.056
78.5-d	^{56}Co	*C*	847	1.00	1.41 ± 0.12	1.46 ± 0.17
271.4-d	^{57}Co	*C*	122	0.859	6.80 ± 0.75	4.58 ± 0.30
71.3-d	^{58}Co	*I*	811	1.00	11.3 ± 1.2	7.90 ± 0.40
5.26-y	^{60}Co	*I*	1173/1332	1.00/1.00	6.35 ± 0.85	5.55 ± 0.33
1.65-h	^{61}Co	*C*	67	0.90	2.71 ± 0.40	2.89 ± 0.24
8.3-h	^{52}Fe	*C*	168	1.00	0.0028 ± 0.0004	0.002 ± 0.002
44.6-d	^{59}Fe	*C*	1099/1292	0.562/0.432	1.37 ± 0.15	2.19 ± 0.21
5.63-d	^{52}Mn	*I*	1434	1.00	0.42 ± 0.05	0.34 ± 0.08
313-d	^{54}Mn	*I*	835	1.00	4.41 ± 0.60	3.24 ± 0.25
2.58-h	^{56}Mn	*C*	847	1.00	1.66 ± 0.20	2.23 ± 0.21
21.6-h	^{48}Cr	*C*	308	0.99	0.0011 ± 0.0003	[a]
42-min	^{49}Cr	*C*	91	0.539	0.023 ± 0.004	0.002 ± 0.002
27.7-d	^{51}Cr	*C*	320	0.098	1.23 ± 0.18	0.46 ± 0.10
16.0-d	^{48}V	*C*	983	1.00	0.087 ± 0.010	0.01 ± 0.01
3.93-h	^{44}Sc	*I*	1157	1.00	0.0062 ± 0.0008	[a]
58.6-h	^{44}Sc^m	*I*	1157	1.07		
83.8-d	^{46}Sc	*I*	889	1.00	0.056 ± 0.009	0.004 ± 0.004
3.35-d	^{47}Sc	*I*	159	0.73	0.041 ± 0.008	0.018 ± 0.018
43.7-h	^{48}Sc	*I*	1037	1.00	0.020 ± 0.004	0.028 ± 0.024
22.2-h	^{43}K	*C*	373	0.87	0.0029 ± 0.0006	[a]
1.83-h	^{41}Ar	*C*	1294	0.99	0.0006	[a]
15.0-h	^{24}Na	*C*	1369	1.00	0.0037 ± 0.0020	[a]

[a] No events occurred for these products in the calculations.

emerging nucleons will decrease this ratio[26] so that $R_e < R$. The experimental errors are large and can accommodate any value of R_0 ranging from 1.6 to 3.4. This uncertainty, coupled with $R_e < R$, does not fix R_0 very well. In this work, we have used predominantly the value $R_0 = 2$, which corresponds to absorption being equally probable on neutron-proton pairs as on proton-proton pairs.

In the present calculations, the two nucleons which absorb the pion are distributed uniformly in a momentum sphere with the Fermi momentum determined by the local density. The pion energy is transferred to the center of mass of the two nucleons, and the subsequent escape or collisions of the two nucleons with other nucleons is determined by the VEGAS intranuclear cascade model.[17,18] After the original two nucleons plus the subsequently struck nucleons escape or are captured by the average nucleon potential, a heated nucleus remains. This excited nucleus evaporates off neutrons, protons, deuterons, tritons, ^{3}He, and α particles, and the residual nuclei are the observed spallation products. The evaporation stage is calculated with the DFF (Ref. 11) evaporation code. Angular momentum effects are ignored in the evaporation calculation.

IV. RESULTS

The absolute yields of residual products from the interactions of stopped π^- with Cu and Ta are given in Tables I and II. The relative yields from the high-intensity target exposures were put on an absolute basis by normalization to several high-yield, nearly saturated, monitor products. For Cu, the monitors were ^{55}Co, ^{56}Mn, and ^{48}Cr, and for Ta they were ^{170}Hf, ^{171}Hf, and ^{172}Lu. The photopeak energies, branching ratios, and the half-lives of the radioactive products,

TABLE II. Yields of products from stopped-π^- interaction with Ta.

Nuclide		Yield type	E_γ (keV)	γ/dis	Measured yield (%)	Calculated yield (%)
16-h	^{170}Hf	I	165/621	0.35/0.23	4.2 ± 0.7	0.98 ± 0.14
12.2-h	^{171}Hf	I	662	0.15	5.1 ± 0.7	2.48 ± 0.22
1.9-y	^{172}Hf	I	1093	0.65	6.9 ± 0.6	4.76 ± 0.31
23.6-h	^{173}Hf	I	124	0.995	9.0 ± 1.5	6.62 ± 0.36
70-d	^{175}Hf	I	343	0.82	11 ± 0.7	8.50 ± 0.41
52-min	^{177}Hf^m	I	277	0.93	0.068 ± 0.020	<5.2
29-d	^{179}Hf^m	I	363/454	0.39/0.67	0.31 ± 0.06	<3.6
55-min	^{167}Lu	I	239	0.12	0.028 ± 0.009	0.026 ± 0.023
1.42-d	^{169}Lu	C	960	0.237	3.0 ± 0.3	1.10 ± 0.16
2.02-d	^{170}Lu	I	987	0.067	2.3 ± 0.25	2.60 ± 0.23
8.22-d	^{171}Lu	I	741	0.527	3.26 ± 0.31	3.98 ± 0.28
6.70-d	^{172}Lu	I	1093	0.65	3.33 ± 0.36	5.26 ± 0.32
512-d	^{173}Lu	I	271	0.22	3.6 ± 0.35	5.10 ± 0.32
142-d	^{174}Lu^m	I	67.1	0.16	3.7 ± 0.4	5.11 ± 0.32
1204-d	^{174}Lu^g	I	76.5			
3.69-h	^{176}Lu^m	I	88.4	0.087	1.2 ± 0.2	3.1
6.61-d	^{177}Lu^g	I	208	0.0994	1.55 ± 0.22	1.88 ± 0.19
160-d	^{177}Lu^m	I	208	0.04		
23-min	^{178}Lu^m	I	426	0.95	0.27 ± 0.11	1.3
4.6-h	^{179}Lu	I	214	0.123	0.28 ± 0.04	0.36 ± 0.08
56.7-h	^{166}Yb	C	82	0.15	0.45 ± 0.12	0.058 ± 0.034
31-d	^{169}Yb	C	198	0.36	4.4 ± 0.5	2.28 ± 0.30
4.21-d	^{175}Yb	I	396	0.065	0.34 ± 0.04	0.33 ± 0.08
1.9-h	^{177}Yb	I	150	0.22	0.018 ± 0.003	0.076 ± 0.039
30.6-h	^{165}Tm	C	243	0.433	0.11 ± 0.013	0.026 ± 0.023
7.70-h	^{166}Tm	I	778	0.20	0.079 ± 0.018	0.144 ± 0.054
9.29-d	^{167}Tm	C	208	0.403	1.1 ± 0.1	0.77 ± 0.21
93-d	^{168}Tm	I	816	0.482	0.13 ± 0.02	0.50 ± 0.10
126-d	^{170}Tm	~I	β^-		0.10 ± 0.01	0.39 ± 0.09
63.6-h	^{172}Tm	~I	1093	0.060	0.028 ± 0.004	0.13 ± 0.05
8.24-h	^{173}Tm	~I	399	0.806	0.013 ± 0.003	0.096 ± 0.044
9.3-d	^{169}Er	~I	β^-		0.0043 ± 0.0006	0.040 ± 0.028
7.52-h	^{171}Er	~I	308	0.658	0.0012 ± 0.0002	0.012 ± 0.012

used in the yield calculations, are included in the tables. Cumulative or independent yields are denoted by *C* or *I*.

The experimental errors quoted in the tables are due chiefly to uncertainties in photopeak intensity measurements. Smaller error contributions arise from corrections for photon absorption in the target foil, extended source geometry, and detector photopeak efficiency. The quoted errors do not include a possible systematic uncertainty, estimated to be less than ±12%, due to the determination of pion stops in the absolute yield measurements. In the calculations, 5000 stops were followed and the errors are statistical, ranging from ±5% for yields of about 10% to ±50% for yields near 0.1%.

The experimental independent yields of products from Cu are plotted in Fig. 3 and compared with calculations; smooth curves are drawn through calculated yields to guide the eye.

For Ta, measured independent yields are compared with calculations in Figs. 4 and 5. Smooth curves have been drawn through the calculated points to guide the eye. In the case of Ta, we were able to measure about two thirds of the total mass yields, compared to about 38% of the total for Cu. We have estimated the missing Ta yields (mainly the stable isotopes) by applying the computer code RUDSTAM[28] to our measured data. This code was developed at Brookhaven to calculate missing spallation product yields, using Rudstam's original empirical formulation.[29] The resultant total mass yields for Ta are compared with the stopped-pion model calculations in Fig. 6.

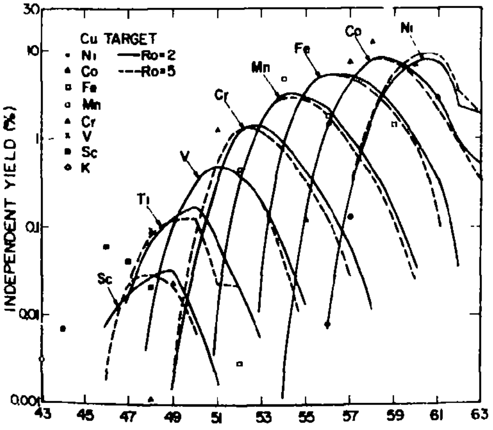

FIG. 3. Independent yields of residual spallation products from stopped-π^- interactions with Cu. Experimental alues are shown as points and smooth curves are drawn rough the calculated points (not shown). The solid and ashed curves are for $R_0 = 2$ and 5, respectively, where $_0$ is the ratio of the probabilities for absorption on an $-p$ pair to absorption on a p-p pair.

Contributions to the observed yields due to secondary reactions can be estimated by measuring Z (Cu) and $Z+1$ (Zn) radioactivities in the Cu target foils and in secondary target foils placed downstream behind sufficient absorber so they are beyond the range of the pions. The Z and $Z+1$ products are unique to secondary reactions because π^- absorption leads to species with $Z < 29$. These statements apply equally well to the Ta targets.

The results of measurements of secondary reaction products are given in Table III. In Cu, (p, xn), (n, xn), (n, p), and $(n$, spall) products were detected, while in Ta only (n, xn) and (n, p) products were observed. Products due to (n, α) reactions $(Z-2)$ were not observed in the secondary targets; however, contributions from this

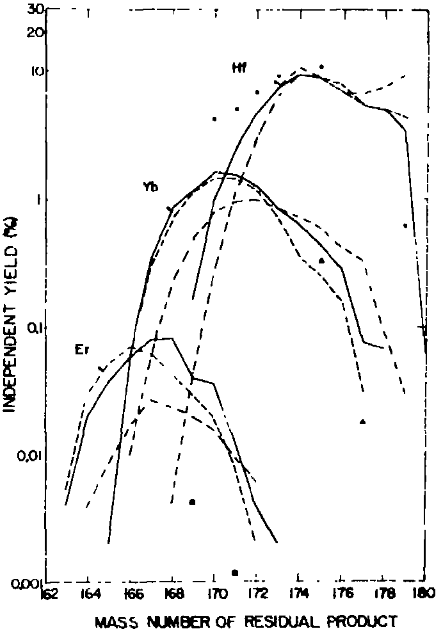

FIG. 4. Independent yields for residual Hf, Yb, and Er products from the interaction of stopped π^- with Ta. The measured yields are shown as circles (Hf), triangles (Yb), and squares (Er). Curves are established from the calculated yields. Solid and dashed curves are for $R_0 = 2$ and 5, respectively. The dash-dot curves are for $R_0 = 2$, but with an absorption probability arbitrarily peaked closer to the nuclear surface (see Fig. 2). The measured yield for ^{175}Hf represents a lower limit because only the high-spin isomer was detectable.

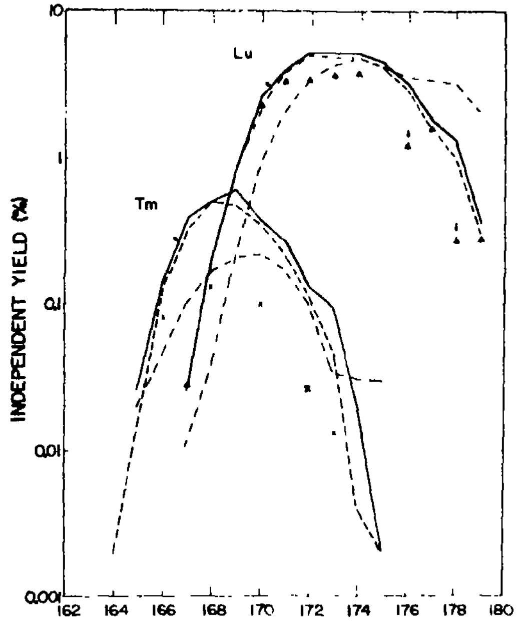

FIG. 5. Independent yields for residual Lu and Tm products from the interaction of stopped π^- with Ta. The measured yields are shown as triangles (Lu) and crosses (Tm). Curves are established from the calculated yields. Solid and dashed curves are for $R_0 = 2$ and 5, respectively. The dash-dot curves are for $R_0 = 2$, but with the absorption probability arbitrarily peaked closer to the nuclear surface (see Fig. 2).

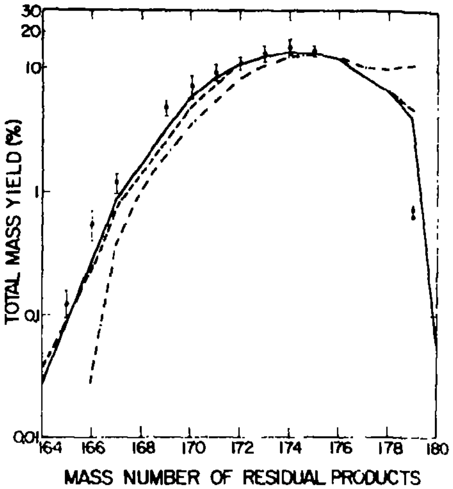

FIG. 6. Total mass yields for residual products from the interaction of stopped π^- with Ta. The points are the sums of experimentally determined yields with estimates of missing yields from the semi-empirical fitting routine described in Sec. IV. The smooth curves are established from the calculated yields. The solid and dashed curves are for $R_0 = 2$ and 5, respectively. The dash-dot curve is for $R_0 = 2$, but with the absorption probability peaked closer to the nuclear surface (see Fig. 2). The $A = 179$ yield is shown as a lower limit because only the high-spin isomer of ^{179}Hf was detectable

reaction were estimated by comparing published (n, α) cross sections with $(n, 2n)$ or (n, p) excitation functions in the 8- to 20-MeV region. In Table III the yield per pion stop of ^{60}Co from the (n, α) reaction is estimated to be 0.1% which is to be compared with a total measured ^{60}Co yield of 7.05% per pion stop; this is about a 1.5% contribution from the secondary reaction. Presumably, about the same amount of (n, α) contribution occurs in Ta adding to the ^{178}Lu yield.

Due to the combination of low reaction cross sections and poor geometry, the only $Z < 29$ product we detected in the secondary Cu target foils was ^{56}Mn, presumably due to high-energy nucleon-induced spallation. The other $Z < 29$ species observed from the stopped π^- interactions must also be made to some extent by the high-energy secondary nucleons, but our measure-

TABLE III. Yields of products from secondary reactions.

	Cu target			Ta Target	
Product	Yield (% per π^- stop)	Predominant reaction	Product	Yield (% per π^- stop)	Predominant reaction
^{62}Zn	0.014	^{63}Cu$(p, 2n)$	^{178}Ta^m	0.22	$(n, 4n)$
^{63}Zn	0.052	^{63}Cu(p, n)	^{176}Ta	0.14	$(n, 6n)$
^{61}Cu	0.23	^{63}Cu$(n, 3n)$	^{181}Hf	0.040	(n, p)
^{64}Cu	0.64	^{65}Cu$(n, 2n)$	^{178}Lu	0.012 (est)	(n, α)
^{65}Ni	0.047	^{65}Cu(n, p)			
^{60}Co	0.10 (est)	^{63}Cu(n, α)			
^{62}Co	0.05 (est)	^{65}Cu(n, α)			
^{56}Mn	0.016	Cu $(n$, spall)			

ments indicate that these contributions amount to about 1% and, therefore, are negligible for the ~1 g/cm^2 targets.

During the course of this work several measurements were made with Fe and Cu targets in order to determine the difference in residual product distributions when the charge on the incoming pion was changed from minus to plus. Of course, a positively charged pion cannot be Coulomb captured by a nucleus and must have sufficient kinetic energy to overcome the Coulomb barrier. For these measurements the π^+ were degraded with 4.45-cm-thick graphite plates, from an incident energy of 50 MeV down to about 20 MeV at the center of the target foil. Since the interaction cross section for π^+ drops rapidly with decreasing energy, below 100 MeV, we adopted a π^+ energy of 20 MeV for this comparison, although this energy is considerably higher than the Coulomb barrier. At 20 MeV, the π^+ interaction is predominantly absorption and inelastic scattering is relatively unimportant. The small amount of kinetic energy which can add to the pion rest-mass energy (140 MeV) upon absorption should not alter the π^+ yield distributions to any measurable degree.

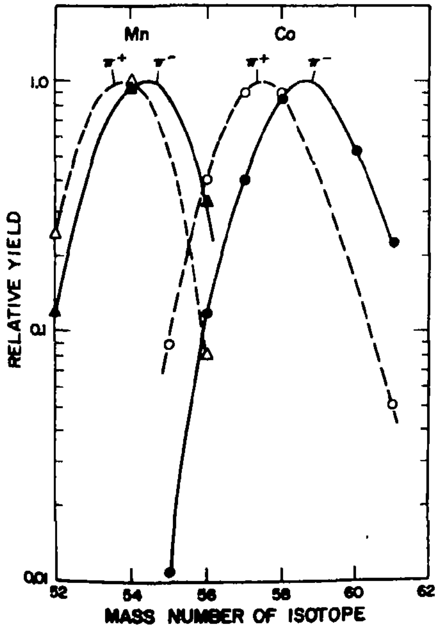

FIG. 7. Relative yields of Co and Mn spallation products from stopped π^- (solid points) and 20-MeV π^+ (open points) incident on Cu. The centroids are normalized to unity for easier comparison.

The Mn and Co yields from Cu are shown in Fig. 7. For Co the shift is about 1.2 mass units. However, for Mn the shift is only about one half this amount; the reason for this smaller shift is not obvious.

In order to utilize the set of five measurable Sc isotopes to determine the extent of the shift expected due to changing the charge of the incoming pion, Fe was selected for the target material. Cu was not as suitable a target since the expected ^{61}Cu product from secondary nucleon reactions would preclude a determination of the ^{43}Sc yield. This is because ^{61}Cu has a strong γ transition in its decay which is identical in energy to the 373-keV γ ray of ^{43}Sc. The Sc yields from Fe, shown in Fig. 8, illustrate the shift in yield distributions between absorption of π^+ and π^-; here the shift in the centroids is again about 1.2 mass units. Although not shown here, measurements from a 20-MeV π^+ irradiation of Cu, compared with stopped-π^- results, indicate that from those Sc isotope yields that could be determined unambiguously, a shift of about 1.2 mass units occurs in the estimated centroids.

The centroid shifts in cross sections of Co, Mn, and Sc isotopes from fast π^+ and π^- reactions with Cu are, as one would expect, considerably smaller. The ΔA values decrease from 0.6 to approximately 0.2 mass units in going from 100 to 350 MeV.[30]

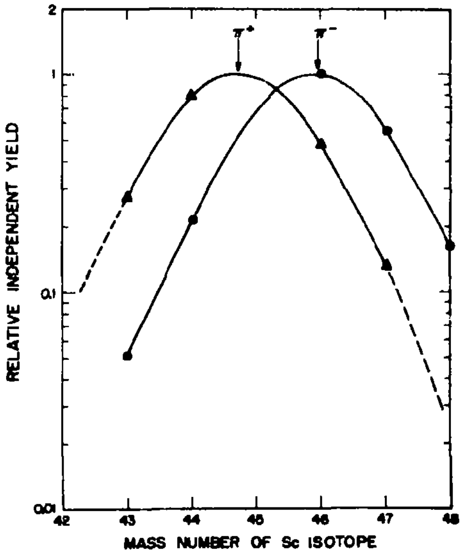

FIG. 8. Relative yields of Sc isotopes from stopped π^- (circles) and 20-MeV π^+ (triangles) incident on Fe. The centroids are normalized to unity for easier comparison.

V. DISCUSSION

A. Comparison of measured and calculated yields

For the independent yields shown in Fig. 3, those for cobalt are underestimated by the model. The greatest discrepancies, however, are the underestimations of the Cr, V, and Sc isotopic yields. Increasing the ratio R_0 from 2 to 5 does not change these results; the model does not seem to deposit enough energy in the Cu nucleus.

The agreement of the calculations with the measured total yields from Ta (Fig. 6) is quite good, although the products far removed from the target are somewhat underestimated. The experimental data for products near the target are less complete for comparison purposes. In Figs. 4 and 5, the individual isotopes are compared and we see a different situation than for copper. Only the isotopes of Hf, far removed from the target, are underestimated. The isotopes of Lu and Yb are predicted fairly well, but those of Tm and Er are severely overestimated. Changing R_0 from 2 to 5 does not significantly affect the calculated yields. We have also calculated the products with a pion absorption distribution which is peaked farther out on the edge of the nucleus, where the density is 25% of central density. This distribution, given in Fig. 2, improves the results for Tm and Er but gives poor results for the remaining isotopes.

The results on Cu and Ta indicate that the basic absorption mechanism used may not be the only mechanism involved. The neutron-deficient isotopes are being underestimated. The flatness of the Hf isotope curve and the low yields of the Tm and Er isotopes are difficult to reconcile in a simple model of pion absorption.

B. Comparison with previous studies

We show in Table IV a comparison of our ^{181}Ta results with yield data for stopped-π^- absorption in ^{181}Ta and nearby heavy nuclei, as reported by other investigators. The mean numbers of emitted neutrons and protons ($\langle n\rangle$ and $\langle p\rangle$) that we calculate for ^{181}Ta are very similar to those for ^{197}Au and ^{209}Bi reported by Pruys *et al.*[15] Also, these authors presented systematics that showed the centroids of the isotopic yield distributions (Gaussians) for (π^-, xn) products remain constant at $x \approx 6$ for $A = 165$ to 209, and the FWHM of all isotopic yield curves increase with target mass number. Our data for ^{181}Ta fit these systematics rather well. However, when we compare our data with those of Beetz *et al.*[16] for ^{181}Ta we find rather poor agreement. Why this is so we cannot say for certain, although, we suspect it may be due in part to the complexity of the prompt γ-ray spectrum in the 200-keV energy region. They report[16] absolute yields (per π^- stop) for the $4^+ - 2^+$ γ transitions in the ground-state rotational bands of the even-even Hf isotopes. We note, for example, that the 207.4-keV $\frac{7}{2}^+[633] - \frac{5}{2}^-[523]$ γ transition in high-yield ^{175}Hf might enhance the 206.5-keV photopeak from ^{174}Hf; the Table of Isotopes lists many γ rays in this energy region for the odd-mass Hf isotopes.

In the case of Cu, where we measured only 38% of the mass yield, we find that after correcting for the two isotopes of natural copper, the yield distributions are quite similar to those for ^{59}Co and ^{75}As reported by Pruys *et al.*[15], and the FWHM for the Mn and Co isotopic yield distributions (2.8 mass units) fit their systematics quite well.

C. Angular momentum considerations

The angular momentum brought into the nucleus by the Coulomb captured π^- is quite small since the pion itself has zero spin and only the pionic orbital momentum can be transferred. A large amount of angular momentum, however, can be imparted to the nucleus when a pion is absorbed near the surface and one of the absorbing nucleons escapes without further interaction, while the other nucleon, through collisions with other nucleons in the nucleus, imparts its kin-

TABLE IV. Comparison of isotopic yield data for π^- absorption in heavy nuclei.

Target	Centroid of (π^-, xn) isotopic yield (x)	FWHM of isotopic yield curves (ΔA)	$\langle n\rangle$	$\langle p\rangle$
^{165}Ho (Ref. 31)	6	6.1		
^{175}Lu (Ref. 31)	7	7.0		
^{181}Ta (Ref. 16)	8	5.2		
^{181}Ta (this work)	6	7.3	6.4 ± 0.5	0.40 ± 0.16
^{197}Au (Ref. 15)	6	8.9	6.6 ± 0.4	0.32 ± 0.14
^{209}Bi (Ref.15)	6	8.9	6.8 ± 0.4	0.37 ± 0.16
^{209}Bi (Ref. 16)	6	8.0		

TABLE V. Isomer ratios for ^{174}Lu and ^{177}Lu from ^{181}Ta.

Product	$I^{\pi}(m)/I^{\pi}(g)$	100-MeV protons	500-MeV protons	Stopped π^-
^{174}Lu	$6^-/1^-$	0.65±0.08	0.65 ±0.07	0.69±0.07
^{177}Lu	$\frac{23}{2}^-/\frac{7}{2}^+$	0.19±0.12	0.088±0.030	0.15±0.04

etic energy to the nucleus. This twisting of the nucleus can transfer about 11 $\hbar$ units of angular momentum in Cu if the two nucleons recoil perpendicularly to a radius vector near the nuclear surface. Conversely, if a pion is absorbed deep in the nucleus, on the average, very little angular momentum will be imparted by the recoiling pair of nucleons, although much larger nuclear excitation energy will result compared with surface absorption.

Several authors[12, 13] have emphasized the observed production of high-spin isomers of residual products by the stopped-pion interaction. Our measurements agree with this observation; however, we wish to point out the fact that this production of high-spin isomers is about the same as that which would be observed if the target nucleus were irradiated with ~70-MeV nucleons. One can visualize essentially the same impact parameters for 70-MeV nucleon-induced reactions and for stopped-π^- interactions near the nuclear surface.

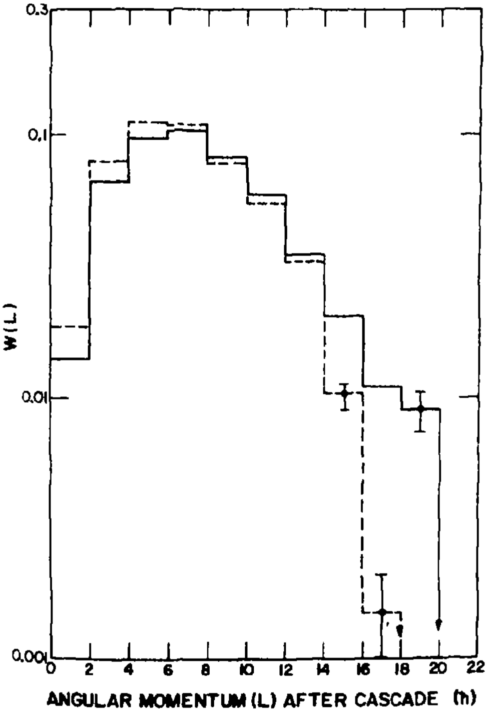

FIG. 9. The distributions of calculated angular momenta left in residual-product nuclei after the intranuclear cascade process for 70-MeV protons (solid line) and for stopped π^- (dashed line) incident on ^{181}Ta.

We have determined isomer ratios in ^{174}Lu and ^{177}Lu from stopped-π^- and 100- and 500-MeV proton reactions with Ta, and the data are given in Table V. The nuclear spin difference in the ^{174}Lu isomers is not very large and considerable particle evaporation occurs to erode the effect; however, the spin difference for the ^{177}Lu isomers is large, and these isomers lie within a few mass numbers of the ^{181}Ta target. Our measurements show, within the rather large uncertainties, that the isomer yields from stopped-π^- reactions with Ta are about the same as for fast-proton reactions. The fact that the isomer ratios are about the same for both 100- and 500-MeV protons and for stopped pions indicates that 70-MeV nucleons have essentially saturated the population of spin states with $\Delta I \leq 8$. This would probably not be the case if ΔI were much larger.

Angular momentum calculations using the stopped-pion interaction model and the VEGAS code for 70-MeV protons indicate that the angular momentum transfers to ^{181}Ta are very nearly the same for both projectiles. The calculated results are shown in Fig. 9.

VI. CONCLUSIONS

The data from this study are consistent with the smoothly increasing widths of the isotopic yield distributions with target mass number, and with a maximum in the (π^-, xn) yield distributions at $x = 6$ for heavy mass targets, discussed in Ref. 15.

The stopped-pion interaction model discussed in Sec. III reproduces the experimental data fairly well. In the case of the Cu target it appears to underestimate the yields below $A = 54$, suggesting that these calculations put too little excitation energy into the nucleus, and that the absorption of the pion occurs deeper, on the average, in the Cu nucleus than the model predicts. Also, when we compare the calculated yields with the measured independent yields given in Fig. 3, we notice that the measured yields for Sc isotopes peak near $A\approx 45$ while the calculations show the maximum near $A\approx 47$. This may be due to a deficiency in the DFF (Ref. 11) evaporation code which appears to overreact to the $N=28$ neutron shell in both fast-pion and proton reaction studies.

Although for Ta the calculated total mass yields reproduce the observed yields quite well, there is considerable room for improvement in the calculated independent yields shown in Figs. 4 and 5. A new, more sophisticated evaporation code (JULIAN) has been written by Hillman and Eyal,[32] and its substitution for the DFF code may improve the agreement in the independent yield calculations for products many mass numbers removed from the target mass.

Comparisons of our experimental and calculated spallation-product yields indicate that the latter are rather insensitive to R_0, the ratio of pion absorption on n-p to p-p pairs. On the other hand, the calculated yields are quite sensitive to the radial depth of absorption, with the calculated half-central-density radius providing the best fit in Ta. In the case of Cu a slightly deeper absorption distribution than calculated would provide a better fit for the product yields.

Our measurements indicate that high-spin isomers are produced by π^- absorption in ^{181}Ta. However, both our measurements of isomer ratios in ^{177}Lu from ^{181}Ta targets irradiated with stopped π^- and with fast protons and our angular momentum calculations with the stopped-pion interaction model and the VEGAS code for 70-MeV protons, indicate that the angular momentum transfers to ^{181}Ta are very nearly the same for both projectiles.

From the results of the investigation of the influence of pion charge on the product yield distributions from Cu, the "memory" effect is clearly exhibited in yields of products from 2 to at least 8 units of Z from the target.

ACKNOWLEDGMENTS

We gratefully acknowledge the work of the LAMPF technical staff and operating crews for enabling the target exposures to be carried out. We thank G. A. Cowan and J. E. Sattizahn for their encouragement and support of this study. This work was performed under the auspices of the U.S. Department of Energy.

---

[1] J. Hüfner, Phys. Rep. **21C**, 1 (1975).

[2] A. L. Turkevich and J. B. Niday, Phys. Rev. **84**, 1253 (1951).

[3] T. T. Sugihara and W. F. Libby, Phys. Rev. **88**, 587 (1952).

[4] A. L. Turkevich and S. Fung, Phys. Rev. **92**, 521 (1953).

[5] A. L. Turkevich and J. B. Niday, Phys. Rev. **90**, 342 (1953).

[6] N. Sugarman and A. Haber, Phys. Rev. **92**, 730 (1953).

[7] L. Winsberg, Phys. Rev. **95**, 198 (1954).

[8] E. Gadioli and E. Gadioli-Erba, Nucl. Phys. **A256**, 414 (1976).

[9] A. S. Iljinov, V. I. Nazaruk, and S. E. Chigrinov, Nucl. Phys. **A268**, 513 (1976).

[10] H. W. Bertini, Phys. Rev. C **1**, 423 (1970).

[11] I. Dostrovsky, Z. Fraenkel, and G. Friedlander, Phys. Rev. **116**, 683 (1959).

[12] V. S. Butsev, Yu. K. Gavrilov, Dz. Ganzorig, S. M. Polikanov, and D. Chultem, Pis'ma Zh. Eksp. Teor. Fiz. **21**, 400 (1975) [JETP Lett. **21**, 182 (1975)].

[13] V. M. Abazov, S. R. Avramov, V. S. Butsev, E. P. Cherevatenko, D. Chultem, W. D. Fromm, Dz. Ganzorig, Yu. K. Gavrilov, and S. M. Polikanov, Nucl. Phys. **A274**, 463 (1976).

[14] H. D. Engelhardt, C. W. Lewis, and H. Ullrich, Nucl. Phys. **A258**, 480 (1976).

[15] H. S. Pruys, R. Engfer, R. Hartmann, U. Sennhauser, H.-J. Pfeiffer, H. K. Walter, J. Morgenstern, A. Wyttenbach, E. Gadioli, and E. Gadioli-Erba, Nucl. Phys. **A316**, 365 (1979).

[16] R. Beetz, F. W. N. de Boer, J. K. Panman, J. Konijn, P. Pavlopoulos, G. Tibell, K. Zioutas, I. Bergstrom, K. Fransson, L. Tauscher, P. Blum, R. Guigas, H. Koch, H. Poth, and L. M. Simons, Z. Phys. **A286**, 215 (1978).

[17] K. Chen, Z. Fraenkel, G. Friedlander, J. R. Grover, J. M. Miller, and Y. Shimamoto, Phys. Rev. **166**, 949 (1968).

[18] K. Chen, G. Friedlander, G. D. Harp, and J. M. Miller, Phys. Rev. C **4**, 2234 (1971).

[19] R. Gunnink and J. B. Niday, Lawrence Livermore Laboratory Report No. UCRL-51061 (1971–1972).

[20] S. Charalambus, Nucl. Phys. **A166**, 145 (1971).

[21] A. Wyttenbach, P. Baertschi, S. Bajo, J. Hadermann, K. Junker, S. Katcoff, E. A. Ermes, and H. S. Pruys, Nucl. Phys. **A294**, 278 (1978).

[22] G. Backenstoss, Annu. Rev. Nucl. Sci. **20**, 467 (1970)

[23] D. K. Anderson, D. A. Jenkins, and R. J. Powers, Phys. Rev. **188**, 9 (1969).

[24] C. W. de Jager, H. de Vries, and C. de Vries, At. Data and Nucl. Data Tables **14**, 479 (1974).

[25] M. Leon, private communication.

[26] J. N. Ginocchio, Phys. Rev. C **17**, 195 (1978).

[27] M. E. Nordberg, Jr., K. F. Kinsey, and R. L. Burman, Phys. Rev. **165**, 1096 (1965).

[28] J. B. Cumming, P. E. Haustein, R. W. Stoenner, L. Mausner, and R. A. Naumann, Phys. Rev. C **10**, 739 (1974).

[29] G. Rudstam, Z. Naturforsch. **21a**, 1027 (1966).

[30] C. J. Orth, B. J. Dropesky, R. A. Williams, G. C. Giesler, and J. Hudis, Phys. Rev. C **18**, 1426 (1978).

[31] P. Ebersol, B. Aas, W. Dey, R. Eichler, H. J. Leisi, W. W. Sapp, and H. K. Walter, Phys. Lett. **58B**, 428 (1975).

[32] M. Hillman and Y. Eyal, Amer. Chem. Soc. 174th National Meeting, Chicago, 1977. Abstract No. 47, Nucl. Chem. and Technology Bulletin.

PHYSICAL REVIEW C VOLUME 21, NUMBER 6 JUNE 1980

Proton-deuteron elastic scattering at 800 MeV

E. Winkelmann,* P. R. Bevington, M. W. McNaughton,† and H. B. Willard‡
Case Western Reserve University, Cleveland, Ohio 44106

F. H. Cverna, E. P. Chamberlin, and N. S. P. King
Los Alamos Scientific Laboratory, Los Alamos, New Mexico 87545

(Received 28 January 1980)

Differential cross sections and polarization analyzing powers for proton-deuteron elastic scattering have been measured at 800 MeV incident proton kinetic energy over the range of center-of-mass angles from 14.1° to 153.6°. The differential cross sections are described by the Glauber theory of impulse approximation at forward angles ($-t < 0.5$) and exhibit the exponential dependence on $\cos\theta_{c.m.}$ typical for these energies at backward angles ($\cos\theta_{c.m.} < -0.5$). The analyzing power shows considerable structure with strong positive peaks at forward and backward angles and a sharp dip at $t = -0.4$ typical at intermediate energies. There is no evidence for correspondence of the angular dependence of the analyzing power with that for the $pp \rightarrow d\pi^+$ reaction. At large momentum transfer the data favor calculations based on multiple scattering with a modified deuteron form factor rather than N^* exchange.

[NUCLEAR REACTIONS ^{2}H$(p,p)^2$H, E = 800 MeV, measured $\sigma(\theta)$ and $A_y(\theta)$.]

I. INTRODUCTION

There has been considerable interest in the proton-deuteron interaction as the simplest possible between protons and nuclei. Proton-deuteron elastic scattering, moreover, should show some correspondence with other proton-deuteron interactions such as pion production from the $pp \rightarrow d\pi^+$ reaction. We have measured both the differential cross section and the polarization analyzing power A_y, the asymmetry in the scattering of a polarized proton by an unpolarized target (which equals the polarization P if time reversal holds), for the elastic scattering of protons by deuterons for $T_p = 800$ MeV and $14° < \theta_{c.m.} < 154°$, with emphasis on precision measurements of the analyzing power.

The status of proton-deuteron elastic scattering at intermediate energies has been reviewed recently.[1] The differential cross section has been measured extensively[2-8] from 316 MeV to 5.73 GeV, with emphasis on backward angles. The analyzing power has been studied over as wide an energy range,[3-5,9,10] but with less precision. In addition, there have been efforts recently to determine the spin orientation of the scattered deuteron[11] and the tensor analyzing power.[12]

At forward angles, where the transferred momentum is small, the interaction should be dominated by the impulse approximation, and the differential cross section is expected to agree with that predicted by the theory of Glauber[13,14] and Watson.[15] The incident proton is considered to scatter successively from one or both of the individual nucleons in the deuteron with essentially a free nucleon-nucleon interaction. Interference between single and double scattering should produce a sharp dip when the four-momentum transfer squared $t = -0.4\ (\text{GeV}/c)^2$. The observed smoothing of the dip to the shape of a shoulder has been ascribed to either differences in the ratios of real to imaginary parts of the n-p and p-p forward scattering amplitudes[6] or to the admixture of d state in the deuteron.[14]

The analyzing power should also be large and positive in the forward direction as in free nucleon-nucleon scattering, though the angle at which the analyzing power peaks should be smaller than that of $\theta_{c.m.} = 40°$ for p-p scattering[16] or $\theta_{c.m.} = 30°$ for p-n scattering[17] as observed for other light nuclei.

It is at back angles that we might hope to learn more about the details of the deuteron wave function and its form factor, since they depend on the small radial components whose effects can only be observed for large momentum transfer.[7] Below 300 MeV, i.e., below the threshold for pion production, the reaction is well described by one nucleon exchange (ONE). There is a well-defined peaking at back angles, which is characteristic of nucleon-deuteron scattering from low energies to the GeV region.[1] Such a rise can be obtained with a calculation based on single scattering, since the cross section for free nucleon-nucleon scattering also rises at back angles.[18] At intermediate energies, however, the magnitude observed at back angles is larger than can be pre-

© 1980 The American Physical Society

dicted with so simple a calculation.

Kerman and Kisslinger[19] proposed a 1%–2% admixture of excited nucleon state component in the ground state wave function, specifically the $N^*(\frac{5}{2}, \frac{1}{2})$ nucleon isobar with an invariant mass of 1688 MeV. The exchange of these components in proton-deuteron scattering would augment neutron exchange sufficiently to fit the observed yields. The mechanism almost entirely responsible for elastic scattering is thus fermion transfer (pick-up), because the momentum transfer required at the deuteron vertex is much smaller than that for single or double impulse collisions.[20]

Craigie and Wilkin[21] proposed that the reaction $pp \to d\pi^+$ should play a significant role, and they adapted a calculation of Yao[22] which related the $pp \to d\pi^+$ and $\pi p \to p\pi$ reactions. Since the latter correspondence held well above resonant energy, the correspondence between proton-deuteron scattering and the $pp \to d\pi^+$ reaction might hold above the pronounced resonance in that reaction corresponding to the mass of the $\Delta(\frac{3}{2}, \frac{3}{2})$ at 1236 MeV in the pion-nucleon system. They characterized the scattering as a two-step process in which the virtual reaction $pp \to d\pi^+$ is followed by absorption of the pion,[18] calculated from the so-called triangular graph which includes as input the $pp \to d\pi^+$ amplitude.[21]

Barry[23] obtained excellent fits to the available data with a corrected version of Craigie and Wilkin's calculations. He noted, however, that the excited nucleon theory of Kerman and Kisslinger[19] and the triangle graph of Craigie and Wilkin[21] were both different facets of the same one pion exchange (OPE) process. Kolybasov and Smordinskaya[18] extended the work of Craigie and Wilkin and added a smooth background to achieve excellent fits. Noble and Weber[24] found no convincing need for either exchange of excited N^* isobars in the deuteron wave function or pion-nucleon exchange contributions beyond the usual ONE. They claimed that Kerman and Kisslinger[19] incorrectly evaluated their wave functions in terms of $|\Delta| = |\vec{d}'/2 - \vec{p}|$ rather than $Q = [(p \cdot d')^2/M_d^2 - M_p^2]^{1/2}$. One really different alternative is that of Remler and Miller,[25] who took a multiple scattering approach, using knowledge of the deuteron structure and the nucleon-nucleon interaction, neglecting exchange terms. More recently Gurvitz and Rinat[26] have successfully fitted back angle pd scattering data above 1 GeV/c with a calculation based on single scattering plus neutron exchange, yielding a reasonable form factor for the deuteron, with no N^* content.

The observed cross section has passed many of the tests of comparison with the $pp \to d\pi^+$ reaction at back angles. The cross section at very back angles falls rapidly with energy except for a pronounced bump at about 600 MeV, which has been reproduced in calculations.[1,18] Furthermore, the shapes of the angular distributions have been fitted with the various recipes based on OPE, except for the lack of a dip at extreme back angles.[5]

Still, the ultimate test is to compare the analyzing powers for the two reactions. The reaction mechanism in proton-deuteron scattering is sensitive to the proton polarization.[18] We would thus expect the asymmetries resulting from incident polarized protons to be the same for both reactions at back angles and the same energies. Otherwise, if OPE is not dominant, the scattering of polarized protons by deuterons should be dominated by three-baryon exchange.[24]

One comparison at 425 MeV (Refs. 3 and 27) showed little agreement. Another measurement at 544 MeV (Refs. 4 and 28) was inconclusive because of poor statistics in the analyzing power for proton-deuteron scattering. Hence, we felt the need for precise measurements of the analyzing power for proton-deuteron elastic scattering at the same energy as recent measurements of the asymmetry in the $pp \to d\pi^+$ reaction,[29] i.e., 800 MeV.

II. EXPERIMENTAL PROCEDURE

The experimental method has been described elsewhere.[16,30] A floor plan of the experimental arrangement is given in Fig. 1. Measurements were made with the external proton beam (EPB) of the Los Alamos Meson Physics Facility (LAMPF). The position of the beam was monitored with a profile monitor, and its intensity (about 20 pA) was determined relatively with an Ar-CO_2 ion chamber and a Faraday cup,[31] with absolute normalization obtained by comparison of interspersed measurements of elastic proton-proton scattering with earlier highly accurate determinations.[16] The polarization of the incident beam was monitored with a polarimeter,[32] which was normalized absolutely by quenching the polarized beam at the source. The polarization was typically of the order of 0.75, reversed every three minutes, with an uncertainty of about 0.5%.

The targets were slabs of CD_2 ranging from 18 mg/cm^2 to 556 mg/cm^2, with corresponding slabs of pure C to investigate the contributions from quasielastic scattering, and CH_2 to determine if CH_2 contamination gave spurious information. All but the desired data were rejected kinematically. Both the scattered proton and the recoil deuteron were detected (for right and left

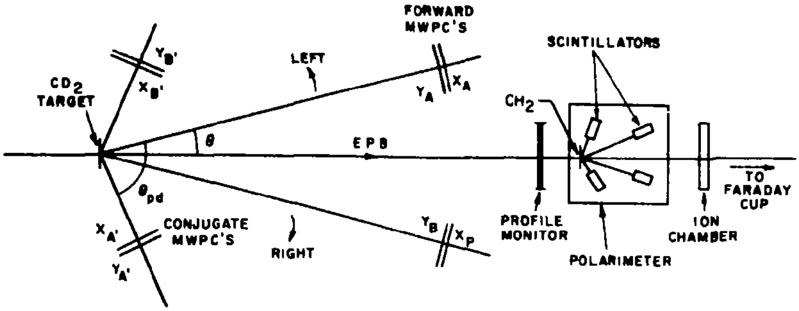

FIG. 1. Floor plan of experimental arrangement.

scattering) with x-y pairs of MWPC's.[33] The products of elastic scattering reactions were identified by kinematical constraints of the polar (θ_{pd}) and azimuthal angles with interpolation and subtraction of contributions from other sources such as quasielastic scattering from nucleons in the carbon nuclei. The backgrounds constituted from 25% to 90% with uncertainties from 2% to 4%. The data-acquisition system[34] was developed to minimize dead time, which was monitored for correction of the cross-section measurements; typical values of dead time were from 1% to 8%. The differential cross section was also corrected for the finite opening of the MWPC's with corrections from +2% to −11% and uncertainties of 1% to 4%. The only significant uncertainties in the analyzing power were those of counting statistics.

III. RESULTS

The observed differential cross section $d\sigma(\theta_{c.m.})/d\Omega$ for the elastic scattering of 800 MeV protons by deuterons is listed in Table I and plotted against $\cos\theta_{c.m.}$ in Fig. 2. The shape is typical of those observed at intermediate energies: The cross section decreases by several orders of magnitude at very forward angles, then with a sharp break it decreases more slowly until at very back angles it rises sharply again.

TABLE I. Differential cross sections and analyzing powers for proton-deuteron elastic scattering at $T_p = 800$ MeV. (Quantities with an asterisk are in the center-of-mass system.)

θ (°)	$d\sigma/d\Omega$ (μb/sr)	θ^* (°)	$\cos\theta^*$	t (GeV/c)^2	$d\sigma/dt$	$(d\sigma/d\Omega)^*$ (μb/sr)	$A_y(\theta^*)$
8.0		14.1	0.970	−0.042			0.340 ± 0.049
9.4		16.4	0.959	−0.055			0.450 ± 0.023
10.1	4920	17.8	0.952	−0.066	67 850	14 900 ± 4800	
10.9		19.2	0.945	−0.076			0.459 ± 0.026
12.4	2390	21.7	0.929	−0.098	32 600	7 160 ± 1500	0.426 ± 0.006
14.9	745	26.2	0.898	−0.141	9 970	2 190 ± 260	0.418 ± 0.007
17.4	398	30.3	0.864	−0.188	5 240	1 150 ± 90	0.364 ± 0.015
19.9	114	34.6	0.823	−0.244	1 470	322 ± 37	0.246 ± 0.013
22.4	57.7	38.7	0.780	−0.303	724	159 ± 18	0.096 ± 0.032
24.9	34.4	43.0	0.731	−0.371	420	92.2 ± 7.4	0.005 ± 0.006
27.4	34.2	47.0	0.682	−0.439	406	89.1 ± 4.9	0.056 ± 0.016
29.9	25.9	51.2	0.627	−0.515	297	65.3 ± 4.1	0.107 ± 0.023
35.0	25.4	59.2	0.512	−0.673	271	59.6 ± 3.9	0.225 ± 0.020
40.0	18.5	66.9	0.392	−0.839	182	40.0 ± 2.9	0.218 ± 0.036
45.0	17.3	74.4	0.269	−1.009	156	34.3 ± 2.4	0.149 ± 0.026
55.5	11.2	89.0	0.017	−1.357	82.4	18.1 ± 1.7	0.092 ± 0.031
60.0	11.8	94.9	−0.085	−1.497	78.8	17.3 ± 1.8	0.066 ± 0.029
68.9		105.7	−0.271	−1.754			−0.076 ± 0.029
69.8	10.4	106.8	−0.289	−1.778	56.0	12.3 ± 1.2	−0.137 ± 0.033
79.9	8.7	117.8	−0.467	−2.024	36.9	8.1 ± 1.0	−0.360 ± 0.028
89.9	11.7	127.6	−0.610	−2.222	38.7	8.5 ± 1.0	−0.220 ± 0.030
99.9	23.1	136.2	−0.722	−2.376	59.7	13.1 ± 1.3	0.071 ± 0.030
109.9	47.7	143.7	−0.806	−2.492	97.5	21.4 ± 1.8	0.217 ± 0.021
119.7	97.3	150.3	−0.869	−2.579	160	35.1 ± 2.9	0.230 ± 0.020
124.8	135.7	153.5	−0.895	−2.614	200	44.0 ± 4.7	0.190 ± 0.044

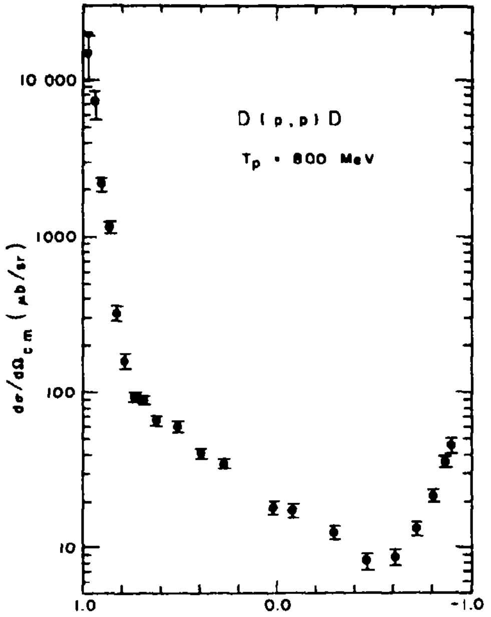

FIG. 2. Differential cross section $\sigma(\theta_{c.m.})$ vs $\cos\theta_{c.m.}$ for $T_p = 800$ MeV.

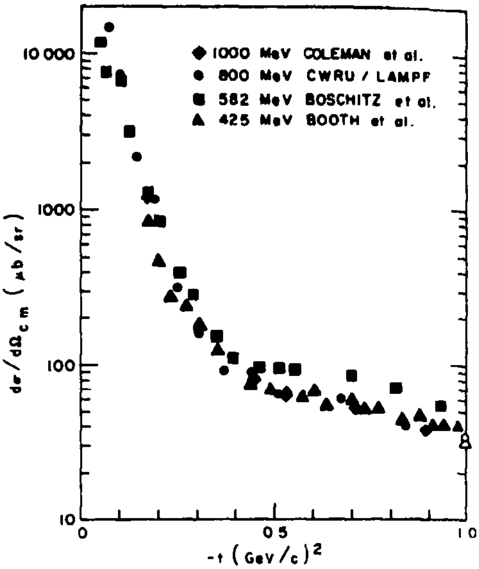

FIG. 3. Comparison of $\sigma(\theta_{c.m.})$ vs $-t$ at forward angles with data of Coleman *et al.* (Ref. 7), Boschitz *et al.* (Ref. 4), and Booth *et al.* (Ref. 3).

The behavior at forward angles is compared in Fig. 3 with other measurements between 400 and 1000 MeV, plotted against the four-momentum transfer squared t (in GeV$^2/c^2$). To the extent that the impulse approximation of Glauber theory[13,14] holds, the dependence on t should be independent of incident proton energy. This is true for $-t < 0.5$ GeV$^2/c^2$, beyond which the data at different energies begin to diverge. The predicted dip at $t \approx -0.4$ is barely perceptible as a shoulder.

For comparison with other measurements between 400 MeV and 2.6 GeV at back angles, the cross section is plotted in Fig. 4 vs $\cos\theta_{c.m.}$. Alder[2] noted that over a wide energy range, for $\cos\theta_{c.m.} < -0.5$, there was an exponential dependence on $\cos\theta_{c.m.}$, which might result from exponential dependence on $t = (\vec{p} - \vec{p}\,')^2 = 2p_{c.m.}^2(\cos\theta_{c.m.} - 1)$. He also noted that the exponential coefficient was s dependent (i.e., varied with incident proton kinetic energy), which could be avoided by plotting vs the Fermi momentum of the nucleon exchanged $|\Delta| = |\vec{d}\,'/2 - \vec{p}|$, although the fit is not as good. Dubal[8] also observed a decrease in s dependence when the backward cross section $\sigma(180°)$ is plotted vs Δ.

Also plotted in Fig. 4 are the neutron-deuteron scattering data of Bonner *et al.*[35] at 794 MeV; the straight line is their fit to an exponential dependence on momentum transfer, indicative of particle exchange. The excellent agreement verifies the absolute normalization of the *nd* scattering data, which in turn support the normalization of the *pd* data of Dubal *et al.*,[8] undermining the justification for introducing N^* con-

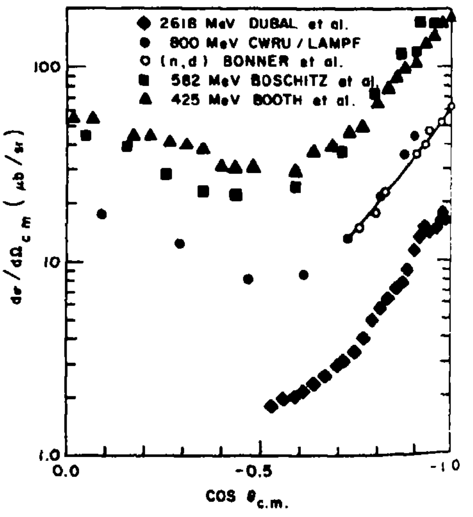

FIG. 4. Comparison of $\sigma(\theta_{c.m.})$ vs $\cos\theta_{c.m.}$ at backward angles with data of Dubal *et al.* (Ref. 8), Boschitz *et al.* (Ref. 4), and Booth *et al.* (Ref. 3) and with *nd* data of Bonner *et al.* (Ref. 35). Line is fitted to *nd* data.

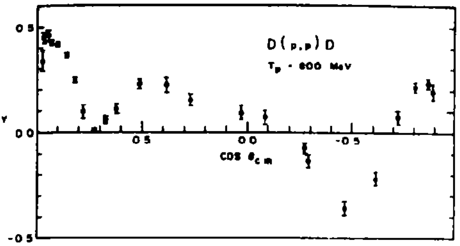

FIG. 5. Analyzing power $A_y(\theta_{c.m.})$ vs $\cos\theta_{c.m.}$ for $T_p = 800$ MeV.

tent in the deuteron. The measurements of Bonner *et al.*[36] of *nd* scattering at 180° raised serious doubts about the validity of the triangular diagram technique of Craigie and Wilkin.[31] The shoulder they observed in the excitation function has been shown[37] to overlap that found at 180° in π^-d scattering when plotted at the same momentum transfer, which implies that neither the triangle diagram nor N^* exchange contributes significantly to Nd scattering at large momentum transfer.

The polarization analyzing power $A_y(\theta_{c.m.})$ is listed in Table I and plotted vs $\cos\theta_{c.m.}$ in Fig. 5. The value fluctuates rapidly between +0.5 and −0.5. The measurements are compared with those at lower energies in Fig. 6, plotted against t to emphasize agreement with the impulse approximation. As expected, there is a strongly positive peak at forward angles, with a maximum value of 0.46 at 18° for the 800 MeV data. A sharp dip occurs at $t = -0.4$ at all energies, much sharper than in the cross section at the same value of t, but not so deep at higher energies. For $-t > 0.5$, the data at different energies diverge considerably, with those at 800 MeV generally more positive.

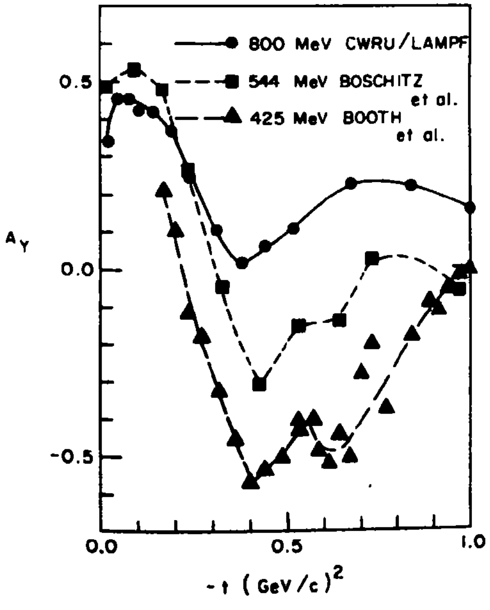

FIG. 6. Comparison of $A_y(\theta_{c.m.})$ vs $-t$ at forward angles with data of Boschitz *et al.* (Ref. 4) and Booth *et al.* (Ref. 3). Lines are to guide the eye.

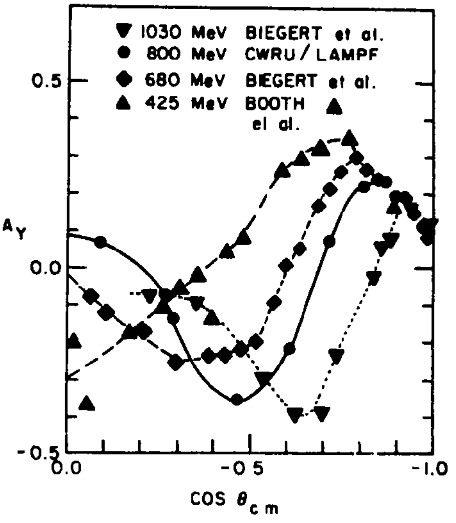

FIG. 7. Comparison of $A_y(\theta_{c.m.})$ vs $\cos\theta_{c.m.}$ at back angles with data of Biegert *et al.* (Ref. 9) and Booth *et al.* (Ref. 3). Lines are to guide the eye.

The back-angle behavior is compared in Fig. 7, plotted vs $\cos\theta_{c.m.}$. At intermediate angles the behavior is strikingly different, but the analyzing power always manages to reach a positive peak with $A_y \simeq 0.3$ before dropping to zero at 180°. There is an apparent tendency for that peak to be crowded more towards backward angles at higher energies, which is exactly opposite what Anderson[10] found below 600 MeV. Curiously enough, A_y seems to have a minimum just at $\cos\theta_{c.m.} = 0.5$, where the cross section also shows a definite break in shape.

The wild fluctuations with angle of the analyzing power for proton-deuteron elastic scattering are in stark contradiction with the always positive, smooth, nearly $\cos^2\theta_{c.m.}$ angular variations of the analyzing power recently measured for the $pp \to d\pi^+$ reaction.[38,39] The latter can be described best with a Legendre polynomial series containing only s-, p-, and d-wave contributions. However, the energy dependence of the polynomial coefficients exhibits the same peaking at 600 MeV as the cross section.[28] The only correspondence between the angular distributions of the analyzing powers for the two reactions is that they are both positive at very backward angles, but that comparison is better below[3] the resonance energy of 600 MeV than at[9] or equally far above (800 MeV).

Gurvitz[30] has recently calculated the analyzing power for *pd* scattering for comparison with the data of Biegert *et al.*[9] at $T_p \geq 1.03$ GeV. *They* find excellent agreement with their model of noneikonal multiple scattering; at very back angles the positive peaking requires the inclusion of neutron pickup. Their calculation yields a form factor for the deuteron which is quite different from that obtained from conventional deuteron wave functions. The results appear consistent with our measurements at 800 MeV, but may not hold at lower energies.

It appears that the analyzing power for *pd* scattering at 800 MeV is best described at large momentum transfer by multiple scattering plus *n* exchange, and the differential cross section no longer justifies considering N^* exchange and the triangle diagram. But it should be noted that the measurements of tensor analyzing power by Igo *et al.*[12] are in disagreement with both models, and it may well be that the calculations suffer from insufficient knowledge of the *NN* amplitudes, which therefore requires measurements of more elastic scattering observables.

ACKNOWLEDGMENTS

The authors are particularly indebted to the injector group of LAMPF, who provided an excellent polarized proton beam, to Dr. Helmut Baer, who participated in the early stages of this experiment, and to the entire staff of LAMPF for their assistance throughout the course of this experiment. We are also grateful to Dr. B. E. Bonner for many helpful suggestions and comments, and to Mrs. M. W. McNaughton for checking the results of the data reduction. This work was supported in part by the Department of Energy.

---

*Present address: Physik Institut der Universität Zürich, 8001 Zürich, Switzerland.

†Present address: Los Alamos Scientific Laboratory, Los Alamos, New Mexico 87545.

‡Present address: National Science Foundation, Washington D. C. 20550.

[1] J. E. Simmons, in *Proceedings of the Sixth International Conference on High Energy Physics and Nuclear Structure*, edited by D. E. Nagle *et al.* (AIP, New York, 1975), p. 103.

[2] J. C. Alder, W. Dollhoff, C. Lunke, C. F. Perdrisat, W. K. Roberts, P. Kitching, G. Moss, W. C. Olsen, and J. R. Priest, Phys. Rev. C 6, 2010 (1972).

[3] N. E. Booth, C. Dolnick, R. J. Esterling, J. Parry, J. Scheid, and D. Sherden, Phys. Rev. D 4, 1261 (1971).

[4] E. T. Boschitz, W. K. Roberts, J. S. Vincent, M. Blecher, K. Gotow, P. C. Gugelot, C. F. Perdrisat, L. W. Swenson, and J. R. Priest, Phys. Rev. C 6, 457 (1972).

[5] M. G. Albrow, M. Borghini, B. Bosnjakovic, F. C. Erné, Y. Kimura, J. P. Lagnaux, J. C. Sens, and F. Udo, Phys. Lett. 35B, 247 (1971).

[6] G. W. Bennett, J. L. Friedes, H. Palevsky, R. J. Sutter, G. J. Igo, W. D. Simpson, G. C. Phillips, R. L. Stearns, and D. M. Corley, Phys. Rev. Lett. 19, 387 (1967).

[7] E. Coleman, R. M. Heinz, O. E. Overseth, and D. E. Pellett, Phys. Rev. Lett. 16, 761 (1966); E. Coleman, R. M. Heinz, O. E. Overseth, and D. E. Pellett, Phys. Rev. 164, 1655 (1967).

[8] L. Dubal, C. K. Hargrove, E. P. Hincks, R. J. McKee, H. Mes, A. C. Thompson, L. Bird, C. H. Halliwell, R. W. Morrison, J. Walters, J. B. McCaslin, and A. R. Smith, Phys. Rev. D 9, 597 (1974).

[9] E. Biegert, J. Carroll, W. Dragoset, Jr., R. Klem, J. Lesikar, M. L. Marshak, J. McClelland, T. Mulera, E. A. Peterson, J. B. Roberts, K. Ruddick, R. Talaga, and A. Wriekat, Phys. Rev. Lett. 41, 1098 (1978).

[10] A. N. Anderson, J. M. Cameron, D. A. Hutcheon, J. Källne, B. K. S. Koene, B. T. Murdoch, W. T. H. van Oers, and A. W. Stetz, Phys. Rev. Lett. 40, 1553 (1978).

[11] G. Bunce, O. E. Overseth, J. Walker, H. Halpern, R. Handler, L. Pondrom, and S. Olsen, Phys. Rev. Lett. 28, 120 (1972).

[12] G. J. Igo, M. Bleszynski, J. B. Carroll, A. Sagle, C. L. Morris, R. Klem, T. Joyce, Y. Makdisi, M. Marshak, B. Mossberg, E. A. Peterson, K. Ruddick, and J. Whittaker, Phys. Rev. Lett. 43, 425 (1979).

[13] R. J. Glauber, in *Lectures in Theoretical Physics*, edited by W. E. Britten *et al.* (Interscience, New York, 1959), Vol. 1, p. 315.

[14] V. Franco and R. J. Glauber, Phys. Rev. 142, 1195 (1966); V. Franco, Phys. Rev. Lett. 16, 944 (1966); V. Franco and E. Coleman, *ibid.* 17, 827 (1966); V. Franco and R. J. Glauber, *ibid.* 22, 370 (1969).

[15] M. L. Goldberger and K. M. Watson, *Collision Theory* (Wiley, New York, 1964).

[16] H. B. Willard, B. D. Anderson, H. W. Baer, R. J. Barrett, P. R. Bevington, A. N. Anderson, H. Willmes, and N. Jarmie, Phys. Rev. C 14, 1545 (1976).

[17] J. E. Simmons, private communication.

[18] V. M. Kolybasov and N. Ya. Smordismkaya, Yad. Fiz. 17, 1211 (1973) [Sov. J. Nucl. Phys. 17, 630 (1973)].

[19] A. K. Kerman and L. S. Kisslinger, Phys. Rev. 180, 1483 (1969).

[20] J. S. Vincent, W. K. Roberts, E. T. Boschitz, L. S.

Kisslinger, K. Gotow, P. C. Gugelot, C. F. Perdrisat, L. W. Swenson, and J. R. Priest, Phys. Rev. Lett. 24, 236 (1970).

[21] N. S. Craigie and C. Wilkin, Nucl. Phys. B14, 477 (1969).

[22] T. Yao, Phys. Rev. 134, B454 (1964).

[23] G. W. Barry, Ann. Phys. 73, 482 (1972).

[24] J. V. Noble and H. J. Weber, Phys. Lett. 50B, 233 (1974).

[25] E. A. Remler and R. A. Miller, Ann. Phys. (N.Y.) 82, 189 (1974).

[26] S. A. Gurvitz and S. A. Rinat, Phys. Lett. 60B, 405 (1976).

[27] C. L. Dolnick, Nucl. Phys. B22, 461 (1970).

[28] M. G. Albrow, S. Andersson-Almehed, B. Bošnjaković, F. C. Erné, Y. Kimura, J. P. Lagnaux, J. C. Sens, and F. Udo, Phys. Lett. 34B, 337 (1971).

[29] R. Joseph, F. Cverna, H. Willard, M. McNaughton, E. Winkelmann, C. Hwang, B. Bonner, and N. King, Bull. Am. Phys. Soc. 24, 688 (1979); F. Cverna, M. McNaughton, C. Hwang, B. Bonner, N. King, H Willard, E. Winkelmann, and R. Joseph, in the Proceedings of the Second Conference on Meson-Nuclear Physics, 1979, Houston, Texas (to be published), p. 64.

[30] P. R. Bevington, M. W. McNaughton, H. B. Willard, H. W. Baer, E. Winkelmann, F. Cverna, E. P. Chamberlin, N. S. P. King, R. R. Stevens, H. Willmes, and M. A. Schardt, Phys. Rev. Lett. 41, 384 (1978).

[31] R. J. Barrett, B. D. Anderson, H. B. Willard, A. N. Anderson, and N. Jarmie, Nucl. Instrum. Methods 129, 441 (1975).

[32] M. W. McNaughton *et al* , unpublished; E. P. Chamberlin *et al*., Bull. Am. Phys. Soc. 23, 540 (1978).

[33] P. R. Bevington, R. J. Barrett, B. D. Anderson, F. H. Cverna, and A. N. Anderson, Nucl. Instrum. Methods 129, 373 (1975).

[34] P. R. Bevington and R. A. Leskovec, Nucl. Instrum. Methods 147, 431 (1977).

[35] B. E. Bonner, J. E. Simmons, M. L. Evans, G. Glass, J. C. Hiebert, Mahavir Jain, L. C. Northcliffe, C. W. Bjork, P. J. Riley, and C. G. Cassapakis, Phys. Rev. C 17, 671 (1978).

[36] B. E. Bonner, C. L. Hollas, C. R. Newson, P. J. Riley, and G. Glass, Phys. Rev. Lett. 39, 1253 (1977).

[37] E. Myrher and B. E Bonner, private communication.

[38] S. A. Gurvitz, Phys. Lett. 85B, 5 (1979).

PHYSICAL REVIEW C VOLUME 21, NUMBER 6 JUNE 1980

Off-shell rescattering effects in the reaction $\pi^- + d \rightarrow 2n + \gamma$

G. F. de Téramond, J. Páez, and C. W. Soto Vargas
Escuela de Física, Universidad de Costa Rica, San José, Costa Rica

(Received 30 November 1979)

We have reexamined the multiple scattering corrections to the reaction $\pi^- + d \rightarrow 2n + \gamma$ in order to extend the validity of previous calculations to a larger neutron-neutron relative momentum interval and to determine the effective range parameter. This extension has been carried out analytically by studying the off-shell properties and energy dependence of the pion-nucleon amplitude. The sensitivity of the photon spectral curves for various approximations is shown, and the importance of the different effects in the values of the neutron-neutron scattering length and effective range is indicated.

[NUCLEAR REACTIONS $\pi^- + d \rightarrow 2n + \gamma$, analytical treatment of multiple scattering. Off-shell extension of pion-nucleon amplitude.]

I. INTRODUCTION

In view of the recent experimental study of the reaction

$$\pi^- + d \rightarrow 2n + \gamma \qquad (1)$$

by the Lausanne-Munich-Zurich (LMZ) group,[1] prompted by the utilization of meson factories and improved detection techniques to determine the $^1S_0$ neutron-neutron scattering length a_{nn} as a test of the charge symmetry of the nuclear forces, it appears of interest to examine some approximations considered in different theoretical models used to analyze the data; in particular, the off-shell nature and energy dependence of the pion-nucleon amplitude which has not been included in previous theoretical analysis of reaction (1).[2-5] The effect of final-state interactions between the outgoing neutrons has been discussed in the frame of potential theory[4] and also in a model-independent way using dispersion relations.[2,5]

Bander[2] has calculated multiple scattering corrections where the pion collides elastically with a nucleon before being absorbed radiatively by the second nucleon, as well as elastic proton-neutron intermediate-state interactions and corrections to the impulse approximation. His calculation showed that the dominant correction came from first order pion-nucleon rescattering processes. Shklyarevskii later confirmed that the sum of an infinite series of diagrams which take into account multiple scattering corrections has a negligible effect on the first order calculation.[3] These calculations describe the πN scattering by a constant amplitude (effectively the scattering length). Although these calculations showed small rescattering effects on the normalized energy spectrum, mainly because they considered only S-wave contributions to the final n-n scattering state, there is a substantial difference in the spectrum at large relative n-n momenta when higher n-n partial waves are included. The effect of the rescattering is to modify the S-wave amplitude relative to higher waves.

One of the reasons for reexamining the rescattering problem is to extend the validity of the theory to higher neutron-neutron relative momenta in order to determine the presently unknown effective range parameter r_{nn} using the very high statistics photon spectrum measured at SIN by the LMZ group.[1] Experimental results are sensitive to the extracted value of r_{nn} depending on how the rescattering effects are treated. In the present work we are concerned primarily with the analytical treatment of initial state interactions. We have studied the dependence of the spectral shapes on the off-shell extension of the πN amplitude, and a closed-form solution for the rescattering corrections is obtained.

II. THE RESCATTERING AMPLITUDE

The diagrams of the relevant processes to be discussed in reference to reaction (1) are depicted in Fig. 1, corresponding to the dominant process [Fig. 1(a)], pion rescattering [Fig. 1(b)], and proton-neutron intermediate-state rescattering [Fig. 1(c)]. The contribution of the third diagram is of order m_π/m_N with respect to the rescattering correction shown in the second diagram.[2-3] In Fig. 1(b) we neglect the charge exchange process described by the amplitude $T(\pi^- p \rightarrow n\pi^0)\ T(n\pi^0 \rightarrow n\gamma)$ since to leading orders the photoproduction of π^0 vanishes at threshold energies.[6] The important rescattering contribution left is given by the elastic pion-neutron and the inverse charged pion photoproduction amplitudes via the process $T(\pi^- n \rightarrow \pi^- n)T(\pi^- p \rightarrow n\gamma)$. Other impulse approximation corrections consid-

© 1980 The American Physical Society

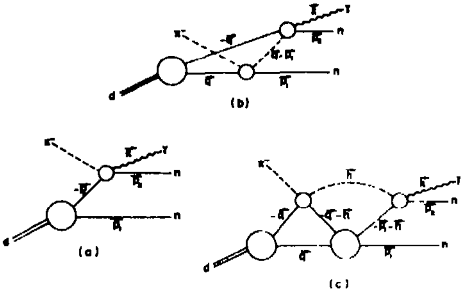

FIG. 1. Diagrams for the reaction $\pi^- + d \to 2n + \gamma$: (a) dominant contribution, (b) pion rescattering, and (c) proton-neutron rescattering.

ered by Bander are of order m_π/m_N relative to the rescattering term. If the terms of order m_π/m_N with respect to the rescattering correction are neglected, we are then able to calculate analytically the rescattering contribution to the spectrum.

We will follow the notation used by one of us, Ref. 5, henceforth referred to as I. In particular, the structure of the deuteron is described by the analytical wave function given in the latter reference and the spin structure of the transition matrix is displayed by the rotational invariants listed in the same reference.

In the impulse approximation, the transition matrix element corresponding to Figs. 1(a) and 1(b) is given by

$$T = T_{\pi\gamma}(\vec{p}_2, -\vec{p}_1)\phi_d(-\vec{p}_1) + \int \frac{T_{\pi\gamma}(\vec{p}_2, -\vec{q})\phi_d(-\vec{q})T_{\pi N}(\vec{p}_1, \vec{q})}{(\vec{q}^2 - \vec{p}_1^{\,2})/2m_N - (\vec{q} - \vec{p}_1)^2/2m_\pi + i\epsilon} \frac{d^3q}{(2\pi)^3} . \tag{2}$$

The form of the deuteron wave function is

$$\phi_d(\vec{q}) = (2\pi)^{3/2} N\chi^* \left[u(q)\vec{\sigma}\cdot\vec{\eta} + \frac{\rho}{\sqrt{2}} w(q) \times \left(\frac{3(\vec{\sigma}\cdot\vec{q})(\vec{\eta}\cdot\vec{q})}{q^2} - \vec{\sigma}\cdot\vec{\eta}\right)\right] i\sigma_2\chi^* , \tag{3}$$

where the S and D momentum space wave functions are

$$u(q) = \sum_\lambda \frac{C_\lambda}{q^2 + \gamma_\lambda^2} , \tag{4}$$

$$w(q) = \frac{q^2}{\gamma^2} \sum_\lambda \frac{C_\lambda}{q^2 + \gamma_\lambda^2} , \tag{5}$$

and ρ is the asymptotic D to S ratio. We have utilized the parametrizations of γ_λ and C_λ given in I. The amplitude $T_{\pi\gamma}$ is the threshold pion photoproduction transition matrix

$$T_{\pi\gamma} \sim \vec{\sigma}\cdot\vec{\epsilon} , \tag{6}$$

and $T_{\pi N}$ is the pion-nucleon amplitude to be discussed in the next section. In the above expressions $\vec{\epsilon}$ and $\vec{\eta}$ are, respectively, the photon and deuteron polarization vectors.

Since the pion capture is at rest, it is justifiable to use nonrelativistic kinematics. The relative momenta before and after the collision in the π-N center-of-mass system are given in terms of the relative N-N momentum $\vec{q}$ in the intermediate N-N center-of-mass system by

$$\vec{q}_i = -\frac{m_\pi \vec{q}}{m_\pi + m_N} \tag{7}$$

and

$$\vec{q}_f = \frac{m_N(\vec{q} - \vec{p}_1) - m_\pi \vec{p}_1}{m_\pi + m_N} ; \tag{8}$$

thus neglecting corrections of order m_π/m_N the rescattering term T^R reduces to the simple form

$$T^R = -(\vec{\sigma}\cdot\vec{\epsilon})(\vec{\sigma}\cdot\vec{\eta}) \int \frac{u(q)\langle \vec{q} - \vec{p}_1 | T_{\pi N} | \vec{0} \rangle}{(\vec{q} - \vec{p}_1)^2/2m_\pi - i\epsilon} \frac{d^3q}{(2\pi)^3} , \tag{9}$$

where we have not included the D state of the deuteron, this being a small contribution.

III. THE PION-NUCLEON AMPLITUDE

In view of the strong enhancement in the ${}^1S_0$ partial wave due to the final-state interaction, we limit our rescattering calculation to the processes that lead to the ${}^1S_0$ final state. Under this consideration we are left with the S_{31} channel for the πN amplitude. Thomas[7] has introduced a separable potential which reproduces the πN data up to 300 MeV, and has the following form:

$$v(q) = \frac{A}{q^2 + a^2} + \frac{B}{q^2 + b^2} , \tag{10}$$

where the adjustable parameters A, B, a, and b are respectively, 28.228, -1.136, 4.4575, and 1.2584 (in fm^{-1}). Our values differ from those given by Thomas because we use different conventions and nonrelativistic kinematics when fitting the data.

In the πN center-of-mass system, the expression for the half-on-shell amplitude in each partial wave is given by[8]

$$\langle q' | T_{\pi N}(q^2) | q \rangle = v(q')v(q)/D(q^2) , \tag{11}$$

where

$$D(q^2) = 1 + \sigma\frac{2\mu}{\pi} \int_0^\infty \frac{dq'^2 q' v^2(q')}{q'^2 - q^2 - i\epsilon} , \tag{12}$$

μ being the reduced mass of the pion-nucleon system and $\sigma = \pm 1$ depending on the attractive (-1) or repulsive (+1) character of the interaction (+1 for the S_{31} channel).

A useful relation follows from (11) when the amplitude is taken on-shell,

$$D(q^2)e^{i\delta(q)}\sin\delta(q) = -2\mu q v^2(q)\ , \tag{13}$$

and taking the real and imaginary part of (12),[8] we obtain

$$\tan\delta(q) = -\frac{2\mu q v^2(q)}{1+2\mu G(p)}\ , \tag{14}$$

where $G(q)$ is the principal value integral

$$G(q) = \frac{1}{\pi} P\int_0^\infty \frac{dq'^2 q' v^2(q')}{q'^2 - q^2}\ . \tag{15}$$

The pion-nucleon scattering length is obtained from the above expressions in the limit $q \to 0$,

$$a_{\pi n} = -\frac{2\mu v^2(0)}{D(0)}\ , \tag{16}$$

and has the value $a_{\pi n} = -0.096/m_\pi$.

For the separable potential given in Eq. (10), $G(q)$ is calculated analytically and has the following form:

$$G(q) = \frac{A^2}{2a}\frac{(a^2-q^2)}{(q^2+a^2)^2} + \frac{B^2}{2b}\frac{(b^2-q^2)}{(q^2+b^2)^2} + \frac{2AB}{a^2-b^2}\left(\frac{b}{q^2+b^2} - \frac{a}{q^2+a^2}\right)\ . \tag{17}$$

Expanding the pion-nucleon amplitude in partial waves and retaining only the S_{31} channel amplitude (11), we obtain after integration over the angular variables

$$T^R = (\vec\sigma\cdot\vec\epsilon)(\vec\sigma\cdot\vec\eta)a_{\pi n}\sum_\lambda C_\lambda\Bigg[I(q_-,\gamma_\lambda,0) - \frac{1}{A/a^2+B/b^2} \times\left(\frac{A}{a^2}I(q_-,\gamma_\lambda,a) + \frac{B}{b^2}I(q_-,\gamma_\lambda,b)\right)\Bigg]\ , \tag{18}$$

where

$$\begin{aligned} I(q,\gamma,\kappa) &= \frac{1}{2\pi q}\int_0^\infty \frac{q'\,dq'}{q'^2+\gamma^2}\ln\left[\frac{(q'+q)^2+\kappa^2}{(q'-q)^2+\kappa^2}\right] \\ &= I(q,\gamma+\kappa,0) \\ &= \frac{1}{q}\tan^{-1}\left(\frac{q}{\gamma+\kappa}\right) \end{aligned} \tag{19}$$

and

$$\vec q_+ = \vec p + \tfrac{1}{2}\vec k = \vec p_1,\quad \vec q_- = \vec p - \tfrac{1}{2}\vec k = -\vec p_2\ .$$

The relative n-n momentum is $\vec p = \frac{1}{2}(\vec p_1 - \vec p_2)$ and $\vec k$ is the photon momentum. In the above expressions we have substituted the deuteron wave function (4) and the expression for $a_{\pi n}$ (16). To take into account the Pauli exclusion principle for the two final neutrons, we further decompose Eq. (18) into the rotational invariants defined in Table I of I, thus obtaining

$$f^R_{1,7} = 4\pi a_{\pi n}\sum_\lambda C_\lambda\Bigg[I(q_-,\gamma_\lambda,0) \pm I(q_+,\gamma_\lambda,0) - \frac{1}{A/a^2+B/b^2} \times\left(\frac{A}{a^2}[I(q_-,\gamma_\lambda,a) \pm I(q_+,\gamma_\lambda,a)] + \frac{B}{b^2}[I(q_-,\gamma_\lambda,b) \pm I(q_+,\gamma_\lambda,b)]\right)\Bigg]\ , \tag{20}$$

where the amplitudes f^R_i are scalar functions of the kinematic variables as defined in Eq. (2.3) of I.

In the zero range limit ($a, b \to \infty$), the above expressions reduce to

$$f^R_{1,7} = 4\pi a_{\pi n}\sum_\lambda C_\lambda\left(\frac{1}{q_-}\tan^{-1}\frac{q_-}{\gamma_\lambda} \pm \frac{1}{q_+}\tan^{-1}\frac{q_+}{\gamma_\lambda}\right)\ , \tag{21}$$

which correspond to the on-shell constant πN amplitude rescattering corrections.[2,9] It should be noted however, that we obtain a different sign with respect to Bander's calculation.[2]

IV. FINAL-STATE INTERACTIONS

The final-state interactions (FSI) are described in a model independent way by studying the analytical structure of the rescattering amplitude in the complex p plane, appearing in the dispersion integrals at fixed photon energy k as treated in I.

The final-state enhancement to a given partial wave amplitude $T_l(p,k)$ is given by the Muskhelishvili-Omnès equation[10]

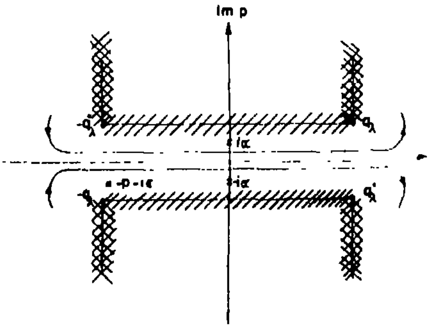

FIG. 2. The analytic properties of the rescattering amplitude in the complex plane, $q_\lambda = \frac{1}{2}k + i\gamma_\lambda$.

$$T_l^{\mathrm{FSI}}(p,k)=T_l(p,k)+\frac{1}{f_l(-p)}\,\frac{1}{\pi}\int_{-\infty}^{\infty}\frac{T_l(p',k)\,\mathrm{Im}f_l(p')}{p'+p+i\epsilon}\,dp', \tag{22}$$

where $f_l(p)$ is the Jost function,[11] and p is the relative momentum of the two outgoing neutrons. For the ${}^1S_0$ final state

$$f_0(p)=\frac{p-i\beta}{p-i\alpha}, \tag{23}$$

with

$$a_{nn}=\frac{\alpha-\beta}{\alpha\beta},\quad r_{nn}=\frac{2}{\alpha-\beta}.$$

We take the S-wave projection of the rescattering amplitude (20), thus obtaining

$$T_0^R(p,k)=\frac{16\pi}{kp}\,a_{\pi n}\sum_\lambda C_\lambda\left[S_R(\gamma_\lambda,p,\tfrac{1}{2}k)-\frac{1}{A/a^2+B/b^2}\left(\frac{A}{a^2}S_R(\gamma_\lambda+a,p,\tfrac{1}{2}k)+\frac{B}{b^2}S_R(\gamma_\lambda+b,p,\tfrac{1}{2}k)\right)\right] \tag{24}$$

where

$$S_R(\gamma,p,q)=\frac{1}{2}\left[(p+q)\tan^{-1}\left(\frac{p+q}{\gamma}\right)-(p-q)\tan^{-1}\left(\frac{p-q}{\gamma}\right)\right]-\frac{1}{4}\gamma\ln\frac{\gamma^2+(p+q)^2}{\gamma^2+(p-q)^2}. \tag{25}$$

In the complex p plane, Eq. (24) presents for each term branch points at $\pm\frac{1}{2}k\pm i\gamma_\lambda$ and $\pm\frac{1}{2}k+i\infty$. We separate the integrand appearing in Eq. (22) in order to avoid the branch cuts as indicated in Fig. 2. The result is the following:

$$\begin{aligned}T_0^{\mathrm{FSI}\,(R)}=\frac{16\pi}{kp}\,e^{i\delta_0}\sin\delta_0\sum_\lambda C_\lambda\Bigg\{&C_R(\gamma_\lambda,\gamma_\lambda,p,\tfrac{1}{2}k)\\&-\frac{1}{A/a^2+B/b^2}\left(\frac{A}{a^2}C_R(\gamma_\lambda+a,\gamma_\lambda+a,p,\tfrac{1}{2}k)+\frac{B}{b^2}C_R(\gamma_\lambda+b,\gamma_\lambda+b,p,\tfrac{1}{2}k)\right)\\&+\cot\delta_0\left[S_R(\gamma_\lambda,p,\tfrac{1}{2}k)-\frac{1}{A/a^2+B/b^2}\left(\frac{A}{a^2}S_R(\gamma_\lambda+a,p,\tfrac{1}{2}k)+\frac{B}{b^2}S_R(\gamma_\lambda+b,p,\tfrac{1}{2}k)\right)\right]\\&-C_R(\gamma_\lambda,\gamma_\lambda+\alpha,0,\tfrac{1}{2}k)+\frac{1}{A/a^2+B/b^2}\Bigg(\frac{A}{a^2}C_R(\gamma_\lambda+a,\gamma_\lambda+a+\alpha,0,\tfrac{1}{2}k)\\&\qquad+\frac{B}{b^2}C_R(\gamma_\lambda+b,\gamma_\lambda+b+\alpha,0,\tfrac{1}{2}k)\Bigg)\\&+\alpha\tan^{-1}\left(\frac{\frac{1}{2}k}{\gamma_\lambda+\alpha}\right)-\frac{\alpha}{A/a^2+B/b^2}\left[\frac{A}{a^2}\tan^{-1}\left(\frac{\frac{1}{2}k}{\gamma_\lambda+a+\alpha}\right)+\frac{B}{b^2}\tan^{-1}\left(\frac{\frac{1}{2}k}{\gamma_\lambda+b+\alpha}\right)\right]\Bigg\},\end{aligned} \tag{26}$$

where

$$C_R(\sigma,\gamma,p,q)=-\tfrac{1}{4}\{(p+q)\ln[\gamma^2+(p+q)^2]-(p-q)\ln[\gamma^2+(p-q)^2]\}-\sigma C(\gamma,p,q), \tag{27a}$$

with

$$C(\gamma,p,q)=\frac{1}{2}\left[\tan^{-1}\left(\frac{2\gamma q}{\gamma^2+p^2-q^2}\right)+\epsilon\pi\right]. \tag{27b}$$

In the above expression

$\epsilon=0$ if $\gamma^2+p^2-q^2\geq 0$,

$\epsilon=1$ if $\gamma^2+p^2-q^2<0$.

We have not included the ${}^3P$-wave enhancement since this effect has been shown to be very small.[4]

V. RESULTS AND CONCLUSIONS

We have reexamined the existing rescattering calculations of reaction (1) and extended the validity of such analysis to large n-n relative momenta, by including the off-shell and energy dependence of the πN amplitude. The analytical formalism developed in this paper allows us to

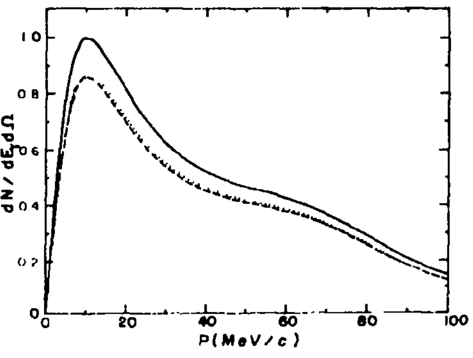

FIG. 3. Photon energy spectra as a function of the relative n-n momentum p for $a_{nn} = -18$ fm and $r_{nn} = 2.8$ fm; —— without rescattering, — — constant πN amplitude, ···· including off-shell effects.

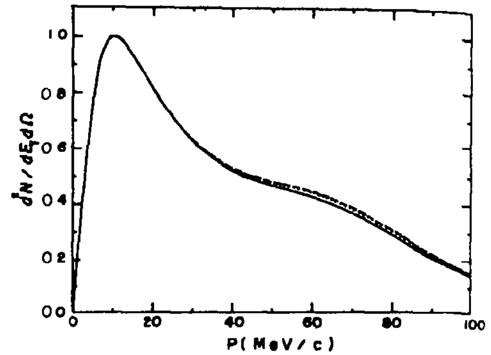

FIG. 4. Normalized photon spectra (curves same as in Fig. 3).

examine in a very simple and concise form the sensitivity of the photon spectrum to the different contributions, such as the n-n phase shifts, the deuteron wave function, and πN parameters. This is particularly useful in the analysis of the experimental data since it avoids extensive numerical work.

The effect of final-state interactions and different deuteron wave functions were included in I and are discussed extensively in a recent work.[12] It should be noted that in this paper we are not concerned with final-state interactions and they are treated here in a model independent way.

The effects of pion-nucleon rescattering are shown in Figs. 3 and 4. The different photon spectra in these figures correspond to the calculation without rescattering, with a constant πN amplitude, and lastly including the off-shell effects. In Fig. 4 the spectra has been normalized. We notice that the constant amplitude rescattering gives essentially the correct results. The error in the scattering length a_{nn} without including rescattering can be as large as 1 fm at n-n relative momenta of the order of 80 MeV/c, whereas the constant amplitude rescattering reduces this error to 0.2 fm (these two errors evaluated with respect to the rescattering calculation which includes off-shell effects). The corresponding errors in the effective range r_{nn} are 0.3 fm without rescattering and 0.05 fm with a constant πN amplitude.

We hope that the analytical treatment described here will be useful in the study of nonradiative pion capture reactions such as $\pi + d \to N + N$, where the impulse approximation is no longer valid and the off-shell rescattering contributions can be important.[13,14]

ACKNOWLEDGMENTS

We wish to thank Dr. B. Gabioud for his continued interest and collaboration. This work was supported in part by CONICIT, Costa Rica.

---

[1] B. Gabioud *et al.*, Phys. Rev. Lett. 42, 1508 (1979).

[2] M. Bander, Phys. Rev. 134, B1052 (1964).

[3] G. M. Shklyarevskii, Yad. Fiz. 16, 1270 (1972 [Sov. J. Nucl. Phys. 16, 700 (1973)].

[4] W. R. Gibbs, B. F. Gibson, and G. J. Stephenson, Jr., Phys. Rev. C 11, 90 (1975).

[5] G. F. de Téramond, Phys. Rev. C 16, 1976 (1977). Because of a different normalization, the amplitudes f_l defined in Eq. (2.11) of this reference should be multiplied by a factor 4π.

[6] N. M. Kroll and M. A. Ruderman, Phys. Rev. 93, 233 (1954).

[7] A. W. Thomas, Nucl. Phys. A258, 417 (1976).

[8] F. Tabakin, Phys. Rev. 177, 1433 (1969).

[9] G. F. de Téramond, Thèse d'Etat, University of Paris, 1977 (unpublished).

[10] J. Gillespie, *Final-State Interactions* (Holden-Day, San Francisco, 1964).

[11] R. G. Newton, J. Math. Phys. 1, 319 (1960).

[12] B. Gabioud, Thèse d'Etat, University of Lausanne, 1979 (unpublished).

[13] F. Hachenberg, J. Hüfner, and H. J. Pirner, Phys. Lett 66B, 425 (1977).

[14] G. F. Bertsch and D. O. Riska, Phys. Rev. C 18, 317 (1978).

PHYSICAL REVIEW C VOLUME 21, NUMBER 6 JUNE 1980

Decay of ^{180}Re: Search for octupole states in ^{180}W

L. G. Mann, J. B. Carlson, R. G. Lanier, G. L. Struble, W. M. Buckley, R. K. Sheline,* and Z. Singh†
Nuclear Chemistry Division, Lawrence Livermore Laboratory, Livermore, California 94550

(Received 2 January 1980)

Study of the decay of 2.45-min ^{180}Re leads to the observation of about 90 γ rays and a number of new levels in ^{180}W. Spins and parities of many of the levels observed are determined using the logft values of positron population and/or the γ-ray depopulation. The allowed unhindered decay from the $(\pi 5/2^+[402\uparrow]\text{-}\nu 7/2^-[514\downarrow])_{1-}$ ^{180}Re ground state indicates fragmentation of the $(\pi 5/2^+[402\uparrow]\text{-}\pi 9/2^-[514\uparrow])_2$ configuration among a number of 2 states in ^{180}W. We find tentative observation of the $K = 1^-$ and 0^- components of the octupole vibration. This would establish the excitation energy of all four expected octupole components in ^{180}W.

[RADIOACTIVITY ^{180}Re [from ^{182}W(p, $3n$), natural targets]; measured E_γ, I_γ, γ-γ coinc.; deduced logft; ^{108}W deduced levels E, J, π.]

I. INTRODUCTION

In a study of the high-spin states in ^{180}W from the ^{181}Ta(p, $2n\gamma$)^{180}W reaction,[1] we observed both the $K^\pi = 2^-$ and 3^- components of the octupole vibration. However, no evidence was found for the $K^\pi = 0^-$ and 1^- components. Goudsmit *et al.*[2] have shown that the ground state of the 2.45-min positron/electron-capturing ^{180}Re activity must have the configuration $(\pi 5/2^+[402\uparrow] - \nu 7/2^-[514\downarrow])_{1-}$ because of its superallowed decay into the $K^\pi = 2^-$ octupole band with an appreciable component of the configuration $(\pi 5/2^+[402\uparrow] - \pi 9/2^-[514\uparrow])_{2-}$. This proton configuration also strongly influences the β decay, with log$ft = 5.0$, to a level of 1832 keV, and it might be expected to influence the β decay to other 2^- levels. Although Goudsmit *et al.*[2] failed to identify the $K^\pi = 0^-$ and 1^- octupole components, the large β decay Q value of 3828 keV suggests that they might be populated from the ^{180}Re decay. Identification of these components would allow a study of the interactions among all four of the octupole bands and a comparison with the study of Neergård and Vogel,[3] who have predicted the detailed properties based on microscopic calculations. With these purposes in mind, we have reinvestigated the decay of ^{180}Re.

II. EXPERIMENTS

Single detector γ-ray spectra were accumulated using a 15% coaxial Ge(Li) detector and a low-energy photon (LEP) pure Ge detector. Gamma-gamma coincidence spectra were also obtained using two 10% coaxial Ge(Li) detectors. Three-parameter coincidence data (E, E, t) were stored event by event on magnetic tape. Absorbers of 0.22-g/cm^2 Cd and 0.48-g/cm^2 Cu were used with the coaxial detectors to reduce the low-energy counting rates. Energy resolution was 2.0 to 2.5 keV full width at half-maximum (FWHM) at 900 keV for the coaxial detectors and 550 eV at 100 keV for the LEP detector.

Sources of ^{180}Re were produced by the ^{182}W(p, $3n$)^{180}Re reaction using 27-MeV protons from the Livermore cyclograaff. Target foils were natural W metal of 102 mg/cm^2 (coaxial detectors) or 51 mg/cm^2 (LEP detector). The sources were hand carried from their irradiation position in the external beam to the γ-ray spectroscopy detectors located outside the irradiation area. Longer-lived background activities were almost entirely due to other Re isotopes. These activities were held to a minimum in the single detector γ-ray spectrum measurements by using a new W foil for each irradiation. (About 40 sources were used in accumulating the singles spectrum.) Under these conditions, background activities in percent of the ^{180}Re activity at the start of data accumulation were as follows: 19-h ^{181}Re, 0.3%; ^{182}Re, 0.15% (mostly 12.7 h); 38-d ^{184}Re, 0.02%.

In the singles γ-ray spectrum experiments, two 4096-channel spectra, separated in time by 2.5 to 3.3 min, were accumulated for each source. The computer code GAMANAL[4] was used for analysis of the spectra. Gamma rays which exhibited the proper 2.45-min decay in these spectra were assigned to ^{180}Re decay. Our data are most consistent with a half-life of 2.38 min for ^{180}Re, in good agreement with previously published values.[5]

Only one spectrum was accumulated in the coincidence experiment. A 180° detector geometry was used, with the detectors separated by ~5 mm of Pb shielding, and with the sources axially located in a 5-mm diameter hole in the shield.

The spectra in coincidence with 50 γ-ray energy gates were generated by off-line sorting of the event-mode data; coincidences due to chance and to the Compton continuum underlying the γ-ray peaks were subtracted during the sorting process.

Energy calibrations were based on the ^{180}W γ rays of 233.98, 744.78, 902.84, 1006.41, 1117.24, and 1129.09 keV which were measured in the ^{181}Ta(p, $2n\gamma$) experiments,[1] and which are prominent in the ^{180}Re decay spectrum. We used standard γ-ray sources of ^{56}Co, ^{133}Ba, ^{152}Eu, and ^{182}Ta for energy nonlinearity and efficiency calibrations.

III. RESULTS

The γ-ray spectra obtained during the first count are shown in Fig. 1. The lines at 365.5 keV and at 1121.4, 1189.2, 1221.5, and 1231.1 keV are impurities from ^{181}Re and ^{182}Re, respectively. Spectra in coincidence with the 2^+-0^+ transition (103.6 keV) in the ground-state band, the 902.8-keV γ ray that depopulates the octupole $K^\pi = 2^-$ level at 1006.4 keV, and the 1013.7- and 1117.3-keV γ rays that depopulate the $K^\pi = 2^+$ level at 1117.2 keV, are shown in Fig. 2. Table I summarizes the data and shows for comparison (on an independent intensity scale) the γ-ray intensities reported by Goudsmit *et al.*[2]

Using the energy and coincidence data in Table I together with existing information about the ^{180}W levels,[1] we have constructed the decay scheme shown in Fig. 3 for ^{180}W levels populated by ^{180}Re decay. The strongly populated level at 1831.71 keV was established in the early studies[3] of ^{180}Re decay. None of the other levels above 1233 keV have been reported previously.

The three states at 1587.25, 1632.90, and 1814.9 keV are the only states we find in the region between 1.0 and 2.0 MeV that could possibly belong to the $K^\pi = 0^-$ or $K^\pi = 1^-$ octupole bands. Although they are only weakly populated in the ^{180}Re decay, these levels are quite firmly established by our γ-ray energy and coincidence data. The 1632.90-keV state cannot be the same level as the one observed at 1634.56 keV and interpreted as $K^\pi = 3^-$ in the ^{181}Ta(p, $2n\gamma$)^{180}W study[1] because the decay modes are entirely different.

There is evidence that all three of these states were populated in the ^{181}Ta(p, $2n\gamma$)^{180}W reaction.[1] The 1483.6-, 1529.8-, and possibly the 1786.4-keV γ rays reported in Ref. 1 agree in energy with γ rays which depopulate the levels at 1587, 1633, and 1815 keV, respectively. Also, the 808.9-keV γ ray which depopulates the 1815-keV level appeared in coincidence with the 902.8-keV γ ray. These data indicate that the populations of the three levels in the ^{181}Ta(p, $2n\gamma$) reaction were as follows, relative to the population of the $K^\pi = 2^-$ band head at 1006 keV: 4% (1587-keV level), 3% (1633-keV level), and 4% (1815-keV

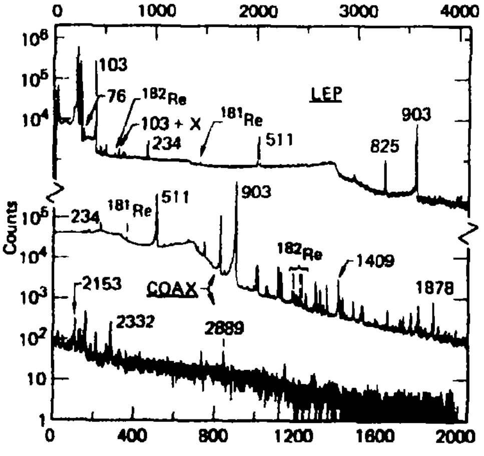

FIG. 1. Gamma-ray spectra obtained with a pure Ge (LEP) detector (top scale) and a coaxial Ge (Li) detector (bottom scale, 0–4096 channels overlapped). Energy calibrations are approximately 0.25 keV/channel (LEP) and 1.00 keV/channel (coax).

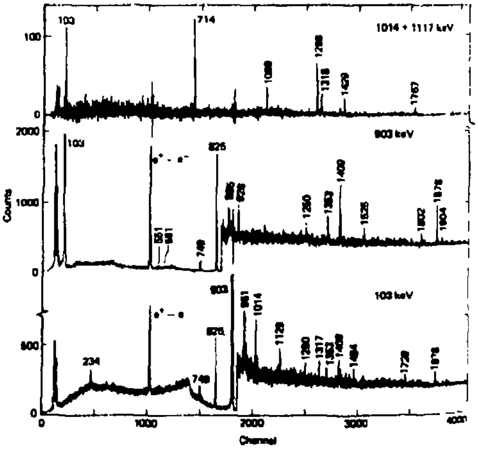

FIG. 2. Gamma-ray spectra in coincidence with three different energy gates, showing γ rays which populate the ground-state band, the octupole band head at 1006 keV (903-keV gate), and the 2^+ band head at 1117 keV (1014-+ 1117-keV gates). The changes which occur in the ordinate scale in the region between channels 1500 and 2000 are by a factor of 20 in the 903-keV gated spectrum and by a factor of 10 in the 103-keV gated spectrum. A constant of 20 counts per channel has been added to the data from the 903- and 103-keV gates in order to eliminate negative numbers arising from the chance coincidence subtractions.

TABLE I. Gamma rays from ^{180}Re decay.

	$I_\gamma(\Delta I_\gamma)$			Transition	
$E_\gamma(\Delta E)$ (keV)[a]	Goudsmit *et al.*[b]	This work[c]	Coincidence γ rays (keV)	E_i	E_f
75.99	~0.7	19 (1)	104, 749, 903, (1353)	1082	1006
(102.51)[d]		(1.7)[d]		1185	1082
103.567	23.0(25)	2390 (70)	234, 511[e], 749, 825, 903, (970) 1014, 1121, 1130, 1250, 1318, (1332), 1353, 1409, (1484) (1529), 1727, (1766), 1877	104	0
131.54		11.7(5)			
173.91(7)		10 (2)	None		
178.74(9)		7.7(8)	1250	1185	1006
233.983	0.5(1)	85 (3)	104, (551), 669, 745, 749, 825 (847), 895, (1250), (1333), 1353, 1477, (1802)	338	104
511[e]			104, 511[e], 570, 669, 825, 903, 1006		
550.52(4)		18.1(15)	104, (745), 903	1633	1082
580.8(1)		12 (2)	(828), 848, 903, (935)	1587	1006
599.0(1)		16 (2)	(104), 234, 1129	1832	1233
626.7(2)		6.4(23)		1633	1006
668.80(3)		14 (3)	234, (749), (825), (1333), (1353), (1878)	1006	338
699.7(2)		10 (3)	None	(2532	1832)
714.43(3)		30(2)	1014, 1117	1832	1117
744.84(4)	[0.7(2)]	28 (2)	104, 234, (551), 749, (1353)	1082	338
749.34(1)	1.4(4)	120 (4)	(76), 104, 234, 745, 903	1832	1082
782.6(2)		2.9(10)		2416	1633
808.9(3)		3.1(6)		1815	1006
825.36(1)	11.8(5)	1070 (30)	104, (234), 511[e], 903, (971), 1006, 1052	1832	1006
828.5		4 (2)[f]		(2416	1587)
847.80(9)		3 (1)	581, 1484, (1587)	1185	338
		4.5(10)		2435	1587
(895.26)[d]		7.6[d]	234, (1651)	1233	338
902.838	100	9690 (290)	104, 162, 511[e], 551, (581), (627) 749, (809), 825, 929, 1250 (1333), 1353, 1409, 1429, (1516), (1525), 1802, (1816), 1878, (1904)	1006	104
935.2(2)		3.5(9)	(581), (903)	2523	1587
995.14(8)		7.6(8)	104, 234, 1129	2228	1233
1006.31(2)	0.6(1)	53 (2)	511[e], 825, (1409)	1006	0
1013.73(2)	1.2(3)	79 (3)	104, 714, 1059, 1298, 1318, 1405, 1429, (1767)	1117	338
1036.0(3)		1.1(4)			
1052.42(5)		9.9(6)	104, 825, 903	2884	1832
1059.42(4)	0.20(7)	12.7(7)	(104), 1014, 1117	2177	1117
1069.4(2)		3.3(6)	104, (1711)	2884	1815
1082.6(3)		1.5(5)			
1110.7(2)		5.9(7)		2228	1117
1117.28(2)	0.7(2)	67 (2)	714, 1059, 1298, 1318, (1405), 1429, 1767	1117	0
1129.14(2)	0.6(2)	48 (2)	104, 599, 995, 1183, 1203 (1290), 1651	1233	104
1145.4(4)		1.1(6)		2228	1082
1183.11(5)		12 (1)	1129	2416	1233
1202.6(1)	0.27(8)	8.6(7)	1129	2435	1233
1250.22(4)		6 (1)	104, 179, 903	2435	1185
		6 (1)		2257	1006
1290.0(1)		4.2(6)		2523	1233

TABLE I. (*Continued.*)

	$I_\gamma(\Delta I_\gamma)$				
$E_\gamma(\Delta E)$ (keV)[a]	Goudsmit *et al.*[b]	This work[c]	Coincidence γ rays (keV)	E_i	E_f
1298.44(2)	0.47(9)	37 (1)	104,1014,1117	2416	1117
		<3		2532	1233
1314.2(1)		4 (1)		2547	1233
1317.85(3)	0.30(7)	19 (1)	1014,1117	2435	1117
1333.4(1)		5.8(6)	(745)	2416	1082
1352.80(2)	0.37(8)	30 (2)	104,234,903	2435	1082
1405.2(1)		6.7(7)		2523	1117
1409.40(2)	1.2(1)	50 (2)	104,903	2416	1006
1429.22(4)[g]	0.26(8)	11 (2)	903,1014,1117	2547	1117
		4 (1)		2435	1006
1449.2(2)		1.7(6)		2532	1082
1477.3(3)		1.4(5)		1815	338
1483.69(4)	0.29(6)	11 (1)	104,848,(935)	1587	104
1516.0(5)		5 (1)		2523	1006
1525.14(6)		8.1(5)	(104),903	2532	1006
1529.30(6)	0.32(6)	8.4(5)	(104)	1633	104
1561.0(4)		0.6(4)			
1587.2(2)		1.9(4)		1587	0
1595.5(3)		1.1(4)			
1651.45(6)		7.1(5)	104,1129	2884	1233
1678.0(3)		2.2(6)		(2910	1233
1694.0(4)[h]		1.4(8)			
1711.3(2)		2.5(4)		1815	104
1727.8(1)		6.1(8)	104	1832	104
1766.74(6)	0.15(4)	9.2(9)	1014,1117	2884	1117
1792.3(3)		1.8(5)	None	(2910	1117)
1801.75(5)	0.2(1)	15.2(10)	104,903,(745)	2884	1082
1815.6(3)		1.8(4)	(903)		
1839.6(2)		1.8(4)			
1877.70(3)	0.25(3)	22.4(10)	104,903	2884	1006
1903.6(1)		3.1(4)	(903)	(2910	1006)
1939.1(2)		1.1(3)			
1991.1(2)		2.1(4)			
2027.2(4)	0.04(2)	1.4(4)			
2066.9(4)		1.3(3)			
2073.5(2)	0.084(30)	2.5(4)		2177	104
2096.0(2)		1.3(3)			
2142.2(3)		1.7(3)			
2153.24(6)	0.11(2)	9.2(6)		2257	104
2165.7(4)		0.4(2)			
2176.9(1)		3.6(4)		2177	0
2182.3(1)		2.9(3)			
2196.0(5)		0.3(2)			
2204.64(4)	0.13(2)	15.3(7)			
2232.9(2)		1.3(3)			
2258.4(1)	0.05(2)	4.4(4)			
2312.1(2)		1.9(4)		2416	104
2331.87(6)	<0.12(2)	9.1(5)		2435	104
2408.4(3)	0.02(2)	0.6(2)			
2475.5(3)		0.7(2)			
2780.6(2)		1.4(2)		2884	104
2889.8(2)		1.6(3)			
3340.7(5)		0.6(2)			

TABLE I. (*Continued.*)

---

[a] Errors in the least significant digits are shown in parentheses. They reflect only the statistical uncertainties in peak positions. Approximately 50 eV should be added in quadrature for γ rays below 1500 keV, and 100 eV for γ rays above 1500 keV, in order to include systematic errors.

[b] Reference 2. These authors also report γ rays which we do not confirm at 1024.9, 1228, (1545), 1820.5, 1838.4, 1867.4, 2033.6, 2241.9, and 2341 keV.

[c] Intensities are the number of γ rays per 10 900 Re decays. Errors include our estimate of systematic errors. The statistical errors on intense lines (104, 825, and 903 keV) are much smaller than the errors shown.

[d] Energy and intensity from Ref. 1.

[e] e^+-e^- annihilation radiation.

[f] This line was seen marginally only in coincidence data.

[g] Complex peak. From coincidence data the γ rays to the 1117- and 1006-keV levels have energies of 1429.5(2) and 1428.8(1) keV, respectively.

[h] This peak might be due to the pair effect of the 2204.6-keV γ ray with single 511 escape.

level). The Hauser-Feshbach calculation discussed in Ref. 1 predicts populations of the $K^\pi = 0^-$ and 1^- bands which agree well with the above observations.

The level at 1814.9 keV agrees very closely in energy with a level that is strongly populated in the (d,d') reaction.[8] Our coincidence data support the decay of this level to the 4^+ and 2^+ members of the ground-state band and also to the $K^\pi = 2^-$ octupole band head at 1006.4 keV. A weak γ ray of 1815.6 keV suggests that the 1814.9-keV level might also decay to the ground state. Because of the low intensities, the data are not good enough to reject this possibility completely. However, both the energy fit, which is off by 2 standard deviations, and the coincidence data, which show weak evidence of coincidences between the 1815.6- and 902.8-keV γ rays, suggest that the 1815.6-keV γ ray does not depopulate the 1814.9-keV state.

Beta decay intensities shown in Table II were determined from a detailed intensity balance at each level. In general, we used theoretical values of the conversion coefficients[7] for each γ ray based on its most probable multipolarity. (We used the measured conversion coefficient of Konijn *et al.*[8] for the 902.8-keV γ ray.) Uncertainties in the conversion coefficients had only a minor effect on the intensity balances. The log*ft* values in Table II were obtained from the tables of Gove and Martin[9] using the $\beta^+ + e^-$-capture intensities, the β-decay Q value of 3828 ± 60 keV determined by Goudsmit *et al.*,[2] and a ^{180}Re half-life of 2.45 min. We assumed there is no β decay to the ^{180}W ground state. If an upper limit of intensity corresponding to log ft = 6.0 is assumed

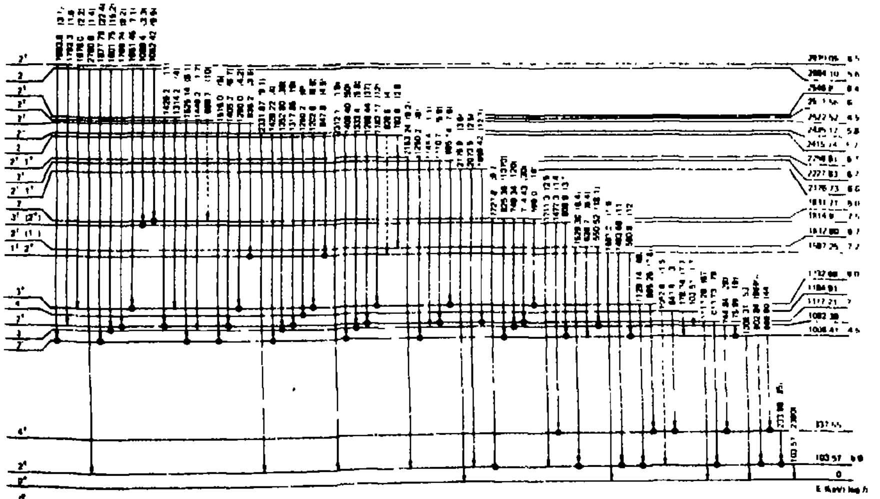

FIG. 3. Decay scheme of ^{180}Re. Gamma-ray intensities per 10 900 Re decays are shown in parentheses following the transition energy label (in keV). A dot at the arrowhead of a γ-ray transition indicates that the γ ray was seen in coincidence with one or more of the γ rays which depopulate the level.

TABLE II. Log*ft* values for ^{180}Re decay to levels in ^{180}W.

Level (keV)	$\beta^+ + K$-cap. Intensity[a]	$\log f_0 t$[b]
103.57	730(430)	5.9
337.65	14(7)	7.5[c]
1006.41	8410(290)	4.50
1082.39	62(20)	6.6[c]
1117.21	12(4)	7.3
1184.91	17(5)	7.1[c]
1232.68	−2(4)	$>$9.0[d]
1587.25	11(4)	7.2
1632.90	30(3)	6.7
1814.9	3.7(11)	7.5
1831.71	1240(30)	5.0
2176.73	19(1)	6.6
2227.83	15(1)	6.7
2256.81	15(2)	6.7
2415.74	112(4)	5.7
2435.17	82(5)	5.8
2522.52	16(2)	6.5
2531.55	10(1)	6.7[e]
2546.8	17(2)	6.4
2884.10	65(2)	5.6
2910.05	7(1)	6.5

[a] Errors in the least significant digits are shown in parentheses.

[b] Uncertainties in log*ft*'s can be inferred from the β-decay intensity errors in column 2. The uncertainty in Q_β introduces an error of 0.02 to 0.04 in log*ft*.

[c] These are at least 2nd forbidden. The log*ft* differences, by ~2σ (337-keV level) and ~3σ (1082- and 1185-keV levels) from the large expected values, are presumably due to unplaced weak γ rays.

[d] $\log f_1 t$.

[e] This log*ft* would be 6.4 if the 699.7-keV γ ray depopulated the 2531.55-keV level.

for the ground-state transition, then the log*ft*'s in Table II would increase by a maximum of 0.1.

Spins and parities of the levels up to 1232.68 keV are known from previous work. For the other levels we used log*ft* values and γ-ray branchings to deduce the possible spins and parities, as shown in Fig. 3. The levels at 1831.71, 2415.74, 2435.17, and 2884.10 keV are restricted to the unique value $I^\pi = 2^-$ because of the low log*ft* values, indicating allowed β decay[10] from the 1^- ground state of ^{180}Re, and because they all have γ-ray branches to the 3^+ state at 1232.68 keV. All of the remaining levels have uncertain parity based on their log*ft* values, which are consistent with either allowed or first-forbidden β decay. Several of these levels, at 2227.83, 2522.52, 2531.55, 2546.8, and 2910.05 keV, are rather clearly restricted to $I = 2$ because of γ-ray branches to 3^+ and/or 3^- levels and the absence of observable γ branches to the ground-state band. If these levels had $I = 1$, we would expect the high energy ΔK-allowed dipole transitions to the ground-state band to be the dominant mode of decay.

The possible spins for the other five levels above 1233 keV are more ambiguous (see Fig. 3). The two levels at 1587.25 and 1632.90 are particularly interesting because of the possibility that they may be the $I = 1$ and 2 members of the $K^\pi = 1^-$ octupole band (see Sec. IV). Both levels decay to the ground-state band; the 1587.25-keV level decays to both the 0^+ and the 2^+ members, and the 1632.90-keV level decays to the 2^+ member only. This would be consistent with a $K = 1$ assignment for them. However, the other J^π possibilities shown in Fig. 3 cannot be rejected on the basis of the β- and γ-decay properties.

Since the level at 1814.9 keV decays to the 2^+ and 4^+ levels of the ground-state band, but probably not to the 0^+ level, its spin is most likely 3. That interpretation would conflict with the log*ft* value in Table II, which is too low for a β decay with $\Delta I > 1$. However, this discrepancy could easily be due to undetected weak γ rays which populate the 1814.9-keV level, causing our measured log*ft* to be too low.

IV. DISCUSSION

One interesting aspect of the ^{180}Re decay to levels in ^{180}W is the low log*ft* values to five 2^- states with energies of 1006, 1832, 2416, 2435, and 2884 keV. The log*ft* values to these states are 4.5, 5.0, 5.7, 5.8, and 5.6, respectively. It is clear from the low log*ft* values that the allowed unhindered decay from the $(\pi 5/2^+[402\uparrow]-\nu 7/2^-[514\downarrow])_1$- configuration of the ^{180}Re ground state to the $(\pi 5/2^+[402\uparrow]-\pi 9/2^-[514\uparrow])_2$- configuration in ^{180}W dominates these decay modes. If one makes the simplifying assumption that these are the only configurations involved in the decay to the five 2^- states, one can calculate the fragmentation of the $(\pi 5/2^+[402\uparrow]-\pi 9/2^-[514\uparrow])_2$- configuration among these five states. Based on the measured log*ft* values, the percentages of this configuration in the 1006-, 1832-, 2416-, 2435-, and 2884-keV states are 66, 21, 4, 3, and 5, respectively. It is interesting that such a large fraction (approximately 66%) of the $(\pi 5/2^+[402\uparrow]-\pi 9/2^-[514\uparrow])_2$- configuration is in the 1006-keV state, which is the $K^\pi = 2^-$ component of the octupole vibration. This is somewhat surprising, since the band is known to be quite collective and is expected therefore to be made up from a large number of small contributions of the quasiparticle states. Most of the rest of the $(\pi 5/2^+[402\uparrow]-\pi 9/2^-[514\uparrow])_2$- configuration (21%) resides in the 1832-keV state. Smaller fractions (but enough to influence the log*ft* values significantly) reside in the other three 2^- states.

States in ^{180}W with possible spin-parity of 1^- and 2^- are observed at 1587.25 and 1632.90 keV, respectively. If these two states are assumed to be members of the same rotational band, a rotational constant $\hbar^2/2\mathscr{I}=11.4$ keV is calculated in substantial agreement with the value $\hbar^2/2\mathscr{I}=12.6$ keV calculated from the 2^- and 3^- members of the $K^\pi=2^-$ octupole band. It is therefore tempting to suggest that the states at 1587.25 and 1632.90 keV are the 1^- and 2^- members of the $K^\pi=1^-$ octupole band. This interpretation receives support from the possible observation in the (d,d') and the $(p,2n\gamma)$ studies[1,6] of the 3^- member of the $K^\pi=1^-$ band. A state observed at 1693.6 keV in the $(p,2n\gamma)$ reaction decays to the 4^+ member of the ground-state band and corresponds closely in energy to the state at 1692 keV reported in the (d,d') reaction. This energy agrees very well with the predicted energy of the 3^- state in our proposed $K^\pi=1^-$ band, especially if we allow for some depression of the odd-spin energies due to Coriolis-induced mixing with the $K^\pi=0^-$ band.

A state which is observed at 1814.9 keV with spin $3^\pm(2^+)$ corresponds almost exactly with the state observed at 1814 keV in the (d,d') studies of Günther *et al.*[6] This is the most strongly populated state in the (d,d') reaction above the 3^- member of the $K^\pi=2^-$ band at 1082.39 keV. The (d,d') strength and our observation of γ-ray decay to the 2^+ and 4^+ members of the ground-state band would be consistent with an assignment for the 1814.9-keV state as the 3^- member of the $K^\pi=0^-$ octupole band. In that case the γ-ray branching to the ground-state band members might agree reasonably well with the Alaga rules,[11] because the $\Delta K=1$ $E1$ transitions due to any admixed $K=1$ components in the 1815-keV level are expected to be rather strongly hindered with respect to the $\Delta K=0$ transitions.[12] The predicted ratio of reduced $E1$ transition probabilities to the 2^+ and the 4^+ members of the ground band is 0.75, in satisfactory agreement with the observed ratio of 1.1 ± 0.4.

The 1814.9-keV level decays to the $K^\pi=2^-$ octupole band head at 1006.4 keV with an intensity roughly equal to its decay to the ground-state band. This branching requires a hindrance of the $E1$ transitions to the ground band of $\sim4\times10^4$ if we assume an $E2$ strength of one single-particle Weisskopf unit for the $\Delta K=2$ decay to the $K^\pi=2^-$ band head. Such a large hindrance for a $\Delta K=0$ transition weakens the $K^\pi,I=0^-,3$ assignment,[12] but it may not be sufficient cause to reject the possibility entirely. In ^{236}U, for example,[5] the transitions from the 688-keV level to the ground-state band appear to be $\Delta K=0$ $E1$'s with hindrances exceeding 10^6. If the inertial parameter $\hbar^2/2\mathscr{I}$ in this proposed $K^\pi=0^-$ band is the same as in the $K^\pi=2^-$ octupole band, then the $K^\pi,I=0^-,1$ band head would be at 1688 keV.

Using random-phase approximation (RPA) calculations with an octupole-octupole force and including Coriolis mixing, Neergård and Vogel[3] have been able to reproduce both the approximate energies of band heads and the $B(E3)$ strengths in the 3^- members of the $K^\pi=0^-$, 1^-, 2^-, and 3^- octupole bands in the rare earth nuclei. In view of the previous qualitative success of these calculations, it may be of value to compare their calculations with the two previously observed[1] octupole bands ($K^\pi=2^-$ and 3^-) and with the tentatively assigned $K^\pi=0^-$ and 1^- bands from the present research. Unfortunately, Neergård and Vogel did not report calculations on ^{180}W in Ref. 3. However, the results of a calculation by Neergård on ^{180}W are reported by Günther *et al.*[6] for the $K^\pi=2^-$ and 3^- bands. For the $K^\pi=0^-$ and 1^- bands, we have extrapolated the Neergård and Vogel results on Hf and other W isotopes to obtain approximate predictions of the band head energies and the $B(E3)$ values in ^{180}W. The calculated values for the $K^\pi=0^-$, 1^-, 2^-, and 3^- bands, respectively, are 2000, 1400, 1290, and 1740 keV for the band head energies, and 1, 0.1, 12.4, and 3.8, in units of 10^{-2} e^2b^3, for the $B(E3)$ values to the $I=3$ states. The systematics in this nuclide region suggest that the extrapolations used for $K=0$ and 1 might introduce errors of $\gtrsim10\%$ in the energy predictions and of a factor of 2 or more in the $B(E3)$ predictions. Considering the large uncertainties in these predictions and the uncertainties in extracting $B(E3)$ values from the (d,d') experiments,[6] the agreement between measured $B(E3)$ values and the predictions seems acceptable for our proposed octupole 3^- states.

Recent calculations[1] have been carried out for ^{180}W directly. In these calculations the data available on the $K^\pi=2^-$ and 3^- octupole bands from in-beam measurements were used with a Coriolis interaction model in an attempt to obtain better estimates for the positions of the missing $K^\pi=0^-$ and 1^- octupole band heads. The data from the present experiments suggest a disparity of several hundred keV in the positions of these octupole bands when compared to the results of the simple Coriolis interaction calculation of Ref. 1. The calculation was repeated and the additional experimental data from the present study were used to fix the positions of the four octupole band heads. No realistic set of Coriolis interaction matrix elements could be found which would accurately accommodate both the known energies of the octupole bands and the measured rotational spacings in the $K^\pi = 1^-$ and 2^- bands. Nevertheless, a set of reasonable parameters was obtained which give a best fit to all the experimental data. The calculated values of the lowest-lying states in each octupole band are compared in Table III with the experimental data and with the calculations of Neergård and Vogel.[3]

With the wave functions derived from these calculations, we can estimate the log*ft* value for the $K^\pi, I = 1^-, 2$ octupole state tentatively assigned as the level at 1632.9 keV. The calculated wave function for this state is $|1633, I=2\rangle = 0.9992|1^-, 2\rangle - 0.0389|2^-, 2\rangle$. If we assume that the $K^\pi = 1^-$ octupole band head is essentially unmixed, then we can use the Alaga rules[11] with the observed *ft* value to the 1587-keV state to determine the β-decay matrix element for the $|1^-, 2\rangle$ component. The *ft* value for the $|2^-, 2\rangle$ component is determined directly from the observed *ft* value to the $K^\pi = 2^-$ octupole band head at 1006 keV. Depending on the undetermined relative signs of the two matrix elements, the calculated log*ft* to the $K^\pi, I = 1^-, 2$ state is 6.8 or 7.2. This result agrees well with the observed value of 6.7 for the level at 1632.9 keV, and is therefore consistent with the assignment of the 1587.2- and 1632.9-keV levels as the spins 1 and 2 members of the $K^\pi = 1^-$ octupole band.

V. CONCLUSIONS

We have identified 11 (and possibly 2 other) new low-spin states in ^{180}W. Low log*ft* values to five 2^- states, including the $K^\pi = 2^-$ octupole band head, indicate fragmentation of the $(\pi 5/2^+[402] - \pi 9/2^-[514])_{2^-}$ configuration among the five states. Tentative identification of a state at 1814.9 keV as the $K^\pi, I = 0^-, 3$ octupole vibrational component is compatible with the γ-decay branching and the previously reported[6] strength of excitation in the (d, d') reaction. This assignment is a very speculative possibility, however, and requires confirmation by identification of other members of the rotational band. Two states at 1587.25 and 1632.90 keV and a previously reported state at 1693.6 keV[1,6] have γ-decay branchings, log*ft*'s from ^{180}Re β decay, (d, d') excitation (to the 1693.6-keV state), and energy spacings which are fully compatible with their assignments as the spins 1, 2, and 3 members of the $K^\pi = 1^-$ octupole vibrational band. If these assignments can be finally confirmed, then the energies of all four components of the octupole vibration in ^{180}W would be quite firmly established. In that case, our extrapolations of the calculations in this nuclide region suggest there are significant discrepancies between the microscopic calculations and the observed band head energies, particularly for the $K = 0$ and $K = 2$ components.

TABLE III. Calculated and tentatively observed energies (in keV) of the lowest-lying states in each octupole band in ^{180}W.

	Energy (keV)			
	$K^\pi = 0^-$	$K^\pi = 1^-$	$K^\pi = 2^-$	$K^\pi = 3^-$
Experiment	1814.9[a]	1587.3	1006.4	1634.6[b]
Calculation[c]	1807[a]	1578	1006.8	1632
Calculation[d]	2100[a]	1400	1290	1740

[a] This is the energy of the K^π, $I = 0^-, 3$ state. The K^π, $I = 0^-, 1$ state has not been observed.

[b] See Ref. 1.

[c] Results from a semiempirical Coriolis interaction calculation. See text.

[d] Calculations of Neergård and Vogel (Ref. 3) extrapolated as described in the text. A value of $\hbar^2/2\mathfrak{J} = 12.8$ has been assumed for the $K^\pi = 0^-$ band.

ACKNOWLEDGMENTS

We wish to acknowledge the contribution of the operations staff of the Livermore cyclograaff in producing the ^{180}Re sources. This work was performed under the auspices of the U. S. Department of Energy by the Lawrence Livermore Laboratory under Contract No. W-7405-ENG-48. The work of one of us (R.K.S.) was supported in part by National Science Foundation Grant No. PHY-77-12876.

---

*Permanent address: The Florida State University, Tallahassee, Florida 32306.

†Permanent address: Southern University, Baton Rouge, Louisiana 70813.

[1] L. G. Mann, J. B. Carlson, R. G. Lanier, G. L. Struble, W. M. Buckley, D. W. Heikkinen, I. D. Proctor, and R. K. Sheline, Phys. Rev. C 19, 1191 (1979).

[2] P. F. A. Goudsmit, J. Konijn, and F. W. N. de Boer, Nucl. Phys. A104, 497 (1967).

[3] K. Neergård and P. Vogel, Nucl. Phys. A145, 33 (1970).

[4] R. Gunnink and J. B. Niday, Lawrence Livermore Laboratory Report No. UCRL-51061, 1972 (unpublished).

[5] C. M. Lederer and V. S. Shirley, *Table of Isotopes* (Wiley, New York, 1978).

[6] F. Günther, P. Kleinheinz, R. F. Casten, and B. Elbek, Nucl. Phys. A172, 273 (1971).

[7] F. Rösel, H. M. Fries, K. Alder, and H. C. Pauli, At. Data Nucl. Data Tables 21, 291 (1978).

[8] J. Konijn, B. J. Meyer, and G. Van Middelkoop, Phys. Lett. 35B, 567 (1971).

[9] N. B. Gove and M. J. Martin, Nucl. Data Tables 10, 205 (1971).

[10] S. Raman and N. B. Gove, Phys. Rev. C 7, 1995 (1973).

[11] G. Alaga, K. Alder, A. Bohr, and B. R. Mottelson, K. Dan. Vidensk. Selsk. Mat. Fys. Medd. 29, No. 9, 2 (1955).

[12] L. Kocbach and P. Vogel, Phys. Lett. 32B, 434 (1970).

PHYSICAL REVIEW C VOLUME 21, NUMBER 6 JUNE 1980

Systematics of quasirotational states in $N = 88$ nuclei

D. R. Zolnowski, M. B. Hughes, J. Hunt, and T. T. Sugihara
Cyclotron Institute, Texas A&M University, College Station, Texas 77843

(Received 3 December 1979)

The decays of 4.2-min ^{152}Tb, 3.3-min ^{154}Ho, 11.8-min ^{154}Ho, and 82-sec ^{156}Tm have been studied by γ-ray and conversion electron spectroscopy using the He-jet technique. High-spin states in ^{152}Gd were also studied in the ^{152}Sm$(\alpha,4n\gamma)$ reaction at 50 MeV and the ^{150}Sm$(\alpha,2n\gamma)$ reaction at 28 MeV. The systematic behavior of quasirotational bands in $N = 88$ nuclei has been studied, and observed features in the location of β- and γ-band states are shown to be explainable from a consideration of available orbitals in a Nilsson diagram. Microscopic calculations employing fourth and sixth order versions of the boson expansion model of Tamura, Kishimoto, and Weeks reproduce the known low-lying positive parity states in ^{150}Sm, ^{152}Gd, ^{154}Dy, and ^{156}Er. Experimentally observed negative-parity states are explained remarkably well by a quadrupole-octupole coupling model, but a backbending plot suggests a possible change in intrinsic structure above spin 11.

RADIOACTIVITY ^{152}Tb^{m}, ^{154}Ho^{m1}, ^{154}Ho^{m2}, ^{156}Tm; I_γ, E_γ, I_{ce}, E_{ce}, γ-γ coin. ^{152}Gd, ^{154}Dy, ^{156}Er deduced levels, ICC, J, π; systematics, comparison with microscopic theory.
NUCLEAR REACTIONS ^{152}Sm$(\alpha,4n)$, $E_\alpha = 50$ MeV; ^{150}Sm$(\alpha,2n)$, $E_\alpha = 28$ MeV; measured E_γ, I_γ, $I_\gamma(\theta)$, I_{ce}, γ-γ coin. ^{152}Gd deduced levels, ICC, J, π. Enriched targets, Ge(Li), Si(Li) detectors.

I. INTRODUCTION

The systematics of low-lying vibrational bands in the $N = 88$ nuclei are for the most part unknown, largely due to the difficulty involved in studying short-lived nuclides such as ^{154}Ho and ^{156}Tm. In-beam studies[1,2] of $N = 88$ nuclei have provided information on high-spin backbending phenomena in yrast states and have succeeded in locating an odd-spin negative-parity band (NPB). In ^{156}Er this band has been interpreted as having two-quasineutron rotationally-aligned character.[3] In ^{152}Gd, however, where low-spin states are also known, a simple quadrupole-octupole coupling (QOC) model has been shown to explain remarkably well all known negative-parity states.[2,4] The NPB in the QOC picture is basically octupole vibrational. To aid in clarifying this issue, information on low-lying negative-parity states in ^{154}Dy and ^{156}Er seemed essential.

To locate these low-lying negative-parity states and to study the systematics of vibrational bands in $N = 88$ nuclei, decay studies of 4-min ^{152}Tb, 3.3-min ^{154}Ho, 11.8-min ^{154}Ho, and 82-sec ^{156}Tm were undertaken. To add to high-spin information, an in-beam investigation of ^{152}Gd was also performed. Parts of the latter results have already been reported.[2]

II. EXPERIMENTAL PROCEDURE

The radioactive nuclides were produced by bombardment with α particle or HI beams from the Texas A&M variable energy cyclotron. The reactions and beam energies are summarized in Table I. Through the use of the He-jet technique, reaction products were thermalized in helium gas, transported approximately 30 m to a low background area, successively collected on Mylar tape, and counted. An exploded view of the He-jet reaction chamber is given in Fig. 1. The chamber is modular in design and permits use of additional capillary bundles if desired. Although the figure shows a bundle consisting of three separate capillaries, only a single polyethylene capillary with 1.7 mm interior diameter was employed. The helium gas was bubbled through benzene to increase greatly the transmission of recoiling nuclei through the capillary. Targets consisted of sep-

TABLE I. Reaction data.

Nuclide	Reaction	Bombardment energy (MeV)
^{152}Tb (4.2 min)	^{151}Eu$(\alpha, 3n)$	40
^{154}Ho (3.3 min)	^{148}Sm$(^{11}$B$, 5n)$	83
^{154}Ho (11.8 min)	^{148}Sm$(^{12}$C$, 6n)^{154}$Er $\xrightarrow{\beta}$ ^{154}Ho	93
^{156}Tm (82 sec)	^{148}Sm$(^{14}$N$, 6n)$	109, 113, 119

© 1980 The American Physical Society

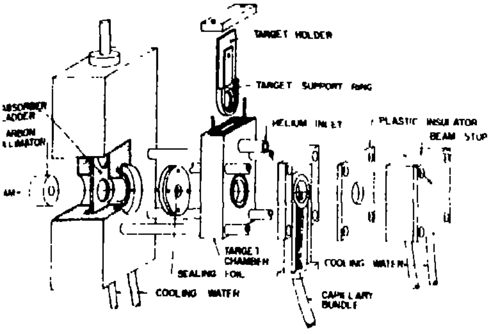

FIG. 1. Exploded view of He-jet target chamber. In ie present experiments a single capillary was used to ansport reaction products.

rated isotopes in oxide form on a 0.635 mm Al oil. Bonding to the foil was achieved by forming slurry from the oxide and a small amount of lear plastic spray.

Singles spectra were taken with 30 and 55 cm^3 ie(Li) detectors with respective resolutions of .86 and 1.78 keV at 1332 keV. A 1 cm^3 Ge(Li) lanar detector [700 eV full width at half maximum FWHM) at 122 keV] was also used in some cases. The energies of stronger transitions were determined using standard sources and these subsequently served as internal standards in the singles pectra. Conversion-electron spectra were obained with a 3 mm×2 cm^2 Si(Li) detector with esolution of 2.1 keV at 975 keV. The details of conversion-electron spectroscopy of short-lived nuclides by use of the He-jet technique have been given previously.[6] Event-by-event γ-γ-t coincidence experiments were performed using the two large detectors. Resolving times were typically 12 ns. Energy gates were subsequently set on almost every γ ray reported in this work.

In-beam γ-ray measurements on ^{152}Gd were made using the 55 cm^3 detector. Targets consisting of self-supporting metal foils of enriched ^{152}Sm were bombarded with 50 MeV α particles. Angular distribution data were taken at 90°, 125°, 145°, and 160° at a distance of 29 cm. A pulser triggered by a monitor detector was used to normalize the data at the various angles. In-beam conversion-electron measurements were made with a broad range electron spectrometer consisting of a cooled Si(Li) detector and an electron steering magnet. Details of the spectrometer have already been given elsewhere.[7] In-beam γ-γ coincidence experiments were also performed for the $^{152}\mathrm{Sm}(\alpha,4n\gamma)$ and $^{150}\mathrm{Sm}(\alpha,2n\gamma)$ reactions at 40 and 28 MeV, respectively.

III. EXPERIMENTAL RESULTS

A. Decay of 4.2-min $^{152}\mathrm{Tb}^m$

The 4.2-min $^{152}\mathrm{Tb}^m$ activity was previously investigated by Bowman *et al.*[8] No isomeric transitions in Tb other than the eight reported in that investigation were observed. Of 47 transitions in Gd reported in the present work, 22 are previously unreported in the short-lived-isomer decay. The small contribution from 17.5 h ^{152}Tb (Ref. 9) to the

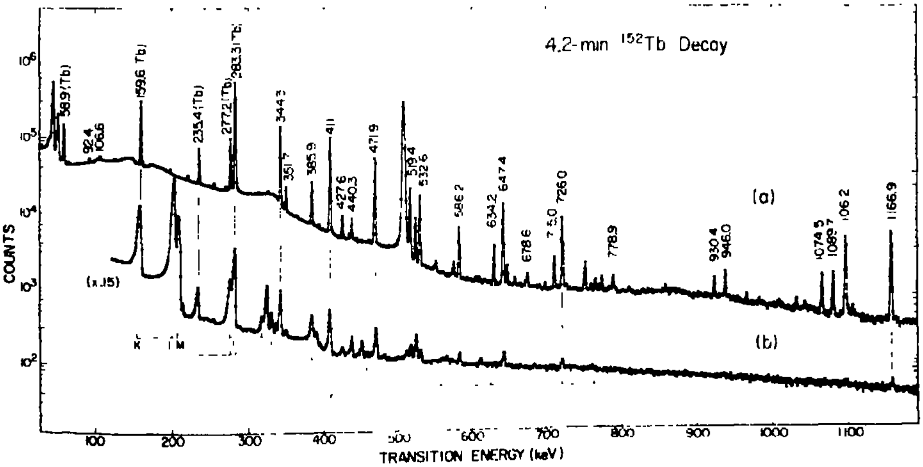

FIG. 2. Gamma-ray (a) and conversion-electron (b) spectra for the decay of 4.2-min^{152}Tb. A total of 140 sources were counted for 2 min each (using the 30 cm^2 detector) to obtain spectrum (a). To obtain spectrum (b), 375 sources were counted for 28 sec each [with a 3 mm×2 cm^2 Si(Li) detector.] Shorter collection times were used for conversion-electron measurements to minimize source thickness and thus to improve resolution.

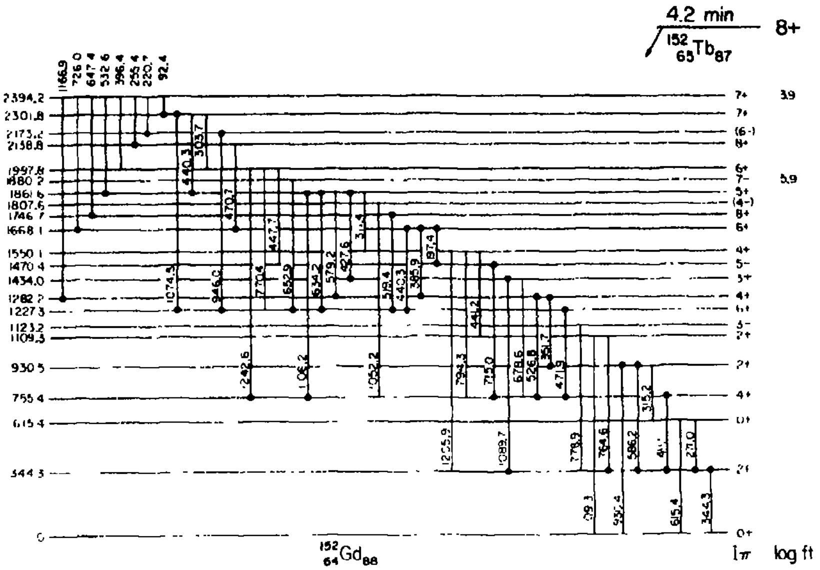

FIG. 3. Levels in ^{152}Gd populated in the decay of 4.2-min^{152}Tb. Dots at bottom (top) of transition indicate placement is confirmed by coincidence with succeeding (preceding) transition(s).

γ-ray spectrum was determined from the intensity imbalance for the 1282.3 keV level in ^{152}Gd.

Conversion-electron data permitted multipolarity assignments to be made for 20 transitions. Preliminary results were reported previously.[8] The quality of γ-ray and electron data is indicated in Fig. 2, and intensities and energies are summarized in Table II. The γ-γ-t coincidence data were used to locate the ^{152}Gd levels shown in Fig. 3. Of the proposed levels, seven were previously unobserved in this decay. The two possible level schemes given by Bowman *et al.*[8] for the Tb states populated in the 4.2-min decay are given in Fig. 4. The presence of a 48-keV transition depopulating

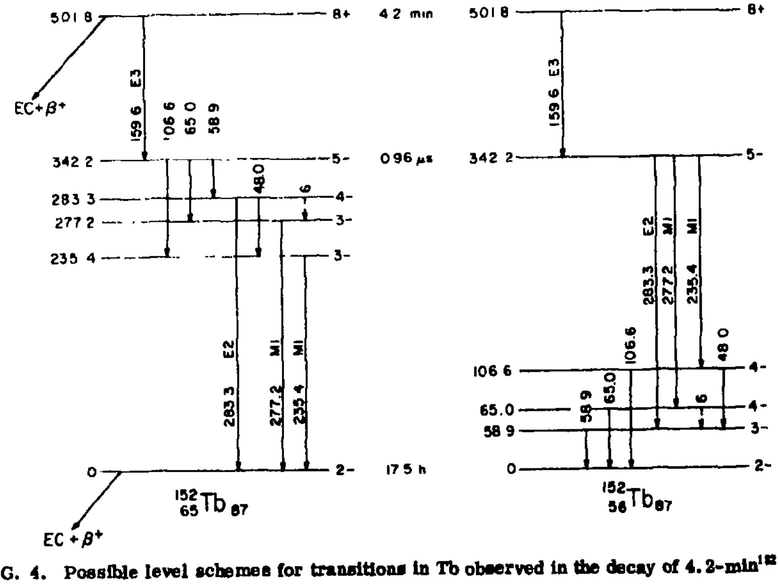

FIG. 4. Possible level schemes for transitions in Tb observed in the decay of 4.2-min^{152}Tb.

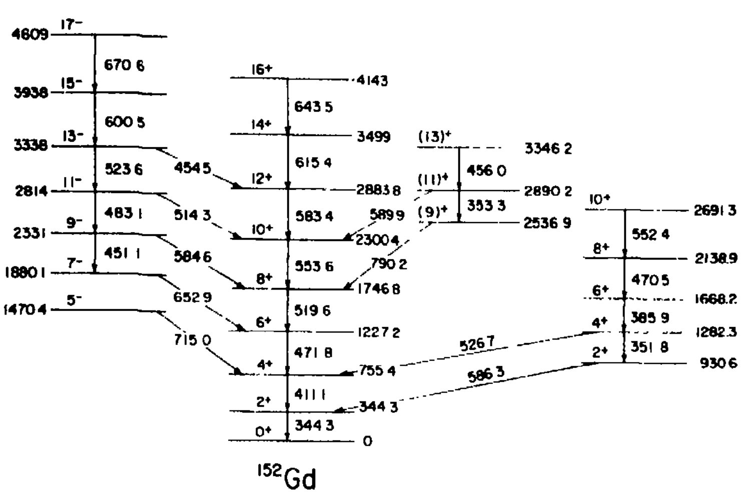

FIG. 5. Levels in ^{152}Gd observed in the ^{152}Sm(α, 4$n\gamma$) reaction at 50 MeV.

the 283.2-keV state has also been confirmed in spectra taken with the high resolution Ge(Li) planare detector.

It is possible that a ^{154}Gd(p, 3$n\gamma$)^{152}Tb in-beam study could be used to determine which of the two schemes is correct. Specifically, the in-beam relative intensities of the 235.4-, 277.2-, and 283.3-keV γ rays will be the same as those observed in the 4.2-min decay if they depopulate the same level. In the alternate scheme, these transitions de-excite three distinct levels. As a result, different relative intensities are expected if the reaction succeeds in populating these states in ways other than through the 4.2-min isomer decay.

All of the EC+β^+ decay intensity of ^{152}Tb^m appears to occur to the 7^+ state at 2394.2 keV, although some states such as the 1880.2-keV (7^-) state may be weakly fed. If one assumes total feeding to the 2394.2-keV state, the logft value for $Q_{EC}=4.3$ MeV is 3.9. This allowed unhindered value can be explained[8] by interpreting the latter state as the two neutron configuration $\frac{5}{2}^-[532]+\frac{11}{2}^-[505]$ and the 8^+ isomeric state in Tb as $\pi\frac{5}{2}^-[532]+\nu\frac{11}{2}^-[505]$.

The Tb isomeric state decays also via an $E3$ transition to a 5^- level at 342.2 keV which has a measured half-life of 0.96 μsec.[10] This state may be the $\pi\frac{5}{2}^-[532]+\nu\frac{5}{2}^+[642]$ configuration. In ^{152}Eu an $E3$ transition involving the $\frac{11}{2}^-[505]$ and $\frac{5}{2}^+[642]$ neutron orbitals has also been reported[11] with a Weisskopf hindrance factor $F_W=7.5\times10^3$. In our case a similar value, $F_W=4.5\times10^3$ is obtained.

B. In-beam results for ^{152}Gd

In-beam γ-ray, conversion-electron, γ-γ-t coincidence, excitation function, and angular distribution measurements were performed to study high-spin states in ^{152}Gd. The observed level scheme and proposed band structure is shown in Fig. 5. Supportive experimental results are summarized in Table III.

That part of the data relevant to the ground-state and negative-parity bands has been reported in a previous publication.[2] The ground-state band (gsb) has been observed to spin 16. In ^{154}Dy, "forking" was reported to occur above the 14^+ yrast state,[12] but similar structure is not observed in ^{152}Gd in the present work. The odd-spin negative-parity band occurring in several $N=88$ nuclei will be discussed in a subsequent section.

A new band is observed which consists of states at 2536.9, 2890.2, and 3346.2 keV. The angular distribution results are consistent with quadrupole character for the 353.3- and 456.0-keV intraband transitions. The conversion coefficient for the 589.9-keV interband transition indicates $E2$ character and confirms positive parity for the band.

At very similar energies (9^+, 2490 keV; 11^+, 2904 keV; 13^+, 3385 keV) a band has been reported in ^{156}Er up to spin 21 (Ref. 1). The ^{152}Gd band is most likely this same band. The 9-11-13 spin sequence is also consistent with the angular distribution results for the 589.9- and 790.0-keV interband transitions. An attempt to explain this band in ^{156}Er as arising from an incompletely aligned $(i_{13/2})^2$ quasineutron configuration[3] produced poor agreement with experiment. An adequate characterization of this band is lacking at this time.

The quasi-beta band has also been observed in the present work up to spin 10. Analysis of some transitions within this band was made particularly

TABLE II. Transition data for 4.2-min ^{152}Tb^m data.

E	I_γ		$\alpha_K(\times 10^3)$			
(keV)	1 cm^3	30 cm^3	exp.	theo.[f]	Multipolarity	Placement
Tb						g
48.0(2)	19.7(15)					
58.9(2)	121(9)	108(9)				
65.0(3)	3.1(2)	2.8(6)				
106.6(3)	5.4(3)	4.6(5)				
159.59(10)[a]	277(14)	274(20)	971(115)	$E3$:1140	$E3$	
235.4(1)	71.1(45)	73.3(52)	159(13)	$M1$:172	$M1$	
277.2(1)	142(6)	140(10)	105(8)	$M1$:111	$M1$	
283.29(5)	≡1000	≡1000	54.1(43)	$E2$:56.0	$E2$	
Gd						
92.4(2)	5.3(3)	4.9(5)				2394.2 → 2301.8
197.4(3)	4.7(4)	4.9(4)				1668.1 → 1470.4
220.7(3)	7.3(5)	7.3(6)				2394.2 → 2173.2
255.4(3)	6.2(4)	6.1(5)	96(24)	$E2$:73.0, $M1$:125	$M1, E2$	2394.2 → 2138.8
271.0(3)		1.3(8)				615.4 → 344.3
303.7(4)[b]		1.0(5)				2301.8 → 1997.8
311.4(4)[b,e]		1.3(5)				1861.6 → 1550.1
315.2(3)		2.3(5)				930.5 → 615.4
344.26(7)[a]		336(17)	≡31.0	$E2$:31.0	$E2$	344.3 → 0
351.7(1)		30.5(20)	31.0(37)	$E2$:29.3	$E2$	1282.2 → 930.5
385.9(1)		54.7(30)	31(12)	$E2$:23.5	$E2$	1668.1 → 1282.2
396.4(3)		2.2(5)				2394.2 → 1997.8
411.1(1)		304(15)	20.4(15)	$E2$:19.1	$E2$	755.4 → 344.3
427.6(2)		15.6(9)	17(8)	$E2$:17.2	$E2$	1861.6 → 1434.0
440.3(2)	12.9(10)	6.7(25)[d] 5.8(29)[d]				1668.1 → 1227.3 2301.8 → 1861.6
441.2(5)[b]		3(2)				1550.1 → 1109.2
447.7(4)		1.6(4)				1997.8 → 1550.1
470.7(5)		7.7(30)				2138.8 → 1668.1
471.9(1)		198(10)	14.5(12)	$E2$:13.2	$E2$	1227.3 → 755.4
519.4(1)		79.2(57)	11.4(18)	$E2$:10.3	$E2$	1746.7 → 1227.3
526.8(2)		27.5(20)	76.3(84)	$M1$:19.2	$E0+E2+(M1)$	1282.2 → 755.4
532.6(1)		71.6(38)	9.9(12)	$E2$:9.7	$E2$	2394.2 → 1861.6
579.2(3)		3.7(3)				1861.6 → 1282.2
586.2(2)		23.0(19)	23.3(28)	$M1$:14.7	$E0+E2+(M1)$	930.5 → 344.3
615.4[c]					$E0$	615.4 → 0
634.2(2)		15.8(12)				1861.6 → 1227.3
647.4(2)		72.3(52)	10.2(12)	$M1$:11.4	$M1+(E2)$	2394.2 → 1746.7
652.9(3)		5.7(4)				1880.2 → 1227.3
678.6(3)		3.2(4)				1434.0 → 755.4
715.0(2)		9.8(7)				1470.4 → 755.4
726.0(2)		53.1(27)	7.7(7)	$M1$:8.6	$M1+(E2)$	2394.2 → 1668.2
764.6(4)[b]		0.2(2)				1109.2 → 344.3
770.4(3)		2.6(4)				1997.8 → 1227.3
778.9(3)		1.2(8)				1123.2 → 344.3
794.3(3)		3.1(5)				1550.1 → 755.4
930.4(3)		4.6(4)				930.5 → 0
946.0(2)		8.0(6)				2173.2 → 1227.3
1041.0(4)		2.3(4)				
1052.2(4)		1.2(6)				1807.6 → 755.4
1074.5(2)		11.1(8)				2301.8 → 1227.3
1089.7(2)		11.3(8)				1434.0 → 344.3
1106.2(2)		46.9(28)	1.9(9)	$E2$:1.9	$E2+(M1)$	1861.6 → 755.4
1109.3(4)[b]		0.5(4)				1109.2 → 0
1166.9(2)[a]		62.1(35)	2.5(7)	$M1$:2.8	$M1$	2394.2 → 1227.3
1205.9(5)		1.0(4)				1550.1 → 344.3
1242.6(4)		1.7(3)				1997.8 → 755.4

TABLE II. *(Continued.)*

[a] Energy adopted from Ref. 8.
[b] Tentatively assigned to the decay.
[c] Energy taken from Ref. 9.
[d] Intensity determined from coincidence experiment.
[e] Alternate placement is between 2173.2- and 1861.7-keV levels.
[f] Reference 27.
[g] For placement of transitions in Tb see Fig. 4.

TABLE III. Intensities, angular distributions, and conversion coefficients of γ rays in ^{152}Gd observed in the ^{152}Sm($\alpha,4n$) reaction at 50 MeV and γ-ray intensities for the ^{150}Sm($\alpha,2n$) reaction at 28 MeV.

E_γ keV	I_γ ($\alpha,2n$) 125°	I_γ ($\alpha,4n$) 125°	A_2	A_4	$\alpha_K(\times 10^2)$ exp.	$\alpha_K(\times 10^2)$ theo.[a]/mult.	Placement
271.1	1.1						$2^+_\beta \to 2^+$
344.3	≅100	≡100	0.22(4)	−0.08(5)	≡3.05	3.05/$E2$	$2^+ \to 0^+$
351.8	5.5	6.5	0.25(7)	−0.13(10)			$4^+_\beta \to 2^+_\beta$
353.3	0.9	2.8	0.38(11)	−0.01(15)			$11^+ \to 10^+$
385.9	8.1	7.8	0.19(4)	−0.14(6)			$6^+_\beta \to 4^+_\beta$
411.1	84.9	90.6	0.23(4)	−0.10(6)	1.97(17)	1.94/$E2$	$4^+ \to 2^+$
451.1	0.9	3.9	0.27(4)	−0.15(6)			$9^- \to 7^-$
454.5		2.8	−0.21(7)	0.03(9)			$13^- \to 12^+$
456.0		5.0	0.18(7)	−0.21(10)			$13^+ \to 12^+$
470.5	7.6	11.3	0.50(15)	−0.02(16)	1.30(18)	1.35/$E2$	$8^+_\beta \to 6^+_\beta$
471.8	60.8	76.0	0.21(4)	−0.13(5)			$6^+ \to 4^+$
483.1	1.8	6.3	0.24(4)	−0.16(6)			$11^- \to 9^-$
514.3	7.8	11.6	−0.17(6)	0.14(8)			$11^- \to 10^+$
519.6	38.8	65.8	0.25(3)	−0.05(4)	1.05(10)	1.04/$E2$	$8^+ \to 6^+$
523.6	1.7	12.1	0.22(9)	−0.02(13)			$13^- \to 11^-$
526.7	4.5	4.1	−0.34(6)	−0.09(8)			$4^+_\beta \to 4^+$
552.4	1.7	8.9	0.54(13)	−0.12(16)			$10^+_\beta \to 8^+$
553.6	19.6	47.3	0.21(4)	−0.11(4)			$10^+ \to 8^+$
583.4	2.2	20.6	0.29(8)	−0.08(10)			$12^+ \to 10^+$
584.6	10.3	14.0	−0.25(7)	0.16(10)			$9^- \to 8^+$
586.3	6.1	3.6	−0.37(18)	−0.10(25)			$2^+_\beta \to 2^+$
589.9	1.9	4.5	0.24(6)	−0.03(10)	0.66(19)	0.75/$E2$	$11^+ \to 10^+$
600.5		6.7	0.20(4)	−0.07(6)	0.72(11)	0.73/$E2$	$15^- \to 13^-$
615.4	1.1	11.1	0.23(4)	−0.09(6)			$14^+ \to 12^+$
643.5		4.4	0.21(4)	−0.07(5)	0.55(11)	0.61/$E2$	$16^+ \to 14^+$
652.9	7.9	4.8	−0.31(5)	0.06(8)	0.22(4)	0.23/$E1$	$7^- \to 6^+$
670.6		3.4	0.19(7)	0.03(10)	0.41(21)	0.56/$E2$	$17^- \to 15^-$
715.0	4.8	1.9	−0.27(10)	0.24(15)			$5^- \to 4^+$
778.9	1.4						$3^- \to 2^+$
790.2	2.9	2.9	0.31(7)	0.11(9)			$9^+ \to 8^+$

[a] Reference 27.

difficult due to similarity in energy to gsb transitions.

C Decay of 3.3-min ^{154}Ho

Transition data for this decay are given in Table IV. Of 32 transitions assigned to this decay, 14 are newly observed and have been incorporated into a decay scheme consisting of 17 levels (Fig. 6). A conversion-electron spectrum obtained via the He-jet technique (Fig. 7) allowed multipolarity assignments to be made for 16 transitions.

The data support a probable spin of 7 or 8 for the ^{154}Ho parent, with most of the EC$+\beta^+$ decay occurring with an allowed log*ft* value (≤ 4.6) to a 7^+ level at 2472.9 keV in ^{154}Dy. The two states involved are probably identical in character to those observed in the high-spin isomer decay of ^{152}Tb where they are interpreted as having the configurations $(\pi\frac{5}{2}^-|532| + \nu\frac{11}{2}^-|505|)\,8^+$ and $(\nu\frac{3}{2}^-[532] + \nu\frac{11}{2}^-[505])\,7^+$. Unlike ^{152}Tb, however, no isomeric transitions in ^{154}Ho were observed.

In a previous work,[13] weak transitions at 158, 472, and 911 keV were tentatively proposed. The were not observed in our data and probably are n associated with this decay. The former two transitions undoubtedly belong to the decay of 4.2-min ^{152}Tb, which is a principal impurity for the reaction chosen.

Higher-spin members of vibrational bands are populated in this decay, with the quasirotational beta, gamma, and $K=0$ octupole bands observed to the 8^+, 7^+, and 7^- states, respectively.

D. Decay of 11.8-min ^{154}Ho

The 11.8-min ^{154}Ho activity was obtained via the β decay of ^{154}Er produced in the ^{148}Sm(^{12}C, 6*n*) reaction. The decay of the 0^+ ground state of ^{154}Er ensures that only the low-spin isomer of ^{154}Ho is

TABLE IV. Transition data for 3.3-min ^{154}Ho decay.

E_γ (keV)		I_γ		I_K	$\alpha_K(\times 10^2)$ exp.	$\alpha_K(\times 10^2)$ theo.[b]	Multipolarity	Placement
280.4		1.4(2)						2472.9 → 2192
289.4(2)		5.2(4)		9.9(9)	19.1(21)	$M1$:10.8	$E0+(M1+E2)$	2472.9 → 2183.
309.5(2)		4.1(3)		3.9(4)	9.4(11)	$M1$:9.00	$M1$	2472.9 → 2163.4
334.6(1)		≡100		≡36	3.60	$E2$:3.60	$E2$	334.6 → 0
346.6(2)		10.5(7)		3.7(9)	3.5(9)	$E2$:3.25	$E2$	1251.8 → 905.2
405.8(4)		3.1(5)		4.4(3)	1.9(2)	$E2$:2.10		1740.0 → 1334.3
406.9(1)		20.2(14)					$E2$	1658.8 → 1251.8
412.4(1)		84.3(51)		17.3(10)	2.05(17)	$E2$:2.05	$E2$	747.0 → 344.6
434.7(2)		2.7(3)		6.3(4)	23(3)	$M1$:3.68	$E2+E0+(M1)$	1658.8 → 1224.1
443.3(2)		5.5(4)		0.8(2)	1.5(4)	$E2$:1.73	$E2$	2183.3 → 1740.0
477.1(1)		58.7(31)		7.6(10)	1.3(2)	$E2$:1.39	$E2$	1224.1 → 747.0
504.7(2)	504.6	17.4(10)	13.5[a]	10.9(7)	6.26(52)	$M1$:2.50		2163.4 → 1658.8
	504.8						$E2+E0+(M1)$	1251.8 → 747.0
515.6(3)		2.0(3)						1740.0 → 1224.1
523.8(1)		19.5(11)		2.2(3)	1.1(2)	$E2$:1.10	$E2$	1747.9 → 1224.1
570.6(1)		11.2(6)		2.3(3)	2.1(3)	$M1$:1.83	$M1, E2+E0+(M1)$	905.2 → 334.6
587.3(3)		1.3(2)						1334.3 → 747.0 2472.9 → 1885.6
661.5(3)		1.9(5)		0.25(13)	1.3(8)	$M1$:1.28	$M1, E2$	1885.6 → 1224.1
725.1(1)		13.3(8)		0.92(15)	0.69(12)	$E2$:0.52	$M1+E2$	2472.9 → 1747.9
732.8(2)		3.3(3)						2472.9 → 1740.0
740.6(2)		2.5(3)						1964.7 → 1224.1
798.9(3)		1.5(3)						1545.9 → 747.0
814.1(1)		15.0(9)		0.85(14)	0.57(10)	$E2$:0.39	$M1+E2$	2472.9 → 1658
905.2(3)		1.8(3)						905.2 → 0
959.1(3)		2.6(3)						2183.3 → 1224.1
968.3(3)		2.7(3)						2192.5 → 1224.1
992.9(3)		5.3(5)						1740.0 → 747.0
999.7(3)		2.5(3)						1334.3 → 334.6
1072.2(4)		0.3(1)						1819.0 → 747.0
1138.5(3)		1.0(2)						1885.6 → 747.0
1248.8(2)		18.9(10)		0.60(13)	0.32(8)	$M1$:0.28	$M1$	2472.9 → 1224.1

[a] Intensity estimated from spectrum of γ rays coincident with 814.1-keV transition.

[b] Reference 27.

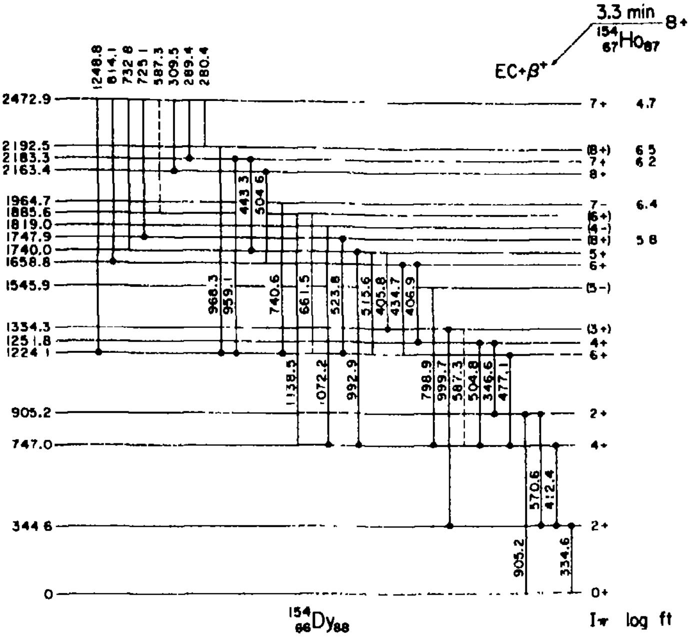

FIG. 6. Levels in ^{154}Dy observed in the decay of 3.3-min ^{154}Ho. Placements supported by coincidence data are indicated as in Fig. 4. Dashes indicate alternate placements.

observed. The energies and intensities of the 64 assigned transitions are given in Table V and have been placed in a decay scheme consisting of 34 excited states (Table VI).

The probable parent spin consistent with the observed data is 3^+. This conclusion is somewhat perplexing since an atomic beam measurement indicates spin 1 for the 11.8-min activity.[14] In contradiction to this, 0^+ states appear not to be fed, while the 4^+ level of the gsb is clearly populated in the decay. A strong 158-keV transition tentatively postulated in a previous work[13] to account for the intensity imbalance for the 4^+ state is not supported by our singles or coincidence data. Furthermore, the existence of a third isomer with similar half-life and spin 1 is unlikely, since it would have been dominantly produced in the ^{154}Er decay. Consequently, we are forced to the conclusion that the atomic beam results are somehow in error.

Conversion-electron data, summarized in Table VII, indicate seven transitions totally or partially $E0$ in character. These data were crucial in locating the second excited 0^+ state at 1057.9 keV.

E. Decay of 82-sec ^{156}Tm

Previously, two ^{156}Tm isomers were proposed from an α-decay study—a lower-spin isomer with $T_{1/2}=80$ sec and a high-spin isomer with $T_{1/2}=19$

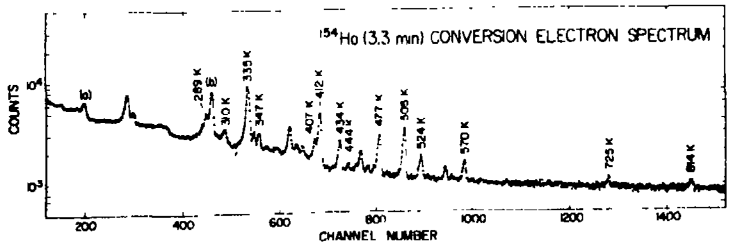

FIG. 7. Conversion-electron spectrum for the decay of 3.3-min ^{154}Ho using the He-jet technique. A total of 386 sources was counted for 30 sec each. The peak labeled (a) is the K-conversion line from the 160 keV $E3$ transition in ^{152}Tb^m decay, while that labeled (b) is the 296K-conversion line originating from ^{153}Ho decay.

TABLE V. Transition data for 11.8-min ^{154}Ho decay.

E_γ (keV)	I_γ	Placement	E_γ (keV)	I_γ	Placement
152.7(3)	0.59(10)	1057.9 → 905.2	876.6(3)	0.72(10)	1903.8 → 1027.1
182.0(4)	0.76(15)	1390.4 → 1208.0	905.2(2)	2.60(24)	905.2 → 0
244.2(4)	0.50(15)	905.2 → 660.8	999.7(2)	3.86(24)	1334.3 → 334.6
326.2(3)	5.60(90)	660.8 → 334.6	1027.1(2)	6.76(41)	1027.1 → 0
334.6(1)	100^{N}	334.6 → 0	1056.8(3)	1.14(14)	1390.4 → 334.6
346.6(3)	1.19(12)	1251.9 → 905.2	1058.4(6) [a]		1057.9 → 0
363.4(4)	0.42(20)	1390.4 → 1027.1	1072.2(3)	1.18(15)	1818.9 → 747.1
366.2(3)	1.27(16)	1027.1 → 660.8	1085.9(3)	1.94(17)	1420.5 → 334.6
397.3(2) [a]		1057.9 → 660.8	1108.0(4)	0.80(20)	1442.6 → 334.6
412.5(1)	17.8(10)	747.0 → 334.6	1156.8(4)	0.57(28)	1903.8 → 747.1
415.8(4)	0.47(11)	1442.6 → 1027.1	1173.2(2)	2.11(18)	1507.6 → 334.6
429.1(4)	0.53(13)	1334.3 → 905.2	1244.6(3)	0.40(10)	2272.2 → 1027.1
460.9(3)	1.09(10)	1208.0 → 747.1	1300.6(2)	4.48(28)	1635.2 → 334.6
480.0(4)	0.26(10)	1507.6 → 1027.1	1390.0(4)	0.58(13)	1390.4 → 0
485.3(3)	0.66(10)	1390.4 → 905.2	1420.3(3)	2.41(23)	1420.5 → 0
504.9(3)	1.78(17)	1251.9 → 747.1	1431.0(3)	0.67(13)	2178.2 → 747.1
515.2(4)	0.48(20)	1420.5 → 905.2	1447.1(4)	0.59(13)	1782.0 → 334.6
569(1)	13.2(7)	1903.8 → 1334.3	1498.3(3)	1.68(16)	1832.9 → 334.6
570.6(2)		905.2 → 334.6	1502.5(4)	0.77(13)	2249.6 → 747.1
587.4(3)	0.94(10)	1334.3 → 747.1	1507.6(4)	0.89(18)	1507.6 → 0
602.9(4)	0.36(10)	1507.6 → 905.2	1510.3(3)	2.21(19)	1844.9 → 334.6
610.6(5)	0.35(16)	1818.9 → 1208.0	1542.7(5)	1.05(14)	1877.2 → 334.6
642.8(4)	0.54(25)	1390.4 → 747.1	1611.2(5)	0.37(15)	2272.2 → 660.8
660.8(2) [a]		660.8 → 0	1623.7(5)	0.80(15)	1958.3 → 334.6
692.5(2)	6.07(40)	1027.1 → 334.6	1656.5(3)	1.65(16)	1991.1 → 334.6
695.5(3)	1.28(11)	1442.6 → 747.1	1813.8(5)	0.64(12)	2148.4 → 334.6
723.6(5)	0.2(1)	1057.9 → 334.6	1834.1(4)	1.19(14)	2168.7 → 334.6
729.7(3)	1.46(12)	1390.4 → 660.8	1843.8(5)	0.60(13)	2178.2 → 334.6
755.1(5)	0.65(13)	1782.0 → 1027.1	1849.3(4)	1.09(14)	2183.9 → 334.6
799.0(3)	0.66(10)	1546.1 → 747.1	1877.1(6)	0.55(14)	1877.2 → 0
846.6(3)	1.12(11)	1507.6 → 660.8	1937.8(5)	0.73(15)	2272.2 → 334.6
873.4(1)	14.8(10)	1208.0 → 334.6	2010.3(6)	0.62(12)	2344.9 → 334.6

[a] $E0$ transition. Energy determined from conversion-electron data.

sec.[15] In a heavy-ion reaction, such as the ^{148}Sm(^{14}N, 6n) reaction used by us to produce ^{156}Tm, the production of the high-spin isomer should dominate. However, several multispectral-scaling measurements performed over time-bin ranges of 5–20 sec showed only the presence of a single ^{156}Tm activity with $T_{1/2}=82\pm5$ sec. This failure to observe a short-lived component in any of the transitions in ^{156}Tm suggests an error was probably made in assigning the 19-sec α branch to this nucleus.

A total of 37 transitions have been assigned to the 82-sec activity. The γ-ray and conversion-electron data are summarized in Tables VIII and IX, respectively. The decay scheme is presented in Fig. 8. Based on a consideration of the spin and parity of the states populated in the EC $+\beta^+$ decay, the probable J^π assignment for the ^{156}Tm parent is 3^+, and could be explained as the $\pi\frac{5}{2}^+[402]+\nu\frac{1}{2}^+[660]$ configuration.

During the course of our investigation, a study of the decay of the ^{156}Tm was reported in which the activity was produced via the Er(p, xn) reaction.[16] While this work failed to locate the 3^+ state at 1243.0 keV and, consequently, was in error in some band assignments (see next section), the transition data are in good agreement with ours.

IV. DISCUSSION

A. Systematics

Since the $N=88$ nuclei lie just outside the permanently deformed region which begins at $N=90$, they exhibit transitional character. Although rotational spacings are not observed between levels, it has been demonstrated that quasirotational bands can be constructed in ^{152}Gd which correspond to the rotational bands in ^{154}Gd (Ref. 9). The quasirotational bands for all $N=88$ nuclei (Fig. 9) are strikingly similar, with the gsb in ^{152}Gd and ^{154}Dy

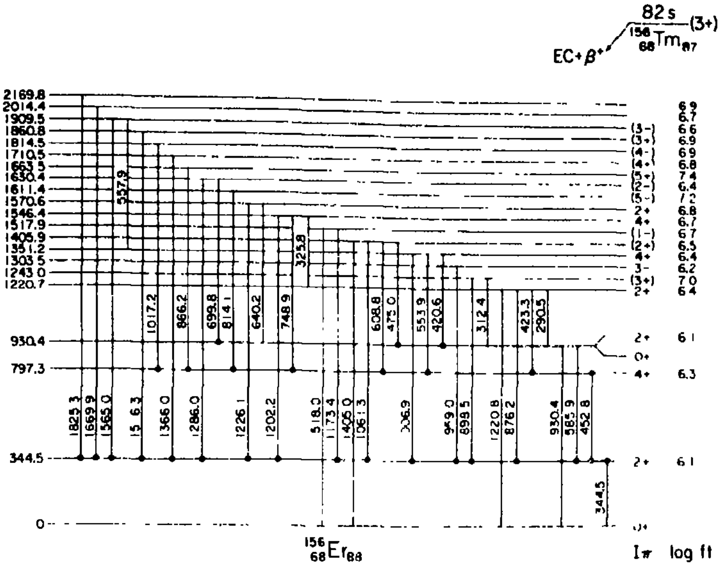

FIG. 8. Levels in ^{156}Er observed in the decay of 82-sec ^{156}Tm. Placements confirmed by coincidence data are indicated as in Fig. 4. Note that there are two levels at 930.4 keV.

being nearby identical. The new information obtained in this investigation for ^{152}Gd, ^{154}Dy, and ^{156}Er, together with that known previously for ^{150}Sm (Ref. 1), now permits a discussion of the systematics of $N=88$ nuclei and a clearer picture of the effects of increasing proton number on level structure.

It is believed that the main trends in the location of the vibrational bands in nuclei can be understood from a consideration of available orbitals in a Nilsson diagram.[17] For each vibrational type, selection rules exist for the asymptotic quantum numbers $Nn_z\Omega\Sigma$. These are given in Table X for the beta, gamma, and octupole ($K=0$) vibrational bands. The operator associated with each vibrational field is also listed. A discussion of the success of these selection rules in accounting for the observed systematics follows.

Quasi-gamma band

The systematic behavior of the members of the quasi-gamma states in $N=88$ nuclei is shown in Fig. 10. A bunching of pairs of states is observed and can be associated with a small difference in the prolate and oblate well depths (near-γ instability).[18] The smooth monotonic decrease in energy with increasing proton number, which is observed for all the band members, can be easily understood from a consideration of the Nilsson diagram for protons shown in Fig. 11. Applying the selection rules given in Table X, one finds that only two pairs of states, $\{\frac{5}{2}^+[413], \frac{1}{2}^+[411]\}$ and $\{\frac{3}{2}^+[411], \frac{1}{2}^+[411]\}$, will lead to large strength for γ vibrations. Consequently, the lowest-lying gamma bands should occur for $Z=66$ or $Z=68$, since both orbital pairs are contributing at these proton numbers. The $N=88$ systematics merely reflect this, showing a smooth decrease to a minimum at $Z=68$. It follows from this argument, that the γ-vibrational bandhead in ^{158}Yb ($Z=70$) when located, should show an upturn in energy.

The same selection rules, of course, can also be applied to neutrons, where the $\{\frac{3}{2}^-[523], \frac{1}{2}^-[521]\}$ and $\{\frac{5}{2}^-[523], \frac{1}{2}^-[521]\}$ orbital pairs are found to be the important ones. Large contributions to γ vibrations are therefore expected for $N\approx 98$. The combined contributions from protons and neutrons are thus expected to produce the lowest-lying γ bands in ^{164}Dy and ^{166}Er. As seen in Fig. 12, this has been verified experimentally.

Quasi-beta band

The relative location of the members of the quasi-beta bands in $N=88$ nuclei is depicted in Fig. 13. The bandheads are observed to occur at rather low energies. This can again be understood

TABLE VI. Decay scheme for 11.8-min ^{154}Ho(3$^+$).

Level (keV)	I^π	I(EC + β^+) (%)	log*ft*[a]	Depopulating transitions (level fed)[b] (keV)
334.6	2^+	15.27	6.8	334.6(g.s.)
660.8	0^+			326.2(334.6), $\underline{660.8}$(g.s.)
747.1	4^+	7.29	7.0	412.5(334.6)
905.2	2^+	10.43	6.7	244.2(660.8), 570.6(334.6), 905.2(g.s.)
1027.1	2^+	9.59	6.7	366.2(660.8), 692.5(334.6), 1027.1(g.s.)
1057.9	0^+	1.95[c]	7.4	152.7(905.2), $\underline{397.1}$(660.8), $\underline{723.6}$(334.6), $\underline{1058.4}$(g.s.)
1208.0	3^-	12.55	6.5	460.9(747.1), 873.4(334.6)
1251.9	4^+	2.63	7.2	346.6(905.2), 504.9(747.1)
1334.3	3^+	4.50	6.9	429.1(905.2), 587.4(747.1), 999.7(334.6)
1390.4	2^+	4.84	6.9	182.0(1208.0), 363.4(1027.1), 485.3(905.2), 642.8(747.1), 729.7(660.8), 1055.8(334.6), $\underline{1390.0}$(g.s.)
1420.5	1^-	4.07	6.9	515.2(905.2), 1085.9(334.6), $\underline{1420.3}$(g.s.)
1442.6	4^+	2.21	7.2	415.8(1027.1), 695.5(747.1), 1108.0(334.6)
1507.6	2^+	3.99	6.9	$\underline{480.0}$(1027.1), 602.9(905.2), 846.6(660.8), 1173.2(334.6), $\underline{1507.6}$(g.s.)
1545.9	(5^-)	0.56	7.7	799.0(747.1)
1635.2	2^-	3.80	6.9	1300.6(334.6)
1782.0	(3^+)	1.20	7.3	755.1(1027.1), 1447.1(334.6)
1818.9	(4^-)	1.30	7.3	610.6(1208.0), 1072.2(747.1)
1832.9		1.43	7.2	1498.3(334.6)
1844.9		1.87	7.1	1510.3(334.6)
1877.2		1.36	7 2	1542.7(334.6), 1877.1(g.s.)
1903.8	(3^-)	1.09	7.3	569(1334.3), 876.6(1027.1), 1156.8(747.1)
1958.3		0.68	7.5	1623.7(334.6)
1991.1		1.40	7.1	1656.5(334.6)
2148.4		0.54	7.5	1813.8(334.6)
2168.7		1.01	7.2	1834.1(334.6)
2178.2		1.08	7.2	1431.0(747.1), 1843.8(334.6)
2183.9		0.92	7.2	1849.3(334.6)
2249.6		0.65	7.4	1502.5(747.1)
2272.2		1.27	7.1	1244.6(1027.1), 1611.2(660.8), 1937.8(334.6)
2344.9		0.53	7.4	2010.3(334.6)

[a] Reference 28. Q_{EC} is taken as 5.76 MeV.

[b] Transitions underlined are placed on the basis of energy sums and differences. All other placements are based on coincidence experiment results.

[c] The apparent weak EC + β^+ population of the 1057.9-keV state may principally originate from an unresolved transition from the 1390.4-keV state.

TABLE VII. Conversion coefficient data for 11.8-min ^{154}Ho.

Transition energy (keV)		I_K	$\alpha_K(\times 10^2)$ exp.	$\alpha_K(\times 10^2)$ theo.[a]	Multipolarity
334.6		≈1000	≈3.60	$E2$:3.60	$E2$
397.3		352(21)			$E0$
412.5		108(8)	2.18(20)	$E2$:2.05	$E2$
485.3		32.3(48)	17.6(37)	$M1$:2.75	$E0+(E2)+(M1)$
504.9		38.0(41)	7.9(12)	$M1$:2.50	$E0+(E2)+(M1)$
570.6		70.0(57)	>1.91(15)	$M1$:1.83	$E0+(E2)+(M1)$
660.8		131(8)			$E0$
692.5		22.6(50)	1.34(31)	$M1$:1.14	$M1$
695.5		4.1(22)	1.15(58)	$E2$:0.55	$M1+(E2)$
873.4		5.7(28)	0.14(7)	$E1$:0.139	$E1$
1055.8	13.2(30)	4.9(20)	1.55(65)	$M1$:0.41	$E0+(E2)+(M1)$
1058.4		8.3(25)			$E0$

[a] Reference 27.

TABLE VIII. Transition data for 82-sec ^{156}Tm decay.

E_γ (keV)	I_γ	Placement	E_γ (keV)	I_γ	Placement
290.5(5) [a]	0.5(2)	1220.7 → 930.4	930.4(1)	5.9(4)	930.4 → 0
312.4(4) [a]	0.3(1)	1243.0 → 930.4	959.0(1)	10.8(7)	1303.5 → 344.5
325.8(4) [a]	0.4(2)	1546.4 → 1220.7	1006.9(2)	3.6(4)	1351 2 → 344.5
344.5(1)	≅100	344.5 → 0	1017.2(3)	1.3(2)	1814.5 → 797.3
420.6(3)	2.1(2)	1351.2 → 930.4	1061.3(4)	1.0(3)	1405.9 → 344.5
423.3(3)	0.7(3)	1220.7 → 797.3	1173.4(3)	0.7(4)	1517.9 → 344.5
452.8(1)	20.5(11)	797.3 → 344.5	1202.2(3)	1.2(2)	1546.4 → 344.5
475.0(6)	0.9(2)	1405.9 → 930.4	1220.8(2)	3.6(4)	1220.7 → 0
553.9(3)	1.2(2)	1351.2 → 797 3	1226.1(3)	1.4(2)	1570.6 → 344.5
557.9(4) [a]	0.4(2)	1909.5 → 1351.2	1286.0(2)	3.1(4)	1630.4 → 344.5
585.9(1)	17.3(9)	930.4 → 344.5	1366.0(3)	1.7(3)	1710.5 → 344.5
608.8(3)	1.8(2)	1405.9 → 797.3	1405.0(5)	0.5(2)	1405.9 → 0
640.2(4)	0.7(3)	1570.6 → 930.4	1516.3(6)	1.4(5)	1860.8 → 344.5
699.8(3)	1.5(2)	1630.4 → 930.4	1518.0(4)	2.2(5)	1517.9 → 0
748.9(4)	1.0(5)	1546.4 → 797.3	1565.0(3)	1.9(3)	1909.5 → 344.5
814.1(6)	0.7(4)	1611.4 → 797.3	1663.9(4)	1.3(3)	
866.2(4)	0.5(2)	1633.5 → 797.3	1669.9(3)	1.7(3)	2014.4 → 344.5
876.2(2)	2.8(3)	1220.7 → 344.5	1825.3(3)	1.0(2)	2169.8 → 344.5
898.5(3)	1.6(2)	1243.0 → 344.5			

[a] Tentatively assigned to decay.

from a consideration of the selection rules in Table X. The set of appropriate selection rules indicates no change in the asymptotic quantum numbers. This means that the relevant quantity for a given orbital ν is its quadrupole moment $\langle \nu | r^2 Y_{20} | \nu \rangle$. Enhancement of the beta-vibrational mode is therefore expected where two orbitals with markedly different quadrupole moments cross. Recalling that orbitals with large N and n_z values have the largest prolate quadrupole moments and that those with N large but n_z small are the most oblate, one can see that low-lying beta bands should occur when a low-Ω state from a high-j orbital (downsloping, that is, larger-deformation driving) crosses a high-Ω state from a high-j orbital (upsloping, or, smaller-deformation driving). Pairing correlations result in states which are mixed, and the competition between a component favoring smaller deformation and another favoring a larger deformation enhances the β-vibrational mode. The low-lying β bands in the $N=88-90$ nuclei are, therefore, readily explained, resulting from the crossing of the $\frac{11}{2}^-[505]$ and $\frac{1}{2}^-[660]$ neutron orbitals as seen in Fig. 14. Similarly, the minimum observed for the beta bandhead at $Z=64$ can be principally ascribed to crossing of the $\frac{5}{2}^-[532]$ prolate orbital and the $\frac{5}{2}^+[413]$ weakly oblate orbital at that proton number.

Second excited 0^+ states

The second excited 0^+ states in $N=88$ nuclei are observed to follow the same systematic trends as the β-band states (Fig. 13) and occur at energies 1.6 to 1.7 times that of the β-band 0^+ state. They also show a large preference to decay to the one-phonon beta-vibrational states, as is evident from the ratios of reduced transition probabilities given in Table XI. This leads to an interpretation of these states as having two-phonon beta-vibrational character.

A consideration of available two-nucleon transfer data, however, suggests the situation may be more complicated. In deformed nuclei, one would expect the two-particle transfer strength to collect in the ground state, since these nuclei are generally superconducting. In spherical nuclei, however, the strength may be shared with an excited 0^+ state usually considered to be pairing vibrational. Data

TABLE IX. Conversion-electron data for 82-sec ^{156}Tm decay.

Transition energy (keV)	I_K	$\alpha_K(\times 10^2)$ exp.	$\alpha_K(\times 10^2)$ theo. [a]	Multipolarity
344.5	≈35	≈3.50	$E2$:3.50	$E2$
420.6	0.5(2)	2.4(10)	$E2$:2.05	$E2$
452.8	3.2(3)	1.56(17)	$E2$:1.70	$E2$
585.9	1.3(2)	0.75(16)	$E2$:0.90	$E2$
876.2	0.9(2)	3.2(8)	$M1$:0.75	$E0+E2+(M1)$
930.4	0.4(2)	0.68(34)	$M1$:0.64	$M1, E2$
959.0	<0.2	<0.19	$E1$:0.13	$E1$

[a] Reference 27.

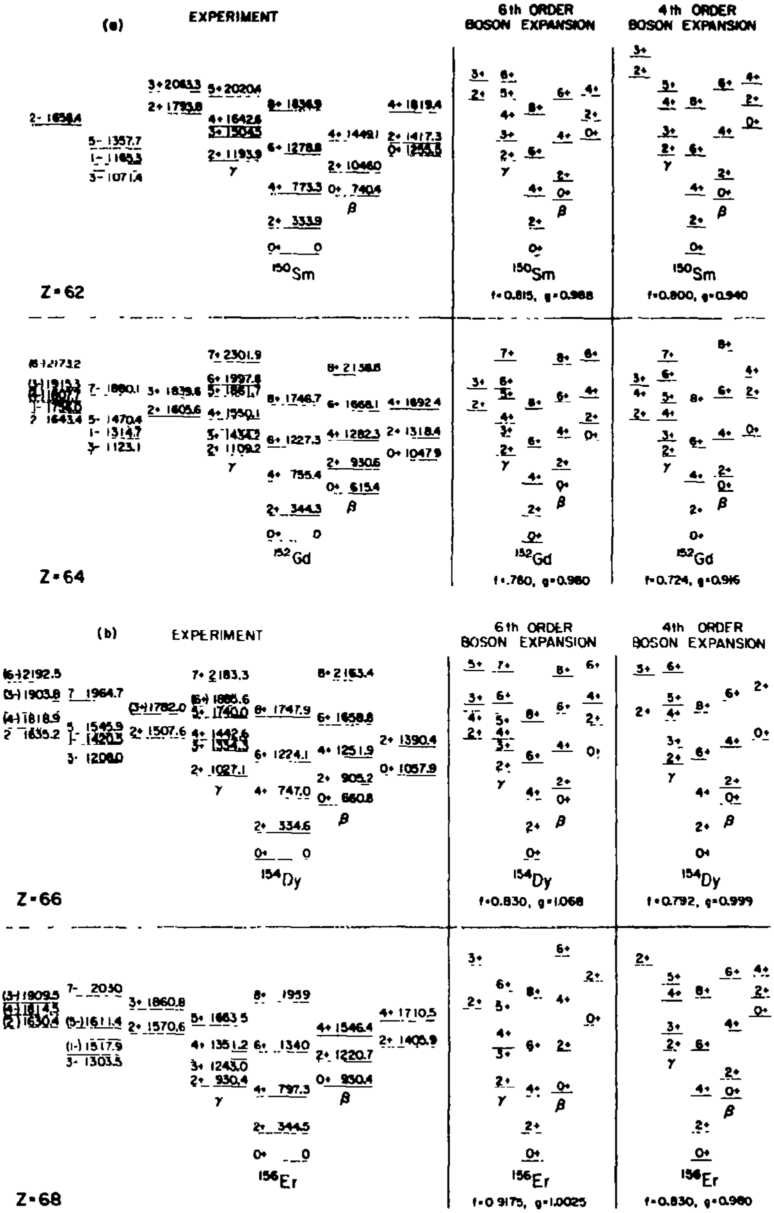

FIG. 9. (a) Comparison of quasirotational bands in ^{150}Sm and ^{152}Gd with results from microscopic fourth- and sixth-order boson-expansion calculations. Data for ^{150}Sm are from Ref. 1. (b) Same as Fig. 9(a) for ^{154}Dy and ^{156}Er.

obtained for the ^{154}Gd(p, t)^{152}Gd and ^{152}Sm(p, t)^{150}Sm reactions, however, show two excited 0^+ states, accompanied by a decrease in the ground-state population strength as compared to that of their higher mass isotopes.[19] Poor shape overlap between the A and $A \pm 2$ ground states is generally invoked to explain the results obtained in the N=88–90 region. For example, failure to observe the 1255-keV 0^+ state in the ^{148}Sm(t, p)^{150}Sm reaction led to the proposal that this was a deformed state existing in a more or less spherical nucleus.[19] Although one might then expect such a

TABLE X. Asymptotic quantum number selection rules and operators for vibrational bands.

Vibration	Operator	Selection rules
β	r^2Y_{20}	$\Delta N=0, \Delta n_z=0$ $\Delta\Lambda=0, \Delta\Sigma=0$
γ	$r^2Y_{2\pm2}$	$\Delta N=0, \Delta n_z=0$ $\Delta\Lambda=2, \Delta\Sigma=0$
Octupole ($K=0$)	r^3Y_{30}	$\Delta N=1, \Delta n_z=1$ $\Delta\Lambda=0, \Delta\Sigma=0$

deformed state to be isomeric, this has not been reported.

A microscopic calculation of the competition between the pairing- and beta-vibrational modes has been performed by Mikoshiba.[20] Interestingly, these two states were found in the transition region around $N=90$ to occur at similar energies and to couple significantly. The beta-vibrational state would, therefore, contain a certain admixture of the pairing vibration and vice versa. Thus, the second excited 0^+ states in the $N=88$ nuclei could be pairing vibrational in character. No definitive interpretation of these states, however, seems possible at this time on the basis of available data.

Negative-parity states

In-beam investigations of $N=88$ nuclei[1] had previously identified to high spin a negative-parity odd-spin band of unknown character. The absence of even-spin states lead Gono *et al.*[1] to interpret the ^{156}Er negative-parity band as a $K=0$ band. Flaum and Cline,[3] however, interpreted the same

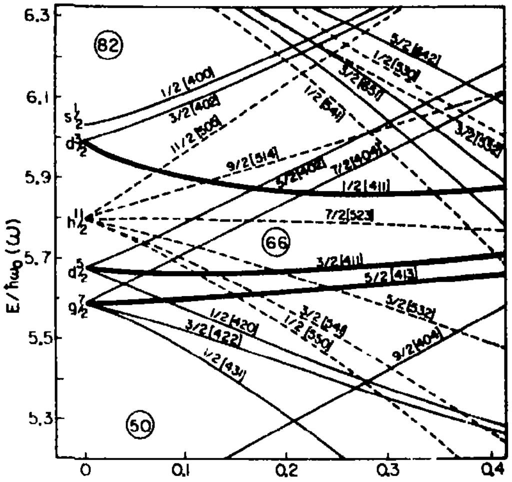

FIG. 11. Portion of Nilsson diagram for protons. Bold orbitals are those which are responsible for low-lying γ bands at $Z=66-68$. See text for details.

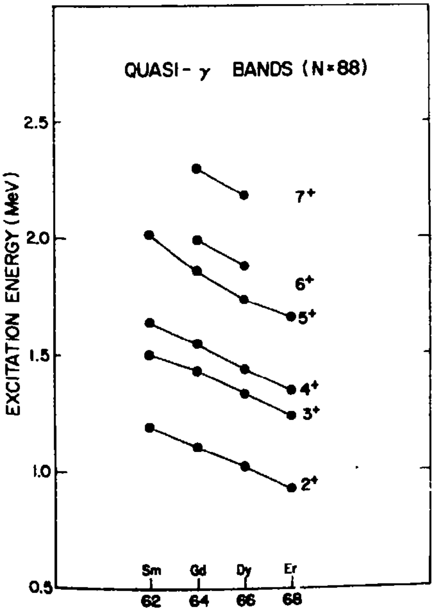

FIG. 10. γ-band systematics for several $N=88$ nuclei.

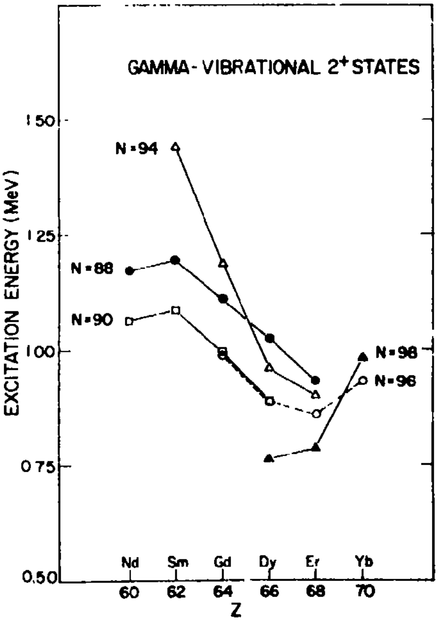

FIG. 12. Systematics of γ-vibrational 2^+ states in the region $Z=60-70$ and $N=88-94$.

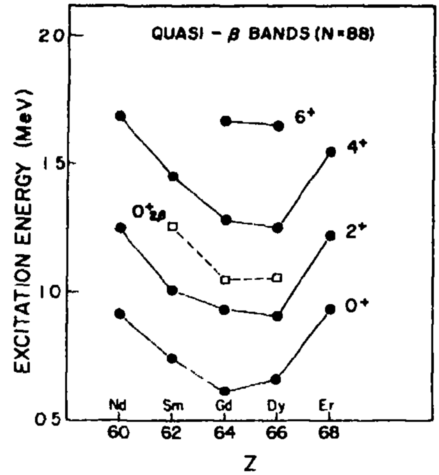

FIG. 13. Systematics for β-band members for several $N=88$ nuclei. The second excited 0^+ states are also indicated with open squares.

states as members of a two-quasiparticle aligned band composed of $i_{13/2}$ and $f_{7/2}$ quasineutrons. For ^{152}Gd, where several additional negative-parity states below 2 MeV were also known, it was shown by Zolnowski *et al.*[2] and Nomura[4] that all the known negative-parity states in this nucleus could be explained remarkably well in the framework of a simple quadrupole-octupole coupling model (QOC). The so-called interacting-boson-approximation model (IBA) of Arima and Iachello[21] when treating negative-parity states is basically similar to the QOC model. Owing to a different choice of interaction term in the Hamiltonian, however, the IBA model requires five parameters to describe all the negative-parity states in ^{152}Gd, whereas the QOC model requires only one after gsb parametrization.

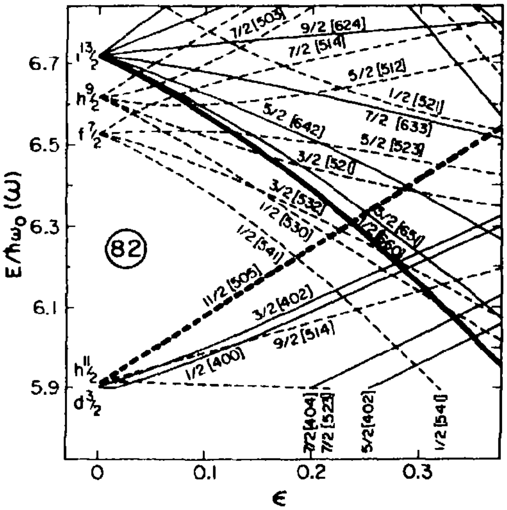

FIG. 14. Portion of Nilsson diagram for neutrons. The crossing of the bold $\frac{1}{2}$ [660] and $\frac{11}{2}$ [505] orbitals is responsible for the low-lying β bands observed in the $N=88-90$ region.

In this investigation we were successful in locating the lower-spin negative-parity states in other $N=88$ nuclei. The data obtained revealed the systematic trends for negative-parity states as summarized in Fig. 15. The odd-spin states decrease in energy with decreasing proton number. The tendency of the 1^- state to move below the first 3^- state for lower Z suggests an increase in deformation for these nuclei. The even-spin states and the second 3^- state, however, proved insensitive to changes in proton number. All of these systematic trends are successfully reproduced by the QOC model (Fig. 15) and indicate, as one might expect, octupole vibrational character for these states.

The selection rules given in Table X for $K=0$ octupole vibrational states do not give, as they did for the γ- and β-vibrational bands, a simple explanation of the systematic behavior of the low-lying negative-parity states. Upon perusal of the Nilsson diagram, the reason for this becomes clear. Unlike the situation for the quadrupole vibrational bands, a large number of states satisfy the selection rules. Consequently, it is impossible to locate visually the regions of maximum effect.

The high-spin negative-parity states in ^{150}Sm, ^{152}Gd, and ^{154}Dy are also remarkably reproduced by a QOC calculation. The fit to ^{154}Dy levels is shown in Fig. 16. However, the model produces, in comparison, only a fair fit to ^{156}Er (Table XII). The reason is not clear since the experimental evidence indicates that this band has the same character in all the $N=88$ nuclei.

A model introduced by Vogel[22] proposes that above a certain critical spin value, the negative-parity yrast states should be interpreted as decoupled two-quasiparticle states. He notes that at high angular momenta, independent alignment of the participating quasiparticles along the axis of rotation might be energetically favored over correlated octupole motion. Thus, the low-lying negative-parity states would be octupole, but the higher ones would be decoupled two-quasiparticle states. A plot of $2\mathscr{I}/\hbar^2$ vs $\hbar^2\omega^2$, the ordinary backbending plot, is shown in Fig. 17 for the negative-parity band. The moment of inertia for the lower states of the band is found to change abruptly and then assume an approximately constant value.

TABLE XI. Experimental and theoretical $B(E2)$ ratios in $N=88$ nuclei. The notation BE4 and BE6 refers to fourth-order and sixth-order boson-expansion calculations.

Initial	Final		^{150}Sm			^{152}Gd			^{154}Dy			^{156}Er	
state	states	exp.[a]	BE4	BE6	exp.[a]	BE4	BE6	exp.[a]	BE4	BE6	exp.[a]	BE4	BE6[b]
2_β	$4g/2g$	3.87(48)	0.32	0.30	2.04(27)	0.24	0.27		0.23	0.27	9.5(42)	0.22	101
	$0g/2g$	0.084(10)	0.10	0.10	0.020(2)	0.099	0.097	0.016(3)	0.10	0.10	0.25(4)	0.10	7.1
	$0\beta/0g$	27.6(39)	7.6	7.6	107(11)	5.4	6.7	135(42)	5.7	6.8		6.4	28.2
4_β	$2g/4g$	0.0024(5)	0.056	0.056		0.081	0.054		0.067	0.052	0.11(6)	0.053	2.2
	$2\beta/4g$	5.93(85)	2.66	2.8	8.4(8)	2.2	2.6	4.39(61)	2.2	2.7	26(18)	2.4	78.9
6_β	$4\beta/6g$		5.1		16(6)	4.5	6.4	10.4(14)	4.4	6.6		4.6	
2_γ	$2g/0g$	4.4(6)	0.66	1.1	7.05(70)	0.75	1.3	6.4(6)	0.55	1.2		0.40	10.7
	$2g/4g$	2.0(7)	0.083	0.18		0.071	0.21		0.055	0.20		0.042	29.5
	$0\beta/0g$	5.2(7)	9.6	8.3	2.93(35)	13.4	8.2		13.0	7.3		13.0	3.2
	$2\beta/2g$	12(6)	25.0	14.5		21.0	11.1		27 4	12.1		39.6	0.26
	$0\beta/2\beta$	0.10(5)	0.59	0.51		0.85	0.55		0.85	0.53		0.81	1.14
3_γ	$2g/4g$	0.29(6)	0.94	0.88	0.45(5)	0.85	0.83	0.29(4)	0.83	0.90		0.82	0.56
	$2\beta/2g$	11(3)	3.1	2.8	2.8(3)	3.4	2.8	9.4(24)	3.6	2.6		4.0	2.9
4_γ	$2g/4g$	0.050(7)	1.3	0.72	0.071(15)	1.3	0.73	0.061(16)	1.5	0.81	0.15(3)	1.7	0.068
	$2\beta/4g$	2.95(59)	0.0077	0.085		0.0018	0.36		0.050	0.34		0.059	2.4
	$4\beta/2\beta$	70(21)	525	52.9		1714	11.0		60.4	10.2		48.0	
	$4\beta/4g$	10.3(27)	5.1	3.3		4.0	2.9		4.6	2.9		4.85	
	$3\gamma/2\gamma$	2.7(13)	0.34	0.42		0.30	0.44		0.27	0.49		0.297	0.50
	$2\gamma/2g$		17.2	13.2		13.9	8.3	79(27)	17.2	7.1		22.0	24.9
5_γ	$6g/4g$		1.2		5.44(53)	1.08	1.15	10.0(18)	1.25	1.04		1.43	2.1
	$4\beta/4g$		1.2	0.72	2.00(20)	1.02	0.44		1.35	0.36		1.83	2.9
	$3\gamma/4g$		6.1	5.5	36.5(32)	4.9	4.7	51(10)	5.8	4.4		7.08	7.3
$0_{2\beta}$	$2\beta/2g$	24.7(69)	981		237(71)	989	20.7	7049(3720)	21 455	10.6		3.45×10^6	0.37

[a] This work and/or Ref. 9.

[b] The $h_{11/2}$ shell has been raised 1 MeV in the calculation. See text for details.

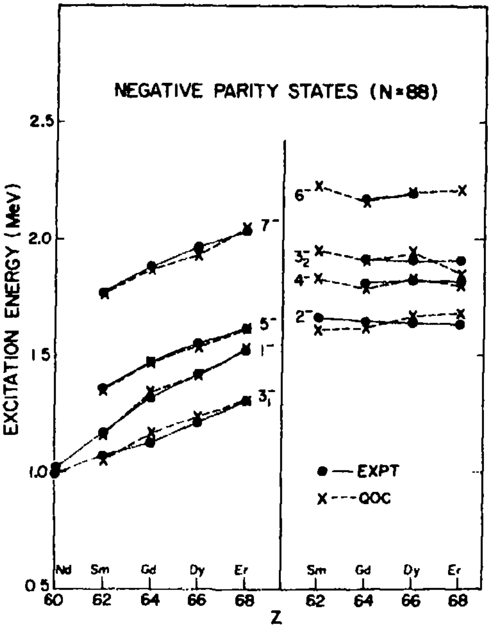

FIG. 15. Systematics of low-lying negative-parity states in several $N = 88$ nuclei and comparison with results of a quadrupole-octupole coupling model (QOC).

This may indicate, as pointed out by Lieder and Ryde,[23] that a fundamental change in the intrinsic structure has occurred, lending some support to Vogel's picture.

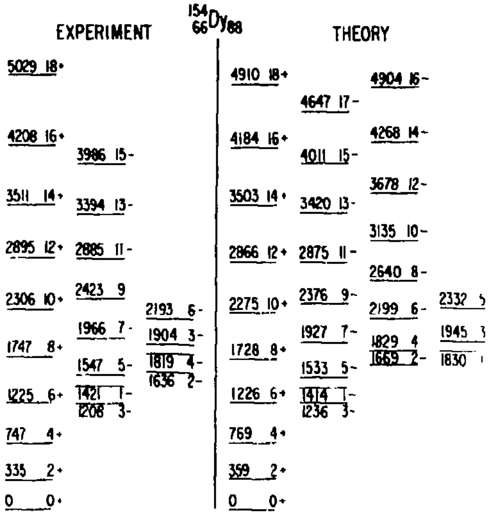

FIG. 16. Comparison of experimental ground-state band and negative-parity states in ^{154}Dy with the results obtained using the QOC model.

B. Microscopic calculations

The microscopic code of Tamura, Weeks, and Kishimoto[24] which describes nuclear collective motions in terms of the boson-expansion technique was used to calculate the level structure and electromagnetic properties of the $N = 88$ nuclei. In the

TABLE XII. Comparison of energies (in keV) of experimental negative-parity states in ^{150}Sm, ^{152}Gd, and ^{156}Er with theoretical values obtained with the quadrupole-octupole coupling model (QOC).

	^{150}Sm		^{152}Gd		^{156}Er	
I^π	theo.	exp.[a]	theo.	exp.	theo.	exp.[b]
1^-	1161, 1668	1166, 1713	1341, 1767	1315, 1756	1531, 1969	1518
3^-	1053, 1960	1071, 1952	1166, 1910	1123, 1915	1306, 1850	1304, 1910
5^-	1348, 2398	1358	1468, 2300	1470	1612, 2283	1611
7^-	1760, 2899	1764	1866, 2749	1880	2044, 2810	2029
9^-	2239, 3452	2232	2317, 3245	2331	2573, 3432	2489
11^-	2773, 4055	2744	2812, 3783	2814	3197, 4147	2923
13^-	3360, 4640	3293	3348, 4363	3338	3913, 4627	3431
15^-	3998, 5121	3914	3926, 4826	3938	4720, 5152	4035
17^-	4686, 5659	4606	4545, 5320	4609	5619, 5774	4712
2^-	*1610, 2281*	*1658*	*1618, 2054*	*1643*	*1679, 2080*	*1630*
4^-	1831, 2621		1786, 2349	1803	1797, 2278	1814
6^-	2225, 3113		2159, 2812	2173	2211, 2821	
8^-	2699, 3658		2600, 3314		2733, 3449	
10^-	3233, 4254		3091, 3856		3353, 4167	
12^-	3821, 4900		3627, 4438		4067, 4889	
14^-	4462, 5595		4204, 5060		4873, 5387	
16^-	5153, 6149		4822, 5658		5771, 5991	

[a] Reference 1.

[b] Reference 3.

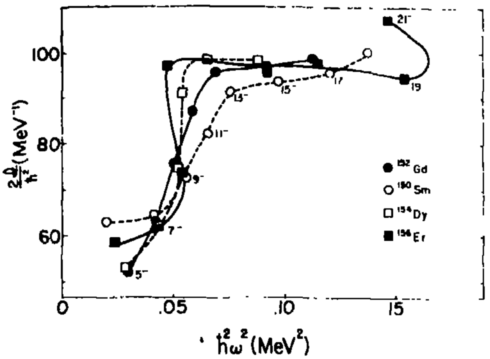

FIG. 17. Backbending plot for the negative-parity band in ^{150}Sm, ^{152}Gd, ^{154}Dy, and ^{156}Er.

theory, the microscopic Hamiltonian is written as the sum of a single-particle term, a particle-hole quadrupole-quadrupole interaction, and a pairing interaction of both monopole and quadrupole types. The expansion is carried out to sixth order and uses the single-particle states of Klinkenberg.[25] The only parameters of the model are the relative strengths of the quadrupole particle-hole and the quadrupole-pairing interaction, designated f and g, respectively. These quantities are constrained to have a value near unity. Their values for these calculations are shown in Fig. 9. For the sake of comparison, the calculations were also performed using the fourth-order boson-expansion code of Kishimoto and Tamura.[26] Klinkenberg single-particle energies were again used.

The experimental and theoretical level structure for ^{150}Sm, ^{152}Gd, ^{154}Dy, and ^{156}Er is compared in Fig. 9. The agreement with experiment is remarkably good for both microscopic calculations. The sixth-order results, however, are clearly superior, reproducing not only the ground-state band and bandhead energies of the β and γ bands but also more subtle features such as the bunching of the 3^+ and 4^+, 5^+ and 6^+, etc., states in the γ band. Poorest agreement generally occurred for the ^{156}Er case, which, as can be seen in the fourth-order calculation, places the γ band at much too high an energy. Consequently, the apparent degeneracy between the bandheads of the β and γ bands which has been observed experimentally is not reproduced. The calculations also generated a potential for ^{156}Er indicating a deformation which was too large. To correct this, the $h_{11/2}$ states were arbitrarily raised 1 MeV and the sixth-order calculation repeated. The latter ^{156}Er calculation is the one presented in this work. A great improvement in the fit to the energy levels was obtained. To check if the movement of the $h_{11/2}$ states would adversely affect the results for ^{154}Dy, this calculation also was repeated. A fit to the known energy levels as good as the original was obtained, indicating the location of the $h_{11/2}$ states becomes critically important only with ^{156}Er.

The ratios of reduced transition probabilities are compared with experimental values in Table XI. Overall, the agreement is rather good, with the largest deviations usually arising where the weakest transitions are involved. It is also interesting to note that both the fourth- and sixth-order calculations produce similar results. For the ^{156}Er case, however, it is seen that the movement of the $h_{11/2}$ shell has produced significant changes in the branching ratios, although agreement with experiment is still about as good as the fourth-order results.

The properties of transitional nuclei have proved in the past to be extremely difficult to reproduce microscopically. This has resulted in use of purely parametrized models such as the variable moment of inertia model (VMI) and the interacting-boson-approximation model (IBA). The success with which the boson-expansion calculations reproduce the experimental results for the $N=88$ nuclei shows the great progress recently made in microscopically describing collective motions.

V. CONCLUSIONS

The study of the decays of 4.2-min ^{152}Tb, 3.3-min ^{154}Ho, 11.8-min ^{154}Ho, and 82-sec ^{156}Tm has provided considerable information on the systematics of quasirotational states in $N=88$ nuclei. No evidence is found for a previously proposed high-spin 19-sec isomer in ^{156}Tm. The trends observed in the location of the β- and γ-vibrational bands can be explained from a consideration of available Nilsson orbitals. The low-lying positive-parity states are reproduced very well by the microscopic boson-expansion model. While all the negative-parity states can be explained as octupole vibrational in character by a simple quadrupole-octupole coupling model, some evidence suggests a change in intrinsic structure at higher spins.

ACKNOWLEDGMENTS

The authors wish to thank T. Kishimoto for help in interpreting the experimental results and for providing the fourth-order boson-expansion code. We are also grateful to K. Weeks and T. Tamura for their help in performing the sixth-order boson-expansion calculations at the University of Texas at Austin and for the hospitality extended to one of us (D.R.Z.) during his visit there. W. W. Bowman, D. R. Haenni, and M. Devous also provided valuable assistance with various aspects of data acquisition and reduction during the course of this work. This work was supported in part by the U. S. Department of Energy and the Robert A. Welch Foundation.

---

[1] Y. Gono, D. R. Zolnowski, D. R. Haenni, and T. T. Sugihara, Phys. Lett. 49B, 338 (1974); H. Beuscher, W. F. Davidson, R. M. Lieder, C. Mayer-Böricke, and H. Ihle, Z. Phys. 263, 201 (1973); A. W. Sunyar, E. der Mateosian, O. C. Kistner, A. Johnson, A. H. Lumpkin, and P. Thelberger, Phys. Lett. 62B, 283 (1976); M. J. A. DeVoigt, Z. Sujkowski, D. Chmielewska, J. F. W. Jansen, J. Van Klinken, and S. J. Feenstra, Phys. Lett. 59B, 137 (1975); C. M. Baglin, Nucl. Data Sheets 18, 223 (1976).

[2] D. R. Zolnowski, T Kishimoto, Y. Gono, and T. T. Sugihara, Phys. Lett. 55B, 453 (1975).

[3] C. Flaum and D. Cline, Phys. Rev. C 14, 1224 (1976).

[4] M. Nomura, Phys. Lett. 55B, 357 (1975).

[5] W. W. Bowman, T. T Sugihara, and R. D. Macfarlane, Nucl. Instrum. Methods 103, 61 (1972).

[6] D. R. Zolnowski and T. T Sugihara, Nucl. Instrum. Methods 114, 341 (1974).

[7] Y. Gono, R. L. Watson, T. T. Sugihara, and R. A. Kuebbing, Nucl. Instrum. Methods 127, 391 (1975).

[8] W. W. Bowman, T. T. Sugihara, and F. R. Hamiter, Phys. Rev. C 3, 1275 (1971).

[9] D. R. Zolnowski, E. G. Funk, and J. W. Mihelich, Nucl. Phys. A177, 513 (1971).

[10] W. W. Bowman, Nuclear Spectroscopy Progress Report No. ORO-4322-4 1972, Texas A&M Cyclotron Institute, p. 14.

[11] K. Takahashi, M. McKeown, and G. Scharf-Goldhaber, Phys. Rev. 137, B763 (1965).

[12] H. Beuscher, W. F. Davidson, R. M. Lieder, and C. Mayer-Böricke, in *Proceedings of the International Conference on Reactions between Complex Nuclei, Nashville, Tennessee, 1974*, edited by R. L. Robinson, F. K. McGowan, J. B. Ball, and J. H. Hamilton (North-Holland, Amsterdam, 1974), Vol. 1, p. 189.

[13] W. D. Schmidt-Ott, K. S. Toth, E. Newman, and C. R. Bingham, Phys. Rev. C 10, 296 (1974).

[14] C. Eckström, T. Noreland, M. Olmstats, and B. Wannberg, Nucl. Phys. A135, 289 (1969).

[15] K. S. Toth, R. L. Hahn, and M. A. Ijaz, Phys. Rev. C 4, 2223 (1971).

[16] P. Aguer, C. F. Liang, J. Libert, P. Paris, A. Peghaire, A. Charvet, R. Duffait, and G. Marguier, Nucl. Phys. A252, 293 (1975).

[17] A. Bohr and B. R. Mottelson, *Nuclear Structure* (Benjamin, New York, 1975), Vol. II, p. 550.

[18] R. J. Turner and T. Kishimoto, Nucl. Phys. A217, 317 (1973); L. Wilets and M. Jean, Phys. Rev. 102, 788 (1956); S. G. Rohozinski, J. S. Srebrny, and K. Horbaczewska, Z. Phys. 268, 401 (1974).

[19] D. G. Fleming, C. Günther, G. B. Hagemann, B. Herskind, and P. O. Tjøm, Phys. Rev. Lett. 27, 1235 (1971); Phys. Rev. C 8, 806 (1973); W. McLatchie, W. Darcey, and J. E. Kitching, Nucl. Phys. A159, 615 (1970); J. H. Bjerregaard, O. Hansen, and O. Nathan, *ibid.* 86, 145 (1966).

[20] O. Mikoshiba, R. K. Sheline, T. Udagawa, and S. Yoshida, Nucl. Phys. A101, 202 (1968).

[21] A. Arima and F. Iachello, Phys. Rev. Lett. 57B, 39 (1975).

[22] P. Vogel, Phys. Lett. 60B, 431 (1976).

[23] R. M. Lieder and H. Ryde, *Advances in Nuclear Physics*, edited by M. Baranger and E. Vogt (Plenum, New York, 1977), Vol. 10.

[24] T. Tamura, K. Weeks, and T. Kishimoto, Phys. Rev. C 20, 307 (1979).

[25] P. F. A. Klinkenberg, Rev. Mod. Phys. 24, 63 (1952).

[26] T. Kishimoto and T. Tamura, Nucl. Phys. A192, 264 (1972); A270, 317 (1976).

[27] R. S. Hager and E. C. Seltzer, Nucl. Data A4, 1 (1968).

[28] N. B. Gove and M. J. Martin, Nucl. Data Tables 10, 205 (1975).

PHYSICAL REVIEW C VOLUME 21, NUMBER 6 JUNE 1980

g factors of the 80 and 1094 keV states of ^{168}Er

Akira Furusawa
Department of Physics, Faculty of Science, Niigata University, Niigata, Japan

Masaaki Kanazawa and Shogo Hayashibe
Department of Physics, Faculty of Science, Tohoku University, Sendai, Japan

(Received 22 October 1979)

The g factors of the first excited and 1.094 MeV states of ^{168}Er have been obtained by the time integral and time differential perturbed angular correlation methods using two large volume Ge(Li) detectors. The results are found to be $g(2+) = 0.31 \pm 0.03$ for the first excited state and $g(4-) = 0.24 \pm 0.01$ for the 1.094 MeV state. These values are compared to the experimental results reported previously and to theoretical predictions.

[RADIOACTIVITY ^{168}Er level; measured $\gamma\gamma$ coin., $\gamma\gamma(\theta,t)$, deduced $T_{1/2}$, relaxation constants; measured $\gamma\gamma(\theta,H)$, $\gamma\gamma(\theta,H,t)$. TIPAC, TDPAC methods, deduced g.]

I. INTRODUCTION

^{168}Er is one of the typical deformed even-even nuclei, and excited states of this nucleus are described fairly well by the rotation-vibration model.

Besides the usual ground-state rotational band, three other bands have been identified in the spectrum, having $K\pi = 2+$, $4-$, and $3-$, respectively. The 1.094 MeV level has been identified as the band head of a $K\pi = 4-$ rotational band and may be represented by a configuration involving two neutrons in the Nilsson orbits ($633\ \frac{7}{2}^+$) and ($521\ \frac{1}{2}^-$).[1,2] This observation is supported mainly by reaction studies,[3,4] but there is only one measurement of the g factor for this level that has reasonably small experimental errors.[5] Recently, two neutron resonance measurements have been reported, but these have large experimental errors.[6,7]

In general, the spin rotation method on gamma adiation from radioisotope decay can be carried t with rather small experimental errors comred with the results of the neutron resonance ethod. However, it is fairly difficult to measure e g factor of the 1.094 MeV level populated in the Tm decay, as the strong 448–198 keV cascade s a very small anisotropy.

In the present work, two large volume Ge(Li) tectors were used, and the time differential spin tation measurement has been performed in HI lution for the 448-830 keV cascade whose anisoopy was expected to be larger, by about a factor 7 than that of the 448-198 keV cascade. The me integral rotated angular correlation measureent for the 816-80 keV cascade has also been rried out, and the g factor of the first excited ate was evaluated.

These results were compared with others obtained so far.[8–11] Furthermore, the results from the time differential perturbed angular correlation measurement have been examined in order to determine the relaxation time in the HI solution.

The time integral rotated angular correlation and time differential spin rotation measurements were carried out at the Research Laboratory of Nuclear Science, Tohoku University, while the time differential perturbed angular correlation was measured at the Faculty of Science, Niigata University.

II. EXPERIMENTS

A. Source preparation

A source of about 30 μCi of the 93 day ^{168}Tm isotope was produced by the electron linac at the Research Laboratory of Nuclear Science, Tohoku University. A Tm target was bombarded with 60 MeV photons for 48 hours.

The measurements were carried out about two months after irradiation, in order to let the ^{167}Tm ($T_{1/2} = 9.6$ d) activity decay. The source needed for the time integral measurement was dissolved in HNO_3 solution, while the source used for the time differential measurements was dissolved in HI solution. The liquid solutions were then placed in plastic source holders which had holes with 0.4 cm inner diameter and 0.7 cm length. The source to detector distance was 6.8 cm.

B. Experimental apparatus and measurements

Two large volume Ge(Li) detectors were used for the time integral angular correlation and the time differential spin rotation measurements. One detector was a true coaxial type, 80 cm^3 in vol-

© 1980 The American Physical Society

ume, having a resolution of 2.2 keV [full width at half maximum (FWHM) at 1.33 MeV]; the other was a single ended coaxial type, 70 cm^3 in volume, having a resolution of 2.4 keV (FWHM at 1.33 MeV).

Coincidence data were taken with a fast-slow coincidence system utilizing constant fraction timing. The resulting data were corrected for accidental coincidence and for finite solid angle of the detectors. The finite solid angle corrections were calculated with a high speed computer by the Monte Carlo method for each energy and source-detector distance.

An external magnetic field directed either up or down with respect to the plane of the gamma rays was applied to the source, which was placed in the gap of the pole pieces of the magnet.

For the time integral angular correlation measurement, the coincidence counting rates for the 816-80 keV cascade were accumulated automatically at seven angles from 90–225° with respect to the symmetry axis of the two detectors. The magnitude of the external magnetic field, 7300 ±100 Gauss, was maintained constant throughout the time period of data accumulation.

The energy was taken from a timing single channel analyzer with a window set at 816 ±3 keV, and the time to pulse height converter was adjusted to provide a resolving time of about 60 nsec. The measurements were carried out in 10 runs of 8192 sec duration for each angle and for each field direction, and about 20 000 counts were obtained at 90°. The data were then least square fitted to derive $\Delta\theta_2$, $\Delta\theta_4$, b_{22}, and b_{44} values which were defined by equations (1) and (2),[12-14]

$$W(\theta,B)=1+\frac{b_{22}}{[1+(2\omega_B\tau)^2]^{1/2}}\cos 2(\theta-\Delta\theta_2)$$

$$+\frac{b_{44}}{[1+(4\omega_B\tau)^2]^{1/2}}\cos 4(\theta-\Delta\theta_4)\ , \qquad (1)$$

$$\tan(N\Delta\theta_N)=N\omega_B\tau\ , \qquad (2)$$

where ω_B and τ are the Larmor precession frequency and the mean life of the intermediate state, respectively.

On the other hand, for the time differential spin rotation measurements, the two detectors were separated by constant angle 135°, and the total coincidence counting rates of seven days for each field direction were obtained for the 448-830 keV cascade. An external magnetic field of 8900 ±100 G was applied in this case. Let the coincidence rates be $W(t,\ B+,\ 135°)$, $W(t,\ B-,\ 135°)$ for the up and down directions of the magnetic field, respectively; a ratio $C(t,\ B,\ 135°)$ was defined the usual way be Eq. (3)[13,14]:

$$C(t,B,\ 135°)=\frac{2[W(t,B+,135°)-W(t,B-,135°)]}{W(t,B+,135°)+W(t,B-,135°)}\ . \qquad (3)$$

For the two Ge(Li) detectors system, the prompt time distribution was measured by taking two pairs of energy bands selected with ^{22}Na source. One pair involved the two photopeaks of the positron annihilation 511 keV γ rays and the other was taken by selecting the photopeak of the positron annihilation 511 keV γ ray in the 70 cm^3 Ge(Li) detector, and the 99.0 ±1.5 keV region of its Compton continuum in the 80 cm^3 Ge(Li) detector. In the former case, a resolving time of 9.2 ±0.2 nsec was obtained, and it was assumed to be roughly equal to the resolving time for the 448-830 keV cascade case. In the latter case, a time resolution of 16.2 ±0.5 nsec was obtained.

For the relaxation time measurement, a 35 cm^3 Ge(Li) detector for the 448 keV transition and a 3.8 cm × 0.64 cm NaI(Tl) crystal for the 99 keV transition were used.

The coincidence counting rates for the 448-99 keV cascade were taken at 90° and 180°, with respect to the symmetry axis of the two detectors, and the measurements were carried out in 7 runs of two days for each angle. Let the coincidence rates be $W(t,90°)$, $W(t,180°)$ for the 90° and 180° angle settings, respectively; a ratio $\bar{A}(t)$ was defined by Eq. (4):

$$\bar{A}(t)=\frac{2[W(t,180°)-W(t,90°)]}{W(t,90°)+W(t,180°)}\ . \qquad (4)$$

A prompt time distribution was measured with a ^{60}Co source. The resolving time in this case was 6.0 ±0.5 nsec.

III. RESULTS

Figure 1 shows the partial level scheme of ^{168}Er in which the thick arrows are related to several transitions measured in this experiment.[1]

The single spectra measured with the 80 cm^3 Ge(Li) detector and with the NaI(Tl) crystal are shown in Figs. 2 and 3, respectively. Again, only the energy values which are related to present experiments are indicated with arrows.

The time integral angular correlations are shown in Fig. 4. The angular coefficients A_{22} and A_{44} for the 816-80 keV cascade have been measured by several authors. The values

$$A_{22}=-0.157\pm0.008,$$

$$A_{44}=-0.09\pm0.02\ ,$$

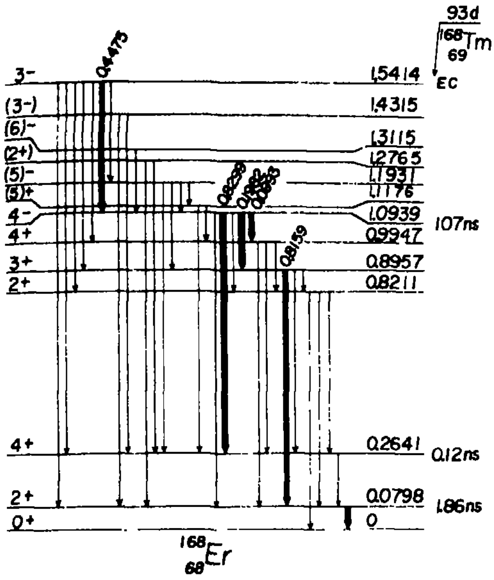

FIG. 1. Partial level scheme of ^{168}Er taken from Table of Isotopes (Ref. 15).

have been obtained by Behar *et al.* recently.[16]

Because the A_{44} value is not negligibly small, it is necessary to take into account the $k = 4$ term in the polynomial expansion for the data analysis and to use explicitly Eqs. (1) and (2). The fitted values for Eq. (1) were as follows:

$\Delta\theta_2 = 0.195 \pm 0.015$ rad ,

$\Delta\theta_4 = 0.176 \pm 0.042$ rad ,

$b_{22} = -0.105 \pm 0.004$ (not corrected for solid angle),

$b_{44} = -0.022 \pm 0.005$ (not corrected for solid angle).

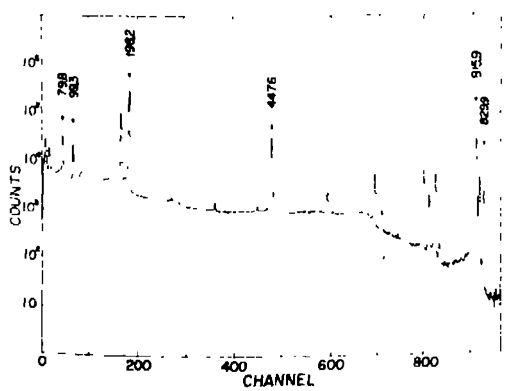

FIG. 2. Single spectrum of γ radiation from ^{168}Tm decay obtained with the 80 cm^3 Ge(Li) detector.

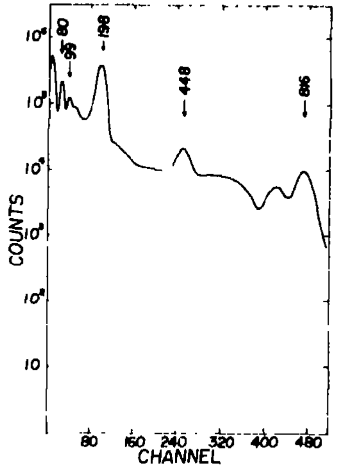

FIG. 3. Single spectrum of γ radiation from ^{168}Tm decay obtained with an NaI(Tl) detector of 3.8 cm diameter by 0.64 cm long.

Using Eq. (2), $\omega_B\tau$ was calculated:

$$\omega_B\tau = 0.206 \pm 0.016 \text{ rad (from } \Delta\theta_2) ,$$

$$\omega_B\tau = 0.21 \pm 0.05 \text{ rad (from } \Delta\theta_4) .$$

The mean life $\tau = 2.68$ nsec was taken from the Table of Isotopes.[15] A paramagnetic correction factor 6.97 (20°C) (Ref. 17) was used to obtain the g factor of the first excited state:

$$g(2+) = 0.31 \pm 0.03 .$$

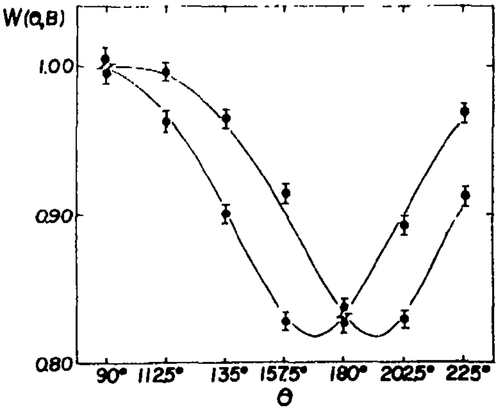

FIG. 4. Time integral angular correlation for the 816–80 keV cascade obtained with two Ge(Li) detectors. The open and closed circles indicate the up and down magnetic field directions, respectively. No correction is made for finite solid angle in this figure.

This result is shown in Table I and is compared with the measured values by several authors; each experimental method is also indicated.

Comparing experimentally obtained b_{22} and b_{44} values with A_{22} and A_{44} values, and taking into account the solid angle corrections, the attenuation coefficients G_{22}, G_{44} and the relaxation constants λ_2, λ_4 can be assigned.

If we adopt the values by Behar *et al.* for A_{22} and A_{44} coefficients,

$$G_{22}=0.90^{+0.03}_{-0.04}\ ,\quad G_{44}=0.70^{+0.15}_{-0.16}\ ,$$

$$\lambda_2=(4.3\pm1.6)\times10^{7}\ \text{sec}^{-1}$$

and

$$\lambda_4=(1.6^{+1.0}_{-1.0})\times10^{8}\ sec^{-1}$$

are obtained.

From these results, it is inferred that the magnetic interaction is predominant in the HNO_3 solution.[18]

The prompt distribution curve obtained with the two Ge(Li) detectors system is shown in Fig. 5, and the delayed curve of 1.094 MeV level for the *intense 448-198 keV cascade is shown in Fig. 6.* From this delayed curve, we assign the half-life $T_{1/2}=112.5\pm1.0$ nsec, which agrees with previous results.[5,19]

Sufficiently long relaxation time is needed in order to observe clearly the spin rotation effect by the time differential method. Until recently, several reports pointed out the long relaxation time in the HF solution in which minimum extra perturbations are seen.[16,20] So we tried to measure with the source in the HF solution, but since HF acid has very small solubility for Tm metal, we could not have sufficiently intense source activity.

TABLE I. The results of *g*-factor measurements for the first excited state by several authors and present experiments. Experimental methods for each measurement are shown also.

Level energy (keV)	*g* factor	Method	Reference
79.8	0.31 ± 0.03	IPAC[a]	Present
	0.27 ± 0.03	IPAC[a]	8
	0.333 ± 0.0008	ME[b]	9
	0.305 ± 0.010	RIGV[c]	10
	0.348 ± 0.029	CETD[d]	11

[a] IPAC: Time-integral perturbed (rotated) angular correlation.

[b] ME: Mössbauer effect.

[c] *RIGV: Recoil into gas and/or vacuum.*

[d] CETD: Time-differential perturbed angular distribution of γ rays following Coulomb excitation.

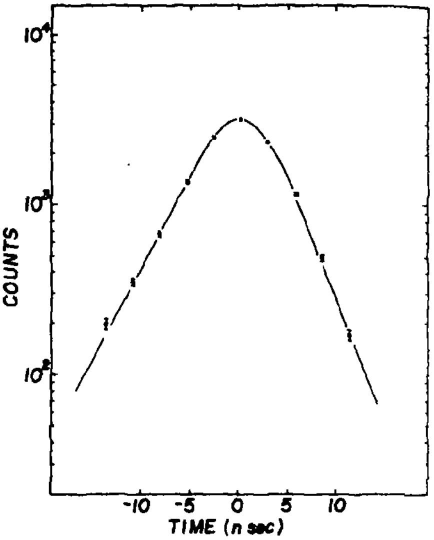

FIG. 5. Prompt time distribution for the 511-511 keV positron annihilation γ rays obtained with two Ge(Li) detectors and an ^{22}Na source.

In several relaxation time measurements with various kinds of solutions, we found that the relaxation time in the HI solution, which has a large solubility for Tm metal, was as long as in the HF solution. The time dependence behavior of the anisotropy $\bar{A}(t)$ for the 448-99 keV cascade in the HI solution is shown in Fig. 7. Since the coefficient A_{44} is negligible small in this cascade, it is sufficient to consider only the attenuation coefficient $G_{22}(t)$ for the attenuation. $G_{22}(t)$ would be *expressed by relaxation constant λ_2 as follows:*

$$G_{22}(t)=e^{-\lambda_2 t}\ .$$

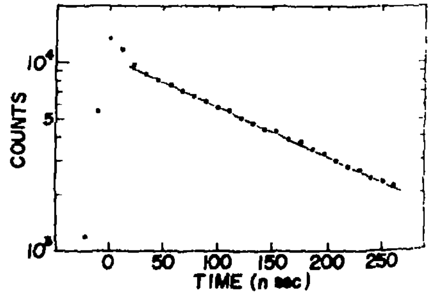

FIG. 6. Delayed time coincidence spectrum for the 448-198 keV cascade obtained with two Ge(Li) detector

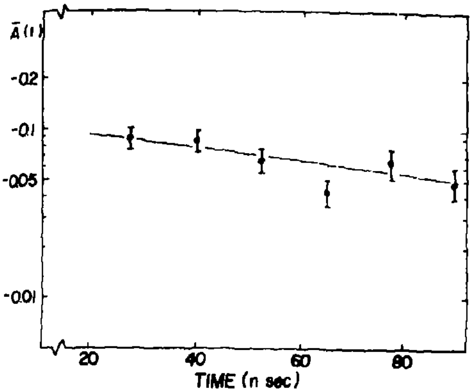

FIG. 7. Time differential perturbed angular correlation for the 448-99 keV cascade obtained with the 35 cm^3 Ge(Li) detector and the NaI(Tl) detector. No correction is made for finite solid angle in this figure.

The best fit obtained from the curve in Fig. 7 gives

$$\lambda_2 = (0.81 \pm 0.25) \times 10^7 \text{ sec}^{-1} .$$

This result corresponds to the value (0.75 ±0.10) ×10^7 obtained in HF solution by Behar *et al.*

The spin rotation measurement for the 448-830 keV cascade by the time differential method is shown in Fig. 8. The spin rotation effect is clearly seen. Since the two Ge(Li) system was utilized, a narrow energy region for the two γ transitions could be selected, and, moreover, since the resolving time was approximately as short as for large Ge(Li) detectors, it is assumed that this measurement was not much affected by the competing γ-γ cascades.

The mixing ratios δ of the 448 and 830 keV transitions have been reported recently to be $-0.06 \geq \delta \geq -0.17$ and $0.01 \geq \delta \geq -0.09$ by Behar *et al.*, and using these values, the angular coefficient A_{22} is evaluated to be $-0.098 \leq A_{22} \leq 0.002$. Moreover, Behar *et al.* have assigned the coefficient $A_{22} = -0.07 \pm 0.01$ for the 448-99 keV cascade and the mixing ratio $\delta = -0.06 \pm 0.05$ for the 99 keV transition. If these values are taken into account, the A_2 value is calculated to be $0.18 \geq A_2 \geq 0.12$ for the 448 keV transition and then, the coefficient A_{22} for the 448-830 keV cascade is evaluated as $-0.051 \geq A_{22} \geq 0.088$. Our result is approximately consistent with this value.

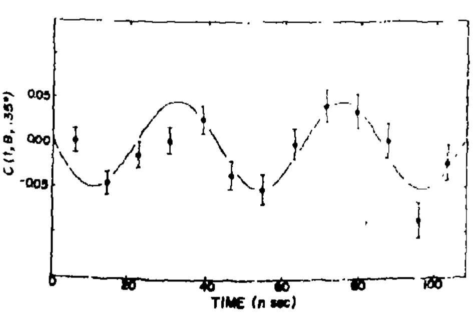

FIG. 8. Time differential spin rotation behavior for the 448-830 keV cascade obtained with two Ge(Li) detectors. No correction is made for finite solid angle in this figure.

It is expected that the coefficient A_{44} is negligibly small in this cascade and the time dependence behavior would be expressed by Eq. (5):

$$C(t, B, 135°) = \frac{12A_{22}\sin 2\omega_B t}{8 + 2A_{22}} . \tag{5}$$

From the best fit of the data to Eq. (5), the precession frequency was obtained in an external applied magnetic field:

$$\omega_B = (7.3 \pm 0.3) \times 10^7 \text{ sec}^{-1} .$$

This value yields $g(4-) = 0.24 \pm 0.01$, and the sign is assigned to be positive from the observation of the direction of the spin rotation with respect to the applied field direction and of the sign of the A_{22} coefficient. This result is shown in Table II and is compared again to the values measured up to now.

IV. DISCUSSION

The g factor for the first excited state of the present experiment agrees with the previous data shown in Table I, and particularly agrees with the results of the RIGV (recoil into gas and/or vacuum) and ME (Mössbauer effect) methods. We think that our result is better than previous results by the IPAC [time-integral perturbed (rotated) angular correlation] method, because we measured with two Ge(Li) detectors and the data analysis was done by solving explicitly the relevant equations; the error in the $\Delta\theta_z$ assignment due to the

TABLE II. The results of g-factor measurements for the 1.094 MeV state by several authors and present experiments. Experimental methods for each measurement are shown also.

Level energy (keV)	g factor	Method	Reference
1093.9	0.24 ± 0.01	DPAC[a]	Present
	0.45 ± 0.02	DPAC[a]	5
	−0.11 ± 0.18	NRES[b]	6
	0.22 ± 0.[illegible]0	NRES[b]	7

[a] DPAC: Time-differential perturbed (spin rotation) angular correlation.

[b] NRES: Neutron resonance energy shift.

perturbation effect by internal fields,[13] and to the contribution from the $k=4$ term in the polynomial expansion, is very small.

On the other hand, it is found that there are considerable differences in the results for the g factor of the 1.094 MeV state, as shown in Table II. Our result is consistent with the data by Alfimenkov *et al.*, who utilized a NRES method, but is inconsistent with the data by Kim *et al.*, who used the ^{168}Tm decay.

The 1.094 MeV level has been assigned to be $I=4$ and identified as the band head of a $K\pi=4-$ rotational band as mentioned before, and the (d,p) reaction studies suggest this level to be represented by a configuration involving two quasineutrons in Nilsson orbits having $\Omega=(633\ \frac{7}{2}^+)+(521\ \frac{1}{2}^-)$. The g factor for this configuration can be obtained from so-called additive theory which is given by Eq. (6),[21-23]

$$g(I)=\tfrac{1}{2}(g_1+g_2)+\frac{j_1(j_1+1)-j_2(j_2+1)}{2I(I+1)}(g_1-g_2)\,, \quad (6)$$

where $g(I)$ is the g factor of a state I, which is a two particle configuration with the spins j_1 and j_2 and the g factors g_1 and g_2, respectively. The value of the g factor is thus calculated to be $g(4-)=-0.013$ using $g[^{167}\mathrm{Er},\ (633\ \frac{7}{2}^+)_n]=-0.162$ and $g[^{169}\mathrm{Er},\ (521\ \frac{1}{2}^-)_n]=1.03$, which were obtained experimentally for the neighboring odd neutron nuclei. It appears that the resulting g cannot be interpreted with the above configuration completely, and therefore one should take into account the two quasiprotons state, which is reasonably assigned to be $(523\ \frac{7}{2}^-)_p$ and $(411\ \frac{1}{2}^+)_p$. Then the g factor of the 1.094 MeV state can be explained by a mixture of about 30% of the quasiprotons state configuration, with $g[^{165}\mathrm{Ho},\ (523\ \frac{7}{2}^-)_p]=1.19$ and $g[^{169}\mathrm{Tm},\ (411\ \frac{1}{2}^+)_p]=-0.643$ which were obtained experimentally in neighboring proton odd mass nuclei.

ACKNOWLEDGMENTS

We are indebted to Professor M. Yagi, Dr. K. Kondo, Mr. A. Kurihara, and others at the Research Laboratory of Nuclear Science, Tohoku University, for preparing the sources and electronic circuits.

---

[1] A. Bohr and B. R. Mottelson, *Nuclear Structure* (Benjamin, Reading, Mass., 1975), Vol. II.

[2] W Michaelis, H. Ottmar, and F. Weller, Nucl. Phys. A150, 161 (1970).

[3] L. M. Bollinger and G. E. Thomas, Phys. Rev. C 2, 1851 (1970).

[4] R. A. Harlan and R. K. Sheline, Phys. Rev. 160, 1005 (1967).

[5] B. T. Kim, W. K. Chu, and J. C. Glass, Phys. Rev. C 8, 1920 (1973).

[6] K. H. Bockurts and G. Brunhart, Phys. Rev. C 1, 726 (1970).

[7] U. P. Alfimenkov *et al.*, Yad. Fiz. 17, 13 (1973) [Sov. J. Nucl. Phys. 17, 6 (1973)].

[8] E. Bodenstedt, H. J. Korner, E. Gerdau, J. Radeloff, L. Mayer, R. Auerbach, J. Braunsfurth, and G. Mielken, Z. Phys. 170, 355 (1962).

[9] E. Münck, Z. Phys. 208, 184 (1968).

[10] I. Ben-zvi, M. B Goldberg, G. Goldring, K. H. Speidel, and A. Sprinzak, Nucl. Phys. A151, 401 (1970).

[11] J. D. Kurfess and R. P. Scharenberg, Phys. Rev. 161, 1185 (1967).

[12] E. Bodenstedt, in *The Electromagnetic Interaction in Nuclear Spectroscopy*, edited by W. D. Hamilton (North-Holland, Amsterdam, 1975), p. 738.

[13] E. Bodenstedt, in *Perturbed Angular Correlations*, edited by E. Karlsson, E. Matthias, and K. Siegbahn (North-Holland, Amsterdam, 1964), p. 217.

[14] H. Frauenfelder and R. M. Steffen, in *Alpha-Beta-and Gamma-Ray Spectroscopy*, edited by K. Siegbahn (North-Holland, Amsterdam, 1974), Vol. 2, p. 1153.

[15] *Table of Isotopes, 7th edition*, edited by C. M. Lederer and V. S. Shirley (Wiley, Interscience, New York, 1978).

[16] M. Behar, L. M. Quinones, and Z. W. Gravowski, Z. Phys. 274, 359 (1975).

[17] C. Günther and I. Lindgen, in *Perturbed Angular Correlations*, edited by E. Karlsson, E. Matthias, and K. Siegbahn (North-Holland, Amsterdam, 1964), p. 357.

[18] H. F. Wagner, M. Popp, and M. Forker, Z. Phys. 248, 195 (1971).

[19] C. Günther and D. R. Parsignault, Phys. Rev. 153, 1297 (1967).

[20] F. C. Zawislak, D. E. Brandao, A. Vasquez, and F. P Livi, Phys. Lett. 7, 337 (1963).

[21] E. Bodenstedt, Hyp. Int. 2, 1 (1976).

[22] P. J. Brussaard and P. W. M. Glaudemans, *Shell Model Applications in Nuclear Spectroscopy* (North-Holland, Amsterdam, 1977), p. 256.

[23] E. Ejiri, G. B. Hagemann, and T. Hammer, in *Proceedings of the International Conference on Nuclear Moments and Nuclear Structure*, edited by H. Horie and K. Sugimoto (Physical Society of Japan, Tokyo, 1972), p. 426.

PHYSICAL REVIEW C VOLUME 21, NUMBER 6 JUNE 1980

Ground-state nuclear g factor of ^{97}Ru

K. Leuthold, E. Hagn, H. Ernst, and E. Zech
Physik-Department, Technische Universität München, D-8046 Garching, West Germany

(Received 15 June 1979)

The magnetic hyperfine splitting constant $g\mu_N H_{HF}/h$ of ^{97}Ru as a dilute impurity in Fe has been determined by the technique of nuclear magnetic resonance on oriented nuclei to be 117.69 ± 0.02 MHz. With the known hyperfine field for Ru*Fe* of -504 ± 12 kG the ground-state nuclear g factor of ^{97}Ru is deduced to be $(-)0.306 \pm 0.008$. The resonance shift and the spin-lattice-relaxation time have been measured as functions of an external magnetic field.

[RADIOACTIVITY ^{97}Ru from ^{96}Ru(n,γ); NMR on oriented nuclei. Deduced μ. Knight shift, relaxation times.]

I. INTRODUCTION

The deviations of nuclear magnetic moments from the single-particle Schmidt values are qualitatively well understood for nuclear states with configurations of few nucleons outside of closed shells. The main deviations are believed to be due to $j^{\pi} = 1^{+}$ polarization of the core[1,2] and, in addition, to mesonic effects.[3,4] In the region $A \sim 90$, where $^{90}_{40}\mathrm{Zr}_{50}$ or $^{88}_{38}\mathrm{Sr}_{50}$ are assumed to be fairly good magic nuclei, the states with few protons in the $g_{9/2}$ shell and few neutrons in the $d_{5/2}$ shell are well suited for systematic studies of these effects. Most experiments have been done for a better understanding of the $\pi g_{9/2}$ magnetic moments, which have shown that the additivity of magnetic moments is violated, and that an anomalous orbital magnetism due to mesonic effects exists.[5-7] For the interpretation of the data from odd-odd nuclei, precise data for the neutron contributions to the magnetic moments have to be available. In this context, a systematic study of $d_{5/2}$ neutron magnetic moments is of interest.

In addition to these aspects the magnetic moments of ruthenium nuclei are interesting for the following reason. The ground-state spin of the lighter isotopes ^{96,97,99,101}Ru is $j^{\pi} = \frac{5}{2}^{+}$, which can be understood as a pure $d_{5/2}$ shell model configuration. The ground-state spins of the heavier isotopes ^{103}Ru and ^{105}Ru have not been determined experimentally in a direct way. From indirect arguments, however, the most probable assignment is $j^{\pi} = \frac{3}{2}^{+}$, which could be understood in the frame of the shell model as a $(d_{5/2})^{3}_{3/2^{+}}$ configuration. A measurement of the magnetic moments could possibly yield some information on this subject. First nuclear orientation experiments on ^{97}Ru*Fe*, ^{103}Ru*Fe*, and ^{105}Ru*Fe* (Ref. 8) showed, however, that the γ anisotropies of ^{103}Ru and ^{105}Ru are very small, so that no unique conclusions could be drawn. A combination of the nuclear orientation (NO) measurements with NMR-ON experiments (nuclear magnetic resonance on oriented nuclei detected by the anisotropy of radiation), however, would yield a precise value for the nuclear g factors and would thus allow a *unique* spin determination. (This feature is based on the fact that the NO method yields the magnetic moment μ, while the NMR-ON method yields the g factor.) In order to clarify whether the NMR-ON method is well applicable to Ru*Fe* systems, the first experiments have been performed on ^{97}Ru*Fe* for which the γ anisotropy is comparatively large. These experiments are described in this paper.

II. PRINCIPLE OF MEASUREMENT

A. Nuclear orientation

The angular distribution of oriented nuclei is most conveniently written as[9]

$$W(\Theta) = 1 + \sum_{k=2,4} U_k F_k B_k^{(I)}(gB/kT) P_k(\cos\Theta) Q_k . \qquad (1)$$

The different coefficients have the following meaning. The F_k are the usual angular correlation coefficients, and the U_k take into account the deorienting effect of preceding unobserved (γ, $\beta^{\pm}$, EC) transitions. The U_k and F_k depend on the parameters of the nuclear decay, i.e., on spins, multipolarities, and mixing ratios of different multipolarities if the transitions are not pure. The B_k describe the degree of orientation of the initial state. They depend on gB/kT and on the spin j of the state. If the B_k are calculated as a function of $\mu B/kT$ instead of gB/kT, it is found, that the j dependence of B_k is rather weak in the region $gB/kT < 1$. This has the consequence that μ can be determined rather reliably, even if no unique spin assignment is possible. (The asymp-

© 1980 The American Physical Society

totic values $\bar{B}_k^{(j)}$, which are obtained for $gB/kT \gg 1$, depend, of course, on j). The temperatures which are necessary for the corresponding saturation of the anisotropy are extremely low in most cases and cannot be obtained in most NO experiments. The $P_k(\cos\Theta)$ in formula (1) are Legendre polynomials, Θ being the angle between the quantization axis, which, in the present case of pure magnetic interaction, coincides with the direction of the magnetic field, and the direction of observation. The Q_k take into account the solid angle of the detectors, they are normally in the region near unity. The sum in formula (1) runs on even k only, the maximum value k_{max} depending on the spins and multipolarities which are involved in the decay cascade. It is in most cases given by $k_{max}=4$.

To get a considerable degree of orientation at $T\sim 10$ mK, magnetic fields of the order of >100 kG are necessary. This is obtained by utilizing the internal hyperfine fields B_{HF}, which act on dilute impurities in ferromagnetic host lattices (Fe, Co, Ni, Gd). The value of B_{HF} is dependent on the type of impurity-host system; a compilation of most presently known hyperfine fields is given in Ref. 10.

To get rid of several disturbing effects, such as the decrease of the counting rate due to the finite lifetime of the parent nucleus, the ratio

$$\epsilon=\frac{W(0)}{W(90)}-1 \tag{2}$$

is normally calculated and analyzed as a function of the temperature T.

The precision to which magnetic moments can be determined from the temperature dependence of the γ anisotropy depends strongly on the particular case, a typical value being ~5%. Some limiting factors are imprecisely known mixing ratios of different tensor ranks of the preceding β^{+} or EC transitions, nonalignment of the hyperfine field (Aharoni effect), different spin-lattice-relaxation times in comparison to those of the thermometers, etc. A very much higher precision is obtainable with the NMR-ON method which is described in the next subsection.

B. Fast-sweep nuclear magnetic resonance on oriented nuclei

In the NMR-ON method[11] the γ anisotropy is used as a detector for nuclear magnetic resonance. As a precise knowledge of the absolute value of the γ anisotropy is not necessary, an accurate determination of the temperature of the sample is also not necessary. The only restriction is that the γ anisotropy is so large that the resonant destruction can be observed. The resonance condition is given by

$$h\nu=g\mu_N[B_{HF}+(1+K)B_0]\,, \tag{3}$$

where g is the nuclear g factor, μ_N the nuclear magneton, B_{HF} the magnetic hyperfine field, K the Knight shift, and B_0 the external magnetic field, which is necessary to orient the ferromagnetic domains, and which thus establishes a unique quantization direction with respect to which the γ anisotropy is observed. If the Knight shift can be neglected, formula (3) reduces to

$$h\nu=g\mu_N(B_{HF}+B_0)\,. \tag{4}$$

In this case the nuclear g factor can be determined from the resonance shift with the external field, i.e., without the knowledge of B_{HF}.

Besides the static resonance condition, which is given by formula (3), dynamic effects have to be considered in the experiment. The rf field, which has the "correct" frequency ν_0, induces rf transitions between the m sublevels, the effect being a total or at least partial destruction of the polarization with the corresponding change in the γ anisotropy. If the rf field is now switched off, the system returns to the thermal equilibrium with a characteristic time constant T_1'. This time constant, which is normally denoted as spin-lattice-relaxation time, is not uniquely defined as will be shown in the following. The spin-lattice-relaxation mechanism can be described by a set of rate equations for the sublevel populations, the essential parameter being a reduced matrix element which describes the strength of the coupling between the nuclei and the lattice.[12] In the high-temperature region $kT \gg gB$, the rate equations can be solved analytically. In this approach, the polarization, and all physical quantities which are proportional to it such as the magnetization, decay exponentially to the equilibrium value, the time constant being the spin-lattice-relaxation time T_1 which follows the Korringa law $T_1T=\mathcal{K}$, where $\mathcal{K}$ is the Korringa constant. In the low-temperature region $kT \ll gB$, and also in the region of intermediate temperature $kT \approx gB$, the rate equations have to be solved numerically. The time dependence of the polarization or the alignment consists of a sum of exponential functions with different time constants. It is found, however, that the return of the γ anisotropy to the equilibrium value can be described in a fairly good approximation by a single-exponential decay with a time constant T_1', which is different from the above T_1 and, in addition, which is dependent on the initial conditions, i.e., on the deviation of the system from the thermal equilibrium. This means, however, that a proportionality holds between T_1 and T_1', the proportionality constant being fixed if the temperature and the deviation from the equilibrium are kept constant. Thus, a functional dependence of T_1 on any parameter, such as the external magnetic field, can be detected by observing the corresponding dependence of T_1', which can be measured more easily.

The resonance frequency ν_R and the relaxation time constant T_1' can be measured *simultaneously* if a sweep-mode technique for the applied rf field is used. This nonconventional technique will be described in the following. The main features are shown in Fig. 1. Starting at $\nu = \nu_1 < \nu_R$ the frequency of the applied rf field is swept continuously over the resonance with a constant sweep rate $d\nu/dt = +p$. At $\nu = \nu_2 > \nu_R$ the sweep direction is reversed, the rf frequency is swept continuously over the resonance again, the sweep rate being now $d\nu/dt = -p$. At $\nu = \nu_1$ the sweep direction is reversed again, initiating a new cycle. This is shown in the lower part of Fig. 1. Before discussing the response of the nuclear spin system, the effect of inhomogeneous broadening has to be considered. It is found experimentally that the hyperfine field does not have a sharp value but a certain distribution. Assuming a Gaussian shape, which is a good approximation in most cases, the distribution of the resonance around the center frequency ν_R is given by

$$G(\nu) = f\left(\frac{\ln 2}{\pi}\right)^{1/2} \frac{1}{\Gamma_0} \exp[-\ln 2(\nu - \nu_R)^2/\Gamma_0^2] , \quad (5)$$

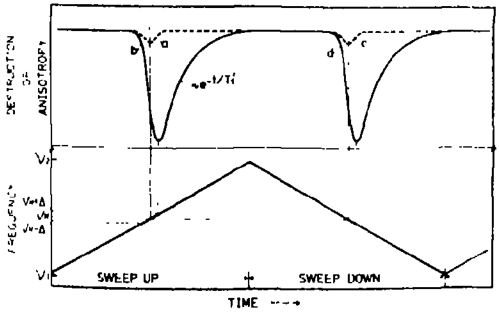

FIG. 1. Details of the sweep-mode technique for NMR-ON measurements. The rf center frequency is swept continuously up and down between the boundary frequencies ν_1 and ν_2 with a constant sweep rate $d\nu/dt = \pm p$ (bottom). The response of the γ anisotropy (top) depends on the choice of the sweep velocity (see text). In the adiabatic case, two symmetric resonances with the same center at ν_R are observed (curves *a* and *c*). In the nonadiabatic case, an integrating effect is active which leads to asymmetric resonances with a shift of the center and an exponential decay in sweep direction (curves *b* and *d*).

where Γ_0 is the inhomogeneous linewidth and f is the fraction of nuclei which can be affected by the rf. The normalization is chosen in such a way that

$$\int G(\nu)d\nu = f \quad (6)$$

is given. In the ideal case, $f = 1$ is expected. To get a reasonable resonance effect, the rf field has to be frequency modulated. Assuming that all time-dependent effects can be neglected the observed resonance effect at a frequency ν is then given by

$$R_a(\nu) = \int_{\nu-\Delta f}^{\nu+\Delta f} G(\nu')d\nu' , \quad (7)$$

where Δf is the modulation width, and a stands for adiabatic approximation. If Δf is small in comparison to Γ_0 the shape of $R_a(\nu)$ is approximately Gaussian again, the linewidth and the amplitude being dependent on the value of Δf. For a precise determination of ν_R, the modulation width Δf has to be chosen properly as a compromise between a large resonance effect and a small resonance linewidth.

If the resonances are measured with a sweep-mode technique the time-dependent effects of the spin-lattice relaxation have to be taken into account. The resonance effect is then given by

$$R(\nu) = R_a(\nu) + \int_{\nu_0}^{\nu} R_a(\nu') \exp\{-|t(\nu) - t'(\nu')|/T_1'\} d\nu' . \quad (8)$$

The second term describes the resonance effect obtained at earlier times, which is decaying with the anisotropy relaxation time. The far-off-resonance frequency ν_0 is either ν_1 or ν_2 (see Fig. 1) for the upward or downward sweep direction, respectively. If we introduce the time during which a frequency interval Γ_0 is passed,

$$\tau = \int_{-\Gamma_0/2}^{\Gamma_0/2} (d\nu/dt)^{-1}\, dt = \frac{\Gamma_0}{d\nu/dt} . \quad (9)$$

Formula (8) can be written as

$$R(\nu) = R_a(\nu) + \int_{\nu_1}^{\nu} R_a(\nu') \exp\left(-\frac{\nu - \nu'}{\Gamma_0} \frac{\tau}{T_1'}\right) d\nu' \quad (10a)$$

for the sweep up and

$$R(\nu) = R_a(\nu) - \int_{\nu_2}^{\nu} R_a(\nu') \exp\left(-\frac{\nu' - \nu}{\Gamma_0} \frac{\tau}{T_1'}\right) d\nu' \quad (10b)$$

for the sweep down. This shows that an asymmetry of $R(\nu)$ is introduced, depending on the sweep direction, the essential asymmetry parameter being τ/T_1', i.e., the (experimentally choosable) sweep velocity. In the slow-sweep limit

$\tau/T_1' \gg 1$, $R(\nu)$ reduces to the "adiabatic" case $R_a(\nu)$. This is illustrated by the curves a and c of Fig. 1. Both resonances have the same center frequency ν_R. In the ultrafast limit $\tau/T_1' \ll 1$, the structure of $R(\nu)$ would be that of the error function. In this case all information on T_1' would be lost, too.

For $\tau/T_1' \approx 1$, the measured resonance effect $R(\nu)$ has an asymmetric shape, with an exponential decay in sweep direction. This is illustrated in Fig. 1 (curves b and d). Moreover, the "center" frequency (the frequency at which the destruction of the anisotropy has its maximum value) is shifted to $\nu_R + \Delta$ or to $\nu_R - \Delta$, depending on the sweep direction. For the determination of ν_R from slow-sweep mode measurements, where Δ is small, but not negligible, an equal number of spectra with opposite sweep direction are usually added together. With this procedure the observed linewidth is slightly increased, but the center frequency, which is the main result, is not affected by the sweeping. Because of the integrating effect of the fast-sweep technique, the rf modulation width can be chosen small, allowing a highly precise determination of ν_R. Moreover, the relaxation time T_1' can be determined simultaneously.

In the presence of a small quadrupole interaction, which may be superimposed to the magnetic hyperfine splitting, deviations of the observed resonance behavior from that given by formula (7) are expected. The main effect results then in the (observable) fact that the resonance amplitudes are different for both sweep directions. Conversely, if these amplitudes are found to be equal, one can conclude that quadrupole effects have not to be considered in the determination of the magnetic hyperfine splitting constant from the observed resonance frequency.

III. EXPERIMENTAL DETAILS

The ^{97}Ru*Fe* samples were prepared in the following way. Inactive ^{96}Ru*Fe* alloys were produced by melting isotopically enriched ^{96}Ru (enrichment 98.1%) with highly pure iron (purity >99.999%) in an electron beam furnace. For the concentration of ^{96}Ru the relatively high value of 1 at % was chosen because of the small neutron capture cross section of $\sigma \sim 0.3$ b. The alloys were cold rolled with intermediate annealing steps until a final thickness of ~2 μm was reached. Foils with an area of 8×8 mm^2 were irradiated at the Karlsruhe research reactor FR2 for five days in a neutron flux of $\phi = 10^{14}$ n/sec cm^2 to produce the radioactive isotope ^{97}Ru ($T_{1/2} = 2.9$ d; $I^\pi = \frac{5}{2}^+$). After the irradiation the foils were annealed again at a temperature of ~700 °C under high-vacuum atmosphere (~10^{-7} torr). Special care was taken in slowly cooling down the samples to room temperature. Two foils were then soldered with Ga-In solder, which has the low melting point of 15 °C, to both sides of the Cu coldfinger of a demagnetization cryostat. With Cr-K alum as cooling salt, the samples were cooled to a temperature of ~0.01 K. To orient the ferromagnetic domains a small external magnetic field (<7 kG), which was provided by superconducting split coils, was applied in a direction parallel to the foil plane. The γ radiation was analyzed with four 7.6 cm diam × 7.6 cm NaI(Tl) detectors which were placed at 0°, 90°, 180°, and 270° with respect to the direction of the magnetic field.

The rf field was applied using a one-turn coil, the direction being perpendicular to the static field and parallel to the foil plane. The constant frequency sweep was achieved by driving the mechanical tuning of the rf oscillator with a stepping motor. Using different gearing units, the sweep rate $d\nu/dt$ could be varied over a large range. In comparison to electrically tuned oscillators this method has the advantage of a very much better constancy of the sweep rate. The rf field was frequency modulated with a modulation width of 100 kHz and a modulation frequency of 1 kHz. The output of the oscillator was measured continuously using a high-precision frequency counter operating with a repetition rate of 1 kHz. The frequency modulation of the oscillator was synchronized with the frequency counter. Thus a unique determination of the effective center frequency is possible, independent of the modulation width. The output of the frequency counter was used to synchronize a multichannel analyzer, which operated in multiscaling mode.

IV. RESULTS

In the decay of ^{97}Ru only one strong γ transition with an energy of 216 keV is present. A simplified decay scheme is illustrated in Fig. 2. For ^{97}Ru*Fe*,

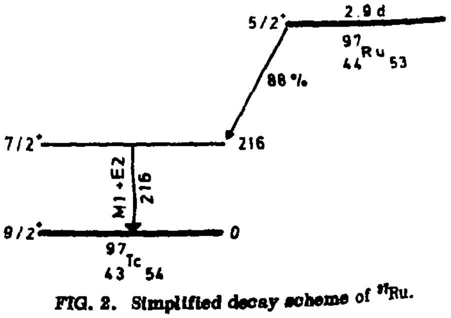

FIG. 2. Simplified decay scheme of ^{97}Ru.

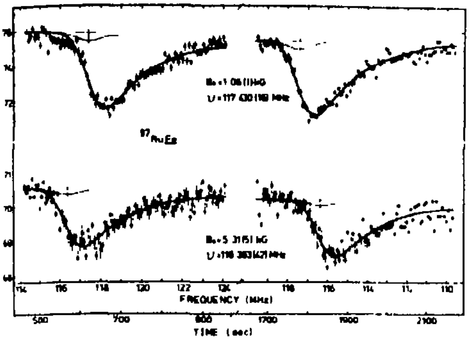

FIG. 3. Fast-sweep-NMR-ON resonances for two different values of the polarizing field B_0. The scale of the abscissa is a time scale (bottom) which has been converted to frequency (top). The left-hand resonances have been measured during the sweep up, the right-hand resonances during the sweep down. The dashed curves are the "adiabatic" resonances as obtained from the least-squares fit utilizing Eq. (10).

the corresponding γ-ray anisotropy is $\epsilon \sim 20\%$ at $T \sim 10$ mK. Figure 3 shows resonance spectra, measured at 0° (with respect to B_0) for two different values of the external magnetic field. The solid curves are the results of least-squares fits, utilizing Eq. (10) as theoretical curve and a Gaussian line shape for the inhomogeneous broadening. The dashed curves in Fig. 3 are the "adiabatic" resonances, which have been added to demonstrate the large enhancement of the observed resonance effect by the fast-sweep technique. The shift of the resonance towards smaller frequencies with increasing polarization field is due to the negative sign of the hyperfine field. More details of the resonance spectra for a measurement with $B_0 = 1.06(1)$ kG can be seen in Fig. 4. It is clearly demonstrated that the maximum of the resonance destruction is shifted by $\Delta = 0.8$ MHz in sweep direction. Thus a folding of both spectra to get rid of the asymmetric line shape would not be a good procedure for the precise determination of ν_R. The upper part of Fig. 5 shows the resonance frequencies as a function of the external magnetic field. The solid line is the result of a least-squares fit, which yields

$$g\mu_N B_{hf}/h = 117.69(2)\ \mathrm{MHz}$$

for the hyperfine splitting and

$$g\mu_N(1+K)/h = 0.246(3)\ \mathrm{MHz/kG}$$

for the resonance shift. The lower part of Fig. 5 illustrates the deviation of the measured points from the fitted line, thus demonstrating the good accuracy obtainable with the fast-sweep technique. The quoted error for the resonance shift is mostly

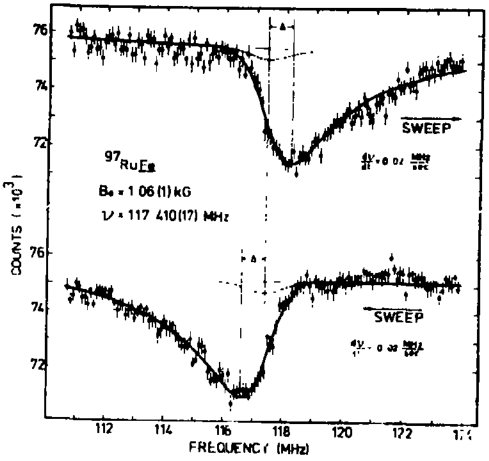

FIG. 4. Details of a fast-sweep-NMR-ON resonance run for $B_0 = 1.06$ (1) kG versus frequency. The maxima of the resonance curves are clearly shifted by $\Delta = 0.80$ MHz in sweep direction (upper spectrum: sweep up; lower spectrum: sweep down). The full curves are the results of a least-squares fit utilizing Eq (10); the dashed curves are the "adiabatic" resonance, which is also a result of the fit.

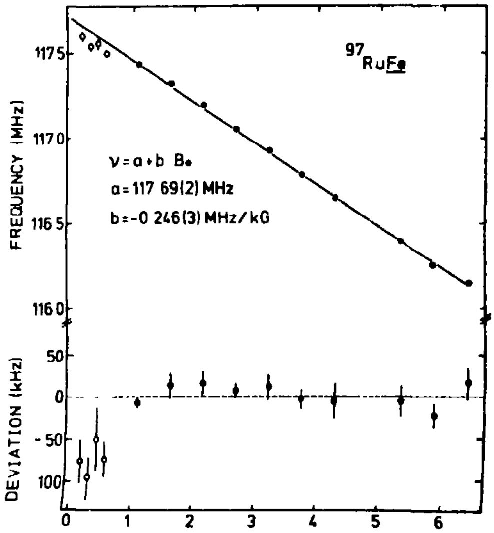

FIG. 5. NMR-ON center frequencies (top) and deviation of these frequencies from the fitted straight line (bottom). The values for $B_0 < 1$ kG have been added for demonstration; they are not used for the fit of the resonance shift because of the incomplete magnetic saturation of the samples in this region.

due to an (absolute) uncertainty of ~1% in the calibration of the external magnetic field. This calibration has been performed by measuring the resonance shift of ^{60}Co*Fe*, which was found to be reproducible within an accuracy of ~1%.

For the interpretation of our hyperfine splitting, the knowledge of the hyperfine field for Ru*Fe* is necessary. From Mössbauer-effect measurements on ^{99}Ru*Fe* (Ref. 13) the splitting of the $\frac{3}{2}^+$ state at 90 keV has been measured as $\nu_M = 72.8(1.3)$ MHz. With the known magnetic moment of $\mu_{3/2} = -0.284(6)\ \mu_N$ (Ref. 14) for this $\frac{3}{2}^+$ state, $B_{HF} = -504(14)$ kG is calculated. (The negative sign has been measured with the use of an external magnetic field.)[13] From NMR investigations of ^{99}Ru and ^{101}Ru as impurities in Fe, Co, and Ni (Ref. 15) the ground-state splitting of ^{99}Ru*Fe* (1 at %) has been found to be $\nu_M = 95.75(10)$ MHz. With $\mu_{5/2} = -0.623(19)\ \mu_N$ the corresponding hyperfine field is deduced to be $B_{HF} = -504(15)$ kG. These two values are not completely independent, however, as $\mu_{5/2}$ is calculated using $\mu_{3/2}$ and the measured g-factor ratio $g_{3/2}/g_{5/2} = 0.759(16)$.[13] Thus,

$$B_{HF} = -504(12)\ \text{kG}$$

[instead of the usual tabular value of −500 (10) kG (Ref. 10)] is adopted to deduce the ground-state g factor of ^{97}Ru, which yields

$$|g| = 0.306(8).$$

Much more precise results are obtained for the ratios of the ground-state g factors of ^{97}Ru, ^{99}Ru, and ^{101}Ru. These, together with the resonance frequencies, are compiled in Table I.

From the resonance shift we get

$$|g(1+K)| = 0.315(7),$$

which can be used to deduce the value

$$K = +2.9(3.4)\%$$

for the Knight shift of ^{97}Ru*Fe*. This value, which is consistent with $K = 0$, lies well within the usual range of Knight shifts for dilute iron host alloys[16,17] in the mass region $A < 100$.

Figure 6 shows the linewidth (bottom), the resonance effect (middle), and the anisotropy relaxation time T_1' (top) as a function of the external magnetic field B_0. The linewidth is found to be rather constant in the whole range. This behavior is quite normal, the mean value $\Gamma = 1.4(2)$ MHz is, however, relatively large in comparison to other NMR-ON data on other systems in this frequency range. This could be caused by the relatively high Ru concentration of ~1 at.%, which had to be chosen because of the small neutron capture cross section of ^{96}Ru.

The dependence of the resonance effect on B_0 can be understood easily: The increase between $B_0 = 0$ and $B_0 = 1$ kG is due to the increasing degree of orientation, which reaches the saturation value at ~1 kG. [In this region of incomplete saturation the measured center frequencies are not described properly by Eq. (3) because of the finite angle between B_0 and B_{HF}, which, in addition, depends on B_0. Thus the resonance frequencies for $B_0 < 1$ kG have been omitted for the analysis of the hyperfine

TABLE I. Magnetic hyperfine splitting and ratios of ground-state g factors of ^{97,99,101}Ru.

System	ν_M(MHz)	g/g (^{97}Ru)[a]	Reference
^{97}Ru*Fe*	117.69(2)	1.0	b
^{99}Ru*Fe*	95.75(10)	0.8136(8)	c
^{101}Ru*Fe*	107.30(10)	0.9117(8)	c

[a] Possible hyperfine anomalies are neglected in this ratio. This is possible, as only differences of hyperfine anomalies would enter, which are expected to be smaller than the quoted error.

[b] This work.

[c] J. J. Murphy, T. J. Burch, and J. I. Budnick, J. Phys. Soc. Jpn. 36, 634 (1974).

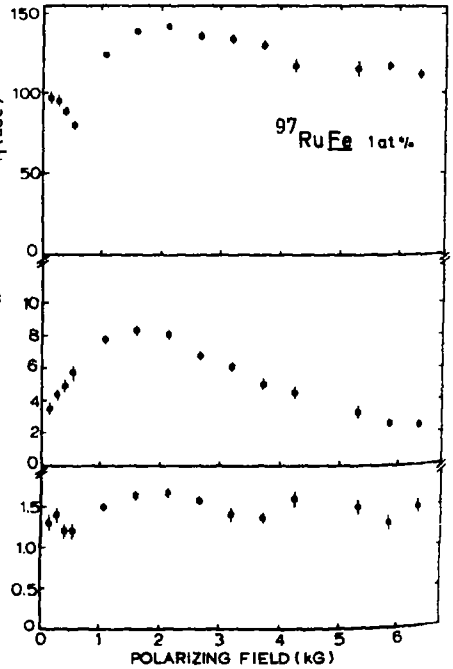

FIG. 6. Observed linewidth (bottom), resonance effect (middle), and anisotropy relaxation time (top) versus the applied external magnetic field.

splitting and the resonance shift.] The decrease of the resonance effect for $B_0 > 1.5$ kG is probably due to the decreasing enhancement factor for the rf field, which is proportional to B_{hf}/B_0 in first approximation.

The behavior of the relaxation time T_1' in dependence of B_0 is anomalous in comparison to that of other systems in this mass region. Neglecting the data points for the magnetization region $B_0 \lesssim 1$ kG, T_1' is found to be rather constant, with a slightly decreasing trend for $B_0 > 2$ kG. This decrease is partly caused by the smaller deviation of the sublevel populations from the equilibrium value, as observed by the decreasing resonance effect. An increase of T_1' by a factor ~5 between 0 and 5 kG, as observed, e.g., on ^{90}Nb*Fe* and ^{94}Tc*Fe*,[18] is clearly not present for ^{97}Ru*Fe*.

TABLE II. Magnetic moments of neutron $\frac{5}{2}^+$ states in the mass region $A > 90$.

Isotope	μ (μ_N)	Reference
$^{91}_{40}$Zr$_{51}$	−1.30362(2)	a
$^{93}_{42}$Mo$_{51}$	−1.20(5)	b
$^{95}_{42}$Mo$_{53}$	−0.9142(1)	c
$^{97}_{42}$Mo$_{55}$	−0.9335(1)	c
$^{97}_{44}$Ru$_{53}$	−0.765(20)	d
$^{99}_{44}$Ru$_{55}$	−0.623(19)	e
$^{101}_{44}$Ru$_{57}$	−0.698(24)	f
$^{105}_{46}$Pd$_{59}$	−0.642(3)	g
$^{105}_{48}$Cd$_{57}$	−0.7393(2)	h
$^{107}_{48}$Cd$_{59}$	−0.615055(1)	j, k
$^{109}_{48}$Cd$_{61}$	−0.827846(1)	j, l
$^{111}_{48}$Cd$_{63}$	−0.7656(25)	m

[a] E. Brun, J. Oeser, and H. H. Staub, Phys. Rev. 05, 1929 (1957).

[b] E. Hagn, E. Zech, and G. Eska, Hyp. Int. 4, 201 1978).

[c] W. G. Proctor and F. C. Yu, Phys. Rev. 81, 20 1951).

[d] This work.

[e] E. Matthias, S. S. Rosenblum, and D. A. Shirley, Phys. Rev. 139, B532 (1965).

[f] J. J. Murphy, T. J. Burch, and J. I. Budnick, J. Phys. Soc. Jpn. 36, 634 (1974).

[g] J. A. Seitchik, A. C. Gossard, and V. Jaccarino, Phys. Rev. 136, A1119 (1964).

[h] N. S. Laulainen and M. N. McDermott, Phys. Rev. 177, 1615 (1969).

[j] P. W. Spence and M. N. McDermott, Phys. Lett. 12A, 273 (1972).

[k] F. W. Byron, Jr., M. N. McDermott, and R. Novick, Phys. Rev. 132, 1181 (1963).

[l] M. N. McDermott and R. Novick, Phys. Rev. 131, 707 (1963).

[m] H. Bertschat, H. Haas, F. Pleiter, E. Recknagel, E. Schlodder, and B. Spellmeyer, Z. Phys. 270, 203 (1974).

V. DISCUSSION

With $J^\pi = \frac{5}{2}^+$, the magnetic moment of ^{97}Ru is found to be

$$\mu = (-)0.765(20)\ \mu_N .$$

The negative sign has been adopted from the systematics of magnetic moments of $\frac{5}{2}^+$ states in this mass region. A compilation of magnetic moments of $\frac{5}{2}^+$ states is given in Table II for the mass region $A > 90$, where the neutron $d_{5/2}$ shell is successively filled. With the exception of ^{111}Cd, all data originate from measurements on ground states. The value for $^{93}_{51}$Mo$_{42}$ has been deduced in the following way: Assuming $^{92}_{50}$Mo$_{42}$ to be the "core," the isotopes $^{93}_{51}$Mo$_{42}$, $^{93}_{50}$Tc$_{43}$, and $^{94}_{51}$Tc$_{43}$ have the configurations $|\nu d_{5/2}\rangle$, $|\pi g_{9/2}\rangle$, and $|\nu d_{5/2}\pi g_{9/2}\rangle_{7^+}$. As the magnetic moments of ^{93}Tc and ^{94}Tc are known,[19] the neutron contribution to the magnetic moment of ^{94}Tc can be calculated:

$$\mu(\nu d_{5/2}) = \mu(7^+) - \mu(\pi g_{9/2}) .$$

This procedure is based on the assumption that the magnetic moments of the one-particle states remain unchanged for the two-particle state, which is valid in most cases to an accuracy of several percent. Figure 7 illustrates the behavior of the $d_{5/2}$ neutron magnetic moments versus the neutron number. The relatively large values for $N = 51$ are quite normal for states with one particle outside closed shells. The strong deviation from

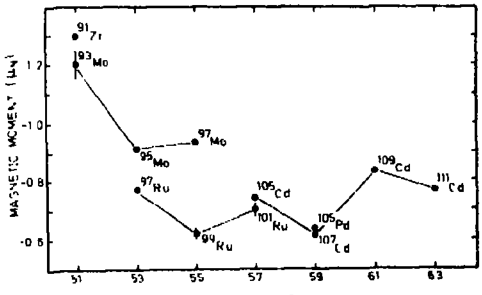

FIG. 7. Magnetic moments of $\frac{5}{2}^+$ states in the mass region $A > 90$ versus neutron number. A similar structure of μ for ^{93,95,97}Mo, ^{97,99,101}Ru, and ^{105,107,109}Cd can be seen. This yields a strong evidence for the fact that the addition of proton pairs in the $\pi g_{9/2}$ shell, by going from Mo to Cd, is accompanied by a simultaneous addition of the same number of neutron pairs into the $\nu g_{7/2}$ shell.

TABLE III. Calculated magnetic moments of $\frac{5}{2}^+$ states for different neutron configurations.

Nucleus	Proton configuration [a]	Neutron configuration [a]	μ_{cal} (μ_N) [b]	μ_{exp} (μ_N) [c]
^{91}Zr		$(d_{5/2})^1$	−1.44	−1.30
^{93}Mo	$(g_{9/2})^2$	$(d_{5/2})^1$	−1.42	−1.20
^{95}Mo	$(g_{9/2})^2$	$(d_{5/2})^3$	−0.95	−0.91
		$(g_{7/2})^2\ (d_{5/2})^1$	−1.53	
^{97}Mo	$(g_{9/2})^2$	$(d_{5/2})^5$	−0.50	−0.93
		$(g_{7/2})^2\ (d_{5/2})^3$	−1.07	
^{97}Ru	$(g_{9/2})^4$	$(d_{5/2})^3$	−0.93	−0.77
		$(g_{7/2})^2\ (d_{5/2})^1$	−1.51	
^{99}Ru	$(g_{9/2})^4$	$(d_{5/2})^5$	−0.50	−0.62
		$(g_{7/2})^2\ (d_{5/2})^3$	−1.05	
^{101}Ru	$(g_{9/2})^4$	$(g_{7/2})^2\ (d_{5/2})^5$	−0.61	−0.70
		$(g_{7/2})^4\ (d_{5/2})^3$	−1.16	

[a] Configuration above the core $^{90}_{40}Zr_{50}$.

[b] Calculated with parameters of Ref. 20.

[c] For references see Table II.

the Schmidt value ($\mu = -1.91\mu_N$) is probably due to the fact that the $\nu g_{9/2}$ shell is filled completely at $N = 50$, the $\nu g_{7/2}$ shell, however, is empty. Consequently, the $g_{9/2} \rightarrow g_{7/2}$ core polarization may be active, thus reducing the magnetic moments. For $N > 51$ the $d_{5/2} \rightarrow d_{3/2}$ excitations are responsible for a further reduction of μ. In a simple shell model picture the $d_{5/2}$ shell should be filled at $N = 56$, and thus, no $j^\pi = \frac{5}{2}^+$ ground-state configurations should be present for $N > 56$. It is experimentally found, however, that $j^\pi = \frac{5}{2}^+$ ground states occur up to $N = 61$ ($^{109}_{48}Cd_{61}$). This is due to the fact that the energy spacing between the $\nu d_{5/2}$ and $\nu g_{7/2}$ shell is relatively small, so that the filling of these two shells does not take place independently. In principle, the quasiparticle occupation probabilities u^2 and v^2 should be used for a proper description of the ground-state configurations. However, such data are not available with sufficient accuracy. Experimental values of magnetic moments of $\frac{5}{2}^+$ states can provide further information as a strong dependence of μ on the nuclear configuration is expected. Applying the core-polarization theory of Arima and Horie,[1] theoretical magnetic moments for the different extremal configurations are obtained. The result for ^{91}Zr, ^{93,95,97}Mo, and ^{97,99,101}Ru is listed in Table III. Although the absolute values are not described properly for ^{91}Zr and ^{93}Mo for which the neutron configuration is fixed, a similarity of the qualitative trend can be seen. For the Mo isotopes ^{93}Mo, ^{95}Mo, and ^{97}Mo the main neutron configuration is given by $(\nu d_{5/2})^1$; $(\nu d_{5/2})^3$, and $(\nu g_{7/2})^2 (\nu d_{5/2})^3$, respectively. The main neutron configuration of the Ru isotopes ^{97}Ru, ^{99}Ru, and ^{101}Ru should then be $(\nu d_{5/2})^3$, $(\nu d_{5/2})^5$, and $(\nu g_{7/2})^2 (\nu d_{5/2})^5$, respectively. The slight increase of the magnetic moments of the heaviest isotopes in these series is then explained consistently by the blocking of the $g_{9/2} \rightarrow g_{7/2}$ core polarization due to the more filled $\nu g_{7/2}$ shell. To investigate, whether the Pd isotopes fit into such a scheme, too, the magnetic moments of ^{101}Pd and ^{103}Pd would be interesting. NMR-ON measurements concerning this subject are in progress.

Moreover, our experiments have shown that the NMR-ON method is well suited for the precise determination of the hyperfine splitting constants of Ru*Fe* systems. The application to ^{103}Ru and ^{105}Ru could thus lead to a better understanding of the structure of these anomalous ground states.

ACKNOWLEDGMENTS

We want to thank Professor T. Yamazaki for discussions and Dr. P. Maier-Komor for the preparation of the Ru*Fe* alloys. We also thank the Gesellschaft für Kernforschung, Karlsruhe, for performing the neutron irradiations. This work was supported by the Bundesministerium für Forschung und Technologie.

[1] A. Arima and H. Horie, Prog. Theor. Phys. 12, 623 (1951).

[2] H. A. Mavromatis, L. Zamick, and G. E. Brown, Nucl. Phys. 80, 545 (1966); H. A. Mavromatis and L. Zamick, Nucl. Phys. A104, 17 (1967).

[3] H. Miyazawa, Prog. Theor. Phys. 6, 801 (1951).

[4] M. Chemtob, Nucl. Phys. A123, 449 (1969); M. Chemtob and M. Rho, *ibid.* A163, 1 (1971).

[5] S. Nagamiya, T. Katou, T. Nomura, and T. Yamazaki, Phys. Lett. 33B, 574 (1970); T. Yamazaki, in *Proceedings of the International Conference on Nuclear Structure and Spectroscopy, Amsterdam, 1974*, edited by H. P. Blok and A. E. L. Dieperink (Scholar's Press, Amsterdam, 1974), Vol. 2, p. 554 and references therein.

[6] E. Hagn, P. Kienle, and G. Eska, in *Proceedings of the International Conference on Nuclear Structure and Spectroscopy, Amsterdam, 1974*, edited by H. P. Blok and A E. L. Dieperink (Scholar's Press, Amsterdam, 1974), Vol. 2, p. 576.

[7] O. Häusser, I. S. Towner, T Faestermann, H. R. Andrews, J. R. Beene, D. Horn, D. Ward, and C. Broude, Nucl. Phys. A293, 248 (1977).

[8] J. Wese, E. Hagn, P. Kienle, and G. Eska (unpublished).

[9] S. R. de Groot, H. A. Tolhoek, and W. J. Huiskamp, *Alpha, Beta, and Gamma Ray Spectroscopy*, edited by K. Siegbahn (North-Holland, Amsterdam, 1965), Vol. 2, p. 1199.

[10] G. N. Rao, Nucl. Data Tables 15, 553 (1975).

[11] E. Matthias and R. J. Holliday, Phys. Rev. Lett. 17, 897 (1966).

[12] F. Bacon, J. A. Barclay, W. D. Brewer, D. A. Shirley, and J. E. Templeton, Phys. Rev. B 5, 2397 (1972).

[13] O. C. Kistner, Phys. Rev. 144, 1022 (1966).

[14] E. Matthias, S. S. Rosenblum, and D. A Shirley, Phys. Rev. 139, B532 (1965).

[15] J. J. Murphy, T. J. Burch, and J. I. Budnick, J. Phys. Soc. Jpn. 36, 634 (1974).

[16] E Hagn and G Eska, in *Proceedings of the International Conference on Hyperfine Interactions Studied in Nuclear Reactions and Decay, Uppsala, Sweden, 1974*, edited by E. Karlsson and R. Wäppling (Uplands Grofiska AB, Uppsala, 1974), p. 148.

[17] M. Kopp and W. D. Brewer, Hyp. Int. 3, 321 (1978).

[18] E. Hagn, E. Zech, and G. Eska (unpublished).

[19] E Hagn, E. Zech, and G Eska, Hyp. Int. 4, 201 (1978).

[20] H. Noya, A. Arima, and H. Horie, Prog. Theor. Phys. Suppl. 8, 33 (1958).

Level properties of $^{85}_{37}\mathrm{Rb}_{48}$ from the decay of the ^{85}Kr and ^{85}Sr isomers and the cluster-vibration model

R. A. Meyer, J. E. Fontanilla, N. L. Smith, C. F. Smith, and R. C. Ragaini
Lawrence Livermore Laboratory, Livermore, California 94550

V. Paar
Priordoslovno-matematički Fakultet, Zavod Za Teorijsku Fiziku, Marulićev TRG 19/I, 41000 Zagreb, Croatia, Yugoslavia

(Received 30 October 1978; revised manuscript received 21 December 1979)

We have investigated the decay of $^{85}\mathrm{Kr}^m$, $^{85}\mathrm{Kr}^g$, $^{85}\mathrm{Sr}^m$, and $^{85}\mathrm{Sr}^g$ using Ge(Li) spectroscopy and intrinsic Ge Compton-suppression spectroscopy techniques. We observe levels at (J^π in parentheses) g.s. (5/2$^-$), 151.18 (3/2), 281.01 (1/2), 513.998 (9/2$^+$), 731.79 (3/2), 868.05 (7/2$^-$), and 921 (1/2$^-$,3/2$^-$) keV. Our data suggest that the ~880 keV level observed in (t,α) and (^{3}He,d) reactions is the known 868-keV level. The Q_{EC} value for the $^{85}\mathrm{Sr}^m$ decay is calculated to be 1323±20 keV from our EC/β^+ intensity data. We use the cluster-vibration model to calculate the ^{85}Rb level structure and electromagnetic decay properties. For the latter, we discuss the role of the *M*1 tensor operator.

NUCLEAR STRUCTURE Cluster-vibration model, influence of *M*1 tensor term.

RADIOACTIVITY ^{85}Kr, $^{85}\mathrm{Kr}^m$, ^{85}Sr, and $^{85}\mathrm{Sr}^m$. Measured E_γ, I_γ. ^{85}Rb deduced levels, E_γ, I_γ, J, π. Ge(Li) detector, Compton-suppression spectrometer.

I. INTRODUCTION

A major problem in predicting the level structure of odd-mass spherical nuclei is the inability of the simple single-particle shell model to account for the large number of experimentally observed levels below the pairing gap.[1,2] Some of the "extra" levels in odd-mass nuclei have been accounted for in a phenomenological way by using a weak coupling model.[3-5] Recently, some success has been achieved in accounting for all the levels and their properties by incorporating explicit multiparticle excitations and their interaction with the vibrational field.[6-17] The odd-mass Rb nuclei with $Z = 37$ provide a test of these calculations for, as shown in Fig. 1, their level density below 800 keV changes drastically as the number of neutron pairs are changed.[18-40] Here we present our experimental studies which were aimed at clarifying the number and decay properties of the ^{85}Rb levels below 1 MeV. We then compare the results of cluster-vibration model calculations with the ^{85}Rb levels and their properties. Finally, we discuss the role of the tensor term in l-forbidden *M*1 transitions.

Since the last published compilation on $A = 85$ nuclei by Horen,[28] several studies of ^{85}Rb have been reported. The levels of ^{85}Rb have been studied by (^{3}He,d), (Ref. 29), (t, α) (Ref. 24) and (d, ^{3}He) (Ref. 31) reactions, Coulomb-excitation,[26] (n,$n'\gamma$) reactions,[23,25] and decay studies,[18-21] including our initial reports.[28,30] A number of the levels observed in reaction spectroscopy have l-value assignment inconsistent with the decay properties observed i the two (n,$n'\gamma$) studies. In addition, a level of approximately 880 keV has been reported in some transfer reaction studies but not in all the related studies.

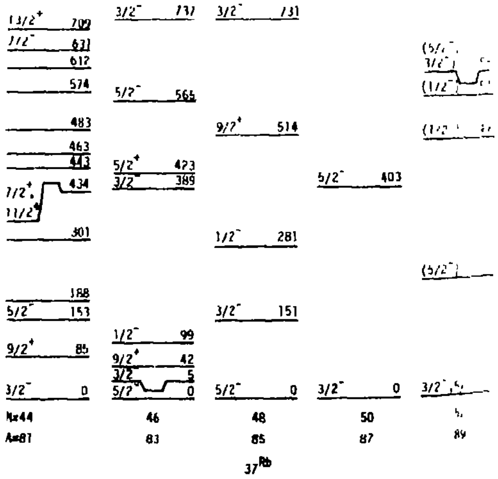

FIG. 1. Experimentally observed levels of odd-mass Rb nuclei below 800 keV. These levels have been taken from the data presented in Refs. 18 to 44, inclusive.

II. EXPERIMENTAL

Using gas-chromatography techniques, we prepared sources of 10.37-y ^{85}Kr^{g} from the gross fission products of an underground nuclear detonation.[41,42] A commercially available source was also used. Approximately 1 Ci of ^{85}Kr^{g} was adsorbed onto 1 g of charcoal and sealed in a quartz counting ampule.

Two types of 4.48-h ^{85}Kr^{m} sources were made. The first source was mass separated after gas-chromatographic separation of krypton from gross fission products.[41,42] Since this source was too weak, a second source was prepared from gaseous fission products but was not mass separated in order to achieve reasonable counting statistics.

The ^{85}Kr^{g} was counted several times using two different Compton-suppression spectrometers: one with a Ge(Li) detector,[43] the other with an intrinsic-Ge detector.[44] The ^{85}Kr^{m} spectra were taken with an LEPS, a large-volume Ge(Li) detector, and Compton-suppression spectrometers. In addition, the sources were counted simultaneously with known energy standards.[45,46] All spectra in this study were analyzed on CDC-7600 computers using the GAMANAL code developed by Gunnink and Niday.[47]

Sources of 69.5-min ^{85}Sr^{m} were produced by irradiating enriched ^{84}Sr in the Livermore Pool-Type Reactor (LPTR). Since the initial experiments showed the presence of major non-Sr contaminants, the enriched ^{84}Sr was chemically purified by adsorbing Sr ions out of an aqueous solution of ^{84}Sr(NO$_3$)$_2$ on a Dowex-50 cation column. Any impurities adsorbed on the column were stripped off with 0.5 M α-hydroxy isobutyric acid (α-HIBA) with pH 5.2. The Sr was eluted with 1 M α-HIBA at pH 5.2 and precipitated as SrCO$_3$ using NH$_3$ and CO$_2$. The SrCO$_3$ was washed, dried, weighed, divided into several vials, and sealed for irradiation. Upon completion of irradiation, the SrCO$_3$ was removed from the irradiation vial and sealed in a counting planchette. A new source was produced every 60 minutes, and during each 60-min period spectra were taken sequentially on four separate Ge(Li) spectrometers. Each spectrometer accumulated data for approximately 500 min.

Sources of 65.19-d ^{85}Sr^{g} were produced by the ^{85}Rb(α,4n)^{85}Y^{m+g} $\rightarrow$ ^{85}Sr^{g} sequence using enriched ^{85}Rb targets at the Lawrence Berkeley Laboratory (LBL) 223-cm cyclotron. The ^{85}Sr^{g} sources were chemically purified by the same technique as above to eliminate any possible contaminants. Again, singles, Compton-suppression, and energy-calibration spectra were taken.

III. RESULTS AND DECAY SCHEMES

A. ^{85}Kr^{m} decay

In Table I we present the energies and intensities of the γ rays we assign to the decay of ^{85}Kr^{m}. A portion of the Ge(Li)-LEPS spectra showing the 129- and 151-keV γ rays is given in Fig. 2. The decay scheme deduced from our data is shown in Fig. 3(a). The logft values were calculated using a Q_β of 991 ± 2 keV and a half-life of 4.475 ± 0.010 hr as reported by Wohn *et al.*[20]

We observe population of the 732-keV level observed in Coulomb excitation.[26] Bond and Kumbartski[26] have shown that the J^π value for this level is $\frac{3}{2}^-$; thus, the implied β transition from ^{85}Kr^{m}($\frac{1}{2}^-$) is *allowed*. We also observe population of the 732-keV level in the decay of ^{85}Sr^{m} (see Sec. III C).

B. ^{85}Kr^{g} decay

The energies and intensities of the γ rays from the decay of ^{85}Kr^{g} are listed in Table II. The ^{85}Kr^{g} decay scheme is shown in Fig. 3(b). The Compton-suppression spectra of the decay of ^{85}Kr^{g} and details of the 151-, 362-, and 514-keV peaks from the intrinsic-Ge Compton-suppression spectrometer are shown in Figs. 4(a)–4(d). From our limit on the intensity of any 129-keV γ ray, obtained with the Compton-suppression system, we calculate a lower limit of 17 for the logft value for the unique third-forbidden β decay from ^{85}Kr^{g} to the 281-keV level. We have observed for the first time the $E3$ transition from the 514-keV $\frac{9}{2}^+$ level to the 151-keV $\frac{3}{2}^-$ level in ^{85}Rb. Our branching ratio of five 362-keV γ rays per 10^6 decays of the 514-keV level ($T_{1/2}$ = 1 μs) gives an $E3$ hindrance of 75 relative to the Moszkowski estimate.[48] This value is quite different from the enhancement of 3 spu for similar transitions in the indium nuclei.[49,50] More data of a systematic nature are needed before the role of the octupole vibration in these types of transitions can be discussed.

TABLE I. γ rays from the decay of ^{85}Kr^{m}.

$E_\gamma(\Delta E_\gamma)$ (keV)	$I_\gamma(\Delta I_\gamma)$ (relative)	Assignment From	To
129.81 (2)	4.0 (1)	281	151
151.19 (3)	1000 (5) [a]	151	GS
281.01 (4)	$\lesssim$0.01	281	GS
304.87 (2)	187 (2)	I.T.	
451.0 (1)	0.15 (5)	732	281
580.6 (1)	$\leq$0.01	732	151
731.6 (3)	0.10 (4)	732	g.s.

[a] Fiducial value. The error represents statistical and fitting error only.

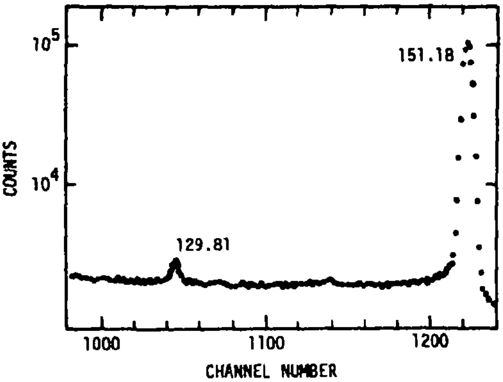

FIG. 2. Portion of γ-ray spectrum from the decay of ^{85}Kr^m showing the 129- and 151-keV γ rays. (N.B.: small peak at channel 1140 is the 151-keV Ge escape peak.)

C. ^{85}Sr^m decay

In Figs. 5(a) and 5(b) we show the ^{85}Sr^m spectra. In Table III we present the γ-ray intensities for the decay of ^{85}Sr^m. In Fig. 6 we show the decay scheme of ^{85}Sr^m. If we use our values for the positron intensity and E.C. feeding of the 151-keV level, we obtain an EC/β^+ ratio of $(1.9 \pm 0.3) \times 10^3$. This corresponds to a Q value of 1323 ± 20 keV for the decay of the isomer.[34] Previously, only an estimated Q value of 1308 keV was available.[28]

D. ^{85}Sr^g decay

The γ-ray energies and intensities for the decay of ^{85}Sr^g are given in Table IV, and Fig. 7 shows the ^{85}Sr^g decay scheme. The observation of the 951-keV γ ray was not unambiguous; therefore, we report an upper limit for its intensity and do not include it in our decay scheme.

Bubb *et al.*[21] have stated that the decay of ^{85}Sr^g populates only the $\frac{9}{2}^+$ level at 514 keV in ^{85}Rb. They did not observe γ rays at 880 and 356 keV, which were previously reported[22,23] and assumed to deexcite a level at approximately 880 keV. They further claimed that the ^{85}Sr^m decay populates only the 151-keV $\frac{3}{2}^-$ level in ^{85}Rb. Our results, as shown in Table V and Fig. 7, disagree with those of Bubb *et al.*[21] We do observe 868-, 716-, and 354-keV γ rays that deexcite a level at 868 keV.[18] This level has been observed in recent Coulomb-excitation and $(n, n'\gamma)$ experiments.[25,26,28] We note that Vatai *et al.*[19] found tentative evidence for 868-keV γ rays; however, they did not have enough sensitivity in their measurement to observe the 716- or 354-keV γ rays and hence definitely establish a level.

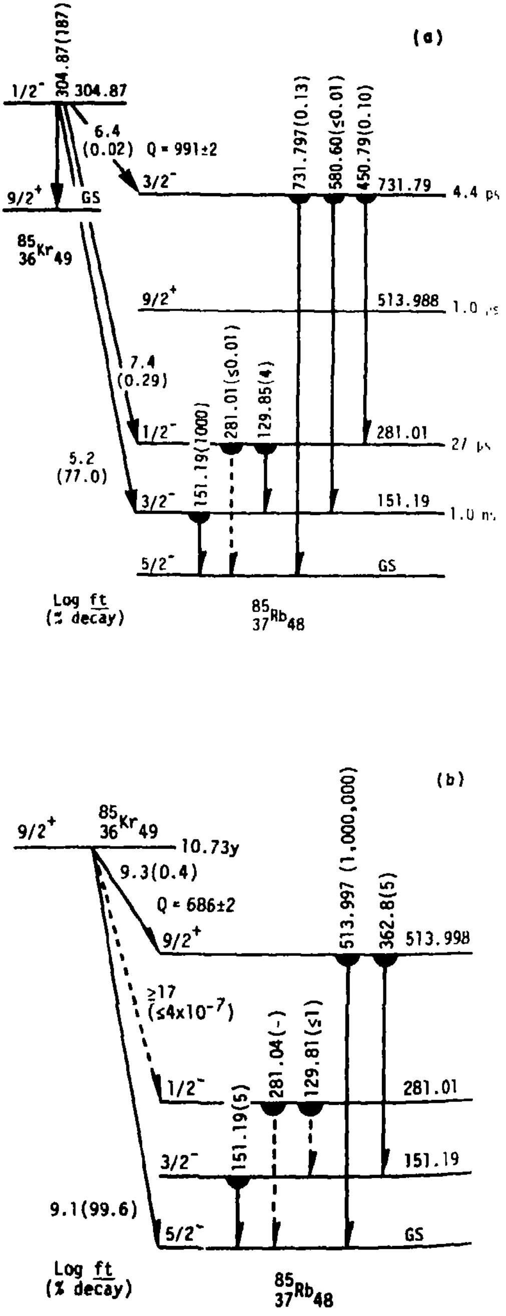

FIG. 3. (a) Decay scheme for ^{85}Kr^m. (b) Decay scheme for ^{85}Kr^g. The 281-keV γ ray is not observed in either of these decays; however, it is observed in the decay of ^{85}Sr^m with a branching ratio of 2.7×10^{-3} (see Fig. 6).

TABLE II. γ rays from the decay of ^{85}Kr^{g}.

$E_\gamma(\Delta E_\gamma)$ (keV)	$I_\gamma(\Delta I_\gamma)$ (relative)	Assignment From	To
129.81 (2)	≤ 1	281	151
151.18 (3)	5 (3)	151	GS
362.81 (4)	5 (1)	513	151
513.997 (5)	10^6	513	GS

E. ^{85}Rb level assignments

In Table V we present a compendium of the ^{85}Rb levels observed in the various studies. The 868- and 919-keV levels have been observed in several studies[25,26,32] while a level at approximately 880 keV has been suggested.[24,29] Our work supports the levels at 868 and 919 keV but we obtain no evidence for a level at 880 keV. The 868-keV level has been observed in Coulomb-excitation studies[26] as well as in (d, ^{3}He) (Ref. 31) and (n,$n'\gamma$) studies.[25,32] The 919.7-keV level is observed in both (n,$n'\gamma$) studies[25,32] and is reported to have an $l = 3$ value in (d,^{3}He) studies[31] and an $l = 1$ value in (t,α) studies.[24] None of the decay, Coulomb excitation,[26] (d,^{3}He), (Ref. 31) or (n,$n'\gamma$) studies[25,32] report a level at approximately 880 keV. However, both (t,α) (Ref. 24) and (^{3}He,d) (Ref. 29) studies report a single peak at about 880 keV. Presumably this 880-keV peak is due to the 868-keV level, the energy discrepancy being due to the rather poor energy resolution of the charged-particle spectrometers. Our ^{85}Sr^{g} decay data imply a J^π of $\frac{7}{2}^-$ for the 868-keV level, in contrast to the ($\frac{1}{2}^-$, $\frac{3}{2}^-$) assignment suggested by the charged-particle reaction experiments.[24,29,31] In the case of the 919-keV level, the possible β-decay feeding from ^{85}Sr^{m} ($\frac{1}{2}^-$) and the $l = 1$ (t,α) result suggest a

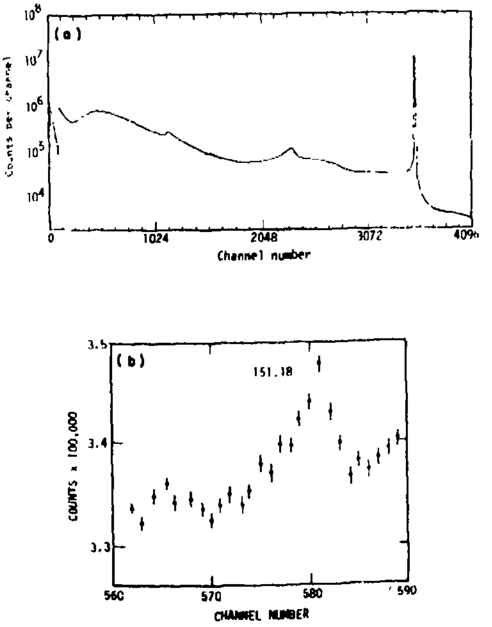

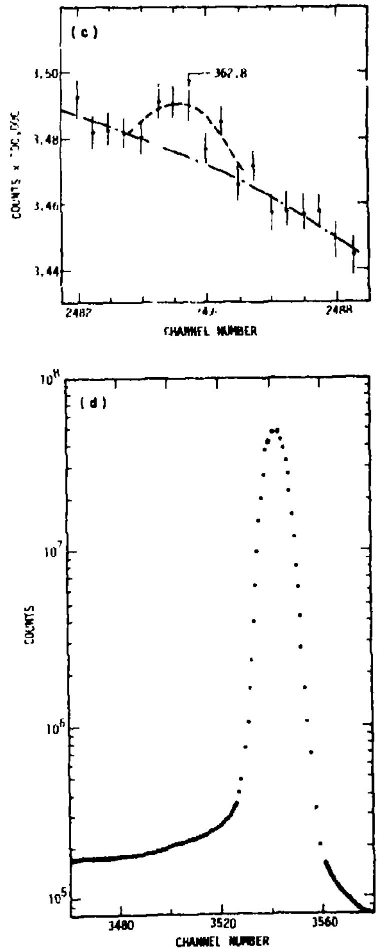

FIG. 4. (a) Early spectra of the ^{85}Kr^{g} decay taken with an intrinsic Ge Compton-suppression spectrometer (CSS). Large hump at low energy is bremsstrahlung from the intense β branch. (b) Detail from CSS showing 151.18-keV γ ray. (c) Detail from CSS showing 362.8-keV γ rays. (d) Detail from CSS showing the shape and statistics of 514-keV γ ray. The duration of count for Fig. 1(a) is approximately one week, while here (b) and (c) are from a 30-day counting period; the values given in Table II are average values of five long-duration Compton-suppression measurements.

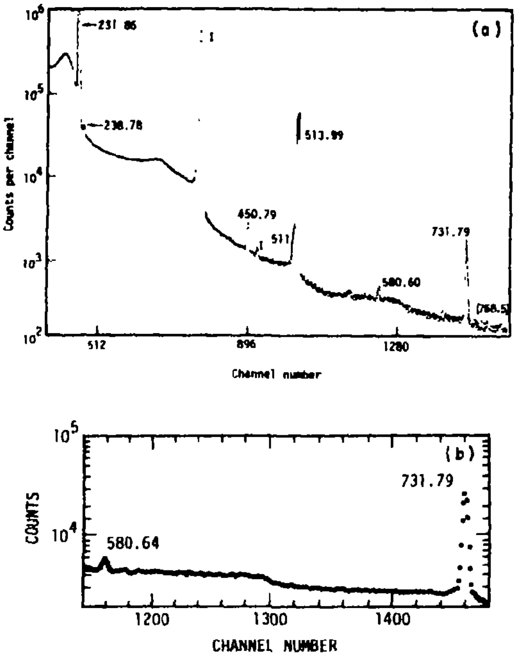

FIG. 5. (a) ^{85}Sr^m Ge(Li) spectrum accumulated with a graded absorber between source and detector during the second half-life period. The peaks labeled I are the impurity lines from the decay of ^{87}Sr^m; (b) ^{85}Sr^m spectra taken with Pb-Cd absorbers in front of a large-volume Ge(Li) detector during first half-life period.

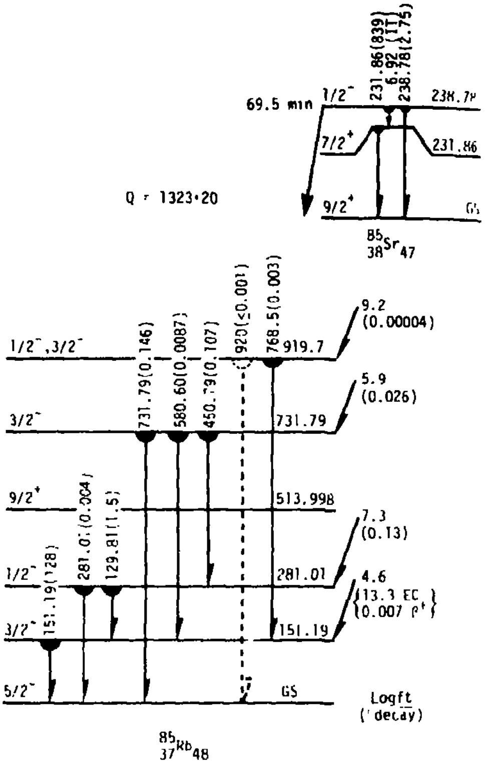

FIG. 6. Decay scheme of ^{85}Sr^m.

$\frac{1}{2}^-$ or $\frac{3}{2}^-$ assignment.

A unique J^π assignment for the 951.2-keV level cannot be made on the basis of the available evidence. The (t, α) study gives $l = 3$ or 4, the $(d, {}^3\text{He})$ an $l = 1$ value, and the $({}^3\text{He}, d)$ an $l = 2$ value. The two $(n, n'\gamma)$ studies each give somewhat different information. In the $(n, n'\gamma)$ studies of Torti *et al.*,[25] enriched ^{85}Rb targets were used and only two transitions out of this level were observed, of energy 951.3 and 800.2 keV. Barnard

TABLE III. γ rays from the decay of ^{85}Sr^m.

$E_\gamma(\Delta E_\gamma)$ (keV)	$I_\gamma(\Delta I_\gamma)$ (per 1000 decays)	Assignment From	To
129.815 (35)	1.5 (4)	281	151
151.194 (15)	128 (3)	151	GS
231.860 (20) [a]	839 (16)		
238.78 (5) [a]	2.75 (5)		
281.01 (3)	0.004 (2)	281	GS
450.79 (5)	0.107 (5)	731	281
511.00 (–) [b]	0.14 (2)		
580.64 (5)	0.0087 (9)	732	281
731.797 (15)	0.146 (8)	732	281
768.5 (10) [c]	0.0030 (25)	922	151
[919.8 (9)] [c,d]	0.0010 (5)	919	g.s.

[a] Transition occurs in the parent nucleus.

[b] Annihilation radiation.

[c] Measured from first half-life data.

[d] Evidence for this γ ray is tentative.

TABLE IV. γ rays from the decay of ^{85}Sr^g.

γ-ray energy (ΔE) (keV)	Relative intensity (ΔI)	Assignment From	To
129.80 (5)	≤0.005	281	151
151.18 (3)	0.012 (9)	151	GS
513.997 (2)	997.0 [a]	514	GS
354.06 (5)	0.005 (2)	868	514
362.82	≤0.01	514	151
716.87 (5)	0.0032 (3)	868	151
868.05 (5)	0.126 (5)	868	g.s.
(951.0 (5)) [b]	(≤0.0003) [b]	(951)	(g.s.)

[a] Total transition intensity taken as 1000.

[b] A γ ray of 951 keV was observed in two spectra taken with high counting statistics. However, the evidence for its assignment to ^{85}Sr decay is tentative.

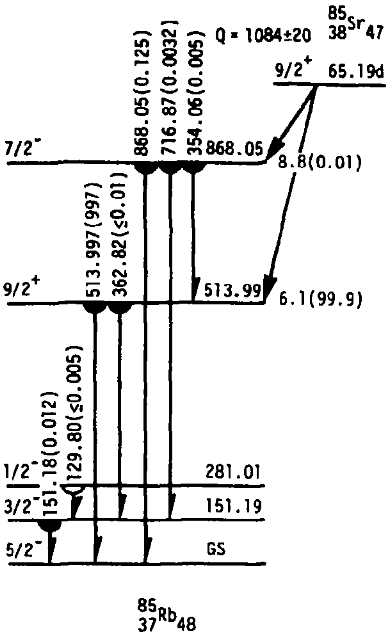

FIG. 7. Decay scheme of ^{85}Sr^g. Although unmeasured and not shown in this figure, it should be noted that the possibility of unique first-forbidden (u1f) beta decay exists between the $J^\pi = \frac{9}{2}^+$ ^{85}Sr^g and the $J^\pi = \frac{5}{2}^-$ ground state of ^{85}Rb. A logf_1t value of 9.7 is consistent with u1f beta decay in this mass region (e.g., ^{84}Rb has a 9.6 and ^{86}Rb has a 9.8 logf_1t value). Using this value, the half-life and measured Q value, the branching ratio to the ground state, would be one percent.

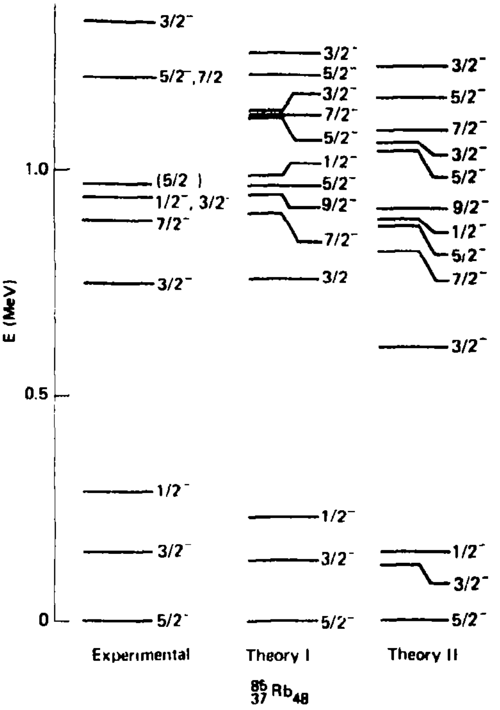

FIG. 8. Comparison of the experimental negative-parity levels of ^{85}Rb and the theoretical levels calculated in the cluster-vibration model (see text for a description of parametrization I and II).

TABLE V. Comparison of experimental results from ^{85}Rb level studies.

Level energy (keV)	J	Log ft Parent J Kr $\frac{1}{2}^-$	Sr $\frac{1}{2}^-$	Sr $\frac{9}{2}^+$	Kr $\frac{9}{2}^+$	l[a] p (t,α)	l[b] p $(d,{}^3\mathrm{He})$	l[c] p $({}^3\mathrm{He},d)$	$(n,n'\gamma)$ Ref. d	$(n,n'\gamma)$ Ref. e
0.0	$\frac{5}{2}^-$				9.1	3	3	3		
151.19	$\frac{3}{2}^-$	5.2	4.6			1	1	1	151.2	151.2
280.01	$\frac{1}{2}^-$	7.4	7.3		6.3	1	1	1	281.0	281.0
513.998	$\frac{9}{2}^+$			6.1	9.3	4	4	4	514.0	514.0
731.79	$\frac{3}{2}^-$	6.4	5.9			(3, 4)	1	1	731.9	732.0
868.05	$\frac{7}{2}^-$			8.8		1[f]	1	1[g]	868.7	868.5
919.7	$(\frac{1}{2}^-, \frac{3}{2}^-)$		≥9.2			1[h]	3		919.6	919.8
951.2	$(\frac{5}{2}^-)$			(?)		(3, 4)	1	2	951.3	951.1
1175.8	$\frac{5}{2}^-, \frac{7}{2}^-$					(4)	(3)	4	1176	1175.7

[a] See Ref. 24.
[b] See Ref. 31.
[c] See Ref. 29.
[d] See Ref. 32.
[e] See Ref. 25.
[f] Value for "880-keV" level.
[g] Value for "883-keV" level.
[h] Value for "925-keV" level.

TABLE VI. Wave functions of the low-lying negative-parity states. Only amplitudes larger than 4% are listed. The assignment of the total angular momentum is omitted from the basis vectors.

$\frac{5}{2}^-_1$	
$\vert[(p_{1/2}^{-2})0,f_{5/2}^{-1}]\frac{5}{2},00\rangle$	−0.357
$\vert[(p_{3/2}^{-2})0,f_{5/2}^{-1}]\frac{5}{2},00\rangle$	−0.483
$\vert(f_{5/2}^{-3})\frac{5}{2},00\rangle$	−0.628
$\frac{3}{2}^-_1$	
$\vert[(p_{1/2}^{-2})0,p_{3/2}^{-1}]\frac{3}{2},00\rangle$	−0.315
$\vert(p_{3/2}^{-3})\frac{3}{2},00\rangle$	−0.275
$\vert[(f_{5/2}^{-2})0,p_{3/2}^{-1}]\frac{3}{2},00\rangle$	−0.719
$\vert[(f_{5/2}^{-2})0,p_{3/2}^{-1}]\frac{3}{2},12\rangle$	−0.209
$\frac{1}{2}^-_1$	
$\vert[(p_{3/2}^{-2})0,p_{1/2}^{-1}]\frac{1}{2},00\rangle$	−0.410
$\vert[(f_{5/2}^{-2})0,p_{1/2}^{-1}]\frac{1}{2},00\rangle$	−0.693
$\vert[(f_{5/2}^{-2})0,p_{3/2}^{-1}]\frac{3}{2},12\rangle$	0.289
$\vert(f_{5/2}^{-3})\frac{5}{2},12\rangle$	0.292
$\frac{3}{2}^-_2$	
$\vert[(p_{1/2}^{-2})0,f_{5/2}^{-1}]\frac{5}{2},12\rangle$	−0.270
$\vert[(f_{5/2}^{-2})2,p_{1/2}^{-1}]\frac{3}{2},00\rangle$	0.310
$\vert[(p_{3/2}^{-2})0,f_{5/2}^{-1}]\frac{5}{2},12\rangle$	−0.293
$\vert(f_{5/2}^{-3})\frac{3}{2},00\rangle$	0.298
$\vert(f_{5/2}^{-3})\frac{3}{2},12\rangle$	−0.513
$\frac{7}{2}^-_1$	
$\vert[(p_{5/2}^{-2})0,f_{5/2}^{-1}]\frac{5}{2},12\rangle$	0.335
$\vert[(f_{5/2}^{-2})4,p_{1/2}^{-2}]\frac{7}{2},00\rangle$	−0.328
$\vert[(p_{3/2}^{-2})0,f_{5/2}^{-1}]\frac{5}{2},12\rangle$	0.386
$\vert(f_{5/2}^{-3})\frac{5}{2},12\rangle$	0.565
$\frac{7}{2}^-_2$	
$\vert[(p_{1/2}^{-2})0,f_{5/2}^{-1}]\frac{5}{2},12\rangle$	0.211
$\vert[(p_{1/2}^{-1}p_{3/2}^{-1})2,f_{5/2}^{-1}]\frac{7}{2},00\rangle$	−0.316
$\vert[(p_{3/2}^{-2})0,f_{5/2}^{-1}]\frac{5}{2},12\rangle$	0.392
$\vert[(f_{5/2}^{-2})2,p_{3/2}^{-1}]\frac{7}{2},00\rangle$	0.268
$\vert[(f_{5/2}^{-2})0,p_{3/2}^{-1}]\frac{3}{2},12\rangle$	−0.448
$\vert(f_{5/2}^{-3})\frac{5}{2},12\rangle$	0.301
$\frac{5}{2}^-_2$	
$\vert[(p_{1/2}^{-2})0,f_{5/2}^{-1}]\frac{5}{2},12\rangle$	−0.269
$\vert[(f_{5/2}^{-2})2,p_{1/2}^{-1}]\frac{5}{2},00\rangle$	−0.260
$\vert[(f_{5/2}^{-2})0,p_{1/2}^{-1}]\frac{1}{2},12\rangle$	−0.430
$\vert[(p_{3/2}^{-2})0,f_{5/2}^{-1}]\frac{5}{2},12\rangle$	−0.340
$\vert(f_{5/2}^{-3})\frac{5}{2},12\rangle$	−0.424

et al.,[32] who used a natural Rb target (72.2% abundant in ^{85}Rb), report an additional 670.3-keV γ ray that decays to the $\frac{1}{2}^-$, 281-keV level with a 4% branching ratio, as well as a 438-keV transition to the $\frac{9}{2}^+$ 514-keV level with a 1% branching ratio. We note that the weak 438- and 670-keV γ rays could be masked in the study of Torti *et al.*[25] by the relatively high background. The observation of a transition to the 151-keV $\frac{3}{2}^-$ level does rule out the $l=4$ assignment. The possible β-decay feeding from ^{85}Sr^g ($J^\pi=\frac{9}{2}^+$) and the γ-ray branching observed in the $(n,n'\gamma)$ work of Bernard *et al.*[33] lead us to suggest a J^π value of $\frac{5}{2}^-$ for the 951-keV level.

IV. DISCUSSION

The 37 neutron nuclei have been treated by the cluster-vibration model (CVM).[31,32] Negative-parity states in ^{69}Ge and ^{67}Zn were described by coupling three holes in the subshell with single-particle configurations $p_{1/2}$, $p_{3/2}$, and $f_{5/2}$ to the quadrupole vibration; i.e., it was assumed that for these nuclei $N=40$ plays the role of a closed subshell. Here we extend this approach to $^{85}_{37}$Rb$_{38}$, which is a $Z=37$ nucleus. In the present calculation the following parametrization is used: The proton single-hole energies are $\epsilon(p_{1/2}^{-1})-\epsilon(f_{5/2}^{-1})=0.5$ MeV and $\epsilon(p_{3/2}^{-1})-\epsilon(f_{5/2}^{-1})=0.3$ MeV, the experimental energy of the first excited state in $^{88}_{40}$Zr$_{48}$ is taken as 1.06 MeV, the pairing strength is $G=0.4$ MeV, and the adopted value for the particle-vibration coupling strength is $a=0.3$ (parametrization I). The calculation is also performed for a slightly different parametrization, with $p_{1/2}^{-1}$ being lowered by 0.1 MeV and the parameter "a" being increased by 0.1 (parametrization II). The cluster-vibration Hamiltonian is diagonalized in the bases $|[(j_1j_2)J_{12},j_3]J,NR;I\rangle$. Here N represents the number and R the angular momentum of phonons, J is the angular momentum of the three-proton cluster, and I is the total angular momentum. Figure 8 shows the spectra calculated for parametrizations I and II, and Table VI presents the largest components (≥4%) in the wave functions of the low-lying states calculated in parametriza-

TABLE VII. Calculated $B(E2)$ and $B(M1)$ values for parametrizations I and II. For description see the text.

	I		II	
	$B(E2)$ (e^2b^2)	$B(M1)$ (μ_N^2)	$B(E2)$ (e^2b^2)	$B(M1)$ (μ_N^2)
$\frac{3}{2}_1^- \to \frac{5}{2}_1^-$	0.0020	0.0220	0.0038	0.0226
$\frac{1}{2}_1^- \to \frac{5}{2}_1^-$	0.0063		0.0061	
$\frac{1}{2}_1^- \to \frac{3}{2}_1^-$	0.0066	1.0846	0.0072	1.0006
$\frac{3}{2}_2^- \to \frac{5}{2}_1^-$	0.0138	0.0002	0.0156	0.0004
$\frac{3}{2}_2^- \to \frac{3}{2}_1^-$	0.0008	0.0299	0.0023	0.0639
$\frac{3}{2}_2^- \to \frac{1}{2}_2^-$	0.0011	0.0260	0.0018	0.0509
$\frac{7}{2}_1^- \to \frac{5}{2}_1^-$	0.0115	0.0004	0.0136	0.0010
$\frac{7}{2}_1^- \to \frac{3}{2}_1^-$	0.0001		0.0048	
$\frac{7}{2}_1 \to \frac{3}{2}_2^-$	0.0023		0.0126	
$\frac{1}{2}_2^- \to \frac{5}{2}_1^-$	0.0049		0.0054	
$\frac{1}{2}_2^- \to \frac{3}{2}_1^-$	0.0066	0.0743	0.0074	0.0550
$\frac{1}{2}_2^- \to \frac{1}{2}_1^-$		0 0143		0.0137
$\frac{1}{2}_2^- \to \frac{3}{2}_2^-$	0.0029	0.1228	0.0055	0.2242
$\frac{5}{2}_2^- \to \frac{5}{2}_1^-$	0.0072	0.0009	0.0064	0.0025
$\frac{5}{2}_2^- \to \frac{3}{2}_1^-$	0.0002	0.0001	0.0007	0.0002
$\frac{5}{2}_2^- \to \frac{1}{2}_1^-$			0.0062	
$\frac{5}{2}_2^- \to \frac{3}{2}_2^-$	0.0001	0.0001	0.00003	0.0017
$\frac{5}{2}_2^- \to \frac{7}{2}_1^-$	0.0010	0.0121	0.0013	0.0504
$\frac{5}{2}_2^- \to \frac{1}{2}_2^-$	0.0031		0.0066	

TABLE VIII. Comparison of the experimental and calculated electromagnetic properties of ^{85}Rb. Γ, $B(E2)$, Q (electric quadrupole moment), and μ (magnetic dipole moment) are expressed in units ps, e^2b^2, eb, and μ_N, respectively. The calculated transitions from each state are normalized to the corresponding experimental transition with strongest intensity (underlined values).

	I_γ			I_γ	
	Experiment	Theory (II)		Experiment	Theory (II)
			$\Gamma(\frac{3}{2}_1^-)$	1000	5000
			$\Gamma(\frac{1}{2}_1^-)$	27	18
$\frac{1}{2}_1^- \to \frac{5}{2}_1^-$	0.004 (2)	0.005	$\Gamma(\frac{3}{2}_2^-)$	4	2
$\to \frac{3}{2}_1^-$	1.5 (4)	1.5	$\Gamma(\frac{7}{2}_1^-)$	4	8
$\frac{3}{2}_2^- \to \frac{5}{2}_1^-$	0.10 (4)	0.08	$B(E2)$ $(\frac{3}{2}_1^- \to \frac{5}{2}_1^-)$	0.0053 (6)	0.0038
$\to \frac{3}{2}_1^-$	0.01	0.4	$B(E2)$ $(\frac{1}{2}_1^- \to \frac{5}{2}_1^-)$	0.0048 (6)	0.0061
$\to \frac{1}{2}_1^-$	0.15 (6)	0.15	$B(E2)$ $(\frac{3}{2}_2^- \to \frac{5}{2}_1^-)$	0.0151 (5)	0.0156
$\frac{7}{2}_1^- \to \frac{5}{2}_1^-$	0.125 (5)	0.125	$B(E2)$ $(\frac{7}{2}_1^- \to \frac{5}{2}_1^-)$	0.027 (3)	0.0136
$\to \frac{3}{2}_1^-$	0.0032 (3)	0.004	$Q(\frac{5}{2}_1^-)$	+0.27	+0.10
			$\mu(\frac{5}{2}_1^-)$	+1.35	+1.26

tion II. These wave functions were used to calculate the electromagnetic properties. The effective charges and gyromagnetic ratios are as follows: $e^{\text{s.p.}}=1$, $e^{\text{vib}}=3.5$, $g_R=Z/A$, $g_l=1$, $g_s=0.7\,g_s^{\text{free}}$, and $g_p=1.33$. The quenching of the g_s value was taken from Ref. 17 and the gyromagnetic ratio for the tensor $M1$ operator $(Y_2\times s)_1$ was taken in accordance with Refs. 53 and 54. The calculated $B(E2)$ and $B(M1)$ values for transitions between low-lying states are presented in Table VII, and a comparison of the experimental and calculated electromagnetic properties, branching ratios, half-lives, reduced transition probabilities, and static moments is given in Table VIII. The overall agreement between the experimental and calculated energy spectra and electromagnetic properties is reasonably good. However, the calculated branching ratio for the $\tfrac{3}{2}{}_2^-\rightarrow\tfrac{3}{2}{}_1^-$ transition is too large because $B(M1)$ $(\tfrac{3}{2}{}_2^-\rightarrow\tfrac{3}{2}{}_1^-)$ is not small enough. In fact, in the CVM, the $\tfrac{3}{2}{}_1^-\rightarrow\tfrac{5}{2}{}_1^-$ $M1$ transition is exactly forbidden in the zeroth-order approximation ($a=0$). However, in the present parametrization, which assumes an intermediate particle-vibration coupling strength, the $B(M1)$ $(\tfrac{3}{2}{}_2^-\rightarrow\tfrac{3}{2}{}_1^-)$ value is hindered only by two orders of magnitude. This value is rather sensitive to the parametrization used owing to the interference of many small partial contributions and therefore should not be interpreted too rigidly. In addition, in ${}^{85}_{37}\text{Rb}_{48}$, the parametrization is adjusted to reproduce the experimental levels and such a treatment may not be the optimum one for the electromagnetic properties.

In the present calculation we also include the tensor term in the $M1$ operator. Generally, it drastically affects the $M1$ transitions, which are l-forbidden in zeroth order. In our case, such a transition is the $\tfrac{3}{2}{}_1^-\rightarrow\tfrac{5}{2}{}_1^-$ $M1$ transition, which is in zeroth order of the type $|[(f_{7/2}{}^{-2})0,p_{3/2}{}^{-1}]\tfrac{3}{2},00;\tfrac{3}{2}\rangle\rightarrow|[(f_{7/2}{}^{-3})\tfrac{5}{2},00;\tfrac{5}{2}\rangle]$. In this case, the destructive interference between the higher-order contributions to the $M1$ transition moment for a standard $M1$ operator is large, and such a transition is therefore strongly hindered in the presence of mixed wave functions.[54] Our calculated value for a standard $M1$ operator is $B(M1)$ $(\tfrac{3}{2}{}_1^-\rightarrow\tfrac{5}{2}{}_1^-)=0.000\,03$ μ_N^2; the calculated half-life of the $\tfrac{3}{2}{}_1^-$ state would then exceed the experimental value by three orders of magnitude, and the branching to the $\tfrac{5}{2}{}_1^-$ state would be too small by three orders of magnitude. However, inclusion of the tensor term in the $M1$ operator, with the usual value of the gyromagnetic ratio, $g_p=1.33$,[53,54] results in the calculated value $B(M1)$ $(\tfrac{3}{2}{}_1^-\rightarrow\tfrac{5}{2}{}_1^-)=0.023$ μ_N^2. This leads to a correct order of magnitude for the half-life $\tau(\tfrac{3}{2}{}_1^-)$. On the other hand, the other $M1$ transitions, which are not l-forbidden in zeroth order, are much less affected by the tensor $M1$ term. For comparison, we show in Table IX the calculated $B(M1)$ values for a standard $M1$ operator and those for the $M1$ operator with the tensor term included.

TABLE IX. Effect of the tensor term on $M1$ transitions.

Transition (From To)	Tensor term Without	With
	$B(M1)$ (μ_N^2)	
l forbidden		
$\tfrac{3}{2}{}_1^-\rightarrow\tfrac{5}{2}{}_1^-$	0.000 03	0.023
Not l forbidden		
$\tfrac{1}{2}{}_1^-\rightarrow\tfrac{3}{2}{}_1^-$	1.100 7	1.000 6
$\tfrac{1}{2}{}_2^-\rightarrow\tfrac{3}{2}{}_1^-$	0.062 4	0.055 0
$\tfrac{3}{2}{}_2^-\rightarrow\tfrac{3}{2}{}_1^-$	0.063 9	0.063 9
$\tfrac{7}{2}{}_1^-\rightarrow\tfrac{5}{2}{}_1^-$	0.000 3	0.000 6

This work was performed under the auspices of the U. S. Department of Energy, under Contract No. W-7405-Eng-48.

---

[1] R. A. Meyer, in *Problems in Vibrational Nuclei*, edited by G. Alaga, V. Paar, and L. Sips (North-Holland, Amsterdam, 1975), Chap. 7.

[2] R. A. Meyer, in *Proceedings of the International Conference on Gamma-Ray Transition Probabilities*, New Delhi, India, 1974; also in Lawrence Livermore Laboratory Report No. UCRL-76207, 1974.

[3] A. DeShalit, Phys. Rev. 122, 1530 (1961).

[4] S. Wahlborn, Nucl. Phys. 58, 209 (1964).

[5] L. S. Kisslinger and R. A. Sorensen, Rev. Mod. Phys. 35, 853 (1963).

[6] A. Kuriyama, T. Marumori, and K. Matsuyanagi, Prog. Theor. Phys. Suppl. 58, 100 (1975).

[7] A. Kuriyama, T. Marumori, and K. Matsuyanagi, Prog Theor. Phys. 51m, 779 (1974).

[8] A. Kuriyama, T. Marumori, K. Matsuyanagi, and R. Okamata, Prog. Theor. Phys. Suppl. 58, 1 (1975).

[9] G. Vanden Berghe, Z. Phys. 266, 139 (1974), and private communication.

[10] R. Almar, O. Civitarese, and F. Krmpotic, Phys. Rev. C 8, 1518 (1973).

[11] M. L. Rustgi, J. G. Lucas, and S. N. Mukherjee, Nucl. Phys. A117, 321 (1968).

[12] K. Heyde and P. J. Brussaard, Nucl. Phys. A104, 81 (1967).

[13] B. S. Reehal and R. A. Sorensen, Phys. Rev. C 2, 819

(1970).

[14] G. Alaga and G. Ialongo, Nucl. Phys. **A97**, 600 (1965).

[15] V. Paar, Phys. Lett. **39B**, 466 (1972); **39B**, 587 (1972).

[16] R. A. Meyer, A. L. Prindle, W. A. Myers, P. K. Hopke, D. Deterly, and J. E. Koops, Phys. Rev. C **17**, 1822 (1978).

[17] V. Paar, Nucl. Phys. **A211**, 29 (1973).

[18] R. C. Ragaini, C. F. Smith, and R. A. Meyer, Bull. Am. Phys. Soc. **17**, 444 (1972).

[19] E. Vatai, A. C. Xenoulis, K. R. Baker, F. Tolea, and F. W. Fink, Nucl. Phys. **A219**, 595 (1974).

[20] F. K. Wohn, W. L. Talbert, Jr., and J. K. Halbig, Nucl. Phys. **A152**, 561 (1970).

[21] I. F. Bubb, S. I. H. Naqvi, and J. L. Wolfson, Nucl. Phys. **A167**, 252 (1971).

[22] M. K. Ramaswany, B. A. Bishara, and P. S. Jastram, Bull. Am. Phys. Soc. **7**, 341 (1962).

[23] A. R. Sattler, Phys. Rev. **127**, 854 (1962).

[24] R. C. Ragaini, J. D. Knight, and W. T. Leland, Phys. Rev. C **8**, 988 (1973).

[25] R. C. Torti, V. M. Cottles, V. R. Dave, J. A. Nelson, and R. M. Wilenzick, Phys. Rev. C **6**, 1686 (1972).

[26] P. Bond and G. Kumbartski, Nucl. Phys. **A205**, 239 (1973).

[27] P. M. Endt and C. van der Leun, Nucl. Phys. **A105**, 1 (1967).

[28] D. J. Horen, Nucl. Data Sheets **5**, 131 (1971).

[29] L. R. Medsker, J. N. Bishop, S. G. Headly, and H. T. Fortune, Phys. Rev. C **10**, 2117 (1974).

[30] R. C. Ragaini, C. F. Smith, and R. A. Meyer, Lawrence Livermore Laboratory Report No. UCRL-73654, 1972 (unpublished).

[31] J. R. Comfort, J. R. Puray, and W. J. Braithwaite, Phys. Rev. C **8**, 1354 (1973).

[32] E. Barnard, N. Coetzee, J. A. M. de Villiers, D. Reitmann, and P. van der Merwe, Z. Phys. **260**, 197 (1973).

[33] H. C. Friedericks, A. Gelberg, B. Heits, K. O. Zell, and P. von Brentano, Phys. Rev. C **13**, 2247 (1976).

[34] C. M. Lederer and V. Shirley, *Table of Isotopes*, 7th ed. (Wiley, New York, 1978).

[35] J. F. Lemming, Nucl. Data **B15**, 132 (1975).

[36] D. C. Kocher, Nucl. Data **B15**, 169 (1975).

[37] F. K. Wohn, J. K. Halbig, W. L. Talbert, Jr., and J. R. McConnell, Phys. Rev. C **7**, 160 (1973).

[38] H. Verheul, Nucl. Data **B5**, 46 (1971).

[39] E. A. Henry, W. L. Talbert, Jr., and J. R. McConnell, Phys. Rev. C **7**, 222 (1973).

[40] D. C. Kocher, Nucl. Data **B16**, 445 (1975).

[41] C. F. Smith, U. S. Atomic Energy Commission Report No. UCRL-74710, 1973.

[42] C. F. Smith and F. F. Momyer, Jr., Report No. NAS-NS 3025, 1960.

[43] D. C. Camp, in *Radioactivity in Nuclear Spectroscopy*, edited by J. E. Hamilton and J. C. Manthuruthil (Gordon and Breach, New York, 1972), Vol. I, p. 135.

[44] D. C. Camp, Proceedings of the ERDA Symposium on x- and γ-Ray Sources and Applications, Ann Arbor, Mich. Report Nos. Conf-760539 and UCRL-77697, 1976, p. 76.

[45] R. A. Meyer, in Proceedings of the ERDA Symposium on x- and γ-Ray Spectroscopy, University of Michigan, Report No. Conf-760539, 1976, p. 61.

[46] R. A. Meyer, Multigamma-Ray Calibration Sources, LLL Manual, M-100 (1978).

[47] R. Gunnink and J. B. Niday, Lawrence Livermore Laboratory Report No. UCRL-51061, Vols. I, II, and III, 1972 (unpublished).

[48] S. A. Moszkowski, in *Alpha-, Beta-, and Gamma-Ray Spectroscopy*, edited by K. Siegbahn (North-Holland, Amsterdam, 1968), p. 881.

[49] A. A. Delucchi and R. A. Meyer, J. Inorg. Nucl. Chem. **38**, 2135 (1976).

[50] K. Heyde, M. Waroquier, and R. A. Meyer, Phys. Rev. C **17**, 1219 (1978).

[51] V. Paar, U. Eberth, and J. Eberth, Phys. Rev. C **13**, 2532 (1976).

[52] V. Paar, E. Coffou, U. Eberth, and J. Eberth, J. Phys. G **2**, 917 (1976).

[53] I. Hamamoto, Phys. Lett. **61B**, 343 (1976).

[54] V. Paar and S. Brant, Nucl. Phys. **A297**, 471 (1978), and to be published.

PHYSICAL REVIEW C VOLUME 21, NUMBER 6 JUNE 1980

Inelastic scattering $E4$ transition probabilities in the $0d$, $1s$ shell

B. A. Brown
Nuclear Physics Laboratory, Oxford University, Oxford OX1 3RH, England

W. Chung
Cyclotron Laboratory, Michigan State University, East Lansing, Michigan 48824

B. H. Wildenthal
Nuclear Physics Laboratory, Oxford University, Oxford OX1 3RH, England
and Cyclotron Laboratory, Michigan State University, East Lansing, Michigan 48824*

(Received 25 January 1980)

Theoretical $E4$ transition matrix elements calculated in the full $d_{5/2}$-$s_{1/2}$-$d_{3/2}$ shell-model space are presented for excitations of some ground states of stable nuclei for $18 \leq A \leq 38$. These matrix elements have been used to calculate inelastic transition probabilities for electromagnetic and hadronic probes. Available data on the relative magnitudes and energy distributions of $E4$ excitation strengths are found to be well reproduced theoretically thereby. Based on several experimentally measured transition strengths, the empirical isoscalar $E4$ effective charge is found to be $e_p + e_n = (2.0 \pm 0.2)e$. This is similar in magnitude to the analogous isoscalar $E2$ effective charge, but is much larger than existing theoretical estimates.

[NUCLEAR STRUCTURE ^{18}O, ^{19}F, ^{20}Ne, ^{22}Ne, ^{24}Mg, ^{25}Mg, ^{26}Mg, ^{28}Si, ^{30}Si, ^{32}S, ^{34}S, ^{36}Ar, ^{38}Ar; *calculations for the strengths of $E4$ inelastic scattering transitions and their proton and neutron components*; complete $0d_{5/2}$-$1s_{1/2}$-$0d_{3/2}$ shell-model wave functions; Chung-Wildenthal Hamiltonians.]

I. INTRODUCTION

In this paper we present calculations for the strengths of $\Delta J^\pi = 4^+(E4)$ excitations of ground states in the region $18 \leq A \leq 38$. The one-body transition density matrix elements for these excitations were calculated from the $d_{5/2}$-$s_{1/2}$-$d_{3/2}$ shell-model wave functions of Chung and Wildenthal.[1,2] These transition densities were then used to calculate matrix elements for electromagnetic excitation of these transitions and for the relative strengths of these same transitions as they are excited by various hadronic probes. The present calculations systematically employ harmonic-oscillator single-particle wave functions. The effects of using different (e.g., Hartree-Fock) radial dependences for the single-particle states were examined and found to be significant, but no alternative clearly preferable to harmonic-oscillator dependence was determined.

Our present study focuses on three aspects of $E4$ phenomena. The first issue we address presumes reasonably good theoretical-experimental agreement between *relative* values of several large measured transition strengths. In such a context it is meaningful to speak of the "effective charges" appropriate to the model space which serve to produce agreement between calculation and experiment in the absolute as well as relative sense. By comparing values from the extant body of measured $E4$ rates to our calculated values we are able to extract a value of the isoscalar $E4$ effective charge for the sd-shell space of $e_p + e_n = (2.0 \pm 0.2)e$.

We then proceed to deal with the general questions of what type of $E4$ phenomena are predicted by the Chung-Wildenthal wave functions and how well these accord with experimental facts. There are several aspects to be considered, such as the dependence of the aggregate $E4$ strength on the A value, the distribution of strength within a given nucleus as a function of excitation energy, and the A dependence of this distribution.

Lastly, we consider the individual neutron and proton components of the transitions in the $T \neq 0$ nuclei. From the values of these components the relative strengths by which a given state is excited by various hadronic probes, as well as electronmagnetically, can be predicted. We consider in particular, alphas, protons, and pions.

In Sec. II the calculation of the shell-model transition-density matrix elements is described as well as their combination with the single-particle matrix elements (which incorporate the radial wave function dependence) to obtain the theoretical $B(E4)$ values. In Sec. III these values are compared with the strong experimental $B(E4)$ values to obtain $E4$ effective charges. In addition, the

© 1980 The American Physical Society

distributions of calculated $E4$ strengths for all stable even-even nuclei are presented in comparison with available experimental data, together with some selected results for odd-even nuclei. In Sec. IV a method for calculating the hadronic excitation strengths is presented. The conclusions of the present study constitute Sec. V.

II. SHELL-MODEL CALCULATIONS OF THE TRANSITION DENSITIES

The reduced matrix element for a one-body operator between initial and final sd-shell wave functions for N valence particles is expressed as a linear combination of reduced matrix elements between single-particle states ρ_j and the one-body transition densities $D^{N;JT,J'T'}_{\Delta T,\Delta T}$ by the relation

$$\left\langle \psi^{NJT} \left|\left|\left| \sum_{i=1}^{N} O(\Delta J, \Delta T) \right|\right|\right| \psi^{NJ'T'} \right\rangle = \sum_{jj'} D^{N;JT,J'T'}_{\Delta T,\Delta T}(j,j') \langle \rho_j ||| O(\Delta J, \Delta T) ||| \rho_{j'} \rangle , \tag{1}$$

where

$$D^{N;JT,J'T'}_{\Delta T,\Delta T}(j,j') = \frac{\langle \psi^{NJT} ||| (a_j^\dagger \times \tilde{a}_{j'})_{\Delta J \Delta T} ||| \psi^{NJ'T'} \rangle}{[(2\Delta J+1)(2\Delta T+1)]^{1/2}} . \tag{2}$$

The operator $O(\Delta J, \Delta T)$ has associated with it a unit operator in isospin space when $\Delta T = 0$ and the operator τ in isospin space when $\Delta T = 1$; our isospin convention is such that

$$O(\Delta J)_{p/n} = \tfrac{1}{2}[1(+/-)\tau_3] O(\Delta J) . \tag{3}$$

The proton and neutron matrix elements for these operators between the sd-shell wave functions are given by

$$\begin{aligned} A_{p/n}(T_z) = {} & \frac{(-1)^{T_f - T_z}}{2} \begin{pmatrix} T_f & 0 & T_i \\ -T_z & 0 & T_z \end{pmatrix} \left\langle \psi^{J_f T_f} \left|\left|\left| \sum_{i=1}^{N} O(\Delta J, \Delta T = 0)_i \right|\right|\right| \psi^{J_i T_i} \right\rangle \\ & (+/-) \frac{(-1)^{T_f - T_z}}{2} \begin{pmatrix} T_f & 1 & T_i \\ -T_z & 0 & T_z \end{pmatrix} \left\langle \psi^{J_f T_f} \left|\left|\left| \sum_{i=1}^{N} O(\Delta J, \Delta T = 1)_i \right|\right|\right| \psi^{J_i T_i} \right\rangle . \end{aligned} \tag{4}$$

It is well known in the case of $E2$ transitions that core-polarization corrections are important and we anticipate that they will also be important for $E4$ transitions. Thus we introduce proton and neutron effective charges e_p and e_n which relate the total proton matrix element M_p to the proton and neutron matrix elements in the model space A_p and A_n:

$$M_p = A_p e_p + A_n e_n = A_p(1 + \delta e_p) + A_n \delta e_n . \tag{5}$$

In terms of M_p the $B(E4)$ value is given by

$$B(E4, J_i \to J_f) = (2J_i + 1)^{-1} M_p^2 . \tag{6}$$

The quantity δe_p represents the effect of virtual excitation of core protons by the valence protons and the quantity δe_n represents the effect of the virtual excitation of core protons by the valence neutrons. If we denote δe_p by δ_{pp} and δe_n by δ_{pn}, then the generalizations of Eq. (5) for both the proton and neutron matrix elements take the form

$$\begin{aligned} M_p &= A_p(1 + \delta_{pp}) + A_n \delta_{pn} , \\ M_n &= A_n(1 + \delta_{nn}) + A_p \delta_{np} . \end{aligned} \tag{7}$$

(The neutron matrix elements will be needed to calculate strengths for hadronic excitations.) For nuclei with approximately equal numbers of neutrons and protons $\delta_{np} = \delta_{pn}$ and, since the nuclear interaction is charge symmetric, $\delta_{nn} = \delta_{pp}$. Thus we can express the neutron matrix element in terms of the proton and neutron effective charges,

$$M_n = A_n e_p + A_p e_n . \tag{8}$$

The values of the one-body transition densities D for some of the transitions discussed in the following sections are given in Table I. These quantities constitute the total information content of the shell-model wave functions insofar as these $E4$ excitations are concerned. The matrix elements

$$\left\langle \psi^{NJT} \left|\left|\left| \sum_{i=1}^{N} O(\Delta J, \Delta T)_i \right|\right|\right| \psi^{NJ'T'} \right\rangle$$

or the equivalent $A_{p/n}$ can be calculated from these entries once a set of single-particle matrix elements are specified.

The triply reduced single-particle matrix elements are

$$\langle \rho_j ||| O(\Delta J, \Delta T = 0) ||| \rho_{j'} \rangle = (2)^{1/2} \langle \rho_j || O(\Delta J) || \rho_{j'} \rangle$$

and

$$\langle \rho_j ||| O(\Delta J, \Delta T = 1) ||| \rho_{j'} \rangle = (6)^{1/2} \langle \rho_j || O(\Delta J) || \rho_{j'} \rangle . \tag{9}$$

The electric multipole operator is given by

$$O(\Delta J)_i = r_i^{\Delta J} Y_m^{(\Delta J)}(\hat{r}_i) . \tag{10}$$

TABLE I. Calculated values of the one-body transition densities for some selected $E4$ transitions.

A	$T_i \to T_f$	$J_i \to J_f$	j-j' $\Delta T = 0$ $\frac{5}{2}$-$\frac{5}{2}$	$\frac{5}{2}$-$\frac{3}{2}$	$\frac{3}{2}$-$\frac{5}{2}$	$\Delta T = 1$ $\frac{5}{2}$-$\frac{5}{2}$	$\frac{5}{2}$-$\frac{3}{2}$	$\frac{3}{2}$-$\frac{5}{2}$
18	$1 \to 1$	$0^+ \to 4^+(1)$	−0.8266	−0.0726	0.1817	−0.6749	−0.0593	0.1483
19	$\frac{1}{2} \to \frac{1}{2}$	$\frac{1}{2}^+ \to \frac{9}{2}^+(1)$	0.4483	0.3411	−0.1715	0.2398	−0.0377	−0.1721
20	$0 \to 0$	$0^+ \to 4^+(1)$	0.4033	0.2714	−0.3061			
		$0^+ \to 4^+(2)$	0.0141	−0.1054	0.0695			
22	$1 \to 1$	$0^+ \to 4^+(1)$	−0.0210	−0.2009	0.3206	0.6233	0.0303	−0.0638
		$0^+ \to 4^+(2)$	0.8423	0.0269	−0.2217	0.3384	−0.0610	−0.0218
24	$0 \to 0$	$0^+ \to 4^+(1)$	−0.3057	−0.0076	−0.0426			
		$0^+ \to 4^+(2)$	0.2402	0.3082	−0.4845			
		$0^+ \to 4^+(3)$	0.3469	−0.0976	0.0327			
25	$\frac{1}{2} \to \frac{1}{2}$	$\frac{5}{2}^+ \to \frac{9}{2}^+(1)$	0.4962	−0.2212	0.0778	−0.1159	−0.0182	0.0257
		$\frac{5}{2}^+ \to \frac{9}{2}^+(2)$	0.2396	0.4615	−0.2587	−0.0123	0.0056	0.0323
		$\frac{5}{2}^+ \to \frac{13}{2}^+(3)$	−0.2156	−0.2610	0.5347	0.1647	0.0585	−0.0318
26	$1 \to 1$	$0^+ \to 4^+(1)$	0.7231	0.1225	−0.3194	−0.5609	0.0920	−0.1292
		$0^+ \to 4^+(2)$	−0.0417	−0.3206	0.7093	0.0043	−0.0235	0.1286
		$0^+ \to 4^+(3)$	0.1833	0.1277	−0.2988	0.3690	−0.0097	−0.1744
28	$0 \to 0$	$0^+ \to 4^+(1)$	−0.0065	−0.4561	0.2478			
		$0^+ \to 4^+(2)$	0.2267	0.4496	−0.1517			
		$0^+ \to 4^+(3)$	−0.2008	0.1694	−0.1190			
30	$1 \to 1$	$0^+ \to 4^+(1)$	0.2305	0.6219	−0.3076	−0.0978	0.3469	−0.1662
		$0^+ \to 4^+(2)$	−0.1606	−0.8941	0.3455	−0.0534	0.2664	−0.0551
		$0^+ \to 4^+(3)$	−0.0122	−0.0787	−0.0178	0.3036	0.3685	−0.0363
32	$0 \to 0$	$0^+ \to 4^+(1)$	−0.0911	−0.5652	0.3328			
		$0^+ \to 4^+(2)$	0.0917	0.3303	−0.1418			
	$0 \to 1$	$0^+ \to 4^+(2)$				0.0288	0.4918	−0.0858
34	$1 \to 1$	$0^+ \to 4^+(1)$	0.1361	0.8449	−0.4448	0.0049	−0.0445	−0.0372
		$0^+ \to 4^+(2)$	−0.1047	0.1241	−0.0464	−0.0690	−0.3905	0.1371
36	$0 \to 0$	$0^+ \to 4^+(1)$	−0.1252	−0.4596	0.3211			
	$0 \to 1$	$0^+ \to 4^+(3)$				−0.0089	−0.4011	0.1070
38	$1 \to 1$	$0^+ \to 4^+(1)$	−0.0345	−0.8156	0.1947	0.0281	0.6659	−0.1589

For $\Delta J = 4$ there are only two possible independent single-particle matrix elements in the sd-shell space and these are given by

$$\langle d_{5/2} \| r^4 Y^{(4)} \| d_{5/2} \rangle = \left(\frac{9}{7\pi}\right)^{1/2} \langle d_{5/2} | r^4 | d_{5/2} \rangle ,$$
$$\langle d_{5/2} \| r^4 Y^{(4)} \| d_{3/2} \rangle = \left(\frac{18}{7\pi}\right)^{1/2} \langle d_{5/2} | r^4 | d_{3/2} \rangle . \tag{11}$$

Since the $E4$ matrix elements are weighted by r^4, the relation between experiment and theory is very sensitive to the specification of the radial integrals in Eqs. (11). We have chosen to evaluate these integrals independently for each nucleus we consider by choosing harmonic-oscillator wave functions parametrized to reproduce the individual measured values of the rms charge radii. The rms charge radii r_{ch} for essentially all stable sd-shell nuclei are now known to high accuracy, a rather recent development. These values are

TABLE II. Rms charge radii and the extracted harmonic oscillator parameter b.

	r_{ch} (fm)	b (fm)	$\hbar\omega$ (MeV)
^{16}O	2.794(3)[a]	1.820	12.50
^{19}F	2.898(10)[b]	1.833	12.34
^{20}Ne	3.020(20)[c]	1.869	11.87
^{22}Ne	2.949(20)[d]	1.821	12.50
^{24}Mg	3.035(18)[e]	1.813	12.61
^{25}Mg	3.003(11)[f]	1.793	12.90
^{26}Mg	3.017(32)[g]	1.802	12.77
^{28}Si	3.127(3)[b,h]	1.827	12.42
^{30}Si	3.139(3)[i]	1.834	12.33
^{32}S	3.264(2)[b]	1.881	11.72
^{34}S		1.881	11.72
^{36}Ar	3.399(5)[i]	1.938	11.04
^{38}Ar	3.414(10)[j]	1.947	10.94

[a] Reference 26.
[b] Reference 27.
[c] Reference 28, Table I.
[d] Reference 10; $r_{ch}(^{22}\mathrm{Ne}) - r_{ch}(^{20}\mathrm{Ne}) = -0.071$ fm.
[e] Reference 29.
[f] Reference 30.
[g] Reference 28, Table II.
[h] For natural Si, $r_{ch} = 3.129$ (3).
[i] Reference 31, Table IV.
[j] Reference 31, Table III.

listed in Table II.

For the harmonic-oscillator potential $V(r) = \frac{1}{2}m\omega^2 r^2$, the point proton rms radius for nuclei in the sd shell is given by

$$r_p^{\,2} = \left[\frac{18 + (Z-8)\frac{7}{2}}{Z}\right] b^2 - \frac{3b^2}{2A},$$

where

$$b^2 = \hbar/m\omega. \tag{12}$$

The last term is the correction for center-of-mass motion.[3,4] The charge radius is obtained by folding r_p with the rms charge radii for the protons and neutrons and adding relativistic corrections. Ignoring the relativistic spin-orbit correction, which is important only for nuclei with a large neutron or proton excess of spin unsaturated nucleons, the rms charge radii are given by[3]

$$r_{ch}^{\,2} = r_p^{\,2} + r_{\mathrm{proton}}^{\,2} + \frac{N}{Z} r_{\mathrm{neutron}}^{\,2} + \frac{3}{4}\left(\frac{\hbar}{mc}\right)^2, \tag{13}$$

where $r_{\mathrm{proton}}^{\,2} = (0.86)^2$ and $r_{\mathrm{neutron}}^{\,2} = -(0.35)^2$. The values of b and $\hbar\omega$ extracted from the experimental charge radii are given in Table II. In terms of b, the radial matrix elements of Eqs. (11) are expressed as

$$\langle d_{5/2}|r^4|d_{5/2}\rangle = \langle d_{5/2}|r^4|d_{3/2}\rangle = 15.75b^4. \tag{14}$$

The procedure we have adopted obviously takes into account all of the new precisely known variations in the sizes of sd-shell ground states. The conventional prescriptions for either harmonic-oscillator or Saxon-Woods potentials, which assume some smoothly varying mass dependence, e.g., $\hbar\omega = 41A^{-1/3}$, fail to account for these variations, sometimes by significant amounts. In our opinion it is appropriate to remove this source of noise in the comparison of theoretical to experimental elements by abandoning size formulas altogether and using instead the individual measured radii.

We utilize harmonic-oscillator radial dependence rather than Saxon-Woods or Hartree-Fock prescriptions because these latter, supposedly more "realistic," presciptions do not in fact offer improvements over the harmonic oscillator sufficient to justify the additional complexity and ambiguity their use introduces into the problems at hand. The problem inherent in specifying single-particle wave functions for open-shell nuclei such as concern us here is that the experimental separation energies are inconsistent with the energies of the shell-model single-particle potential, e.g., for ^{28}Si the $1s_{1/2}$ separation energy is greater than that for $0d_{5/2}$, and $0d_{3/2}$ is greater than $1s_{1/2}$, in inverse order to the shell-model sequence. In the full shell-model calculation this effect comes out of the two-body part of the Hamiltonian, but simple single-particle models are helpless to deal with it. Moreover, by going from the infinite harmonic-oscillator well to finite wells, one runs the risk of obtaining more realistic surface behavior in some wave functions at the cost of introducing more serious errors in others.

In our judgement it is advisable to retain the advantages of harmonic-oscillator dependence, where possible, until rigorous treatments of the single-particle problem, treatments which will presumbably follow along the paths explored in the treatment of single-nucleon transfer reactions,[5] become available. At the same time, it is also advisable to ascertain the degree to which conclusions based on the harmonic oscillator are subject to change when alternate models are used. To this end we have explored the consequence of using the radial-matrix elements of r^4 which are obtained from the Hartree-Fock calculations of Brown and Massen.[6] Some results from this study are presented in the Appendix.

III. RESULTS AND COMPARISON WITH EXPERIMENT

We first consider the strongest experimentally measured $E4$ transitions together with the matrix elements A_p and A_n in order to determine the empirical effective charges from the relationship

$$B(E4) = (2J_i + 1)^{-1} M_p^2$$
$$= (2J_i + 1)^{-1} (A_p e_p + A_n e_n)^2 .$$

This comparison is made in Table III in which the matrix elements M_p have been rewritten in the form

$$M_p = \tfrac{1}{2}(A_p + A_n)(e_p + e_n) + \tfrac{1}{2}(A_p - A_n)(e_p - e_n) \qquad (15)$$

in order to show that the isovector quantity $A_p - A_n$ is usually small relative to the isoscalar quantity $A_p + A_n$. (An exception to this occurs in ^{22}Ne.) For this reason e_p-e_n cannot be reliably determined from the existing experimental data and we have set it equal to the bare value $e_p - e_n = e$.

The values of $e_p + e_n$ which serve to equate the shell-model predictions to the measured value for each experimentally observed transition are listed as the last column in Table III. All cluster around a value of $e_p + e_n = 2.0e$. This empirical value is much larger than the theoretical value of $e_p + e_n = 1.15e$ calculated by Horikawa *et al.*[7] Part of this discrepancy may be due to the fact that Horikawa *et al.* assumed unperturbed energies ($\Delta E \simeq 2\hbar\omega$, $4\hbar\omega, \ldots$) for the one-particle–one-hole states and if there were a collective "giant" 4^+, $T = 0$ state it could occur lower in energy, which would thus enhance its admixture into the model-space wave functions and make the isoscalar effective charge larger.

Analyses of the experimentally measured $B(E4)$ for the $\frac{19}{2}^- \rightarrow \frac{11}{2}^-$ transition in ^{53}Fe have suggested that the $E4$ effective charge is small and the $E6$ effective charge is even negative.[8] The present results suggest that these "anomalies" in ^{53}Fe may originate within the valence (fp) shell configurations via effects which have not been accurately calculated in previous shell-model calculations because of the large dimensions involved, rather than being a consequence of systematic, state-independent quenching of the effective charge.

We present in Tables IV–VII calculated energies and values of A_p, A_n, M_p, M_n, and $B(E4)$ for $\Delta J^\pi = 4^+$ excitations, along with what experimental information exists. Rather complete sets of predictions are given for $\Delta T = 0$ and $\Delta T = 1$ excitations in $N = Z$ nuclei (Tables IV and V, respectively) and for the $\Delta T = 0 + 1$ excitations of the $T = 1$ states in $T_z = -1$ nuclei (Table VI). For stable even-odd nuclei we present (in Table VII) results only for ^{19}F and ^{25}Mg, for which some experimental data exist. The values of M_p, M_n, and $B(E4)$ are based upon the values of the added effective charges $\delta_{pp} = \delta_{nn} = \delta_{np} = \delta_{pn} = 0.5$ as motivated by the results of Table III.

In comparing theoretical and experimental values of $B(E4)$ it is important to note that there are several theoretical sources of uncertainty in the values quoted for the experimental $B(E4)$. The $B(E4)$ values are obtained from inelastic electron scattering data by an extrapolation of the form factors measured at finite values of the momentum transfer q to the value for $q = \omega$ by using a model for the shape of the form factor. All results which we quote have been obtained with the Tassie model,[9] which is probably quite adequate for the strong $E4$ transitions but potentially questionable for the weak $E4$ transitions, where unusual shapes in the transition density may result from cancellation between single-particle form factors. In

TABLE III. Isoscalar effective charges for the stronger experimentally measured $E4$ transitions.

	$J_i \rightarrow J_f$	$[B(E4)]^{1/2}(e^2\mathrm{fm}^4)$ Theory	Experiment[a]	$\frac{e_p + e_n}{e}$[b]
^{19}F	$\frac{1}{2}^+ \rightarrow \frac{9}{2}^+ (1)$	$46.8(e_p + e_n)$ $-17.2(e_p - e_n)$	69 ± 8	1.8 ± 0.2
^{20}Ne	$0^+ \rightarrow 4^+(1)$	$106(e_p + e_n)$	195 ± 20	1.8 ± 0.2
^{22}Ne	$0^+ \rightarrow 4^+(1)$	$34.4(e_p + e_n)$ $+42.0(e_p - e_n)$	130 ± 15	2.6 ± 0.4
^{24}Mg	$0^+ \rightarrow 4^+(2)$	$105(e_p + e_n)$	207 ± 15	2.0 ± 0.2
^{26}Mg	$0^+ \rightarrow 4^+(2)$	$65.0(e_p + e_n)$ $-11.2(e_p - e_n)$	161 ± 22	2.7 ± 0.3
^{28}Si	$0^+ \rightarrow 4^+(1)$	$79.6(e_p + e_n)$	134 ± 7	1.7 ± 0.1

[a] For experimental references see Tables IV, VI, and VII.

[b] $(e_p - e_n) = e$ assumed.

TABLE IV. $\Delta T = 0$ $E4$ transitions in N-Z nuclei.

	$J_i \rightarrow J_f$	E_f (MeV) th	E_f (MeV) exp[c]	A_p[a] (fm^4)	M_p[b] (fm^4)	$B(E4)$ (e^2fm$^8 \times 10^3$) th	$B(E4)$ (e^2fm$^8 \times 10^3$) exp	Method of exp. analysis
^{20}Ne	$0^+ \rightarrow 4^+(1)$	4.13	4.25[d]	106.1	212	45	38 ± 8[e]	DUELS[h]
	$4^+(2)$	9.86	9.03[d]	−20.2	−40	1.6		
	$4^+(3)$	10.97		−3.8	−8	0.06		
	$4^+(4)$	11.70		−1.1	−2	0.004		
	$4^+(5)$	14.29		−1.4	−3	0.009		
	$4^+(6)$	14.63		13.3	27	0.7		
^{24}Mg	$0^+ \rightarrow 4^+(1)$	4.42	4.12	−19.7	39	1.6	2.0 ± 0.3[f]	DUELS[h]
	$4^+(2)$	5.89	6.01	104.9	210	44	43 ± 6[f]	DUELS[h]
	$4^+(3)$	8.79		12.5	25	0.6		
	$4^+(4)$	9.62		−0.8	1.7	0.003		
	$4^+(5)$	11.15		12.8	26	0.7		
	$4^+(6)$	12.18		−9.1	−18	0.3		
	$4^+(7)$	12.25		−14.1	−28	0.8		
	$4^+(8)$	12.63		−6.8	−14	0.2		
^{28}Si	$0^+ \rightarrow 4^+(1)$	4.88	4.62	−79.6	−159	25	27 ± 5[g]	g
	$4^+(2)$	7.49	6.89	85.5	171	29		
	$4^+(3)$	9.70		16.4	33	1.1		
	$4^+(4)$	10.15		16.3	33	1.1		
	$4^+(5)$	10.50		−13.0	−26	0.7		
	$4^+(6)$	11.06		1.3	3	0.009		
	$4^+(7)$	11.29		−3.8	−8	0.06		
	$4^+(8)$	11.93		7.8	16	0.3		
^{32}S	$0^+ \rightarrow 4^+(1)$	4.82	4.46	−121.4	−243	59		
	$4^+(2)$	6.65	6.41	67.7	135	18		
	$4^+(3)$	7.55		20.0	40	1.6		
	$4^+(4)$	7.94		−8.7	−17	0.3		
	$4^+(5)$	9.00		17.2	34	1.2		
	$4^+(6)$	9.36		−14.8	−30	0.9		
	$4^+(7)$	9.98		19.6	39	1.5		
	$4^+(8)$	10.40		7.8	16	0.3		
^{36}Ar	$0^+ \rightarrow 4^+(1)$	4.74	4.41	−123.5	−248	62		
	$4^+(2)$	6.81		3.3	6.5	0.04		
	$4^+(3)$	9.07		−30.5	−61	3.7		
	$4^+(4)$	9.98		18.6	37	14		
	$4^+(5)$	11.75		16.6	33	1.1		
	$4^+(6)$	12.64		22.7	45	2.0		

[a] $A_n = A_p$.

[b] $M_n = M_p$.

[c] From Ref. 21 except where noted.

[d] Reference 32.

[e] Reference 10.

[f] Reference 11.

[g] The results given in Ref. 17 for the PWBA $B(E4)$ values in ^{24}Mg and ^{28}Si are 28.7×10^3 and $(17.8 \pm 2.0) \times 10^3$ e^2fm^8, respectively, whereas a DWBA value of $(43 \pm 6) \times 10^3$ e^2fm^8 is given in Ref. 11 for ^{24}Mg. For ^{28}Si we have used $B(E4) = [(43 \pm 6)/28.7] \times (17.8 \pm 2.0) \times 10^3$ e^2fm^8.

[h] Reference 16.

addition, the $E4$ transition strengths have been extracted from simple one-step, plane-wave Born approximation (PWBA) calculations. The results we quote from Refs. 10–15 have been corrected for distorted-wave effects with the computer code DUELS.[16] For a few cases, only the PWBA analysis is available (Refs. 17–19). $B(E2)$ values extracted from a distorted-wave Born approximation (DWBA) analysis are typically about 30% larger than those extracted from a PWBA analysis[17] and the difference is probably larger for $B(E4)$ values (see Sec. 5.5 in Ref. 15). Two-step excitations such as $0 \rightarrow 2 \rightarrow 4$ have not been considered and this must be important on some level for the transi-

TABLE V. $\Delta T = E4$ transitions in $N = Z$ nuclei.[a]

	$J_i \to J_f$	E_f (MeV) th	E_f (MeV) exp	A_p[b] (fm^4)	M_p[c] (fm^4)	$B(E4)$ (e^2fm$^8\times 10^3$) th
^{20}Ne	$0^+ \to 4^+(1)T=1$	10.86	11.07[d]	27.7	27.7	0.77
	$4^+(2)T=1$	13.88		8.4	8.4	0.07
	$4^+(3)T=1$	15.74		−3.9	−3.9	0.015
	$4^+(4)T=1$	16.22		−9.7	−9.7	0.09
^{24}Mg	$0^+ \to 4^+(1)T=1$	9.74	9.51[e]	16.4	16.4	0.27
	$4^+(2)T=1$	12.28		26.5	26.5	0.70
	$4^+(3)T=1$	12.89		25.1	25.1	0.63
	$4^+(4)T=1$	13.36		−1.1	−1.1	0.001
^{32}S	$0^+ \to 4^+(1)T=1$	10.08	10.15[f]	−20.6	−20.6	0.42
	$4^+(2)T=1$	10.78		−75.5	−75.5	5.7
	$4^+(3)T=1$	11.85		15.7	15.7	0.25
	$4^+(4)T=1$	12.41		26.3	26.3	0.69
^{36}Ar	$0^+ \to 4^+(1)T=1$	10.32		−7.5	−7.5	0.06
	$4^+(2)T=1$	12.50		31.0	31.0	0.96
	$4^+(3)T=1$	12.76		73.1	73.1	5.3
	$4^+(4)T=1$	14.67		13.3	13.3	0.18

[a] The theoretical results for ^{28}Si have not been calculated.

[b] $A_n = -A_p$.

[c] $M_n = -M_p$.

[d] Reference 32.

[e] Based on the energy of the $1^+T=1$ state in ^{32}S and the $4^+T=1$ state in ^{32}P (Ref. 21).

[f] Reference 21.

TABLE VI. $E4$ transitions for $T_z = -1$ nuclei ($T=1 \to T=1$).

	$J_i \to J_f$	E_f (MeV) th	E_f (MeV) exp[a]	A_p (fm^4)	A_n (fm^4)	M_p (fm^4)	M_n (fm^4)	$B(E4)$ (e^2fm$^8\times 10^3$) th	$B(E4)$ (e^2fm$^8\times 10^3$) exp	Method of exp analysis
^{18}O	$0^+ \to 4^+(1)$	3.52	3.56[b]	0	−107.1	−54	−161	2.9	1.04 ± 0.20[c]	DUELS[f]
	$4^+(2)$	8.21		0	−81.5	−41	−122	1.7		
^{22}Ne	$0^+ \to 4^+(1)$	3.42	3.36	−76.3	7.6	−111	−27	12.3	17 ± 4[d]	DUELS[f]
	$4^+(2)$	5.40	5.52	38.4	69.7	92	124	8.5		
	$4^+(3)$	6.22	6.34	−50.9	−51.6	−102	−103	10.4		
	$4^+(4)$	7.21	(7.34)	−13.9	62.9	11	87	0.3		
^{26}Mg	$0^+ \to 4^+(1)$	4.59	4.32	71.6	45.3	130	104	16.9		
	$4^+(2)$	5.41	4.90	−53.8	−76.2	−119	−141	14.1	26 ± 7[e]	DUELS[f]
	$4^+(3)$	5.87	5.47	2.1	86.1	36	100	1.3	3.4[e]	DUELS[f]
	$4^+(4)$	6.13	5.72	−60.0	−8.2	−94	−42	8.8	13 ± 5[e]	DUELS
^{30}Si	$0^+ \to 4^+(1)$	5.40	5.28	36.1	107.6	108	180	11.7		
	$4^+(2)$	6.02	5.95	111.9	66.2	201	155	40		
	$4^+(3)$	7.52	7.22	54.5	45.3	59	41	3.5		
	$4^+(4)$	8.23		15.4	−9.2	18	−6	0.3		
^{34}S	$0^+ \to 4^+(1)$	4.88	4.69	101.3	100.6	202	201	41		
	$4^+(2)$	6.90	6.25	58.4	−44.4	65	37	4.2		
	$4^+(3)$	7.23		37.6	59.1	86	107	7.4		
	$4^+(4)$	7.76		56.8	−34.6	68	23	4.6		
^{38}Ar	$0^+ \to 4^+(1)$	7.79	5.35	−172.9	0	−259	−86	67		
	$4^+(2)$	14.88		−11.4	0	−17	−6	0.3		

[a] From Ref. 21 except as noted.

[b] Reference 32.

[c] Reference 12.

[d] Reference 13.

[e] Reference 14.

[f] Reference 16.

TABLE VII. Selected $E4$ transitions in odd-even nuclei ($T=1/2 \to T=1/2$).

		E_f (MeV)						$B(E4)$ ($e^2\mathrm{fm}^8\times10^3$)		
	$J_i \to J_f$	th	exp[a]	A_p (fm^4)	A_n (fm^4)	M_p (fm^4)	M_n (fm^4)	th	exp	Method of exp analysis
^{19}F	$\frac{1}{2}^+ \to \frac{7}{2}^+(1)$	4.64	4.38[b]	−13.1	−2.3	−21	−10	0.44		
	$\frac{7}{2}^+(2)$	5.95	5.46[b]	−36.6	−66.2	−88	−118	7.7		
	$\frac{7}{2}^+(3)$	6.43	6.07[b]	−26.6	−35.1	−57	−66	3.2		
	$\frac{7}{2}^+(4)$	8.36		10.7	23.2	28	40	0.8		
	$\frac{1}{2}^+ \to \frac{9}{2}^+(1)$	2.56	2.78[b]	42.3	91.2	109	158	5.9	4.7 ± 1.1[c]	PWBA
	$\frac{9}{2}^+(2)$	6.73	6.59[b]	−16.0	−33.6	41	58	0.8		
	$\frac{9}{2}^+(3)$	8.27		14.7	−5.9	18	−1.7	0.17		
	$\frac{9}{2}^+(4)$	10.74		−7.9	43.1	9.6	61	0.05		
^{25}Mg	$\frac{5}{2}^+ \to \frac{3}{2}^+(1)$	1.17	0.97	−16.7	−43.5	−47	−74	0.37		
	$\frac{3}{2}^+(2)$	3.08	2.80	−16.9	19.2	−16	20	0.043	(1.5 ± 0.4)[d,e]	PWBA
	$\frac{3}{2}^+(3)$	4.71	4.36	−2.9	−10.1	−9	−17	0.014		
	$\frac{3}{2}^+(4)$	6.04		12.8	18.6	28	34	0.13		
	$\frac{5}{2}^+ \to \frac{5}{2}^+(2)$	2.06	1.96	−27.3	16.4	−33	11	0.18		
	$\frac{5}{2}^+(3)$	4.24	3.91	65.2	91.5	144	170	3.5	1.9 ± 0.4[d]	PWBA
	$\frac{5}{2}^+(4)$	5.06		−6.6	0.6	−10	−2.4	0.017		
	$\frac{5}{2}^+ \to \frac{7}{2}^+(1)$	1.75	1.61	−27.0	−20.3	−51	−44	0.43		
	$\frac{7}{2}^+(2)$	3.02	2.74	−59.1	−101.8	−140	−182	3.3	1.5 ± 0.4[d,e]	PWBA
	$\frac{7}{2}^+(3)$	5.18	5.01	−42.7	12.1	−58	−3.2	0.56		
	$\frac{7}{2}^+(4)$	5.94	5.98	−14.6	−4.3	−24	−14	0.010		
	$\frac{5}{2}^+ \to \frac{9}{2}^+(1)$	3.62	3.41	13.0	−5.4	17	−1.7	0.05		
	$\frac{9}{2}^+(2)$	4.08	4.06	68.1	63.0	135	127	3.0	1.3 ± 0.3[d]	PWBA
	$\frac{9}{2}^+(3)$	4.85	4.71	−21.0	15.9	−24	13	0.09		
	$\frac{9}{2}^+(4)$	6.56	5.97	54.1	66.1	115	125	2.2		
	$\frac{5}{2}^+ \to \frac{11}{2}^+(1)$	5.26	(5.25)	139.5	123.3	271	255	12.2	5.8 ± 1.2[d] 13 ± 6[f]	PWBA DWBA[g]
	$\frac{11}{2}^+(2)$	5.80	5.53	−6.1	6.2	−6	6	0.006		
	$\frac{11}{2}^+(3)$	6.28	(6.04)	20.5	−19.3	21	−19	0.074		
	$\frac{11}{2}^+(4)$	7.70		6.1	−11.7	3.3	−14	0.003		
	$\frac{5}{2}^+ \to \frac{13}{2}^+(1)$	5.73	5.46	37.0	−0.2	56	17	0.5		
	$\frac{13}{2}^+(2)$	7.87		17.1	19.1	34	37	0.2		
	$\frac{13}{2}^+(3)$	8.09		−85.0	−54.6	−154	−125	3.9		
	$\frac{13}{2}^+(4)$	8.96		−38.9	−26.7	−71	−76	0.8		

[a] From Ref. 21 except where noted.

[b] Reference 32.

[c] Reference 18.

[d] Reference 19.

[e] The $\frac{3}{2}^+(2)$ and $\frac{7}{2}^+(2)$ states were not resolved in the electron scattering experiment of Ref. 19.

[f] Reference 15.

[g] Reference 16.

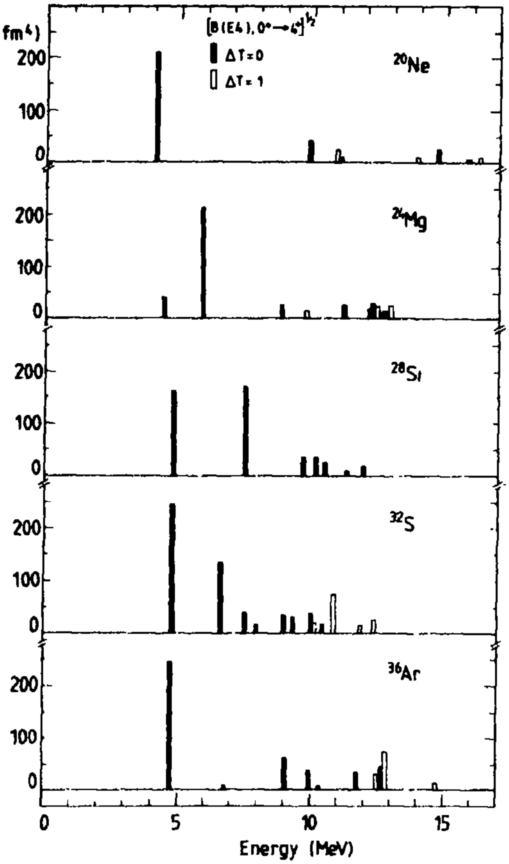

FIG. 1. Theoretical values for the $[B(E4), 0^+\to 4^+]^{1/2}$ matrix elements as a function of excitation energy for $N=Z$ nuclei in the sd shell. Both $\Delta T=0$ and $\Delta T=1$ transitions are shown. The numbers are taken from Tables IV and V; $\Delta T=1$ transitions in ^{28}S have not been calculated.

tions which have a very weak one-step $E4$ matrix element.

The calculated $E4$ strength distributions for $N=Z$ nuclei are shown in Fig. 1 and compared with experiment in Tables IV and V. The identities of the observed strong transitions in the $T=0$ nuclei ^{20}Ne, ^{24}Mg, and ^{28}Si are correctly predicted, in particular the shift of the dominant $E4$ strength from the lowest 4^+ state in ^{20}Ne to the second 4^+ state in ^{24}Mg and back (partially) to the lowest 4^+ state in ^{28}Si. Moreover, the magnitudes of these three strong transitions are reproduced to within experimental error. To pursue this particular aspect of the $E4$ picture further it is important to obtain experimental measurements of the second 4^+ state in ^{28}Si, of the first two 4^+ states in ^{32}S, and of the first 4^+ state in ^{36}Ar. It would also be valuable to measure or to set experimental upper bounds on the strength of the higher excited 4^+ states in the systems. Future experimental studies on these $T=0$ nuclei should also concentrate efforts on attempting the formidable task of extracting strengths for $\Delta T=1$ excitations to J^π, $T=4^+$, 1 states, the predictions for which are given in Table IV.

The predicted distributions of $E4$ strength in the $T_z=-1$ nuclei are more complex than for the $T_z=0$ systems and the individual values are smaller. The experimental data, single values for ^{18}O and ^{22}Ne and three values for ^{26}Mg, confirm these predictions about fragmentation and average magnitudes, but except for ^{18}O the experimental $B(E4)$ values tend to be larger than the predicted values by about 1 to 1.5 standard deviations. However, because of the varying structure of these excitations, this trend is not to be attributed to any simple isovector effective charge renormalization. More experimental measurements of $E4$ strength values of these systems would go far toward firmly validating the general picture of $E4$ strengths in $T=1$ systems predicted by the present stage of nuclear structure theory as well as to provide specific and unique information on the salient characteristics of the individual $J^\pi=4^+$ states.

The spectra of $E4$ excitations which can be obtained with odd-mass targets are, of course, potentially richer and more complex than for the $T_z=-1$, let alone the $T_z=0$ systems. Experimental electron scattering data have been reporte for ^{19}F (Ref. 18) and ^{25}Mg (Refs. 15 and 19); results of our calculations for these two nuclei are presented in Table VII. Experiment and theory are in good agreement for the $\frac{1}{2}^+\to\frac{9}{2}^+(1)$ transition in ^{19}F; other $\frac{1}{2}^+\to\frac{9}{2}^+$ $E4$ transitions up to 11 MeV in excitation are predicted to be weak. Only a few of the $\frac{5}{2}^+\to J^\pi$ transitions in ^{25}Mg are predicted to be strong and these are in general not to the lowest level of each spin. The relative strengths of the $B(E4)$ values reported by Okazaki *et al.* (Ref. 19) are in excellent agreement with the calculations. There is an overall factor of 2 discrepancy between experiment and theory. However, this is probably associated with the fact that a PWBA analysis was used by Okazaki *et al.* to extract the $B(E4)$ values (see the remarks in Sec. 5.5 of Ref. 15); the experimental $B(E4)$ which we have used for other nuclei have been obtained using a DWBA analysis.[16] Experimental results for two other transitions which are predicted to be strong in ^{25}Mg have not been reported [the $\frac{5}{2}^+\to\frac{9}{2}^+(2)$ and $\frac{5}{2}^+\to\frac{13}{2}^+(3)$ transitions]. There is obviously an extensive amount of work to be done on this component of the $E4$ picture. Ultimately, the experimental delineation of the distributions and magnitudes of $E4$ strength in odd-mass nuclei as a function of A, excitation energy, and final state spin, and the concurrent testing of the analogous nuclear structure model predictions will significantly enlarge our understanding both of nuclear wave functions and the foundations of the $E4$ excitation mode.

IV. STRENGTH RATIOS FOR EXCITATION BY ELECTROMAGNETIC AND VARIOUS HADRONIC PROBES

In this section we derive some estimates of the matrix elements associated with inelastic hadron scattering and present some sample results for proton, alpha, and pionic probes. The calculations are based upon the assumption, which has proved to be remarkably successful in describing alpha scattering,[20] that the cross sections for hadronic excitation are proportional to the same matrix elements which enter into the calculations of electromagnetic transition rates. Thus these cross sections are proportional to

$$B'(a)=(2J_i+1)^{-1}[C_p(a)M_p+C_n(a)M_n]^2\,, \tag{16}$$

where $C_{p/n}$ represents the interaction strengths of probe (a) with the protons/neutrons of the nucleus.

Since we are concerned here with nuclear structure effects rather than the details of the probe-specific absolute interaction strengths we choose to work with normalized strength factors $B(a)$ defined so as to yield a value for $T=0\to T=0$ transitions (for which $M_p-M_n=0$) which is unique, independent of probe (a):

$$\begin{aligned} B(a)&=B'(a)/[C_p(a)+C_n(a)]^2\\ &=(2J_i+1)^{-1}[\tfrac{1}{2}(M_p+M_n)+\tfrac{1}{2}R(a)(M_p-M_n)]^2\,, \end{aligned} \tag{17}$$

here

$$R(a)=\frac{C_p(a)-C_n(a)}{C_p(a)+C_n(a)}\,. \tag{18}$$

or the electromagnetic probes, $C_p=e$ and $C_n=0$ nd hence $R(a=e)=1$, and Eq. (17) reduces to Eq. 3),

$$B(E4)=B(e)=(2J_i+1)^{-1}M_p{}^2\,. \tag{19}$$

or the alpha particle, $C_p=C_n$ and hence $R(a$ alpha$)=0$ and

$$B(\text{alpha})=(2J_i+1)^{-1}[\tfrac{1}{2}(M_p+M_n)]^2\,. \tag{20}$$

or pions at energies near the (3, 3) resonance $(a=\pi^\pm)=\pm 0.5$ and

$$B(\pi^\pm)=(2J_i+1)^{-1}[\tfrac{1}{2}(M_p+M_n)\pm\tfrac{1}{4}(M_p-M_n)]^2\,. \tag{21}$$

ion inelastic scattering experiments are currently designed to yield the ratios of excitation rengths with π^- and π^+ projectiles. This quantity is expressed in our model as

$$\frac{B(\pi^-)}{B(\pi^+)}=\left(\frac{M_p+3M_n}{3M_p+M_n}\right)^2. \tag{22}$$

This precise result depends, of course, upon the assumption that near resonance the π^--n and π^+-p interaction amplitudes are 3.0 times stronger than the π^--p and π^+-n amplitudes, but analogous expressions are easily obtained for different assumptions about these elementary-particle features.

Many strongly excited 4^+ states at high excitation energy have been reported in alpha inelastic scattering experiments. In Table VIII are listed some strengths from alpha scattering on ^{24}Mg (Ref. 20) in comparison with the present theoretical predictions for the first nine 4^+ states. Above 9.0 MeV there is complete disagreement between experiment and theory. This could be due to experimental errors in the spin assignments (in Endt and van der Leun[21] no definite 4^+ assignments have been made above 9.0 MeV) or to two-step contributions to the inelastic scattering cross sections which were not considered in the DWBA analysis, rather than a failure of the nuclear structure wave functions.

Some predicted values for $B(\alpha)$ and $B(\pi^\pm)$ in $T_z=-1$ nuclei are given in Table IX. It should be quite interesting to carry out the corresponding experimental measurements since several quite strong deviations from isoscalar behavior are predicted. Inelastic alpha scattering to 4^+ states in ^{22}Ne and ^{26}Mg as well as in several $N=Z$ nuclei has been measured by Rebel *et al.*[22] but the extraction of $B(\alpha)$ values via the methods of Ref. 20 have not been carried out.

As a final example of hadronic excitations we compare some experimentally measured proton

TABLE VIII. Alpha scattering transition strengths for $0^+\to 4^+$ transitions in ^{24}Mg.

$J_f(T_f)$	Energy (MeV) th	Energy (MeV) exp[a]	B(alpha) (fm$^8\times 10^3$) th	B(alpha) (fm$^8\times 10^3$) exp[a]
$4^+(0)$	4.42	4.12	1.6	
$4^+(0)$	5.89	6.01	44.0	21.4 ± 3.2
$4^+(0)$	8.79	8.64	0.6	3.0 ± 0.5
4^+		9.12		8.1 ± 1.4
(4^+)		9.30		12.2 ± 1.9
4^+		10.03		16.0 ± 2.4
$4^+(0)$	9.62		0.002	
$4^+(1)$	9.74			
$4^+(0)$	11.15		0.6	
$4^+(0)$	12.17		0.3	
$4^+(0)$	12.24		0.7	
$4^+(1)$	12.28			

[a] $B(\text{alpha})=(A/2Z)^2B(IS)$ where $B(IS)$ are taken from Table IX in Ref. 20.

TABLE IX. Alpha scattering and pion scattering strengths for the $0^+ \to 4^+$ transitions in $T_z = -1$ nuclei.

Nucleus	$J_i \to J_f$	B(alpha) (fm$^8 \times 10^3$)	$\frac{B(\text{alpha})}{B(E4)}$	$\frac{B(\pi^-)}{B(\pi^+)}$
^{18}O	$0^+ \to 4^+(1)$	11.5	4.00	2.78
^{22}Ne	$0^+ \to 4^+(1)$	4.7	0.38	0.28
	$4^+(2)$	11.7	1.37	1.34
^{26}Mg	$0^+ \to 4^+(1)$	13.7	0.80	0.80
	$4^+(2)$	16.9	1.20	1.19
^{30}Si	$0^+ \to 4^+(1)$	20.7	1.77	1.65
	$4^+(2)$	31.8	0.78	0.77
^{34}S	$0^+ \to 4^+(1)$	40.8	1.00	1.00
	$4^+(2)$	0.2	0.05	0.09
^{38}Ar	$0^+ \to 4^+(1)$	30.0	0.44	0.36

scattering strengths in ^{26}Mg (Ref. 23) with estimates for 30 MeV proton scattering. From the microscopic optical model of Brieva and Rook[24] we obtain values for the interaction strengths at this energy of $C_p = 0.3$ and $C_n = 0.7$. This yields

$$B(\text{proton}, 30\ \text{MeV}) = (2J_i + 1)^{-1}(0.3M_p + 0.7M_n)^2 . \quad (23)$$

The predicted and measured B values are presented in Table X. The experimental $0^+ - 4_2^+$ strength is twice as large as the predicted value. This is probably a real discrepancy since, in addition, the experimental electron scattering $B(E4)$ value is larger than predicted (see Table V). The predicted ratio $B(p)/B(E4)$ is consistent with experiment. The situation for the weaker $0^+ - 4_1^+$ transition is not so clear since the $B(E4)$ value has not yet been extracted from the experimental data; the calculated $B(p)$ value is in fair agreement with experiment. The proton scattering strength to the third 4^+ state is predicted to be much stronger than the electromagnetic excitation strength.

V. SUMMARY AND CONCLUSIONS

The Chung-Wildenthal wave functions for the *sd*-shell nuclei have been used to calculate hexadecapole transition densities. These have been combined with harmonic-oscillator radial wave functions to predict proton and neutron $E4$ matrix elements within the *sd*-shell model space. There is at present no good theoretical prescription for obtaining radial wave functions for open-shell nuclei which are more realistic than those of the harmonic-oscillator potential.

The effects of model-space truncation on the $E4$ operator have been taken into account by introducing empirical effective charges. The experimental values for strong electromagnetic excitations are all consistent with a isoscalar effective charge of $e_p + e_n \simeq 2.0e$. This is much larger than the results of microscopic core-polarization calculations of Horikawa *et al.*,[7] which gave $e_p + e_n \simeq 1.15e$.

These empirical effective charges were used to calculate the proton and neutron matrix elements M_p and M_n; electromagnetic excitation strengths are determined by M_p while hadronic scattering strengths depend on both M_p and M_n. Predicted electromagnetic $B(E4)$ values are in good agreement with existing experiments over a wide range of magnitudes. However, experimental electron scattering results are lacking for the upper *sd* shell as well as for pure $\Delta T = 1$ excitations in $N = Z$ nuclei.

It is more difficult to extract nuclear structure information from the hadronic scattering cross sections. For transitions which are characterized by small direct matrix elements, two-step contributions are certainly important; this may be responsible for the disagreement between the very small isoscalar excitation strengths predicted to 4^+ states above 9 MeV in ^{24}Mg compared with experiment. A systematic analysis of alpha, proton, or pion scattering for $0^+ - 4^+$ transitions in many *sd*-shell nuclei is needed to confirm our predic-

TABLE X. Proton scattering transition strengths $B(p) = B$(proton, 30 MeV) for the $0^+ \to 4^+$ transitions in ^{26}Mg.

Energy (MeV)		$B(p)$ (fm$^8 \times 10^3$)		$B(p)/B(E4)$	
th	exp[a]	th[b]	exp[c]	th	exp[d]
4.59	4.32	12.5	18 ± 2	0.74	
5.41	4.90	18.1	41 ± 2	1.28	1.6 ± 0.3
5.87	5.47	6.5		5.0	
6.13	5.72	3.3		0.38	

[a] Reference 21.
[b] $B(p) = (0.3M_p + 0.7M_n)^2$.
[c] Reference 23.
[d] For $B(E4)_{\text{exp}}$ see Table VI.

TABLE XI. Hartree-Fock results for ^{20}Ne.

	Harmonic oscillator	Hartree-Fock Skyrme III	Hartree-Fock Skyrme IV
$\langle d_{5/2}\lvert r^4\rvert d_{5/2}\rangle_p$ (fm^4)[a]	179	181	198
$\langle d_{5/2}\lvert r^4\rvert d_{3/2}\rangle_p$ (fm^4)[a]	179	236	274
r_p (fm)[b]	2.905	2.905	2.902
$BE(d_{5/2})_p$ (MeV)[c]		−5.42	−5.62
$BE(d_{3/2})_p$ (MeV)[c]		−0.02	0.78

[a] Proton radial-matrix elements.

[b] Point proton rms radii.

[c] Proton single-particle energies.

tions for the relative sizes and phases of the proton and neutron matrix elements.

APPENDIX

In this section we discuss the Hartree-Fock calculations for ^{20}Ne and ^{36}Ar which have recently been carried out by Brown and Massen.[6] For these calculations a Skyrme interaction[25] was used and a self-consistent spherical potential was constructed out of the monopole densities obtained by adding the squares of the radial wave functions weighted by the orbit occupation probabilities, which in turn had been obtained from the sd-shell-model calculations. The spin-orbit parameter was chosen to reproduce the $d_{5/2}$-$d_{3/2}$ spin-orbit splitting of about 5 MeV in $A=17$.

The results using Skyrme III and Skyrme IV interactions for ^{20}Ne are given in Table XI. Under the column labeled "harmonic oscillator" we give the r^4 matrix elements which we would obtain if we took the theoretical value of $r_p = 2.905$ fm and interpreted it as a sum of harmonic oscillators extract b and then to calculate $\langle r^4\rangle = 15.75b^4$. or the $d_{5/2}$ orbit the Hartree-Fock results are very close to the harmonic-oscillator results, but the Hartree-Fock results for the off-diagonal, $d_{5/2}$-$d_{3/2}$ matrix element are much larger than the harmonic-oscillator result and they depend strongly on the value of the binding energy. (The radial wave function for the unbound $d_{3/2}$ state obtained with the Skyrme IV interaction was obtained by the method described by Beiner *et al.*[35])

The experimental separation energies of the $d_{5/2}$ and $d_{3/2}$ orbits in ^{20}Ne, −16.87 and −18.42 MeV, respectively, are very different from the Hartree-Fock single-particle energies because of the residual interactions. Thus, the tails of the wave functions, which are important for the r^4 matrix elements and which are determined by the separation energy, cannot be reliably calculated with spherical Hartree-Fock or any other smoothly mass dependent single-particle wave functions. These large separation energies may even result in $\langle r^4\rangle$ matrix elements which are smaller than the harmonic-oscillator results. There is at present no rigorous theoretical prescription for taking the residual interactions into account.

The situation is different when the orbits are more deeply bound. In Table XII the Hartree-Fock

TABLE XII. Hartree-Fock results for ^{36}Ar.[a]

	Harmonic oscillator	Hartree-Fock Skyrme III	Hartree-Fock Skyrme IV
$\langle d_{5/2}\lvert r^4\rvert d_{5/2}\rangle_p$ (fm^4)	220	201	196
$\langle d_{5/2}\lvert r^4\rvert d_{3/2}\rangle_p$ (fm^4)	220	213	219
r_p (fm)	3.318	3.318	3.298
$BE(d_{5/2})_p$ (MeV)		−13.51	−17.52
$BE(d_{3/2})_p$ (MeV)		−7.26	−6.93

[a] See footnotes to Table XI.

results for ^{36}Ar are given. For both Skyrme III and Skyrme IV the results are close to the harmonic-oscillator values, even though the $d_{5/2}$ single-particle energies are quite different in the two cases. In this case the experimental separation energies for the $d_{5/2}$ and $d_{3/2}$ orbits of −17.01 and −15.25 MeV, respectively, are fairly close to the Hartree-Fock single-particle energies.

ACKNOWLEDGMENTS

This material is based upon work supported in part by the U. S. National Science Foundation unde Grant No. Phy-7822696. One of the authors (B.H.W.) wishes to thank Prof. K. W. Allen and Dr. P. E. Hodgson for their hospitality during his stay at Oxford.

---

[*] Permanent address.

[1] W. Chung, thesis, Michigan State University, 1976 (unpublished); W. Chung and B. H. Wildenthal (unpublished).

[2] B. H. Wildenthal, *Elementary Modes of Excitation in Nuclei*, edited by R. Broglia and A. Bohr (Soc. Italiana de Fisica, 1977); B. H. Wildenthal and W. Chung, *Mesons in Nuclei*, edited by M. Rho and D. H. Wilkinson (North-Holland, Amsterdam, 1979); B. A. Brown, W. Chung, and B. H. Wildenthal, Phys. Rev. Lett. 40, 1631 (1978); B. H. Wildenthal, Nucleonika 23, 459 (1978).

[3] J. L. Friar and J. W. Negele, *Advances in Nuclear Physics*, edited by M. Baranger and E. Vogt (Plenum, New York, 1975), Vol. 8, p. 219.

[4] L. J. Tassie and F. C. Barker, Phys. Rev. 111, 940 (1958).

[5] R. J. Philpott, W. T. Pinkston, and G. R. Satchler, Nucl. Phys. A119, 241 (1968); G. M. McAllen, W. T. Pinkston, and G. R. Satchler, Part. Nucl. 1, 412 (1971); A. Prakash and N. Austern, Ann. Phys. (N.Y.) 51, 418 (1969).

[6] B. A. Brown and S. E. Massen (unpublished).

[7] Y. Horikawa, T. Hoshino, and A. Arima, Phys. Lett. 63B, 134 (1976).

[8] D. F. Geesaman, R. L. McGrath, J. W. Noé, and R. E. Malmin, Phys. Rev. C 19, 1938 (1979); H. Sagawa, *ibid.* 19, 506 (1979).

[9] L. J. Tassie, Aust. J. Phys. 9, 407 (1956); 11, 481 (1958).

[10] R. P. Singhal, H. S. Caplan, J. R. Moreira, and T. E. Drake, Can. J. Phys. 51, 2125 (1973).

[11] H. Zarek, S. Yen, B. O. Pich, T. E. Drake, C. F. Williamson, S. Kowalski, C. P. Sargent, W. Chung, B. H. Wildenthal, M. Harvey, and H. C. Lee, Phys. Lett. 80B, 26 (1978).

[12] B. E. Norum, thesis, Massachusetts Institute of Technology, 1979 (unpublished).

[13] K. K. Maruyama, F. J. Kline, J. W. Lightbody, S. Penner, W. J. Briscoe, M. Lunnan, and H. Crannell, Phys. Rev. C 19, 1624 (1979).

[14] E. W. Lees, A. Johnson, S. W. Brain, C. S. Curran, W. A. Gillespie, and R. P. Singhal, J. Phys. A 7, 936 (1974).

[15] E. W. Lees, C. S. Curran, T. E. Drake, W. A. Gillespie, A. Johnston, and R. P. Singhal, J. Phys. G 5, 341 (1976).

[16] S. T. Tuan, L. E. Wright, and D. S. Onley, Nucl. Instrum. Methods 60, 70 (1968).

[17] A. Nakada and Y. Torizuka, J. Phys. Soc. Jpn. 32, 1 (1972).

[18] M. Oyamada, T. Terasawa, K. Nakahara, Y. Endo, H. Saito, and E. Tanaka, Phys. Rev. C 11, 1578 (1975)

[19] Y. Okazaki, K. Hayakawa, K. Nakahara, M. Oyamada, T. Terasawa, and H. Saito, Phys. Lett. 55B, 373 (1975).

[20] A. M. Bernstein, *Advances in Nuclear Physics*, edited by M. Baranger and E. Vogt (Plenum, New York, 1969), Vol. 3, p. 325.

[21] P. M. Endt and C. van der Leun, Nucl. Phys. A235, 27 (1974).

[22] H. Rebel, G. W. Schweimer, G. Schatz, J. Specht, R. Löhken, G. Hauser, D. Habs, and H. Klewe-Nebentus, Nucl. Phys. A182, 145 (1972).

[23] P. W. F. Alons, H. P. Blok, and J. F. A. van Hienen, Phys. Lett. 83B, 34 (1979).

[24] F. A. Brieva and J. R. Rook, Nucl. Phys. A307, 493 (1978).

[25] M. Beiner, H. Flocard, N. van Giai, and P. Quentin, Nucl. Phys. A238, 29 (1975).

[26] M. Miska, B. Norum, M. W. Hynes, W. Bertozzi, S. Kowalski, F. N. Rad, C. P. Sargent, T. Sasanuma, and B. L. Berman, Phys. Lett. 83B, 165 (1979).

[27] L. A. Schaller, T. Dubler, K. Kaeser, G. A. Rinker, B. Robert-Tissot, L. Schellenberg, and H. Schneuwly, Nucl. Phys. A300, 225 (1978).

[28] C. W. de Jager, H. de Vries, and C. de Vries, At. Data Nucl. Data Tables 14, 479 (1974).

[29] C. G. Li, M. R. Yearian, and I. Sick, Phys. Rev. C 9, 1861 (1974); I. Sick, private communication.

[30] H. Euteneuer, H. Rothhaas, O. Schwentker, J. R. Moreira, C. W. de Jager, L. Lapikas, H. de Vries, J. Flanz, K. Itoh, G. A. Peterson, D. V. Webb, W. C. Barber, and S. Kowalski, Phys. Rev. C 16, 1703 (1977).

[31] R. Engfer, H. Schneuwly, J. L. Vuilleumier, H. K. Walter, and A. Zehnder, At. Data Nucl. Data Tables 14, 509 (1974).

[32] F. Ajzenberg-Selove, Nucl. Phys. A300, 1 (1978).

PHYSICAL REVIEW C VOLUME 21, NUMBER 6 JUNE 1980

Single-particle states in nuclear matter and in finite nuclei

R. Sartor

Institut für Theoretische Physik, Universität Tübingen, 7400 Tübingen, West Germany and Institut de Physique, Université de Liège, Sart Tilman, 4000 Liège 1, Belgium

C. Mahaux

Institut de Physique, Université de Liège, Sart Tilman, 4000 Liège 1, Belgium

(Received 7 November 1979)

The complex single-particle field in nuclear matter is computed in the framework of Brueckner's theory, in the case of the realistic nucleon-nucleon interaction of Hammann and Ho-Kim The Hartree-Fock, the core polarization, and the correlation contributions are calculated; renormalization corrections are also evaluated. The results are compared with those derived from a dispersion relation approach. Particular attention is paid to the behavior of the effective mass near the Fermi surface, where it presents a narrow enhancement. Following a recent suggestion by Orland and Schaeffer, the nuclear matter results are adapted to finite nuclei by assuming that the relevant variable is the difference between the single-particle energy and the Fermi energy. This yields fair agreement between the strength functions for quasihole states calculated here and those measured from $(e,e'p)$ knockout processes.

[NUCLEAR STRUCTURE Potential energy and width of single-particle states from Hammann–Ho-Kim interaction.]

I. INTRODUCTION

Bethe[1] emphasized that "the most striking feature of finite nuclei is the validity of the shell model. Nuclei can be very well described by assigning quantum numbers to individual nucleons." In the simple case of nuclear matter, the latter sentence amounts to stating that one can associate a well-defined energy to nucleons with a given wavelength. Landau[2-4] explained the success of the shell model by the fact that for small excitation energies the spectrum of an interacting Fermi gas can be described in terms of excitations of nucleons surrounded by their polarization clouds, i.e. of quasiparticles; these move independently in a smooth mean potential, possibly nonlocal. For soft phenomenological nucleon-nucleon interactions, this static potential i usually identified with the Hartree-Fock field, hich is represented by graph (IA) in Fig. 1.

The validity of the concept of quasiparticles has een justified theoretically for single-particle tates close to the Fermi surface. The empirical uccess of the optical model shows that this conept is also valid for scattering states.[5] Besides, ıe quasiparticle model is often used for deeply ound single-particle states, for instance when sing a Hartree-Fock description of nuclear round states. It is of interest to investigate 'hether this extension is valid. Experimentally, nost information in this respect is obtained from ,e'p) or $(p,2p)$ knockout reactions. Theoretiially, one must study whether for a deeply bound state the single-particle strength is still sharply peaked about the single-particle energy. This problem involves the study of the "true" energy dependence of the mean field. The existence of this energy dependence reflects the interaction between quasiparticle states. The dispersion relation (2.6) below, which connects the real and imaginary parts of the mean field, shows that the energy dependence is intimately related to the fact that the mean field is complex. The imaginary part of the field accounts for the spreading of the single-particle strength.

A theoretical investigation of these properties of the mean field implies that one carries the calculation beyond the Hartree-Fock approximation, since the latter is real and static. If one uses a soft phenomenological nucleon-nucleon interaction, the natural way to proceed is to add to the first-order field (IA) the second-order contributions, represented by the "polarization" diagram (IIA) and by the "correlation" graph (IIB).[6] In the case of nuclear matter, the energy dependence of these second-order contributions has recently been investigated by Orland and Schaeffer[7] on the basis of the dispersion relation (2.6). In Ref. 8, we show that part of their discussion is marred by the use of a somewhat arbitrary parametrization of the energy dependence of the imaginary part of the mean field. This led us to perform an explicit evaluation of the real and imaginary parts of graphs (IA), (IIA), and (IIB). More precisely, we have computed the Brueckner-Hartree-Fock approximation, which is rep-

© 1980 The American Physical Society

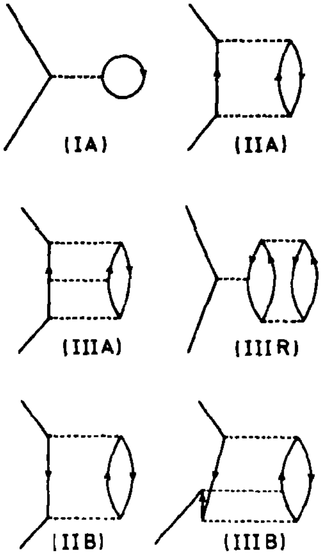

FIG. 1. Graphical representation of the leading terms of the perturbation expansion of the mass operator. Only direct terms are drawn. Graph (IA) is the Hartree-Fock approximation, (IIA) is the polarization graph, and (IIB) the correlation graph. Diagram (IIIR) yields the renormalization of graph (IA).

resented by graph (BHF) in Fig. 2. This is the sum of a series of particle-particle ladders of which graphs (IA), (IIA), and (IIIA) of Fig. 1 are the leading terms. We have also computed the real and the imaginary parts of the graph (CO) of Fig. 2, which is the sum of a series of diagrams of which graphs (IIB) and (IIIB) of Fig. 1 are the leading terms.

The input of our calculation is the nucleon-nucleon interaction of Hammann and Ho-Kim.[9] This interaction is a realistic one since it renders with good accuracy the S, P, and D nucleon-nucleon scattering phase shifts. However, it is in some sense only semirealistic because it has finite rank, i.e., is strongly nonlocal. This influences the nonlocality of the corresponding single-particle mean field. Moreover, the average binding energy per nucleon at normal density as calculated from the Brueckner-Hartree-Fock approximation is larger than the empirical value; we note that the Hartree-Fock approximation yields good agreement with the empirical binding energy. These deficiencies have to be kept in mind when discussing our results. They are overshadowed by the following two features. Firstly, the interaction is sufficiently soft for using a perturbation expansion. Secondly, Brueckner's reaction matrix can be computed faster and more accurately than for a local interaction.

The interaction of Hammann and Ho-Kim has already been used in Refs. 10 and 11 to investigate some properties of bound single-particle states. In the present paper, we take advantage of the two features mentioned above to calculate separately the contributions to the single-particle mean field of specific graphs of the perturbation expansion, and to compare these results with those recently obtained by Orland and Schaeffer[7] who used the dispersion relation (2.6). Moreover, we investigate the shape of the enhancement of the effective mass near the Fermi surface in more detail than was previously possible in the case of the local Reid's hard core interaction.[5] Finally, the comparison between quantities calculated in nuclear matter and empirical data is performed by assuming that the relevant variable that provides a link between the two cases is the difference between the single-particle energy and the Fermi energy. This method is based on a suggestion by Orland and Schaeffer.[7] It yields better agreement between calculated and measured quantities than the approach used in Refs. 10–12, and which consisted in identifying the momentum of a particle in nuclear matter with the average momentum of a single-particle state in a finite nucleus.

A few useful formulas and concepts are briefly recalled in Sec. II. Section III is devoted to the real part of the mean field. In Secs. III A–III C, we successively discuss some properties of the Hartree-Fock approximation, of the core polarization contribution, and of the correlation graph. We pay particular attention to the vicinity of the Fermi surface, where the empirical effective mass is known to be enhanced.[13] The size of the renormalization corrections is evaluated in Sec. III D. Our results are compared with the dispersion approach of Orland and Schaeffer[7] in Sec. III E and with empirical values in Sec. III F.

The imaginary part of the mean field is investi-

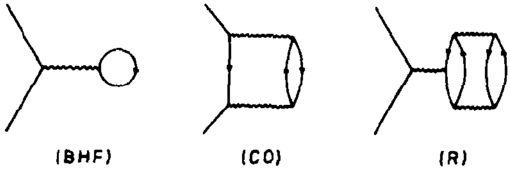

FIG. 2. Graphical representation of some contributions to the low-density expansion of the mass operator. Graph (BHF) represents the Brueckner-Hartree-Fock approximation (CO) shows the correlation contribution. The sum of graphs (BHF) and (R) yields the renormalized Brueckner-Hartree-Fock approximation.

gated in Sec. IV, where we compare it with the value used by Orland and Schaeffer, and also with a compilation of empirical data.

In Sec. V, we calculate the strength function of quasihole states, i.e., the distribution of the spread single-particle states. We obtain fair agreement between calculated and measured strength functions by equating in the two cases the difference between the single-particle energy and the Fermi energy. As mentioned above, this method follows a suggestion by Orland and Schaeffer.[7] It presents over that used in Refs. 10–12 the advantages of identifying the main relevant variable, and of compensating part of the deficiencies of the interaction of Hammann and Ho-Kim.

II. BASIC FORMULAS

A. Definitions

The equations and results given in Secs. II–IV refer to infinite nuclear matter with equal number of neutrons and protons. Insofar as possible, we follow the notation of Ref. 5, where proofs or references to the original papers can be found. We denote by ρ the nucleon density and by k_F the Fermi momentum. They are related by

$$\rho = 2(3\pi^2)^{-1} k_F^3 . \tag{2.1}$$

The mass operator

$$\lim_{\eta\to 0} M(k;E-i\eta) = M(k;E) = V(k;E) + iW(k;E) \tag{2.2}$$

depends on k_F. It can be identified with the single-particle field felt by a nucleon with momentum k and energy E. One has $W(k;E) \leq 0$.

Most physical processes can be described in terms of quasiparticles. A quasiparticle with momentum k has a well-defined energy $E(k)$ given by the relation ($\hbar = 1$)

$$E(k) = k^2/2m + V(k;E(k)). \tag{2.3a}$$

The mean field felt by a quasiparticle with momentum k is the on-shell value of the mass operator:

$$M(k;E(k)) = \tilde{M}(k) = \tilde{V}(k) + i\tilde{W}(k). \tag{2.4}$$

The Fourier transform $\tilde{\mathfrak{M}}(|\vec{r}-\vec{r}\,'|)$ of $\tilde{M}(k)$ yields a static nonlocal field. Equivalently, one may specify the energy E of a quasiparticle, and determine its momentum $k(E)$ by the energy-momentum relation

$$E = [k(E)]^2/2m + V(k(E);E). \tag{2.3b}$$

The corresponding mean field is the on-shell value

$$M(k(E);E) = \bar{M}(E) = \bar{V}(E) + i\bar{W}(E), \tag{2.5}$$

which is a local energy-dependent field.

The fields $\bar{M}(E)$ and $\tilde{M}(k)$ are equivalent in the sense that they yield the same quasiparticle properties. In a finite system, they are phase equivalent since they yield practically the same phase shifts, though the corresponding scattering wave functions are different in the nuclear interior. In nuclear reaction analyses, one normally uses a local energy-dependent optical-model potential which should thus be identified with $\bar{M}(E)$. In bound state calculations, one often uses a nonlocal static shell-model potential (e.g., in a Hartree-Fock model); it should be identified with $\tilde{M}(k)$.

When the nucleon-nucleon interaction has no hard core, the following dispersion relation holds:

$$V(k;E) = M_{(\mathrm{IA})}(k) + \frac{\mathcal{P}}{\pi} \int_{-\infty}^{\infty} \frac{W(k;E')}{E-E'}\,dE' , \tag{2.6a}$$

where $\mathcal{P}$ denotes a principal value integral. The energy-independent background $M_{(\mathrm{IA})}(k)$ is the Hartree-Fock contribution to the real part of the mean field. In the presence of a hard core repulsion, one must use the subtracted dispersion relation[8]

$$V(k;E) = V(k;E_0) + \frac{E_0-E}{\pi}\mathcal{P} \int_{-\infty}^{\infty} \frac{W(k;E')}{(E-E')(E_0-E')}\,dE' , \tag{2.6b}$$

where E_0 is arbitrary.

B. Perturbation expansion

The nucleon-nucleon potential of Hammann and Ho-Kim[9] is sufficiently soft for using a perturbation expansion in powers of the strength of the interaction. Some contributions are represented in Fig. 1. The first-order term is the Hartree-Fock (HF) approximation

$$M_{(\mathrm{IA})}(k) = M_{(\mathrm{I})}(k) = \sum_{j<k_F} \langle \vec{k},\vec{j}\,|v|\,\vec{k},\vec{j}\,\rangle_{\mathfrak{a}} . \tag{2.7}$$

Here, v is the nucleon-nucleon potential and $\mathfrak{a}$ refers to antisymmetrization. Note that $M_{(\mathrm{I})}(k)$ is real and independent of E.

There exist two second-order terms. They are energy dependent and complex. The "polarization" contribution is represented by graph (IIA); its algebraic expression reads

$$M_{(\mathrm{IIA})}(k;E) = \tfrac{1}{2} \sum_{j<k_F} \sum_{a,b>k_F} \frac{|\langle \vec{k},\vec{j}\,|v|\,\vec{a},\vec{b}\,\rangle_{\mathfrak{a}}|^2}{E+E(j)-E(a)-E(b)-i\eta} . \tag{2.8}$$

We recall that the function $E(n)$ is defined by the energy-momentum relation (2.3). The "correlation" contribution is represented by graph (IIB):

$$M_{(\mathrm{IIB})}(k;E)=\tfrac{1}{2}\sum_{l,j<k_F}\sum_{a>k_F}\frac{|\langle\vec{j},\vec{l}\,|v|\vec{k},\vec{a}\rangle_a|^2}{E+E(a)-E(j)-E(l)-i\eta}. \tag{2.9}$$

C. Low-density expansion

The sum of the one-hole line graphs (IA), (IIA), (IIIA),... of Fig. 1 yields the Brueckner-Hartree-Fock (BHF) approximation

$$M_{\mathrm{BHF}}(k;E)=\sum_{j<k_F}\langle\vec{k},\vec{j}\,|g[E+E(j)]|\vec{k},\vec{j}\rangle_a . \tag{2.10}$$

Here, $g[E+E(j)]$ is the reaction matrix. It is the solution of the integral equation

$$g[E+E(j)]=v+v\sum_{a,b>k_F}\frac{|\vec{a},\vec{b}\rangle\langle\vec{a},\vec{b}|}{E+E(j)-E(a)-E(b)-i\eta}\times g[E+E(j)] . \tag{2.11}$$

The BHF approximation is represented by the graph denoted by (BHF) in Fig. 2.

The sum of the graphs (IIB), (IIIB),... of Fig. 1 yields the diagram labeled (CO) in Fig. 2. It reads

$$M_{(\mathrm{CO})}(k;E)=\tfrac{1}{2}\sum_{l,j<k_F}\sum_{a>k_F}\frac{|\langle\vec{j},\vec{l}\,|g[E(j)+E(l)]|\vec{k},\vec{a}\rangle_a|^2}{E+E(a)-E(j)-E(l)-i\eta}. \tag{2.12}$$

By analogy with Eq. (2.9), we also call $M_{(\mathrm{CO})}$ a correlation graph.

Graph (IIIR) in Fig. 1 is the progenitor of a series of graphs whose sum is represented by graph (R) in Fig. 2. The sum of graphs (BHF) and (R) yields the "renormalized" Brueckner-Hartree-Fock approximation; it reads

$$M^{\mathrm{R}}_{\mathrm{BHF}}(k;E)=(1-\kappa)M_{\mathrm{BHF}}(k;E) . \tag{2.13}$$

Here, $1-\kappa$ denotes the average occupation number in the Fermi sea. In the case of the interaction of Hammann and Ho-Kim one has[10]

$$\kappa\simeq 0.08 \tag{2.14}$$

for $k_F=1.17\ \mathrm{fm}^{-1}$ as well as for $k_F=1.36\ \mathrm{fm}^{-1}$. Engelbrecht and Weidenmüller[14] have argued that the correlation contribution (2.12) can also be renormalized, with the result

$$M^{\mathrm{R}}_{(\mathrm{CO})}(k;E)=(1-\kappa)^2M_{(\mathrm{CO})}(k;E) . \tag{2.15}$$

Unless otherwise specified, the single-particle energy $E(k)$ will henceforth be approximated by its BHF value ($\hbar=1$)

$$E(k)=k^2/2m+V_{\mathrm{BHF}}(k;E(k)). \tag{2.16a}$$

The Fermi energy E_F will be identified with $E(k_F)$:

$$E_F=E(k_F) . \tag{2.17}$$

Occasionally, we shall also consider the second-order approximation

$$E^{(2)}(k)=k^2/2m+V_{\mathrm{BHF}}(k;E(k))+V_{(\mathrm{CO})}(k;E(k)), \tag{2.16b}$$

and the renormalized second-order approximation

$$E^{\mathrm{R}}(k)=k^2/2m+V^{\mathrm{R}}_{\mathrm{BHF}}(k;E(k))+V^{\mathrm{R}}_{(\mathrm{CO})}(k;E(k)). \tag{2.18}$$

III. REAL PART OF THE MEAN FIELD

A. Hartree-Fock approximation

The short dashes in Fig. 3 represent the value of the Hartree-Fock approximation

$$\tilde{V}_{(\mathrm{IA})}(k)=\overline{V}_{(\mathrm{IA})}(E(k)) \tag{3.1}$$

to the mean field felt by a quasiparticle with momentum k [and thus with energy $E(k)$]. At the Fermi surface, one has $V_{(\mathrm{IA})}(k)=-50$ MeV. The empirical value of the Fermi energy is

$$\epsilon_F=-16\ \mathrm{MeV} \tag{3.2}$$

for $k_F=1.36\ \mathrm{fm}^{-1}$. This yields the following depth for the quasiparticle potential at the Fermi surface and for $k_F=1.36\ \mathrm{fm}^{-1}$:

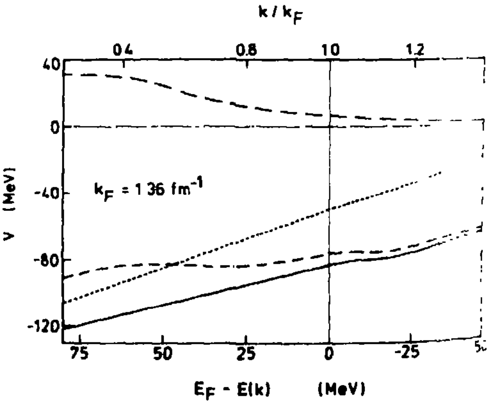

FIG. 3. Dependence upon k/k_F (upper scale) and upon $E_F-E(k)$ (lower scale) of various contributions to the real part $V(k;E(k))$ of the quasiparticle field, in the case of the interaction of Hammann and Ho-Kim and for $k_F=1.36\ \mathrm{fm}^{-1}$. The short dashes represent the Hartree-Fock approximation. The full curve shows the BHF approximation. The long dashes give the correlation contribution. The dash and dots represent the sum of the correlation contribution and of the BHF approximation.

$$V(k_F) = -16 - k_F^2/2m = -54.4 \text{ MeV}. \qquad (3.3)$$

This is in fair agreement with the Hartree-Fock value. However, we shall see in the next sections that this agreement between theory and experiment is spoiled when higher-order contributions are taken into account.

The dependence of the mean field upon the quasiparticle energy is characterized by the effective mass $m^*(E)$, which is defined by the equivalent relations

$$m^*(E)/m = 1 - \frac{d}{dE}\bar{V}(E) \qquad (3.4a)$$

$$= \left[1 + \frac{m}{k}\frac{d}{dk}\tilde{V}(k)\right]^{-1}. \qquad (3.4b)$$

Figure 3 shows that the dependence of $\bar{V}_{(\mathrm{IA})}(E)$ upon E is approximately linear. Hence, the effective mass is almost independent of E in the Hartree-Fock approximation. In the case of the Hammann–Ho-Kim interaction and for $k_F = 1.36$ fm^{-1}, the dotted curve in Fig. 3 yields

$$m^*_{(\mathrm{IA})}(E)/m \approx 0.35 \text{ for } |E - E_F| < 50 \text{ MeV}. \qquad (3.5)$$

The property that the Hartree-Fock approximation yields an effective mass which is almost independent of energy is largely independent of the nature of the nucleon-nucleon interaction. It reflects the static nature of the Hartree-Fock field, i.e., the fact that $V_{(\mathrm{IA})}(k)$ is independent of E. In the case of the interaction of Hammann and Ho-Kim, the value of the effective mass calculated in the Hartree-Fock approximation is particularly small. This is due to the strongly nonlocal nature of the interaction, which has finite rank. This should be kept in mind when comparing the calculated effective mass with the empirical value.

Empirical data will be compared with theory in Sec. III F. Here, we only summarize some of their main features. In the domain $E - E_F > 20$ MeV, the effective mass can be determined accurately by investigating the energy dependence of the real part of the optical-model potential. This yields

$$m^*(E)/m = 0.68 \text{ for } E - E_F > 20 \text{ MeV}. \qquad (3.6)$$

Information on the effective mass near the Fermi energy can be obtained from the density of weakly bound single-particle states. One finds

$$m^*(E)/m \approx 1 \text{ for } |E - E_F| < 10 \text{ MeV}. \qquad (3.7)$$

The value of the effective mass at the bottom of the Fermi sea is poorly known, because the corresponding single-particle states are widely spread. It appears that

$$m^*(E)/m \approx 0.7 \text{ for } E - E_F < -20 \text{ MeV}. \qquad (3.8)$$

Equations (3.6)–(3.8) show that the empirical effective mass is not independent of energy; it has a maximum near the Fermi surface. It has recently been pointed out that this local enhancement should be taken into account when investigating, e.g., the root mean square radius of valence orbits,[15-18] the empirical value of the Landau parameters,[19] the nuclear gyromagnetic ratios,[20] the gravitational collapse of stars,[21] etc. Hence a detailed theoretical investigation of this enhancement is fully justified. Since it is not present in the Hartree-Fock approximation, it requires the investigation of higher-order contributions.

B. Polarization graph

The BHF approximation $V_{\mathrm{BHF}}(k;E(k))$ to the real part of the quasiparticle field is represented by the full curve in Fig. 3, for $k_F = 1.36$ fm^{-1}. At $k = k_F$, one has

$$\tilde{V}_{\mathrm{BHF}}(k_F) \simeq -83 \text{ MeV}; \qquad (3.9)$$

the corresponding approximation to the Fermi energy is

$$E(k_F) = -44.6 \text{ MeV}. \qquad (3.10)$$

These numbers are much larger, in absolute magnitude, than the empirical values given by Eqs. (3.3) and (3.2). This shows that the interaction of Hammann and Ho-Kim is on the average too attractive; we shall have to correct for this when comparing calculated and measured single-particle energies and widths.

The matrix elements of the reaction matrix g are also larger in absolute magnitude than those of bare nucleon-nucleon interaction v, with a typical ratio

$$\langle g \rangle / \langle v \rangle \approx 83/50 = 1.66 \qquad (3.11)$$

for $k_F = 1.36$ fm^{-1}. This shows that the convergence rate of the perturbation expansion is fairly slow. For the simplicity of the discussion, we shall nevertheless assume that the BHF field is well approximated by the sum of graphs (IA) and (IIA) in Fig. 1:

$$V_{\mathrm{BHF}}(k;E) \approx V_{(\mathrm{IA})}(k) + V_{(\mathrm{IIA})}(k;E). \qquad (3.12)$$

Then, the on-shell quantity

$$V_{(\mathrm{IIA})}(k;E(k)) = \tilde{V}_{(\mathrm{IIA})}(k) = \bar{V}_{(\mathrm{IIA})}(E(k)) \qquad (3.13)$$

of the polarization graph is given by the difference between the ordinates of the full and dotted curves in Fig. 3. The resulting value of expression (3.13) is represented by the short dashes in Fig. 4. The attractive nature of $\tilde{V}_{(\mathrm{IIA})}(k)$ for $k < k_F$ directly de-

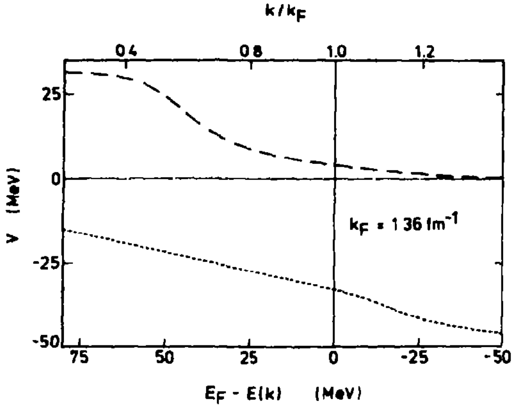

FIG. 4. Dependence upon k/k_F (upper scale) and upon the difference $E_F - E(k)$ (lower scale of the contributions of the polarization graph (short dashes) and of the correlation graph (long dashes) to the potential energy of a quasiparticle, in the case of the interaction of Hammann and Ho-Kim and for $k_F = 1.36\ \mathrm{fm}^{-1}$.

rives from Eq. (2.8). Equivalently, it can be understood on the basis of the dispersion relation

$$V_{(\mathrm{IIA})}(k;E) = \pi^{-1}\mathcal{P}\int_{E_F}^{\infty} \frac{W_{(\mathrm{IIA})}(k;E')}{E-E'}\,dE' , \tag{3.14}$$

and of the fact that

$$W_{(\mathrm{IIA})}(k;E') = 0 \text{ for } E' < E_F , \tag{3.15a}$$

$$W_{(\mathrm{IIA})}(k;E') < 0 \text{ for } E' > E_F . \tag{3.15b}$$

The dependence of $\tilde{V}_{(\mathrm{IIA})}(k)$ upon k can also be characterized by an effective mass, namely

$$m^*_{(\mathrm{IIA})}(E)/m = 1 - \frac{d}{dE}\overline{V}_{(\mathrm{IIA})}(E) \tag{3.16a}$$

$$= \left[1 + \frac{m}{k}\frac{d}{dk}\tilde{V}_{(\mathrm{IIA})}(k)\right]^{-1} . \tag{3.16b}$$

The value of $m^*_{(\mathrm{IIA})}$ is influenced by the dependence of $V_{(\mathrm{IIA})}(k;E)$ upon k on the one hand, and upon E on the other hand. This is exhibited by the following identities, which are also valid for indexed quantities:

$$\frac{m^*(E)}{m} = \frac{\overline{m}(E)}{m}\,\frac{\tilde{m}(E)}{m} , \tag{3.17}$$

where the E mass $m(E)$ is defined by

$$\overline{m}(E(k))/m = \left[1 - \frac{\partial}{\partial E}V(k;E)\right]_{E=E(k)} , \tag{3.18}$$

while the k mass $\tilde{m}(E)$ is given by

$$\tilde{m}(E(k))/m = \left[1 + \frac{m}{k}\frac{\partial}{\partial k}V(k;E)\right]^{-1}_{E=E(k)} . \tag{3.19}$$

We first discuss the dependence of $\overline{m}_{(\mathrm{IIA})}(E)$ upon E. Equation (3.12) shows that

$$\overline{m}_{\mathrm{BHF}}(E) = \overline{m}_{(\mathrm{IIA})}(E) . \tag{3.20}$$

The quantity $\overline{m}_{\mathrm{BHF}}(E)$ is represented by the long dashes in Figs. 5 and 6, for $k_F = 1.36\ \mathrm{fm}^{-1}$ and $1.18\ \mathrm{fm}^{-1}$, respectively. In the domain $E < E_F$, the inequalities

$$\overline{m}_{\mathrm{BHF}}(E) > m, \quad \frac{d}{dE}[\overline{m}_{\mathrm{BHF}}(E)] > 0 \tag{3.21}$$

directly follow from the dispersion relation (3.14), from which one can also find that

$$\left(\frac{d}{dE}[\overline{m}_{\mathrm{BHF}}(E)]\right)_{E=E_F} = +\infty , \tag{3.22}$$

independently of the nature of the nucleon-nucleon interaction. The fact that $\overline{m}_{\mathrm{BHF}}(E)$ becomes equal to the bare mass m at some energy $E_m > E_F$ is also a rather general feature, valid for all interactions for which the dispersion relation (3.14) holds, i.e., in the absence of a hard core. It follows from the fact that $W_{(\mathrm{IIA})}(k;E')$ vanishes for $E' < E_F$ and for $E' \to \infty$. The value of E_m depends on the nature of the interaction. It would be of interest to clarify what are the main properties of the interaction that determine the value of E_m. In the case of the potential of Hammann and Ho-Kim, Figs. 5 and 6 show that $E_m - E_F \approx 30$ MeV. This implies that the width of the peak of $\overline{m}_{\mathrm{BHF}}(E)$ is about 15 MeV.

The results obtained here are similar to those presented in Ref. 5 in the case of Reid's hard core potential. They are more detailed, because the g matrix can be computed more accurately for the interaction of Hammann and Ho-Kim, hence the interest of the present study. We note that the value of $m/\overline{m}_{\mathrm{BHF}}(E_F)$ calculated here is close to the spectroscopic factors recently computed by Birbrair, Alkhazov, Lapina, and Sadovnika[22] and by Bernard and Van Giai[23] for single-particle levels close to the Fermi surface in $^{208}\mathrm{Pb}$.

The value of the BHF approximation to the k mass (3.19) is represented by the short dashes in Figs. 6 and 7. At the Fermi surface, one has

$$\tilde{m}_{\mathrm{BHF}}(E_F)/m = 0.36 \tag{3.23}$$

for $k_F = 1.36\ \mathrm{fm}^{-1}$. This is very close to the value of $m^*_{(\mathrm{IIA})}(E_F)/m = \tilde{m}_{(\mathrm{IIA})}(E_F)/m$ given by Eq. (3.5). Hence the dependence of $V_{(\mathrm{IIA})}(k;E)$ upon k is much smaller than that of $V_{(\mathrm{IIA})}(k)$. This result supports the accuracy of the approximation recently made by Bernard and Nguyen Van Giai,[23] who neglected the dependence upon k of the polarization term (IIA). The value of $\tilde{m}_{\mathrm{BHF}}(E)$ calculated here is approximately 20% smaller than that derived from

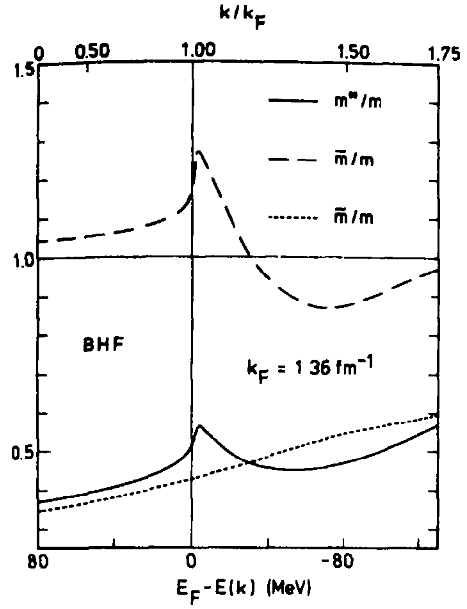

FIG. 5. Dependence upon k/k_F (upper scale) and upon the difference $E_F-E(k)$ (lower scale) of the E mass (long dashes), of the k mass (short dashes), and of the effective mass (full curve), measured in units of the bare mass and evaluated in the framework of the BHF approximation from the interaction of Hammann and Ho-Kim. The value of the Fermi momentum is k_F =1.36 fm^{-1}.

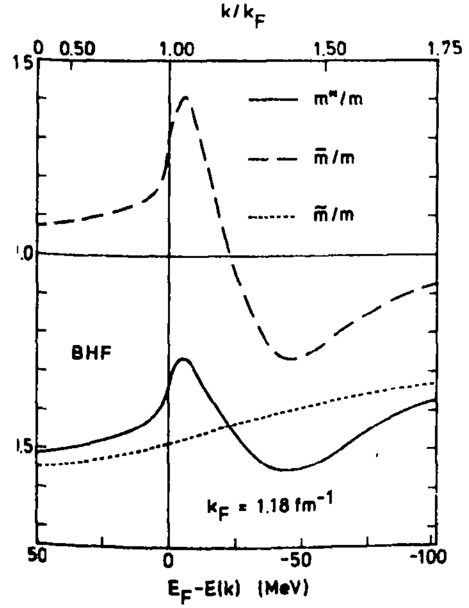

FIG. 6. Same as Fig. 5, for k_F=1.18 fm^{-1}.

Reid's hard core interaction. We argued in Sec. IIIA that this is mainly due to the strongly nonlocal character of the interaction of Hammann and Ho-Kim.

The BHF approximation of the effective mass is obtained from the Eq. (3.17):

$$\frac{m^*_{\rm BHI}(E)}{m}=\frac{\tilde m_{\rm BHI}(E)}{m}\,\frac{\bar m_{\rm BHI}(E)}{m}\,. \qquad (3.24)$$

The value of $m^*_{\rm BHI}(E)/m$ is represented by the full curves in Figs. 5 and 6. The enhancement that it displays near the Fermi surface reflects that of $\bar m_{\rm BHI}(E)$. This feature is in qualitative agreement with the empirical evidence summarized by Eqs. (3.6)–(3.8). However, the calculated value of $m^*_{\rm BHI}(E)$ is too small for all $E(k)$. This is mainly due to the fact that $\tilde m_{\rm BHI}(E)$ is too small in the case of the interaction of Hammann and Ho-Kim.

The fact that the enhancement of $\bar m_{\rm BHI}(E)$ is located near the Fermi surface must be ascribed to the Pauli principle. This is confirmed by the fact that the enhancement also exists in the case of the hard sphere dilute Fermi gas,[8] in which the shape of $\bar m(E)$ is entirely determined by the available phase space for two-particle–one-hole or two-hole–one-particle excitations. The long dashes in Fig. 7 show the value of $\bar m_{\rm BHI}(E)$ in the

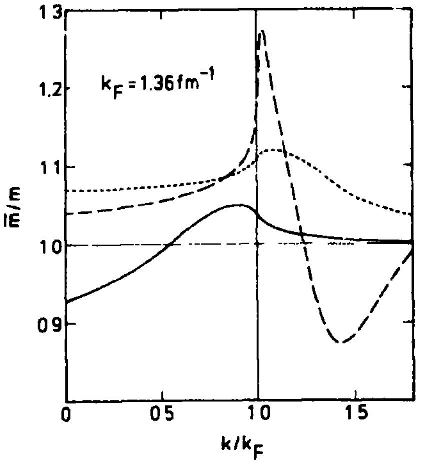

FIG. 7. The long dashes represent the dependence upon k/k_F of $\bar m_{\rm BHF}/m \approx \bar m_{\rm (IIA)}/m$ in the case of the interaction of Hammann and Ho-Kim and for k_F=1.36 fm^{-1}. The other curves correspond to the value that $\bar m/m$ would take in a hard sphere dilute Fermi gas if one would take into account either the analog of the polarization graph (IIA) (short dashes) or the analog of the correlation graph (IIB) (full curves) (Ref. 8). The hard sphere radius has been adjusted to yield the same average depletion of the Fermi sea for the two interactions.

case of the interaction of Hammann and Ho-Kim. The short dashes correspond to the hard sphere dilute Fermi gas,[8] in which the parameter ($k_F c = 0.426$) has been adjusted in such a way as to yield the same average occupation number below the Fermi surface in the correlated ground state as in the case of the interaction of Hammann and Ho-Kim. Here, c refers to the hard sphere radius. The difference between the shape of $\bar{m}_{\rm BHF}(E)$ for the two interactions is quite striking. It exhibits the fact that the narrowness of the enhancement peak is largely determined by the long-range part of the nucleon-nucleon interaction.

For $k_F = 1.36$ fm^{-1}, the effective mass as calculated in the Brueckner-Hartree-Fock approximation decreases by 15% when $E(k) - E_F$ increases from 5 to 25 MeV. The enhancement is more pronounced at low density: For $k_F = 1.18$ fm^{-1}, the effective mass decreases by 40% when $E(k) - E_F$ increases from 5 to 25 MeV. Although the variation of m^* is impressive, its influence on the dependence of $V(k;E(k))$ upon $E(k)$ is barely visible in Figs. 3 and 4. In Fig. 4, the enhancement corresponds to the feature that the slope of $V_{\rm (IIA)}(k;E(k))$ (short dashes) is steeper in the energy interval $0 > E_F - E(k) > -25$ MeV than elsewhere. Correspondingly, the single-particle level density is increased in this energy interval, since it is proportional to the product (km^*).[5] We emphasize that this effect is due to the *variation* of the slope of $V_{\rm (IIA)}(k;E(k))$. If the dependence of this quantity upon $E(k)$ could be approximated by a linear law, the polarization graph would increase the Hartree-Fock single-particle level density by the same amount for all energies.

C. Correlation graph

The expression of the correlation graph (CO) in Fig. 2 is given by Eq. (2.12). Its formal similarity with Eq. (2.9) also justifies our use of the expression "correlation graph" for diagram (IIB) in Fig. 1. However, Eq. (3.11) shows that these two graphs are not equal and that their ratio is approximately given by

$$\frac{M_{\rm (CO)}(k;E)}{M_{\rm (IIB)}(k;E)} \approx (1.66)^2 \simeq 2.75 \,. \qquad (3.25)$$

The on-shell value $V_{\rm (CO)}(k;E(k))$ of the correlation graph in the case of the interaction of Hammann and Ho-Kim has been calculated in Refs. 10 and 11. It is represented by the long dashes in Fig. 4. When added to the BHF approximation, it yields the dash and dots in Fig. 3. The corresponding value of the Fermi momentum is

$$E_F^{(2)} = E_F + V_{\rm (CO)}(k_F;E(k_F)) = -37.6 \text{ MeV} \,.$$

The accuracy of the calculated value of $V_{\rm (CO)}(k;E(k))$ is unfortunately not sufficient to reliably evaluate its derivative, i.e., its influence on the value of the effective mass, nor *a fortiori* its second derivative, i.e., its influence on the energy dependence of the effective mass. From the dispersion relation

$$V_{\rm (CO)}(k;E) = \pi^{-1} \mathcal{P} \int_{-\infty}^{E_F} \frac{W_{\rm (CO)}(k;E')}{E - E'} dE' \,, \qquad (3.26$$

and from the asymptotic behavior for E' close to E_F

$$W_{\rm (CO)}(k;E') \sim (E' - E_F)^2 \qquad (3.27$$

for $k < 3k_F$.[11] It can easily be checked that

$$W_{\rm (CO)}(k;E_F + 0) > 0 \,, \qquad (3.28$$

$$[\partial V_{\rm (CO)}(k;E)/\partial E]_{E > E_F} < 0 \,, \qquad (3.29$$

$$[\partial^2 V_{\rm (CO)}(k;E)/\partial^2 E]_{E = E_F + 0} = \infty \,. \qquad (3.30$$

Inequality (3.29) shows that above the Fermi surface the correlation graph increases the value of the effective mass, as compared to the BHF approximation. The singularities (3.22) and (3.30) cancel one another; the quantity $d\bar{m}(E)/dE$ is therefore finite at $E = E_F$. The hard sphere dilute Fermi gas model suggests that the contribution of the correlation graph to the effective mass essentially amounts to symmetrizing the BHF enhancement peak about E_F, and to increasing its maximum value by about 20%. In the present case, these rough estimates indicate that the enhancement peak of $m^*(E)$ should be almost symmetric about E_F, and that its width at half maximum is approximately equal to 40 MeV. The maximum values would be approximately equal to $m^*(E_F)/m \approx 0.7$ for $k_F = 1.36$ fm^{-1}, and $m^*(E_F)/m \approx 0.9$ for $k_F = 1.18$ fm^{-1}. These are likely to be underestimates of the physical reality, since the k mass $\bar{m}$ is anomalously small in the case of the interaction of Hammann and Ho-Kim.

D. Renormalization corrections

The sum of the graphs (BHF) and (R) in Fig. 2 yields the renormalized BHF approximation (2.13). In Fig. 8, we plot for $k_F = 1.36$ fm^{-1} the renormalized quantities $(1-\kappa)\, V_{\rm HF}(k)$, $V^{\rm R}_{\rm BHF}(k;E(k))$, $V^{\rm R}_{\rm (CO)}(k;E(k))$, and $V^{\rm R}_{\rm BHF}(k;E(k)) + V^{\rm R}_{\rm (CO)}(k;E(k))$ versus the difference $E^{\rm R}_F - E^{\rm R}(k)$, with

$$E^{\rm R}_F = E^{\rm R}(k_F) = -49.5 \text{ MeV} \,. \qquad (3.31$$

As expected from the smallness of κ [Eq. (2.14)], the curves shown in Fig. 8 are quite similar to those which appear in Fig. 3. The main origin of the differences is that the renormalized single-particle energy $E^{\rm R}(k)$ contains the contribu-

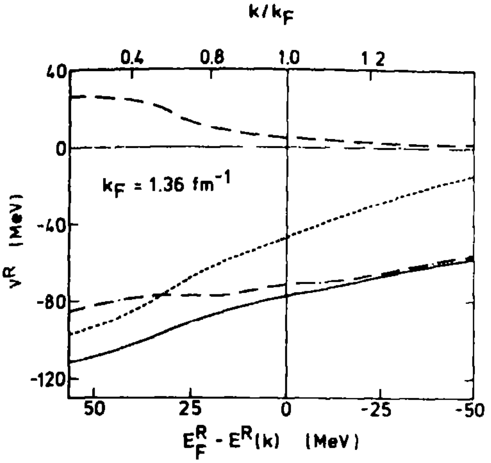

FIG. 8. Dependence upon the difference $E_F^R - E^R(k)$ of the renormalized quantities $(1-\kappa)\, V_{HF}(k)$ (short dashes), $V_{\rm BHF}^R(k; E(k))$ (full curve), $V_{\rm (CO)}^R(k, E(k))$ (long dashes), and $V_{\rm BHF}^R(k;E(k)) + V_{\rm (CO)}^R(k;E(k))$ (dash and dots), for $k_F = 1.36$ fm^{-1} and in the case of the interaction of Hammann and Ho-Kim.

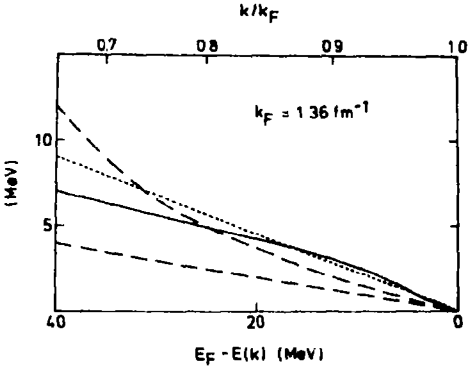

FIG. 9. The quantities (3.32a) and (3.33a) as evaluated by Orland and Schaeffer (Ref. 7) are represented by the full curve and the dash and dots, respectively. The short dashes and the long dashes show the value of (3.32b) and of (3.33b), respectively, for $k_F = 1.36$ fm^{-1} and in the case of the interaction of Hammann and Ho-Kim.

tion of the (renormalized) correlation graph; see Eq. (2.18). In particular, this is responsible for the steep rise of $(1-\kappa)\, V_{\rm HF}$ for $E_F^R - E^R(k) \approx 30$ MeV.

E. Comparision with a dispersion relation approach

Orland and Schaeffer[7] recently evaluated the quantities

$$V_{\rm (IIA)}(k;E) - V_{\rm (IIA)}(k;E_F)\,, \tag{3.32a}$$

and

$$V_{\rm (IIB)}(k;E) - V_{\rm (IIB)}(k;E_F)\,. \tag{3.33a}$$

They used the subtracted dispersion relation (2.6b); see also Eqs. (3.14) and (3.26) where they inserted for $W(k;E')$ algebraic expressions suggested by the hard sphere dilute Fermi gas model. In Fig. 9, we compare their results with the quantities

$$V_{\rm (IIA)}(k;E(k)) - V_{\rm (IIA)}(k_F;E_F)\,, \tag{3.32b}$$

$$V_{\rm (CO)}(k;E(k)) - V_{\rm (CO)}(k_F;E_F)\,, \tag{3.33b}$$

as calculated here from the interaction of Hammann and Ho-Kim. This comparison is legitimate, since Orland and Schaeffer neglected the dependence upon k of the quantities (3.32a) and (3.33a). The overall agreement between the two approaches is fair, despite the fact that both of them suffer from weaknesses. These mainly consist in the parametric expression of $W(k;E')$ used by Orland and Schaeffer on the one hand,[8] and in the finite rank nature of the interaction of Hammann and Ho-Kim on the other hand.

F. Comparison with empirical values

The comparison between our calculated depths and empirical depths can only bear on their energy dependence, since the interaction of Hammann and Ho-Kim yields too much attraction. Accordingly, we shall add to the calculated value of the depth a constant equal to

$$\Delta_{\rm BHF} = \epsilon_F - E_F = 28.6 \text{ MeV} \tag{3.34}$$

in the case of the BHF approximation, and to

$$\Delta_{\rm BHF}^{(2)} = \epsilon_F - E_F^{(2)} = 21.6 \text{ MeV} \tag{3.35}$$

in the case of the sum of the BHF and of the correlation graphs. One should also keep in mind that the empirical depth depends on the geometry adopted for the mean field, and that moreover the interaction of Hammann and Ho-Kim yields a too large value for the nonlocality range. Despite these reservations, a comparison between calculated and empirical depths is useful, in particular, since it offers an opportunity to show to what extent the experimental data indeed exhibit that the effective mass is enhanced near the Fermi surface.

Bear and Hodgson[24] recently fitted the centroid energies of bound single-particle states with a shell-model potential well whose Woods-Saxon geometry was kept fixed, but whose depth was adjusted in order to reproduce each centroid energy. The resulting empirical depths are represented by open dots (protons) and by crosses (neutrons) in Figs. 10 and 11. The vertical bars

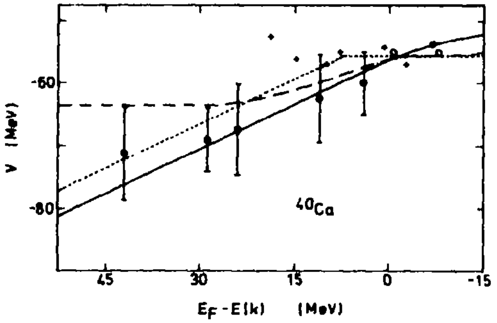

FIG. 10. The dots represent the depth of a Woods-Saxon potential which reproduces the experimental single-particle centroid energy $E(k)$, in the case of ^{40}Ca (Ref. 24). We took $E_F = -8$ MeV. The short dashes show the trend indicated by Bear and Hodgson (Ref. 24). The full curve is the BHF approximation (plus $\Delta_{\rm BHF} = 28.6$ MeV) in the case of nuclear matter with $k_F = 1.36$ fm^{-1} and of the interaction of Hammann and Ho-Kim. The dash and dots correspond to the sum of the BHF approximation and of the correlation term, plus $\Delta^{(2)}_{\rm BHF} = 21.6$ MeV.

indicate the size of the width of the single-particle states. Bear and Hodgson argued that these results suggest the existence of a plateau near the Fermi surface; they accordingly represented this trend by the short dashes, which follow two straight lines. The full curve represents the calculated BHF mean field, plus $\Delta_{\rm BHF} = 28.6$ MeV. The dash and dots corresponds to the sum of the BHF field and of the correlation graph, plus 21.6 MeV.

The overall agreement between calculated and empirical energy dependence is fair. However, several difficulties should be mentioned. Firstly, the empirical depths for proton single-particle states do not exhibit a plateau near the Fermi surface: it is only by combining proton and neutron data that this trend appears. Secondly, the trend is rendered somewhat hazy by the large width of the bound single-particle states. Finally the energies of the single-particle states close to the Fermi surface are particularly sensitive to the nature of the low-lying core excitations in the case of light and medium-light nuclei. Accordingly, one would expect that the existence of a plateau in the energy dependence of the potential depth should be better exhibited in the case of a heavy nucleus and in the framework of a study that encompasses scattering states. In the case of ^{208}Pb, for instance, the experimental single-particle levels close to the Fermi surface are well reproduced by a static and local Woods-Saxon potential ($m^* = m$). The elastic scattering data require $m^* = 0.7$ m for $E > 20$ MeV.[25] Thus, the combination of bound and scattering data clearly shows that m^* is larger near the Fermi surface than at positive energy. The Skyrme-III interaction ($m^*_{\rm III} = 0.75$) yields a satisfactory agreement between the Hartree-Fock approximation and bulk nuclear properties; it is thus probably reliable for most bound single-particle states. However, it yields a too small single-particle level density near the Fermi surface.[26] These features suggest that the enhancement of the empirical effective mass is local.

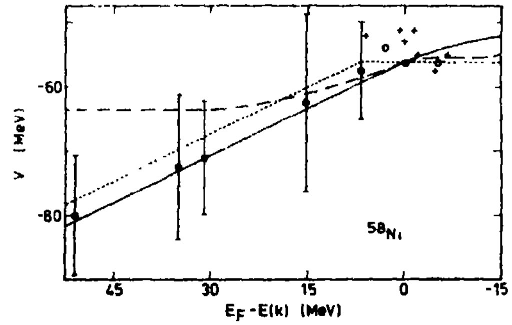

FIG. 11. Same as Fig. 10, in the case of ^{58}Ni.

Giannini, Ricco, and Zucchiatti[27] have recently rendered the energies of bound single-particle states and nucleon elastic scattering data for nuclei ranging from C to Sn. The dots in Fig. 12 represent the corresponding empirical depths. We note that in this compilation, the existence of a plateau near $E(k) = E_F$ is better pronounced than in Figs. 10 and 11, owing to the availability of positive energies $E(k)$. As in Figs. 10 and 11, the full curve and the dash and dots correspond

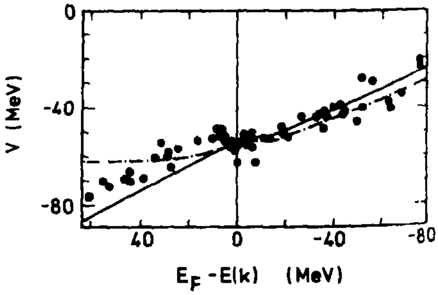

FIG. 12. The dots represent the depth of a Woods-Saxon potential which fits bound single-particle centroid energies $[E(k) < 0]$ or elastic scattering data $[E(k) > 0]$ (Ref. 27). We took $E_F = -8$ MeV. The full curve is the BHF approximation plus $\Delta_{\rm BHF} = 28.6$ MeV, for nuclear matter with $k_F = 1.36$ fm^{-1} and for the interaction of Hammann and Ho-Kim. The dash and dots correspond to the sum of the Brueckner-Hartree-Fock approximation and of the correlation term, plus $\Delta^{(2)}_{\rm BHF} = 21.6$ MeV.

to the BHF and to the BHF + correlation graph approximation, respectively, including the shifts $\Delta_{\rm BHF}$ and $\Delta^{\rm (CO)}_{\rm BHF}$. The comparison with the data indicates that the calculated enhancement of m^* is somewhat too narrow, and that it should, moreover, be centered on E_F rather than somewhat above E_F. As we discussed in Sec. III C, the hard sphere dilute Fermi gas model suggests that these deficiencies would be largely corrected by a better evaluation of the value of the correlation graph in the vicinity of the Fermi surface.

G. Discussion

There exists experimental evidence that the energy dependence of the depth of the single-particle potential is weaker near the Fermi energy than elsewhere. This corresponds to a local enhancement of the effective mass. This cannot be obtained in the framework of a static description like the Hartree-Fock approximation. One must introduce the dynamics of the shell model by taking into account the coupling of the single-particle states to core excitations, and also the blocking of ground state correlations due to the existence of a valence nucleon. The results presented here confirm and extend the conclusions that had been reached in Ref. 5 from the investigation of the Brueckner-Hartree-Fock calculations in the case of Reid's hard core nucleon-nucleon interaction.

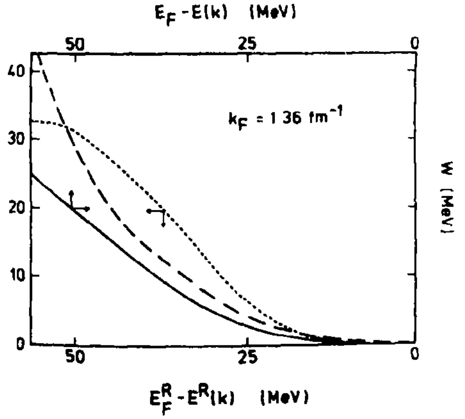

FIG. 13. The full curve (right-hand scale) represents e dependence upon $E_F - E(k)$ (upper scale of the imanary part of the quasiparticle mean field as calculed for $k_F = 1.36\ \mathrm{fm}^{-1}$ from the interaction of Hammann d Ho-Kim and in the framework of the BHF approxiation. The dashed curve (left-hand scale) corresponds the dependence of the renormalized second-order proximation, Eq. (4.3), upon the energy distance to e Fermi energy as calculated from Eq. (2.18). The ng dashes show the result obtained by Orland and haeffer (Ref. 7).

One may wonder whether the finiteness of nuclei strongly influences the local enhancement of the effective mass. Hamamoto and Siemens[28] evaluated the increase of the single-particle level density near the Fermi surface of ^{208}Pb in the framework of a particle-vibration coupling model. They found an enhancement which saturates only very slowly with increasing excitation energy of the vibrations. Thus, it appears rather unlikely that the particle-vibration coupling leads to an increase of m^* that would be confined near the Fermi energy. This suggests that the local enhancement of m^* is mainly due to the coupling of single-particle states to one particle-one hole excitations. This is in keeping with the finding that the local enhancement of m^* exists in the limit $A \to \infty$, i.e., for infinite nuclear matter.[5] We note that the effect of the particle vibration is $O(A^{-2/3})$ while the shell spacing in the independent particle approximation is $O(A^{-1/3})$.[28] Hence, the effect of the particle-vibration coupling vanishes in the limit $A \to \infty$, as expected from the surface nature of the vibrations.

IV. IMAGINARY PART OF THE MEAN FIELD

A. Numerical results

The imaginary part of the mean field felt by a quasiparticle with energy $E(k)$ is given by

$$W(E(k)) = W(k; E(k)). \qquad (4.1)$$

We shall see in Sec. V that in first approximation the corresponding width of the quasiparticle state is given by

$$\Gamma(E(k)) = 2\overline{W}(E(k)). \qquad (4.2)$$

We calculated this quantity from the interaction of Hammann and Ho-Kim. The solid line in Fig. 13 shows the dependence upon the difference $E_F - E(k)$ of the BHF approximation $\overline{W}_{\rm BHF}(E(k))$. In the energy range $|E_F - E(k)| < 50$ MeV, which is of physical interest, our results are quite close to those obtained by Orland and Schaeffer[7] from their dispersion relation approach, and which are represented by the long dashes in Fig. 13. The short dashes correspond to the dependence upon $E^R_F - E^R(k)$, Eq. (2.18), of the renormalized BHF approximation, i.e., of

$$(1-\kappa)^2 W_{\rm BHF}(E(k)). \qquad (4.3)$$

We note that the renormalized approximation lies higher than the BHF approximation despite the reduction factor $(1-\kappa)^2$; this reflects the difference between the two energy scales used in the abscissa to characterize the quasiparticle state.

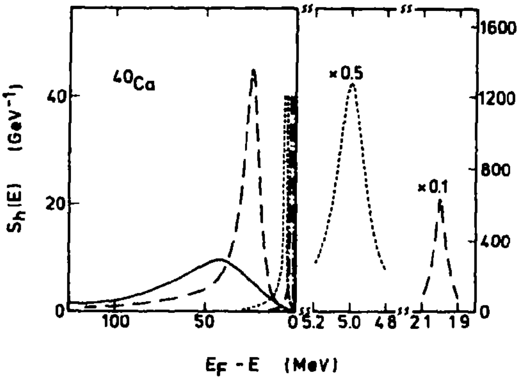

FIG. 18. Spectral functions for single-particle states in ^{40}Ca, as calculated at $k_F = 1.36$ fm^{-1} from Eq. (5.2). The quasiparticle energy $E(k)$ in Eq. (5.2) has been adjusted to the empirical peak energy of the hole states with quantum numbers 1*s* (full curve), 1*p* (long dashes), 1*d* (short dashes), and 2*s* (dash and dots).

have adjusted the quasiparticle energy $E(k)$ in such a way that the difference $E_F - E(k)$ is equal to the empirical value.

In Fig. 17, we show the dependence upon $E_F - E$ of the spectral function $S_h(k;E)$ calculated in this way, with the energy $E(k)$ adjusted to the experimental value of the difference $E_F - E(k)$ for the 1*s* state in the nuclei ^{8}Be, ^{12}C, ^{16}O, and ^{27}Al. We note that the peaks are asymmetric. This is due to the term proportional to $R(k)$ in the numerator on the right-hand side of Eq. (5.2), and reflects the fact that $S_h(k;E_F) = 0$. The width of the peaks increases with increasing binding energy and, correspondingly, their height decreases.

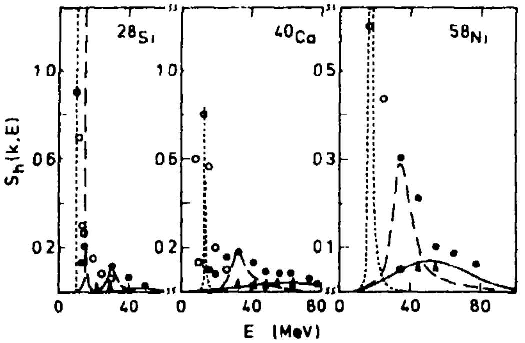

FIG. 19. Comparison between empirical strength functions (Ref. 33) and spectral functions calculated from Eq. (5.2) for $k_F = 1.36$ fm^{-1} ($\rho = 0.17$ nucleons/fm^3). The ordinate scale is in arbitrary units. The peak energy $E(k)$ in Eq. (5.2) has been adjusted to the empirical value for the single-particle states with quantum numbers 1*s* (triangles and continuous curves), 1*p* (full dots and long dashes), and 1*d* (open circles and short dashes). In the case of ^{28}Si, the two dashed curves correspond to the $1p_{3/2}$ and $1p_{1/2}$ levels, respectively.

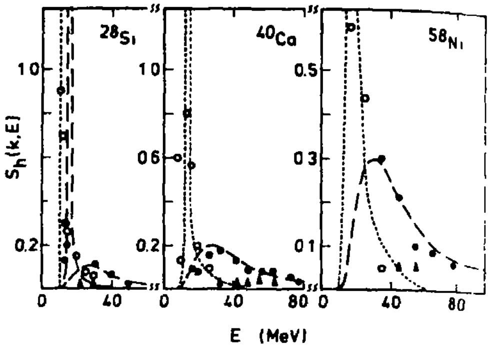

FIG. 20. Same as Fig. 19, for $k_F = 1.18$ fm^{-1} ($\rho = 0.11$ nucleons/fm^3).

In Fig. 18, we plot the spectral function $S_h(k,E)$, as calculated from the right-hand side of Eq. (5.2) in which we adjusted the value of $E(k)$ to the empirical energy of the 1*s*, 1*p*, 1*d*, and 2*s* hole states in ^{40}Ca; we took $k_F = 1.36$ fm^{-1}. These results are compared with empirical data in Fig. 19, where we also show results pertaining to ^{28}Si and ^{58}Ni. The units in the ordinate scale are arbitrary. Since the data do not directly yield the normalized spectral function, we had to attach to the theoretical curves one normalization coefficient, chosen in such a way that the height of the 1*p* peak is in keeping with the empirical value. We note that the agreement between the calculated and the empirical strength distributions is fair in the case of the 1*s* state, but that the calculated peaks are too narrow for the 1*d* and 1*p* levels. This may be partly ascribed to the fact that for these two orbits the mean nuclear density (ρ) is smaller than for the deeply bound 1*s* level. This is illustrated in Fig. 20 where we show the spectral functions calculated as in Fig. 19, but for the Fermi momentum $k_F = 1.18$ fm^{-1}.

VI. DISCUSSION

In the present paper, we studied several properties of the mean single-particle field and of hole state strength functions in nuclear matter and in finite nuclei. The input of our calculation is the semirealistic nucleon-nucleon interaction of Hammann and Ho-Kim.[9] This interaction presents two advantages over a more realistic nucleon-nucleon potential, such as Reid's for instance[34]: (a) Firstly, it is sufficiently soft for enabling one to use a perturbation expansion for the mean field, although the rate of convergence of this expansion is not fast (Sec. III B). Thus, we have been able to display the contributions to the real part of the mean field of the Hartree-Fock term (Sec. III A), of the polarization graph (Sec. III B), and of the correlation graph (Sec. III C). The two latter contributions had not yet been calculated in the case of nuclear matter. We compared our results with those of Orland and Schaeffer[7] (Sec. III E), with empirical potential depths (Sec. III F), and with empirical absorptive potentials (Sec. IV B). (b) Secondly, the interaction of Hammann and Ho-Kim is of finite rank. This allows an accurate calculation of Brueckner's reaction matrix, and enabled us to investigate in detail the energy dependence of the effective mass in the Brueckner-Hartree-Fock approximation (Sec. III B), and the spectral function of hole states (Sec. V).

The interaction of Hammann and Ho-Kim suffers from the following two drawbacks: (a) It is of finite rank, i.e., is highly nonlocal. This leads to an underestimate of the effective mass in the Hartree-Fock approximation (Sec. III A), and more generally to an underestimate of the k mass $\tilde{m}(k)$ [Eq. (3.19)]. (b) The strength of the interaction of Hammann and Ho-Kim is too large. Indeed, the calculated Fermi energy is larger in absolute magnitude than the empirical value when calculated in the Brueckner-Hartree-Fock approximation.

We argued that the advantages overshadow the drawbacks. However, the latter must be kept in mind, and if possible corrected for, when comparing calculated and empirical values (Secs. III F, IV B, and V). This comparison is semiquantitatively satisfactory, if one adopts a suggestion due to Orland and Schaeffer[7] for mapping nuclear matter values onto finite nuclei properties. These authors proposed to identify in the two cases the difference between the Fermi energy and the quasiparticle energy. This prescription amounts to acribing a major role to the phase space available for the decay of the scattering state. Moreover, it largely corrects the error introduced by drawback (b) above.

This work was supported by the Institut Interuniversitaire des Sciences Nucléaires, Belgium.

---

[1] H. A. Bethe, Annu. Rev. Nucl. Sci. 21, 93 (1971).

[2] L. D. Landau, Sov. Phys.—JETP 8, 70 (1959).

[3] A. B. Migdal, *Theory of Finite Fermi Systems and Applications to Atomic Nuclei* (Interscience, New York, 1967).

[4] G. E. Brown, Rev. Mod. Phys. 43, 1 (1971).

[5] J. P. Jeukenne, A. Lejeune, and C. Mahaux, Phys. Rep. 25C, 83 (1976).

[6] G. F. Bertsch and T. T. S. Kuo, Nucl. Phys. A112, 204 (1968).

[7] H. Orland and R. Schaeffer, Nucl. Phys. A299, 442 (1978).

[8] R. Sartor and C. Mahaux, Phys. Rev. C 21, 1546 (1980).

[9] T. F. Hammann and Q. Ho-Kim, Nuovo Cimento 64B, 356 (1969); 14A, 633(E) (1973).

[10] R. Sartor, Nucl. Phys. A267, 29 (1976).

[11] R. Sartor, Nucl. Phys. A289, 329 (1977).

[12] H. S. Köhler, Nucl. Phys. 88, 529 (1966).

[13] G. E. Brown, J. H. Gunn, and P. Gould, Nucl. Phys. 46, 598 (1963).

[14] C. A. Engelbrecht and H. A. Weidenmüller, Nucl. Phys. A184, 385 (1972).

[15] B. Castel and K. Goeke, Phys. Lett. 82B, 160 (1979).

[16] L. Zamick, in *Common Problems in Low- and Medium-Energy Nuclear Physics*, edited by B. Castel, B. Goulard, and F. C. Khanna (Plenum, New York, 1979), p. 397.

[17] A. Lejeune and C. Mahaux, in *What do we know about the Radial Shape of Nuclei in the Ca-Region?* edited by H. Rebel, H. J. Gils, and G. Schatz (Kernforschungszentrum Karlsruhe GmBH, Karlsruhe, 1979).

[18] A. Lejuene, private communication.

[19] G. E. Brown, J. S. Dehesa, and J. Speth, Nucl. Phys. A330, 290 (1979).

[20] G. E. Brown and M. Rho, Nucl. Phys. (to be published).

[21] H. A. Bethe, G. E. Brown, J. Applegate, and J. M. Lattimer, Nucl. Phys. A324, 487 (1979).

[22] B. L. Birbrair, G. D. Alkhazov, L. P. Lapina, and V. A. Sadovnikova, Yad. Fiz. 28, 625 (1978) [Sov. J. Nucl. Phys. 28, 321 (1978)].

[23] Nguyen Van Giai, in Proceedings of the 77th Enrico Fermi Summer School (to be published); V. Bernard and Nguyen Van Giai, private communication.

[24] K. Bear and P. E. Hodgson, J. Phys. G 4, L287 (1978).

[25] J. P. Jeukenne, A. Lejeune, and C. Mahaux, Phys. Rev. C 16, 80 (1977).

[26] M. Beiner, H. Flocard, Nguyen Van Giai, and P. Quentin, Nucl. Phys. A238, 29 (1975).

[27] M. M. Giannini, G. Ricco, and A. Zucchiatti, Ann. Phys. (N.Y.) 124, 208 (1980).

[28] I. Hamamoto and P. Siemens, Nucl. Phys. A269, 199 (1976).

[29] P. Doll, G. J. Wagner, K. T. Knöpfle, and G. Mairle, Nucl. Phys. A263, 210 (1976).

[30] G. Jacob and T. A. J. Maris, Rev. Mod. Phys. 45, 6 (1973).

[31] T. A. Hughes, S. Fallieros, and B. Goulard, Nuclei and Particles 1, 93 (1971).

[32] Q. Ho-Kim, unpublished, quoted in Ref. 31.

[33] J. Mougey, M. Bernheim, A. Bussière, A. Gillebert, Phan Xuan Hô, M. Priou, D. Royer, I. Sick, and G. J. Wagner, Nucl. Phys. A262, 461 (1976).

[34] J. Mougey, J. Phys. Soc. Jpn. 44, Suppl., 420 (1978).

[35] R. V. Reid, Ann. Phys. (N.Y.) 50, 411 (1968).

PHYSICAL REVIEW C VOLUME 21, NUMBER 6 JUNE 1980

Short-range correlations and the nuclear momentum density distribution for ^{16}O

J. W. Van Orden, W. Truex, and M. K. Banerjee
Department of Physics and Astronomy, University of Maryland, College Park, Maryland 20742

(Received 19 November 1979)

The leading-order correlation corrections to the independent particle shell model momentum density distribution for ^{16}O are calculated using the Brueckner theory of finite nuclei. The Pauli corrected defect functions are calculated using Reid soft core B and de Tourreil-Sprung interaction potentials with harmonic oscillator starting wave functions and experimental shell model starting energies. The short-range correlations are found to modify significantly the independent particle shell model momentum density distribution for low momenta and to dominate it for high momenta. Comments are made concerning the selection of ground state nuclear wave functions for calculating quasielastic scattering processes.

[NUCLEAR STRUCTURE ^{16}O, calculated momentum density distribution. Brueckner method finite nuclei; Reid soft core, Sprang potentials used.]

The experiments of Frankel *et al.*[1] with 180° proton production from quasielastic proton-nucleus scattering have stimulated interest in the nuclear momentum density distribution. A simplified calculation of this process which is roughly dependent upon the nuclear momentum distribution has been used in an attempt to extract this distribution from the data.[2]

As a result of this interest in the momentum distribution, Zabolitzky and Ey[3] have produced theoretical calculations of the momentum density distribution using the coupled-cluster or exp(S) form of many-body theory[4] in the generalized Brueckner-Hartree-Fock approximation. The calculations in Ref. 3 show that the momentum distribution is dominated by two-nucleon correlation contributions at momenta greater than 2 fm^{-1}. This suggests the value of an experimental determination of the nuclear momentum distribution as a possible means of studying two-body correlations. Therefore, it is necessary to perform more realistic calculations of 180° proton production or similar processes such as quasielastic electron scattering in order to determine whether it is possible to obtain the nuclear momentum distribution, or comparable information concerning nuclear correlations, from such experiments.

With this eventual object in mind, we will present first the simpler approach of the Brueckner theory of finite nuclei[5] to introduce two-nucleon correlations. This approach will be used to calculate the momentum density distributions for ^{16}O using Reid soft core B and de Tourreil-Sprung potentials. These will be shown to be essentially equivalent to those of Ref. 3. We will then make use of the momentum distributions to discuss whether it is necessary to use more realistic single-nucleon ground state wave functions such as those due to a Woods-Saxon potential.

We define the momentum density distribution $n(p)$ with the following normalization:

$$A=\frac{1}{(2\pi)^3}\int d^3p\, n(p)\,, \tag{1}$$

where A is the total number of nucleons.

Using the Brueckner theory for finite nuclei, the nuclear momentum density distribution including the lowest-order two-nucleon correlation corrections is represented by the Goldstone diagrams of Figs. 1(a)–(e), where the cross repre-

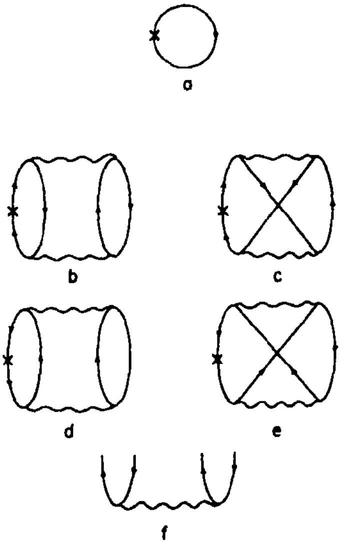

FIG. 1. Goldstone diagrams representing momentum density distribution with lowest order two-nucleon correlation corrections.

© 1980 The American Physical Society

sents the nonlocal operator $e^{i\vec{k}\cdot(\vec{r}\,'-\vec{r})}$, the wavy lines represent the two-nucleon interaction resulting from the sum of ladder diagrams, and the upward and downward pointing arrows represent particles and holes, respectively.

Diagram 1(a) represents the independent particle shell-model result for the momentum distribution while diagrams 1(b)–1(e) represent the lowest-order two-nucleon correlation corrections to the momentum density. Diagrams 1(d) and 1(e) serve to renormalize diagram 1(a) such that the total number of nucleons remains unchanged by the introduction of correlations. The actual calculation of these diagrams can be simplified by recognizing that the parts of each of the diagrams 1(b)–1(e) corresponding to Fig. 1(f) represent the two-nucleon defect function which is defined as the difference between the Brueckner-Hartree-Fock (BHF) pair wave function and the exact, correlated pair wave function. The defect function can be determined from the equation

$$|\chi\rangle = |\phi\rangle - |\psi\rangle = -\frac{Q}{\omega - H_0} V|\psi\rangle\,, \tag{2}$$

where $|\psi\rangle$ and $|\phi\rangle$ are the exact and BHF two-nucleon wave functions, V is the interaction potential, H_0 is the BHF Hamiltonian, ω is the energy of the two-nucleon propagator, and Q is the Pauli operator.

The evaluation of Eq. (2) is simplified in this work by introducing several approximations. The most important of these is the replacement of the BHF wave functions by harmonic oscillator ground state wave functions where the oscillator parameter is chosen to provide a good fit to the low momentum ($\leq$400 MeV) portion of the elastic charge form factor. This eliminates the problem of actually finding solutions to the self-consistent BHF equations. Such solutions do not always give accurate binding energies and do not always provide a good description of the elastic charge form factor.[3,4,6] A more practical consideration is the obvious convenience of having an analytical expression for these wave functions and of being able to separate exactly pair wave functions into relative and center-of-mass factors by means of Moshinsky brackets. The additional approximations are made that the experimental shell-model binding energies are substituted for the eigenvalues of H_0 in Eq. (2), and that the Pauli operator Q is treated in the Eden-Emery approximation.

Using the above approximations, Eq. (2) is solved in coordinate space for both the Reid soft core B and de Tourreil-Sprung supersoft core potentials. The momentum distribution for ^{16}O is calculated using the momentum space Fourier transform of the defect function corresponding to each potential. The accuracy of these calculations is tested by computing the norm of the defect functions calculated in both coordinate and momentum spaces, and by verifying that Eq. (1) is satisfied for each distribution. The resulting momentum distributions for ^{16}O are shown in Figs. 2 and 3 where line A represents the correlated distribution using the Reid potential, and line B is the correlated distribution using the Sprung potential. Line C is the IPSM harmonic oscillator momentum distribution and line D is the IPSM Woods-Saxon momentum distribution. Distributions A, B, and C have been corrected for spurious center-of-mass motion as in Ref. 3. Calculation of such a correction for the Woods-Saxon distribution is considerably more complicated

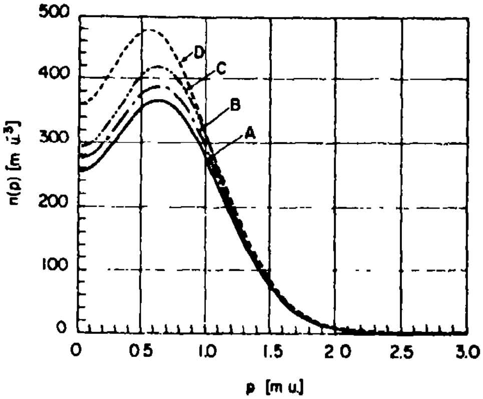

FIG. 2. Momentum density distribution for ^{16}O: 1 m.u. = $m_\pi c$ = 139.57 MeV.

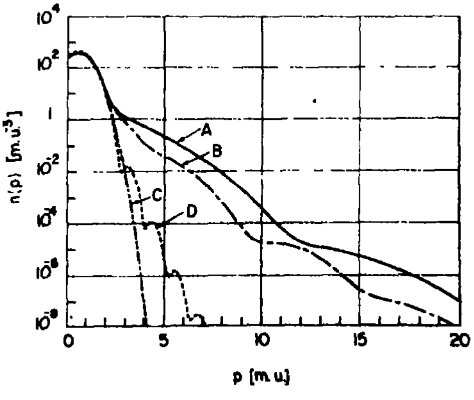

FIG. 3. Momentum density distribution for ^{16}O.

than for the distributions A through C, and is beyond the scope of this paper. For this reason the Woods-Saxon distribution (D) does not include corrections for spurious center-of-mass motion and is included only for the purpose of comparison with C. The momentum distributions displayed in Figs. 2 and 3 are in good agreement with the corresponding distributions in Ref. 3.

At low momenta the primary effect of the correlation is the renormalization of the IPSM distribution (C). At a momentum of approximately 2 mesic units (m.u., 1 m.u. $= m_\pi c = 139.57$ MeV) the correlated distributions (A and B) become larger than the uncorrelated distribution (C). At a momentum of 3 mesic units the correlated distributions are almost an order of magnitude larger than the uncorrelated distribution. At small momenta the Sprung distribution (B) is larger than the Reid distribution (A) and is smaller than the Reid distribution at large momenta, as would be expected.

It is interesting to consider the IPSM Woods-Saxon distribution (D). This distribution is larger at low momenta (less than 1 m.u.) than the harmonic oscillator distribution (C) since the Woods-Saxon potential is broader than the harmonic oscillator potential. As the momentum increases above 1 m.u. the harmonic oscillator distribution becomes larger than the Woods-Saxon distribution. At approximately 3 m.u. the Woods-Saxon distribution begins to show the oscillatory behavior which reflects the range parameter of the Woods-Saxon potential,[7] and again becomes larger than the harmonic oscillator distribution at approximately 4 m.u. Examination of Fig. 3 shows the essentially exponential falloff of the Woods-Saxon density as opposed to the much more rapid Gaussian falloff of the harmonic oscillator density. The high momentum behavior of the Woods-Saxon wave functions is often considered to be more realistic than that of the harmonic oscillator wave function. However, at momenta above 2 m.u. the Woods-Saxon density (D) is much smaller than the correlated densities (A and B). The slower falloff and extra structure of the Woods-Saxon wave functions at large momenta is totally obscured by the two-nucleon correlations. Therefore, for processes which are roughly dependent upon the ground state momentum distribution, such as quasielastic proton or electron scattering, the ground state may be well described by harmonic oscillator wave functions and two-nucleon correlations.

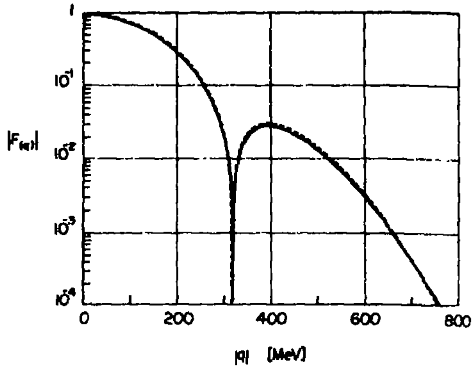

FIG. 4. Elastic charge form factor for ^{16}O.

The effect of correlations is quite different in the case of the elastic charge form factor than in the case of the momentum distribution. Figure 4 shows the elastic charge form factor for ^{16}O as calculated using the harmonic oscillator wave functions with (solid line) and without (dashed line) correlations. The correlations are included by evaluating a set of diagrams similar to Figs. 1(a)–1(e) where the cross represents the local operator $e^{i\vec{q}\cdot\vec{r}}$. Clearly in this case the inclusion of two-nucleon correlations results in negligible change to the elastic charge form factor. This tends to justify our use of the form factor as a means of selecting the oscillator parameter. Zabolitzky and Ey[3] argue that the form factor is relatively insensitive to correlations since it is a measure of density fluctuations whereas the momentum density distribution is a measure of density correlations and is therefore much more sensitive to the inclusion of correlations.

In summary, we make the following conclusions:

(1) The simplified approach of Brueckner theory used in this paper provides a good description of the nuclear momentum density distributions. These distributions are in good agreement with those calculated in Ref. 3, using the much more complicated exp(S) method.

(2) At momenta less than 3 mesic units the renormalized single-particle momentum distribution dominates, whereas at momenta greater than 3 mesic units the correlation contributions to the momentum distribution dominate.

(3) Since correlation contributions dominate the momentum distribution at momenta greater than 3 mesic units, the high momentum behavior of the Woods-Saxon distribution is totally obscured by the correlations. Therefore, for processes which are roughly dependent upon the ground state momentum distribution, such as quasielastic proton or electron scattering, the ground state may be well described by harmonic oscillator wave functions and two-nucleon correlations.

(4) Since the elastic charge form factor is in-

sensitive to correlations, single-particle ground state wave functions may be selected by fitting the lower momentum ($|q| \lesssim 400$ MeV) portion of the elastic charge form factor.

The authors wish to acknowledge the support of the U. S. Department of Energy and the University of Maryland Computer Science Center for this work.

---

[1] S. Frankel *et al.*, Phys. Rev. Lett. 36, 642 (1976).

[2] R. D. Amado and R. M. Woloshyn, Phys. Rev. Lett. 36, 1435 (1976).

[3] J. G. Zabolitzky and W. Ey, Phys. Lett. 76B, 527 (1978).

[4] J. G. Zabolitzky, Nucl. Phys. A228, 272 (1974).

[5] M. Baranger, *Proceedings of the International School of Physics "Enrico Fermi," Vol. 40*, Varena, Italy (Academic, New York, 1969), p. 511.

[6] M. Gari, H. Hyuga, and J. G. Zabolitzky, Nucl. Phys. A271, 365 (1976).

[7] The oscillatory behavior of line D in Fig. 3 reflects the well radius of the Woods-Saxon potential. The oscillations have a periodicity of 2π/(well radius). A well radius of 2.68 m.u. was used in the calculation displayed in Figs. 2 and 3.

PHYSICAL REVIEW C VOLUME 21, NUMBER 6 JUNE 1980

Use of the boson-expansion theory for the description of collective nuclei

K. J. Weeks and T. Tamura
Department of Physics, University of Texas, Austin, Texas 78712

(Received 26 December 1979)

A clear understanding of how to construct the boson expansion of a collective fermion pair operator is given. The criteria for the applicability of the procedure are also discussed. Following this prescription, the Pauli-principle violation is made negligible for the low-lying states of collective nuclei.

[NUCLEAR STRUCTURE Boson expansion; criteria for truncation and convergence; collective motions.]

I. INTRODUCTION

In the past several years, we have been using the Belyaev-Zelevinsky[1] type boson-expansion theory (BET) as a tool for describing states arising from quadrupole vibrations and/or deformations in even-even nuclei.[2-6] The first paper[2] and a part of the second paper[3] in this series dealt with the formal aspects of the problem along the lines developed earlier by Sorensen,[7] with a few key improvements. Succeeding papers were mostly of an application-minded nature. In Ref. 4, extension of BET to a higher order (sixth) was made to show the convergence *per se*. This convergence, i.e., the possibility of truncating the series expansion, was verified numerically and was seen to hold consistently in later applications.

Recently, Silvestre-Brac and Piepenbring[8] followed the prescription of Ref. 2, in treating the $K=0^+$ bands of deformed nuclei, and claimed that the boson expansion breaks down. Our most recent applications,[4-6] however, are based on a somewhat different understanding of the boson expansion[6] than in Ref. 2. The purpose of the present paper is to clarify, first, the difference in understanding between Refs. 2 and 6, and then show that the use of the latter is more correct for practical applications of BET. Discussion will also be presented on how the boson expansion should, in fact, be made and what are its limits. It will become clear why the problem, pointed out by Silvestre-Brac and Piepenbring, was not encountered in our applications,[4-6] and why it will probably disappear in their application as well, if they switch to the newer understanding of Ref. 6.

II. BRIEF SUMMARY OF THE BOSON EXPANSION METHOD

We begin by recapitulating a few formulas of Ref. 2. As done there, we first define the two-quasiparticle-pair operators which are needed:

$$B^\dagger_{\beta\lambda\mu}=\sum_{j_1<j_2} D_{j_1j_2}^{-1}\,\psi^{\beta}_{j_1j_2\lambda}[\alpha^\dagger_{j_1}\alpha^\dagger_{j_2}]_{\lambda\mu}\,, \tag{1}$$

$$C^\dagger_{j_1j_2 2\mu}=[\alpha^\dagger_{j_1}\alpha_{\tilde{j}_2}]_{2\mu}\,, \tag{2}$$

where

$$D_{j_1j_2}=(1+\delta_{j_1j_2})^{1/2}\,. \tag{3}$$

Here $\alpha^\dagger_{jm}$ is a quasiparticle fermion creation operator and $\psi^{\beta}_{j_1j_2\lambda}$ is an element of some $N\times N$ unitary matrix, where N is the number of ways to couple two of the quasiparticle states to an angular momentum λ, as denoted by square brackets in Eqs. (1) and (2). In practice this matrix is chosen to be the result of a Tamm-Dancoff calculation, which results in a single collective mode and $N-1$ noncollective modes.[2,9] Using the abbreviated notation $a=\{\alpha\lambda\mu\}$ and $p=\{j_1j_2kq\}$, we may summarize the commutation relations between fermion operators as[2]

$$[B_a,B^\dagger_b]=\delta_{ab}-\sum_p P^p_{ab}C^\dagger_p\,, \tag{4a}$$

$$[C^\dagger_p,B^\dagger_a]=\sum_b P^p_{ab}B^\dagger_b\,, \tag{4b}$$

$$P^p_{ab}=\hat{\lambda}_a\hat{\lambda}_b(\bar{\lambda}_a\bar{\mu}_a\lambda_b\mu_b|kq)\times\sum_j \psi^{\alpha}_{jj_2\lambda_a}\psi^{\beta}_{j_1j\lambda_b}W(j_2j_1\lambda_a\lambda_b;kj)D_{j_1j}D_{j_2j}\,. \tag{5}$$

See Ref. 2 for more details of notation.

In order to convert a fermion Hamiltonian, which may be written as products of the $B^\dagger$ and $C^\dagger$ operators, into boson expanded form, we begin by writing series expressions for the fermion pair operators as

$$B^\dagger_a=xA^\dagger_a+\sum_{bcd}X_3(abc\bar{d})A^\dagger_bA^\dagger_cA_d+\sum_{bcdef}X_5(abcd\bar{e}\bar{f})A^\dagger_bA^\dagger_cA^\dagger_dA_eA_f+\cdots\,, \tag{6a}$$

$$C_p^\dagger = X_0(p) + \sum_{ab} X_2(p, a\bar{b}) A_a^\dagger A_b + \sum_{abcd} X_4(p, ab\bar{c}\bar{d}) A_a^\dagger A_b^\dagger A_c A_d + \cdots , \qquad (6b)$$

in terms of boson operators A and $A^\dagger$ that satisfy

$$[A_a, A_b^\dagger] = \delta_{ab} . \qquad (7)$$

By substituting $B^\dagger$ and $C^\dagger$ of (6) into (4), the latter becomes a set of equations for the expansion coefficients X, which can be solved analytically.[2]

One nice property found[2,7] is that

$$X_0 = \tfrac{1}{2}\hat{j}_1 \delta_{j_1 j_2} \delta_{\mu 0}(1 - x^2), \quad X_2(p; ab) = P^{p}_{ba} ,$$
$$X_4 = X_6 = \cdots = 0 , \qquad (8)$$

i.e., that $C^\dagger$ has a finite expansion. The general forms for X_3 and X_5 are given as

$$X_3(abc\bar{d}) = r(\delta_{ab}\delta_{cd} + \delta_{ac}\delta_{bd}) + sY(abcd) , \qquad (9a)$$

$$X_5(abcd; \bar{e}\bar{f}) = u\Delta_{\delta\delta}(abcdef) + v\Delta_{\delta Y}(abcdef) + w\Delta_{YY}(abcdef) , \qquad (9b)$$

where

$$Y(abcd) = \sum_p P^{p}_{ab} P^{p}_{\bar{c}d} ,$$
$$\Delta_{\delta\delta}(abcdef) = P_{bcd}(\delta_{ab}\delta_{ce}\delta_{df} + \delta_{ab}\delta_{cf}\delta_{de}) ,$$
$$\Delta_{\delta Y}(abcdef) = P\delta_{ab} Y(cefd) , \qquad (10)$$
$$\Delta_{YY}(abcdef) = P\sum_g Y(abge)Y(cfgd) ,$$

with

$$P = P_{bcd} P_{aef} \qquad (11)$$
$$P_{aef} = 1 + P_{ae} + P_{af} \quad P_{bcd} = 1 + P_{bc} + P_{bd} .$$

The operator P_{ab} exchanges the indices a and b.

The coefficients r, s, u, v, and w in (9) can be expressed[2] in terms of x. One can then substitute the boson expansion series, (6), into the Hamiltonian. This gives an infinite boson Hamiltonian defined on the boson space spanned by all states of the form

$$|B\rangle = (A_{a_1}^\dagger)^{n_1}(A_{a_2}^\dagger)^{n_2} \cdots (A_{a_K}^\dagger)^{n_K} |0\rangle_B ,$$

where K is the number of multipoles possible, and $a_1, \ldots, a_K$ distinguish between different modes of each multipole. The solution of such a problem would yield exactly the same answers as the original fermion problem, but obviously is even harder to solve. One realizes then that some truncation is necessary. If one begins truncation at this stage, however, then one has begun too late, and it is at this juncture that the prescription given in Ref. 2 could have been misleading.

III. TRUNCATION OF THE BOSON EXPANSION

In our applications[3-8] of BET, we intended to describe the properties of the positive parity low-lying states of even-even nuclei, which show collective quadrupole behavior. In practice, we may restrict ourselves to only a few modes of excitation, and describe many of the low-lying states of nuclei as superpositions of these modes. Whether or not this ansatz allows us to describe data, is shown *a posteriori* by comparing the obtained results with experiment.

Before continuing, we clarify why the fermion pairs must be expanded in a possibly infinite number of boson terms. The answer is the need to satisfy the Pauli principle and this becomes clear if one considers the following example. Let a given fermion state be denoted by $|F\rangle$. Suppose that this state definitely (with occupation probability of unity) contains two quasiparticles in the single-particle states $(j_1 m)$ and $(j_2 \text{-} m)$. Now consider a state $[\alpha_{j_1}^\dagger \alpha_{j_2}^\dagger]_{2\mu} |F\rangle$. By the Pauli principle, this expression contains some terms which vanish; e.g., for $\mu = 0$ and $j_1 \leq j_2$, one term out of $2j_1 + 1$ vanishes. Now the state $|F\rangle$ must have a counterpart (or image) in the boson space of the form $|B\rangle$, as given above. If we let only a single boson term represent the pure configuration $[\alpha_{j_1}^\dagger \alpha_{j_2}^\dagger]_{2\mu}$, i.e., consider only the first term of (6a), then when we construct $A^\dagger |B\rangle$, we find that the cancellation of Pauli-principle violating amplitudes does not take place. Thus, in some cases, the operation of $A^\dagger$ results in a state which has components violating the Pauli principle. It is the succeeding terms of Eq. (6a) which check the fermion content of $|B\rangle$ and cancel out any Pauli-principle violating terms. Thus the expansion is necessary to strictly satisfy the Pauli principle.

The above example hints at why it is inadvisable to boson expand pure fermion pair states such as $[\alpha_{j_1}^\dagger \alpha_{j_2}^\dagger]$. Things can go bad very quickly if one does not expand to very high order. The interested reader is referred to the work of Marshalek.[10]

We now return to the question of truncation which comes into our discussion in two ways. To discuss the first, we will begin with Eq. (6). We consider the $\lambda = 2$ collective solution of the Tamm-Dancoff problem. It defines a fermion operator $B_{\text{coll}}^\dagger$ of physical interest, the other $B^\dagger$ operators corresponding to excitations which lie at or above twice the energy gap.[9] In the summations in Eq. (6) over all different bosons, we will restrict ourselves to the above $\lambda = 2$ boson which has the collective nature. Thus the expressions to be substituted into Eq. (4) are those in Eq. (6), but with the indices $a, b, \ldots,$ subject to the restrictions that $\alpha = \beta = \cdots = \text{coll}$, and $\lambda_a = \lambda_b = \cdots = 2$. Thus the summations in fact disappear. The solutions, for the coefficients which define the X_n, are then easily found to be[4,6]

$$r = 0, \quad s \simeq -1/(4x), \quad u = v = 0, \quad w \simeq -s^2/(18x), \tag{12}$$

with the results for the coefficients of $C^\dagger$ unchanged from Eq. (8).

In (12), the relation $r = u = v = 0$ is exact, while the expressions for s and w are approximate. They can be used for practical calculations since they are obtained by neglecting terms which have been found to add corrections to these expressions of a few percent which subsequently have been seen to have virtually no effect on the final energies or wave functions in practical cases. The result that $r = 0$ eliminates large terms which appear in the Hamiltonian when the expression of Ref. 2 is used, i.e., when we set

$$r = [2(x^2 - 1)^{1/2} + (x^2 + 2)^{1/2} - 3x]/6 . \tag{13}$$

The danger of the r term is more evident if one notes the following. Instead of just retaining the collective mode with $\lambda = 2$, suppose we start picking up more modes, one by one, and repeatedly resolve the commutation relations for $B^\dagger$ and $C^\dagger$. One finds that $r = u = v = 0$ is exactly true continually, until one has decided to pick up all possible modes of every single multipole. Then, and only then, r changes discontinuously from 0 to that expression given in Eq. (13). Note that during this procedure, s and w are deviating a little bit from their simple form in Eq. (12), but that presents no problem or trouble in the calculations. At this final stage, the other problem that the expressions given in Ref. 2 for u, v, and w, demand $x^2 \geqslant 2$ and so on, also reappear.[2,8]

One may wonder what roles the terms in (9) play in the full general calculation. For this purpose we give a diagrammatic representation of the quadrupole collective operator $B^\dagger_{\text{coll}}$ in Fig. 1. The smooth lines represent single bosons while the dotted lines represent the quasiparticles. From Fig. 1 and Eq. (6), we see that the first diagram describes or creates the boson excitation of collective nature. The third diagram (s term) checks the fermion nature of all single bosons present in the basis state or sample boson state $|B\rangle$ and adds a correction (subtraction) according to the nature of the bosons in $|B\rangle$. Similarly, the sixth diagram (w term) checks the fermion nature of all possible boson pairs and makes corrections. The second diagram (r term) does not check anything as regards the fermion content of the bosons in the sample state. It picks out and counts all the bosons that are already present in the sample boson state and excites the collective boson onto that state. The purpose of this term in the most general case (of Ref. 2) is to effectively renormalize the coefficient of the linear boson operator, to account for higher order corrections to the Pauli principle, which because of indice permutations and contractions come in with large coefficients. If, by the physics of the problem, one knows that one does not desire to consider all possible multipoles of bosons as well as all possible modes of these multipoles, then it is incorrect to include these r, u, and v coefficients in a truncated calculation; they are necessary to preserve the Pauli principle only when all the fermion operators are to be handled. As an aside, we see that the vanishing of the r, u, and v coefficients in the truncated problem can be expressed, in the language of this diagrammatic representation, by saying that we ignore unconnected diagrams in Fig. 1.

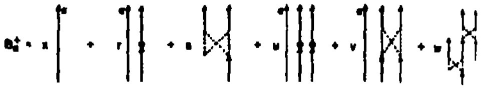

FIG. 1. *First six terms of a diagrammatic expansion of the fermion pair operator* $B_i^\dagger$ *(i labels all quantum numbers). Smooth (dotted) lines represent bosons (quasiparticles). Permutation of indices in the* r, s, v, *and* w *terms and summations over all quasiparticle pair components of the bosons are omitted from the figure for clarity.*

Once we recognize that the unconnected diagrams are to be omitted in a realistic calculation, we may put the boson series in a more convenient form, and we begin to prepare for the second aspect of our truncation problem. We let ξ represent the diagram in the s term of Fig. 1. We will consider all boson lines to be collective bosons. Then we have

$$B^\dagger_{\text{coll}} = xA^\dagger - \frac{\xi}{4x} - \frac{\xi^2}{2 \times 4^2 \times x^3} - \frac{\xi^3}{3 \times 4^3 \times x^5} - \frac{\xi^4}{4 \times 4^4 \times x^7} - \cdots , \tag{14}$$

where $A^\dagger$ creates the collective boson. Permutation of indices which gave identical terms when the restriction to one collective boson was made, reduced the numbers in the denominators of the expressions for the w term, for instance. Before discussing convergence we digress to cover a few points.

The choice of x itself has invoked some controversy. Sorensen[7] had advocated both $x \gg 1$ and $x \ll 1$ on different occasions. Naively, from Eq. (14), one might suppose that large x improves convergence. However, when plugging the boson expansion for $B^\dagger$ into Eq. (4a), the leading term is $x^2\delta_{ab}$, to be compared to δ_{ab} on the right-hand side. The choice $x=1$ is naturally suggested and is in fact consistent with the derivation of Eq. (12). The only way x can be chosen larger is if all modes are being considered in $B^\dagger$. Then δ_{ab} terms can drop out of the commutators of the higher order terms to reduce $x^2\delta_{ab}$ from the left-hand side of Eq. (4a) to the δ_{ab} as required by the right-hand side. The choice of $x=1$ was used in all our previous applications.. Nevertheless, the results are relatively insensitive to changes in x of at least 20%. As an aside, we note that if one were to take the boson expansion out to high order and include all modes, thus forcing the choice of x to be much greater than unity, the following happens.[2] The r coefficient is for large x a factor of x^2 smaller than s while u (v) is x^4 (x^2) smaller than w. Thus r, u, v, become more and more negligible as the full calculation is taken to higher and higher order. In addition, the exact expressions for s and w approach $-1/(4x)$ and $-s^2/(22.5x)$, respectively. These expressions are similar to Eq. (12), except in this case $x \gg 1$ while in Eq. (12), as pointed out above, only $x=1$ is consistent.

We now consider, under what conditions, the boson expansion can be useful in nuclear physics applications. Looking at Eq. (14), the only way the boson expansion can converge quickly is when it is applied for a collective mode (i.e., a fermion mode in which a large number of pairs of single-particle orbits are contributing coherently with individually small amplitudes). If all single-particle levels are degenerate, then the magnitude of the quantity ξ^n (which checks the fermion content of n boson configurations) is equal to $[1/\sum_j(2j+1)]^n$ which is very small even for $n=1$. Of course, in nuclear physics the single-particle levels are not degenerate; thus full collectivity is not reached. The quantity ξ is then figuratively $[1/\sum_j a_j(2j+1)]$, where a_j are coefficients less than unity, they are largest for states near the Fermi surfaces, and decrease to zero for states farther away. In practical applications,[4-6] where numerical convergence has been demonstrated, this quantity has a magnitude of about 0.2, making the net expansion coefficient of the series as small as 0.05. In particular in Ref. 4, it was pointed out and confirmed in later work that for nuclei which are mildly deformed, the fourth order results differed negligibly from the sixth order results. (In the present paper's terminology, e.g., fourth order means a calculation made by ignoring w terms in $B^\dagger_{\mathrm{coll}}$ and s^2 terms in the product of $B^\dagger$ operators in the Hamiltonian.) Only when the nucleus is well deformed is there appreciable difference, but it can be safely said that the results (for low-lying states) have converged by sixth order, except for very fine details.

Thus, if one encounters a problem where one needs to treat the multiple excitations of a collective fermion mode, the boson expansion can work quite nicely. To put it another way, the spreading of the collective fermion operator over many single-particle orbits ensures that the Pauli-principle violating components are but a small fraction of the total boson state which is obtained when a truncated boson representation of a collective fermion operator operates on a boson state comprised of a finite number of purely collective bosons. It is possible to cut off the number of terms in Eqs. (6a) or (14), because the terms which are dropped add either very small or exactly zero contributions for the states of interest. However, if one envisions the boson expansion of several modes of basically pure quasiparticle pair nature, then Pauli-principle violations can become insurmountable if one tries to cut the order of the expansion at a calculationally reasonable point.[10]

IV. CONCLUSION

The correct procedure for using the boson expansion method has been set forth. Namely, that one represents the physical fermion operators by boson expanded expressions which do not involve boson excitations of nonphysical interest. One solves the commutation relations for the coefficients of this expansion and then converts the fermion Hamiltonian into boson expanded form. A second truncation may then be made as regards limiting the number of bosons in each boson product operator of the Hamiltonian.

From a graphical description, we were able to see that the r, u, and v terms do not check the fermion nature of the bosons and, in fact, violate the Pauli principle, if they are allowed to remain in a truncated calculation. The s, w, and higher order (connected diagram) terms do indeed take care of the Pauli principle and, for some problems, it may be possible to truncate this series and still describe the fermion nature accurately. Nuclear collective motion, wherein a large number of particle-hole excitations contribute coherently to produce low-lying energy states, is a good example of such a problem.

ACKNOWLEDGMENTS

The authors gratefully thank Dr. T. Udagawa for many useful conversations throughout the course of this work. This work was supported in part by the U. S. Department of Energy.

[1] S. T. Belyaev and V. G. Zelevinsky, Nucl. Phys. 39, 582 (1962).

[2] T. Kishimoto and T. Tamura, Nucl. Phys. A192, 246 (1972).

[3] T. Kishimoto and T. Tamura, Nucl. Phys. A270, 317 (1976).

[4] T. Tamura, K. Weeks, and T. Kishimoto, Phys. Rev. C 20, 307 (1979).

[5] K. J. Weeks and T. Tamura, Phys. Rev. Lett. 44, 533 (1980); Phys. Rev. C 21, 2632 (1980).

[6] K. Weeks, Ph.D. thesis, The University of Texas, 1978 (unpublished).

[7] B. Sorensen, Nucl. Phys. A97, 1 (1967); A119, 65 (1968); A142, 392 (1970); A142, 411 (1970).

[8] B. Silvestre-Brac and R. Piepenbring, Phys. Rev. C 20, 1161 (1979).

[9] D. J. Rowe, *Nuclear Collective Motion* (Methuen, London, 1970), pp. 198, 219.

[10] E. R. Marshalek, Nucl. Phys. A161, 401 (1971).

PHYSICAL REVIEW C VOLUME 21, NUMBER 6 JUNE 1980

Shape of eigenvalue distribution for bosons in scalar space

V. K. B. Kota
Physical Research Laboratory, Navrangpura, Ahmedabad 380 009, India

V. Potbhare
Department of Physics, Faculty of Science, M. S. University, Baroda 390 002, India

(Received 7 February 1979; revised manuscript received 7 November 1979)

Analytic expressions for obtaining first four moments of noninteracting as well as interacting bosons have been given in terms of matrix elements. These expressions have been utilized to obtain general conditions under which the eigenvalue distributions for bosons tend towards the Gaussian distribution. Results for pairing and $Q\cdot Q$ operators in an s-d boson shell have also been given.

NUCLEAR STRUCTURE Analytic expressions, first four moments, noninteracting and interacting bosons, eigenvalue distribution, conditions leading to Gaussian distribution, pairing and Q-Q operators, s-d boson space.

The assumption of applicability of a strong central limit theorem (CLT) to two-body interactions has brought forth a tremendous simplification in the nuclear shell model spectroscopy.[1] The conditions on traces of matrix elements, which give rise to normal eigenvalue distributions (EVD) for fermion systems (noninteracting and interacting), have been clearly formulated.[2,3] The question of normality of EVD for boson systems was recently raised by Bortignon *et al.*[4,5] They have given analytical expressions for the first four moments of noninteracting boson EVD. These expressions, however, do not reveal the conditions for normality of EVD; also, the more interesting and more realistic case of interacting bosons was not treated. In this paper, we present simple analytic expressions for the first four moments of EVD for noninteracting and interacting bosons. We shall also discuss the conditions under which EVD for bosons tend to Gaussian distribution.

The m-particle scalar average $\langle H(k)\rangle^m$ of a k-body operator $H(k)$ in the space defined by N single-particle states, corresponds to the average of expectation values of $H(k)$ over all the states of m particles, and can be expressed in terms of $\langle H(k)\rangle^k$:

$$\langle H(k)\rangle^m=\binom{m}{k}\langle H(k)\rangle^k\,, \tag{1}$$

where $\binom{m}{k}$ is the usual binomial factor. Equation 1 is valid for both the fermions and the bosons. The number of states of m bosons in the space of N single-particle states is given by $\binom{N+m-1}{m}$; hence, in terms of the trace of $H(k)$ in k-particle space $\langle\langle H(k)\rangle\rangle^k$, we obtain

$$\langle H(k)\rangle^m=\binom{m}{k}\binom{N+k-1}{k}^{-1}\langle\langle H(k)\rangle\rangle^k\,, \tag{2}$$

where the double bracket $\langle\langle\ \rangle\rangle$ indicates the trace. For noninteracting bosons, the Hamiltonian H is a one-body operator $H=\sum_i\epsilon_i n_i$; here ϵ_i is single-particle energy and n_i is the number operator for the ith single-particle state. Except for the centroid which defines the location of a distribution, the shape of the EVD is determined by its central moments. Therefore, we shall deal only with traceless single-particle energies $\tilde{\epsilon}_i=\epsilon_i-N^{-1}\sum\epsilon_i$, and shall evaluate moments of $\tilde{H}=H-nN^{-1}\sum\epsilon_i$, where $n=\sum_i n_i$, for noninteracting bosons. We evaluate the second moment of H by separating $(\tilde{H})^2$ into its one-body and two-body parts:

$$(\tilde{H})^2=\sum_i\tilde{\epsilon}_i^{\,2}n_i+\sum_i\tilde{\epsilon}_i^{\,2}n_i(n_i-1)$$
$$+\sum_{i\neq j}\tilde{\epsilon}_i\tilde{\epsilon}_j n_i n_j\,. \tag{3}$$

The first term above is the one-body part of $(\tilde{H})^2$ and its scalar average in m-particle space is given by $m\sum\epsilon_i^2/N$. The remaining terms form the two-body part of $(\tilde{H})^2$ and their scalar average equals $[m(m-1)/N(N+1)]\sum_i\tilde{\epsilon}_i^{\,2}$. Hence the average value of $(\tilde{H})^2$ in m-particle space can be expressed as

$$\langle\tilde{H}^2\rangle^m=\frac{m(N+m)}{N(N+1)}\sum\tilde{\epsilon}_i^{\,2}\,. \tag{4}$$

Similarly the scalar averages of $(\tilde{H})^3$ and $(\tilde{H})^4$

© 1980 The American Physical Society

can be obtained by separating $\bar{H}^3$ into (1+2+3)-body parts and $\bar{H}^4$ into (1+2+3+4)-body parts. Adding the contributions from different k-body parts gives us the following expressions:

$$\langle \bar{H}^3 \rangle^m = \frac{m(N+m)(N+2m)}{N(N+1)(N+2)} \sum_i \tilde{\epsilon}_i^{\,3} ,$$
$$\langle \bar{H}^4 \rangle^m = \frac{m(N+m)}{N(N+1)} \sum_i \tilde{\epsilon}_i^{\,4} + \frac{m(m-1)(N+m)(N+m+1)}{N(N+1)(N+2)(N+3)} \times \left[3\Big(\sum_i \tilde{\epsilon}_i^{\,2}\Big)^2 + 6 \sum_i \tilde{\epsilon}_i^{\,4} \right] . \tag{5}$$

It is quite interesting to note that, by substituting $-N$ for N in the corresponding expressions for fermions, and then by taking the absolute value of each term, one obtains the above expressions for the boson systems. For example,

$$\langle \bar{H}^3 \rangle^m_{\text{fermions}} = \frac{m(N-m)(N-2m)}{N(N-1)(N-2)} \sum_i \tilde{\epsilon}_i^{\,3} \tag{6}$$

goes to its boson counterpart by substituting $-N$ for N and taking modulo of the final result (however, one cannot obtain moments of EVD for fermions from those of bosons as we will be left with phase ambiguities). This was previously conjectured by Nomura[6]; using this principle one can obtain several new results. For example, a class of Wigner coefficients of the O(N) group can be obtained from those of the Sp(N) group via moments in quasispin subspaces.[7]

Another interesting one-body Hamiltonian is $H = \sum \epsilon_{ij} A_i B_j$, where ϵ_{ij} is an off diagonal single-particle matrix element when $i \neq j$, ϵ_{ii} is the usual single-particle energy, and A_i, B_j are single-particle creation and destruction operators, respectively. Such a Hamiltonian is widely used in solid-state physics, where ϵ_{ij} $(i \neq j)$ can be identified with the exciton hopping integral between sites i and j. The traceless single-particle matrix elements $\tilde{\epsilon}_{ij}$, in this case, are given by $\tilde{\epsilon}_{ij} = \epsilon_{ij} - \delta_{ij} N^{-1} \sum_k \epsilon_{kk}$. The expressions for second, third, and fourth central moments of this Hamiltonian can be obtained by substituting $\sum \tilde{\epsilon}_i^{\,2}$, $\sum \tilde{\epsilon}_i^{\,3}$, and $\sum \tilde{\epsilon}_i^{\,4}$ by $\sum \tilde{\epsilon}_{ij} \tilde{\epsilon}_{ji}$, $\sum \tilde{\epsilon}_{ij} \tilde{\epsilon}_{jk} \tilde{\epsilon}_{ki}$, and $\sum \tilde{\epsilon}_{ij} \tilde{\epsilon}_{jk} \tilde{\epsilon}_{kl} \tilde{\epsilon}_{li}$, respectively, in Eqs. 4 and 5 given above.

The preceding treatment of a one-body Hamiltonian was simple and elementary. We shall start with some general results before going to the case of moments of EVD for bosons interacting via two-body interactions. A number conserving, k-body operator for bosons in the space defined by N single-particle states can be decomposed according to the irreducible (IR) representations of the U(N) group; $F(k) = \sum_{\nu=0}^{k} F^{\nu}(k)$, where $F^{\nu}(k)$ is the rank-ν part of $F(k)$ and transforms as a $[2\nu, \nu^{N-2}]$ partition under a U(N) transformation. $F^{\nu}(k)$ can be written as a product of a unitary scalar operator and a completely IR ν-body and rank-ν operator $\mathfrak{F}(\nu)$:

$$F^{\nu}(k) = \binom{n-\nu}{k-\nu} \mathfrak{F}(\nu) . \tag{7}$$

In order to find out the different unitary IR parts systematically, we introduce a contraction operator D_-, defined by the following double commutator:

$$D_- F = \sum_{i=1}^{N} \Big[[B_i, F]_-, A_i \Big]_- . \tag{8}$$

The operator D_- reduces the particle rank (or the body rank) of F by one, without altering its unitary rank. Since $\mathfrak{F}(\nu)$ is completely irreducible, any reduction of its particle rank by D_- destroys it; $D_- \mathfrak{F}(\nu) = 0$. It should be noted that this contraction operator is different from similar contraction operators for fermions.[1,8] Contracting $F(k)$ r times by D_- gives us

$$D_-^r F(k) = \sum_{\nu} r! \binom{N+k+\nu-1}{r} F^{\nu}(k-r) . \tag{9}$$

By inverting this expression we obtain

$$\mathfrak{F}(\nu) = \frac{1}{(k-\nu)!} \binom{N+\nu+k-1}{k-\nu}^{-1} \times \sum_{t=k-\nu}^{k} \frac{(-1)^{t-k+\nu}}{(t-k+\nu)} \binom{N+2\nu-2}{t-k+\nu}^{-1} \times \binom{n-k+t}{t-k+\nu} D_-^t F(k) . \tag{10}$$

Application of this to a one-body operator $H = \sum \epsilon_i n_i$ gives us the IR $\nu = 0$ part as $n \sum \epsilon_i / N$, and the IR $\nu = 1$ part as $\sum \tilde{\epsilon}_i n_i$ in terms of the traceless single-particle energies $\tilde{\epsilon}_i$. Similar application of Eq. (10) to the two-body interaction given by $\frac{1}{4} \sum V_{ijkl} A_i A_j B_k B_l$, expressed in terms of the two-body matrix elements V_{ijkl}, gives us the following three parts: (i) the IR $\nu = 0$ part

$$n(n-1) \sum V_{ijij} / [2N(N+1)] ,$$

(ii) the IR $\nu = 1$ part

$$\sum_{i,k} (n-1)(N+2)^{-1} \left[\sum_j \Big(V_{ijkj} - \delta_{ik} \sum_{ij} V_{ijij} / N \Big) A_i B_k \right] ,$$

and (iii) the IR $\nu = 2$ part

$$\tfrac{1}{4} \sum \bar{V}_{ijkl} A_i A_j B_k B_l .$$

Here $\tilde{V}_{ijkl}$ is the IR $\nu = 2$ matrix element, obtained by subtracting $\nu = 0$ and $\nu = 1$ contributions from V_{ijkl}.

We have already given expressions for the first four central moments of EVD generated by the one-body (which is essentially IR $\nu = 1$) interaction. Now we give the final expressions for second, third, and fourth central moments of EVD generated by a two-body, IR rank $\nu = 2$ Hamiltonian H. The procedure leading to these final expressions is straightforward, and consists of (a) decomposing H^m into parts according to the body (particle) rank, and (b) using Eq. (2) separately for each part. In order to take care of the bookkeeping of various terms, which is the only difficult part in the whole procedure, we use the Feynman diagram type approach.[8,9] The following is the expression for the ith central moment μ_i [$\mu_i^m = \langle\langle(\tilde{H})^i\rangle\rangle^m$, $\tilde{H}$ is the traceless part of H in m-particle scalar space] of EVD for m bosons interacting via two-body, IR rank $\nu = 2$ interaction $\tilde{V}$:

$$\langle\langle(\tilde{V})^i\rangle\rangle^m = \sum_{s=2}^{i} \binom{m}{s}\binom{N+s+m-1}{s} \times \binom{2s}{s}^{-1}\binom{N+2s-1}{2s} C_i^s . \qquad (11)$$

Here i goes from 2 to 4. All the necessary information about the two-body, $\nu = 2$ interaction goes in the evaluation of coefficients C_i^s. The expressions for these in terms of the two-body matrix elements are given below:

$$\begin{aligned}
&C_2^{\,2} = \tfrac{1}{4}\sum \tilde{V}_{ijkl}\tilde{V}_{klij}, \quad C_3^{\,2} = \tfrac{1}{8}\sum \tilde{V}_{ijkl}\tilde{V}_{klmn}\tilde{V}_{mnij},\\
&C_3^{\,3} = 2C_3^{\,2} + \sum \tilde{V}_{iljk}\tilde{V}_{knlm}\tilde{V}_{mjni},\\
&C_4^{\,2} = \tfrac{1}{16}(AA1),\\
&C_4^{\,3} = \tfrac{1}{4}(AA1) + CC1 + \tfrac{1}{2}BA1 + 2(CA1),\\
&C_4^{\,4} = \tfrac{3}{8}(AA1) + 6(CC1) + 3(BA1) + 6(CA1)\\
&\qquad + 3(AB1) + 3(C_2^{\,2})^2,
\end{aligned} \qquad (12)$$

where

$$\begin{aligned}
AA1 &= \sum \tilde{V}_{ijkl}\tilde{V}_{klmn}\tilde{V}_{mnop}\tilde{V}_{opij},\\
AB1 &= \sum \tilde{V}_{ijkl}\tilde{V}_{lmjn}\tilde{V}_{nomp}\tilde{V}_{pkoi},\\
BA1 &= \sum \tilde{V}_{ijkl}\tilde{V}_{klin}\tilde{V}_{mnop}\tilde{V}_{opmj},\\
CA1 &= \sum \tilde{V}_{ijkl}\tilde{V}_{kmno}\tilde{V}_{olmp}\tilde{V}_{npij},\\
CC1 &= \sum \tilde{V}_{ijkl}\tilde{V}_{mnjo}\tilde{V}_{olnp}\tilde{V}_{pkmi}.
\end{aligned} \qquad (13)$$

Here the summation is over all labels. These results can be very easily extended to evaluation of the moments of EVD generated by a general (1+2)-body interaction H; the corresponding expressions are given in the Appendix.

The necessary information C_i^s for the evaluation of the ith moment of EVD in the m-boson space, generated by IR $\nu = 2$ interaction, can also be obtained from the ith moment in 2 to the i-boson spaces only. One, however, would expect, due to the two-body character of the interaction, that the ith moments in 2 to $2i$ particle spaces would have been necessary[10] for evaluation of the ith moment of EVD in m-boson space. The validity of this fact in fermion spaces[1,10] can be attributed to the particle-hole symmetry of the IR $\nu = 2$ interaction. There is no concept of hole for bosons, and hence one can see that the IR $\nu = 2$ nature of interaction is responsible for this simplicity, and in fermion spaces, the particle-hole symmetry is a consequence of the IR $\nu = 2$ nature of the interaction.

We shall now discuss the conditions for the normality of the EVD. The first two moments of the EVD tell us about the location (centroid) and the spread (width) of the EVD. The information about the shape of the spectrum is given by the third and higher central moments of the EVD. In principle, all the higher moments are necessary for determining the shape of EVD; but here we shall deal only with the moments up to fourth order. The corresponding shape parameters are the skewness $\gamma_1 = \mu_3/(\mu_2)^{3/2}$, and the excess $\gamma_2 = \mu_4/(\mu_2)^2 - 3$. For the Gaussian or the normal distribution, both γ_1 and γ_2 are equal to zero.

Let us start with a pure one-body interaction; the central moments for such an interaction are given by Eqs. (4) and (5). In the dilute limit, defined by $m \to \infty$, $N \to \infty$, but $m/N \ll 1$, we find that the shape parameters $\gamma_1(m)$ and $\gamma_2(m)$ for m-boson EVD approach asymptotically to values given by the expressions

$$\begin{aligned}
&\gamma_1(m) = m^{-1/2}\gamma_1(1),\\
&\gamma_2(m) = [\gamma_2(1) + 3](m^{-1} + 6N^{-1}).
\end{aligned} \qquad (14)$$

Thus, in the dilute limit, both $\gamma_1(m)$ and $\gamma_2(m)$ approach zero if the shape parameters $\gamma_1(1)$ and $\gamma_2(1)$ for one-boson EVD are finite. The same result was obtained for the fermion EVD in the dilute limit.[2] Thus in the dilute system, one gets the same result irrespective of the fermion or the boson nature of particles, since the Pauli's exclusion principle has negligibly small effect when $N \gg m$. However, for bosons, since there is no limit to the number of particles in any single-particle state, unlike fermions, we can consider the limit $m \rightarrow \infty$ with finite N. This is called the dense limit; the second central moment and the shape parameters in this limit are given by

$$\begin{aligned} \langle(\tilde{H})^2\rangle^m &= \sigma^2(m) = m^2\sigma^2(1)/(N+1)\,, \\ \gamma_1(m) &= 2\gamma_1(1)\frac{(N+1)^{1/2}}{(N+2)}\,, \\ \gamma_2(m) &= 6\frac{\{[\gamma_2(1)+3](N+1)-(2N+3)\}}{(N+2)(N+3)}\,. \end{aligned} \tag{15}$$

The width of the m-boson EVD $\sigma(m)$ increases linearly with m. The shape parameters, however, approach values which are independent of m, but which very much depend on the shape parameters for one-boson EVD and the size of the single-boson space N. For large values of N again, the EVD can be considered Gaussian if $\gamma_1(1)$ and $\gamma_2(1)$ are reasonably small. For example, in the case of noninteracting particles, with N equidistant single-particle states, we have $\gamma_1(1)=0$ and $\gamma_2(1)=-1.2\ [(N^2+1)/(N^2-1)]$. We can see that for $N=5$, the absolute value of excess in the dense limit is less than 0.24; for $N=10$ it is less than 0.12. Thus, the EVD in this case approaches Gaussian in the dense limit if $N>5$.

We now consider the dilute and the dense limits of the shape of EVD generated by a purely two-body, IR rank-2 interaction V, by introducing dimensionless quantities $P(m,n)$, defined by

$$P(m,n) = \frac{C_m^n}{(C_2^2)^{m/2}}\,. \tag{16}$$

These are the ratios of traces of various combinations of the matrix elements, and are characteristic of the interaction used to generate the EVD. In the dilute limit, $\gamma_1(m)$ approaches $NP(3,2)/m + P(3,3)$ and $[\gamma_2(m)+3]$ tends to $N^2P(4,2)/m^2 + NP(4,3)/m + P(4,4)$. Thus the EVD approach Gaussian distribution if $P(3,2) \ll m/N$, $P(3,3) \ll 1$, $P(4,2) \ll m^2/N^2$, $P(4,3) \ll m/N$, and $(P(4,4)-3) \ll 1$. One can translate these conditions to conditions on the shape parameters of EVD for 2, 3, and 4 bosons. The skewness and excess in dilute limit approach constant values $-\sqrt{2}\gamma_1(2)+\sqrt{6}\gamma_1(3)$, and $\gamma_2(2)-6\gamma_2(3)+6\gamma_2(4)$, respectively. Thus the approach to Gaussian distribution in the dilute limit is decided by these shape parameters of EVD for 2, 3, and 4 bosons. Since in the dilute limit, bosons and fermions behave similarly, the same conditions will apply for fermions. This clearly shows that for purely two-body, IR rank-2 interaction, the assumption of applicability of a strong central limit theorem is not valid. The shape of the EVD in the dilute limit does not necessarily approach the Gaussian distribution with increasing m, as the limiting values of $\gamma_1(m)$ and $\gamma_2(m)$ reach constant values depending on the shape parameters of the EVD for $m=2$, 3, and 4. Of course, the addition of the one-body part of the interaction and the IR rank-1 part of the two-body interaction to the two-body IR rank-2 interaction is likely to alter the whole picture, and the conditions for normality of the EVD will have complicated structures. It is known that the IR rank-1 part of the interaction is quite important for the nuclear structure studies.[11]

In the dense limit ($m \rightarrow \infty$, N finite) valid only for bosons, the values of $P(3,3)$ and $P(4,4)$ completely determine the shape of the EVD. For,

$$\begin{aligned} \gamma_1(m) &\rightarrow \frac{P(3,3)[N(N+1)(N+2)(N+3)]^{1/2}}{(N+4)(N+5)}\,, \\ \gamma_2(m)+3 &\rightarrow \frac{P(4,4)N(N+1)(N+2)(N+3)}{(N+4)(N+5)(N+6)(N+7)}\,. \end{aligned} \tag{17}$$

For large N, we get $\gamma_1(m) \simeq P(3,3)$ and $\gamma_2(m)+3 \simeq P(4,4)$ in the dense limit. Again one can express these conditions in terms of the shape parameters of EVD for 2, 3, and 4 bosons, using the following expressions for $P(3,3)$ and $P(4,4)$:

$$\begin{aligned} P(3,3) &= (N+4)\left(\frac{2}{N(N+1)}\right)^{1/2} \\ &\quad\times\left[\left(\frac{3(N+4)}{(N+2)}\right)^{1/2}\gamma_1(3)-\gamma_1(2)\right], \\ P(4,4) &= \frac{(N+4)}{N(N+1)}\left(6[\gamma_2(4)+3]\frac{(N+4)(N+5)^2}{(N+2)(N+3)}\right. \\ &\quad -6[\gamma_2(3)+3]\frac{(N+6)(N+4)}{(N+2)} \\ &\quad \left.+[\gamma_2(2)+3](N+7)\right). \end{aligned} \tag{18}$$

So in the dense limit also, the skewness and the excess of EVD for m bosons approach constant values depending on the values of $\gamma_1(i)$ for $i=2,3$ and $\gamma_2(j)$ for $j=2,3,4$. The approach to Gaussian limit depends only on these numbers.

Two sets of matrix elements have been given by Bortignon *et al.*[4] for the d bosons of the interacting boson approximation model.[12] Using these two sets of matrix elements, we obtain $P(3,3) = 1.78$ and $P(4,4) = 23.12$ for one interaction, while the second one gives $P(3,3) = 2.09$ and $P(4,4) = 25.55$. The size of the single-particle space is given by $N=5$. So, in the dense limit, the limiting values of the shape parameters are

$\gamma_1(m)=0.81, 0.95$ and $\gamma_2(m)=0.27, 0.61$, for the two interactions, respectively; hence the shape of the EVD is nowhere near Gaussian. A pairing interaction in the space of s-d bosons with $N=6$ gives $P(3,3)=1.46$ and $P(4,4)=15.64$; hence the limiting values of γ_1 and γ_2 in the dense limit are 0.73 and -0.24, respectively. Similarly, a $Q\cdot Q$ interaction in the s-d boson space (having both IR rank-1 and IR rank-2 parts) gives the following limiting values for $\gamma_1(m)=-0.76$ and $\gamma_2(m)=0.86$ in the dense limit. Incidentally, for fermions and the $Q\cdot Q$ interaction in a large j orbit, the values of γ_1 and γ_2 in the middle of the shell have been obtained by Nomura,[13] and these are 1.26 and -0.6, respectively.

One interesting feature of the boson systems is the complete domination of the two-body part of the interaction, over the one-body part for large m. This can be seen from the expressions given in the Appendix for moments of the (1+2)-body interaction; each factor containing the external single-particle energy term (ϵ) gets multiplied by m, while each factor containing a two-body matrix element (V) has a coefficient proportional to m^2 in the large m limit. For example, the one-body contribution to μ_4 has a coefficient which goes as m^4, and the corresponding coefficient for the two-body contribution to μ_4 goes as m^8 in the dense limit. One also sees that in this limit the shape parameters approach constant values, which are not necessarily those of a Gaussian distribution. For the dilute limit, one can get the result of noninteracting particles only if the one-body part (external single-particle energies) is dominant over the two-body part.

Finally, let us consider the shape of ensemble-averaged EVD, using an ensemble of random interactions. The ensemble averaged skewness will be zero for any ensemble (with matrix element mean = 0) of random interactions, because each necessary matrix element trace for the evaluation of the ensemble averaged third moment will have an odd number of matrix elements. We therefore need to consider only the ensemble averaged excess in this case. For the dilute limit one can show that the ensemble averaged eigenvalue distribution is Gaussian. For the lense limit, one gets the Gaussian distribution if V is sufficiently large; the shape parameters for inite N in the dense limit have complicated itructure and shall be discussed elsewhere.

In conclusion, we have obtained analytic ex- ressions for the first four moments of the EVD f interacting (via two-body interactions) and oninteracting boson systems. The conditions eading to normality of the EVD have been discussed. Extension of the present work for configuration subspaces is straightforward.

APPENDIX

Here we give expressions for the first four moments of the EVD of a general (1+2)-body Hamiltonian (H):

$$
\begin{aligned}
H &= \sum \epsilon_{ij} A_i B_j + \tfrac{1}{4} \sum V_{ijkl} A_i A_j B_k B_l \\
&= H^{\nu=0} + H^{\nu=1} + H^{\nu=2} \\
&= H_0 + \tilde{H} ,
\end{aligned}
\tag{A1}
$$

$$
\begin{aligned}
H^{\nu=0} &= H_0 = n \sum \epsilon_{ii}/N + \frac{n(n-1)}{N(N+1)} \sum_{i\leq j} V_{ijij} , \\
H^{\nu=1} &= h = \sum \xi_{ij} A_i B_j , \\
\xi_{ij} &= \epsilon_{ij} - \frac{1}{N} \sum \epsilon_{ii}\delta_{ij} + \frac{n-1}{N+2} \\
&\quad \times \left[\sum_k \left(V_{ikjk} - \frac{\delta_{ij}}{N} \sum V_{mnmn} \right) \right] , \\
H^{\nu=2} &= \tilde{V} = \tfrac{1}{4} \sum \tilde{V}_{ijkl} A_i A_j B_k B_l ,
\end{aligned}
\tag{A2}
$$

$$
\begin{aligned}
\langle H\rangle^m &= \frac{m}{N} \sum \epsilon_{ii} + \frac{m(m-1)}{N(N+1)} \sum_{i\leq j} V_{ijij} , \\
\langle (H)^2\rangle^m &= \frac{m(N+m)}{N(N+1)} \sum \xi_{ij}\xi_{ji} + \langle (\tilde{V})^2\rangle^m , \\
\langle (H)^3\rangle^m &= \frac{m(N+m)(N+2m)}{N(N+1)(N+2)} \sum \xi_{ij}\xi_{jk}\xi_{ki} \\
&\quad + \frac{\binom{m}{2}\binom{N+m+1}{2}}{\binom{4}{2}\binom{N+3}{4}} \left(3D_1 + \tfrac{3}{2}E_1\right) \\
&\quad + \frac{\binom{m}{3}\binom{N+m+1}{2}}{\binom{5}{2}\binom{N+4}{5}} (3E_1) + \langle (\tilde{V})^3\rangle^m ,
\end{aligned}
$$

where

$$
\begin{aligned}
D_1 &= \sum \tilde{V}_{ijkl}\xi_{ik}\xi_{jl} , \\
E_1 &= \sum \tilde{V}_{ijkl}\tilde{V}_{kmij}\xi_{lm} ,
\end{aligned}
\tag{A3}
$$

$$\langle\langle (H)^4\rangle\rangle^m = \frac{m(N+m)}{N(N+1)} M_2 + \frac{\binom{m}{2}\binom{N+m+1}{2}}{\binom{4}{2}\binom{N+3}{4}}[12K_1+2G_1+2G_2+2G_3+F_1+3(M_1)^2+6M_2]$$

$$+\frac{\binom{m}{3}\binom{N+m+1}{2}}{\binom{5}{2}\binom{N+4}{5}}[24K_1+2F_1]+\frac{\binom{m}{3}\binom{N+m+2}{3}}{\binom{6}{3}\binom{N+5}{6}}[12G_1+6G_2+12G_3+12G_4+\tfrac{3}{2}G_5+2F_1+12F_2+6F_3]$$

$$+\frac{\binom{m}{4}\binom{N+m+2}{3}}{\binom{7}{3}\binom{N+8}{7}}[4F_1+24F_2+12F_3]+\langle\langle(\tilde{V})^4\rangle\rangle^m ,$$

where

$$M_1=\sum \xi_{ij}\xi_{ji}, \quad M_2=\sum \xi_{ij}\xi_{jk}\xi_{kl}\xi_{li} ,$$

$$K_1=\sum \tilde{V}_{ijkl}\xi_{ik}\xi_{jm}\xi_{ml} ,$$

$$G_1=\sum \tilde{V}_{ijkl}\tilde{V}_{knij}\xi_{lm}\xi_{mn} ,$$

$$G_2=\sum \tilde{V}_{ijkl}\tilde{V}_{mnij}\xi_{km}\xi_{ln} ,$$

$$G_3=\sum \tilde{V}_{ijkl}\tilde{V}_{kmin}\xi_{lm}\xi_{nj} ,$$

$$G_4=\sum \tilde{V}_{ijkl}\tilde{V}_{kmln}\xi_{ji}\xi_{mn} ,$$

$$G_5=\sum \xi_{ij}\xi_{ji}\sum \tilde{V}_{klmn}\tilde{V}_{mnkl} ,$$

$$F_1=\sum \tilde{V}_{ijkl}\tilde{V}_{kpmn}\tilde{V}_{mnij}\xi_{lp} , \tag{A4}$$

$$F_2=\sum \tilde{V}_{ijkl}\tilde{V}_{lmjn}\tilde{V}_{npmi}\xi_{kp} ,$$

$$F_3=\sum \tilde{V}_{ijkl}\tilde{V}_{klmj}\tilde{V}_{mpin}\xi_{np} .$$

Note that the expressions for $\langle\langle(\tilde{V})^4\rangle\rangle^m$ are given in Eq. (11) of the text.

---

[1] F. S. Chang, J. B. French, and T. H. Thio, Ann. Phys. (N.Y.) 66, 137 (1971).

[2] K. K. Mon and J. B. French, Ann. Phys. (N.Y.) 95, 90 (1975).

[3] M. Nomura, Prog. Theor. Phys. 59, 1199 (1978).

[4] P. F. Bortignon, M. Dalla Francesca, and V. R. Manfredi, Lett. Nuovo Cimento 19, 15 (1977).

[5] P. F. Bortignon, V. R. Manfredi, and S. Spitz, Lett. Nuovo Cimento 23, 210 (1978).

[6] M. Nomura, Ann. Phys. (N.Y.) 91, 83 (1975).

[7] V. K. B. Kota, J. Phys. Lett. (Paris) (to be published).

[8] J. N. Ginocchio, Phys. Rev. C 8, 135 (1973); S. Ayik and J. N. Ginocchio, Nucl. Phys. A221, 285 (1974).

[9] V. Potbhare, Ph.D. thesis, University of Rochester, 1975.

[10] J. B. French and K. F. Ratcliff, Phys. Rev. C 3, 94 (1971).

[11] V. Potbhare and S. P. Pandya, Nucl. Phys. A256, 253 (1976); V. K. B. Kota and V. Potbhare, *ibid.* (to be published).

[12] A. Arima and F. Iachello, Ann. Phys. (N.Y.) 99, 253 (1976).

[13] M. Nomura, Prog. Theor. Phys. 48, 442 (1972).

PHYSICAL REVIEW C VOLUME 21, NUMBER 6 JUNE 1980

Nucleon-nucleon interaction as derived from the De Rújula, Georgi, Glashow phenomenological quark-quark potential

C. S. Warke and R. Shanker
Tata Institute of Fundamental Research, Homi Bhabha Road, Bombay 400005, India

(Received 3 July 1979)

The nucleon-nucleon interaction, originating from the phenomenological quark-quark interaction: one gluon exchange with an *ad hoc* confining potential, is rigorously derived. The coupling constants of this potential and the quark masses—which determine the strengths of the *NN* potentials in the various channels—had been previously reliably determined from the masses of the *s*-wave baryons. Two distinguishing features of this study are the reliable nature of the coupling constants and quark masses used and the inclusion of the detailed radial dynamics of quarks. The main results are as follows: (i) exchange of colored quarks among other things leads to short-range strongly repulsive central *NN* potentials in the odd channels alone, i.e., it yields the saturation property of nuclear forces; (ii) the spin-orbit (tensor) potential between quarks goes over to the spin-orbit (tensor) potential between nucleons, (iii) both these spin-orbit and tensor potentials between nucleons are found to have the correct signatures but they are very weak; (iv) there is insufficient attraction in the *NN* potentials in the intermediate range, so that the colored quark-exchange mechanism is not adequate to keep the deuteron bound. The *NN* potentials derived from one gluon exchange with an *ad hoc* confining potential are compared finally with the corresponding phenomenological ones.

[NUCLEAR STRUCTURE *NN* interaction from nonrelativistic quantum chromodynamics. Quark exchange, spin-orbit and tensor potentials, short-range repulsive core.]

I. INTRODUCTION

The problem of the nucleon-nucleon (*NN*) interaction has engaged the attention of numerous physicists over the last five decades; nevertheless a satisfactory theoretical understanding encompassing all its features has not yet emerged.[1,2] This interaction between two nucleons, at low energies (<400 MeV projectile energy) can be imagined to be mediated by a nonrelativistic potential. The use of a potential is justified provided only low energy *NN* collisions are considered, and moreover, such a potential description of the interaction is both intuitively appealing and familiar through its long use in classical electrodynamics and gravitation. At higher energies however, such a description—being unable to cope with the phenomenon of creation and annihilation of particles—has been superseded by a eld theoretic or a dispersion-theoretic descrip- on of the interaction. The field-theoretic de- ription of the interaction is the most general ie, and the potential description can be derived om the former, in particular from the con- ructs of vertex functions and propagators, in e nonrelativistic limit. The *NN* interaction has en described in all three languages mentioned ove appropriate to the energy of the colliding cleons. But in this study attention will be confined solely to the potential description, valid at low energies.

The interaction between nucleons observed at low energies obviously has its genesis in the strong-interaction dynamics of hadrons.[1,2] Novel strides in strong-interaction dynamics have, understandably, given rise to corresponding ones in the *NN* interaction. The meson-exchange *NN* potentials and the reggeon exchanges are striking examples.[3,4] In recent years the spectacular success of the non-Abelian color gauge field theory in explaining hadron spectra (especially the spectra of the charmed mesons) suggests that the successful models of the new strong-interaction theory of quantum chromodynamics (QCD) be brought to bear upon this long standing problem of the *NN* interaction.

The pertinent question now is this: What exactly is lacking and unsatisfactory in the present understanding of the *NN* interaction at low energies? At a phenomenological level, there is a fairly reliable description of the *NN* interaction. The most modern of such descriptions use, for the *NN* interaction, a sum of one-meson-exchange potentials.[3,4] The forms of these meson-exchange potentials, as obtained from the nonrelativistic reduction of meson field theory, are employed in these descriptions, and often the meson-nucleon coupling constants are determined only from a

© 1980 The American Physical Society

fit to the phase-shift data.[5] Furthermore, all the mesons belonging to the SU(3) octets and singlets are included, thus tremendously complicating the description of the phenomena. If one admits of such a complex description, then a very good χ^2 fit to the phase-shift data is possible.[4,5] The reasons for considering such a phenomenological description unsatisfactory are twofold. Firstly, a description involving numerous mesons, notwithstanding its success, goes counter to the aesthetic principle of simplicity. Secondly, the objection that the meson-exchange potentials—coming as they do from meson field theory—ignore completely the quark constitution of hadrons (which is now well established[6,7]) is unassailable.[3]

At the level of microscopic theories, only the long-range part of the *NN* interaction can be said to have been understood. And this is attributed to the exchange of a single pion.[1,2] To explain the hard core at very short distances, physicists have had to invoke the exchange of the heavier vector mesons ρ and ω and ϕ.[4,8] To account for every specific aspect of the *NN* interaction, a new meson is brought in thereby making the theoretical framework very complex. Indeed, it would be more satisfying to have a simpler theory of the phenomenon, one in which all that which is achieved here by meson nonets is achieved by one or, at the most, two "elementary" quanta or particles. In view of the tremendous success of QCD or the potential models thereof,[8] the question arises as to the possibility of deriving the *NN* potential from this modern theory of strong-interaction dynamics. This question is not an entirely new one and has been in existence for a couple of years.[7,9-11] The aim of this study is to provide a satisfactory answer to this question. Quite apart from these reasons, the new emerging ideology of D. Robson in nuclear structure based on the exchange of colored quarks[12] suggests that the *NN* interaction comes about precisely, through the exchange of constituent quarks. The preliminary success of a phenomenological bond model based on colored quarks[12,13] points to the fact that there is some measure of truth in the concept of quark exchange between nucleons.

Therefore, the objective of this study is to calculate rigorously the *NN* potential which arises from the exchange of colored quarks. The interaction between nucleons which arise in this way can be likened to the van der Waals interaction between atoms. Just as this van der Waals interaction stems from the Coulomb potentials between electrons and protons, the present *NN* interaction originates from the potential (arising from one-gluon exchange with confinement) between colored quarks which constitute colorless (i.e., color singlet) hadrons. Because baryons are colorless, the interaction between them, based on color, can only be a feeble vestige of that between colored quarks themselves, even as the interaction between two He atoms (which are electronically saturated and therefore "colorless") is only a pale vestige of the electrostatic interactions between the constituent electrons and protons.[3]

The theoretical framework employed here can be dubbed the one-gluon exchange with an *ad hoc* confining potential (OGEC) model. The precise meaning of this terminology will become clear in Sec. II A. The starting point is the quark-quark (*qq*) phenomenological interaction, used by De Rújula, Georgi, and Glashow,[6] together with an *ad hoc* confining potential. The calculation of the potential between two clusters of three quarks each is then performed more or less along the lines of the resonating group method of Wheeler.[14] But in order to carry out this calculation, it becomes necessary to determine the quark masses and coupling constants in a reliable way, for the strength of the quark-exchange potential (QEP) in the various channels would depend critically on these values. This determination is analogous to the determination of the pionic mass and the pion-nucleon coupling constant, which are inputs to the meson field-theoretic potentials. As already mentioned, there have been few attempts to calculate the *NN* potential arising from quark exchanges.[7,9-11] The serious drawbacks of these calculations are that the quark masses and the coupling constants have been sloppily determined and the radial dynamics of quarks in nucleons has either been parametrized or treated unrealistically. On account of this, statements concerning the strengths of the potential in various channels cannot be taken to be authentic. The OGEC constants used in this study have been reliably determined from the masses of the *s*-wave baryons, and their consistency with some other *s*-wave baryonic data has also been checked.[15] The space-wave functions which describe the radial dynamics of quarks in nucleons have also been determined from a dynamical approach to *s*-wave baryon spectra.[15] Using these reliable OGEC constants and cluster wave functions (WF's), the *NN* potential arising from quark exchanges has been calculated.

The emergence of the general structure for the NN interaction in the form

$$V=V_c(R)+V_{ls}(R)\vec{\mathrm{L}}\cdot(\vec{\mathrm{S}}_a+\vec{\mathrm{S}}_b)+V_t(R)\frac{\hat{\mathrm{S}}_{ab}}{4} \qquad (1.1)$$

(though not explicitly shown, all the *V*'s include the various exchanges) ***from the qq OGEC potential has been here rigorously demonstrated for the first time.*** The salient results of this calculation are as follows: (i) The central part of the QEP in the odd channels is strongly repulsive at short distances, *thereby showing that the colored quark-exchange mechanism is capable of yielding the property of saturation of nuclear forces*; (ii) the distance at which strong repulsion abruptly sets in tallies with the *core* radius of the nucleon calculated in a previous study[15]; (iii) the spin-orbit part of the QEP has the "inverted" character, which is observed experimentally, and the tensor part in the various channels has the right signatures; and (iv) the QEP suffers from the serious drawback *of insufficient attraction in the intermediate range*. In view of this limitation, it does not qualify to be the sole mechanism behind all the observed features of the *NN* interactions.

The organization of the paper is as follows. In Sec. II, the theoretical framework is set up. Firstly, the theoretical basis for the phenomenological OGEC *qq* potential is discussed. Subsequently, the six-quark WF is constructed, and a definition is given for the nonrelativistic *NN* QEP. In the third section, the structure of the QEP in the spaces of spin, isospin, and color spin is discussed. The spin-isospin (SI) structure of the spin-spin, spin-orbit, tensor, and central interactions are discussed in that order. In Sec. IV, the radial structure of the QEP is considered. The radial dependence of the central, spin-orbit, and tensor interactions are examined, in that order. Having been assembled, the QEP's central, spin-orbit, and tensor parts are separately compared with the corresponding pieces of the phenomenological potentials in Sec. V. In the same section, the possibility of including the L^2 interaction and the quadratic spin-orbit interaction in the QEP is pointed out. The results obtained here are then compared with those of four other contemporary calculations in Sec. VI. The present work must be considered the most reliable among these in view of the careful determination of the OGEC constants and the inclusion of quark radial dynamics. Lastly, in Sec. VII, a retrospective survey is made.

II. THEORETICAL FRAMEWORK

A. OGEC Potential between quarks

A nucleon is a cluster of three valence quarks, each of them having a distinct color, so that the nucleon WF in color space is a fully antisymmetric 3×3 Slater determinant. In high energy phenomena the interaction between hadrons (which are bound states of quarks) is described by the non-Abelian field theory of QCD. According to this theory, the dynamics of quarks is induced by the color, rather than by the flavor degrees of freedom. As hadrons are color singlets (i.e., they are colorless), it would appear on the face of it that there can be no color interaction between hadrons. It turns out that in OGEC, the direct part of the *NN* color interaction vanishes, as intuitively expected, whereas the exchange part of the color interaction between colorless hadrons is nonvanishing and contributes to the *NN* potential [see Eq. (3.1)]. The two characteristic features of this non-Abelian field theory of QCD are asymptotic freedom and infrared slavery. Asymptotic freedom is tantamount to the logarithmic vanishing of the QCD coupling constant when the quarks are very close together, and infrared slavery is the property by virtue of which quarks are unable to be isolated, i.e., quarks are always confined within hadrons. If the nonrelativistic image of the QCD field theory is to be faithful then it is essential that the OGEC potential between quarks must possess both the aforementioned non-Abelian features. While the artifice of a linear (or harmonic oscillator) confinement potential simulates very well the property of infrared slavery, a corresponding artifice for asymptotic freedom has been generally lacking.[6,7,16] But recently Richardson[17] has considered the question "Can both asymptotic freedom and infrared slavery be incorporated in a $q\bar{q}$ potential in a unified manner?" and has provided a preliminary answer to it. In the light of this investigation it is found that a potential, which incorporates asymptotic freedom, differs only in so far as being softer than a Coulomb potential, near the origin. Consequently the discrepancy between such an asymptotically free potential and the one used here is rather small. In the present analysis, the justification for ignoring asymptotic freedom is this small discrepancy between the two potentials. The question raised by J. L. Richardson deserves further investigation but this falls outside the ambit of this study.

Starting from a *part* of the total interaction Lagrangian of QCD[7];

$$\mathcal{L}'_{\text{int}} = ig \sum_{k=1}^{8} \bar{\psi} \gamma^{\mu} \lambda_k \psi (\mathcal{G}_{\mu})_k , \qquad (2.1)$$

one can derive the potential between quarks in the nonrelativistic limit be retaining terms in (2.1) to order $1/c^2$. This procedure, being almost parallel to that used in the derivation of the Fermi-Breit interaction in QED,[18] suffices to give the final result. This potential corresponds to a static one-gluon exchange between quarks, which was popularized through the work of De Rújula, Georgi, and Glashow.[6] To get the complete OGEC *qq* potential, one must add a linear (or a harmonic oscillator) confinement potential. The only other vestige of the non-Abelian nature of QCD is the color-spin scalar $\vec{F}_i \cdot \vec{F}_j$. The qq OGEC potential is then

$$V(ij)=\alpha_s\vec{F}_i\cdot\vec{F}_j\Big[b+\frac{1}{r}\Big(1-\frac{r^3}{a^3}\Big)-\frac{1}{2m^2c^2}\Big(\frac{\vec{P}_i\cdot\vec{P}_j}{r}+\frac{\vec{r}\cdot(\vec{r}\cdot\vec{P}_i)\vec{P}_j}{r^3}\Big)-\frac{\pi\hbar^2}{m^2c^2}\delta^3(\vec{r})(1+\tfrac{4}{3}\vec{S}_i\cdot\vec{S}_j)$$
$$-\frac{\hbar}{2m^2c^2r^3}[\vec{r}\times(\vec{P}_i-2\vec{P}_j)\cdot\vec{S}_i-\vec{r}\times(\vec{P}_j-2\vec{P}_i)\cdot\vec{S}_j]+\frac{\hbar^2}{m^2c^2}\Big(\frac{\vec{S}_i\cdot\vec{S}_j-3(\vec{S}_i\cdot\hat{n})(\vec{S}_j\cdot\hat{n})}{r^3}\Big)\Big]. \quad (2.2)$$

Several remarks about this potential are necessary. Here α_s represents the strong-coupling constant and is independent of the energy (logarithmic dependence of α_s on the energy is tantamount to asymptotic freedom). If this energy dependence is included before Fourier transforming the momentum space interaction from (2.1), then one arrives at a coordinate space potential which obeys asymptotic freedom.[17] In the present analysis however, with a view to avoid complications in the radial matrix element this energy dependence has been overlooked. b is a constant which is included because the confinement potential is asymptotically nonvanishing. a is the confinement constant; it is the distance at which the sum of the Coulomb and confinement potentials in (2.1) vanish. $\vec{r}=\vec{r}_i-\vec{r}_j$ and $\vec{P}_i(\vec{S}_i)$ is the momentum (spin) vector of the ith quark. Since the nucleons are composed of only the nonstrange n and p quarks (which have the same mass since the assumption is made that the electromagnetic interaction between quarks is switched off), the mass m is that which corresponds to nonstrange quarks.

It is important to note that in the OGEC potential the dominant short-range interaction is the Coulomb potential arising from the exchange of a massless gluon of the color gauge field. The spin-orbit, tensor, spin-spin, and momentum dependent potentials are only corrections to this dominant term, as borne out by their multiplicative factors $1/c^2$. The long-range dominant part is the confinement potential, which has been taken to be quadratic. Lattice gauge theories give some justification for the linear choice of a confinement potential, whereas the oscillator confinement potential has only a phenomenological basis. From a previous, careful study[15] of baryon spectroscopy based on OGEC however, it has been found that these two forms of confinement potentials are equally reliable.

The distinguishing feature of this investigation is that the OGEC constants, namely, m, α_s, a, and b, have been carefully determined from a dynamical approach to baryon spectroscopy.[15] In that approach both the linear and oscillator confinement potentials were used along with the one-gluon–exchange qq potential. The radial wave functions which were variationally determined were of two types: Exponential $[\psi \propto R^{5/2}\exp(-\beta R/2)]$ and Gaussian $[\psi \propto R^{5/2}\exp(-\frac{1}{2}\beta^2R^2)]$. The arguments R in these were again chosen to be of the following two types: $R=r_{12}+r_{23}+r_{31}$ and $R=(r_{12}^2+r_{23}^2+r_{31}^2)^{1/2}$. Thus, in all, eight cases were studied. These eight cases can be denoted by VCT, with V standing for the variational wave function $[E(G)$ for exponential (Gaussian)], C for the confinement potential $[L(H)$ for linear (harmonic oscillator) types], and T for the arguments of type I and type II indicated above. Table I exhibits the values of the OGEC constants that go in as inputs into this theory of the NN interaction.

B. The six-quark wave function

Having defined the OGEC potential between constituent colored quarks, the ground must next be prepared for the definition of the NN QEP. The

TABLE I. The four OGEC constants (α_s, a, b, m_p) determined from a dynamical approach to baryon spectroscopy (Ref. 15). The meaning of VCT is explained in Sec. II A. The constants in the qq potential (2.2) are thus accurately known. The somewhat larger value for the nonstrange quark mass (m_p = 575 MeV) is vindicated in Ref. 15. The quark mass has the same value for all the eight cases studied. The quantity β is a property of the quark radial wave function, i.e., of the dynamics; even though it varies with the cases, the rms charge radius of the proton is roughly constant for all the eight cases (Ref. 15). The case relevant to this study is GH II.

Case: *VCT*	$\frac{\alpha_s}{\hbar c}$	a (fm)	$-2\alpha_s b$ (MeV)	β (fm^{-1})
GH I	0.4584	0.4332	−1886.52	1.14
GL I	0.4672	0.2748	−2431.82	1.12
GH II	0.5918	0.4655	−1710.68	2.02
GL II	0.5932	0.3100	−2251.43	2.00
EH I	0.3241	0.3998	−2077.32	3.82
EL I	0.3786	0.2372	−2609.23	3.72
EH II	0.4424	0.4417	−1894.77	6.69
EL II	0.4569	0.2757	−2420.43	6.60

intuitive concept of this potential is the following. Imagine two nucleons separated by a distance $\vec{R}$. By virtue of the qq interaction defined in (2.2), this configuration of the two nucleons corresponds to a certain potential energy, and when we change $\vec{R}$, this potential energy follows this change, and the NN QEP is just this potential energy. Mathematically, if $\hat{V}$ is the potential energy between six quarks and $|\Psi\rangle$ is the state of six quarks, then the potential energy is $\propto\langle\Psi|\hat{V}|\Psi\rangle$. Essentially, if we sharpen this definition, we would have the NN QEP, which can then be subsequently calculated. The above argument suggests that first of all the six quark wave function be constructed, corresponding to the two-nucleon spatial configuration specified above.

Let $\phi_a(123)$, $\phi_b(456)$ be the completely antisymmetric WF's for the two-nucleon clusters a and b situated at a distance $\vec{R}$ apart. The completely antisymmetric wave function Ψ for six quarks (i.e., for the two nucleon system) can be built up) from the basis function ϕ_a, ϕ_b for three-quark subsystems,

$$\Psi=\frac{1}{\sqrt{20}}\sum_{\alpha=1}^{20}(-1)^{\alpha}\hat{P}_{\alpha}[\phi_a(123)\phi_b(456)]_{ST}\times F_{ST}\left(\frac{\vec{r}_1+\vec{r}_2+\vec{r}_3-\vec{r}_4-\vec{r}_5-\vec{r}_6}{3}\right). \tag{2.3}$$

In (2.3) the cluster WF's ϕ_a, ϕ_b are coupled to total spin (isospin) $S(T)$ so that Ψ is a state of sharp spin (isospin) $S(T)$. And F_{ST} is the WF describing the relative motion of the clusters a and b. The operators $\{\hat{P}_{\alpha}\}$ are all possible *inter-cluster* permutations, and the sign $(-1)^{\alpha}$ is the signature of the permutation $\hat{P}_{\alpha}$. This six-quark WF can be cast in a more convenient "cluster-antisymmetrized" form

$$\Psi=\frac{1}{\sqrt{10}}\left(1-\sum_{\substack{i\in a\\ j\in b}}\hat{P}_{ij}\right)[\phi_a(123)\phi_b(456)]_{ST}\times\psi_{ST}\left(\frac{\vec{r}_1+\vec{r}_2+\vec{r}_3-\vec{r}_4-\vec{r}_5-\vec{r}_6}{3}\right), \tag{2.4}$$

ere

$$\psi_{ST}(\vec{R})=\frac{1}{\sqrt{2}}[F_{ST}(\vec{R})+(-1)^{S+T+1}F_{ST}(-\vec{R})],$$

and

$$a(b)=\{1,2,3\}(\{4,5,6\}).$$

An advantage of the cluster-antisymmetrized form is that it is an illustration of the validity of the spin-statistics theorem of Ehrenfest and Oppenheimer.[19]

C. Definition of the NN quark exchange potential

Let H be a six-quark Hamiltonian defined through the two-body interactions (2.2), i.e.,

$$H=\sum_{i=1}^{6}T_i+\tfrac{1}{2}\sum_{i=1}^{6}\sum_{j=1}^{6}{}'V(ij). \tag{2.5}$$

Considering the sum of the kinetic energies (KE) of the three quarks in nucleon $a(b)$, this sum is equal to the KE of these three quarks *about* the center of mass of nucleon $a(b)$ together with the KE of the center of mass of nucleon $a(b)$.[20] Calling the latter parts T_a, T_b, their sum can again be split up into two parts, namely, the KE of the reduced mass particle of the nucleons a and b and the KE of the center of mass of nucleons a and b. If all calculations are performed in the center-of-mass frame of the nucleons a and b, then the latter term in the KE drops out giving

$$\sum_{i=1}^{6}T_i=t_a+t_b+\frac{\vec{p}^{\,2}}{3m}. \tag{2.6}$$

Here $t_a(t_b)$ denote the KE of three quarks *about* the center of mass of their respective nucleon $a(b)$, i.e., it is the internal KE while $\vec{p}^{\,2}/3m$ represents the KE of the reduced mass particle of nucleons a and b each having a mass $3m$ (m being the quark mass).

Before the potential energy term in (2.5) is considered, we observe a result which will be used in the sections to follow. If $\hat{P}$ is the sum of the nine permutation operators $\hat{P}_{ij}$ in (2.4), then

$$\begin{aligned}\langle\Psi|\Psi\rangle&=\tfrac{1}{10}\langle\phi_a\overrightarrow{(123)}\phi_b^{S,T}(456)\psi_{ST}|(1-\hat{P})(1-\hat{P})|\phi_a\overrightarrow{(123)}\phi_b^{S,T}(456)\psi_{ST}\rangle\\&=\langle\phi_a\overrightarrow{(123)}\phi_b^{S,T}(456)\psi_{ST}|(1-\hat{P})|\phi_a\overrightarrow{(123)}\phi_b^{S,T}(456)\psi_{ST}\rangle.\end{aligned} \tag{2.7}$$

is norm $\mathfrak{N}$ is invariant under the two sets of rmutations of the indices i,j; i, $j\in a$ and of the lices k,l; $k,l\in b$. Use of these two symmetries duces (2.7) to the form

$$\mathfrak{N}=\langle\phi_a\phi_b\psi_{ST}|(1-9\hat{P}_{36})|\phi_a\phi_b\psi_{ST}\rangle. \tag{2.8}$$

To prevent the notation from becoming clumsy, from this point onwards, the arguments of ϕ_a and

ϕ_b can be suppressed, and also the coupling symbol $\overset{S,T}{\_}$ —which indicates that the nucleonic cluster functions have been coupled to have a total spin (isospin) of $S(T)$—can be dropped. For the expectation value (EV) of the potential energy operator in (2.5) in the state Ψ, one has

$$\left\langle\Psi\left|\tfrac{1}{2}\sum_{i=1}^{6}\sum_{j=1}^{6}{}' V(ij)\right|\Psi\right\rangle$$

$$=\tfrac{1}{10}\left\langle\phi_a\phi_b\psi_{ST}\left|(1-\hat{P})\tfrac{1}{2}\sum_{ij}{}' V(ij)(1-\hat{P})\right|\right.$$

$$\left.\times\,\phi_a\phi_b\psi_{ST}\right\rangle .$$

So long as the indices i,j in the above sum span all the six quarks, $\hat{P}$ commutes with the total potential energy operator. In this way, the operator in the EV becomes $\frac{1}{2}\sum'_{ij}V(ij)(1-\hat{P})$; using again the two symmetries of the indices pertaining to the two clusters, this EV can be reduced to the form

$$\left\langle\phi_a\phi_b\psi_{ST}\left|\tfrac{1}{2}\sum_{i=1}^{6}\sum_{j=1}^{6}{}' V(ij)(1-9\hat{P}_{36})\right|\phi_a\phi_b\psi_{ST}\right\rangle . \qquad (2.9)$$

The qq interactions in the above sum can be divided into two sets: *intercluster interactions* and *intracluster interactions*. These intracluster qq interactions together with the internal KE's t_a+t_b in (2.6) contribute to the rest mass of the two nucleon clusters, namely, $2M_N$. Subtracting out this rest mass from the EV $\langle\Psi|H|\Psi\rangle$, one has

$$\langle\Psi|H|\Psi\rangle-\varepsilon\langle\Psi|\Psi\rangle$$

$$=\left\langle\phi_a\phi_b\psi_{ST}\left|\frac{\vec{p}^{\,2}}{3m}(1-9\hat{P}_{36})\right|\phi_a\phi_b\psi_{ST}\right\rangle$$

$$+\left\langle\phi_a\phi_b\psi_{ST}\left|\sum_{\substack{i\,\in\,a\\ j\,\in\,b}} V(ij)(1-9\hat{P}_{36})\right|\phi_a\phi_b\psi_{ST}\right\rangle$$

$$-\varepsilon\langle\phi_a\phi_b\psi_{ST}|(1-9\hat{P}_{36})|\phi_a\phi_b\psi_{ST}\rangle . \qquad (2.10)$$

Functional variation of this expression with respect to Ψ_{ST} yields the following Schrödinger equation for the relative motion of the two nucleons:

$$\frac{\vec{p}^{\,2}}{3m}\psi_{ST}+\left\langle\phi_a\phi_b\left|\sum_{\substack{i\,\in\,a\\ j\,\in\,b}} V(ij)(1-9\hat{P}_{36})\right|\phi_a\phi_b\psi_{ST}\right\rangle\Big/\mathfrak{N}$$

$$=\varepsilon\psi_{ST} \qquad (2.11)$$

In this formulation, the QEP is defined by the second term on the left hand side of (2.11). The identification of the QEP with this term would have been exact had the bare reduced mass $3m/2$ been equal to $\frac{1}{2}M_N$. This equality can come about only if mass renormalization is performed, but this is outside the scope of the present nonrelativistic framework. In any case, the NN interaction can be defined by the second term on the left-hand side of (2.11). The remainder of this paper is concerned with the calculation of this EV. Robson's definition of the QEP[12] is a particular case of the definition given here, and it suffers from the drawback of ignoring all but the $V(36)$ term in the summation in (2.11). The error involved in this omission will be discussed in subsequent sections.

III. GENERAL STRUCTURE OF THE QEP

The evaluation of the QEP in the subspaces of color, spin-isospin (SI) and ordinary space is considered now in that order. The EV defining the QEP is invariant under two sets of symmetry operations: permutations of any pair of indices $\in$ nucleon a and permutations of any pair of indices $\in$ nucleon b. Using these two symmetries, the direct part of the QEP can be brought to the form

$$\mathcal{V}_D=9\langle\phi_a\phi_b|V(36)|\phi_a\phi_b\rangle .$$

This direct term vanishes on account of ϕ_a,ϕ_b being color singlets.

Thus the NN interaction arises solely from the antisymmetrization of the six-quark WF, i.e., only when quarks are exchanged between the two nucleons. Using the two symmetries specified above and the additional $(123)\longleftrightarrow(456)$ symmetry of the EV, the exchange part of the QEP can be reduced to

$$\mathcal{V}=-9\left\langle\phi_a\phi_b\left|\sum_{\substack{i\in a\\ j\in b}} V(ij)\hat{P}_{36}\right|\phi_a\phi_b\right\rangle$$

$$=-9\langle\phi_a\phi_b|[4V(14)+4V(16)+V(36)]\hat{P}_{36}|\phi_a\phi_b\rangle . \qquad (3.1)$$

A. Evaluation of the color EV's

The permutation operator in (3.1) acts on all the subspaces: color, SI, and ordinary space,

$$\hat{P}_{36}=\hat{P}^{C}_{36}\hat{P}^{\sigma}_{36}\hat{P}^{\tau}_{36}\hat{P}^{x}_{36} . \qquad (3.2)$$

For the group $\mathrm{SU}_C(3)$, the permutation operator is

$$\hat{P}^{C}_{36}=\tfrac{1}{3}+2\vec{\mathbf{F}}_3\cdot\vec{\mathbf{F}}_6 . \qquad (3.3)$$

The form given in Robson's paper[12] is incorrect. Considering first the 14 term in (3.1) as an illustration, the EV in color subspace is (suppressing the arguments of ζ_a,ζ_b),

$$\Gamma(14)=\langle\zeta_a\zeta_b|\vec{\mathbf{F}}_1\cdot\vec{\mathbf{F}}_4(\tfrac{1}{3}+2\vec{\mathbf{F}}_3\cdot\vec{\mathbf{F}}_6)|\zeta_a\zeta_b\rangle .$$

Direct calculations gives

$$\Gamma(14)=\tfrac{2}{9}\sum_{\alpha,\beta}\tfrac{1}{4}\,\mathrm{Tr}^2(F(\alpha)F(\beta))=\tfrac{1}{9} ,$$

since[21]

$$\mathrm{Tr}(F(\alpha)F(\beta))=\tfrac{1}{2}\delta_{\alpha\beta} . \qquad (3.4)$$

Thus the QEP, after completing the color algebra for the remaining two cases, acquires the form

$$\mathcal{V} = -4\langle \phi_a\phi_b | [V(14) + V(36) - 2V(16)] \times \hat{P}^{\sigma\tau x}_{36} | \phi_a\phi_b\rangle . \quad (3.5)$$

B. Evaluation of the spin-isospin EV's

The first step will consist in the calculation of the norm defined in (2.8). It will be helpful to remember that the cluster functions therein are coupled to total spin (isospin) $S(T)$. Color algebra (namely, the EV $\langle \zeta_a\zeta_b | \hat{P}^C_{36} | \zeta_a\zeta_b\rangle$) gives a factor $\frac{1}{3}$, and disentangling the space part from the SI part, one has

$$\mathfrak{N} = 1 - 3\langle \phi_a\phi_b | \hat{P}^x_{36} | \phi_a\phi_b\rangle \langle \phi_a\phi_b | \hat{P}^{\sigma\tau}_{36} | \phi_a\phi_b\rangle . \quad (3.6)$$

In Appendix A, it is shown that the SI EV in (3.6) possesses a factorization property, and calculating the various $9-j$ symbols therein, one has

$$\begin{aligned}\mathfrak{N} = 1 - 3\langle \phi_a\phi_b | \hat{P}^x_{36} | \phi_a\phi_b\rangle &\times[(S-\tfrac{1}{2})(T-\tfrac{1}{2}) + 2(\tfrac{1}{2}-S/3)(\tfrac{1}{2}-T/3) \\ &+ \tfrac{1}{9}(\tfrac{1}{2}+S/3)(\tfrac{1}{2}+T/3)] . \end{aligned} \quad (3.7)$$

This expression is symmetric in S and T, as it ought to be, and the factorization of the EV into space and SI parts, being a property common to all the EV's in the six-quark state, will be frequently encountered in the following paragraphs. It will be worthwhile to remember that all spin-independent qq interactions in (2.2), when averaged in the six-quark state Ψ, will have their SI structure identical to that of the norm in (3.7).

The interactions between quarks, which depend on their spins, are of the spin-spin, spin-orbit, and tensor types [see Eq. (2.2)]. Each of these types is considered separately now.

1. *The spin-spin interaction*

The starting point will be always the "color independent" form of the *NN* QEP, namely (3.5).

$$\mathcal{V}_{ss} = -4\langle \phi_a\phi_b | [V_{ss}(14) + V_{ss}(36) \times -2V_{ss}(16)] \hat{P}^{\sigma\tau x}_{36} | \phi_a\phi_b\rangle .$$

By inserting the qq interaction (2.2) in the above expression,

$$V_{ss}(ij) = -\frac{8\pi\hbar^2\alpha_s}{3m^2c^2}\delta^3(\vec{r}_{ij})\vec{S}_i\cdot\vec{S}_j , \quad (3.8)$$

and evaluating the SI EV using the result of Appendix A, one has

$$\mathcal{V}_{ss}(16) = 8\left(-\frac{8\pi\hbar^2\alpha_s}{3m^2c^2}\right) \times\langle \phi_a\phi_b | \delta^3(\vec{r}_{16})\hat{P}^x_{36} | \phi_a\phi_b\rangle f_{16}(S,T) , \quad (3.9)$$

with

$$f_{16}(S,T) = \left(\frac{3-2T}{72}\right)[S(S+1)-3] - \left(\frac{3+2T}{36}\right)\left(\frac{S(S+1)+3}{18}\right) . \quad (3.10)$$

Repeating this calculation for the 14 and 36 cases, one has

$$\mathcal{V}_{ss}(14) = -4\left(-\frac{8\pi\hbar^2\alpha_s}{3m^2c^2}\right) \times\langle \phi_a\phi_b | \delta^3(\vec{r}_{14})\hat{P}^x_{36} | \phi_a\phi_b\rangle f_{14}(S,T) , \quad (3.11)$$

with

$$f_{14}(S,T) = -\frac{(3+2S)}{36}\frac{(3+2T)}{36} + \frac{5S(3+2T)}{6(81)} + \frac{(-1)^S(3+2T)}{12(81)}(\tfrac{3}{2} - S(S+1)^2 , \quad (3.12)$$

and

$$\mathcal{V}_{ss}(36) = -4\left(-\frac{8\pi\hbar^2\alpha_s}{3m^2c^2}\right) \times\langle \phi_a\phi_b | \delta^3(\vec{r}_{36})\hat{P}^x_{36} | \phi_a\phi_b\rangle f_{36}(S,T) , \quad (3.13)$$

with

$$\begin{aligned} f_{36}(S,T) = \frac{3+2T}{9} &- 2\left(\frac{(3+2T)(2-S)(S+3)}{36\times 36} + \frac{S(S+1)(3-2T)}{72} + \frac{(2T-1)(1-S)}{8}\right) \\ &- 3\left(\frac{(2S-1)(2T-1)}{16} + \frac{(3-2S)(3-2T)}{72} + \frac{(3+2S)(3+2T)}{36\times 36}\right) . \end{aligned} \quad (3.14)$$

The spin-spin interaction between nucleons a and b can now be cast in the canonical form of a central potential with the Wigner, Bartlett, Heisenberg, and Majorana exchanges.[32] Inserting the foregoing results into (3.5),

$$\mathcal{V}_{SS} = V^{ss}_C + V^{ss}_\sigma \vec{\sigma}_a\cdot\vec{\sigma}_b + V^{ss}_\tau \vec{\tau}_a\cdot\vec{\tau}_b + V^{ss}_{\sigma\tau}(\vec{\sigma}_a\cdot\vec{\sigma}_b)(\vec{\tau}_a\cdot\vec{\tau}_b) , \quad (3.15)$$

and taking the trace of both sides of (3.15), one obtains

$$\begin{aligned} V^{ss}_C &= -\tfrac{1}{4}[3m_s(36) + \tfrac{1}{3}m_s(14) + 2m_s(16)] , \\ V^{ss}_\sigma &= -\tfrac{1}{36}[-m_s(36) + m_s(14) - 2m_s(16)] , \\ V^{ss}_\tau &= -\tfrac{1}{108}[9m_s(36) + m_s(14) - 6m_s(16)] , \\ V^{ss}_{\sigma\tau} &= -\tfrac{1}{324}[-25m_s(36) + m_s(14) + 10m_s(16)] , \end{aligned} \quad (3.16)$$

where the $m_s(ij)$ are the radial EV's given by

$$m_s(ij)=-\frac{8\pi\hbar^2\alpha_s}{3m^2c^2}\langle\phi_a\phi_b|\delta^3(\vec{r}_{ij})\hat{P}^{x}_{36}|\phi_a\phi_b\rangle\,. \quad (3.17)$$

2. The spin-orbit interaction

The starting point is again (3.5) with the qq spin-orbit potential being given by

$$V_{ls}(ij)=\frac{-\hbar\alpha_s}{2m^2c^2}\times\left(\frac{\vec{r}_{ij}\times(\vec{p}_i-2\vec{p}_j)\cdot\vec{S}_i-\vec{r}_{ij}\times(\vec{p}_j-2\vec{p}_i)\cdot\vec{S}_j}{r_{ij}^3}\right). \quad (3.18)$$

It is shown starting from this interaction that it implies a spin-orbit interaction between the two nucleons. As has been the practice up to now, the 16 calculation is carried out in some detail, and subsequently the corresponding results for the remaining two cases are presented. The general EV for the 16 case has the structure

$$\mathcal{V}_{ls}(16)=8\left(\frac{-\hbar\alpha_s}{2m^2c^2}\right)\times\langle\phi_a\phi_b|(\vec{A}\cdot\vec{S}_1+\vec{B}\cdot\vec{S}_6)\hat{P}^{\sigma\tau}_{36}\hat{P}^{x}_{36}|\phi_a\phi_b\rangle\,. \quad (3.19)$$

From (3.18) it is seen that the vectors $\vec{A}$, $\vec{B}$ act only upon the O(3) states so that, as far as the SI space is concerned, they may be treated as constant vectors.

The factorization property embodied in (A11) of Appendix A leads to the following structure of the SI EV:

$$\langle\phi_a\phi_b|\vec{A}\cdot\vec{S}_1\hat{P}^{\sigma\tau}_{36}|\phi_a\phi_b\rangle=\frac{1}{4}\sum_{ll'}4\left\{\begin{array}{ccc} l & \frac{1}{2} & \frac{1}{2}\\ \frac{1}{2} & l' & \frac{1}{2}\\ \frac{1}{2} & \frac{1}{2} & T\end{array}\right\}\mu_{\vec{A}\cdot\vec{s}_1}(16)\,, \quad (3.20)$$

with

$$\mu_{\vec{A}\cdot\vec{s}_1}(16)=\langle(l\tfrac{1}{2})\tfrac{1}{2},(l\tfrac{1}{2})\tfrac{1}{2};S,M|\vec{A}\cdot\vec{S}_1\hat{P}^{\sigma}_{36}|\times(l\tfrac{1}{2})\tfrac{1}{2},(l'\tfrac{1}{2})\tfrac{1}{2};S,M\rangle\,,$$

$$\mu_{\vec{A}\cdot\vec{s}_1}(16)=\vec{A}\cdot\vec{S}\left[l(l+1)\left\{\begin{array}{ccc} l & \frac{1}{2} & \frac{1}{2}\\ \frac{1}{2} & l' & \frac{1}{2}\\ \frac{1}{2} & \frac{1}{2} & 1\end{array}\right\}-\frac{l(l+1)}{6}\left\{\begin{array}{ccc} \frac{1}{2} & l' & \frac{1}{2}\\ \frac{1}{2} & l & \frac{1}{2}\end{array}\right\}\right], \quad (3.21)$$

and

$$\mu_{\vec{B}\cdot\vec{s}_6}(16)=\vec{B}\cdot\vec{S}\left[\frac{[3-2l'(l'+1)]}{3}\left\{\begin{array}{ccc} l & \frac{1}{2} & \frac{1}{2}\\ \frac{1}{2} & l' & \frac{1}{2}\\ \frac{1}{2} & \frac{1}{2} & 1\end{array}\right\}-\tfrac{1}{2}[3-2l(l+1)]\left\{\begin{array}{ccc} \frac{1}{2} & \frac{1}{2} & l\\ \frac{1}{2} & \frac{1}{2} & l'\end{array}\right\}\right], \quad (3.22)$$

and the EV of $\vec{B}\cdot\vec{S}_6$ has the structure similar to that of $\vec{A}\cdot\vec{S}_1$ [see Eq. (3.20)]. The results corresponding to (3.21) and (3.22) for the 14 and 36 cases are

$$\mu_{\vec{C}\cdot\vec{s}_4}(14)=\vec{C}\cdot\vec{S}\left[l'(l'+1)\left\{\begin{array}{ccc} l & \frac{1}{2} & \frac{1}{2}\\ \frac{1}{2} & l' & \frac{1}{2}\\ \frac{1}{2} & \frac{1}{2} & 1\end{array}\right\}-\frac{l'(l'+1)}{6}\left\{\begin{array}{ccc} \frac{1}{2} & \frac{1}{2} & l\\ \frac{1}{2} & \frac{1}{2} & l'\end{array}\right\}\right], \quad (3.23)$$

$$\mu_{\vec{D}\cdot\vec{s}_3}(36)=\vec{D}\cdot\vec{S}\left[\frac{[3-2l(l+1)]}{3}\left\{\begin{array}{ccc} l' & \frac{1}{2} & \frac{1}{2}\\ \frac{1}{2} & l & \frac{1}{2}\\ \frac{1}{2} & \frac{1}{2} & 1\end{array}\right\}-\frac{[3-2l'(l'+1)]}{6}\left\{\begin{array}{ccc} \frac{1}{2} & \frac{1}{2} & l\\ \frac{1}{2} & \frac{1}{2} & l'\end{array}\right\}\right]. \quad (3.24)$$

These could have been obtained from (3.21) and (3.22)—in so far as their ll' dependence is concerned—by interchanging l and l'. This symmetry stems from the (123) ⟷ (456) symmetry which is possessed by all these EV's. Performing the ll' summation in (3.20), after substituting for (3.21) and (3.22), one has

$$\mathcal{V}_{ls}(16)=-\frac{8\hbar\alpha_s}{2m^2c^2}\langle\phi_a\phi_b|\hat{O}_{16}\hat{P}^{x}_{36}|\phi_a\phi_b\rangle\,, \quad (3.25)$$

where

$$\hat{O}_{16}=\vec{A}(16)\cdot\vec{S}f_1(T)+\vec{B}(16)\cdot\vec{S}f_2(T)\,,$$

and

$$\vec{A}(16)[\vec{B}(16)]=\frac{\vec{r}_{16}\times\vec{p}_1-2\vec{r}_{16}\times\vec{p}_6}{r_{16}^3}\left[\frac{2\vec{r}_{16}\times\vec{p}_1-\vec{r}_{16}\times\vec{p}_6}{r_{16}^3}\right], \quad (3.26)$$

$$f_1(T)=\frac{8(3+2T)}{36\times 36},$$

$$f_2(T)=\frac{(2T-1)}{8}-\frac{(2T+3)}{54\times 36}-\frac{(3-2T)}{12\times 9}.$$

The spin-orbit NN interaction arising from the 14 and 36 exchanges are, using (3.23) and (3.24),

$$\mathcal{V}_{ls}(14)=\frac{4\hbar\alpha_s}{2m^2c^2}\langle\phi_a\phi_b|\hat{O}_{14}\hat{P}_{36}^{x}|\phi_a\phi_b\rangle\,, \qquad (3.27)$$

with

$$\hat{O}_{14}=[\vec{\mathrm{A}}(14)+\vec{\mathrm{B}}(14)]\cdot\vec{\mathrm{S}}f_1(T)\,,$$

and

$$\mathcal{V}_{ls}(36)=\frac{4\hbar\alpha_s}{2m^2c^2}\langle\phi_a\phi_b|\hat{O}_{36}\hat{P}_{36}^{x}|\phi_a\phi_b\rangle\,, \qquad (3.28)$$

with

$$\hat{O}_{36}=[\vec{\mathrm{A}}(36)+\vec{\mathrm{B}}(36)]\cdot\vec{\mathrm{S}}f_2(T)\,.$$

The total spin-orbit potential is the sum of (3.25), (3.27), and (3.28).

The total spin-orbit interaction between nucleons can be cast in the canonical form. Firstly,

$$\begin{aligned}\mathcal{V}_{ls}&=\mathcal{V}_{ls}(16)+\mathcal{V}_{ls}(14)+\mathcal{V}_{ls}(36)\\&=\mathcal{V}_{ls}^{\text{even}}+\mathcal{V}_{ls}^{\text{odd}}\\&=\langle\phi_a\phi_b|\vec{\alpha}^{\text{even}}\cdot(\vec{\mathrm{S}}_a+\vec{\mathrm{S}}_b)\hat{P}_{36}^{x}|\phi_a\phi_b\rangle\\&\quad+\langle\phi_a\phi_b|\vec{\alpha}^{\text{odd}}\cdot(\vec{\mathrm{S}}_a+\vec{\mathrm{S}}_b)\hat{P}_{36}^{x}|\phi_a\phi_b\rangle\,,\end{aligned}$$

where the even and odd parts are given by

$$\begin{aligned}\vec{\alpha}^{\text{even (odd)}}=\frac{2\hbar\alpha_s}{m^2c^2}\Bigg[&\left(\frac{\vec{\mathrm{A}}(14)+\vec{\mathrm{B}}(14)}{r_{14}^{\;3}}-\frac{2\vec{\mathrm{A}}(16)}{r_{16}^{\;3}}\right)\tfrac{5}{162}\left(\tfrac{1}{54}\right)\\&+\left(\frac{\vec{\mathrm{A}}(36)+\vec{\mathrm{B}}(36)}{r_{36}^{\;3}}\right.\\&\left.-\frac{2\vec{\mathrm{B}}(16)}{r_{16}^{\;3}}\right)\tfrac{55}{486}\left(-\tfrac{100}{243}\right)\Bigg]. \qquad (3.29)\end{aligned}$$

To bring out the NN spin-orbit potential in the canonical form $\propto\vec{\mathrm{L}}_R\cdot\vec{\mathrm{S}}$, it is necessary to carry out the radial EV's in the foregoing equations. This will be taken up in the section on radial EV's (see Sec. IV C).

3. The tensor interaction

The NN interaction arising from the qq tensor potential also turns out to be tensorial. The calculation of the SI parts starts from (3.5) with the qq interactions given by

$$V_t(ij)=\frac{\hbar^2\alpha_s}{m^2c^2}\left(\frac{\vec{\mathrm{S}}_i\cdot\vec{\mathrm{S}}_j-3(\vec{\mathrm{S}}_i\cdot\hat{n})(\vec{\mathrm{S}}_j\cdot\hat{n})}{r_{ij}^{\;3}}\right),$$

and the NN tensor potential (anticipating the result) is

$$\begin{aligned}\mathcal{V}_t=-4\langle\phi_a\phi_b|[&V_t(14)+V_t(36)\\&-2V_t(16)]\hat{P}_{36}^{\sigma\tau x}|\phi_a\phi_b\rangle\,. \qquad (3.30)\end{aligned}$$

The proof is first given—for the above statement—for the case of the 16 term, and then the corresponding results for the other two cases are presented. The tensor potential (3.30) is actually a scalar obtained by contracting two second rank tensors.[23] One of these is compounded from the vector operator $\hat{n}_{ij}$ ($\hat{n}_{ij}$ is the unit vector in the direction $\vec{\mathrm{r}}_{ij}$), while the other is a second rank tensor compounded from two vector spin operators of the two particles $\vec{\mathrm{S}}_i$ and $\vec{\mathrm{S}}_j$. Therefore (3.30) can be written as

$$V_t(ij)=\frac{\hbar^2\alpha_s}{m^2c^2}\frac{1}{r_{ij}^{\;3}}T_2(\vec{\mathrm{S}}_i,\vec{\mathrm{S}}_j)\cdot T_2(\hat{n}_{ij})\,. \qquad (3.31)$$

The NN potential $\mathcal{V}_t$ arising from this, if it is truly tensorial, will have the same general structure as in (3.31), i.e., $\propto T_2(\vec{\mathrm{S}}_a,\vec{\mathrm{S}}_b)\cdot T_2(\hat{n})$, where $\hat{n}$ is a unit vector in the direction $\vec{\mathrm{R}}$. In attempting to derive the "macroscopic" tensor potential from the "microscopic" one, it will be useful to bear in mind that this derivation must necessarily proceed in two stages. The SI calculations will lead to the replacement

$$T_2(\vec{\mathrm{S}}_i,\vec{\mathrm{S}}_j)\to T_2(\vec{\mathrm{S}}_a,\vec{\mathrm{S}}_b)\,,$$

and the radial calculations to the replacement $T_2(\hat{n}_{ij})\to T_2(\hat{n})$ for all the (ij)'s in (3.31). Therefore the proof will be completed only towards the end of the section on the evaluations of the radial EV's (see Sec. IV D). For the present, the proof is carried out only for the SI parts. For illustration, the 16 case is considered in some detail and the corresponding results for the remaining two cases are then presented.

$$\begin{aligned}\mathcal{V}_t(16)=\frac{8\hbar^2\alpha_s}{m^2c^2}\Bigg\langle\phi_a\phi_b\Bigg|&\frac{1}{r_{16}^{\;3}}T_2(\vec{\mathrm{S}}_1,\vec{\mathrm{S}}_6)\cdot T_2(\hat{n}_{16})\\&\times\hat{P}_{36}^{\sigma\tau}\hat{P}_{36}^{x}\Bigg|\phi_a\phi_b\Bigg\rangle. \qquad (3.32)\end{aligned}$$

Using the factorization property of the SI EV, embodied in (A11) of Appendix A,

$$\begin{aligned}\langle\phi_a\phi_b|T_2(\vec{\mathrm{S}}_1,\vec{\mathrm{S}}_6)\cdot T_2(\hat{n}_{16})\hat{P}_{36}^{\sigma\tau}|\phi_a\phi_b\rangle\\=\tfrac{1}{4}\sum_{ll'}4\begin{Bmatrix}l&\tfrac{1}{2}&\tfrac{1}{2}\\\tfrac{1}{2}&l'&\tfrac{1}{2}\\\tfrac{1}{2}&\tfrac{1}{2}&T\end{Bmatrix}\mu_t(16)\,, \qquad (3.33)\end{aligned}$$

where

$$\mu_t(16)=\langle(l\tfrac{1}{2})\tfrac{1}{2},(l'\tfrac{1}{2})\tfrac{1}{2};S,M|T_2(\vec{\mathrm{S}}_1,\vec{\mathrm{S}}_6)\cdot T_2(\hat{n}_{16})\hat{P}_{36}^{\sigma}|(l\tfrac{1}{2})\tfrac{1}{2},(l'\tfrac{1}{2})\tfrac{1}{2};S,M\rangle\,, \qquad (3.34)$$

and after some manipulation, (3.34) can be reduced to the form

$$\left\langle S,M\left|\tfrac{1}{2}\sum_{e}(-1)^{e}T_{2-e}(\hat{n}_{16})T_{2e}(\vec{S}_1,\vec{S}_6)\right|S,M\right\rangle .$$

By successive application of Wigner-Eckart theorem and more powerful ones derived thereof,[24] one has, for this matrix element,

$$\tfrac{1}{2}\left(\frac{T_{20}(\hat{n}_{16})2[3M^2-S(S+1)]}{[(2S+3)(2S+2)(2S+1)(2S)(2S-1)]^{1/2}}\right.$$

$$\left.\times[S]\sqrt{[2]}\,\delta_{S,1}\begin{Bmatrix}\frac{1}{2} & \frac{1}{2} & 1\\ \frac{1}{2} & \frac{1}{2} & 1\\ 1 & 1 & 2\end{Bmatrix}\right)$$

$$\times\tfrac{1}{2}\langle(l)\tfrac{1}{2}\|\vec{S}_{12}\|(l\tfrac{1}{2})\tfrac{1}{2}\rangle$$

$$\times\langle(l'\tfrac{1}{2})\tfrac{1}{2}\|\vec{S}_6\|(l'\tfrac{1}{2})\tfrac{1}{2}\rangle . \tag{3.35}$$

By considering now the EV $\langle S,M|\hat{T}_2(\vec{S}_a,\vec{S}_b)\cdot T_2(\hat{n}_{16}|S,M\rangle$, it can be shown to be $=\frac{3}{2}\times$ the quantity in the curly brackets in (3.35). Finally evaluating the two reduced matrix elements in (3.35), the EV $\mu_t(16)$ can be written as a tensor interaction between the two nucleons a and b, in so far as the spin structure is concerned,

$$\mu_t(16)=T_2(\vec{S}_a,\vec{S}_b)\cdot T_2(\hat{n}_{16})$$
$$\times\{\tfrac{1}{5}l(l+1)[\tfrac{3}{2}-l'(l'+1)]\} . \tag{3.36}$$

The remainder of the proof will be carried out in the section on the radial EV's (see Sec. IVD). The results analogous to (3.36) for the 14 and 36 cases are

$$\mu_t(14)=T_2(\vec{S}_a,\vec{S}_b)\cdot T_2(\hat{n}_{14})\left(\frac{l(l+1)l'(l'+1)}{9}\right), \tag{3.37}$$

$$\mu_t(36)=T_2(\vec{S}_a,\vec{S}_b)\cdot T_2(\hat{n}_{36})\{\tfrac{2}{3}[\tfrac{3}{2}-l(l+1)]$$
$$\times\tfrac{2}{3}[\tfrac{3}{2}-l'(l'+1)]\} . \tag{3.38}$$

Inserting (3.36) in (3.33) and carrying out the l, l' summation, one has

$$\mathcal{V}_t(16)=\frac{8\hbar^2\alpha_s}{m^2c^2}\frac{1}{36}\left((3-2T)-\frac{(3+2T)}{9}\right)$$
$$\times\langle\phi_a\phi_b|\frac{T_2(\vec{S}_a,\vec{S}_b)\cdot T_2(\hat{n}_{16})}{r_{16}{}^3}\hat{P}^x_{36}|\phi_a\phi_b\rangle , \tag{3.39}$$

$$\mathcal{V}_t(14)=-\frac{4\hbar^2\alpha_s}{m^2c^2}\left(\frac{3+2T}{81}\right)$$
$$\times\langle\phi_a\phi_b|\frac{T_2(\vec{S}_a,\vec{S}_b)\cdot T_2(\hat{n}_{14})}{r_{14}{}^3}\hat{P}^x_{36}|\phi_a\phi_b\rangle , \tag{3.40}$$

and

$$\mathcal{V}_t(36)=-\frac{4\hbar^2\alpha_s}{m^2c^2}\left(\frac{(3+2T)}{9\times 36}+\frac{(2T-1)}{4}+\frac{(2T-3)}{18}\right)$$
$$\times\langle\phi_a\phi_b|\frac{T_2(\vec{S}_a,\vec{S}_b)\cdot T_2(\hat{n}_{36})}{r_{36}{}^3}\hat{P}^x_{36}|\phi_a\phi_b\rangle . \tag{3.41}$$

The tensor interaction is generally decomposed into even ($T=1$) and odd ($T=0$) parts,

$$\mathcal{V}_t=\mathcal{V}_t^{\text{even}}+\mathcal{V}_t^{\text{odd}},$$

$$\mathcal{V}_t^{\text{even (odd)}}=\frac{4\hbar^2\alpha_s}{m^2c^2}\langle\phi_a\phi_b|T_2(\vec{S}_a,\vec{S}_b)\cdot\mathcal{T}^{\text{even (odd)}}$$
$$\times\hat{P}^x_{36}|\phi_a\phi_b\rangle ,$$

where

$$\mathcal{T}^{\text{even (odd)}}=\tfrac{3}{81}(\tfrac{12}{81})\frac{T_2(\hat{n}_{16})}{r_{16}{}^3}-\tfrac{8}{81}(-\tfrac{3}{81})\frac{T_2(\hat{n}_{14})}{r_{14}{}^3}$$
$$-\tfrac{17}{81}(+\tfrac{32}{81})\frac{T_2(\hat{n}_{36})}{r_{36}{}^3} . \tag{3.42}$$

When the evaluation of these radial EV's is complete, it will be found that $T_2(\hat{n}_{ij})\rightarrow T_2(\hat{n})$ where $\hat{n}$ = unit vector in the direction of $\vec{R}$.

4. The central interaction

The SI structure of the central interactions will obviously be the same as that of the norm $\mathfrak{N}$ of the six-quark WF. There are essentially four different types of central interactions between quarks: Coulombian, oscillator, $\delta(\vec{r})$, and the momentum dependent potential [see (2.2)]. The last of these is the most difficult to evaluate, as will be seen in the forthcoming section on the radial EV's.

The central qq interactions give rise to central NN potentials with all the four types of exchanges. It is customary to cast this interaction in the standard form, analogous to (3.15). The direct part of the interaction is absent on account of nucleons being color singlets [see the text preceeding (3.1)]; only the exchange interaction contributes. From the starting point (3.5), one has

$$\mathcal{V}_c=-4\langle\phi_a\phi_b|[V_c(14)+V_c(36)-2V_c(16)]\hat{P}^x_{36}|\phi_a\phi_b\rangle$$
$$\times\left(\frac{(2S-1)(2T-1)}{4}+\frac{2(3-2S)(3-2T)}{36}\right.$$
$$\left.+\frac{(3+2S)(3+2T)}{9\times 36}\right), \tag{3.43}$$

with the SI dependence being identical to that in the norm $\mathfrak{N}$ given by (3.7). Putting this equal to

$$V_c+V_\sigma\cdot\vec{\sigma}_a\cdot\vec{\sigma}_b+V_\tau\cdot\vec{\tau}_a\cdot\vec{\tau}_b$$
$$+V_{\sigma\tau}(\vec{\sigma}_a\cdot\vec{\sigma}_b)(\vec{\tau}_a\cdot\vec{\tau}_b) . \tag{3.44}$$

The component V's can be evaluated by trace methods already outlined [see sequel to (3.15)]. Finally, substituting these values of V's back into (3.44),

$$\mathcal{V}_c = -\rho - \tfrac{1}{9}\rho\cdot\vec{\sigma}_a\cdot\vec{\sigma}_b - \tfrac{1}{9}\rho\cdot\vec{\tau}_a\cdot\vec{\tau}_b - [illegible]\,\rho\cdot(\vec{\sigma}_a\cdot\vec{\sigma}_b)(\vec{\tau}_a\cdot\vec{\tau}_b)\,, \tag{3.45}$$

with

$$\rho = \langle\phi_a\phi_b|[V_c(14)+V_c(36)-2V_c(16)]\hat{P}^x_{36}|\phi_a\phi_b\rangle\,,$$

where V_c is the sum of the four central interactions mentioned earlier. This structure of ρ is very crucial, in making the *NN* interaction independent of the OGEC constant b in (2.2). The $[11-2]$ structure of the *NN* interaction [see (3.5)] is responsible for b being totally absent in the *NN* potential. Contrary to this, the role played by b in baryon spectroscopy was very decisive in obtaining a good fit to the baryonic levels.[15]

Having determined the SI structure of the *NN* QEP, attention is now turned to the determination of the radial dependence of the QEP.

IV. THE STRUCTURE OF THE QEP IN COORDINATE SPACE

Since the EV's are the averages in a six-quark state, the radial matrix elements are really 18-dimensional integrals. As in the treatment of the SI EV's, the various types of interactions can be examined sequentially. Before embarking on this program, it is proper that the nucleon radial WF ϕ_a be accurately defined. Up to this point, these WF's were kept quite general, but for calculational purposes these must be given specific forms. In the work on baryon spectroscopy, carried out by these authors,[15] two arguments R were used for ϕ_a, as were two forms for ϕ_a. The arguments were of a collective nature: $r_{12}+r_{23}+r_{31}$, $(r_{12}^2+r_{23}^2+r_{31}^2)^{1/2}$. For ϕ_a, both exponential and Gaussian forms were used. Without going into the reasons for this choice here, the following definition of ϕ_a suffices:

$$\phi_a(123) = \eta\exp[-\tfrac{1}{2}\beta^2(r_{12}^2+r_{23}^2+r_{31}^2)]\,, \tag{4.1}$$

where η, the normalization factor, $=(3\sqrt{3}/\pi^3)^{1/2}\beta^3$. In the present calculation only the normalized WF in (4.1) is used. Physicists have long since been familiar with Gaussian integrals, which can be evaluated in closed form; this is their main advantage. The value of β, which characterizes the WF and is compatible with s-wave baryonic data, is given in Table I.

A. The radial norm

A glance at (3.6) suggests the following definition for the radial norm:

$$\mathfrak{N}(R) = \langle\phi_a(123)\phi_b(456)|\hat{P}^x_{36}|\phi_a(123)\phi_b(456)\rangle\,. \tag{4.2}$$

The structure of the radial EV's appears in (2.11). The value of such a matrix element will depend critically upon the definition of the exchange operator $\hat{P}^x_{36}$. This exchange operator not only exchanges $\vec{r}_3$ and $\vec{r}_6$ between $\phi_a(123)$ and $\phi_b(456)$, but also interchanges these two coordinates in the argument of the WF $\psi_{ST}(\vec{R})$, for the relative motion. Since $\vec{R}=\frac{1}{3}(\vec{r}_4+\vec{r}_5+\vec{r}_6-\vec{r}_1-\vec{r}_2-\vec{r}_3)$, one has

$$\hat{P}^x_{36}\phi_a(123)\phi_b(456)\psi_{ST}(\vec{R}) = \phi_a(126)\phi_b(453)\psi_{ST}\left(\frac{\vec{r}_4+\vec{r}_5+\vec{r}_3-\vec{r}_1-\vec{r}_2-\vec{r}_6}{3}\right).$$

Taylor expanding the WF of relative motion to first order,

$$\psi_{ST}(\hat{P}^x_{36}\vec{R}) = \psi_{ST}(\vec{R}) + \tfrac{2}{3}\vec{r}_{36}\cdot\vec{\nabla}_R\psi_{ST}(\vec{R})\,, \tag{4.3}$$

and the omission of the higher order terms is justified since $\psi_{ST}(\vec{R})$ is expected to vary slowly with $\vec{R}$. Now it turns out that *for all interactions excepting the spin-orbit one*, the contribution of the gradient term to the radial EV vanishes by virtue of the parity selection rule, whereas for the spin-orbit interaction, the matrix element corresponding to the first term vanishes while that corresponding to the second makes a nonzero contribution. Thus the action of $\hat{P}^x_{36}$ on $\vec{R}$ is included here contrary to the practice in molecular physics, and this action can be consistently defined for all the parts of the *qq* interactions in (2.2).

The radial norm (4.2) falls in the first category of EV's which do not receive any contribution from the second term in (4.3). This amounts to ignoring the action of $\hat{P}^x_{36}$ on $\psi_{ST}(\vec{R})$. All the calculations are performed in the center-of-mass frame of the dinucleon system. Thus (4.2) has the structure, if (4.1) is used,

$$\mathfrak{N}(R) = \eta^4\int\prod_{i=1}^{6}d\vec{r}_i\exp(-\tfrac{1}{2}\beta^2\{\rho_a^2+\rho_b^2+\rho_a'^2+\rho_b'^2\})\times\delta\left(\frac{\vec{r}_1+\vec{r}_2+\vec{r}_3}{3}+\frac{\vec{R}}{2}\right)\times\delta\left(\frac{\vec{r}_4+\vec{r}_5+\vec{r}_6}{3}-\frac{\vec{R}}{2}\right), \tag{4.4}$$

with

$$\begin{aligned}\rho_a^2(\rho_a'^2) &= r_{12}^2+r_{23}^2(r_{26}^2)+r_{13}^2(r_{16}^2)\,,\\ \rho_b^2(\rho_b'^2) &= r_{45}^2+r_{46}^2(r_{43}^2)+r_{56}^2(r_{53}^2)\,.\end{aligned} \tag{4.5}$$

The presence of the two delta functions needs some explanation. Going back to (2.11) and remembering that the QEP is defined at a fixed value of the argument of ψ_{ST}, namely $\vec{R}$, it can be seen that all these radial EV's must be carried out for a fixed value of $\vec{R}$. This is achieved by inserting a delta function $\delta[\vec{R}-\frac{1}{3}(\vec{r}_1+\vec{r}_2+\vec{r}_3-\vec{r}_4-\vec{r}_5-\vec{r}_6)]$ in the EV. The fact that all calculations are carried out in the center-of-mass frame of reference, when stated mathematically, is tantamount to the insertion of another delta function in the radial EV, $\delta[\frac{1}{3}(\vec{r}_1+\vec{r}_2+\vec{r}_3)-\frac{1}{3}(\vec{r}_4+\vec{r}_5+\vec{r}_6)]$. The pair of delta functions appearing in (4.4) are entirely equivalent to the ones mentioned above, as can be verified by inspection. These Gaussian three-dimensional integrals are easily evaluated in closed form using the results of Appendix B. The radial norm is thus found to be

$$\mathfrak{N}(R)=\frac{64}{27\times5\times\sqrt{5}}\exp(-\tfrac{3}{5}\beta^2R^2). \tag{4.6}$$

B. The EV's of central potentials

The central potentials are four in number: Coulomb, oscillator (confinement), delta function, and the potential bilinear in the quark momenta. The Coulomb potential will be considered first. From (3.5), it is seen that three distinct EV's contribute to the *NN* potential. Calculations show that a Coulomb potential between quarks leads to a $\operatorname{erf}(CR)/R$ potential between the nucleons. Contrary to the practice of illustrating the calculation for a specific pair of quark indices, only the final results of the calculations are presented for the EV's of the central potentials.

The Coulomb radial EV's, which enter into (3.45), are proportional to

$$M_{ch}(ij)=\alpha_s\left\langle\phi_a\phi_b\left|\frac{1}{|\vec{r}_{ij}|}\hat{P}^x_{36}\right|\phi_a\phi_b\right\rangle. \tag{4.7}$$

The general structure of these EV's is found to be

$$M_{ch}(ij)=\alpha_s\times\mathfrak{N}(R)\frac{C_{ij}}{R}\operatorname{erf}(A_{ij}\beta R), \tag{4.8}$$

where $\operatorname{erf}(x)$ is the error function (see Appendix B). The values of the coefficients in (4.8) for all the three cases appear in Table II.

The radial EV's of the next central potential, namely, that of the harmonic oscillator, are proportional to

$$M_{cn}(ij)=-\frac{\alpha_s}{a^3}\langle\phi_a\phi_b|r_{ij}^2\hat{P}^x_{36}|\phi_a\phi_b\rangle. \tag{4.9}$$

Calculations show that these EV's can be brought to the form

$$M_{cn}(ij)=-\frac{\alpha_s}{a^3}\frac{\mathfrak{N}(R)}{\beta^2}\left(C'_{ij}+\frac{\beta^2R^2}{C_{ij}^2}\right). \tag{4.10}$$

The coefficients C'_{ij} for the three cases are listed in Table II. It can be seen from this expression that the harmonic confinement potential between quarks leads to a harmonic potential between the nucleons.

The radial EV's of delta-function potentials are proportional to

$$M_d(ij)=-\frac{\alpha_s\pi\hbar^2}{m^2c^2}\langle\phi_a\phi_b|\delta(\vec{r}_{ij})\hat{P}^x_{36}|\phi_a\phi_b\rangle, \tag{4.11}$$

and the radial spin-spin EV's are simply related to these

$$M_s(ij)=\tfrac{2}{3}M_d(ij). \tag{4.12}$$

Calculations yield the structure

$$M_d(ij)=-\frac{\alpha_s\pi\hbar^2}{m^2c^2}\mathfrak{N}(R)\beta^3\times C_{ij}^{3/2\,(1)}\exp(\beta^2A_{ij}^2R^2). \tag{4.13}$$

The presence of the Gaussian factors, over and above that in the radial norm, indicates that the *qq* delta-function interaction leads to an extremely short range *NN* potential. And even the strength of this potential is quite small, in view of the c^2 factor in the denominator.

The last of the central potentials whose radial EV's are necessary is the potential between the quarks which is bilinear in the momenta of the quarks. From the mathematical point of view, the evaluation of these EV's is extremely laborious. The EV's are proportional to

$$M_{pp}(ij)=-\frac{\alpha_s}{2m^2c^2}\langle\phi_a\phi_b|\left(\frac{\vec{p}_i\cdot\vec{p}_j}{|\vec{r}_{ij}|}+\frac{\vec{r}_{ij}\cdot(\vec{r}_{ij}\cdot\vec{p}_i)\vec{p}_j}{|\vec{r}_{ij}|^3}\right)\times\hat{P}^x_{36}|\phi_a\phi_b\rangle. \tag{4.14}$$

The calculations (with suppressed details) show that these EV's have a structure given by

TABLE II. The entries in the table [see Eqs. (4.8), (4.10), and (4.13)] define completely the radial part of the *NN* potential arising from the indicated *qq* interactions.

ij	Coulomb: $1/r$		Confinement: r^2		Delta function: $\delta(\vec{r})$	
	C_{ij}	A_{ij}	C'_{ij}	$(1/C_{ij}^2)$	$C_{ij}^{(1)}$	A_{ij}
14	$\frac{10}{12}$	$3(\frac{3}{10})^{1/2}$	$\frac{4}{5}$	$(\frac{6}{5})^2$	$15/8\pi$	$3(\frac{3}{16})^{1/2}$
36	$\frac{10}{6}$	$3(\frac{1}{30})^{1/2}$	$\frac{6}{5}$	$(\frac{3}{5})^2$	$5/4\pi$	$3(\frac{1}{20})^{1/2}$
16	$\frac{10}{9}$	$3(\frac{27}{140})^{1/2}$	$\frac{7}{10}$	$(\frac{9}{10})^2$	$15/7\pi$	$3(\frac{27}{140})^{1/2}$

TABLE III. The entries in the table [see (4.15)] define completely the radial part of the NN potential arising from the qq potential bilinear in the quark momenta.

ij	A_{ij}	C_{ij}	D_{ij}	G_{ij}	F_{ij}
14	$3(\frac{3}{10})^{1/2}\beta R$	$5/9\beta^2$	$\frac{9}{32}$	$\frac{15\sqrt{15}}{90\sqrt{2\pi}}\frac{1}{\beta}$	0
36	$3\beta R/\sqrt{20}$	$44/3\beta^2$	$\frac{14}{5}$	$\frac{72}{\sqrt{20\pi}}\frac{1}{\beta}$	0
16	$9\sqrt{3}/2\sqrt{35}\,\beta R$	$146/27\beta^2$	1	$\frac{17\sqrt{15}}{21\sqrt{7\pi}}\frac{1}{\beta}$	$\frac{45\sqrt{15}}{98\sqrt{7\pi}}\beta$

$$M_{pp}(ij)=\frac{\alpha_s\hbar^2}{2m^2c^2}\beta^4\mathfrak{N}(R)$$
$$\times\left(\frac{\operatorname{erf}(A_{ij})}{R}(C_{ij}-D_{ij}R^2)\right.$$
$$\left.-\exp(-A_{ij}^2)\{G_{ij}+F_{ij}R^2\}\right). \qquad (4.15)$$

The values of these coefficients are tabulated in Table III. It is seen that this relativistic correction term leads to a Coulomb-type interaction between the nucleons. There is an additional contribution which resembles a delta-like interaction [see (4.13)] between nucleons. And yet another contribution which amounts to a damped harmonic interaction between the two nucleons.

C. The radial EV's of the spin-orbit term

The proof for the qq spin-orbit interaction going over to the NN spin-orbit interaction was suspended halfway in Sec. III B 2. Here, in this section, this remainder of the proof is carried to its conclusion. In essence it must be shown now that the radial EV's of the vectors $\vec{\alpha}^{\text{even(odd)}}$ in (3.29) are proportional to the angular momentum $\vec{L}_R$ of the relative motion of the two nucleons.

Recapitulating the discussion in Sec. IV A on the definition of $\hat{P}^x_{36}$, this operator must now be made to act on $\psi_{ST}(\vec{R})$, the WF for the relative motion of the two nucleons. The radial spin-orbit EV's are proportional to

$$M_{1s}(ij)=-\frac{\hbar\alpha_s}{2m^2c^2}\langle\phi_a\phi_b|\left(\frac{\vec{A}(ij)+\vec{B}(ij)}{|\vec{r}_{ij}|^3}\right)\cdot\vec{S}$$
$$\times\hat{P}^x_{36}|\phi_a\phi_b\psi_{ST}\rangle, \qquad (4.16)$$

where the vectors $\vec{A}(ij)$, $\vec{B}(ij)$ are defined in (3.26), and $\vec{S}$ is the total spin of the two nucleons, i.e., $=\vec{S}_a+\vec{S}_b$. The result of the calculations of the radial EV's is

$$M_{1s}(ij)=\frac{\alpha_s\hbar^2}{2m^2c^2}\frac{\mathfrak{N}(R)}{R}C_{ij}\frac{d}{dR}$$
$$\times\left\{\frac{D'_{ij}}{R}\operatorname{erf}(A_{ij}\beta R)\right\}\vec{L}_R\cdot\vec{S}\psi_{ST}\,. \qquad (4.17)$$

TABLE IV. The entries in the table define completely the radial structure [see (4.17) and (4.23)] of the NN spin orbit and tensor potentials arising from the corresponding qq potentials.

ij	Spin-orbit potential C_{ij}	D'_{ij}	A_{ij}	Tensor potential C_{ij}	A_{ij}
14	$\frac{5}{6}$	$\frac{10}{6}$	$3(\frac{3}{10})^{1/2}$	$\frac{5}{6}$	$3(\frac{3}{10})^{1/2}$
36	$\frac{5}{3}$	$\frac{10}{3}$	$3(\frac{1}{20})^{1/2}$	$\frac{5}{3}$	$3(\frac{1}{20})^{1/2}$
16	$\frac{10}{9}$	$\frac{10}{9}$	$\frac{9}{2}(\frac{3}{35})^{1/2}$	$\frac{10}{9}$	$\frac{9}{2}(\frac{3}{35})^{1/2}$

The coefficients occurring in this result are all listed in Table IV. The constant $\hbar$ that usually goes with an angular momentum operator has been lumped, in this case, along with the multiplicative constants. Thus the spin-orbit NN interaction has now been finally put in the canonical form.

D. The radial EV's of the tensor interaction

A glance at the end of Sec. III B 3 shows that when the radial EV's are evaluated. It would amount to the quantities $T^{\text{even(odd)}}$ being replaced by $T_2(\hat{n})$. In this section the latter half of this proof is carried through.

With the aid of the identity

$$\frac{\vec{S}_a\cdot\vec{S}_b-3(\vec{S}_a\cdot\hat{n})(\vec{S}_b\cdot\hat{n})}{r^3}$$
$$=-(\vec{S}_a\cdot\vec{\nabla})(\vec{S}_b\cdot\vec{\nabla})\left(\frac{1}{r}\right)-\frac{4\pi}{3}\vec{S}_a\cdot\vec{S}_b\delta(\vec{r}), \qquad (4.18)$$

the EV of (3.31) can be put in the form

$$t_{ij}=\langle\phi_a\phi_b|\tfrac{1}{3}T_2(\vec{S}_a,\vec{S}_b)\cdot T_2(\vec{\nabla}_{ij})\frac{1}{r_{ij}}\hat{P}^x_{36}|\phi_a\phi_b\rangle\,. \qquad (4.19)$$

Using Fourier integral representations and completeness expansions, the EV (4.19) can be calculated, and the results are

$$t_{36}=\frac{1}{2\pi^2}\left(\frac{4\pi}{3}\right)\mathfrak{N}(R)T_2(\vec{S}_a,\vec{S}_b)\cdot T_2(\hat{R})$$
$$\times\int K^2dK\,j_2\left(\frac{3KR}{5}\right)\exp\left(\frac{-K^2}{5\beta^2}\right). \qquad (4.20)$$

For the remaining two cases, one has

$$t_{14}=\frac{1}{2\pi^2}\left(\frac{4\pi}{3}\right)\mathfrak{N}(R)T_2(\vec{S}_a,\vec{S}_b)\cdot T_2(\hat{R})$$
$$\times\int K^2dK\,j_2\left(\frac{6KR}{5}\right)\exp\left(\frac{-2K^2}{15\beta^2}\right), \qquad (4.21)$$

$$t_{16}=\frac{1}{2\pi^2}\left(\frac{4\pi}{3}\right)\mathfrak{N}(R)T_2(\vec{S}_a,\vec{S}_b)\cdot T_2(\hat{R})$$
$$\times\int K^2dK\,j_2\left(\frac{9KR}{10}\right)\exp\left(\frac{-7K^2}{60\beta^2}\right). \qquad (4.22)$$

Defining $m_t(ij) = -(\alpha_s\hbar^2/m^2c^2)t_{ij}$ and carrying out the $\vec{K}$ integrations, one obtains

$$m_t(ij) = -\frac{\alpha_s\hbar^2}{m^2c^2}\mathfrak{N}(R)\left(\frac{C_{ij}}{R}\right)^2 n\gamma(\tfrac{5}{2}, A_{ij}{}^2\beta^2R^2)$$

$$\times T_2(\vec{S}_a, \vec{S}_b)\cdot T_2(\hat{R}), \qquad (4.23)$$

where $n\gamma(\frac{5}{2}, x)$ is the normalized incomplete Gamma function[26] of order $\frac{5}{2} = \gamma(\frac{5}{2}, x)/\Gamma(\frac{5}{2})$, and the coefficients C_{ij}, A_{ij} are the ones listed in Tabel IV. At this stage it can be appreciated that the occurrence of the incomplete Gamma function of order $\frac{5}{2}$ can be traced to the use of the Gaussian quark WF's. If some other choice had been made for these quark WF's then there would be, correspondingly, a different function in place of $n\gamma(\frac{5}{2}, x)$. In any case, whichever quark radial WF's one might use, the tensorial character of the *NN* interaction will not be perturbed and will emerge finally, as in (4.23). From (4.23) it is possible to evaluate the even and the odd parts of the *NN* tensor potentials $\mathcal{V}^{\text{even(odd)}}$ defined towards the end of Sec. III B3.

Up to this point all the effort has gone into the derivation of the *NN* potential—starting with the *qq* interaction—and its casting in the canonical form. Now it remains to be seen whether this *NN* potential, arising from the exchange of colored quarks, has any measure of truth in it. For this purpose the 14, 16, and 36 parts which have been separately calculated must be brought together according to (3.5), the general expression for the *NN* QEP. Once this is done, it will be possible to numerically calculate the strengths of these *NN* potentials in the various channels.

V. COMPARISON OF THE QEP WITH PHENOMENOLOGICAL POTENTIALS

The three main parts of the QEP, appearing in (1.1), are now assembled with a view to compare their radial profiles with the corresponding ones of phenomenological potentials.

A. The central part of the QEP

Both the central potential (i.e., all the four types of *qq* potentials discussed in Sec. III B4) and the spin-spin potential contribute to the total *NN* central potential $V_c^{\text{tot}}(R)$ in (1.1). The detailed structure is given by (3.5),

$$V_c^{\text{tot}}(R) = V_c(R) + V_\sigma(R)\vec{\sigma}_a\cdot\vec{\sigma}_b + V_\tau(R)\vec{\tau}_a\cdot\vec{\tau}_b$$

$$+ V_{\sigma\tau}(R)(\vec{\sigma}_a\cdot\vec{\sigma}_b)(\vec{\tau}_a\cdot\vec{\tau}_b), \qquad (5.1)$$

where

$$V_c(R) = -\tfrac{2}{3}[3m_c(36) + \tfrac{1}{3}m_c(14)$$

$$+ 2m_c(16)] + \phi(R), \qquad (5.2)$$

$$V_\sigma(R) = -\tfrac{2}{27}[-m_c(36) + m_c(14)$$

$$- 2m_c(16)] + \tfrac{1}{9}\phi(R), \qquad (5.3)$$

$$V_\tau(R) = -\tfrac{2}{81}[9m_c(36) + m_c(14)$$

$$- 6m_c(16)] + \tfrac{1}{9}\phi(R), \qquad (5.4)$$

$$V_{\sigma\tau}(R) = -\tfrac{2}{243}[-25m_c(36) + m_c(14)$$

$$+ 10m_c(16)] + \tfrac{32}{81}\phi(R). \qquad (5.5)$$

In the above four equations the quantities occurring in the square brackets represent the spin-spin-delta-function interaction, while $\phi(R)$ represents the contribution arising from the four types of central potentials. This latter quantity is given by

$$\phi(R) = 2[m_d(16) + m_{cn}(16) + m_{cb}(16) + m_{pp}(16)]$$

$$- [m_d(14) + m_{cn}(14) + m_{cb}(14) + m_{pp}(14)]$$

$$- [m_d(36) + m_{cn}(36)$$

$$+ m_{cb}(36) + m_{pp}(36)], \qquad (5.6)$$

and these matrix elements $m_x(ij)$ have already been calculated in Secs. III and IV. The phenomenological *NN* potentials[1,2,8] are known in each of

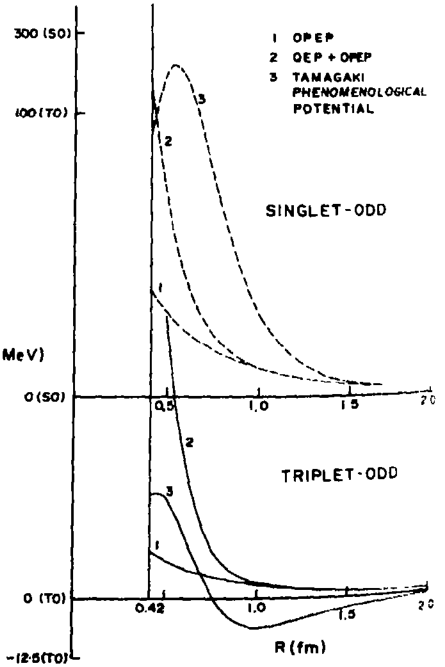

FIG. 1. A comparison of the central components of the QEP+OPEP, OPEP (Ref. 1) and the Tamagaki phenomenological potentials (Ref. 8) in the singlet-odd (SO) and the triplet-odd (TO) channels. The Tamagaki hard-core radius is at 0.42 fm.

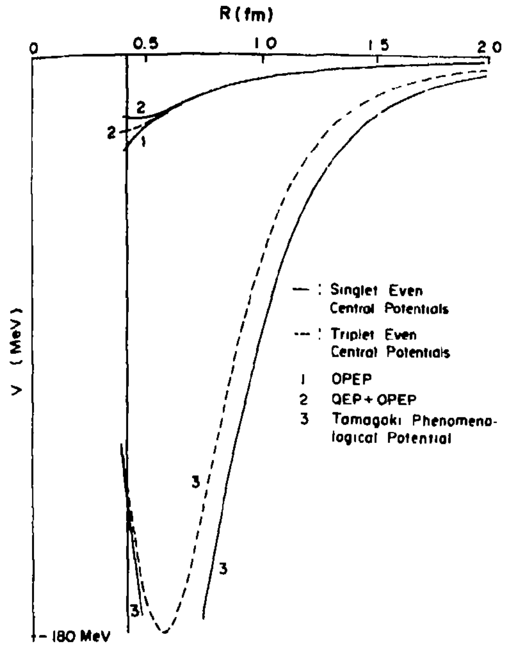

FIG. 2. A comparison of the central components of the QEP+OPEP, OPEP (Ref. 1) and the Tamagaki phenomenological potentials in the even channels. The OPEP has the same radial variation for both the even channels. The Tamagaki hard-core radius is at 0.42 fm.

the four dinucleon states: singlet even, singlet odd, triplet even, and triplet odd. To compare the QEP with such potentials, it is necessary to take the EV of Eq. (5.1) in each of these four states $|S,T\rangle$. Doing this, one has

$$\begin{aligned}\langle V_c^{\text{tot}}(R)\rangle_{SE}&=V_c(R)-3V_\sigma(R)+V_\tau(R)-3V_{\sigma\tau}(R)\,,\\ \langle V_c^{\text{tot}}(R)\rangle_{SO}&=V_c(R)-3V_\sigma(R)-3V_\tau(R)+9V_{\sigma\tau}(R)\,,\\ \langle V_c^{\text{tot}}(R)\rangle_{TE}&=V_c(R)+V_\sigma(R)-3V_\tau(R)-3V_{\sigma\tau}(R)\,,\\ \langle V_c^{\text{tot}}(R)\rangle_{TO}&=V_c(R)+V_\sigma(R)+V_\tau(R)+V_{\sigma\tau}(R)\,.\end{aligned}\tag{5.7}$$

Here, S and T stand for the singlet and triplet, and E and O stand for even and odd, respectively. These four potentials are plotted as function of R in Figs. 1 and 2. In these same figures one can contrast the QEP with the one-pion exchange potential (OPEP) and the phenomenological potentials. The contributions to the central part of the QEP from only the spin-spin interactions are also exhibited in Figs. 3 and 4.

1. The hard core

The phenomenological $^1S_0$ phase-shift data show that beyond about 250 MeV the phase shift changes from a positive to a negative value. With the phase shift being roughly the difference between the perturbed action and the unperturbed one, it is easy to see that its sign will be opposite to that of the scattering potential.[26] What this means is that at higher energies the NN interaction acquires a repulsive component. The occurrence of such a repulsion is welcome since it is found adequate to explain the saturation property of nuclei. The onset of such a repulsion only at higher energies can be simulated by a potential which is very strongly repulsive at short distances (the hard

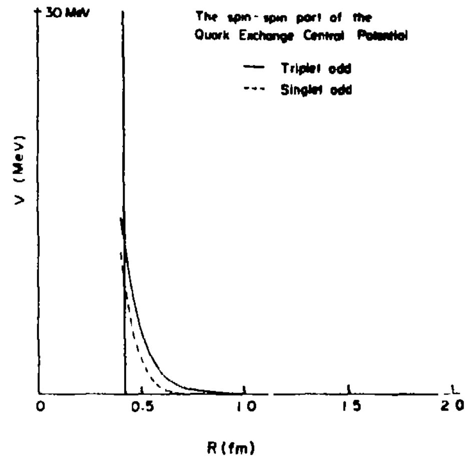

FIG. 3. The spin-spin qq interaction (Eq. 3.12) leads to the above repulsive central NN interaction in the odd channels. The potentials continue to be more repulsive within the Tamagaki hard-core radius at 0.42 fm.

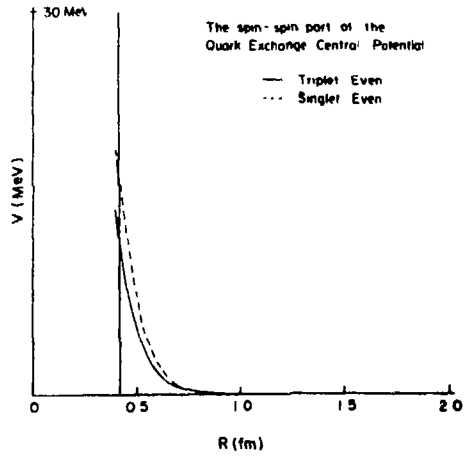

FIG. 4. Same as Fig. 3, but for the even channels.

core). This particular representation of the energy dependence of the $^1S_0$ phase shift is by no means unique, even within the potential framework. Finite repulsive potentials (i.e., soft core) at short distances, as also momentum dependent potentials, are capable of reproducing this phase-shift data. In the following it will be seen that the QEP gives the short-range strong repulsion and hence the property of saturation of nuclear forces.

The central part of the QEP in the odd channels is strongly repulsive at short distances. This is shown in Fig. 1. Also, there is reasonable agreement with the Tamagaki phenomenological potential.[8] However, the central part is only weakly attractive in the even channels (see Fig. 2), contrary to the behavior of the pehnomenological potentials. The insignificant attraction in the triplet even state suggests that the colored quark exchange mechanism is not adequate to keep the deuteron bound. The spin-spin interaction is found to contribute repulsion in all the four channels of the central potential (see Figs. 3 and 4). It is also found that in the even channels the QEP is repulsive inside the hard core, a feature which also appears in the investigation of Ribeiro.[27] Whereas, in Ribeiro's analysis this short-range repulsion is ascribed to the *qq* confinement interaction; in the present model it arises from the short-range spin-spin *qq* intreaction. Similar conclusions are also reached in the work of Liberman[9] and in a calculation of the *NN* potential as given by the MIT[28] bag model of QCD.

As regards the origin of this repulsion, Machida and Namiki[29] had ascribed the hard core of the *NN* interaction to the exclusion principle. However, it turns out that when color is introduced one can construct[7] a six-quark wave function with the spatial structure $(1s)^6$ so that the exclusion principle in itself does not rule out six quarks being localized—as in a *NN* collision. The repulsion observed in the QEP at short distances originates from the gluon interaction rather than from the exclusion principle. Lastly, if one were to define the radius of the short-range repulsion in the QEP to be nearabout the point of steepest rise, it is seen from Fig. 1 that this $\simeq 0.55$ fm. The consistency of this value with the hard-core radius expected on the grounds that the nucleon core size is $\simeq 0.3$ fm (Ref. 15) is indeed noteworthy.

2. *The intermediate range*

As pointed out above, the QEP's central part falls short of providing sufficient attraction in the triplet even and singlet even states in the intermediate range. The implication is that the deuteron cannot be bound by this mechanism of exchange of colored quarks. As it is impossible to alter the shape of the QEP curves—since the theory is truly microscopic and all the OGEC constants have been reliably fixed once for all—this conclusion of insufficient binding is irrevocable.

B. Spin-orbit part

Putting together the 14, 16, and 36 terms of the spin-orbit potentials into (3.5), one has in the various dinucleon states

$$\langle V^{\text{tot}}_{ls}(R)\rangle_{\text{TO}} = \tfrac{2}{243}[140m_{ls}(16) - 15m_{ls}(14) - 55m_{ls}(36)], \tag{5.8}$$

$$\langle V^{\text{tot}}_{ls}(R)\rangle_{\text{TE}} = \tfrac{1}{81}[-88m_{ls}(16) - 6m_{ls}(14) + 50m_{ls}(36)], \tag{5.9}$$

and the spin-orbit potential obviously vanishes in both the singlet states. It is seen from Figs. 5 and 6 that the spin-orbit potential arising from the exchange of colored quarks is very weak, contrary to that observed in phenomenological potentials. However, the inverted signature of this interaction, as demanded by experiment, emerges correctly from the present theory. Within the framework of meson theory, a close connection exists between the hard-core repulsion (produced by the exchange of vector mesons) and the inverted signature of the spin-orbit *NN* potential.[30] Even though the QEP yields both the hard-core and the inverted spin-orbit interaction, the link between these two features is not transparent.

At this stage one might suppose that this deficiency of the QEP might be overcome by introducing a spin-dependent confinement potential.[18,31] Already, to have a OGEC theory of the states of charmonium—that explains all the observed splittings of levels—it has been found necessary to postulate a spin-dependent confinement potential. One therefore wonders whether a similar correction is necessary here, too. Moreover, the inclusion of this correction to the spin-orbit potential does not vitiate the values of the OGEC constants, since, for *s*-wave baryons, there is no contribution to their mass from the spin-orbit potential. Thus, replacing the quantity $-(1/r_{ij})^3$ by $(1/r_{ij})(d/dr_{ij})V(r_{ij})$ in the spin-orbit terms, one can see that if $V(r_{ij}) = (1/r_{ij}) - (r_{ij}/a)^2(1/a)$, then $-(1/r_{ij})^3 \to -(1/r_{ij})^3 - (2/a^3)$. This correction does not perturb the already right signatures obtained for the spin-orbit potential. Carrying out a little algebra, it can be seen that the correction amounts to the replacement

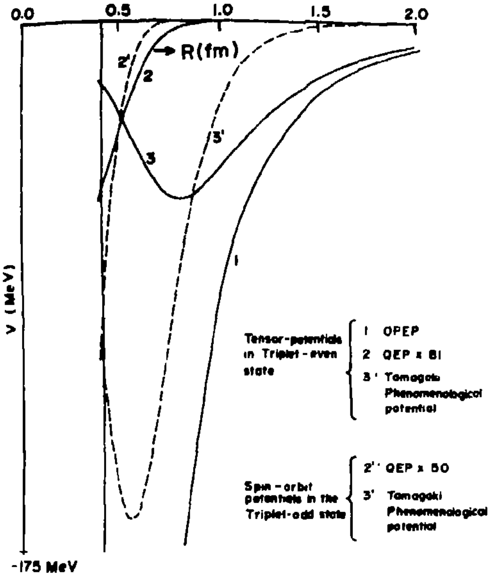

FIG. 5. A comparison of the respective tensor components and the respective spin-orbit components of the QEP, OPEP, and the Tamagaki phenomenological potential. The large magnification of the QEP indicates that its strength is quite weak. The signatures of the QEP are nevertheless correct.

$$m_{ls}(ij) \rightarrow m_{ls}(ij) - \frac{\alpha_s \hbar^3}{2m^2c^3}\left(\frac{2}{a^3}\right)\mathcal{H}(R)\eta(ij), \qquad (5.10)$$

where $\eta(14)=\frac{14}{5}$, $\eta(16)=\frac{9}{10}$, and $\eta(36)=\frac{6}{5}$. It has been found that this correction is too insignificant to alter the conclusions already reached regarding the spin-orbit potential.

It is not out of place here to record also the futility of applying a similar correction to the central part of the QEP, due to the additional spin-dependent confinement potential. This correction is tantamount to replacing $\delta(\vec{r})$—multiplying $\vec{S}_i \cdot \vec{S}_j$ in the qq interaction—by $\delta(\vec{r})+3/2\pi a^3$. In terms of the radial EV's, the replacement is $m_s(ij) \rightarrow m_s(ij) + (4/a^3)(-\alpha\hbar^2/m^2c^2)\mathcal{H}(R)$. That is to say, the correction is independent of (ij) and consequently, in view of the structure in (3.5), the total correction averages to zero. As regards the tensor potential, it can be seen that an oscillator confinement potential cannot possibly lead to a tensor potential.

C. The tensor part

The total tensor potential is found to be

$$\langle V_t^{\text{tot}}(R)\rangle_{\text{TO}} = \frac{1}{81}[2m_t(16) - 17m_t(36) - 5m_t(14)], \qquad (5.11)$$

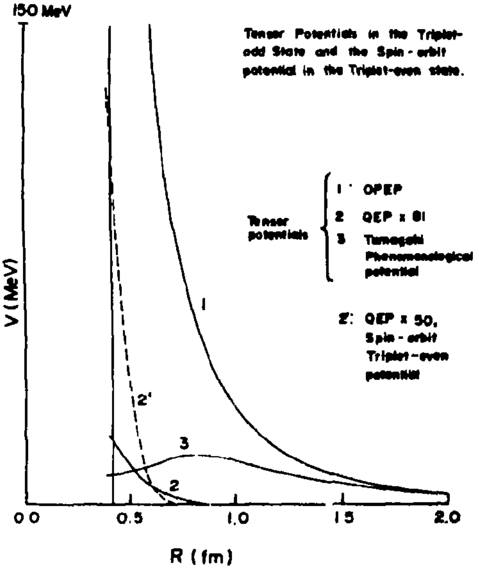

FIG. 6. See caption to Fig. 5.

$$\langle V_t^{\text{tot}}(R)\rangle_{\text{TE}} = \frac{1}{27}[4m_t(16) + 11m_t(36) - m_t(14)]. \qquad (5.12)$$

Figures 5 and 6 exhibit these plots, in comparison with those of OPEP and the phenomenological potential.[8] The QEP is seen to suffer from the drawback of insufficient strengths, even though the signatures in both the channels come out right. The weak nature of the quark-exchange tensor potentials is, however, a happy circumstance, since the OPEP supplies most of what is called for by experiment. Neither of the theoretical potentials by themselves are close to reality, but their sum, however, provides a better approximation to what is observed.

D. The L^2 and the quadratic spin-orbit terms within the QEP

In defining the action of the exchange operator on coordinate space WF's, the higher order gradient operators acting on the WF of relative motion $\psi_{ST}(R)$ were neglected on the grounds that $\psi_{ST}(\vec{R})$ varies slowly with R. If the higher order gradient operators are retained then one will arrive at the $\hat{L}^2$ term which is often included in the analysis of the phase-shift data.[1,2] The way to include the quadratic spin-orbit interaction at the NN level is straightforward. In the derivation of the qq interaction (the Fermi-Breit interaction), if the relativistic corrections $O(1/c^4)$

are also included, this term will naturally come about. In the interests of simplicity, many of such finer refinements have not been included in the present analysis.

VI. COMPARISON WITH CONTEMPORARY CALCULATIONS BASED ON QUARKS

Except for the work of Barry,[10] all the approaches to the *NN* interaction via the quark model have used colored quarks. In the work of Barry, the assumption is made that a diquark is a fermion, and the problem is thus reduced to that of two "hydrogenic atoms" interacting with each other. This treatment, moreover, lacks the merit of using reliable coupling constants and quark masses. The defect in the work of Libermann[9] is that the constants have not been well determined, and for the *qq* interaction, too restricted a choice is used. (The *qq* potential is taken to be just the sum of an oscillator potential and a "confinement" spin-spin potential.) These are probably the reasons which lead to a strong repulsion in the even channels as well of the central *NN* potential, calculated by Libermann. Kislinger[11] has calculated the *NN* force arising from the exchange of a massive dressed gluon. By arguing that interquark distances (when the quarks are in different nucleons) are nearly the same as the distance between the nucleonic clusters, he replaces the *qq* interaction by the *NN* interaction. While this assumption is justified for the radial coordinates, the same cannot be said of the spin-isospin coordinates. Moreover, the constants used have no authenticity, and quark dynamics is totally ignored. The basic observations made by Robson[12] and Ribeiro[27] are borne out in the present study—regarding the signs of the central part of the QEP in the various dinucleon channels.

VII. CONCLUSION

These labors having drawn to a close, one must examine with hindsight what ground one has covered and learn the lessons one can. What measure of reality is there in the colored quark exchange mechanism as a possible origin of the nuclear force? Certainly OGEC is not the whole story in so far as all the aspects of the *NN* interaction are concerned. Its chief merit lies in the strong short-range repulsion that it gives in the odd channels of the central part, i.e., quark exchange yields the property of saturation of nuclear forces. Its weak tensor part ties in well with the close agreement between the OPEP's tensor potential and the tesnor potential of the phenomenological potential. Considering the lack of sufficient attraction in the intermediate range, one can say that the QEP is somewhat complimentary to the OPEP.

If QCD is to be taken as the path leading to reality, then one must show on its basis how meson exchanges can exist. A preliminary step in this direction has been taken by Lovas,[3] who has shown by a simple generalization of the Okubo-Zweig-Iizuka (OZI) rule that the mesons δ, S^* will have the weak coupling strengths they have. The next step ought to be in the direction of deriving the OPEP from a possible generalization of the present OGEC model so as to include the sea quarks as well in baryons.

APPENDIX A

In evaluating the SI EV's, it is found that all of them share a common factorization property which can be brought to light by studying the structure of a typical EV,

$$M(\hat{O};S,T)=\langle\phi_a\phi_b|\hat{O}(\text{spin})\hat{P}^{\sigma}_{36}\hat{P}^{\tau}_{36}|\phi_a\phi_b\rangle\,. \tag{A1}$$

The state $|\phi_a\phi_b\rangle$ is a six-quark state of total spin (isospin) $=S(T)$. ϕ_a,ϕ_b are three quark states of spin (isospin) $=\frac{1}{2}(\frac{1}{2})$. The structure of this cluster state (being totally symmetric in the spin, isospin coordinates of three quarks) is

$$\phi_a=\frac{1}{\sqrt{2}}[\chi^{\sigma}_{S}(\tfrac{1}{2})\chi^{\tau}_{S}(\tfrac{1}{2})+\chi^{\sigma}_{A}(\tfrac{1}{2})\chi^{\tau}_{A}(\tfrac{1}{2})]\,, \tag{A2}$$

where $\chi_{S(A)}$ is a three-quark state which is symmetric (antisymmetric) in the labels of the first and second quarks and has total spin or isospin $=\frac{1}{2}$, i.e.,

$$\chi_{S(A)}=|[1(0)\tfrac{1}{2}]\tfrac{1}{2}\rangle\,. \tag{A3}$$

If the state is symmetric (antisymmetric) in the first two-quark coordinates, then the total spin or isospin of the first two quarks will be 1(0).

The structure of $|\phi_a\phi_b\rangle$ is now seen to be

$$|\phi_a\phi_b\rangle=\frac{1}{2}\sum_{l l'}|(l\tfrac{1}{2})\tfrac{1}{2},(l'\tfrac{1}{2})\tfrac{1}{2};S,M\rangle \times|(l\tfrac{1}{2})\tfrac{1}{2},(l'\tfrac{1}{2})\tfrac{1}{2};T,M_T\rangle\,. \tag{A4}$$

The EV (A1) is now seen to possess the factorization property

$$M(\hat{O};S,T)=\frac{1}{4}\sum_{l,l',l_1,l_1'}\langle(l_1\tfrac{1}{2})\tfrac{1}{2},(l_1'\tfrac{1}{2})\tfrac{1}{2};S,M|\hat{O}(\text{spin})\hat{P}^{\sigma}_{36}|(l\tfrac{1}{2})\tfrac{1}{2},(l'\tfrac{1}{2})\tfrac{1}{2};S,M\rangle \times\langle(l_1\tfrac{1}{2})\tfrac{1}{2},(l_1'\tfrac{1}{2})\tfrac{1}{2};T,M_T|\hat{P}^{\tau}_{36}|(l\tfrac{1}{2})\tfrac{1}{2},(l'\tfrac{1}{2})\tfrac{1}{2};T,M_T\rangle\,. \tag{A5}$$

Considering the simpler of these matrix elements, i.e., the one in isospin space, it can be seen that it will be diagonal in $l_1, l; l_1' l'$. The reason is that the operator $\hat{P}^{\tau}_{36}$ does not act on the coordinates 1, 2; 4, 5, which are characterized by $l_1, l; l_1', l'$. Thus, even though the spin operator $\hat{O}$ (spin) may act on the quarks 1, 2; 4, 5, the presence of the isospin-matrix element makes the spin-matrix element also diagonal in the ls. Therefore

$$M(\hat{O};S,T)=\tfrac{1}{4}\sum_{ll'}\langle (l\tfrac{1}{2})\tfrac{1}{2},(l'\tfrac{1}{2})\tfrac{1}{2};S,M\,|\,\hat{O}(\text{spin})\hat{P}^{\sigma}_{36}\,|\,(l\tfrac{1}{2})\tfrac{1}{2},(l'\tfrac{1}{2})\tfrac{1}{2};S,M\rangle$$
$$\times\langle (l\tfrac{1}{2})\tfrac{1}{2},(l'\tfrac{1}{2})\tfrac{1}{2};T,M_T\,|\,\hat{P}^{\tau}_{36}\,|\,(l\tfrac{1}{2})\tfrac{1}{2},(l'\tfrac{1}{2})\tfrac{1}{2};T,M_T\rangle\,. \tag{A6}$$

Again considering the isospin-matrix element, denoting the states by $|l,l';T,M_T\rangle$ and changing the basis to one in which $\hat{P}^{\tau}_{36}$ diagonal, one has

$$\eta_T(l,l')=\langle l,l';T,M_T\,|\,\hat{P}^{\tau}_{36}\,|\,l,l';T,M_T\rangle$$
$$=\sum_{\substack{j_{1245},j'_{1245}\\ j_{36},j'_{36}}}4\{[j_{1245}][j_{36}][j'_{1245}][j'_{36}]\}^{1/2}\begin{Bmatrix} l & l' & j_{1245}\\ \tfrac{1}{2} & \tfrac{1}{2} & j_{36}\\ \tfrac{1}{2} & \tfrac{1}{2} & T\end{Bmatrix}\begin{Bmatrix} l & l' & j'_{36}\\ \tfrac{1}{2} & \tfrac{1}{2} & j'_{36}\\ \tfrac{1}{2} & \tfrac{1}{2} & T\end{Bmatrix}$$
$$\times\langle (ll')j'_{1245},(\tfrac{1}{2}\tfrac{1}{2})j'_{36};T,M_T\,|\,\hat{P}^{\tau}_{36}\,|\,(ll')j_{1245},(\tfrac{1}{2}\tfrac{1}{2})j_{36};T,M_T\rangle\,,$$

where the last matrix-element is equal to

$$(-1)^{1+j_{36}}\delta(j_{1245},j'_{1245})\delta(j_{36},j'_{36})\,.$$

Therefore,

$$\eta_T(l,l')=\sum_{j_{36},j_{1245}}4[j_{1245}][j_{36}]\times\begin{Bmatrix} l & l' & j_{1245}\\ \tfrac{1}{2} & \tfrac{1}{2} & j_{36}\\ \tfrac{1}{2} & \tfrac{1}{2} & T\end{Bmatrix}^2(-1)^{1+j_{36}}\,, \tag{A7}$$

and $[l]=2l+1$. Using the theorem[32]

$$\sum_{j_{13},j_{24}}\begin{Bmatrix} j_1 & j_4 & j_{14}\\ j_3 & j_2 & j_{23}\\ j_{13} & j_{24} & j\end{Bmatrix}^2[j_{13}][j_{24}](-1)^{2j_2+j_{24}+j_{23}-j_{34}}$$
$$=\begin{Bmatrix} j_1 & j_4 & j_{14}\\ j_2 & j_3 & j_{23}\\ j_{14} & j_{23} & j\end{Bmatrix}. \tag{A8}$$

Equation (A7) reduces to

$$\eta_T(l,l')=4\begin{Bmatrix} l & \tfrac{1}{2} & \tfrac{1}{2}\\ \tfrac{1}{2} & l' & \tfrac{1}{2}\\ \tfrac{1}{2} & \tfrac{1}{2} & T\end{Bmatrix}. \tag{A9}$$

If $\hat{O}(\text{spin})=1$, then one has perfect symmetry between spin and isospin,

$$\eta_s(l,l')=4\begin{Bmatrix} l & \tfrac{1}{2} & \tfrac{1}{2}\\ \tfrac{1}{2} & l' & \tfrac{1}{2}\\ \tfrac{1}{2} & \tfrac{1}{2} & S\end{Bmatrix}. \tag{A10}$$

Thus (A6) becomes

$$M(\hat{O};S,T)=\tfrac{1}{4}\sum_{ll'}4\begin{Bmatrix} l & \tfrac{1}{2} & \tfrac{1}{2}\\ \tfrac{1}{2} & l' & \tfrac{1}{2}\\ \tfrac{1}{2} & \tfrac{1}{2} & T\end{Bmatrix}\times\text{spin matrix element}\,. \tag{A11}$$

Equation (A11) embodies the factorization property for the SI EV's. Repeated use will be made of this result in the text.

APPENDIX B

In evaluating the radial EV's, the following three-dimensional definite integrals are found to be useful:

$$\int d\vec{K}\exp(-B\vec{K}^2+iA\vec{K}\cdot\vec{R})=\left(\frac{\pi}{B}\right)^{3/2}\exp\left(-\frac{A^2R^2}{4B}\right), \tag{B1}$$

$$\int\frac{d\vec{K}}{\vec{K}^2}\exp(-B\vec{K}^2+iA\vec{K}\cdot\vec{R})=\pi^{3/2}\left(\frac{AR}{2}\right)^{-1}\gamma\left(\frac{1}{2},\frac{A^2R^2}{4B}\right), \tag{B2}$$

$$\int\vec{K}^2d\vec{K}\exp(-B\vec{K}^2+iA\vec{K}\cdot\vec{R})=\frac{\pi^{3/2}}{2B^{5/2}}\left(3-\frac{A^2R^2}{2B}\right)\exp\left(-\frac{A^2R^2}{4B}\right), \tag{B3}$$

$$\int\frac{d\vec{K}}{\vec{K}^2}(\vec{K}\cdot\vec{R})\exp(-B\vec{K}^2+iA\vec{K}\cdot\vec{R})=\frac{i\pi^{3/2}}{2}\times\frac{8}{A^3R}\gamma\left(\frac{3}{2},\frac{A^2R^2}{4B}\right), \tag{B4}$$

$$\int \vec{K}\cdot\vec{R}\,d\vec{K}\exp(-B\vec{K}^2+iA\vec{K}\cdot\vec{R}) = \frac{i\pi^{3/2}}{2}\frac{AR^2}{B^{5/2}}\exp\left(-\frac{A^2R^2}{4B}\right), \quad \text{(B5)}$$

$$\int \frac{(\vec{K}\cdot\vec{R})^2}{\vec{K}^2}d\vec{K}\cdot\exp(-B\vec{K}^2+iA\vec{K}\cdot\vec{R}) = \frac{8\pi^{3/2}}{A^3R}\left[-\frac{1}{2}\gamma\left(\frac{1}{2},\frac{A^2R^2}{4B}\right)+\exp\left(-\frac{A^2R^2}{4B}\right) \times\left\{\left(\frac{A^2R^2}{4B}\right)^{1/2}+\left(\frac{A^2R^2}{4B}\right)^{3/2}\right\}\right], \quad \text{(B6)}$$

$$\int \vec{x}\exp(-B\vec{x}^2-i\vec{K}\cdot\vec{x})d\vec{x} = \left(\frac{-i\vec{K}}{2B}\right)\left(\frac{\pi}{B}\right)^{3/2}\exp\left(-\frac{\vec{K}^2}{4B}\right), \quad \text{(B7)}$$

$$\int \vec{x}^2\exp(-B\vec{x}^2-A\vec{K}\cdot\vec{x})d\vec{x} = \frac{\pi^{3/2}}{2B^{5/2}}\left(3+\frac{A^2K^2}{2B}\right)\exp\left(\frac{A^2\vec{K}^2}{4B}\right), \quad \text{(B8)}$$

$$\int x_i x_j\exp(-B\vec{x}^2-i\vec{K}\cdot\vec{x})d\vec{x} = \left(\frac{-1}{4B^2}\right)(K_iK_j-2B\delta_{ij})\left(\frac{\pi}{B}\right)^{3/2}\exp\left(-\frac{\vec{K}^2}{4B}\right), \quad \text{(B9)}$$

where

$$\gamma(\tfrac{1}{2},x^2)=\sqrt{\pi}\,\mathrm{erf}(x)=2\int_0^x \exp(-t^2)dt, \quad \text{(B10)}$$

and

$$\gamma(n,x^2)=\int_0^{x^2}\exp(-t)t^{n-1}dt \quad \text{(B11)}$$

is the incomplete Gamma function of order n.

---

[1] A. Bohr and B. R. Mottelson, *Nuclear Structure* (Benjamin, Reading, 1969), Vol. I.

[2] M. J. Moravcsik, Rep. Prog. Phys. 35, 587 (1972).

[3] I. Lovas, Report No. IAEA-SMR-45 (1978).

[4] M. A. Nagels, T. A. Rijkin, and J. J. deSwart, Phys. Rev. D 12, 744 (1975); J. J. deSwart and M. M. Nagels, Report No. THEF-NYM-77.4 (1977).

[5] M. M. Nagels *et al.*, Nucl. Phys. B109, 1 (1976).

[6] A. De Rújula, H. Georgi, and S. Glashow, Phys. Rev. D 12, 147 (1975).

[7] R. H. Dalitz, in *Topics in Quantum field theory and Gauge theories (Lecture Notes in Physics), Proceedings of the 8th International Seminar on Theoretical Physics, Salamanca, Spain, 1977*, edited by J. A. de Azcárraga (Springer, New York, 1977), Vol. 77, p. 336.

[8] R. Tamagaki, Prog. Theor. Phys. 39, 91 (1968).

[9] D. A. Liberman, Phys. Rev. D 16, 1542 (1977).

[10] G. W. Barry, Phys. Rev. D 16, 2886 (1977).

[11] M. B. Kisslinger, Phys. Lett. 79B, 474 (1978).

[12] D. Robson, Nucl. Phys. A308, 381 (1978).

[13] D. Robson, Phys. Rev. Lett. 42, 876 (1979).

[14] J. A. Wheeler, Phys. Rev. 52, 1083 (1937).

[15] R. Shanker, Ph.D. dissertation, Bombay Univ., 1979 (unpublished).

[16] D. Gromes and I. O. Stamatescu, Nucl. Phys. B112, 213 (1976). L. J. Reinders, J. Phys. G 4, 241 (1978).

[17] J. L. Richardson, SLAC Report No. SLAC-PUB-2229, (1978).

[18] V. B. Berestetskii *et al.*, *Relativistic Quantum Theory* (Pergamon, New York, 1971), Vol. 4, part I, Sec. 83.

[19] D. M. Brink, *Nuclear Forces* (Pergamon, New York, 1965), p. 5.

[20] H. Goldstein, *Classical Mechanics* (Addison-Wesley, Reading, Mass., 1968), p. 8.

[21] P. Carruthers, *Introduction to Unitary Symmetry* (Interscience, New York, 1966), p. 30.

[22] Reference 1, p. 66.

[23] A. R. Edmonds, *Angular momentum in Quantum Mechanics* (Princeton University Press, Princeton, New Jersey, 1960), p. 73.

[24] Reference 23, Chap. 7.

[25] I. S. Gradshteyn and I. W. Ryzhik, *Table of Integrals, Series and Products* (Academic, New York, 1965), p. 940.

[26] L. D. Landau and E. M. Lifshitz, *Quantum Mechanics, Course of Theoretical Physics* (Pergamon, New York, 1965), Vol. III, Chap. XVII.

[27] J. Ribeiro, Ph.D. dissertation, Oxford Univ. (1978), mentioned in Ref. 7.

[28] C. DeTar, in *Fewbody Systems and Nuclear Forces*, edited by H. Zingl *et al.* (Springer, Berlin, 1978), Vol. II, p. 121.

[29] S. Machida and M. Namiki, Prog. Theor. Phys. 33, 125 (1965).

[30] G. E. Brown and A. D. Jackson, *Nordita 1971-1972 Lectures, Part I* (Nordita, Denmark, 1973), p. 11.

[31] H. J. Schnitzer, Phys. Rev. Lett. 35, 1540 (1975).

[32] A. R. Edmonds, Ref. 23, p. 103.

PHYSICAL REVIEW C VOLUME 21, NUMBER 6 JUNE 1980

Comments

The Comments section is for short papers which comment on papers previously published in **The Physical Review** *Manuscripts intended for this section must be accompanied by a brief abstract for information retrieval purposes and a keyword abstract*

Search for nuclear structure dependence of analyzing powers for the $(\vec{t},p)$ reaction in medium mass nuclei

Ronald E. Brown, J. A. Cizewski, J. W. Sunier, and E. R. Flynn
Los Alamos Scientific Laboratory, Los Alamos, New Mexico 87545

P. Alford and E. Sugarbaker
University of Colorado, Boulder, Colorado 80305

D. Ardouin
University of Nantes, Nantes, France

(Received 10 August 1979)

Recent measurements of the $(\vec{p},t)$ reaction on targets in the mass range $106 \leq A < 128$ have shown a change in the sign of the analyzing power at forward angles for transitions to the lowest 2^+ states. The $(\vec{t},p)$ reaction has been used in a similar search for corresponding effects on targets of ^{96}Mo, ^{106}Pd, and ^{126}Te. In contrast to the $(\vec{p},t)$ results, the analyzing power for $L = 2$ transitions in the $(\vec{t},p)$ measurements does not show a sign change and the data are fitted with standard distorted-wave Born approximation calculations.

[NUCLEAR REACTIONS ^{96}Mo, ^{106}Pd, ^{126}Te $(\vec{t},p)$ measured $\sigma(\theta)$ A_y DWBA analysis.]

It is well known that analyzing powers (A_y) are usually more sensitive to the detailed description of nuclear reactions than are the shapes of the differential cross sections. This is in part due to the approximate derivative of the cross section behavior of these analyzing powers and, more directly, due to the spin dependent features of the interaction. In the study of the $(\vec{t},p)$ reaction it has been found that A_y may be quite sensitive to the reaction mechanism[1] and attempts have been made to see if the effects of multistep processes would be evident in the measurement of A_y values.[2,3] However, no clear distinction was found between multistep and direct distorted wave (DW) calculations fitted to data involving transitions which were not forbidden. Recent $(\vec{p},t)$ results by Yagi *et al.*[4] indicate a systematic nuclear structure dependence of A_y for 2^+ states in a series of vibrational nuclei. This dependence was explained as the result of a phase change due to interference between one- and two-step processes in the reaction mechanism, the indirect process being primarily inelastic scattering to the 2^+ state followed by an $L=0$ transfer. This interference goes from onstructive in the ^{128}Te$(\vec{p},t)^{126}$Te reaction to destructive in the ^{110}Pd$(\vec{p},t)^{108}$Pd reaction. Such a sensitivity to nuclear structure effects could make A_y measurements an important tool.

The present paper describes an attempt to observe effects analogous to those reported in Ref. 4 namely, the study of the reactions ^{126}Te$(\vec{t},p)^{128}$Te and ^{106}Pd$(\vec{t},p)^{108}$Pd as well as the ^{96}Mo$(\vec{t},p)^{98}$Mo reaction. The principal purpose was to look for similar interference effects for reactions to the 2^+ states, especially as no such strong effects had previously been noted in the Ni nuclei,[2] or the Zr and Pb nuclei.[3]

The experiment was carried out using a quadrupole-dipole-dipole-dipole (Q3D) spectrometer[5] for detecting the reaction protons produced by the incident 17 MeV polarized triton beam.[6] Details of this arrangement are given in Refs. 2 and 3. Analyzing powers and cross sections were measured at ten angles from 15° to 60° in 5° steps. Beams averaging 60 na were used with typical polarizations of 0.75. A solid-state monitor detector at 30° served to provide relative normalizations as well as absolute cross sections based on optical-model calculations. The Mo and Pd targets were self-supported metallic foils of thickness about 0.5 and 1.0 mg/cm^2, respectively. The Te target was about 0.5 mg/cm^2 in thickness prepared by evaporation of tellurium on a thin carbon foil.

This communication deals only with the data directly relevant to the results discussed in Ref. 4. Data for other transitions will appear in a later publication. Our measured cross sections and A_y values for transitions to the lowest 0^+ and 2^+ states are shown in Figs. 1 and 2, respectively, for the targets ^{96}Mo, ^{106}Pd, and ^{128}Te. The error bars are from counting statistics only, and the absolute accuracy of the cross section data is ±20%. As the data indicate, the ^{128}Te has cross sections to the 2^+ states considerably smaller than the other targets, and this is reflected in the larger error bars.

In the $(\vec{p},t)$ measurements of Ref. 4, A_y for the $L=2$ transitions showed a change of sign between Pd and Te at forward angles. Examination of the present data indicates that no dramatic differences exist among the three targets. The angular shifts that show up for both the cross section and A_y results exhibit a smooth variation with mass. In the case of the $(\vec{p},t)$ data, the Te A_y measurements represent picking up particles from almost a full shell and the Pd A_y results are from the middle of the shell. This means that the Te 2^+ states are very strongly populated in this reaction, as the results of Ref. 4 indicate, and the Pd 2^+ states correspondingly have smaller cross sections. The Pd 2^+ states are also more collective as there are more particle-hole components available near the middle of the shell. It is this fact, coupled with a destructive phase between the direct and indirect paths, that leads to the change in sign of A_y in the $(\vec{p},t)$ data.

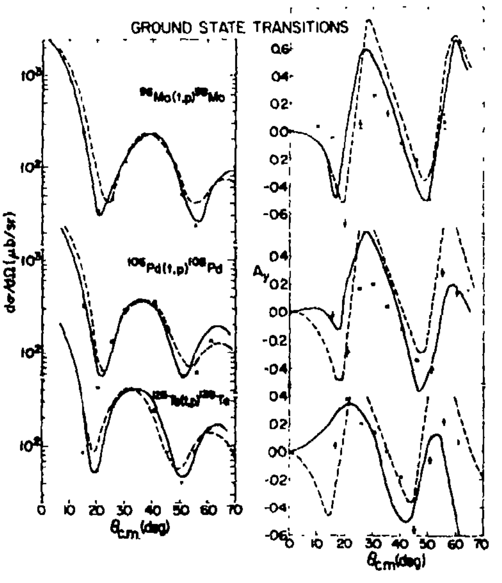

FIG. 1. Differential cross sections and A_y values for ground state transitions. The lines are DW calculations with the solid line using the parameter set of Ref. 8 and the dashed line Ref. 9.

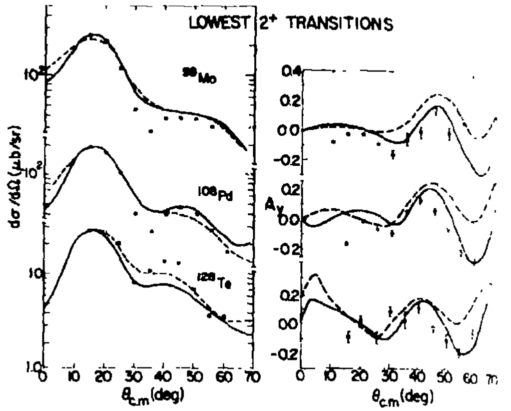

FIG. 2. Differential cross sections and A_y values for 2^+ transitions. See also the caption to Fig. 1.

The corresponding situation in the $(\vec{t},p)$ reaction would be to compare the other end of the $N=50-82$ shell to the Pd nuclei. Therefore, the ^{96}Mo target was included in the present experiment. This target represents adding neutrons to an approximately empty shell, although still to a reasonably collective nucleus, which parallels the ^{128}Te situation. Thus the Mo-Pd comparison in the $(\vec{t},p)$ reaction is analogous to the Te-Pd comparison in the $(\vec{p},t)$ reaction. In spite of this, the data for the $(\vec{t},p)$ case do not show the anomaly in the A_y shapes to the 2^+ states that the $(\vec{p},t)$ data do.

Distorted wave (DW) calculations were performe to determine if these could adequately describe the $(\vec{t},p)$ data. These results are shown in Figs. 1 and 2. These calculations are extremely sensitive to the proton optical potential and very insensitive to the triton potential.[7] Therefore, several sets of proton potentials were tried to see how they would affect the overall fit. The standard parameter sets of Becchetti *et al.*[8] and Perey[9] were used, with slight adjustments in the real well depth in some cases in order to fit the positions of the $L=0$ minimum. The parameter values use are listed in Table I. The best overall fit to both the $L=0$ and $L=2$ A_y results are obtained with the Becchetti parameters.[8] The opposite result was found in the Ni region[3] where the Perey paramete gave the best fit. In all of the angular distributio examined here, the quality of the DW fits is only fair but it does reproduce the general features of

TABLE I. Optical-model parameters used in DW calculations. The values shown are for Mo with those for Pd and Te extrapolated using the formulas given in Refs. 8 and 9.

Particle	V (MeV)	r_r (fm)	a_r (fm)	W (MeV)	r_i (fm)	a_i (fm)	V_{so} (MeV)	r_{so} (fm)	a_{so} (fm)
t	166.7	1.16	0.752	21.8	1.498	0.817	6.0	1.10	0.83
p^a	56.4	1.17	0.75	2.6	1.32	0.51	6.2	1.01	0.75
				8.15^c	1.32	0.51			
p^b	51.6	1.25	0.60	13.8^c	1.25	0.47	7.5	1.25	0.47

^{a}From Ref. 8.
^{b}From Ref. 9.
^{c}Derivative form.

the data. Indeed both sets of optical potentials do reproduce the gross features of the data and there is no evidence for the complete out-of-phase behavior that was noted in the $(\vec{p},t)$ A_y data.

To examine the effect of the present optical-model parameters on the $(\vec{p},t)$ data of Ref. 4, DW calculations using the parameter sets in Table I were used in a $(\vec{p},t)$ calculation. Fits for the $L=0$ transitions comparable to Fig. 1 were obtained. For the $L=2$ situation the ^{128}Te$(\vec{p},t)^{126}$Te was also adequately described, but for the ^{108}Pd target the DW calculation was out of phase with the data. This result concurs with the analysis of Yagi *et al.*[4] The present analysis assumes that the reactions studied are all direct reactions with minimal compound nucleus contributions. It is also worth noting that the present triton energy corresponds very closely to the outgoing triton energy of the $(\vec{p},t)$ study so ingoing and outgoing channels are very similar.

The authors of Ref. 4 were able to describe their $(\vec{p},t)$ results with a coupled-channel formalism involving the inelastic excitation of the 2^+ state followed by an $L=0$ transfer. The wave functions for the ground and 2^+ states were calculated in a BCS and quasi-particle RPA formalism.[10,11] In the $(\vec{p},t)$ study the differences between the Pd and Te measurements are based on an increase in the ground state correlations in Pd. This results in a sign difference in the spectroscopic amplitudes between the indirect and direct transfer processes for the Pd target, while no sign difference is manifested in Te. According to our present measurements, to be correct this same formalism must predict that for a $(\vec{t},p)$ measurement, the direct and indirect transfer process are in phase. This test is critical to the success of the interpretation of Yagi *et al.*[4]

Although the present results do not show a dependence on the underlying nuclear structure as did the $(\vec{p},t)$ measurements, there are presumably other nuclear regions where the microscopic structure of low lying states will be such that a cancellation of $(\vec{t},p)$ strength will occur similar to that in $(\vec{p},t)$. Such a cancellation should produce anomalous A_y angular distributions for the stripping reaction. It is planned to examine other regions between closed shells for such effects in the $(\vec{t},p)$ reaction.

These results were obtained under the auspices of the U.S. Department of Energy.

---

[1] R. N. Boyd, W. P. Alford, E. R. Flynn, and R. A. Hardekopf, Phys. Rev. C 15, 1160 (1977).

[2] W. P. Alford, R. N. Boyd, E. Sugarbaker, D. L. Hanson, and E. R. Flynn (unpublished).

[3] E. R. Flynn, R. A. Hardekopf, J. D. Sherman, and J. W. Sunier, Phys. Lett. 61B, 433 (1976).

[4] K. Yagi, S. Kunori, Y. Aoki, Y. Higashi, J. Sanada, and Y. Tagishi, Phys. Rev. Lett. 40, 161 (1978); K. Yagi, S. Kunori, Y. Aoki, K. Nagano, Y. Tagishi, and Y. Toba, Phys. Rev. C 19, 285 (1979).

[5] E. R. Flynn, S. Orbesen, J. D. Sherman, J. W. Sunier, and R. Woods, Nucl. Instrum. 128, 35 (1975).

[6] R. A. Hardekopf, G. G. Ohlsen, R. V. Poore, and N. Jarmie, Phys. Rev. C 13, 2127 (1976).

[7] E. R. Flynn, D. D. Armstrong, J. G. Beery, and A. G. Blair, Phys. Rev. 182, 1113 (1969).

[8] F. D. Becchetti and G. W. Greenlees, Phys. Rev. 182, 1190 (1969).

[9] F. G. Perey, Phys. Rev. 131, 745 (1963).

[10] T. Izumoto, Prog. Theor. Phys. 52, 1214 (1974).

[11] T. Udagawa, Phys. Rev. C 9, 270 (1974).

PHYSICAL REVIEW C VOLUME 21, NUMBER 6 JUNE 1980

Communications

The Communications section is for brief reports on completed research. A Communication may be no longer than the equivalent of 2800 words, i.e., the length to which a **Physical Review Letter** *is limited. (See the editorial in the 21 December 1970 issue of* **Physical Review Letters**.*) Manuscripts intended for this section must be accompanied by a brief abstract for information retrieval purposes and a keyword abstract.*

Large absorption potential for the Ag+p reaction at sub-Coulomb energies

A. Feigel, E. Finckh, K. Rüskamp, and U. Weise
Physikalisches Institut der Universität Erlangen-Nürnberg, D-8520 Erlangen, Germany

(Received 19 December 1979)

The analyzing power of the ^{109}Ag($\vec{p}$,p_0) reaction has been measured in the sub-Coulomb region. The volume integral of the imaginary potential deduced from this measurement has a much larger value than for Zr and Sn, confirming the value $W_D = 20$ MeV obtained in an ^{109}Ag(p,n) investigation by Johnson *et al.* The large volume integral is probably an indication of shell effects in the optical model. The volume integral does not determine the absorption cross section uniquely.

[NUCLEAR REACTIONS ^{109}Ag($\vec{p}$,p_0), $E = 6.06$ MeV; measured $A(\theta)$; deduced optical-model parameters; enriched target $\theta = 30$–$160°$; $\Delta\theta = 5°$.]

Johnson *et al.*[1] investigated the (p,n) cross section in medium weight nuclei, $89 \le A \le 130$, in the energy range $E_p = 3$–6 MeV. The data were fitted with optical model calculations of the total reaction cross section. The parameters for the imaginary potential (derivative of Woods-Saxon potential) were $r_D = 1.31A^{1/3}$, $a_D = 0.4$ fm, and W_D was fitted to the data. The results for W_D showed a resonancelike behavior with A, rising from $W_D \approx 12$ MeV around $A = 120$ to a maximum value of $W_D \approx 28$ MeV at $A = 103$. The volume integral of the imaginary potential shows of course the same unexpected A dependence. This result induced us to investigate other experimental evidence for such a deep imaginary potential.

Besides the cross section, the analyzing power of the elastic proton scattering is strongly influenced by the absorption potential. We, therefore, measured this quantity for the ^{109}Ag($\vec{p}$,p_0) reaction. The target was a self-supporting ^{109}Ag foil, enriched to 92%. The proton energy chosen, $E_p^{\text{lab}} = 6.06$ MeV, lies well below the first isobaric analog resonance of ^{109}Ag ($E_{\text{IAR}}^{\text{lab}} = 6.496$ MeV) and of ^{107}Ag ($E_{\text{IAR}}^{\text{lab}} = 6.189$ MeV). Polarized protons from the Erlangen Lamb shift source were accelerated by our EN tandem, energy analyzed, and focused on the target through a 2 mm diameter aperture. The beam current on the target was 15 nA. The polarization was continuously monitored by a ^{4}He-filled polarimeter. The scattered protons were measured with 12 detectors on the left and right sides of the beam. The angular distribution was determined from $\Theta = 30°$ to $160°$ in 5° steps.

Since the analyzing power is rather small at this low energy, care had to be taken to avoid systematic errors. The beam position on the target was, therefore, stabilized and the polarization of the beam was switched on and off with a frequency of 10 Hz. The angular distribution was measured in this way for both spin directions. The proton spectra were taken using a routing system and a PDP 11/40 computer. The data are shown in Fig. 1 together with a calculation

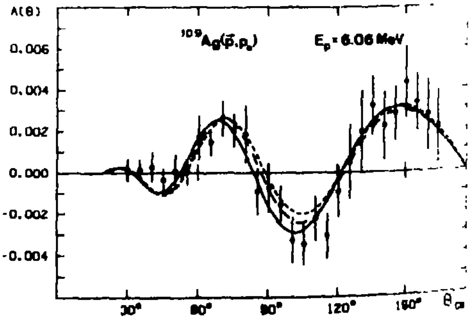

FIG. 1. Analyzing power of the reaction ^{109}Ag($\vec{p}$,p_0) measured at $E_p^{\text{lab}} = 6.06$ MeV. The curves are calculated with the parameters of Table I (—— column 1, ---- column 2, —— column 3).

© 1980 The American Physical Society

using the optical model parameters of Johnson *et al.*[1] (see first column in Table I). The agreement is remarkably good. Using the parameters of Becchetti and Greenlees[2], the analyzing power can be fitted equally well with small changes in the depth of the real and imaginary potential (second column in Table I and Fig. 1). The calculated curve shows a systematic departure from the data in the angular region around 90° and 120°. To improve the fit, the parameter r_0 of the real potential has to be increased to $r_0 = 1.20$ fm. At energies above the Coulomb barrier such small changes in r_0 can be compensated by the Vr^n ambiguity; perhaps, the sensitivity is larger at low energies.

The analyzing power can be reproduced in the calculation with different combinations of the depth W_D and the diffuseness a_D; only the product is determined $W_D a_D \approx 8$ MeV fm. The volume integral of the imaginary potential has nearly the same value. However, the (p,n) cross section in the energy range $E_p = 3$–6 MeV is reproduced in the calculation only for $a_D = 0.4$ fm and, therefore, $W_D = 20$ MeV is the correct value. This example shows clearly that the volume integral of the imaginary potential fixes the analyzing power but not the absorption cross section uniquely. That is to be considered when optical model parameter sets are used for the analysis of compound reactions.

Larger values of a_D and smaller ones of the imaginary potential increase the calculated cross section and the necessary reduction would lead to a diffuseness of the real potential $a_v \doteq 0.52$ fm. This value seems to be more unreasonable than the large value of W_D. Therefore, starting from the parameter set of Becchetti and Greenlees we have chosen $a_D = 0.4$ fm and $r_0 = 1.20$ fm and varied V and W_D. A good fit to the analyzing power and to the reduced cross section is obtained (see Fig. 1 and third column in Table I).

TABLE I. Optical model parameters. The usual notation is used, all potentials are in MeV, all lengths in fm. The volume integrals and the absorption cross section are calculated for $E_p = 6$ MeV. The real potential is given by the formula $V = V_0 - b \cdot E + 0.4\, Z/A^{1/3} + 24(N-Z)/A$. The energy dependence was chosen in all cases $b = 0.32$ MeV^{-1}. Johnson *et al.* (Ref. 1) use the factor 0.45 in the Coulomb correction term.

	(a)	(b)	(c)
V_0	55.4	55.61	54.18
r_0	1.20	1.17	1.20
a_v	0.73	0.75	0.75
W_D	20	13.56	21.12
r_D	1.30	1.32	1.32
a_D	0.40	0.606	0.40
V_{so}	6.4	6.2	6.[illegible]
r_{so}	1.03	1.01	1.01
a_{so}	0.63	0.75	0.75
r_c	1.22	1.21	1.21
$\frac{1}{A}\int V dr$	510	481	503
$\frac{1}{A}\int W dr$	144	151	157
σ_{abs}	0.3315	0.4730	0.3445

[a] Johnson *et al.*, Ref. 1

[b] See text.

[c] See text.

The large depth of the imaginary potential found by Johnson *et al.* is in agreement with our polarization data. The volume integral is independently determined and, in spite of the small diffuseness a_D, its value $J_w/A = 147$ MeV fm^3 is above the values of other elements.[3] This large value together with the smaller-than-average values for the magic nuclei tin[4] and zirconium[5] confirm the results of Eder *et al.*[6] that at low energies the imaginary surface potential shows large shell effects.

---

[1] C. H. Johnson, A. Galonsky, and R. L. Kernell, Phys. Rev. Lett. 39, 1604 (1977).

[2] F. D. Becchetti and G. W. Greenlees, Phys. Rev. 182, 1196 (1969).

[3] S. Kailas and S. K. Gupta, Phys. Lett. 71B, 271 (1977).

[4] W. Drenckhahn, A. Feigel, E. Finckh, G. Gademann, K. Hüskamp, M. Wangler, and L. Zemlo, Nucl. Phys. A (to be published).

[5] B. Badum, Zulassungsarbeit, University Erlangen-Nürnberg, 1979.

[6] G. Eder, H. Leeb, and H. Oberhummer, J. Phys. G 3, L127 (1977).

PHYSICAL REVIEW C VOLUME 21, NUMBER 6 JUNE 1980

Importance of the breakup mechanism for composite particle scattering

G. Baur and R. Shyam
Institut für Kernphysik, Kernforschungsanlage Jülich, D-5170 Jülich, West Germany

F. Rösel and D. Trautmann
Institut für Theoretische Physik, Universität Basel, CH-4056 Basel, Switzerland

(Received 16 October 1979)

We calculate in our formulation of the elastic and inelastic breakup process in nucleus-nucleus collisions the corresponding flux removed from the elastic channel. It is the dominant reaction mode for surface partial waves. Strongly reminiscent of the Serber model, the absorption can be characterized by "geometrical" quantities (radius of the projectile and target nucleus) and a "strength parameter" which becomes constant for energies much larger than the binding energy of the projectile.

NUCLEAR REACTIONS $A(d,p)$ breakup at $E_d = 25.5$, 80 MeV, $A = 27$, 62, 93, 181, 197; $A(\alpha, {}^3\text{He})$ breakup at $E_\alpha = 100$, 140, 172.5 MeV, $A = 58$, 62, 90; calculated breakup probabilities, total cross sections, deduced gross properties.

It has long been suspected that in deuteron nucleus collisions the breakup process has a strong influence on other channels. Whereas recent investigations[1,2,3] have emphasized the study of the feedback of the breakup channel on the elastic channel, the real breakup has been calculated theoretically[4,5,6] and compared to very complete experiments recently.[5,6] Of course, the breakup mode will also have an influence on stripping channels as shown in detailed investigations by Johnson and Soper.[7] Since the distorted-wave Born approximation (DWBA) theory for elastic and inelastic breakup is in rather good agreement with experiment,[6] we feel that it is now possible to take this approach as a starting point for the investigation of the effect of breakup on other reaction channels. It is the purpose of this paper to determine the influence of the breakup process on the absorption in the elastic channel. The breakup mode is not only important for the weakly bound deuteron but also, at sufficiently high incident energies, for all other composite particles. As an example, we study the α-particle breakup process on medium mass nuclei at $E_\alpha = 100$–172 MeV.[8,9] It turns out in our calculations that the absorption due to breakup is very important in the surface region. Similar to the Serber model,[10] where the breakup cross section is determined by geometrical quantities (the radii of projectile and target nucleus), we find simple scaling properties for the breakup probability.

We consider a projectile a to be composed of $b+n$ (e.g., $a=d$, $b=p$; for more complex particles, of course, different modes of fragmentation exist). The inclusive $A(a,b)$ spectrum consists of the elastic and inelastic modes[6] (depending on whether the target nucleus A stays in the ground state or not during the reaction). It is calculated following the procedure described in Ref. 6. In this first order theory, only the coupling of the elastic channel to the breakup channel is considered, whereas the coupling of the breakup channel back to the elastic channel or to other channels is neglected.

Even without introducing such a coupling we can determine an influence of the breakup process on the elastic scattering. We consider the transmission coefficient T_{l_a}, which determines the total reaction cross section of $a+A$ scattering, as given by

$$T_{l_a} = 1 - |S_{l_a l_a}|^2 = \sum_{c \neq l_a} |S_{l_a c}|^2 . \tag{1}$$

Here l_a denotes the elastic channel. For simplicity of notation we take a and A to be spinless; hence l_a corresponds to the total spin, and c describes any other channel with total angular momentum l_a. Because of the unitarity of the S-matrix, we can express the transmission coefficient T_{l_a} as a sum (or integral for continuous channels) over all reaction channels. This allows us to study the effect of the breakup channel on T_{l_a} in an explicit way, even in a first order theory.

We define the "probability of break-up" $T_{l_a}^{\text{breakup}}$ by

$$\sigma_{\text{total}}^{\text{breakup}(a,b)} = \frac{\pi}{q_a^2} \sum_{l_a} (2l_a+1) T_{l_a}^{\text{breakup}(a,b)} = \iint dE_b\, d\Omega_b \frac{d^2\sigma(a,b)}{d\Omega_b\, dE_b} , \tag{2}$$

where $d^2\sigma(a,b)/d\Omega_b dE_b$ denotes the inclusive

© 1980 The American Physical Society

double differential cross section; it is calculated as described in Refs. 6 and 9. The integration over Ω_b can be done analytically and the energy integration is performed numerically. Enough partial waves are used to ensure convergence, and we go substantially beyond the grazing partial waves, in order to make sure that the long-range Coulomb effects are also taken into account.

In Fig. 1 we show our results for the reaction ^{93}Nb(d,p) at the incident deuteron energy of 25.5 MeV. The potential parameters used are the same as described in Ref. 6, where it is shown that our theory is in good agreement with the experimental breakup spectra. Whereas the transmission coefficient (which is calculated with a standard optical model potential) shows a "smooth cutoff" behavior, $T_{l_d}^{\text{b-up}(d,p)}$ shows a distinct peak around grazing partial waves ($l_d \simeq 11$). With increasing projectile energy our calculations show that the localization of the breakup probability in l space becomes much more pronounced because of the smaller wavelength of the incident particle. Thus we have established the peripheral nature of the breakup process. It is worthwhile to compare our results with other approaches. Whereas in Rawitscher's approach there is some surface peaking of the breakup probability,[11] we have close resemblance with Austern *et al.*,[1] as can be seen in Fig. 3 of Ref. 1. (Although these authors consider in a very sophisticated model a different target nucleus and rather simple types of interactions, a qualitative comparison of our results with those of Ref. 1 seems meaningful.) However, we cannot corroborate their "$L=9$ effect" (see Ref. 1); instead, we have a rather smooth dependence of $T_{l_d}^{\text{b-up}(d,p)}$ on l_d, which is expected if semiclassical concepts are meaningful. The surface peaking of the breakup probability is also present in the results of Ref. 3. In these calculations, only the elastic breakup is included, and a large part of the absorption, which is due to the inelastic breakup, is thereby missed.

Another interesting feature of Fig. 1 is the fact that for $l_d > 13$, $T_{l_d}^{\text{b-up}(d,p)}$ exceeds the total transmission coefficient. Of course, we must always have $T_{l_d} \geq T_{l_d}^{\text{b-up}(d,p)}$. This is not a deficiency of our breakup calculations; rather, it shows the inadequacy of the phenomenological deuteron optical model potential used to determine transmission coefficients T_{l_d} for large values of l_d. The fitting procedures to obtain such optical model parameters are too restricted in their radius dependence: The Woods-Saxon shape precludes the slow decrease of T_{l_d} for large l_d. Thus our calculations provide direct evidence for a large extension of absorption in deuteron nucleus scattering.

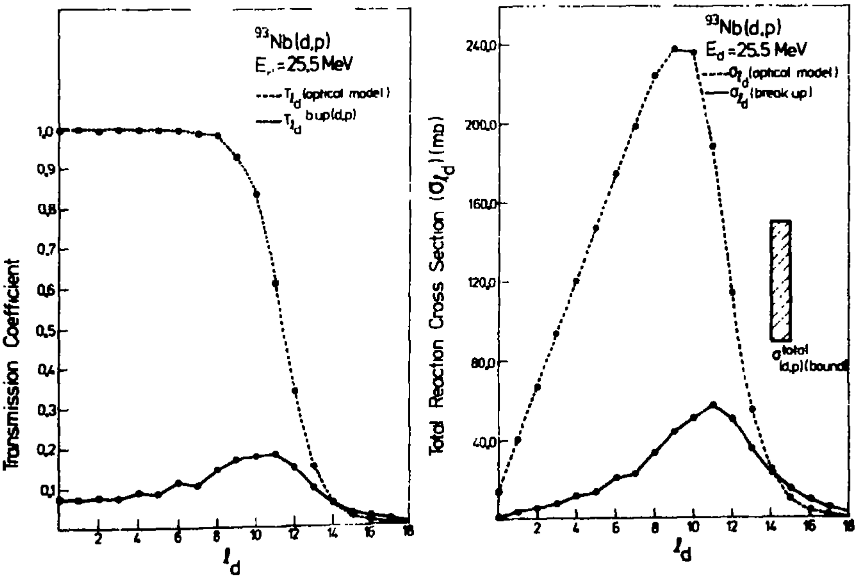

G. 1. On the left-hand side, the transmission coefficient as calculated from a standard optical model potential and (d,p) breakup probability are shown for the deuteron induced reaction on ^{93}Nb at $E_d = 25.5$ MeV. On the right-hand , the corresponding total breakup and reaction cross sections are shown. For the sake of comparison we show e shaded area the magnitude of the experimental total cross section for (d,p) stripping to bound states, as taken n Ref. 6.

In model calculations,[18] where we have switched off the nuclear part of the projectile target interaction, we could explicitly see that this long range deuteron absorption is entirely due to the Coulomb breakup. In Fig. 1 we also show the experimentally observed total cross section for (d,p) stripping to bound states ($E_n<0$). It is only a minor fraction of the direct (d,p) processes.

As another example, we calculate the breakup probability $T_{l_\alpha}^{\text{b-up}(\alpha,{}^3\text{He})}$. For simplicity we consider here only the $(\alpha,{}^3\text{He})$ breakup process; a similar effect is expected for (α,t) breakup. (In addition, there will be other fragmentation modes like $\alpha\to d+d$, etc.) In Fig. 2 we show the impact parameter dependence of the total $(\alpha,{}^3\text{He})$ breakup cross section defined by

$$\sigma_{\text{total}}^{\text{break-up}(\alpha,{}^3\text{He})}=\frac{\pi}{q_\alpha^2}\sum_{l_\alpha}(2l_\alpha+1)T_{l_\alpha}^{\text{b-up}(\alpha,{}^3\text{He})}$$
$$\simeq 2\pi\int db\,bT_{l_\alpha}^{\text{b-up}(\alpha,{}^3\text{He})}, \qquad (3)$$

where $b=(l_\alpha+\frac{1}{2})/q_\alpha$ is the impact parameter. The optical model parameters used are taken from Ref. 9. Even more strongly than in the (d,p) case, we note in Fig. 2 the localization of the breakup probability at peripheral impact parameters. We can see that for increasing α-particle energy the shape of the breakup probability curve remains unchanged; only its magnitude increases, with some kind of "saturation." This shows the geometrical nature of the breakup process. Thus it is established that the breakup is an important absorption effect in the surface region for α-induced reactions (at least for α-particle energies much larger than the breakup threshold). Therefore all kinds of theories which disregard the possibility of the breakup of the α particle must lead to quite appreciable deviations of the theoretical transmission coefficients as compared to the experimental ones. Since the grazing angular momenta determine the angular distributions, the possibility of breakup has to be included in all optical model theories for composite particles. This holds especially for the α-nucleus optical potentials calculated in Ref. 13, where absorption is assumed to be only due to the excitation of target states treating the α particle as an elementary particle.

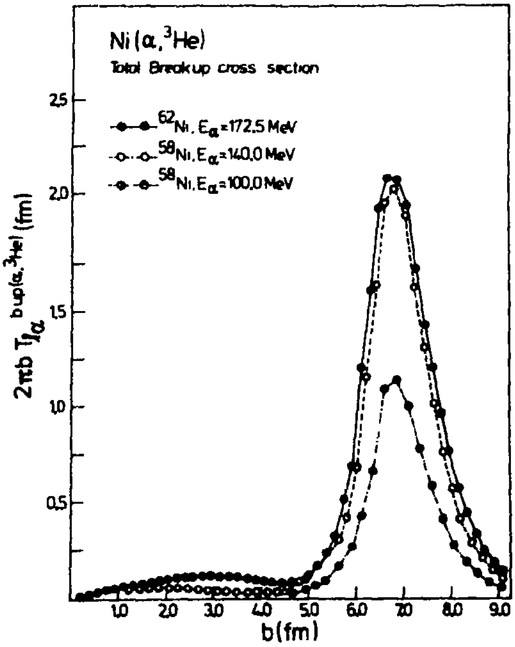

FIG. 2. Impact parameter dependence of the total $(\alpha,{}^3\text{He})$ breakup cross section on Ni targets for various α-energies E_α.

Finally we try to extract some "gross properties" of the breakup reaction. We introduce a simple parametrization of our numerical results, which shows a remarkable similarity to the Serber picture. We write

$$T_l^{\text{b-up}(a,b)}=\beta(E_a,E_{\text{bind}})e^{-(l-l_0)^2/(\Delta l)^2}$$
$$=\beta(E_a,E_{\text{bind}})e^{-(b-b_0)^2/(\Delta R)^2}, \qquad (4)$$

with $b=l/q_a$, $b_0=l_0/q_a$, $\Delta R=\Delta l/q_a$, and q_a being the wave number of the projectile. E_a and E_{bind} correspond to the incident and binding energies of the projectile, respectively. The breakup probability has a peak at a partial wave l_0 with a width Δl. The impact parameter b_0 and ΔR are almost independent of the incident energy. The factor β describes the strength of the breakup process, which is expected to show a saturation for suffici-

TABLE I. Simple parametrization of the breakup probability, Eq. (4). The numbers are determined by fitting our numerical results to Eq. (4).

A	r_0	ΔR	β
	(d,p) breakup at $E_d=25.5$ MeV		
27	1.29	1.85	0.205
62	1.25	1.90	0.185
93	1.24	1.89	0.185
181	1.13	1.96	0.185
	(d,p) breakup at $E_d=80.0$ MeV		
27	1.09	1.63	0.420
93	1.15	1.92	0.315
197	1.19	1.90	0.280
	$(\alpha,{}^3\text{He})$ breakup at $E_\alpha=140$ MeV		
58	1.18	1.05	0.048
90	1.16	1.15	0.047

ently high incident energies and vanish for small incident energies. We relate b_0 to the size of the target and projectile by $b_0 = r_0(A^{1/3} + a^{1/3})$. In Table I we show the values of r_0 and ΔR extracted from the cases we have studied in deuteron scattering at $E_d = 25.5$ MeV and 80.0 MeV, and α scattering at $E_\alpha = 100$, 140, and 172.5 MeV. *These numbers are remarkably independent of A and E_α*; this supports the Serber picture. The slight decrease of r_0 with A for $E_d = 25.5$ MeV deuteron breakup can be explained[12] by destructive nuclear Coulomb interference which becomes more important for increasing A. The optical model parameters used in these calculations are of the standard type; extensive details will be given in Ref. 12.

In conclusion, we want to say that we have studied the influence of the breakup channel on the elastic channel. We use our method[8,9,12] to calculate the real breakup, which reproduces the experimental breakup cross sections. Then we use unitarity to determine quantitatively the influence of breakup on the elastic channel. Since $T_l^{\text{b-up}(a,b)}$ is smaller than 1, our first order theory gives reliable results. On the other hand, these breakup probabilities are large enough to be of great importance as a surface absorption mechanism. Finally we give a very simple geometrical interpretation of our numerical results for the breakup process, which confirms some of the concepts of the Serber model.

One of us (R. S.) acknowledges gratefully an Alexander von Humboldt fellowship.

---

[1] N. Austern, C. M. Vincent, and J. P. Farrell, Jr., Ann. Phys. (N.Y.) 114, 93 (1978).

[2] G. H. Rawitscher, Phys. Rev. C 9, 2210 (1974); 11, 1152 (1975).

[3] H. Yamakawa, S. Yamaji, A. Mori, and K. Yazaki, Phys. Lett. 82B, 13 (1979).

[4] G. Baur and D. Trautmann, Phys. Rep. 25C, 293 (1976).

[5] G. Baur, F. Rösel, and D. Trautmann, Nucl. Phys. A255, 101 (1976).

[6] J. Pampus, J. Bisplinghoff, J. Ernst, T. Mayer-Kuckuk, J. Rama Rao, G. Baur, F. Rösel, and D. Trautmann, Nucl. Phys. A311, 141 (1978); G. Baur, F. Rösel, D. Trautmann, J. Pampus, J. Bisplinghoff, J. Ernst, T. Mayer-Kuckuk, J. Rama Rao, A. Budzanowski, and R. Shyam, Proceedings of the International Workshop on Reaction Models for Continuous Spectra of Light Particles, Bad Honnef, 1978 (unpublished).

[7] R. C. Johnson and P. J. R. Soper, Phys. Rev. C 1, 976 (1970).

[8] J. R. Wu, C. C. Chang, and H. D. Holmgren, Phys. Rev. Lett. 40, 1013 (1978).

[9] A. Budzanowski, G. Baur, C. Alderliesten, J. Bojowald, C. Mayer-Böricke, W. Oelert, P. Turek, F. Rösel, and D. Trautmann, Phys. Rev. Lett. 41, 635 (1978).

[10] R. Serber, Phys. Rev. 72, 1008 (1947).

[11] G. H. Rawitscher, private communication.

[12] G. Baur, R. Shyam, F. Rösel, and D. Trautmann (unpublished).

[13] N. Vinh Mau, in *Proceedings of the Workshop on Microscopic Optical Potentials, Hamburg, 1978*, edited by H. V. von Geramb (Springer, Heidelberg, 1978).

PHYSICAL REVIEW C VOLUME 21, NUMBER 6 JUNE 1980

Evidence for statistical fluctuation in the fragmentation of ^{16}O at intermediate energies

Che Ming Ko
Nuclear Science Division, Lawrence Berkeley Laboratory, University of California, Berkeley, California 94720

(Received 21 January 1980)

The asymmetry in the parallel and transverse momentum distributions for fragments produced by the fragmentation of ^{16}O at intermediate energies has been partially explained previously by the deflection of the projectile trajectory. The remaining discrepancy of ~25% between theory and experiment is suggested here as due to the scattering angle fluctuation as a result of the damping of the projectile kinetic energy. A model is introduced to study quantitatively this effect.

[NUCLEAR REACTIONS Momentum distributions of projectile fragments studied including the effect of statistical fluctuations.]

Recently, Van Bibber *et al.*[1] have measured the parallel and transverse momentum distributions for fragments of $Z \geq 3$ produced by the fragmentation of ^{16}O at 90 and 120 MeV/nucleon with Au and Al targets. They have fitted the energy spectra and angular distributions assuming a Gaussian distribution in both $p_\parallel$ and $p_\perp$ in the projectile frame of reference, i.e.,

$$P(\vec{p}) \propto \exp\left(-\frac{p_\parallel^2}{2\sigma_{p_\parallel}^2} - \frac{p_\perp^2}{2\sigma_{p_\perp}^2}\right). \tag{1}$$

The distribution of $\sigma_{p_\parallel}$ as a function of fragment mass F is in good agreement with the parabolic form $\sigma_{p_\parallel}^2 = \sigma_0^2 F(A-F)/(A-1)$ expected from momentum conservation.[2] Here, A is the projectile atomic number. They found that σ_0 agrees with the value 88 MeV/c found at 2.1 GeV/A averaged over many targets.[3]

For the $\sigma_{p_\perp}$ distribution, however, they found that it is more than 200 MeV/c. This behavior is in sharp contrast with that at 2.1 GeV/A where $\sigma_{p_\parallel} = \sigma_{p_\perp}$ to within 10%. Van Bibber *et al.* attributed the large value of $\sigma_{p_\perp}$ as evidence for orbital deflections. Extending the derivations of Ref. 2, they obtained

$$\sigma_{p_\perp}^2 = \frac{F(A-F)}{A-1}\,\sigma_1^2 + \frac{F(F-1)}{A(A-1)}\,\sigma_2^2, \tag{2}$$

where $\sigma_1^2 = \sigma_0^2$ is the usual form due to the intrinsic nucleon motion, while $\sigma_2^2 = \frac{1}{2}\langle \vec{P}_{A_\perp}^2\rangle$ is the variance of transverse momentum of the projectile at the time of fragmentation.

Fitting the experimental data with Eqs. (1) and (2), they obtained $\sigma_1 \sim \sigma_0$ while $\sigma_2 \sim$ (200–240) MeV/c. Using a Woods-Saxon nuclear potential and a point charge Coulomb potential, they calculated the classical deflection function $\theta(b)$, from which they obtained the σ_2 according to

$$\sigma_2^2 = \frac{1}{2} P_A^2 \int_{b_1}^{R} N(b) \sin^2\theta(b)\,db. \tag{3}$$

In the above, $N(b) = 2b/(R^2 - b_1^2)$ is the geometrical weighting factor, P_A is the momentum of the projectile, R is the sum of target and projectile radii, and b_1 serves as a cutoff in impact parameter such that the fraction of the total cross section which appears as fragmentation is 0.6 ± 0.1.[4] The resulting theoretical value for σ_2 obtained in Ref. 1 is ~(170–200) MeV/c, which is systematically smaller than the experimental value by 25%. This happens at both energies and for both targets.

We feel that the discrepancies mentioned above are interesting and point to other important physical effects which were not considered in Ref. 1. For instance, the trajectory of the projectile is not only deflected classically, but may also be dispersed due to quantal effects. Furthermore, the motion of the projectile is damped, resulting in a decrease of its velocity, which is indeed experimentally verified. Due to the excitation of the nuclei, we expect modifications of the classical trajectories also from dissipation and fluctuation effects. These effects are well studied in deep inelastic heavy ion collisions at relatively low incident kinetic energies. Both quantal and statistical effects would lead to a dispersion of the classical deflection function. Therefore we expect that they would increase the value of σ_2 calculated according to Eq. (3).

To formulate the problem explicitly, let us assume that the classical scattering angle has a Gaussian distribution

$$P(\theta, b) = \frac{1}{\sqrt{2\pi}\,\Delta(b)} \exp\{-[\theta - \theta(b)]^2/2\Delta^2(b)\}, \tag{4}$$

where $\theta(b)$ is the scattering angle obtained from a classical calculation for a given impact parameter b, and $\Delta(b)$ is the width of the angular spread due to both quantal and statistical fluctuations. Equation (3) is then rewritten as

$$\bar{\sigma}_2^2 = \tfrac{1}{2} P_A^2 \int_{b_1}^{R} db\, N(b) \int d\theta \sin^2\theta P(\theta, b) d\theta$$
$$= \sigma_2^2 + \Delta\sigma_2^2 , \qquad (5)$$

where σ_2^2 is given by Eq. (3) and

$$\Delta\sigma_2^2 = \tfrac{1}{4} P_A^2 \int_{b_1}^{R} db\, N(b) [\cos^2\theta(b) - \sin^2\theta(b)]$$
$$\times (1 - e^{-2\Delta^2(b)}) . \qquad (6)$$

In the case we are considering, we have from Ref. 1, $|\theta(b)| < 5°$. This immediately shows that $\Delta\sigma_2^2 > 0$. Hence, any fluctuation of the scattering angle will lead to an increase of the value of σ_2 calculated in Ref. 1. For such small deflection angles, we can approximate $\sin^2\theta \approx 0$, $\cos^2\theta \approx 1$. For simplicity, we assume that $\Delta(b) \approx \text{const} \approx \Delta_M$, then

$$\Delta\sigma_2^2 \approx \tfrac{1}{4} P_A^2 (1 - e^{-2\Delta_M^2}) . \qquad (7)$$

To increase σ_2 by 25% in order that $\bar{\sigma}_2$ agree with the experimental value, we need $\Delta\sigma_2^2 \approx 0.56\,\sigma_2^2$, i.e.,

$$\frac{1 - e^{-2\Delta_M^2}}{2} \cong 0.56 \int_{b_1}^{R} db\, N(b) \sin^2\theta(b) . \qquad (8)$$

From the deflection function calculated in Ref. 1, which is shown by the long-short dashed curve in Fig. 1, the integral on the right-hand side of Eq. (8) is $\sim 4.5 \times 10^{-3}$. Then Eq. (8) leads to

$$\Delta_M \approx 3° . \qquad (9)$$

At the energy we consider, the quantal fluctuation in angle is expected to be small. As the dominant angular momentum is $\sim 200\,\hbar$, the angular spread from the uncertainty principle is only $\sim 0.3°$, which is indeed negligible. We therefore suggest that the required angular fluctuation of 3° is mainly of statistical origin.

In the following, we shall perform a model calculation to study quantitatively such an angular fluctuation. The model we shall use is an extension of the transport theory employed for the study of deep inelastic heavy ion reactions at low incident kinetic energy ~ 10 MeV/A.[5] The transport equation can be approximately reduced to equations for the mean trajectory and its spread. The former is similar to the classical Newtonian equation of motion with frictional force. The latter describes the evolution of the angular and momentum widths. Using the same Woods-Saxon nuclear potential as in Ref. 1 and similar statistical input ($W_0 = 30$ MeV, $\sigma = 4$ fm, $\Delta = 14$ MeV) as in Ref. 5, we obtain the scattering angle, final kinetic energy, and angular width as functions of the impact parameter. These are shown in Fig. 1 for the reaction ^{16}O + ^{27}Al at 92.5 MeV/A. In the range of the impact parameter we are interested in, i.e., 4 fm $\lesssim b \lesssim$ 7 fm, the angular width is indeed of the right magnitude.

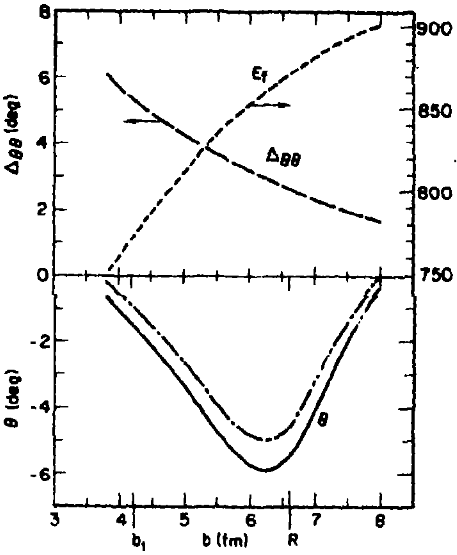

FIG. 1. Scattering angle θ (——), final kinetic energy E_f (– – – –), and angular width $\Delta_{\theta\theta}$ (— —) as functions of the impact parameter b. Calculations are done with the nuclear potential of Ref. 1 and statistical theory of Ref. 5. The long-short dashed curve is the deflection function obtained without frictional force.

From Fig. 1, we see that the scattering angle becomes larger when the frictional force is introduced in the evaluation of the orbital deflection. This effect by itself would lead to a slight increase of σ_2 according to Eq. (3). However, this increase of σ_2 is largely canceled by the decrease of the projectile momentum P_A because of the kinetic energy damping. Furthermore, the final projectile momentum also has a statistical distribution. But it affects only slightly the calculated value of σ_2.

In this paper, we have shown that the experimental data suggest strongly that the transverse momentum distributions of the fragments from projectile fragmentation are influenced by the scattering angle fluctuation of the projectile's trajectory. Its magnitude can be explained by a model which is derived for deep inelastic heavy ion collisions at much lower energy. Since the reaction time at the energy range we are considering is comparable to the time a perturbed nucleus requires to achieve global equilibrium, we expect that only local excitation is realized in the course of the reaction. The parameter Δ in the statistical model characterizes the energy dependence of the nuclear transition matrix element. The normal value as used in the deep inelastic heavy ion collisions is ~7 MeV. Here we use a larger value ~14 MeV because of the stronger energy dependence of nuclear transition matrix elements when only local excitations prevail. If we used $\Delta = 7$ MeV, the angular width would be substantially reduced, and the total kinetic energy loss would also be too small compared to the experimental value.

The author appreciates useful discussions with Dr. K. Van Bibber, Dr. D. K. Scott, and Dr. C. Y. Wong. He especially thanks Dr. D. K. Scott for encouragement which led to the writing of this report. This work was supported by the Nuclear Physics Division of the U. S. Department of Energy.

---

[1] K. Van Bibber *et al.*, Phys. Rev. Lett. 43, 840 (1979).

[2] A. S. Goldhaber, Phys. Lett. 53B, 306 (1974).

[3] D. E. Greiner, P. J. Lindstrom, H. H. Heckman, Bruce Cork, and F. S. Bieser, Phys. Rev. Lett. 35, 152 (1975).

[4] Paul J. Karol, Phys. Rev. C 11, 1203 (1975).

[5] D. Agassi, C. M. Ko, and H. A. Weidenmüller, Ann. Phys. (N.Y.) 107, 140 (1977); 117, 237 (1979); 117, 407 (1979); Phys. Lett. 73B, 284 (1978); Phys. Rev. C 18, 223 (1978).

PHYSICAL REVIEW C VOLUME 21, NUMBER 6 JUNE 198

Projection operator method for finding energies and widths of shape resonances in heavy-ion collisions

Thomas L. Larry* and William P. Beres
Department of Physics, Wayne State University, Detroit, Michigan 48202

(Received 27 December 1979)

A projection operator approach is presented for the determination of energies and widths of shape resonances in low-energy heavy-ion scattering. The method produces essentially the same results as standard S-matrix techniques in much less time, and works best for narrow virtual and quasibound resonances that could easily be missed by a scan. Examples for $^{12}C + ^{12}C$ are given.

NUCLEAR REACTIONS Shape resonances in low-energy heavy-ion collisions; calculated E_{RES} and Γ. Projection operators, no scanning. Comparison with S-matrix methods.

To find the resonance energies of the Jth partial wave $\psi_J^{(+)}$ of the scattering state wave function generally requires a scan over the S matrix or phase shift. This is a time consuming procedure which could in fact miss narrow resonances. A projection operator treatment of shape resonances has been developed which eliminates the need for such a phase shift analysis and is particularly useful for narrow resonances. In its original form as developed by Lev and Beres[1] the method was appropriate for nucleons scattered by nuclei. In the present paper we adopt the method to the treatment of heavy-ion scattering. The technique determines not only the positions but also the widths of resonances in an optical potential well. The method of Ref. 1 was a variation on an earlier paper by Wang and Shakin[2] that used projection operators to extract single-particle resonances from the continuum.

If a spinless heavy ion is scattered from a spinless target, then the resulting equation of Ref. 1 can be written as

$$E_{RES} - \mathrm{Re}\langle\phi_{nJ}|h_{RR}|\phi_{nJ}\rangle - \mathrm{Re}\langle\phi_{nJ}|h_{Rp}|G_p^{(+)}(E)h_{pR}|\phi_{nJ}\rangle = 0\,, \quad (1)$$

where E_{RES} is the resonance energy, J is the total angular momentum, h is the real one body Hamiltonian, R and p are projection operators that divide the single-particle Hilbert space into orthogonal resonant and nonresonant subspaces, respectively, and the notation $h_{RR} = RhR$, etc., is used. We assume that the resonant radial wave function can be approximated by the harmonic oscillator wave function ϕ_{nJ} without affecting the energy and width of the resonance. In Eq. (1) the term involving $G_p^{(+)}$, the Green's function for php, represents an important real part or shift that depends on E itself. The calculation of this shift constitutes the main point of this article. The width at E_{RES} is given by

$$\Gamma(E_{RES}) = -2\,\mathrm{Im}\langle\phi_{nJ}|h_{Rp}G_p^{(+)}(E_{RES})h_{pR}|\phi_{nJ}\rangle\,. \quad (2)$$

The choice of the harmonic oscillator wave functions is somewhat different for heavy-ion scattering than it is for nucleon scattering. In the latter case, a well known relation for $\hbar\omega$ is used.[3] It is

$$\hbar\omega = 40A^{-1/3}\,\mathrm{MeV}\,. \quad (3)$$

The reasoning which led to Eq. (3) is based on the shell model and is not appropriate for the case of heavy ions. The choice of $\hbar\omega$ for the present case is guided by the fact that ϕ_{nJ} is to approximate the actual radial wave function for the shape resonance. The latter wave function is normalized, vanishes beyond a certain cutoff radius, and will look like a bound state in the interaction region.

The following method for choosing $\hbar\omega$ has proved to work very well. The harmonic oscillator potential is given by

$$V(r) = \tfrac{1}{2}m\omega^2 r^2\,, \quad (4)$$

where ω is the classical angular frequency of the oscillator. The eigenvalues associated with the potential of Eq. (4) are given by

$$E_{nl} = \hbar\omega(2n + l - \tfrac{1}{2})\,, \quad (5)$$

where n signifies the number of nodes of the eigenstate, and l the orbital angular momentum. The potential of Eq. (4) is drawn in Fig. 1. The horizontal line in the figure represents the energy of the state with quantum numbers (n, l). At the radial distance r_0 the relationship

© 1980 The American Physical Society

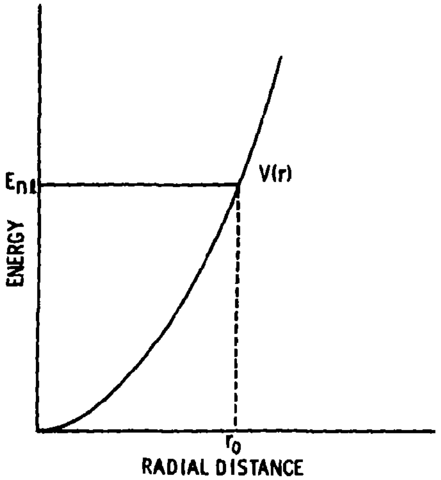

FIG. 1. Plot of the harmonic oscillator potential $V(r)=\frac{1}{2}m\omega^2r^2$. The horizontal line E_{nl} represents an energy eigenvalue.

$$E_{nl} = V(r_0) \tag{6}$$

is satisfied. From Eqs. (4) and (5) it follows that

$$\hbar\omega = \frac{2\hbar^2(2n+l-\frac{1}{2})}{mr_0^2} . \tag{7}$$

Equation (7) can be considered from another point of view. For a given specification of (n, l) this formula specifies the harmonic oscillator wave function in terms of the single parameter r_0. The physical significance of r_0 is clear. Beyond this radial distance the amplitude of the wave function drops off very rapidly with increasing r. Thus if ϕ_{nJ} is to approximate the resonant radial wave function, the value of r_0 should be chosen to correspond to the distance at which the latter is expected to begin "dropping off." If the results of the method were extremely sensitive to the value chosen for r_0, then it would have little value. As it turns out, all that is required is a reasonable guess. Varying r_0 by one or two fermi's does not significantly affect the results.

Figure 2 compares this method with an S-matrix scan. The potential chosen is a Woods-Saxon well plus a Coulomb repulsion term. The parameters chosen are almost the same as those used by Gobbi *et al.*[4] in an optical model calculation of the $^{12}C+^{12}C$ cross section. The object here is to compare the two methods for finding resonances and thus no attempt was made to produce an experimental fit.

In Fig. 2 the $J=10$ partial wave was examined. Part (a) shows a plot of $E-E_{RES}$ vs E, where E_{RES} is obtained from Eq. (1). The intersection with

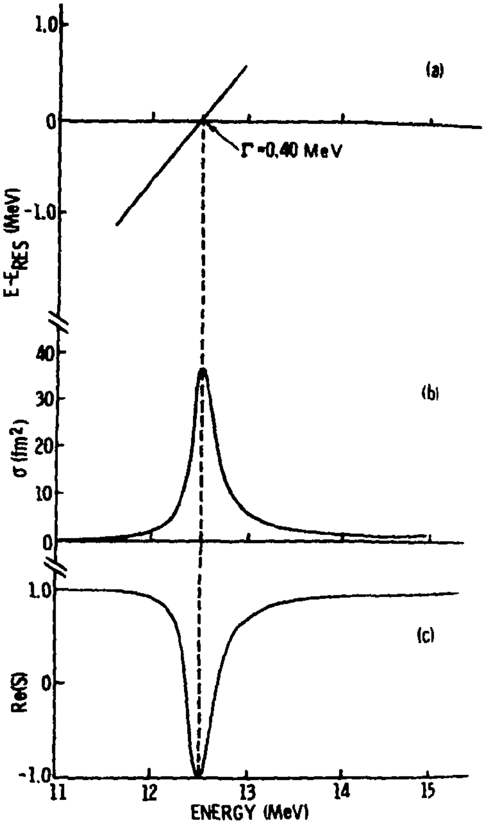

FIG. 2. $^{12}C+^{12}C$ elastic scattering. Comparison of the projection operator method Eq. (1) in part (a) and the S-matrix scan in part (c) for the $L=10$ partial wave. The cross section based on the S matrix is shown in part (b). In part (a) a resonance was found at 12.53 MeV with a width Eq. (2) of 0.40 MeV. This can be compared with parts (b) and (c).

the zero ordinate line gives a resonance energy of 12.5 MeV. Equation (2) then readily yields a width $\Gamma(E_{RES})=0.40$ MeV. We note that $E-E_{RES}$ is essentially a straight line and only a few points are needed to find the intersection. In part (b) of Fig. 2 the traditional cross section based on the S matrix is shown vs E, and in part (c) $Re(S)$ vs E is displayed. The S matrix predicts a resonance at 12.5 MeV in agreement with our simpler method. In addition, the S-matrix method yields a width of about 0.40 MeV, which agrees with our results. In a similar calculation for the $J=12$ partial wave, our method yielded $E_{RES}=17.35$ MeV and $\Gamma(E_{RES})=1.55$ MeV. In comparison, the S-matrix results were less than 2% greater.

In summary, since only a few points are needed to determine the position of a resonance, our method is much less time consuming than the standard techniques. Furthermore, since our approach is most accurate for narrow resonances, it can be used for finding both virtual and quasibound heavy-ion resonances. The latter tend to be very narrow and could easily be missed by a scan. We emphasize that although narrow single-particle resonances are not expected to be seen directly in heavy-ion data, they are often necessary as inputs to more detailed nuclear reaction and structure calculations.

This work was supported in part by the National Science Foundation under Grant No. PHY 78-00925.

---

*Present address: Dynamics Technology Inc., Torrance, California 90505.

[1] A. Lev and W. P. Beres, Phys. Rev. C 14, 354 (1976).

[2] W. L. Wang and C. M. Shakin, Phys. Lett. 32B, 421 (1970).

[3] A. Bohr and B. R. Mottelson, *Nuclear Structure* (Benjamin, New York, 1969), Vol. 1, p. 209.

[4] A. Gobbi, in Proceedings of the Symposium on Heavy Ion Scattering, Argonne, Illinois, 1971, edited by R. H. Siemssen *et al.*, ANL Report No. ANL-7837 (unpublished).

PHYSICAL REVIEW C VOLUME 21, NUMBER 6 JUNE 1980

P-wave dispersive contribution to low-energy elastic $\pi^+ {}^2H$ scattering

R. M. Rockmore
Department of Physics, Rutgers University, New Brunswick, New Jersey 08903

(Received 31 January 1980)

The *P*-wave dispersive contribution to the elastic scattering of low-energy positive pions ($T_{\pi^+}^{\text{lab}} \sim 50$ MeV) by deuterons is studied in a simple model with pion and ρ-meson rescattering via isobar excitation. For *S*-state deuterons it is found that only the tensor part of the effective potential for one-boson exchange contributes, and the resulting interference with the single scattering is a sensitive function of the ρ parameter, κ.

[NUCLEAR REACTIONS $d(\pi^+, \pi^+)$, $E = 49$ MeV; *P*-wave dispersive contribution; π, ρ rescattering; interference with single scattering; ρ parameter.]

The calculation of the effects of the absorption of *P*-wave pions on low-energy elastic $\pi^+ {}^2H$ scattering (via $\pi^+ {}^2H \to pp \to \pi^+ {}^2H$) is a problem of long standing in medium-energy physics.[1,2] In the low-energy domain (40 MeV $\leq T_{\pi^+}^{\text{lab}} \lesssim 60$ MeV), the quantitative resolution of the problem is further complicated by the fact that the single-scattering $\pi^+ {}^2H$ amplitude is nearly real there, so that the interference with the "absorptive" amplitude will be determined by the *dispersive* contribution of the latter.[2] More recently, McMillan and Landau[3] have performed an extensive numerical study of the single-scattering contribution to the elastic $\pi^+ {}^2H$ cross section in the 25–100 MeV region, examining effects due to the presence of the *D*-state component of the deuteron wave function, to internal motion of the target nucleons, and to uncertainties in the off-energy-shell pion-nucleon scattering amplitudes and the pion-nucleon phase shifts. They[3] find that the contribution from the *D*-state component becomes fairly sizable for pion lab energies above 49 MeV, e.g., raising the backward elastic angular distribution at 49 MeV by 12% in the case of the Moravcsik-Gartenhaus[4] wave function with a 6.7% *D*-state probability; moreover, McMillan and

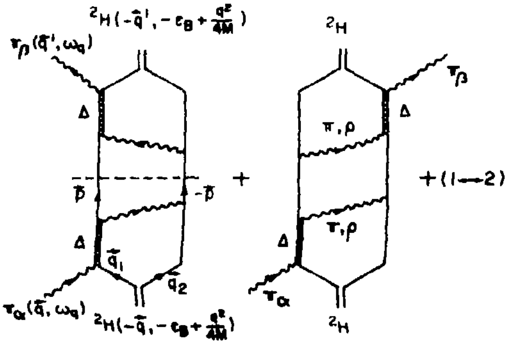
$^2H(-\vec{q}', -\epsilon_B + \frac{q^2}{4M})$
$\pi_\beta(\vec{q}', \omega_q)$
Δ
$\vec{p}$
$-\vec{p}$
Δ
$\vec{q}_1$
$\vec{q}_2$
$\pi_\alpha(\vec{q}, \omega_q)$
$^2H(-\vec{q}, -\epsilon_B + \frac{q^2}{4M})$
+
^2H
π_β
Δ
π, ρ
π, ρ
Δ
π_α
^2H
+ (1 ⟷ 2)

FIG. 1. (π, ρ)-rescattering graphs used in calculating the *P*-wave dispersive contribution to elastic $\pi^+ {}^2H$ scattering. The nucleon momenta are $\vec{q}_1 = \vec{p} + \vec{k} - \vec{q}$ and $\vec{q}_2 = -\vec{p} - \vec{k}$, where $\vec{k}$ is the rescattered meson momentum.

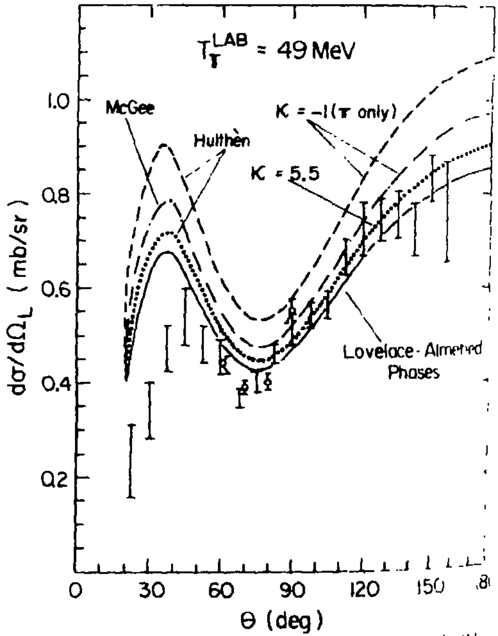

FIG. 2. $\pi^+ {}^2H$ elastic differential cross section (solid line) for a pion lab kinetic energy of 49 MeV in the single-scattering approximation (Ref. 3). In the calculation of the *P*-wave dispersive correction, an *S*-state Hulthén wave function with $\alpha_1 = 0.326$ and $\beta_1 = 2.029$ is used with the dashed and dotted curves indicating the effect of the *P*-wave dispersive contribution for $\kappa = -1$ (π exchange only) and 5.5. The dashed-dotted curve indicates the effect of the *P*-wave dispersive contribution for $\kappa = -1$ (π exchange only) using McGee's wave function (Ref. 9). I also take $\Lambda_\pi = 1200$ MeV and $\Lambda_\rho = 1600$ MeV. Data shown are taken from D. Axen *et al.* (Ref. 11) and B. Balestri *et al.* (circles) (Ref. 12).

© 1980 The American Physical Society

Landau show that Beder's[2] approximations in the single-scattering terms (neglecting entirely the D-state contributions) produce at this same energy results which differ from those where complex phase-shift functions are used by about the same amount. The elastic cross section within the single-scattering approximation is found[3] not significantly affected by the choice of the off-energy-shell function. Note that the possibility of a non-negligible contribution from absorption does not enter into their[3] considerations. The subsequent calculation of the $\pi^+\,{}^2\mathrm{H}$ elastic cross section at 47.5 MeV by McMillan and Landau was observed by Burman[5] to "represent the data (of Axen *et al.*) reasonably well"; indeed, it was remarked[6] "that a simple single-scattering approach is so close to the data... is encouraging." Thus it would be useful to provide some theoretical justification for ignoring this bothersome contribution in discussions of single-scattering fits to the low-energy elastic data.

The boson (π,ρ)-rescattering model of Brack *et al.*,[6] which has lately proved successful in fitting $\pi^+\,{}^2\mathrm{H}$ absorption, is the basis for the calculation of the P-wave dispersive contribution to elastic $\pi^+\,{}^2\mathrm{H}$ scattering I sketch here. In my adaptation of this model to the present diagonal situation $[\pi^+\,{}^2\mathrm{H}$ (absorption) $\to pp \to \pi^+\,{}^2\mathrm{H}$ (reemission)], I make the following reasonable approximations:

(1) In the energy domain of interest, i.e., 40 MeV $\leq T_{\pi^+}^{\mathrm{lab}} \leq 60$ MeV, only the rescattering terms via Δ excitation are kept. (The relevant graphs are shown in Fig. 1.)

(2) As in Ref. 6, my considerations are limited to *static* boson exchanges.

(3) The dependence of the absorption (reemission) "form factor" on the initial (final) π^+ momentum is neglected ("threshold approximation"[7]). In spite of the quantitative shortcomings alluded to above, I have for simplicity carried out the calculation in terms of Beder's approximations,[2,3] i.e., the real approximate phase-shift functions,

$$\exp[i\delta^{l}_{2t,2j}(k_0)]\sin\delta^{l}_{2t,2j}(k_0) \to a^{l}_{2t,2j}(k_c/m_\pi)^{2l+1}\,, \qquad (1)$$

with $a^0_{11}=0.18$, $a^0_{31}=-0.12$, $a^1_{11}=-0.048$, $a^1_{13}=-0.01$, $a^1_{31}=-0.032$, $a^1_{33}=0.205$, are used. First, for convenience I use a Hulthén (S-state) wave function with $\alpha_1=0.326$ and $\beta_1=2.029$ in calculating the effect of this perturbation on the single-scattering prediction of Ref. 3. The graphs of Fig. 1 yield the amplitude

$$\langle T=0|\mathfrak{A}_{\mathrm{dispersive}}|T=0\rangle = -i(2\omega_q,2\omega_q)^{-1/2}\tfrac{16}{81}\{\tfrac{4}{3}[4\vec{q}\,'\cdot\vec{q} - i(\vec{\sigma}_1+\vec{\sigma}_2)\cdot\vec{q}\,'\times\vec{q}\,] - \tfrac{1}{3}(\vec{\sigma}_1+\vec{\sigma}_2)\cdot\vec{q}\,'(\vec{\sigma}_1+\vec{\sigma}_2)\cdot\vec{q}\}$$

$$\times\iiint d\vec{p}\,d\vec{k}\,d\vec{k}\,'(2\pi)^{-9}(a'_\pi-a'_\rho)(a_\pi-a_\rho)P_2(\hat{k}'\cdot\hat{p})P_2(\hat{k}\cdot\hat{p})P/[\omega_q+(q^2/4M)-\epsilon_B-(p^2/M)]\,, \qquad (2)$$

where $(i=\pi,\rho)$

$$a_i=(f^*_\pi/m_\pi)[(f^*_if_i)/m_i^2](\omega_q-\omega_\Delta+i\Gamma_{\Delta/2})^{-1}[(\Lambda_i^2-m_i^2)^2/(\Lambda_i^2+k^2)^2]k^2(m_i^2+k^2)^{-1}(4\pi)^{1/2}N$$

$$\times\{[\alpha_1^2+(\vec{k}+\vec{p})^2]^{-1}-[\beta_1^2+(\vec{k}+\vec{p})^2]^{-1}\}\,. \qquad (3)$$

With approximation (3) the integrals over $\vec{k}$ and $\vec{k}'$ can now be obtained *in closed form. Thus the evaluation of the perturbation reduces to a single numerical integration.*

As in Ref. 6, I take[8] $f^*/f=2$, $f^*/f=1.7$. In my calculation I set $\Lambda_\pi=1200$ MeV, $\Lambda_\rho=1600$ MeV. N is the normalization constant of the deuteron S-state wave function. *Note that only the tensor part of the effective potential for one boson exchange contributes.* Next, with slight formal modification of expression (2), I calculate the effect using the more physical McGee wave function[9] (7% D-state probability). For π exchange only I find a 50% reduction in the Hulthén results; nevertheless, the perturbation in this case is still quite substantial at all angles. (I also find the D-state contribution to be negligible here.) The expectation that the resulting interference with the single-scattering amplitude

$$\langle T=0|\mathfrak{A}_{ss}|T=0\rangle \cong -i\left\langle T=0\right|\int d\vec{p}(2\pi)^{-3}\sum_{i=1,2}\left[\frac{(\omega'_c+E'_c)(\omega_c+E_c)}{\omega'_L\omega_LE'_LE_L}\right]^{1/2}$$

$$\times\left\{-\frac{8\pi^2}{k_c^{(0)}}\sum(2l+1)\delta^{l}_{2t,2j}[k_c^{(0)}]\kappa_j^{(i)}(\hat{k}'_c|\mathfrak{F}^{(i)}_{l,j}|\hat{k}_c) + \left[\frac{\omega'_c\omega_cE'_cE_c}{(\omega'_c+E'_c)(\omega_c+E_c)}\right]^{1/2}\frac{\pi\alpha}{[k_c^{(0)}]^2(1-\cos\theta_c)}I_z(1+\tau_z^{(i)})\right\}$$

$$\times\phi_D(|\vec{p}+\tfrac{1}{2}(\vec{k}_L-\vec{k}'_L)|)\phi_D(\vec{p})|T=0\rangle\,, \qquad (4)$$

where my notation follows those of earlier works[1-3] [with $(\epsilon_j)\mathfrak{F}_{i,j}$ denoting the appropriate (iso)spin projection operator; $L(c)$, laboratory (center-of-mass) frame; $\omega(E)$, meson (nucleon) energy, etc.[10]] depends sensitively on the ρ-meson parameter, κ; is confirmed in the dashed and dotted Hulthén plots of Fig. 2. One sees that as the currently favored value of $\kappa = 5.5$ is approached, the perturbation on $(d\sigma^{el}/d\Omega_L)_m$ arising from the P-wave dispersive contribution becomes negligible and the good fit to experiment already provided by the single-scattering approximation of Ref. 3 is preserved. The perturbation is plotted on the single-scattering prediction of Landau and McMillan with the 47.5 MeV data of Axen *et al.*[11] and the 47 MeV data of Balestri *et al.*[12] shown for comparison.

I am happy to acknowledge the use of the PDP-11 computer of the Rutgers Nuclear Physics Laboratory. This work was supported in part by the Rutgers Research Council under Grant No. 07-2330.

---

[1] R. M. Rockmore, Phys. Rev. 105, 256 (1957).

[2] D. S. Beder, Nucl. Phys. B34, 189 (1971).

[3] M. McMillan and R. H. Landau, TRIUMF Report No. TRI-74-1 (unpublished).

[4] M. Moravcsik, Nucl. Phys. 7, 113 (1958); S. Gartenhaus, Phys. Rev. 100, 900 (1955).

[5] R. L. Burman, *High Energy Physics and Nuclear Structure—1975*, proceedings of the Sixth International Conference, Santa Fe and Los Alamos, edited by D. E. Nagle *et al.* (AIP, New York, 1975), pp. 41–51.

[6] M. Brack, D. O. Riska, and W. Weise, Nucl. Phys. A287, 425 (1977).

[7] A. E. Woodruff, Phys. Rev. 117, 1113 (1960); D. S. Koltun and A. Reitan, *ibid.* 141, 1413 (1966); C. Lazard, J. L. Ballot, and F. Becker, Nuovo Cimento 65, 117 (1970); G. A. Miller, Phys. Rev. C 16, 2325 (1977). I do not find any significant change in the results reported here when, following Woodruff, I use $j_0(qr/2)$ for the meson wave function in place of 1 (threshold approximation).

[8] I take $f_\pi^2/4\pi = 0.08$, $f_\rho^2/4\pi = (g_\rho^2/4\pi)\,[m_\rho/(2M)]^2(1+\kappa)^2$, with $g_\rho^2/4\pi = 0.52$.

[9] I. J. McGee, Phys. Rev. 151, 772 (1966).

[10] Note that in evaluating the perturbation, to simplify matters, I set the nucleon momentum $\vec{p}$ equal to the Carlson value $\vec{p}_{av} = -\frac{1}{4}(\vec{k}_L - \vec{k}_L')$ in the two-body amplitude and take the ambiguous frame denoted by $c^{(0)}$ to be the initial (unprimed) center-of-mass frame. Thus my calculation ***underestimates*** the interference with the single-scattering amplitude.

[11] D. Axen *et al.*, Nucl. Phys. A256, 387 (1976).

[12] B. Balestri *et al.*, *Few Body Systems and Nuclear Forces*, proceedings of the VIII International Conference on Few Body Systems and Nuclear Forces, Graz, Austria, 1978, edited by H. Zingl, M. Haftel, and H. Zankel (Springer, Berlin, 1978), p. 227.

PHYSICAL REVIEW C   VOLUME 21, NUMBER 6   JUNE 19

(π,p) absorption in ^{6,7}Li at 75 and 175 MeV

Jan Källne, J. Davis, P. C. Gugelot, and J. S. McCarthy
Department of Physics, University of Virginia, Charlottesville, Virginia 22901

G. R. Smith
Department of Physics, University of Colorado, Boulder, Colorado 80309

R. L. Boudrie, B. Höistad, and C. L. Morris
Los Alamos Scientific Laboratory, Los Alamos, New Mexico 87545

(Received 21 May 1979)

Differential cross sections are reported for (π^+,p) reactions to discrete final states over the range $\theta = 20$–95 (116°) and for the inclusive $(\pi^\pm,p)$ reactions in ^{6}Li at $\theta = 20°$ to the continuum. The continuum cross sections indicate the predominance of the two-nucleon pion absorption mechanism when $(\pi\ ,p)$ shows the importance of multiple (charge-exchange) scattering. The combined use of the exclusive and inclusive cross sections is discussed.

[NUCLEAR REACTIONS ^{6,7}Li$(\pi^+,p)^{5,6}$Li, $T_\pi = 75$ MeV, $\theta = 20$–116°, $T_\pi = 175$ MeV. $\theta_p = 20$–95° measured $\sigma(\theta)$; ^{6}Li$(\pi^\pm,p)$, T_π 75, 175 MeV, $\theta_p = 20°$ measured $\sigma(T_p)$; discussed reaction mechanism effects.]

A significant part of the pion-nucleus interaction is true pion absorption, but only a fraction thereof represents (π,p) reactions to discrete final states, $A(\pi,p)A-1$. There is no definitive interpretation of such reactions [or of the related pion production reactions $A-1(p,\pi)A$] and most progress towards an understanding of the pion absorption mechanism has been realized for the two-nucleon system.[1] The dissipation of the pion energy requires the involvement of large off-shell momenta (≥ 0.5 GeV/c) which is a little known regime of the nuclear dynamics. Studies of (π^+,p) in ^2H indicate that, rather than coming from the nuclear single particle motion, such momenta are the result of π-(NN) interactions which can be described, for instance, in terms of $\pi+N$ off-shell scattering preceding the $\pi N \rightarrow N$ annihilation on the second nucleon. In the interpretation of (π,p) reactions in many-body systems ($A>2$) one has to consider the possibility of pion off-shell scattering from several nucleons besides the effects of ordinary (on-shell) multiple scattering. Theoretical attempts have been made to connect the $A(\pi,p)A-1$ reactions in ^2H and heavier nuclei by using the two-nucleon and pion-rescattering models.[2,3] The treatment of the dependence on nuclear structure presents a problem in these reactions but is of lesser importance in inclusive reactions $A(\pi,p)X$, particularly in regions where few-nucleon interactions are kinematically allowed, for instance, $\pi NN \rightarrow Np$. The other reaction aspects of the $A(\pi,p)A-1$ reaction models can in part be tested in this part of the spectrum just as it connects to the more ambitious efforts to predict the full $A(\pi,p)X$ spectrum (for instance, the intranuclear cascade model[4]). In this note we report on the first measurements of the full (π,p) absorption spectra with results on ^{6,7}Li$(\pi^+,p)^{5,6}$Li and ^{6}Li$(\pi^\pm,p)X$. We discuss the information extractable from these exclusive and inclusive reactions separately and the additional information power that lies in their combined use.

The experiment was carried out with the EPICS channel and spectrometer system at LAMPF. Using fairly thick targets (314 and 245 mg/cm^2 of 98% pure ^{6}Li and ^{7}Li) we obtained (π,p) spectra such as the example shown in Fig. 1. All cross sections were normalized by measuring the π^+d

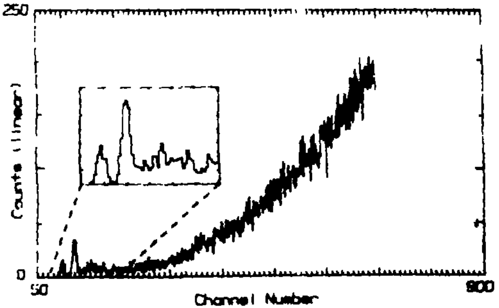

FIG. 1. A typical ^{7}Li(π^+,p) spectrum obtained at $\theta = 20°$ and $T = 175$ MeV. The insert shows an enlargement with the 0 and 2.18 MeV states in ^{6}Li.

[1] W. R. Gibbs, *Nucleon-Nucleon Interactions*, in Proceedings of the Second International Conference on Nucleon-Nucleon Interactions, Vancouver, 1977, edited by D. F. Measday, H. W. Fearing, and A. Strathede (American Institute of Physics, Vol. 41, New York, 1978), p. 314.

[2] H. W. Fearing, Phys. Rev. C 16, 313 (1977).

[3] W. R. Gibbs and A. T. Hess, Phys. Lett. 68B, 205 (1977).

[4] J. N. Ginocchio, Phys. Rev. C 17, 195 (1978).

[5] G. Jones, *Nucleon-Nucleon Interactions*, in Proceedings of the Second International Conference on Nucleon-Nucleon Interactions, Vancouver, 1977, edited by D. F. Measday, H. W. Fearing, and A. Strathede (American Institute of Physics, Vol. 41, New York, 1978), p. 292; C. Richard-Serre *et al.*, Nucl. Phys. B20, 413 (1970).

[6] H. A. Thiessen *et al.*, Los Alamos Scientific Laboratory, Informal Report, LA-6663-MS, 1977.

[7] E. Aslanides *et al.*, Phys. Lett. 69B, 433 (1977).

[8] Jan Källne *et al.*, Phys. Rev. Lett. 40, 378 (1978).

[9] J. Källne *et al.*, Phys. Lett. 52B, 313 (1974); B. Fagerström *et al.*, Phys. Scr. 13, 101 (1976).

[10] M. M. Sternheimer and R. R. Silbar, Phys. Rev. D 6, 3117 (1972).

[11] Equations (A6) and (A7) of Ref. 4 give the ratio 16:1 for $^6\mathrm{Li}(\pi^+,p)$ to $^6\mathrm{Li}(\pi^-,p)$ which changes to 31:1 considering the fact that the $np(\pi^+,p)p$ channel produces two detectable protons.

[12] H. E. Jackson *et al.*, Phys. Rev. C 16, 730 (1977); Phys. Rev. Lett. 39, 1601 (1977).

PHYSICAL REVIEW C VOLUME 21, NUMBER 6 JUNE 1980

Comparison of analyzing powers and polarizations for the charge symmetric reactions $^2\mathrm{H}(\vec{d},p)^3\mathrm{H}$ and $^2\mathrm{H}(\vec{d},n)^3\mathrm{He}$

J. J. Bevelacqua
Planning Division, United States Department of Energy, P. O. Box E, Oak Ridge, Tennessee 37830

(Received 16 October 1979)

Analyzing powers and polarizations for the $^2\mathrm{H}(\vec{d},n)$ and $^2\mathrm{H}(\vec{d},p)$ charge symmetric reactions were calculated in a $4\hbar\omega$ model space within the framework of the generalized R-matrix methodology of Lane and Robson. The calculated differences are approximately an order of magnitude smaller than those quoted by Dries *et al*.

[NUCLEAR REACTIONS Calculated analyzing power and polarization differences for the charge symmetric reactions $^2\mathrm{H}(\vec{d},p)$ and $^2\mathrm{H}(\vec{d},n)$ for $E_d \leq 10.0$ MeV.]

In a recent letter Dries *et al.*[1] measured the vector and tensor analyzing powers for the $^2\mathrm{H}(\vec{d},n)^3\mathrm{He}$ and $^2\mathrm{H}(\vec{d},p)^3\mathrm{H}$ reactions for low energies ($E_d \leq 5.5$ MeV), where effects due to the Coulomb interaction should be enhanced. On the basis of their data, Dries *et al.* conclude that the energy trends of all the analyzing powers are inconsistent with a simple energy shift correction for Coulomb effects proposed by Hardekopf *et al.*[2] Dries *et al.* also conclude that there are real differences in the magnitude of the comparable analyzing powers and polarizations in the two reactions when the data are compared at equal projectile energies. Typically, $A_{zz}(0°)$ and $A_y(120°)$ differ by about 0.05 when the $^2\mathrm{H}(\vec{d},p)$ and $^2\mathrm{H}(\vec{d},n)$ reactions are compared at equal incident energies. The neutron data is larger (less negative) than the proton data,[1] and this trend holds for all deuteron energies considered in Ref. 1. Unfortunately, the conclusions of Dries *et al.* are clouded because there is considerable scatter in the $^2\mathrm{H}(\vec{d},n)$ data.[3-6]

In addition to experimental uncertainties, the $(\vec{d},n)$ and $(\vec{d},p)$ reactions are of interest because they can be used to explore charge symmetry violations of the nuclear force. Polarizations are expected to be identical when exact charge symmetry holds.[7] This exact symmetry can be broken by the Coulomb interaction, but its effect on observables is not well known.[8] The author notes that questions of charge symmetry violation have been frequently raised in the ^{4}He system.[9,10] The large $^3\mathrm{H}(p,n)\ P^y - A_y$ differences were found by Donoghue *et al.*[9] to be small, and the apparent discrepancy was removed by additional experimental effort. The (p,n) results are consistent with Coulomb effects and one would expect the $(\vec{d},p)$ and $(\vec{d},n)$ polarization results to likewise show a normal Coulomb breaking effect of about 0.01–0.02, and not be as large as reported by Dries *et al.*

The model used in the analysis of $(\vec{d},n)$ and $(\vec{d},p)$ scattering is based on the generalized R-matrix formalism of Lane and Robson.[11] Details of the formalism have been given elsewhere[10-12] and only salient features will be outlined here. The internal states for the ^{4}He system are expanded on a basis of properly symmetrized translationally invariant harmonic oscillator eigenstates including all states of up to $4\hbar\omega$ of oscillator excitation. All three two-body breakup channels, namely $p+{}^3\mathrm{H}$, $n+{}^3\mathrm{He}$, and $d+{}^2\mathrm{H}$, are explicitly included. The model predicts at most a 3% breaking of isospin purity for states above the $d+{}^2\mathrm{H}$ channel.[8] The $^2\mathrm{H}(\vec{d},n)$ and $^2\mathrm{H}(\vec{d},p)$ reactions require the calculation of both ^{3}H and ^{3}He bound state properties, and the model predicts binding energies which are 5% less than the experimental values for both clusters. The calculated rms radius is within 8% of data for ^{3}He and within 2% for ^{3}H.

Calculations of the ^{3}H and ^{3}He ground state wave functions yield a 0.01% Coulomb prompted isospin breaking effect in the $A=3$ system. In addition, our previous calculations suggest that Coulomb forces will have a small effect on level[8] as well as reaction properties[10-12] in the $A=4$ system. In particular, the $P_y - A^y$ difference in the $^3\mathrm{H}(p,n)$ reaction was found to be typically 0.015 or less. Thus, we are led to the conclusion that the $^2\mathrm{H}(\vec{d},n)$ and $^2\mathrm{H}(\vec{d},p)$ reactions will show a similar effect with expected differences being less than the 0.05 result of Dries *et al.*

Calculations of both polarization and analyzing power differences have been performed for $E_d \leq 10$ MeV and are summarized in Table I. The calculations are performed at $\theta_{c.m.} = 120°$ which shows the largest difference of experimental A^y values.[1] The values in Table I are based on the E_R^{shifted} spectrum[10] which corresponds to the

TABLE I. Analyzing power and polarization differences for the ^{2}H($\vec{d}$,p) and ^{2}H($\vec{d}$,n) reactions (E_R^{shifted} spectrum).

E_d (MeV)	$A^y(\vec{d},p)-A^y(\vec{d},n)$	$P_y(\vec{d},p)-P_y(\vec{d},n)$
1.0	−0.004 25	−0.000 34
1.5	−0.006 54	−0.001 92
2.0	−0.006 79	−0.001 61
2.5	−0.006 70	−0.001 40
3.0	−0.005 33	−0.001 27
5.0	−0.003 73	−0.002 06
9.0	+0.006 93	−0.000 11
10.0	+0.006 68	−0.000 01

level scheme of Fiarman and Meyerhof.[13] The use of the $E_R^{\text{unshifted}}$ spectrum, which lies several MeV above the experimental levels,[10] leads to differences which are about a factor of 4 smaller than those summarized in Table I. Variations in these spectra emphasize that the level positions, both near the $d+{}^2$H channel and lying higher in the continuum, can have a significant impact on the calculated polarization and analyzing power values.

The ^{4}He levels above the $d+{}^2$H channel are broad and overlapping.[13] This feature suggests that significant variation in polarization values will not be encountered in the vicinity of the levels above the deuteron threshold in the ^{4}He system. The level character will also favor smaller polarization differences which are expected in the vicinity of broad energy levels. This feature is reflected in the results summarized in Table I. The calculated values are generally less than 0.007 which is about an order of magnitude smaller than the differences of Dries *et al.* The 0.007 model result is reasonable when compared with the 0.015 difference in the (p,n) reaction below the $d+{}^2$H threshold. The (p,n) reaction estimate was made in an energy region where narrow resonances predominate.

It should be noted that polarization differences as large as 0.05 can occur in the ^{3}H($\vec{p}$,p) and ^{3}He($\vec{n}$,n) reactions,[14-16] but even differences this large do not require charge symmetry violations as an explanation. The differences can be attributed to channel as well as level effects.[14] Model calculations[14] predict these trends and are in agreement with $(\vec{p},p)$ and $(\vec{n},n)$ data.[15,16] In view of the fairly wide qualitative agreement between our calculated results[10,14] and the $(\vec{p},p)$, $(\vec{n},n)$, and (p,n) data,[9,15,16] we conclude that the data set of Dries *et al.* suggests trends which are not consistent with observed ^{4}He properties. These inconsistencies may be attributed to either the $(\vec{d},p)$ or $(\vec{d},n)$ data. As noted earlier, considerable scatter exists in the $(\vec{d},n)$ data. Since there is only one set of (d,p) data, additional measurements would aid in determining if the anomalous differences between the proton and neutron data are real.

---

[1] L. J. Dries, H. W. Clark, R. Detomo, Jr., and T. R. Donoghue, Phys. Lett. 80B, 176 (1979).

[2] R. A. Hardekopf, R. L. Walter, and T. B. Clegg, Phys. Rev. Lett. 28, 760 (1972).

[3] J. E. Simmons *et al.*, Phys. Rev. Lett. 27, 113 (1971).

[4] G. C. Salzman *et al.*, Phys. Lett. 45B, 123 (1973).

[5] P. W. Lisowski, R. L. Walter, C. E. Busch, and T. B. Clegg, Nucl. Phys. A242, 298 (1975).

[6] H. Paetz gen. Schieck, Cl. Petitjean, H. R. Striebel, and P. Huber, Helv. Phys. Acta. 40, 414 (1967).

[7] M. Simonius, in *Lecture Notes in Physics*, edited by D. Fick (Springer, Berlin, 1974), Vol. 30, p. 38.

[8] J. J. Bevelacqua, Phys. Rev. C 18, 591 (1978).

[9] T. R. Donoghue, Sr. M. A. Doyle, H. W. Clark, L. J. Dries, J. L. Regner, W. Tornow, R. G. Byrd, P. W. Lisowski, and R. L. Walter, Phys. Rev. Lett. 37, 981 (1976) and references therein.

[10] J. J. Bevelacqua, Phys. Rev. C 16, 107 (1977).

[11] A. M. Lane and D. Robson, Phys. Rev. 151, 774 (1966); 178, 1715 (1969); 185, 1403 (1969).

[12] J. J. Bevelacqua and R. J. Philpott, Nucl. Phys. A275, 301 (1977).

[13] S. Fiarman and W. E. Meyerhof, Nucl. Phys. A206, 1 (1973).

[14] J. J. Bevelacqua, Phys. Rev. C 16, 1782 (1977).

[15] R. A. Hardekopf, P. W. Lisowski, T. C. Rhea, and R. L. Walter, Nucl. Phys. A191, 481 (1972).

[16] P. W. Lisowski, T. Rhea, R. L. Walter, C. E. Bush, and T. B. Clegg, Nucl. Phys. A259, 61 (1976).

PHYSICAL REVIEW C VOLUME 21, NUMBER 6 JUNE 1980

High energy scattering from a bound nucleon: Unitarity and closure approximation

F. Cannata
Physics Department, Weizmann Institute of Science, Rehovot, Israel
*and Instituto di Fisica dell'Universita and Istituto Nazionale de Fisica Nucleare, Bologna, Italy**

S. A. Gurvitz
Physics Department, Weizmann Institute of Science, Rehovot, Israel

(Received 23 May 1979)

The scattering of high energy hadrons from nuclei is treated in a generalized closure approximation for inclusive cross sections which takes into account some Fermi motion and binding potential effects. The consistency with unitarity is demonstrated.

[NUCLEAR REACTIONS High energy scattering, single scattering amplitude, inclusive cross section, closure approximation, unitarity.]

An approach to the projectile-nucleus elastic scattering which utilizes in a systematic way the compensation of Fermi motion and bindings effects has recently been derived.[1-3] Its application to the analysis of pd high energy backward scattering[3,4] revealed remarkable agreement with the data.

Here we investigate the unitarity of this approach concentrating on the analysis of the single scattering amplitude. Consider a model where a projectile (mass μ and momentum $\vec{p}$) scatters (with a scattering matrix τ) on a nucleon (mass m and momentum $\vec{P}-\vec{p}$) which is bound by a local potential $\tilde{V}$ to a core of infinite mass. Using this model we present an approximate treatment of inclusive cross sections (excluding, however, true absorption or charge exchange processes). We thus assume that the projectile does not interact with the core.

We denote by ϵ_n the eigenvalues corresponding to eigenstates ϕ_n of the nuclear Hamiltonian $H_N=K_{\text{nucleon}}+\tilde{V}$, and set $E=\vec{p}^2/2\mu+\epsilon_0$ and $\vec{V}=\vec{p}/\mu$. The inclusive differential cross section is

$$\frac{d\sigma_{\text{total}}}{d\Omega_{p'}}=\frac{(2\pi)^4}{v}\sum_n\int p'^2dp'\,\delta\!\left(E-\epsilon_n-\frac{\vec{p}'^2}{2\mu}\right)\times|\langle\Phi_n,\vec{p}'|\tau|\Phi_0,\vec{p}\rangle|^2\,. \tag{1}$$

Using the spectral representation of the Green's function $[G=(E-H_N-K_{\text{projectile}})^{-1}]$ we can express σ_{total} as

$$\sigma_{\text{total}}=\frac{(2\pi)^3}{iv}\langle\Phi_0,\vec{p}|\tau^+(G^+-G)\tau|\vec{p},\Phi_0\rangle\,. \tag{2}$$

In our approach we approximate the Green's function G in Eq. (2) by G_ϵ:

$$\langle\vec{p}'',\vec{P}''|G_\epsilon(E)|\vec{p}',\vec{P}'\rangle=\frac{\delta^3(\vec{p}''-\vec{p}')\delta^3(\vec{P}''-\vec{P}')}{E-\vec{p}'^2/2\mu-\epsilon(\vec{p}',\vec{\chi})+i\delta}\,, \tag{3}$$

where $\vec{p}'$, $(\vec{p}'')$, $\vec{P}'$, $(\vec{P}'')$ denote projectile and total nucleon plus projectile momenta, respectively. The approximation in Eq. (3) is very similar to the generalized closure approximation defined in Ref. 5, for the treatment of inclusive cross sections. However, we must use the same approximation for the Green's function in the Lippmann-Schwinger equation for the scattering matrix τ. This consistent approximation is crucial to implement unitarity. The closure energy $\epsilon(\vec{p}',\vec{\chi})$ is assumed to depend on $\vec{p}'$ and an external vector $\vec{\chi}$ but not on $\vec{P}'$ $(\vec{P}'')$.[1,2] It is defined to be chosen in such a way as to lead to vanishing first order corrections to σ_{total}.

Defining $h_\epsilon=G_\epsilon^{-1}-G^{-1}$ one has $G=G_\epsilon+\Delta^1G_\epsilon+\Delta^2G_\epsilon+\cdots$, $\Delta^1G_\epsilon=G_\epsilon h_\epsilon G_\epsilon$, $\Delta^2G_\epsilon=G_\epsilon h_\epsilon G_\epsilon h_\epsilon G_\epsilon$. In a similar way one can look for a closure energy $\bar{\epsilon}$ (which may differ from ϵ) for the Green's function entering the Lippmann-Schwinger equation $\tau=\tilde{U}+\tilde{U}G\tau$ where $\tilde{U}$ is the projectile-nucleon potential. This approximate Green's function is $G_{\bar{\epsilon}}$. We also define

$$t_{\bar{\epsilon}}=\tilde{U}+\tilde{U}G_{\bar{\epsilon}}t_{\bar{\epsilon}}\,, \tag{4}$$

$$\langle\vec{p}',\vec{P}'|t_{\bar{\epsilon}}|\vec{p},\vec{P}\rangle=\langle\vec{p}'|\hat{t}_{\bar{\epsilon}}|\vec{p}\rangle\delta^3(\vec{P}'-\vec{P})\,, \tag{5a}$$

where $t_{\bar{\epsilon}}$ does not depend on $\vec{P}$ $(\vec{P}')$.[1,2] [One sees from Eqs. (3) and (4) that the approximate scattering matrix $t_{\bar{\epsilon}}\cong\tau$ contains only a two-body cut whose position depends on $\bar{\epsilon}$ ($t_{\bar{\epsilon}}$ does not contain many body cuts which appear in τ).]

The first order correction $\tau-t_{\bar{\epsilon}}=\Delta^1\tau+\cdots$ is given by $\Delta^1\tau=t_{\bar{\epsilon}}G_{\bar{\epsilon}}h_{\bar{\epsilon}}G_{\bar{\epsilon}}t_{\bar{\epsilon}}$ where $h_{\bar{\epsilon}}=G_{\bar{\epsilon}}^{-1}-G^{-1}$. Including the correction $\Delta^1\tau$ we have

$$\sigma_{\text{total}}=\langle t_{\bar{\epsilon}}^{\pm}(G_\epsilon^+-G_\epsilon)t_{\bar{\epsilon}}\rangle+\langle t_{\bar{\epsilon}}^{+}(\Delta^1G_\epsilon^+-\Delta^1G_\epsilon)t_{\bar{\epsilon}}\rangle+\langle\Delta^1\tau^+(G_\epsilon^+-G_\epsilon)t_{\bar{\epsilon}}\rangle+\langle t_{\bar{\epsilon}}^{+}(G_\epsilon^+-G_\epsilon)\Delta^1\tau\rangle\,.$$

We now determine ϵ and $\bar{\epsilon}$ so that the Δ^1G and $\Delta^1\tau$ terms vanish. First examine the Δ^1G correction

© 1980 The American Physical Society

$$\int \phi_0(\vec P-\vec p)|\langle\vec p|\hat t_{\bar\epsilon}|\vec p'\rangle|^2\frac{\{[(\vec P-\vec p')^2/2m-\epsilon(\vec p',\vec\chi)]\delta^3(\vec P-\vec P')+\tilde V(\vec P-\vec P')\}}{[E-\vec p'^2/2\mu-\epsilon(\vec p',\vec\chi)]^2}\,\phi_0(\vec P'-\vec p)d^3P\,d^3P'd^3p'\,. \tag{5b}$$

For a local potential $\tilde V$ we have

$$\int \tilde V(\vec P_1-\vec P_2)\phi_0(\vec P_2-\vec p)d^3P_2=[-(\vec P_1-\vec p)^2/2m+\epsilon_0]\phi_0(\vec P_1-\vec p)$$

If we then set

$$\epsilon(\vec p',\vec\chi)_{\vec\chi=\vec p}=\epsilon_0+\frac{1}{2m}(\vec p-\vec p')^2 \tag{6}$$

and perform the integration in (5b) the integral is seen to vanish. Proceeding in the same way with the $\Delta^1\tau$ corrections we obtain $G_\epsilon=G_{\bar\epsilon}$ and from Eq. (3):

$$\langle\vec p'',\vec P''|G_\epsilon|\vec p',\vec P'\rangle=\delta^3(\vec P''-\vec P')\delta^3(\vec p''-\vec p')\left(\frac{\vec p^2}{2\mu}-\frac{\vec p'^2}{2\mu}-\frac{(\vec p-\vec p')^2}{2m}\right)^{-1}. \tag{7a}$$

The Lippmann-Schwinger equation for $\hat t_\epsilon$ [see Eq. (4)] is

$$\langle\vec p|\hat t_\epsilon|\vec p'\rangle=\tilde v(\vec p-\vec p')+\int\tilde v(\vec p-\vec p'')d^3p''\frac{\langle\vec p''|\hat t|\vec p'\rangle}{\vec p^2/2\mu-\vec p''^2/2\mu-(\vec p-\vec p'')^2/2m}\,, \tag{7b}$$

which therefore corresponds to the free on shell projectile nucleon t matrix with the kinematics of the initial nucleon at rest.[6] So neglecting second order corrections we have

$$\frac{d\sigma_{\text{total}}^{(\epsilon,\bar\epsilon=\epsilon)}}{d\Omega_{p'}}=\frac{(2\pi)^4}{v}\int p'^2dp'|\langle\vec p'|\hat t_\epsilon|\vec p\rangle|^2\delta\left(\frac{\vec p^2}{2\mu}-\frac{\vec p'^2}{2\mu}-\frac{(\vec p-\vec p')^2}{2m}\right). \tag{8}$$

The integration over d^3P was already performed in (8) where we used $\int|\phi_0(\vec P-\vec p)|^2d^3P=1$.

Equations (7b) and (8) manifest the compensation of Fermi motion and binding potential effects[7] which results in a *freezing* of the Fermi motion of the struck nucleon in Eq. (8).

A similar calculation has previously been done for elastic scattering,[1] where the first order corrections to the elastic amplitude t_{elastic} were set equal to zero. The result [Eq. (20) of Ref. 1] coincides with Eq. (7b) for $\vec p=\vec p'$, i.e., forward elastic scattering. Therefore, the optical theorem

$$\sigma_{\text{total}}^{(\epsilon,\bar\epsilon=\epsilon)}=\frac{(2\pi)^3}{iv}\langle\phi_0,\vec p|t^+_{\text{elastic}}-t_{\text{elastic}}|\phi_0,\vec p\rangle \tag{9}$$

is preserved within the generalized closure approximation for σ_{total} and t_{elastic}. This is seen by comparison of Eqs. (8) and (9).

In calculating higher order corrections for the Green's function discontinuity we have to consider the term

$$\begin{aligned}\langle t^+_{\bar\epsilon}[\Delta^2G^+_\epsilon-\Delta^2G_\epsilon]t_{\bar\epsilon}\rangle=\frac{(2\pi)^3}{iv}&\int\phi_0(\vec P-\vec p)|\langle\vec p'|\hat t_\epsilon|\vec p\rangle|^2\left\{\left[\frac{(\vec P-\vec p')^2}{2m}-\frac{(\vec p-\vec p')^2}{2m}-\epsilon_0\right]\delta^3(\vec P-\vec P'')+\tilde V(\vec P-\vec P'')\right\}\\&\times\left\{\left[\frac{(\vec P''-\vec p')^2}{2m}-\frac{(\vec p-\vec p')^2}{2m}-\epsilon_0\right]\delta^3(\vec P''-\vec P')+\tilde V(\vec P''-\vec P')\right\}\phi_0(\vec P'-\vec p)\\&\times\frac{d^3Pd^3P'd^3P''d^3p'}{[\vec p^2/2\mu-\vec p'^2/2\mu-(\vec p-\vec p')^2/2m-i\delta]^3}-(G^+\to G)\,.\end{aligned}$$

Integrating over d^3Pd^3P' one can eliminate $\tilde V$ obtaining

$$\begin{aligned}\langle t^+_{\bar\epsilon}[\Delta^2G^+_\epsilon-\Delta^2G_\epsilon]t_{\bar\epsilon}\rangle=\frac{(2\pi)^3}{iv}&\int|\phi_0(\vec P''-\vec p)|^2|\langle\vec p'|t_{\bar\epsilon}|\vec p\rangle|^2\left(\frac{\vec p^2}{2\mu}-\frac{\vec p'^2}{2\mu}-\frac{(\vec p-\vec p')^2}{2m}-i\delta\right)^{-3}\\&\times\left[\frac{(\vec P''-\vec p)(\vec p-\vec p')}{m}\right]^2d^3P''-(G^+\to G)\,.\end{aligned}$$

So by neglecting all terms involving commutators of the potential $\tilde V$ with the kinetic energy of the nucleon which appear in third and higher orders[8] we obtain

$$\frac{d\sigma_{\text{total}}}{d\Omega_{p'}}=\frac{(2\pi)^4}{v}\int p'^2dp'd^3P|\phi_0(\vec P-\vec p)|^2|\langle\vec p'|\,\hat t_\epsilon\,|\vec p\rangle|^2\delta\left(\frac{\vec p^2}{2\mu}-\frac{\vec p'^2}{2\mu}+\frac{(\vec P-\vec p)^2}{2m}-\frac{(\vec P-\vec p')^2}{2m}\right). \tag{10}$$

By a similar consideration $\tilde{t}_\epsilon$ fulfills the Lippmann-Schwinger equation

$$\langle\vec{p}|\tilde{t}_\epsilon(\vec{P})|\vec{p}'\rangle=\tilde{v}(\vec{p}-\vec{p}')+\int\tilde{v}(\vec{p}-\vec{p}'')\frac{\langle\vec{p}''|\tilde{t}_\epsilon(\vec{P})|\vec{p}'\rangle d^3p''}{\vec{p}^2/2\mu+(\vec{P}-\vec{p})^2/2m-\vec{p}''^2/2\mu-(\vec{P}-\vec{p}'')^2/2m}\,.$$

It is therefore an on-shell t matrix with the initial and final momenta of projectile and bound nucleon to be $\vec{p},\vec{p}',\vec{P}-\vec{p},\vec{P}-\vec{p}'$, respectively[6] and again one can show that unitarity has been implemented.

We would like to comment briefly on the structure of Eq. (10). It is manifestly a quasifree approximation in which the binding effects compensate the final state nucleon core interaction. Since both effects are due to $\tilde{V}$ such a compensation is understandable. One is thus left [contrary to Eq. (8)] with a Fermi broadening effect only. For comparison we consider the plane wave approximation where the nucleon core interaction in the final state is neglected (for a discussion see also Refs. 7 and 10). In this approximation we evaluate the free Green's function for an off-shell energy $E=\vec{p}^2/2\mu+\epsilon_0$ both in the discontinuity and in the Lippmann-Schwinger equation obtaining

$$\frac{d\sigma_{\text{total}}^{\text{impulse}}}{d\Omega_{p'}}=\frac{(2\pi)^4}{v}\int|\phi_0(\vec{P}-\vec{p})|^2|\langle\vec{p}'|t(E=\vec{p}^2/2\mu+\epsilon_0)|\vec{p}\rangle|^2\delta\left(\frac{\vec{p}^2}{2\mu}+\epsilon_0-\frac{\vec{p}'^2}{2\mu}-\frac{(\vec{P}-\vec{p}')^2}{2m}\right)p'^2dp'd^3P\,, \tag{11}$$

where $\langle\vec{p}'|t|\vec{p}\rangle$ is a free t matrix evaluated at the off-shell energy $E=\vec{p}^2/2\mu+\epsilon_0$. Note that there is an energy shift $\epsilon_0-(\vec{P}-\vec{p})^2/2m$ in the δ function of Eq. (11) as compared to Eq. (10). This shift may be appreciable.

If we now consider a core of finite mass $M-m$, rather than the infinite mass core considered before, the wave function will depend on relative momenta. Equation (3) is modified to[11]

$$\langle\vec{p}',\vec{P}'|G_\epsilon|\vec{P}'',\vec{p}''\rangle=\frac{\delta^3(\vec{P}'-\vec{P}'')\delta^3(\vec{p}'-\vec{p}'')}{E-\dfrac{\vec{p}''^2}{2\mu}-\dfrac{(\vec{p}-\vec{p}'')^2}{2M}-\epsilon(\vec{p}'',\chi)}\,.$$

Calculating ϵ in the standard way (such as to have vanishing first order corrections to σ_{total}) we obtain

$$\epsilon(\vec{p}'',\vec{\chi})_{\vec{\chi}=\vec{p}}=\epsilon_0+\frac{(\vec{p}-\vec{p}'')^2(M-m)}{2mM}\,.$$

Equations (7a) and (7b) are not modified and higher order corrections leading to Eq. (10) can be calculated with no additional complications.

In principle the same procedure may be applied to a first order optical potential theory $U=\sum\tau_i$, $\tau_i=\tilde{v}_i+\tilde{v}_iG(1-P_0)\tau_i$, P_0 being the ground state projection of a many body system treated in the single particle approximation without correlations. However, one cannot have an equation such as (5a) since the Green's function appearing in the calculation of τ_ϵ has the structure

$$\delta^3(\vec{p}''-\vec{p}')\frac{\delta^3(\vec{P}''-\vec{P}')-\phi_0(\vec{P}''-\vec{p}')\phi_0(\vec{P}'-\vec{p}')}{E-p'^2/2\mu-\bar{\epsilon}+i\delta}\,,$$

which is more complicated than Eq. (3). This fact does not allow the elimination of $\tilde{V}$ from the equation corresponding to (5b). One can overcome this difficulty and construct an approximation for U starting from the auxiliary matrix t_i^ϵ fulfilling Eq. (4) with ϵ as in Eq. (6). Defining $\tau_i^\epsilon=t_i^\epsilon-t_i^\epsilon G_\epsilon P_0\tau_i^\epsilon$, one can consider $U\cong U^\epsilon=\sum\tau_i^\epsilon$. A simple expression for σ_{reactive} can then be obtained taking all $\tilde{v}_i$ to be equal, neglecting $1/A$ effects and setting $\tau_i^\epsilon=t_i^\epsilon$,

$$\frac{d\sigma_{\text{reactive}}}{d\Omega_{p'}}\cong\frac{(2\pi)^4}{v}A\int p'^2dp'|\langle\vec{p}'|\tilde{t}_\epsilon|\psi_{\vec{p}}^{+}\rangle|^2\times\delta\left(\frac{\vec{p}^2}{2\mu}-\frac{\vec{p}'^2}{2\mu}-\frac{(\vec{p}-\vec{p}')^2}{2m}\right), \tag{12}$$

where ψ_p^+ is the projectile distorted wave function.

One of us (F.C.) would like to thank the Weizmann Institute for warm hospitality and financial support.

---

*Permanent address.

[1] S. A. Gurvitz, J. P. Dedonder, and R. D. Amado, Phys. Rev. C 19, 142 (1979).

[2] S. A. Gurvitz, Phys. Rev. C 20, 1256 (1979).

[3] S. A. Gurvitz, Phys. Rev. C (to be published).

[4] S. A. Gurvitz, Phys. Lett. 85B, 5 (1979).

[5] M. L. Goldberger and K. M. Watson, *Collision Theory* (Wiley, New York, 1964), p. 690.

[6] For fixed $\vec{p}'$ the knocked out nucleon remains in the plane determined by the projectile $\vec{p},\vec{p}'$ momenta.

[7] R. Rosenfelder, Phys. Lett. 79B, 15 (1978). In this paper a near cancellation of binding potential and Fermi motion effects for an energy independent local potential $\tilde{V}$ has been found as far as the peak position of quasielastic electron scattering is concerned.

[8] From an order of magnitude type of estimate the effects one is neglecting are expected to be of order $(\langle\vec{\nabla}^2\tilde{V}\rangle/mE^2)(\mu/m)$.

[9] In Eq. (10) the quasifree kinematics does not mean that the plane identified by the projectile initial and final momenta $\vec{p}, \vec{p}\,'$ contains also the final nucleon momentum $\vec{P}-\vec{p}\,'$ due to the fact that $\vec{P}$ need not be in the plane.

[10] F. Lenz, Proc. Top. Meet. Intern. Energy Phys., Zuoz 1976, Vol. 2, SIN report, p. 379 and following.

[11] $\vec{P}$ should be viewed here as the total projectile plus nucleus momentum (we are working in the laboratory frame).

PHYSICAL REVIEW C VOLUME 21, NUMBER 6 JUNE 1980

Time-dependent quadrupole interactions in ^{129}I

S. L. Gupta, Ashok Kumar, S. K. Soni, and S. C. Pancholi
Department of Physics and Astrophysics, University of Delhi, Delhi-110007, India

(Received 11 September 1979)

γ-γ time-differential directional correlation studies have been carried out on the $5/2^+$ (459.6 keV) $5/2^+$ (27.8 keV) $7/2^+$ cascade in ^{129}I using a ^{129}Te^{m+g} source in 4*N* HCl. The measurements reveal time-dependent electric quadrupole perturbation of the correlation. From the plot of $A_2(\bar{t})$ vs $\bar{t}$ (finite time resolution corrected), the obtained values of the relaxation parameter λ_2^{el} and the unperturbed $A_2(0)$ coefficient (solid angle corrected) are $(0.21\pm0.01)\times10^9$ sec^{-1} and $-(0.068\pm0.002)$, respectively. The observed λ_2^{el} is consistent with that deduced from the theory of Abragam and Pound.

[RADIOACTIVITY ^{129}Te^{m+g} [from ^{128}Te (n,γ)]; measured γ-$\gamma(\theta,t)$; deduced $\lambda_2^{el}, A_2(0), \bar{G}_2(\infty)$.]

I. INTRODUCTION

Tellurium radicals are known to have ionic structure in HCl solution and generate strong electric field gradients due to electrons in covalent bonds. The field gradients are made time dependent due to the Brownian motion of the ions in the liquid. The interaction of these fields with the electric quadrupole moments of nuclei in their intermediate states is expected to cause time-dependent perturbation of the γ-γ angular correlation. In our earlier work[1] we carried out time-differential directional correlation measurements on the $\frac{5}{2}^+$ (360.3 keV) $\frac{7}{2}^+$ (57.6 keV) $\frac{5}{2}^+$ cascade using ^{127}Te^{m+g} source in HCl solution. A time-dependent electric quadrupole perturbation of the correlation was found. Similar time-differential perturbed angular correlation (PAC) measurements are performed on the (459.6–27.8 keV) γ-γ cascade using ^{129}Te^{m+g} activity in 4*N* HCl solution and are presented in this paper. This work has been undertaken to search for any quadrupole interaction similar to that observed in ^{127}I. Our data in this case also clearly indicate a time-dependent quadrupole perturbation of the correlation.

II. EXPERIMENTAL DETAILS

The ^{129}Te^{m+g} source of high specific activity was obtained from New England Nuclear, U.S.A. It was in the form of concentrated solution in 4*N* HCl. The radiometric purity of the source was >99%. The counting source was prepared by taking a few drops of this chloride solution in a perspex vial of dimensions 3 mm diam × 4 mm.

The timing coincidence spectrometer consisted of 2.54 cm diam × 1.27 cm NE111 plastic scintillator and 3.81 cm diam × 3.81 cm NaI(Tl) detector both coupled to XP-1021 photomultipliers. The fast output on the side of the plastic scintillator was further coupled to a constant fraction pulse height trigger. Aluminum absorbers of appropriate thickness were used in front of both the scintillators to cut off the conversion electrons and ~1.5 MeV β's feeding the 27.8 keV level in ^{129}I. The 459.6 keV gamma photopeak was gated in the NaI(Tl) detector whereas the upper ~75% of the Compton distribution of the 27.8 keV γ transition was gated in the plastic scintillator. The calibration of the TPHC-ADC system was carried out by observing the shift of the prompt resolution curve using a ^{60}Co source with the introduction of accurately calibrated GR874-L30 air dielectric coaxial delay lines and was found to be (0.62 ± 0.01) nsec/channel.

The full width at half maximum (FWHM) of the prompt curve at the above energy settings using a ^{60}Co source was 2.9 nsec with a slope ($\frac{1}{2}$) of 0.2 nsec. The delayed time coincidence spectra were recorded at 90°, 120°, 150°, 180°, 180°, 210°, 240°, and 270° and the data from the corresponding angles in the two quadrants were stored in the 256 channel subgroups of a 4096 channel analyzer. Simultaneously, the singles counts from both detectors were also recorded for normalization purposes.

Figure 1 shows the chance subtracted delayed time coincidence spectra recorded at 90°(I), 120°(II), 150°(III), and 180°(IV). The prompt part in the spectra arises due to the counter-to-counter scattering and other prompt γ-γ cascades. After normalizing with the gate counts, the data at each corresponding channel of the delayed region were analyzed by the weighted least squares method for obtaining $A_2(t)$ coefficients. The delayed region so chosen was well outside the prompt part.

© 1980 The American Physical Society

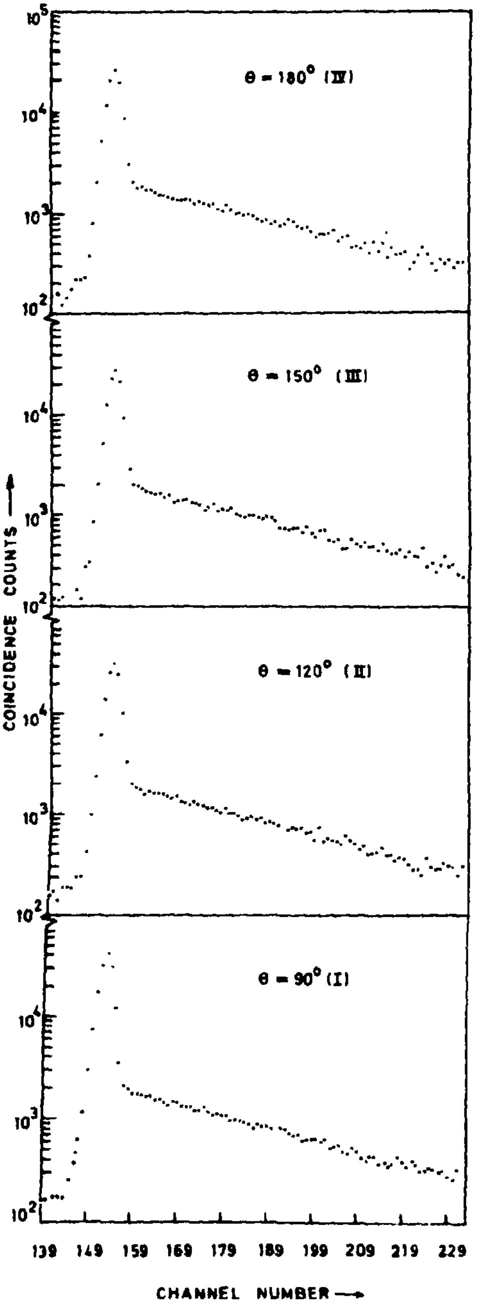

FIG. 1. The chance subtracted delayed time coincidence spectra recorded at $\theta = 90°$ (I), 120° (II), 150° (III), and 180° (IV) for the (459.6–27.8) keV γ-γ cascade in ^{129}I.

The main contribution to the (459.6–27.8) keV γ-γ cascade appears to come from the $\frac{3}{2}^{+}\xrightarrow{1083.6\ \gamma}\frac{5}{2}^{+}\xrightarrow{27.8\ \gamma}\frac{7}{2}^{+}$ interfering cascade. This was estimated to be $\leq 1\%$ and hence no correction was applied. The contributions from other γ rays coincident with the 27.8 keV γ ray are negligible because of their weak photon intensities.

The differential nonlinearity (DNL) curve for the system was also recorded. The nonlinearity was estimated to be $< 1\%$ and hence no correction was applied.

An estimate of self-absorption for the 27.8 keV γ ray within the thickness of the liquid ^{129}Te^{m+g} source employed for the present measurements was also made.[2] It was found to be ~0.4% and hence no correction for this effect was applied to the cascade anisotropy.

The solid angle correction factor (Q_2) for the correlation geometry and at the energy settings mentioned above was determined experimentally by the method given in Ref. 3. The instrumental angular resolution curve was obtained by recording 511–511 keV coincidences using a ^{22}Na source. The correction factor (Q_2), obtained by direct numerical integration over the experimental resolution curve, is 0.816 ± 0.002.

III. RESULTS

After applying finite time resolution correction[4] to the $A_2(t)$ coefficients, a plot of $A_2(\bar{t})$ vs $\bar{t}$ is shown in Fig. 2, which exhibits the exponential behavior of the perturbation. The $A_2(\bar{t})$ values were least squares fitted to the equation

$$A_2(\bar{t}) = A_2(0)\exp(-\lambda_2^{ef}\bar{t}) , \tag{1}$$

yielding λ_2^{ef} (the relaxation parameter) $= (0.21 \pm 0.01) \times 10^9\ \mathrm{sec}^{-1}$ and the solid angle uncorrected unperturbed expansion coefficient $A_2(0) = -0.056 \pm 0.002$. After solid angle correction, $A_2(0) = -(0.068 \pm 0.002)$. This is compared with the earlier results in Table I. Using our λ_2^{ef} and known λ_0 [$T_{1/2} = 16.8 \pm 0.2$ nsec (Ref. 5)] and using the relation

$$\bar{G}_2(\infty) = \frac{\lambda_0}{\lambda_2^{ef} + \lambda_0} \tag{2}$$

for a time-dependent perturbation, the integral attenuation coefficient $\bar{G}_2(\infty) = 0.16 \pm 0.01$ is obtained. This value of $\bar{G}_2(\infty)$ is quite small and is, therefore, indicative of a strong perturbation of the correlation.

IV. DISCUSSION

The results of the present time-differential PAC measurements in ^{129}Te^{m+g} decay and those of our earlier work[1] in ^{127}Te^{m+g} decay both show a time-

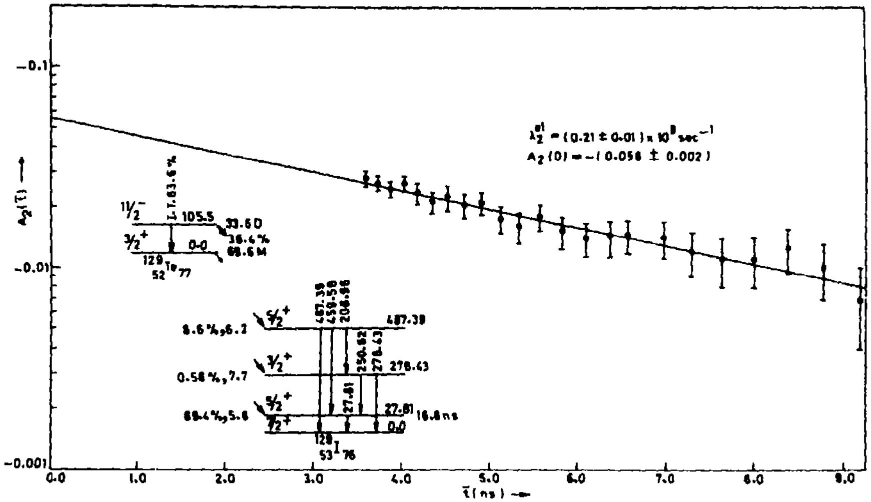

FIG. 2. Plot of $A_2(\bar{t})$ (uncorrected for solid angle) vs $\bar{t}$ from time-differential measurements in ^{129}I for a concentrated ^{129}Te^{m+g} source in 4*N* HCl. The relevant decay scheme (Ref. 15) is also shown as an insert.

dependent quadrupole perturbation of the correlations. The source forms used in these measurements are similar. The time-dependent interactions seemingly arise as a result of the rapidly fluctuating electric field gradients due to the Brownian motion of the complex tellurium chloride ions. These fields interact with the nuclear electric quadrupole moments of the first excited states[Q(57.6 keV level in ^{127}I) = −0.71 b and Q(27.8 keV level in ^{129}I) = −0.68 b].

Abragam and Pound[12] have shown that for time-dependent electric quadrupole interactions in the liquid sources, the relaxation parameter λ_2^{el} is given by

$$\lambda_2^{el} = \left(\frac{3}{80}\right)\left(\frac{eQ}{\hbar}\right)^2 \left\langle\left(\frac{\partial^2 V}{\partial Z^2}\right)^2\right\rangle \tau_c \times \frac{k(k+1)[4I(I+1)-k(k+1)-1]}{I^2(2I-1)^2}\,. \tag{3}$$

TABLE I. A_2 coefficients ($A_4 \approx 0$ within experimental error) for the (459.6–27.8) keV γ-γ cascade in ^{129}I.

Reference	Source form	Detectors used	Integral A_2
6	Te metal	NaI-NaI	−0.160 ± 0.033
7		NaI-NaI	−0.0489 ± 0.0090
8	HNO$_3$ solution	NaI-NaI	−0.0148 ± 0.0029
9	HNO$_3$ solution	NaI-NaI	+0.056 ± 0.018
10	HNO$_3$ solution (dilute)	NaI-Si(Li)	−0.033 ± 0.011
		Ge(Li)-Si(Li)	−0.035 ± 0.017
		Detectors used	Differential $A_2(0)$
10	Te in Ni matrix	NaI plastic	−0.028 ± 0.007
11	Te metal; ZnTe powder; aqueous solution of K_2TeO_3	NaI plastic	Isotropic
Present work	4*N* HCl solution	NaI-NE 111 plastic	−0.068 ± 0.002

Here, the coupling factor $eQ\langle(\partial^2 V/\partial Z^2)\rangle/\hbar = 2\pi\Delta\nu_Q$, where $\Delta\nu_Q$ is the electric quadrupole interaction frequency. τ_c represents the correlation time for the ions in the liquid. Substituting $\tau_c \approx 2\times10^{-11}$ sec (Refs. 13 and 1) for the concentrated $4N$ HCl solution, $\Delta\nu_Q = 3000$ MHz (Ref. 14) and $I = \frac{5}{2}$ for the 27.8 keV level in ^{129}I in Eq. (3), λ_2^{el} (theory) $= 0.40\times10^9$ sec^{-1} has been obtained. This is roughly in agreement with our λ_2^{el} (expt) $= (0.21\pm0.01)\times10^9$ sec^{-1}. The difference in the two values could perhaps arise due to the uncertainties involved in the estimation of τ_c and $\Delta\nu_Q$. In any case, our differential correlation measurements clearly indicate the presence of time-dependent electric quadrupole interactions in the HCl solution.

---

[1] Ashok Kumar, S. K. Soni, S. L. Gupta, and S. C. Pancholi, Phys. Rev. C 16, 2027 (1977).

[2] C. M. Davisson and R. D. Evans, Rev. Mod. Phys. 24, 79 (1952).

[3] E. L. Church and J. J. Kraushaar, Phys. Rev. 88, 419 (1952).

[4] E. Bodenstedt, H. J. Körner, C. Günther, and J. Radeloff, Nucl. Phys. 22, 145 (1961).

[5] D. J. Horen, Nucl. Data Sheets for $A = 129$, B8, 123 (1972).

[6] S. L. Gupta and N. K. Saha, Nucl. Phys. 73, 461 (1965).

[7] A. P. Arya and N. Nicholson, Bull. Am. Phys. Soc. 10, 588 (1965).

[8] R. Sanders, Nucl. Phys. A138, 583 (1969).

[9] E. K. Makariuniene and K. V. Makariunas, Yad. Fiz. 10, 440 (1969) [Sov. J. Nucl. Phys. 10, 251 (1970)].

[10] M. Rots, H. Van de Voorde, H. Ooms, F. Namavar, R. Coussement, and J. de Raedt, Z. Phys. 270, 51 (1974).

[11] N. Kaplan, S. Ofer, and H. Zmora, Nucl. Phys. 52, 249 (1964).

[12] A. Abragam and R. V. Pound, Phys. Rev. 92, 943 (1953).

[13] G. E. Pake, *Solid State Physics* (Academic, New York, 1956), Suppl. 2, p. 68.

[14] W. Gordy, W. V. Smith, and R. F. Trambarulo, *Microwave Spectroscopy* (Wiley, New York, 1953), p. 258.

[15] L. G. Mann, W. B. Walters, and R. A. Mayer, Phys. Rev. C 14, 1141 (1976).

PHYSICAL REVIEW C VOLUME 21, NUMBER 6 JUNE 1980

Composite particle emission from ^{65}Zn*

H. Machner
Institut für Kernphysik, Kernforschungsanlage Jülich, D-5170 Jülich, West Germany

(Received 10 October 1979)

Calculations within the framework of the exciton-coalescence model of angle integrated spectra as well as of angular distributions for light charged particles with $A \le 4$ from ^{65}Zn* with $E^* = 37.4$ MeV have been made. These reproduce well the influence of different projectiles (deuterons, helions, alphas) leading to the same compound system. The analysis indicates projectile and ejectile dependent radii of the coalescence spheres.

NUCLEAR REACTIONS ^{63}Cu(d,X), E = 24.7 MeV; ^{62}Ni(^{3}He,X), E = 24.3 MeV; ^{61}Ni(α,X), E = 35.5 MeV; Calculation of pre-equilibrium angle integrated spectra, angular distributions, and comparison with experiment.

In a recent paper[1] we have shown that complex particle emission from proton induced reactions could be treated in the exciton model assuming the coalescence of excited nucleons to clusters (exciton-coalescence model). There is only one additional parameter with respect to nucleon spectra, namely, the radius of a coalescence sphere. Within the framework of this approach, even the angular distributions of complex particles could be reproduced surprisingly well. A more stringent test of the model would be to compare its predictions with data from complex particle induced reactions.

For this purpose we have chosen the data of Ref. 2. These are of special interest because they are from a Ghoshal type experiment[3]: The intermediate system ^{65}Zn was produced via three different entrance channels leading to approximately the same excitation energy 37.4 MeV of the composite system. This was done by the following reactions: ^{63}Cu + 24.7 MeV d, ^{62}Ni + 24.3 MeV ^{3}He, and ^{61}Ni + 35.5 MeV α. Light charged particles up to α's have been measured.

Although in the original Ghoshal experiment[3] no influence of the entrance channel has been observed according to Bohr's compound nucleus hypothesis,[4] the spectra under discussion here show strong entrance channel dependence.

A main feature of the model in Ref. 1 is the condensation of those excited nucleons into clusters which are within a sphere in momentum space. This gives the initial exciton numbers for states from which complex particle emission is possible. For proton induced reactions these values are 3p (particles) + 2h (holes), 4p + 3h, and 5p + 4h for deuterons, tritons, and alphas, respectively. This is in contrast to the work of Refs. 5–7, where complex particle emission was allowed if the number of excited particles equaled the number of nucleons in the corresponding cluster. Of course, this influences the shape of the spectra. On the other hand, the coalescence picture gives the direction of the emitted clusters. The emission rates are given by

$$W_x(p,h,\varepsilon,\vartheta) = W_x(p,h,\varepsilon)\,A(p+p_y-p_x,h,\vartheta) \times \theta\,(p+h+p_y-p_x)\,d\varepsilon. \qquad (1)$$

The angular distribution functions A are given by the recursion relation[8]

$$A(p,h,\Omega_{p,h}) = \int d\Omega_{p-1,h-1}\,w(\Omega_{p-1,h-1}-\Omega_{p,h}) \times A(p-1,h-1,\Omega_{p-1,h-1}). \qquad (2)$$

The transition rate w is calculated from the nucleon-nucleon cross section.

The angle independent emission rates $W_x(p,h,\varepsilon)$ are those from Ref. 6 with the following correction. In counting all possible states for a composite system with excitation energy E which is divided into a residual system with excitation energy U and p_x unbound particles with energy $E-U$, one looks for the number of ways to distribute the energy U to $p+h-p_x$ excitons, and the energy $E-U$ to p_x excitons.[6] Because there are p particles the number of possible configurations has to be multiplied by p. On the other hand, fermions are indistinguishable. Therefore, the number of possible configurations has to be divided by $\binom{p}{p_x}$. In the case of nucleon spectra the latter factor was introduced by Blann in Ref. 9, while the first one was given by him in Ref. 10. Also Gadioli has taken these factors into account by deriving transition rates.[11] In the hybrid model,[9,10] taking only nucleon emission into account which leads to $\binom{p}{1} = p$ these two factors cancel out. On the other hand, these arguments when

© 1980 The American Physical Society

also applied to the statistics of holes, influence averaged nuclear transition rates. Whereas the influence of the factors given above in the exciton model approach of nucleon spectra is weak, they are of great importance for complex particle emission.

The quantity p_y denotes the number of nucleons in the projectile. The cross sections are given by

$$\frac{d^2\sigma_x(\varepsilon,\vartheta)}{d\varepsilon\, d\Omega}=\sigma_0\sum_{n=n_0,\,\Delta n=2}^{\bar{n}} W_x(p,h,\varepsilon,\vartheta)\tau_n(E)\ , \qquad (3)$$

with $\tau_n(E)$ the average n exciton lifetime including depletion derived from the integration of the master equation,[12] and σ_0 the total reaction cross section. The calculations were carried out with projectile dependent initial exciton numbers n_0. The summation was stopped when the system reached thermal equilibrium characterized by the exciton number $\bar{n}$.

We have assumed in all cases that $n_0=(p_y+1)p+1h$ as in previous work.[1] To reproduce angle integrated proton spectra, the nucleon mean free path has been multiplied by a factor of 4 (Fig. 1). Examples for the deuteron and alpha in the exit channel are given in Figs. 2 and 3. The radii of the coalescence spheres have been treated as free parameters and are derived from fitting the angle integrated spectra. The deduced values are given in Table I. From this analysis it turns out that in cases where projectile and ejectile are the same particle type, the radii P_0 are larger than in the other cases. Larger P_0 values mean, under the assumption of phase space relations, a smaller volume in the nucleus from which the particle is being emitted. Therefore, a possible explanation of large P_0 values may be the fact that a part of the projectile particle survives nucleon interactions. Thus in the case of alpha emission, the difference between deuteron and alpha induced reactions results in a change of ≈30% in the emitting volume. The radii R of the interaction regions are also given in Table I. They are obtained from radii $\tilde{P}_0$ in momentum space from which phase factors and spin alignment have been explicitly removed by using the relation[13]

$$(\tilde{P}_0{}^3)^{\pi+\nu-1}=(P_0{}^3)^{\pi+\nu-1}\,\frac{2^{\pi+\nu}}{(\pi+\nu)^3\,(2s+1)}\ , \qquad (4)$$

with π, ν, s the number of protons, neutrons, and the spin of the ejectile. A comparison of the radii

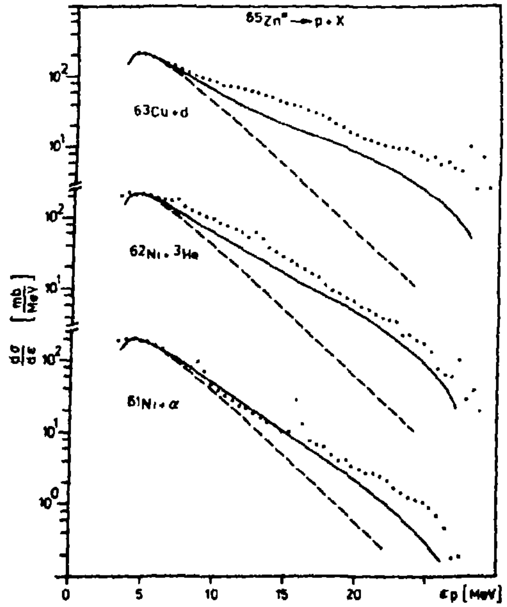

FIG. 1. Proton decay of $^{65}Zn^*$ with $E^*=37.4$ MeV. The data (Ref. 2) are represented by dots while the evaporative contribution is dashed line drawn. The sum of evaporation plus pre-equilibrium contribution is solid line drawn. Different entrance channels are indicated next to the appropriate curves.

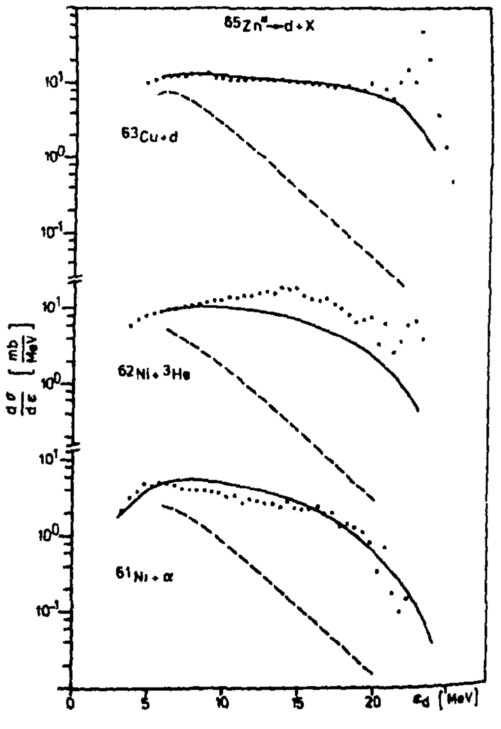

FIG. 2. Same as Fig. 1 but for deuteron emission.

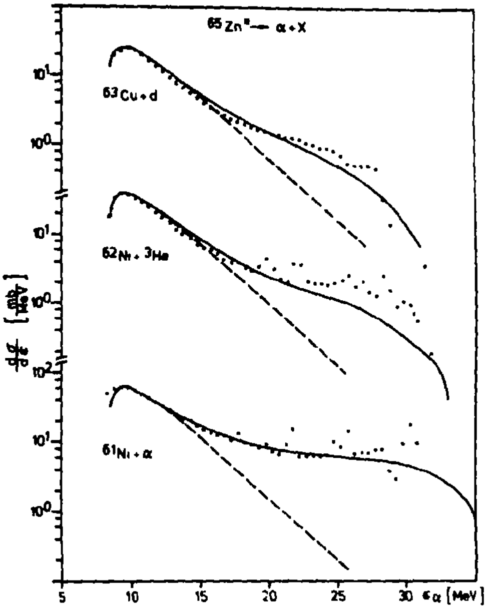

FIG. 3. Same as Fig. 1 but for alpha emission.

of the emitting volume with those of the ejectiles indicates a strong ejectile dependence (Table I). It turns out that the radii of the emitting volume are roughly equal to the radii of the free clusters.

The compound contributions to the spectra are calculated by the evaporation approximation[14,15]

$$\frac{d\sigma_a}{d\varepsilon} \propto \varepsilon^{5/11}\,\sigma_{\mathrm{inv}}(\varepsilon)e^{-\varepsilon/T}, \qquad (5)$$

and by using effective Coulomb barriers.[16] The absolute height has been derived by first adjusting the pre-equilibrium contribution at the high energy part and then adjusting the compound contribution to the low energy part of the spectra. This procedure implies a relatively large uncertainty in the case of triton emission which has been measured only up to 19 MeV. It should be further mentioned that triton emission is a weak channel. Therefore, the deviations between the free triton radius and radii of the emitting volume are largest in this case.

TABLE I. Radii of coalescence spheres in momentum space P_0 and of emitting volume R; in the last column the ejectile radii R_x from Ref. 18 are given.

Entrance channel	Exit channel	P_0 (MeV/c)	R (fm)	R_x (fm)
d	d	251	3.46	3.24
^{3}He		247	3.51	−4.31
α		207	4.15	
d	t	288	2.28	
^{3}He		261	2.52	1.82
α		242	2.71	
^{3}He	^{3}He	365	1.80	1.97
d	α	327	1.70	
^{3}He		315	1.77	1.63
α		360	1.55	

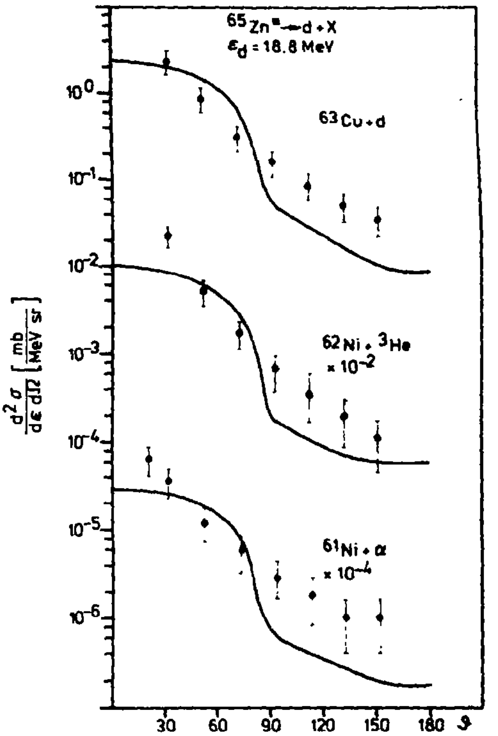

FIG. 4. Angular distributions for deuterons emitted from ^{65}Zn* with E^* = 37.4 MeV: The data (dots) for ϵ_d = 18.8 MeV are from Ref. 2. The calculations are solid line drawn. Different projectile and targets are indicated next to the appropriate curves.

From Figs. 2 and 3 it is obvious that the model reproduces the shape of the complex particle spectra very well. Small deviations occur due to direct reactions and breakup of the projectile as in the (^{3}He, dx) case which is not included in the present calculation.

In Figs. 4–6, angular distributions are compared with data. We used an initial distribution function

$$A(p_o, h_o, \Omega_{p_o,h_o}) = \frac{1}{\pi}\cos\vartheta\ \theta(\pi/2-\vartheta). \qquad (6)$$

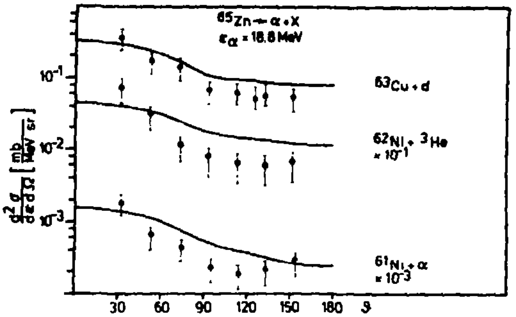

FIG. 5. Same as Fig. 4 but for alpha emission.

The agreement between data and experiment is satisfactory although not as good as in the case of proton induced reactions.[1] But the agreement is in the same accuracy as for proton emission.[17] The deviations between the theoretical curves and the data are largest at backward angles where the contribution of compound emission to the cross sections is largest. This contribution has been assumed to be emitted isotropically.

Thus the coalescence model, previously applied to high energy data and modified to fit in the frame of the exciton model can well describe the influence of different entrance channels on different exit channels. Data analysis suggests that complex particles do survive in part interactions with nucleons in nuclear matter. The emitting volume of the excited nucleus has approximately the same size as the emitted complex particle.

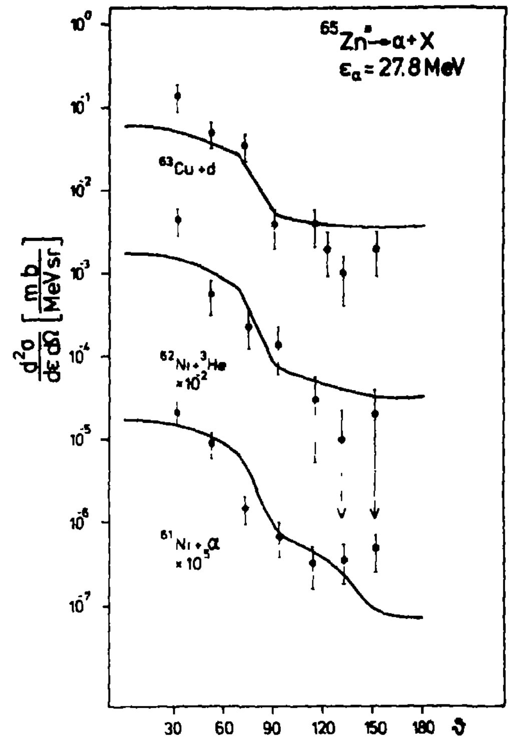

FIG. 6. Same as Fig. 5 but for $\epsilon_\alpha = 27.8$ MeV.

The author is grateful to Dr. M. Blann for bringing the factor $\binom{p}{p_x}^{-1}$ as discussed above to his attention. He also thanks Dr. Mayer-Böricke for his continuing and encouraging support.

---

[1] H. Machner, Phys. Lett. 86B, 129 (1979).

[2] J. Bisplinghoff, J. Ernst, R. Löhr, T. Mayer-Kuckuk, and P. Meyer, Nucl. Phys. A269, 147 (1976); J. Bisplinghoff, private communication.

[3] S. N. Ghoshal, Phys. Rev. 80, 939 (1950).

[4] N. Bohr, Nature 137, 344 (1936).

[5] C. K. Cline, Nucl. Phys. A193, 417 (1972).

[6] I. Ribanský and P. Obložinský, Phys. Lett. 45B, 318 (1973).

[7] J. R. Wu, C. C. Chang, and D. H. Holmgren, Phys. Rev. C 19, 370 (1975); 19, 659 (1975); 19, 698 (1975).

[8] G. Mantzouranis, Phys. Lett. 63B, 25 (1976).

[9] M. Blann, Phys. Rev. Lett. 27, 337 (1971).

[10] M. Blann, Phys. Rev. Lett. 27, 1550 (1971).

[11] E. Gadioli, E. Gadioli Erba, and P. G. Sona, Nucl. Phys. A217, 589 (1973).

[12] C. K. Cline and M. Blann, Nucl. Phys. A172, 225 (1971).

[13] A. Mekjian, Phys. Rev. C 17, 1051 (1978).

[14] V. F. Weisskopf, Phys. Rev. 52, 295 (1937).

[15] J. M. B. Lang and K. J. Le Couteur, Proc. Phys. Soc. London 67, 586 (1954).

[16] T. Ericson, Adv. Phys. 9, 425 (1960).

[17] G. Mantzouranis, H. A. Weidenmüller, and D. Agassi, Z. Phys. A276, 145 (1976).

[18] P. Marmier and E. Sheldon, *Physics of Nuclei and Particles* (Academic, New York, 1970).

PHYSICAL REVIEW C VOLUME 21, NUMBER 6 JUNE 1980

Cumulative Author Index

Abbas, Afsar and Larry Zamick — Effective charge in the large A limit. C **21**, 738
Abegg, R. — (see Datta, S.K.) C **21**, 1687
Abou-Zeid, O. A. — (see Datta, S.K.) C **21**, 1687
Adams, G. S., Th. S. Bauer, G. Igo, G. Pauletta, C. A. Whitten, Jr., A. Wriekat, G. W. Hoffman, G. R. Smith, and M. Gazzaly — 800-MeV inelastic proton scattering from ^{40}Ca, ^{48}Ca, and ^{54}Fe. C **21**, 2485
____(see Bauer, T.S.) C **21**, 757
____(see Hoffmann, G.W.) C **21**, 1488
Adhikari, Sadhan K. and W. Glöckle — Three-body Lippmann-Schwinger equations. C **21**, 54
Adler, L. — (see Namboodiri, M.N.) C **21**, 1680(E)
Aggarwal, S. K. and H. C. Jain — Half-life of ^{241}Pu. C **21**, 2033
Ahmad, I., A. M. Friedman, and S. W. Yates — Vibrational states in ^{250}Cf excited by the (d,d') reaction. C **21**, 874
Alburger, D. E., P. Richards, and T. H. Ku — Beta decay of ^{99}Tc^m. C **21**, 705
Alexander, John M. — (see Catchen, Gary L.) C **21**, 940
____(see McMahan, M.A.) C **21**, 1261
Alford, P. — (see Brown, Ronald E.) C **21**, 2663
Alford, W. P., R. N. Boyd, E. Sugarbaker, D. L. Hanson, and E. R. Flynn — $(\vec{t},p)$ reaction on ^{56}Fe, ^{58,60,64}Ni: Structure and reaction-mechanism effects. C **21**, 1203
Alt, E. O. and W. Sandhas — Scattering amplitudes and integral equations for the collision of two charged composite particles. C **21**, 1733
Alvarez, R. A. — (see Caldwell, J.T.) C **21**, 1215
Amado, R. D., J. -P. Dedonder, and F. Lenz — Explicit formula for hadron-nucleus elastic scattering in the eikonal approximation. C **21**, 647
Amann, J. F. — (see Hoffmann, G.W.) C **21**, 1488
____(see Olmer, C.) C **21**, 254
Amsler, C. — (see Axen, D.) C **21**, 998
____(see Bugg, D.V.) C **21**, 1004
____(see Clough, A.S.) C **21**, 988
Anand, J. D., V. S. Bhasin, and V. K. Gupta — Photoproduction of pions by deuterons at medium energies C **21**, 2010
Anderson, A. N. — (see Källne, Jan) C **21**, 675
Anderson, B. D. — (see Cecil, R.A.) C **21**, 2471
Anderson, R. E. — (see Bauer, T.S.) C **21**, 757
Andreozzi, F., A. Covello, and A. Porrino — Equations-of-motion method and pairing correlations in doubly even nuclei. C **21**, 1094
Andritsopoulos, G., X. Aslanoglou, P. Bakoyeorgos, and G. Vourvopoulos — ^{12}C-^{12}C resonances studied through γ decay. C **21**, 1648
Ansari, A. and S. C. K. Nair — Second and third backbending in ^{160}Yb. C **21**, 1674
Anttila, A. and J. Keinonen — Analog $E2$ transitions in the $A=30$ nuclei, lifetime and branching ratio measurements of levels in ^{30}P. C **21**, 1196
Apagyi, B. and T. Vertse — Configuration mixing effect in the ^{12}C(^{6}Li,d)^{16}O* α-transfer reaction. C **21**, 779
Ardouin, D. — (see Brown, Ronald E.) C **21**, 2663
Argan, P., G. Audit, A. Bloch, N. de Botton, J. -L. Faure, C. Schuhl, G. Tamas, C. Tzara, E. Vincent, J. Deutsch, D. Favart, R. Prieels, and B. Van Oystaeyen — π^+ photoproduction near threshold on ^{12}C. C **21**, 662
____, **G. Audit, A. Bloch, N. de Botton, J. L. Faure, C. Schuhl, G. Tamas, C. Tzara, E. Vincent, J. Deutsch, D. Favart, R. Prieels, and B. Van Oystaeyen** — π^0 photoproduction near threshold on hydrogen, deuterium, ^{3}He, and ^{4}He. C **21**, 1416
Arnold, L. G., B. C. Clark, and R. L. Mercer — Diffraction structure in back angle p-^{4}He elastic scattering. C **21**, 1899
Arnold, Raymond G., Carl E. Carlson, and Franz Gross — Elastic electron-deuteron scattering at high energy. C **21**, 1426
Asai, J., J. J. Murphy II, and D. M. Skopik — Reactions ^{7}Li$(e,{}^6\mathrm{He})pe'$ and ^{7}Li$(e,{}^6\mathrm{Li})ne'$ at intermediate excitation energies. C **21**, 469
____(see Skopik, D.M.) C **21**, 1746
Aslanoglou, X. — (see Andritsopoulos, G.) C **21**, 1648
Audit, G. — (see Argan, P.) C **21**, 662
____(see Argan, P.) C **21**, 1416
Auerbach, N., V. Bernard, and Nguyen Van Giai — ^{41}Sc-^{41}Ca Coulomb displacement energy. C **21**, 744
Austern, N. — (see Silver, M.) C **21**, 272
Austin, Sam M. — (see Comfort, J.R.) C **21**, 2147
____(see Fox, S.H.) C **21**, 1133
Axen, D., R. Dubois, R. Keeler, G. A. Ludgate, C. J. Oram, L. P. Robertson, N. M. Stewart, C. Amsler, D. V. Bugg, J. A. Edgington, W. R. Gibson, N. Wright, and A. S. Clough — Neutron-proton elastic scattering between 200 and 500 MeV. II. Measurement of R_t and A_t. C **21**, 998
____(see Bugg, D.V.) C **21**, 1004
____(see Clough, A.S.) C **21**, 988

Badelek, B. — (see Jonsson, S.) C **21**, 306
Bagchi, B., B. Mulligan, and T. O. Krause — Redundant states, reduced potentials, and extra nodes in the radial wave function. C **21**, 1
Bakoyeorgos, P. — (see Andritsopoulos, G.) C **21**, 1648
Baktash, C. — (see Kreiner, A.J.) C **21**, 933

Balagna, J. P. — (see Hoffman, Darleane C.) C **21**, 637
Baldwin, A. R. — (see Cecil, R.A.) C **21**, 2471
Banerjee, M. K. and S. J. Wallace — Local field corrections in π-nucleus scattering. C **21**, 1996
———(see Van Orden, J.W.) C **21**, 2628
Barbarino, S., M. Lattuada, F. Riggi, C. Spitaleri, and D. Vinciguerra — Impulse distribution of the α-d motion in ^{6}Li. C **21**, 1104
Bargholtz, Chr., J. Becker, S. Beshai, M. El-khoshi, K. Fransson, and B. Sundström — Anomalous gamma-ray–L-x-ray directional correlations in ^{160}Dy. C **21**, 1078
Barlett, M. — (see Hoffmann, G.W.) C **21**, 1488
Barrette, J. — (see Paul, M.) C **21**, 1802
———(see Tserruya, I.) C **21**, 1864
Bass, R. — (see Eyal, Y.) C **21**, 1377
Bates, G. M. — (see Pitthan, R.) C **21**, 147
Bauer, Th. S., G. S. Adams, G. J. Igo, G. Pauletta, C. A. Whitten, G. R. Smith, J. R. Shepard, R. E. Anderson, R. L. Boudrie, N. J. DiGiacomo, J. J. Kraushaar, R. J. Peterson, and G. Hoffmann — ^{7}Li and ^{13}C(p,d) reactions at $T_p = 800$ MeV. C **21**, 757
———(see Adams, G.S.) C **21**, 2485
———(see Chrien, R.E.) C **21**, 1014
Baur, G., R. Shyam, F. Rösel, and D. Trautmann — Importance of the breakup mechanism for composite particle scattering. C **21**, 2668
Bazzacco, D., A. M. I. Haque, K. O. Zell, P. von Brentano, and C. Protop — Core coupled states in ^{145}Eu. C **21**, 222
Beachy, J. S. — (see Pitthan, R.) C **21**, 147
Becchetti, F. D., K. T. Hecht, J. Jänecke, D. Overway, and G. Kekelis — Systematics of (α,^{12}C) in light nuclei and implications for multi-α-cluster transfer reactions. C **21**, 444
Bechtold, G. — (see Gils, H.J.) C **21**, 1239
Becker, J. — (see Bargholtz, Chr.) C **21**, 1078
Beckerman, M. — (see Sikora, B.) C **21**, 614
Beene, J. R., R. M. DeVries, D. Shapira, and M. R. Clover — m-substate populations in resonant heavy-ion reactions. C **21**, 167
Beer, H. and F. Käppeler — Neutron capture cross sections on ^{138}Ba, ^{140,142}Ce, ^{175,176}Lu, and ^{181}Ta at 30 keV: Prerequisite for investigation of the ^{176}Lu cosmic clock. C **21**, 534
——— **and F. Käppeler** — Erratum: Neutron capture cross sections on ^{138}Ba, ^{140,142}Ce, ^{175,176}Lu, and ^{181}Ta at 30 keV: Prerequisite for investigation of the ^{176}Lu cosmic clock [C 21, 534 (1980)]. C **21**, 2139(E)
Behera, B., K. C. Panda, and R. K. Satpathy — Imaginary part of the ion-ion interaction potential. C **21**, 1883
Belehrad, R. H. — (see Vary, J.P.) C **21**, 1626
Bellicard, J. B., P. Bounin, R. F. Frosch, R. Hofstadter, J. S. McCarthy, F. J. Uhrhane, B. C. Clark, and R. Herman — Elastic cross sections for $e^- + {}^{48}$Ca at 757.5 MeV. C **21**, 1652
Benczer-Koller, N. — (see Brennan, J.M.) C **21**, 574
———(see Shu, N.K.B.) C **21**, 1828
Bendel, W. L. — (see Jones, E.C., Jr.) C **21**, 1162
Benenson, W. — (see Pardo, R.C.) C **21**, 462
Beres, William P. — (see Larry, Thomas L.) C **21**, 2126
———(see Larry, Thomas L.) C **21**, 2675
Bergstrom, J. C. — *Electroexcitation of* ^{6}Li with application to the reactions ^{6}Li(π^-,γ)$_{ts}$^{6}He(0$^+$,2$^+$). C **21**, 2496
Berman, B. L. — (see Caldwell, J.T.) C **21**, 1215
———(see Jury, J.W.) C **21**, 503
Bernard, V. — (see Auerbach, N.) C **21**, 744
Berrier-Rousin, G. — (see Gerlic, E.) C **21**, 124
———(see Rotbard, G.) C **21**, 1232
———(see Rotbard, G.) C **21**, 2293
Berthot, J. — (see Jonsson, S.) C **21**, 306
Bertrand, F. E. — (see Harakeh, M.N.) C **21**, 768
Beshai, S. — (see Bargholtz, Chr.) C **21**, 1078
Betts, R. R., M. M. Hindi, S. B. DiCenzo, and P. D. Parker — Search for fusion oscillations in the ^{16}O + ^{28}Si system. C **21**, 175
Betts, R. R. — (see Mortensen, M.H.) C **21**, 2275
———(see Mortensen, M.H.) C **21**, 2288
Betz, M. and F. Coester — Phenomenological relativistic quantum mechanics of the $NN\pi$ system. C **21**, 2505
Bevelacqua, J. J. — Comparison of analyzing powers and polarizations for the charge symmetric reactions ^{2}H($\vec{d}$,p)^{3}H and ^{2}H($\vec{d}$,n)^{3}He. C **21**, 2685
Beveridge, J. L. — (see Clough, A.S.) C **21**, 988
———(see Källne, Jan) C **21**, 675
Bevington, P. R. — (see Winkelmann, E.) C **21**, 2535
Bhalerao, R. S., L. C. Liu, and C. M. Shakin — Systematic features of the pion-nucleus interaction. C **21**, 1903
———, **L. C. Liu, and C. M. Shakin** — Self-energy of the Δ resonance in finite nuclei and Fermi broadening. C **21**, 2103
Bhasin, V. S. — (see Anand, J.D.) C **21**, 2010
Bimbot, R. — (see Gardes, D.) C **21**, 2447
Bini, M., A. M. Bizzeti-Sona, P. Blasi, M. Lorini, and N. Taccetti — Isomeric transitions in ^{100}Tc. C **21**, 116
Birkelund, J. R. — (see Wilcke, W.W.) C **21**, 2019
Bisplinghoff, J. — (see Sikora, B.) C **21**, 614
Bizzeti-Sona, A. M. — (see Bini, M.) C **21**, 116
Bland, L. C. and H. T. Fortune — ^{10}B from ^{9}Be(^{3}He,d) C **21**, 11
———, **H. T. Fortune, O. K. Gorpinich, Yu S. Stryuk, V. N. Shcherbin, and V. V. Tokarevski** — Reaction ^{27}Al(α,d)^{29}Si at 27.2 MeV. C **21**, 2227
Blann, Marshall — Decay of deformed and superdeformed nuclei formed in heavy ion reactions. C **21**, 1770
———(see Sikora, B.) C **21**, 614
Blanpied, G. S. — (see Burleson, G.R.) C **21**, 1452
———(see Hoffmann, G.W.) C **21**, 1488
Blasi, P. — (see Bini, M.) C **21**, 116
Blatt, S. L. — (see Linck, I.) C **21**, 791
Bloch, A. — (see Argan, P.) C **21**, 662
———(see Argan, P.) C **21**, 1416
Boal, David H. — Probing inclusive production mechanisms with the (p,2p) reaction. C **21**, 1913
Bock, R. — (see Eyal, Y.) C **21**, 1377
Bockelman, C. K. — (see Mortensen, M.H.) C **21**, 2275
———(see Mortensen, M.H.) C **21**, 2288
Bond, A. H., Jr. — (see Trail, C.C.) C **21**, 2131
Bond, P. D. — (see Kubono, S.) C **21**, 459
Bonetti, R., L. Colli Milazzo, A. De Rosa, G. Inglima, E. Perillo, M. Sandoli, and F. Shahin — Statistical multistep compound emission in the ^{27}Al(^{3}He,p)^{29}Si reaction. C **21**, 816
Börner, H. G. — (see Casten, R.F.) C **21**, 65
Boudrie, R. L. — (see Bauer, T.S.) C **21**, 757

____(see Hoffmann, G.W.) C 21, 1488
____(see Källne, Jan) C 21, 2681
____(see Olmer, C.) C 21, 254
____(see Peterson, R.J.) C 21, 1030
Bounin, P. — (see Bellicard, J.B.) C 21, 1652
Bowman, C. D. and R. A. Schrack — Influence of vibrations of gas molecules on neutron reaction cross sections. C 21, 58
Boyd, R. N. — (see Alford, W.P.) C 21, 1203
Brady, F. P. — (see Fitzgerald, D.H.) C 21, 1190
____(see Garrett, R.) C 21, 1149
____(see King, N.S.P.) C 21, 1185
Braga, R. A. — (see Gnade, B.E.) C 21, 2025
Braithwaite, W. J. — (see Peterson, R.J.) C 21, 1030
Braun-Munzinger, P. — (see Tserruya, I.) C 21, 1864
Breitig, D. — (see Casten, R.F.) C 21, 65
Brennan, J. M., M. Hass, N. K. B. Shu, and N. Benczer-Koller — Magnetic moments of 2_1^+ states of even-even Pd, Cd, and Ba isotopes. C 21, 574
____(see Shu, N.K.B.) C 21, 1828
Briscoe, W. J. — (see Sober, D.I.) C 21, 1495
Britt, H. C., E. Cheifetz, D. C. Hoffman, J. B. Wilhelmy, R. J. Dupzyk, and R. W. Lougheed — Fission barriers for ^{255}Es, ^{256}Es, and ^{255}Fm. C 21, 761
Bronson, J. D. — (see Rozsa, C.M.) C 21, 1252
Brown, B. A. and B. H. Wildenthal — Relative importance of neutron and proton components of nuclear transitions and comparative π^-/π^+ inelastic scattering C 21, 2107
____, **W. Chung, and B. H. Wildenthal** — Inelastic scattering $E4$ transition probabilities in the $0d,1s$ shell. C 21, 2600
Brown, Ronald E., J. A. Cizewski, J. W. Sunier, E. R. Flynn, P. Alford, E. Sugarbaker, and D. Ardouin — Search for nuclear structure dependence of analyzing powers for the $(\vec{t},p)$ reaction in medium mass nuclei C 21, 2663
Browne, J. C. — (see Wilcke, W.W.) C 21, 2019
Buckley, W. M. — (see Mann, L.G.) C 21, 2547
Buenerd, M. — (see Guillot, J.) C 21, 879
Bugg, D. V., J. A. Edgington, W. R. Gibson, N. Wright, N. M. Stewart, A. S. Clough, D. Axen, G. A. Ludgate, C. J. Oram, L. P. Robertson, J. R. Richardson, and C. Amsler — Neutron-proton elastic scattering between 200 and 500 MeV. III. Phase shift analysis C 21, 1004
____(see Axen, D.) C 21, 998
____(see Clough, A.S.) C 21, 988
Bülow, B. — (see DeCarlo, V.) C 21, 1460
Burleson, G. R., G. S. Blanpied, J. Davis, J. S. McCarthy, R. C. Minehart, C. Goulding, C. L. Morris, H. A. Thiessen, W. B. Cottingame, S. Greene, and C. F. Moore — Quasielastic scattering of pions from ^{12}C and ^{40,44,48}Ca C 21, 1452
____(see Olmer, C.) C 21, 254
Burq, J. P. — (see Jonsson, S.) C 21, 306
Burt, P. E. — (see Sober, D.I.) C 21, 1495
Buschmann, J. — (see Gils, H.J.) C 21, 1239
Buskirk, F. R. — (see Pitthan, R.) C 21, 28
____(see Pitthan, R.) C 21, 147
Butler, P. A. — (see Yates, S.W.) C 21, 2366
Caffrey, A. J. — (see Robinson, R.L.) C 21, 603
Caldwell, J. T., E. J. Dowdy, B. L. Berman, R. A. Alvarez, and P. Meyer — Giant resonance for the actinide nuclei Photoneutron and photofission cross sections for ^{235}U, ^{236}U, ^{238}U, and ^{232}Th C 21, 1215
Callender, W. D. — (see Cleary, T.P.) C 21, 2244
Cambi, A., B. Mosconi, and P. Ricci — Consistency between pion exchange currents and N-N potential in doubly radiative π-p capture. C 21, 1921
Cameron, J. M. — (see Moss, G A.) C 21, 1932
Cannata, F. and S. A. Gurvitz — High energy scattering from a bound nucleon Unitarity and closure approximation. C 21, 2687
Canto, L. F. — (see Hussein, M S.) C 21, [illegible]
Canty, M. J. — (see Spanhoff, R.) C 21, 36[illegible]
Caretto, A. A., Jr. — (see Church, [illegible] B.) C 21, 246
Carey, T. A. — (see Roos, P.G.) C 21, 799
____(see Wang, C W.) C 21, 1705
Carlson, Carl E. — (see Arnold, Raymond G.) C 21, 1426
Carlson, J. B. — (see Mann, L G.) C 21, 2547
Cassidy-Aaquist, Denise and Boris Castel — Isomeric states and spin polarization in $A \sim 90$ nuclei C 21, 1538
Castaneda, C. M., H. A. Smith, Jr., P. P. Singh, and H. Karwowski — Mechanisms of production of fast particles with $Z=1,2$ in ^{6}Li-induced reactions far above the Coulomb barrier C 21, 179
Castel, Boris — (see Cassidy-Aaquist, Denise) C 21, 1538
Casten, R. F., G. J. Smith, M. R. Macphail, D. Breitig, W. R. Kane, M. L. Stelts, S. F. Mughabghab, J. A. Cizewski, H. G. Börner, W. F. Davidson, and K. Schreckenbach — ^{109}Pd Difficulties in particle-rotor models for unique-parity states and revision of spectroscopic factors. C 21, 65
Catchen, Gary L., Morton Kaplan, John M. Alexander, and M. F. Rivet — Semiempirical methods for estimating fragment spins from studies of ^{4}He and ^{1}H emission. C 21, 940
Cecil, R. A., B. D. Anderson, A. R. Baldwin, R. Madey, A. Galonsky, P. Miller, L. Young, and F. M. Waterman — Neutron angular and energy distributions from 710-MeV alphas stopping in water, carbon, steel, and lead and 640-MeV alphas stopping in lead. C 21, 2471
Cerruti, C. — (see Namboodiri, M N.) C 21, 1680(E)
Cha, D. — Transverse electromagnetic form factor in ^{12}C C 21, 1672
Chakravarti, S. — (see Olmer, C.) C 21, 254
Chamberlin, E. P. — (see Winkelmann, E.) C 21, 2535
Chant, N. S. — (see Roos, P G.) C 21, 799
____(see Wang, C W.) C 21, 1705
Chasman, R. R. — ^{147}Tb and proton single particle states near $Z=64$ C 21, 456
Chauvin, J. — (see Guillot, J.) C 21, 879
Cheifetz, E. — (see Britt, H.C.) C 21, 761
Chemarin, M. — (see Jonsson, S.) C 21, 306
Cheng, W. K., B. Lorazo, and B. Goulard — Interplay between mesonic-exchange corrections and nuclear structure in the weak transitions $^{16}\mathrm{O}(0^+) \rightleftarrows {}^{16}\mathrm{N}(0^-)$. C 21, 374
Chéry, R. — (see Sau, J.) C 21, 405
Chevallier, M. — (see Jonsson, S.) C 21, 306
Childs, J. D. — (see Dachnick, W.W.) C 21, 2253
Chisholm, A., J. C. Duder, R. Garrett, and J. L. Poletti — Interpretation of a recent neutron-proton analyzing

power measurement. C 21, 1653

Chrien, R. E., T. J. Krieger, R. J. Sutter, M. May, H. Palevsky, R. L. Stearns, T. Kozlowski, and T. Bauer — Proton spectra from 800 MeV protons on selected nuclides. C 21, 1014

____(see Greenwood, R.C.) C 21, 498

Chung, W. — (see Brown, B.A.) C 21, 2600

Church, L. B. and A. A. Caretto, Jr. — $(\pi^{\pm}, xn)$ reactions. C 21, 246

Cioffi degli Atti, C., E. Pace, and G. Salmè — Realistic nucleon-nucleon interactions and the three-body electrodisintegration of ^{3}H. C 21, 805

Cizewski, J. A. — (see Brown, Ronald E.) C 21, 2663

____(see Casten, R.F.) C 21, 65

Clark, B. C. — (see Arnold, L.G.) C 21, 1899

____(see Bellicard, J.B.) C 21, 1652

Clark, H. W. — (see Dries, L.J.) C 21, 475

Clark, P. D. — (see Eck, J.S.) C 21, 2352

Clark, Robert Beck — (see Dominguez, C.A.) C 21, 1944

Cleary, T. P., W. D. Callender, and R. K. Sheline — ^{210}Bi$^{m}(d,t)$ reaction; ^{210}Bi(9^{-}) parentage of states in ^{209}Bi. C 21, 2244

____(see Ford, J.L C., Jr.) C 21, 764

Clements, J. S., L. R. Medsker, L. H. Fry, Jr., and L. V. Theisen — High-spin $E2$ bands in Kr isotopes. C 21, 1285

Cline, D. — (see Yates, S.W.) C 21, 2366

Clough, A. S., D. R. Gibson, D. Axen, R. Dubois, L. Felawka, R. Keeler, G. A. Ludgate, C. J. Oram, C. Amsler, D. V. Bugg, J. A. Edgington, L. P. Robertson, N. M. Stewart, J. Beveridge, and J. R. Richardson — Neutron-proton elastic scattering between 200 and 500 MeV. I. Experimental details and measurements of the D_t and P parameters. C 21, 988

____(see Axen, D.) C 21, 998

____(see Bugg, D.V.) C 21, 1004

Clover, M. R. — (see Beene, J.R.) C 21, 167

Coester, F. — (see Betz, M.) C 21, 2505

Colli Milazzo, L. — (see Bonetti, R.) C 21, 816

Collins, M. T. — (see Roos, P.G.) C 21, 799

Colombani, P. — (see Yates, S.W.) C 21, 2366

Comfort, J. R., Sam M. Austin, P. T. Debevec, G. L. Moake, R. W. Finlay, and W. G. Love — Inelastic excitation of ^{12}C and ^{14}N by 122 MeV protons and implications for the effective nucleon-nucleon interaction. C 21, 2147

____ **and B. C. Karp** — Scattering and reaction dynamics for the $^{12}\mathrm{C}+p$ system. C 21, 2162

Conzett, H. E. — (see Stephenson, E.J.) C 21, 44

Cormier, T. M. — (see Fulton, B.R.) C 21, 198

Cosman, E. R., R. Ledoux, and A. J. Lazzarini — $^{12}\mathrm{C}+{}^{12}\mathrm{C}$ intermediate structures correlated among elastic and reaction channels. C 21, 2111

Cotanch, Stephen R. — Interior probing capability in kaon-nucleus inelastic scattering. C 21, 2115

Côté, J. — (see Lacombe, M.) C 21, 861

Cotte, P. — (see Jonsson, S.) C 21, 306

Cottingame, W. B. — (see Burleson, G.R.) C 21, 1452

Courtemanche, A. N. — (see Lichtenstadt, J.) C 21, 1128(E)

Courtney, L. H. — (see Parks, L.A.) C 21, 217

Covello, A. — (see Andreozzi, F.) C 21, 1094

Cramer, J. G. — (see Zisman, M.S.) C 21, 2398

Crannell, Hall — (see Sober, D.I.) C 21, 1495

Cseh, J. — (see Sanders, S.J.) C 21, 1810

Cugnon, J. and R. Sartor — Factorization in high-energy nucleus-nucleus fragmentation cross sections. C 21, 2342

Cunsolo, A., A. Foti, G. Immè, G. Pappalardo, G. Raciti, F. Rizzo, and N. Saunier — $^{13}\mathrm{C}(^{6}\mathrm{Li},t)^{16}\mathrm{O}$ reaction in the 20–32 MeV incident energy range. C 21, 952

____**, A. Foti, G. Immè, G. Pappalardo, G. Raciti, and N. Saunier** — $^{12}\mathrm{C}(^{6}\mathrm{Li},d)^{16}\mathrm{O}\rightarrow\alpha+{}^{12}\mathrm{C}$ reaction mechanism by means of angular correlation measurements. C 21, 2345

Cutler, R. I., K. W. Kemper, and A. Roy — $(^{7}\mathrm{Li},t)$ on $1f$-$2p$ shell nuclei. C 21, 1799

Çverna, F. H. — (see Winkelmann, E.) C 21, 2535

Ćwiok, S., W. Nazarewicz, J. Dudek, and Z. Szymański — Analysis of the backbending effect in ^{166}Yb, ^{168}Yb, and ^{170}Yb within the Hartree-Fock-Bogolyubov cranking method. C 21, 448

Daehnick, W. W., J. D. Childs, and Z. Vrcelj — Global optical model potential for elastic deuteron scattering from 12 to 90 MeV. C 21, 2253

Dahlgren, S. — (see Jonsson, S.) C 21, 306

Dally, E. B. — (see Pitthan, R.) C 21, 147

Daneshvar, K. — (see Prosser, F.W., Jr.) C 21, 1819

Dange, S. P. — (see Datta, Tarun) C 21, 1411

Daniels, W. R. — (see Hoffman, D.C.) C 21, 972

____(see Orth, C.J.) C 21, 2524

Das Gupta, S. — (see Forest, E.) C 21, 1989

Datta, S. K., W. R. Falk, S. P. Kwan, R. Abegg, and O. A. Abou-Zeid — $^{12}\mathrm{C}(p,\alpha^{*})^{9}\mathrm{B}$ reaction in the finite range microscopic distorted-wave Born-approximation formalism. C 21, 1687

Datta, Tarun, S. P. Dange, S. B. Manohar, A. G. C. Nair, Satya Prakash, and M. V. Ramaniah — Charge distribution in the thermal neutron fission of ^{245}Cm: Fractional cumulative yields of ^{135}I and ^{140}Ba. C 21, 1411

Davidson, W. F. — (see Casten, R.F.) C 21, 65

Davis, J. — (see Burleson, G.R.) C 21, 1452

____(see Källne, Jan) C 21, 2681

Davis, S. — (see Kolata, J.J.) C 21, 776

Debevec, P. T. — (see Comfort, J.R.) C 21, 2147

____(see Moake, G.L.) C 21, 25

____(see Moake, G.L.) C 21, 2211

de Botton, N. — (see Argan, P.) C 21, 662

____(see Argan, P.) C 21, 1416

DeCarlo, V., N. Freed, W. Rhodes, B. Bülow, G. G. Jonsson, K. Lindgren, and R. Petersson — Photoproduction of π^{-} on ^{14}N. C 21, 1460

Dechargé, J. and D. Gogny — Hartree-Fock-Bogolyubov calculations with the $D1$ effective interaction on spherical nuclei. C 21, 1568

De Clercq, A. — (see De Frenne, D.) C 21, 629

____(see D'hondt, P.) C 21, 963

____(see Jacobs, E.) C 21, 237

Dedonder, J. -P. — (see Amado, R.D.) C 21, 647

De Frenne, D., H. Thierens, E. Jacobs, P. De Gelder, A. De Clercq, P. D'hondt, and A. J. Deruytter — Charge distribution for the photofission of ^{238}U with 20-MeV bremsstrahlung. C 21, 629

———(see D'hondt, P.) C 21, 963
———(see Jacobs, E.) C 21, 237
De Gelder, P. — (see De Frenne, D.) C 21, 629
———(see D'hondt, P.) C 21, 963
———(see Jacobs, E.) C 21, 237
del Campo, J. Gomez — (see Shapira, D.) C 21, 1824
De Leo, R. — (see Fabrici, E.) C 21, 830
———(see Fabrici, E.) C 21, 844
de Lima, A. P. — (see Kawakami, H.) C 21, 1311
Deloff, A. — Low-energy kaon-nucleus interaction. C 21, 1516
——— **and J. Law** — Sturmian expansion method for bound state problems. C 21, 2048
de Passos, E. J. V. and A. F. R. de Toledo Piza — Properties of Griffin-Hill-Wheeler spaces. II. One-parameter and two-conjugate-parameter families of generator states. C 21, 425
D'Erasmo, G. — (see Fabrici, E.) C 21, 830
———(see Fabrici, E.) C 21, 844
der Mateosian, E. — (see Kreiner, A.J.) C 21, 933
De Rosa, A. — (see Bonetti, R.) C 21, 816
Deruytter, A. J. — (see De Frenne, D.) C 21, 629
———(see D'hondt, P.) C 21, 963
———(see Jacobs, E.) C 21, 237
de Saint Simon, M. — (see Morrissey, D.J.) C 21, 1783
de Saussure, G. — (see Difilippo, F.C.) C 21, 1400
de Téramond, G. F., J. Páez, and C. W. Soto Vargas — Off-shell rescattering effects in the reaction $\pi^- + d \to 2n + \gamma$. C 21, 2542
de Toledo Piza, A. F. R. — (see de Passos, E.J.V.) C 21, 425
Detomo, R. , Jr. — (see Dries, L.J.) C 21, 475
de Tourreil, R. — (see Lacombe, M.) C 21, 861
Deutsch, J. — (see Argan, P.) C 21, 662
———(see Argan, P.) C 21, 1416
Devereux, M. J. — (see Olmer, C.) C 21, 254
deVries, H. — (see Hicks, R.S.) C 21, 2177
DeVries, R. M. — (see Beene, J.R.) C 21, 167
———(see Zisman, M.S.) C 21, 2398
DeYoung, P. A. — (see Kolata, J.J.) C 21, 776
D'hondt, P., E. Jacobs, A. De Clercq, D. De Frenne, H. Thierens, P. De Gelder, and A. J. Deruytter — Emission of long-range alpha particles in the photofission of ^{235}U with 20-MeV bremsstrahlung. C 21, 963
———(see De Frenne, D.) C 21, 629
———(see Jacobs, E.) C 21, 237
Diamond, R. M. — (see Yates, S.W.) C 21, 2366
DiCenzo, S. B. — (see Betts, R.R.) C 21, 175
Didelez, J. P. — (see Guillot, J.) C 21, 879
Dietrich, F. S. — (see Howell, R.H.) C 21, 1153
———(see Howell, R.H.) C 21, 1158
Dietzsch, O. — (see Takagui, E.M.) C 21, 1667
Difilippo, F. C., R. B. Perez, G. de Saussure, D. K. Olsen, and R. W. Ingle — ^{238}U neutron-induced fission cross section for incident neutron energies between 5 eV and 3.5 MeV. C 21, 1400
DiGiacomo, N. J. — (see Bauer, T.S.) C 21, 757
DiRienzo, A. C., H. A. Enge, S. B. Gazes, M. K. Salomaa, A. Sperduto, W. Schier, and H. E. Wegner — New isotope ^{199}Rn and evidence for an isomeric state ^{199}Rn^m. C 21, 2101
Di Toro, M., G. Russo, and F. Duggan — Alternative methods for the solution of static Hartree-Fock and related problems. C 21, 2054
Dodd, L. R. and K. J. Nieukerke — Adiabatic limit of the Faddeev equations. C 21, 1724
Dominguez, C. A. and Robert Beck Clark — Extraction of the πNN form factor from charged pion photoproduction. C 21, 1944
Donangelo, R. — (see Hussein, M.S.) C 21, 772
Donoghue, T. R. — (see Dries, L.J.) C 21, 475
Doré, C. — (see Jonsson, S.) C 21, 306
Dover, Carl B. and J. M. Richard — Elastic, charge exchange, and inelastic $\bar{p}p$ cross sections in the optical model. C 21, 1466
Dowdy, E. J. — (see Caldwell, J.T.) C 21, 1215
Dracoulis, G. D. — (see Walker, P.M.) C 21, 464
Drake, D. M. — (see Nilsson, L.) C 21, 902
Dressler, E. T., N. Freed, and H. B. Miska — Pion electroproduction from the nucleon near threshold. C 21, 2119
Dries, L. J., H. W. Clark, R. Detomo, Jr., J. L. Regner, and T. R. Donoghue — $A_{zz}(0°)$ for the charge-symmetric ^{3}He$(\vec{d},p)^4$He and ^{3}H$(\vec{d},n)^4$He reactions below 6.75 MeV C 21, 475
Dropesky, B. J. — (see Orth, C.J.) C 21, 2524
Drosg, M. — (see Nilsson, L.) C 21, 902
Dubois, D. H. — (see Pitthan, R.) C 21, 147
Dubois, R. — (see Axen, D.) C 21, 998
———(see Clough, A.S.) C 21, 988
Dudek, J. — (see Ćwiok, S.) C 21, 448
Duder, J. C. — (see Chisholm, A.) C 21, 1653
Duggan, F. — (see Di Toro, M.) C 21, 2054
Duhamel, G. — (see Gerlic, E.) C 21, 124
———(see Guillot, J.) C 21, 879
Dumbrajs, Olgierd — Analyticity and model-independent determination of the nuclear charge density. C 21, 1677
Dupzyk, R. J. — (see Britt, H.C.) C 21, 761
———(see Hoffman, D.C.) C 21, 972
Dworzecka, Maria — (see Griffin, James J.) C 21, 1351
———(see Kan, K.-K.) C 21, 1098
Dyer, J. N. — (see Pitthan, R.) C 21, 147

Earle, E. D. — (see Saha, S.K.) C 21, 2322
Eck, J. S., J. R. Leigh, T. R. Ophel, and P. D. Clark — Total fusion cross section for the ^{9}Be + ^{28}Si system. C 21, 2352
Edgington, J. A. — (see Axen, D.) C 21, 998
———(see Bugg, D.V.) C 21, 1004
———(see Clough, A.S.) C 21, 988
Eggers, R. — (see Namboodiri, M.N.) C 21, 1680(E)
Eichler, E. — (see Yates, S.W.) C 21, 2366
Eisen, Y. — (see Eyal, Y.) C 21, 1377
———(see Stokstad, R.G.) C 21, 2427
Ekelöf, T. — (see Jonsson, S.) C 21, 306
El Hage, Y. — (see Galès, S.) C 21, 98
El-khosht, M. — (see Bargholtz, Chr.) C 21, 1078
Elwyn, A. J. — (see Gronemeyer, S.A.) C 21, 1290
Enge, H. A. — (see DiRienzo, A.C.) C 21, 2101
Ernst, D. J. and Gerald A. Miller — Relativistic kinematics for elastic pion-nucleus scattering. C 21, 1472
Ernst, H. — (see Leuthold, K.) C 21, 2581
Escudié, J. L. — (see Fabrici, E.) C 21, 830
Eyal, Y., A. Gavron, I. Tserruya, Z. Fraenkel, Y. Eisen, S. Wald, R. Bass, C. R. Gould, G. Kreyling, R. Ren-

fordt, K. Stelzer, R. Zitzmann, A. Gobbi, U. Lynen, H. Stelzer, I. Rode, and R. Bock — Neutron emission in deep-inelastic collisions induced by ^{86}Kr on ^{166}Er at 5.7, 7.0, and 7.9 MeV/nucleon. C 21, 1377

Fabrici, E., S. Micheletti, M. Pignanelli, F. G. Resmini, R. De Leo, G. D'Erasmo, A. Pantaleo, J. L. Escudié, and A. Tarrats — Proton elastic scattering on light nuclei. I. Energy dependence. C 21, 830
——, **S. Micheletti, M. Pignanelli, F. G. Resmini, R. De Leo, G. D'Erasmo, and A. Pantaleo** — Proton elastic scattering on light nuclei. II. Nuclear structure effects. C 21, 844
Fagg, L. W. — (see Jones, E.C., Jr.) C 21, 1162
Fäldt, G. — (see Jonsson, S.) C 21, 306
Falk, W. R. — (see Datta, S.K.) C 21, 1687
Faul, D. D. — (see Jury, J.W.) C 21, 503
Faure, J. -L. — (see Argan, P.) C 21, 662
——(see Argan, P.) C 21, 1416
Favart, D. — (see Argan, P.) C 21, 662
——(see Argan, P.) C 21, 1416
Fayard, C. — (see Giraud, N.) C 21, 1959
Fearing, Harold W. — *Relativistic calculation of radiative* muon capture in hydrogen and ^{3}He. C 21, 1951
Feigel, A., E. Finckh, K. Rüskamp, and U. Weise — Large absorption potential for the Ag + *p* reaction at sub-Coulomb energies. C 21, 2666
Felawka, L. — (see Clough, A.S.) C 21, 988
Filevich, A. — (see Kreiner, A.J.) C 21, 933
Finckh, E. — (see Feigel, A.) C 21, 2666
Fink, R. W. — (see Gnade, B.E.) C 21, 2025
Finlay, R. W. — (see Comfort, J.R.) C 21, 2147
Fitzgerald, D. H., F. P. Brady, R. Garrett, S. W. Johnsen, J. L. Romero, T. S. Subramanian, J. L. Ullmann, and J. W. Watson — Neutron-proton scattering. II. Spin correlation parameter $A_{yy}(\theta)$ at 50 MeV. C 21, 1190
——(see Garrett, R.) C 21, 1149
——(see King, N.S.P.) C 21, 1185
Flanz, J. B. — (see Hicks, R.S.) C 21, 2177
Fleury, A. — (see Gardes, D.) C 21, 2447
Fliessbach, Torsten — Justification of local potentials in coupled channel problems. C 21, 919
Flynn, D. S. — (see Hershberger, R.L.) C 21, 896
Flynn, E. R. — (see Alford, W.P.) C 21, 1203
——(see Brown, Ronald E.) C 21, 2663
Fodor, I. and J. Sziklai — Analog doorway and its effect in the different channels. C 21, 787
Fontanilla, J. E. — (see Meyer, R.A.) C 21, 2590
Ford, G. P. — (see Hoffman, Darleane C.) C 21, 637
Ford, J. L. C., Jr., T. P. Cleary, J. Gomez del Campo, D. C. Hensley, D. Shapira, and K. S. Toth — First 8^+ state in ^{28}Si and level systematics of *sd* shell nuclei. C 21, 764
——(see Shapira, D.) C 21, 1824
Forest, E., S. Das Gupta, and C. S. Lam — Proton-proton correlations, the fireball model, and inclusive pion spectrum. C 21, 1989
Fortier, S. — (see Galès, S.) C 21, 98
Fortney, D. R. and N. T. Porile — Differential ranges of Sc fragments from the interaction of ^{238}U with 0.8–400 GeV protons. C 21, 664
—— **and N. T. Porile** — Angular distributions of Sc fragments from the interaction of ^{238}U with 0.8–400 GeV protons. C 21, 2511
Fortune, H. T. — (see Bland, L.) C 21, 11
——(see Bland, L.C.) C 21, 2227
Fossan, D. B. — (see Sjoreen, T.P.) C 21, 1838
Foti, A. — (see Cunsolo, A.) C 21, 952
——(see Cunsolo, A.) C 21, 2345
Fox, S. H. and Sam M. Austin — ^{14}N$(p,p')^{14}$N reaction between 25 and 40 MeV and the tensor part of the effective interaction. C 21, 1133
Fraenkel, Z. — (see Eyal, Y.) C 21, 1377
——(see Yariv, Y.) C 21, 2139(E)
Frahn, W. E. — Closed-form description of heavy-ion transfer reactions based on distorted-waves theory. C 21, 1870
Fransson, K. — (see Bargholtz, Chr.) C 21, 1078
Freed, N. — (see DeCarlo, V.) C 21, 1460
——(see Dressler, E.T.) C 21, 2119
Freedman, M. S. — (see Schupp, G.) C 21, 348
Freeman, R. M. — (see Kolata, J.J.) C 21, 579
Friedman, A. M. — (see Ahmad, I.) C 21, 874
Friedman, E. — (see Gils, H.J.) C 21, 1239
——(see Gils, H.J.) C 21, 1245
Friedman, William A. and Alvin M. Saperstein — Glauber theory and *N-N* inelasticity. C 21, 2098
Frisbee, P. E. — (see Roos, P.G.) C 21, 799
Frosch, R. F. — (see Bellicard, J.B.) C 21, 1652
Fry, L. H., Jr. — (see Clements, J.S.) C 21, 1285
Fuda, Michael G., B. A. Girard, and J. S. Whiting — Parametrization of *N/D* input. C 21, 18
——Feshbach-Villars formalism and pion-nucleon scattering. C 21, 1480
Fulton, B. R., T. M. Cormier, and B. J. Herman — Resonances in ^{12}C + ^{12}C inelastic scattering to the 0_2^+, 3_1^-, and 4_1^+ states. C 21, 198
Funk, E. G. — (see Rakel, D.A.) C 21, 595
Furuno, Kohei — (see Katori, Kenji) C 21, 1387
Furusawa, Akira, Masaaki Kanazawa, and Shogo Hayashibe — *g* factors of the 80 and 1094 keV states of ^{168}Er. C 21, 2575
Fuschini, E., F. Malaguti, A. Uguzzoni, and E. Verondini — Axial blocking measurement of the ^{28}Si 12.291 MeV level width. C 21, 1646

Gabbard, F. — (see Hershberger, R.L.) C 21, 896
Gal, M. — (see Tserruya, I.) C 21, 1864
Galès, S., Y. El Hage, J. P. Schapira, S. Fortier, H. Laurent, and J. M. Maison — High-spin analog resonances near the $N = 50$ neutron shell. C 21, 98
——(see Gerlic, E.) C 21, 124
Gallmann, A. — (see Kolata, J.J.) C 21, 579
Galloway, R. B. and A. S. Hall — Angular dependence of neutron polarization for the ^{2}H$(d,n)^3$He reaction for deuteron energies less than 500 keV. C 21, 453
Galonsky, A. — (see Cecil, R.A.) C 21, 2471
——(see Williamson, C.) C 21, 1344
Gambhir, Y. K., S. Haq, and J. K. Suri — Quadrupole moments and $E2$ transition rates in the Zr region with wave functions of the broken pair approximation. C 21, 1124
—— **and R. Parthasarathy** — Total muon capture rates in

neon. C 21, 1637

García Bermúdez, G. — (see Kreiner, A.J.) C 21, 933

Garcilazo, Humberto — Pion-nucleus optical potential including the nuclear Hamiltonian. C 21, 2094

Gardes, D., R. Bimbot, J. Maison, M. F. Rivet, A. Fleury, F. Hubert, and Y. Llabador — Angular distributions and ranges of heavy products from quasi-elastic transfer reactions induced by heavy ions in ^{209}Bi. C 21, 2447

Garg, U. — (see Rozsa, C.M.) C 21, 1252

Garg, U. — (see Sjoreen, T.P.) C 21, 1838

Garrett, R., J. W. Watson, F. P. Brady, D. H. Fitzgerald, J. L. Romero, J. L. Ullmann, and C. Zanelli — Neutron-proton analyzing power at 50 MeV. C 21, 1149

——(see Chisholm, A.) C 21, 1653

——(see Fitzgerald, D.H.) C 21, 1190

Gavron, A. — Statistical model calculations in heavy ion reactions. C 21, 230

——(see Eyal, Y.) C 21, 1377

Gazes, S. B. — (see DiRienzo, A.C.) C 21, 2101

Gazzaly, M. — (see Adams, G.S.) C 21, 2485

Geerts, R., C. Nuytten, E. Schoeters, R. Silverans, and L. Vanneste — Magnetic moments of ^{125}Te^{m}, ^{127}Te^{m}, and ^{129}Te^{m}. C 21, 439

Geesaman, D. F. — (see Olmer, C.) C 21, 254

——(see Paul, M.) C 21, 1802

——(see Prosser, F.W., Jr.) C 21, 1819

——(see Sanders, S.J.) C 21, 1810

Gerlic, E., G. Berrier-Ronsin, G. Duhamel, S. Galès, E. Hourani, H. Langevin-Joliot, M. Vergnes, and J. Van de Wiele — Neutron-hole distributions in ^{111,115,119}Sn as observed in the (^{3}He,α) reaction. C 21, 124

——(see Guillot, J.) C 21, 879

Giai, Nguyen Van — (see Auerbach, N.) C 21, 744

Giannoni, M. J. and P. Quentin — Mass parameters in the adiabatic time-dependent Hartree-Fock approximation. I. Theoretical aspects: the case of a single collective variable. C 21, 2060

—— **and P. Quentin** — Mass parameters in the adiabatic time-dependent Hartree-Fock approximation. II. Results for the isoscalar quadrupole mode. C 21, 2076

Gibson, D. R. — (see Clough, A.S.) C 21, 988

Gibson, W. R. — (see Axen, D.) C 21, 998

——(see Bugg, D.V.) C 21, 1004

Giesler, G. C. — (see Orth, C.J.) C 21, 2524

Gilat, J., S. Katcoff, and L. K. Peker — Levels of ^{230}Ac and ^{230}Th populated by decay of ^{230}Ra and ^{230}Ac. C 21, 2041

Gils, H. J., E. Friedman, H. Rebel, J. Buschmann, S. Zagromski, H. Klewe-Nebenius, B. Neumann, R. Pesl, and G. Bechtold — Nuclear sizes of ^{40,42,44,48}Ca from elastic scattering of 104 MeV alpha particles. I. Experimental results and optical potentials. C 21, 1239

——, **E. Friedman, Z. Majka, and H. Rebel** — Nuclear sizes of ^{40,42,44,48}Ca from elastic scattering of 104 MeV alpha particles. II. Nuclear density distributions. C 21, 1245

Ginocchio, Joseph N. and Mikkel B. Johnson — Effect of the pion and Δ optical potential on deep inelastic pion-nuclear reactions. C 21, 1056

——(see Orth, C.J.) C 21, 2524

Girard, B. A. — (see Fuda, M.G.) C 21, 18

Giraud, B. G., B. Grammaticos, and M. Rosina — Time-dependent Hartree-Fock theory and the Rayleigh-Ritz principle. C 21, 391

Giraud, N., C. Fayard, and G. H. Lamot — Relativistic description of πd elastic scattering in the (3,3) resonance region. C 21, 1959

Glashausser, C. — (see Hoffmann, G.W.) C 21, 1488

Gleeson, A. M. and S. Raha — Shock waves in relativistic nuclear matter. I C 21, 1065

Glendenning, Norman K. and Yasha J. Karant — Assessment of the possibility of discovering the asymptotic hadron spectrum through ultrarelativistic nuclear collisions. C 21, 1501

Glöckle, W. — (see Adhikari, Sadhan K.) C 21, 54

Gnade, B. E., R. A. Braga, and R. W. Fink — $L_{2,3}$-subshell x-ray fluorescence and Coster-Kronig yields at $Z=64$ and 67. C 21, 2025

Gobbi, A. — (see Eyal, Y.) C 21, 1377

Gogny, D. — (see Dechargé, J.) C 21, 1568

Goldberg, D. A. — (see Zisman, M.S.) C 21, 2398

Goldflam, R. and K. L. Kowalski — Multiple scattering and few-body Hamiltonian models of nuclear reactions. C 21, 483

Gomez del Campo, J. — (see Ford, J.L.C., Jr.) C 21, 764

Gonthier, P. — (see Namboodiri, M.N.) C 21, 1680(E)

Gorpinich, O. K. — (see Bland, L.C.) C 21, 2227

Gosset, J. — (see Sandoval, A.) C 21, 1321

Goulard, B. — (see Cheng, W.K.) C 21, 374

Gould, C. R. — (see Eyal, Y.) C 21, 1377

Goulding, C. — (see Burleson, G.R.) C 21, 1452

Grafström, P. — (see Jonsson, S.) C 21, 306

Grammaticos, B. — (see Giraud, B.G.) C 21, 391

Greene, S. — (see Burleson, G.R.) C 21, 1452

Greeniaus, L. G. — (see Moss, G.A.) C 21, 1932

Greenwood, R. C. and R. E. Chrien — Neutron mass: Measurement of the ^{1}H(n,γ)^{2}H γ ray and revised values for selected neutron binding energies. C 21, 498

Greiner, Walter — (see Park, Jae Y.) C 21, 958

Griffin, James J., Peter C. Lichtner, and Maria Dworzecka — Time-dependent-S-matrix Hartree-Fock theory of complex reactions. C 21, 1351

——(see Kan, K.-K.) C 21, 1098

Griffin, P. J. — (see Roos, P.G.) C 21, 799

Gronemeyer, S. A., L. Meyer-Schützmeister, A. J. Elwyn, and G. Hardie — Gamma-ray studies in ^{45}V. C 21, 1290

Gross, Franz — (see Arnold, Raymond G.) C 21, 1426

Gugelot, P. C. — (see Jonsson, S.) C 21, 306

——(see Källne, Jan) C 21, 2681

Guidry, M. W. — (see Yates, S.W.) C 21, 2366

Guillot, J., J. Van de Wiele, H. Langevin-Joliot, E. Gerlic, J. P. Didelez, G. Duhamel, G. Perrin, M. Buenerd, and J. Chauvin — Neutron hole states in ^{207,206,205}Pb isotopes via the (^{3}He,α) reaction at 100 MeV. C 21, 879

Günther, C. — (see Kleinrahm, A.) C 21, 1670

Gupta, Raj K. — Binary decay process in the reaction ^{84}Kr$+^{238}$U within the dynamical fragmentation theory. C 21, 1278

Gupta, S. L., Ashok Kumar, S. K. Soni, and S. C. Pancholi — Time-dependent quadrupole interactions in ^{129}I. C 21, 2691

Gupta, V. K. — (see Anand, J.D.) C 21, 2010

Gurvitz, S. A. — (see Cannata, F.) C 21, 2687
Gutay, L. J. — (see Moske, G.L.) C 21, 2211
Gutbrod, H. H. — (see Sandoval, A.) C 21, 1321

Haas, F. — (see Kolata, J.J.) C 21, 579
Hagberg, E. — (see Jonsson, S.) C 21, 306
Haglund, R. F. , Jr. — (see Hardekopf, R.A.) C 21, 906
Hagn, E. — (see Leuthold, K.) C 21, 2581
Hall, A. S. — (see Galloway, R.B.) C 21, 453
Hallgren, A. — (see Jonsson, S.) C 21, 306
Halperin, J., C. H. Johnson, R. R. Winters, and R. L. Macklin — Resonance structure of ^{32}S + n from measurements of neutron total and capture cross sections. C 21, 545
____(see Winters, R.R.) C 21, 563
Hamilton, J. H. — (see Kawakami, H.) C 21, 1311
____(see Robinson, R.L.) C 21, 603
____(see Yates, S.W.) C 21, 2366
Hanashima, Susumu — (see Katori, Kenji) C 21, 1387
Hanson, D. L. — (see Alford, W.P.) C 21, 1203
Haq, S. — (see Gambhir, Y.K.) C 21, 1124
Haque, A. M. I. — (see Bazzacco, D.) C 21, 222
Harakeh, M. N., H. P. Morsch, K. van der Weg, A. van der Woude, and F. E. Bertrand — Isoscalar giant resonances in ^{232}Th. C 21, 768
Hardekopf, R. A., R. F. Haglund, Jr., G. G. Ohlsen, W. J. Thompson, and L. R. Veeser — Polarized triton elastic scattering at 17 MeV. C 21, 906
Hardie, G. — (see Gronemeyer, S.A.) C 21, 1290
Hass, M. — (see Brennan, J.M.) C 21, 574
Hayashibe, Shogo — (see Furusawa, Akira) C 21, 2575
Hecht, K. T. — (see Becchetti, F.D.) C 21, 444
Heikkinen, D. W. — (see Howell, R.H.) C 21, 1153
Heisenberg, J. — (see Lichtenstadt, J.) C 21, 1128(E)
Henderson, D. J. — (see Urbon, J.A.) C 21, 1048
Henning, W. — (see Paul, M.) C 21, 1802
____(see Prosser, F.W., Jr.) C 21, 1819
____(see Sanders, S.J.) C 21, 1810
Hensley, D. C. — (see Ford, J.L.C., Jr.) C 21, 764
Herman, B. J. — (see Fulton, B.R.) C 21, 198
Herman, R. — (see Bellicard, J.B.) C 21, 1652
Hernandez, E. S. and S. A. Moszkowski — Effect of the Pauli principle on ion-ion cross sections in the impulse approximation. C 21, 929
Hershberger, R. L., D. S. Flynn, F. Gabbard, and C. H. Johnson — Systematics of proton absorption deduced from (p,p) and (p,n) cross sections for 2.0- to 6.7-MeV protons on ^{107,109}Ag and ^{115}In. C 21, 896
Heusch, B. — (see Kolata, J.J.) C 21, 579
Heyde, K. — (see Sau, J.) C 21, 405
____(see Sau, J.) C 21, 419
Hichwa, R. D. — (see Yates, S.W.) C 21, 2366
Hicks, R. S., A. Hotta, J. B. Flanz, and H. deVries — Electroexcitation of odd-parity states in ^{27}Al. C 21, 2177
Higashi, Y. — (see Mikumo, T.) C 21, 620
Hill, John C., R. F. Petry, and K. H. Wang — Identification and decay of neutron-rich ^{39}S. C 21, 384
Hilscher, D. — (see Wilcke, W.W.) C 21, 2019
Hindi, M. M. — (see Betts, R.R.) C 21, 175
Hintz, N. M. — (see Hoffmann, G.W.) C 21, 1488
Hirooka, M. — (see Tamae, T.) C 21, 1758
Hoffman, Darleane C., G. P. Ford, J. P. Balagna, and L. R. Veeser — Neutron multiplicity measurements of Cf and Fm isotopes. C 21, 637
____, **J. B. Wilhelmy, J. Weber, W. R. Daniels, E. K. Hulet, R. W. Lougheed, J. H. Landrum, J. F. Wild, and R. J. Dupzyk** — 12.3-min ^{256}Cf and 43-min ^{258}Md and systematics of the spontaneous fission properties of heavy nuclides. C 21, 972
____(see Britt, H.C.) C 21, 761
____(see Hulet, E.K.) C 21, 966
Hoffmann, G. W., L. Ray, M. Barlett, J. McGill, G. S. Adams, G. J. Igo, F. Irom, A. T. M. Wang, C. A. Whitten, Jr., R. L. Boudrie, J. F. Amann, C. Glashausser, N. M. Hintz, G. S. Kyle, and G. S. Blanpied — 0.8 GeV p + ^{208}Pb elastic scattering and the quantity Δr_{np}. C 21, 1488
____(see Adams, G.S.) C 21, 2485
____(see Bauer, T.S.) C 21, 757
Hofstadter, R. — (see Bellicard, J.B.) C 21, 1652
Höistad, B. — (see Källne, Jan) C 21, 2681
Holt, R. J., R. M. Laszewski, H. E. Jackson, J. E. Monahan, and J. R. Specht — Photoneutron studies of $E1$, $M1$, and $E2$ excitations in ^{13}C. C 21, 1699
Horn, D. — (see Kubono, S.) C 21, 459
Hotta, A. — (see Hicks, R.S.) C 21, 2177
Houk, W. A. — (see Pitthan, R.) C 21, 28
Hourani, E. — (see Gerlic, E.) C 21, 124
Howell, R. H., F. S. Dietrich, D. W. Heikkinen, and F. Petrovich — $(p,p'\gamma)$ spin-flip measurement for 1^+ states in ^{12}C at $E_p = 23.5$–27 MeV. C 21, 1153
____, **F. S. Dietrich, and F. Petrovich** — Effect of the tensor force on gamma-ray de-excitation angular distributions from dipole states populated in the ^{12}C(p,p') reaction. C 21, 1158
Hübel, H. — (see Kleinrahm, A.) C 21, 1670
Hubert, F. — (see Gardes, D.) C 21, 2447
Huck, A., G. Klotz, A. Knipper, C. Miehé, G. Walter, and C. Richard-Serre — Levels in ^{45}K and ^{46}K excited by the β decay of ^{45}Ar and ^{46}Ar. C 21, 712
Huffman, R. — (see Williamson, C.) C 21, 1344
Hughes, M. B. — (see Zolnowski, D.R.) C 21, 2556
Huizenga, J. R. — (see Wilcke, W.W.) C 21, 2019
Hulet, E. K., R. W. Lougheed, J. H. Landrum, J. F. Wild, D. C. Hoffman, J. Weber, and J. B. Wilhelmy — Spontaneous fission of ^{259}Fm. C 21, 966
____(see Hoffman, D.C.) C 21, 972
Hummel, Parl C. — (see Laird, C.E.) C 21, 723
Hunt, J. — (see Zolnowski, D.R.) C 21, 2556
Hussein, M. S., L. F. Canto, and R. Donangelo — Static and dynamic deformation effects in the fusion cross section of light heavy ions at sub-barrier energies. C 21, 772
Hutcheon, D. A. — (see Källne, Jan) C 21, 675
____(see Moss, G.A.) C 21, 1932
Hwang, W-Y. P. — Impulse approximation with current conservation. C 21, 1086

Igo, G. J. — (see Adams, G.S.) C 21, 2485
____(see Bauer, T.S.) C 21, 757
____(see Hoffmann, G.W.) C 21, 1488
Ille, B. — (see Jonsson, S.) C 21, 306
Immè, G. — (see Cunsolo, A.) C 21, 952
____(see Cunsolo, A.) C 21, 2345

Ingle, R. W. — (see Difilippo, F.C.) C 21, 1400
Inglima, G. — (see Bonetti, R.) C 21, 816
Irom, F. — (see Hoffmann, G.W.) C 21, 1488

Jackson, H. E. — (see Holt, R.J.) C 21, 1699
Jacobs, E., H. Thierens, D. De Frenne, A. De Clercq, P. D'hondt, P. De Gelder, and A. J. Deruytter — Product yields for the photofission of ^{235}U with 12-, 15-, 20-, 30-, and 70-MeV bremsstrahlung. C 21, 237
____(see De Frenne, D.) C 21, 629
____(see D'hondt, P.) C 21, 963
Jacobs, W. W. — (see Schwandt, P.) C 21, 1656
Jahnel, Lucia C. — (see Saxena, R.N.) C 21, 1531
Jain, H. C. — (see Aggarwal, S.K.) C 21, 2033
Jänecke, J. — (see Becchetti, F.D.) C 21, 444
Jastrzebski, J. — (see Sadler, M.E.) C 21, 2303
Johnsen, S. W. — (see Fitzgerald, D.H.) C 21, 1190
Johnson, C. H. and R. R. Winters — Neutron total cross section of sulfur: Single level to multilevel to optical model. C 21, 2190
____(see Halperin, J.) C 21, 545
____(see Hershberger, R.L.) C 21, 896
Johnson, M. W. — (see Orth, C.J.) C 21, 1967
____(see Wilcke, W.W.) C 21, 2019
Johnson, Mikkel B. — (see Ginocchio, Joseph N.) C 21, 1056
Johnson, N. R. — (see Yates, S.W.) C 21, 2366
Johnston, A. — (see Walker, P.M.) C 21, 464
Jones, E. C., Jr., W. L. Bendel, L. W. Fagg, and R. A. Lindgren — Magnetic electron scattering from deuterium at low-momentum transfer. C 21, 1162
Jonsson, G. G. — (see DeCarlo, V.) C 21, 1460
Jonsson, S., S. Dahlgren, T. Ekelöf, G. Grafström, E. Hagberg, A. Hallgren, S. Kullander, B. Badelek, J. Nassalski, J. Berthot, P. Cotte, C. Doré, L. Meritet, M. Querrou, F. Vazeille, J. P. Burq, M. Chemarin, M. Chevallier, B. Ille, M. Lambert, G. Fäldt, and P. C. Gugelot — Production and knockout of nucleon isobars from helium by 5 GeV pions. C 21, 306
Jourdain, J. -C. — (see Sandoval, A.) C 21, 1321
Jury, J. W., B. L. Berman, D. D. Faul, P. Meyer, and J. G. Woodworth — Photoneutron cross sections for ^{17}O. C 21, 503

Kaczarowski, R. — (see Rakel, D.A.) C 21, 595
Kahler, A. C. — (see Yates, S.W.) C 21, 2366
Kallas, S. — (see Schwandt, P.) C 21, 1656
Kaitchuck, M. D. — (see Schwandt, P.) C 21, 1656
Kakiuchi, S. — (see Mazaki, H.) C 21, 344
Kalifa, J. — (see Rotbard, G.) C 21, 1232
Källne, Jan, A. N. Anderson, J. L. Beveridge, J. Rogers, D. A. Hutcheon, and W. J. McDonald — Some dynamical aspects of pickup reactions studied in ^{13}C$(p,d)^{12}$C at 200–500 MeV. C 21, 675
____, **J. Davis, P. C. Gugelot, J. S. McCarthy, G. R. Smith, R. L. Boudrie, B. Höistad, and C. L. Morris** — (π,p) absorption in ^{6,7}Li at 75 and 175 MeV. C 21, 2681
Kan, K. -K., P. C. Lichtner, M. Dworzecka, and J. J. Griffin — Time-dependent Hartree-Fock dynamics and phase transition in Lipkin-Meshkov-Glick model. C 21, 1098

Kanazawa, Masaaki — (see Furusawa, Akira) C 21, 2575
Kane, W. R. — (see Casten, R.F.) C 21, 65
Kaplan, Morton — (see Catchen, Gary L.) C 21, 940
Kaplanis, S. — (see Stokstad, R.G.) C 21, 2427
Kapoor, S. S. — (see Ramamurthy, V.S.) C 21, 752
Käppeler, F. — (see Beer, H.) C 21, 534
____(see Beer, H.) C 21, 2139(E)
Kapusta, Joseph I. — Mechanisms for deuteron production in relativistic nuclear collisions. C 21, 1301
Karant, Yasha J. — (see Glendenning, Norman K.) C 21, 1501
Karp, B. C. — (see Comfort, J.R.) C 21, 2162
Karwowski, H. — (see Castaneda, C.M.) C 21, 179
Kashy, E. — (see Pardo, R.C.) C 21, 462
Kasiraj, P. — (see Namboodiri, M.N.) C 21, 1680(E)
Katcoff, S. — (see Gilat, J.) C 21, 2041
Katori, Kenji, Kohei Furuno, Takao Ooi, and Susumu Hanashima — Alpha-particle doorway states in ^{28}Si. C 21, 1387
Kaufman, S. B. — (see Urbon, J.A.) C 21, 1048
Kawakami, H., A. P. de Lima, R. M. Ronningen, A. V. Ramayya, J. H. Hamilton, R. L. Robinson, H. J. Kim, and L. K. Peker — High-spin states in ^{65}Ga and possible triaxial structure. C 21, 1311
Keeler, R. — (see Axen, D.) C 21, 998
____(see Clough, A.S.) C 21, 988
Keinonen, J. — (see Anttila, A.) C 21, 1196
Kekelis, G. — (see Becchetti, F.D.) C 21, 444
Kemper, K. W. — (see Cutler, R.I.) C 21, 1799
____(see Parks, L.A.) C 21, 217
Kim, H. J. — (see Kawakami, H.) C 21, 1311
____(see Robinson, R.L.) C 21, 603
King, C. H. — (see Sandoval, A.) C 21, 1321
King, G. — (see Sandoval, A.) C 21, 1321
King, N. S. P., J. D. Reber, J. L. Romero, D. H. Fitzgerald, J. L. Ullmann, T. S. Subramanian, and F. P. Brady — Neutron-proton scattering. I. Differential cross section at 63.1 MeV. C 21, 1185
____(see Peterson, R.J.) C 21, 1030
____(see Winkelmann, E.) C 21, 2535
Klein, Jeffrey — (see Stephens, William) C 21, 1664
Kleinrahm, A., C. Günther, and H. Hübel — g factor of the 14 ms 8^+ isomeric state in ^{88}Y. C 21, 1670
Klewe-Nebenius, H. — (see Gils, H.J.) C 21, 1239
Klotz, G. — (see Huck, A.) C 21, 712
Knight, J. D. — (see Orth, C.J.) C 21, 1967
Knipper, A. — (see Huck, A.) C 21, 712
Ko, Che Ming — Evidence for statistical fluctuation in the fragmentation of ^{16}O at intermediate energies C 21, 2672
Koene, B. K. S. — (see Moss, G.A.) C 21, 1932
Kok, L. P. and H. van Haeringen — Off-shell Coulomb T matrix in connection with the exact solution of three-particle equations with Coulomb interaction. C 21, 512
Kolata, J. J., R. M. Freeman, F. Haas, B. Heusch, and A. Gallmann — Reaction cross sections for ^{12}C + ^{12}C. C 21, 579
____, **R. E. Malmin, P. A. DeYoung, S. Davis, and R. Lahn** — Inclusive α-particle production in the ^{12}C + ^{12}C reaction. C 21, 776
Koshel, R. D. — (see Roos, P.G.) C 21, 799
Kota, V. K. B. and V. Potbhare — Shape of eigenvalue distribution for bosons in scalar space. C 21, 2637

Kovar, D. G. — (see Paul, M.) C 21, 1802
——(see Prosser, F.W., Jr.) C 21, 1819
——(see Sanders, S.J.) C 21, 1810
Kowalick, S. J. — (see Pitthan, R.) C 21, 147
Kowalski, K. L. — Truncated pion-nucleon amplitudes and pion-nucleus interactions. C 21, 2122
——(see Goldflam, R.) C 21, 483
Kozlowski, T. — (see Chrien, R.E.) C 21, 1014
Kozub, R. — (see Sanders, S.J.) C 21, 1810
Kraus, L. — (see Linck, I.) C 21, 791
Krause, T. O. — (see Bagchi, B.) C 21, 1
Kraushaar, J. J. — (see Bauer, T.S.) C 21, 757
——(see Peterson, R.J.) C 21, 1030
Kreiner, A. J., A. Filevich, G. García Bermúdez, M. A. J. Mariscotti, C. Baktash, E. der Mateosian, and P. Thieberger — High-spin band structure of ^{192}Tl. C 21, 933
Krewald, S. and J. W. Negele — Creation and observation of a pion condensate in high-energy heavy-ion collisions C 21, 2385
Kreyling, G. — (see Eyal, Y.) C 21, 1377
Krieger, T. J. — (see Chrien, R.E.) C 21, 1014
Ku, T. H. — (see Alburger, D E.) C 21, 705
Kubono, S., P. D. Bond, D. Horn, and T. R. Renner — Energy dependence of ^{40}Ca + ^{12}C elastic scattering at 90° and 180°. C 21, 459
——(see Tserruya, I.) C 21, 1864
Kuehner, J. A. — (see Shahabuddin, M.A.M.) C 21, 1116
Kullander, S. — (see Jonsson, S.) C 21, 306
Kumar, Ashok — (see Gupta, S.L.) C 21, 2691
Kurath, D. — (see Lee, T.-S.H.) C 21, 293
Kusahara, M. — Photoreaction mechanism of ^{6}Li. C 21, 1165
Kwan, S. P. — (see Datta, S K.) C 21, 1687
Kyle, G. S. — (see Hoffmann, G W.) C 21, 1488

Lacombe, M., B. Loiseau, J. M. Richard, R. Vinh Mau, J. Côté, P. Pirès, and R. de Tourreil — Parametrization of the Paris *N-N* potential C 21, 861
Lagu, A. V. — (see Maheshwari, C.) C 21, 1120
Laird, C. E., Parl C. Hummel, and Hsing-Chung Liu — *K*-shell autoionization accompanying the beta decays of ^{99}Tc, ^{147}Pm, ^{151}Sm, and ^{204}Tl. C 21, 723
Lakshminarayana, S. — (see Srinivasa Rao, M.) C 21, 728
Lam, C. S. — (see Forest, E.) C 21, 1989
Lambert, M. — (see Jonsson, S.) C 21, 306
Lamot, G. H. — (see Giraud, N.) C 21, 1959
Landrum, J. H. — (see Hoffman, D C.) C 21, 972
——(see Hulet, E.K) C 21, 966
Landsberger, S., R. Lecomte, P. Paradis, and S. Monaro — Quadrupole moments of the first excited states of ^{96}Ru, ^{98}Ru, ^{100}Ru, ^{102}Ru, and ^{104}Ru. C 21, 588
Langevin-Joliot, H. — (see Gerlic, E.) C 21, 124
——(see Guillot, J) C 21, 879
Lanier, R. G. — (see Mann, L.G.) C 21, 2547
Larimer, R. M. — (see Stephenson, E.J.) C 21, 44
Larry, Thomas L. and William P. Beres — Projection operator method for heavy ion reactions and application to ^{12}C + ^{12}C. C 21, 2126
—— **and William P. Beres** — Projection operator method for finding energies and widths of shape resonances in heavy-ion collisions. C 21, 2675
Laszewski, R. M. — (see Holt, R.J.) C 21, 1699
Lattuada, M. — (see Barbarino, S.) C 21, 1104
Laurent, H. — (see Galès, S.) C 21, 98
Law, J. — (see Deloff, A.) C 21, 2048
Lawson, R. D. — (see Lee, T.-S. H.) C 21, 679
Lazzarini, A. J. — (see Cosman, E.R.) C 21, 2111
Lecomte, R. — (see Landsberger, S.) C 21, 588
Ledoux, R. — (see Cosman, E.R.) C 21, 2111
Lee, I. Y. — (see Yates, S.W.) C 21, 2366
Lee, M. A. and W. L. Talbert, Jr. — Decays of mass-separated ^{139}Xe and ^{139}Cs. C 21, 328
Lee, T. -S. H. and D. Kurath — Inelastic pion scattering for 1*p* -shell targets. C 21, 293
—— **and R. D. Lawson** — Inelastic pion scattering from ^{18}O. C 21, 679
——(see Olmer, C.) C 21, 254
Leemann, B. T. — (see Stephenson, E.J.) C 21, 44
——(see Roos, P.G.) C 21, 799
Leigh, J. R. — (see Eck, J.S.) C 21, 2352
Lejeune, A. — Low-energy optical model potential in finite nuclei from Reid's hard core interaction. C 21, 1107
LeMere, M. and Y. C. Tang — Resonating-group study and odd-even features in the ^{3}He + ^{6}Li system. C 21, 1170
Lenz, F. — (see Amado, R.D.) C 21, 647
Lesser, P. M. S. — (see Liou, M.K.) C 21, 518
——(see Trail, C.C) C 21, 2131
Leuthold, K., E. Hagn, H. Ernst, and E. Zech — Ground-state nuclear *g* factor of ^{97}Ru. C 21, 2581
Levin, F. S. — Wave-function formalisms in the channel coupling array theory of many-body scattering. C 21, 2199
LeVine, M. J. — (see Paul, M.) C 21, 1802
Levit, S. — Time-dependent mean-field approximation for nuclear dynamical problems. C 21, 1594
——**, J. W. Negele, and Z. Paltiel** — Time-dependent mean-field theory and quantized bound states. C 21, 1603
Lichtenstadt, J., J. Heisenberg, C. N. Papanicolas, C. P. Sargent, A. N. Courtemanche, and J. S. McCarthy — High-spin states of $J^{\pi} = 12^{-}$, 14^{-} in ^{208}Pb studied by (e,e') [C 20, 497 (1979)]. C 21, 1128(E)
Lichtner, Peter C. — (see Griffin, James J.) C 21, 1351
——(see Kan, K.-K.) C 21, 1098
Liljestrand, R. L. — (see Moss, G.A.) C 21, 1932
Linck, I., L. Kraus, and S. L. Blatt — Radiative capture of tritons by ^{14}N and ^{17}O levels above 19 MeV. C 21, 791
Lindgren, K. — (see DeCarlo, V.) C 21, 1460
Lindgren, R. A. — (see Jones, E.C., Jr.) C 21, 1162
Lindholm, A. — (see Nilsson, L.) C 21, 902
Liou, M. K., C. K. Liu, P. M. S. Lesser, and C. C. Trail — Proton-carbon bremsstrahlung calculation. C 21, 518
——(see Trail, C.C.) C 21, 2131
Liu, C. K. — (see Liou, M.K.) C 21, 518
——(see Trail, C.C.) C 21, 2131
Liu, Hsing-Chung — (see Laird, C.E.) C 21, 723
Liu, L. C. — (see Bhalerao, R.S.) C 21, 1903
——(see Bhalerao, R.S.) C 21, 2103
Llabador, Y. — (see Gardes, D.) C 21, 2447
Lo Bianco, G. — (see Mandò, P.A.) C 21, 2135
Logan, B. A. — (see Pisk, K.) C 21, 1525

Loiseau, B. — (see Lacombe, M.) C 21, 861
Lokan, K. H. — (see Sherman, N.K.) C 21, 2328
Lorazo, B. — (see Cheng, W.K.) C 21, 374
Lorini, M. — (see Bini, M.) C 21, 116
Lougheed, R. W. — (see Britt, H.C.) C 21, 761
____(see Hoffman, D.C.) C 21, 972
____(see Hulet, E.K.) C 21, 966
Love, W. G. — (see Comfort, J.R.) C 21, 2147
____(see Petrovich, F.) C 21, 1718
Loveland, W. — (see Morrissey, D.J.) C 21, 1783
Ludgate, G. A. — (see Axen, D.) C 21, 998
____(see Bugg, D.V.) C 21, 1004
____(see Clough, A.S.) C 21, 988
Luhn, R. — (see Kolata, J.J.) C 21, 776
Lui, Y.-W. — (see Rozsa, C.M.) C 21, 1252
Lukner, Ch. — (see Sandoval, A.) C 21, 1321
Lynen, U. — (see Eyal, Y.) C 21, 1377

MacDonald, William M. — Reply to "Comment on 'Statistical significance of spreading widths for doorway states'
Macfarlane, M. H. — (see Rhoades-Brown, M.) C 21, 2417
____(see Rhoades-Brown, M.) C 21, 2436
Machner, H. — Composite particle emission from ^{65}Zn*. C 21, 2695
Macklin, R. L. — (see Halperin, J.) C 21, 545
____(see Winters, R.R.) C 21, 563
Macphail, M. R. — (see Casten, R.F.) C 21, 65
Madey, R. — (see Cecil, R.A.) C 21, 2471
Mahaux, C. — (see Sartor, R.) C 21, 1546
____(see Sartor, R.) C 21, 2613
Maheshwari, C., P. C. Sood, and A. V. Lagu — Parametrization of half-shell functions in triplet *S* channel. C 21, 1120
Maison, J. M. — (see Galès, S.) C 21, 98
____(see Gardes, D.) C 21, 2447
Majka, Z. — (see Gils, H.J.) C 21, 1245
Malaguti, F. — (see Fuschini, E.) C 21, 1646
Malmin, R. E. — (see Kolata, J.J.) C 21, 776
Mando, P. A., G. Poggi, G. Lo Bianco, and N. Molho — Levels in ^{44}K via the ^{48}Ca($p, \alpha n$) reaction. C 21, 2135
Mann, L. G., J. B. Carlson, R. G. Lanier, G. L. Struble, W. M. Buckley, R. K. Sheline, and Z. Singh — Decay of ^{180}Re: Search for octupole states in ^{180}W. C 21, 2547
Manohar, S. B. — (see Datta, Tarun) C 21, 1411
Mariscotti, M. A. J. — (see Kreiner, A.J.) C 21, 933
Markham, R. — (see Williamson, C.) C 21, 1344
Matsui, M. — (see Mazaki, H.) C 21, 344
May, M. — (see Chrien, R.E.) C 21, 1014
Maynard, M. J. — (see Saha, S.K.) C 21, 2322
Mazaki, H., S. Kakiuchi, T. Mukoyama, and M. Matsui — Effect of chemical state on the decay constant of ^{99}Tc^{m}. C 21, 344
McCarthy, J. S. — (see Bellicard, J.B.) C 21, 1652
____(see Burleson, G.R.) C 21, 1452
____(see Källne, Jan) C 21, 2681
____(see Lichtenstadt, J.) C 21, 1128(E)
McCarthy, R. J. — (see Petrovich, F.) C 21, 1718
____(see Vary, J.P.) C 21, 1626
McDonald, A. B. — (see Saha, S.K.) C 21, 2322
McDonald, W. J. — (see Källne, Jan) C 21, 675
McGill, J. — (see Hoffmann, G.W.) C 21, 1488
McMahan, M. A. and John M. Alexander — Barrier to complete fusion for ^{4}He and ^{1}H and that for evaporation from ^{194}Hg. C 21, 1261
McNaughton, M. W. — (see Winkelmann, E.) C 21, 2535
Medsker, L. R. — (see Clements, J.S.) C 21, 1285
Mehta, G. K. — (see Sinha, A.K.) C 21, 2467
Melnik, D. — (see Shu, N.K.B.) C 21, 1828
Mennenga, G. — (see Spanhoff, R.) C 21, 361
Mercer, R. L. — (see Arnold, L.G.) C 21, 1899
Meritet, L. — (see Jonsson, S.) C 21, 306
Mermaz, M. C. — Direct transfer reaction to discrete and continuum states. C 21, 2356
Meyer, P. — (see Caldwell, J.T.) C 21, 1215
____(see Jury, J.W.) C 21, 503
Meyer, R. A., J. E. Fontanilla, C. F. Smith, N. L. Smith, R. C. Ragaini, and V. Paar — Level properties of $^{85}_{37}$Rb$_{48}$ from the decay of the ^{85}Kr and ^{85}Sr isomers and the cluster-vibration model. C 21, 2590
Meyer, W. G. — (see Sandoval, A.) C 21, 1321
Meyer-Schützmeister, L. — (see Gronemeyer, S.A.) C 21, 1290
Micheletti, S. — (see Fabrici, E.) C 21, 830
____(see Fabrici, E.) C 21, 844
Miché, C. — (see Huck, A.) C 21, 712
Mihelich, J. W. — (see Rakel, D.A.) C 21, 595
Mikumo, T., M. Sasagase, M. Sato, T. Ooi, Y. Higashi, Y. Nagashima, and M. Yamanouchi — *Q*-value dependence of inelastic scattering and multinucleon transfer reactions ^{27}Al + ^{16}O at 88 MeV Optimum *Q* values and *Q*-value dependence of angular distributions of reaction products. C 21, 620
Miller, C. A. — (see Moss, G.A.) C 21, 1932
Miller, Gerald A. and J. V. Noble — Low-energy absorption of pions on nuclei and the real $\rho^2(r)$ potential. C 21, 2519
____(see Ernst, D.J.) C 21, 1472
Miller, P. — (see Cecil, R.A.) C 21, 2471
Milner, W. T. — (see Robinson, R.L.) C 21, 603
Minehart, R. C. — (see Burleson, G.R.) C 21, 1452
Miska, H. B. — (see Dressler, E.T.) C 21, 2119
Moake, G. L. and P. T. Debevec — Determination of the optical potential for elastic proton scattering on ^{6}Li, ^{12}C, and ^{14}N at 144 MeV. C 21, 25
____, **L. J. Gutay, R. P. Scharenberg, P. T. Debevec, and P. A. Quin** — Proton-nucleus charge exchange measurements at 144 MeV as a test of one-pion exchange and the partially conserved axial vector current C 21, 2211
____(see Comfort, J.R.) C 21, 2147
Molho, N. — (see Mandò, P.A.) C 21, 2135
Monahan, J. E. — (see Holt, R.J.) C 21, 1699
Monaro, S. — (see Landsberger, S.) C 21, 588
Moore, C. F. — (see Burleson, G.R.) C 21, 1452
____(see Peterson, R.J.) C 21, 1030
Moore, R. W. — (see Pitthan, R.) C 21, 28
Moretto, Luciano G. and Richard P. Schmitt — Equilibrium statistical treatment of angular momenta associated with collective modes in fission and heavy-ion reactions. C 21, 204
Morris, C. L. — (see Burleson, G.R.) C 21, 1452
____(see Källne, Jan) C 21, 2681
____(see Olmer, C.) C 21, 254

——(see Peterson, R.J.) C 21, 1030

Morrissey, D. J., W. Loveland, M. de Saint Simon, and G. T. Seaborg — Target residues from the reaction of 8 GeV ^{20}Ne with ^{181}Ta and ^{197}Au. C 21, 1783

Morsch, H. P. — (see *Harakeh, M.N.*) *C 21, 768*

Mortensen, M. H., R. R. Betts, and C. K. Bockelman — W(*p,t*) reactions. I. Even targets. C 21, 2275

——, **R. R. Betts, and C. K. Bockelman** — W(*p,t*) reactions. II. Odd target. C 21, 2288

Mosconi, B. — (see Cambi, A.) C 21, 1921

Moss, G. A., L. G. Greeniaus, J. M. Cameron, D. A. Hutcheon, R. L. Liljestrand, C. A. Miller, G. Roy, B. K. S. Koene, W. T. H. van Oers, A. W. Stetz, A. Willis, and N. Willis — Proton-^{4}He elastic scattering at intermediate energies. C 21, 1932

Moszkowski, S. A. — (see Hernandez, E.S.) C 21, 929

Mughabghab, S. F. — (see Casten, R.F.) C 21, 65

Mukoyama, Takeshi — (see Mazaki, H.) C 21, 344

——(see Watanabe, Yoshihisa) C 21, 1753

Mulligan, B. — (see Bagchi, B.) C 21, 1

Murphy, J. J., II — (see Asai, J.) C 21, 469

——(see Skopik, D.M.) C 21, 1746

Nadasen, A. — (see Roos, P.G.) C 21, 799

——(see Wang, C.W.) C 21, 1705

Nagarajan, M. A. — (see Werby, M.F.) C 21, 2235

Nagashima, Y. — (see Mikumo, T.) C 21, 620

Nair, A. G. C. — (see Datta, Tarun) C 21, 1411

Nair, S. C. K. — (see Ansari, A.) C 21, 1674

Namboodiri, M. N., J. B. Natowitz, P. Kasiraj, R. Eggers, L. Adler, P. Gonthier, C. Cerruti, and S. Simon — Angular momentum transfer in the deep inelastic reactions of 237 MeV ^{40}Ar with ^{89}Y [C 20, 982 (1979)]. C 21, 1680(E)

Nassalski, J. — (see Jonsson, S.) C 21, 306

Natowitz, J. B. — (see Namboodiri, M.N.) C 21, 1680(E)

Nazarewicz, W. — (see Ćwiok, S.) C 21, 448

Negele, J. W. — (see Krewald, S.) C 21, 2385

——(see Levit, S.) C 21, 1603

Neumann, B. — (see Gils, H.J.) C 21, 1239

Nieukerke, K. J. — (see Dodd, L.R.) C 21, 1724

Nigam, B. P. — (see Payne, Gerald L.) C 21, 1177

Nilsson, L., M. Drosg, D. M. Drake, and A. Lindholm — Isospin structure of the giant dipole resonance in ^{41}Ca. C 21, 902

Nix, J. Rayford and Arnold J. Sierk — Macroscopic description of isoscalar giant multipole resonances. C 21, 396

——(see Sierk, Arnold J.) C 21, 982

Noble, J. V. — (see Miller, Gerald A.) C 21, 2519

Norman, Eric B. — Half-life of ^{176}Lu. C 21, 1109

Nuytten, C. — (see Geerts, R.) C 21, 439

O'Brien, J. T. — (see Sober, D.I.) C 21, 1495

Ohlsen, G. G. — (see Hardekopf, R.A.) C 21, 906

Olmer, C., D. F. Geesaman, B. Zeidman, S. Chakravarti, T.-S. H. Lee, R. L. Boudrie, R. H. Siemssen, J. F. Amann, C. L. Morris, H. A. Thiessen, G. R. Burleson, M. J. Devereux, R. E. Segel, and L. W. Swenson — Elastic and inelastic scattering of 162 MeV pions by ^{28}Si, ^{58}Ni, and ^{208}Pb. C 21, 254

——(see Paul, M.) C 21, 1802

——(see Sanders, S.J.) C 21, 1810

Olsen, D. K. — (see Difilippo, F.C.) C 21, 1400

Oei, Takao — (see Katori, Kenji) C 21, 1387

——(see *Mikumo, T.*) *C 21, 620*

Ophel, T. R. — (see Eck, J.S.) C 21, 2352

Oram, C. J. — (see Axen, D.) C 21, 998

——(see Bugg, D.V.) C 21, 1004

——(see Clough, A.S.) C 21, 988

Orth, C. J., J. D. Knight, K. Wolfsberg, and M. W. Johnson — Nuclear disintegration of some complex nuclei by 60-MeV muons. C 21, 1967

——, **W. R. Daniels, B. J. Dropesky, R. A. Williams, G. C. Giesler, and J. N. Ginocchio** — Products of stopped-pion interactions with Cu and Ta. C 21, 2524

Overway, D. — (see Becchetti, F.D.) C 21, 444

Paar, V. — (see Meyer, R.A.) C 21, 2590

Pace, E. — (see Ciofi degli Atti, C.) C 21, 805

Páez, J. — (see de Téramond, G.F.) C 21, 2542

Palevsky, H. — (see Chrien, R.E.) C 21, 1014

Paltiel, Z. — (see Levit, S.) C 21, 1603

Pancholi, S. C. — (see Gupta, S.L.) C 21, 2691

Panda, K. C. — (see Behera, B.) C 21, 1883

Pantaleo, A. — (see Fabrici, E.) C 21, 830

——(see Fabrici, E.) C 21, 844

Papanicolas, C. N. — (see Lichtenstadt, J.) C 21, 1128(E)

Pappalardo, G. — (see Cunsolo, A.) C 21, 952

——(see Cunsolo, A.) C 21, 2345

Paradis, P. — (see Landsberger, S.) C 21, 588

Pardo, R. C., L. W. Robinson, W. Benenson, E. Kashy, and R. M. Ronningen — Mass and excited states of the nucleus ^{89}Mo. C 21, 462

Park, Jae Y., Walter Greiner, and Werner Scheid — Signatures of molecular single-particle states by level crossings in heavy ion collisions. C 21, 958

Parker, P. D. — (see Betts, R.R.) C 21, 175

Parks, L. A., D. P. Stanley, L. H. Courtney, and K. W. Kemper — Quadrupole contributions to ^{10,11}B + ^{16}O elastic scattering. C 21, 217

Parthasarathy, R. — (see Gambhir, Y.K.) C 21, 1637

Pašagić, V. — (see Pisk, K.) C 21, 1525

Paul, M., S. J. Sanders, D. F. Geesaman, W. Henning, D. G. Kovar, C. Olmer, J. P. Schiffer, J. Barrette, and M. J. LeVine — ^{24}Mg(^{16}O,^{12}C)^{28}Si and ^{24}Mg(^{16}O,^{16}O)^{24}Mg reactions at backward angles. C 21, 1802

——(see Sanders, S.J.) C 21, 1810

Pauletta, G. — (see Adams, G.S.) C 21, 2485

——(see Bauer, T.S.) C 21, 757

Payne, Gerald L. and B. P. Nigam — Elastic and inelastic charge form factors for $^9_3$Li from electron scattering. C 21, 1177

Peker, L. K. — (see Gilat, J.) C 21, 2041

——(see Kawakami, H.) C 21, 1311

Pelte, D. — (see Stokstad, R.G.) C 21, 2427

Perez, R. B. — (see Difilippo, F.C.) C 21, 1400

Perillo, E. — (see Bonetti, R.) C 21, 816

Perrin, G. — (see Guillot, J.) C 21, 879

Perry, D. G. — (see Wilcke, W.W.) C 21, 2019

Pesl, R. — (see Gils, H.J.) C 21, 1239

Peterson, R. J., R. L. Boudrie, J. J. Kraushaar, R. A.

Ristinen, J. R. Shepard, G. R. Smith, C. F. Moore, W. J. Braithwaite, N. S. P. King, C. L. Morris, H. A. Thiessen, and J. Piffaretti — Spin and isospin transfer in the ^{12}C(π^+, $\pi^{+\prime}$) reaction. C 21, 1030
____(see Bauer, T.S.) C 21, 757
Petrovich, F., W. G. Love, and R. J. McCarthy — Separation of current and spin contributions to isovector $M1$ excitations by means of the (e,e') and (p,n) reactions. C 21, 1718
____(see Howell, R.H.) C 21, 1153
____(see Howell, R.H.) C 21, 1158
Petry, R. F. — (see Hill, John C.) C 21, 384
Pettersson, R. — (see DeCarlo, V.) C 21, 1460
Pieper, Steven C. — (see Rhoades-Brown, M.) C 21, 2417
____(see Rhoades-Brown, M.) C 21, 2436
Piercey, R. B. — (see Robinson, R.L.) C 21, 603
Piffaretti, J. — (see Peterson, R.J.) C 21, 1030
Pignanelli, M. — (see Fabrici, E.) C 21, 830
____(see Fabrici, E.) C 21, 844
Pilt, A. A. — (see Shahabuddin, M.A.M.) C 21, 1116
Pirès, P. — (see Lacombe, M.) C 21, 861
Pisk, K., V. Paśagić, and B. A. Logan — Internal bremsstrahlung in s-electron capture. C 21, 1525
Pitthan, R., F. R. Buskirk, W. A. Houk, and R. W. Moore — Giant multipole resonances in the deformed fissionable nucleus ^{238}U. C 21, 28
____, **G. M. Bates, J. S. Beachy, E. B. Dally, D. H. Dubois, J. N. Dyer, S. J. Kowalick, and F. R. Buskirk** — Comparison of giant multipole resonances of multipolarity $E1$ to $E4$ in ^{58}Ni ($T_0 = 1$) and ^{60}Ni ($T_0 = 2$) with inelastic electron scattering. C 21, 147
Plougher, W. — (see Schwandt, P.) C 21, 1656
Poggi, G. — (see Mandò, P.A.) C 21, 2135
Poletti, J. L. — (see Chisholm, A.) C 21, 1653
Porile, N. T. — (see Fortney, D.R.) C 21, 664
____(see Fortney, D.R.) C 21, 2511
Perrino, A. — (see Andreozzi, F.) C 21, 1094
Poskanzer, A. M. — (see Sandoval, A.) C 21, 1321
Postma, H. — (see Spanhoff, R.) C 21, 361
Potbhare, V. — (see Kota, V.K.B.) C 21, 2637
Prakash, M. — (see Ramamurthy, V.S.) C 21, 752
Prakash, Satya — (see Datta, Tarun) C 21, 1411
Price, D. — (see Udagawa, T.) C 21, 1891
Prieels, R. — (see Argan, P.) C 21, 662
____(see Argan, P.) C 21, 1416
Priyadarsini, D. K. — (see Srinivasa Rao, M.) C 21, 728
Prosser, F. W., Jr., R. A. Racca, K. Daneshvar, D. F. Geesaman, W. Henning, D. G. Kovar, K. E. Rehm, and S. L. Tabor — Complete fusion of ^{15}N + ^{27}Al. C 21, 1819
Protop, C. — (see Bazzacco, D.) C 21, 222

Quentin, P. — (see Giannoni, M.J.) C 21, 2060
____(see Giannoni, M.J.) C 21, 2076
Querrou, M. — (see Jonsson, S.) C 21, 306
Quin, P. A. — (see Moake, G.L.) C 21, 2211

Racca, R. A. — (see Prosser, F.W., Jr.) C 21, 1819
Raciti, G. — (see Cunsolo, A.) C 21, 952
____(see Cunsolo, A.) C 21, 2345
Ragaini, R. C. — (see Meyer, R.A.) C 21, 2590
Raha, S. — (see Gleeson, A.M.) C 21, 1065
Rakel, D. A., R. Kaczarowski, E. G. Funk, and J. W. Mihelich — High spin states in the $N = 82$ nucleus ^{145}Eu. C 21, 595
Ramamurthy, V. S., M. Prakash, and S. S. Kapoor — Magnitude of energy dissipation in fission. C 21, 752
Ramaniah, M. V. — (see Datta, Tarun) C 21, 1411
Ramayya, A. V. — (see Kawakami, H.) C 21, 1311
____(see Robinson, R.L.) C 21, 603
Ray, L. — (see Hoffmann, G.W.) C 21, 1488
Rebel, H. — (see Gils, H.J.) C 21, 1239
____(see Gils, H.J.) C 21, 1245
Reber, J. D. — (see King, N.S.P.) C 21, 1185
Regner, J. L. — (see Dries, L.J.) C 21, 475
Rehm, K. E. — (see Prosser, F.W., Jr.) C 21, 1819
Renfordt, R. — (see Eyal, Y.) C 21, 1377
Renner, T. R. — (see Kubono, S.) C 21, 459
Resmini, F. G. — (see Fabrici, E.) C 21, 830
____(see Fabrici, E.) C 21, 844
Rhoades-Brown, M., M. H. Macfarlane, and Steven C. Pieper — Techniques for heavy-ion coupled-channels calculations. I. Long-range Coulomb coupling. C 21, 2417
____, **M. H. Macfarlane, and Steven C. Pieper** — Techniques for heavy-ion coupled-channels calculations. II. Iterative solution of the coupled radial equations. C 21, 2436
Rhodes, W. — (see DeCarlo, V.) C 21, 1460
Ricci, P. — (see Cambi, A.) C 21, 1921
Richard, J. M. — (see Dover, Carl B.) C 21, 1466
____(see Lacombe, M.) C 21, 861
Richards, P. — (see Alburger, D.E.) C 21, 705
Richard-Serre, C. — (see Huck, A.) C 21, 712
Richardson, J. R. — (see Bugg, D V.) C 21, 1004
____(see Clough, A.S.) C 21, 988
Riedinger, L. L. — (see Yates, S.W.) C 21, 2366
Riggi, F. — (see Barbarino, S.) C 21, 1104
Rinat, A. S. and Y. Starkand — Some convergence tests on medium-energy pion-deuteron elastic scattering amplitudes. C 21, 324
Ristinen, R. A. — (see Peterson, R.J.) C 21, 1030
Rivet, M. F. — (see Catchen, Gary L.) C 21, 940
____(see Gardes, D.) C 21, 2447
Rizzo, F. — (see Cunsolo, A.) C 21, 952
Roberson, N. R. — (see Turner, J D.) C 21, 525
Robertson, B. C. — (see Saha, S.K.) C 21, 2322
Robertson, L. P. — (see Axen, D.) C 21, 998
____(see Bugg, D.V.) C 21, 1004
____(see Clough, A.S.) C 21, 988
Robinson, E. L. — (see Yates, S.W.) C 21, 2366
Robinson, L. W. — (see Pardo, R.C.) C 21, 462
Robinson, R. L., H. J. Kim, R. O. Sayer, W. T. Milner, R. B. Piercey, J. H. Hamilton, A. V. Ramayya, J. C. Wells, Jr., and A. J. Caffrey — High-spin levels and band structure in ^{78}Kr. C 21, 603
____(see Kawakami, H.) C 21, 1311
Rockmore, R. M. — P-wave dispersive contribution to low-energy elastic $\pi^{+}{}^{2}$H scattering. C 21, 2678
Rode, I. — (see Eyal, Y.) C 21, 1377
Rogers, J. — (see Källne, Jan) C 21, 675
Romero, J. L. — (see Fitzgerald, D.H.) C 21, 1190
____(see Garrett, R.) C 21, 1149
____(see King, N.S.P.) C 21, 1185

Ronningen, R. M. — (see Kawakami, H.) C 21, 1311
——(see Pardo, R.C.) C 21, 462
——(see Yates, S.W.) C 21, 2366
Roos, P. G., A. Nadasen, P. E. Frisbee, N. S. Chant, T. A. Carey, M. T. Collins, B. T. Leemann, P. J. Griffin, and R. D. Koshel — ^{3}He+^{4}He elastic scattering at $E_{\mathrm{c.m.}}=60.2$ and 113.1 MeV. C 21, 799
——(see Wang, C.W.) C 21, 1705
Rösel, F. — (see Baur, G.) C 21, 2668
Rosina, M. — (see Giraud, B.G.) C 21, 391
Ross, C. K. — (see Sherman, N.K.) C 21, 2328
Rotbard, G., G. Berrier-Ronsin, M. Vergnes, J. Kalifa, J. Vernotte, and R. K. Sheline — States in ^{193}Pt using the (p,t) reaction. C 21, 1232
——, **M. Vergnes, G. Berrier-Ronsin, and J. Vernotte** — Neutron rich ^{73}Ga and ^{79}As isotopes via the (α,p) reaction. C 21, 2293
Roy, A. — (see Cutler, R.I.) C 21, 1799
Roy, G. — (see Moss, G.A.) C 21, 1932
Roy, R. — (see Stephenson, E.J.) C 21, 44
Rozsa, C. M., D. H. Youngblood, J. D. Bronson, Y.-W. Lui, and U. Garg — Isoscalar breathing mode state in ^{90}Zr and ^{116}Sn. C 21, 1252
Rüskamp, K. — (see Feigel, A.) C 21, 2666
Russo, G. — (see Di Toro, M.) C 21, 2054
Rutledge, L. L., Jr. — (see Sadler, M.E.) C 21, 2303

Sadler, M. E., P. P. Singh, J. Jastrzebski, L. L. Rutledge, Jr., and R. E. Segel — Interaction of 80–164 MeV protons with nickel isotopes. C 21, 2303
Saha, S. K., M. J. Maynard, B. C. Robertson, A. B. McDonald, and E. D. Earle — Gamma-ray lifetimes for parity doublets in ^{41}K, ^{41}Ca. C 21, 2322
Saharia, A. N. and R. M. Woloshyn — Application of the isobar-doorway model to pion charge exchange reactions. C 21, 1111
Salmè, G. — (see Ciofi degli Atti, C.) C 21, 805
Saloman, M. K. — (see DiRienzo, A.C.) C 21, 2101
Sanders, S. J., M. Paul, J. Cseh, D. F. Geesaman, W. Henning, D. G. Kovar, R. Kozub, C. Olmer, and J. P. Schiffer — Resonant behavior of the ^{24}Mg(^{16}O,^{12}C)^{28}Si reaction. C 21, 1810
——(see Paul, M.) C 21, 1802
Sandhas, W. — (see Alt, E.O.) C 21, 1733
Sandoli, M. — (see Bonetti, R.) C 21, 816
Sandoval, A., H. H. Gutbrod, W. G. Meyer, R. Stock, Ch. Lukner, A. M. Poskanzer, J. Gosset, J.-C. Jourdain, C. H. King, G. King, Nguyen Van Sen, G. D. Westfall, and K. L. Wolf — Spectra of p,d, and t from relativistic nuclear collisions. C 21, 1321
Saperstein, Alvin M. — (see Friedman, William A.) C 21, 2098
Sargent, C. P. — (see Lichtenstadt, J.) C 21, 1128(E)
Sartor, R. and C. Mahaux — Self-energy, momentum distribution, and effective masses of a dilute Fermi gas. C 21, 1546
—— **and C. Mahaux** — Single-particle states in nuclear matter and in finite nuclei. C 21, 2613
——(see Cugnon, J.) C 21, 2342
Sasagase, M. — (see Mikumo, T.) C 21, 620
Sastry, D. L. — (see Srinivasa Rao, M.) C 21, 728
Sato, M. — (see Mikumo, T.) C 21, 620
Satpathy, R. K. — (see Behera, B.) C 21, 1883
Sau, J., K. Heyde, and R. Chéry — Shell-model description of the nucleus ^{132}Te. C 21, 405
—— **and K. Heyde** — Method for calculating matrix elements for shell-model calculations. C 21, 419
Saunier, N. — (see Cunsolo, A.) C 21, 952
——(see Cunsolo, A.) C 21, 2345
Saxena, R. N., Lucia C. Jahnel, and F. C. Zawislak — Gamma-gamma directional correlations for transitions in ^{84}Kr. C 21, 1531
Sayer, R. O. — (see Robinson, R.L.) C 21, 603
Schapira, J. P. — (see Galès, S.) C 21, 98
Scharenberg, R. P. — (see Moake, G.L.) C 21, 2211
Scheid, Werner — (see Park, Jae Y.) C 21, 958
Schier, W. — (see DiRienzo, A.C.) C 21, 2101
Schiffer, J. P. — (see Paul, M.) C 21, 1802
——(see Sanders, S.J.) C 21, 1810
Schmid, E. W. — N-cluster dynamics and effective interaction of composite particles. I. The dynamical equation. C 21, 691
Schmitt, Richard P. — (see Moretto, Luciano G.) C 21, 204
Schoeters, E. — (see Geerts, R.) C 21, 439
Schrack, R. A. — (see Bowman, C.D.) C 21, 58
Schreckenbach, K. — (see Casten, R.F.) C 21, 65
Schröder, W. U. — (see Wilcke, W.W.) C 21, 2019
Schuhl, C. — (see Argan, P.) C 21, 662
——(see Argan, P.) C 21, 1416
Schultheis, H. and R. Schultheis — Reply to "Magnitude of energy dissipation in fission". C 21, 755
Schultheis, R. — (see Schultheis, H.) C 21, 755
Schupp, G. and M. S. Freedman — K-shell ionization in the electron and positron decays of ^{64}Cu. C 21, 348
Schwandt, P., S. Kailas, W. W. Jacobs, M. D. Kaitchuck, W. Ploughe, and P. P. Singh — Optical potential for ^{6}Li+^{28}Si elastic scattering at 154 MeV. C 21, 1656
Scobel, W. — (see Sikora, B.) C 21, 614
Seaborg, G. T. — (see Morrissey, D.J.) C 21, 1783
Segel, R. E. — (see Olmer, C.) C 21, 254
——(see Sadler, M.E.) C 21, 2303
Semmler, W. — (see Shu, N.K.B.) C 21, 1828
Sen, Nguyen Van — (see Sandoval, A.) C 21, 1321
Seshagiri Rao, V. — (see Srinivasa Rao, M.) C 21, 728
Sesma, Javier — Existence of strongly bound states of pions in nuclei. C 21, 2130
Shahabuddin, M. A. M., A. A. Pilt, and J. A. Kuehner — (t,α) reaction on ^{124}Te, ^{126}Te, ^{128}Te and ^{130}Te nuclei. C 21, 1116
Shahin, F. — (see Bonetti, R.) C 21, 816
Shakin, C. M. — (see Bhalerao, R.S.) C 21, 1903
——(see Bhalerao, R.S.) C 21, 2103
Shanker, R. — (see Warke, C.S.) C 21, 2643
Shapira, D., J. L. C. Ford, Jr., J. Gomez del Campo, and P. H. Stelson — Backward angle cross sections for ^{27}Al + ^{16}O reaction products. C 21, 1824
——(see Beene, J.R.) C 21, 167
——(see Ford, J.L.C., Jr.) C 21, 764
Shcherbin, V. N. — (see Bland, L.C.) C 21, 2227
Sheline, R. K. — Character of the low-lying 0^- and 0^+ states in the even Rn, Ra, Th, U, and Pu isotopes. C 21, 1660
——(see Cleary, T.P.) C 21, 2244

____(see Mann, L.G.) C 21, 2547
____(see Rotbard, G.) C 21, 1232
Shepard, J. R. — (see Bauer, T.S.) C 21, 757
____(see Peterson, R.J.) C 21, 1030
Sherman, N. K., C. K. Ross, and K. H. Lokan — Photon-absorption cross sections between 3 and 30 MeV. C 21, 2328
Shimizu, Sakae — (see Watanabe, Yoshihisa) C 21, 1753
Shu, N. K. B., D. Melnik, J. M. Brennan, W. Semmler, and N. Benczer-Koller — Velocity dependence of the dynamic magnetic field acting on swift O and Sm ions. C 21, 1828
____(see Brennan, J.M.) C 21, 574
Shyam, R. — (see Baur, G.) C 21, 2668
Siemssen, R. H. — (see Olmer, C.) C 21, 254
Sierk, Arnold J. and J. Rayford Nix — Fission in a wall-and-window one-body-dissipation model. C 21, 982
____(see Nix, J. Rayford) C 21, 396
Sikora, B., M. Blann, W. Scobel, J. Bisplinghoff, and M. Beckerman — Comparisons of experimental and theoretical nucleus-nucleus potentials for heavy ion reactions. C 21, 614
Silbar, Richard R. — (see Sternheim, Morton M.) C 21, 1974
Silver, M. and N. Austern — Pion-nucleus scattering using finite binding potentials. C 21, 272
Silverans, R. — (see Geerts, R.) C 21, 439
Simon, R. S. — (see Yates, S.W.) C 21, 2366
Simon, S. — (see Namboodiri, M.N.) C 21, 1680(E)
Singh, P. P. — (see Castaneda, C.M.) C 21, 179
____(see Sadler, M.E.) C 21, 2303
____(see Schwandt, P.) C 21, 1656
Singh, Z. — (see Mann, L.G.) C 21, 2547
Singham, M. K. and F. Tabakin — Role of Gamow-Teller suppression and $M1$ radiative widths on π^- photoproduction from ^{14}N. C 21, 1039
Sinha, A. K. and G. K. Mehta — Scission-point configuration of ^{252}Cf. C 21, 2467
Sjoreen, T. P., U. Garg, and D. B. Fossan — Spectroscopy of ^{213}At, ^{212}Po, and ^{210}Pb following ^{208}Pb + ^{7}Li. C 21, 1838
Skopik, D. M., J. Asai, and J. J. Murphy II — ^{56}Fe(e,α) reaction and its relevance to the $E2$ isoscalar sum rule. C 21, 1746
____(see Asai, J.) C 21, 469
Smilansky, U. — (see Stokstad, R.G.) C 21, 2427
Smith, C. F. — (see Meyer, R.A.) C 21, 2590
Smith, G. J. — (see Casten, R.F.) C 21, 65
Smith, G. R. — (see Adams, G.S.) C 21, 2485
____(see Bauer, T.S.) C 21, 757
____(see Källne, Jan) C 21, 2681
____(see Peterson, R.J.) C 21, 1030
Smith, H. A., Jr. — (see Castaneda, C.M.) C 21, 179
Smith, N. L. — (see Meyer, R.A.) C 21, 2590
Sober, D. I., W. J. Staper, W. J. Briscoe, P. E. Burt, Hall Crannell, and J. T. O'Brien — Absorption in flight of positive pions in carbon. C 21, 1495
Soni, S. K. — (see Gupta, S.L.) C 21, 2691
Sood, P. C. — (see Maheshwari, C.) C 21, 1120
Spanhoff, R., M. J. Canty, H. Postma, and G. Mennenga — Nuclear orientation study of ^{182}W in the decay of ^{182}Re isomers. C 21, 361
Specht, J. R. — (see Holt, R.J.) C 21, 1699
Sperduto, A. — (see DiRienzo, A C.) C 21, 2101
Spitaleri, C. — (see Barbarino, S.) C 21, 1104
Srinivasa Rao, M., D. K. Priyadarsini, S. Lakshminarayana, V. Seshagiri Rao, and D. L. Sastry — 3^--2^+ first-forbidden beta transitions in the decay of $^{72}_{31}\text{Ga}_{41}$. C 21, 728
Stanley, D. P. — (see Parks, L.A.) C 21, 217
Staper, W. J. — (see Sober, D.I.) C 21, 1495
Starkand, Y. — (see Rinat, A.S.) C 21, 324
Stearns, R. L. — (see Chrien, R.E.) C 21, 1014
Steinberg, E. P. — (see Urbon, J.A.) C 21, 1048
Stelson, P. H. — (see Shapira, D.) C 21, 1824
Stelts, M. L. — (see Casten, R.F.) C 21, 65
Stelzer, H. — (see Eyal, Y.) C 21, 1377
Stelzer, K. — (see Eyal, Y) C 21, 1377
Stephens, F. S. — (see Yates, S.W.) C 21, 2366
Stephens, William, Jeffrey Klein, and Robert Zurmühle — Search for naturally occurring superheavy element $Z = 110$, $A = 294$. C 21, 1664
Stephenson, E. J., H. E. Conzett, R. M. Larimer, B. T. Leemann, R. Roy, and P. von Rossen — Tensor analyzing powers in ^{4}He(d,d)^{4}He elastic scattering between 17 and 45 MeV. C 21, 44
Sternheim, Morton M. and Richard R. Silbar — Interpretation of quasielastic pion scattering coincidence experiments. C 21, 1974
Stetz, Albert W. — Analysis of quasi-free scattering data in the impulse approximation C 21, 1979
____(see Moss, G.A.) C 21, 1932
Stewart, N. M. — (see Axen, D.) C 21, 998
____(see Bugg, D V.) C 21, 1004
____(see Clough, A.S.) C 21, 988
Stock, R. — (see Sandoval, A.) C 21, 1321
Stokstad, R. G., Y. Eisen, S. Kaplanis, D. Pelte, U. Smilansky, and I. Tserruya — Fusion of ^{16}O + ^{148,150,152,154}Sm at sub-barrier energies. C 21, 2427
Strayer, M. R. — (see Werby, M.F.) C 21, 2235
Struble, G. L. — (see Mann, L.G.) C 21, 2547
Stryuk, Yu S. — (see Bland, L.C.) C 21, 2227
Subramanian, T. S. — (see Fitzgerald, D.H.) C 21, 1190
____(see King, N.S.P.) C 21, 1185
Sugarbaker, E. — (see Alford, W.P.) C 21, 1203
____(see Brown, Ronald E.) C 21, 2663
Sugawara, M. — (see Tamae, T.) C 21, 1758
Sugihara, T. T. — (see Zolnowski, D.R.) C 21, 2556
Sundström, B. — (see Bargholtz, Chr.) C 21, 1078
Sunier, J. W. — (see Brown, Ronald E.) C 21, 2663
Suri, J. K. — (see Gambhir, Y K.) C 21, 1124
Sutter, R. J. — (see Chrien, R.E.) C 21, 1014
Swenson, L. W. — (see Olmer, C.) C 21, 254
Sziklai, J. — (see Fodor, I) C 21, 787
Szymański, Z. — (see Ćwiok, S) C 21, 448

Tabakin, F. — (see Singham, M.K.) C 21, 1039
Tabor, S. L. — (see Prosser, F W., Jr.) C 21, 1819
Taccetti, N. — (see Bini, M.) C 21, 116
Takagui, E. M. and O. Dietzsch — ^{111}In–^{109}In mass difference. C 21, 1667
Talbert, W. L., Jr. — (see Lee, M.A.) C 21, 328
Tamae, T., T. Urano, M. Hirooka, and M. Sugawara — Statistical and pre-equilibrium (γ,α) cross sections of

^{90}Zr and their multipolarities via the ^{90}Zr(e, α) reaction. C 21, 1758
Tamas, G. — (see Argan, P.) C 21, 662
____(see Argan, P.) C 21, 1416
Tamura, T. — (see Udagawa, T.) C 21, 1271
____(see Udagawa, T.) C 21, 1891
____(see Weeks, K.J.) C 21, 2632
Tang, Henry H. K. and Cheuk-Yin Wong — Exactly central heavy-ion collisions by nuclear hydrodynamics. C 21, 1846
Tang, Y. C. — (see LeMere, M.) C 21, 1170
Tarrats, A. — (see Fabrici, E.) C 21, 830
Theisen, L. V. — (see Clements, J.S.) C 21, 1285
Thieberger, P. — (see Kreiner, A.J.) C 21, 933
Thierens, H. — (see De Frenne, D.) C 21, 629
____(see D'hondt, P.) C 21, 963
____(see Jacobs, E.) C 21, 237
Thiessen, H. A. — (see Burleson, G.R.) C 21, 1452
____(see Olmer, C.) C 21, 254
____(see Peterson, R.J.) C 21, 1030
Thompson, W. J. — (see Hardekopf, R.A.) C 21, 906
Tilley, D. R. — (see Turner, J.D.) C 21, 525
Tokarevski, V. V. — (see Bland, L.C.) C 21, 2227
Toth, K. S. — (see Ford, J.L.C., Jr.) C 21, 764
Trail, C. C., P. M. S. Lesser, A. H. Bond, Jr., M. K. Liou, and C. K. Liu — Bremsstrahlung from *$^{12}C + p$* near the 1.7-MeV resonance. C 21, 2131
____(see Liou, M.K.) C 21, 518
Trautmann, D. — (see Baur, G.) C 21, 2668
Truex, W. — (see Van Orden, J.W.) C 21, 2628
Tserruya, I., J. Barrette, S. Kubono, P. Braun-Munzinger, M. Gai, and C. D. Uhlhorn — Complete fusion of ^{12}C with ^{20}Ne. C 21, 1864
____(see Eyal, Y.) C 21, 1377
____(see Stokstad, R.G.) C 21, 2427
Turner, J. D., N. R. Roberson, S. A. Wender, H. R. Weller, and D. R. Tilley — Polarized proton capture on ^{13}C C 21, 525
Tzara, C. — (see Argan, P.) C 21, 662
____(see Argan, P.) C 21, 1416

Udagawa, T. and T. Tamura — Breakup of strongly absorptive projectiles. Application to *(h,dp)* reaction. C 21, 1271
____, **T. Tamura, and D. Price** — Parametrization of exact-finite-range distorted-wave Born approximation overlap integral for reactions induced by heavy ions. C 21, 1891
Uguzzoni, A. — (see Fuschini, E.) C 21, 1646
Uhlhorn, C. D. — (see Tserruya, I.) C 21, 1864
Uhrhane, F. J. — (see Bellicard, J.B.) C 21, 1652
Ullah, Nazakat — Angular-momentum-dependent inertia parameter. C 21, 466
Ullmann, J. L. — (see Fitzgerald, D.H.) C 21, 1190
____(see Garrett, R.) C 21, 1149
____(see King, N.S.P.) C 21, 1185
Urano, T. — (see Tamae, T.) C 21, 1758
Urbon, J. A., S. B. Kaufman, D. J. Henderson, and E. P. Steinberg — *Angular and energy distributions of ^{24}Na fragments formed by the reaction of 11.5-GeV protons with ^{197}Au.* C 21, 1048

van der Weg, K. — (see Harakeh, M.N.) C 21, 768
van der Woude, A. — (see Harakeh, M.N.) C 21, 768
Van de Wiele, J. — (see Gerlic, E.) C 21, 124
____(see Guillot, J.) C 21, 879
van Haeringen, H. — (see Kok, L.P.) C 21, 512
Vanneste, L. — (see Geerts, R.) C 21, 439
van Oers, W. T. H. — (see Moss, G.A.) C 21, 1932
Van Orden, J. W., W. Truex, and M. K. Banerjee — Short-range correlations and the nuclear momentum density distribution for ^{16}O. C 21, 2628
Van Oystaeyen, B. — (see Argan, P.) C 21, 662
____(see Argan, P.) C 21, 1416
Vargas, C. W. Soto — (see de Téramond, G.F.) C 21, 2542
Vary, J. P., R. H. Belehrad, and R. J. McCarthy — Valence-core self-consistency in the $A = 17$ system. C 21, 1626
Vazeille, F. — (see Jonsson, S.) C 21, 306
Veeser, L. R. — (see Hardekopf, R.A.) C 21, 906
____(see Hoffman, Darleane C.) C 21, 637
Vergnes, M. — (see Gerlic, E.) C 21, 124
____(see Rotbard, G.) C 21, 1232
____(see Rotbard, G.) C 21, 2293
Vernotte, J. — (see Rotbard, G.) C 21, 1232
____(see Rotbard, G.) C 21, 2293
Verondini, E. — (see Fuschini, E.) C 21, 1646
Vertse, T. — (see Apagyi, B.) C 21, 779
Vincent, E. — (see Argan, P.) C 21, 662
____(see Argan, P.) C 21, 1416
Vinciguerra, D. — (see Barbarino, S.) C 21, 1104
Vinh Mau, R. — (see Lacombe, M.) C 21, 861
von Brentano, P. — (see Bazzacco, D.) C 21, 222
von Rossen, P. — (see Stephenson, E.J.) C 21, 44
Vourvopoulos, G. — (see Andritsopoulos, G.) C 21, 1648
Vrcelj, Z. — (see Daehnick, W.W.) C 21, 2253

Wald, S. — (see Eyal, Y.) C 21, 1377
Walker, P. M., G. D. Dracoulis, and A. Johnston — Band crossing in ^{172}Hf. C 21, 464
Wallace, S. J. — (see Banerjee, M.K.) C 21, 1996
Walter, G. — (see Huck, A.) C 21, 712
Wang, A. T. M. — (see Hoffmann, G.W.) C 21, 1488
Wang, C. W., N. S. Chant, P. G. Roos, A. Nadasen, and T. A. Carey — Quasi-free $(\alpha,2\alpha)$ reaction induced by 140 MeV alpha particles on ^{9}Be, ^{12}C, ^{16}O, and ^{20}Ne. C 21, 1705
Wang, K. H. — (see Hill, John C.) C 21, 384
Warke, C. S. and R. Shanker — Nucleon-nucleon interaction as derived from the De Rújula, Georgi, Glashow phenomenological quark-quark potential. C 21, 2643
Watanabe, Yoshihisa, Takeshi Mukoyama, and Sakae Shimizu — Nuclear excitation of ^{111}Cd by positron annihilation. C 21, 1753
Waterman, F. M. — (see Cecil, R.A.) C 21, 2471
Watson, J. W. — (see Fitzgerald, D.H.) C 21, 1190
____(see Garrett, R.) C 21, 1149
____(see Zisman, M.S.) C 21, 2398
Weber, J. — (see Hoffman, D.C.) C 21, 972
____(see Hulet, E.K.) C 21, 966
Weeks, K. J. and T. Tamura — Use of the boson-expansion theory for the description of collective nuclei C 21, 2632

Wegner, H. E. — (see DiRienzo, A.C.) C 21, 2101
Weise, U. — (see Feigel, A.) C 21, 2666
Weller, H. R. — (see Turner, J.D.) C 21, 525
Wells, J. C., Jr. — (see Robinson, R.L.) C 21, 603
Wender, S. A. — (see Turner, J.D.) C 21, 525
Werby, M. F., M. R. Strayer, and M. A. Nagarajan — Finite range distorted-wave Born approximation analysis of (p,t) reactions with a realistic triton wave function. C 21, 2235
Westfall, G. D. — (see Sandoval, A.) C 21, 1321
Whiting, J. S. — (see Fuda, M.G.) C 21, 18
Whitten, C. A., Jr. — (see Adams, G.S.) C 21, 2485
____(see Bauer, T.S.) C 21, 757
____(see Hoffmann, G.W.) C 21, 1488
Wilcke, W. W., M. W. Johnson, W. U. Schröder, D. Hilscher, J. R. Birkelund, J. R. Huizenga, J. C. Browne, and D. G. Perry — Actinide muonic atom lifetimes deduced from muon-induced fission. C 21, 2019
Wild, J. F. — (see Hoffman, D.C.) C 21, 972
____(see Hulet, E.K.) C 21, 966
Wildenthal, B. H. — (see Brown, B.A.) C 21, 2107
____(see Brown, B.A.) C 21, 2600
Wilhelmy, J. B. — (see Britt, H.C.) C 21, 761
____(see Hoffman, D.C.) C 21, 972
____(see Hulet, E.K.) C 21, 966
Willard, H. B. — (see Winkelmann, E.) C 21, 2535
Williams, R. A. — (see Orth, C.J.) C 21, 2524
Williamson, C., A. Galonsky, R. Huffman, and R. Markham — Inelastic scattering of ^{6}Li from ^{58}Ni at 71 MeV. C 21, 1344
Willis, A. — (see Moss, G.A.) C 21, 1932
Willis, N. — (see Moss, G.A.) C 21, 1932
Winkelmann, E., P. R. Bevington, M. W. McNaughton, H. B. Willard, F. H. Cverna, E. P. Chamberlin, and N. S. P. King — Proton-deuteron elastic scattering at 800 MeV. C 21, 2535
Winters, R. R., R. L. Macklin, and J. Halperin — ^{186,187,188}Os(n,γ) cross sections and galactic nucleosynthesis. C 21, 563
____(see Halperin, J.) C 21, 545
____(see Johnson, C.H.) C 21, 2190

Wolf, K. L. — (see Sandoval, A.) C 21, 1321
Wolfsberg, K. — (see Orth, C.J.) C 21, 1967
Woloshyn, R. M. — (see Saharia, A.N.) C 21, 1111
Wong, Cheuk-Yin — (see Tang, Henry H K.) C 21, 1846
Woodworth, J. G. — (see Jury, J.W.) C 21, 503
Wriekat, A. — (see Adams, G.S.) C 21, 2485
Wright, N. — (see Axen, D.) C 21, 998
____(see Bugg, D.V.) C 21, 1004

Yamanouchi, M. — (see Mikumo, T.) C 21, 620
Yariv, Y. and Z. Fraenkel — Erratum: Intranuclear cascade calculation of high-energy heavy-ion interactions [C 20, 2227 (1979)]. C 21, 2139(F)
Yates, S. W., I. Y. Lee, N. R. Johnson, E. Eichler, L. L. Riedinger, M. W. Guidry, A. C. Kahler, D. Cline, R. S. Simon, P. A. Butler, P. Colombani, F. S. Stephens, R. M. Diamond, R. M. Ronningen, R. D. Hichwa, J. H. Hamilton, and E. L. Robinson — High-spin properties of ^{164}Er in the multiple band crossing region. C 21, 2366
____(see Ahmad, I.) C 21, 874
Young, L. — (see Cecil, R A.) C 21, 2471
Youngblood, D. H. — (see Rozsa, C M.) C 21, 1252

Zagromski, S. — (see Gils, H.J.) C 21, 1239
Zamick, Larry — (see Abbas, Afsar) C 21, 738
Zanelli, C. — (see Garrett, R.) C 21, 1149
Zawislak, F. C. — (see Saxena, R.N.) C 21, 1531
Zech, E. — (see Leuthold, K.) C 21, 2581
Zeidman, B. — (see Olmer, C.) C 21, 254
Zell, K. O. — (see Bazzacco, D.) C 21, 222
Zisman, M. S., J. G. Cramer, D. A. Goldberg, J. W. Watson, and R. M. DeVries — Dominance of strong absorption in ^{9}Be + ^{28}Si elastic scattering. C 21, 2398
Zitzmann, R. — (see Eyal, Y.) C 21, 1377
Zolnowski, D. R., M. B. Hughes, J. Hunt, and T. T. Sugihara — Systematics of quasirotational states in $N = 88$ nuclei. C 21, 2556
Zurmühle, Robert — (see Stephens, William) C 21, 1664

CONTENTS—*Continued*

PHYSICAL REVIEW C **THIRD SERIES, VOLUME 21, NUMBER 6** **JUNE 198**

Level properties of $^{85}_{37}\mathrm{Rb}_{48}$ from the decay of the ^{85}Kr and ^{85}Sr isomers and the cluster-vibration model . . . . . . R. A. Meyer, J. E. Fontanilla, N. L. Smith, C. F. Smith, R. C. Ragaini, and V. Paar 259

Nuclear Structure

Inelastic scattering E4 transition probabilities in the 0d, 1s shell . . . . B. A. Brown, W. Chung, and B. H. Wildenthal 2600
Single-particle states in nuclear matter and in finite nuclei . . . . R. Sartor and C. Mahaux 2613
Short-range correlations and the nuclear momentum density distribution for ^{16}O . . . . . . J. W. Van Orden, W. Truex, and M. K. Banerjee 2628
Use of the boson-expansion theory for the description of collective nuclei . . . . K. J. Weeks and T. Tamura 2632
Shape of eigenvalue distribution for bosons in scalar space . . . . V. K. B. Kota and V. Potbhare 2637
Nucleon-nucleon interaction as derived from the De Rújula, Georgi, Glashow phenomenological quark-quark potential . . . . C. S. Warke and R. Shanker 2643

Comments

Search for nuclear structure dependence of analyzing powers for the $(\vec{t},p)$ reaction in medium mass nuclei . . . . Ronald E. Brown, J. A. Cizewski, J. W. Sunier, E. R. Flynn, P. Alford, E. Sugarbaker, and D. Ardouin 2663

Communications

Large absorption potential for the Ag + p reaction at sub-Coulomb energies . . . . A. Feigel, E. Finckh, K. Rüskamp, and U. Weise 2666
Importance of the breakup mechanism for composite particle scattering . . . . G. Baur, R. Shyam, F. Rösel, and D. Trautmann 2668
Evidence for statistical fluctuation in the fragmentation of ^{16}O at intermediate energies . . . . Che Ming Ko 2672
Projection operator method for finding energies and widths of shape resonances in heavy-ion collisions . . . . Thomas L. Larry and William P. Beres 2675
P-wave dispersive contribution to low-energy elastic $\pi^{+\,2}$H scattering . . . . R. M. Rockmore 2678
(π,p) absorption in ^{6,7}Li at 75 and 175 MeV . . . . Jan Källne, J. Davis, P. C. Gugelot, J. S. McCarthy, G. R. Smith, R. L. Boudrie, B. Höistad, and C. L. Morris 2681
Comparison of analyzing powers and polarizations for the charge symmetric reactions $^2\mathrm{H}(\vec{d},p)^3\mathrm{H}$ and $^2\mathrm{H}(\vec{d},n)^3\mathrm{He}$ . . . . J. J. Bevelacqua 2685
High energy scattering from a bound nucleon: Unitarity and closure approximation . . . . F. Cannata and S. A. Gurvitz 2687
Time-dependent quadrupole interactions in ^{129}I . . . . S. L. Gupta, Ashok Kumar, S. K. Soni, and S. C. Pancholi 2691
Composite particle emission from ^{65}Zn* . . . . H. Machner 2695

Cumulative Author Index 2699